

Mechanisms and Machine Science

Shaofan Li *Editor*

Computational and Experimental Simulations in Engineering

Proceedings of ICCES 2023 - Volume 2




 Springer

The Springer logo consists of a white chess knight icon on a red background, followed by the word "Springer" in a white serif font.

Mechanisms and Machine Science

Volume 145

Series Editor

Marco Ceccarelli , Department of Industrial Engineering, University of Rome Tor Vergata, Roma, Italy

Advisory Editors


Sunil K. Agrawal, Department of Mechanical Engineering, Columbia University, New York, NY, USA

Burkhard Corves, RWTH Aachen University, Aachen, Germany

Victor Glazunov, Mechanical Engineering Research Institute, Moscow, Russia

Alfonso Hernández, University of the Basque Country, Bilbao, Spain

Tian Huang, Tianjin University, Tianjin, China

Juan Carlos Jauregui Correa , Universidad Autonoma de Queretaro, Queretaro, Mexico

Yukio Takeda, Tokyo Institute of Technology, Tokyo, Japan

This book series establishes a well-defined forum for monographs, edited Books, and proceedings on mechanical engineering with particular emphasis on MMS (Mechanism and Machine Science). The final goal is the publication of research that shows the development of mechanical engineering and particularly MMS in all technical aspects, even in very recent assessments. Published works share an approach by which technical details and formulation are discussed, and discuss modern formalisms with the aim to circulate research and technical achievements for use in professional, research, academic, and teaching activities.

This technical approach is an essential characteristic of the series. By discussing technical details and formulations in terms of modern formalisms, the possibility is created not only to show technical developments but also to explain achievements for technical teaching and research activity today and for the future.

The book series is intended to collect technical views on developments of the broad field of MMS in a unique frame that can be seen in its totality as an Encyclopaedia of MMS but with the additional purpose of archiving and teaching MMS achievements. Therefore, the book series will be of use not only for researchers and teachers in Mechanical Engineering but also for professionals and students for their formation and future work.

The series is promoted under the auspices of International Federation for the Promotion of Mechanism and Machine Science (IFTOMM).

Prospective authors and editors can contact Mr. Pierpaolo Riva (publishing editor, Springer) at: pierpaolo.riva@springer.com

Indexed by SCOPUS and Google Scholar.

Shaofan Li
Editor

Computational and Experimental Simulations in Engineering

Proceedings of ICCES 2023—Volume 2

 Springer

Editor
Shaofan Li
Department of Civil and Environmental
Engineering
University of California, Berkeley
Berkeley, CA, USA

ISSN 2211-0984 ISSN 2211-0992 (electronic)
Mechanisms and Machine Science
ISBN 978-3-031-42986-6 ISBN 978-3-031-42987-3 (eBook)
<https://doi.org/10.1007/978-3-031-42987-3>

© The Editor(s) (if applicable) and The Author(s), under exclusive license to Springer Nature Switzerland AG 2024

This work is subject to copyright. All rights are solely and exclusively licensed by the Publisher, whether the whole or part of the material is concerned, specifically the rights of translation, reprinting, reuse of illustrations, recitation, broadcasting, reproduction on microfilms or in any other physical way, and transmission or information storage and retrieval, electronic adaptation, computer software, or by similar or dissimilar methodology now known or hereafter developed.

The use of general descriptive names, registered names, trademarks, service marks, etc. in this publication does not imply, even in the absence of a specific statement, that such names are exempt from the relevant protective laws and regulations and therefore free for general use.

The publisher, the authors, and the editors are safe to assume that the advice and information in this book are believed to be true and accurate at the date of publication. Neither the publisher nor the authors or the editors give a warranty, expressed or implied, with respect to the material contained herein or for any errors or omissions that may have been made. The publisher remains neutral with regard to jurisdictional claims in published maps and institutional affiliations.

This Springer imprint is published by the registered company Springer Nature Switzerland AG
The registered company address is: Gewerbestrasse 11, 6330 Cham, Switzerland

Paper in this product is recyclable.

Preface

We are thrilled to present the Conference Proceedings of the 29th International Conference on Computational & Experimental Engineering and Sciences (ICCES) held in Shenzhen, China. This book showcases the latest advances, innovations, and applications in computational engineering, as shared by renowned international researchers and engineers during this prestigious event.

The contributions in this volume cover diverse areas such as Biomedical Engineering, Sound & Vibration, Computational & Experimental Materials & Design, Engineering and Experimental Sciences, Modern Computational Methods, Modern Developments in Mechanics of Materials & Structures.

We extend our appreciation to the authors for their exceptional contributions and the reviewers for their diligent evaluations. We also thank the conference organizing committee, sponsors, and volunteers for their invaluable support, which made ICCES 2023 a remarkable success.

We hope that this volume will inspire readers to explore new frontiers, embark on groundbreaking research, and cultivate fruitful collaborations. We believe that the multidisciplinary approach fostered by ICCES will continue to drive innovation and excellence in the years to come.

Shaofan Li
Conference Chair/Editor-in-Chief
University of California
Berkeley, USA

Contents

1	A Peridynamic Micro-Scale Model for Predicting Mechanical Properties of Graphene	1
	Dan Wu, Yin Yu, and Y. L. Hu	
2	Three-Dimensional Temperature Field Prediction in Double-Wall Cooling Structure Using Deep Learning Method	11
	Junjie Huang, Jianqin Zhu, Yanjia Wang, Zeyuan Cheng, and Lu Qiu	
3	A Neural Network-Based Method for Solving the Mass Flow Related Forward and Inverse Problems of Laminate Cooling Structures	25
	Yanjia Wang, Jianqin Zhu, Zeyuan Cheng, and Kaihang Tao	
4	Experimental Research of Ultra High Performance Concrete in Supersized Rectangle Pipe Jacking Project	41
	Tao Fang, Linxing Guan, and Wei Sun	
5	Mechanical Performance and Experimental Research on Plug-in Fast Connector of Shield Tunnel	53
	Tao Fang, Linxing Guan, and Mengxi Zhang	
6	The Advancement of Knowledge Graphs in Cybersecurity: A Comprehensive Overview	65
	Yuke Ma, Yonggang Chen, Yanjun Wang, Jun Yu, Yanting Li, Jinyu Lu, and Yong Wang	
7	Active Disturbance Rejection Control of Hypersonic Vehicle Based on Q-Learning Algorithm	105
	Jie Yan and Liang Zhang	

8 Deformation and Crack Monitoring of RC Beams Based on Computer Vision 117
 Ruilin Wang, Weiping Zhang, Shuting Zhang, and Youling Yu

9 Numerical Simulation of Enhancing the Solar-Thermal Conversion and Storage Performance for Expanded Perlite/Paraffin Wax Composites by Introducing Expanded Graphite and Carbon Nanotubes 133
 Xinbo Zhao and Zhi Guo Qu

10 Effect of Natural Fracture Clusters on Hydraulic Fracture Propagation in Fractured Reservoirs: A Numerical Simulation Study 155
 Guchang Zhang, Bo Wang, Ying Zhang, Wenxia Li, and Fujian Zhou

11 Molecular Dynamics Investigations of Hydrogen-Enriched Natural Gas Permeation in Polyethylene 175
 Dukui Zheng, Jingfa Li, Bo Yu, Yafan Yang, Dongxu Han, Jianli Li, Zhiqiang Huang, and Yindi Zhang

12 Estimation of Hourly Solar Radiation in Australia Using Machine Learning Models 185
 Shuting Zhao and Youzhen Xiang

13 Theoretical Calculation and Parametric Study of Floating and Sinking Process of the Steel Tube with a Large Diameter 195
 Jianbo Yi, Qing Chong, Yu Huang, and Xuan Xing

14 A Stable Method for Multi-component Gas Darcy Flow in Porous Media 205
 Wendi Xue, Yi Wang, and Yuanyuan He

15 Optimal Control of Vehicle Queue Following Based on Wireless Communication 215
 ZhaoWei Ding, FaZhan Tao, MengYang Li, and Zhou Tao

16 Fatigue Crack Quantification Model for Metallic Structures Based on Strain Monitoring 225
 Kunpeng Li, Xin Qi, and Biao Li

17 A Study of a Confucius Culture Learning Environment Based on a 3D Metaverse 233
 Miaolei Deng, Kai Yang, Zhibin Zuo, and Haonan Zhai

18 Optimization on Aerodynamic Performances of Pantograph Combined with Sample Infill Criterion 243
 Zhiyuan Dai, Tian Li, Weihua Zhang, Ning Zhou, and Jiye Zhang

19	Measuring Fire Spread Rate with Digital Image Processing Method	257
	Juan Chen and Yunping Yang	
20	Metaverse Standardization: System Planning, Current Status and Prospects	269
	Zunbo Wei, Qiang Ge, Xiangjuan Jia, Yijian Zhang, Mengwei Han, and Xiaofeng Chen	
21	Generating Second-Order Stokes Waves Using a Cylinder-Shaped Plunger—Theoretical Derivations and SPH Simulations	281
	Yu-cheng Sui, Ming He, Xue-yan Li, and Yu-jie Meng	
22	Design of Construction Mode of Offshore Gas Storage in the Whole Sea—Taking H Gas Field in Liaodong Bay, Bohai Sea as an Example	297
	Shixin Jiang, Zhan Su, Jingyao Sun, Youwu Li, Yixin Yu, and Jiaojiao Yu	
23	Machine Learning-Based Models for Predicting the Depth of Concrete Penetration	311
	Meng Li, Haijun Wu, Heng Dong, Guang Ren, Peng Zhang, and Fenglei Huang	
24	Model Test Research on Pressure Wave in the Subway Tunnel	327
	Xu Zhang, Honglin Wang, Haiquan Bi, Yuanlong Zhou, Nanyang Yu, and Yi Fang	
25	Numerical Investigation of Isotropic and Transverse Isotropic Rock Failure Under Semi-circular Bending Test Using Peridynamic	353
	Kaiwei Tian, Zeqi Zhu, and Qian Sheng	
26	Field Tests of Bridge Damage Detection by Using the Passive Tap-Scan Method	367
	Ping Lin, Zhuyou Hu, He Guo, Lei Qiao, and Zhihai Xiang	
27	Research on High-Velocity Perforation Characteristics of Elliptical Cross-Section Truncated Ogive Projectile	379
	Ximin Deng, Heng Dong, Hao Wang, Haijun Wu, and Fenglei Huang	
28	Study on Downhole Torque Prediction Method Combining Machine Learning and Mechanism Model	395
	Chuanjie Ren, Wenjun Huang, and Deli Gao	

29 Wellbore Temperature and Pressure Field Model Considering the Segmented Rheological Model 411
Xingao Liao, Jun Li, Gonghui Liu, and Hongwei Yang

30 Enhancing Effect of Leeward Side Deflector on High-Speed Trains Aerodynamic Performance Under Crosswinds 425
Zheng-Wei Chen, Guang-Zhi Zeng, and Zhan-Hao Guo

31 Consideration and Technical Feasibility Research of Multi-source Collaborative Gas Supply in China 437
Jingyao Sun, Jiaojiao Yu, Shixin Jiang, Youwu Li, Yongxin Ma, Zhan Su, Mihong Zhong, and Jiqiang Zhang

32 Study on Constitutive Relation of PVC Foam Based on Microstructure Model 451
Yong Zhou, Bin Xue, and Renpeng Wang

33 A Bitcoin Address Multi-classification Mechanism Based on Bipartite Graph-Based Maximization Consensus 473
Lejun Zhang, Junjie Zhang, Kentaroh Toyoda, Yuan Liu, Jing Qiu, Zhihong Tian, and Ran Guo

34 DSBT: Research on Soulbound Token Mechanism Based on Consortium Blockchain and Decentralized Identity 489
Yijian Zhang, Lu Zhang, Qing Zhang, Peiyu Zheng, Xiangjuan Jia, and Xiaofeng Chen

35 Hydraulic Fracture Propagation in Layered Rocks: Research Combining 3D FEM Modeling and Laboratory Experiments 507
Fei Wang, Wei Liu, Kaiqi Wang, Kaikai Xu, Jingen Deng, Chaowei Xing, and Ke Yan

36 Numerical Calculation of Equivalent Continuum Model for Fractured Reservoir Based on Meshless Generalized Finite Difference Method 527
Wenming Hu, Deng Liu, and Wentao Zhan

37 Numerical Simulation Methods for Nonlinear Mechanical Behaviors of Confined Prestressed Hollow Core Wall Panels 537
Rui Wang, Ying Zhou, and Yiqiu Lu

38 Design and Experimental Study of Raindrop High-Speed Emission System 551
Zhibo Wu, Chengyu Ma, Lanting Liu, Jianping Yin, and Yinggang Miao

39 Design of Long-Span Continuous Beam Bridge with Corrugated Steel Webs Constructed by Cantilever Assembly 559
 Qing Wang, Wenyao Peng, Wen Zhong, Lizhi Lu, Yong Liu, and Rong Liu

40 Meshless Generalized Finite Difference Method for Gas–Water Two-Phase Flow Equation of Complex-Shape Shale Gas Reservoirs 571
 Wentao Zhan, Liang Pu, Sheng Lei, Zhao Hui, Hao Huang, and Yunfeng Xu

41 Cuttings Transport: Tripping Analysis Based on a Dynamic Layering Method via CFD 583
 Na Zhu, Chenliang Ruan, Heming Zhu, Huang Wenjun, and Deli Gao

42 SPH Simulation of Solitary Wave Impact on Coastal Bridge Superstructures 595
 Guozhen Cai, Zhisheng Xia, Yi Zhan, and Min Luo

43 Numerical Study on Smoke Diffusion Distance Induced by a Moving Vehicle in Road Tunnel Using Dynamic Mesh 607
 Longyue Li, Yi Lu, Lin Xu, Yong Yang, Hao Wang, and Shao Chen

44 Static Aeroelastic Analysis of Electric Vertical Takeoff and Landing Aircraft ET480 617
 Shuai Zhang, Junqi Zhang, Jiayong Zhang, and Jielong Wang

45 Study on Stress Variation and Sealing of Casing-Cement Ring-Strata Assemblies Under Sour Gas Production Conditions 629
 Dingyuan Liu, Jun Li, and Wei Lian

46 RLGBG: A Reachable Landmark Grouping Based IP Geolocation Method for Unreachable Target 643
 Shuodi Zu, Chong Liu, Fan Zhang, and Shichang Ding

47 Deepwater Choke and Well Killing Manifold Automatic Control Pressure System and Simulation Experiments 657
 Zhenyu Long, Jun Li, Hongwei Yang, and Wang Chen

48 Prediction of Horizontal and Vertical Distribution Trend of Formation Pressure and Characteristics of Safety Density Window in Yinggehai Basin 669
 Reyu Gao, Yi Cui, Jinzhao Fan, Guang Yang, and Hongwei Yang

49 Development of Multi-level Substructure Analysis and Solution Framework Based on SiPESC.FEM 681
 Dianheng Jiang, Sheng Zhang, Biaosong Chen, and Na Li

50 Simulation Study on the Displacement Characteristics of an Ultra-Low Permeability Reservoir by CO₂-WAG Flooding 697
 Zhizeng Xia, Hongjun Yin, Xuewu Wang, and Zhaoming Li

51 Well Test Model for Double-Porosity Media Three-Zone Composite Reservoir Considering Interface Resistance 715
 Baotong Li, Hongjun Yin, and Cuiqiao Xing

52 Production Characteristics Analysis of CO₂ Huff-And-Puff Development in Tight Oil Reservoirs 731
 Zhaoming Li, Hongjun Yin, Zhizeng Xia, and Guohan Xu

53 Under the Blast Impact Load Study of Analytical Prediction Method for Plastic Response of Stiffened Plate 747
 TianBo Huang, Shuai Zong, Kun Liu, JiaXia Wang, and ZhenGuo Gao

54 A Blockchain-Based Method for Power-Related Data Quality Auditing 773
 Minjie Fu, Fuqiang Tao, Weiping Li, Rundong Shao, and Zhe Sun

55 FEDSET: Federated Random Forest Based on Differential Privacy 791
 Fuqiang Tao, Zhe Sun, Rui Liang, Rundong Shao, Yuhan Chai, and Yangyang Wang

56 Study on Analytical Prediction Method for Plastic Response of Folded Sandwich Plates Under Explosion Impact Loads 807
 Yimei Xia, Shuai Zong, Kun Liu, Jiaxia Wang, and Zhenguo Gao

57 Numerical Simulation and Experimental Analysis of Two-Dimensional Wedge-Shaped Structure’s Water Entry with Boulder Impact 827
 Zong Shuai, Huang Tianbo, Liu Kun, Wang Jiaxia, and Gao Zhenguo

58 Fuzzy-Logic-Based Integrated Orbit-Attitude-Vibration Prescribed-Time Control for Large-Scale Flexible Spacecraft 839
 Xiaokui Yue, Bailiang Lyu, and Chuang Liu

59 Study on the Classification Method of the Usage Severity of Aircraft Structures 851
Weiye Guo, Yanjun Zhang, Bintuan Wang, and Chengjian Che

60 Six Degrees of Freedom Simulation for Skipping Stones Based on Quaternion Method in SPH Framework 865
Xiang-Shan Guan, Peng-Nan Sun, Yu-Xiang Peng, and Nian-Nian Liu

61 Deep Reinforcement Learning-Based Intelligent Decision-Making for Orbital Game of Satellite Swarm 875
Weizhuo Yu, Xiaokui Yue, Panxing Huang, and Chuang Liu

62 Numerical Studies on the Temperature and Pressure Changes of a Maglev Train Surface Moving Dynamically in a Vacuum Tube 891
Yunfeng Bi, Haiquan Bi, and Honglin Wang

63 A Model-Based Pre-feedback Decoupling Control Framework for Ground Flutter Simulation Test 907
Guiwei Zhang, Weiguang Li, Ximing Zhu, and Zhichun Yang

64 Evaluating Contribution of Training Samples for Differentially Private Machine Learning 923
Yang Lv, Yufu Zou, Simin Wang, Zhe Sun, and Ran Li

65 Research on Fire Smoke Control of an Ultra-wide Road Tunnel with Lateral Exhaust 937
Jing Wang, Haiquan Bi, Bo Lei, Zhicheng Mu, Zhe Liu, and Qingxun Zeng

66 Deformable Special-Shaped Projectile Impacting Basalt Target: Experiments and Analysis 953
Guang Ren, Haijun Wu, Heng Dong, Yingqing Lv, and Fenglei Huang

67 Research on the THMC Coupling Model for Enhanced Geothermal Systems Based on the Framework of EDFM 963
Weitao Zhang, Dongxu Han, Kaituo Jiao, Yujie Chen, Qing Yuan, Liang Gong, and Bo Yu

68 Synthetic Data: Development Status and Prospects for Military Applications 979
Jinhui Huang, Junsong Yin, Shuangshuang Wang, and Dezhao Kong

69 Experimental Study on Aeroacoustic of Counter-Rotating Propeller in Ground Acoustic Environment 993
Wei Kai, Cao Qi, Yan Qun, Xu Jian, and Xue Dongwen

70 Enhanced Geothermal System Performance Prediction Based on Deep Learning Neural Networks 1007
 Chuan-Yong Zhu, Di Huang, Bo Yu, Liang Gong, and Ming-Hai Xu

71 The Influence of the Mesh Size on Numerical Simulations of Dynamic Buckling of the Stiffened Cylindrical Shell Subjected to Underwater Explosion Shock Wave 1023
 Chen-Xing Qu, Shao-Fei Ren, Peng-Fei Zhao, and Qi Wang

72 DDoS Detection Based on Sliding Window Entropy and Decision Tree with Programmable Switch 1037
 Shurong Zhang, Tianyu Gao, and Junxing Zhang

73 Supply Forecast of Shared Parking Spaces in Social Parking Lots Around Primary Schools Based on Shared Parking Spaces 1051
 Lu Chu, Jingyuan Wang, and Xiaoyu Ji

74 Review on the Development of Multi-lateral Well Technology 1075
 Qirui Yan, Jianfang Jiang, and Na Zhu

75 A Robust Nonsingular Double-Boundary CHIEF Method for Full Wave Numbers 1087
 Jie Chen, Yu Xiang, and Ziyu Shi

76 Numerical and Experimental Study on the Construction Process of the Pedestrian Bridge with a Curved Beam and Inclined Arch 1097
 Shaocai Zhu, Dan Liu, and Zhiyong Yao

77 Numerical Study on Fracture Formation and Propagation Law in the Perforating Process Based on FEM-SPH Coupling 1107
 Xianbo Liu, Jun Li, Wei Lian, Gonghui Liu, Yunfeng Zhao, Shiyuan Xie, Penglin Liu, and Dian Wang

78 Study on Degradation of Prestressed Concrete Beams in Hydrochloric Acid Environment Based on Stochastic Process 1121
 Yuwei Wang, Zuanfeng Pan, and Chengye Zhao

79 Prediction Model of Wellbore Temperature Field in Ultra-deep Shale Oil Horizontal Well During Managed Pressure Cementing 1139
 Jinlu Liu, Jun Li, Hongwei Yang, Hui Li, and Gonghui Liu

80 A Blockchain Based Documentation Sharing Framework for Copyright Protection 1153
 Huanqin Zheng, Yue Xue, Wanjuan Xie, and Zhengzheng Shi

81 Research on the Design of Blockchain-Based Aviation Physical and Chemical Testing System 1165
 Yijian Zhang, Lu Zhang, Jing Xu, Jingyi Du, Zunbo Wei, and Xiaofeng Chen

82 Coupled Axial-Rotational Motion of the Pipe on Cuttings Transport via CFD 1185
 Na Zhu, Chenliang Ruan, Heming Zhu, Zhiquan Nie, Wenjun Huang, and Deli Gao

83 Design of General SDN Controller System Framework for Multi-domain Heterogeneous Networks 1195
 Wenxiao Li, Jianhua Zhao, Huicong Fan, Shijia Zhu, Wandi Liang, Hongguang Yu, and Peng Lin

84 Systematic Evaluation of the Efficacy and Safety of Rivastigmine in Combination with Memantine for Mild to Moderate Alzheimer’s Disease Based on MCMC Algorithm 1211
 Hui Yue, Hong-rui Bao, Yan-yin Cui, Wen-xin Hou, and Hong-juan Wen

85 Perlite Pressure Calculation and Finite Element Simulation Study of LNG Storage Tank 1223
 Xu Chen, Juan Su, Shuqian Tong, Ye Chen, and Cheng Chen

86 Study on the Steel Lazy Wave Riser Configuration via a Simplified Static Model Considering Critical Sensitive Factors 1231
 Hui Wang, Ye Chen, Song Liu, Ning He, Zhen Tian, and Jianwen He

87 Numerical Simulation of Breathing Effect Induced by Drilling in Deep-Water Shallow Formations 1243
 Honglin Huang, Jun Li, Wentuo Li, Geng Zhang, Hongwei Yang, Jianming Li, Jintao An, Shujie Liu, and Ming Luo

88 A Review on Vector Form Intrinsic Finite Element Method and Its Application 1257
 Y. F. Duan, Y. Fang, S. M. Wang, S. K. Wu, and H. M. Zhang

89 Insight into the Mechanical Behaviour of Cooling Rate-Dependent Blistering Failures in Alumina Films 1289
 Ke Wang, Bo Yuan, Xiaofeng Guo, Christopher Harvey, and Simon Wang

90 Search for Universal Minimum Drag Resistance Underwater Vehicle Hull Using CFD 1297
 Harsh Vardhan and Janos Sztipanovits

91 Additive Manufacturing Simulation: A Review 1305
 Citlaly Castillo, Félix R. Saucedo-Zendejo, and Adrian García

92 A Novel Immersed Framework of Computational Fluid Structure Interaction 1313
 Wang Xinyu, Chennakesava Kadapa, and Mei Yue

93 Mechanical Modeling and Structural Optimization of Spindle System of Static Bias Point the Bit Rotary Steerable System 1327
 Tian Chen, Jun Li, and Gonghui Liu

94 Calculation Model of Annular Pressure Loss in Slim Hole Considering Drill String Rotation, Eccentricity and Joint 1339
 J. T. An, J. Li, G. H. Liu, H. L. Huang, and H. W. Yang

95 A Simulation Model of Resilience Evaluation for Natural Gas Pipeline Network Systems 1357
 Zhaoming Yang, Qi Xiang, Qian He, Enrico Zio, Michael Havbro Faber, Huai Su, and Jinjun Zhang

96 Staged Deployment of LEO Communication Satellite Constellation Based on Real Option Theory 1371
 Xuefeng Wang and Shijie Zhang

97 Multiphase Flow Model of Gas Hydrate Production Wellbore Based on Double-Layer Continuous Pipe 1385
 Geng Zhang, Jun Li, Hongwei Yang, Gonghui Liu, Hui Zhang, Honglin Huang, Jintao An, Wang Chen, and Chao Chen

98 Multiphase Flow Behaviors and Wellhead Backpressure Responses During Managed Pressure Drilling Well Control Considering Gas Dissolution 1401
 Wang Chen, Jun Li, Hongwei Yang, Geng Zhang, and Honglin Huang

99 Bilinear Auto-Bäcklund Transformation, Shock Waves, Breathers and X-Type Solitons for a (3 + 1)-Dimensional Generalized B-Type Kadomtsev-Petviashvili Equation in a Fluid 1419
Lu Zheng, Bo Tian, Dan-Yu Yang, and Tian-Yu Zhou

100 Study on Stress Area Law and Detection Range at Key Locations of Natural Gas Station 1433
Gang Liu, Rui Liu, Yang Qin, Fang Yang, and Hang Song

101 Numerical Simulation of Impact Response of Board-Level Packaging Structure 1443
Xu Long, Yuntao Hu, Tianxiong Su, and Chao Chang

102 A Graphical Computing-Based Image Registration Method for LED Chips 1455
Pengfei Zheng, Bo Wang, Xiyuan Wan, Jingjing Lou, Jun Lv, Qingdong Luo, and Linsheng Xie

Chapter 1

A Peridynamic Micro-Scale Model for Predicting Mechanical Properties of Graphene



Dan Wu, Yin Yu, and Y. L. Hu

Abstract Graphene, a honeycomb-like sheet of carbon just one atom thick, is used as a new reinforcement to make high-performance composites due to its unprecedented physical and chemical properties. Here we focus on the elastic properties of multi-layer graphene to simulate the mechanical properties of their composites. On the basis of the methods of state-based peridynamics and periodic boundary conditions, a unit cell model of graphene was established at the microscopic scale. Considering six pure load cases, the response of the periodic material under the action of macroscopically uniform deformation gradient is obtained. The effect of van der Waals forces and Brenner interatomic potentials with optimized parameters has been taken into account in the analysis of interaction between carbon atoms in graphene. The results obtained from the present numerical solution are in good agreement with the data in the existing literature, indicating that the model can well simulate the elastic properties of graphene, and give a significant reference for the further studies of the properties of graphene-based composites.

Keywords Graphene · State-based peridynamics · Periodic boundary condition · Van der Waals forces · Brenner empirical potentials

D. Wu · Y. Yu · Y. L. Hu (✉)

Aerospace Structure Research Center, School of Aeronautics and Astronautics, Shanghai Jiao
Tong University, Shanghai 200240, China
e-mail: yilehu@sjtu.edu.cn

Lab of Civil Aircraft Structures Testing, School of Aeronautics and Astronautics, Shanghai Jiao
Tong University, Shanghai 200240, China

D. Wu

e-mail: eterno@sjtu.edu.cn

Y. Yu

e-mail: yuyin@sjtu.edu.cn

1.1 Introduction

Graphene sheets are the lightest, thinnest and hardest two-dimensional nanostructures known at present. As reinforcement materials, graphene can greatly improve the mechanical properties of matrix materials, and have a wide range of application prospects in aviation, navigation and civil engineering fields.

For nanomaterials such as graphene, efforts have been made to develop a better technique to predict and test their mechanical properties in the study of solid mechanics. Frank et al. experimentally obtained Young's modulus of graphene sheets with less than 5 layers as high as 0.5TPa Frank I W [1]. However, limitations of experimental methods make the mechanical properties of graphene difficult to test when preparing high-quality graphene materials. Therefore, more researchers use numerical simulation and theoretical methods to study graphene, such as molecular mechanics method [2], Monte Carlo method [3–5]. Reddy et al. obtained the Young modulus of single-layer graphene by using continuum mechanics method as 0.669TPa [6]. However, due to the large computational domain, the molecular dynamics method is prone to non-convergence and low computational efficiency. Therefore, if the number of graphene layers is large and the number of carbon atoms is large, the calculation speed and accuracy will be reduced when the graphene model contains a large number of carbon atoms and graphene layers. The peridynamic (PD) theory proposed by Silling in 2000 is a continuum mechanics method with integral operator [7]. They discrete materials into several particles, and the motion analysis of each particle is in a given computational domain, rather than the whole material as the analytical domain, which can greatly reduce the computational workload. In addition, this method can effectively simulate discontinuous phenomena such as cracks by breaking the bond between material points.

In the study of properties of graphene, we focus on the way carbon atoms interact with each other. In 1990, Brenner et al. proposed a potential energy functions based on Tersoff's covalent-bonding for modeling intramolecular chemical bonding [8], and In 2002, a second-generation potential energy function (REBO) for solid carbon and hydrocarbon molecules was presented [9]. Those potentials can better describe the bond energy, length, elastic properties and gap defect energy between carbon and carbon atoms, but without being parameterized, the Young's modulus predicted by REBO are considerably different from the values obtained by experimental [10]. Then, L. Lindsay and D. A. Broido found a parameter set for Brenner empirical potential, which can offer a better prediction of the elastic properties of graphene [11]. He et al. [12] analyzed the deformation of axially compressed multi-walled carbon nanotubes (CNTs) by establishing the Van der Waals (vdW) force model. They note that the influence between adjacent layers are mainly affected by the van der Waals interactions, while the force between remote layers can be ignored.

In this study, a state-based peridynamic model considering the interaction forces between carbon atoms of graphene sheets was developed. The interaction mode between atoms in different layers and carbon atoms in the same layer is described by van der Waals force and Brenner empirical potentials with optimized parameters.

The mechanical properties of graphene were analyzed by applying specific boundary conditions and solving the model elastic matrix. This paper lays a foundation for analyzing graphene containing defects and predicting the properties of graphene composites.

1.2 Interaction

The various characteristics of C–C covalent bonds are characterized by Brenner empirical potentials with optimized parameters (REBO_LB). It can be expressed as

$$E_{rebo-LB} = \sum_i \sum_{j(>i)} [V^R(r_{ij}) - b_{ij}V^A(r_{ij})] \quad (1.1)$$

The functions $V^R(r_{ij})$ and $V^A(r_{ij})$ represent the interatomic repulsive term and attraction term in the potential function, respectively. The form of bond order function b_{ij} contains some information about the interaction between atoms.

The long distance interaction between atoms is characterized by the Lennard–Jones (L–J) potential proposed by Jones [13], which describes the potential energy between two atoms in the same molecular system that have no direct chemical bond interaction [14, 15]. The expression of L–J potentials used to calculate the energy of vdW forces is thus

$$E_{vdW}(r) = 4\varepsilon \left(\left(\frac{\sigma}{r} \right)^{12} - \left(\frac{\sigma}{r} \right)^6 \right) \quad (1.2)$$

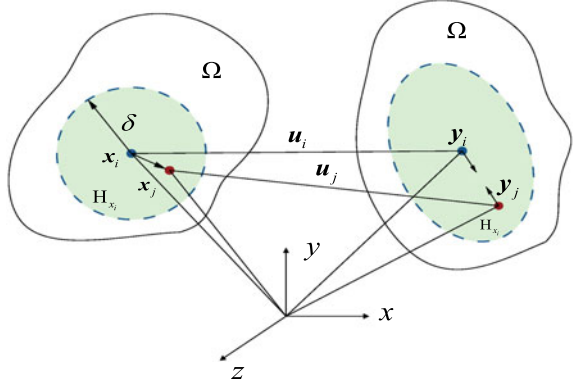
where r is the distance between the interacting atoms, ε is the interaction potential between two atoms at equilibrium, and σ is a parameter determined by equilibrium distance.

Especially, in the case of multilayered graphene, the mechanical behavior between layers is mainly considered by vdW forces.

1.3 PeriDynamics

In PeriDynamics (PD), a body is discretized into an infinite number of material points that can be subjected to prescribed body loads, displacement, or velocity. Usually, each material point has a range of influence, which is called “horizon” denoted as $H_{x_i} = \{|\mathbf{x}' - \mathbf{x}| \leq \delta, \mathbf{x} \in H_{x_i}, H_{x_i} \in \Omega\}$, as shown in Fig. 1.1. The equilibrium equations of peridynamic theory is shown as

Fig. 1.1 The interaction between \mathbf{x}_i and \mathbf{x}_j within peridynamic model



$$\rho(\mathbf{x})\ddot{\mathbf{u}}(\mathbf{x}, t) = \int_H [\mathbf{t}(\mathbf{x}_j - \mathbf{x}_i, \mathbf{u}_j - \mathbf{u}_i, t) - \mathbf{t}'(\mathbf{x}_j - \mathbf{x}_i, \mathbf{u}_j - \mathbf{u}_i, t)]dH + \mathbf{b}(\mathbf{x}, t) \quad (1.3)$$

where $\mathbf{u} = \mathbf{u}(\mathbf{x}, t)$, $\ddot{\mathbf{u}}(\mathbf{x}, t)$, $\mathbf{b}(\mathbf{x}, t)$, $\rho(\mathbf{x})$ represent the displacement, acceleration, body force density, and mass density, of the material point x_j , respectively. \mathbf{t} refers to the interaction force or PD force.

1.4 Unit Cell

Buryachenko V. A. pointed out that the intrinsic properties and microstructure of a material can be represented by the effective material properties of a unit [16]. The material and geometric properties of graphene platelets containing a large number of atoms are repeated periodically on a macroscopic scale. Selecting a single unit rather than a whole for analysis can significantly reduce the amount of calculation, as shown in Fig. 1.2. For a periodically arranged element, we assume that physical quantities such as displacement field, stress field and strain field on the boundary surface of the element after deformation are still continuous. In order to reflect this periodic characteristic, Erdogan Madenci [17] solves this problem by completing a family of material points near the surface or corners, as shown in Fig. 1.3. In this paper, the supplementary part of the horizon is called “virtual horizon”.

For the periodic model, the state of a material point near the boundary is related to the state of the point k in the “virtual horizon” which is not directly available, as shown in Fig. 1.3. Therefore, the displacement of the point k calculated by considering the corresponding point k' in the internal of the unit cell. The motion states of points k and k' are defined in the theory of elastic mechanics, i.e.

$$u_{i(k)} = H_{ij}x_{j(k')}, \quad i, j = 1, 2, 3 \quad (1.4)$$

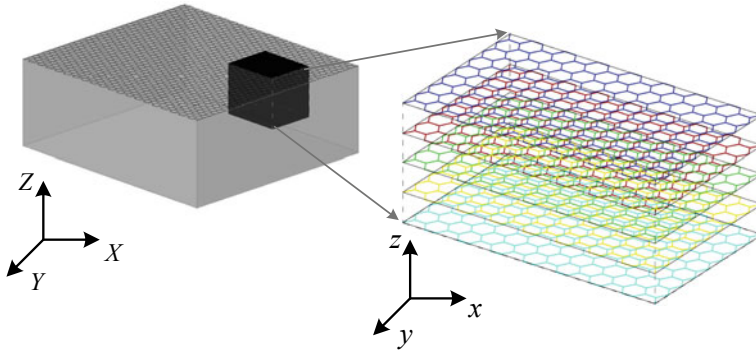
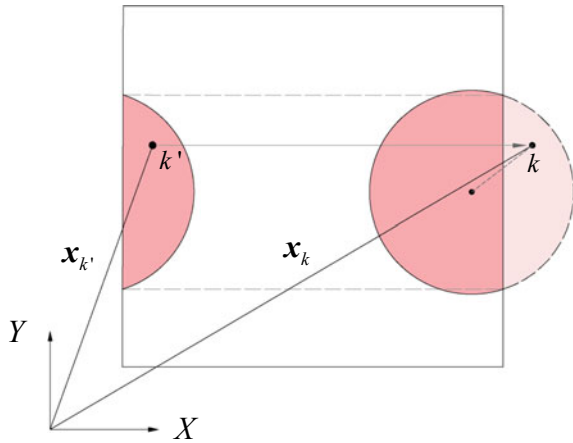


Fig. 1.2 Unit cell of graphene platelets

Fig. 1.3 The method to complete the families of material points near a surface or a corner



$$u_{i(k)} = H_{ij}x_{j(k)}, \quad i, j = 1, 2, 3 \tag{1.5}$$

where $x_{j(k)}$ is the coordinate, H_{ij} is the displacement gradient tensor and is constructed as

$$H_{ij} = \frac{\partial u_i}{\partial x_j}, \quad i, j = 1, 2, 3 \tag{1.6}$$

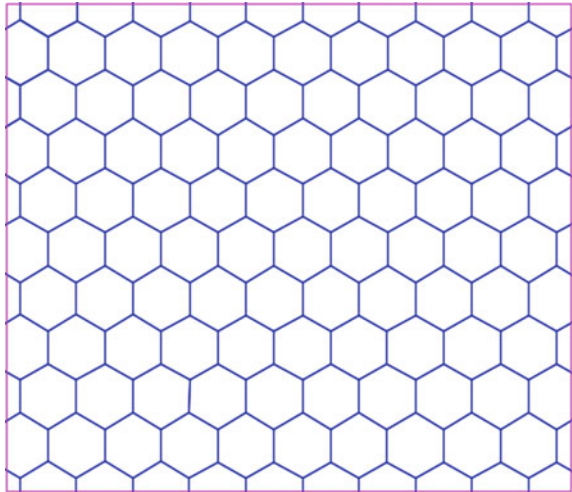
1.5 Results and Discussion

Firstly, consider a single layer graphene cell in Fig. 1.4, with a length of 24.595121 Å and a width of 21.3 Å, which is assumed to have thickness 3.4 Å [18]. By analyzing the response of the unit under the action of equivalent load, the response of the periodic material under the action of macroscopic uniform deformation gradient can be obtained, so as to analyze the elastic properties of graphene and calculate its elastic matrix. Therefore, the two-dimensional model is taken as an example here, and the three pure load boundary cases considered are shown in Fig. 1.5 to obtain the central tensor of strain concentration. Similarly, for the three-dimensional model, we have three stretch and three shear deformation conditions, where six uniform load cases are specified by

$$\left\{ \begin{array}{l} \boldsymbol{\varepsilon}_1 = \{\varepsilon, 0, 0, 0, 0, 0\}^T \\ \boldsymbol{\varepsilon}_2 = \{0, \varepsilon, 0, 0, 0, 0\}^T \\ \boldsymbol{\varepsilon}_3 = \{0, 0, \varepsilon, 0, 0, 0\}^T \\ \boldsymbol{\varepsilon}_4 = \{0, 0, 0, \varepsilon, 0, 0\}^T \\ \boldsymbol{\varepsilon}_5 = \{0, 0, 0, 0, \varepsilon, 0\}^T \\ \boldsymbol{\varepsilon}_6 = \{0, 0, 0, 0, 0, \varepsilon\}^T \end{array} \right. \quad (1.7)$$

Figure 1.6 shows the displacement fields in the x and y directions of the single-layer graphene in the case of Fig. 1.5a, and the position of carbon atoms in the figure indicates the distribution of particles after deformation. Figures 1.7 and 1.8 shows the results in the case of Fig. 1.5b, c respectively. It can be clearly seen that when the tensile load is applied to the model only in the x direction, the displacement in

Fig. 1.4 A single layer graphene cell



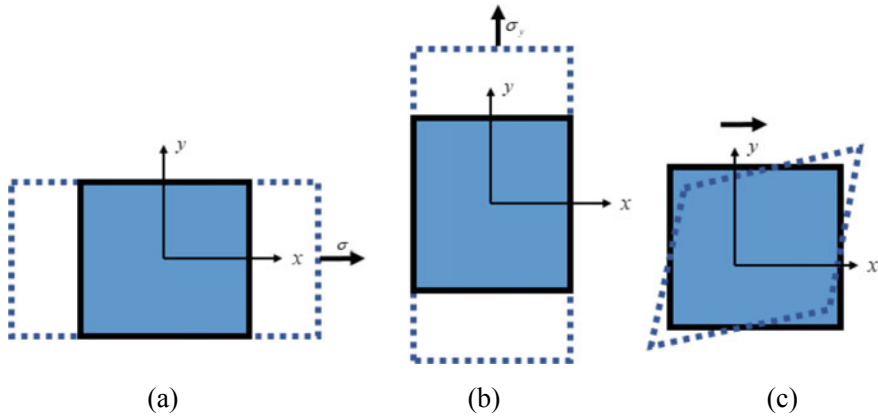


Fig. 1.5 Three boundary conditions

this direction changes uniformly in the whole cell, while the displacement in the y direction of the two adjacent rows of carbon atoms presents different directions, indicating the overall internal self-equilibrium state. Similarly, for the boundary conditions in Fig. 1.7, the graphene displacement field presents a uniform change in the y direction, while in the x direction, it varies little as in Fig. 1.6, but the values on the relative boundary still show a symmetric feature. Finally, under shear loads, the displacement fields in both directions vary evenly.

Therefore, combined with the previous description, we set the ε to be small, the elastic coefficient matrix values of single-layer graphene with different sizes are obtained as Table 1.1. Significantly, the elastic properties vary over a wide range depending on the dimensions. the material exhibits anisotropic characteristics and the calculated value of the elastic coefficient is smaller. This phenomenon shows that graphene exhibits isotropic properties under small displacement loading, while the material becomes nonlinear elastic when subjected to relatively large deformations [10].

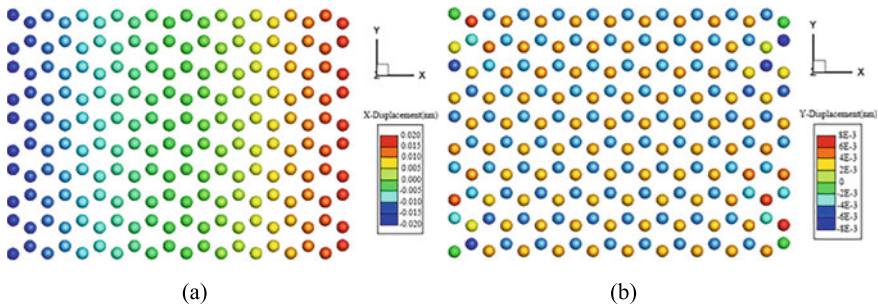


Fig. 1.6 The displacement fields of single-layer graphene in the x and y directions in the case of Fig. 1.5a. (a) The displacement fields in the x directions (b) The displacement fields in the y directions

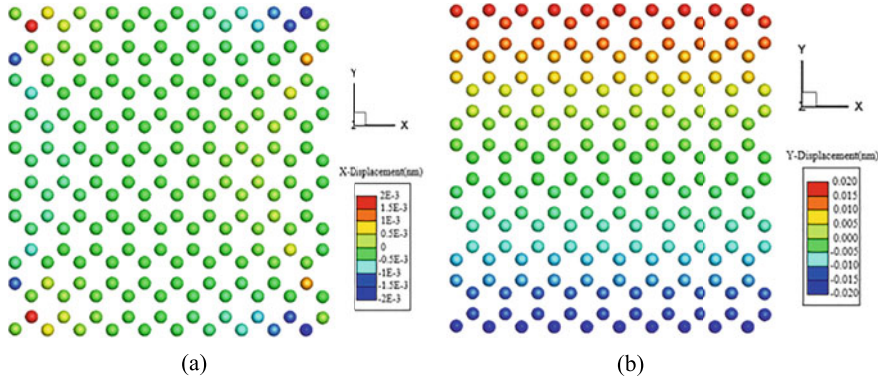


Fig. 1.7 The displacement fields of single-layer graphene in the x and y directions in the case of Fig. 1.5b. (a) The displacement fields in the x directions (b) The displacement fields in the y directions

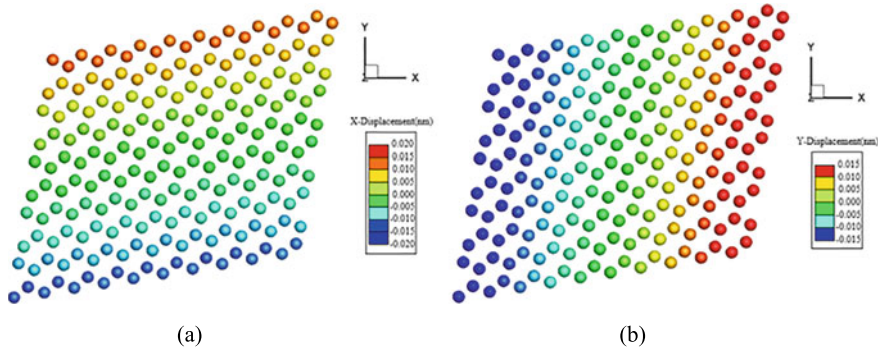


Fig. 1.8 The displacement fields of single-layer graphene in the x and y directions in the case of Fig. 1.5c. (a) The displacement fields in the x directions (b) The displacement fields in the y directions

Table 1.1 The elastic coefficient matrix values of single-layer graphene

L (\AA)	W (\AA)	C_{11} (TPa)	C_{22} (TPa)
22.136	17.04	1.12	0.92
24.595	21.30	1.12	0.92
73.785	63.90	1.21	1.02
122.976	106.50	1.23	1.13

1.6 Conclusion

This study proposes a simulation method for the analysis of graphene sheets based on the state-based peridynamics. Carbon atoms in graphene are treated as discrete material points in this model. The vdW forces and REBO potential functions are introduced into the equation of motion of material points to study the response of graphene under six pure loads. The results show that the presented method can well predict the mechanical properties of graphene materials. Therefore, it is feasible to extend the proposed method to complex graphene structures and other graphene composites in future studies.

Credit Authors Contribution Statement **Dan Wu:** Conceptualization, Methodology, Simulation, Analysis, Original draft, Graphs, Editing, Review. **Yin Yu:** Analysis, Resources, Review. **Yile Hu:** Methodology, Software, Simulation, Analysis, Review, Editing.

Declaration of Competing Interest

The authors declare that they have no known competing financial interests or personal relationships that could have appeared to influence the work reported in this paper.

Data Availability

The datasets generated and/or analyzed during the current study are available from the corresponding author on reasonable request.

Acknowledgements

This work is supported by National Natural Science Foundation of China under Grant No. 11902197 and Ye Qisun Fund under Grant No. U2241266. The corresponding author is grateful to the research grant for young scholar by Shanghai Jiao Tong University.

References

1. Frank, I.W.T.D.M., Van der Zande, A.M., et al.: Mechanical properties of suspended graphene sheets. *J. Vacuum Sci. Technol. B Microelectron. Nanometer Struct.* **25**(6), 2558–2561 (2007)
2. Burkert, U.A.N.L.: *Molecular Mechanics*. American Chemical Society, Washington, DC (1982)
3. Berg, B.A.: *Markov Chain Monte Carlo Simulations and Their Statistical Analysis: With Web-Based Fortran Code*. World Scientific (2004)
4. Doucet, A.D.F.N., Gordon, N.: *Sequential Monte Carlo Methods in Practice*. Springer, New York (2001)
5. Binder, K.: The Monte Carlo method in condensed matter physics. In: *The Monte Carlo Method in Condensed Matter Physics*, p. 1 (1995)
6. Reddy, C.D.R.S., Liew, K.M.: Equilibrium configuration and continuum elastic properties of finite sized graphene. *Nanotechnology* **17**(3), 864–870 (2006)
7. Silling, S.A.: Reformulation of elasticity theory for discontinuities and long-range forces. *J. Mech. Phys. Solids.* **48**(1), 175–209 (2000)
8. Brenner, D.W.: Empirical potential for hydrocarbons for use in simulating the chemical vapor deposition of diamond films. *Phys. Rev. B* **42**(15), 9458–9471 (1990)
9. Brenner, D.W., et al.: A second-generation reactive empirical bond order (REBO) potential energy expression for hydrocarbons. *J. Phys. Condensed Matter.* **14**(4), 783–802 (2002)

10. Deji Akinwande, C.J.B., Scott Bunch, J., Egberts, P., Felts, J.R., Gao, H., Huang, R., Kim, J.-S., Li, T., Li, Y., Liechti, K.M., Lu, N., Park, H.S., Reed, E.J., Wang, P., Yakobson, B.I., Zhang, T., Zhang, Y.-W., Zhou, Y., Zhu, Y.: A review on mechanics and mechanical properties of 2D materials—graphene and beyond. *Extreme Mech. Lett.* **13**, 42–77 (2017)
11. Lindsay, L., Broido, D.A.: Optimized Tersoff and Brenner empirical potential parameters for lattice dynamics and phonon thermal transport in carbon nanotubes and graphene. *Phys. Rev. B* **81**(20), 205441 (2010)
12. He, X.Q., et al.: Modeling of van der Waals force for infinitesimal deformation of multi-walled carbon nanotubes treated as cylindrical shells. *Int. J. Solids Struct.* **42**(23), 6032–6047 (2005)
13. Jones, J.E.: The determination of molecular fields: from the variation of the viscosity of a gas with temperature. *Proc. Royal Soc.* **106A**, 441 (1924)
14. Girifalco, L.A., Lad, R.A.: Energy of cohesion, compressibility, and the potential energy function of graphite system. *J. Chem. Phys.* **25**, 693–697 (1956)
15. Girifalco, L.A.: Interaction potential for C₆₀ molecules. *J. Phys. Chem.* **95**, 5370–5371 (1991)
16. Buryachenko, V.A.: *Micromechanics of Heterogeneous Materials*. Springer, NY (2007)
17. Madenci Erdogan, A.B., Phan, N.D.: Peridynamic unit cell homogenization. In: 58th AIAA/ASCE/AHS/ASC Structures, Structural Dynamics, and Materials Conference, AIAA SciTech Forum. AIAA, Grapevine, TX (2017)
18. Arroyo, M.B.T.: Finite crystal elasticity of carbon nanotubes based on the exponential Cauchy–Born rule. *Phys. Rev. B. Condensed Matter.* **69**, 115415 (2004)

Chapter 2

Three-Dimensional Temperature Field Prediction in Double-Wall Cooling Structure Using Deep Learning Method



Junjie Huang, Jianqin Zhu, Yanjia Wang, Zeyuan Cheng, and Lu Qiu

Abstract The double-walled cooling structure can achieve high cooling efficiency but has a higher risk of failure compared to traditional structures. In order to optimize the structural variables of the structure, a fast and accurate temperature field prediction method is urgently proposed. This study establishes a deep learning model using MLPs and SRCNN modules to predict the 3D temperature field of the outer wall of a double-walled cooling structure (DWCS) unit. The model takes in geometric structure variables and working condition variables as inputs. To train the model, a temperature field dataset is generated by CFD numerical simulation. The results demonstrate that the deep learning method can accurately predict the 3D temperature field of the DWCS unit at multiple scales, and the model training can be convergent with the proper design of the model architecture and training strategies. Compared to numerical simulation, the deep learning model can predict the temperature field quickly and be combined with machine learning optimization algorithms for the optimization of DWCS variables.

Keywords Deep learning model · Double-walled cooling structure · 3D temperature field prediction

2.1 Introduction

As the inlet temperature of the turbine continues to rise, the turbine blades are subjected to high-temperature gas that exceeds the melting point of the manufacturing materials. To ensure the operation of the turbine blades, a highly efficient cooling structure is used as an effective thermal protection measure. A double-wall cooling structure integrates cooling forms such as impingement cooling, convective cooling, and film cooling, making it an efficient means of thermal protection. The double-wall cooling structure has been applied to high-temperature components such

J. Huang · J. Zhu (✉) · Y. Wang · Z. Cheng · L. Qiu
Beihang University, Beijing, China
e-mail: buaahjj@buaa.edu.cn

as combustion chambers and turbine blades, and its heat transfer characteristics have been extensively studied.

The heat transfer capacity of the double-wall cooling structure mainly depends on the internal impingement cooling and external film cooling. Internal impingement cooling is achieved by guiding cold air through impingement holes to impact the inner side of the outer wall of the double-wall structure. For the heat transfer characteristics of internal impact cooling, An experimental study conducted by Brigham et al. [1] focused on the impact of pin-fins on the cooling of the turbulence inside a cylinder. The researchers compared the effects of short and long pins and concluded that longer pin-fins contribute to greater heat transfer than their shorter counterparts. Rao et al. [2] conducted a study to investigate the combined effect of pin fin-dimple arrays on heat transfer enhancement and compared it with the effects of a pin-fin channel. The results of their study were similar to those reported by Shevchenko et al. [3], who also studied the combination of pin-fins with dimples. Su et al. [4] studied the entropy generation of staggered pin-fins, which is crucial for reducing energy loss. Their findings revealed that thermal diffusion dominates the entropy generation at small Reynolds numbers, whereas fluid friction dominates at large Reynolds numbers.

The principle of film cooling is to create openings on the outer wall of the double-wall and guide coolant to flow out of the wall surface, the coolant forms a thin layer of coolant on the wall surface, which insulates the gas from direct burning and erosion. Chang et al. [5] investigated the effects of effusion hole placement and coolant discharge on the thermal performance of a gas turbine blade. Effusion improved heat transfer rates by suppressing crossflow, and reducing tip discharge further improved performance. Three sets of heat transfer and pressure drop correlations were developed for leading-edge cooling applications.

Double-wall cooling structure has excellent cooling performance, which brings the increase of failure risk [6–8]. The temperature change on the double wall cooling structure is very severe, which can't be ignored. The stress concentration occurs in the cavity structure, which makes the influence of thermal stress in the cavity area further increase and the probability of structural failure further increase. Therefore, it is very necessary to optimize the structural parameters of double-wall cooling in industrial design [9–11]. The calculation accuracy and efficiency of the temperature field determine the period of optimization and the quality of optimization results.

The traditional calculation method of the temperature field of the double-wall cooling structure depends on theoretical analysis and numerical simulation. The traditional method can't take into account the calculation speed and calculation accuracy. For the optimal design of the double-wall cooling structure, a fast and accurate temperature field calculation method is urgently needed. The artificial intelligence method has a unique advantage in speed and accuracy. Many scholars have applied artificial intelligence algorithms to the study of heat transfer characteristics of double-walled cooling structures. Yang et al. [12] established a proxy model based on convolutional neural network (CNN) for two-dimensional cooling effect prediction of a large number of randomly combined film holes on a plate. After training, the relative error of the prediction of two-dimensional cooling effect distribution is 4.04%. A figure-graph translation model based on conditional generation adversarial

network (CGAN) was established [13] to achieve rapid prediction of cooling efficiency under different end-wall film hole arrangement locations. Wang et al. [14] established the mapping relationship between flow structure parameters and two-dimensional temperature field on the surface of a flat plate based on deconvolution neural network for flat plate single-hole film cooling structure, and the prediction error of the test set was less than 0.7%. Xing et al. [15] parameterized the flat panel film cooling unit into five structure and flow parameters and realized the cooling effect prediction of two-dimensional flat film cooling structure based on CNN, and used the deconvolution network to achieve the reverse prediction of the two-dimensional cooling effect to structure and flow parameters.

The present study considered a double-walled cooling structure (DWCS) unit. Based on the numerical simulation results of computational fluid dynamics (CFD), the three-dimensional (3D) temperature field dataset of the DWCS unit is established. A 3D temperature field prediction model based on the deep learning method is proposed, which includes a multi-layer perceptron (MLPs) module composed of the fully connected network and super resolution convolutional neural network (SRCNN) module composed of the convolutional network. The model can quickly and accurately reconstruct the 3D temperature field of the structure under the condition of given geometric structure variables and working condition variables.

2.2 Methodology

2.2.1 Numerical Simulation for DWCS Unit

Geometry Define. The geometric structure of the DWCS unit is shown in Fig. 2.1. D_f is the diameter of the film hole, α is the inclination angle of the film hole, P is the spanwise direction spacing of the film hole, S is the stream direction spacing of the film hole, H_o is the thickness of the outer wall, and H is the impact distance. The structure includes a fluid domain and a solid domain, and the fluid domain includes an external mainstream channel, an internal cool air channel and an internal impact cooling channel. Considering that the outer wall is the failure zone, only the outer wall in contact with the main stream is retained in the solid domain, and the inner wall is not considered for the time being. In order to ensure the full development of the main stream, the length of the external main stream passage is extended by $5D_f$ at the inlet and outlet. Specific structural parameters are described in Sect. 2.2.

Heat Transfer Analyses. Commercial software Fluent was used for CFD numerical simulation. The reynolds average navier-stokes (RANS) method was used to simulate the flow and coupled heat transfer processes of geometric structures. The $k - \omega$ shear stress transport (SST) model was used for the turbulence model. Figure 2.2 shows the boundary conditions of the computing domain. The main flow inlet and coolant inlet are set as mass inlet conditions, the main flow outlet is set as pressure

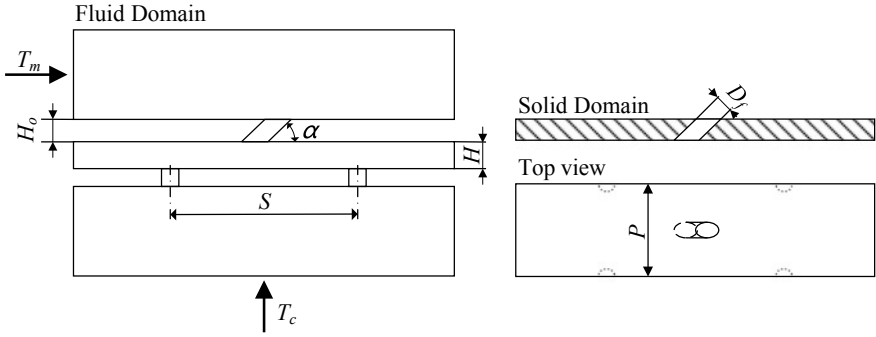


Fig. 2.1 The geometric structure of the DWCS unit

outlet conditions. The left and right sides of the computing domain are set as periodic boundaries. The whole structure consists of two parts: fluid domain and solid domain, and the solid domain only includes the outer wall of the DWCS unit. The calculation is considered convergent when the temperature field remains stable for 2000 steps and the maximum residual is less than 1×10^{-6} .

The computing domain mesh was generated by the commercial software FluentMeshing. In order to realize automatic mesh division, unstructured mesh was used, and the poly-hexcore volume mesh generation method was used for mesh generation. This method can effectively increase the number of hexahedral mesh, thus improving the overall quality of the grid. In order to meet the requirements of SST $k - \omega$ turbulence model, the mesh size near the wall was adjusted to ensure that y^+ is less than 1. The mesh in the hole column area and wall area is refined, and the expansion layer is set at the fluid–solid interface. In order to verify grid independence, three sets of different mesh of 0.06 million, 0.2 million and 1.2 million were

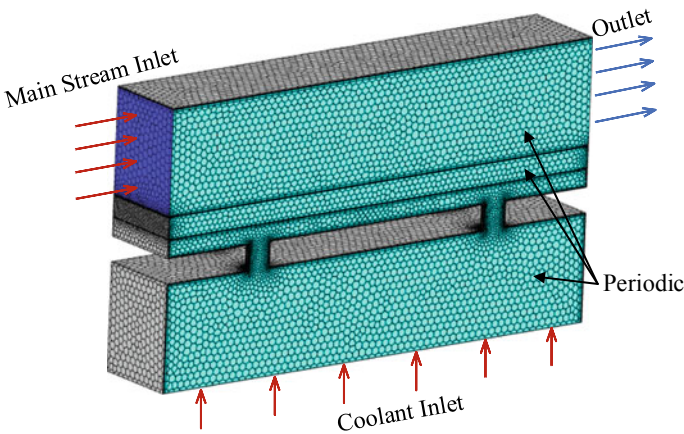


Fig. 2.2 The boundary conditions of the computing domain

compared. Table 2.1 shows the specific size Settings of the three sets of mesh. The comprehensive cooling efficiency is adopted as the metric of the cooling efficiency of the DWCS unit. The comprehensive cooling efficiency is defined as follows:

$$\phi = \frac{T_m - T_w}{T_m - T_c} \quad (2.1)$$

Figure 2.3 shows the comparison results of the distribution of comprehensive cooling effect along the stream direction of the three sets of mesh. The results show that the distribution of the comprehensive cooling effect of the three sets of mesh is similar. Considering that the training of neural networks requires a large amount of data, 0.2 million mesh can save a lot of computing resources under the condition of ensuring accuracy, The 0.2 million mesh Settings are selected in the subsequent mesh division.

2.2.2 Dataset Building

Variable Combinations Determined. The training of deep learning models depends on large amounts of data generated by numerical simulation. This paper aims to propose a model to predict the 3D temperature field of the DWCS unit. The variable parameters of the data set are designed to ensure the trained model can be applied to most structural parameter Spaces and working condition Spaces. Six important structural parameters were selected as variables, and the sampling range of each parameter is constrained, as shown in Table 2.2.

The sampling range of parameters is formulated as follows: (1) Considering the constraints of processing and manufacturing, the minimum diameter of the film hole is 0.4 mm; considering the experience values of common film diameters of turbine blades, the maximum diameter is 0.9 mm; and the wall thickness is between 0.7 and 1.2 mm according to design experience; (2) In order to ensure the effective covering of the film cooling, the incidence angle of the film hole varies from 20° to 70°; (3) In order to increase the parameter space of geometric structure variables, the stream direction spacing and spanwise spacing vary between $1D_f$ and $5D_f$, and the impact distance varies between $0.7D_f$ and $1.2D_f$. The Latin hypercube sampling method was adopted to sample the above 6 variables in the parameter space, forming 25 groups of geometric structure parameter combinations. Finally, commercial software UG was used to construct 25 geometric structures.

Three working condition parameters with significant influence on the temperature field are selected as variables, and the values of the variables are shown in Table 2.3. By permutation and combination of the values of the three variables, a total of 12 groups of working condition parameter combinations was formed. The numerical simulation under 12 groups of working condition parameter combinations was performed for each geometric structure. Finally, we generated a simulation dataset with 300 outer wall temperature fields of the DWCS unit.

Table 2.1 The specific size Settings of the three sets of meshes

Mesh	Local size		Surface mesh		Boundary layers		Volume mesh		Total mesh
	Wall-holes	Wall-solid	Minimum	Maximum	Number	First height	Min cell length	Max cell length	
1	1.00E-04	1.60E-04	2.00E-04	4.00E-04	4	2.00E-06	7.00E-05	2.80E-04	67,844
2	5.00E-05	8.00E-05	1.00E-04	3.00E-04	5	2.00E-06	5.00E-05	2.00E-04	202,566
3	1.00E-05	5.00E-05	5.00E-05	1.00E-04	8	2.00E-06	1.00E-05	1.60E-04	1,241,452

Fig. 2.3 The distribution of comprehensive cooling effect along the stream direction of the three sets of mesh

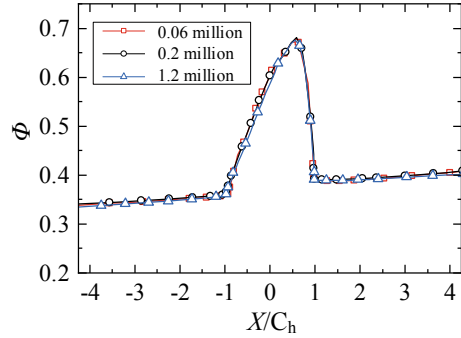


Table 2.2 The sampling range of each parameter

Parameter	Range
Film hole diameter D_f /mm	0.4–0.9
Inclination angle of the film hole α (°)	20–70
Spanwise spacing of the film hole P /mm	$3 D_f$ – $5 D_f$
Stream spacing of the film hole S /mm	$3 D_f$ – $13 D_f$
Outer wall thickness H_o /mm	0.7–1.2
Impact distance H /mm	0.7–1.2

Table 2.3 Working condition parameters

Parameter	Range
Main stream temperature T_m /K	1700, 1900, 2100
Main stream velocity V_m /(m/s)	400, 800
Blow ratio M	0.75, 1.25

Data Processing. The data format that convolutional neural networks can learn directly is the high-dimensional tensor structure. The numerical simulation method adopted in this paper is based on unstructured mesh. The calculated temperature field data is a linked list structure composed of grid-node-coordinates. Therefore, the numerical data cannot be directly trained in the convolutional neural network model. The usual practice is to process the numerical results into a contour and convert them into a picture format. Naturally, the picture is a tensor structure composed of RGB, so it can be directly put into model training. For the work in this paper, we preprocessed the numerical simulation results and converted them into 3D tensor structure. The element of the tensor is a physical quantity, which is characteristic of the physical mechanism better than the RGB value. The griddata method of scipy python library was used for data processing, and the nearest method was chosen as the interpolation parameter. Each sample was processed into a temperature field tensor with the size of $16 \times 256 \times 64$ and a temperature characteristic field tensor with size of $4 \times 64 \times 16$ for the training of different modules in the model.

2.2.3 Deep Learning Algorithm

As shown in Fig. 2.4, the model consists of the following two parts: MLPs module, which is composed of the fully connected neural network, predicts the temperature characteristic field from the label vector. The SRCNN module, composed of the upsampling layer and the convolutional network layer, predicts the final temperature field. The two modules and the evaluation metrics are described below.

MLP module. The label vector is the original input in the entire model. It is composed of 6 geometric parameter variables and 3 working condition parameter variables. The temperature field contains too many elements ($16 \times 256 \times 64 = 262,144$), thus the construction of MLPs that directly predict the temperature field will lead to the explosion of trainable parameters of the model, making it difficult to train convergence. Therefore, the task of MLPs is lightened to predict the temperature characteristic field ($4 \times 64 \times 16 = 4096$). The module consists of 4 subnetworks of the same size. The subnetwork is a fully connected neural network with a one-dimensional tensor of 1024 length output. The outputs of the four subnetworks are reshaped into a two-dimensional tensor with the size of 64×16 and then stacked into a 3D tensor with the size of $16 \times 256 \times 64$. The task of upsampling and predicting the final temperature field is assigned to SRCNN module.

SRCNN module. SRCNN is proposed to solve the problem of image super resolution. In this paper, from the temperature characteristic field with size of $4 \times 64 \times 16$ to the temperature field with the size of $16 \times 256 \times 64$, it can be regarded as a 3D super resolution problem with a magnification of 4. The module takes the temperature characteristic field tensor as input and expands the input tensor to the same size as the temperature field tensor using transpose convolution. Three layers of CNN were used to extract and reassemble the features, and finally output the temperature field. See the literature [16] for the principle and details of SRCNN.

Loss function and metrics. We used L_1 loss function to train the model. The loss is described as:

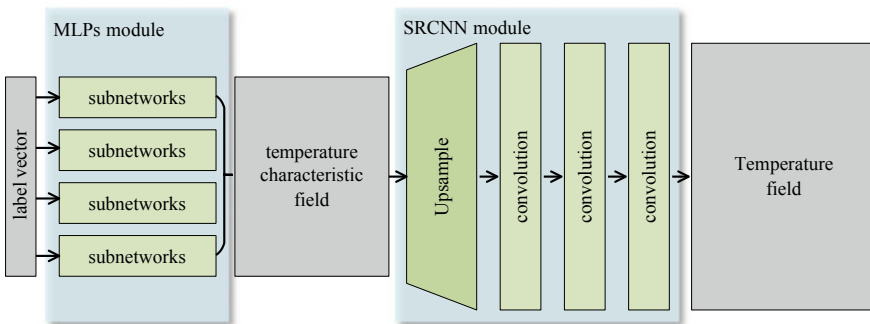


Fig. 2.4 The deep learning network architecture

$$L_1 = \frac{1}{n} \sum_{i=1}^n |y_i - \hat{y}_i| \quad (2.2)$$

where n is the point number of samples, y_i is the ground truth, and \hat{y}_i is the module predicted value.

To evaluate the model, the mean relative error (E_{MRE}) and the accuracy rate (E_{acc}) shown in Eqs. (2.3) and (2.4) for measuring the deviation between the predicted data and the ground truth.

$$E_{MRE} = \frac{1}{n} \sum_{i=1}^n \frac{y_i - \hat{y}_i}{\epsilon + \max(y_i, \hat{y}_i)} \times 100\% \quad (2.3)$$

$$E_{acc} = 1 - E_{MRE} \quad (2.4)$$

where ϵ is a minimum value to prevent the divisor from being 0, which takes 1×10^{-4} . Other variables are defined the same as Eq. (2.2).

2.3 Experiment and Results

Our model is implemented by PyTorch-1.11.0, and trained on GPU (NVIDIA GeForce GTX 3060Ti). Adam optimizer was used to optimize the parameters of the model training process. In order to verify the performance of the model, the model is evaluated and discussed after the model converges in the training set.

2.3.1 Model Evaluation

In the training process of the model, we selected an adaptive learning rate attenuation method ReduceLROnPlateau, which helps the model to converge better in the training. In order to promote model convergence, we used a two-stage training strategy. Firstly, the MLPs module was trained separately, and only the temperature characteristic field data set was used. The learning rate was selected as 1×10^{-3} , and a total of 3000 epochs were trained. As shown in Fig. 2.5, at the time of the 2000 epoch, the MLPs module has converged, and the prediction accuracy of the temperature characteristic field has reached 99.3%. Then, the SRCNN module is added for training. At this time, temperature characteristic field data is used as the truth value of the MLPs module, and temperature field data is used as the truth value of the SRCNN module. As shown in Fig. 2.5, at the time of the 4000 epoch, the entire model training has converged, and the accuracy of temperature field prediction has reached 99%.

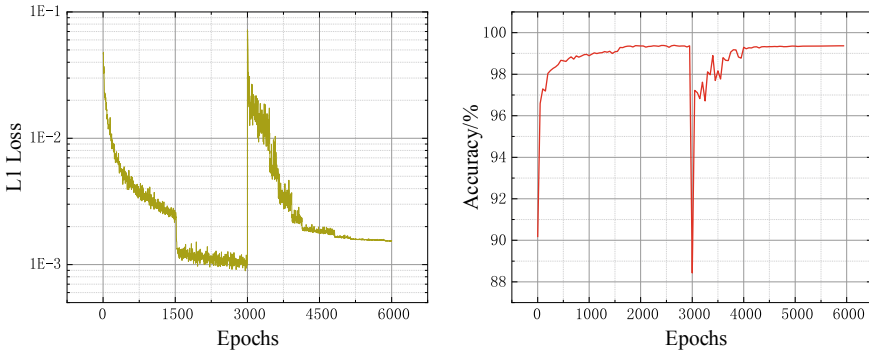


Fig. 2.5 Loss function curve and test set accuracy curve in training process

After completing the training of the model, we demonstrated the prediction effect of the model from multiple scales and compared the prediction results of the model with the numerical simulation results (ground truth). The average absolute error and average relative error of the established model on the test set are 42 K and 2.5%. This proves that the deep learning method has excellent ability in 3D temperature field prediction. Figure 2.6 shows the contour of the test sample at different sections. The film surface, mid-section and impact surface are selected respectively. It can be found that for different sections, the convolution kernel can well predict the temperature distribution, which is highly consistent with the temperature distribution obtained by CFD, and the prediction effect is also good for the region with a large temperature gradient at the hole region. To make a quantitative comparison between the model prediction data and the numerical simulation results, we show the cooling effect distribution trend of the predicted results and the numerical simulation results on the film surface in Fig. 2.7. On the film surface, one curve was selected along the stream direction and one curves along the spanwise direction. The distribution of cooling efficiency along these curves can characterize the condition of film covering so that the prediction ability of the model to the film cooling effect can be observed. The distribution of the cooling effect predicted by the model coincides with the numerical simulation results. By evaluating the model and comparing it with numerical data, we demonstrate that our model can predict accurate 3D temperature fields under multiple scales.

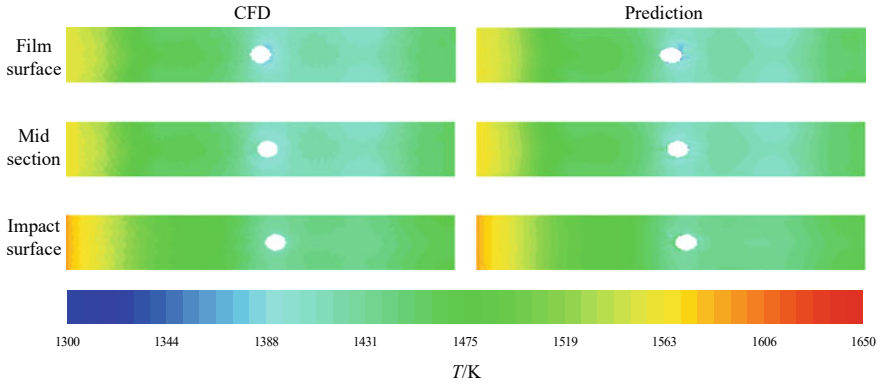


Fig. 2.6 Numerical simulation results and model prediction results of a test sample at different sections

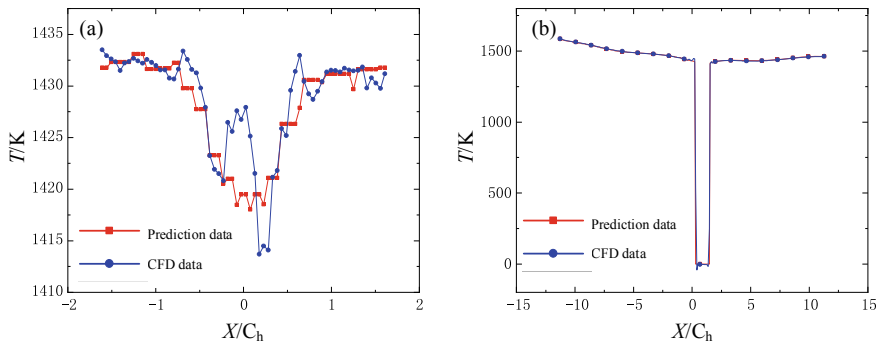


Fig. 2.7 The cooling effect distribution trend of the predicted results and the numerical simulation results on the film surface

2.4 Conclusion

To predict the 3D temperature field of the outer wall of the DWCS unit, a deep learning model is established based on the MLPs module and SRCNN module. The model takes geometric structure variables and working condition variables as inputs. Firstly, the temperature characteristic field is predicted by the MLPs module, and then the 3D temperature field is reconstructed by the SRCNN module. To support the model training, a temperature field dataset was generated by CFD numerical simulation. Results indicated the following conclusions:

1. The deep learning method can establish the mapping relationship between the label vector composed of geometric structure variables and working condition variables and the 3D temperature field. Through the design of the model architecture and the reasonable selection of training strategies, the model training can be convergent.
2. Our model can accurately predict the 3D temperature field of the outer wall of the double-walled cooling structure at multiple scales. Model performance evaluation shows that the average absolute error and average relative error of the established model on the test set are 42 K and 2.5% respectively. The temperature contour on different sections and the one-dimensional distribution of the cooling efficiency of the film surface are highly consistent with the ground truth.

Compared with numerical simulation, the deep learning model can predict the temperature field quickly. Based on the model proposed in this paper, combined with the machine learning optimization algorithm, the optimization of the double-wall cooling structure variables can be completed in a relatively short time. In future work, the model architecture will be further optimized, the prior knowledge related to heat transfer will be used to constrain the learning process of the model, and a temperature field prediction model with higher precision and stronger generalization will be generated around the heat transfer mechanism.

References

1. Brigham, B.A., VanFossen, G.J.: Length to diameter ratio and row number effects in short pin fin heat transfer (1984)
2. Rao, Y., Xu, Y., Wan, C.: An experimental and numerical study of flow and heat transfer in channels with pin fin-dimple and pin fin arrays. *Exp. Therm. Fluid Sci.* **38**, 237–247 (2012)
3. Shevchenko, I., Kindra, V., Bychkov, N.: A numerical study of heat and mass transfer in a narrowing channel with pin fin-dimple arrays. In: 2018 International Multi-Conference on Industrial Engineering and Modern Technologies (FarEastCon), pp. 1–4. IEEE (2018, October)
4. Su, Y., Liu, Z., Jiang, F.: Entropy generation of staggered short pin fin arrays. In: 2011 International Conference on Remote Sensing, Environment and Transportation Engineering, pp. 300–303. IEEE (2011, June)
5. Chang, S.W., Chiang, P.A., Cai, W.L.: Thermal performance of impinging jet-row onto trapezoidal channel with different effusion and discharge conditions. *Int. J. Therm. Sci.* **159**, 106590 (2021)
6. Guo, Z., Song, Z., Fan, J., Yan, X., Huang, D.: Experimental and analytical investigation on service life of film cooling structure for single crystal turbine blade. *Int. J. Fatigue* **150**, 106318 (2021)
7. Elmukashfi, E., Murray, A.V., Ireland, P.T., Cocks, A.C.: Analysis of the thermomechanical stresses in double-wall effusion cooled systems. *J. Turbomach.* **142**(5), 051002 (2020)
8. Wang, S., Zhang, Z.: Failure mechanism of turbine guide vane and oxide composition analysis on the surface of failure vane cracks. *Eng. Fail. Anal.* **117**, 104763 (2020)
9. Kim, K.M., Moon, H., Park, J.S., Cho, H.H.: Optimal design of impinging jets in an impingement/effusion cooling system. *Energy* **66**, 839–848 (2014)
10. Moon, M.A., Kim, K.Y.: Analysis and optimization of fan-shaped pin-fin in a rectangular cooling channel. *Int. J. Heat Mass Transf.* **72**, 148–162 (2014)

11. Skamniotis, C., Cocks, A.C.: Minimising stresses in double wall transpiration cooled components for high temperature applications. *Int. J. Mech. Sci.* **189**, 105983 (2021)
12. Yang, L., Min, Z., Yue, T., Rao, Y., Chyu, M.K.: High resolution cooling effectiveness reconstruction of transpiration cooling using convolution modeling method. *Int. J. Heat Mass Transf.* **133**, 1134–1144 (2019)
13. Yang, L., Dai, W., Rao, Y., Chyu, M.K.: Optimization of the hole distribution of an effusively cooled surface facing non-uniform incoming temperature using deep learning approaches. *Int. J. Heat Mass Transf.* **145**, 118749 (2019)
14. Wang, Y., Wang, W., Tao, G., Zhang, X., Luo, S., Cui, J.: Two-dimensional film-cooling effectiveness prediction based on deconvolution neural network. *Int. Commun. Heat Mass Transfer* **129**, 105621 (2021)
15. Xing, H., Luo, L., Du, W., Wang, S.: Direct and inverse model for single-hole film cooling with machine learning. *J. Turbomach.* **144**(4) (2022)
16. Yoon, Y., Jeon, H.G., Yoo, D., Lee, J.Y., So Kweon, I.: Learning a deep convolutional network for light-field image super-resolution. In: Proceedings of the IEEE International Conference on Computer Vision Workshops, pp. 24–32 (2015)

Chapter 3

A Neural Network-Based Method for Solving the Mass Flow Related Forward and Inverse Problems of Laminate Cooling Structures



Yanjia Wang, Jianqin Zhu, Zeyuan Cheng, and Kaihang Tao

Abstract Laminate cooling structures are extensively used in the design of turbine blades for aircraft engines. There are two types of mass flow related problems in the design of laminate cooling structures: the forward problem of predicting the mass flow rate of cooling air, and the inverse problem of designing the geometric parameters given the target mass flow rate. The present study constructed a dataset for neural network training and testing using numerical simulation methods. A neural network model was established to solve the forward problem of predicting the mass flow rate, with four hidden layers and 64 neurons per layer. The average relative error of the predicted mass flow rate was 1.46%. A solution method for the inverse problem based on predicting the diameter of the film cooling holes was proposed. Using this method, six sets of geometric parameters for the laminate cooling structure were designed under known target mass flow rate conditions, with a design time of 0.014 s. Numerical simulation verification showed that the maximum relative error and average relative error between the designed mass flow rate and the target value were 2.9% and 1.54%, respectively, demonstrating the practicality of the proposed method.

Keywords Laminate cooling structures · Mass flow rate · Forward problem · Inverse problem · Neural networks

3.1 Introduction

Laminate structures are widely used cooling structures in turbine blades for aircraft engines. By exchanging heat between the structure and the cooling air, the temperature of the blade is kept below the material melting point. The more cooling air flow used by the cooling structure, the more adverse effects it has on the engine

Y. Wang · J. Zhu (✉) · Z. Cheng · K. Tao
Beihang University, Beijing, China
e-mail: zhujianqin@buaa.edu.cn

thrust. Therefore, the design of the cooling structure often needs to achieve better cooling effect under the condition of ensuring that the use of cooling air does not exceed the given limit. The laminate structure is a type of cooling structure that can efficiently utilize cooling air. On the one hand, the laminate structure has two or more heat exchange surfaces, which results in a large heat exchange area. On the other hand, multiple cooling structures can be arranged on the wall surface and adjacent walls of the laminate structure, which is beneficial for realizing a composite cooling method. The advantages of laminate structures in flow and heat transfer have attracted extensive attention and research.

The mass flow rate of cooling air is an important parameter in the design of laminate structures. Mass flow related problems in laminate structures can be divided into two categories. The first category is the forward problem, which asks how to evaluate the mass flow rate through the laminate structure given the boundary conditions and geometric parameters. The second category is the inverse problem, which asks how to design the geometric parameters of the laminate structure given the boundary conditions and target mass flow rate. Solving these two types of mass flow related problems in laminate structures is essential for achieving precise control of the cooling structure's mass flow rate in the design process, which is crucial for improving the performance and reliability of turbine blades.

The evaluation of mass flow rate in laminate cooling structures can be achieved through experimental measurements and numerical simulations. Alexander [1] designed a new type of recirculating double wall experimental device and studied the relationship between the internal and external pressure ratios of four different geometric structures and the dimensionless cold air flow rate, finding that high porosity structures require a lower pressure ratio to reach a specific cooling air flow rate. Fujio [2] conducted experimental studies on simplified turbine blade leading edges with laminate cooling structures and found that the presence of pin-fins has little effect on the pressure loss for the same cooling mass flow rate. Chen [3] conducted experimental research on laminate cooling structures on flat plates and found that the placement of pin-fins increases pressure loss and decreases the overall flow coefficient. Lu [4] conducted numerical simulations on 1N1-type laminate cooling structures and established an exponential function relationship between the pressure drop and the dimensionless mass flow rate, which can predict the cooling mass flow rate through the structure given the known internal and external pressure for a fixed geometric parameter of the laminate cooling structure. Both experimental measurements and numerical simulations have high accuracy, but the disadvantage is that the computational time is often long, making it difficult to achieve rapid evaluation.

The fluid network method based on empirical formulas [5] is a fast calculation method for cooling airflow, which simplifies the complex structure into nodes and flow resistance elements. The conservation equations between nodes are established and solved to obtain the pressure and flow parameters of the nodes. Robert [6] proposed that the flow resistance characteristics of laminate cooling structures can be described by two parameters: the viscous resistance coefficient and the inertial resistance coefficient. The flow resistance characteristics of 15 different structures were obtained through experimental studies on laminate cooling structures on turbine

blades. Zhang [7] evaluated the cooling airflow rate through laminate cooling structures by establishing a fluid network for the laminate structure. Compared with numerical simulation results, the error of mass flow rate evaluation is 17%. The fluid network method introduces a lot of simplification and approximation in solving process, and can only be used as a rough mass flow rate estimation method.

The general method for designing the geometric parameters of the laminate cooling structure is the trial-and-error method [8–10]. By repeatedly changing the values of the design parameters and verifying them through numerical simulations, a structure that meets the design requirements can be obtained. The trial-and-error method relies heavily on the experience of the designer, and the design time is long. Moreover, it does not have the ability to search for the optimal design within a certain design parameter space. In order to have search capability within parameter space, current research has established surrogate models between the target parameters and the design parameters through a large number of experiments or numerical simulations, and then used optimization algorithms to search for the optimal design based on the surrogate models [11]. The surrogate models combined with optimization methods can match the geometric parameter design with the design target requirements very well. However, when there are multiple solutions that meet the design requirements within the parameter space, this method can only randomly find one solution, and the optimization process takes a certain amount of time, which cannot achieve real-time design.

Neural networks can automatically learn patterns and rules from historical data through training, and demonstrate good performance in new similar tasks. Existing studies have used neural networks to solve various problems related to flow and heat transfer characteristics, such as predicting the surface pressure field of turbine blades [12], predicting the surface cooling efficiency of transpiration cooling structures [13, 14], and predicting the cooling efficiency of multi-row film cooling hole structures [15]. Meanwhile, neural networks can also serve as a surrogate model in geometric parameter design tasks. By combining with optimization algorithms based on the established neural network surrogate model, the best parameter combination can be found within a certain parameter space [16–18]. Existing studies have shown that the use of neural networks can effectively accelerate the prediction and design of cooling structures. However, the solution to the current geometric parameter design problem still relies on the establishment of forward prediction surrogate models and the optimization method, and the problem of strong design randomness and difficulty of real-time design has not been solved.

The current study focuses on a 161-type laminate cooling structure as the research object. For the mass flow rate forward problem, a fully connected neural network is established to predict the cooling air mass flow rate per unit area. For the inverse problem, a neural network is established to directly predict the geometric parameters that satisfy the target mass flow rate. The training data set for the neural networks consists of 300 sets of data obtained from numerical simulations. The proposed method for the laminate cooling structure mass flow rate prediction can achieve fast and accurate prediction. The proposed method for the inverse problem can provide

multiple reasonable designs that meet the target cooling mass flow rate, which has a positive effect on accelerating the design process of laminate cooling structures.

3.2 Dataset Preparation

3.2.1 Geometries, and Computational Setups

The present study selected a series of laminate cooling structures for numerical simulation and used the simulation results as the dataset for the neural network that solved the mass flow related problem. The laminate cooling structure used in the simulation was shown in Fig. 3.1, where the ratio of the number of impingement holes, pin-fins, and film cooling holes was 1:6:1, and the structure was therefore referred to as the 161-type laminate. In the 161-type laminate cooling structure, the cooling gas first entered through the impingement holes on the inner wall, then flowed around the pin-fins, and finally exited through the film cooling holes on the outer wall. Figure 3.1 showed the geometric parameters of the 161 laminate cooling structure, where the thickness of the inner wall t_1 was 0.8 mm, the distance between the inner and outer walls t_2 was 0.7 mm, the thickness of the outer wall t_3 was 0.7 mm, and the diameter of the pin-fin d_p was 0.8 mm. The five geometric parameters that varied were the diameter of the film cooling holes (d_f), the streamwise spacing (S_f), the spanwise spacing (L_f), the incidence angle of the film cooling holes (α), and the diameter of the impingement holes (d_i), and their ranges were shown in Table 3.1.

Latin hypercube sampling (LHS) method was used to sample within the geometric design parameter space, and a total of 100 geometric models were generated for subsequent numerical simulations. LHS is a stratified sampling method that ensures full coverage of the sampling points in the parameter space, avoiding the situation where training data cannot be collected in the edge area, which has a positive impact on the accuracy of the neural network trained using the dataset in the entire parameter space.

To save computational resources, the minimum calculation unit of the laminate structure was selected for calculation, as shown in the dashed box in Fig. 3.1. The length in the streamline direction of the minimum calculation unit was $2S_f$, and the length in the spanwise direction was $1/2L_f$. Since the study mainly focused on cooling air mass flow related issues of the laminate structure and did not consider heat transfer in the solid domain, only the fluid domain was modeled and calculated. Figure 3.2 shows the boundary conditions used in the simulation. The inlet of the cooling air was set as a pressure inlet with a given total temperature of 836.9 K, and the inlet total pressure $P1^*$ was shown in Table 3.2. The outlet of the cooling air was set as a pressure outlet with a pressure of 2,400,000 Pa. Two side faces in the spanwise direction were set as symmetric boundaries, and the side faces in the streamline direction were set as periodic boundaries. All other surfaces were adiabatic. The fluid was set as ideal gas, and its properties were described using

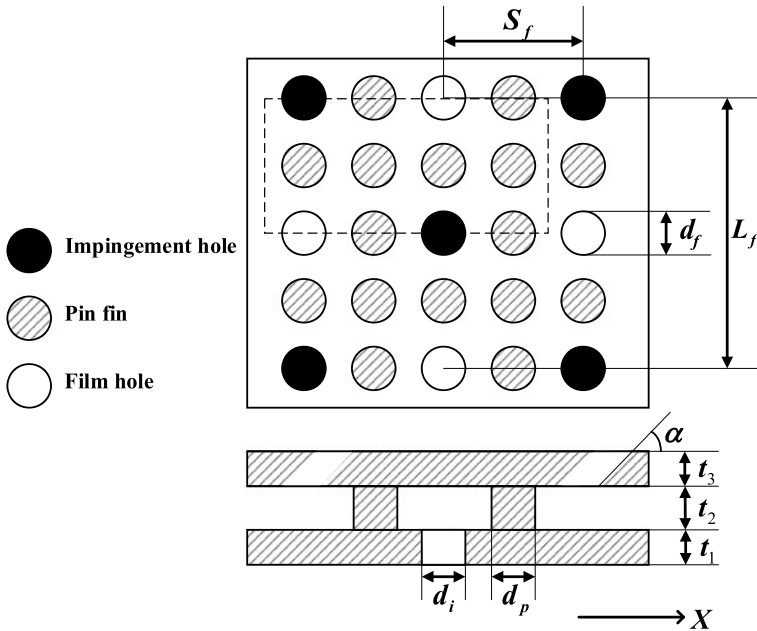


Fig. 3.1 Geometric parameters of type 161 laminate structure

Table 3.1 Geometric parameters design ranges

Parameter	Range
d_f	0.50–0.81 mm
S_f	3.4–6.0 mm
L_f	5.5–9.0 mm
α	25–60°
d_i	1.0–1.3 mm

a sixth-order polynomial function of temperature for the thermal conductivity and viscosity.

A Fluent solver using Reynolds averaged Navier–Stokes (RANS) model was utilized to simulate the flow through the laminate structure under given inlet and outlet pressure. The k- ω SST turbulence model was employed, which has been shown to have high accuracy in numerical simulations of double-walled cooling structures. The SIMPLC algorithm was used in the calculation, and the second-order scheme was adopted for the discretization of the equations. Figure 3.2 shows the computational mesh generated using Fluent Meshing, which employed the ploy-hexcore volume mesh generation method. This method generates hexahedral mesh as much as possible in the computational domain, and the generated result often has fewer grids than the tetrahedral mesh division method. Boundary layer meshes were generated in the near-wall area, with the first layer grid height of 2×10^{-4} mm, a

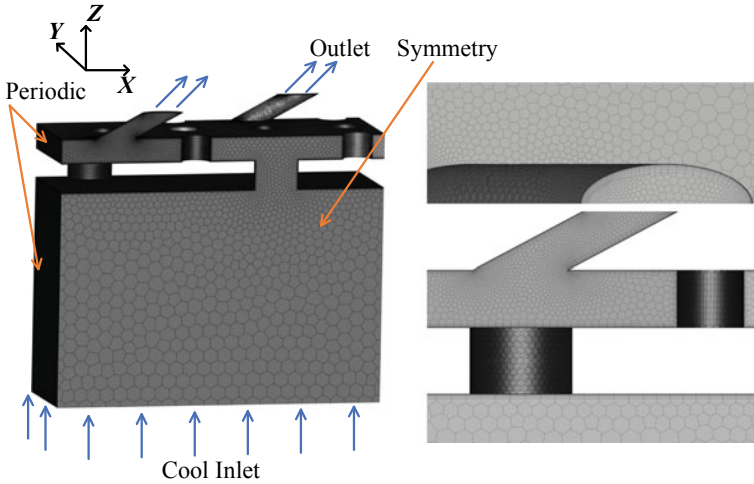


Fig. 3.2 Mesh overview and local views

Table 3.2 Pressure parameter design ranges

Parameter	Value (Pa)
P_1^*	2,600,000, 2,750,000, 2,930,000
P_2	2,400,000

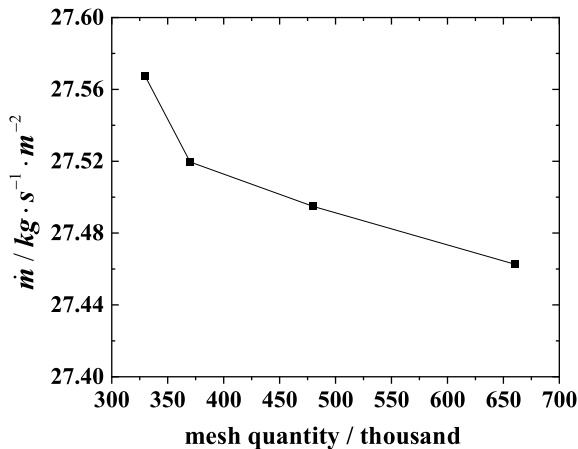
growth rate of 1.5, and 13 layers. The non-dimensional wall distance y^+ of the first boundary layer grid was less than 1.0, meeting the requirements of the $k\text{-}\omega$ SST turbulence model.

The mass flow rate per unit area was defined as shown in Eq. (3.1), where m_c was the total mass flow rate of cooling air through the laminate unit, which could be obtained by numerical simulation. There was one complete film cooling hole in a 161-type laminate unit structure, so the mass flow rate per unit area was equivalent to the mass flow rate through a single film cooling hole.

$$\dot{m} = \frac{m_c}{S_f L_f} \tag{3.1}$$

By discretizing the porous and pillar regions, four different mesh quantities were obtained, which were 330,000, 370,000, 480,000, and 660,000, respectively. Numerical calculations were performed to obtain the mass flow rate for the laminate unit structure with four different mesh quantities, as shown in Fig. 3.3. It can be seen that when the number of mesh quantities reached 370,000, the relative error of the unit mass flow rate was less than 0.3%. Therefore, the corresponding mesh quantity of 370,000 grids was selected for mesh division of all models.

Fig. 3.3 Mesh independence verification



3.2.2 Flow Data for Training

The pressure difference between inlet and outlet was defined as P_{gap} in Eq. (3.2), while the average pressure was defined as P_{ave} in Eq. (3.3).

$$P_{\text{gap}} = P_1^* - P_2 \quad (3.2)$$

$$P_{\text{ave}} = \frac{P_1^* + P_2}{2} \quad (3.3)$$

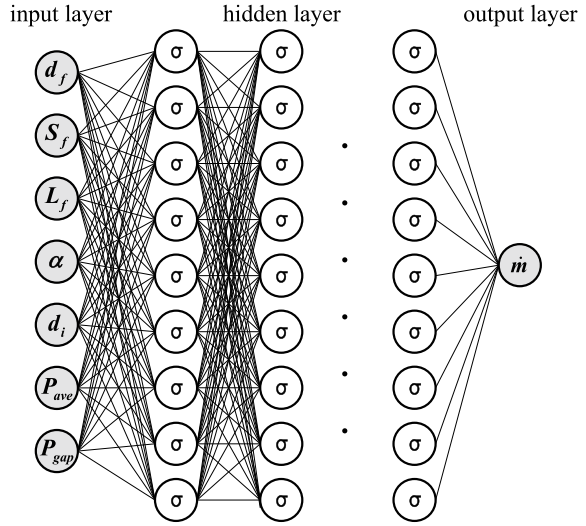
Numerical simulations were conducted on the 100 laminate geometries under three different inlet–outlet pressure conditions. After post-processing, 300 sets of data were obtained, and the form of each data set was $(d_f, S_f, L_f, \alpha, d_i, P_{\text{gap}}, P_{\text{ave}}, \dot{m})$. The acquisition of data sets laid a data foundation for the subsequent training of the neural networks.

3.3 Methodology

3.3.1 Network Architecture for Solving Forward Problems

The forward problem of laminate structure can be expressed as: how to predict the cooling air mass flow rate under the condition that the inlet and outlet pressure of the structure and the geometric parameters of the laminate are known. Neural networks show strong predictive ability by establishing the mapping relationship between input and output parameters under sufficient data training. An artificial neural network (ANN) was established to solve the forward problem, as shown in Fig. 3.4. The

Fig. 3.4 Artificial neural network structure for solving the forward problem



input layer contained 7 neurons representing 5 geometric parameters of the laminar structure, the pressure difference between inlet and outlet and the pressure average. The output layer had one neuron representing the mass flow rate per unit area. There were several hidden layers connected between the input layer and the output layer, and the activation function of the neurons adopted the ReLU function. To verify the influence of network hyperparameters on the prediction accuracy, the number of hidden layers (depth) was set to 2, 4, 6, respectively. The number of neurons per layer (width) was set to 16, 32, 64, respectively.

The mean square error (MSE) function was used to define the loss function of the neural network, as shown in Eq. (3.4). Here, N represented the number of training data, the subscript “pred” represented the predicted value of the neural network, and the subscript “dat” represented the numerical simulation result value. The closer the loss function was to 0, the closer the predicted value of the neural network was to the actual numerical simulation result.

$$Loss = \frac{1}{N} \sum_1^N (\dot{m}_{pred} - \dot{m}_{dat})^2 \quad (3.4)$$

The proposed artificial neural network was built using the open-source deep learning framework Pytorch 1.11. The dataset obtained in Sect. 3.2 was divided into training and validation sets, which contained 80% and 20% of the training data, respectively. The neural network was trained on the training set until convergence using the backpropagation algorithm. Firstly, the algorithm calculated the loss function value through forward computation, and then it calculated the derivatives of weights and biases in the network through backward computation, updating the network weights and biases using the gradient descent method. The gradient descent

method was implemented using the adaptive moment estimation (Adam) algorithm, with the initial learning rate set to 1×10^{-2} . During the training process, the learning rate was reduced to half of its previous value every 1000 training iterations. To determine the optimal network hyperparameters, different depths and widths of neural networks were validated using the mean relative error (MRE) on the validation set, and the network structure with the smallest error was chosen as the final one. The MRE was calculated as shown in Eq. (3.5).

$$MRE = \frac{1}{N} \sum_1^N \left| \frac{\dot{m}_{pred} - \dot{m}_{dat}}{\dot{m}_{dat}} \right| \quad (3.5)$$

3.3.2 Network Architecture for Solving Inverse Problems

The inverse problem of laminate structure can be expressed as: how to design the geometric parameters under the condition that the inlet and outlet pressure of the structure and the target cooling air mass flow rate are known. The present study proposed a method for solving the inverse problem, and the technical route of the method was shown in Fig. 3.5. Given the inlet and outlet pressure and the target cooling air mass flow rate, the partial geometric parameter values are given based on engineering experience. In this study, the partial geometric parameters referred to the geometric parameters of laminate structure other than the diameter of the film cooling hole. Then, the initial design parameters and the partial geometric parameter values are input into the artificial neural network for solving the inverse problem. The network outputs the diameter value of the film cooling hole. A complete geometric description of the laminate structure conforming to the target cooling air mass flow rate is then obtained.

The ANN for solving the inverse problem was established, as shown in Fig. 3.6. The input parameters of the network include the cooling air mass flow rate per unit area, the partial geometric parameters, the pressure difference between inlet and outlet and the pressure average. The output parameter was the diameter of the film cooling hole. The activation function, data set source, and training method of the inverse problem solving neural network were the same as those of the forward problem solving network in Sect. 3.3.1. The loss function and MRE of the ANN were defined as shown in Eqs. (3.6) and (3.7), respectively.

$$Loss = \frac{1}{N} \sum_1^N (d_f^{pred} - d_f^{dat})^2 \quad (3.6)$$

$$MRE = \frac{1}{N} \sum_1^N \left| \frac{d_f^{pred} - d_f^{dat}}{d_f^{dat}} \right| \quad (3.7)$$

Fig. 3.5 Technical route for solving the forward problem

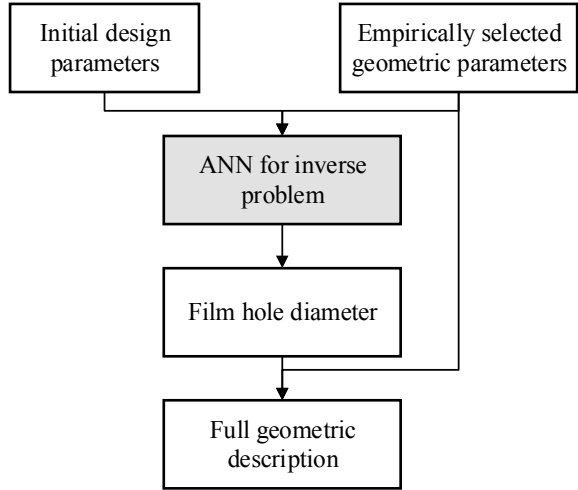
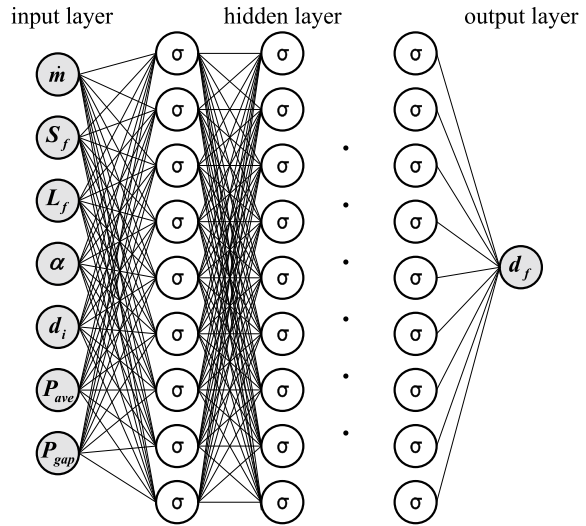


Fig. 3.6 Artificial neural network structure for solving the inverse problem



3.4 Results and Discussion

3.4.1 Forward Problem

The forward problem of laminate structure was realized by building and training the ANN for predicting cooling air mass flow rate per unit area. The depth and width of ANN were changed, and the pre-training network was obtained by training the ANN with the training set. The MRE of the pre-training network prediction results

Table 3.3 The impact of depth and width on the MRE of the predicted value of the neural network for solving the forward problem

	16 (%)	32 (%)	64 (%)
2	1.73	1.68	1.15
4	1.68	1.29	1.07
6	1.24	1.51	1.45

on the validation data set was observed, and the results were shown in Table 3.3. It could be seen that the influence of changing the network depth and width on the prediction accuracy of the neural network was small, and the MRE on the validation set was within 2.0%. The hyperparameters with the best network fitting degree was selected, with 4 layers in the hidden layer and 64 neurons in each hidden layer. The pre-training network was retrained with a combined set of training and validation sets, and the final ANN model for solving the forward problem was obtained.

Using the random sampling method, a test dataset of 50 sets of parameters ($d_f, S_f, L_f, \alpha, d_i, P_{gap}, P_{ave}, \dot{m}$) generated within the parameter space was shown in Table 3.4, which was used to test the accuracy of the final ANN model. The comparison of ANN predicted values of cooling air mass flow rate per unit area and numerical simulation results was shown in Table 3.5. The maximum relative error of the predicted values was less than 3%. The MRE of the neural network prediction on the entire test set was calculated to be 1.46%, indicating that the neural network has high prediction accuracy within the specified parameter space.

The ANN for mass flow rate per unit area prediction could effectively solve the forward problem of the laminate structure within a certain range of design parameters. Given the inlet and outlet pressure and the geometric parameters of the laminate structure, the ANN model can predict the unit cooling air mass flow rate per unit area \dot{m}_{pred} . The total cooling air mass flow rate can be calculated by Eq. (3.8), where n_f represents the total number of film holes in the laminate structure.

$$m_c = n_f \dot{m}_{pred} S_f L_f \quad (3.8)$$

in this study, the values of geometric parameters and pressure parameters were in line with the actual engineering application of aero-engine turbine blade, especially the

Table 3.4 Geometric and pressure parameter ranges

Parameter	Range
d_f	0.50–0.81 mm
S_f	3.4–6.0 mm
L_f	5.5–9.0 mm
α	25–60°
d_i	1.0–1.3 mm
P_1^*	2,750,000, 2,900,000 Pa
P_2	2,400,000 Pa

Table 3.5 Comparison of ANN predicted values and numerical simulation results of cooling air mass flow rate per unit area

	Geometric parameters	Boundary conditions	$\dot{m}_{dat} / \text{kg s}^{-1} \text{ m}^{-2}$	$\dot{m}_{pred} / \text{kg s}^{-1} \text{ m}^{-2}$	MRE (%)
1	$d_f = 0.565 \text{ mm}$, $S_f = 4.52 \text{ mm}$, $L_f = 7.00 \text{ mm}$, $\alpha = 60^\circ$, $d_i = 1.16 \text{ mm}$	$P_1^* = 2750000 \text{ Pa}$ $P_2 = 2400000 \text{ Pa}$	13.66	13.67	0.07
2	$d_f = 0.559 \text{ mm}$, $S_f = 5.97 \text{ mm}$, $L_f = 6.30 \text{ mm}$, $\alpha = 53^\circ$, $d_i = 1.28 \text{ mm}$	$P_1^* = 2750000 \text{ Pa}$ $P_2 = 2400000 \text{ Pa}$	10.87	11.04	1.56
3	$d_f = 0.732 \text{ mm}$, $S_f = 4.01 \text{ mm}$, $L_f = 7.08 \text{ mm}$, $\alpha = 56^\circ$, $d_i = 1.05 \text{ mm}$	$P_1^* = 2750000 \text{ Pa}$ $P_2 = 2400000 \text{ Pa}$	23.50	22.94	2.38
4	$d_f = 0.640 \text{ mm}$, $S_f = 5.14 \text{ mm}$, $L_f = 6.80 \text{ mm}$, $\alpha = 39^\circ$, $d_i = 1.13 \text{ mm}$	$P_1^* = 2900000 \text{ Pa}$ $P_2 = 2400000 \text{ Pa}$	18.43	18.68	1.36
5	$d_f = 0.751 \text{ mm}$, $S_f = 4.83 \text{ mm}$, $L_f = 7.98 \text{ mm}$, $\alpha = 54^\circ$, $d_i = 1.15 \text{ mm}$	$P_1^* = 2900000 \text{ Pa}$ $P_2 = 2400000 \text{ Pa}$	22.43	22.61	0.80
6	$d_f = 0.596 \text{ mm}$, $S_f = 5.30 \text{ mm}$, $L_f = 8.12 \text{ mm}$, $\alpha = 30^\circ$, $d_i = 1.21 \text{ mm}$	$P_1^* = 2900000 \text{ Pa}$ $P_2 = 2400000 \text{ Pa}$	13.39	13.34	0.37

values of geometric parameters cover the vast majority of commonly used values in engineering. Therefore, the model obtained in this study can effectively be applied in engineering practice. However, the range of values for the inlet and outlet pressure in the dataset is small, which leads to poor generalization performance of the ANN model under different pressure conditions. The next step is to expand the range of pressure conditions in the dataset to improve the model's generalization performance.

3.4.2 Inverse Problem

The inverse problem in laminate structure was addressed by constructing and training a neural network to predict the diameter of film cooling holes. By combining engineering expertise with ANN model, multiple sets of geometric parameters for achieving target cooling air mass flow rate can be designed. The film cooling hole diameter prediction network was trained and tested.

The depth and width of the ANN model were varied, and the model was trained with the training dataset to obtain a pre-trained network. The MRE of the pre-trained network predictions on the validation dataset was observed, as shown in Table 3.6. It can be seen that the network with the lowest complexity (depth of 2 and width of 16) exhibits the largest MRE, with a maximum value of 1.15%. Increasing the complexity of the network (depth or width) can improve the accuracy of the network on the validation set. However, when the complexity of the network reaches a certain level, the prediction accuracy on the validation set will not increase further. The best-fitting set of network parameters was selected from all pre-trained networks, with a hidden layer consisting of 2 layers and 32 neurons in each hidden layer. The pre-trained network was then trained by merging the training and validation sets to obtain the final neural network model for solving the inverse problem in laminate structure.

The proposed method for solving the inverse problem of laminate structures was tested by designing geometric structures given the target cooling air mass flow rate and inlet/outlet pressure conditions. The test results are shown in Table 3.7. The first column of the table represents the initially given parameters, the second column represents the partial geometric parameter values given based on engineering experience, the third column gives the design results of the neural network for the film cooling hole diameter, the fourth column gives the numerical simulation results, and the last column gives the relative error between the target values and numerical simulation values of the cooling air mass flow rate per unit area. The maximum relative

Table 3.6 The impact of depth and width on the MRE of the predicted value of the neural network for solving the inverse problem

	16 (%)	32 (%)	64 (%)
2	1.15	0.63	0.74
4	0.73	0.82	0.71
6	0.76	0.90	0.92

Table 3.7 The design result of the inverse problem solving method

Initial conditions	Empirical parameters	d_f /mm	$\dot{m}_{dat}/\text{kg s}^{-1} \text{m}^{-2}$	MRE (%)
$\dot{m} = 17.0 \text{ kg}/(\text{s m}^2)$ $P_1^* = 2,750,000 \text{ Pa}$ $P_2 = 2,400,000 \text{ Pa}$	$S_f = 4.8 \text{ mm}, L_f = 7.0 \text{ mm}$ $\alpha = 45^\circ, d_i = 1.2 \text{ mm}$	0.668	17.50	2.9
	$S_f = 5.0 \text{ mm}, L_f = 6.0 \text{ mm}$ $\alpha = 60^\circ, d_i = 1.25 \text{ mm}$	0.618	17.11	0.64
	$S_f = 5.2 \text{ mm}, L_f = 8.8 \text{ mm}$ $\alpha = 38^\circ, d_i = 1.22 \text{ mm}$	0.778	16.89	0.63
	$S_f = 6.0 \text{ mm}, L_f = 8.0 \text{ mm}$ $\alpha = 45^\circ, d_i = 1.3 \text{ mm}$	0.783	16.54	2.7
	$S_f = 3.5 \text{ mm}, L_f = 7.8 \text{ mm}$ $\alpha = 40^\circ, d_i = 1.24 \text{ mm}$	0.599	17.38	2.2
	$S_f = 3.8 \text{ mm}, L_f = 8.5 \text{ mm}$ $\alpha = 30^\circ, d_i = 1.15 \text{ mm}$	0.649	17.03	0.17

error and average relative error of cooling air mass flow rate per unit area were 2.9% and 1.54% respectively, indicating that the design results meet the requirements very well.

The proposed method for solving the inverse problem has the advantage of quickly providing multiple structural designs that meet the design requirements. Comparing to the trial-and-error method that requires multiple iterations to achieve the desired design requirements, the proposed method significantly reduces the design time cost, with a design time of only 0.014 s. Compared to the optimization method combined with surrogate mode, the proposed method has a shorter design time and less randomness, and easier to integrate engineering experience into the design process. In addition, no additional data set construction costs are introduced because the training data sets of the model solving the inverse problem and the model solving the forward problem use the same data set.

3.5 Conclusion

The present study proposes solutions to the mass flow rate prediction problem (forward problem) and the structural design problem under known target flow conditions (inverse problem) for laminate structures. To solve the forward problem, a neural network is built to map geometric parameters and inlet/outlet pressure to the cooling air mass flow rate per unit area. A group of 300 data sets generated by numerical simulation are used for network training. The impact of the network hyperparameters on prediction accuracy is investigated, and the network with the highest prediction

accuracy has a depth of 4 layers and a width of 64 neurons per hidden layer. The final convergence network is taken as the network that solves the forward problem, and tested on the test set containing 50 groups of data. The mean relative error of the predicted cooling air mass flow rate per unit area is 1.46%.

To solve the inverse problem, a neural network is built and trained to predict the diameter of the film cooling hole. The network hyperparameters is selected with a depth of 2 layers and a width of 32 neurons per hidden layer. The training data set for solving the inverse problem is the same as that for solving the forward problem neural network, which means no additional data generation cost is introduced. Using the proposed method, six sets of geometric parameters are quickly designed under the condition of a target cooling air mass flow rate per unit area of $17 \text{ kg}/(\text{s m}^2)$, an inlet total pressure of 2,750,000 Pa, and an outlet pressure of 2,400,000 Pa. The design process takes 0.014 s. The maximum relative error and mean relative error between the numerical simulation result values of cooling air mass flow rate per unit area and the target value are 2.9% and 1.54%, respectively. The laminate structure design method proposed in this paper has the advantages of fast design speed, low design randomness, and high design accuracy. Future research can focus on adding more design parameter conditions, expanding the design parameter space, and incorporating physical prior knowledge to further improve the engineering practicality of the model.

References

1. Murray, A.V., Ireland, P.T., Romero, E.: Experimental and computational methods for the evaluation of double-wall, effusion cooling systems. *J. Turbomach.* **142**(11), 111003 (2020)
2. Bamba, T., Kumagai, T., Mimura, F., et al.: Leading edge cooling performance of an integrated cooling configuration. In: *Turbo Expo: Power for Land, Sea, and Air*, pp. 553–561. American Society of Mechanical Engineers, Berlin (2008)
3. Chen, Y., Wei, H., Zu, Y.Q.: Experimental study on the conjugate heat transfer of double-wall turbine blade components with/without pins. *Therm. Sci. Eng. Prog.* **8**, 448–456 (2018)
4. Lv, D.: *Study on Flow Heat Transfer Mechanism and Optimization Design of Laminate Structure*. Beihang University, Beijing (2007)
5. Zhongran, C.: *Heat Transferring Design for Air-Cooled Turbine Blades*. Harbin Institute of Technology, Harbin (2011)
6. Hickel, R.O., Warren, E.L., Kaufman, A.: Experimental investigation of the flow, oxidation, cooling, and thermal-fatigue characteristics of a laminated porous sheet material (No. E-5872). NASA, USA (1972)
7. Zhang, S.C., Xia, S.C., Chi, Z.R.: Study on the modeling method and cooling design procedure of double-wall turbine blades. *J. Eng. Therm. Energ. Power* **36**(10), 11–17 (2021)
8. Rao, Y., Liu, Y., Wan, C.: Multiple-jet impingement heat transfer in double-wall cooling structures with pin fins and effusion holes. *Int. J. Therm. Sci.* **133**, 106–119 (2018)
9. Liu, Y., Rao, Y., Yang, L.: Numerical simulations of a double-wall cooling with internal jet impingement and external hexagonal arrangement of film cooling holes. *Int. J. Therm. Sci.* **153**, 106337 (2020)
10. Liu, Y., Rao, Y., Yang, L., Xu, Y.: Flow and heat transfer characteristics of double-wall cooling with multi-row short film cooling hole arrangements. *Int. J. Therm. Sci.* **165**, 106878 (2021)

11. Zhang, G., Zhu, R., Xie, G.: Optimization of cooling structures in gas turbines: a review. *Chin. J. Aeronaut.* **35**(6), 18–46 (2022)
12. Wang, Q., Yang, L., Rao, Y.: Establishment of a generalizable model on a small-scale dataset to predict the surface pressure distribution of gas turbine blades. *Energy* **214**, 118878 (2021)
13. Yang, L., Min, Z., Yue, T.: High resolution cooling effectiveness reconstruction of transpiration cooling using convolution modeling method. *Int. J. Heat Mass Transf.* **133**, 1134–1144 (2019)
14. Yang, L., Dai, W., Rao, Y.: Optimization of the hole distribution of an effusively cooled surface facing non-uniform incoming temperature using deep learning approaches. *Int. J. Heat Mass Transf.* **145**, 118749 (2019)
15. Yang, L., Wang, Q., Huang, K.: Establishment of a long-short-term-memory model to predict film cooling effectiveness under superposition conditions. *Int. J. Heat Mass Transf.* **160**, 120231 (2020)
16. García, J.C., Dávalos, J.O., Urquiza, G.: Film cooling optimization on leading edge gas turbine blade using differential evolution. *Proc. Inst. Mech. Eng. Part G J. Aerospace Eng.* **233**(5), 1656–1666 (2019)
17. Mostofizadeh, A.R., Adami, M., Shahdad, M.H.: Multi-objective optimization of 3D film cooling configuration with thermal barrier coating in a high pressure vane based on CFD-ANN-GA loop. *J. Braz. Soc. Mech. Sci. Eng.* **40**, 1–15 (2018)
18. El Ayoubi, C., Hassan, O., Ghaly, W.: Aero-thermal optimization and experimental verification for the discrete film cooling of a turbine airfoil. In: *Turbo Expo: Power for Land, Sea, and Air*, pp. V03BT13A050. American Society of Mechanical Engineers, San Antonio (2013)

Chapter 4

Experimental Research of Ultra High Performance Concrete in Supersized Rectangle Pipe Jacking Project



Tao Fang, Linxing Guan, and Wei Sun

Abstract In recent years, supersized rectangle pipe-jacking method has been widely used and the monolithic pre-cast pipe tube is extensively adopted. However, the application of supersized rectangle pipe-jacking method in the urban area is severely limited, because of the oversized volume and weight as well as the difficulty of transportation and lifting. Therefore, it is imperative to explore the new structure of the supersized rectangular pipe tube. This paper introduces two-half-assembled precast concrete tube to reduce the aforementioned difficulties. Depending on the excellent early-strength performance, mechanical performance, and durability performance of ultra-high performance concrete (UHPC), quick connection of the wet-joint can be achieved on-site and maintenance only needs 3 days before propulsion operation. The mechanical and waterproofing performance of the interface between UHPC and PC are explored by prototype test. The main conclusions are summarized as follows: (1) the bearing capacity of the wet-joint is much higher than the actual need after 3-day maintenance; (2) the waterproofing performance of the interface by the laboratory test meets the design requirements; (3) the interface of the prototype test has barely waterproofing performance; (4) after special treatment on the interface, waterproofing performance is improved and meets the demands, which it is successfully applied to the actual project.

Keywords Supersized rectangle pipe-jacking method · Prototype tests · Interface · Mechanical performance · Waterproofing performance

4.1 Introduction

The traditional open-cut method has gradually been replaced by non-excavation technology because of the influence of urban aesthetics and interrupting ground traffic. Rectangle Pipe Jacking Method (RPJM), as a trenchless construction technology,

T. Fang (✉) · L. Guan · W. Sun
Shanghai Municipal Engineering Design Institute (Group) Co., Ltd., Shanghai 200092, China
e-mail: submit_tao_fang@163.com

plays a vital role in guaranteeing traffic smoothness and maintaining the urban style. In the 1970s, rectangular pipe jacking technology was successfully applied for the first time in crossing passages of the Tokyo subway in Japan. Though this technology is rather late in China, the momentum of development is rapid. Especially with the upsurge of development and utilization of underground space in domestic cities, rectangular pipe jacking technology has been widely used in urban underground pedestrian crossing tunnels [1], entrance tunnels of subway stations [2, 3], municipal roads under roads and railways [4–6], utility tunnels [7–9] and so on.

Rectangular pipe jacking tunnels show a trend of a supersized cross-section to meet the demands of expressways and large traffic flow. However, as the section continues to increase, the size of a tube also increases accordingly. For example, the weight of a tube of the project in Zhengzhou [1] exceeds 70t while that in Jiaxing [10] Astonishingly reaches 135t. Such amazing size and weight of tubes put forward strict requirements on the transportation conditions, which limits the application prospect of the rectangle pipe jacking technology in urban area. Thus, it is imperative to replace the intact tube with the assembled one.

Japanese engineers have proposed to the assembled tube and jacked after assembly on-site [11]. However, it is necessary to use the internal prestress for assembly, which is verbose. Due to the supersized cross-section of Box Culvert Method (BCM), the main structure is poured partly and connected by the wet joint in some domestic projects [12]. However, disadvantages of the conventional wet joint by the concrete are obvious, Long maintenance time and inefficiency. Ultra-high performance concrete (UHPC), used in the connection of a prefabricated bridge deck, has high-early strength.

Based on a supersized rectangle pipe jacking project in Hangzhou, the feasibility of an assembled precast concrete tube and connection by UHPC is analyzed. Then, the mechanical and waterproof properties of UHPC-PC joints are studied through tests. Finally, reasonable design optimization suggestions are put forward for the actual project and the first supersized rectangle pipe jacking tunnel with assembled tubes has been successfully realized.

4.2 Background

4.2.1 Project Review

With the increasing number of private cars, parking becomes a prominent problem in urban area, especially for large commercial complexes and office areas. In order to improve the urban supporting facilities, a new underground garage under construction in Hangzhou should be connected to the underground garage of the Science and Technology Innovation Center on the north side, as shown in Fig. 4.1. The connecting tunnel passes under a traffic artery and there are many underground pipelines. Therefore, the supersized rectangular pipe jacking method is proposed.

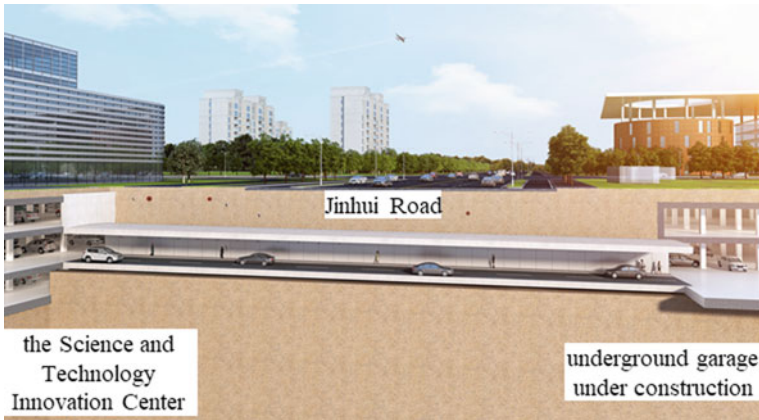


Fig. 4.1 Diagram of the project

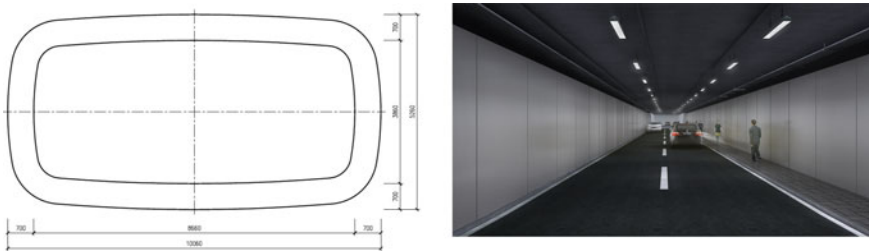


Fig. 4.2 Illustration of the cross-section of the connecting tunnel

The tube size of the connecting tunnel is shown in Fig. 4.2, which meets the demands of both vehicles and pedestrians. The buried depth of the tunnel, which goes through typical water-rich soil layers is 6 m and the groundwater level is located 1–2 m below the surface.

4.2.2 Design of an Assembled Tube

There are two main factors affecting the segmentation scheme of a tube, mechanical performance and waterproof performance. Mechanical performance determines the number of segments and the position of the joint, while waterproof performance determines the connection method adopted at the joint.

Boundary conditions of transportation should be determined before studying segmentation scheme. According to Specification CJJ37-2012, the width of large vehicles and mixed lanes is 3.5–3.75 m, and the minimum net height of vehicles is 4.5 m. Owing to the restriction of municipal road conditions, the width and height

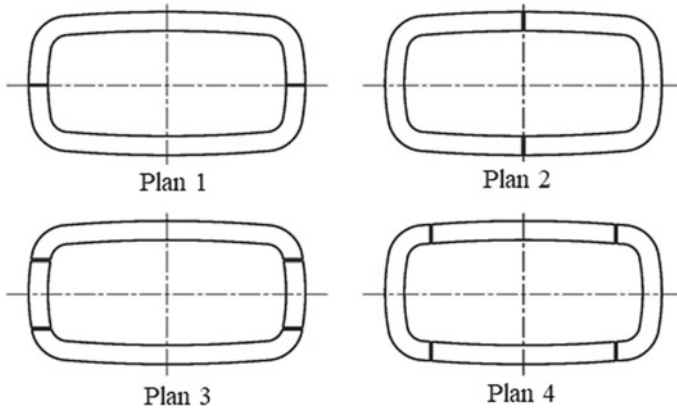


Fig. 4.3 Illustration of segmentation schemes of tubes

of a tube segment should be less than 3.5 m and 4 m respectively. The segmentation schemes, as shown in Fig. 4.3, can be considered for the rectangle tube.

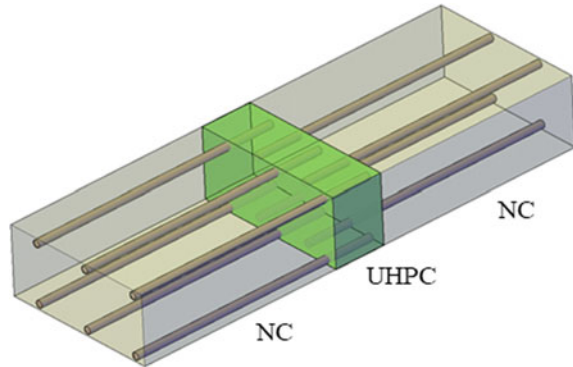
According to the calculation of the background project, the shear force in the middle of side-walls is almost 0 and N/M is relatively large. Therefore, it is reasonable that the joint is located in the middle of side-walls. In addition, joints reduce waterproof performance. Therefore, the scheme of the two-half-assembled tube, whose segments are longitudinal asymmetrical to each other, is adopted.

4.2.3 Connection Method

The connection method adopted for joints not only determines force mode but also the waterproof performance of the whole tunnel. Conventional in-situ casting (also called wet-joint) is widely used in prefabricated residential and prefabricated bridge structures. However, conventional cement-based materials cannot meet the construction requirements of timeliness of RPJM and a new medium is required to connect the segments.

The concept of ultra-high performance concrete (UHPC), a new generation of cement-based building materials, is first proposed by Larrard [13] based on the principle of maximum bulk density [14]. It not only has self-leveling characteristics but also has excellent mechanical properties [15]. The strength after 3 days' maintenance can reach 70–80% of the final strength, which meets all of the demands for the construction of RPJM. In addition, the reinforcement anchorage length is $3D$ – $4D$, which is 1/10 of its length in ordinary concrete. Therefore, a steel connector is abandoned, which greatly reduces the construction difficulty and operation time. In summary, it is the feasibility that two segments of a tube are connected by UHPC, as shown in Fig. 4.4.

Fig. 4.4 Diagram of connection by UHPC



There are many literatures related to the interface between UHPC and normal concrete (NC) and most of them focus on mechanics performance. However, they barely mention the mechanical and waterproof performance after 3-days' maintenance. It is necessary to carry out experimental research on the mechanical and waterproof performance of UHPC-NC joints.

4.3 Mechanical Performance

4.3.1 Test Scheme

Specimen Design. Full-scale model tests are carried out to verify the mechanical performance of the joints, when UHPC has been cured for only 3 days. As shown in Fig. 4.5, the length of the beam is 3000 mm, while the thickness and width are 700 mm and 1500 mm, which is the same as those in the actual project. The loading scheme, shown in Fig. 4.5, ensures the wet joint under compression-bending loading without shear force. The specimens after two-step pouring are shown in Fig. 4.6 respectively.

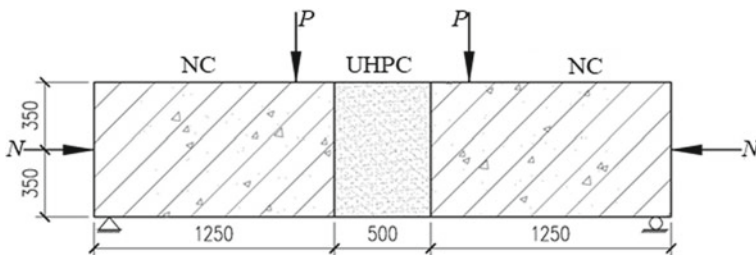


Fig. 4.5 Layout of specimens (Unit: mm)



Fig. 4.6 Pictures of specimens

Fig. 4.7 Picture of measuring points of steel bar

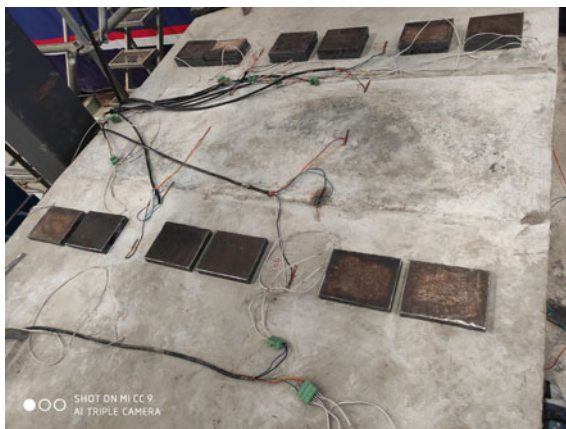


Monitoring Design. There are three kinds of measuring points for steel bars, the interface between UHPC and NC, and Displacement. As shown in Fig. 4.7, strain gauges are arranged on the all of longitudinal steel bars at the edge of the interface. As shown in Fig. 4.8, special strain gauges, which can detect the crack and Collect relevant data, are arranged on the surface uniformly of UHPC, NC, and interface between UHPC and NC. In addition, Eight measuring points are arranged to monitor the vertical displacements.

4.3.2 Results

With the increase of vertical load, visible cracks first appear on the bottom of the interface between UHPC and NC, and gradually expand upward along the interface. Then, visible cracks appeared on the bottom of ordinary concrete at about 300 mm from the interface, and gradually expanded upward. When the vertical load is Finally

Fig. 4.8 Picture of measuring points of UHPC, NC and interface



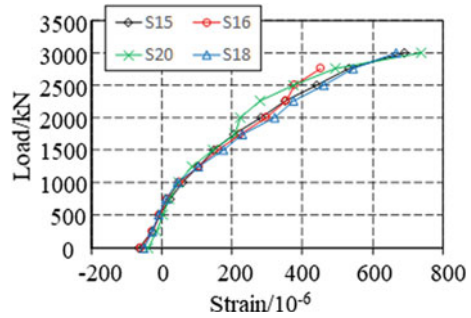
loaded to 3000 kN, as shown in Fig. 4.9, the cracks at the interface are very significant, which are perforated at the bottom. Only a few visible micro-cracks on the bottom and side face of NC, while there is no crack on the surface of UHPC. In addition, there was no crushing of concrete in the upper compression zone.

Figure 4.10 shows the strain variation of tensile bars with the loading process. At the initial stage, the deformation of concrete and steel bars is coordinated and the growth rate of strain is slow. The growth of strain is accelerating when cracks on concrete appear. However, steel bars are still within the range of elastic deformation when the vertical load reaches 3000 kN. It is drawn that the mechanical performance of the joint is reliable under the design load.

Fig. 4.9 Crack in the side face of specimen



Fig. 4.10 Strain with loading of tensile bars



4.4 Waterproofing Performance

4.4.1 Laboratory Test

Test Scheme. According to Specification GB/T 50082-2009, all of blocks are frustum of cone with a height of 150 mm, an upper diameter of 175 mm and a bottom diameter of 185 mm. As shown in Fig. 4.11, two types of UHPC and two types of interface are studied. Plate-Shaped blocks are consisted of half-piece NC and half-piece UHPC while circular-ring-shaped blocks are cylinder of UHPC wrapped by NC. all of blocks are not poured UHPC until concrete maintenance is completed.

Results. Taken 1.2 MPa as the expected anti-permeability strength, 8 blocks of four groups are carried out. As control groups, an NC block and a UHPC block are tested simultaneously. It can be seen from the results that there is no penetration in control groups while the phenomenon occurs in all other blocks during the experiment. When the pressure reaches 0.4 MPa, penetration first occurs in blocks of P-C and H-C. Then the pressure reaches 0.6 MPa, it also occurs in blocks of P-L and H-L.

As shown in Fig. 4.12, the entire interface of each block is soaked in water. It is indicated that the waterproofing Performance of the interface between UHPC and NC is far lower than that of NC or UHPC.

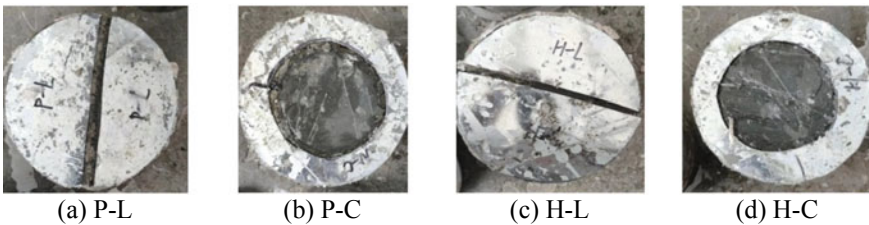


Fig. 4.11 Diagram of test blocks for impermeability. P and H represent different UHPC while L and C represent different interface

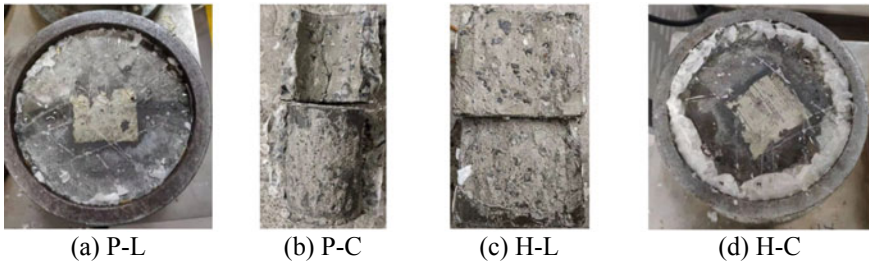


Fig. 4.12 Experimental phenomena of blocks

It is the main reason that strong shrinkage of UHPC produces tensile stress and cracks at the interface, which decreases anti-permeability strength. In addition, the influence of a smooth interface on impermeability may be also significant. Therefore, it is recommended that the steel bars are properly arranged at the interface to offset the shrinkage of UHPC and artificial Chiseling is adopted on the interface of NC before pouring UHPC.

4.4.2 *Prototype Test*

Test Scheme. The loading method for the waterproof test of a shield tunnel segment is adopted to verify the waterproof performance of interface with actual sizes. Due to the size, the impermeability test device is customized, as shown in Fig. 4.13.

Specimens are the same as those for the bending test. Considering the penetration path, single-component polyuria waterproofing coating is used to change the length,



Fig. 4.13 Customized impermeability test device

as shown in Fig. 4.14. The impermeability test is carried out when UHPC has been cured for 3 days.

Test Results. According to the actual situation, 0.1 MPa is taken as the expected anti-permeability strength. The loading scheme from Specification CJJ/T164-2011 is adopted. Results meet expectations that there is no penetration in both two specimens with a holding pressure of 0.1 MPa and holding-pressure time of 2 h. Afterward, pressure is increased to explore the ultimate anti-permeability strength. However, when the pressure reaches 0.15 MPa, penetration occurs on the side of the interface, then on the top of the interface after a while. Results indicate that the anti-permeability strength of assembled tubes just meets the requirements. An improved waterproofing design should be adopted to ensure long-term performance (Fig. 4.15).

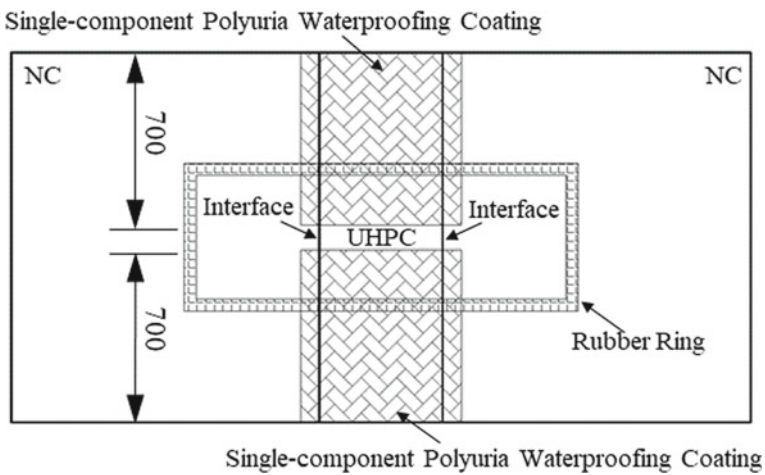


Fig. 4.14 Diagram of single-component polyuria waterproofing coating on a specimen



Fig. 4.15 Phenomena of prototype impermeability tests

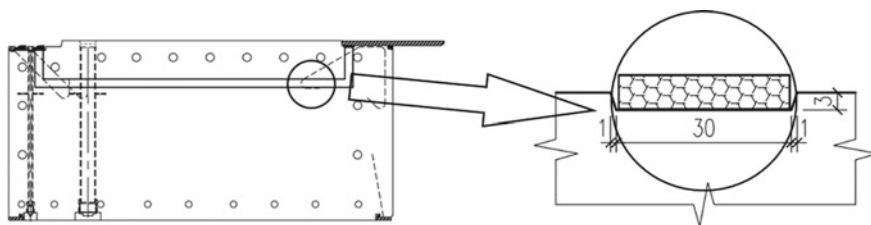


Fig. 4.16 Diagram of improved waterproof design



Fig. 4.17 Application of two-half-assembled precast concrete tube in RPJM

4.4.3 Improved Waterproofing Design

In order to enhance the waterproof performance of the interface of two-half-assembled precast concrete tubes, a hydro-swelling rubber-sealing strip is added to the interface, as shown in Fig. 4.16. It is connected to the rubber olecranon-shaped sealing ring, and the rubber sealing ring beneath the steel plat, which forms a closed sealing system.

As shown in Fig. 4.17, the two-half-assembled precast concrete tube of RPJM has been successfully applied to the project, which realizes the convenient transportation of segments of tubes and rapid assembly on-site.

4.5 Conclusion

The main conclusions are summarized as follows:

- (1) The bearing capacity of the wet joint is much higher than the actual need after 3-day maintenance.
- (2) The waterproof performance of the interface by the laboratory test is far lower than expectations.
- (3) The waterproof performance of the interface by the prototype test just meets the design requirements.

- (4) In order to ensure long-term performance, an improved waterproofing design is adopted, which it is successfully applied to the actual project.

References

1. Sun, Y., Xu, Z., Li, A., Wang, C.: Analysis of influence factors on end soil reinforcement effect of rectangular pipe jacking. *Proc. Inst. Civil Eng. Geotech. Eng.* **2021**, 1–10 (2021)
2. Zhu, H.: Structural design and research of exit passage by rectangular pipe-jacking construction for underground subway station. *Undergr. Eng. Tunnels* **2010**(1), 1–4, 52 (2010)
3. Shi, W.: Protective technology of large-sectional rectangle jacking pipe construction pipeline. *Urban Roads Bridges Flood Control* **2011**(07), 179–182, 16 (2011)
4. Rong, L., Yang, H.: Settlement control technology for tunnel crossing underneath Zhongzhou Avenue in Zhengzhou constructed by super-large rectangular cross-section pipe-jacking machine. *Tunnel Constr.* **35**(12), 1338–1344 (2015)
5. Zhang, Z., Huang, A., Wang, C.: Construction scheme of rectangular pipe jacking method for metro station in soft soil area. *Urban Mass Transit* **23**(7), 163–166, 171 (2019)
6. Zhen, L., Yu, W., Xu, W., Yue, X.: Deformation analysis of pipe-jacking process for a large-section shallow-covered project crossing highway. *IOP Conf. Ser. Earth Environ. Sci.* **861**(5), 052109 (2021)
7. Chen, X., Ma, B., Najafi, M.: Long rectangular box jacking project: a case study. *Undergr. Space* **6**(2), 101–125 (2019)
8. Han, J.: Construction technology of shallow buried river with super large section rectangular jacking pipe. *Eng. Technol. Res.* **2019**(10), 47–48 (2019)
9. Xue, Q.: Calculation and measurement analysis of jacking force of large cross-section rectangular pipe jacking machine used in Suzhou Chengbei Road. *Tunnel Constr.* **40**(12), 1717–1724 (2020)
10. Xue, G., Jia, L., Fan, L., Chen, W.: Research on soil pressure balance control technology of rectangular TBM with large section. *Constr. Mech.* **41**(10), 41–45 (2020)
11. Shiomi, M.: Supersized pipe jacking using segmental pipes. *Tunnels Tunnel. Int.* **10**, 21–22 (2006)
12. Guo, S., Lu, Y., Wei, X.: Connection design of precast concrete box-culvert fabricated pedestrian underground passage with transverse joints. *Urban Roads Bridges Flood Control* **2019**(3), 191–194, 22 (2019)
13. Larrard, F.D., Sedran, T.: Optimization of ultra-high-performance concrete by the use of a packing model. *Cem. Concr. Res.* **24**(6), 997–1009 (1994)
14. Reda, M., Shrive, N., Gillott, J.: Microstructural investigation of innovative UHPC. *Cem. Concr. Res.* **29**(3), 323–329 (1999)
15. Li, J., Luo, B., Luo, Z.: Research and application of ultra-high performance concrete. *Municipal Eng. Technol.* **39**(5), 155–158 (2021)

Chapter 5

Mechanical Performance and Experimental Research on Plug-in Fast Connector of Shield Tunnel



Tao Fang, Linxing Guan, and Mengxi Zhang

Abstract Urban development and renewal reduce the performance of shield tunnels and may cause structural safety hazards. Thus, a new plug-in fast connector is developed for shield tunnels to improve structural resilience. The connector does not require additional tightening, and the segment opening and dislocation are small. Taking a 650 mm thick segment as the prototype, this paper conducts the tensile and shearing tests of the plug-in fast connector, to investigate the structural form, material properties, and the force transmission between the connection and concrete segment. In addition, the theoretical value of the connector is employed to compare experimental values. The main conclusions are as follows: (1) The insufficient bond strength between the embedded sleeves and concrete causes the fast connector to be pulled out and the tensile failure of concrete is occurred. (2) The yield strength of the connector is about 150 kN, and the failure strength is about 200 kN, which is slightly lower than the design value. (3) With the increase of the shearing displacement, damage occurs inside the embedded sleeves and then the concrete of the upper surface is crushed. Finally, the tightness between CR and sleeves is invalid and the shear strength of each connector is 210 kN. (4) The shear stiffness of the plug-in fast connector is fitted by two straight lines, and K_1 and K_2 are 2.611 kN/mm and 18.544 kN/mm respectively. (5) The new plug-in fast connector can improve the longitudinal mechanical performance of a shield tunnel. The subsequent research should focus on the selection of materials for embedded sleeves and the bond strength between the sleeve and concrete.

Keywords Shield tunnel · Plug-in fast connector · Tensile test · Shearing test

T. Fang (✉) · L. Guan
Shanghai Municipal Engineering Design Institute (Group) Co., Ltd., Shanghai 200092, China
e-mail: submit_tao_fang@163.com

M. Zhang
Department of Civil Engineering, Shanghai University, Shanghai 200444, China

5.1 Introduction

Owing to high safety and environmental protection, Shield tunneling method has been widely used in municipal engineering at home and abroad in recent years [1]. The connection between rings of a tunnel, which is composed of bolts and shear pins, is common in China. However, there are many disadvantages. First of all, different from the construction condition of the steel structure, the small space inside the tunnel and artificial dependence make the bolt installation difficult. Secondly, it is hard to keep the high quality of construction during the whole process because of multi-step installation such as tightening, blocking, etc. In addition, the gap between the bolt and hole, commonly 3–6 mm, which is convenient for construction, can easily lead to the wrong platform between rings and reduce the waterproof performance. Therefore, many researchers explore the new connection way between rings of shield tunnels for security, automation, and rapidity [2–9].

Japanese have developed plenty of fast connectors between rings and conducted extensive research and application [10–12]. In China, a Japanese plug-in fast connector is introduced by Shanghai Metro for the first time and successfully applied to the shield tunnel of the entry line in Line 18 [13, 14]. Compared with bolts, a plug-in fast connector has many advantages, such as fast assembly, simple process, good waterproofing, and small wrong platform. But there are no case so far in China that the plug-in fast connector is used in a super-large-diameter shield tunnel. Due to the difference in materials and processing technology, basic research need to be carried out before the application of plug-in fast connector in a super-large-diameter shield tunnel.

A shield tunnel with an outer diameter of about 15 m is emerging in recent years, which is usually adopted as underground expressways. Taking the thickness of a segment of these tunnels, 650 mm, as the prototype, this paper conducts the tensile and shearing tests of the plug-in fast connector, to investigate the structural form, material properties, and the force transmission between the connection and concrete segment.

5.2 Background

5.2.1 Project Overview

Shanghai Nanbei Channel Project intends to be constructed as an underground expressway with multiple ramps in urban core zones. As shown in Fig. 5.1, the main line is 16 km and is set up along Quyang Road, North Linping Road, Gaoyang Road, South Pudong Road, Pusan Road, and South Yanggao Road, which passes through 2 districts, Hongkou and Putuo. Shanghai Nanbei Channel is mainly underground roads, and the shield method is widely implemented.

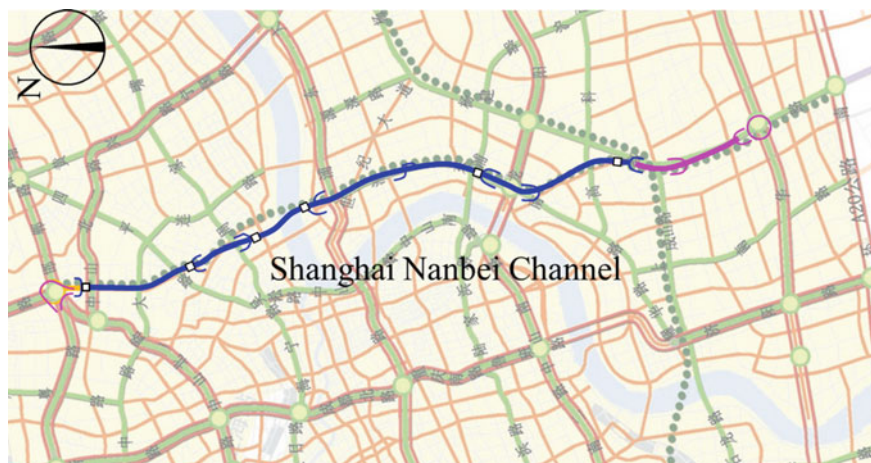


Fig. 5.1 Diagram of Shanghai Nanbei Channel

Shanghai Nanbei Channel Project crosses the urban center, where there are lots of buildings around and the shallow underground space has been fully used. Therefore, the main line is deeply buried. Due to the characteristics of the typical water-rich and soft stratum, the deeper the tunnel is buried, the worse mechanical performance is shown. In addition, the channel may be located in a confined aquifer and strict requirements should be met for waterproofing. The connection by the conventional bolt is hard to be competent and the researchers intend to use a plug-in fast connector.

5.2.2 *Plug-in Fast Connector*

The circular seam, which is a gap between lining rings, is vertical to the axis of a tunnel. A plug-in fast connector, used for the connection of the circular seam, mainly undertakes tensile and shear force. At present, there are many kinds of plug-in fast connectors but according to the mechanism, they are divided into two types, the friction-type and the wedge-type. As shown in Fig. 5.2, one of wedge-type connectors, that is adopted for tests, contains three parts, a core rod (CR), a threaded sleeve (TS), and a wedge sleeve (WS). While TS and WS are shaped by the high-strength and tough polyamide material, CR is a steel screw wrapped by the polyamide material. The inner diameter of sleeves is slightly larger than the nominal diameter of CR. The production error of all components is 1 mm.

TS and WS are buried in pairs on sides of a circular seam before pouring segments. When assembling a tunnel lining, a CR is tightened into TS firstly and then pushed into WS by the external jack force. Mechanical transmission is relied on hangnail fixed After installation.

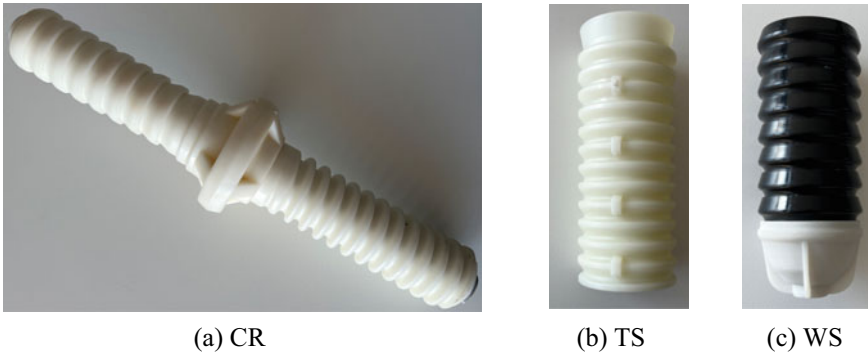


Fig. 5.2 Pictures of the plug-in fast connector used for tests

The ideal destruction state of the plug-in fast connector is that the steel screw is yielded and fractured. The strength grade and the diameter of the steel screw are 8.8 and 22 mm respectively. According to the calculation, the yield strength of the connector is about 240 kN and the failure strength exceeds 300 kN. All the specimens of tests are designed by the data above.

5.3 Tensile Test Scheme

5.3.1 Specimen Design

The T-shaped loading beam is designed, as shown in Fig. 5.3, to determine the tensile performance of this plug-in fast connector. The length and width of a beam are 1500 mm and 1000 mm respectively and the thickness of 650 mm is set the same as that of shield tunnels with an outer diameter of 15 m. All of specimens are made of C60 concrete and HRB400 steel bars.

5.3.2 Apparatus

Two jacks with a maximum tonnage of 100t are applied for tests to reduce the impact of eccentricity, which are pressurized synchronously with one oil pump, as shown in Fig. 5.4.

Due to the large size, the specimens are laid on the ground to ensure safety during tests. As shown in Fig. 5.5, two parallel rectangular steel tubes are placed at the bottom of the specimens to reduce friction. Jacks, placed between wings of beams, are raised by steel to reduce the impact of eccentricity. Before tests, it is ensured by the measurement that the jacks are located at the center of beam.

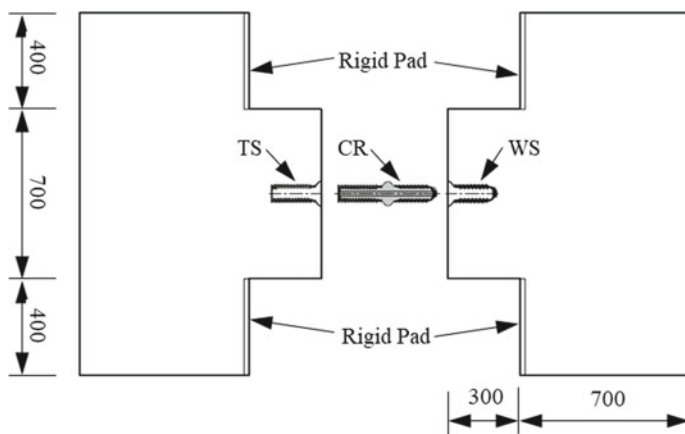


Fig. 5.3 Plan view of T-shape loading beam (Unit: mm)



Fig. 5.4 Jack and oil pump of tensile tests

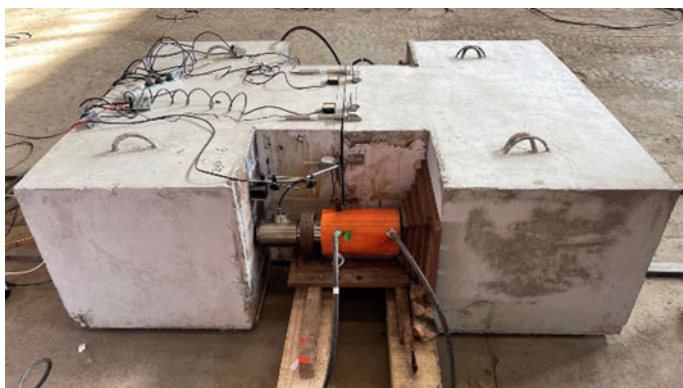


Fig. 5.5 Apparatus of tensile tests after installation

Loading keeps at a constant speed and each stage is kept for 10 min. In the initial stage (0–20 kN), the loading rate is slow and set to 5 kN, which is beneficial to reduce the effect of friction. Subsequently, before 100 kN, the loading rate is set to 20 kN. Lastly, the loading rate is set to 10 kN until destruction.

5.3.3 Monitoring Scheme

The axial pressure applied by jacks is collected by the pressure sensor, whose accuracy level is 0.1 and the sensitivity is 2.0 mV/V. The relative displacement between specimens is measured by the laser displacement sensor. Four sensors are symmetrically arranged at the seam as shown in Fig. 5.5. All the data is collected by the acquisition instrument and the acquisition frequency is 1 Hz.

5.4 Shearing-Test Scheme

5.4.1 Introduction of Scheme

The shearing test is carried out to determine the shearing performance of the plug-in fast connector, Diagram of the test scheme is shown in Fig. 5.6. Both right and left specimens should not be tied and rotated, while the middle one is just restricted by two connectors and friction. In addition, a rigid pad is put on the upper surface of the middle specimen to ensure a balanced load of two connectors.

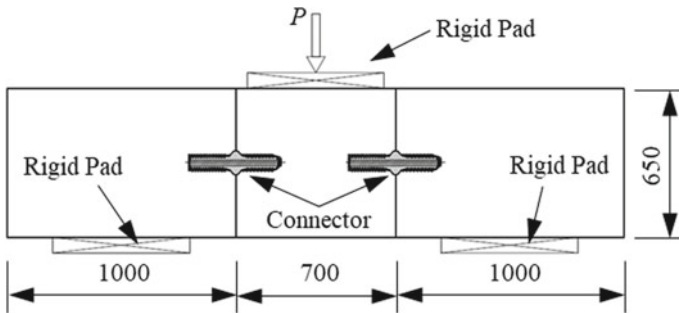


Fig. 5.6 Layout of shearing tests (Unit: mm)

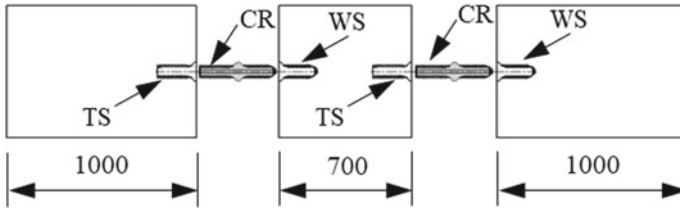


Fig. 5.7 Plan view of loading beam for shearing tests

5.4.2 Specimen Design

In order to determine the shearing performance of this plug-in fast connector, two kinds of size of specimens are designed as shown in Fig. 5.7. The thickness and width of three specimens is the same, 650 mm and 700 mm respectively, while the length of the middle specimen is 700 mm, 300 mm shorter than that of others. All of specimens are made of C60 concrete and HRB400 steel bars.

5.4.3 Apparatus and Loading Scheme

The common multifunctional structure testing machine is adopted for the tests. The loading process is controlled by displacement and the loading rate is 2 mm/min. The specimen after installation is shown in Fig. 5.8.

With an increment of shear force, there will be a certain amount of dislocation between the specimens. The LVDT displacement sensor is used to measure a wrong platform.

Fig. 5.8 Apparatus of shearing tests after installation



5.5 Results

5.5.1 Tensile Test

As the force of jacks continues to grow, the relative movement between specimens occurs. Figure 5.9 shows the changing trend of the relative movement with force. The ultimate relative movement and load capability of the first group are 8.8 mm, and 192.7 kN respectively, while those of the second group are 11.2 mm and 207.5 kN respectively. As shown in Fig. 5.9, the process can be divided into three stages. When the load is less than 30 kN, the movement increased rapidly because of the gap between CR and sleeves. Then the load–displacement curve is approximately linear when the load is between 30 and 150 kN. When the load is greater than 150 kN, the tensile stiffness decreases and the movement increases rapidly. Finally, the failure of the connector occurred with an angle of 45°.

As shown in Fig. 5.10, the failure modes of the tests are the same. There is huge noise after the load is greater than 150 kN. According to phenomena after tests, crack damage occurs in WS at this time. Then, the insufficient bond strength between sleeves and the reinforce concrete is occurred, and part of WS is pulled out from RC. At the same time, tensile damage of RC is occurred with an angle of 45°. The ultimate bearing capacities of tests are 192.7 kN and 207.5 kN respectively, which is far lower than the calculation value.

In summary, the yield strength of the connector is about 150 kN, and the failure strength is about 200 kN.

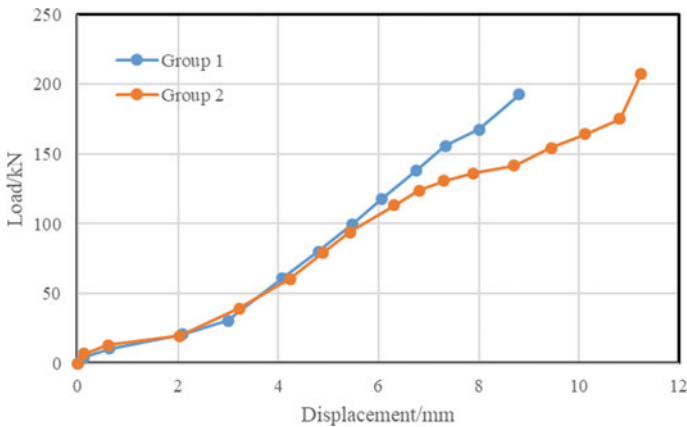


Fig. 5.9 Figure of load–displacement curve



Fig. 5.10 Failure mode of tensile tests

5.5.2 *Shearing Test*

During the loading process, the upper surface of the seam is gradually tightly bonded, while the lower is gradually opened. As shown in Fig. 5.11, RC on the upper surface is crushed, but there is no obvious damage to RC around the connector. The plug-in fast connector has a certain inclination and CR is pulled out from sleeves.

Figure 5.12 shows the changing trend of the displacement with shearing force. The process can be divided into three stages. Firstly, the displacement increases rapidly and the shear-displacement curve is almost a horizontal line when the force is lower than 50 kN. Secondly, the curve shows a linear growth trend and the growth of displacement slows down until the force reaches 430 kN. After that, the force



Fig. 5.11 Failure mode of shearing tests

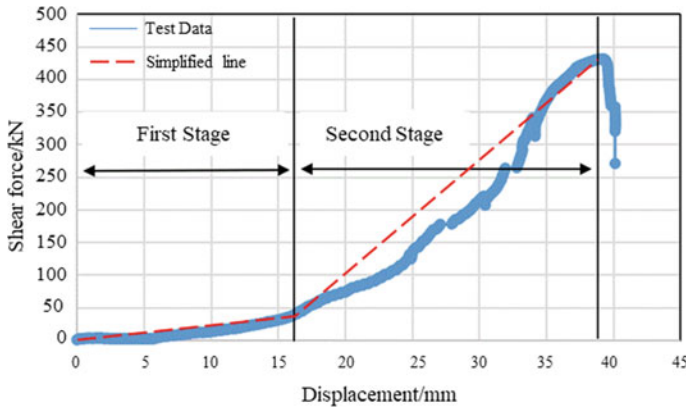


Fig. 5.12 Figure of shearing force–displacement curve

decreases and damage occurs. It is concluded that the shear performance of the plug-in fast connector is good.

The curve is fitted by two straight lines as shown in Fig. 5.12. the shear stiffness for the first two stages are $K_1 = 2.611$ kN/mm and $K_2 = 18.544$ kN/mm respectively.

5.6 Conclusion

The main conclusions are drawn as follows:

- (1) The damage mode of two groups of tensile tests is the same. The insufficient bond strength between the embedded sleeves and concrete causes the fast connector to be pulled out and the tensile failure of concrete is occurred.
- (2) the yield strength of the connector is about 150 kN, and the failure strength is about 200 kN, which is slightly lower than the design value.
- (3) With the increase of the shearing displacement, damage occurs inside the embedded sleeves and then the concrete of the upper surface is crushed. Finally, the tightness between CR and sleeves is invalid and the shear strength of each connector is 210 kN.
- (4) The shear stiffness of the plug-in fast connector is fitted by two straight lines, and K_1 and K_2 are 2.611 kN/mm and 18.544 kN/mm respectively.
- (5) The new plug-in fast connector can improve the longitudinal mechanical performance of a shield tunnel. The subsequent research should focus on the selection of materials for embedded sleeves and the bond strength between the sleeve and concrete.

References

1. Knights, M.: Tunneling projects in London: Olympic City 2012. *Tunnel Constr.* **32**(4), 604–612 (2012)
2. Yue, S., Zhou, Z., Peng, F.: Mechanism analysis of plug-in quick-joint connector for shield tunnel segment. *Chin. J. Undergr. Space Eng.* **6**(3), 532–536 (2010)
3. Yan, Z., Ding, W., Shen, B., Peng, Y.: Structural model for radial joints of water-conveyance shield tunnels. *Chin. J. Geotech. Eng.* **33**(8), 1185–1191 (2011)
4. Nie, J., Li, Y., Tao, M., Zhang, Z., Tang, H.: Experimental research on uplift performance of a new type of uplift restricted-slip free connector. *China J. Highway Transp.* **27**(4), 38–45 (2014)
5. Zheng, Z., Zhang, Z.: A study on flexural rigidity and optimization of segment joint with anchored rebar. *Chin. J. Undergr. Space Eng.* **11**(S2), 462–468 (2015)
6. Cheng, B.: Experimental research on cast iron embedded part applied in segment ring connection of water tunnel. *China Municipal Eng.* **2016**(3), 108–110 (2016)
7. Ju, J., Meng, H., Yan, Z., Zhou, L., Zhu, H., Guan, L., Shen, Y.: Test of tensile performance for embeded part with high bearing capability of segment joints in shield tunnel. *China J. Highway Transp.* **30**(8), 149–155 (2017)
8. Guan, P., Yang, Z.: Research and development of new fast segment connector and mechanical property analysis of segment joint. *Tunnels Rail Transit* **2018**(1), 1–6 (2018)
9. Geng, P., Wang, Q., Guo, X., Zeng, G., Chen, C., He, C.: Pull-out test of longitudinal joints of shield tunnel. *China J. Highway Transp.* **33**(7), 124–134 (2020)
10. Fujiki, I., Oishi, K., Saitou, M., Takaki, K.: Development and construction on automatically constricted segment. *J. Japan Soc. Civil Eng.* **67**(1), 16–34 (2011)
11. Shirato, M., Furuichi, K., Takimoto, K., Yoshida, K.: Development of new composite segment and application to the tunneling project. *Doboku Gakkai Ronbunshu* **2003**(728), 157–174 (2003)
12. Yuasa, Y., Masuno, M., Koizumi, A.: Study on water tightness of RC segment for underground river shield tunnel. *Doboku Gakkai Ronbunshuu F* **66**(4), 578–592 (2010)
13. Liu, X., Li, H., Guan, P., Yang, Z.: Research on design parameters for shield tunnel lining structure with quick connectors. *Modern Tunnel. Technol.* **56**(6), 19–26 (2019)
14. Bi, X., Liu, X., Li, W., Cao, W., Wang, X., Chen, B.: Research on the application of new connecting segment technology in metro shield tunnel. *Urban Mass Transit* **23**(7), 1–11 (2020)

Chapter 6

The Advancement of Knowledge Graphs in Cybersecurity: A Comprehensive Overview



Yuke Ma, Yonggang Chen, Yanjun Wang, Jun Yu, Yanting Li, Jinyu Lu, and Yong Wang

Abstract With the increasing complexity of artificial intelligence technology and network environments, cybersecurity is facing massive and complex data. Knowledge graphs have the potential to aggregate, represent, manage, and reason with this knowledge. Therefore, applying knowledge graphs to cybersecurity can help to characterize and present security situations, support security decision-making, and predict warnings. Over the past two decades, research on knowledge graphs for cybersecurity has received growing attention in data processing, construction, and visualization. This review provides a comprehensive comparative analysis of key technologies and application scenarios of cybersecurity knowledge graphs. Firstly, basic concepts of knowledge graphs and cybersecurity knowledge graphs are outlined, and the required datasets for their construction are compared and analyzed from both general-purpose and specialized perspectives. On this basis, a framework for building cybersecurity knowledge graphs is summarized, and key techniques for building cybersecurity knowledge graphs, including ontology construction, information extraction, and knowledge reasoning, are detailed. Finally, application scenarios of knowledge graphs in the field of cybersecurity are sorted out from the perspective of application objectives. The challenges knowledge graphs face and future development trends in this field are also pointed out.

Keywords Cybersecurity · Knowledge graph · Knowledge representation · Ontology construction · Information extraction · Knowledge reasoning

Y. Ma · Y. Wang (✉) · J. Yu · Y. Li
College of Computer and Communication Engineering, Zhengzhou University of Light Industry,
Zhengzhou 450002, China
e-mail: wyl@zzuli.edu.cn

Y. Chen
The State Information Center, Beijing 100045, China

J. Lu
Henan Province Platform Economy Development Guidance Center, Zhengzhou 450008, China

Y. Wang
Zhengzhou Aiwon Computer Technology Co., Ltd., Zhengzhou 450000, China

6.1 Introduction

In recent years, the global cybersecurity situation is not optimistic. Cyber security is the act of protecting computer systems from attacks or illegal access, and with the increase of new technologies and devices, the causes of cyber attacks and the focus on prevention have diversified. Under the influence of the epidemic, cyber security threats such as security vulnerabilities, ransomware, ransomware, cloud services, obsolete and inefficient systems against infrastructure and important information systems are becoming increasingly serious, and the means of attack are escalating, bringing huge risks to people's lives, economic production, social stability, and national security [1]. With the rapid development of big data and artificial intelligence, new cybersecurity solutions have emerged, leveraging the vast amount of security-related data available in cyberspace. This data includes monitored cybersecurity alert data, vulnerability information repositories, and security notices. By mining the information in these data, security analysts can provide support for cybersecurity situational awareness, realize security alert predictions, and support cybersecurity decisions. However, the characteristics of network security data of massive quantification, decentralization, fragmentation, and hidden relationships make how to analyze and process these massive data in a timely and accurate manner a major problem in the field of network security. Therefore, there is a need to find effective big data analysis technologies and algorithms to achieve rapid processing and analysis of cybersecurity data to better protect cybersecurity.

Cybersecurity knowledge graph is a method that uses knowledge mapping technology to model and expresses knowledge in the field of cybersecurity, aiming to model the concepts of attackers, targets, tools, vulnerabilities, threats, risks, and other concepts involved in cyberspace and the connections between them into a unified knowledge system, to achieve a comprehensive understanding and effective control of the security posture of cyberspace to support the cyber attack and defense posture perception, threat prediction, risk assessment, and other tasks. The cybersecurity knowledge graph has the following advantages: (1) it can integrate multi-source heterogeneous data and improve data quality and credibility; (2) it can express complex semantic relationships and improve information expressiveness and readability; (3) it can support ontology-based reasoning and improve knowledge discovery and utilization; (4) it can support graph-based analysis and improve data mining and visualization.

At present, some progress has been made in cybersecurity knowledge graph research [2]. Some scholars have proposed ontology-based methods for constructing cybersecurity knowledge graphs, including knowledge extraction, ontology construction, entity identification, and other techniques, as a way to construct cybersecurity knowledge graphs. Meanwhile, some researchers are also exploring how to integrate multi-source heterogeneous data into the cybersecurity knowledge graph, to improve the completeness and accuracy of the graph. In addition, some scholars

are also studying how to use knowledge graph technology for cybersecurity situational awareness and threat intelligence analysis to achieve cybersecurity intelligence. Overall, there are still many challenges and problems in the research of cybersecurity knowledge graphs, which need further in-depth exploration. In this paper, we focus on various key technologies and application scenarios of knowledge graphs in cybersecurity, conduct a more complete and in-depth review, and give some issues that may exist or are worth exploring in the future.

This paper is organized as follows: Sect. 6.2 of this paper provides a brief overview of the development of general knowledge graph construction techniques as well as their application in the field of cybersecurity knowledge graph construction; Sect. 6.3 summarizes and analyzes the relevant datasets of cybersecurity knowledge graph; Sect. 6.4 proposes a framework for cybersecurity knowledge graph construction and sorts out the key technologies for cybersecurity knowledge graph construction; Sect. 6.5 gives the application scenarios of cybersecurity knowledge graph; Sect. 6.6 looks forward to the cybersecurity The future research direction of the knowledge graph. Finally, the whole paper is summarized.

6.2 Background Knowledge

6.2.1 Knowledge Graph

The early idea of the Knowledge Graph originated from the vision of Tim Berners-Lee, the father of the World Wide Web, on Semantic Web [3]. The core idea of the Semantic Web is to add machine-understandable semantic information to web data, thus improving the comprehension ability of machines. In 2012, Google introduced the concept of Knowledge Graph to enhance the search quality and user experience of search engines [4]. Subsequently, Knowledge Graph has been extensively utilized in diverse domains, including but not limited to finance, education, and medicine.

Knowledge graph is a structured data model for representing and storing knowledge, which organizes knowledge elements such as entities, concepts, relationships, and attributes in graph form to achieve description, query, reasoning and application of knowledge [5]. In essence, a knowledge graph is a semantic network that shows entities and relationships between entities and is a formal description of things and relationships in the real world. Knowledge graphs are generally represented by a triad, i.e. $K = (E, R, S)$ where K denotes the knowledge base; $E = \{e_1, e_2, \dots, e_{|E|}\}$ denotes the set of entities in K . There are $|E|$ kinds of entities in the set of entities $|E|$ kinds. $R = \{r_1, r_2, \dots, r_{|R|}\}$ denotes the set of relations in K , and There are $|R|$ different kinds of relations in the set of relations. The basic forms of the triples are <concept, attribute, attribute value> and <entity1, relationship, entity2>, etc. The most fundamental components of knowledge graph K are entities, which are interconnected through different types of relationships. Concepts are used to describe the category or type of things, objects, or collections, including place names and individuals.

Attributes, such as birthplace and birth year, refer to the inherent characteristics and features of entities. Attribute values represent the specific values of the attributes assigned to entities or relationships, such as “Beijing.” A unique identifier can be assigned to each entity, while attribute and value pairs are used to describe the entity’s intrinsic characteristics. Relationships connect entities and indicate the associations between them.

The logical structure of the knowledge graph can be divided into a schema layer and a data layer. The schema layer is the basis of knowledge graph construction, which defines the meta-information and meta-structure of data and is usually designed through an ontology library. Ontology is a structured knowledge representation, which describes the relationships and attributes between different concepts. Data layers are concrete knowledge instances, including entities, relationships, and attributes, generated according to the ontology specification of the schema layer. They describe specific knowledge facts of a class or a concept. The schema layer and the data layer can be compared to the relationship between the skeleton and the flesh and blood.

Figure 6.1 illustrates the general process of constructing a knowledge graph, which is continually updated and refined through cognitive ability. Generally, there are two methods for building knowledge graphs: top-down and bottom-up. The top-down approach involves defining ontology and the knowledge graph data model first, and then adding knowledge to the database. On the other hand, the bottom-up approach involves extracting knowledge from open unstructured data and selecting those with higher confidence levels to add to the knowledge graph. This approach also involves building the top-level ontology model.

There are two main categories of knowledge graphs based on their knowledge scope and application scenarios, namely general knowledge graphs and domain-specific knowledge graphs. General knowledge graphs are extensive knowledge

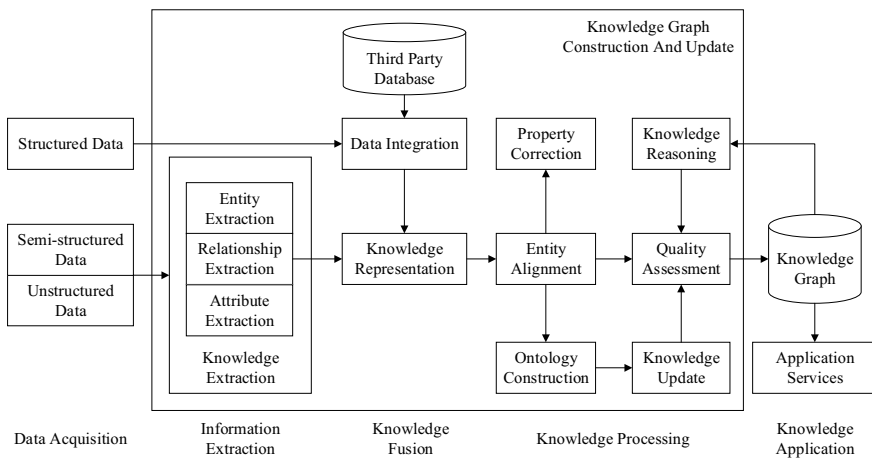


Fig. 6.1 The general construction process of knowledge graph

bases, such as Freebase [6], Yago [7], DBpedia [8], etc., which are mainly used for pervasive intelligent search and recommendation scenarios and provide broad basic knowledge associations. Domain-specific knowledge graphs, on the other hand, build a knowledge space with depth based on a certain knowledge sub-domain to serve specific query and analysis requirements in the domain. The cybersecurity knowledge graph can be positioned as a domain-specific knowledge graph in this classification system, providing deep knowledge space and specific query and analysis demand services in the cybersecurity domain, and we will introduce the cybersecurity knowledge graph in Sect. 6.2.2.

6.2.2 *Cybersecurity Knowledge Graph*

The technology of knowledge graphs has broad applications in the field of cybersecurity [9]. As the network environment becomes increasingly complex, the amount of data involved in cybersecurity is also rapidly expanding. Consequently, there is a pressing need to identify correlations and attack patterns from the vast, fragmented, and heterogeneous data related to cyberspace that come from multiple sources. Network security knowledge mapping is to organize and manage a massive amount of network security knowledge with the technology of knowledge mapping. The present challenge in conducting cybersecurity posture analysis is not the absence of available information, but rather, the difficulty in integrating heterogeneous information from multiple sources into a single model. This integration is crucial in obtaining a comprehensive understanding of the cybersecurity posture and providing decision support. Knowledge graph technology can effectively integrate heterogeneous cybersecurity data from multiple sources, build a security knowledge ontology architecture, and support tasks such as cybersecurity situational awareness and early warning prediction.

The role of knowledge graph technology in the cybersecurity field is mainly in the following aspects: integrating multi-source heterogeneous cybersecurity data to build a unified and structured cyberspace situational portrait; revealing the intrinsic connections and influencing factors among different entities to provide rich cyberspace correlation analysis capabilities; supporting intelligent reasoning capabilities to realize dynamic perception and prediction of cyber threat behaviors and risk states; and providing other cybersecurity technologies with reliable data sources and decision bases. When introducing knowledge graph into the cybersecurity field, core concepts and relationships can be defined based on ontology and threat modeling methods, entity and relationship information can be extracted from multi-source heterogeneous cybersecurity data, and data in the security knowledge graph can be stored and managed using graph databases and graph computing frameworks, and complex reasoning tasks can be performed based on methods such as logical reasoning or machine learning, such as attack path analysis, risk assessment, and anomaly detection, etc.

The construction of cybersecurity knowledge graph generally starts with ontology construction and the design of the conceptual structure of cybersecurity knowledge graph, including the definition of entity types, attribute types and relationship types, as well as the hierarchical relationships and constraints among entities. Reference can be made to existing standards and frameworks in the field of cybersecurity, such as STIX, ATT&CK, CAPEC, etc. Next, knowledge extraction is performed to identify named entities and relationships from unstructured or semi-structured cybersecurity data and map them to ontologies. Natural language processing, machine learning, rule matching, and other methods are generally used. Then, knowledge storage is performed, and the extracted entities and relations are stored in the knowledge graph database to form a cybersecurity knowledge graph. Suitable data models and query languages, such as RDF, SPARQL, etc., can be selected. Finally, knowledge inference is performed using logical reasoning, path search, and machine learning to generate new knowledge to support prediction and inference tasks by using the existing cybersecurity knowledge graph. In the latest study, Ren et al. [10] designed a complete knowledge graph framework including knowledge extraction, knowledge storage, knowledge inference, and knowledge visualization, and used deep learning and expert knowledge to complement and update the knowledge graph.

Relevant cybersecurity knowledge bases have been constructed in the field of cybersecurity [11]. Building a cybersecurity knowledge graph can integrate cybersecurity-related information from different sources, analyze and mine them to understand the cybersecurity posture, and provide a basis for decision-making. This is very important for detecting intrusions and monitoring the cybersecurity posture. Given the increasingly systematic knowledge available in the field of network security, the construction of network security knowledge graphs typically employs a top-down approach. Compared to foreign countries, domestic research on knowledge graphs in the field of cybersecurity has been relatively limited and started later. Iannacone et al. proposes the cyber threat intelligence platform STUCCO [12], which is dedicated to cyber attack detection and contextual understanding; MITRE, the National Security Engineering Center, develops a Neo4j-based cyber attack knowledge graph tool CyGraph [13], which is mainly oriented to cyber warfare task analysis, visualization analysis and knowledge management.

Previous review articles on cybersecurity knowledge graphs are mainly in the areas of building key technologies and cybersecurity assessment. Zhang et al. [14] reviewed the application and development of knowledge graphs in the field of cybersecurity assessment, analyzed the advantages and challenges of knowledge graphs, proposed a framework for cybersecurity assessment based on knowledge graphs, and gave a case study, but only limited to the field of cybersecurity assessment. Li et al. [15] summarize the current research progress of knowledge graph-related technologies at home and abroad and their application status in the field of network security, but only confine to the key technical aspects and do not cover the application scenarios of network security knowledge graph. Ding et al. [16] briefly elaborate on several application directions of network security knowledge graph on the basis of introducing the construction technology of network security knowledge graph. Liu et al. [9] provide an overview of A comparative review of different works describing recent advances

in cybersecurity knowledge application scenarios is presented. Other articles mainly review the research on cybersecurity knowledge graphs in the dimensions of graph-based approaches [17], knowledge inference approaches [18], etc. However, there is still a lack of literature that comprehensively reviews cybersecurity knowledge graph construction techniques and application scenarios. The primary objective of this paper is to offer a comprehensive and in-depth review of the datasets, key technologies, and application scenarios of knowledge graphs in the field of cybersecurity, incorporating the latest advancements.

6.3 Cybersecurity Knowledge Graph Dataset

The internet comprises numerous elements related to cybersecurity, and several security companies have made significant strides in collecting and integrating cyberspace resources [19]. For instance, KnownSec has developed ZoomEye, a cyber radar system; FOFA, a web search engine launched by the 100 Club; and Shodan, a web device search engine. Shodan is a well-known open web search engine that scans internet devices and identifies information about them. Censys is a free search engine that scans IPV4 addresses, domain names and certificates. ZoomEye is a cyberspace search engine with two detection engines that can identify Internet devices and websites.

Cybersecurity knowledge mapping data must usually be obtained from many different sources, the first source is structured data, such as structured intelligence databases and intelligence from STIX. The second source is semi-structured data, such as the knowledge base under MITRE, including CVE, CWE, CAPEC, CPE, ATT&CK and CTI [20]. Such information is typically collected and stored in semi-structured vulnerability databases, including NVD, CNVD, and CNNVD [21]. Public disclosure of important security information also appears in the databases of well-known companies, such as Kaspersky (Kaspersky Anti-Virus [22] is one of the world's most technologically advanced antivirus software), IBM, VERIS Community [23], and other open-source intelligence community sites. Third, security engineers can also find some key information from cybersecurity blogs (such as Talos blog [24]), cybersecurity reports (such as GitHub APT report [25]), Internet chat rooms, and any publicly available cybersecurity texts. These are better resources that can be mined for concepts, abstractions, entities, attributes, and relationships.

In this paper, based on the purpose of constructing knowledge graphs, the cybersecurity knowledge graph datasets are divided into two categories: general-purpose and professional-purpose. The general-purpose knowledge graph aims to cover all aspects of the cybersecurity domain, including threat intelligence, vulnerability information, security events, etc.; while the specialized knowledge graph focuses on a specific domain, such as industrial control system security, cloud security, etc.

6.3.1 *Generalized Dataset of Cybersecurity Knowledge Graph*

To improve the analysis and decision-making capability of cybersecurity, the literature [26] introduces the SEPSES knowledge graph. The knowledge graph integrates a variety of cybersecurity data and knowledge resources, including data on threat intelligence, vulnerabilities, attack patterns, and security events, and shows the relationships and semantics among them. The SEPSES knowledge graph is represented by RDF/OWL specification and supports cybersecurity analysis and decision-making by providing SPARQL endpoints and web interfaces to query and visualize the data. Among other things, SEPSES Knowledge Graph can help users discover attackers' strategies, assess system vulnerabilities, predict future threats, etc., and improve the visualization and operability of cybersecurity.

To build a comprehensive cybersecurity knowledge graph (CSKG), knowledge mapping techniques and multi-source heterogeneous security knowledge bases are utilized, as discussed in the literature [27]. Publicly available vulnerability and threat bases on the network are analyzed to extract knowledge and form a multi-source heterogeneous information security knowledge graph for threat analysis. The article presents a description of the security knowledge ontology model during the construction process, as well as methods such as threat modeling, which enable the processing and integration of multi-source heterogeneous cyber security domain information into a structured intelligent security domain knowledge base. Among the datasets are NVD, CAPEC, CWE, etc. The article also explores applications of this knowledge graph, such as threat intelligence analysis, malicious activity detection, and advanced persistent threat (APT) organization attribution.

Literature [28] introduces a unique dataset containing manually labeled cybersecurity-related terms in six categories: attackers, targets, vulnerabilities, attack methods, consequences, and solutions. The dataset helps organizations and government agencies to automatically extract cybersecurity terms, quickly understand and discover vulnerabilities in their systems, and take appropriate measures to strengthen security, while also tracking unofficial data sources to discover potential threats. Data sources include open blogs and official company security bulletins, among others.

The data sources used in the study [29] were structured data from the cyber security domain, including the National Vulnerability Database (NVD), the Open Source Vulnerability Database (OSVDB), and the Exploit Database (Exploit-DB). These data sources provide a number of entity tags associated with text descriptions, such as vulnerability name, software name, attack type, etc. The article uses these tags to automatically tag text descriptions with entities, thus generating a corpus containing cybersecurity entities, and exposing the corpus. The application scenario of the article is to use this corpus to train a supervised learning algorithm based on a maximum entropy model to extract cybersecurity entities from other unlabeled texts, such as blogs, news articles, and tweets.

6.3.2 *Cybersecurity Knowledge Graph Professional Type Dataset*

The literature [30] discusses the construction of a new annotated malware text database. The article presents an annotation framework for defining malware features based on MAEC vocabularies and a database containing 39 annotated APT reports with 6819 sentences. The authors also use this database to construct models that can help cybersecurity researchers in data collection and analysis. The advantage of this approach is that it can help cybersecurity researchers to better collect and analyze data, but the disadvantage is that it requires a large amount of annotated data.

Sun et al. [31] use CWE (Common Weakness Enumeration) based knowledge graphs to analyze Twitter data to discover and predict cybersecurity-related events and trends. The article describes the method of constructing CWE knowledge graphs and how to use knowledge graphs and machine learning techniques to classify, cluster, correlate, and visualize Twitter data. The article also shows some experimental results to demonstrate the effectiveness and application value of the CWE knowledge graph-based Twitter data analysis method in the field of cybersecurity.

In [32], a novel approach for the automatic extraction of core information from CTI reports is presented, using a Named Entity Recognition (NER) system. The study also includes the publication of a dataset containing 498,000 tagged examples. With countless CTI reports being used by companies worldwide for security purposes, it is essential to extract useful information from large volumes of textual data to secure critical cybersecurity information. The advantage of this approach is the ability to quickly extract useful information from large amounts of text data, but the disadvantage is the large amount of labeled data required.

Open-CyKG [33] is an open-source knowledge graph framework that aims to extract valuable cyber threat intelligence (CTI) from unstructured advanced persistent threat (APT) reports using an attention mechanism-based neural open information extraction (OIE) model. The framework consists of three modules: data preprocessing, entity recognition and relation extraction. The NER model is designed to identify security-related entities, such as malware names, IP addresses, and file names, while the RE model identifies the relationships between these entities. The attention mechanism is used to improve the accuracy of the extraction by giving more attention to important parts of the text. The extracted information is then represented as a knowledge graph, which can be used for various cybersecurity applications, such as threat analysis and attack prediction. The article also shows some application cases, such as APT organization attribution, attack vector analysis, and vulnerability exploitation analysis using knowledge graphs.

The literature [34] presents MalKG: a framework for generating and predicting knowledge graphs (KGs) related to malware threat intelligence. The article describes methods for collecting and processing malware-related data from different open data sources, and how to use relational extraction (RE) techniques to generate malware knowledge graphs. The article also describes how to use graph neural network

(GNN)-based models to predict missing entities and relationships in the knowledge graph and how to use the knowledge graph for threat intelligence analysis.

Kurniawan et al. [35] proposed a knowledge graph-based dataset, ATT&CK-KG, that includes 665 attack techniques and 14 attack tactics from the MITRE ATT&CK framework. Each technique and tactic has unique attributes such as ID, name, description, platform, data source, and impact. The dataset is stored and represented in RDF format and can be integrated with other cybersecurity-related knowledge graphs to form a larger and more comprehensive cybersecurity knowledge graph. The literature [10] proposes a cybersecurity knowledge graph dataset CSKG4APT for APT organization attribution. The dataset is based on ontology, and by collecting and analyzing APT organization information in open source threat intelligence and combining threat intelligence data standards such as STIX and CYBOX, a security knowledge graph model containing APT organizations, attack activities, attack techniques, vulnerabilities, malware and other entities and their relationships is constructed. A security knowledge graph model containing APT organizations, attack activities, attack techniques, vulnerabilities, malware and other entities and their relationships. The data sources of this dataset are mainly MITRE's ATT&CK framework and Threat Group Cards, as well as other publicly available threat intelligence platforms and reports, providing cybersecurity analysts with an intelligent knowledge graph-based auxiliary platform that can help analysts quickly identify the characteristics of APT organizations through query, inference and visualization, etc. and behavior patterns, thereby improving the efficiency and accuracy of cyber attack attribution.

Li et al. [36] developed AttacKG, a method for constructing technical knowledge graphs (TKGs) from cyber threat intelligence (CTI) reports to analyze cyber-attacks. They used two datasets: the publicly available MISP CTI dataset and a private CTI Corpus collected and labeled by the authors. The datasets were preprocessed and labeled to extract attack techniques and relationships, which were then aligned with the MITRE ATT&CK framework. Hanks et al. [37] proposed a new cybersecurity entity annotation dataset for identifying and extracting cybersecurity-related entities, such as attackers, attack techniques, vulnerabilities, etc., from cyber threat intelligence (CTI) texts. This dataset is an unstructured CTI corpus collected from multiple open sources and contains texts of different types and styles (Table 6.1).

The Cybersecurity Knowledge Graph dataset is a very valuable resource that provides a common, scalable, and reusable cybersecurity knowledge base for academia and industry. By modeling and constructing the knowledge graph, we can better understand and master the knowledge and technologies in the field of cybersecurity, thus improving our ability to identify and respond to cybersecurity issues. In this paper, we introduce two types of general-purpose and professional cybersecurity knowledge graphs, and their establishment will provide valuable support and help for researchers and practitioners in different fields. It is believed that the release and use of these datasets will greatly contribute to the development and progress of the cybersecurity field.

Table 6.1 Cybersecurity knowledge graph dataset

Year	Knowledge graph	References	Data sources	Purpose
2019	SEPSSES CKB	[26]	CVE, CWE, CAPEC, CPE, CVSS	Security event prediction
2020	CSKG	[27]	CVE, CWE, CAPEC	Cybersecurity knowledge graph
2019	CWE-KG	[31]	CWE, CAPEC, Twitter data	Twitter data analysis
2021	Open-CyKG	[33]	APT reports, CTI reports	Open cyber threat intelligence knowledge graph
2021	MalKG	[34]	CVE, Malware reports	Malware threat intelligence
2021	ATT&CK-KG	[35]	ATT&CK	Network security event detection and analysis
2022	AttacKG	[36]	AlienVault OTX, Emerging threats, and CTI reports et al	Cyber attack
2022	CSKG4APT	[10]	STIX, CYBOX	Cyber attack attribution

6.4 Cybersecurity Knowledge Graph Construction Techniques

6.4.1 Technical Architecture of CyberSecurity Knowledge Graph

The construction process of a cybersecurity knowledge graph follows a common framework similar to that of a general knowledge graph. A top-down construction model is typically adopted due to the relative maturity and completeness of the cybersecurity domain's knowledge system [38]. In this model, existing cybersecurity knowledge maps are combined to link fragmented knowledge. Information extraction and fusion techniques are used to separate entities and relationships from original data, which are then connected into the knowledge graph representation under the guidance of the ontology framework. Knowledge inference techniques are applied to generate new knowledge based on the existing knowledge graphs to support prediction and inference tasks. The resulting cybersecurity knowledge graph can be used in several application scenarios, including cyberspace situational awareness, attack path analysis, risk assessment, and anomaly detection. Figure 6.2 shows the construction framework of a cybersecurity knowledge graph.

The focus of this chapter is to provide a comparative analysis of the current research status of key technologies in the field of cybersecurity knowledge graphs, including ontology modeling, knowledge extraction, and knowledge inference.

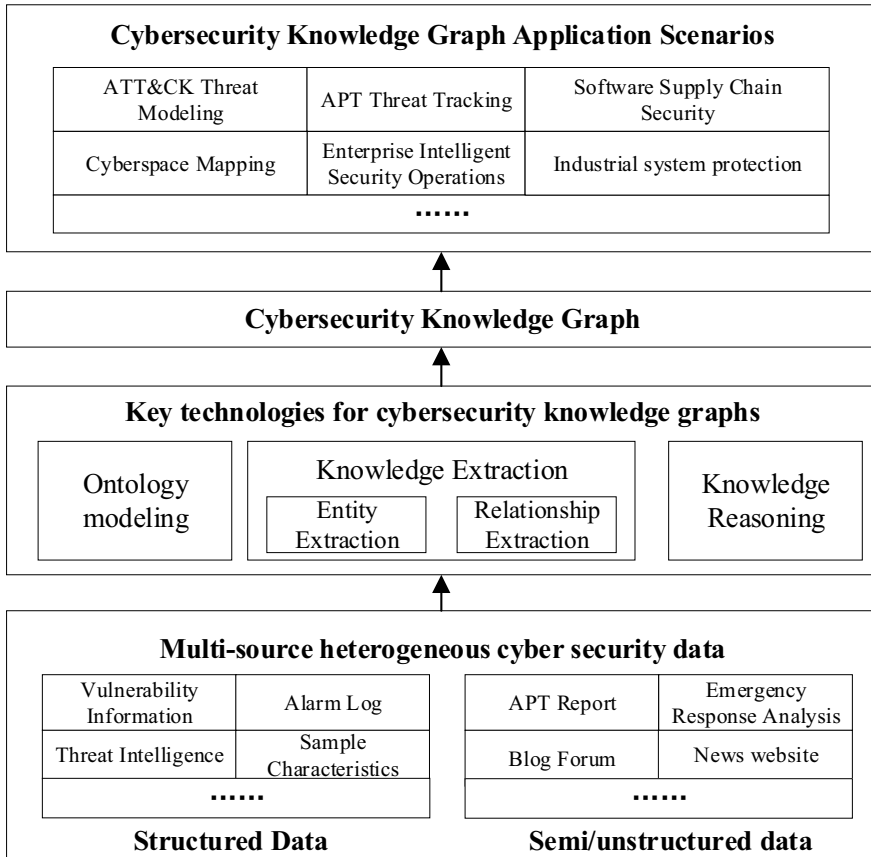


Fig. 6.2 Framework for constructing cybersecurity knowledge graph

6.4.2 Network Security Domain Ontology Modeling

Ontology Definition

Ontologies are the schema layer of knowledge graphs, derived from the philosophical domain [39], which philosophically refers to the discipline of inquiring into the nature of things in the world, and in the fields of computer science and information, science refers to the representation of categories, properties and relationships among concepts, data and entities. Ontologies are commonly used to organize data from different domains into information and knowledge, in order to reduce complexity, improve knowledge sharing, and promote reuse. Ontologies can be categorized into three types based on their scope of application: top-level ontology, domain ontology, and hybrid ontology. A top-level ontology represents generic domain concepts and relationships that are suitable for all domains. Domain ontology represents domain-specific concepts and relationships that are restricted to a particular domain. Hybrid

ontology lies between top-level ontology and domain ontology. This chapter focuses on cyber security domain ontology construction. The modeling meta-language of ontology includes five elements: class (or concept), instance, relationship, function and axiom, which are the basic elements to compose the ontology model.

The ontology model is usually represented by a five-tuple (C, I, R, F, A) , where C denotes the set of classes or concepts, I denotes the set of class instances, R denotes the set of relationships between classes and classes, F denotes the set of special relationships of function classes, and A denotes the set of axioms that constrain classes and relationships. The set of relations R contains four basic types: whole and local relations (part-of), parent and subclass relations (kind-of), class and instance relations (instance-of), and attribute relations (attribute-of), which can be customized according to the specific domain relations.

Ontology construction methods can be classified into manual construction, semi-automatic construction, and automatic construction [40]. Manual construction of domain ontology relies on the knowledge of domain experts but lacks standardization and evaluation criteria for results. The semi-automatic approach reuses existing ontology libraries for extension, which can reduce the cost of ontology construction, but can also result in ontology conflict problems. The automatic construction approach is challenging because of the difficulty in handling noisy data, which makes it challenging to ensure the quality of the ontology. There are six more mature ontology construction methods, including IDEF5, skeleton method, TOVE Methodology, Methodology method, seven-step method and cyclic acquisition method. Based on the W3C standard specification, the ontology description language can be divided into RDF [41], RDFS [42] and OWL [43]. When building the domain ontology, the domain characteristics and the corresponding description language should be fully considered.

Cybersecurity Domain Ontology

In the field of cyber security, ontologies are widely researched, but there is no unified security ontology for reference [44]. Current research mainly focuses on specific areas of security, such as malware classification [45], threat intelligence analysis [46], etc. These research results provide the basis for the construction of network security knowledge graphs. At present, ontologies are mainly constructed by manual editing, because the data types involved are small and manual editing is more efficient [47].

According to the level and granularity of ontologies, this paper divides cybersecurity ontologies into three levels: (1) The highest level, unified security ontology, describes the most fundamental and core concepts and relationships in the cybersecurity domain, such as security policies, security events, security threats, etc. Ontologies at this level can provide an overall security knowledge framework and provide the basis for higher-level ontologies. (2) Intermediate level, including intrusion detection ontology, malware classification and behavior modeling ontology, vulnerability analysis ontology, etc. These ontologies describe instances or events with high generality and importance, such as different types of malware, common intrusion detection methods, and vulnerability analysis tools. Ontologies at this level can provide support

for specific security application scenarios. (3) The lowest level of the cybersecurity ontology includes several sub-ontologies, such as cyber threat intelligence analysis, cyber attack analysis, threat and security assessment, and threat actor analysis, etc. These ontologies describe situations or behaviors in network security with high detail and specificity, such as specific attack methods, attacker behavior patterns, threat intelligence analysis methods, etc. Ontologies at this level can provide more detailed knowledge support for cybersecurity professionals.

Each of these three levels is described below to provide content experience for the construction of security ontologies.

The highest level ontology in cyber security

The highest-level ontology in the network security domain includes the most fundamental and core concepts and relationships in the network security domain, such as security policy, authentication, access control, encryption and decryption, etc. The construction of the unified security ontology requires deep excavation of the nature and purpose of network security, analysis and abstraction of various security mechanisms and security protocols, as well as modeling and prediction of network attacks and threats.

Iannacone et al. proposed STUCCO [12], an ontology for cybersecurity knowledge graph databases. STUCCO is designed to integrate multiple structured and unstructured data sources and contains concepts, relationships, and rules related to cybersecurity. It mainly includes the following: (1) defines the core concepts in the cyber security domain, such as attacker, target, event, behavior, tool, etc.; (2) defines the relationships among these concepts, such as belong, cause, use, etc.; (3) defines the attributes of these concepts and relationships, such as name, time, type, etc.; (4) uses OWL language to represent the ontology and uses SPARQL query language for data retrieval. Such ontologies can help to extract meaningful cybersecurity information from data of different sources and formats, and to integrate and analyze them. Meanwhile, the article introduces the design method and implementation process of the ontology, and how to use the ontology for knowledge graph construction, querying and reasoning. In a practical case, the application effect of the ontology is demonstrated and how to use the knowledge graph to support cybersecurity analysis and decision-making is shown.

Syed et al. proposed the Unified Cybersecurity Ontology (UCO) to facilitate information integration and cyber situational awareness in cybersecurity systems [48]. The UCO combines and integrates heterogeneous data and knowledge models from different cybersecurity systems and standards, including CAPEC, CVE, CWE, STIX, TAXII [49], and Att&ck [50]. This integration makes UCO a comprehensive and practical cybersecurity ontology for information sharing and exchange. Although STIX was designed with the integration of other framework standards in mind, STIX is mainly oriented to threat intelligence information and does not cover some data representations with low information content, while its XML format representation of information is not conducive to automatic information inference. The UCO ontology, through the study of existing threat intelligence standards and ontologies, merges multiple standards into a unified standard by merging similar categories and

parent class abstraction, and covers the data ontologies represented by the current mainstream standards. operations. While many of the ontologies discussed in the literature are not publicly available, the Unified Cybersecurity Ontology (UCO) provides downloads at [51], including some example instances from industry standard repositories. However, the instance data in the dumps are not complete or updated, and there are no available public endpoints. Another example of an RDF ontology available for download is the Cyber Intelligence Ontology [52], which provides classes, properties, and many industry-standard constraints, but no instance data.

Intermediate level ontology in cyber security

Intermediate-level ontologies in the network security domain, i.e., instantiated ontologies, describe instances or events with high generality and importance in network security, such as intrusion detection, malware classification, vulnerability analysis, etc. The construction of instantiated ontology needs to focus on common security problems in practical application scenarios, extract the features and relationships through analysis and modeling of existing instances, and build the corresponding ontology model.

The role of an intrusion detection ontology is to describe and represent the concepts, properties, relationships and rules of the intrusion detection domain, as well as the semantic connections between them. The literature [53] proposes a target-centric ontology for intrusion detection to describe the composition, state and behavior of computer systems, as well as the goals, strategies and means of attackers. The article first analyzes the needs and challenges in the field of intrusion detection, and then introduces the design principles and methods of the ontology, as well as the concepts, properties, and relationships contained in the ontology. Then, the article shows how to use ontologies for knowledge representation, reasoning, and querying for intrusion detection, and how to integrate ontologies with other information sources. Finally, the article discusses the strengths and limitations of ontologies and points out future research directions. The shortcomings of this article are that the ontology may not be complete and general enough, and needs to be extended and updated for different computer systems and attack types.

The role of malware ontologies is to represent malware types, behaviors and prevention methods with semantic knowledge to improve malware identification, analysis and defense. The literature [45] focuses on an ontology-based knowledge representation approach for processing and storing complex behavioral knowledge of a large number of malware families and individuals. Using the ontology-based malware knowledge base can support a variety of research tasks, such as malware sample analysis, infection process understanding, and potential damage level assessment. In addition, the paper proposes an ontology-based reasoning approach for malware classification, which uses malware behavioral features and similarity calculations to achieve automatic categorization of unknown malware individuals. However, the specific steps and tools for extracting behavioral features from malware samples and building an ontology knowledge base are not detailed. The literature [54] mainly introduces an ontology model based on malware behavior,

which can describe the details of the malware infection process, attack target, execution mode and impact range, as well as the association between malware and threat actors and attack techniques. This ontology model can support tasks such as malware detection, analysis, and classification to improve the understanding and identification of malware behavior. However, the paper does not explain how to extract relevant information from malware samples and populate the ontology knowledge base.

Qin et al. proposed an Automated Analysis and Reasoning Model (AARV) based on a vulnerability knowledge graph [55] for vulnerability analysis. AARV consists of three components: knowledge graph construction, vulnerability description analysis, and security domain knowledge graph inference. The model can extract and store vulnerability knowledge from several widely used vulnerability databases, process and analyze the latest vulnerability descriptions using natural language processing techniques, and perform security domain knowledge graph inference using graph database query language. Based on the model, security personnel can quickly locate vulnerabilities, assess their impact and make remediation recommendations to improve cybersecurity defenses.

Lowest level ontology in cyber security

The lowest-level ontology in cybersecurity describes situations or behaviors in cybersecurity with high detail and specificity, such as cyber threat intelligence analysis, cyber attack analysis, threat and security assessment, and threatener analysis. The construction of event ontology requires an in-depth study of the details of various events in cyber security, and analysis and modeling of the source, purpose, means, and characteristics of events to better understand and predict the occurrence and evolution of cyber security events.

To provide a unified representation of multi-source heterogeneous cyber threat intelligence, Philpot et al. [56] introduce a Cyber Intelligence Ontology (CIO) to support the collection, analysis, and sharing of cyber threat intelligence. The ontology employs the OWL language for formal representation and the SPARQL language for querying and reasoning. The ontology provides an open-source knowledge model for different application scenarios and requirements. The advantage of the article is that it provides a generic web intelligence ontology. The literature [57] proposes an ontology-based information security assessment model that can describe knowledge about the structure, functionality, vulnerabilities and threats of information systems. The authors construct an information security knowledge graph based on the ontology model to store and manage information security-related data and rules. And based on the knowledge graph, a rule-based inference engine is designed to automate and automate the information security assessment. Recently, Gao et al. [46] proposed an ontology-based technique for cyber threat intelligence analysis, which uses a general ontology modeling approach to abstract the elements involved in cyber threat intelligence, such as entities, attributes, relationships, and rules, into ontology concepts and use the OWL language for formal representation. The technique can structure, semantically and logically process cyber threat intelligence and improve cyber security situational awareness. Its advantage is that it realizes the unified description and storage of cyber threat intelligence from different sources

and formats. The article also designs an ontology-based network threat intelligence analysis system for the collection, storage, query and visualization of network threat intelligence, and verifies the effectiveness and feasibility of the technique through experiments.

For cyber attacks, the literature [58] presents an ontology of cybersecurity attacks intended to represent and organize knowledge of relevant concepts, services, threats, vulnerabilities, and failure modes in the cybersecurity domain to support cybersecurity analysis and assessment. The strength of the paper is that it provides a framework for cybersecurity attacks based on standard literature and accepted methods that classify attacks into five dimensions: attack target, attack source, attack method, attack outcome, and attack defense. The literature [59] introduces an ontology-based security framework for detecting and defending zero-day attacks and complex attacks against web applications. The article proposes two ontology models that store information about application layer attacks and HTTP communication protocols, respectively, and uses this information for content filtering and attack identification. The article also demonstrates the effectiveness of the framework in a real-world environment, proving its outperformance over traditional security solutions. More recently, the literature [60] proposes a cybersecurity ontology to support the collection and representation of risk-related information in cyber-physical systems. This cybersecurity ontology includes concepts such as components, attributes, vulnerabilities, threats, attacks, and impacts of cyber-physical systems, and the relationships among them. It can be used to construct risk models of cyber-physical systems, analyze possible attack paths, and assess risk levels and impact levels. It also demonstrates the effectiveness and scalability of this cybersecurity ontology in practical applications through a case study of a smart grid.

The literature [61] presents a framework for creating a knowledge graph of threat actors, including the construction of a threat actor ontology and a named entity identification system. The threat actor ontology is used to describe the attributes, relationships, and categories of threat actors, as well as their associations with other cybersecurity-related entities. The named entity recognition system is used to extract cybersecurity-related entities from articles and generate knowledge graphs based on the threat actor ontology. And with a case study, it is demonstrated that the framework can help understand cybersecurity threat posture, especially information about threat actors. Similarly, the literature [62] proposes an ontology-based knowledge graph model that can accurately describe cybersecurity threats, vulnerabilities, attacks, and defenses, and can support complex reasoning and analysis.

In the domain of social engineering in cybersecurity, Wang et al. [63] define 11 core entity concepts and the relationships among them, as well as attributes describing social engineering attack scenarios and events; and demonstrates the usefulness of ontologies and knowledge graphs for understanding and analyzing social engineering attacks through knowledge graph applications to evaluate the effectiveness of ontologies. The strengths of this paper are: a systematic, standardized, and formalized ontology for the social engineering domain is proposed, filling the gap of lacking a unified conceptual framework in the field.

Summary and Discussion

The research on security ontology provides the reference for the construction of cybersecurity knowledge graphs in terms of content and methods. Although the above ontologies have proposed ontologies covering various security elements from various perspectives, they are relatively independent and do not consider the interconnection and integration with other ontology standards, which is still slightly insufficient for building a comprehensive knowledge ontology. This chapter proposes three levels of cybersecurity ontologies and points out their respective roles and meanings, as shown in Fig. 6.3. Establishing a network security ontology model can improve the description and understanding of knowledge and practices in the field of network security, leading to enhanced automation and intelligence of network security. Cybersecurity ontologies will continue to play a crucial role in various application scenarios and provide robust support for research and practice in the cybersecurity domain. However, due to the continuous changes and evolutions in the security domain, the design and updates of ontologies need to be constantly followed up, otherwise, they may lose their proper value and usefulness. In addition, although ontologies can provide formal representation and reasoning of security knowledge, specific customization, and adaptation are still needed for some practical application scenarios to suit different needs and situations. Therefore, how to improve the scalability and practicality of ontology is a problem that needs to be further explored and solved.

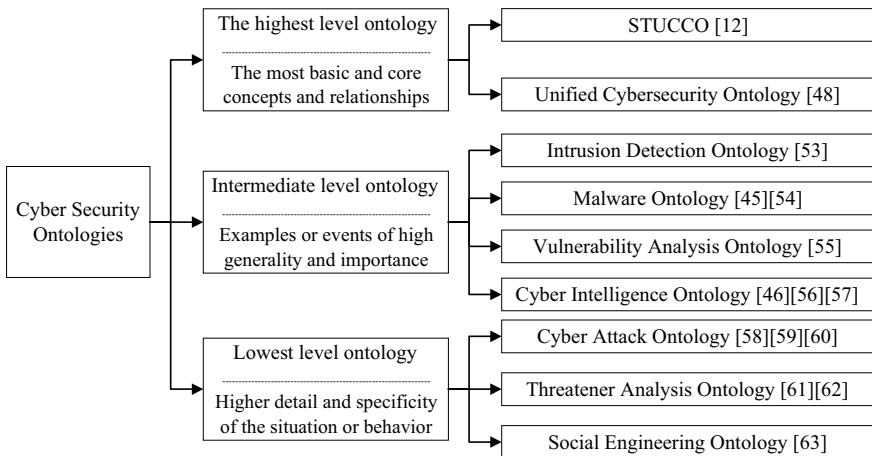


Fig. 6.3 Different levels of cybersecurity ontology

6.4.3 *Knowledge Extraction for CyberSecurity Knowledge Graph*

The construction of cybersecurity knowledge graphs needs to rely on knowledge extraction techniques. Currently, the core tasks of knowledge extraction include Named Entity Recognition (NER) and Relationship Extraction (RE). In the entity recognition task, traditional knowledge extraction methods can be categorized into three types: rule-based, statistical machine learning-based, and deep learning-based methods [64].

Entity extraction in the field of cybersecurity

Cybersecurity entity recognition is a type of named entity recognition (NER) specifically focused on identifying and classifying security-related entities within cybersecurity text data. These entities can include things like computers, domain names, hacker organizations, and vulnerabilities, among others. The goal of cybersecurity entity recognition is to extract and classify relevant cybersecurity vocabulary from unstructured text data, allowing for better analysis and understanding of cybersecurity threats and trends.

Rule-based approach

Most of the initial studies used rule-based approaches, whose main advantages are their high accuracy, close to the human way of thinking, intuitive presentation, and ease of machine reasoning. However, the disadvantage of the rule-based approach is that it is costly because most rules are only applicable to specific domains and cannot be extended to a wider range of domains.

In the field of intrusion detection, deep packet inspection techniques in products such as Snort, I7-filter, and Bro use a rule-based matching approach for attack type identification [65].

The paper [66] presents an improved Bootstrapping method for extracting secure entities from texts such as blogs and tweets. The traditional Bootstrapping method requires two full-text searches in one cycle, but PACE improves it by requiring only one full-text search in one cycle. First, an entity library with context is used instead of an entity library and a rule library (pattern library). When using the initial rules to extract entities, not only the entities are extracted, but also a certain number of words before and after them are selected as contextual words together to form the extraction result. Secondly, the rule generation process is changed from searching in the full text to generating in the entity database containing contextual words, thus reducing the time of searching the full text at a time. In addition, PACE relaxes the restrictions on rule generation and improves the selection of relevant contextual words to increase the recall rate and maintain a high accuracy rate.

The literature [67] proposes a combination of regular expressions and ontologies to extract entities from log files. The method first uses a support vector machine to determine whether a log file is security-relevant, then uses a separator to slice and dice paragraphs with the same format, and then uses a regular expression generated by a

genetic algorithm to tag the information in the paragraphs, and finally converts the tagged information into entities by ontology matching. The advantage of this method is that the format of semi-structured documents is used as features for type recognition and regular expression generation, and the accuracy of extraction is improved by the method of information extraction and ontology matching verification. However, this method cannot be applied to the extraction of unstructured documents. In contrast, the literature [68] proposes an approach that combines regular expressions and syntax trees to extract Indicators of Compromise (IoC) from blog text. The method first uses regular expressions and lexicons to locate web security entities and relations, and then uses grammar tree similarity to determine whether the content contains entities and relations. However, this method cannot be applied to the extraction of unstructured documents.

Statistical machine learning-based approach

Traditional machine learning-based entity extraction methods require a combination of a large number of manually designed features that are converted into a multiclassification or sequence labeling task, thus making full use of the contextual and internal features of the entities. This approach is more flexible and robust, but requires a large amount of feature engineering and manually labeled data, and also suffers from the problem of data sparsity. Several papers [69] also point out these problems.

The literature [70] proposes a weakly supervised approach based on security event extraction, but this approach relies heavily on the setting of seed samples while ignoring the entity information in the text itself.

Joshi et al. [71] developed a named entity recognition method for cybersecurity-related entities and relationships in web text data using Conditional Random Fields (CRF); Lal [72] proposed an SVM-based method for identifying cybersecurity-related entities and concepts in the unstructured text; Mulwad et al. [73] designed an SVM-based information extraction system for identifying vulnerability and attack information in web text.

The article [29] proposes an entity extraction method that uses structured data from the cybersecurity domain to automatically annotate the unstructured text. The method generates a large-scale annotated corpus by writing a script that matches entities from structured data sources with relevant text descriptions. The method then uses this corpus to train a supervised learning algorithm based on a maximum entropy model and an average perceptron to identify the desired entities from other cybersecurity documents. The method achieves a high level of accuracy, recall and efficiency. Similarly, Hanks et al. [37] present a new dataset for cybersecurity entity annotation, and the article also provides an online tool for visually and interactively annotating cybersecurity entities. This work has important implications for building artificial intelligence-based cyber defense systems and cybersecurity knowledge graphs.

Deep learning-based approach

Deep learning methods based on neural networks have shown promising results in named entity recognition and can be applied to cybersecurity as well. Compared with traditional entity recognition methods, deep learning methods are able to better

learn the feature and semantic combination capabilities of data to improve recognition accuracy by automatically discovering features and performing the potential representation and processing required for classification or detection. The current mainstream research direction is based on deep learning entity extraction methods. Deep neural networks are able to capture features and perform entity recognition automatically without excessive human intervention.

Neural networks are capable of feature extraction from data by building multi-layer network structures. The Collobert [74] model based on Convolutional Neural Networks (CNN) was first used in the field of general named entity recognition and achieved good results. Since then, neural networks have been widely used for feature extraction in various domains, including cybersecurity. Hochreiter [75] proposed an LSTM model for filtering historical information using a threshold mechanism. Peng [76] uses a short text classification model based on convolutional neural network to extract features from microblogging text data and classify them by CRF, and achieves better results. Qin et al. [77] proposed a feature template-based FT-CNN-BiLSTM-CRF cybersecurity entity recognition algorithm based on a neural network model, which achieved an F-value of 86% on a large-scale cybersecurity dataset.

The main content of the literature [78] is about cybersecurity named entity recognition using LSTM recurrent neural networks. The aim of this work is to convert cybersecurity information from unstructured online sources, such as blogs and articles, into a more formal representation, which is necessary for applications in many domains. Named Entity Recognition (NER) is one of the early stages in achieving this goal, and it involves detecting relevant information.

Related research is mainly based on deep learning methods [29, 79] for threat intelligence data extraction in cyberspace. In recent years, Ranade et al. [80] proposed a contextual word embedding method CyBERT for the cybersecurity domain, which has significant performance advantages in four cybersecurity tasks, namely named entity recognition, relationship extraction, sentiment analysis and threat intelligence generation, and can capture specific semantic and syntactic information in the cybersecurity domain. Chen et al. [81] proposed a BERT model-based cybersecurity named entity identification method for extracting relevant entity information from cyber threat intelligence texts and constructing cybersecurity knowledge graphs. The authors first define and classify six types of named entities in the cybersecurity domain, including attackers, attack techniques, attack targets, vulnerabilities, malware, etc. Then, the authors design a joint learning framework based on the BERT model to decompose the named entity identification task into two subtasks: entity boundary detection and entity type classification.

Relationship extraction in the field of cyber security

Cybersecurity entity relationship extraction involves extracting relationships between entities in a specific cybersecurity domain. While named entity recognition can identify discrete entities, it does not capture the relationships between them. Entity relationship extraction aims to address this issue. With the advancement of information extraction and big data technologies, entity relationship extraction is increasingly used in information retrieval, relationship mining, knowledge graphs,

and other domains. Relationships between entities are an essential component of knowledge graphs, and different relationships connect distinct entities to form a knowledge graph. Identifying relationships between entities from unstructured text is a critical task in knowledge graph construction [82]. Early research on relation extraction mainly used templates to discriminate semantic relations among entities in text, but it is impossible to exhaust all templates for multiple types of relations by manual methods.

Machine learning-based approach

With the development of machine learning, more and more researchers have adopted supervised learning methods to extract relationships among entities, such as feature and kernel function-based methods for supervised learning, bootstrap, collaborative training, label propagation methods for semi-supervised learning and clustering-centered methods for unsupervised methods. The model performance of traditional machine learning is very dependent on the size and quantity of manually labeled feature data, and therefore a method that can extract features automatically is needed.

Jones et al. [83] proposed a framework for semi-supervised security entity and relationship extraction for cybersecurity concept extraction. The goal of the framework is to help security analysts access relevant information, such as new vulnerabilities, attacks, or patches, for their networks. However, annotated text data in the cybersecurity domain is scarce and expensive. Therefore, the paper follows the development of semi-supervised natural language processing and implements a bootstrapping algorithm to extract security entities and their relationships from the text. The algorithm requires only a small amount of input data, specifically, some relations or patterns (heuristic rules for identifying relations), and contains an active learning component that prompts the user for feedback on the correctness of the automatically extracted relations. The paper describes a preliminary implementation of the algorithm and applies it to cybersecurity concepts such as vulnerabilities and attacks.

Deep learning-based approach

With the development of deep learning, neural network models have brought new breakthroughs for entity relationship extraction. Liu et al. [84] proposes to classify relationships based on CNN sentence semantic coding model, which has significant performance improvement compared with traditional statistical machine learning methods; [85, 86] proposes relationship extraction based on recurrent neural network (RNN) and long short-term memory neural network (LSTM); [87] proposes to use recurrent neural network for syntactic analysis tree modeling of sentences, which takes into account the lexical and syntactic features of sentences while extracting semantic features. However, manual annotation becomes expensive in the face of large-scale data. Subsequently, scholars proposed a relation extraction method based on far-supervised learning [88], which would introduce noise to the training set. Other scholars have further proposed relational extraction methods such as multiple example learning, sentence-level attention mechanism, adversarial training, and reinforcement learning mechanism [89, 90].

Many algorithms use deep learning models for entity relationship extraction, allowing for automatic feature learning without the need for manual feature templates. While these methods achieve excellent performance on entity relationship extraction tasks, they often require large amounts of annotated data and lack annotated datasets for specific fields. To address the problem of insufficient annotated data, researchers have begun to explore remotely supervised approaches to entity relationship extraction. Zeng [91] extended the relationship extraction model based on the segmented convolutional neural network PCNN to remotely supervised data, using a remote extraction strategy based on multi-instance learning to reduce the workload of manual data labeling. However, this method's performance on relationship extraction is not very high. To address this issue, Lin et al. [92] added an attention mechanism to address noise during encoding. In 2018, a few researchers [93] found that reinforcement learning can address the noise problem during remote monitoring with good results, and this method may become a trend for future research.

For cyberspace entity relationship extraction, literature [94] extracts cyberspace knowledge from malware action reports based on Stanford extractor; literature [95] defines entity relationship extractor based on deep learning method to determine which pre-defined relationship between two entities belongs to; literature [96] proposes a CASIE system based on BERT pre-training model to achieve classification and extraction of cyber security event-related elements, and similarly, Li et al. [36] use a BERT-based sequence annotation model to identify attack techniques from each CTI report and use a GCN-based relationship classification model to predict the relationship type from each pair of neighboring techniques. The literature [26] proposes an ETL serial knowledge extraction-based approach to transforming existing public cyberspace knowledge such as CWE, CVE, CAPEC, and Common Vulnerability Scoring System (CVSS) into the triples needed for knowledge mapping.

In a recent study, Agrawal et al. [97] proposed a method for constructing knowledge graphs in the cybersecurity domain from unlabeled unstructured text and applied it to cybersecurity education. The method uses pre-trained language models and graph neural networks to extract entities and relations and uses a rule-based approach to filter and correct erroneous entities and relations. Table 6.2 summarizes and compares the methods and extraction content of representative cybersecurity knowledge extraction efforts.

6.4.4 CyberSecurity Knowledge Graph Reasoning

Regarding knowledge graph inference in cyberspace, several studies have been conducted. For example, [98] constructed a knowledge graph using MITRE's CWE knowledge base and utilized the TransE model to learn the representation of structural and textual description information in the knowledge graph, which enables inference applications such as CWE link prediction and vulnerability damage prediction. In addition, [99] developed a vulnerability knowledge graph based on the Unified Cybersecurity Ontology (UCO) ontology and implemented the inference of vulnerability

Table 6.2 Cybersecurity knowledge extraction method

Literature and year	Method	Extraction content
[65], 2011	Rule matching	Attack type identification
[66], 2013	Improved Bootstrapping method	Security entities in the blog text
[67], 2015	Regular expressions and ontologies combined	Entities in the log text
[68], 2016	Combining regular expressions and syntax trees	Missing indicators in the blog text
[70], 2015	Weak supervision method	Security events
[71], 2013	CRF	Web text data entity
[72], 2013	SVM	Entities in unstructured text
[73], 2011	SVM	Vulnerability and attack information
[29], 2013	Automatic labeling based on machine learning	Name of person, organization, etc
[37], 2022	Automatic labeling based on machine learning	Vulnerabilities, attack categories, etc
[77], 2019	Feature templates and CNN-BiLSTM-CRF	Cybersecurity entities
[78], 2018	LSTM	Security entities in blogs and articles
[80], 2021	BERT	Threat intelligence entities
[81], 2021	BERT	Threat intelligence entities
[83], 2015	Bootstrapping method	Correlation between vulnerabilities and attacks, etc
[95], 2019	Feed-forward neural networks	Malware relationships
[96], 2020	BERT	Cyber security events
[36], 2022	BERT, GCN	Attack technology relationships

hiding relationships. Moreover, [100] proposed an embedding and prediction method for software security entities and relationships. This study constructed a knowledge graph based on public knowledge bases, such as CWE, CVE, and CAPEC, and proposed a knowledge graph embedding method to embed software security entities, relationships, and description information into a continuous vector space. The study performed knowledge inference based on the open-world assumption to discover hidden relationships among software security entities.

The existing inference methods include rule-based methods, representation learning-based inference and neural network-based inference methods, etc. Graph inference mainly involves graph association retrieval, graph data mining algorithms, graph representation learning methods, relational inference, etc. Graph association retrieval provides responses to a specified entity, relationship, and attribute feature queries through the shortest path, similarity analysis, and other methods. Graph data

mining algorithms include node clustering on graphs, association discovery, significant node discovery, path mining, and so on, to provide in-depth data insight for knowledge graphs. Graph representation learning acquires vectorized representations of key elements of the knowledge graph through learning methods of structure, attributes, and other dimensions, which can be used to support knowledge retrieval, knowledge inference, and other types of technical implementations. Relational reasoning provides inference results such as knowledge semantic derivation and relational link prediction based on representation learning results or through end-to-end graph neural network model design.

Rule-based approach

Rule-based reasoning methods achieve deductive reasoning of knowledge with the help of rules, axioms and other logical forms. In security research, rule-based inference methods mainly include first-order logic rule-based methods and ontology rule-based methods [101]. Among them, the first-order logic-based approach achieves knowledge inference by constructing predicate logic formulas, which has a long research history, but the use of predicate logic formulas is narrow and the application process is more complicated. The ontology rule-based approach has been more fully researched in recent years. Rule constraints defined in OWL and SWRL or other formal languages are used to build inference relations on the basis of ontology, which has the characteristics of concise definition and rich description [102].

The literature [103] proposes a method using SQL as a rule for determining whether an access policy is misconfigured in Android. The method uses access patterns to associate specific access behaviors with explicitly defined access policies and identifies access policies that do not follow the minimization principle. Although SQL as a rule carrier can achieve simple truth-value judgment, it cannot carry complex semantics and has limited reasoning power. In contrast, SWRL is a language for Semantic Web reasoning that enables rich logical reasoning based on ontology-based OWL representations.

The literature [104] proposes a UCO ontology-based approach that uses SWRL rules to combine security content in Twitter with internal asset intelligence to generate targeted alerts. The method automatically discovers security information on social media by matching security content on the ontology and generating alerts based on SWRL rules for a specific system portrait. However, the rule defined in this method is too flat and not conducive to management. In order to effectively manage a large number of rules, rules can be defined in multiple dimensions such as time and space to improve management efficiency.

The literature [105] proposes an SWRL rule approach based on multiple processes to determine the threat risk from the time dimension. The method divides the asset risk analysis process into multiple steps, defines SWRL rules through different processes, and finally obtains asset analysis results in series. In the specific implementation, the asset analysis process is divided into four processes: element association, calculation of threat likelihood, identification of affected assets and their degree, and analysis of threat propagation paths, which has the characteristics of clear organization and rigorous logic. The literature [106] proposes a method to construct SWRL rules

based on multiple levels to identify erroneous IoT security configurations from the spatial dimension. The method checks configuration information through different levels of constraints to achieve multiple inference judgments on the correctness of configuration information and detect configurations with risks. In the specific implementation, the configuration constraints are divided into two aspects: foundational constraints and user-driven constraints, and SWRL rules are constructed at different levels. Foundational constraints include constraints for internal information such as reachability, sampling, resources, etc.; user-driven constraints include constraints for external information such as capabilities and conditions, and the rules can be extended according to specific attack behaviors.

Recently, Yi et al. [107] used knowledge graph and rule-based inference techniques to model and infer entities, attributes, relationships, and events in satellite networks to enable understanding and assessment of the security posture of satellite networks.

Representation-based learning approach

Representation learning-based inference learns a representation in vector space for each element by mapping the elements of the knowledge graph containing entities and relationships into a continuous vector space, where the representation in vector space can be one or more vectors or matrices. Representation learning allows the algorithm to automatically capture the information required for inference in the process of learning vector representations, and encodes the information of discrete symbolic representations in the knowledge graph in different vector space representations through training learning, enabling the inference of the knowledge graph to be automatically implemented through the computation between predefined vector space representations, without the need for a displayed inference step. Relational inference based on knowledge graph representation learning consists of knowledge graph representation learning and potential relationship prediction. The commonly used representation learning methods for relational inference are TransE (Translating Embedding) family of algorithms, RESCAL, DistMult, etc.

Bordes et al. [108] proposed TransE, the first transfer-based representation model for knowledge graph representation learning. The main idea of TransE is that the sum of the head entity vector and the relation vector is similar to the tail entity vector if the triple (h, r, t) holds, otherwise, it is far away. This basic transfer assumption is the foundation of subsequent research works. The score function is obtained based on this assumption, measuring the distance in terms of L1 or L2 parametrization. During the learning process, negative examples are obtained by replacing the head or tail entity, and a Margin-based loss is minimized so that the score of positive examples is at least one Margin higher than that of negative examples, similar to support vector machines. The candidate entity/relationship with the larger value of the score function is the inference result during inference. However, TransE has some limitations, such as not considering rich semantic information, lack of further adjustment of vector distribution positions in space, and not considering rich relationships, which limit its application in security scenarios.

The knowledge graph representation-based learning method is a simple and efficient relational reasoning method due to its effective and reasonable vector space assumption. For the problem of the security knowledge graph, knowledge graph representation-based learning methods have been applied in security knowledge complementation and attack path investigation. In a recent study, Wang et al. proposed a cybersecurity knowledge graph complementation method CSEA based on integrated learning and adversarial training, which integrates multiple projection and rotation operations to model the relationships between entities and uses angular information to distinguish entities. The method achieves better results than existing methods on knowledge graphs in cybersecurity and is robust to noisy data.

Neural network-based approach

Graph representation learning enables single-step relational reasoning, which can be applied to investigate individual attack events and fix broken chains. However, complex multi-step attacks require multi-step relational inference. The PRA algorithm (path ranking algorithm) is a classic multi-step relational inference algorithm that uses paths as features to predict the existence of specified relationships between entities. PATH-RNN [109] is an example of a PRA-based algorithm for multi-step relational inference. In PATH-RNN, the input is a path between two entities, and the output is the inferred new relationship between the two. The connections between relationships are represented by RNN for inference, and the representation of the path is given by the final hidden state of the RNN after processing all the relations in the path.

Ren et al. [10] proposed a deep learning-based APT knowledge graph inference method for extracting feature vectors of APT organizations from the knowledge graph and using cosine similarity and clustering algorithms to calculate the similarity and attribution relationships among APT organizations. This method can effectively utilize the structured and unstructured information in the knowledge graph to improve the accuracy and interpretability of APT attribution analysis.

Yi et al. [107] proposed a knowledge graph inference method combining rules and neural networks, which is applicable to satellite network anomaly detection and threat assessment. First, a knowledge graph of the satellite network is constructed, including entity types, attribute types and relationship types, as well as the association relationships among entities. Secondly, anomaly detection rules and threat assessment rules are defined and trained and optimized based on historical data, and finally, a neural network model is designed. The model can transform the rules into trainable parameters and use historical data for training optimization. Finally, the trained neural network model is used to reason about the new input satellite network data and output anomaly detection results, threat assessment results and response suggestion results. This approach can help the satellite network detect anomalies and take effective response measures in a timely manner.

In recent years, graph neural networks have attracted a lot of attention, and Garrido et al. [110] proposed a method for context-aware security monitoring using knowledge graphs to represent data and background knowledge related to network security and combining graph neural networks and anomaly detection algorithms. The method

is effective in detecting potential attacks and reducing false positives and misses. Yin et al. [111] proposed a knowledge graph inference method for discovering software vulnerability co-exploitation behavior, which is a type of cyber attack that exploits multiple vulnerabilities at the same time. The method uses a graph neural network model to learn embedding representations of vulnerability entities and relationships from the cybersecurity knowledge graph and then predicts co-exploitation links between vulnerabilities based on these embedding representations. The method also combines attention mechanisms and graph convolutional networks to enhance the learning process. The article claims that the method can achieve better performance than existing methods and provide interpretable results for cybersecurity intelligence.

6.5 Application Scenarios of Network Security Knowledge Graph

Currently, knowledge graph has been widely adopted in many fields, including big data analysis and natural language processing. With the development of knowledge graph technology, there are also more and more applications of network security knowledge graph in various scenarios, such as threat detection, intelligent security decision-making, vulnerability management, and attack path analysis. In this paper, the application scenarios are classified from the perspective of application objectives into the following categories.

6.5.1 CyberSecurity Knowledge Graph Defense Class Application Scenarios

The defense class application scenario aims to improve network defense capability by using network security knowledge mapping. Among them, situational awareness and security assessment can realize visual display and analysis of multi-dimensional data such as network environment, threat intelligence, and attack events to assess network security risks and threats by constructing a network security situational knowledge graph. Vulnerability management and prediction, on the other hand, can collect, organize, analyze and push vulnerability information, predict potential vulnerability exploitation and attack methods, and formulate effective protective measures by constructing a vulnerability knowledge map. Intrusion detection, on the other hand, realizes the description, representation and reasoning of intrusion behavior by constructing an intrusion detection knowledge graph, and improves the accuracy and efficiency of intrusion detection.

The use of knowledge graph-based network security situational awareness models has various practical applications. For example, Chen et al. [112] proposed a KG-based attack situational detection scheme to detect network security threats by

abstracting attack events, which improves the accuracy of network security situational detection. Similarly, Wang et al. [113] proposed a KG-NSSA model that utilizes similarity estimation and attribute graph mining methods to effectively reflect network attack scenarios in the case of asset nodes. Pang et al. [114] developed a KG-based security assessment method for power IoT terminals based on the specific application scenarios and security threat characteristics of power IoT terminals. Moreover, Chen et al. [115] generated extended attack graphs to obtain the maximum probability vulnerability paths, providing insights into attack success rates and losses.

Garrido et al. [110] propose a knowledge graph-based machine learning approach for context-aware security monitoring. The approach uses knowledge graphs to represent entities and relationships in cyberspace, as well as attackers' behavior patterns and uses graph neural networks and anomaly detection algorithms to generate meaningful and interpretable security alerts. Recently, Yin et al. [111] proposed a model based on graph neural networks and attention mechanisms that can effectively capture semantic and structural information among vulnerabilities to predict potential co-option behaviors. The model is also capable of generating interpretable co-exploitation paths to help security experts understand and prevent cyber attacks. Li et al. [116] proposed a knowledge graph-based approach for automated cyber threat intelligence analysis (K-CTIAA) that can extract threat behaviors by parsing the semantic information of cybersecurity terms. They introduced a visibility matrix and modified the formula for self-attention to reduce the negative impact of knowledge insertion, i.e., the knowledge noise problem. They also used the mapping relationship between ATT&CK and D3fend (cybersecurity knowledge graph) to provide countermeasures for the extracted threat behaviors, which can help security experts respond quickly to upcoming threats.

6.5.2 CyberSecurity Knowledge Graph Attack Class Application Scenarios

The attack class application scenarios aim to improve attack capabilities or simulate attack behaviors by using network security knowledge graphs. Among them, attack investigation can realize the tracing, analysis and attribution of attack events and reveal the identity, motive and target of attackers by constructing the attack investigation knowledge graph. Attack prediction is to achieve the prediction and early warning of possible future attacks by constructing the attack prediction knowledge map, so as to prepare for prevention or countermeasures in advance. Attack strategy generation is to realize deep analysis and mining of target systems or organizations to generate effective and covert attack strategies by building an attack strategy generation knowledge map.

For different types of attacks, Sun et al. proposed a 0-day attack path prediction method based on network defense KG, which can accurately predict the potential attack paths of 0-day attacks by using graph neural networks and knowledge graph

embeddings [117]. For distributed DDoS attacks, Liu et al. constructed a malicious behavior knowledge base, which includes a malicious traffic detection database and a network security knowledge base [118]. The authors of [119] proposed a method for generating optimal penetration paths that consider both insider and unknown attacks. The method utilizes a two-layer threat penetration graph (TLTPG), consisting of a host threat penetration graph (HTPG) in the lower layer and a network threat penetration graph (NTPG) in the upper layer. This approach can effectively generate optimal attack paths and improve the efficiency of security response. The method uses genetic algorithms and heuristic search algorithms to find the optimal host path in the HTPG and the optimal network path in the NTPG and combines the two into an optimal penetration path.

Kurniawan et al. [120] proposed a knowledge graph-based framework for discovering and analyzing the tactical behavior of cyber attacks from audit data. The authors used knowledge graph techniques to formally represent concepts, relationships, and rules in the cybersecurity domain and combined the ATT&CK knowledge base and security event log data to construct a cyber attack knowledge graph (ATT&CK-KG). The authors design a graph pattern matching-based algorithm for detecting subgraphs associated with known attack tactics from ATT&CK-KG and calculate the confidence level of tactical behavior based on the node and edge attributes in the subgraphs. The authors evaluate the framework on a real cybersecurity audit dataset and compare it with other approaches. The results show that the framework has high accuracy, efficiency, and interpretability in discovering and analyzing the tactical behavior of cyber attacks.

6.5.3 CyberSecurity Knowledge Graph Optimization Class Application Scenarios

Using cybersecurity knowledge graphs, optimization of cybersecurity operations or decision processes can be achieved. Among them, the optimization categories include intelligent operation, security policy verification, and result prediction. By constructing intelligent operation knowledge graphs, resources such as data, tools, and tasks in the process of network security operations can be managed and scheduled, thus improving the efficiency and quality of operations. By constructing the security policy validation knowledge map, the validation and evaluation of existing or newly formulated security policies in terms of legitimacy, effectiveness, and consistency can be verified and evaluated. By constructing the result prediction knowledge map, it realizes the simulation and prediction of possible results under different scenarios and gives corresponding optimization suggestions.

Yi et al. [107] used a domain knowledge-based reasoning approach to achieve automatic correlation analysis of multi-source intelligence to understand the status of satellite networks. The authors analyze the needs and challenges of satellite network

situational awareness, design a framework for satellite network situational awareness based on knowledge graphs, and give a concrete application case to demonstrate the advantages of the approach in improving satellite network security defense capabilities.

Gao et al. [121] proposed ThreatRaptor, a log-based cyber threat-hunting system that leverages external threat knowledge from OSCTI. It features an unsupervised natural language processing method that extracts structured threat behaviors from unstructured OSCTI text. ThreatRaptor also includes a domain-specific query language TBQL for hunting malicious system activities, a query synthesis mechanism that automatically generates TBQL queries, and an efficient query execution engine for searching large-scale audit log data.

Existing intrusion detection methods often suffer from generating an excessive number or poor quality of alerts. To address these issues, Garrido et al. applied machine learning to knowledge graphs to detect unexpected activities in industrial automation systems integrating IT and OT elements [110]. In the area of cyber intelligence support, Wang et al. propose a method to build a cyber attack KG based on CAPCE and CWE and implement it in the graph database Neo4j and present the directional aspects of KG in the area of secure operations, challenges faced by intelligent operations, and technical prospects [122, 123].

The cybersecurity knowledge graph also acts in logical analysis of security policies, filtering false information: Vassilev et al. propose a four-layer framework and use it for validation of the most common security threat scenarios in digital banking and implement a prototype event-driven engine for intelligent graph navigation [124]. Mitra et al. proposed a system that captures and integrates source information with Cyber Threat Intelligence (CTI) by enhancing the existing Cyber Security Knowledge Graph (CSKG) model. The system incorporates an information source graph with CSKG to improve its inference capability, enforcing rules that preserve trusted information and discard the rest [125]. Table 6.3 summarizes the latest applications of knowledge graphs in security.

6.6 Challenges and Future Trends

6.6.1 Challenges to the Cybersecurity Knowledge Graph

Cybersecurity knowledge graph is a technology for representing and managing knowledge in the cybersecurity domain, which can improve the intelligence, automation and visualization of cybersecurity. However, there are some challenges and problems with cybersecurity knowledge graphs, mainly in the following aspects.

Cybersecurity knowledge acquisition and representation

How to extract, integrate and standardize cybersecurity knowledge from multiple sources of heterogeneous data, how to select appropriate models and methods to

Table 6.3 Cybersecurity knowledge application scenarios

Year	Ref.	Application purpose
2020	[112]	Knowledge graph-based attack posture detection
2020	[113]	Network security situational awareness model (KG-NSSA)
2021	[114]	Power IoT terminal security assessment
2021	[110]	Security monitoring
2022	[111]	Preventing cyber attacks
2023	[116]	Automated cyber threat intelligence analysis (K-CTIAA)
2022	[117]	0day attack path prediction
2019	[119]	Generate optimal penetration paths
2022	[120]	Analyzing the tactical behavior of cyber attacks
2022	[107]	Satellite network security defense
2021	[121]	Log-based network threat hunting
2021	[110]	Detection of unexpected activities in industrial automation systems
2021	[123]	DDos flood attacks and multi-stage attacks
2021	[124]	Validation of the most common security threat scenarios in digital banking
2021	[125]	Filtering Cybersecurity Intelligence

represent cybersecurity knowledge, and how to deal with incomplete, inconsistent, uncertain and dynamically changing cybersecurity knowledge. Maintaining data sources related to cybersecurity research is a prerequisite for achieving efficient access to information. Due to the specialized nature of the security field, it is important for the information sources to both cover a wide range of security information and reduce the presence of security irrelevant information.

Construction and update of cybersecurity knowledge graph

How to construct a cybersecurity knowledge graph quickly, accurately and effectively, how to realize real-time updates and maintenance of cybersecurity knowledge graph, how to solve the problems of scale, complexity, and openness of cybersecurity knowledge graph and how to better improve the quality and trustworthiness of the knowledge graph. Recently, there has been related research in improving the quality of cybersecurity knowledge graphs, such as the problem of co-referential disambiguation of cybersecurity entities [126].

Reasoning and analysis of cybersecurity knowledge graph

How to use cybersecurity knowledge graph for deep-level semantic reasoning and analysis, how to support multiple types of query, retrieval, matching and recommendation functions, and how to improve the reasoning efficiency and accuracy of cybersecurity knowledge graph.

Evaluation and application of cybersecurity knowledge graph

How to evaluate the quality, reliability, validity and impact of cybersecurity knowledge graph, how to apply cybersecurity knowledge graph to various scenarios, such as threat intelligence analysis, attack traceability, risk assessment, etc., and how to improve user experience and satisfaction.

6.6.2 Future Trends of Knowledge Graph in Cybersecurity

Knowledge graph is a knowledge representation and management method based on Semantic Web technology, which can integrate structured and unstructured data into a unified, queryable, reasonable and visualized knowledge network. Knowledge graphs have a wide application prospect in the field of cybersecurity and can improve the efficiency and effectiveness of cybersecurity analysis and decision-making. This paper summarizes the development trend of the knowledge graph in the field of cybersecurity in the following aspects.

Knowledge graphs will be combined with other artificial intelligence techniques, such as machine learning, natural language processing, and computer vision, to enable deep mining and intelligent analysis of cybersecurity data. For example, Sleeman et al. [127] use more advanced graph neural network (GNN) methods to extract deeper information and knowledge from cybersecurity knowledge graphs to support more complex cybersecurity tasks.

Moreover, there will be a greater emphasis on interoperability and integration between different knowledge graphs, allowing for the creation of larger, more comprehensive knowledge repositories that can support more complex and sophisticated cybersecurity analysis. This will require the development of standardized data models and knowledge representation formats that can be used across different domains and contexts.

Finally, there will be a growing focus on the development of knowledge graphs that are tailored to specific cybersecurity domains, such as critical infrastructure protection, Internet of Things (IoT) security, and cloud security. This will require the integration of domain-specific knowledge and expertise into the knowledge graph, as well as the development of specialized algorithms and analytical techniques that are optimized for the specific cybersecurity domain.

6.7 Conclusion

In recent years, the research and development of cybersecurity have received wide attention from academia and industry, but its development process faces problems such as discrete data distribution, inaccurate information content, and difficulties in comprehensive intelligence analysis, and the emergence of knowledge graph

provides an effective solution to the above problems. This review comprehensively reviews the key technologies and application scenarios of cybersecurity knowledge graphs. We first outline the basic concepts of cybersecurity knowledge graphs, analyze the basic datasets required to build knowledge graphs, including general-purpose and specialized datasets, and summarize a framework for building them. Then we detail the key techniques for building cybersecurity knowledge graphs, including ontology construction, information extraction, and knowledge inference. Finally, we review the applications of knowledge graphs in cybersecurity and point out the challenges and future development trends of cybersecurity knowledge graphs.

References

1. Kaur, J., Ramkumar, K.R.: The recent trends in cyber security: a review. *J. King Saud Univ.-Comput. Inform. Sci.* **34**(8), 5766–5781 (2022)
2. Sani, M.: Knowledge graph on cybersecurity: a survey (2020)
3. Berners-Lee, T., Hendler, J., Lassila, O.: The semantic web. *Sci. Am.* **284**(5), 34–43 (2001)
4. Singhal, A.: Introducing the knowledge graph: things, not strings. *Official Google Blog* **5**(16), 3 (2012)
5. Chen, X., Jia, S., Xiang, Y.: A review: knowledge reasoning over knowledge graph. *Exp. Syst. Appl.* **141**, 112948 (2020)
6. Bollacker, K., Evans, C., Paritosh, P., et al.: Freebase: a collaboratively created graph database for structuring human knowledge. In: *Proceedings of the 2008 ACM SIGMOD International Conference on Management of Data*, pp. 1247–1250. ACM Press, New York, NY, USA
7. Suchanek, F.M., Kasneci, G., Weikum, G.: Yago: a large ontology from Wikipedia and WordNet. *J. Web Semant.* **6**(3), 203–217 (2008)
8. Auer, S., Bizer, C., Kobilarov, G., et al.: Dbpedia: a nucleus for a web of open data. In: Cruz, I.F., Decker, S., Allemang, D., et al. (eds.) *The Semantic Web: 6th International Semantic Web Conference, 2nd Asian Semantic Web Conference, ISWC 2007+ ASWC 2007*, Busan, Korea, 11–15 Nov. 2007, *Proceedings*, pp. 722–735. Springer, Berlin, Heidelberg
9. Liu, K., Wang, F., Ding, Z., et al.: A review of knowledge graph application scenarios in cyber security (2022). arXiv preprint [arXiv:2204.04769](https://arxiv.org/abs/2204.04769)
10. Ren, Y., Xiao, Y., Zhou, Y., et al.: CSKG4APT: a cybersecurity knowledge graph for advanced persistent threat organization attribution. *IEEE Trans. Knowl. Data Eng.* (2022)
11. CyberSecurity Knowledge graph. Available at https://github.com/HoloLen/CyberSecurity_Knowledge_graph
12. Iannacone, M., Bohn, S., Nakamura, G., et al.: Developing an ontology for cyber security knowledge graphs. In: *Proceedings of the 10th Annual Cyber and Information Security Research Conference*, pp. 1–4 (2015)
13. Noel, S., Harley, E., Tam, K.H., et al.: CyGraph: graph-based analytics and visualization for cybersecurity. In: *Handbook of Statistics*, vol. 35, pp. 117–167. Elsevier (2016)
14. Zhang, K., Liu, J.: Review on the application of knowledge graph in cyber security assessment. *IOP Conf. Ser. Mater. Sci. Eng.* **768**(5), 052103 (2020). IOP Publishing
15. Li, X., Lian, Y., Zhang, H., Huang, K.: Key technologies of cyber security knowledge graph. *Frontiers Data Comput.* **3**(3), 9–18 (2021)
16. Ding, Z., Liu, K., Liu, B., et al.: Survey of cyber security knowledge graph. *J. Huazhong Univ. Sci. Tech. (Natural Science Edition)* **49**(07), 79–91 (2021)
17. Noel, S.: A review of graph approaches to network security analytics. In: *From Database to Cyber Security*, pp. 300–323 (2018)
18. Dong, C., Jiang, B., Lu, Z.G., et al.: Knowledge graph for cyberspace security intelligence: a survey. *J. Cyber Sec.* **5**, 56–76 (2020)

19. Liu, H., Yao, W.J., Che, S., et al.: Classification and application of cyberspace surveying and mapping system. *Inform. Technol. Netw. Sec.* **40**(10), 16–21+28 (2021)
20. MITRE: CTI for MITRE in GitHub (2023). Available at <https://github.com/mitre/cti>
21. CNNVD: CNNVD list (2023). Available at <https://www.cnnvd.org.cn/home/childHome>
22. Kaspersky: Vulnerability (2023). Available at <https://threats.kaspersky.com/en/vulnerability/>
23. Verizon Security Research & Cyber Intelligence Center: The VERIS framework (2023). Available at <http://veriscommunity.net/>
24. TALOS: Talos threat source newsletters (2023). Available at <https://talosintelligence.com>
25. CyberMonitor: APT cybercriminal campaign collections (2022). Available at https://github.com/CyberMonitor/APT_CyberCriminal_Campagin_Collections
26. Kiesling, E., Ekelhart, A., Kurniawan, K., et al.: The SEPSSES knowledge graph: an integrated resource for cybersecurity. In: *International Semantic Web Conference*, pp. 198–214. Springer (2019)
27. Wang, D.: CyberSecurity Knowledge graph (2020). Available at https://github.com/HoloLen/CyberSecurity_Knowledge_graph
28. Lal, R.: Information Extraction of Security related entities and concepts from unstructured text (2013)
29. Bridges, R.A., Jones, C.L., Iannacone, M.D., et al.: Automatic labeling for entity extraction in cyber security (2013). arXiv preprint [arXiv:1308.4941](https://arxiv.org/abs/1308.4941)
30. Lim, S.K., Muis, A.O., Lu, W., et al.: Malwaretextdb: a database for annotated malware articles. In: *Proceedings of the 55th Annual Meeting of the Association for Computational Linguistics (Volume 1: Long Papers)*, pp. 1557–1567 (2017)
31. Sun, N.: CWE-knowledge-graph-based-Twitter-data-analysis-for-cybersecurity (2019). Available at <https://github.com/nansunsun/CWE-Knowledge-Graph-Based-Twitter-Data-Analysis-for-Cybersecurity>
32. Kim, G., Lee, C., Jo, J., et al.: Automatic extraction of named entities of cyber threats using a deep Bi-LSTM-CRF network. *Int. J. Mach. Learn. Cybern.* **11**(10), 2341–2355 (2020)
33. Sarhan, I., Spruit, M.: Open-cykg: an open cyber threat intelligence knowledge graph. *Knowl.-Based Syst.* **233**, 107524 (2021)
34. Rastogi, N., Dutta, S., Christian, R., et al.: Predicting malware threat intelligence using KGs (2021). arXiv preprint [arXiv:2102.05571](https://arxiv.org/abs/2102.05571)
35. Kurniawan, K., Ekelhart, A., Kiesling, E.: An ATT&CK-KG for linking cybersecurity attacks to adversary tactics and techniques (2021)
36. Li, Z., Zeng, J., Chen, Y., et al.: AttacKG: constructing technique knowledge graph from cyber threat intelligence reports. In: *Computer Security Copenhagen, Denmark, 26–30 Sept. 2022, Proceedings, Part I*. Springer International Publishing, Cham (2022)
37. Hanks, C., Maiden, M., Ranade, P., et al.: Recognizing and extracting cybersecurity entities from text. In: *International Conference on Machine Learning Workshop on Machine Learning for Cybersecurity* (2022)
38. Yang, Y.J., Xu, B., Hu, J.W., Tong, M.H., Zhang, P., Zheng, L.: Accurate and efficient method for constructing domain knowledge graph. *Ruan Jian Xue Bao/J. Softw.* **29**(10), 2931–2947 (2018)
39. Wikipedia: Ontology (2023). Available at <https://en.wikipedia.org/wiki/Ontology>
40. Khadir, A.C., Aliane, H., Guessoum, A.: Ontology learning: grand tour and challenges. *Comput. Sci. Rev.* **39**, 100339 (2021)
41. Manola, F., Miller, E., McBride, B.: RDF primer. w3c recommendation **10**(1–107), 6 (2004)
42. McBride, B.: The resource description framework (RDF) and its vocabulary description language RDFS. In: *Handbook Ontologies*, pp. 51–65 (2004)
43. McGuinness, D.L., Van Harmelen, F.: OWL web ontology language overview. w3C recommendation **10**(10), 2004 (2004)
44. Mavroeidis, V., Bromander, S.: Cyber threat intelligence model: an evaluation of taxonomies, sharing standards, and ontologies within cyber threat intelligence. In: *Proceedings of the 2017 European Intelligence and Security Informatics Conference (EISIC)*, pp. 91–98. IEEE, Athens (2017)

45. Ding, Y., Wu, R., Zhang, X.: Ontology-based knowledge representation for malware individuals and families. *Comput. Secur.* **87**, 101574 (2019)
46. Gao, J., Wang, A.: Research on ontology-based network threat intelligence analysis technology. *Comput. Eng. Appl.* **56**(11), 112–117 (2020)
47. Liu, J., Li, Y., Duan, H., et al.: Knowledge graph construction techniques. *J. Comput. Res. Dev.* **53**(3), 582–600 (2016)
48. Syed, Z., Padia, A., Finin, T., et al.: UCO: a unified cybersecurity ontology. In: *Workshops at the Thirtieth AAAI Conference on Artificial Intelligence* (2016)
49. Cyber Threat Intelligence (2023). Available at <https://oasis-open.github.io/cti-documentation/>
50. MITRE ATT&CK (2023). Available at <https://attack.mitre.org>
51. Unified-Cybersecurity-Ontology (2019). Available at <https://github.com/Ebiquity/Unified-Cybersecurity-Ontology>
52. Cyber Intelligence Ontology (2015). Available at <https://github.com/daedafusion/cyber-ontology>
53. Jeffrey, U., John, P., Anupam, J., et al.: A target centric ontology for intrusion detection. In: *The IJCAI-03 Workshop on Ontologies and Distributed Systems*, pp. 47–58. IJCAI, Acapulco (2004)
54. Grégio, A., Bonacin, R., Nabuco, O., et al.: Ontology for malware behavior: a core model proposal. In: *2014 IEEE 23rd International WETICE Conference*, pp. 453–458. IEEE (2014)
55. Qin, S., Chow, K.P.: Automatic analysis and reasoning based on vulnerability knowledge graph. In: *Cyberspace Data and Intelligence, and Cyber-Living, Syndrome, and Health*, pp. 3–19. Springer, Singapore (2019)
56. Philpot, M.: *Cyber Intelligence Ontology* (2015). <https://github.com/daedafusion/cyber-ontology>, 18 Oct.
57. Gao, J.B.: *Research on ontology model and its application in information security evaluation*. Shanghai Jiao Tong University (2015)
58. Simmonds, A., Sandilands, P., van Ekert, L.: An ontology for network security attacks. In: *Applied Computing*, pp. 317–323. Springer (2004)
59. Razzaq, A., Anwar, Z., Ahmad, H.F., et al.: Ontology for attack detection: an intelligent approach to web application security. *Comput. Secur.* **45**(S1), 124–146 (2014)
60. Grigoriadis, C., Berzovitis, A.M., Stelios, I., et al.: A cybersecurity ontology to support risk information gathering in cyber-physical systems. In: *Computer Security. ESORICS 2021 International Workshops: CyberICPS, SECPRE, ADIoT, SPOSE, CPS4CIP, and CDT&SECOMANE*, pp. 23–39, Darmstadt, Germany, 4–8 Oct. Springer International Publishing, Cham (2022)
61. Hooi, E.K.J., Zainal, A., Maarof, M.A., et al.: TAGraph: knowledge graph of threat actor. In: *International Conference on Cybersecurity (ICoCSec)*, pp. 76–80. IEEE (2019)
62. Kaloroumakis, P.E., Smith, M.J.: *Toward a knowledge graph of cybersecurity countermeasures*, p. 11. The MITRE Corporation (2021)
63. Wang, Z., Zhu, H., Liu, P., et al.: Social engineering in cybersecurity: a domain ontology and knowledge graph application examples. *Cybersecurity* **4**, 1–21 (2021)
64. Li, J., Sun, A., Han, J., et al.: A survey on deep learning for named entity recognition. *IEEE Trans. Knowl. Data Eng.* **99**, 1–11 (2020)
65. Zhang, S.Z., Luo, H., Fang, B.X.: Regular expressions matching for network security. *J. Softw.* **22**(8), 1838–1854 (2011)
66. McNeil, N., Bridges, R.A., Iannacone, M.D., et al.: Pace: pattern accurate computationally efficient bootstrapping for timely discovery of cyber-security concepts. In: *Machine Learning and Applications (ICMLA)*, pp. 60–65 (2013)
67. Kushner, S.: Ontology-driven data semantics discovery for CyberSecurity. In: *Practical Aspects of Declarative Languages (PADL)*, pp. 1–16 (2015)
68. Liao, X., Yuan, K., Li, Z., et al.: Acing the IOC game: toward automatic discovery and analysis of open-source cyber threat intelligence. In: *ACM Sigsac Conference on Computer and Communications Security (ACM SIGSAC)*, pp. 755–766 (2016)

69. Georgescu, T.M.: Natural language processing model for automatic analysis of cybersecurity-related documents. *Symmetry* **12**(3), 20–35 (2020)
70. Ritter, A., Wright, E., Casey, W., et al.: Weakly supervised extraction of computer security events from Twitter. In: *The 24th International Conference on World Wide Web*, pp. 896–905 (2015)
71. Joshi, A., Lal, R., Finin, T., et al.: Extracting cybersecurity related linked data from tex. In: *2013 IEEE Seventh International Conference on Semantic Computing*, pp. 252–259 (2013)
72. Lal, R.: *Information extraction of cyber security related terms and concepts from unstructured text*. University of Maryland, Baltimore County (2013)
73. Mulwad, V., Li, W., Joshi, A., et al.: Extracting information about security vulnerabilities from web text. In: *2011 IEEE/WIC/ACM International Conferences on Web Intelligence and Intelligent Agent Technology*, pp. 257–260 (2011)
74. Collobert, R., Weston, J., Bottou, L., et al.: Natural language processing (almost) from scratch. *J. Mach. Learn. Res.* **12**(ARTICLE), 2493–2537 (2011)
75. Graves, A., Graves, A.: Long short-term memory. In: *Supervised Sequence Labelling with Recurrent Neural Networks*, pp. 37–45 (2012)
76. Peng, N., Dredze, M.: Named entity recognition for Chinese social media with jointly trained embeddings. In: *The 2015 Conference on Empirical Methods in Natural Language Processing*, pp. 548–554 (2015)
77. Qin, Y., Shen, G., Zhao, W., et al.: A network security entity recognition method based on feature template and CNN-BiLSTM-CRF. *Frontiers Inform. Technol. Electron. Eng.* **20**(6), 872–884 (2019)
78. Gasmı, H., Bouras, A., Laval, J.: LSTM recurrent neural networks for cybersecurity named entity recognition. *ICSEA* **11**, 2018 (2018)
79. Yu, H., Zhang, N., Deng, S., et al.: Bridging text and knowledge with multi-prototype embedding for few-shot relational triple extraction (2020). arXiv preprint [arXiv:2010.16059](https://arxiv.org/abs/2010.16059)
80. Ranade, P., Piplai, A., Joshi, A., et al.: Cybert: contextualized embeddings for the cybersecurity domain. In: *2021 IEEE International Conference on Big Data (Big Data)*, pp. 3334–3342. IEEE (2021)
81. Chen, Y.X., Ding, J., Li, D., et al.: Joint BERT model based cybersecurity named entity recognition. In: *2021 The 4th International Conference on Software Engineering and Information Management*, pp. 236–242 (2021)
82. Fisher, J., Vlachos, A.: Merge and label: a novel neural network architecture for nested NER (2019). arXiv preprint [arXiv:1907.00464](https://arxiv.org/abs/1907.00464)
83. Jones, C.L., Bridges, R.A., Huffer, K.M.T., et al.: Towards a relation extraction framework for cyber-security concepts. In: *the 10th Annual Cyber and Information Security Research Conference*, pp. 1–4 (2015)
84. Liu, C.Y., Sun, W.B., Chao, W.H., et al.: Convolution neural network for relation extraction. In: *9th International Conference on Advanced Data Mining and Applications (ADMA)*, China, pp. 231–242, Hangzhou (2013)
85. Zhang, D., Wang, D.: Relation classification via recurrent neural network (2015). arXiv preprint [arXiv:1508.01006](https://arxiv.org/abs/1508.01006)
86. Zhou, P., Shi, W., Tian, J., et al.: Attention-based bidirectional long short-term memory networks for relation classification. In: *The 54th Annual Meeting of the Association for Computational Linguistics (Volume 2: Short papers)*, pp. 207–212 (2016)
87. Socher, R., Huval, B., Manning, C.D., et al.: Semantic compositionality through recursive matrix-vector spaces. In: *The 2012 Joint Conference on Empirical Methods in Natural Language Processing and Computational Natural Language Learning*, pp. 1201–1211 (2012)
88. Mintz, M., Bills, S., Snow, R., et al.: Distant super-vision for relation extraction without labeled data. In: *The International Joint Conference on ACL Association for Computational Linguistics*, pp. 1003–1011. Association for Computational Linguistics, Singapore (2009)
89. Feng, J.: Reinforcement learning for relation classification from noisy data. In: *The Thirty-Second AAAI Conference on Artificial Intelligence*, pp. 5779–5786. Louisiana, New Orleans (2018)

90. Han, X., Zhu, H., Yu, P., et al.: FewRel: a large-scale supervised few-shot relation classification dataset with state-of-the-art evaluation. In: The 2018 Conference on Empirical Methods in Natural Language Processing, pp. 4803–4809. Association for Computational Linguistics, Brussels (2018)
91. Zeng, D., Liu, K., Chen, Y., et al.: Distant supervision for relation extraction via piecewise convolutional neural networks. In: The 2015 Conference on Empirical Methods in Natural Language Processing, pp. 1753–1762 (2015)
92. Lin, Y., Shen, S., Liu, Z., et al.: Neural relation extraction with selective attention over instances. In: The 54th Annual Meeting of the Association for Computational Linguistics (Volume 1: Long Papers), pp. 2124–2133 (2016)
93. Qin, P., Xu, W.Y., Wang, W.Y.: Robust distant supervision relation extraction via deep reinforcement learning (2018). arXiv preprint [arXiv:1805.09927](https://arxiv.org/abs/1805.09927)
94. Gupta, M., Abdelsalam, M., Khorsandroo, S., et al.: Security and privacy in smart farming: challenges and opportunities. *IEEE Access* **8**, 34564–34584 (2020)
95. Pingle, A., Piplai, A., Mittal, S., et al.: Relext: relation extraction using deep learning approaches for cybersecurity knowledge graph improvement. In: The 2019 IEEE/ACM International Conference on Advances in Social Networks Analysis and Mining, pp. 879–886 (2019)
96. Satyapanich, T., Ferraro, F., Finin, T.: Casie: extracting cybersecurity event information from text. In: The AAAI Conference on Artificial Intelligence, vol. 34(05), pp. 8749–8757 (2020)
97. Agrawal, G., Deng, Y., Park, J., et al.: Building knowledge graphs from unstructured texts: applications and impact analyses in cybersecurity education. *Information* **13**(11), 526 (2022)
98. Han, Z., Li, X., Liu, H., et al.: Deepweak: reasoning common software weaknesses via knowledge graph embedding. In: 2018 IEEE 25th International Conference on Software Analysis, Evolution and Reengineering (SANER), pp. 456–466. IEEE (2018)
99. Qin, S., Chow, K.P.: Automatic analysis and reasoning based on vulnerability knowledge graph. In: Cyberspace Data and Intelligence, and Cyber-Living, Syndrome, and Health: International 2019 Cyberspace Congress, CyberDI and CyberLife, Beijing, China, 16–18 Dec. 2019, Proceedings, Part I 3, pp. 3–19. Springer, Singapore (2019)
100. van Gerven, M.A.J., Bohte, S.M.: Artificial neural networks as models of neural information processing. *Frontiers Comput. Neurosci.* (2017)
101. Saiping, G., Xiaolong, J., Yantao, J., et al.: Knowledge graph oriented knowledge inference methods: a survey. *J. Softw.* **29**(10), 2966–2994 (2018)
102. Yu, L., Yu, L.: OWL: web ontology language. In: A Developer’s Guide to the Semantic Web, pp. 155–239 (2011)
103. Wang, R., Azab, A.M., Enck, W., et al.: Spoke: scalable knowledge collection and attack surface analysis of access control policy for security enhanced android. In: The 2017 ACM on Asia Conference on Computer and Communications Security, pp. 612–624 (2017)
104. Mittal, S., Das, P.K., Mulwad, V., et al.: Cybertwitter: using Twitter to generate alerts for cybersecurity threats and vulnerabilities. In: 2016 IEEE/ACM International Conference on Advances in Social Networks Analysis and Mining (ASONAM), pp. 860–867. IEEE (2016)
105. Qamar, S., Anwar, Z., Rahman, M.A., et al.: Data-driven analytics for cyber-threat intelligence and information sharing. *Comput. Secur.* **67**, 35–58 (2017)
106. Mohsin, M., Anwar, Z., Zaman, F., et al.: IoTChecker: a data-driven framework for security analytics of Internet of Things configurations. *Comput. Secur.* **70**, 199–223 (2017)
107. Yi, J., Liu, B., Yao, L.: Satellite cyber situational understanding based on knowledge reasoning. *Syst. Eng. Electron.* (2022)
108. Bordes, A., Usunier, N., Garcia-Duran, A., et al.: Translating embeddings for modeling multi-relational data. In: Advances in Neural Information Processing Systems, p. 26 (2013)
109. Das, R., Zaheer, M., Reddy, S.: Chains of reasoning over entities, relations, and text using recurrent neural networks. In: Proceedings of the 15th Conference of the European Chapter of the Association for Computational Linguistics: Volume 1, Long Papers, pp. 132–141 (2017)
110. Garrido, J.S., Dold, D., Frank, J.: Machine learning on knowledge graphs for context-aware security monitoring. In: 2021 IEEE International Conference on Cyber Security and Resilience (CSR), pp. 55–60. IEEE (2021)

111. Yin, J., Tang, M.J., Cao, J., et al.: Knowledge-driven cybersecurity intelligence: software vulnerability co-exploitation behaviour discovery. *IEEE Trans. Ind. Inform.* (2022)
112. Chen, J.: Design and implementation of network attack situation detection system based on knowledge graph. Beijing University of Posts and Telecommunications (2020)
113. Wang, Y.: Research and implementation of NSSA technology based on knowledge graph. University of Electronic Science and Technology of China (2020)
114. Pang, T., Song, Y., Shen, Q.: Research on security threat assessment for power IOT term terminal based knowledge graph. In: 2021 IEEE 5th Information Technology, Networking, Electronic and Automation Control Conference (ITNEC), pp. 1717–1721. IEEE (2021)
115. Chen, Z., Dong, N., Zhong, S., et al.: Research on the power network security vulnerability expansion attack graph based on knowledge map. *Inform. Technol.* **46**(02), 30–35 (2022)
116. Li, Z.X., Li, Y.J., Liu, Y.W., et al.: K-CTIAA: automatic analysis of cyber threat intelligence based on a knowledge graph. *Symmetry* **15**(2), 337 (2023)
117. Sun, C., Hu, H., Yang, Y., et al.: Prediction method of 0 day attack path based on cyber defense knowledge graph. *Chin. J. Netw. Inform. Sec.* **8**(01), 151–166 (2022)
118. Liu, F., Li, K., Song, F.: Distributed DDoS attacks malicious behavior knowledge base construction. *Telecommun. Sci.* **37**(11), 17–32 (2021). 111
119. Wang, S., Wang, J.H., Tang, G.M., et al.: Intelligent and efficient method for optimal penetration path generation. *J. Comput. Res. Dev.* **56**, 929–941 (2019)
120. Kurniawan, K., Ekelhart, A., Kiesling, E., et al.: KRYSTAL: knowledge graph-based framework for tactical attack discovery in audit data. *Comput. Secur.* **121**, 102828 (2022)
121. Gao, P., Shao, F., Liu, X., et al.: Enabling efficient cyber threat hunting with cyber threat intelligence. In: 2021 IEEE 37th International Conference on Data Engineering (ICDE), pp. 193–204. IEEE (2021)
122. NEFOCUS: Security Knowledge Graph Technology White Paper (2022). https://www.nsfocus.com.cn/html/2022/92_0105/166.html
123. Wang, W., Zhou, H., Li, K., et al.: Cyber-attack behavior knowledge graph based on CAPEC and CWE towards 6G. In: International Symposium on Mobile Internet Security, pp. 352–364. Springer (2021)
124. Vassilev, V., Sowinski-Mydlarz, V., Gasiorowski, P., et al.: Intelligence graphs for threat intelligence and security policy validation of cyber systems. In: Proceedings of International Conference on Artificial Intelligence and Applications, pp. 125–139. Springer (2021)
125. Mitra, S., Piplai, A., Mittal, S., et al.: Combating fake cyber threat intelligence using provenance in cybersecurity knowledge graphs. In: 2021 IEEE International Conference on Big Data (Big Data), pp. 3316–3323. IEEE (2021)
126. Liu, Z., Su, H., Wang, N., et al.: Coreference resolution for cybersecurity entity: towards explicit, comprehensive cybersecurity knowledge graph with low redundancy. In: 18th EAI International Conference on Security and Privacy in Communication Networks (SecureComm 2022), pp. 89–108. virtual Event, October 2022, Proceedings. Springer Nature Switzerland, Cham
127. Sleeman, J., Finin, T., Halem, M.: Understanding cybersecurity threat trends through dynamic topic modeling. *Frontiers Big Data* **4**, 601529 (2021)

Chapter 7

Active Disturbance Rejection Control of Hypersonic Vehicle Based on Q-Learning Algorithm



Jie Yan and Liang Zhang

Abstract The control of hypersonic vehicle is characterized by strong coupling, large parameter fluctuation, nonlinearity and uncertainty. To solve the above technical difficulties, active disturbance rejection control (ADRC) is presented to track the expected pitch angle of hypersonic vehicles. Due to the problem that extended state observer (ESO) and nonlinear state error feedback (NLSEF) parameters in ADRC need to be debugged many times, this paper develops a Q-learning algorithm to adjust the optimal parameters of ADRC within a certain range. Simulation results indicate that the proposed control strategy has a better tracking performance.

Keywords Hypersonic vehicle · Active disturbance rejection control · Q-learning · Reinforcement learning

7.1 Introduction

The hypersonic vehicle is a space transportation vehicle with a speed of more than Mach 5. The earliest research in this field can be traced back to the 1940s, when the concept of this type of vehicle was first proposed by the United States. Since its high speed, stealth, and rapid response, it has become an important research object in the field of aviation in various countries in recent years.

For the control of hypersonic vehicles, there are characteristics of strong coupling, fast time change, large parameter fluctuation, nonlinearity and nondeterminism. Numerous research projects have been carried out at home and abroad. Schmidt [1] performed control configurations for heating problems and trajectory performance problems in the control system of hypersonic vehicles. Hu [2] adopted the approach of nonlinear adaptive control for the hypersonic vehicle's downward pressure segment attitude control, which solved the influence of aerodynamic dynamic pressure on the stability and accuracy of the attitude control system. Hu and Liu

J. Yan · L. Zhang (✉)

School of Aeronautics and Astronautics, Sun Yat-Sen University, Shenzhen 518107, China

e-mail: zhangliang8@mail.sysu.edu.cn

[3] adopted a fuzzy adaptive attitude control approach with fuzzy approximation to solve the coupling uncertainty in the attitude angle dynamics. Qi et al. [4] adopted an ADRC-PID control approach and introduced a tracking differentiator to investigate the pitch attitude control of hypersonic vehicles under strong disturbances. Pei et al. [5] designed ADRC based on trajectory linearization control for attitude control of hypersonic vehicles. Ping et al. [6] used neural network PID control to effectively suppress the effects of changes in aerodynamic parameters of hypersonic vehicles. However, there are some problems in the above research, for example, the parameter adjustment of the control method is a difficult problem, which requires the experimental personnel to artificially debug the experimental parameters and requires repeated trials to cope with different environments. Therefore, it is worthwhile to design a machine training method that allows the controller parameters to be adaptively adjusted to satisfy the control requirements in different environments.

Q-learning [7], as a reinforcement learning algorithm, is selected to obtain the suitable parameters under a large number of machine training by designing a reasonable reward mechanism. Hao et al. [8] designed a novel algorithm called dynamic and fast Q-learning to solve the path planning problem for USV in partially known maritime environments. Kankashvar et al. [9] presented a novel approach based on Q-learning for spacecraft formation flying reconfiguration tracking problems. In this paper, Q-learning is applied in nonlinear ADRC to achieve the pitch channel attitude control of the hypersonic vehicle.

This paper is organized as follows. In Sect. 7.2, the attitude dynamics of the hypersonic vehicle is established. In Sect. 7.3, this essay proposes the design methodology of ADRC, including tracking differentiator, extended state observer and nonlinear state error feedback control law. The ADRC controller parameters are adapted using the Q-learning algorithm in Sect. 7.4. Finally, simulation results and analysis of ADRC, Q-ADRC and PID are presented in Sect. 7.5.

7.2 Pitch Channel Dynamics Model of Hypersonic Vehicles

The dynamics model of the pitch channel of the hypersonic vehicle is established as follows [10]:

$$\begin{cases} \dot{V} = \frac{P \cos \alpha - X}{m} - g \sin \theta \\ \dot{\theta} = \frac{P \sin \alpha + Y}{mV} + \cos \theta \left(\frac{V}{R_c + y} - \frac{g}{V} \right) \\ \dot{\omega}_z = \frac{M_z}{I_z} \\ \dot{\vartheta} = \omega_z \\ \dot{x} = V \cos \theta \left(\frac{R_c}{R_c + y} \right) \\ \dot{y} = V \sin \theta \\ \dot{m} = -m_c \\ \alpha = \vartheta - \theta \\ \delta_e = f(\bullet) \end{cases} \quad (7.1)$$

where V , P , α , m , X , Y denotes the hypersonic vehicle speed, the engine thrust, the angle of attack, the mass, the air drag and the vehicle lift, respectively. g is the gravitational acceleration, θ , ϑ , x , y represents the ballistic inclination angle, the pitch angle, the sailing distance and the altitude, respectively. R_c , ω_z , M_z , I_z denotes the earth radius, pitch speed, the pitch moment and the pitch moment of inertia. m_c denotes the fuel consumption rate, and δ_e is the elevator deflection angle.

7.3 ADRC Controller Design for the Pitch Channel of Hypersonic Vehicle

7.3.1 Pitch Channel State Equation

For pitch angle control of a hypersonic vehicle, Eq. (7.1) can be rewritten as:

$$\begin{cases} \alpha = \vartheta - \gamma \\ \dot{\vartheta} = r \\ \dot{r} = \frac{M_z}{I_z} \\ M_z = \frac{1}{2} \rho V^2 S [CM(\alpha) + CM(\delta_e) + CM(r)] \end{cases} \quad (7.2)$$

where ϑ , r denote the pitch angle and pitch angular velocity of the vehicle, respectively. M_z , I_z are the pitch moment and pitch rotational inertia, respectively. S , δ_e denote the reference aerodynamic area and rudder deflection angle, respectively [11].

7.3.2 Design of ADRC Controller

The main components of the self-turbulent controller are the tracking differentiator (TD), the extended state observer (ESO), and the nonlinear state error feedback control law (NLSEF) [12]. TD generates a transition signal and a differential of the

transition signal. ESO will observe the state variables and system disturbances and transfer the results to the control law to obtain the desired control commands [13]. For the attitude control problem of the hypersonic vehicle studied in this paper, ADRC can solve the problem of rapid recovery of the vehicle attitude to the steady state under the external disturbance.

A. Design of TD

The tracking differentiator in this paper is developed as follows:

$$\begin{cases} \dot{x}_1 = x_2 \\ \dot{x}_2 = u \\ u = fhan(x_1, x_2, r, h) \end{cases} \quad (7.3)$$

where $fhan(\bullet)$ is defined as

$$\begin{cases} d = rh^2 \\ a_0 = hx_2 \\ y = x_1 + a_0 \\ a_1 = \sqrt{d(d + 8|y|)} \\ a_2 = a_0 + \text{sign}(y)(a_1 - d)/2 \\ fsg(x, d) = (\text{sign}(x + d) - \text{sign}(x - d))/2 \\ a = (a_0 + y - a_2)fsg(y, d) + a_2 \\ fhan = fsg(a, d)(r\text{sign}(a) - r\frac{a}{d}) - r\text{sign}(a) \end{cases} \quad (7.4)$$

where r is the speed factor which will affect the speed of convergence. h is the integral step size [14].

B. Design of ESO

According to Eqs. (7.1) and (7.2), define $x_1 = \vartheta$, $x_2 = \dot{\vartheta} = r$, and define the total perturbation $f(x_2, x_2, \delta_e)$ as a new state variable x_3 , then the system can be expanded into a new system as follows:

$$\begin{cases} \dot{x}_1 = x_2 \\ \dot{x}_2 = x_3 + b\delta_e \\ \dot{x}_3 = g \end{cases} \quad (7.5)$$

where g is the differential of the total disturbance.

We can design an extended state observer in Eq. (7.6) to observe the state variables of the vehicle and the total disturbance of the system [15].

$$\begin{cases} e = z_1 - \vartheta \\ \dot{z}_1 = z_2 - \beta_1 e \\ \dot{z}_2 = z_3 - \beta_1^2 |e|^{\frac{1}{2}} \text{sign}(e) + bu \\ \dot{z}_3 = -\beta_2 |e|^{\frac{1}{4}} \text{sign}(e) \end{cases} \quad (7.6)$$

where e denotes the pitch angle error of the vehicle. z_1, z_2, z_3 are the estimated value of the state variable x_1, x_2, x_3 , and β_1, β_2 is the parameter of the expansion state observer.

C. Design of NLSEF

NLSEF is a method of linearizing system. In this system, the nonlinear function is eliminated by nonlinear feedback in a system with model, thus the system is transformed into a series integrator type system. The specific control law is designed as follows [16]:

$$\begin{cases} e_1 = v_1 - z_1 \\ e_2 = v_2 - z_2 \\ u_0 = \beta_{01}fal(e_1, \alpha, \delta) + \beta_{02}fal(e_2, \alpha, \delta) \end{cases} \quad (7.7)$$

The final control command is presented as follows:

$$u = u_0 - z_3/b \quad (7.8)$$

According to the above equations, it can be seen that the parameter will directly affect the performance of the controller.

7.4 Q-Learning Algorithm for Attitude Controller Parameter Tuning

7.4.1 Q-Learning Theory

The Q-learning algorithm is a “semi-supervised” machine learning algorithm that learns from a dataset or trains from the environment in advance based on the input data and analyzes the results of the training. In this algorithm, there is an agent-like “Q” role, which will select actions according to the current system state. It will select actions according to the current system state and reward or punish the “agent Q” according to the results of the actions. It means that “Q” is encouraged to continue to move in the direction of the goal. Getting a penalty means that its behavior may be deviating from the goal and needs to find the optimal path direction. In addition, in order to keep “Q” from falling into a cycle of local optimality, “Q” is given a certain curiosity to explore new and better paths. Finally, “Q” becomes a mature “agent” to guide the actual problem and find the best solution [17].

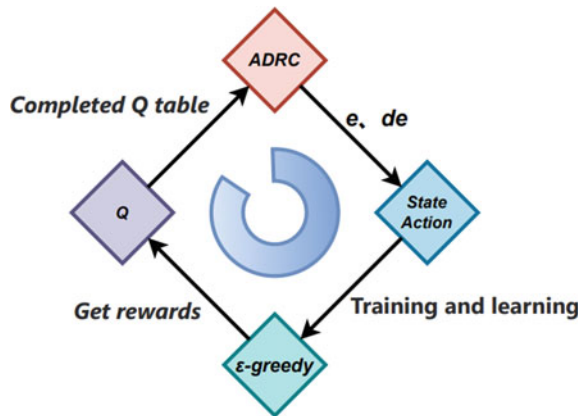
7.4.2 The Design Process of Q-learning Algorithm

The Q-learning algorithm can help us quickly determine the hypersonic vehicle attitude controller parameters. The algorithm will make the controller parameters have the ability to adaptively adjust when the vehicle encounters external disturbances. The pitch angle error of the vehicle and the error change rate are used as the state variables in the Q-learning training process. Each combination of parameters in the controller will be an action in the Q-learning training process. The Q will obtain the reward and punishment of each step action according to the state variables. Finally, through multiple training to obtain the table, the aircraft will be able to achieve optimal control through the trained Q table [18]. The specific steps are given as follows in Fig. 7.1.

1. The pitch angle error of the aircraft and the rate of change of the error are monitored in real time.
2. The values of e and \dot{e} are divided into A and B intervals. They represent the state of the system. They are used as e and \dot{e} to develop performance indicators to judge the performance of the controller.
3. There are $A*B$ possibilities for determining the combination of system states (e, \dot{e}).
4. Determine the number of actions of the system. There are four parameters $M = \{\beta_1, \beta_2, \beta_{01}, \beta_{02}\}$ that the controller needs to control.
5. The $\epsilon - greedy$ strategy is used to perform the selection of greedy behavior in order to keep Q from falling into a kind of local optimum loop and to give the machine some curiosity during the training process. The $\epsilon - greedy$ strategy is developed as follows:

$$Action = \begin{cases} \arg \max_{a \in A} \hat{Q}(a), & p < \epsilon \\ R \text{ and } \hat{Q}(a), & p < \epsilon \end{cases} \quad (7.9)$$

Fig. 7.1 The design process of Q-learning algorithm



where Q denotes the trained Q-table, p is a random number from 0 to 1, ε is the set greedy parameter.

6. The parameters selected in step 5 are applied to the controller. The action is given certain incentives and penalties based on the values returned by the feedback.

$$\begin{cases} J = \sum_{k=t}^{k-i+100} e^2(k)/100 \\ R = \begin{cases} 1, & J \leq \lambda \\ -1, & J > \lambda \end{cases} \end{cases} \quad (7.10)$$

where J is a performance function and λ is a set parameter, both of which are used to determine the controller performance under certain behaviors.

7. Set the number of training sessions, start training, and finally obtain the Q table.
8. The trained table is used to guide the parameter setting of the hypersonic vehicle ADRC controller.

7.4.3 Design of Q-Algorithm Behavior and State

The value range of pitch angle error is set to $(-1, 1)$, and the interval is divided into 7 parts, that is, $A = 7$, and the value range of change rate is set to $(-500, 500)$, and the interval is also divided into 7 parts, $B = 7$, so the table has a total of $A*B = 49$ states as shown in Table 7.1.

In this paper, the control parameters to be rectified by the controller are $M_1 = \{\beta_1, \beta_2\}$, $M_2 = \{\beta_{01}, \beta_{02}\}$, where $\beta_1 \in [1, 41]$, $\beta_2 \in [1, 41]$, $\beta_{01} \in [90, 130]$, $\beta_{02} \in [1, 41]$. The two groups M_1, M_2 are calculated separately to obtain Q_1, Q_2 .

As a result, the table should be a matrix of 1600×49 and the expression of the table is

Table 7.1 State table

e	\dot{e}						
	$[-500, -150)$	$[-150, -50)$	$[-50, -10)$	$[-10, 10)$	$[10, 50)$	$[50, 150)$	$[150, 500]$
$[-1, -0.5)$	1	2	3	4	5	6	7
$[-0.5, -0.3)$	8	9	10	11	12	13	14
$[-0.3, -0.05)$	15	16	17	18	19	20	21
$[-0.05, 0.05)$	22	23	24	25	26	27	28
$[0.05, 0.03)$	29	30	31	32	33	34	35
$[0.3, 0.5)$	36	37	38	39	40	41	42
$[0.5, 1]$	43	44	45	46	47	48	49

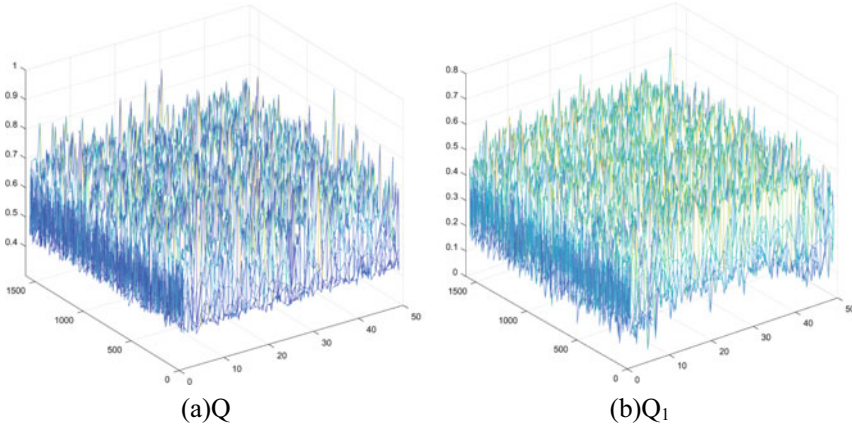


Fig. 7.2 Trained Q and Q_1

$$Q = \begin{bmatrix} Q_1(s, a) & \dots & Q_{49}(s, a) \\ \vdots & & \vdots \\ Q_{1551}(s, a) & \dots & Q_{1600}(s, a) \end{bmatrix} \quad (7.11)$$

The number of training times is set to 100,000, and the completed training table is obtained, which can be used to guide the selection of parameters for the controller. The results are shown in Fig. 7.2.

7.5 Simulation Test

To verify the effectiveness of the proposed algorithm in this paper, this simulation assumes that the hypersonic vehicle has entered the level flight segment. The pitch angle is 0° . It receives an input signal that adjusts the pitch angle of the vehicle to 5° and resumes the level flight command at the 10 s. To verify the performance of Q-ADRC, the conventional ADRC and PID controllers are selected for comparison, and the specific parameters are designed as shown in Table 7.2.

The external disturbance is added and can be simulated as a sine disturbance, there is

$$w(t) = 0.1 \sin(t) \quad (7.12)$$

Simulation results are shown in Fig. 7.3.

From the Fig. 7.3, it can be seen that maximum overshoot of the pitch angle of Q-ADRC is about 0.3° (Fig. 7.4). The convergence time is about 11 s. Moreover,

Table 7.2 Parameter design

Parameter	Value
$\{\beta_1, \beta_2\}(ADRC)$	{20,20}
$\{\beta_{01}, \beta_{02}\}(ADRC)$	{100,20}
Kp	5
Ki	0.8
Kd	1
$\{\beta_1, \beta_2\}(Q - ADRC)$	~
$\{\beta_{01}, \beta_{02}\}(Q - ADRC)$	~
δ	0.01
α	0.75

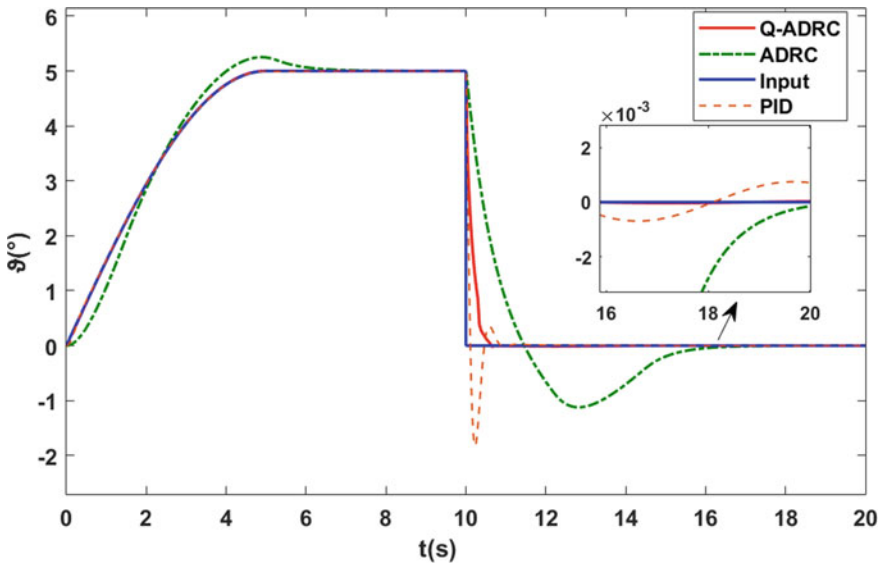


Fig. 7.3 The response of pitch angle

the steady-state error is approximately -0.001° . ADRC and Q-ADRC have smaller rudder declination changes than PID. Compared with PID and ADRC, the rudder declination angle of Q-ADRC will keep changing all the time. The overshoot is significantly reduced and the regulation time is optimized. It demonstrates that the addition of the Q algorithm can improve the performance of the controller.

As shown in Fig. 7.5, it can be seen that the controller parameters under the Q algorithm are no longer static when aircraft receives the command to resume level flight near 10 s. They will adjust the control strategy in real time according to the Q table trained in advance to complete the command as soon as possible. Therefore, the robustness of the controller is improved.

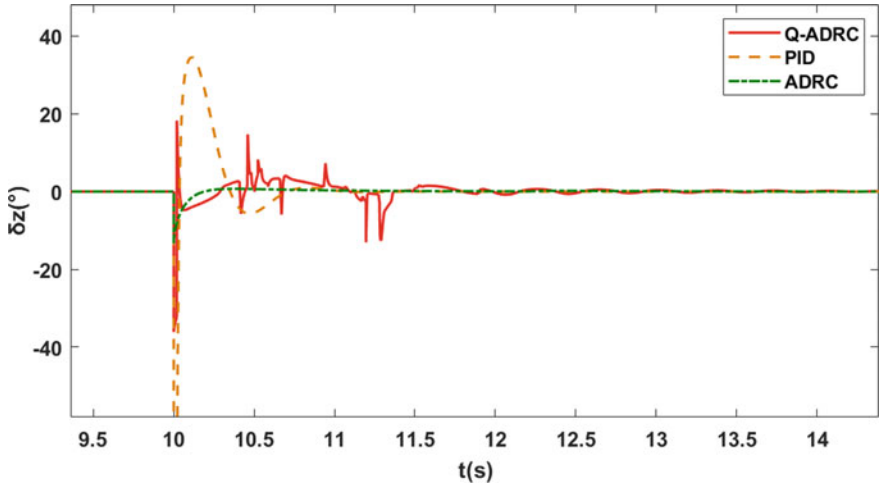


Fig. 7.4 The curve of δ_z

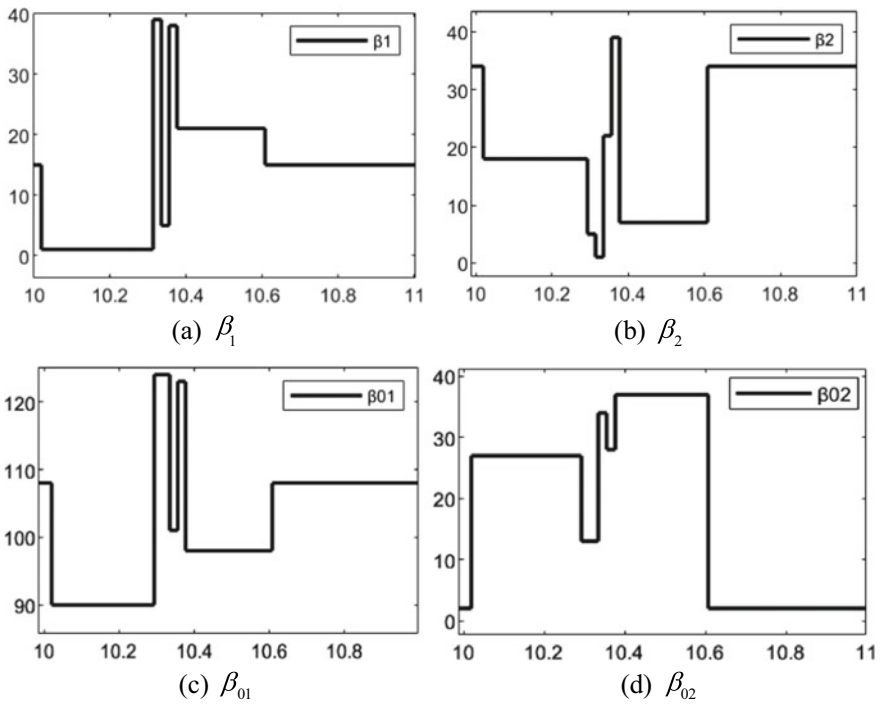


Fig. 7.5 The curve of M

7.6 Conclusion

Considering the nonlinearity and uncertainty of the hypersonic vehicle during flying, this paper designs a new ADRC scheme combined with Q-learning algorithm to achieve the better tracking performances. The results show that the Q-learning algorithm-based ADRC oscillates no more than 1° , with a regulation time of about 10.5 s and a steady-state error of about -0.001 . It has better control accuracy, strong robustness and adaptive capability to different environments than traditional ADRC and PID controller.


References

1. Schmidt, D. K.: Problems in control system design for hypersonic vehicles. In: *Automatic Control in Aerospace 1992*, pp. 89–96. Pergamon (1993)
2. Hu, J.: The nonlinear adaptive attitude control for hypersonic vehicle. *J. Astronaut.* **38**(12), 1281–1288 (2017)
3. Hu, C., Liu, Y.: Fuzzy adaptive attitude control based on ESO for hypersonic vehicles. *Aerosp. Control* **33**(3), 47–53 (2015)
4. Qi, N., Song, Z., Qin, C.: ADRC PID attitude control of a hypersonic flight vehicle. *J Project Rockets Missiles Guid* **30**(05), 66–68 (2010)
5. Pei, Y., Wang, H., Zhang, H., Shao, X., Su, Z.: ADRC attitude control based on TLC for hypersonic aircraft. *Tact Missile Technol.* **162**(06), 79–84 (2013)
6. Ping, G., He, Z., Ge, X.: Neural network PID control of hypersonic vehicle. *Aerosp. Control* **36**(01), 8–13 (2018)
7. Zheng, Y., Sun, Q., Chen, Z., Sun, M., Tao, J., Sun, H.: Deep Q-Network based real-time active disturbance rejection controller parameter tuning for multi-area interconnected power systems. *Neurocomputing* **460**, 360–373 (2021)
8. Hao, B., Du, H., Yan, Z.: A path planning approach for unmanned surface vehicles based on dynamic and fast Q-learning. *Ocean Eng.* **270**, 113632 (2023)
9. Kankashvar, M., Bolandi, H., Mozayani, N.: Multi-agent Q-Learning control of spacecraft formation flying reconfiguration trajectories. *Adv. Space Res.* **71**(3), 1627–1643 (2023)
10. Han J.: Improved PID control law using nonlinear properties. *Inform. Control* **06**, 356–364 (1995)
11. Gao, Q., Li, X., Ji, Y.-h., Liu, J.-j. Research on active disturbance rejection control of hypersonic vehicle based on Q-learning. *Control Eng. China* 21–1476 (2022)
12. Du, H., Fan, Y., Yan, J.: Active disturbance rejection control for airbreathing hypersonic vehicle. *Comput. Modern.* **214**(06), 1–4 (2013)
13. Han, J.: Auto disturbances rejection control technique. *Front. Sci.* **1**(01), 24–31 (2007)
14. Shu, L., Qing, S., Wan, W., Ming, S., Zeng, C., Ying, H.: Accurate flight path tracking control for powered parafoil aerial vehicle using ADRC-based wind feedforward compensation. *Aerosp. Sci. Technol.* **84**, 904–915 (2019)
15. Zhang, L., Cui, N., Wei, C., Han, P., Lu, B.: Active disturbance rejection control for reusable launch vehicle. *J. Chin. Inertial Technol.* **25**(03), 387–394 (2017)
16. Zhang, L.: Adaptive attitude control for a heavy-lift launch vehicle. Harbin: Harbin Institute of Technology (2019)
17. Han, J.: Nonlinear state error feedback control law. *Control Decis.* **3**, 221–225+231 (1995)
18. Wang, T., Gao, J., Xie, O.: Sliding mode disturbance observer and Q learning-based bilateral control for underwater teleoperation systems. *Appl. Soft Computing* **130**, 1568–4946 (2022)

Chapter 8

Deformation and Crack Monitoring of RC Beams Based on Computer Vision



Ruilin Wang , Weiping Zhang, Shuting Zhang, and Youling Yu

Abstract Deformation and cracks are valuable clues for evaluating the condition of existing concrete structures. In previous studies, computer vision technology has been proven to be an efficient and accurate means for detailed deformation and crack information acquisition. But there is still a gap in determining the functional level of structures directly from the extracted information. In this study, six concrete beams with different reinforcements were loaded to failure, and the loading processes were recorded by cameras. The dynamic evolution of deformation and cracks under different load steps was analyzed by our designed image processing pipeline. It was found deformation and crack evolution were strongly related to failure mode. On this basis, a crack characteristic parameter system used for structure monitoring was established, which is composed of the initial position, width, length, direction, and occurrence time of the fracture, corresponding characterization and extraction methods also were proposed. The established parameter system can be used to solve reverse problems such as failure mode prediction and load estimating.

Keywords Crack characteristic · Deflection measurement · Dynamic monitoring · Subpixel edge detection · DBSCAN

8.1 Introduction

Deformation and cracks are important information for structural assessment of concrete structures, implying the stress state to a certain extent. However, obtaining detailed deformation and crack information is always labor and time consuming, and there are often omissions and errors in the manually collected information, which leads to misjudgment of the structural state.

R. Wang · W. Zhang (✉) · S. Zhang
Department of Structural Engineering, Tongji University, Shanghai, China
e-mail: weiping_zh@tongji.edu.cn

Y. Yu
Department of Control Science and Engineering, Tongji University, Shanghai, China

In order to accelerate the information acquisition process, a significant amount of research has attempted to adopt computer-vision (CV) techniques to identify surface damage and to measure deformation [1]. Much of the early work on vision-based crack detection deployed digital image processing algorithms such as canny edge detection [2], adaptive threshold segmentation [3, 4], and active contour model [5, 6]. To improve the robustness of the vision algorithm in changing environments, convolutional neural networks (CNN) were also introduced into this task. Classification and object detection networks only could locate the defect regions [7–10], while segmentation networks such as Mask R-CNN [11] and FCN [12, 13] could achieve pixel-level identification. As for displacement measurement, most studies used template matching to track target markings affixed to the structure surface [14, 15]. When the random speckle can be drawn on the surface, digital image correlation was another prior choice, since it could capture full-field deformation [16, 17]. In the situation without marks, the contours of the specimen could be used to extract displacement [18, 19]. The aforementioned automated approaches have been proven to be effective in indoor or field tests.

Utilizing the output crack maps and displacements for structural assessment and maintenance decision-making is the important research topic that follows. A simple path is to compare the extracted crack widths and displacements with the serviceability criteria specified in codes such as ACI318 [20]. To further take full advantage of the information contained in crack maps, quantifying methods such as fractal dimension were used to characterize crack patterns. The obtained quantities were more suitable to construct machine-learning models compared to the original maps, bridging the gap between CV and structural assessment. Momeni proposed a Bayesian regression model to predict the peak drift ratio that RC shear walls have experienced during an earthquake based on the fractal dimension surface cracks [21]; Farhidzadeh and Rezaie used a similar characterization method to assess post-earthquake reinforced concrete shear walls and rubble stone masonry piers, respectively [22, 23]. Davoudi [24–26] conducted a series of research on load level estimation of beams, slabs, and panels based on the combinations of the total number, polar moment of inertia, and total length of cracks.

Generally, there will be monitoring or multiple inspections within a building's service life, the sequence of images in which the extra dimension of time can provide more information, but these previous studies ignored the information implicit in the dynamic evolution of deformation and cracks.

This study analyzed the features of cracks and deflection of six simply supported RC beams under various load steps, expanded the original crack characteristic parameter system with time-related parameters, and proposed automatic image processing methods for extracting all parameters. It was found that the parameters of beams with different reinforcements evolved in distinct ways, and the proposed parameter system could help to predict failure modes and make decisions about the optimal technological measures that are needed to keep the structure at the desired level of functionality.

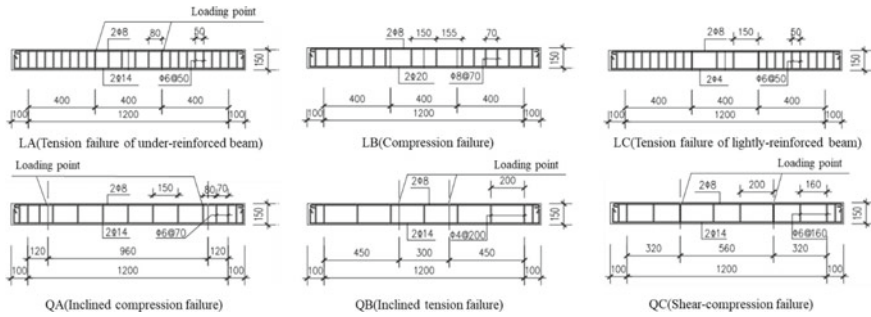


Fig. 8.1 Configuration of longitudinal reinforcements and stirrups in concrete beams (unit in mm)

8.2 Image Acquisition

8.2.1 Experimental Specimens

To study the crack dynamic monitoring and characteristic parameters extraction methods, six RC beams with different target failure modes were tested. These specimens were numbered LA–LC and QA–QC, and their structural details are shown in Fig. 8.1. In addition, the width of the cross-section was 100 mm, and the thickness of concrete cover was 15 mm.

According to the material test results, the compressive strength f_c of the standard cube concrete specimens was 31.2 MPa, and the yield strength f_k of the reinforcing steel bars with different diameters (d) was 570 MPa ($d = 20$ mm)/389 MPa ($d = 14$ mm)/368 MPa ($d = 8$ mm)/462 MPa ($d = 6$ mm)/330 MPa ($d = 4$ mm).

The load was applied through the electro-hydraulic servo loading system. 20% of the estimated cracking load was taken as the load increment of a loading step before cracking, while 5–15% of the ultimate load was taken as the load increment of a loading step after cracking. The load was held unchanged between two load steps for photographing the beam surface, and meanwhile, cracks were observed using a tape measure and crack microscope to record the cracks’ maximum width and position for method validation. A laser displacement sensor was arranged in the middle of the beam bottom to record the deflection development during the whole loading process, and the measured mid-span deflection was used to validate the CV method, too.

8.2.2 Cameras Set-Up

Two Prosilica GT6400 industrial cameras were used to record the deflection of the entire beam during loading. The diagonal length of their photosensitive element is 27.9 mm, the aspect ratio of the photosensitive element is 4:3, the resolution is 6480 (H) × 4860 (V), and the focal length of the lens is 28 mm. In order to achieve a

shooting range greater than 1.7 m, the working distance was set to 1.4 m. And the distance between the two cameras was 0.6 m to ensure that the overlap rate of the field of view exceeds 65%. Throughout the loading process, the cameras were stationary and continuously recorded images at 1 frame per second.

The two cameras were arranged primarily for a wide field of view, which is suitable for calculating deformation based on beam contours, but the image obtained is too blurry for crack measurement. So, a Sony Alpha 7 SLR camera was used to photograph the cracks at close range. The diagonal length of their photosensitive element is 35 mm, the aspect ratio of the photosensitive element is 3:2, the resolution is 6000 (H) \times 4000 (V), and the focal length of the lens is 24 mm. In order to make a pixel in the image correspond to an actual size of less than 0.1 mm, the working distance was set to 0.35 m, and the corresponding field of view is about 577 mm \times 385 mm. The camera needs to be moved on the slider to capture cracks in all locations, and the single movement distance was set to 200 mm to ensure the image stitching effect.

All cameras were calibrated before testing, and their layout during loading is shown in Fig. 8.2.

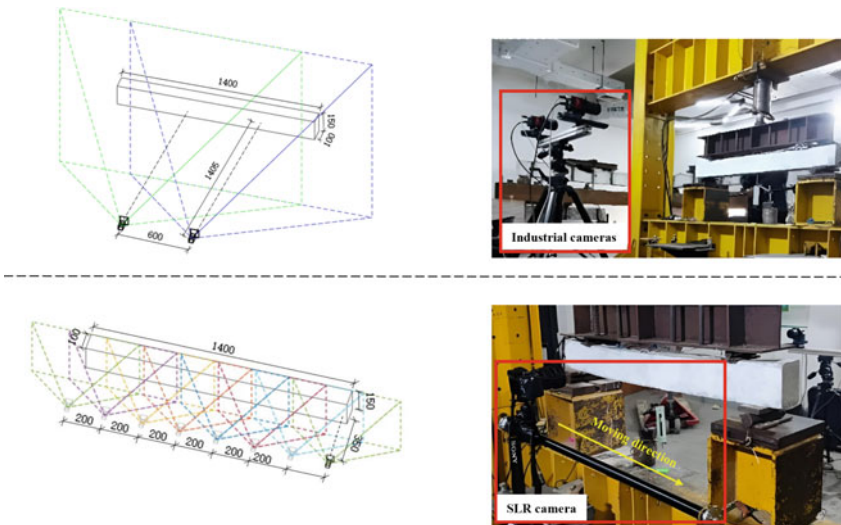


Fig. 8.2 Set-up of cameras in the loading experiment

8.3 Method and Result

8.3.1 Mid-Span Deflection Extraction

The displacement of the middle point of the beam bottom contour with respect to the support point equals the mid-span deflection of the beam. By stitching together overlapping images, the target beam's panoramic image was created. The beam contour was then determined by segmenting the image according to the gray threshold. The mid-span deflection could be calculated by identifying the contour's key points, then subtracting those points' displacements.

SURF-based image stitching. Speeded-Up Robust Features (SURF) algorithm was employed for detecting and describing local features in images because it is fast and robust to changes in illumination, scale, and rotation. Then, the extracted features in adjacent images were matched by RANSAC-based matching. Based on the matched feature points, homography matrixes were estimated and decomposed for obtaining rotation matrixes and translation vectors between adjacent images. Using estimated geometric transformation, images taken from different views were aligned and blended together, resulting in a seamless panoramic image of the target beam.

Beam's key points extraction and deflection calculation. Directly irradiate the surface of the beam with high-lumen lights, increasing the brightness difference between the beam and the background. With the aid of light, a simple global threshold method was used to identify the beam in the image. The fixed threshold depended on the lighting conditions and was selected manually.

To simplify deflection calculations, the segmented panoramic image was rotated to be horizontal. The four corner points of the contour were found by seeking the point that makes the sum and difference of the horizontal and vertical coordinates take the maximum and minimum values. Connect the two points on the bottom edge, then the arc tangent of the slope of the connecting line is the rotation angle which can rotate the picture to be horizontal. The left support position is the point with a cumulative length of 100 mm from the lower left corner on the bottom contour. And the mid-span point is the curve's midpoint. The whole process of key points extraction is summarized in Fig. 8.3.

The difference between the vertical coordinates of the two points was taken as the mid-span deflection. Finally, the deflections in pixel space were transformed into physical space by multiplying a conversion coefficient determined in camera calibration.

Result and validation. Considering that the loading speed is only 1 kN/min, the mid-span displacement was calculated every 50 s using the method described above. The obtained displacements of five beams are compared with the measured displacements in Fig. 8.4 (the displacement sensor failed when QB was loaded). The mean relative errors are listed in Table 8.1.

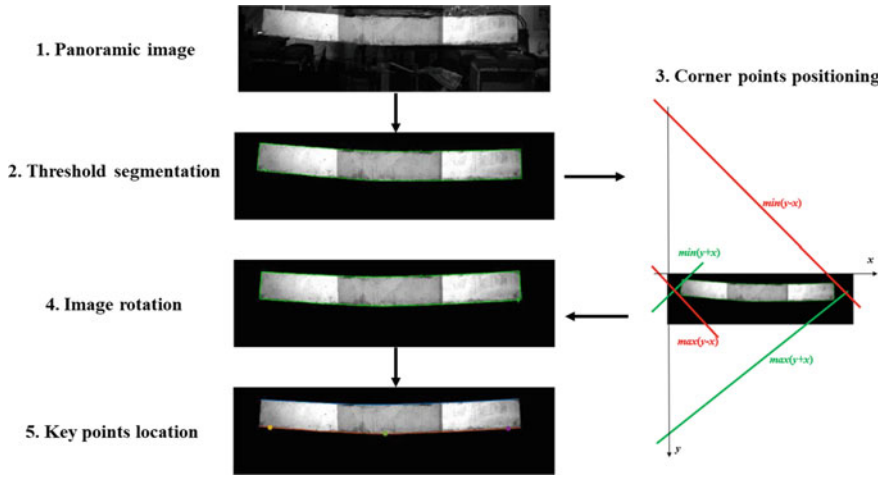


Fig. 8.3 Process of key points extraction

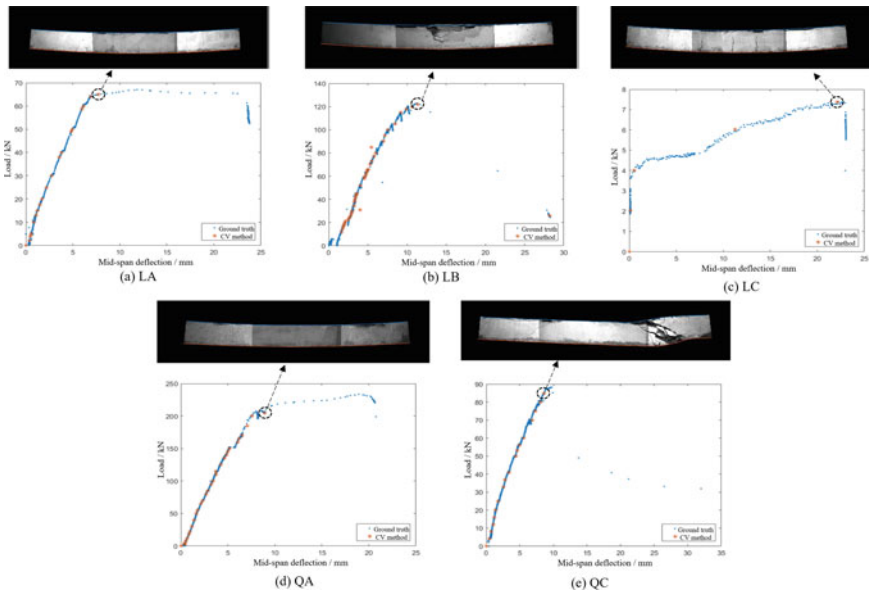


Fig. 8.4 Load–displacement curves of five beams

8.3.2 Crack Detection on Sequential Images

A subpixel edge detector [27] was used to detect cracks considering the fineness requirements of crack measurement. Then, density-based spatial clustering of applications with noise (DBSCAN) [28] was adopted to filter out noise edge points caused

Table 8.1 Mean relative errors of mid-span deflection

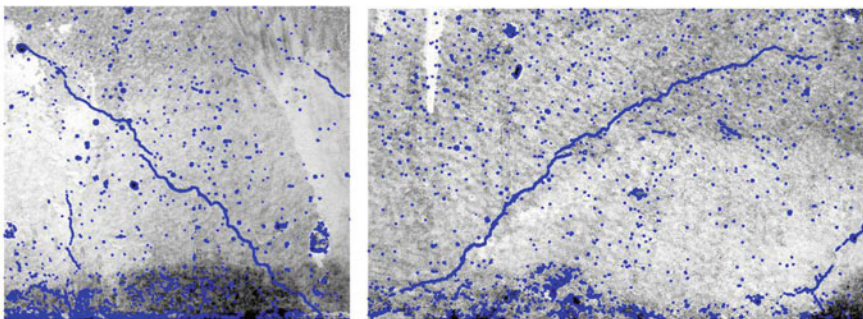
Beam number	Mean relative error (%)
LA	2.06
LB	3.31
LC	5.82
QA	2.15
QC	2.72

by pores and uneven texture on the surface. It was also challenging to spot cracks when the load is low because they are so tiny and their features are not visually apparent. As the load increases, new cracks appear, and cracks become wider and longer, making cracks in previous frames encircled by the contours of cracks in the last frame. So, for sequential images, crack identification is performed in frames with obvious cracks, and the obtained crack map is used as mask to filter out the noise edge points of previous frames.

Subpixel edge detection. Subpixel edge detection can identify edges that are not aligned with pixel boundaries, providing edge information with greater precision than traditional edge detection methods that work at the pixel level. This feature is beneficial to the measurement of crack geometric information.

First, the pixel-level edges of cracks are located by seeking maximum gradients. Then, the pixel-level edges are refined to obtain subpixel edges, with the assumption that the intensities and areas on each side of the subpixel edge are proportionate to the pixel values recorded by light sensors. That is, when a pixel is divided into two sub-regions by a subpixel edge, its intensity captured by the camera is the weighted average of the pixel intensity on either side of the edge, with the weight being the ratio of the sub-region to a single pixel. Figure 8.5 shows the detected subpixel edge points on typical concrete surface images.

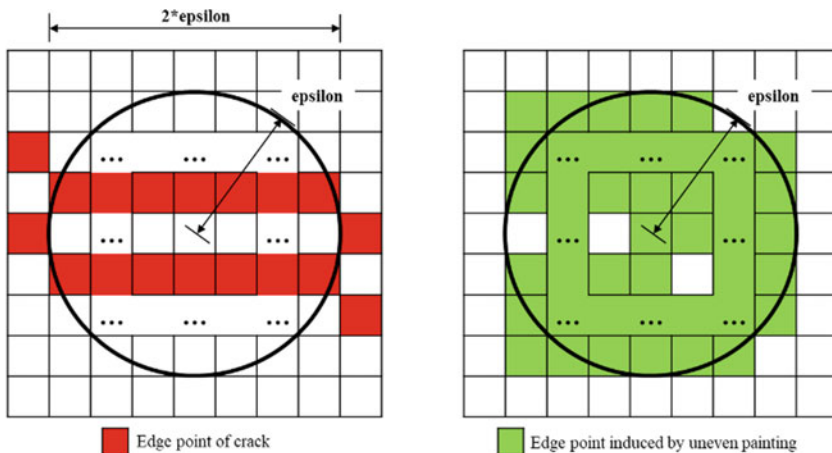
Noise edge point identification and elimination with DBSCAN. Noise edge points induced by surface holes, uneven paint, etc. should be removed before calculating

**Fig. 8.5** Detected sub-pixel edge points on typical concrete surface images

the crack parameters based on the edge points. The edge points induced by cracks are relatively dense because the intensities of crack edges change drastically, and the point set made up of them has the elongated shape characteristic. According to this characteristic, the disordered edge points in crack images were first clustered into several clusters, and the noise points were then filtered out using the morphological properties of the clusters.

Since cracks come in arbitrary sizes and shapes, DBSCAN, an algorithm that does not require the assumption of a particular distribution of data points, was employed for edge point clustering. DBSCAN works by defining a neighborhood around each point and then identifying high-density regions as clusters. Specifically, the algorithm defines two parameters: “epsilon”, which is the radius of the neighborhood around each point, and “minPoints”, which is the minimum number of points required to form a cluster.

The choice of two parameters “epsilon” and “minPoints” have a significant impact on the performance of the algorithm. In this study, “epsilon” was determined by the empirical maximum discontinuity distance of surface cracks, which states that when two edge points are separated by more than this distance, they are not regarded as being a part of the same crack. For our imaging system, the empirical maximum distance of 3 cm corresponds to 41 pixels, so “epsilon” is set as 40. For a continuous crack, when it passes through an area within a radius of “epsilon” around a certain edge point, there are at least 4 times “epsilon” edge points in this area, as shown in Fig. 8.6a. Considering that surface crack will have discontinuities, the “minPoints” was reduced to 80. But if there are more than 240 edge points in the area, they might be noise points brought on by uneven painting, as shown in Fig. 8.6b.



(a) Numbers of crack edge points in the circle region (b) Numbers of noise edge points in the circle region

Fig. 8.6 Diagram of the edge points counting in the circular area

So, DBSCAN was first applied to eliminate isolated noise points, with the “epsilon” of 30 and “minPoints” of 80; then DBSCAN was used to identify spot-shape point clusters with the “epsilon” of 30 and “minPoints” of 240. Figure 8.7 shows the result of the two-step clustering method on a typical concrete surface image.

Crack identification using constraints between multiple frames. The cracks in the last frame are developed from those in previous frames. So it is possible to obtain an inter-frame constraint, which states that the edge points of the previous frames must be encircled by those of the subsequent frame. In order to maintain this constraint relationship when structural displacement is present, it is necessary to align the images of various frames, as shown in Fig. 8.8a.

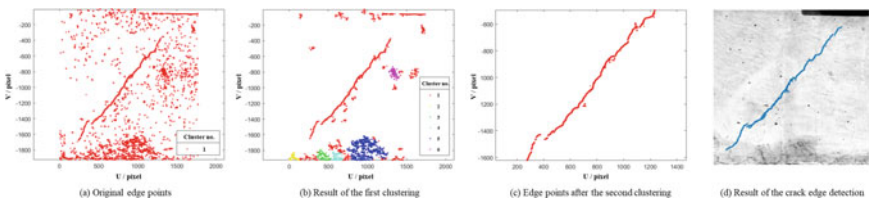


Fig. 8.7 Noise edge point elimination using the two-step clustering method

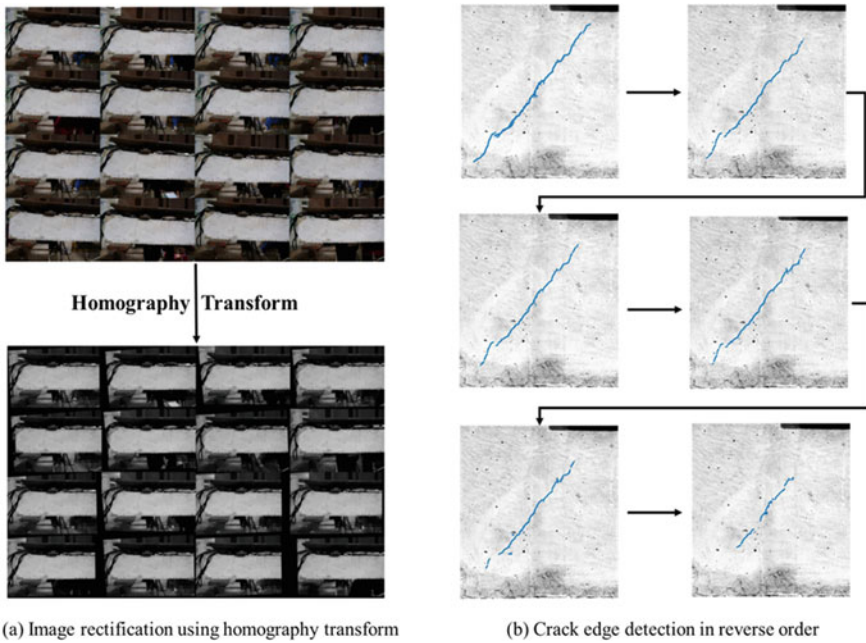


Fig. 8.8 Crack edge points identification in reverse order

This constraint can be used to eliminate noise points by masking out edge points based on the crack edge points in the most recent frame, especially when the cracks are relatively tiny. In addition to assisting in the identification of developing cracks, the crack identification procedure in reverse order can significantly increase the algorithm's calculation efficiency. The reverse order recognition method was carried out on the images after rectification, the results are shown in Fig. 8.8b.

8.3.3 Crack Characteristic Parameters Extraction

The characteristic parameters are the quantitative expression of the crack map, and the parameter system should contain all information needed by the assessment task such as cracking causes analysis, failure mode prediction, or load estimation. The physical characteristics of cracks, including the orientation, length, and width, are necessary. Table 8.2 compares the crack patterns induced by different external effects. It could be concluded that historical information on crack developments including the first occurrence time, starting position, terminal position, and development direction of each crack, also could contribute to the assessment. For instance, the starting position and development direction of the crack can be used to analyze the crack cause; the crack terminal position indicates that the principal stress at this point is exactly equal to the concrete tensile strength, representing a specific stress state.

Physical Characteristics of Cracks

Crack width. Crack width is defined as the distance between the nearest edge points on either side of the crack. However, the edge points within the crack contour will bring obstacles to the width calculation. The contour points could be separated from the edge points using the alpha shape. A line connecting two points, p and q belonging to the point set s , is considered to be a part of the alpha shape if a circle with radius r passes through the two points, and no other points in set s are located inside of this circle.

Table 8.2 Crack patterns induced by different external effects

Crack cause	Crack pattern
Bending moment	Cracks first appear at the side under tension induced by the bending moment and propagate toward the other side, with a gradual decrease in width
Shear-compression/inclined tension	Inclined cracks initiate at the supports of the beam and propagate toward the loading points, with a gradual increase in width
Inclined compression	Inclined cracks initiate at the web of the beam and propagate toward the loading points and the supports, with a gradual decrease in width
Pure torsion	Spiral cracking

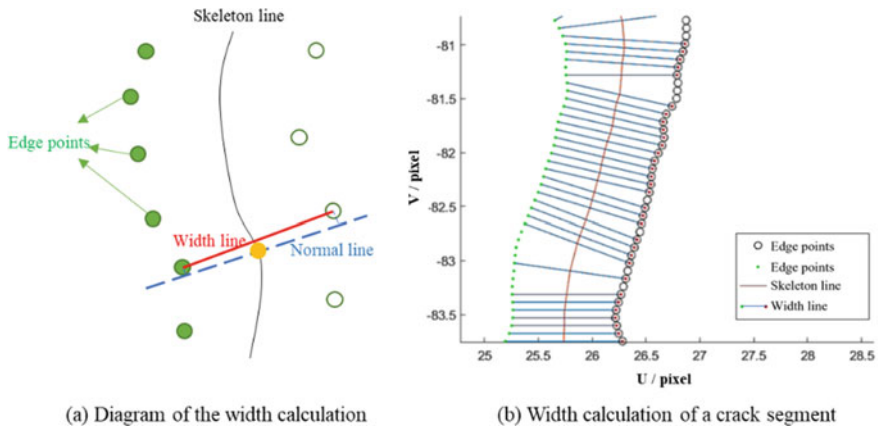


Fig. 8.9 Width calculation based on the nearest edge points

The extracted contour is first skeletonized, and then each point on the crack skeleton line is assigned a normal line using SVD. The two edge points closest to a normal line are regarded as the nearest edge points, and their distance is the crack width according to this definition of the nearest edge point method, as shown in Fig. 8.9.

Crack length. Crack length is defined as the cumulative length of the crack skeleton line. The skeleton line forks make it difficult to choose which route to take in order to calculate the length. For such complex cracks with secondary branches, the depth-first algorithm was used to find the main path to calculate the crack length.

Figure 8.10 showed the entire procedure. First, identify intersections and endpoints using the template matching method; then starting from the endpoint with the largest width, find its closest point to calculate their distance, and repeat this process until the intersection point is discovered; Calculate the length of each branch starting at the intersection point as the last step did and continuing until all branches have been calculated; in the end, store the length results in a tree data structure, and use the depth-first algorithm to find the longest path as the crack length. The longest path could be called the principal skeleton line.

Width change along the principal skeleton line. Cracking indicates that the concrete’s principal stress at this location has exceeded its tensile strength, and the more it exceeds, the wider the crack. So the width change along the principal skeleton line reveals the development process of the crack, that is, the maximum crack width can be regarded as the starting point of the crack, and the direction from wide to narrow crack can be regarded as the crack development direction.

Draw a curve that fits the scatterplot of the crack width with the length of the crack skeleton line, the outcomes are displayed in Fig. 8.11. With the increase in the skeleton line, the bending crack becomes narrower; the inclined compression crack is typically wide in the middle and narrow at both ends.

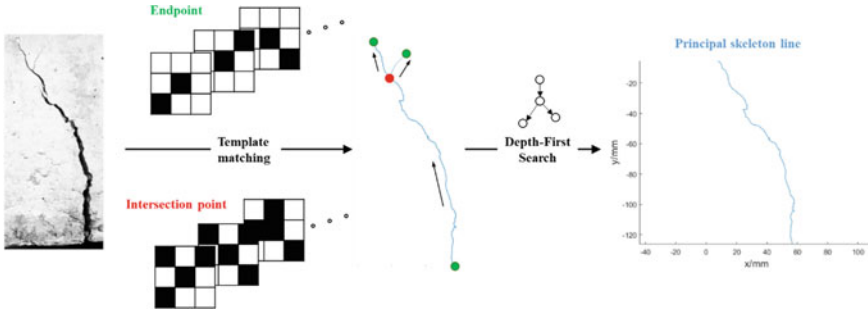


Fig. 8.10 Diagram of the principal skeleton line extraction

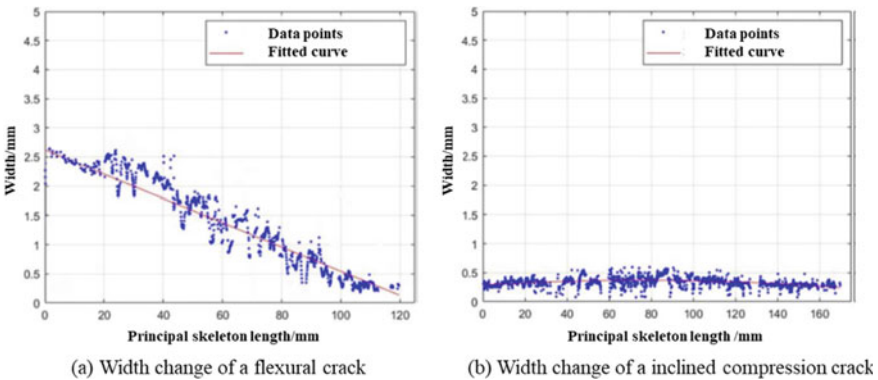


Fig. 8.11 Width change features of two types of crack

Crack orientation. The approximate orientation of the crack can be determined by fitting the principal skeleton line of the crack linearly using the least square method.

Historical information. The dynamic monitoring of concrete cracks could provide more information about crack development, such as the time corresponding to the occurrence, demonstrated in Fig. 8.12. In the case of monotonous loading, the cracks are most numerous and most noticeable on the last frame of the sequence images. Therefore, cracks were identified first on the last frame, and the crack clusters were positioned and numbered according to the abscissa. Then, the physical characteristics of each numbered crack were extracted from earlier frames and recorded. The crack characteristic changes during the monitoring time could also be determined.

The aforementioned crack characteristic parameters were chosen in accordance with the requirements of structural evaluation and can be applied to load estimation, crack cause analysis, and other tasks.

Result and validation. Manual measured crack information was recorded in the form of crack maps under different loads. Figure 8.13 lists the crack maps when the beams reached the bearing capacity, containing the maximum width of the major cracks.

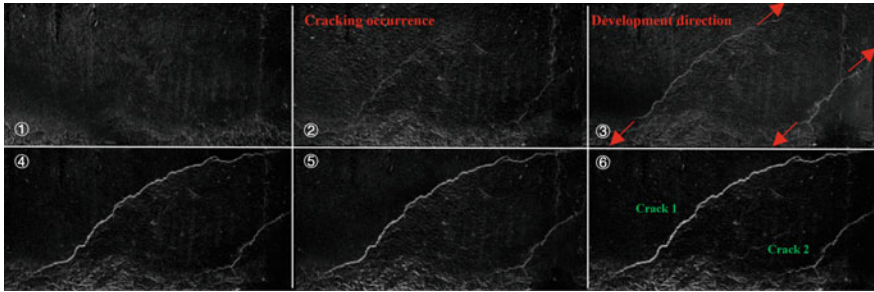


Fig. 8.12 Example of historical information from sequence images

For each beam, only the evolution of the first occurred major crack was recorded for validating the suggested crack monitoring method. Figure 8.13 also shows the edge points of selected cracks in the last frame, which were extracted by the pipeline described in 3.2. On this basis, edge point detection was performed on the previous frames in reverse order. The crack information under different loads was extracted from edges and compared with the measured results.

For the physical characteristics, the results show that the deviation of the extracted maximum crack width does not exceed 0.05 mm, which is within the allowable range of errors. When the crack width is above 0.35 mm, the relative error is within 5%; when the crack width is 0.15–0.35 mm, the detection absolute error is within 0.03 mm, and the relative error is within 22%; when the crack width is 0.05–0.15 mm, the absolute error is within 0.03 mm. Table 8.3 takes the comparison of crack 1 on

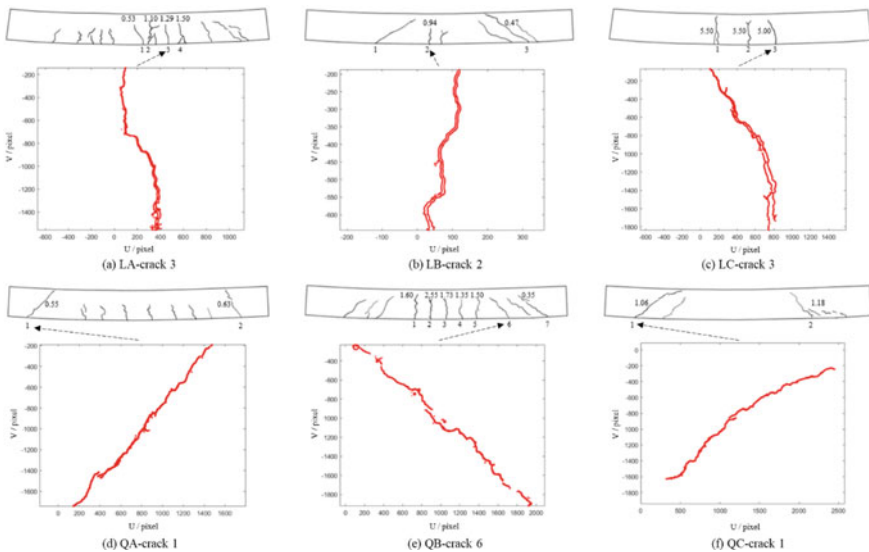


Fig. 8.13 Detected edge points of the first occurred major crack on six beams

Table 8.3 Example validation of maximum width on QA-crack 1

Load (kN)	Orientation (°)	Length (mm)	Extracted maximum width (mm)	Actual maximum width (mm)	Absolute error (mm)
200	50.07	169.48	1.0980	1.06	0.04
165	49.65	131.15	0.6092	0.59	0.02
150	50.27	140.34	0.4795	0.46	0.02
130	50.36	134.06	0.1643	0.14	0.02
115	50.89	127.47	0.1537	0.13	0.02
100	52.62	79.04	0.1203	0.10	0.02

Table 8.4 Validation of first cracking time

Beam No	Actual cracking load (kN)	Extracted cracking load (kN)	Initial position
LA	18	30	Beam bottom in mid-span
LB	21	66	Beam bottom in mid-span
LC	4	6	Beam bottom in mid-span
QA	22	100	Near support point
QB	16	36	Beam bottom in mid-span
QC	20	41	Near support point

beam QC as an example. For the cracks' first occurrence time and initial position, the comparison is shown in Table 8.4, where the time is represented by the load at the first cracking moment. It could be found that there is a delay between the cracking time recognized in the image and the actual cracking time. This is due to the fact that our vision algorithms still cannot detect very tiny cracks.

8.4 Conclusion

In this paper, the whole process of the crack and deformation evolution of six RC beams with different failure modes was simulated by loading tests. Based on the captured sequential images, research on CV-based deformation and crack information extraction was carried out. The main contributions are as follows:

- (1) A mid-span displacement extraction method based on the lower edge of the beam contour line was proposed. The panoramic image of the test beam could be obtained by SURF-based image stitching method, and the contour of the test beam could be extracted based on the threshold segmentation method under suitable lighting conditions. The vertical displacement difference between the midpoint of the lower edge and the support point could be taken into account

as the mid-span deflection of the beam, after translating the image coordinates to the physical dimensions. Compared with the measured results, the average deviation of mid-span displacement extracted by the suggested method does not exceed 3.22%.

- (2) Combining subpixel edge detection and edge point denoising based on DBSCAN, a crack edge point recognition method was developed. On this basis, in order to further improve the extraction efficiency of crack edges in sequential images, a reverse sequence analysis method based on image rectification and inter-frame constraints is proposed. The absolute error of cracks in each test beam is about 0.02 mm, which is within the allowable range.
- (3) A crack characteristic parameter system used for structure assessment was established. The system consists of physical characteristics like width, and historical information like initial position and occurrence time of the fracture. Corresponding extraction methods also were proposed. The comparative verification results show that the average accuracy of the maximum crack width reaches 97.82%.

Acknowledgements Sponsored by Program of Shanghai Science and Technology Committee (22dz1203600).

References

1. Spencer, B.F., Hoskere, V., Narazaki, Y.: Advances in computer vision-based civil infrastructure inspection and monitoring. *Engineering* **5**, 199–222 (2019)
2. Abdel-Qader, I., Abudayyeh, O., Kelly, M.E.: Analysis of edge-detection techniques for crack identification in bridges. *J. Comput. Civ. Eng.* **17**, 255–263 (2003)
3. Kim, H., Ahn, E., Cho, S., Shin, M., Sim, S.H.: Comparative analysis of image binarization methods for crack identification in concrete structures. *Cem. Concr. Res.* **99**, 53–61 (2017)
4. Kamaliardakani, M., Sun, L., Ardakani, M.K.: Sealed-crack detection algorithm using heuristic thresholding approach. *J. Comput. Civ. Eng.* **30**, 1–10 (2016)
5. Wang, W., Li, H., Wang, K., He, C., Bai, M.: Pavement crack detection on geodesic shadow removal with local oriented filter on LOF and improved level set. *Constr. Build Mater.* **237**, 117750 (2020)
6. Li, S., Cao, Y., Cai, H.: Automatic pavement-crack detection and segmentation based on steerable matched filtering and an active contour model. *J. Comput. Civ. Eng.* **31**, 1–9 (2017)
7. Yang, L., Li, B., Li, W., Liu, Z., Yang, G., Xiao, J.: Deep concrete inspection using unmanned aerial vehicle towards CSSC database. In: *Proceedings of the IEEE/RSJ International Conference on Intelligent Robots and Systems*, pp. 24–28 (2017)
8. Cha, Y.J., Choi, W., Suh, G., Mahmoudkhani, S., Büyüköztürk, O.: Autonomous structural visual inspection using region-based deep learning for detecting multiple damage types. *Comput. Civ. Infrastruct. Eng.* **33**, 731–747 (2018)
9. Maeda, H., Sekimoto, Y., Seto, T., Kashiyama, T., Omata, H.: Road damage detection and classification using deep neural networks with smartphone images. *Comput. Civ. Infrastruct. Eng.* **33**, 1127–1141 (2018)
10. Deng, J., Lu, Y., Lee, V.C.S.: Concrete crack detection with handwriting script interferences using faster region-based convolutional neural network. *Comput. Civ. Infrastruct. Eng.* **35**, 373–388 (2020)

11. Yuan, C., Xiong, B., Li, X., Sang, X., Kong, Q.: A novel intelligent inspection robot with deep stereo vision for three-dimensional concrete damage detection and quantification. *Struct. Health Monit.* **21**, 788–802 (2022)
12. Li, S., Zhao, X., Zhou, G.: Automatic pixel-level multiple damage detection of concrete structure using fully convolutional network. *Comput. Civ. Infrastruct. Eng.* **34**, 616–634 (2019)
13. Yang, X., Li, H., Yu, Y., Luo, X., Huang, T., Yang, X.: Automatic pixel-level crack detection and measurement using fully convolutional network. *Comput. Civ. Infrastruct. Eng.* **33**, 1090–1109 (2018)
14. Feng, D., Feng, M.Q.: Computer vision for SHM of civil infrastructure: from dynamic response measurement to damage detection—a review. *Eng. Struct.* **156**, 105–117 (2018)
15. Bolognini, M., Izzo, G., Marchisotti, D., Fagiano, L., Limongelli, M.P., Zappa, E.: Vision-based modal analysis of built environment structures with multiple drones. *Autom. Constr.* **143**, 104550 (2022)
16. Sen, Y.Y., Lin, W.C., Hsu, T.T.C., Yang, H.C., Lu, H.J., Chang, C.C.: Image analysis method for crack distribution and width estimation for reinforced concrete structures. *Autom. Constr.* **91**, 120–132 (2018)
17. Ghyabi, M., Timber, L.C., Jahangiri, G., Lattanzi, D., Shenton, H.W., III., Chajes, M.J., Head, M.H.: Vision-based measurements to quantify bridge deformations. *J. Bridg. Eng.* **28**, 1–12 (2023)
18. Han, Q., Liu, X., Xu, J., Sun, T.: Research on the feasibility of visual measurement using first-person perspective based on smartphones. *Comput. Civ. Infrastruct. Eng.* 1–15 (2022)
19. Bhowmick, S., Nagarajaiah, S., Lai, Z.: Measurement of full-field displacement time history of a vibrating continuous edge from video. *Mech. Syst. Signal Process* **144**, 106847 (2020)
20. ACI Committee: Building code requirements for structural concrete (ACI 318–08) and commentary. American Concrete Institute (2008)
21. Momeni, H., Dolatshahi, K.M.: Predictive equations for drift ratio and damage assessment of RC shear walls using surface crack patterns. *Eng. Struct.* **190**, 410–421 (2019)
22. Rezaie, A., Godio, M., Achanta, R., Beyer, K.: Machine-learning for damage assessment of rubble stone masonry piers based on crack patterns. *Autom. Constr.* **140**, 104313 (2022)
23. Farhidzadeh, A., Dehghan-Niri, E., Moustafa, A., Salamone, S., Whittaker, A.: Damage assessment of reinforced concrete structures using fractal analysis of residual crack patterns. *Exp. Mech.* **53**, 1607–1619 (2013)
24. Davoudi, R., Miller, G.R., Kutz, J.N.: Automation in construction data-driven vision-based inspection for reinforced concrete beams and slabs: quantitative damage and load estimation. *Autom. Constr.* **96**, 292–309 (2018)
25. Davoudi, R., Miller, G.R., Kutz, J.N.: Structural load estimation using machine vision and surface crack patterns for shear-critical RC beams and slabs. *J. Comput. Civ. Eng.* **32**, 04018024 (2018)
26. Davoudi, R., Miller, G.R., Calvi, P., Kutz, J.N.: Computer vision-based damage and stress state estimation for reinforced concrete and steel fiber-reinforced concrete panels. *Struct. Health Monit.* **19**, 1645–1665 (2020)
27. Trujillo-Pino, A., Krissian, K., Alemán-Flores, M., Santana-Cedrés, D.: Accurate subpixel edge location based on partial area effect. *Image Vis. Comput.* **31**, 72–90 (2013)
28. Ester M, Kriegel H-P, Sander J, Xu X, et al. A density-based algorithm for discovering clusters in large spatial databases with noise. In: *KDD*, pp. 226–231 (1996)

Chapter 9

Numerical Simulation of Enhancing the Solar-Thermal Conversion and Storage Performance for Expanded Perlite/Paraffin Wax Composites by Introducing Expanded Graphite and Carbon Nanotubes



Xinbo Zhao and Zhi Guo Qu

Abstract In this study, the expanded perlite (EP) powder and expanded graphite (EG) were used as supports to stabilize paraffin wax (PW) for preparing composite phase change materials (PCMs). The impregnation method was used to prepare PW/EP, PW/EP/EG1, PW/EP/EG3 and PW/EP/EG5. The enhancement effect of EG with different mass proportions on the heat storage/release performance of PW/EP, and the improvement effect of carbon nanotubes (CNTs) on the solar-thermal conversion performance of pure PW and composite PCMs were studied by three-dimensional numerical simulation. The thermal conductivities of composite phase change materials were 1.26–2.13 times higher than the pure PW. The PW/EP/EG5 had wonderful thermal physical property in heat energy storage and release process. The solar-thermal conversion performance could be effectively improved by adding CNTs cover; Compared to C-PW, the phase change time of C-PW/EP, C-PW/EP/EG1, C-PW/EP/EG3 and C-PW/EP/EG5 decreased by 4%, 19%, 26% and 31%, respectively; the performance of PW/EP was improved the most and that PW/EP/EG5 was improved the least; but C-PW/EP/EG5 had the best solar-thermal conversion and storage performance.

Keywords Phase change materials · Expanded perlite · Expanded graphite · Carbon nanotubes · Solar-thermal conversion

X. Zhao · Z. G. Qu (✉)

School of Energy and Power Engineering, Xi'an Jiaotong University, Xi'an 710049, Shaanxi, China

e-mail: zgqu@mail.xjtu.edu.cn

9.1 Introduction

With the development of economy, the quantity demand of energy continues to grow. The environment pollution limited the sustainable development and produced a lot of destroyers due to the large number of fossils were used [1]. In order to use energy by various ways and realize green sustainable development, it is becoming more and more important and urgent to develop renewable energy [2]. The status of renewable energy is increasing day by day, and has become an important part of the energy development strategy. But the renewable energy such as solar and wind energy are intermittent and unstable in the collection and use process, which improve the difficulty of energy utilization. In addition, the inadequate use of traditional fossil energy also causes a huge waste of heat energy.

Energy storage technology can solve the contradiction of time, geographical location and quantity in the process of energy development, conversion and utilization, improve energy utilization and optimize energy structure [3]. Energy storage technology mainly focus on the storage the mechanical, electric, thermal energy and so on. Thermal energy storage (TES) is an important part of energy science and technology. TES can be implemented in three main different ways: chemical reaction, sensible, and latent heat storage [4]. The latent thermal energy storage (LTES) depends on the phase change enthalpy of phase change material (PCM) to storage and release a massive amount of thermal energy within a small temperature range, which is superior sensible thermal energy storage [5]. LTES stores heat energy through solid–solid, solid–liquid, solid–gas, liquid–gas phase transitions of matter [6]. The solid–liquid phase change material with the advantages of high thermal capacity, lower volume change in phase transition process is used for various applications [7]. Nowadays, solid–liquid PCM has been widely used in solar energy storage (concentrating solar power plants [8], solar energy water heater [9], solar heating of ventilation air equipment [10], solar energy assisted desiccant air conditioning system [11], solar regulation and storage for smart window [12]), building energy conservation (passive composite PCMs wall [13], passive net-zero energy building [14], floor heating system [15]) thermal management (battery [16], electric device [17]) waste heat recovery [18].

The PCM can divided into organic, inorganic and eutectic PCM according different chemical component [19], and divided into low, middle, high temperature PCM according different temperature range [20]. The solid–liquid PCM has been extensively used due to its advantages in chemical and physical properties. However, most solid–liquid PCMs have low thermal conductivity, leak easily when in liquid state, which limits its extension of application. There has been lots of researches to solve the problems by adding high thermal conductivity material, preparing stabilized composite PCM and encapsulating PCM. However, in the process of using solar energy directly, the solar absorptance of PCM is low, effective solar-thermal conversion and storage cannot be achieved. At present, there are few researches focus on this problem. Researchers mainly optimize matrix materials to develop composite PCMs with better solar absorption. Some researchers used rGO [21], Mxene nanosheet

[22, 23], black phosphorus nanosheet [24], carbon nano-material [25] to modify polyurethan, melamine and metal foam matrix. Shao et al. [23] fabricated a novel PCM composites with superior solar-to-thermal conversion efficiency and shape memory function by introducing MXene-coated melamine foam into poly(ethylene glycol) (PEG). Minority researchers used CdS [26], TiO₂ [27] to modify microcapsule shell in order obtain better solar absorption. Zheng et al. [28] acquired microencapsulated phase change materials within the nanocarbon microcapsules to improve solar-thermal conversion system. In addition, some three-dimensional structure materials such as cellulose nanofiber aerogel [29], graphene aerogel [30], graphene foam [31] were used for preparing solar-thermal conversion composite PCMs. Wu et al. [32] selected cellulose as a carbon source precursor, and three-dimensional (3D) directional cellulose-based carbon aerogels (CBCA) are constructed through an immersion expansion, orientation, freeze-drying, and carbonization process.

However, the preparation process of these method is more complex, not easy to large-scale produce, and expensive. This paper starts from the surface and interior of material, takes low-cost expand perlite as the matrix material, paraffin wax as phase change material, to prepared the shaped composite PCM, and different mass proportions of expand graphite is added to improve the overall thermal conductivity of composite PCMs. The surface of materials is treated with high solar-absorbing carbon nanotubes to enhance the solar-thermal conversion performance of composites. Finally, the solar-thermal conversion and storage composite PCMs with good comprehension performance is constructed.

9.2 Material and Characterization

9.2.1 Materials

The expanded perlite powder was supplied by Nanyang Houpu Mining Industry Co., Ltd. The expanded Graphite with a mean size of 325 mesh were supplied by Shuqian Xigu Nanotechnology Co., Ltd., China. Shenzhen Hongdachang Technology Co., Ltd. provided water-based multiwalled carbon nanotubes. Paraffin wax with a phase transition temperature of 45–58 °C provided by Sinopec Asset Management Co., Ltd.

9.2.2 Preparation of Composites

All the materials were dried in the drying oven at 105 °C for 2 h. The different masses of EP were separately mixed with EG at mass ratio of 1%, 3%, 5% in a flat-bottomed beaker respectively. Mass fraction of each material in different composite PCMs are listed in the Table 9.1. Then a certain mass of PW was added in the beaker and then

Table 9.1 Mass fraction of each material in different composite PCMs

Samples	PW (%)	EP (%)	EG (%)
PW	100	0	0
PW/EP	71	29	0
PW/EP/EG1	71	28	1
PW/EP/EG3	72	25	3
PW/EP/EG5	73	22	5

sealing the mouth of the beaker. After putted beaker into a water bath with a stable temperature of 95 °C for 90 min to impregnate PW. The samples were heated and filtered to obtain form stable composite PCMs at 80 °C in the drying oven by hot filtration method. The three different composites based on EP, EG, and PW were obtained and denoted as PW/EP/EG1, PW/EP/EG3, and PW/EP/EG5. And the PW/EP also used same preparation method.

When preparing composites with photo-thermal conversion coating, the samples were placed into a cylindrical mold with a diameter of 12 mm to shape the powder under a certain pressure. Then the block samples were coated with water-based multi-wall carbon nanotubes on its surface. After put the sample into drying oven for 4 h to make its surface dry completely. The samples were marked as C-PW, C-PW/EP, C-PW/EP/EG1, C-PW/EP/EG3, and C-PW/EP/EG5.

9.2.3 Characterization

The microstructure images and morphology were obtained by scanning electron microscopy (SEM, ZEISS EVO10, Germany) at an accelerating voltage of 3 kV. The thermal behaviors, including latent heat and phase change point, were obtained by differential scanning calorimeter (DSC, TA Instruments DSC250, America) under nitrogen with a flow rate of 50 ml min⁻¹ at a scanning rate of 5 °C from 5 °C to 80 °C min⁻¹, the test error is ±0.05%. Thermal stability was evaluated by thermogravimetric analysis (TGA, METTLER TOLEDO TGA/DSC3+, Switzerland) from room temperature to 800 °C with a heating rate of 10 °C min⁻¹ under nitrogen, the mass error is ±0.1%. The solar absorptance of the composite PCMs are measured by a Lambda950 spectrophotometer.

9.2.4 Morphologies and Microstructure

The SEM images of EP, EG, PW/EP, PW/EP/EG1, PW/EP/EG3, PW/EP/EG5 are showed in Fig. 9.1.

The irregular flake structure of EP can be observed in Fig. 9.1a. And the EG particle consist of lot of cross-linking graphite layer with flocculence microstructure

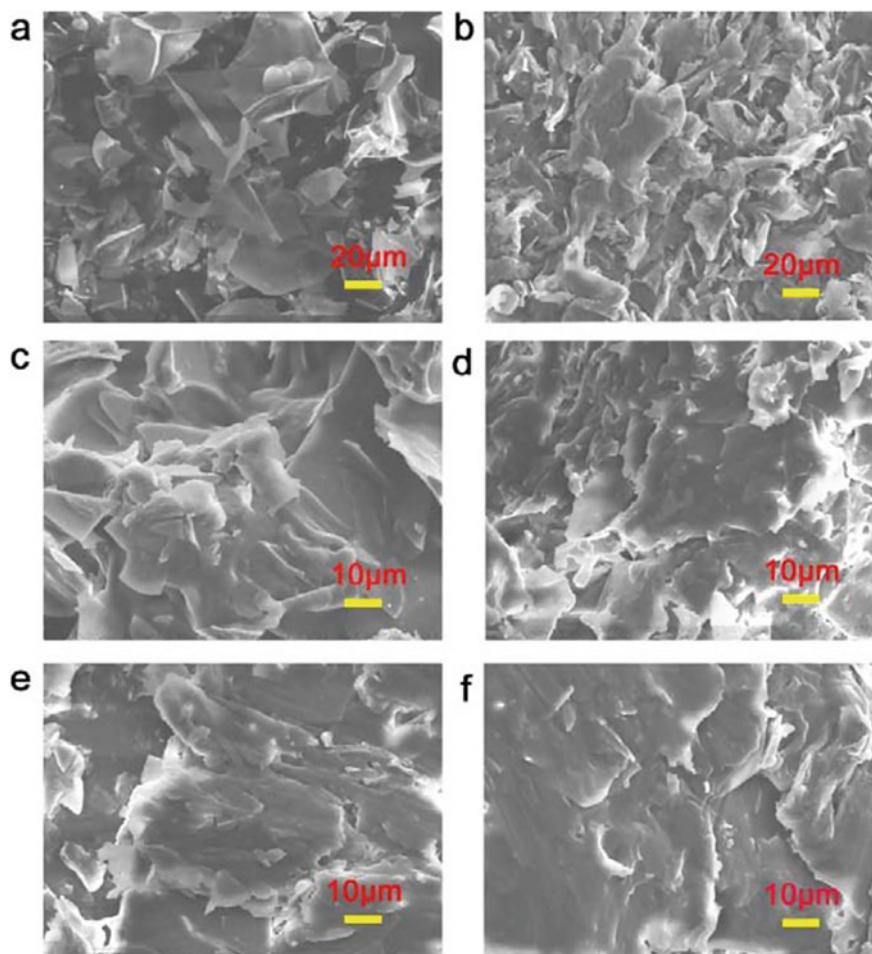


Fig. 9.1 SEM images of **a** EP; **b** EG; **c** PW/EP; **d** PW/EP/EG1; **e** PW/EP/EG3; **f** PW/EP/EG5

can be observed in Fig. 9.1b. The PW was impregnated into the EP successfully. It was already difficult to observe the existence of EP (Fig. 9.1c). It is observed that PW was impregnated into the layer framework of EP and the pores of EG successfully (Fig. 9.1d–f). The PW was distributed homogeneous without leaking due to the capillary and surface tension force of EP and EG. And the microstructure of EP and EG is disappear. With the increasing of the mass of EG, the load of PW in composites increase. The PW/EP/EG5 is flatter than PW/EP/EG1 and PW/EP/EG3, which can be observed in Fig. 9.1f. The interfaces between the matrix and PW combined compactly respectively, there is no obvious phase separation showing a good compatibility.

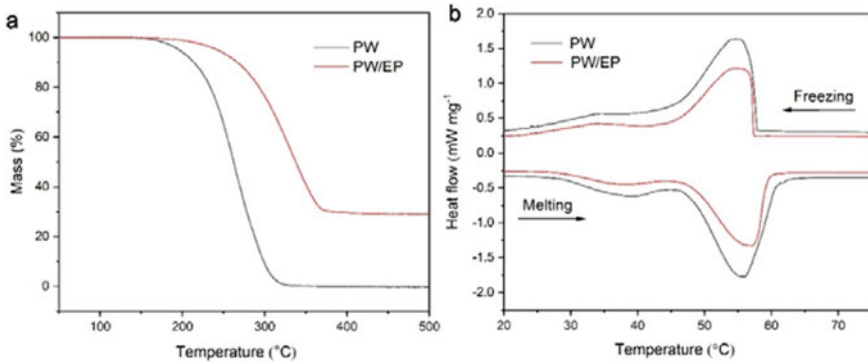


Fig. 9.2 The thermal properties curves of PW and PW/EP in **a** TG and **b** DSC test

9.2.5 Thermal Properties of PW and Composites

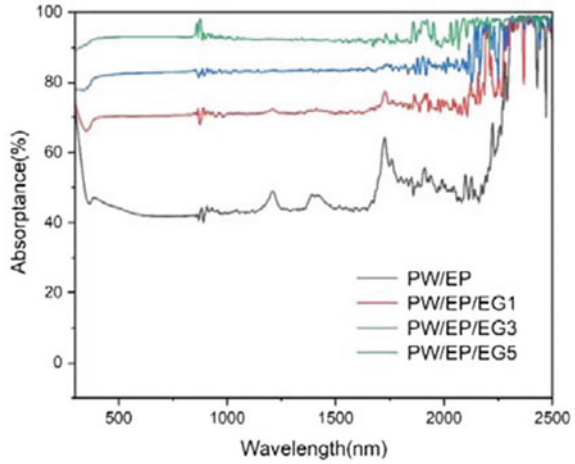
The TG and DSC curves of pure PW and the PW/EP are illustrated in the Fig. 9.2. As shown in Fig. 9.2a, the pure PW and the PW/EP began decomposed at about 150 °C, and all the samples had only one-stage decomposition process. The load of PW was 71.03% for PW/EP. The complete decomposition temperature of pure PW was about 300 °C. The final decomposition temperature of composites (360 °C) was higher than pure PW. It showed that composites were more stable.

The freezing temperature and melting temperature of pure PW were 57.83 and 46.98 °C. The latent heat value of composite phase change materials is one of a crucial factor for engineering application of thermal energy storage equipment. The latent heat of melting and freezing of pure PW were 195.5 and 203.3 J g⁻¹, respectively.

9.2.6 The Solar Absorbance of PW and Composites

Considering the utilization of the composite PCMs in the solar-thermal storage system, the solar absorbance are important factors which affect the light-to-thermal conversion rate. The solar absorbance of the composite PCMs are measured. As shown in Fig. 9.3, the absorbance of PW/EP/EG1, PW/EP/EG3 and PW/EP/EG5 in the wavelengths from 0.3 to 2.5 μm is above 0.7, 0.8 and 0.9. And the absorbance of PW/EP is above 0.4. The absorbance of pure PW is above 0.67 [33]. Carbon nanotubes has high solar absorbance. Jin et al. [34] report a perfect absorber based on CNTs and carbon black particles with omnidirectional high absorption efficiency beyond 99.9% over the broad wavelength range from 400 to 20 mm. For C-PW, C-PW/EP, C-PW/EP/EG1, C-PW/EP/EG3, and C-PW/EP/EG5, it can consider the solar absorption rate to be about 0.95 in the surface of materials.

Fig. 9.3 The solar absorptance of the composite PCMs



9.3 Numerical Model

9.3.1 Physical Model

The heat storage and release process and solar-thermal process of pure PW and composite PCMs were simulated. The physical model is schematically illustrated in Fig. 9.4, Fig. 9.4a is 3D model, and Fig. 9.4b is cross section of plane of X0Z, which has two temperature probe points of A and B. Five samples of the same shape and size (cylinder with diameter 12 mm and height 10 mm) are filled into a glass tube (the inside diameter of 16 mm, the wall thickness of 2 mm and the height of 12 mm) and the bottom is sealed with copper tape as shown in Fig. 9.4a.

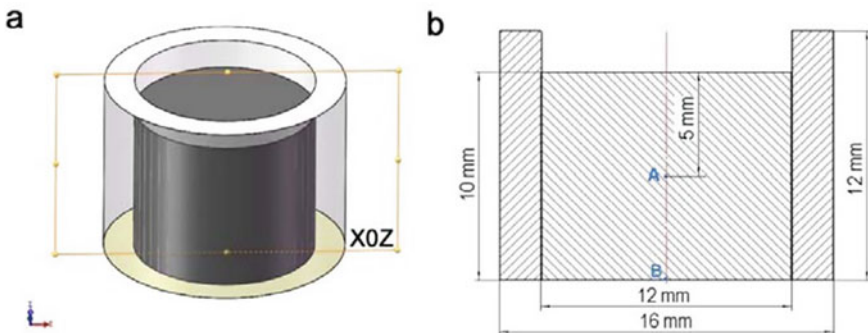


Fig. 9.4 Schematic diagram of **a** 3D physical model, **b** cross section and geometric dimensioning

9.3.2 Governing Equations

The heat transfer mainly including heat conduction and heat convection during the phase change process for the composite PCMs, the governing equations include continuity, momentum and energy equations, which can be expressed as Eqs. (9.1)–(9.10). The momentum equation of liquid phase change materials in the porous media is expressed by extensions of Darcy's law.

The main assumptions of mathematical model are: (1) The liquid PCM is considered as Newtonian and incompressible; (2) The natural convection caused by buoyancy obeys Boussinesq approximation, which is subject to temperature change; (3) The thermo-physical properties of pure PW and composite PCMs are constant, the volumetric expansion is negligible in the phase change temperature range; (4) The pure PW and composites are considered as homogenous and isotropic; (5) The phase change material and porous media are always in local thermal equilibrium state and the viscous dissipation ignored.

The governing equations are listed as follow:

Continuity equation:

$$\varepsilon \frac{\partial \rho_f}{\partial t} + \nabla \cdot (\rho_f \vec{U}) = 0 \quad (9.1)$$

Momentum equations:

$$\frac{\rho_f}{\varepsilon} \frac{\partial u}{\partial t} + \frac{\rho_f}{\varepsilon^2} (\vec{U} \cdot \nabla) u = -\nabla P + \frac{\mu_f}{\varepsilon} \nabla^2 u + S_u \quad (9.2)$$

$$\frac{\rho_f}{\varepsilon} \frac{\partial v}{\partial t} + \frac{\rho_f}{\varepsilon^2} (\vec{U} \cdot \nabla) v = -\nabla P + \frac{\mu_f}{\varepsilon} \nabla^2 v + S_v \quad (9.3)$$

$$\frac{\rho_f}{\varepsilon} \frac{\partial w}{\partial t} + \frac{\rho_f}{\varepsilon^2} (\vec{U} \cdot \nabla) w = -\nabla P + \frac{\mu_f}{\varepsilon} \nabla^2 w + S_w \quad (9.4)$$

where u , v , w are the velocity components in the x , y , z directions; The μ_f is viscosity of liquid PCM; ρ_f is density of liquid PCM, ε is the porosity of porous media. The source terms are listed in the Eqs. (9.5)–(9.7). The physical property parameters of pure PW and composites PCMs are listed in the Table 9.2.

$$S_u = -\left(\frac{\mu_f}{K} + \frac{\rho_f c_F}{\sqrt{K}} |\vec{U}|\right) u + A_{mush} \frac{(1-\beta)^2}{\beta^3 + \omega} u \quad (9.5)$$

$$S_v = -\left(\frac{\mu_f}{K} + \frac{\rho_f c_F}{\sqrt{K}} |\vec{U}|\right) v + A_{mush} \frac{(1-\beta)^2}{\beta^3 + \omega} v \quad (9.6)$$

Table 9.2 Physical property parameters of pure PW and composites PCMs

Samples	ρ (kg m ⁻³)	C_p (J kg ⁻¹ K ⁻¹)	k (W m ⁻¹ K ⁻¹)	ε (%)	μ_f (Pa s)	γ (K ⁻¹)
PW	933	2000	0.26	–	0.00318	0.01
EP	2035	800	0.07	–	–	–
EG	2090	710	137	–	–	–
PW/EP	1252.6	1652.0	0.23	84.24	0.00318	0.01
PW/EP/EG1	1253.1	1651.1	0.33	85.26	0.00318	0.01
PW/EP/EG3	1243.2	1661.3	0.47	88.72	0.00318	0.01
PW/EP/EG5	1233.3	1671.5	0.55	90.89	0.00318	0.01

$$S_w = -\left(\frac{\mu_f}{K} + \frac{\rho_f C_F}{\sqrt{K}} |\vec{U}|\right)w + A_{mush} \frac{(1-\beta)^2}{\beta^3 + \omega} w + \rho_{ref} g \gamma (T - T_{ref}) \quad (9.7)$$

Porous media are modeled by the addition of a momentum source term to the standard fluid flow equations. The source term is composed of viscous loss and inertial loss term [the first term on the right-hand side of Eqs. (9.5)–(9.7)]. The enthalpy-porosity technique treats the mushy region as a porous media, a momentum sink due to the reduced porosity in the mushy zone takes the second term on the right-hand side of Eqs. (9.5)–(9.7). Where β is liquid fraction as shown in Eq. (9.8), ω is small number (0.001) to prevent division by zero, A_{mush} is mushy zone constant (10^5) that represent the momentum limiting factor of fluid flow during phase change. The K is the permeability, described by the Carman-Kozeny equation in formula (9.9). C_F is inertial coefficient (0.55), T_{ref} is reference temperature (297.15 K).

$$\beta = \begin{cases} 0 & T < T_s \\ 1 & T > T_l \\ (T - T_s)/(T_l - T) & T_s \leq T \leq T_l \end{cases} \quad (9.8)$$

$$K = \frac{d_p^2 \varepsilon^3}{180(1 - \varepsilon)^2} \quad (9.9)$$

Energy equation:

$$(\rho C_p)_{eff} \frac{\partial T}{\partial t} + (\rho C_p)_f \vec{U} \cdot \nabla T = \nabla \cdot (k_{eff} \nabla T) - \varepsilon \rho_f L \frac{\partial \beta}{\partial t} \quad (9.10)$$

The temperature of liquid PCM in porous media was evaluated using the local thermal equilibrium hypothesis, ignoring the temperature difference between the liquid and porous media. $(\rho C_p)_{eff}$ is the effective volumetric heat capacity of composite PCMs, $(\rho C_p)_f$ is heat capacity of the liquid PCM in the porous medium. L is the latent heat of PCM. k_{eff} is the effective thermal conductivity of composite PCMs. In this research, the volume average method is used to calculate the effective

conductivity of the solid–fluid system as the weighted arithmetic mean of fluid and porous matrix conductivities:

$$k_{eff} = \theta_p k_p + (1 - \theta_p)k \quad (9.11)$$

where θ_p and k_p are volume fraction and thermal conductivity of solid material, respectively. The k is thermal conductivity of pure PCM.

When the extended porous matrix models include more than one solid, the averaging model is modified in the following way:

$$k_{eff} = \sum_i \theta_{pi} k_{pi} + (1 - \sum_i \theta_{pi})k \quad (9.12)$$

9.3.3 Boundary Conditions

Thermal convection exists between physical model and environment, the convection flux on the entire outer surface is follow:

$$\mathbf{q}_0 = h \cdot (\mathbf{T}_{ext} - \mathbf{T}) \quad (9.13)$$

The heat transfer coefficient h is set as 6 W/(m² K). The environment temperature is 295.15 K.

The initialization boundary condition of computational domain is:

$$T(x, y, z, t = 0) = T_0 \quad (9.14)$$

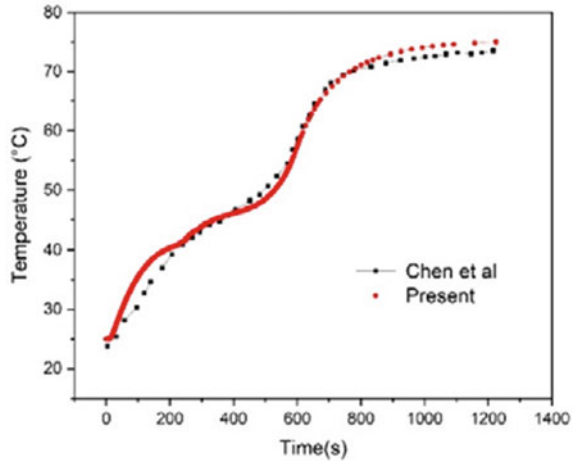
The T_0 is set as 295.15 K.

9.3.4 Numerical Approach and Module Validation

This study used non-isothermal flow module of Comsol Multiphysics 5.6 to simulate the solid–liquid phase change in the porous media. The porous media domain is used in the computational, and the transient solver is PARDISO.

The experiment of Chen et al. was verified. As shown in Fig. 9.5, the numerical model has a high accuracy in the phase change stage and beyond period, the temperature difference between the two outputs can be ignored. The error in the initial heating stage is large, the maximum error is about 8%. In general, the numerical model established had better reliability and accuracy.

Fig. 9.5 Experimental and numerical results of the temperature curve



9.3.5 Grid and Time Steps Independence Verification

In this simulation, four groups of grids are divided according to the two-fold increasing principle of grid number, and the grid number are 11,401, 36,643, 71,544 and 129,112, respectively. Under the premise of the same solver parameter setting, the above numerical models with four groups mesh number are calculated respectively. The changes of the liquid phase rate of PCM with different mesh number with time are obtained by volumetric weighted average method. It can be seen from Fig. 9.6a that when the number of grids increases from 11,401 to 129,112, there is almost no significant change of liquid phase ratio. It is considered that the grid-independent requirement has been achieved, and the mesh number is finally determined to be 36,643.

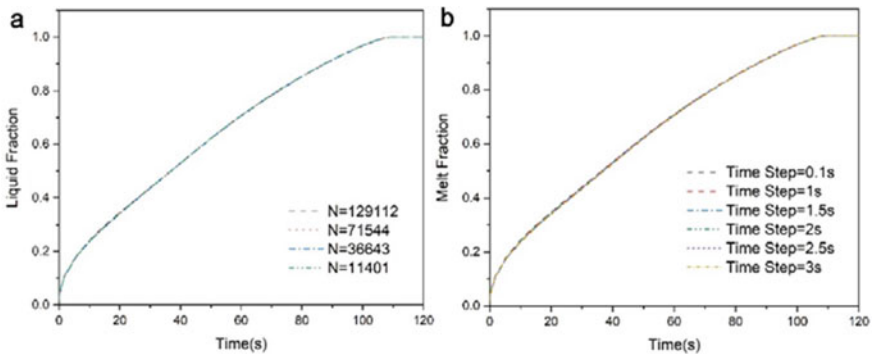


Fig. 9.6 The liquid fraction curve in **a** different mesh number and **b** different time steps

Another important factor in the setting of transient numerical study is reliability of the time step, which is closely related to the accuracy and convergence. Therefore, it is necessary to verify the independence of the time step before performing the calculation. Figure 9.6b shows the change of liquid fraction of PCM with time at six different time steps. During the melting process of PCM, the liquid-phase rate evolution is roughly same under different time steps. As a result, time steps of 1 s and 2 s are sufficient to provide higher accuracy and lower analysis costs.

9.4 Results and Discussion

9.4.1 Heat Storage and Release

The heat storage process of the samples on a constant temperature plate of 80 °C for 900 s was simulated. The initial temperature of samples was 22 °C. The temperature change curves of heat storage in the point A and liquid fraction of pure PW and composite PCMs are shown in Fig. 9.7a, b, respectively. From Fig. 9.7a, it can be seen that the temperature of the PW and composite PCMs grows rapidly at the beginning. The PW and PW/EP have almost the same temperature increasing curve at the beginning and latent heat storage stage. The temperature increase rates of PW/EP/EG1, PW/EP/EG3 and PW/EP/EG5 increase successively with the increase of EG content in the initial sensible heat storage stage. The temperature increase rates of PW/EP/EG1, PW/EP/EG3 and PW/EP/EG5 are faster than PW and PW/EP. This is because PW/EP/EG1, PW/EP/EG3 and PW/EP/EG5 have higher thermal conductivity than pure PW and PW/EP. It takes 130 s and 134 s for PW and PW/EP to reach 46.98 °C, and 104, 82, and 74 s for PW/EP/EG1, PW/EP/EG3 and PW/EP/EG5, respectively. Compared to pure PW, the sensible thermal energy storage time of PW/EP/EG1, PW/EP/EG3 and PW/EP/EG5 decreased by 20%, 0.37% and 43%, respectively. At the latent heat storage stage, the pure PW had longest period. The storage periods of PW/EP/EG1, PW/EP/EG3 and PW/EP/EG5 decreased in turn, although the content of PW in them increased successively. After the latent heat stages, the sensible heat storage stages begin, and the temperatures tend to equilibrium state finally. PW/EP/EG1, PW/EP/EG3 and PW/EP/EG5 reached equilibrium temperature at 775 s (about 73.1 °C), at 698 s (about 73.8 °C) and at 660 s (about 74.2 °C), respectively. Pure PW reached equilibrium temperature at 870 s (about 73.8 °C), and PW/EP not reached equilibrium temperature at 900 s, it indicated that PW/EP had poor thermal property in the whole heat storage period.

As shown in Fig. 9.7b, the increase rates of liquid fraction of PW/EP/EG1, PW/EP/EG3 and PW/EP/EG5 faster than pure PW and PW/EP. PW/EP/EG1, PW/EP/EG3 and PW/EP/EG5 melted completely at 570, 458 and 417 s, respectively, and faster than PW (685 s) and PW/EP (773 s). This is because the PW/EP/EG1, PW/EP/EG3 and PW/EP/EG5 have higher thermal conductivities and lower content of

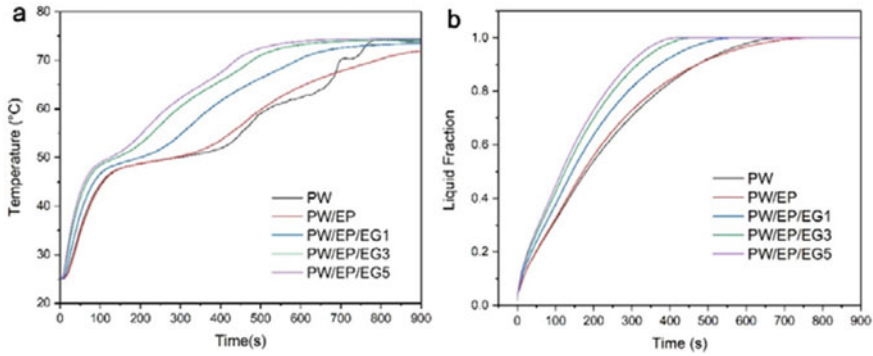


Fig. 9.7 Temperature–time curves **a** in heat charge process and **b** liquid fraction of pure PW and composites

PW than pure PW. Although the PW/EP has least content of PW, it also has lowest thermal conductivity, therefore it takes the longest time.

Figure 9.8 shows the temperature cloud images of PW, PW/EP, PW/EP/EG1, PW/EP/EG3 and PW/EP/EG5 at different times in heat storage process from top to bottom. As shown in Fig. 9.8, at 50 s, there are large temperature difference between bottom and top for pure PW and composite PCMs, which have distinct different temperature layers. At 250 s, the PW/EP/EG3 and PW/EP/EG5 exhibit uniform temperature distribution in the half bottom, while PW, PW/EP still have bigger temperature difference. At 450 s, the PW/EP/EG5 display the uniform temperature distribution in the whole region, while PW, PW/EP, PW/EP/EG1 still have distinct temperature difference. At 650 s, the temperatures of PW/EP/EG1, PW/EP/EG3 and PW/EP/EG5 are higher and evenly distribution in the whole area. PW/EP/EG5 with high effective thermal conductivity can transfer the heat from the bottom to the top level faster and avoid long time local high temperature phenomena such as PW and PW/EP.

From the above results, it can be seen that the thermal storage property of composite PCMs with EG were better than pure PW and PW/EP, and PW/EP/EG5 had the best heat storage property. After adding same 2% mass fraction of EG, the heat storage performance of PW/EP/EG3 was greatly improved, while that of PW/EP/EG5 was slightly improved.

The heat release process of the samples on a constant temperature plate of 20 °C for 900 s was simulated. The temperature change curves of heat storage in the point A and liquid fraction of pure PW and composite PCMs are shown in Fig. 9.9a, b, respectively. As shown in Fig. 9.9a, the temperatures of all samples decline rapidly at initial sensible heat discharge stage, temperature of PW/EP drops the slowest, and the temperature of PW/EP/EG5 drops the fastest. The PW and PW/EP have almost same curves in the subsequent phase change and heat release period, and they have longer phase change stage than other samples. After the liquidus-solidus phase stage, the temperatures of samples descend rapidly again. The pure PW and PW/EP take

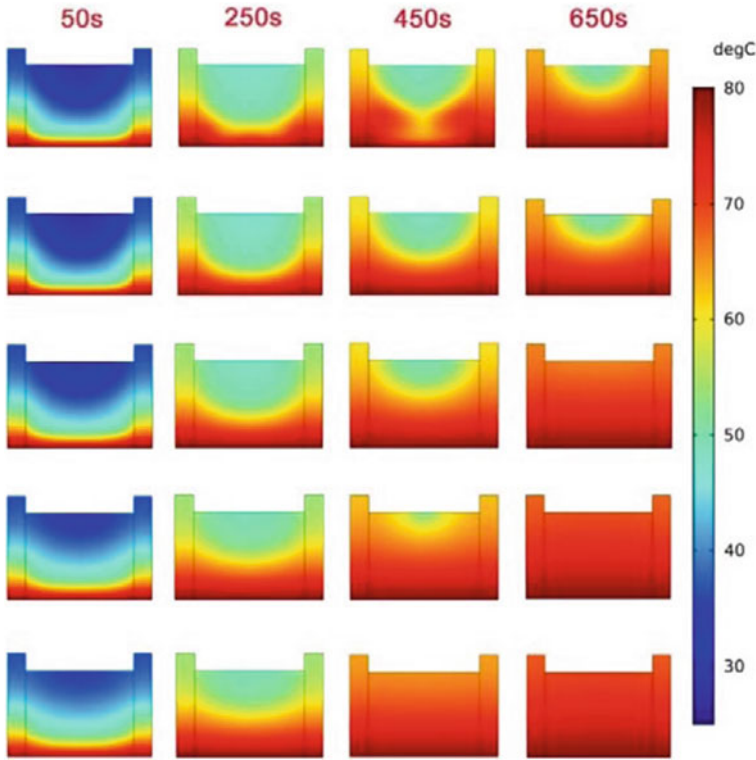


Fig. 9.8 Temperature cloud images in heat charge process of pure PW and composites

about 700 s to complete heat discharge, while PW/EP/EG1, PW/EP/EG3 and PW/EP/EG5 take ~550 s, respectively. The heat release times reduced by 21%. It can be seen from Fig. 9.9b, the liquid fraction of PW/EP/EG1, PW/EP/EG3 and PW/EP/EG5 decrease faster than pure PW and PW/EP. PW/EP/EG1, PW/EP/EG3 and PW/EP/EG5 solidification completely at 334, 250 and 237 s, respectively, and faster than PW (381 s) and PW/EP (434 s). Above results is also due to different thermal conductivities and content of PW. The PW/EP/EG1, PW/EP/EG3 and PW/EP/EG5 have higher thermal conductivities and lower content of PW than pure PW.

Figure 9.10 shows the temperature cloud images of PW, PW/EP, PW/EP/EG1, PW/EP/EG3 and PW/EP/EG5 at different times in heat discharge process from top to bottom. As shown in Fig. 9.10, at 50 s, the bottom temperatures of pure PW and composite PCMs drop rapidly, there are large temperature difference between bottom and top. At 150 s, the PW/EP/EG3 and PW/EP/EG5 exhibit almost same temperature distribution, and bottom half get cold, while PW, PW/EP still have bigger temperature in the most region. At 250 s, the PW/EP/EG5 display the lower temperature in the whole district, while PW, PW/EP, PW/EP/EG1 still have higher temperature in the upper central position. At 350 s, the temperatures of PW/EP/EG1, PW/EP/EG3 and

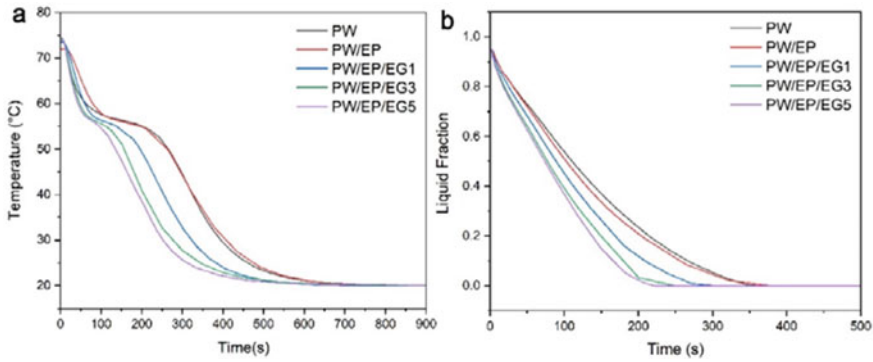


Fig. 9.9 Temperature–time curves **a** in heat discharge process and **b** liquid fraction of pure PW and composites

PW/EP/EG5 are evenly distributed throughout the area. The results show that PW/EP/EG3 and PW/EP/EG5 had better heat release performance in the first 250 s, due to high effective thermal conductivity.

From the above analysis, it can be seen that the thermal discharge performance could be improved by adding EG, and PW/EP/EG5 had the best heat release property. After adding same 2% mass fraction of EG, the heat discharge performance of PW/EP/EG3 was greatly improved, while that of PW/EP/EG5 was slightly improved.

9.4.2 Solar-Thermal Conversion and Storage Process

At 1535 W/m² vertical solar radiation, the temperature change curves and liquid fraction in the point A of pure PW and composite PCMs are shown in Fig. 9.11a and b, respectively. As shown in Fig. 9.11a, after rapidly increase of temperature, the temperatures of PW, PW/EP and PW/EP/EG1 are hardly growing. The PW/EP does not undergo phase change in the entire process. It takes 982 s for PW to reach 46.98 °C, and 938, 680, and 560 s for PW/EP/EG1, PW/EP/EG3 and PW/EP/EG5, respectively. Compared to pure PW, the time of PW/EP/EG3 and PW/EP/EG5 were decreased by 31% and 43%, respectively. Only PW/EP/EG5 has an obvious phase change platform, at about 3500 s, the phase change period end, the temperature increases fast again, it also can be seen from Fig. 9.11b, the liquid fraction already reaches 100%. At 5400 s, the liquid fraction of PW, PW/EP, PW/EP/EG1 and PW/EP/EG3 is 0.5, 0.02, 0.5 and 0.97, respectively.

Figure 9.12 shows the temperature cloud images of PW, PW/EP, PW/EP/EG1, PW/EP/EG3 and PW/EP/EG5 at different times in solar-thermal conversion and storage process from top to bottom. At 500 s, the whole temperature of PW/EP is the lowest, and PW/EP/EG5 is the highest. PW and PW/EP/EG1 have almost same temperature distribution in different times. From 3500 to 4500 s, the temperature

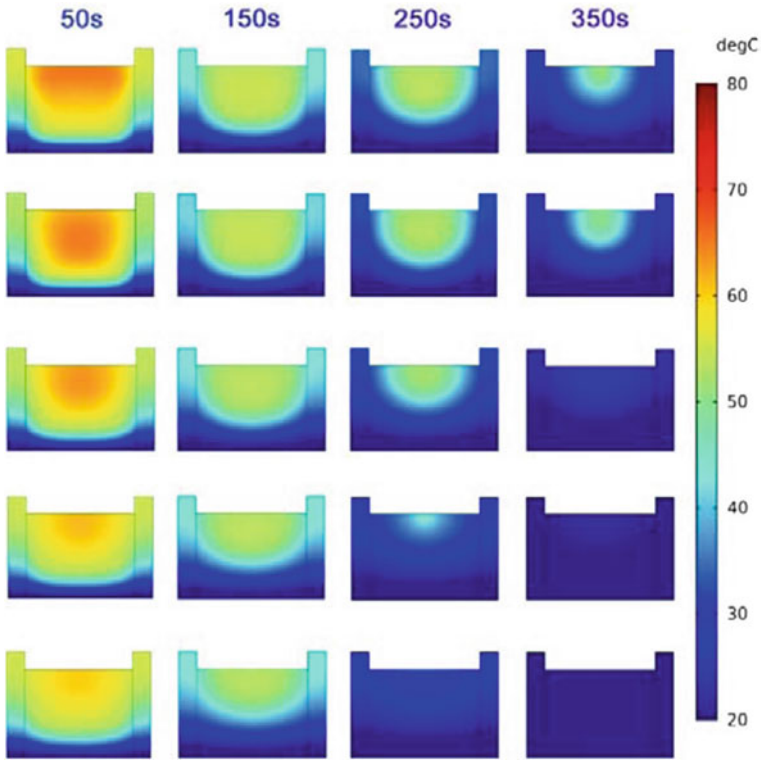


Fig. 9.10 Temperature cloud images in heat discharge process of pure PW and composites

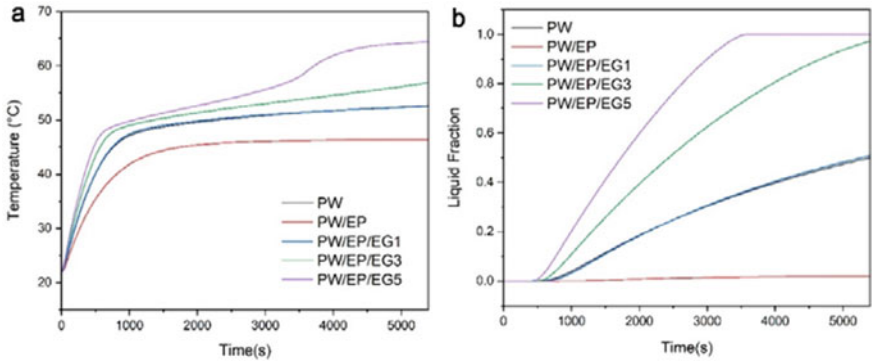


Fig. 9.11 Temperature–time curves **a** in solar-thermal conversion and storage process and **b** liquid fraction of pure PW and composites

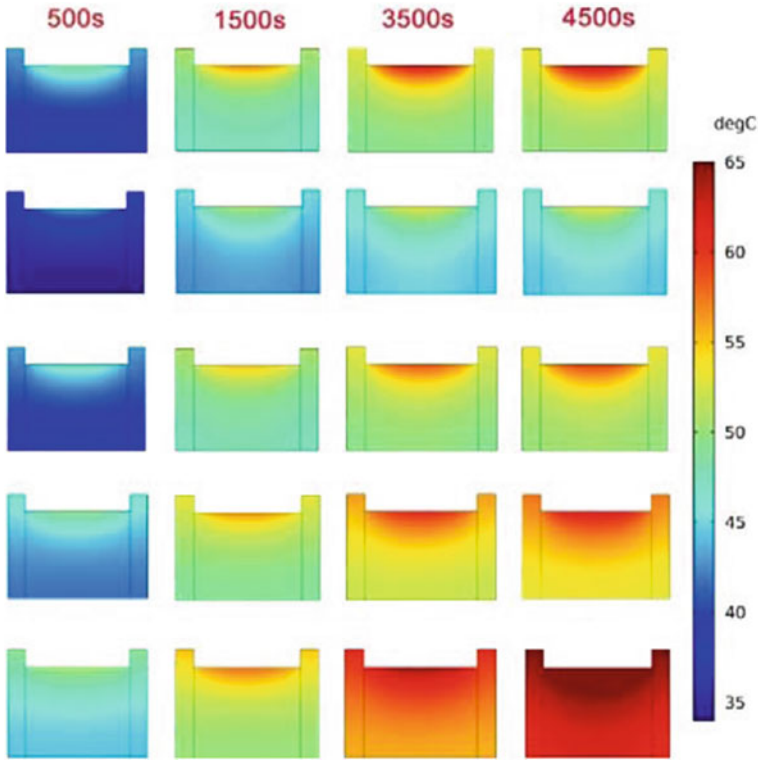


Fig. 9.12 Temperature cloud images in solar-thermal conversion and storage process of pure PW and composites

distributions of PW, PW/EP, PW/EP/EG1 almost unchanged, while the temperature of PW/EP/EG5 increase sharply in entire region.

The results indicated that the addition of EP negative effected the performance of solar-thermal conversion and storage, and EG had positive effect. PW/EP/EG5 had better solar-thermal conversion and storage performance.

The temperature change curves and liquid fraction in the point A of C-PW and composite PCMs with CNTs cover are shown in Fig. 9.13a and b, respectively. As shown in Fig. 9.13a, at first 500 s, the temperatures of samples rapidly increase. At first 2500 s, the C-PW and composites PCMs have almost same curves. All the samples experience entire phase change process, C-PW takes 3178 s finish phase change process, and it takes 3040, 2575, 2365 and 2193 s for C-PW/EP, C-PW/EP/EG1, C-PW/EP/EG3 and C-PW/EP/EG5, respectively. Compared to C-PW, the phase change time of C-PW/EP, C-PW/EP/EG1, C-PW/EP/EG3 and C-PW/EP/EG5 decreased by 4%, 19%, 26% and 31%, respectively. It also can be seen from Fig. 9.13b, the liquid fraction of C-PW, C-PW/EP, C-PW/EP/EG1, C-PW/EP/EG3 and C-PW/EP/EG5 reaches 100% at 3935, 3695, 3190, 3002 and 2885 s, respectively. Compared to C-PW, the time of C-PW/EP, C-PW/EP/EG1, C-PW/EP/EG3 and C-PW/EP/EG5

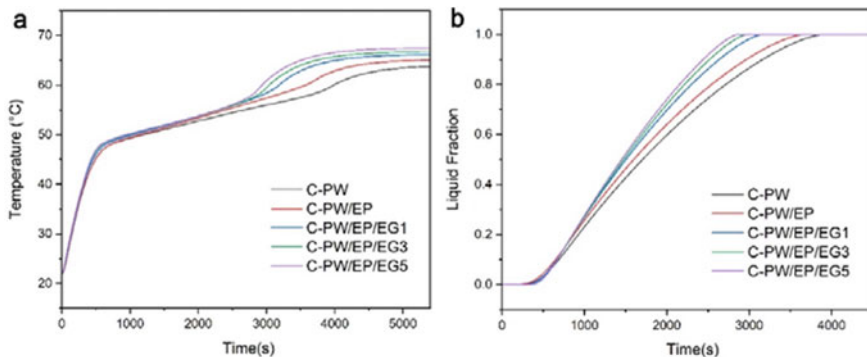


Fig. 9.13 Temperature–time curves **a** in solar-thermal conversion and storage process and **b** liquid fraction of C-PW and composites

decreased by 6%, 19%, 24% and 27%, respectively. This is because C-PW/EP/EG1, C-PW/EP/EG3 and C-PW/EP/EG5 have higher thermal conductivities and lower content of PW than C-PW.

Figure 9.14 shows the temperature cloud images of C-PW, C-PW/EP, C-PW/EP/EG1, C-PW/EP/EG3 and C-PW/EP/EG5 at different times in solar-thermal conversion and storage process from top to bottom. At 500 and 1500 s, the surface temperatures of C-PW, C-PW/EP, C-PW/EP/EG1 are obviously higher than PW/EP/EG3 and C-PW/EP/EG5. This is because the surface heat cannot rapidly transfer from top to underneath region due to lower thermal conductivity. At 3500 s, C-PW and C-PW/EP have distinct temperature difference for different region, while C-PW/EP/EG3 and C-PW/EP/EG5 is uniform relatively. At 4500 s, the C-PW/EP/EG1, C-PW/EP/EG3 and C-PW/EP/EG5 have similar temperature distribution, but C-PW/EP/EG5 accumulate less temperature in the upper region. The results indicated that it indicated that C-PW/EP/EG1, C-PW/EP/EG3 and C-PW/EP/EG5 had higher solar-thermal conversion and storage performance, and C-PW/EP/EG5 is best of them.

Figure 9.15 is temperature difference of pure PW and composites PCM with and without CNTs cover in solar-thermal conversion and storage process. As shown in the picture, the temperature differences of PW, PW/EP and PW/EP/EG1 with and without CNTs cover have similar tendency, which increase first, then decrease and increase again. While the temperature differences of PW/EP/EG3 and PW/EP/EG5 with and without CNTs cover have similar tendency. The maximum temperature difference is about 18.7 °C between PW/EP with and without cover, followed by PW/EP/EG1 (13.7 °C), followed by PW (11.1 °C) and PW/EP/EG3 (11.2 °C), and the smallest is PW/EP/EG5 (7 °C). The results indicated that the solar-thermal performance can be effective improved by adding CNTs cover, and performance of PW/EP was improved the most and that PW/EP/EG5 was improved the least.

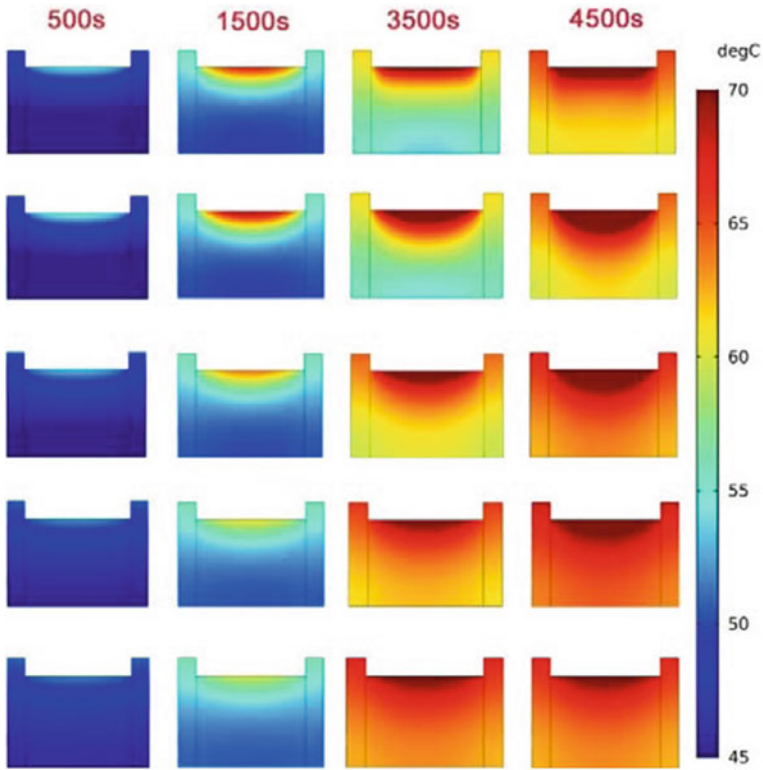
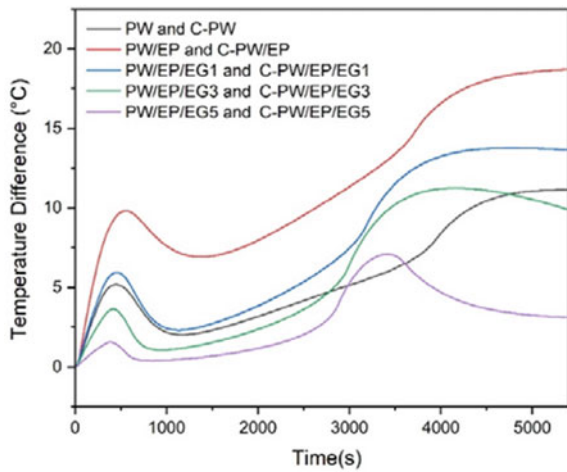


Fig. 9.14 Temperature cloud images in solar-thermal conversion and storage process of C-PW and composites

Fig. 9.15 Temperature difference of samples with and without CNTs converts in solar-thermal conversion and storage process



9.5 Conclusion

A three-dimensional numerical simulation model for composite phase change materials was established and verified by experimental data. The strengthening effects of different proportions of EG on the heat storage and release performance were studied by numerical method, and the pure PW and composite PCMs coated with CNTs were studied in depth in order to improve the overall solar-thermal conversion and storage performance, the following conclusions were obtained:

- (1) PW/EP/EG5 had the best heat storage and release performance, and the heat storage performance of the composites with the addition of EG is better than that of PW and PW/EP; After adding same 2% mass fraction of EG, the heat storage performance of PW/EP/EG3 was greatly improved, while that of PW/EP/EG5 was slightly improved.
- (2) The solar-thermal performance could be effectively improved by adding CNTs cover; C-PW/EP/EG1, C-PW/EP/EG3, C-PW/EP/EG5 had better photothermal conversion and storage performance than C-PW and C-PW/EP; C-PW/EP/EG5 had the best solar-thermal conversion and storage performance.
- (3) When adding the CNTs coat, the performance of PW/EP was improved the most and that PW/EP/EG5 was improved the least. On the premise of considering the cost, PW/EP/EG5 with higher solar absorptance could be chosen as the object.

Acknowledgements This work was supported by National Natural Science Foundation Innovation Group of China (51721004).

References

1. da Cunha, S.R.L., de Aguiar, J.L.B.: Phase change materials and energy efficiency of buildings: a review of knowledge. *J. Energy Storage* **27**, 101083 (2020)
2. Eanest Jebasingh, B., Valan Arasu, A.: A comprehensive review on latent heat and thermal conductivity of nanoparticle dispersed phase change material for low-temperature applications. *Energy Storage Mater.* **24**, 52–74 (2020)
3. Li, C., Xie, B., Chen, J., He, Z., Chen, Z., Long, Y.: Emerging mineral-coupled composite phase change materials for thermal energy storage. *Energy Convers. Manage.* **183**, 633–644 (2019)
4. Pereira da Cunha, J., Eames, P.: Thermal energy storage for low and medium temperature applications using phase change materials—a review. *Appl. Energy* **177**, 227–238 (2016)
5. Li, C., Wang, M., Chen, Z., Chen, J.: Enhanced thermal conductivity and photo-to-thermal performance of diatomite-based composite phase change materials for thermal energy storage. *J. Energy Storage* **34**, 102171 (2021)
6. Mahdi, J.M., Lohrasbi, S., Nsofor, E.C.: Hybrid heat transfer enhancement for latent-heat thermal energy storage systems: a review. *Int. J. Heat Mass Transf.* **137**, 630–649 (2019)
7. Schmit, H., Rathgeber, C., Hoock, P., Hiebler, S.: Critical review on measured phase transition enthalpies of salt hydrates in the context of solid-liquid phase change materials. *Thermochim. Acta* **683**, 178477 (2020)

8. Prieto, C., Cabeza, L.F.: Thermal energy storage (TES) with phase change materials (PCM) in solar power plants (CSP) concept and plant performance. *Appl. Energy* **254**, 113646 (2019)
9. Huang, H., Xiao, Y., Lin, J., Zhou, T., Liu, Y., Zhao, Q.: Improvement of the efficiency of solar thermal energy storage systems by cascading a PCM unit with a water tank. *J. Clean. Prod.* **245**, 118864 (2020)
10. Kabeel, A.E., Khalil, A., Shalaby, S.M., Zayed, M.E.: Experimental investigation of thermal performance of flat and v-corrugated plate solar air heaters with and without PCM as thermal energy storage. *Energy Convers. Manage.* **113**, 264–272 (2016)
11. Kabeel, A.E., Abdelgaied, M.: Solar energy assisted desiccant air conditioning system with PCM as a thermal storage medium. *Renew. Energy* **122**, 632–642 (2018)
12. Zhou, Y., Wang, S., Peng, J., Tan, Y., Li, C., Boey, F.Y.C., Long, Y.: Liquid thermo-responsive smart window derived from hydrogel. *Joule* **4**(11), 2458–2474 (2020)
13. Kong, X., Wang, L., Li, H., Yuan, G., Yao, C.: Experimental study on a novel hybrid system of active composite PCM wall and solar thermal system for clean heating supply in winter. *Sol. Energy* **195**, 259–270 (2020)
14. Stropnik, R., Koželj, R., Zavrl, E., Stritih, U.: Improved thermal energy storage for nearly zero energy buildings with PCM integration. *Sol. Energy* **190**, 420–426 (2019)
15. Lu, S., Xu, B., Tang, X.: Experimental study on double pipe PCM floor heating system under different operation strategies. *Renew. Energy* **145**, 1280–1291 (2020)
16. Safdari, M., Ahmadi, R., Sadeghzadeh, S.: Numerical investigation on PCM encapsulation shape used in the passive-active battery thermal management. *Energy* **193**, 116840 (2020)
17. Tomizawa, Y., Sasaki, K., Kuroda, A., Takeda, R., Kaito, Y.: Experimental and numerical study on phase change material (PCM) for thermal management of mobile devices. *Appl. Therm. Eng.* **98**, 320–329 (2016)
18. Royo, P., Ferreira, V.J., Ure, Z., Gledhill, S., López-Sabirón, A.M., Ferreira, G.: Multiple-Criteria Decision Analysis and characterisation of phase change materials for waste heat recovery at high temperature for sustainable energy-intensive industry. *Mater. Des.* **186**, 108215 (2020)
19. Tauseefur, R., Ali, H. M., Janjua, M. M., Sajjad, U., Yan, W.-M.: A critical review on heat transfer augmentation of phase change materials embedded with porous materials/foams. *Int. J. Heat Mass Transf.* **135**, 649–673 (2019)
20. Sharma, A., Tyagi, V.V., Chen, C.R., Buddhi, D.: Review on thermal energy storage with phase change materials and applications. *Renew. Sustain. Energy Rev.* **13**(2), 318–345 (2009)
21. Tao, Z., Chen, X., Yang, M., Xu, X., Sun, Y., Li, Y., Wang, J., Wang, G.: Three-dimensional rGO@sponge framework/paraffin wax composite shape-stabilized phase change materials for solar-thermal energy conversion and storage. *Solar Energy Mater. Solar Cells* **215**, 110600 (2020)
22. Du, X., Qiu, J., Deng, S., Du, Z., Cheng, X., Wang, H.: Ti3C2Tx@PDA-integrated polyurethane phase change composites with superior solar-thermal conversion efficiency and improved thermal conductivity. *ACS Sustain. Chem. Eng.* **8**(14), 5799–5806 (2020)
23. Shao, Y.-w., Hu, W.-w., Gao, M.-h., Xiao, Y.-y., Huang, T., Zhang, N., Yang, J.-h., Qi, X.-d., Wang, Y.: Flexible MXene-coated melamine foam based phase change material composites for integrated solar-thermal energy conversion/storage, shape memory and thermal therapy functions. *Compos. Part A Appl. Sci. Manuf.* **143**, 106291 (2021)
24. Du, X., Qiu, J., Deng, S., Du, Z., Cheng, X., Wang, H.: Flame-retardant and solid-solid phase change composites based on dopamine-decorated BP nanosheets/polyurethane for efficient solar-to-thermal energy storage. *Renew. Energy* **164**, 1–10 (2021)
25. Ye, Q., Tao, P., Chang, C., Zhou, L., Zeng, X., Song, C., Shang, W., Wu, J., Deng, T.: Form-stable solar thermal heat packs prepared by impregnating phase-changing materials within carbon-coated copper foams. *ACS Appl. Mater. Interfaces* **11**(3), 3417–3427 (2019)
26. Liu, H., Wang, X., Wu, D.: Tailoring of bifunctional microencapsulated phase change materials with CdS/SiO₂ double-layered shell for solar photocatalysis and solar thermal energy storage. *Appl. Therm. Eng.* **134**, 603–614 (2018)

27. Pornea, A. M., Kim, H.: Design and synthesis of SiO₂/TiO₂/PDA functionalized phase change microcapsules for efficient solar-driven energy storage. *Energy Convers. Manage.* **232**, 113801 (2021)
28. Zheng, Z., Chang, Z., Xu, G.K., McBride, F., Ho, A., Zhuola, Z., Michailidis, M., Li, W., Raval, R., Akhtar, R., Shchukin, D.: Microencapsulated phase change materials in solar-thermal conversion systems: understanding geometry-dependent heating efficiency and system reliability. *ACS Nano* **11**(1), 721–729 (2017)
29. Du, X., Qiu, J., Deng, S., Du, Z., Cheng, X., Wang, H.: Flame-retardant and form-stable phase change composites based on black phosphorus nanosheets/cellulose nanofiber aerogels with extremely high energy storage density and superior solar-thermal conversion efficiency. *J. Mater. Chem. A* **8**(28), 14126–14134 (2020)
30. Sun, K., Dong, H., Kou, Y., Yang, H., Liu, H., Li, Y., Shi, Q.: Flexible graphene aerogel-based phase change film for solar-thermal energy conversion and storage in personal thermal management applications. *Chem. Eng. J.* **419**, 129637 (2021)
31. Zhang, L., Li, R., Tang, B., Wang, P.: Solar-thermal conversion and thermal energy storage of graphene foam-based composites. *Nanoscale* **8**(30), 14600–14607 (2016)
32. Wu, N., Bing, G., Li, Y., Xie, H., Yu, W.: Three-dimensional directional cellulose-based carbon aerogels composite phase change materials with enhanced broadband absorption for light-thermal-electric conversion. *Energy Conv. Manage.* **256**, 115361 (2022)
33. Chen, G., Su, Y., Jiang, D., Pan, L., Li, S.: An experimental and numerical investigation on a paraffin wax/graphene oxide/carbon nanotubes composite material for solar thermal storage applications. *Appl. Energy* **264**, 114786 (2020)
34. Jin, Y., Zhang, T., Zhao, J., Zhao, Y., Liu, C., Song, J., Hao, X., Wang, J., Jiang, K., Fan, S., Li, Q.: Spray coating of a perfect absorber based on carbon nanotube multiscale composites. *Carbon* **178**, 616–624 (2021)

Chapter 10

Effect of Natural Fracture Clusters on Hydraulic Fracture Propagation in Fractured Reservoirs: A Numerical Simulation Study



Guchang Zhang, Bo Wang, Ying Zhang, Wenxia Li, and Fujian Zhou

Abstract The presence of a large number of natural fracture clusters in fractured reservoirs has a significant impact on fracture propagation during hydraulic fracturing. A two-dimensional fluid–solid coupled hydraulic fracture intersection extension finite element model was established considering the coupling between the deformation of rock and the fluid flow inside the fracture as well as the interaction between natural fracture (NF) and hydraulic fracture (HF). The results indicate that when HF intersects NF with a high approach angle at a low horizontal stress difference, HF tends to pass through NF directly, and vice versa, HF tends to activate NF; with the increase of horizontal stress difference, the fracture as a whole extends in a zigzag shape along the direction of maximum principal stress. As the NF angle is higher, HF is prone to divert to activate the NF and the fracture extends in a step-like shape along the NF, and the higher the NF angle the straighter the fracture is, and the greater the fracture initiation pressure. The higher the injection rate, the more HF tends to penetrate the NF, and the straighter the HF morphology. The fracturing fluid viscosity has less influence on the expansion of HFs, and the HF morphology is approximately similar. This study has certain theoretical guiding significance for clarifying the propagation path of hydraulic fractures under natural fracture distribution and formulating the stimulation plan of fractured reservoirs.

Keywords Fractured reservoirs · Natural fractures · Fracture propagation · Finite element method

G. Zhang · Y. Zhang · F. Zhou
State Key-Laboratory of Petroleum Resources and Prospecting, China-University of Petroleum (Beijing), Beijing 102249, China

B. Wang (✉)
China University of Petroleum-Beijing at Karamay, Karamay 83400, Xinjiang, China
e-mail: wangbo@cupk.edu.cn

W. Li
The Tuha Downhole Service Company, CNPC, Western-Drilling Engineering Co. Ltd., Xinjiang 838200, China

10.1 Introduction

With the further increase in global energy demand, unconventional energy has gradually become an important field for oil and gas exploration and development. Due to the characteristics of large burial depth, low porosity and permeability, unconventional oil and gas reservoir resources are difficult to be used and poorly developed [1–3]. Hydraulic fracturing is the key and core technology to improve the oil and gas development effect of unconventional reservoirs, and hydraulic fracturing can increase the channel of oil and gas transportation and improve oil and gas production and recovery [4–7]. Geological investigation and field research has found that there are more NFs in some reservoirs, and the interaction with NFs during hydraulic fracture expansion will affect the expansion path of hydraulic fractures, and the change of expansion path will have an impact on the flow of fracturing fluid and proppant in the fractures, which will then affect the scale of fracturing transformation and the benefit of product enhancement and development. Therefore, it is important to consider the HF expansion law under the influence of NF clusters for the product enhancement and transformation of fractured reservoirs.

The propagation law of HF under the influence of NF has been a hot topic of research by many scholars. Numerous studies have shown that the interaction between hydraulic fractures and natural fractures is specifically manifested in three forms: through natural fracture type, activated natural fracture type and stopped expansion type when encountering natural fractures. Blanton [8] conducted experiments on the interaction between HFs and NFs under different stress differences and NF angles. Jeffrey et al. [9, 10] found that HFs can divert to activate NFs and extend in a stepwise manner along an inclined shear zone with proppant distributed throughout the fracture. Zhou et al. investigated the effect of NFs and stress differences on HF extension in fractured reservoirs by indoor true triaxial hydraulic fracturing tests, which showed that at high levels of stress differences, HFs tend to be dominant fractures with random multiple branches [11, 12]. Wang et al. [4] studied the expansion path of samples with cemented fractures by using semicircular bending tests and found that the larger the shear strength of NFs, the larger the angle of approximation between HFs and NFs, and the easier it is for HFs to pass through NFs. Liu et al. [7] established different inclination angle pre-fractures and studied the effect of different types of NFs on fracture propagation in dense reservoirs during hydraulic fracturing. The above scholars studied the HF expansion law under the influence of NFs through indoor experiments, but the physical model experiments are limited by the scale of the samples and cannot eliminate the influence of boundary effects in stress loading, resulting in a certain gap between the fracture propagation law and the reality.

With the development of numerical simulation techniques, the displacement discontinuity method (DDM), discrete element method (DEM), finite element method (FEM), finite difference method (FDM), and cohesive zone model (CZM) can be used to simulate the expansion behavior of fractures intersecting with NFs in hydraulic fracturing. Wu et al. [13, 14] investigated the interaction law between HF and NF based on the three-dimensional DDM and FDM. Song et al. considered the

shear and tensile damage mechanism of rocks, used theoretical analysis and DEM numerical simulation to verify the expansion law of HF under the influence of NF, and investigated the effects of approach angle, principal stress difference, NF tensile strength and length, reservoir elastic modulus, and Poisson's ratio on the expansion pattern of HFs [15]. Guo et al. [16] developed a new model based on the coupled stress-seepage damage field using the viscous zone method to simulate the interaction between HFs and NFs without introducing a cross-criterion. Among them, CZM uses bilinear intrinsic relationships to describe the damage and destruction processes of hydraulically fractured fractures [17], which has been widely used to simulate HF extensions due to its unique advantages. Chen et al. [18] used CZM to study the interaction between HFs and pre-existing NFs. However, the CZM method must pre-define the crack expansion path, which makes it difficult to simulate the artificial HF expansion in bedrock along arbitrary directions. Most of the current results mainly focus on the study of the initiation and propagation of a single HF, or the intersection form of two fractures. Thus, Nguyen et al. [19] established a new method for stochastic expansion of HFs based on zero-thickness CZM. Wang et al. [20] established a NF formation model and studied the fracture expansion pattern in naturally fractured reservoirs using a numerical simulation method with globally embedded CZM. In summary, numerical simulation methods are favored by many scholars due to their superiority in time and cost, but although these studies obtained the overall expansion forms and paths of HFs, there are fewer studies on the fracture expansion variation laws after the intersection of HFs and NFs, and also fewer studies on the expansion behavior of HFs in fractured reservoirs under different NF angles and the injection pressure response characteristics.

In this paper, based on the finite element and global cohesion zone methods, a batch embedding cohesive element method using Python secondary development technique is used to characterize the potential expansion paths of HFs. At the same time, NFs with the same angle are embedded to study the HF expansion law and injection pressure response characteristics under the influence of NF clusters. The research in this paper has some theoretical guidance significance to clarify the HF expansion paths under the distribution of NFs.

10.2 Governing Equations

In the hydraulic fracturing process, the interaction between HFs and NFs is a complex fluid–solid coupling process, which mainly includes rock deformation and fluid percolation process, fracture initiation and propagation process, intra-seam fluid flow, and the interaction behavior of HFs and NFs. In this study, the interaction behavior between NFs and HFs in finite element simulation does not introduce a fixed determination criterion. The interaction behavior of activating or crossing the NF depends on the stress-percolation-damage field during the fracture propagation. The controlling equations in the HF propagation process mainly include the rock deformation and

fluid flow equations, the fracture initiation and propagation equations, and the fluid flow equations within the fracture.

10.2.1 Rock Deformation and Fluid Flow Equations

The reservoir is a porous medium including rock skeleton and pore fluid, the deformation of the rock is not only related to the stress acting on the rock but also related to the fluid pressure in the pore, the stress and strain off relationship can be characterized by the linear poroelastic equation [21].

$$\delta_{ij} = \lambda \varepsilon_{vol} \delta_{ij} + 2G \varepsilon_{ij} - C \zeta \delta_{ij} \quad (10.1)$$

where λ and G are Larmé parameters for porous media, respectively, dimensionless; ε_{vol} is the volume strain; and ζ is the volume strain parameter of fluid to solid.

$$p = C \varepsilon_{vol} - M \zeta \quad (10.2)$$

where C and M are the additional modulus of elasticity required to describe the two-phase medium, GPa; p is the pore pressure, Pa.

The fluid in the pores of the rock conforms to the mass conservation equation as follows:

$$\frac{\partial \zeta}{\partial t} + q_{i,j} = 0 \quad (10.3)$$

where $q_{i,j}$ is the fluid flux in the pore space, m^2/s .

10.2.2 Fracture Tip Initiation and Propagation Control Equation

The fracture initiation and propagation behavior is characterized by the cohesive zone model (CZM), which considers the existence of a process zone at the fracture tip (Fig. 10.1a tip region). In this region, the fracture interface gravitational force is bilinearly related to the interface distance (T-S criterion), and the cohesion zone model can accurately simulate the tangential flow and normal filtration loss of fluid in the fracture, which becomes an effective method to simulate fracture initiation and propagation.

For fracture element initiation, the quadratic stress criterion is used for control, i.e., initial damage to the fracture element occurs when the sum of the squares of the ratios of the actual stresses in the three directions and the critical stresses in the corresponding directions is equal to 1.

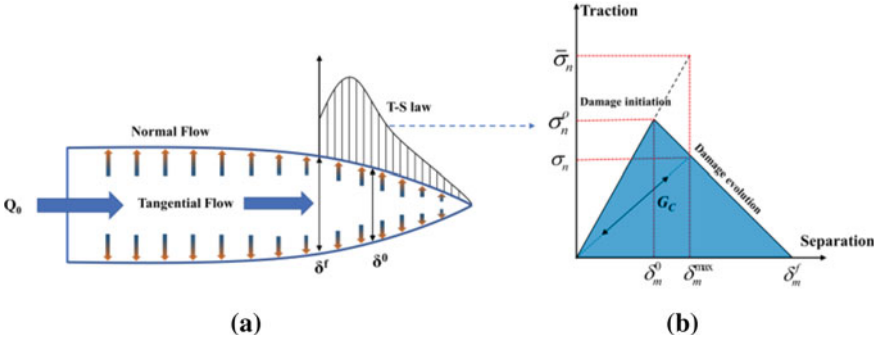


Fig. 10.1 CZM model **a** fracture initiation in cohesive zone model. **b** A bilinear cohesive traction–separation law

$$\left\{ \frac{\sigma_n}{\sigma_n^o} \right\}^2 + \left\{ \frac{\sigma_s}{\sigma_s^o} \right\}^2 + \left\{ \frac{\sigma_t}{\sigma_t^o} \right\}^2 = 1 \tag{10.4}$$

where, $\sigma_n^o, \sigma_s^o, \sigma_t^o$ represent the tensile strength and shear strength in both directions, respectively, MPa. The symbol $\langle \rangle$ indicates that the compressive stress does not cause damage. $\sigma_n, \sigma_s, \sigma_t$ represent the actual normal and tangential stresses in the crack unit, MPa.

After the initial damage, the fracture element interface stress can be calculated by the following equation:

$$\sigma_n = \begin{cases} (1 - D)\bar{\sigma}_n, & \bar{\sigma}_n \geq 0 \\ \bar{\sigma}_n & \end{cases} \tag{10.5}$$

$$\begin{aligned} \sigma_s &= (1 - D)\bar{\sigma}_s \\ \sigma_t &= (1 - D)\bar{\sigma}_t \end{aligned} \tag{10.6}$$

where, $\bar{\sigma}_n, \bar{\sigma}_s, \bar{\sigma}_t$ represent the stresses calculated in the normal direction and two tangential directions according to the linear elasticity criterion before the damage. D is the dimensionless damage factor, which takes the value between 0 and 1, when $D = 0$, the material is not damaged; $D = 1$, the material is completely damaged.

The expression of the damage factor D is as follows:

$$D = \frac{\delta_m^f \cdot (\delta_m^{\max} - \delta_m^0)}{\delta_m^{\max} \cdot (\delta_m^f - \delta_m^0)} \tag{10.7}$$

where, δ_m^{\max} is the current interface distance, mm. δ_m^0, δ_m^f are the corresponding interface distance when the initial damage and complete damage, mm, respectively.

10.2.3 Fluid Flow Equation in the Fracture

After the formation of HFs, the flow equation along the fracture direction satisfies Poiseuille's law.

$$q = -\frac{w^3}{12\mu}\nabla p \quad (10.8)$$

The flow equation for filtration loss in the vertical fracture direction is defined as follows:

$$\begin{cases} q_t = c_t(p_i - p_t) \\ q_b = c_b(p_i - p_b) \end{cases} \quad (10.9)$$

The fluid within the fracture conforms to the mass conservation equation.

$$\frac{\partial w}{\partial t} + \nabla \cdot q + (q_t + q_b) = Q(t)\delta(x, y) \quad (10.10)$$

where q is the flow rate in the fracture, m^3/s ; q_t, q_b is the filtration loss flow rate into the top and bottom of the fracture, m^3/s , respectively; p_i, p_t, p_b is the fluid pressure at the top, center, and bottom of the fracture, Pa, respectively; c_t, c_b is the fluid filtration loss coefficient at the top and bottom of the fracture, $\text{m}^3/\text{s}/\text{Pa}$, respectively; w is the fracture width, m; μ is the fracturing fluid viscosity, $\text{mPa}\cdot\text{s}$.

10.3 Numerical Simulation Method Validation and Model Building

10.3.1 Numerical Simulation Method Validation

Blanton conducted an indoor experiment of hydraulic fracturing under triaxial stress and studied the propagation of HFs and NFs under different horizontal stress differences and fracture intersection angles [8]. To verify the correctness of this model when considering the intersection effect of HF and NF, the finite element model with the angle between HF and NF of 45° and 60° , and the stress difference of 9 and 15 MPa, respectively, was established concerning Blanton's experimental model and parameters.

Figure 10.2 compares the numerical simulation results with Blanton's experimental results. In Fig. 10.2a, the angle between HF and NF is 45° , the horizontal stress difference is 15 MPa, HF is arrested by NF and no longer expands forward; keeping the horizontal stress difference constant at 15 MPa, the angle between HF

and NF is 60° (Fig. 10.2b), the HF crosses the NF and continues to expand in the original direction; keeping the angle between HF and NF constant at 60°, reducing the horizontal stress difference to 9 MPa, the HF can divert to activate NF (Fig. 10.2c).

Table 10.1 shows the comparison results of numerical simulations with Blanton’s experiments. The results show that the numerical simulations are consistent with the experimental results, proving the accuracy of the fracture intersection propagation model used in this study.

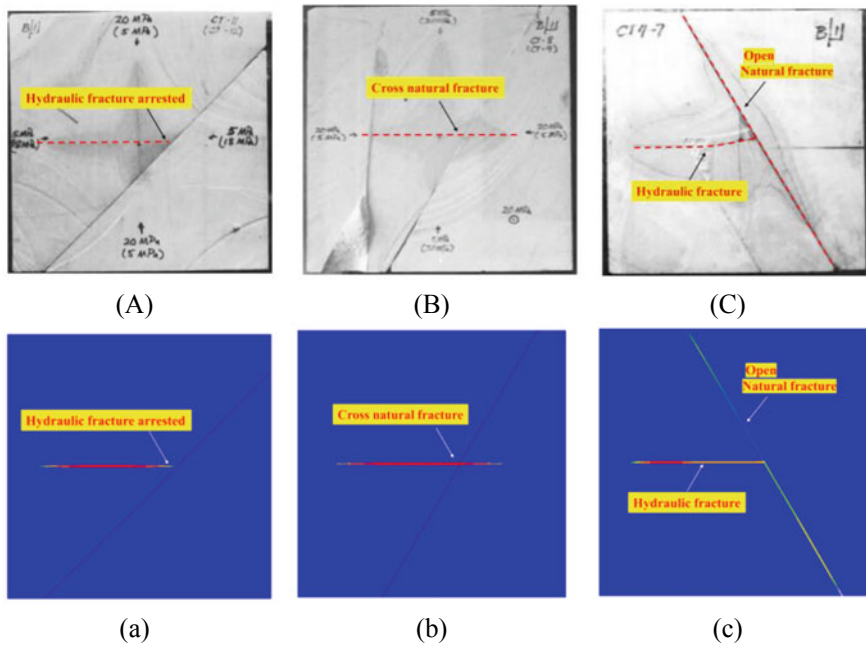


Fig. 10.2 Blanton experiment results and corresponding numerical simulation results. **A–C** Blanton experiment results. **a–c** Numerical simulation results

Table 10.1 Comparison between numerical simulation and Blanton’s experiment

Angle	$\Delta\sigma$ (MPa)	Blanton’s experiment	Numerical simulation
45°	15	Arrest	Arrest
60°	15	Crossing	Crossing
60°	9	Opening	Opening

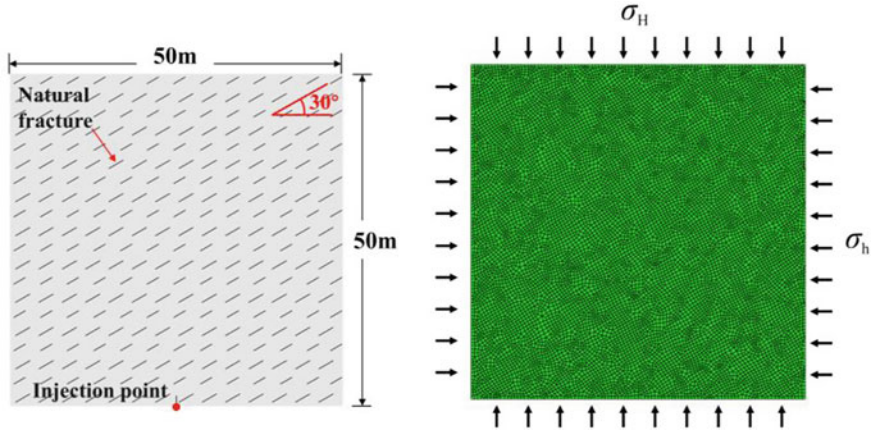


Fig. 10.3 Model diagram and finite element mesh division

10.3.2 Model Building

Based on the finite element method and the global cohesion zone model, a two-dimensional fluid–solid coupling model is established with pre-set fixed angle NF clusters to study the influence law of different NF clusters on HF propagation. Considering the symmetry of the model, to shorten the computation time, the unilateral fracture propagation is designed and the established model size is 50 m \times 50 m. In addition, the element types: two-dimensional four-node bilinear displacement and pore pressure element (CPE4P) is used for the matrix rock body, and six-node displacement and pore pressure bonding element (COH2D4P) is used for the fracture propagation path, with a total number of 34,351 meshes. The displacement degrees of freedom of the finite element model boundary is fixed, and a constant pore pressure boundary is set. Figure 10.3 shows the model size, injection point location, NF distribution, and the division of finite element mesh, and Table 10.2 shows the model base input parameters.

10.4 Simulation Results

10.4.1 Fracture Propagation Morphology and Injection Pressure Response Characteristics

In order to investigate the HF propagation morphology and injection pressure response characteristics of the fractured reservoir, based on the basic data in Table 10.2, a NF angle of 30° and a horizontal stress difference of 2.5 MPa are used as an example. Figures 10.4 and 10.5 demonstrate the fracture propagation morphology

Table 10.2 Input parameters of the base model

Category	Input parameters	Value
Reservoir rock parameters	Elastic modulus	30 GPa
	Poisson's ratio	0.25
	Tensile strength of rock	6 MPa
	Shear strength of rock	20 MPa
	Tensile strength of natural fracture	4 MPa
	Shear strength of natural fracture	10 MPa
	Formation effective permeability	1 md
	Leak-off coefficient	$1e^{-14}$ m ³ /s/Pa
In-situ stress parameters	Maximum horizontal stress	42.5 MPa
	Minimum horizontal stress	40 MPa
Pumping fluid parameters	Fluid viscosity	1 mPa·s
	Injection rate	0.001 m ² /s
Initial condition	Initial pore pressure	30 MPa
	Porosity	0.2

and injection pressure response characteristics at different injection times (the fracture morphology is enlarged by 75 times in the figure). It can be seen that the HF first expands in the direction of the maximum principal stress, and when it intersects with the NF ($t = 15$ s), the injection pressure increases rapidly, and the HF turns to activate the NF. The HF then continues to expand in the direction of the maximum principal stress until it encounters the NF again and reactivates ($t = 50$ s, 90 s, 120 s, 150 s). In addition, it can be noticed that when the HF and NF approach angle is large (close to 90°), the injection pressure increase is significant, while when the HF and NF approach angle is small, the HF is prone to activate the NF and the injection pressure increase is slight. When HF encountered NF again ($t = 180$ s), HF is not enough to divert to activate NF, and HF expands through NF along the direction of maximum principal stress.

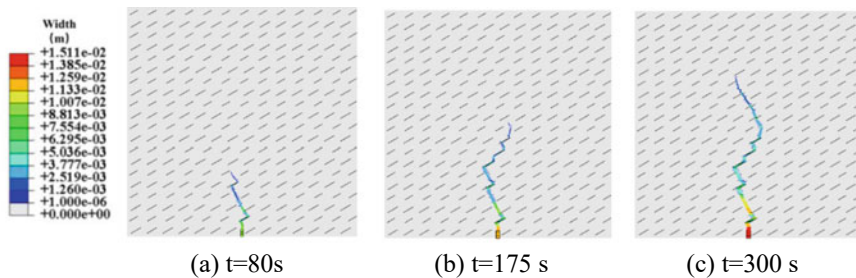
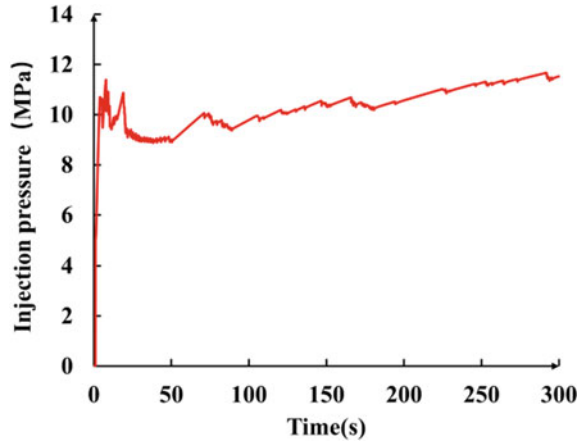


Fig. 10.4 Fracture propagation morphology under different injection times

Fig. 10.5 Injection pressure response characteristic curve



In summary, in the reservoir with the NF angle of 30° , at the early stage of HF propagation, due to the relatively low fluid filtration and energy consumption, when HF encounters NF, HF tends to divert to activate the NF, and then under the action of the maximum principal stress, the fracture continues to expand in the direction of the maximum principal stress, and the fracture expands in a zigzag shaped meander, and the injection pressure continuously changes. On the whole, there are three forms when HFs intersect with NFs, namely, fully activating NF, activating part of NF, and passing through NF. In the later stage of HF propagation, with the continuous injection of fluid, due to the increase of fracture length and the filtration of fluid in the fracture, the net pressure of fluid in the fracture decreases, and the fracture width becomes narrower. The fracture width in the near-wellbore area is about 1.5 cm, while the fracture width in the fracture tip area is about 0.45 cm. Reduce by about 70.95%. In the later stage of fracture propagation, the fracture shape is relatively straight, and the injection pressure fluctuates little.

10.4.2 Influence of Horizontal Stress Difference on Hydraulic Fracture Propagation

Based on the base data in Table 10.1, the NF angle is fixed at 30° , the minimum horizontal principal stress (5 MPa) is kept constant, the maximum horizontal principal stress (5, 7.5, 10 MPa, respectively) is changed, and other parameters are kept consistent to study the HF propagation law under the influence of different horizontal stress differences (0, 2.5, 5 MPa).

The horizontal principal stress difference has a significant effect on the fracture propagation pattern of hydraulic fracturing. When the horizontal principal stress difference is 0 MPa, the in-situ stress has no control effect on the fracture propagation direction. It can be seen from Fig. 10.6a that after the hydraulic fracturing fracture

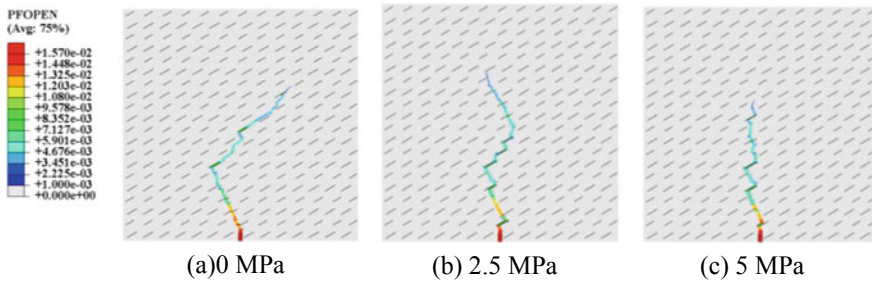


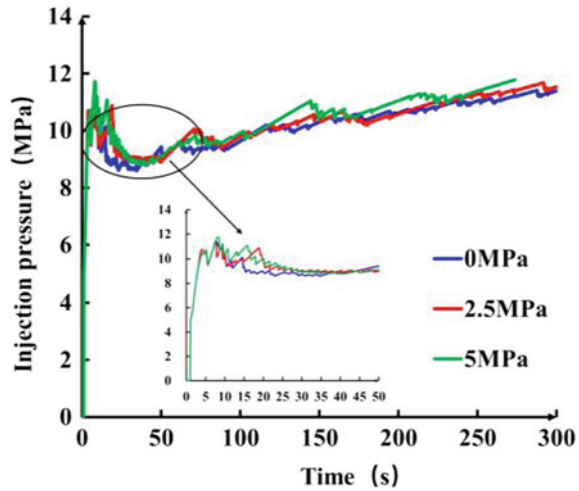
Fig. 10.6 Fracture propagation patterns under different horizontal stress difference

initiates, it first extends through the NF with a high approximation angle, and then activates the NF with a low approximation angle and extends along the NF. The overall extension direction of the latter section is roughly the same as that of the NF. Therefore, when the horizontal stress difference is 0, the fracture extension can be extended in any direction, and the approach angle when HF and NF intersect becomes the key factor to control the HF extension behavior. When the horizontal stress difference is 2.5 MPa, the HF extension direction is dominated by the maximum horizontal principal stress direction. In the early stage of extension, HF can turn to activate the NF even when it intersects NF at a high approach angle; in the late stage of extension, HF passes through NF if it intersects NF at a high approach angle due to the decrease of net pressure in the fracture. With the increase of horizontal stress difference to 5 MPa, the controlling effect of ground stress is further enhanced. As can be seen from Fig. 10.6c, when HF intersects with the first NF, the fracture does not fully activate the NF under the action of ground stress but expands along the direction of maximum principal stress. Subsequently, when the HF encountered the NF, it turned to activate the NF, but the fracture expansion direction changed to the maximum principal stress direction in a short time, and the fracture as a whole expanded in a zigzag shape along the maximum principal stress direction. In addition, from the pumping pressure curve in Fig. 10.7, it can be seen that the fracture initiation pressure is about the same under different horizontal stress differences, which is about 11.52 MPa, but the greater the horizontal stress difference, the higher the fracture extension pressure and the injection pressure curve under different horizontal stress differences shows the characteristic of constant fluctuation due to the continuous penetration of HF and activation of NF.

10.4.3 Influence of Natural Fracture Angle on Hydraulic Fracture Propagation

Different NF angles affect the approach angle when HF and NF intersect, which in turn affects the propagation pattern of HF. Based on the data in Table 10.1, the

Fig. 10.7 I Injection pressure response characteristics under different horizontal stress differences and local magnification



horizontal stress difference of 2.5 MPa is kept constant and other parameters are kept the same to investigate the fracture propagation pattern under different NF angles. When the angle of NF is 30° , the approach angle is larger when HF intersects with NF, and in the early stage of HF extension, HF can turn to activate the NF when HF intersects with NF at a high approach angle or low approach angle due to the small energy consumption in the fracture (Fig. 10.8); in the late stage of HF extension, HF will pass through NF if HF intersects with NF at a high approach angle due to the decrease of net pressure in the fracture; when the angle of NF is 45° or 60° , HF intersects the NF with a smaller approach angle, the energy required for HF to activate the NF is smaller, and HF easily turns to activate the NF, and the fracture extends in a step-like manner along the inclined NF, which is consistent with the results of Jeffrey's study [10]. And when the NF angle is higher (45° , 60°), the overall morphology of HF is approximately the same as the NF direction, and the higher the NF angle is, the straighter the fracture is. Figure 10.9 shows the characteristics of injection pressure curves under different NF angles. It can be noticed that the higher the NF angle is, the higher the fracture initiation pressure is, and the NF angle increases from 30° to 60° , the fracture initiation pressure increases from 11.67 MPa to 19.35 MPa, about 39.68%, which is a large increase. And the fracture extension pressure does not differ much, and the overall pressure curve shows fluctuating characteristics.

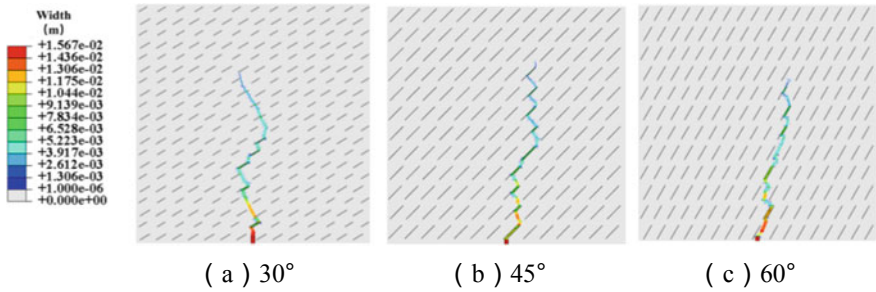
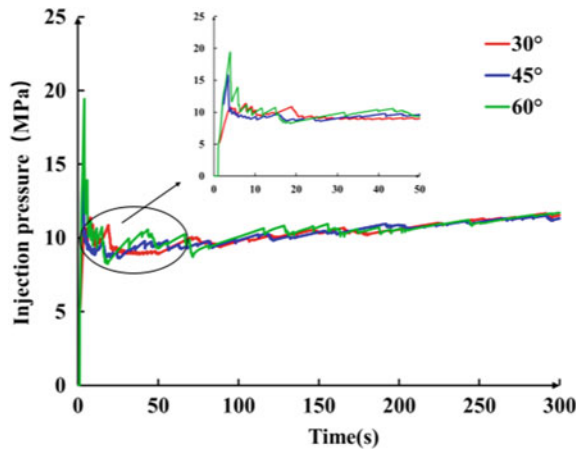


Fig. 10.8 Fracture propagation patterns under different natural fracture angles

Fig. 10.9 Injection pressure response characteristics under different natural fracture angles and local magnification



10.4.4 Influence of Injection Rate and Fracturing Fluid Viscosity on Hydraulic Fracture Propagation

The effects of two major formation parameters on the HF propagation pattern and injection pressure in fractured reservoirs, including horizontal stress difference and NF angle, have been investigated above. This section investigates the effects of injection rate and fracture fluid viscosity on HF extension in fractured reservoirs, as they are critically important and controllable factors in the fracturing process. Therefore, this section investigates the effects of injection rate and fracturing fluid viscosity on HF extension in fractured reservoirs. The horizontal stress difference of 2.5 MPa, the fracturing fluid viscosity of 1 mPa s is kept constant, the NF angle is fixed at 30°, and the injection rate of 4 and 8 m³/min are varied to investigate the fracture propagation pattern and injection pressure response characteristics. From Fig. 10.10, it can be seen that the low rate of 4 m³/min HF near wellbore area turns to activate the NF, and the distal HF penetrates the NF, the fracture width gradually decreases, and the HF has a tortuous shape. Increasing the rate to 8 m³/

min, the injection rate becomes the dominant factor to control the HF morphology, HF mostly penetrates the NF, and the HF morphology is straighter and the longer the fracture length. This is due to the reduction of fluid filtration loss in the fracture under high injection rate, high energy at the fracture tip, the fast fluid flow rate in the fracture, and HF penetrating NF in a short time, which is consistent with the concept of raising the rate to create long fractures in the field. From the injection pressure curve in Fig. 10.12a, it can be seen that the injection rate increases from 4 to 8 m³/min, the fracture initiation pressure increases from 11.52 to 14.03 MPa, about 17.89%, and the higher the injection rate, the higher the overall fracture extension pressure. Figure 10.11 shows the HF morphology under different fracturing fluid viscosities, and it can be seen that the fracturing fluid viscosity has less influence on the HF extension, and the HF morphology under different fracturing fluid viscosities is approximately the same as the injection pressure curve (Fig. 10.12).

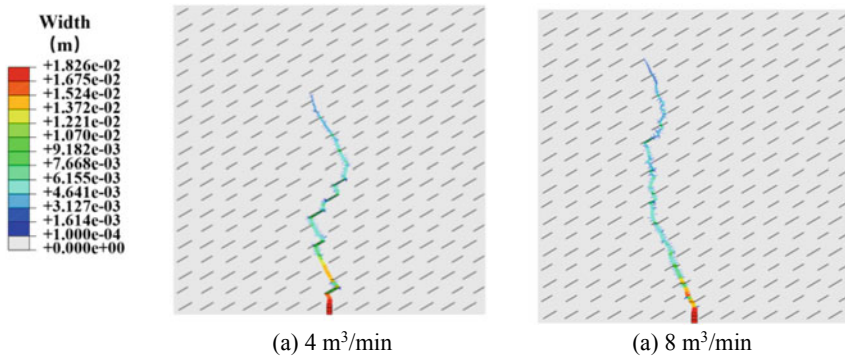


Fig. 10.10 Fracture propagation patterns under different injection rates

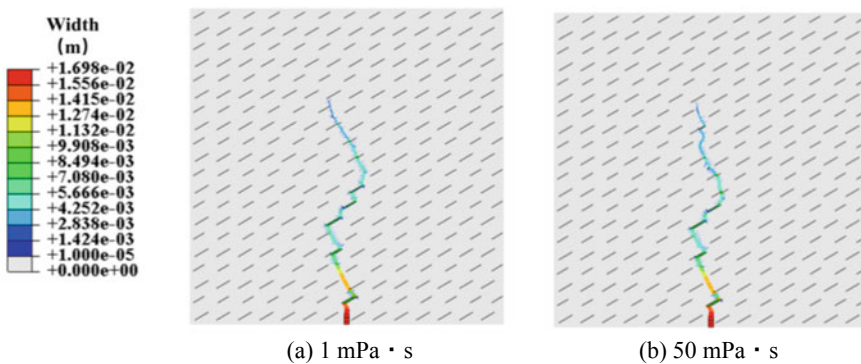


Fig. 10.11 Fracture propagation patterns under different fracturing fluid viscosity

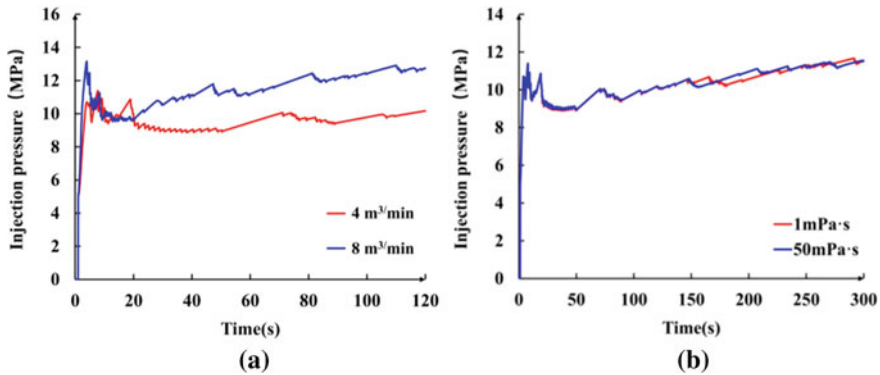


Fig. 10.12 Injection pressure curve **a** different injection rates, **b** different fracturing fluid viscosity

10.5 Discussion

When the reservoir is homogeneous and there are no NFs, the HFs tend to form symmetric biplane fractures and expand perpendicular to the minimum principal stress direction. However, when there are a large number of NFs, there are three patterns when HF intersects with NF, i.e., fully activated NF, partially activated NF, and through NF. Various factors jointly affect the expansion pattern when HF intersects with NF, and this paper discusses the expansion pattern of HFs under the influence of different horizontal stress differences, different NF angles, and different injection rates and fracturing fluid viscosity. The horizontal stress difference controls the overall fracture direction. With low horizontal stress difference, the fracture steering amplitude is greater and the fracture ripple area is wider, while with high-level stress difference the fracture expands along the direction of the maximum principal stress in the central axis and the fracture ripple area is narrower. Different NF angles affect the approach angle when HF intersects with NF, the higher the NF angle is, the smaller the approach angle when HF intersects with NF, and HF tends to activate NF and expand along the NF direction (Fig. 10.8c). When the horizontal stress difference is 0 (Fig. 10.6a), the in-situ stress has no controlling effect on the fracture propagation direction. Therefore, the approach angle when HF intersects with NF becomes the dominant factor controlling the direction of HF; when intersecting at a high approach angle, HF passes through NF; conversely, HF activates NF and expands along NF. In addition, the effects of two construction factors on the HF extension pattern in fractured reservoirs are explored. The higher the injection rate, the easier the HF crosses the NF and the fracture pattern is straighter. In contrast, the fracturing fluid viscosity has less influence on the HF morphology, and the fracture morphology is generally consistent when the viscosity is increased.

From the above discussion, it is clear that NF can change the expansion direction of HF, so the overall fracture morphology in fractured reservoirs can be expressed in two forms. One is HFs forming tortuous fractures with major flow channels, and the other

is forming complex fractures with mesh-like structures. Both patterns can be realized under some specific conditions. Wang et al. [20] argued that the former case is easier to achieve. Wang compared multiple clusters of fracture expansion with branching fracture expansion in a horizontal well section to illustrate that the stress shadow effect inhibits fracture expansion when the cluster spacing is small. Furthermore, since the distance of branching fractures from the main fracture is much smaller than the shot-hole cluster spacing, the stress-shadowing effect between fracture branches is much larger than that between shot-hole clusters. This paper also confirms through numerical simulation that HFs in fractured reservoirs are more likely to form tortuous fractures with major flow channels. To form a complex fracture network, the fracture network can be shifted to fracturing technology by temporary plugging, i.e., when the HF is sufficiently extended, a small particle size temporary plugging agent is pumped in and the temporary plugging agent is bridged and sealed inside the fracture or at the end of the fracture to form a dense temporary plugging body, which prevents the fluid pressure in the HF from transferring to the fracture tip area. The net pressure inside the fracture rises, forcing the fluid to flow to the NF and fully activating the NF to form a complex fracture network [22].

For tortuous fractures, more attention is paid to the difficulty of sand addition in field fracturing construction, the greater the tortuosity of the fracture, the more difficult it is to add sand. The fracture tortuosity is the ratio of the fracture centerline length to the straight line distance between the beginning and end of the fracture. Therefore, this paper extracts the path of the fracture unit through the secondary development technique of Python, to calculate the fracture tortuosity (Fig. 10.13). The tortuosity of HFs under different NF angles and horizontal stress difference conditions is shown in Fig. 10.14. It can be found that as the horizontal stress difference increases, the tortuosity of the fracture increases, and the stress difference increases from 0 to 2.5 MPa, the fracture tortuosity increases greatly; the stress difference increases from 2.5 to 5 MPa, the growth is gentle. In addition, the smaller the NF angle is, the larger the intersection angle of HF and NF is, and the larger the fracture tortuosity is. With the decrease of NF angle, the difference of fracture tortuosity under the same horizontal stress difference is smaller.

10.6 Conclusions

In this paper, a two-dimensional fluid–solid coupled fracture expansion model is established through a finite element method with the global embedding of cohesive elements, and the effect of NF clusters in fractured reservoirs on the fracture morphology and pumping pressure response characteristics of HF propagation is simulated and studied. The main findings are as follows:

- (1) In reservoirs with dense distribution of NFs, three forms exist when the HF intersects with the NF, i.e., fully activated NF, partially activated NF, and through NF. In the late stage of HF expansion, the net fluid pressure inside the fracture

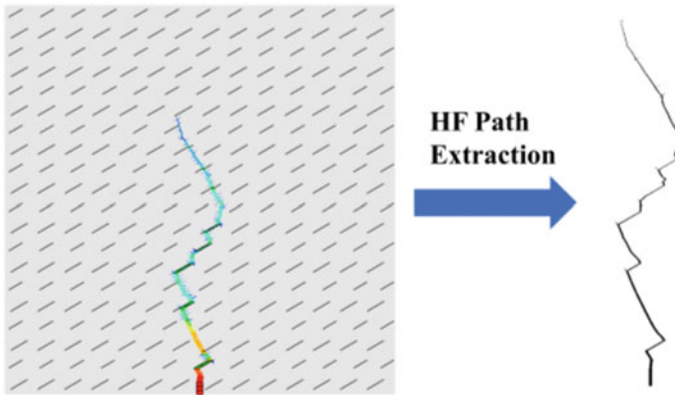
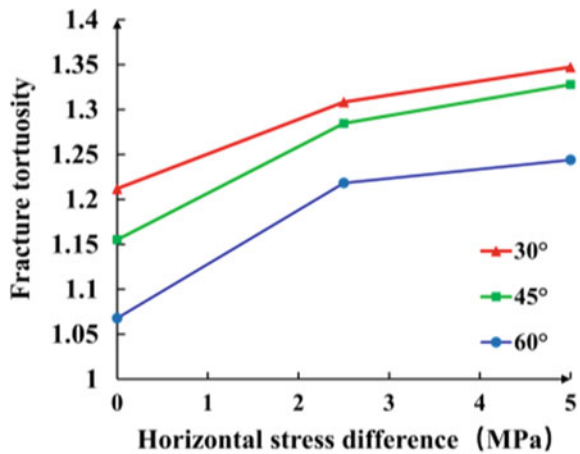


Fig. 10.13 Hydraulic fracture extraction

Fig. 10.14 Fracture tortuosity under different conditions



decreases due to the filtration loss of fluid inside the fracture, and the fracture width keeps narrowing. Due to the influence of the intersecting expansion of HF and NF, the injection pressure curve shows the characteristic of constant fluctuation.

- (2) When HF intersects NF with a high approach angle at a low-level stress difference, HF tends to pass through NF directly; when HF intersects NF with a low approach angle, HF tends to activate NF. At high-level stress difference, the fractures as a whole extend in a zigzag-shaped tortuous direction along the maximum principal stress. The fracture initiation pressure is approximately the same for different horizontal stress differences, but the higher the horizontal stress difference, the higher the fracture extension pressure.

- (3) When the NF angle is higher, the approach angle is smaller when HF intersects with NF, HF is prone to turn to activate NF, the fracture extends in a step-like manner along the inclined NF, and the overall shape of HF is approximately the same as the NF direction, and the higher the NF angle is, the straighter the fracture is, the greater the fracture initiation pressure, while the difference in fracture extension pressure is not large.
- (4) At a low injection rate, HF turns to activate NF in the area near the wellbore and HF penetrates NF at the distal end; at a high injection rate, HF mostly penetrates NF and the HF pattern is straighter. The higher the injection rate, the higher the overall fracture initiation pressure and extension pressure; the fracture fluid viscosity has less influence on the HF extension, and the HF morphology and injection pressure curves are approximately the same for different fracture fluid viscosities.
- (5) Hydraulic fractures in fractured reservoirs are more likely to form tortuous fractures with major flow channels. With the increase of horizontal stress difference, the fracture tortuosity keeps increasing, as well as the smaller the natural fracture angle under the same horizontal stress difference, the larger the fracture tortuosity.

Acknowledgements This work was funded by the National Natural Science Foundation of China (No. 52104011), the Natural Science Foundation of Xinjiang Uygur Autonomous Region (2022D01B77), and the Karamay Innovative Environment Construction Plan (Innovative talents) project (NO. 20232023hjcxrc0037).

References

1. Sun, L., Zou, C., Jia, A., Wei, Y., Zhu, R., Wu, S., Guo, Z.: Development characteristics and orientation of tight oil and gas in China. *Pet. Explor. Dev.* **46**, 1073–1087 (2019). [https://doi.org/10.1016/S1876-3804\(19\)60264-8](https://doi.org/10.1016/S1876-3804(19)60264-8)
2. Tong, X., Zhang, G., Wang, Z., Wen, Z., Tian, Z., Wang, H., Ma, F., Wu, Y.: Distribution and potential of global oil and gas resources. *Pet. Explor. Dev.* **45**, 779–789 (2018). [https://doi.org/10.1016/S1876-3804\(18\)30081-8](https://doi.org/10.1016/S1876-3804(18)30081-8)
3. Dahi-Taleghani, A., Olson, J.E.: Numerical modeling of multistranded-hydraulic-fracture propagation: accounting for the interaction between induced and natural fractures. *SPE J.* **16**, 575–581 (2011). <https://doi.org/10.2118/124884-PA>
4. Wang, W., Olson, J. E., Prodanovic, M.: Natural and hydraulic fracture interaction study based on semi-circular bending experiments. *OnePetro* (2013)
5. Baykin, A.N., Golovin, S.V.: Application of the fully coupled planar 3D poroelastic hydraulic fracturing model to the analysis of the permeability contrast impact on fracture propagation. *Rock Mech. Rock Eng.* **51**, 3205–3217 (2018). <https://doi.org/10.1007/s00603-018-1575-1>
6. Xu, W., Zhao, J., Rahman, S.S., Li, Y., Yuan, Y.: A comprehensive model of a hydraulic fracture interacting with a natural fracture: analytical and numerical solution. *Rock Mech. Rock Eng.* **52**, 1095–1113 (2019). <https://doi.org/10.1007/s00603-018-1608-9>
7. Liu, Z., Pan, Z., Li, S., Zhang, L., Wang, F., Han, L., Zhang, J., Ma, Y., Li, H., Li, W.: Study on the effect of cemented natural fractures on hydraulic fracture propagation in volcanic reservoirs. *Energy* **241**, 122845 (2022). <https://doi.org/10.1016/j.energy.2021.122845>

8. Blanton, T. L.: An experimental study of interaction between hydraulically induced and pre-existing fractures. In: SPE Unconventional Gas Technology Symposium Society of Petroleum Engineers (1986)
9. Jeffrey, R. G., Zhang, X., Thiercelin, M.: Hydraulic fracture offsetting in naturally fractures reservoirs: quantifying a long-recognized process. *OnePetro* (2009)
10. Jeffrey, R. G., Bungler, A. P., Lecampion, B., Zhang, X., Chen, Z. R., van As, A., Allison, D. P., de Beer, W., Dudley, J. W., Siebrits, E., Thiercelin, M., Mainguy, M.: Measuring hydraulic fracture growth in naturally fractured rock. *OnePetro* (2009)
11. Zhou, J., Xue, C.: Experimental investigation of fracture interaction between natural fractures and hydraulic fracture in naturally fractured reservoirs. *OnePetro* (2011)
12. Yan, T., Li, W., Bi, X.: An experimental study of fracture initiation mechanisms during hydraulic fracturing. *Pet Sci.* **8**, 87–92 (2011). <https://doi.org/10.1007/s12182-011-0119-z>
13. Wu, K., Olson, J.: Mechanics analysis of interaction between hydraulic and natural fractures in shale reservoirs. In: Unconventional Resources Technology Conference, Denver, Colorado, 25–27 August 2014. Society of Exploration Geophysicists, American Association of Petroleum Geologists, Society of Petroleum Engineers, pp 1824–1841 (2014)
14. Wu, K., Olson, J.E.: Numerical investigation of complex hydraulic-fracture development in naturally fractured reservoirs. *SPE Prod. Oper.* **31**, 300–309 (2016). <https://doi.org/10.2118/173326-PA>
15. Yaobin, S., Weiyong, L., Changchun, H., Erhu, B.: Numerical simulation of the influence of natural fractures on hydraulic fracture propagation. *Geofluids* **2020**, 1–12 (2020). <https://doi.org/10.1155/2020/8878548>
16. Guo, J., Zhao, X., Zhu, H., Zhang, X., Pan, R.: Numerical simulation of interaction of hydraulic fracture and natural fracture based on the cohesive zone finite element method. *J. Natural Gas Sci. Eng.* **25**, 180–188 (2015). <https://doi.org/10.1016/j.jngse.2015.05.008>
17. Wang, H.: Numerical modeling of non-planar hydraulic fracture propagation in brittle and ductile rocks using XFEM with cohesive zone method. *J. Petrol. Sci. Eng.* **135**, 127–140 (2015). <https://doi.org/10.1016/j.petrol.2015.08.010>
18. Chen, Z., Jeffrey, R.G., Zhang, X., Kear, J.: Finite-element simulation of a hydraulic fracture interacting with a natural fracture. *SPE J.* **22**, 219–234 (2016). <https://doi.org/10.2118/176970-PA>
19. Nguyen, V.P., Lian, H., Rabczuk, T., Bordas, S.: Modelling hydraulic fractures in porous media using flow cohesive interface elements. *Eng. Geol.* **225**, 68–82 (2017). <https://doi.org/10.1016/j.enggeo.2017.04.010>
20. Wang, H.: Hydraulic fracture propagation in naturally fractured reservoirs: Complex fracture or fracture networks. *J. Nat. Gas Sci. Eng.* **68**, 102911 (2019). <https://doi.org/10.1016/j.jngse.2019.102911>
21. Chen, M., Zhang, S., Xu, Y., Ma, X., Zou, Y.: A numerical method for simulating planar 3D multi-fracture propagation in multi-stage fracturing of horizontal wells. *Pet. Explor. Dev.* **47**, 171–183 (2020). [https://doi.org/10.1016/S1876-3804\(20\)60016-7](https://doi.org/10.1016/S1876-3804(20)60016-7)
22. Wang, B., Zhou, F., Yang, C., Wang, D., Yang, K., Liang, T.: Experimental study on injection pressure response and fracture geometry during temporary plugging and diverting fracturing. *SPE J.* **25**, 573–586 (2020). <https://doi.org/10.2118/199893-PA>

Chapter 11

Molecular Dynamics Investigations of Hydrogen-Enriched Natural Gas Permeation in Polyethylene



Dukai Zheng, Jingfa Li, Bo Yu, Yafan Yang, Dongxu Han, Jianli Li, Zhiqiang Huang, and Yindi Zhang

Abstract It is the trend of future energy development to blend a certain proportion of hydrogen into natural gas for utilization due to the zero carbon emissions characteristic of hydrogen after combustion. The hydrogen embrittlement and other hydrogen damages caused by metal pipelines can be effectively avoided by using non-metallic pipelines to transport hydrogen-enriched natural gas (HENG). However, due to the material characteristics, the degree of gas permeation of non-metal pipelines is greater than that of metal pipelines. In the study, the molecular dynamics combined with Giant Canonical Monte Carlo method is used to investigate the dissolution, diffusion and permeation characteristics of HENG with different hydrogen blending ratios (HBR, 5–20%) in amorphous polyethylene at temperatures of 270–310 K and pressures of 0.1–0.7 MPa. Results show that the solubility coefficient of hydrogen increases with increasing temperature and HBR, while the solubility coefficient of methane presents the opposite trend. The diffusion coefficients of hydrogen and methane increase with the rise of temperature and pressure but decrease with the increase of HBR. The permeability coefficients of hydrogen and methane increase with the increase of temperature. In addition, with the increase of HBR, the permeability coefficient of hydrogen increases, while that of methane decreases.

Keywords Hydrogen-enriched natural gas · Hydrogen blending ratio · Polyethylene · Solubility · Diffusion · Permeation coefficient

D. Zheng · Z. Huang · Y. Zhang
College of Petroleum Engineering, Yangtze University, Wuhan 430100, China

J. Li (✉) · B. Yu · D. Han · J. Li
School of Mechanical Engineering and Hydrogen Energy Research Center,
Beijing Institute of Petrochemical Technology, Beijing 102617, China
e-mail: lijingfa@bipt.edu.cn

Y. Yang
State Key Laboratory for Geomechanics and Deep Underground Engineering,
China University of Mining and Technology, Xuzhou 221116, China

11.1 Introduction

With the increasing impact of Greenhouse Effect on ecology, the development of clean energy to reduce carbon emissions has become an important trend in the future. Hydrogen is a kind of renewable and clean energy with great development potential. Therefore, the development of hydrogen energy has been an important measure to reduce the carbon emissions due to its zero-carbon emission characteristic after combustion, among which the hydrogen-enriched natural gas (HENG) is the research hotspot in the field of hydrogen energy. The HENG can be transported economically and efficiently through pipelines, but the hydrogen embrittlement and other hydrogen-induced damages will occur when using metal pipelines, which may lead to serious safety problems [1]. The non-metal pipelines can effectively avoid the occurrence of above problems, but due to the characteristics of material properties, there will be a large degree of gas permeation compared with metal pipelines. The long-term gas permeation and leakage will cause energy loss and waste. Therefore, it is of great significance to study the permeation characteristics of HENG in non-metallic PE pipelines. At present, the molecular dynamics (MD) is the main method to study the gas permeability in polymers. Therefore, the MD combined with Grand Canonical Monte Carlo (GCMC) method is used to study the dissolution, diffusion and permeation characteristics of HENG with different hydrogen blending ratios (HBR, 5–20%) under PE pipeline working conditions (temperature of 270–310 K and pressure of 0.1–0.7 MPa) in this paper.

11.2 Molecular Dynamics Model

The PE single chain with 100 polymerization degrees, H₂ molecule and CH₄ molecule are constructed by the all-atom model with high precision. Then, their structures are optimized with 500 steps. The 10 PE cells composed of 5 PE single chains are constructed based on the Theodorou and Suter's modified Rotational Isomeric State method, and then three PE cells with the lowest energy are selected as the final research cells. They are optimized with 20,000 steps to eliminate unreasonable structures. Subsequently, a series of dynamic operations are carried out for further optimization. (1) The NVT ensemble is used for 500 ps relaxation at 300 K. (2) Annealing: the PE cell is heated from 300 to 600 K with a step of 60 K, and then cooled from 600 to 300 K with the same temperature step. (3) The NPT ensemble is used to relax the PE cells for 500 ps at 300 K and 1 GPa. (4) The NPT ensemble is used to balance for 1000 ps at 298 K and 0.1 MPa. The Polymer Consistent Force Field (PCFF) with a cutoff radius of 12.5 Å is used in the MD simulation process.

11.3 Molecular Dynamics Simulation Process

11.3.1 Simulation of Dissolution/Sorption Process

The “NPT + GCMC” method [2] is used to study the solubility coefficients of H₂ and CH₄ in the gas mixture in PE, so as to consider the swelling effect of PE after gas sorption and the sorption of PE after swelling. Finally, the adsorption isotherms of H₂ and CH₄ in PE at different temperatures are obtained, in which each model is simulated at least three times to eliminate the error. The adsorption isotherm of H₂ is fitted by Henry model, as shown in Eq. (11.1). The adsorption isotherm of CH₄ is fitted by Dual Mode model, as shown in Eq. (11.2). When the fugacity f tends to 0, the limit slope of the fitted model is the solubility coefficient, as shown in Eqs. (11.3) and (11.4), respectively.

$$C = K_H \cdot f \quad (11.1)$$

$$C = K_H \cdot f + \frac{abf}{1 + bf} \quad (11.2)$$

$$S = \lim_{f \rightarrow 0} \frac{C}{f} = K_H \quad (11.3)$$

$$S = \lim_{f \rightarrow 0} \frac{C}{f} = K_H + ab \quad (11.4)$$

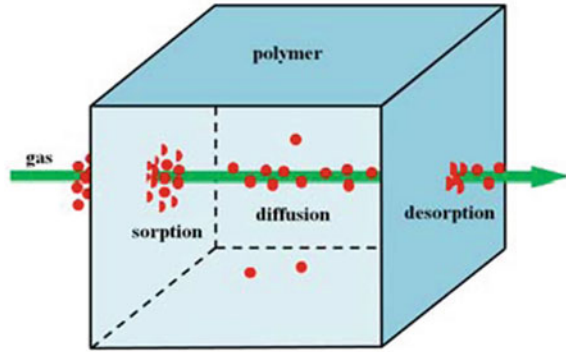
Here, C is the dissolved concentration of the gas molecules in the polymer, cm³ (STP)/cm³; K_H is the Henry constant; f is the fugacity, MPa; a is the Langmuir adsorption capacity; b is the Langmuir constant; S is the solubility coefficient, cm³ (STP)/(cm³·MPa).

11.3.2 Simulation of Diffusion Process

The diffusion coefficients of gas molecules in PE are obtained by long-time NVT operations on the PE cell which adsorbs gas molecules. Through 10 ns NVT, the mean square displacement (MSD)-time (t) figure of gas molecules in PE is obtained. Then, the diffusion coefficients can be obtained by calculating the normal diffusion part of the MSD- t figure by Einstein equation. The Einstein equation is shown in Eq. (11.5).

$$D = \frac{a}{6} \quad (11.5)$$

Fig. 11.1 Permeation process of the gas molecules in polymer



Here, D is the diffusion coefficient, cm^2/s ; N_a is the number of gas molecules; a is the slope of the normal diffusion part of the MSD- t figure.

11.3.3 Simulation of Permeation Process

The permeation process of gas molecules in polymer can be described by the “dissolution–diffusion” theory [3], as shown in Fig. 11.1. The gas molecules dissolve into the polymer through surface, then diffuse through the polymer, and finally are desorbed on the other surface to escape the polymer. Therefore, the permeation of H_2 and CH_4 in PE includes dissolution/sorption and diffusion, and the relationship between them is shown in Eq. (11.6).

$$P = SD \quad (11.6)$$

Here, P is the permeability coefficient, cm^3 (STP)· $\text{cm}/(\text{cm}^2\cdot\text{s}\cdot\text{MPa})$; S is the solubility coefficient, cm^3 (STP)/ $(\text{cm}^3\cdot\text{MPa})$; D is diffusion coefficient, cm^2/s .

11.4 Analysis of Simulation Results

11.4.1 Study of Gas Dissolution

The adsorption isotherms of H_2 and CH_4 in PE are studied at HBR of 20%, as shown in Fig. 11.2. They are fitted by the Henry model of Eq. (11.1) and the Dual Mode model of Eq. (11.2), respectively, and then the solubility coefficients are calculated by Eqs. (11.3) and (11.4), respectively, as shown in Fig. 11.3. Figure 11.3 shows that the solubility coefficient of H_2 increases with increasing temperature, while that of CH_4 shows an opposite trend. At low temperature, the solubility of H_2 in PE is

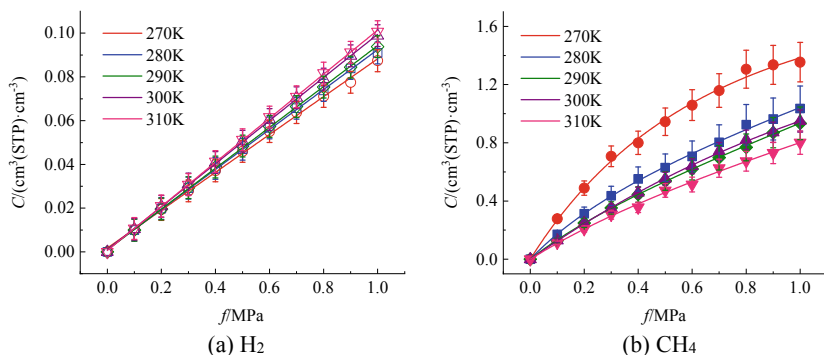


Fig. 11.2 Adsorption isotherms of H₂ and CH₄ in PE at HBR of 20%

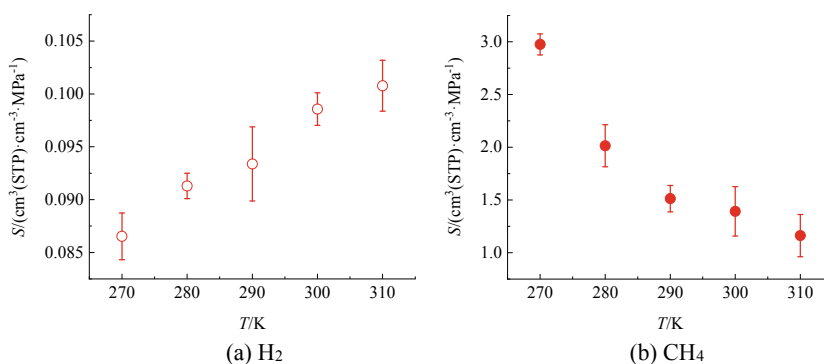


Fig. 11.3 Influence of temperature (270–310 K) on solubility coefficients of H₂ and CH₄ in PE at HBR of 20%

weak. With the increase of temperature, the free volume in PE expands to increase the probability of H₂ dissolution. For CH₄, when the temperature increases, the diffusion rate of CH₄ increases, so that the amount of CH₄ remaining in PE decreases, which makes the solubility coefficient of CH₄ decrease with the increase of temperature.

The influences of HBR (5–20%) on the solubility coefficient at temperature of 270 K are studied, as shown in Fig. 11.4. Figure 11.4 displays that the solubility coefficients of H₂ and CH₄ increase with the rise of their own content, because the greater the concentration of gas molecules, the greater the dissolution amount.

11.4.2 Study of Gas Diffusion

The influences of temperature (270–310 K) on the diffusion coefficient at pressure of 0.1 MPa and HBR of 20% are studied, as shown in Fig. 11.5. It indicates that the

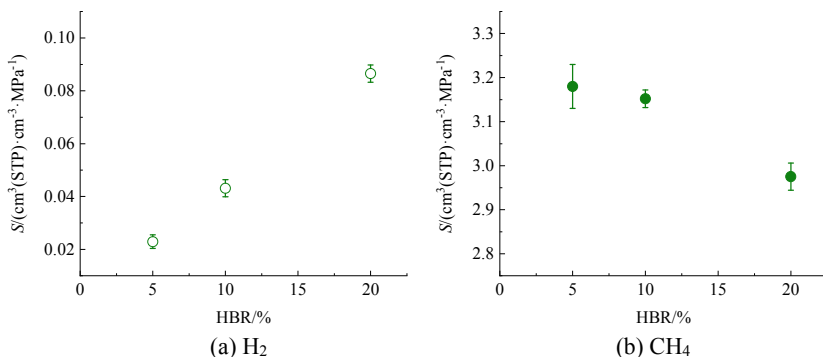


Fig. 11.4 Influence of HBR (5–20%) on solubility coefficients of H₂ and CH₄ in PE at 270 K

diffusion coefficients increase with increasing temperature, because the temperature increases the dynamic energy of gas molecules and the activity ability of PE chains, which makes the gas molecules diffuse faster and PE has more free volume for gas molecules to diffuse.

Similarly, the influences of pressure (0.1–0.7 MPa) on the diffusion coefficient at temperature of 270 K and HBR of 20% are studied, as shown in Fig. 11.6. Figure 11.6 explains that the diffusion coefficients increase with increasing pressure, because the molecular weight of gas adsorbed by PE increases with the rise of pressure. Therefore, under the swelling effect, the volume of PE increases, providing more free volume for gas molecules to diffuse.

The influences of HBR (5–20%) on the diffusion coefficient at temperature of 270 K and pressure of 0.1 MPa are investigated, as shown in Fig. 11.7. It can be seen that the diffusion coefficients decrease with the increase of HBR. This is because the solubility coefficient of CH₄ in PE is greater than that of H₂, which makes the swelling effect of CH₄ greater than that of H₂. Consequently, with the increase of

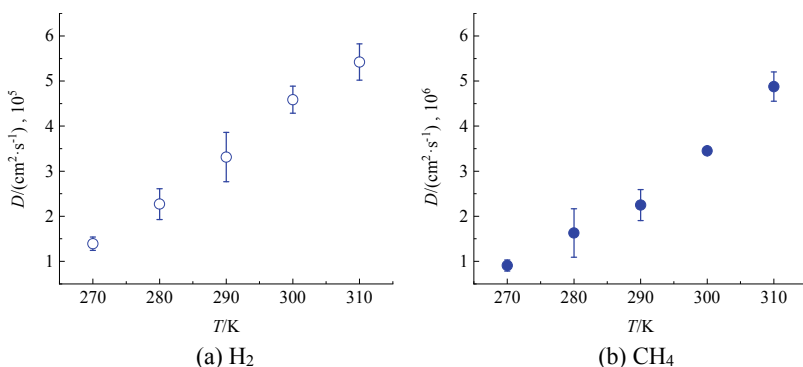


Fig. 11.5 Influence of temperature (270–310 K) on diffusion coefficients of H₂ and CH₄ in PE at 0.1 MPa and HBR of 20%

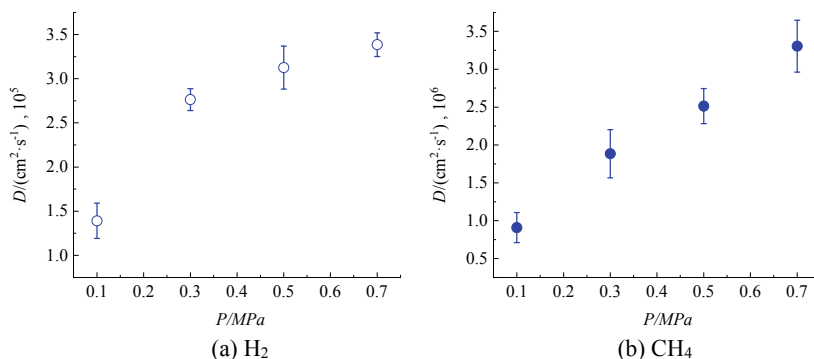


Fig. 11.6 Influence of pressure (0.1–0.7 MPa) on diffusion coefficients of H₂ and CH₄ in PE at 270 K and HBR of 20%

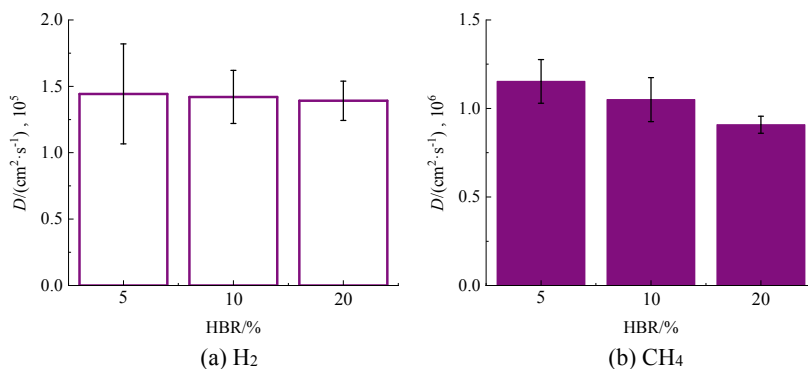


Fig. 11.7 Influence of HBR (5–20%) on diffusion coefficients of H₂ and CH₄ in PE at 270 K and 0.1 MPa

HBR, the content of CH₄ decreases, which weakens the swelling effect of PE. The free volume of PE also decreases, eventually leading to the reduction of diffusion coefficient.

11.4.3 Permeation Characteristics

Firstly, the results in Figs. 11.3 and 11.5 are calculated by Eq. (11.6) to study the influence of temperature (270–310 K) on the permeation coefficient, as shown in Fig. 11.8. It indicates that the permeation coefficients of H₂ and CH₄ increase with increasing temperature. For H₂, there is due to that both the solubility coefficient and diffusion coefficient of H₂ increase with the increase of temperature. For CH₄, it is

because the increase of diffusion coefficient is greater than the decrease of solubility coefficient with the rise of temperature.

As presented in Fig. 11.9, the results in Figs. 11.4 and 11.7 are calculated by Eq. (11.6) to reveal the influence of HBR (5–20%) on the permeation coefficient. It shows that the permeation coefficient of H_2 increases with increasing HBR, because the increase of solubility coefficient is greater than the decrease of diffusion coefficient. However, the permeation coefficient of CH_4 shows the opposite trend, because both solubility and diffusion coefficients decrease with increasing HBR.

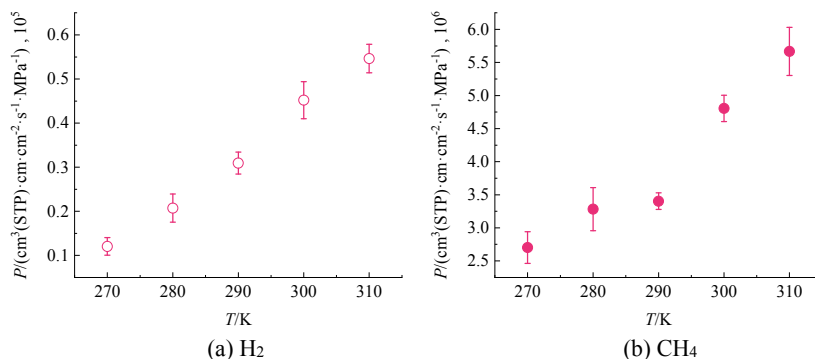


Fig. 11.8 Influence of temperature (270–310 K) on permeation coefficients of H_2 and CH_4 in PE at 0.1 MPa and HBR of 20%

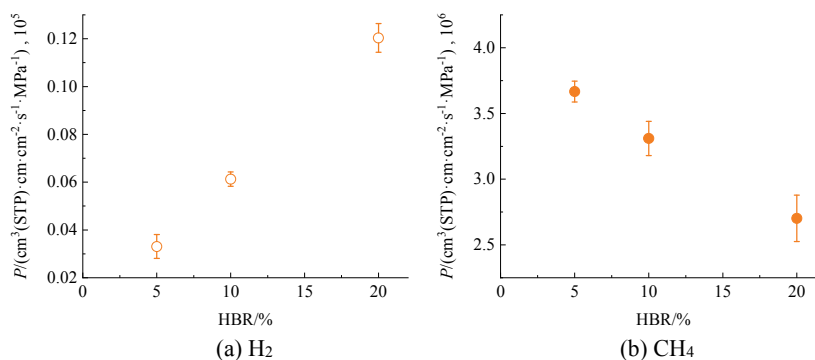


Fig. 11.9 Influence of HBR (5–20%) on permeation coefficients of H_2 and CH_4 in PE at 270 K and 0.1 MPa

11.5 Conclusions

The influences of temperature (270–310 K), pressure (0.1–0.7 MPa) and hydrogen blending ratio (5–20%) on the dissolution, diffusion and permeation of H₂ and CH₄ in PE are studied by molecular dynamics simulations, and the following conclusions are obtained.

- (1) The solubility coefficient of H₂ increases with the increase of temperature and hydrogen blending ratio, while the solubility coefficient of CH₄ show the opposite trend.
- (2) The diffusion coefficients of H₂ and CH₄ increase with increasing temperature and pressure, as well as decrease with the rise of hydrogen blending ratio.
- (3) The permeability coefficients of H₂ and CH₄ increase with increasing temperature. With the increase of hydrogen blending ratio, the permeability coefficient of H₂ increases, while that of CH₄ decreases.

Acknowledgements This study is supported by the National Key R&D Program of China (2021YFB4001601), the State Key Laboratory of Engines, Tianjin University (K2022-02), and Hubei Provincial Department of Science and Technology Project: Natural Gas Blending Hydrogen Transmission Technology (2022EJD031).

References

1. Li, J.F., Su, Y., Zhang, H., et al.: Research progresses on pipeline transportation of hydrogen-blended natural gas. *Nat. Gas. Ind.* **41**(04), 137–152 (2021)
2. Yang, Y.F., Nair, A.K.N., Sun, S.Y.: Adsorption and diffusion of methane and carbon dioxide in amorphous regions of cross-linked polyethylene: a molecular simulation study. *Ind. Eng. Chem. Res.* **58**, 8426–8436 (2019)
3. Zheng, D.K., Li, J.F., Liu, B., et al.: Molecular dynamics investigations into the hydrogen permeation mechanism of polyethylene pipeline material. *J. Mol. Liq.* **368**, 120773 (2022)

Chapter 12

Estimation of Hourly Solar Radiation in Australia Using Machine Learning Models



Shuting Zhao and Youzhen Xiang

Abstract The prediction of global hourly solar radiation is of great significance for the development of solar energy resources in energy conversion countries. Based on this view, this study used RF and SVM models to simulate solar radiation data distributed at three weather stations in Australia based on different input combinations. In the training of the model, the meteorological data included in the parameter combination selected in this study include average temperature, relative humidity, extraterrestrial radiation and precipitation. The results showed that the simulation accuracy of SVM model was better than that of RF model, and the average RMSE was 0.61 and 0.68 MJ m⁻² h⁻¹, respectively. The model with Z2 input was significantly better than the model with Z1 input. The RMSE was reduced by 25% and the R² was increased by 10%. Temperature had an important influence on solar radiation.

Keywords Solar radiation · Machine learning model · SVM · RF

12.1 Introduction

The continuous development of the world economy has led to a sharp increase in human demand for energy. In order to alleviate the pressure of the earth's energy shortage and reduce the adverse effects of fossil energy consumption on the environment, solar energy resources and other clean energy have become the goals pursued by most countries and have great potential [1, 2]. In order to make full use of and understand the solar energy potential of an area, it is necessary to master the solar radiation data of the area [3]. In general, solar radiation is measured by instruments with

S. Zhao · Y. Xiang (✉)

Key Laboratory

of Agricultural Soil and Water Engineering in Arid and Semiarid Areas of Ministry of Education, Northwest A&F University, Yangling 712100, China

e-mail: youzhenxiang@nwsuaf.edu.cn

Institute of Water-Saving Agriculture in Arid Areas of China, Northwest A&F University, Yangling 712100, China

high installation and maintenance costs, which makes most of the world's regions do not have the conditions to set up solar radiation stations. For example, there are only more than one hundred stations in China that can record solar radiation data, and these stations obviously cannot provide sufficient solar radiation data for research [4]. Therefore, using other common meteorological data combined with machine learning to establish a solar radiation model to predict the solar radiation value of the target site is a commonly used and accurate data source.

At first, many scholars used empirical models to predict solar radiation. However, due to the influence of bad weather conditions and the complex nonlinear relationship between independent variables and dependent variables, empirical models cannot predict solar radiation well [5–7]. With the rapid development of artificial intelligence in recent years, machine learning models have become the mainstream of predicting solar radiation [8]. The research of these scholars shows that machine learning models can provide more accurate results than empirical models. For example, Quej et al. [9] used three models (SVM, ANN and ANFIS) to predict daily solar radiation in Mexico, and the results showed that the SVM model well estimated the solar radiation in the region. Mohammadi et al. proposed a method of combining SVM and wavelet transform (WT) algorithm to simulate solar radiation. The results show that the combination of sunshine duration, temperature, relative humidity and extraterrestrial radiation is the best [10]. In another study, Meenal and Selvakumar evaluated the accuracy of SVM models, ANN models and empirical models under different parameter combinations in India. The results showed that SVM models performed better than ANN and empirical models [11].

Although previous scholars have evaluated many machine learning models, the performance of the models still varies under different locations and input conditions. Especially in mainland China, the systematic comparison between related research and models is very scarce. Therefore, this study proposes two machine learning models to estimate solar radiation in mainland China based on different parameter combinations, aiming to provide reference for selecting appropriate inputs and models for predicting solar radiation in regions with similar climatic conditions.

12.2 Study Site and Data Collection

In this study, some meteorological data from three sites in Australia were collected from Fluxnet2015 flux data set. The general orientation of these sites in Australia is shown in Fig. 12.1. The site is represented by an asterisk. The specific latitude and longitude and other detailed meteorological data of the site are shown in Table 12.1. The data obtained include the measured value of solar radiation (R_s), the measured value of solar radiation in the previous hour (R_{s_P}), wind speed (WS), average temperature (TA), temperature difference (TA_D), precipitation (P) and relative humidity (RH). The extraterrestrial radiation (R_a) is calculated based on the article of Allen et al. [12].



Fig. 12.1 Locations of three meteorological stations in Australia

According to previous scholars' research, temperature is not only a key meteorological factor for simulating solar radiation, but also easier to obtain than other parameters, such as clarity index. Therefore, based on the input R_s , P , WS , P and RH , this study considers the simulation of solar radiation combined with average temperature and temperature difference (see Table 12.2), aiming to explore the influence of different machine learning models on solar radiation simulation based on different parameter combinations.

In the process of processing data, if the data part is missing, the row is deleted. Finally, 80% of the total data set is used as the training set for model training, and 20% is used as the test set. All the statistical index results of this paper are displayed by the simulated values of the test set.

12.3 Machine Learning Models and Statistical Indicators

12.3.1 *RF*

Random forest (RF) is a representative Bagging ensemble algorithm [13], which further introduces random feature selection into the training process of decision tree. In the random forest, for each node of the base decision tree, a subset containing k features is randomly selected from the feature set of the node, and then an optimal feature is selected for partitioning. The algorithm has high accuracy, can effectively run on large data sets, handle input samples with high-dimensional features, and can

Table 12.1 Geographical location and meteorological data of three weather stations in Australia

Stations	Latitude (N)	Longitude (E)	Rs_P (MJ m ⁻¹ h ⁻¹)	Ra (MJ m ⁻¹ h ⁻¹)	TA (°C)	P (mm)	RH (%)	WS (m/s)	TA_D (°C)
AU-Ade	-13.08	131.12	921.45	1501.79	28.88	0.13	43.54	1.98	-0.0022
AU-ASM	-22.28	133.25	939.40	1613.89	21.94	0.04	31.18	3.01	-0.0001
AU-Cum	-33.62	150.72	654.03	1574.35	18.73	0.09	61.05	1.81	-0.0016

Table 12.2 The selected models and input combinations

No.	Model	Combinations	
Z1	RF1	SVM1	Rs_P, Ra, RH, P, WS
Z2	RF2	SVM2	Rs_P, Ra, RH, P, WS, TA, TA_D

also obtain good results for default value problems. The details of RF can be found in Breiman’s article [13].

12.3.2 SVM

Support vector machine (SVM) is a kind of generalized linear classifier that classifies data by supervised learning. SVM can perform linear and nonlinear classification, and even outlier monitoring tasks, which is suitable for the classification of small and medium-sized complex data sets. Its basic idea is to solve the separation hyperplane that can correctly divide the training set and has the largest geometric interval. It can use only a part of support vectors to make hyperplane decisions without relying on all data. In addition, SVM can use a large number of kernel functions to solve various nonlinear classification regression problems more flexibly. Even if the sample size is not sufficient, it can have higher classification accuracy and strong generalization ability. The details of SVM can be found in Vapnik’s article [14].

12.3.3 Statistical Indicators

In this study, root mean square error (RMSE) and coefficient of determination (R^2) were used to analyze and evaluate the model simulation results. Their mathematical formulas are described as follows:

$$RMSE = \sqrt{\frac{1}{n} \sum_{i=1}^n (Y_i - X_i)^2} \tag{12.1}$$

$$R^2 = \frac{[\sum_{i=1}^n (X_i - \bar{X})(Y_i - \bar{Y})]^2}{\sum_{i=1}^n (X_i - \bar{X})^2 \sum_{i=1}^n (Y_i - \bar{Y})^2} \tag{12.2}$$

where n is the number of samples, i is the number of measurement days, Y_i represents the predicted value of the i-th day, X represents the measured value of the i-th day, \bar{Y} and \bar{X} represent the average of the predicted value and the measured value respectively. The closer the RMSE value is to 0 and the closer the R^2 is to 1, the better the model effect is.

12.4 Results and Discussion

In this study, two machine learning models, random forest and support vector machine, were used to evaluate and analyze the hourly solar radiation value based on some meteorological data of three surface meteorological stations in Australia. The statistical results are shown in Table 12.3. It can be seen from the table that the SVM model (average RMSE = $0.61 \text{ MJ m}^{-2} \text{ h}^{-1}$ for all sites, $R^2 = 0.89$) is numerically superior to the RF model (average RMSE = $0.68 \text{ MJ m}^{-2} \text{ h}^{-1}$ for all sites, $R^2 = 0.87$). The SVM model at the AU-ASM site showed the highest simulation accuracy compared to the other two sites, with an average RMSE = $0.53 \text{ MJ m}^{-2} \text{ h}^{-1}$ and $R^2 = 0.93$. In the Z2 combination, the SVM model has a good performance at most of the sites selected in this study (R^2 values are >0.9), and the simulation results are relatively poor only at the AU-Cum site ($R^2 = 0.81$), but still better than the RF model ($R^2 = 0.78$), which indicates that the SVM model estimates the solar radiation value more accurately than the RF model. Bellido-Jiménez et al. developed and evaluated several machine learning models for predicting solar radiation in nine locations with different climatic and geographical conditions, such as Spain and the United States. The results show that SVM model and RF model have good prediction performance in the most arid and humid areas. In terms of NSE, RF model is equal to 0.897, while SVM can reach 0.924 [15]. Fan et al. evaluated the performance of SVM model and four tree-based machine learning models including RF model to simulate solar scattering radiation. The results show that SVM model still shows good generalization ability in the absence of R_s , and its prediction results are significantly better than RF model [16]. The above studies are consistent with the results of this study.

Comparing the results of all statistical indicators, it can be found that in the Z1 combination, the RMSE range of all sites is $0.6\text{--}0.81 \text{ MJ m}^{-2} \text{ h}^{-1}$, and the R^2 is $0.75\text{--}0.91$. In the Z2 combination, the RMSE range of all sites is $0.45\text{--}0.61 \text{ MJ m}^{-2} \text{ h}^{-1}$, and the R^2 is $0.86\text{--}0.95$. The average RMSE of Z2 combination was $0.55 \text{ MJ m}^{-2} \text{ h}^{-1}$, $R^2 = 0.91$, and the RMSE value was 25% lower than that of Z1 combination, and the R^2 value was increased by 10%. The above analysis shows that the Z2 combination has a better prediction effect as the input of the model. Temperature is one of the important

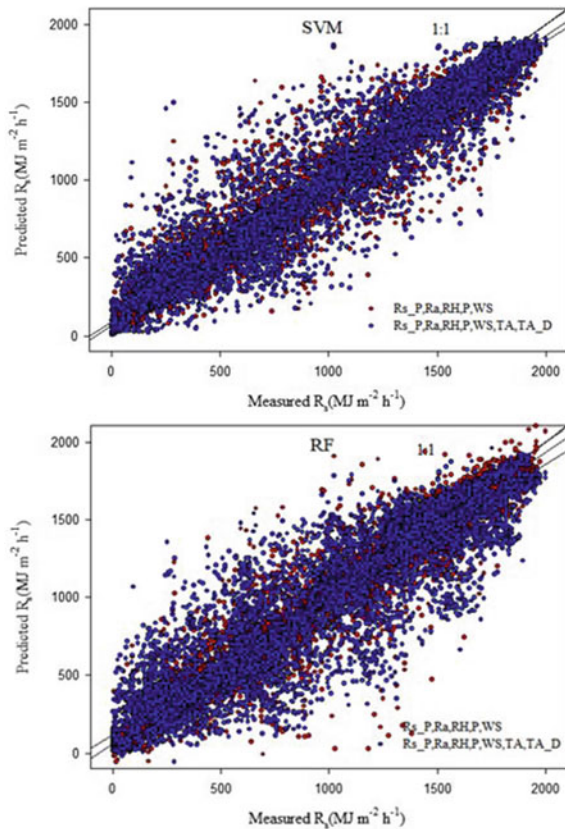
Table 12.3 Results of statistical indicators of simulated solar radiation at three sites in Australia using machine learning models

Stations	Statistical indicators	RMSE ($\text{MJ m}^{-2} \text{ h}^{-1}$)		R^2	
	Models/combinations	1	2	1	2
AU-Ade	SVM	0.63	0.53	0.91	0.93
	RF	0.71	0.57	0.88	0.92
AU-ASM	SVM	0.60	0.45	0.91	0.95
	RF	0.76	0.51	0.85	0.93
AU-Cum	SVM	0.81	0.61	0.75	0.86
	RF	0.89	0.63	0.71	0.85

meteorological factors for simulating solar radiation, which can significantly improve the simulation effect of the model. Wu et al.'s study evaluated the performance of Bayesian additive regression trees in predicting solar diffuse radiation under different parameter combination inputs at four sites in arid and humid regions of the world. Their study also considered that the input combination with average temperature performed best in predicting global solar diffuse radiation [17].

In order to more clearly see the performance of the combination of Z1 and Z2 in the RF and SVM models, we take the AU-ASM site as an example, and further draw a scatter plot based on the simulated solar radiation value of the meteorological data at the site and the measured solar radiation value of the site (see Fig. 12.1). It can be clearly seen from the figure that in the Z1 combination, the RF model has the highest degree of dispersion, and the measured value of the SVM model is closer to the 1:1 line in the figure, while in the Z2 combination, the SVM model has the highest degree of fitting (Fig. 12.2).

Fig. 12.2 Scatter plots of solar radiation at AU-ASM site are simulated using machine learning models



12.5 Conclusion

Solar radiation has important scientific research and application value in many fields such as engineering and agriculture. However, its acquisition needs to consider local weather station conditions and other meteorological factors. This study proposes two machine learning models to simulate hourly solar radiation at three sites in Australia with different parameter input combinations. The results show that: (1) The SVM model is better than the RF model in simulating solar radiation; (2) TA and TA_D as input can bring significant improvement to the model.

References

1. Ak, A., As, B., Ci, C., Adtc, D., Age, F.: Performance enhancement of a greenhouse dryer: analysis of a cost-effective alternative solar air heater—ScienceDirect. *J. Clean. Prod.* **251**, 119672 (2020)
2. Edenhofer, Pichsmadruga, R., Sokona, Y., Farahani, E., Kadner, S., Seyboth, K., Adler, A., Baum, I., Brunner, S.: IPCC, 2014: Climate Change 2014: Mitigation of Climate Change. Contribution of Working Group III to the Fifth Assessment Report of the Intergovernmental Panel on Climate Change (2014)
3. Yadav, A.K., Malik, H., Chandel, S.S.: Selection of most relevant input parameters using WEKA for artificial neural network based solar radiation prediction models. *Renew. Sustain. Energy Rev.* **31**, 509–519 (2014)
4. Zang, H., Xu, Q., Bian, H.: Generation of typical solar radiation data for different climates of China. *Energy* **38**(1), 236–248 (2012)
5. Fan, J., Wang, X., Wu, L., Zhang, F., Bai, H.: New combined models for estimating daily global solar radiation based on sunshine duration in humid regions: A case study in South China. *Energy Conv. Manage.* **156**, 618–625 (2018)
6. Feng, Y., Gong, D., Jiang, S., Cui, N.: Evaluation of temperature-based machine learning and empirical models for predicting daily global solar radiation. *Energy Conv. Manage.* **198**, 111780 (2019)
7. Kisi, O., Parmar, K.S.: Application of least square support vector machine and multivariate adaptive regression spline models in long term prediction of river water pollution. *J. Hydrol.* **534**, 104–112 (2016)
8. Liu, Y., Zhou, Y., Chen, Y., Wang, D., Wang, Y., Zhu, Y.: Comparison of support vector machine and copula-based nonlinear quantile regression for estimating the daily diffuse solar radiation: a case study in China. *Renew. Energy* **146**, 1101–1112 (2020)
9. Quej, V.H., Almorox, J., Arnaldo, J.A., Saito, L.: ANFIS, SVM and ANN soft-computing techniques to estimate daily global solar radiation in a warm sub-humid environment. *J. Atmos. Solar Terr. Phys.* **155**, 62–70 (2017)
10. Mohammadi, K., Shamshirband, S., Tong, C.W., Arif, M., Petković, D., Ch, S.: A new hybrid support vector machine–wavelet transform approach for estimation of horizontal global solar radiation. *Energy Convers. Manage.* **92**, 162–171 (2015)
11. Meenal, R., Selvakumar, A.I.: Assessment of SVM, empirical and ANN based solar radiation prediction models with most influencing input parameters. *Renew. Energy* **2018**, S0960148117312016 (2018)
12. Allen, R., Pereira, L., Raes, D., Smith, M., Allen, R.G., Pereira, L.S., Martin, S.: Crop evapotranspiration: guidelines for computing crop water requirements. FAO Irrigation and Drainage Paper 56. FAO 56 (1998)
13. Breiman. Random forests. *Mach. Learn.* **45**(1), 5–32 (2001)

14. Vapnik, V.N.: *The Nature of Statistical Learning Theory*. Springer (1995)
15. Bellido-Jiménez, J.A., Gualda, J.E., García-Marín, A.P.: Assessing new intra-daily temperature-based machine learning models to outperform solar radiation predictions in different conditions. *Appl. Energy* **298**, 117211 (2021)
16. Jf, A., Xw, B., Fz, A., Xin, M.C., Lw, D.: Predicting daily diffuse horizontal solar radiation in various climatic regions of China using support vector machine and tree-based soft computing models with local and extrinsic climatic data. *J. Clean. Prod.* **248**, 119264 (2019)
17. Wu, W., Tang, X., Lv, J., Yang, C., Liu, H.: Potential of Bayesian additive regression trees for predicting daily global and diffuse solar radiation in arid and humid areas. *Renew. Energy* **177**, 148–163 (2021)

Chapter 13

Theoretical Calculation and Parametric Study of Floating and Sinking Process of the Steel Tube with a Large Diameter



Jianbo Yi, Qing Chong, Yu Huang, and Xuan Xing

Abstract In order to study the influence of different condition parameters on the process of floating transportation of steel guard cylinder, taking the floating transportation and sinking of 3.9 m super-large diameter steel guard cylinder of a continuous rigid frame bridge pile in Suichang, Zhejiang Province as an example, the basic working principle of the floating transportation method of super-large diameter steel guard cylinder and the process of floating transportation and sinking in the construction process are studied. The water entry depth of the steel sheath under different equilibrium tilt angles is discussed and the corresponding theoretical calculation formula is given. When the balance tilt Angle is fixed, the influence of the water inlet velocity and water inlet area on the speed and water entry time of the steel sheath is studied, and the corresponding theoretical calculation formula is put forward respectively. The results show that the floating method of steel protecting tube sinking construction can effectively guarantee the accuracy of the liners of the large diameter into the water, improve the overall stability of the sinking process of the steel liners, reduce the risk of the steel liners capsized, for rational selection of the steel liners of the construction conditions to provide the corresponding theoretical support, and for the future similar steel protecting tube into the water sink to provide the corresponding reference.

Keywords Steel tube · Floating and sinking · Equilibrium · Bridge construction · The theoretical calculation

J. Yi · Y. Huang · X. Xing
CCCC First Highway Engineering Group Co. Ltd., Lishui 323000, Zhejiang, China

Q. Chong (✉)
School of Civil Engineering, Changsha University of Science and Technology, Changsha 410114, Hunan, China
e-mail: 1620562076@qq.com

13.1 Introduction

In the process of pile foundation construction of bridge engineering, steel casing is an important auxiliary pore-forming measure and has been widely used in engineering [1]. The water entry of large-diameter steel protective tube, transportation of large equipment on the water and construction of immersed tube tunnel mostly adopt the floating transportation method [2]. The floating method is to assemble the steel guard cylinder into a whole and seal it in turn on the site. The sliding speed should be controlled by laying air bags on the river side. It is transported to the sinking site with the buoyancy of water, and positioned by repeated filling and deflating of steel guard cylinder. After the completion of the positioning, the plane position of the steel shield is measured to strictly control the construction quality; after each construction index is qualified, vibration hammer is used to vibrate the steel protective cylinder to the designed elevation [3].

At present, the design trend of bridge bored pile is large diameter, large hole depth, some pile diameter even more than 3.5 m, resulting in the diameter and length of steel drum increase. In the process of some important bored pile construction, the construction quality of steel shield has become one of the key links affecting the whole bridge.

When the difference between the water level and the day setting is relatively small and there are anchorage places for ships on both sides of the river, the floating transportation method can be adopted for construction [4]. The key of this technology is the floating and sinking of steel shield during construction. Aiming at the key construction processes such as floating transport and subsidence of the river crossing pipeline, the methods and ideas of subsection floating transport, overall irrigation subsidence and multi-lifting point winch control are adopted to realize the safe and accurate construction of floating transport and subsidence of large river crossing pipeline, providing favorable guarantee for the smooth implementation of subsequent underwater construction [5]. The floating transportation method has good economic and technical performance. When the floating transportation method is applied to the transportation of electric single piles in the sea, the construction procedure can be optimized and the cost can be reduced [6]. The structural facility of “Hollow drum axle type automobile inner tube inflation” proposed by Wang Houqiang has been adopted in the transportation of steel pipe piles (53.4–60 m in length of 1200 mm and 30 t in weight) at Beilun Port transit terminal [7]. In the article, Wu Kailui systematically introduced the plug installation method adopted in floating transportation, and analyzed its advantages [8]. The patent “Method of Air bag floating tubular member” discloses a method of placing an air bag in the inner cavity of pipe pile to seal or penetrate the air bag in the inner cavity to make the member meet the floating requirements [9]. Large-diameter single pile floating technology has been developed very mature abroad, and has been applied to Walney offshore wind field in the Irish Sea of the United Kingdom [10].

In the process of literature research, it is found that the existing articles have a very detailed discussion on a series of construction processes of steel protective

cylinder, but the specific details of the floating and sinking of steel protective cylinder are rarely described in the articles. In this paper, based on the actual construction situation, the theoretical calculation and the solution of the floating process of steel drum into water are given.

13.2 Floating and Sinking Process of Steel Guard Cylinder

The engineering background of this paper is (7 × 58) m composite continuous rigid frame bridge. Pier No.2#-5 of the bridge is the construction of deep-water pile foundation. By taking full advantage of the favorable conditions of site construction and combining with the principle of mechanical balance, the construction technology of steel guard cylinder charging and exhaust floating and sinking installation is designed. The floating transportation method is relatively simple in construction operation, wide in application range, high in safety and reliability, good in use effect, and can significantly reduce costs.

The bottom of the protective cylinder first enters the water. After the bottom of the protective cylinder submerges into the water for a certain distance, the bottom of the protective cylinder slowly floats under the action of buoyancy until the whole protective cylinder floats horizontally on the water surface. The protective cylinder bears the buoyancy generated by the structure's self-weight displacing the lake water. In the process of sinking, the stress condition of the steel casing is relatively complicated. The steel casing bears the buoyancy generated by the dead weight of the casing and the dead weight of the water injected into the casing. In the process of overturning the steel casing, the length of the cantilever of the casing also changes gradually with the constant change of the tilt Angle, resulting in greater internal force of the casing. In the upright suspension state, the gravity of the guard cylinder is balanced under the combined action of the reaction produced by the compressed air inside the guard cylinder and certain buoyancy force.

13.3 Establishment of Equilibrium Equation

The calculation diagram is shown in Fig. 13.1. It is assumed that the depth of the casing immersed in water is H , the height of the liquid surface in the casing is h , the tilt Angle of the casing in water is θ , the radius of the outer wall of the casing is R_1 , the radius of the inner wall is R_2 , the total length of the casing is L , the length of the surface is l , the weight of the casing is G , and the bulk density of water is γ . Taking the drum and the water in the drum as the research object, Eq. (13.1) can be obtained according to the mechanical balance, where F_f is the buoyancy force on the steel drum, G_h is the gravity of the drum, and G_w is the gravity of the water in the drum.

$$F_f = G_h + G_w \quad (13.1)$$

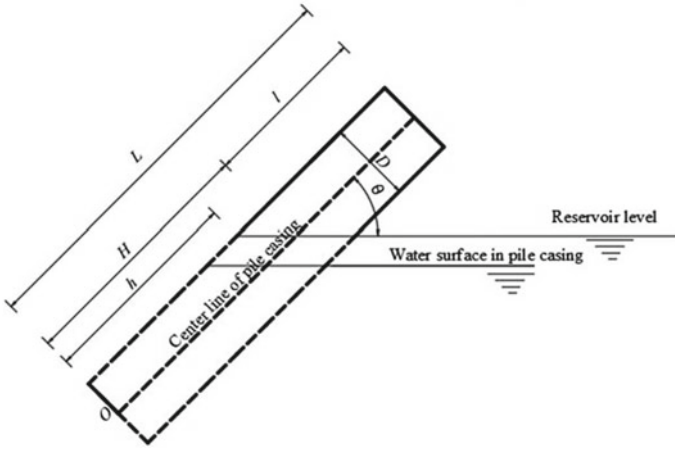


Fig. 13.1 Schematic diagram of buoy floating

It is can be obtained,

$$\gamma\pi R_1^2 \times (H + R_1ctg\theta) = G + \gamma\pi R_2^2 \times (h + R_2ctg\theta) \tag{13.2}$$

According to the balance of buoyancy and gravity on moment of O point, it can be obtained:

$$F_f \times L_f = G_h \times L/2 + G_w \times L_w \tag{13.3}$$

Let the distance between the centroid of the triangle caused by θ and the base edge be, then, from Eq. (13.3):

$$\begin{aligned} &\gamma\pi R_1^2 \times H^2 \cos\theta/2 + \gamma\pi R_1^2 R_1(H + a)ctg\theta \cos\theta \\ &= G \times L \cos\theta/2 + \gamma\pi R_2^2 \times h^2 \cos\theta/2 \\ &+ \gamma\pi R_2^2 R_2(H + a)ctg\theta \cos\theta \end{aligned} \tag{13.4}$$

After simplification we get

$$\begin{aligned} &\gamma\pi R_1^2 \times H^2/2 + \gamma\pi R_1^2 R_1(H + a)ctg\theta \\ &= G \times L/2 + \gamma\pi R_2^2 \times h^2/2 + \gamma\pi R_2^2 R_2(H + a)ctg\theta \end{aligned} \tag{13.5}$$

13.4 Analysis and Discussion

In the second part, according to the principle of mechanical balance, the balance equations of force and moment are established respectively. According to Eqs. (13.2) and (13.5), the conclusion can be drawn: the solution of the equilibrium equation is related to three parameters: H , the depth of the casing immersed in water; h , the height of the liquid level in the casing from the bottom of the casing, and θ , the tilt Angle of the casing in water. Any one of the three parameters can be determined in the solution process to solve the equation. In the following research and discussion, a series of parameters will be solved from several special equilibrium tilt angles of 30° , 45° , 60° and 90° , and corresponding theoretical calculation formulas will be given.

13.4.1 The Relationship Between the Immersion Depth of the Protection Cylinder and the Depth of the Liquid Level in the Barrel

The maximum length of steel drum for one installation on site is $L = 37.5$ m, the wall thickness of the drum is 30 mm, the outer wall $R_1 = 1.95$ m, the inner wall $R_2 = 1.92$ m, the steel bulk weight is 78.5 kN/m³, the water bulk weight is 10 kN/m³, and the radius of the sealing plate at both ends of the drum is 2.05 m (0.1 m larger than the outer diameter of the drum, Ensure the installation space of the sealing bolt tie rod), and the thickness is 3 cm. When the guard cylinder floats, the sealing plates at both ends are included in the calculation, and auxiliary facilities such as valves and gas pipes are ignored. The weight of the drum $G = 1095.346$ kN.

According to Eq. (13.2), the deformation Eq. (13.6) is obtained, and the relation between H and h is further studied when the balance tilt Angle is determined.

$$h = H \bullet \frac{R_1^2}{R_2^2} - \frac{G + \gamma \pi R_2^3 ctg\theta - \gamma \pi R_1^3 ctg\theta}{\gamma \pi R_2^2} \quad (13.6)$$

When the tilt of the guard cylinder is balanced, assuming that the balance inclination Angle is $\theta = 30^\circ$, the value of, is, then Eqs. (13.2) and (13.5) can be simplified to:

$$\gamma \pi R_1^2 \times (H + \sqrt{3}R_1) = G + \gamma \pi R_2^2 \times (h + \sqrt{3}R_2) \quad (13.7)$$

$$\begin{aligned} & \gamma \pi R_1^2 \times H^2/2 + \gamma \pi R_1^2 R_1 (H + \sqrt{3}R_1/3)\sqrt{3} \\ & = G \times L/2 + \gamma \pi R_2^2 \times h^2/2 + \gamma \pi R_2^2 R_2 (H + \sqrt{3}R_1/3)\sqrt{3} \end{aligned} \quad (13.8)$$

It can be obtained from Eq. (13.6):

Table 13.1 $H(h)$ values corresponding to different equilibrium tilt angles

Θ	H (m)	h (m)
30°	21.65	13.02
45°	22.16	13.48
60°	22.39	16.68
90°	22.77	14.02

$$h = H \bullet \frac{R_1^2}{R_2^2} - \frac{G + \sqrt{3}\gamma\pi R_2^3 - \sqrt{3}\gamma\pi R_1^3}{\pi\gamma R_2^2} \tag{13.9}$$

It can be calculated from Eq. (13.9) that:

$$h = 1.031H - 9.301 \tag{13.10}$$

Substituting Eq. (13.10) into Eq. (13.8), H and h are 21.65 and 13.02 m, respectively. According to the calculation results of different balance tilt angles, it is drawn as Table 13.1.

13.4.2 Relation Between Water Inlet Speed and Rotational Speed

In the calculation of 13.4.1, it can be concluded that when the balance tilt Angle is determined, the height between the liquid level in the protective cylinder and the bottom of the cylinder is also determined, so that the volume of water entering the steel protective cylinder can be calculated. According to the calculation formula of the inlet flow rate Q , it can be seen that the inlet volume in the steel shield cylinder has a certain relationship with the inlet area, inlet rate and speed, and the formula can be deformed to obtain the expression of the relationship between v , ω and θ .

$$v = \frac{180\omega R_2^2 h}{A\theta} \tag{13.11}$$

Under the condition that the equilibrium tilt angle is known, the relation between the inlet speed and the rotational speed is discussed by assuming that the inlet area of the steel guard cylinder is fixed. In the calculation process, two different influent conditions are assumed respectively to get the expression of the relation between influent velocity and rotational speed. When the inlet area A_1 of steel sheath is 0.5 m^2 , $v = k\omega$ can be obtained according to Eq. (13.11), k_1 and k_2 under different conditions can be calculated successively, and the relationship diagram between inlet velocity v and rotational speed ω under different balance tilt angles is drawn, and the values of k_1 and k_2 calculated under different balance tilt angles are sorted into Table 13.2.

Table 13.2 Corresponding K values under different inlet water areas

θ	k_1	k_2
30°	576	288
45°	400	200
60°	304	152
90°	207	104

It can be seen from Fig. 13.2 that the influent velocity increases with the increase of rotational speed. Compared with the results of different influent areas under the same equilibrium inclination Angle, it can be seen that the larger the influent area is, the larger the slope is. This indicates that when the influent velocity is constant, the larger the influent area is, the less time it takes to reach the equilibrium inclination Angle. With the increasing of the balance tilt Angle, the ratio between water inlet speed and rotational speed gradually decreases.

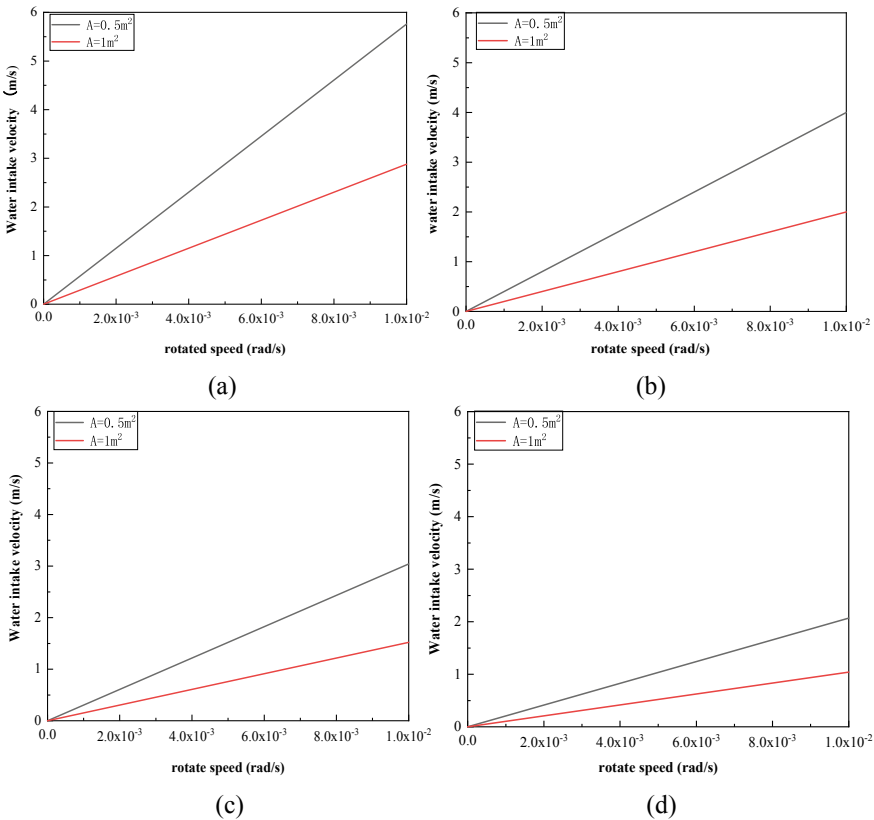


Fig. 13.2 Relation between water inlet velocity and rotational speed at different angle

13.4.3 Relation Between Water Inlet Area and Rotational Speed and Time

In Sect. 13.4.2, the relation between inlet speed and rotational speed is studied according to inlet flow rate. In Sect. 13.4.3, the relation expression between speed ω and inlet area A is discussed according to deformation Eq. (13.12).

$$\omega = \frac{vA\theta}{180R_2^2h} \tag{13.12}$$

Because the bottom plate of the steel guard is bolted to the guard and water inlet valve is installed at the bottom of the guard, the water inlet area of the steel guard is limited. In the construction process of the river flow rate is relatively stable. In the calculation process, it is assumed that the bottom of the water speed is 1 m/s, the water area is 0.5 and 1 m², so as to obtain different balance Angle, different water area of the corresponding speed (Tables 13.3, 13.4).

According to Fig. 13.3, it can be concluded that when the water inlet speed is constant, the larger the water inlet area, the greater the corresponding speed value. Under the same water inlet area, with the increase of the balance tilt Angle, the speed of the inclined sinking of the steel guard cylinder also increases. According to the deformation formula of Q , it can be obtained Eq. (13.13). It can be seen that when the inlet area of the guard cylinder changes, the inlet time also changes accordingly.

$$t = \frac{\pi R_2^2h}{vA} \tag{13.13}$$

The water inlet time corresponding to the equilibrium inclination Angle of steel sheath under different water inlet areas can be obtained by keeping the water inlet

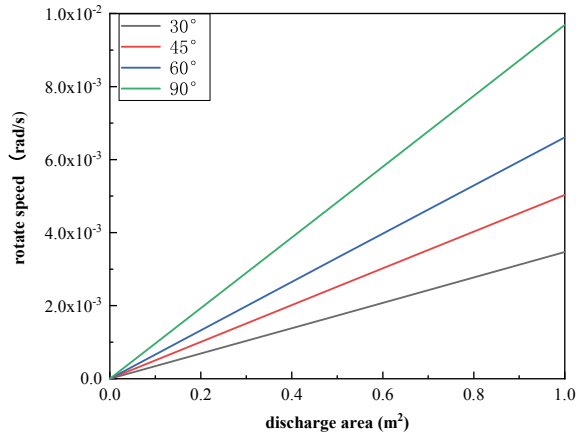
Table 13.3 Rotational speed corresponding to the balanced tilt Angle under different influent areas

θ	ω_1	ω_2
30°	1.73×10^{-3}	3.47×10^{-3}
45°	2.52×10^{-3}	5.03×10^{-3}
60°	3.31×10^{-3}	6.61×10^{-3}
90°	4.83×10^{-3}	9.69×10^{-3}

Table 13.4 Time to reach equilibrium under different inlet water areas

θ	t_1 (s)	t_2 (s)
30°	302	151
45°	313	156
60°	317	159
90°	325	163

Fig. 13.3 Relationship between inlet water area and rotational speed



velocity and water inlet area unchanged. It can be seen from the calculation results that the larger the water inlet area at the bottom of the steel sheath, the less time it takes for the steel sheath to reach the corresponding balance tilt Angle.

13.5 Conclusion

This paper mainly studies and discusses the application of floating transport method in the construction process of steel shield can effectively ensure the positioning of large diameter steel shield into water, calculates the depth of steel shield into water under different balance inclination angles, discusses the relationship between water inlet speed and speed and the relationship between water inlet area and speed, and solves a series of parameters. It provides theoretical conditions for rational selection of structural parameters of steel casing, reduces the risk of steel casing overturning during construction, and provides reference for sinking construction of similar steel casing into water in the future.

References

1. He, C., Peng, L.: Key technology for construction of 4.1m super-large diameter steel sheath of Jiaxiao Bridge. *China Harbor Construct.* **35**(01), 55–58 (2015)
2. Wang, G., Wang, J., Huang, Y.: Construction technology of large diameter single pile floating for offshore wind power. *China Harbor Construct.* **42**(03), 63–66 (2022)
3. Zhang, X.: Discussion on drilling pile construction of deepwater floating platform. *Eng. Construct. Design* **04**, 126–129 (2015)
4. Long, H.: Application of floating method in erection of 80m railway steel girder. *Bridge Construct.* **S1**, 58–61 (2007)

5. Zhao, Z., Sheng, S.: Research on the key process of surface floating transportation of large-scale water transfer immersed pipe. *Pearl River Water Transp.* **09**, 108–109 (2020)
6. Liu, Y., Zhang, C.: Design and research of floating and plugging system for large diameter single pile foundation of offshore wind power. *Mach. Res. Appl.* **33**(03), 156–160 (2020)
7. Wang, H.: Floating Steel Pipe Pile. *Water Transp. Eng.* **7**, 40–42 (2019)
8. Wu, K.-R., Li, J.: Application of aerated capsule plug floating transportation method in water transportation construction of steel pipe pile. *Water Transp. Eng.* **8**, 99–101 (2015)
9. Zhong, A.: Method of Floating Tubular Component by Air Bag: China, 200910016526.8 (2010)
10. Crol, J.B.: Upending of a monopile for an offshore wind turbine foundation. Delft University of Technology, Holland (2015)

Chapter 14

A Stable Method for Multi-component Gas Darcy Flow in Porous Media



Wendi Xue , Yi Wang , and Yuanyuan He

Abstract A numerical model for multi-component gas Darcy flow in porous media is proposed in this paper. The model is capable of simulating underground gas storage operations and cushion gas flow while accounting for gas compressibility and coupling gas density and pressure. Gas properties are calculated using the Benedict–Webb–Rubin–Starling (BWRS) equation and the non-polar gas viscosity equation. The finite volume method is employed for discretization. Moreover, the computational stability of the proposed method is analyzed and verified. Compared to classical methods, the proposed method exhibits faster convergence with larger time steps. This is a significant advantage as it allows for more efficient simulations and faster results. To demonstrate the applicability of our model, we simulate two cases of UGS: a single well injection and a multiple wells injection. We find that the multiple wells injection method can effectively reduce the diffusion of cushion gas and increase the gas storage capacity.

Keywords Underground gas storage · Multi-component · Cushion gas

14.1 Introduction

The focus of current research is on the multi-component gas flow model in porous media and its solving method, which is a key model for cushion gas in underground gas storage. Ewing et al. [1] presented the multi-component gas mass equations and incorporated non-Darcy flow into the model. Liang and Zhou [2] proposed a novel conservative splitting decomposition method (S-DDM) that retains the benefits of non-overlapping domain decomposition and splitting techniques. Chen et al. [3]

W. Xue · Y. Wang (✉)

National Engineering Research Center of Oil and Gas Pipeline Transportation Safety/MOE Key Laboratory of Petroleum Engineering/Beijing Key Laboratory of Urban Oil and Gas Distribution Technology, China University of Petroleum (Beijing), Beijing 102249, China
e-mail: wangyi1031@cup.edu.cn

Y. He

PetroChina Research Institute of Petroleum Exploration and Development, Beijing 100083, China

developed a fully mass-conservative numerical method that ensures the positivity preservation of each component's molar concentration. Tenthorey et al. [4] utilized the Otway Basin underground gas storage as a simulation model to compare CO₂ storage capacity under varying operating conditions. Davarpanah et al. [5] focused on the impact of nitrogen cushion gas on natural gas underground storage operations using underground gas storage in Iran as a simulation model. Sadeghi and Sedaei [6] examined the influence of gas diffusion on cushion gas distribution and found that diffusion must be considered due to extended operation times. Gamal Rezk and Foroozesh [7] analyzed the effect of uncertain diffusion coefficients on production rates and gas storage capacity. Xue [8] proposed an integrated model for fractured underground gas storage, but this model just applies to single component gas.

Combining the above researches, we proposed a stable method for multi-component gas Darcy flow in porous media. The method linearizes the gas equation of state and incorporates Darcy flow into the mass conservation equation, reducing model complexity and enhancing computational efficiency. The model is suitable for simulation of seepage of work gas and cushion gas in underground gas storage.

14.2 Mathematical Model

We consider the multi-component gas and Darcy law in porous media [1], the mass conservation for component i is as follow:

$$\frac{\partial}{\partial t}(\phi\rho_i) + \nabla \cdot (\rho_i\mathbf{u}) = \nabla \cdot (D\nabla\rho_i) + q_i \quad (14.1)$$

where ϕ is the porosity, ρ_i is the density of component i , \mathbf{u} is the velocity, D is the diffusion coefficient, q_i is the source items for component i .

By superimposing the equations for all components, the mass conservation equation is obtained:

$$\frac{\partial}{\partial t}(\phi\rho) + \nabla \cdot (\rho\mathbf{u}) = \nabla \cdot (D\nabla\rho) + q \quad (14.2)$$

The gas velocity obeys the Darcy's law [8, 9]:

$$\mathbf{u} = -\mathbf{k}\frac{\nabla p}{\mu} \quad (14.3)$$

where p is the gas pressure, μ is the viscosity, \mathbf{k} is the permeability tensor.

Due to the wide range of gas pressure variations and the significant differences in the physical properties of different components, it is not feasible to assign constant values to these properties. This study introduces gas property equations commonly used in engineering, such as the BWRS equation [10], which can calculate the

relationship between gas pressure and density:

$$p = \left[\rho RT + \left(B_0 RT - A_0 - \frac{C_0}{T^2} + \frac{D_0}{T^3} + \frac{E_0}{T^4} \right) \rho^2 + \left(bRT - \alpha - \frac{d}{T} \right) \rho^3 + \alpha \left(a + \frac{d}{T} \right) \rho^6 + \frac{c\rho^3}{T^3} (1 + \gamma\rho^2) \exp(-\gamma\rho^2) \right] \quad (14.4)$$

A semi-empirical formula [10] is used to calculate the gas viscosity:

$$\mu = C \exp \left[x \left(\frac{\rho}{1000} \right)^y \right] \quad (14.5)$$

$$x = 2.57 + 0.2781\Delta + \frac{1063.6}{T} \quad (14.6)$$

$$y = 1.11 + 0.04x \quad (14.7)$$

$$C = \frac{2.415 \times (7.77 + 0.1844\mu)T^{1.5}}{122.4 + 377.58\Delta + 1.8T} \times 10^{-4} \quad (14.8)$$

14.3 Proposed Method

In this section, we present an analysis of the classical method and introduce a novel approach. The classical iteration process involves the following steps:

1. Calculation of gas component density using Eq. (14.1).
2. Calculation of gas pressure using Eq. (14.4).
3. Calculation of gas velocity using Eq. (14.3).
4. Repetition of steps 1–3 until convergence is achieved.

Above steps (2) and (3) can reduce the computational stability. We combine these steps and gas properties. As density is monotonically related to pressure, a linear equation obtained by Eq. (14.4) is proposed as follow:

$$\rho = \eta p \quad (14.9)$$

By introducing Eqs. (14.3) and (14.9) into Eq. (14.2), the equation complexity can be reduced from the original three equations to two equations. Moreover, the gas pressure equation is obtained as follows:

$$\frac{\partial}{\partial t}(\phi\eta p) = \nabla \cdot [\rho \mathbf{k} \mu^{-1} \nabla p + D \nabla(\eta p)] + q \quad (14.10)$$

By utilizing Eq. (14.10), gas pressure can be directly calculated. It is important to note that the coefficient η must be recalculated during iterations, which is equivalent to calculating Eq. (14.4). Compared to the classical method, the proposed approach can mitigate instability caused by the source term. The iterative process involves the following steps:

1. Initialization of the coefficient η using the gas pressure from the previous step.
2. Calculation of gas pressure using Eq. (14.10) and direct calculation of gas velocity.
3. Calculation of gas component density using Eq. (14.1) and updating of the coefficient η .
4. Repetition of steps 1–3 until convergence is achieved

14.4 Stability Verification

The stability of the proposed method will be verified through simulation results. The injected gas mass flow is 10 kg/s at position 1 as shown in Sect. 14.5.1. We simulate the convergence for different time steps and obtain the max relaxation factors (Table 14.1).

Compared with the classical method, the proposed method is extremely stable. The proposed method still converges at a larger time step with a relaxation factor of 1.0. We further analyze the pressure and density (time step 1000 s).

From Fig. 14.1, the gas injection can cause a pressure rise in the initial iterative step. As the iterative steps increase, the pressure diffuses into the reservoir, resulting in the pressure drop. Moreover, the high pressure in the initial iterative step can cause more pressure to diffuse the reservoir. After about 50 iteration steps, the pressure gradually rises to convergence.

From Fig. 14.2, the density variations are more stable than the pressure variations. The density gradually rises to convergence as iteration steps increase.

Table 14.1 Stability verification

Time step (s)	Method	Max relaxation factor for convergence
10	Classical method	0.2
100	Classical method	0.01
1000	Classical method	*NAN
10	Proposed method	1.0
100	Proposed method	1.0
1000	Proposed method	1.0

* NAN : Not a Number; Relaxation factor of 1.0: Normal Iteration

Fig. 14.1 Pressure variations during iterations

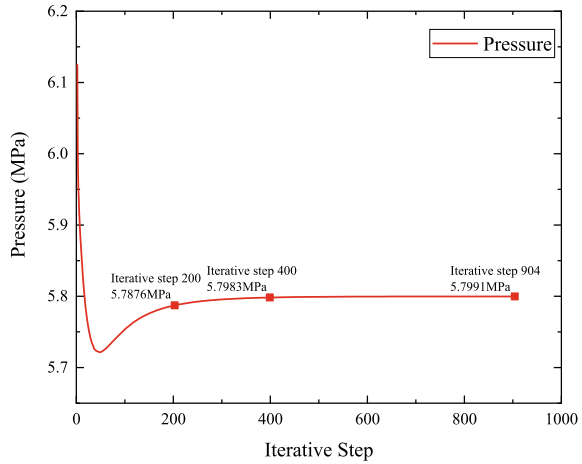
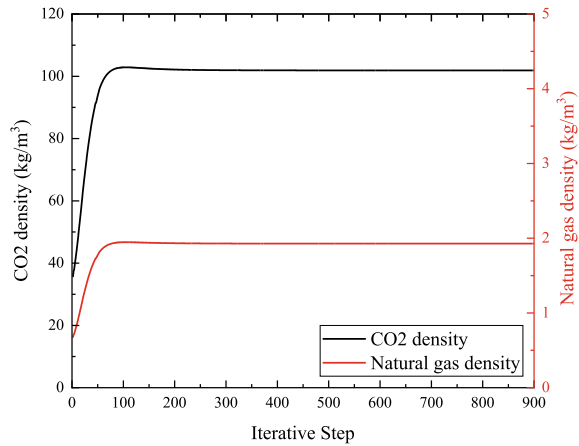


Fig. 14.2 Density variations in iterations



14.5 Case Study

14.5.1 Parameters of the Simulation

The size of reservoir model is 100 m × 100 m × 10 m with mesh number 71 × 71 (neglecting the effect of reservoir thickness). The gas injection wells are set to 5 positions (as shown in Table 14.2). The other parameters are shown in Table 14.3.

The reservoir physical properties is shown in Table 14.3.

In this study, the work gas is natural gas and the cushion gas is carbon dioxide. The convergence criterion is that the absolute deviation of the gas density is $<10^{-3}$.

Table 14.2 Well position

Well position	x position (m)	y position (m)
1	50	50
2	10	10
3	90	10
4	10	90
5	90	90

Table 14.3 Reservoir physical properties

Parameter	Value	Unit
Initial gas pressure $p^{(0)}$	5	MPa
Porosity ϕ	0.3	1
Permeability k_{xx}	100	md
Permeability k_{yy}	100	md
Diffusion coefficient D	2×10^{-5}	m^2/s

14.5.2 Case for a Single Well Gas Injection

Case 1:

- Injecting cushion gas at 10 kg/s for 48 h at position 1.
- Injecting work gas at 10 kg/s for 24 h at position 1.
- Stopped injecting gas for 24 h.

From Fig. 14.3, the red region is carbon dioxide and the blue region is natural gas. The initial work gas in the reservoir flows towards the boundary due to cushion gas injection. The single well gas injection method can result in the loss of this work gas. This part of the work gas will not be produced.

From Fig. 14.4, the injection of work gas leads to a ring structure of cushion gas. Due gas injection suddenly stops at the operation 72 h, gas flows back to the center. The gas mixing region becomes larger.

14.5.3 Case for Multiple Wells Gas Injection

Case 2:

- Injecting cushion gas at 2.5 kg/s for 48 h at position 2, 3, 4, 5.
- Injecting work gas at 10 kg/s for 24 h at position 1.
- Stopped injecting gas for 24 h.

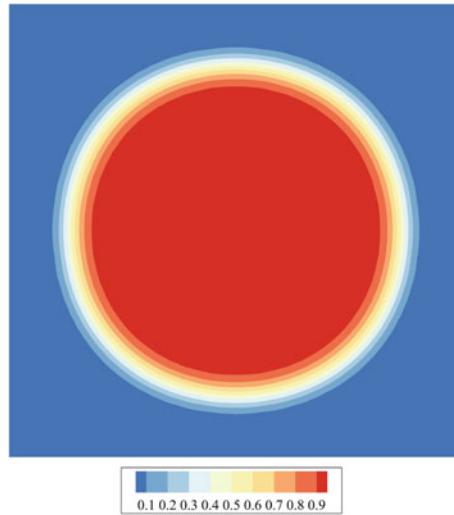


Fig. 14.3 Component distribution of a single well gas injection

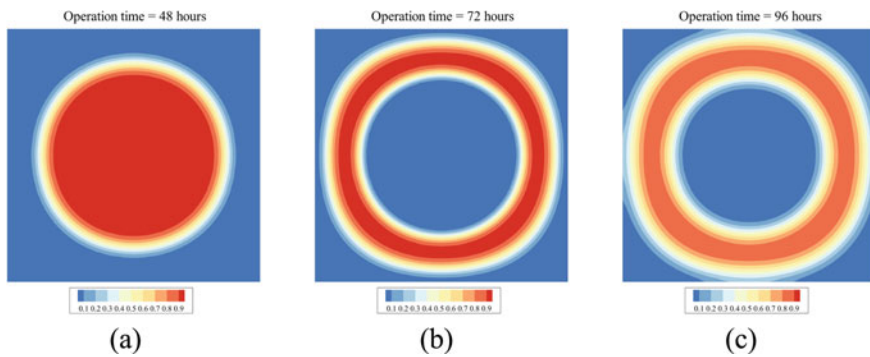


Fig. 14.4 Component distribution of a single well gas injection: **a** Operation 48 h; **b** Operation 72 h; **c** Operation 96 h

From Fig. 14.5, the red region is carbon dioxide and the blue region is natural gas. The initial work gas in the reservoir flows towards the center due to cushion gas injection. The multiple wells gas injection method can minimize the loss of work gas.

From Fig. 14.6, the injection of work gas leads to the accumulation of cushion gas. The cushion gas is basically not flowing. Multiple wells gas injection is better compared to a single well gas injection. The study only includes the four corners of gas injection. Better positions for gas injection can be selected based on the real reservoir geometry. This method can reduce the diffusion of cushion gas.

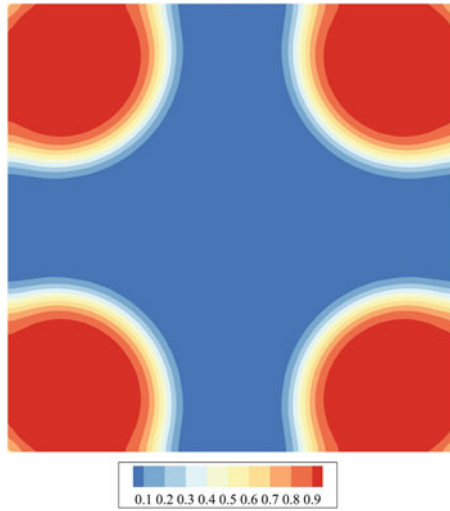


Fig. 14.5 Component distribution of multiple wells gas injection

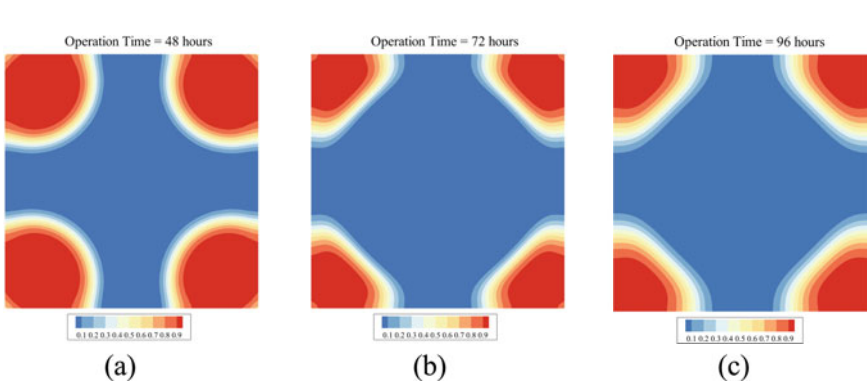


Fig. 14.6 Component distribution of multiple wells gas injection: **a** Operation 48 h; **b** Operation 72 h; **c** Operation 96 h

14.6 Conclusion

In this study, we propose a stable method for multi-component gas Darcy flow in porous media. Our model integrates the gas mass conservation equation, gas state equation, and Darcy flow law to the gas pressure equation. Simulation results demonstrate that our method exhibits greater stability than classical method. We simulate the cases of a single well and multiple wells gas injection. Our findings indicate that, compared to single-well injection, multiple-well injection can more effectively preserve the initial working gas in the reservoir. As such, multiple-well injection may serve as a primary approach for cushion gas injection.

Acknowledgements The study is supported by National Natural Science Foundation of China (No. 51576210).

CRedit Authorship Contribution Statement Wendi Xue: Conceptualization, Methodology, Software, Formal analysis, Visualization, Writing—original draft, Writing—review and editing. Yi Wang: Supervision, Writing—review & editing. Yuanyuan He: Visualization, Writing—review & editing.

Data Availability No data was used for the research described in the article.

Declaration of Competing Interest The authors declare that they have no known competing financial interests or personal relationships that could have appeared to influence the work reported in this paper.

References

1. Ewing, R.E., Wang, J., Weekes, S.L.: On the simulation of multicomponent gas flow in porous media. *Appl. Numer. Math.* **31**(4), 405–427 (1999). [https://doi.org/10.1016/S0168-9274\(99\)00006-9](https://doi.org/10.1016/S0168-9274(99)00006-9)
2. Liang, D., Zhou, Z.: The conservative splitting domain decomposition method for multicomponent contamination flows in porous media. *J. Comput. Phys.* (2020). <https://doi.org/10.1016/j.jcp.2019.108974>
3. Chen, H., Fan, X., Sun, S.: A fully mass-conservative iterative IMPEC method for multicomponent compressible flow in porous media. *J. Comput. Appl. Math.* **362**, 1–21 (2019). <https://doi.org/10.1016/j.cam.2019.05.012>
4. Tenthorey, E., Nguyen, D., Vidal-Gilbert, S.: Applying underground gas storage experience to geological carbon dioxide storage: a case study from Australia's Otway Basin. *Energy Proc.* **4**, 5534–5540 (2011). <https://doi.org/10.1016/j.egypro.2011.02.540>
5. Davarpanah, A., Mazarei, M., Mirshekari, B.: A simulation study to enhance the gas production rate by nitrogen replacement in the underground gas storage performance. *Energy Rep.* **5**, 431–435 (2019). <https://doi.org/10.1016/j.egy.2019.04.004>
6. Sadeghi, S., Sedaee, B.: Mechanistic simulation of cushion gas and working gas mixing during underground natural gas storage. *J. Energy Storage* (2022). <https://doi.org/10.1016/j.est.2021.103885>
7. Gamal Rezk, M., Foroozesh, J.: Uncertainty effect of CO₂ molecular diffusion on oil recovery and gas storage in underground formations. *Fuel* (2022). <https://doi.org/10.1016/j.fuel.2022.124770>
8. Xue, W., Wang, Y., Chen, Z., Liu, H.: An integrated model with stable numerical methods for fractured underground gas storage. *J Clean Prod* **393** (2023). <https://doi.org/10.1016/j.jclepro.2023.136268>
9. Darcy, H.: Les fontaines publiques de la ville de Dijon. Recherche, p 647 (1856)
10. Li, C., Wang, Y., Chen, Z., Liang, G., Huang, Z.: Natural gas pipeline transportation (in Chinese), 2nd edn. Petroleum Industry Press, Beijing (2008)

Chapter 15

Optimal Control of Vehicle Queue Following Based on Wireless Communication



ZhaoWei Ding, FaZhan Tao, MengYang Li, and Zhou Tao

Abstract In this paper, to solve the problem of vehicle following tracking control in the vehicle following scenario, an intelligent queue following optimization control method is proposed based on the Internet of Things communication network. Firstly, the Internet of Things network is used to obtain the network information, based on which optimization algorithm is designed for car following distance to improve the driving safety, road traffic capacity and driving safety. Secondly, the following controller is given by using the backstepping method to achieve the following of the optimal following distance. Finally, the validity of the proposed scheme is verified via a simulation example.

Keywords Queue following · Wireless communication · Optimal control · Vehicle

15.1 Introduction

The rapid development of Internet of Things provides the key technology for the realization of intelligent transportation system [1–4]. As an important component of the intelligent transportation system technology, the vehicle queue driving control technology enables vehicles in the same lane to drive at a small safe distance, which can reduce the air resistance during vehicle driving and fuel consumption, improve road capacity and traffic flow, and remission traffic congestion. Therefore, the team driving technology has receive more and more attention [5, 6]. It is worth that how to design the distance optimization algorithm based on Internet of Things network communication for following driving control [7].

Z. Ding · F. Tao

College of Information Engineering, Henan University of Science and Technology, Kaiyuan Avenue, Luoyang 471023, Henan, China

M. Li (✉) · Z. Tao

College of Physics and Electronic Information, Luoyang Normal University, Yibin, Luoyang 471000, Henan, China
e-mail: limengyang8801@163.com

The spacing control strategy can be divided into fixed spacing strategy and variable spacing strategy according to whether the spacing changes or not. Nevertheless, the fixed distance control strategy ignores the use of network communication information, which could cause security problems and waste traffic flow. To solve those problems, many researchers have proposed the variable spacing algorithm. In the constant workshop time distance control strategy, in [8] authors address the adaptive control and identification of heterogeneous fleets under a variety of topologies. An adaptive cruise control method is proposed to overcome sensor/actuator delays in [9]. In [10], author adopt a new definition of queue stability in the fleet control, which can be used for not only linear but also nonlinear systems. In addition, it can be used for analyzing independently of the fleet topology.

Based on the fleet control method of variable time distance strategy, an adaptive control method is designed to reduce the distance between adjacent vehicles and improve traffic capacity [11]. PID control method [12] is proposed to reduce fuel consumption and ensure the stability of the fleet. It is worth pointing out that the existing vehicle spacing strategies have their own advantages and disadvantages, so that they are applicable to different fleet composition, roads and communication conditions. This paper proposes Sequential Quadratic Programming (SQP) algorithm to optimize the following distance based on the Internet of Things network communication technology. Then, the backstepping strategy is used to design the following controller to improve driving safety, road traffic capacity and driving comfort.

15.2 Problem Formulation and System Modeling

Considering the Fig. 15.1 about the networked vehicle following control system, the controlled vehicle is equipped with a laser radar sensor to obtain the following distance between the controlled vehicle and the vehicle in front, using V2V and V2I communication technology to obtain the information of the vehicle in front (position S_p , speed V_p), road adhesion coefficient, road roughness and other information. The following distance is directly related to fuel economy, driving safety, driving comfort and traffic capacity.

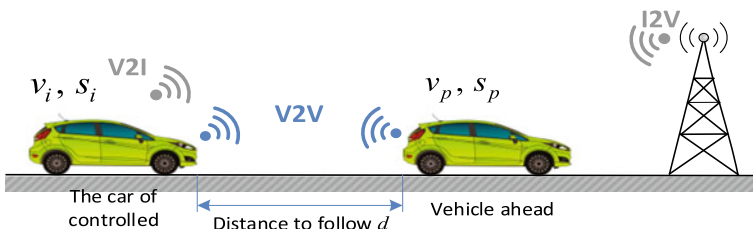


Fig. 15.1 Car following control system of networked

15.3 Vehicle Longitudinal Dynamics Model

The longitudinal dynamic model of the vehicle is given as follows:

$$\begin{cases} \dot{s} = v_i \\ \dot{v}_i = \frac{1}{m}(F_t - F_a - F_r - F_g) \end{cases} \quad (15.1)$$

where s_i , v_i , m_i are the position, speed and mass of the current vehicle, respectively. F_g is the traction or braking force of vehicle. F_a , F_r and F_g are the air resistance, rolling resistance and ramp resistance during vehicle driving, respectively. The air resistance is determined by the speed of the vehicle, the air resistance coefficient C_d , the air density ρ , and the windward area A of the vehicle.

$$F_a = \frac{1}{2}C_d\rho Av_i^2 \quad (15.2)$$

Rolling resistance is defined as follows:

$$F_r = f_r m_i g \cos \theta \quad (15.3)$$

where f_r is the rolling resistance coefficient, g is the gravity acceleration. θ is the road grade.

The ramp resistance of the vehicle is defined as follows:

$$F_g = m_i g \sin \theta \quad (15.4)$$

15.4 Car Following Distance Optimization and Nonlinear Control

15.4.1 Follow Distance Optimization

For the following process, proper following distance can effectively avoid rear end collision, ensure driving safety and improve traffic capacity. The purpose of car following distance optimization is to generate a variable car following distance track based on traffic conditions, taking into account driving safety and comfort.

To ensure traffic safety and traffic capacity, the minimum and maximum following distances are defined as follows:

$$\begin{cases} d_{\min}(v_i(k)) = 2 + 0.5v_i(k) + 0.0625v_i(k)^2 \\ d_{\max}(v_i(k)) = 10 + v_i(k) + 0.0825v_i(k)^2 \end{cases} \quad (15.5)$$

where d_{\min} , d_{\max} are the max and min follow distance under the speed v_i of the controlled vehicle, respectively.

In order to ensure the actual following distance is within the above safety range, the cost functions of driving safety and traffic capacity are defined as follows:

$$J_{safety} = \left(d - \frac{d_{\max}(v_i(k)) - d_{\min}(v_i(k))}{2} \right)^2 \quad (15.6)$$

where d is the follow distance.

In the process of following, frequent acceleration and deceleration of the vehicle in front will affect the driving comfort of the controlled vehicle. Therefore, the cost function of driving comfort is defined as Eq. (15.7).

$$J_{comfort} = (v_i(k) - v_i(k-1))^2 \quad (15.7)$$

where $v_i(k-1)$ and $v_i(k)$ are the speeds of the controlled vehicle at and time, respectively.

To sum up, the total cost function and constraints are defined as follows:

$$\begin{aligned} \min_d J_1 &= w_1 J_{safety} + w_2 J_{comfort} \\ s.t. \quad &d_{\min}(v_i(k)) \leq d \leq d_{\max}(v_i(k)) \end{aligned} \quad (15.8)$$

where w_1 and w_2 are weighting factors.

After all the parameters are defined and constraints in the cost function, the tracking distance optimization problem can be transformed into a nonlinear optimization problem. In order to ensure that the optimal following distance algorithm can be used online, SQP method is used to solve the optimal following distance.

15.4.2 Nonlinear Tracking Control Based on Optimal Following Distance

For the nonlinear model of vehicle, the controller is designed by backstepping method to ensure the controlled vehicle follows the vehicle ahead at the optimal following distance.

First, introducing the position error function:

$$Z_1 = s_i - (s_p - d) \quad (15.9)$$

By taking the derivative of (15.9), obtain:

$$\dot{Z}_1 = \dot{s}_i - \dot{s}_p + \dot{d} = v_i - v_p + \dot{d} \quad (15.10)$$

Then design a Lyapunov function as follows:

$$V_1 = \frac{1}{2} Z_1^2 \quad (15.11)$$

According to (15.10) and (15.11), obtain

$$\dot{V}_1 = Z_1(v_i - v_p + \dot{d}) \quad (15.12)$$

Z_2 is defined as the virtual error:

$$Z_2 = v_i - a \quad (15.13)$$

where $a = -k_1 z_1 - \dot{d} + \dot{s}_p$, k_1 is a positive constant, then $Z_2 = v_i + k_1 z_1 + \dot{d} - \dot{s}_p$.

Take the derivative of Z_2 , get:

$$\begin{aligned} \dot{Z}_2 = & \frac{1}{m_i} u - \frac{1}{2m_i} C_d \rho A v_i^2 - f_r g \cos \theta \\ & - g \sin \theta + k_1 \dot{Z}_1 + \ddot{d} - \ddot{s}_p \end{aligned} \quad (15.14)$$

Then design a Lyapunov function as follows:

$$V_2 = V_1 + \frac{1}{2} Z_2^2 \quad (15.15)$$

According to (15.12)–(15.14), one can get

$$\dot{V}_2 = -k_1 Z_1^2 + Z_2(Z_1 + \dot{Z}_2) \quad (15.16)$$

Backstepping controller is designed as follows:

$$\begin{aligned} F_t = & m_i - k_2 Z_2 - Z_1 + \frac{1}{2m_i} C_d \rho A v^2 \\ & + f_r g \cos \theta + g \sin \theta - k_1 \dot{Z}_1 - \ddot{d} + \dot{v}_p \end{aligned} \quad (15.17)$$

Substitute (15.17) into (15.16), obtain

$$\dot{V} \leq -k_1 Z_1^2 - k_2 Z_2^2 \leq 0 \quad (15.18)$$

Theorem 15.1 If $\Omega(t)$ is a uniformly continuous function, and $\lim_{x \rightarrow \infty} \int_0^t \Omega(t) dt$ existing and limited, then we can get $\Psi(t) \rightarrow 0$ when $t \rightarrow \infty$.

In order to analyze the stability of system (15.15), the following function is defined:

$$\Theta(t) = -V_2(t) \quad (15.19)$$

Integral of (15.19) can get

$$\int_0^t \Phi(t)dt = V_2(0) - V_2(t) \quad (15.20)$$

where $Z_1(0), Z_2(0)$ and $V_2(0)$ are bounded. According to (15.15), $V_2(t)$ is nonadditive and bounded.

Therefore, $\lim_{x \rightarrow \infty} \int_0^t \Omega(t)dt$ exists and is limited. From Theorem (15.1), we can get $\Theta(t) \rightarrow 0$ when $t \rightarrow \infty$. It means that $Z_1(t)Z_2(t)$ converge to zero when $t \rightarrow \infty$.

Thus, the designed backstepping controller can asymptotically stabilize the error system (15.15).

15.5 Simulation Studies

In order to verify the above design method, a small fleet consisting of a front vehicle and a controlled vehicle is selected for computer simulation. The initial spacing between two vehicles is set as 24 m. The simulation analysis is carried out under the conditions of acceleration and deceleration of the vehicle ahead.

Acceleration of the front car: the initial state of the front car, including position, speed and acceleration, are set to [24 m, 20 m/s, 2 m/s²], respectively.

In addition, the initial state of the rear car is defined as [0 m, 20 m/s, 0 m/s²], and the front car accelerates from 20 to 30 m/s with an acceleration value of 2 m/s². The speed curve of the front car is shown in Fig. 15.2a. Deceleration of the front car: the initial state of the front car, including position, speed and acceleration, is set to [24 m, 20 m/s, -2 m/s²], respectively. In addition, the initial state of the rear car is defined as [0 m, 20 m/s, 0 m/s²], the front car decelerates from 20 to 0 m/s, and the acceleration value is -2 m/s². The speed curve of the front car is shown in Fig. 15.3a. Two strategies are adopted to track vehicle behavior, namely fixed spacing control and the optimal following distance control proposed in this paper. The simulation results are shown in Figs. 15.2 and 15.3.

Figures 15.2a and 15.3a show the vehicle speed curves under the two strategies. The tracking effect of fixed spacing control is better, but the vehicle speed changes more smoothly under the optimal following distance control, and the driving comfort is higher.

Figures 15.2b and 15.3b shows the change of the following distance under the two strategies. The fixed distance control follows the car at a constant distance of 30 m.

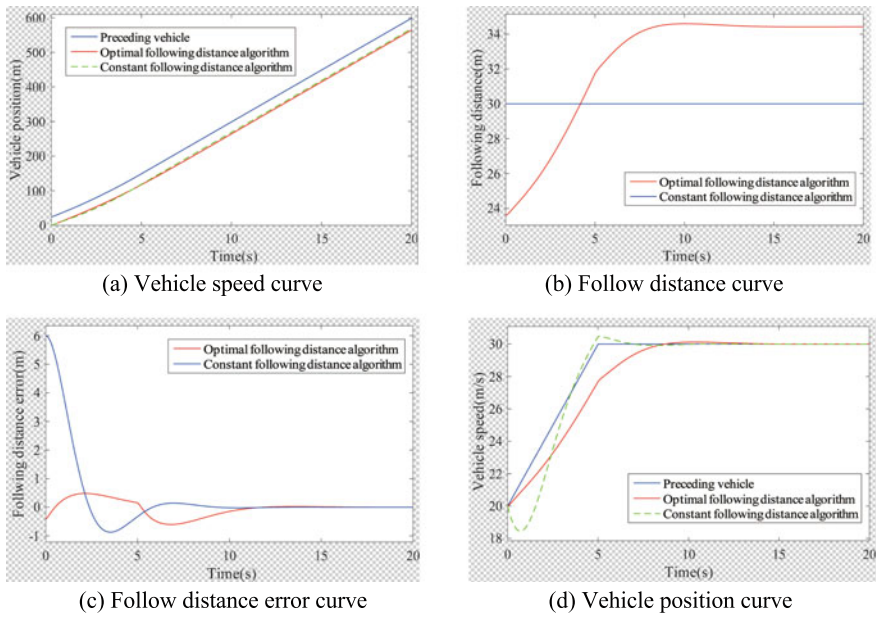


Fig. 15.2 Comparison of car following control strategies during acceleration of the front car

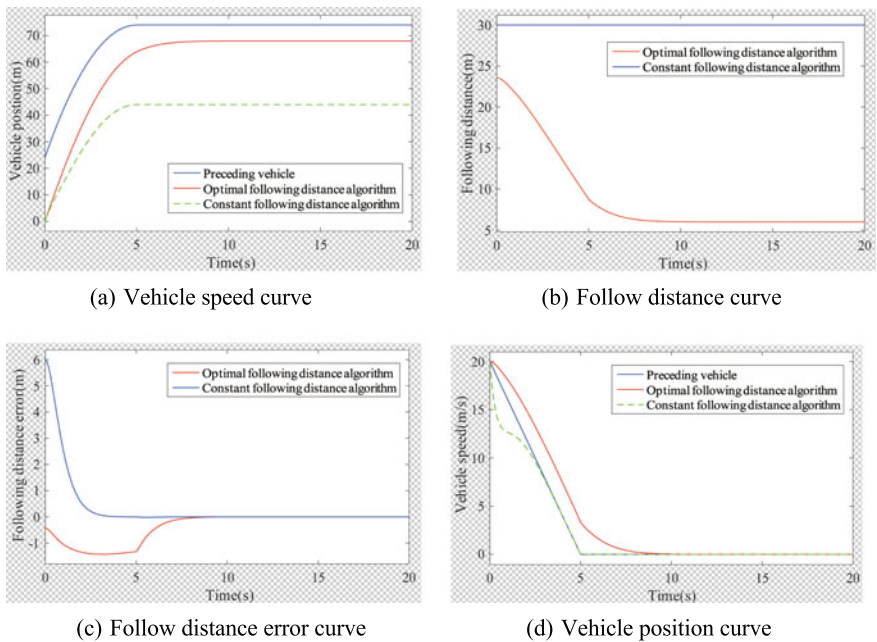


Fig. 15.3 Comparison of following control strategies in deceleration process of front vehicle

The ideal workshop distance under the optimal following distance control varies with the vehicle speed and acceleration and deceleration.

Figures 15.2c and 15.3c show the following distance error under the two strategies. The distance error given to me under the two strategies can converge to zero, and the convergence speed is faster under the control of fixed spacing.

Figures 15.2d and 15.3d show the vehicle position curves under the two strategies. With the fixed spacing strategy, the driving positions of vehicles are basically symmetrical, and the vehicle spacing is about 30 m. Under the control of the optimal following distance, the distance between workshops changes with the road traffic conditions, which is safer, and the road traffic capacity is also guaranteed.

15.6 Conclusion

In order to ensure the driving safety of car following, improve the driving comfort and road traffic capacity, this paper proposes a car following optimization control method based on the intelligent network environment. The state information of the vehicle in front and the controlled vehicle according to the network information was obtained. Then, the optimization algorithm of the following distance and the following error model was designed. The following controller using the reverse stepping method to realize the controlled vehicle to follow the vehicle in front with the optimal following distance was proposed. Based on this strategy, the following stability was analyzed. From the simulation results, the following control strategy show effectness in terms of vehicle spacing safety, road traffic capacity and impact degree Suppression.

References

1. Zhang, G., Shi, C., Han, C., Li, X., Wang, D., Rabie, K., Kharel, R.: Implementation-friendly and energy-efficient symbol-by-symbol detection scheme for IEEE 802.15.4 O-QPSK receivers. *IEEE Access* **8**, 158402–158415 (2020)
2. Zhang, G., Ma, C., Chen, K., Li, Y., Li, H., Han, C.: Multiple-symbol noncoherent learning detection of coded QAM signals in IEEE 802153 Wireless Multi-media Networks. *Phys. Commun.* **55**, 1–11 (2022)
3. Zhang, Y., He, W., Li, X., Peng, H., Rabie, K., Nauryzbayev, G., ElHalawany, B.M., Zhu, M.: Covert communication in downlink NOMA systems with channel uncertainty. *IEEE Sens. J.* **22**(19), 19101–19112 (2022)
4. Li, X., Li, J., Liu, Y., Ding, Z., Nallanathan, A.: Residual transceiver hardware impairments on cooperative NOMA networks. *IEEE Trans. Wireless Commun.* **19**(1), 680–695 (2020)
5. Tithi, T., Deka, B., Gerdes, R.M., Winstead, C., Li, M., Heaslip, K.: Analysis of friendly jamming for secure location verification of vehicles for intelligent highways. *IEEE Trans. Veh. Technol.* **67**(8), 7437–7449 (2018)
6. Wang, F.Y., Zheng, N.N., Cao, D., Martinez, C.M., Li, L., Liu, T.: Parallel driving in CPSS: a unified approach for transport automation and vehicle intelligence. *IEEE/CAA J. Autom. Sin.* **4**(4), 577–587 (2017)

7. Li, L., Peng, X., Wang, F.Y., Cao, D., Li, L.: A situation-aware collision avoidance strategy for car-following. *IEEE/CAA J. Autom. Sin.* **5**(5), 1012–1016 (2018)
8. Gao, F., Li, S.E., Zheng, Y., Kum, D.: Robust control of heterogeneous vehicular platoon with uncertain dynamics and communication delay. *IET Intel. Transport Syst.* **10**(7), 503–513 (2016)
9. Liu, B., Gao, F., He, Y., Wang, C.: Robust control of hetero-generous vehicular platoon with non-ideal communication. *Electronics* **8**(2), 207–221 (2019)
10. Bekiaris-Liberis, N., Roncoli, C., Papageorgiou, M.: Predictor-based adaptive cruise control design. *IEEE Trans. Intell. Transp. Syst.* **19**(10), 3181–3195 (2018)
11. Ploeg, J., Nathan, V.D.W., Nijmeijer, H.: string stability of cascaded systems: application to vehicle platooning. *IEEE Trans. Control Syst. Technol.* **22**(2), 786–793 (2014)
12. Yanakiev, D., Kanellakopoulos, I.: Nonlinear spacing policies for automated heavy-duty vehicles. *IEEE Trans. Veh. Technol.* **47**(4), 1365–1377 (1998)

Chapter 16

Fatigue Crack Quantification Model for Metallic Structures Based on Strain Monitoring



Kunpeng Li, Xin Qi, and Biao Li

Abstract The real-time monitoring of fatigue crack length is crucial for estimating the damage tolerance and the residual lifetime of aircraft metallic structures. This paper proposed a deep learning-based approach for predicting the fatigue crack size of metallic structures using strain monitoring data. By constructing learning models for Cycle Consistent Adversarial Networks, crack sizes are classified and quantified, and the correlation between the measured strain data and finite element simulation data was established. The proposed approach was applied for monitoring the growth of fatigue crack in a central hole plate subjected to random fatigue loads. The predictions show that the proposed model can monitor the fatigue crack lengths with high accuracy, where the prediction error of the crack length is less than 1 mm. This approach provides a reliable and accurate method for predicting the fatigue crack size of metallic structures, which may have important practical applications in aviation industry.

Keywords Fatigue crack · Strain monitoring · Deep learning · Data driven model · Fatigue crack prediction

16.1 Introduction

In recent years, the rising cost of development and manufacturing of advanced aircraft has posed challenges to their durability, reliability, and economy [1, 2]. The ability to monitor and assess the damage of aircraft structures during their service life is essential for conducting health assessments, life consumption calculations, maintenance scheduling, life extension planning, and other related tasks [3–5]. Traditional crack growth prediction methods based on physical models were developed using appropriate crack growth rate models such as Paris, Walker, Forman, and others. However, the accuracy of these models heavily relies on the rationality of the physical basis, and

K. Li · X. Qi · B. Li (✉)

School of Aeronautics, Northwestern Polytechnical University, Xi'an 710072, Shaanxi, China
e-mail: libiao@nwpu.edu.cn

there may be inconsistencies between the service process and the experiment process, resulting in errors in crack growth length prediction even for the same formula and the same structure. To address these issues, new approaches based on machine learning and data-driven methods have emerged. These approaches can take into account the uncertainties and variations in real-world conditions and improve the accuracy and efficiency of crack growth prediction. These methods offer promising alternatives to traditional physical models and have the potential to significantly enhance the safety, reliability, and cost-effectiveness of aircraft structures.

The appearance of cracks in a structure can cause changes in its stiffness and load transfer path, leading to significant changes in local strain fields. Researchers have explored the use of surface strain measurements to correlate crack characteristics with its infer information such as length, direction, and form of the crack. For instance, Crocombe et al. [6] used strain measurements on the back side of a bonded structure to establish a relationship between strain and damage and infer the fatigue damage evolution of the structure. However, it can be challenging to establish a clear relationship between crack length, strain, and load for structures with complex geometries. This is because the mapping relationship between these parameters may not be unique, and determining the location of strain measurement can be difficult. To address this challenge, numerical modeling and simulation techniques can be used to predict the strain field and crack behavior under different loading conditions. This can guide the placement of sensors to identify critical areas for strain measurement. In addition, advancements in sensor technology and data analysis methods, such as machine learning algorithms, can improve the accuracy and efficiency of crack detection using strain measurements. Overall, the use of strain measurements for crack detection and damage assessment is a promising approach that requires careful consideration of the specific characteristics and challenges of each structure.

Machine learning methods have become increasingly popular in the field of structural lifetime prediction. The method can effectively establish nonlinear relationships between input and output data, which improves the prediction accuracy. Wang et al. [7] used Back Propagation (BP) neural networks to identify the flight load of missile models. They used flight parameters such as speed, altitude, and response angle as the input, and the load at key structural components as the output. This approach provides the measurement of the structural load during flight and ensure the safety and reliability of the missile. Trivailo and Carn [8] used neural networks to predict the fatigue load of aircraft tail fins. They inputted the monitored strain values into the neural network and predicted the load of aircraft tail fins. The fatigue life of aircraft structures was obtained, and the maintenance schedule was optimized to ensure the safety and reliability of aircraft operations. Overall, the use of machine learning methods for structural lifetime prediction has great potential to improve the accuracy and efficiency of structural lifetime prediction and ensure the safety and reliability of structures in various applications.

The development of online detection methods is crucial for realizing real-time, continuous, and long-term evaluation of structural performance. This approach is the main direction of intelligent development for future aircraft, such as self-sensing and self-diagnosis [9]. Traditional crack prediction methods based on physical models

can be affected by the inconsistency between the service process and the test process. To address this issue, a real-time fatigue crack prediction method based on strain monitoring data using deep learning has been proposed. This method allows for the crack length to be obtained by inputting the strain data collected in real-time. With this approach, the problem of inaccurate crack length prediction caused by deviations between testing and service can be solved, providing a theoretical basis for aircraft overhaul and maintenance, life management, and life monitoring.

16.2 Model Development

This work proposes a quantitative model for predicting the growth of structural fatigue cracks based on strain monitoring data. The model is developed by establishing a relationship between strain data at a monitoring location and the length of the specific crack. To enhance the accuracy of the model, a mapping relationship between test data and finite element simulation data is established, which reduces deviation caused by test processes and finite element modeling. Furthermore, the paper introduces a classification system for crack sizes and establishes a crack quantization model for different size ranges for further improving the prediction precision of the crack size.

Figure 16.1 illustrates the process of the model development, which includes four main steps: identification of strain monitoring sites, establishment of Cycle-Consistent Adversarial Networks (CycleGAN), establishment of a Classifying Model (CM) for crack size range, and establishment of a Quantifying Model (QM) for crack length. Three types of deep learning models were developed with different purposes, which are outlined.

- (1) The CycleGAN model was utilized to establish a mapping relationship between experiment data and Finite Element Analysis Strain Data (FSD). Given the presence of discrepancy between the experiment and the Finite Element Analysis (FEA), the strain data measured during the experiment was inputted into CycleGAN's Generator to produce Fake Finite Element Analysis Strain Data (Fake-FSD), which closely approximates the FSD. This approach helps to reduce the impact of differences between experiment data and FSD on the precision of the crack prediction model.
- (2) The CM is developed based on an Artificial Neural Network (ANN), which is used to classify the size range of structural cracks. The Fake-FSD is inputted into the CM model, while outputs the size range of the crack. When the crack size is relatively small, the short-term strain value may not be sensitive to changes in the crack length. In order to enhance the predictive ability of short cracks, it is necessary to reduce the interference of long crack strain data. To achieve this, the threshold value was set according to the crack growth range, and the crack size range was divided accordingly. The CM model was then used to classify the crack size based on these threshold values.

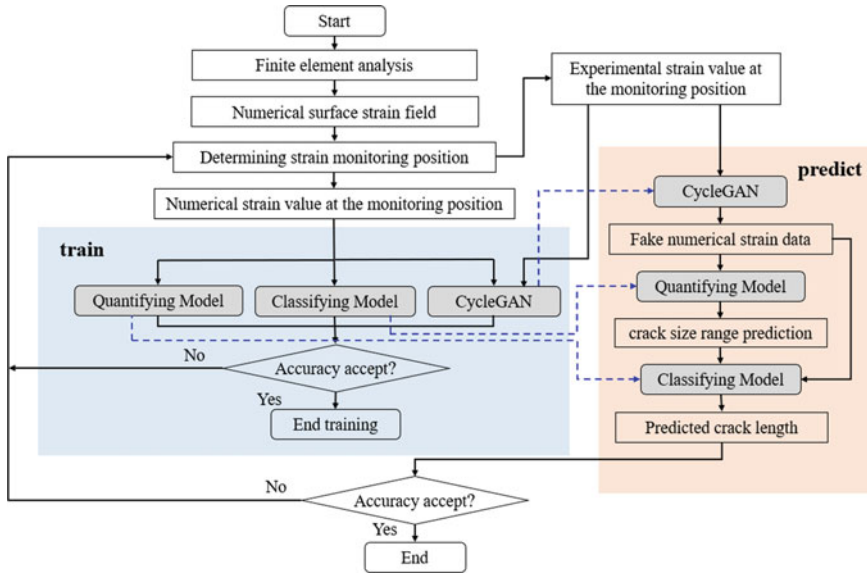


Fig. 16.1 Flow chart of fatigue crack quantification model of metallic structures based on strain monitoring

(3) The QM is also developed based on ANN and is used to predict the length of structural cracks. The model input is the Fake-FSD, while the output is a quantitative prediction of the crack length. The QM model contains several sub-QMs for crack length quantization. The Fake-FSD obtained from CycleGAN is substituted into the appropriate sub-QM.

Due to the insensitivity of strain data to changes in crack length when the crack is short, the training data from long cracks can interfere with the prediction of short crack lengths. To improve the overall prediction accuracy, multiple models were trained using different strain values for different crack length ranges. To achieve this, it was necessary to divide the crack sizes into several ranges.

In this study, the CM was developed to classify cracks into short and long ones. To determine the threshold of the short and long cracks, a crack length quantization model was trained, and the precision between the predicted and actual crack lengths was evaluated. The threshold value a_0 was set to identify short cracks when the length is less than a_0 , and long cracks when it exceeds a_0 . The CM model was built using the *ReLU* activation function for interneurons, and the results were activated by the Sigmoid function. The cross-entropy loss function was adopted as the loss function.

The proposed approach in this paper involves a neural network-based deep learning model to train data that conforms to short crack conditions in equivalent strain and establish a short crack sub-QM, and train data that conforms to long crack conditions to establish a long crack length quantization model. The *ReLU* activation function is used to activate the regression problem. Once the crack size range

is classified by CM, the equivalent strain is substituted into the corresponding sub-QM based on the crack size range classification, and the predicted crack length is obtained.

16.3 Application Examples of the Model

In this study, a central hole plate with a dimensions of 300 mm (length) \times 60 mm (width) \times 2 mm (thickness) was used as a sample. The plate contained a 4 mm diameter hole and was made of LY12-CZ material with an elastic modulus of 71,000 MPa and a Poisson's ratio of 0.33. Two predefined cracks were located on both side of the center hole with the lengths denoted with a_1 and a_2 . Two crack length combinations were compared: (1) symmetric crack (SC) with $a_1 = a_2 = 1$ mm and (2) non-symmetric crack (NSC) with $a_1 = 3$ mm and $a_2 = 1$ mm, as shown in Fig. 16.2. The FEA model is presented in Fig. 16.3.

To establish a deep learning model, a large amount of data is required. By using FEA models, many simulation data can be quickly obtained, which significantly reduces the cost. In this study, surface strain data from all established FEA models were output, and the variance of strain values at the same strain monitoring location in different FEA models was calculated. When the variance was large, the location was considered to be highly sensitive to the existence of the cracks, and the strain data contained more crack information such as crack length and crack direction. The strain monitoring locations were preferentially set at the locations with higher sensitivity. The location and number of strain measurement sites were determined according to the structural feature and the strain collection method. The strain monitoring point $X = 6$ was selected for the training and testing. The random load spectrum was used in the test.

After the model training was completed, the SC and NSC samples were tested and labelled as SC_1, SC_2, NSC_1, and NSC_2. Strain data at the monitoring locations were collected in real-time, and the equivalent strain values were processed and inputted into the trained model. The predicted crack length results were obtained and analyzed.

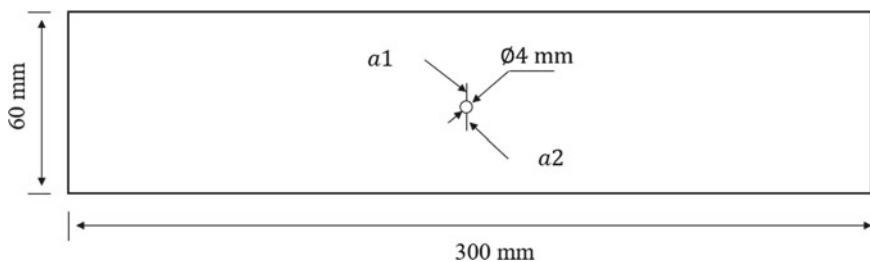


Fig. 16.2 Geometry of the open-hole plate sample

Figures 16.4 and 16.5 show the SC and NSC samples with and without CycleGAN model-revised predictive data (prd. data) and corresponding experiment data (exp. data). The hole center is used as the origin, and the transverse axis represents the distance from the crack tip to the hole center. The vertical axis represents the number of the cyclic spectral blocks. The results show that the accuracy of the uncorrected predictions for long cracks is superior to the those of short cracks. The accuracy of the short crack length range is improved by using the CycleGAN model. The SC sample has simpler change in strain dataset, and so the less crack information, leading to slightly worse crack prediction precision than that of the NSC sample. The predicted error of the model is less than 1 mm, and the proposed method achieves high accuracy in predicting the crack length of a central hole plate. However, it should be noted that the prediction precision under short crack conditions is insufficient even with CycleGAN model modification. The main reason is that the strain data collected by the strain monitoring site contains insufficient crack information to accurately reflect the crack length under short crack conditions. Future research may explore measures such as increasing the number of strain gauges and adding information on crack growth direction to training data to address this issue.

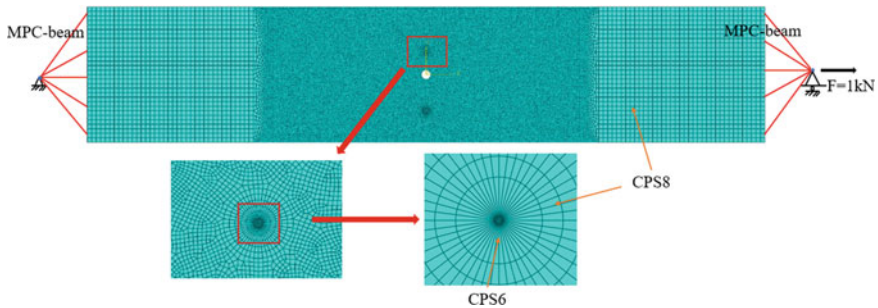


Fig. 16.3 Finite element mesh of the sample

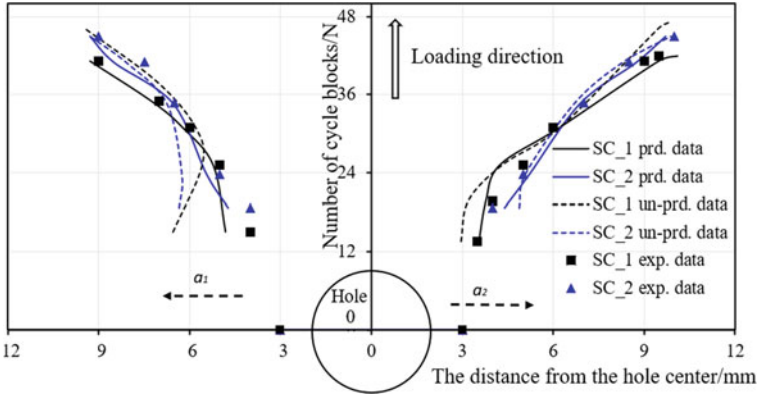


Fig. 16.4 Measured and predicted crack length of SC samples versus the number of cycle blocks

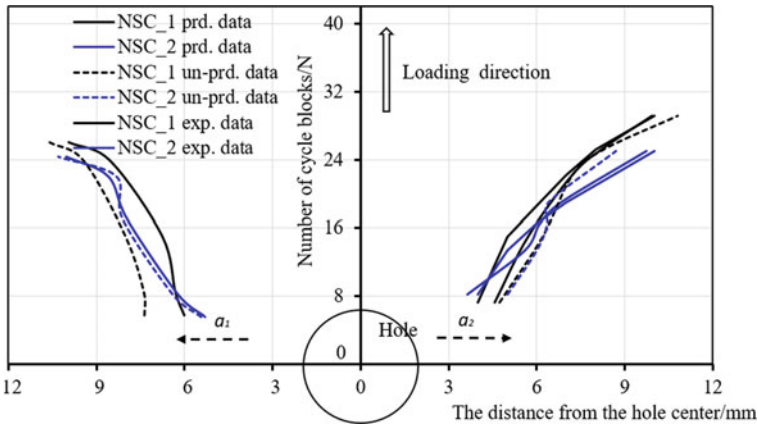


Fig. 16.5 Measured and predicted crack length of NSC samples versus the number of cycle blocks

16.4 Conclusion

In this paper, a deep learning-based quantitative model for structural fatigue crack has been established, which enables accurate real-time prediction of crack length with strain monitoring data, even when the external load is unknown. A correction model using the CycleGAN network structure was developed to reduce the discrepancy between the experimental data and numerical calculation data. The crack size was divided into two ranges with an established classification model, and the corresponding sub-models were further developed for predicting the crack lengths, forming the quantization model to achieve accurate prediction of the full crack size. By comparing with experimental results, the prediction error of crack length was less

than 1 mm. The proposed model enables real-time online prediction of crack length, providing a theoretical basis for aircraft overhaul and maintenance, life management, and monitoring.

Acknowledgements This work was supported by the National Natural Science Foundation of China (12072272) and the National Science and Technology Major Project (J2019-I-0016-0015).

References

1. Chen, Z.M., Tang, N., Fang, H.F.: Flight load modeling method optimized for complex structures. *Adv. Aeronaut. Sci. Eng.* **13**(2), 45–50 (2022)
2. Li, B., Fan, X.L., Zhou, K., Wang, T. J.: Effect of oxide growth on the stress development in double-ceramic-layer thermal barrier coatings. *Ceram. Int.* **43**(17), 14763–14774 (2017)
3. Chang, Q., Yang, W.X., Zhao, H., et al.: A multi-sensor based crack propagation monitoring research. *Acta Aeronaut. Astronaut. Sin.* **41**(2), 226–237 (2020)
4. Li, B., Yang, B.S., Wang, S.Y., Chen, J., Jiang, W.: Numerical study of thermomechanical delamination mechanisms in segmented high-temperature coatings. *Eng. Fail. Anal.* **153**, 107577 (2023)
5. Li, B., Shu, Y.X., Li, Y.Z.: Interface cracking behavior in high-temperature coatings with non-uniformly distributed segmentation cracks. *Eur. J. Mech. A-Solid*, **96**, 104674 (2022)
6. Crocombe, A.D., Ong, C.Y., Chan, C.W.M., et al.: Investigating fatigue damage evolution in adhesively bonded structures using backface strain measurement. *J. Adhes.* **78**, 745–776 (2020)
7. Wang, H. W.: Research on load identification algorithm of aircraft based on neural network. ZheJiang University (2018)
8. Trivailo, P.M., Carn, C.L.: The inverse determination of aerodynamic loading from structural response data using neural networks. *Inverse Prob. Sci. Eng.* **14**(4), 379–395 (2006)
9. Renaud, G., Liao, M., Bombardier, Y.: Demonstration of an airframe digital twin framework using a CF-188 full-scale component test. ICAF 2019—Structural Integrity in the Age of Additive Manufacturing (2019)

Chapter 17

A Study of a Confucius Culture Learning Environment Based on a 3D Metaverse



Miaolei Deng, Kai Yang, Zhibin Zuo, and Haonan Zhai

Abstract With the development of technology, the term metaverse is becoming more known. Metaverses hope to turn imagination into reality through the integration of various technologies. Metaverses are the latest stage in the development of visual immersive technology with four characteristics: spatio-temporality, authenticity, independence, and connectivity. The purpose of this paper is to study the construction of a Confucian culture learning environment in a 3D metaverse, where students connect to a platform constructed by a 3D virtual world through a Head-Mounted Display (HMD). Students can learn about Confucianism, Confucius' life and stories, as well as visit Confucian cultural buildings. The platform is based on a virtual scene built on The Sims 4, and the HMD is used as a connection between the metaverse and the real world enriching the user's experience with the same features and perceptions as the real world, which will make the online learning approach more meaningful. Finally, this paper presents the content of the metaverse exhibition through an experimental approach.

Keywords Metaverse · Immersion · Virtual world · HMD · Online learning · Confucian culture

17.1 Introduction

Globalization has led to the rise of “Chinese language fever” around the world, and more and more people are using Chinese as a second language. Learning about Confucian culture is becoming more popular and the ways of learning about it are diversifying. Since the beginning of 2020, the impact of the new coronavirus (COVID-19) has caused great inconveniences for life and study, and non-face-to-face [1], online

M. Deng · K. Yang · Z. Zuo (✉) · H. Zhai
College of Information Science and Engineering, Henan University of Technology,
Zhengzhou 450001, China
e-mail: zzbin_2000@163.com

educational learning methods have become a viable alternative to real-world classrooms. Current web-based online learning [2] is insufficient and a new solution is needed.

With access to many digital devices it is difficult for students to be able to focus on one thing, and even though students are studying a lot, their learning efficiency is low. The effective combination of the web and virtual reality extends the offline learning approach to immersive 3D virtual learning in the metaverse as a new way of learning [3, 4]. The research platform here is based on *The Sims 4*, which provides virtual libraries, laboratories, classrooms, and other learning environments, as well as work, play, and other real-life experiences. Learning in the metaverse provides a more realistic experience and interaction, which allows learners to focus on learning more so than via traditional e-learning [5] methods, makes them more interested in participating in the learning process, and allows them to become immersed quickly. The avatars in the metaverse can perform various activities and in interactive experiences in the virtual world. The most important feature of the metaverse is interactive, immersive and situated learning [6], which is difficult to achieve via traditional e-learning methods.

The purpose of this paper is to study the construction of a learning environment for Confucius culture in a metaverse. The main goal of this study is firstly to provide an environment and platform for students and teachers to learn about Confucian culture [7]. First, the international community's perception of Confucian culture and Confucianism is still superficial, so it will be very helpful to spread Confucianism and further promote Chinese culture to the outside world. Secondly, we discuss the status of existing online learning methods and show the future direction of learning in virtual environments.

17.2 Metaverse

Neal Stephenson describes a metaverse as “a computer simulation of an artificial space that runs parallel to the real world by putting on headphones and goggles, connecting to a terminal, and entering it as an avatar”. A metaverse is a synthesis of the words beyond (meta) in virtual space and universe in real space [8–10], meaning a world in a 3D virtual space. A metaverse has elements such as 3D space, virtual characters, and interactive entertainment, which are different from what is found in Virtual Reality (VR) [11]. A metaverse is an experience based on extended reality that provides immersive reality, a reflection of the real world generated based on digital technology. In short, metaverses have three characteristics: immersive experience [12], a virtualized body, and open creation.

Immersion theory (also called “mind flow theory”) was proposed by Mihaly Csikszentmihalyi and others to describe a state of mind in which the individual user is fully engaged in an activity, unaffected by the surrounding environment and other factors. Immersive experience includes sensory experience and cognitive experience [13]. Sensory experience stimulates the human sensory nervous system through

changes in the outside world, so that the five senses of hearing, sight, touch, smell and taste are simulated using immersive technology. However, the sensory experience of being there and being in the environment is only short-lived and sometimes does not allow people to be fully immersed in it and achieve the feeling of being one with the environment. Cognitive experience is the use of people's habitual thinking and experience to enhance their cognition of the environment [4, 14, 15]. Therefore, to achieve the best immersion experience, both rich sensory experience and sufficient cognitive experience activities must be available, and the organic combination of both can create an engaging state of mind flow.

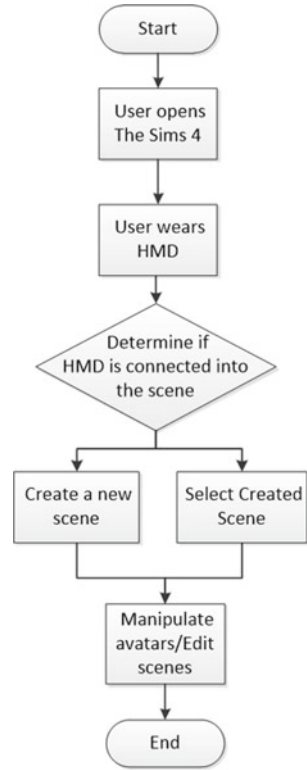
A virtual avatar is a real-world user who enters a virtual world through a device that can have one or more identities within an ID. For example, like in the movie *Avatar*, the subject controls the avatar in the virtual world through some external device and through his or her mind. Multiple avatars can be created in a virtual world, such as in *Second Life* or *The Sims 4*, and the user can control these avatars simultaneously or individually, and switch seamlessly between avatar controls.

Open creation means that users can enter the digital world through a terminal, and can use massive resources to start creative activities. The essence of a metaverse is to digitize human sensory experience, including not only hearing and vision but also touch, taste and smell, so that there is almost no difference between the sensory experience in the virtual world and the real world. In general, a metaverse is a conceptualization of new technologies such as extended reality (XR), augmented reality (AR), virtual reality (VR), artificial intelligence (AI), and digital twin, and will be the next stage of the Internet.

17.3 Based on HMD Interaction Technology

This 3D model is implemented on *The Sims 4* platform by writing scripts in the model to create interactive content. The virtual space of each scene should be built based on a real space, thus improving the user's experience of realism. Augmented reality technology based on HMD (Head-Mounted Display) allows for an interactive experience between the virtual space and reality in a dynamically changing real space [16]. The user enters the virtual space through the HMD and can touch the avatar in the virtual space to realize the basic operations of the avatar according to the skills it has now [17]. The scenes and objects in the virtual space are created automatically, but of course, users can also add their own models, such as flowers, chairs, bells, etc. The user enters the virtual space to control the avatar in reality as shown in Fig. 17.1.

Fig. 17.1 HMD operation flow chart



17.4 Experimental Platform

First, a virtual environment was built for the experiments. The Sims 4 software, developed by Maxis Software, contains the materials needed to build the environment, including walls, windows, doors, tables, flowers, trees, and so on. One can also create multiple avatars in the pin-up system. The virtual world avatars can carry out a number of behaviors, making friends, sleeping, entertainment, etc. These functions in the virtual world serve as an experimental way of contextual learning, which is difficult to achieve in traditional learning methods and online learning methods.

17.5 Experimental Method

17.5.1 Abbreviations and Acronyms

First, a preliminary survey of 30 students' learning and perceptions of Chinese culture was conducted. The survey was conducted to investigate the students' knowledge of Confucius thought and traditional Chinese culture, ignoring differences in age, gender, nationality, and perceptions among these students. The results of the survey showed that each person's knowledge of Chinese culture varied, and each person's needs and wants for learning about Chinese culture varied. According to the survey data, male students were interested in traditional Chinese martial arts, tea ceremonies, and various handicrafts, while female students were interested in Chinese qin, chess, calligraphy and painting, classical costumes (e.g., Hanfu), and Chinese silk. Common for both was a strong interest in traditional ancient Chinese architecture and famous sites, such as the Confucius Temple and the Confucius Mansion. Also, they both had a strong interest in traditional Chinese culture.

17.5.2 Building the Virtual Learning Environment

Based on the results of the survey, we discussed what was of common interest to the students, and we decided to build a part of two traditional Chinese architectural scenes, one a part of the Confucius Temple and the other a part of the Confucius Mansion. The environment was built for this experiment so that learners could learn about Confucian culture and the rituals of Confucianism etc., while visiting these ancient buildings. The learning environment constructed in The Sims 4 is shown in Figs. 17.2 and 17.3.

17.5.3 Conducting Experience and Analysis

Experiments were conducted on the two learning environments in the 3D meta-verse and 100 students were selected for the survey experiment. In the experiment, we mainly studied the following questions: Can students' learning immersion be enhanced in virtual space? Are students learning better? [18] And student feedback was analyzed.

Experiment 1: 10 students, including international students and Chinese students, were selected to conduct the first experiment of visiting the Confucius Temple. No students conducting the experiment had used The Sims 4 software. Each participant sat in front of a computer with The Sims 4 software. Each experimental environment had avatars and the experimenter in front of the computer controlled each avatar. The learning experience lasted about half an hour. Before the experiment started, each



Fig. 17.2 Schematic diagram of the Confucius Temple built in The Sims 4



Fig. 17.3 Schematic diagram of the Confucius Mansion built in The Sims 4

participating student was given a guide to visit the temple, and the Chinese students explained the life story of Confucius, Confucian culture, and the story behind each item in the temple according to their knowledge, as well as the order of the tour and the rituals of worship according to custom. The international students operated their own

virtual experience while listening to the explanation. At the same time, they discussed and communicated with each other about the questions they did not understand. The entire experiment was recorded. At the end of the experiment, the participants discussed and filled out a questionnaire [19] and exchanged their experiences of learning in the 3D metaverse environment.

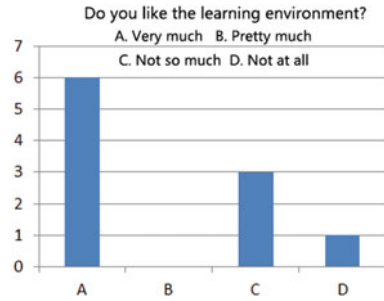
Experiment 2: The 2 international students in the first experiment remained the same and continued to participate in the second experiment, while eight students were selected from the remaining students to participate in the second experiment. As in the first experiment, no participants had used *The Sims 4*, and the duration of the experiment was again half an hour. The international students who had experienced the first experiment clearly had an understanding of Confucius' culture, and when they visited the Confucius Mansion, they manipulated their avatars while exploring according to the tour guide they were given. At the same time, the international students who had experienced the first experiment explained to the inexperienced international students what they knew about the cultural etiquette and the contents of the tour. During the experiment, the international students and Chinese students discussed and learned about Confucius culture, and consulted relevant materials when they disagreed. The whole experiment was recorded and at the end of the experiment the participants discussed and shared their feelings about learning Confucian culture in the 3D metaverse environment.

17.6 Experiment Results

Experiment 1: Through the first experiment, the analysis was conducted based on the recorded experiment. Six of the Chinese students felt immersed in the learning in the 3D virtual environments and were very interested in this new way of learning. The other two Chinese students felt uncomfortable, experiencing 3D vertigo and feeling it as different from the real-world experience. One of the two international students thought that learning about Chinese culture in the virtual environment was better and more relaxing than in the traditional way; the other one thought that the content in the virtual environment was not so rich compared with the real world, and more content was needed to increase the experience of the participants. The results of the experiment are shown in Fig. 17.4.

Experiment 2: In Experiment 2, the international students who had participated in the first experiment were able to gradually immerse themselves in the learning, and even the one student who thought the content was singular began to be interested in and use it. The other two international students expressed a strong interest in the Chinese culture they experienced and hoped that more virtual environments could be added for learning. The remaining six Chinese students all said that learning in the virtual environment of this metaverse was more effective than traditional learning methods because they could not only learn but also operate the virtual characters and feel the experience, which could improve their understanding of Chinese culture. At the same time, the Chinese students thought that the communication and discussion

Fig. 17.4 Experiment1 results



with international students stimulated their inner interest and pride. The results of the experiment are shown in Fig. 17.5.

On the basis of the above two experiments, the experimental process was described, screenshots of the experimental environment were taken, a questionnaire was made based on these contents, and 100 students were randomly surveyed to reveal the feelings of students with different values [20], and further improvements were made according to different views and suggestions. The results of the questionnaire are shown in Fig. 17.6.

Fig. 17.5 Experiment 2 results

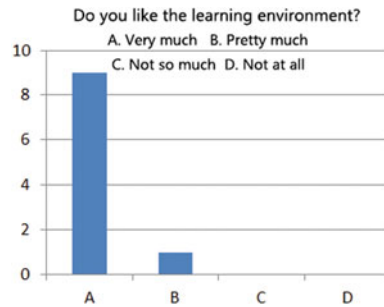
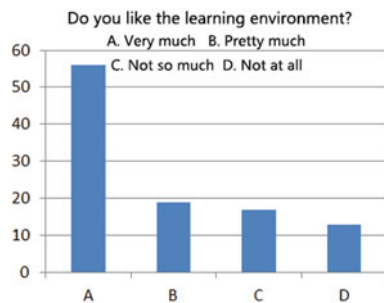


Fig. 17.6 Survey results



17.7 Conclusion

The experiment shows that participation and collaborative learning are the basis of the collective, and that using a metaverse as a new online learning method is the trend of global development. The experiments used 5G technology as the underlying support technology for the metaverse, which features low latency, ultra-high speed, and ubiquitous networking. The low latency keeps the user experience coherent and increases the user's sense of reality. Ultra-high speed guarantees the ability to meet the needs of ultra-high traffic services such as VR and AR, which provides the possibility of extended range (XR). Ubiquitous networking is able to reduce the limitation of space usage, which can allow users to experience learning anytime and anywhere. According to the students' feedback, most expressed more interest in learning in the virtual environment of the 3D metaverse compared with learning in the traditional way, and were more able to enter into immersive learning and improve their understanding of Confucian culture and various rituals. A small number of students said that they could not experience the virtual environment as well as they could the real environment. The subjects of this experiment included different students, and by allowing students from different cultures to communicate, new values are better cultivated. The study used simulation technology to generate a virtual space with a high degree of simulation of the real world, and used AI, XR, and 3D to achieve a cross-generational and diverse reshaping of the hyper-real space. It solved the inconvenience of not being able to go out to study in the field during the current epidemic, and students can study and visit in the virtual space of a 3D metaverse anytime and anywhere. Finally, although learning and experiencing can be done in a 3D metaverse virtual environment, there are still subtle differences from the real world, so users can achieve better learning results by learning in the virtual environment and then physically experiencing it again in the real world.

Acknowledgements This research is supported by the National Natural Science Foundation of China (62276091) and the Major Public Welfare Project of Henan Province (201300311200).

References

1. Mukkavar, V.V., Netak, L.D., Nikam, V.B.: Architectural view of non-face-to-face experiential learning through the immersive technologies. In: 2021 13th International Conference on Intelligent Human Computer Interaction (IHCI), vol. 13184, pp. 282–291 (2021)
2. Kovačević, I., Anđelković Labrović, J., Petrović, N., Kužet, I.: Recognizing predictors of students' emergency remote online learning satisfaction during COVID-19. *Educ. Sci.* **11**, 693 (2021)
3. Won, K.: A study on metaverse learning using telepresence and gamification as educational scaffolding. *J. Korean Assoc. Comput. Educ.* **24**(6), 69–80 (2021)
4. Araiza-Alba, P., Keane, T., Chen, W.S., Kaufman, J.: Immersive virtual reality as a tool to learn problem-solving skills. *Comput. Educ.* **164**, 104121 (2021)

5. Jeong, J.S., González-Gómez, D., Cañada-Cañada, F.: Prioritizing elements of science education for sustainable development with the MCDA-FDEMATEL method using the flipped e-learning scheme. *Sustainability* **11**(11), 3079 (2019)
6. Lave, J., Wenger, E.: *Situated learning: legitimate peripheral participation*. Cambridge University Press (1991)
7. Tamai, M., Inaba, M., Hosoi, K., Thawonmas, R., Uemura, M., Nakamura, A.: Constructing situated learning platform for Japanese language and culture in 3D metaverse. In: 2011 Second International Conference on Culture and Computing, pp. 189–190 (2011)
8. Yoo, G.S., Chun, K.: A study on the development of a game-type language education service platform based on metaverse. *J. Digital Contents Soc.* **22**(9), 1377–1386 (2021)
9. Park, S., Kim, S.: Identifying world types to deliver gameful experiences for sustainable learning in the metaverse. *Sustainability* **14**, 1361 (2022)
10. Duan, H., Li, J., Fan, S., Lin, Z., Wu, X., Cai, W.: Metaverse for social good: a university campus prototype. In: *Proceedings of the 29th ACM International Conference on Multimedia*, pp. 153–161 (2021)
11. Ho, K.C., Jhin, C.S.: A study on metaverse construction and use cases for non-face-to-face education. *J. Conver. Cult. Technol.* **8**(1), 483–497 (2022)
12. Sun, Y.: Immersive experience design path of memorial architectural space based on augmented reality technology. In: 2021 4th International Conference on Information Systems and Computer Aided Education (ICISCAE 2021), pp. 2361–2365 (2021)
13. Xu, R., Chen, W., Zheng, S., Zhang, Y., Yuan, F., Ge, W., Wei, H.: Integration of environment and body: the connotation construction, realization mechanism and educational application of immersive experience: also discuss the new form of AI+immersive learning. *J. Dist. Educ.* **39**, 28–40 (2021)
14. Li, Y.: Application of immersive experience in carrying forward Chinese traditional culture. In: *JinGu Creative Literature*, pp. 76–78 (2022)
15. De Paolis, L.T., De Luca, V. The effects of touchless interaction on usability and sense of presence in a virtual environment. In: *Virtual Reality* (2022)
16. Choi, H., Kim, S.: A content service deployment plan for metaverse museum exhibitions—centering on the combination of beacons and HMDs. *Int. J. Inf. Manage.* **37**(1), 1519–1527 (2016)
17. Wei, Y., Tan, X., Qin, X., Yu, X., Sun, B., Zhu, X.: Exploring the use of a 3D virtual environment in chinese cultural transmission. In: 2014 International Conference on Cyberworlds, pp. 345–350 (2014)
18. Jin, Z., Meiyu, Z.: Research on the effectiveness of experiential learning in immersive virtual reality. In: 2020 International Conference on Modern Education and Information Management (ICMEIM), pp. 828–831 (2020)
19. Barry, D., Ogawa, N., Dharmawansa, A., Kanematsu, H., Fukumura, Y., Shirai, T., Yajima, T., Kobayashi, T.: Evaluation for students' learning manner using eye blinking system in metaverse. In: *Procedia Computer Science*. 2015 19th International Conference on Knowledge Based and Intelligent Information and Engineering Systems, vol. 60, pp. 1195–1204 (2015)
20. Nakahira, K.T., Rodrigo, N.R., Taguchi, R., Kanematsuy, H., Fukumural, Y.: Design of a multilingualistic Problem Based Learning environment in the metaverse. In: 2010 2nd International Symposium on Aware Computing, pp. 298–303 (2010)

Chapter 18

Optimization on Aerodynamic Performances of Pantograph Combined with Sample Infill Criterion



Zhiyuan Dai, Tian Li, Weihua Zhang, Ning Zhou, and Jiye Zhang

Abstract The increase in the running speed aggravated the influence of the pantograph aerodynamic uplift force on the pantograph-catenary contact force. Moreover, the longitudinal asymmetry of the pantograph makes the aerodynamic uplift force vary greatly under the operating conditions of the knuckle-downstream and knuckle-upstream. Therefore, it is of great significance to optimize the aerodynamic characteristics of the pantograph and ensure the consistency of the aerodynamic uplift force of the pantograph under the two operating conditions. A hybrid infill criterion (HIC) is proposed combining the improved expectation infill criterion (EIC) and the Pareto solution infill criterion (PIC) to improve the optimization efficiency, and the multi-objective aerodynamic optimization of the high-speed pantograph is carried out based on the HIC surrogate model. Taking the single- and multi-objective test function as an example, the convergence speed of EIC, PIC and HIC surrogate models is compared. The results show that the optimization efficiency of the HIC surrogate model is improved by 50.0% compared with the EIC and the PIC surrogate model in the single-objective optimization. For the multi-objective test function, the efficiency of the HIC surrogate model is improved by 62.5%. Further, the Pareto solution set of the pantograph multi-objective optimization is obtained using the PIC surrogate model and genetic algorithm, and the aerodynamic uplift forces of the optimal pantograph under the knuckle-downstream and knuckle-upstream are 36.1 N and 39.9 N, respectively. The pantograph-catenary contact force satisfies the standard considering the static uplift force. Meanwhile, the difference in the aerodynamic uplift forces of the pantograph under two operating conditions is only 3.8 N, and the aerodynamic resistance of the knuckle-downstream and knuckle-upstream operating conditions of the pantograph has been reduced by 1.2%.

Keywords High-speed pantograph · Aerodynamic characteristic · Surrogate model · Multi-objective optimization · Sample infill criterion

Z. Dai · T. Li (✉) · W. Zhang · N. Zhou · J. Zhang
State Key Laboratory of Traction Power, Southwest Jiaotong University, Chengdu 610031, China
e-mail: litian2008@home.swjtu.edu.cn

18.1 Introduction

The pantograph, as the hub through which electricity is transmitted from the catenary to the train, serves as the power source of the electric multiple units (EMU) train. The quality of its current receiving is critical to the operation of the train, and it is also seriously affecting the running safety of the high-speed train. The aerodynamic drag force of the pantograph accounts for about 10%–12% of the total aerodynamic resistance of the train at speeds of 250–300 km/h. Meanwhile, the performance of the pantograph is greatly affected by the airflow when the train is travelling at high speeds [1–3]. Furthermore, the impact of high-speed airflow on the aerodynamic uplift force of the pantograph will be exacerbated as the running speed of the train increases, which in turn will affect the current received by the pantograph. In addition, the longitudinal structure of the pantograph is asymmetrical, resulting in different aerodynamic uplift forces under the operating conditions of the knuckle-downstream and knuckle-upstream. The airbag system needs to be adjusted to adjust the static lift forces as the train reverses the running direction. Therefore, optimizing the aerodynamic characteristics of the pantograph and adjusting the uplift forces of the knuckle-downstream and knuckle-upstream conditions to close will ensure better current reception, slow down the fatigue damage of the airbag system, reduce the incidence of pantograph-catenary accidents, and ensure the operation safety.

The study of pantographs primarily focuses on pantograph-catenary coupling dynamics and aerodynamic performances at present. The research on the pantograph-catenary coupling dynamics is mainly concerned with analyzing the effects of the pantograph on the catenary or the impact of the catenary on the pantograph under the excited state, the vibration acceleration of the pantograph head and the catenary, and the pantograph-catenary coupling equations, wear and tear of carbon strips, etc. [4, 5]. The earliest research on the aerodynamics of the pantograph was a wind tunnel test on the pantograph conducted by Cai [6]. The test results revealed that the pantograph has a relatively large aerodynamic resistance, for which the aerodynamic head accounted about 15–20%. Therefore, aerodynamic performance must be considered when designing the pantograph. Guo et al. [7] studied the unsteady aerodynamic characteristics of the pantograph by using the method of Detached-Eddy Simulation (DES). The aerodynamic lift coefficient of the pantograph is greatly affected by the vortex shedding frequency and vortex shedding strength. Carnevale et al. [1, 8] found that the aerodynamic lift force of the pantograph is correlated with the speed of the high-speed train, and the aerodynamic resistance of the pantograph accounts for about 8–14% of the total aerodynamic resistance of the train. Li et al. [9] studied aerodynamics and acoustic scale effects on the pantographs, and the model scales are 1/1, 1/2, 1/4 and 1/8 respectively. The energy concentration range of radiated noise will change from low frequency to medium high frequency as the model scale decreases. Dai et al. [10] investigated the effect of strip spacing on the aerodynamic performance of a high-speed pantograph with a double-strip. The results show that the drag and lift forces of the strip increase with the strip spacing, while the lift force on the first strip tends to be stable as the spacing reaches up to a certain distance.

Studies of aerodynamics mainly generally concentrate on drag force reduction, the shape optimization of the strip and the wind deflector, and the aerodynamic noise characteristics, etc. However, there is relatively little research on the aerodynamic uplift force of the pantograph when subjected to aerodynamic action, and there is no research on the optimization of the aerodynamic characteristics of the pantograph using the surrogate model method.

The surrogate model was initially applied to the structural optimization, and the response surface model was mainly used. It entered the field of aerodynamic optimization design after the development of multidisciplinary design [11]. The radial basis model (RBF), Kriging model, neural network, and support vector regression (SVR) are widely used in aerodynamic multi-objective optimization [12, 13]. Optimization results largely depend on the prediction accuracy of the surrogate model when aerodynamic optimizations are carried out. The surrogate model could improve the accuracy through reasonable sample infill criteria and then converge to the optimal solution [14]. The surrogate model is currently widely used in the nose shape optimization of high-speed trains. Lee and Kim [15] employed the support vector machine method to optimize the two-dimensional linearity of the longitudinal profile of the train, involving 9 design variables. The optimization goal was to reduce the micro pressure wave, and a model with better performance is obtained. Yao et al. [16] established the standard SVR model using 66 initial samples and selected six samples in the Pareto solution set for verification. One of the verification points did not meet the requirements, so researchers added 30 samples to the initial sample set and established a second-generation model, which achieved excellent results. Li et al. [17] employed the FFD method and five design variables to realize the control of the tip of the nose and the driver's cab and combined it with the genetic algorithm to optimize the nose shape of the CRH2. The aerodynamic drag force of the whole vehicle and the lift force of the head and tail car in the optimal solution are reduced by 3.6%, 9.6%, and 10.9%, respectively. Zhang et al. [18] adopted the basic NSGA-II algorithm to optimize a specific type of HST in China. The initial population was set to 50, the crossover probability was 0.9, and the genetic algebra was 30. The Pareto optimal solution set was obtained. The aerodynamic resistance of the optimal model was reduced by 2.6%, and the lift force of the tail car was reduced by 9.9%.

Therefore, the mature surrogate model method used in the field of high-speed train nose shape optimization can be applied to the optimization of aerodynamic characteristics in the pantograph. Furthermore, the pantograph has a complex shape structure, numerical simulations take time, the optimization cycle is lengthy, and establishing a high-precision surrogate model necessitates a large number of samples. Therefore, the surrogate model construction scheme based on the sample infill criterion can be adopted. The samples needed to update the surrogate model and improve its prediction accuracy are obtained through some strategy. The improved expectation infill criterion (EIC) and the Pareto front infill criterion (PIC) are combined to form the hybrid infill criterion (HIC) in this paper. Additionally, a Pareto front point selection technique is suggested. In this way, the updated algebra of the surrogate model is reduced, and the optimization efficiency is improved. Furthermore, the efficient

optimization strategy can improve the performance of the pantograph and make it more adaptable to high-speed trains with increasing speed levels.

18.2 Kriging Model and Sample Infill Criterion

18.2.1 Kriging Model

The establishment of the standard Kriging surrogate model is as follows:

The basis function of the Kriging model is [19]

$$\psi = \exp\left(-\sum_{j=1}^k \theta_j |x_j^{(i)} - x_j| \right) \quad (18.1)$$

where x is the design variables of the optimization problem, k is the number of variables, θ is the weight.

Assuming the response comes from a random process, the correlation between random variables is correlated with each other using basis functions, and the relationship is as follows,

$$\text{cor}[Y(x^{(i)}), Y(x^{(l)})] = \exp\left(-\sum_{j=1}^k \theta_j |x_j^{(i)} - x_j^{(l)}| \right) \quad (18.2)$$

Then for an unknown vector \mathbf{x}' , its response value can be expressed as [19]

$$\hat{y}(\mathbf{x}') = \hat{\mu} + \boldsymbol{\psi}^T \boldsymbol{\Psi}^{-1} (\mathbf{y} - \mathbf{1}\hat{\mu}) \quad (18.3)$$

where $\boldsymbol{\varphi}$ is the correlation vector between the point \mathbf{x} and the prediction point \mathbf{x}' , $\boldsymbol{\Psi}$ the correlation matrix, \mathbf{y} is the true response, $\hat{\mu}$ is the mean of the random process.

18.2.2 Sample Selections in Pareto Front and Hybrid Infill Criterion

The EIC employed in this paper is a commonly used standard method without improvement [19]. For the PIC method, a new strategy of selecting samples from the Pareto front is proposed. Assuming that all optimization objectives are to search for the minimum value, define the comprehensive optimization rate T_j of the j th sample in the Pareto front solution set.

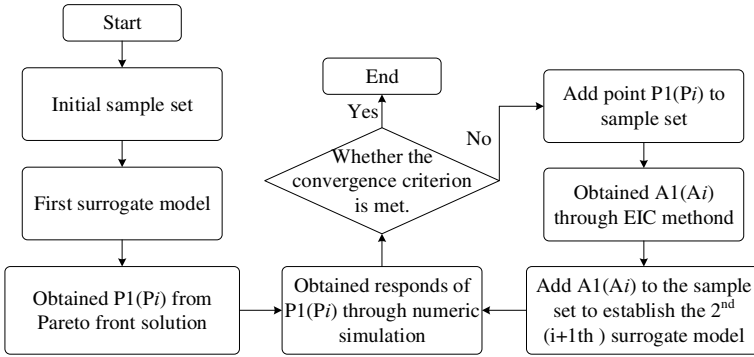


Fig. 18.1 Process of establishing the HIC surrogate model

$$T_j = - \sum_{i=1}^n w_i t_{ij} \tag{18.4}$$

where n is the number of optimization objectives; t_{ij} is the rate of change for the j th sample on the optimization objective i ; w_i is the weight of the optimization objective i .

Calculate the T_j of all samples in the Pareto front solution set, and take the one with the largest comprehensive optimization rate as P_i . This criterion guarantees the surrogate model has higher accuracy in the optimal position of the preferred objective and is more conducive to finding the desired optimal solution.

The construction process of the HIC model is shown in Fig. 18.1.

18.3 Kriging Model and Sample Infill Criterion

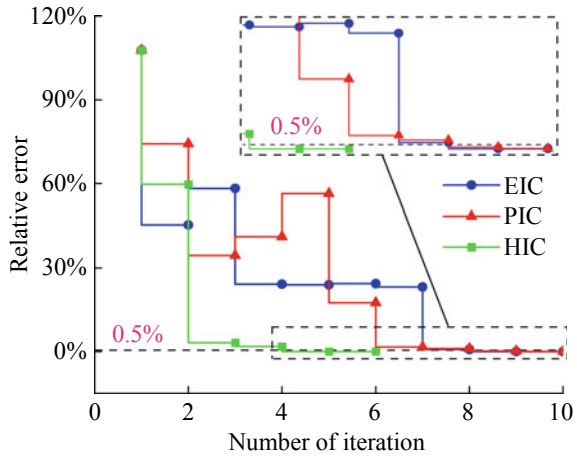
The single-objective and multi-objective test functions are used to compare and study the construction and optimization efficiency of EIC, PIC, HIC three surrogate models.

18.3.1 Single-Objective Function Branin

The Branin function is a classic example of the global optimization problem, and the mathematical model [19] is

$$\begin{cases} f(x) = \left(x_2 - \frac{5.1}{4\pi^2} x_1^2 + \frac{5}{\pi} x_1 - 6 \right)^2 + 10 \left[\frac{8\pi - 1}{8\pi} \cos x_1 + 1 \right] + 5x_1 \\ x_1 \in [-5, 10], x_2 \in [0, 15] \end{cases} \tag{18.5}$$

Fig. 18.2 Error convergence process of the optimal solution



This optimization problem adds an item to the classic Branin function so that it has two local optimal solutions and one global optimal solution (that is, the minimum value of the function). The function obtains the global optimal solution at the point (0.0874, 0.9086), and the value is -16.6440 . The intervals of the two independent variables of the Branin function are scaled to $[0, 1]$ to facilitate sampling and the establishment of subsequent surrogate models. EIC, PIC and HIC methods are adopted to build surrogate models, and model updates and optimization calculations are carried out. In order to compare the performance of each sample infill criterion in the case of fewer initial samples, only 6 samples were selected using the optimal Latin hypercube design (OLHD) method to establish the first-generation surrogate model. The Branin function is a single-objective function, so the convergence criterion is set more strictly. The convergence criterion is that the error between the optimal solution of the surrogate model and the real optimal solution is less than 0.5%. Figure 18.2 shows the error convergence process of the optimal solution for the three methods of sample infill criteria to establish the surrogate model.

The optimal solution obtained by the optimization calculation of the 4th generation HIC surrogate model meets the error criteria, as shown in Fig. 18.2. Both EIC and PIC surrogate models satisfied the criteria only when the results of the 8th generation are obtained, and the optimization efficiency is 50.0% lower than that of the HIC method. Furthermore, the convergence process of the PIC surrogate model exhibits strong oscillations when the number of initial samples is minimal, which limits the accuracy of the model and causes huge error fluctuations. The surrogate models of three infill criteria can eventually converge to the optimal solution for the single-objective test function. After the error requirement is reached, the PIC approach adds a total of 6 samples, comprising 3 improved expectation samples and 3 Pareto front samples, while EIC and PIC surrogate models both add 7 samples. The HIC surrogate model converges to the optimal solution by updating the surrogate model fewer

times, and the number of simulations required is also reduced, implying improved optimization efficiency.

18.3.2 Multi-objective Function Poloni

The Poloni function [20] has multi-peak characteristics, it is difficult to establish a surrogate model, and it is easy to fall into a local optimum during the optimization process, so it is often used as a test function to examine the quality of the surrogate model. The f_1 and f_2 of the Poloni function are

$$f_1(x, y) = -[1 + (A_1 - B_1)^2 + (A_2 - B_2)^2] \quad (18.6)$$

$$f_2(x, y) = -[(x + 3)^2 + (y + 1)^2] \quad (18.7)$$

where $(x, y) \in (-\pi, \pi)$

$$A_1 = 0.5 \sin 1 - 2 \cos 1 + \sin 2 - 1.5 \cos 2 \quad (18.8)$$

$$A_2 = 1.5 \sin 1 - \cos 1 + 2 \sin 2 - 0.5 \cos 2 \quad (18.9)$$

$$B_1 = 0.5 \sin x - 2 \cos x + \sin y - 1.5 \cos y \quad (18.10)$$

$$B_2 = 1.5 \sin x - \cos x + 2 \sin y - 0.5 \cos y \quad (18.11)$$

The OLHD method is adopted to extract 10 samples as the initial sample set, and the efficiency of EIC, PIC and HIC to construct surrogate models is compared. The weights of the two objectives are set to 0.5 when calculating the comprehensive optimization rate of the Pareto front adding samples. Because the value of the function is in the range $[0, 70]$, including 0, and the relative error cannot be used as the standard, the error criterion is set as the average difference between all points of the Pareto front solution set obtained by optimization and the real value is less than 0.2. Meanwhile, the error between the Pareto front obtained by the optimization and the real front is within 5.0%, and the error is represented by the difference in the integral area between the Pareto front and the x -axis. Figure 18.3 shows the error convergence process of the three methods of sample infill criteria to establish the surrogate model.

The Pareto front produced by the third-generation HIC surrogate model can satisfy two error criteria simultaneously. A total of four samples are added when the error criteria are met, including two improvement expectation samples and two Pareto front samples, and four numerical simulations are carried out. The EIC surrogate model has been updated to the tenth generation and still fails to meet any error criteria. Only the second error criterion is met by updating the PIC surrogate model to the eighth

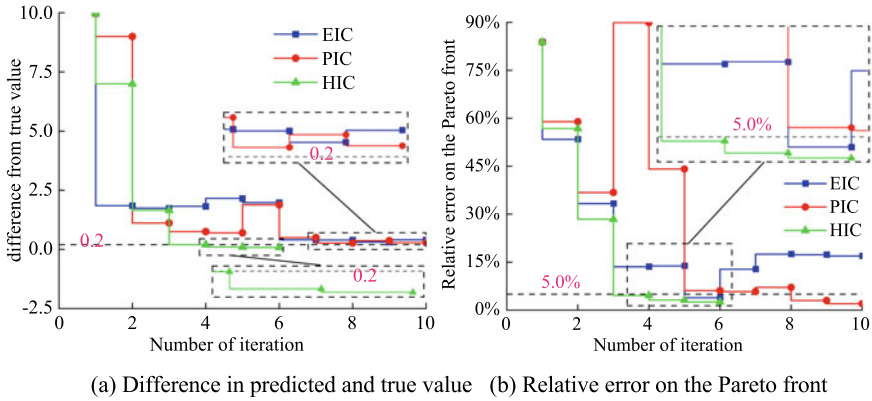


Fig. 18.3 Convergence process of the three methods

generation. At this point, 8 samples have been added, and 8 simulation calculations have been performed. The optimization efficiency of the HIC surrogate model is 62.5% lower. When the PIC surrogate model is updated to the 10th generation, it still cannot satisfy another error criterion, and there are strong oscillations in the optimization process. The comparison of the three types of surrogate models for the multi-objective test function shows that the HIC performs better, and can obtain the Pareto front quickly and accurately.

18.4 Optimization on the Pantograph

Taking the angle of the baffle and the diameter of the upper and lower arms as design variables. The large-diameter end of the upper arm of the original pantograph model is 90 mm, and the small-diameter end is 65 mm. The large-diameter end of the lower arm is 100 mm, and the small-diameter end is 70 mm. Both the upper and lower arms are changed based on the small-diameter end, and the diameter ratio of the large- and small-diameter ends remains unchanged. The initial angle of the baffle is 0°. Figure 18.4a shows the models of the pantograph and baffle.

Figure 18.4b shows the computational domain, the length direction of the domain is 60 m, and the height and width directions are 10 m and 20 m, respectively. A boss is set on the bottom surface of the domain to simulate the high-speed train body, and the pantograph is placed on top of the boss. Meanwhile, the pantograph is 30 m from both the entrance and exit boundaries. The numerical simulation methods and validation, the calculation method of aerodynamic uplift force can be found in reference [21]. The aerodynamic uplift forces of the pantograph under the knuckle-downstream and knuckle-upstream operating conditions are calculated to be 48.7 N and 10.1 N respectively, the difference is 38.6 N. Moreover, the sum of the aerodynamic resistance of the pantograph under the two operating conditions is 3223 N.

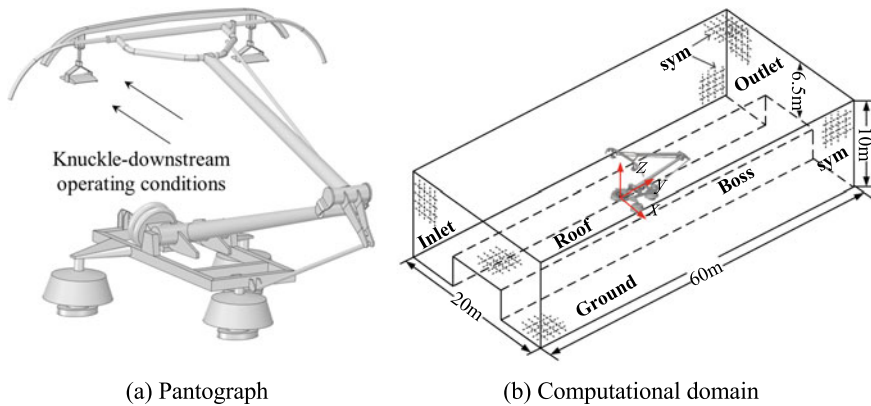
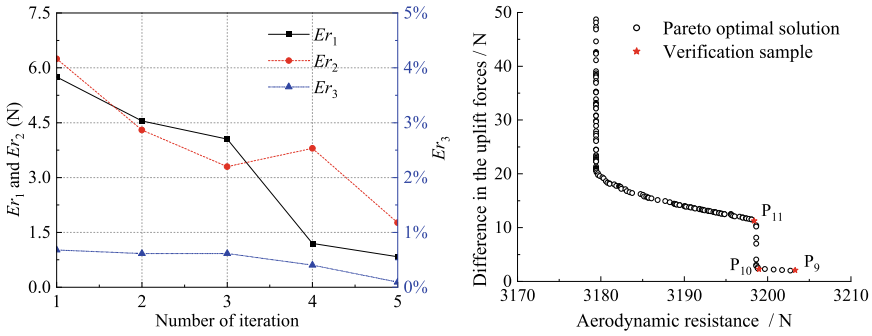


Fig. 18.4 Models of the pantograph and computational domain

The optimization is to minimize the difference in the aerodynamic uplift forces and the aerodynamic resistance of the pantograph under the knuckle-downstream and knuckle-upstream operating conditions, and one constraint is that the aerodynamic uplift force satisfies the standard EN5036720-12. There are three error criteria, which must be satisfied at the same time. The error of the aerodynamic uplift force under the knuckle-downstream condition is less than 3 N, denoted as Er_1 . The error of the difference between the aerodynamic uplift forces at the knuckle-downstream and knuckle-upstream conditions is less than 5 N, denoted as Er_2 . The error of the aerodynamic resistance of the pantograph under the two operating conditions is less than 1%, denoted as Er_3 . The OLHD method is employed to extract 25 initial samples, and the surrogate model is established according to the process in Fig. 18.1. In order to further ensure the accuracy of multi-objective optimization, two samples are selected from the Pareto front each time to add to the next-generation surrogate model. The average value of two samples is taken for error evaluation. The convergence process of the three error criteria is shown in Fig. 18.5a. Since the initial surrogate model Er_1 has satisfied the error requirements, it is because the diameter of the upper and lower arms and the angle of the baffle have relatively little influence on the aerodynamic resistance of the pantograph. Therefore, the standard deviation of this target is very small, and the prediction of the surrogate model is more accurate. The optimization results based on the fourth-generation surrogate model have met the three error criteria at the same time, as shown in Fig. 18.5a. However, to ensure the stability of the optimization system and increase the possibility of obtaining better samples, the surrogate model will continue to be updated to the fifth generation. The Pareto front obtained on the basis of the fifth-generation surrogate model is shown in Fig. 18.5b.

P9 and P10 are preferred for the small difference in aerodynamic uplift force, and P11 is additionally employed as a verification sample. Numerical simulations are carried out and compared with the predicted values, and the three samples all meet the convergence criteria, as shown in Fig. 18.5a. P10 is selected as the optimal



(a) Error convergence history (b) Pareto front solution set and verification sample

Fig. 18.5 Multi-objective optimization process

solution for the multi-objective optimization of the aerodynamic performance of the pantograph. The aerodynamic uplift forces under the knuckle-downstream and knuckle-upstream conditions are 36.1 N and 39.9 N respectively, and the difference between the aerodynamic uplift forces of the two conditions is only 3.8 N. Moreover, the aerodynamic resistance of the whole pantograph is reduced by 1.2%.

The surface pressure distribution of the strip and the baffles under the knuckle-downstream and knuckle-upstream conditions of the optimal pantograph is shown in Fig. 18.6. Under the knuckle-downstream operation condition, there is a large positive pressure on the edge of the windward side of the baffles, and its component force in the vertical direction is downward, indicating negative lift. There is also a positive pressure area on the windward side of the baffles under the knuckle-upstream operation condition, and its component force in the vertical direction is upward, providing positive lift. The lift force of the baffles is directly converted into the aerodynamic uplift force of the pantograph, and its influence is greater than that of the upper and lower arms. The baffles of the optimal solution model reduce the aerodynamic uplift force of the pantograph under the knuckle-downstream condition and increase that under the knuckle-upstream condition, thereby resolving the problem of the large difference in aerodynamic uplift between the two operating conditions.

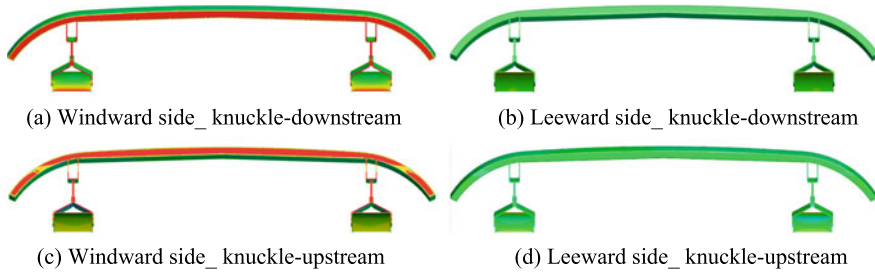


Fig. 18.6 Pressure distribution on the surface of the strip and wind baffles

18.5 Conclusion

The accuracy and optimization efficiency of EIC, PIC and HIC methods to construct surrogate models are compared using single- and multi-objective test functions, and the feasibility of the HIC method to establish surrogate models are validated. Finally, the HIC surrogate model is employed to perform multi-objective optimization of the aerodynamic characteristics of the pantograph, and the following main conclusions are obtained:

- (1) For the single-objective test function, the optimal solution obtained through optimization meets the error criterion after the HIC surrogate model is updated to the fourth generation, and the other two criteria surrogate models must be updated to the eighth generation. The optimization efficiency of the HIC surrogate model has been increased by 50%. In the meantime, the HIC surrogate model necessitates fewer samples.
- (2) The Pareto front obtained by the third-generation HIC surrogate model can satisfy the error criterion for the multi-objective test function, and the PIC surrogate model must be iterated to the eighth generation. The HIC surrogate model has a 62.5% higher optimization efficiency. The EIC surrogate model has been updated to the tenth generation but continues to fail to meet the error criterion. The HIC technique performs better, as evidenced by the comparison of the three sample infill criteria.
- (3) The angle of the baffle and the diameter of the upper and lower arms are employed as the design variables to establish a HIC surrogate model. The optimal solution of the multi-objective optimization is obtained by considering each optimization objective comprehensively. The aerodynamic uplift forces of the optimal model under the knuckle-downstream and knuckle-upstream conditions are 36.1 N and 39.9 N respectively, and the difference between the aerodynamic uplift forces of the two conditions is only 3.8 N. Moreover, the aerodynamic resistance of the pantograph is reduced by 1.2%.

Funding Statement This project was supported by the Sichuan Science and Technology Program (2023JDRC0062), National Natural Science Foundation of China (52072319) and Project of State Key Laboratory of Traction Power (2023TPL-T05).

Conflicts of Interest

The authors declare that they have no conflicts of interest to report regarding the present study.

References

- Carnevale, M., Facchinetti, A., Maggiori, L., Rocchi, D.: Computational fluid dynamics as a means of assessing the influence of aerodynamic forces on the mean contact force acting on a pantograph. *Proc. Instit. Mech. Eng. Part F: J. Rail Rapid Transit* **230**(7), 1698–1713 (2016)
- Tan, X.M., Yang, Z.G., Tan, X.M., Wu, X.L., Zhang, J.: Vortex structures and aeroacoustic performance of the flow field of the pantograph. *J. Sound Vib.* **432**, 17–32 (2018)
- Li, T., Liang, H., Zhang, J., Zhang, J.: Numerical study on aerodynamic resistance reduction of high-speed train using vortex generator. *Eng. Appl. Comput. Fluid Mech.* **17**(1), e2153925 (2023)
- Zhou, N., Zhang, W.H., Li, R.P.: Dynamic performance of a pantograph-catenary system with the consideration of the appearance characteristics of contact surfaces. *J. Zhejiang Univer.-Sci. A* **12**(12), 913–920 (2011)
- Guan, J.F., Wu, J.Q.: Dynamic coupling equations between pantograph and overhead rigid conductor rail by using numerical method. *J. Railway Sci. Eng.* **2**, 362–368 (2016)
- Cai, G.H.: Aerodynamic characteristic measurements on pantograph of super express train. *Exp. Measur. Fluid Mech.* **18**(1), 53–56 (2004)
- Guo, D.L., Yao, S.B., Liu, C.H., Yang, G.W.: Unsteady aerodynamic characteristics of high-speed pantograph. *J. China Railway Soc.* **34**(11), 20–25 (2012)
- Zhang, L., Zhang, J., Li, T., Zhang, W.H.: Influence of pantograph fixing position on aerodynamic characteristics of high-speed trains. *J. Mod. Transp.* **25**, 34–39 (2017)
- Li, T., Qin, D., Zhou, N., Zhang, J., Zhang, W.H.: Numerical study on the aerodynamic and acoustic scale effects for high-speed train body and pantograph. *Appl. Acoust.* **196**, 108886 (2022)
- Dai, Z.Y., Li, T., Deng, J., Zhou, N., Zhang, W.H.: Effect of the strip spacing on the aerodynamic performance of a high-speed double-strip pantograph. *Veh. Syst. Dyn.* **60**(10), 3358–3374 (2022)
- Jeong, S., Murayama, M., Yamamoto, K.: Efficient optimization design method using kriging model. *J. Aircr.* **42**(2), 413–420 (2005)
- Forrester, A.I., Keane, A.J.: Recent advances in surrogate-based optimization. *Prog. Aerosp. Sci.* **45**(1–3), 50–79 (2009)
- Wang, Q., Moin, P., Iaccarino, G.: A rational interpolation scheme with superpolynomial rate of convergence. *SIAM J. Numer. Anal.* **47**(6), 4073–4097 (2010)
- Han, Z.H.: Kriging surrogate model and its application to design optimization: a review of recent progress. *Acta Aeronautica ET Astronautica Sinica* **37**(11), 3197–3225 (2016)
- Lee, J., Kim, J.: Approximate optimization of high-speed train nose shape for reducing micropressure wave. *Struct. Multidiscip. Optim.* **35**, 79–87 (2008)
- Yao, S.B., Guo, D.L., Sun, Z.X., Chen, D.W., Yang, G.W.: Parametric design and optimization of high-speed train nose. *Optim. Eng.* **17**(3), 605–630 (2016)
- Li, R., Xu, P., Peng, Y., Ji, P.: Multi-objective optimization of a high-speed train head based on the FFD method. *J. Wind Eng. Ind. Aerodyn.* **152**, 41–49 (2016)
- Zhang, L., Zhang, J.Y., Li, T., Zhang, Y.D.: Multi-objective aerodynamic optimization design of high-speed train head shape. *J. Zhejiang Univer.-Sci. A* **18**(11), 841–854 (2017)

19. Sobester, A., Forrester, A., Keane, A.: *Engineering Design Via Surrogate Modelling: A Practical Guide*. John Wiley and Sons, Ltd., Publication (2008)
20. Poloni, C., Giurgevich, A., Onesti, L., Pediroda, V.: Hybridization of a multi-objective genetic algorithm, a neural network and a classical optimizer for a complex design problem in fluid dynamics. *Comput. Meth. Appl. Mech. Eng.* **186**(2–4), 403–420 (2000)
21. Dai, Z.Y., Li, T., Zhou, N., Zhang, J., Zhang, W.H.: Numerical simulation and optimization of aerodynamic uplift force of a high-speed pantograph. *Railway Eng. Sci.* **30**(1), 117–128 (2022)

Chapter 19

Measuring Fire Spread Rate with Digital Image Processing Method



Juan Chen and Yunping Yang

Abstract In the past few years, forest fire and building fire accidents occurred frequently, which has been attracting more and more attentions on the prevention and control of such kind of fire. In view of the timeliness and accuracy limitations of typical early fire spread measurement and detection methods, this paper proposes a new digital image processing based fire spread rate measurement method. The color and motion characteristics of flame images has been examined to perform image segmentation, resulting in the extracted fires in image space. Then, fire spreading rate is calculated after geometric correction. Results indicate that the proposed method has the advantages of simple implementation, rapid acquisition and accurate results.

Keywords Digital image processing · Geometric space correction · Fire color · Image binarization · Fire spread rate

19.1 Introduction

Forest fire and building fire accidents caused great damage each year, as a consequence, researchers have been paid a lot of attentions on the topic of fire prevention and control in the past decades. In order to prevent and control fire, it is necessary to detect fire action as quickly and accurately as possible in the early stage of fire development. Fire actions can be described by heat release rate, smoke spread rate, fire spread rate and some other parameters. Among all these parameters, fire spread rate is directly related to the fire intensity and the geometric shape of the flame front, so fire spread rate has been used as an indicator to quantify fire risk degree. Therefore, how to find a fast and accurate method to measure the fire spread rate became more and more important.

Traditionally, fire spread rate can be determined by methods include Bunsen burner laminar flow method [1], nylon line method [2], benchmark method [3] and so

J. Chen (✉) · Y. Yang
Department of Fire Protection Engineering, Southwest Jiaotong University, Chengdu 610000, China
e-mail: 153103158@qq.com

on. Some of these measuring methods have timeliness limitations while some others have accuracy limitations. For example, the Bunsen burner method is suitable for determining the fire spread rate of laminar premixed flames. And most of the other methods are suitable for laboratory-scale experimental fires. With the rapid development in digital image processing technology, new fire detection and measurement has been proposed in the past decades. Chen et al. [4] analyzed color and motion features of fire flame in video sequences. They formulized a mathematical model to describe these features and proposed a multi-feature fusion based flame detection method. Zhao et al. [5] proposed a flame recognition method for forest fire based on the difference between the early flame color and the forest background color. Li et al. [6] developed a flame extraction software by combining digital image processing with BP neural network, relying on digital image processing. Sebastien et al. [7] proposed a new network structure for smoke and fire detection and location based on convolutional neural network by dividing the RGB image. Mishra et al. [8] used ImageJ programming software to detect the position of flame edge and then calculate the flame height. According to the previous study of a multi-feature flame recognition algorithm, Qiu et al. [9] algorithm a novel flame recognition based on free radical emission spectroscopy during combustion is investigated.

Summarizing the current studies on the topic of fire detection and measurement with digital image processing methods, it can be found that image processing technology has been widely used to detect fire and smoke features in images, however, measuring fire spread rate is still rare. As a consequence, in this paper, we firstly study the flame color and movement characteristics in video frames, and then put forward a fire detection method based on digital image processing, at last, the fire spread rate calculation method will be discussed. In the last section, we conclude our paper.

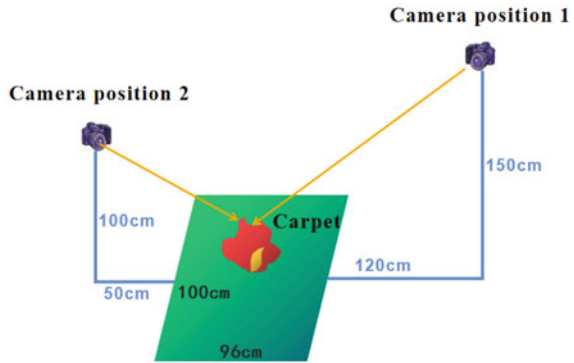
19.2 Flame Image Acquisition and Spatial Correction

To measure fire spread rate, a fire spread experiment was designed in this study. To get rid of the influence of environmental factors such as wind direction and wind speed, the experiment was performed in a relatively closed room. Polyurethane fiber carpet was adopted as burning material, while several cameras were set at different positions to capture and record the fire spread scenarios. The experimental setup can be found in Fig. 19.1, where the camera setting parameters were presented.

The reason why we choose several shooting positions was that it is nearly impossible to record fire flame from a completely vertical static position above the forward flame front during the fire spreading process. There will be always a certain projection angle for our daily installed CCTV cameras [10]. Therefore, to explore the effect of shooting angle on the measurement results, we set in total 2 positions in the present study.

For the video recordings we got, the burning surface show some geometric distortions that need to be corrected. Therefore, the most important step in calculating

Fig. 19.1 Scheme of experimental setup



the rate of fire spread is to determine the correspondence between the points on the captured image and the real scene plane.

In the present study, we assume that the fire spread on plain area and there is no varied topography. Then, control points method can be applied to describe the transformation relation between fire spread surface X' and the projected image X . Here, control points are those points whose real world physical coordinates are known and whose features are obvious in the image space. With these points, the mapping relationship between the original image coordinate X and the target coordinate X' can be established as follows,

$$X' = H \cdot X \tag{19.1}$$

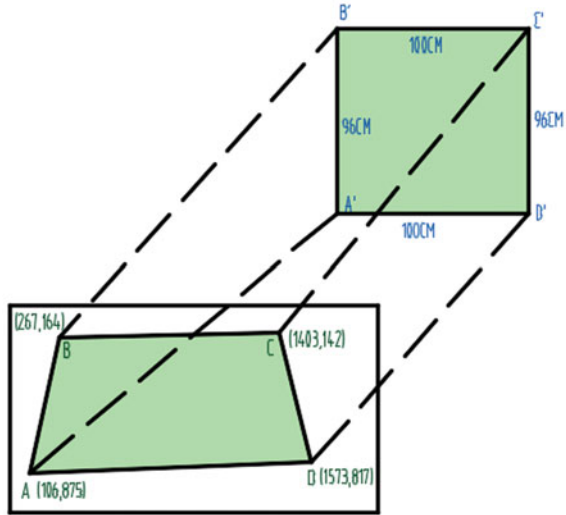
In the present study, the Direct Linear Transform (DLT) algorithm has been selected to calculate mapping relationship, i.e., the plane identity matrix H [11]. For the sake of completeness, this method is briefly described below.

Given that X'_i is a homogeneous column vector that contains the coordinates of the control point i (for $i = 1, \dots, 4$) of the real surface (values are expressed in cm), and X_i is a column vector that contains the coordinates of the control point i (for $i = 1, \dots, 4$) on the image (values are expressed in pixels). In accordance with the example shown in Fig. 19.2, vectors X'_i and X_i take the following values,

$$X_1 = \begin{bmatrix} 106 \\ 875 \\ 1 \end{bmatrix} \quad X_2 = \begin{bmatrix} 267 \\ 164 \\ 1 \end{bmatrix} \quad X_3 = \begin{bmatrix} 1403 \\ 142 \\ 1 \end{bmatrix} \quad X_4 = \begin{bmatrix} 1573 \\ 817 \\ 1 \end{bmatrix} \tag{19.2}$$

$$X'_1 = \begin{bmatrix} 0 \\ 0 \\ 1 \end{bmatrix} \quad X'_2 = \begin{bmatrix} 0 \\ 96 \\ 1 \end{bmatrix} \quad X'_3 = \begin{bmatrix} 100 \\ 96 \\ 1 \end{bmatrix} \quad X'_4 = \begin{bmatrix} 100 \\ 0 \\ 1 \end{bmatrix} \tag{19.3}$$

Fig. 19.2 Corresponding relation between pixel coordinates and real plane



$$X = [X_1 X_2 X_3 X_4] = \begin{bmatrix} 106 & 267 & 1403 & 1573 \\ 875 & 164 & 142 & 817 \\ 1 & 1 & 1 & 1 \end{bmatrix} \tag{19.4}$$

$$X' = [X'_1 X'_2 X'_3 X'_4] = \begin{bmatrix} 0 & 0 & 100 & 100 \\ 0 & 96 & 96 & 0 \\ 1 & 1 & 1 & 1 \end{bmatrix} \tag{19.5}$$

To ensure that the resulting identity matrix H is independent of the coordinate system representing the points, the two sets of points X' and X should be normalized separately before the direct linear transformation algorithm is applied to calculate H . Firstly, we put the matrix in Eqs. (19.4) and (19.5) in row echelon form by performing elementary transformation, then we put them back in the standard form to get the unit matrix shown in Eqs. (19.6) and (19.7).

$$\hat{X} = [\hat{X}_1 \hat{X}_2 \hat{X}_3 \hat{X}_4] = \begin{bmatrix} 0.1203 & 0.8521 & 0.9949 & 0.8874 \\ 0.9927 & 0.5234 & 0.1007 & 0.4609 \\ 0.0011 & 0.0032 & 0.0007 & 0.0006 \end{bmatrix} \tag{19.6}$$

$$\hat{X}' = [\hat{X}'_1 \hat{X}'_2 \hat{X}'_3 \hat{X}'_4] = \begin{bmatrix} 0 & 0 & 0.7214 & 1.0000 \\ 0 & 0.9999 & 0.6925 & 0 \\ 1.000 & 0.0104 & 0.0072 & 0.0100 \end{bmatrix} \tag{19.7}$$

In the calculation of H , the expression of direct linear transformation can be expressed as:

$$\widehat{X}'_l = \widehat{H} \cdot X_l \quad (19.8)$$

All the four control points previously referenced must fulfill this condition. Therefore, the above Eq. (19.7) can also be written in the following format,

$$\begin{bmatrix} \widehat{X}'_1 & \widehat{X}'_2 & \widehat{X}'_3 & \widehat{X}'_4 \end{bmatrix} = \begin{bmatrix} h_{11} & h_{12} & h_{13} \\ h_{21} & h_{22} & h_{23} \\ h_{31} & h_{32} & h_{33} \end{bmatrix} \cdot \begin{bmatrix} \widehat{X}_1 & \widehat{X}_2 & \widehat{X}_3 & \widehat{X}_4 \end{bmatrix} \quad (19.9)$$

From this expression can be seen that only \widehat{H} needs to be calculated. To ensure that the above formula is always valid, the relation can be rewritten in terms of a cross product in Eq. (19.9),

$$\widehat{H}_l \times \widehat{H} \cdot \widehat{X}_l = 0 \quad (19.10)$$

A linear solution \widehat{H} to a simple equation can be found to the simple equation. After that, we take the inverse normalization procedure and get the matrix H .

With the matrix H , the original image captured by the video camera as shown in Fig. 19.3a can be corrected. In this study, the corrected image was further cut to remove the background part and keep the burning area, as shown in Fig. 19.3b and d.

19.3 Flame Target Segmentation

When compared with the image in RGB color space, the one expressed in HSI color space is more natural and intuitive because the later one is more suitable for human perception and more convenient for artificial designation of color [12]. Therefore, in this study, in order to reduce the complexity of image processing and speed up the processing, the flame image is firstly converted from RGB color space to HSI color space following the formula shown below,

$$I = \frac{1}{3}(R + G + B) \quad (19.11)$$

$$S = 1 - \frac{3 \min(R, G, B)}{R + G + B} \quad (19.12)$$

$$\theta = \cos^{-1} \left[\frac{\frac{1}{2}[(R - G) + (R - B)]}{\sqrt{(R - G)^2 + (R - B)(G - B)}} \right] \quad (19.13)$$

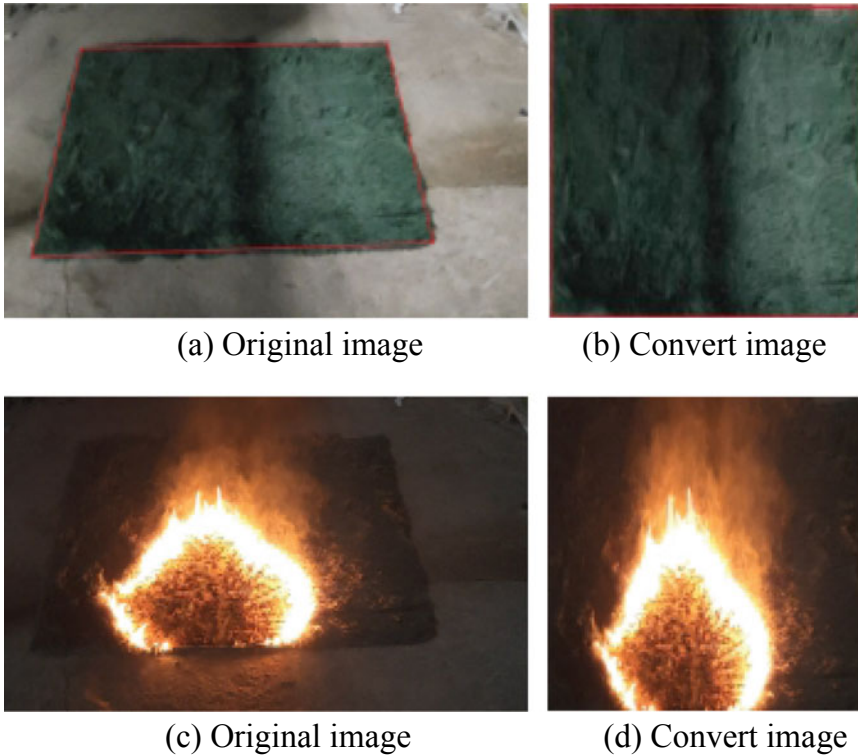


Fig. 19.3 The original image and the corrected image

$$H = \begin{cases} \theta & G \geq B \\ 360^\circ - \theta & G < B \end{cases} \quad (19.14)$$

In this way, the image shown in Fig. 19.3d can be mapped into HIS space as shown in Fig. 19.4a. Then, this figure is further processed to get the grayscale image. The result can be found in Fig. 19.4b. Based on the grayscale image, we can select a threshold T to complete image binarization process, i.e., the pixel point in the image is larger than the threshold, it is turned to white, and vice versa. Result with a threshold $T = 180$ can be found in Fig. 19.4c. Due to the reason that the threshold is artificially set, we tried several times and finally set $T = 220$ in the following study because the binary image is the closest to the shape of the fire front.

Since there is a certain influence of noise on the image after binarization, the morphological principle is adopted for image denoising. When using the algorithms of corrosion, expansion, open operation and close operation to reprocess the binary image shown in Fig. 19.5b, it is found that the open operation is better for the processing effect of the experimental image by contrasting. Compared with other morphological operations, the opening operation [13] first carries out corrosion and

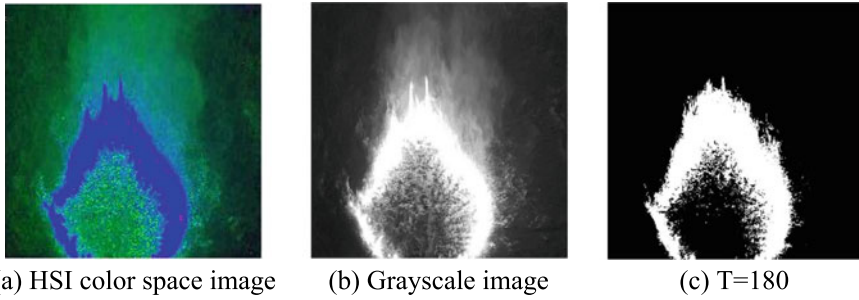


Fig. 19.4 Image in HSI color space, grayscale and after binarization

then expansion, which can remove isolated small points, burrs and small bridges, and the overall position and shape are inconvenient, making the image clearer. Therefore, in this experiment, open operation was used to process the binary image before we search for the maximum connected region.

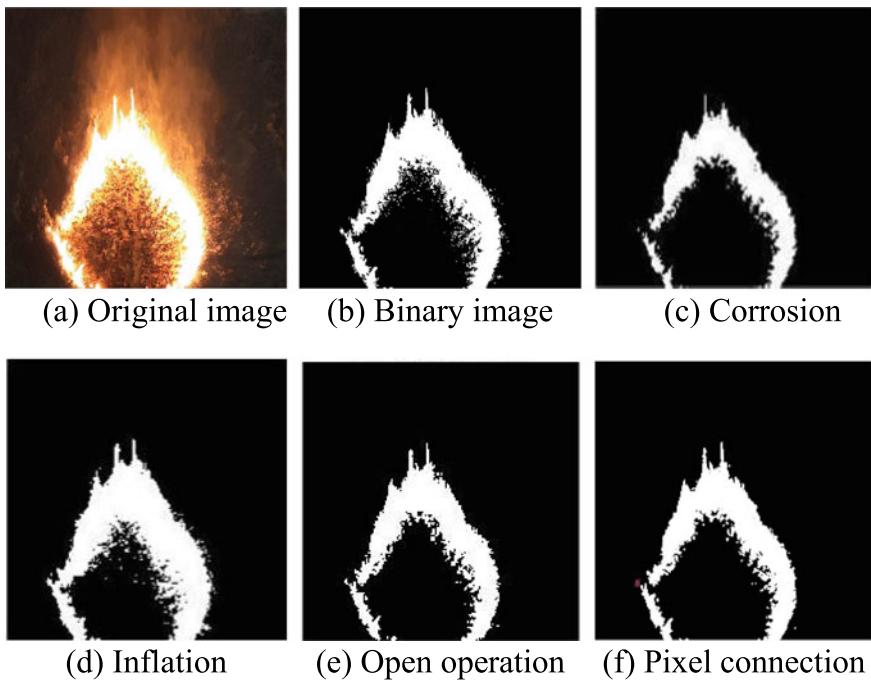


Fig. 19.5 Binary image with different processing

19.4 Fire Spread Rate Calculation

Since the color of the flame is completely different from that of the background in the processed image, this color information can be used to search the position of the flame front. The pixel coordinate position of the flame front can be recorded, as shown in Fig. 19.6. From Fig. 19.6 it can be seen that the flame front extracted at different moments after ignition keeps growing. With the position coordinates of the flame front obtained from the red box in the figure, we can calculate the fire spread rate.

The image has been corrected in geometric space before segmentation, so a point in the corrected image can be selected as the origin of coordinates to establish a Cartesian coordinate system, and pixel coordinates can be converted to actual length coordinates according to the actual geometric length of the carpet,

$$L = \frac{n}{m} \times L_0 \quad (19.15)$$

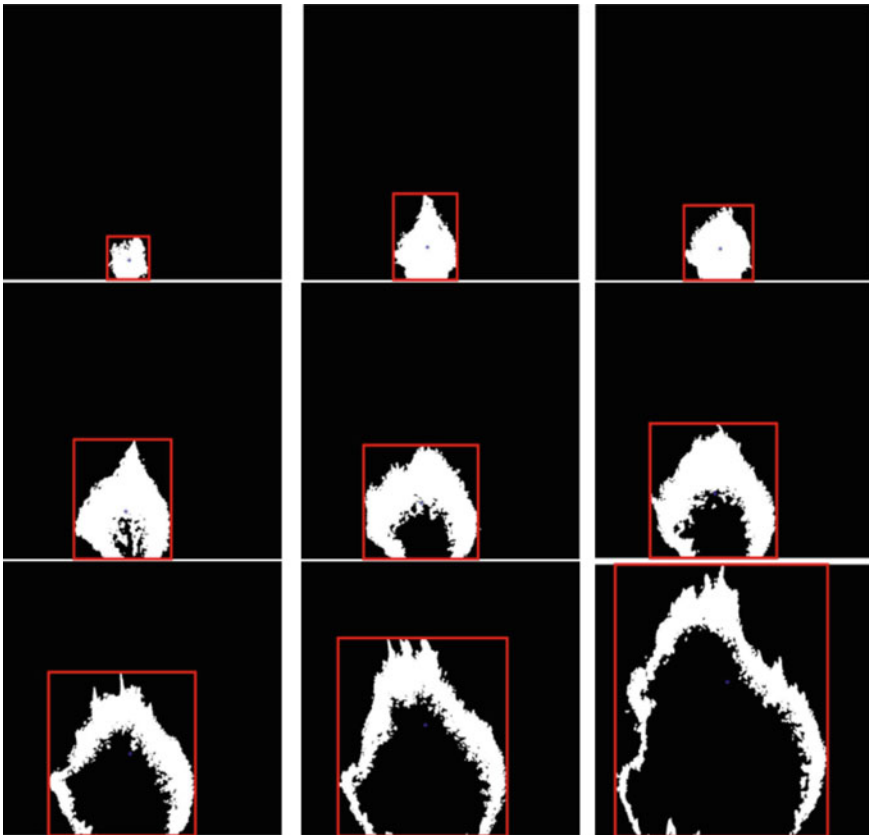


Fig. 19.6 Extraction of flame front coordinates

In Eq. (19.15), L —The actual distance the fire spread;

n —The farthest pixel value of the flame;

m —The pixel value of the image’s edge length;

L_0 —The actual geometric length of the carpet;

In this paper, the position of ignition source was selected as the origin of coordinates, and the pixel coordinates were converted into actual length coordinates. The fire spread distance with increasing time and the instantaneous fire spread rate can then be calculated and shown in Figs. 19.7 and 19.8.

From Fig. 19.7 it can be found that the average fire spread rate of camera position 1 was calculated as 0.21 cm/s. From Fig. 19.8, it can be found that the instantaneous fire spread rate fluctuates with time, and there are very few times when the fire spread rate is negative. The reason for the negative spread rate of fire is that the initial flame is unstable and the shape of flame changes greatly, which leads to the large fluctuation range.

Fig. 19.7 Relationship between fire spread distance with time

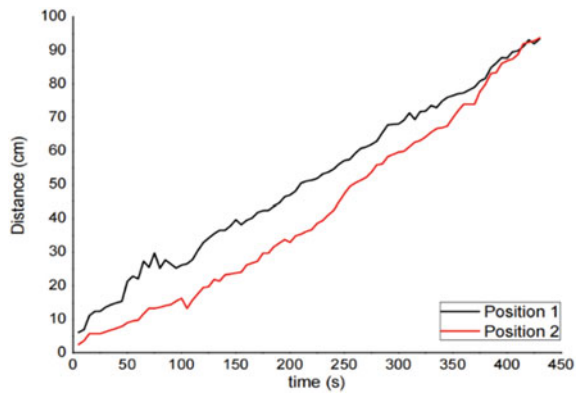


Fig. 19.8 Instantaneous fire spread rate

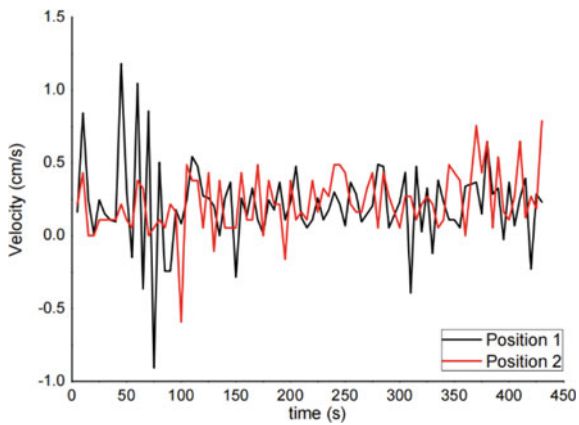
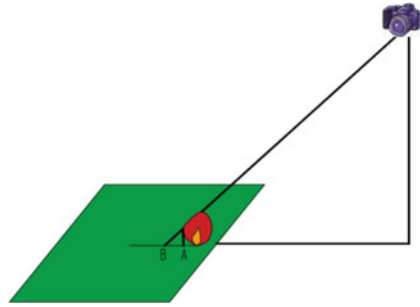


Fig. 19.9 Schematic diagram of error generation



When we compare the fire spread rate obtained at different camera positions, it can be found that the error caused by the shooting angle is also one of the main reasons for the negative fire spread rate. In the shooting process, as the camera is shooting from overhead, the projection of part of the flame height will be shot as the fire spreading front. Figure 19.9 describes the reasons for the error. Due to the unstable flame at the beginning of combustion, the data in the early stage fluctuates greatly.

In order to make the calculated fire spread rate more accurate and eliminate the above errors, the fire spread video sequence images taken by machine position 2 were also processed by the above image geometric space transformation and image segmentation. The calculated average fire spread rate at camera position 2 is 0.22 cm/s, and the graph of the change of fire spread distance with time and the graph of instantaneous fire spread rate are shown in Fig. 19.8. From Fig. 19.8, it can be found that there is little difference in the fire spread rate between the two machines. However, in order to make the data more accurate, the average value of the two machines is taken as the fire spread rate of the experiment, and the fire spread rate of the carpet is 0.22 cm/s.

19.5 Conclusion

In this study, a fire spread rate measuring method based on digital image processing technology is proposed. The video images of fire spread were collected from multiple directions, and the fire spread rate was calculated by extracting the position of the flame front through geometric space correction, color space conversion and image segmentation. By comparing the fire spread rate calculated by different camera positions, the error was estimated, and results indicated that the feasibility and accuracy of the fire spread rate measuring method was acceptable. Compared with the traditional methods to measure fire spread rate, the method proposed in this paper has the advantages of simple implementation, fast acquisition and high accuracy.

Acknowledgements The authors deeply acknowledge the support from the National Natural Science Foundation of China (Nos. 72104205, 71871189).

References

1. Xu, T.M.: Combustion Theory. China Machine Press, Beijing (2011)
2. Pastor, E., Águeda, A., Andrade-Cetto, J., Muñoz, M., Pérez, Y., Planas, E.: Computing the rate of spread of linear flame fronts by thermal image processing. *Fire Saf. J.* **41**(8), 569–579 (2006)
3. Balbi, J.H., Santoni, P.A., Dupuy, J.L.: Dynamic modeling of fire spread across a fuel bed. *Int. J. Wildland Fire* **9**(4), 275–284 (1999)
4. Chen, J., He, Y.P., Wang, J.: Multi-feature fusion based fast video flame detection. *Build. Environ.* **45**(5), 1113–1122 (2009)
5. Zhao, Y.Q., Zhou, Z., Xu, M.M.: Forest fire smoke video detection using spatiotemporal and dynamic texture features. *J. Electric. Comput. Eng.* **706187**(1–706187), 7 (2015)
6. Li, J.: Research on the Method of Forest Fire Recognition Based on Digital Image Processing. Beijing Forestry University (2009)
7. Sebastien, F., Moez, B., Ginoux, J.M., Moreau, E., Sayadi, M.: Convolutional neural network for smoke and fire semantic segmentation. *IET Image Proc.* **15**(3), 634–647 (2021)
8. Mishra, D.P., Kumar, P.: Experimental investigation of laminar LPG–H₂ jet diffusion flame with preheated reactants. *Fuel* **87**(13), 3091–3095 (2008)
9. Qiu, X.B., Xi, T.Y., Sun, D.Y., Zhang, E.H., Li, C.L., Peng, Y.M., Wei, J.L., Wang, G.: Fire detection algorithm combined with image processing and flame emission spectroscopy. *Fire Technol.* **54**(5), 1249–1263 (2018)
10. Zheng, L., Liu, Y.G., Li, J.: The mapping-adaptive convolution a fundamental theory for homography or perspective invariant matching methods. *SIAM J. Imag. Sci.* **10**(4), 1767–1803 (2017)
11. <http://certec.upc.es/articles/forestal/rateofspread.htm>
12. Huang, W.H., Chen, J.X., Liu, K., Lu, M.: Research on color image classification based on HSV color space. In: 2012 Second International Conference on Instrumentation, Measurement, Computer, Communication and Control, pp. 944–947. Harbin, China.
13. Zhao, X.C.: MATLAB Image Processing: Program Implementation and Modular Simulation. Beijing University of Aeronautics and Astronautics Press, Beijing (2018)

Chapter 20

Metaverse Standardization: System Planning, Current Status and Prospects



Zunbo Wei, Qiang Ge, Xiangjuan Jia, Yijian Zhang, Mengwei Han,
and Xiaofeng Chen

Abstract In recent years, metaverse has become one of the frontier fields that countries around the world pay attention to and has gradually entered the public's field of vision. The emergence of metaverse brings new consumption scenarios and models to industrial digitization, and will bring together more industrial resources such as social networking, entertainment, finance, and education, thereby creating a brand new digital world. However, since the metaverse is an emerging technology and business form, it is not perfect in terms of laws, regulations and regulatory policies. At the same time, there are many industry participants in the metaverse, with various business forms, and its development is still in its early stages. There are uncertainties in the global supervision of the metaverse. Standards need to be used to guide it to promote the healthy development of the metaverse. Therefore, it is particularly important to do a good job in the forward-looking analysis of metaverse standardization. From the perspective of standardization, this paper proposes a metaverse standard system based on the current situation of the metaverse, sorts out the existing standards related to the metaverse, and gives some suggestions on the standardization construction of the metaverse.

Keywords Metaverse · Development status · Standard system · Standardization

20.1 Introduction

The term “metaverse” was born in the science fiction *Snow Crash* in 1992. The novel depicts a huge virtual reality world, where people use digital avatars to control and compete with each other to improve their status. As for the metaverse, the recognized ideological source is Professor Vernor Vinge, an American mathematician

Z. Wei · Q. Ge · X. Jia · Y. Zhang · M. Han · X. Chen
Hangzhou Qulian Technology Co., Ltd., Hangzhou, China

X. Chen (✉)
State Key Laboratory of Blockchain and Data Security, Zhejiang University, Hangzhou, China
e-mail: chenxf.alfred@zju.edu.cn

and computer expert. In his novel *True Names* published in 1981, he creatively conceived a virtual world that entered and gained sensory experience through the brain-computer interface [1].

To realize the real application of the metaverse, it is necessary to use many cutting-edge technologies such as blockchain, artificial intelligence, AR/VR/XR/MR, big data, interactive technology and digital twinning. At present, the global Internet giants have paid unprecedented attention to the metaverse, and have turned their attention to actual investment and research and development, and the new track of the metaverse has been initially revealed. The concept of metaverse is highly sought after, and a large amount of capital flows into the metaverse ecology, which makes the metaverse blossom everywhere in the fields of manufacturing, entertainment, social interaction and finance, and produces a large number of start-up companies [6].

Metaverse is of great significance to the future social and economic development and digital transformation of various industries, and many countries around the world have successively formulated development strategies related to metaverse [7].

In July 2021, the Ministry of Economy, Trade and Industry of Japan issued the Investigation Report on the Future Possibilities and Topics of Virtual Space Industry, and planned to improve the laws and policies on the development of metaverse to guide and standardize the development of metaverse industry and strive to occupy a leading position in the global virtual space industry [8].

In November 2021, the Seoul City Government of South Korea issued a five-year Metaverse Seoul Basic Plan, announcing that from 2022, it will be divided into three stages to build a metaverse service ecosystem in business areas such as economy, education, tourism and public services [9].

The US government is still in a wait-and-see state for the metaverse, especially paying special attention to the data security and privacy protection issues that may be brought about by the development of the metaverse industry.

Due to the lack of large-scale original ecological Internet companies, some European countries are highly cautious about the development of metaverse, and focus on the supervision and rules of metaverse to prevent the new application model from bringing high risks [12].

Chinese government attaches great importance to the deep integration of digital economy and real economy. At the beginning of 2022, the Ministry of Industry and Information Technology proposed to vigorously promote the digital development of small and medium-sized enterprises, and cultivate a number of innovative small and medium-sized enterprises to enter emerging fields such as the metaverse, blockchain and artificial intelligence. By December 2022, many provinces in China have issued policies to support or develop parks related to the metaverse.

Although many countries in the world strongly support the construction of the metaverse, it is undeniable that the development of the global metaverse is still in its infancy, and the metaverse industry is growing wildly, lacking standardization guidance. The existing related standardization foundations are mainly concentrated in the technical fields such as blockchain and artificial intelligence [14].

On the one hand, the standardization development in the existing technical fields is still not perfect. For example, technologies such as blockchain are still emerging technologies, and the standard system planning is still short. There are still many problems in the development of a single technical standard. On the other hand, the metaverse is supported by many technologies. However, at present, there is a lack of standards for fusion technologies and standardized guidance for the development of related technologies.

In addition, the metaverse also involves many aspects, such as content, assets, supervision and so on, which are easily used by economic crimes with a little negligence, and these aspects also need to be standardized and guided.

20.2 Metaverse Standard System

MetaOpera: A Cross-Metaverse Interoperability Protocol written by Huawei Huang, Zibin Zheng et al. mentions that the purpose of interoperability is to provide users with a seamless experience interacting with the metaverse. However, the development of cross-metaverse interoperability is still in its infancy in industry and academia, and a practical cross-metaverse interoperability protocol cannot yet be found. Finally, this paper proposes MetaOpera, a generalized cross-metaverse interoperability protocol. The standardization of metaverse interoperability is a standard field with strong demand [15].

By combining some of the above materials to summarize the judgment of most experts on the development trend of the metaverse, and based on the existing technologies and application fields of the metaverse in the market, we have conducted in-depth thinking on the metaverse standard system [16].

The standard system is a conceptual system, which is an artificial system formed by artificially organizing standards. It should have the functions of finding and solving problems and guiding the development and application of standards [17].

Based on the standardization requirements of the metaverse, and the analysis and refinement of the development of the metaverse and the global related technical standard system, we think that the metaverse technical standard system structure includes four parts: A foundation, B technology, C application field and D governance, and the metaverse standard system structure is shown in Fig. 20.1.

Among them, foundation standards mainly include AA terms and definitions, AB reference architecture, AC coding and identification, AD classification and guidance, which are located at the bottom of the standard architecture of metaverse and provide support for other parts.

Technology standards mainly include BA infrastructure, BB key technologies, BC interoperability and BD security assurance, which are in the middle layer of the metaverse standard architecture and provide support for application fields and governance.

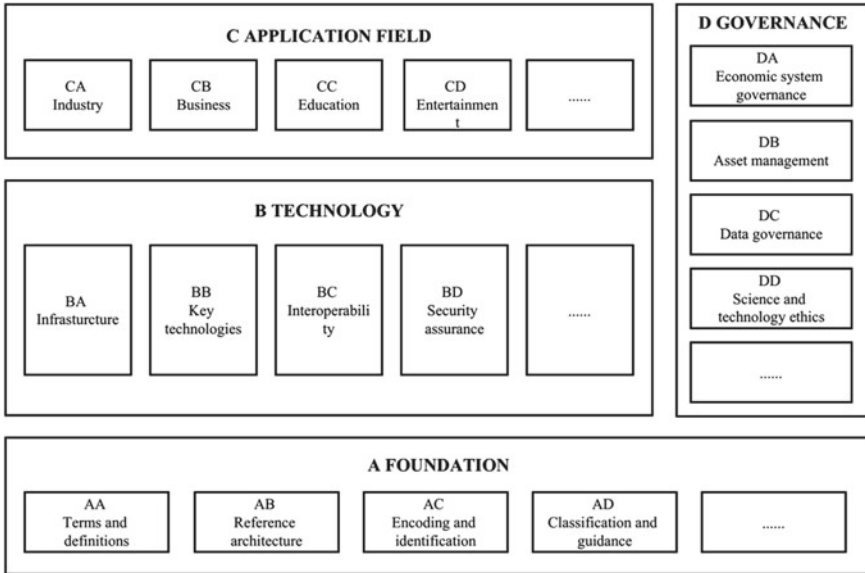


Fig. 20.1 Metaverse standard system structure

Application field standards include CA industry, CB business, CC education, CD entertainment and other categories, which are located at the top of the metaverse standard architecture and provide support for related industry applications.

Governance standards mainly include DA economic system governance, DB asset management, DC data governance, and DD science and technology ethics, which are located on the side of the standard system structure of metaverse and are mainly used to standardize and guide the development of metaverse technology.

20.3 Metaverse Standardization

Technologies such as blockchain, artificial intelligence, and virtual reality are important components of the metaverse. So let us briefly introduce the standardization of these technologies.

In general, the standardization of blockchain technology has received worldwide attention, and most of the international standards are developed and released by the three major standards organizations, ISO, ITU, and IEEE. Among them, ISO pays more attention to basic standards, such as general-purpose basic standards such as ontology, terminology, reference architecture, security, and smart contracts, while IEEE focuses more on engineering-oriented standards, such as guidelines for the Internet of Things and energy [20].

From the perspective of distribution, the blockchain standard focuses on technology and data foundation, security and privacy, but lags behind in the core technology fields such as smart contracts, cross-chain, sharding and the next main development direction. In addition, the standards for the specific application of the blockchain are relatively insufficient. Overall, the global blockchain standard system is still in the initial stage of construction, and many subdivided standards still need to be improved.

At present, the entire international standard of artificial intelligence mainly emphasizes term definitions, reference frames and related general requirements, as well as data and models. In the latest artificial intelligence standardization, artificial intelligence is defined from two latitudes of system set and engineering discipline, and artificial intelligence related systems including generation cycle, system function, application, etc. are introduced. From the perspective of the artificial intelligence ecosystem, the relevant data and related supporting technologies involved in artificial intelligence are clearly defined, and the concept of the artificial intelligence ecosystem is stipulated.

In the field of virtual reality, many video and audio technology standard organizations and groups around the world are conducting technical research and related standard formulation work. Through the tracking research on the latest situation of these standard organizations, virtual reality technology standards can be divided into three categories: system application, quality experience and data presentation. At present, virtual reality technology has not formed a complete and complete standard system. Most of the standards are still in the stage of proposal, research and formulation, and there are few related standards officially released.

20.3.1 Current Status of Metaverse Standardization in China

On July 26, 2022, the Metaverse Working Committee of the China Electronics Standardization Association was formally established. This organization is jointly carried out by the China Electronics Standardization Institute and a group of advantageous companies to carry out standardization work related to the metaverse. In addition, the Metaverse Working Committee of China Electronics Standardization Association also launched two group standards, Metaverse Reference Architecture and Industrial Metaverse Construction Guidelines.

At the same time, local associations are also speeding up the deployment of metaverse-related standards. ShenZhen information service Blockchain Association released two group standards, Metaverse Identity Authentication Specification System Based on Blockchain and Metaverse Payment and Clearing Specification System Based on Blockchain. The Zhongguancun Digital Media Industry Alliance released the group standard Metaverse Terminology and Communication Specifications.

Table 20.1 Group standards of metaverse in China

No.	Name of group standard
1	Metaverse reference architecture
2	Industrial metaverse construction guidelines
3	Metaverse identity authentication specification system based on blockchain
4	Metaverse payment and clearing specification system based on block-chain
5	Metaverse terminology and communication specifications
6	Blockchain-based metaverse part 1: technical requirements for ac-count security
7	Blockchain-based metaverse part 2: technical requirements for digital commodity circulation security
8	Blockchain-based metaverse part 3: technical requirements for data security
9	Blockchain-based metaverse part 4: technical requirements for inter-connection security
10	Technical specifications for virtual digital humans supporting voice and visual interaction
11	Guidelines for the evaluation of digital humans
12	Information classifying and coding specifications of industrial metaverse
13	Guidelines for the construction and operation of metaverse industrial bases
14	Basic capability requirements and evaluation methods of digital human systems

More metaverse-related standards are under development. China Institute of Communications, Shenzhen Artificial Intelligence Industry Association, Zhong-guancun Big Data Industry Alliance, and China Academy of Information and Communications Technology have all announced some metaverse-related standards that have been successfully approved. All the group standard names mentioned above are shown in Table 20.1.

20.3.2 *Current Status of International Metaverse Standardization*

In terms of international standards related to the metaverse, International Organization for Standardization (ISO), International Electrotechnical Commission (IEC), International Telecommunication Union (ITU), Institute of Electrical and Electronics Engineers (IEEE) and other world-renowned international organizations have begun to lay out metaverse-related standards.

ISO's metaverse-related research at this stage mainly consists of blockchain (TC590), artificial intelligence (ISO/IEC JTC1 SC42), Internet of Things (ISO/IEC JTC1 SC41), digital twins (ISO/IEC JTC 1/SC 41/WG6), cloud computing (ISO/IEC JTC1 SC38) and other technical committees and working groups, and has not yet formed a special metaverse standardization committee [21].

IEC established the Standardization Evaluation Group 15 on Metaverse in January 2023, aiming to propose the concept and definition of the metaverse, study the standardization requirements in the metaverse field, and formulate a standardization roadmap for the metaverse field.

Prior to this, IEC mainly focused on the development of virtual reality hardware equipment standards. At present, research on standards related to interface specifications of virtual reality head-mounted devices is being carried out. IEC 63145-20-10 is the first international standard in the field of virtual reality for eye-mounted displays (VR/AR), as shown in Table 20.2.

ITU-T established SG16 to focus on the formulation of international standards for multimedia, including blockchain, artificial intelligence, immersive experience, intelligent vision, audio and video codec, etc. These technologies are closely related to metaverse [23]. At the same time, ITU-T Focus Group on AI and Metaverse Open and Ubiquitous Systems was established under SG16. In January 2022, ITU-T formally froze two digital human standards at the SG16 plenary meeting, Framework and metrics for digital human application systems and Requirements and evaluation methods of non-interactive 2D real-person digital human application systems. At the same time, the SG16 plenary meeting also approved the Requirements and evaluation methods of digital human platform and the international standard for blockchain digital collections technical framework of DLT-based digital collection services, laying a good foundation for metaverse-related research [25]. The above standards are shown in Table 20.3.

The Standards Association (IEEE-SA) under IEEE is an advanced standardization operation department in the field of electronic technology science. On June 21, 2022, the IEEE Computer Society held a working meeting on the standardization of the metaverse. After discussion and voting, the No. 2022-023 bill was approved, and the establishment of the IEEE Computer Society Metaverse Research Group was approved. IEEE P2048 Standard for Metaverse: Terminology, Definitions, and Taxonomy, IEEE P3812.1 Standard for General Requirements for Identity

Table 20.2 International standards of metaverse in IEC

No.	Name of IEC standard
63145-20-10	Eyewear display—part 21–20: specific measurement methods for VR image quality—screen door effect

Table 20.3 International standards of metaverse in ITU-T

No.	Name of ITU-T standard
F.748.15	Framework and metrics for digital human application systems
F.748.14	Requirements and evaluation methods of non-interactive 2D real-person digital human application systems
F.DH-PE	Requirements and evaluation methods of digital human platform
H.DLT-DCS	Technical framework of DLT-based digital collection services

Table 20.4 International standards of metaverse in IEEE

No.	Name of IEEE standard
P2048	Metaverse: terminology, definitions, and taxonomy
P3812.1	General requirements for identity framework for metaverse
P7016	Ethically aligned design and operation of metaverse systems
P3221	Technical requirements of digital collection services based on blockchain technologies

Framework for Metaverse and IEEE P7016 Standard for Ethically Aligned Design and Operation of Metaverse Systems have been successfully approved. In addition, the IEEE SA Standards Committee officially passed the Technical Requirements of Digital Collection Services Based on Blockchain Technologies, which is the first international standard for blockchain digital collections in IEEE. The above standards are shown in Table 20.4. In the future, the Metaverse Research Group will accelerate the promotion of metaverse standardization research, clarify the scope and objects of metaverse standardization, and lay the foundation for the development of key standards in the metaverse field [26].

On June 21, 2022, the Khronos Group, an open standards industry organization in the United States, and Meta (formerly Facebook), Microsoft, Epic Games, Nvidia, Sony, Unity, Alibaba, Huawei and other technology giants jointly formed an organization called Metaverse Standards Forum. The purpose is to formulate metaverse industry standards and build interoperability standard services for cooperation, so that the metaverses of various companies can be compatible with each other [28].

From the above content, we can see that the existing metaverse-related standards mainly focus on the foundation standards and application field standards of the metaverse standard system, and rarely involve technical standards and governance standards. In addition, most existing standards are in the project approval stage.

20.4 Prospects of Metaverse Standardization

Based on the analysis of the above-mentioned existing metaverse-related standards, we believe that the direction and focus of future metaverse standard development should first be the consensus on metaverse concept standards, followed by technical standards such as underlying protocols, integration of key technologies, interoperability protocols, and Governance standards such as economic models, asset management, and technology ethics. Because the governed technology can stimulate the real vitality of the metaverse. In addition, we also put forward several suggestions.

20.4.1 Strengthen the Design of Metaverse Standard System

Different from a single technology system, the metaverse involves many technical fields, and the application scenarios involve a lot of extremely sensitive information such as assets and private data. Based on the basic principles of reasonable structure, advanced science and international compatibility, all countries in the world should systematically analyze the characteristics and development trends of metaverse technology and industry, and systematically consider the cooperative and mutual recognition relationship among various key technical standards systems such as artificial intelligence, blockchain, Internet of Things and XR, and strengthen the development and improvement of metaverse standard systems [29].

20.4.2 Promote the Interactive Development of Standardization and Technological Innovation

All countries in the world should strengthen the standard research in the key technical fields of metaverse, and improve the standard level through technological innovation, and actively explore the advanced and applicable scientific and technological innovation achievements in the metaverse field, and focus on the network, data, interface and platform required for virtual-real interaction. It is also necessary to actively organize the transformation of relevant standards, improve relevant standards and link protocols, and enhance the overall technical capabilities of the industry [34].

20.4.3 Cultivate New Standards for Developing Emerging Industries

Countries around the world should carry out research on standardization of emerging industries and future industries led by the metaverse, formulate a number of new standards suitable for various application scenarios in the fields of infrastructure, interactive terminals, digital content and system integration, and foster the development of new formats and new models [37]. For example, establish standards and specifications for data resource property rights, transaction circulation and IoT traffic and privacy security [40].

20.4.4 Promote the Pilot and Application of Standards

The development law of standards shows that if we want to improve the influence of standards, we need to carry out pilot promotion of standards. Especially in the face

of emerging things like the metaverse, the standardization foundation is relatively weak, and the implementation of the new standard needs to be verified in advance. At this stage, according to the progress of standard development, the relevant enterprises of metaverse should carry out standard verification work in the process of building the underlying development platform, application research and development and business expansion around the typical scenes of the metaverse, such as industry, medical care, education, commerce and entertainment, and summarize and form experiences that can be replicated and popularized.

20.4.5 Improve the Existing Standard System in Time

In the pilot promotion stage of standards, countries all over the world should collect suggestions on relevant issues, put forward measures to improve the standard system of metaverse by analyzing, seeking and verifying the causes of problems or potential causes, and track and evaluate the improvement effect of the standard system of metaverse [42].

In addition, countries around the world should also strengthen personnel training and communication and cooperation, and at the same time reach a consensus on the development of key standards such as terminology and reference framework, so as to lay the foundation for the healthy development of the metaverse.

20.5 Conclusion

In this paper, according to the present situation and possible development trend of metaverse, the framework of metaverse standard system is put forward, and the current status of metaverse standardization in China and the world is analyzed. At the same time, this paper also puts forward some suggestions for the future construction of metaverse standardization.

Acknowledgements This work was supported by the National Key R&D Program of China (Grant No. 2020YFB1005400) and the Key R&D Program of Guangdong Province (Grant NO. 2020B0101090003).

References

1. Dionisio, J.D.N., III, W.G.B., Gilbert, R.: 3D virtual worlds and the metaverse: current status and future possibilities. *ACM Comput. Surv. (CSUR)* **45**(3), 1–23 (2013)
2. Lee, J., Yeo, I., Lee, H.: Metaverse current status and prospects: focusing on metaverse field cases. In: 2022 IEEE/ACIS 7th International Conference on Big Data, Cloud Computing, and Data Science (BCD), pp. 330–336. IEEE (2022)

3. Falchuk, B., Loeb, S., Neff, R.: The social metaverse: battle for privacy. *IEEE Technol. Soc. Mag.* **37**(2), 52–66 (2018)
4. Gillespie, T.: *Custodians of the Internet: Platforms, Content Moderation, and the Hidden Decisions that Shape Social Media*. Yale University Press (2018)
5. Stephenson, N.: *Snowcrash*. ROC. Penguin, London (1992)
6. Ning, H., Wang, H., Lin, Y., Wang, W., Dhelim, S., Farha, F., Ding, J., Daneshmand, M.: A Survey on Metaverse: The State-of-the-Art, Technologies, Applications, and Challenges. arXiv preprint [arXiv:2111.09673](https://arxiv.org/abs/2111.09673) (2021)
7. Cheng, R., Wu, N., Chen, S., Han, B.: Will Metaverse be Next G internet? Vision, Hype, and Reality. arXiv. arXiv preprint [arXiv:2201.12894](https://arxiv.org/abs/2201.12894) (2022)
8. Radoff, J.: The Metaverse Value-Chain. Medium. <https://medium.com/building-the-metaverse/themetaverse-value-chain-afcf9e09e3a7> (2021). Last accessed 3 Apr 2023
9. Wang, Y., Su, Z., Zhang, N., Xing, R., Liu, D., Luan, T. H., Shen, X.: A survey on metaverse: fundamentals, security, and privacy. *IEEE Commun. Surv. Tutorials* (2022)
10. Gadekallu, T.R., Huynh-The, T., Wang, W., Yenduri, G., Ranaweera, P., Pham, Q.V., da Costa, D.B., Liyanage, M.: Blockchain for the Metaverse: A Review. arXiv preprint [arXiv:2203.09738](https://arxiv.org/abs/2203.09738) (2022)
11. Ng, D.T.K.: What is the metaverse? Definitions, technologies and the community of inquiry. *Australas. J. Educ. Technol.* **38**(4), 190–205 (2022)
12. Fernandez, C.B., Hui, P.: Life, the Metaverse and everything: an overview of privacy, ethics, and governance in Metaverse. In: 2022 IEEE 42nd International Conference on Distributed Computing Systems Workshops (ICDCSW), pp. 272–277. IEEE (2022)
13. Kraus, S., Kanbach, D.K., Krysta, P.M., Steinhoff, M.M., Tomini, N.: Facebook and the creation of the metaverse: radical business model innovation or incremental transformation? *Int. J. Entrepr. Behav. Res.* (2022)
14. Pine, B.J., Korn, K.C.: *Infinite Possibility: Creating Customer Value on the Digital Frontier*. Berrett-Koehler Publishers (2011)
15. Li, T., Yang, C., Yang, Q., Zhou, S., Huang, H., Zheng, Z.: MetaOpera: A Cross-Metaverse Interoperability Protocol. arXiv preprint [arXiv:2302.01600](https://arxiv.org/abs/2302.01600) (2023)
16. Mystakidis, S.: Metaverse. *Encyclopedia* **2**(1), 486–497 (2022)
17. Damar, M.: Metaverse shape of your life for future: a bibliometric snapshot. *J. Metaverse* **1**(1), 1–8 (2021)
18. The Khronos Group Inc website. <https://www.khronos.org>. Last accessed 03 Apr 2023
19. Metaverse Standards Forum. <https://metaverse-standards.org>. Last accessed 03 Apr 2023
20. Shafiq, M., Tian, Z., Bashir, A.K., Du, X., Guizani, M.: CorrAUC: a malicious bot-IoT traffic detection method in IoT network using machine-learning techniques. *IEEE Internet Things J.* **8**(5), 3242–3254 (2020)
21. Hackl, C., Lueth, D., Di Bartolo, T.: *Navigating the metaverse: a guide to limitless possibilities in a Web 3.0 world*. John Wiley & Sons (2022)
22. Ball, M.: *The Metaverse: and How it Will Revolutionize Everything*. Liveright Publishing (2022)
23. Wang, D., Yan, X., Zhou, Y.: Research on metaverse: concept, development and standard system. In: 2021 2nd International Conference on Electronics, Communications and Information Technology (CECIT), pp. 983–991. IEEE (2021)
24. Tian, Z., Li, M., Qiu, M., Sun, Y., Su, S.: Block-DEF: A secure digital evidence framework using blockchain. *Inf. Sci.* **491**, 151–165 (2019)
25. Rothbaum, B.O., Hodges, L., Anderson, P.L., Price, L., Smith, S.: Twelve-month follow-up of virtual reality and standard exposure therapies for the fear of flying. *J. Consult. Clin. Psychol.* **70**(2), 428 (2002)
26. Wang, M., Jing, Z.: Research on cultural influence based on the immersive entertainment IP experience project. In: 6th Annual International Conference on Social Science and Contemporary Humanity Development (SSCHD 2020), pp. 124–130. Atlantis Press (2021)
27. Winston, M., Edelbach, R.: *Society, Ethics, and Technology*. Cengage Learning (2013)

28. The Metaverse Needs Standards Too. <https://spectrum.ieee.org/metaverse-standards-forum>. Last accessed 03 Apr 2023
29. Wild, F., Perey, C., Hensen, B., Klamma, R.: IEEE standard for augmented reality learning experience models. In: 2020 IEEE International Conference on Teaching, Assessment, and Learning for Engineering (TALE), pp. 1–3. IEEE (2020)
30. Vadakital, V.K.M., Dziembowski, A., Lafruit, G., Thudor, F., Lee, G., Alfaced, P.R.: The MPEG immersive video standard—current status and future outlook. *IEEE Multimedia* **29**(3), 101–111 (2022)
31. The International Organization for Standardization website. <https://www.iso.org/standards.html>. Last accessed 03 Apr 2023
32. The International Electrotechnical Commission website. <https://iec.ch/homepage>. Last accessed 03 Apr 2023
33. Qiu, J., Tian, Z., Du, C., Zuo, Q., Su, S., Fang, B.: A survey on access control in the age of internet of things. *IEEE Internet Things J.* **7**(6), 4682–4696 (2020)
34. The International Organization for Standardization website, <https://www.itu.int/en/ITU-T/Pages/default.aspx>. Last accessed 23 Apr 2023
35. The Institute of Electrical and Electronics Engineers website. <https://www.ieee.org/>. Last accessed 03 Apr 2023
36. Blackwell, L., Ellison, N., Elliott-Deflo, N., Schwartz, R.: Harassment in social virtual reality: challenges for platform governance. *Proc. ACM Human-Comput. Interact.* **3**(CSCW), 1–25 (2019)
37. Horizon Worlds | Virtual reality worlds and communities. <https://www.oculus.com/horizon-worlds/>. Last accessed 03 Apr 2023
38. Pham, Q.V., Pham, X.Q., Nguyen, T.T., Han, Z., Kim, D.S. Artificial intelligence for the metaverse: a survey. arXiv e-prints, arXiv-2202 (2022)
39. Chen, D., Zhang, R.: Exploring research trends of emerging technologies in health metaverse: a bibliometric analysis. Available at SSRN 3998068 (2022)
40. Tian, Z., Luo, C., Qiu, J., Du, X., Guizani, M.: A distributed deep learning system for web attack detection on edge devices. *IEEE Trans. Industr. Inf.* **16**(3), 1963–1971 (2019)
41. Shafiq, M., Tian, Z., Sun, Y., Du, X., Guizani, M.: Selection of effective machine learning algorithm and Bot-IoT attacks traffic identification for internet of things in smart city. *Futur. Gener. Comput. Syst.* **107**, 433–442 (2020)
42. V Ramesh, U., Harini, A., Gowri, C.S.D., Durga, K. V., Druvitha, P., Kumar, K.S.: Metaverse: future of the internet. *J. Homepage. www.ijrpr.com* ISSN 2582, 7421 (2022)
43. Xu, M., Ng, W.C., Lim, W.Y.B., Kang, J., Xiong, Z., Niyato, D., Miao, C.: A full dive into realizing the edge-enabled metaverse: visions, enabling technologies, and challenges. *IEEE Commun. Surv. Tutor.* (2022)
44. Mozumder, M.A.I., Sheeraz, M.M., Athar, A., Aich, S., Kim, H.C.: Overview technology roadmap of the future trend of metaverse based on IoT, blockchain, AI technique, and medical domain metaverse activity. In: 2022 24th International Conference on Advanced Communication Technology (ICACT), pp. 256–261. IEEE (2022)

Chapter 21

Generating Second-Order Stokes Waves Using a Cylinder-Shaped Plunger—Theoretical Derivations and SPH Simulations



Yu-cheng Sui, Ming He, Xue-yan Li, and Yu-jie Meng

Abstract Plunger-type wavemakers have been and will be utilized in numerous wave tanks around the world, mainly due to their high efficiency in relatively deep water, space-saving in the wave direction, etc. Although theoretical methods for generating second-order Stokes waves based on a piston-type wavemaker are nearly mature, they cannot be extended to the plunger-type wavemaker. How to control the plunger motion to produce high-quality second-order Stokes waves is still an unsolved but practically meaningful issue. In this study, new formulae that relate the vertical motion of a cylinder-shaped plunger to the target second-order Stokes waves are derived, based on the conservation between the change in the immersion volume of the cylinder and the volume of the generated waves. Constraints on the generation of second-order Stokes waves are also proposed. Then, a numerical wave flume is established based on the Smoothed Particle Hydrodynamics (SPH) method. After examining its accuracy and analyzing its convergence by reproducing a physical experiment reported in the literature, the flume is used to simulate the second-order Stokes wave generation. The computed wave profiles, flow velocities, and pressures are compared with analytical solutions to verify the reliability of the proposed wave-making theory. The results show that the second-order Stokes waves produced by a plunger-type wavemaker are both precise and stable. Besides, high-quality second-order Stokes waves can be generated within a short distance, saving the precious laboratory space and computational domain between the wavemaker and the structure if exists.

Keywords Plunger-type wavemaker · Cylinder-shaped plunger · Second-order Stokes wave · Smoothed particle hydrodynamics (SPH)

Y. Sui · X. Li (✉) · Y. Meng

School of Hydraulic Engineering and Shandong Marine Aerospace Equipment Technology Innovation Center, Ludong University, Yantai 264025, China
e-mail: yanzi03@126.com

M. He

Tianjin Key Laboratory of Port and Ocean Engineering, Tianjin University, Tianjin 300350, China

21.1 Introduction

A second-order Stokes wave is a weakly nonlinear surface wave. Compared with a small-amplitude wave, it reflects the nonlinearity of natural waves, and compared with higher-order Stokes waves, it has a simpler form. Thus, it is often used in the studies on the hydrodynamics of marine and coastal structures. At present, theoretical methods of second-order Stokes wave-making have been proposed mainly regarding piston-type wavemakers [1, 2]. However, plunger-type wavemakers have been and will be widely mounted in worldwide wave tanks because of their high efficiency in relatively deep water and space-saving in the wave direction [3], to which the existing piston-type wave-making theories are not applicable.

In fact, there have been a number of studies dedicated to nonlinear wave-making using a plunger. For example, Yim et al. [4] respectively utilized the Reynolds-averaged Navier–Stokes and SPH methods to investigate the impulse wave generation by a freely falling rigid body. Based on the real-time equivalence between the immersion volume of the plunger and the volume of the target waves, He et al. [3] proposed the theoretical method for solitary wave-making using an arbitrary-geometry plunger. Then, the wedge-shaped, box-shaped, and cylinder-shaped plungers were taken as examples to examine the reliability of the theory. Following He et al. [3], Sun et al. [5] established the implicit equations describing the relation between the vertical displacement of a wedge-shaped plunger and the highly-nonlinear fifth-order Stokes waves. However, theories of second-order Stokes wave-making are still lacking.

As per the conservation between the change in the immersion volume of a cylinder-shaped plunger and the volume of the generated waves, this study derives new equations connecting the cylinder motion to the second-order Stokes waves. Moreover, constraints on the wave generation are also proposed. As a Lagrangian meshfree numerical method, the SPH [6, 7] is naturally good at treating the moveable water-cylinder interface and the nonlinear wave motion. Therefore, it is adopted herein to simulate the second-order Stokes wave generation so as to verify the proposed theory.

The rest of this paper is structured in the following manner. Section 21.2 derives the theory of generating second-order Stokes waves as well as the wave-making constraints. Then, the SPH method is introduced in Sect. 21.3, along with the validation of the established SPH model. Section 21.4 simulates the second-order Stokes wave generation using a cylinder-shaped plunger. The computed wave profiles, flow velocities, and pressures are compared with analytical solutions to examine the proposed theory. Finally, main conclusions are drawn in Sect. 21.5.

21.2 Wave-Making Theory

21.2.1 Equations of Plunger Motion

As Fig. 21.1 shows, a cylinder-shaped plunger is initially immersed. When the cylinder moves downward, the water surface rises and a wave crest will be produced. Then, as the cylinder moves upward, the water surface declines and a subsequent wave trough will be generated. As per the conservation between the change in the immersion volume of the cylinder and the volume of the generated second-order Stokes waves, we have

$$V_t - V_0 = V_1 + V_2 \tag{21.1}$$

where V_t and V_0 symbolize the immersion volume of the cylinder at time t and at the initial instant, respectively; V_1 represents the water volume between the wave profile and the still water level (SWL); V_2 stands for the water volume enclosed by the SWL, the cylinder boundary, and the vertical line from the transition point between the dry and wet boundaries of the cylinder to the SWL.

Taking the wave-front toe as the origin, a coordinate system $o-xy$ moving with the second-order Stokes wave is established. Thus, V_1 can be calculated by

$$V_1 = \int_0^{x_c} \eta(x) dx \tag{21.2}$$

where x_c signifies the horizontal position of the intersection between the wave surface and the cylinder; $\eta(x)$ indicates the wave profile defined as

$$\eta(x) = \bar{\eta} + \frac{H}{2} \cos(kx + \varphi) + \frac{kH^2 \cosh(kd)[\cosh(2kd) + 2] \cos 2(kx + \varphi)}{16 \sinh^3(kd)} \tag{21.3}$$

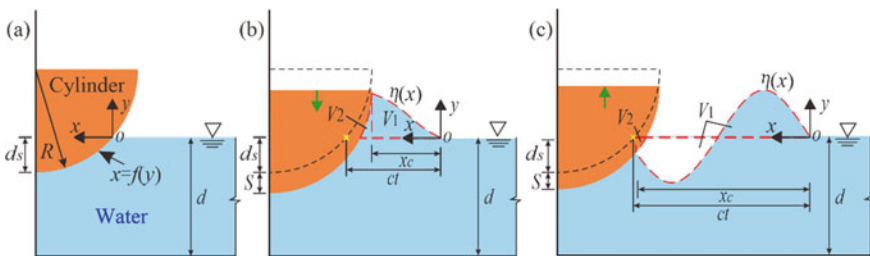


Fig. 21.1 Sketch of second-order Stokes wave generation due to the motion of a cylinder-shaped plunger (a) at the initial instant, (b) when the cylinder is moving downward, and (c) when the cylinder is moving upward

In the above equation, H and k refer to the wave height and wave number, respectively. φ denotes the wave phase and is approximately taken as $-\pi/2$ to satisfy $\eta(0) = 0$. d symbolizes the water depth. $\bar{\eta}$ is a set-down term written as

$$\bar{\eta} = -\frac{kH^2}{8 \sinh(2kd)} \tag{21.4}$$

Substituting Eq. (21.3) into Eq. (21.2), we obtain

$$V_1 = \frac{H}{2k} [1 - \cos(kx_c)] - \frac{kH^2x_c}{8 \sinh(2kd)} - \frac{H^2 [2 \cosh^3(kd) + \cosh(kd)]}{32 \sinh^3(kd)} \sin(2kx_c) \tag{21.5}$$

V_2 is given by integrating the surface function of the cylinder $x = f(y)$ along the y -axis:

$$V_2 = \int_0^{\eta(x_c)} [f(y) - x_c] dy \tag{21.6}$$

The surface function is defined as

$$f(y) = \sqrt{2Rd_s - d_s^2} + ct - \sqrt{R^2 - [y - (R - d_s - S)]^2} \tag{21.7}$$

where R , d_s , and S signify the radius, initial immersion depth, and vertical displacement of the cylinder, respectively; c is the wave celerity. Thus, Eq. (21.6) is rewritten as

$$V_2 = \left(\sqrt{2Rd_s - d_s^2} + ct - x_c \right) \eta(x_c) - \frac{R^2}{2} \arcsin \frac{R - S - d_s}{R} - \frac{\eta(x_c) - R + S + d_s}{2} \sqrt{R^2 - [\eta(x_c) - R + S + d_s]^2} - \frac{R^2}{2} \arcsin \frac{\eta(x_c) - R + S + d_s}{R} - \frac{R - S - d_s}{2} \sqrt{R^2 - (R - S - d_s)^2} \tag{21.8}$$

V_0 and V_t are calculated by the following equations, respectively.

$$V_0 = \int_{-d_s}^0 \left[\sqrt{2Rd_s - d_s^2} - f(y) \right] dy$$

$$= \frac{\pi R^2}{4} - \frac{R - d_s}{2} \sqrt{2Rd_s - d_s^2} - \frac{R^2}{2} \arcsin \frac{R - d_s}{R} \tag{21.9}$$

$$V_t = \int_{-(d_s+S)}^0 \left[\sqrt{2Rd_s - d_s^2} + ct - f(y) \right] dy \tag{21.10}$$

$$= \frac{\pi R^2}{4} - \frac{R - S - d_s}{2} \sqrt{R^2 - (R - S - d_s)^2} - \frac{R^2}{2} \arcsin \frac{R - S - d_s}{R}$$

Substituting Eq. (21.5) and Eqs. (21.8)–(21.10) into Eq. (21.1) yields

$$\begin{aligned} \frac{R^2}{2} \arcsin \frac{R - d_s}{R} + \frac{R - d_s}{2} \sqrt{2Rd_s - d_s^2} &= \frac{H}{2k} [1 - \cos(kx_c)] - \frac{kH^2 x_c}{8 \sinh(2kd)} \\ &- \frac{H^2 [2 \cosh^3(kd) + \cosh(kd)]}{32 \sinh^3(kd)} \sin(2kx_c) + \left(\sqrt{2Rd_s - d_s^2} + ct - x_c \right) \eta(x_c) \\ &- \frac{\eta(x_c) - R + S + d_s}{2} \sqrt{R^2 - [\eta(x_c) - R + S + d_s]^2} \\ &- \frac{R^2}{2} \arcsin \frac{\eta(x_c) - R + S + d_s}{R} \end{aligned} \tag{21.11}$$

In the above equation, S and x_c are two unknown variables with respect to the time. Therefore, another equation needs to be supplemented. Taking $[x_c, \eta(x_c)]$, which represents the position of the intersection between the wave surface and cylinder, into $x = f(y)$, we have

$$x_c = \sqrt{2Rd_s - d_s^2} + ct - \sqrt{R^2 - [\eta(x_c) - R + S + d_s]^2} \tag{21.12}$$

By solving Eqs. (21.11) and (21.12), the real-time displacement of the cylinder can be obtained.

21.2.2 Constraints on the Generated Wave

There are four constraints on the generation of second-order Stokes wave using a cylinder-shaped plunger. First, the volume of the generated second-order Stokes wave crest V_c cannot exceed the maximum increment of the immersion volume of the cylinder. This constraint can be further divided into

$$\begin{aligned} V_c \leq & \frac{R - d_s}{2} \sqrt{2Rd_s - d_s^2} - \frac{R - d}{2} \sqrt{2Rd - d^2} \\ & + \frac{R^2}{2} \arcsin \frac{R - d_s}{R} - \frac{R^2}{2} \arcsin \frac{R - d}{R}, \text{ if } R \geq d \end{aligned} \tag{21.13a}$$

$$V_c \leq \frac{R - d_s}{2} \sqrt{2Rd_s - d_s^2} + \frac{R^2}{2} \arcsin \frac{R - d_s}{R}, \text{ if } R < d \tag{21.13b}$$

where V_c is calculated by

$$\begin{aligned} V_c &\approx \int_0^{\lambda/2} \left\{ \bar{\eta} + \frac{H}{2} \sin(kx) - \frac{kH^2 \cosh(kd) [\cosh(2kd) + 2]}{16 \sinh^3(kd)} \cos(2kx) \right\} dx \\ &= \frac{H\lambda}{2\pi} - \frac{\pi H^2}{16 \sinh(kd) \cosh(kd)} \end{aligned} \tag{21.14}$$

with λ representing the wavelength.

Substituting Eq. (21.14) into Eqs. (21.13a) and (21.13b), we have

$$\begin{aligned} \frac{H\lambda}{\pi} - \frac{\pi H^2}{8 \sinh(kd) \cosh(kd)} &\leq (R - d_s) \sqrt{2Rd_s - d_s^2} - (R - d) \sqrt{2Rd - d^2} \\ &+ R^2 \arcsin \frac{R - d_s}{R} - R^2 \arcsin \frac{R - d}{R}, \text{ if } R \geq d \end{aligned} \tag{21.15a}$$

$$\begin{aligned} \frac{H\lambda}{\pi} - \frac{\pi H^2}{8 \sinh(kd) \cosh(kd)} &\leq (R - d_s) \sqrt{2Rd_s - d_s^2} \\ &+ R^2 \arcsin \frac{R - d_s}{R}, \text{ if } R < d \end{aligned} \tag{21.15b}$$

Second, Le Mehaute [8] put forward the scope of various wave theories. The parameters of the second-order Stokes wave to be produced should be located in the corresponding region. That is

$$\frac{H}{\lambda \tanh\left(\frac{2\pi d}{\lambda}\right)} > 0.006 \tag{21.16a}$$

$$\frac{H}{\lambda \tanh\left(\frac{2\pi d}{\lambda}\right)} < 0.05 \tag{21.16b}$$

$$\frac{H\lambda^2}{d^3} < 26 \tag{21.16c}$$

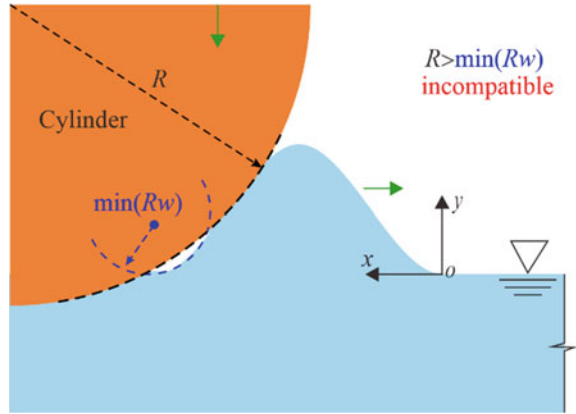
Third, the curvature radius of the cylinder R should not exceed the minimum one of the wave profile $\min(R_w)$, i.e.

$$R \leq \min(R_w) \tag{21.17}$$

Otherwise, as shown in Fig. 21.2, the wave surface will detach from the cylinder and collapse under the action of gravity.

R_w has the following form:

Fig. 21.2 Constraint on the curvature radius of the cylinder-shaped plunger



$$R_w = \frac{[1 + (\eta')^2]^{3/2}}{|\eta''|} \tag{21.18}$$

where η' and η'' stand for the first and second derivatives of $\eta(x)$ with respect to the x -axis, respectively. Since the calculation of $dR_w/dx = 0$ is quite complex, an approximation formula for R_w is used:

$$R_w \approx \frac{1}{|\eta''|} = \frac{1}{\left| -\frac{k^2 H \sin(kx)}{2} + \frac{k^3 H^2 [2 \cosh^3(kd) + \cosh(kd)] \cos(2kx)}{4 \sinh^3(kd)} \right|} \tag{21.19}$$

Thus,

$$\begin{aligned} \frac{dR_w}{dx} &\approx \frac{\frac{k^3 H \cos(kx)}{2} + \frac{k^4 H^2 [2 \cosh^3(kd) + \cosh(kd)] \sin(2kx)}{2 \sinh^3(kd)}}{\left\{ -\frac{k^2 H \sin(kx)}{2} + \frac{k^3 H^2 [2 \cosh^3(kd) + \cosh(kd)] \cos(2kx)}{4 \sinh^3(kd)} \right\}^2} \\ &\text{sgn} \left\{ -2k^2 H \sinh^3(kd) \sin(kx) + k^3 H^2 [2 \cosh^3(kd) + \cosh(kd)] \cos(2kx) \right\} \\ &= 0 \end{aligned} \tag{21.20}$$

Two solutions are obtained:

$$x_1 = \frac{\pi}{2k}, x_2 = \frac{\pi + \arcsin \left[\frac{\sinh^3(kd)}{4kH \cosh^3(kd) + 2kH \cosh(kd)} \right]}{k} \tag{21.21}$$

x_1 locates at the peak point of the wave and the circle of curvature is under the wave profile, so the interface incompatibility can only exist at x_2 . The use of $x = x_2$ in Eq. (21.19) yields

$$\min(R_w) = \frac{16 \sinh^3(kd)[2 \cosh^3(kd) + \cosh(kd)]}{[4k^{3/2}H \cosh^3(kd) + 2k^{3/2}H \cosh(kd)]^2 + 2k \sinh^6(kd)} \quad (21.22)$$

Substituting Eq. (21.22) into (21.17), we have

$$R \leq \frac{16 \sinh^3(kd)[2 \cosh^3(kd) + \cosh(kd)]}{[4k^{3/2}H \cosh^3(kd) + 2k^{3/2}H \cosh(kd)]^2 + 2k \sinh^6(kd)} \quad (21.23)$$

Fourth, owing to the set-down term in Eq. (21.3), the total volume of a second-order Stokes wave is less than zero. The cylinder then moves to a higher position after each wave generation, according to the conservation between the change in the immersion volume of the cylinder and the volume of the generated waves. Thus, we need to ensure that the cylinder will not rise above the SWL during the wave generation, i.e.

$$-\frac{t_m}{T} \lambda \bar{\eta} = \frac{ckH^2 t_m}{8 \sinh(2kd)} \leq \frac{\pi R^2}{4} - \frac{R - d_s}{2} \sqrt{2Rd_s - d_s^2} - \frac{R^2}{2} \arcsin \frac{R - d_s}{R} \quad (21.24)$$

where t_m is the total wave-making time; T indicates the wave period.

21.3 Numerical Model and Its Validations

21.3.1 The SPH Method

In the weakly compressible SPH framework, the Navier–Stokes equations can be expressed by [9]

$$\frac{D\rho_i}{Dt} = -\rho_i \sum_j (u_j - u_i) \cdot \nabla_i W_{ij} V_j + \delta h c_0 \sum_j \psi_{ij} \frac{(r_j - r_i) \cdot \nabla_i W_{ij}}{\|r_j - r_i\|^2} V_j \quad (21.25)$$

$$\frac{D\mathbf{u}_i}{Dt} = -\frac{1}{\rho_i} \sum_j (p_j + p_i) \nabla_i W_{ij} V_j + \mathbf{g} + \alpha h c_0 \frac{\rho_0}{\rho_i} \sum_j \pi_{ij} \nabla_i W_{ij} V_j \quad (21.26)$$

where subscripts i and j denote a target particle and its neighbouring particle, respectively; ρ , p , \mathbf{u} , \mathbf{r} , \mathbf{g} , and V symbolize the density, pressure, velocity, position, gravitational acceleration, and volume, respectively; $\delta = 0.1$ is the diffusive coefficient [10]; $h = 2\delta_p$ refers to the smoothing length [11] with δ_p being the initial particle spacing; $c_0 = 10(gd)^{1/2}$ indicates the numerical speed of sound [12]; $\rho_0 = 1000 \text{ kg/m}^3$ represents the reference density; $\alpha = 8\nu/(hc_0)$ is the artificial viscosity coefficient

[13] and $\nu = 10^{-6} \text{m}^2/\text{s}$ signifies the kinematic viscosity; W symbolizes the Wendland C2 kernel function [14].

ψ_{ij} in Eq. (21.25) is defined as

$$\psi_{ij} = 2(\rho_j - \rho_i) - [(\nabla\rho)_j^L + (\nabla\rho)_i^L] \cdot (\mathbf{r}_j - \mathbf{r}_i) \quad (21.27)$$

where $(\nabla\rho)^L$ stands for the renormalized density gradient [15] calculated by

$$(\nabla\rho)_i^L = \sum_j (\rho_j - \rho_i) \left[\sum_j (\mathbf{r}_j - \mathbf{r}_i) \otimes \nabla_i W_{ij} V_j \right]^{-1} \nabla_i W_{ij} V_j \quad (21.28)$$

π_{ij} in Eq. (21.26) is written as

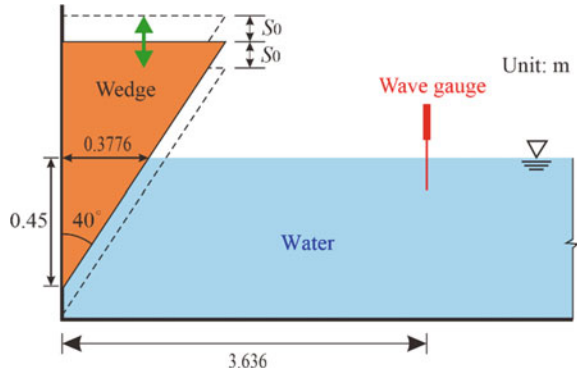
$$\pi_{ij} = \frac{(\mathbf{u}_j - \mathbf{u}_i) \cdot (\mathbf{r}_j - \mathbf{r}_i)}{\|\mathbf{r}_j - \mathbf{r}_i\|^2} \quad (21.29)$$

Equations (21.25) and (21.26) are not yet closed; thus, a state equation is supplemented [16] to build a connection between ρ and p :

$$p_i = c_0^2(\rho_i - \rho_0) \quad (21.30)$$

Since the Lagrangian meshfree nature of the SPH method, the free-surface boundary condition can be automatically satisfied without any special treatments [17, 18]. The solid boundary condition is implemented using the dynamic boundary particles (DBPs). Specifically, three layers of DBPs are placed along the framework of the solid domain. They participate in the same continuity and state equations as fluid particles, but remain stationary or move following the cylinder. Besides, the densities of the DBPs are modified to overcome the unphysical boundary layers on the solid surface [19].

Fig. 21.3 Sketch of the experimental setup of Kashiwagi [20]



21.3.2 Model Validations

Before using the SPH method to verify the proposed wave-making theory, the laboratory experiment of Kashiwagi [20] was numerically reproduced. The experiment was conducted in a wave tank of 65 m long, 4 m wide, and 7 m deep. Regular waves of $H = 0.1$ m and $T = 0.96$ s were produced by a wedge-shaped plunger whose dimensions and movement pattern are illustrated in Fig. 21.3.

The oscillation equation of the wedge is defined as

$$y_p = S_0 \sin \frac{2\pi t}{T} \left[\exp\left(\frac{-t^2}{1.75^2}\right) - 1 \right] \tag{21.31}$$

where y_p represents the instantaneous displacement of the wedge with a negative value referring to a downward displacement; $S_0 = 0.0373$ m is the oscillation amplitude.

As illustrated in Fig. 21.4, a numerical wave flume equipped with the same wedge-shaped plunger and wave gauge as Kashiwagi [20] was established. To guarantee high computational efficiency in a deep-water condition, the numerical water depth d was taken to be $0.5\lambda_0$ with $\lambda_0 = 1.44$ referring to the deep-water wavelength. A sponge layer of length λ_0 was placed on the downstream of the flume to absorb the outgoing waves. Three different particle resolutions $H/\delta_p = 5, 10,$ and 20 were used to check the numerical convergence, resulting in 40 k, 151 k, and 587 k particles, respectively.

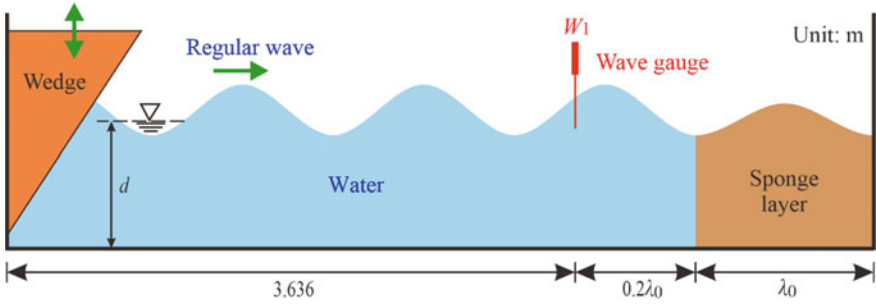


Fig. 21.4 The SPH wave flume used to reproduce the laboratory experiment of Kashiwagi [20]

Figure 21.5a compares the time histories of computed and measured wave profiles under various particle resolutions. Figure 21.5b further shows their root-mean-square deviations (RMSDs), which are defined by the following equation:

$$RMSD = \sqrt{\frac{1}{N_s} \sum_{l=1}^{N_s} \left[\left(\frac{\eta}{S_0} \right)_{SPH,l} - \left(\frac{\eta}{S_0} \right)_{Exp,l} \right]^2} \quad (21.32)$$

where N_s signifies the total number of sample points within $3 \leq t/T \leq 13$; l indicates the sequence number. From Fig. 21.5, it can be seen that the computational results are almost identical to the measurement data, tends to converge with the increase of H/δ_p . Considering the balance between the computational accuracy and efficiency, $H/\delta_p = 10$ is regarded as an appropriate particle resolution.

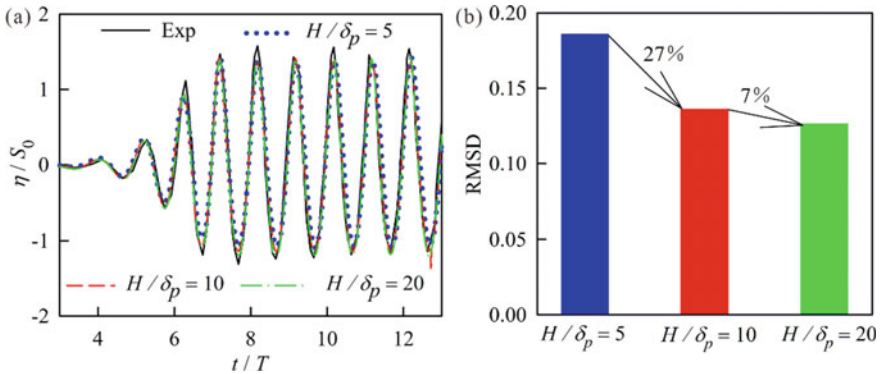


Fig. 21.5 Comparisons between the computed and measured wave profiles under different particle resolutions. **a** Time histories. **b** Root-mean-square deviations (RMSDs)

21.4 Examination of Cylinder-Induced Waves

The validated SPH wave flume was then adjusted to verify the proposed theory of second-order Stokes wave-making. As shown in Fig. 21.6, the flume was 4.5λ in length, which was equipped with a cylinder-shaped plunger with radius being 0.5 m and initial immersion depth being 0.2 m. The cylinder motion was controlled by Eqs. (21.11) and (21.12). Six gauges W_1-W_6 were mounted to measure the wave profiles. They had equal spacing of 0.5λ and the foremost gauge was 0.5λ away from the upstream boundary of the flume. Four probes PV_1-PV_4 were placed to capture the flow pressures and velocities. As per the four constraints mentioned in Sect. 21.2.2, $H = 0.05$ m, $T = 2$ s, and $d = 0.4$ m were chosen as the target wave parameters.

Figure 21.7 compares the computed wave profiles measured by $W_1 - W_6$ with the analytical ones described in Eq. (21.3). Satisfactory agreement on the wave height, period, and phase can be seen. It demonstrates that, by applying the proposed theory, second-order Stokes waves with stable waveform and precise wave parameters can be produced. In addition, the produced wave achieves its target form within a short distance, saving the precious laboratory space and computational domain between the wavemaker and the structure if exists.

Figures 21.8 and 21.9 compare the computed flow velocities and pressures measured by PV_1-PV_4 with the analytical ones calculated by

$$u_x = A\omega \left[\frac{\cosh k(y+d)}{\sinh(kd)} \sin(kx_2 - \omega t) - \frac{3Ak \cosh 2k(y+d)}{4 \sinh^4(kd)} \cos 2(kx_2 - \omega t) \right] \tag{21.33}$$

$$u_y = A\omega \left[\frac{\sinh k(y+d)}{-\sinh(kd)} \cos(kx_2 - \omega t) - \frac{3Ak \sinh 2k(y+d)}{4 \sinh^4(kd)} \sin 2(kx_2 - \omega t) \right] \tag{21.34}$$

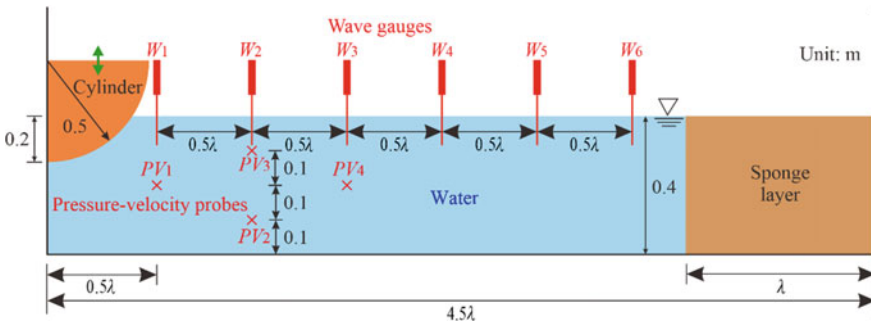


Fig. 21.6 The SPH wave flume used to verify the theory of second-order Stokes wave generation using a cylinder-shaped plunger

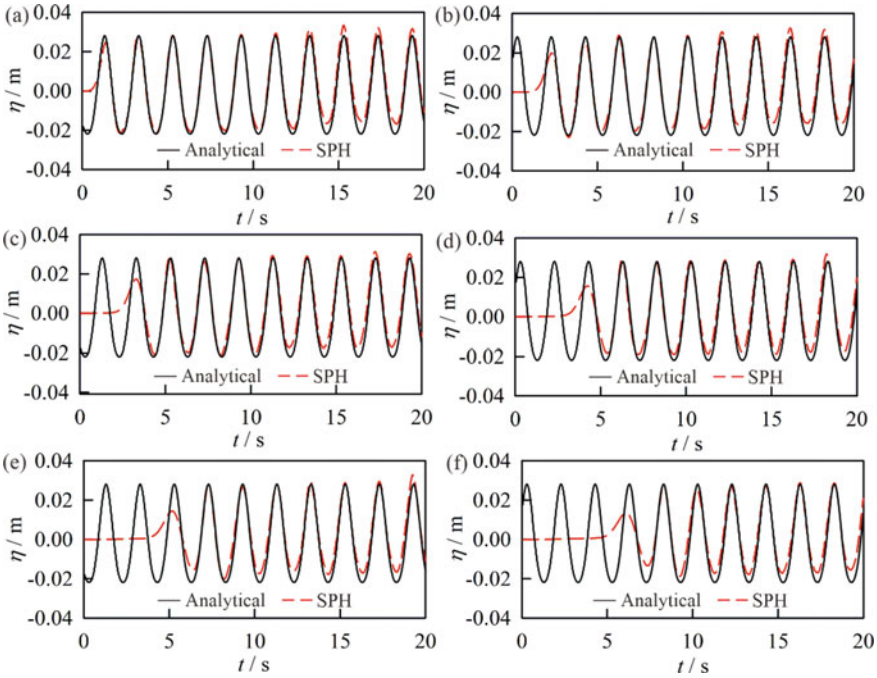


Fig. 21.7 Comparisons between the computed and analytical wave profiles at **a** W_1 , **b** W_2 , **c** W_3 , **d** W_4 , **e** W_5 , and **f** W_6

$$\begin{aligned}
 p = & -\rho g y + \rho g A \frac{\cosh k(y+d)}{\cosh(kd)} \sin(kx_2 - \omega t) - \frac{\rho g A^2 k}{\sinh(2kd)} \sinh^2[k(y+d)] \\
 & - \frac{3\rho g A^2 k}{2 \sinh(2kd)} \left[\frac{\cosh 2k(y+d)}{\sinh(2kd)} - \frac{1}{3} \right] \cos 2(kx_2 - \omega t) \tag{21.35}
 \end{aligned}$$

where u_x and u_y symbolize the horizontal and vertical velocities of the flow, respectively; A refers to the wave amplitude; $\omega = 2\pi/T$ represents the angular frequency; x_2 is the abscissa with its origin being fixed at the upstream boundary of the flume, and points to the wave direction. Except the early stage of wave generation, the overall agreement between the computational and analytical results is satisfactory. Moreover, the numerical flow velocity and pressure are stable, which further verifies the reliability of the proposed wave-making theory.

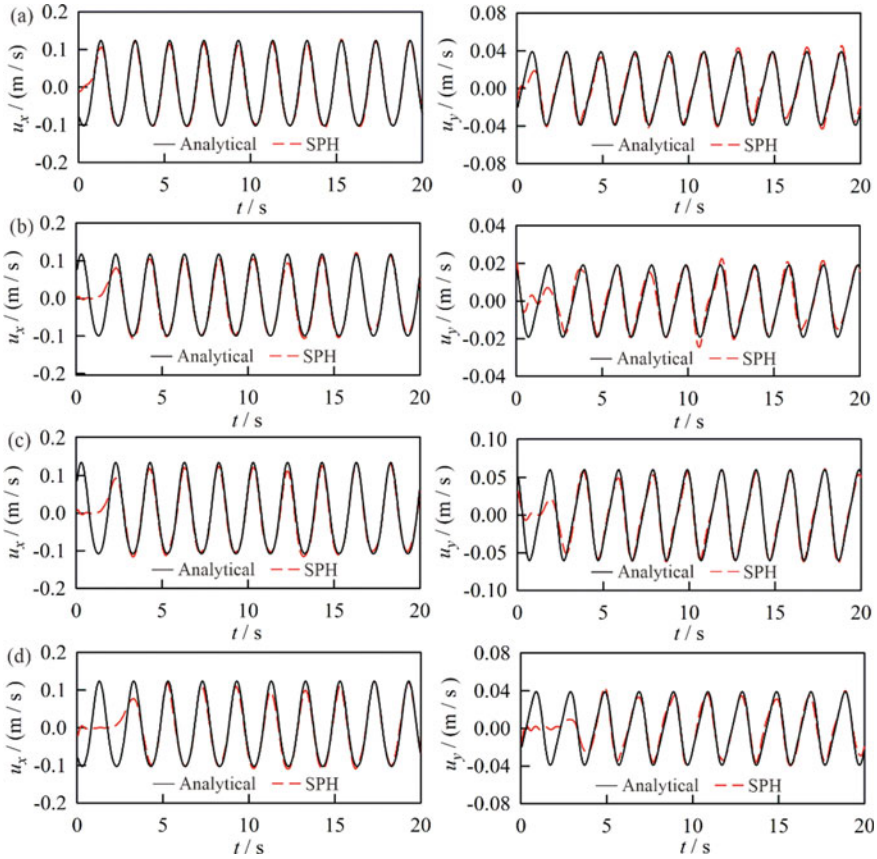


Fig. 21.8 Comparisons between the computed and analytical flow velocities at **a** PV_1 , **b** PV_2 , **c** PV_3 , and **d** PV_4

21.5 Conclusions

For better use of plunger-type wavemakers, a theory of second-order Stokes wave-making regarding a cylinder-shaped plunger was proposed. The theory was then examined in a SPH wave flume which was validated in advance by reproducing a laboratory experiment in the literature. The computed wave profiles, flow velocities, and pressures were compared with analytical solutions, respectively. Satisfactory agreements were observed. Moreover, the produced wave achieves its target form within a short distance, saving the precious laboratory space and computational domain between the wavemaker and the structure if exists.

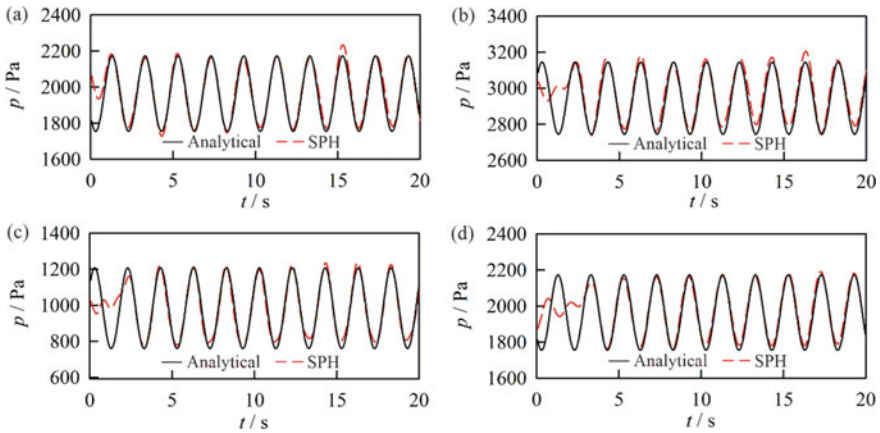


Fig. 21.9 Comparisons between the computed and analytical flow pressures at **a** PV_1 , **b** PV_2 , **c** PV_3 , and **d** PV_4

Funding Statement X.-y. Li acknowledges the support by the Natural Science Foundation of Shandong Province (Grant No. ZR202110280004). M. He acknowledges the support by the National Natural Science Foundation of China [Grant No. 51709201] and the TianHe Qingsuo open research fund of TSYS in 2022 & NSCC-TJ (Grant No. P-THQS-22-ZD-No. 0008).

Conflicts of Interest

The authors declare that they have no conflicts of interest to report regarding the present study.

References


1. Madsen, O.S.: On the generation of long waves. *J. Geophys. Res.* **76**(36), 8672–8683 (1971)
2. Schäffer, H.A.: Second-order wavemaker theory for irregular waves. *Ocean Eng.* **23**(1): 47–88 (1996)
3. He, M., Khayyer, A., Gao, X., Xu, W., Liu, B.: Theoretical method for generating solitary waves using plunger-type wavemakers and its Smoothed Particle Hydrodynamics validation. *Appl. Ocean Res.* **106**, 102414 (2021)
4. Yim, S.C., Yuk, D., Panizzo, A., Risio, M.D., Liu, P.L.-F.: Numerical simulations of wave generation by a vertical plunger using RANS and SPH models. *J. Waterw. Port Coast. Ocean Eng.* **134**(3), 143–159 (2008)
5. Sun, B., Li, C., Yang, S., Zhang, H.: A simplified method and numerical simulation for wedge-shaped plunger wavemaker. *Ocean Eng.* **241**, 110023 (2021)
6. Gotoh, H., Khayyer, A.: On the state-of-the-art of particle methods for coastal and ocean engineering. *Coast. Eng. J.* **60**(1), 79–103 (2018)
7. Luo, M., Khayyer, A., Lin, P.: Particle methods in ocean and coastal engineering. *Appl. Ocean Res.* **114**, 102734 (2021)
8. Le Méhauté, B.: *An Introduction to Hydrodynamics and Water Waves*. Springer-verlag (1976)
9. Antuono, M., Colagrossi, A., Marrone, S., Molteni, D.: Free-surface flows solved by means of SPH schemes with numerical diffusive terms. *Comput. Phys. Commun.* **181**(3), 532–549 (2010)

10. Antuono, M., Marrone, S., Colagrossi, A., Bouscasse, B.: Energy balance in the δ -SPH scheme. *Comput. Meth. Appl. Mech. Eng.* **289**, 209–226 (2015)
11. Chen, Y., Liu, Y., Meringolo, D.D., Hu, J.: Study on the hydrodynamics of a twin floating breakwater by using SPH method. *Coast. Eng.* **179**, 104230 (2023)
12. Monaghan, J.J., Kos, A.: Solitary waves on a Cretan beach. *J. Waterw. Port Coast. Ocean Eng.* **125**(3), 145–155 (1999)
13. Monaghan, J.J., Kajtar, J.B.: SPH particle boundary forces for arbitrary boundaries. *Comput. Phys. Commun.* **180**(10), 1811–1820 (2009)
14. Wendland, H.: Piecewise polynomial, positive definite and compactly supported radial functions of minimal degree. *Adv. Comput. Math.* **4**(1), 389–396 (1995)
15. Randles, P.W., Libersky, L.D.: Smoothed particle hydrodynamics: some recent improvements and applications. *Comput. Meth. Appl. Mech. Eng.* **139**(1–4), 375–408 (1996)
16. Molteni, D., Colagrossi, A.: A simple procedure to improve the pressure evaluation in hydrodynamic context using the SPH. *Comput. Phys. Commun.* **180**(6), 861–872 (2009)
17. Colagrossi, A., Antuono, M., Le Touzé, D.: Theoretical considerations on the free-surface role in the smoothed-particle-hydrodynamics model. *Phys. Rev. E* **79**(5), 056701 (2009)
18. Colagrossi, A., Antuono, M., Souto-Iglesias, A., Le Touzé, D.: Theoretical analysis and numerical verification of the consistency of viscous smoothed-particle-hydrodynamics formulations in simulating free-surface flows. *Phys. Rev. E* **84**(2), 026705 (2011)
19. Ren, B., He, M., Dong, P., Wen, H.: Nonlinear simulations of wave-induced motions of a freely floating body using WCSPH method. *Appl. Ocean Res.* **50**, 1–12 (2015)
20. Kashiwagi, M.: Full-nonlinear simulations of hydrodynamic forces on a heaving two-dimensional body. *J. Soc. Naval Archit. Jpn.* **180**, 373–381 (1996)

Chapter 22

Design of Construction Mode of Offshore Gas Storage in the Whole Sea—Taking H Gas Field in Liaodong Bay, Bohai Sea as an Example



Shixin Jiang , Zhan Su, Jingyao Sun, Youwu Li, Yixin Yu, and Jiaojiao Yu

Abstract Offshore LNG import has become one of the four major natural gas import channels. One of the potential targets of gas reservoir reconstruction around coastal developed areas is offshore near-exhausted gas reservoir resources. Therefore, in recent years, the related research on offshore gas storage is gradually carried out. In view of the congested shipping lanes in China's coastal areas, the “onshore gas reverse transport” mode used in the construction of offshore gas storage abroad may be difficult to solve the gas source problem of offshore gas storage due to the scarce resources of LNG receiving stations, busy sea lanes and other problems. Therefore, this paper innovated and proposed a brand new storage construction mode—the whole-sea offshore gas storage construction mode, which provides a new idea for offshore gas storage construction. The main difference between this model and other offshore gas storage models is that in this model, the gasification storage units are located at sea, and the main gasification units used are floating gasification storage units (FSRU, Floating Storage and re-to-feedstock Unit); GBS (Gravity Based Structure). Taking H gas field in Bohai Sea as an example, this paper studies the scheme of reservoir construction under this model. The research results show that H gas field can be converted into “whole sea” offshore gas storage, which can provide reference for other offshore gas storage construction.

Keywords Gas storage · Offshore gas storage · Database building mode · Full sea type · LNG · Marine engineering · FSRU · GBS

S. Jiang (✉) · Z. Su · J. Sun · Y. Li · Y. Yu · J. Yu
Research and Development Center of CNOOC Gas and Power Group, Beijing 100028, China
e-mail: jiangshx@cnooc.com.cn

22.1 Introduction

In recent years, with the increasing dependence on external natural gas, the country is accelerating the construction of natural gas reserve capacity. As the ballast stone of natural gas reserve capacity construction, gas storage can effectively guarantee the security of our natural gas supply. At present, China mainly imports natural gas through four channels: China-Myanmar, Central Asia, China-Russia pipeline gas and coastal LNG import channel. Among them, three onshore pipeline gas import channels have been built with several large gas storage facilities, which can be used for long-term pipeline gas storage peak adjustment. However, coastal LNG import channels are still dominated by receiving stations and rely on storage tanks for storage rotation. Therefore, large gas storage tanks should also be built for imported LNG. In view of the limited resources of high-quality onshore storage sites around China's coastal areas, relevant enterprises are actively exploring the construction of gas storage targeting near depleted offshore oil and gas fields [1–6].

22.2 Overseas Offshore Gas Storage Construction Cases and Construction Modes

22.2.1 Overseas Offshore Gas Storage Construction Cases and Construction

Up to now, four offshore natural gas storage have been built in the world, which are located in Europe, namely Rough gas storage in the UK, Kinsale Southwest Gas storage in Ireland, Gaviota gas storage in Spain and K. Mara gas storage in Turkey, as shown in Table 22.1.

(1) Rough gas storage in the UK

Rough is the largest gas storage in the United Kingdom. It was converted into a gas storage in 1985. Its working capacity is 3.65 billion cubic meters, accounting for 77% of the UK's total gas storage capacity. The daily gas supply capacity is 44 million m³/day, accounting for 34% of the UK's natural gas peak regulating capacity. At the end of 2017, it was announced to shut down permanently due to the expiration of its service life. But it was reopened in May 2022 due to the international situation.

Rough gas storage consists of two offshore platforms: the 47/3B built in 1983 with 24 Wells, and the 47/8A built in 1977 with 5 Wells. The two platforms are connected to each other via a 2 km 18 in subsea line; The offshore platform is connected to the onshore processing terminal via a 29 km 36 in pipeline. The Easington terminal on shore is used to process the injection-production fluid. The produced natural gas is dried, separated and measured into the national pipe network system, and the condensate oil is transported through the special pipeline and the water is hauled away by tank trucks.

Table 22.1 Summary of global offshore natural gas storage information

Gas storage indicators	Rough, UK	K. Marmara, Turkey	Gaviata, Spain	Kinsale southwest, Ireland
Type of reservoir	Condensate gas reservoir	Condensate gas reservoir	Condensate gas reservoir	Condensate gas reservoir
Formation	Permian sandstone	/	/	/
Porosity (%)	12	20	8.86–13.86	4.3–23.2
Permeability (mD)	75	50	0.27–17.12	19
Reservoir thickness (m)	35	65	90–120	22
Elevation depth (m)	2743	1150	2400	1083
Geological reserves of natural gas (million cubic meters)	4500	/	/	/
Design storage capacity (million cubic meters)	5240	/	/	/
Design working capacity (million cubic meters)	3340	4600	730	230

(2) K. Marmara gas storage in Turkey

The K. Mara gas field was developed in 1997 and discontinued in 2001. In 2007, it was converted into a storage facility and connected to the onshore Degirmenkoy storage facility, operated by TPAO (Turkey's leading LNG importer).

The gas reservoir has a water depth of 43 m, a reservoir depth of 1150 m, a reservoir thickness of 65 m, a porosity of 20% and a permeability of 50 mD. The 11 injection-production Wells (5 old Wells + 6 new Wells) have a working gas capacity of 1.6 billion cubic meters. The maximum gas injection capacity is 11.8 million cubic meters per day, and the export capacity is 15 million cubic meters per day. The third phase of the expansion project will start in June 2018, and the working gas capacity will be increased to 4.6 billion cubic meters.

(3) Gaviata gas storage in Spain

Gaviata was developed in 1986, stopped production in 1994, and converted into a gas storage facility currently operated by Enagas (acquired from Repsol in 2010 for approximately \$140 million).

The average water depth is 100 m, the reservoir depth is 2400 m, the reservoir thickness is 90–120 m, and the working gas volume is 730 million cubic meters. Gas injection in summer and gas production in winter, with a maximum gas injection capacity of 4.25 million cubic meters per day and transport capacity of 5.66 million cubic meters per day.

(4) Kinsale southwest gas storage, Ireland

Kinsale southwest is a small gas field located under the main Kinsale gas field, which has been converted to gas storage after depletion, about 80 km offshore. The field was discovered in 1995, started production in 1999, and converted to storage in 2001. The average water depth is 93 m, the reservoir depth is 1083 m, and the thickness is 22 m. It has 1 gas injection well and 2 gas production Wells, and the working gas volume is 230 million cubic meters. Gas source: In the early stage, it came from the adjacent main gas field. In 2006, it could also be reversed from the land through renovation.

22.2.2 Construction Mode of Offshore Gas Storage Abroad

The four gas storage reservoirs are all gas reservoir reconstruction, and the gas source is mainly LNG. The storage construction mode is mainly “onshore gas reverse transport” mode, that is, LNG is gasified through the onshore receiving terminal and then returned to the gas storage through pipe network, and the onshore processing terminal, sea and land pipe network and surrounding oil and gas fields are interconnected, as shown in Fig. 22.1.

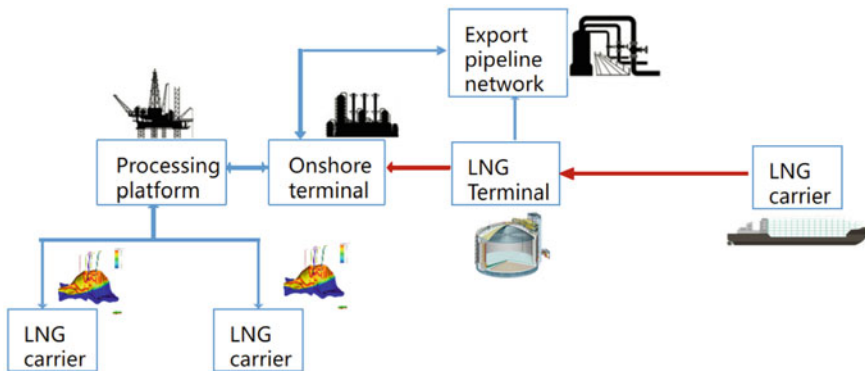


Fig. 22.1 Design of “onshore gas reverse transport” construction mode for offshore gas storage

22.3 Construction Mode of Offshore Gas Storage

At present, new LNG receiving stations in China have high requirements for port site selection, and the construction cost of special terminals is high. Suitable station sites will become increasingly scarce in the future. On the one hand, the expansion of LNG receiving station is limited by the size of the reserved site, and the expansion scale is limited. If some high-quality storage sites are designed according to the “onshore gas reverse transport” mode, there is no suitable LNG receiving station or expansion of existing LNG receiving stations to support it. On the other hand, with the improvement of docking and unloading capacity, LNG carriers’ occupation of port channel resources will be more and more prominent, and the timeliness of docking and unloading gasification of LNG carriers will be affected by more and more uncertain factors, as shown in Fig. 22.2.

Therefore, on the basis of learning from foreign models, the construction mode of the whole sea gas storage is proposed, that is, during the gas injection period, LNG ships are directly gasification through the gasification storage device and then injected into the gas storage, and the whole gasification docking and unloading process is completed offshore. This design mode is not restricted by the site, nor does it affect the navigation of the port. It is an effective receiving way to further expand the scale of LNG import in the future. Under the guidance of this model, a new integrated gas storage of “offshore LNG receiving terminal + offshore gas storage” can be built, named “all offshore” for short. Without considering the use of sea lanes, part of the production capacity can be directly connected and unloaded

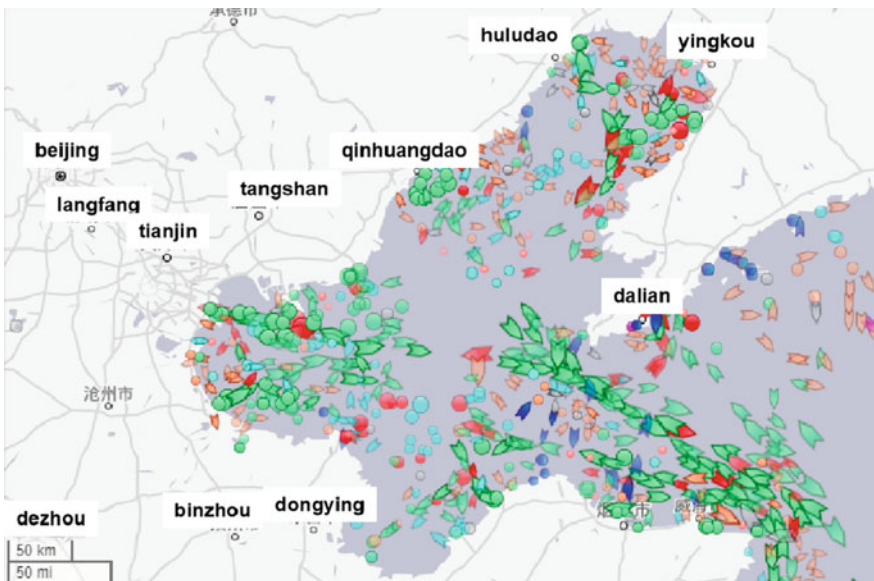


Fig. 22.2 Usage of port and channel in Bohai Bay

at sea to gasify LNG into gas storage for storage in off-season, thus solving the gas source problem of offshore gas storage. Other spare production capacity can be regarded as offshore LNG receiving terminal direct gasification export to improve equipment utilization rate and economy.

Therefore, on the basis of learning from foreign models, the construction mode of the whole sea gas storage is proposed, that is, during the gas injection period, LNG ships are directly gasification through the gasification storage device and then injected into the gas storage, and the whole gasification docking and unloading process is completed offshore. This design mode is not restricted by the site, nor does it affect the navigation of the port. It is an effective receiving way to further expand the scale of LNG import in the future. Under the guidance of this model, a new integrated gas storage of “offshore LNG receiving terminal + offshore gas storage” can be built, named “all offshore” for short. Without considering the use of sea lanes, part of the production capacity can be directly connected and unloaded at sea to gasify LNG into gas storage for storage in off-season, thus solving the gas source problem of offshore gas storage. Other spare production capacity can be regarded as offshore LNG receiving terminal direct gasification export to improve equipment utilization rate and economy, as shown in Fig. 22.3.

The difference between this model and the traditional model mainly lies in the gasification storage unit, in which the gasification storage unit is located at sea. In this mode, the selection of the gasification storage device in the sea area is generally carried out first.

At present, the gasification Storage system mainly consists of FSRU(Floating storage and Re-gasification Unit) and GBS (Gravity Based Structure) that can be used as feedstocks.

GBS is a sitting-bottom structure that uses steel or concrete. The entire structure is anchored to the sea floor, while docks, tanks and regasification facilities are mounted on the structure above the water. Conventional onshore regasification equipment, small LNG storage tanks, etc., can be used.

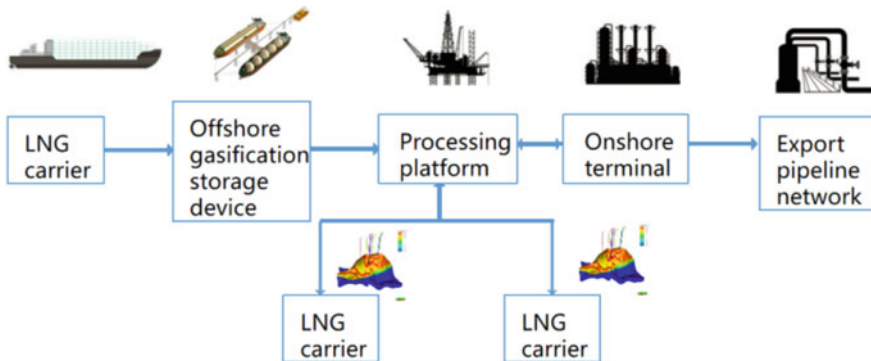


Fig. 22.3 Offshore gas storage “all offshore” construction mode design

FSRU is a floating vessel that stores and regasifies LNG. It requires LNG transport to ship the LNG, unload the LNG into the FSRU storage tank, and regasify the LNG and transfer the gas to a subsea pipeline [7–9].

If both types of gasification devices can be realized, other schemes will be designed around the two types of gasification devices and schemes will be compared for optimization; If only one way can be realized. The model design is carried out around the selection of gasification storage device.

22.4 Application Cases

Bohai H Gas field is located in the northern waters of Liaodong Bay, Bohai Sea, 50 km from the nearest coast. H gas field is located in a sea area with a depth of 16–20 m. The gas field was discovered in November 1984, officially started construction in 1990, and successfully put into operation in 1992. The annual production capacity is 500 million cubic meters of natural gas and 100,000 tons of condensate oil. It has a daily production capacity of 1.5 million cubic meters of natural gas and has entered the late stage of development. According to the investigation, the surrounding sea gas exploitation volume is not enough to support the gas source demand for the construction of reservoir, and the onshore distance of the gas field is close to the coast, there is no LNG receiving station and other supporting facilities, so it is difficult to use the “onshore gas reverse transport” mode to design, so the storage site is designed according to the “all offshore” mode.

22.4.1 Gas Reservoir Engineering

The main target of the gas field reconstruction is Shahejie Formation, with a buried depth of 2000–2200 m. Two large faults are developed in the area, both of which are sealed faults and the original formation pressure is 34.5 Mpa. The cap bed is a semi-deep water lacustrine deposit with nearly 437 m thick mudstone reservoir covering the entire Shahejie Formation of the gas field. It is a regional cap bed with stable distribution and wide range. It thickens from southwest to east in plane. The existing data predict that the large set of mudstone has good sealing property. The reservoirs are mainly carbonate rocks, most of which are dissolution pores. The reservoir porosity is 26%. Permeability of 232 mD, mainly high porosity and high permeability, good physical property. The reservoir thickness ranges from 0 to 72 m, with an average of 19.0 m. The total proved reserves of natural gas after reserve review are $77 \times 10^8 \text{ m}^3$. In summary, the geological condition of the site is good, which can be used as the offshore gas storage site target.

The design is based on the injection and production cycle days of the main domestic gas storage. Combined with reservoir engineering research and evaluation, the construction parameters of gas storage are predicted as a whole. It is estimated

Table 22.2 Main storage capacity parameters design of gas storage in H gas field

Gas injection period	120 days
Gas recovery period	180 days
Balancing period	35 days in spring, 30 days in fall
Daily gas injection	12 million cubic meters per day
Daily gas production	15 million cubic meters per day
Operating pressure	24–34.5 MPa
Storage capacity	$64.6 \times 10^8 \text{ m}^3$
Working volume	$18.1 \times 10^8 \text{ m}^3$
Cushion volume	$46.3 \times 10^8 \text{ m}^3$
Refill pad volume	$23 \times 10^8 \text{ m}^3$

that the operating pressure of gas storage is 24–34.5 MPa and the capacity of gas storage is $64.6 \times 10^8 \text{ m}^3$, working volume $18.1 \times 10^8 \text{ m}^3$, cushion volume $46.3 \times 10^8 \text{ m}^3$, refill pad volume $23 \times 10^8 \text{ m}^3$, the specific parameters are shown in Table 22.2 [10–13].

22.4.2 Overall Deployment Scheme

The new facilities of H gas field offshore gas storage project include gasification storage device (if it is FSRU, mooring system should also be considered), injection and production wellhead integrated platform WHPA, processing and export platform CEP and three sea pipes. The natural gas produced from the gas storage formation is dehydrated to reach the piped gas delivery standard, and mixed with the FSRU gas, it is transported to the land terminal through this pipeline. The offshore pipeline can also realize the reverse transport of the land terminal to the platform for gas injection. The other new offshore pipeline will transport the qualified condensate from the CEP treatment to the onshore terminal, as shown in Figure 22.4.

Gasified gas from the gasified storage unit is transported to the WHPA platform via sea pipeline and pressurized into the formation by gas compressors placed on the WHPA platform. Electric drive centrifugal compressor is selected. Two compressors are used and one is in standby mode. The compressor is powered by the turbine generator set of the CEP platform.

During gas production, the production fluid comes out from the gas production well of WHPA platform through manifold and trestle to the CEP platform for treatment, and carries on gas-liquid separation in the condensate oil separator. The gas is further dehydrated by triethylene glycol and then exported through the gas offshore pipeline. The liquid is separated by oil and water, and the condensate oil is exported through the condensate offshore pipeline.

The electricity consumption of the CEP platform and WHPA platform is provided through the turbine generator set of the CEP platform. Four 16 MW gas turbine

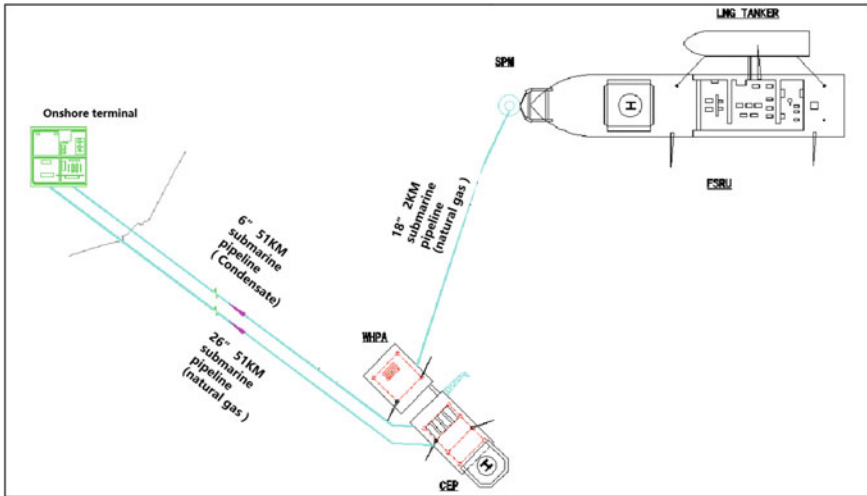


Fig. 22.4 General plan layout of gas field (FSRU Plan)

generating sets are set on the CEP platform. During gas injection, the turbine runs in the state of 3 used and 1 standby or all 4 units are put into operation. During the gas production period, the operation state of the gas turbine is 2 in use and 2 in standby.

Combined with the requirements of gas storage operation parameters, the processing capacity of the main process system is determined as shown in Table 22.3. The offshore pipeline transportation capacity of natural gas supports 15 million cubic meters per day of gas storage, and the remaining 15 million cubic meters per day is used to meet the emergency reverse transportation of natural gas from main lines to the revolving storage of offshore gas storage or the direct gasification of FSRU.

Table 22.3 Main process system design processing capacity

System	Design capabilities
Gas injection system	12 million m ³ /day
Produce a single well metering system	20.3–1.615 million m ³ /day (gas) 5–106 m ³ /day (oil) 3–28 sq/day (water)
Condensate treatment system	18.46 million m ³ /day (gas) 1110 m ³ /day (oil) 284 SQM/day (water)
Natural gas treatment system	18.46 million m ³ /day
Production water treatment system	480 m ³ /day
FSRU to pressurized reinjection platform sea pipe	20 million m ³ /day
Condensate offshore pipeline	1200 m ³ /day
Natural gas offshore pipeline	30 million m ³ /day

22.4.3 Gasification Storage Device Scheme

The gasification storage device mainly adopts GBS and FSRUs. In view of the conflict between CGB and the environmental protection requirements of the sea area where the gas field is located, relevant schemes are mainly studied for FSRU [9].

(1) FSRU design condition

According to the gas field environment, the FSRU design conditions mainly include:

Extreme working condition: The FSRU cannot be relieved in position under the condition of a typhoon once every 100 years.

Function requirements: releasable, can be connected back.

Design life: 25 years.

Design water depth: 91 m.

(2) FSRU scheme

According to the survey, there is no FSRU that fully meet the project working conditions in the world, so it is suggested that the project FSRUs should be newly built. The following parameters must be met.

The length of the ship is 292 m, the width of the ship is 43.4 m, the type depth is 26.3 m, and the design maximum draft is 12 m. The loading capacity of LNG is 147,000 square meters and DWT is 83,000 tons. It has its own propulsion system, equipped with LNG regasification module, STL single point cabin and equipment, and offhand unloading system (rigid arm unloading system or STS connection transfer system with low temperature hose), as shown in Table 22.3.

(3) System selection

FSRU usually has two moorings, multi-point moorings and single-point moorings.

The characteristics of multi-point mooring system are large positioning constraints for floating bodies, simple system and low cost, but small load bearing capacity for wave. It is usually applicable to the sea area with mild wave environment, and the water depth is generally less than 15 m, so it is not applicable to the target sea area of the project in the South China Sea.

Single point mooring means that the ocean engineering ship is connected to the undersea mooring chain through a single point structure on the ship, around which the ship can turn 360° with the effect of wind-wave-current load. Due to the weather beacon effect, the bow of the moored ship will be stable at the position with the minimum environmental force, so it has strong bearing capacity to the wave load and can withstand the once-in-a-century typhoon. Applicable water depth from 20 to 2000 m. The application of single point mooring system originated from FPSO, which has more than 40 years of technical development history and has been widely used in the global sea area. With high technical maturity, it is suitable for the Bohai Sea target area of this project.

In summary, the design of the single point mooring system.

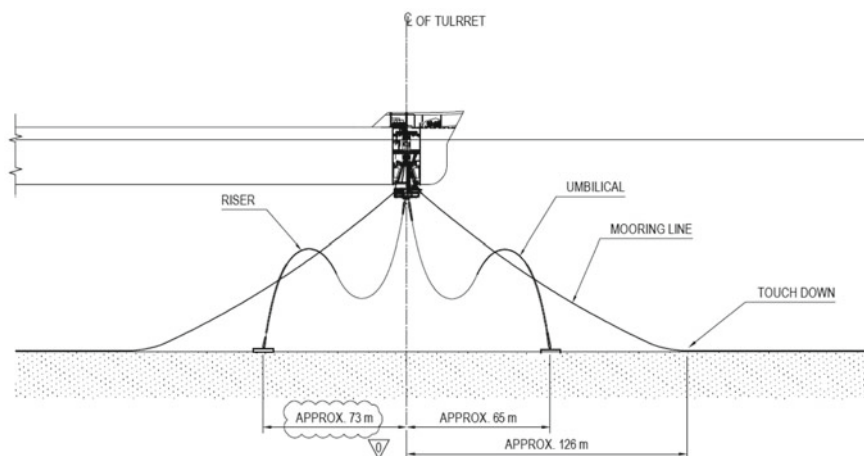


Fig. 22.5 General layout of gas field (FSRU)

(4) General layout design of mooring system

The design of the single point mooring system of this project adopts 9 catenary anchors, arranged 3×3 , three groups of three in each group, with a spacing of 120° . The upper end is connected with the STL single point buoy, and the lower end is connected with the submarine anchor pile. The size of the natural gas export submarine pipeline (steel) is 16–20 inches. The underwater PLET and the STL buoy are connected by a 14–18 inch flexible dynamic riser. The overall arrangement is shown in Fig. 22.5.

(5) Discharge method at sea

There are usually two kinds of shipping methods for unloading LNG at sea. The first is STS, Ship to Ship, which has the advantages of mature technology and low cost. The disadvantage is that the operation risk is high, and it is only suitable for the sea conditions of less than 2.5 m meaningful wave height. The second type is Tandem Loading, where the FSRU ship is connected to the LNGC ship head and tail. Its advantage is that the operation risk is lower and it can be applied to the sea conditions with 4.5 m meaningful wave height. The disadvantage is that the technology is new, there is no commercial application and the cost is high. At present, 90% of the world's LNG carriers are using the method of ship unloading, mainly for the delivery of LNG terminals. All of the FSRUs in operation are using the method of ship unloading through the LNG unloading arm or hose end to end connection.

Considering the technical maturity, mature ship to ship midship offloading is recommended for offshore offloading systems. The offloading time is usually around 16 h. The equipment selection can be flexible unloading arm connection or cryogenic hose end to end connection.

22.4.4 Upper Module Process

Two new platforms are designed for offshore gas storage, namely WHPA platform and CEP platform. WHPA platform is mainly equipped with gas injection compressor and supporting facilities, and is equipped with injection and production Wells, monitoring Wells and sewage injection Wells, etc. After the LNG gasification raw gas delivered from the FSRUs is transported to the booster platform, it can be pressurized into the formation through the gas injection compressor, or it can be directly exported. The project also considers meeting the demand for reverse gas injection into the reservoir formation from the land terminal. The booster reinjection platform has a designed injection capacity of 12 million cubic meters per day. Production well metering facilities are also located on the WHPA platform).

The CEP platform is adjacent to the WHPA platform and connected by trestle. The main facilities are oil, gas and water treatment facilities, utilities, living buildings, and rescue and escape systems.

The CEP platform and WHPA platform share the power supply system, and adopt the self-generating scheme of offshore natural gas fuel.

22.4.5 Offshore Pipeline Technology

This project needs to build three new offshore pipelines (as shown in the blue line in Fig. 22.4), single point natural gas transmission pipeline to WHPA platform, CEP platform to land terminal condensate transmission pipeline and CEP platform to land terminal natural gas transmission pipeline. The transportation scale of the single point to WHPA platform natural gas transmission pipeline is about 20 million m^3/day . In the gas injection condition, after the gasification of FSRU, natural gas is transported to WHPA platform through the sea gas transmission pipeline, and pressurized into the gas storage by natural gas compressor. In the gas production condition, the mixture of oil, gas and water produced from the wellhead of WHPA platform is transported to the condensate treatment system of CEP platform. After the condensate treatment is qualified, it is transported to the land terminal through the condensate offshore pipeline, with a transportation scale of about 1200 m^3/day . Natural gas can be transferred to the land terminal after the dewatering treatment reaches the standard of pipeline gas transmission, with a transportation scale of about 30 million m^3/day . The newly built natural gas transmission pipeline is designed to realize two-way transportation, and relevant parameters are shown in Table 22.4.

22.5 Conclusions

The following conclusions can be drawn in this paper.

Table 22.4 Marine management information sheet

No.	Pipe name	Pipe length (km)	Pipe diameter (in)	Conveying capacity	Remarks
1	FSRU single point to WHPA natural gas transmission line	2	18	2000×10^4 S m ³ /d	Newly build
2	CEP to terminal natural gas transmission pipeline	51	26	3000×10^4 S m ³ /d	Newly build
3	CEP to terminal condensate transmission pipeline	51	6	1200 m ³ /d	Newly build

- (1) The “all offshore” construction mode is a feasible design model for offshore gas storage construction, which can provide reference for other offshore gas storage project design.
- (2) For offshore gas storage which is applicable to both “onshore gas reverse transport” and “all offshore” construction mode, it is suggested to design two schemes and carry out relevant economic comparison, so as to choose the best construction design mode.
- (3) The core point of the design of the “whole sea” mode is mainly the selection of the gasification storage device. It is necessary to give priority to the selection of the gasification storage device according to the project conditions, and carry out other scheme design around the gasification storage device.

Acknowledgments Fund support: Part of the research results of China National Offshore Oil Corporation science and technology research project “Study on the scheme of underground gas storage for offshore near-exhausted gas reservoir” (NO: CNOOC-KJ135KJXMQD2020-004)

References

1. Su, Z.: Research on the development trend of global underground gas storage and Its Enlightenment to the construction of gas storage peak shaving system in China. *Q. Mark.* **07**, 143–145 (2021)
2. Zeng, D.: Sinopec’s UGS construction achievement and development prospect. *Nat. Gas. Ind.* **09**, 125–133 (2021)
3. Zhang, G., Li, B., Zheng, D., et al.: Challenges to and proposals for underground gas storage (UGS) business in China. *Nat. Gas. Ind.* **37**(1), 153–159 (2017)
4. Zhang, G.: Underground gas storage of sinopec: construction status analysis and development proposals. *Nat. Gas. Ind.* **38**(8), 112–118 (2018)
5. Zeng, D., Zhang, J., Zhang, G., et al.: Research progress of Sinopec’s key underground gas storage construction technologies. *Nat. Gas. Ind.* **40**(6), 115–123 (2020)

6. Ding, G., Wei, H.: Review on 20 years' UGS construction in China and the prospect. *Oil Gas Store. Transp.* **39**(1), 25–31 (2020)
7. Chen, Y.Y.U.Z., et al.: Experimental study on heat transfer performance of printed circuit plate heat exchanger in FSRU. *Nat. Gas. Ind.* **41**(6), 120–126 (2021)
8. Tian, B.H., Ju, Y.: Optimal synthesis of expansion liquefaction cycle for distributed-scale LNG(liquefied natural gas) plant. *Energy* (2015)
9. Ye, D., Jia, T.: Process of LNG floating storage and regasification terminal and the revelation on China LNG import. *J. Chem. Ind. Eng. (China)* **60**(S1), 22–26 (2009)
10. Zheng, D., Zhao, T., Zhang, G., Tian, J., Wei, H.: Enlightenment from European and American UGS operation management modes. *Nat. Gas Ind.* **35**(11), 97–101 (2015)
11. Xu, D., Tang, G.: Policy evolution and research progress of investment, construction and operation management of gas storage in China. *Oil Gas Stor. Transp.* **39**(5), 481–491 (2020)
12. Wei, H., Tian, J.: Research on natural gas storage and peak-shaving modes in China. *Nat. Gas. Ind.* **36**(8), 145–150 (2016)
13. Shen, X., Chen, J.: European and American NG peak-shaving system and its enlightenment. *Int. Petrol. Econ.* **25**(3), 43–52 (2017)

Chapter 23

Machine Learning-Based Models for Predicting the Depth of Concrete Penetration



Meng Li, Haijun Wu, Heng Dong, Guang Ren, Peng Zhang, and Fenglei Huang

Abstract In the domain of concrete penetration, test data are often limited in quantity and unevenly distributed, which leads to poor accuracy of the machine learning-based model for predicting the depth of concrete penetration. This paper aims to improve the accuracy of the model within the constraints of limited penetration test data. In this paper, based on collecting a large amount of penetration test data, the penetration data was extended by data augmentation methods such as linear interpolation and adding Gaussian noise. The genetic algorithm and greedy algorithm were used to optimize four common machine learning models' hyperparameters: multilayer perceptron (MLP), radial basis neural network (RBF), support vector regression (SVR), and extreme gradient boosting tree (XGBoost). The results show that using linear interpolation and adding Gaussian noise can effectively alleviate the problems of insufficient data and uneven data distribution. The average error of MLP, RBF, and XGBoost decreases by 2.7%, 3%, and 0.8%, respectively, after using data augmentation. In addition, the average error of the optimal machine learning-based method is 8.4%, and the global accuracy of this model is better than the commonly used empirical formulas. The machine learning-based model can effectively predict the depth of concrete penetration and meet engineering applications' requirements.

Keywords Depth of concrete penetration · Machine learning · Data augmentation · Neural network

M. Li · H. Wu · H. Dong (✉) · G. Ren · F. Huang
State Key Laboratory of Explosion Science and Technology, Beijing Institute of Technology,
Beijing 100081, China
e-mail: 7520210180@bit.edu.cn

P. Zhang
Institute of Hongdu Aviation Industry Group, AVIC, No.660, Nanchang 330024, China

23.1 Introduction

As a common engineering and protective material, concrete has been widely used in military and civil engineering in recent years. Predicting the concrete penetration depth is an essential task of engineering protection. However, the existing prediction methods of penetration depth are often complicated and tedious with low accuracy. The existing research methods for predicting penetration depth include theoretical analysis, experimental studies, and numerical calculations. The theoretical analysis generally requires a certain degree of simplification and more complex iterative calculations, numerical calculations are limited by computer performance and are time-consuming, and experimental studies are costly [1]. Therefore, there is a need to find a fast and accurate method to predict concrete penetration depth. Machine learning models such as neural networks with powerful automatic extraction of nonlinear relations are well suited to solve such complex nonlinear problems as concrete penetration.

In recent years, scholars have carried out a series of research works on predicting the effect of projectile penetration by applying machine learning models and have achieved certain results. Ryan et al. [2–4] used neural networks to predict the damage pattern of metal target plates. Xiong [5], Zhang [6], and Wang et al. [7] accurately calculated the destruction effect by neural networks. Hosseini et al. [8], Li et al. [8], and Zhang et al. [1] applied neural networks and support vector machines to predict the penetration depth of plain concrete accurately. All the above works have achieved good results, but the small amount and discrete nature of concrete penetration test data limit the applicability and accuracy of machine learning models [9, 10]. Therefore, some researchers have focused on improving the accuracy of machine learning models under the restrictions of limited test data. Gonzalez-Carrasco et al. [11–13] systematically compared the effects of selecting machine learning models, sampling methods of data, and hyperparameter optimization methods on the accuracy of concrete penetration models. Yang et al. [14] and Jin et al. [15] applied data mining and data fusion methods to process the penetration data, respectively, to improve the accuracy and extend the applicability of the neural networks for predicting the penetration depth of plain concrete. Thompson et al. [16] used generative adversarial neural networks to generate the penetration data and accurately predicted the damaging effect of steel plates. These studies have improved the accuracy of machine learning models for penetration problems to varying degrees. The increasing velocity of the projectile and the widespread use of high-strength concrete and steel fiber concrete in recent years have put forward new requirements for the prediction model of penetration depth. Therefore, there is still a need to investigate further the methods to improve the accuracy of machine learning models with limited test data and to obtain a realistic and credible model for predicting the depth of concrete penetration with wide application and high prediction accuracy. This study collects a large amount of concrete penetration test data. The amount of available data is improved by using data augmentation means such as linear interpolation and adding Gaussian noise. Furthermore, the changes in the accuracy of different

machine learning models before and after data augmentation are studied. A model for predicting the depth of concrete penetration is obtained that meets the engineering requirements.

23.2 Data Augmentation

23.2.1 Data Collection of Penetration Tests

In order to ensure the authenticity of the data, this paper collected 618 published test data of projectile penetration into the concrete. The impactors are ogive-nose head projectiles with normal penetration, and the concrete target slabs cover plain concrete, reinforced concrete, and steel fiber concrete. The primary references and parameter ranges are shown in Table 23.1. This information constituted the data's characteristics and was input into the subsequent model.

23.2.2 Detection and Cleaning of Abnormal Penetration Data

In the impact test, due to the difference in test conditions and measurement errors, some samples inevitably do not conform to the general rules of the data model and have significant deviations from other samples, which are called "abnormal data". The existence of these samples will reduce the speed and accuracy of neural network model training and even produce wrong results, so the samples are detected and removed before training the neural network. This paper used a deviation-based abnormality detection method to detect and remove anomalies from the penetration test data. That is, a neural network is trained with all the samples to obtain a nonlinear function model with minimum deviation from all the samples, and then the Euclidean distance from all the samples to this model is calculated. The data with a distance greater than a set threshold is considered abnormal and removed from the data set. The multilayer perceptron was trained with the collected 618 samples, and the absolute percentage error was used for abnormal data detection, as shown in Fig. 23.1. 5% of the total number of samples were marked data, i.e., abnormal data. After cleaning the abnormal data, the number of valid samples is 589.

After the above abnormal data detection and removal, the range of penetration data parameters is shown in Table 23.2.

Table 23.1 Data sources and parameter distribution of the penetration test

References	Test No.	m (kg)	d (mm)	CRH	v (m/s)	f_c (MPa)	r/ρ_v (%)
[17]	11	0.906	26.9	2	239–780	85,157	0/2–3
[18]	19	0.472	30	1	60–463	34	4.31/1.3
[19]	31	0.33–0.395	25.3	3	510–1320	35–142	0/4
[20]	14	0.341	25.3	3	503–846	103–129	0/2
[21]	16	0.33–0.35	25.3	3	491–858	67–125	0/1.5–3
[22]	11	8.4	80	0.5	64.1–89.7	44	1.43/0
[23]	13	5.9	76.2	1.5	307–828	35	0/0
[24]	17	0.9–0.91	26.9	2	277–800	32–108	0/0
[25]	15	12.9–13.2	76.2	3,6	139–456	23,39	0/0
[26]	18	0.48–1.62	20,31	3	442–1225	58.4	0/0
[27]	22	3.65–4.5	50	3–12	406–464	48–146	0/0
[28]	77	0.87–454	11–307	0.7–1.5	160–908	24–200	0/0
[29]	26	0.1	15	3	615–1325	35–117	0/0
[30]	11	0.46–6.2	10,40	3	206–657	15,17	0/0
[31]	16	0.48–1.6	13,31	3,4.25	405–1201	51,63	0/0
[32]	16	0.1–0.13	15	3	498–1373	28,35	0/0
[33]	40	0.12–7.81	15–60	4	338–709	31–71	0/0
[34]	19	0.24–1.12	27,46	5.3	148–465	24,30	0/0
[35]	10	0.168	20	2.5	479–675	31,40	0/0
[36]	12	0.29–0.32	27,30	3	885–1872	40.8	0/0
[37]	15	0.31–4.73	30–60	3	841–1872	48	0/0
[38]	10	0.168	20	2.5	465–671	35	0/0
Others	179	–	–	–	–	–	–
Total	618	0.1–454	10–307	0.5–12	45–1872	15–157	0–4.31/0–4

Note m , d , CRH , v , f_c , r , ρ_v indicate the projectile's mass, diameter, caliber-radius-head, impact velocity, compressive strength of concrete, the ratio of the volume of reinforcement, the ratio of the volume of steel fibers

23.2.3 Linear Interpolation

Research has shown that acquiring large amounts of data is the key to improving the performance of neural networks. However, due to the high cost of penetration tests, collecting a sufficient amount of test data is impossible. Existing studies have shown that the lack of training data can be significantly alleviated by processing existing samples using data augmentation methods [39].

Linear interpolation is a typical means of data augmentation. The penetration depth is approximately proportional to the projectile's velocity in a specific range when other parameters are constant [40]. Therefore, it was chosen to generate new penetration data based on the penetration results at different velocities for the same

Fig. 23.1 Serial numbers of available data and abnormal data

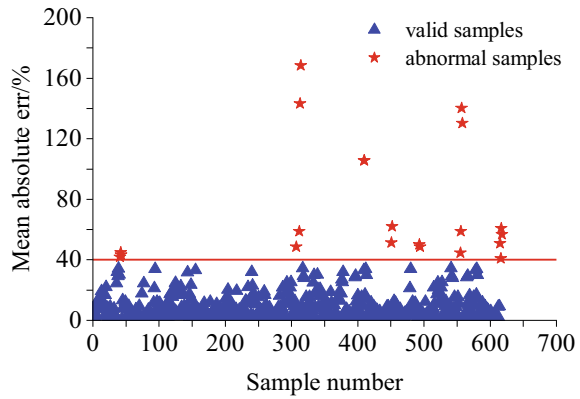


Table 23.2 Parameter distribution of penetration test data

m (kg)	d (mm)	CRH	v (m/s)	f_c (MPa)	r (%)	ρ_v (%)
0.1–89.9	10–155	0.5–12	45–1280	14.6–120	0–4.31	0–4

projectile target conditions. Due to the uneven distribution of the test data samples and the small amount of data for projectiles above 1 kg, data augmentation was performed mainly in this data distribution interval. This paper uses the continuous uniform interpolation method to calculate the mean values of velocity and penetration depth at two adjacent points. The obtained results are used as new data for data filling to realize the expansion of the penetration data. For example, the 13 5.9 kg projectile penetration test data in the literature [23] were extended by 12, and the measured data were compared with the extended data generated by interpolation, as shown in Fig. 23.2.

Figure 23.2 shows no significant difference between the extended and measured data, and the trend of penetration depth with velocity is the same. The data distribution

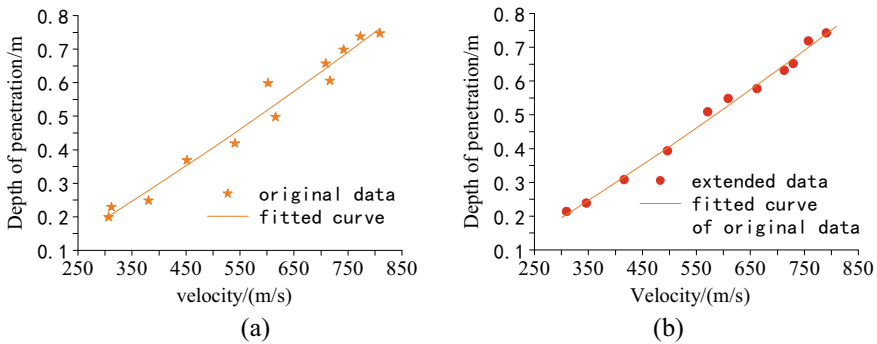


Fig. 23.2 Original data and linear interpolation extended data. **a** Original data. **b** Extended data

Table 23.3 Comparison of sample distribution before and after data augmentation

	m/kg	Test No.	m/kg	Test No.	m/kg	Test No.
Before interpolation	0.1–1	337	1–10	180	10–100	72
After interpolation	0.1–1	337	1–10	281	10–100	102

of each quality interval before and after linear interpolation is shown in Table 23.3. Table 23.3 shows that selective linear interpolation alleviates the problem of uneven data distribution, and the sample is extended while increasing the data diversity.

23.2.4 Adding Noise

Adding random noise to the samples is also a typical means of data augmentation and facilitates model regularization, improves the model's generalization ability, and enhances the robustness of the model [13, 39]. In the case of this paper, Gaussian noise with distribution $N = N(0, 0.012)$ was added to the training sample to generate new data, and the new data was merged with the original data. For example, Gaussian noise with a standard deviation of 0.012 was added to the penetration data of the 5.45 kg projectile in the literature [30]. Figure 23.3 shows the mapping relationship between the dimensionless penetration depth and the Teland dimensionless velocity. The Teland dimensionless velocity characterizes the impact momentum of the projectile on the concrete target. Its expression is given in Eq. (23.1), where N is the coefficient related to the shape of the projectile, v refers to the velocity, m refers to the mass of the projectile, d refers to the diameter of the projectile, and f_c refers to the compressive strength of the concrete. Figure 23.3 shows that the extended data differ slightly from the measured data. However, the trends of the dimensionless penetration depth and dimensionless velocity are still the same, and the extended data are still roughly distributed along the fitted curve of the measured data.

$$\bar{V} = Nv(m/d^3 f_c)^{0.5} \quad (23.1)$$

The 589 penetration test data were extended to 720 by linear interpolation. 70% of the data were randomly selected as the training set, totaling 505, and the remaining 30% as the test set, totaling 215. Gaussian noise was added to the training set to generate the extended data and merged with the original training set data to form a new training set, totaling 1008 data. No noise was added to the test set, totaling 215 data. The training set was applied to train the machine learning model, and the test set was not involved in training but was applied to evaluate the completed machine learning model after training.

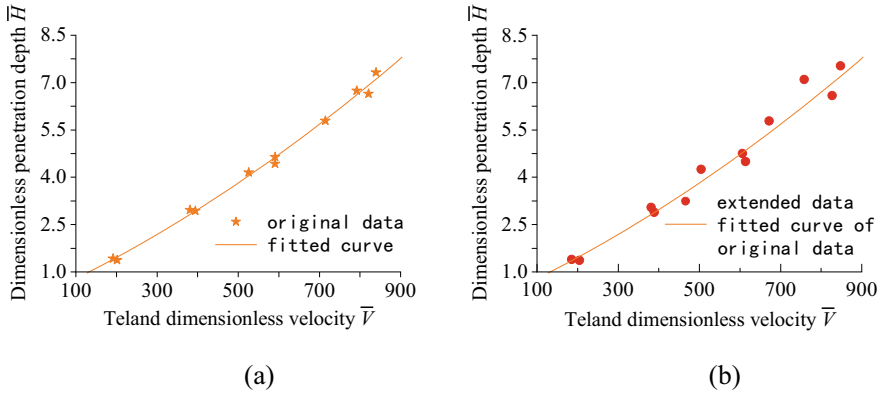


Fig. 23.3 Original data and extended data obtained by adding noise. **a** Original data. **b** Extended data

23.3 Machine Learning Model Selection and Hyperparameter Optimization Methods

23.3.1 Selection of Machine Learning Models

In this paper, four commonly used machine learning models, multilayer perceptron (MLP), radial basis neural network (RBF), support vector regression (SVR), and extreme gradient boosting tree (XGBoost), were selected for predicting concrete penetration depth. MLP is one of the most widely used neural network models consisting of input, output, and hidden layers. During training, the MLP adjusts the connection weights between neurons in each layer by the backpropagation algorithm to achieve a fit to a regression or classification model. This study selected a multilayer perceptron with two hidden layers. Its key parameters include the number of neurons n_1 and n_2 in the hidden layer and the learning rate l_r . RBF neural network is an efficient feed-forward neural network that achieves fitting to the input and output by adjusting the center and width of the Gaussian function. The key parameters include the number of radial basis neurons n and the learning rate l_r . The SVR model is generated by applying support vector machines to regression problems. Its key parameters include the kernel function, the relaxation variable ξ , and the regularization parameter C . XGBoost can be understood as combining multiple regression trees and fitting the residuals generated in the previous time by continuously adding new trees to reduce the error. Its key parameters include the number of regression trees n , the maximum depth d , and the learning rate l_r . These key parameters, called hyperparameters, need to be artificially given prior to training and significantly impact the model's accuracy.

23.3.2 Hyperparametric Optimization Methods

Different values of hyperparameters have a large impact on the model performance. Usually, it is necessary to continuously debug and optimize the hyperparameters to determine a set of optimal values to improve the learning ability and efficiency of the models [39]. Considering the training time and computational cost of each machine learning model, this paper applied the greedy algorithm to optimize the hyperparameters of MLP and SVR and applied the genetic algorithm to optimize the hyperparameters of XGBoost and SVR.

The greedy algorithm divides the whole problem into a series of subproblems. At each step, the algorithm chooses the optimal solution, and the final solution obtained is considered to apply to the whole problem. Taking the optimization of the hyperparameters of the MLP as an example, the number of neurons in the hidden layer of the first layer is n_1 , the number of neurons in the second layer is n_2 , the learning rate is l_r , and the error of the model is $E(n_1, n_2, l_r)$. Then the optimization process of the greedy algorithm can be described in Fig. 23.4. When the computation is finished, the algorithm exchanges the hyperparameters' order and computes again, and saves the one with the minor error.

The genetic algorithm [41] is an evolutionary algorithm based on natural selection and natural genetics mechanisms. This paper uses hyperparameters as chromosomes and uses the model's accuracy as the optimization goal. At each iteration, genetic operations are performed to obtain a set of better-performing chromosomes, such as selection, crossover, and mutation. Repeat the above operations until the maximum number of genetic generations, i.e., the optimized hyperparameters, are obtained. The whole optimization process is shown in Fig. 23.5.

The hyperparameters of each model were obtained after optimization, as shown in Table 23.4 These hyperparameters will be used in the subsequent calculations and analysis.

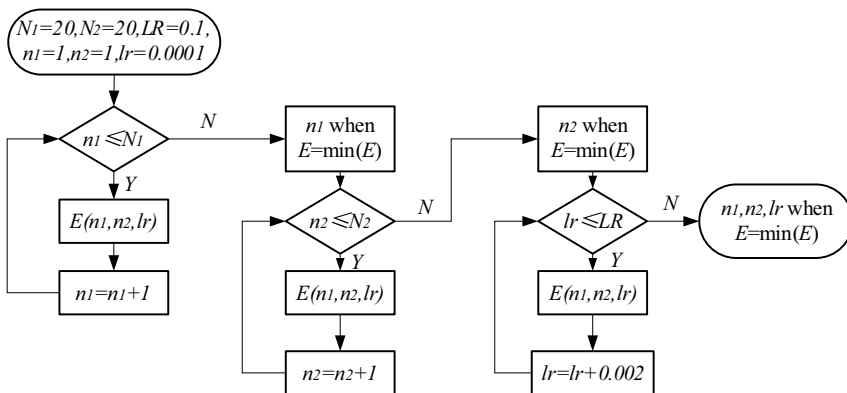


Fig. 23.4 Diagram of the greedy algorithm

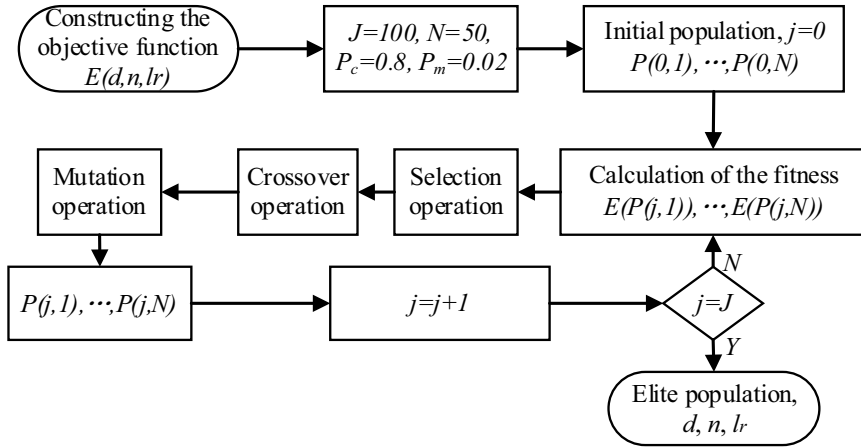


Fig. 23.5 Diagram of the genetic algorithm

Table 23.4 Each model’s hyperparameters

Model	Hyperparameter	Value	Hyperparameter	Value	Hyperparameter	Value
MLP	n_l	17	n_2	15	l_r	0.002
XGBoost	d	5	n	100	l_r	0.09
RBF	n	30	l_r	0.015	/	/
SVR	C	20	ξ	0.0005	Kernel	‘rbf’

23.3.3 Loss Function Selection

The loss function reflects the difference between the model and the actual data and guides the optimization of the model parameters during the training phase. The loss functions commonly used in regression problems include mean square error (MSE) and mean absolute percentage error (MAPE). Let the predicted value be $\tilde{y} = \{\tilde{y}_1, \tilde{y}_2, \dots, \tilde{y}_n\}$, and the true value be $y = \{y_1, y_2, \dots, y_n\}$, then MSE and MAPE can be expressed as

$$MSE = \frac{1}{n} \sum_{i=1}^n (\hat{y}_i - y_i)^2 \tag{23.2}$$

$$MAPE = \frac{100\%}{n} \sum_{i=1}^n \left| \frac{\hat{y}_i - y_i}{y_i} \right| \tag{23.3}$$

This paper chose MSE and MAPE as the loss functions of the multilayer perceptron and the radial basis neural network, respectively, and compared the accuracy of the models when different loss functions were used.

23.4 Prediction Results and Analysis of Machine Learning Models

The collection, detection, cleaning, and augmentation of the penetration data were completed in the above sections. The hyperparameters of each machine learning-based model were also optimized. The obtained data were used to establish the machine learning-based model for predicting concrete penetration depth, and the whole process is shown in Fig. 23.6.

For example, this paper used the original training set without data augmentation to training the MLP. The changes in the training error and test error of the MLP during the training process are shown in Fig. 23.7. After 2000 training epochs, the training error of MLP stabilizes at 6.5%, and the testing error stabilizes at 11.1%.

This paper applied the same method to train each machine learning-based model and compared the differences in its results. The training set consists of the original data and the data after data augmentation. The machine learning-based models for predicting the depth of concrete penetration were realized. And the errors of each machine learning model and empirical formula were calculated using the test set, and Table 23.5 shows the calculation results. In order to reduce the randomness,

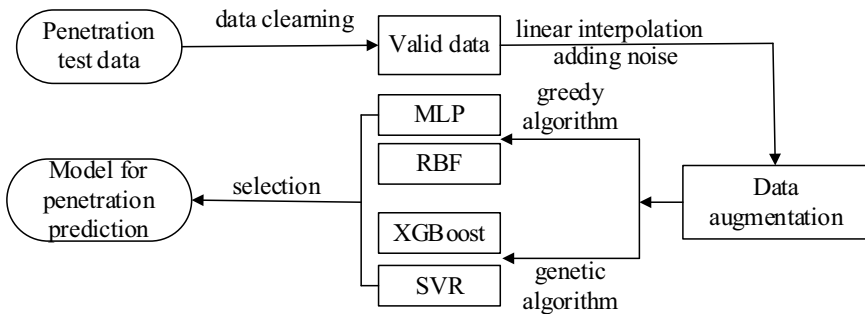
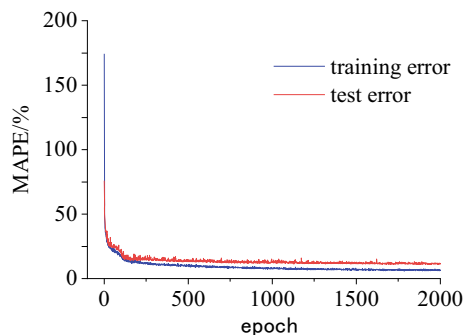


Fig. 23.6 Flowchart of this paper

Fig. 23.7 Training process of MLP



this paper trained each model 11 times and took the median error as the calculation result. The error refers to the average absolute percentage error, and its expression is Eq. 23.2.

As shown in Table 23.5, it can be seen that the accuracy of all four penetration depth prediction models is improved to different degrees after using data augmentation. MLP’s error decreases by about 2.7%, with a minimum error of 8.4%, RBF’s error decreases by about 3%, with a minimum error of 10.4%, SVR’s error decreases by about 0.8%, with a minimum error of 10.1%, and XGBoost’s error decreases by about 0.8%, with a minimum error of 11.5%. The result indicates that data augmentation effectively alleviates the problem of insufficient penetration test data and low accuracy of the penetration depth prediction machine learning-based models.

Comparing the models’ errors when different loss functions are used in Table 23.5, it can be seen that the errors of the models all decrease to different degrees when using MAPE as the loss function. The error of MLP decreases by about 2.8% in the original data set and by about 4.9% after data enhancement. The error of RBF decreases by about 1.4% in the original data set and by about 3% after data enhancement. It is because the penetration test data are discrete and abnormal data still exist, while MAPE is insensitive to abnormal data when used as a loss function.

The errors of the empirical formulas in Table 23.5 are greater than 20%. It is because the range of test data is wide, some of the test speed is high, and the mass is small, which is beyond the applicability of the empirical formula. This leads to a significant global error in the empirical formula.

The error distribution of each machine learning-based model for predicting the depth of concrete penetration and Young’s formula are plotted, as shown in Fig. 23.8. Analysis of Fig. 23.8 shows that among all models, the error of MLP is more concentrated at 0%, and the majority of errors are less than 50%, which is the best performance among all models.

In addition, histograms of the error distributions of MLP, RBF, XGBoost, and SVR are plotted, as shown in Fig. 23.9. Analysis of Fig. 23.9 shows that MLP has

Table 23.5 The relative error of each depth before and after data enhancement

Test error	Young	ACE	MLP + MSE	MLP + MAPE	RBF + MSE	RBF + MAPE	SVR	XGBoost
Original data/%	21.4	22.5	13.9	11.1	14.0	13.4	10.9	12.1
After data augmentation/%	22.3	23.1	13.3	8.4	12.6	10.4	10.1	11.5

Note MLP + MSE refers to the MLP model using MSE as the loss function
 MLP + MAPE refers to the MLP model using MAPE as the loss function

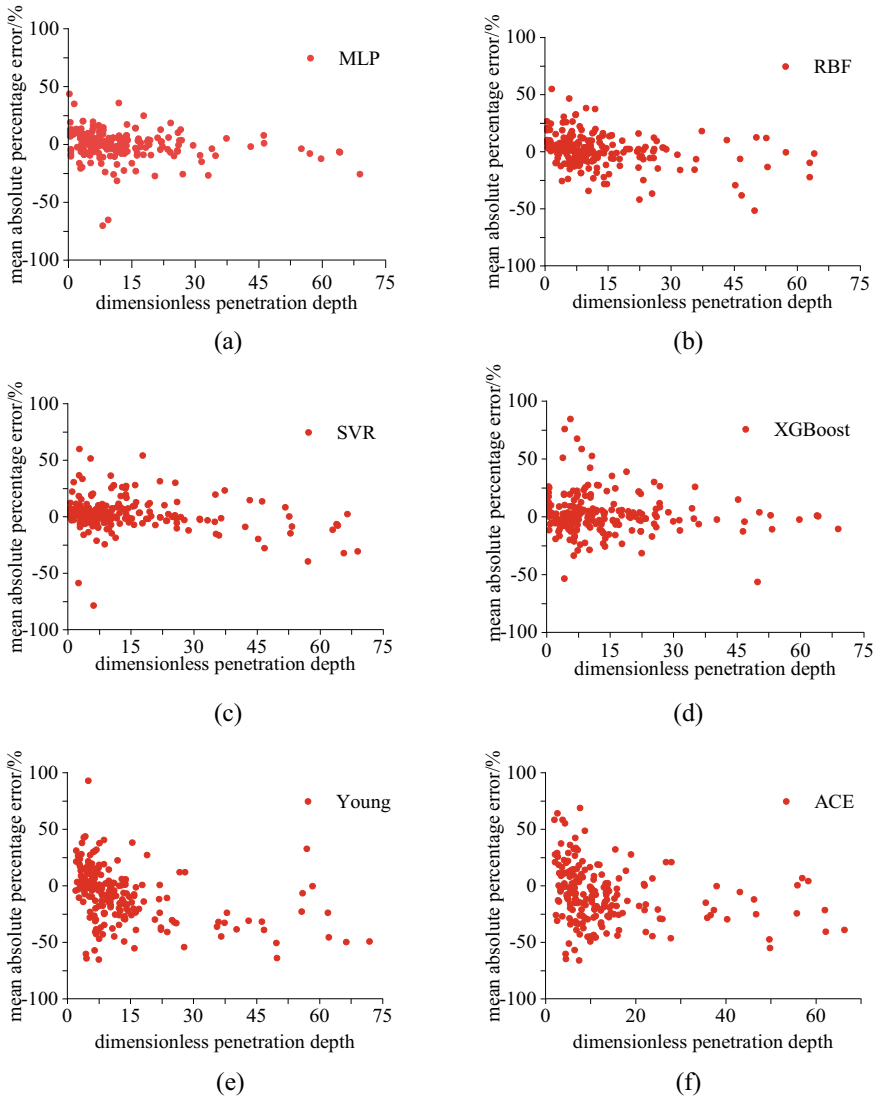


Fig. 23.8 Error distribution for each model. **a** Multilayer perceptron (MLP). **b** Radial basis neural network (RBF). **c** Support vector regression (SVR). **d** Extreme gradient boosting tree (XGBoost). **e** Young formula. **f** ACE formula

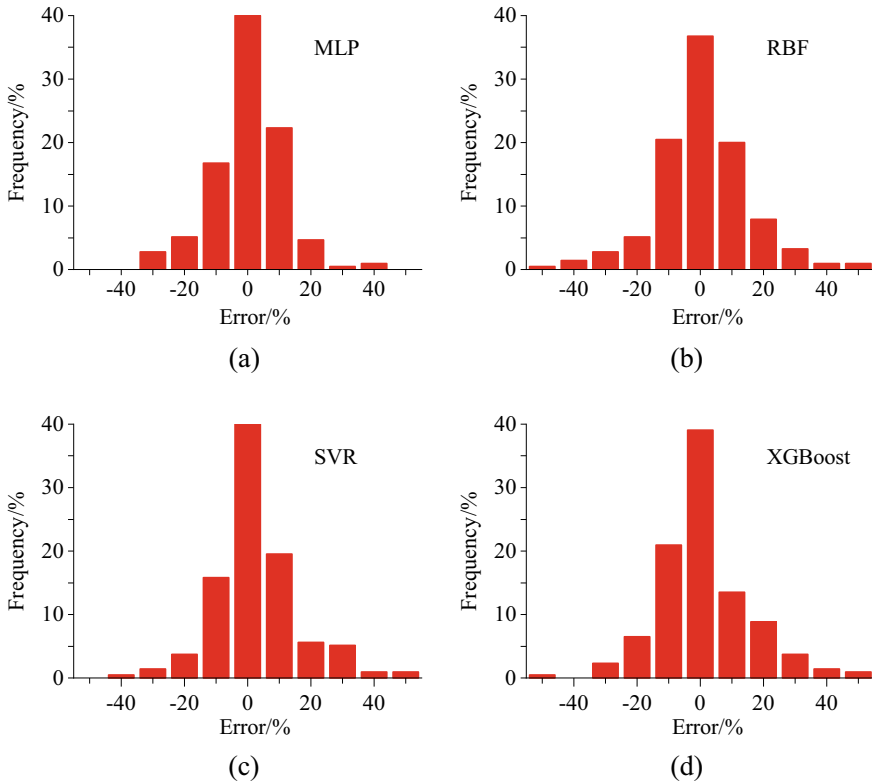


Fig. 23.9 Histogram of error distribution. **a** Multilayer perceptron (MLP). **b** Radial basis neural network (RBF). **c** Support vector regression (SVR). **d** Extreme gradient boosting tree (XGBoost)

the most concentrated error, with a minor error greater than 40% among all models. Therefore, its average error is the smallest.

23.5 Conclusion

This paper collects a large amount of publicly published, authentic, and credible experimental data and cleans the abnormal data using a bias-based detection method. Data augmentation methods such as linear interpolation and adding Gaussian noise are applied to extend the penetration data and increase the number of data while alleviating the uneven distribution. The greedy and genetic algorithms optimize the hyperparameters of four machine learning models, and the machine learning-based models are used to predict the penetration depth. This paper investigates the changes

in the accuracy of each machine learning model before and after using data augmentation and the accuracy of machine learning models when different loss functions are used. The following conclusions are obtained from this paper:

- (1) MLP, XGBoost, RBF, and SVR's accuracy is improved by 0.8–3% by extending penetration data through data augmentation methods such as linear interpolation and adding Gaussian noise. It indicates that data augmentation effectively alleviates the lack of penetration test data and improves the accuracy of the machine learning-based model for predicting concrete penetration.
- (2) For the data collected in this paper, the use of different loss functions has an impact on the results of the models for predicting the depth of penetration. When MLP and RBF are employed to predict the penetration depth, the accuracies of the models are about 1.4–4.9% higher when MAPE rather than MSE is used as the loss function.
- (3) The average error of the best model for predicting the penetration depth is 8.4%. The global accuracy of the model is better than the common-used empirical formulas for predicting penetration depth, which can meet the needs of engineering applications.

Acknowledgements This work was supported by the National Natural Science Foundation of China (Grant number 12202067) and the State Key Laboratory of Explosion Science and Technology (Grant number QNKT22-03).

Conflicts of Interest

The authors declare that they have no conflicts of interest to report regarding the present study.

References

1. Zhang, S.X., Zhao, H.D., Han, Z.G.: Method of penetrate result prediction based on PSO-SVM. *J. North Univer. China (Nat. Sci. Ed.)* **36**(2), 6 (2015)
2. Ryan, S., Thaler, S.: Artificial neural networks for characterising Whipple shield performance. *Int. J. Impact Eng.* **56**, 61–70 (2013)
3. Ryan, S., Kandanaarachchi, S., Smith, M.K.: Support vector machines for characterising Whipple shield performance. *Proc. Eng.* **103**, 522–529 (2015)
4. Ryan, S., Thaler, S., Kandanaarachchi, S.: Machine learning methods for predicting the outcome of hypervelocity impact events. *Exp. Syst. Appl.* **45**, 23–39 (2016)
5. Xiong, P.Q.: Research on space debris damage pattern recognition based on neural network technology (Master's Thesis). Harbin Institute of Technology, China (2012)
6. Zhang, S.: Numerical simulation analysis of projectile penetration into reinforced concrete multilayer target slab (Master's Thesis). Nanjing University of Science & Technology, China (2017)
7. Wang, S., Shi, Q.: Penetration pattern recognition based on artificial neural network. *J. Ordnance Equip. Eng.* **10**, 60–64 (2017)
8. Li, J.G., Li, Y.C., Wang, Y.L.: Penetration depth of projectiles into concrete using artificial neural network. *Strat. Study Chin. Acad. Eng.* **9**(8), 77–81 (2007)

9. Kiliç, N., Ekici, B., Hartomacıoğlu, S.: Determination of penetration depth at high velocity impact using finite element method and artificial neural network tools. *Defence Technol.* **11**(2), 110–122 (2015)
10. Auten, S., Hammell, R.: Comparing the prediction capabilities of an artificial neural network vs a phenomenological model for predicting the terminal ballistics of kinetic energy projectiles. In: *Proceedings of the Conference on Information Systems Applied Research* ISSN. 2167:1508 (2015)
11. Gonzalez-Carrasco, I., Garcia-Crespo, A., Ruiz-Mezcua, B., et al.: Dealing with limited data in ballistic impact scenarios: an empirical comparison of different neural network approaches. *Appl. Intell.* **35**(1), 89–109 (2011)
12. Gonzalez-Carrasco, I., Garcia-Crespo, A., Ruiz-Mezcua, B., et al.: A neural network-based methodology for the recreation of high-speed impacts on metal armours. *Neural Comput. Appl.* **21**(1), 91–107 (2012)
13. Gonzalez-Carrasco, I., Garcia-Crespo, A., Ruiz-Mezcua, B., et al.: An optimization methodology for machine learning strategies and regression problems in ballistic impact scenarios. *Appl. Intell.* **36**(2), 424–441 (2012)
14. Yang, J., Zhang, L., Wang, J., M., et al.: Prediction of concrete penetration depth based on data fusion. *Ordnance Mater. Sci. Eng.* **04** (2020)
15. Jin, S., Liu, J., Zhang, L., et al.: The application of data mining technology in the analysis of the projectile penetration depth in concrete. *J. PLA Univer. Sci. Technol. (Nat. Sci. Ed.)*. **06** (2017)
16. Thompson, S., Teixeira-Dias, F., Paulino, M., et al.: Ballistic response of armour plates using generative adversarial networks. *Defence Technol.* **18**(9), 1513–1522 (2022)
17. Cargile, J., O'Neil, E., Neeley, B.: Very-high-strength concretes resistant for use in blast- and penetration-resistant structures. *AMPTIAC Q.* **6**(4), 61–66 (2002)
18. Goel, R., Chandra, S., Chandola, U., et al.: *Behaviour of Concrete Under High Velocity Impact*. Defence Research and Development Organization New Delhi (India) (1990)
19. Wu, H., Fang, Q., Chen, X.W., et al.: Projectile penetration of ultra-high performance cement based composites at 510–1320 m/s. *Constr. Build. Mater.* **74**, 188–200 (2015)
20. Wu, H., Fang, Q., Gong, J., et al.: Projectile impact resistance of corundum aggregated UHP-SFRC. *Int. J. Impact Eng.* **84**, 38–53 (2015)
21. Wu, H., Fang, Z., Gong, Z.: Experiments and theoretical analyses on HSFRC target under the impact of rigid projectile. *J. Ballistics* **24**(03), 19–24+53 (2012)
22. Kataoka, S., Beppu, M., Ichino, H., et al.: Failure behavior of reinforced concrete slabs subjected to moderate-velocity impact by a steel projectile. *Int. J. Protect. Struct.* **8**(3), 384–406 (2017)
23. Canfield, J., Clator, I.: *Development of a scaling law and techniques to investigate penetration in concrete*. United States Naval Weapons Laboratory (1966)
24. Forrestal, M.J., Altman, B., Cargile, T., et al.: An empirical equation for penetration depth of ogive-nose projectiles into concrete targets. *Int. J. Impact Eng.* **15**(4), 395–405 (1994)
25. Forrestal, M.J., Frew, D., Hickerson, J., Rohwer, T.: Penetration of concrete targets with deceleration-time measurements. *Int. J. Impact Eng.* (2003)
26. Frew, D.J., Hanchak, S.J., Green, M.L., Forrestal, M.J.: Penetration of concrete targets with ogive-nose steel rods. *Int. J. Impact Eng.* (1998)
27. Hansson, H.: *Penetration in Concrete for Projectiles with L/D=9*. FOI-R-1659-SE (2005)
28. Sjø, H., Teland, J.A., Kaldheim, Ø.: Penetration into concrete-analysis of small scale experiments with 12 mm projectiles. *FFI/RAPPORT-2002/04867* (2002)
29. Zhang, X.Y.: *Research on constitutive model and anti-penetration mechanism of high-strength concrete* (Ph.D. Thesis). Beijing Institute of Technology, China (2021)
30. Xv, J.B.: *Investigations on Long Projectiles Penetrating into concrete Targets* (Ph.D. Thesis). National University to Defense Technology, China.
31. Xv, J.B., Lin, J.D., Tang, R.L., Chu, Z.: Experimental study on penetration of long rod projectile into concrete. *Explos. Shock Waves* **02**, 174–178 (2002)
32. Wu, H.J., Zhang, X.Y., Zhang, S., Huang, F.L.: Prediction of trajectory of rigid projectile penetrating/perforating a finite-thick reinforced concrete target. *Acta Armamentarii* **41**(S2), 12–25 (2020)

33. Wu, C.: Research on anti-penetration performance of concrete target at mesoscale (Ph.D. Thesis). Nanjing University of Science & Technology, China (2020)
34. Shen, Z.W., Sun, Y.X., Li, Y.C., Li, X.J.: Experimental study on concrete target plate penetration of airport runway. *J. Exp. Mech.* **03**, 264–269 (2001)
35. Lu, H., Yue, S., Sun, S., Song, C., Xiong, Z.: Model test study on damage depth of concrete target under penetration and explosion. *Explos. Shock Waves* **41**(07), 80–87 (2021)
36. Song, M., Li, W., Wang, X., Feng, J., Liu, Z.: Experimental and dimensional analysis of high speed penetration efficiency of projectile body. *Explos. Shock Waves* **36**(06), 752–758 (2016)
37. Feng, J., Song, M., Sun, W., et al.: Thick plain concrete targets subjected to high speed penetration of 30CrMnSiNi2A steel projectiles: tests and analyses. *Int. J. Impact Eng.* **122**, 305–317 (2018)
38. Geng, H., Lu, H., Sun, S., et al.: Experimental study and damage effect analysis of concrete structures under the combined loadings of penetration and explosion. *Shock Vib.* (2020)
39. Fang, A., Li, R.: Penetration fuze accurate layer recognition neural network data enhancement method. *J. Detection Control* 044–001 (2022)
40. Zhao, H.Y., Wu, H.J., Dong, H., et al.: Experimental study on anti-penetration performance of concrete-filled steel tubular with honeycomb structure. *Explos. Shock Waves* 1–13 (2022)
41. Lei, Y.J., Zhang, S.W.: MATLAB genetic algorithm toolbox and its application. Xi'an Electronic Technology Publishing House, China (2014)

Chapter 24

Model Test Research on Pressure Wave in the Subway Tunnel



Xu Zhang, Honglin Wang, Haiquan Bi, Yuanlong Zhou, Nanyang Yu, and Yi Fang

Abstract As the subway lines are rapidly developing in the cities, the pressure wave in different subway tunnel constructs is urgently needed to be studied and receded. In this study, a subway tunnel pressure wave experimental system was designed, constructed, and tested. The influence of train model head shape, train model speed, shaft number in the tunnel, and bypass number in the tunnel on the pressure wave amplitude were experimented with and analyzed. The results show that the train model head shapes significantly impact the amplitude of the initial compression wave in the tunnel. The blunter train model head generates a greater amplitude of the initial compression wave. When the train passes through a single-track tunnel, the maximum positive pressure amplitude of the pressure wave in the tunnel is at the first compression wave at the tunnel entrance. The maximum negative pressure value in the tunnel is at the superposition of the initial compression wave reflected from the first time and the train's body, which is related to the length of the train's body, tunnel length, train's speed, and sound speed. The shaft set in the tunnel decreases the amplitude of the initial compression wave in the tunnel space behind, but it will increase the pressure wave's amplitude reflected in the tunnel when the train passes through the shaft. After the bypass tunnel is added, the initial compression wave propagation in the tunnel behind the bypass tunnel is receded. It also increases the negative pressure amplitude when the train passes.

Keywords Subway tunnel · Pressure wave · Model test · Intermediate air shaft · Bypass tunnel

Abbreviation

φ Diameter of traction rope and guide rope (mm)
 M Mach number

X. Zhang · H. Wang (✉) · H. Bi · Y. Zhou · N. Yu · Y. Fang
School of Mechanical Engineering, Southwest Jiaotong University, Chengdu 610031, China
e-mail: honglinwang305@hotmail.com

Re	Reynolds number
ρ	Density of the air when the actual train is running
V	Actual train velocity (km/h)
L	Size of the actual train
μ	Dynamic viscosity coefficient of the air when the actual train is running
S_1	Area of section 1 (m^2)
$P_{P,1}$	Positive pressure peak of section 1 (Pa)
$P_{N,5}$	Negative pressure peak of section 5 (Pa)
S	The distance between the first and the second photoelectric switch (m)
t	Time recorded by timer (s)
v_1	Velocity of train model to enter the tunnel (m/s)
ρ'	Density of the air when the train model is running
V'	Train model velocity (km/h)
L'	Size of the train model
μ'	Dynamic viscosity coefficient of the air when the train model is running
S_2	Windward area of train model (m^2)
$P_{P,5}$	Positive pressure peak of section 5 (Pa)
$P_{N,1}$	Negative pressure peak of section 1 (Pa)

24.1 Introduction

With the rapid development of the modern city scale, the number of urban populations is increasing, and the ground traffic is becoming more and more congested. To alleviate the urban traffic congestion, cities across the country are actively planning and building a more scientific and perfect traffic network system, among which, subway, one of the effective tools to relieve urban traffic congestion, has developed rapidly in recent years. By the end of 2021, 40 cities in China have opened 250 operating lines, with a total length of 8116 km. The design of subway lines requires longer and more numerous tunnel sections, where different tunnel structures complicate aerodynamic problem.

When the train enters the tunnel, the internal air will be strongly squeezed by the train due to the closed space of the subway tunnel, and the gas at the tunnel entrance will be compressed, which leads to rapidly rising pressure, forming a pressure pulse [1, 2]. As is shown in Fig. 24.1, the phenomenon when the pressure pulse travels along the tunnel at speed close to that of sound is called compression wave [3]. When the compression wave reaches the entrance of the tunnel, part of it propagates to the outside of the tunnel, forming a so-called micro-pressure wave [4, 5]; the other part is reflected back and propagates in the opposite direction, called expansion wave, which reflects again when it encounters the front of the car [6]. This process is repeated, and a tunnel pressure wave is formed in the tunnel [7]. The generation of pressure waves will greatly affect passengers' safety and comfort, as well as the normal operation of auxiliary equipment in the station [8].

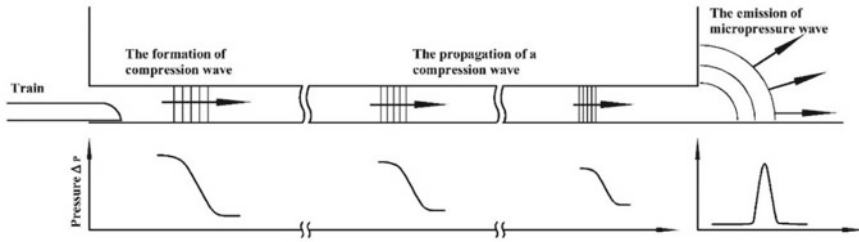


Fig. 24.1 Schematic diagram of pressure wave caused by train passing through tunnel

The pressure wave generated by train operation is affected by many factors [9–12]. Among them, the shape of the front of the subway train greatly influences the amplitude of the pressure wave in the tunnel [13, 14]. The train's running resistance with a blunt head is the largest, and the longer the shape of the head is, the smaller the resistance will be, but the slowing effect is gradually decreasing [15, 16]. The peak value and gradient of the initial compression wave generated by the common China Railway High-speed (CRH) 3 and CRH380A trains in China are also different at the same speed, the change of which in the CRH3 train is more severe than that of the CRH380A train [17]. Also, the velocity of the train has a great influence on the pressure wave. At present, most of the subway lines in China operate at 80 km/h. In recent years, 100 km/h and more than 100 km/h subway lines have been gradually put into operation, and many high-speed subways are under construction. After the subway speed reaches above 100 km/h, many aerodynamic problems, especially the tunnel pressure wave [18, 19] at the low speed of the subway, will be aggravated [20–22].

To prevent two trains from running in the tunnel at the same time, it is necessary to set up an intermediate air shaft in the interval tunnel when it is long [23]. Its function is to ensure that only one train runs in a ventilation section, avoiding multiple trains running when the breakdown of a certain vehicle or a fire may affect other vehicles [24]. Changing the basal area and position of the shaft set in the tunnel can effectively reduce the maximum pressure wave amplitude and gradient. The pressure wave amplitude will decrease as the basal area of the tunnel increases [25]. The optimal shaft position in the tunnel can make itself have the best decompression effect [26]. In addition, the height of the shaft also has a certain effect on the reduction of the pressure wave amplitude in the tunnel, which will decrease as the height of the shaft decreases [27].

The increase in the number of tunnels also has a great influence on the pressure wave in the subway tunnel [28, 29]. For safety reasons, two tunnels connected with pressure relief pipes near the tunnel should be the first choice. When the train runs in a tunnel, the bypass tunnel can play a certain role of ventilation [30] and serve as a rescue channel in an emergency [31]. Therefore, it is necessary to study the effect of increasing bypass tunnels on pressure waves in the tunnel.

In this study, the model test analyzes the influence of locomotive shape and running speed on the pressure wave. The influence of the number of shafts in the tunnel and

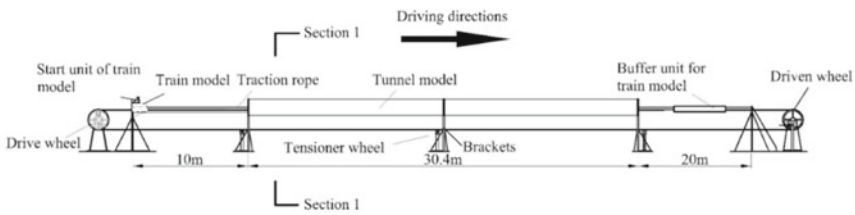
the bypass tunnel is also studied. Section 24.2 of this paper introduces the working principle of the test system in detail. Section 24.3 analyzes the errors in the model test. Section 24.4 analyzes the influence of various factors on the tunnel pressure wave. Section 24.5 draws the conclusion of this paper.

24.2 Model Test

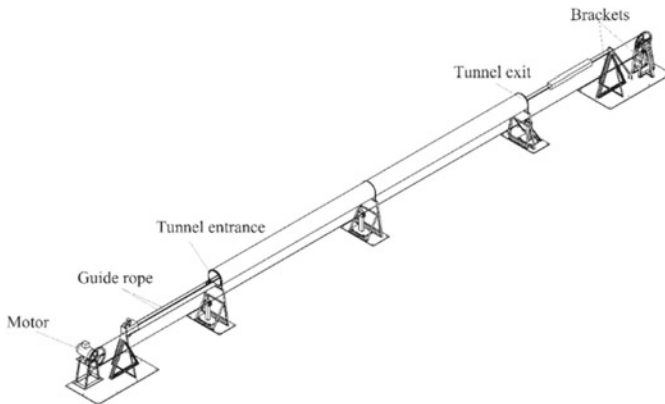
24.2.1 The Bench of Model Test

Overview of the model test stand. Figure 24.2a shows the main view of the schematic diagram of the pressure wave model test bench of this subway tunnel. The length of the tunnel model is 30.4 m. The train model is 10 m from the tunnel entrance, and the deceleration section at the tunnel exit is 20 m long.

The three-dimensional view of the model test bench is shown in Fig. 24.2b. The model test bench mainly includes the drive wheel, tunnel model, driven wheel, two



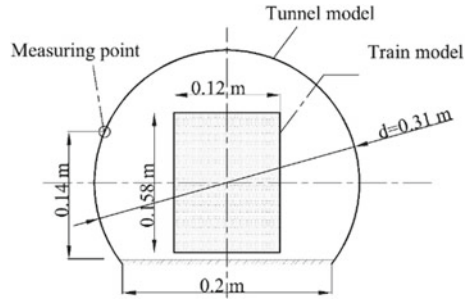
(a) Main view



(b) Three-dimensional view

Fig. 24.2 Schematic diagram of the model test bench

Fig. 24.3 The longitudinal section 1 of the tunnel when train model enters the tunnel



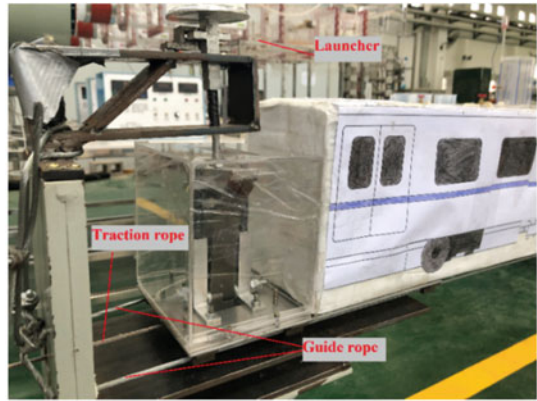
3 mm guide ropes, one 3 mm traction rope which tows train model, brackets, and train model. The drive wheel is directly fixed on the output shaft of the variable frequency motor. The tunnel model is replaced with PVC pipes, and the mechanical fixing device of the tunnel is designed with the matching fixed clamp to fasten the pipe. Two $\phi 3$ smooth wire ropes are fixed on the brackets at both ends at the same height and pass through the train model's body, which is used as the positioning track to determine the driving route of the train model. Traction rope uses $\phi 3$ wire rope passing through drive wheel, driven wheel and tensioner wheel. The height of the tensioner wheel can be adjusted to achieve the tension of the traction rope. The train is connected to the traction rope, and the motor drives the drive wheel to rotate so as to drive the traction rope and train model.

The longitudinal section 1 of the tunnel when train model enters the tunnel is shown in Fig. 24.3. The diameter of the tunnel's circular part is 0.31 m, the cross-sectional area of which is 0.0704714 m^2 , and the width of the bottom is 0.2 m. The length of the model car is 1.4 m, the cross-sectional area of which is 0.01896 m^2 . The train/tunnel area ratio is 0.269. The measuring points are arranged on the inner side of the pipeline with a horizontal distance of 0.14 m from the bottom.

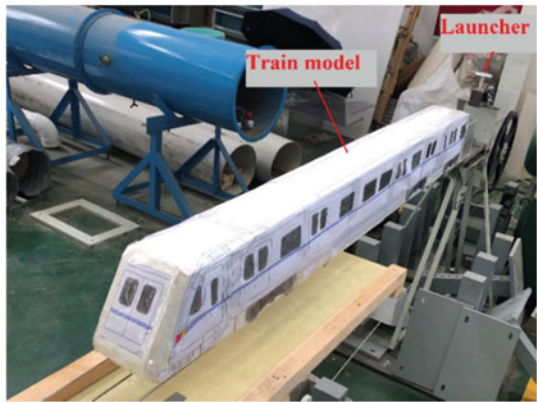
Train operation system and its working principle. As is shown in Fig. 24.4, the train operation system includes the launcher for train model, train model, motor, drive wheel, driven wheel, traction rope, guide rope, tensioner wheel and other equipment.

The working principle of the model test stand is as follows. Firstly, set the test speed in the PLC control system before the test, then press the launcher to separate the traction rope from the train model. Thirdly, control the motor to start working to drive the traction rope to accelerate it to the required traction speed. At this point, the release launcher connects the traction rope with the train model, driving the train model to run into the tunnel at speed required by the test in a short time. The two sensors at the entrance of the tunnel, which is shown in Fig. 24.5, detect the speed at which the model car enters the tunnel, and the sensor at the exit of the tunnel, which is shown in Fig. 24.6, monitors the speed at which the model car leaves the tunnel. Meanwhile, the pressure sensor arranged on the inner wall of the tunnel monitors the pressure generated by the train model. When the train model passes through the sensor at the exit, it will give a feedback signal to the PLC control system to stop the operation of the motor, which makes the traction wire rope to decelerate immediately,

Fig. 24.4 Main unit of train operation system



(a) Launcher for train model

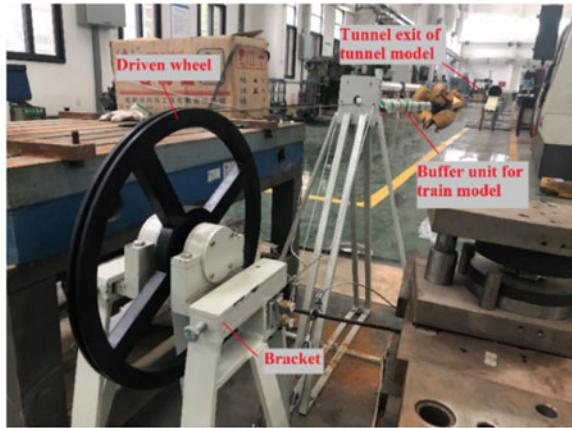


(b) Train model



(c) Drive wheel and motor

Fig. 24.4 (continued)



(d) Driven wheel



(e) Tensioner wheel

thus driving the train model to slow down at once after driving out and finally hit the buffer mechanism not far from the tunnel exit to stop completely for the next test.

The specific deceleration plan is as follows. As is shown in Fig. 24.6, the train's deceleration is realized by the motor brake and the train's connection multi-stage buffer device. When the train leaves the tunnel at high speed, the photoelectric switch, installed at the tunnel exit, senses and feeds back to the PLC. In the early stage, active deceleration is achieved through motor reversal and energy consumption braking given by frequency converter controlled by PLC, while in the later stage, the train is decelerated passively by setting a multi-stage buffer sponge. Two kinds of deceleration not only protect the body but also achieves an efficient speed reduction. When the test is completed, the motor is reversed at low speed to allow the train to run from the tunnel exit to the tunnel entrance to achieve rapid train recovery.

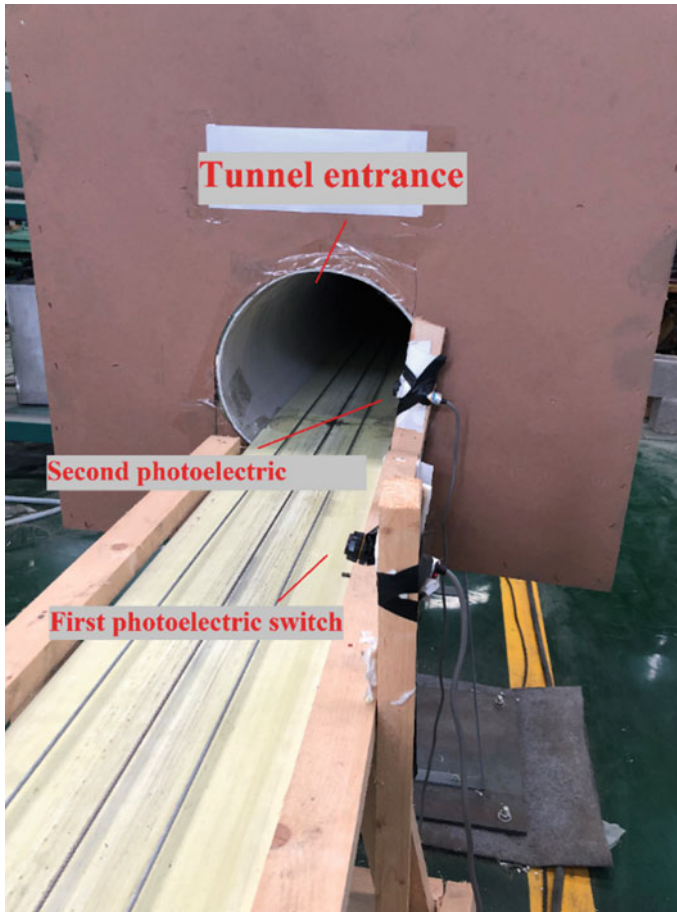


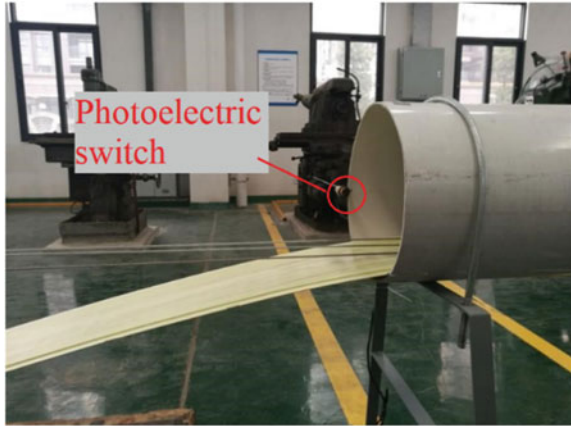
Fig. 24.5 Sensors at tunnel entrance

24.2.2 Test Instrument

Pressure Sensor. As is shown in Fig. 24.7, this test uses a durable, robust miniature piezoresistive pressure sensor with high sensitivity- Endevco® model 8515C-15. Its surface mounting thickness is only 0.76 mm, and the diameter is 6.3 mm. The Endevco® model 8515C-15 can be installed on curved surfaces due to its small dimensions, with little disturbance to laminar or hot airflow, and installed in grooves on the test surface. Therefore, the pressure sensor is widely used in local pressure measurement in wind tunnel tests and surface aerodynamic measurement in flight test.

Data collection system. As is shown in Fig. 24.8, this test uses DTS's SLICE to collect test data. SLICE is an ultra-small modular data acquisition system with

Fig. 24.6 Damping system of the model test bench

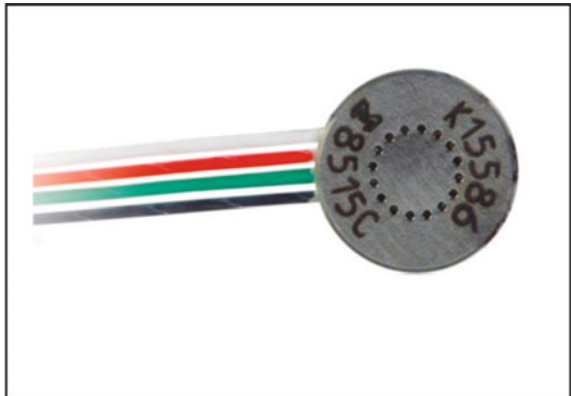


(a) Sensor at tunnel exit



(b) The buffer structure of tunnel exit

Fig. 24.7 Pressure sensor Endeveco 8515C-15



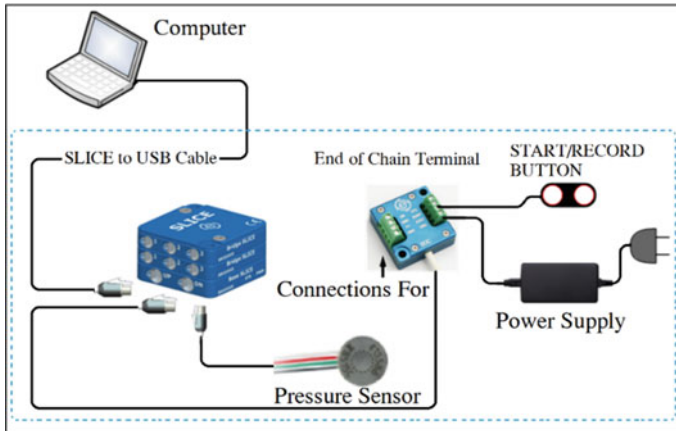


Fig. 24.8 Data acquisition system SLICE

excellent flexibility, technology, and reliability. The basic module BASE SLICE of the data acquisition system contains a microprocessor, memory, and control circuit. It can be connected to a computer and a pressure sensor at the same time. Besides, the acquisition system uses supporting SLICEW are software to complete sensor information storage and data acquisition. During the test, the pressure sensor sensing the pressure signal converts it into an electrical signal, and the pressure value is displayed in the computer test supporting software after being processed in the data acquisition system.

Train speed test system. The train speed test scheme is shown in Fig. 24.5. Two diffused photoelectric switches of the same type and batch are arranged in front of the tunnel entrance at a distance of S and are connected to two high-speed counter ports of PLC. When the train passes the first photoelectric switch at high speed, the counting of the first high-speed counter is interrupted, and the PLC immediately enters the interrupt program to start the timer. At this time, the train's speed entering the tunnel is the ratio of S to the time t just recorded by the timer, i.e., $v_1 = S/t$. Figure 24.9 shows the appearance of the photoelectric switch.

During the test, a Programmable logic controller (hereinafter referred to as PLC) controls the motor operation, speed setting, and train recovery. Figure 24.10 shows the operation interface of PLC in which the acceleration time, deceleration time, and the reverse time for the motor to decelerate are set. Taking the first photoelectric switch position in Fig. 24.5 as the reference, position 1 for velocity measurement is where the velocity sensor at the entrance lies, and position 2 is where the velocity sensor at the exit lies. The train model's speed entering the tunnel is determined by the distance value entered at position 1 for velocity measurement in the PLC and the time difference between the first photoelectric switch and the second photoelectric switch. Similarly, the speed of the train model exiting the tunnel can be obtained. The two speeds can be shown on the interface in Fig. 24.10. Before we start a new test, the speed required for the test is set on the equipment. When we click the start



Fig. 24.9 Photoelectric switch

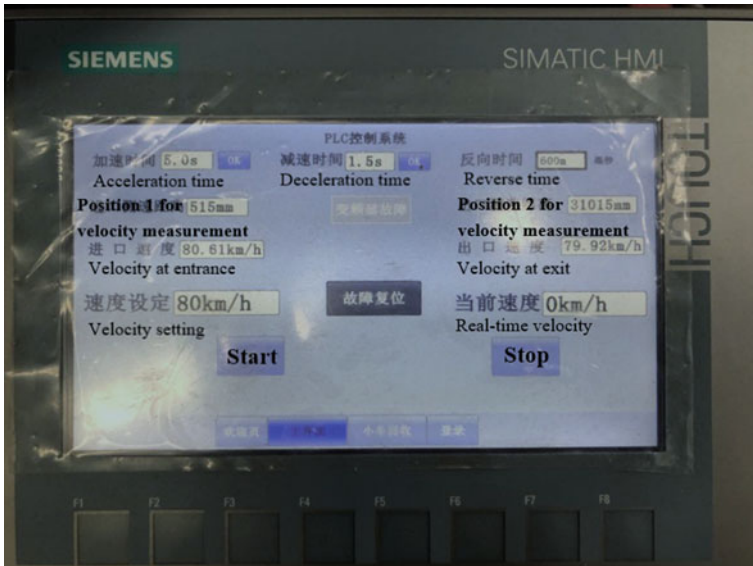


Fig. 24.10 The interface of PLC control system

button, the motor starts to run, driving the traction system, and the real-time speed is displayed on the interface. When the model car passes through the sensor at the tunnel's exit, the PLC receives the signal and immediately controls the motor to stop and decelerate by reversing. During the test, you can also press the stop button to stop the motor immediately.

24.2.3 Layout of Measuring Points

Figure 24.11 is a schematic diagram of the arrangement of each pressure measuring point in this test. In this test, a total of 6 test sections were arranged along the tunnel, and the distance between each was 3.8 m. Specifically, Fig. 24.11a shows the arrangement of measuring points under the condition of no shaft and no bypass tunnel. Figure 24.11b and c show the schematic diagram of the measuring point layout when one and two shafts are set without a bypass tunnel. Figure 24.11d and e show the schematic diagrams of measuring point layout when testing one and two bypass tunnels without shafts.

24.2.4 Determination of Similarity Criterion

Certain similar conditions must be met to make the test data comparable and useful in the scale model experiment, which includes the similarity of dynamics, geometry, and motion [31]. The thermal similarity when the train enters the tunnel is temporarily ignored because the energy loss and temperature change are minimal.

It is vital to consider the dynamic similarity criterion because geometric motion similarity is easily satisfied. When simulating gas flow in a tunnel, the two most important parameters are the Mach number (hereinafter referred to as M) and the Reynolds number (hereinafter referred to as Re). The physical meaning of Re is the ratio of characteristic inertial force to viscous force, namely

$$Re = \frac{\rho V^2 / L}{\mu V / L^2} = \frac{\rho V L}{\mu} \quad (24.1)$$

Re is a similar criterion that reflects the effect of fluid viscosity on flow. If the two flow fields are similar, the effect of inertia force and viscous force should be the same, so is the Reynolds number of the two flow fields the Reynolds number of the two flow fields.

$$Re = \frac{\rho V L}{\mu} = Re' = \frac{\rho' V' L'}{\mu'} \quad (24.2)$$

In this formula, ρ is the density of the air when the actual train is running, V is the velocity of the actual train, L is the size of the actual train, and μ is the dynamic viscosity coefficient of the air. ρ' is the density of the air when the train model is running, V' is the speed of train model, L' is the size of the actual train, and μ' is the dynamic viscosity coefficient of the air. In the model test, ρ/μ is related to the ambient temperature of the test site. So, when the temperature has less changes, ρ/μ can be regarded as a fixed value. Therefore, V and L should be equal to make Re equal. If the Re is to be equal, the speed of the train model should be higher than 20

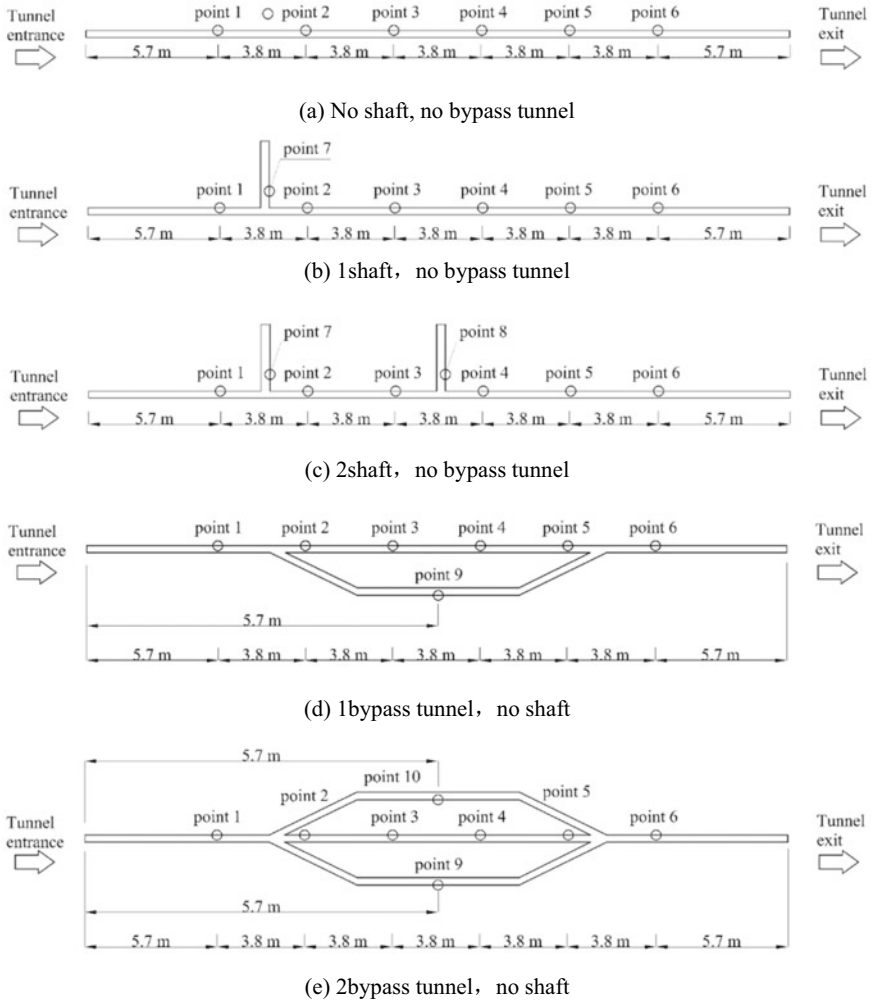


Fig. 24.11 Layout of measuring points in tunnels (the circles in the figure are the measuring points arranged)

times the actual train speed because the size similarity ratio of the model is less than 1/20, which cannot be achieved in the model test.

However, people found that in applying the dynamic similarity criterion, the flow field has a “self-modeling region” [32]. The phenomenon that the flow state and velocity distribution are similar to each other and not depend on the Re 's change when it is in a certain range is called “self-modeling”. When Re is less than a certain value (the first critical value), the flow is laminar. When it is greater than the first critical value, the flow changes from laminar to turbulent flow. It gradually enters a turbulent state when the change of Re has a greater impact on the flow state and

velocity distribution. When Re increases to a certain value (the second critical value), the flow state and velocity distribution are similar to each other and do not change with the change of the Re . That is, the flow enters the “self-modeling region”, and the corresponding flow is fully developed turbulence. When the train model and the actual train are in the same self-modeling region, the model test results can be used in the actual object. Because the speed range studied here belongs to subsonic speed and is already in a highly turbulent state, it can be considered that the flow field is in the self-model region. At this time, researchers can start the model test without considering the restriction of Re 's similarity condition.

24.3 Error Analysis

In the test process, various links will produce certain errors, which will lead to deviations in the experimental results. The major influencing factors are the sensor's errors, the running speed of the train model, and the test environment temperature.

Before the start of this model test, pressure sensors used in the test have been calibrated in the national legal metrological verification agency. The calibration method is as follows. During the calibration process, the pressure sensor was placed in the calibration environment for more than 2 h. Then the pressure sensor and the standard digital pressure gauge were installed on the pressure pump at the same time. Starting from the lower measurement limit of the pressure sensor, according to the calibration point setting, the pressure was raised to the upper limit of measurement point by point. Then the pressure was reduced from the upper measurement limit point by point to the lower measurement limit. During this process, the output value of the pressure sensor was recorded in turn. Finally, the basic error of the pressure sensor was within $\pm 0.2\%$. A standard voltage value which is input into the data acquisition system is compared with the actual voltage value reading, the error of the which is within 0.5%.

In this test, the PLC control system controls the motor to reach the required rotation speed, and the traction rope is pulled to accelerate to the required speed. And the train model and the traction rope are combined to run at the test speed. Before the start of the test, different operating speeds are set in the PLC control system, and the passing time of the train model is tested and recorded by sensors installed at the entrance and exit of the tunnel. Therefore, the actual running speed of the model car is calculated. Speed errors are all within 1% through multiple comparisons between the set running speed and the actual measured speed.

The model test bench is set up in an indoor laboratory to minimize the impact of the test environment on this test. As shown in Table 24.1, the on-site ambient temperature is recorded before each test, and the maximum change in each case doesn't exceed 10%. For the same test case, the experimental data are obtained after repeated testing three times, the relative error of whose pressure amplitude is within 3%.

Table 24.1 Test case ambient temperature chart

Case	1	2	3	4	5	6	7	8	9
Temperature	22.3	22.4	22.4	20.7	20.7	20.8	21.6	21.5	21.5

24.4 Results and Discussion

The pressure wave in the tunnel is affected by many factors. This study mainly discusses the influence of the shape of the train’s head, train speed, the establishment of the shaft, and the bypass tunnel in the tunnel on the pressure wave.

24.4.1 The Influence of the Shape of Locomotive on the Tunnel Pressure Wave

Differentiation in the locomotive’s shape will affect the amplitude and maximum positive and negative pressure wave extremum formed when the train enters the tunnel. In order to study the influence of trains with different locomotive shapes on the pressure wave in the tunnel, train models with locomotive angles of 45°, 60°, and 75° were used in the test. Figure 24.12 shows the schematic diagram of the train model in each test case. The train model’s length is 1.4 m, and the cross-sectional area is the same.

Detailed parameters of each train are given in Table 24.2. During the test, the model train’s running speed is 80 km/h, and the model tunnel is not equipped with intermediate air shafts and bypass tunnels.

Figure 24.13 shows the dynamic pressure change curve of measuring point 1. The first wave crest and wave trough are generated when the model train’s head and tail pass the tunnel entrance, respectively. It can be seen that with the increase of locomotive angle, the amplitude of the initial pressure wave generated by the train

Fig. 24.12 Comparison of locomotive of different shapes

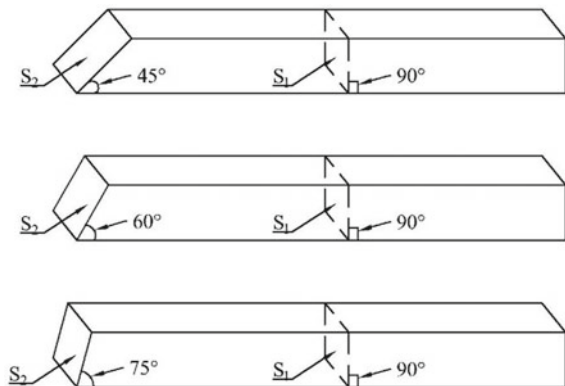
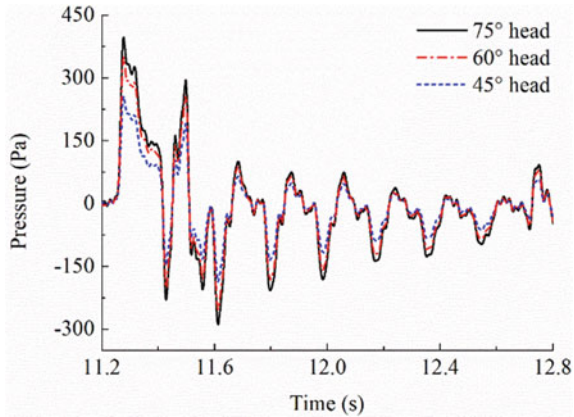


Table 24.2 Parameters of different train shapes

Train type	$S_1(m^2)$	$S_2(m^2)$	S_1/S_2
45°	0.01896	0.02681	0.707
60°	0.01896	0.02189	0.866
75°	0.01896	0.01963	0.966

Fig. 24.13 Comparison of dynamic pressure changes at measuring point 1 (Case of different car head)



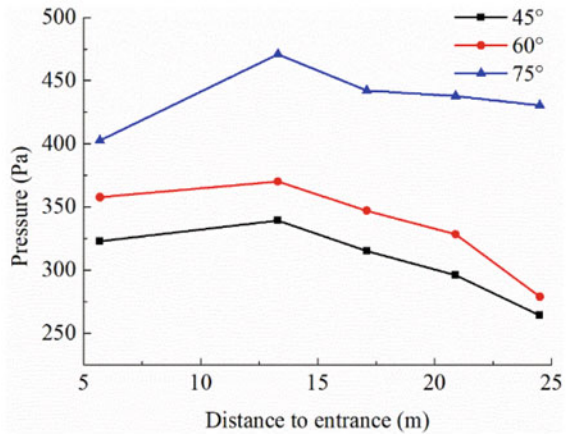
model passing through the tunnel also increases gradually, among which the pressure amplitude of the train model with 75° locomotive head is the largest, reaching 400 Pa.

Figure 24.14 shows the comparison of the aerodynamic pressure peaks at different measuring points of the three different car head shapes when passing through the model tunnel. Figure 24.14a shows the positive pressure peak, Fig. 24.14b shows the negative one. It can be seen from the figure that with the increase of the train head angle, the maximum positive and negative values generated by the train passing through the measuring points are increased. It can be seen from Table 24.2 that the windward area of the front of the car decreases with the increase of the angle of the windward surface, thus increasing the resistance encountered by the air flowing through the front and increasing the positive amplitude of the initial compression wave.

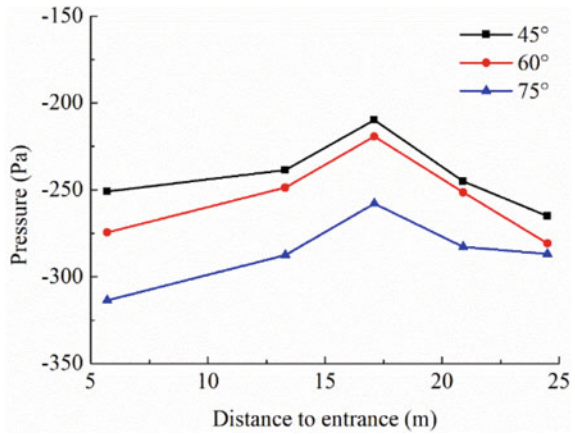
24.4.2 The Influence of Train Speed on Tunnel Pressure Wave

The size of the initial compression waves generated when the subway enters the tunnel depends on the train’s speed. This section studies the variation of aerodynamic pressure generated when the model train passes through the model tunnel at different speeds to study the influence of velocity on compression waves. During the test, a

Fig. 24.14 Peak pressure generated by train models with different head shapes



(a) Positive pressure

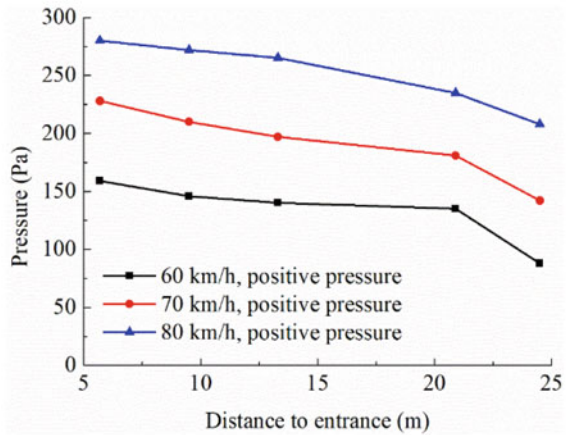


(b) Negative pressure

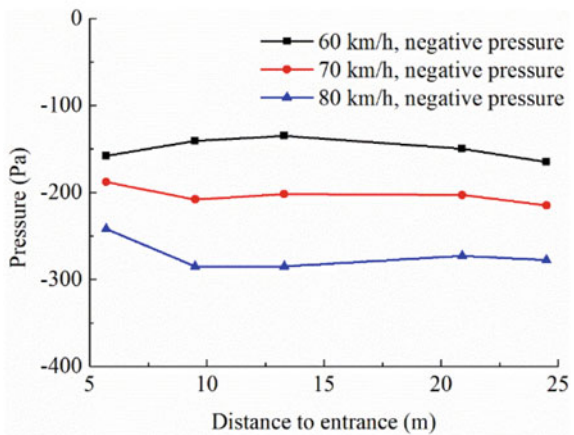
train model with a head angle of 60° was used, and the tunnel model was not equipped with an intermediate air shaft and a bypass tunnel.

Figure 24.15 shows each section wall's pressure amplitude when the train model passes through the tunnel at three different speeds (60, 70, 80 km/h). The measuring point with the largest positive pressure amplitude is point 1, arranged on section 5.7 m away from the tunnel entrance. The maximum positive pressures at three speeds (60, 70, 80 km/h) are 172 pa, 228 pa, and 280 pa, respectively. The measuring point with the largest negative pressure amplitude is on the section 9.5 m away from the tunnel entrance. The maximum negative pressure amplitudes at the three speeds are -142, -240, and -305 Pa.

Fig. 24.15 Pressure peaks generated by the model car under different speed cases



(a) Positive pressure value



(b) Negative pressure value

The positive pressure fluctuation in the tunnel is generated by the compressed air when the train model enters the tunnel and will gradually decrease along the tunnel model's length due to the influence of the tunnel model wall friction and running resistance. Therefore, the maximum positive pressure value monitored by the measuring point in the tunnel model is located in section 1. The compression wave formed by the train model entering the tunnel model will propagate in the tunnel model at speed close to that of sound and propagate back when an expansion wave is generated at the exit, propagating back and forth in the tunnel. An expansion wave will be generated when the rear of the car enters the tunnel, whose propagation path is the same as the compression wave. A large negative pressure is generated when the train model passes through the measuring point because the pressure will be superimposed when the expansion wave propagating back and forth in the tunnel encounters the car body.

Figure 24.16 shows the analysis diagram of pressure fluctuations in the tunnel model. It can be seen from Fig. 24.16 that when the train model passes through section 2 or Section 3, it encounters the expansion wave propagating in the tunnel model, making the negative pressure value at this point larger. Therefore, the theoretical analysis is consistent with the experimental results.

It can also be seen from Fig. 24.15 that the positive and negative pressure amplitudes of each measuring point increase as the speed of the train model increases. Select the data at the measurement points of Section 1 and Section 5 for function fitting. It can be seen from Fig. 24.17 that the pressure value at the measuring point is proportional to the square of the train model speed.

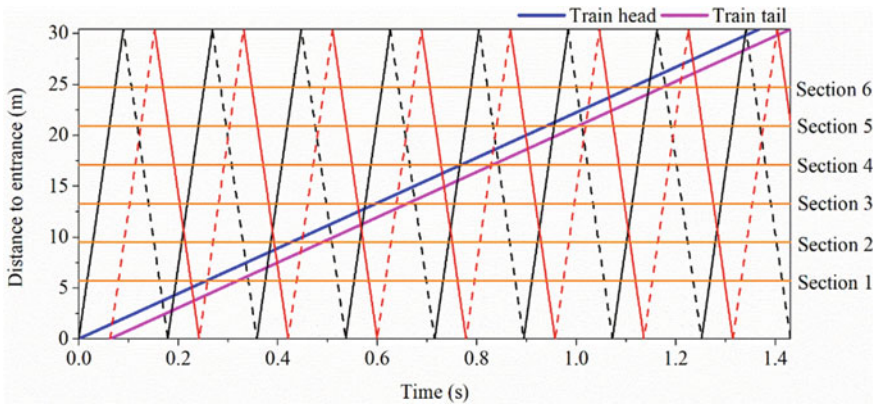
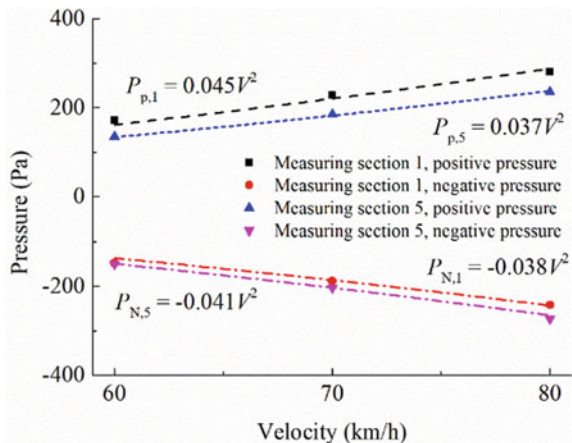


Fig. 24.16 Pressure fluctuation analysis diagram

Fig. 24.17 Pressure peak fitting diagram



24.4.3 Influence of Shaft on Pressure Wave in Tunnel

The tunnel structure changes after the intermediate air shafts are installed in the interval tunnel, so it is necessary to analyze the influence of the intermediate air shaft on the change of the tunnel pressure wave. This section examines this effect. The conditions of one and two wind shafts are set up in the model tunnel, respectively, for research, whose positions are shown in Fig. 24.11b and c. During the test, the diameter of the shaft is 0.11 m, and the height is 2.6 m, and a model train with a head shape of 60° was used, running speed of which was 80 km/h, and no bypass tunnel was set in the model tunnel.

Figure 24.18 shows the dynamic pressure curve of the initial compression wave at section 1 when the train enters the tunnel under three different working conditions, namely, the shaft number is 0, 1, and 2. Under the three working conditions, the positive pressure amplitude of the initial compression wave is 287 Pa, 281 Pa, and 278 Pa, respectively, with a small difference in the peak value of the pressure wave due to the air wells set after section 1. Therefore, whether a shaft is set in the tunnel has little influence on the initial pressure wave at the tunnel entrance.

Figure 24.19 shows the dynamic change curve of the pressure wave on point 3. Under the three working conditions, the positive pressure amplitude of the initial compression wave is 300 Pa, 244 Pa, and 233 Pa, respectively, with little change, and the negative one is -177 , -128 , and -137 Pa. However, when the train model passes through the first shaft, it can be seen that the pressure amplitude of the measuring point is the largest under the condition of setting a shaft while the smallest under no shaft. This is because the measuring point is behind the first vertical shaft. When the train model passes through the shaft, not only the compression wave is not reduced, but the pressure fluctuation is increased.

Figure 24.20 shows the dynamic change curve of the pressure wave on section 4. Under the three working conditions, the positive pressure amplitude of the initial compression wave is 285 Pa, 230 Pa, and 198 Pa, respectively, with little change,

Fig. 24.18 Comparison of dynamic pressure changes at measuring point 1 (Case of different number of shafts)

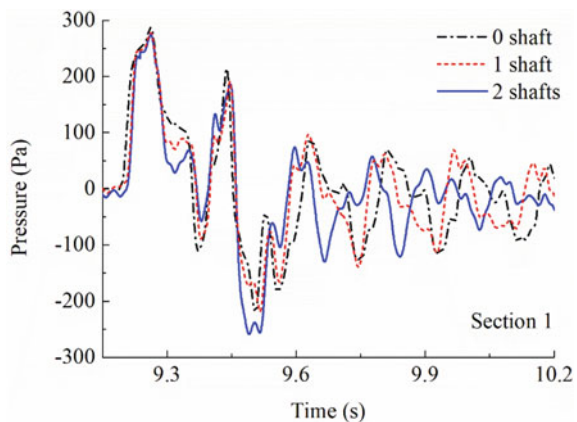
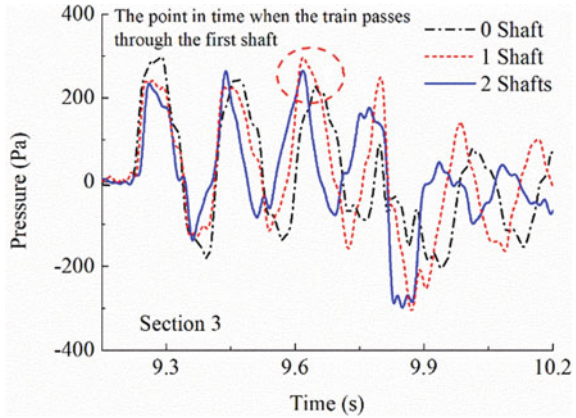


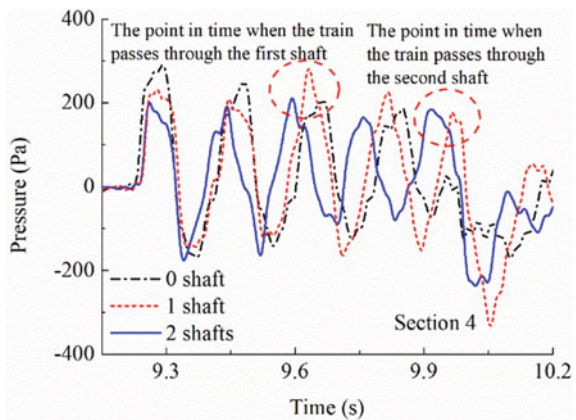
Fig. 24.19 Comparison of dynamic pressure changes at measuring point 3



and the negative one is -170 , -146 , and -177 Pa. When the train model passes through the first shaft, the rule is the same as that in the measuring point of section 3. When the model train passes through the second shaft, it can be seen that the pressure amplitude of the measuring points in the working conditions under two shafts has also increased, which is similar to the situation when a model train passes through the first shaft. The reason for this phenomenon is the increase of the air shaft's number. When the train passes through the shaft, a pressure wave will be generated and superimposed with the pressure wave reflected in the tunnel so that the pressure monitored at the measuring point will increase.

It can be clearly seen from Figs. 24.18, 24.19, and 24.20 that when the train model passes through the measuring point, the amplitude of negative pressure generated under the condition of one shaft and two shafts is larger than that under the condition of no shaft. The reason for this phenomenon is that the air velocity in the tunnel increases with the increase of the shaft, and the negative pressure generated by the train passing through the measuring point also increases due to the existence of the

Fig. 24.20 Comparison of dynamic pressure changes at measuring point 4



shaft. The pressure wave will also be superimposed with the negative pressure of the train passing by, making the pressure amplitude increase or decrease, which is related to the shaft position, train speed, and tunnel length.

24.4.4 Influence of Bypass Tunnel on Tunnel Pressure Wave

This section studies the influence of the number of bypass tunnels on the pressure wave in the tunnel. The conditions are studied by setting 1 and 2 bypass tunnels in the tunnel model. The layouts of measuring points are shown in Fig. 24.11d and e. During the test, the diameter of the bypass tunnel is 0.25 m, and a model train with a head shape of 60° was used, the running speed of which was 80 km/h. No air shaft was set in the tunnel model.

Figure 24.21 shows the pressure dynamic change curve at the measuring point of section 1 when the train model passes through the tunnel model under three different conditions, that is, straight, one bypass, and two bypass tunnels. The positive pressure amplitudes of the initial compression wave under the three test conditions are 286, 264, and 250 Pa, and the negative ones are -100 Pa, -40 Pa, and -30 Pa, respectively. The positive pressure of the initial compression wave changes little, but the negative pressure amplitude decreases with the increase of the bypass tunnel at measuring point 1, which indicates that the increased bypass tunnel plays a role in reducing the negative pressure amplitude of the initial compression wave. The reason for this phenomenon is that the initial compression wave generated by the front of the train model is reflected back and forth in the tunnel between the bypass tunnel and the tunnel entrance, and the expansion wave generated at the measuring point 1 and the rear of the vehicle entering the tunnel is just superimposed to offset, which makes the negative pressure amplitude of the initial compression wave decrease.

Fig. 24.21 Comparison of dynamic pressure changes at measuring point 1 (Case of different number of bypass tunnels)

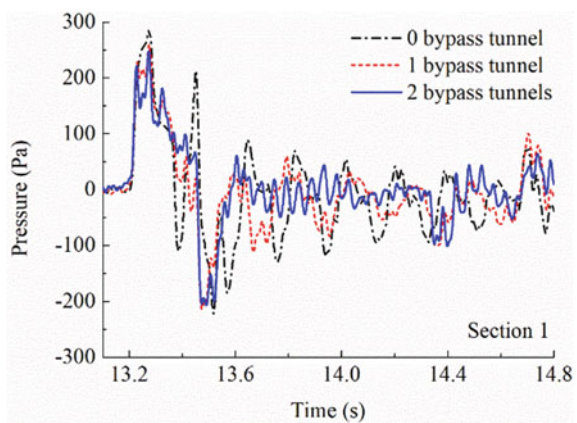


Figure 24.22 shows the pressure dynamic change curve of the measuring point in test section 5. The positive pressure amplitudes of the initial compression wave under the three working conditions are 275, 245, and 186 Pa and the negative ones are -165 , -130 , and -22 Pa, which means both the positive pressure amplitude and negative pressure amplitude of the initial compression wave have decreased. This is because after the bypass tunnel is added when the initial compression wave passes through the bypass tunnel, the air flowable area in the tunnel increases, which has a certain pressure relief effect on the initial compression wave. However, when the train model passed the measuring point, the negative pressure amplitudes were -189 Pa, -250 Pa, and -230 Pa, respectively, which shown the increase of the bypass tunnel increased the pressure amplitude change in the tunnel.

Figure 24.23 shows the dynamic pressure change curve at the measuring points of the test section 6. It can be seen that the change rule of the initial compression wave is consistent with that of section 5. The increase of the bypass tunnel slows down the amplitude of the initial compression wave, and the mitigation effect of two bypass tunnels is greater than that of one bypass tunnel. When the train model passes through the measuring points of three different structure tunnels (no bypass tunnel, one bypass tunnel, and two bypass tunnels), the negative pressure amplitudes generated are -227 Pa, -300 Pa, and -306 Pa, respectively. The results are the same as those on section 5 similar. The main reason is that the air circulation area becomes larger after the bypass tunnel is added, and the drag coefficient encountered by the model car when traveling decreases, which will increase the air velocity and static pressure at the section.

Fig. 24.22 Comparison of dynamic pressure changes at measuring point 5

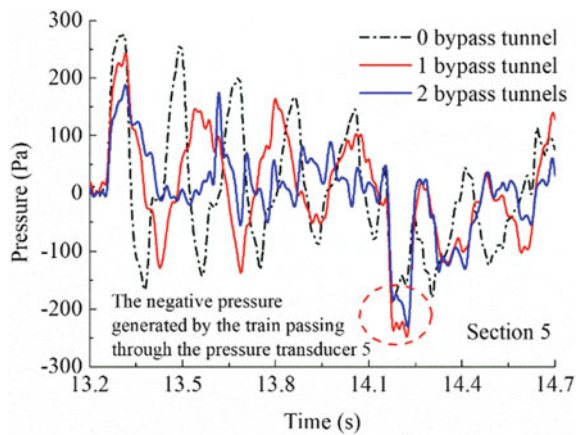
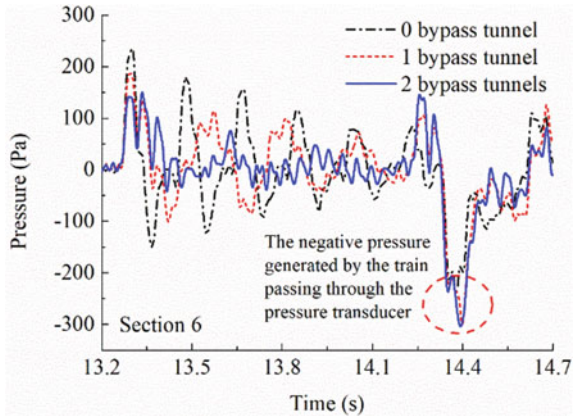


Fig. 24.23 Comparison of dynamic pressure changes at measuring point 6



24.5 Conclusion

This study uses the research method of model test to study the influence factors of the pressure wave in the subway tunnel by analyzing the influence of the locomotive shape, the speed of the train, the middle air shaft, and the bypass tunnel on the change rule of the pressure wave in the tunnel. The main conclusions are as follows:

When the train runs at a speed of 80 km/h, the blunter the locomotive shape is, the larger the initial compression is. The pressure amplitude generated by the locomotive angle of 75° is 43.6% higher than that generated by the 60° locomotive angle.

After the train enters the tunnel from outside, the place with the largest positive pressure amplitude of the pressure wave is the tunnel entrance, and the amplitude will continuously attenuate along the tunnel length. The maximum negative pressure amplitude is related to the length of the tunnel and the train as well as the train itself. When the train encounters the expansion, a wave reflected back and forth in the tunnel as the train is running, the negative pressure amplitude will increase and may become the maximum one.

After the middle air shaft is set in the tunnel, the amplitude of the initial compression wave in the tunnel space in front of the air shaft is less slow down, and the amplitude of the initial compression wave in the space behind the air shaft will be slowed down, but the amplitude value of the pressure wave propagating in the space behind the air shaft will be enhanced.

After the bypass tunnel is added to the tunnel, the positive pressure amplitude of the initial compression wave will not be affected for the tunnel space in front of the bypass tunnel, but the negative pressure amplitude will be affected due to the reflection of the initial compression wave propagating to the bypass tunnel, and the specific impact is related to the train length, tunnel length and train speed. For the tunnel space behind the bypass tunnel, the set of bypass the tunnel will slow down the impact of the initial compression wave but will enhance the amplitude of negative pressure generated by the train passing by.

Acknowledgements This study was supported by the Sichuan Provincial Science and Technology Program [grant number 2021YFG0208; 2021YFG0214], and the Fundamental Research Funds for the Central Universities [grant number 2682021ZTPY121].

References

1. Zhang, L., Yang, M., Liang, X., Zhang, J.: Oblique tunnel portal effects on train and tunnel aerodynamics based on moving model tests. *J. Wind Eng. Ind. Aerodyn.* **167**, 128–139 (2017)
2. Li, Z., Yang, M., Huang, S., Liang, X.: A new method to measure the aerodynamic drag of high-speed trains passing through tunnels. *J. Wind Eng. Ind. Aerodyn.* **171**, 110–120 (2017)
3. Li, T., Dai, Z., Yu, M., Zhang, W.: Numerical investigation on the aerodynamic resistances of double-unit trains with different gap lengths. *Eng. Appl. Comput. Fluid Mech.* **15**(1), 549–560 (2021)
4. Wang, H., Vardy, A.E., Bi, H.: Characteristics of pressure waves radiated from tunnel portals in cuttings. *J. Sound Vib.* **521**, 116664 (2022)
5. Wang, H., Vardy, A.E., Bi, H.: Micro-pressure wave radiation from tunnel portals in deep cuttings. *Proc. Instit. Mech. Eng. Part F: J. Rail Rapid Transit.* 09544097221099393 (2022)
6. Bi, H., Wang, Z., Wang, H., Zhou, Y.: Aerodynamic phenomena and drag of a maglev train running dynamically in a vacuum tube. *Phys. Fluids* **34**(9), 096111 (2022)
7. Iliadis, P., Soper, D., Baker, C.: Experimental investigation of the aerodynamics of a freight train passing through a tunnel using a moving model. *Proc. Instit. Mech. Eng. Part F: J. Rail Rapid Transit.* **233**(8), 857–868 (2019)
8. Raghunathan, R.S., Kim, H.D., Setoguchi, T.: Aerodynamics of high-speed railway train. *Prog. Aerosp. Sci.* **38**(6–7), 469–514 (2002)
9. Yuan, H., Zhou, D., Meng, S.: Study of the unsteady aerodynamic performance of an inter-city train passing through a station in a tunnel. *Tunn. Undergr. Space Technol.* **86**, 1–9 (2019)
10. Liang, H., Sun, Y., Li, T.: Influence of marshalling length on aerodynamic characteristics of urban emus under crosswind. *J. Appl. Fluid Mech.* **16**(1), 9–20 (2023)
11. Li, X., Wu, Z., Yang, J.: Experimental study on transient pressure induced by high-speed train passing through an underground station with adjoining tunnels. *J. Wind Eng. Ind. Aerodyn.* **224**, 104984 (2022)
12. Liu, T., Jiang, Z., Li, W.: Differences in aerodynamic effects when trains with different marshalling forms and lengths enter a tunnel. *Tunn. Undergr. Space Technol.* **84**, 70–81 (2019)
13. Chen, X., Liu, T., Zhou, X.: Analysis of the aerodynamic effects of different nose lengths on two trains intersecting in a tunnel at 350 km/h. *Tunn. Undergr. Space Technol.* **66**, 77–90 (2017)
14. Niu, J., Zhou, D., Liu, F.: Effect of train length on fluctuating aerodynamic pressure wave in tunnels and method for determining the amplitude of pressure wave on trains. *Tunn. Undergr. Space Technol.* **80**, 277–289 (2018)
15. Wang, J.: Aerodynamic study on the high-speed railway tunnel with large cross-sections. Thesis of master, Southwest Jiaotong University Chengdu China (2006)
16. Heine, D., Ehrenfried, K., Heine, G.: Experimental and theoretical study of the pressure wave generation in railway tunnels with vented tunnel portals. *J. Wind Eng. Ind. Aerodyn.* **176**, 290–300 (2018)
17. Wang, R.: Numerical study on aerodynamic effect of high speed train entering tunnel. Thesis of master, Lanzhou Jiaotong University Lanzhou China (2015)
18. William-Louis, M., Tournier, C.: A wave signature based method for the prediction of pressure transients in railway tunnels. *J. Wind Eng. Ind. Aerodyn.* **93**(6), 521–531 (2005)
19. Zhang, L., Yang, M., Niu, J.: Moving model tests on transient pressure and micro-pressure wave distribution induced by train passing through tunnel. *J. Wind Eng. Ind. Aerodyn.* **191**, 1–21 (2019)

20. Zhou, Y., Wang, H., Bi, H.: Experimental and numerical study of aerodynamic pressures on platform screen doors at the overtaking station of a high-speed subway. *Build. Environ.* **191**, 107582 (2021)
21. Wang, F., Weng, M., Xiong, K.: Study on aerodynamic pressures caused by double-train tracking operation in a metro tunnel. *Tunn. Undergr. Space Technol.* **123**, 104434 (2022)
22. Khayrullina, A., Blocken, B., Janssen, W.: CFD simulation of train aerodynamics: train-induced wind conditions at an underground railroad passenger platform. *J. Wind Eng. Ind. Aerodyn.* **139**, 100–110 (2015)
23. Ran, T., Xiong, X.: Study of the change of the shaft shape on the influence to aerodynamics effect of the high-speed metro tunnel. *DEStech Trans. Eng. Technol. Res.* 2475-885X:678-687 (2017)
24. Fujii, K., Ogawa, T.: Aerodynamics of high speed trains passing by each other. *Comput. Fluids* **24**(8), 897–908 (1995)
25. Xiong, X., Zhu, L., Zhang, J.: Field measurements of the interior and exterior aerodynamic pressure induced by a metro train passing through a tunnel. *Sustain. Cities Soc.* **53**, 101928 (2020)
26. Li, Z., Liang, X., Zhang, J.: Influence of shaft on alleviating transient pressure in tunnel. *J. Central South Univer. (Sci. Technol.)* **42**(8), 2514–2519 (2011)
27. Li, Z., Liang, X., Zhang, J.: Study of alleviating transient pressure with cross passage in a tunnel. *J. Railway Sci. Eng.* **7**(4), 37–41 (2010)
28. Li, X., Wang, M., Xiao, J.: Experimental study on aerodynamic characteristics of high-speed train on a truss bridge: a moving model test. *J. Wind Eng. Ind. Aerodyn.* **179**, 26–38 (2018)
29. Ouyang, D., Yang, W., Deng, E.: Comparison of aerodynamic performance of moving train model at bridge–tunnel section in wind tunnel with or without tunnel portal. *Tunn. Undergr. Space Technol.* **135**, 105030 (2023)
30. Baron, A., Mossi, M., Sibilla, S.: The alleviation of the aerodynamic drag and wave effects of high-speed trains in very long tunnels. *J. Wind Eng. Ind. Aerodyn.* **89**(5), 365–401 (2001)
31. Zhang, H., Zhu, C., Liu, M.: Mathematical modeling and sensitive analysis of the train-induced unsteady airflow in subway tunnel. *J. Wind Eng. Ind. Aerodyn.* **171**, 67–78 (2017)
32. Heine, D., Ehrenfried, K., Kühnelt, H.: Influence of the shape and size of cavities on pressure waves inside high-speed railway tunnels. *J. Wind Eng. Ind. Aerodyn.* **189**, 258–265 (2019)

Chapter 25

Numerical Investigation of Isotropic and Transverse Isotropic Rock Failure Under Semi-circular Bending Test Using Peridynamic



Kaiwei Tian, Zeqi Zhu, and Qian Sheng

Abstract In this work, we present a peridynamic-based simulation method for modeling quasi-static fracture propagation in isotropic and transverse isotropic rock within the framework of peridynamic least square minimization (PDLSM). The isotropic elastic PDLSM is further extended to investigate the elastic deformation and fracture propagation in transverse isotropic materials. The proposed model naturally employs Hooke's law for transverse isotropic material to determine peridynamic internal force and uses a transverse isotropic maximum bond stretch failure criterion to judge the bond breakage, thereby characterizing crack propagation and damage evolution. To demonstrate the effectiveness of the proposed model, simulations of elastic deformation of a transverse isotropic plate and fracture evolution in rock under semi-circular bending (SCB) tests are presented and compared with finite element method (FEM) analysis and experimental results, respectively. It is shown that the proposed model effectively simulates transverse isotropic elastic deformation and captures the fracture trajectory of isotropic and transverse isotropic SCB specimens.

Keywords Peridynamic · Fracture propagation · SCB test · Isotropy · Transverse isotropy

25.1 Introduction

Most rocks can be regarded as isotropy at the macro-scale, however sedimentary rocks such as shale and coal should be considered transverse isotropic materials due to the inner transverse isotropic structures, such as bedding plane and foliation, generated by geological deposition. The fracture propagation behavior of transverse

K. Tian · Z. Zhu (✉) · Q. Sheng

Institute of Rock and Soil Mechanics, Chinese Academy of Sciences, Wuhan 430071, China
e-mail: 329130217@qq.com

University of Chinese Academy of Sciences, Beijing 100049, China

isotropic rocks differs from that of isotropic rocks. Considering that fracture propagation plays a key role in the failure process of rocks, it has significant influence on the stability of underground excavation, efficiency of hydraulic fracture and other geotechnical engineering applications [18]. Consequently, in rock engineering, a thorough understanding of the inside mechanism of fracture propagation in isotropic rocks and transverse isotropic rocks is essential.

In recent years, numerous numerical methods have been developed to analyze the crack propagation and fracture process in isotropic and transverse isotropic materials, such as the extended finite element method (XFEM) [11] and phase-field method (PF) [15]. Nevertheless, these methods are based on classical (local) continuum mechanics and necessarily require additional processing methods to deal with the spatial discontinuities like cracks. Peridynamic (PD) theory is a kind of non-local mechanics that has been found to be suited better for modeling fracture processes than classical continuum mechanics (CCM) because its governing equations are integral equations rather than partial differential equations. There are three types of PD theory, bond-based theory [13], ordinary state-based theory [14] and non-ordinary state-based theory [16]. Bond-based PD has a fixed Poisson's ratio, whereas the other two types have no restriction. The advantage of NOSB PD is obvious as it inherits PD's ability to deal with cracks while allowing convenient implementations of existing failure models in CCM. The traditional NOSB PD, on the other hand, suffers from numerical oscillation, which may have a significant impact on simulation results. To overcome this limitation, PD least squares minimization (PDLSM) [10] and revised non-ordinary state-based PD (RNOSBPD) [6] model have been proposed. In light of these considerations, we employ the PDLSM theory as the base framework for modeling elastic deformation and fractures propagation in isotropic and transverse isotropic rock in this paper.

In this paper, we propose a new model named T-PDLSM for transverse isotropic material based on PDLSM and weighted residual method (WRM), and conduct simulations for elastic deformation of a square plate and quasi-static crack propagation under semi-circular bending test, respectively. The proposed T-PDLSM can be easily reduced into an isotropic model and provides an efficient way to analysis the crack propagation in isotropic and transverse isotropic materials. The peridynamic internal force is calculated according to the Hooke's law for transverse isotropic material and bond breakage is determined by a transverse isotropic maximum bond stretch failure criterion.

The remainder of this paper is organized as follows. First, the basic theory of PDLSM is introduced in Sect. 25.2. The extended model T-PDLSM for 2D transverse isotropic materials based on PDLSM and WRM is developed and presented in Sect. 25.3. Three numerical examples are performed in Sect. 25.4 to validate the proposed model and its capability of simulating fracture propagation in both isotropic and isotropic rocks. Finally, concluding remarks are summarized in Sect. 25.5.

25.2 Brief Introductions to PDLMS

The peridynamic least square minimization (PDLMS) was first developed by Madenci et al. [10], which combines the concept of peridynamic differential operator (PDDO) [9] and LSM. In contrast to standard PD theory, which is limited to sphere interaction domains, PDLMS is applicable to any arbitrary interaction domain. As a result, the PDLMS is free of surface effect and volume correction, and it could provide non-local stress and strain similar to CCM.

In PDLMS, the equation of motion for linear isotropic material is given by

$$\rho(\mathbf{x})\ddot{\mathbf{u}}(\mathbf{x}, t) = \mathbf{L}^{\text{pd}} + \mathbf{b}(\mathbf{x}, t) = \int_{H_x} \omega(|\boldsymbol{\xi}|) \mathbf{G} \cdot \boldsymbol{\eta} dV_{x'} + \mathbf{b}(\mathbf{x}, t) \quad (25.1)$$

where ρ is the mass density, $\ddot{\mathbf{u}}$ is the acceleration of node \mathbf{x} , \mathbf{b} is the external force vector, $\boldsymbol{\xi} = \mathbf{x}' - \mathbf{x}$ and $\boldsymbol{\eta} = \mathbf{u}(\mathbf{x}') - \mathbf{u}(\mathbf{x})$ are the relative position and relative displacement of nodes \mathbf{x}' and \mathbf{x} , respectively, $\omega(|\boldsymbol{\xi}|)$ is the weight function, and the integral part is the internal force vector \mathbf{L}^{pd} , which is calculated by the integration of bond force between node \mathbf{x} and \mathbf{x}' over the interaction domain H_x of node \mathbf{x} , as shown in Fig. 25.1. The matrix \mathbf{G} connects linear elastic Hooke's law and peridynamic, which is defined for plane stress problems as

$$[\mathbf{G}] = \begin{bmatrix} \frac{E}{2(1-\nu)}d_1 + S(d_1 + d_2) & \frac{E}{2(1-\nu)}d_3 \\ \frac{E}{2(1-\nu)}d_3 & \frac{E}{2(1-\nu)}d_2 + S(d_1 + d_2) \end{bmatrix} \quad (25.2)$$

and for plane strain problems

$$[\mathbf{G}] = \begin{bmatrix} (\lambda + S)d_1 + S(d_1 + d_2) & (\lambda + S)d_3 \\ (\lambda + S)d_3 & (\lambda + S)d_2 + S(d_1 + d_2) \end{bmatrix} \quad (25.3)$$

where λ is the Lamé's material constant, S is the shear modulus, ν is Poisson's ratio, E is Young's modulus, and d_1, d_2, d_3 are PDDO, which is defined as

$$\left[\frac{\partial}{\partial x} \frac{\partial}{\partial y} \frac{\partial^2}{\partial x^2} \frac{\partial^2}{\partial y^2} \frac{\partial^2}{\partial xy} \right] \mathbf{u}(\mathbf{x}, t) = \int_{H_x} \omega(|\boldsymbol{\xi}|) [d_1 d_2 d_3 g_1 g_2] \cdot \boldsymbol{\eta} dV_{x'} \quad (25.4)$$

The non-local displacement gradient can be expressed as

$$\nabla \otimes \mathbf{u}(\mathbf{x}, t) = \int_{H_x} \omega(|\boldsymbol{\xi}|) \boldsymbol{\eta} \otimes \mathbf{g} dV_{x'} \quad (25.5)$$

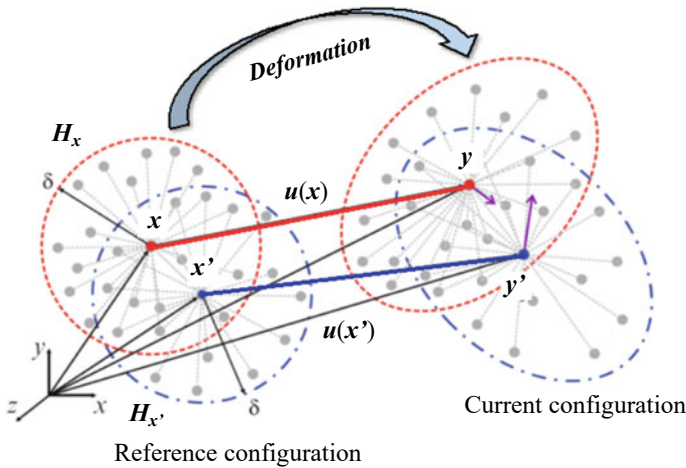


Fig. 25.1 Deformation of peridynamic node x and x'

where \otimes is the inner product, $\mathbf{g} = [g_1 \ g_2]$ is the PDDO vector, as explained in Liu et al. [7] and Madenci et al. [10].

According to the CCM, the stain tensor $\boldsymbol{\varepsilon}$ in the framework of infinitesimal deformation is expressed as

$$\boldsymbol{\varepsilon} = \frac{1}{2}(\nabla \otimes \mathbf{u} + \mathbf{u} \otimes \nabla) \tag{25.6}$$

25.3 Transverse Isotropic PDLSM Model T-PDLSM

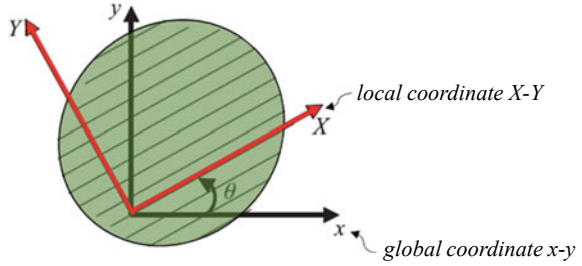
25.3.1 Review of Transverse Isotropic Elasticity

In the case of transverse isotropic material, the relationship between strain and stress in the plane stress condition is defined by the well-known generalized Hooke’s law in the Voigt notation as

$$[\boldsymbol{\sigma}] = [\mathbf{C}][\boldsymbol{\varepsilon}] \rightarrow \begin{bmatrix} \sigma_1 \\ \sigma_2 \\ \tau_{12} \end{bmatrix} = \begin{bmatrix} \frac{E_1}{1-\nu_{12}\nu_{21}} & \frac{\nu_{12}E_1}{1-\nu_{12}\nu_{21}} & 0 \\ \frac{\nu_{12}E_1}{1-\nu_{12}\nu_{21}} & \frac{E_2}{1-\nu_{12}\nu_{21}} & 0 \\ 0 & 0 & G_{12} \end{bmatrix} \begin{bmatrix} \varepsilon_1 \\ \varepsilon_2 \\ \gamma_{12} \end{bmatrix} \tag{25.7}$$

where $\nu_{12} = \nu_{21}E_1/E_2$, \mathbf{C} is the elastic stiffness matrix, and all the quantities in Eq. (25.7) is expressed in the local coordinate frame X–Y, as shown in Fig. 25.2.

Fig. 25.2 Local coordinate X–Y and global coordinate x–y of transverse isotropic rock



The elastic stiffness matrix C' of transverse isotropic materials with a material orientation angle θ in the global coordinate could be obtained using a coordinate transformation method,

$$[C'] = [Q]^{-1}[C][Q]^{-T} = \begin{bmatrix} C'_{11} & C'_{12} & C'_{16} \\ C'_{12} & C'_{22} & C'_{26} \\ C'_{16} & C'_{26} & C'_{66} \end{bmatrix} \tag{25.8}$$

Here the matrix C' is symmetric and note that there are tension (or compression) deformation and shear deformation coupling components C'_{16} and C'_{26} , and Q is the transformation matrix given as,

$$[Q] = \begin{bmatrix} \cos^2 \theta & \sin^2 \theta & 2 \sin \theta \cos \theta \\ \sin^2 \theta & \cos^2 \theta & -2 \sin \theta \cos \theta \\ -\sin \theta \cos \theta & \sin \theta \cos \theta & \cos 2\theta \end{bmatrix} \tag{25.9}$$

Considering that the analysis in this paper is primarily aimed at plane stress problems, we only discuss these types of problems; however, the plane strain problem could also be analyzed in a similar way.

25.3.2 Derivation of PD Inner Force for Transverse Isotropy

Considering the simplicity and effectiveness of Voigt notation in handling transverse isotropy problems compared to tensor calculation, the PD inner force for transverse isotropy is expressed in Voigt notation as,

$$L_{ti}^{pd} = \begin{bmatrix} \frac{\partial}{\partial x} & 0 & \frac{\partial}{\partial y} \\ 0 & \frac{\partial}{\partial y} & \frac{\partial}{\partial x} \end{bmatrix} [C'] \begin{bmatrix} \varepsilon_x \\ \varepsilon_y \\ \tau_{xy} \end{bmatrix}$$

$$= \begin{bmatrix} \frac{\partial}{\partial x} & 0 & \frac{\partial}{\partial y} \\ 0 & \frac{\partial}{\partial y} & \frac{\partial}{\partial x} \end{bmatrix} [C'] \begin{bmatrix} \int_{H_x} \omega(|\xi|) g_1 \eta_1 dV_{x'} \\ \int_{H_x} \omega(|\xi|) g_2 \eta_2 dV_{x'} \\ \int_{H_x} \omega(|\xi|) (g_1 \eta_2 + g_2 \eta_1) dV_{x'} \end{bmatrix} \quad (25.10)$$

By using the definition of transverse isotropic stiffness C' in Eq. (25.8) and the definition of PDDO in Eq. (25.4), the matrix $G_{\bar{ii}}$ of transverse isotropic case is obtained as,

$$[G_{\bar{ii}}] = \begin{bmatrix} C'_{11}d_1 + 2C'_{13}d_3 & C'_{12}d_3 + C'_{23}d_2 + \\ +C'_{33}d_2 & C'_{13}d_1 + C'_{33}d_3 \\ C'_{12}d_3 + C'_{23}d_2 + & C'_{22}d_2 + 2C'_{23}d_3 \\ C'_{13}d_1 + C'_{33}d_3 & +C'_{33}d_1 \end{bmatrix} \quad (25.11)$$

It should be noted that the matrix $G_{\bar{ii}}$, like matrix G in the isotropic case in Eq. (25.2), is symmetric. In the case of isotropic materials $E_1 = E_2 = E$, $\nu_{12} = \nu_{21} = \nu$, and $G_{12} = E/2(1 + \nu)$, the tension and shear deformation coupling component C'_{16} and C'_{26} vanish, and the matrix $G_{\bar{ii}}$ is reduced to matrix G of isotropic case in Eq. (25.2) for plane stress condition.

25.3.3 Fracture Criterion

In PD, the fracture process is accomplished by breaking the bond that links two nodes. The interaction force on the bond vanishes once the bond is broken, and the bond breakage is recorded by a scalar variable $\mu(\xi, t)$ defined as,

$$\mu(\xi, t) = \begin{cases} 1 & (\text{if the bond is intact}) \\ 0 & (\text{if the bond is broken}) \end{cases} \quad (25.12)$$

As a consequence, the damage $D(x, t)$ for a node x could be determined by the proportion of broken bonds and intact bond in the interaction domain H_x .

$$\mu(\xi, t) = 1 - \frac{\int_{H_x} \mu(\xi, t) dV_{x'}}{\int_{H_x} dV_{x'}} \quad (25.13)$$

The most common failure criterion for isotropic materials in PD is the critical bond stretch failure criterion, which means that the bond will break when its stretch s reaches critical stretch S_c ,

$$S_c = \begin{cases} \sqrt{4\pi G_0/9E\pi\delta} \text{ (plane stress)} \\ \sqrt{5\pi G_0/12E\pi\delta} \text{ (plane strain)} \end{cases} \quad (25.14)$$

where G_0 is the fracture energy, δ is the radius of the interaction domain H_x .

There are various bond failure criteria for transverse isotropic materials. For example, the Tsai-Hill stress criterion is adopted by Hattori et al. [3] to model damage in composite materials. However, unlike the critical stretch criterion, the failure criterion based on stress may be strongly influenced by the mesh condition [6]. Thus, the transverse isotropic critical stretch criterion proposed by Ghajari et al. [2] is adopted in this paper for its simplicity, which is given by,

$$S_c^2 = S_{c2}^2 + (S_{c1}^2 - S_{c2}^2)\cos^2\theta \quad (25.15)$$

where S_{c1} and S_{c2} are the critical stretch of bond at two different material orientation angles $\theta = 0^\circ$ and 90° , respectively.

$$\begin{aligned} S_{c1}^2 &= \frac{2(G_{Ic1}-G_{Ic2})c_1+(8G_{Ic1}-3G_{Ic2})c_2}{5t\delta^4(2c_1^2+11c_1c_2+2c_2^2)} \\ S_{c2}^2 &= \frac{(8G_{Ic2}-3G_{Ic1})c_1+2(G_{Ic2}-3G_{Ic1})c_2}{5t\delta^4(2c_1^2+11c_1c_2+2c_2^2)} \end{aligned} \quad (25.16)$$

Here G_{Ic1} and G_{Ic2} are critical fracture energies in the plane normal to the X and Y axes in the local coordinate in Fig. 25.2, respectively. c_1 and c_2 are parameters defined as,

$$\begin{aligned} c_1 &= \frac{15.41C_{11}-7.41C_{22}}{\pi t\delta^3} \\ c_2 &= \frac{8.08C_{22}-0.08C_{11}}{\pi t\delta^3} \end{aligned} \quad (25.17)$$

Note that this transverse isotropic failure criterion can be reduced to the critical bond stretch failure criterion i.e. Equation (25.13) if the material is isotropic.

25.3.4 Numerical Implementation

The quasi-static fracture problem is widely studied in the fields of rock mechanics and rock engineering, and this paper aims to model quasi-static fracture process. The explicit adaptive dynamic relaxation method (ADR) [5] is widely used and preferred for the analysis of quasi-static problems. However, comparing to the ADR, the implicit algorithm is better suited for quasi-static problems [12]. For the purpose of accomplish the implicit algorithm for T-PDLSM, the weak form of T-PDLSM is obtained by applying the weighted residual method (WRM) on the equation of motion and the boundary conditions (B.C.),

$$\int_{V_{pd}} \delta \mathbf{u} \cdot (\mathbf{L}_{pd} + \mathbf{b} - \rho \ddot{\mathbf{u}}) dV - \int_{S_{pd}} \delta \mathbf{u} \cdot (\boldsymbol{\sigma}_{pd} \cdot \mathbf{n} - \mathbf{T}) dS = 0 \quad (25.18)$$

where \mathbf{T} is the external traction on the boundary, \mathbf{n} is the unit normal vector of the boundary, and $\delta \mathbf{u}$ is a virtual displacement.

According to the study of Liu et al. [7], the matrix form of the governing Eq. (25.18) for quasi-static analysis can be written in the same form as linear elastic FEM,

$$\mathbf{K} \mathbf{u} = \mathbf{F} \quad (25.19)$$

where \mathbf{u} is the node displacement vector, \mathbf{K} is the global stiffness matrix, and \mathbf{F} is the global equivalent node force.

In traditional PD theory, applying boundary conditions is more complex than in FEM. In those PD theories, a fictitious layer with nonzero volume is required for applying boundary conditions. However, using the framework of PDLSM, the constraint and traction boundary conditions can be treated as same way as the FEM method, which is more convenient than the traditional PD theories.

25.4 Numerical Verification and Simulation

Three plane stress examples are performed to demonstrate the capability of this proposed T-PDLSM model to analyze isotropic and transverse isotropic materials. The first example verifies the elastic deformation of a transverse isotropic square plate, the second and third examples simulate the fracture process of isotropic and transverse isotropic SCB specimen, respectively.

25.4.1 Elastic Deformation of a Transverse Isotropic Plate Under Tension

As shown in Fig. 25.3, a transverse isotropic square plate with dimensions $L = W = 1$ m and unitary thickness is subjected to a uniaxial displacement loading $u_0 = 0.1$ m along the left and right boundary surfaces. The four independent material constants are specified in Table 25.1 corresponding to a type of transverse isotropic shale. The material orientation angle is defined as $\theta = 30^\circ$. The entire PD domain is discretized using a non-uniform mesh of 7140 PD nodes (Fig. 25.3), and the horizon size is specified as $\delta = 3d$, where d is the characteristic length. The deformed configuration and the displacement field calculated by the proposed T-PDLSM model are compared to those obtained by 2D FEM calculation and show good agreement, as shown in Fig. 25.4. It is demonstrated that the displacements results u_x and u_y predicted by the

Fig. 25.3 2D plate PD mesh

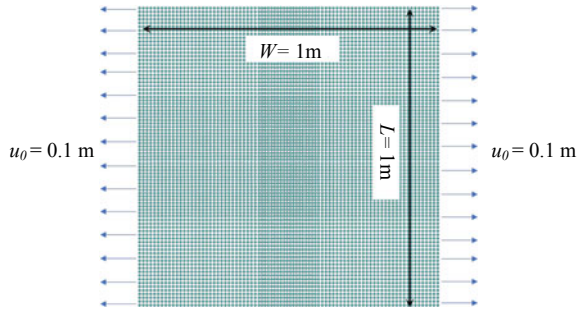


Table 25.1 Parameter selection for the transverse isotropic plate

Parameter	E_1 (GPa)	E_2 (GPa)	ν_{12}	G_{12} (GPa)
Value	45.8	16.5	0.31	12

T-PDLSM model are identical to the FEM solution, and the displacement results do not display surface effect in the boundary part, which could cause significant errors in other PD models [8]. In addition, the uniform distributed displacement contour indicates that the proposed T-PDLSM is suitable for non-uniform mesh. This is due to the fact that the T-PDLSM model is applicable to an arbitrary shape of interaction domain, not limited to a circular domain, so surface correction and volume correction are not required. The consistency between the results obtained by T-PDLSM model and the FEM solution confirms the high accuracy of T-PDLSM model in simulating the transverse isotropic elasticity problem.

25.4.2 Fracture Analysis of Isotropic SCB Tests

As a benchmark problem, an isotropic SCB specimen made of Polymethylmethacrylate (PMMA) with a pre-existing flaw is simulated to validate the capability of the T-PDLSM model for capturing crack evolution in isotropic materials, as shown in Fig. 25.5. If the material is isotropic, the T-PDLSM model is reduced to the PDLSM model, as described in Sect. 25.3. And the bond breakage is determined using the isotropic fracture criterion described in Sect. 25.3.3. The isotropic SCB plate is subjected displacement loading u increasing form zero with incremental $\Delta u = 1.6e-5$ m on the top of numerical model. The displacement in the x and y directions of the left support pin is fixed, while the y direction of the right pin is fixed and the x direction is free (Fig. 25.5a). The angel of the pre-existing flaw and the vertical line is denoted by α . The dimensions of the specimen are determined as radius $R = 50$ mm, crack length $a = 15$ mm, support distance $2S = 43$ mm, and thickness $t = 5$ mm. The mechanical properties of PMMA are specified as Young’s Modulus $E = 3.75$ GPa, Poisson’s ratio $\nu = 0.31$, Fracture Toughness $K_{IC} = 2.13$ MPa·m^{1/2}. As

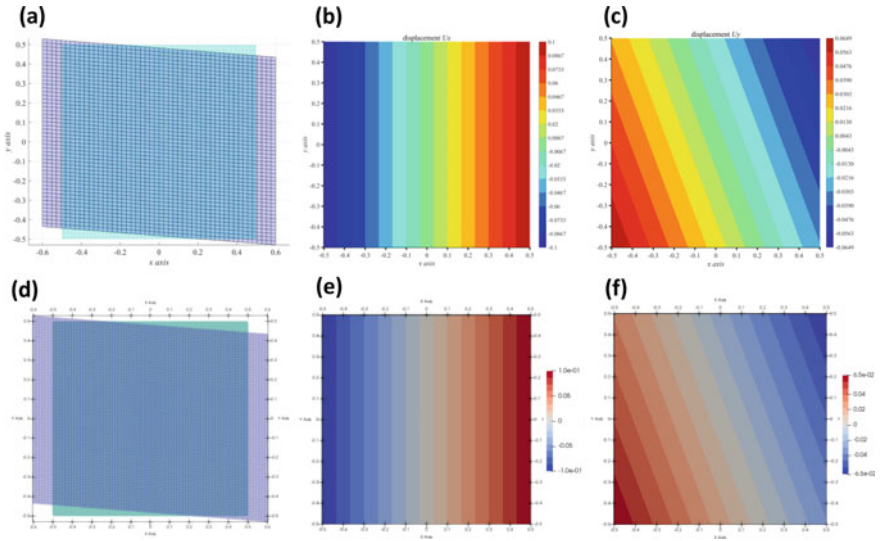


Fig. 25.4 **a** Deformed configuration obtained by FEM. **b** Displacements u_x obtained by FEM. **c** Displacements u_y obtained by FEM. **d** Deformed configuration obtained by T-PDLSM. **e** Displacements u_x obtained by T-PDLSM. **f** Displacements u_y obtained by T-PDLSM

shown in Fig. 25.5b, the entire domain is discretized with 10,512 PD nodes, and the horizon size is specified as $\delta = 3d$, where d is the characteristic length.

Figures 25.6 and 25.7 illustrate the critical load and fracture trajectory of specimens associated with two different angles $\alpha = 0^\circ$ and 30° . When $\alpha = 0^\circ$, the fracture propagates along the direction of the pre-existing flaw, resulting in pure model I fracture pattern. The simulated critical load is 2482N, which is close to the experimental results of 2400N. When $\alpha = 30^\circ$, the fracture propagate starts from the flaw tip as a wing crack and eventually aligns with the horizontal direction. The simulated critical

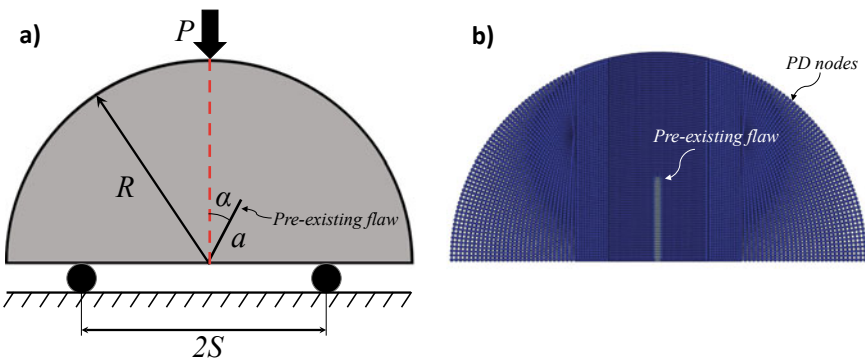


Fig. 25.5 **a** Schematic of a SCB specimen with a pre-existing flaw. **b** PD mesh

load 2822N is nearly identical to the experimental results of 2800N. The fracture trajectories of the two cases obviously agree with the experiment results of Ayatollahi and Aliha [1]. Consequently, the proposed T-PDLSM model can be reduce to the isotropic case and effectively simulate the fracture process of an isotropic SCB test.

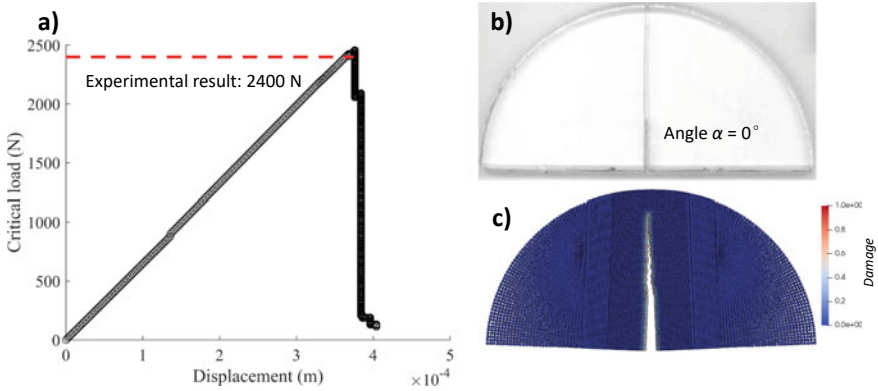


Fig. 25.6 Simulation of critical load and crack trajectory for an isotropic SCB specimen with a pre-existing flaw angle $\alpha = 0^\circ$. **a** Load–displacement curve. **b** Experimental crack path [1]. **c** Simulated fracture trajectory

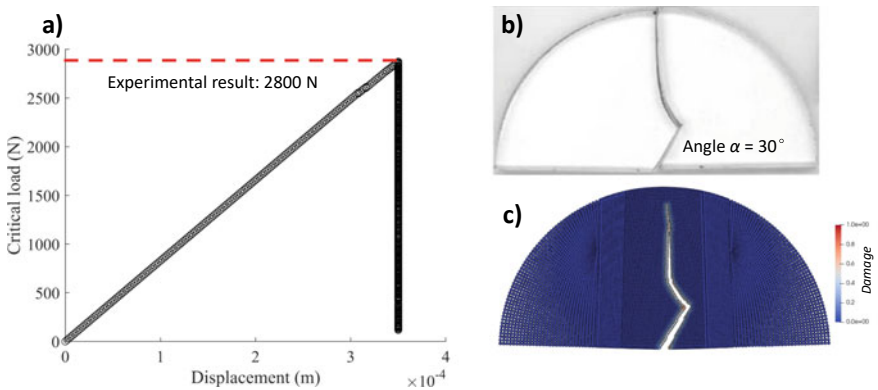


Fig. 25.7 Simulation of critical load and crack trajectory for an isotropic SCB specimen with a pre-existing flaw angle $\alpha = 30^\circ$. **a** Load–displacement curve. **b** Experimental crack path [1]. **c** Simulated fracture trajectory

25.4.3 Fracture Analysis of Transverse Isotropic SCB Tests

In this section, the T-PDLSM equipped with the transverse isotropic fracture criterion described in Sect. 25.3.3 is used to analyze the crack propagation path in the transverse isotropic rock subjected to SCB test. The transverse isotropic semi-circular plate is subjected to displacement loading u increasing from zero with incremental $\Delta u = 1.6 \times 10^{-5}$ m on the top of the specimen. The dimensions and the boundary conditions of this specimen are determined in the same way as the isotropic model described in Sect. 25.4.2. The mechanical properties of the specimen are specified according to the study of Wang et al. [17] as $E_1 = 2326.31$ MPa, $E_2 = 1887.59$ MPa, $\nu_{12} = 0.31$, $G_{12} = 767.65$ MPa, $K_{IC1} = 0.3$ MPa·m^{1/2}, $K_{IC2} = 0.1$ MPa·m^{1/2}. The whole domain is discretized with 10,512 PD nodes, and the horizon size is specified as $\delta = 3d$, where d is the characteristic length.

Figure 25.8 illustrate the fracture trajectory of a specimen with flaw angles $\alpha = 0^\circ$ and orientation angle $\theta = 30^\circ$. Figure 25.9 exhibits the fracture trajectory of a specimen with flaw angles $\alpha = 30^\circ$ and orientation angle $\theta = 60^\circ$. Compared to the isotropic case in Sect. 25.4.2, it can be seen clearly that the crack trajectory of transverse isotropic model is more complicated than that of the isotropic model due to the presence of the oscillation cracks and transition zones, which have been reported in transverse isotropic rocks [4]. According to the experimental results of Wang et al. [17], the fracture starts from the flaw tip and develops along the bedding angle before deflecting in the opposite direction in the transition zone, resulting in complicated oscillation cracks, shown in Figs. 25.8 and 25.9. This complex crack path can be well captured by the proposed T-PDLSM model, demonstrating the approach's effectiveness in simulating crack propagation in transverse isotropic rock under SCB test.

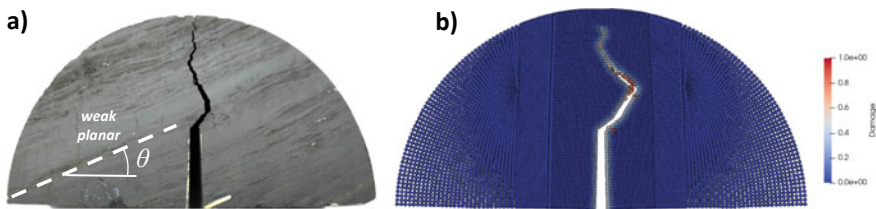


Fig. 25.8 Simulation of critical load and crack trajectory for an isotropic SCB specimen with pre-existing flaw angle $\alpha = 0^\circ$ and orientation angle $\theta = 30^\circ$. **a** Experimental crack path [17]. **b** Simulated fracture trajectory

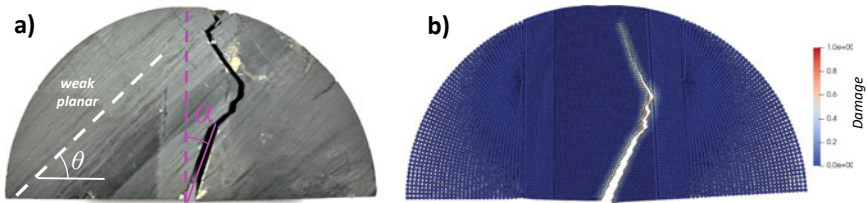


Fig. 25.9 Simulation of crack trajectory in transverse isotropic SCB specimen with pre-existing flaw angle $\alpha = 30^\circ$ and orientation angle $\theta = 60^\circ$. **a** Experimental crack path [17]. **b** Simulated fracture trajectory

25.5 Conclusion

In this study, peridynamic least square minimization (PDLSM) have been extended to transverse isotropic materials named T-PDLSM model, based on the weighted residual method. The proposed T-PDLSM model is characterized by four independent elastic parameters corresponding to the transverse isotropic elasticity. Based on the transverse isotropic critical stretch failure criterion, a complete numerical simulation model for linear elastic transverse isotropic material is proposed. The T-PDLSM could apply boundary conditions the same as FEM and does not require surface correction and volume correction, thus improving the computation accuracy. One square plate under displacement tension is performed to calculate its displacement, which show a good accuracy compared to the FEM solution. Crack propagation in isotropic and transverse isotropic semi-circular plates under SCB tests is simulated, and the results show the ability of the T-PDLSM model to capture the complex crack path. In conclusion, the proposed T-PDLSM model is capable of analyzing the elastic deformation and fracture propagation in both isotropic and isotropic rocks.

Funding Statement The work was financially supported by the National Natural Science Foundation of China (Grant No. U21A20159).

Conflicts of Interest

The authors declare that they have no conflicts of interest to report regarding the present study.

References

1. Ayatollahi, M., Aliha, M.: Wide range data for crack tip parameters in two disc-type specimens under mixed mode loading. *Comput. Mater. Sci.* **38**(4), 660–670 (2007)
2. Ghajari, M., Iannucci, L., Curtis, P.: A peridynamic material model for the analysis of dynamic crack propagation in orthotropic media. *Comput. Methods Appl. Mech. Eng.* **276**, 431–452 (2014)
3. Hattori, G., Trevelyan, J., Coombs, W.: A non-ordinary state-based peridynamics framework for anisotropic materials. *Comput. Methods Appl. Mech. Eng.* **339**, 416–442 (2018)

4. Ju, M., Li, J., Li, J., Zhao, J.: Loading rate effects on anisotropy and crack propagation of weak bedding plane-rich rocks. *Eng. Fract. Mech.* **230**, 106983 (2020)
5. Kilic, B., Madenci, E.: An adaptive dynamic relaxation method for quasi-static simulations using the peridynamic theory. *Theoret. Appl. Fract. Mech.* **53**, 194–204 (2010)
6. Liu, Q., Xin, X.: Revised non-ordinary state-based peridynamics and a new framework for coupling with finite element method. *Eng. Fract. Mech.* **242**, 107483 (2021)
7. Liu, Q., Xin, X., Ma, J., Wang, Y.: Simulating quasi-static crack propagation by coupled peridynamics least square minimization with finite element method. *Eng. Fract. Mech.* **252**, 107862 (2021)
8. Madenci, E., Oterkus, E.: *Peridynamic Theory and Its Applications*. Springer, New York (2014)
9. Madenci, E., Barut, A., Futch, M.: Peridynamic differential operator and its applications. *Comput. Meth. Appl. Mech. Eng.* **304**, 408–451 (2016)
10. Madenci, E., Dorduncu, M., Gu, X.: Peridynamic least squares minimization. *Comput. Meth. Appl. Mech. Eng.* **348**, 846–874 (2019)
11. Motamedi, D., Mohammadi, S.: Dynamic crack propagation analysis of orthotropic media by the extended finite element method. *Int. J. Fract.* **161**, 21–39 (2010)
12. Ni, T., Zaccariotto, M., Zhu, Q., Galvanetto, U.: Static solution of crack propagation problems in Peridynamics. *Comput. Meth. Appl. Mech. Eng.* **346**, 126–151 (2019)
13. Silling, S.: Reformulation of elasticity theory for discontinuities and long-range forces. *J. Mech. Phys. Solids* **48**(1), 175–209 (2000)
14. Silling, S., Epton, M., Weckner, O., Xu, J., Askari, E.: Peridynamic states and constitutive modeling. *J. Elast.* **88**(2), 151–184 (2007)
15. Wang, L., Zhou, X.: Phase field model for simulating the fracture behaviors of some disc-type specimens. *Eng. Fract. Mech.* **226** (2020)
16. Warren, T., Silling, S., Askari, A., Weckner, O., Epton, M., Xu, J.: A non-ordinary state-based peridynamic method to model solid material deformation and fracture. *Int. J. Solids Struct.* **46**(5), 1186–1195 (2009)
17. Wang, W., Teng, T.: Experimental study on anisotropic fracture characteristics of coal using notched semi-circular bend specimen. *Theoret. Appl. Fract. Mech.* **122**, 103559 (2022)
18. Xie, Y., Cao, P., Jin, J., Wang, M.: Mixed mode fracture analysis of semi-circular bend (scb) specimen: a numerical study based on extended finite element method. *Comput. Geotech.* **82**, 157–172 (2017)

Chapter 26

Field Tests of Bridge Damage Detection by Using the Passive Tap-Scan Method



Ping Lin, Zhuyou Hu, He Guo, Lei Qiao, and Zhihai Xiang

Abstract In recent years, using a passing vehicle to detect damage has attracted extensive attention. Among these works, the tap-scan damage detection method can achieve a high signal to noise ratio by applying the tapping force at a sensitive frequency that is higher than the frequency band of environmental noises. Further analysis shows that this method can detect the stiffness transition of beam structures, because the vehicle acceleration is very sensitive to the stiffness gradient. This paper will further report the new design of the passive tap-scan damage detection vehicle updated for practical implementations. The results from two field tests are used to demonstrate that this vehicle can not only find the damage on beam surface, but also give the quantitative estimation of damage severity. All these findings demonstrate the practical potential of the passive tap-scan method.

Keywords Tap-scan method · Bridge damage detection · Field test

26.1 Introduction

Damage detection is very important for bridge health evaluation and management [1, 2]. In daily maintenance, visual inspection can be routinely used to find surface damage. While for special inspections, dynamical testing should be conducted [3]. However, these two methods are time-consuming and sometimes need traffic blocking. Real-time monitoring under normal traffic is possible with the fast development of sensing technology [4–6]. But these monitoring systems are mainly based on global properties of the bridge, such as natural frequencies and mode shapes, so that they are still difficult to give reliable information on the presence of local damage

P. Lin · H. Guo · L. Qiao

CCCC Road & Bridge Inspection & Maintenance Co., Ltd, Beijing, China

CCCC Infrastructure Maintenance Group Co., Ltd, Beijing, China

Z. Hu · Z. Xiang (✉)

Department of Engineering Mechanics, Tsinghua University, Beijing 100084, China

e-mail: xiangzhihai@tsinghua.edu.cn

[4–9]. Under such circumstances, it calls for a new technology that can screening out local damage in an efficient and economical way.

Since the pioneering work of Yang et al. [10, 11], the vehicle scanning method (VSM) has attracted intensive interest to obtain bridge conditions by using an accelerometer mounted on a passing vehicle [12, 13]. The original purpose of the VSM is extracting the fundamental frequency of bridge [10, 11]. But it soon extends to extract other bridge information, such as mode shapes [14, 15], damping [16, 17], road roughness [18, 19], and damage [13, 20–27].

It seems that the VSM is a good bridge inspection technology complement to the aforementioned visual inspection, dynamical testing and health monitoring systems. However, the success of the VSM in practical implementations is strongly dependent on the denoising method. Inspired by the hunting behavior of woodpeckers, one can add tapping forces to ensure a high signal to noise ratio (SNR) and extract the damage information through the high frequency responses. This is called the tap-scan damage detection method. The tapping force can be actively applied by using a shaker [21–23], or passively generated by a toothed wheel [24, 27]. Although the active method is flexible, it suffers from cumbersome tapping systems. Therefore, this paper just discusses the performance of the vehicle based on the passive method, which is more portable and cheaper.

Since the theoretical basis of the passive method has been extensively discussed in [24, 27], this paper just gives a brief revisit in Sect. 26.2. Then, the design of the vehicle system is introduced in more detail in Sect. 26.3. This vehicle has been used for many on-site inspections, two of them are reported in Sect. 26.4 to demonstrate its practical performance. Finally, conclusions are given in Sect. 26.5.

26.2 A Brief Revisit to the Basis of the Passive Tap-Scan Damage Detection Method

As Fig. 26.1 shows, the passive tap-scan method can be discussed based on a vehicle-bridge interaction model, in which the vehicle (represented by a sprung-mass system) passes through a bridge (represented by a simply-supported beam) at a constant velocity v . This system is governed by the following equations:

$$M \ddot{y}_V + k_V (y_V - y_B|_{x=vt}) + \mu_V \left(\dot{y}_V - \frac{dy_B}{dt} \right) = 0 \quad (26.1)$$

$$m \ddot{y}_B + EI \frac{\partial^4 y_B}{\partial x^4} + \mu_B \dot{y}_B = -(F + Mg) \delta(x - vt) \quad (26.2)$$

where y_V and y_B are vehicle and beam displacements in y direction, respectively; M is the mass of vehicle body; k_V and μ_V are the stiffness and damping constant of the vehicle suspension system, respectively; and the beam is characterized by the bending stiffness EI , mass per unit length m , and damping constant μ_B . The overhead

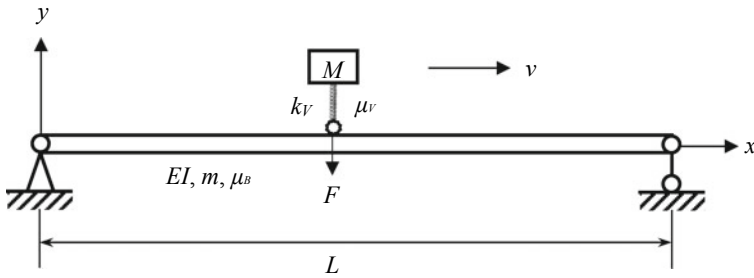


Fig. 26.1 The theoretical model

dot represents the derivative over time; and $d/dt = \partial/\partial t + v\partial/\partial x$ is the material derivative evaluated at $x = vt$. δ is the Dirac delta function. Mg is the static weight force of the vehicle. F is the beam support force, which is in equilibrium with the passive tapping force F_T and the vehicle-beam interaction force:

$$F = F_T - k_V(y_V - y_B|_{x=vt}) - \mu_V \left(\dot{y}_V - \frac{dy_B}{dt} \right) \tag{26.3}$$

According to Eqs. (26.1)–(26.3), one can obtain the point-impedance Z of the beam at position x :

$$Z(x) = -\frac{F + Mg}{y_B} \delta(x - vt) = -\frac{M \ddot{y}_V + Mg + F_T}{y_B} \tag{26.4}$$

Equation (26.4) clearly shows that the vehicle acceleration is the function of $Z(x)$, which contains the information of local damage.

The damage in the beam can be regarded as an abnormal bending stiffness $(EI)_A$. In order to find the analytical solution of the vehicle passing through the damage, one can convert the damage in the beam at position x to the effective stiffness $k(x)$ of the vehicle:

$$k(x) = \frac{k_V}{1 - [\theta(x) - 1]D_s(x)} \tag{26.5}$$

where $\theta(x) \equiv (EI)_A/EI$ is the stiffness ratio; and D_s is a position dependent coefficient. The effectiveness of Eq. (26.5) has been verified by numerical and experimental examples in [27].

The passive tapping force F_T can be generated by a toothed wheel moving at constant velocity v and is simply represented as:

$$F_T \approx \frac{A}{\pi} + \frac{A \sin(\omega_0 t)}{2} \tag{26.6}$$

where A and ω_0 are the amplitude and angular frequency of the tapping force.

The vehicle displacement at time $t = t_0 + \Delta t$ can be easily solved by using the Duhamel integration method [27]. The most significant components of y_V are:

$$y_V^*(t) = \left[\frac{\dot{y}_V(t_0) + \xi_V \omega_V y_V(t_0)}{\bar{\omega}_V} \sin(\bar{\omega}_V \Delta t) + y_V(t_0) \cos(\bar{\omega}_V \Delta t) \right] e^{-\xi_V \omega_V \Delta t} + \sum_{j=1}^{\infty} \frac{H_j^0}{R_0} [\sin(\omega_0 t) + e^{-\xi_V \omega_V \Delta t} \sin(\bar{\omega}_V \Delta t)] \quad (26.7)$$

where ξ_V is the damping ratio of the vehicle; $\omega_V = \sqrt{k/M}$ is the effective vehicle frequency; $\bar{\omega}_V = \sqrt{1 - \xi_V^2} \omega_V$; H_j^0 is the function of ω_V ; and:

$$R_0 = (\omega_V^2 + \omega_0^2)^2 - 4(1 - \xi_V^2) \omega_0^2 \omega_V^2 \quad (26.8)$$

Since the damaged region has different ω_V due to the different k , the vehicle acceleration \ddot{y}_V^* should be different from that in intact regions. According to Eqs. (26.7) and (26.8), this difference will be significant if the tapping frequency ω_0 is close to ω_V . In addition, \ddot{y}_V^* will have a pulse when the vehicle enters or leaves the damaged region, because \ddot{y}_V^* contains $\ddot{\omega}_V$.

With the above understanding, the vehicle velocity should be adjusted to generate tapping force at frequency around ω_V . Then, the damage can be identified from the abnormal amplitude in the power spectral density (PSD) of the vehicle acceleration in the sensitive frequency range (SFR) covering ω_V . The details of the damage identification algorithm can be found in [27]. Here just emphasize two important issues for practical implementations. The first issue is about the time–frequency analysis. Usually, the short time Fourier transformation can be utilized to calculate the PSD at low computational cost. However, one should set a proper window length (WL) to make the tradeoff between the time and frequency resolutions according to the uncertainty criterion. For example, one meter WL is adopted in this paper, which is good enough to locate damage with acceptable frequency resolution, although the pulse on the boundary of the damaged region is smoothed out by this setting. The second issue is about the filtering parameter B_f , which is used to remove small fluctuations in the damage detection results. Usually, $B_f = 1.5$ is a good setting, which is also adopted in this paper.

26.3 Vehicle Design

With the experience obtained from the preliminary tests reported in [27], the prototype vehicle was updated to an engineering version. The main objects of this new design are mainly of two folds: portability and safety. As Figs. 26.2 and 26.3 show, this vehicle is in a compact dimension, so that it just occupies a single lane on the

bridge free of complete traffic blocking. It can be easily put into a conventional SUV or a pick-up truck in transfer transportation. In order to warn other drivers in nearby passing vehicles, a red flash light is raised up when the vehicle is working on the bridge.

As Fig. 26.4 shows, the main frame of the vehicle is a welded structure made of stainless steel. The tapping wheel serves as the sprung-mass system shown in Fig. 26.1. Two front wheels driven by in-wheel electric motors provide differential steering capability. With the help of a gyroscope, the vehicle can pass through a single lane semi-automatically. A heavy battery pack is placed in the center of the vehicle, so that the axial weight of the tapping wheel is large enough to generate sufficient tapping force.

In accordance with the theoretical model in Fig. 26.1, the accelerator is mounted near the center of the tapping wheel (see Fig. 26.5). The structure of the tapping wheel system is carefully designed to ensure that the sensitive vehicle frequency ω_V is well above the environmental noises. The ω_V of this vehicle is about 126 Hz, so that the SFR is set as [120, 135] Hz in the field tests reported in the next section. Because the tapping wheel of 250 mm in diameter contains 72 rubber teeth, the vehicle velocity is about 1.4 m/s to generate the tapping frequency of 127 Hz.



Fig. 26.2 The vehicle in working state and transport state



Fig. 26.3 The three-view of the vehicle

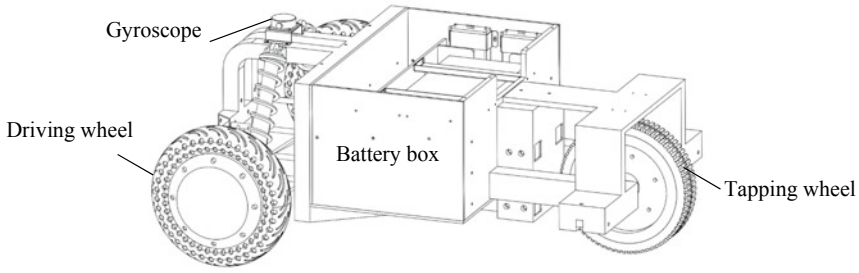


Fig. 26.4 The internal structure of the vehicle

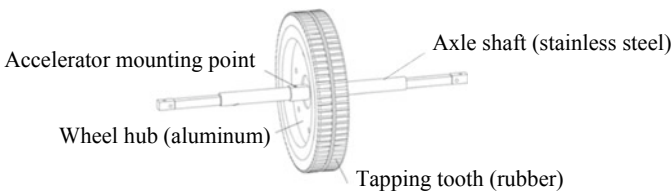


Fig. 26.5 The details of the tapping wheel assembly

26.4 Field Tests

26.4.1 Cai-Jia-He-Zhi-Liu Bridge

Cai-Jia-He-Zhi-Liu bridge is located on the Muyan Road in Beijing, China. As Fig. 26.6 shows, this simply-supported bridge has a single span of 20 m in length and is composed of 16 concrete plate beams.

In the field inspection, the vehicle tested one beam in each scan. The identified results of beam 2#, 3#, 4# and 7# in the north to south scans are shown in Fig. 26.7. One can clearly identify the signal at 127 Hz in the PSD graph. This means that the high SNR can be achieved in this test, so that one can expect reliable results. According to the theoretical basis of tap-scan method introduced in Sect. 26.2, the high amplitude in PSD graph implies the presence of damage. Actually, many crystalline blooms

Fig. 26.6 The elevation view of Cai-Jia-He-Zhi-Liu bridge



were found in the visual inspection, which are marked in the red boxes in Fig. 26.7, corresponding to the locations of the high PSD signals.

26.4.2 *Yan-Zi-Yan Bridge*

Yan-Zi-Yan bridge is located on the Huiyuan Road in Guiyang city, China. As Fig. 26.8 shows, this simply-supported 6-span bridge has a dimension of 240 m in length and 17.25 m in width. Each span of 40 m in length has five prestressed concrete box-beams with a middle diaphragm.

In the field inspection, the vehicle tested one beam in each scan (see Figs. 26.8 and 26.9). For demonstration, Fig. 26.10 just shows the inspection results of the inner side beams in span 4, 5 and 6, which are marked in the red box in Fig. 26.8. One can find that each pier and diaphragm can be clearly identified from the PSD graph. Besides, there are four strong signals that imply severe damage. In the regions marked as Damage 1 and Damage 2, one can find continuous abnormal PSD signals. Actually, in visual inspection, one could find many continuous micro-cracks on the beam bottom in the region of Damage 1 and a long crack with the exposed tendon in the region of Damage 2. The exposed tendon could also be found in the location of Damage 3, which has the strongest PSD signal. However, although a long crack was found in the location of Damage 4, the corresponding PSD signal is very concentrated. All these findings demonstrate that this inspection vehicle can not only scan out the damage, but also give quantitative evaluation of the damage severity, which is beyond the capability of visual inspection.

26.5 Conclusions

This paper gives a detailed report on the design of a damage inspection vehicle based on the passive tap-scan method. The field test results of two real bridges demonstrate that high SNR can be achieved in practical implementations, because the sensitive frequency of this vehicle is higher than the frequencies of noises including the influence of other passing vehicles. The identified results have good agreement with the visual inspections. Besides, this method can give reliable estimation of the damage severity, which is hard to obtain only from the symptom shown in surface damage.

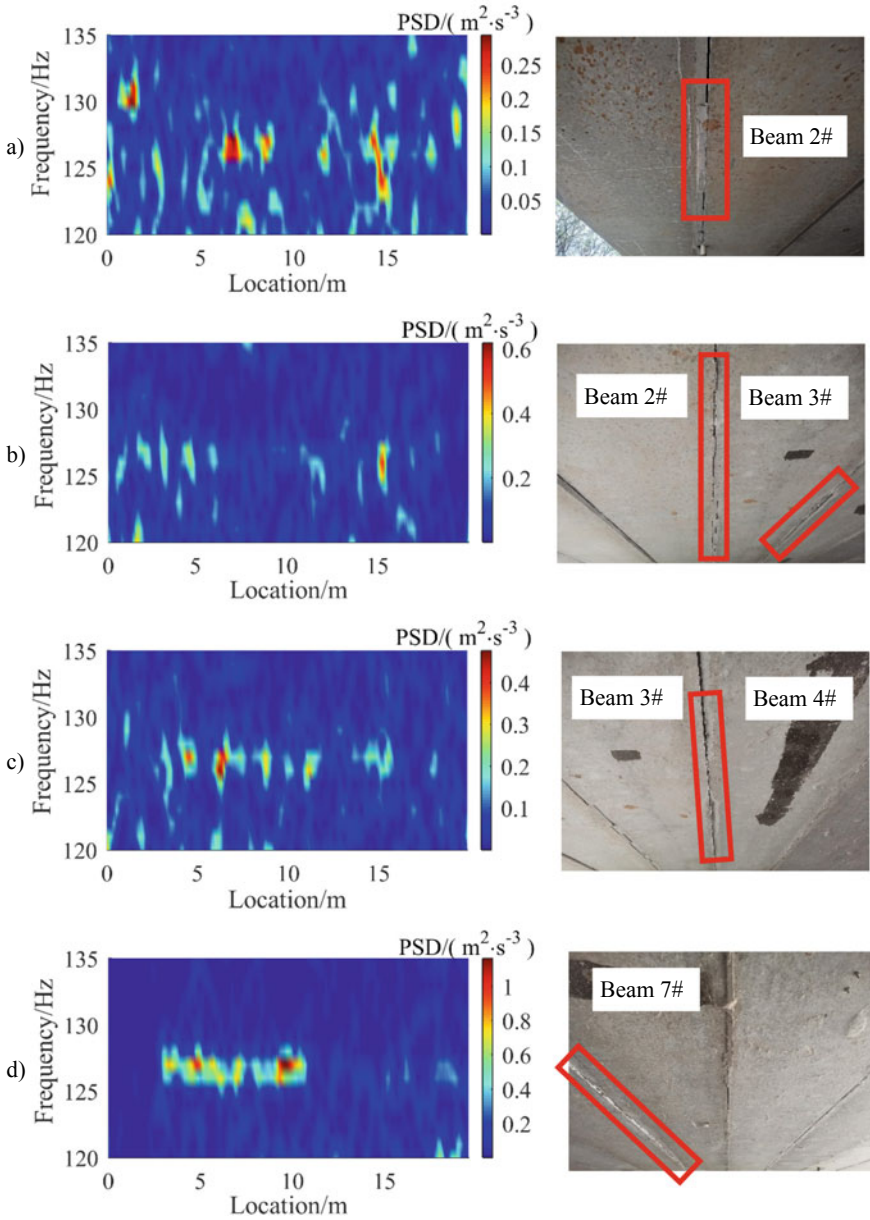


Fig. 26.7 The PSD graph and the corresponding damage of Cai-Jia-He-Zhi-Liu bridge: **a** beam 2#; **b** beam 3#; **c** beam 4# and **d** beam 7#

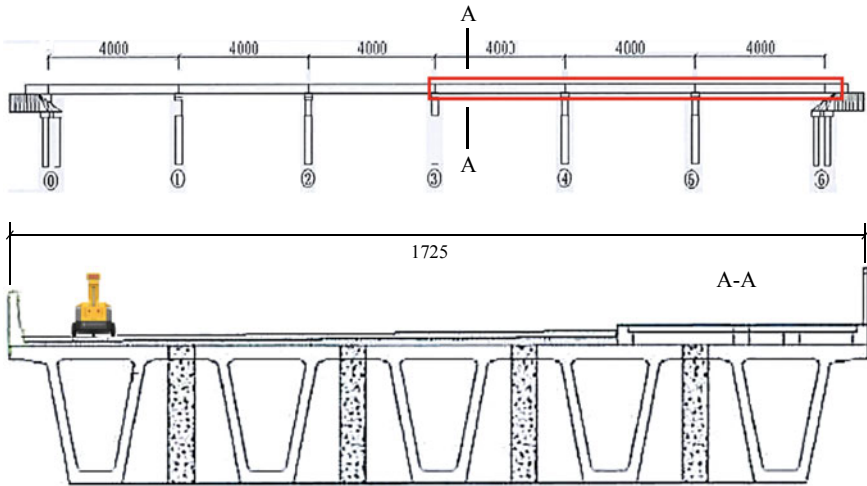


Fig. 26.8 The drawing of Yan-Zi-Yan bridge (unit: cm). Red box indicates the inspection spans

Fig. 26.9 The field inspection of Yan-Zi-Yan bridge



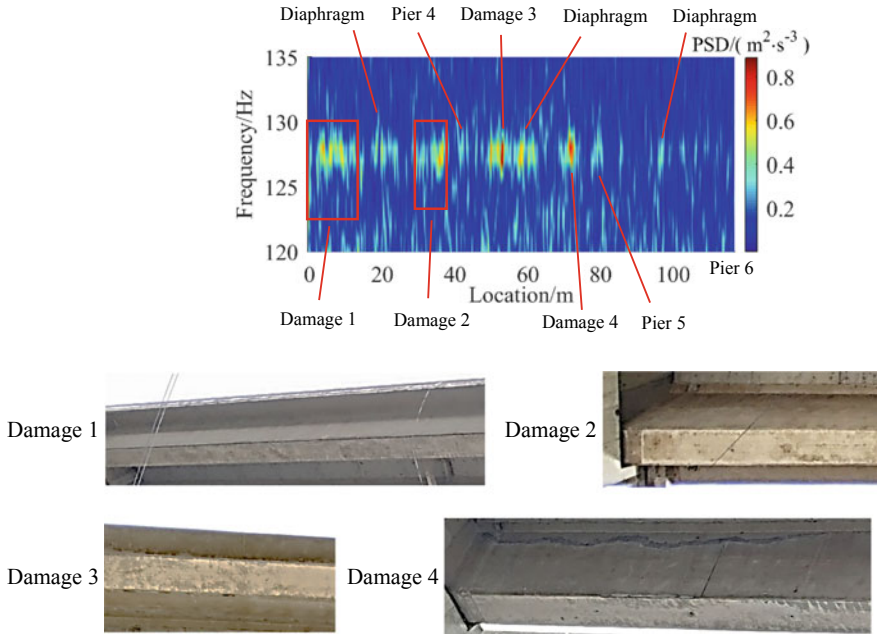


Fig. 26.10 The inspection results of Yan-Zi-Yan bridge

Funding This work was supported by the grant 2021-ZJYHZDXM-06 from CCCC Infrastructure Maintenance Group Co., Ltd., China.

Conflict of Interest The authors declare that they have no conflicts of interest to report regarding the present study.

References

1. Rehman, S.K.U., Ibrahim, Z., Memon, S.A., et al.: Nondestructive test methods for concrete bridges: a review. *Constr. Build. Mater.* **107**, 58–86 (2016)
2. AASHTO: *The Manual for Bridge Evaluation*, 3rd edn. American Association of State Highway and Transportation Officials, Washington, DC (2018)
3. Cunha, A., Caetano, E., Magalhães, F., Moutinho, C.: Recent perspectives in dynamic testing and monitoring of bridges. *Struct. Control. Health Monit.* **20**, 853–877 (2013)
4. Carden, E.P., Fanning, P.: Vibration based condition monitoring: a review. *Struct. Health Monit.* **3**(4), 355–377 (2004)
5. Fujino, Y., Siringoringo, D.M., Ikeda, Y., et al.: Research and implementations of structural monitoring for bridges and buildings in Japan. *Engineering* **5**, 1093–1119 (2019)
6. Figueiredo, E., Brownjohn, J.: Three decades of statistical pattern recognition paradigm for SHM of bridges. *Struct. Health Monit.* **21**(6), 3018–3054 (2022)
7. Farrar, C.R., Jauregui, D.A.: Comparative study of damage identification algorithms applied to a bridge: I. experiment. *Smart Mater. Struct.* **7**, 704–719 (1998)

8. Xiang, Z.H., Zhang, Y.: Change of modal properties of simply-supported plane beams due to damages. *Interact. Multiscale Mech.* **2**, 153–175 (2009)
9. Xiang, Z.H., Wang, L.Q., Zhou, M.S.: Suppressing damage identification errors from selected natural frequencies and mode shape points. *Inverse Probl. Sci. Eng.* **20**, 871–890 (2012)
10. Yang, Y.B., Lin, C.W., Yau, J.D.: Extracting bridge frequencies from the dynamic response of a passing vehicle. *J. Sound Vib.* **272**, 471–493 (2004)
11. Lin, C.W., Yang, Y.B.: Use of a passing vehicle to scan the fundamental bridge frequencies: an experimental verification. *Eng. Struct.* **27**, 1865–1878 (2005)
12. Yang, Y.B., Yang, J.P., Zhang, B., Wu, Y.: *Vehicle scanning method for bridges*. Wiley, Hoboken (2019)
13. Malekjafarian, A., Corbally, R., Gong, W.: A review of mobile sensing of bridges using moving vehicles: progress to date, challenges and future trends. *Structures* **44**, 1466–1489 (2022)
14. Zhang, Y., Wang, L.Q., Xiang, Z.H.: Damage detection by mode shape squares extracted from a passing vehicle. *J. Sound Vib.* **33**, 291–307 (2012)
15. Jin, N., Dertimanis, V.K., Chatzi, E.N., et al.: Subspace identification of bridge dynamics via traversing vehicle measurements. *J. Sound Vib.* **523**, 116690 (2022)
16. González, A., O'Brien, E.J., McGettrick, P.J.: Identification of damping in a bridge using a moving instrumented vehicle. *J. Sound Vib.* **331**, 4115–4131 (2012)
17. Yang, Y.B., Zhang, B., Chen, Y., et al.: Bridge damping identification by vehicle scanning method. *Eng. Struct.* **183**, 637–645 (2019)
18. González, A., O'Brien, E.J., Li, Y.Y., et al.: The use of vehicle acceleration measurements to estimate road roughness. *Veh. Syst. Dyn.* **46**, 483–499 (2008)
19. Zhan, Y., Au, F.T.K.: Bridge surface roughness identification based on vehicle-bridge interaction. *Int. J. Struct. Stab. Dyn.* **19**, 1950069 (2019)
20. Bu, J.Q., Law, S.S., Zhu, X.Q.: Innovative bridge condition assessment from dynamic response of a passing vehicle. *J. Eng. Mech.* **132**, 1372–1378 (2006)
21. Xiang, Z.H., Dai, X.W., Zhang, Y., et al.: The tap-scan method for damage detection of bridge structures. *Interact. Multiscale Mech.* **3**, 173–191 (2010)
22. Zhang, Y., Lie, S.T., Xiang, Z.H.: Damage detection method based on operating deflection shape curvature extracted from dynamic response of a passing vehicle. *Mech. Syst. Signal Process.* **35**, 238–254 (2013)
23. Xiang, Z.H., Lu, Q.H.: Elasto-dynamic damage evaluation of bridges. In: *Handbook of Damage Mechanics: Nano to Macro Scale for Materials and Structures*, pp. 589–618. Springer, New York (2015)
24. Hu, Z.Y., Xiang, Z.H., Lu, Q.H.: Passive Tap-scan damage detection method for beam structures. *Struct. Control. Health Monit.* **27**, e2510 (2020)
25. Yang, D.S., Wang, C.M.: Bridge damage detection using reconstructed mode shape by improved vehicle scanning method. *Eng. Struct.* **263**, 114373 (2022)
26. Corbally, R., Malekjafarian, A.: Bridge damage detection using operating deflection shape ratios obtained from a passing vehicle. *J. Sound Vib.* **537**, 117225 (2022)
27. Hu, Z.Y., Lin, P., Guo, H., Zhang, Y.M., Xiang, Z.H.: Detect the stiffness transition in beam structures by using the passive tap-scan method. *Mech. Syst. Signal Process.* **192**, 110211 (2023)

Chapter 27

Research on High-Velocity Perforation Characteristics of Elliptical Cross-Section Truncated Ogive Projectile



Ximin Deng, Heng Dong, Hao Wang, Haijun Wu, and Fenglei Huang

Abstract With the development of the hypersonic weapon system, the non-circular cross-section projectile with more space utilization has attracted extensive attention. The high-velocity penetration mechanism of the non-circular cross-section projectile is a crucial issue that must be solved. Based on the truncated conical head structure of a typical anti-ship warhead and the elliptical section projectile shape, the resistance characteristics of the projectile and the damage mechanism of the metal sheet are studied by numerical simulation. The load of the projectile is divided into two parts: shear punching resistance and ductile enlargement resistance. The results show that the elliptical cross-section truncated ogive projectile (ETOP) penetrating the metal sheet can be divided into the head and body penetration stages. In the head invasion stage, the failure mode of the sheet is decomposed into the shear plugging caused by the truncated cone platform and the ductility enlargement of the curved surface of the head. Under high-velocity impact, the damage to the sheet caused by the ogive/blunt projectile with the elliptic-section is different from that caused by low-velocity impact. When the ogive projectile penetrates the sheet, ductile enlargement failure occurs. When a blunt projectile impacts the sheet at high velocity, the coupled failure mode of shear punching and ductile enlargement occurs. The resistance of the elliptical cross-section projectile is the same as that of the circular cross-section projectile with the same area. The difference is that the asymmetric structure of the elliptical cross-section leads to non-uniform load distribution.

Keywords Elliptical cross section projectile · Perforation · Plugging · Enlargement

X. Deng · H. Dong · H. Wu (✉) · F. Huang
State Key Laboratory of Explosion Science and Technology, Beijing Institute of Technology,
Beijing 100081, China
e-mail: wuhj@bit.edu.cn

H. Wang
Beijing Research Institute of Mechanical and Electrical Technology, Beijing 100074, China

27.1 Introduction

With the development of hypersonic weapon systems, the velocity range studied in the field of perforation/penetration has changed from medium–low velocity to high-velocity. To improve the aircraft's space utilization rate of the damage load, the non-circular section projectile structure is proposed in the engineering design. Therefore, the high-velocity perforation/penetration mechanism of non-circular cross-section projectiles on targets has attracted extensive attention. Dong [1, 2] and Wang [3–5] conducted systematic research on the perforation/penetration of concrete and metal targets by special-shaped projectiles and gave the loading and deflection model in the medium and low-velocity range. Based on the cavity expansion theory, Dai [6] and Wei [7] proposed a ballistic model of an ogive projectile with an elliptical cross-section penetrating the thick target. There are few studies on elliptical cross-section projectiles penetrating thin metal targets at high velocity. However, the armor-piercing theory of circular-section projectiles in the medium and low-velocity range has been widely studied.

Through two-dimensional numerical simulation, Rosenberg [8] studied the penetration process to the ductile metal plate and found that the plate had ductile enlargement and petalling when it was impacted by conical and ogive projectile at low velocity. The enlargement mainly occurred in the penetration process of the medium-thick target (thick-diameter ratio of 1/3–1). Chen [9] compared the model proposed by Chen and Li [10] and Forrestal and Warren [11] of the conical projectile. The results show that the former is suitable for almost all ogive and conical projectiles, while the Forrestal and Warren [11] model is only suitable for the ductile enlargement problem of elongated ogive and conical projectiles. In addition, Chen [9] further analyzed the plate material and thickness on the armor-piercing ability and found that the piercing machine would change with the increase of thickness and material strength.

The resistance characteristics of the non-circular cross-section projectile and the failure mode of the plate are critical issues in researching the basic theory of perforation mechanics. According to the main geometric characteristics of non-circular cross-section projectile and simplifying the modeling of theoretical analysis, taking elliptical cross-section truncated ogive projectile (ETOP) as the research object. Through the numerical simulation of the projectile perforation the metal plate at high velocity, analyzed the resistance characteristics of the projectile and the failure mode of the plate. The high-velocity perforation process of the projectile with elliptic cross-section is studied. The resistance function and residual velocity analytical models of two typical projectiles are proposed.

27.2 Simulation Method and Verification

Based on the truncated ogive nose of the conventional anti-ship warhead and the shape of the elliptical cross-section formed the ETOP. The specific geometry is shown in Fig. 27.1, where the ratio of the major and minor axes of the elliptical section is $\lambda = 1.6$. The projectile mass is 265.2 g, the impact velocity is 700–1000 m/s, and the materials of 3 mm plate is 945 steel.

Abaqus/Explicit was used for simulation calculation. To improve the computational efficiency and the accuracy of numerical simulation, the grid in the center area of the board was locally refined, and the full-size 3D model was used for calculation with the grid size of $0.02 \times 0.02 \times 0.02$ cm [3, 12]. In addition, considering that the width of the shear band is about 10–100 μm [13, 14], to characterize the crack propagation process of the blunt projectile compression process, the mesh size of the impact area in Sect. 1.3 is 0.01 cm [15]. An 8-node reducing integral element C3D8R is used and fixed constraint boundary conditions are applied to the boundary of the plate. The general contact algorithm is adopted for projectile and target contact, and ignores the friction between projectile and target [12, 16, 17]. Considering that the projectile diameter is much larger than the plate thickness and small projectile deformation, assumed that the projectile is rigid material for the convenience of subsequent theoretical analysis.

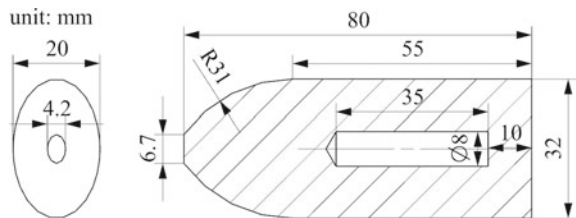
The improved Johnson–Cook constitutive model describes the stress–strain relationship of the plate material:

$$\bar{\sigma} = [A + B(\bar{\epsilon}^p)^n][1 + (C_1 + C_2 \ln \dot{\epsilon}^*) \ln \dot{\epsilon}^*][1 - T^{*m_T}] \tag{27.1}$$

$$\dot{\epsilon}^* = \frac{\dot{\epsilon}}{\dot{\epsilon}_0}, T^* = \frac{T - T_0}{T_m - T_0} \tag{27.2}$$

where $\bar{\epsilon}^p$ is the equivalent plastic strain, $\dot{\epsilon}_0$ and $\dot{\epsilon}$ are the reference strain rate and equivalent plastic strain rate, respectively. T , T_0 , and T_m are the material deformation temperature, reference temperature, and melting temperature, respectively. A is the initial yield stress at reference strain rate and reference temperature. B and n are strain hardening modulus and hardening index of the material, respectively. C_1 and C_2 are strain rate strengthening parameters. m_T is the thermal softening index of materials.

Fig. 27.1 Geometry of the ETOP



Due to the high temperature in the shear zone of the plate during high-velocity penetration, the local softening effect caused by adiabatic temperature rise should be considered. Temperature rise caused by introducing local plastic work to produce heat [18]

$$\Delta T = \frac{\chi}{\rho c} \int_0^{\varepsilon_p} \sigma(\varepsilon_p) d\varepsilon_p \tag{27.3}$$

where χ is the plastic work-heat transfer factor, ρ is the material density, and c is the specific heat capacity at constant pressure.

The damage characteristics of plates are characterized by a three-stage damage model proposed by Wierzbick [19] which considers the stress triaxial η . Assuming that the damage parameter D increases linearly with the equivalent plastic strain,

$$D = \int_0^{\bar{\varepsilon}_f} f(\eta) d\bar{\varepsilon}^p \tag{27.4}$$

$$\bar{\varepsilon}_f = \begin{cases} \frac{D_1}{1 + 3\eta} & -\frac{1}{3} \leq \eta \leq 0 \\ \varepsilon_{f,t} + (\varepsilon_{f,t} - \varepsilon_{f,s})(3\eta - 1) & 0 < \eta \leq \frac{1}{3} \\ D_2 \exp(D_3\eta + D_4) & \eta > \frac{1}{3} \end{cases} \tag{27.5}$$

where $D_1 \sim D_4$ is the material parameters, $D_1 = \varepsilon_{f,s}$ is the shear failure strain ($\eta = 0$), $\varepsilon_{f,t}$ is the uniaxial tensile failure strain ($\eta = 1/3$), $\bar{\varepsilon}_f$ is the average failure strain, and $d\bar{\varepsilon}^p$ is the equivalent plastic strain increment.

By fitting experimental data [20, 21], the parameters of 945 steel are shown in Table 27.1.

A VUMAT subroutine is used to characterize the mechanical properties of 945 steel. The comparison between the numerical simulation and the experiment is shown in Table 27.2 and Fig. 27.2, which verifies the effectiveness of the simulation model.

27.3 The Penetration Characteristics of the ETOP

27.3.1 Perforation Progress

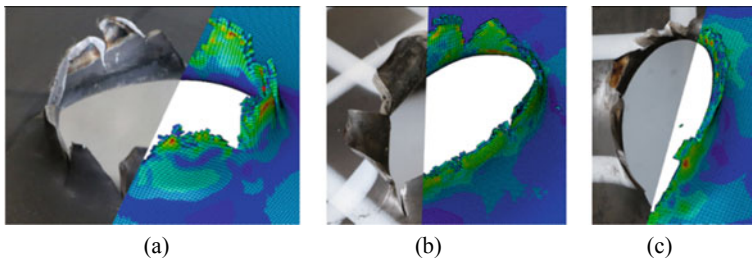
Figure 27.3a shows the velocity and acceleration curves of the ETOP perforating the 3 mm 945 steel plate with an initial velocity of 1000 m/s. According to the change of acceleration, the projectile perforation process includes the stage of head invasion (stage I) and perforation (stage II). Stage I is the primary interaction period between the projectile and plate, and there is no load on the projectile in stage II. By comparing

Table 27.1 Material parameters of 945 steel

Parameters	A (MPa)	B (MPa)	n	C_1	C_2	E (GPa)	ν	$\dot{\varepsilon}_0$ (s^{-1})	T_0 (K)	T_m (K)
Value	451.16	797.73	0.75	- 0.1589	0.012	210	0.33	3E-4	293	1800
Parameters	m	χ	ρ ($g \cdot cm^{-3}$)	c_p ($J \cdot kg^{-1} \cdot K^{-1}$)	D_1	D_2	D_3	D_4	$\varepsilon_{f,t}$	
Value	0.859	0.9	7.85	452	0.35	1.11	- 0.806	0.10	0.996	

Table 27.2 Comparison of experimental [4] and simulation results

No	Impact angle	Initial velocity/(m s ⁻¹)	Residual velocity/(m s ⁻¹)		Deviation/%
			Experimental	Simulation	
1	0°	293.24	261.23	267.90	2.55
2	0°	308.34	279.95	286.32	2.28
3	30°	268.49	254.23	248.58	- 2.22
4	30°	260.03	239.16	225.17	- 5.85
5	30°	542.86	529.81	516.47	- 2.52

**Fig. 27.2** Comparison of failure modes of the plate. **a** The first target of No. 1; **b** the first target of No. 4; **c** the second target of No. 5

the acceleration of the projectile at different moments and the position relationship between the projectile and the plate, stage I can be further refined into four periods, as shown in Figs. 27.3b and 27.4.

Period I–I: After the head invades the plate, the plate forms a plug with a similar area to the truncated cone, and the velocity of the plug increases rapidly and exceeds the projectile velocity. It reaches its maximum value at time ①. The resistance is generated by the shear failure and the radial expansion of the hole.

Period I–II: At time ①, the plug reaches its maximum velocity and separates from the projectile, continuing to move forward due to inertia. The relative motion of the plug and the plate causes a bulge on the back of the plate, resulting in a decrease in the resistance of the projectile.

Period I–III: The plug is completely separated from the plate at time ③. When the projectile invades the inner wall of the hole, the failure mode of ductile enlargement appears. The resistance increases with the increase of the contact area between the projectile and the plate.

Period I–IV: The plug detached from the plate and no longer affected the projectile. At this stage, it can be approximately equivalent to the ogive projectile with an elliptical cross-section penetrating the metal plate with an initial hole, the projectile and the inner wall of the hole are entirely fitted, and the deformation of the plate is radial expanding.

According to elastic–plastic mechanics, the plastic deformation and failure of materials are related to the stress state. The work done by the stresses in different

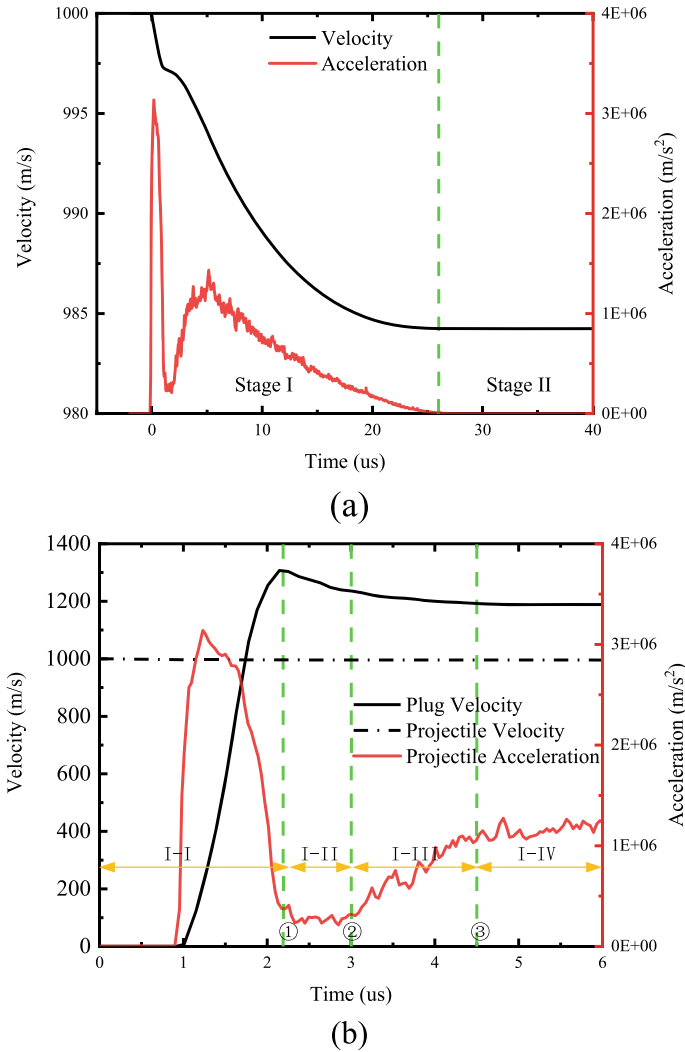


Fig. 27.3 The response of ETOP during penetration. **a** The velocity/acceleration curve of the ETOP; **b** velocity and acceleration curves of ETOP and plug

directions will lead to the difference in the plastic work done components. Therefore, the failure mode of the plate can be quantitatively analyzed according to the distribution of plastic work done components. Taking the initial impact point as the origin point, the cylindrical coordinate system $r\theta z$ is established, in which the r axis points to the inner wall of the hole and the z axis points to the tail along the axis of the projectile. The stress and strain components of the elements under the cylindrical coordinate system are shown in Fig. 27.5.

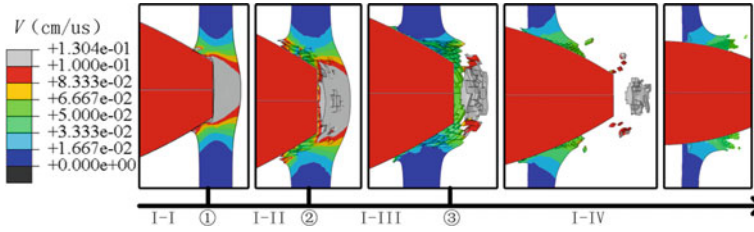


Fig. 27.4 Velocity distributions at different times in stage I

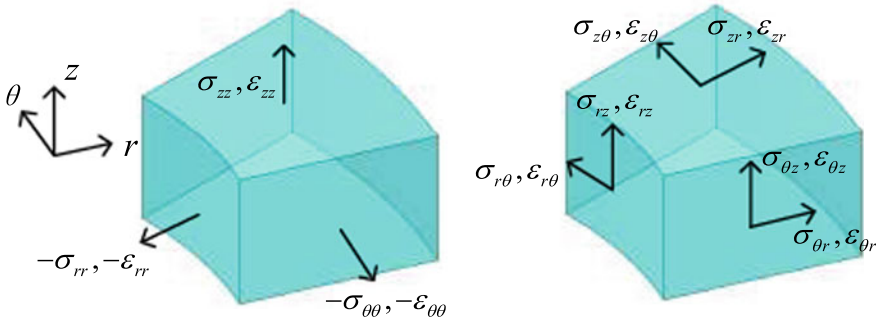


Fig. 27.5 Stress and strain components in cylindrical coordinates

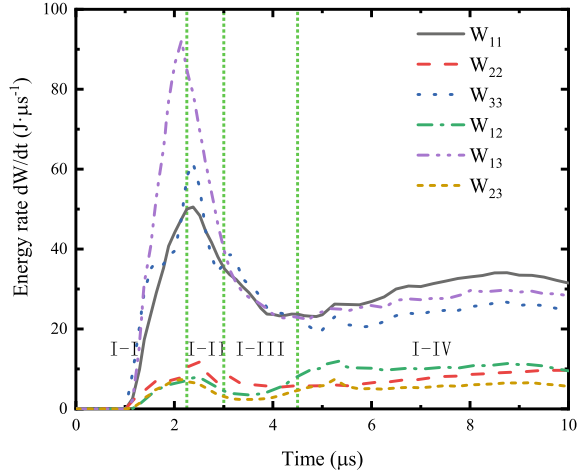
Based on the cylindrical coordinate system shown in Fig. 27.5, the plastic work done by the plate elements in all directions can be expressed as

$$\begin{aligned}
 W_{ii} &= \sigma_{ii} \times \epsilon_{ii}^p \times Vol \\
 W_{ij} &= \sigma_{ij} \times \gamma_{ij} \times Vol
 \end{aligned}
 \tag{27.6}$$

where the subscript ij represents the axis direction, W_{ij} are the plastic work done components in the cylindrical coordinate system, σ and ϵ^p are the stress and plastic strain components, $\gamma_{ij} = 2\epsilon_{ij}^p$ are the shear strain components, and Vol is the element volume. Equation (27.6) is programmed into VUMAT and output as a state variable. At the same time, the relevant data were extracted with a Python subroutine during post-processing. Then the sum of plastic work done components of plate elements under the cylindrical coordinate system was obtained.

Figure 27.6 shows the energy rate curve of the plate in stage I. In I-I and I-II periods, the energy ratio corresponding to shear stress σ_{13} and axial stress σ_{33} is the largest, indicating that the response of plates in this period is mainly shear and axial compression, and the failure mode is shear plugging. During the I-III period, the energy rate corresponding to shear stress σ_{13} decreases, and the change rates of W_{11} , W_{33} , and W_{13} tend to be consistent. During the I-IV period, the change of radial energy rate accounted for the most significant proportion, indicating that the radial

Fig. 27.6 Energy rate curve of the plate in stage I



compression dominated the plate response, and the failure mode was the ductile enlargement.

According to the above analysis, when the ETOP penetrates the metal plate at a high velocity, the failure mode of the plate can be divided into shear plugging caused by the truncation cone at the initial stage of penetration and ductility enlargement by the ogive nose. To obtain the resistance characteristics of the projectile corresponding to the two types of failure modes, the blunt/ogive projectiles with elliptical cross-section are taken as the research objects to carry out further simulation research.

27.3.2 High-Velocity Perforation Characteristics of Elliptical Cross-Section Projectile

Defining the equivalent circle whose area is equal to that of the ellipse, and its radius is the equivalent radius r_{p0} . The r_{p0} of the two types of projectiles is 1.5 cm, and the length is about 10 cm. The major and minor axes of the ellipse are $2r_{p0}\sqrt{\lambda}$ and $2r_{p0}/\sqrt{\lambda}$. λ is 1, 1.5, 1.8, and 2. The mass of the blunt and the ogive projectiles are 554.6 g and 453.9 g, respectively. Figures 27.7 and 27.8 show the geometry of projectiles.

The acceleration curves of the four types of ogive projectiles with elliptical cross-section penetrated the 945-steel plate with an initial velocity of 700–1000 m/s are shown in Fig. 27.9. Where $\lambda(_)$ is the ratio of the major and minor axes of the ellipse, and $V(_)$ is the initial velocity. The results show that the acceleration curves of the projectile with circular section ($\lambda = 1$) and elliptical cross-section are coincident when it impacts the plate at the initial velocity of 900 m/s. In range $\lambda \in [1, 2]$ [1, 2], the projectile has the same resistance when it impacts the thin plate at high velocity. In other words, under the same initial velocity, the resistance of the projectile with

Fig. 27.7 Geometric relation between equivalent circle and ellipse

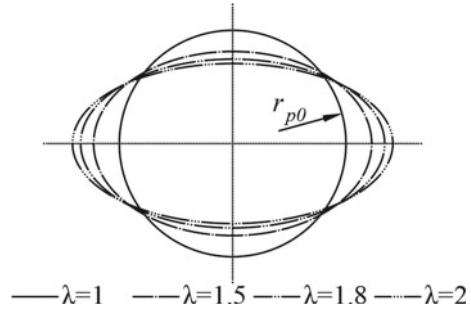
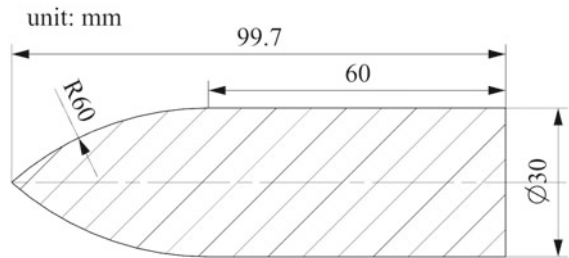


Fig. 27.8 The geometry of the ogive projectile



an elliptical cross-section is the same as that of the projectile with the equivalent radius. In addition, the resistance is related to the impact velocity during ductile enlargement, and the increase of the velocity leads to the increase of the peak load and the decrease of the load duration.

It is worth noting that the axial resistance of the projectile with an elliptical cross-section is the same as that of the equivalent radius. However, the stress of the elliptical cavity is not uniformly distributed in the process of hole enlargement, as shown in Fig. 27.10. In reference [5, 22–24], the stress distribution on the inner wall of the cavity when the elliptical cross-section projectile penetrates the thick concrete target, the thin metal target, and the elliptical cavity under the action of detonation wave is studied. It is found that the stress on the major axis is higher than that on the minor axis.

The acceleration curves of the blunt projectile with the elliptic-section penetrating the 3 mm 945 steel sheet with the initial velocity of 700–1000 m/s are similar to the curves in Fig. 27.6. The results show that the elliptic projectile's resistance curves coincide when the equivalent section area is the same under the same impact velocity. Therefore, the analysis method of the projectile with the circular section can be used to calculate the plugging resistance of the elliptic section projectile. Figure 27.11b verifies the applicability of the above conclusions under the conditions of 700–1000 m/s. In addition, the resistance of the projectile in the shear plug mode is positively correlated with the initial velocity. The projectile takes 1.25 μs to penetrate a 0.3 cm sheet, and the maximum displacement of the projectile is 0.12 cm, which is

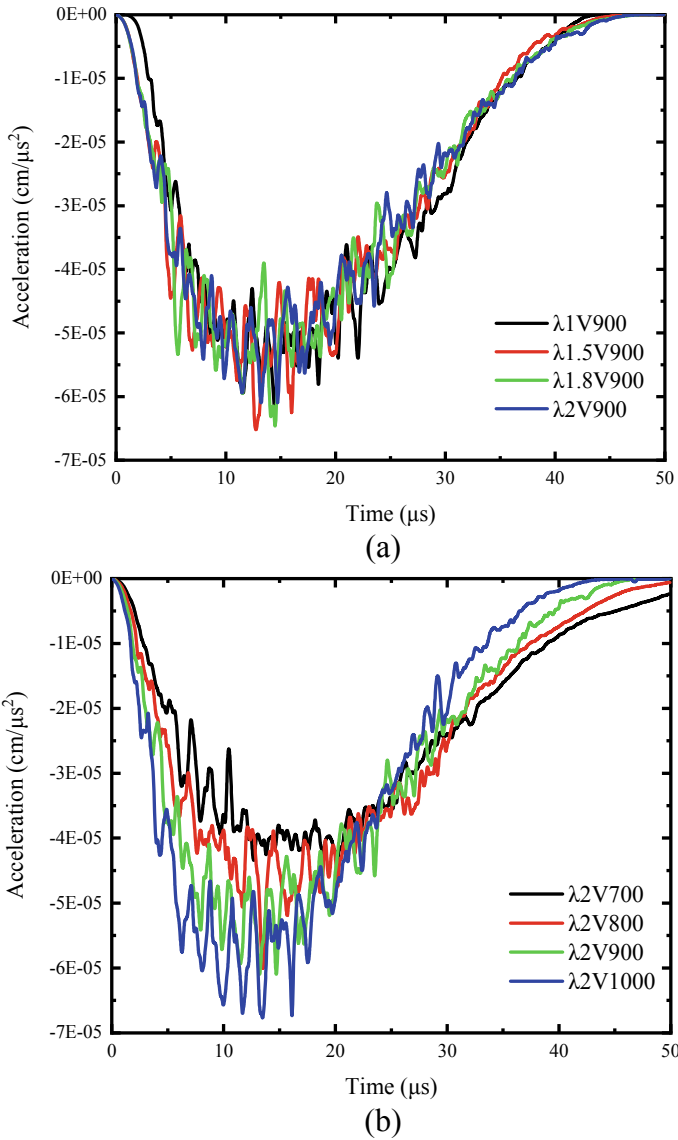


Fig. 27.9 Ogive projectile acceleration curves. **a** At the same velocity; **b** at the different velocity

half of the thickness of the plate. It indicates that the projectile and plate interaction does not end when the head passes through the sheet.

The progress of the blunt projectile penetrating the sheet can be divided into several stages [25, 26], such as local pressing (t_1), crack propagation (t_2), and plug formation (t_3), as shown in Fig. 27.12, where the red arrow represents the direction of crack propagation. When the blunt projectile penetrates the sheet at high velocity,

Fig. 27.10 Stress distribution of elliptic cavity

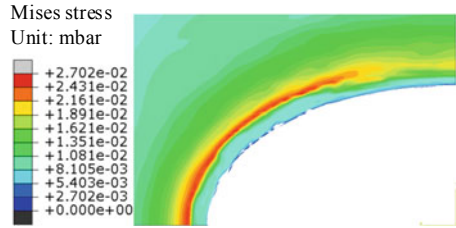
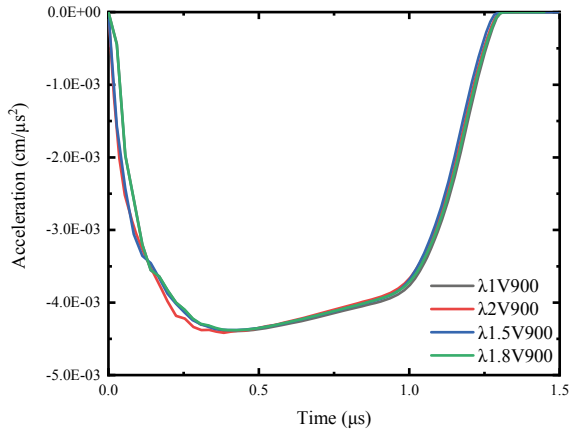
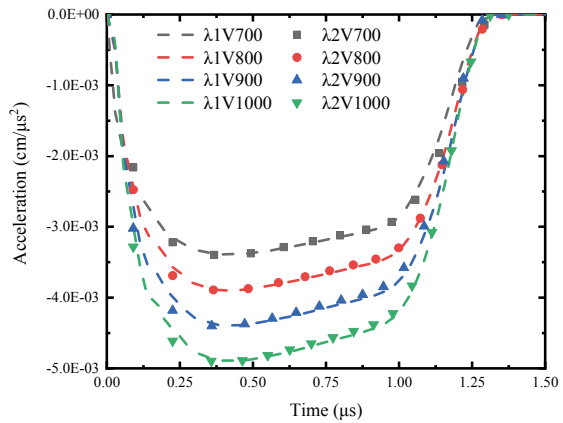


Fig. 27.11 Flat projectile acceleration curves. **a** At the same velocity; **b** at the different velocity



(a)



(b)

the failure mode of the sheet is the coupling mode of ductile enlargement and shear plugging. The resistance of the projectile includes axial pressure, shear force, and the resistance caused by the radial expansion of the sheet.

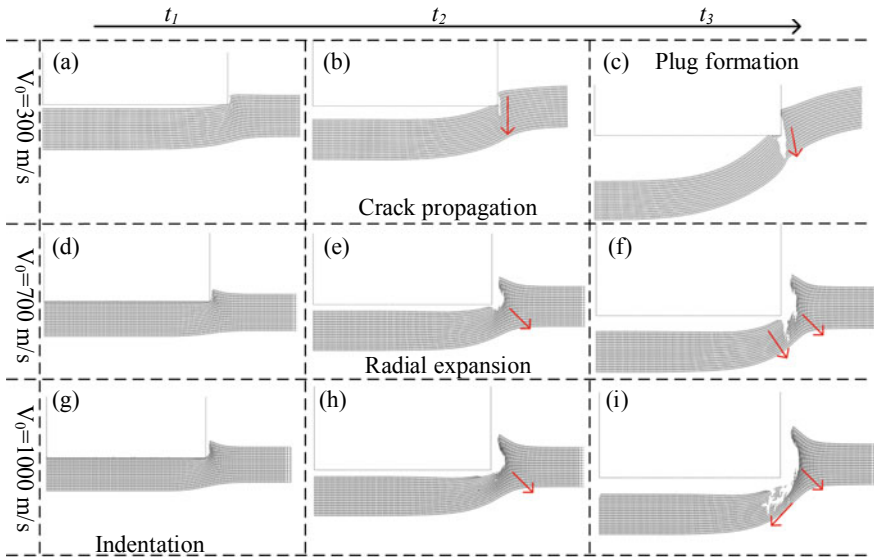


Fig. 27.12 Failure mode of target at different impact velocities

As can be seen from Fig. 27.12a–c, cracks occur after the projectile penetrates the sheet and propagate to the back of the sheet at a higher speed than the projectile. When cracks come through the sheet, a plug is formed. Figure 27.12d–f and g–i shows the process of the projectile with the elliptic section penetrating the sheet at 700 m/s and 1000 m/s, respectively. At t_1 , that is, during the penetrating stage of the projectile head, the sheet near the bullet hole expands radially except for the compression deformation. No cracks occurred at t_2 , and the inner wall of the bullet hole expanded radially, showing the characteristics of ductile enlargement. In addition, at t_2 , the radial expansion of the bullet hole stopped, and cracks appeared where the plug connected to the sheet. With the increased sheet velocity, the crack direction gradually shifted to the inside of the plug.

The above phenomenon indicates that the failure mode of the sheet under the impact of a blunt projectile at high velocity is different from that under low-speed impact. The failure mode is like the combined form of ductile enlargement and shear plugging. The resistance of the projectile includes axial pressure, shear force, and the resistance caused by the radial expansion of the sheet.

Combined with the above analysis, the resistance characteristics of the blunt/ogive projectile with an elliptic section are like those of a circular section projectile when penetrating the metal sheet. However, the response characteristics of the sheet at high-velocity impact are no longer the same as those at low speed. According to the sheet's failure mode and the projectile's resistance characteristics, the resistance of ETOP in the process of perforation can be divided into shear plugging and ductile enlargement.

27.4 Conclusion

Based on the numerical simulation method, the penetration process of the ETOP and the ogive/blunt projectile with an elliptic-section penetrating metal sheet was studied. The main conclusions can be drawn as follows:

- (1) The ETOP penetrating the metal sheet can be divided into the head penetration stage and the body penetration stage without load. In the head invasion stage, the failure mode of the projectile to the sheet is decomposed into the shear plugging caused by the truncated cone platform and the ductility enlargement of the curved surface of the head.
- (2) Under high-velocity impact, the damage to the sheet caused by the ogive/blunt projectile with the elliptic-section differs from that caused by low-velocity impact. When the ogive projectile penetrates the sheet, ductile enlargement failure occurs. When a blunt projectile impacts the sheet at high velocity, the coupled failure mode of shear punching and ductile enlargement occurs.
- (3) The resistance of the elliptical cross-section projectile is the same as that of the circular cross-section projectile with the same cross-sectional area. The difference is that the asymmetric structure of the elliptical cross-section projectile leads to non-uniform load distribution.

Acknowledgements This work was supported by the National Natural Science Foundation of China (grant No. 12072039), the National Natural Science Foundation Youth Project (grant No. 12202067), and the State Key Laboratory of Explosion Science and Technology (grant No. QNKT22-03).

Conflict of Interest The authors declare that they have no conflicts of interest to report regarding the present study.

References

1. Dong, H.: Penetration mechanism and structural response of elliptical cross-sectional projectile penetrating into concrete target. Ph.D. Thesis, Beijing Institute of Technology, Beijing (2021)
2. Dong, H., Wu, H., Liu, Z., et al.: Penetration characteristics of pyramidal projectile into concrete target. *Int. J. Impact Eng.* **143**, 103583 (2020)
3. Wang, H.: The failure mode and deflection mechanism of projectiles with tapered-elliptic cross-section perforation into stiffened plates. Ph.D. Thesis, Beijing Institute of Technology, Beijing (2020)
4. Wang, H., Wu, H.J., Yan, L., et al.: Failure mode of oblique perforation of truncated ogive-nosed projectiles with elliptic cross-section into double-layered thin steel plate with gap space. *Acta Armamentarii* **41**(S2), 1–11 (2020)
5. Tian, Z., Wang, H., Wu, H.J., et al.: Attitude deflection mechanism of projectiles with variable elliptical cross-sections obliquely perforating thin targets. *Acta Armamentarii* **43**(7), 1537–1552 (2022)
6. Dai, X.H., Wang, K.H., Li, M.R., et al.: Rigid elliptical cross-section ogive-nose projectiles penetration into concrete targets. *Def. Technol.* **17**(3), 800–811 (2021)

7. Haiyang, W., Xianfeng, Z., Wei, X., et al.: Oblique penetration of elliptical cross-section projectile into metal target. *Explos. Shock Waves* **42**(2), 023304 (2022)
8. Rosenberg, Z., Dekel, E.: Revisiting the perforation of ductile plates by sharp-nosed rigid projectiles. *Int. J. Solids Struct.* **47**(22–23), 3022–3033 (2022)
9. Chen, X.W., Huang, X.L., Liang, G.J.: Comparative analysis of perforation models of metallic plates by rigid sharp-nosed projectiles. *Int. J. Impact Eng.* **38**(7), 613–621 (2011)
10. Chen, X.W., Li, Q.M.: Perforation of a thick plate by rigid projectiles. *Int. J. Impact Eng.* **28**(7), 743–759 (2003)
11. Forrestal, M.J., Warren, T.L.: Perforation equations for conical and ogival nose rigid projectiles into aluminum target plates. *Int. J. Impact Eng.* **36**(2), 220–225 (2009)
12. Borvik, T., Hopperstad, O.S., Berstad, T., et al.: Perforation of 12 mm thick steel plates by 20 mm diameter projectiles with flat, hemispherical and conical noses part II: numerical simulations. *Int. J. Impact Eng.* **27**(1), 37–64 (2002)
13. Børvik, T., Leinumb, J.R., Solberg, J.K., et al.: Observations on shear plug formation in Weldox 460 E steel plates impacted by blunt-nosed projectiles. *Int. J. Impact Eng.* **25**, 553–572 (2001)
14. Chen, X.W., Li, Q.M., Fan, S.C.: Initiation of adiabatic shear failure in a clamped circular plate struck by a blunt projectile. *Int. J. Impact Eng.* **31**(7), 877–893 (2005)
15. Borvik, T., Hopperstad, O.S., Langseth, M., et al.: Effect of target thickness in blunt projectile penetration of Weldox 460 E steel plates. *Int. J. Impact Eng.* **28**(4), 413–464 (2003)
16. Børvik, T., Langseth, M., Hopperstad, O.S., et al.: Perforation of 12 mm thick steel plates by 20 mm diameter projectiles with flat, hemispherical and conical noses: part I: experimental study. *Int. J. Impact Eng.* **27**, 37–64 (2002)
17. Rusinek, A., Rodríguez-Martínez, J.A., Zaera, R., et al.: Experimental and numerical study on the perforation process of mild steel sheets subjected to perpendicular impact by hemispherical projectiles. *Int. J. Impact Eng.* **36**(4), 565–587 (2009)
18. Chen, X.W., Liang, G.J., Yao, Y., et al.: Perforation modes of metal plates struck by a blunt rigid projectile. *Chin. J. Theor. Appl. Mech.* **41**(1), 84–90 (2009)
19. Mae, H., Teng, X., Bai, Y., et al.: Comparison of ductile fracture properties of aluminum castings: sand mold vs. metal mold. *Int. J. Solids Struct.* **45**(5), 1430–1444 (2008)
20. Li, Y.: Fragment resistant mechanism research of safety liquid cabin. M.D. Thesis, Wuhan University of Technology (2014)
21. Li, Y.: Damage and protective mechanism of cabins under anti-ship missile internal blast. Ph.D. Thesis, Wuhan University of Technology (2017)
22. Dong, H., Liu, Z.H., Wu, H.J., et al.: Study on penetration characteristics of high-speed elliptical cross-sectional projectiles into concrete. *Int. J. Impact Eng.* **132**, 103311 (2019)
23. Wang, H., Pan, X., Wu, H.J., et al.: Energy dissipation analysis of elliptical truncated oval rigid projectile penetrating stiffened plate. *Explos. Shock Waves* **39**(10), 69–80 (2019)
24. Deng, X., Wu, H., Yang, X., et al.: Preformed fragment velocity distribution of elliptical cross-section projectile. *Latin Am. J. Solids Struct.* **19**(1), 1–29 (2022)
25. Teng, X., Wierzbicki, T.: Dynamic shear plugging of beams and plates with an advancing crack. *Int. J. Impact Eng.* **31**(6), 667–698 (2005)
26. Vershinin, V.V.: Validation of metal plasticity and fracture models through numerical simulation of high velocity perforation. *Int. J. Solids Struct.* **67–68**, 127–138 (2015)

Chapter 28

Study on Downhole Torque Prediction Method Combining Machine Learning and Mechanism Model



Chuanjie Ren, Wenjun Huang, and Deli Gao

Abstract Long horizontal Wells have been widely used in the development and utilization of unconventional oil and gas resources such as shale oil and gas. However, excessive torque has been a limiting factor for the length of horizontal Wells. Accurate prediction of downhole torque is a key technique to improve the rate of penetration and achieve safe drilling in the horizontal section. However, it is currently difficult to directly measure downhole torque due to the limitations of downhole measuring tools. Therefore, a new downhole torque prediction method based on soft sensing ideas combining artificial intelligence with string mechanics is proposed in this paper. Firstly, GA-BP with field-measured data is used to predict rotary torque. Then, the downhole torque is inverted by the soft rope model. Finally, the efficiency of torque transfer during drilling is evaluated. The results show that the downhole torque only accounts for 27.6% of surface torque due to the presence of drag and torque. The research results have important guiding significance for the safety control and optimization of long horizontal well drilling.

Keywords Downhole torque prediction · Machine learning · Mechanism model · Soft rope model · Soft sensing

C. Ren · W. Huang (✉) · D. Gao (✉)

MOE Key Laboratory of Petroleum Engineering, China University of Petroleum, Beijing 102249, China

e-mail: huangwenjun1986@126.com

D. Gao

e-mail: gaodeli_team@126.com

State Key Laboratory of Petroleum Resources and Prospecting, China University of Petroleum, Beijing 102249, China

28.1 Introduction

Drag and torque have become important factors affecting the operation safety of complex structural wells such as horizontal wells and extended-reach wells. Downhole torque is one of the important energy sources of drill bit rock breaking. Therefore, accurate prediction of downhole torque is a key technology to achieve safe drilling and improve drilling efficiency. Many drag and torque models have been proposed by different scholars until now. Johancsik et al. [1] established a classic soft rope model to calculate drag and torque, which simplified downhole pipe string into a rope without bending stiffness. Ho [2] regarded downhole drill string as an elastic thin rod and proposed a stiff rod model. Aadnoy and Djurhuus [3] presented a generalized drag and torque calculation model, which could be used in vertical sections, build-up bends, drop-off bends, and straight sections. Mitchell and Samuel [4] established a more accurate stiff rod model considering the influence of the contact case between the tubular string and wellbore. Considering the influence of viscous force caused by cuttings bed, eccentricity, and joint, Sun and Gao [5] proposed a more complicated stiff rod model. Huang et al. [6] established an amended drag torque model by introducing the lock-sticking effect, which can more accurately simulate the complex mechanical behavior of drill string with connectors in a borehole. Considering the effects of curvature discontinuity of well trajectory and stiffness discontinuity of tubular string, Zhao et al. [7] proposed an improved torque and drag model.

With the development of computer and artificial intelligence technology, there are some attempts to use machine learning algorithms for torque prediction. Hedge et al. [8] established a downhole torque prediction model using multi-layer perceptron, random forest, and other algorithms, in which downhole torque must be known in advance. Song et al. [9] established an intelligent prediction model of hook load and rotary torque by using BP neural network and long and short-term memory neural network, considering the complex and diverse factors affecting hook load and torque and the timing characteristics of the drilling process.

Direct measurement of downhole torque and direct prediction using artificial intelligence techniques is very difficult due to the high cost of downhole measurement and poor data stability. The soft sensing technology uses easily measurable process variables as a bridge and applies computer technology to calculate and estimate variables that are difficult to be directly measured, which makes it possible to predict downhole torque [10, 11].

Therefore, a prediction method of downhole torque based on soft sensing is proposed in this paper. The artificial intelligence is combined with tubular mechanics to calculate downhole torque, and the mechanical characteristics are analyzed in the drilling process. Among them, GA-BP combined with field-measured data was used to predict the rotary torque. Then, the downhole torque is inverted by the soft rope model. Finally, the efficiency of torque transfer during drilling is evaluated.

28.2 Prediction of Rotary Torque

Rotary torque is the result of the interaction of drill string, drilling parameters, and formation, and it is also one of the important energy sources of drilling rock breaking. Therefore, it can be used as an important representation of downhole BHA working conditions at the surface. By accurately predicting rotary torque, drilling risks can be predicted and intervention measures can be implemented in advance, which can reduce the occurrence of drilling accidents. In this paper, a GA-BP rotary torque prediction model is established by using a genetic algorithm (GA) to optimize BP neural network.

BP neural network is a multi-layer forward feedback neural network trained with an error back propagation algorithm. Due to its powerful nonlinear fitting ability, it has become one of the most widely used neural network models [12]. The structure of the BP neural network generally includes an input layer, hidden layers, and an output layer; the basic hidden layer unit is composed of input data, weight coefficient, deviation, activation function, and output data, as shown in Fig. 28.1.

BP neural networks have a powerful nonlinear fitting ability, which can fully exploit the mechanism existing inside the data. However, BP neural network is easily influenced by model hyperparameters with the disadvantages of slow learning convergence, unstable network structure, and falling easily into a local minimum. The genetic algorithm is a heuristic optimization algorithm with a strong global search ability, and its use for the optimization of network parameters can effectively improve the shortcomings of the BP neural network [13].

The establishment of GA-BP rotary torque prediction model is divided into three steps: BP neural network structure determination, genetic algorithm optimization

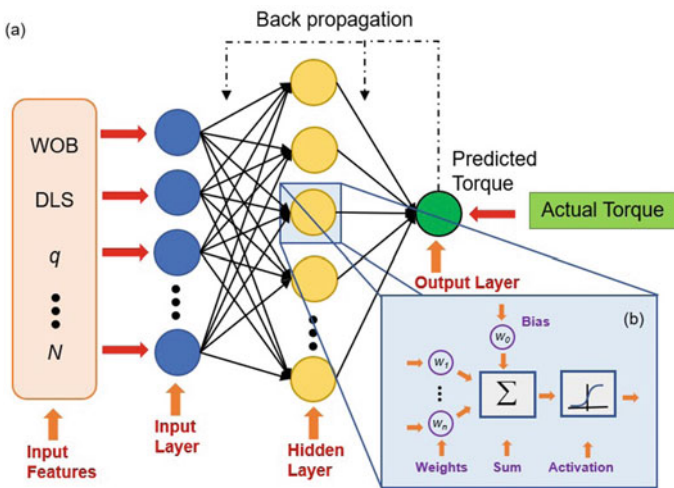


Fig. 28.1 BP neural network structure

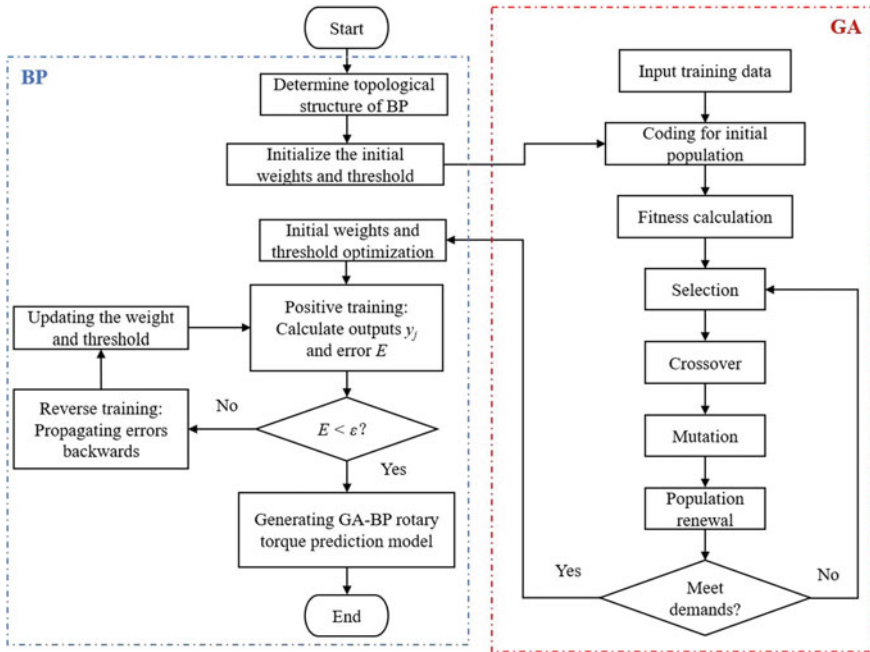


Fig. 28.2 GA-BP rotary torque prediction model

weights and thresholds, and BP neural network training and prediction, as shown in Fig. 28.2. The BP neural network topology structure is determined according to the feature selection and prediction objectives in the feature engineering, which determines the number of neurons in the input layer and the output layer of the network. The length of the genetic algorithm individual could also be known. The genetic algorithm is used to optimize the initial weights and thresholds of the BP neural network. Each individual in the population contains weights and thresholds of a network model, which represents a particular prediction model, and each fitness value is calculated by the fitness function. The optimal individual with the best fitness value could be found by a genetic algorithm through selection, crossover, and mutation operations, which is selected as the current neural network. It is trained by the training data to obtain a GA-BP rotary torque prediction model that meets the accuracy requirements.

28.3 Mechanical Model of Tubular in Rotary Drilling

In tubular mechanics, the existing calculation models of drag and torque are mainly divided into three categories: soft rope model, stiff rod model, and finite element model. The soft rope model is widely used in the calculation of drag and torque for

various types of wells due to its simplicity and reliability. It is assumed that the drill pipe is a soft rope that cannot bear bending moments but can withstand torque. Before the mechanical analysis of the pipe string, the following assumptions are made on the model:

- ① Drill string is similar to the soft rope, ignoring its stiffness, and the wall is rigid;
- ② The drill string is in continuous contact with the wellbore, and the drill string axis coincides with the wellbore axis;
- ③ The influence of local shapes of drill string on drag and torque is neglected;
- ④ Ignoring the dynamic effect of the drill string, the deformation of the string is in an elastic range.

A micro-element segment with arc length of ds is selected as the research unit on the whole pipe string, and the force analysis is carried out; the schematic diagram is shown in Fig. 28.3.

In rotary drilling, the axial feed rate of the drill string is much smaller than its rotation speed, and the axial friction resistance of the drill string is much smaller than its torsional friction resistance under the compound effect of axial vibration. Therefore, the axial friction resistance can be ignored when analyzing the friction force of drill string in rotary drilling conditions, and the main problem becomes the torque loss of the drill string. Therefore, the force balance equation of rotary drilling string is as follows [14]:

$$\frac{dF}{ds} = -q \cos \alpha \tag{28.1}$$

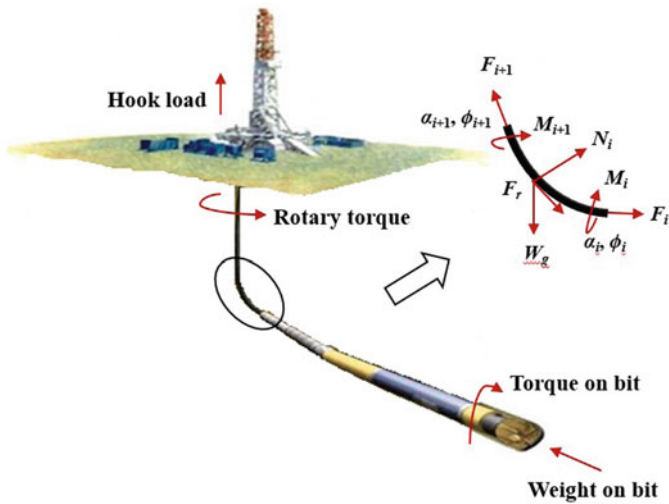


Fig. 28.3 Force analysis diagram of drill string micro-segment

$$\frac{dM_t}{ds} = \mu \cdot N \cdot D_t / 2 \quad (28.2)$$

$$N = \sqrt{[A_s^2 + B_s^2] / (1 + \mu^2)} \quad (28.3)$$

$$A_s = -k_b(F + k_n M_t) + q \frac{K_\alpha}{K_b} \sin \alpha \quad (28.4)$$

$$B_s = \frac{d}{ds}(k_b M_t) - q \frac{K_\varphi}{K_b} \sin^2 \alpha \quad (28.5)$$

where N is the positive pressure of the string to the wellbore, N/m; F is the axial force, N, and the tension is positive; μ is the sliding friction coefficient between the string and the wellbore; D_t is the outer diameter of the pipe joint, m; ds is the arc length of the micro-segment, m; q is the effective weight per unit length of the string in the drilling fluid, N/m; M_t is the torque loss caused by the sliding friction of the string, N·m.

α , φ , K_α , K_φ , and K_b are the inclination angle, inclination azimuth, inclination change rate, inclination azimuth change rate, and borehole curvature respectively. k_b and k_n are the curvature and deflection of the elastic deformation line of the string, respectively, which can be calculated by the curvature (K_b) and torsion (K_n) formula of the wellbore axis according to the assumption that the elastic deformation of the string coincides with the borehole axis:

$$K_b = \sqrt{K_\alpha^2 + K_\varphi^2 \sin^2 \alpha} \quad (28.6)$$

$$K_n = \frac{K_\alpha K'_\varphi - K_\varphi K'_\alpha}{K_b^2} \sin \alpha + K_\varphi \left(1 + \frac{K_\alpha^2}{K_b^2}\right) \cos \alpha \quad (28.7)$$

28.4 Downhole Torque Calculation Based on Soft Rope Model

During rotary drilling, the downhole weight on bit is considered to be equal to the WOB measured on the ground because the axial friction is too small to be detected. Without downhole power drilling tools in the bottom hole assembly, the bit rotational speed is equal to the surface rotary speed; the torque on bit can be estimated by subtracting the theoretical torque lost along the drill string from the rotary torque. Therefore, there are the following relationship expressions between surface drilling parameters and downhole drilling parameters:

$$WOB_{bit} \approx WOB_{surf}$$

$$\begin{aligned} N_{bit} &\approx N_{surf} \\ T_{bit} &\approx T_{surf} - T_{strings} \end{aligned} \quad (28.8)$$

The finite difference method is used to solve the overall force differential equation of rotary drilling established in Sect. 28.3. Firstly, according to the geometric structure characteristics of the borehole and the string, the whole string is divided into n units with the wellhead as the starting point, with a total of $n + 1$ nodes. Then the forward difference method is used to transform the transfer equations of axial force and torque in the overall force model into a different format, namely:

$$F_{i+1} = F_i + q_i \cdot \cos \alpha_i \cdot \Delta s_i \quad (28.9)$$

$$M_{i+1} = \frac{1}{2} \mu_i \cdot N_i \cdot D_{ti} \cdot \Delta s_i + M_{ti} \quad (28.10)$$

where F_i , M_i , F_{i+1} , and M_{i+1} are the axial force and torque of the i -th section of the pipe string near the ground and the section near the drill bit, respectively; α_i , q_i , μ_i , N_i , D_{ti} and Δs_i are the average inclination angle, the effective weight per unit length of the string in the drilling fluid, the sliding friction coefficient, the contact force between the string with borehole wall, the outer diameter of string joint and the length of unit string, respectively.

Based on the above assumptions, the axial force at any point of the string can be calculated from the bottom of the well by the axial force transfer formula for a given WOB. Secondly, the rotary torque can be predicted by the GA-BP intelligent prediction model according to the working conditions, given drilling parameters and formation characteristics. Finally, according to the torque transfer formula, the torque on bit can be calculated with the wellhead as the starting calculation point. The specific process is shown in Fig. 28.4.

28.5 Case Study

The prediction of rotary torque, the calculation of downhole torque and the transmission efficiency of torque are carried out for a horizontal well A. In this case, the rotary torque is predicted by the established GA-BP prediction model, and the prediction accuracy is evaluated. Secondly, the downhole torque is calculated according to the soft rope model. Finally, the transmission efficiency of torque is quantitatively evaluated.

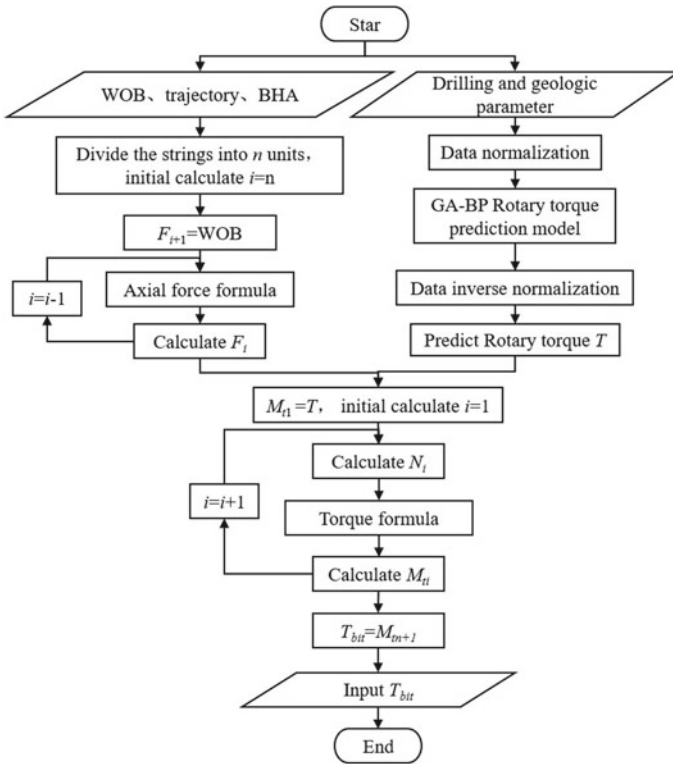


Fig. 28.4 Flow chart of downhole torque calculation

28.5.1 Basic Information of Well A

The basic information of the well is as follows: the well adopts a “vertical-kickoff-stable” three-stage wellbore trajectory type, as shown in Fig. 28.5; its whole depth is 5610 m, of which the length of the kick-off section is 1253 m and the length of the horizontal section is 1150 m. The wellbore structure of the well adopts the two types of structure. The first is drilled to a depth of 1750 m by using a 15” drill bit, and the 10-3/6” surface casing is used to block the formation that is easy to leak and collapse. In the second section, the 8-1/2” drill bit is used to drill to the target of 5610 m, and the 5-1/2” productive casing is run. As shown in Table 28.1, the drill assembly of “PDC bit + RSS + LWD + MWD” is used to complete the ‘one-trip drilling’ operation in the kill-off section and the horizontal section.

Fig. 28.5 Bore trajectory diagram

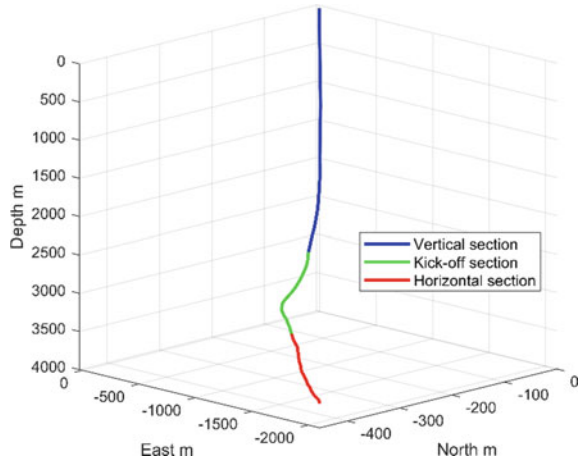


Table 28.1 Well A's drilling assembly

Well type	Started depth (m)	Finished depth (m)	Footage (m)	Drilling assembly
Horizontal section	4460	5610	1150	8-1/2" PDC Bit + RSS + LWD + MWD + 5" NMDC + 5" HWDP × 3 + 5" DP × 80 + 5" HWDP × 24 + 5" DP

28.5.2 Prediction of Rotary Torque

Data Pre-processing

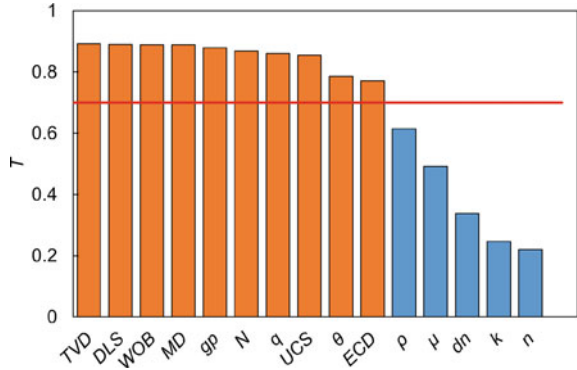
Feature Selection

The selection of characteristic parameters determines the performance of the neural network model. When the features with strong correlations are used as input parameters, the neural network model can fully identify the intrinsic relationship between input parameters and target features. Therefore, mutual information method is introduced to measure the correlation between drilling parameters and torque in this paper.

Mutual information $I(x, y)$ is the relative entropy between the joint distribution $p(x, y)$ and the producing distribution $p(x)p(y)$, which is an important method to measure the correlation of two nonlinear random variables. It can be defined as follows:

$$\begin{aligned}
 I(X; Y) &= \sum_{x \in X} \sum_{y \in Y} p(x, y) \log \frac{p(x, y)}{p(x)p(y)} \\
 &= D(p(x, y) \| p(x)p(y))
 \end{aligned}
 \tag{28.11}$$

Fig. 28.6 Correlation results of drilling parameters and rotary torque



where X and Y are two random drilling variables; $p(x)$ and $p(y)$ are the marginal probabilities of x and y , respectively; and $p(x, y)$ is the joint probability of x and y .

The mutual information calculation results of drilling parameters and torque are shown in Fig. 28.6. The drilling parameters are sorted according to the mutual information value, and 0.7 is selected as the threshold of feature selection. If the mutual information value between drilling parameters and torque is greater than 0.7, it is selected as the input parameter of GA-BP. Thus, vertical depth (TVD), dogleg severity (DLS), weight on bit (WOB), measuring depth (MD), formation pressure gradient (g_p), rotational speed (N), displacement (q), rock compressive strength (UCS), inclination angle (θ) and drilling fluid equivalent circulation density (ECD).

Normalization Process

To eliminate the influence of data amplitude on the performance of GA-BP prediction model, the Z-score standardization method is used to normalize the input training data. The method is based on the mean and standard deviation of the original data standardizes for the standardization. The processed data conforms to the standard normal distribution, that is, the mean is 0, the standard deviation is 1, and the transformation function is:

$$x^* = \frac{x - \mu}{\sigma} \tag{28.12}$$

where μ is the mean of the sample data and σ is its standard deviation.

Evaluation Indexes of Prediction Accuracy

To evaluate the accuracy of the model, mean absolute error, root mean square error, mean absolute percentage error and R^2 correlation coefficient are taken to measure the prediction accuracy.

Mean absolute error (MAE)

$$MAE = \frac{\sum_{i=1}^n |\hat{y}_i - y_i|}{n} \tag{28.13}$$

Root mean square error (RMSE)

$$RMSE = \sqrt{\frac{\sum_{i=1}^n (\hat{y}_i - y_i)^2}{n}} \tag{28.14}$$

Mean absolute percentage error (MAPE)

$$MAPE = \frac{\sum_{i=1}^n |(y_i - \hat{y}_i)/y_i|}{n} \times 100\% \tag{28.15}$$

R² correlation coefficient

$$R^2 = \frac{(n \sum_{i=1}^n \hat{y}_i y_i - \sum_{i=1}^n \hat{y}_i \cdot \sum_{i=1}^n y_i)^2}{[n \sum_{i=1}^n \hat{y}_i^2 - (\sum_{i=1}^n \hat{y}_i)^2] \cdot [n \sum_{i=1}^n y_i^2 - (\sum_{i=1}^n y_i)^2]} \tag{28.16}$$

where \hat{y}_i is the predicted value; y_i is the actual value; n is the number of samples.

Structure design of GA-BP prediction model

The hyperparameters of machine learning model have an important influence on its performance. In this paper, Bayesian optimization algorithm is used to optimize the hyperparameters. The optimal number of hidden layer neurons and learning rate of the GA-BP neural network model is adopted by it. The optimization results are: the number of hidden layer neurons is 20 and the learning rate is 0.2459. The Bayesian optimization algorithm is also used to optimize the hyperparameters of other prediction models, and the optimization results are shown in Table 28.2.

Table 28.2 Hyperparameters of rotary torque prediction models

	Hyperparameter		Hyperparameter	
<i>BP</i>			<i>GA-BP</i>	
Number of neurons in hidden layer(s)	20	Number of neurons in hidden layer(s)	20	
Activation function	Logistic	Activation function	Logistic	
Learning rate	0.0168	Learning rate	0.3077	
<i>SVM</i>			<i>ELM</i>	
Kernel function	RBF	Number of neurons in hidden layer(s)	600	
Penalty coefficient	0.0243	Activation function	Sig	
Kernal coefficient	0.1000			

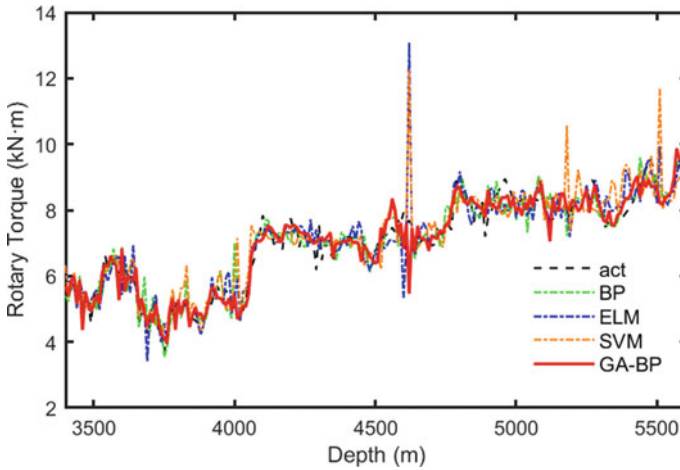


Fig. 28.7 Rotary torque prediction results

Results of GA-BP Rotary Torque Prediction

The rotary torque prediction model was established based on the above feature selection and optimal hyperparameters, and the prediction model was verified and compared by ELM, SVM and BP using the horizontal section data of well A. The results are shown in Fig. 28.7. As can be seen from Fig. 28.7, the prediction accuracy of ELM and SVM models is low, and the prediction results are easy to generate outliers. BP and GA-BP models have higher prediction accuracy, and the GA-BP model can accurately portray the change of rotary torque. Compared with the BP model, the GA-BP model is more stable. Meanwhile, the prediction accuracy of the GA-BP model is the highest among the four prediction models.

According to the above four evaluation indexes, the prediction accuracy of the rotary torque is evaluated, and the results are shown in Fig. 28.8. The R^2 coefficients of BP, SVM, ELM, and GA-BP models were 0.9820, 0.9644, 0.9798, and 0.9833, respectively. From the prediction results, these four models have achieved good prediction accuracy, and the GA-BP model is the best. Its root mean square error (0.5700), mean absolute error (0.4010) and mean absolute percentage error (0.0352) are better than the other models.

Results of torque on bit prediction

Based on the predicted data of GA-BP rotary torque, the torque on bit is calculated using the soft rope model and compared with the calculating results of the empirical formula. The empirical formula for calculating the torque on bit is shown in “Appendix A”, and the results are shown in Fig. 28.9. Due to the long build-up section and horizontal section of the well, there is large friction during the drilling process, resulting in excessive torque loss when the torque input from the ground is transmitted to the bit along the drill string. There is a great difference between rotary torque and torque on bit.

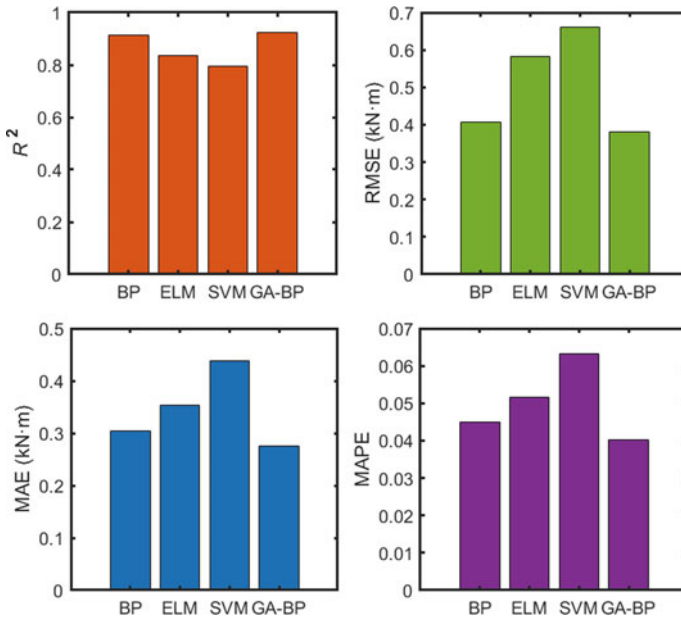


Fig. 28.8 Evaluation indexes results of rotary torque prediction models

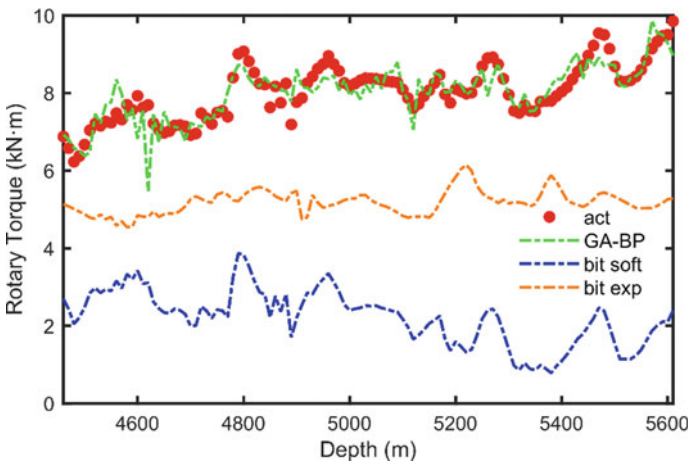


Fig. 28.9 Downhole torque at bit prediction results

Torque Transfer Efficiency Evaluation

In the drilling process of horizontal wells, the torque generated by the ground equipment is finally transmitted through the drill string to the drill bit for rock breaking, as shown in Fig. 28.2. Due to the existence of friction, there is a huge loss of surface

Fig. 28.10 Average torque of Well A

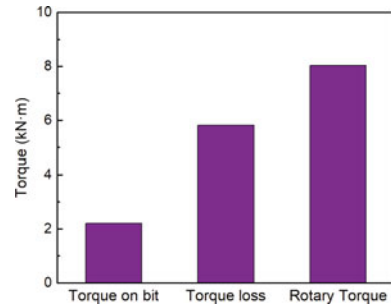
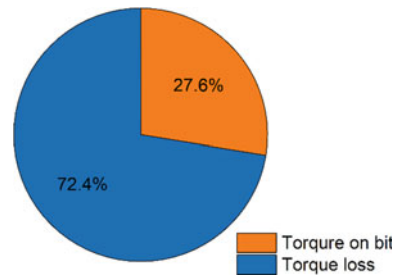


Fig. 28.11 Torque distribution percentage chart



torque in the process of transmission along drill strings. Thus, a torque transfer efficiency was quantitatively evaluated, the results are shown in Fig. 28.10. The average rotary torque on the ground is 8.0389 kN m, the average torque on bit is 2.2167 kN m, and the average torque loss is 5.822 kN m.

Compared with the torque used for effective rock breaking and loss torque, 72.4% of the torque generated on the ground is used to overcome the friction effect, only 27.6% of the torque is used for rock breaking, and the torque transmission efficiency is only 27.6%, as shown in Fig. 28.11.

28.6 Conclusion

Based on the above studies, the following conclusions are drawn:

- (1) A rotary torque prediction model based on GA-BP is established, which can accurately predict rotary torque through ground measurement data. The prediction accuracy can reach 98.33%.
- (2) The downhole torque calculation model established based on soft sensing in this paper can analyze the transmission of torque during drilling. Most of the torque input by ground equipment is used to overcome friction.
- (3) According to the flow analysis of torque in the drill string, only 27.6% of the torque is used for rock breaking, so it is necessary to use friction reduction technology to improve the efficiency of torque transmission.

Acknowledgements The authors gratefully acknowledge the financial support from the Natural Science Foundation of China (Grant No. 52222401, 52234002 and 51904317), Science Foundation of China University of Petroleum, Beijing (Grant No. ZX20180414) and other projects (Grant No. ZLZX2020-01-07-01). We also wish to thank Xinjiang Oilfield Company Engineering Technology Research Institute, CNPC, for technical support of this work.

Appendix A: Empirical Model of Torque on Bit in Horizontal Well

The torque on bit cannot be easily measured by surface instruments in engineering until now. Therefore, the torque on bit can be calculated using the WOB and sliding friction coefficient. According to the double integral correlation theorem, the bottom-hole torque on bit during drilling can be obtained as [15]:

$$\begin{aligned}
 T_b &= \int_0^{D_b/2} \int_0^{2\pi} r^2 \frac{4\mu_b \cdot \text{WOB}_b}{\pi D_b^2} dr d\theta \\
 &= \int_0^{D_b/2} \frac{8\mu_b \cdot \text{WOB}_b}{D_b^2} r^2 dr \\
 &= \frac{\mu_b \cdot \text{WOB} \cdot e^{-\mu\gamma_b} D_b}{3}
 \end{aligned} \tag{28.17}$$

where D_b is the bit diameter, kN; μ is the friction coefficient between drill string and well wall; γ_b is the bottom hole inclination angle; μ_b is the bit sliding friction coefficient.

References

1. Johancsik, C.A., Friesen, D.B., Dawson, R.: Torque and drag in directional wells—prediction and measurement. *J. Pet. Technol.* **36**, 987–992 (1984)
2. Ho, H.-S.: An improved modeling program for computing the torque and drag in directional and deep wells. In: *Annual Technical Conference and Exhibition*, pp. 407–418. SPE, Houston, TX (1988)
3. Aadnoy, B.S., Djurhuus, J.: Theory and application of a new generalized model for torque and drag. In: *IADC/SPE Asia Pacific Drilling Technology Conference*, pp. 1–9. Society of Petroleum Engineers, Jakarta, Indonesia (2008)
4. Mitchell, R.F., Samuel, R.: How good is the torque/drag model? *SPE Drill. Complet.* **24**, 62–71 (2009)
5. Sun, L., Gao, D.: A numerical method for determining the stuck point in extended reach drilling. *Pet. Sci.* **8**, 345–352 (2011)

6. Huang, W., Gao, D., Liu, Y.: Mechanical model and optimal design method of tubular strings with connectors constrained in extended-reach and horizontal wells. *J. Petrol. Sci. Eng.* **166**, 948–961 (2018)
7. Zhao, J., Huang, W., Gao, D.: Research on dynamic prediction of tubular extension limit and operation risk in extended-reach drilling. *J. Nat. Gas Sci. Eng.* **107**, 104542 (2022)
8. Hegde, C., Wallace, S., Gray, K.: Real time prediction and classification of torque and drag during drilling using statistical learning methods. In: *SPE Eastern Regional Meeting Morgantown*, pp. 1–13. SPE, West Virginia (2015)
9. Song, X., Zhu, S., Li, G., et al.: Prediction of hook load and rotary drive torque during well-drilling using a BP-LSTM network. *J. China Univ. Petrol.* **46**, 76–84 (2022)
10. Fortuna, L., Graziani, S., Rizzo, A., et al.: *Soft Sensors for Monitoring and Control of Industrial Processes*. Springer, London (2007)
11. Souza, F.A.A., Araújo, R., Mendes, J.: Review of soft sensor methods for regression applications. *Chemom. Intell. Lab. Syst.* **152**, 69–79 (2016)
12. Rumelhart, D.E., Hinton, G.E., Williams, R.J.: Learning representations by back-propagating errors. *Nature* **323**, 533–536 (1986)
13. Ashena, R., Rabiei, M., Rasouli, V., et al.: Drilling parameters optimization using an innovative artificial intelligence model. *J. Energy Res. Technol.* **143**, 1–8 (2021)
14. Gao, D., Liu, X., Xu, B.: *Well Trajectory Control*. Petroleum University Press, Dongying (1994)
15. Pessier, R.C., Fear, M.J.: Quantifying common drilling problems with mechanical specific energy and a bit-specific coefficient of sliding friction. In: *Annual Technical Conference and Exhibition*, pp. 373–388. SPE, Washington, DC (1992)

Chapter 29

Wellbore Temperature and Pressure Field Model Considering the Segmented Rheological Model



Xingao Liao, Jun Li, Gonghui Liu, and Hongwei Yang

Abstract With the advancement of oil and gas exploration at home and abroad in the direction of deep-sea, deep and unconventional resources, it is increasingly difficult to calculate the wellbore pressure accurately during the drilling process. Moreover, a large number of studies have shown that the traditional rheological models such as Bingham model and power-law model are not very consistent with the actual rheology of drilling fluid in the wellbore. Besides, temperature and pressure have a great influence on the rheology of drilling fluid. Therefore, it is important to select the optimal rheological model at different temperatures and pressures to describe the rheology of drilling fluid for accurate calculation of wellbore pressure. In this study, FannIX77 high temperature and high pressure automatic rheometer is used to carry out rheology test experiments of water-based and oil-based drilling fluids. It is found that the rheology of drilling fluid is greatly affected by temperature and pressure, and the influence of temperature is more significant. Using the 1st OPT software and regression fitting algorithm, it is found that the rheology of water-based drilling fluid is more in line with the Herschel-Bulkley model when the temperature is less than 100 °C, and more in line with the four-parameter model when the temperature is greater than 100 °C. The rheology of oil-based drilling fluid is more in line with the Herschel-Bulkley model when the temperature is less than 140 °C, and more in line with the four-parameter model when the temperature is greater than 140 °C. Therefore, this study establishes a wellbore temperature and pressure field model considering the segmented rheological model. Then, this study uses example well data to compare with the calculation results of wellbore friction pressure drop of the model and under wellbore temperature and pressure field model with different rheological models. It is found that the calculation results of the wellbore temperature and pressure field model considering the segmented rheological model are more

X. Liao · J. Li · G. Liu · H. Yang (✉)
China University of Petroleum (Beijing), Beijing 102200, China
e-mail: 13617299166@163.com

J. Li
China University of Petroleum (Beijing), Karamay Campus, Karamay 834000, China

G. Liu
Beijing University of Technology, Beijing 100022, China

consistent with the actual data in the field. This study provides theoretical guidance for accurate calculation of wellbore pressure.

Keywords Rheological model · Rheological test experiments · Segmented · Wellbore temperature and pressure field

29.1 Introduction

As oil and gas exploration at home and abroad gradually advances to the direction of deep-sea, deep and unconventional difficult to exploit, the drilling process often leads to complex situations such as bore instability, overflow and leakage due to inaccurate grasp of wellbore pressure, so accurate calculation of wellbore pressure is particularly important to prevent the occurrence of complex accidents downhole. The calculation of wellbore pressure mainly consists of three parts: vertical pressure, wellbore hydrostatic column pressure and wellbore friction pressure drop. The vertical pressure can be measured by the on-site pressure gauge, and the hydrostatic column pressure is often obtained by calculating the wellbore temperature and pressure field model, but the calculation of frictional pressure drop is often obtained by using the hydraulic equations in Bingham mode and power-law mode, ignoring the influence of temperature pressure on the rheology of drilling fluid, resulting in the inability to accurately calculate the wellbore friction pressure drop. A large number of studies have shown that the shape of the rheological curve of drilling fluid has a certain degree of similarity with the rheological curve of plastic fluid and pseudo-plastic fluid, and the traditional rheological mode such as Bingham mode and power law mode are not very consistent with the actual rheology of drilling fluid in the wellbore, and temperature and pressure have a great influence on the rheology of drilling fluid [1]. Therefore, it is important to select the optimal rheological mode at different temperatures and pressures to describe the rheology of drilling fluids for accurate calculation of wellbore pressure.

The known rheological modes of drilling fluids include Bingham mode, power law mode, Carson mode, He-Ba mode, Rowe mode, Sisko mode, four-parameter mode, hyperbolic mode and Linberheng mode. These nine rheological modes vary in form and the fluid rheological properties described are also emphasized, which makes it difficult to select the appropriate rheological mode on site. In order to characterize the actual flow of drilling fluid, this study summarizes the research status of high temperature and high pressure rheology of drilling fluid and the applicability of drilling fluid rheological mode, and uses FannIX77 high temperature and high pressure automatic rheometer to carry out rheological test experiments of water-based and oil-based drilling fluid, and uses 1st OPT software and regression algorithm to fit the rheological experimental data of water-based and oil-based drilling fluids under different rheological modes, and obtains the rheological mode of each rheological mode for water-based and oil-based According to the experimental results, a wellbore temperature and pressure field model with segmented rheological mode

was established, and the calculation results of wellbore friction pressure drop under wellbore temperature and pressure field models with different rheological mode were compared with the example well data. This study provides theoretical guidance for accurately calculating wellbore pressure, provides new solutions for actual drilling operations on site, and promotes the development of wellbore pressure.

29.2 Study on Rheological Patterns of Drilling Fluids

29.2.1 Existing Rheological Patterns and Their Characteristics

Rheology of drilling fluid refers to the characteristics of flow and deformation of drilling fluid under the action of external force, in which fluidity is the main aspect. According to the relationship between drilling fluid shear stress and shear rate, rheological modes are used to characterize the rheology of drilling fluids, and different rheological modes have corresponding rheological equations. Accurate characterization of drilling fluid rheology plays a very important role in maintaining wellbore stability, controlling the pressure agitation of the liquid column in the well, improving the drilling speed and calculating the wellbore friction pressure drop.

The known rheological modes of drilling fluids include Bingham mode, power law mode, Carson mode, He-Ba mode, Roth mode, Sisko mode, four-parameter mode, hyperbolic mode and Lin Boheng mode to characterize the rheology of drilling fluids. The rheological equations for the different rheological modes and their characteristics are shown in Table 29.1.

The rheological equations of each rheological mode mainly characterize the rheology of drilling fluids based on whether the drilling fluid has yield value and

Table 29.1 Rheological equations and their characteristics for different rheological modes

Rheological mode	Rheological equations	Number of parameters
Bingham model	$\tau = \tau_0 + \mu_p \gamma$	Two parameters
Power law model	$\tau = K \gamma^n$	Two parameters
Carson model	$\tau^{1/2} = \tau_c^{1/2} + \eta_\infty^{1/2} \gamma^{1/2}$	Two parameters
Heba model	$\tau = \tau_y + K \gamma^n$	Three parameters
Ross model	$\tau = A(\gamma + C)^B$	Three parameters
Sisko model	$\tau = a\gamma + b\gamma^c$	Three parameters
Four parameters model	$\tau = \tau_0 + a\gamma + b\gamma^c$	Four parameters
Hyperbola model	$\tau = \tau_0 + \frac{a\gamma}{1+b\gamma}$	Three parameters
Lin Boheng model	$\tau = \tau_s + \eta_p \gamma \left(1 + \frac{\beta}{\gamma}\right)^{1/2}$	Three parameters

the relationship between shear stress and shear rate. The Bingham model mainly reflects the rheological equation of the plastic fluid, and its non-Newtonian nature is reflected in the fact that the plastic fluid has a yield value, and the shear stress of the fluid is greater than the minimum shear stress, and the plastic fluid will flow. After the shear rate increases to a certain value, the rheological curve is a straight non-Newtonian fluid. The power-law mode mainly reflects the pseudoplastic fluid, and its non-Newtonian nature is reflected in the relationship between shear stress and shear rate, and the slope of the tangent of the curve decreases with the increase of shear rate. The Heba mode is a power-law mode with yield value, which is a three-parameter mode that combines the characteristics of Bingham mode and power-law mode, which reflects both the yield value and the power-law nature, which is closer to the drilling fluid reality. The four-parameter mode is an improvement on the Heba mode, which reflects the ultimate viscosity of the drilling fluid. The Carson mode, Ross mode, Sisko mode, hyperbolic mode, and Lin Boheng mode are the rheological equations fitted by other scholars through the experimental data of different drilling fluid rheology tests.

Secondly, according to the existing research, temperature and pressure have a great influence on the rheology of drilling fluid, and the temperature and pressure range applicable to the rheological equation of the above rheological mode are limited, with the increase of temperature and pressure, the drilling fluid treatment agent in the cycle will occur high temperature crosslinking, polymer thermal degradation, desorption, bentonite formation gelling and other problems, and the physical and chemical reactions between treatment agents and between treatment agents and other materials will change, resulting in significant changes in the rheology of drilling fluid [2]. Therefore, it is necessary to study the applicability of drilling fluid rheological patterns in the full temperature and pressure range to provide more direct and practical theoretical guidance in the field.

29.2.2 Research Status of Rheology of Drilling Fluid at High Temperature and High Pressure and Applicability of Rheological Mode of Drilling Fluid

Regarding the effects of temperature and pressure on drilling fluid, scholars at home and abroad such as Bailey and Yan Jiannian used high temperature and high pressure rheometers to conduct experiments on the rheology of drilling fluids, and it was found that the rheology of drilling fluids was greatly affected by temperature and pressure, and the influence of temperature was more significant. Wang Haige et al. found that the power-law mode found at room temperature had the best description of the rheology of drilling fluid. Amani et al. found that oil-based drilling fluids have better tolerance to high temperature and high pressure conditions; Gao Yu et al. used the high temperature and high pressure rotational viscometer to conduct rheological experiments on 4 water-based drilling fluids and 3 oil-based drilling

fluids used in the field within a large temperature and pressure range, and analyzed the effects of temperature and pressure on the rheology of drilling fluids, and found that the hyperbolic mode had a better effect on the rheology of drilling fluids under normal temperature conditions, and the four-parameter mode described the rheology of drilling fluids better under high temperature conditions.

Most of the scholars such as Wang Haige, J. E. Cloud, Zhou Fujian, Wang Fuhua, etc. compared and optimized the rheological mode through drilling fluid rheology experiments, pointing out that the Heba mode has the best description of drilling fluid rheology. Some scholars also pointed out that the power-law mode, Carson mode and four-parameter mode have the best description of the rheology of drilling fluid. Due to the differences in the characteristics of drilling fluids and rheological modes themselves, and the rheological modes recommended by different studies for different drilling fluids, how to optimize the rheological mode of drilling fluids has been widely concerned.

In summary, based on a large number of experiments and related studies of predecessors, the following conclusions can be summarized:

- (1) The shape of the rheological curve of drilling fluid is similar to the rheological curve of plastic fluid and pseudoplastic fluid, and the traditional rheological mode such as Bingham mode and power law mode is not very consistent with the actual rheology of drilling fluid in the wellbore.
- (2) Temperature and pressure have a great influence on the rheology of drilling fluid, and it is necessary to study the applicability of drilling fluid rheology mode in the full temperature and pressure range, and optimize the rheological mode of drilling fluid.
- (3) It is of great significance to select the best rheological mode at different temperatures and pressures to describe the rheology of drilling fluids, which is of great significance for accurately calculating wellbore pressure.

29.3 Rheological Test Experiments of Water-Based and Oil-Based Drilling Fluids

In this study, six typical rheological modes of drilling fluids were selected for study according to the characteristics of nine rheological modes, regardless of the Ross mode, Sisko mode and hyperbolic mode. The reason is: Ross mode—Ross mode can be transformed into Bingham mode and power-law mode under certain conditions, but the physical meaning of the parameters in the mode is not clear, and its parameter calculation is complex, and the value cannot be determined, which is not universal for engineering practice, so it cannot be considered; Sisko mode—this is a three-parameter mode proposed by Sisko when studying the fluidity of lubricating oil, which is pointed out that this mode can better describe the flow characteristics of lubricating oil in the range of 0.04-22,000 s⁻¹ s⁻¹ shear rate, so it does not conform to the characteristics of drilling fluid, is not universal, and can be disregarded; Hyperbolic mode—if the shear rate is infinite, the apparent viscosity will be infinitely close

Fig. 29.1 FannIX77 High temperature and high pressure automatic rheometer



to 0, and most of the actual drilling fluid has a limit viscosity, which is contrary to the actual drilling fluid, so it can be ignored.

Based on the above research, this study uses FannIX77 high temperature and high pressure automatic rheometer to carry out the rheological test experiment of water-based and oil-based drilling fluid, and its built-in software can realize the operation and data acquisition of the instrument (see Fig. 29.1).

Separately measure the rheology of water-based and oil-based drilling fluids with an initial density of 2.3 g/cm^3 under the commonly used drilling fluid system in the field, the reason why 2.3 g/cm^3 drilling fluid is selected for testing is because its rheology is more obviously affected by temperature and pressure, and the test conditions are tested $\text{Ø}3$, $\text{Ø}6$, $\text{Ø}100$, $\text{Ø}200$, $\text{Ø}300$, $\text{Ø}600$ five points for each temperature and pressure point, the specific temperature and pressure range is shown in Table 29.2.

The specific test process is as follows:

- (1) Stir the drilling fluid to be measured at high speed for 10 min;
- (2) Pour the drilling fluid to be tested into the test cup, install the float combination, torque combination, etc., and cover the cover;
- (3) Operate the computer, enter the data acquisition interface, input temperature, pressure and speed, after the experiment starts, the instrument will automatically rise/cool down and increase/decompress at 300 rpm, and when the set temperature is reached $\pm 2 \text{ }^\circ\text{C}$ and the set pressure $\pm 200 \text{ psi}$ range, the instrument

Table 29.2 Rheology test conditions for drilling fluids

Serial number	Sample type	Temperature range/ $^\circ\text{C}$	Pressure range/MPa
1	Water-based	20–220	0.1–90
2	Oil-based	20–220	0.1–90

will automatically start the test, and the test results will be displayed on the test interface;

- (4) After the experiment, adjust the speed to zero, cool and relieve pressure.

The rheological test results of water-based and oil-based drilling fluids are shown (see Figs. 29.2 and 29.3), respectively:

It can be seen from Figs. 29.2 and 29.3 that the rheology of drilling fluid is greatly affected by temperature and pressure, and the influence of temperature is more significant than that of pressure. In the same temperature and pressure range, the fluctuation of oil-based drilling fluid phase under the influence of temperature and pressure is slightly smaller than that of water-based drilling fluid, indicating that oil-based drilling fluid phase has certain tolerance compared with water-based drilling fluid. The rheological curves of drilling fluids are clearly different from those at high and low temperatures, so it is necessary to study the applicability of drilling fluids at different temperatures.

Since the effect of pressure compared with temperature on the rheology of drilling fluid is too small, the maximum pressure experimental data at the same temperature were selected in this study, and the agreement of the experimental data of six rheological modes in the experimental temperature and pressure range was analyzed, and

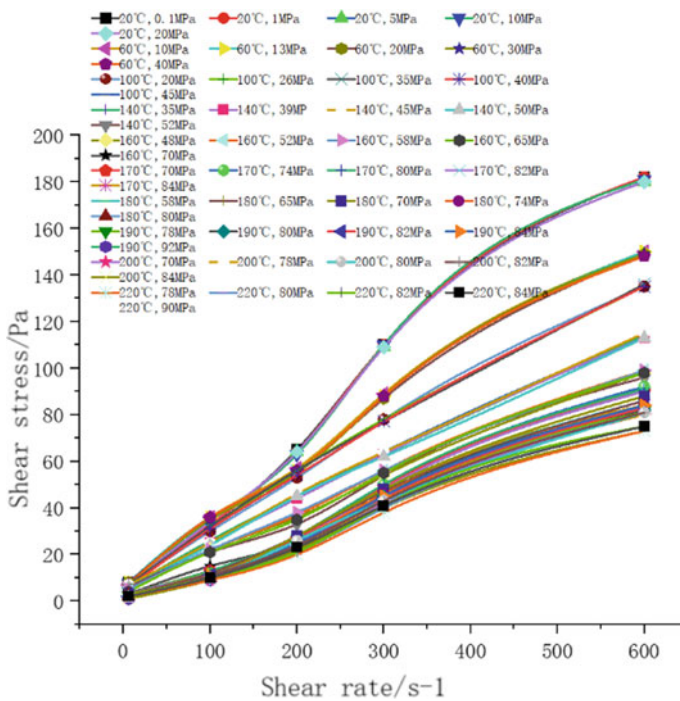


Fig. 29.2 Rheological test results of water-based drilling fluids

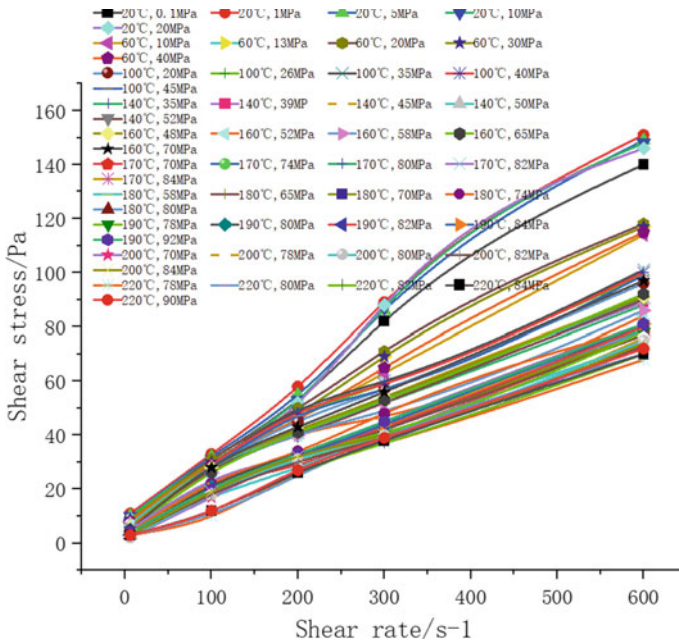


Fig. 29.3 Rheological test results of oil-based drilling fluids

the 1st OPT software and regression fitting algorithm were used to fit, and the test results are shown (see Fig. 29.4 and 29.5).

It can be seen from Fig. 29.4 that when the temperature is less than 100 °C, the coefficient of determination (R^2) of the Heba mode for fitting the experimental data of water-based drilling fluid is the largest. When the temperature is greater than 100 °C, the four-parameter mode has the largest coefficient of determination (R^2) for fitting the experimental data of water-based drilling fluid. When the temperature is greater than 100 °C, the fitting effect of each rheological mode on the experimental data of water-based drilling fluid decreases.

It can be seen from Fig. 29.5 that when the temperature is less than 140 °C, the coefficient of determination (R^2) of the Heba mode for the fitting of oil-based drilling fluid experimental data is the largest. When the temperature is greater than 140 °C, the four-parameter mode has the largest coefficient of determination (R^2) for the fitting of oil-based drilling fluid experimental data.

When the temperature is greater than 140 °C, the fitting effect of each rheological mode on the experimental data of oil-based drilling fluid decreases.

Combining Figs. 29.4 and 29.5, it can be found that when the temperature is less than 140 °C, the coefficients of determination of the power-law mode and the Heba mode on the fitting of the experimental data of water-based and oil-based drilling fluids will be higher than the Heba mode in a small temperature range, but it is still slightly lower than the Heba mode overall. Compared with other rheological

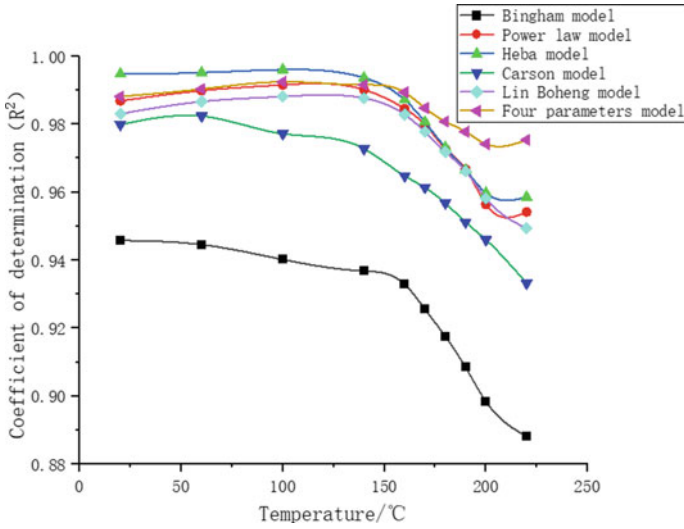


Fig. 29.4 Six rheological modes curved the coefficient of determination (R^2) of the fitting of water-based drilling fluid experimental data with temperature

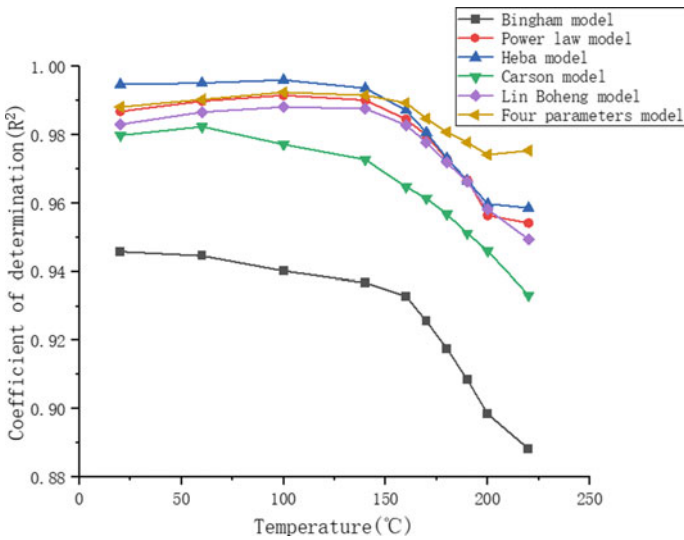


Fig. 29.5 Six rheological modes curved the coefficient of determination (R^2) of the fitting of oil-based drilling fluid experimental data with temperature

modes, the Heba mode and the four-parameter mode have better fitting effects on the experimental data of drilling fluid. Compared with other rheological modes, the Bingham mode and the Carson mode have poor fitting effect on the experimental data of drilling fluid. When the temperature exceeds 200 °C, the fitting effect of each rheological mode on the experimental data of drilling fluid increases slightly, which may be related to the endpoint effect of the fitting curve and the small internal denaturation of the drilling fluid. From the perspective of the fitting equation coefficient, the rheology of drilling fluid under high temperature and high pressure varies greatly in the same rheological mode, so it is of great significance to consider the calculation of wellbore temperature and pressure field under segmented rheological mode for accurate calculation of wellbore pressure.

29.4 Wellbore Thermobaric Field Model in Segmented Rheological Mode

For field practice, an ideal rheological mode should meet three basic conditions: (1) the parameters in the rheological equation can reflect the rheology of the drilling fluid; (2) In a wide range of temperature and pressure conditions and shear rates, the experimental data of different types of drilling fluids are in good agreement; (3) Facilitate relevant hydraulic calculations [3–5].

Therefore, in this study, the Heba model was chosen to describe the rheology of water-based drilling fluids at temperatures less than 100 °C. When the temperature is greater than 100 °C, the rheology of water-based drilling fluid is described by the four-parameter mode, and the wellbore temperature and pressure field model in segmented rheological mode is established, and the calculation of drilling fluid layer flow pressure loss and Leiro number under different rheological modes can refer to related research [6–9]. Based on the rheological data of water-based drilling fluid of well X-well in Yibin, Sichuan, the fitted equations in different rheological modes were obtained by using the inline equation fitting method in the Matlab calculation software, and then the wellbore temperature and pressure field calculation was carried out, and the basic input parameters of the wellbore temperature and pressure field model under each rheological mode are shown in Table 29.3.

Because the calculation of wellbore pressure is mainly composed of three parts: vertical pressure, wellbore hydrostatic column pressure and wellbore friction pressure drop. Among them, the wellbore friction pressure drop is most significantly affected by the rheological mode of the drilling fluid, so the calculation results of the annular friction under different rheological modes are used to characterize the effect of the rheology of the drilling fluid on the calculation of wellbore pressure, and the calculation results are shown (see Fig. 29.6).

According to Bernoulli's principle, the annular friction is 1.8 MPa at a well depth of 2000 m, 2.5 MPa at a well depth of 4000 m, and 3.8 MPa at a well depth of 6000 m. It can be seen from Fig. 29.6 that the annular friction calculated by considering

Table 29.3 Basic input parameters of wellbore thermobaric field model in each rheological mode

Parameter	Value	Parameter	Numeric value
Well depth	6000 m	Drill collar length	198 m
Drill string inner diameter	82.3 mm	Casing diameter	200 mm
Drill string outer diameter	101.6 mm	Glasses-free diameter	171.5 mm
Weighted drill pipe inner diameter	63.5 mm	Drilling fluid inlet temperature	30 °C
Drill collar diameter	50.8 mm	Surface temperature	20 °C
Drill collar outer diameter	120.7 mm	Geothermal gradient	0.03 °C/m
The upper casing is deep below	4600 m	Drilling fluid density	2.3 g/cm ³
Emphasize the length of the drill pipe	141 m	Displacement	18 L/s
Weighting the outside diameter of the drill pipe	113.9 mm	Nozzle acreage	268 mm ²
Stratigraphic rock density	2.64g/cm ³	Thermal conductivity of drilling fluid	1.73 W/(m °C)
Thermal conductivity of drill pipe	43.75 W/(m °C)	Thermal conductivity of rocks	2.25 W/(m °C)
Specific heat of drilling fluid	900 J/(kg °C)	Specific heat of the drill pipe	400 J/(kg °C)
Rocks are specific heat	800 J/(kg °C)	Rotate speed	70 r

the piecewise rheological mode is the most consistent with the actual situation, which shows that the wellbore temperature and pressure field model considering the segmented rheological mode can calculate the wellbore pressure more accurately.

The main reason for the calculation of the wellbore friction pressure drop in the Carson mode is that the rheological parameters of the Carson mode are calculated irregularly, and the change of the rheological parameters of drilling fluid often has a clear trend with the temperature change, so the fitting effect is poor. The results of the wellbore friction pressure drop calculated in the Bingham mode are large, mainly because the rheological curve of the Bingham mode is straight and the fitting effect is poor. The main reason for the large friction pressure drop of the wellbore calculated in the Lin Boheng mode is that the rheological parameters of the Carson mode are calculated irregularly, and the change of the rheological parameters of drilling fluid often has a clear trend with the temperature change, so the fitting effect is poor. The wellbore friction pressure drop calculated in Heba mode and four-parameter mode is close to the actual data, and the actual data is also obviously segmented, and the wellbore friction pressure drop calculated in the segmented rheological mode is more consistent with the actual data.

Therefore, by setting the same parameters, it is found that the wellbore temperature and pressure field model considering the segmented rheological mode is more consistent with the actual field data than the calculation results of the wellbore temperature

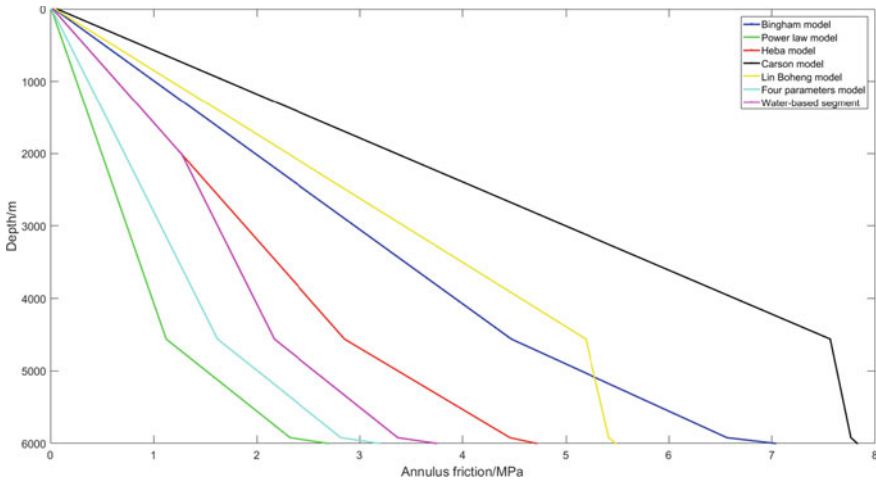


Fig. 29.6 The variation of annular friction with well depth under different rheological modes

and pressure field model under other rheological modes, and can better reflect the influence of the rheology of drilling fluid on the wellbore pressure.

29.5 Conclusion

Through the study of drilling fluid rheological patterns, six typical drilling fluid rheological modes in the existing research were selected and studied. In this study, FannIX77 high temperature and high pressure automatic rheometer was used to carry out the rheological test experiment of water-based and oil-based drilling fluid, and the rheological experimental data of water-based and oil-based drilling fluid under different rheological modes were fitted by using 1st OPT software and regression algorithm, and the coefficient of determination of the fitting of water-based and oil-based drilling fluid experimental data by each rheological mode was obtained with temperature. The calculation results of wellbore friction pressure drop under wellbore temperature and pressure field models with different rheological modes were compared. Based on the above research, the following conclusions are drawn:

- (1) The shape of the rheological curve of drilling fluid is similar to that of plastic fluid and pseudoplastic fluid, so the traditional rheological mode such as Bingham mode and power law mode is not very consistent with the actual rheology of drilling fluid in the wellbore;
- (2) The rheology of drilling fluid is greatly affected by temperature and pressure, and the influence of temperature is more significant;

- (3) The rheology of water-based drilling fluid is more in line with the Heba mode when the temperature is less than 100 °C, and more in line with the four-parameter mode when the temperature is greater than 100 °C; The rheology of oil-based drilling fluid is more in line with the Heba mode when the temperature is less than 140 °C, and the four-parameter mode when the temperature is greater than 140 °C.
- (4) The calculation results of the wellbore temperature and pressure field model considering the segmented rheological mode are more consistent with the actual data on site, and the established wellbore temperature and pressure field model considering the segmented rheological mode can better reflect the actual rheology of the drilling fluid in the wellbore, which is of great significance for the accurate calculation of wellbore pressure.

References

1. Fan, H.: Practical Drilling Fluid Mechanics. Petroleum Industry Press (2014)
2. Zhao, S., Yan, J., Ding, T., et al.: Study on rheological properties of high-temperature high-density water based drilling fluid. *Nat. Gas Indus.* **27**(5), 78–80 (2007)
3. Yang, X., Li, S., Yan, J., et al.: Temperature pattern modelling and calculation and analysis of ECD for horizontal wellbore. *Drill. Fluid Compl. Fluid* **31**(5), 63–66 (2014)
4. Galindo, K.A., Zha, W., Zhou, H., et al.: High temperature, high performance water-based drilling fluid for extreme high temperature wells. In: SPE/IADC Drilling Conference and Exhibition. Society of Petroleum Engineers, London (2015) (SPE-173017-MS)
5. Sukhoboka, O.: Drilling fluid rheology under high pressure high temperature conditions and its impact on the rate of penetration. In: SPE Bergen One Day Seminar. Society of Petroleum Engineers, Bergen (2017) (SPE-185916-MS)
6. Fu, J., Feng, J., Chen, P., et al.: Simulation on wellbore pressure during dynamic kill drilling in deep water. *Acta Petrol. Sinica* **36**(2), 232–237 (2015)
7. He, M., Liu, G., Li, J., et al.: Solution and analysis of fully transient temperature and pressure coupling model for multiphase flow. *Petrol. Drill. Tech.* **43**(2), 25–32 (2015)
8. Zhang, J.: Drilling Fluid Mechanics. Petroleum Industry Press, Beijing (1994)
9. Yang, L., Li, Z., Nie, Q., et al.: Study on effects of temperature and pressure on density of oil based drilling fluids and the mathematical model thereof. *Drill. Fluid Compl. Fluid* **39**(2), 151–157 (2022)

Chapter 30

Enhancing Effect of Leeward Side Deflector on High-Speed Trains Aerodynamic Performance Under Crosswinds



Zheng-Wei Chen , Guang-Zhi Zeng , and Zhan-Hao Guo

Abstract To enhance the aerodynamic performance of high-speed trains in crosswinds, the aerodynamic forces and flow structures of the high-speed train with the deflector are investigated in this work, while the influence of deflectors on the train's leeward side in various positions on the train's aerodynamic performance is also compared. The results show that the deflector configured on the leeward side of the train has a notable effect on reducing the rolling moment coefficient (C_{Mx}), as compared to the case without a deflector, resulting in a decrement of 4.39%, 11.66%, and 19.80% at position A, position B and position C, respectively. The flow structures around the train further reveal that the deflector plate inhibits the winding and acceleration of vortices formed in the leeward side of the train and weakens the concentration as well as strong energy of the vortices, compared to the case without deflector, and therefore leading to an improvement in the train's aerodynamic performance in crosswind environments.

Keywords CFD · Crosswind environment · High-speed train · Deflector · Aerodynamic performance

30.1 Introduction

High-speed trains, nowadays, revolutionize the way most people travel, owing to their fast, comfortable, convenient and increasingly sophisticated railway network planning. While high-speed trains bring convenience to commuting, the safe operation of

Z.-W. Chen · G.-Z. Zeng · Z.-H. Guo

National Rail Transit Electrification and Automation Engineering Technology Research Center (Hong Kong Branch), Hung Hom, Kowloon, Hong Kong, China

Z.-W. Chen (✉) · G.-Z. Zeng · Z.-H. Guo

Department of Civil and Environmental Engineering, The Hong Kong Polytechnic University, Hung Hom, Kowloon, Hong Kong, China

e-mail: zhengwei.chen@polyu.edu.hk

trains in complex environments still comes with challenges [1–5], particularly under crosswinds, which may cause significant side forces as well as overturning moments variation on trains [6, 7]. The potential for aerodynamic instability under crosswinds has raised concerns about the safety of high-speed trains, especially in light of recent high-profile overturn accidents caused by strong crosswinds. Based on this, research efforts have been devoted to developing various methods to understand the aerodynamic behavior of trains and the factors that contribute to their instability under crosswinds, including full-scale tests [6, 8–11], wind tunnel tests [12–14], moving model tests [15], and numerical simulations [16–22].

To improve the aerodynamic performance of high-speed trains under crosswind environments, aerodynamic designs of high-speed trains, including micro-structures, head shapes and active control strategy, have been developed and optimized by scholars at home and abroad. For instance, Li et al. [23] investigated the unsteady aerodynamic performance of a high-speed train's pantograph with different dome shapes subjected to crosswind based on the delayed detached eddy simulation method. Ezoji and Talaei [24] analyzed airflow structures induced by crosswinds around high-speed trains featuring various nose shapes and compared their aerodynamic performances through parametric analysis. Chen et al. [25] adopted active control strategies by considering different positions of blowing slots on the high-speed train's surface, which indicated that the blowing positions on the lower half of the windward side and upper half of the leeward side would delay the vortex separation and improve train's aerodynamic performance under crosswinds.

Most investigations currently, regarding improving the aerodynamic performance of trains in crosswind environments based on passive control methods, are adopted methods via changing the head shape or local shape of the train. In this study, an innovative leeward side deflector configuration on a high-speed train is proposed to improve the aerodynamic performance under crosswind environments. The aerodynamic forces and moments of the high-speed trains are analyzed in relation to leeward side deflector positions. Also, the flow mechanisms are explored under different leeward side deflector positions of the high-speed train.

The numerical model is described in Sect. 30.2 of this work. Section 30.3 provides the results of the analysis and discussions. Section 30.4 concludes by summarizing the main findings of this work.

30.2 Method and Model

30.2.1 Geometry of the Train

Previous study indicates that alternations in the flow field surrounding the head car have the most significant impact on its aerodynamic performance [5, 26]. In light of this, a high-speed train is examined in the current work, including the head car with a streamlined head shape and half of the middle car. The inclusion of the half-car,

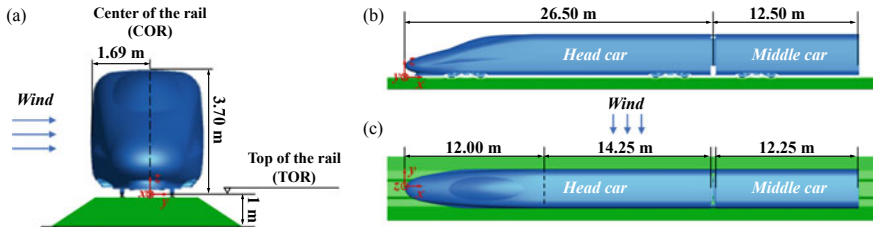


Fig. 30.1 The geometry of the high-speed train model: **a** the front view, **b** the side view, and **c** the top view

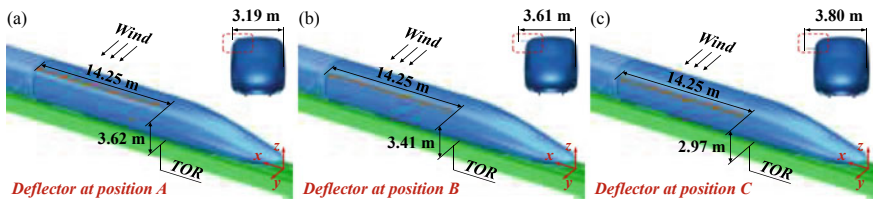


Fig. 30.2 The positions of the leeward side deflector: **a** position A, **b** position B, and **c** position C

which is behind the head car, is primarily to ensure the development of a flow field around the head car, as suggested in previous investigations [27–29].

Figure 30.1 shows the high-speed train model addressed in this work, which comprises the head car and a half of the middle car with lengths of 26.50 and 12.50 m, respectively; the width of the train is 3.38 m, and the train height from the top of the rail is 3.70 m.

This study focuses on various positions of leeward side deflector to improve the aerodynamic performance of a train, as shown in Fig. 30.2. The deflector configuration is applied to the leeward side of the head car, with three different heights from the top of the rail, namely 3.62 m (position A), 3.41 m (position B) and 2.97 m (position C), respectively. Also, all deflector adopted in the current work features a length of 14.25 m and a thickness of 0.05 m, while the width from the deflector edge to the windward side of trains is 3.19, 3.61 and 3.80 m in the position A, B and C, respectively, based on their individual positions on the leeward side of the train.

30.2.2 Computational Domain and Boundary Conditions

Figure 30.3 portrays the computational domain with dimensions of $42.97H$, $32.43H$ and $11.08H$ for length, width and height, respectively, where H donates the train height from the top of the rail. The nose of the streamlined head of the train is positioned $10.81H$ away from the front face (Face AEHD) of the domain longitudinally and the center of the rail is positioned at a transverse distance of the left face (Face

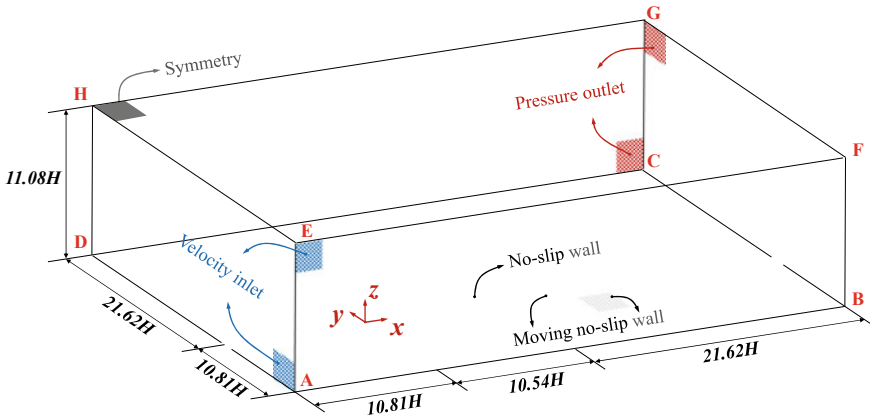


Fig. 30.3 The computational domain and boundary conditions

ABFE) of the domain. To ensure the full development of the flow field, the distance between the end point of the train and the back face (Face BFGC) of the domain is given a value of $21.62H$, as well as the distance between the center of the rail and right face (Face CGHD) of the domain. A uniform and constant synthetic velocity of $U_t = 60$ m/s of overtime is used on the boundary of the velocity inlet, while the zero-pressure outlet boundary condition is implemented at the opposite. On the upper face of the computational domain, a symmetry boundary condition is adopted; the no-slip wall boundary condition is used on the train surface, while the moving no-slip wall conditions are adopted on the ground and subgrade, setting the velocity component along the flow direction equal to the free flow velocity in the longitudinal direction.

30.2.3 Mesh Strategy

To ensure accurate capture of detailed flow separations, three refinement boxes (i.e., coarse, fine, and extra-fine boxes) are employed, as illustrated in Fig. 30.4a. Due to the wall effect, the velocity gradient would change gradually near the train surface. Therefore, ten-layer prism meshes are attached to the concerned object to compute this change. The first layer's non-dimensional wall distance y^+ is in the range of 30–40. Additionally, the grid on the train and subgrade surface as well as the bogie surface are shown in Fig. 30.4b.

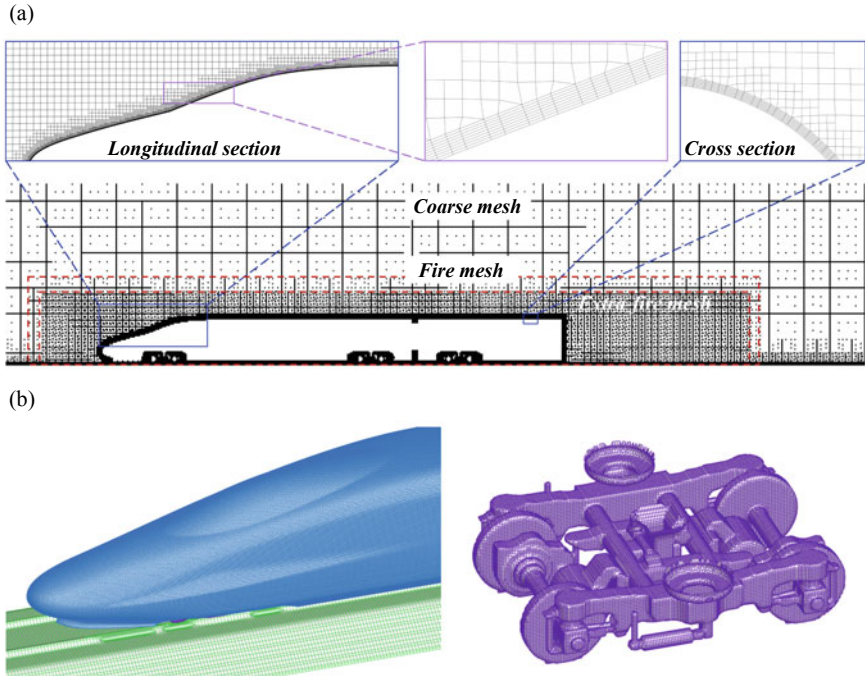


Fig. 30.4 The computational mesh: **a** mesh of the side view, and **b** mesh of the head car and bogie

30.3 The Flow Mechanism of Different Deflector Positions

Under crosswinds, the side force F_y , lift force F_z , rolling moment around the leeward side rail M_x , the pressure distribution P , and space wind speed V , etc., are important parameters for quantifying the aerodynamic performance of trains. To facilitate analysis, the following dimensionless parameters are defined:

$$\text{Side force coefficient } C_{F_y} = F_y / (0.5\rho U_t^2 A) \quad (30.1)$$

$$\text{Lift force coefficient } C_{F_z} = F_z / (0.5\rho U_t^2 A) \quad (30.2)$$

$$\text{Rolling moment coefficient } C_{M_x} = M_x / (0.5\rho U_t^2 A l) \quad (30.3)$$

$$\text{Pressure coefficient } C_p = (P - P_0) / (0.5\rho U_t^2) \quad (30.4)$$

$$\text{Velocity coefficient } C_v = V / U_t \quad (30.5)$$

where, ρ is the dry air density under the standard atmospheric pressure condition, which is equal to 1.225 kg/m^3 ; A is the reference area, which is the projected area of the train's cross-section and is 11.22 m^2 for the full-scale size; l is the reference length, which is 3 m for a full-scale size [30]; P_0 is the reference pressure, which is 0 Pa .

30.3.1 Aerodynamic Forces

Figure 30.5 depicts the aerodynamic coefficients of side fore, lift force and overturning moment. Note that in Fig. 30.5a–c, the number mark without the box represents the variation ratio compared to the case without deflector, while the number mark with the box means the variation ratio compared to the previous case.

In Fig. 30.5a and c, the inclusion of deflectors on the leeward side of the train trims down the impact of wind loads and results in a decreased trend in C_{Fy} and C_{Mx} compared to the case without deflectors. Additionally, it was observed that C_{Fy} decreases as the height of the deflector decreases, as well as C_{Mx} . For example, for the head car, the reduction ratios are 3.55%, 8.36%, and 14.34% in C_{Fy} when the deflector is configured at position A, B, and C, respectively, while the reduction ratios are 4.39%, 11.66%, and 19.80% in C_{Mx} , respectively. In cases with leeward side deflectors, positioning the deflector at B instead of A results in reduction ratios of 4.99% in C_{Fy} and 7.63% in C_{Mx} . Further lowering the deflector to position C results in decrement ratios of 6.53% in C_{Fy} and 9.19% in C_{Mx} for the head car. On the other hand, when leeward side deflectors are included on the train, there is an increasing trend in C_{Fz} , which is opposite to the trends observed for C_{Fy} and C_{Mx} , as illustrated in Fig. 30.5b. Compared to the original train, when the deflector is positioned at A, B, and C, the increment in C_{Fz} is 1.65%, 5.96%, and 12.00%, respectively. Meanwhile, relocating the deflector in various positions also triggers to C_{Fz} increase. The position of the deflector from A to B causes an increase of 4.24% in C_{Fz} , while a further increase of 5.70% is observed as the deflector is positioned even lower at position C.

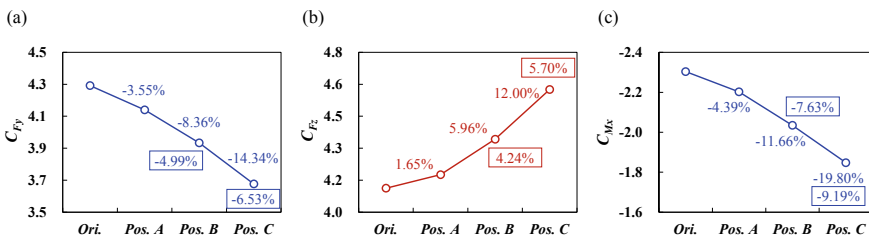


Fig. 30.5 Comparison of time-averaged aerodynamic force coefficients: a C_{Fy} , b C_{Fz} , and c C_{Mx}

30.3.2 *The Time-Averaged Flow Structures*

The magnitude of aerodynamic forces on the train is directly affected by the pressure distribution on its surface. Figure 30.6 depicts the 3-D pressure distribution for trains without deflector configuration and trains equipped with deflectors in three different positions, namely position A, position B, and position C. As demonstrated in Fig. 30.6a, a significant pressure change can be observed in the top area of the train. Owing to the installation of the deflector and the airflow separation in its vicinity, a significant negative pressure region is generated on the upper of the train (Region I), and this region is enlarged compared to the case without a mounted deflector. Furthermore, in comparison to the case without a deflector, the guiding effect of the deflector on the airflow results in a gradual reduction of the negative pressure area that forms from the streamlined head to the leeward side of the train's head car, as illustrated in Fig. 30.6b. The variation in Region II, which is near the bottom of the train, is particularly pronounced. As shown in the dotted boxes, compared to the case without a deflector, as the deflector is configured in position A, the decrement of pressure coefficient can be observed on the leeward side of the train, especially in the area near the end of the head car. Further, this phenomenon is also presented in other cases with deflectors, where the negative pressure coefficient exhibits the same continuous decrease when the deflector continuously drops to position B and position C.

30.3.3 *Instantaneous Flow Structures*

To facilitate a better understanding of the vortex separation, attachment, rotation, and development around the train, the 3-D transient flow structures in the cases for trains without deflector configuration and trains configured with deflectors in three different positions are illustrated in Fig. 30.7. In Fig. 30.7, there are massive vortices generated in the leeward side of the train, owing to the vortexes winding and separation. Further, in all cases, two distinct vortices, labeled *V1* and *V2*, are formed on the leeward side of the train. However, *V1* quickly dissipates, while *V2* persists for a longer distance, extending beyond the end of the train. Finally, in the cases configured deflector on the leeward side of the train, the relatively steady structure of *V2* is weakened, due to the deflector plate inhibiting vortexes winding and acceleration. Furthermore, as depicted by the dotted boxes in Fig. 30.7, when the deflector's height is lowered from position A to position C, the concentrated and potent energy of *V2* gradually dissipates and disintegrates, resulting in more effective mitigation of the crosswind effect.

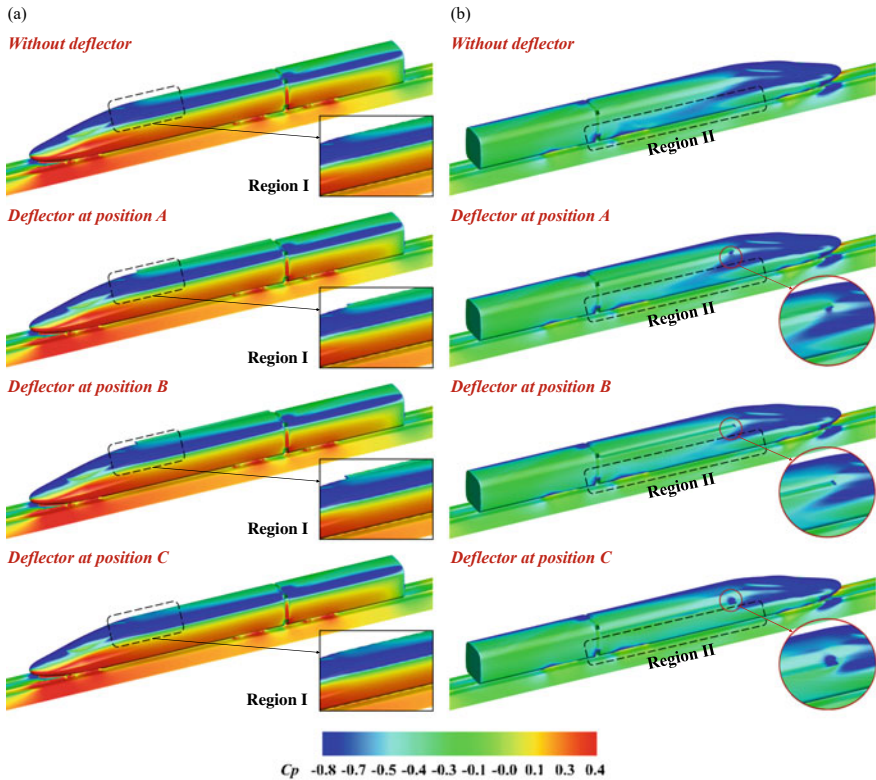


Fig. 30.6 The time-averaged distribution of C_p on the train surface: **a** windward side, and **b** leeward side

30.4 Conclusion

This paper presents a study and comparison of various positions of deflectors installed on the leeward side of a train, aimed at mitigating the crosswind effect. Based on the cases proposed in this work, the study draws the following conclusions and observations:

- (1) Compared to the case without a deflector, the aerodynamic side force coefficient C_{F_y} and rolling moment coefficient C_{M_x} of the head car exhibit a significant decline in those cases configured deflector on the leeward side of the train. When the deflector is configured at positions A, B, and C, C_{F_y} reduces by 3.55%, 8.36%, and 14.34%, respectively, while the reduction ratios in C_{M_x} are 4.39%, 11.66%, and 19.80%, respectively. However, equipping the deflector on the leeward side of the train causes a rising trend for the lift force coefficient C_{F_z} of the train, which portrays an increment ratio of 1.65%, 5.96%, and 12.00% as the deflector installed at positions A, B, and C, respectively.

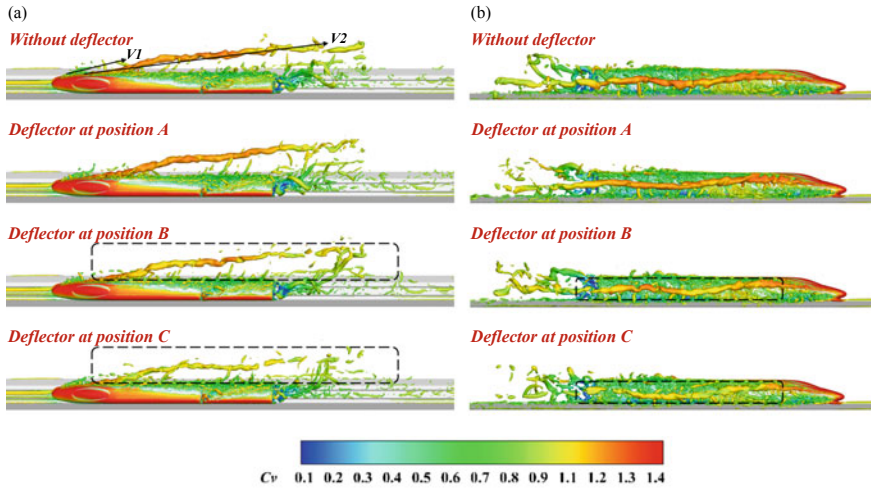


Fig. 30.7 The vortex development along the train ($Q = 100,000$): **a** top view, and **b** the view of the leeward side

- (2) Due to the deflector plate inhibiting vortices winding and acceleration on the leeward side of the train, compared to the original case, the negative pressure coefficient on the leeward side of the train with the deflector decreases significantly and continues to decrease as the height of the deflector decreases (from position A–C). The instantaneous flow structures also indicate that the deflector on the leeward side of the train weakens the concentrated and strong energy of the vortex in the leeward side of the train, leading to the better aerodynamic performance of the train in crosswind environments.

References

1. He, X., Li, H.: Review of aerodynamics of high-speed train-bridge system in crosswinds. *J. Central South Univ.* **27**(4), 1054–1073 (2020)
2. Li, W., Liu, T., Martinez-Vazquez, P., Guo, Z., Huo, X., Xia, Y., Chen, Z.: Effects of embankment layouts on train aerodynamics in a wind tunnel configuration. *J. Wind Eng. Ind. Aerodyn.* **220**, 104830 (2022)
3. Mohebbi, M., Rezvani, M.A.: Analysis of the effects of lateral wind on a high speed train on a double routed railway track with porous shelters. *J. Wind Eng. Ind. Aerodyn.* **184**, 116–127 (2019)
4. Niu, J., Zhang, Y., Li, R., Chen, Z., Yao, H., Wang, Y.: Aerodynamic simulation of effects of one-and two-side windbreak walls on a moving train running on a double track railway line subjected to strong crosswind. *J. Wind Eng. Ind. Aerodyn.* **221**, 104912 (2022)
5. Tian, H.: Review of research on high-speed railway aerodynamics in China. *Transp. Safety Environ.* **1**(1), 1–21 (2019)
6. Baker, C., Jones, J., Lopez-Calleja, F., Munday, J.: Measurements of the cross wind forces on trains. *J. Wind Eng. Ind. Aerodyn.* **92**(7–8), 547–563 (2004)

7. Chen, Z., Liu, T., Yan, C., Yu, M., Guo, Z., Wang, T.: Numerical simulation and comparison of the slipstreams of trains with different nose lengths under crosswind. *J. Wind Eng. Ind. Aerodyn.* **190**, 256–272 (2019)
8. Gallagher, M., Morden, J., Baker, C., Soper, D., Quinn, A., Hemida, H., Sterling, M.: Trains in crosswinds—comparison of full-scale on-train measurements, physical model tests and CFD calculations. *J. Wind Eng. Ind. Aerodyn.* **175**, 428–444 (2018)
9. Gao, H., Liu, T., Gu, H., Jiang, Z., Huo, X., Xia, Y., Chen, Z.: Full-scale tests of unsteady aerodynamic loads and pressure distribution on fast trains in crosswinds. *Measurement* **186**, 110152 (2021)
10. Liu, T., Wang, L., Chen, Z., Gao, H., Li, W., Guo, Z., Xia, Y., Huo, X., Wang, Y.: Study on the pressure pipe length in train aerodynamic tests and its applications in crosswinds. *J. Wind Eng. Ind. Aerodyn.* **220**, 104880 (2022)
11. Xu, J., Chen, Z., Liu, T.: Experimental and numerical research on the safety of an EMU running on a normal-speed railway line under strong wind. In: *IOP Conference Series: Materials Science and Engineering*. IOP Publishing (2019)
12. Hashmi, S.A., Hemida, H., Soper, D.: Wind tunnel testing on a train model subjected to crosswinds with different windbreak walls. *J. Wind Eng. Ind. Aerodyn.* **195**, 104013 (2019)
13. He, X., Zuo, T., Zou, Y., Yan, L., Tang, L.: Experimental study on aerodynamic characteristics of a high-speed train on viaducts in turbulent crosswinds. *J. Central South Univ.* **27**(8), 2465–2478 (2020)
14. Mohebbi, M., Rezvani, M.A.: 2D and 3D numerical and experimental analyses of the aerodynamic effects of air fences on a high-speed train. *Wind Struct.* **32**(6), 539–550 (2021)
15. Soper, D., Baker, C., Sterling, M.: An experimental investigation to assess the influence of container loading configuration on the effects of a crosswind on a container freight train. *J. Wind Eng. Ind. Aerodyn.* **145**, 304–317 (2015)
16. Chen, Z., Liu, T., Jiang, Z., Guo, Z., Zhang, J.: Comparative analysis of the effect of different nose lengths on train aerodynamic performance under crosswind. *J. Fluids Struct.* **78**, 69–85 (2018)
17. Chen, Z., Liu, T., Li, M., Yu, M., Lu, Z., Liu, D.: Dynamic response of railway vehicles under unsteady aerodynamic forces caused by local landforms. *Wind Struct.* **29**(3), 149–161 (2019)
18. Hemida, H., Krajnović, S.: LES study of the influence of a train-nose shape on the flow structures under cross-wind conditions. *J. Fluids Eng.* **130**(9), 091101 (2008)
19. Liu, T., Chen, Z., Guo, Z., Krajnović, S.: Reasonable pressure tap layout to measure the aerodynamic forces of a train at different yaw angles. *Measurement* **166**, 108255 (2020)
20. Mohebbi, M., Rezvani, M.A.: Two-dimensional analysis of the influence of windbreaks on airflow over a high-speed train under crosswind using lattice Boltzmann method. *Proc. Inst. Mech. Eng. Part F J. Rail Rapid Transit* **232**(3), 863–872 (2018)
21. Noguchi, Y., Suzuki, M., Baker, C., Nakade, K.: Numerical and experimental study on the aerodynamic force coefficients of railway vehicles on an embankment in crosswind. *J. Wind Eng. Ind. Aerodyn.* **184**, 90–105 (2019)
22. Rezvani, M.A., Mohebbi, M.: Numerical calculations of aerodynamic performance for ATM train at crosswind conditions. *Wind Struct.* **18**(5), 529–548 (2014)
23. Li, X., Zhou, D., Jia, L., Yang, M.: Numerical study of the influence of dome shape on the unsteady aerodynamic performance of a high-speed train's pantograph subjected to crosswind. *J. Traffic Transp. Eng.* **10**, 13–30 (2023)
24. Ezoji, R., Talaei, M.R.: Analysis of overturn of high-speed train with various nose shapes under crosswind. *Iran. J. Sci. Technol. Trans. Mech. Eng.* **46**, 1–14 (2021)
25. Chen, Z.-W., Ni, Y.-Q., Wang, Y.-W., Wang, S.-M., Liu, T.-H.: Mitigating crosswind effect on high-speed trains by active blowing method: a comparative study. *Eng. Appl. Comput. Fluid Mech.* **16**(1), 1064–1081 (2022)
26. Liu, T., Chen, Z., Zhou, X., Zhang, J.: A CFD analysis of the aerodynamics of a high-speed train passing through a windbreak transition under crosswind. *Eng. Appl. Comput. Fluid Mech.* **12**(1), 137–151 (2018)

27. Schober, M., Weise, M., Orellano, A., Deeg, P., Wetzel, W.: Wind tunnel investigation of an ICE 3 endcar on three standard ground scenarios. *J. Wind Eng. Ind. Aerodyn.* **98**(6–7), 345–352 (2010)
28. Huo, X., Liu, T., Yu, M., Chen, Z., Guo, Z., Li, W., Wang, T.: Impact of the trailing edge shape of a downstream dummy vehicle on train aerodynamics subjected to crosswind. *Proc. Inst. Mech. Eng. Part F J. Rail Rapid Transit* **235**(2), 201–214 (2021)
29. Gu, H., Gao, H., Liu, T., Cheng, S., Li, J., Liu, Z.: Effects of windbreak wall model lengths on aerodynamic characteristics of trains on different tracks in wind tunnel tests—a measurement strategy. *J. Wind Eng. Ind. Aerodyn.* **228**, 105104 (2022)
30. EN14067-6: Railway Applications Aerodynamics-Part 6: Requirements and Test Procedures for Cross Wind Assessment (2018)

Chapter 31

Consideration and Technical Feasibility Research of Multi-source Collaborative Gas Supply in China



Jingyao Sun , Jiaojiao Yu, Shixin Jiang, Youwu Li, Yongxin Ma, Zhan Su, Mihong Zhong, and Jiqiang Zhang

Abstract In recent years, due to the impact of COVID-19, international geopolitics, market supply and demand, the international DES spot price of liquefied natural gas (LNG) has fluctuated dramatically. At the same time, China's imported LNG accounts for about 65% of total imported gas. To minimize the impact of international prices on China, the idea of a "multi-source collaborative gas supply" was proposed by LNG terminal, underground gas storage (UGS), and domestic produced gas. To study the feasibility of a "multi-source collaborative supply", the domestic gas infrastructure construction and pipeline connectivity, gas well production system, underground gas storage capacity and other aspects of collaborative supply technical feasibility were analyzed. The idea of a multi-source collaborative supply and gas resource swap was put forward, and from this, the full life cycle management of "production, injection, storage and sale" of high-quality gas reservoirs could be realized. It also provided ideas for integrating gas field development and UGS construction, which can avoid the repeated construction of UGS after gas reservoir exhaustion and improve China's ability to ensure a long-term stable supply of gas.

Keywords Collaborative gas supply · LNG · Underground gas storage · Gas swap · UGS engineering mode

J. Sun (✉) · J. Yu · S. Jiang · Y. Li · Z. Su · M. Zhong
CNOOC Gas and Power Group LTD, Beijing 100028, China
e-mail: sunjy@cnooc.com.cn

Y. Ma
CNOOC China LTD Zhanjiang Branch, Zhanjiang 524000, China

J. Zhang
CNOOC China LTD Hainan Branch, Haikou 570000, China

31.1 Introduction

Under the “dual carbon targets” of China’s carbon reduction and carbon neutrality, natural gas is favored as a relatively clean and low-carbon fossil energy. According to the statistics of the National Bureau of Statistics, domestic gas consumption has continued to grow in recent years, and the consumption of gas in 2021 is about 372.6 billion cubic meters, of which domestic produced gas accounts for 55%, imported LNG accounts for 29%, and imported pipeline gas accounts for 16%. It is predicted that in the future, imported LNG will reach more than 30% of the total consumption of gas, which will be an important source to meet the domestic demand. According to the Argus statistics, the prices for spot LNG deliveries to northeast Asia have been as low as \$2/mm Btu and as high as more than \$50/mm Btu in two years due to the influence of COVID-19, geopolitics, market supply and demand and other factors, and the price fluctuates dramatically, thus putting great pressure on domestic gas suppliers and end users [11, 21]. Therefore, it is of great significance to improve the long-term stable supply of gas in China by utilizing domestic gas pipeline network system, adopting domestic produced gas, imported gas and stored gas to supply the downstream market in synergy with each other and forming a “multi-source collaborative gas supply” mode when the international gas price fluctuates violently.

31.2 China’s Natural Gas Consumption Status and Main Sources

In the past ten years, China’s gas consumption has maintained rapid growth, with an average annual growth rate of 11.6%. In 2021, the gas consumption was about 372.6 billion cubic meters, up 13% yearly, accounting for 8.3% of domestic primary energy consumption. With the promotion of China’s “dual-carbon goal”, gas, as an important transition energy to achieve the goal, will have a large room for improvement in the future. It is predicted that the proportion of gas in domestic primary energy consumption will reach 15% in 2035 [22].

The supply of gas mainly comes from domestic producing gas and imported gas. Domestic-produced gas is mostly conventional gas. In 2021, the output of conventional gas was about $170.7 \times 10^9 \text{ m}^3$, accounting for 82% of the total produced gas, which is the primary source of gas production and increase, but the growth rate is slowing down. In 2021, $167.5 \times 10^9 \text{ m}^3$ of gas was imported, with a dependence of 45%. It is expected that in 2025, the imported gas will reach $235 \times 10^9 \text{ m}^3$, with a dependency of more than 50%. Imported gas includes pipeline gas and LNG. In 2021, $108.9 \times 10^9 \text{ m}^3$ (in the standard state after gasification, the same as below) of LNG was imported by sea, accounting for 65% of the total imported gas. In 2025, imported LNG will reach $140 \times 10^9 \text{ m}^3$, accounting for about 60% of the total imported gas. In the winter of 2017, there was a severe “gas shortage” in the north of China, which resulted in high gas prices and an imbalance between supply and demand. In early

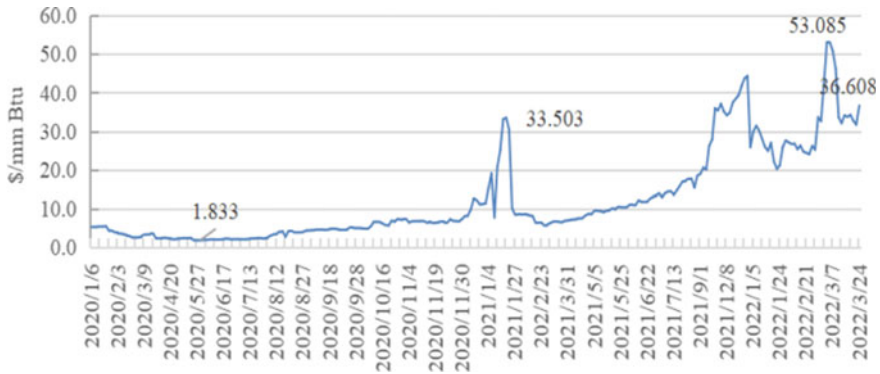


Fig. 31.1 Prices for spot LNG deliveries to northeast Asia (data from Argus)

2020, due to the impact of the COVID-19 pandemic, supply over demand, and price wars among supplier countries, the international DES spot LNG price fell off a cliff. The spot price of LNG in Northeast Asia was once lower than US\$2/mm Btu, far lower than the cost of wellhead gas or imported pipeline gas, while the spot price of LNG has been high since 2021, even more than US\$50/mm Btu (Fig. 31.1).

Under the trend of continuous growth of domestic gas consumption demand and tight local balance, to ensure energy supply, it is important to strengthen domestic underground gas storage (UGS) capacity construction and multi-source combined adjustment and supply. LNG storage tanks and UGS are the main gas storage facilities, and the important infrastructure for peak regulation and supply stabilization. Therefore, when the price of imported LNG fluctuates sharply, the imported LNG from the coastal terminal, the working gas in UGS, and the produced gas in domestic gas fields can be used for multi-source collaborative gas supply to ensure the stability of the market.

31.3 Feasibility of Land Infrastructure for Multi-source Collaborative Gas Supply

31.3.1 China's LNG Terminal Capacity

LNG import by the sea in the southeast coastal areas is one of China's four major gas import channels. Except for the LNG terminals in the Bohai Bay area, which have been in a tight equilibrium state in recent years when the demand surges in winter, the terminal receiving capacity of LNG in other coastal regions is rich. By the end of 2021, 22 LNG terminals have been put into operation, with a receiving capacity of 102.2×10^6 t/yr [22]. 29 projects under construction with a receiving capacity of 102.1×10^6 t/yr. The total receiving capacity achieves 204.3×10^6 t/yr

(Fig. 31.2). According to statistics, China’s LNG receiving capacity is expected to reach 247×10^6 t/yr in 2025 if approved and ongoing projects are put into production as scheduled.

Based on the conversion of LNG imports and the receiving capacity of existing LNG terminals, the terminal’s utilization rate in 2021 was about 77%, which will decrease with the commissioning of new terminals. It is estimated that the terminal’s utilization rate will be 46% in 2025 and 69% in 2040. The terminal will have a large surplus receiving capacity (Fig. 31.3). There is ample capacity for volume control to import LNG.

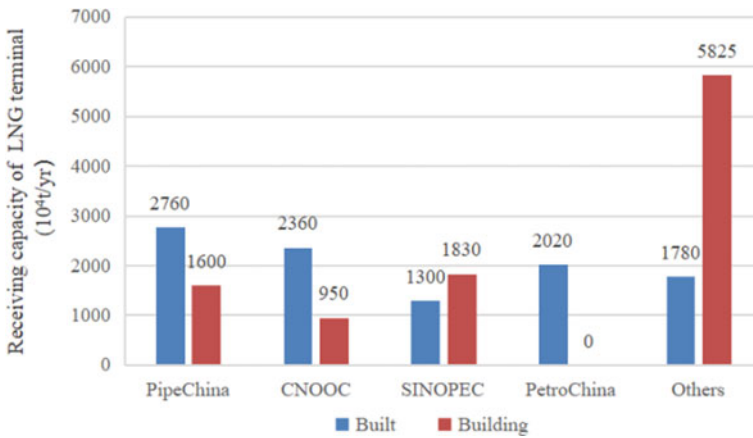


Fig. 31.2 China’s coastal LNG terminal

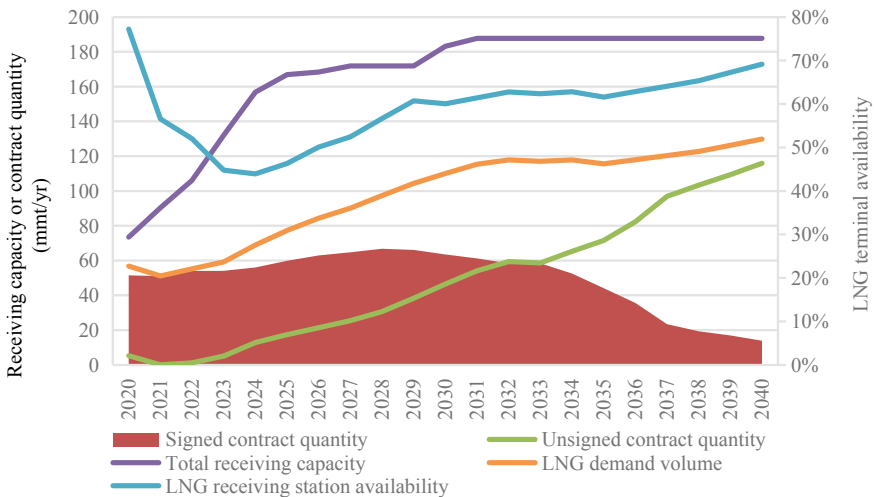


Fig. 31.3 LNG contract volume and offloading capacity in China (data from [18])

31.3.2 China's UGS Construction Situation

Currently, 27 UGS have been built in China (Fig. 31.4), with a peak load balancing capacity of about $14 \times 10^9 \text{ m}^3$ [4]. The total number is 45, including planned construction projects. There are 22 CNPC gas storage projects with an entirely designed working gas capacity of about $30 \times 10^9 \text{ m}^3$, 13 Sinopec projects with total designed working gas of about $3.6 \times 10^9 \text{ m}^3$, and 9 Pipechina projects with a total intended working gas capacity of about $14.2 \times 10^9 \text{ m}^3$, and 1 Ganghua project, with designed working gas of about $0.3 \times 10^9 \text{ m}^3$. In recent years, UGS has played a vital role in gas supply and peak regulation.

In response to the requirements of the state to strengthen the UGS capacity and the need of peak adjustment and guaranteed supply of gas, the upstream oil and gas companies actively layout and prepare the medium and long-term development plans of UGS, adapt to UGS conditions, and speed up the UGS capacity building by the principle of “first east, then west, first easy, then difficult.” The construction and planning of these UGS facilities provide a robust infrastructure for collaborative gas supply.

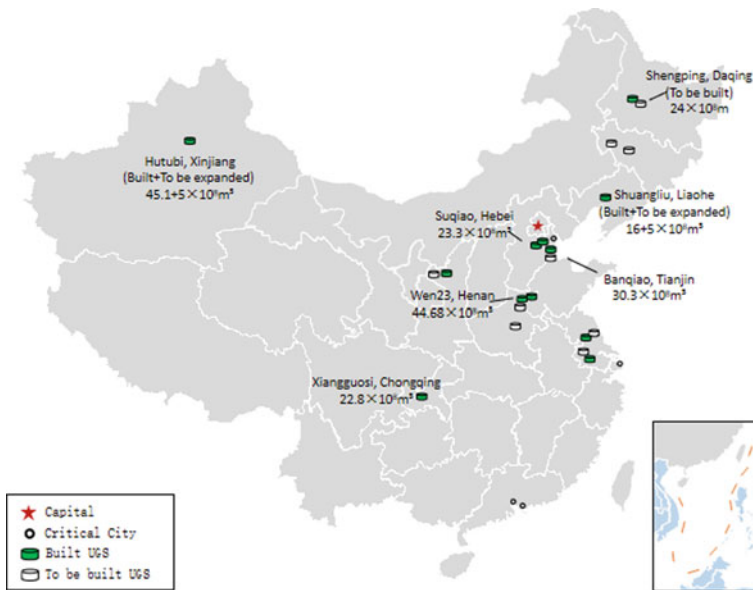


Fig. 31.4 The locations of partial UGS in China

31.3.3 The Connectivity of the Onshore Pipeline Network

The onshore pipeline network is an important channel connecting LNG terminals, tanks, UGS and gas fields to end users. The domestic onshore pipeline network system is gradually improving, especially in the eastern coastal areas. Taking Jiangsu Province as an example, there are several LNG terminals built or under construction in its coastal areas, which have been connected to the onshore pipeline network [6]. In addition, Jintan and Liuzhuang UGS, with a total capacity of $2.9 \times 10^9 \text{ m}^3$ have been built in Jiangsu Province. In 2022, two new salt cavern UGS facilities (clusters) will be built in Chuzhou and Huai'an, Jiangsu Province. The UGS facilities built and planned are respectively connected with the Jini-Nanjing tie-line trunk and the West–east Gas transmission pipeline. The interconnection between the onshore pipeline network, LNG terminal and gas storage makes it possible to supply gas from multiple sources.

31.4 Technical Feasibility of Gas Well Production Control

In 2021, China produced gas $205.3 \times 10^9 \text{ m}^3$. Except for the total output of coal seam gas, shale gas, and coal-to-gas, about $31.4 \times 10^9 \text{ m}^3$ [15], the primary major output comes from conventional gas reservoirs. This part mainly analyzes the technical feasibility of decreasing or increasing the production of conventional gas wells, and according to the study [7–13], UGS is also mainly converted from conventional gas reservoirs (including condensate gas reservoirs).

According to the changes of supply and demand in the downstream gas market, gas wells decrease or increase production operations occasionally. The most direct measure to adjust gas well production is to adjust the size of the wellhead nozzle. For one gas well, with other parameters unchanged, the pressure P_t at the wellhead and bottom hole flow pressure can be controlled by adjusting the size of the oil nozzle, to control the production pressure difference between the formation and the bottom hole and change the output of the gas well.

31.4.1 Effect of Decrease or Increase on Gas Well Productivity

Gas well production decreases or increases have different effects on ultimate recovery under different gas reservoir types and gas well production conditions. This paper analyzes the production effect in two kinds of varying well conditions.

Non-water producing well. For gas Wells that do not produce water without edge bottom water, gas production is driven mainly by the elasticity generated by gas expansion in the formation. After a while of gas well exploitation, the formation

energy in the near well zone will be firstly exhausted. If the energy in the far well zone can't be replenished in time, the pressure drop funnel in a particular range will be formed. Intermittent production or shutdown of gas wells during decreased production can effectively replenish the near-well formation energy, thus increasing the gas well production to a certain extent without affecting the overall gas reservoir's ultimate recovery. During production enhancement, if the formation permeability is high, the formation energy near the wellbore can be replenished in time. However, if the formation permeability is very low, the regional velocity sensitivity may occur, resulting in gas production only near the wellbore, and the gas ultimate recovery will probably decrease.

For gas reservoirs with edge and bottom water, the bottom hole flow pressure of the gas well increases after production decrease or shut-in, and the formation pressure drops slowly, which can slow down the advancing speed of gas-water or gas-oil contact and increase the production time of no-water/oil for gas well. On the contrary, production may accelerate water/oil discovery. For condensate gas reservoirs, decreased production can decrease the formation pressure drop rate and delay condensate water production, but rapid production is vice versa.

Water and gas producing Wells. There are two types of produced water for gas wells condensate water and formation water. Condensate water refers to the water produced after the formation pressure drops to the critical condensate pressure of water in the condensate gas reservoir production process. In this case, the daily water production of a single well is generally small, and the water production is stable. When formation water exists in the gas reservoir, the boundary water of the formation water and bottom water will advance to the gas well with the decrease of formation pressure in the production process so that the gas well will be invaded by water. In this case, water production will show an apparent upward trend. Both condensate water and edge or bottom water affect the production of gas wells, and border or bottom water is usually more important. The gas production of the water-producing gas well must meet a specific liquid-carrying capacity and carry the produced water out of the wellbore to ensure the normal production of the gas well.

Specific analysis can be divided into the following situations:

- (1) Gas Wells that have not been flooded and only a small amount of condensate water is produced. A short period of shut-in or reopening after a decrease in production has little impact on gas well production. As shown in Fig. 31.5, well A of a gas field YC in the South China sea, with a daily production of about 80 m³ condensate water, only reduced gas production within 10% after the well was reopened after 3 months of shut-in compared with that before shut-in. However, the actual influence degree should be analyzed according to different condensate gas reservoir conditions and different condensate water production degrees.
- (2) Gas Wells that have been flooded have high production of formation or condensate water. If the gas well's production is reduced or the well is shut down without any measures, it will cause serious fluid accumulation in the wellbore. On the one hand, the fluid accumulation in the wellbore will reduce the production

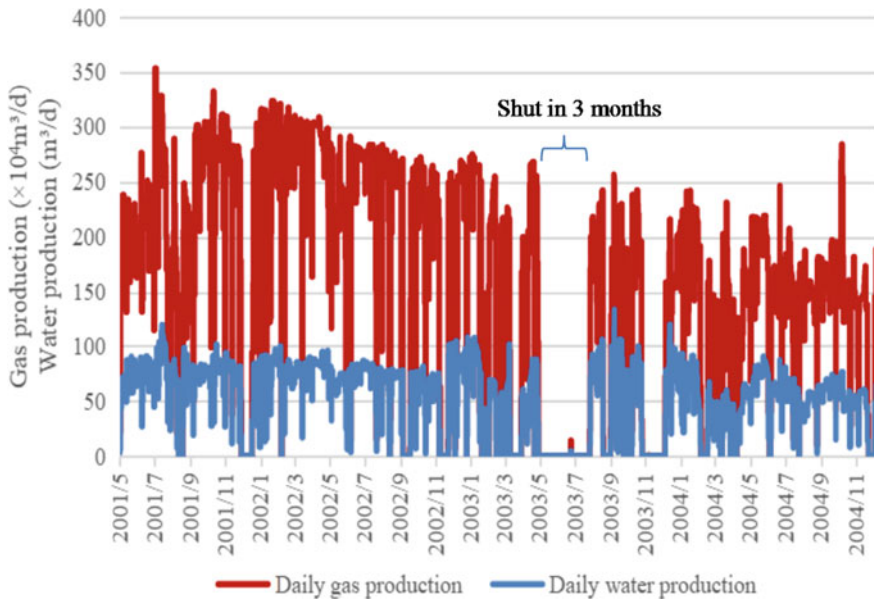


Fig. 31.5 The well A production profile of YC gas field

pressure difference during the re-opening of the well, resulting in the decrease of the liquid carrying capacity of the gas well, which significantly increases the difficulty of the well opening and affects the normal production of the gas well. On the other hand, under the effect of the shut-in pressure difference, the fluid will be injected back into the formation (Fig. 31.6), which makes the water saturation in a particular range near the well higher. The formation water occupies the gas phase seepage channel, resulting in the water lock effect, which leads to a substantial decrease in the gas phase permeability, thus seriously affecting the productivity of the gas well and even causing suspend production.

Due to the additional pressure caused by the two-phase separation of gas and liquid in the wellbore, the fluid in the wellbore is injected back into the formation, resulting in the phenomenon of fluid in the wellbore, as shown in the hump in Fig. 31.6. However, in some cases, formation pressure is also recovering when gas and liquid are separated in the wellbore. If both are carried out simultaneously, the hump phenomenon in Fig. 31.6 will not occur, so the accumulation of liquid in the gas well will not happen. Therefore, the factors that affect the occurrence of wellbore drainage backflow include formation permeability, wellbore fluid viscosity, skin coefficient near the wellbore and gas solubility, etc. If the formation permeability is high, the wellbore liquid viscosity is large, the skin coefficient is large, and the gas solubility is high, effective measures must be taken to prevent the occurrence of the wellbore fluid backflow phenomenon.

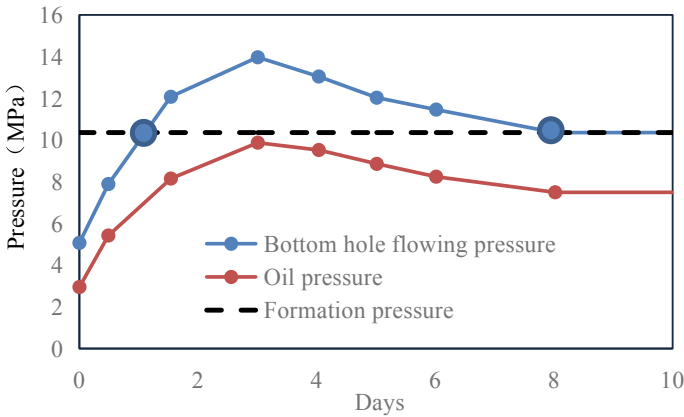


Fig. 31.6 Pressure recovery curve of gas well with accumulation liquid

- (3) For gas wells with both water and sand production, a pollution zone will be formed between the near-well zone and the sand control pipe in a certain range. The fine sand and mud in the formation will form non-Newtonian fluid under high water saturation, and the formation permeability will decrease rapidly. In severe cases, the formation permeability after pollution is even less than 20% of the original permeability, which will have a massive impact on the productivity of gas Wells [10].

31.4.2 Solution Measures Affecting Gas Recovery

The measures discussed in this paper are mainly for water-bearing gas wells. For gas wells without water production and dry gas reservoirs without being affected by edge or bottom water, adjustment production has no or little effect on the ultimate recovery factor of the whole gas field.

Reasonable design of gas production. Regardless of the downstream market demand or the working gas requirements of the surface compressor, decreased production has the greatest impact on the well production of the gas well that has already produced water, as opposed to increasing production. Therefore, the main objective is to prevent fluid accumulation in the wellbore after decreased production. To achieve the purpose, the minimum gas production after the decrease production should meet the requirements of liquid carrying, i.e. $Q_{min} \geq Q_{sc}$.

According to the research results of scholars, the formula for calculating the critical liquid-carrying velocity of conventional gas wells [3] is as follows:

$$v_{sg} = \frac{Ku}{3.73} \left\{ 6.6 \left[\frac{\sigma(\rho_l - \rho_g)}{\rho_g^2} \right]^{0.25} \right\} \tag{31.1}$$

where

v_{sg} is the critical liquid carrying velocity, m/s;
 $\frac{Ku}{3.73}$ is the correction coefficient.

In practical application, the corresponding correction coefficient can be queried from Table 31.1 [3] according to the actual parameter of the gas field,

$6.6 \left[\frac{\sigma(\rho_l - \rho_g)}{\rho_g^2} \right]^{0.25}$ is the classic Turner model;
 σ is gas–liquid surface tension, N/m;
 ρ_l is the liquid phase density, kg/m³;
 ρ_g is the gas phase density, kg/m³.

According to the gas conversion coefficient under standard conditions, the critical liquid carrying velocity of gas calculated by the above formula is converted into gas production under standard conditions, and the critical liquid-carrying flow of gas is obtained [16–8]:

$$Q_{sc} = 2.5 \times 10^8 \frac{Ap}{ZT} v_{sg} \tag{31.2}$$

Table 31.1 Correction coefficient table

Hole deviation angle (°)	Correction coefficients for different tubing inner diameters			
	50.67 mm	62.00 mm	75.9 mm	100.53 mm
0	0.769	0.79	0.808	0.829
5	0.768	0.789	0.807	0.828
10	0.765	0.786	0.805	0.825
15	0.76	0.782	0.8	0.821
20	0.753	0.775	0.793	0.814
25	0.745	0.766	0.785	0.806
30	0.733	0.755	0.774	0.795
35	0.72	0.742	0.761	0.782
40	0.704	0.726	0.745	0.767
45	0.686	0.708	0.727	0.749
50	0.664	0.686	0.706	0.728
55	0.638	0.661	0.681	0.704
60	0.609	0.632	0.652	0.675
65	0.574	0.597	0.618	0.641
70	0.531	0.555	0.576	0.601
75	0.479	0.503	0.524	0.55
80	0.41	0.434	0.456	0.482
85	0.308	0.331	0.352	0.379
90	0.032	0.035	0.039	0.045

where

- Q_{sc} is the critical liquid-carrying flow of gas, m^3/d ;
 A is the tubing area, m^2 ;
 P is the pressure, MPa;
 T is the temperature, K;
 Z is the gas deviation coefficient, dimensionless.

Measures to reduce the influence of fluid accumulation on gas production well.

Different measures can be taken according to the amount of fluid accumulated in the wellbore [2, 1]:

(1) Active drainage before shut-in

Before shutting in a gas well, the fluid accumulation in the wellbore should be detected in advance. Suppose the fluid accumulation in the wellbore is serious. In that case, it is necessary to take active drainage measures to avoid the backflow of the fluid accumulation in the wellbore after shut-in.

(2) Change the shut-in operation method

Suppose the fluid accumulation in the wellbore is not much and the formation pressure is small. In that case, the gas well can be slowly closed by gradually reducing the opening of the oil nozzle, so that the pressure between the wellbore and the near wellbore can be restored to the equilibrium state. The liquid accumulation backflow phenomenon can be avoided.

(3) Reasonable design of well opening and blowout inducement

Given the pressure and fluid accumulation in the wellbore of gas wells, the applicability of various production processes, such as coiled tubing with liquid nitrogen, bubble drainage, and membrane nitrogen production was tried. The gas storage capacity in the limited space of the wellbore was used to improve the foaming effect and form continuous drainage to increase the amount of induced blowout.

31.5 Discussion on Multi-source Collaborative Gas Supply Measures

31.5.1 Early Gas Drive Oil Recovery and Late Gas Production

The condensate gas reservoir with depletion development mode can be adjusted to gas injection to develop condensate oil in the early stage, and converted to UGS in the later stage, which can enhance the recovery rate of condensate oil without affecting the production and recovery rate of gas. For the oil field developed by water injection, if the conditions of later conversion to storage are available, it should be adjusted to

early gas injection to drive oil development and later gas recovery. To achieve the integration effect of oil and gas field development and UGS construction [17].

31.5.2 Domestic Produced Gas and “Production, Injection, Storage and Sales” Full Life Reservoir Management

When the international LNG price is much lower than the domestic gas production cost, gas produced from wells that can't be shut down or decreased could be injected back into gas reservoirs through a pipeline network, which could be regarded as UGS with high permeability reservoir and wall rock sealing. The downstream market relies on imported LNG supply, especially the purchase of low-cost spot LNG supply, for resource swap to gain super profit and reserve gas resources. When the international LNG price is high or the downstream market demand increases, domestically produced gas and gas storage will be used to supply the market at the same time, and spot LNG will be purchased as little as possible to mitigate the impact of high prices in the international market. On the premise of not considering the factors of “buy low and sell high” of international and domestic gas, only the method of “summer injection and winter production” can be used to obtain the national regulation of winter supply of gas gate station prices of provinces of 20% increase in the price difference.

It is planned to establish a regional data control center for gas in the long term. Guided by the downstream gas market, the linkage and dynamic digital management of UGS, domestic gas fields and LNG terminals will be formed, the linkage effect of “multi-source regulation and collaboration” of gas storage, domestic produced gas and imported gas will be brought into play. Large high-quality gas reservoirs (UGS) will be built into a platform for gas operation. According to the needs of market and peak regulating, gas reservoirs have been dynamically managed throughout the whole life cycle from single “production and marketing” to “production, injection, storage and marketing”, meanwhile prolonging the life cycle of the peripheral marginal gas field, improving the industrial chain of “production, supply, storage and sales”, thus increasing the supply guaranteeing ability and suppressing the international price fluctuation. For high-quality gas reservoirs, the feasibility of “injection, storage and production” should be planned and studied as early as possible. Especially in the research stage of gas field development and construction, the planning and layout of UGS research should be involved to complement the LNG terminal and gas field production to realize the dynamic management of gas reservoir development, production, and injection during the whole life cycle. At the same time, supporting facilities such as pipeline networks should be arranged and constructed to meet the overall design function positioning needs.

31.6 Conclusions and Recommendations

- (1) The basic requirements for realizing a “multi-source collaborative gas supply” are a perfect pipeline network system and a highly unified regional dispatching operation center. LNG terminal and UGS need to be connected to the gas pipeline network, which can provide convenient conditions for the cooperative import of LNG and domestic gas supply.
- (2) From the perspective of gas reservoir characteristics and gas field production, it is necessary to conduct in-depth research on the reservoir construction mode of the “multi-source collaborative gas supply” pilot according to the production situation of different gas fields and gas wells. For large undeveloped gas reservoirs, through the combination of the gas drive recovery project and UGS project, “overall layout and phased implementation” in advance to avoid repeated construction of UGS reconstruction in the later stage to maximize investment benefits. The developed gas reservoir can be used for rich gas injection reserves, realizing the transformation of the gas reservoir from production to injection and the construction of gas reserve capacity to enhance the value of high-quality and scarce enormous gas reservoir resources.

Funding Part of the research results of CNOOC group Ltd. science and technology research project “Study on the scheme of UGS for offshore near-exhausted gas reservoir” (NO: CNOOC-KJ135KJXMJD2020-004).

References

1. Bai, X., Tian, W., Tian, S., Li, K.: Optimization on wellbore flow parameters of gas lift deliquification in low production and liquid loading gas wells. *Fault-Block Oil Gas Field* **21**(1), 125–128 (2014)
2. Chen, X.: New resumed production technique for low pressure low production gas wells with liquid loading. *Special Oil Gas Reserv.* **24**(3), 160–163 (2017)
3. Chen, D., Yao, Y., Han, H., Gang, F., Song, T., Xie, S.: A new prediction model for critical liquid-carrying flow rate of directional gas wells. *Nat. Gas. Ind.* **36**(6), 40–44 (2016)
4. Ding, G., Ding, Y., Li, Y., Tang, L., Wu, Z., Qiqi, W., et al.: Prospects of underground gas storage in China under the strategy of carbon neutrality. *Oil Gas Storage Transp.* **4**(1), 1–9 (2022)
5. Ding, G., Li, C., Wang, J., Xu, H., Zheng, Y., Qiqi, W., et al.: The status quo and technical development direction of underground gas storages in China. *Nat. Gas. Ind.* **35**(11), 107–112 (2015)
6. Zihang, F., Shan, T., Yang, Y., Liu, F.: Interoperability of LNG terminals and gas pipeline networks. *Nat. Gas. Ind.* **40**(7), 97–105 (2020)
7. Gong, W., Tian, L., Wang, D., Wang, H., Wang, J., Zhang, Y.: Evaluation of the economic benefits of gas storage based on the whole natural gas industry chain. *Nat. Gas. Ind.* **40**(3), 157–163 (2020)
8. Guan, H., Jifei, Y., Fang, Z., Li, W.: A new method of the critical liquid carrying flow rate for highly deviated gas well. *China Offshore Oil Gas* **23**(1), 50–52 (2011)

9. Guo, B., Jing, J., Wang, X.: Calculation improvement of critical liquid-carrying flow rate for gas well. *Fault Block Oil Gas Field* **25**(4), 484–487 (2018)
10. He, Z., Hao, Y.: Analysis of effects of permeability on gas well productivity equation and open flow capacity. *Pet. Explor. Dev.* **28**(5), 46–48 (2001)
11. Hu, Y., He, S., Han, Q., Zhong, H., Wang, H.: Construction of a big data platform for gas storage and peak shaving. *Nat. Gas. Ind.* **40**(6), 157–163 (2020)
12. Liu, J., Liu, Y.: Development status and prospects of China's underground gas storage construction. *Appl. Chem. Ind.* **51**(4), 1136–1140 (2022)
13. Ma, X., Zheng, D., Shen, R., Wang, C., Luo, J., Sun, J.: Key technologies and practice for gas field storage facility construction of complex geological conditions in China **45**(3), 489–499 (2018)
14. Ming, R., He, H., Qiangfa, H.: A new predicting method of the critical liquid-loading flow rate for horizontal gas wells. *Petrol. Geol. Oilfield Dev. Daqing* **37**(5), 81–85 (2018)
15. National Energy Administration: China Natural Gas Development Report. Petroleum Industry Press, Beijing (2021)
16. Ran, L., Zheng, D., Luo, T., Wanyan, Q., Hou, Y.: Construction & operation characteristics of salt cavern underground gas storages. *Oil Gas Storage Transp.* **38**(7), 778–781+787 (2019)
17. Sun, C., Zhai, L., Luo, M., Hong, B.: Study on economic evaluation model and economy for collaborative construction of gas storage and oilfield development. *Petrol. New Energy* **33**(3), 53–59 (2021)
18. Woodmac (2020) LNG short term outlook [M]. Publisher unknown (2020)
19. Zhang, S., Liu, G., Liao, W., Chen, Y., Zhang, Y., Zheng, Q.: Problems and technical countermeasures in multi-cycle operation of large gas storage with edge and bottom water: a case study of Hutubi gas storage. *Sino-Global Energy* **25**(2), 50–57 (2020)
20. Zhang, F., Zeng, P, Zhou, L., Li, B., Zhang, S.: Underground gas storage research status quo and application expectations at home and abroad. *Coal Geol. China* **33**(10), 39–42+52 (2021)
21. Zheng, D., Zhang, G., Wei, H., Ding, G., Qi, H., Li, D.: Countermeasures and suggestions on natural gas peak shaving and supply guarantee in China. *Nat. Gas. Ind.* **38**(4), 153–160 (2018)
22. Zhou, S., Zhu, J., Shan, T., Qiang, F., Zhang, D., Wang, J.: Development status and outlook of natural gas and LNG industry in China. *China Offshore Oil Gas* **34**(1), 1–8 (2022)

Chapter 32

Study on Constitutive Relation of PVC Foam Based on Microstructure Model



Yong Zhou, Bin Xue, and Renpeng Wang

Abstract The mechanical properties of foam materials are closely related to the mechanical properties of the matrix material and the geometrical characteristics of the microstructure. In this paper, a novel method of constructing a microstructural model of transverse isotropic closed-cell foam is proposed and uniaxial tensile simulations of PVC foam are carried out based on this model. The simulation results of the established finite element model are in good agreement with the experimental results. The effect of the change in aspect ratio and relative density on the mechanical properties in compression of the isotropic microstructure into a transverse isotropic microstructure is then investigated through numerical simulations, and the prediction equations for the tensile modulus and tensile yield strength of the closed-cell PVC foam are established. Finally, a relatively simple uniaxial tensile constitutive equation is proposed, so that the tensile stress–strain curve can be determined by as few parameters as possible. The parameters in the equation are related to the relative density and aspect ratio, and the phenomenological tensile constitutive equation is established.

Keywords Finite element analysis · Transversely isotropic foam · Bulk mechanical properties · Constitutive relation

32.1 Introduction

PVC foam is increasingly used as a lightweight core material in composite sandwich structures due to its light weight and superior energy absorption properties. The compressive mechanical properties of PVC foam have been widely studied, but there are few studies on the tensile mechanical properties. However, as a common form of force, tensile behavior should be studied. The deformation characteristics of foam under tensile load are typical, which mainly experience two stages, namely linear elastic stage and plastic rising stage [1]. The tensile strain of PVC foams of

Y. Zhou · B. Xue · R. Wang (✉)
College of Civil Engineering, Tongji University, Shanghai 200092, China
e-mail: renpengwang@126.com

© The Author(s), under exclusive license to Springer Nature Switzerland AG 2024
S. Li (ed.), *Computational and Experimental Simulations in Engineering, Mechanisms and Machine Science* 145, https://doi.org/10.1007/978-3-031-42987-3_32

concern is usually very small because the elastic stage and the tensile yield strength corresponding to 0.2% plastic strain occur within 3% strain [2]. The research on the tensile mechanical properties of PVC foam is mainly focused on experiments. The tensile and compressive tests of four kinds of high-performance closed-cell PVC foams with different densities were carried out by Colloca et al. [2]. It was found that the tensile elastic modulus was greater than the compressive elastic modulus, and the tensile yield strength was greater than the compressive yield strength. However, the energy absorbed by PVC foam under compressive load was 5 times more than that under tensile load. Viana et al. [3] tested the tensile mechanical properties of PVC foam in the rising direction of cell pore and the direction perpendicular to the rising direction of cell pore, and found that the tensile mechanical properties in the two directions were different, and the elastic modulus and yield strength in the rising direction of cell pore were greater than those in the direction perpendicular to the rising direction of cell pore. Deshpande et al. [4] used SEM to observe the deformation of foam under tensile and compressive loads, and found that the deformation of foam under compressive load was determined by the buckling of cell wall, while the deformation under tensile load was controlled by the bending of cell wall, which led to the difference of tensile and compressive elastic modulus and yield strength. Kabir et al. [5] studied the tensile fracture behavior of polymer foams with different densities, polymer materials and loading rates, and determined the empirical relationship between tensile yield strength, tensile elastic modulus and fracture toughness and foam density. Although there are few studies on the tensile mechanical properties of foam, a large number of compression studies can provide guidance for the study of tensile mechanical properties. Gibson and Ashby [6] proposed formulas for predicting the elastic modulus and yield strength of isotropic foam under compression as follows:

$$\frac{E^*}{E_s} = C_1 \phi^2 \left(\frac{\rho^*}{\rho_s} \right)^2 + C_2 (1 - \phi) \frac{\rho^*}{\rho_s} \quad (32.1)$$

$$\frac{\sigma_{pl}^*}{\sigma_{ys}} = C_3 \left(\phi \frac{\rho^*}{\rho_s} \right)^{3/2} + C_4 (1 - \phi) \frac{\rho^*}{\rho_s} \quad (32.2)$$

where ρ^* and ρ_s were the densities of the foam and the base material, respectively; ϕ was the volume fraction of the base material in the struts; C_1 – C_4 were empirical. The Young's modulus E^* and plastic collapse strength σ_{pl}^* belong to foam while the Young's modulus E_s and yield strength σ_{ys} belong to solid substrate. However, when loading in different material directions, the mechanical properties of polymer foams may be very different [7–9]. This is mainly due to the fact that the cell tends to elongate along the rising direction of the foam in the mold, resulting in a large difference in mechanical properties between parallel and perpendicular to the rising direction, forming transverse isotropy. Gibson and Ashby [6] through the analysis of simple geometric cubic hole, put forward the properties of different two direction compression elastic modulus and yield strength ratio formula is as follows:

$$\frac{E_3^*}{E_1^*} = \frac{2R^2}{1 + \left(\frac{1}{R}\right)^3} + (1 - \phi) \frac{2R}{1 + \frac{1}{R}} \quad (32.3)$$

$$\frac{\left(\sigma_{pl}^*\right)_3}{\left(\sigma_{pl}^*\right)_1} = \frac{2R}{1 + 1/R} \quad (32.4)$$

where E_3^* and E_1^* are the Young's moduli in the rise direction and the transverse direction, respectively; $\left(\sigma_{pl}^*\right)_3$ and $\left(\sigma_{pl}^*\right)_1$ are the plastic collapse strengths in the rise direction and the transverse direction, respectively. However, Zhou et al. [10] found that this formula could not accurately predict the mechanical properties both directions, and established a phenomenological mechanical property prediction equation through finite element simulation.

It is a common method to study the macroscopic compressive behavior of foams by fine microscopic finite element simulation. Many models have been developed to establish the relationship between microstructure and macroscopic properties of foams. Using a tetrahedral Kelvin unit to simulate a foam structure is one of the simplest methods. Based on the finite element model of regular Kelvin element arrangement, Jang et al. [11] determined the elastic modulus and yield strength of open-cell foam under compression load. Based on the finite element model of Kelvin element. However, this single structure cannot represent the randomness of the real foam microstructure, and this model often overestimates the mechanical properties of the foam [2, 12]. For this reason, many scholars have used random partition models to construct the three-dimensional structure of the foam, and combined with the finite element method to study the influence of the geometric characteristics of the microstructure on the macroscopic mechanical properties of the foam. Among them, the Voronoi partition model and the Laguerre partition model are commonly used. These models can be used to quantify the influence of different microscopic parameters (cell size distribution, hole wall thickness, mass distribution of faces and edges, irregularity, etc.) on mechanical properties [13–16]. Many scholars have studied the anisotropy and transverse isotropy in foam structures. Sadek et al. [17] constructed an anisotropic foam microstructure by stretching the periodic Kelvin tetrahedral closed-cell foam model in three directions with different proportions, and studied the influence of anisotropy on the elastic modulus and yield strength in three orthogonal directions. Ayyagari and Shafiq [18, 19] constructed transversely isotropic foams by introducing a geometric stretch factor into the periodic Kelvin open-cell foam model, and studied the effect of the geometric stretch factor on the strength and stiffness of the Kelvin foam model. Mashhadi et al. [20, 21] introduced a geometric stretching factor based on the Laguerre partition model and carried out a high-fidelity simulation of PU closed-cell foam under compression load until densification and established a new model to predict the stress–strain curve of closed-cell foam. Pei et al. [22, 23] established a rate constitutive model of transversely isotropic PU foam

by testing a self-made transversely isotropic PU foam and stretching an open-celled Kelvin tetrahedron. Zhou et al. [10, 24] studied the relative density and aspect ratio under the premise of ensuring the volume of the model cells. However, the above studies are basically limited to uniaxial compression. This paper studies the tensile behavior of transversely isotropic foam.

There are few tensile constitutive relations for foams, and most of the current literatures use polynomials to fit the stress–strain curves [25, 26], and the results are cumbersome. Therefore, this paper proposes a simple tensile constitutive equation to characterize the tensile mechanical behavior of tensile strain within 3%, so that the tensile stress–strain curve can be determined with only a few parameters. Based on the finite element simulation results, an equation for predicting the tensile elastic modulus and tensile yield strength of PVC closed-cell foam was proposed. This equation considers the influence of relative density and aspect ratio R . Combined with the proposed prediction equation, the tensile constitutive equation prediction model considering the influence of relative density and aspect ratio R was summarized to characterize the uniaxial tensile mechanical properties of PVC foam.

32.2 Materials and Experiments

32.2.1 Materials

The foams studied in this paper are H100 and H250 foams produced by Diab, which are now widely used in aviation and shipbuilding industries. H series foams are made of polyvinyl chloride (PVC). The microscopic geometric characteristics of H100 foam and H250 can be found in [24]. The measured densities of H100 and H250 were 95.06 kg/m^3 and 294.86 kg/m^3 , respectively, and the measured cell wall thicknesses were $11.5 \text{ }\mu\text{m}$ and $30.2 \text{ }\mu\text{m}$, respectively. H100 foam and H250 micro-solid PVC properties and macroscopic compressive mechanical properties can be found in [10]. The elastic modulus of solid PVC is 2700 MPa and the yield strength is 64 MPa .

The foam studied is transversely isotropic, where the mechanical properties in the direction of cell ascent (Z direction) are different from those in the direction perpendicular to the cell ascent (X/Y direction) (Fig. 32.1). The aspect ratio R was used to quantitatively analyze the difference. The R values of H100 and H250 were 1.2 and 1.4, respectively.

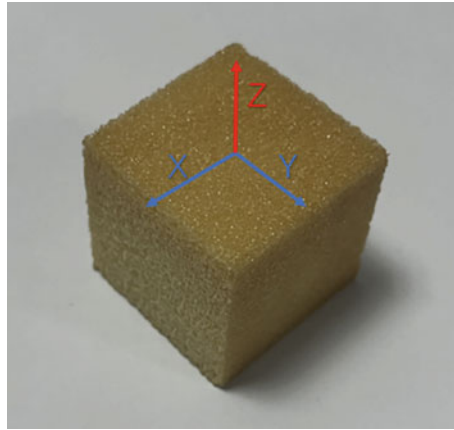


Fig. 32.1 Transversely isotropic PVC foam schematic

32.2.2 Experiments

Shafiq et al. [19] carried out the quasi-static uniaxial tensile test of H100 foam using dog-bone specimens, and the loading strain rate was 5×10^{-4} . Daniel et al. [27] carried out the quasi-static uniaxial tensile test of H250 foam using cubic specimens, and the loading strain rate was 10^{-4} . Each foam was tested in Z and X/Y directions. The test results are shown in Fig. 32.2. It can be found that the tensile mechanical properties in the Z direction are quite different from those in the X/Y direction, so the effect of transverse isotropy cannot be ignored in PVC foam, and this effect is related to density and aspect ratio R .

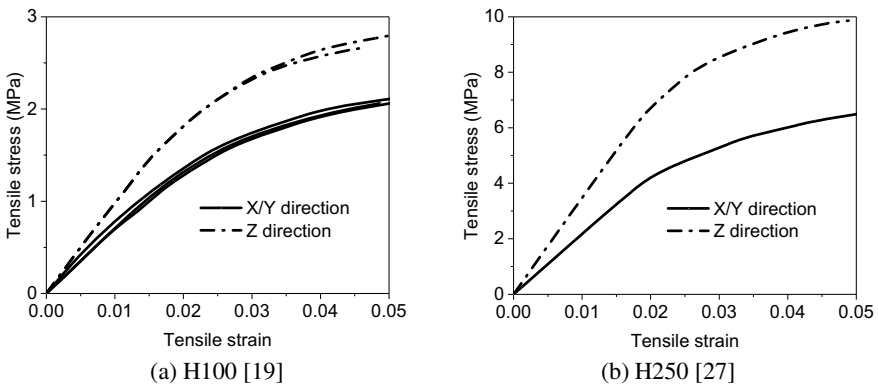


Fig. 32.2 Stress–strain curves of foam samples under uniaxial tension

32.3 Finite Element Simulation

In this study, the forward surface algorithm is used to closely accumulate the spheres, and the Laguerre tessellation is used to establish the microstructure finite element model of the foam. The specific microstructure construction method is described in detail in [24]. Because the difference of microscopic geometric characteristics of different types of foam is mainly the difference of cell wall thickness and R value, different types of foam can be constructed by giving different cell wall thickness and R value without changing the cell volume. The specific practice is shown in Fig. 32.3. When the Z direction is elongated, both the X and Y directions are shortened and $a \times b^2 = 1$ is guaranteed, then R can be defined as a/b .

32.3.1 Parameter Setting

In the finite element model, solid PVC is set as an ideal elastoplastic material and the cell wall is meshed by shell elements (S4R, S3R). Because Abaqus/Explicit is stable in simulating cell wall buckling and contact, Abaqus/Explicit is used to simulate the tensile simulation of the finite element model. For the uniaxial test, two analytical rigid shells with reference points are created and placed at the top and bottom of the RVE model. The general contact is established in Abaqus/Explicit to consider the surface-to-surface contact between the foam hole walls. The tangential behavior of the contact is set to a friction coefficient of 0.2, and the normal behavior is ‘hard’ contact and allows post-release separation. At the same time, in order to make the analytical rigid shell not separate from the RVE during tension, the analytical rigid shell and the adjacent nodes are set to ‘tie’.

The velocity loading is set to describe the engineering stress and strain of the model by obtaining the reaction force of the reference point RP on the moving rigid shell and the displacement in the loading direction. In order to simulate the mechanical behavior of foam under quasi-static and compare with the experiment, the loading rate of 0.002 mm/s is selected, and the strain rate corresponding to the 2 mm cube

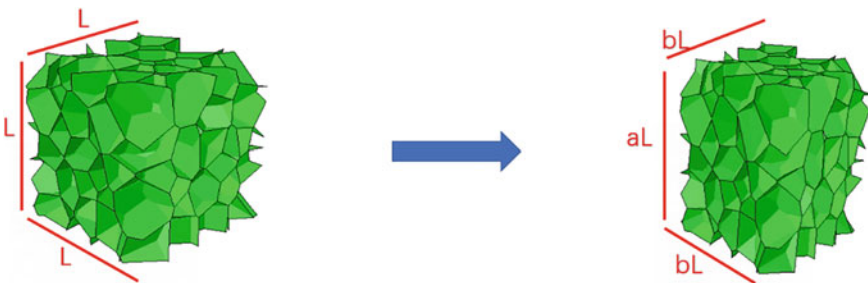


Fig. 32.3 Schematic diagram of the iso-volume transformation

model is 0.001/s. At the same time, in order to reduce the operation time as much as possible, the mass scaling is performed when the kinetic energy/internal energy is less than 5%.

32.3.2 FEA Results

In order to determine the minimum size of the RVE, the side length of 2, 3, 4 mm cube tensile simulation. Taking H100 as an example, the simulation results are shown in Fig. 32.4. It can be found from the figure that RVE of 2 mm size can already represent the overall tensile mechanical behavior. Therefore, the later analysis of this study is carried out with RVE of 2 mm size.

Figure 32.5 compares the finite element results with the experimental results. It can be found that the finite element results are in good agreement with the experimental results.

32.4 Effect of Different R Value and Relative Density

Since the main differences between different types of foams are relative density $\frac{\rho^*}{\rho_s}$ and aspect ratio R , these two factors are considered as undetermined parameters for analysis. The aspect ratio R of PVC foam is basically between 1.2 and 1.6 [7], so $R = 1, 1.2, 1.4, 1.6$ are selected for calculation. At the same time, in order to consider the influence of relative density, $\frac{\rho^*}{\rho_s} = 0.07, 0.14, 0.21$ and 0.28 are selected for calculation under each R . In order to consider the transverse isotropy, the X/Y direction and Z direction were tested. Figure 32.6 shows the finite element simulation results for different R and $\frac{\rho^*}{\rho_s}$.

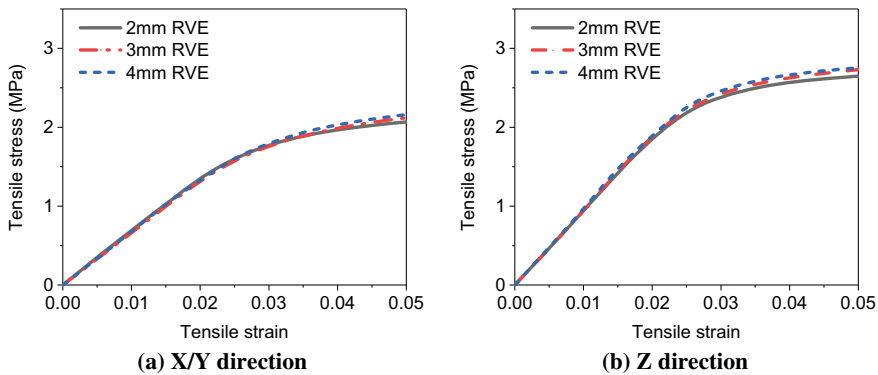


Fig. 32.4 Comparison of the FEA results of three RVEs

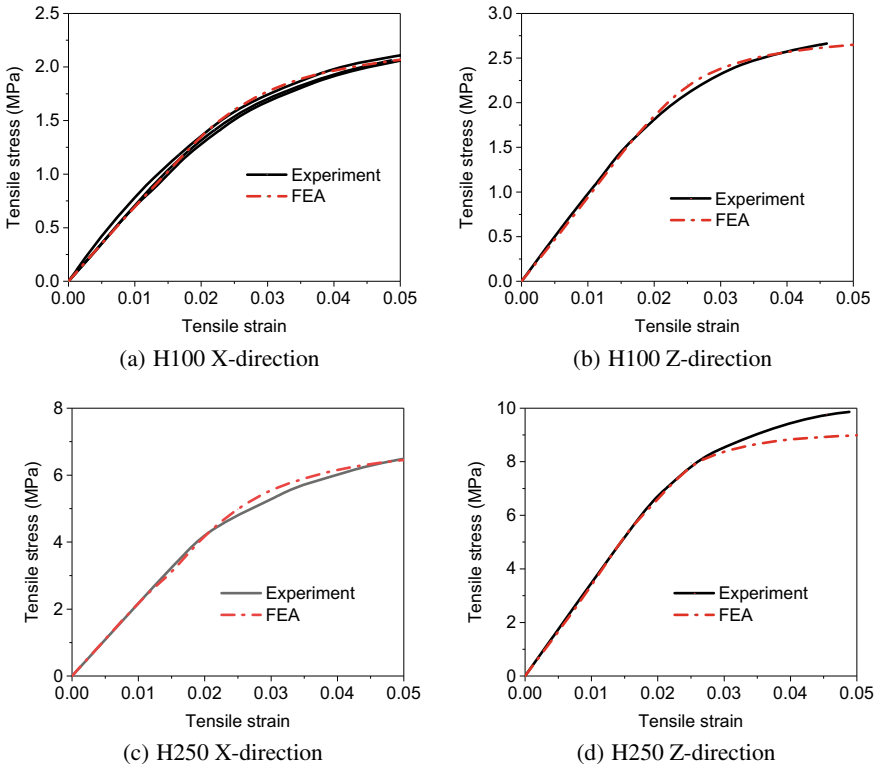


Fig. 32.5 Comparison of FEA and experimental results

It can be found from Fig. 32.6 that when $R > 1$, the elastic modulus in the Z direction and the tensile yield strength determined by 0.2% plastic strain are higher than those in the X/Y direction, and the degree of difference is related to R and $\frac{\rho^*}{\rho_s}$. For simplicity, the elastic modulus and yield strength at a relative density of 0.07 are extracted for analysis. Figure 32.7 shows the change in elastic modulus at different R values.

E_3^*/E_1^* is linearly related to R and conforms to the relationship of Eq. (32.5).

$$\frac{E_3^*}{E_1^*} = 1.795 \times R - 0.795 \tag{32.5}$$

E_3^* is the tensile modulus of Z direction and E_1^* is the tensile modulus of X/Y direction.

At the same time, there is an Eq. (32.6) relationship between the tensile modulus of the model with $R > 1$ and the model with $R = 1$, and when $R > 1$, the product of the tensile modulus E_3^* in the Z direction and the tensile modulus E_1^* in the X/Y direction is equal to the square of the tensile modulus E_{iso}^* of the model with $R = 1$.

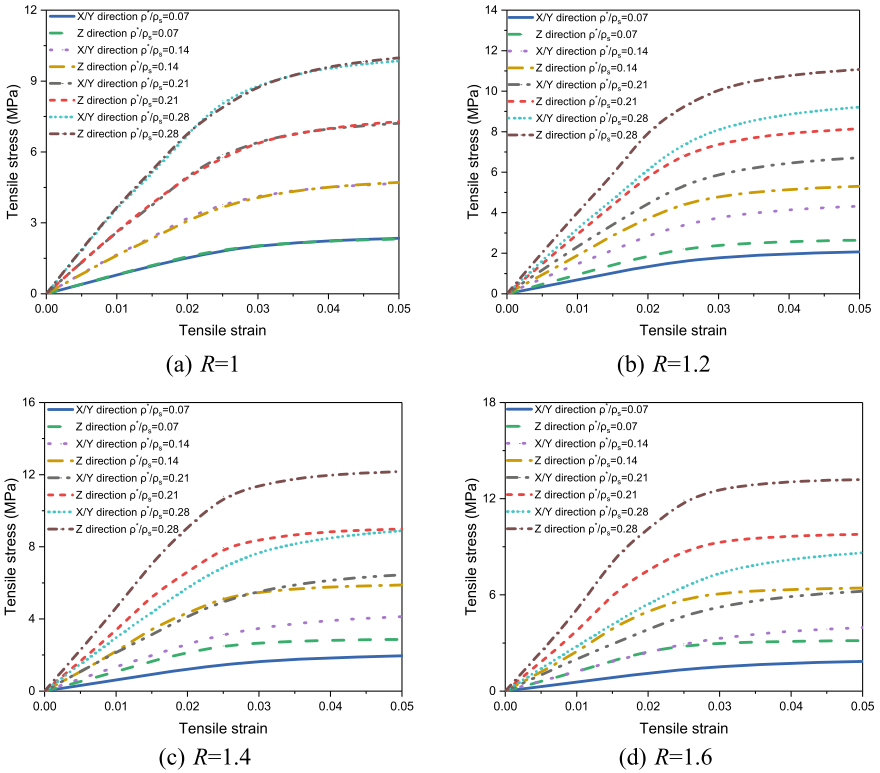


Fig. 32.6 FEA results of different R and $\frac{\rho^*}{\rho_s}$

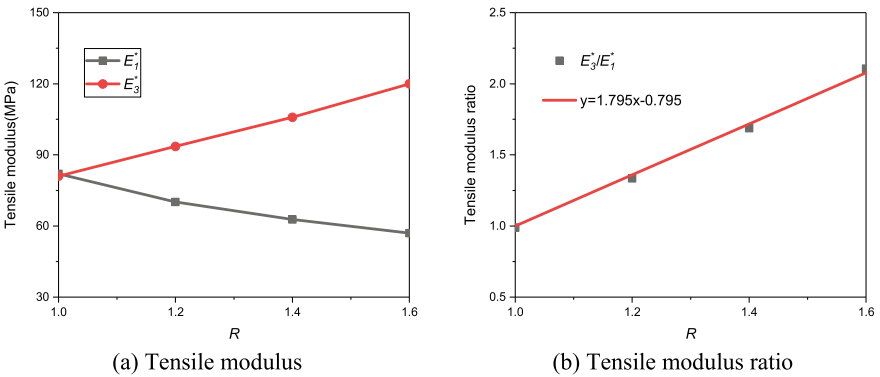


Fig. 32.7 Variation of tensile modulus

Table 32.1 lists the product results in detail.

$$E_3^* \times E_1^* = (E_{iso}^*)^2 \tag{32.6}$$

A similar treatment is applied to the tensile yield strength determined by 0.2% plastic strain. Figure 32.8 shows the variation of tensile yield strength under different R .

σ_3^*/σ_1^* is linearly related to R and conforms to the relationship of Eq. (32.7).

$$\frac{\sigma_3^*}{\sigma_1^*} = 1.716 \times R - 0.716 \tag{32.7}$$

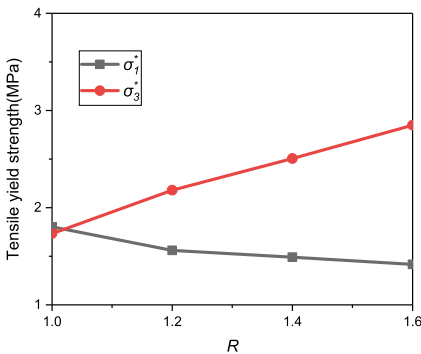
σ_3^* is the tensile yield strength of Z direction and σ_1^* is the tensile yield strength of X/Y direction. Similarly, the tensile yield strength obeys the product relationship of Eq. (32.8). Table 32.2 lists the product results in detail.

$$\sigma_1^* \times \sigma_1^* \times \sigma_3^* = (\sigma_{iso}^*)^3 \tag{32.8}$$

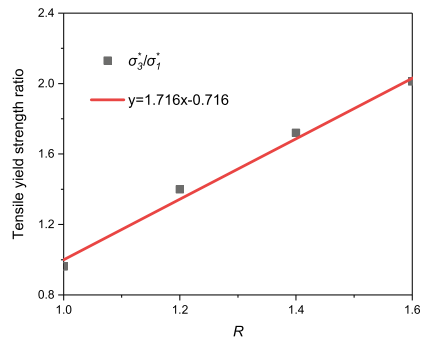
Table 32.1 Comparison of $E_3^* \times E_1^*$ and $(E_{iso}^*)^2$

R	E_3^*	E_1^*	$E_3^* \times E_1^*$	$(E_{iso}^*)^2$	Error (%)
1.0	81.94	81.00	6637.63	6637.63	0.00
1.2	70.14	93.57	6562.88	6637.63	- 1.13
1.4	62.74	105.85	6641.07	6637.63	0.05
1.6	56.97	119.98	6834.78	6637.63	2.97

Note Error = $[E_3^* \times E_1^*/(E_{iso}^*)^2 - 1] \times 100\%$



(a) Tensile yield strength



(b) Tensile yield strengths ratio

Fig. 32.8 Variation of tensile yield strength

Table 32.2 Comparison of $\sigma_1^* \times \sigma_1^* \times \sigma_3^*$ and $(\sigma_{iso}^*)^3$

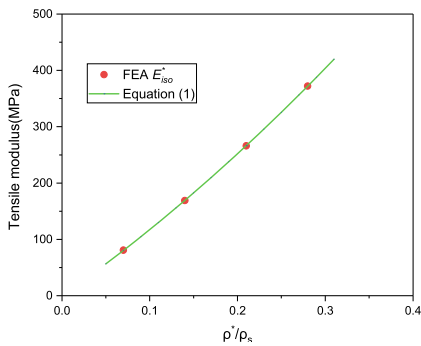
R	σ_1^*	σ_3^*	$\sigma_1^* \times \sigma_1^* \times \sigma_3^*$	$(\sigma_{iso}^*)^3$	Error (%)
1	1.80	1.73	5.63	5.63	0.00
1.2	1.56	2.18	5.31	5.63	5.68
1.4	1.49	2.51	5.56	5.63	- 1.27
1.6	1.42	2.85	5.71	5.63	1.51

Note Error = $[\sigma_1^* \times \sigma_1^* \times \sigma_3^*/(\sigma_{iso}^*)^3 - 1] \times 100\%$

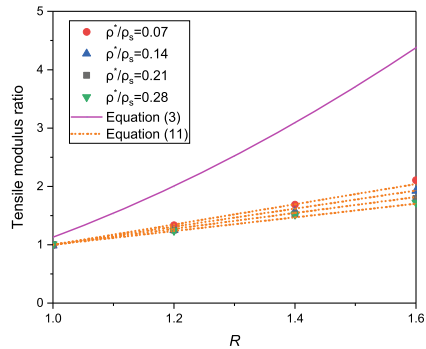
For other relative density foams, Eq. (32.6) is still valid. The linear relationship between the compression modulus ratio E_3^*/E_1^* and the R in Eq. (32.5) is also the same, but the coefficients in Eq. (32.5) are different. The equation of Gibson and Ashby [6] can well fit the Young’s modulus calculated by FEA based on isotropic model, with coefficients $C_1 = 0.42$, $C_2 = 3.1$ and $\phi = 0.87$ (Fig. 32.9a), but cannot predict the change of compression modulus ratio E_3^*/E_1^* with shape-anisotropy ratio (Fig. 32.9b).

Therefore, a coefficient k is introduced to consider the influence of relative density, and in order to make the curve pass through the (1, 1) corresponding to $R = 1$, Eq. (32.9) is set as

$$\frac{E_3^*}{E_1^*} = k \times R - k + 1 \tag{32.9}$$



(a) isotropic model



(b) transversely isotropic model

Fig. 32.9 Comparison of FEA calculated Young’s moduli with the equations by Gibson and Ashby [6]

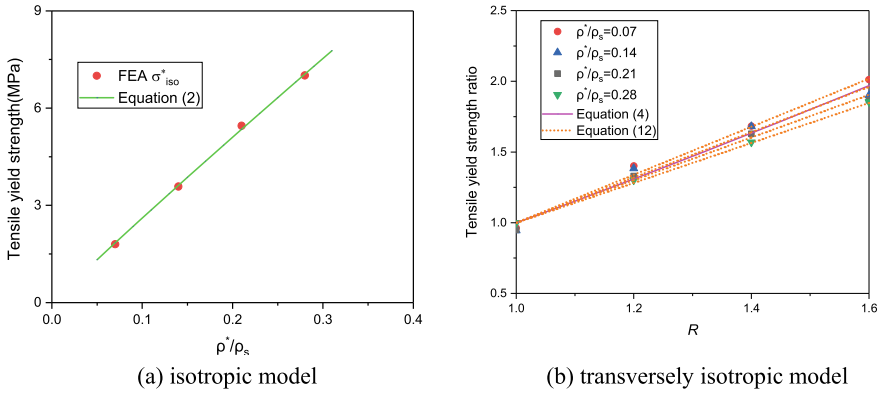


Fig. 32.10 Comparison of FEA calculated yield strength with the equations by Gibson and Ashby [6]

And the coefficient k can be determined by

$$k = -2.667 \frac{\rho^*}{\rho_s} + 1.922 \tag{32.10}$$

Therefore, the equation for predicting the modulus ratio eventually becomes

$$\frac{E_3^*}{E_1^*} = \left(-2.667 \frac{\rho^*}{\rho_s} + 1.922 \right) \times R + 2.667 \frac{\rho^*}{\rho_s} - 0.922 \tag{32.11}$$

A similar method is also applicable to the analysis of tensile yield strength σ_{iso}^* . The finite element results are brought into Eq. (32.2) and fitted to obtain $C_3 = -0.08$, $C_4 = 3.29$ and $\phi = 0.87$ (Fig. 32.10a). After applying a series of treatment methods similar to elastic modulus, the equation for predicting the tensile yield strength ratio eventually becomes

$$\frac{\sigma_3^*}{\sigma_1^*} = \left(1.796 - 1.367 \frac{\rho^*}{\rho_s} \right) \times R + 1.367 \frac{\rho^*}{\rho_s} - 0.796 \tag{32.12}$$

Different from the tensile elastic modulus, Eq. (32.4) can basically predict the ratio of tensile yield strength, but Eq. (32.12) is more accurate (Fig. 32.10b).

Table 32.3 Comparison of predicted and experimental values of elastic modulus

Foam specification	H100	H250
R	1.2	1.4
$E_3^*/E_1^*(EXP)$	1.47	1.6
$E_3^*/E_1^*(FEA)$	1.33	1.53
$E_3^*/E_1^*(EQU)$	1.35	1.54
$E_3^*(EXP)$	98.36 MPa	322 MPa
$E_3^*(FEA)$	93.57 MPa	330.76 Mpa
$E_3^*(EQU)$	90.38 MPa	332.08 MPa
$E_1^*(EXP)$	66.69 MPa	201 MPa
$E_1^*(FEA)$	70.14 MPa	216.87 MPa
$E_1^*(EQU)$	67.04 MPa	215.06 MPa

32.5 Prediction Formula of Tensile Elastic Modulus and Yield Strength

32.5.1 Tensile Elastic Modulus

According to the Eqs. (32.1), (32.5) and (32.11), the tensile elastic modulus of the cell in the upward direction and perpendicular to the upward direction of the transversely isotropic PVC foam can be predicted. For the PVC foam in this study, the fitting coefficients were $C_1 = 0.42$, $C_2 = 3.1$ and $\phi = 0.87$. The density of H100 was 95.06 kg/m^3 , $R = 1.2$, the density of H250 was 294.86 kg/m^3 , $R = 1.4$, the density of substrate PVC was 1400 kg/m^3 , and the elastic modulus of substrate PVC was 2700 MPa. Table 32.3 shows the comparison of experimental results, finite element results and predicted results.

It can be seen from the table that the elastic modulus prediction results are in good agreement, with a maximum error of 7% (H250 E_1^*).

32.5.2 Tensile Yield Strength

According to the Eqs. (32.2), (32.8) and (32.12), the tensile elastic modulus of the cell in the upward direction and perpendicular to the upward direction of the transversely isotropic PVC foam can be predicted. For the PVC foam in this study, the fitting coefficients were $C_3 = -0.08$, $C_4 = 3.29$ and $\phi = 0.87$. The yield strength of substrate PVC was 64 MPa. Table 32.4 shows the comparison of experimental results, finite element results and predicted results.

Table 32.4 Comparison of predicted and experimental values of yield strength

Foam specification	H100	H250
R	1.2	1.4
$\sigma_3^*/\sigma_1^*(EXP)$	1.39	1.67
$\sigma_3^*/\sigma_1^*(FEA)$	1.41	1.63
$\sigma_3^*/\sigma_1^*(EQU - Gibson)$	1.31	1.63
$\sigma_3^*/\sigma_1^*(EQU)$	1.34	1.60
$\sigma_3^*(EXP)$	2.13 MPa	8.28 MPa
$\sigma_3^*(FEA)$	2.18 MPa	8.09 MPa
$\sigma_3^*(EQU)$	2.17 MPa	7.35 MPa
$\sigma_1^*(EXP)$	1.53 MPa	4.96 MPa
$\sigma_1^*(FEA)$	1.56 MPa	4.97 MPa
$\sigma_1^*(EQU)$	1.62 MPa	4.58 MPa

It can be seen from the table that the prediction accuracy of yield strength is not as good as that of elastic modulus, but the result is still good, with a maximum error of 11.23% (H250 σ_3^*).

32.6 Tensile Constitutive Equation

From the comparison between the previous finite element simulation and the experiment, it can be found that when $R = 1.2$, the finite element model is in good agreement with the experiment. When $R = 1.4$, the finite element results are greatly different from the experiment when the strain is $> 3\%$. In addition, the elastic modulus and yield strength of the important factors in the tensile mechanical behavior appear within 3% strain. Therefore, the tensile constitutive model of this study is limited to within 3% strain.

32.6.1 Proposed Constitutive Model

Under tensile load, the foam first passes through the linear elastic stage until the strain reaches the elastic limit strain, which changes with R and relative density. Between the elastic limit strain and 3% strain, it is a nonlinear rising stage. It is found that this stage is the same as the rising stage of concrete compression. Therefore, the stress–strain curve equation of the nonlinear rising stage is established as

$$\sigma_t = A * [1 - (1 - \varepsilon_t/0.03)^B] \tag{32.13}$$

A is the tensile stress corresponding to the strain of 0.03 and B is the fitting coefficient.

Therefore, the tensile constitutive equation can be established as

$$\begin{aligned} \sigma_t &= E \varepsilon_t & 0 \ll \varepsilon_t < \varepsilon_0 \\ \sigma_t &= A * [1 - (1 - \varepsilon_t/0.03)^B] & \varepsilon_0 \ll \varepsilon_t \ll 0.03 \end{aligned} \quad (32.14)$$

ε_0 is the elastic limit strain. In this constitutive equation, in order to ensure the continuity of the stress–strain curve, it is necessary to ensure that the two curves pass through the same point when the strain is elastic limit, so the B can be solved as

$$B = \frac{\log(1 - E\varepsilon_0/A)}{\log(1 - \varepsilon_0/0.03)} \quad (32.15)$$

It can be found from Eqs. (32.14) and (32.15) that the whole tensile stress–strain curve can be determined only by knowing the elastic ultimate strain ε_0 , so the elastic ultimate strain becomes an important parameter of the curve form. After many tests, it is found that when the elastic limit strain conforms to the Eq. (32.16), the established stress–strain curve is in good agreement with the finite element results. There is little difference in elastic limit strain of different densities under the same R , so do not consider the effect of density on the elastic limit strain.

$$\begin{aligned} \varepsilon_0 &= 0.005R + 0.01 \quad Z\text{-direction} \\ \varepsilon_0 &= 0.02 - 0.005R \quad X/Y\text{-direction} \end{aligned} \quad (32.16)$$

Figure 32.11 compares the tensile stress–strain curve directly obtained by this constitutive relationship with the finite element and experimental stress–strain curves. Figure 32.11 compares the tensile stress–strain curve directly obtained by this constitutive relationship with the finite element and experimental stress–strain curves. It can be seen from the results that the two-parameter formula can well fit the tensile stress–strain curves of transversely isotropic foam in two directions.

32.6.2 Prediction of Constitutive Model

The tensile stress–strain curve has elastic stage and nonlinear rising stage. For the elastic stage, Sect. 32.5 summarizes the prediction formula of elastic modulus. Section 32.6 summarizes the relationship between elastic ultimate strain and R . Therefore, the stress–strain curve of elastic stage can be predicted when only R and relative density are known. In order to obtain the stress–strain curve of elastic limit to 3% strain, parameters A and B need to be known. In the case of known stress–strain curve, it is easy to get the value of parameter A , and inversely calculate the value of B . However, in the case of unknown curve, B is difficult to solve, so it is impossible to predict the curve of nonlinear ascent. But through a large number of fitting found that the A has a certain rule. Figure 32.12 shows A at different R and relative densities.

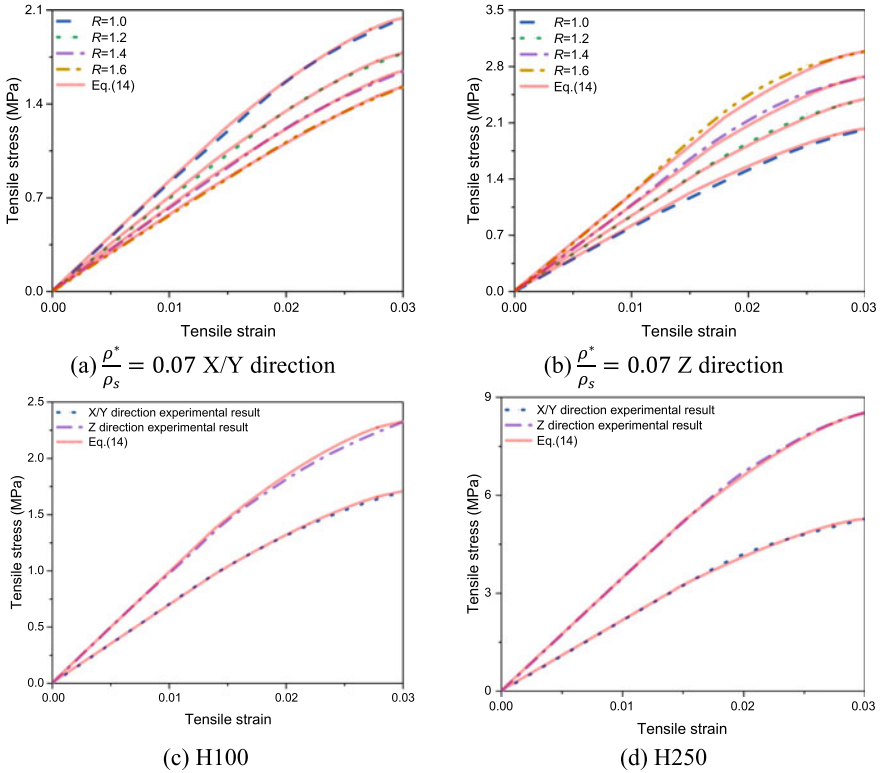


Fig. 32.11 Comparison of fitting results with experimental and finite element results

It is difficult to analyze the A directly, so the method of separating parameters is used for analysis. Firstly, the A rule in X/Y direction is discussed. Figure 32.13 shows A with different relative densities at $R = 1$. It can be found that the relationship between A and relative density basically obeys the Eq. (32.17).

$$A_{iso} = \sigma_{ys} \left(C_3 \left(\phi \frac{\rho^*}{\rho_s} \right)^{3/2} + C_4 (1 - \phi) \frac{\rho^*}{\rho_s} \right) \tag{32.17}$$

with coefficients $C_1 = 0.212$, $C_2 = 3.078$ and $\phi = 0.87$.

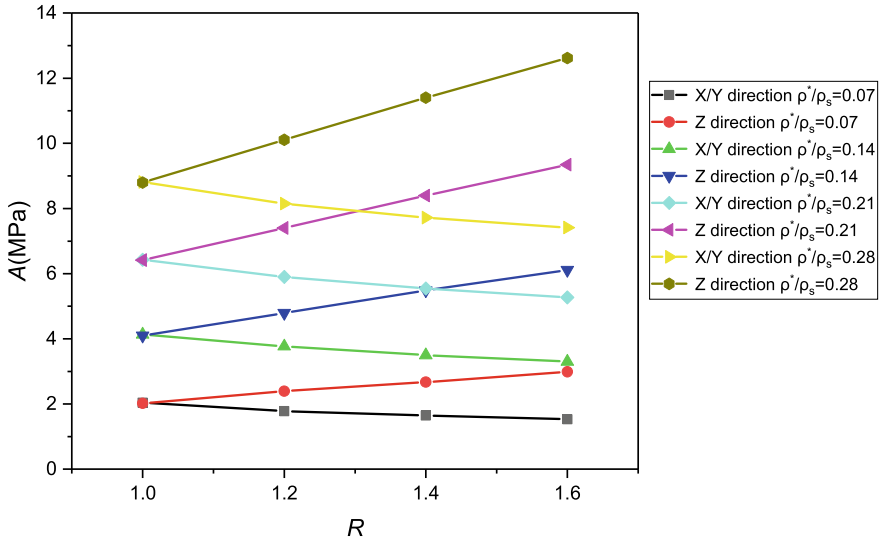
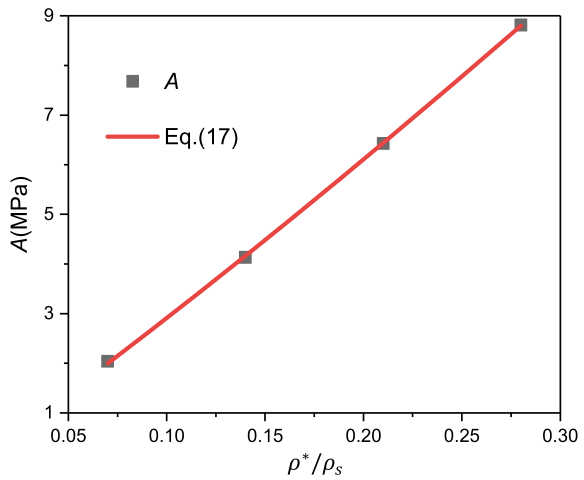


Fig. 32.12 A at different R and relative densities

Fig. 32.13 A at different relative densities when R = 1



A and tensile yield strength are characteristic points on the tensile stress–strain curve, so similar treatment method is adopted. It is found that the A value has the same product with the tensile yield strength, as shown in Eq. (32.18).

$$A_1 \times A_1 \times A_3 = (A_{iso}) \tag{32.18}$$

Similarly, with reference to Eq. (32.12), the relationship between A_3/A_1 and relative density and R is established as shown in Eq. (32.19).

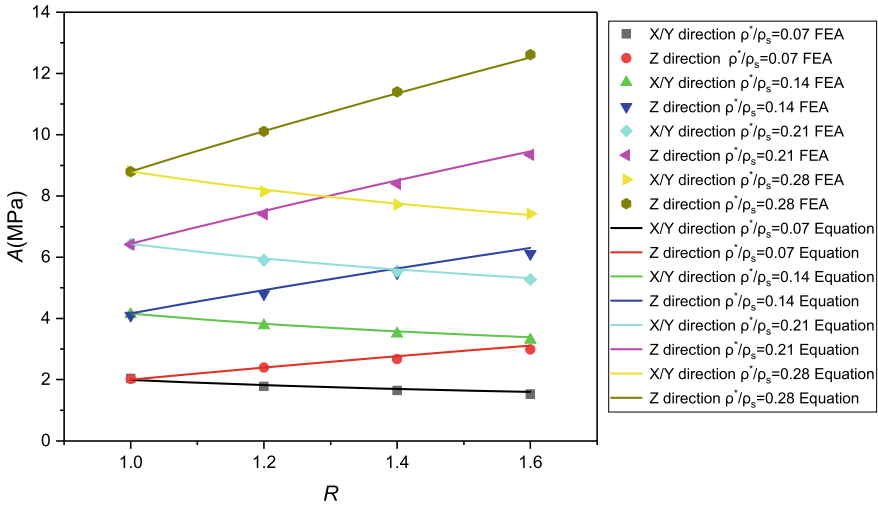


Fig. 32.14 Comparison of inverse parameters and fitting results

$$\frac{A_3}{A_1} = (1.711 - 1.961 \frac{\rho^*}{\rho_s}) \times R + 1.961 \frac{\rho^*}{\rho_s} - 0.711 \quad (32.19)$$

The inverse A from Eqs. (32.17) and (32.19) are compared with the direct fitting results (Fig. 32.14).

Combining Eqs. (32.1), (32.6), (32.11) and (32.14–32.19), the form and size of the tensile stress–strain curve within 3% strain can be predicted. The comparison of predicted results with finite element results and experimental results are shown in Fig. 32.15. It can be found that the prediction results are in good agreement with the finite element results and experimental results, and whether in the X/Y direction or the Z direction, the smaller the R , the better the prediction results. In general, this model can be used to predict the tensile constitutive curve of transversely isotropic foam.

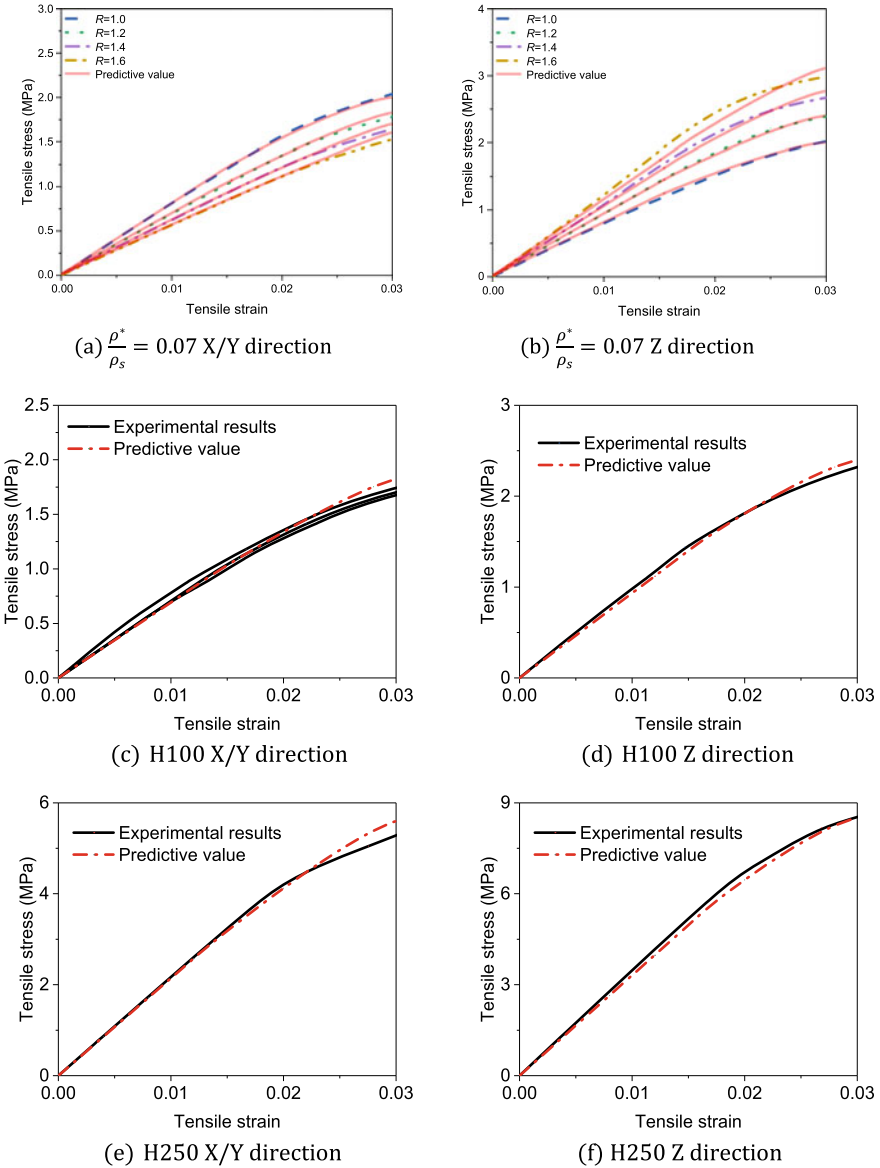


Fig. 32.15 Comparison of predictive results with experimental and finite element results

32.7 Conclusion

In this paper, the finite element model is used to study the influence of R and relative density on the tensile mechanical behavior of transversely isotropic foam. It is found that the tensile elastic modulus and tensile yield strength of transversely isotropic foam in different directions are consistent with R and relative density. An equivalent formula is proposed so that the tensile elastic modulus and yield strength of transversely isotropic foam with $R > 1$ can be predicted by the properties of $R = 1$ (isotropic) model.

In addition, this paper proposes a two-parameter tensile constitutive equation, which can better characterize the tensile mechanical behavior within 3% strain by extracting the elastic limit strain and inverting the two parameters. Moreover, for the PVC foam studied in this paper, R and relative density are connected with two parameters, so that the tensile stress–strain curve can be predicted only when R and relative density are known. The predicted results are in good agreement with the finite element results and experimental results.

Acknowledgements This research was supported by the National Key Research and Development Project (Grant No. 2016YFB1200601-16).

References

1. Khan, M.B., et al.: The mechanical property and micro-mechanism of nanoparticle-contained graphene foam materials under uniaxial tension. *Comput. Mater. Sci.* **206**, 111277 (2022)
2. Colloca, M., et al.: Mechanical properties and failure mechanisms of closed-cell PVC foams. *Int. J. Crashworthiness* **17**(3), 327–336 (2012)
3. Viana, G.M., et al.: Mechanical properties and fracture characterization of cross-linked PVC foams. *J. Sandwich Struct. Mater.* **4**, 99–113 (2002)
4. Deshpande, V.S., Fleck, N.A.: Multi-axial yield behaviour of polymer foams. *Acta Mater.* **49**(10), 1859–1866 (2001)
5. Kabir, M.E., Saha, M.C., Jeelani, S.: Tensile and fracture behavior of polymer foams. *Mater. Sci. Eng. A* **429**(1), 225–235 (2006)
6. Gibson, L.J., Ashby, M.F.: *Cellular Solids: Structure and Properties*. Cambridge University Press (1997)
7. Liu, Y., Rahimidehghan, F., Altenhof, W.: Anisotropic compressive behavior of rigid PVC foam at strain rates up to 200 s⁻¹. *Polym. Test.* **91**, 106836 (2020)
8. Marvi-Mashhadi, M., Lopes, C.S., LLorca, J.: Effect of anisotropy on the mechanical properties of polyurethane foams: an experimental and numerical study. *Mech. Mater.* **124**, 143–154 (2018)
9. Pei, L., et al.: Response of anisotropic polyurethane foam to compression at different loading angles and strain rates. *Int. J. Impact Eng.* **127**, 154–168 (2019)
10. Zhou, Y., et al.: Prediction of bulk mechanical properties of PVC foam based on microscopic model: part II-Material characterization and analytical formulae. *Polym. Test.* **117**, 107846 (2023)
11. Jang, W.Y., Kyriakides, S., Kraynik, A.M.: On the compressive strength of open-cell metal foams with Kelvin and random cell structures. *Int. J. Solids Struct.* **47**(21), 2872–2883 (2010)

12. De Giorgi, M., et al.: Aluminium foams structural modelling. *Comput. Struct.* **88**(1–2), 25–35 (2010)
13. Chen, Y.M., Das, R., Battley, M.: Effects of cell size and cell wall thickness variations on the stiffness of closed-cell foams. *Int. J. Solids Struct.* **52**, 150–164 (2015)
14. Chen, Y.M., Das, R., Battley, M.: Effects of cell size and cell wall thickness variations on the strength of closed-cell foams. *Int. J. Eng. Sci.* **120**, 220–240 (2017)
15. Song, Y.Z., et al.: Dynamic crushing behavior of 3D closed-cell foams based on Voronoi random model. *Mater. Des.* **31**(9), 4281–4289 (2010)
16. Zhu, H.X., et al.: The effects of regularity on the geometrical properties of Voronoi tessellations. *Phys. Stat. Mech. Appl.* **406**, 42–58 (2014)
17. Sadek, E., Fouad, N.A.: Finite element modeling of compression behavior of extruded polystyrene foam using X-ray tomography. *J. Cell. Plast.* **49**(2), 161–191 (2013)
18. Ayyagari, R.S., Vural, M.: Multiaxial yield surface of transversely isotropic foams: part I modeling. *J. Mech. Phys. Solids* **74**, 49–67 (2015)
19. Shafiq, M., et al.: Multiaxial yield surface of transversely isotropic foams: part II-experimental. *J. Mech. Phys. Solids* **76**, 224–236 (2015)
20. Marvi-Mashhadi, M., Lopes, C.S., LLorca, J.: Modelling of the mechanical behavior of polyurethane foams by means of micromechanical characterization and computational homogenization. *Int. J. Solids Struct.* **146**, 154–166 (2018)
21. Marvi-Mashhadi, M., Lopes, C.S., LLorca, J.: Surrogate models of the influence of the microstructure on the mechanical properties of closed- and open-cell foams. *J. Mater. Sci.* **53**(18), 12937–12948 (2018)
22. Li, P., Guo, Y.B., Shim, V.P.W.: Micro and meso-scale modelling of the response of transversely isotropic foam to impact—a structural cell-assembly approach. *Int. J. Impact Eng.* **135**, 103404 (2020)
23. Li, P., Guo, Y.B., Shim, V.P.W.: A rate-sensitive constitutive model for anisotropic cellular materials—application to a transversely isotropic polyurethane foam. *Int. J. Solids Struct.* **206**, 43–58 (2020)
24. Zhou, Y., et al.: Prediction of bulk mechanical properties of PVC foam based on microscopic model: part I-microstructure characterization and generation algorithm. *Polym. Test.* **117**, 107872 (2023)
25. Lu, Z.: Investigation into the tensile constitutive relation and failure mechanism of pur foamed plastics. *Acta Aeronaut. Astronaut. Sinica* **23**(2), 151–154 (2002)
26. Rao, C., et al.: Research on constitutive relation of high-density polyethylene structural foam under tensile. *China Plastics* **26**(7), 66–69 (2012)
27. Daniel, I.M., Cho, J.M.: Characterization of anisotropic polymeric foam under static and dynamic loading. *Exp. Mech.* **51**(8), 1395–1403 (2011)

Chapter 33

A Bitcoin Address Multi-classification Mechanism Based on Bipartite Graph-Based Maximization Consensus



Lejun Zhang, Junjie Zhang, Kentaroh Toyoda, Yuan Liu, Jing Qiu, Zhihong Tian, and Ran Guo

Abstract Bitcoin is widely used as the most classic electronic currency for various electronic services such as exchanges, gambling, marketplaces, and also scams such as high-yield investment projects. Identifying the services operated by a Bitcoin address can help determine the risk level of that address and build an alert model accordingly. Feature engineering can also be used to flesh out labeled addresses and to analyze the current state of Bitcoin in a small way. In this paper, we address the problem of identifying multiple classes of Bitcoin services, and for the poor classification of individual addresses that do not have significant features, we propose a Bitcoin address identification scheme based on joint multi-model prediction using the mapping relationship between addresses and entities. The innovation of the method is to (1) Extract as many valuable features as possible when an address is given to facilitate the multi-class service identification task. (2) Unlike the general supervised model approach, this paper proposes a joint prediction scheme for multiple learners based on address-entity mapping relationships. Specifically, after obtaining the overall features, the address classification and entity clustering tasks are performed separately, and the results are subjected to graph-based maximization consensus. The final result is made to baseline the individual address classification results while satisfying the constraint of having similarly behaving entities as far as possible. By testing

L. Zhang · J. Zhang

College of Information Engineering, Yangzhou University, Yangzhou 225127, China

L. Zhang (✉) · Y. Liu · J. Qiu · Z. Tian

Cyberspace Institute Advanced Technology, Guangzhou University, Guangzhou 510006, China

e-mail: zhanglejun@gzhu.edu.cn

L. Zhang

Research and Development Center for E-Learning, Ministry of Education, Beijing 100039, China

K. Toyoda

Institute of High Performance Computing (IHPC), Agency for Science, Technology and Research (A*STAR), 1 Fusionopolis Way, #16-16 Connexis, Singapore 138632, Republic of Singapore

R. Guo

School of Physics and Materials Science, Guangzhou University, Guangzhou 510006, China

and evaluating over 26,000 Bitcoin addresses, our feature extraction method captures more useful features. In addition, the combined multi-learner model obtained results that exceeded the baseline classifier reaching an accuracy of 77.4%.

Keywords Bitcoin · Multi-service classification · Graph maximization consensus · Data security

33.1 Introduction

In recent years, Bitcoin [1] has gained popularity worldwide as the most valuable cryptographic digital currency currently on the market. Figure 33.1 shows a line graph of the price change of Bitcoin from its launch to the present day. As the graph shows, the price of Bitcoin has not changed significantly for a long time since its launch, however, with the advent of various online services, the value of the electronic currency has gradually become apparent and the price of Bitcoin has reached its peak in the last few years.

Tasca et al. [2] have analyzed the evolution of the Bitcoin economy and summarized three distinguishable economic regimes as the Bitcoin economy has developed and matured. Firstly, Bitcoin’s early phase was dominated by mining and proof-of-concept without much substantial economic activity. Followed by a period of criminal growth, when early participants were attracted to the unique properties of cryptocurrencies, hence the proliferation of “criminal” enterprises (gambling, black markets, etc.) under this phase. The third stage is led by legitimate exchanges, which are businesses that convert digital currencies into fiat currency to cover costs and avoid price fluctuations. They found that different business categories populate the various

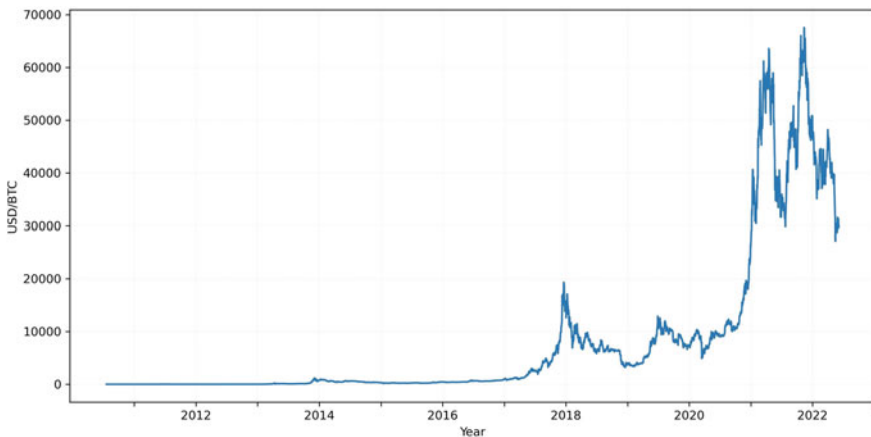


Fig. 33.1 Bitcoin price curve

stages of Bitcoin's development and that each business category has its different transaction flow patterns.

Bitcoin has so many commercial categories because it has properties that traditional currencies do not have. Bitcoin has a decentralized nature, it is not controlled by governments or financial institutions, and it can even be traded directly across borders. Besides, openness, transparency, immutability and anonymity are also its key features. Everyone can see all the transactions that have taken place, which makes bitcoin transactions open and transparent. Blockchain utilizes cryptography and consensus mechanisms so that all blocks retain the hash of their previous block, and if one block is changed, then all subsequent blocks must be changed, so that transaction information cannot tamper with. The addresses involved in Bitcoin transactions are obtained as pseudonyms through layers of cryptographic calculations with the user's public key and do not contain any identifiers to verify their identity, so the user has a certain degree of anonymity. While all these features are guaranteed to improve blockchain security, the fact is that blockchain is not secure. Zhang et al. [3] investigate that only a small percentage of blockchain platforms can achieve a set of security goals in practice. Xu et al. [4] argue that blockchain can prevent only a portion of fraudulent and malicious activities and remains vulnerable to attacks, they suggest appropriate defensive measures and call for further research to combat malicious activities associated with blockchain.

Recently, the website blockchain.info distinguished the existing mainstream bitcoin cryptocurrency services based on their risk factors, as shown in Fig. 33.2. Due to the lack of regulation and investigation by law enforcement, many services come with a certain amount of risk. For example, with high-risk exchanges and coin-mixing companies, sometimes we have no way of knowing whether they are providing a legitimate service or engaging in illegal fundraising, while lost virtual currency property is difficult to retrieve without credentials. In traditional anti-fraud or anti-money laundering efforts, the government monitors the behavior of suspicious people through financial services institutions that must verify the identity of customers before providing financial services, at which point the government can accurately track down suspicious people based on perfect knowledge of the user's identity. In contrast, Bitcoin user identities are difficult to identify, with no real identity information embedded in the address for any participant, and worse, new addresses can be generated at will. Möser et al. [5] have attempted to establish blacklisting policies for dangerous addresses in Bitcoin to make transaction recipients as risk-averse as possible, but early Bitcoin services were incomplete compared to today, the use of taint propagation techniques to assess reputation is not effective for new transaction models. Therefore, the identification of the possible identity of the target address needs to be completed before the transaction to avoid risks and help the blockchain ecosystem develop healthily.

The rest of the paper is structured as follows, Sect. 33.2 will briefly introduce the work related to address clustering and address classification in Bitcoin, as well as the innovation points of this paper. Section 33.3 will introduce the general steps and specifics of the model, Sect. 33.4 will describe the experimental process of this



Fig. 33.2 Bitcoin service category risks published by blockchain.info

paper, organize and evaluate the experimental results, and Sect. 33.5 will conclude the whole paper and provide an outlook on future work.

33.2 Related Work

This section presents related work on address clustering and address classification, pointing out the problems of existing research as well as the motivation and innovation of the scheme in this paper.

33.2.1 Bitcoin Address Clustering

In the Bitcoin system, any entity can manage more than one Bitcoin address. The de-anonymization of addresses is a key issue in analyzing addresses and a focus on the detection of illegal activities such as anti-money laundering, not only by detecting anomalous entities through address clustering but also by using tagged addresses to trace other addresses and transactions of the entity. Several de-anonymization techniques have emerged in the past, often referred to as address clustering algorithms. Androulaki et al. [6] showed that despite not knowing the true identity of the owner,

there are two heuristics to associate a bitcoin address with its owner, the multiple-input heuristic and the zero-finding heuristic, respectively. The first heuristic states that all transaction addresses in a transaction belong to the same user entity. The second heuristic is that only when the output address is two, if one of the addresses appears in the blockchain for the first time, it is a change address automatically generated by the system for the user and therefore belongs to the same entity as all the input addresses. Initially, these two address clustering methods were able to cope with most bitcoin address analysis efforts, but the consequent creation of hybrid coin services has somewhat impacted this approach [7]. The main idea of the mixed coin service is that multiple users transfer coins to the same transaction at the same time, rendering the multi-input heuristic rule ineffective. Some research on anti-mixed coins has also been carried out, Wu et al. [8] analyzed mixed coin transactions in Bitcoin, and they found that there are two main types of mixed coin transactions, exchange, and obfuscation, and designed heuristic rules to detect mixed coin transactions. In summary, the main limitation in identifying the controlling entity behind Bitcoin addresses is that they do not involve any identifying information linking them to the owner, and even if multiple addresses were known to be controlled by one person or one entity, it would still be unable to determine their true identity. Nevertheless, address clustering techniques can often bring a different analysis from a more macro perspective, e.g. Meiklejohn et al. [9] studied the usage of Bitcoin transactions through address clustering-based transaction graph analysis, and they showed that different clustered entities correspond to various services such as mining pools, wallets, exchanges, gambling, and money laundering, among others. For the identification work of multiple services of bitcoin addresses, obtaining some characteristic information of the address entity helps the performance of the classifier. Since the zero-finding heuristic is more likely to synthesize too large clusters and experience cluster crashes, in this paper, we only use the multiple-input heuristic for address clustering to obtain the entity where the address is located and other addresses of that entity.

33.2.2 Address Service Classification

Training a transaction flow feature model for Bitcoin services to identify the services performed by an address as accurately as possible before the transaction completes is a reliable solution to hedge risk and secure transactions. Several studies have been conducted on the service category identification problem, which can be broadly divided into two directions, respectively, classification of addresses and classification of entities (heuristic clustering). They usually start with feature extraction of the dataset addresses or entities, and subsequently, put the features and labeled data into the classifier for model training and result validation. For example, Akcora et al. [10] proposed a novel and effective prediction framework for ransom transactions that can automatically predict emerging ransom transactions in a limited amount of relevant historical transaction data. Jourdan et al. [11] define some new features

related to the characteristics of entities on the Bitcoin blockchain and study their efficacy in practice. Toyoda et al. [12] summarized the historical transactions of addresses and computed the features to train the model from both address and entity perspectives, concluding that the classification results were better with entities as samples, possibly due to the greater randomness of selecting individual addresses, which made the classification results lower. Unlike Toyoda's extracting features separately for addresses and entities, Zola et al. [13] used cascaded machine learning to characterize entities, and they used the classification results of addresses within entities to vote and enriched the features of entities with the voting results as new features so that the classification results of entities followed the results of most of the addresses within them to achieve good classification results. Fusing the classification results of addresses and entities can improve the classification of entities. However, transactions are often sent to a single address rather than an entity, and sometimes we are more concerned with the nature of the service for a single address, so we worked to address the following issues: Can the classification result of a single address be corrected using information about the entity of this address to improve the classification accuracy of a single address? A voting strategy may not solve this problem because entities may participate in multiple services and it cannot simply be determined that all addresses within an entity participate in the same service. To solve the above problems, we were inspired by the article by Gao et al. [14] which combines heterogeneous source information to correct the original classification results. This paper proposes a consensus method for maximizing address and entity classification results. Firstly, we ensure high prediction accuracy by extracting a large number of address features, secondly, we cluster highly similar entities using a small number of features of the entity where the address is located, so that entities exhibiting similarity appears in the same clusters, and finally, we perform consensus on the classification results and clustering results at the output level to counteract the randomness of individual address features and optimize the classification results of individual addresses to improve the accuracy.

33.2.3 Motivation and Contribution

Yang et al. [15] used a Gaussian distribution unsupervised clustering method to cluster Bitcoin entities into six clusters, representing six groups of users exhibiting different features. It is not rigorous to use unsupervised clustering alone to obtain class labels for addresses within clusters, but we can gain some insight that entities within the same cluster do have similar features. The similarity of entities in the same service is more obvious, and if using it as a constraint on the classification results of individual addresses, individual addresses that do not match the service representation can be corrected, thus improving the accuracy of the overall prediction. Note that we should still focus on the classification results of individual addresses, and the entity label correction only serves as a constraint. To implement the above ideas, the open and transparent nature of Bitcoin and the existing mature machine learning

methods can be of good help, however, two efforts remain to improve the accuracy of the predictions as much as possible. (1) How to accurately describe the behavior patterns of addresses through the transaction history of individual addresses? In this paper, based on previous research, the historical transactions of Bitcoin addresses and the complex structure of the inter-address transaction graph are described, and both explicit and implicit features are summarized. (2) How to choose a machine learning model? In this paper, we use the current best-integrated learning models Random Forest and Gradient Boosting as the comparison models and use their outputs as the input for consensus. In contrast, unsupervised clustering uses spectral clustering, as it is suitable for dealing with sparse data with low dimensionality and a small number. The contribution of this paper can be summarized as follows.

- (a) In this paper, we summarize previous research and conduct comprehensive mining of features based on a single address. 111 features are extracted in this paper, including explicit features based on address transaction history and implicit features describing connections between addresses.
- (b) In this paper, we propose a consensus scheme for correcting address supervised classification results with entity unsupervised clustering results, which, to our knowledge, is the first scheme to combine multivariate model joint prediction with the Bitcoin multi-class service detection problem.
- (c) In this paper, the selected features are ablated to verify and analyze the feature importance through experimental comparative analysis. Next, the proposed method is compared and analyzed with advanced machine learning methods to prove the effectiveness of the scheme.

33.3 Proposed Method

The address service identification approach proposed in this paper can be summarized in four steps: (1) retrieving and preprocessing historical transactions of addresses, (2) feature extraction, (3) training a baseline model, and (4) consensus of results at the output level.

33.3.1 *Transaction Retrieval and Pre-processing*

In this paper, we use the labeled address dataset [16] published in the article [12]. There are a total of 26,309 addresses and labels, of which the labels are divided into seven categories, namely Exchange, Faucet, Gambling, HYIP, Market, Mixer, and Mining Pool.

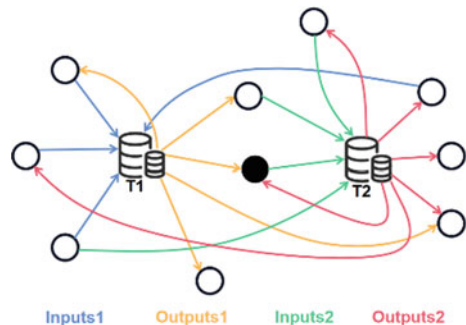
We use sampling to retrieve historical transactions because we find that some addresses even have more than 400,000 transactions, which is wasteful for analyzing the behavior of that address and would substantially increase the feature extraction time, which is not conducive to training a timely and usable model, so we randomly

sample no more than 500 transactions for each address. The preprocessing of the transactions is mainly the conversion of the exchange rate, and due to the high volatility of the BTC price, it will negatively affect the classification effect of the amount feature, so we use the API provided by coindesk [17] to import the exchange rate of USD and Bitcoin to ensure the stability of the amount feature.

33.3.2 Feature Extraction

This paper mines address features from two perspectives, which can be broadly divided into explicit features that summarize historical transactions and implicit features that describe relationships between addresses. Among them, the explicit feature extraction method retrieves all historical transactions of an address to get single features such as balance, life cycle, the total number of transactions, etc. In addition, we also summarize the historical transactions of an address, bring together data such as the amount of each transaction into a list, and obtain its statistical features such as maximum and minimum values, mean value, variance, standard deviation, etc. In this paper, 93 explicit features are extracted. The implicit feature is then based on Ranshous et al.'s study [18], as shown in Fig. 33.3, where we make the following definition. The black circle represents the address A to be analyzed. Taking a set of transactions as an example, when A is used as the output of a transaction, all input addresses of that transaction are called ancestor addresses of that address, i.e., the address connected by the blue line in the figure. And so on, the addresses connected by yellow, green, and red are output sibling address, input sibling address, and successor address, respectively. The diagram describes only the two transactions in which the target address is involved, and we collect the proximity addresses for all its transactions and calculate 12 features related to the number of proximity addresses, after which we extract six transaction pattern features by the merge set operation on the proximity addresses, and obtain a total of 18 implicit features.

Fig. 33.3 Diagram of the neighborhood address in the Bitcoin directed hypergraph



33.3.3 Results Consensus Model

The inclusion of unsupervised clustering models in the classification combination can increase the diversity of the models, thus improving the accuracy and robustness of the predictions. This paper considers the similarity of entity behaviors of the same services and proposes a scheme to correct the supervised classification results of address features with the unsupervised clustering results of entity features. The method is a good remedy for the shortcomings of supervised or unsupervised learning only. For supervised learning, since bitcoin addresses are generated without cost, some addresses that are used only a few times do not match the features of their participating services and thus are inevitably misclassified, while entities are representational as mappings of real participants that are not easily generated or discarded. For unsupervised learning, clustering methods can only obtain the indexes of clusters, not the labels directly, and it is too absolute to simply group the addresses within a cluster into one category. However, the entities within the clusters obtained by unsupervised clustering have some correlation, which can be exploited for joint prediction in combination with supervised learning classifiers, and the entities are the ties that associate address objects of the same service. The ensemble problem can be viewed as an optimization problem on a bipartite graph, where the misclassified addresses in the entities are corrected by iterative propagation of probability estimates between neighboring entities. Achieving this optimization problem requires two things: first, the labels of the predictions should be consistent with the baseline of the supervised learning results as much as possible, which can be achieved by penalizing deviations from the predictions provided by supervised learning in an abstract bipartite graph optimization problem. Second, the unsupervised constraint needs to be satisfied to the maximum extent possible, and stable entity features replace their internally fluctuating address features for iterative propagation of probability estimates until they are stable and finally a smooth prediction result is obtained.

In this paper, we use the following identifiers to denote the important parameters in the algorithm, the set of addresses to be predicted is $X = x_1, x_2, \dots, x_n$, the addresses participate in c service categories. A total of m models are involved in joint prediction, where r models are supervised models that provide prediction data and the remaining $m - r$ unsupervised models provide clustering *id* s for the addresses. In a bitcoin address multi-classification task, each model divides the data points into groups, so there will be a total of $v = m * c$ groups. The supervised learning model divides the addresses into $s = r * c$ groups with the same predictive labels, while the unsupervised model divides the addresses into $v - s$ groups with similar behavior. Note that the cluster *id* number z may not be the same as the category z because cluster *id* only distinguishes between different clusters to provide category constraints, and does not represent a specific service classification. In this paper, the $n \times m$ matrix is denoted by $B_{n \times m}$, and b_{ij} denotes the elements in row i and column j of the matrix. \vec{b}_i and \vec{b}_j denote the vectors of the i -th row and j -th column, respectively. If x_i is assigned to group g_j by one of the algorithms then $a_{ij} = 1$, otherwise 0. The matrix $A_{n \times v}$ formed by a_{ij} is called the affinity matrix.

Our goal is to compute the conditional probability u_{iz} that each address node x_i belongs to category z and the conditional probability q_{jz} that each group node g_j belongs to category z . The conditional probability matrix consisting of these two conditional probabilities is denoted as $U_{n \times c}$ and $Q_{v \times c}$, respectively. Since the first s groups are obtained from the supervised learning model and they have some initial class label estimates, we use $y_{jz} = 1$ to indicate that the group node g_j belongs to the class z and 0 otherwise, and the matrix consisting of y_{jz} is denoted as $Y_{v \times c}$. Finally, the number of categories assigned to each group is denoted as k_j and $k_j = \sum_{z=1}^c y_{jz}$. Table 33.1 summarizes the important notations.

To reach a consensus among all models, an optimization problem is defined in a bipartite graph with an objective function that penalizes deviations from the base classifier predictions and differences in predicted class labels between nearby nodes. As Eq. (33.1) is shown, where $|\cdot|$ and $\|\cdot\|$ denote the L1 and L2 paradigms of the vector, respectively.

$$f(Q, U) = \sum_{i=1}^n \sum_{j=1}^v a_{ij} \|\vec{u}_i - \vec{q}_j\|^2 + \alpha \sum_{j=1}^v k_j \|\vec{q}_j - \vec{y}_j\|^2 \quad (33.1)$$

The first part of this formula is to ensure that if an address object x_i is assigned to group g_j by one of the algorithms, i.e., when $a_{ij} = 1$, their conditional probability estimates must be close. The second part is the constraint that the consensus class label estimate for group g_j should not significantly deviate from its initial class label prediction y_j , which ensures that the algorithm is dominated by the classification result. α is the penalty for violating that constraint, The group node g_j participates in the constraint only if $j = 1, \dots, s$, because it is generated by the classifier with $k_j = 1$. And the group node generated by unsupervised clustering does not participate in this constraint. Finally, \vec{u}_i and \vec{q}_j are probability vectors, so each component must be greater than or equal to 0 and sum to 1. The update formula for the matrix is shown in Algorithm 1.

Table 33.1 Important notations

Symbol	Definition
$A_{n \times v} = [a_{ij}]$	a_{ij} —indicator of object i in group j
$U_{n \times c} = [u_{iz}]$	u_{iz} —probability of object i with respect to class z
$Q_{v \times c} = [q_{jz}]$	q_{jz} —probability of group j with respect to class z
$Y_{v \times c} = [y_{jz}]$	y_{jz} —indicator of group j predicted as class z

Algorithm 1 : BGCM algorithm

Input : group-object affinity matrix A ,
initial labeling matrix Y , parameters α and ϵ ;
Output : consensus matrix U

- 1) Initialize U^0, U^1 randomly
- 2) $t \leftarrow 1$
- 3) **while** $\|U^t - U^{t-1}\| > \epsilon$ **do**
- 4) $Q^t = (D_v + \alpha K_v)^{-1} (A^T U^{t-1} + \alpha K_v Y)$
- 5) $U^t = D_n^{-1} A Q^t$
- 6) **end while**
- 7) **return** U^t

In this algorithm, $D_v = \text{diag}\{(\sum_{i=1}^n a_{ij})\}_{v \times v}$ and $D_n = \text{diag}\{(\sum_{j=1}^v a_{ij})\}_{n \times n}$ act as the normalization factor, $K_v = \text{diag}\{(\sum_{z=1}^c y_{jz})\}_{v \times v}$ denotes the constraints on the group nodes. During each iteration, the probability estimation of each group node (i.e., Q) receives information from its neighboring object nodes while retaining its initial value Y . In return, the updated probability estimate of the group node propagates information back to its neighboring object nodes when updating U . ($Q^{(t)}, U^{(t)}$) both converge to the stationary point of the optimization problem.

33.4 Experiment and Evaluation

In this paper, we use bitcoin-core [19] to obtain bitcoin block information and use the blocksci library [20] to process and retrieve historical bitcoin transactions. The experimental code is written in python 3.7 and mainly uses the blocksci, pandas, numpy, and scikit-learn libraries. In this paper, we evaluate the feature contribution, model accuracy, and confusion matrix, respectively.

33.4.1 Feature Contribution Analysis

In this section, we perform ablation validation of feature selection for both categories, and we divide the tests into accuracy comparisons using only explicit features, using only implicit features, and using all features. Random forest was chosen as the machine learning algorithm, and the number of estimators was set to 100. A tri-fold cross-validation method was used to obtain the accuracy for each evaluation, and the average value was taken as the result of each evaluation. Due to the imbalance of the dataset, we sampled the same number of addresses for each category for each experiment, and 100 addresses were extracted from each category of data to constitute the dataset; thus, 700 addresses were used as the dataset for each evaluation.

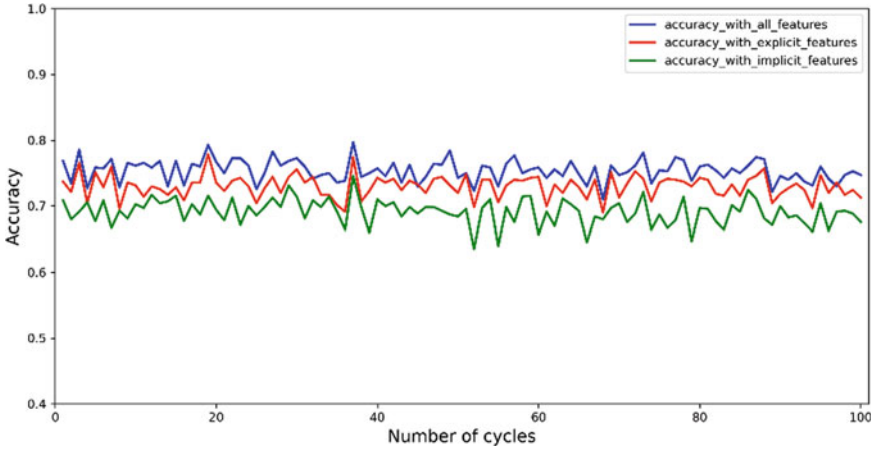


Fig. 33.4 Accuracy under different feature selection methods

For each method, we repeated the accuracy assessment 100 times. To better show the difference, we plotted the accuracy as a line graph and the final result is shown in Fig. 33.4.

Since the sample set of addresses is randomly sampled in each round, the accuracy rate fluctuates, and the average accuracy results are 0.754, 0.73, and 0.691 in that order. The high accuracy rate can be obtained with a small number of features using only implicit features, which indicates that the inter-address transaction relationship is an important factor.

33.4.2 Model Accuracy Evaluation

In this experiment, BGCM is compared with the two best result algorithms, random forest and gradient boosting, to test the accuracy improvement. The number of estimators in the compared algorithms both set to 100, and the rest of the parameters are set to default values. These two results are used as inputs for the first two supervised learning results in the BGCM algorithm, and the rest of the unsupervised clustering inputs are generated by spectral clustering. The alpha parameter in the BGCM algorithm is set to 3, and the number of iterations is 30. Table 33.2 shows the accuracy, recall, and F1 score under different methods. Our method can obtain better classification results and can successfully correct the few addresses that are misclassified because they do not match the service features, thus improving the overall accuracy. And our algorithm has some applicability and can be applied to other anonymous transaction scenarios.

Table 33.2 Performance comparison of different algorithms

Methods	Precision	Recall	F1-score
Random forest	0.758	0.753	0.753
Gradient boosting	0.767	0.761	0.760
BGCM	0.774	0.773	0.774

Table 33.3 Confusion matrix under the algorithm BGCM

	Exchange	Faucet	Gambling	HYIP	Market	Mixer	Pool
Exchange	0.63	0.04	0.12	0.05	0.07	0.01	0.07
Faucet	0.04	0.86	0.06	0.06	0.01	0.0	0.01
Gambling	0.11	0.03	0.58	0.07	0.04	0.0	0.03
HYIP	0.04	0.05	0.07	0.74	0.01	0.01	0.06
Market	0.11	0.02	0.09	0.02	0.84	0.02	0.02
Mixer	0.02	0.0	0.03	0.01	0.02	0.96	0.0
Pool	0.05	0.0	0.05	0.05	0.01	0.01	0.81

33.4.3 Confusion Matrix

Table 33.3 shows only the confusion matrix of classification results based on the BGCM algorithm, where each row of the table represents the actual service, while each column represents the predicted service. Bold numbers represent the probability of correct prediction for that category.

It is not difficult to find that exchanges and gambling sites have the lowest detection accuracy, probably due to the high number of addresses for these two services in the dataset, resulting in a wide distribution of their features and therefore uneven sampling. Moreover, there are many similarities between the two categories, with 12% of exchange addresses being misclassified as gambling and 11% of gambling addresses being misclassified as exchanges, this result is also acceptable as the number of addresses within these services is too high to guarantee that their features are similar. Nevertheless, our method still shows some improvement in classification effectiveness.

33.5 Conclusion

In this paper, we propose a new approach to improve the prediction of bitcoin address service classes by combining the analysis of the features of addresses and the features of the entities they are located in to identify address-involved services. Identifying address-involved services has many benefits, such as dangerous transaction prevention and statistical analysis of bitcoin services. Specifically, we show how

a multi-model maximization consensus mechanism can be combined with bitcoin addresses and entities to obtain better classification performance. With the tri-fold cross-validation method, we can obtain a global average accuracy of 77.4%. In future work, we would like to focus our work on studying the detection of suspicious addresses using unsupervised learning algorithms, because in real life, most bitcoin addresses or transactions are made by normal users and it is difficult to obtain labels, using supervised learning algorithms tends to generate a large number of false positive addresses, so our idea is to use outlier detection algorithms to filter out a large number of normal nodes, and further perform outlier nodes for fraud category detection to minimize the number of misclassified users. Nevertheless, in this paper, we were able to classify the seven classes of addresses that have been tagged for services with high accuracy, and we believe that this research can help investigate crimes and assist law enforcement agencies in detecting illegal activities in the Bitcoin network.

References

1. Nakamoto, S.: Bitcoin: a peer-to-peer electronic cash system. In: *Decentralized Business Review*, p. 21260 (2008)
2. Tasca, P., Hayes, A., Liu, S.: The evolution of the bitcoin economy: extracting and analyzing the network of payment relationships. *J. Risk Finance* **19**(2), 94–126 (2018)
3. Zhang, R., Xue, R., Liu, L.: Security and privacy on the blockchain. *ACM Comput. Surv.* **52**(3), 1–34 (2019)
4. Xu, J.J.: Are blockchains immune to all malicious attacks? *Finan. Innov.* **2**(1), 1–9 (2016)
5. Möser, M., Böhme, R., Breuker, D.: Towards risk scoring of Bitcoin transactions. In: *Financial Cryptography and Data Security: FC 2014 Workshops, BITCOIN and WAHC 2014*, Christ Church, Barbados, March 7, 2014, Revised Selected Papers, vol. 18, pp. 16–32. Springer Berlin Heidelberg (2014)
6. Androulaki, E., Karame, G.O., Roeschlin, M., Scherer, T., Capkun, S.: Evaluating user privacy in bitcoin. In: *Financial cryptography and data security: 17th international conference, FC 2013*, Okinawa, Japan, April 1–5, 2013, Revised Selected Papers, vol. 17, pp. 34–51. Springer Berlin Heidelberg (2013)
7. Bonneau, J., Narayanan, A., Miller, A., Clark, J., Kroll, J.A., Felten, E.W. Mixcoin: anonymity for bitcoin with accountable mixes. In: *Financial Cryptography and Data Security: 18th International Conference, FC 2014*, Christ Church, Barbados, March 3–7, 2014, Revised Selected Papers, vol. 18, pp. 486–504. Springer Berlin Heidelberg (2014)
8. Wu, L., Hu, Y., Zhou, Y., Wang, H., Luo, X., Wang, Z., et al.: Towards understanding and demystifying bitcoin mixing services. In: *Proceedings of the Web Conference 2021*, pp. 33–44 (2021)
9. Meiklejohn, S., Pomarole, M., Jordan, G., Levchenko, K., McCoy, D., Voelker, G. M., Savage, S.: A fistful of bitcoins: characterizing payments among men with no names. In: *Proceedings of the 2013 Conference on Internet Measurement Conference*, pp. 127–140 (2013)
10. Akcora, C.G., Li, Y., Gel, Y.R., Kantarcioglu, M. (2019). Bitcoinheist: topological data analysis for ransomware detection on the bitcoin blockchain. arXiv preprint [arXiv:1906.07852](https://arxiv.org/abs/1906.07852)
11. Jourdan, M., Blandin, S., Wynter, L., Deshpande, P.: Characterizing entities in the bitcoin blockchain. In: *2018 IEEE International Conference on Data Mining Workshops (ICDMW)*, pp. 55–62. IEEE (2018)

12. Toyoda, K., Ohtsuki, T., Mathiopoulos, P.T.: Multi-class bitcoin-enabled service identification based on transaction history summarization. In: 2018 IEEE International Conference on Internet of Things (iThings) and IEEE Green Computing and Communications (GreenCom) and IEEE Cyber, Physical and Social Computing (CPSCoM) and IEEE Smart Data (SmartData), pp. 1153–1160. IEEE (2018)
13. Zola, F., Eguimendia, M., Bruse, J.L., Urrutia, R.O.: Cascading machine learning to attack bitcoin anonymity. In: 2019 IEEE International Conference on Blockchain (Blockchain), pp. 10–17. IEEE (2019)
14. Gao, J., Liang, F., Fan, W., Sun, Y., Han, J.: Graph-based consensus maximization among multiple supervised and unsupervised models. In: Proceedings of the 22nd International Conference on Neural Information Processing Systems (NIPS'09), pp. 585–593. ACM (2009)
15. Yang, L., Dong, X., Xing, S., Zheng, J., Gu, X., Song, X.: An abnormal transaction detection mechanism on bitcoin. In: 2019 International Conference on Networking and Network Applications (NaNA), pp. 452–457. IEEE (2019)
16. <https://goo.gl/sQJKdx>. Accessed 23 Feb 2023
17. Coindesk: <https://www.coindesk.com/price/>. Accessed 23 Feb 2023
18. Ranshous, S., Joslyn, C.A., Kreyling, S., Nowak, K., Samatova, N.F., West, C.L., Winters, S.: Exchange pattern mining in the bitcoin transaction directed hypergraph. In: Financial Cryptography and Data Security: FC 2017 International Workshops, WAHC, BITCOIN, VOTING, WTSC, and TA, Sliema, Malta, April 7, 2017, Revised Selected Papers, vol. 21, pp. 248–263. Springer International Publishing (2017)
19. bitcoin-core: <https://bitcoin.org/en/bitcoin-core/>. Accessed 23 Feb 2023
20. Blocksci: <https://citp.github.io/BlockSci/>. Accessed 23 Feb 2023

Chapter 34

DSBT: Research on Soulbound Token Mechanism Based on Consortium Blockchain and Decentralized Identity



Yijian Zhang, Lu Zhang, Qing Zhang, Peiyu Zheng, Xiangjuan Jia, and Xiaofeng Chen

Abstract Issues such as technology, application and future development based on blockchain have always been hot topics. Future forms such as Web3.0 and the Metaverse are inseparable from digital identities and virtual tokens. This paper focuses on the recently popular Soulbound Token (SBT), introduces the concepts of digital identity, blockchain, and Decentralized Identity (DID) related to it, analyzes the shortcomings and challenges of SBT, and combines the consortium blockchain and DID. A new concept of Soulbound Token (DSBT) based on the decentralized identity of the consortium blockchain is proposed, which aims to make up for the technical deficiencies of SBT, and through the new concept of Displayable Credentials (DCs), DSBT combines DID for identity authentication, The advantages of access, in turn, can realize the concept of “programmable privacy” expected by SBT. Finally, the coping mechanism is proposed for the possible risks of DSBT, the application scenarios of DSBT in the active health intelligent care platform for the elderly are listed, and the future development of blockchain, DID and DSBT is expected.

Keywords Blockchain · Consortium blockchain · Decentralized identity · Decentralized identity soulbound token · Aged care

34.1 Introduction

In today’s world, the Internet has entered the era of big data. The world is at a new historical intersection of the technological revolution and the production revolution. With the globalization of information networks and the increase in the number of netizens, more and more “cloud data” is generated by the network. Especially since

Y. Zhang · L. Zhang · Q. Zhang · P. Zheng · X. Jia · X. Chen (✉)
Hangzhou Qulian Technology Co., Ltd., Hangzhou, China
e-mail: chenxf.alfred@zju.edu.cn

X. Chen
State Key Laboratory of Blockchain and Data Security, Zhejiang University, Hangzhou, China

the outbreak of Covid-19 in 2020, the growth of netizens in various countries around the world has increased year-on-year to varying degrees, with China as the For example, in 2020, the growth rate of Chinese netizens exceeded 10% over the previous year, the first time since 2013 [1].

The ever-increasing number of Internet users is also accompanied by the continuous problems of network security and personal information leakage. Although countries are constantly promulgating new laws and regulations [2], on the other hand, it is also accompanied by more and more problems, such as personal information leakage accident. For example, well-known application providers such as Microsoft, Twitter, and Marriott International have experienced hundreds of millions of data-level user information leakage incidents. Centralized application providers hijack a large amount of user data and cause security problems, making the voice of user autonomy more and more powerful. Among them, decentralized identity based on blockchain and distributed ledgers is one of the implementation forms. This paper introduces the concept of “DSBT” into decentralized identity, hoping to provide some ideas for the future development of the field of decentralized identity and DSBT research.

Our main contributions in this paper are as follows:

First, we studied the latest research results in the fields of blockchain, digital identity, SBT, etc., gave the main components and operation process of decentralized identity, and focused on the Verifiable Credentials (VCs).

Secondly, we introduce SBT into decentralized identity, combine the on-chain and off-chain data of the SBT and the components of decentralized identity, and propose a new concept of Soulbound Token (Decentralized Identity Soulbound Token, DSBT) based on decentralized identity, making it a part of decentralized identity.

Next, based on the inspiration of the VCs, we give the concept of “Displayable Credentials (DCs)” which is crucial for DSBT. Presentable credential is an important part of DSBT’s “programmable” privacy mechanism.

Finally, we enumerate the application scenarios of DSBT in the elderly intelligent care platform, and put forward an outlook on the future development of decentralized identity and DSBT.

34.2 Related Technology Research

34.2.1 Digital Identity

Digital identity refers to the digital characterization of network entities. Offline individuals or entities enable a set of network data to describe their identity through registration, binding, etc. The network has characteristics such as virtuality and concealment [3]. In the process of rapid development of the network, there is also a problem that the identity of the main body of the network digital identity is difficult to correspond one-to-one. The confirmation of digital identity is essentially the answer

to “who am I”, and it is expressed in the network as a way of proving the mapping relationship. By proving the ownership of the account, the user can make the service provider confirm that the operation is from him.

In its development process, digital identity is roughly divided into three stages: centralized digital identity, alliance digital identity, and self-sovereign digital identity [4].

34.2.2 Blockchain and Web3.0 Technology Research

Blockchain is a technology that appeared with Bitcoin. It first appeared in the article “Bitcoin: A Peer-to-Peer Electronic Cash System” by Satoshi Nakamoto. The core of the blockchain is decentralization [5], is a distributed ledger technology (DLT). The characteristics of the blockchain are “decentralized distribution”, high security, and data cannot be tampered with it, the consensus mechanism is used to ensure the immutability of the data, and the security of the data is guaranteed by the cryptographic algorithm [6].

Blockchains are classified into the following three categories according to their uses and actual manifestations:

Public Blockchain. The Public Blockchain has the characteristics of open source code and unlimited access. The public chain and other nodes conduct transactions based on the consensus mechanism. The common consensus mechanisms of the public chain are: Proof of Work (POW), Proof of Stake (POS). Applications such as Bitcoin and Ethereum are typical public blockchains. Every Internet node user has the right to conduct transactions and record blocks on the public blockchain. Typical application scenarios of public blockchains include decentralized application scenarios such as digital assets (virtual currency) and anonymous transactions. Public blockchains are open source and anonymous, and are difficult to control in terms of network supervision.

The biggest feature of the public chain is that it has value incentives, that is, virtual tokens (Tokens). Therefore, the application of public blockchain basically revolves around financial payment, such as payment, electronic commercial insurance, mining machine mining, virtual wallet and other industries developing rapidly on public blockchain.

Private Blockchain. Private Blockchain is generally not open to the outside world. It is built within an institution or enterprise and has high privacy and security. It is generally limited to a small number of nodes, because its network is closed, and it is not suitable for deployment on large-scale landing applications. However, due to its characteristics, the private chain also has certain advantages: the private chain benefits from the internal open mechanism, and nearly 100% trust between each node, so its transaction cost is very low.

Consortium Blockchain. Consortium Blockchain refers to a blockchain consisting of permissioned accounting nodes that is managed by a limited number of related parties and managed in an alliance manner. It is especially suitable for use by related parties with regulatory needs.

Compared with public and private blockchains, consortium blockchain has the following advantages:

- It has a wide range of operation space and application, and can support the landing of large-scale applications (such as various web3.0 social applications).
- Compared with the public chain, it is easy to supervise and has less uncontrollable factors. At the same time, having supervision does not mean centralization. There can be different degrees of supervision in different countries. Most of them still require different levels of supervision when it comes to application scenarios such as credit, finance, government, and military. Therefore, the consortium blockchain can be used as a flexible and bottom-up mechanism to expand the scope of use to a large extent.
- Compared with the public blockchain, there are fewer nodes, and the consensus and block generation time is shorter, which is convenient for fast transactions.
- For node access, the reliability of multiple nodes is high, and the probability of being maliciously attacked by internal nodes is small [7].

The earliest concept of Web3.0 came from Dr. Gavin Wood, the co-founder of Ethereum and the founder of Polkadot, who proposed a revolutionary idea in 2014, and initiated and established the Web3 Foundation. Today, web 3.0 is mainly used to describe a “decentralized” Internet running on blockchain and distributed ledger technology [8], in this environment, users can use a decentralized digital identity, which is available on every network platform in the world. As a blockchain application method with certain advantages, consortium blockchain is a fertile soil for realizing user autonomy and decentralized digital identity. Based on the consortium blockchain, this article will explore the operation mechanism and broad future of decentralized identity and DSBT proposed below.

34.3 Decentralized Identity Technology

34.3.1 DID Structure and Operation Process

On November 7, 2019, the W3C Decentralized Identifier Working Group released Decentralized Identifiers: first public working draft of Decentralized Identifiers (DIDs) v1.0 specification, which is the beginning of W3C research on decentralized identity (DID) [9], on July 19, 2022, Decentralized Identifiers v1.0 was officially released as a recommended standard.

Compared with the general identity system, the differences in the elements included in the DID system are shown in Table 34.1.

Table 34.1 Comparison of elements of general identity system and DID system

Generic identity system contains elements	DID system contains elements
Identity (identifier)	Decentralized identifiers
Management of identity information: storage, acquisition, etc.	DID document
Authentication	Universal resolver
Data authorization	Verifiable credentials (VCs)
Management of private data: storage, acquisition, etc.	Identity hubs

As shown in the table above, a complete DID system consists of five meta-components:

- **Distributed Identifiers (DIDs):** It is a new form of verifiable digital identity identifiers with user autonomy [10]. Through it, a verifiable, decentralized digital identity can be manipulated, which is a string of three-part data forms. For example `did:btc:21tDAKCERh95uGgKbJNHYP`.
- **DID doc** is similar to a digital certificate. It does not store any private information of the user, but only stores the version number, DID identifier, public key, verification method, service information and other information.
- The function of **Universal Resolver (identifier resolver)** is to connect the DIDs and the DID doc to prove that the user of the DID identifier is the user himself. The parser obtains the DID file, the application provider generates a random encrypted nonce through the public key in the DID doc and provides it to the user, and the user decrypts it with his own private key to prove the ownership of the DIDs [11].

The following will focus on verifiable credentials and Identity Hub.

34.3.2 Verifiable Credentials

Verifiable credentials are composed of several related parties: consortium blockchain regulator, issuer, holder (where holder is bound to the Identity Hub that stores its private data), verifier, and identifier registry. Verifiable credentials are the core of DID. The relationships of the five related parties of the class are shown in Fig. 34.1.

The Consortium Blockchain Regulator, according to the application environment, is mainly composed of the founder of the consortium blockchain or the public credibility agencies such as the government and public security organs. In the application scenario of VCs, it can not only exercise the supervisory power as a regulator, but also inherit and exercise the issuer and flag. Part or all the rights of the registry, regulator is the exclusive authority of the consortium blockchain.

The Consortium Blockchain Issuer can be either a consortium blockchain regulator or a government agency authorized by the consortium blockchain regulator. In addition to the status quo of non-government agencies accessing and mastering

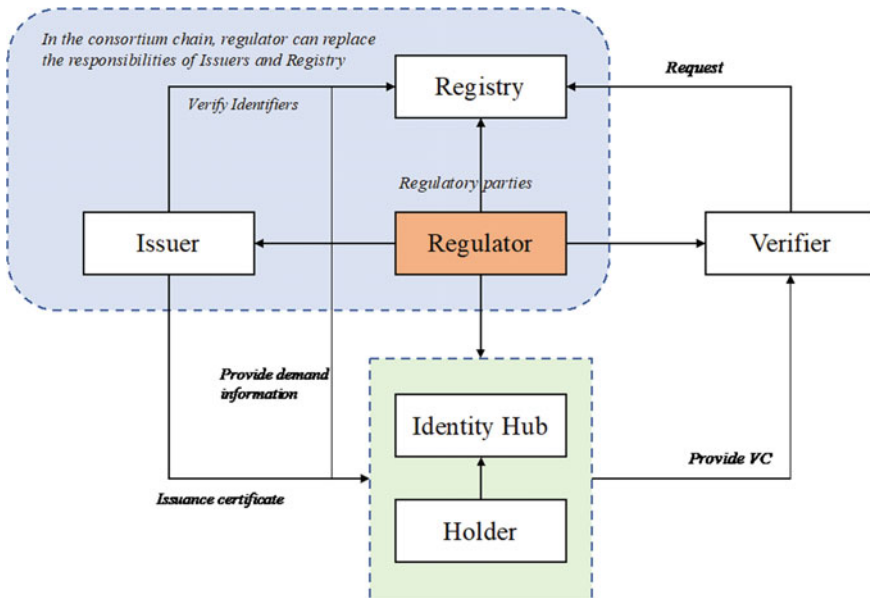


Fig. 34.1 Verifiable credentials parties

user data, Issuer can access user data and issue VCs, and national agencies such as the government can access user data, authoritative and credible. It is worth noting that although Issuer is qualified to issue VCs, it does not mean the centralization of personal data, and users have the right to decide whether their private data is stored in the cloud or on personal devices [12].

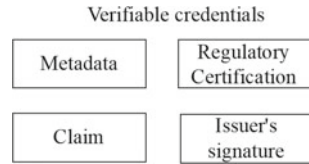
The Consortium Blockchain Holder is the user himself. The holder is bound to the Identity Hub that stores its private data. The main responsibility of the holder is to request, obtain, use, and hold VCs from the Issuer. In addition, to avoid the user’s repeated requests and waiting, the VCs can be stored in the user’s Identity Hub, and the same type of VCs can be used repeatedly.

The Consortium Blockchain Verifier is mainly composed of user VCs demanders [13], that is, various service application providers (such as various APPs, and even offline entities). It is mainly responsible for verifying VCs and providing corresponding services to users who comply with VC declarations.

The Consortium Blockchain Registry is responsible for maintaining the distributed database of DIDs and DID doc. The exercise of its powers is under the supervision of the consortium blockchain regulator to avoid arbitrariness and evil, while providing services and responsibility for the other three types of parties [14].

Vcs based on consortium blockchain consists of metadata, claim, consortium blockchain regulatory certification, and consortium blockchain issuer signature [15], as shown in Fig. 34.2. Among them, the metadata includes: issuer, certificate issuance

Fig. 34.2 Verifiable credentials composition



time, validity period, expiration time, public key used for verification and other data [16]. The consortium blockchain supervisor authentication mainly includes the hash display information uploaded to the supervisor, the authentication time, etc., in the scenario where the supervisor exercises the power of the issuer, the supervisor can include authentication information and signature information.

Verifiable credentials based on the consortium blockchain have the following characteristics:

Have privacy. The verifier cannot read the real private information of the holder.

Mainly used for authentication, difficult or impossible to have social attributes. On the premise of distributed social applications, D.A.O. community autonomy, financial mortgage and other Web3.0 applications, most of them rely on a certain degree of privacy disclosure. Due to the privacy characteristics of verifiable credentials themselves, it is difficult to use them in the above scenarios, and it is more difficult to use them.

Authoritative and authentic validity. The VCs regulator of the consortium blockchain are composed of public credibility agencies such as the government and the public security, and can effectively endorse the effectiveness of VCs.

34.3.3 *DID Verifiable Representation*

A verifiable representation is a way of organically combining verifiable credentials of different types and persons in a structure and showing their compliance to the verifier [17]. In a separate did system, it can be used to enhance privacy protection, and users can complete the required verification operations based on zero-knowledge proof without revealing any information other than the representation. In the decentralized identity system that introduces DSBT, which we discuss below, verifiable representations can serve as important “passports” for users’ web 3.0 social activities.

34.3.4 *DID Identity Hub*

The above-mentioned DIDs, DID doc, VCs, etc., can only display encrypted data related to identity, while the Identity Hub is responsible for storing the user’s real

private data. Identity Hub is distributed, off-chain storage data, which can realize the control and control of personal data by users, and ensure security through encryption algorithms [18], as long as the user does not have explicit authorization, the third-party service provider cannot obtain the user's private data. Even if the user is authorized, the authentication operation can be completed by means of verifiable credentials, with limited or even no need to disclose any private data.

In addition, Identity Hub does not mean centralization. The location of Identity Hub is determined by the user, which can be stored in the cloud or in the user's personal local port (mobile phone, computer, IOTs [19], etc.). Access to all data needs to be requested in Identity Hub [20].

34.3.5 Summary

In this section, we mainly discuss the basic meta-components of decentralized identity based on consortium blockchain, which detail: VCs based on consortium blockchain, verifiable representations, and Identity Hub. Learn about these three basic logic of meta-components helps us to understand the introduction of SBT into DID, that is, DSBT. As can be seen from the above, the most important function of DID is to correspond to the identity and complete the authentication of digital identity, but when it comes to social applications of Web3.0, such as unsecured loans, DAO community qualification access, real property rights transactions and leases, etc., Relying on DID alone may be impossible. As we mentioned above, DID is like a dot, giving you and me a place on web3.0, but it seems that others see you and me like a black dot, a black hole, if there is no DSBT to replenish flesh and blood, we are on the Internet may not be a perfect digital identity.

34.4 Add SBT to DID—DSBT Based on Decentralized Identity

34.4.1 Conception

Before mentioning the concept of DSBT, let us briefly introduce the concept of SBT (Soulbound Token), which was first seen in May 2022, jointly released by Ethereum founder Vitalik Buterin, economist Glen Weyl and Flashbots researcher Puja Ohlhaver In the paper: "Decentralized Society: Finding Web3's Soul".

In this paper, the account or wallet that holds publicly visible, non-transferable tokens is called "soul", and the tokens held in the account/wallet are called SBT, which stands for commitment, personal qualifications, asset proof, and attribution [21]. The biggest difference between SBT and NFT is "soul bound". Once SBT is bound, it cannot be sold or traded.

SBT is essentially a token issued by the issuer on the public chain to the user's wallet. It can include birth certificate, work certificate, income certificate, education certificate and certificate, participation in competition experience, personal loan history, etc. A series of attribution relationships, each proof corresponds to an SBT. The issuer of SBT can be an individual, a company or an authoritative institution.

However, SBT under the public chain has the following problems that need to be solved urgently:

- **Lack of certain regulation.** Freedom is often accompanied by a certain degree of restraint. Without restraint, freedom does not have much meaning. In the Web3.0 scenario, although there are blockchains and distributed accounting technology to protect, but if there is no appropriate supervision mechanism as the bottom line, there may be problems such as the proliferation of SBTs, the low availability, and the mixing of false SBTs and real SBTs, on the contrary, it can truly expand the application scenarios of web3.0 underlying mechanisms such as SBT to a large extent.
- **SBT lacks the technical means of “programmable privacy”.** In the paper on the concept of SBT, the author discusses the idea of “programmable privacy” of SBT, that is, access rights, but it is difficult to achieve “programmable” privacy only by relying on the public chain and SBT itself.
- **SBT is not suitable for carrying identity sensitive information.** Due to the characteristics (openness) of the public chain and SBT, SBT is not suitable for carrying sensitive information such as personal identification. That is to say, the situation of SBT is like duckweed, which can only be used in the application scenario after the identity information is confirmed, and it is difficult to undertake the functions of confirmation and access of the identity information itself.

Therefore, we propose the concept of DSBT based on consortium blockchain + decentralized identity + SBT. Compare the basic concepts in Table 34.2.

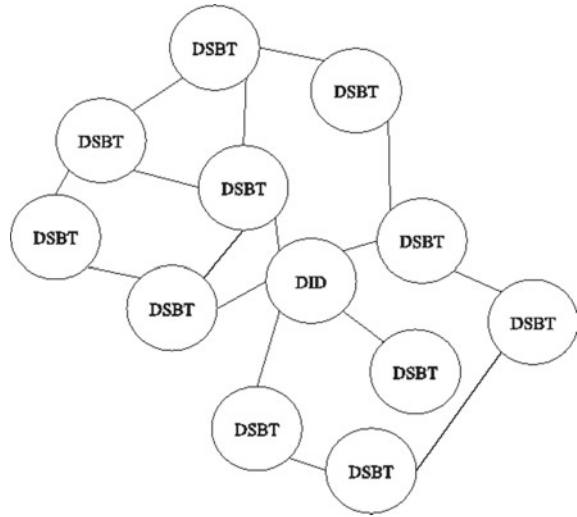
DSBT has the following advantages:

- **Easy to supervise.** According to the usage scenarios and the national conditions of different countries, DSBT and its corresponding certification relationship can be generated and used to give different degrees of supervision to improve the usability of DSBT. In addition, it can greatly expand the application scenarios of DSBT in financial lending, property rights, government affairs [22], etc.
- **Reduced chance of Sybil attack.** A major feature of the consortium blockchain is the access mechanism for nodes and users. The nodes and users of the consortium

Table 34.2 Comparison of the basic concepts of the two papers

Basic concepts	Original paper	In this paper
Operating environment	Public blockchain	Consortium blockchain
Soul	Public blockchain wallet	Consortium blockchain based wallet
SBT	Public blockchain token	Consortium blockchain token

Fig. 34.3 DID and DSBT relationship



blockchain need to pass the access audit before they can access and use them normally. Therefore, the probability of Sybil attack can be reduced to a certain extent [23].

- **Ability to “program” private information.** Below we will mention, how DSBT realizes the “programmability” of personal privacy information.
- **Possess proof of identity information.** DSBT is a DID based component. Therefore, DSBT can not only realize the confirmation/access work of identity information, but also realize the role of all individuals to prove the attribution relationship.

If DID solves the problem of user autonomy in digital identity, DSBT is a process of continuously giving users a means of flesh and blood online on the basis of user autonomy. If DID is a point to form a user’s network digital identity, then DSBT is a surface that contains all the information that the user has and will have, and together constitute the user’s network portrait, as shown in Fig. 34.3. At the same time, based on DID, it avoids the traditional web2.0, in which centralized applications master the form of user digital identity and user portrait.

34.4.2 Identity Hub Based on DSBT—The Real Body of DSBT

Above, we mentioned that the Identity hub is responsible for storing the real private data of users, and no private data is displayed on the chain, although it is assumed in Vitalik Buterin et al.’s paper that both the soul and DSBT are public, the author also admits and it is obvious that not many people will be willing to display all their

proofs (i.e. DSBT and private data itself) on the chain. Therefore, Identity hub, one of the meta-components of the decentralized identity system based on consortium blockchain and distributed ledgers, is very suitable as a storage point for DSBT privacy data, which is the real body of DSBT.

Of course, it cannot be ruled out that there will be some DSBT contents, and the owner of DSBT wants to show them. Therefore, DSBT and its linked attribution proof are designed in the following two forms, as shown in Fig. 34.4.

At the same time, the identity hub that introduces DSBT needs to have the following functions:

- DID privacy data and DSBT privacy data are stored separately. DID data is relatively fixed and hardly needs to be modified, and it is also the data with the highest privacy for users. It should have a similar isolation mechanism or sandbox mechanism, as shown in Fig. 34.5.

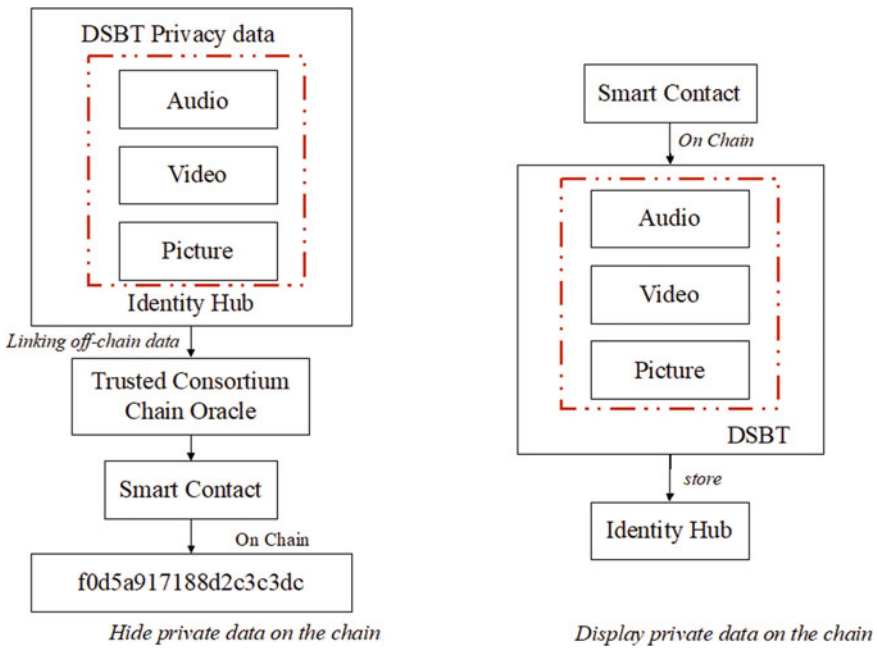
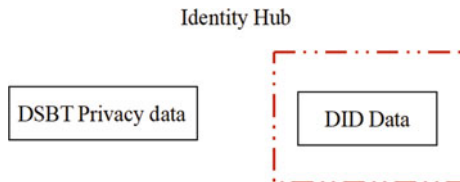


Fig. 34.4 Two DSBT on-chain and off-chain display forms [21]

Fig. 34.5 DSBT and DID data



- Thanks to the introduction of DSBT, frequent updates of Identity Hub and data synchronization between different devices are also important considerations, and Identity Hub needs to have these functions [24].

34.4.3 *Displayable Credentials—DSBT Veil of Free Choice*

After the above understanding, we know that a verifiable credential mechanism is required in a DID system. The verifiable credential mechanism is the center of the operation of the decentralized identity system and an important means of authentication and access. However, in the face of complex social scenarios, mortgage transactions for offline items, financial loans, D.A.O. community autonomy, etc., the privacy protection mechanism of VCs makes it difficult for the holder to use it effectively. Most credit scenarios and C2C, etc., people rely more on And trust those “seeable” proofs [21]. Therefore, for DSBT, we propose the concept of “Displayable Credentials (DCs)”. DCs are the core of implementing DSBT’s “programmable privacy”. Displayable credentials have the following advantages and characteristics.

DCs are presentable. The displayable certificate can display all kinds of electronic certificates, signatures, etc. owned by the holder, which can be displayed in the required scene.

DCs are composable. Displayable credentials can be combined with verifiable credentials into verifiable representations to support authentication requirements in complex polymorphic environments.

DCs have a high degree of freedom. Holder can arbitrarily combine all its DSBTs (linked and expressed certificates, qualification information) to form a combined displayable certificate, or can use a single DSBT as a displayable certificate according to requirements. And can freely decide the degree of privacy of the displayable certificate according to the holder’s needs.

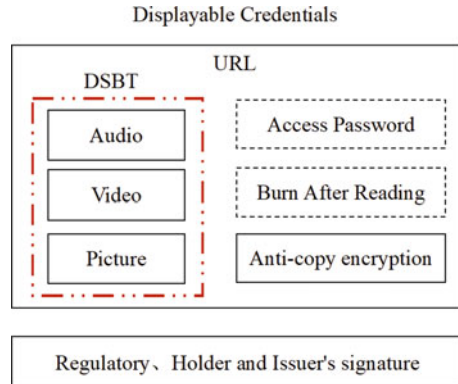
DCs owns property rights. DCs can play the property rights of DSBT by setting access thresholds, access rights, etc. to obtain property rights such as disposal and income [25].

34.4.4 *DCs Meta Component*

The DCs based on the consortium blockchain and decentralized identity contains the URL and signature, as shown in the Fig. 34.6.

- Linkable URL (the holder can freely decide the valid time of the URL and can close it at any time), for privacy settings, the holder can choose the following two ways:

Fig. 34.6 DCs architecture diagram



- (1) A settable access password (the holder decides whether to set it or not, according to their own sensitivity to the display DSBT);
- (2) It will be burned after reading, only the Displayable credentials shared by the holder can be browsed [26].

- Signatures of the consortium blockchain regulator, holder and issuer.

The differences between DCs and VCs are as follows:

- **Privacy presentation.** The VCs do not reveal the private data itself in the process of its generation and use. During its use, the private data is “available and invisible”. DCs directly display the private data in the Identity Hub linked by DSBT (it is worth noting that such a link does not directly submit the private data itself, and the display in the URL is only a mirror image in the Identity Hub [27]);
- **Component Architecture.** VCs are mainly composed of metadata without private data, declarations, certifications and signatures. DCs are composed of URL URLs that display private data, anti-copy encryption methods, and related party signatures.
- **Usage scenarios.** As the core of the DID system, VCs are mainly used for identity access scenarios such as identity provision and verification, and there are few usage scenarios. DCs can be used in various scenarios such as D.A.O autonomous voting, social relations in DeSoc decentralized society, social scenarios in the metaverse, mortgage transactions of real objects, and property rights changes.

34.4.5 DCs Operating Mechanism

Holders can choose VCs based on homomorphic encryption and zero-knowledge proof [28], but in most secondary application scenarios, such as unsecured loans and other financial fields, it may be difficult for Verifier to recognize zero-leak credentials. It may be a more convincing way to display DSBT through DID DCs, combined

with verifiable representations, to collect and integrate several DCs and VCs into one representation and provide it to Verifier, as shown in Fig. 34.7.

The Issuer of DSBT receives the requirements of DCs, generates DCs and returns them to Holder, which can be displayed in the form of URL links including pictures, videos, etc. Verifier can access these URLs to determine whether Holder meets the verification requirements, the operating mechanism of DCs is shown in Fig. 34.8. DCs should have certain anti-copying and encryption methods, such as unauthorized screenshots, visitor watermarks, anti-crawlers.

At present, Web 3.0 is still in the emerging stage, facing problems such as imperfect infrastructure and insufficient application fields. Such external URL links actually have certain network security problems [29], but it is still a choice in the development process [30].

In the future, DCs can be nested in wallet applications (such as accessing hot wallets in the form of components) [31], and the actual real data is still stored in the identity hub. The time and form are determined by the DCs. The DSBT content

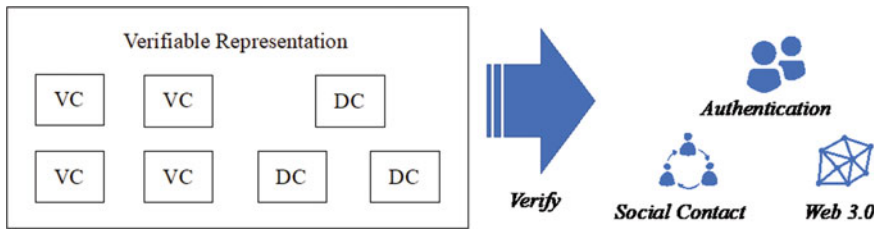


Fig. 34.7 Verifiable representations and application scenarios combined with DCs

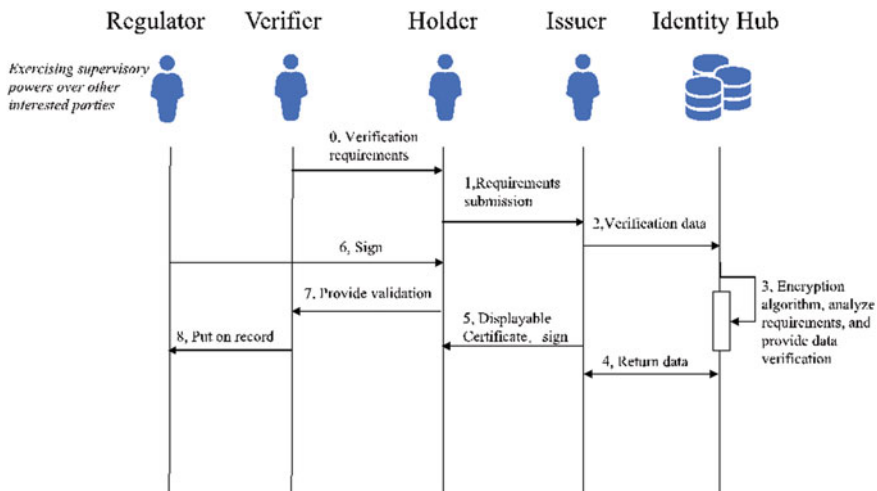


Fig. 34.8 DCs operation diagram

that the holder wants to be displayed is directly displayed in the application, and the visitor can only browse. In this process, Holder can realize the “benefit” operation, that is, set the access threshold and access cost to obtain benefits. Similarly, technical means should also be used to prevent visitors from having the right to “save” Holder’s DSBT images in the form of screenshots, downloads, etc. If the visitor has such a demand, it must be approved by Holder.

34.5 Application of DSBT

34.5.1 Risks and Coping Mechanisms of DSBT

If DID is the entry ticket to web 3.0, then DSBT and DCs are the passports for major social applications, D.A.O. governance, financial lending and mortgages, etc. in the future. Among them, it is very important to prevent Sybil attacks. Sybil attacks generate a large number of robots disguised as real users in an attempt to confuse the order, muddle through and master the right to vote autonomously, which is very harmful [32].

Vitalik Buterin believe that it can be circumvented in the form of a Personality Proof Protocol (PoP), but it is undoubtedly costly and time-consuming for everyone to register such an additional protocol. However, combined with the decentralized identity based on the consortium blockchain, DSBT can evade the Sybil attack relatively well:

The “soul” that DSBT relies on, that is, the decentralized identity based on the consortium blockchain, is the entity in the consortium blockchain that can be traced back to its real identity. Verifier can prove that the user is a real user, not a robot generated by a Sybil attack, through various verification methods such as VCs, DCs, and verifiable representations. Therefore, Verifier can formulate its own verification specification and initiate random verification within an appropriate time period. Of course, the advantages of the consortium blockchain are also shown at this moment [33]: that is, the consortium blockchain Regulator has the right to monitor whether Verifier “abuses” its verification authority.

34.5.2 Application of DSBT in the Scenario of Active Health Intelligent Care Platform for the Elderly

In the application scenario of the elderly active health intelligent care platform, elderly users can register the elderly care blockchain and big data platform through DID, and obtain the health status DSBT issued by a number of health institutions and hospitals, big data knowledge base through DSBT, intelligently recommend the required knowledge map, knowledge base and other materials. At the same time,

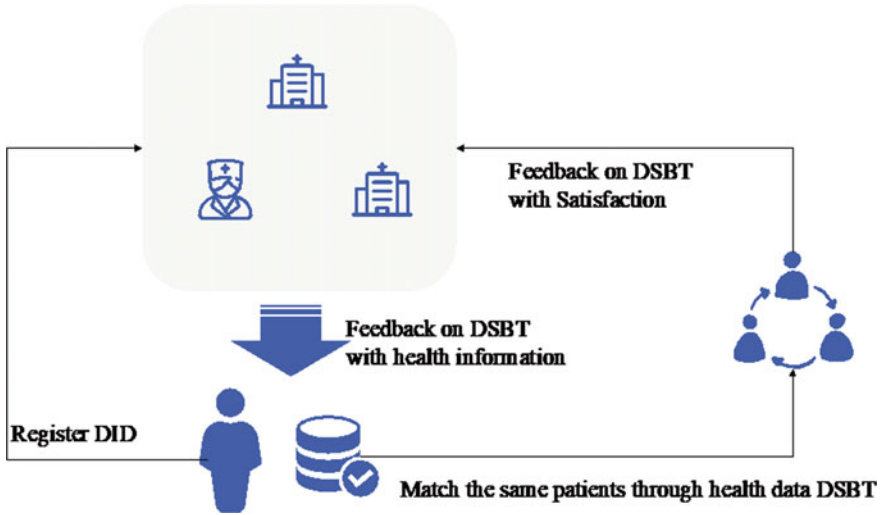


Fig. 34.9 Application of DSBT in elderly care scenarios

elderly users with the same DSBT can form a social community to communicate and discuss health issues together. Elderly users can also issue DSBTs to health institutions and hospitals to give feedback on their satisfaction [34]. DSBTs are of great benefit in elderly care scenarios [35].

The basic realization of DSBT and the elderly active health care platform is shown in Fig. 34.9.

34.6 Summary and Prospect

This article mainly introduces the basic concepts and basic technologies of digital identity, blockchain technology, and DSBT. Analyzed the meta-component technology of decentralized identity based on blockchain, combined DSBT with DID based on consortium blockchain, and proposed a new concept of “DSBT”, it not only summarizes the reasonable technical use methods of DSBT, but also expands the use scenarios of DID, so that DID can not only be used in the field of identity authentication, but also can also use DSBT to play the “digital portrait” function of its users’ autonomous rights in scenarios such as social applications, financial lending, and elderly care in web3.0. The future will be an era of awakening, distributed and decentralized user autonomy. Metaverse, Internet of Things [36], and Web3.0 based on infrastructures such as DID and DSBT will certainly be able to show its attractive appeal.

Acknowledgements This work was supported by the National Key R&D Program of China (Grant No.2020YFC2008700) and the Key-Area Research and Development Program OF Guangdong Province 2020B0101090003.

References

1. Yu, Z.: The 45th “statistical report on internet development in China” was released. *China Broadcasting* **05**, 27 (2020)
2. Zhou, L., Chen, Q.: Current status and enlightenment of foreign network information security governance systems. *Soc. Govern.* **9**, 71–78 (2020)
3. Sullivan, C., Burger, E.: Blockchain, digital identity, e-government. *Bus. Transform. Blockchain* **II**, 233–258 (2019)
4. Cui, J., Lv, Y., Wang, H.: Development status of digital identity based on blockchain. *Cyberspace Secur.* **11**(6), 25–29 (2020)
5. Nakamoto, S.: Bitcoin: A peer-to-peer electronic cash system. *Decentral. Bus. Rev.* 21260 (2008)
6. Zhang, K.: Research on logistics user privacy data protection and access rights management (Master’s thesis, Southeast University) (2018)
7. Su, H., Wang, Y.: Research on trust-based service routing system in P2P environment. *Comput. Appl. Res.* **23**(9), 230–233 (2006)
8. Potts, J., Rennie, E.: Web3 and the creative industries: how blockchains are reshaping business models. In: *A Research Agenda for Creative Industries*, pp. 93–111. Edward Elgar Publishing (2019)
9. Zhao, Y., Qiao, Z.: Research on the development status of digital identity management based on blockchain. *China Secur.* (2022)
10. Drumond, R., Manu, S.Y., Dave, L., Christopher, A., Ryan, G., Markus, S.: Decentralized Identifiers (DIDs) v1.0 (2019). <https://www.w3.org/TR/did-core/>
11. DID Development Center: DID Resolver (2020). <http://did.baidu.com/did-resolver/>
12. Yao, Q.: A Preliminary study on self-management identity. *Tsinghua Fin. Rev.* (2022)
13. Yang, G., Liu, Y., Xu, H., Xing, H., Zhang, J., Li, E.: A blockchain-based trusted distributed identity authentication system for power grids. *J. Netw. Inf. Secur.* **7**(6), 88–98 (2021)
14. Xia, Y., Che, L., Wang, G., Liu, J.: Application of blockchain-based self-sovereign identity in learning behavior data management. *Inf. Technol. Inform.* (2021)
15. Manu, S.Y., Dave, L., David, C.: Verifiable Credentials Data Model 1.0. Technical Report. W3C, pp. 1–115 (2019). <https://w3c.github.io/vcdata-model>, <https://www.w3.org/TR/vc-data-model/>
16. Sedlmeir, J., Smethurst, R., Rieger, A., Fridgen, G.: Digital identities and verifiable credentials. *Bus. Inf. Syst. Eng.* **63**(5), 603–613 (2021)
17. Li, W., Jiang, Z.: Research on the development and supervision of distributed accounts, blockchain and digital currency. *Fin. Supervis. Res.* **6**(1), 12 (2018)
18. Yao, Q., Zhang, D.: A review of identity management technology in blockchain systems. *J. Softw.* **32**(7), 2260–2286 (2021)
19. Shafiq, M., Tian, Z., Bashir, A.K., Du, X., Guizani, M.: CorrAUC: a malicious bot-IoT traffic detection method in IoT network using machine-learning techniques. *IEEE Internet Things J.* **8**(5), 3242–3254 (2020)
20. Decentralized Identifiers (DIDs) v1.0 (2020). <https://www.w3.org/TR/did-core/>
21. Weyl, E.G., Ohlhaber, P., Buterin, V.: Decentralized society: finding web3’s soul (2022). Available at SSRN 4105763
22. Wang, M., Lu, J.: Blockchain technology and its application research in government governance. *E-Govern.* **2**, 1–14 (2018)

23. Zhu, L., Yu, H., Zhan, S., Qiu, W., Li, Q.: Research on high performance alliance blockchain technology. *J. Softw.* **30**(6), 1577–1593 (2019)
24. Hao, K., Xin, J., Huang, D., Wang, G.: A decentralized distributed storage model. *Comput. Eng. Appl.* **53**(24), 1–7 (2017)
25. Long, W.: Research on the construction and system of new data property rights. *Tribune Polit. Sci. Law* **35**(4) (2017)
26. Tian, Z., Luo, C., Qiu, J., Du, X., Guizani, M.: A distributed deep learning system for web attack detection on edge devices. *IEEE Trans. Industr. Inf.* **16**(3), 1963–1971 (2019)
27. Ye, L.: Storage data mirroring technology and financial industry application analysis. *Fin. Electron.* **4**, 60–62 (2009)
28. Wang, R., Tang, Y., Pei, X., Guo, S., Zhang, F.: Blockchain privacy protection scheme based on lightweight homomorphic encryption and zero-knowledge proof. *Comput. Sci.* **S2**, 547–551 (2021)
29. Qiu, J., Tian, Z., Du, C., Zuo, Q., Su, S., Fang, B.: A survey on access control in the age of internet of things. *IEEE Internet Things J.* **7**(6), 4682–4696 (2020)
30. Mao, Z.: Research and implementation of web application vulnerability detection method based on Web Crawler (Master's thesis, Beijing Jiaotong University) (2020)
31. Dwivedi, Y.K., Hughes, L., Baabdullah, A.M., Ribeiro-Navarrete, S., Giannakis, M., Al-Debei, M.M., Dennehy, D., Metri, B., Buhalis, D., Cheung, C.M., Conboy, K.: Metaverse beyond the hype: multidisciplinary perspectives on emerging challenges, opportunities, and agenda for research, practice and policy. *Int. J. Inf. Manage.* **66**, 102542 (2022)
32. Liu, H., Ruan, N.: Research on attack methods in blockchain. *J. Comput. Sci.* **44**(4), 786–805 (2021)
33. Chen, C.: The key technology of consortium blockchain and the regulatory challenges of blockchain. *Power Equipment Manage.* **11**, 20–21 (2019)
34. Tian, Z., Li, M., Qiu, M., Sun, Y., Su, S.: Block-DEF: a secure digital evidence framework using blockchain. *Inf. Sci.* **491**, 151–165 (2019)
35. Sun, J.: Elderly care service system from the perspective of healthy aging: theoretical discussion and system conception. *J. Huazhong Univ. Sci. Technol. (Soc. Sci. Edn.)* **35**(5), 1–8 (2021)
36. Shafiq, M., Tian, Z., Sun, Y., Du, X., Guizani, M.: Selection of effective machine learning algorithm and Bot-IoT attacks traffic identification for internet of things in smart city. *Futur. Gener. Comput. Syst.* **107**, 433–442 (2020)

Chapter 35

Hydraulic Fracture Propagation in Layered Rocks: Research Combining 3D FEM Modeling and Laboratory Experiments



Fei Wang, Wei Liu, Kaiqi Wang, Kaikai Xu, Jingen Deng, Chaowei Xing,
and Ke Yan

Abstract The complex morphology of hydraulic fractures has been reported in layered formations due to the frequent occurrence of bedding. The success of hydraulic fracturing heavily depends on the vertical growth of hydraulic fractures. However, hydraulic fracture propagation in laminated rocks poses a complex problem due to the heterogeneity of the formations and bedding plane properties. This study employs a 3D finite element modeling considering bedding plane properties to simulate hydraulic fracture propagation in multi-lithologic interbedded strata and then validate the results with laboratory experiments. The hydromechanical coupled model proposed in this paper accounting for contact types, bedding friction coefficient and conductivity, rock layer distribution, stress and viscous fluid flow, which can well simulate the mutual interaction between hydraulic fractures and bedding planes. Numerical predictions are in good agreement with true triaxial fracturing experiments conducted. According to the numerical simulation and experiments results, the hydraulic fracture can exhibit one of the following behaviors: it may pass through the interface directly, extend along the interface after turning, or stop before reaching the interface. The results indicate that higher overburden pressure promotes the cross-layer propagation of hydraulic fractures. Only when the coefficient of variation between the vertical stress and the minimum horizontal stress reaches a certain threshold can the fracture penetrate the bedding. Hydraulic fractures may be arrested at the interface due to weak bedding strength or roughness. In the presence of multiple interfaces, hydraulic fractures may propagate along weakly-bonded interfaces with conductivity, which can lead to a decrease in the effective fracture area and a reduced efficiency of hydraulic fracturing. This study conducts

F. Wang · W. Liu · K. Wang · K. Xu · J. Deng (✉) · C. Xing · K. Yan
College of Petroleum Engineering, China University of Petroleum (Beijing), 18 Fuxue Road,
Beijing 102249, China
e-mail: dengjg@cup.edu.cn

State Key Laboratory of Petroleum Resources and Engineering, 18 Fuxue Road, Beijing 102249,
China

further investigations and discussions on the influence of parameters, such as inter-layer roughness and strength, interface permeability, on the fracture propagation. This research can provide insights into the mechanics of hydraulic fracture propagation in layered rocks and contribute to the development of unconventional reservoirs with more effective hydraulic fracturing techniques.

Keywords Hydraulic fracturing · Fracture propagation · Layered rocks · Weak-bonded interface · Bedding plane properties

35.1 Introduction

Hydraulic fracturing is a technique that injecting high-pressure fluids into rocks to create fractures and increase permeability. The LinXing area is a tight gas field located in the northeastern margin of the Ordos Basin, with sandstones of the Benxi, Taiyuan, and Shihezi Formation [1]. Due to its low porosity and permeability, hydraulic fracturing is necessary to improve production. The LinXing area has extensive interbedded mudstone and coal strata, forming a multi-lithologic stratigraphic formation vertically. In Lining area, the main production layers are widely composed of interbedded mudstones and coal seams, forming a multi-lithological layered formation vertically.

The colored-sand proppant mineback experimental results reported in a volcanic reservoir showed that the fracture exhibits complex morphological features, including branching, closing, overlapping, etc., and that the proppant distribution is uneven, with gaps and blockages [2]. It is important to note that the propagation path of hydraulic fractures in layered rocks is influenced by bedding planes, which is different from homogeneous isotropic formations [3]. Whether effective fractures can be created is crucial for effectively stimulating such reservoirs.

Previous researchers have conducted numerous laboratory experiments to determine the factors that influence the propagation of hydraulic fractures in layered formations. Athavale et al. conducted hydraulic fracturing experiments on homogeneous specimens and layered composite specimens, and the results showed that planar bi-wing fractures appeared in homogeneous cement blocks, while complex fractures occurred in layered composite specimens: wandering fracture paths, fracture branching, and possible shear sliding along unconsolidated interfaces [4]. Casas conducted fracturing experiments with Colton sandstone to evaluate the influence of discontinuities on the propagation of hydraulic fractures. Using fixed pressure probes at the interface, they observed significant fluid lag zones [5]. Suarez-Rivera conducted fracturing experiments using a fractured glass plate to study the arrest and propagation behavior of hydraulic fractures encountering interfaces [6]. Related triaxial fracturing experiments [7–10] have shown that the fracture propagation path in laminated formations is influenced by factors such as interface properties, interface inclination angle, in-situ stresses, fracturing fluid viscosity, and injection rate.

Currently, there are many numerical methods for simulating hydraulic fracturing, including FEM, FDM, BEM, DDM, DEM, GFEM, and XFEM. In Tang's study, A 3D hydraulic fracturing model was developed by Tang et al., which considered the layering of rock to analyze the impact of different parameters on the fracturing results [11]. Xie used fully three-dimensional displacement discontinuity method combined with FDM to simulate shale fracturing of the Longmaxi area. The study showed that when a hydraulic fracture vertically intersects a bedding plane, some fluid enters the bedding, resulting in slip of the bedding plane [12]. A fully three-dimensional model was established taking into account the longitudinal flow of fluids, fluid filtration, and the influence of bedding planes, and a criterion for identifying hydraulic fractures crossing bedding planes was obtained in Huang's study [13].

In this study, laminated composite specimens with different interface strengths and rock combinations were prepared based on similarity criteria, and fracturing experiments were conducted on a liquid pressure testing machine. In addition, a three-dimensional finite element model considering fluid–solid coupling, nonlinear seepage and interface effects was established and compared with the indoor test results to verify the reliability of the model. The study analyzed the influence of factors such as interface strength and roughness, and in situ stress on the direction, morphology, and failure mode of hydraulic fracturing, and revealed the mechanism and laws of hydraulic fracturing in layered rocks.

35.2 Numerical Model

35.2.1 Numerical Simulation Method

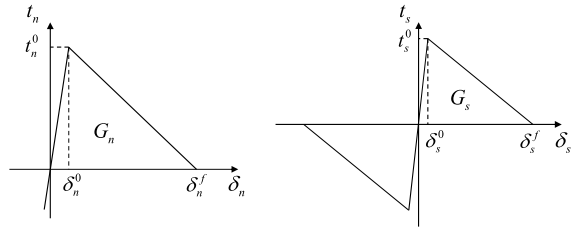
Constitutive model of cohesive element. The cohesive element's constitutive relation encompasses both the initial linear elastic behavior and damage evolution. The cohesive element is based on the assumption that there exists a process zone at the crack tip, and the failure of the process zone is described by the Traction-separation (T-S) constitutive model, which avoids the stress singularity at the crack tip in linear elastic fracture mechanics. The classic bilinear T-S model (as shown in Fig. 35.1) can be expressed as:

$$\left(\frac{t_n}{t_n^0}\right)^2 + \left(\frac{t_{s1}}{t_{s1}^0}\right)^2 + \left(\frac{t_{s2}}{t_{s2}^0}\right)^2 = 1 \quad (35.1)$$

t_n, t_{s1}, t_{s2} are the nominal stresses in the normal, first tangential, and second tangential directions of the cohesive element, respectively; $t_n^0, t_{s1}^0, t_{s2}^0$ are the corresponding critical nominal stresses.

After the cohesive elements are completely damaged, fluid enters these elements and applies fluid pressure to the crack wall, simulating the behavior of hydraulic fracture propagation.

Fig. 35.1 Bilinear traction–separation constitutive law for tensile (left) and shear failure of the (right) cohesive element



Fluid Within the Cohesive Element. For incompressible Newtonian fluids, tangential fluid flow within the crack can be described using the Poiseuille law:

$$q = -\frac{w^3}{12\mu} \nabla p \tag{35.2}$$

For Eq. (35.2), q is the fluid flow velocity within the fracture, p is the fluid pressure within the fracture; w is the fracture width; μ is the viscosity of the fracturing fluid (Fig. 35.2).

The loss of fracturing fluid can be described by Eq. (35.3), q_t and q_b are the filtration velocities through the upper and lower surfaces of the cohesive element, respectively. c_t and c_b are the filtration coefficients of the upper and lower surfaces, respectively. p_i is the pressure at the middle node of the cohesive element. p_t and p_b are the pore pressures at the upper and lower surfaces of the cohesive element, respectively.

$$\begin{cases} q_t = c_t(p_i - p_t) \\ q_b = c_b(p_i - p_b) \end{cases} \tag{35.3}$$

Interaction between hydraulic fractures and interfaces. The encounter of hydraulic fractures with bedding planes causes complex propagation paths. In the finite element model, the pressure transmission problem of cohesive elements is

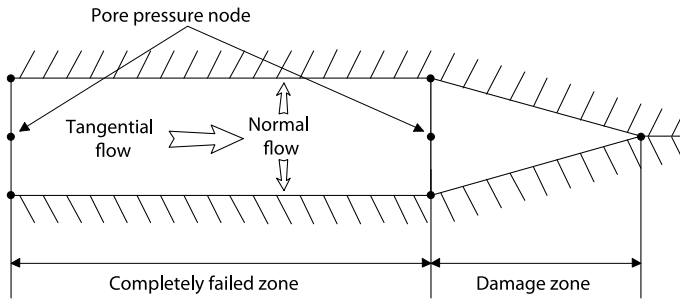


Fig. 35.2 Sketch of fluid flow within cohesive elements

solved by sharing the fluid pressure nodes at the intersection of the cohesive element corresponding to the hydraulic fracture surface and the cohesive element of the bedding plane.

Differences in flow distribution in the three directions result in different expansion paths due to the distinct parameter properties of the cohesive elements.

The strength of bedding planes comes from both the strength of the bonding material between interfaces and the frictional force caused by the pressure of overlying rock and the roughness of the interface. The shear strength of bedding planes can be studied using the weak plane criterion (Eq. 35.4), where τ_s is the shear stress, C is the shear strength, μ is the friction coefficient, and σ_t is the normal stress on the bedding plane. When the shear stress on a bedding plane exceeds the shear strength of the rock, the upper and lower boundaries of the bedding plane will undergo relative displacement, resulting in slipping.

$$\tau_s = C + \mu\sigma_t \quad (35.4)$$

Criteria for hydraulic fracture penetrating through the bedding plane. Whether a hydraulic fracture can penetrate a bedding plane depends not only on the stress field at the fracture tip but also on the shear strength of the bedding plane. Two conditions must be satisfied for a hydraulic fracture to penetrate a bedding plane [14, 15]: (1) the maximum tensile stress at the crack tip is greater than the critical strength of the rock ahead; and (2) there is no shear slip on the bedding planes. In Eq. 35.5, K_e is the equivalent stress intensity factor when the hydraulic fracture penetrates the interface, K_{IC} is the fracture toughness of the rock ahead of the propagation direction, and τ_{xy} is the tangential stress component at the hydraulic fracture tip on the interface.

$$\begin{cases} K_e \geq K_{IC} \\ \tau_{xy} < \tau_0 + \mu\sigma_v \end{cases} \quad (35.5)$$

35.2.2 FEM Numerical Model and Parameter Setting

Based on the exploration of the Lin-Xing block, it has been found that layered rocks are widely distributed at depths ranging from 1230 to 2000 m, as demonstrated in Fig. 35.3. The Taiyuan Formation contains coal beds in both its upper and lower sections, and there are interfaces between the coal and sandstone.

A 3D finite element model of $40 \times 50 \times 80$ m was established as shown in Fig. 35.4. Cohesive elements were embedded in advance, in which the longitudinal cohesive elements simulate the hydraulic fracturing propagation in the layered rocks, and the horizontal cohesive elements simulate the interlayer interfaces.

Fracturing fluid is injected at the injection node with a constant injection volume, and the initial damaged elements near the injection node are set as the perforation in

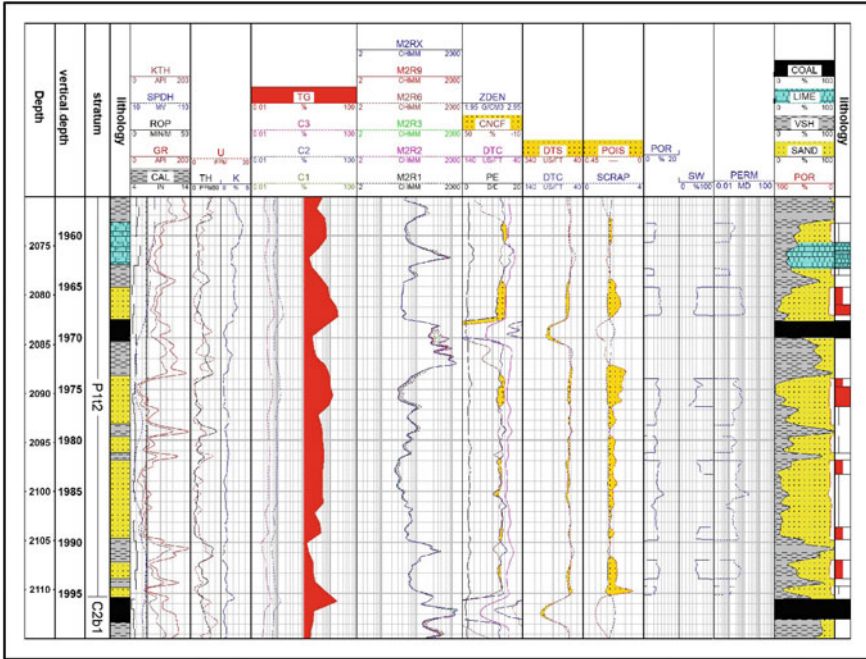


Fig. 35.3 The logging interpretation for a well in Lin-Xing block

Fig. 35.4 The finite element model of fracture propagation

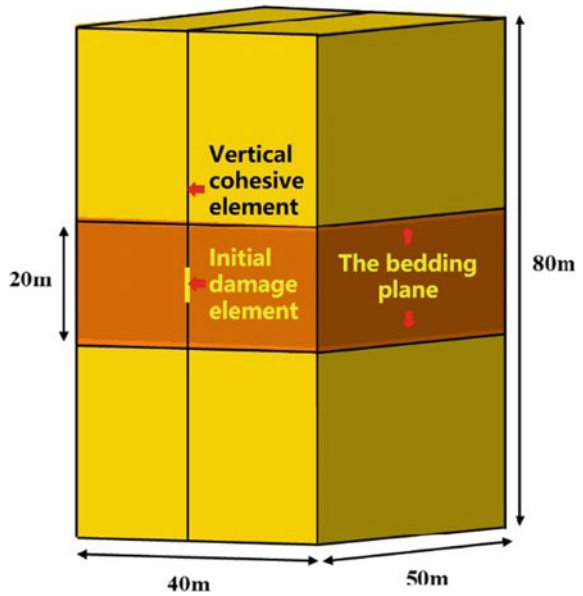


Table 35.1 Basic parameters of the numerical model

Parameter	Value
Young's modulus/GPa	25
Poisson ratio	0.22
Permeability/md	0.5
Minimum horizontal stress/MPa	20
Tensile strength of matrix/MPa	4.5
Shear strength of matrix/MPa	15
Normal, tangential fracture energy of matrix/J m ⁻²	2000
Normal, tangential fracture energy of the interface/J m ⁻²	150
Tensile strength of the interface/MPa	0.1
Shear strength of the interface/MPa	5
Fracturing fluid viscosity/MPa s	3.0
Fracturing fluid density/g cm ⁻³	1.0

well completion. The basic data in the model are shown in Table 35.1. To achieve the transfer of pressure and fluid, the intersection between the bedding plane and hydraulic fracturing propagation is established by defining the element nodes.

35.2.3 Numerical Simulation Results and Discussion

The hydraulic fracture propagation path interacting with the interface is affected by factors such as the properties of the interface, geological conditions, and parameters of the fracturing fluid. In this study, parameters such as the in-situ stress, interface roughness and strength, injection rate, and fracturing fluid viscosity were analyzed. During the analysis, only one parameter was varied while the other parameters remained constant based on the fundamental model.

In-situ Stress. To accurately quantify the influence of in-situ stress on hydraulic fracture propagation, the friction coefficient of the bedding plane was set to 0.6, and the minimum horizontal stress was maintained at 20 MPa. With constant injection rate and fracturing fluid viscosity, the crack propagation path at the same expansion time was analyzed by varying the overlying rock pressure.

As shown in Fig. 35.6a, a cross-layer crack was formed when the difference between the vertical stress and the minimum horizontal stress reached 30 MPa. The maximum width of the crack was 1.206 cm, and the crack initiation pressure was 35.4 MPa, with an expansion pressure of 26.2 MPa. When hydraulic fracture propagation reached the bedding plane, some of the fracturing fluid entered the bedding plane after it sliding a certain distance along the bedding plane, and ultimately crossed the bedding plane upward. The simulation results were consistent with the results of Xing et al.'s laboratory visualization experiment [16], as shown in Fig. 35.6.

As depicted in Fig. 35.5b, when the difference between the vertical stress and the minimum horizontal stress is 20 MPa, the crack does not completely cross the bedding plane. The maximum width of the crack is 1.198 cm, the crack initiation pressure is 34.3 MPa, and the extension pressure of the crack is approximately 28.4 MPa.

When the difference between the vertical stress and the minimum horizontal stress is 10 MPa. The reduction of overlying rock pressure prevents the fracture from overcoming the resistance caused by interface. The crack is confined to grow within the bedding plane, with its height being inhibited (see Fig. 35.5c).

When the difference between the vertical stress and the minimum horizontal stress is 0 MPa, the fracture turns to expand along the bedding plane (see Fig. 35.5d). The extension pressure of the crack is only 22 MPa, decreasing by 4.2 MPa. A large amount of fracturing fluid enters the interface, causing the crack width to decrease by 50%. Such a crack propagation path leads to a decrease in fracturing efficiency.

Simulation results indicate that the smaller difference between minimum horizontal stress and the vertical stress can induce a turning fracture to form after meeting bedding plane. Furthermore, research on the damage of rock around the fracture, as shown in Fig. 35.7, indicates that tensile damage mainly occurs around the fracture area, i.e. the green region $MMIXDEM = 0-0.5$. Correspondingly, shear damage mainly occurs in bedding plane close to the fracture, i.e. the $MMIXDEM = 0.5-1.0$ region in Fig. 35.7b which presents red. When the vertical stress is 30 MPa, the shear damage area is only generated at the intersection of the hydraulic fracture and the bedding plane. When the vertical stress is 20 MPa, the shear stress acting on the bedding plane is greater than the friction resistance, causing a large range of shear damage area (see Fig. 35.7c). As mentioned above, when the difference is 0, the fracture turns and extends along the bedding plane. With the fracturing fluid injecting, the friction resistance of the bedding plane is greater than the tensile strength of the interface, and the bedding plane presents tensile damage.

The behavior of the bedding plane under different fracture propagation paths was further elucidated by monitoring the displacement of the intersection node between the bedding plane and the hydraulic fracture (Fig. 35.8). When the difference was 30 MPa, in stage A, the tip of the crack met the bedding plane; in stage B, the crack tip slid and the displacement at the intersection increased from 0 to 0.7 mm; in stage C, the crack crossed the bedding plane and continued to expand upward, with the relative displacement of the bedding plane gradually decreasing to 0 mm.

When the difference was 10 MPa, the height of the fracture stopped increasing and the crack expanded along the bedding plane in the length direction, with the displacement at the intersection remaining constant. When the difference was 0 MPa, the crack turned and expanded along the bedding plane, with the displacement at the intersection stabilizing at 0.4 mm.

Friction coefficient of bedding plane. The tangential frictional force between the upper and lower rocks is crucial for the crack propagation behavior. By setting the difference in two-directional stress to be 20 MPa and changing the friction coefficient, the influence of the friction coefficient on the crack propagation path was studied (see Fig. 35.9). The numerical simulation results show that when the local stress

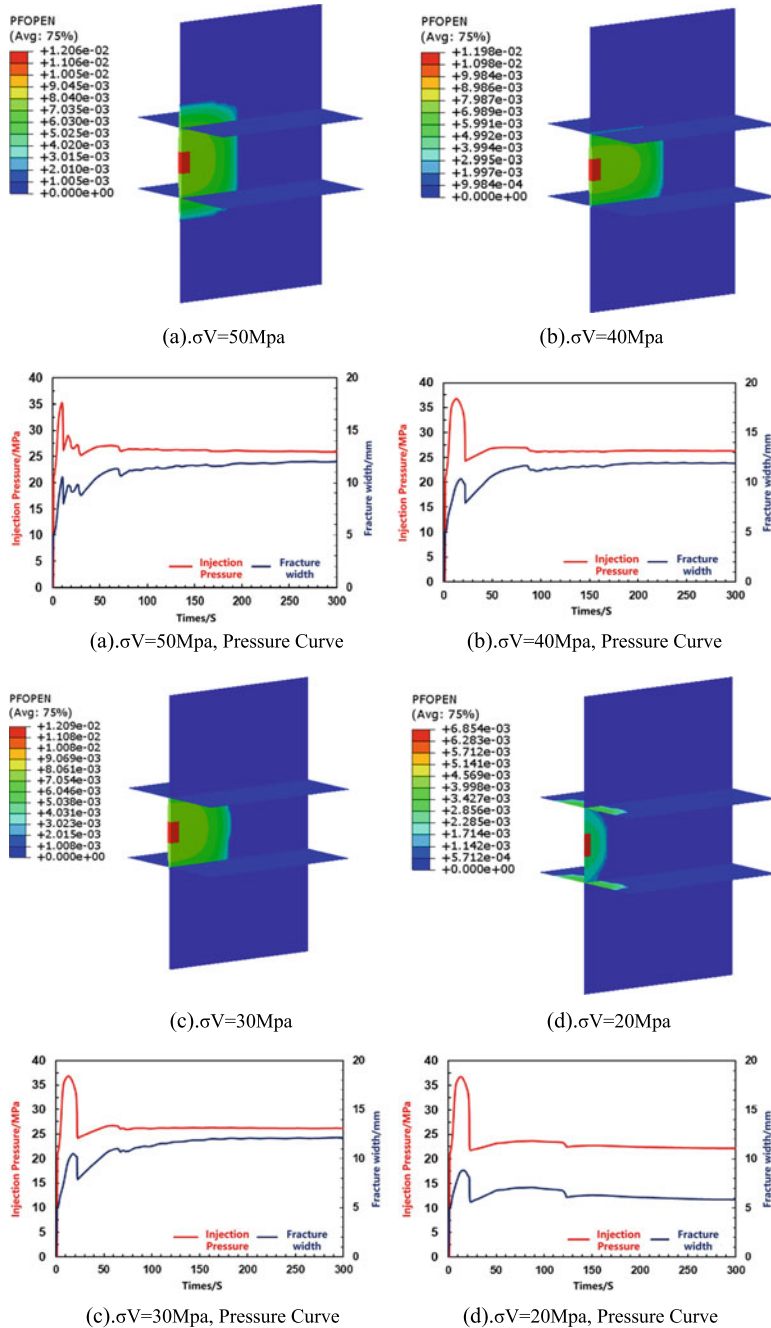


Fig. 35.5 Numerical simulation results under different stress conditions

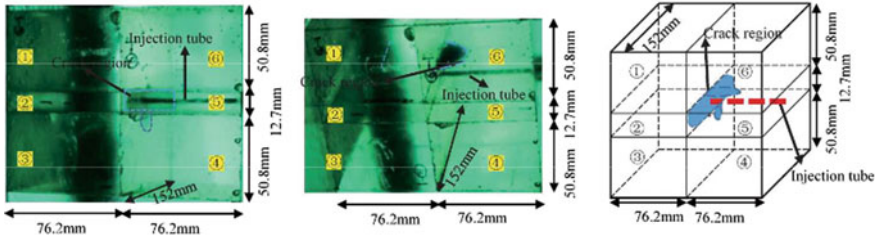


Fig. 35.6 Visualization experiment results of lamination seam in Xing et al.'s study [16]

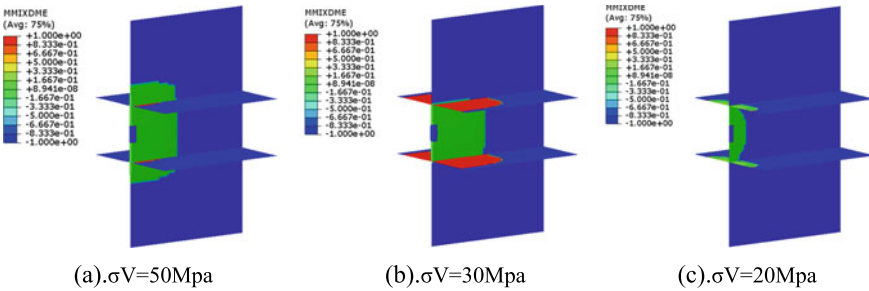


Fig. 35.7 Numerical simulation results of the rock failure forms under different stress

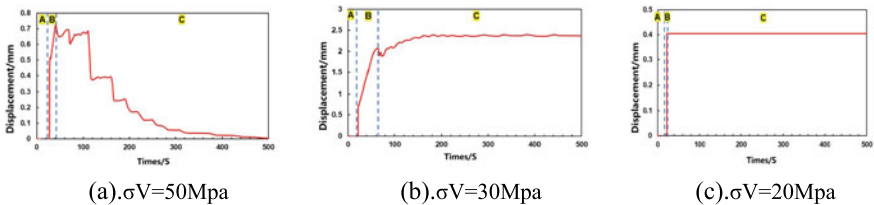


Fig. 35.8 Numerical simulation results of the displacement of the crossing nodes under different stress

difference is constant, a larger friction coefficient is favorable for the crack to cross the interface. When the friction coefficient is between 0.7 and 0.8, the crack crosses the interface. When the friction coefficient is between 0.4 and 0.6, the crack slips along the bedding plane and reaches a dynamic equilibrium, forming a slip-strike crack. Comparing the crack cloud maps in Fig. 35.9, under the condition that the crack crosses the interface, the greater the friction coefficient, the greater the crack height.

The cloud diagrams shown in Fig. 35.10 depict the rock failure patterns with friction coefficients of 0.6 and 0.7, respectively. It can be seen from the figures that as the friction coefficient increases, the shear failure area on the bedding plane decreases.

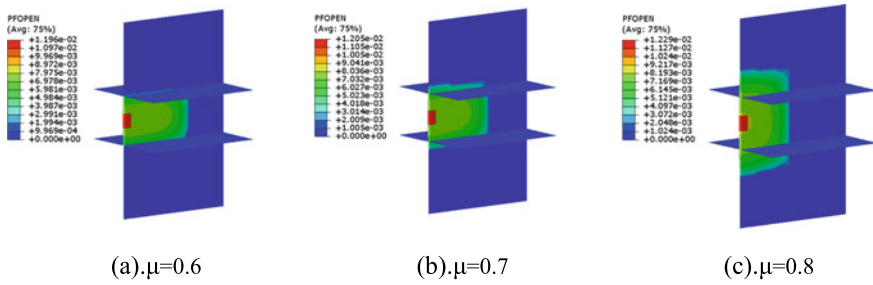


Fig. 35.9 Numerical simulation results under different friction coefficient

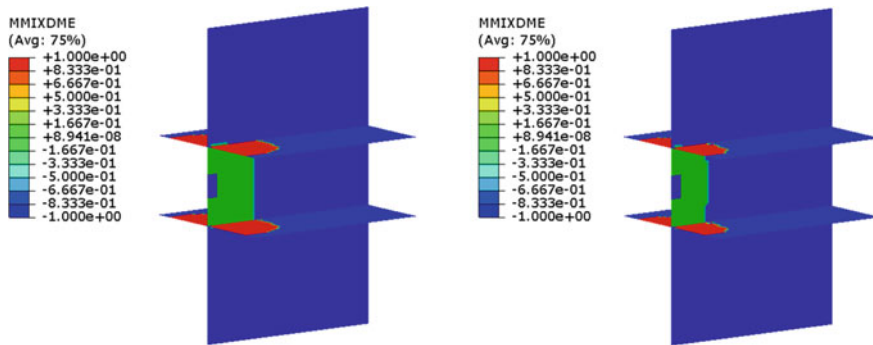


Fig. 35.10 Numerical simulation results of the rock failure forms under different friction coefficient

Drawing the influence factors chart of the biaxial stress difference and friction coefficient, it can be seen from Fig. 35.11 that with the increase of biaxial stress difference, the corresponding friction coefficient for cross-layer fracturing decreases. Increasing the friction coefficient will reduce the minimum biaxial stress difference required for forming cross-layer fractures.

Bedding strength. With the minimum horizontal stress set to 20 MPa, the difference between the two horizontal stresses set to 10 MPa, and the friction coefficient set to 0.6, the influence of the strength difference between the bedding plane and the matrix rock on the hydraulic fracture propagation is studied. The relative strength parameter δ is defined, and the calculation method is shown in Eq. (35.6). δ is defined as the ratio of tensile/shear strength of bedding plane to the tensile/shear strength of rock. Numerical simulations are conducted for δ values of 0.1, 0.3, and 0.5, and the results for the crack propagation paths are shown in Fig. 35.12.

$$\delta = \frac{\sigma_B}{\sigma_R} \tag{35.6}$$

As shown in Fig. 35.13, as the friction coefficient increases, the critical strength required for the crack to propagate across layers decreases, making it easier for the

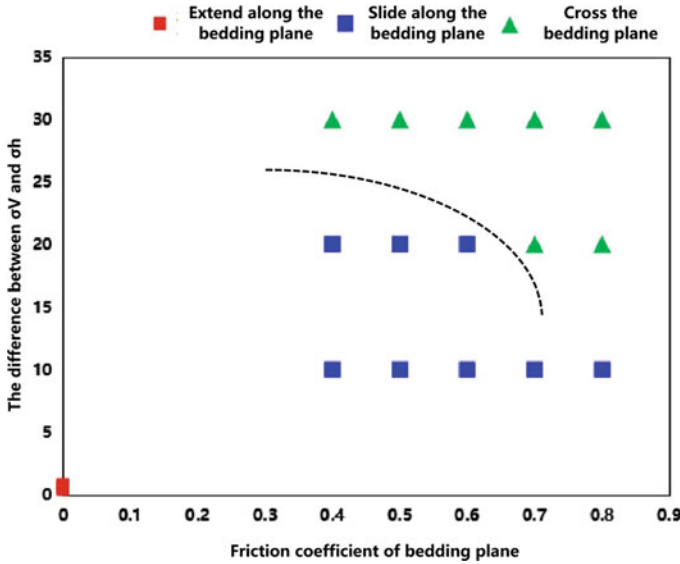


Fig. 35.11 Comprehensive impact diagram of different bedding plane friction coefficients and differential stresses

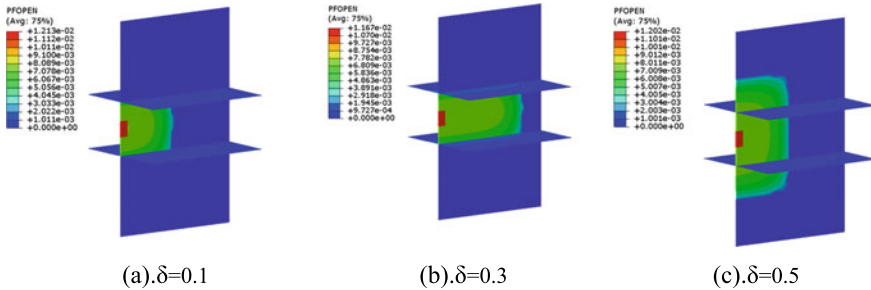


Fig. 35.12 Numerical simulation results of the rock failure forms under different friction coefficient

crack to propagate across layers. And as the relative strength increases, the minimum friction coefficient required for interlayer propagation decreases.

35.3 Experimental Comparison

The laboratory experiments conducted in this study are consistent with the numerical simulation results. The experimental design mainly focuses on the effects of factors such as in-situ stress and interface properties on the hydraulic fracture propagation paths.

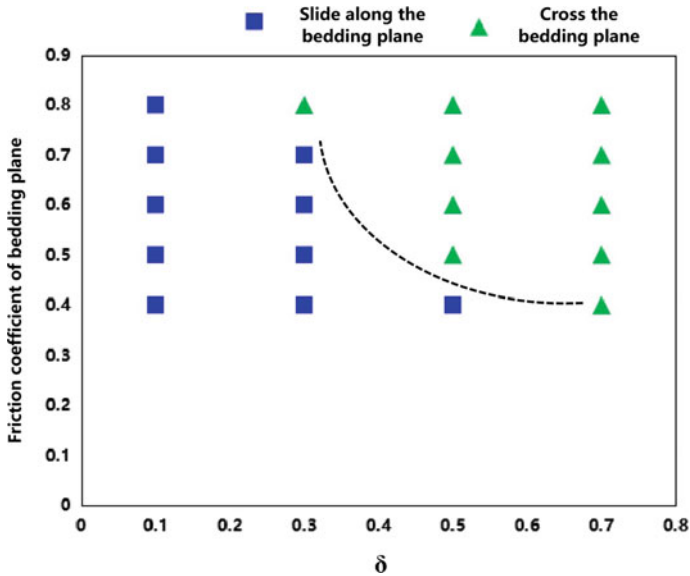


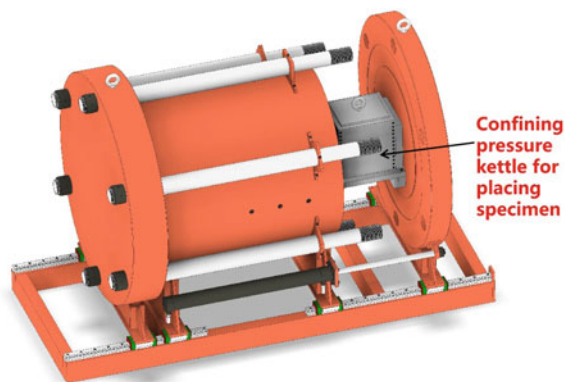
Fig. 35.13 Comprehensive impact diagram of different friction coefficients and δ

35.3.1 Experimental Apparatus

Some laboratory experiments were conducted in this research using a true-triaxial hydraulic fracturing test system, as illustrated in Fig. 35.14. The equipment comprises a hydraulic voltage pump, MTS pressure controller, three flattened jacks oriented in different directions, and a data acquisition system.

Cube-shaped specimens, measuring between 300 and 400 mm, are placed on a confined pressure vessel and positioned atop a cantilevered frame, which smoothly slides on rails. The experimental system is capable of applying a maximum confining

Fig. 35.14 The major component of the true-triaxial hydraulic fracturing apparatus



pressure of up to 50 MPa and a maximum injection pressure of up to 70 MPa. Injection of the fracturing fluid begins after completing the confining pressure loading step. Data collection was terminated when the injection pressure abruptly decreased to a low value and remained steady for an extended period. Subsequently, the specimens were cautiously opened to observe the fracture propagation path and the fracture geometries surrounding the transition zone.

35.3.2 Specimen Preparation

The laminated composites of sandstone and coal were employed to investigate hydraulic fracture propagating behavior in a layered rock. The interface between the sandstone and coal rock was positioned perpendicular to the vertical stress applied in the experiment. Epoxy resin and water-permeable stone materials were utilized to simulate the bedding planes with different properties. The specimen sketh diagrams are shown in Fig. 35.16a, and a stainless steel pipe with a diameter of 12 mm was made to represent a vertical wellbore during this experiment. In addition, specimen #6 is a three-layer specimen with an interlayer-sandstone-interlayer structure, as shown in Fig. 35.15b.

To realistically simulate the hydraulic fracture propagation behavior in the LINXING oilfield, rock mechanics tests were conducted on the cores using the MTS816 equipment. This provided the triaxial compressive strength, elastic modulus, and Poisson’s ratio of the formation rocks. Suitable rocks were selected to replace them in the specimens. Table 35.2 shows the specific parameters of the rocks used in the specimens. The plasticity characteristics of coal and simulated interlayer rocks are significantly stronger than those of sandstone.

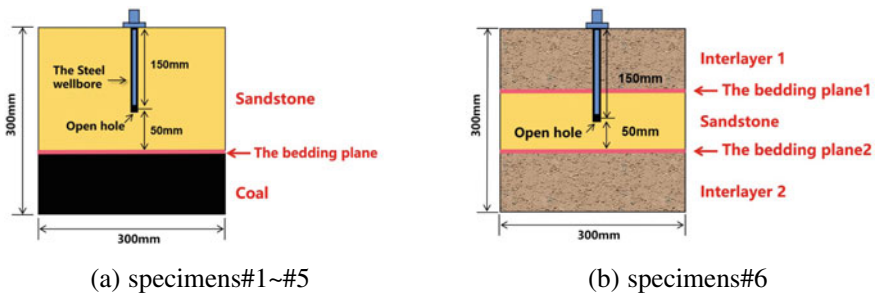


Fig. 35.15 Schematic diagrams of the specimens #1–#6

Table 35.2 Mechanical parameters of rock outcrops used in specimens

Rock in specimens	Compressive strength	Young’s modulus	Poisson ratio
Sandstone	48.30	13.5	0.15
Coal	19.68	5.57	0.27
Interlayer	30.47	9.47	0.32

35.3.3 Experimental Scheme

Table 35.3 presents a detailed experimental schemes and fractures geometries observed in the specimens. The injection rate was set to 10 ml/min, and the viscosity of the fracturing fluid was 21.3 MPa·s. The perforation interval was located in sandstone in the specimens. The fracture geometries are in Figs. 35.16, 35.17 and 35.18.

Table 35.3 The hydraulic fracturing experiments schemes fracture simple description of the specimens after fracturing

Sample No.	In-situ stress MPa	Injection rate ml/min	Fluid viscosity MPa s	Interface type	Fracture geometries
#1	15/10/30	10	21.3	Epoxy resin	Simple double wing fracture with crossing the bedding interface
#2	15/10/30	10	21.3	Epoxy resin, but the interface has broken	Double wing fracture not only propagated in the sandstone but also extended along the interface
#3	15/10/30	10	21.3	Lubricating grease	The fracture propagation path is the same as #2
#4	15/10/30	10	21.3	Permeable interface	The fracture propagation path is the same as #1
#5	15/10/20	10	21.3	Permeable interface	The fracture arrest at the interface
#6	15/10/20	10	21.3	Permeable interface	The cracks initiate in the sandstone, the permeable interface 1 is opened and completely broken, and the cracks stop at the resin interface 2



Fig. 35.16 Fracture geometry of the specimens #1–#2

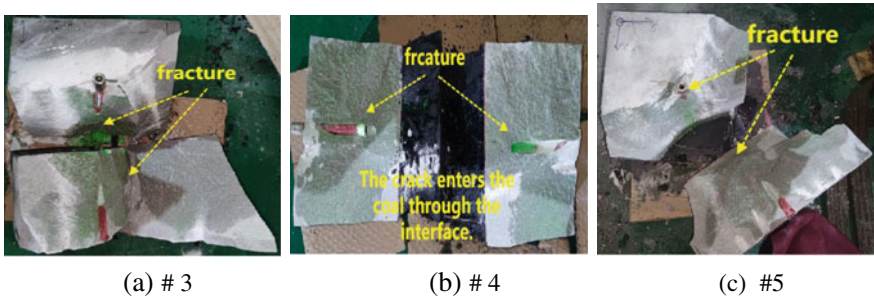


Fig. 35.17 Fracture geometry of the specimens #3–#5



Fig. 35.18 Fracture geometry of #6 after fracturing

35.3.4 Experimental Results and Discussion

#1 specimen had a well-bonded epoxy resin interface, while #2 specimen had a fractured epoxy resin interface, which means the interface lost its bonding strength and had gaps that cannot be avoided. The hydraulic fracturing experiment results of #1 and #2 specimens showed that under the same stress and fracturing fluid parameters,

reducing the interface bonding strength would cause hydraulic fractures to propagate and turn at the interface.

The interface of specimen #3 is a greasy lubricant, with a certain thickness of lubricant applied between the sandstone and coal seams, and the interface has no adhesive effect. Compared with specimens #1 and #2, the friction coefficient between the upper and lower rock layers is reduced. The results of the hydraulic fracturing experiment of #3 and #1 specimens show that under the same experimental conditions, smaller interface roughness also leads to hydraulic fractures turning and propagating along the interlayer interface. Rough interlayer interfaces are favorable for the cross-layer propagation of hydraulic fractures.

#4 and #5 hydraulic fracturing experiments were conducted by varying the vertical pressure to study the effect of the difference between the overburden stress and the minimum horizontal stress on the fracture propagation path. The experimental results are consistent with the numerical simulation results: under the same interface type and fracturing parameters, the fracture can only penetrate the interface directly when the vertical stress reaches a certain threshold.

#6 specimen has two types of interfaces: interface 1 is a weak permeable interface, and interface 2 is bonded with epoxy resin. Figure 35.18 shows the appearance, fracture photo, and reconstructed fracture geometry after the fracturing experiment of the #6 specimen, respectively.

The fracture in #6 specimen propagates vertically in the direction of the wellbore, cracks the sandstone, and extends to the lithological interface 2. Before the crack tip stress satisfies the interlayer penetration condition or opens the strongly bonded interface 1, the crack extends vertically to interface 1 and the fracturing fluid turns along interface 1 and stops extending vertically. Then, the crack extends along interface 1 until interface 1 is completely opened. The experimental results show that the weak permeable interface has a significant inhibitory effect on the extension of the crack in the height direction.

35.4 Conclusions

In this study, hydraulic fracture propagation in interbedded strata with multiple lithologies was simulated using a 3D finite element model that takes into account bedding plane properties. The simulation results were then validated through laboratory experiments. The main conclusions are shown as follows.

- (1) The increase in differential stress, layer strength, and friction coefficient can effectively increase the possibility of cracks crossing the interface. Higher overburden stress favors hydraulic fracture propagation through the interface, and a certain threshold of bidirectional stress difference is required for the fracture to cross. Therefore, it can be inferred that hydraulic fractures are not easily cross interface in shallow formations. As the strength of the the interface increases, the friction coefficient required for cross-bedding fractures decreases. The increase

in friction coefficient reduces the stress differentials and the critical strength required to across the interface. If the fracture can cross the interface, its height increases as the friction coefficient increases.

- (2) Slip along the bedding plane is one of the important factors limiting the height growth of fractures. Slip along bedding planes is influenced by the stresses differential, friction coefficient, and the bedding strength. When the stress differential is large, the effect of friction and bedding strength on the behavior of fracture propagation is reduced. Therefore, in reservoirs with large stress differential, hydraulic fracture behavior is primarily characterized by cross-bedding propagation. When the resistance to fracture extension along bedding is less than that of slip, hydraulic fractures tend to turn and propagate along bedding planes.
- (3) For fractures that cross bedding, the failure zone of the bedding only occurs within a certain area where the hydraulic fractures intersect with the bedding planes. For sliding fractures, the shear failure area of the bedding planes is larger. For fractures that extend along the bedding planes, the damage to the bedding planes takes the form of tensile failure, and the efficiency of fracturing fluid is lowest, resulting in half the fracture width compared to the other two types of fractures.
- (4) In actual fracturing operations, weaker strength and roughness of interfaces can cause hydraulic fractures to propagate along or deflect towards the bedding planes, inhibiting vertical growth. Due to the permeability and slip effects along the bedding planes, hydraulic fractures maybe confined to the formation between the bedding planes, leading to lower fracturing efficiency.

References

1. Mi, L., Zhu, G.: Geological characteristics and exploration breakthrough in Linxing-Shenfu tight gas field, northeastern Ordos Basin. *China Petrol. Explor.* **26**(3), 53–67 (2021)
2. Warpinski, N.R., Tyler, L.D., Vollendorf, W.C., Northrop, D.A.: Direct observation of a sand-propped hydraulic fracture. United States (1981)
3. Huang, B., Liu, J.: Experimental investigation of the effect of bedding planes on hydraulic fracturing under true triaxial stress. *Rock Mech. Rock Eng.* (2017)
4. Athavale, A.S., Miskimins, J.L.: Laboratory Hydraulic Fracturing Tests on Small Homogeneous and Laminated Blocks. ARMA-08-067 (2008)
5. Casas, L., Miskimins, J.L., Black, A., Green, S.: Laboratory hydraulic fracturing test on a rock with artificial discontinuities. In: LSPE Annual Technical Conference and Exhibition (2006)
6. Suarez-Rivera, R., Connor, B., Kieschnick, J., Green, S.: Hydraulic fracturing experiments help understanding fracture branching on tight gas shales. In: Proceedings of the 41st U.S. Rock Mechanics Symposium—ARMA's Golden Rocks 2006—50 Years of Rock Mechanics (2006)
7. Teufel, L.W., Clark, J.A.: Hydraulic fracture propagation in layered rock: experimental studies of fracture containment. *Soc. Petrol. Eng. J.* **24**(01), 19–32 (1984)
8. Hou, B., Zhu, P., Xu, D., Yao, Z., Li, Z., Chen, M., Zhou, Z.: Experimental investigation of longmaxi shale core: hydraulic fracture initiation and propagation in vertical plane. In: 5th ISRM Young Scholars' Symposium on Rock Mechanics and International Symposium on Rock Engineering for Innovative Future, Okinawa, Japan (2019)

9. Wang, T., Chen, M., Wu, J., Lu, J., Luo, C., Ju, Y.: Experimental study on the hydraulic fracture behavior when meeting large particle, layer interface and natural fractures. In: Abu Dhabi International Petroleum Exhibition & Conference, Abu Dhabi, UAE (2020)
10. Chen, J., Li, X., Cao, H., Huang, L.: Experimental investigation of the influence of pulsating hydraulic fracturing on pre-existing fractures propagation in coal. *J. Petrol. Sci. Eng.* **189**, 107040 (2020)
11. Tang, J., Zuo, L., Xiao, L., Wu, K., Qian, B., Yin, C., Ehlig-Economides, C., You, X.: A 3D hydraulic fracture propagation model applied for multiple-layered formation. **2019**(3), 1–21 (2019)
12. Xie, J., Tang, J., Yong, R., Fan, Y., Zuo, L., Chen, X., Li, Y.: A 3-D hydraulic fracture propagation model applied for shale gas reservoirs with multiple bedding planes. *Eng. Fract. Mech.* **228**, 106872 (2020)
13. Huang, B., Liu, J.: Fully three-dimensional propagation model of horizontal borehole hydraulic fractures in strata under the effect of bedding planes. *Energy Explor. Exploit.* **36**(5), 1189–1209 (2018)
14. Wan, C.: Mechanism of hydraulic fracture propagation in fractured shale reservoir in three dimensional space. Ph.D. thesis in China University of Petroleum, Beijing (2016)
15. Taleghani, A.D.: Analysis of hydraulic fracture propagation in fractured reservoir: an improved model for the interaction between induced and natural fractures. Ph.D. thesis in the University of Texas at Austin (2009)
16. Pengju, X., Keita, Y., Jose, A., Amr, E.-F., Bungler, A.P.: Laboratory demonstration of hydraulic fracture height growth across weak discontinuities. *Geophysics* **83**(2), MR93–MR105 (2018)

Chapter 36

Numerical Calculation of Equivalent Continuum Model for Fractured Reservoir Based on Meshless Generalized Finite Difference Method



Wenming Hu, Deng Liu, and Wentao Zhan

Abstract Low permeability fractured reservoir has the characteristics of non-even and non-continuous fracture distribution. In this paper, the equivalent permeability tensor is used to characterize fractured reservoirs based on the equivalent continuum media model. The initial fracture network model is generated based on the geological fracture description data, and then the equivalent permeability tensor is determined by the equal flow fundamental. Therefore, the fractured reservoir can be approximated as an anisotropic reservoir by the continuous equivalent media model. The meshless generalized finite difference method is a natural multi-point flow calculation scheme. It uses Taylor's formula and weighted least squares method to obtain a generalized difference approximation scheme for the spatial derivative of an unknown function in the node influence domain. Compared with the multi-point flow approximation, this method can deal with the anisotropic permeability tensor more conveniently and reduce the calculation cost to some extent. In addition, the computational domain discretization scheme based on the meshless point cloud is more suitable for the irregular geometry of the actual reservoir. This method avoids the difficulty of grid-like numerical computation, which is to generate high quality matched mesh characterizing boundary to ensure the stability of computation at the boundary. The effectiveness and computational performance of the proposed method are verified by the examples of complex boundary crack networks, and the sensitivity of the influence radius to the computational accuracy is discussed. In summary, this work provides a new idea for numerical simulation of low permeability fractured reservoir.

W. Hu

Underground Surface Engineering Emergency Maintenance Center in Liutun Town, Puyang County, Puyang, Henan, China

D. Liu

PetroChina Tarim Oilfield Company, Korla, China

W. Zhan (✉)

School of Petroleum Engineering, Yangtze University, Wuhan, Hubei, China
e-mail: zhanwt1996@163.com

Keywords Generalized finite difference method · Equivalent continuum model · Reservoir simulation

36.1 Introduction

As the degree of exploration and development of oil and gas resources in the world is gradually deepening, low-permeability fractured reservoirs are more important reservoir types for oil and gas supply. The influence of natural fractures on low-permeability reservoirs is very strong, and the development of natural fractures will significantly increase the permeability of reservoirs, which can make the reservoirs developable. However, the complex natural fracture distribution will aggravate the anisotropy of the reservoir and increase the difficulty of oil field development. The continuous media model is able to describe the complexity of subsurface flow at the macroscopic scale and is suitable for numerical simulation of large-scale reservoirs.

The equivalent continuous model is an anisotropic continuous media characterized by the equivalent permeability tensor instead of the original non-homogeneous media, and then analyzed based on the full tensor permeability continuous media seepage theory. The key to the equivalent continuous model is the determination of the equivalent permeability tensor and the flow simulation considering the full tensor permeability form. Snow [1] created the theory of permeability tensor for rock fractures. Kamath et al. [2] used the boundary element method to calculate single-phase fluid flow in naturally fractured reservoirs, which can handle complex fracture networks and flow coupling between matrix and fractures. Teimoori [3] considered different length fractures (e.g., short, medium, and long fractures) on this basis. They considered short fractures to improve matrix permeability and medium-length fractures as matrix source-sink terms. Li [4] used the boundary element method to find the equivalent permeability tensor for fractured reservoirs. For flow simulations considering the full tensor permeability form, spatial coordinate transformation theory and multi-point flow approximation are commonly used to deal with the anisotropy problem. Muskat [5] investigated the steady-state percolation theory for planar anisotropic reservoirs and gave the analytical solution of the steady-state percolation model for anisotropic reservoirs by coordinate transformation. This scheme converts the flow problem in anisotropic porous media into an isotropic reservoir problem. Yildiz [6] used coordinate transformation to solve a semi-analytical mathematical model of a three-dimensional branching horizontal well in a rectangular anisotropic porous media. The spatial transformation theory is to transform anisotropic problems into isotropic problems by coordinate transformation. The method is simple and efficient, but the spatial transformation increases the complexity of the boundary conditions and the method is not very general. The multi-point flow approximation [7–10] calculates contact surface flow and conductivity coefficients at intersection surfaces over multiple interaction zones around the grid under conditions of continuity of flow and pressure.

The generalized finite difference method (GFDM) is a meshless method that has emerged in recent years. This method starts with any point in the solution domain (called the centroid) as the object of study. In the vicinity of the center point, the support domain (the set of the nearest points to the center point) is formed according to the criterion of “shortest distance”. Finally, based on the idea of Taylor series expansion and weighted least squares, the derivatives of each order of the function at the center point are expressed as a differential approximation of the function values at the nodes of its support domain. This approximation scheme is a multi-point approximation format that can handle anisotropy problems. In addition, the coefficient matrix generated by this method is a sparse matrix, which can be easily and quickly solved by various sparse matrix solvers. Some scholars have applied it to engineering fields such as fluid mechanics [11–13], higher order equations [14], heat source problems [15] fluid–solid coupling, etc. In this paper, we equate fractured reservoirs to anisotropic reservoirs based on the equivalent continuous medium model, and use the GFDM method to solve the full permeability tensor to provide a concise and efficient computational method for the fractured reservoir number model.

36.2 Basic Principles

36.2.1 Equivalent Permeability Tensor Calculation Principle

According to the principle of flow equivalence, under the same pressure gradient and external boundary conditions, the flow rates of the same fluid through the same size fractured porous media body and homogeneous anisotropic media body are equal, respectively. Therefore, the cracked porous media can be replaced by the homogeneous anisotropic media equivalently. In other words, the overall permeability of the fractured porous media can be expressed by the permeability of the homogeneous anisotropic media. The permeability of a homogeneous anisotropic media body is not a scalar, but a second-order tensor, which is called the equivalent permeability tensor in the equivalent continuous media model. The equivalent permeability tensor of a fractured porous medium is determined by the spatial distribution, physical property values of the matrix and fractures.

$$K = \begin{pmatrix} K_{xx} & K_{xy} \\ K_{yx} & K_{yy} \end{pmatrix} \quad (36.1)$$

According to Darcy's law, the relationship between the percolation velocity v of a fluid through an equivalent homogeneous anisotropic medium body and the pressure gradient is as follows:

$$v = -\frac{K}{\mu} \nabla P = \left(-\frac{K}{\mu} \frac{\partial P}{\partial x}, -\frac{K}{\mu} \frac{\partial P}{\partial y} \right) \quad (36.2)$$

where μ is fluid viscosity. $v = (v_x, v_y)^T$ is flow velocity. ∇P is pressure gradient operator.

If the component of the average flow velocity at the outer boundary of a fractured porous media body under the same conditions is known, combined with the flow equivalence principle and Darcy's formula.

$$\begin{aligned} \bar{v}_x &= -\frac{1}{\mu} \left(K_{xx} \frac{\partial P}{\partial x} + K_{xy} \frac{\partial P}{\partial y} \right) \\ \bar{v}_y &= -\frac{1}{\mu} \left(K_{yx} \frac{\partial P}{\partial x} + K_{yy} \frac{\partial P}{\partial y} \right) \end{aligned} \quad (36.3)$$

If a unit pressure gradient $\nabla P = (1, 0)^T$ is applied to the grid block, the first column components K_{xx} and K_{yx} can be obtained. Similarly, the second column component K_{xy} and K_{yy} can be found when the pressure gradient is $\nabla P = (0, 1)^T$.

36.2.2 Generalized Finite Difference Theory

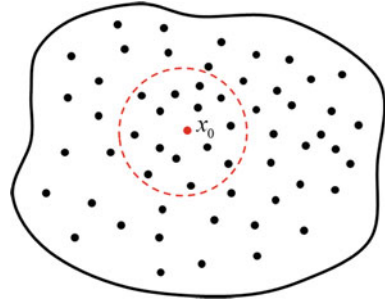
The two-dimensional pressure diffusion equation is expressed as follows:

$$\nabla \cdot \left(\frac{K}{\mu} \nabla P \right) = \frac{\partial P}{\partial t} \quad (36.4)$$

When the permeability is a tensor, Eq. (36.3) can be rewritten according to the chain rule of derivation.

$$\begin{aligned} \frac{k_{xx}}{\mu} \frac{\partial^2 P}{\partial x^2} + \frac{2k_{xy}}{\mu} \frac{\partial P}{\partial x \partial y} + \frac{k_{yy}}{\mu} \frac{\partial^2 P}{\partial y^2} + \frac{1}{\mu} \left(\frac{\partial k_{xx}}{\partial x} + \frac{\partial k_{xy}}{\partial y} \right) \frac{\partial P}{\partial x} \\ + \frac{1}{\mu} \left(\frac{\partial k_{xy}}{\partial x} + \frac{\partial k_{yy}}{\partial y} \right) \frac{\partial P}{\partial y} = \frac{\partial P}{\partial t} \end{aligned} \quad (36.5)$$

Fig. 36.1 GFDM-based local point cloud



Time derivatives are approximated using the central difference scheme.

$$\frac{\partial P}{\partial t} = \frac{P(t + \Delta t) - P(t)}{\Delta t} \tag{36.6}$$

The approximation of the spatial derivatives is done by the generalized finite difference method. The method is based on Taylor function expansion and weighted least squares method, as shown in Fig. 36.1, and the computational domain is discretely inscribed by using uniform or non-uniform matching points in combination with the specific shape of the solution domain. For a central node x_0 , a local point cloud of the central node is constructed by selecting a suitable radius of the influence domain according to the principle of Euclidean distance minimization, denoted as $E_m = \{x_0, x_1, \dots, x_m\}$.

The physical quantity corresponding to node x_i is u_i , and the Taylor expansion of the central node x_0 based on the local point cloud is as follows:

$$u_i = u_0 + (h_i \partial_x + k_i \partial_y)u_0 + \frac{1}{2}(h_i \partial_x + k_i \partial_y)^2 + \dots, i = 1, 2, \dots, m \tag{36.7}$$

where ∂_x and ∂_y is the partial derivative of unknown function u_0 with respect to x and y .

Define the weighted residual function:

$$B(u) = \sum_{i=1}^m \left(u_0 - u_i + (h_i \partial_x + k_i \partial_y)u_0 + \frac{1}{2}(h_i \partial_x + k_i \partial_y)^2 + \dots \right)^2 \omega_i^2 \tag{36.8}$$

where, w is the weight function, Taylor approximation has a local nature, the closer the points in the point cluster are to the center point, the higher the approximation accuracy of Taylor expansion, the greater the weight of the weight function, and vice versa, the smaller the weight function.

In order to obtain the partial derivatives of each order of the unknown quantity, the bias guide is introduced.

$$D_u = \left\{ \frac{\partial u}{\partial x}, \frac{\partial u}{\partial y}, \frac{\partial^2 u}{\partial x^2}, \frac{\partial^2 u}{\partial y^2}, \frac{\partial^2 u}{\partial x \partial y} \right\} \tag{36.9}$$

In order to minimize the residuals to obtain gen higher approximation accuracy, for this purpose the Eq. (36.7) is polarized to the bias vector to obtain the following linear algebraic equations.

$$AD_u = b \tag{36.10}$$

The vector of partial derivatives at node $\times 0$ can be obtained as

$$D_u = A^{-1}b = E\{u_0, u_1, \dots, u_m\}^T \tag{36.11}$$

As seen in Eq. (36.11), the derivatives of each order of the physical quantities of the nodes can be approximated by a weighted linear accumulation of the functions of adjacent point sets. This is also the core idea of generalized finite difference, and this approximation is a multi-point computational format, also called its approximation scheme as generalized difference operator. Solving the system of linear equations gives the expression of the generalized difference approximation for the unknown function.

$$\begin{aligned} \frac{\partial u}{\partial x} &= \sum_{j=1}^m e_{1j}u_j, \quad \frac{\partial u}{\partial y} = \sum_{j=1}^m e_{2j}u_j, \quad \frac{\partial^2 u}{\partial x^2} = \sum_{j=1}^m e_{3j}u_j, \\ \frac{\partial^2 u}{\partial y^2} &= \sum_{j=1}^m e_{4j}u_j, \quad \frac{\partial^2 u}{\partial x \partial y} = \sum_{j=1}^m e_{5j}u_j. \end{aligned} \tag{36.12}$$

The pressure diffusion equation can be rewrite with Eq. (36.12)

$$\begin{aligned} \frac{k_{xx}}{\mu} \sum_{i=1}^n e_{3i} P_i + \frac{2k_{xy}}{\mu} \sum_{i=1}^n e_{5i} P_i + \frac{k_{yy}}{\mu} \sum_{i=1}^n e_{4i} P_i \\ + \frac{1}{\mu} \left(\frac{\partial k_{xx}}{\partial x} + \frac{\partial k_{xy}}{\partial y} \right) \sum_{i=1}^n e_{1i} P_i + \frac{1}{\mu} \left(\frac{\partial k_{xy}}{\partial x} + \frac{\partial k_{yy}}{\partial y} \right) \sum_{i=1}^n e_{2i} P_i = \frac{\partial P}{\partial t} \end{aligned} \tag{36.13}$$

The process of solving the anisotropic pressure diffusion equation using the generalized finite difference method requires only the coordinate information of the discrete nodes, with no requirement for the connection information of the spatial nodes. This makes the method flexible and more adaptable to complex models.

36.3 Numerical Example

Figure 36.2 shows a reservoir with complex boundaries. The left and right boundaries, and the upper and lower boundaries are curves with different bending degrees. The left side is a constant pressure boundary condition of 30 MPa, the right side is a constant pressure boundary condition of 15 MPa, and the upper and lower boundaries are closed boundary conditions.

Consider the following basic control equation for an unsteady seepage problem in a two-dimensional porous media.

$$\nabla \cdot \left(\frac{\mathbf{k}}{\mu} \nabla P \right) = \frac{\partial P}{\partial t} \tag{36.14}$$

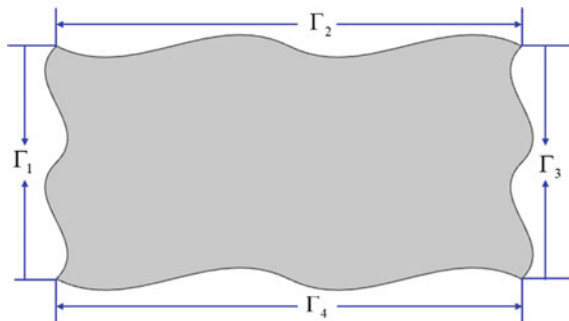
where the fluid viscosity may be taken as $\mu = 1 \text{ m Pa s}$. \mathbf{k} is the permeability tensor.

$$\mathbf{k} = \begin{bmatrix} k_{xx} & k_{xy} \\ k_{xy} & k_{yy} \end{bmatrix} = \begin{bmatrix} 50 & 100 \\ 120 & 300 \end{bmatrix} mD \tag{36.15}$$

According to Eq. (36.12), the following equation is obtained by bringing in the parameter values.

$$\left(50 \frac{\partial^2 P}{\partial x^2} + 220 \frac{\partial P}{\partial x \partial y} + 300 \frac{\partial^2 P}{\partial y^2} \right) = \frac{\partial P}{\partial t} \tag{36.16}$$

Fig. 36.2 Irregular boundary calculation domain



The first type of boundary conditions and the second type of boundary conditions are as follows:

$$\begin{aligned}
 P|_{\Gamma_1} &= 30 \text{ MPa} \\
 P|_{\Gamma_3} &= 15 \text{ MPa} \\
 (\mathbf{k}\nabla P) \cdot \mathbf{n}_y|_{\Gamma_2} &= \left(100 \frac{\partial P}{\partial x} + 300 \frac{\partial P}{\partial y}\right)|_{\Gamma_2} = 0 \\
 (\mathbf{k}\nabla P) \cdot \mathbf{n}_y|_{\Gamma_4} &= \left(100 \frac{\partial P}{\partial x} + 300 \frac{\partial P}{\partial y}\right)|_{\Gamma_4} = 0
 \end{aligned} \tag{36.16}$$

The pressure is calculated as the reference solution using the FEM under the fine triangular dissection grid, and the L_2 relative error formula is introduced to illustrate the effectiveness of the method in this paper. Using the matching point scheme as shown in Fig. 36.3, the pressure in the 1 day and 20 day calculated by GFDM are compared with the reference solution (in Fig. 36.4). Relative to the FEM-based reference solution, the computational error of the GFDM is within 0.3% using 1.6 times of the average distribution distance as the radius of the influence domain. The average distance of 1.6, 2.6, 3.6, 4.6 and 5.6 times is used as the influence radius respectively. It is found that with the increase of the influence radius, the calculation accuracy decreases gradually. Therefore, when GFDM is used to calculate the pressure equation, it is necessary to select the smallest radius of the influence domain as long as the non-singular calculation is guaranteed (Table 36.1).

$$error = \sqrt{\sum_{i=1}^{n_p} \frac{(P_{GFDM,i} - P_{ref,i})^2}{P_{ref,i}^2}} \tag{36.17}$$

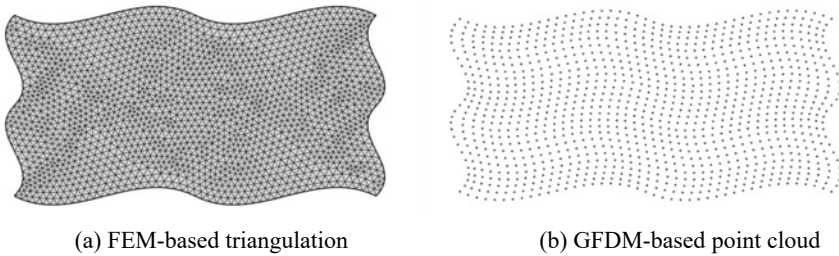


Fig. 36.3 Computational domain discretization

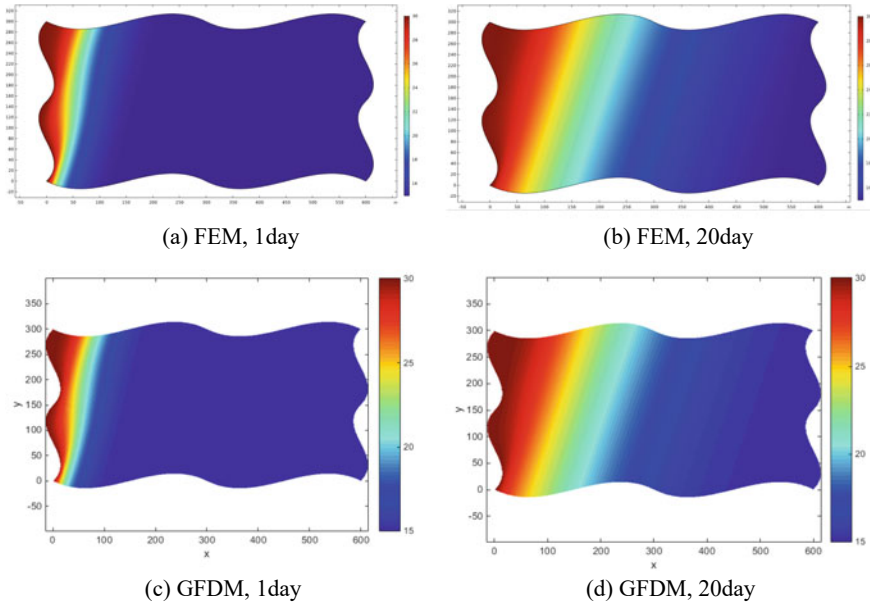


Fig. 36.4 Pressure profiles

Table 36.1 The influence of the radius of influence domain on calculational accuracy

Radius of influence domain	$1.6 r_e$	$2.6 r_e$	$3.6 r_e$	$4.6 r_e$	$5.6 r_e$
Relative error (%)	0.21	0.39	0.62	0.83	1.13

36.4 Conclusion

This paper presents a computational framework for fractured reservoirs based on the continuous equivalent model and meshless GFDM. Compared with the traditional numerical simulation method, the discrete computation domain of this method is free and flexible, and the discrete solution of the equation is simple and efficient, which provides a new idea for fractured reservoirs.

References

1. Snow, D.: Anisotropic permeability of fractured media. *Water Resour. Res.* **5**(6), 1273–1289 (1969)
2. Kamath J., Lee S. H., Jensen C. L., et al.: Modeling fluid flow in complex naturally fractured reservoirs. In: *SPE India Oil and Gas Conference and Exhibition*. OnePetro (1998)

3. Teimoori, A., Chen, Z., Rahman, S.S., et al.: Effective permeability calculation using boundary element method in naturally fractured reservoirs. *Pet. Sci. Technol.* **23**(5–6), 693–709 (2005)
4. Li, Y.J., Yao, J., Huang, Z.Q., et al.: Calculation of equivalent permeability tensor and study on representative element volume for modeling fractured reservoirs. *Chin. J. Hydrodyn.* **25**(1), 1–7 (2010)
5. Muskat, M., Meres, M.W.: The flow of heterogeneous fluids through porous media. *Physics* **7**(9), 346–363 (1936)
6. Yildiz, T.: Multilateral pressure-transient response. *SPE J.* **8**(01), 5–12 (2003)
7. Aavatsmark, I.: An introduction to multipoint flux approximations for quadrilateral grids. *Comput. Geosci.* **6**, 405–432 (2002)
8. Kim, J., Tchelep, H.A., Juanes, R.: Stability, accuracy, and efficiency of sequential methods for coupled flow and geomechanics. *SPE J.* **16**(02), 249–262 (2011)
9. Chen, Q.Y., Wan, J., Yang, Y., et al.: Enriched multi-point flux approximation for general grids. *J. Comput. Phys.* **227**(3), 1701–1721 (2008)
10. Sandve, T.H., Berre, I., Nordbotten, J.M.: An efficient multi-point flux approximation method for discrete fracture–matrix simulations. *J. Comput. Phys.* **231**(9), 3784–3800 (2012)
11. Rao, X., Liu, Y., Zhao, H.: An upwind generalized finite difference method for meshless solution of two-phase porous flow equations. *Eng. Anal. Boundary Elem.* **137**, 105–118 (2022)
12. Liu, Y., Rao, X., Zhao, H., et al.: Generalized finite difference method based meshless analysis for coupled two-phase porous flow and geomechanics. *Eng. Anal. Boundary Elem.* **146**, 184–203 (2023)
13. Zhan, W., Rao, X., Zhao, H., et al.: Generalized finite difference method (GFDM) based analysis for subsurface flow problems in anisotropic formation. *Eng. Anal. Boundary Elem.* **140**, 48–58 (2022)
14. Ureña, F., Salet, E., Benito, J.J., et al.: Solving third- and fourth-order partial differential equations using GFDM: application to solve problems of plates. *Int. J. Comput. Math.* **89**(3), 366–376 (2012)
15. Gu, Y., Wang, L., Chen, W., et al.: Application of the meshless generalized finite difference method to inverse heat source problems. *Int. J. Heat Mass Transf.* **108**, 721–729 (2017)

Chapter 37

Numerical Simulation Methods for Nonlinear Mechanical Behaviors of Confined Prestressed Hollow Core Wall Panels



Rui Wang , Ying Zhou , and Yiqiu Lu 

Abstract Concrete prefabrication techniques have been popularized and utilized in building construction industry for years. To further improve the construction efficiency and quality for low-rise buildings, a prestressed hollow core wall system is proposed. Nonlinear mechanical behaviors of such a structural system are strongly determined by the occurrence timing and order of splitting and sliding of joints as well as cracking of concrete wall panels. In this paper, a detailed finite element model was developed in ANSYS to provide a tool for investigating the seismic behaviors of prestressed hollow core wall structures. Contact elements were applied to simulate the interaction between material interfaces. Techniques including coupling of degrees of freedom of overlapped nodes and deactivation of concrete elements were adopted, along with restart analysis to simulate nonlinear mechanical behaviors of the structural system. The developed modeling method was verified by experimental test results and was shown to accurately predict the global and local behaviors such as failure modes and load bearing capacities of precast hollow core walls. Pros and cons of the proposed simulation method were summarized, and suggestions were provided so as to improve the accuracy and versatility of this method to predict the global seismic behaviors of prestressed hollow core wall structures.

Keywords Prestressed hollow core slab · Prestressed hollow core wall structure · Precast concrete structure · Numerical simulation · Nonlinear analysis · Innovative structural system

R. Wang (✉) · Y. Zhou · Y. Lu
State Key Laboratory of Disaster Reduction in Civil Engineering, College of Civil Engineering,
Tongji University, Shanghai, China
e-mail: ruiwang_richardw@outlook.com

37.1 Introduction

Concrete prefabrication techniques have been popularized and utilized in building construction industry for years. Mechanized manufacture of standard concrete members guarantees a steady and controllable product quality and simplifies installation process from formworks, which helps improve construction efficiency.

Prefabricated shear wall structures have been popularized due to its excellent strength, stiffness and construction efficiency. In order to enhance the integrity of the structure, prefabricated shear walls are usually anchored with grouted sleeves or metal ducts for inter-story joints. The grouted joint is not economic due to the complexity of the manufacturing and the strict requirements of machining accuracy. In order to improve the construction efficiency, the research team has been putting great effort into exploring the feasibility of confined prestressed hollow core wall panels in building structures.

A brand new precast concrete structural system named prestressed hollow core wall structure is proposed. The main vertical components resisting gravity and lateral loads are precast prestressed hollow core wall panels. The panels are confined by a precast constructional frame that is composed of precast concrete ring beams and tie columns to improve its ductility and strength. Binding materials are employed to fill the interfacial gaps between structural components, and grouting materials together with reinforcements are used for vertical connections. The majority of the hollow cores are never filled throughout the construction process. It is worth noting that, the aim of proposing prestressed hollow core wall structures is for rapid construction of low-rise buildings in rural areas rather than for higher seismic performance requirements such as resilience.

The design philosophy of precast concrete structures can be roughly subdivided into two categories, emulative design and non-emulative design [1]. For conventional precast concrete structures, emulative design is preferred, and nonlinear mechanical behaviors of structures are mainly induced by elastoplastic deformation of structural concrete and reinforcement. However, such a situation is no longer feasible for prestressed hollow core wall structures. To address the lack of mechanical experimental data on this type of system, experimental tests of 19 pieces of wall panel specimens were conducted by Tongji University and Shanghai CITI-RAISE Construction Group, to systematically investigate its axial, in-plane and out-of-plane mechanical behaviors.

The test results revealed that the failure mechanism of the structural system was tremendously altered as a consequence of the specially designed weak joints between structural members, both horizontal ones and vertical ones. Nonlinear mechanical behaviors of the structure are strongly determined by the occurrence timing and order of splitting and sliding of joints as well as cracking of concrete wall panels, of which geometrical and mechanical parameters including shear span ratio and axial load ratio, etc. serve as the main influential factors. To study a wide range of influential factors as well as to provide solid proof for practical feasibility of prestressed hollow

core wall structures, a numerical model that could accurately predict the structural behaviors is required.

Simulation of elastoplastic behaviors of reinforced concrete materials has been researched for years and relevant achievements have already been incorporated in commercial software. Mainstream mechanical models for concrete damage description include Discrete Crack Model (DCM), Smeared Crack Model (SCM), and Plastic Damage Model (PDM), etc. DCM treats concrete cracks as geometrical entities and gives accurate description of cracking shapes, which constantly alter mesh systems of the finite element model. Discrete element method is sometimes adopted to study the meso-scopic failure mechanism of concrete in consideration of aggregates [2]. Zhang et al. [3] carried out fracture simulation of plain-concrete beams with notches and took distribution and contribution of aggregates into account. SCM maintains a continuum calculation assumption and simulates stiffness degradation caused by concrete cracking through adjustment of element stiffness matrices. Crack widths can be numerically predicted according to gird partition and strain distribution [4]. PDM adopts more sophisticated three-dimensional constitutive models for materials and is able to reproduce stiffness degradation and restoring of concrete under cyclic or dynamic loads. Under such circumstances, concrete cracking and crushing details are not reflected, while comprehensive indices such as damage parameter are utilized for description of material behaviors [5].

As for numerical simulation of prestressed hollow core slabs, a large amount of research have been conducted. Souza et al. [6] applied SCM in DIANA software for out-of-plane shear capacity evaluation, and simulated concrete cracks through a total strain criterion. Brunesi et al. [7] and Nguyen et al. [8] studied web-strength of prestressed hollow core slabs with SCM and PDM, respectively, and analyzed cracking patterns through axial and shear stress distribution. Li et al. [9] adopted SCM in ABAQUS for verification of slab strengthening techniques. Sarkis et al. [10] modelled prestressed hollow core slabs in MIDAS with SCM and suggested that moduli of rupture, crack bandwidths of concrete and sizes of solid mesh elements were critical factors in numerical simulation. Most of the above researches focused on single prestressed hollow core unit and neglected the interaction between structural members. Besides, geometrical nonlinearity was rarely considered in simulation, which made large deformation and accurate contact analysis impossible. In addition, establishment of 3-D finite element models adds to the work for parametric analysis, as well as challenges the mathematical algorithms for numerical convergence. Lateef et al. [11] utilized the phase-field approach, which is an advanced modification of DCM, to study the crack propagation in a 2-D beam of plain concrete, but still admitted the complaint of high computational cost. As a consequence, it is worthwhile developing an accurate simplified numerical modeling method for prestressed hollow core wall structures.

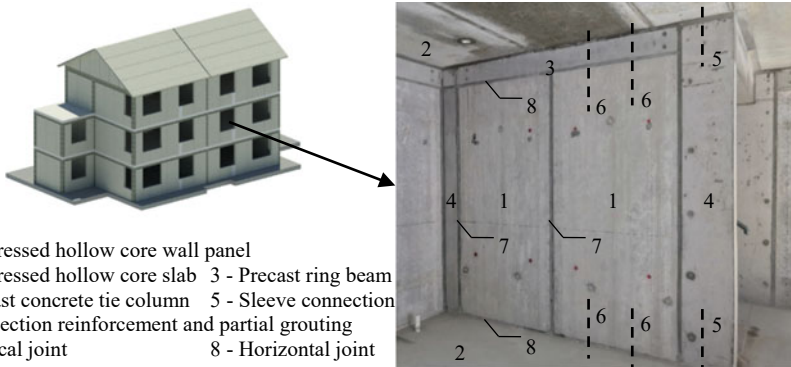
The objective of this paper is to develop a numerical modeling method to accurately capture mechanical behaviors of prestressed hollow core walls, so as to provide a solution for seismic performance evaluation of prestressed hollow core wall structures. Firstly the experimental works were reviewed in brief to grasp the conceptualization and mechanical properties of the proposed structural system. Then the

numerical modeling method was introduced in detail. 2-D models were developed in ANSYS software, with contact elements involved and the element birth-and-death technique utilized. The numerical simulation results were compared with the test results and a discussion was made. Finally, the pros and cons of the developed numerical simulation methods were summarized, through which its application prospect for future research was concluded.

37.2 Prestressed Hollow Core Wall Structures

The configuration of the proposed structural system named prestressed hollow core wall structures can be illustrated through a pilot construction project as shown in Fig. 37.1. Wall panels 1 are confined with boundary elements that consist precast ring beams 3 and precast concrete tie columns 4, to enhance structural integrity, ductility and strength. For each wall panel only two hollow cores 6 are partially grouted with the inserted reinforcement to form horizontal joints. Mortar pad is utilized to establish the horizontal joints 8 between ring beams and wall panels, and the vertical joints 7 are filled with low-strength materials. The prestressed hollow core slabs 2 are also used as floor systems. Therefore, the proposed system only consists of three standardized precast components: prestressed hollow core units, precast ring beams and precast tie columns, which accelerates both the component manufacture and on-site construction speed.

To address the lack of experimental data on this type of system, physical tests of 19 pieces of wall panel specimens were conducted, incorporating specimens of different sizes and configurations. A standard specimen employed in the experiment was mainly composed of one or two pieces of precast hollow core wall panels, two concrete tie columns, one ring beam, a top loading beam and a bottom foundation beam. Configuration and size information of a typical specimen are depicted in detail



- 1 - Prestressed hollow core wall panel
- 2 - Prestressed hollow core slab
- 3 - Precast ring beam
- 4 - Precast concrete tie column
- 5 - Sleeve connection
- 6 - Connection reinforcement and partial grouting
- 7 - Vertical joint
- 8 - Horizontal joint

Fig. 37.1 The pilot construction project

in Fig. 37.2. Two types of standard prestressed hollow core wall panels were tested in the experiments, including SP panels and HC panels, as shown in Fig. 37.3.

Detailed test results and evaluation of the structural system can be accessed in a separate paper by the research team, while some basic experimental phenomena are outlined as follows for better understanding of the lateral resistance mechanism of the system. For specimens under in-plane monotonic loading as shown in Fig. 37.4a, the following cracking sequence was observed during the test: (1) a horizontal crack throughout the bottom joint of the specimen at the lateral drift around 0.28%; (2) a diagonal crack at the wall toe, extending from the compressive side of the bottom section to the vertical joint on the tensile side at the lateral drift around 0.52%; (3) a

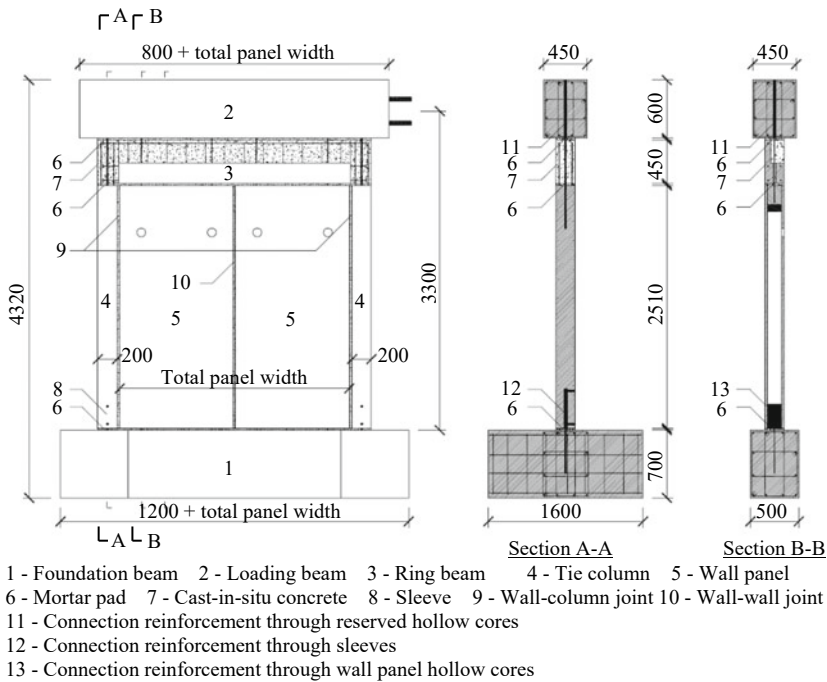


Fig. 37.2 Geometrical configuration of specimens (mm)

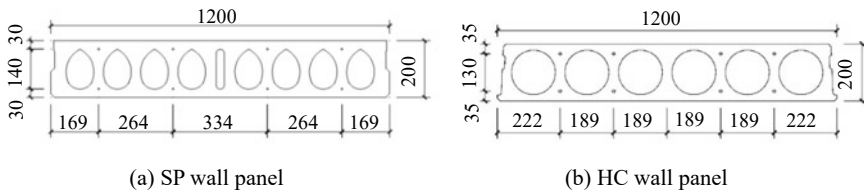


Fig. 37.3 Cross sections of wall panels (mm)

vertical crack through the vertical wall-column joint on the tensile side at the lateral drift around 0.62%; (4) multiple horizontal cracks across the concrete tie column on the tensile side at the lateral drift around 0.77%. Occurrence of the above mentioned continuous major crack generally led to the inflexion point on the force-drift curve, as shown in Fig. 37.5a.

Specimens that were subjected to cyclic loads had similar deformation modes and damage patterns with that of the specimens subjected to monotonic tests, as shown in Fig. 37.4b. Strength dropped down due to the failure of the vertical joint materials and separation between wall panels and concrete tie columns on the tensile side.

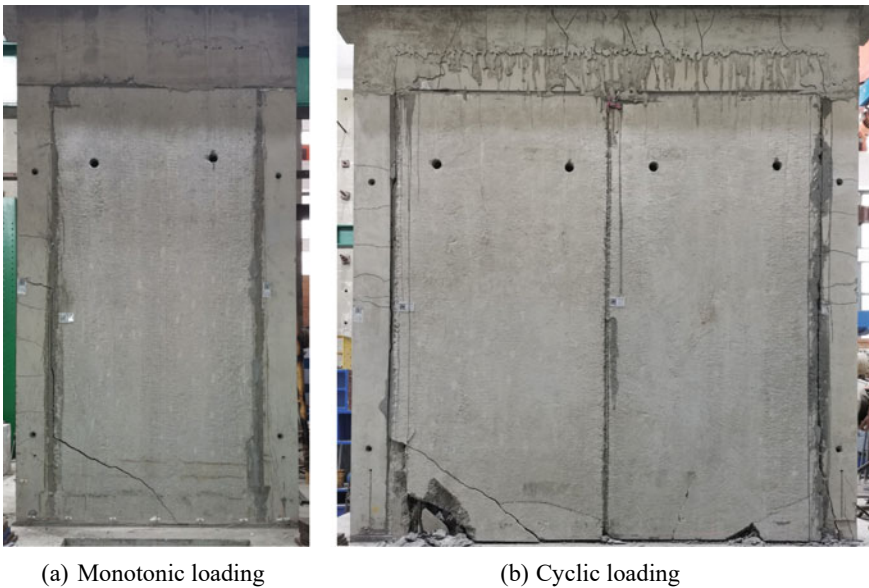


Fig. 37.4 Failure modes of typical specimens

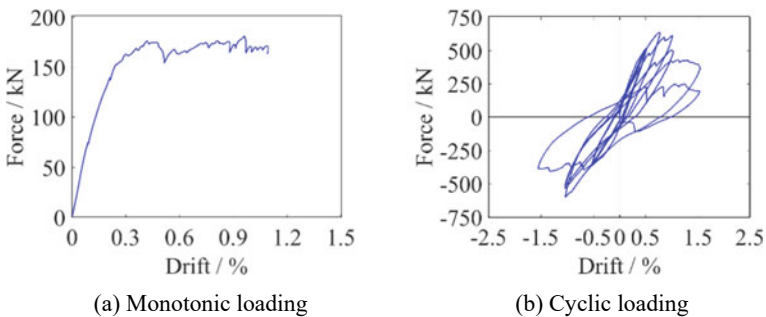


Fig. 37.5 Force-deformation curves of typical specimens

However, strength still kept stable and a ductile post-cracking mechanical behaviors could be maintained in their final conditions, as shown in Fig. 37.5b.

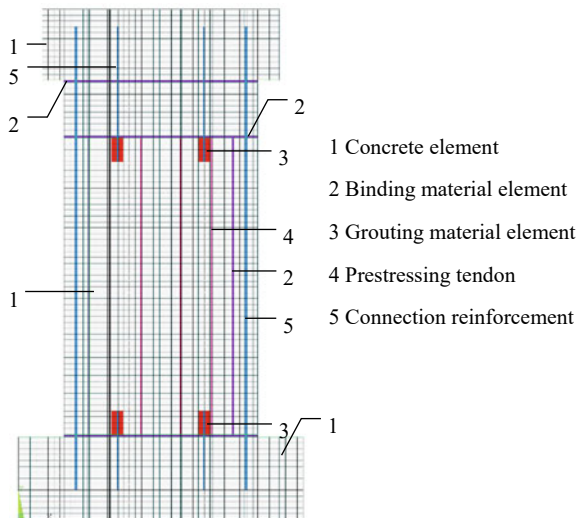
The test results indicate that nonlinear mechanical behaviors of the structure are strongly determined by the occurrence timing and order of splitting and sliding of joints and cracking of concrete wall panels. In order to study the influence of geometrical and mechanical parameters, e.g. shear span ratio and axial load ratio, etc., on the lateral resistance properties of the structural system, a numerical model that could accurately predict the structural behaviors is required.

37.3 Numerical Simulation Methods

Ansys Mechanical Finite Element Analysis Software for Structural Engineering (ANSYS) was utilized in this study to model prestressed hollow core walls. The finite element model of a prestressed hollow core wall was simplified into a 2-D mechanical problem, with several modeling techniques adopted to model the real behaviors. A direct generation method of modeling was adopted in ANSYS and the technique of command stream was used [12, 13]. PLANE42 2-D Structural Solid element were utilized to establish the model, serving as plane stress elements. The configuration of the numerical model is illustrated in Fig. 37.6.

Geometry of concrete and binding materials was based on the physical experimental specimens, and thicknesses of wall panel elements were calculated as the average thicknesses of concrete within their respective element regions. Prestressing tendons and connection reinforcement were modelled separately using plane

Fig. 37.6 Configuration of the numerical model



elements, overlapping elements of concrete or binding materials at the same position. Thicknesses of such elements were calculated based on equivalent cross section areas. Since a direct generation method was adopted, locations of nodes within the overlapping areas could be one-to-one matched and thus the overlapped nodes were coupled respectively, on both degrees of freedom (UX and UY) to simulate the deformation compatibility between reinforcement and concrete or binding materials. In particular, the partially grouted hollow cores were modelled using the same technique since the grouting materials and concrete wall panel occupied the same plane location.

As for the splitting and sliding of joint interfaces within the model, contact elements (CONTA171 and TARGE169) were adopted for the simulation. Adjacent structural components were modelled separately, and both degrees of freedom of the overlapped interfacial nodes were coupled respectively as the initial condition. Once debonding occurred, the coupled degree of freedom sets were deleted, and splitting or sliding between interfaces might occur. Friction coefficient between interfaces was consistently taken as 0.8 in this study.

A bilinear kinematic hardening material model (BKIN) was used for connection reinforcement, with the post-yield stiffness set to zero to simulate an elastic-perfectly plastic mechanical behavior, as shown in Fig. 37.7a. Prestressing tendons were modelled with linear elastic materials since elastoplastic behaviors were not expected for strands. The ascending section of the stress–strain curve consistent with the current Chinese national code, Code for design of concrete structures (GB 50010-2010) [14], was adopted for concrete as well as other cement-based materials, but the residual strength was reduced to 85% of the peak strength to form the descending section, as shown in Fig. 37.7b. Since a descending section of the curve exists, the multi-linear isotropic hardening material model (MISO) was no longer feasible. As a consequence, a multi-linear elasticity material model (MELAS) was applied, and the nonlinear behaviors of concrete were simulated through an element birth-and-death technique.

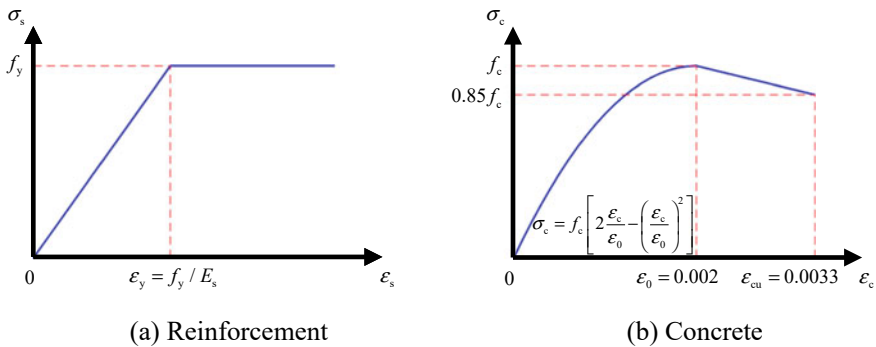


Fig. 37.7 Material constitutive models

The previous physical test results indicated that damages of the specimen were concentrated at the interfaces between different materials as well as concrete of the inner hollow core wall panels. Therefore, two failure criteria were defined. For interfacial failure, debonding of interfacial materials was determined based on the first principal stress (S_1) exceeding tensile strength of the weaker material. Debonding of interfacial materials led to release of the coupled degree of freedom sets of corresponding interfacial nodes, as mentioned above, and thus deformation compatibility of interfaces no longer existed. For concrete failure, damages were only considered for concrete of the inner hollow core wall panels, and a four-parameter failure criterion proposed by Ottosen was adopted [15], which can be expressed as Eq. (37.1).

$$f(I_1, J_2, \cos 3\theta) = A \frac{J_2}{f_c^2} + \lambda \frac{\sqrt{J_2}}{f_c} + B \frac{I_1}{f_c} - 1 = 0$$

where $\lambda = K_1 \cos \left[\frac{1}{3} \arccos(K_2 \cos 3\theta) \right]$ for $\cos 3\theta \geq 0$

$$\lambda = K_1 \cos \left[\frac{\pi}{3} - \frac{1}{3} \arccos(-K_2 \cos 3\theta) \right]$$
 for $\cos 3\theta < 0$ (37.1)

Within this expression, stress state correlated variants I_1, J_2 and θ are the first stress invariant, the second deviatoric stress invariant, and the Lode angle, respectively, and f_c is the material characteristic of compressive strength. The value of the index $f < 0$ corresponds to stress states inside the failure surface. A, B, K_1 and K_2 are the four parameters considered, and were predefined as 1.2759, 3.1962, 11.7365, and 0.9801, respectively, according to relevant national codes and experimental results. It is worth noting that the tensile strength of concrete f_c used in the expression is uniaxial compressive cylinder strength, so an empirical coefficient of 1.2 should be multiplied to the uniaxial compressive prism strength regulated by the Chinese code GB 50010-2010 [16]. Due to the element birth-and-death technique, concrete elements of which stress states exceeded the failure surface were deactivated (EKILL), removing their contribution to the global stiffness matrix.

Vertical loads were exerted on the top surface of the loading beam, and gravity loads were exerted through global acceleration in ANSYS. Bottom surface of the foundation beam was restrained to simulate a fixed boundary condition, and structural displacements were horizontally exerted to nodes of the top surface of the loading beam, to simulate the displacement-controlled loading protocols. Stretching and releasing of prestressing tendons were realized in separate models to create the initial stress file for the current model. The largest element size was restricted to $0.05 \text{ mm} \times 0.05 \text{ mm}$, and the loading step increment was chosen as 0.02 mm , in order to not only achieve a higher calculation efficiency, but also avoid distortion of simulation of complex mechanical behaviors, including splitting and sliding, cracking, and crushing, etc. After each load step, calculation process was suspended and stress distribution of nodes and elements was obtained. The aforementioned failure criteria were evaluated and the coupled degree of freedom to be released as well as the concrete elements to be deactivated were documented. Then the calculation process

was restarted, documented coupled sets were deleted and concrete elements were deactivated. Displacement of the loading beam was increased, and the solution of the next load step began.

37.4 Simulation Results

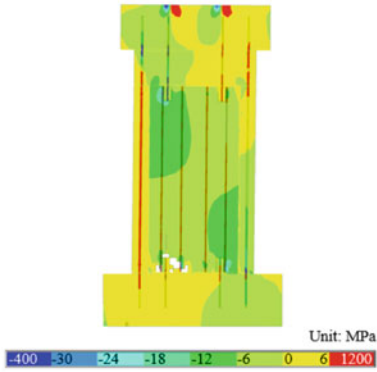
Specimens 07, 11 and 12 in the experimental study of this research were taken as the standard specimens for numerical simulation and calibration. Specimen 07 and Specimen 11 were both monotonically loaded in plane, but were with different shear span ratios. Specimen 12 was cyclically loaded in plane. Deformation and stress states at the maximum drifts are compared in Fig. 37.8, with images of the final conditions of corresponding specimens presented. Deformation is plotted in real scales, and vertical stress (SY) distribution is illustrated in color. Deactivated concrete elements are removed from the diagrams for better illustration. Force-drift curves or skeleton curves are compared in Fig. 37.9.

37.5 Discussion

37.5.1 *Simulation for Monotonically Loaded Specimens*

In Fig. 37.8a, splitting and sliding of material interfaces and damages of concrete at the bottom ends of the inner wall panel are observed, which is consistent with the phenomena of the concrete wall toe crushing and the diagonal crack of Specimen 07, as shown in Fig. 37.8b. The stress diagram reflects that tie columns on each side were either in compression or in tension, while the inner wall panel mainly served as a diagonal truss member at the maximum drift. The tensile cracking of the concrete wall panel can be predicted in the numerical simulation in accordance with the initial occurrence of concrete material failure beyond the grouting portions. Simulated initiation of tensile cracking is at the lateral drift of 0.46%, which is close to the test result of 0.52%, when cracking of the concrete wall panel was first observed. Similar deformation pattern and vertical stress distribution can be found for Specimen 11 with a smaller shear span ratio as well, as shown in Fig. 37.8c, d.

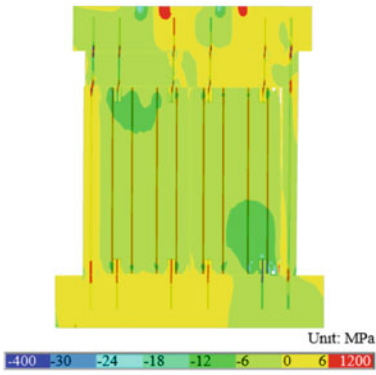
Force-drift curves produced by numerical simulations are compared to the test results as well in Fig. 37.9a, b. The simulated initial stiffness is higher than that of the test one, which might be due to the unintended movement of anchoring and loading facilities. Load bearing capacities of numerical models are close to the test results, with the errors typically less than 15%. The modeling technique is regarded feasible for engineering application.



(a) Simulation result of Specimen 07



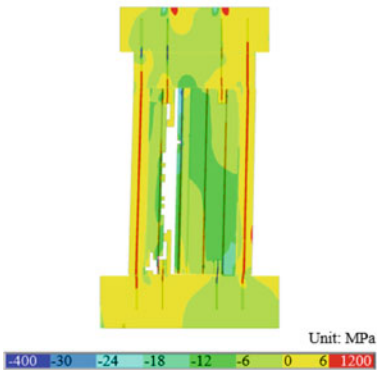
(b) Final condition of Specimen 07



(c) Simulation result of Specimen 11



(d) Final condition of Specimen 11



(e) Simulation result of Specimen 12



(f) Final condition of Specimen 12

Fig. 37.8 Deformation and vertical stress distribution of Specimens 07, 11 and 12, in comparison with their final conditions in physical tests

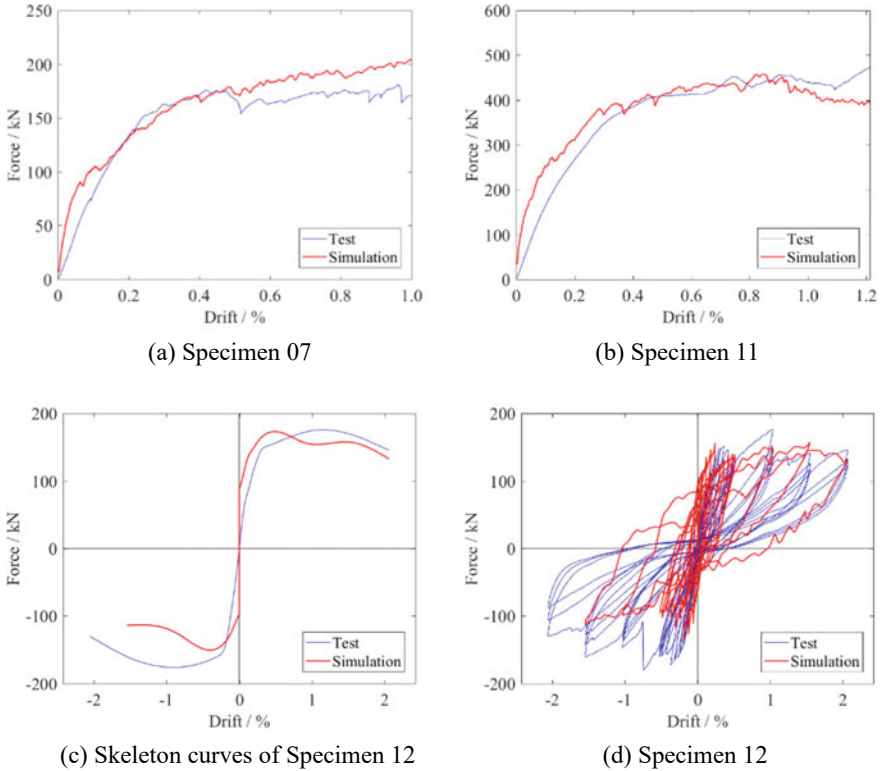


Fig. 37.9 Comparison of force-drift curves or skeleton curves

37.5.2 Simulation for Cyclically Loaded Specimens

For cyclic loading, it is worth noting that the utilized version of ANSYS Software (version 19.1) has a limitation in the number of restart files of 999, enabling at most 1000 load steps for restart analysis. As a consequence, the number of loading loops was reduced, and the load step increment was also increased from 0.2 to 1.0 mm. Figure 37.8e is the state where maximum lateral drift of Specimen 12 was achieved. One piece of the inner modelled wall panel was split thoroughly from bottom to top, which is very similar to the test result as shown in Fig. 37.8f. As for the force-drift curves in the cyclically loaded scenario as shown in Fig. 37.9c, positive sections of skeleton curves of the numerical simulation and the test result are similar. However, negative section of the numerical simulation is lower than the observed curve, mainly attributed to the fact that the deactivated concrete elements were never reactivated, and thus closure of concrete cracks and transfer of normal or shear stresses was impossible when the specimen was loaded in the negative direction. According to Fig. 37.9d, pinching effects of concrete components cannot be simulated with the adopted techniques. Pinching effects are generally related to

crack closure, shear lock and slipping of longitudinal reinforcement [17], and should be further studied experimentally and numerically, possibly utilizing material models such as Bouc-Wen-Baber-Noori (BWBN) hysteretic model [18], etc. In addition, the current modeling techniques are not applicable for dynamic analysis, since energy dissipation contributed by hysteretic behaviors of materials will be overestimated, and other issues should also be taken into consideration, such as increment of material strength and structural stiffness under dynamic loading, alteration of cracking order, and the limitation of number of restart analysis, etc.

37.6 Conclusion

The precast concrete structural system named prestressed hollow core wall structure was proposed by the research team, whose nonlinear mechanical behaviors are strongly determined by the occurrence timing and order of splitting and sliding of joints and cracking of concrete wall panels. In order to systematically study the influence of geometrical and mechanical parameters on the lateral resistance properties of the structural system, a numerical model was developed for prestressed hollow core walls. 2-D finite element models were established and contact elements were applied to simulate the interaction between material interfaces. Techniques including coupling of degrees of freedom of overlapped nodes and deactivation of concrete elements were adopted, and restart analysis was utilized for realization of nonlinear mechanical behaviors.

According to the test and simulation results, failure modes, cracking patterns and load bearing capacities of confined prestressed hollow core wall panels under monotonic loading can be well predicted by the developed numerical model. The diagonal bracing mechanism can be reflected through vertical stress distribution, and brittle failure order of wall panels can be tracked in accordance with the deactivated concrete elements. The proposed numerical simulation methods are able to capture skeleton curves under cyclic loads, but the pinching behaviors of concrete material are not available. The numerical model still has to be further developed for its application in dynamic analysis, so as to acquire a more comprehensive knowledge of the prestressed hollow core wall structural system.

Acknowledgements The authors gratefully acknowledge the financial support from the Distinguished Young Scientists Fund of National Natural Science Foundation of China (Grant No. 52025083), and the technical support of Shanghai CITI-RAISE Construction Group.

References

1. PCI Industry Handbook Committee: PCI Design Handbook, 7th edn. Precast/Prestressed Concrete Institute, Illinois (2010)
2. Huang, P., Pan, X., Niu, Y., Du, L.: Concrete failure simulation method based on discrete element method. *Eng. Fail. Anal.* **139**, 106505 (2022)
3. Zhang, C., Yang, X., Gao, H., Zhu, H.: Heterogeneous fracture simulation of three-point bending plain-concrete beam with double notches. *Acta Mech. Solida Sin.* **29**, 232–244 (2016)
4. Cervenka, V., Rimkus, A., Gribniak, V., Cervenka, J.: Simulation of the crack width in reinforced concrete beams based on concrete fracture. *Theoret. Appl. Fract. Mech.* **121**, 103428 (2022)
5. Yu, T., Teng, J.G., Wong, Y.L., Dong, S.L.: Finite element modeling of confined concrete-II: plastic-damage model. *Eng. Struct.* **32**(3), 680–691 (2010)
6. Souza, J.R., Araújo, D.L.: Shear capacity of prestressed hollow core slabs in flexible support using computational modelling. *Eng. Struct.* **260**, 114243 (2022)
7. Brunesi, E., Nascimbene, R.: Numerical web-shear strength assessment of precast prestressed hollow core slab units. *Eng. Struct.* **102**, 13–30 (2015)
8. Nguyen, T.N.H., Tan, K.H., Kanda, T.: Investigations on web-shear behavior of deep precast, prestressed concrete hollow core slabs. *Eng. Struct.* **183**, 579–593 (2019)
9. Li, X., Wu, G., Popal, M.S., Jiang, J.: Experimental and numerical study of hollow core slabs strengthened with mounted steel bars and prestressed steel wire ropes. *Constr. Build. Mater.* **188**, 456–469 (2018)
10. Sarkis, A.I., Sullivan, T.J., Brunesi, E., Nascimbene, R.: Critical modelling criteria for precast pre-stressed hollow-core slabs. *J. Build. Eng.* **54**, 104545 (2022)
11. Lateef, H.A., Laftah, R.M., Jasim, N.A.: Investigation of crack propagation in plain concrete using Phase-field model. *Mater. Today Proc.* **57**(2), 375–382
12. Wang, X.: ANSYS Numerical Analysis of Engineering Structures, 1st edn. China Communications Press, Beijing (2007). (in Chinese)
13. Wang, X., Li, Y., Xu, H.: ANSYS Structural Analysis Elements and Application, 1st edn. China Communications Press, Beijing (2011). (in Chinese)
14. China Academy of Building Research: Code for Design of Concrete Structures. GB 50010-2010. China Architecture Publishing & Media, Beijing (2015). (in Chinese)
15. Ottosen, N.S.: A failure criterion for concrete. *J. Eng. Mech. Div.* **103**(4), 527–535 (1977)
16. Gu, X.: Fundamentals of Concrete Structures, 3rd edn. Tongji University Press, Shanghai (2015). (in Chinese)
17. Yu, J., Yu, K., Shang, X., Lu, Z.: New extended finite element method for pinching effect in reinforced concrete columns. *ACI Struct. J.* **113**(4), 689–699 (2016)
18. Foliente, G.C., Singh, M.P., Noori, M.N.: Equivalent linearization of generally pinching hysteretic, degrading systems. *Earthquake Eng. Struct. Dynam.* **25**(6), 611–629 (1996)

Chapter 38

Design and Experimental Study of Raindrop High-Speed Emission System



Zhibo Wu, Chengyu Ma, Lanting Liu, Jianping Yin, and Yinggang Miao

Abstract When aircrafts fly through thunderstorm areas, it is inevitable to suffer the impact of raindrops. The structures may be damaged by the multiple impacts. Therefore, rain erosion test is very important to evaluate the safety and service life of aerospace structures and involved materials. In the work, a multistage system is designed for high-speed raindrop emission based on the split Hopkinson bar technique, and is achieved experimentally. The high-speed camera is used to record the experimental process, and the size and velocity of raindrop are obtained. The results show that the velocity of the raindrop jet increased with the enhancement of loading speed, and the increase is greater than the loading speed. When the velocity of the striker bar is up to 28.22 m/s, the jet velocity can reach 50.90 m/s via acceleration of the emission system. Meanwhile, the raindrop mass is 365.03 mg, and the interval times can be up to more than 5 times. This work could fill the gap of the current high-speed raindrop impact loading technique, and provide the experimental techniques for the anti-raindrop properties of materials and structures from aeronautics and astronautics.

Keywords Raindrop high-speed emission · Stress wave · Hopkinson pressure bar

38.1 Introduction

With the development of high speed vehicles, they are faced with more stringent service conditions, such as aircrafts, which requires high-speed and all-weather service capabilities. When the aircraft passes through the rain area, the impact from the high speed raindrops, causes the damage or even spalling of the structural surface

Z. Wu · L. Liu · J. Yin · Y. Miao (✉)

Joint International Research Laboratory of Impact Dynamics and Its Engineering Applications, Xi'an, China

e-mail: ygmiao@nwpu.edu.cn

C. Ma

School of Aeronautics, Northwestern Polytechnical University, Xi'an 710072, Shaanxi, China

materials, and even finally ruins the structural integrity of the aircraft. Therefore, the raindrop impact on aircraft structure is a growing problem to affect the aircraft integrity. Experimental investigations work as the fundamental and efficient methods, which require the loading apparatus to simulate the actual engineering conditions. Nowadays, methodologies for the high-speed raindrop tests consist mainly of below:

- (1) Rocket sled method [1, 2], which places specimens on rocket sled to accelerate through artificial rain field, is mainly used for supersonic test, and can simulate the damage of specimens in real rain field. However, the test cost is too high.
- (2) Rotating arm method [3–5], which requires the specimen place at the end of the rotating arm, with the rotation of the rotating arm to accelerate the specimen, so that the specimen through the nozzle or needle made artificial rain field. This method has low cost and can simulate the damage condition of the specimen in real rain field, but the size and speed of the specimen are limited by the strength of the rotating arm.
- (3) Jet method [6–8], which impacts specimen through high-speed jet generated by high-speed bullet impacting the water storage nozzle in the device. Due to low cost and wide range of jet velocity, this method has been used to analyze the damage behaviors and mechanism of materials.

At present, the jet method is the best method to study the corrosion of high-speed raindrop on aerospace materials at present. However, there is few literature available about the raindrop high-speed emission system in China, which can achieve series of rain drop impact with controllable loading intervals in one test, as the actual working conditions of the aircrafts flying through thunderstorm area. Considering the accuracy and requirements of the jet method, it is necessary based on it, to further improve the performance of the raindrop emission system. Therefore, this paper designs an experimental system for the raindrop high-speed emission, which can realize a series of raindrops impacts with different mass, wide impact velocity and controlling loading interval, to simulate the real rain erosion.

38.2 Methodologies

38.2.1 Loading Principle

Based on one-dimensional stress wave propagation theory, the stress wave can be optimized to propagate periodically in the incident bar, and push intermittently the incident bar to move forward for extruding the liquid. Then it forms a multiple water jetting, thus consequently achieve a controllable multi-jet rain erosion loading for materials and structures.

As shown in Fig. 38.1, a series of compression stress waves are generated when the striker bar impacts the incident bar. The compression stress waves propagate forward along the incident bar and push forward the piston in the water storage cavity. The

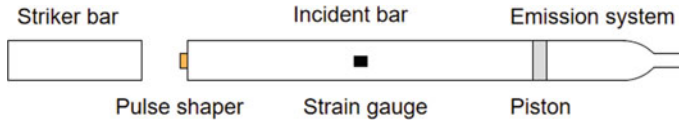


Fig. 38.1 Schematic diagram of loading equipment

liquid in the water storage cavity is extruded and ejected from the tip nozzle, thus forming a high-speed water jet. Since the wave impedance of the incident bar is much higher than that of the piston, the stress waves in the incident bar are nearly totally reflected back to the bar. The compressive stress wave is then reflected from the end face of the incident bar to form a tensile stress wave, which propagates in the opposite direction to the impacting end. On the other end face, it is reflected back again to be the second compressive stress wave, which pushes the piston to squeeze the liquid in the water storage cavity again, and then forms a the second high-speed water jet at the tip nozzle to eject. According to the one-dimensional stress wave propagation theory, the stress wave propagates repeatedly in the incident bar, repeats the above process, intermittently pushes the incident bar to move forward, and then pushes the piston to extrude the liquid in the water storage cavity to form high-speed water jet, and finally realizes a controllable multistage jet emission.

38.2.2 Raindrop Emission Adapter Designing

The experimental device is designed based on the split Hopkinson pressure bar apparatus. During the experiment, the high pressured gas pushes the striker bar to impact the incident bar to move forward for a certain distance, and the water in the rigid water storage cavity is extruded from the nozzle. Due to the repeating propagation of stress waves in the incident bar, the incident bar extrudes the water for several times and ejects multiple water jets, thus forming multistage water jets. In addition, a high-speed camera is used to monitor the shape and loading process of the water jet at the jet ejection end. The schematic diagram of the device is shown in Fig. 38.2.

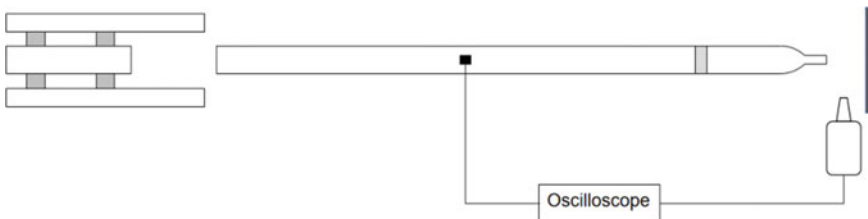


Fig. 38.2 Raindrop emission adaptation design schematic diagram

38.2.3 Achievements of Controllable Parameters

When the loading stress wave propagates to the right end of the incident bar, it can be reflected nearly totally to be a tensile wave, and the end face velocity at the bar end is doubled based on stress wave loading theory [9, 10]. At the same time, the dispersion effect is ignored during the process of stress wave propagation due to the pulse shaping technique [11–13], and the speed and distance of the incident bar are nearly same for each stress wave loading. Consequently, the shape, volume, velocity of the water jet are stable. The volume of liquid extruded by the incident bar is equal to the volume of liquid ejected by the nozzle, and formulated below.

$$v_1 t \cdot \frac{\pi D^2}{4} = v_2 t \cdot \frac{\pi d^2}{4} \quad (38.1)$$

where v_1 is the impact velocity of the striker bar, D is the inner diameter of the rigid water storage cavity, d is the diameter of the nozzle, and v_2 is the velocity of the water jet, respectively. Therefore, the relation between outflow jet velocity and incident bar end velocity can be deduced by Eq. (38.1).

$$v_2 = v_1 \cdot \frac{D^2}{d^2} \quad (38.2)$$

It is found from the Eq. (38.2) that, the water jet velocity can be controlled both by the velocity of the striker bar and the ratio of the inner cavity diameter/the nozzle diameter. The volume of the ejected water jet is defined as Eq. (38.3).

$$V = \frac{\pi D^2 L v_1}{2C} \quad (38.3)$$

where L is the length of the striker bar, and C is the wave velocity of the stress wave propagating in the incident bar, respectively. Therefore, the volume of a single water jet can also be controlled by the length and speed of the striker bar.

After the acceleration by the designed raindrop emission system, the final ejection velocity of the jet could be more than 50 m/s, the multiple emission times are more than 5, and the maximum mass of the single ejection raindrop is not more than 370 mg.

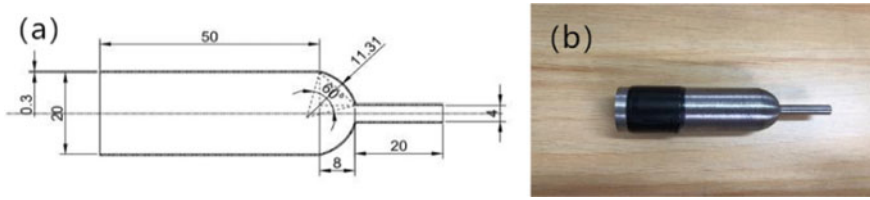


Fig. 38.3 Raindrop high-speed emission experimental system processing diagram and physical diagram

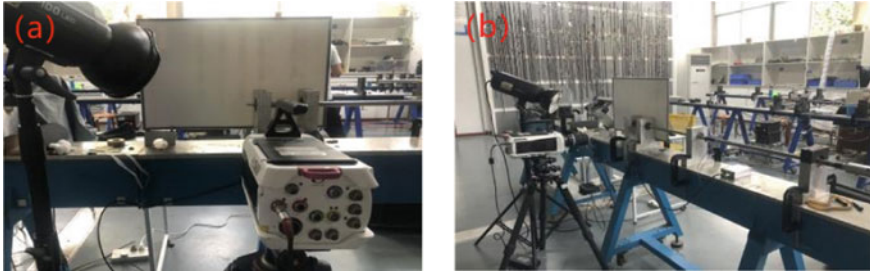


Fig. 38.4 Raindrop high-speed emission experimental system loading diagram

38.3 Experiments and Results

38.3.1 *Experimental Realization*

The raindrop high-speed emission experimental system and its physical diagram are designed to illustrate in Fig. 38.3. The system is connected at the end of the incident bar, and the loading apparatus and its camera are together shown in Fig. 38.4.

38.3.2 *Processing and Interpretation of Experimental Data*

It is indicated from Eq. 38.2 that the water jet velocity can be controlled both by the velocity of the striker bar and the ratio. According to the Hopkinson bar loading theory, the striker bar speed can be controlled by the pressure and the length of the striker bar. In this experiment, the length of the striker bar is constant, so the striker bar speed can be controlled only by the pressure.

In experimenting, four loading conditions are investigated with each condition repeating for three times. Figure 38.5. shows the emission processes recorded by the high-speed camera under different conditions.

For different conditions, different pressures are used to produce the speed of the striker bar, and the stress wave signal in the incident bar is measured. Then the average

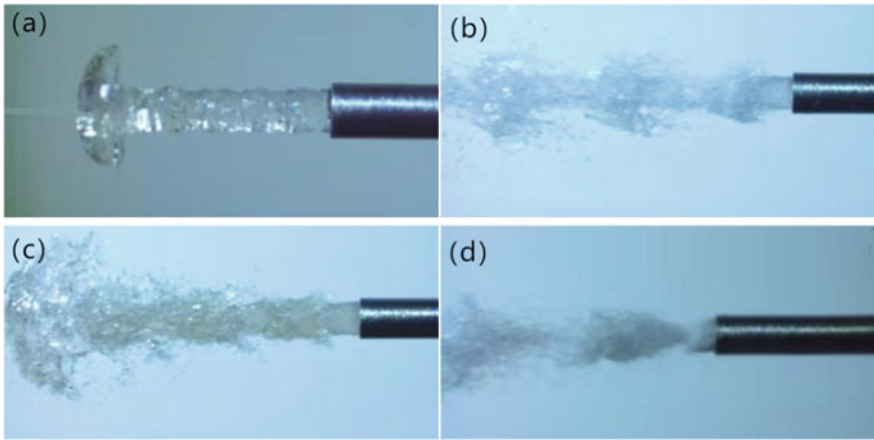


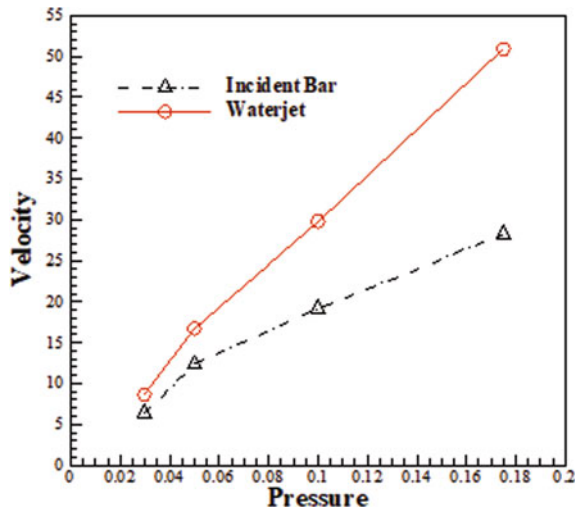
Fig. 38.5 Jet recorded by high-speed cameras under different conditions, **a** 0.03 MPa; **b** 0.05 MPa; **c** 0.10 MPa; **d** 0.175 MPa

value of the peak velocity is calculated at the end of the incident bar. Alternatively, the jet velocity is also measured by the photos taken by the high-speed camera, and the average value of the three experiments is obtained to depict in Fig. 38.6.

It is found that the velocity of the raindrop jet increased with the enhancement of loading speed, and the increase is greater than the loading speed the raindrop velocity increases, and the final jet velocity can reach 50 m/s. The mass of the high-speed raindrop emission system designed in this paper can be calculated by Eq. 38.4.

$$m = \rho \cdot V \tag{38.4}$$

Fig. 38.6 Comparison of peak velocity of incident bar end and jet



where ρ is the density of water, V is the volume of water jet ejected by the emission system under the action of each stress wave, respectively. It can be calculated by Eq. 38.3, and the mass of raindrop is calculated to be 365.03 mg.

38.4 Conclusions

Based on the experimental investigations of multistage high-speed raindrop emission system, the main findings are summarized as follows:

- (1) Based on Hopkinson pressure bar, a high speed raindrop emission system is built and implemented for raindrop emissions.
- (2) An intermittent multistage high speed raindrop emission system is constructed. The multistage emission can be observed by high-speed camera. The results show that the raindrop velocity increases to a certain extent under different loading speeds. The specifications can be achieved as 50.90 m/s of the ejection velocity, 365.03 mg of raindrop mass and more than 5 times of the interval times.

References

1. Hong, Y.K., Moon, K.H.: Experimental research on a waterjet to simulate erosion by impact of a water drop. *Wear* **368–369**, 116–123 (2016)
2. Field, J.E.: ELSI conference: invited lecture: liquid impact: theory, experiment, applications. *Wear* **233–235**, 1–12 (1999)
3. Adler, W.F.: Rain impact retrospective and vision for the future. *Wear* **233–235**, 25–38 (1999)
4. Carolyn, W., et al.: A discussion of rain erosion testing at the United States air force rain erosion test facility. *Wear* **186–187**, 384–387 (1995)
5. Adler, W.F., Boland, P.L.: Multiparticle supersonic impact test program. *Proc. SPIE Int. Soc. Opt. Eng.* **1326**, 268–279 (1990)
6. Seward, C.R., Pickles, C., Marrah, R., et al.: Rain erosion data on window and dome materials. Window and Dome Technologies and Materials III. International Society for Optics and Photonics, 1992, 1760
7. Seward, C.R., Coad, E.J., Pickles, C., et al.: The liquid impact resistance of a range of IR-transparent materials. *Wear* **186–187**(part-P2), 375–383 (1995)
8. Obara, T., Bourne, N.K., Field, J.E.: Liquid-jet impact on liquid and solid surfaces. *Wear* **186–187**(part-P2), 388–394 (1995)
9. Ying-Gang, M., Yu-Long, L., Hong-Yuan, L., Qiong, D., Luming, S., Yiu-Wing, M., Ya-Zhou, G., Tao, S., Hai-Tao, H., Fa-Qin, X., Long, Z., Yong-Jian, M., Wei, Q.: Determination of dynamic elastic modulus of polymeric materials using vertical split Hopkinson pressure bar. *Int. J. Mech. Sci.* **108–109**, 188–196 (2016)
10. Miao, Y., Du, W., Yin, J., Zeng, Y., Wang, C.: Characterizing multi mechanical behaviors for epoxy-like materials under wide strain rate range. *Polymer Test.* **116**, 107804 (2022)
11. Miao, Y.: On loading ceramic-like materials using split Hopkinson pressure bar. *Acta Mechanica* **229**, 3437–3452 (2018)

12. Miao, Y.: Critical appraising of Hopkinson bar techniques for calibrating high accelerometers. *Metrol. Measur. Syst.* **26**(2), 335–343 (2019)
13. Han, Z., Song, Y., Liu, Y., He, H., Chai, M., Miao, Y.: Coupling effect of hydrogen and strain rate on 2.25Cr1Mo0.25V steel deformed over wide strain rate ranges. *Int. J. Hydro. Energy* **48**(2), 798–815 (2023)

Chapter 39

Design of Long-Span Continuous Beam Bridge with Corrugated Steel Webs Constructed by Cantilever Assembly



Qing Wang, Wenyao Peng, Wen Zhong, Lizhi Lu, Yong Liu, and Rong Liu

Abstract Bridge prefabrication and assembly construction technology has been popularized and applied from normal span bridges to large span bridges. The Nanyang Xiangjiang River Bridge in Wushi-Yiyang Highway is facing severe challenges such as: extreme environmental protection requirements in Dongting Lake area, deep and soft foundation and short construction period etc. The bridge adopts $(76.3 + 3 \times 120 + 76.3)$ m span corrugated steel web composite box girder with variable cross-section depth, erecting by factory prefabrication and site assembly. The design concept innovation and detailed structure of the bridge are introduced in this paper. In addition, the construction process and operation state of the bridge are simulated by finite element methods. The calculation results show that the overall bearing capacity of the bridge, the shear bearing capacity of the corrugated steel webs, the horizontal shear bearing capacity of the corrugated steel web connectors, and the bending bearing capacity of the corners of the corrugated steel web connectors meet the stress requirements. And the anti-slip margin coefficient of the corrugated steel web connectors is above 1.29, while the maximum tensile stress of the external prestressed steel strand of the bridge is 1043 MPa. At present, the bridge has been completed and opened to traffic, saving the construction period of 4 months, providing a significant reference for similar projects.

Keywords Cantilever assembled bridge · Composite beam with corrugated steel webs · Structural design · Construction technology · Finite element simulation · External prestress

Q. Wang · L. Lu · Y. Liu (✉) · R. Liu
Hunan Provincial Communications Planning, Survey and Design Institute Co., Ltd., Changsha, China
e-mail: liushahust@163.com

W. Peng · W. Zhong
Hunan Pingyi Expressway Construction and Development Co., Ltd., Yueyang, China

Y. Liu
School of Civil Engineering, Central South University, Changsha, China

39.1 Introduction

The Wushi-Yiyang Highway is located in the northeast of Hunan Province and the south edge of Dongting Lake. The Nanyang Xiangjiang River Bridge of Wushi-Yiyang Highway crosses the west branch of Xiangjiang river in Hunan Province. The bridge site belongs to the Dongting Lake plain landform, with flat terrain and extensive farmland. The construction of the bridge faces the following severe challenges: the ecological environment protection is extremely important in the lake area; at the same time, the foundation overburden in the lake area is very deep, and the pile foundation in the gravel layer is difficult to form holes. As the control project of the highway project, the construction period of the bridge is relatively short.

Bridge prefabrication and assembly can effectively reduce the impact on the environment, shorten the construction period and ensure the construction quality, which is an important direction of bridge engineering development [1–4]. Bridge prefabrication and assembly technology has gradually been popularized and applied from small and medium span bridges to large span bridges. There have been construction of long-span concrete cantilever girder bridges in China, such as Xiushan Bridge in Daishan County, Zhejiang Province. At the same time, the segmental assembled corrugated steel webs bridge is mainly used in small and medium span bridges of equal height [5–10]. The construction of Nanyang Xiangjiang River Bridge is facing great technological challenges.

The bridge adopts $(76.3 + 3 \times 120 + 76.3)$ m span corrugated steel web composite box girder with variable cross-section depth, erecting by factory prefabrication and site assembly. The design concept innovation and detailed structure of the bridge are introduced in this paper. A comprehensive and systematic finite element simulation is carried out for the construction and operation of the bridge. The results show that the design parameters of the bridge are reasonable and feasible.

39.2 Bridge Scheme

Nanyang Xiangjiang River Bridge crosses the west branch of the Xiangjiang River. The main channel of the bridge site is about 400 m wide. The provincial highway S308 Linzikou Xiangjiang River Bridge, about 5 km downstream, is a 4×100 m continuous beam. From the perspective of controlling the project cost, two one-way navigation holes are adopted to reduce the span of the main bridge. Taking into account the river terrain, flood control needs and other factors, the plan of $(76.3 + 3 \times 120 + 76.3)$ m continuous beam is proposed.

According to the previous bridge design experience in the lake area, the continuous beam with a span of about 120 m is a more economical bridge type structure. Considering the current construction level of bridges, the comparison and selection of two structural schemes, corrugated steel web PC composite beam and prestressed concrete box beam, are emphasized (Table 39.1).

Table 39.1 Comparison and selection of main bridge schemes

Bridge schemes	Composite beam with corrugated steel webs	Prestressed concrete continuous beam
Economy	Good	Good
Progressiveness technology	Relatively advanced	Traditional
Stress performance	The bending resistance of the top and bottom plates and the shear resistance of the steel webs avoid the web cracking problem. The structure has a light dead weight, the torsion resistance of the main girder is weak, and the bending resistance is reduced. The beam height needs to be appropriately increased	The overall rigidity of the structure is large, and there is a risk of cracking in the concrete web, so it is necessary to pay attention to the vertical prestress tension control
Construction difficulty	The construction technology is relatively mature, which saves the binding of web reinforcement, concrete pouring and web steel tendon tensioning. However, the construction of top and bottom plate connection is relatively complicated. The beam section is relatively light and suitable for segmental assembly construction	The construction technology is mature and the construction difficulty is small. The weight of the section is slightly heavier during the cantilever construction
Pile length	The pile length is relatively short due to the lighter dead weight of the girder	The pile length is relatively long due to the heavier dead weight of the girder
Durability	Good durability due to no cracking risk of the corrugated steel web	If the construction and maintenance are improper, the concrete web is easy to crack, and the durability of the structure will be significantly reduced after the cracks occur
Repair and maintenance	The extracorporeal cable can be replaced with good maintainability; Corrugated steel webs need regular anti-corrosion coating, and the cost is high	The maintenance and maintenance technology is mature, and the maintenance cost of the whole life cycle is high
Landscape effect	Good	Poor
Scheme selection	Selected	

The composite beam with corrugated steel webs can completely avoid that the webs of traditional all-concrete box girder are easy to crack, and improve the durability of the structure. The dead weight of the girder with corrugated steel webs is significantly lower than that of the concrete girder, which is more convenient for the use of prefabricated segmental cantilever construction. The light dead weight of the girder segment can effectively shorten the length of the pile foundation, making the



Fig. 39.1 Aerial view of the Nanyang Xiangjiang bridge

corrugated steel web composite box girder reflect better economy. In comprehensive consideration, the 120 m corrugated steel web composite box girder scheme is recommended for the main bridge (Fig. 39.1).

39.3 Design Parameters

39.3.1 Technical Standards

- (1) Highway grade: Expressway;
- (2) Design speed: 100 km/h;
- (3) Design reference period: 100 years;
- (4) Design safety level: Level 1;
- (5) Subgrade width: Standard width 26 m;
- (6) Load class: Highway—class I;
- (7) Bridge width: Sidewalk is set in the river-crossing section. The total width of the bridge is 29.5 m, while the width of the single bridge is 14.5 m. The spacing between the two bridges is 0.5 m;
- (8) Channel grade: the planned channel grade of the west branch of the Xiangjiang River is II (3), and the one-way navigation clearance is 75×10 m;
- (9) Design flood: 1/300.

39.3.2 Building Materials

Concrete. The concrete of 120 m span composite box girder is C60 concrete, and the concrete of main bridge hollow pier is C50 concrete according to Chinese codes.

Steel. The tensile strength standard of low relaxation prestressed steel strand is 1860 MPa, while the external prestressed steel strand is made of epoxy steel strand with diameter of 15.2 mm and standard strength of 1860 MPa.

Q345qD is adopted for the corrugated steel webs and their connectors of the main bridge. The embedded steel pipe of steering gear is seamless steel pipe. Shear nails are cylindrical head welding nails. Grade 10.9 is used for high-strength bolts.

Structure joint adhesive. The 120 m box girder segment assembly joint adopts the prefabricated segment assembly structure joint adhesive, whose main characteristics shall meet the following requirements: high strength, high elastic modulus, low creep, waterproof and corrosion resistance; High thixotropy, no sagging, no dripping. It is easy to compact, the glue joint has no water seepage, and the bonding strength is not higher than the concrete body strength. It has good applicability, can be used for damp surface and low temperature construction, and can be operated for a long time, but it has rapid curing and rapid strength development; Good toughness, fatigue resistance and impact resistance; Safe and non-toxic.

The technical performance shall comply with FIP standards, and the main indicators are as follows:

Applicable period: ≥ 20 min.

Thixotropy: no sagging above 3 mm.

Compressive strength: 12h ≥ 20 MPa, 24h ≥ 60 MPa, 7d ≥ 75 MPa.

Creep: instantaneous compression ≥ 8000 MPa, delayed compression ≥ 6000 MPa.

Shear strength (oblique shear): ≥ 12 MPa.

Bending strength: completely damaged by concrete body.

Damp-heat aging resistance (strength reduction rate): 90 days (50°, 95% RH) $\leq 12\%$.

39.3.3 Structural Parameters

Girder design. The main bridge is (76.3 + 3 × 120 + 76.3) m rigid frame-continuous composite system, the main girder is corrugated steel web variable cross-section PC composite girder, prefabricated cantilever assembly construction, a total of 13 cantilever assembly segments.

Single-box single-chamber section is adopted for single main girder. The height of the main girder section and the thickness of the bottom plate vary according to 1.8 times parabola. The height of the root beam of the standard section of the main girder is 7.5 m, and the thickness of the bottom plate is 0.9 m. The height of the cast-in-place girder section of the midspan and side span is 3.5 m, and the thickness of the bottom plate is 0.3 m. The top plate of the box girder is 14.5 m wide, the bottom plate is 8.1 m wide, and 2% one-way cross slope is adopted. The center distance of corrugated steel webs on both sides of the box girder is 7.5 m, and the cantilever length is 3.5 m. The thickness of the top plate is 0.3 m, the thickness of

the cantilever end is 0.2 m, and the thickness of the linear thickening is 0.5 m, and then the thickness of the cantilever root is 0.7 m; The webs are made of corrugated steel plates, with the thickness of 12, 16, 20, 22 and 24 mm from the cast-in-place section of the middle or side span to the root of the box girder (Fig. 39.2).

The corrugated steel webs of each section are connected by lap continuous fillet welding joints and high-strength bolts during construction. The connection between corrugated steel web and bottom plate adopts angle steel connectors. The connection with the top plate adopts double-hole steel plate connector (Twin-PBL connection) (Fig. 39.3).

Cast-in-situ concrete lining is set on the inside of the corrugated steel web of the box girder 1 and 2# girder segments and the end support segments. The bonding between the corrugated steel web and the lining concrete is realized by welding studs. The 0# girder section of the main girder is provided with a pier top diaphragm with a thickness of 3.2 m; The beam end is provided with an end diaphragm with a thickness of 1.8 m, and two sliding bearings are arranged in the transverse direction of the bridge under the end beam. One transverse diaphragm is set for the 6# and 11# midspan girder segments respectively, and the 11# girder segment diaphragm

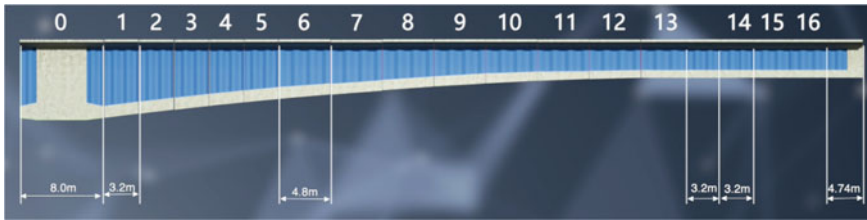


Fig. 39.2 Overview of girder segment division

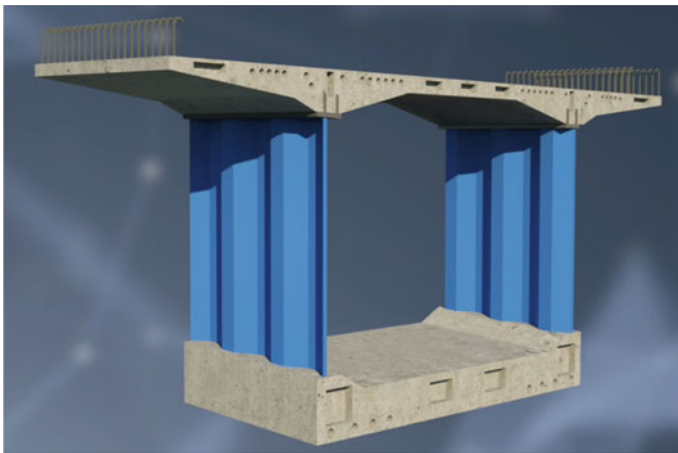


Fig. 39.3 3D model of girder segment

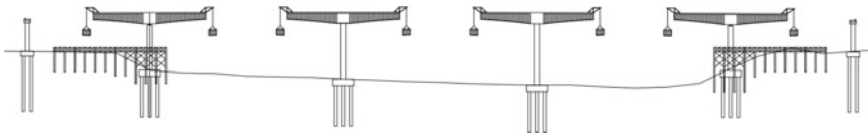


Fig. 39.4 Diagram of girder segment cantilever assembly

is also used as the external pre-stressed steering block of the midspan; A transverse diaphragm is set at girder sections 6, 11 and 14 of side span, and the diaphragm of girder sections 11 and 14 is also used as external prestressed steering block of side span.

The main girder is divided into 4 cantilever “T” structures, one “T” structure is divided into 13 girder segments on one side, the length of girder segment 0# is 8.0 m, and the 1–13 girder segments are $5 \times 3.2 \text{ m} + 8 \times 4.8 \text{ m}$ (Fig. 39.4). The cast-in-place section at the side span is 4.74 m long, and the length of 14–16# beam sections is 3.2 m. The 0# girder section is cast-in-place on the pier top bracket, the side span cast-in-place section is cast-in-place on the bracket, the side span 14–16# girder section is assembled on the bracket, and the rest of the beam sections are cantilever assembled, the maximum weight of the cantilever section is 1520 kN.

In order to facilitate maintenance during construction and operation, each partition is provided with manhole.

Prestressed system. The main girder adopts longitudinal, transverse and vertical prestress, and the longitudinal internal prestress tendon is divided into the early tendon of the top plate, the late tendon of the top plate and the late tendon of the bottom plate. In view of the limited space for placing the prestress on the top and bottom of the box girder, the external cable is used to replace part of the internal cable. The outer cable steering block is in the form of diaphragm.

39.3.4 Construction Process of Cantilever Assembly of Box Girder

The overall process of cantilever assembly construction of 120 m box girder is as follows: install temporary bracket to cast the 0# section of the main girder, install the bridge deck crane, install the 1–13# girder section symmetrically, cast in situ at the end of the side span, lift the 14–16# beam section, lift the side span closure section, and lift the middle span closure section.

The segmental prefabrication of box girder shall be carried out in advance according to the schedule of assembly construction period.

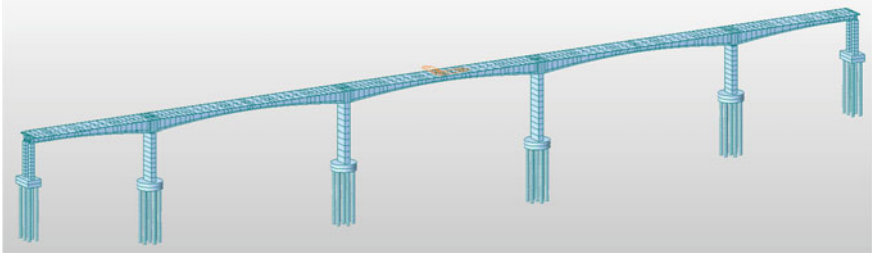


Fig. 39.5 Finite element model of Nanyang Xiangjiang bridge

39.4 Finite Element Simulation

39.4.1 Model Establishment

Midas Civil is used to establish the finite element model of the whole bridge. The calculation model is shown in Fig. 39.5.

The model simulates the stress state of the bridge during construction and the load combination during operation in detail. In the calculation, permanent actions such as structural dead weight, concrete shrinkage and creep, foundation displacement, and variable actions such as vehicle load, impact force, braking force, crowd load, temperature action and bearing friction are considered.

The main girder and pier in the calculation model are simulated by beam element. The boundary conditions are as follows: the middle 2 piers are consolidated by pier and girders, and the rest piers are supported by bearings.

39.4.2 FEM Simulation Results

Calculation results of ultimate limit state. The checking calculation results of the bending capacity of the normal section of the main girder at the ultimate limit state are shown in Table 39.2.

The maximum shear stress of the corrugated steel web of the main girder in the ultimate state of bearing capacity is 122.5 MPa, which meets the relevant requirements of strength and combined buckling resistance. The design value of the maximum horizontal shear force per unit length at the connection between the corrugated steel web and the top and bottom plates is 1685.8 kN, and the checking calculation of the horizontal shear bearing capacity of the connector meets the requirements of relevant specification.

Calculation results of serviceability limit state. The normal section crack resistance calculation of the main girder top and bottom slab concrete in the normal service limit state meets the requirements, in which the minimum compressive stress at the

Table 39.2 Checking calculation of bending bearing capacity of normal section of Nanyang Xiangjiang river bridge

Control section	Design value of bending moment (kN * m)	Bending capacity (kN * m)	Safety factor
Section of main pier top	969,488	1,363,077	1.41
Mid-span	189,883	226,663	1.19
Secondary midspan midspan	170,445	211,103	1.24
Midspan of side span	124,156	165,507	1.33

lower edge of the midspan is 2.0 MPa, and the minimum compressive stress at the upper edge of the pier top is 0.2 MPa.

The design value of the maximum horizontal shear force per unit length at the connection between the corrugated steel web of the main girder and the top and bottom plates in the serviceability limit state is 1126.1 kN, and the anti-slip and stress checking calculation of the connectors meet the requirements of this specification.

The maximum tensile stress of the internal prestressed steel strand in the tension zone is 1202.9 MPa, and the maximum tensile stress of the external prestressed steel strand is 1043.0 MPa, which meets the specification requirements.

After eliminating the long-term deflection caused by the dead weight of the structure, the maximum deflection of the main girder is 6.1 cm, $f/L = 1/1967 < 1/600$, which meets the specification requirements.

Stress checking calculation of components under persistent and transient conditions. The maximum compressive stress of the normal section of the concrete at the top of the main girder and the bottom plate under the standard combination of persistent conditions meet the requirements of the specification, of which the maximum compressive stress at the upper edge of the top plate is 17.5 MPa, and the maximum compressive stress at the lower edge of the bottom plate is 13.9 MPa.

During the construction stage, the maximum compressive stress of the top and bottom concrete sections of the main girder meet the requirements of the specification, including the maximum compressive stress of the upper edge of the top plate of 16.5 MPa and the maximum compressive stress of the lower edge of the bottom plate of 17.1 MPa.

The maximum tensile stress of internal prestressed strand is 1261.5 MPa, and the maximum tensile stress of external prestressed strand is 1091.0 MPa, meeting the specification requirements.

39.5 Conclusion

Based on the engineering background of the Nanyang Xiangjiang River Bridge of Wushi-Yiyang Highway, a long-span cantilever composite continuous beam with corrugated steel webs is proposed creatively in this paper, which successfully overcomes the difficulties of high environmental protection requirements, thick foundation coverage and short construction period, and obtains the following conclusions:

- (1) Based on the construction conditions of the bridge, the main girder types of the bridge are compared and analyzed, and the long-span cantilever corrugated steel web composite continuous beam scheme is determined.
- (2) The design parameters of the bridge are comprehensively introduced from the aspects of design standards, building materials, structural details and construction methods.
- (3) The finite element analysis for the construction and operation stages of the bridge shows that all indicators of the bridge meet the relevant requirements and have sufficient bearing capacity and good service performance.
- (4) The Nanyang Xiangjiang River Bridge has been completed and opened to traffic, and has achieved good social response, providing an important reference for similar projects.

Acknowledgements This research was supported by the Transportation Technology Project of Hunan Province (201914).

References

1. Hunan Provincial Communications Planning, Survey and Design Institute Co., Ltd.: Detailed design drawing of Nanyang Xiangjiang bridge (2018)
2. Zhang, Z.C., Liu, X.L., Hu, L.Y., et al.: Zig-zag theory for concrete beams with corrugated steel webs. *Eng. Struct.* **258** (2022)
3. Dai, G.L., Su, M., Liu, W.S., Chen, Y.F.: New Songhua river bridge: a continuous girder, tied arch, hybrid bridge with four rail tracks in Harbin, China. *Struct. Eng. Int.* **26**(3), 254–259 (2016)
4. Zhao, H., Gou, H., Ni, Y.S., Xu, D.: Reinforcement design of the top and bottom slabs of composite box girder with corrugated steel webs. *Steel Compos. Struct.* **33**(4), 537–550 (2019)
5. Su, Q., Zhang, C., Zhao, W., Wan, S.: Parametric analysis of seismic response of PC continuous beam bridge with corrugated steel webs. In: AIP Conference Proceedings. AIP Publishing LLC AIP Publishing (2019)
6. Cheng, Z.Q., Liang, S.H., Lv, G.B., Zhao, Z.D.: Analysis on Local Mechanical Behavior in Incremental Launching Method of Pre-pressed Concrete Composite Box Girder with Corrugated Steel Webs. *DEStech Publications* (2017)
7. Su, M., Gong, S., Liu, Y., Peng, H.: Flexural behavior of RC beams strengthened with fully or partially prestressed near-surface mounted FRP strips: an experimental investigation. *Eng. Struct.* **262**, 114345 (2022)

8. Lu, Y.: Effect of different connectors on concrete composite box-girders with corrugated steel webs. *J. Harbin Inst. Technol. (New Ser.)* **25**(02), 77–88 (2018)
9. Yuan, Z.Y., Li, L., Liu, Q., Hou, J.: Analysis and experimental study of transverse internal force in composite box girder with corrugated steel webs. *China J. Highway Transp.* **28**(147(11)), 77–85 (2015)
10. Chen, Y., Dong, J., Xu, T.: Composite box girder with corrugated steel webs and trusses—a new type of bridge structure. *Eng. Struct.* (2018)

Chapter 40

Meshless Generalized Finite Difference Method for Gas–Water Two-Phase Flow Equation of Complex-Shape Shale Gas Reservoirs



Wentao Zhan, Liang Pu, Sheng Lei, Zhao Hui, Hao Huang, and Yunfeng Xu

Abstract In this paper, the meshless generalized finite difference method (GFDM) is applied to the gas–water two-phase flow equation of complex-shape shale gas reservoirs. GFDM is a regional meshless method, in which the partial derivatives of unknown functions at any node can be expressed as differential approximations of other node functions in the node influence domain by using Taylor series expansion of multiple functions and least squares approximation. It overcomes the dependence of the discrete fracture method (DFM) on the grids and can obtain the finite difference approximation with higher precision. Compared with DFM, the meshless GFDM is based on the point cloud discretization which is more flexible to describe the complex geometric of the field case. Thus, reducing the computational freedom of the numerical model and the calculation cost. In the last, the numerical examples of the complex boundary demonstrate the computational performance of the proposed method for gas–water two-phase flow in shale gas reservoirs. In conclusion, this work provides an efficient meshless GFDM-based calculation method for solving the gas–water two-phase flow problem with the complex boundary conditions in shale gas reservoirs, and reveals the tremendous application potential of meshless GFDM in the numerical simulation of shale reservoirs with the complex boundary conditions.

Keywords Generalized finite difference method · Shale gas reservoirs · Gas–water two-phase simulation

W. Zhan · L. Pu · S. Lei · Z. Hui · H. Huang (✉) · Y. Xu (✉)
School of Petroleum Engineering, Yangtze University, Wuhan, Hubei, China
e-mail: 2022730022@yangtzeu.edu.cn

Y. Xu
e-mail: 201972114@yangtzeu.edu.cn

40.1 Introduction

Shale gas resources are abundant and widely distributed in the world. Shale gas plays an extremely important role in energy supply structure. It is a kind of clean and efficient energy resource and chemical raw material, and it has many values to accelerate the exploration, development and utilization of shale gas. Shale gas plays an important role in meeting the huge demand for clean energy for social and economic development, controlling greenhouse gas emissions, and building resource-saving and environment-friendly production and consumption patterns.

At present, numerical simulation technology is the most economical and effective means to reproduce oil and gas migration in the process of shale gas development. The matrix porosity and permeability of shale gas reservoir are poor, and the natural fracture heterogeneity is obvious, and fracturing is a common technical means of exploitation. During the fracturing process, fracturing fluid can easily invade the reservoir, resulting in a low flowback rate. Therefore, it is very necessary to study the gas–water two-phase seepage and the law of gas–water production in shale gas reservoirs to guide the optimization of shale gas production measures and the prediction of shale gas production. Xia et al. [1] considered the non-equilibrium effect of the interaction between adsorbed gas and free gas in shale reservoir. Fan et al. [2] defined a new parameter representing the ratio of adsorption and desorption gas to elastic release of free gas in shale reservoir, and established a mathematical model of unstable seepage in shale gas reservoir considering the adsorption and desorption process. Yin et al. [3] applied Langmuir isothermal adsorption curve and Fick's quasi-steady-state diffusion law to describe mathematically the desorption characteristics and diffusion characteristics of adsorbed gas, and established a mathematical model of gas–water two-phase seepage in shale gas reservoir. Zhou et al. [4] established a dimensionless imbibition velocity calculation method based on the basic gas–water two-phase seepage theory and considering the influence of various factors. However, this model is aimed at extremely low permeability reservoir, and it needs to be verified whether it is applicable to shale gas reservoir. The trilinear flow model of multi-fractured horizontal Wells proposed by Brown et al. [5] has been widely used. This model assumes that the reservoir is a homogeneous dual medium. However, later studies have shown that the heterogeneity of reservoir porosity/permeability after fracturing is very obvious [6, 7]. In the reformed area, due to the retention of fracturing fluid, the water saturation in the pores is higher than the bound water saturation, that is, there is body phase water. As a result, obvious gas–water two-phase flow exists in shale production, and its migration law is relatively complex [8, 9].

Generalized finite difference method (GFDM) is a grid-free method emerging in recent years. The initial generalized finite difference method was developed by Jesen [10], Perrone [11] and Liszka [12] under the framework of finite difference calculation. These methods are based on the grid and the application of distance function to capture the necessary nodes to implement operations. The main core idea of the GFDM is to use the weighted least squares method to find the minimal value of the residual function and introduce the weight function to characterize the degree of influence of the nodes at different distances to the central node [13]. In other words, the partial derivatives of the unknown parameters in the differential equation are expressed as linear combinations of the values of the functions of the adjacent nodes, overcoming the dependence of the traditional method on the grid. The method can construct applicable forms of field node distribution according to different geological models, and the generated nodes fit to the undulating surface or boundary, which is suitable for dealing with irregular boundary or undulating interface problems. Some scholars have applied GFDM to fluid mechanics [14–16], heat conduction equations [17], and interface problems [18]. Numerous research results show that the generalized finite difference method has unique advantages and broad application prospects in dealing with complex problems. In this paper, the meshless method is applied to the numerical simulation of gas–water two-phase flow in shale gas reservoirs to provide new ideas for the numerical simulation of gas–water two-phase flow in shale gas reservoirs.

40.2 Control Equations for Gas–Water Two-Phase Flow in Shale Gas Reservoirs

It is assumed that the model of horizontal shale gas wells is a dual media model of fracture-matrix, which is divided into two systems of fracture and matrix. Shale gas is mainly stored in the matrix system, and the fracture network is the main seepage channel. Both water and gas phases can flow in the fractures, but only single-phase flow of gas phase flows in the matrix, without considering the flow of water phase in the matrix. The flow between substrates is neglected, the effects of gravity, gas slippage and the capillary forces are ignored. Fluid and rock is assumed to be slightly compressible. The gas- water phases flow control equations in the fracture system are given below.

Gas-phase mass conservation equation:

$$\nabla(\rho_{fg}v_{fg}) + q_g + q_{mfg} = \frac{\partial}{\partial t}(\phi_f \rho_{fg} S_g) \quad (40.1)$$

Gas-phase flow equation

$$v_{fg} = -\frac{K_f K_{rg}}{\mu_{fg}} \nabla p_{fg} \quad (40.2)$$

where, v_{fg} is the gas percolation rate in the fracture. ρ_{fg} is the density of natural gas in the fracture. q_g is the source and sink term of gas and represents the mass flow rate of injected or produced fluid per unit volume of rock. ϕ_f is the fracture porosity of shale reservoir. K_f is the permeability of shale reservoir fractures. S_g is the gas saturation in the fracture. p_{fg} is the gas phase pressure in the crack. K_{rg} is the relative permeability of gas phase in fracture system. μ_{fg} is the viscosity of natural gas in fractures.

Therefore, the mathematical model of gas phase flow in shale reservoir fractures is as follows:

$$\nabla \left(\alpha \frac{K_f K_{rg} \rho_{fg}}{\mu_{fg}} \nabla p_{fg} \right) + \alpha \frac{\sigma K_m \rho_{mg}}{\mu_m} (p_m - p_{fg}) + q_g = \alpha \frac{\partial}{\partial t} (\phi_f \rho_{fg} S_g) \quad (40.3)$$

Similarly, the water phase flow equation in fractures can be rewritten as:

$$\nabla \left(\alpha \frac{K_f K_{rw} \rho_w}{\mu_w} \nabla p_w \right) + q_w = \alpha \frac{\partial}{\partial t} (\phi_f \rho_w S_w) \quad (40.4)$$

where K_{rw} is water phase relative permeability. ρ_w is the density of water in the crack. μ_w is the viscosity of water in the crack. p_w is the water phase pressure in the fracture. q_w is the output term of water. S_w is the water saturation in the fracture.

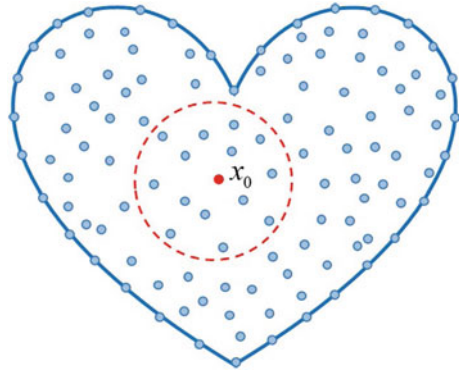
40.3 Basic Theory of Generalized Finite Differences

As shown in Fig. 40.1, combined with the specific shape of the solution domain, the computational domain is described discretely by uniform or non-uniform matching nodes. For the node x_0 in the solution domain, the neighboring points are selected to form a sub-region (circular region in Fig. 40.1), and the point is taken as the central point. The Taylor expansion of any point in the sub-region at the central point is expressed as:

$$\begin{aligned} u_i = u_0 &+ h_i \frac{\partial u_0}{\partial x} + l_i \frac{\partial u_0}{\partial y} + \frac{h_i^2}{2} \frac{\partial^2 u_0}{\partial x^2} + \frac{l_i^2}{2} \frac{\partial^2 u_0}{\partial y^2} \\ &+ h_i l_i \frac{\partial^2 u_0}{\partial x \partial y} + o(x^3, y^3), \quad i = 1, 2, \dots, S \end{aligned} \quad (40.5)$$

where $h_i = x_i - x_0$, $l_i = y_i - y_0$ represent the distance between node i in the subdomain and the central node in the x and y directions respectively.

Fig. 40.1 Computational domain discretization and influence domain



The problem considered in this paper requires the unknown function to have second-order continuity, where the Taylor expansion is retained to the second-order term, i.e., second-order accuracy. To improve the differential accuracy, the Taylor expansion can be retained to a higher order. Define the error weight function

$$B_u = \sum_{i=1}^S \left(u_0 - u_i + h_i \frac{\partial u_0}{\partial x} + l_i \frac{\partial u_0}{\partial y} + \frac{h_i^2}{2} \frac{\partial^2 u_0}{\partial x^2} + \frac{l_i^2}{2} \frac{\partial^2 u_0}{\partial y^2} + h_i l_i \frac{\partial^2 u_0}{\partial x \partial y} \right)^2 \omega_i^2(h_i, l_i) \tag{40.6}$$

where ω_i is the weight function at node i . The weight function is generally taken as a quartic spline function [13].

$$\omega_i = \begin{cases} 1 - 6\left(\frac{r_i}{r_m}\right)^2 + 8\left(\frac{r_i}{r_m}\right)^3 - 3\left(\frac{r_i}{r_m}\right)^4 & r_i \leq r_m \\ 0 & r_i > r_m \end{cases} \tag{40.7}$$

where r_i is the Euclidean distance from node x_i to node x_0 . r_m is the radius of the influence domain of node x_0 .

Let D_u u be all the partial derivatives that can occur at the center point.

$$D_u = \left(\frac{\partial u_0}{\partial x}, \frac{\partial u_0}{\partial y}, \frac{\partial^2 u_0}{\partial x^2}, \frac{\partial^2 u_0}{\partial y^2}, \frac{\partial^2 u_0}{\partial x \partial y} \right)^T \tag{40.8}$$

According to the principle of weighted least squares, the minimum value of the error weight function is taken. Take the partial derivative of the error function with respect to D_u and make the value of the partial derivative to zero.

$$\frac{\partial B_u}{\partial D_u} = 0 \tag{40.9}$$

The following matrix equation can be obtained.

$$A_u \cdot D_u = b_u \tag{40.10}$$

where

$$A_u = \begin{pmatrix} \sum_{i=1}^S h_i^2 \omega_i^2 & \sum_{i=1}^S h_i l_i \omega_i^2 & \sum_{i=1}^S \frac{h_i^3}{2} \omega_i^2 & \sum_{i=1}^S \frac{h_i l_i^2}{2} \omega_i^2 & \sum_{i=1}^S h_i^2 l_i \omega_i^2 \\ \sum_{i=1}^S h_i l_i \omega_i^2 & \sum_{i=1}^S l_i^2 \omega_i^2 & \sum_{i=1}^S \frac{h_i^2 l_i}{2} \omega_i^2 & \sum_{i=1}^S \frac{l_i^3}{2} \omega_i^2 & \sum_{i=1}^S h_i l_i^2 \omega_i^2 \\ \sum_{i=1}^S \frac{h_i^3}{2} \omega_i^2 & \sum_{i=1}^S \frac{h_i^2 l_i}{2} \omega_i^2 & \sum_{i=1}^S \frac{h_i^4}{4} \omega_i^2 & \sum_{i=1}^S \frac{h_i^2 l_i^2}{4} \omega_i^2 & \sum_{i=1}^S \frac{h_i^3 l_i}{2} \omega_i^2 \\ \sum_{i=1}^S \frac{h_i l_i^2}{2} \omega_i^2 & \sum_{i=1}^S \frac{l_i^3}{2} \omega_i^2 & \sum_{i=1}^S \frac{h_i^2 l_i^2}{4} \omega_i^2 & \sum_{i=1}^S \frac{l_i^4}{4} \omega_i^2 & \sum_{i=1}^S \frac{h_i l_i^3}{2} \omega_i^2 \\ \sum_{i=1}^S h_i^2 l_i \omega_i^2 & \sum_{i=1}^S h_i l_i^2 \omega_i^2 & \sum_{i=1}^S \frac{h_i^3 l_i}{2} \omega_i^2 & \sum_{i=1}^S \frac{h_i l_i^3}{2} \omega_i^2 & \sum_{i=1}^S h_i^2 l_i^2 \omega_i^2 \end{pmatrix} \tag{40.11}$$

$$b_u = \left(\sum_{i=1}^S h_i (u_i - u_0) \omega_i^2 \quad \sum_{i=1}^S l_i (u_i - u_0) \omega_i^2 \quad \sum_{i=1}^S \frac{h_i^2}{2} (u_i - u_0) \omega_i^2 \quad \sum_{i=1}^S \frac{l_i^2}{2} (u_i - u_0) \omega_i^2 \quad \sum_{i=1}^S h_i l_i (u_i - u_0) \omega_i^2 \right)^T \tag{40.12}$$

The partial derivatives can be found everywhere in space.

$$\begin{cases} D_u = A_u^{-1} b_u = -M_0 u_0 + \sum_{i=1}^S M_i u_i \\ M_0 = \sum_{i=1}^S M_i \end{cases} \tag{40.13}$$

where M_i is the generalized finite difference coefficient of adjacent nodes.

40.4 The Control Equation Discretization and Boundary Conditions

Take upwind scheme for the mobility term. According to formula (40.3) and derivation rule, the governing equation of gas phase flow in fracture can be rewritten as

$$\begin{aligned} \frac{\partial}{\partial x} \left(\alpha \frac{k_f k_{rg} \rho_{fg}}{\mu_{fg}} \frac{\partial p}{\partial x} \right) + \frac{\partial}{\partial y} \left(\alpha \frac{k_f k_{rg} \rho_{fg}}{\mu_{fg}} \frac{\partial p}{\partial y} \right) + \alpha \frac{\sigma k_m \rho_{mg}}{\mu_m} (p_m - p_{fg}) \\ + q_g = \alpha \frac{\partial}{\partial t} (\phi_f \rho_{fg} S_g) \end{aligned} \tag{40.14}$$

The discrete scheme of formula (40.14) is obtained according to formula (40.13).

$$\alpha \frac{k_{f,ij}^{t+\Delta t} k_{rg,ij}^{t+\Delta t} \rho_{fg}^{t+\Delta t}}{\mu_{fg,ij}^{t+\Delta t}} \left(\sum_{i=0}^S (M_{3,i} + M_{4,i}) u_i \right) + \alpha \frac{\sigma k_{m,ij}^{t+\Delta t} \rho_{mg,ij}^{t+\Delta t}}{\mu_{m,ij}^{t+\Delta t}} (p_m^{t+\Delta t} - p_{fg}^{t+\Delta t}) + q_g^{t+\Delta t} = \alpha \frac{\phi_f^{t+\Delta t} \rho_{fg}^{t+\Delta t} S_g^{t+\Delta t} - \phi_f^t \rho_{fg}^t S_g^t}{\Delta t} \quad (40.15)$$

Similarly, the discrete scheme of generalized difference of water phase is obtained

$$\alpha \frac{k_{f,ij}^{t+\Delta t} k_{rw,ij}^{t+\Delta t} \rho_w^{t+\Delta t}}{\mu_{w,ij}^{t+\Delta t}} \left(\sum_{i=0}^S (M_{3,i} + M_{4,i}) u_i \right) + q_w^{t+\Delta t} = \alpha \frac{\phi_f^{t+\Delta t} \rho_w^{t+\Delta t} S_w^{t+\Delta t} - \phi_f^t \rho_w^t S_w^t}{\Delta t} \quad (40.16)$$

where the harmonic average of permeability and the arithmetic average of viscosity were used.

$$k_{f,ij}^{t+\Delta t} = \frac{2}{1/k_{f,i}^{t+\Delta t} + 1/k_{f,j}^{t+\Delta t}}$$

$$\mu_{\sigma,ij}^{t+\Delta t} = \frac{\mu_{\sigma,i}^{t+\Delta t} + \mu_{\sigma,j}^{t+\Delta t}}{2}, \quad \sigma = g, w \quad (40.17)$$

For the relative permeability of oil phase and water phase, the upwind format is adopted, i.e.

$$k_{r\sigma,ij}^{t+\Delta t} = \begin{cases} k_{r\sigma,i}(S_{w,i}^{t+\Delta t}) & \text{if } p_{\sigma,(i,j)}^{t+\Delta t} \geq p_{\sigma,i}^{t+\Delta t} \\ k_{r\sigma,i}(S_{w,i}^{t+\Delta t}) & \text{if } p_{\sigma,(i,j)}^{t+\Delta t} < p_{\sigma,i}^{t+\Delta t} \end{cases}, \quad \sigma = g, w \quad (40.18)$$

The first boundary condition can be expressed as:

$$p_{fg}(x, y, t)|_{\Gamma} = p_e(x, y, t) \quad (40.19)$$

There are two production modes of oil and gas well: constant bottom-hole pressure production and constant rate production. When the shale gas well is produced by the method of constant bottom-hole pressure, its boundary condition is as follows.

$$p_{wf}(x, y, t) = p_{wf}(t) \quad (40.20)$$

When a shale gas well is produced at a fixed rate, the boundary conditions are as follows

$$\begin{aligned} Q_g(x, y, t) &= Q_g(t) \\ Q_w(x, y, t) &= Q_w(t) \end{aligned} \tag{40.20}$$

40.5 Numerical Example

As shown in Fig. 40.2, this is a reservoir with complex boundaries. Γ_1, Γ_2 are the left and right boundaries, which are arcs with a radius of 100 m, and Γ_3, Γ_4 are the upper and lower boundaries, which are straight lines with a length of 200 m. All boundaries are constant pressure boundary conditions. There is a horizontal well in the middle of the reservoir that shoots 10 fractures in the formation. Figure 40.3 is the fine DFM model, which is used as the reference solution. Figure 40.4 is the meshless point cloud model with GFDM. The formation physical parameters are given below, as shown in Table 40.1.

Figure 40.5 shows the calculated fracture pressures for day 10 and day 100. Figure 40.6 draws the curves of daily gas production and water production calculated by the proposed method and the finite difference method respectively. It can be seen that the calculated results of the proposed method are very close to those of DFM on the whole, indicating the effectiveness of the proposed method. The proposed method can achieve the same accuracy as the finite difference method, but compared with the traditional finite difference method, the meshless method in this paper can be adapted to reservoirs with complex boundaries or geological conditions.

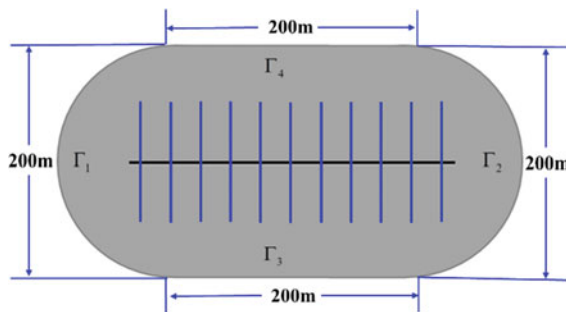


Fig. 40.2 Reservoir model

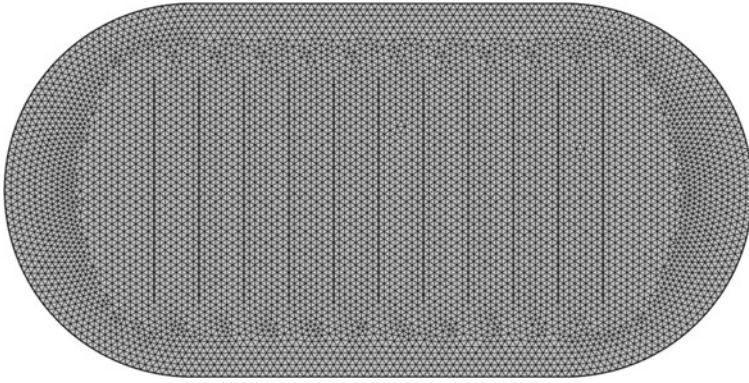


Fig. 40.3 Computational domain discretization by DFM

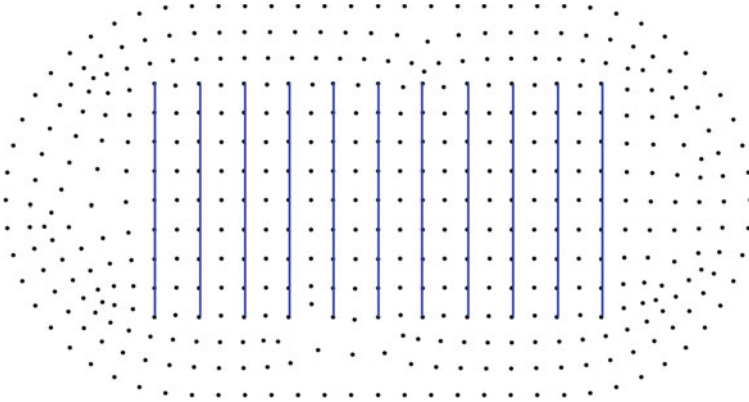


Fig. 40.4 Computational domain discretization by GFDM

Table 40.1 Physical parameters

Physical parameters	Value	Physical parameters	Value
Initial pressure p_i , MPa	20	Fracture system porosity ϕ_f	0.4
Fracture Permeability, mD	10	Initial water saturation, fraction	0.5
Crossflow coefficient, m^{-2}	0.2	Constant BHP p_{wf} , MPa	10
Matrix permeability, mD	0.01	Matrix porosity, fraction	0.2

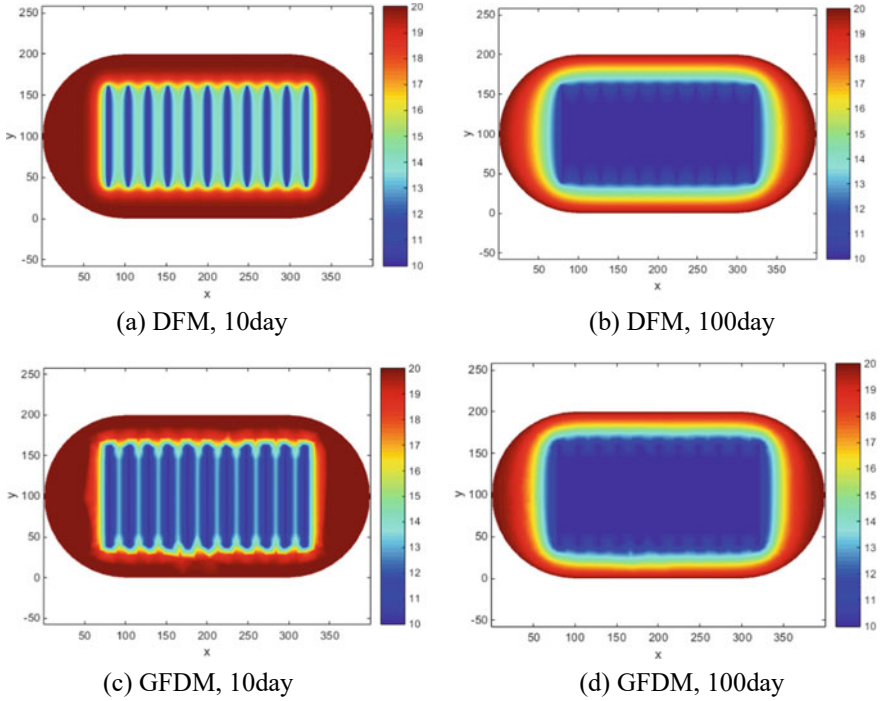


Fig. 40.5 Comparisons of the pressure profiles calculated by DFM and GFDM

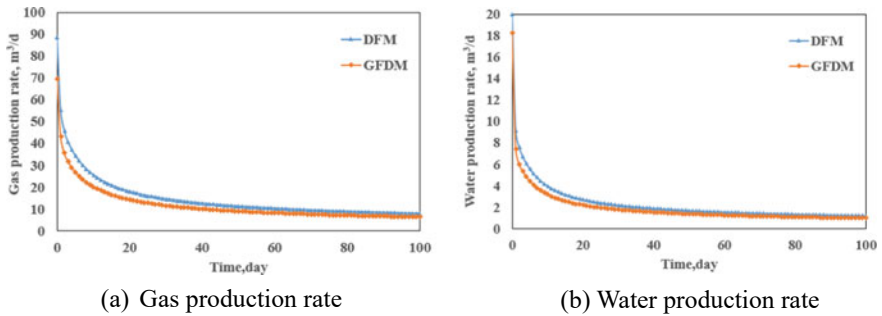


Fig. 40.6 Comparisons of gas and water production rates calculated by GFDM and DFM

40.6 Conclusion

In this paper, the meshless generalized finite difference method is used to calculate the gas–water two-phase flow problem in the dual medium of shale gas reservoirs with complex boundary. The discrete fracture model method of fine mesh generation is used as the reference solution. By comparing with the reference solution, it is

found that the proposed method is basically consistent with the reference solution in the case of irregular reservoir boundaries. Compared with traditional methods, the proposed method is free and flexible in describing reservoirs with complex boundaries or geological conditions, and can deal with complex geometry better. This work provides a new idea for numerical simulation of shale gas reservoirs with complex boundary.

References

1. Xia, Y., Jin, Y., et al.: The coupling of multi-physics for gas flow in shale reservoirs. *SCIENTIA SINICA Physica. Mechanica & Astronomica* **09**, 30–43 (2015)
2. Fan, D.Y., Yao, J., et al.: Transient flow model of stage-fractured horizontal wells in shale gas reservoirs. *J. China Univ. Petrol.* **38**(5), 116–123 (2014)
3. Yin, H., Wang, X.H., et al.: Influence of adsorbed gas on bottom hole pressure of shale gas wells with gas–water two-phase flow. *Fault-Block Oil Gas Field* **20**(1), 72–75 (2013)
4. Zhou, L.B., Cheng, L.S., et al.: Scaling model of imbibition in fractured ultra-low permeability reservoir. *Petrol. Drilling Techn.* **03**, 83–86 (2010)
5. Brown, M., Ozkan, E., Raghavan, R., et al.: Practical solutions for pressure-transient responses of fractured horizontal wells in unconventional shale reservoirs. *SPE Res. Eval. Eng.* **14**(6), 663–676 (2011)
6. Cai, J.C., Sun, S.Y.: Fractal analysis of fracture increasing spontaneous imbibition in porous media with gas-saturated. *Int. J. Mod. Phys. C* **24**(8), 1350056 (2013)
7. Sun, H., Yao, J., Zhang, L., et al.: A computing method of shale permeability based on pore structures. *J. China Univ. Pet. (Nat. Sci.)* **38**(2), 92–98 (2014)
8. Li, L., Sheng, G.L., Su, Y.L.: Water-gas two-phase flow behavior of multi-fractured horizontal wells in shale gas reservoirs. *Processes* **7**(10), 19 (2019)
9. Dejam, M., Hassanzadeh, H., Chen, Z.: Semi-analytical solution for pressure transient analysis of a hydraulically fractured vertical well in a bounded dual-porosity reservoir. *J. Hydrol.* **565**, 289–301 (2018)
10. Jensen, P.S.: Finite difference techniques for variable grids. *Comput. Struct.* **2**(1–2), 17–29 (1972)
11. Perrone, N., Kao, R.: A general finite difference method for arbitrary meshes. *Comput. Struct.* **5**(1), 45–57 (1975)
12. Liszka, T., Orkisz, J.: The finite difference method at arbitrary irregular grids and its application in applied mechanics. *Comput. Struct.* **11**(1–2), 83–95 (1980)
13. Benito, J.J., Urena, F., Gavete, L.: Influence of several factors in the generalized finite difference method. *Appl. Math. Model.* **25**(12), 1039–1053 (2001)
14. Zheng, Z.Y., Li, X.L.: Theoretical analysis of the generalized finite difference method. *Comput. Math. Appl.* **120**, 1–14 (2022)
15. Liu, Y., Rao, X., Zhao, H., et al.: Generalized finite difference method based meshless analysis for coupled two-phase porous flow and geomechanics. *Eng. Anal. Boundary Elem.* **146**, 184–203 (2023)
16. Zhan, W., Rao, X., Zhao, H., et al.: Generalized finite difference method (GFDM) based analysis for subsurface flow problems in anisotropic formation. *Eng. Anal. Boundary Elem.* **140**, 48–58 (2022)
17. Rao, X.: An upwind generalized finite difference method (GFDM) for meshless analysis of heat and mass transfer in porous media. *Comput. Particle Mechan.* 1–22 (2022)
18. Qin, Q.S., Song, L.N., Liu, F.: A meshless method based on the generalized finite difference method for three-dimensional elliptic interface problems. *Comput. Math. Appl.* **131**, 26–34 (2023)

Chapter 41

Cuttings Transport: Tripping Analysis Based on a Dynamic Layering Method via CFD



Na Zhu, Chenliang Ruan, Heming Zhu, Huang Wenjun, and Deli Gao

Abstract Insufficient hole cleaning is one of the main reasons for pipes stuck in extended-reach drilling, especially while tripping. The mechanism of cuttings transport while tripping is with this investigated. First, a dynamic layering method with the Eulerian-Granular approach is established and verified. The dynamic layering method can simulate the axial movement of the pipe, and the Eulerian-Granular approach can simulate the two-phase flow. Next, the tripping operations of a connector-furnished pipe with and without circulation are simulated, and the sensitive parameter analysis is conducted. The results demonstrate that cuttings dune piles up in front of the connector (lower right corner), and the dune's height increases with time. Moreover, the cuttings concentration around the connector when tripping with circulation is higher than that without circulation. So, it is safe to use the large flow rate after the cuttings have passed through the connector while tripping. Furthermore, the highest cuttings concentration decreases with the connector's length, while increases with the connector's diameter. This exploration is an essential guide to predicting and controlling tight spots while tripping.

Keywords Drill cuttings transport · Tripping · Dynamic layering method · Hole cleaning · Connector

N. Zhu · C. Ruan · H. Zhu (✉)
SINOPEC Research Institute of Petroleum Engineering Co., Ltd., No. 197 Baisha Road,
Changping, Beijing 102206, China
e-mail: 931819658@qq.com

H. Wenjun · D. Gao
MOE Key Laboratory of Petroleum Engineering, China University of Petroleum, Beijing 102249,
China

41.1 Introduction

Drilling projects are more efficient and profitable if holes are cleaned [1]. Inadequate hole cleaning can lead to a variety of problems, including increased equivalent circulating density and formation leakage, low ROP, high drag and torque, and even pipe stuck. Tripping and back reaming account for up to 54% of stuck pipe events [2, 3].

Drilling and washing are the main methods of hole cleaning, but cuttings transport under tripping conditions has not been adequately investigated. Cutting transport research is most commonly conducted experimentally and theoretically [4].

Numerous variables can be directly investigated in experiments to determine how they affect hole cleaning. A shortcoming arises from the variations in wellbore geometry, solid characteristics, flow parameters, etc., which make testing difficult under any flow conditions. It is common to combine flow and drilling rates in the study of drilling and washing. Despite this, tripping experiments, which couple both the flow and axial motion of a pipe, are still complex and rare to conduct [5–8].

Researchers have been studying the CFD method to determine how cuttings travel in the annular wellbore in recent years [9, 10]. A benefit of this method is that it provides detailed and desired properties without limiting the experimental conditions and layer modeling. Despite this, there have not been any models that can forecast the cuttings concentration during the tripping process due to the complexity of the flow.

In CFD simulations, two types of methods can be used, namely Eulerian-Eulerian and Eulerian-Lagrangian. Fluids and particles are considered continuum phases in the former [11, 12]. Despite its efficiency in representing many particles, this approach does not provide comprehensive information regarding micro- and mesoscale flow. Eulerian-Lagrangian methodology is used to treat particles as discrete phases, allowing each particle's motion to be determined separately and collisions between particles to be taken into account. Its disadvantage is that it has a much higher computational cost, especially for flows with many particles. Using Eulerian-Granular, the particles are viewed as continuous phases. Flows involving liquids and solids can be studied using this method without requiring large computational resources [13–16].

Hence, an analysis of tripping operations using dynamic layering meshes and Eulerian-Granular methods. Simulation of the pipe's axial motion can be achieved using dynamic layering.

41.2 Concept of Tripping and Methodology

Tripping is defined as a mechanical operation combining pipe extraction from the hole and/or pumping (Fig. 41.1), which is widely used in drilling. To simulate the motion of the pipe, the dynamic layering mesh method is employed.

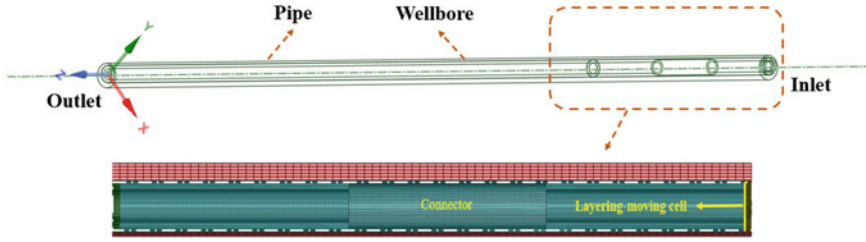


Fig. 41.1 Concept illustration of the tripping operation with a connector

Besides, a Eulerian-Granular method is applied to simulate the two-phase flow. This method requires less computational resources than CFD-DEM method and has been extensively used in liquid–solid flows. The detailed equations are shown in Table 41.1.

Thus, a wellbore with a total length of 3 m is simulated and the length of the connector is 0.25 m. The diameters of the wellbore, pipe, and the connector are 0.074, 0.033 and 0.046 m. The fluid uses water and the solid is the sand particle, with

Table 41.1 Principal and constitutive equations of the Eulerian-Granular model

Equations	Equation expression	No.
Mass conservation equation	$\frac{\partial}{\partial t} (\alpha_q \rho_q) + \nabla \cdot (\alpha_q \rho_q \vec{v}_q) = \sum_{s=1}^n (\dot{m}_{sq} - \dot{m}_{qs})$	(41.1)
Conservation of momentum	$\begin{aligned} \frac{\partial}{\partial t} (\alpha_q \rho_q \vec{v}_q) + \nabla \cdot (\alpha_q \rho_q \vec{v}_q \vec{v}_q) = & -\alpha_q \nabla p + \nabla \cdot \bar{\tau}_q + \alpha_q \rho_q \vec{g} \\ & + \sum_{s=1}^n (\vec{R}_{sq} + \dot{m}_{sq} \vec{v}_{sq} - \dot{m}_{qs} \vec{v}_{qs}) \\ & + (\vec{F}_q + \vec{F}_{lift,q} + \vec{F}_{wl,q} + \vec{F}_{vm,q} + \vec{F}_{id,q}) \end{aligned}$	(41.2)
Granular temperature	$\Theta_s = \frac{1}{3} u_s u_s$	(41.3)
Transport equation	$\begin{aligned} \frac{3}{2} \left[\frac{\partial}{\partial t} (\rho_s \alpha_s \Theta_s) + \nabla \cdot (\rho_s \alpha_s \vec{v}_s \Theta_s) \right] = & \left(-\rho_s \bar{I} + \bar{\tau}_s \right) : \\ \nabla \cdot \vec{v}_s + \nabla \cdot (k_{\Theta_s} \nabla \Theta_s) - \gamma_{\Theta_s} + \phi_{I_s} \end{aligned}$	(41.4)
Solids pressure	$p_s = \alpha_s \rho_s \Theta_s + 2\rho_s (1 + e_{ss}) \alpha_s^2 g_{0,ss} \Theta_s$	(41.5)
Solids shear stresses	$\mu_s = \mu_{s,col} + \mu_{s,kin} + \mu_{s,fr}$	(41.6)
Collisional viscosity	$\mu_{s,col} = \frac{4}{5} \alpha_s \rho_s d_s g_{0,ss} + (1 + e_{ss}) \left(\frac{\Theta_s}{\pi} \right)^{1/2}$	(41.7)
Kinetic viscosity	$\mu_{s,kin} = \frac{d_s \rho_s \sqrt{\Theta_s \pi}}{6(3 - e_{ss})} \left[1 + \frac{2}{5} (1 + e_{ss}) (3e_{ss} - 1) \alpha_s g_{0,ss} \right]$	(41.8)
Bulk viscosity	$\lambda_s = \frac{4}{3} \alpha_s^2 \rho_s d_s g_{0,ss} (1 + e_{ss}) \left(\frac{\Theta_s}{\pi} \right)^{1/2}$	(41.9)

a density of 2500 kg/m^3 , and a diameter of 0.003 m . The eccentricity of the pipe is 0.3 . The tripping velocity is 0.1 m/s , and the rotational speed of the pipe is 120 RPM .

41.3 Results and Discussion

41.3.1 Tripping Without Circulation

The tripping process without circulation is simulated and the cuttings concentration when the time increases from 0.2 to 0.8 s is presented in Fig. 41.2. As shown in Fig. 41.2, the overall cuttings concentration changes slightly. Besides, the velocity contour of water is also given in Fig. 41.3. It can be seen that the water velocity in the lower annular is smaller than that of the upper annular, and the moving pipe mainly affects the water velocity near the pipe wall. Regarding the flow region far from the pipe, the impact on the water velocity is mild.

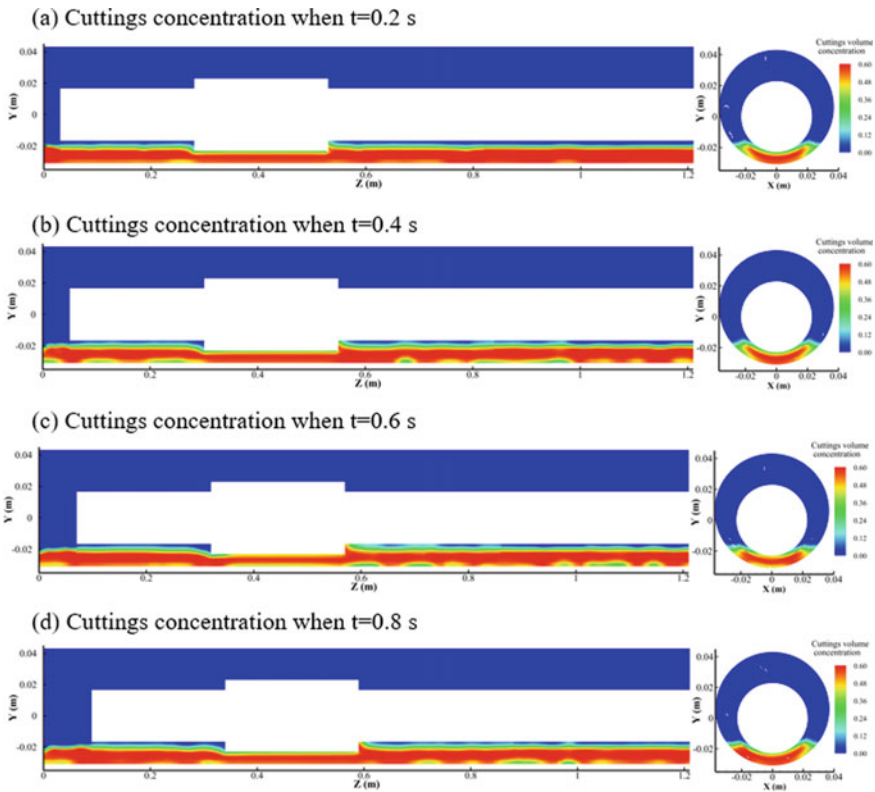


Fig. 41.2 Cuttings concentration under different circulation time

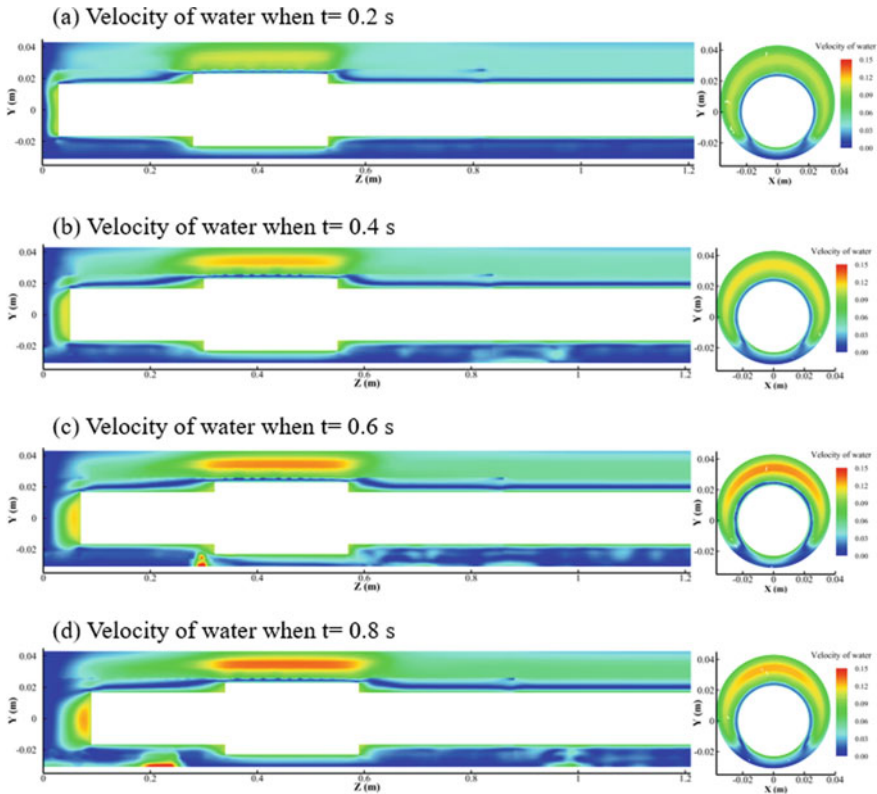


Fig. 41.3 Velocity of water under different circulation time

However, a cuttings dune piles up in front of the connector (lower right corner), and the dune’s height increases with time (see Fig. 41.4). The reason is that the connector has a pushing effect on the cuttings dune when the dune height is higher than the lower side of the connector. The cuttings dune has not been removed in time, so its height becomes higher, which poses a significant risk while tripping. Thus, before tripping, the annular should be cleaned as much as possible to avoid the cuttings pipe up around the connector.

41.3.2 Tripping with Circulation

The tripping process with circulation is simulated and the cuttings concentration when the time increases from 0.2 to 0.8 s is presented in Fig. 41.5. As depicted in Fig. 41.5, the cuttings move forward when the time increases and the overall cuttings concentration decreases.

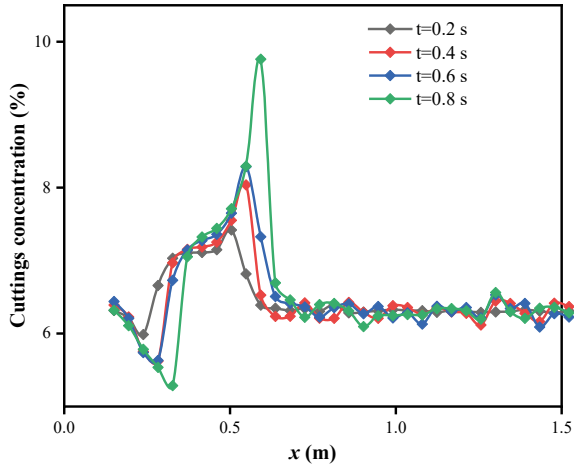


Fig. 41.4 Average cuttings concentration under different circulation time

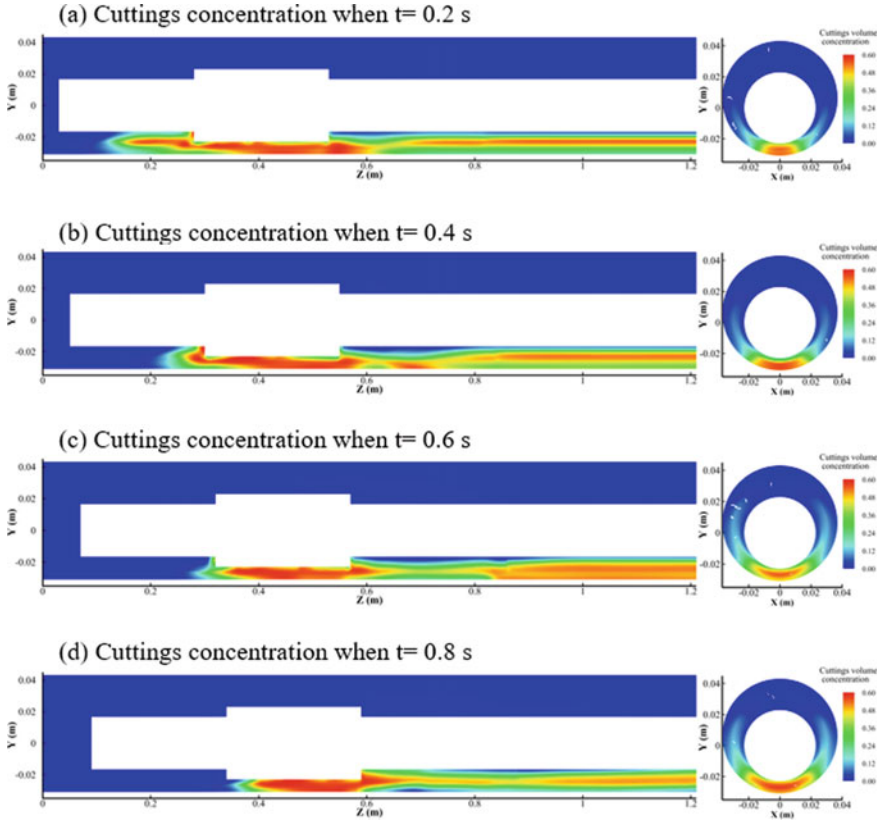


Fig. 41.5 Cuttings concentration under different circulation time

Figure 41.6 shows the contour of the water velocity and the streamline. The water velocity is the smallest in front of the connector (the lower right corner), the reason is that the cross-sectional area at the position of the connector is smaller than that of the pipe body, and the water velocity becomes higher at the position of the connector and then decreases after the connector. As a result, the cuttings pile up like a dune when the water velocity decreases after the connector, which would pose a risk of the pipe getting stuck. As can be seen in Fig. 41.7, the cuttings concentration in front of the connector increases with time, and are higher than that of tripping without circulation, indicating that the circulation can also play a dangerous role in the pipe stuck, so it is safe to use the large flow rate after the cuttings have passed through the connector while tripping.

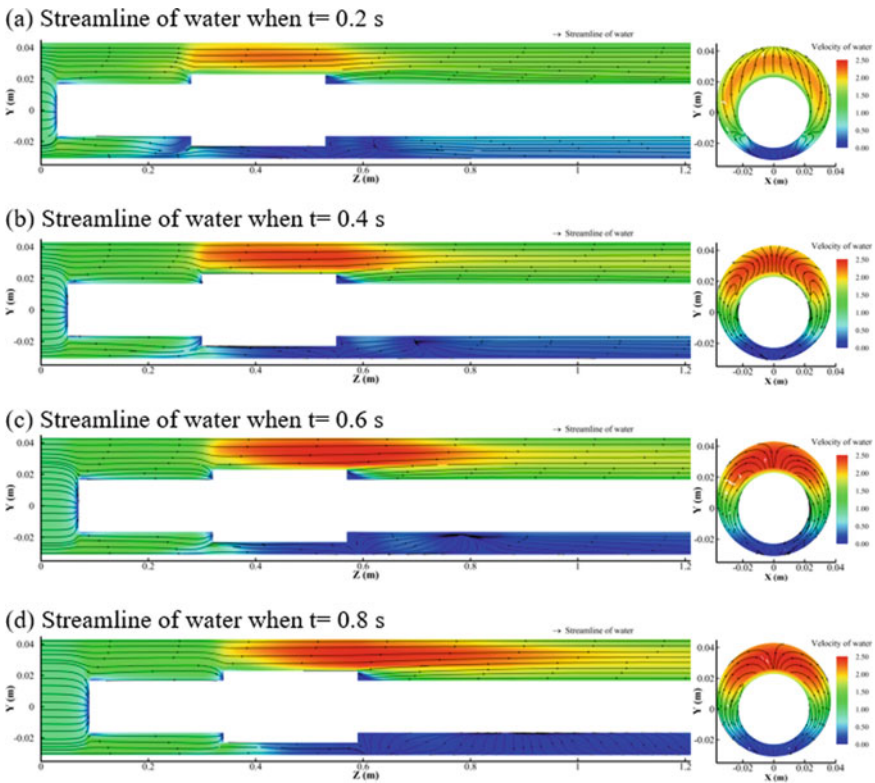


Fig. 41.6 Velocity of water and the streamline of water under different circulation time

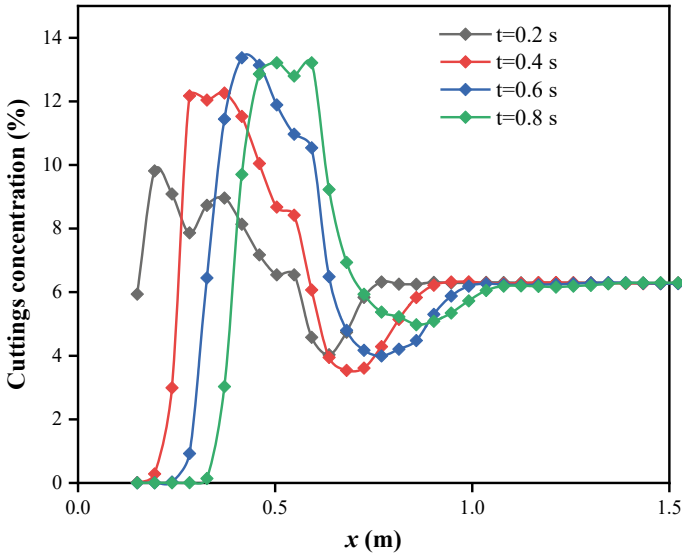


Fig. 41.7 Average cuttings concentration under different circulation time

41.3.3 Impact of the Connector's Length

The effect of the connector's length is investigated in Fig. 41.8. The highest cuttings concentration in front of the connector with different connector's length is calculated. It can be seen from Fig. 41.8 that the highest cuttings concentration decreases with the connector's length. The reason is that with the increase in the connector's length, it takes more cuttings to pass through the connector, and the remaining cuttings in front of the connector decrease.

41.3.4 Impact of the Connector's Diameter

The effect of the connector's diameter is investigated in Fig. 41.9. The highest cuttings concentration in front of the connector with different connector's diameter is calculated. It can be seen from Fig. 41.9 that the highest cuttings concentration increases with the connector's diameter significantly. The reason is that a larger connector's diameter leads to a bigger differential water velocity between the location of the connector and the pipe body, resulting in a higher cuttings concentration.

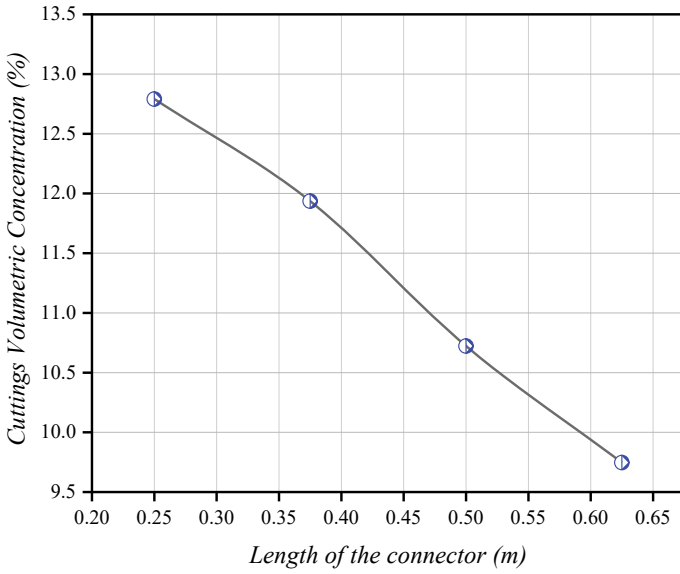


Fig. 41.8 The highest cuttings concentration around the connector under different lengths of the connector

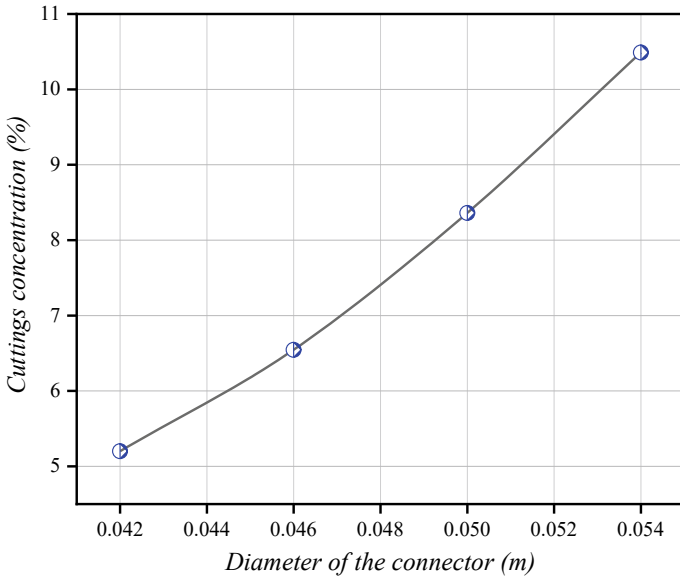


Fig. 41.9 The highest cuttings concentration around the connector under different diameters of the connector

41.4 Results and Discussion

- (1) A dynamic layering mesh method with a Eulerian-Granular approach is proposed to investigate the cuttings transport while tripping. The dynamic layering method can simulate the axial movement of the pipe, and the Eulerian-Granular approach can simulate the two-phase flow.
- (2) The tripping processes with and without circulation are investigated. The results show that cuttings dune piles up in front of the connector (lower right corner) and the dune's height increases with time. Moreover, the cuttings concentration around the connector when tripping with circulation is higher than that without circulation. So, it is safe to use the large flow rate after the cuttings have passed through the connector while tripping.
- (3) The effects of the connector's length and diameter are investigated. The highest cuttings concentration decreases with the connector's length, while increases with the connector's diameter.

Acknowledgements The authors gratefully acknowledge the financial support from the Natural Science Foundation of China (Grant Nos. 52222401, 52234002, 51904317 and 52174012), Science Foundation of China University of Petroleum, Beijing (Grant No. ZX20180414), and other projects (ZLZX2020-01-07-01).

References

1. Alshaikh, A.A., Albassam, M.K., Al Gharbi, S.H., and Al-Yami, A.S.: Detection of stuck pipe early signs and the way toward automation. In: Abu Dhabi International Petroleum Exhibition and Conference, pp. 12–15. Onepetro, Abu Dhabi, UAE (2018). <https://doi.org/10.2118/192975-MS>
2. Epelle, E.I., Gerogiorgis, D.I.: Drill cuttings transport and deposition in complex annular geometries of deviated oil and gas wells: a multiphase flow analysis of positional variability. *Chem. Eng. Res. Des.* **151**, 214–230 (2019). <https://doi.org/10.1016/j.cherd.2019.09.013>
3. Yarim, G., Uchytel, R.J., May, R.B., Trejo, A.: Stuck pipe prevention—a proactive solution to an old problem. In: SPE Annual Technical Conference and Exhibition, pp. 11–14. Onepetro, California, USA (2007). <https://doi.org/10.2118/109914-MS>.
4. Zhu, N., Huang, W., Gao, D.: Numerical analysis of the stuck pipe mechanism related to the cutting bed under various drilling operations. *J. Pet. Sci. Eng.* **208**, 109783 (2022). <https://doi.org/10.1016/j.petrol.2021.109783>
5. Pandya, S., Ahmed, R., Shah, S.: Effects of particle density on hole cleanout operation in horizontal and inclined wellbores. In: SPE/ICoTA Well Intervention Conference and Exhibition, pp. 26–27. Onepetro, The Woodlands, Texas, USA (2019). <https://doi.org/10.2118/194240-MS>
6. Song, X., Xu, Z., Wang, M., Li, G., Shah, S.N., Pang, Z.: Experimental study on the wellbore-cleaning efficiency of microhole-horizontal-well drilling. *SPE J.* **22**(4), 1189–1200 (2017). <https://doi.org/10.2118/185965-PA>
7. Ozbayoglu, M.E., Saasen, A., Sorgun, M., Svanes, K.: Effect of pipe rotation on hole cleaning for water-based drilling fluids in horizontal and deviated wells. In: IADC/SPE Asia Pacific Drilling Technology Conference and Exhibition, pp. 25–27. Onepetro, Jakarta, Indonesia (2008). <https://doi.org/10.2118/114965-MS>

8. Paranhos Sobrinho, E.S., Escarpini Filho, R.S., Lages, E.N., Anjos, J.L.R., Almeida, L.F.M., Gonçalves, C.: Consideration of backreaming in vertical wells closure model-ing in salt rock. *SPE J.* **26**(3), 1092–1109 (2021). <https://doi.org/10.2118/204209-PA>
9. Li, J., Luft, B.: Overview of solids transport studies and applications in oil and gas industry-experimental work. In: *SPE Russian Oil and Gas Exploration and Production Technical Conference and Exhibition*, pp. 14–16. Onepetro, Moscow, Russia (2014). <https://doi.org/10.2118/171285-MS>.
10. Gavignet, A., Sobey, I.: Model aids cuttings transport prediction. *J. Pet. Tech-nol.* **41**(9), 916–921 (1989). <https://doi.org/10.2118/15417-PA>
11. Zhang, F., Wang, Y., Wang, Y., Miska, S., Yu, M.J.S.J.: Modeling of dynamic cuttings transportation during drilling of oil and gas wells by combining 2D CFD and 1D discretization approach. *SPE J.* **25**(3), 1220–1240 (2020). <https://doi.org/10.2118/199902-PA>
12. Heydari, O., Sahraei, E., Skalle, P.: Investigating the impact of drillpipe’s rota-tion and eccentricity on cuttings transport phenomenon in various horizontal annuluses using computational fluid dynamics (CFD). *J. Pet. Sci. Eng.* **156**, 801–813 (2017). <https://doi.org/10.1016/j.petrol.2017.06.059>
13. Akhshik, S., Behzad, M., Rajabi, M.: CFD-DEM approach to investigate the effect of drill pipe rotation on cuttings transport behavior. *J. Pet. Sci. Eng.* **127**, 229–244 (2015). <https://doi.org/10.1016/j.petrol.2015.01.017>
14. Capecelatro, J., Desjardins, O.: An Euler-Lagrange strategy for simulating par-ticle-laden flows. *J. Comput. Phys.* **238**, 1–13 (2013). <https://doi.org/10.1016/j.jcp.2012.12.015>
15. Basu, D., Das, K., Smart, K., Ofoegbu, G.: Comparison of Eulerian-Granular and discrete element models for simulation of proppant flows in fractured reservoirs. In: *ASME International Mechanical Engineering Congress and Exposition*, pp. 13–19, American Society of Mechanical Engineers, Houston, Texas (2015). <https://doi.org/10.1115/IMECE2015-50050>
16. Bonamy, D., Chavanis, P.H., Cortet, P.P., Daviaud, F., Dubrulle, B., Renouf, M.: Euler-like modelling of dense granular flows: application to a rotating drum. *Eur. Phys. J. B* **68**, 619–627 (2009). <https://doi.org/10.1140/epjb/e2009-00123-6>

Chapter 42

SPH Simulation of Solitary Wave Impact on Coastal Bridge Superstructures



Guozhen Cai, Zhisheng Xia, Yi Zhan, and Min Luo

Abstract Sea-crossing bridges are built for connecting important coastal cities. These bridges are subjected to extreme ocean wave actions, which pose serious threats to the bridges. In this context, this study examines the solitary wave impacts on a suspended flat plate and a coastal-bridge deck numerically by using the SPH (Smoothed Particle Hydrodynamics) open-source code SPHinXsys. The physical quantities including the wave profile, the velocity distribution near superstructures and the impact load on superstructures will be investigated. The research findings will provide some guidance on how to consider the extreme wave impacts in the design and maintenance of sea-crossing bridges.

Keywords Particle method · Extreme wave · SPHinXsys · Impact load · Coastal bridge

42.1 Introduction

As an important part of the infrastructure, more and more sea-crossing bridges have been built. The bridge superstructures are often impacted by waves, which poses a huge threat to the structural safety sea-crossing bridges. Tsunami is a kind of catastrophic wave that has a destructive effect on sea-crossing bridges, which should be fully considered in structural design and maintenance [3, 9, 16]. In this context, this work considers a suspended flat plate and a coastal-bridge deck that represent the bridge superstructures and investigates their interaction with the solitary wave, which represents the tsunami due to their resemblance.

G. Cai · Y. Zhan · M. Luo (✉)
Ocean College, Zhejiang University, Zhoushan, China
e-mail: min.luo@zju.edu.cn

Z. Xia
Shandong Energy Group, New Energy Co., Ltd., Jinan, China

M. Luo
Donghai Laboratory, Zhoushan, China

CFD (Computational Fluid Dynamics) modelling, due to its rapid development, has becoming an important tool in analyzing wave-structure interaction problems. Among the various numerical models, Smoothed Particle Hydrodynamics (SPH) [7], being a typical Lagrangian particle method, has been rapidly developed and widely used due to their intrinsic advantages in handling large deformation, moving interface, etc. The theories and numerical technologies of particle methods have been developed significantly in the last two decades [4–6, 12, 15, 17, 19].

The particle methods have been extensively used for simulating wave interaction with coastal structures. For example, [13] studied the effect of tsunami impacting on bridge piers with the SPH code GPUSPH. The flow field and bed shear stress around the pier, as well as the hydrodynamic loading on the pier, were investigated. Aristodemo et al. [1] studied the wave force impacting on a submerged horizontal circular cylinder by the solitary wave using δ -SPH model. Tripepi et al. [11] studied the semi-analytical estimation of the solitary-wave induced horizontal loads on a square barrier. Pringgana et al. [8] studied the influence of differentiation in the orientations and arrangements of onshore structures on tsunami impacts using the SPH open-source code DualSPHysics.

This study adopts the weakly-compressible SPH code SPHinXsys [18] to study the solitary interaction with a suspended flat plate and a coastal-bridge deck. The key hydrodynamic parameters including wave elevation, wave profile and impact load on bridge superstructures will be elaborated in comparison with the results produced by the experiment. The physics behind the wave-structure interaction process is discussed, as well as the accuracy of SPHinXsys is verified. In what follows, Sect. 42.2 presents the key mathematical formulations of SPHinXsys; Sect. 42.3 presents model validation as well as results and discussion; Sect. 42.4 concludes the study.

42.2 Mathematical Formulations

42.2.1 Governing Equations

The present works adopt the weakly-compressible-SPH open-source code SPHinXsys. The governing equations are the conservation equations of mass and momentum in the Lagrangian form:

$$\begin{cases} \frac{D\rho}{Dt} = -\rho\nabla \cdot \mathbf{v} \\ \frac{D\mathbf{v}}{Dt} = -\frac{1}{\rho}\nabla p + \nu\nabla^2\mathbf{v} + \mathbf{g} \end{cases} \quad (42.1)$$

where ρ is the density of a fluid, \mathbf{v} the particle velocity vector, p the fluid pressure, ν the kinematic viscosity, \mathbf{g} the gravity acceleration, and t is the time. Discretized non-connecting particles comprise the fluid domain. Each particle possesses the constant

mass and moves under the combined effect of the gravity, pressure gradient, viscous force as described in Eq. (42.1).

The fluid pressure is related to density through an equation of state [18]:

$$p = c_0^2(\rho - \rho_0) \quad (42.2)$$

where ρ_0 is the reference density, c_0 is the artificial speed of sound. The fluid density varies around 1% if c_0 is adopted to be 10 times of the projected maximum particle velocity during the simulation

42.2.2 Numerical Formulations of SPHinXsys

The governing equations are discretized by particle interpolation [18]:

$$\begin{cases} \frac{D\rho_i}{Dt} = 2\rho_i \sum_j \frac{m_j}{\rho_j} (\mathbf{v}_i - \overline{\mathbf{v}}_{ij}) \cdot \nabla_i W_{ij} \\ \frac{D\mathbf{v}_i}{Dt} = -2 \sum_j m_j \frac{\overline{p}_{ij}}{\rho_i \rho_j} \nabla_i W_{ij} + 2 \sum_j m_j \frac{\eta}{\rho_i \rho_j} \frac{\mathbf{v}_{ij}}{r_{ij}} \nabla_i W_{ij} + \mathbf{g}_i \end{cases} \quad (42.3)$$

where $\overline{\mathbf{v}}_{ij} = (\mathbf{v}_i + \mathbf{v}_j)/2$, $\overline{p}_{ij} = (p_i + p_j)/2$, η the dynamic viscosity, m_j is the mass of particle j which is fixed during the simulation, and W is the kernel function used in particle interpolation. A Wendland C2 kernel function [14] is used in the present study:

$$W = \alpha_d \begin{cases} (1 - \frac{1}{2}q)^4(1 + 2q), & 0 \leq q < 2 \\ 0, & q \geq 2 \end{cases} \quad (42.4)$$

where α_d is a constant equal to $21/16\pi h^3$ for three-dimensional simulations, and $q = |\mathbf{r}_i - \mathbf{r}_j|/h = r_{ij}/h$ with h being the smoothing length.

SPHinXsys uses the Riemann solver [18] to mitigate numerical noises (e.g. the spurious pressure fluctuation). In the Riemann solver, an imaginary interface is constructed between two particles, and the states are mutually defined at the left and right sides of the interface (more details in [18]):

$$\begin{cases} (\rho_L, U_L, P_L, c_L) = (\rho_i - \mathbf{v}_i \cdot \mathbf{e}_{ij}, p_i, c_i) \\ (\rho_R, U_R, P_R, c_R) = (\rho_j - \mathbf{v}_j \cdot \mathbf{e}_{ij}, p_j, c_j) \end{cases} \quad (42.5)$$

where L and R is left and right, respectively.

A low-dissipation Riemann solver is adopted:

$$\begin{aligned}
\mathbf{v}^* &= \frac{1}{2}(\mathbf{v}_i + \mathbf{v}_j) - (U^* - \frac{1}{2}(U_L + U_R)) \cdot \mathbf{e}_{ij} \\
U^* &= \frac{(\rho_{LC}U_L + \rho_{RC}U_R + P_L - P_R)}{\rho_{LC} + \rho_{RC}} \\
p^* &= \frac{(\rho_{LC}P_R + \rho_{RC}P_L + \rho_{LC}\rho_{RC}\beta(U_L - U_R))}{\rho_{LC} + \rho_{RC}}
\end{aligned} \tag{42.6}$$

where $\beta = \min(3\max(U_L - U_R, 0)/c, 1)$ denotes the low dissipation limiter and $c = (\rho_{LC} + \rho_{RC})/(\rho_L + \rho_R)$. The variables of p^* and \mathbf{v}^* are then used to replace the terms \overline{p}_{ij} and $\overline{\mathbf{v}}_{ij}$ in Eq. (42.3). This leads to the particle-interpolated continuity and momentum equations.

For the time propagation, the time step size is calculated by the CFL condition:

$$\Delta t = CFL \frac{h}{c + v_{\max}} \tag{42.7}$$

where the coefficient CFL is adopted to be 0.6 and h is the smoothing length.

The wall boundaries of the surface-piercing cylinder and the computational domain are represented by dummy particles in SPHinXsys. Through these, the velocity of the boundary particles is subjected to non-slip and impermeable conditions, and the pressure is solved by Neumann boundary condition. Specifically, the pressure values on wall particles are obtained by $P_R = P_L + \rho_f g \cdot r_{fw}$, where $r_{fw} = r_w - r_f$ with r_w and r_f representing the locations of a wall particle and its relating fluid particle [18].

42.3 Results and Discussion

42.3.1 Solitary Wave Interaction with a Suspended Flat Plate

The case of solitary wave interaction with a suspended flat plate is studied [10]. As sketched in Fig. 42.1, the effective length of the computational domain is $L = 7.84$ m and a piston-type wave maker is placed on the left side of the domain. A fixed flat plate of width 0.305 m and thickness of 0.0127 m (0.013 m is adopted herein) is placed such that its leading edge (facing the incident wave) is 2.62 m from the initial location of the wave maker. Other parameters considered are: water depth $h = 0.114$ m, elevations ratio $z^*/h = 0.1$ (z^* is measured from the bottom of the plate to the still-water level) and solitary wave height $H = 0.301h$. In simulations, a fixed particle size is adopted to be $dp = 0.003$ m by considering the particle size convergence and by letting each dimension of the structure be the integer multiplies of particle size. With this particle size, the numerical domain contains a total of 115,600 particles and the computational time is about 9.3 min for simulating 1 s physical process based on a computer with Intel(R) i7-10700 CPU (8-Cores 2.90 GHz). The wave elevations

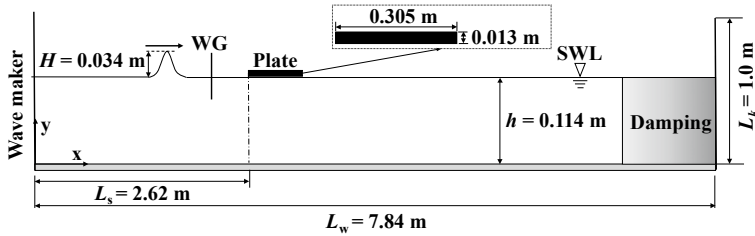


Fig. 42.1 Computational domain of solitary wave interaction with a suspended flat plate

at $x = 2.01$ m (WG in Fig. 42.1), as well as the horizontal and vertical components of the wave force applied on the plate, are studied.

The predicted wave elevation at WG is compared with the analytical solution in Fig. 42.2 and the relative error is only 1.18%. The wave profiles and velocity fields at typical time instants are presented in Figs. 42.3 and 42.4. As can be seen, the wave crest reaches the upper side of the plate at $t = 5.5$ s. After that, the wave velocity underneath the plate is almost horizontal due to the obstructive of the plate, while the wave above the plate shows the shoaling characteristics because of the decrease of the effective water depth. At $t = 5.7$ s, water surface on the rear edge of the plate gradually surges and produces a counterclockwise vortex of the initial state. The present SPH captures the whole process satisfactorily with regular particle and smooth pressure distributions.

The wave force components obtained by the present two-dimensional simulation are multiplied by the width of the physical plate (i.e. 0.149 m), as shown in Fig. 42.5. For the vertical force F_V , the overall trend and magnitude predicted by SPH agree well with the experimental data. For the horizontal force F_H , the positive horizontal force predicted by SPH lasts longer and has a larger magnitude than that of the experimental result. From the instantane wave profile at $t = 5.7$ s, the particle distribution near the leading and trailing edges of the plate is irregular. This results in inaccuracy of

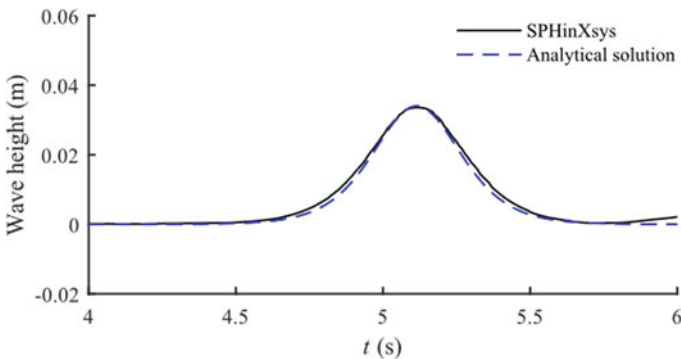


Fig. 42.2 Wave elevation at WG in the case of solitary wave interaction with a flat plate

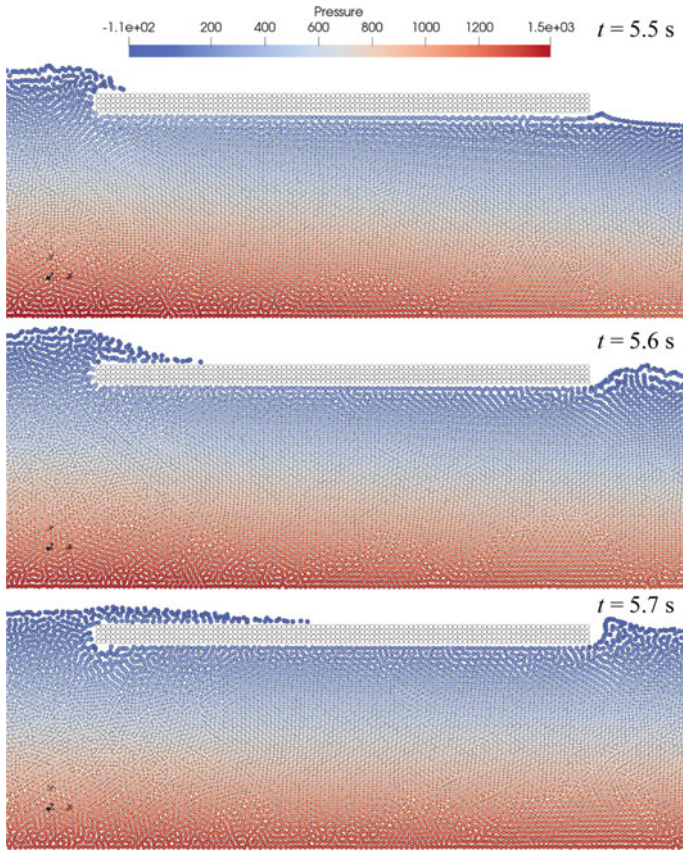


Fig. 42.3 Particle distributions with pressure contours near the plate at $t = 5.5, 5.6$ and 5.7 s

pressure and hence wave force computation, which may be the reason for the above distinction.

42.3.2 Solitary Wave Interaction with a Coastal-Bridge Deck

This section studies the case of solitary wave interaction with a coastal-bridge deck [2]. As sketched in Fig. 42.6, the effective length of the computational domain is $L_w = 12$ m and a piston-type wave maker is placed on the left side of the domain. A fixed bridge model (detailed coordinates in Fig. 42.6) is placed such that its leading edge (facing the incident wave) is 6 m from the initial location of the wave maker. Other parameters considered are: water depth $h = 0.623$ m, the bottom of the model being close to the still water level, and solitary wave height $H = 0.167$ m. In simulations, a fixed particle size of $dp = 0.005$ m is adopted and the particle distribution of the

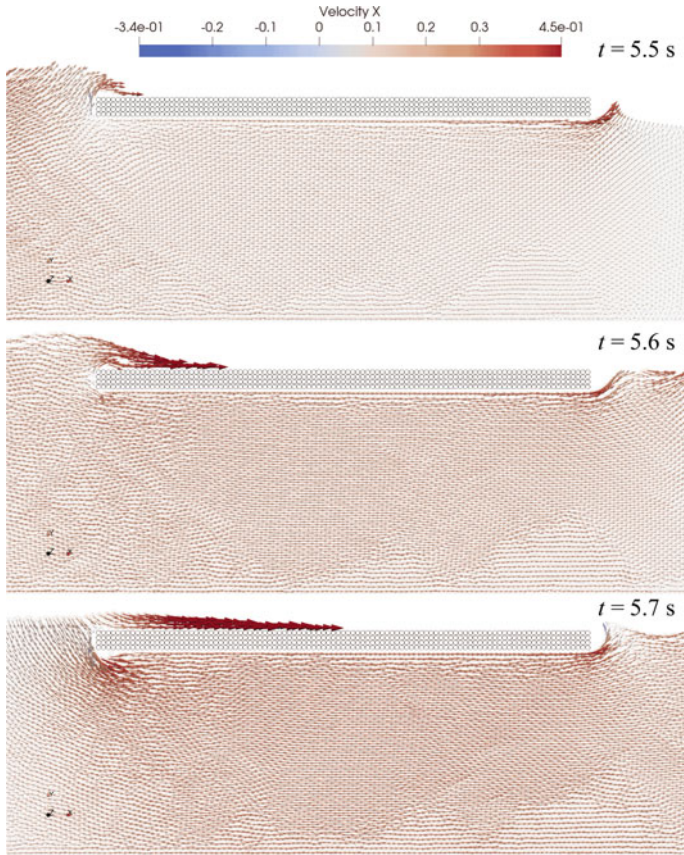


Fig. 42.4 Velocity fields near the plate at $t = 5.5, 5.6$ and 5.7 s

deck is produced by the body-fitted particle generator [20]. The wave elevations at $x = 4$ m (WG in Fig. 42.6), as well as the horizontal and vertical components of the wave force applied on the plate, are studied. Note that the length of the flume has been reduced by 21.75 m in SPHinXsys simulation for saving computational cost, and the arrival time of the SPH-simulated wave crest has been shifted by the ratio of the reduced flume length to the solitary wave celerity.

The wave profiles and velocity fields at typical time instants of the wave-deck interaction process are presented in Figs. 42.7 and 42.8. The wave crest reaches the upper side of the bridge deck at $t = 4.0$ s and forms a gap at the leading edge of the deck. After that, a counterclockwise vortex is generated on the lower right side of the deck $t = 4.2$ s, and a new vortex is also generated on the free surface at the lower edge of the deck, which surges up to the deck and travels upstream to meets the downstream breaking wave. Above the deck, the shoaling process happens similarly to that in the flat plate case. Again, the particle distribution and pressure distribution

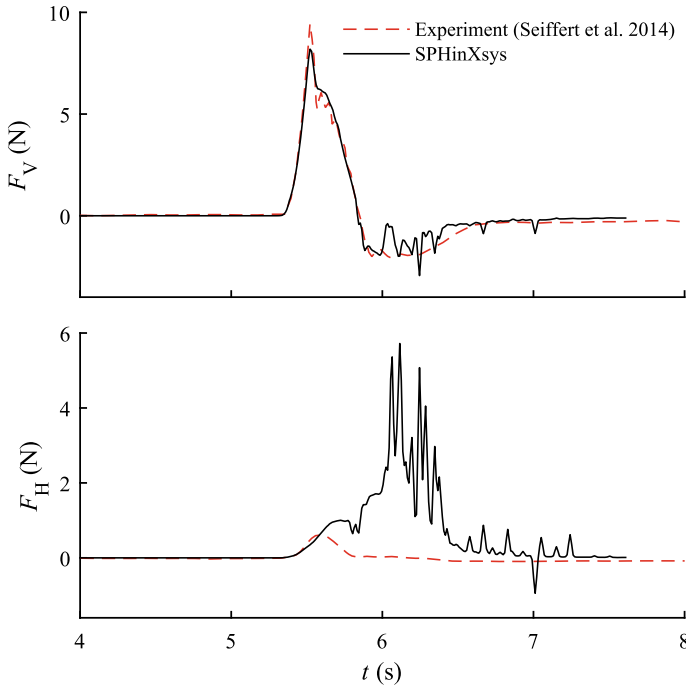


Fig. 42.5 Wave force components applied on the flat plate

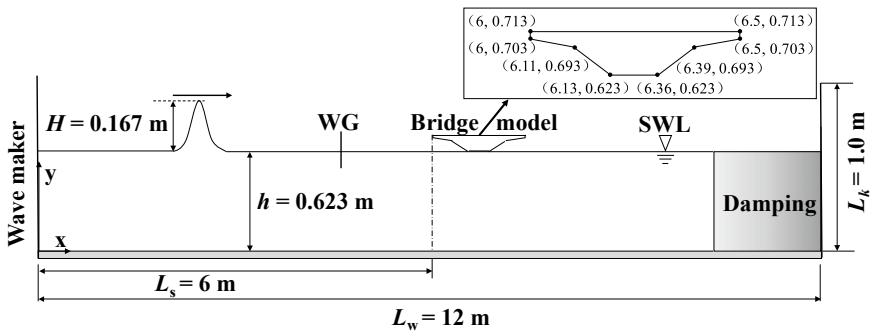


Fig. 42.6 Computational domain of solitary wave interaction with a coastal-bridge deck

are generally smooth in the whole domain except for the regions near the four corners of the deck.

The predicted wave elevation at WG is compared with the analytical solution in Fig. 42.9 and the relative error is only 2.1%. The wave forces that the solitary apply on the deck are shown in Fig. 42.10. For the vertical force F_V , the overall trend and magnitude predicted by SPH are in good agreement with the published

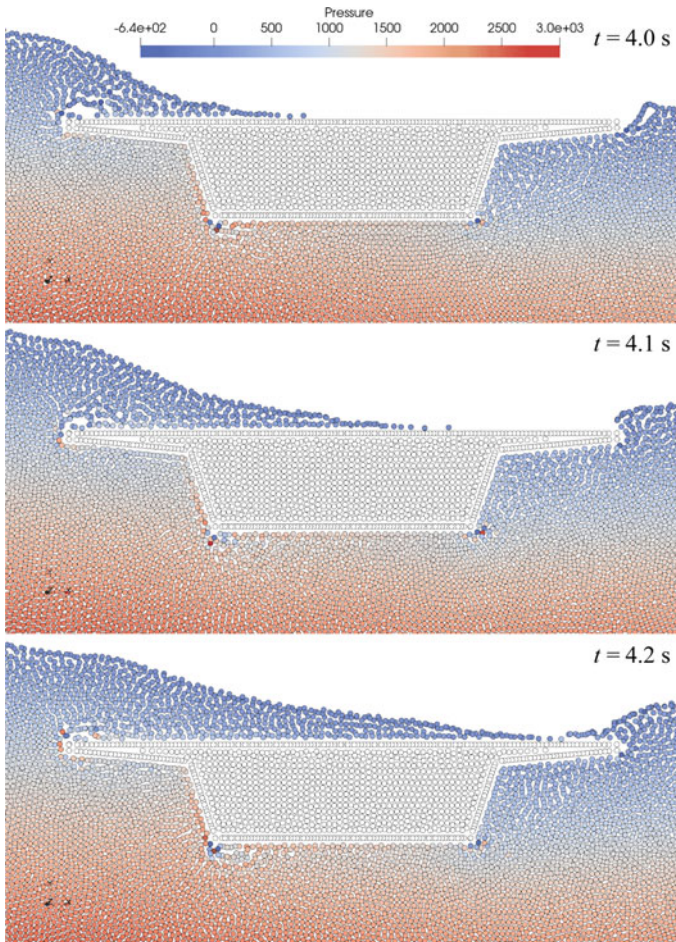


Fig. 42.7 Particle distributions with pressure contours near the deck at $t = 4.0, 4.1$ and 4.2 s

experimental results. For the horizontal force F_H , the positive peak predicted by SPH is larger compared to the experimental results, and the predicted negative peak is much smaller. The irregular pressure distribution of the four corners of the bridge has an impact on the capture of wave forces, as can be seen in Fig. 42.10. It is worth noting that there are double peaks in the wave force in both directions predicted by SPH (see a–d in Fig. 42.1). The two points of a and c represent that the wave strikes the entire bottom structure of the deck. With the wave propagation, the wave acts on the upper edge of the deck, and the wave force gradually increases to the largest magnitude (point b and point d). The first peak of horizontal force occurs earlier than that of vertical force, while the second peak of force in both directions occurs almost at the same moment.

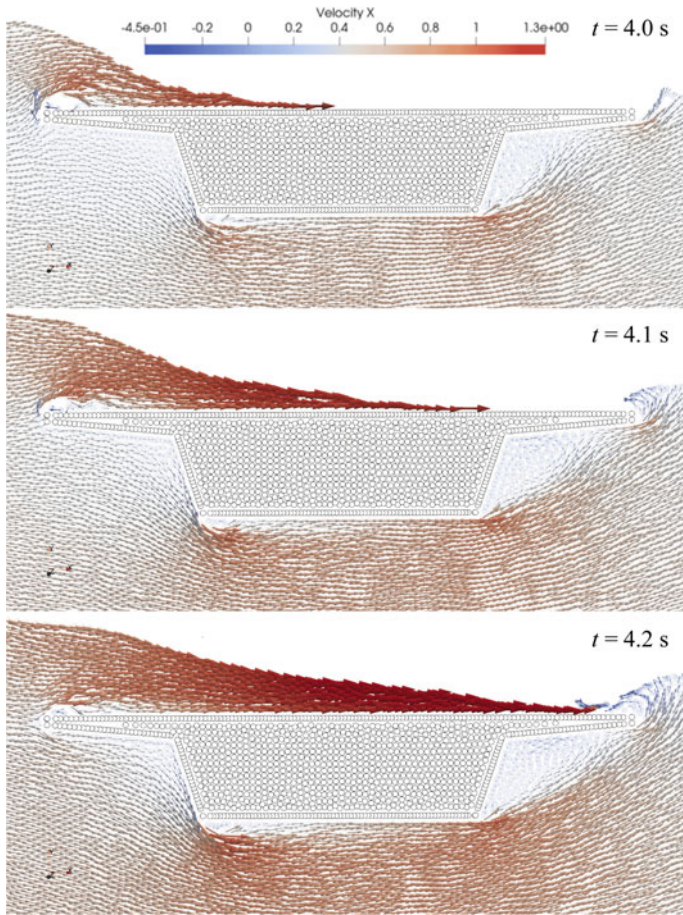


Fig. 42.8 Velocity fields near the deck at $t = 4.0, 4.1$ and 4.2 s

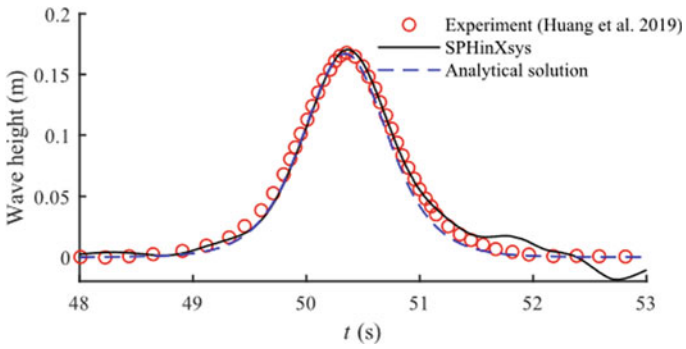


Fig. 42.9 Wave elevation at WG in the case of solitary wave interaction with a coastal-bridge deck

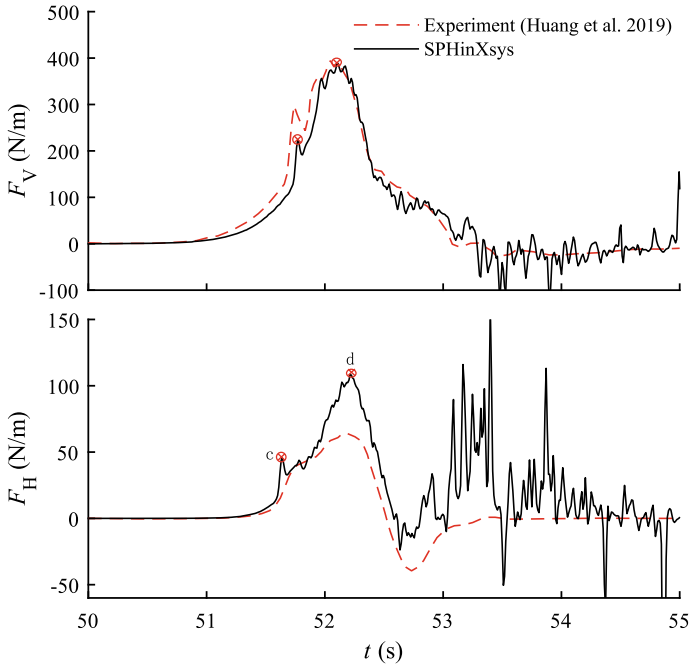


Fig. 42.10 Wave force components applied on the bridge deck by the solitary wave

42.4 Concluding Remarks

This work adopts the SPH open source code SPHinXsys to study the interaction process of solitary wave passing through a suspended flat plate and a coastal-bridge deck.

The wave heights of the solitary wave simulated by SPH agree well with the theoretical values in two cases. The simulated pressure contours and velocity distributions near the structures are smooth, which demonstrate the performance of the present SPH model in mitigating pressure noises. The vertical forces predicted by SPH are in good agreement with the experiment. Regarding the horizontal wave force, the SPH model over-predicts the positive peak. The difference in horizontal wave force may be related to the minor non-physical pressure distribution near the corners of structures and the small thickness of the structure edges.

Funding The Science Foundation of Donghai Laboratory (No. DH-2022KF0311); the start-up funding provided by Zhejiang University (to the corresponding author); Research grant of SNDJKJ2023B02.

References

1. Aristodemo, F., Tripepi, G., Meringolo, D.D., Veltri, P.: Solitary wave-induced forces on horizontal circular cylinders: laboratory experiments and SPH simulations. *Coast. Eng.* **129**, 17–35 (2017)
2. Huang, B., Yang, Z., Zhu, B., Zhang, J., Kang, A., Pan, L.: Vulnerability assessment of coastal bridge superstructure with box girder under solitary wave forces through experimental study. *Ocean Eng.* **189**, 106337 (2019)
3. Huang, B., Zhu, B., Cui, S., Duan, L., Zhang, J.: Experimental and numerical modelling of wave forces on coastal bridge superstructures with box girders, part I: Regular waves. *Ocean Eng.* **149**, 53–77 (2018)
4. Khayyer, A., Gotoh, H., Shimizu, Y.: On systematic development of FSI solvers in the context of particle methods. *J. Hydrodyn.* **34**(3), 395–407 (2022)
5. Luo, M., Khayyer, A., Lin, P.: Particle methods in ocean and coastal engineering. *Appl. Ocean Res.* **114** (2021)
6. Lyu, H.-G., Sun, P.-N., Huang, X.-T., Peng, Y.-X., Liu, N.-N., Zhang, X., Xu, Y., Zhang, A.-M.: SPHydro: promoting smoothed particle hydrodynamics method toward extensive applications in ocean engineering. *Phys. Fluids* **35**(1), 017116 (2023)
7. Monaghan, J.J.: Simulating free surface flows with SPH. *J. Comput. Phys.* **110**(2), 399–406 (1994)
8. Pringgana, G., Cunningham, L.S., Rogers, B.D.: Influence of orientation and arrangement of structures on Tsunami impact forces: numerical investigation with smoothed particle hydrodynamics. *J. Waterw. Port Coast. Ocean Eng.* **147**(3), 04021006 (2021)
9. Qu, K., Wen, B., Yao, Y., Sun, W., Jiang, C.: Numerical study on hydrodynamic characteristics of movable coastal bridge deck under joint action of solitary wave and current. *Ocean Eng.* **262**, 112143 (2022)
10. Seiffert, B., Hayatdavoodi, M., Ertekin, R.C.: Experiments and computations of solitary-wave forces on a coastal-bridge deck. Part I: flat plate. *Coast. Eng.* **88**, 194–209 (2014)
11. Tripepi, G., Aristodemo, F., Meringolo, D.D., Gurnari, L., Filianoti, P.: Hydrodynamic forces induced by a solitary wave interacting with a submerged square barrier: physical tests and δ -LES-SPH simulations. *Coast. Eng.* **158**, 103690 (2020)
12. Vacondio, R., Altomare, C., De Leffe, M., Hu, X., Le Touzé, D., Lind, S., Marongiu, J.-C., Marrone, S., Rogers, B.D., Souto-Iglesias, A.: Grand challenges for smoothed particle hydrodynamics numerical schemes. *Comput. Particle Mech.* **8**(3), 575–588 (2020)
13. Wei, Z., Dalrymple, R.A., Hérault, A., Bilotta, G., Rustico, E., Yeh, H.: SPH modeling of dynamic impact of tsunami bore on bridge piers. *Coast. Eng.* **104**, 26–42 (2015)
14. Wendland, H.: Piecewise polynomial, positive definite and compactly supported radial functions of minimal degree. *Adv. Comput. Math.* **4**(1), 389–396 (1995)
15. Xu, F., Wang, J., Yang, Y., Wang, L., Dai, Z., Han, R.: On methodology and application of smoothed particle hydrodynamics in fluid, solid and biomechanics. *Acta. Mech. Sin.* **39**(2), 1–36 (2023)
16. Xu, G., Cai, C., Han, Y.: Investigating the characteristics of the solitary wave-induced forces on coastal twin bridge decks. *J. Perform. Constr. Facil.* **30**(4), 04015076 (2016)
17. Ye, T., Pan, D., Huang, C., Liu, M.: Smoothed particle hydrodynamics (SPH) for complex fluid flows: Recent developments in methodology and applications. *Phys. Fluids* **31**(1), 011301 (2019)
18. Zhang, C., Rezavand, M., Zhu, Y., Yu, Y., Wu, D., Zhang, W., Wang, J., Hu, X.: SPHinXsys: an open-source multi-physics and multi-resolution library based on smoothed particle hydrodynamics. *Comput. Phys. Commun.* **267**, 108066 (2021)
19. Zhang, C., Zhu, Y.-j., Wu, D., Adams, N.A., Hu, X.: Smoothed particle hydrodynamics: methodology development and recent achievement. *J. Hydrodyn.* **34**(5), 767–805 (2022)
20. Zhu, Y., Zhang, C., Yu, Y., Hu, X.: A CAD-compatible body-fitted particle generator for arbitrarily complex geometry and its application to wave-structure interaction. *J. Hydrodyn.* **33**(2), 195–206 (2021)

Chapter 43

Numerical Study on Smoke Diffusion Distance Induced by a Moving Vehicle in Road Tunnel Using Dynamic Mesh



Longyue Li, Yi Lu, Lin Xu, Yong Yang, Hao Wang, and Shao Chen

Abstract The occurrence of fire in tunnel results in significant human losses and economic damages. The smoke propagation mechanism in tunnel has attracted a lot of attentions all over the world. Most of the previous studies focus on the stationary fire source scenario. However, few researches consider the transient movement of a burning vehicle and its effect on smoke propagation in tunnel. Therefore, to fill the research gap, this paper studies the influence of the moving vehicle on the smoke diffusion distance in tunnel using the dynamic mesh. Based on the geometrical parameters of an urban road tunnel, a 520 m long tunnel model is established. The dynamic mesh method used in this paper is verified by the experimental results by Kim. Multiple variables including the fire heat release rate and the vehicle speed are considered in the simulation. The results show that the propagation of smoke inside tunnel is mainly affected by the vehicle moving speed. Based on the simulation results, an empirical equation of smoke diffusion length is proposed to be used in the practical engineering application.

Keywords Tunnel · Moving vehicle · Smoke diffusion distance · Fire heat release rate · Vehicle speed · Dynamic mesh

L. Li · L. Xu · Y. Yang (✉) · S. Chen
Department of Thermal Engineering, Shandong Jianzhu University, Jinan 250000, China
e-mail: yangyong@sdjzu.edu.cn

Y. Lu
Shandong Quality Inspection and Testing Center of Construction Engineering Corp., Ltd.,
Jinan 250000, China

H. Wang
Shandong Electric Power Engineering Consulting Institute Corp., Ltd., Jinan 250000, China

43.1 Introduction

Smoke propagation in the case of tunnel fire has attracted the interest of the researchers in the last two decades [1, 2]. Most of the previous researches are conducted under the stationary fire scenario. Few researches are concerned with the moving fire source scenarios. The piston wind induced by the moving vehicle and its effect on the diffusions of heat and pollutants inside tunnel have been widely proved [3, 4]. Similarly, the movement of an undetected burning vehicle (such as the Mont Blanc Tunnel Fire in 1999) will also influence the smoke propagation inside tunnel. Therefore, the smoke diffusion characteristics inside tunnel under the moving vehicle scenario is also worthy studying.

Unfortunately, few researches focus on this. For the metro fires, Wang et al., Zhang et al., Zhou et al. study the effects of the train speed, tunnel slope and blockage ratio of the cross-section on smoke diffusion in tunnel [4–7]. However, there exists large differences of wind velocity and the blockage ratio between the metro tunnel and the road tunnel. The results of the previous studies may not be applicable to that of road tunnel.

In this paper, the smoke diffusion distances both upstream and downstream the moving vehicle are studied by use of the dynamic mesh model [8–13]. Two variables including the fire heat release rate and the vehicle speed are considered in the simulation. The results can provide a reference for fire prevention and smoke exhaust strategies for tunnel.

43.2 Numerical Model

43.2.1 Tunnel Model

The tunnel model is based on the geometrical parameters of an urban road tunnel in Jinan City, China. It is about 520 m long, 12 m wide and 5 m high. As exhibited in Fig. 43.1a, a vehicle [4 m (distance) \times 2 m (width) \times 1.5 m (height)] enters the tunnel at a fixed speed, and the rear section of the vehicle catches fire at 10 m away from the tunnel entrance. However, the fire size is small and is not detected by the driver in time, the vehicle keeps driving at a fixed speed.

43.2.2 Dynamic Mesh Model

The modelling and meshing are conducted by the preprocessor software GAMBIT. To maintain the meshes quality of the calculating domain during the mesh updating process, the computational domain is divided into five parts including sub-region 1, sub-region 2, sub-region 3, sub-region 4 and the moving vehicle region (see

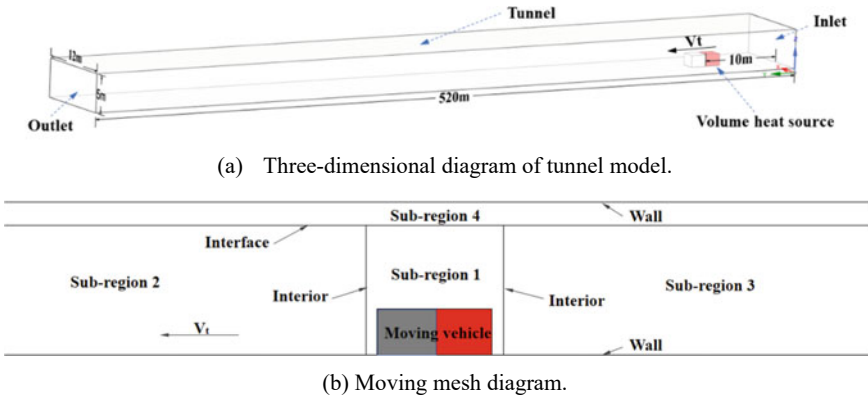


Fig. 43.1 Schematic diagram of tunnel

Fig. 43.1b). The sub-region 4 is less affected by the vehicle movement, its mesh does not change with time. The meshes in sub-region 1 move synchronously with the vehicle. By comparison, the meshes in sub-region 2 and sub-region 3 disappear and split with time, respectively. The moving vehicle is divided into two parts, the unburning front section and the burning rear section. The numerical simulation conducted in this work are implemented by the software FLUENT. Considering the influence of calculation accuracy and calculation time, the 0.02 s time step and 1,996,800 mesh schemes are chosen in the simulation.

43.2.3 CFD Methods and Boundary Conditions

The governing equations adopted in the simulation are based on the combination of 3D compressible unsteady N-S equations and the SST $k-\omega$ turbulence model [14]. The fire source is set as a volumetric heat source (2 m × 2 m × 1.5 m). The initial temperature is set as 27 °C. The tunnel inlet and outlet are set as the pressure inlet and pressure outlet with zero static pressure. The no-slip wall conditions are applied in the top, side and ground faces of the computational domain. The vehicle surfaces for the unburning section are also set as the no-slip wall boundary. Different values of vehicle speed (V_t) and fire heat release rate (Q) are designed to study their effects on the smoke diffusion distance inside tunnel. The regarding fire scenarios are listed in Table 43.1.

Table 43.1 Summary of all fire scenarios

Case	V_t /km/h	Q /MW	Case	V_t /km/h	Q /MW
1–3	0	10/15/20	11–12	15	10/20
4–6	5	10/15/20	13–15	20	10/15/20
7–8	8	10/20	16–18	40	10/15/20
9–10	10	10/20	19–21	60	10/15/20

43.2.4 Verification of Numerical Model

To verify the accuracy of dynamic mesh, the measurement data of Kim [15] are compared with the predicted results by CFD. As shown in Fig. 43.2a, Kim measures the transient pressure variation induced by a high-speed moving train in a model tunnel. By use of the dynamic mesh model mentioned above, the pressure values at the measuring points of Kim's experiment are predicted, and the resistance coefficients of C_p are further calculated. Figure 43.2b presents the comparison between the experimental and predicted values of C_p . The results show that the numerical results fit relatively well with the experimental data. The error between the simulation and Kim's experimental data is within 5%, and the maximum error is no more than 20%. It confirms the reliability of the numerical scheme.

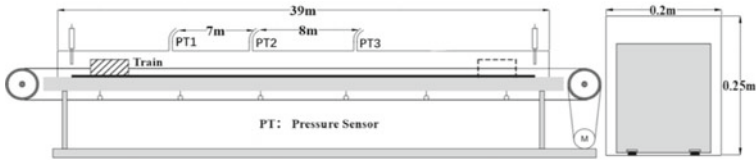
43.3 Results and Discussion

43.3.1 Dynamic Smoke Diffusion

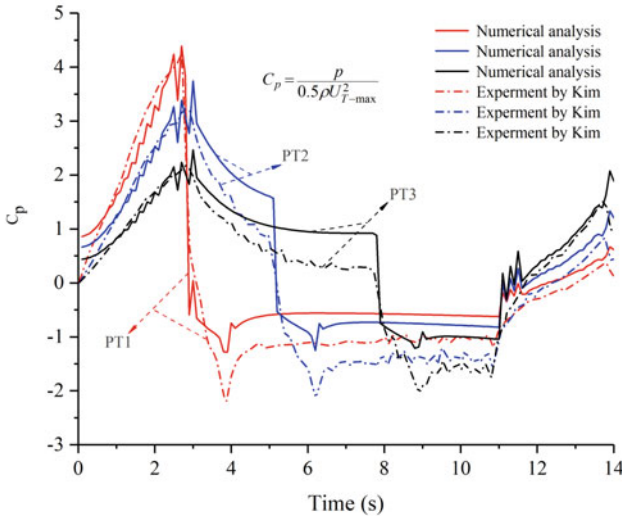
For convenient analysis, the variables of S_u and S_d are introduced to locate the real-time position of smoke diffusion front upstream and downstream the fire source, as shown in Fig. 43.3. The variable S_t representing the smoke diffusion distance inside tunnel is the length between the smoke diffusion front upstream and downstream the fire source.

For the case 13, the temperature distribution at the longitudinal central section of the tunnel is shown in Fig. 43.4. The arrival of smoke is defined by the significant temperature increase [16]. Obviously, the smoke propagates upstream inside the tunnel with the moving vehicle. The value of S_t increases from 28 m (at $t = 3$ s), 64 m (at $t = 10$ s) to 116 m (at $t = 20$ s). Moreover, the smoke flows downstream the fire source take on obvious fluctuation trend. This is due to the coupled effect of buoyancy and inertia force. At $t = 20$ s, the smoke descends to the floor at about 80 m downstream the vehicle, endangering the personal evacuation.

In the following section, the effects of vehicle speed and fire heat release rate on the smoke diffusion inside tunnel are detailed analyzed based on the temperature distribution at $t = 20$ s.



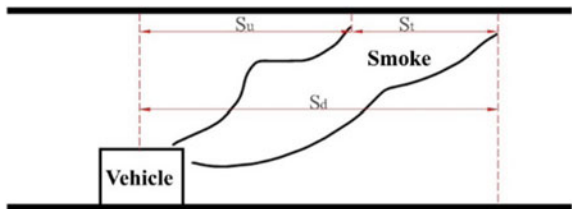
(a) Experimental schematic of Kim



(b) Comparison of Cp values between the simulation and experiment.

Fig. 43.2 Validation of numerical method by experiment [15]

Fig. 43.3 Schematic diagram of smoke diffusion from moving fire source



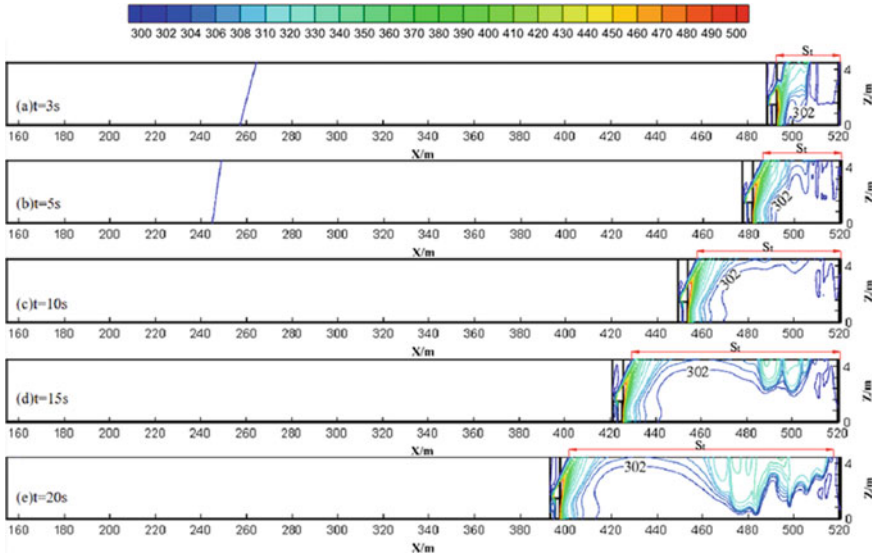


Fig. 43.4 Dynamic temperature distribution on the longitudinal central section in tunnel ($Q = 10$ MW, $V_t = 20$ km/h)

43.3.2 Moving Vehicle Speed

Figure 43.5 depicts the variation of temperature distribution with the vehicle speed for a given heat release rate ($Q = 20$ MW). It is shown that the value around 20 km/h is an important critical point to distinguish the smoke front position relative to the moving vehicle. With the increase of vehicle speed, the smoke front position transfers from upstream to downstream the fire source. The value of S_u firstly decreases to zero and then reversely increases. The smoke diffusion distance downstream the fire source (S_d) keeps increasing gradually with the increasing vehicle speed. As mentioned above, the smoke propagation downstream the fire source is controlled by the coupled effect of buoyancy and inertia force. When $V_t < 5$ km/h, the piston wind induced by vehicle is weak, the smoke distributes in the upper zone of the tunnel. When 20 km/h $< V_t < 40$ km/h, the inertia force grows to be equivalent with the buoyancy force, leading to the evident fluctuation of smoke flow. When $V_t = 60$ km/h, the inertia force due to the moving vehicle is large enough to sufficiently mix the smoke on the whole cross-section of tunnel.

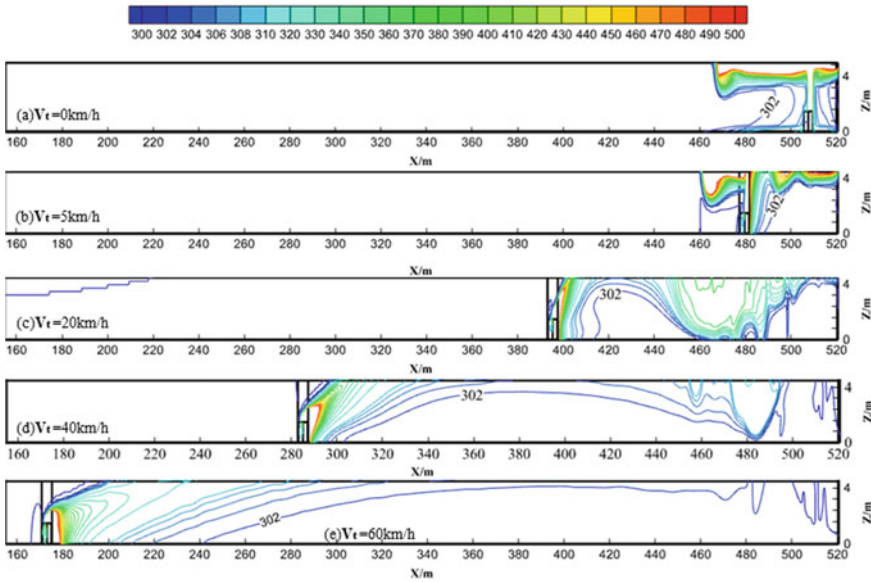


Fig. 43.5 Longitudinal central section of the smoke temperature at $t = 20$ s in tunnel ($Q = 20$ MW and $V_t = 0-60$ km/h)

43.3.3 Fire Heat Release Rate

The variation of temperature distribution with the fire heat release rate is exhibited in Fig. 43.6. For the stationary fire source, the S_u value increases by about 10 m with the Q increasing of 10 MW (see Fig. 43.6a, b). For the cases of $V_t = 60$ km/h, no obvious difference is found in the temperature distribution at the longitudinal central section of tunnel with the Q increasing of 10 MW (see Fig. 43.6c, d). This demonstrates that the fire heat release rate has negligible impact on the values of S_u , S_d and S_t , for the higher vehicle speed cases. This is because two reasons: (1) the piston wind; (2) much eddies behind the vehicle.

As shown in Fig. 43.7, The piston wind and the eddies behind the vehicle strengthens the mixing effect of the smoke downstream the moving vehicle.

For different vehicle speed and fire heat release rate, the values of S_u and S_t are presented in Fig. 43.8. The variation of S_u with V_t can be divided into two regions. In region I, the value of S_u decreases rapidly to zero with the increasing V_t . In region II, the smoke front location moves to downstream the vehicle and S_u value increases with V_t . The critical V_t value at the interface of two regions is about 10 km/h. The piston wind induced by the vehicle at 10 km/h succeeds to prevent the backflow of the smoke. This is similar with the critical velocity for the longitudinal ventilation.

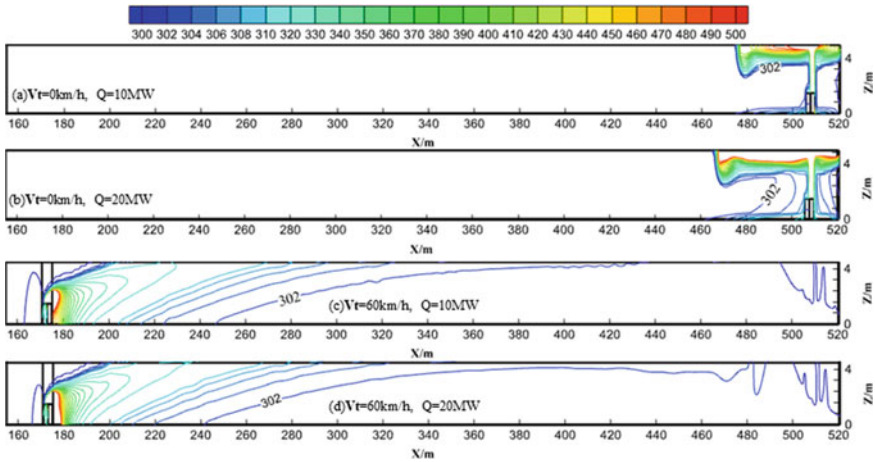


Fig. 43.6 Longitudinal central section of the smoke temperature ($Q = 10$ and 20 MW, $V_t = 0$ and 60 km/h) and velocity ($Q = 20$ MW and $V_t = 60$ km/h) in tunnel

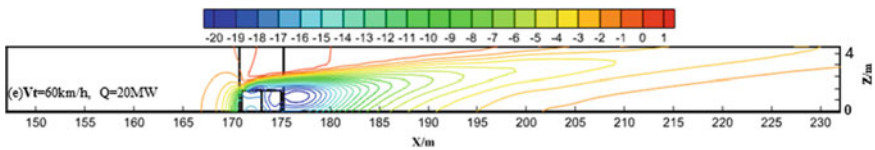


Fig. 43.7 Longitudinal central section of the smoke velocity ($Q = 20$ MW and $V_t = 60$ km/h) in tunnel

By comparison, the fire heat release rate has little effect on the values of S_u and S_t especially for the higher vehicle speed ($V_t > 20$ km/h). The smoke propagation length inside tunnel (S_t) shows an exponential increasing trend with the increasing vehicle speed. The fitting curve in Fig. 43.8 is expressed as Eq. (43.1):

$$S_t = 512.44e^{\frac{V_t}{153.40}} - 472.77 \tag{43.1}$$

The fitting correlation coefficient of Eq. (43.1) is 0.991, which justifies the accuracy of fitting curve.

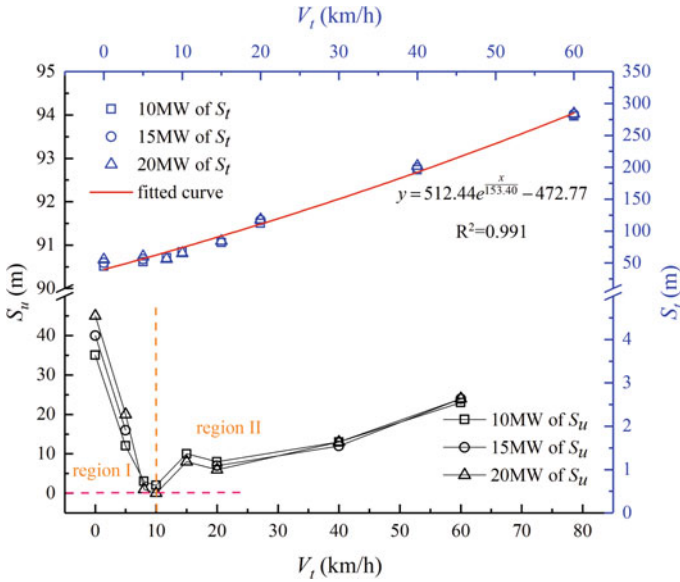


Fig. 43.8 The variation of S_u and S_t with the vehicle speed

43.4 Conclusion

This paper studies the smoke diffusion characteristics inside tunnel for a moving burning vehicle scenario. The influences of vehicle speed and fire heat release rate on the smoke propagation are analyzed. The major conclusions are summarized as follows:

The accuracy of the adopted dynamic mesh method is verified by the experimental results by Kim. The error between the simulation and Kim’s experimental data is within 5%, the maximum error is no more than 20%. With the movement of the burning vehicle, the smoke gradually propagates upstream. The smoke-filled region inside tunnel becomes larger with time. The vehicle speed has an evident effect on the smoke diffusion inside tunnel. The variation of S_u with V_t is divided into two regions. In region I, S_u decreases rapidly to zero with the increasing V_t . At $V_t = 10$ km/h, the induced piston wind prevents the backflow of smoke. In region II, the smoke front location moves to downstream the vehicle and S_u value increases with V_t . The fire heat release rate has negligible influence on the values of S_u and S_t , especially for the higher vehicle speed ($V_t > 20$ km/h). An empirical correlation of S_t is proposed based on the simulated results, which can be used in the practical engineering application.

Acknowledgements The work was supported by the Natural Science Foundation of Shandong Province of China (Grant numbers: ZR2021ME200, ZR2020QE279) and National Natural Science Foundation of China (Grant numbers: 51108254).

References

1. Gao, Y.J., Zhu, G.Q., et al.: Experimental and numerical studies on ceiling maximum smoke temperature and longitudinal decay in a horseshoe shaped tunnel fire. *Case Stud. Thermal Eng.* **12**, 134–142 (2018)
2. Chen, C.K., Zhu, C.X., Liu, X.Y., Yu, N.H.: Experimental investigation on the effect of asymmetrical sealing on tunnel fire behavior. *Int. J. Heat Mass Transf.* **92**, 55–65 (2016)
3. Liu, M.Z., Zhu, C.G., et al.: The environment and energy consumption of a subway tunnel by the influence of piston wind. *Appl. Energy* **246**, 11–23 (2019)
4. Wang, X.M., Zhang, T.T., Tan, Y.F., Liu, Z.: Piston-wind ventilation strategy for thermal environment improvement of heat-supply compartment in utility tunnels. *Case Stud. Thermal Eng.* **30**, 101790 (2022)
5. Wang, Z., Zhou, D., et al.: Moving model test of the smoke movement characteristics of an on-fire subway train tunneling through a tunnel. *Tunn. Undergr. Space Technol.* **96**, 103211 (2020)
6. Zhang, Z.Q., Tan, Y.J., et al.: Experimental investigation of tunnel temperature field and smoke spread under the influence of a slow moving train with a fire in the carriage. *Tunnell. Undergr. Space Technol. Incorpor. Trenchless Technol. Res.* **131**, 104844 (2023)
7. Zhou, D., Hu, T.E., et al.: Influence of tunnel slope on movement characteristics of thermal smoke in a moving subway train fire. *Case Stud. Thermal Eng.* **28**, 101472 (2021)
8. Dimitri, J., Mavriplis, Y.Z.: Construction of the discrete geometric conservation law for high-order time-accurate simulations on dynamic meshes. *J. Comput. Phys.* **213**(2), 557–573 (2006)
9. Tan, Z.J., Tang, T., Zhang, Z.R.: A simple moving mesh method for one and two dimensional phase-field equations. *J. Comput. Appl. Math.* **190**(1–2), 252–269 (2006)
10. Li, Y.H., Kong, S.-C.: Integration of parallel computation and dynamic mesh refinement for transient spray simulation. *Comput. Methods Appl. Mech. Eng.* **198**(17–20), 1596–1608 (2009)
11. Nkonga, B.: On the conservative and accurate CFD approximations for moving meshes and moving boundaries. *Comput. Methods Appl. Mech. Eng.* **190**(13–14), 1801–1825 (2000)
12. Tenchev, R.T., Mackenzie, J.A., Scanlon, T.J., et al.: Finite element moving mesh analysis of phase change problems with natural convection. *Int. J. Heat Fluid Flow* **26**(4), 597–612 (2005)
13. Quan, S.P., Lou, J., Schmidt, D.P.: Modeling merging and breakup in the moving mesh interface tracking method for multiphase flow simulations. *J. Comput. Phys.* **228**(7), 2660–2675 (2009)
14. Zhou, Y., Qian, W.Q., Deng, Y.Q., Ma, M.: Introductory analysis of the influence of Menter’s $k-\omega$ SST turbulence model’s parameters. *Acta Aerodynamica Sinica* **28**(02), 213–217 (2010)
15. Kim, J.Y., Kim, K.Y.: Experimental and numerical analyses of train-induced unsteady tunnel flow in subway. *Tunnell. Undergr. Space Technol. Incorpor. Trenchless Technol. Res.* **22**(2), 166–172 (2007)
16. Ahmed, K., Yuan, Z.Y., Lei, B.: Ceiling temperature distribution and smoke diffusion in tunnel fires with natural ventilation. *Fire Safety J.* **62**(C), 249–255 (2013)

Chapter 44

Static Aeroelastic Analysis of Electric Vertical Takeoff and Landing Aircraft ET480



Shuai Zhang, Junqi Zhang, Jiayong Zhang, and Jielong Wang

Abstract This paper presents the static aeroelastic analysis of the electric vertical takeoff and landing aircraft (eVTOL) ET480 by using the inner-house code AeLasV2.0.4. Firstly, the structure modeling of complete configuration for this type of eVTOL are implemented by using the geometrical nonlinear beam elements. The structural deformations are then predicted according to this finite element model. Secondly, when affording the high resolution CFD meshes, the aerodynamic performance is simulated accurately by solving the Reynolds-Averaged-Navier-Stokes (RANS) equations. Third, the data interface between structural deformations and aerodynamic pressures are carefully designed to transfer information for the CFD/CSD coupling simulation. Finally, the static aeroelastic analysis is performed by AeLasV2.0.4 to estimate the aeroelastic behavior of ET480 to support its aerodynamic designing and structural designing.

Keywords Static aeroelastic analysis · Aerodynamic load · Deformation · Cruising performance

44.1 Introduction

In general, aeroelastic problems of civil aircraft due to the interactions between elastic deformations and aerodynamic forces are determined by flow nonlinearities and at times by the deformations of sub-structures, such as wings, tails and control surfaces. Therefore, coupled approaches are necessary to solve such problems [1], accurately. These approaches are usually categorized in two types, loosely-coupled or fully-coupled. The loosely-coupled methods iteratively solve the fluid and structure equations by introducing the coupling scheme without altering the source code of either fluid or structure analysis tool. Because it allows the use of a variety of existing

S. Zhang · J. Zhang · J. Zhang · J. Wang (✉)
COMAC Beijing Civil Aircraft Technology Research Institute, No.3 North Street of Future Science City, Changping, Beijing 102201, P.R. China
e-mail: jelon.wang@gmail.com

fluid/structure codes, the loosely-coupled methods have developed quickly. Fully-coupled methods [2, 3] require the solution of the fluid and structure equations simultaneously, which necessitates the reformulation of the governing equations of each discipline [4]. The stiffness matrices associated with the structures are orders of magnitude stiffer than those associated with fluids. Thus, it is numerically inefficient to solve both systems by using a monolithic numerical algorithm [1, 5, 6]. Till now, the fully-coupled methods are still the research hot topics. In view of this situation, we paid a special attention to the loosely-coupled approaches, and explored the available loosely-coupled tools [7–9]. For example, the structured NASA code CFL3D v6.44 [10] developed as a means of aeroelastic simulation, and the unstructured NASA code FUN3D v5.6 [11] was given aeroelastic capability as well. These NASA CFD codes simulated the aeroelastic phenomena by using a nonlinear flow field solver and a modal representation of the structural equations. The fluids and structures were modeled independently and exchanged boundary information to obtain aeroelastic solutions in an efficient manner. In Refs. [12, 13], a loosely-coupled approach based on high-fidelity numerical fluid dynamics and structural analysis methods performed aeroelastic analyses. An in-house simulation procedure was built around DLR's flow solver TAU and the commercial finite-element analysis code NASTRAN, and the numerical results were validated against experimental data. Similarly, a static fluid–structure simulation [14] on a complete aircraft configuration has been performed using the commercial CFD++ Navier-Stokes code and the NASTRAN structural analysis code. Soon after, a numerical static aeroelastic analysis procedure [15] is presented by applying a modal approach in coupling the fluid dynamic and structural solutions. This approach constructed a modal model for aircraft wind-tunnel model through a preliminary structural modal analysis from which a number of natural modes are selected. Recently, the fluid structure interaction methodology [16] couples high-fidelity computational fluid dynamics to a simplified beam representation of the finite element model. The correlation between the numerical simulations and wind tunnel data for varying angles of attack is analyzed and the results revealed the importance of considering structural model deformations in the aerodynamic simulations.

The above investigations show that CFD solvers with high resolution was commonly applied in a loosely-coupled approach. Whereas, the modal representation based on linear structural assumption or simplified beam representation were popular selections describing the structural deformations that had been limited to deal with deformations with small amplitudes. This paper presents the result of a static aeroelastic analysis implemented by using inner-house code AeLasV.2.0.4 method which with high fidelity that takes into accounts the nonlinearity of flow and geometric nonlinearity of structural deformation.

44.2 Aeroelastic Modeling of ET480

The aeroelastic modeling of ET480 includes structural modeling and aerodynamic modeling. Through structural modeling, the whole aircraft model is preliminarily verified, and then through aerodynamic modeling, the data exchange interface between the aerodynamics and the structure is established to complete the preparation work for aeroelastic analysis.

44.2.1 Structure Modeling

The self-developed software HBEM was used to create a geometrically nonlinear two-dimensional plate-shell—one-dimensional beam hybrid element model. HBEM program is used to solve structural deformation, vibration mode, dynamic response and control unit design by finite element method. The concrete modeling process consists of six steps:

(1) Extraction of two-dimensional cross-section input data for the whole machine

The software CATIA V5 R20.0 was used to extract the wing, fuselage, flat tail and vertical tail of ET480. Refer to Fig. 44.1 for the extracted two-dimensional cross sections. After extracting the two-dimensional section, the curve needs to be closed, and then the section plane shape is constructed. It need to keep the main geometric features constant. Each cross section is a structural control section of the subsequent nonlinear finite element model. The more there are, the more accurate the nonlinear beam finite element model is and the more accurately it can simulate the stiffness characteristics of the model wing. After the section extraction, the curve should be closed and the section plane shape should be constructed successively, as shown in Fig. 44.2.

After that, the output data was imported into ABAQUS to divide the finite element mesh into quadrilateral structure mesh and complete the mesh quality check. After

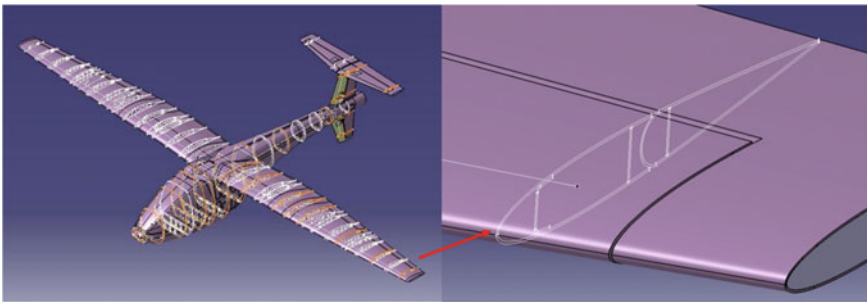


Fig. 44.1 Two-dimensional cross-section of aircraft structure



Fig. 44.2 Plane shape of two-dimensional airfoil section

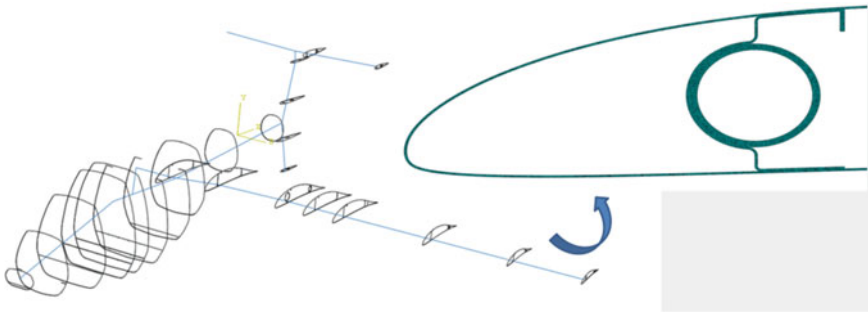


Fig. 44.3 A two-dimensional cross-section grid of ET480

completing multiple two-dimensional cross-section meshing of the wing, fuselage, flat tail and vertical tail of ET480, a total of 400,000 quadrilateral elements are included, as shown in Fig. 44.3. It is not difficult to find from the figure that ET480 is a thin-walled structure.

(2) Create HBEM nonlinear finite element model

Use MatLab script files to generate flx data files and finite element model dat data files.

(3) Create a two-dimensional cross-section finite element model

With the ABAQUS finite element grid data stored in the inp file as the input, the MatLab script file was run to create a new format of two-dimensional section digital model ios data file.

(4) Structural stiffness prediction of the whole machine

The above finite element model data file is read through the proprietary intellectual property program CroSect or HBEM. The program CroSect or HBEM will automatically establish finite element discrete models, calculate the torsional stiffness, bending stiffness, tensile stiffness and stiffness coupling terms, and determine the position of the stiffness center, the corresponding compliance matrix, the full-rank mass matrix and the position of the section centroid.

(5) Perfect the finite element model of the whole machine structure

The stiffness prediction results of the whole machine structure were assigned to the finite element beam model to complete the whole machine structure model.

(6) Numerical and modular static loading verification of the whole machine structure

Given the appropriate load, the nonlinear deformation of the structure is predicted and the rationality of the deformation is checked.

44.2.2 Aerodynamic Modeling

Firstly, structured fluid mesh generation and related aerodynamic CFD calculation of ET480 half mode were carried out. The preliminary meshing of half mode is divided into 30 million nodes, turbulence model SST, including fuselage, wing, tail thrust, strut, landing gear, flat tail, vertical tail and other grids. Complete the CFD calculation and check of the half mode, and map the half mode to the complete model after confirmation. The structured surface mesh of half- and full-mode can be referenced in Fig. 44.4.

AeLas aeroelastic calculation will automatically establish the interface for load and displacement data exchange between aerodynamics and structure, but it needs to define the mapping relationship between aerodynamics grid points on aircraft surface and structural finite element beams, rigid bodies or plates and shells, as shown in Fig. 44.5.

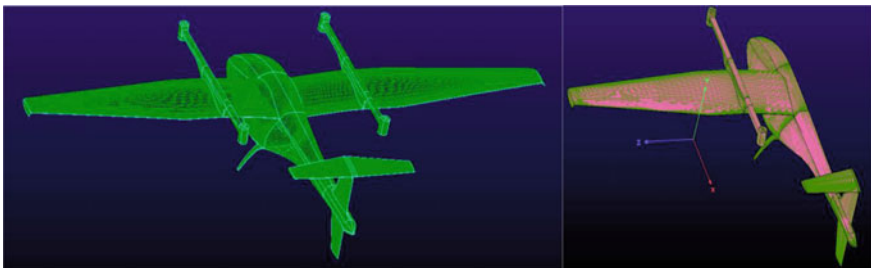


Fig. 44.4 Structured surface grids for half and full modes

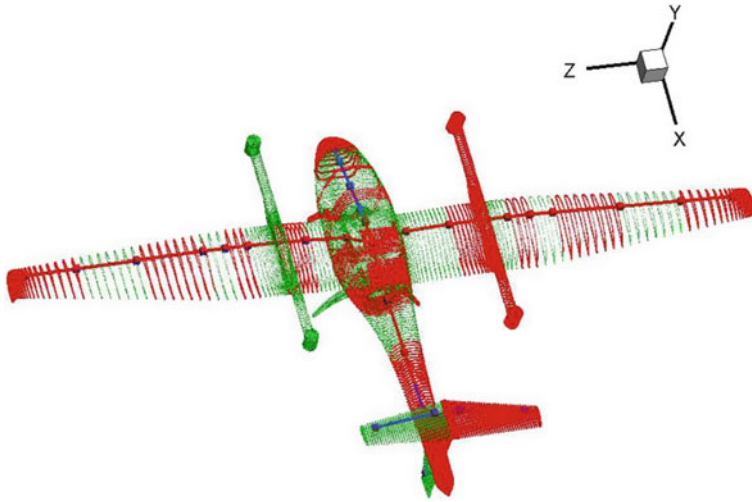


Fig. 44.5 Different color surface grid points in the figure belong to different structural units

44.3 Aeroelastic Analysis of ET480

After the aerodynamic and structural modeling are completed respectively, the static aeroelastic analysis model is formed by coupling the two models. AeLas will automatically call HBEM to complete the structural deformation calculation, and calculate the surface auxiliary point deformation according to the deformation of the main node of the structure, which is used to calculate the exchange displacement and aerodynamic load data with the pneumatic Sflow.

44.3.1 Calculation Working Condition

The calculation conditions are shown in Table 44.1. Assuming a flight speed of 110 km/h, the flight Angle of attack ranges from -2° to 4° .

44.3.2 Analysis of Fluid–Structure Coupling Calculation Results

AeLas (V2.0.4 Linux version), an independent intellectual property tool, was used for static aeroelastic analysis of ET480. The static aeroelasticity calculation starts from the shape of the frame (0-G shape) and considers the effect of gravity. The fluid–structure coupling iterative calculation was carried out until convergence, and the elastic

Table 44.1 Calculated working condition

Ma	T/(Rankian temperature)	Alpha/(°)	Beta/(°)
0.09	518	- 2	0
0.09	518	1	0
0.09	518	0	0
0.09	518	1	0
0.09	518	2	0
0.09	518	3	0
0.09	518	4	0

shape calculation results were obtained (see Table 44.2). Not taking into account the elastic deformation, that is, the rigid shape calculation results (see Table 44.3).

From the above two data tables, it can be seen that, due to the small structural deformation, the aerodynamic parameter reduction is low, that is, the average elastic-stiffness ratio is 99.04%. In addition, in order to intuitively study the aerodynamic distribution of the ET480 cruise flight structure after deformation. Figure 44.6 shows the aircraft surface pressure and direction at 0° Angle of attack. It can be seen from the pressure distribution that the aerodynamic pressure of the inner wing between the rotor struts decreases obviously.

Table 44.2 Calculation results of elastic shape (body shafting)

Ma	T/(Rankian temperature)	Alpha/(°)	CL	CD	CMZ
0.09	518	- 2	0.1549	0.0201	0.0159
0.09	518	- 1	0.2055	0.0205	0.0266
0.09	518	0	0.2568	0.0214	0.0375
0.09	518	1	0.3094	0.0227	0.0483
0.09	518	2	0.3616	0.0245	0.0592
0.09	518	3	0.4127	0.0266	0.0702
0.09	518	4	0.4625	0.0291	0.0809

Table 44.3 Calculation result of rigid contour (body shafting)

Ma	T/(Rankian temperature)	Alpha/(°)	CL	CD	CMZ
0.09	518	- 2	0.1572	0.0200	0.0166
0.09	518	- 1	0.2081	0.0205	0.0272
0.09	518	0	0.2599	0.0214	0.0379
0.09	518	1	0.3127	0.0227	0.0487
0.09	518	2	0.3649	0.0245	0.0595
0.09	518	3	0.4162	0.0266	0.0703
0.09	518	4	0.4666	0.0292	0.0809

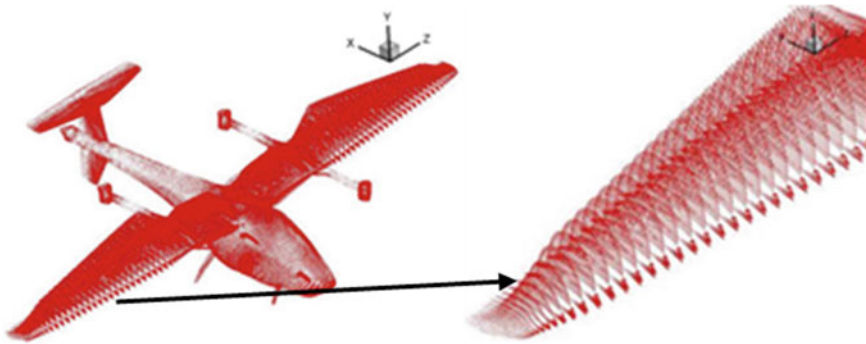


Fig. 44.6 Aerodynamic distribution on the whole aircraft surface

The aeroelastic analysis tool will automatically interpolate the above aerodynamic pressure FEM into the structural finite element node, as shown in Fig. 44.7. The calculation results show that the lift spanwise distribution of ET480 is inconsistent with the assumption of elliptical distribution, as shown in Fig. 44.8.

In the calculation of the ultimate load of ET480, the elliptic hypothesis of lift spanwise distribution is used, and the shape of drag distribution along the spanwise distribution is consistent with that of lift. Therefore, the calculation of the ultimate load of ET480 is quite different from the real load distribution.

The total air lift of the whole aircraft can be calculated by static airelastic analysis (see Table 44.4).

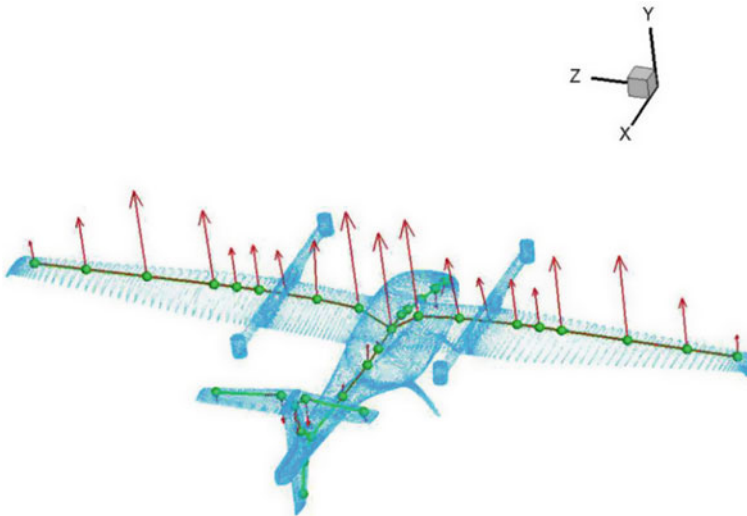


Fig. 44.7 Aerodynamic load transfer of whole structure

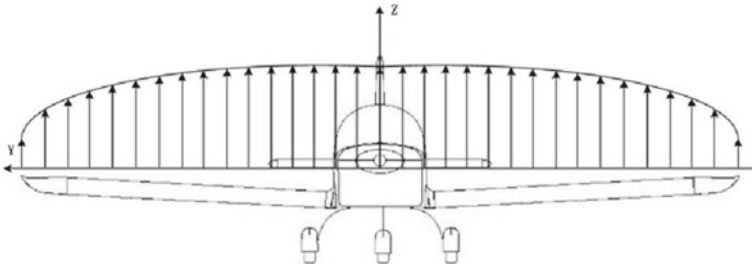


Fig. 44.8 Wing lift extensional elliptic distribution hypothesis

Table 44.4 Aerodynamic calculation results of the whole engine (body shafting)

Ma	T/(Rankian temperature)	Alpha/(°)	FY(N)
0.09	518	0	3.50739e + 03
0.09	518	2	4.93067e + 03
0.09	518	4	6.30581e + 03

ET480 has defined the maximum take-off weight of the aircraft at 480 kg. When the Angle of attack is 2°, the aerodynamic force $F_y = 4930.67 \text{ N} > G = 4708.8 \text{ N}$, which meets the lift requirements for cruise flight. After the aerodynamic pressure is loaded into the finite element node of the structure, the structural statics analysis is carried out to predict the structural deformation. Figure 44.9 shows the aerodynamic profile of the whole aircraft before and after deformation during cruise flight at an Angle of attack of 4°. Green is the pre-deformation configuration and red is the post-deformation configuration. Figure 44.10 shows the deformation of the left wing.

The calculation shows that the vertical displacement at the node on the left wing is 11.4 mm. Small deformation indicates that the design of structural stiffness is too conservative and there is still a large space for structural weight reduction.

The analysis of aerodynamic and structural coupling effects shows that there is a weak coupling effect between aerodynamic and structural deformation for the current aerodynamic and structural design configurations. In other words, the structural stiffness is too large and the deformation is small, which has little influence on the magnitude, direction and distribution of aerodynamic force. The elasto-rigid ratio of aerodynamic lift coefficient is 99.04%. However, the vertical take-off and landing system has obvious influence on the aerodynamic performance of cruise flight, which increases the flight drag and reduces the lift force, thus affecting the aerodynamic efficiency.

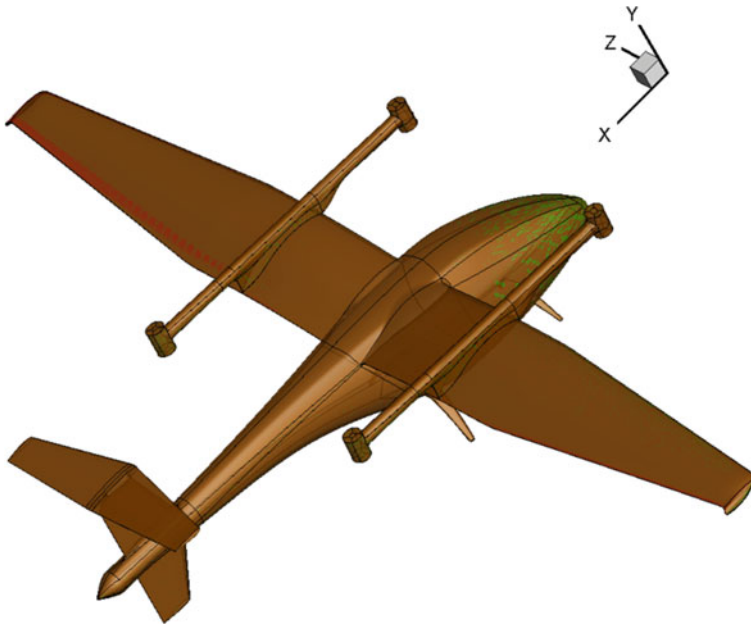


Fig. 44.9 Aerodynamic surface deformation of the whole machine

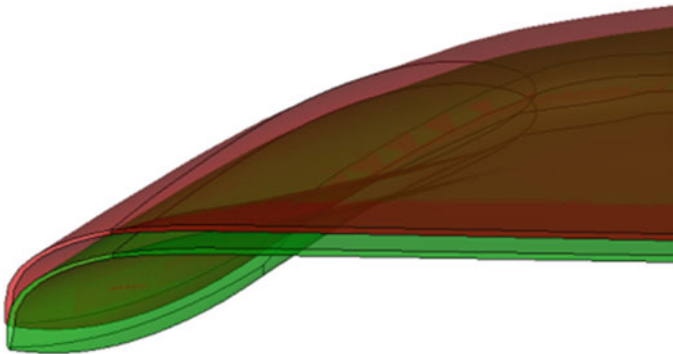


Fig. 44.10 The deformation of the left wing

44.4 Conclusion

According to the above Static aeroelasticity analysis, the conclusions are as follows:

- (1) Static aeroelastic analysis shows that the coupling effect between the rotor strut and the fixed wing affects the aerodynamic efficiency. The aerodynamic surface pressure distribution of the whole aircraft indicates that the aerodynamic lift of the inner wing segment (the part of the wing between the rotor struts) is

significantly reduced. The rotor strut of the rotor has a large drag, which reduces the aerodynamic efficiency during cruise flight, so it needs to be optimized accordingly.

- (2) Based on static aeroelastic analysis, the longitudinal distribution of lift force at the finite element node of the wing structure does not meet the elliptic distribution, so it is too conservative to use the elliptic longitudinal distribution of lift resistance to calculate the limit load for strength check.
- (3) Static aeroelastic analysis shows that the structure has little deformation during cruise flight, and the structure of the outer wing segment can be optimized to reduce weight.

References

1. Guruswamy, G.P. (ed.): Coupled Finite-Difference/Finite-Element Approach for Wing-Body Aeroelasticity. AIAA Paper 92-4680 (1992)
2. Bendiksen, O.O. (ed.): A New Approach to Computational Aeroelasticity. AIAA Paper 91-0939 (1991)
3. Felker, F.F. (ed.): A New Method for Transonic Static Aeroelastic Problems. AIAA Paper 92-2123 (1992)
4. Bauchau, O.A., Ahmad, J.U. (eds.): Advanced CFD and CSD Methods for Multidisciplinary Applications in Rotorcraft Problems. AIAA Paper 96-4151 (1996)
5. Dunne, T., Rannacher, R., Richter, T.: Numerical simulation of fluid-structure interaction based on monolithic variational formulations. In: Galdi, G.P., Rannacher, R. (eds.) *Fundamental Trends in Fluid-Structure Interaction. Contemporary Challenges in Mathematical Fluid Dynamics and Its Applications*, World, pp. 1–75, 552. Scientific, Singapore (2010)
6. Hoffmana, J., Janssona, J., Janssona, N. (eds.): Simulation of 3D unsteady incompressible flow past a NACA 0012 wing section, KTH-CTL-4023 (2012)
7. Guruswamy, G.P.: Vortical flow computations on swept flexible wings using Navier-Stokes equations. *AIAA J.* **28**(12), 2077–2084 (1990). <https://doi.org/10.2514/3.10524>
8. Bond, V.L., Canfield, R.A., Suleman, A., Blair, M.: Aeroelastic scaling of a joined wing for nonlinear geometric stiffness. *AIAA J.* **50**(3), 513, 522 (2012). <https://doi.org/10.2514/1.41139>
9. Prananta, B.B., Meijer, J.J., Muijden, J.V. (eds.): *Static Aeroelastic Simulation Using CFD, Comparison with Linear Method*, NLR-TP-2003-530 (2003)
10. Bartels, R.E. (ed.): *Development of Advanced Computational Aeroelasticity Tools at NASA Langley Research Center*, AVT-154-003 (2008)
11. Silva, W.A., Vatsa, V.N., Biedron, R.T. (eds.): *Development of Unsteady Aerodynamic and Aeroelastic Reduced-Order Models Using the FUN3D Code*, IFASD 2009-030 (2009)
12. Keye, S., Rudnik, R.: Aeroelastic effects in maximum lift prediction of a transport aircraft and comparison to flight data. In: 32nd AIAA Applied Aerodynamics Conference, pp. 1–11. AIAA, Washington, DC (2014)
13. Keye, S., Rudnik, R.: Validation of wing deformation simulations for the NASA CRM model using fluid-structure interaction computations. In: 53rd AIAA Aerospace Sciences Meeting, pp. 1–13. AIAA, Washington, DC (2015)

14. Cella, U., Biancolini, M.E.: Aeroelastic analysis of aircraft wind-tunnel model coupling structural and fluid dynamic codes. *J. Aircr.* **49**(2), 407–414 (2012). <https://doi.org/10.2514/1.C031293>
15. Biancolini, M.E., Evangelos, M., Cella, U., Groth, C., Genta, M.: Static aeroelastic analysis of an aircraft wind-tunnel model by means of modal RBF mesh updating. *J. Aerosp. Eng.* **29**(6), 04016–04061 (2016). [https://doi.org/10.1061/\(ASCE\)AS.1943-5525.0000627](https://doi.org/10.1061/(ASCE)AS.1943-5525.0000627)
16. Bdeiwi, H., Ciarella, A., Peace, A., Hahn, M.: Model structure effect on static aeroelastic deformation of the NASA CRM. *Int. J. Numer. Methods Heat Fluid Flow* **30**(9), 4167 (2019). <https://doi.org/10.1108/HFF-07-2018-0352>

Chapter 45

Study on Stress Variation and Sealing of Casing-Cement Ring-Strata Assemblies Under Sour Gas Production Conditions



Dingyuan Liu, Jun Li, and Wei Lian

Abstract During the exploitation of deep and ultra-deep sour gas-bearing gas wells in Sichuan, the casing-cement sheath-formation combination has been under high pressure and acidic environment for a long time. The stress variation law of the combination is complex, and the problem of sealing failure annulus pressure is serious. In this paper, the finite element software is used to establish a model of casing-cement sheath-formation combination with corrosion defects under high-pressure acid gas production conditions. The stress variation law of the combination under the change of casing internal pressure and formation pressure is clarified, and the sealing failure mechanism of casing-cement sheath-formation combination is revealed. The results show that corrosion is the key factor affecting the sealing failure caused by the stress change of the assembly, and the sealing failure of the assembly is related to the corrosion position. When the casing is subjected to uniform corrosion, as the degree of corrosion increases, the overall stress of the combination becomes larger, resulting in plastic strain between the cement sheath and the casing, and debonding between the plastic strain and the cement-well interface. The two factors together aggravate the continuous expansion of the microannulus at the cement-well interface. When the cement sheath is corroded, the cementation strength of the local cementing interface will be destroyed. With the expansion of the corrosion range, the stress of the combination is redistributed, and the stress distribution is gradually complicated. A certain degree of stress concentration is easy to occur at the corrosion position, resulting in plastic strain between the cement sheath and the casing, which in turn aggravates the failure risk of the cementing interface. In the design of gas well cement slurry containing acid gas, the corrosion resistance and the sealing performance of the cementing interface should be considered.

Keywords Corrosion · Assembly · Variation of stress · Seal integrity

D. Liu · J. Li (✉) · W. Lian
China University of Petroleum-Beijing, Changping, Beijing 102200, China
e-mail: lijun446@vip.163.com

45.1 Instruction

In recent years, the oil and gas industry is facing the current situation of market turmoil and complex downhole environment, which brings severe challenges to safe, lasting and stable well conditions. Wellbore integrity is a key issue in the wellbore life cycle, which affects the safety of operators, the environment around the site and the benefits of oil and gas wells [1]. The deep and ultra-deep formations in the Sichuan Basin of China are the most complex natural gas producing areas in the world, with ultra-high pressure (160 MPa in Well Longgang 70), high salinity formation water and strong corrosion (for example, H_2S : 7.1–13.7%, CO_2 : 5.1–10.4% in the Luojiashai gas field in northeastern Sichuan; the characteristics of H_2S : 5–15%, CO_2 : 5–10%) in Puguang gas field. Due to the complex regional geological environment, the casing-cement ring-formation combination has been in the environment of high pressure and acidic gas interaction for a long time, which leads to the complex stress variation law of the combination and the serious problem of sealing failure annulus pressure (the annulus pressure of some gas wells in Puguang gas field exceeds 20 MPa), which poses a serious threat to production and life. Therefore, it is necessary to study the stress variation law and sealing integrity of casing-cement sheath-formation combination to reduce or avoid major economic losses in the production process of high-pressure sour gas wells.

For the high-pressure acid gas environment, Condor-Tarco et al. [2] found through a large number of experiments that compared with the uncorroded cement stone, the strength of the cement stone is greatly reduced with the increase of the corrosion age. The higher the concentration of corrosive medium, the more easily the cement stone is corroded. Omosebi et al. [3] found that when the temperature and pressure in the formation reach or even exceed the critical temperature and critical pressure of CO_2 , this supercritical state of CO_2 will accelerate the corrosion of cement stone, thereby increasing the risk of cement stone sealing failure. Some researchers have also studied the change of casing in corrosive environment. Wu et al. [4] believed that the product film formed by Cr-containing steel under $\text{CO}_2/\text{H}_2\text{S}$ conditions has a two-layer structure, and Cr is enriched in the inner layer. The enrichment of Cr enhances the compactness of the film and hinders the mass transfer of ions from the solution to the metal surface, thereby reducing the corrosion rate. The corrosion of the steel pipe is gentle and uniform. For the stress distribution of the assembly, Davies et al. [5, 6] studied through experiments that the reduction of the pressure in the casing can cause the redistribution of the cement sheath stress and lead to the failure of the cement sheath. Meng M. et al. [7] found that the change of annular pressure will inevitably lead to the change of the stress of casing-cement sheath-formation combination structure, which may lead to the failure of cement sheath seal and even casing damage.

In this paper, a finite element model of the combination with corrosion defects is established for high-pressure corrosion gas wells. The stress variation law of the combination under the changes of casing internal pressure, annulus pressure and

formation pressure is clarified, and the sealing failure mechanism of the casing-cement sheath-formation combination is revealed. It provides technical support for optimizing production system and wellbore pressure on site, and ensures the integrity of casing-cement sheath-formation combination.

45.2 Numerical Modeling

45.2.1 Cementing Interface Theory and Control Equation

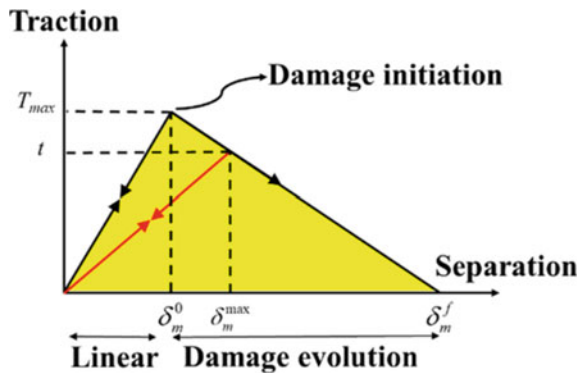
The bilinear cohesion model is used to simulate the cementation of casing-cement sheath-formation cementation surface. In the bilinear cohesion model, the model is divided into four stages: elastic stage, crack initiation stage, crack propagation stage and complete failure stage. The failure behavior of the interface is described according to the Traction–separation criterion. The unit damage mechanism of the Traction–separation criterion is shown in Fig. 45.1.

In the initial elastic stage, the relationship between element displacement and stress is linear, and the elements maintain continuous and coordinated deformation. The constitutive equation of this stage is [8]:

$$\sigma = \begin{pmatrix} \sigma_n \\ \sigma_s \\ \sigma_t \end{pmatrix} = \begin{pmatrix} K_{nn} & & \\ & K_{ss} & \\ & & K_{tt} \end{pmatrix} \begin{pmatrix} \delta_n \\ \delta_s \\ \delta_t \end{pmatrix} = K\delta, \delta < \delta^0 \tag{45.1}$$

σ_n , σ_s and σ_t are the stress of the interface in the normal direction and the two orthogonal tangential directions respectively, MPa, the subscript n represents the normal direction of the cohesive element, and the subscript s and t represent the two tangential directions of the cohesive element K_{nn} , K_{ss} and K_{tt} are the normal and two tangential stiffness of the cohesive interface, MPa.

Fig. 45.1 Constitutive relation of interface mechanical model



In the crack initiation stage, the casing-cement sheath-formation combination is subjected to casing internal pressure, annulus pressure and formation pressure, and the stress form is relatively simple. In this paper, the maximum nominal stress criterion is selected as the damage criterion. As long as the force in one direction reaches the maximum value, the material begins to damage. The governing equations are as follows

$$\max \left\{ \frac{\langle \sigma_n \rangle}{\sigma_n^o}, \frac{\sigma_s}{\sigma_s^o}, \frac{\sigma_t}{\sigma_t^o} \right\} = 1 \quad (45.2)$$

σ_n , σ_s and σ_t are the stresses of the interface in the normal direction and the two orthogonal tangential directions, MPa. The subscript n represents the normal direction of the cohesive element, corresponding to the mode I fracture. The subscripts s and t represent the two tangential directions of the cohesive element, corresponding to the mode II and III fractures. When the interface unit of casing-cement sheath-formation combination satisfies formula (45.2), the cementing interface begins to damage, the interface gradually debonds, and the energy consumed by the interface satisfies the following formula.

$$\Gamma_t = \frac{\sigma_t \delta_t}{2} \quad (45.3)$$

Γ_t is the tangential dissipation energy, J/m^2

In the crack propagation stage, the degradation treatment of the binding force response of the enrichment element is cited. The interface stiffness will be reduced during the degradation process. When the required stress is reduced to 0, the material is completely broken. Taking the tangential direction as an example, the governing equation is:

$$\sigma_t = (1 - D_t) K_t \delta_t, \delta_t^0 < \delta < \delta_t^f \quad (45.4)$$

D_t is the composite fracture energy damage factor. D_t can describe the damage degree of the interface in the crack propagation stage. When $D_t = 0$, the interface has no damage. When $D_t = 1$, the interface is completely damaged. δ_t^0 is the displacement of the interface in the tangential softening, m; δ_t^f is the displacement of the cemented surface when it completely fails tangentially, m.

The complete failure stage is when the cohesive element is completely broken, forming two independent surfaces. At this time, taking the tangential direction as an example, when $\delta_t^f < \delta_t$, $\delta_t = 0$, forming two independent surfaces.

45.2.2 *Model Assumption*

The basic assumptions are as follows:

- (1) The casing is regarded as a linear elastic–plastic material, the cement sheath is an elastic–plastic body conforming to the Mohr–Coulomb constitutive model, and the formation is regarded as an ideal elastic body;
- (2) Defects in the process of well construction, namely casing, cement, formation in the initial state of complete and close contact;
- (3) The corrosion direction is single and constant, that is, corrosion from the casing to the formation, or corrosion from the cement sheath to the casing.

45.2.3 *Finite Element Model Establishment and Parameter Setting*

The annulus pressure between the production casing and the technical casing of the field gas well is the most prominent, that is, the failure of the B-annulus seal is serious. The isotope tracking shows that the B-annulus air body is homologous to the gas in the production layer. Therefore, the research object of the numerical model is the cement ring between the production casing and the technical casing. Therefore, in this paper, a two-dimensional numerical calculation model of casing-cement ring-formation combination with different degrees of corrosion is established according to the rock mechanics profile and the in-situ stress profile data for the most complex production section of the wellbore. In order to control the variables, two directions of corrosion defect simulation were carried out, from the casing to the formation direction of corrosion, and the cement ring to the casing direction of corrosion, for the two clothing directions, four different corrosion degrees were carried out. Defect modeling of the combination. As shown in Fig. 45.2.

The modeling basis is as follows:

- ① Acid gas corrosion from the casing to the formation direction: In the drilling site, Cr-containing casing is often used in a strong corrosion environment. Some scholars have experimentally studied the corrosion rate of Cr-containing casing in a high concentration of corrosive gas environment, and the corrosion form is uniform corrosion [8], so the casing corrosion defect is simulated as uniform corrosion.
- ② Acid gas corrosion from the formation to the casing direction: Formation to the casing direction of the cement sheath corrosion There are also a large number of scholars have studied the corrosion law [9, 10], the site due to cost constraints, the use of anti-corrosion cement will reduce the corrosion rate, but the strength of the corroded part will still be greatly reduced, so the simulation of the corrosion gas to the point of invasion of the cement sheath. Since the rate of acid gas corrosion of cement sheath is much faster than that of corrosion of casing, casing corrosion is not considered in this case.

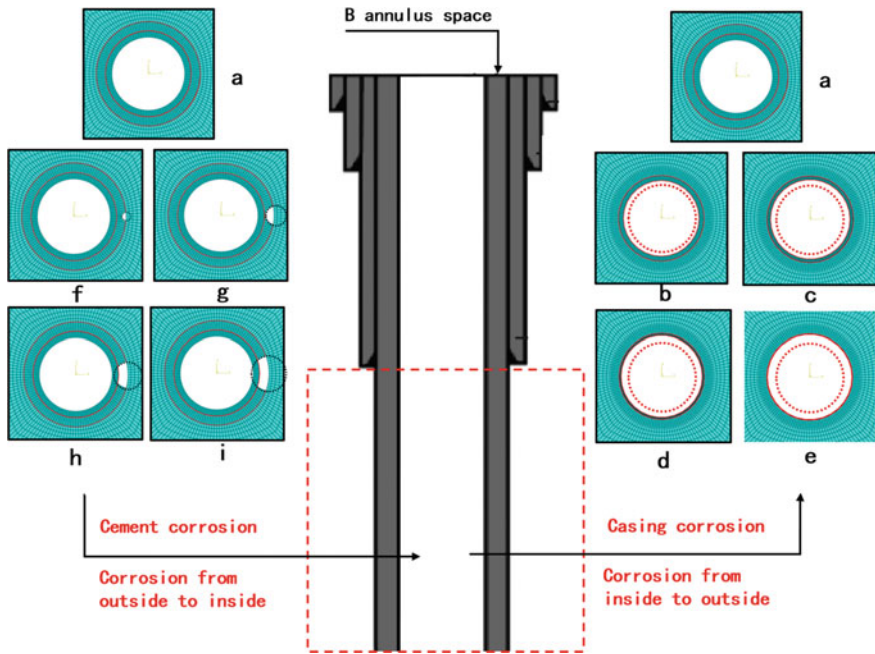


Fig. 45.2 Shaft finite element model diagram

In the numerical model, the contact between casing, cement sheath and formation is simulated by cohesive element combined with friction. That is, when the cohesive element does not fail, the interface is in a bonded state. When the cohesive element fails, the contact interface between casing, cement sheath and formation will produce frictional contact. In terms of grid division, variable density grid division is adopted, and the grid type is CPE4. The formation size is $7\text{ m} \times 7\text{ m}$ to avoid the influence of formation size on the stress of cement sheath. The model material and borehole size parameters are shown in Table 45.1.

Table 45.1 Model material and borehole size parameters

Name	Outer diameter (mm)	Wall thickness (mm)	Elastic modulus (GPa)	Poisson's ratio	Plasticity
Casing	88.9	13.72	206	0.3	758 MPa
Formation	–	–	30	0.15	–
Cement	107.95	19.05	15	Friction angle	Cohesion
				17.1°	21.6 MPa

45.3 Numerical Simulation Results

45.3.1 Corrosion of Casing Pipe

Influence of wellbore pressure

From the stress cloud diagram, it can be seen that the stress of the cement sheath and the casing is gradually increasing under different corrosion degrees of the casing. See Fig. 45.3, the maximum stress of the casing Mises gradually approaches the yield strength, and the maximum stress range gradually expands; at the same time, the stress of cement sheath shows an increasing trend. With the decrease of casing strength, the plasticity of cement sheath near an interface gradually increases, as shown in Fig. 45.4.

The stiffness degradation of the cohesive element can reflect the process of interface cementation failure. In this paper, the CSDMG value in ABAQUS is used to evaluate the degree of stiffness degradation. When CSDMG reaches 1, it means that

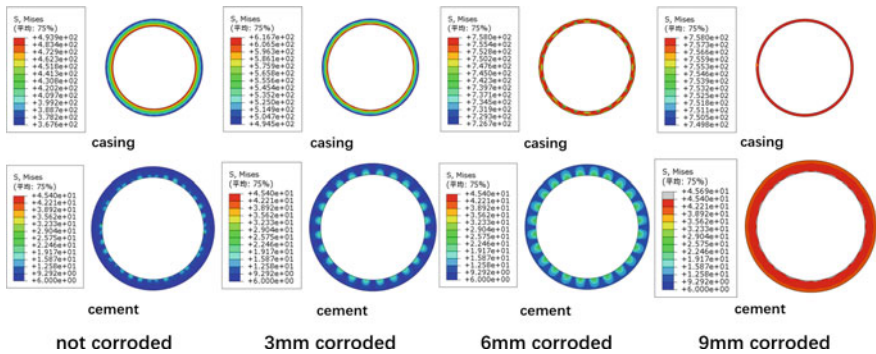


Fig. 45.3 Stress distribution of casing cement sheath under different corrosion depths of 90 MPa internal pressure

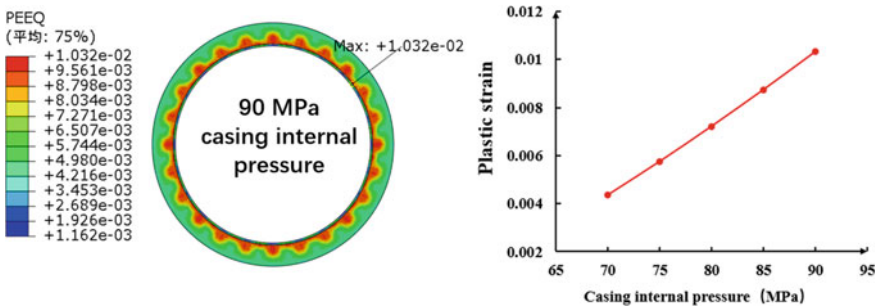


Fig. 45.4 Plastic deformation of cement sheath under 9 mm corrosion depth

the cohesion fails and the interface is debonding. Taking the finite element model of uncorroded casing as an example, it can be seen from the cloud map that when the internal pressure increases from 70 to 90 MPa, the CSDMG value of the cement-well interface reaches 0.99, and the SCDMG value of the cement-well interface is 0. It can be seen that the change of casing internal pressure has a greater impact on the interface.

Therefore, in the case of casing corrosion, the influence of wellbore pressure change on the first interface is greater than that on the second interface. With the increase of casing internal pressure, stiffness degradation occurs first at the first interface of cement sheath, while the second interface has been in a completely cemented state. With the increase of the corrosion depth of the casing, the cohesion of the interface is gradually weakened, the plastic strain of the cement sheath is gradually increased, and the plastic strain of the cement sheath itself is combined with the interface debonding, resulting in a more dangerous interface. Due to the existence of casing internal pressure, there is no obvious gap at the interface, but the cement sheath has produced plasticity, and the cementation of the cement-well interface has also failed. When the casing internal pressure fluctuates or decreases, the casing shrinkage will be much faster than the cement sheath shrinkage, and the interface will produce obvious gaps.

Effect of formation pressure

It can be seen from the stress cloud diagram that the Mises stress distribution of the casing and the cement ring under the 30 MPa ground stress difference of the casing with different corrosion degrees (Fig. 45.5). The maximum Mises stress range of the casing is gradually increasing, and the cement ring stress increases first and then decreases, because the casing gradually yields and causes stress release. From the perspective of plastic deformation (Fig. 45.6), the cement sheath does not produce obvious plastic strain, and the casing with the increase of corrosion depth, the yield strength gradually decreases to produce plasticity, which will affect the cementing interface.

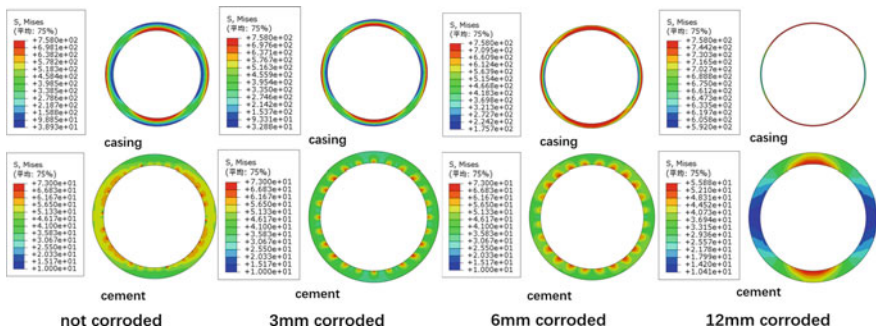


Fig. 45.5 Stress distribution of casing cement sheath under different corrosion depths of 30 MPa ground stress difference

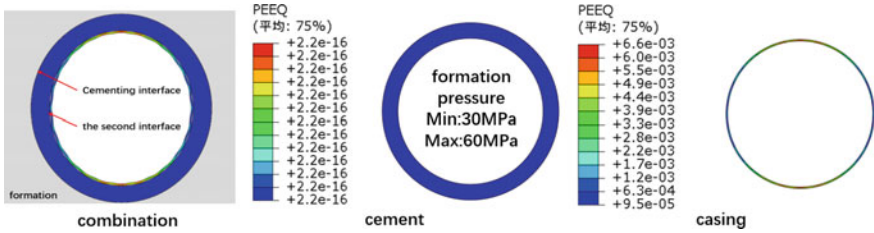


Fig. 45.6 Plastic deformation of the composite at 12 mm corrosion depth

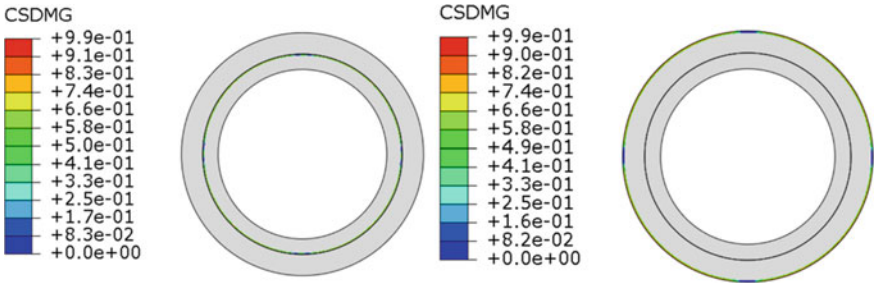
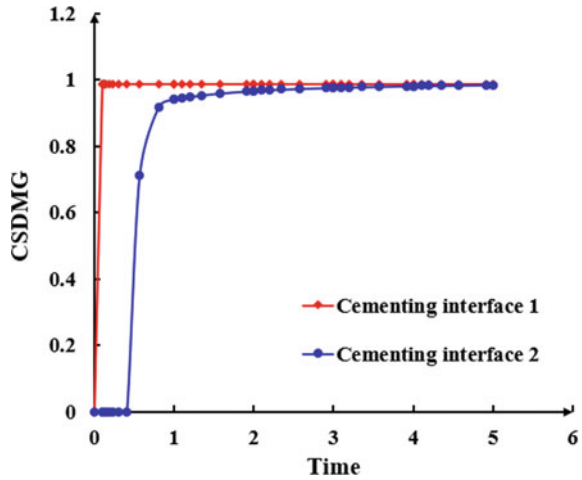


Fig. 45.7 Cloud map of cementing interface stiffness degradation in casing corrosion environments (formation pressure change)

Through the stiffness degradation of the cohesive element, the degree of cementation of the interface can be understood. Taking the finite element model of uncorroded casing as an example, it can be seen from the cloud map that when the formation pressure difference gradually increases from 10 to 30 MPa, the CSDMG values of the first cementing interface and the second cementing interface are both 0.99, that is, both cementing surfaces fail (Fig. 45.7). By extracting the CSDMG in the process of gradual increase of in-situ stress, it can be found that one interface is prior to the two interface failure, as shown Fig. 45.8.

In summary, the change of ground stress has a great influence on the interface. When the casing does not produce plastic strain, the interface bonding stiffness reaches zero first, indicating that the change of in-situ stress has a great influence on the interface bonding. When the casing produces plastic strain, with the increase of casing corrosion depth, the interface debonding, cement sheath plasticity and casing plasticity accumulate, resulting in a more prone to micro-annulus.

Fig. 45.8 CSDMG change trend diagram of cementing interface



45.3.2 Cement Corrosion

Influence of wellbore pressure

From the stress cloud diagram, it can be seen that the stress of cement sheath and casing is gradually increasing under different corrosion degrees, and the stress of cement sheath at the corrosion surface is the largest (Fig. 45.9).

It can be seen from the CSDMG cloud diagram that in the absence of corrosion, when the casing internal pressure increases from 70 to 90 MPa, the value of CSDMG at the first interface of cementing reaches 0.9, and the value of SCDMG at the second interface of cementing is 0 (Fig. 45.10). It can be seen that the change of casing internal pressure has a greater impact on the first interface of the complete combination. With the increase of the corrosion radius of the cement sheath, the cement-well interface also becomes a weak surface, that is, after the cement sheath

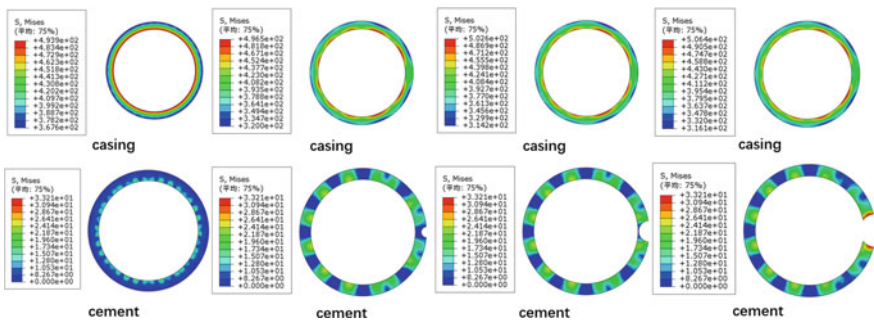


Fig. 45.9 90 MPa ground stress difference stress distribution map of cement sheath casing under different corrosion radius

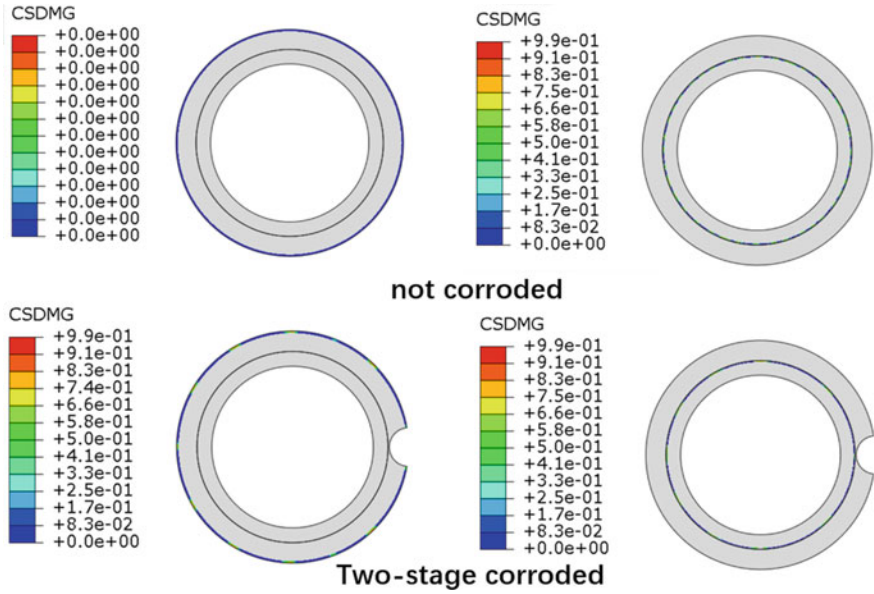
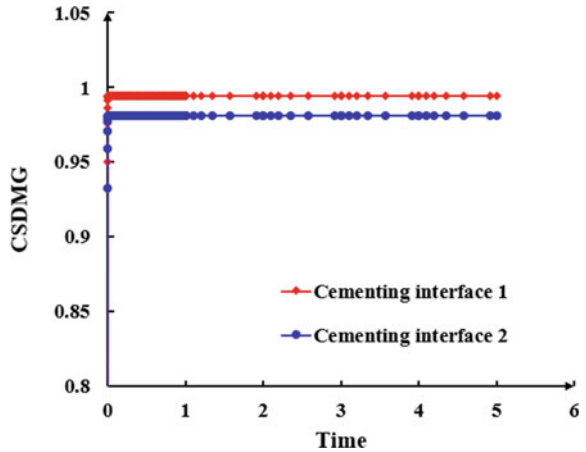


Fig. 45.10 Cloud view of cemented interface stiffness degradation in cement corrosion environments (change in wellbore internal pressure)

is corroded, the cement-well interface becomes more fragile. Compared with the case without corrosion, the cementation strength of the cement-well interface decreases, and the cement-well interface is more prone to failure and debonding (Fig. 45.11).

Therefore, in the case of cement sheath corrosion, the influence of wellbore internal pressure change on the first interface is greater than that on the second interface. With the increase of corrosion degree and corrosion area, the second interface

Fig. 45.11 CSDMG change diagram of interface under cement sheath corrosion



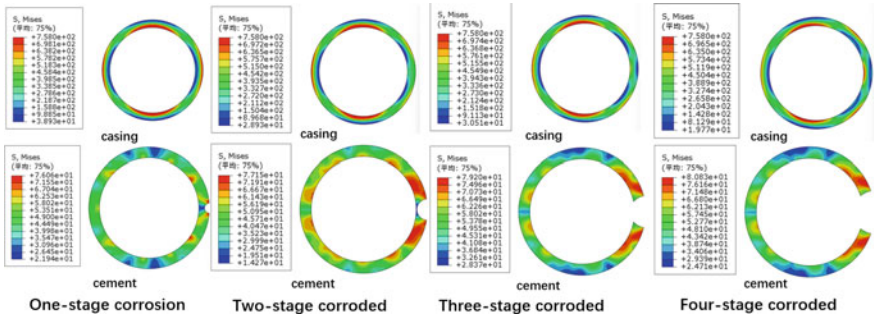


Fig. 45.12 30 MPa ground stress difference stress distribution map of cement sheath casing under different corrosion radius

of cementing becomes easy to fail. The corrosion degree and location of the cement sheath have a great influence on the interface failure, and the corrosion resistance of the cement sheath should be paid attention to in the field.

Effect of formation pressure

It can be seen from the stress cloud diagram that under different degrees of cement ring corrosion, the casing stress does not change much, the casing stress is redistributed, and the maximum stress position shifts to the opposite side of the corrosion. The stress of the cement sheath increases gradually, and the maximum stress is at the corrosion place (Fig. 45.12).

In the stage without corrosion, when the in-situ stress difference increases from 30 to 60 MPa, the previous analysis shows that the first interface of cementing will fail before the second interface of cementing. From the CSDMG cloud diagram after corrosion, taking the the four-stage cement ring corrosion as an example, it can be found that the CSDMG of the first interface of cementing reaches 1 before the second interface of cementing, indicating that the stiffness degradation of the first interface of cementing will be faster than that of the second interface of cementing. However, it should be pointed out that the second interface of cementing is also a dangerous interface under the change of in-situ stress (Fig. 45.13).

In summary, in the case of cement sheath corrosion, the risk of failure of the first interface of cementing is still very large. With the increase of cement sheath corrosion, the second interface of cementing becomes easier to fail than before, but the first interface of cementing is still easier to fail than the second interface of cementing. Therefore, in the design of gas well cement slurry containing acid gas, the corrosion resistance and the sealing performance of the cementing interface should be considered.

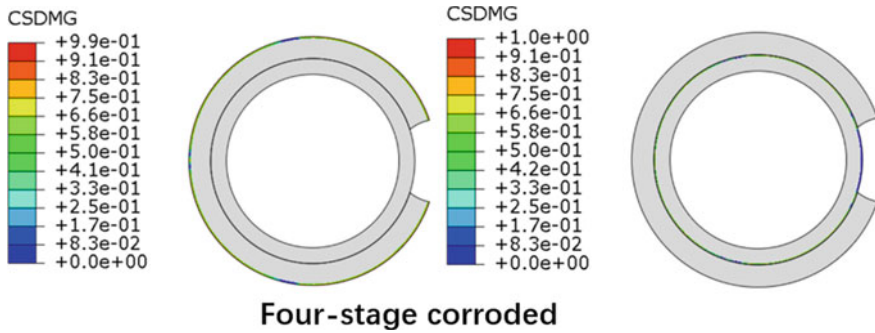


Fig. 45.13 Cloud view of cemented interface stiffness degradation in cement corrosion environment (formation pressure change)

45.4 Conclusion

For high-pressure gas wells containing acid gas, the acid gas will corrode the casing or cement ring during the production process, which will lead to the change of the stress of the casing-cement ring-formation combination, which will affect the sealing integrity of the combination. Based on the corrosion law on site, a finite element model of wellbore combination is established. Considering the changes of casing internal pressure and formation pressure, the stress changes and sealing failure of the combination under different corrosion degrees are analyzed. The conclusions are as follows:

1. Corrosion affects the stress and sealing integrity of the assembly. Casing corrosion will increase the overall stress of the casing-cement sheath-formation combination, resulting in an increase in the plasticity of the cement sheath. At the same time, it will also weaken the casing strength and increase the plasticity, making the cement-well interface more likely to fail; the corrosion of cement sheath will affect the stress distribution of the combination, cause stress concentration locally, and weaken the cementation strength of the cement-well interface.
2. There are three main factors that affect the sealing integrity: the failure of the bonding surface of the combination, the plasticity of the cement ring and the casing. The three factors may exist at the same time and combine with each other to increase the risk of seal failure. The risk of interface failure near the corrosion position is high.
3. When there is no corrosion or uniform corrosion of casing, the change of casing internal pressure and formation pressure has a great influence on the first interface of cementing. When the cement sheath is corroded, the change of casing internal pressure and formation pressure will increase the influence on the second interface of cementing, but the first interface of cementing is still easier to fail than the second interface of cementing.

References

1. Kiran, R., Teodoriu, C., Dadmohammadi, Y., et al.: Identification and evaluation of well integrity and causes of failure of well integrity barriers. *J. Nat. Gas Sci. Eng.* **45**, 511–526 (2017)
2. Condor, J., Asghari, K.: Experimental study of stability and integrity of cement in wellbores used for CO₂ storage. SPE103816 (2010)
3. Omosebi, O.A., Sharma, M., Ahmed, R.M., et al.: Cement degradation in CO₂-H₂S environment under high pressure-high temperature conditions. SPE-185932-MS, Norway, 2017
4. Wu, H.B., Liu, L.F., Wang, L.D., et al.: Influence of chromium on mechanical properties and CO₂/H₂S corrosion behavior of P110 grade tube steel. *J. Iron Steel Res. Int.* **21**(1), 76–85 (2014)
5. Davies, R.J., Almond, S., Ward, R.S., et al.: Oil and gas wells and their integrity: implications for shale and unconventional resource exploitation. *Mar. Pet. Geol.* **56**, 239–254 (2014)
6. Taleghani, A.D., Li, G., Moayeri, M.: Smart expandable cement additive to achieve better wellbore integrity. *J. Energy Resour. Technol. Trans. ASME* **139**(6) (2017)
7. Meng, M., Zamanipour, Z., Miska, S., et al.: Dynamic stress distribution around the wellbore influenced by surge/swab pressure. *J. Petrol. Sci. Eng.* **172**, 1077–1091 (2019)
8. Wang, C., Yang, L., Xue, Y., et al.: Simulation on the second cementing interface bonding characteristics of nature gas hydrate formation in South China Sea. *J. Central South Univ. Sci. Technol.* **53**(3), 993–994 (2022)
9. Aiex, C., Campos, G., et al.: An experimental study on effects of static CO₂ on cement under high-pressure/high-temperature conditions. In: *Offshore Technology Conference*, Houston, USA, 2015
10. Aiex, C., Campos, G., et al.: A Diffusion Controlled Model for Prediction of Long-Term Cement Sheath Carbonation. EUROPEC 2015, Madrid, Spain, June 2015

Chapter 46

RLGBG: A Reachable Landmark Grouping Based IP Geolocation Method for Unreachable Target



Shuodi Zu, Chong Liu, Fan Zhang, and Shichang Ding

Abstract IP geolocation technology can estimate or determine the geographical location of terminal device through IP address, which is an important basis for location-based network services. The existing IP geolocation methods based on network measurement cannot accurately obtain the network environment when the target does not respond to the detection message, so it is difficult to achieve high-precision geolocation. To solve this problem, a reachable landmark grouping based IP geolocation method for unreachable target (RLGBG) is proposed in this manuscript. RLGBG first detects landmark data extensively, filters, evaluates and retains reliable and accessible landmarks. Secondly, RLGBG counts the topological relationship and geographical distribution among the reachable landmarks, groups the landmarks according to the common router, and divides the landmarks into different groups after checking by geographical location. Then, the continuous IP segments are divided into IP blocks according to landmark groups, and the location range of each IP block is calculated by the landmarks within each group. Finally, RLGBG counts the IP blocks containing the target, merges those IP blocks that are geographically coincident and topologically related, and estimates the target's location by calculating the landmark center within the IP blocks. The geolocation experiments based on four cities in China show that RLGBG can effectively estimate the location of unreachable IP targets, and its accuracy and coverage are higher than the existing typical method and IP location databases.

Keywords IP geolocation · Unreachable IP target · Landmark grouping · IP segment division · Network measurement

S. Zu · C. Liu · F. Zhang · S. Ding (✉)
State Key Laboratory of Mathematical Engineering and Advanced Computing,
Zhengzhou 450001, China
e-mail: scdingwork@outlook.com

© The Author(s), under exclusive license to Springer Nature Switzerland AG 2024
S. Li (ed.), *Computational and Experimental Simulations in Engineering, Mechanisms and Machine Science* 145, https://doi.org/10.1007/978-3-031-42987-3_46

643

46.1 Introduction

With the development of the Internet, people's request for location-based services (LBS) has become increasingly strong. When LBS obtains the user's geographical location, it is also a common means to determine the location through the user's IP in addition to the satellite geolocation module of the device itself. IP geolocation is applicable to providing positioning services for PCs, various servers, routers and other fixed network devices with public IP and without satellite positioning module [1, 2].

Network measurement refers to the behavior of acquiring various parameters such as delay, traffic, topology, etc. in the network through network probes, various tools and software [3]. As one of the research hotspots in this field, IP location based on network measurement has the advantage of not requiring the target to actively provide its location information. The IP geolocation based on network measurement combines active detection and passive sniffing to obtain the delay, route, topology and other information of the network where the IP target is located. After comprehensive analysis, the geographical location range of the IP can be determined [4]. During the operation of network measurement based IP geolocation, it is not necessary for the target to actively provide its location, equipment model, user data and other information. As long as the IP address of the target does exist in the Internet, it can be geolocated. Because IP geolocation based on network measurement is independent of user assistance, it has been widely used in commercial advertising, network equipment management, network security and other fields [5–7].

However, in the actual Internet, some firewalls, routing devices and security software cannot respond to ICMP packet and other network control messages due to network security protection or quality of service control. In this case, the geolocators cannot accurately obtain the parameter information of the network where the IP target cannot be detected, and thus cannot achieve high-precision geographical geolocation.

To solve the above problem, a reachable landmark grouping based IP geolocation method for unreachable target (RLGGB) is proposed in this paper. According to the detection and analysis of living landmarks, the proposed method completes the division and location of IP segments, thus achieving the geographical location of unreachable IP targets. The experimental results show that RLGGB is significantly better than the existing typical methods in geolocating unreachable IP targets.

The rest of this paper is organized as follows: Sect. 46.2 introduces the relevant work. The framework and main steps are describes Sect. 46.3. Section 46.4 evaluates the performance of this method. Section 46.5 summarizes the work of this paper.

46.2 Related Work

The IP geolocation based on network measurement collects network delay, topology and other information by deploying detection sources, collecting a large number of network landmarks and detecting each other. The most basic tools to achieve this goal are Ping and Traceroute. The detection source is a device that sends and receives detection messages and has a public IP address. In practice, personal computers and servers are two common types of detection sources. Landmark is a type of network equipment with public IP and known geographical location. Landmarks that can respond to detection messages are able to play the role of reference points in the geolocation process. The existing mainstream geolocation methods can be divided into two categories: delay-based and topology-based.

IP geolocation based on delay measures the time delay between the target and the landmarks after setting up multiple detection sources, and estimates the position of the target through time delay constraints. Typical algorithms include GeoPing [8], CBG [9], Spotter [10], CRLB [11], etc. The GeoPing uses the detection sources to construct delay vectors for both the target and the landmarks, and takes the location of the landmark with the shortest Euclidean distance from the delay vector of the target as the target's location. CBG attempts to convert the time delay between the detection source and the target into geographical distance, and form distance constraints on the target from multiple detection sources to obtain the possible location range of the target. Spotter uses the standard normal function to fit the probability distribution relationship between time delay and distance. When there are multiple detection sources, the distribution of time delay is expressed by the joint probability of independent normal distribution. Ciavarrini et al. analyzed the delay-based geolocation method in detail, and gave the delay-based geolocation method CRLB. The method pointed out that a large number of landmarks need to be used to obtain the geolocation error below 20 km, and it is often impractical to obtain such a large number of landmarks, so the delay-based geolocation method is often difficult to meet the application with high positioning accuracy requirements.

Topology-based IP geolocation determines the location of the target by measuring the network topology around the target and combining the location information of the landmarks. Typical algorithms include TBG [12], SLG [13], PBG [14] and RMPG [15]. TBG uses the time delay data between detection sources and between detection sources and landmarks to estimate the location of the target into a small area, and then estimates its distance by measuring the time delay between adjacent routers on the path from the detection source to the target, and finally determines the final location of the target by minimizing the average geolocation error between the target and the routers. After SLG geolocates the target in a coarse-grained area based on the improved CBG, it adds landmarks in this area, implements topology measurement and further narrows the area, and finally iterates to get the target location results. PBG obtains the access level network, point of presence (PoP), by extracting the "bi-fan structure" [16] of the target city, and realizes the location of the access level network with the help of the landmarks connected by the PoP, thus achieving the geolocation

of the target located in the PoP. RMPG assumes that the service object of each router is stable within a specific time, infers the service range of the router through the geographical distribution of landmarks, and forms the distance constraint caused by the service range to estimate the geographical location of the target IP.

However, when the target is unreachable, that is, unable to respond to the detection message, the geolocator cannot obtain the network delay and topology data around the target, and thus cannot achieve high-precision geolocation based on the network measurement data.

46.3 Proposed Method

In order to facilitate the deployment, management and maintenance of network facilities, Internet service providers (ISP) often divide the entire IP segment into different subnets or address blocks and assign them to different network user groups. RLGBG determines the range of these IP address blocks to achieve geolocation of unreachable IP targets.

46.3.1 Framework and Main Steps

As shown in Fig. 46.1, RLGBG can be logically divided into two parts. The first part completes the grouping of landmarks and geolocation of IP segments through network measurement and geographical location proofreading, and the other part realizes the geolocation of unreachable targets through the combination and location calculation of these IP segments. The rounded rectangles in the figure represent entities, which are the inputs and output of RLGBG. The landmarks and target IP are the inputs, and the geolocation result is the output. The rectangle represents the specific operation.

RLGBG mainly consists of four parts. The method starts with extensive detection of landmarks, and preserves the reachable landmarks, namely, landmarks that respond to the detection message, after which RLGBG evaluates the reliability of landmarks, and preserves the detection path to reliable landmarks (step 1). Then RLGBG groups landmarks according to the common router connected to landmarks in the detection path, and removes landmarks that do not belong to the same city for each group of landmarks (step 2). Next, the proposed method searches the numerical extreme value of IP in each landmark group to determine the IP block boundary, and calculates the center position according to the landmark distribution (step 3–4). Finally, RLGBG finds the IP block containing the landmarks to be located, combines the IP blocks with the same subnet and high geographical range coincidence, and obtain the target location estimation by calculating the landmark center in the IP block (step 5–6). The specific steps of RLGBG are shown below.

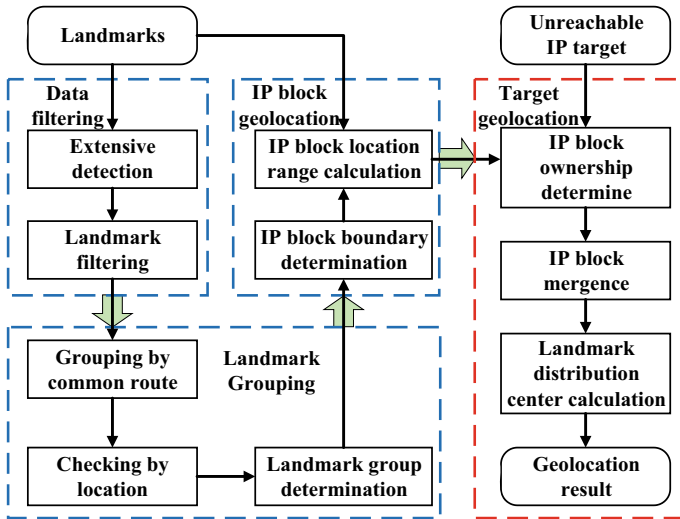


Fig. 46.1 Framework of RLGBG

Input: target IP and landmarks.

Output: geolocation result.

Step 1: Conduct extensive detection of landmarks, screen the reachable landmarks among them, and reserve their detection paths.

Step 2: Groups the landmark according to the last hop router in the detection path. For each group of landmarks, remove the landmarks that are inconsistent with the city-level location of most landmarks.

Step 3: Search the maximum and minimum values of IP in each group of landmarks to determine the IP block boundary.

Step 4: For each IP block, calculate the calculation center of the landmark contained therein, and take the distance between the landmark farthest from the center and the center as the IP block range radius.

Step 5: Find the IP blocks containing the target to be located. For the IP blocks with the primary routing of the included landmarks located in the same/24 subnet, calculate the ratio of the overlap area to the area of each IP block. If the proportion is 100% or more than 90%, the above IP blocks will be merged.

Step 6: Calculate the center of the merged IP blocks, and obtains the average of each IP block by weighting the number of landmarks to obtain the target location estimation.

The key parts of RLGBG will be described in detail in the following sections.

46.3.2 Landmark Grouping

When deploying network equipment, ISPs usually consider deployment costs, management costs, network service quality and other factors. Therefore, in most cases, the geographical distance between access routers and terminals will be very close. For the same reason, ISPs often divide the entire IP segment into several subnets or address blocks and assign them to different network user groups. Although the detection unreachable IP does not respond to the detection message due to the configuration of the terminal equipment or router, it still accesses the Internet according to the geographical distribution in most cases, so it is also applicable to this distribution feature.

The detection path can be expressed as a sequence of IP nodes such as $Path_{v_1 \rightarrow v_n} = (v_1, v_2, \dots, v_n)$, while the IP node that determines the landmark group is the penultimate hop of the path, namely v_{n-1} . RLGGB searches all the paths of the same node with the penultimate hop, and put their endpoints into a group. A landmark group $Group_{v_c}$ formed by node v_c can be expressed as follow:

$$Group_{v_c} = \{v_n | v_n \in Path_{v_1 \rightarrow v_n}, v_{n-1} = v_c\} \quad (46.1)$$

Through the above operations, the landmarks distributed in a specific range can be grouped. Figure 46.2 shows the geographical distribution of the four groups in Beijing. It can be seen that the landmarks can be effectively grouped through common routing.

In the detection, some routing nodes are also unable to respond to the detection message like unreachable terminals. These are called anonymous routing nodes. A large number of anonymous routing nodes will be generated during path detection. Some researchers realized the merging of anonymous routes through the merging of routes, and added these anonymous routing nodes into the topology analysis. We conducted routing detection and landmark grouping for landmarks in four cities in China, and made statistics on the geographical distribution of the groups. The results are shown in Table 46.1.

We only make statistics for groups containing 2 or more landmarks. According to statistics, the average distribution radius of the group formed by non-anonymous nodes is 5.54 km, while the average distribution radius of the group formed by anonymous nodes is 16.93 km. There is a large gap between the two. Therefore, in order to minimize the geolocation error, we only use non-anonymous nodes for landmark grouping.

46.3.3 IP Block Mergence

In the actual Internet, for the sake of quality of service control and network robustness, ISPs usually do not only set up a single router to provide access services for a user

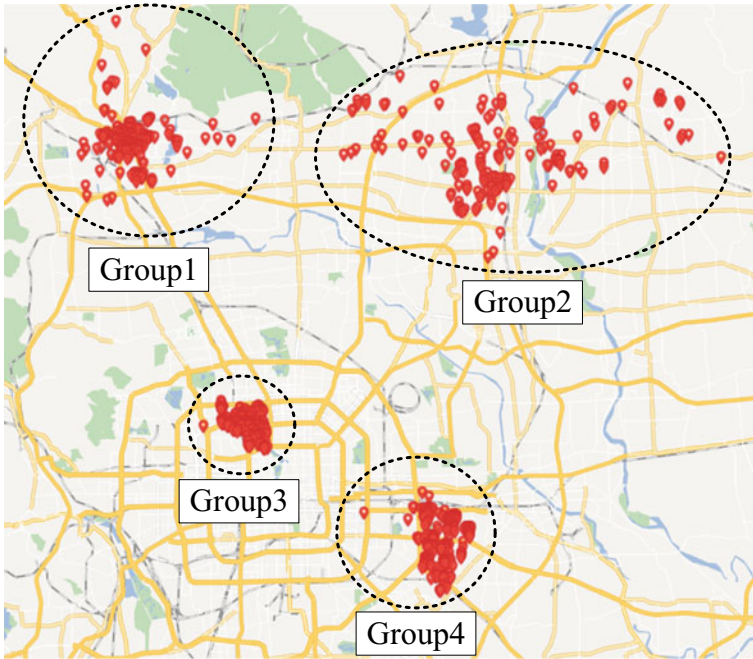


Fig. 46.2 Geographical distribution of four landmark groups in Beijing

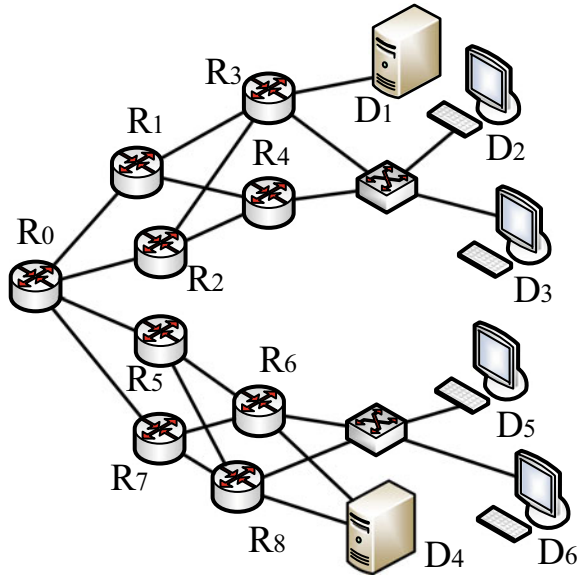
Table 46.1 Comparison of geographical distribution of different landmark groups

City	Average radius of non-anonymous groups (km)	Average radius of anonymous groups (km)
Beijing	4.64	19.17
Chengdu	4.00	12.07
Guangzhou	5.62	15.58
Zhengzhou	7.89	20.97
Average	5.54	16.93

group, but use multiple routers to form an access router group. Therefore, when detecting different terminals belonging to the same user group, their penultimate hop routes may be different. Figure 46.3 shows a schematic diagram of this situation.

As shown in Fig. 46.3, the detection message sent to terminal device D_2 can reach the destination through the forwarding of access router R_3 , or through access router R_4 . Therefore, the detection path is not unique. In order to facilitate deployment, management and maintenance, ISPs will assign adjacent IP addresses to routers with the same or similar responsibilities. Taking Fig. 46.3 as an example, R_3 and R_4 are often in the same subnet, as are R_6 and R_8 . Therefore, RLGBG merges the IP blocks whose common routes are in the same subnet.

Fig. 46.3 Common deployment method of access routers



In order to avoid wrong merging of IP blocks that do not belong to the same user group, RLGBG will check the distribution range of the two IP blocks before merging. As described in Sect. 46.3.1, the center of each IP block is the calculation center of all the included landmark coordinates, and the radius is the distance between the landmark farthest from the center and the center. When the distribution range of the two IP blocks is highly coincident, RLGBG will merge them. Figure 46.4 shows several types of IP block distribution.

As shown in Fig. 46.4, when two IP blocks belong to an inclusive (Fig. 46.4a) or highly coincident (Fig. 46.4b) relationship, combined with the common routing of the last hop in the same subnet, it can be sure that the two IP blocks belong to the same user group and should be merged. When the distribution is slightly coincident (Fig. 46.4c) or separated (Fig. 46.4d), the two IP blocks should not be merged.

During the detection process, due to the settings of the router manufacturer or maintainer, different routers have different tendencies to return the interface when responding to the detection message. Some are the interface IP for receiving the message, and some are the interface IP for forwarding the message. This results in that when probing routers located in the same subnet, the returned IP may not belong to the same subnet. Aliases merging of path detection results during detection can improve to some extent, but cannot completely avoid the occurrence of problems.

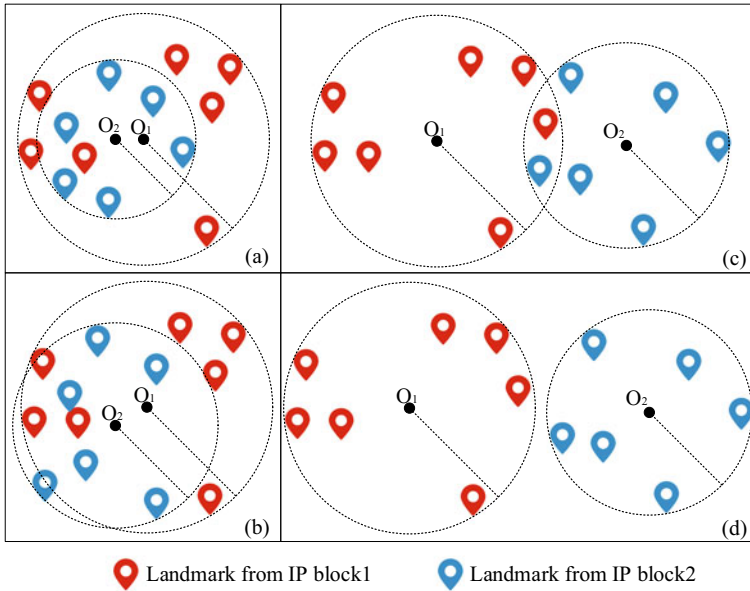


Fig. 46.4 Four distribution of IP blocks

46.3.4 Weighted Geolocation of Target

After determining the IP blocks of the target to be located, this section completes the geolocation of the target by calculating the IP blocks' center. When the number of IP blocks to which the target belongs is one, the process is easy to understand. When the number of IP blocks to which the target belongs is greater than one, we need to calculate the geolocation result by weighting.

For each IP block, the coordinate of its center is $Center_i$. The number of landmarks included is $Count_i$. The final result can be expressed as:

$$Result = \frac{\sum_{i=1}^n Center_i * Count_i}{\sum_{i=1}^n Count_i} \tag{46.2}$$

For example, in Fig. 46.4b, it is assumed that the IP blocks O_1 and O_2 failed to be merged in the previous section, which includes 7 and 6 landmarks respectively. The coordinates of the final result are located on the line between O_1 and O_2 , and the distance from the center of O_1 is 6/13 of the total length of the line.

RLGBG maps the location of the IP block where the target is located to the location of the target. When the location range corresponding to the IP block is small enough, the geolocation error through the IP block will also be smaller, and the geolocation accuracy will be much higher than the city-level.

46.4 Experiment

After introducing the experimental settings, this section evaluates the geolocation performance of RLPBG and explains its specific performance.

46.4.1 Experimental Settings

Data collection. We use the methods in paper [17] and paper [18] to obtain IP with actual geographical location through Internet yellow pages and network maps, and then use the methods in paper [19] to evaluate its reliability and retain IPs with reliable location as landmarks. We randomly take a part of the landmarks, detect them separately, divide them into two groups according to the target accessibility, and then conduct geolocation tests on them respectively. We have deployed detection sources in Beijing, Hohhot, Shanghai and Hong Kong in China. These detection sources are relatively scattered and can obtain more abundant detection path data than single-source detection. In order to improve the accuracy and integrity of the topological information around the landmarks, we used the network measurement tool Scamper [20] developed by CAIDA to detect the path to the IP target. In addition, when detecting the topology information of the target network, we comprehensively used five protocols: ICMP, TCP, UDP, ICMP-Paris and UDP-Paris. By using multi-protocol path detection, it increases the probability of successful forwarding of the detection message and improves the scale of obtaining the topology information. ICMP-Paris and UDP-Paris can also avoid generating incorrect path information [21].

Metric. We use the geolocation success rate and geolocation error to measure the performance of RLGBG. The success rate refers to the ratio of the number of times that the target geolocation results can be successfully returned to the total number of geolocations. The geolocation error is the distance between the geographical location returned by the method and the actual geographical location of the target when the IP target with known location is geographically located. The geolocation error involves the location within the city, so the geographical scale is small. In this case, the calculation error between plane coordinates and spherical coordinates can be ignored, so we directly use the plane coordinate system to calculate the distance between two points.

Comparison methods. We choose PBG [14] and RMPG [15] as the comparison methods. PBG is a typical city-level geolocation algorithm, and it is also a rare method that claims to be able to geolocate unreachable targets. RMPG can implement street-level geolocation for IP targets, which is an effective IP geolocation algorithm in recent years. Because PBG can only give city-level geolocation results, we mark the center of the city as the geolocation result in the experiment, and calculate the geolocation error according to this.

Table 46.2 RLGBG’s overall geolocation performance

City	Mean error of reachable target geolocation (km)	Mean error of unreachable target geolocation (km)	Comprehensive mean error (km)
Beijing	2.58	2.74	2.67
Chengdu	5.29	5.43	5.35
Guangzhou	3.02	3.27	3.15
Zhengzhou	3.24	3.58	3.41
Average	3.53	3.76	3.64

46.4.2 Overall Performance

As shown in Table 46.2, the comprehensive mean error of RLGBG is 4.11 km. When testing different types of IP targets, the mean geolocation errors of reachable and unreachable targets are 3.53 km and 3.76 km respectively. It can be seen that RLGBG has no significant difference in the geolocation effect of reachable and unreachable targets. In addition, due to the geographical distribution of IP terminal users in different cities, the geolocation performance of RLGBG in different cities will be different.

46.4.3 Comparison

First, we tested the geolocation success rate of PBG, RMPG and RLGBG, and the results are shown in Fig. 46.5. In the figure, the column represents the ratio of the number of successful results returned by the geolocation method to the total number of geolocations. The higher the column is, the higher the geolocation success rate of the method.

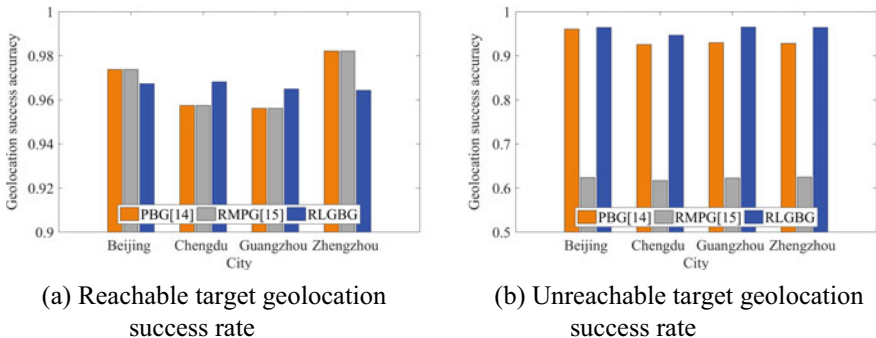


Fig. 46.5 Comparison of geolocation success rate

According to statistics, the success rates of reaching target geolocation of PBG, RMPG and RLGBG are 96.74%, 96.74% and 96.62% respectively, and the success rates of unreachable target location are 93.62%, 62.23% and 96.00% respectively. It can be seen that RMPG has a low success rate in unreachable target geolocation because it needs to determine the adjacent routing of the target IP. Although PBG also achieves geolocation through routing comparison, its PoP level network extracted with the help of the bi-fan structure has more network nodes and larger granularity, which greatly increases the probability of its coincidence with the detection path of the unreachable target, and thus has a high geolocation success rate. RLGBG does not need to geolocate the target IP after calculating the IP block, so the accessibility of the target has no effect on the geolocation success rate. During the implementation of RLGBG, only the number of landmarks (the coverage of IP segments) will affect the final geolocation effect.

Subsequently, we tested the geolocation error, and the results are shown in Fig. 46.6. Because PBG algorithm can only give city-level location results, we mark the center of the city as the target geolocation result in the experiment, and calculate the geolocation error according to this. In the figure, the points on the curve represent the proportion of the results with error less than a specific value in the total. The closer the curve is to the upper left corner of the figure is, the smaller the geolocation error of the method is, and the better the geolocation performance is.

According to statistics, the mean errors of reachable target geolocation of PBG, RMPG and RLGBG are 12.68 km, 4.17 km and 3.20 km respectively, and these of unreachable target geolocation are 12.00 km, 9.25 km and 3.18 km respectively. It can be seen that RLGBG has lower geolocation error than PBG and RMPG. At the same time, RLGBG has the same high geolocation capability for unreachable targets.

Finally, we summarize the comprehensive performance of these three methods, and the contents are shown in Table 46.3. It is easy to see that RLGBG has higher geolocation success rate and lower geolocation error for both reachable and unreachable targets.

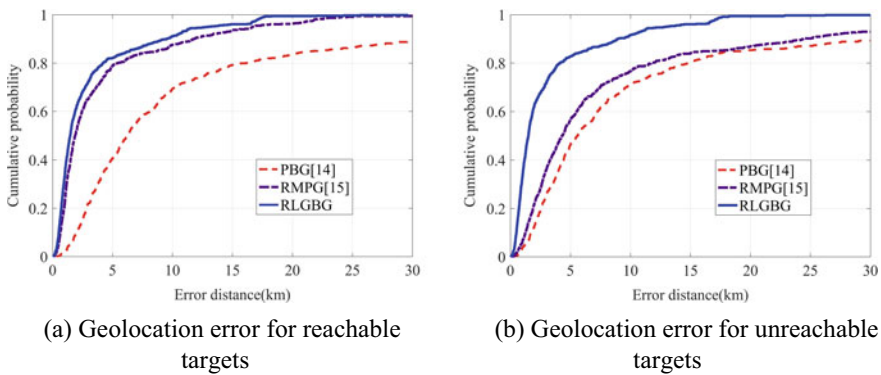


Fig. 46.6 Comparison of geolocation error

Table 46.3 Summary of comparison

Method	PBG [14]	RMPG [15]	RLGBG
Reachable target geolocation success rate (%)	96.74	96.74	96.62
Unreachable target geolocation success rate (%)	93.62	62.23	96.00
Reachable target mean geolocation error (km)	12.68	4.17	3.20
Unreachable target mean geolocation error (km)	12.00	9.25	3.18

46.5 Conclusion

IP geolocation technology is widely used in daily life. In order to solve the problem of unreachable IP target geolocation, a reachable landmark grouping based IP geolocation method for unreachable target (RLGBG) is proposed in this paper. RLGBG realizes the division of multiple IP blocks by grouping the landmarks, calculates the geographical location of the IP blocks by the distribution of the landmarks contained in the IP blocks, and realizes the geolocation of the unreachable IP targets based on the determination of the target ownership and the combination of these IP blocks. The experiment verifies the geolocation ability of RLGBG for unreachable IP targets. In the future, we will test RLGBG in more regions and network environments to further improve the adaptability of the method to different network environments.

Acknowledgements This work was supported by the Henan Key Laboratory of Cyberspace Situation Awareness.

Funding Statement This work was supported by the National Key R&D Program of China (Grant No. 2022YFB3102904), the National Natural Science Foundation of China (Grant No. U1804263, 62172435), the Zhongyuan Science and Technology Innovation Leading Talent Project of China (Grant No. 214200510019), and Key Research, Development and Promotion Project on Tackling Key Scientific Problems of Henan Province (No. 232102211052).

References

1. Niu, B., Li, Q., Zhu, X., Cao, G., Li, H.: Enhancing privacy through caching in location-based services. In: 2015 IEEE Conference on Computer Communications (INFOCOM), 1017–1025. IEEE (2015)
2. Zheng, X., Cai, Z., Li, J., Gao, H.: Location-privacy-aware review publication mechanism for local business service systems. In: IEEE INFOCOM 2017-IEEE Conference on Computer Communications, 1–9. IEEE (2017)
3. Burch, H., Cheswick, B.: Mapping the internet. *Computer* **32**(4), 97–98 (1999)
4. Chen, J., Liu, F., Zhao, F., Zhu, G., Ding, S.: A SC-Vivaldi network coordinate system based method for IP geolocation. *J. Internet Technol.* **17**(1), 119–127 (2016)
5. Liu, C., Luo, X., Yuan, F., Liu, F.: RNBG: a ranking nodes based IP geolocation method. In: IEEE INFOCOM 2020-IEEE Conference on Computer Communications Workshops (INFOCOM WKSHPS), 80–84. IEEE (2020)

6. Zhang, F., Liu, F., Xu, R., Luo, X., Ding, S., Tian, H.: Street-level IP geolocation algorithm based on landmarks clustering. *Comput. Mater. Cont.* **66**(3), 3345–3361 (2021)
7. Ding, S., Luo, X., Wang, J., Fu, X.: GNN-Geo: A Graph Neural Network-Based Fine-grained IP Geolocation Framework. arXiv preprint [arXiv:2112.10767](https://arxiv.org/abs/2112.10767) (2021)
8. Li, D., Chen, J., Guo, C., Liu, Y., Zhang, J., Zhang, Z., Zhang, Y.: IP geolocation mapping for moderately connected internet regions. *IEEE Trans. Parallel Distrib. Syst.* **24**(2), 381–391 (2012)
9. Gueye, B., Ziviani, A., Crovella, M., Fdida, S.: Constraint-based geolocation of internet hosts. *IEEE/ACM Trans. Netw.* **14**(6), 1219–1232 (2006)
10. Laki, S., Mátray, P., Hága, P., Sebők, T., Csabai, I., Vattay, G.: Spotter: a model based active geolocation service. In: *Proceedings of IEEE INFOCOM*, pp. 3173–3181 (2011)
11. Ciavarrini, G., Greco, M.S., Vecchio, A.: Geolocation of Internet hosts: accuracy limits through Cramér–Rao lower bound. *Elsevier Comput. Netw.* **135**, 70–80 (2018)
12. Katz-Bassett, E., John, J.P., Krishnamurthy, A., Wetherall, D., Anderson, T., Chawathe, Y.: Towards IP geolocation using delay and topology measurements. In: *Proceedings of ACM IMC*, pp. 71–84 (2006)
13. Wang, Y., Burgener, D., Flores, M., Kuzmanovic, A., Huang, C.: Towards street-level client-independent IP geolocation. In: *Proceedings of USENIX NSDI*, p. 27 (2011)
14. Zu, S., Luo, X., Liu, S., Liu, Y., Liu, F.: City-level IP geolocation algorithm based on pop network topology. *IEEE Access* **6**, 64867–64875 (2018)
15. Zhao, F., Xu, R., Li, R., Zhu, M., Luo, X.: Street-level geolocation based on router multilevel partitioning. *IEEE Access* **2019**(7), 59237–59248 (2019)
16. Milo, R., Shen-Orr, S., Itzkovitz, S., Kashtan, N., Chklovskii, D., Alon, U.: Network motifs: simple building blocks of complex networks. *Science* **298**(5594), 824–827 (2002)
17. Li, D., Chen, J., Guo, C., Liu, Y., Zhang, J., Zhang, Z., Zhang, Y.: IP-geolocation mapping for moderately connected internet regions. *IEEE Trans. Parallel Distrib. Syst.* **24**, 381–391 (2012)
18. Ma, T., Liu, F., Luo, X., Yin, M., Li, R.: An algorithm of street-level landmark obtaining based on yellow pages. *J. Internet Technol.* **20**, 1415–1428 (2019)
19. Li, R., Sun, Y., Hu, J., Ma, T., Luo, X.: Street-level landmark evaluation based on nearest routers. *Secur. Commun. Netw.* (2018)
20. Luckie, M.: Scamper: a scalable and extensible packet prober for active measurement of the internet. In: *Proceedings of the 10th ACM SIGCOMM Conference on Internet Measurement*, pp. 239–245 (2010)
21. Augustin, B., Cuvellier, X., Orgogozo, B., Viger, F., Friedman, T., Latapy, M., Magnien, C., Teixeira, R.: Avoiding traceroute anomalies with Paris traceroute. In: *Proceedings of the 6th ACM SIGCOMM Conference on Internet Measurement*, pp. 153–158 (2006)

Chapter 47

Deepwater Choke and Well Killing Manifold Automatic Control Pressure System and Simulation Experiments



Zhenyu Long, Jun Li, Hongwei Yang, and Wang Chen

Abstract Offshore oil and gas resources are hot spots for development in various countries, but developing deepwater formations will inevitably encounter problems such as ultra-HTHP (high temperature and pressure), narrow safety density window, and complex formation structures. Improper handling can cause kick, blowout and other drilling complications, which will not only cause environmental pollution, but also threaten engineers' lives. At present, the basic means to deal with kick is still through the engineer to control the opening of choke valve, but the manual control has long adjustment time, large pressure fluctuations, and extremely dependent on the engineer's work experience. With the development and advancement of artificial intelligence and automation technology, oil and gas well pressure control also needs to integrate artificial intelligence and automation technology to carry out research on automatic control system for choke and well killing manifold in deep water for accurate and fast control of wellbore pressure. In this paper, we designed a deepwater choke and well killing manifold automatic control pressure system based on the optimized PID control method and built equipment to conduct simulation experiments to test the ability of the system to track the target pressure stably and quickly as well as the ability to track the continuous pressure curve. The results show that the system can adjust choke valve in place within 35 s during the experimental process of simulating kick and automatic pressure control, at which time the system pressure is stable and the pressure fluctuation is less than 0.02 MPa. This indicates that the deepwater choke and well killing manifold automatic control pressure system established in this paper has the advantages of fast pressure adjustment and high adjustment accuracy, which can replace engineers in automatic control to a certain extent and provide a guarantee for the safe development of offshore It provides a guarantee for the safe development of oil and gas.

Keywords Choke and well killing manifold · Automatic pressure control · Optimized PID control method

Z. Long (✉) · J. Li · H. Yang · W. Chen
China University of Petroleum (Beijing), No. 18 Fuxue Road, Changping District,
Beijing 102249, China
e-mail: longzhenyu@foxmail.com

47.1 Introduction

As oil and gas resources continue to degrade, ultra-deep and ultra-deepwater oil and gas reservoirs have become crucial areas for oil and gas development in China [1–4]. These reservoirs present significant challenges due to their complex geological conditions and narrow safety density windows. As a result, controlling wellbore pressure becomes challenging, leading to frequent complex situations such as downhole kick and leakage that pose serious threats to wellbore safety [5]. To address such issues during offshore drilling, controlling wellbore pressure by choking the pressure sink has become an important approach to dealing with kick, well surge, or blowout accidents [6, 7]

Currently, engineers still need to manually control the choke opening during well killing operations. However, this approach heavily relies on their experience, which may lead to inaccuracies. Additionally, when gas–liquid mixing occurs under multi-phase flow conditions, it becomes even more challenging to control the choke opening accurately. As a result, wellbore pressure can fluctuate widely, and the pressure response may be slow during well control. These fluctuations can easily break the narrow safety density window, leading to more severe downhole complex conditions and even malignant well blowout accidents. To overcome these challenges, artificial intelligence and automation technology need to be integrated into oil and gas well pressure control. Research on automatic well killing control systems is necessary for precise and rapid control of wellbore pressure in deep water. By integrating artificial intelligence and automation technology, well killing operations can be carried out more accurately and quickly, leading to improved safety and reduced risks during offshore drilling.

In this paper, we present an automatic control system for the Deepwater choke and kill manifold based on the optimized PID control method. We built a simulation experiment to test the system's ability to track the target pressure steadily and quickly and to track the continuous well killing curve. We also studied the effect of the system on tracking pressure under single-phase flow and gas–liquid two-phase flow conditions with varying target pressure and gas–liquid ratio. Based on the experimental results, we analyze the control effect of the self-built well killing manifold automatic control system. The second part of the paper introduces the self-built well killing manifold automatic control system. The third part describes the well killing manifold automatic control device and the experimental procedure. The fourth part analyzes the experimental results under different conditions. In the last part, we draw conclusions from the study's findings. By using the Deepwater choke and kill manifold automatic control system, we can effectively track the target pressure and continuously control the wellbore pressure curve, providing a safer and more efficient solution for well killing operations in deep water. The system's ability to adapt to varying gas–liquid ratios and different target pressures highlights its potential for widespread application in the oil and gas industry.

47.2 Choke and Kill Manifold Automatic Control System

The automatic control system of choke and well killing manifold in this paper mainly consists of data acquisition module (pressure and displacement sensors and choke valve opening displacement sensors), PID control module, actuation module (electro-hydraulic proportional valve and solenoid reversing valve and hydraulic system), and the system composition and signal transmission are shown in Fig. 47.1.

In the process of well killing automatic control, the PID control module collects the actual pressure data (signal source) through the sensor of the data acquisition module, transmits it to the proportional amplifier to realize the signal amplification and processing, and then compares the actual pressure with the set target pressure data through the PID controller to get the output signal, which is transmitted to the actuation system (electro-hydraulic proportional valve + electromagnetic reversing valve) to control the liquid-operated choke [8–10]. During the control process, the displacement of the choke and the feedback pressure signal will be returned to the PID control module for further analysis, and when the error signal is processed by the PID controller, it will continue to be transmitted to the actuation system. Among them, the electro-hydraulic proportional reversing valve is mainly controlled by the proportional solenoid, according to the direction and size of the signal of the control current to produce the corresponding action to change the position of the spool, so as to establish different hydraulic channels, adjust the size of the valve port, so as to complete the flow output proportional to the input current and finally precisely adjust the displacement of the choke hydraulic cylinder, the choke opening will be changed, so as to achieve the purpose of automatic control of the well killing.

PID controller is a linear controller, including proportional, integral and differential control algorithms [11–14]. First, the proportional-integral, differential system two links to calculate the corresponding output control function to regulate the controlled object, and then the feedback data formed by the variable error for appropriate adjustment so as to achieve closed-loop control, its control principle is shown in Fig. 47.2.

The system constitutes the control deviation based on the given $r(t)$ value and the actual output value $y(t)$, as shown in Eqs. (47.1). The proportional (P), integral (I) and differential (D) of the deviation are combined linearly to form a control quantity

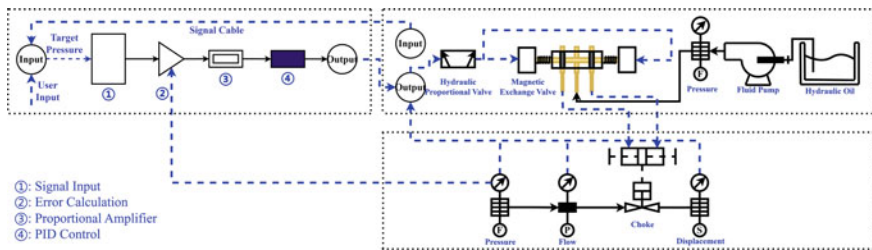


Fig. 47.1 Choke and kill manifold automatic control system composition and signaling

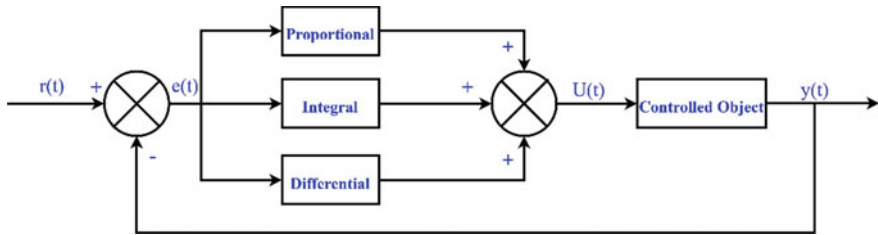


Fig. 47.2 PID control principle

to control the object under control, so it is called a PID controller.

$$e(t) = r(t) - y(t) \tag{47.1}$$

The control law of this controller is shown in Eqs. (47.2).

$$u(t) = K_p \left[e(t) + \frac{1}{T_i} \int_0^t e(t) dt + T_d \frac{de(t)}{dt} \right] \tag{47.2}$$

Rewriting the above equation into transfer function form, we can obtain Eqs. (47.3):

$$G(s) = \frac{U(s)}{E(s)} = K_p \left(1 + \frac{1}{T_i S} + T_d S \right) \tag{47.3}$$

In Eqs. (47.3), K_p is the scale factor; T_i is the integration time constant; T_d is the differential constant.

In the process of automatic well killing control, the actual pressure at the well-head collected by the pressure sensor is $y(t)$ and the target pressure is $r(t)$. The PID controller controls the operation of the electro-hydraulic proportional valve and the electromagnetic reversing valve through the calculated differential pressure, thus controlling the flow direction and flow rate of the hydraulic oil in the hydraulic line and realizing the control of the choke and automatic wellhead pressure control.

47.3 Indoor Simulation Experiment System

In order to verify the control effect and stability of the choke and well killing manifold automatic control system, an indoor physical simulation experimental system for well killing automatic control was constructed, and its schematic and physical diagrams are shown in Figs. 47.3 and 47.4. The whole experimental system includes well killing automatic control system, simulated wellbore system, hydraulic choke system, circulation system and data acquisition system. The experimental system can be used

to study the control effect of the automatically controlled well killing system with variable target pressure, variable gas–liquid injection and variable gas content under different gas–liquid two-phase flow conditions. In order to verify the control effect and stability of the choke and well killing manifold automatic control system, an indoor physical simulation experimental system for well killing automatic control was constructed, and its schematic and physical diagrams are shown in Figs. 47.3 and 47.4. The whole experimental system includes automatic well killing control system, simulated wellbore system, hydraulic choke system, circulation system and data acquisition system. The experimental system can be used to study the control effect of the automatically controlled well killing system with variable target pressure, variable gas–liquid injection and variable gas content under different gas–liquid two-phase flow conditions.

In this well killing automatic control indoor physical simulation experimental system, the simulated wellbore is made of stainless steel tubing with a height of 2 m and an inner diameter of 133 mm, and is designed to withstand a pressure of 2 MPa. The fluids circulating in the simulated wellbore include gas and liquid. By adjusting the gas phase injection rate (0–18 m³/h) and the liquid phase injection rate (0–20 m³/h), a gas–liquid two-phase flow with gas content between 0 and 65% can be injected into the simulated wellbore. The choke is a commonly used needle type choke with different openings corresponding to spool strokes of 0–44 mm, and the spool displacement strokes are acquired through sensors attached to the spool. The data acquisition system includes pressure sensors mounted at the top and bottom of the wellbore, gas and liquid flow sensors, and choke displacement sensors to collect pressure, valve opening, and other data in real time at various locations in the installation.

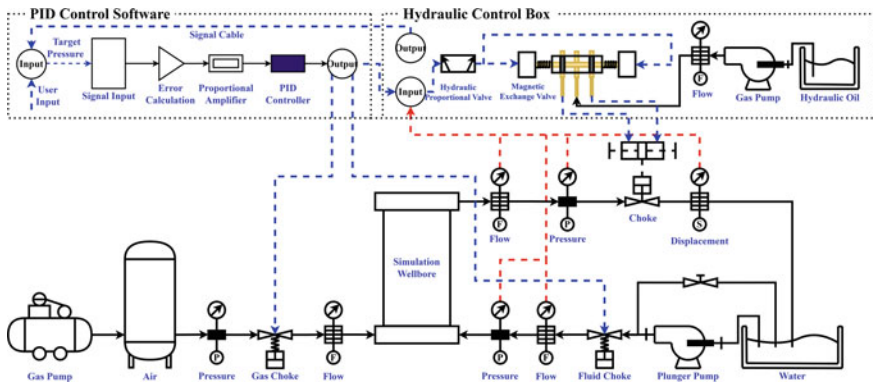


Fig. 47.3 Indoor simulation experimental device connection schematic



Fig. 47.4 Physical diagram of indoor simulation experimental device: **a** hydraulic control box; **b** hydraulic lines; **c** PID control software; **d** piston pump; **e** gas phase injection system (including gas pump and storage tank); **f** choke; **g** simulated wellbore

47.4 Well Killing Automatic Control Simulation Experiment

During conventional well pressurization, the target pressure is adjusted according to the pre-construction designed pressure curve and the wellhead back pressure so that the bottomhole pressure can be kept stable at different stages of well pressurization. In order to ensure that the bottomhole pressure does not change abruptly during the pressurization process, the automatic pressure control system needs to adjust the choke opening in the shortest possible time after the target pressure changes to adjust the pressure to the target pressure and keep it stable.

The control pressure in this paper is the casing pressure, and the system's control capability is tested by testing the system's fast control capability and the stability after controlling to the target pressure.

47.4.1 Fast Control and Stability Tests Under Single-Phase Flow Conditions

To test the ability of the choke and well killing manifold automatic control system to quickly track the target pressure under single-phase flow conditions, the fluid

injection rate was set constant and different target pressures were varied, and the duration of control and pressure fluctuations were recorded. The results of the simulation experiments are shown in Fig. 47.5 and Table 47.1. In the experiment shown in Fig. 47.5, the fluid injection rate was set at 18 m³/h and the target pressure was adjusted within 0.1 MPa to 0.6 MPa.

See Fig. 47.5 and Table 47.1, single-phase flow conditions to test the system control ability of the experimental results show that a wide range, a small range of changing the target pressure, the system in most conditions can be adjusted to the choke in place within 35 s, the absolute value of pressure fluctuations is basically less than 0.02 MPa, the process of adjustment only the target pressure from 0.6 adjustment to 0.1 group overshoot phenomenon. After the system adjusted the casing pressure to the target pressure, there were certain fluctuations in the set pressure, but the choke

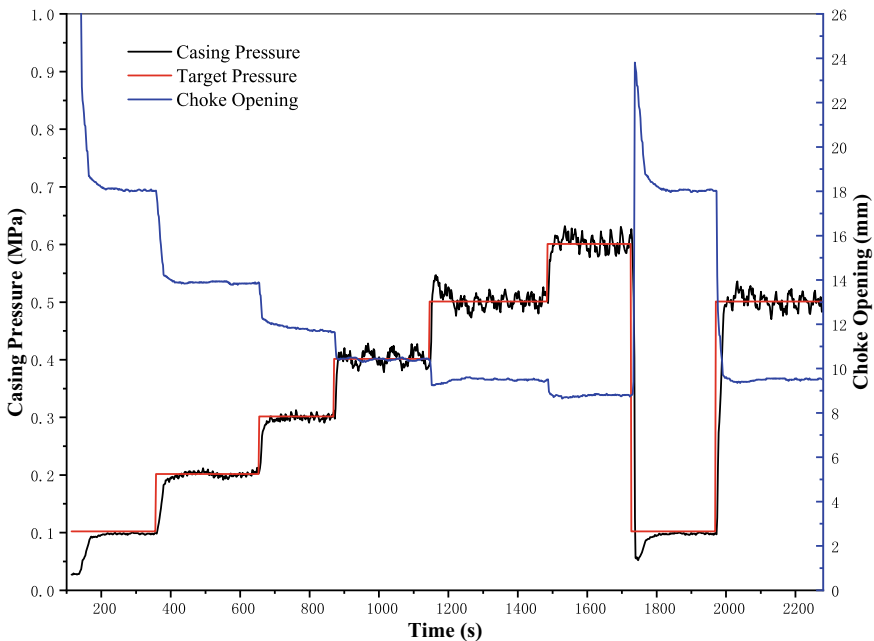


Fig. 47.5 Simulation experiments with constant liquid injection velocity and varying target pressure under single-phase flow conditions

Table 47.1 Control time and pressure fluctuation under single-phase flow and varying target pressure

Target pressure (MPa)	0.1	0.2	0.3	0.4	0.5	0.6	0.1	0.5
Control time (s)	34	32	30	12	32	16	50	26
Absolute fluctuation (MPa)	0.006	0.007	0.010	0.017	0.018	0.020	0.006	0.018

opening remained stable at this time, which could be judged to be caused by the pressure fluctuations in the simulated wellbore and the fluid delivery steel pipe.

Then, the target pressure was fixed and different liquid injection rates were varied, when the set pressure would increase or decrease suddenly, and the time to recover to the target pressure after the set pressure change and the range of pressure fluctuation were measured. The results of the simulation experiments are shown in Fig. 47.6 and Table 47.2. In the experiment shown in Fig. 47.6, the target pressure is set at 0.2 MPa and the liquid injection rate is set to vary between 11 and 18 m³/h.

According to the experimental results in Fig. 47.6, the system was able to produce a response within 5 s for both large and small changes in liquid injection rate and control the choke to the desired position within 25 s, and there was no overshoot during the whole process of the experiment. However, it is worth mentioning that the stability of the system in this experiment has decreased, and there have been several fine adjustments in the process of maintaining the target pressure, and the opening was not stable the choke and well killing manifold automatic control system in the test of variable target pressure, in most cases in 10–35 s time to adjust the choke

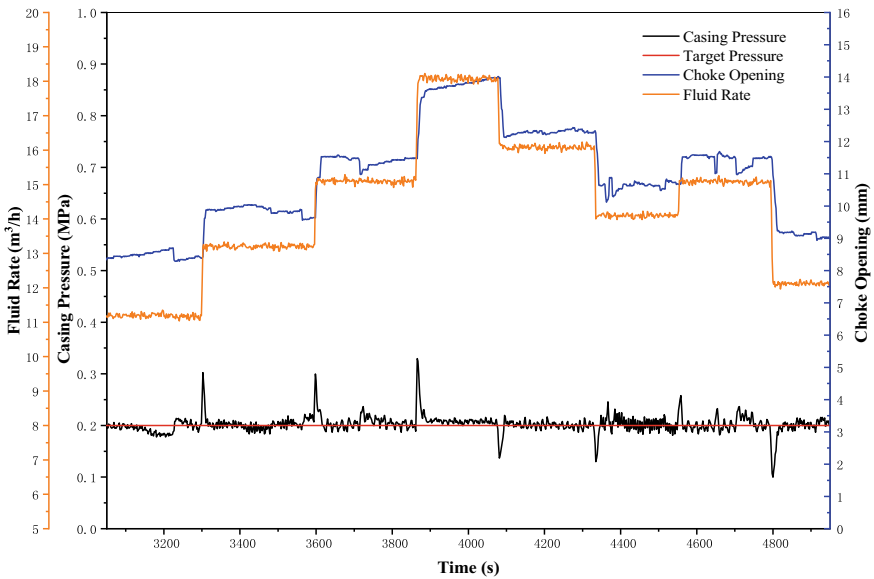


Fig. 47.6 Simulation experiments with constant target pressure and variable liquid injection rate under single-phase flow conditions

Table 47.2 Control time and pressure fluctuation under single-phase flow and varying fluid rate

Fluid rate (m ³ /h)	11→13	13→15	15→18	18→16	16→14	14→15	15→12
Control time (s)	12	10	18	25	15	12	18
Absolute fluctuation (MPa)	0.018	0.015	0.008	0.015	0.019	0.016	0.015

opening in place, the adjustment process set pressure fluctuations are basically less than 0.02 MPa; in the system of variable liquid injection rate of anti-interference test, the control system are within 5 s corresponding, and in 15–30 s the sudden change of pressure back to the target pressure, the pressure fluctuations are less than 0.02 MPa. All pressure fluctuations are less than 0.02 MPa.

In summary, it shows that the automatic control system can accurately, quickly and stably track the target pressure for single-phase flow conditions, and has good stability and automatic control against interference.

47.4.2 Fast Control and Stability Tests Under Two-Phase Flow Conditions

The fast control capability and stability of the choke and well killing manifold automatic control system was tested under the conditions of gas–liquid two-phase flow injected into the simulated wellbore. See Fig. 47.7 for fixed liquid and gas injection rates of 12 m³/h and 200 L/min, respectively, i.e., the gas content of the fluid entering the simulated wellbore was fixed at 50%, and then the control time and pressure fluctuations were measured by varying the target pressure in a wide and small range, as detailed in Table 47.3.

See Fig. 47.7 and Table 47.3. The experimental results of testing the control capability of the system under gas–liquid two-phase flow conditions show that the

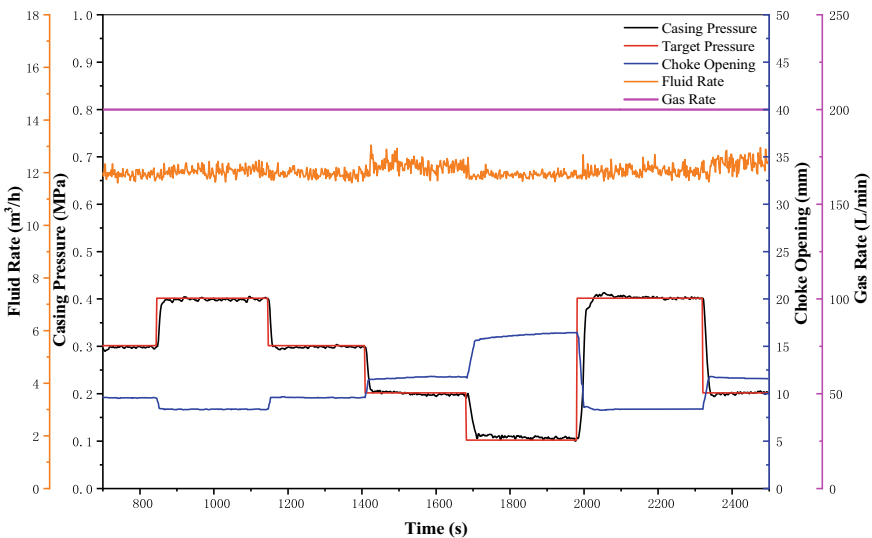


Fig. 47.7 Simulation experiments for gas–liquid two-phase flow with 50% gas content and varying target pressure

Table 47.3 Gas–liquid two-phase flow, control time and pressure fluctuation for varying target pressure

Target pressure (MPa)	0.4	0.3	0.2	0.1	0.4	0.2
Control time (s)	26	14	22	25	35	18
Absolute fluctuation (MPa)	0.004	0.008	0.007	0.010	0.012	0.006

system can adjust the choke in place within 35 s under most conditions for large and small changes in target pressure, and the absolute value of pressure fluctuation is basically less than about 0.01 MPa, and there is basically no overshoot in the process of adjustment. Compared with the experiments under single-phase flow conditions, the pressure fluctuation in the simulated wellbore under gas–liquid two-phase flow conditions is not obvious, which is reflected in the experimental results that the stability of the system control has been significantly improved.

Then the target pressure is fixed and the gas injection rate is varied for different gas injection rates, i.e., the gas content of the injected fluid is changed, at which time the set pressure changes abruptly, and the time to recover to the target pressure after the set pressure changes and the range of pressure fluctuations are measured. The results of the simulation experiments are shown in Fig. 47.8 and Table 47.4. In the experiment shown in Fig. 47.8, the target pressure is set at 0.3 MPa and the gas injection rate is set to vary between 50 and 300 L/min.

According to the experimental results in Fig. 47.8, large and small changes in the gas content rate of the injected fluid, the system is able to produce a response within 6 s and control the choke to the desired position within 10 s with almost no

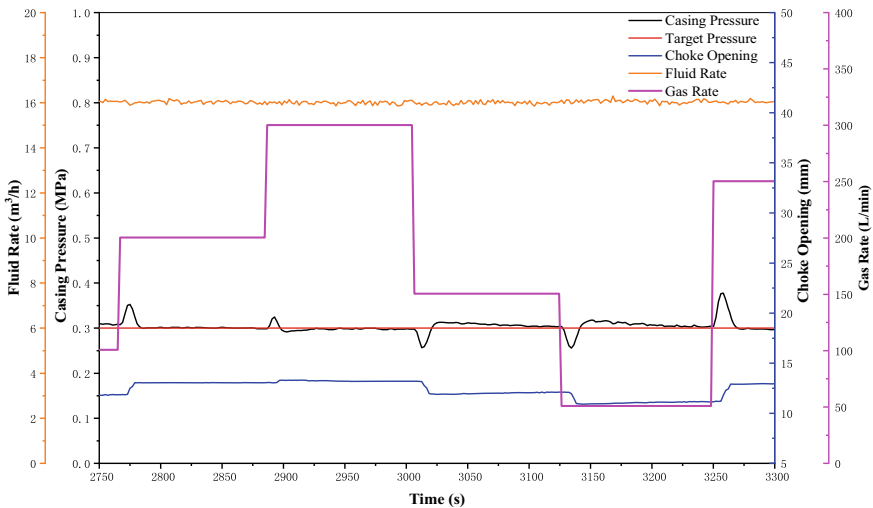


Fig. 47.8 Simulation experiments of varying gas injection velocity under two-phase flow conditions with constant target pressure

Table 47.4 Gas–liquid two-phase flow, control time and pressure fluctuations for varying gas injection rate

Gas rate (L/min)	100→200	200→300	300→150	150→50	50→250
Control time (s)	8	6	8	6	10
Absolute fluctuation (MPa)	0.001	0.007	0.011	0.014	0.003

fluctuation in pressure, and the system is able to stabilize the set pressure near the target pressure.

In summary, the ability of the choke and well killing manifold automatic control system to quickly, steadily, track the target pressure and the ability of the system to recover sudden pressure changes and resist disturbances when the fluid changes was tested under single-phase flow and gas–liquid two-phase flow conditions. Comparing the two different fluids into the simulated wellbore, the experiment of gas–liquid two-phase flow is closer to the realistic scenario of well killing after kick is found, and the system has better response time and control time, better stability and lower pressure fluctuation in the control of gas–liquid two-phase flow, which can replace engineers for automatic control to a certain extent and provide a guarantee for safe development of offshore oil and gas.

47.5 Conclusion

In this paper, a deepwater choke and kill manifold automatic control system based on the optimized PID control method is established, and the fast and stable tracking capability and anti-interference capability of the system are tested in combination with the indoor simulation experimental device for variable target pressure, variable fluid injection rate and gas injection rate, respectively. The experimental results show that the choke and kill manifold automatic control system can adjust the choke opening to the appropriate position within 35 s for the sudden change of set pressure caused by variable target pressure or variable fluid injection rate, and there is no serious overshoot phenomenon during the control process, and the control pressure remains stable. The deepwater choke and kill manifold automatic control system established in this paper has the advantages of fast pressure adjustment speed and high adjustment accuracy, which can replace engineers for automatic control to a certain extent and provide a guarantee for the safe development of offshore oil and gas.

References

1. Wang, Z., Jiang, Q., Dong, X.. Oil, C.: Gas industry development analysis and outlook report blue book (2019–2020) (2020)

2. Tian, Z.: Sustainable development of china's oil and gas resources in the 21st century. *Petrol. Sci. Technol. Forum* **6**, 25–30 (2000)
3. Lei, Q., Xu, Y., Yang, Z., et al.: Progress and development directions of stimulation techniques for ultra-deep oil and gas reservoirs. *Petrol. Explor. Devel.* **48**(01), 193–201 (2021)
4. Jia, C.: Development challenges and future scientific and technological researches in China's petroleum industry upstream. *Acta Petrolei Sin.* **41**(12), 1445–1464 (2020)
5. Zhang, G., Ma, F., Liang, Y., et al.: Domain and theory-technology progress of global deep oil and gas exploration. *Acta Petrolei Sin.* **36**(09), 1156–1166 (2015)
6. Zhang, G.: Discuss one-cycle killing process from typical blowout cases. *Pet. Drill. Tech.* **46**(4), 1–10 (2018)
7. Ma, Z., Vajargah, A.K., Chen, D., et al.: Gas kicks in non-aqueous drilling fluids: a well control challenge. In: IADC/SPE Drilling Conference and Exhibition. OnePetro (2018)_
8. Li, Y., Xia, W., Luo, F., et al.: Experimental study on automatic well killing system of driller's method. *J. Saf. Sci. Technol.* **15**(03), 30–36 (2019)
9. Yi, B., Li, X., Sui, X., et al.: Research and application of computer optimization open-loop well killing software system. *Petrol. Drill. Tech.* **39**(01), 110–114 (2011)
10. Ma, R., Dou, Y., Li, L.: Research on throttle manifold pressure control and its simulation model. *Comput. Digi. Eng.* **45**(09), 1785–1789 (2017)
11. Åström, K.J., Hägglund, T.: The future of PID control. *Control. Eng. Pract.* **9**(11), 1163–1175 (2001)
12. Desborough, L., Miller, R.: Increasing customer value of industrial control performance monitoring-Honeywell's experience[C]. In: AICHE Symposium Series, (326), pp 169–189. American Institute of Chemical Engineers, New York, (1998, 2002)
13. Bennett, S.: The past of PID controllers. *Annu. Rev. Control.* **25**, 43–53 (2001)
14. Wu, H., Shen, S.: Basis of theory and applications on PID Control. *Control Eng. China* (01), 37–42 (2003)

Chapter 48

Prediction of Horizontal and Vertical Distribution Trend of Formation Pressure and Characteristics of Safety Density Window in Yinggehai Basin



Reyu Gao, Yi Cui, Jinzhao Fan, Guang Yang, and Hongwei Yang

Abstract The formation pressure system of Yinggehai Basin has the characteristics of poor horizontal distribution regularity and severe vertical distribution changes. This paper proposes a new method for predicting the horizontal and vertical distribution trend of formation pressure for the situation of limited offshore drilling data. The method is based on the topological triangulation algorithm, combined with the data set to fit the multivariate interpolation function, and conveniently realizes the prediction and visualization of the three-dimensional horizontal and vertical distribution trend of regional formation pressure. On this basis, through the analysis of the relevant data of the complex accident points that have been drilled, the characteristics of the single well safety density window and the regional safety density window are clarified. The study found that there is no high pressure in the shallow layer of the block, and the formation pressure spreads smoothly in the lateral direction; the high pressure top surface is at 3500 m, and the formation pressure gradually increases with the increase in longitude and decrease in latitude in the lateral direction. The formation pressure rises extremely rapidly with the increase of depth in the longitudinal direction, which has the characteristic of “broken line pressurization”. The safety density window of single well is in the shape of funnel with the characteristic of turning back, and the turning section is between 3500 and 4000 m. The safety density window feature of the block can be divided into three stages according to the depth, and the window appears extremely narrow after 3500 m ($< 0.3 \text{ g/cm}^3$).

Keywords Deepwater · Yinggehai Basin · Mud loss · Formation pressure · Safety density window

R. Gao (✉) · Y. Cui · J. Fan · G. Yang · H. Yang
CNPC Engineering Technology R&D Company Limited, Beijing 102206, China
e-mail: gaoreyudr@cnpc.com.cn

© The Author(s), under exclusive license to Springer Nature Switzerland AG 2024
S. Li (ed.), *Computational and Experimental Simulations in Engineering, Mechanisms and Machine Science* 145, https://doi.org/10.1007/978-3-031-42987-3_48

669

48.1 Regional Background

48.1.1 Regional Formation Pressure Characteristics

The Yinggehai Basin has been the main battlefield for natural gas exploration in the western South China Sea in recent years [1, 2]. However, the formation pressure coefficients of the Huangliu Formation and Meishan Formation, which are the main reservoirs in the region, are above 2.20, the formation temperature also exceeds 180 °C, and the safety density window is extremely narrow. At the same time, as the depth of the formation increases, there are significant differences in the pore pressure between the pressure bodies in different layers [3]. Judging from the previous exploration practice, the formation pressure system in this area is extremely complex, with the characteristics of poor horizontal distribution regularity and severe vertical distribution changes. The existence of these problems has also greatly increased the difficulty of determining a reasonable wellbore structure and severely restricted the efficiency of oil and gas development [4, 5]. However, due to the particularity of offshore drilling, it is impossible to obtain a large amount of formation data, which causes the problem of unclear regional formation pressure distribution [6, 7]. Therefore, clarifying the regional formation pressure distribution trend and the distribution law of the safe density window is an important prerequisite for promoting safe and efficient drilling [7–9].

Table 48.1 shows the types of formation pressure curves in the Yinggehai Basin. According to the various characteristics of pressure coefficient with depth, the overall formation pressure curve of the Yinggehai Basin is mainly characterized by three types: “diaper-S pressurization type”, “broken line pressurization type” and “slow pressurization type” [10].

Table 48.1 Characterization types of formation pressure curves in Yinggehai Basin

Formation pressure curve type	Specific definition
Diaper-S pressurization type	Refers to the thick transition section between the atmospheric pressure system and the ultra-high pressure system in the formation. As the depth increases, it can show overpressure characteristics at 1200–2000 m, and the pressure coefficient “return” phenomenon can be found in the overpressure zone
Broken line pressurization type	It means that there are two or more pressure systems in the longitudinal direction, which are mainly manifested in the formation of different pressure systems in the middle and deep parts
Slow pressurization type	This type of pressure distribution system is mainly distributed in the central depression zone and non-diapir areas of the Yinggehai Basin. It is related to the compaction before rapid deposition in the basin and the hydrocarbon generation in the later period

48.1.2 Depth of Overpressure Top Surface

A large number of research results have shown that in areas with abnormally high pressures, formations are rarely rich in natural gas, especially when the pressure coefficient in the transition zone above the overpressure top surface is between 1.2 and 1.5. The reason is mostly related to the fracture of most of the rock formations in the high pressure layer. Especially in areas where clastic rocks are developed, when the formation pressure reaches 75–95% of the overburden pressure, the overlying strata will be fractured, which causes the loss of oil and gas in the reservoir. In the Yinggehai Basin, although the high pressures caused by different abnormal high pressure mechanisms are not the same, they are generally shallower than other basins. Drilling data revealed that the pressure coefficient of the formation near 2000 m has reached 1.5, and the pressure coefficient of the formation below 3000 m is usually greater than 1.8, reaching the category of super-strong pressure.

48.2 Measured Data Analysis and “Horizontal and Vertical” Distribution Trend of Formation Pressure

This section mainly summarizes and analyzes the horizontal and vertical trends of formation pressure in the block, based on the measured formation pressure data and recorded data of multiple wells in the LDx area, combined with the block formation conditions. By using the Delaunay triangulation algorithm, the horizontal and vertical distribution trend of the block is obtained, and a three-dimensional horizontal and vertical distribution trend map of the formation pressure is formed. This lays the foundation for grasping the changing trend of formation pressure in the block. Figure 48.1 is the well location distribution map of 6 wells in the LDx gas field.

48.3 Summary of Measured Formation Pressure Data

Table 48.2 Summary of measured formation pressure data in the LDx gas field. It can be seen that the formation pressure coefficient of LDx-1 at 3982.4 m reaches 2.17, and the formation temperature is 174.3 °C; the formation temperature of LDx-2 at 3964 is 155.5 °C; LDx-12 is at 4391.5 m The formation pressure coefficient is 2.33, and the formation temperature is 193.8 °C. Therefore, most of the wells that have been drilled in this block are ultra-high temperature and ultra-high pressure wells, and the formation data of this well cannot be obtained even if the VSP measurement method is used in the well LDx-2 due to excessive formation pressure and other formation conditions.

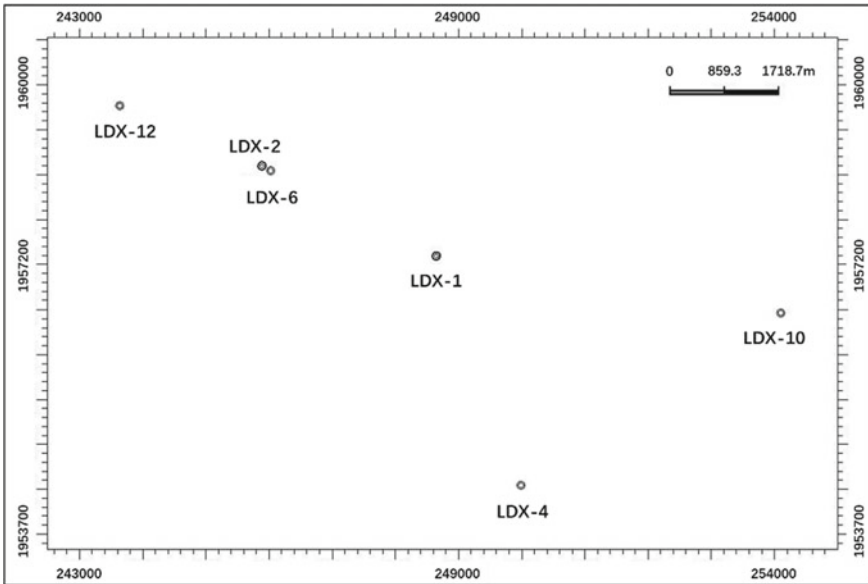


Fig. 48.1 Well location distribution map of LD-x area

Table 48.2 Measured formation pressure data

Well number	Depth m	Formation pressure coefficient g/cm ³	Formation temperature °C	Measurement method
LDx-1	3982.4	2.17	174.3	MDT
LDx-2	3964	The formation pressure is too high and no data can be measured	155.5	VSP
LDx-12	4391.5	2.33	193.8	MDT

48.3.1 Prediction of the Trend of Horizontal and Vertical Formation Pressure Distribution in the Block

In this section, by using Delaunay triangulation and combining with multivariate interpolation function based on basic data set fitting, the horizontal and longitudinal distribution trend of regional formation pressure is predicted. Its advantage lies in the fact that when there are fewer data types and limited sources, a simple and efficient method can be used to predict the horizontal and vertical distribution trend of regional formation pressure and realize visualization. The basic concepts and specific implementation methods will be briefly introduced below.

48.3.1.1 Introduction to Basic Concepts and Forecasting Methods

(1) Triangulation

Triangulation is an effective method and tool to realize data visualization, and it plays a pivotal role in geographic information, medicine, weather forecasting, and other disciplines. Its specific definition is: suppose V is a finite point set on a two-dimensional real number field, edge e is a closed line segment formed by the points in the point concentration as the endpoint, and E is a set of e [11]. Then a triangulation $T = (V, E)$ of the point set V is a plane graph G , which satisfies the conditions:

- ① Except for the endpoints, the edges in the plan view do not contain any points in the point set.
- ② There are no intersecting edges.
- ③ All the faces in the plan view are triangular, and the collection of all triangular faces is the convex hull of the set V of scattered points (Fig. 48.2).

(2) Convex hull

Convex Hull is a concept in computational geometry (graphics). It is specifically defined as: in a real vector space V , for a given set X , the intersection S of all convex sets containing X is called the convex hull of X . The convex hull of X can be constructed by the convex combination of all points (X_1, \dots, X_n) in X . In the two-dimensional Euclidean space, the convex hull can be imagined as a rubber ring that

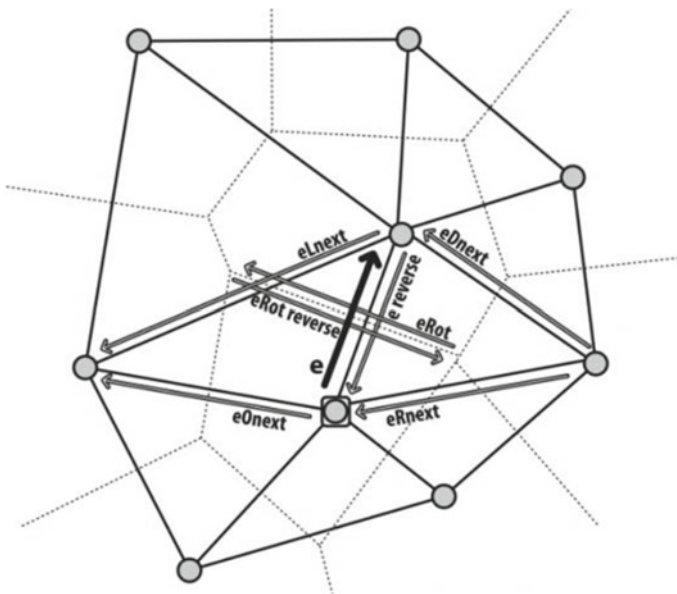


Fig. 48.2 Schematic diagram of triangulation

just covers all the points. In layman's terms, a convex hull is a convex polygon formed by connecting the outermost points of a point set on a given two-dimensional plane, and it can contain all the points in the point set.

(3) Prediction and visualization method of regional formation pressure horizontal and vertical distribution trend

- ① Filter and count the data of each well to form a data set.
- ② Form the data well location distribution map in the plane coordinate system and wrap all the involved well locations in the form of convex hulls by convex polygons.
- ③ If the formed convex polygon is a triangle, skip this step; if the formed convex polygon is non-triangular, the polygon needs to be divided to ensure that every part of the divided is a triangle.
- ④ Triangulate the formed convex polygons and combine the calculation accuracy of the algorithm to use the platform to make the convex polygons shrink inward to a very small value. To ensure that all well coordinate points are in the triangular grid divided by convex polygons, and then determine the specific mesh points.
- ⑤ Use the Delaunay triangulation algorithm to mesh the convex hull.
- ⑥ Based on the basic data set (such as longitude, latitude, pressure, etc.) given by the data well, combined with the required output conditions (such as depth, pressure, etc.), fit an interpolation function that returns the given data set, and use it to disperse Perform interpolation on a two-dimensional or three-dimensional data set of point data.
- ⑦ Choose the output pressure surface to obtain the prediction map of the regional formation pressure horizontal and vertical distribution trend.

48.3.1.2 Prediction of Regional Formation Pressure Distribution Trend in LDx Gas Field

By summarizing and screening the actual use of drilling fluid and measured point data of the six existing wells in the LDx gas field, a data source point set is formed after invalid data is eliminated. The data is integrated through Matlab, using the method mentioned in the previous section, and each pressure level is individually colored, and the formation pressure horizontal and vertical distribution trend graph is obtained, as shown in Fig. 48.3.

Figure 48.3 is based on the Delaunay triangulation algorithm to obtain the LDx gas field formation pressure horizontal and vertical distribution trend prediction map, composed of two different perspectives. The vertical axis in the figure is the depth below sea level, ranging from 0 to 4500 m; the two horizontal axes are longitude and latitude, ranging from 108.57° to 108.70° and 17.64° to 17.7°. In the figure, the formation pressure 0–100 MPa is divided into different colors from blue to red, and 30 pressure surfaces are uniformly selected among them. The points arranged vertically in the figure represent the pressure values of the data points from different depths of each well. It can be seen that there is no high pressure in the shallow layer of this area,

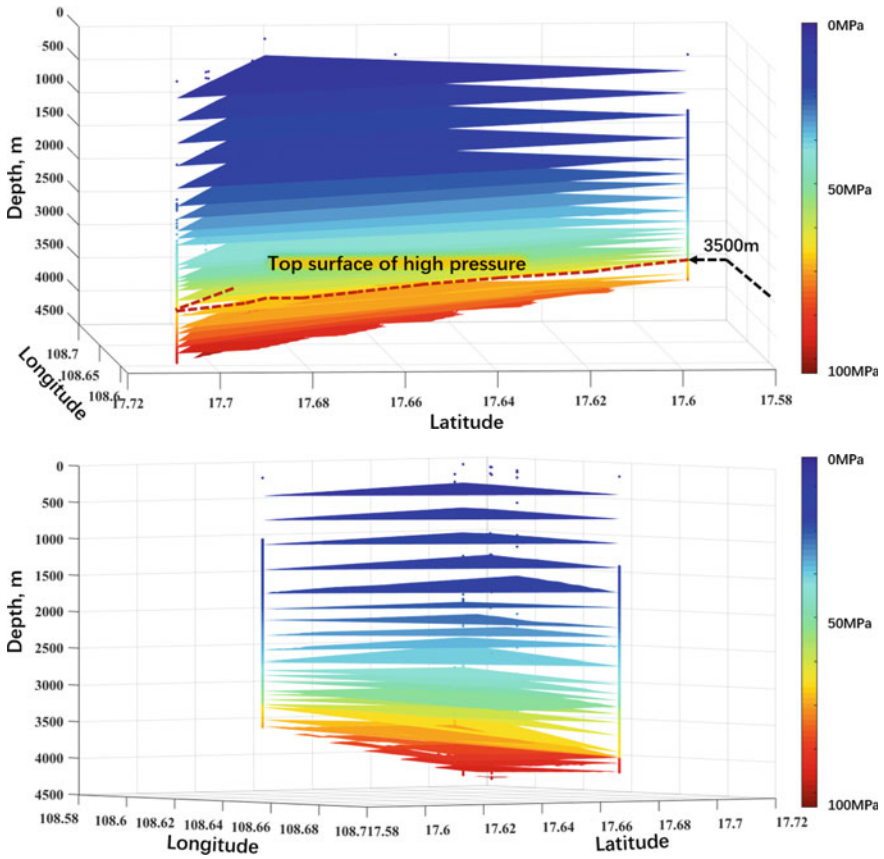


Fig. 48.3 Prediction of the horizontal and vertical distribution trend of formation pressure in LDx block

and the formation pressure spreads horizontally; the top surface of the high pressure layer is about 3500 m (yellow interval, about 70 MPa), and the overall vertical trend shows a slow pressurization type. After the formation depth is greater than 3500 m, with the increase of longitude and the decrease of latitude in the lateral direction, the formation pressure gradually increases from the northwest to the southeast and is relatively gentle. In the longitudinal direction, the formation pressure rises extremely rapidly with the increase of depth. For example, the formation pressure of the well LDx-12 reaches 96 MPa at 4300 m.

48.4 Analysis of Characteristics of Block Security Density Window

48.4.1 Statistics and Analysis of the Safety Density Window of Complex Accident Points

Due to the complexity of the formation pressure system and overpressure mechanism in this area, complex accidents are frequently encountered when traditional drilling and well control measures are used. This section sorts out and analyzes the complex accidents encountered during the drilling process, paving the way for better obtaining the characteristics of the regional safety window and better avoiding risks in the later drilling process. Combining the field data, the depth of the complex accident site, the mud density at the time of drilling, the adjusted mud density, the corresponding leakage pressure, and the width of the window have been sorted out and summarized, as shown in Table 48.3.

By sorting out and analyzing the complex accident points, the safety density window at the complex accident point is extremely narrow, and the pressure coefficient is often less than 0.1 g/cm^3 , and even the width of the window is less than zero. At the same time, the formation temperature is between 180 and $205 \text{ }^\circ\text{C}$, and the formation pressure density equivalent is above 2 g/cm^3 , which belongs to the ultra-high temperature and ultra-high pressure well section.

Table 48.3 Relevant data of complex accident points

Well number	Depth m	Density equivalent of formation fracture pressure g/cm^3	Temperature $^\circ\text{C}$	Mud density before drilling g/cm^3	Adjusted mud density g/cm^3	Density equivalent of leakage pressure g/cm^3	Window width g/cm^3
LDx-1	4085.67		187	2.19	2.23	2.19	Windowless
LDx-2	4103	2.315	191	2.15	2.27	2.27–2.28	Less than 0.1
LDx-4	4052.89		185	2.2	2.6	2.2	Windowless
LDx-6	4105.77	2.35	190	2.24	2.23	2.24	Less than 0.1
	4329.79		192	2.25	2.26	2.25	
LDx-10	3936.2	2.38	192	2.24	2.26	2.24	Less than 0.1
	3972.5		194	2.28	2.28	2.355	
LDx-12	4070.66		205	2.06	2.06	2.11	

48.4.2 Safety Density Window Characteristics for Individual Wells and Zones

It can be seen from Fig. 48.4 that the safety density window of the wellbore in the block gradually decreases with the increase of depth. As the depth of the three wells of LDx-1, LDx-2, and LDx-6 increases, the density window keeps decreasing, reaching a minimum in the target layer. The high pressure top surface at 3500 m is located in the T29 water sand channel, while the ultrahigh-pressure top surface at 4000 m is distributed on the top boundary of the T31 layer. This is consistent with the horizontal and vertical distribution trend of formation pressure predicted in the second section.

In the ultra-high pressure formation, the formation pressure coefficient suddenly increases, and the window is extremely narrow, as shown in the red box in the figure. At a depth of about 3500 m, the “safe density window back section” appeared, as shown in the green box. This is similar to the situation of the two pressure systems described in the formation “broken line pressurization”, that is, there are two sets of formation overpressure systems at 3500 and 4000 m. At the back of the window, after the density window is slightly enlarged, the formation pressure increases sharply and the window becomes smaller. The safety window at 4000 m of the destination layer is extremely small, even less than 0.1, or there is no window. Therefore, the safety density window of a single well in this block is generally funnel-shaped, and the window decreases as the depth increases; at the same time, it is mainly characterized by the cyclotron type, with starting and ending points of 3500 and 4000 m.

Table 48.4 shows the horizontal and vertical trend statistical results of the block safety density window. It can be seen that the security density window of the LDX block can be mainly divided into three stages: (1) When the formation depth is less than 2000 m, the security density window is greater than 0.6 g/cm³. (2) After 2000 m, the overall trend is to reduce the window by about 0.1 g/cm³ per 500 m. (3) The first

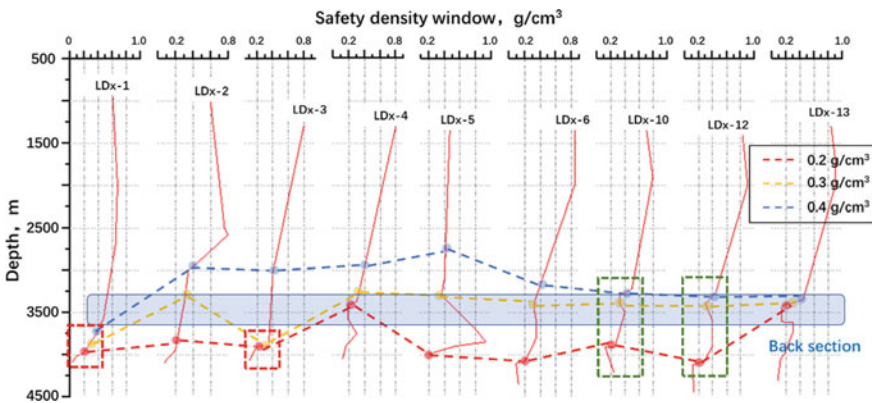


Fig. 48.4 Trend distribution diagram of security density window

Table 48.4 Horizontal and vertical trend statistics of safety density window

Depth, m	Safety density window, g/cm ³
< 2000	> 0.6
2000–2500	0.5–0.6
2500–3000	0.4–0.5
3000–3500	0.3–0.4
3500–4000	0.2–0.3
>4000	<0.2

round of extremely narrow windows ($<0.3 \text{ g/cm}^3$) appeared at the 3500 m layer, and the window values at 4000 m were all reduced to within 0.2 g/cm^3 .

48.5 Conclusion

This paper proposes a new method for predicting the three-dimensional horizontal and vertical distribution trend of regional formation pressure. Aiming at the dilemma of limited offshore drilling data, this method is based on the topological triangulation algorithm and uses the sorted data set to fit a multivariate interpolation function, which can easily realize the prediction and visualization of regional formation pressure. On this basis, the characteristics of the single well and the regional safety density window are clarified by analyzing the relevant data of the complex accident points that have been drilled. The main conclusions are as follows:

- (1) There is no high pressure in the shallow layer of the LDx block, and the formation pressure spreads horizontally; the top surface of the ultrahigh pressure is located at 3500 m. In the interval below 3500 m, the formation pressure gradually increases from the northwest to the southeast in the horizontal direction; in the vertical direction, the formation pressure rises extremely rapidly with the increase of depth, which has the characteristic of “broken line pressurization”.
- (2) The safety density window of a single well is in the shape of a funnel with the characteristic of turning back. The turning section is between 3500 and 4000 m. The block security density window is mainly divided into three stages according to the depth, and a very narrow window ($<0.3 \text{ g/cm}^3$) appears after 3500 m.

Acknowledgements This research work was supported by the Science Foundation of China University of Petroleum, Beijing (Grant No. 2462020XKBH011), the Key Program of the National Natural Science Foundation of China (Grant No. 51734010), the Scientific Research and Technology Development Project of China National Petroleum Corporation (Number 2020B-4019).

References

1. Liang, H., Guo, S., Liao, G.: Application of pressure-monitoring technology while drilling in non-undercompaction overpressure formation in Ledong area of Yingqiong basin. *Chin. Offshore Oil Gas* **32**(04), 147–151 (2020)
2. Fan, C.: The identification and characteristics of migration system induced by high pressure, and its hydrocarbon accumulation process in the Yingqiong Basin. *Oil Gas Geol.* **39**(02), 254–267 (2018)
3. Liu, A., Zhou, J., Fan, C., et al.: Pre-drilling pressure prediction problems and solutions in the HTHP strata of the Yinggehai-Qiongdongnan Basin. *Nat. Gas. Ind.* **35**(02), 21–26 (2015)
4. Li, Y., Ai, C., et al.: Analysis on influential factors for safe window of drilling fluid density in deep well. *Petrol. Geol. Recovery Effi.* **20**(01), 107–110 (2013)
5. Qin, S., Hou, X.: Research on drilling design techniques for narrow mud weight window. *Petrol. Drill. Tech.* **39**(03), 62–65 (2011)
6. Li, W., Li, Z., Liu, B., et al.: The status quo and prospects for pore pressure prediction technology in Yingqiong Basin of South China Sea. *Offshore Oil* **40**(03), 8–12 (2020)
7. Luo, M., Jiang, W., Chen, H., et al.: Ultra-High Temperature High Pressure Drilling Technology for Narrow Safety Density Window Strata in the Western South China[J]. *PETROLEUM DRILLING TECHNIQUES* **47**(01), 8–12 (2019)
8. Liao, M., Yitao, H.: Application of formation pressure monitoring while drilling in D Block, South Sea. *Mud Logging Eng.* **24**(03), 19–25 (2013)
9. Sun, D., Yang, J., et al.: Application of formation pressure prediction while drilling technology in HTHP wells. *Oil Drill. Prod. Technol.* **38**(06), 746–751 (2016)
10. Xie, Y.: Application of formation pressure prediction while drilling technology in HTHP wells. *Nat. Gas. Ind.* **31**(12), 21–25 (2011)
11. Li, L.: Study and Application of Three-dimensional Delaunay Triangulation Algorithm. Dalian Maritime University (2010)

Chapter 49

Development of Multi-level Substructure Analysis and Solution Framework Based on SiPESC.FEM



Dianheng Jiang, Sheng Zhang, Biaosong Chen, and Na Li

Abstract A multi-level substructure framework is built on the SiPESC (Software Integration Platform for Engineering and Scientific Computation).FEM. The framework separates the essential functions of the substructure method, such as domain decomposition, static condensation, and task scheduling, from the software function design perspective. The functionalities of multi-process computing and multi-threaded computing are separated into multiple plug-ins by separating task management and calculation. The framework is used to compute static analysis, transient response analysis, frequency response analysis, vibration eigenvalue analysis, and buckling eigenvalue analysis, among others. The framework is explained in three layers: software architecture design, component design, and parallel design. This article investigated and discussed graph partitioning, memory control in large-scale computing, and the computation of comparable structures. This article demonstrates the domain decomposition, various analysis type simulation, cluster-based parallel computing examples, and hundreds of millions of degrees of freedom examples to demonstrate the framework's practicability and dependability.

Keywords Multi-level substructure · SiPESC · Parallel · Large-scale model analysis

49.1 Introduction

The substructure method is a classical numerical method for solving FEA problems that is widely used in almost all commercial finite element software [1–3], including ANSYS [4], MSC.NASTRAN [5], ABAQUS, and others. The substructure method originates from the idea of domain decomposition techniques. Unlike classical domain decomposition method based on the iterative method, the substructure method focuses on the direct method for solving linear algebraic equations based

D. Jiang · S. Zhang (✉) · B. Chen · N. Li
Department of Engineering Mechanics, Dalian University of Technology, Dalian, China
e-mail: zhangs@dlut.edu.cn

on static condensation (also known as Guyan condensation) and modal reduction [6]. For static analysis, researchers have developed the basic substructure method, the multi-level substructure method, and the substructure method for material nonlinear analysis. For transient analysis, the condensation method is used to solve the linear algebraic equations in the Newmark method and other methods. The generalized eigenvalue problem is at the heart of modal and buckling analysis. In order to solve the generalized eigenvalue problem, researchers have developed an eigenvalue solving algorithm based on multilevel substructure methods and mode synthesis method based on the idea of model reduction. To construct the modal subspace and solve the eigenvalue problem, the modal synthesis method combines the static condensation method and the modal reduction method. The multilevel substructure solution for the frequency response problem uses the same substructure solution as the transient response.

The substructure method is easy to parallelize because of its domain decomposition characteristics, and is often used as a parallel framework to decompose the overall domain solving task into sub-domain. Because the substructure method only needs to condense the structural information on the interface during synthesis, this method is suitable for confidential cooperative simulation among various departments and suitable for joint simulation with component experimental data. Therefore, the substructure analysis method is widely used in aerospace, vehicles, ships and other fields. The development of a general substructure analysis framework is of great importance.

Despite significant progress in substructure over the last 30 years, a mature software framework for substructure calculations is barely developed [7]. The substructure method is designed as an add-on module in all commercial finite element software only for certain analysis types. Wanxie Zhong and his research team attempted to develop generic FEM software based on the substructure method in the late 1970s, resulting in the commercial software “Jifex.” [8]. With the development of hardware computing platforms, the research team of Hongwu Zhang and Biaosong Chen reconstructed Jifex based on C programmer language and named it “SiPESC”. The work herein is based on the SiPESC.FEM, the finite element analysis sub-module of the SiPESC platform.

In this paper, the following work is introduced:

- (1) Static condensation method and unified solution frame design of multi-level substructure solution frame.
- (2) Software design of multi-level substructure solution framework, including software architecture design, component design, and parallel framework design
- (3) Discussion of some key development points of multi-level substructures, such as graph partitioning, memory management, and repeated structure computation.

49.2 The Multi-level Substructure Algorithm

The primary idea behind the multi-level substructures method is to employ the condensation method to solve large-scale linear algebraic problems. Large-scale linear algebraic equations are decomposed into subtasks using domain decomposition methods. The non-boundary structure of each subtask is condensed to the boundary structure, and finally the overall condensed boundary structure problem is solved to achieve a hierarchical block solution to the overall problem.

In this section, we first introduce the static condensation method of multi-layer substructure, and then introduce the unified analysis framework of substructure with this method as the core solution method.

49.2.1 Static Condensation

The static condensation method was inspired by the Gaussian elimination method, and any variables that have no relationship to others are eliminated [9]. Similarly, structures are divided into interior and boundary degrees of freedom. The degrees of freedom of the internal structure (not related to other substructures) are eliminated, and only the boundary structure degrees of freedom remain. This is called the static condensation method [10]. Using linear algebra matrices, the following can be expressed:

$$\mathbf{K}_{se} = \mathbf{K}_{bb} - \mathbf{K}_{bi}\mathbf{K}_{ii}^{-1}\mathbf{K}_{ib}. \quad (49.1)$$

Equation (49.1) is the condensation equation of stiffness matrix and it also called Schur complement in matrix algebra [11]. In Eq. (49.1), the subscript i represents the internal degree of freedom, and the subscript b represents the boundary degree of freedom. \mathbf{K}_{se} means the condensed stiffness matrix. Considering the symmetry of the stiffness matrix, the static condensation of the stiffness matrix can be written as the congruent transformation form Eq. (49.2) with the numerical basis functions \mathbf{N}

$$\mathbf{K}_{se} = \mathbf{N}^T\mathbf{K}\mathbf{N}, \quad \mathbf{N} = \begin{bmatrix} -\mathbf{K}_{ii}^{-1}\mathbf{K}_{ib} \\ \mathbf{I} \end{bmatrix}. \quad (49.2)$$

The congruent transformation is the standard linear space transformation method. Therefore, the force vector \mathbf{F} on right hand term can be transformed into a condensed boundary force vector \mathbf{F}_{se} in Eq. (49.3).

$$\mathbf{F}_{se} = \mathbf{N}^T\mathbf{F} \quad (49.3)$$

The displacement of the boundary \mathbf{u}_b can be obtained by solving the Eq. (49.4)

$$\mathbf{K}_{se}\mathbf{u}_b = \mathbf{F}_{se} \quad (49.4)$$

The displacement vector of the internal structure \mathbf{u}_i can be expressed as the sum of the displacement deformation caused by the boundary displacement and the displacement deformation caused by the force on the internal structure in Eq. (49.5).

$$\mathbf{u}_i = \mathbf{K}_{ii}^{-1}\mathbf{F}_i - \mathbf{K}_{ii}^{-1}\mathbf{K}_{ib}\cdot\mathbf{u}_b \quad (49.5)$$

Substructure solving for global displacements has been done. Equation (49.1)–(49.5) can be directly used to solve the static substructure analysis problem, and when the stiffness matrix \mathbf{K} is replaced by the dynamic equivalent stiffness matrix, the method can be used for the calculation of transient problems and frequency response problems.

49.2.2 A Unified Substructure Analysis Framework

The static condensation method solves the challenging problem of solving the domain decomposition problem: the solution of the linear algebraic equation system problem of the overall solution domain. The static condensation method, like domain decomposition methods based on iterative methods, can be applied to any analysis flow.

Various analysis processes are organized in Fig. 49.1. The calculation process for coupling and solving each substructure is distinguished from the decoupling process for independent calculation of each structure using different boxes. The mathematical formulations of modal analysis and buckling analysis are both generalized eigenvalue analysis. Generalized eigenvalue analysis has a variety of solution methods, and each solution method is quite different. The subspace iteration method is used in Fig. 49.1 as an example. Transient response analysis and frequency response analysis can abstract a unified calculation process.

Obviously, the calculations of the substructures in most analysis workflows are decoupled (independent of each other). Except for generalized eigenvalue analysis, all coupling calculations between substructures are done by solving linear algebraic equations. These substructure-related computations can be accomplished by a number of typical matrix calculation operations, such as Schmidt orthogonalization, static condensation, matrix multiplication, and so on. Therefore, a core substructure algorithm class can be used to implement matrix calculation operations for all analysis types.

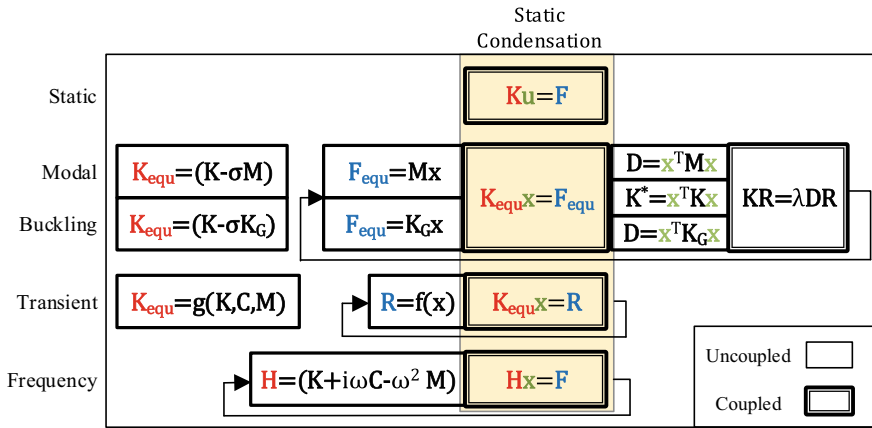


Fig. 49.1 Algorithm flow of various analysis types

49.3 Software Design

This section will introduce the software architecture design of the multi-level substructure framework from the software design sight. This section first introduces the multi- scaled architecture design of the substructure analysis framework based on the SiPESC platform, and then briefly describes the design of component related to substructure calculation according to the required functions in different architecture layers. At last, the parallel computing strategy of multilevel substructure is introduced.

49.3.1 Architecture Design

The software architecture of a Large-scale software is often multi-scaled. To achieve scalability, the SiPESC platform employs a “micro-kernel + plug-in” architecture design to create the basic software architecture. On this foundation, a layered architecture is utilized to complete the separation and aggregation of plug-in functions. A sub-architecture that separates algorithms and models is implemented in each computing plug-in. As a result, the SiPESC platform has implemented three-scale software architecture design.

The software architecture of “microkernel + plug-in” is used in many common software projects, such as Chrome, VS Code, Eclipse, etc. But different from the microkernel strategy of the above program: “The core system of the microkernel architecture pattern traditionally contains only the minimal functionality required to make the system operational” [12], the microkernel of the SiPESC platform means the smallest organizational module that allows the system to run (Fig. 49.2).

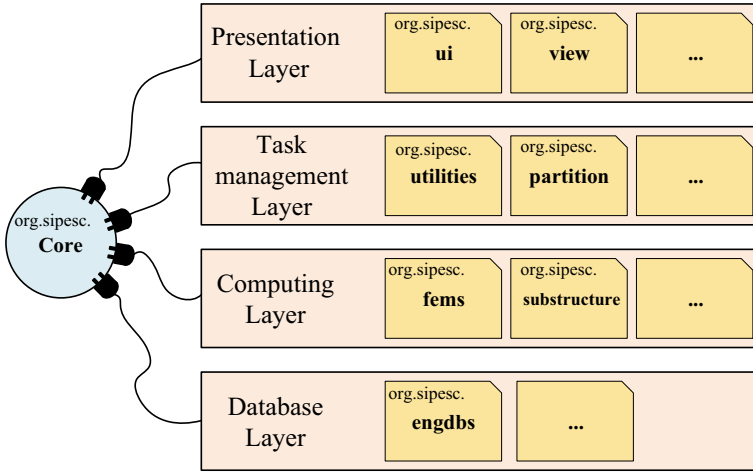


Fig. 49.2 Software architecture diagram

Based on the organizational module of the microkernel, the plug-in system is divided into four logical layers according to functions, namely, the presentation layer, the organization layer, the computing layer, and the database layer.

- (1) The display layer is responsible for the interaction and pre- and post-processing functions, and provides functions such as user interface, console, and finite element module-related model display, load application, and result cloud image display.
- (2) The organization layer is responsible for task process organization, including task process arrangement in factory mode and constructor mode, task division (substructure division) based on graph partition algorithm, MPI parallel task process organization and other functions.
- (3) The calculation layer is responsible for basic finite element calculations and other functions, including element calculations, load calculations, static condensation calculations, and other calculation-related functions.
- (4) The database layer undertakes the information exchange and data storage between plug-ins. The software architecture of micro-core + plug-in basically strips off the large-scale information interaction function between plug-ins in the context of finite element simulation requiring a large amount of data interaction. The database not only undertakes the data storage function of the finite element, but also undertakes a part of the data interaction function between plug-ins.

49.3.2 Component Design

This subsection presents the component design of the substructure framework. The substructure framework can directly calculate the substructure model, or divide the whole structure model into substructure models by using the domain decomposition method for serial calculation or parallel calculation. Therefore, the calculation process of substructure can be divided into two sequential processes, the process of domain decomposition and the process of calculation of substructure (Fig. 49.3).

The “org.sipesc.patition” package is responsible for solving domain decomposition problems of substructures. The package can be divided into the mutual conversion of finite element mesh and graph structure and the solution of graph partition problems. The “org.sipesc.utilities.setask” module is responsible for organizing computation processes using the factory pattern. By managing the running order and process of each task, this component can control the serial-parallel analysis of the multi-level substructure computing framework. The “org.sipesc.substructure” package undertakes the calculation process of the substructure. The relationship between the components in the package is an abstraction of Fig. 49.1. All operations related to substructure calculations are encapsulated in the “org.sipesc.substructure.algorithm” component. Several types of analysis model components can be aggregated or orthogonalized through a small amount of static and other generalized descriptive sentences to complete the realization of the substructure algorithm.

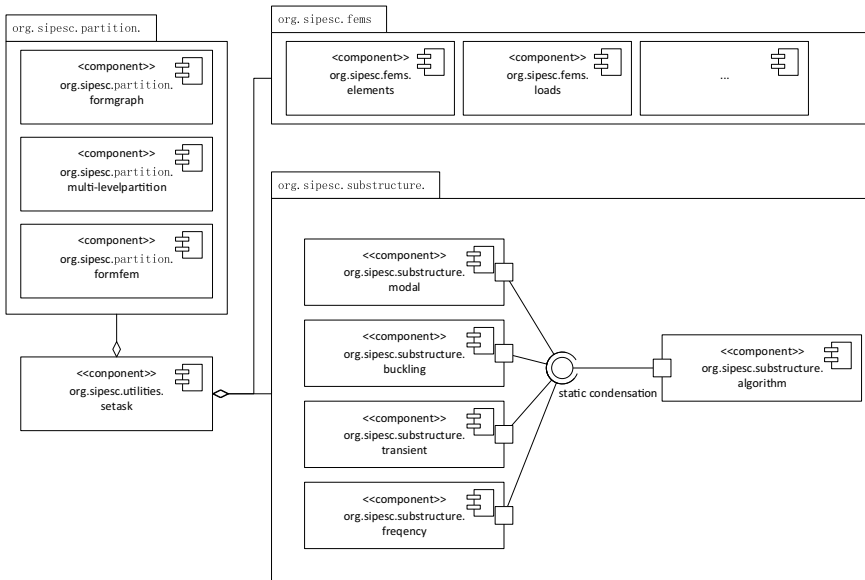


Fig. 49.3 UML component diagram of the substructure calculation plugin

49.3.3 Parallel Design

The parallel framework design of substructure is introduced in this section. The multilevel substructure method adjusts the number of substructure layers according to the topology of the computing hardware environment. A MPI parallel 4-tier structure for clusters is shown in Fig. 49.4.

In actual computing, it is usually the heterogeneous computing of MPI and GPU for personal computer and the distributed memory computing of MPI and OpenMP for cluster. The setask component is in charge of managing the different computing components using MPI connections. The OpenMP parallel module is included in each computing component. The solver directly invokes GPU parallelism [13, 14]. Through the structural separation of the parallel structure, the decoupling design of three types of parallel is completed.

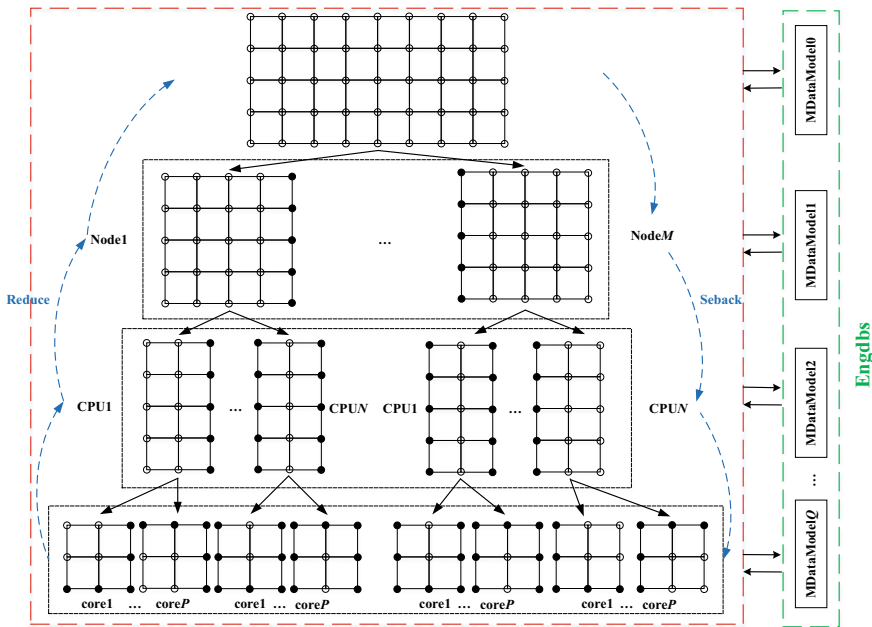


Fig. 49.4 Substructure tree adapted to cluster hardware topology

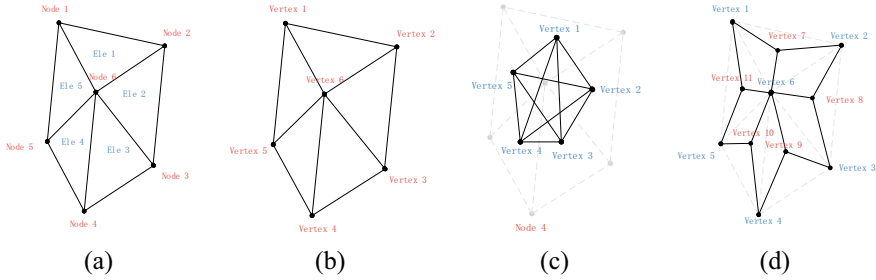


Fig. 49.5 Finite element model and diagram structure description **a** Finite element model; **b** Node-vertex graph; **c** Element-vertex graph; **d** Node element-vertex hypergraph

49.4 Development Key Points

This section focuses on the difficulties encountered when designing numerous multi-level substructure computing frameworks. It consists of graph subdivision for load balancing, memory management for decreasing computation memory, and multi-body dynamics description for minimizing the calculation of comparable structures.

49.4.1 Domain Decomposition

The mathematical form of the domain decomposition problem of substructure can be attributed to the graph partition problem of graph structure [15].

The direct mapping between finite element mesh and graph structure cannot accurately describe the graph partition problem. Mapping the finite element nodes to graph vertices (as shown in Fig. 49.5b) results in the elements being split directly by the style algorithm. Mapping FE elements to graph vertices (as shown in Fig. 49.5c) results in incorrect description of the degrees of freedom of the nodes. A hypergraph model is developed to better properly explain the graph structure of the finite element model. Where the cell is an empty weight vertex, and the node is a weight of degrees of freedom vertex. Using this model more accurately describes the graph partition problem of finite element domain decomposition.

49.4.2 Memory Management

The main challenge of multilevel substructures is the memory management problem in substructure computation. The solution of linear algebraic equations when calculating the numerical basis functions, and the cohesive stiffness matrix being too large due to too many boundary nodes when the top-level stiffness matrix is assembled,

are two parts that cause a large amount of memory usage during the calculation of the substructure.

In the process of calculating the numerical basis function Eq. (49.2), the solution of linear algebraic equations with a large number of right hand terms is involved. Because the numerical basis function N is a dense matrix, the memory occupied by the numerical basis function N grows dramatically as the number of exit nodes grows. This part's memory occupancy can be minimized by utilizing internal and external memory interaction as well as vector component block computation [16].

The upper layer substructure's memory occupancy is more essential. The matrix of the structure will gradually grow denser as the number of static condensation increases. The first crucial element is that the sparsity of the total matrix must be judged at each matrix assembling phase. When the memory used by the sparse matrix representation surpasses the memory occupied by the dense matrix representation (about 50%), it is required to alter the matrix representation or even replace the solver. This is a typical occurrence while calculating a multi-level substructure matrix. The second crucial element is to use some approximation techniques to re-sparse the matrix. The stiffness matrix of the structure is a kind of strictly diagonally dominant matrix, which is called "H matrix" in mathematical expression. The static condensation process is a process of finding the Schur complement of matrix. Because the Schur complement matrix of H matrix is still H matrix (strictly diagonally dominant) [15]. Therefore, a certain threshold can be set, and the elements less than this threshold in all matrices can be omitted, so that the matrix can be sparsely again and meet

$$\frac{\Delta|\mathbf{K}_{sc}|}{|\mathbf{K}_{sc}|} < \epsilon. \quad (49.6)$$

These two memory management strategies can significantly minimize memory use during substructure computation. When the sub-structure has more than five levels, the memory it occupies will certainly increase.

49.4.3 Calculation of Repetitive Structure

Avoiding computations of repeating structures is an efficient technique to speed up calculations. The assembly of substructure described by multi-body dynamics, such as rotation, mirroring translation, etc. for repetitive structures, which has been used since the Jifex version.

The same substructure mode is referred to in the multi-level substructure theory as the substructure with the same structural composition (as determined by spatial transformations such as rotation, mirroring, translation, and so on). The structure correlation matrix only has to be calculated once for the substructure with the same substructure mode, and the substructures with the same substructure mode may be

produced from a single substructure by spatial transformation. The spatial transformation behavior of the substructure may be split into three phases by using stiff body motion representation:

1. Rotation

$$\begin{Bmatrix} x'(i) \\ y'(i) \\ z'(i) \end{Bmatrix} = \begin{bmatrix} \cos \psi & -\sin \psi & & \\ \sin \psi & \cos \psi & & \\ & & 1 & \\ & & & 1 \end{bmatrix} \begin{bmatrix} 1 & & & \\ \cos \psi & -\sin \psi & & \\ \sin \psi & \cos \psi & & \\ & & 1 & \\ & & & 1 \end{bmatrix} \begin{bmatrix} \cos \psi & -\sin \psi & & \\ \sin \psi & \cos \psi & & \\ & & 1 & \\ & & & 1 \end{bmatrix} \begin{Bmatrix} x(i) \\ y(i) \\ z(i) \end{Bmatrix} \quad (49.7)$$

2. Mirroring

$$\{\mathbf{x}''(i)\} = [\mathbf{T}^x]\{\mathbf{x}'(i)\} = \begin{bmatrix} -1 & & \\ & 1 & \\ & & 1 \end{bmatrix} \{\mathbf{x}'(i)\} \quad (49.8)$$

3. Translation

$$\{\mathbf{x}'''(i)\} = \{\mathbf{r}(i)\} + \{\mathbf{x}''(i)\} \quad (49.9)$$

The spatial transformation of the substructure should adhere to the rotation, mirror, and translation descriptions. Using this strategy can save time and minimize the quantity of repeated structure in the computation process.

49.5 Numerical Examples

This section gives some numerical examples of the multi-level substructure analysis framework to show the effectiveness of the multi-level substructure developed in this paper.

49.5.1 Multi-layer Graph Partitioning

This section shows a simplified shell model of an aircraft. The model consists of 226,318 triangular shell elements. The model is divided into three layers substructures. The result of substructure is shown in Fig. 49.6. The structure is divided into 100 sub-structures on the third-layer.

By counting the number of boundary nodes in the 100 substructures of the third layer, draw the balance factor as Fig. 49.7. The error of balance factor is expressed by load imbalance coefficient ϵ_i , which is defined as

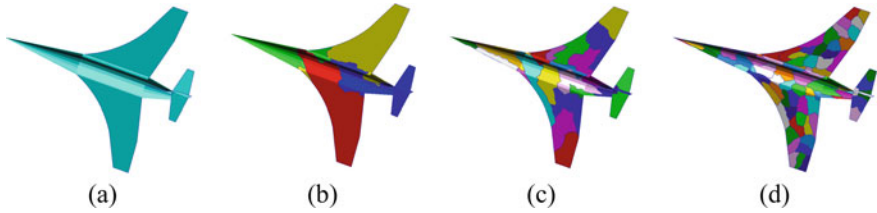


Fig. 49.6 Substructure partition of an airplane. **a** unpartition model; **b** first-layer partition model; **c** second-layer partition model; **d** third-layer partition model

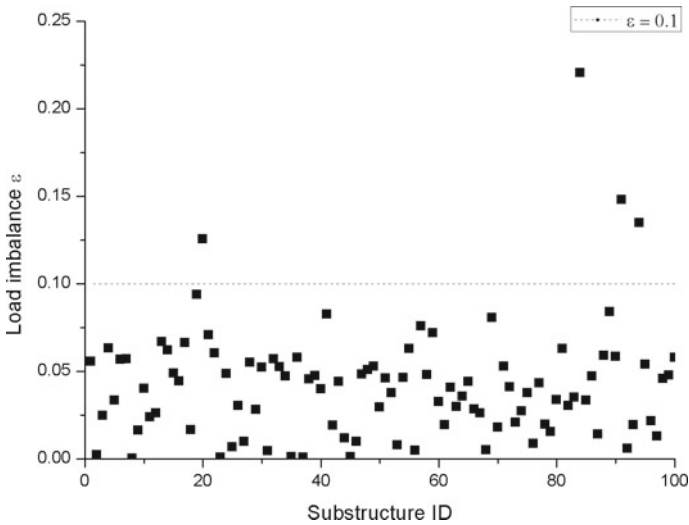


Fig. 49.7 The chart of load imbalance coefficient ϵ_i

$$\epsilon_i = \frac{n_b^i - \frac{\sum n_b^i}{s}}{\frac{\sum n_b^i}{s}} \tag{49.10}$$

The subscript i represents the i th substructure, s represents the number of substructure [17], and n_b represents the number of boundary nodes.

49.5.2 Substructure Calculation for Multiple Analysis Types

This section displays the outcomes of several multi-level substructure analysis. Because the multilevel substructure method does not create any errors, its results are completely consistent with the whole structure analysis. This part just provides the substructure method’s result cloud in Fig. 49.8

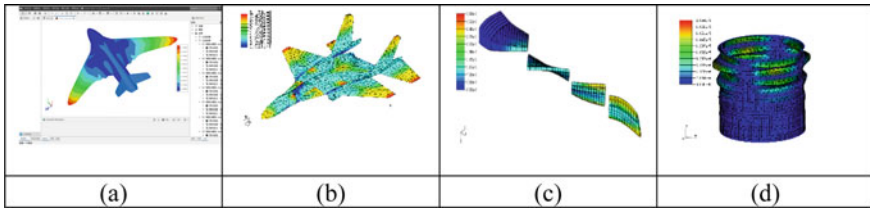


Fig. 49.8 Calculation results of multi-level substructure frames. **a** The static substructure analysis displacement cloud diagram displayed by the operation interface is included; **b** Each substructure displays the cloud diagram independently (transient response problem); **c** The fourth mode of the substructure of the modal analysis problem; **d** First order characteristic displacement of substructure for buckling analysis

The numerical examples in this section prove that the analysis framework can carry out multi-level substructure analysis of various types, and has the whole structure cloud diagram, substructure cloud diagram, explosion diagram and complete user interface.

49.5.3 *Parallel Computing and Large-Scale Computing*

This session demonstrated the parallel computing and large-scale computing capabilities of the multi-level substructure framework. First, based on the Sunway TaihuLight supercomputing cluster in Wuxi, the parallel computation of multi-level substructures from 100 to 1000 threads is calculated. The acceleration ratio curve drawn based on 100 cores [18, 19] is shown in Fig. 49.9. The phenomenon that the acceleration ratio curve of 500 threads to 900 threads is flat is caused by the unbalance distribution of the substructure on the cluster.

In order to verify the effectiveness of the memory management scheme shown in this paper, the research team divided the 107 m DOF aircraft model into 20 substructures for static simulation calculation at a blade node. The memory size of this node is 128 Gb, and the direct solver of the whole structure model problem is difficult to run on this blade node (Fig. 49.10).

The numerical examples in this section prove that the multi-level substructure framework has efficient parallel computing ability and large-scale computing ability.

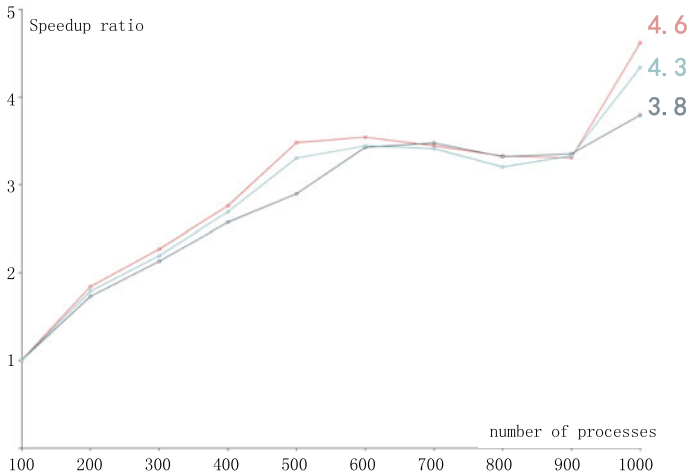


Fig. 49.9 The acceleration ratio curve. The three lines show the highest acceleration ratio, the lowest acceleration ratio and the average acceleration ratio in 20 calculations

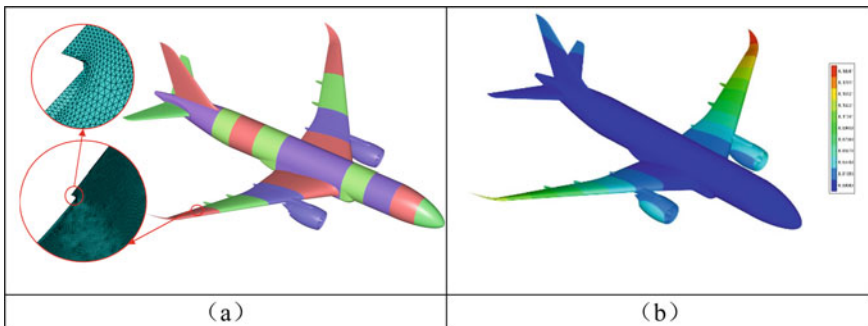


Fig. 49.10 Static analysis example of aircraft with 107 million degrees of freedom

49.6 Conclusion

This paper introduces the design and implementation of a multi-level substructure solution framework based on SiPESC.FEM. Through software framework design, component design, parallel framework design, and software design at three levels, the design idea of solving framework for multilevel substructures is illustrated. Then, the problems of graph subdivision, memory control and repetitive structure calculation are discussed respectively. Finally, some calculation examples calculated using the framework are shown to demonstrate the usability of the framework.

Acknowledgements Funding Statement: The authors are thankful to the financial support of the National Key Research and Development Plan (2021YFB3302501); the National Natural Science

Foundation of China (12072059); the Fundamental Research Funds for the Central Universities (DUT22RC(3)010, DUT20YG125).

Conflicts of Interest: The authors declare that they have no conflicts of interest to report regarding the present study.

References

1. Chao, A., Duoyao, Z., Changchuan, X.: Flutter analysis of large flexible aircraft based on reduced order model. In: Proceedings of the 10th chinese society of aeronautics and astronautics youth forum (pp. 214–223). Springer Nature Singapore, Singapore (2023)
2. Ji, W., Sun, W., Zhang, Y., Wang, D., Wang, B.: Parametric model order reduction and vibration analysis of pipeline system based on adaptive dynamic substructure method. In: Structures (Vol. 50, pp. 689–706). Elsevier (2023)
3. Bennighof, J.K., Kaplan, M.F., Kim, M., Kim, C.W., Muller, M.B.: Implementing automated multi-level substructuring in nastran vibroacoustic analysis. SAE Trans. 1474–1480 (2001)
4. Thompson, M.K., Thompson, J.M.: ANSYS mechanical APDL for finite element analysis. Butterworth-Heinemann (2017)
5. Horne, S.: MSC/NASTRAN (1982)
6. Arndt, D., Bangerth, W., Davydov, D., Heister, T., Heltai, L., Kronbichler, M., et al.: The deal.II finite element library: design, features, and insights. Comput. Math. Appl. Int. J. (Jan.1), 81 (2021)
7. Anderson, R., Andrej, J., Barker, A., Bramwell, J., Camier, J.S., Cerveny, J., et al.: Mfem: a modular finite element methods library. Pergamon (2021)
8. Chen, B., Gang, L., Jian, K., Li, Y.: Design optimization of stiffened storage tank for spacecraft. Struct. Multidiscip. Optim. **36**(1), 83–92 (2008)
9. Khor, M.: Probabilistic finite element analysis using ansys. Struct. Saf. (2006)
10. Shao-Kun, M.A., Miao, Y.U., Cui, H.D.: The basic principle of substructure analysis and the technique of substructure analysis with the software of ansys. J. Guangxi Univ. (2004)
11. Zhang, F. (Ed.): The Schur Complement and Its Applications (Vol. 4). Springer Science & Business Media (2006)
12. Richards, M.: Software architecture patterns (Vol. 4, p. 1005). 1005 Gravenstein Highway North, Sebastopol, CA 95472: O'Reilly Media, Incorporated (2015)
13. Kalinkin, A., Anders, A., Anders, R.: Intel® math kernel library parallel direct sparse solver for clusters. Acm Trans. Math. Softw. (2014)
14. Kalinkin, A., Anders, A., Anders, R.: Schur complement computations in intel math kernel library pardiso. Appl. Math. **2015**(6), 304–311 (2015)
15. Fan, W., Liu, M., Tian, C., Xu, R., Zhou, J.: Incrementalization of graph partitioning algorithms. Proc. VLDB Endowment **13**(8), 1261–1274 (2020)
16. Allison, C.: Intel: Faster Code Faster (2016)
17. Duan, J., Li, Y., Chen, X., et al.: A parallel FEA computing kernel for building structures. In: 2013 Conference on Computational Mechanics (CCM 2013)
18. Snir, M.: MPI: The Complete Reference. MIT (1996)
19. Majeed, R., Farrukh, R., Riaz, O., Ali, S., Samad, A., Khan, M.: Parallel implementation of fem solver for shared memory using openmp. Math. Probl. Eng. (2022)

Chapter 50

Simulation Study on the Displacement Characteristics of an Ultra-Low Permeability Reservoir by CO₂-WAG Flooding



Zhizeng Xia, Hongjun Yin, Xuewu Wang, and Zhaoming Li

Abstract The oil production rate of the ultra-low permeability reservoir decreases rapidly after volume fracturing, and reservoir energy replenishment is in urgent need to enhance the production performance. However, due to the poor reservoir physical property, water injection into the ultra-low permeability reservoir is quite difficult, resulting in unsatisfactory development effect. To evaluate the effectiveness of water alternating CO₂ (CO₂-WAG) flooding in ultra-low permeability reservoir block Z, oil samples from a typical well were used to carry out laboratory experiments, including oil composition analysis, constant composition expansion and CO₂ swelling test. After fitting the experimental results, a numerical simulation model containing four five-point patterns developed by CO₂-WAG flooding was established. The production and seepage characteristics of CO₂-WAG flooding were studied, and the parameter sensitivity analysis was conducted. The results showed that: (1) CO₂-WAG flooding could maintain a longtime stable production with high oil rate, and significantly improve the production effect of the ultra-low permeability reservoir; besides, dynamic CO₂ storage could be achieved with the storage percent of 70% during the flooding process. (2) CO₂-WAG flooding has the following effects, including replenishing reservoir energy, expanding sweeping volume and improving oil displacement efficiency, and the development effect is obviously better than that of water flooding. (3) When the CO₂-WAG flooding was implemented immediately at the reservoir starting production with 6-month alternating cycle and 1:1 CO₂-Water ratio, good

Z. Xia (✉) · H. Yin (✉) · Z. Li
Key Laboratory of Enhanced Oil Recovery (Northeast Petroleum University), Ministry of Education, Daqing 163318, China
e-mail: xzz_cn@aliyun.com

H. Yin
e-mail: yinhj7176@126.com

College of Petroleum Engineering, Northeast Petroleum University, Daqing 163318, China

Z. Xia · X. Wang
Shandong Institute of Petroleum and Chemical Technology, Dongying 257061, China

production performance could be achieved. The results obtained from this research can provide guidance in effectively developing block Z.

Keywords Ultra-low permeability · CO₂ · Water alternating gas · Influencing factors

50.1 Introduction

Ultra-low permeability oil resources are widely distributed, which is believed to be the main part of future crude oil production, and it has become the main target in oil exploration and development [1, 2]. In China, nearly 70% of the newly proved crude oil reserves comes from low-permeability reservoirs in recent years, where the ultra-low-permeability reservoirs are in the majority [3]. The pore throat structure of the ultra-low permeability reservoir is quite complicated [4], which causes poor reservoir physical property. Volume-fracturing technology can significantly improve the flow environment in the near-well area when developing these reservoirs [5], but the reservoir pressure consumption is fast and the production effect is poor [6].

Water flooding and gas flooding are the main measures to replenish reservoir energy. The macroscopic sweep efficiency of water flooding is good, but for conventional water flooding in the ultra-low permeability reservoir, the injection pressure is sometimes too high for water to be injected because of poor reservoir physical property, resulting in low microscopic oil displacement efficiency [7, 8]. Gas flooding can achieve high microscopic oil displacement efficiency, but the gas channeling would easily occur because of unstable displacement front due to the gas's low viscosity, resulting in low macroscopic sweep efficiency [9, 10]. Laboratory and field studies [11–13] show that water alternating gas (WAG) flooding can combine the advantages of water flooding and gas flooding to obtain better mobility control and higher oil recovery.

Most laboratory researches on WAG show good displacement performance. According to the gas type, WAG methods can be classified as water alternating CO₂ (CO₂-WAG), water alternating N₂ (N₂-WAG) and water alternating hydrocarbon gas (HC-WAG), among which CO₂-WAG is the most studied with the best comprehensive effect [14]. Fatemi et al. [15] studied the oil displacement effect on water-wet and mixed-wet cores using CH₄, and the results showed that CH₄-WAG flooding was better than CH₄ flooding or water flooding on both water-wet and mixed-wet cores. Kong et al. [16] studied the recovery effect of N₂-WAG flooding in ultra-high water-cut stage through medium/high permeability coreflood tests and visualization experiments. The results showed that N₂-WAG could improve the irreducible gas saturation and effectively displace the residual oil after water flooding. Ghafoori et al. [17] compared the core flooding effect by N₂-WAG and CO₂-WAG, and the results showed that CO₂-WAG performed better than N₂-WAG with a 13% higher recovery factor. Han et al. [18] evaluated the effects of miscible CO₂-WAG flooding on cores from Bakken formation and the results showed that compared with miscible

CO₂ flooding and water flooding, the miscible CO₂-WAG flooding had the highest recovery with more than 60% of the oil recovered in the first two alternating cycles. Kmalı et al. [19] studied the oil displacement effect by CO₂-WAG flooding under different injection pressures and the results showed that CO₂-WAG had a better effect than CO₂ flooding, and the higher the degree of miscibility, the better the displacement effect. Ahmadi et al [20]. compared the characteristics of N₂-WAG, CO₂-WAG and associated gas-WAG by core flooding and the results showed that the higher the gas content was, the more asphaltene was precipitated; and the associated-gas-WAG had the best effect in consideration of recovery factor and asphaltene precipitation. Wang et al. [21] evaluated the CO₂-WAG performance in multilayer formations by medium and high permeability parallel-core flooding experiments. The results showed that CO₂-WAG flooding could achieve higher oil recovery but with a higher damage degree to core permeability compared with CO₂ flooding.

In recent years, several technologies, including nanofluid alternating gas (NWAG) [22] and chemical-assisted water alternating gas (CWAG) [23], have been developed through modifying the water phase property to improve the effect of WAG. Moradpour et al. [24] studied the displacement characteristics of low-salinity water alternating CO₂ in carbonate cores and the results showed an improvement in the core wettability and sweep efficiency with the oil recovery increased by more than 10%. Moradi et al [25]. carried out experiments on the oil-wet core by SiO₂ water-based nanofluid alternating CO₂ flooding, and the results showed that this method could improve rock wettability, reduce oil–water interfacial tension and achieve higher oil recovery compared with conventional CO₂-WAG flooding. Phukan et al. [26] showed that the surfactant solution alternating CO₂ could increase the oil recovery by more than 16%.

Compared with physical simulation experiments, numerical simulation studies of WAG are relatively few. Afzali et al. [27] studied the characteristics of near-miscible WAG in 1D core scale using IMPES method by considering the hysteresis effects of three-phase relative permeability and capillary pressure. The results showed that the best displacement effect could be achieved when the gas–water ratio was 1:1 and the absolute permeability had little effect on the final displacement effect. Nygård et al. [28] established a 2D layered conceptual model containing one injector and one producer and the results showed that for heterogeneous reservoirs, the existence of gravity segregation helped to improve the sweep efficiency of low-permeability layers and increase the performance of WAG. Wu et al. [29] numerically studied the effect of CO₂-WAG in high-salt reservoirs, and the results showed that a five-spot well pattern with well spacing of 400 m and 150 m could achieve the best oil recovery.

At present, researches on WAG mainly comes from physical simulations, numerical simulations are few especially in a well-pattern scale or field scale; in addition, existing researches are mainly focused on the medium/high permeability reservoir, but few on the ultra-low permeability reservoir. In order to deepen the understanding of the seepage and production characteristics of CO₂-WAG flooding in the ultra-low permeability reservoir, a typical simulation model based on the laboratory experimental results of block Z was established, the production performance and the

oil displacement effect of CO₂-WAG were discussed, and the influence of operation parameters were analyzed. This study is of great significance to improve the exploitation effect of the ultra-low permeability reservoir.

50.2 Numerical Model Establishment

50.2.1 Experimental Results

Block Z is an ultra-low permeability reservoir and the reservoir oil composition of a typical well is shown in Fig. 50.1. High-pressure oil property tests (Figs. 50.2, 50.3 and 50.4) and CO₂ swelling tests (Figs. 50.5 and 50.6) were carried out using typical oil samples with the saturation pressure of 11.53 MPa.

It can be seen that CO₂ has good swelling ability to the tested oil and the physical properties of crude oil can be improved when CO₂ is presented. In this study, the oil composition is divided into six components (i.e., CO₂, CH₄, C₂₋₄, C₅₋₆, C₇₋₁₀, C₁₁₊). CMG-Winprop software is used to fit experimental results, shown in Figs. 50.2, 50.3, 50.4, 50.5 and 50.6. It can be seen that the variation trends of fitting results are consistent with the experimental results, and the average fitting errors are small enough to carried out the following numerical studies.

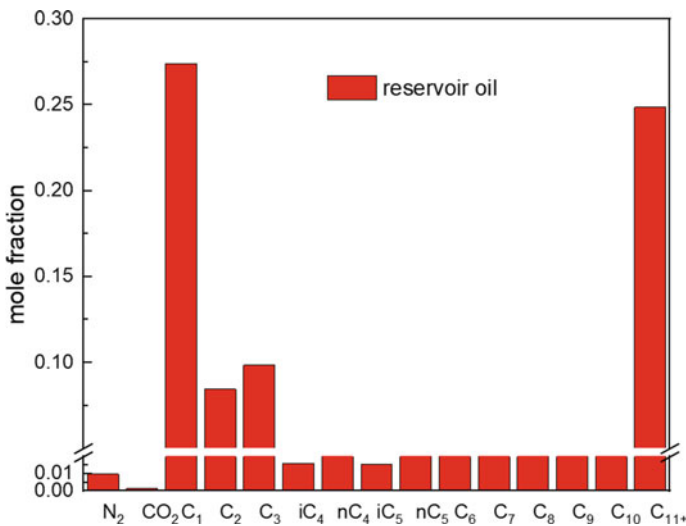


Fig. 50.1 Reservoir oil composition

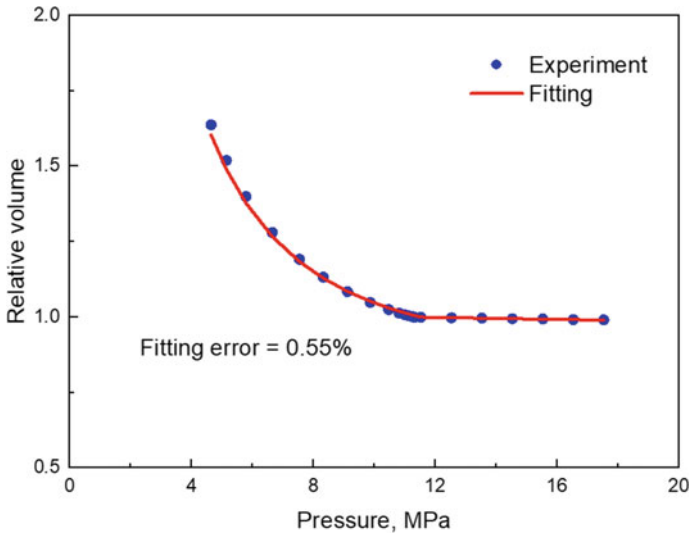


Fig. 50.2 Fitting results of the relative volume in constant composition expansion

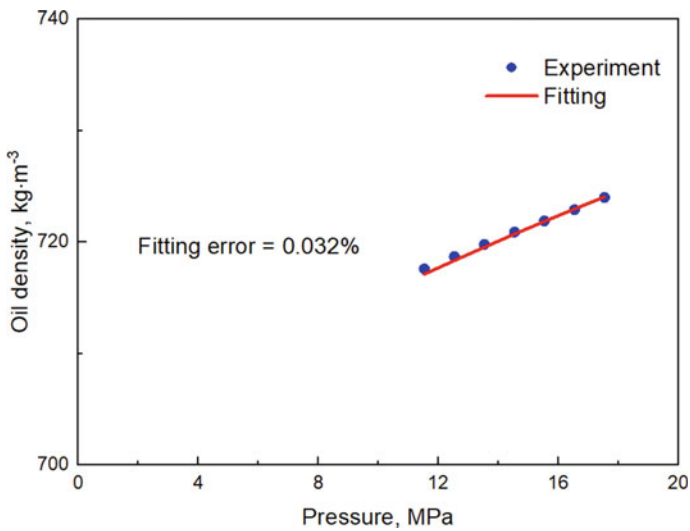


Fig. 50.3 Fitting results of the oil density in constant composition expansion

50.2.2 Numerical Simulation Model

After experimental fitting, a composition simulation model with five-spot well patterns was established based on reservoir parameters of block Z, as shown in Fig. 50.7. The model was 1260 × 900 m in plane size with the reserve of 122.5 ×

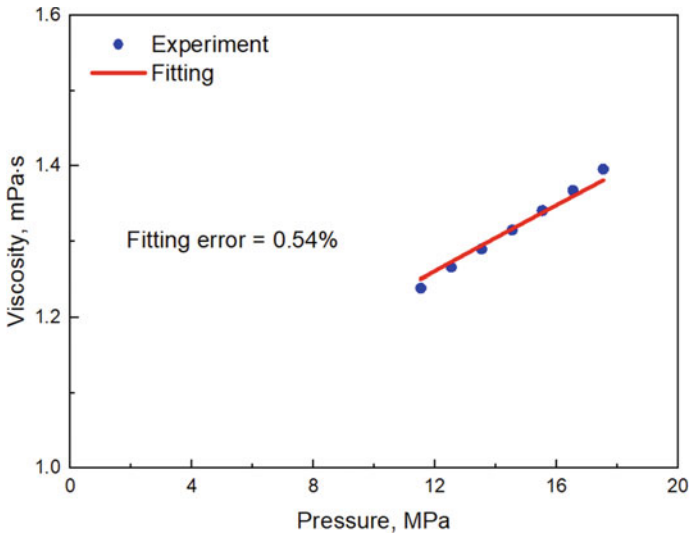


Fig. 50.4 Fitting results of the oil viscosity under reservoir temperature

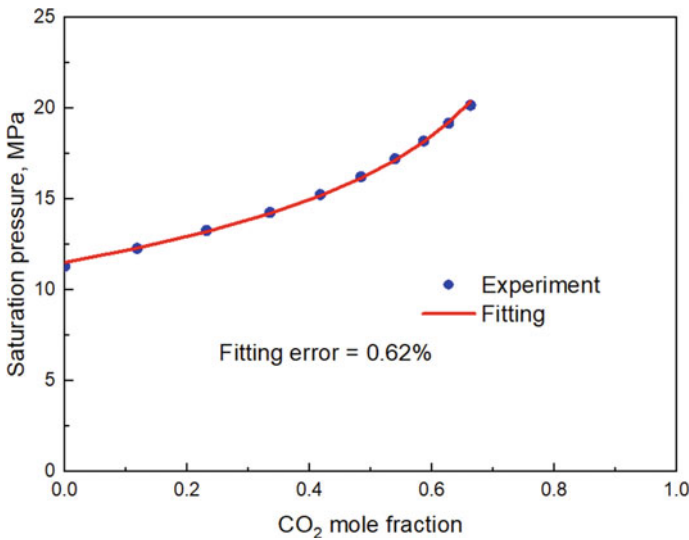


Fig. 50.5 Fitting results of the saturation pressure in CO₂ swelling test

10^4 m^3 . Four horizontal production wells were contained in the model, and each production well was volume-fractured with the half length of the main fracture being 180 m. The grids in the fractured zone were logarithmically spaced-locally refined [24] to model the fluid flow according to the conductivity equivalence, and the equivalent conductivity of the main fracture was $25 \times 10^{-3} \mu\text{m}^2 \text{ m}$.

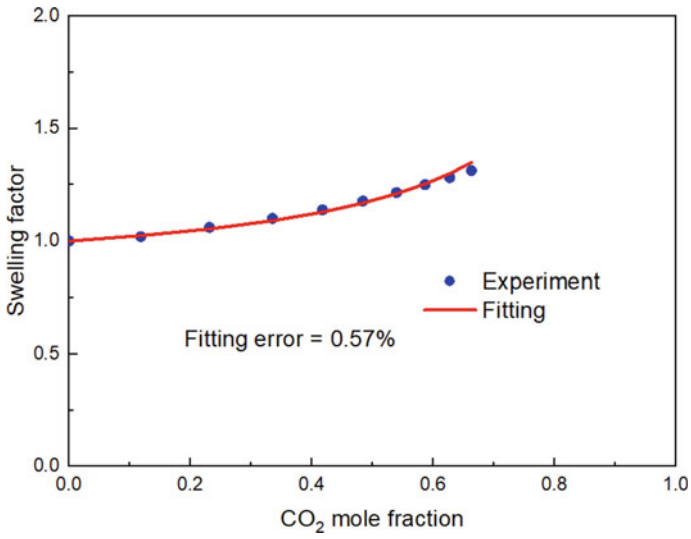


Fig. 50.6 Fitting results of the swelling factor in CO₂ swelling test

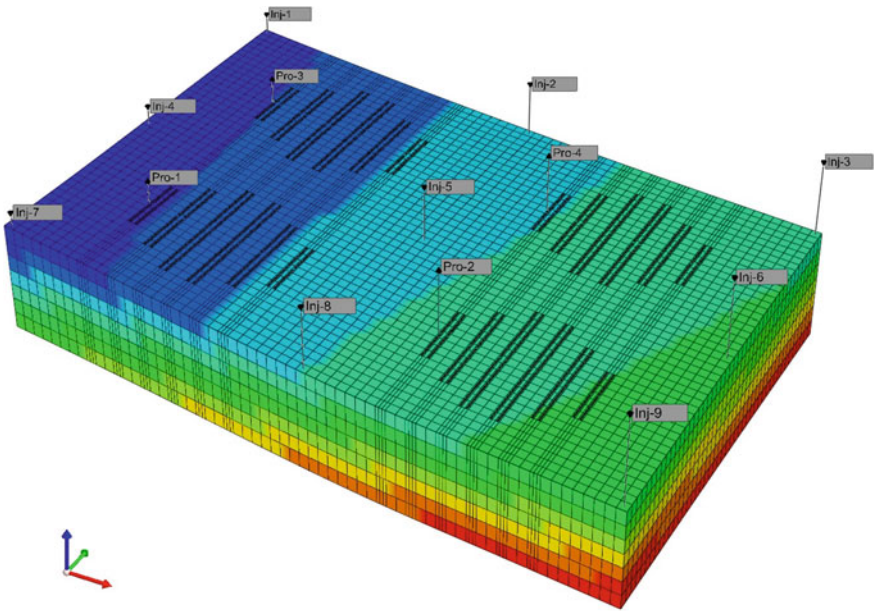


Fig. 50.7 Sketch of the basic model

Table 50.1 Main parameters of the numerical model

Parameter	Value
Initial average reservoir pressure, MPa	15.8
Matrix porosity	0.075–0.164
Matrix permeability, $10^{-3}\mu\text{m}^2$	0.065–1.54
Initial average oil saturation	0.87
Average reservoir thickness, m	18.9
reservoir oil viscosity	1.34

The main parameters are shown in Table 50.1. A 20-year CO₂-WAG flooding simulation process was carried out on the model. The bottomhole pressure of each production well was set to 9.8 MPa slightly lower than the saturation pressure. The injection rates of CO₂ and water were both 20 t/d.

50.3 Production Performance

The oil rates of CO₂-WAG flooding, water flooding and natural depletion are shown in Fig. 50.8, respectively. In the natural depletion production, the oil rate declined rapidly with the increase of time because of the decrease of oil displacement energy (i.e., the decrease of the reservoir pressure). Only one year later, the oil rate dropped to 80 m³/d, which was more than 70% lower than the initial peak value.

In the CO₂-WAG flooding production, the oil rate decline was significantly slowed down, and a long-term stable oil rate of about 80 m³/d was achieved. CO₂ breakthrough occurred after eight years production when the oil rate gradually began to

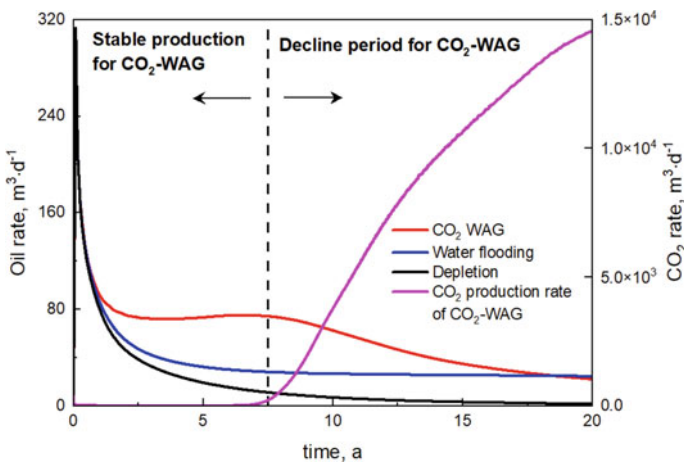


Fig. 50.8 The variations of the oil rate

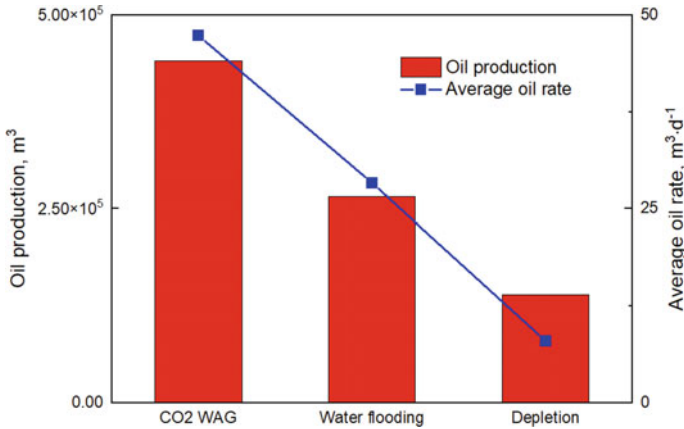


Fig. 50.9 The average oil rate and cumulative oil production under different production methods

decline. In the whole production process, CO₂-WAG flooding maintained a high level of production, and the recovery factor reached about 35.4%. The cumulative oil production was 66% higher than that of water flooding (Fig. 50.9), indicating a significantly improvement of the development effect. In addition, about 70% of the injected CO₂ was stored in the reservoir at the end of the simulation.

The cumulative oil productions are shown in Fig. 50.10. Four production wells showed similar oil production performances, and among these production wells, Pro3 obtained the highest cumulative production because the local reservoir property ensured the most favorable seepage condition.

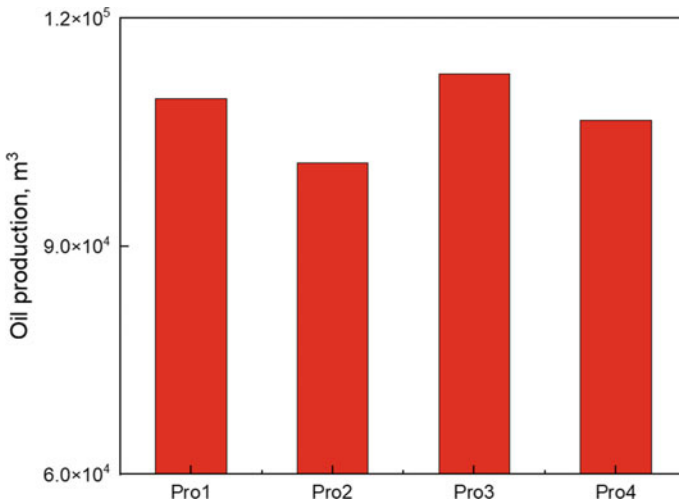


Fig. 50.10 The cumulative oil production of each well group

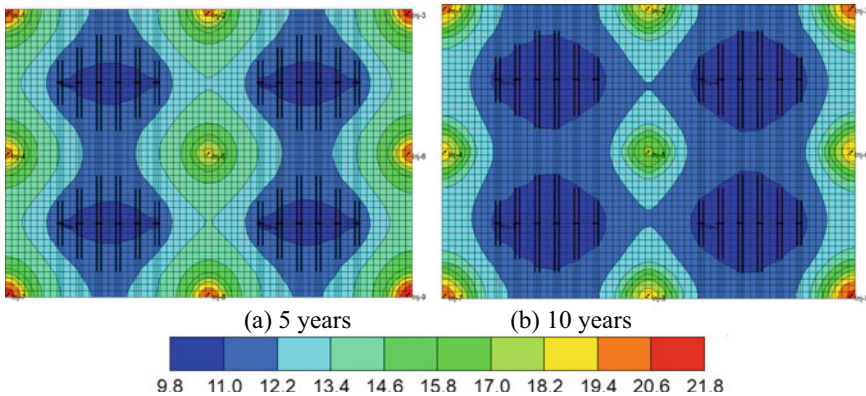


Fig. 50.11 The distribution of the reservoir pressure (unit: MPa)

50.4 CO₂-WAG Effects

50.4.1 Reservoir Energy Replenishment

In the process of CO₂-WAG flooding, the injection of CO₂ and water can refill the pore space caused by the fluid withdrawn to replenish the reservoir energy. Thus, the reservoir pressure will be recovered improving the oil displacement energy. At the end of the simulation, the reservoir pressure distribution is shown in Fig. 50.11. The pressure near injection wells increased significantly, and good displacement system was established between injection-production wells. The average reservoir pressure variations are shown in Fig. 50.12. CO₂-WAG flooding could maintain high pressure level for a long time, and the pressure level gradually decreased after CO₂ breakthrough (Fig. 50.13). Compared with water flooding, CO₂-WAG flooding has better pressure maintenance level and energy replenishment ability, which is more beneficial to improve the development effect.

50.4.2 Expanding Sweeping Volume

At the end of the simulation, the oil saturation distribution of CO₂-WAG flooding is shown in Fig. 50.14. It can be seen that the oil saturation in near-well area of injection wells and inter-well zone between injection and production wells is significantly reduced, indicating good sweep efficiency. From Fig. 50.15, the sweeping degree of the water flooding and CO₂-WAG flooding are similar in bottom layers, but CO₂-WAG flooding have a good sweep efficiency in upper layers due to gravity segregation, so it expands the sweeping volume of water flooding.

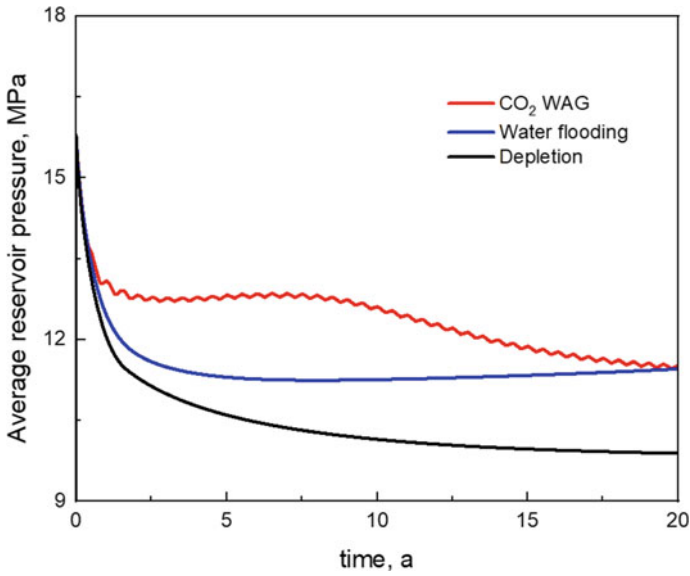


Fig. 50.12 The average reservoir pressure under different production methods

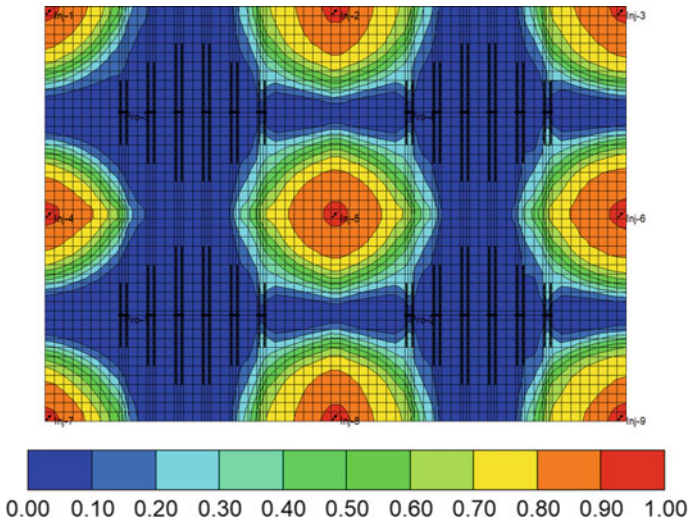


Fig. 50.13 The distribution of the global CO₂ mole fraction

50.4.3 Improving Displacement Efficiency

CO₂ injection into the oil phase has various mechanisms including viscosity reduction, expansion and diffusion [30], which can enhance the recovery effect. In the

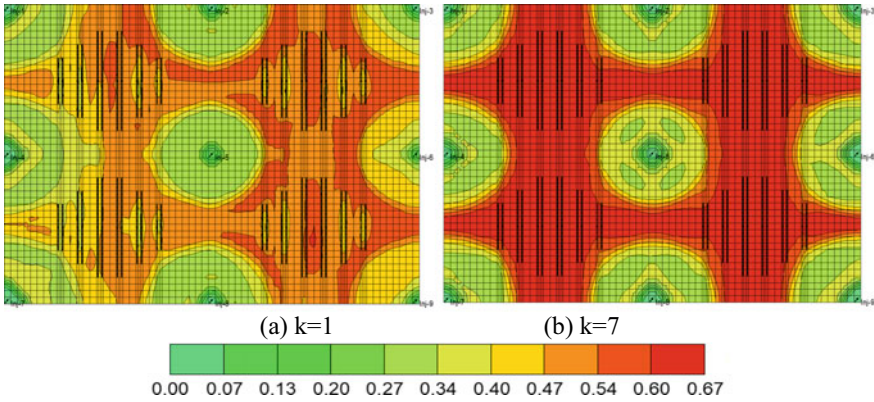


Fig. 50.14 The distribution of oil saturation in the reservoir after CO₂-WAG

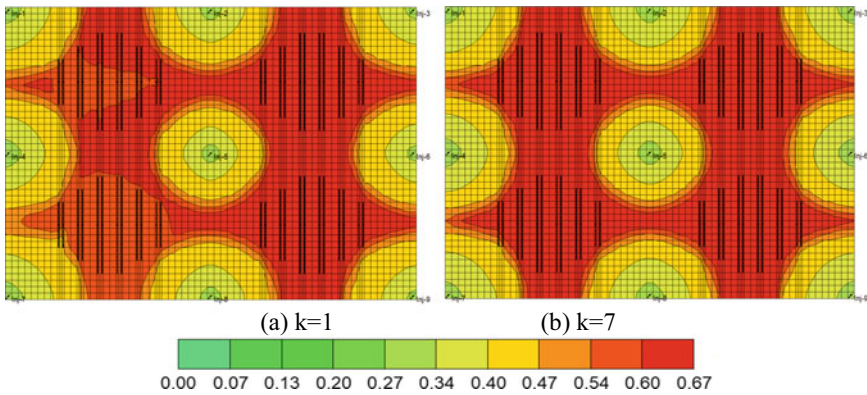


Fig. 50.15 The distribution of oil saturation in the reservoir after water flooding

sweeping area, CO₂'s dissolution (Fig. 50.16) improves the oil's physical property and significantly reduces the oil-gas interfacial tension, enabling more effective displacement. As shown in Fig. 50.17, the existence of CO₂ in the oil phase results in an near-to-zero interfacial tension around injection wells, which can realize miscible CO₂ flooding. Therefore, compared with water flooding, CO₂-WAG flooding has better ability to reduce oil saturation (Figs. 50.14 and 50.15) and can achieve better oil displacement efficiency.

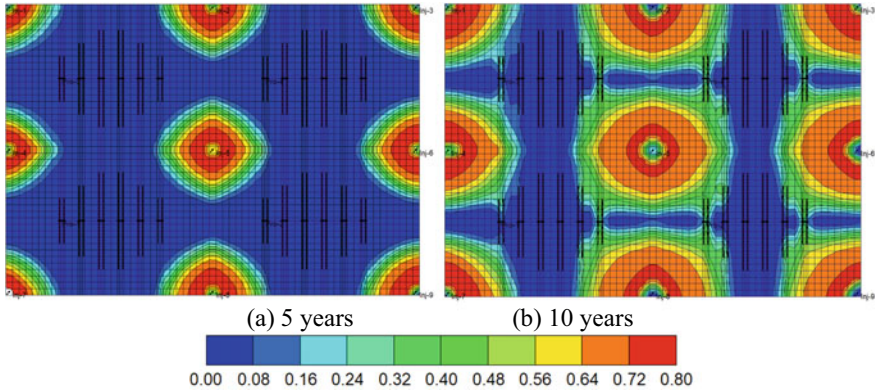


Fig. 50.16 The distribution of the CO₂ in oil phase

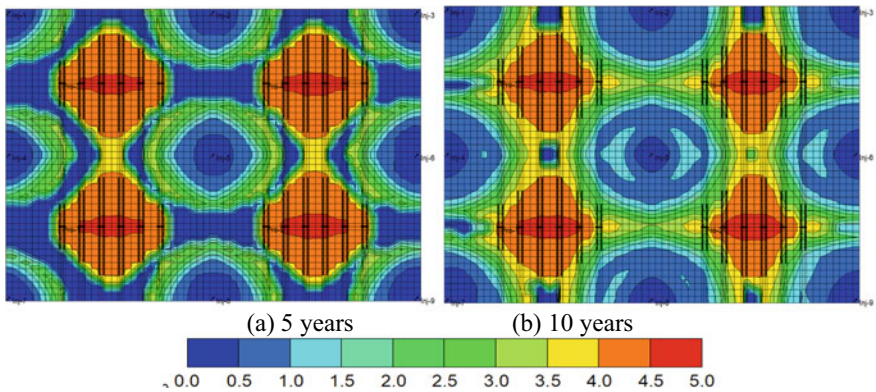


Fig. 50.17 The oil–gas interfacial tension (Unit: mN/m)

50.5 Sensitivity Analysis

50.5.1 Flooding Timing

The flooding timings of CO₂-WAG were set to 0, 2, 4, 6, 8 years after natural depletion, respectively. The simulation results are shown in Fig. 50.18. The earlier the flooding time is, the earlier the reservoir energy is replenished, thus enabling better reservoir exploitation effect. The recovery degree increases as the flooding timing gets earlier. Choosing earlier flooding timing is beneficial to improve the development effect of CO₂-WAG. Therefore, CO₂-WAG flooding can be carried out when the reservoir is put into production for block Z.

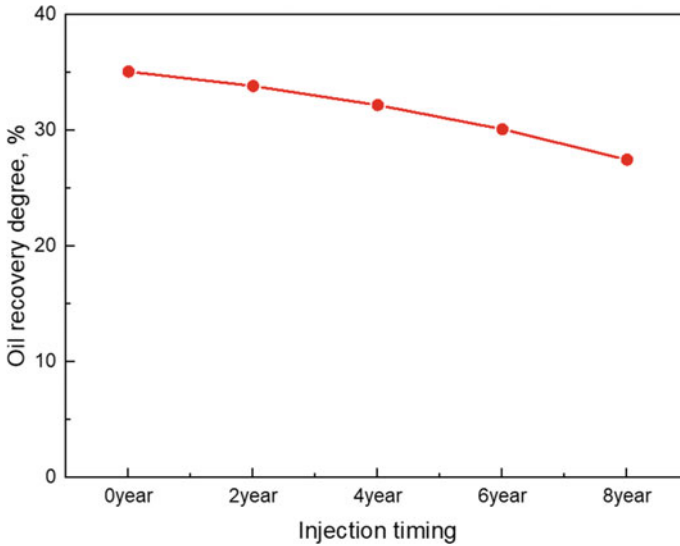


Fig. 50.18 The influence of injection timing on recovery degree

50.5.2 CO_2 -Water Ratio

The CO_2 -water ratios of each injection well were set to 1:3, 1:2, 1:1, 2:1 and 3:1, respectively. The simulation results are shown in Fig. 50.19. The higher the CO_2 -water ratio, the greater the amount of CO_2 injected. It can be seen that the recovery degree decreases significantly when CO_2 -water ratio is small (i.e., 1:3), and when it is at a relatively high level when CO_2 -water ratio is between 1:1 and 2:1. Therefore, the 1:1 CO_2 -water ratio can be selected to save CO_2 consumption for block Z by CO_2 -WAG flooding.

50.5.3 Alternating Cycle

The alternating cycles were set to 2, 4, 6, 8 and 10 months, respectively. The simulation results are shown in Fig. 50.20. The shorter the alternating cycle is, the more beneficial it is to play the synthetic effect of CO_2 and water. It can be seen that the recovery degree gradually increases with the increase of the alternating cycle, and the development effect is the best when the alternating cycle is the shortest. However, too short alternating cycle means frequent alternations of water injection and CO_2 injection, which is often accompanied with high operating costs. Therefore, a 6-month alternating cycle is preferred for block Z by CO_2 -WAG flooding.

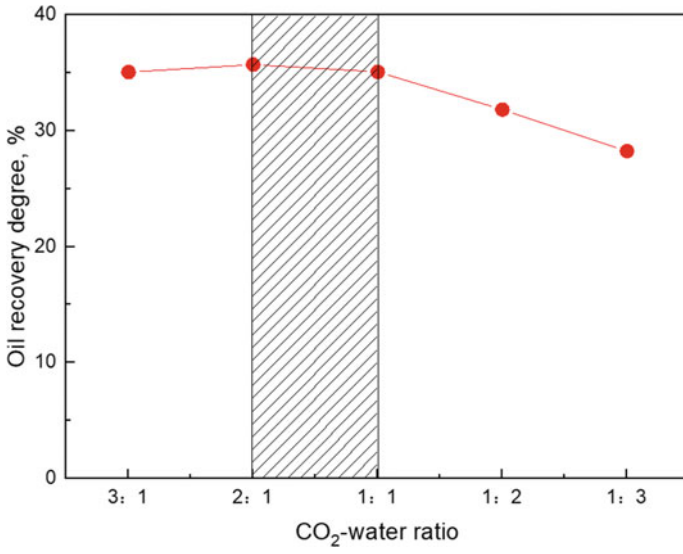


Fig. 50.19 The influence of CO₂-water ratio on recovery degree

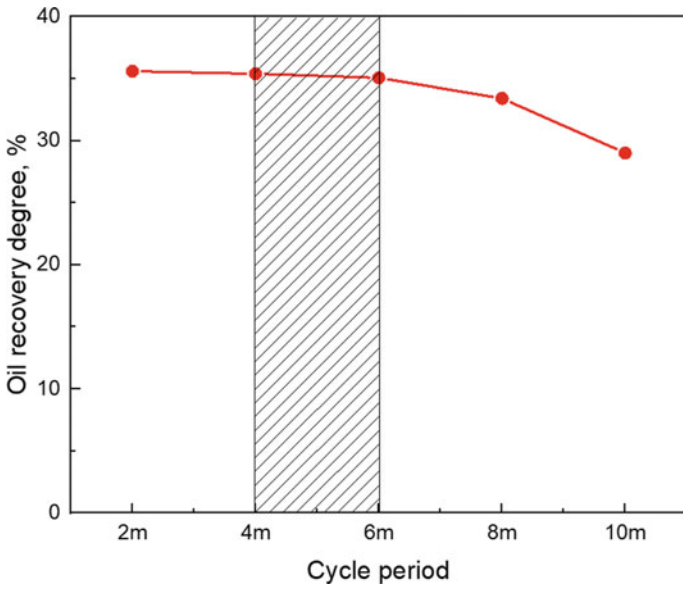


Fig. 50.20 The influence of alternating cycle on recovery degree

50.6 Conclusions

Based on experimental results, the seepage and production characteristics of CO₂-WAG flooding in a typical ultra-low permeability reservoir block Z were numerically studied, and the main conclusions are as follows:

- (1) When applied in the ultra-low permeability reservoir, CO₂-WAG flooding can obtain good development effect. It can slow down the decline of oil rate and maintain a long-time stable production level, but the oil production will decrease after CO₂ breakthrough. About 70% of the injected CO₂ are dynamically stored in the reservoir during CO₂-WAG flooding.
- (2) CO₂-WAG flooding can replenish reservoir energy, expand sweeping volume and improve oil displacement efficiency; and thus, the overall production performance is significantly better compared with water flooding.
- (3) When CO₂-WAG flooding is applied in block Z, good development effect can be achieved when CO₂-WAG flooding begins immediately at the reservoir starting production with 6-month alternating cycle and 1:1 CO₂-Water ratio.

Acknowledgements The authors gratefully acknowledge the Natural Science Foundation of Heilongjiang Province (Grant No. LH2022E023) for the support to present this paper.

References

1. Kang, W.L., Zhou, B.B., Issakhov, M., et al.: Advances in enhanced oil recovery technologies for low permeability reservoirs. *Pet. Sci.* **19**, 1622–1640 (2022)
2. Mahdaviara, M., Sharifi, M., Ahmadi, M.: Toward evaluation and screening of the enhanced oil recovery scenarios for low permeability reservoirs using statistical and machine learning techniques. *Fuel* **325**, 124795 (2022)
3. Wang, Y., Yang, T., Xu, X., et al.: Characteristics of the proved new addition economic recoverable oil and gas reserves in China. *China Petrol. Explor.* **27**(5), 13–26 (2022)
4. Xie, L., You, Q., Wang, E., et al.: Quantitative characterization of pore size and structural features in ultra-low permeability reservoirs based on X-ray computed tomography. *J. Petrol. Sci. Eng.* **208**, 109733 (2022)
5. Li, Q., Xing, H., Liu, J., et al.: A review on hydraulic fracturing of unconventional reservoir. *Petroleum* **1**(1), 8–15 (2015)
6. Bai, H., Zhang, Q., Li, Z., et al.: Effect of fracture on production characteristics and oil distribution during CO₂ huff-n-puff under tight and low-permeability conditions. *Fuel* **246**, 117–125 (2019)
7. Peng, X., Wang, Y., Diao, Y., et al.: Experimental investigation on the operation parameters of carbon dioxide huff-n-puff process in ultra low permeability oil reservoirs. *J. Petrol. Sci. Eng.* **174**, 903–912 (2019)
8. Xiangzeng, W., Hailong, D., Tao, G.A.O.: Method of moderate water injection and its application in ultra-low permeability oil reservoirs of Yanchang Oilfield, NW China. *Petrol. Explor. Dev.* **45**(6), 1094–1102 (2018)
9. Zhang, Y., Gao, M., You, Q., et al.: Smart mobility control agent for enhanced oil recovery during CO₂ flooding in ultra-low permeability reservoirs. *Fuel* **241**, 442–450 (2019)

10. Kulkarni, M.M., Rao, D.N.: Experimental investigation of miscible and immiscible Water-Alternating-Gas (WAG) process performance. *J. Petrol. Sci. Eng.* **48**(1–2), 1–20 (2005)
11. Pal, N., Zhang, X., Ali, M., et al.: Carbon dioxide thickening: a review of technological aspects, advances and challenges for oilfield application. *Fuel* **315**, 122947 (2022)
12. Carpenter, C.: Experimental Program investigates miscible CO₂ WAG injection in carbonate reservoirs. *J. Petrol. Technol.* **71**(1), 47–49 (2019)
13. Christensen, J.R., Stenby, E.H., Skauge, A.: Review of WAG field experience. *SPE Reservoir Eval. Eng.* **4**(2), 97–106 (2001)
14. Afzali, S., Rezaei, N., Zendejboudi, S.: A comprehensive review on enhanced oil recovery by water alternating gas (WAG) injection. *Fuel* **227**, 218–246 (2018)
15. Fatemi, S.M., Sohrabi, M.: Experimental investigation of near-miscible water-alternating-gas injection performance in water-wet and mixed-wet systems. *SPE J.* **18**(1), 114–123 (2013)
16. Kong, D., Gao, Y., Sarma, H., et al.: Experimental investigation of immiscible water-alternating-gas injection in ultra-high water-cut stage reservoir. *Adv. Geo-Energy Res.* **5**(2), 139–152 (2021)
17. Ghafoori, A., Shahbazi, K., Darabi, A., et al.: The experimental investigation of nitrogen and carbon dioxide water-alternating-gas injection in a carbonate reservoir. *Pet. Sci. Technol.* **30**(11), 1071–1081 (2012)
18. Han, L., Gu, Y.: Optimization of miscible CO₂ water-alternating-gas injection in the Bakken formation. *Energy Fuels* **28**(11), 6811–6819 (2014)
19. Kamali, F., Hussain, F., Cinar, Y.: An experimental and numerical analysis of water-alternating-gas and simultaneous-water-and-gas displacements for carbon dioxide enhanced oil recovery and storage. *SPE J.* **22**(02), 521–538 (2017)
20. Ahmadi, Y., Eshraghi, S.E., Bahrami, P., et al.: Comprehensive Water–Alternating–Gas (WAG) injection study to evaluate the most effective method based on heavy oil recovery and asphaltene precipitation tests. *J. Petrol. Sci. Eng.* **133**, 123–129 (2015)
21. Wang, Q., Yang, S., Lorinczi, P., et al.: Experimental investigation of oil recovery performance and permeability damage in multilayer reservoirs after CO₂ and water–alternating–CO₂ (CO₂–WAG) flooding at miscible pressures. *Energy Fuels* **34**(1), 624–636 (2019)
22. Aziz, H., Muther, T., Khan, M.J., et al.: A review on nanofluid water alternating gas (N-WAG): application, preparation, mechanism, and challenges. *Arab. J. Geosci.* **14**(14), 1–12 (2021)
23. Kumar, S., Mandal, A.: A comprehensive review on chemically enhanced water alternating gas/CO₂ (CEWAG) injection for enhanced oil recovery. *J. Petrol. Sci. Eng.* **157**, 696–715 (2017)
24. Moradpour, N., Pourafshary, P., Zivar, D.: Experimental analysis of hybrid low salinity water alternating gas injection and the underlying mechanisms in carbonates. *J. Petrol. Sci. Eng.* **202**, 108562 (2021)
25. Moradi, B., Pourafshary, P., Jalali, F., et al.: Experimental study of water-based nanofluid alternating gas injection as a novel enhanced oil-recovery method in oil-wet carbonate reservoirs. *J. Nat. Gas Sci. Eng.* **27**, 64–73 (2015)
26. Phukan, R., Saha, R.: Low salinity surfactant alternating gas/CO₂ flooding for enhanced oil recovery in sandstone reservoirs. *J. Petrol. Sci. Eng.* **212**, 110253 (2022)
27. Afzali, S., Ghamartale, A., Rezaei, N., et al.: Mathematical modeling and simulation of water-alternating-gas (WAG) process by incorporating capillary pressure and hysteresis effects. *Fuel* **263**, 116362 (2020)
28. Nygård, J.I., Andersen, P.Ø.: Simulation of immiscible water-alternating-gas injection in a stratified reservoir: Performance characterization using a new dimensionless number. *SPE J.* **25**(4), 1711–1728 (2020)
29. Wu, D., Brantson, E.T., Ju, B.: Numerical simulation of water alternating gas flooding (WAG) using CO₂ for high-salt argillaceous dolomite reservoir considering the impact of stress sensitivity and threshold pressure gradient. *Acta Geophys.* **69**(4), 1349–1365 (2021)
30. Jia, B., Tsau, J.S., Barati, R.: A review of the current progress of CO₂ injection EOR and carbon storage in shale oil reservoirs. *Fuel* **236**, 404–427 (2019)

Chapter 51

Well Test Model for Double-Porosity Media Three-Zone Composite Reservoir Considering Interface Resistance



Baotong Li, Hongjun Yin, and Cuiqiao Xing

Abstract Because of the heterogeneity of the formation, different parameters such as formation permeability and porosity may occur in the three zones. Contamination zones exist at the regional intersection due to the mismatch between extraneous fluids and formation fluids meanwhile, especially in low-permeability reservoirs, where the effect of such contamination zones is more obvious. According to the situation of this kind of radial composite reservoir, a test well model for a three-zone dual-porosity radial composite reservoir was established by considering the effects of wellbore storage, interface skin effects, and interfacial resistance, by introducing an “interfacial skin” into the interfacial conditions. Through Laplace transform and numerical inversion method, the typical well test curve was drawn, and the effect of various factors on the typical well test curve was analyzed. Through the analysis of the characteristic curve, it is shown that the interface resistance has certain effect on the bottomhole pressure of the dual-porosity three-zone radial composite reservoir.

Keywords Radial composite reservoir in three-zone · Interfacial resistance · Double-porosity · Well test

51.1 Introduction

A composite reservoir is a reservoir consisting of multiple areas with different rock and fluid properties, that is, two adjacent regions are separated by an interface. However, in the actual development process of oilfield, there is a certain resistance to fluid flow at the intersection of the composite reservoir, and the effect of this

B. Li (✉) · H. Yin (✉) · C. Xing
Key Laboratory of Enhanced Oil Recovery (Northeast Petroleum University), Ministry of Education, Daqing 163318, China
e-mail: 745172903@qq.com

H. Yin
e-mail: yinhj7176@126.com

College of Petroleum Engineering, Northeast Petroleum University, Daqing 163318, China

resistance cannot be ignored. Jiang et al. [1] established three-zone composite horizontal well model for CO₂. Liu et al. [2] introduced “interface skin” into the interface connection conditions to establish a mathematical model for dual-medium composite reservoirs. Zhang et al. [3] deduced the well test model of three-zone composite reservoir considering the effect of temperature effect. Li et al. [4] developed a well test model for the effective well diameter of a triple-media complex reservoir considering the effects of wellbore storage and skin effects, as well as the effect of resistance at the interface. Zhang et al. [5] considering the non-Darcy flow of crude oil, a well test interpretation model for low permeability dual media reservoir was established. Yang et al. [6] considered the difference of bottom water energy and permeability among multiple layers, a dual-media composite numerical well test interpretation was conducted. Chen et al. [7] established a well test interpretation model of radial composite reservoir considering wellbore reservoir and skin effect, in which the inner zone is three-pore medium and the outer zone is two-pore medium. Acosta et al. [8] established a multi-zone composite reservoir model. Jiang et al. [9] established a well test interpretation model of eccentric wells in composite reservoirs considering skin effect and wellbore storage effect. Taking stress sensitivity into account, Zhang et al. [10] established a well test model for dual-medium composite reservoir. Jiang et al. [11] established a new horizontal well testing model considering nonlinear coefficient in dual-medium low permeability reservoir. Wu et al. [12] established the horizontal well test interpretation model of composite reservoir in the third area of heavy oil thermal recovery. Liu et al. [13] established a numerical model of double porosity and double permeability. Zhu et al. [14] established a non-Newton three-zone composite model of polymer flooding. However, the well test interpretation models with additional interfacial resistance are focused on two-zone composite reservoirs, and the research on three-zone composite reservoirs is less. Therefore, this paper establishes a well test interpretation model of three-zone dual-medium radial composite reservoirs affected by additional interfacial resistance.

51.2 Physical Model

The formation is a horizontal, equal-thickness, three-zone radial composite reservoir with a radius of r_f in zone 1, a radius of r_e in zone 2, an infinite outer boundary, a formation thickness of h , fracture permeability K_f in each zone, bedrock permeability K_m , porosity φ , fluid viscosity μ , integrated compression coefficient C_t and other parameters are different and constant, flow ratio between zone 1 and zone 2 is M_{12} , flow ratio between zone 2 and zone 3 is M_{23} , conductivity ratio between zone 1 and zone 2 is η_{12} , and fracture permeability ratio between zone 1 and zone 2 is η_{13} , the storability ratio is ω_1 , ω_2 and ω_3 in turn. The physical model of the three-zone double-porosity media radial composite reservoir is shown in Fig. 51.1.

The model assumes the following conditions:

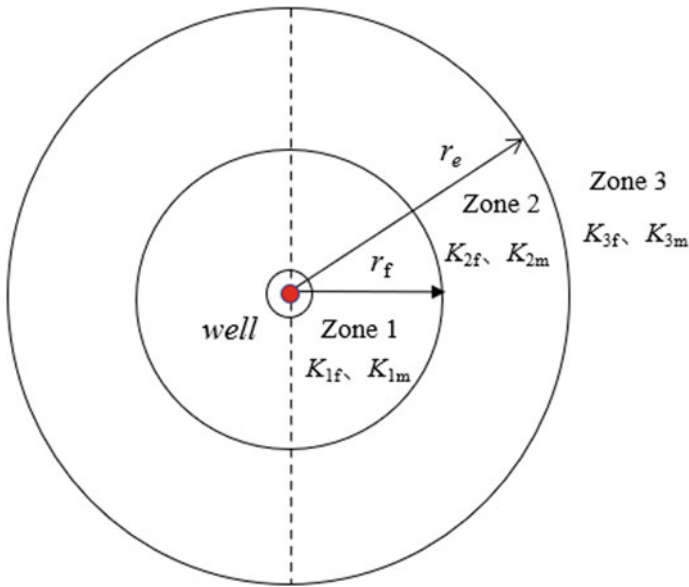


Fig. 51.1 Schematic diagram of a three-zone double-porosity media radial composite reservoir

- (1) The fluid obeys Darcy’s law, where the reservoir fluid is unidirectional and slightly compressible, ignoring the effect of gravity and capillary forces;
- (2) A well is opened for production at a constant production rate q at time $t = 0$. The pressure at all points in the formation before the well is opened is equal to p_i ;
- (3) Considering of interface skin effect and wellbore storage effect;
- (4) Flow as an isothermal process.

51.3 Establishment and Solution of the Mathematical Model

Based on the physical model of flow and the model assumptions, the mathematical model for each zone was developed:

Differential equation for fluid flow in zone 1:

$$\frac{\partial^2 p_{1fD}}{\partial r_D^2} + \frac{1}{r_D} \frac{\partial p_{1fD}}{\partial r_D} = \omega_1 \frac{\partial p_{1fD}}{\partial t_D} + (1 - \omega_1) \frac{\partial p_{1mD}}{\partial t_D} \tag{51.1}$$

$$(1 - \omega_1) \frac{\partial p_{1mD}}{\partial t_D} = \lambda_1 (p_{1fD} - p_{1mD}) \tag{51.2}$$

Differential equation for fluid flow in zone 2:

$$\frac{\partial^2 p_{2fD}}{\partial r_D^2} + \frac{1}{r_D} \frac{\partial p_{2fD}}{\partial r_D} = \eta_{12} \left[\omega_2 \frac{\partial p_{2fD}}{\partial t_D} + (1 - \omega_2) \frac{\partial p_{2mD}}{\partial t_D} \right] \tag{51.3}$$

$$(1 - \omega_2) \eta_{12} \frac{\partial p_{2mD}}{\partial t_D} = \lambda_2 (p_{2fD} - p_{2mD}) \tag{51.4}$$

Differential equation for fluid flow in zone 3:

$$\frac{\partial^2 p_{3fD}}{\partial r_D^2} + \frac{1}{r_D} \frac{\partial p_{3fD}}{\partial r_D} = \eta_{13} \left[\omega_3 \frac{\partial p_{3fD}}{\partial t_D} + (1 - \omega_3) \frac{\partial p_{3mD}}{\partial t_D} \right] \tag{51.5}$$

$$(1 - \omega_3) \eta_{13} \frac{\partial p_{3mD}}{\partial t_D} = \lambda_3 (p_{3fD} - p_{3mD}) \tag{51.6}$$

Initial conditions:

$$p_{jfD}(r_D, 0) = p_{jmD}(r_D, 0) = 0 \quad j = 1, 2, 3 \tag{51.7}$$

Inner boundary conditions:

$$C_D \frac{dp_{wD}}{dt_D} - \left(r_D \frac{\partial p_{1fD}}{\partial r_D} \right) \Big|_{r_D=1} = 1 \tag{51.8}$$

$$p_{wD} = \left(p_{1fD} - S \cdot r_D \frac{\partial p_{1fD}}{\partial r_D} \right) \Big|_{r_D=1} \tag{51.9}$$

Outer boundary conditions:

$$p_{jfD}(\infty, t_D) = p_{jmD}(\infty, t_D) = 0 \quad j = 1, 2, 3 \tag{51.10}$$

Interface connection conditions:

$$\frac{\partial p_{1fD}}{\partial r_D} \Big|_{r_D=r_{fD}} = \frac{1}{M_{12}} \frac{\partial p_{2fD}}{\partial r_D} \Big|_{r_D=r_{fD}} \tag{51.11}$$

$$p_{1fD}(r_{fD}) = \left(p_{2fD} - r_{fD} \cdot S_f \frac{\partial p_{2fD}}{\partial r_D} \right) \Big|_{r_D=r_{fD}} \tag{51.12}$$

$$\frac{\partial p_{2fD}}{\partial r_D} \Big|_{r_D=r_{eD}} = \frac{1}{M_{23}} \frac{\partial p_{3fD}}{\partial r_D} \Big|_{r_D=r_{eD}} \tag{51.13}$$

$$p_{2fD}(r_{eD}) = \left(p_{3fD} - r_{eD} \cdot S_{f2} \frac{\partial p_{2fD}}{\partial r_D} \right) \Big|_{r_D=r_{eD}} \tag{51.14}$$

The dimensionless variables involved in the above mathematical model are defined as follows:

$$\begin{aligned}
 p_{j\text{fD}} &= \frac{2\pi K_{1\text{f}}h}{q\mu}(p_i - p_{j\text{f}}); p_{j\text{mD}} = \frac{2\pi K_{1\text{f}}h}{q\mu}(p_i - p_{j\text{m}}); \\
 t_{\text{D}} &= \frac{K_{1\text{f}}t}{[(\phi C_{\text{t}})_{1\text{f}} + (\phi C_{\text{t}})_{1\text{m}}]\mu r_{\text{w}}^2}; C_{\text{D}} = \frac{C}{2\pi[(\phi C_{\text{t}})_{1\text{f}} + (\phi C_{\text{t}})_{1\text{m}}]hr_{\text{w}}^2}; \\
 \omega_j &= \frac{(\phi C_{\text{t}})_{j\text{f}}}{(\phi C_{\text{t}})_{j\text{f}} + (\phi C_{\text{t}})_{j\text{m}}}; \lambda_j = \alpha \frac{K_{j\text{m}}}{K_{j\text{f}}}r_{\text{w}}^2; r_{\text{D}} = \frac{r}{r_{\text{w}}}; j = 1, 2, 3
 \end{aligned}$$

The dimensionless model is subjected to Laplace transformation about t_{D} , and the Eqs. (51.1) to (51.6) are used to eliminate $\bar{p}_{1\text{mD}}, \bar{p}_{2\text{mD}}, \bar{p}_{3\text{mD}}$:

$$\frac{d^2\bar{p}_{j\text{fD}}}{dr_{\text{D}}^2} + \frac{1}{r_{\text{D}}}\frac{d\bar{p}_{j\text{fD}}}{dr_{\text{D}}} - sf_j(s)\bar{p}_{j\text{fD}} = 0 \tag{51.15}$$

where s is the Laplace variable, \bar{p} is the Laplace transformation of p .

$$\begin{aligned}
 f_1(s) &= \frac{\omega_1(1 - \omega_1)s + \lambda_1}{(1 - \omega_1)s + \lambda_1}; f_2(s) = \eta_{12}\frac{\eta_{12}\omega_2(1 - \omega_2)s + \lambda_2}{\eta_{12}(1 - \omega_2)s + \lambda_2} \\
 f_3(s) &= \eta_{13}\frac{\eta_{13}\omega_3(1 - \omega_3)s + \lambda_3}{\eta_{13}(1 - \omega_3)s + \lambda_3}
 \end{aligned}$$

Equation (51.15) is the Bessel equation of zero-order imaginary parameter, and its general solution is:

$$\bar{p}_{1\text{fD}} = A_1\text{I}_0\left[r_{\text{D}}\sqrt{sf_1(s)}\right] + B_1\text{K}_0\left[r_{\text{D}}\sqrt{sf_1(s)}\right] \tag{51.16}$$

$$\bar{p}_{2\text{fD}} = A_2\text{I}_0\left[r_{\text{D}}\sqrt{sf_2(s)}\right] + B_2\text{K}_0\left[r_{\text{D}}\sqrt{sf_2(s)}\right] \tag{51.17}$$

$$\bar{p}_{3\text{fD}} = B_3\text{K}_0\left[r_{\text{D}}\sqrt{sf_3(s)}\right] \tag{51.18}$$

Combining Eqs. (51.8) to (51.14), the following linear equations can be obtained:

$$\begin{aligned}
 &A_1\sqrt{sf_1(s)}\text{I}_1\left(r_{\text{fD}}\sqrt{sf_1(s)}\right) - B_1\sqrt{sf_1(s)}\text{K}_1\left(r_{\text{fD}}\sqrt{sf_1(s)}\right) \\
 &= \frac{1}{M_{12}}\left[A_2\sqrt{sf_2(s)}\text{I}_1\left(r_{\text{fD}}\sqrt{sf_2(s)}\right) - B_2\sqrt{sf_2(s)}\text{K}_1\left(r_{\text{fD}}\sqrt{sf_2(s)}\right)\right] \\
 &A_1\text{I}_0\left(r_{\text{fD}}\sqrt{sf_1(s)}\right) + B_1\text{K}_0\left(r_{\text{fD}}\sqrt{sf_1(s)}\right) = A_2\text{I}_0\left(r_{\text{fD}}\sqrt{sf_2(s)}\right) + B_2\text{K}_0\left(r_{\text{fD}}\sqrt{sf_2(s)}\right) \\
 &\quad - r_{\text{fD}} \cdot S_{\text{f}}\left[A_2\sqrt{sf_2(s)}\text{I}_1\left(r_{\text{fD}}\sqrt{sf_2(s)}\right) - B_2\sqrt{sf_2(s)}\text{K}_1\left(r_{\text{fD}}\sqrt{sf_2(s)}\right)\right] \\
 &A_2\sqrt{sf_2(s)}\text{I}_1\left(r_{\text{eD}}\sqrt{sf_2(s)}\right) - B_2\sqrt{sf_2(s)}\text{K}_1\left(r_{\text{eD}}\sqrt{sf_2(s)}\right) \\
 &= -\frac{1}{M_{23}}B_3\sqrt{sf_3(s)}\text{K}_1\left(r_{\text{eD}}\sqrt{sf_3(s)}\right)
 \end{aligned}$$

$$\begin{aligned}
 &A_2 I_0\left(r_{eD}\sqrt{s f_2(s)}\right) + B_2 K_0\left(r_{eD}\sqrt{s f_2(s)}\right) \\
 &= B_3 K_0\left(r_{eD}\sqrt{s f_3(s)}\right) + S_{f_2} \cdot r_{eD}\sqrt{s f_3(s)} B_3 K_1\left(r_{eD}\sqrt{s f_3(s)}\right) \\
 &A_1 r_{D}\sqrt{s f_1(s)} I_1\left(r_{D}\sqrt{s f_1(s)}\right) - C_{D s} A_1 I_0\left(r_{D}\sqrt{s f_1(s)}\right) \\
 &\quad + C_{D s} S A_1 r_{D}\sqrt{s f_1(s)} I_1\left(r_{D}\sqrt{s f_1(s)}\right) \\
 &\quad - B_1 r_{D}\sqrt{s f_1(s)} K_1\left(r_{D}\sqrt{s f_1(s)}\right) - C_{D s} B_1 K_0\left(r_{D}\sqrt{s f_1(s)}\right) \\
 &\quad - C_{D s} S B_1 r_{D}\sqrt{s f_1(s)} K_1\left(r_{D}\sqrt{s f_1(s)}\right) = -\frac{1}{s}
 \end{aligned}$$

51.4 Analysis of Typical Curve Characteristics and Sensitivity Factors

By solving the above equations and using Stehfest numerical inversion method, the bottomhole pressure solution p_{wD} in real space can be obtained, and the typical well test curve of three-zone radial composite reservoir can be drawn, as shown in Fig. 51.2.

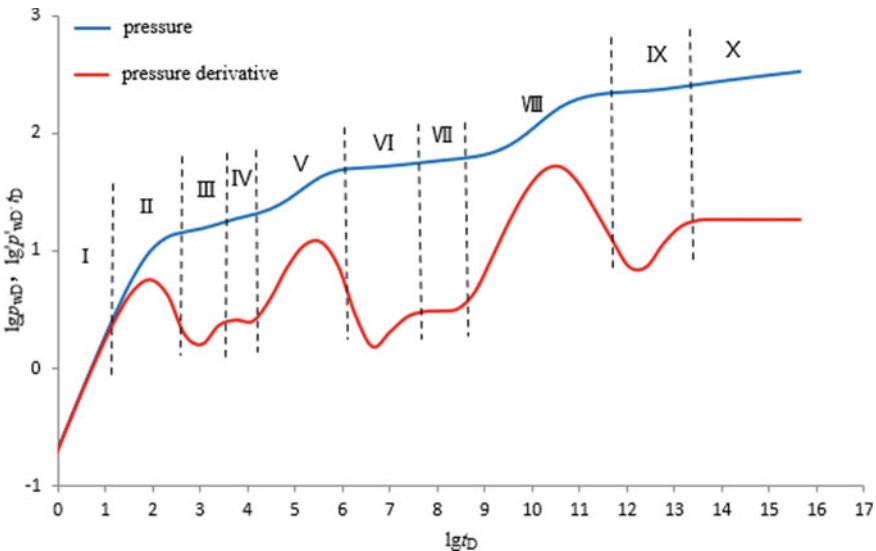


Fig. 51.2 Typical curve of well testing in three-zone double-porosity media radial composite reservoir

As can be seen from Fig. 51.2, the typical curve flow phases of a dual media radial composite reservoir test well in the three zones were divided into ten phases for analysis.

Stage I: wellbore storage regime. On the curve of pressure and its derivative, the double logarithmic curve of pure wellbore reservoir stage shows a straight line with slope of 1 and overlapping each other, which is mainly affected by wellbore storage coefficient.

Stage II: The transitional flow regime. The pressure derivative curve drops to form a "hump", which characterizes the pressure and pressure derivative response from the wellbore storage stage to the zone 1 crossing flow regime, with the size of the "peak" mainly effected by the skin factor.

Stage III: Crossing flow regime in zone 1. The matrix system begins to supply fluid to the fracture system, manifesting itself as a cross from the matrix system to the microfracture system, forming a "concave" in the pressure derivative curve.

Stage IV: The proposed radial flow stage of the total system in zone 1. It reflects the combined characteristics of bedrock system and fracture system, where the pressure in the two media reaches equilibrium, and the radial flow 0.5 horizontal line appears in the pressure derivative curve.

Stage V: Transitional flow regime. It reflects the flow of fluid from zone 2 to zone 1. Due to the existence of interface skin, the resistance of fluid flow increases, the pressure drop consumed by flow increases, and the pressure derivative curve decreases to form a "hump", which describes the pressure and pressure derivative response characteristics from the pseudo-radial flow stage of the total system in Zone 1 to the crossing stage in zone 2, and the "peak" is mainly affected by the interface skin S_f .

Stage VI: Crossing flow regime in zone 2. When the fluid flows from matrix to fracture, the pressure derivative curve exhibits a downward concavity.

Stage VII: Total system proposed radial flow stage in zone 2. Radial flow 0.5 horizontal line in the pressure derivative curve.

Stage VIII: Transitional flow regime. This describes the pressure and pressure derivative response from the proposed radial flow phase of the total system in zone 2 to the crossing phase in zone 3. The size of the "peak" is mainly effected by the interface skin S_{f2} .

Stage IX: Crossing flow regime in zone 3. The stage of fracture of bedrock to fracture in the two-hole media system in zone 3, manifested as a downward concavity of the pressure derivative curve in zone 3, whose depth is mainly effected by the elastic energy storage ratio, and the early and late appearance of fracture is mainly effected by the elastic fracture coefficient.

Stage X: Total system proposed radial flow stage in zone 3. The pressure derivative curve appears as a radial flow 0.5 horizontal line.

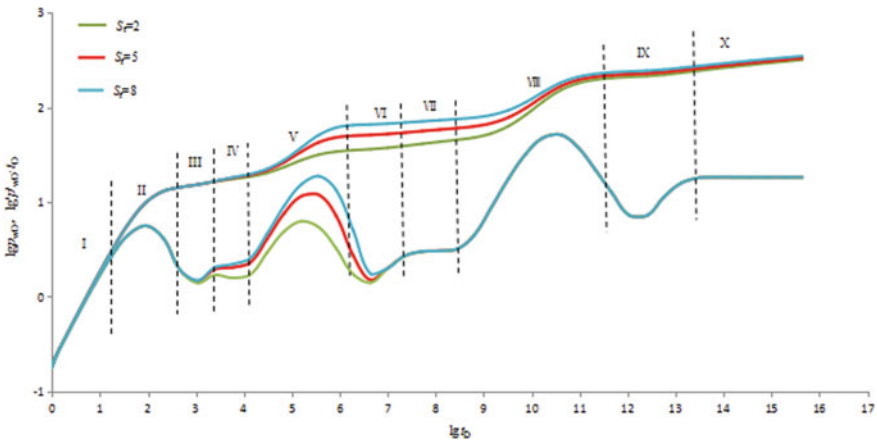


Fig. 51.3 The effect of S_F on typical curve of well testing

51.4.1 Effect of the Interface Skin

As can be seen from Figs. 51.3 and 51.4, when the pressure wave propagates to the regional intersection, the resistance to fluid flow increases due to the presence of the interfacial skin coefficient, the pressure drop consumed by the flow increases, and the position of the dimensionless pressure and pressure derivative curve rises; the larger the skin factor, the relatively more serious the degree of contamination at the intersection, the greater the pressure consumption during production, the higher the hump in the transition phase, and the more the pressure derivative curve leans upwards.

51.4.2 Effect of Storability Ratio

From Figs. 51.5, 51.6 and 51.7, it can be seen that the storability ratio affects the width and depth of the “concave” formed by cross flow. The smaller the storability ratio, the less fluid stored in the fracture, and the fracture system causes great pressure drop in a short period of time. Then the bedrock replenishes fluid to the fracture, so the “concave” is wider and deeper.

51.4.3 Effect of Cross-Flow Coefficient

It can be seen from Figs. 51.8, 51.9 and 51.10 that the cross-flow coefficient mainly affects the time when the cross-flow from bedrock to fracture occurs. The smaller

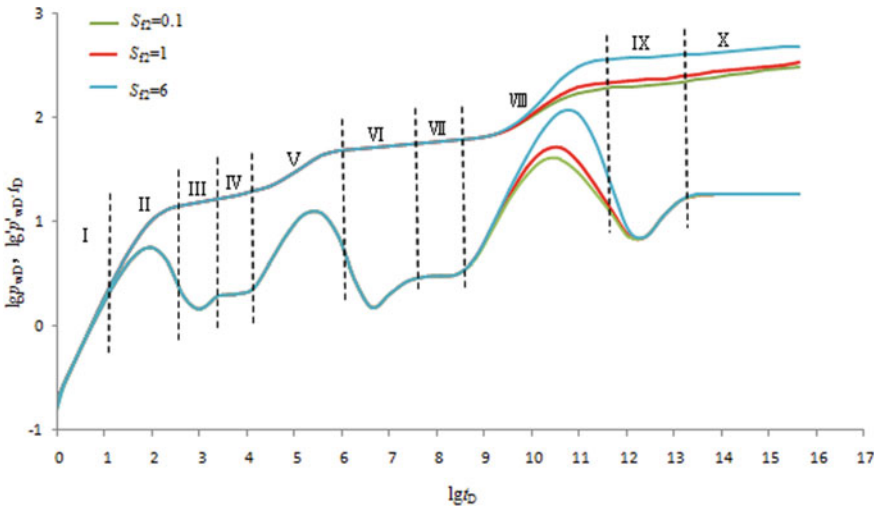


Fig. 51.4 The effect of S_{f2} in Zone 3 and Zone 2 on typical curve of well testing

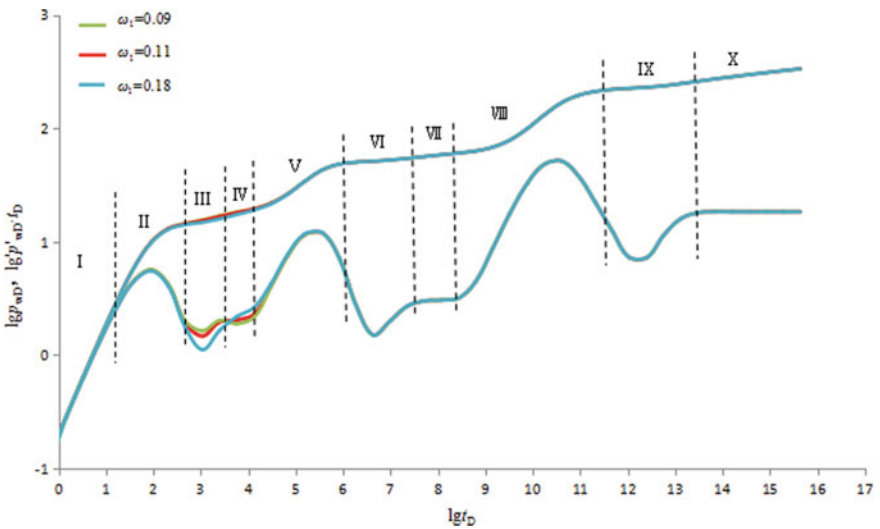


Fig. 51.5 The effect of ω_1 on typical curve of well testing

the cross-flow coefficient, the more difficult it is for fluid to flow into fracture from bedrock. The greater the difference between the permeability of bedrock system and fracture system, the later the cross-flow occurs, and the more the “concave” is to the right.

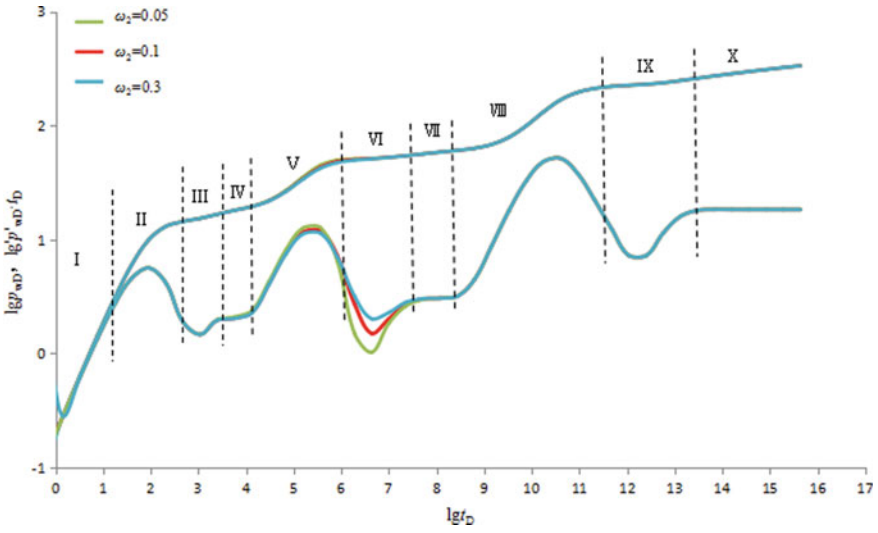


Fig. 51.6 The effect of ω_2 on typical curve of well testing

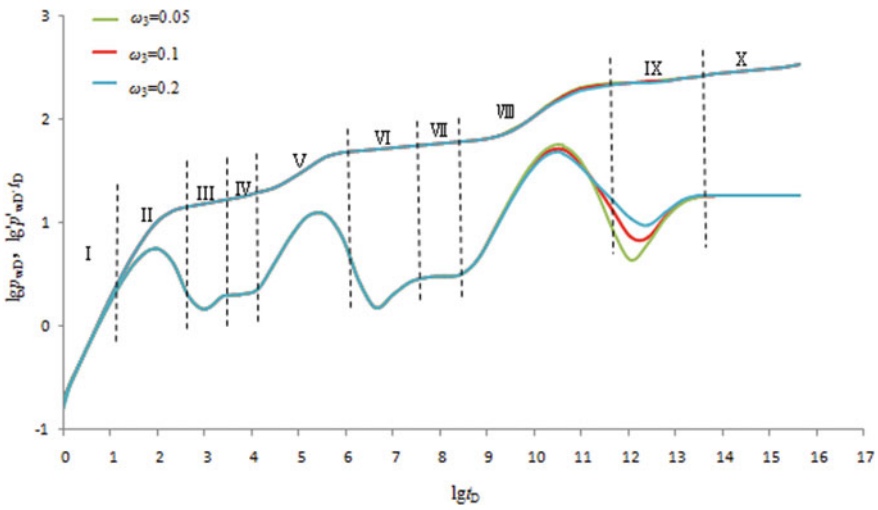


Fig. 51.7 The effect of ω_3 on typical curve of well testing

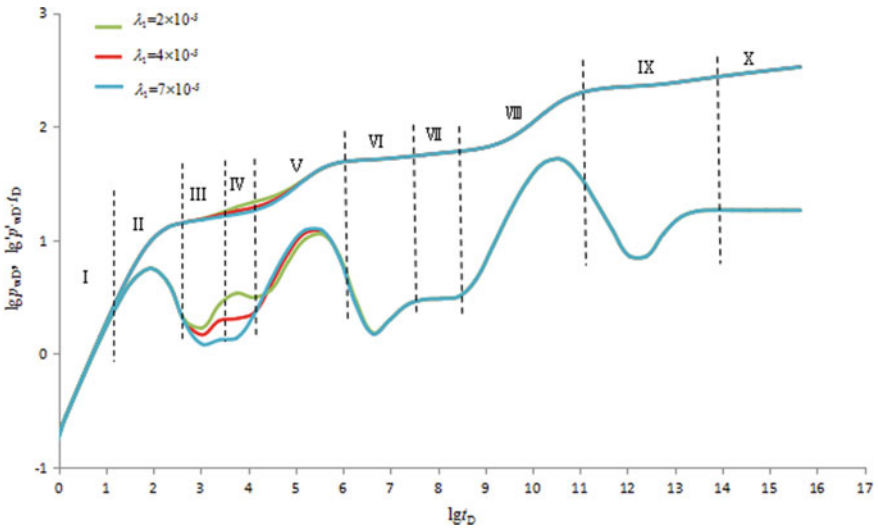


Fig. 51.8 The effect of λ_1 on typical curve of well testing

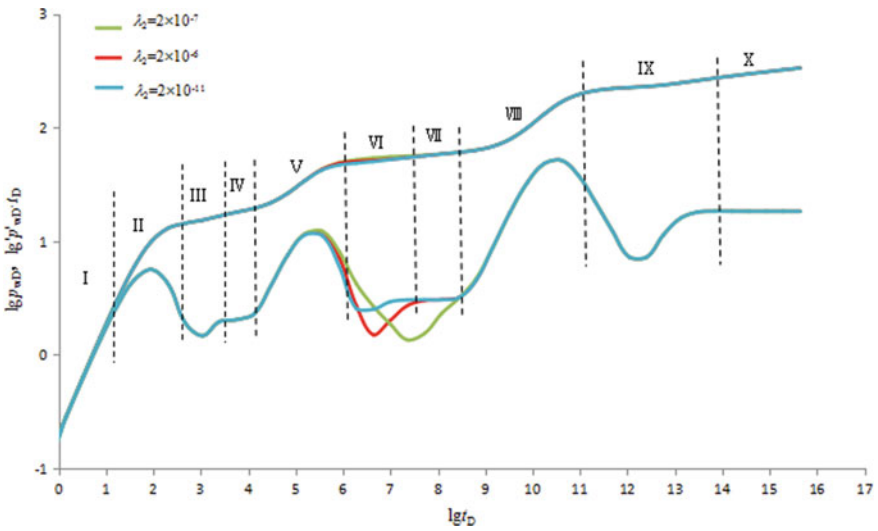


Fig. 51.9 The effect of λ_2 on typical curve of well testing

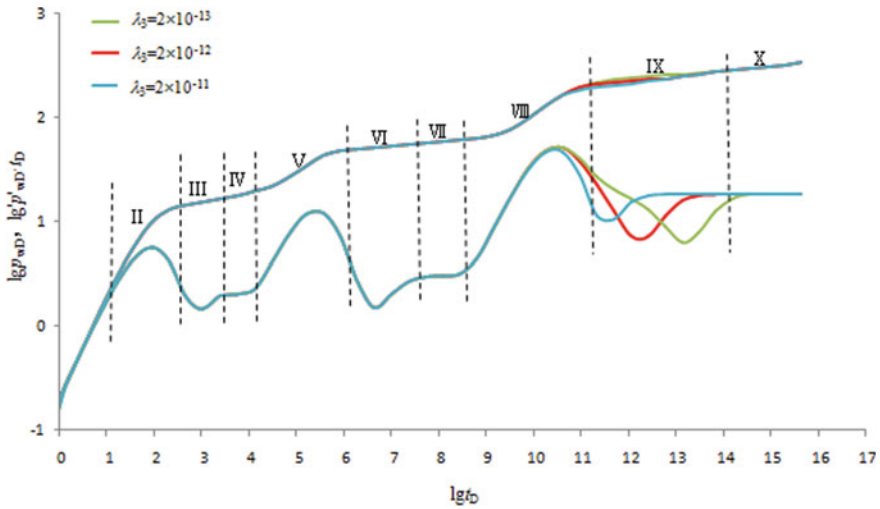


Fig. 51.10 The effect of λ_3 on typical curve of well testing

51.4.4 Effect of Radius of Each Zone

It can be seen from Figs. 51.11 and 51.12 that the radius of each region mainly affects the time when the pressure wave propagates to the interface. As the radius increases, the pressure wave propagation time in the transition zone becomes longer, the later the pressure wave reaches the junction, the longer the radial flow duration, the later the “hump” appears in the transition section, the pressure derivative curve is shifted to the right.

51.4.5 Effect of Mobility ratio

As can be seen from Figs. 51.13 and 51.14, the mobility ratio reflects the flow capacity of the two zones, the larger the mobility ratio, the greater the difference in flow capacity between the two zones, the more pronounced the reflective characteristics of the transition zone and the more pronounced the upward shift in the pressure derivative curve.

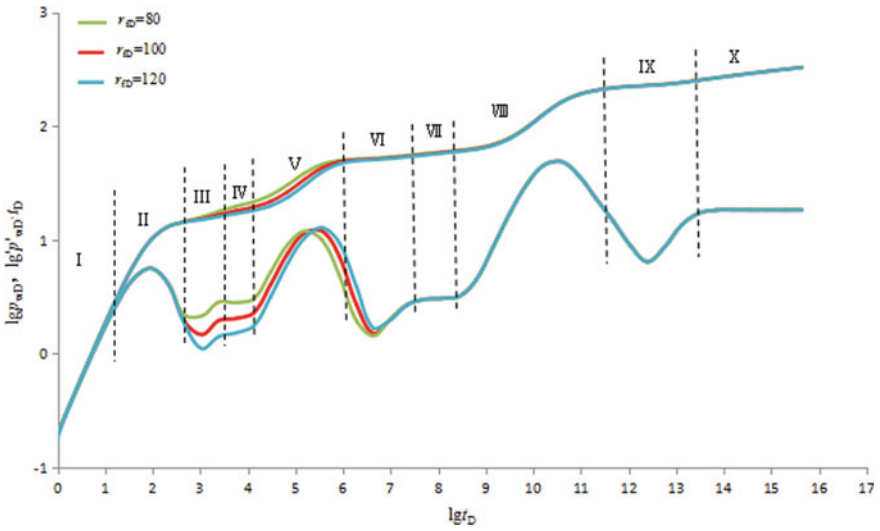


Fig. 51.11 The effect of r_{FD} on typical curve of well testing

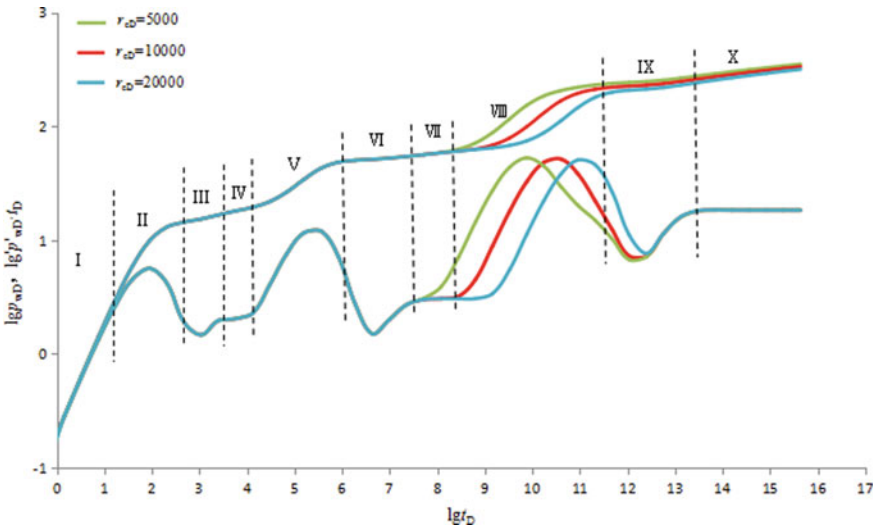


Fig. 51.12 The effect of r_{eD} on the typical curve of well testing

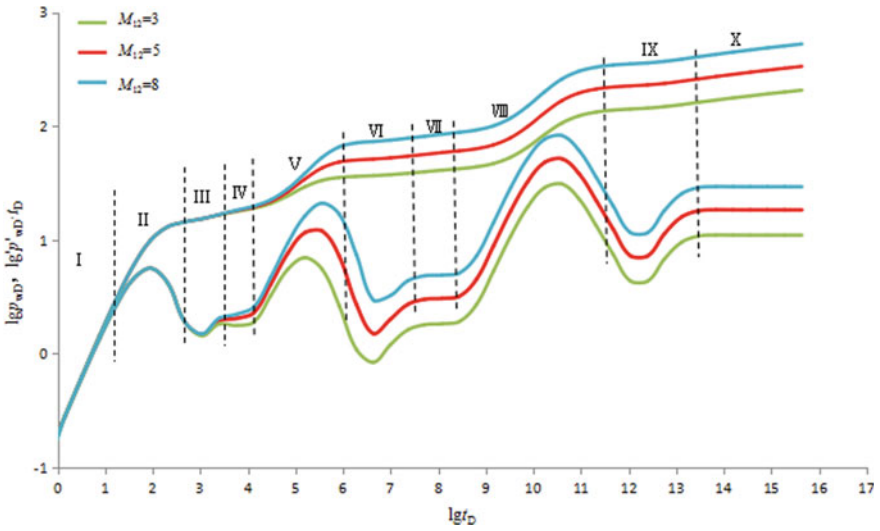


Fig. 51.13 The effect of M_{12} on typical curve of well testing

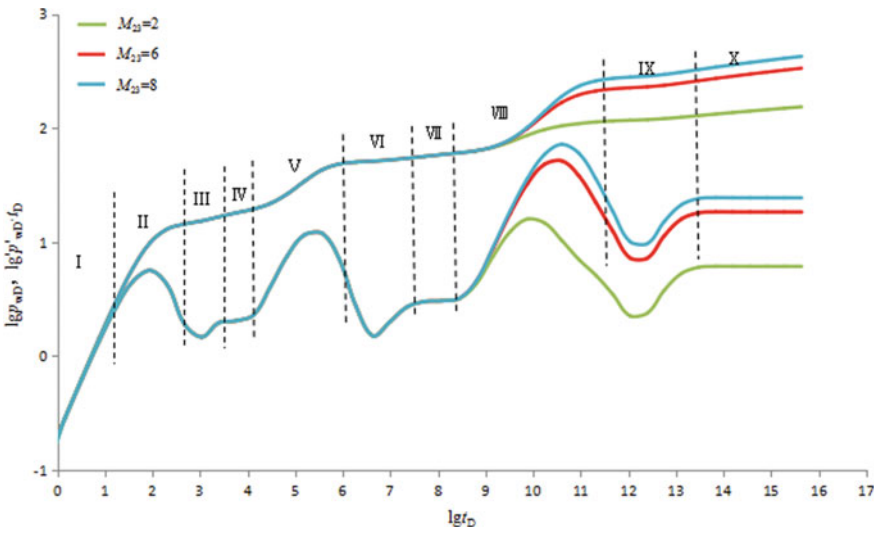


Fig. 51.14 The effect of M_{23} on typical curve of well testing

51.5 Conclusions

- (1) Well test model for a three-zone dual-media radial composite reservoir that takes into account the presence of additional resistance of fluids at the intersection interface is developed by introducing an interfacial skin factor, which is applicable to the interpretation of well test data from heterogeneous reservoirs.
- (2) The analysis of sensitivity factors shows that the resistance at the junction surface mainly affects the transition phase between regions, making a greater differential pressure required for the fluid to flow at the junction surface.
- (3) The effects of different parameters such as storability ratio, cross-flow coefficient and radius of each zone on the typical well test curve of the three-zone composite reservoir is studied, which is significant to the division of the flow stages of the typical well test well in the three-zone composite reservoir.

Acknowledgements The authors gratefully acknowledge the Natural Science Foundation of Heilongjiang Province (Grant No. LH2022E023) for the support to present this paper.

References

1. Ruizhong, J., Haitao, Z., Wei, Z., et al.: Pressure performance analysis of horizontal wells in CO₂ flooding three-zone composite reservoir. *Oil Gas Geol. Recovery* **25**(06), 63–70 (2018). <https://doi.org/10.13673/j.cnki.cn37-1359/te.2018.06.010>
2. Qiguo, L., Yu, F., Fengling, D.: Study on well test interpretation model of dual-medium radial composite reservoir affected by interface additional resistance. *Oil Gas Well Test*. (03), 11–13 +75 (2005)
3. Yan, Z.: Analysis and application of well test interpretation technology and data of composite reservoirs in three areas of heavy oil thermal production. *J. Daqing Normal Univ.* **32**(03), 97–101 (2012)
4. Xiujun, L., Xiaoping, L., Aimin, L.: Well test model of triple medium complex reservoir considering the influence of interface resistance. *Spec. Oil Gas Reservoirs* **16**(03), 74–76 + 109 (2009)
5. Yanyu, Z., Weidong, L., Guoliang, C., et al.: Well test interpretation model of low permeability dual media reservoir. *J. Shaanxi Univ. Sci. Technol. (Nat. Sci. Ed.)* **30**(03), 65–69 (2012)
6. Yong, Y., Ribin, X., Zhenghe, Y., et al.: Application of dual-media composite numerical well testing technology in fractured reef limestone bottom water reservoir. *Spec. Oil Gas Reservoir* **27**(05), 100–105 (2020)
7. Fang-fang, C., Yong-lu, J.: Three-pore and two-pore radial composite reservoir model and well test curve. *Oil Gas Well Test*. (04), 1–4 +7 +75 (2008)
8. Acosta, L.G., Ambastha, A.K.: Thermal well test analysis using an analytical multi-region composite reserve model (2019)
9. Ruizhong, J., Yihua, G., Zhaobo, S., et al.: Well test analysis of eccentric wells in dual-medium composite reservoirs. *Xinjiang Pet. Geol.* **37**(03), 327–331 (2016)
10. Zhang, L.H., Guo, J.J., Liu, Q.G.: A new well test model for stress-sensitive and radially heterogeneous dual-porosity reservoirs with non-uniform thieves. *J. Hydrodyn.* **23**(6), 759–766 (2011)
11. Ruizhong, J., Fulei, Z., Ming, Y., et al.: Horizontal well test model of dual-media low permeability reservoir. *Spec. Oil Gas Reservoir* **26**(03), 79–84 (2019)

12. Minglu, W., Gaolong, Z., Jun, Y., et al.: Well test interpretation model and pressure response characteristics of horizontal wells in composite reservoirs in three areas of heavy oil thermal recovery. *Daqing Petrol. Geol. Dev.* **35**(06), 117–122 (2016)
13. Liu, S., Ni, J., Wen, X., et al.: A dual-porous and dual-permeable media model for imbibition in tight sandstone reservoirs. *J. Pet. Sci. Eng.* **194**, 107477 (2020)
14. Changyu, Z., Shiqing, C., Engao, T., et al.: Well test analysis method of polymer flooding three-zone composite model. *Daqing Pet. Geol. Dev.* **35**(03), 106–110 (2016)

Chapter 52

Production Characteristics Analysis of CO₂ Huff-And-Puff Development in Tight Oil Reservoirs



Zhaoming Li, Hongjun Yin, Zhizeng Xia, and Guohan Xu

Abstract The tight oil reservoir has large resources, but the reservoir has poor physical properties, and there are problems such as rapid decline in oil recovery rate and low recovery rate after volume fracturing. To solve these problems, taking block X as an example, the production characteristics of CO₂ huff-and-puff were numerically studied using CMG software on the basis of experimental data fitting. The results show that: CO₂ huff and puff can significantly increase the daily oil production level, with the highest daily oil production increasing nearly four times, significantly improving the recovery rate of tight oil reservoirs; CO₂ huff and puff can better supplement formation energy, expand swept volume and improve oil flooding efficiency; Higher oil production can be obtained with higher CO₂ injection rate and longer soaking time. With the increase of gas injection rate, the oil production has a certain fluctuation; Under the research conditions of this paper, when the Cumulative oil production is 1500 t/d, the soaking time is 50 d, and the CO₂ injection rate is 50 t/d, the effect of CO₂ huff and puff mining tight reservoir is better. The research results are helpful to strengthen the understanding of the production characteristics of tight reservoirs developed by CO₂ huff and puff.

Keywords Tight oil reservoir · CO₂ huff and puff · Productive features · Injection timing

Z. Li (✉) · H. Yin (✉) · Z. Xia · G. Xu
Key Laboratory of Enhanced Oil Recovery (Northeast Petroleum University), Ministry of Education, Daqing 163318, China
e-mail: 495135554@qq.com

H. Yin
e-mail: yinhj7176@126.com

College of Petroleum Engineering, Northeast Petroleum University, Daqing 163318, China

52.1 Introduction

Tight oil is widely distributed in Ordos, Song liao and other six basins in China, with geological resources of 125.8×10^8 t, which is a hot spot in China's petroleum industry. Relying on the technology of "horizontal well and volume fracturing" [1], the tight oil resources have been exploited on a large scale, and the productivity has reached more than 200×10^4 t [2]. However, with the deepening of development, there are some problems in the process of depletion mining, such as high initial production but rapid decline, insufficient formation energy supplement [3–5], which seriously affect the subsequent mining effect.

The porosity and permeability of tight reservoirs are generally low, and the reservoir properties are poor. CO₂ injection is an important method to improve its development effect, which has been widely concerned and studied. Field practice shows that CO₂ injection is an effective method to improve oil and gas recovery [6–10]. The CO₂ flooding development method achieves the purpose of improving oil recovery through the mechanism of extraction, dissolution, viscosity reduction, expansion and mixing. Compared with conventional water flooding, CO₂ is easier to inject into the formation and can better utilize the crude oil in the small pores of the reservoir [11–13].

The research on carbon dioxide huff and puff oil displacement is mainly based on physical simulation experiments and numerical simulations. Most of the results show good development results. In the experiment, Hawthorne et al. [14] carried out the diffusion experiment of CO₂ in the core matrix, indicating that CO₂ can penetrate into the matrix under pressure, and some crude oil flows from the matrix to the fracture under the action of volume expansion, crude oil viscosity reduction and concentration gradient diffusion. Vega et al. [15] carried out CO₂ displacement and diffusion experiments on low permeability cores under miscible conditions. The results show that CO₂ diffusion greatly improves oil recovery. Zekri et al. [16] believed that CO₂ can improve the oil displacement efficiency of tight core crude oil under immiscible conditions. Ma et al. [17] carried out CO₂ huff and puff experiments and found that the optimal CO₂ huff and puff cycle should be 3 cycles, and the enhanced oil recovery can reach more than 30 percentage points. Song et al. [18] conducted a series of core displacement experiments using core samples collected from the Bakken tight reservoir. The results show that the recovery rate of carbon dioxide huff and puff is better than that of water flooding. Xue-Wu et al. [19] studied the production process of CO₂ huff and puff and the influence of different parameters on the recovery rate of CO₂ huff and puff through physical simulation experiments of CO₂ huff and puff and staged fracturing horizontal wells. Finally, the operating parameters were optimized by numerical simulation. Bai et al. [20] conducted CO₂ huff and puff experiments using fractured cores to evaluate the effects of fractures on CO₂ huff and puff and remaining oil distribution under different permeability. The experimental results show that fracturing can significantly increase the swept volume of core CO₂, and the recovery rate of CO₂ huff and puff in the early and middle stages is significantly improved. Li et al. [6] studied the effect of injection pressure on enhanced oil recovery

of shale oil cores under CO₂ huff and puff injection conditions when the injection pressure is higher than or lower than the minimum miscibility pressure. The results show that the injection pressure has a significant effect on enhancing oil recovery below the minimum miscible pressure. Qian et al. [21] carried out CO₂ huff and puff experiments under different experimental conditions. A fracture-matrix long core system was established. The results show that by increasing the fracture length or density and prolonging the soaking time, the dissolution and diffusion range of injected CO₂ can be significantly increased from both macro and micro aspects.

In terms of numerical simulation, Kong et al. [22] optimized the CO₂ huff and puff process for tight reservoirs, and carried out adaptive CO₂ huff and puff process for tight reservoirs after primary oil recovery. The simulation results show that the adaptive cycle length CO₂ huff and puff process can increase the incremental recovery rate by 11.1% compared with the fixed cycle length CO₂ huff and puff process. Sun et al. [23] established a numerical model to simulate CO₂ huff and puff in Bakken horizontal well. The results show that the CO₂ diffusion coefficient is the most important among the influencing factors of oil displacement effect. CO₂ huff and puff development can improve oil recovery by 6%. Hao et al. [24] studied the sensitivity factors of CO₂ huff and puff in multi-stage fractured horizontal wells in tight reservoirs through experiments and numerical simulations. According to the reservoir parameters of the target reservoir, reasonable well parameters and fracture parameters are obtained. Li et al. [25] established an accurate component numerical model. Well test analysis of CO₂ flooding system was carried out for oil and gas systems with different components. The specific characteristics of CO₂ flooding well test curve are identified and described. Sennaoui et al. [26] studied the process of CO₂ huff and puff to enhance oil recovery, and understood the influence of different parameters on CO₂ enhanced oil recovery. The results show that CO₂ diffusion is very important for enhancing oil recovery in tight oil reservoirs. The undiffused recovery (RF) is 12%, and the diffusion coefficient increases by 4%.

At present, there are few simulation studies on CO₂ huff and puff development at the field scale, and most of the related studies focus on medium–high permeability reservoirs, and there are few studies on tight reservoirs. In order to strengthen the understanding of the application of CO₂ huff and puff in tight permeability reservoirs and clarify its fluid flow and mining dynamic characteristics, based on laboratory experiments, combined with the basic parameters of X block, a typical simulation model was established to study the oil production performance of CO₂ huff and puff oil displacement, and the oil displacement effect was discussed. The effects of injection volume, soaking time, injection speed and other parameters on the mining effect were analyzed. This study is of great significance to improve the mining effect of tight reservoirs.

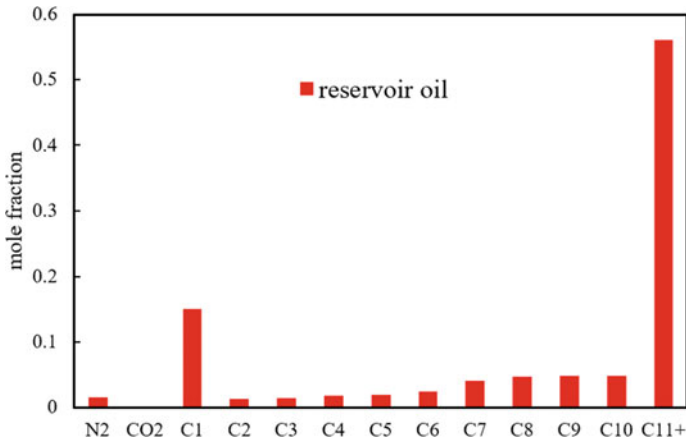


Fig. 52.1 Reservoir oil composition

52.2 Numerical Model Establishment

52.2.1 Experimental Results

Block X is a tight reservoir and the reservoir oil composition of a typical well is shown in Fig. 52.1. CO₂ swelling tests (Figs. 52.2, 52.3 and 52.4) were carried out using typical oil samples with the saturation pressure of 5.6 MPa. It can be seen that CO₂ has good swelling ability to the tested oil and the physical properties of crude oil can be improved when CO₂ is presented. In this study, the oil composition is divided into five components (CO₂, CH₄, C₂₋₇, C₈₋₂₀, C₂₁₋₃₈). CMG-Winprop software is used to fit experimental results, shown in Figs. 52.2, 52.3 and 52.4. It can be seen that the variation trends of fitting results are consistent with the experimental results, and the average fitting errors are small enough to carry out the following numerical studies.

52.2.2 Numerical Simulation Model

After experimental fitting, a single well simulation model was established based on the reservoir parameters of X block, as shown in Fig. 52.5. The model was 2587 × 1300 m in plane size with the reserve of 96.12 × 10⁴ m³. The model is a horizontal well, which is divided into fracture zone and modification zone. The average half length of fracture is 137 m. The grids in the fractured zone were logarithmically spaced-locally refined [23] to model the fluid flow according to the conductivity equivalence. The fracture conductivity and basic parameters are shown in Tables 52.1 and 52.2.

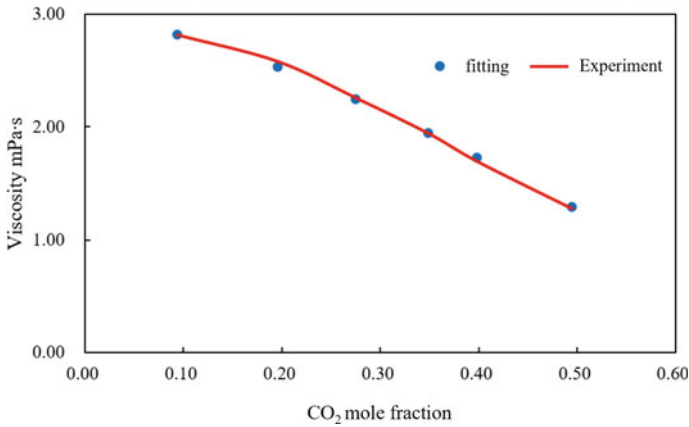


Fig. 52.2 Fitting results of the viscosity in CO₂ swelling test

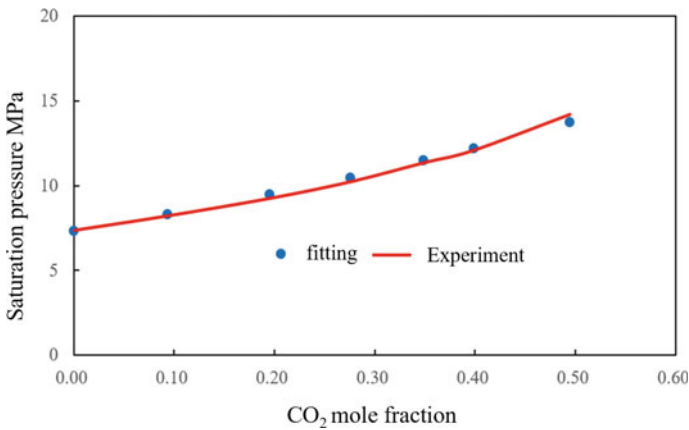


Fig. 52.3 Fitting results of the saturation pressure in CO₂ swelling test

In the simulation study of CO₂ huff and puff mining, the injection time of carbon dioxide was 55 days, the soaking time was 3 months, the average injection rate of CO₂ was 126.53 t/d, and the cumulative injection amount was 7212.21 t.

52.3 Production Performance

The target well was put into production in April 2014. The daily liquid production was 30.8 t/d, the daily oil production was 12.47 t/d, and the flow pressure was 5.33 MPa in the early stage of oil production. It has been put into production for 9 years, with daily liquid production of 4.38 t/d, daily oil production of 1.62 t/d and flow pressure

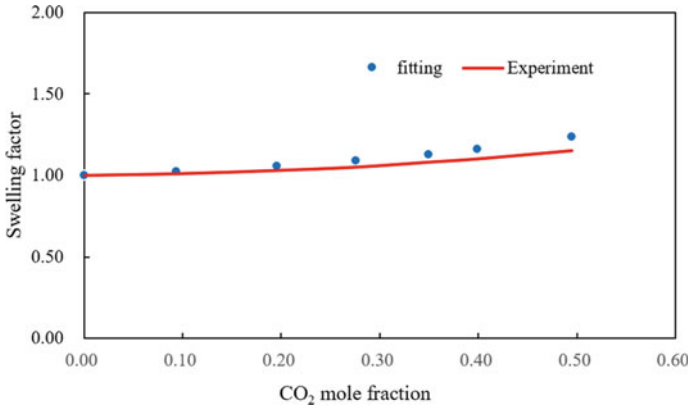


Fig. 52.4 Fitting results of the swelling factor in CO₂ swelling test

Fig. 52.5 Sketch of the basic model

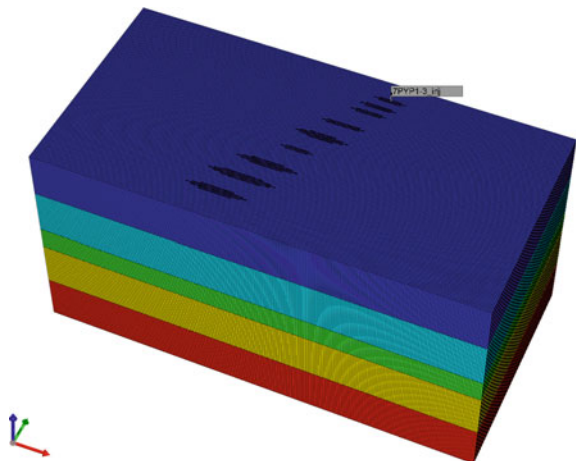


Table 52.1 Main parameters of the numerical model

Parameter	Value
Initial average reservoir pressure, MPa	18.2
Matrix porosity	0.137
Matrix permeability, $10^{-3}\mu\text{m}^2$	2.27
Initial average oil saturation	0.44
Horizontal length, m	1136
Saturation pressure, MPa	5.6
Reservoir oil viscosity	7.02

Table 52.2 Basic model fracture parameter of the reservoir X

Fracturing section	Half length of the main fracture m	Conductivity $\mu\text{m}^2\cdot\text{m}$
1	95	0.26
2	105	0.29
3	105	0.29
4	125	0.29
5	155	0.29
6	105	0.31
7	175	0.31
8	185	0.31
9	175	0.31

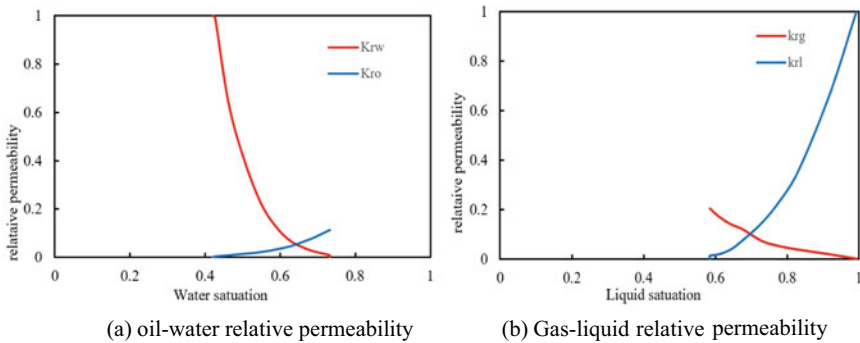


Fig. 52.6 Relative permeability relationship curve of the basic model

of 6.48 MPa. During the period, it experienced a CO₂ huff and puff construction, and the production dynamic curve is as follows (Fig. 52.7).

As of June 30,2022, the cumulative oil production of the target well was 9026.03 m³. The model fitting adopts the constant liquid production system, and the cumulative oil production is 9144.65 m³, with an error of 1.3% (Fig. 52.8).

52.4 CO₂ Huff and Puff Effects

52.4.1 Reservoir Energy Replenishment

In the process of CO₂ huff n puff flooding, the injection of CO₂ can refill the pore space caused by the fluid withdrawn to replenish the reservoir energy. Thus, the reservoir pressure will be recovered improving the oil displacement energy. At the

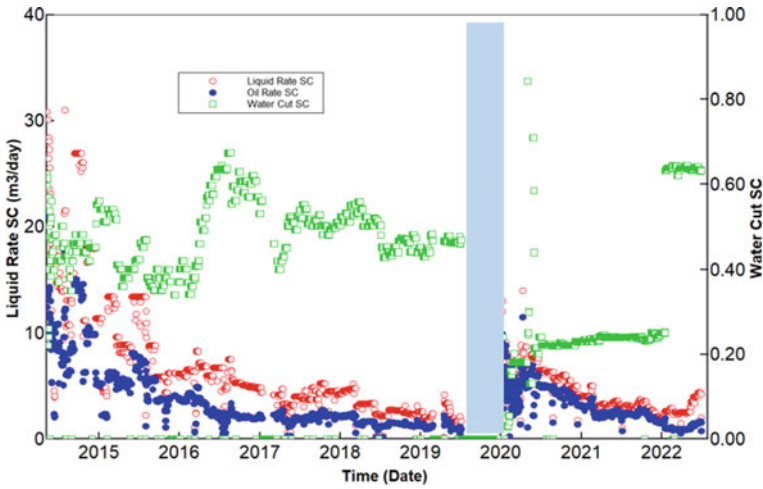


Fig. 52.7 The variation of the production dynamic

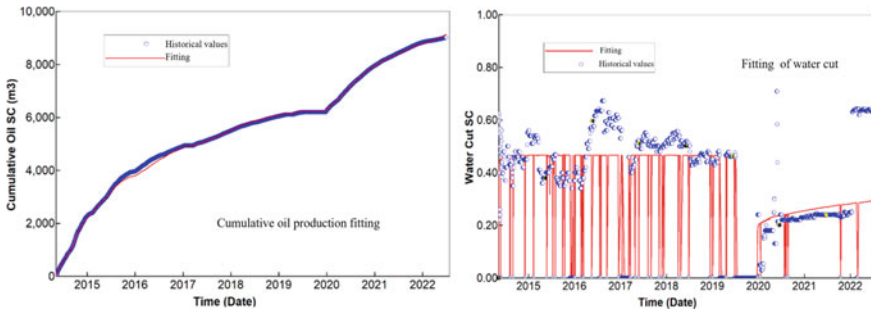


Fig. 52.8 Historical fitting of production performance

end of the simulation, the reservoir pressure distribution is shown in Fig. 52.9. It can be seen that the pressure near the bottom hole increases significantly, the average reservoir pressure increases from 14.45 to 16.84 MPa, and the effective volume accounts for 35.33%. It can be seen that CO₂ huff and puff mining can maintain a high pressure level for a long time, and the effect of supplementing formation energy is significant, which is more conducive to improving the mining effect.

52.4.2 Expanding Sweeping Volume

In the process of CO₂ huff and puff mining simulation, the distribution of oil saturation is shown in Fig. 52.10. It can be seen that the near-wellbore area has achieved

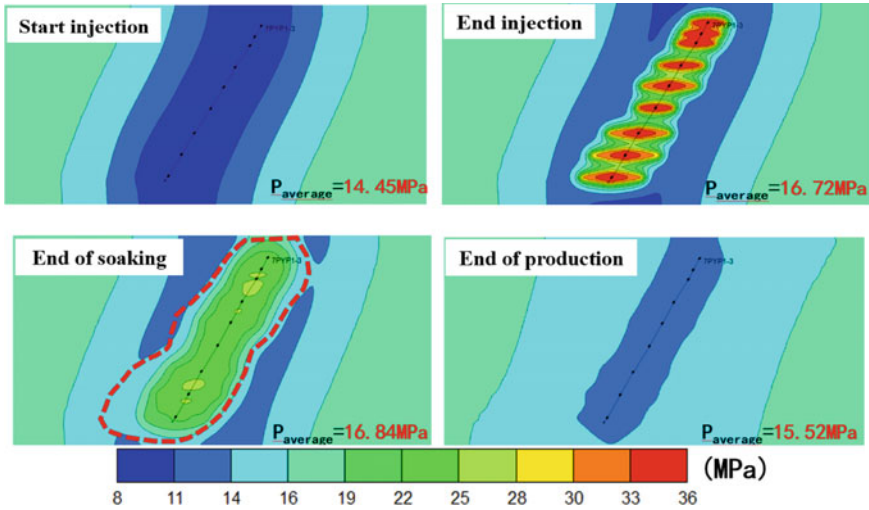


Fig. 52.9 The distribution of the reservoir pressure (unit: MPa)

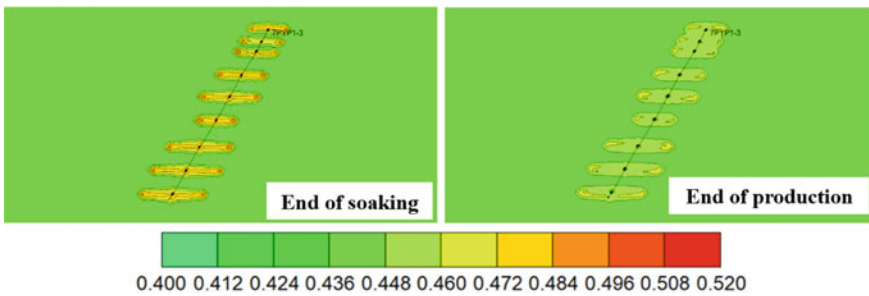


Fig. 52.10 The distribution of the oil saturation

effective sweep, and the volume of crude oil has a large degree of expansion, which makes the oil saturation decrease significantly.

52.4.3 Improving Displacement Efficiency

CO₂ has a variety of mechanisms such as dissolution, viscosity reduction, expansion, and diffusion. The distribution range of CO₂ gradually expands during the process of shut-in and mining. At the end of production, there is still a high content of CO₂ in the crude oil near the well fracturing area (Fig. 52.11).

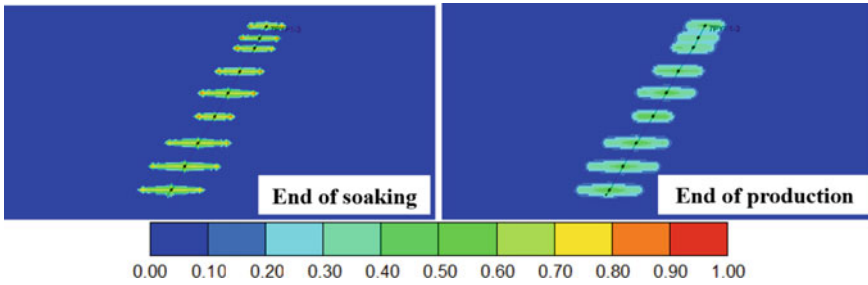


Fig. 52.11 The distribution of the CO₂ in reservoir

52.5 Sensitivity Analysis

The parameters have a significant effect on the exploitation effect of CO₂ huff and puff. On the basis of the basic model, this part keeps other parameters unchanged, selects production parameters such as periodic injection volume, soaking time and gas injection rate, and studies the variation law of oil production and oil change rate under different parameter levels.

52.5.1 Cyclic Injection Rate

Keeping other parameters unchanged, the simulation study of CO₂ huff and puff is carried out when the CO₂ cycle injection amount is 500 t, 1000 t, 1500 t, 2000 t and 2500 t respectively. The simulation results are shown in Fig. 52.12. It can be seen that with the increase of CO₂ cycle injection, the oil production in the huff and puff stage increases obviously. For example, when the CO₂ injection volume increases from 500 to 1000 t, the oil production increases from 1846 m³ to 1961 m³, an increase of about 6%. However, with the increase of cycle injection volume, the growth rate of oil production decreases. The oil change rate gradually decreases with the increase of the periodic injection amount, indicating that the utilization effect of CO₂ gradually becomes worse. This is mainly due to the fact that the higher the injection volume, the better the interaction between CO₂ and crude oil, and the more obvious the development effect; However, when the amount of CO₂ injection is too high, the CO₂ saturation in the near-well fracture area is too high, and it cannot fully play its role in the reservoir matrix, which has a certain impact on the improvement of the development effect. Therefore, it is not appropriate to inject too much or too little CO₂ cycle, and the oil production and oil change rate should be determined to obtain higher oil production and higher oil change rate. In this study, the CO₂ cycle injection amount of 1500 t is appropriate.

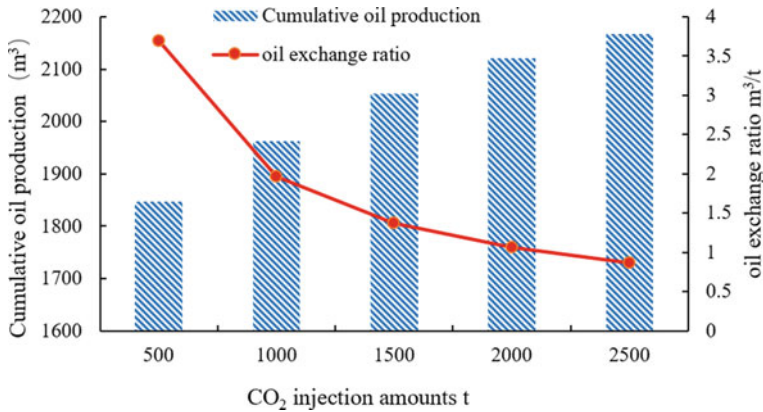


Fig. 52.12 Cumulative oil production and oil exchange ratio under different CO₂ injection amounts

52.5.2 Soaking Time

Keeping other parameters unchanged, the simulation of CO₂ huff and puff is carried out when the soaking time is 10 d, 20 d, 30 d, 40 d and 50 d respectively. The simulation results are shown in Fig. 52.13. It can be seen that the increase of soaking time is beneficial to improve the development effect. The oil production and oil exchange rate in the huff and puff stage increase with the increase of soaking time. When the soaking time increases from 10 to 30 d, the oil production increases by about 5%. However, when the soaking time is longer, the increase of oil production and oil change rate becomes smaller. In the process of soaking, CO₂ and crude oil dissolve and expand. With the increase of soaking time, CO₂ diffuses from the fracture to the deep part of the matrix into the oil phase, which is helpful to the full effect between CO₂ and crude oil and improve the development effect. However, with the extension of soaking time, the overall effect is limited. Therefore, a longer soak time should be selected when conditions permit. In this study, the soaking time is selected as 50 d.

52.5.3 CO₂ Injection Rate

Keeping other parameters unchanged, the gas injection rates of 15 t/d, 30 t/d, 50 t/d, 65 t/d and 80 t/d were selected to carry out the simulation study of CO₂ huff and puff. It can be seen that the oil production and oil change rate in the huff and puff stage fluctuate with the increase of gas injection speed. This is mainly because the increase of gas injection rate is accompanied by the increase of gas injection pressure. Under a certain gas injection rate, it can not only effectively supplement the formation energy, but also facilitate the dissolution of gas in crude oil. When

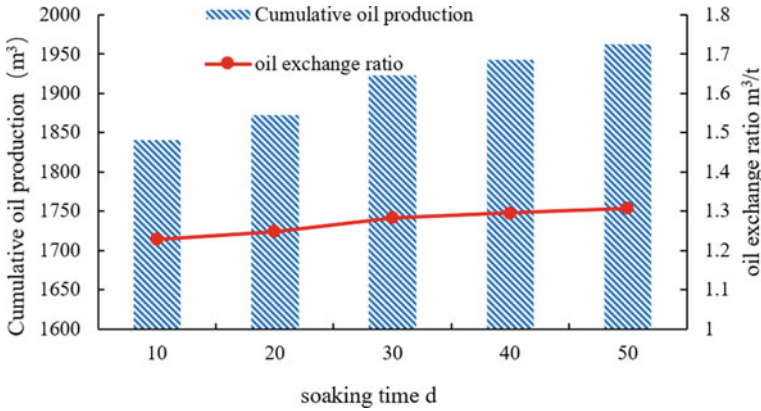


Fig. 52.13 Cumulative oil production and oil exchange ratio under different soaking times

the gas injection rate is very low, it is beneficial for CO₂ to fully dissolve in crude oil, play the role of diffusion and expansion, and improve the development effect. However, when the gas injection rate is very high, the injection time becomes shorter under the condition of a certain amount of injection. Although the pressure near the wellbore increases significantly, the range is limited, and it is possible to squeeze the crude oil near the fracture into the deep matrix, thus affecting the effect. Therefore, when the gas injection amounts is constant, the gas injection rate can't be too high; too low gas injection rate can obtain higher oil production, but it will significantly increase the construction time, so the gas injection rate should't be too low. In this study, the appropriate gas injection rate is 50 t/d (Fig. 52.14).

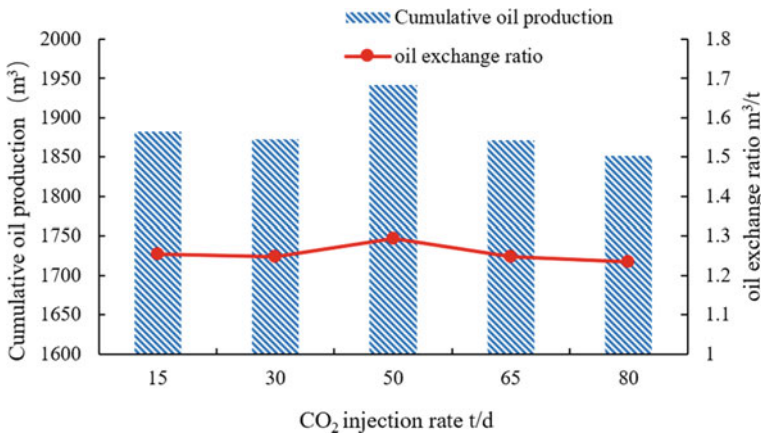


Fig. 52.14 Cumulative oil production and oil exchange ratio under different CO₂ injection rates

52.6 Conclusions

Combined with the experimental results of high pressure physical properties of typical tight reservoir X block, the dynamic law of CO₂ huff and puff mining tight reservoir is studied by numerical simulation method, and the sensitivity analysis of production parameters is carried out. The main understandings obtained under the research conditions of this paper are as follows:

- (1) When natural energy is used for depletion mining, the oil production decreases rapidly. CO₂ huff and puff can improve the decreasing trend of daily oil production in the later stage of depletion mining, significantly improve the daily oil production level, and the maximum daily oil production is increased by nearly 4 times. It can effectively supplement the formation energy, and the formation energy is increased by nearly 19% at the end of the first cycle of gas injection, so as to better improve the mining effect of tight reservoirs.
- (2) The higher the CO₂ cycle injection amount, the higher the cumulative oil production, but the oil change rate gradually decreases. A longer soaking time is beneficial to improve the effect of CO₂ huff and puff mining tight reservoirs. The oil production in the huff and puff stage fluctuates with the increase of gas injection rate.
- (3) In the selection of actual throughput parameters, the injection volume of CO₂ cycle and throughput rounds should not be too high or too low, and the oil production and oil change rate should be taken into account. The gas injection rate should not be too low, and the soaking time should be as large as possible. Therefore, when X block is mined, it is recommended to use a CO₂ cycle injection volume of 1500 t/d, a soaking time of 50 d, and a gas injection rate of 50 t/d, which can achieve better mining results.

Acknowledgements The authors gratefully acknowledge the Natural Science Foundation of Heilongjiang Province (Grant No. LH2022E023) for the support to present this paper.

References

1. Wei, J.G., Zhou, X., Zhou, J., Li, J., Wang, A.: CO₂ Huff-n-Puff after surfactant-assisted imbibition to enhance oil recovery for tight oil reservoirs. *Energy Fuels* **34**, 7058–7066 (2020)
2. Guoxin, L., Rukai, Z.: The development status, challenges and concerns of unconventional oil and gas in PetroChina. *Pet. Explor. Chin.* **25**(2), 1–13 (2020)
3. Xia, Z., Wang, X., Xu, R., Ren, W.: Tight oil reservoir production characteristics developed by CO₂ huff 'n' puff under well pattern conditions. *J. Pet. Explor. Prod. Technol.* **12**, 473–484 (2022)
4. Bai, M., Zhang, Z., Chen, Q., Weifeng, S., Du, S.: Research on the enhanced oil recovery technique of horizontal well volume fracturing and CO₂ Huff-n-Puff in tight oil reservoirs. *ACS Omega* **6**, 28485–28495 (2021)

5. Lei, Z., Wu, S., Yu, T., Ping, Y., Qin, H., Yuan, J., Zhu, Z., Su, H.: Simulation and optimization of CO₂ Huff-n-Puff processes in tight oil reservoir: a case study of Chang-7 tight oil reservoirs in ordos basin. Day 2 Wed, 24 Oct 2018
6. Li, L., Zhang, Y., Sheng, J.J.: Effect of the injection pressure on enhancing oil recovery in shale cores during the CO₂ Huff-n-Puff process when it is above and below the minimum miscibility pressure. *Energy Fuels* **31**, 3856–3867 (2017)
7. Gao, Y., Li, Q., He, X., Yu, H., Wang, Y.: Quantitative evaluation of shale-oil recovery during CO₂ Huff-n-Puff at different pore scales. *Energy Fuels* **35**(20), 16607–16616 (2021)
8. Wei, B., Zhong, M., Gao, K., Li, X., Zhang, X., Cao, J., Lu, J.: Oil recovery and compositional change of CO₂ Huff-n-Puff and continuous injection modes in a variety of dual-permeability tight matrix-fracture models. *Fuel* **276**, 117939 (2020)
9. Afari, S., Ling, K., Sennaoui, B., Maxey, D., Oguntade, T., Porlles, J.: Optimization of CO₂ Huff-n-Puff EOR in the Bakken formation using numerical simulation and response surface methodology. *J. Petrol. Sci. Eng.* **215**, 110552 (2022)
10. Ellafi, A., & Jabbari, H.: Understanding the mechanisms of Huff-n-Puff, CO₂-EOR in liquid-rich shale plays: Bakken case study. In: SPE Canada Unconventional Resources Conference. OnePetro (2020)
11. Tang, Y., Tang, J., Liu, Q., Wang, Y., Zheng, Z., Yuan, Y., He, Y.: Review on Phase behavior in tight porous media and microscopic flow mechanism of CO₂ Huff-n-Puff in tight oil reservoirs. *Geofluids* (2020)
12. Zhang, Y., Hu, J., Zhang, Q.: Simulation study of CO₂ Huff-n-Puff in tight oil reservoirs considering molecular diffusion and adsorption. *Energies* **12**(11), 2136 (2019)
13. Zhang, J., Zhang, H.X., Ma, L., Liu, Y., Zhang, L.: Performance evaluation and mechanism with different CO₂ flooding modes in tight oil reservoir with fractures. *J. Petrol. Sci. Eng.* **188**, 106950 (2020)
14. Hawthorne, S.B., Gorecki, C.D., Sorensen, J.A., Steadman, E.N., Harju, J.A., Melzer, S.: Hydrocarbon mobilization mechanisms from upper, middle, and lower Bakken reservoir rocks exposed to CO (2013)
15. Vega, B., O'Brien, W.J., Kovscek, A.R.: Experimental investigation of oil recovery from siliceous shale by miscible CO₂ injection (2010)
16. Zekri, A.Y., Al-Mehaideb, R.A., Shedid, S.A.: Displacement efficiency of supercritical CO₂ flooding in tight carbonate rocks under immiscible conditions. *Eurosurveillance* (2006)
17. Ma, Q., Yang, S., Lv, D., Wang, M., Chen, J., Kou, G., Yang, L.: Experimental investigation on the influence factors and oil production distribution in different pore sizes during CO₂ Huff-n-Puff in an ultra-high-pressure tight oil reservoir. *J. Pet. Sci. Eng.* (2019)
18. Song, C., Yang, D.: Experimental and numerical evaluation of CO₂ Huff-n-Puff processes in Bakken formation. *Fuel* **190**, 145–162 (2017)
19. Xue-Wu, W., Pufu, X., Zhengming, Y., Xuewei, L., Zhi-zeng, X., Li-qiang, W.: Laboratory and field-scale parameter optimization of CO₂ huff–n–puff with the staged-fracturing horizontal well in tight oil reservoirs. *J. Petrol. Sci. Eng.* **186**, 106703 (2020)
20. Bai, H., Zhang, Q., Li, Z., Li, B., Zhu, D., Zhang, L., Lv, G.: Effect of fracture on production characteristics and oil distribution during CO₂ Huff-n-Puff under tight and low-permeability conditions. *Fuel* **246**, 117–125 (2019)
21. Qian, K., Huang, Y., He, Y., Dou, X., Wu, X.: Experimental study on the oil recovery performance of CO₂ Huff-and-Puff process in fractured tight oil reservoirs. *Geofluids* (2022)
22. Kong, B., Wang, S., Chen, S.: Simulation and optimization of CO₂ Huff-and-Puff processes in tight oil reservoirs (2016)
23. Sun, R., Yu, W., Xu, F., Pu, H., Miao, J.: Compositional simulation of CO₂ Huff-n-Puff process in Middle Bakken tight oil reservoirs with hydraulic fractures. *Fuel* (2019)
24. Hao, M., Liao, S., Yu, G., Lei, X., Tang, Y.: Performance optimization of CO₂ Huff-n-Puff for multifractured horizontal wells in tight oil reservoirs. *Geofluids*, 1–13 (2020)

25. Li, L., Voskov, D., Yao, J., et al.: Multiphase transient analysis for monitoring of CO₂ flooding. *J. Petrol. Sci. Eng.* **160**, 537–554 (2018)
26. Sennaoui, B., Pu, H., Malki, M.L., Afari, A.S., Larbi, A.: Reservoir simulation study and optimizations of CO₂ Huff-n-Puff mechanisms in three forks formation. In: ARMA/DGS/SEG International Geomechanics Symposium. OnePetro (2022)

Chapter 53

Under the Blast Impact Load Study of Analytical Prediction Method for Plastic Response of Stiffened Plate



TianBo Huang, Shuai Zong, Kun Liu, JiaXia Wang, and ZhenGuo Gao

Abstract In this paper, a steel stiffened plate is used as the research object and its blast response under the action of air blast load is simulated and studied. Assuming that the deformation mode of the dynamic response of the reinforced plate is the same as the static limit deformation mode, the energy principle and the plastic deformation principle of the reinforced plate structure are used to analyze and obtain the motion control equations of its plastic dynamic response under the action of the blast impact load. Meanwhile, the simulation analysis of the stiffened plate under the air blast load is carried out using the finite element software ABAQUS, and the deformation theory of the reinforced plate structure is verified according to the simulation analysis results. It provides a reference for the design and impact resistance evaluation of steel stiffened plates.

Keywords Steel stiffened plate · Impact load · Plastic deformation · Analytical calculation · Numerical simulation

53.1 Introduction

Most ship structures are built with reinforced steel plates, which are vulnerable to aerial and underwater explosions during drills and combat. The blast wave acting on the structure of the ship can cause damage, deformation, or structural failure. For this reason, the design of reinforced plates under explosive loads is of great importance. Most of the previous work has focused on analyzing or numerically predicting the dynamic plastic response of reinforced plates and performing experimental studies [1–4]. Despite significant advances in research in this area, further theoretical analysis is required to gain a better understanding of the dynamic response mechanisms of reinforced plates under explosive loads, which can be used as a reference for

T. Huang · S. Zong · K. Liu (✉) · J. Wang · Z. Gao
School of Naval Architecture and Ocean Engineering, Jiang Jiangsu University of Science and Technology, Zhenjiang 212003, Jiangsu, China
e-mail: kunliu@just.edu.cn

initial design, safety research, and risk assessment of reinforced plates. Jones [5–7] pioneered the development of a rigid and perfect plastic method for predicting the permanent displacement of beams and resilient plates. This method was simplified to an approximate yield condition by plotting an exact yield curve. A simplified rigid-plastic model was proposed by Schubak et al. [8, 9] and Olson [10] for reinforced plates subjected to explosive loads. This method was later extended by Jiang and Olson [11] to predict the nonlinear dynamic response of underwater reinforced plates subjected to underwater blast loads. The computational results are consistent with the results of the numerical calculations. Zheng et al. [12, 13] recently investigated the dynamic elastic–plastic response of reinforced plates subjected to constrained explosive loads using experimental, theoretical, and numerical methods. Both the theoretical prediction and the numerical simulation considered the effects of the elastic–plastic effect as well as the position of the reinforcing bars, and the results were in good agreement with the experimental data. Fang et al. [14] recently analyzed the dynamic plastic response of bottom-reinforced plates of a ship under the loading of an underwater blast shock wave using the principle of energy.

Steel-reinforced plates are taken as the object of investigation in this study, and the structural strain criterion for the reinforced plates under static failure conditions is analyzed based on the relative stiffness of the reinforcing bars and the size of the loading peak. On this basis, by using the principles of a body's energy, the theory of the ultimate deformation of structures, and the plastic mechanics of structures, the equation of motion control for the dynamic plastic response of reinforced plates subjected to explosive impact loads is derived and verified using finite element simulation calculations, verifying and enhancing the reliability of the theoretical prediction method.

53.2 Energy Method—Simplified Theoretical Derivation

53.2.1 Determination of Deformation Modes

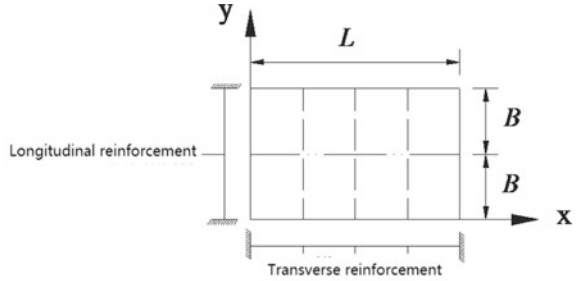
Model of theory analysis

The object of analysis is a rectangular reinforced plate (Fig. 53.1) with length L , width $2B$, thickness t , and a total of n transverse reinforcements and 1 longitudinal reinforcement.

Ribs and reinforced plates undergo plastic deformation together in a reinforced plate framework. For this reinforced plate type, because of the large number of secondary transverse components (i.e., ribs) and the small number of longitudinal resistance components (i.e., chords), as well as the relatively dense array, the following basic assumptions can be made to simplify the analysis [15].

The first fundamental assumption is that During the deformation of the reinforced plate, the deformation of the reinforcement and the plate at the same point are the

Fig. 53.1 Rectangular stiffened plate structure



same, and the reinforcement and plate both enter the plastic state, thus, the plastic hinge will continually pass through the plate and reinforcement;

The second fundamental assumption is that Within the same rigid region, the local grid depression between reinforcement bars is small (ignorable), and the strain of the reinforcing bars and plate is constant.

Under the assumptions above, the transverse reinforcement can be uniformly distributed along the surface of the plate, since the transverse reinforcement is unable to support torsional and axial force in the direction of plate length, and the reinforced plate as a whole can be simplified to an orthotropic plate with a single longitudinal reinforcement.

The ultimate twist moment and membrane force of the plate are, respectively, Before simplification:

$$M_0 = \frac{\sigma_y t^2}{4} \tag{53.1}$$

$$N_0 = \sigma_y t \tag{53.2}$$

where σ_y is the yield stress of the material.

The ultimate bending moment of the plate in the Y-direction and the ultimate membrane force in the X-direction remain unchanged after simplification:

$$M_{0y} = M_0 \tag{53.3}$$

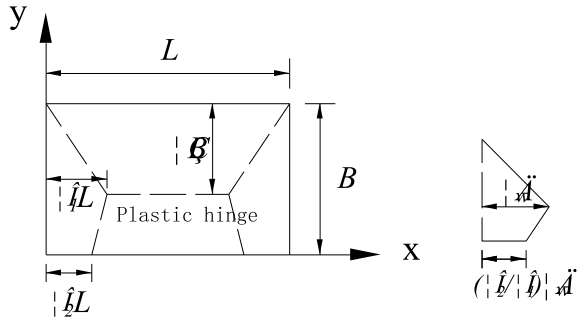
$$N_{0x} = N_0 \tag{53.4}$$

After simplification, the ultimate bending moment of the plate in the X direction and the ultimate membrane force in the Y direction are respectively:

$$M_{0x} = \frac{\sigma_y t_e^2}{4} \tag{53.5}$$

$$N_{0y} = \sigma_y t_e \tag{53.6}$$

Fig. 53.2 Ultimate deformation structure of the stiffened plate



This orthotropic plate has an equivalent thickness in the direction of:

$$t_e = t + \frac{nA_1}{L} \tag{53.7}$$

where \$A\$ is the cross-sectional area of a single transverse reinforcement.

Static Limit Analysis

If we consider that the deformation caused by the symmetric structure and symmetric loading is also symmetric, a 1/2 reinforced plate can be taken for analysis, and its mode of deformation can be determined by static boundary analysis methods. Experience in the analysis of various types of plate structures has led to the assumption that when the reinforced plate is in the ultimate state, its plastic hinges are distributed as shown in Fig. 53.2. \$\xi_1\$, \$\xi_2\$ and \$\eta\$ are dimensionless parameters for determining the position of plastic hinges [16–21].

This is the most general form of the hypothesis, from which it can be derived that longitudinal reinforcement has only one plastic hinge (\$\xi_2 = 0.5\$), or that no plastic deformation occurs (\$\xi_2 = 0\$).

Let \$q\$ be the uniformly distributed external transverse load, and let be the maximum transverse strain on the plate, the total virtual work done by the external force may be obtained:

$$W = qLB\delta w \left(\frac{3\xi_1 - 2\xi_1^2 + (1 - \eta)(3\xi_2 - 2\xi_1\xi_2 - 2\xi_2^2)}{6\xi_1} \right) \tag{53.8}$$

If the degree of boundary fixing is arbitrary, represented by the parameter \$\epsilon\$, then.

- (1) when the boundary is fully fixed, \$\epsilon = 1\$
- (2) when the boundary is simply supported, \$\epsilon = 0\$

The total virtual work done by the internal force is expressed as:

$$\left\{ \begin{array}{l} \frac{M_0 \delta w}{\xi_1 L B} \times (1 + \varepsilon)(k_1 \xi_1 L^2 + 2B^2 + k_2 L B) \quad \eta = 1 \\ \frac{M_0 \delta w}{\xi_1 \eta (1 - \eta) L B} \times (((1 + \varepsilon)(1 - \eta) + 2\eta)k_1 \xi_1 L^2 + 2\eta(1 + \varepsilon)(1 - \eta)B^2) \quad \xi_2 = 0 \\ \frac{M_0 \delta w}{\xi_1 \eta (1 - \eta) L B} \times ((\xi_1(1 + \varepsilon)(1 - \eta) + 2\eta(1 - 2\xi_2)(\xi_1 - \xi_2))k_1 L^2 + \eta(1 + \varepsilon)(1 - \eta)(2B^2 + k_2 L B)) \quad \xi_2 > 0, \eta < 1 \end{array} \right. \quad (53.9)$$

In this equation: $k_1 = \frac{M_{0x}}{M_0}$, $k_2 = \frac{M_b}{M_0 L}$
 M_b is the ultimate torsional moment of longitudinal reinforcement.

$$\beta = \frac{B}{L}, \lambda_1 = \frac{k_1}{\beta^2}, \lambda_2 = 2 + \frac{k_2}{\beta} \quad (53.10)$$

λ_1 and λ_2 represent the stiffness characteristics of the transverse reinforcement and longitudinal reinforcement, respectively.

From $W = U$, the load can be obtained:

$$q = \frac{6M_0 \beta}{L B} \cdot \left\{ \begin{array}{l} \frac{(1+\varepsilon)(\lambda_1 \xi_1 + \lambda_2)}{3\xi_1 - 2\xi_1^2} \eta = 1 \\ ((1+\varepsilon)(1-\eta) + 2\eta)\xi_1 \lambda_1 + 2\eta(1+\varepsilon)(1-\eta) \xi_2 = 0 \\ \frac{\eta(1-\eta)(3\xi_1 - 2\xi_1^2)}{(\xi_1(1+\varepsilon)(1-\eta) + 2\eta(1 - 2\xi_2)(\xi_1 - \xi_2))\lambda_1 + \eta(1+\varepsilon)(1-\eta)\lambda_2} \xi_2 > 0, \eta < 1 \end{array} \right. \quad (53.11)$$

The principle of limit analysis is that the true limit state deformation mode should cause the outer limit load to do the least work, i.e. the corresponding outer load should be the minimum.

We can discuss it in the three cases below:

(1) when $\eta = 1, \xi_1 = \xi_2$

According to $\frac{\partial q}{\partial \xi_1} = 0$, the hinge position of the plate frame in the limit state can be obtained:

$$\xi_p = \frac{\sqrt{\lambda_2^2 + \frac{3}{2}\lambda_1 \lambda_2 - \lambda_2}}{\lambda_1} \quad (53.12)$$

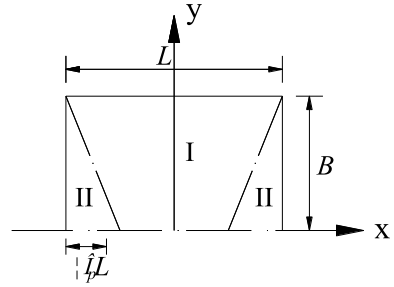
The corresponding limit load is:

$$q_c = \frac{6M_0 \lambda_1 \beta (1 + \varepsilon)}{(3 - 4\xi_p) L B} \quad (53.13)$$

In this mode, it is necessary to have $\xi_p \leq \frac{1}{2}$, so one can get (Fig. 53.3):

$$\frac{\lambda_2}{\lambda_1} \leq \frac{1}{2} \quad (53.14)$$

Fig. 53.3 Deformation mode I



(2) When, $\xi_2 > 0, \eta < 1$:

According to $\begin{cases} \frac{\partial q}{\partial \xi_1} = 0 \\ \frac{\partial q}{\partial \xi_2} = 0 \\ \frac{\partial q}{\partial \eta} = 0 \end{cases}$ and $\begin{cases} 0 \leq \xi_1 \leq \frac{1}{2} \\ 0 \leq \xi_2 \leq \frac{1}{2} \end{cases}$ the hinge position when $\xi_1 = \xi_2 = \frac{1}{2}$ can be obtained:

$$\eta_p = \frac{\sqrt{\lambda_1^2 + 6\lambda_1\lambda_2} - \lambda_1}{2\lambda_2} \tag{53.15}$$

The corresponding limit load is:

$$q_c = \frac{6M_0\lambda_1\beta(1 + \varepsilon)}{\eta_p^2 LB} \tag{53.16}$$

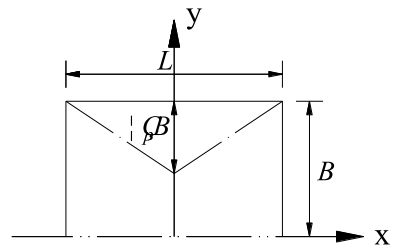
According to $\eta_p \leq 1$, the condition for this mode is as follows (Fig. 53.4):

$$\frac{\lambda_2}{\lambda_1} \geq \frac{1}{2} \tag{53.17}$$

(3) when, $\xi_2 = 0$:

The longitudinal reinforcement in this case does not experience plastic deformation, only when λ_2 is very large.

Fig. 53.4 Deformation mode II



According to $\frac{\partial q}{\partial \eta} = 0$, one can get:

$$\eta_p = \frac{\sqrt{2(1 + \varepsilon)} - (1 + \varepsilon)}{1 - \varepsilon} \tag{53.18}$$

From the equation above, we can see that is related only to the degree of boundary fixing.

When, $\varepsilon = 0$, $\eta_p = \sqrt{2} - 1$

When, $\varepsilon = 1$, $\lim_{\varepsilon \rightarrow 1} \eta_p = \frac{1}{2}$

By substituting $\frac{\partial q}{\partial \xi_1} = 0$ into η_p , we get:

$$\varepsilon_1 = \frac{(1 + \varepsilon)(3 + \varepsilon - 2\sqrt{2(1 + \varepsilon)})}{(1 - \varepsilon)^2} \tag{53.19}$$

When, $\varepsilon = 0$, $\varepsilon_1 = 3 - 2\sqrt{2}$

When, $\varepsilon = 1$, $\lim_{\varepsilon \rightarrow 1} \varepsilon_1 = \frac{1}{4}$

Achieved plastic hinge:

$$\xi_p = \frac{\sqrt{4\varepsilon_1^2 + 3\varepsilon_1\lambda_1 - 2\varepsilon_1}}{\lambda_1} \tag{53.20}$$

The corresponding limit load is:

$$q_c = \frac{6M_0\lambda_1\beta(1 + \varepsilon)}{(3 - 4\xi_p)\varepsilon_1 LB} \tag{53.21}$$

If the minimum load condition is satisfied, then when this deformation pattern occurs, the load obtained in (53.3) should be smaller than the load obtained in (53.2), and the solution to the inequality can be obtained:

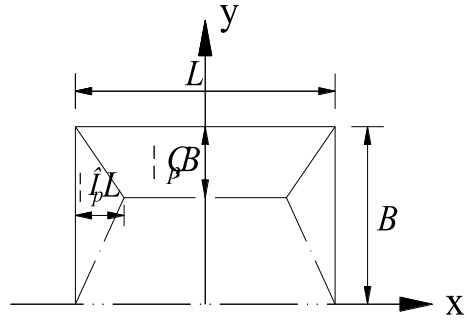
$$\frac{\lambda_2}{\lambda_1} > \lambda^* \tag{53.22}$$

Which (Fig. 53.5):

$$\lambda^* = \frac{(\sqrt{4\varepsilon_1 + 3\lambda_1} - 2\sqrt{\varepsilon_1\lambda_1} + 2\sqrt{\varepsilon_1})(\sqrt{4\varepsilon_1 + 3\lambda_1} + 2\sqrt{\varepsilon_1})}{6\varepsilon_1\lambda_1} \tag{53.23}$$

It can be seen from the above analysis that depending on the different ratios of vertical and horizontal reinforcement stiffnesses, once the reinforced plate is in the static failure state, there are three possible strain patterns I, II, and III, and the corresponding failure loads for these three patterns are as follows:

Fig. 53.5 Deformation mode III



(1) If $\frac{\lambda_2}{\lambda_1} \leq \frac{1}{2}$, it is deformation pattern I: $\xi_p = \frac{\sqrt{\lambda_2^2 + \frac{3}{2}\lambda_1\lambda_2 - \lambda_1}}{\lambda_1}$;

The ultimate loads are as follows: $q_c = \frac{6M_0\lambda_1\beta(1+\varepsilon)}{(3-4\xi_p)LB}$

(2) If $\frac{1}{2} \leq \frac{\lambda_2}{\lambda_1} \leq \lambda^*$, it is deformation pattern II: $\eta_p = \frac{\sqrt{\lambda_1^2 + 6\lambda_1\lambda_2 - \lambda_1}}{2\lambda_2}$

The ultimate loads are as follows: $q_c = \frac{6M_0\lambda_1\beta(1+\varepsilon)}{\eta_p^2 LB}$

(3) If $\xi_2 = 0$, this is the deformation scheme III:

$$\eta_p = \frac{\sqrt{2(1+\varepsilon)} - (1+\varepsilon)}{1-\varepsilon}, \xi_p = \frac{\sqrt{4\varepsilon_1^2 + 3\varepsilon_1\lambda_1 - 2\varepsilon_1}}{\lambda_1}$$

The ultimate load is: $q_c = \frac{6M_0\lambda_1\beta(1+\varepsilon)}{(3-4\xi_p)\varepsilon_1 LB} g$

53.2.2 Dynamic Response Analysis of Plasticity

Plastic hinges will move across the structure during the dynamic plastic response of the structure. As the final residual strain profile of the dynamic response is often close to the static ultimate strain profile, and the energy dissipated by plastic hinge motion is not large, the structure can be assumed to respond in the strain pattern to the static ultimate condition, and remain unchanged throughout the dynamic response process [22–25].

The yield test adopts Johansen’s outer square yield condition, i.e. at the time of the yield,

$$\frac{M}{M_0} = \pm 1 \frac{N}{N_0} = \pm 1 \tag{53.24}$$

In the equation, M_0 and N_0 are the ultimate bending moment and membrane force or the ultimate bending moment and axial force of the longitudinal reinforcement in a certain direction of the plate.

Movement Equation

Applying the Jones-Sawczuk control equation to a reinforced plate, it can be concluded that the total virtual power of external forces is equal to the total virtual power of internal forces:

$$\begin{aligned} & \int_A (q - \rho_1 \ddot{w}) \dot{w} dA + \int_l (-\rho_2 \ddot{w}) \dot{w} dl \\ &= \sum_{i=1}^{m_1} \int_{l_i} (Nw - M) \dot{\theta}_i dl_i + \sum_{j=1}^{m_2} (N_r w - M_r) \dot{\theta}_j \end{aligned} \tag{53.25}$$

In the equation, M and N represent the bending moment and membrane strength of the plate; M_r and N_r represent the bending moment and axial strength of the longitudinal armature; ρ_1 is the unit mass of the surface of the plate; ρ_2 is the mass per unit length of the longitudinal reinforcement; A is the surface area of the plate; l_i is the length of the i th hinge; θ_i is the relative angular velocity of the i th joint on the plate; θ_j is the relative angular velocity of the j th plastic hinge relative to the longitudinal armature; m_1 is the number of hinges on the plate; m_2 is the number of plastic hinges on the reinforcement in the longitudinal direction.

For example, the first deformation mode:

Let $w_0(t)$ be the maximum transverse deformation on the plate at any time t , then the deformation field can be represented as.

$$\text{Rigid region I: } w(x, y, t) = \begin{cases} w_0(t) & 0 \leq x \leq \frac{L}{2} - \xi_p L \\ (1 - \frac{x}{B}) w_0(t) & \frac{L}{2} - \xi_p L \leq x \leq \frac{L}{2} \end{cases} \tag{53.26}$$

$$\text{Rigid region II: } w(x, y, t) = \frac{1 - \frac{2x}{L}}{2\xi_p} w_0(t) \tag{53.27}$$

Substituting the expression for w and the yield condition into the control equation, and defining the following dimensionless parameters

$$\tau = t \sqrt{\frac{M_0}{\rho L^2 h^2}} \quad p(\tau) = \frac{q(\tau) L^2}{M_0} \tag{53.28}$$

Then the motion equation corresponding to the first deformation mode is:

$$\left(\frac{(1 - \xi_p)\mu_1}{3} + \frac{(3 - 4\xi_p)\mu_2}{6\beta} \right) \ddot{u} + 4 \left(\frac{(1 - \xi_p)R_1}{\beta^2} + \frac{\beta + R_2}{\xi_p \beta} \right) u$$

$$= \frac{3 - 2\xi_p}{6} p(\tau) - (1 + \varepsilon) \left(\lambda_1 + \frac{\lambda_2}{\xi_p} \right) \tag{53.29}$$

In the equation, $R_1 = \frac{N_{0v}}{N_0}$ $R_2 = \frac{N_b}{N_0L}$ $\mu_1 = \frac{\rho_1}{\rho h}$ $\mu_2 = \frac{\rho_2}{\rho hL}$

Likewise, the equations of motion corresponding to the other two modes of deformation are respectively.

$$\begin{aligned} & \left(\frac{(1 - \frac{\eta_p}{2})\mu_1}{3} + \frac{\mu_2}{6\beta} \right) \ddot{u} + 4 \left(\frac{R_1}{2\eta_p\beta^2} - 2\eta_p + \frac{4\beta - 2R_2}{\beta} \right) u \\ &= \frac{3 - \eta_p}{6} p(\tau) - (1 + \varepsilon) \left(\frac{\lambda_1}{\eta_p} + 2\lambda_2 \right) \end{aligned} \tag{53.30}$$

$$\frac{(1 - \xi_p)\mu_1}{3} \ddot{u} + 4 \left(\frac{(1 - \xi_p)R_1}{\eta_p(1 - \eta_p)\beta^2} + \frac{1}{\xi_p} \right) u = \frac{3 - 2\xi_p}{6} p(\tau) - (1 + \varepsilon) \left(\frac{\lambda_1}{\varepsilon_1} + \frac{2}{\xi_p} \right) \tag{53.31}$$

The equations of motion for the three modes of deformation can be represented uniformly as a second-order ordinary differential equation.

$$D_1\ddot{u} + D_2u = D_3p(\tau) - D_4 \tag{53.32}$$

Plastic Strain

The explosion load [25] can be represented by an exponential form:

$$p(\tau) = \begin{cases} p_m \left(1 - \frac{\tau}{\tau_d} \right) e^{-\frac{\alpha_0\tau}{\tau_d}} & 0 \leq \tau \leq \tau_d \\ 0 & \tau > \tau_d \end{cases} \tag{53.33}$$

Is the peak of charge in the equation; is the duration of action; is the decay coefficient ($\alpha_0 = 0$ is a triangular load).

The equation of motion corresponding to the deformation mode, i.e., the second order ordinary differential equation, is split into two stages for the solution, depending on the characteristics of the blast load.

(1) The first stage ($0 \leq \tau \leq \tau_d$)

From the initial conditions: $u(0) = 0$ $\dot{u}(0) = 0$

The deformation at any point in time is obtained.:

$$u_1(\tau) = \alpha_1 \cos(\omega\tau) + \alpha_2 \sin(\omega\tau) + (\alpha_3 + \alpha_4\tau) e^{-\frac{\alpha_0\tau}{\tau_d}} - \frac{D_4}{D_2} \tag{53.34}$$

In the equation, $\omega = \sqrt{\frac{D_2}{D_1}}$;

$$\alpha_1 = \frac{D_4}{D_2} - \alpha_3;$$

$$\alpha_2 = \frac{\frac{\alpha_0 \alpha_3}{\tau_d} - \alpha_4}{\omega};$$

$$\alpha_3 = -\alpha_4 \tau_d \left(1 + \frac{2D_1 \alpha_0 \alpha_4}{D_3 p_m \tau_d} \right);$$

$$\alpha_4 = -\frac{D_3 p_m \tau_d}{D_1 \alpha_0^2 + D_2 \tau_d^2}$$

If the peak load is not significant or the duration is longer, the answer can terminate in the first step, and the time $\tau_f = \tau_s$ can be obtained based on $\dot{u}_1(\tau_s) = 0$. Substituting τ_s into Eq. (53.2–53.31), we can calculate the maximum residual strain.

If $\tau_s > \tau_d$ is obtained, when $\tau > \tau_d$, the response enters the second stage, and the maximum deformation $u_1(\tau_d)$ on the plate at the end of the first stage and the velocity $\dot{u}_1(\tau_d)$ at that point can be obtained from Eq. (53.2–53.31).

(2) The second stage ($\tau > \tau_d$)

In this stage, there is no external load, and the initial conditions are:

$$u(\tau_d) = u_1(\tau_d)\dot{u}(\tau_d) = \dot{u}_1(\tau_d) \tag{53.35}$$

The time of motion termination is:

$$\tau_f = \tau_d + \frac{\arctan\left(\frac{\beta_2}{\beta_1}\right)}{\omega} \tag{53.36}$$

In the equation, $\beta_1 = u_1(\tau_d) + \frac{D_4}{D_2}$; $\beta_2 = \frac{\dot{u}_1(\tau_d)}{\omega}$
 The maximum plastic deformation is:

$$u(\tau_f)_1 \cos\omega(\tau_f - \tau_d)_2 \sin\omega(\tau_f - \tau_d) \frac{D_4}{D_2 \max} \tag{53.37}$$

53.2.3 Example Analysis

Calculation Model

Building on the energy method theory above, a reinforced plate structure with one longitudinal reinforcement and several transverse reinforcements is taken as the object of research to investigate the dynamic response of the structure under an explosive load. Figure 53.1 shows the geometric model of the analyzed structure.

Table 53.1 Longitudinal dimensions of strengthening

No.	Height h_2 /mm	Width b_2 /mm
1	80	4
2	180	4
3	300	8

We take the limit of the plate reinforced above with one longitudinal reinforcement and several transverse reinforcements as a fixed support, i.e., the size of the plate and the transverse reinforcement are the same, while the longitudinal reinforcement is taken in three different sizes according to the possible deformation modes, see Table 53.1.

- (1) Table 53.2 shows the main parameters of the truss structure.
- (2) Assuming that the constitutive relationship of the material is elastic-ideal plasticity, the key performance parameters are as follows (Table 53.3).

Based on static limit theory, it is assumed that the deformation mode of the dynamic response is the same as the deformation mode of static limit state. Depending on the material’s elastic–plastic constitutive relation, the mode of the deformation mechanism of the structure and the discriminative condition of that mode of deformation can be derived by the energy method. Using the actual reinforced plate framework from Fig. 53.6 as an example, it is computationally feasible to determine the static limit strain mode of different plate frame designs, i.e., fixed four-sided support and plate and transverse reinforcement with the same size and longitudinal reinforcement with different sizes. The corresponding parameters are simultaneously provided for the subsequent analysis of the dynamic plastic response of the reinforced plate subjected to an explosive load based on the Jones-Sawczuk control equations.

Table 53.2 The main parameters of the plate structure

Component name	Size
Plate	$L \times B \times t = 1600 \text{ mm} \times 500\text{mm} \times 4\text{mm}$
Height of transverse reinforcement	$h_1 = 50 \text{ mm}$
Width of transverse reinforcement	$b_1 = 4 \text{ mm}$
Number of transverse reinforcement	$n = 7$

Table 53.3 The main material parameters of the plate structure

Parameter name	Numerical value
Elastic modulus	$E = 210 \text{ GPa}$
Material density	$\rho = 7850 \text{ kg/m}^3$
Yield limit	$\sigma_y = 235 \text{ MPa}$
Poisson’s ratio	$\nu = 0.3$

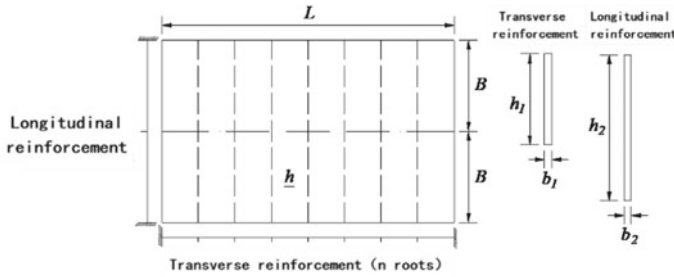


Fig. 53.6 Geometric model

Determining Deformation Modes

Under the basic assumptions of Sect. 53.2.1, if the transverse reinforcement is distributed according to the area along the surface of the panel, equivalent panel thicknesses of the simplified reinforced panel may be obtained:

$$h_e = h + \frac{nA_1}{L} = 4 + \frac{7 \times (50 \times 4)}{1600} = 4.875 \text{ mm} \tag{53.38}$$

If the constitutive relationship of the material is assumed to be elastic-ideal plasticity, the ultimate bending moment of the simplified panel can be obtained based on the material’s elastic limit strength $\sigma_y = 235 \text{ MPa}$:

$$M_0 = \frac{\sigma_y h^2}{4} = \frac{235 \times 4^2}{4} = 940 \text{ N} \tag{53.39}$$

The ultimate bending moment of the simplified panel in the X-direction is:

$$M_{0x} = \frac{\sigma_y h_e^2}{4} = \frac{235 \times 4.875^2}{4} = 1396.23 \text{ N} \tag{53.40}$$

The ultimate bending moment of the longitudinal reinforcement is $M_b = \frac{\sigma_y b_2 h_2^2}{4}$, it can be known that for different sizes of longitudinal reinforcement, their ultimate bending moment is different. Taking the first type of longitudinal reinforcement in Table 53.1 as an example, the ultimate bending moment is calculated to obtain the longitudinal stiffness characteristics of the simplified reinforced panel, thereby determining the deformation mode of the panel. That is, when the height $h_2 = 80 \text{ mm}$ and width $b_1 = 4 \text{ mm}$ of the longitudinal reinforcement is, the ultimate bending moment is:

$$M_b = \frac{\sigma_y b_2 h_2^2}{4} = \frac{235 \times 4 \times 80^2}{4} = 1504000 \text{ N mm} \tag{53.41}$$

Consequently, the coefficients, k_1, k_2 in expression (53.1–53.6) for the total virtual work done by the internal forces are respectively:

$$k_1 = \frac{M_{0x}}{M_0} = \frac{1396.23}{940} = 1.4854 \quad (53.42)$$

$$k_2 = \frac{M_b}{M_0L} = \frac{1504000}{940 \cdot 1600} = 1 \quad (53.43)$$

The panel form factor is:

$$\beta = \frac{B}{L} = \frac{500}{1600} = 0.3125 \quad (53.44)$$

Therefore, the parameters λ_1 and λ_2 characterize the stiffness characteristics of the transverse reinforcement and the longitudinal reinforcement, respectively, as follows:

$$\lambda_1 = \frac{k_1}{\beta^2} = \frac{1.4854}{0.3125^2} = 15.21 \quad (53.45)$$

$$\lambda_2 = 2 + \frac{k_2}{\beta} = 2 + \frac{1}{0.3125} = 5.2 \quad (53.46)$$

So, $\frac{\lambda_2}{\lambda_1} = \frac{5.2}{15.21} = 0.34$

Similarly, it can be obtained that:

The reinforced panel with the second type of longitudinal reinforcement in Table 53.1: $\lambda_1 = 15.21$, $\lambda_2 = 18.2$, $\frac{\lambda_2}{\lambda_1} = 1.20$.

The reinforced panel with the third type of longitudinal reinforcement in Table 53.1: $\lambda_1 = 15.21$, $\lambda_2 = 92$, $\frac{\lambda_2}{\lambda_1} = 6.05$.

From the values of 3 sets of λ_1 and λ_2 , it can be seen that because the three types of panels have the same number and size of transverse reinforcement, the λ_2 values of the three panels are the same, that is, the transverse stiffness characteristics of the panels are the same. However, the longitudinal reinforcement of the three panels is different, and as the size of the longitudinal reinforcement increases, the λ_2 value also increases accordingly, indicating that the longitudinal stiffness characteristics of the panels are related to the longitudinal reinforcement, and the larger the size of the longitudinal reinforcement, the greater the longitudinal stiffness of the panels. The longitudinal and transverse stiffness characteristics of the panels determine the deformation mode of the panels, so the size of the $\frac{\lambda_2}{\lambda_1}$ value can be used as a parameter to determine the deformation mode of the panels.

Based on the fixed support of the reinforced panel on all four sides, i.e. $\varepsilon = 1$, at this time $\varepsilon_1 = \frac{1}{4}$, then Eq. (53.2–53.20) can be simplified to:

$$\lambda^* = \frac{2(\sqrt{1+3\lambda_1} - \sqrt{\lambda_1} + 1)(\sqrt{1+3\lambda_1} + 1)}{3\lambda_1} \quad (53.47)$$

It can be seen that the value of λ^* is only related to the value of λ_1 at this time. Since the λ_1 values of the three types of panels are the same, the λ^* values of the three panels are all:

$$\lambda^* = \frac{2(\sqrt{1 + 3 \times 15.21} - \sqrt{15.21 + 1})(\sqrt{1 + 3 \times 15.21} + 1)}{3 \times 15.21} = 1.35 \quad (53.48)$$

Based on the discussion in Sect. 53.2.1,

For the first type of bracket in Table 53.1, because of $\frac{\lambda_2}{\lambda_1} \leq \frac{1}{2}$, it is a deformation mode I;

For the second type of bracket in Table 53.1, because of $\frac{1}{2} \leq \frac{\lambda_2}{\lambda_1} \leq \lambda^*$, it is a deformation mode II;

For the third type of bracket in Table 53.1, because of $\frac{\lambda_2}{\lambda_1} > \lambda^*$, it is a deformation mode III.

Dynamic Response Analysis of Plasticity

According to the analysis of the plastic dynamic response of the reinforced plate subjected to blast loading in Sect. 53.2.2, the equation of motion for this mode of deformation can be obtained by substituting the strain field and the specific strain mode yield criterion of the reinforced plate into the Jones-Sawczuk control equation. The explosive charge, which is represented as an exponential equation, is then substituted into the above equation of motion, where the parameters of the explosive charge representation, peak value, and duration are dimensionless. The equation of motion is then converted to a second-order constant coefficient differential equation, and the expression for the strain of the reinforced plate at any time can be obtained by solving the second-order constant coefficient differential equation. However, if the peak value of the explosive charge is not large or the duration of the detonation is long, the time corresponding to the maximum deformation can be obtained by finding the zero point of the first derivative of the above deformation expression, and the maximum plastic deformation can be obtained. If the resulting zero-point value is greater than the duration of the outburst, we take the state of the support at the end of the explosion as the initial condition for the next stage of the motion, and solve again for the maximum plastic strain through the expression.

From the theory above, the process of solving for the maximum plastic strain for all three strain modes can be known to be fundamentally the same, only the parameters in the motion equation and equation solution expression are different. Therefore, taking the first type of reinforced plate in Table 53.1 as an example, the dynamic response of the plate under explosive load when it moves in deformation mode I is calculated below.

If the first bracket type is in strain mode I, then its hinge position is:

$$\xi_p = \frac{\sqrt{\lambda_2^2 + \frac{3}{2}\lambda_1\lambda_2} - \lambda_2}{\lambda_1} = \frac{\sqrt{5.2^2 + \frac{3}{2} \times 15.21 \times 5.2} - 5.2}{15.21} = 0.45 \quad (53.49)$$

The motion equation corresponding to deformation mode I is Eq. (53.2–53.26):

$$\begin{aligned} & \left(\frac{(1 - \xi_p)\mu_1}{3} + \frac{(3 - 4\xi_p)\mu_2}{6\beta} \right) \ddot{u} + 4 \left(\frac{(1 - \xi_p)R_1}{\beta^2} + \frac{\beta + R_2}{\xi_p\beta} \right) u \\ & = \frac{3 - 2\xi_p}{6} p(\tau) - (1 + \varepsilon) \left(\lambda_1 + \frac{\lambda_2}{\xi_p} \right) \end{aligned} \quad (53.50)$$

Simplify the ultimate membrane force of the front plate to:

$$N_0 = \sigma_y h = 235 \times 4 = 940 \text{ N/mm} \quad (53.51)$$

Simplify the ultimate membrane force of the rear plate in the direction of y to:

$$N_{0y} = \sigma_y h_e = 235 \times 4.875 = 1145.625 \text{ N/mm} \quad (53.52)$$

The ultimate axial force of the longitudinal reinforcement is:

$$N_b = \sigma_y b_2 h_2 = 235 \times 4 \times 80 = 75200 \text{ N} \quad (53.53)$$

Therefore, the coefficients R_1 and R_2 in Eq. (53.2–53.26) are respectively:

$$R_1 = \frac{N_{0y}}{N_0} = \frac{1145.625}{940} = 1.22 \quad (53.54)$$

$$R_2 = \frac{N_b}{N_0 L} = \frac{75200}{940 \times 1600} = 0.05 \quad (53.55)$$

Because ρ_1 is the mass per unit area of the plate and ρ_2 is the mass per unit length of the longitudinal reinforcement, the coefficients μ_1 and μ_2 in Eq. (53.26) are respectively:

$$\mu_1 = \frac{\rho_1}{\rho h} = \frac{(2\rho L B h)}{(2LB)} = 1 \quad (53.56)$$

$$\mu_2 = \frac{\rho_2}{\rho h L} = \frac{(\rho b_2 h_2 L)}{\rho h L} = \frac{b_2 h_2}{h L} = \frac{4 \times 80}{4 \times 1600} = 0.05 \quad (53.57)$$

At this time, the parameters ξ_p , β , μ_1 , μ_2 , R_1 , R_2 , ε , λ_1 , λ_2 involved in the coefficients before each term in Eq. (53.26) are known, then the coefficients before each term in the second-order constant coefficient differential Eq. (53.29) are respectively:

$$D_1 = \frac{(1 - \xi_p)\mu_1}{3} + \frac{(3 - 4\xi_p)\mu_2}{6\beta}$$

$$= \frac{(1 - 0.45) \times 1}{3} + \frac{(3 - 4 \times 0.45) \times 0.05}{6 \times 0.3125} = 0.215 \quad (53.58)$$

$$D_2 = 4 \left(\frac{(1 - \xi_p) R_1}{\beta^2} + \frac{\beta + R_2}{\xi_p \beta} \right) \\ = 4 \times \left(\frac{(1 - 0.45) \times 1.22}{0.3125^2} + \frac{0.3125 + 0.05}{0.45 \times 0.3125} \right) = 37.647 \quad (53.59)$$

$$D_3 = \frac{3 - 2\xi_p}{6} = \frac{3 - 2 \times 0.45}{6} = 0.349 \quad (53.60)$$

$$D_4 = (1 + \varepsilon) \left(\lambda_1 + \frac{\lambda_2}{\xi_p} \right) = (1 + 1) \times \left(15.21 + \frac{5.2}{0.45} \right) = 53.446 \quad (53.61)$$

Equations (53.30) represent the process of how the impact pressure of the explosive charge changes with time via a function relation, where the important representational parameters are the peak pressure, duration, and decay coefficient. One way to simplify the analytic calculation is to let the decay coefficient $\alpha_0 = 0$, in which the exponential shape of the explosive charge is transformed into a triangular charge, i.e., a charge-time relation in which the initial time is the peak pressure and the pressure decays linearly to zero with time. Equations (53.30) can be simplified as follows;

$$p(\tau) = \begin{cases} p_m \left(1 - \frac{\tau}{\tau_d} \right) & 0 \leq \tau \leq \tau_d \\ 0 & \tau > \tau_d \end{cases} \quad (53.62)$$

As the equations of motion corresponding to the deforming mode have been dimensionless, it is also necessary that the representation parameters for the above explosive charge be dimensionless.

Suppose for the moment that a triangular load with a peak pressure of $q_m = 0.8$ MPa and a duration of $t_d = 1.2$ ms is applied to the reinforced plate carrier, then q_m and t_d are dimensionless:

$$p_m = \frac{q_m L^2}{M_0} = \frac{0.8 \times 1600^2}{940} = 2178.72 \quad (53.63)$$

$$\tau_d = t_d \sqrt{\frac{M_0}{\rho L^2 h^2}} = 1.2 \times \sqrt{\frac{940 \times 10^{-3}}{7.85 \times 10^{-6} \times 1600^2 \times 4^2}} = 0.0649 \quad (53.64)$$

At this time, the relevant coefficients in the expression (53.31) of the solution of the motion equation involve the parameters α_0 , D_1 , D_2 , D_3 , D_4 , p_m , τ_d , which are all known, so the relevant coefficients in the equation are respectively:

$$\omega = \sqrt{\frac{D_2}{D_1}} = \sqrt{\frac{37.647}{0.215}} = 13.24 \quad (53.65)$$

$$\alpha_4 = -\frac{D_3 p_m \tau_d}{D_1 \alpha_0^2 + D_2 \tau_d^2} = -\frac{0.349 \times 2178.72}{37.647 \times 0.0649} = -311.69 \quad (53.66)$$

$$\alpha_3 = -\alpha_4 \tau_d \left(1 + \frac{2D_1 \alpha_0 \alpha_4}{D_3 p_m \tau_d} \right) = -(-311.69) \times 0.0649 = 20.22 \quad (53.67)$$

$$\alpha_2 = \frac{\frac{\alpha_0 \alpha_3}{\tau_d} - \alpha_4}{\omega} = \frac{-311.69}{13.24} = 23.53 \quad (53.68)$$

$$\alpha_1 = \frac{D_4}{D_2} - \alpha_3 = \frac{53.446}{37.647} - 20.22 = -18.80 \quad (53.69)$$

At this time, the expression (53.1–53.31) of the solution of the motion equation can be expressed as:

$$u_1(\tau) = -18.8 \cos(13.24\tau) + 23.53 \sin(13.24\tau) - 311.69\tau + 18.8 \quad (53.70)$$

Taking the first derivative of the above equation gives:

$$\dot{u}_1(\tau) = 248.91 \sin(13.24\tau) + 311.69 \cos(13.24\tau) - 311.69 \quad (53.71)$$

Then, $u_1(\tau_d) = 4.13$, $\dot{u}_1(\tau_d) = 80.46$;

Thus, we can obtain:

$$\beta_1 = u_1(\tau_d) + \frac{D_4}{D_2} = 4.13 + \frac{53.446}{37.647} = 5.55 \quad (53.72)$$

$$\beta_2 = \frac{\dot{u}_1(\tau_d)}{\omega} = \frac{80.46}{13.24} = 6.07 \quad (53.73)$$

Therefore, the time of maximum deformation is:

$$\tau_f = \tau_d + \frac{\arctan\left(\frac{\beta_2}{\beta_1}\right)}{\omega} = 0.0649 + \frac{\arctan\left(\frac{6.07}{5.55}\right)}{13.24} = 0.128 \quad (53.74)$$

From Eq. (53.34), the maximum plastic deformation corresponding to this time is:

$$\begin{aligned} & u_1 \cos \omega(\tau_f - \tau_d) + \frac{D_4}{D_2} \sin \omega(\tau_f - \tau_d) \\ &= 5.55 \times \cos(13.24 \times (0.128 - 0.0649)) \\ &+ 6.07 \times \sin(13.24 \times (0.128 - 0.0649)) - \frac{53.446}{37.647} = 6.81 \end{aligned} \quad (53.75)$$

The τ_f and u_{\max} obtained above are dimensionless, so the actual values are:

$$w_0 = u_{\max} \quad (53.76)$$

$$t_f = \tau_f \sqrt{\frac{\rho L^2 h^2}{M_0}} = 0.128 \times \sqrt{\frac{7.85 \times 10^{-6} \times 1600^2 \times 4^2}{940 \times 10^{-3}}} = 2.4 \text{ ms} \quad (53.77)$$

Likewise, for the second type of support in Table 53.1. 1, it is known from the analysis of the previous section that it is strain mode II, and a triangular-shaped explosive impact charge with a peak pressure of 1.0 MPa and a duration of 1.2 ms is applied. The maximum plastic strain $w_0 = 27.3 \text{ mm}$ and the time $t_f = 2.3 \text{ ms}$ at which the maximum strain occurs can be obtained by solving its equation of motion. The third type of support in Table 53.1 is known from the analysis of the previous section to be strain mode III, and a triangular-shaped explosive impact charge with a peak pressure 1.2 MPa and a duration of 1.2 ms is applied. The maximum plastic strain $w_0 = 19.7 \text{ mm}$ and the time $t_f = 1.4 \text{ ms}$ at which the maximum strain occurs can be obtained by solving its equation of motion.

53.3 Analyzed by Numerical Simulation

We take as our research objects the three reinforced plate frameworks listed in Table 53.1 of the previous section, and numerical simulation computations are carried out using the nonlinear finite element analysis software ABAQUS [26] to obtain the dynamic response of reinforced plate frames subjected to explosive loads. Based on this, the factors affecting the dynamic response of the reinforced plate frames and the response laws of the reinforced plate frames are analyzed, and the results are compared to the theoretical solution based on the energy method of the previous section to check the reliability of the theoretical solution.

53.3.1 Finite Element Model

For the reinforced plate framework constructed using ABAQUS, the geometric dimensions and material properties are the same as those given in the example, and the explicit dynamical method is used to solve it. It is known from the calculations above that the stress conditions of the reinforced plate framework are fixed at all edges, the same constraints are therefore adopted in the finite-element analysis model. The explosive charge can be simplified as a triangular shock charge, and the pressure–time relation of the charge is shown in Fig. 53.7.

Where p_m is the peak pressure of the load, and t_d is the duration of the load. By defining a pressure load, the magnitude of the load can be determined by defining the

Fig. 53.7 Triangular impact load

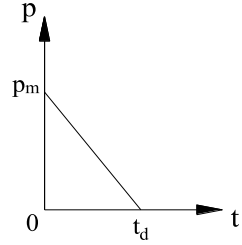


Table 53.4 Load amplitude

Time (s)	Pressure (Pa)
0	p_m
t_d	0
Total time	0

Table 53.5 Applied load

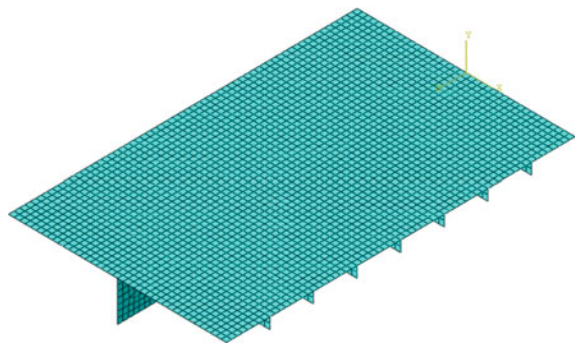
No.	p_m /MPa	t_d /ms
1	0.8	1.2
2	1.0	1.2
3	1.2	1.2

amplitude, and the amplitude Table of the triangular impact load shown in Fig. 53.7 corresponds to the following (Table 53.4):

The shapes of the applied loads for the three longitudinal reinforcements corresponding to Table 53.1 i.e., the three different geometric models of reinforced plate frames, are as follows (Table 53.5):

The characteristic length of the finite element model mesh is chosen to be 20 mm, and the mesh splitting is shown in Fig. 53.8.

Fig. 53.8 Mesh division of stiffened plate frame



53.3.2 Calculation Results Analysis

The use of the finite element model allows the dynamic responses of three different reinforced plate frames to be obtained under the respective explosive load. Figures 53.9, 53.10 and 53.11 show a map of the deformation cloud in the transverse direction.

From the cloud maps above, it can be seen that while the panels and transverse reinforcement of the three reinforced plate frames are the same, the stiffness characteristics of the three plate frames are different because of the differences in the dimensions of the longitudinal reinforcement. Static limit analysis theory predicts that differences in stiffness will result in a different deformation mode of the plate framework. Note that the above three cloud maps correspond to strain modes I, II, and III in the theoretical analysis, i.e. due to the differing relative stiffness of the longitudinal reinforcement, plastic hinges produced on the reinforced plate framework are in different positions, and the shape of the plastic platform area displayed in the cloud map is similar to that of the plastic platform area in the theoretical analysis, indicating the feasibility of the energy-based method for judging the mode of deformation of the reinforced plate structure.

Fig. 53.9 The deformed cloud chart of the first stiffened plate frames

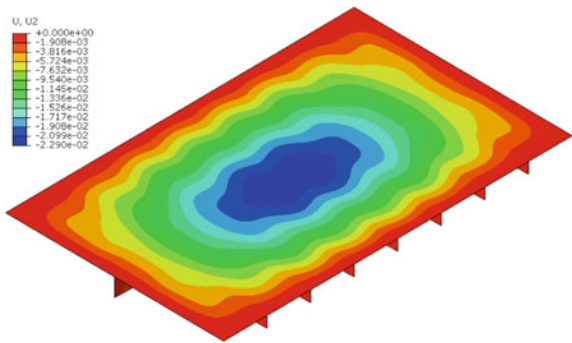


Fig. 53.10 The deformed cloud chart of the second stiffened plate frames

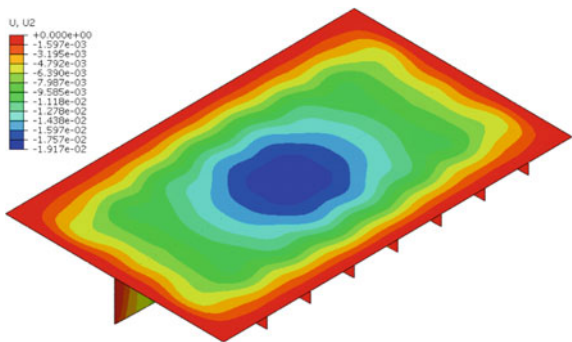
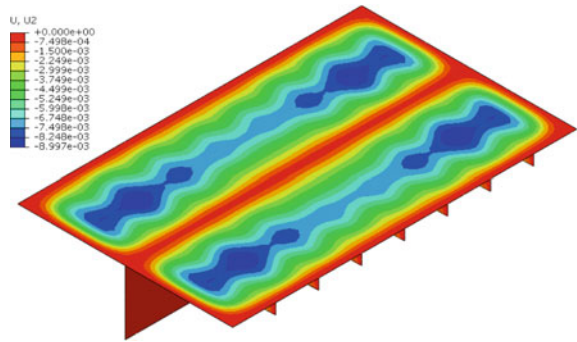


Fig. 53.11 The deformed cloud chart of the third stiffened plate frames



By plotting the deformation versus time of the point with the largest strain in the deformation cloud plot, and comparing it with the theoretical solution, the results are summarized in Figs. 53.12, 53.13 and 53.14 and Table 53.6.

Fig. 53.12 The maximum deformation curve of the first stiffened plate frames

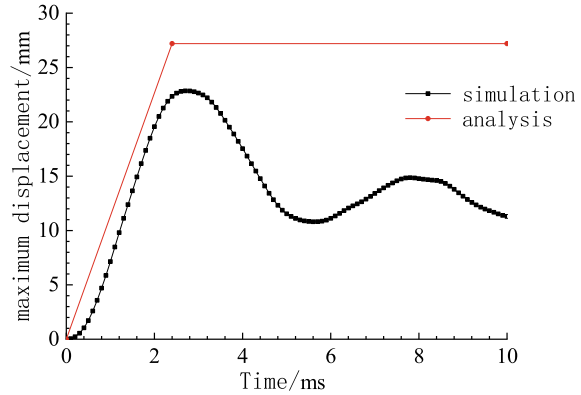
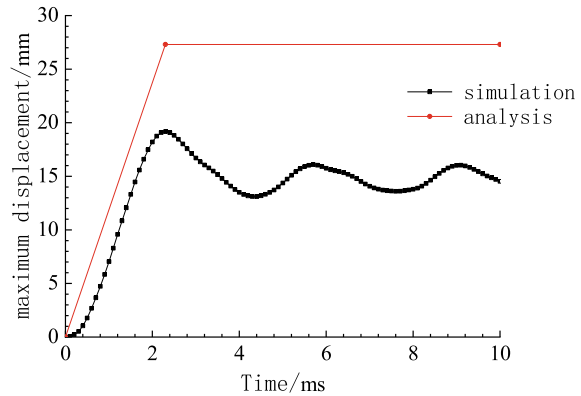


Fig. 53.13 The maximum deformation curve of the second stiffened plate frames



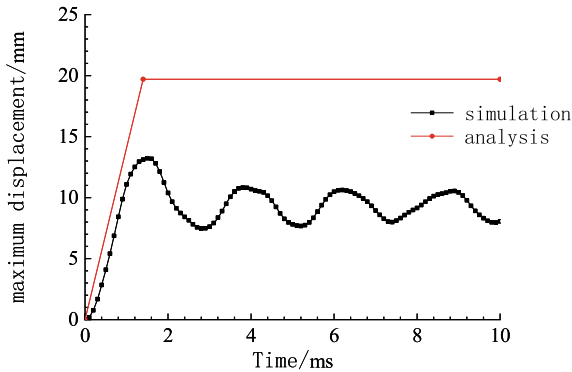


Fig. 53.14 The maximum deformation curve of the third stiffened plate frames

Table 53.6 Analytic results compared with simulation results

No.	Maximum deformation			Time required to reach the maximum deformation		
	Analysis (mm)	Simulation (mm)	Relative error (%)	Analysis (ms)	Simulation (ms)	Relative error (%)
1	27.2	22.9	15.80	2.4	2.7	12.50
2	27.3	19.2	29.70	2.3	2.3	0
3	19.7	13.2	33.00	1.4	1.5	7.10

As can be seen from Table 53.6, there is a relative error between the simulated deformation and the analytical deformation, and the simulated deformation is smaller than the analytical deformation. The reason for this is that the theoretical results are larger than the simulated results, which is because the theoretical results do not take into account the hardening of the structure under explosive loads and the effect of strain rate, and are conservative and applicable for the initial structural strength evaluation in the design stage.

By calculating the maximum strain curve by simulation, it can be known that when the plate frame is subjected to an explosive load, its strain increases rapidly, but after the explosive loading is complete, due to the characteristic of a large peak pressure and a short duration of explosive loading, since there is still considerable acceleration in the reinforced plate frame, the plate frame will deform further. Once the plate frame strain reaches a maximum, the plate frame will enter the free-vibration stage, which corresponds to the stage of oscillation on the strain-curve plot.

It can be seen from the maximum strain curve and the table that the analytical results are relatively conservative, hence more biased toward safety. The time taken to reach maximum strain is relatively close to the simulation results, therefore, the analytical results have important insights for predicting structural failure of the structure under an explosive load.

53.4 Conclusions

Based on the energy principle theory, this study takes reinforced plates as the research object and analyzes the load characteristics and structural response laws for FPSO structure oil and gas explosion accident scenarios. We derive and establish the relevant theoretical prediction methods, and use the nonlinear finite element software ABAQUS for the numerical simulation analysis. To verify and improve the reliability of the theoretical prediction method, the finite element results are compared to the theoretical results. The main findings are:

- (1) Structural deformation criteria were investigated for reinforced plates under static ultimate conditions, and the equation of motion control for the dynamic plastic response of reinforced plates subjected to explosive impact loads was derived using the energy method.
- (2) Using the theoretical formula, the plastic deformation of three reinforced plates of different dimensions was calculated, and the results were compared to the results of finite element calculations to check the reliability of the theoretical solutions.
- (3) This energy method can rapidly analyze and assess the response of structures under blast loads, but this is primarily for plate, beam, and reinforced plate framework structures and requires some simplification which has some limitations.
- (4) The theoretical formula derived from the energy method indicates that the prediction results are slightly conservative concerning the finite element simulation, which makes them more safety-oriented and effective at predicting the response of structures under an explosive load.

References

1. Rudrapatna, N.S., Vaziri, R., Olson, M.D.: Deformation and failure of blast-loads stiffened plates. *Int. J. Impact Eng* **24**(4), 457–474 (2000)
2. Magnanimity, H., Xi, Z., Meibang, G.: Failure mode analysis and structural optimization of stiffened plates under explosive load. *Explos. Impact* **1**, 26–33 (2007)
3. Jinlei, M., Xi, Z., Zhenhua, Z., et al.: Experimental study on deformation and cracking of stiffened plates under underwater explosion load. *Vib. Impact* **27**(1), 57–60 (2008)
4. Zhenhua, Z., Pingyi, C., Wanpeng, Q., et al.: Study on the similarity law of dynamic response of ship partial grillage structure under underwater explosion shock wave. *Vib. Shock* **27**(6), 81–86 (2008)
5. Jones, N.: A theoretical study of the dynamic plastic behavior of beams and plates with finite-deflections. *Int. J. Solids Struct.* **7**, 1007–1029 (1971)
6. Jones, N.: Impact loading of ductile rectangular plates. *Thin-Walled Struct.* **50**, 68–75 (2012)
7. Jones, N.: Dynamic inelastic response of strain rate sensitive ductile plates due to large impact, dynamic pressure and explosive loadings. *Int. J. Impact Eng.* **74**, 3–15 (2014)
8. Schubak, R.B., Olson, M.D., Anderson, D.L.: Rigid-plastic modelling of blast-loaded stiffened plates-Part I: one-way stiffened plates. *Int. J. Mech. Sci.* **35**(3/4), 289–306 (1993)

9. Schubak, R.B., Olson, M.D., Anderson, D.L.: Rigid-plastic modelling of blast-loaded stiffened plates-Part II: partial end fixity, rate effects and two-way stiffened plates. *Int. J. Mech. Sci.* **35**(3/4), 307–324 (1993)
10. Olson, M.D.: Efficient modeling of blast loaded stiffened plate and cylindrical shell structures. *Comput. Struct.* **40**(5), 1139–1149 (1991)
11. Jiang, J., Olson, M.D.: Rigid-plastic analysis of underwater blast loaded stiffened plates. *Int. J. Mech. Sci.* **37**(8), 843–859 (1995)
12. Zheng, C., Kong, X.S., Wu, W.G., Liu, F.: The elastic-plastic dynamic response of stiffened plates under confined blast load. *Int. J. Impact Eng.* **95**, 141–153 (2016)
13. Zheng, C., Kong, X.S., Wu, W.G., Xu, S.X., Guan, Z.W.: Experimental and numerical studies on the dynamic response of steel plates subjected to confined blast loading. *Int. J. Impact Eng.* **113**, 144–160 (2018)
14. Bin, F., Xi, Z., Zhenhua, Z.: Plastic dynamic response of ship bottom grillage under underwater explosion shock wave load. *J. Harbin Eng. Univer.* **29**(4), 326–331 (2008)
15. Kun, L., Yanchang, Z., Pu, W., et al.: Numerical simulation calculation of ultimate bearing capacity of strut structure of semi-submersible drilling platform. *J. Jiangsu Univer. Sci. Technol.* **26**(5) (2012)
16. 2008K24180-02-03-03 Technical Research on Structural Ultimate Strength Analysis, 708 Research Institute of China Shipbuilding Industry Group
17. Ping, Y.: Research on ultimate strength and damaged residual strength of hull structure. Doctoral thesis of Wuhan University of Technology (2005)
18. Baohua, W., Wei, H., Jiameng, W.: Discussion on the application of ultimate strength in ship structure design. *Shanghai Shipbuild.* **3**, 8–10 (2007)
19. Paik, J.K.: *Ultimate Limit State Design of Steel-Plated Structures* (2008)
20. Ueda, Y.: Official Discussion of the Report of Special Task Committee VI.2: Ultimate Hull Girder Strength, Proceeding ISSC 2000, vol. 3, pp. 319–327
21. HSE.: *Analysis of Accident Statistics for Floating Monohull and Fixed Installations*
22. HSE.: *Resistance of Semi-submersibles to Collision*
23. Wang, G., Pedersen, P.T.: *A literature on risk assessment of ship-FPSO collisions*
24. Ali, R.M.M.: *Performance Based Design of Offshore Structures Subjected to Blast Loading*
25. ABAQUS6.6 Basic Course and Case Explanation. China Water Resources and Hydropower Press
26. NORSOK N-004 Structural Steel Design

Chapter 54

A Blockchain-Based Method for Power-Related Data Quality Auditing



Minjie Fu, Fuqiang Tao, Weiping Li, Rundong Shao, and Zhe Sun

Abstract Power big data technology is playing an increasingly important role in the regulation and data analysis of smart grids, which face “data silos” and privacy issues. Federated Learning is a distributed machine learning framework and allows model training to be done without compromising user raw data. To protect private information, the model parameters uploaded by the user are usually trained in cipher text. However, the presence of ciphertext data makes it difficult to audit the quality of data uploaded by users. Smart grid federated analysis tasks are vulnerable to attackers launching attacks such as data poisoning and free-riding, which can have a serious impact on the global model trained. To defend against data poisoning and free-riding attacks, there is a need to audit encrypted grid data uploaded by users. In this paper, we propose a blockchain-based power-related data quality audit method that can ensure the correctness of the smart grid federated analysis model. In particular, we design an efficient noise addition mechanism that makes the aggregation model parameter noise sum to zero, which can protect user data privacy while ensuring the usability of the aggregation model. In addition, we propose a grouped aggregated data quality audit algorithm that can quickly locate users who upload malicious data. We conducted experimental evaluations on both the Real Power dataset and the MNIST dataset, the results showed that our approach is effective against data poisoning and free-riding attacks.

Keywords Data auditing · Blockchain · Secure aggregation · Federated learning

Minjie Fu and Fuqiang Tao are equally contributed.

M. Fu

State Grid Shanghai Information and Telecommunication Company, Shanghai, China

F. Tao · W. Li · R. Shao · Z. Sun (✉)

Cyberspace Institute of Advanced Technology, Guangzhou University, Guangzhou, China

e-mail: sunzhe@gzhu.edu.cn

54.1 Introduction

Power big data technology is playing an increasingly important role in the power industry, and with the popularity of smart grids, power big data analysis has become an important tool for regulating power networks. However, when analyzing power big data, it faces the problems of data silos and privacy leakage, which leads to the power data owned by various power departments or users cannot be effectively integrated and shared, thus affecting the accuracy of data analysis [1–5]. Therefore, solving the problems of data silos and privacy leakage is crucial to improve the effectiveness of smart grid data analysis.

Federated learning [6], as a distributed machine learning framework, allows users to complete model training by uploading only the intermediate model parameters without uploading the original data, effectively solving the data silo problem. To resist model inversion attacks [7], attribute inference attacks [8] and membership inference attacks [9], and to further protect users' privacy information, users upload data usually in ciphertext format for model training. However, when users upload ciphertext data for training, the central server will not be able to audit the quality of user-uploaded data. More seriously, the collaborative analysis task of the smart grid is vulnerable to data poisoning [10] and hitchhiking attacks [11] initiated by malicious attackers, which may affect the correctness of the global model and thus cause serious damage to the smart grid system if the user-uploaded data cannot be audited.

On the other hand, as power data-driven business spans across multiple industries, auditing and evaluating the data uploaded by different participants is imperative to promote the equitable operation of the multi-party data sharing system and encourage more trustworthy participants to engage in collaborative training of power-related data. Several existing research solutions exist to maintain the fairness of multi-party data sharing. One such solution is a game theory-based incentive mechanism. Yin et al. [12] analyzed the critical factors influencing players' decisions in collaborative analysis through an extensive game tree and then derived the Nash equilibrium through iterative games, which encouraged users to submit high-quality data in federated learning. However, this approach can only promote users to submit better quality data and cannot safeguard against data poisoning attacks perpetrated by malicious users. Another solution is a punishment mechanism based on auditing. Sun et al. [13] can identify malevolent data owners and penalize bad actors by introducing two blockchains to record and audit the model parameters uploaded by users. However, homomorphic encryption algorithms are used to protect privacy, which increases the performance overhead of federated learning.

In this paper, we propose a blockchain-based power-related data quality auditing method that uses blockchain to collect model parameters uploaded by clients. The tamper-evident property of blockchain prevents clients from repudiating their actions, while blockchain can also audit model parameters uploaded by users and evaluate the gradient of aggregation. To reduce the additional computational increase from auditing model parameters, we design a progressive federated learning training

model. In the beginning communication rounds, the blockchain only adds noise to the encrypted model parameters and aggregates them, and then audits the user-uploaded model parameters when the global model accuracy produces large fluctuations.

The main contributions of this paper are as follows:

- We propose a blockchain-based power-related data quality audit method that uses blockchain to record user uploads behaviors and perform noise addition and grouping of model parameters uploaded by users through smart contracts.
- We designed an efficient noise addition mechanism to add noise to the model parameters uploaded by users through smart contracts, making it impossible for the auditor to decrypt the original model from the noisy model parameters while ensuring that the added noise will not affect the aggregation results of the encrypted model.
- We design a grouping aggregation quality auditing algorithm that groups multiple model parameters through smart contracts, and the auditor aggregates, decrypts and evaluates the encrypted models in different groups, which can identify and locate malicious data.

The remainder of the paper is structured as follows. Section 54.2 provides an overview of the related work on power-related data quality audits. Section 54.3 outlines the proposed scheme for auditing power-related data quality. The experimental details of the scheme are presented in Sect. 54.4. Finally, Sect. 54.5 provides a summary of the paper.

54.2 Related Work

In this section, we will mainly introduce related work in 3 parts. The first part is some existing automated processing methods for power-related data based on federated learning. The second part is to introduce the research related to the incentive mechanism used in federated learning. The third part is the blockchain-based data quality audit method.

54.2.1 *Power-Related Data Processing Based on Federated Learning*

Federated learning is the optimal technology to solve the collaborative analysis of the smart grid. Taik et al. [14] used federated learning to train long-term short-term memory (LSTM) deep learning networks using residential properties and residential power usage in grid edge devices to achieve short-term prediction of individuals. Wang et al. [15] extracted features from the residential power meter data held by retailers through principal component analysis (PCA), trained a classifier through

federated learning artificial neural networks to predict the social attributes of occupants, and used training data sets based on the global model is aggregated with three weighting strategies of quantity, retailer training dataset average loss and retailer training dataset total loss. Tun [16] et al. used the Ordering points to identify the clustering structure method to cluster users based on residential properties and repeated the federated RNN model training based on residential power data independently for each cluster until convergence. Users used the global model to predict power consumption and send the results to the power company. Gholizadeh et al. [17] clustered the results of adjusting hyperparameters of a training network based on the client and used federated LSTM for short-term load forecasting of a single residence. However, existing federated learning-based data processing for power-related data does not audit the data submitted by each participating party, making it easy for malicious participants to launch data poisoning and free-riding attacks, which could compromise the secure operation of smart grids.

54.2.2 Incentive Mechanisms for Federated Learning

In federated learning, the quality of the model parameters trained can vary due to the differences in data held by each data holder. Without appropriate incentive mechanisms to ensure fairness in federated learning, participants may be unwilling to share model parameters. Doku et al. [18] proposed a new federated learning framework that combines blockchain with federated learning, utilizing proof-of-stake consensus algorithms and IPFS distributed storage to incentivize user participation in training and extract correlations between data. Song et al. [19] defined the contribution index of federated learning participants and proposed a new measure based on the Shapley value to quantify the contribution of each data provider to the joint model of federated learning training based on factors such as local datasets, machine learning algorithms, and test sets. Zhan et al. [20] modeled the total reward of the central server and the total profit of the client as a Stackelberg game, solved the Nash equilibrium to obtain the optimal solution, and dynamically adjusted the incentive strategy using deep reinforcement learning algorithms to encourage participants to provide better quality model parameters. Yin et al. [12] analyzed the key factors that influence player decisions in federated learning using an extensive game tree and then derived a Nash equilibrium through repeated games between users, agents, and servers to encourage users to submit high-quality data in federated learning. However, incentive mechanism schemes can only encourage honest participants to submit high-quality data in collaborative analysis systems. If there are malicious participants who launch data poisoning attacks in the system, the global model analysis results of federated learning will be compromised.

54.2.3 *Blockchain-Based Data Quality Auditing*

In federated learning, local models are typically encrypted and aggregated, which protects the privacy of honest clients but also facilitates poisoning and free-riding attacks, requiring the identification of relevant clients through auditing. Sun et al. [13] use two consortium chains to store the homomorphically encrypted information of interaction and noise models, and by leveraging the encrypted gradient aggregation of different sets, locate the malicious data holders through joint auditing and cross-location, without auditing through decryption of individual gradients. Peng et al. [21] combine blockchain with cryptography, aggregate models through a validator committee, and record corresponding verification proofs on the blockchain, proposing a new authentication data structure to meet the audibility of the VFChain framework while improving efficiency. Xuan et al. [22] compare existing validation methods, propose to combine competitive voting validation with aggregation algorithms and use hierarchical aggregation to reduce the communication overhead of node security verification in blockchain-based federated learning. Mugunthan et al. [23] realize decentralization through blockchain, protect privacy through differential privacy, and propose a responsible federated learning system that can complete the auditing process without a trusted auditor through a novel model contribution auditing mechanism. However, such methods combined with cryptography increase the communication overhead of federated learning or cannot effectively locate the data holders who upload malicious model parameters. Therefore, existing blockchain-based data quality auditing schemes cannot be used for quality auditing of power-related data.

54.3 Method

In this section, we present our method from four aspects. Firstly, in the system architecture, we mainly introduce the system architecture of our approach, which consists of a gradient collection stage, noise addition stage, and group aggregation auditing stage. In the blockchain-based gradient collection stage, we introduce the blockchain framework for gradient collection in federated learning. In the noise addition stage, we describe how the smart contract groups the model parameters uploaded by clients, generate noise and adds noise to the model parameters. In the group aggregation audit phase, we will introduce local models for group aggregation quality audit and locate problem models or possible problem models.

54.3.1 Overall Structure

In the federated learning scenario of power big data, the model parameters uploaded by clients are usually trained in encrypted form. To achieve trustworthy and transparent data auditing, we remove the assumption of the encryption service provider and introduce a decentralized blockchain to organize and manage federated learning. The blockchain records and collects the model parameters uploaded by clients, and the smart contract groups multiple model parameters and adds noise. The aggregation node aggregates, decrypts, and evaluates the encrypted model in different groups, uses the data quality audit algorithm to determine whether there are malicious encrypted model parameters, and accurately locates them. As shown in Fig. 54.1, our framework mainly includes the gradient collection stage, noise addition stage, and group aggregation auditing stage. The process of each round of model training is as follows:

Step 1. System initialization and local model training: The central server creates a genesis block before collaborative training, trains the initial model using a public dataset, and writes the initial model, model parameters, and quality audit test dataset into the genesis block and broadcasts it to all nodes. Each node downloads the initial model in the genesis block and trains it using local data to obtain updated model parameters.

Step 2. The smart contract groups parameters and adds noise: The smart contract groups the locally updated model parameters of clients and adds noise to the model parameters. The smart contract then initiates a quality audit request to the clients, and the clients download the quality audit test dataset from the genesis block and compute the model accuracy locally as a quality declaration. The noise-added model parameters and audit information, including quality declaration, are stored in a new block.

Step 3. Blockchain aggregates and audits model quality: The aggregation node aggregates the noise-added model parameters according to the grouping designed by the smart contract. After the aggregation, the noise result of the model parameters is 0, and the aggregated nodes are submitted to the central server. The noise result of the

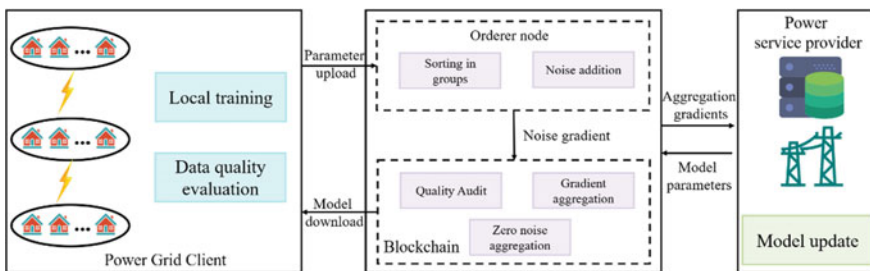


Fig. 54.1 The system architecture of our quality audit approach

aggregated model parameters is zero, and the aggregated model is submitted to the central server. When there is a significant fluctuation in the global model accuracy, the aggregation node audits the quality of the group-aggregated model using the audit test set. During the audit process, the aggregation node compares the test results of different aggregation models with the quality declarations provided by the clients to determine whether there are malicious or poor-quality model parameters in the group.

Step 4. Server updates the model: When the model parameter quality audit is passed, the central server downloads the aggregated global model from the aggregation node and checks whether the model has converged. If the model has not converged, the updated global model is sent to the blockchain for a new round of training until the model converges. If the model parameter quality audit fails, the central server removes the users who uploaded malicious model parameters and conducts a new round of training.

54.3.2 *Blockchain Framework*

Blockchain is a decentralised distributed ledger technology that allows the training parameters of federal learning to be recorded in a tamper-evident manner in a distributed network. In this paper, the reading, group encryption, auditing and aggregation operations of the model gradient information uploaded to the blockchain by users are secured by smart contracts, which audit the model gradient information while ensuring the data privacy of the trainers. As shown in Fig. 54.2, our smart contract solution includes four steps of model parameter reading, group encryption, gradient aggregation and data auditing, with the sorting nodes in the blockchain taking an honest role.

After the client finishes training locally, it will first broadcast to the sorting node in the blockchain. The sorting node will group the gradient information to generate the model matrix, then record the grouping information into the block, and add noise to each model according to the grouping information, and generate two noises corresponding to each model parameter to get two noisy model parameters. The aggregation node will perform aggregation based on the grouping information and audit the aggregation results, the audit method will be described in 3.4. The audit results and aggregation results will be submitted to the central server, which decides on the actors to participate in the next round of training and updates the models.

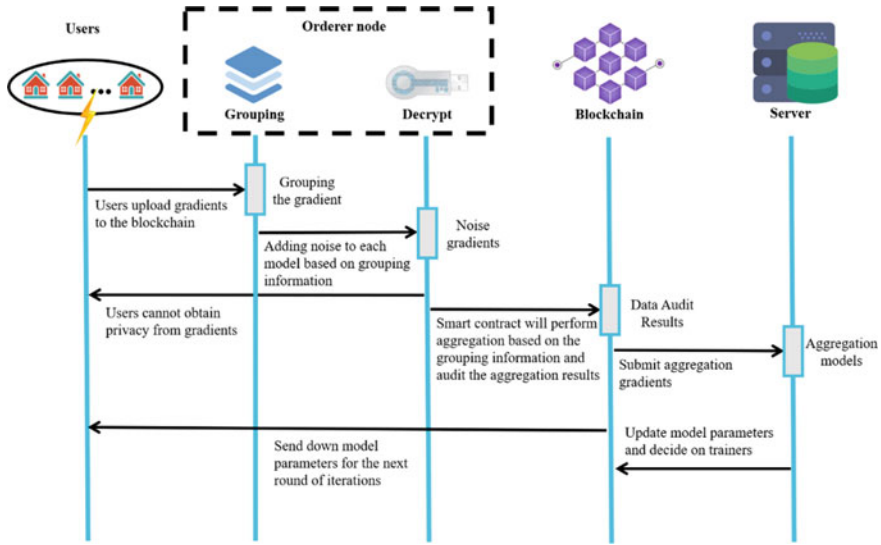


Fig. 54.2 The interactive flow of data auditing

54.3.3 Noise Addition Mechanism

We complete the entire model noise addition process in the smart contract, including three steps: model grouping, noise generation and noise addition. A local model has to be located in both horizontal grouping and vertical grouping, corresponding to the generation of two noises and two noise models.

In model grouping, first, we segment the received local model m_i , divided into $\lfloor n/9 \rfloor$ segments. The number of local models m_i is nine for all segments, only the last segment can have more than nine models, but not more than eighteen models. Segments are only transitional units in the model grouping and are not reflected in the final grouping. We use n to denote the number of local models and seg_j to denote the j th segment. We then ranked all local models m_i in each segment in order from left to right, three columns per row. For each segment, the local models are grouped horizontally and vertically according to the row-first and column-first selection, respectively. When grouping was performed, each segment was divided into $\lfloor |seg_j|/3 \rfloor$ groups, with the number of local models m_i in all groups being three, and only the last group could have more than three models, but less than six models. Uniform numbering of all horizontal and vertical subgroups, with r_x denoting the x th horizontal subgroup and c_y denoting the y th vertical subgroup. The groupings in the non-final and final paragraphs are shown in Figs. 54.3 and 54.4.

In noise generation, we generate the horizontal noise or vertical noise corresponding to the virtual local model in one horizontal grouping or one vertical grouping at a time, with the sum of all the noise in each grouping being zero. In the following we illustrate the noise generation process by generating the corresponding

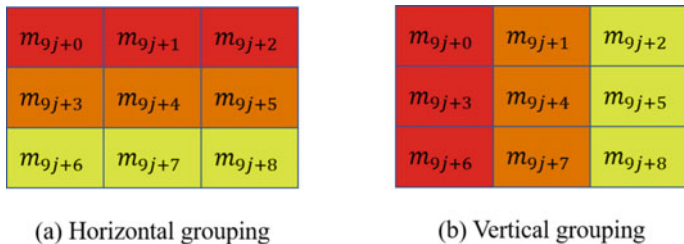


Fig. 54.3 Horizontal and vertical groupings that are not the last segment

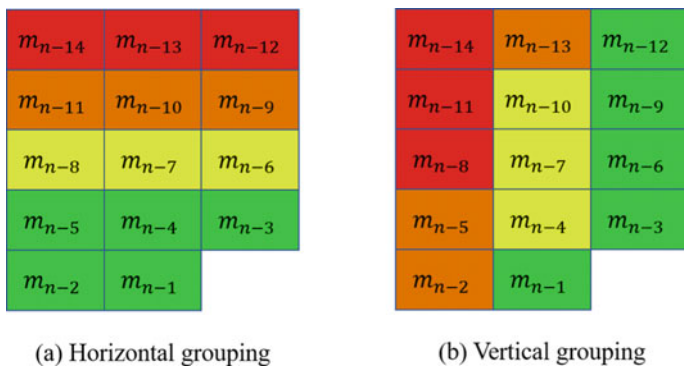


Fig. 54.4 Horizontal and vertical groupings that are the last segment

horizontal noise s_i^r for all local models m_i in a horizontal grouping r_x . First, each local model m_i in the transverse grouping r_x generates a pre-transverse noise cs_i^r that obeys a Gaussian distribution, then all the transverse noise is aggregated and the aggregation result is divided equally according to the number of members in the transverse grouping as a margin to be subtracted from each pre-transverse noise to obtain the final transverse noise s_i^r for noise addition. The formula is expressed as follows:

$$s_i^r = cs_i^r - \frac{1}{|r_x|} \sum_{i \in r_x} cs_i^r \tag{54.1}$$

It can be shown that the sum of all noise in the grouping is equal to zero.

$$\sum_{i \in r_x} s_i^r = \sum_{i \in r_x} cs_i^r - |r_x| \cdot \frac{1}{|r_x|} \sum_{i \in r_x} cs_i^r = 0 \tag{54.2}$$

In the noise addition, we add the horizontal and vertical noise generated in the previous step to the local model to form a horizontal noise model and a vertical noise model respectively.

$$m_i^r = m_i + s_i^r \quad (54.3)$$

$$m_i^c = m_i + s_i^c \quad (54.4)$$

It can be shown that the aggregated results of the noise model for the same horizontal or vertical grouping are equal to the aggregated results of the original model.

$$\sum_{i \in r_x} m_i^r = \sum_{i \in r_x} m_i + \sum_{i \in r_x} s_i^r = \sum_{i \in r_x} m_i \quad (54.5)$$

$$\sum_{i \in c_y} m_i^c = \sum_{i \in c_y} m_i + \sum_{i \in c_y} s_i^c = \sum_{i \in c_y} m_i \quad (54.6)$$

54.3.4 Group Aggregation Quality Audit

We perform a group aggregation quality audit on local models to identify the group in which the anomalous model is located and to further locate the anomalous model. The security objective achieved by this quality auditing algorithm is to accurately locate the problem model or determine the potential scope of the problem model.

The users need to test the unencrypted local model to obtain the model quality statement $state_i$, which is uploaded to the blockchain together with the noisy model. When auditing a grouping, the average value of all models in the grouping is used as the threshold τ to determine whether there is an abnormal model in the grouping. The threshold τ is calculated as follows:

$$\tau_{r_x} = \frac{1}{|r_x|} \sum_{m_i \in r_x} state_i \quad (54.7)$$

$$\tau_{c_y} = \frac{1}{|c_y|} \sum_{m_i \in c_y} state_i \quad (54.8)$$

We audit the local models in the order of horizontal before vertical. In the horizontal grouping audit, the aggregated local model corresponds to the horizontal noise model $m_{r_x} = \frac{1}{|r_x|} \sum_{m_i \in r_x} m_i^r$, and the aggregation results are tested and all models in the horizontal grouping are flagged if the accuracy is below the threshold value τ_{r_x} . After the horizontal grouping audit is completed, a vertical grouping audit is performed for each tagged model. After the horizontal grouping audit is completed, a vertical grouping audit is performed for each tagging model, i.e. aggregating the vertical noise models corresponding to the vertical grouping in which the tagging model is located $m_{c_y} = \frac{1}{|c_y|} \sum_{m_i \in c_y} m_i^c$. and if the test result of the grouped aggregated models is below the threshold τ_{c_y} , then the corresponding tagged models are classified as potentially problematic models.

The potential problem model set PP is obtained after horizontal and vertical grouping auditing, and for each model m_i in it, if only itself in their horizontal or vertical grouping is in the potential problem model set PP , the formula is as follows:

$$|\{m_j | m_j \in PP \text{ and } m_j \in \{r_x | m_i \in r_x\}\}| = 1 \quad (54.9)$$

$$|\{m_j | m_j \in PP \text{ and } m_j \in \{c_y | m_i \in c_y\}\}| = 1 \quad (54.10)$$

Then the model can be explicitly located as a problem model and placed into the set of problem models P , with the remainder output as the set of potential problem models PP . The whole process is described in detail in Algorithm 1, where we divide the possible scenarios into two categories.

Scenario 1: Problem models are all in the same horizontal grouping or vertical grouping in the same segment. In the case of problem models all in the same horizontal grouping, for example, the problem models are classified as potential problem models after the horizontal and vertical grouping audit. In the vertical grouping of problem models, other models are not classified as potential problem models because the test results of the aggregated models in the horizontal grouping are above the threshold, so the only problem model in the vertical grouping of problem models is itself a potential problem model, so that problem model is put into the problem model set P .

Scenario 2: In the same segment, there are problem models in different horizontal and vertical groupings. For example, if the first column of the first row and the second column of the second row are problem models, the models in the second column of the first row and the first column of the second row are classified as potential problem models because the test results of the aggregated models in the horizontal and vertical groupings they are in are below the threshold. In this case, the server can only determine that the problem model is in the potential problem model set PP , but cannot determine exactly which one is the problem model.

Algorithm 1. Group aggregation quality audit algorithm

INPUT: horizontal noise model m_i^r , vertical noise model m_i^c , model quality statement $state_i$

OUTPUT: problem model set P , potential problem model set PP

Initialize the problem model set P and potential problem model set PP as empty set;

In each horizontal and vertical grouping, calculate the mean of the model quality statement $state_i$ as threshold τ_{r_x} and τ_{c_y} ;

For each horizontal grouping r_x :

Aggregating horizontal noise models in horizontal grouping r_x to obtain

$$m_{r_x} = \frac{1}{|r_x|} \sum_{m_i \in r_x} m_i^r;$$

If the accuracy of m_{r_x} below τ_{r_x} , then add r_x to potential problem model set PP ;

End

For each $m_i \in PP$:

Aggregation vertical noise models in vertical grouping c_y , where m_i is located $m_{c_y} =$

$$\frac{1}{|c_y|} \sum_{m_i \in c_y} m_i^c;$$

If the accuracy of m_{c_y} below τ_{c_y} , then then delete m_i from potential problem model set PP ;

End

For each $m_i \in PP$:

If only itself in PP between horizontal grouping or between vertical grouping, then add m_i to problem model set P and delete m_i to potential problem model set PP ;

End

Return P, PP

54.4 Experiments

54.4.1 Experimental Setup

Environment settings: We utilized a total of eight CPU servers (Hygon C86 7159 16-core processors) and two GPU servers (with 8 NVIDIA TESLA T4 GPUs each, with 16 GB of memory), to perform the training for the data holders. The training task for the data holders was image recognition, and we built the client training models, data encoding, and obfuscation using Python (3.8) and PyTorch (1.6) libraries. For data encoding and obfuscation, we used Charm-crypto (0.5.0) library and numpy (1.18.5) library, respectively.

Dataset: *MNIST*: It is a large dataset of handwritten digits commonly used for training various image processing tasks. *CPLID*: It is a dataset of Chinese power line insulators that includes both normal and synthetically generated defective insulator images captured by drones. This dataset is commonly used for image recognition tasks in power-related scenarios.

Metrics: In order to validate the effectiveness of our proposed approach, we used accuracy as the performance metric, defined as $precision = \frac{TP}{TP+FP}$. Additionally,

we compared our approach against the following baselines in our experiments: 1. Comparison between different groups and the global model's accuracy. We used this as our baseline model. 2. Comparison between the accuracy of normal federated learning and federated learning under attack. This was to test whether our auditing algorithm can detect malicious attackers. 3. Time consumption of the blockchain framework. This was to test whether our blockchain framework can be applied in real-world scenarios. 4. Comparison between our obfuscation algorithm and state-of-the-art auditing encryption algorithms. This was to test whether our obfuscation algorithm has a better performance overhead than cryptographic methods.

54.4.2 The Performance of the Data Quality Audit Algorithm

In order to validate the feasibility of our data quality auditing algorithm, we trained a CNN model on the MNIST and CPLID datasets for image classification tasks and evaluated its accuracy. The CNN network consisted of two convolutional layers, two pooling layers, one fully connected layer, and one softmax output layer, and the aggregation algorithm for federated learning was FedAvg. The learning rate for each round was set to 0.0001, the batch size was set to $B = 64$, and the maximum communication rounds Epoch was set to $E = 50$.

In each learning round, nine client machines will undergo local training and submit model parameters to the sorting node. The sorting node will then group clients and add noise to their models before submitting the noisy model parameters to the blockchain. We first evaluated federated learning without any attacks and assessed the global and grouped model accuracy in the CPLID and MNIST datasets. The results, as shown in Fig. 54.5, demonstrate that the accuracy of the grouped model is very close to that of the global model, which is considered the baseline. After 50 iterations, the global model achieved an accuracy of 88.56% on the CPLID dataset and 94.82% on the MNIST dataset.

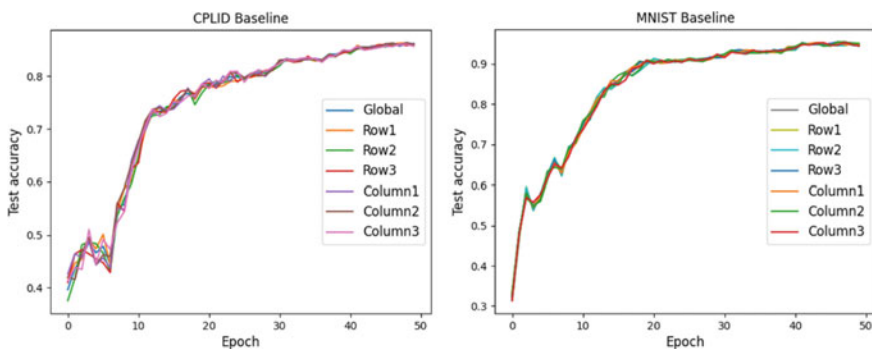


Fig. 54.5 Federated learning without attacks

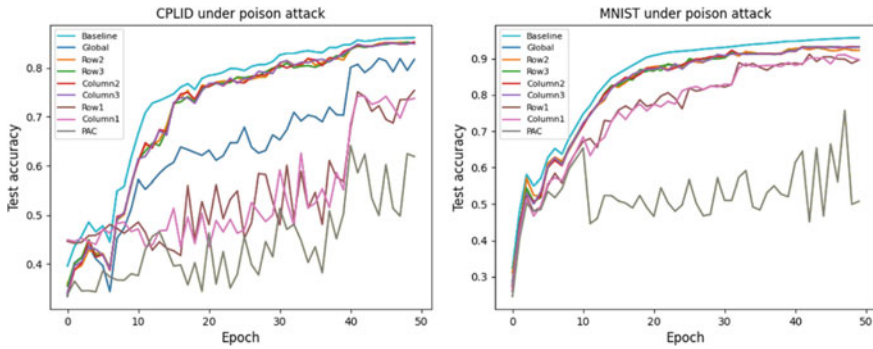


Fig. 54.6 Test accuracy of model under poison attack

In our simulated experiment on data poisoning attacks, we randomly designated one device as a poison attacker (PAC), placing it in the first row and column. This device uploaded the negative gradient information it obtained during training to the sorting node, simulating a data poisoning attack. We evaluated the poisoning behavior using a data quality auditing algorithm, and recorded the impact of the PAC’s attack on the model, as well as the performance of the grouped aggregation model.

As shown in the Fig. 54.6, in both the MNIST and CPLID datasets, the PAC’s poisoning behavior caused fluctuations in the model’s accuracy, which were far below those of the global model and baseline accuracy. Due to the influence of the PAC, the local model accuracy in the first row and column was also lower than the global model and baseline, and they were more difficult to converge. This means that we can locate the PAC from the anomalous behavior in the first row and column, which is the first device in our experiment. This also demonstrates the effectiveness of our data quality auditing algorithm, which can resist data poisoning attacks and accurately locate the attacker.

During the simulation experiments of data hitchhiking attacks, we randomly designated a device as the hitchhiking attacker (FAC) and placed it in the first row and column, which would not participate in normal local training, but only uploaded zero-gradient parameters to the sorting node in each round of iteration to simulate data hitchhiking attacks. We evaluated hitchhiking behavior through data quality auditing algorithms and recorded the impact of the FAC’s hitchhiking attack on the model, as well as the performance of group aggregation of the model. In Fig. 54.7, we can see that in the MNIST and CPLID datasets, the FAC model’s accuracy in the early rounds of iteration was much lower than that of the global model and baseline model. With the increase of iteration times, the FAC model’s accuracy gradually approached that of the global model and began to converge. This demonstrates that hitchhiking attacks can allow attackers to receive high-quality model updates at minimal cost, which is unfair to other honest data holders. On the other hand, we can see that due to the influence of FAC, the local model accuracy in the first row and column was also lower than that of the global model and baseline, especially in the process of iteration from the 5th to the 20th round, and the accuracy of the local model can also

approach that of the global model with the increase of iteration times. The hitchhiking attack launched by the attacker can converge with the increase of iteration times, which means that the hitchhiking attack is more difficult to detect than the poisoning attack. However, we can still detect abnormal behavior in the first row and column in the early stages and locate the FAC accordingly. This demonstrates that our data quality auditing algorithm is effective, and it can resist data hitchhiking attacks and accurately locate data holders who upload low-quality data.

We deployed our data quality audit method in the training process of federated learning, randomly setting some attackers to launch poisoning and data hitchhiking attacks. If we detect malicious behavior, we mark the attackers and no longer accept their uploaded parameter information. As shown in Fig. 54.8, our audit method effectively improves the stability of the model, with the accuracy and convergence speed of the global model approaching the baseline. If there are attackers launching poisoning and data hitchhiking attacks, our audit method can quickly detect and remove them, and the accuracy of the model will gradually improve. This demonstrates that our method is effective in defending against poisoning and data hitchhiking attacks.

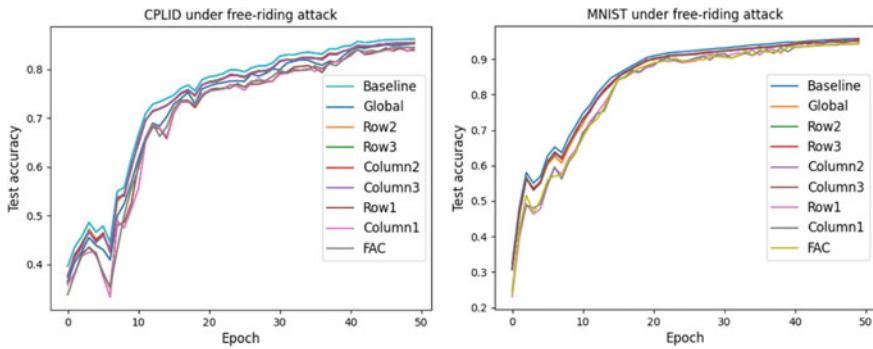


Fig. 54.7 Test accuracy of model under free-riding attack

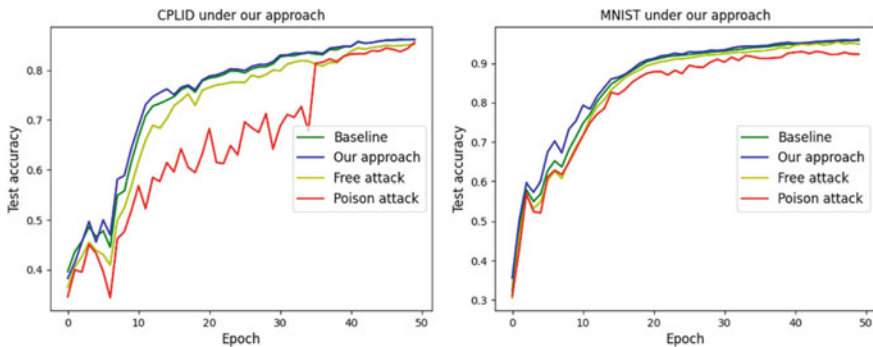


Fig. 54.8 The performance of our audit approach

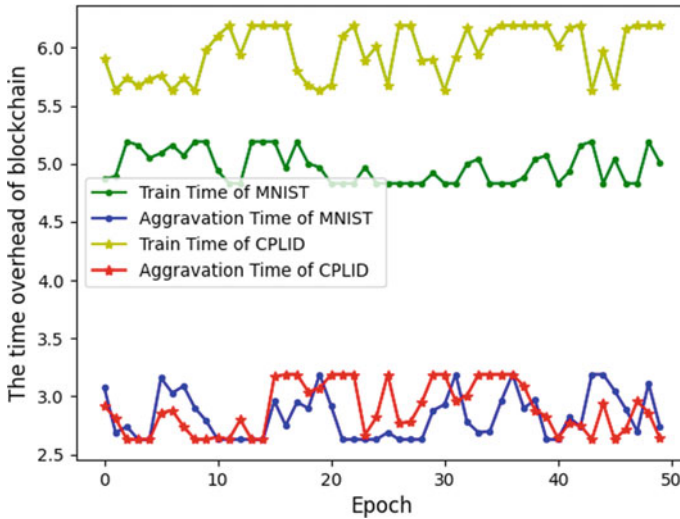


Fig. 54.9 The time overhead of blockchain framework

54.4.3 Time Overhead of Blockchain Framework

To verify the effectiveness of federated learning under a blockchain network, we evaluated the time overhead of the blockchain framework. In this experiment, we recorded the average training time and aggregation time of nodes in each training round. We ran a federated learning method to train a CNN model under the blockchain network using MNIST and CPLID datasets. As shown in Fig. 54.9, the time of the blockchain network fluctuated slightly due to the network environment, but we can conclude that the overall efficiency of the blockchain collaborative training is relatively stable. As the number of iterations increases, the aggregation time of the CNN model does not increase sharply. This indicates that the proposed training method of federated learning under a blockchain network is effective.

54.4.4 Time Overhead of Noise Addition Mechanism

To verify the effectiveness of our noise addition algorithm, we evaluated its performance cost. We added Gaussian noise to the model parameters trained by users, and used the BCP encryption algorithm to encrypt and decrypt the model parameters, evaluating the time cost of this method based on encryption and decryption times. The experimental results, as shown in Table 54.1, indicate that our noise addition scheme had the longest time consumption of 46 s for encryption and 29.28 s for decryption, with 20 clients participating in collaborative training. This demonstrates the usability of our noise addition algorithm, as it remains effective even in larger

Table 54.1 Encryption and decryption times(s)

Clients	5	10	15	20
BCP_Enc _{avg}	24.30	43.59	72.62	96.35
BCP_Dec	45.95	89.03	132.11	175.19
Our_Enc _{avg}	11.55	23.15	34.67	46.26
Our_Dec	7.34	14.66	21.98	29.28

scale collaborative training. This is due to the use of Gaussian noise to add noise to the model parameters trained by users, which greatly reduces computation and communication costs compared to cryptographic methods.

54.5 Conclusions

The quality audit of power-related data plays a critical role in ensuring the fair and efficient operation of smart grids. In this paper, we propose a blockchain-based method for auditing the quality of power related data to guarantee the correctness of the joint analysis model of smart grids. To protect the privacy of users on the blockchain and the availability of the aggregated model, we design an efficient mechanism for adding noise to the model parameters, ensuring that the noise sum of the aggregated model is zero. Additionally, we propose a grouping aggregation data quality audit algorithm that can quickly locate users who upload malicious data. We evaluate our method using real power data sets and the MNIST data set, and the experimental results demonstrate that our approach can effectively resist data poisoning and free-riding attacks. In future work, we will study how to balance the conflict between privacy protection and data mining, and explore an incentive mechanism for sharing parameters that balances privacy preserving and mining value.

Acknowledgements This work was funding by Science and Technology Project of State Grid Limited Science in China (No. SGSHXT00SFJS2200374).

References

1. Shafiq, M., Tian, Z., Bashir, A.K., Du, X., Guizani, M.: CorrAUC: a malicious Bot-IoT traffic detection method in IoT network using machine learning techniques. *IEEE Internet Things J.* **8**(5), 3242–3254 (2021)
2. Tian, Z., Li, M., Qiu, M., Sun, Y., Su, S.: Block-DEF: a secure digital evidence framework using blockchain. *Inf. Sci.* **491**, 151–165 (2019)
3. Qiu, J., Tian, Z., Du, C., Zuo, Q., Su, S., Fang, B.: A survey on access control in the age of internet of things. *IEEE Internet Things J.* **7**(6), 4682–4696 (2020)
4. Tian, Z., Luo, C., Qiu, J., Du, X., Guizani, M.: A distributed deep learning system for web attack detection on edge devices. *IEEE Trans. Industr. Inf.* **16**(3), 1963–1971 (2020)

5. Shafiq, M., Tian, Z., Sun, Y., Du, X., Guizani, M.: Selection of effective machine learning algorithm and Bot-IoT attacks traffic identification for internet of things in smart city. *Futur. Gener. Comput. Syst.* **107**, 433–442 (2020)
6. Konečný, J., McMahan, H.B., Ramage, D., et al.: Federated optimization: Distributed machine learning for on-device intelligence. arXiv preprint [arXiv:1610.02527](https://arxiv.org/abs/1610.02527) (2016)
7. Fredrikson, M., Jha, S., Ristenpart, T.: Model inversion attacks that exploit confidence information and basic countermeasures. In: *Proceedings of the 22nd ACM SIGSAC Conference on Computer and Communications Security*, pp. 1322–1333 (2015)
8. Melis, L., Song, C., De Cristofaro, E., et al.: Exploiting unintended feature leakage in collaborative learning. In: *2019 IEEE Symposium on Security and Privacy (SP)*, pp. 691–706. IEEE (2019)
9. Shokri, R., Stronati, M., Song, C., et al.: Membership inference attacks against machine learning models. In: *2017 IEEE Symposium on Security and Privacy (SP)*, pp. 3–18. IEEE (2017)
10. Chen, X., Liu, C., Li, B., et al.: Targeted backdoor attacks on deep learning systems using data poisoning. arXiv preprint [arXiv:1712.05526](https://arxiv.org/abs/1712.05526) (2017)
11. Kim, H., Park, J., Bennis, M., et al.: Blockchained on-device federated learning. *IEEE Commun. Lett.* **24**(6), 1279–1283 (2019)
12. Yin, L., Lin, S., Sun, Z., et al.: A game-theoretic approach for federated learning: a trade-off among privacy, accuracy and energy. *Digital Commun Netw.* (2023)
13. Sun, Z., Wan, J., Yin, L., et al.: A blockchain-based audit approach for encrypted data in federated learning. *Digit. Commun. Netw.* **8**(5), 614–624 (2022)
14. Taïk, A., Cherkaoui, S.: Electrical load forecasting using edge computing and federated learning[C]. In: *ICC 2020–2020 IEEE International Conference on Communications (ICC)*, pp. 1–6 (2020)
15. Wang, Y., Bennani, I.L., Liu, X., et al.: Electricity consumer characteristics identification: a federated learning approach. *IEEE Trans. Smart Grid* **12**(4), 3637–3647 (2021)
16. Tun, Y.L., Thar, K., Thwal, C.M., et al.: Federated learning based energy demand prediction with clustered aggregation[C]. In: *2021 IEEE International Conference on Big Data and Smart Computing (BigComp)*, 164–167. IEEE (2021)
17. Gholizadeh, N., Musilek, P.: Federated learning with hyperparameter-based clustering for electrical load forecasting. *Internet of Things* **17**, 100470 (2022)
18. Doku, R., Rawat, D.B., Liu, C.: Towards federated learning approach to determine data relevance in big data. In: *2019 IEEE 20th International Conference on Information Reuse and Integration for Data Science (IRI)*, pp. 184–192. IEEE (2019)
19. Song, T., Tong, Y., Wei, S.: Profit allocation for federated learning. In: *2019 IEEE International Conference on Big Data (Big Data)*, pp. 2577–2586. IEEE (2019)
20. Zhan, Y., Li, P., Qu, Z., et al.: A learning-based incentive mechanism for federated learning. *IEEE Internet Things J.* **7**(7), 6360–6368 (2020)
21. Peng, Z., Xu, J., Chu, X., et al.: Vfchain: Enabling verifiable and auditable federated learning via blockchain systems. *IEEE Trans. Netw. Sci. Eng.* **9**(1), 173–186 (2021)
22. Xuan, S., Jin, M., Li, X., et al.: DAM-SE: a blockchain-based optimized solution for the counterattacks in the internet of federated learning systems. *Secur. Commun. Netw.* **2021**, 1–14 (2021)
23. Mugunthan, V., Rahman, R., Kagal, L.: Blockflow: an accountable and privacy-preserving solution for federated learning. arXiv preprint [arXiv:2007.03856](https://arxiv.org/abs/2007.03856) (2020)

Chapter 55

FEDSET: Federated Random Forest Based on Differential Privacy



Fuqiang Tao, Zhe Sun, Rui Liang, Rundong Shao, Yuhan Chai,
and Yangyang Wang

Abstract The rapid development of the federated machine learning paradigm has broken down the data barriers in technology between different organizations and individuals, allowing data that was previously difficult to analyze collaboratively to be used to unimaginable value. Among them, federated random forest has gradually gained popularity among collaborative analysis users for its good adaptability to structured data. However, the contradiction between the demand for collaborative analysis services and users' awareness of privacy-preserving is becoming increasingly prominent and has become a bottleneck hindering the healthy and orderly development of the big data industry. To this end, this paper comprehensively analyzes the privacy preservation and usability requirements faced by federated random forest, and investigates a differential privacy-based federated random forest approach FEDEST. Users design privacy budgets locally, build CART decision trees with noise through a selective noise addition mechanism, and then upload them to the server for aggregation into a random forest, and optimize the random forest model through multiple rounds of iterations. FEDEST can improve the accuracy of business analysis models while safeguarding the privacy information of collaborative analysis participants. Experiments on the Adult and BRFSS datasets show that FEDEST has the highest classification accuracy of 91% and 87%, respectively, which is close to the classification accuracy of non-federated forest.

Keywords Random forest · Federated learning · Privacy-preserving

F. Tao · Z. Sun (✉) · R. Liang · R. Shao · Y. Chai · Y. Wang
Cyberspace Institute of Advanced Technology, Guangzhou University, Guangzhou, China
e-mail: sunzhe@gzhu.edu.cn

R. Liang
Guangxi Key Laboratory of Cryptography and Information Security, Guilin, China

© The Author(s), under exclusive license to Springer Nature Switzerland AG 2024
S. Li (ed.), *Computational and Experimental Simulations in Engineering, Mechanisms and Machine Science* 145, https://doi.org/10.1007/978-3-031-42987-3_55

791

55.1 Introduction

Currently, the big data industry and artificial intelligence applications have been developing rapidly. However, in real-life scenarios, big data is scattered among different government departments and enterprises. There are issues such as conflict of interest and user privacy and security between different departments. Gradually, data silos are formed, hindering data sharing. To address the problem of data silos, Google first introduced the concept of federated learning in 2016 [1–3], with the aim of all parties learning a global model together without sharing data. Federated learning as a deep learning paradigm can work across data structures, across institutions, and without domain and algorithm restrictions, while having the advantages of undamaged model quality, protecting privacy, and ensuring data security. However, big data and artificial intelligence techniques are not limited to deep learning, but also include traditional machine learning algorithms such as decision trees [4], random forest [5], clustering [6], Bayesian classification [7], support vector associative machines [8], EM algorithms [9], and Adaboost algorithms [10]. These algorithms often have already acquired mature models in information services and business, and have been tested over time. And traditional machine learning models based on statistics and probability also have an advantage over deep learning in terms of interpretability, which can help companies analyze the deeper reasons behind the phenomena. Therefore, Google subsequently introduced the concept of federated analytics [11], which was extended to the federated machine learning domain via the federated deep learning framework. Unlike Federated Deep Learning, Federated Machine Learning cannot directly copy the framework of Federated Deep Learning because of the different operation mechanisms but needs to design each machine learning method delicately and carefully, which is one of the reasons why Federated Machine Learning has not been widely used in the Big Data industry (Fig. 55.1).

Random forest [5] is a highly representative machine learning algorithm that contains classifiers with multiple decision trees whose output classes are determined by the plurality of the output classes of individual trees, which is well suited for structured data and is widely used in financial risk control, urban anomaly detection, and smart transportation. However, the widespread diffusion of random forest algorithms in big data applications has encountered two core key problems: first, traditional random forest algorithms need to be centrally trained by servers after collecting raw data from users. However, raw user data is closely related to the individual user and may directly contain sensitive information, such as personal age, race, and disease information. Such data, if leaked, may appear to be maliciously rejected by medical commercial insurance; second, the training data used by users for random forest may indirectly carry implicit sensitive information, which may make the published random forest model be correlated and analyzed for more and deeper private information. Paradoxically, random forest algorithms rely on large amounts of data collection and fusion, and their application will be severely limited if they do not have access to complete and rich information to train models and develop techniques. Therefore, there is an urgent need to design a privacy-enhanced

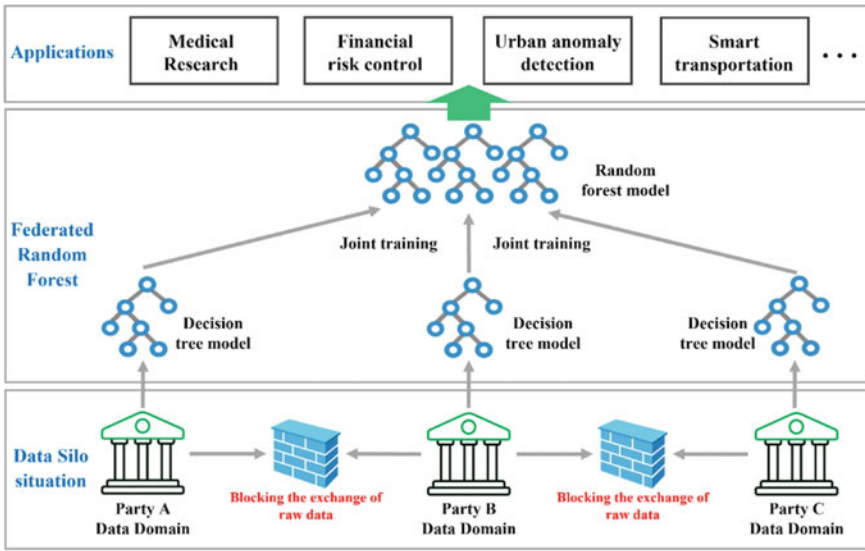


Fig. 55.1 Federated random forest

federated random forest model to bridge the gap between real applications and “data silos” of structured data.

However, there are relatively few studies on federated random forest, which are limited in terms of practicality and privacy-preserving effects. Some proposed cryptography-based federated random forest [12], which effectively solves the data silo problem, but cannot withstand inference attacks initiated by servers [13]. Others have proposed centralized random forest based on differential privacy [14–18], where the server needs to collect raw user data for training and the inclusion of differential privacy noise leads to a significant decrease in the accuracy of the prediction results and poor usability of the model.

To solve the above problems, this paper designs a differential privacy-based federated random forest training scheme, where users train CART decision tree models locally and submit them to the server, avoiding direct data sharing, effectively solving the data silo problem and promoting joint cross-domain data analysis efforts in the big data industry. To resist new privacy attacks such as membership inference attacks and attribute inference attacks, noise satisfying differential privacy is added to the decision tree construction process, and the decision tree model with noise is uploaded to the server, which then aggregates it into a random forest model. To further improve the model usability, the server-client performs multiple rounds of iterations to optimize the random forest model. This results in a usability-strong, privacy-enhanced federated random forest model. Our contributions are three-folds:

- According to the characteristics of the federated random forest, the differential privacy mechanism is fused with the distributed user decision tree model to prevent

inference attacks launched by the server or other potential attackers through the noise mechanism and to improve the privacy-preserving of the participating users' training data.

- In the training process of the client-side decision tree, the Gini index is used to select split points and split features for the decision tree, and randomly select feature points for noise addition by introducing the idea of Bagging integration [19], which effectively reduces the global noise in the federated random forest and thus improves the accuracy of the analysis model.
- The aggregated random forest is evaluated on the server side, and the Gini index threshold is fed back to guide the client to optimize the decision tree model; the client re-establishes the CART decision tree based on the Gini index threshold, privacy budget, and other data sent from the server, and improves the classification accuracy of the federated random forest model through multiple iterations.

This paper will introduce related work in Sect. 55.2, a scheme based on differential privacy federated learning in Sect. 55.3, experiments and analysis of results in Sect. 55.4. Finally, the conclusion will be drawn in Sect. 55.5.

55.2 Related Work

The study of federated machine learning has received a lot of attention from researchers after Google proposed the federated learning paradigm. However, research specifically on federated random forest is still in its infancy. Liu et al. [11] of JD Digital Science designed a federated random forest model that conforms to the federated machine learning paradigm by redesigning the tree-building algorithm, applying encryption methods, and establishing a third-party trusted server to avoid directly sharing the original training data for random forest training. This method can effectively ensure that parameters of the federated random forest are not obtained by malicious attackers or servers during the training process, but it cannot prevent the random forest model released after training from being subjected to an implemented member inference attack. To avoid publishing models that leak private information from users' training data, researchers have prevented inference attacks [13] by adding noise to the construction process of random forest [12]. Since no differential privacy mechanism for federated random forest has been identified yet, most of the existing work is directed at centralized learning of federated random forest. Blum et [14], al proposed a differential privacy-based random forest construction algorithm SuLQ-based ID3 whose main idea is to add noise using the Laplace mechanism whenever the information gain of a feature is computed, and then generate a decision tree and compose a random forest. The addition of noise resulted in a significant deterioration in the accuracy of the forecast results. Although noise-addition optimization methods such as PINQ-based ID3 [15], DiffP-ID3 [16], DiffGen [17], and DiffPRF [18] were proposed continuously, they always had a significant influence on the accuracy of random forest. The reason for this is that, regardless of the grouping and

personalized noise addition, the noise interferes with all the features of the random forest, making the combined noise in the whole random tree too large. In addition, since the current construction scheme of the federated random forest [11] mainly uses one-time aggregation, it makes the aggregation results without feedback to the model training participants, leaving the user with no opportunity to correct for the effects of using differential privacy noise addition, further reducing the usability of the federated random forest.

There are currently two key problems in the federated random forest: first, the resistance to novel privacy attacks in the federated random forest framework is insufficient. Existing cryptography-based federated random forest protection methods cannot resist membership inference attacks launched by central servers and other potential attackers to infer whether a user belongs to a sensitive dataset or has a certain sensitive attribute after publishing the model, and it is not yet consulted to federated random forest-oriented differential privacy preserving scheme, how to design targeted differential privacy noise addition mechanism is the current urgent problem. Second, the existing differential privacy mechanism has a large impact on the usability of the random forest model. The existing differential privacy mechanism in random forest adds a large amount of noise in the construction process, which leads to poor model accuracy; the existing federated random forest algorithm establishes the random forest model with only one round of communication between the client and the server, which lacks the model optimization process and may lead to the poor classification of the final model.

55.3 Method

55.3.1 Overall Structure

In this paper, we argue that there are still two difficulties in privacy-preserving techniques in federated random forest: first, how to design local differential privacy mechanisms for random forest models to meet the requirements of differential privacy theory, to resist new privacy risks such as inference attacks; second, how to achieve a balance between privacy-preserving strength and model accuracy, and reduce the impact of differential privacy plus noise mechanisms on model accuracy in the process of decision tree construction and federated random forest aggregation. Therefore, this paper will mainly address the problems that exist in the above two areas. First, the defense against inference attacks is achieved by designing a differential privacy mechanism applicable to the federated machine learning paradigm, where the privacy budget is locally adjusted by the user; then, the idea of Bagging integration [19] is introduced in the decision tree construction process to randomly select features for noise addition, thus reducing the amount of noise for a single client; finally, the Gini index threshold is carefully designed to guide the client to continuously adjust the decision tree to select split points and split features to improve the

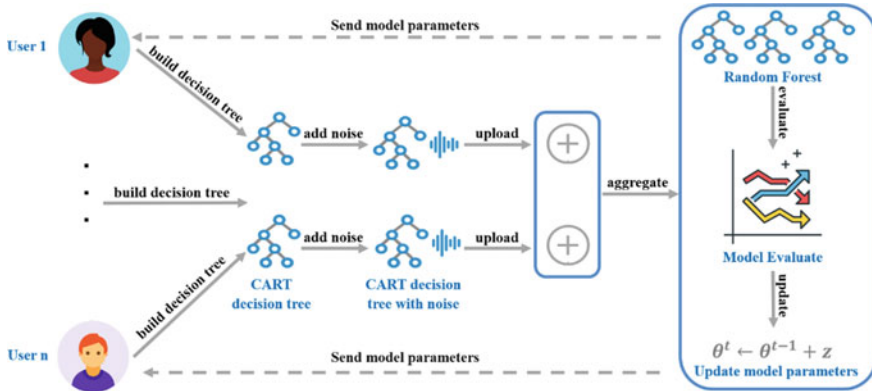


Fig. 55.2 The system architecture of FEDEST

global accuracy of the federated random forest through multiple rounds of iterations. The system architecture of FEDEST is shown in Fig. 55.2.

55.3.2 Privacy Enhancement

In this paper, CART classification trees are used as the base decision trees of the federated random forest project. The random forest consists of multiple decision trees, which are constructed by individual clients, and then the server converges the decision trees of individual clients into a forest, which becomes a global model, which satisfies the federated machine learning paradigm well. The main decision trees are ID3, C4.5, and CART. ID3 can have multiple branches, but cannot handle continuous features, while C4.5 has a preference for features with a small number of values. In contrast, the Gini index is used to select the best splitting features for CART decision tree classification, avoiding the limitations of ID3 and C4.5 which have a preference for the number of features to be taken. Moreover, the CART decision tree construction process can be integrated with differential privacy mechanisms relatively easily, which is an excellent base scheme for framing a privacy-enhanced federated random forest training framework. However, there is no differential privacy-preserving scheme for federated random forest yet.

To address this problem, a federated random forest training framework based on differential privacy is designed in this paper. First, we define the differential privacy mechanism that satisfies the random forest.

Definition 1 (Differential privacy [20]) For any randomized algorithm M such that any subset of its output is Ω . An algorithm M is said to provide ϵ -DP if its output on any of the adjacent data sets D and D' satisfies the following conditions:

$$Pr[M(D) = \Omega] \leq exp(\epsilon) \cdot Pr[M(D') = \Omega] \tag{55.1}$$

where adjacent dataset refers to the two datasets that differ by at most one record. The non-negative parameter ϵ is the privacy budget, and the smaller ϵ is, the higher the degree of privacy preserving.

Definition 2 (*Global sensitivity* [20]) For a function $f: D \rightarrow R^d$, the input is a dataset D and the output is a d -dimensional real vector for arbitrary neighboring datasets D and D' :

$$\Delta f = \max_{D, D'} \|f(D) - f(D')\|_1 \quad (55.2)$$

where Δf is called the global sensitivity of the function f and $\|f(D) - f(D')\|_1$ is the 1-order parametric distance between $f(D)$ and $f(D')$.

Theorem 1 (Laplace mechanism [21]) For any function f , define $M(D) = f(D) + Y$ as the Laplace mechanism, where Y is an independent random variable drawn from the $Lap(0, \Delta f/\epsilon)$. distribution and $Lap(0, \Delta f/\epsilon)$ denotes Laplace random noise with mean 0 and variance $2\Delta f^2/\epsilon^2$.

In the training framework of FEDEST, first, the server announces the number of decision trees n , Gini index thresholds G_{Gini} , and randomly selects n clients to build CART decision trees, and the clients receive the number of decision trees T , Gini index thresholds from the server and customize the privacy budget ϵ . The client builds a CART decision tree based on its dataset and adds Laplace noise to each node in the tree, then uploads the noisy CART decision tree to the server. The server aggregates the decision trees uploaded by T clients into a random forest, and then adjusts the Gini index threshold and the number of features Y according to the model classification effect and sends them to the client, which builds the decision trees according to the Gini index threshold and the number of features Y again and uploads them to the server until the effect of the random forest model aggregated by the server reaches the expected effect.

55.3.3 CART Classification Tree

In this paper, we propose a selective noise addition mechanism for CART decision tree construction for the problem of excess noise addition in the process of decision tree construction by existing differential privacy mechanisms. Most of the current methods combining decision trees with differential privacy use the Laplace mechanism to add noise in each calculation of information gain of features, and then generate decision trees and compose random forest. The added noise will be added for all features of the whole decision tree and repeatedly superimposed in the process of forming the random forest, causing the problem of the sharp decrease in model accuracy.

To solve this problem, this paper adopts the idea of Bagging integration [19] to randomly select feature points for noise addition, which reduces the total noise of the global random forest and improves the accuracy of the model by reducing the noise added during the construction of each decision tree. Specifically, the client defines its differential privacy budget after receiving the number of decision trees T and the Gini index threshold from the server. The rules for client training each CART decision tree are as follows: **Step 1:** Assume that the client training set size is N . For each CART decision tree trained by the client, D training samples are randomly and replayed selected from the training set as the training set of the decision tree; **Step 2:** Assume that the client training set feature dimension is X , then specify the number $Y \ll X$, so that at each node, Y feature dimensions are randomly selected from X and the Gini index is used to compute the best feature among the Y feature dimensions to split the nodes. The value of Y is kept constant during the growth of the random forest; **Step 3:** For the CART decision tree trained by the above M training samples with feature dimension Y , Laplace noise is added to each node in the decision tree.

The Gini index is calculated by dividing D into D_1 and D_2 for each possible value a for each feature A , according to whether $A(x) = a$ holds, and calculating the Gini index when $A(x) = a$ with the following formula.

$$G_{Gini}(D, A) = \frac{|D_1|}{|D|} G_{Gini}(D_1) + \frac{|D_2|}{|D|} G_{Gini}(D_2) \quad (55.3)$$

$$G_{Gini}(D) = 1 - \sum_{k=1}^K \left(\frac{|C_k|}{|D|} \right)^2 \quad (55.4)$$

where D_k represents the subset of samples in D that belong to the k -th class and K is the number of classes. Among all possible features A and all their possible splitting points a , the feature with the smallest Gini index and its corresponding splitting point is selected as the best splitting feature and the best splitting point. The training dataset is assigned to the sub-nodes based on the best splitting feature and the best splitting point. Then the above two steps of division and splitting are performed recursively for the established sub-nodes until the Gini index of the sample dataset is less than the threshold value, then stop. The next step is to assign a privacy budget ε to each node, which is calculated as follows:

$$\varepsilon_p = \frac{\varepsilon_t}{N} \quad (55.5)$$

where ε_t is the custom privacy budget per tree, ε_p is the privacy budget assigned to each node, and N is the number of nodes.

Algorithm 1. CART decision tree building satisfying ϵ -DP privacy-preserving algorithm.

INPUT: Training set D , feature set X , privacy budget ϵ_t
OUTPUT: CART decision tree with noise T^*

Initialize the Gini index threshold G_{Gini} that the client receives from the server, customize the privacy budget ϵ_t for the client;
 From the training set D of capacity N , the self-service sampling method is used to draw N samples as a training set $D_t \subseteq D$;
 For the current training set D_t , m different features Y are randomly selected from the feature set X , $m = \text{Ibsize}(X)$;
 Calculating the Gini index $G_{Gini}(D_t, A)$;
While $G_{Gini}(D_k) > G_{Gini}$ **do**
 Divide D_k into two parts D_1 and D_2 and use Eqs. (55.3, 55.4) to calculate the Gini index while $A(x) = a$;
 Select the feature with the smallest Gini index and its corresponding the splitting point $a\{\min[G_{Gini}(D_k, A)]\}$;
 Assign the training dataset to 2 sub-nodes based on the best split feature and the best split point;
End
 Generate CART decision tree T ;
 Calculate the privacy budget for each node $\epsilon_p = \frac{\epsilon_t}{N}$;
 Add Laplace noise using a mechanism that satisfies ϵ_p -DP
Return CART decision tree with noise $T^* = \text{NoisyCount}(T)$.

55.3.4 Model Evaluation and Optimisation

In this paper, we propose a privacy-preserving parameter optimization method based on multi-round communication federated random forest for the problem of lack of feedback mechanism on the final result in the existing federated random forest. The accuracy of the random forest is mainly related to two factors: first, the greater the correlation of any two decision trees in the random forest, the smaller the accuracy of the random forest; second, the greater the accuracy of each decision tree, the greater the accuracy of the overall random forest. The classification ability of each tree in the random forest is mainly related to the number of randomly selected features Y and the threshold of the Gini index that determines the best features, and by adjusting these two parameters, the correlation and classification ability of the decision trees will change accordingly. So the key problem is how to choose the optimal number of features Y and the Gini index threshold of the best features. However, the current federated random forest framework lacks a mechanism to feed the optimal Gini index threshold to the client.

To solve this problem, this paper uses a multi-round communication-based federated random forest feedback mechanism to pass the optimal Gini index threshold to the client. After the client uploads the CART decision tree with noise to the server. The server aggregates the decision trees uploaded by T clients into a random forest.

The server calculates the Out-of-bag Error (OOB Error) of the random forest, which is calculated as follows: for each unselected sample, the classification of the decision tree for which it is an OOB sample is calculated. The OOB error is an unbiased estimate of the generalization error of the random forest, and its result approximates the k -fold cross-validation that requires extensive computation. The server adjusts the Gini index threshold based on the model effect and sends it to the client, which rebuilds the decision tree based on the Gini index threshold and the number of features Y and uploads it. This process is repeated until the random forest model achieves the expected results.

Algorithm 2. Parameter optimization algorithm for multi-round communication.

INPUT: CART decision tree with noise T^*

OUTPUT: Federated Random Forest FF

Initialize Out-of-bag Error $oob_score(0)$, Maximum iteration number N ;

The server receives the CART decision trees with noise uploaded by the clients $FF_0 = T_1^* \cup T_2^* \cup \dots \cup T_n^*$;

Set $t_0 = oob_score(FF_0), i = 0$;

While $t_i > oob_score(0)$ and $i < N$ do

Update Gini index threshold G_{Gini} and feature number $size(Y)$;

Sending parameters G_{Gini} . and $size(Y)$ to the clients;

Clients update the decision tree model T^* and upload;

Server aggregated decision tree model s $FF_i = T_1^* \cup T_2^* \cup \dots \cup T_n^*$;

Calculating $t_i = oob_score(FF_i)$;

End

Return Federated Random Forest $FF = T_1^* \cup T_2^* \cup \dots \cup T_n^*$.

55.4 Experiments

55.4.1 Experimental Setup

Environment settings: Both the random forest model and the differential privacy algorithm in this paper were compiled using Python (3.8.3) and run on a GPU server (8NVIDIA TELSAs T4 GPUs 16 GB). The machine learning models in this paper's experiments were constructed based on the sklearn library and the numpy (1.18.5) library was used to encode the data.

Set: Adult: The Adult dataset is a dataset from a classic data mining project, which was extracted from the 1994 U.S. Census database. adult contains 48,842 sample sizes and 14 feature sizes. The features are information about the age, type of work, education, and occupation of the individuals. **BRFSS:** The BRFSS is a health-related telephone survey system in the U.S. that collects state data on health-related risk behaviors, chronic health conditions, and preventive service use among U.S. residents.

The BRFS contains a sample size of 50,000 and a number of 36 characteristics. Characteristics are the socioeconomic and lifestyle attributes of individuals.

Baseline Methods: We evaluate the performance of our FEDEST on Adult and BRFS datasets by comparing it with some baseline methods, including (1) *CART decision trees* [4]: CART is a classical implementation of decision tree models that can support both classification and regression tasks. (2) *Random Forest(RF)* [5]: It is a classifier containing multiple CART decision trees whose output is determined by the plurality of the categories output by individual trees.

55.4.2 Matrics

The purpose of the experiment is to study the feasibility and operational efficiency of the federated random forest algorithm based on differential privacy. First, the client constructs and trains the CART decision tree model and adds Laplace noise satisfying differential privacy to obtain the noise-added CART decision tree model, then uploads it to the server for aggregation into a random forest model, and finally uses the aggregated model for classification prediction. The feasibility of the federated random forest privacy-preserving algorithm is demonstrated by comparing the accuracy, recall, *F1* score, and computational efficiency of the federated random forest privacy-preserving algorithm under different parameters.

$$precision = \frac{TP}{TP + FP} \quad (55.6)$$

$$recall = \frac{TP}{TP + FN} \quad (55.7)$$

$$F1 - score = \frac{2 \times precision \times recall}{precision + recall} \quad (55.8)$$

To test the effectiveness of the federated random forest privacy-preserving algorithm, we set up multiple sets of comparisons: (1) between different numbers of iterations; (2) between different depths of decision trees; (3) between different privacy-preserving budgets, and (4) between the federated random forest privacy-preserving algorithm in terms of time consumption.

55.4.3 Experimental Results

According to the definition and implementation mechanism of ϵ -DP privacy-preserving, the size of the privacy-preserving budget determines the size of the added noise. The size of the noise is inversely proportional to ϵ . The larger ϵ is, the smaller

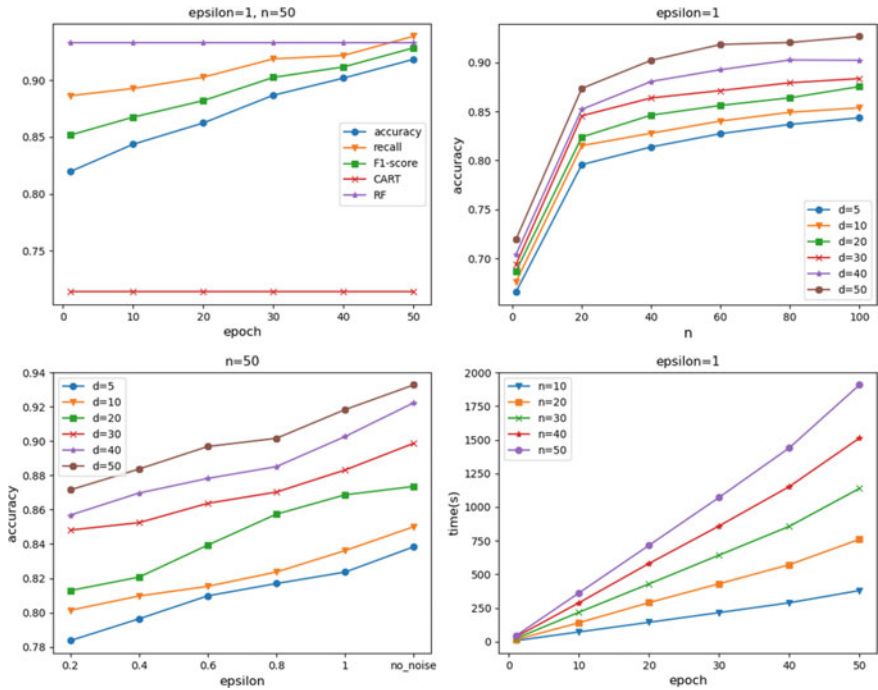


Fig. 55.3 Experimental results for the Adult dataset

of the decision tree in the random forest is small, the classification accuracy is mainly influenced by the privacy-preserving budget because the decision tree divides the dataset more coarsely. As the depth of the decision tree increases, the decision tree divides the dataset more and more finely and the classification results become more and more accurate, resulting in a classification accuracy that is mainly influenced by the depth, the greater the depth, the higher the classification accuracy. When using the Laplace mechanism to add noise to the sample size, the sample size is more affected by the noise, resulting in a generated decision tree that does not reflect the real situation of the dataset and a lower classification accuracy. However, the Gini index has no preference for the number of values available for a feature and uses multiple division operations in its calculation, so using the Gini index as a metric when selecting the best split feature can achieve better results than information gain. It can be seen in the experimental results that FEDEST and the federal forest without privacy preserving have close classification accuracy when the privacy preserving budget is 1 and the tree depth is the same, indicating that our method has good classification ability.

On the other hand, our approach is evaluated from the point of view of efficiency. From the experimental results, it can be seen that when the privacy-preserving budget is 1 and the number of users is the same, the larger the number of iterations epoch, the higher the time consumption of the algorithm. When the number of iterations is

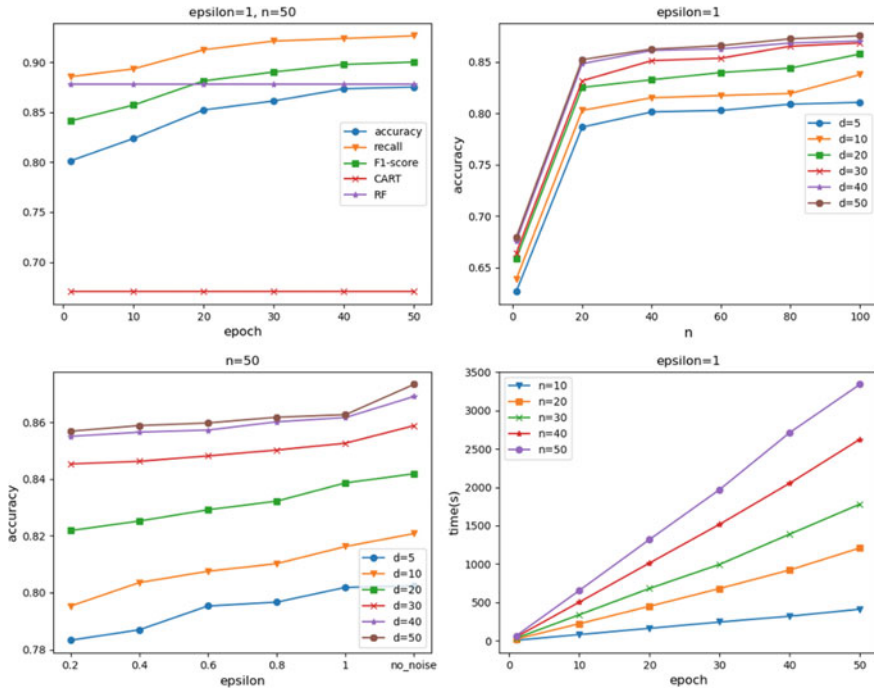


Fig 55.4 Experimental results for the BRFSS dataset

the same, the larger the number of users n , the higher the time consumption of the algorithm. From the experimental results, it can be seen that the algorithm consumes a maximum of 3340s of time when the number of iterations is a maximum of 50 and the number of users is 50. When the number of iterations is 1 and the number of users is 10, the minimum time consumption of the algorithm is 8.53s. The time consumption of the algorithm is mainly in the training of the CART decision tree and the client-server communication.

55.5 Conclusions

In this paper, we propose a differential privacy-based federated random forest model, called FEDEST, in which we design a differential privacy-based federated random forest training scheme, avoid direct data sharing, and effectively solve the problem of data silos. To improve model usability, we design a selective noise addition mechanism for CART decision tree construction, which effectively reduces the amount of noise added to each decision tree. Also, the privacy-preserving parameter optimization method based on multi-round communication federated random forest enables the server and client to perform multiple iterations to optimize the random forest

model. The results of our experimental study show that our FEDEST can reach the accuracy of the non-federated random forest model in overall accuracy on two commonly used datasets.

Acknowledgements This work was supported in part by the National Natural Science Foundation of China (No. 62002077), in part by Guangdong Basic and Applied Basic Research Foundation (No. 2020A1515110385), in part by Guangzhou Science and Technology Plan Project (No. 202102010440), in part by Guangxi Key Laboratory of Cryptography and Information Security (No. GXIS202119).

References

1. McMahan, B., Moore, E., Ramage, D., et al.: Communication-efficient learning of deep networks from decentralized data. *Artif. Intell. Stat.* 1273–1282 (2017)
2. McMahan, B., Ramage, D.: Federated learning: collaborative machine learning without centralized training data. *Google Res. Blog.* 3 (2017)
3. Konečný, J., McMahan, H.B., Ramage, D., et al.: Federated optimization: distributed machine learning for on-device intelligence. *arXiv preprint arXiv:1610.02527.* (2016)
4. Quinlan, J.R.: Induction of decision trees. *Mach. Learn.* **1**(1), 81–106 (1986)
5. Breiman, L.: Random forest. *Mach. Learn.* **45**(1), 5–32 (2001)
6. MacQueen, J.: Classification and analysis of multivariate observations[C]//5th Berkeley Symp. *Math. Statist. Probability.* 281–297 (1967)
7. Webb, G.I., Keogh, E., Miikkulainen, R.: Naïve bayes. *Encycl. Mach. Learn.* **15**, 713–714 (2010)
8. Burges, C.J.C.: A tutorial on support vector machines for pattern recognition. *Data Min. Knowl. Disc.* **2**(2), 121–167 (1998)
9. Dempster, A.P., Laird, N.M., Rubin, D.B.: Maximum likelihood from incomplete data via the EM algorithm *J. Roy. Stat. Soc.: Ser. B (Methodol.)* **39**(1), 1–22 (1977)
10. Freund, Y., Schapire, R.E.: A decision-theoretic generalization of on-line learning and an application to boosting. *J. Comput. Syst. Sci.* **55**(1), 119–139 (1997)
11. Wang, D., Shi, S., Zhu, Y., et al.: Federated analytics: opportunities and challenges. *IEEE Netw.* (2021)
12. Liu, Y., Liu, Y., Liu, Z., et al.: Federated forest. *IEEE Trans. Big Data* (2020)
13. Tramèr, F., Zhang, F., Juels, A., et al.: Stealing machine learning models via prediction {APIs}. In: *25th USENIX Security Symposium (USENIX Security 16)*, pp. 601–618 (2016)
14. Blum, A., Dwork, C., McSherry, F., et al.: Practical privacy: the SuLQ framework[C]. In: *Proceedings of the twenty-fourth ACM SIGMOD-SIGACT-SIGART Symposium on Principles of Database Systems*, pp. 128–138 (2005)
15. McSherry, F.D.: Privacy integrated queries: an extensible platform for privacy-preserving data analysis. In: *Proceedings of the 2009 ACM SIGMOD International Conference on Management of Data*, pp. 19–30 (2009)
16. Friedman, A., Schuster, A.: Data mining with differential privacy. In: *Proceedings of the 16th ACM SIGKDD International Conference on Knowledge Discovery and Data Mining*, pp. 493–502 (2010)
17. Zhu, T., Xiong, P., Xiang, Y., et al.: An effective differentially private data releasing algorithm for decision tree. In: *2013 12th IEEE International Conference on Trust, Security and Privacy in Computing and Communications*, pp. 388–395, IEEE (2013)
18. Patil, A, Singh, S.: Differential private random forest. In: *2014 International Conference on Advances in Computing, Communications and Informatics (ICACCI)*, pp. 2623–2630. IEEE (2014)

19. Breiman, L.: Bagging predictors. *Mach. Learn.* **24**(2), 123–140 (1996)
20. Dwork, C.: A firm foundation for private data analysis. *Commun. ACM* **54**(1), 86–95 (2011)
21. Dwork, C., McSherry, F., Nissim, K., et al.: Calibrating noise to sensitivity in private data analysis. In: *Theory of Cryptography Conference*, pp. 265–284. Springer, Berlin (2006)

Chapter 56

Study on Analytical Prediction Method for Plastic Response of Folded Sandwich Plates Under Explosion Impact Loads



Yimei Xia, Shuai Zong, Kun Liu, Jiaxia Wang, and Zhenguo Gao

Abstract This paper analyzes the structural response of folded steel sandwich plates under an air explosion shock load. According to the analytical calculation method of the sandwich plate's structural deformation, the structural deformation prediction formula under the action of explosion impact load is obtained. At the same time, the nonlinear finite element analysis software ABAQUS was used to simulate the related calculation conditions and verify the structural plastic deformation formula. On this basis, the sensitivity analysis of parameters of sandwich panel structural size was conducted to study the influence of parameters on sandwich panel structural size, and the applicability of the analytical calculation method for folding sandwich panel was verified, providing a reference for the design and impact resistance evaluation of steel folding sandwich panel.

Keywords Folded sandwich plate · Impact load · Plastic deformation · Analytical calculation · Numerical simulation

56.1 Introduction

Ships are frequently threatened by blast impact loads during training and combat, and the blast impact wave acting on the structure of the vessel can cause damage, deformation, or structural failure. As a novel protective device, steel collapsible sandwich panels have advantages such as lightweight, high strength and good impact resistance, and are increasingly being used in industries such as airplanes, ships, and, automobiles [1]. Fleck [2] established a simplified computational method based

Y. Xia

Marine Design and Research Institute of China, Shanghai 200011, China

S. Zong · K. Liu (✉) · J. Wang · Z. Gao

School of Naval Architecture and Ocean Engineering, Jiangsu University of Science and Technology, Zhenjiang 212003, Jiangsu, China

e-mail: kunliu@just.edu.cn

on the elastic–plastic material model for the analysis of the deformation of sandwich beams subjected to impact loading, which can be used to analyze the dynamic response of steel sandwich panels subjected to explosive impact loads. The plastic response of square honeycomb sandwich panels subjected to explosive impact loads was investigated by Jun and Jun [3, 4], and gave the computational formula for the residual strain, and simulated finite element simulation of the square honeycomb sandwich panels via simulation software. The reliability of the theoretical formula was confirmed by comparing the simulation results to the analytical formula. Qiu [5] proposed a simplified analysis model for analyzing the displacement response of four-sided circular rigid multilayer plates subjected to impact loads. Zili et al. [6–8] have investigated the protective performance of collapsible sandwich panels subjected to blast loads underwater using both experimental and simulation methods. The research revealed that the plastic deformation of the sandwich panel facing and the core can effectively absorb the energy of the shock wave. Zhang and Cheng [9–11] carried out experimental studies on the damage mechanism of collapsible sandwich panels under close-range air blast loads, by investigating the large local deformation and failure modes of the sandwich panel, and by discussing the effects of plate thickness, core thickness, core angle and core fillers on the impact strength of the sandwich panel.

From a design point of view, simplified theoretical prediction equations are reliable in helping to evaluate the structural design. Sandwich panels, however, pose computational difficulties due to their diverse core structures, and there is currently a relative paucity of theoretical research on the response analysis of collapsible sandwich panels subjected to impact loads. Since the combination of foldable sandwich panels, which are anisotropic structures, and explosions, which are transient and highly nonlinear processes, further increases the difficulty of the theoretical solution, it is necessary to simplify both the response process and the method of deformation of the sandwich panels. This paper is based on the theorems of kinetic energy, energy conservation, and structural plastic mechanics, and analyzes the structural deformation characteristics of pliable steel sandwich panels subjected to impact loads. From which the analytical plastic strain calculation method for foldable sandwich panels is derived, and verified via finite element simulation calculations. In addition, the influence of the geometric parameters of the sandwich panel on the structural shaping response is discussed by changing the geometric parameters of the sandwich panel, further verifying the reliability of the improved theoretical prediction method.

56.2 Method of Theoretical Analysis and Prediction for Sandwich Panels

56.2.1 Initial Kinetic Energy of the Sandwich Panel

The blow-up impact problem belongs to a strongly nonlinear problem. When the sandwich panel is subjected to blast loading, due to its complex real dynamic response process, it is necessary to simplify it appropriately during the theoretical analysis. The impact of the shock wave on the sandwich panel causes its deformation to rapidly transition from the elastic stage to the plastic stage. For this reason, when analyzing it, the elastic effect of the sandwich panel is ignored and it is treated as an ideal stiff-plastic material.

Where the shock wave generated by the blast impact loading acts on the sandwich panel surface, the incident impulse (I_+) generated by the shock wave per unit area on the sandwich panel is [12]: In this case:

$$I_+ = A_i \frac{\sqrt[3]{m_e^2}}{r} \quad (56.1)$$

$$I = 2I_+ \quad (56.2)$$

where A_i is a coefficient, $A_i = 200 \sim 250$, m_e is the equivalent weight of TNT explosive, r is the explosion distance, and I is the reflected impulse.

When the shock wave acts on the sandwich panel, due to the fast speed and short duration of the shock wave, the core and back-facing panel can be regarded as stationary, and only the facing panel has an initial velocity after the shock wave ends. Based on the momentum theorem, the initial velocity (v_i) of the upper panel is:

$$v_i = \frac{I}{\rho_f t_f} \quad (56.3)$$

According to the kinetic energy theorem of object motion, ignoring the influence of its boundaries, the initial kinetic energy (E_0) obtained by the sandwich panel is:

$$E_0 = \frac{1}{2} S \rho_f t_f v_i^2 = \frac{I^2 S}{2 \rho_f t_f} \quad (56.4)$$

where S is the area of the sandwich panel, ρ_f is the density of the sandwich panel material, and t_f is the thickness of the sandwich panel.

56.2.2 Compression of Sandwich Panel Core

Once the front blast face panel obtains initial kinetic energy, the core of the sandwich panel begins to undergo compressive deformation due to the action of the initial kinetic energy, and at the same time under the action of the reaction force of the nucleus, the forward blast face panel decreases in velocity while the core and aft blast face panel begin to accelerate. The whole sandwich panel will eventually have the same velocity, and, by the law of conservation of momentum, the velocity (v_k) of the whole sandwich panel at that time can be obtained as follows:

$$v_k = \frac{I}{2\rho_f t_f + \rho_c h_c} \tag{56.5}$$

where ρ_c is the equivalent density of the core, $\rho_c = \bar{\rho}\rho_f$, $\bar{\rho}$ represents the relative density coefficient between the core and the material, and h_c is the height of the core.

Referring to Fig. 56.1, for the I-shaped folding sandwich panel, the relative density coefficient $\bar{\rho} = 2t_c/d_p$ is; for the U-shaped folding sandwich panel, the relative density coefficient $\bar{\rho} = 2t_c(d_p - 2d_f)/(h_c d_p \cos \theta)$ is.

Then, according to the law of kinetic energy, the kinetic energy of the sandwich panel is:

$$E_k = \frac{I^2 S}{2(2\rho_f t_f + \rho_c h_c)} \tag{56.6}$$

When the core of the sandwich panel is compressed, energy conversion occurs, and the core layer of the sandwich panel absorbs part of the initial kinetic energy of the sandwich panel, converting it into the plastic deformation energy of the core.

The energy absorbed by the compression of the core layer is:

$$E_a = E_i - E_k \tag{56.7}$$

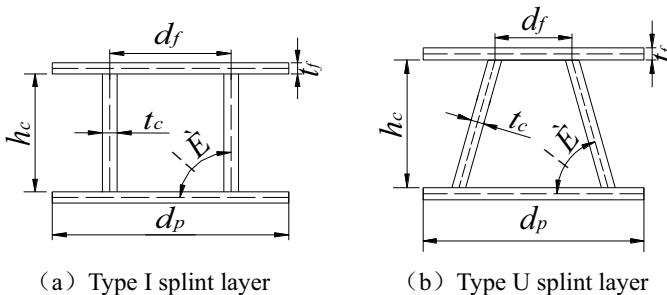


Fig. 56.1 Geometric parameters of folded sandwich plate

For a rectangular sandwich panel with the origin of coordinates at the center of the structure, the deformation of the sandwich panel after the core compression can be represented by a trigonometric function as:

$$w(x, y) = w_c \sin\left(\frac{\pi}{2} + \frac{\pi x}{a}\right) \sin\left(\frac{\pi}{2} + \frac{\pi y}{b}\right) \quad (56.8)$$

Therefore, during the compression process, the relationship between the energy absorbed by the sandwich panel and the compression deformation is:

$$\begin{aligned} E_c &= \sigma_c \int_{-a/2}^{a/2} \int_{-b/2}^{b/2} w_c \sin\left(\frac{\pi}{2} + \frac{\pi x}{a}\right) \sin\left(\frac{\pi}{2} + \frac{\pi y}{b}\right) dx dy \\ &= w_c \frac{4ab}{\pi^2} \sigma_c \end{aligned} \quad (56.9)$$

In the formula, σ_c is the equivalent transverse compressive strength of the core, which can be approximately taken as $\sigma_c = \bar{\rho}\sigma_f$, and σ_f is the yield strength of the material [2].

It can be obtained by simultaneous formulas (56.7) and (56.9):

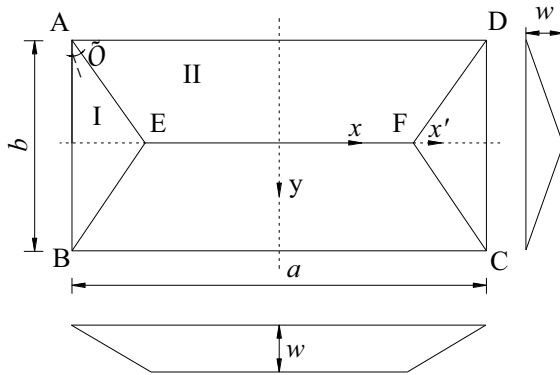
$$w_c = \frac{\pi^2}{4ab\sigma_c} (E_0 - E_a) \quad (56.10)$$

56.2.3 Deformation of the Whole Sandwich Panel

Following the above analysis, the strain and energy absorption of the sandwich panel under impact loading was determined, and the dynamic response of the entire sandwich panel was then analyzed. As the compression of the sandwich panel core ceases, the panels and the core of the sandwich panel gradually become the same velocity, and then the sandwich panel continues to deform. During this period, the sandwich panel undergoes plastic bending and stretching, and its kinetic energy is mainly converted into bending strain energy and tensile strain energy.

To analyze the total deformation of rectangular sandwich plates subjected to explosive impact loads, the total plastic strain is assumed to follow the profile shown in Fig. 56.2 [13]. The sandwich plate is rigidly attached around its edges and deforms into four rigid regions as a result of the impact loading, where two regions are Region I stiffness and two are Region II stiffness, and each rigid region and each rigid region with the boundaries are plastic hinges. Furthermore, it is assumed that the deformation mode of the sandwich panel does not change with time during the process of deformation. The displacement field of each stiffened region can be represented by the following equations: Based on the geometry of the deformed sandwich panel.

Fig. 56.2 Plastic deformation mode of the claimed sandwich plate



Rigid region I:

$$w_i = \frac{\frac{b}{2} \tan \varphi - x'}{\frac{b}{2} \tan \varphi} w = \frac{b \tan \varphi - 2x'}{b \tan \varphi} w \tag{56.11}$$

Rigid region II:

$$w_i = \frac{\frac{b}{2} - y}{\frac{b}{2}} w = \frac{b - 2y}{b} w \tag{56.12}$$

In the equation, a and b are the length and width of the sandwich panel respectively; w is the maximum displacement of the sandwich panel; the angle φ is determined by the following equation [14]:

$$\tan \varphi = \sqrt{3 + \xi^2} - \xi, \xi = \frac{b}{a} \tag{56.13}$$

Taking into account the effects of bending moment and membrane force, the hinge energy dissipation rate of unit length is [15]:

$$D = (M + N w_i) \theta_i \tag{56.14}$$

The total internal virtual work of dynamic plastic deformation of the sandwich panel during deformation is:

$$E_p = \sum_{i=1}^n \int_{l_i} f(M + N w_i) \theta_i dl_i \tag{56.15}$$

where M is the bending moment of the sandwich panel, N is the force exerted by the membrane of the sandwich panel, the parameter w_i is the transverse displacement at

the hinge, θ is the angular velocity of the i -th joint, l_i is the i -th hinge length, and n is the number of hinge points.

The total energy consumption at the hinges of the rectangular deforming sandwich panel structure is given by:

$$\begin{aligned}
 E_p &= 2 \int_{l_{AB}} (M + Nw_i)\theta_{AB}dl_{AB} \\
 &+ 2 \int_{l_{AD}} (M + Nw_i)\theta_{AD}dl_{AD} \\
 &+ 4 \int_{l_{AE}} (M + Nw_i)\theta_{AE}dl_{AE} \\
 &+ \int_{l_{EF}} (M + Nw_i)\theta_{EF}dl_{EF} \quad (56.16)
 \end{aligned}$$

Based on the geometric relationship of the deformed sandwich panel, the values of hinge angular rates θ_{AB} , θ_{AD} , θ_{EF} , and θ_{AE} are approximately taken as:

$$\theta_{AB} = \frac{w}{b \tan \varphi} \quad (56.17)$$

$$\theta_{AD} = \frac{w}{b} \quad (56.18)$$

$$\theta_{EF} = \frac{2w}{b} \quad (56.19)$$

$$\theta_{AE} = \theta_{AB} \cos \varphi + \theta_{AD} \sin \varphi = \frac{w}{b \sin \varphi} \quad (56.20)$$

Substituting Eqs. (56.17) to (56.20) into Eq. (56.16), the total dissipated energy at the hinges during the deformation of the sandwich panel is obtained as:

$$E_p = \left(\frac{2a}{b} + \frac{2 \cos \varphi}{\sin \varphi} - \frac{\tan \varphi}{2} \right) Nw^2 + \left(\frac{4a}{b} + \frac{4 \cos \varphi}{\sin \varphi} \right) Mw \quad (56.21)$$

The membrane force (N) and bending moment (M) are used to describe the plate yield function. The shape of the cross-section and the relative strength and thickness of the panel and core can be seen to affect the shape of the yield surface of the sandwich panel; the sandwich panel calculation is thus different from that of a general planar plate, which may be written in the form [2]:

$$\frac{|M|}{M_0} + \frac{|N|}{N_0} = 1 \quad (56.22)$$

where M_0 is the ultimate bending moment of the sandwich panel; N_0 is the ultimate membrane force of the sandwich panel.

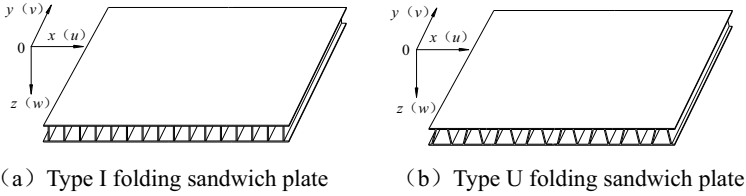


Fig. 56.3 Folded sandwich plate

Sandwich panels are anisotropic structures, and the ultimate bending moment and ultimate membrane force are different in different directions, so they need to be solved separately for different cases.

As shown in Fig. 56.3, for foldable sandwich panels, based on the bending moment and membrane force solution method for flat plates, and combining the characteristics of the sandwich panel structure, the ultimate bending moment and ultimate membrane force perpendicular to the core direction (x-axis direction) can be represented as:

$$M_{0x} = \sigma_f t_f [(h_c - w_{mn}) + t_f] \tag{56.23}$$

$$N_{0x} = 2\sigma_f t_f \tag{56.24}$$

The ultimate bending moment and ultimate membrane force parallel to the core direction (y-axis direction) can be represented as:

$$M_{0y} = \sigma_f t_f [(h_c - w_{mn}) + t_f] + \sigma_c \frac{(h_c - w_{mn})^2}{4} \tag{56.25}$$

$$N_{0y} = 2\sigma_f t_f + \sigma_c (h_c - w_{mn}) \tag{56.26}$$

In the dynamic response problem of sandwich panels, the closed solution of their ultimate deformation is often difficult to obtain. To obtain the most realistic deformation, the yield surface is calculated using the enveloping and inscribed squares of the function [2], as shown in Fig. 56.4.

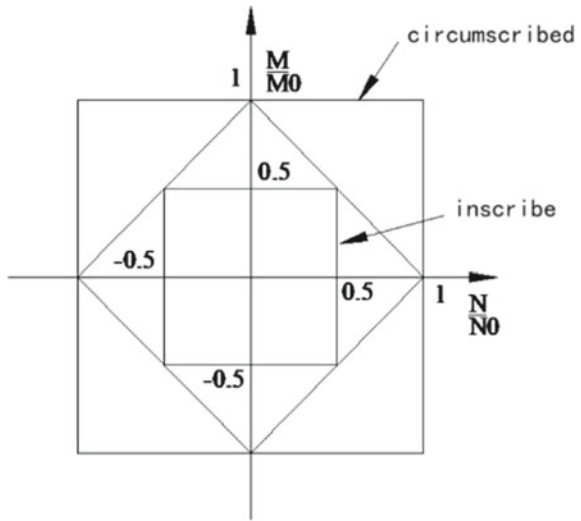
Enveloping square yield surface:

$$|N| = N_0, |M| = M_0 \tag{56.27}$$

Inscribed square yield surface:

$$|N| = 0.5N_0, |M| = 0.5M_0 \tag{56.28}$$

Fig. 56.4 The field curve of the sandwich plate



Using the enveloping square as a yield function will result in a final strain that is smaller than the actual final strain; using the inscribed square as a yield function will result in a final strain that is larger than the actual final strain. Thus, to minimize the error value of the results, the mean value of the results obtained by the formula will be used in the calculation of the final strain of the sandwich panel.

The total energy dissipated when the yield surface is an envelope square is:

$$E_p = \left(\frac{4a}{b} + \frac{2 \cos \varphi}{\sin \varphi} - \tan \varphi \right) N_0 w^2 + \left(\frac{8a}{b} + \frac{8 \cos \varphi}{\sin \varphi} \right) M_0 w \tag{56.29}$$

When the yield surface is an inscribed square, the total dissipated energy is:

$$E_p = \left(\frac{2a}{b} + \frac{\cos \varphi}{\sin \varphi} - \frac{\tan \varphi}{2} \right) N_0 w^2 + \left(\frac{4a}{b} + \frac{4 \cos \varphi}{\sin \varphi} \right) M_0 w \tag{56.30}$$

After the core has finished compressive deformation, its plastic deformation energy will dissipate its initial kinetic energy during overall deformation, so:

$$E_p = E_k \tag{56.31}$$

Substituting Eq. (56.31) into Eqs. (56.29) and (56.30) respectively, we get:

$$\left(\frac{4a}{b} + \frac{2 \cos \varphi}{\sin \varphi} - \tan \varphi \right) N_0 w^2 + \left(\frac{8a}{b} + \frac{8 \cos \varphi}{\sin \varphi} \right) M_0 w = E_k \tag{56.32}$$

The above equation is the final plastic deformation equation for a sandwich panel with an enveloping square as the yield function. Solving this equation gives:

$$w_1 = \frac{-C_1 N_{0i} + \sqrt{(C_2 M_{0i})^2 + 4E_k C_1 N_i}}{2C_1 N_{0i}} \tag{56.33}$$

In the equation, $C_1 = \frac{4a}{b} + \frac{2 \cos \varphi}{\sin \varphi} - 2 \tan \varphi$, $C_2 = \frac{8a}{b} + \frac{8 \cos \varphi}{\sin \varphi}$, $i = x, y$ $C_2 = \frac{8a}{b} + \frac{8 \cos \varphi}{\sin \varphi}$, $i = x, y$

$$\left(\frac{2a}{b} + \frac{\cos \varphi}{\sin \varphi} - \frac{\tan \varphi}{2}\right) N_0 w^2 + \left(\frac{4a}{b} + \frac{4 \cos \varphi}{\sin \varphi}\right) M_0 w = E_k \tag{56.34}$$

The resulting equation is the final plastic strain equation for a sandwich panel with a square inscribed as a yield function. Solving this equation yields:

$$w_2 = \frac{-0.5C_1 N_{0i} + \sqrt{(0.5C_2 M_{0i})^2 + 2E_k C_1 N_{0i}}}{C_1 N_{0i}} \tag{56.35}$$

where the values of C1, and C2 are the same as above, $i = x, y$.

Substitute $M_{0x}, N_{0x}, M_{0y}, N_{0y}$ respectively into Eqs. (56.33) and (56.35) and solve both equations, discarding negative solutions that do not apply. This will give four solutions: $w_{1x}, w_{2x}, w_{1y}, w_{2y}$. The final plastic deformation of the folding sandwich panel under the threat of explosive shock load can then be calculated by taking the average of these results:

$$w = \frac{1}{4}(w_{1x} + w_{2x} + w_{1y} + w_{2y}) \tag{56.36}$$

56.3 Comparison and Analysis of the Results of Theoretical Simulations

To examine the reliability of the above method of analysis, the I-and U-type folding sandwich panels are taken as the objects of investigation, and their dynamic responses are computed and analyzed at different impact loadings. Furthermore, by modifying the aspect ratio, core height, core angle, and material thickness, the influence of the blast load and structural parameters on the structural response is examined, and numerical simulation computations are performed to improve and perfect the theoretical calculation method.

56.3.1 Plastic Response of the Collapsible Sandwich Panels Under Different Impulse Loadings

The first objective is to investigate the dynamic plastic response of a steel folding sandwich plate under different impulse loads. To verify the accuracy of the method in solving for the plastic response of the sandwich plate under different impulsive loads, various sizes of impulsive loads are examined.

For ease of analysis and comparison, momentum is represented by a dimensionless parameter:

$$\underline{I} = \frac{I}{M\sqrt{\frac{\sigma_f}{\rho_f}}} \quad (56.37)$$

where $M = 2\rho_f t_c + h_c \rho_c$ represents the mass per unit area of the sandwich plate.

For the two folding sandwich plates shown in Fig. 56.1, reasonable dimensions are selected according to the structural characteristics of the sandwich plates, and their geometric parameters are shown in Table 56.1:

When using the finite element method to model, the material type is an ideal elastic–plastic material (required for simulation calculation), and the material parameters are as follows: the elastic modulus $E = 2.10 \times 10^5$ MPa, Poisson's ratio $\mu = 0.3$, the material density $\rho_f = 7850$ kg/m³, the yield strength of the material $\sigma_f = 235$ MPa, and the maximum equivalent plastic deformation is taken to be 0.3. A reduced four-node quadrilateral element of integration (S4R) is chosen to model the sandwich plate using shell elements. Since the boundary conditions around the plate and the sandwich plate core boundary stresses are fixed rigidly. To calculate the maximum plastic deformation of the wrinkling sandwich plate under different impulse loads. The central point of the shattered surface may reflect the maximum plastic strain, therefore, when performing a finite element analysis, this point is chosen for numerical analysis.

Combining the results of the analytical calculation with the finite element calculation, we summarize them into the momentum-displacement curves shown in Fig. 56.5. It can be seen from the figure that the displacement curves for the two-fold sandwich plates are identical, and as the loading impulse is increased, the maximum plastic strain of the sandwich plate is gradually increased. There is good agreement between the theoretical solution in this paper and the finite element solution in terms of numerical magnitude and overall trend, with errors typically no greater than 10%,

Table 56.1 Geometric parameter of the folded sandwich plate

Type	a	b	df	dp	hc	tf	tc
	mm	mm	mm	mm	mm	Mm	mm
I-type	23,000	2000	50	50	50	2	2
U-type	3000	2000	25	75	50	2	2

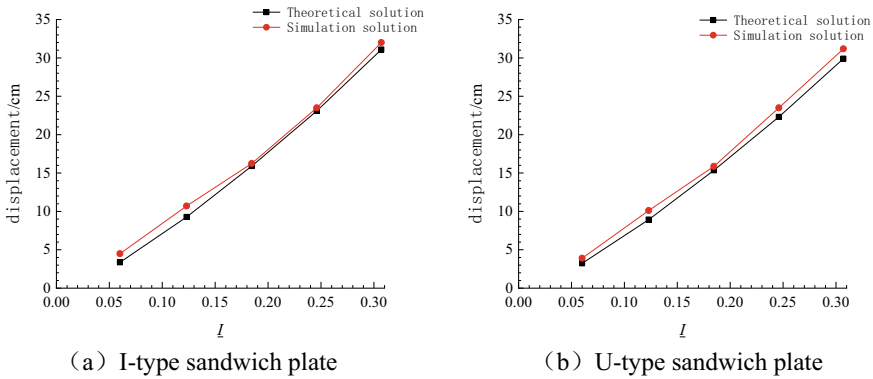


Fig. 56.5 Impulse-displacement curves of folded sandwich plate

which is within an acceptable range, indicating that the solution method proposed in this paper is feasible to implement.

56.3.2 To Determine the Influence of Geometric Parameters on the Plastic Response of the Pliable Sandwich Plates

(1) **To determine the effect of different aspect ratios on the plastic response of the folding sandwich plates**

During the analysis, the size of the impulse is kept constant, and is selected to ensure that the sandwich plates within the scope of the investigation can enter the plastic stage without causing rupture and failure, and the subsequent analysis also uses this impulse. The width of the sandwich plate is fixed and the width is taken to be. The length of the sandwich plate is changed and five length $a = 2000$ mm, $a = 2500$ mm, $a = 3000$ mm, $a = 3500$ mm, and $a = 4000$ mm are selected for analysis, with aspect ratios of 1:1, 1.25:1, 1.5:1, 1.75:1, and 2:1, respectively. For both types of folding sandwich plates, the section size parameters as well as the material type and the finite element input parameters are the same as those for the material parameters of Sect. 2.1. In the following, we analyze the dynamic plastic response of I-type and U-type folding sandwich plates.

Introduction of dimensionless parameters:

$$\lambda = \frac{a}{b} \tag{56.38}$$

λ is the ratio of long side length to short side length.

A comparison of the computational results in this paper with the results of finite element simulation is shown in Fig. 56.6. It can be seen from the displacement plot

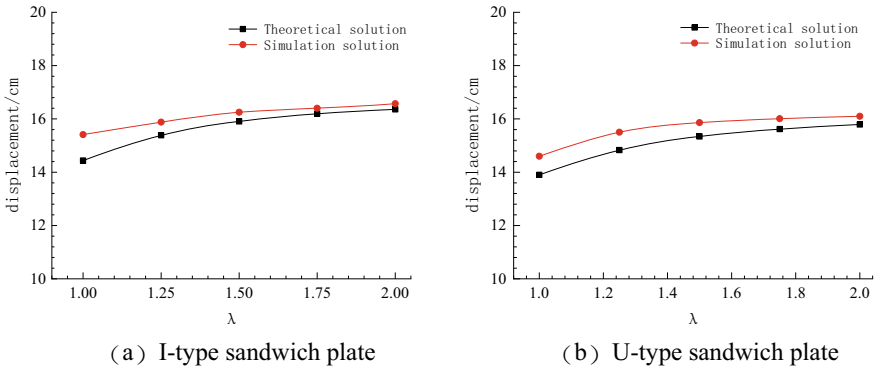


Fig. 56.6 Displacement curves of folded sandwich plate

that the trends of both displacement plots are the same, and increasing the aspect ratio of the sandwich plate will result in a gradual increase in plastic deformation. Since the width of the sandwich plate is constant, the larger the aspect ratio, the larger the area of the impacted sandwich plate, and hence the greater the displacement. Errors between the theoretical solution and the finite element solution for both of these types of wrinkled sandwich plates gradually decrease with increasing aspect ratio over the chosen range. Based on the final trend in the curve, it can be predicted that as the aspect ratio increases up to a certain point, this means that the plastic deformation of the sandwich plate will not change as the aspect ratio is changed. In general, even though the finite element solution is slightly larger than the theoretical solution, the two are relatively close to one another.

(2) **Plastic response of folding sandwich plates with different core heights**

A dimensionless parameter is introduced to fully describe the effect of the core height on the flexural performance of the sandwich plate:

$$\delta = \frac{h_c}{b} \tag{56.39}$$

δ represents the ratio of the core height to the short side of the sandwich plate.

For I-type folding sandwich plates, due to their special structural form, two methods are adopted for further analysis and calculation:

- (1) Keeping the sandwich plate grid square, that is, keeping the core height and the core spacing the same. To ensure the integrity of the sandwich plate grid, some dimensions of the long side of the sandwich plate were fine-tuned. Referring to the size annotation in Fig. 56.1a, the size parameters are shown in Table 56.2:
- (2) In the sandwich plate mesh, the spacing between the cores remains constant, and only the height of the core of the I-type folding sandwich plate is changed. The cross-sectional size of the sandwich plate is shown in Table 56.3:

Table 56.2 Geometric parameters of I-type folded sandwich plate for different spacing

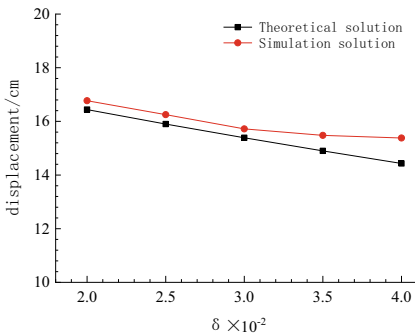
hc	a	b	df	dp	tf	tc
mm	mm	mm	mm	mm	mm	mm
40	3000	2000	40	40	2	2
50	3000	2000	50	50	2	2
60	3000	2000	60	60	2	2
70	3010	2000	70	70	2	2
80	3040	2000	80	80	2	2

Table 56.3 Geometric parameters of I-type folded sandwich plate for same spacing

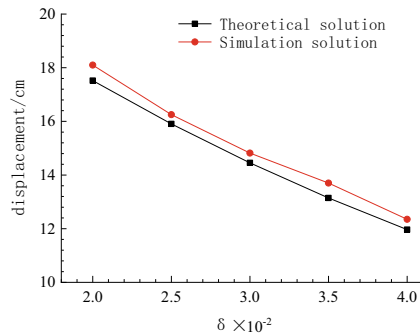
hc	a	b	df	dp	tf	tc
mm	mm	mm	mm	mm	mm	mm
40	3000	2000	50	50	2	2
50	3000	2000	50	50	2	2
60	3000	2000	50	50	2	2
70	3000	2000	50	50	2	2
80	3000	2000	50	50	2	2

The resulting displacement plot is plotted in Fig. 56.7. It can be seen that the displacement trends of the two I-type sandwich plates are generally consistent. For the same impact loading, the displacement of the sandwich plate decreases in a stepwise manner as the height of the sandwich plate increases. The reason for this is that the higher the height, the stronger the ability to resist deformation.

For sandwich panels with different core spacing (Fig. 56.7a), since the grid form of the sandwich panel is always square and the main scale of the sandwich panel does not change, when the core of the sandwich panel is higher, the number of cores



(a) Square grid plate



(b) Rectangular grid plate

Fig. 56.7 Displacement curves of I-type folded sandwich plate for different heights

in the sandwich panel will decrease, resulting in a lower displacement reduction. In comparison, for I-type sandwich panels with fixed core spacing (Fig. 56.7b), the number of cores does not change, only the height of the cores is changed, so the displacement range of the sandwich panel is larger in the selected examples, and the influence of the height of the sandwich panel on the displacement is increased.

In the case of the U-shaped collapsible sandwich panel, based on the cross-sectional diagram shown in Fig. 56.1b, The specific dimensions of five collapsible U-shaped sandwich panels with different core heights are given in Table 56.4. To ensure the rationality of the sandwich panel core structure, different values of d_f and d_p are chosen for different heights.

It can be seen from the computational results shown in Fig. 56.8 that for U-shaped sandwich panels the displacement decreases as the height of the core is increased. The theoretical solution and finite element solution are consistent in trend, with the finite element solution being slightly larger than the theoretical solution, and the error between the two typically does not exceed 7%. Despite the differences in the values of and, the number of U-shaped sandwich panel cores at different heights remains constant, thus, the sandwich panel displacement curve is approximately linear with a large span, which is similar to the displacement curve of I-shaped folding sandwich panels with fixed core spacing (Fig. 56.7b).

(3) The plastic response of the ply sandwich panels at different core angles

As the angle of the I-shaped sandwich panel is always constant, this section only studies U-shaped sandwich panels. For U-shaped sandwich panels, taking into account the rationality of the core structure, the angle is chosen to be between 60° and 80°, and is divided into five structural shapes, each with a range of 5°. The size parameters for the U-shaped sandwich panel are given in Table 56.5

It can be seen from Fig. 56.9 that for the U-shaped sandwich panels, the displacement curves at different angles are relatively smooth. These results indicate that when the height of the core and the number of cores are the same, the plastic deformation of the U-shaped sandwich panel under impact loading is minimally affected by changes in the angle of the cores. Although the theoretical solution in this paper shows a slowly increasing trend, and the finite element solution exhibits slight fluctuations, the overall trend is in agreement with the theoretical solution.

Table 56.4 Geometric parameters of the U-type folded sandwich plate

h_c	a	b	d_f	d_p	t_f	t_c
mm	mm	mm	mm	mm	mm	mm
40	3000	2000	62.5	87.5	2	2
50	3000	2000	59.4	90.6	2	2
60	3000	2000	56.2	93.8	2	2
70	3000	2000	53	97	2	2
80	3000	2000	50	100	2	2

Fig. 56.8 Displacement curves of U-type folded sandwich plate for different heights

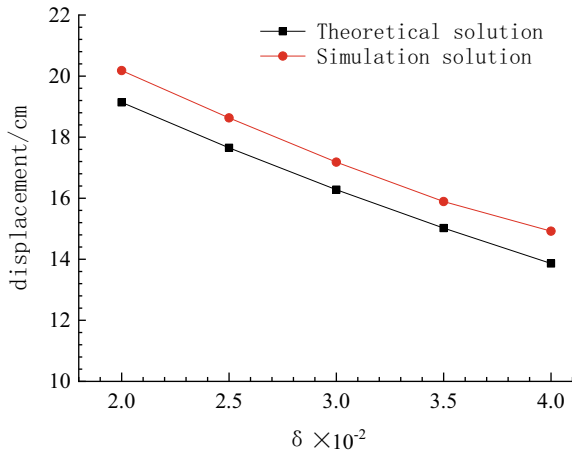
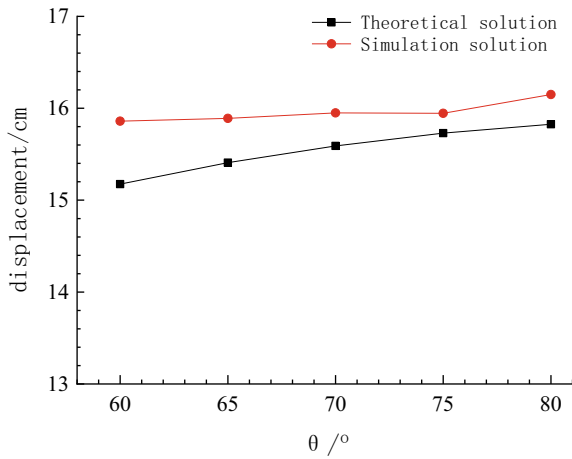


Table 56.5 Geometric parameters of U-type folded sandwich plate for different angles

θ	a	b	hc	df	dp	tf	tc
°	mm	mm	mm	mm	mm	mm	mm
60	3000	2000	50	21.1	78.9	2	2
65	3000	2000	50	27.7	72.3	2	2
70	3000	2000	50	31.8	68.2	2	2
75	3000	2000	50	36.6	63.4	2	2
80	3000	2000	50	41.2	58.8	2	2

Fig. 56.9 Displacement curves of U-type folded sandwich plate for different angles



- (4) The plastic response of the ply sandwich panels with different thicknesses of material

The following analysis is performed from two aspects: For sandwich panels with different material thicknesses:

- (1) The panel and core thickness are the same

If the thickness of the panel and core are the same, five different material thicknesses of $t = 1 \text{ mm}$, $t = 1.5 \text{ mm}$, $t = 2 \text{ mm}$, $t = 2.5 \text{ mm}$, and $t = 3 \text{ mm}$ are analyzed and checked in turn.

Introduction of dimensionless parameters:

$$\gamma = \frac{2t_f + t_c}{d} \tag{56.40}$$

γ represents the ratio of the sum of the upper and lower panel thicknesses to the core thickness relative to the height of the sandwich panel.

It can be seen from the displacement curve in Fig. 56.10 that the theoretical and finite element solutions for types of sandwich ply panels follow a consistent trend, and the shift values are well-matched, with errors of both less than 15%. The impact strength of the sandwich panel gradually improves as the material thickness of the sandwich panel increases, and the plastic strain decreases, but the amount of plastic strain gradually decreases, and the displacement curve shows an exponential decay trend.

- (2) Due to the difference in panel thickness and core

For I-shaped and U-shaped sandwich panels, the core thickness is selected as $t_c = 2 \text{ mm}$, and the upper and lower panel thicknesses are selected as $t_f = 1 \text{ mm}$,

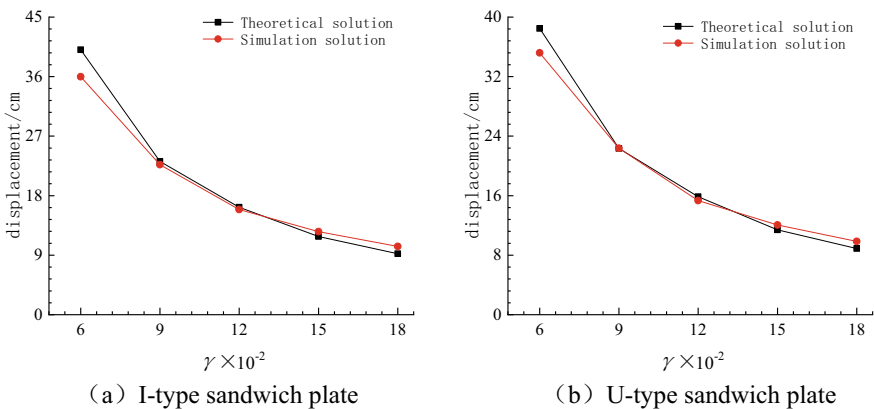


Fig. 56.10 Displacement curves of the folded sandwich plate for different thicknesses of the material

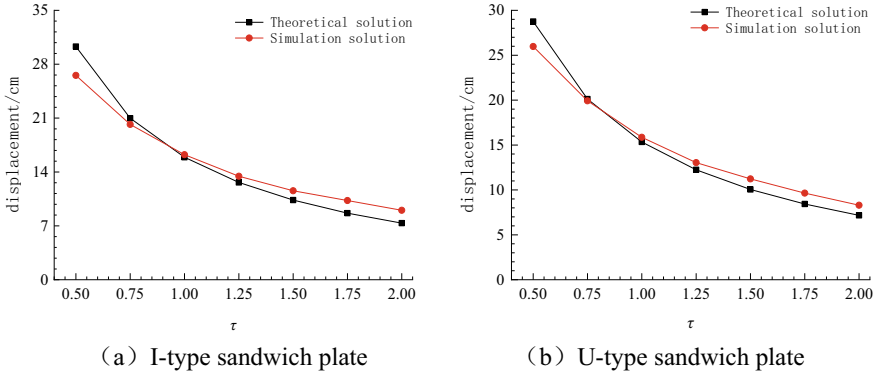


Fig. 56.11 Displacement curves of the folded sandwich plate for different thicknesses of the material

$t_f = 1.5 \text{ mm}$, $t_f = 2 \text{ mm}$, $t_f = 2.5 \text{ mm}$, $t_f = 3 \text{ mm}$, $t_f = 3.5 \text{ mm}$ and $t_f = 4 \text{ mm}$, respectively, for seven different cases. The ratio of the selected panel and core thicknesses covers as much of the range of actual applications as possible:

$$\tau = \frac{t_f}{t_c} \tag{56.41}$$

τ represents the ratio of the panel thickness to the core thickness.

From Fig. 56.11, it can be seen that as the thickness of the panel increases, the impact strength of the sandwich panel increases in a stepwise manner. The trend of the curve is the same as in the first case, and as the thickness ratio of the material increases, the change in the displacement curve gradually decreases and finally approaches a horizontal line. The theoretical result is larger than the finite element result when the thickness ratio of the panel is smaller; the finite element solution gradually becomes larger than the theoretical solution as the thickness ratio of the panel increases. If the ratio of panel thickness to sandwich panel core thickness is in the range of 0.75–1.25, with relatively high computational precision, and good correspondence between the overall results.

56.4 Conclusions

A theoretical solution method for the dynamic response of collapsible sandwich panels under blast loading was investigated, and a numerical simulation was performed using the software ABAQUS, comparing the computational results with the theoretical results, and verifying the practicality of the theoretical method. The main findings are:

- (1) A method for the plastic response solution of collapsible sandwich panels under impact loading was investigated, and the formula, for calculating the plastic strain appropriate for foldable sandwich panels was derived.
- (2) The plastic deformation of I-shaped and U-shaped sandwich panels under different incident impulses was calculated using the theoretical formula, and compared with the finite element calculation results. There is good agreement between the two results, demonstrating the reliability of the computational formula.
- (3) A parameter sensitivity analysis was performed on the sandwich panel, and it was found that the greater the aspect ratio, the higher the plastic deformation of the pliable sandwich panel; the higher the height of the core and the thicker the material, the smaller the plastic deformation of the sandwich panel; when the number of cores is not changed, changing the angle of the core has a small effect on the plastic deformation response of the sandwich panel.
- (4) This derived computational formula can be used for design optimization and evaluation of the impact resistance performance of ship structures based on collapsible sandwich panels, reduce the machine time consumed by finite element modeling and computation, significantly improve computational efficiency, and have some benchmark value for investigating the impact resistance performance of foldable sandwich panels.

References

1. Zili, W., Yanchang, Z.: Crashworthiness design of single hull structure based on sandwich panel. *Chin. Shipbuilding* **49**(1), 60–65 (2008)
2. Zili, W., Yanchang, Z.: Design of crashworthiness of single-shell hull structure based on sandwich plate. *Shipbuilding Chin.* **49**(1), 60–65 (2008)
3. Fleck, N.A., Deshpande, V.S.: The resistance of clamped sandwich beams to shock loading. *J. Appl. Mech.* **71**(3), 386–401 (2003)
4. Jun, L.: Vibration and impact response analysis of square honeycomb sandwich structure. *Huazhong Univ. Sci. Technol.* (2009)
5. Jun, L.: Vibration and Vhock response analysis of square honeycomb sandwich structure. *Huazhong Univ. Sci. Technol.* (2009)
6. Jun, L., Jun, L., Yuansheng, C.: Plastic dynamic response analysis of square honeycomb sandwich panel under impact load. *Ship Mech.* **14**(10), 1165–1172 (2010)
7. Jun, L., Jun, L., YuanSheng, C.: Analysis of plastic dynamic response of square honeycomb sandwich plate under impact load. *Ship Mech.* **14**(10), 1165–1172 (2010)
8. Qiu, X., Deshpande, V., Fleck, N.: Dynamic response of a clamped circular sandwich plate subject to shock loading. *J. Appl. Mech.* **71**(5), 637–645 (2004)
9. Zili, W., Zongwen, H., Yanchang, Z., et al.: Experimental study on underwater explosion of folding sandwich panel. *Chin. Shipbuilding* (3), 74–83 (2014)
10. Zili, W., Zong Wen, H., Yan Chang, Z.: Experimental study on underwater explosion of folding sandwich plate. *Shipbuilding Chin.* (3), 74–83 (2014)
11. Yanchang, Z., Guo, W., Hong, Z. et al.: Numerical simulation analysis of underwater explosion protection performance of folding sandwich panel. *Chin. Shipbuilding* (2), 35–44 (2013)
12. YanChang, Z., Guo, W., Hong, Z.: Numerical simulation analysis of underwater explosion protection performance of folding sandwich plate. *Shipbuilding Chin.* **2**, 35–44 (2013)

13. Zili, W., Yanchang, Z., Jinlan, G.: Dynamic response analysis of laser welded sandwich panel under underwater explosion shock load. In: National Academic Conference on Ship and Marine Engineering (2009)
14. Zili, W., Yanchang, Z., Jinlan, G.: Dynamic response analysis of laser welded sandwich plate under underwater explosion impact load. In: National Conference on Ship and Marine Engineering
15. Zhang, P., Liu, J., Cheng, Y., et al.: Dynamic response of metallic trapezoidal corrugated-core sandwich panels subjected to air blast loading—An experimental study. *Mater. Des.* **65**(65), 221–230 (2015)

Chapter 57

Numerical Simulation and Experimental Analysis of Two-Dimensional Wedge-Shaped Structure's Water Entry with Boulder Impact



Zong Shuai, Huang Tianbo, Liu Kun, Wang Jiaxia, and Gao Zhenguo

Abstract With the rapid development of ships, the problem of bow slamming becomes very prominent. In this paper, based on the impact test data of water entry, a two-dimensional wedge shape test model was established by ANSYS/LS-DYNA finite element software, and simulation analysis was carried out on the model, focusing on the impact of different oblique lifting Angle and water entry speed on the impact load, the change of pressure during the impact process and the liquid level lifting phenomenon of the structure during water entry. The results show that when the wedge contacts the water surface, the slamming pressure increases instantly, then decreases gradually and becomes stable. With the decrease of tilt Angle and the increase of water entry velocity, the slamming pressure increases obviously, and the vertical slamming force also increases. When the inclined rise Angle is small, the peak value of the slamming pressure obtained by numerical simulation and impact test has a slight deviation. In this case, the thinner jet needs to be simulated with a denser grid. The research results can provide a reference for related research.

Keywords Wedge · Slamming · Inclined angle · Slamming load

57.1 Introduction

Water impact problems have the characteristics of multiple impact zones, a short duration of impact, and a relatively large peak impact pressure [1]. To fully understand the phenomenon of water impact on structures, this research is typically focused on the water impact process and load characteristics of local ship structures or wedge-shaped structures. Von Karman [2] simplified the problem of ships' water impact to a two-dimensional wedge-shaped structure impacting a still surface of the water, and

Z. Shuai · H. Tianbo · L. Kun (✉) · W. Jiaxia · G. Zhenguo
School of Naval Architecture and Ocean Engineering, Jiangsu University of Science and Technology, Zhenjiang 212003, China
e-mail: kunliu@just.edu.cn

therefore evaluated and investigated the impact loading. This theory was extended by Wagner [3] in 1932, and through the analysis and calculation of simplified structures, he pointed out the importance of wetted surfaces in the prediction of impact loads. The development of computational technology and computing power has led to the use of numerous high-precision numerical methods to solve complex hydrodynamic impact problems. Zhao [4] and Faltinsen [5] used nonlinear boundary element methods to investigate the water impact problem of a wedge-shaped cross-section at a constant position, and verified the results of the calculation by comparing them to analogous solutions. Stenius [6] used ALE in commercial explicit LS-DYNA to predict the impact loading of a structure in two dimensions. Veen and Gourlay and Seng^[*] used the smooth particle hydrodynamic (SPH) method and the fluid volume method (VOF) to simulate the water impact problem of ships. In China, Xiang et al. [7] used the MPS solver to investigate the water impact problem of a two-dimensional wedge-shaped structure and analyzed the numerical influence of different methods of particle arrangement. Yuwei [8] and Yijun et al. [9] used the simulation software Fluent to numerically simulate the water impact problems of two-dimensional wedge-shaped structures and flat bottom structures respectively. By taking into account factors such as external atmospheric pressure, gravity, and mesh effects, they studied the motion characteristics, impact load characteristics, and water bubble evolution during the free fall of flat objects into the water. Wang and Soares [10–12] used LS-DYNA finite element software to numerically simulate different water entry angles of the bow sections of the vessels, wedged bodies with different angles of attack, 3D hemispheres, and cone-shaped bodies and verified the reliability of the numerical simulation calculation by comparing the theoretical values to the experimental values. The results presented in this paper are based on the two-dimensional inlet water impact test of a wedge-shaped body, and systematically analyze the effect of impact loading on the wedge-shaped body as it impacts the water surface at different angles of attack and velocities via finite element simulation. The model also investigates the process of changing the free liquid surface as the wedge-shaped body impacts the water. The results of the research can provide a reference for the law of change of the impact load under the bow shock of the ship.

57.2 Finite Element Model

For this study, the numerical simulation model is a two-dimensional corner test model, which has undergone a series of tests. This test model has a V-shaped (wedge) bottom profile, with the bottom plate inclined at 10° , 20° , 30° , and 40° (β), and the size and actual shape of the test model are shown in Figs. 57.1 and 57.2, respectively. As part of the experimental process, to measure the impact pressure at various locations on the bottom of the experimental design, the experimental points and the corresponding reference points are arranged at different vertical positions on the bottom of the model of the experiment. The distribution of specific locations is shown in Fig. 57.3, where point O is the center of the bottom plate. Of these, test point P1 is

Fig. 57.1 Size of test models (Unit: mm)

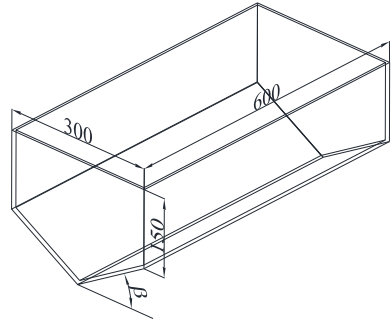


Fig. 57.2 The physical map of test models

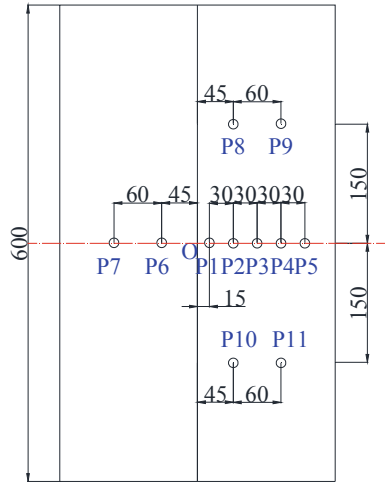


15 mm from point O on the horizontal center line of the bottom plate, and test points P2, P3, P4, and P5 are spaced at a distance of 30 mm from each other. Test points P6 and P7 are symmetrical with test points P2 and P4, and test points P8, and P9 are symmetrical with test points P10, and P11.

In this paper, finite element numerical simulation analysis of wedge-shaped bodies with different tilt angles is performed using ANSYS/LS-DYNA finite element software. The coupling between the structure and the fluid is simulated using the Lagrange-Euler (ALE) algorithm with multiple materials and the penalty function coupling algorithm; a rigid material (*MAT_RIGID) is used to simplify the wedge-shaped body due to its small structural size and inflow velocity of the water. The Gruneisen state equation and linear polynomial Polynomial state equation are used to represent water and air, respectively, and the null material (*MAT_NULL) model is used in combination with the state equation to represent the material in the water area and air area. The 3D Solid 164 element is used in both designs.

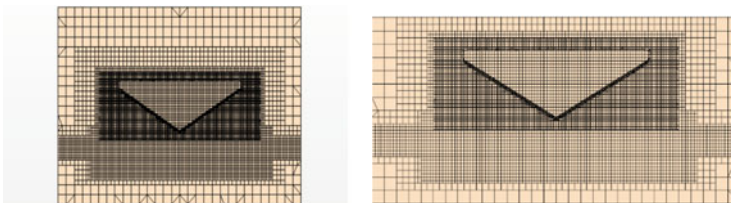
Inside the computational region, the wedge-shaped body mesh is parameterized in a variety of ways. Because errors occur when variables are placed between two cells, the same cell size is used in both the larger surface and the overlapping surface to effectively reduce computational issues caused by the mesh size. The specific mesh configuration of the wedge-shaped body is illustrated in Fig. 57.4a, where the

Fig. 57.3 Distribution and numbering of measure points on wedge bottom (Unit: mm)



background mesh size is set to 0.02 m and the mesh size in the overlapping region is set to 0.008 m. Because, in the process of the wedge-shaped body entering the water, this simulation uses a smaller mesh size at the overlapping mesh to capture the shocking phenomenon that is visible, as shown in Fig. 57.4b. In this case, the mesh in the water surface is refined, and the mesh in the refinement surface is fixed as follows: The longitudinal and transverse meshes in the computational domain are fixed at 8 mm, and the vertical mesh is fixed at 72 mm. The mesh set around the water surface is the same as the mesh set on the water surface, with the longitudinal and transverse mesh sizes set to 8 mm and the vertical mesh size set to 72 mm.

Because the structure under consideration is two-dimensional, only one cell is selected for computation (in the Z direction of the wedge-shaped body), and an unreflective boundary condition is used as the boundary of the fluid which may weaken the effect of sound wave reflection. The wedge-shaped body is located at a distance of 0.01 m from the water surface during the calculation and falls at a velocity of V , and the inlet velocity V of the water can be determined based on the drop height at the test conditions.



(a) Schematic diagram of the overlapping mesh of the wedge-shaped body

(b) Water surface mesh diagram

Fig. 57.4 diagrams of wedge mesh

57.3 Analysis of Calculate Results

57.3.1 *Due to the Effect of Different Tilt Angles on the Impact Pressure of the Wedge*

A comparison curve of test values and shock pressure calculation values at the measurement locations where the maximum wedge shock pressure peak appeared for different tilt angles is shown in Fig. 57.5. 3 shows the shock pressure curve as it falls from a height of 0.4 m. From the figure, we can see that when the wedge angle is 10° , the corner (Fig. 57.5a) has the highest impact loading at the time of impact, and the first measurement location on the wedge will have a higher impact loading and then gradually decrease and level off. For example, the trend of change in the shock pressure peak of the wedge P2 measurement point with a 20° tilt angle in Fig. 57.5b is similar to that of 10° , and it also first increases and then decreases, and the trend of the simulation and test shock pressure change match well. The difference between the wedges with 30° and 40° tilt angles and the first two wedges is that the peak in impact pressure is lower, this is due to the fact that upon the impact of the wedge into the water, if the base of the wedge has a smaller tilt angle, i.e., 10° and 20° wedges, this will affect the uplift of the water surface, so that, when the water surface is continuously uplifted, since the free water surface will be subject to the increasing pressure from the base, the impact loading will also be continuously increasing at this time. If the free surface of the water rises to a certain height, wave breaking will occur, and the peak of the shock loading will appear at that time. Thereafter, the impact loading will gradually decrease, which is due to the separation of the wedge surface from the surface of the water. And when the wedge angle is greater, the free-water surface elevation will not be overly affected by the baseline. In general, the numerical method adopted in this paper can fundamentally satisfy the research on the impact of two-dimensional wedges in the water problem, i.e., the effectiveness of the method is verified.

As the inclination angle of the wedge changes, the impact pressure of the wedge will also change, that is, the larger the angle of the inclination angle, the smaller the impact pressure value of the wedge. Table 57.1 shows the numerical comparison of the experimental and simulated values. From the table, it can be seen that the results of the experimental and simulated values are relatively close to each other, with a small error, except for the wedge results with a tilt angle of 10° , which has a larger error. All errors for the other tilt angles are within 15%.

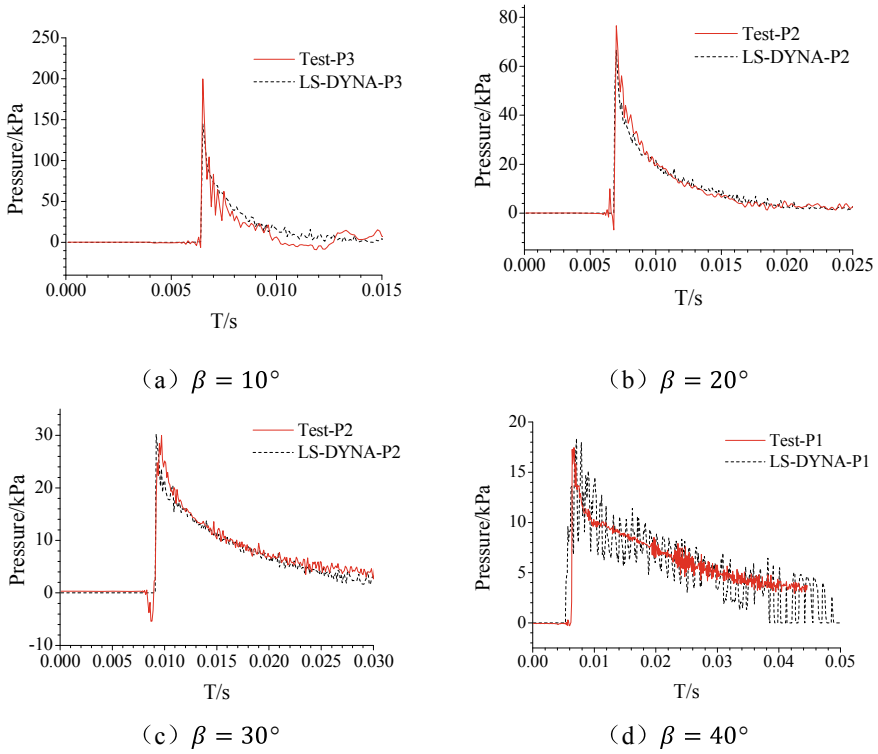


Fig. 57.5 Comparison of slamming pressure for a wedge with different deadrise angles in test and simulation

Table 57.1 Comparison of simulation and experiment

Inclination angle	Experiment/Simulation	P1(P/kPa)	P2(P/kPa)	P3(P/kPa)	P4(P/kPa)
10°	Experimental	130	144	200	184
	Simulation	141.261	/	149.988	143.465
20°	Experimental	56	72	68	38
	Simulation	61.001	57.8324	53.5308	43.2922
30°	Experimental	38	30	24	22
	Simulation	31.8174	30.4179	21.2797	18.6262
40°	Experimental	17.6	14	8.8	9
	Simulation	14.0357	13.3962	11.7048	9.04

57.3.2 To Determine the Effect of Different Water Entry Velocities on the Wedge Impact Pressure

To investigate the comparison of the wedge impact pressure under different water entry velocities, in this paper, the water entry velocity is varied by changing the water entry height of the wedge. In this section, we present the comparison of the wedge impact pressure values with a 10° tilt angle at 0.2 and 0.4 m, the comparison of the impact pressure values of the wedge with an inclination angle of 20° at 0.2, 0.4, and 0.6 m, the comparison of the impact pressure values of the wedge with an inclination angle of 30° at 0.2, 0.4, and 0.6 m, and the comparison of the impact pressure values of the wedge with an inclination angle of 40° at 0.2, 0.4, and 0.6 m. A comparison curve of the experimental and computational values of the impact pressure peak at each measurement location when the wedge is falling from different heights is shown in Fig. 57.6.

From Fig. 57.6, it can be seen that as the water entry velocity increases, i.e., as the water entry height increases, the peak of the impact loading will also become increasingly large. However, at the same speed (i.e. at the same height), when wedges

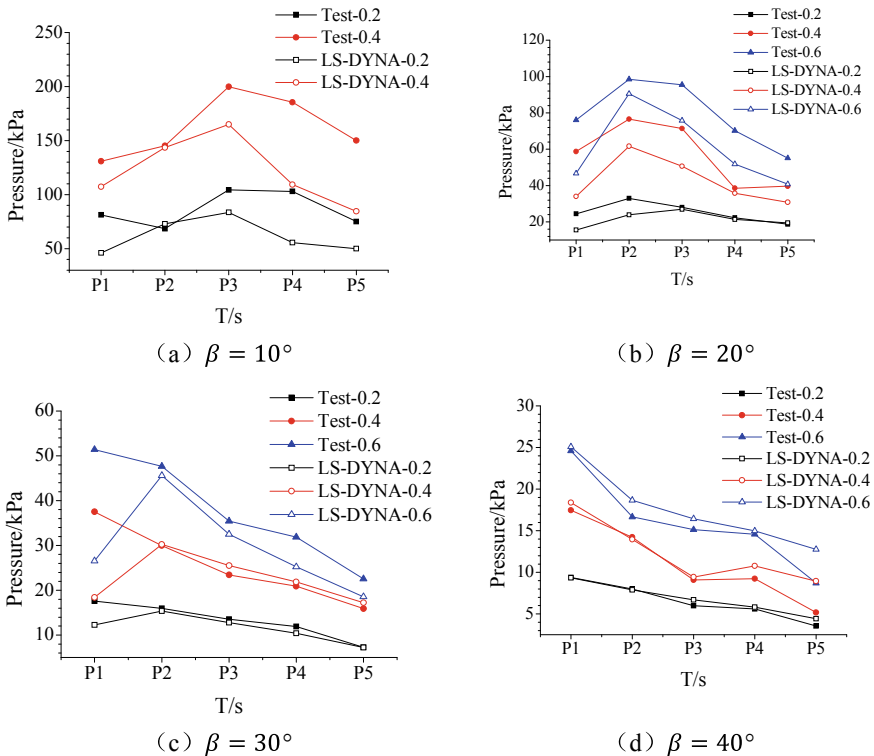


Fig. 57.6 Peak slamming pressure

with different angles enter the water, the final peak in impact loading will become smaller and smaller as their angles get larger and larger. By comparing the peak values of the impact pressure of wedges with different tilt angles at different heights, we can see that when the wedge angle is 10° , at the measurement point P3, the shock pressure value of the wedge is largest, the wedge impact pressure value at measurement point P2 is greatest when the wedge angle is 20° , and when the wedge angle is 30° the value of the wedge impact pressure at measurement point P2 is greatest. The reason for this is that as the tilt angle becomes smaller and smaller, the impact pressure will be more affected by the rise of the free water surface, and the phenomenon of wave breaking will be more evident, whereas, as the angle of tilt of the wedge increases, the impact pressure will become less and less influenced by the rise of the free water surface and the phenomenon of wave breaking.

57.3.3 Vertical Incidence Force

Figure 57.7 shows the vertical impact force received by wedges with different tilt angles as they enter the water at different velocities and impact the static water surface. The numbers in Fig. 57.7 represent the distance from the lowest point of the wedge to the water surface.

The figure above shows that the vertical impact force of wedges with different tilt angles as they enter the water and collide with the water has a tendency to first increase and then decrease, and the change in vertical impact force magnitude is relatively small, since the vertical impact force represents the mean force of the global structure. The vertical impact force starts to decrease significantly as the wedge tilt angle continues to increase; if the angle of tilt of the wedge is the same, as the height of the object's drop increases, the vertical impact force will begin to gradually increase.

57.3.4 Impact Pressure Coefficient

The impact pressure coefficient C_p is a dimensionless measure of the impact pressure P , given by the following expression.:

$$C_p = \frac{P}{\frac{1}{2}\rho V^2} \quad (57.1)$$

where P is the Structural impact pressure, ρ is the Density of water, and V is the Structural in-water velocity.

The impact pressure coefficient of the wet surface of the wedge body obtained from the finite element numerical simulation results is compared with the impact pressure coefficient obtained by Zhao et al. [4] boundary element method (BEM).

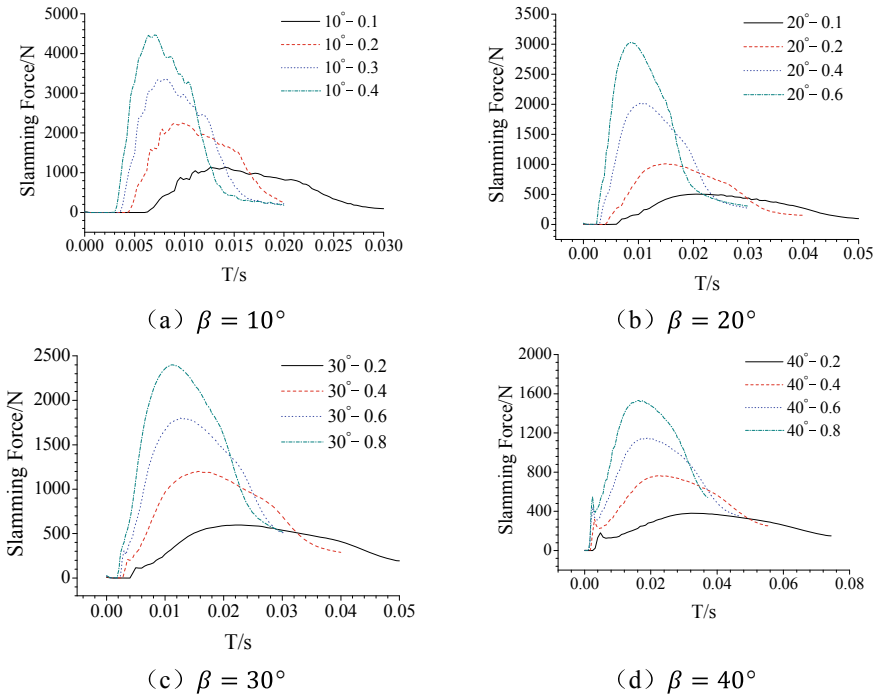


Fig. 57.7 Vertical slamming force of wedges

Where the angle of attack is 20° and 30° , and the impact pressure of the body of the wedge reaches a maximum value, the wetted surface impact pressure coefficient distribution is shown in Fig. 57.8. The abscissa represents the ratio of the vertical coordinates of each point on the wetted surface concerning its draught, with the intersection of the object surface and the water surface represented by 0 and the bottom of the wedge body represented by 1. It can be seen from the figure that the results obtained by the numerical finite element simulation are basically in agreement with the results obtained by the BEM method, and at an angle of attack of 30° the results from the finite element simulation are superior to those from the BEM.

To compare the classical theoretical solution, the experiments, and the finite element simulation results, this paper transforms them into the shock pressure coefficient C_p versus angle of attack β curve shown in Fig. 57.9. Figure 57.9 shows that the trends in the shock pressure curve obtained from the theoretical solution, the experimental results, and the maximum shock pressure coefficient obtained from a finite element numerical simulation is consistent at $\beta \geq 20^\circ$, but that there is a significant difference at $\beta < 20^\circ$. Because of the different ways of treating the liquid-free surface. At $\beta = 10^\circ$, the coefficient of maximum impact pressure obtained from the experiment is in agreement with that obtained by Stavovy and Chuang (1976).

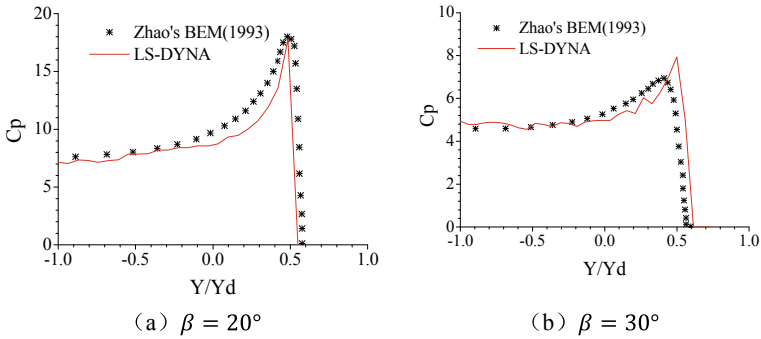
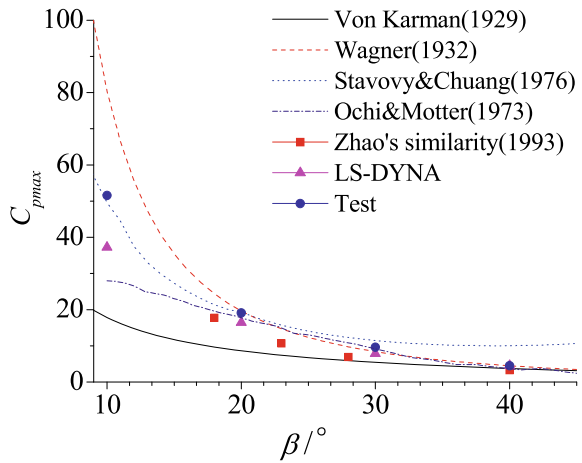


Fig. 57.8 Pressure distributions on wedges when the deadrise angles are 20° and 30°

Fig. 57.9 Comparison of slamming pressure coefficient for a wedge with different deadrise angles



It should be noted that the maximum impact pressure coefficient obtained from the finite element simulation lies between the values obtained by Stavovy et al. (1993).

57.3.5 Raising the Free Liquid Surface of the Wedge Body Upon Entering the Water

The change of the free liquid surface of a wedge body with an angle of attack of 30° falling from a height of 0.4 m is shown in Fig. 57.10. The situation when the wedge body is about to touch the surface of the water is shown in Fig. 57.10a, during which the bottom shock pressure on the wedge body is relatively low. It can be seen from Fig. 57.10b and c that, before jet separation, the maximum pressure value occurs in the jet injection region, and the pressure at the jet is much less than the

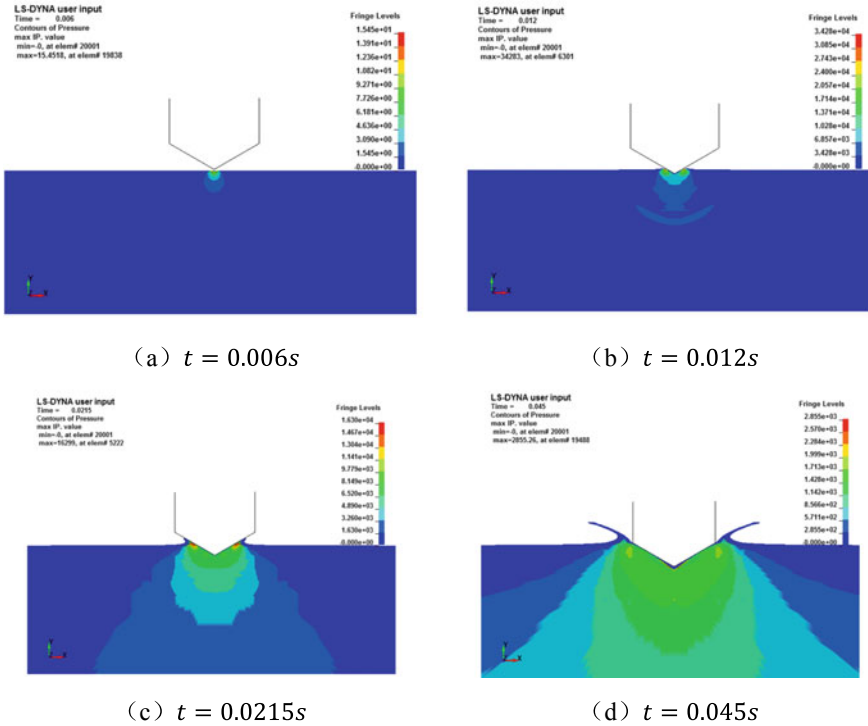


Fig. 57.10 Jet flows and pressure contours of the wedge with 30° deadrise angle

pressure at the root of the jet, which explains the rapid drop in impact pressure after the peak is reached. The pressure distribution along the surface of the wedge body after jet separation is given in Fig. 57.10d. From the figure, it can be seen that the pressure drops very rapidly and the pressure peak shifts to the vicinity of the keel of the wedge body (i.e., the centerline).

57.4 Conclusions

The wedge-shaped body water inlet test is taken as the object of investigation in this study, and the shock pressure variation law and shock force in the vertical direction of the wedge-shaped body during the water entry are analyzed by changing the tilt angle and height of the water entry through ANSYS/LS-DYNA finite element simulation software, and compared to the experimental variation law. The final section discusses and analyzes the free-surface lift phenomenon of water as the wedge-shaped body enters the water. The key findings of this study include the following.

- (1) As the wedge-shaped body surface contacts the water surface again, there is a sudden increase in shock pressure, followed by a gradual decrease before finally leveling off.
- (2) The main factors affecting the size of the shock pressure are the angle of inclination of the wedge-shaped body and the velocity of the inflow of water. As the tilt angle decreases, the inflow velocity of the water increases, and the shock pressure begins to rise significantly.
- (3) When the angle of attack is 30° and 40° , the impact pressure obtained by finite element simulation is consistent with the impact pressure obtained by the experiment. However, when the angle of attack is 10° and 20° , the peak value of the impact pressure obtained by finite element simulation and the impact pressure obtained by the experiment differs significantly, and a finer mesh is required to simulate the thinner jet in this approach.

References

1. Yonghu, W., Xiuhua, S.: Current situation and progress of research on water impact. *Explosion Impact* **03**, 276–282 (2008)
2. Von Karman, T.: The impact on seaplane floats during landing (1929)
3. Wagner, H.: Phenomena associated with impacts and sliding on liquid surfaces. *Z. Angew. Math. Mech.* **12**(4), 193–215 (1932)
4. Zhao, R., Faltinsen, O., Aarsnes J.: Water entry of arbitrary two-dimensional sections with and without flow separation. In: Proceedings of the 21st symposium on naval hydrodynamics, pp 408–423. Trondheim, Norway, National Academy Press, Washington (1996)
5. Faltinsen, O.M.: Water entry of a wedge by hydroelastic orthotropic plate theory. *J. Ship Res.* **43**(03), 180–193 (1999)
6. Stenius, I., Rosén, A., Kuttenukeuler, J.: Explicit FE-modelling of fluid–structure interaction in hull–water impacts. *Int. Shipbuild. Prog.* **53**(2), 103–121 (2006)
7. Xiang, C., Chengping, R., Decheng, W.: Numerical simulation of wedge entering water by MPS method. *J. Comput. Mech.* **34**(3), 356–362 (2017)
8. Yuwei, Z., Zhidong, W., Wenju, J., et al.: Research on two-dimensional wedge slamming load. *Chin. Ship Res.* **5**(3), 34–37 (2010)
9. Yijun, W., Minghai, L., Zhongli, Z., et al.: Simulation of free-falling slamming load of flat-bottomed structure in water based on VOF method. *Vib. Shock* **36**(2), 185–189 (2017)
10. Wang, S., Soares, C.G.: Explicit FE simulation of slamming load on rigid wedges with various deadrise angles during water entry. In: International Conference on Maritime Technology and Engineering (2011)
11. Wang, S., Soares, C.G.: Slam induced loads on bow-flared sections with various roll angles. *Ocean Eng.* **67**(8), 45–57 (2013)
12. Wang, S., Soares, C.G.: Numerical study on the water impact of 3D bodies by an explicit finite element method. *Ocean Eng.* **78**(3), 73–88 (2014)

Chapter 58

Fuzzy-Logic-Based Integrated Orbit-Attitude-Vibration Prescribed-Time Control for Large-Scale Flexible Spacecraft



Xiaokui Yue, Bailiang Lyu, and Chuang Liu

Abstract This paper investigates a fuzzy-logic-based integrated orbit-attitude-vibration prescribed-time controller for large-scale flexible spacecraft to achieve the high-precision orbit-attitude-vibration stabilization. Due to the existence of nonlinear coupling effects, a refined T-S fuzzy model based on the orbit-attitude-vibration dynamics of large-scale flexible spacecraft is constructed to represent the nonlinear characteristics and avoid the calculation singularity. Then, a prescribed-time controller is designed to stabilize the closed-loop system within a prescribed time with precise convergence rate where Lyapunov stability analysis is performed to prove the prescribed-time stability. Simulation results shows the effectiveness of the proposed control strategy.

Keywords Large-scale flexible spacecraft · T-S fuzzy model · Prescribed-time control · Integrated control

58.1 Introduction

Due to the rapid development of space industry worldwide in recent years, the construction and application of large-scale spacecraft has received much attention for various space missions, which has gradually become a research hotspot for future space technology, e.g., deep space exploration, long-term space residency, application for space solar power stations (SSPS), etc. [1]. The large-scale flexible spacecraft

X. Yue · B. Lyu · C. Liu (✉)

National Key Laboratory of Aerospace Flight Dynamics, School of Astronautics, Northwestern Polytechnical University, Xi'an 710072, China

e-mail: liuchuangforever@msn.com

Research and Development Institute of Northwestern Polytechnical University in Shenzhen, Shenzhen 518057, China

is a complex system with strong-integration, thus, due to the effect of space environment disturbance and strong nonlinear coupling effect, the dynamics and control for large-scale spacecraft is a significant challenge [2, 3].

A four-degrees of freedom dynamic model for tethered SSPS is constructed in [4] with the analysis of the connection between the structural vibration and orbital motion. Based on the Absolute Nodal Coordinate Formulation (ANCF) method, the Hamiltonian dynamic equation for the coupled orbit-attitude-vibration of tethered SSPS is derived in [5]. Whereas, due to the selection of generalized coordinates, the derived dynamic equation owns the differential algebraic formulation which is unsuitable for the design of control system directly. As mentioned in [6], the large-scale spacecraft is considered as a deformable flexible beam structure, then using the classical mechanics analysis method, an integrated attitude-orbit dynamic equation is constructed including vibration with dynamic response calculation subject to fourth-order Taylor series. Consequently, the perturbation of the force/moment effect impacted by the sun, moon and Earth oblateness is comprehensively analyzed for further study. The problem of sequence programming for the assembled large-scale spacecraft is investigated in [7] where the proposed improved Genetic Algorithm for multiple constraints is efficient. A distributed cooperative control mechanism with consensus coordination terms for vibration suppression of flexible satellite is developed in [8]. Besides, experimental examples demonstrate the performance of this method which is valuable for the vibration suppression of large-scale spacecraft.

Additionally, though there exists much literature for the modeling dynamics and control, for the practical space mission it is most desirable to reach the required stable state within a preset time, i.e., strong timeliness. Some research has investigated the prescribed time control for spacecraft [9, 10, 11]. The problem of attitude cooperative control with external disturbance for cluster spacecraft in prescribed time is discussed in [12] where the desired attitude observer is introduced to solve this issue. In [13], a nonsingular sliding-mode manifold is designed to achieve the predefined-time predefined-bounded attitude tracking control for rigid spacecraft. As mentioned in [14], a fixed-time disturbance observer is constructed to estimate the model parameters and external uncertainties, the proposed control strategy can stabilize the states in a predefined time which is independent of the initial state. However, the application of the prescribed time control for rigid spacecraft owns good performance. As for the large-scale flexible spacecraft, the system is complex, thus, the achievement of time-guaranteed constraint control is more difficult, the relevant research is few as well.

Above the aforementioned issues, the integrated attitude-orbit-vibration control for large-scale spacecraft in prescribed time with high precision is still an open problem. Accordingly, this paper proposes a fuzzy-logic-based integrated orbit-attitude-vibration prescribed-time controller for large-scale flexible spacecraft to achieve the high-precision stabilization. The main contributions of this work are summarized as follows. First, based on the dynamic analysis, a simplified integrated orbit-attitude-vibration model is constructed in this paper which is suitable for controller design. Second, due to the existence of nonlinear coupling effects, a refined T-S fuzzy model is introduced to represent the nonlinear characteristics and

avoid the singularity of dynamics calculation. Third, a prescribed-time controller is designed to stabilize the complex closed-loop system within prescribed time in high precision, where Lyapunov theory is performed to prove the prescribed-time stability. Simulation results shows the effectiveness of the proposed control strategy.

58.2 Integrated Dynamics

According to [4, 15], it's assumed that the large-scale flexible spacecraft moves in the orbital plane where orbit (R, θ), attitude (ϕ) and vibration (q) degrees of freedom are considered, thus the integrated orbit-attitude-vibration dynamic equation is modelled as Eq. (58.1).

$$\begin{aligned}
 m\ddot{R} - mR\dot{\theta}^2 + d_1 &= u_1 \\
 mR^2\ddot{\theta} + 2mR\dot{R}\dot{\theta} + \left(C_0 + \frac{1}{2}\mathbf{q}^T\mathbf{M}\mathbf{q}\right)(\ddot{\theta} + \ddot{\phi}) \\
 + \mathbf{q}^T\mathbf{M}\dot{\mathbf{q}}(\dot{\theta} + \dot{\phi}) + d_2 &= \Delta u + u_3 = u_2 \\
 \left(C_0 + \frac{1}{2}\mathbf{q}^T\mathbf{M}\mathbf{q}\right)(\ddot{\theta} + \ddot{\phi}) + \mathbf{q}^T\mathbf{M}\dot{\mathbf{q}}(\dot{\theta} + \dot{\phi}) + d_3 &= u_3 \\
 \mathbf{M}\ddot{\mathbf{q}} - \frac{1}{2}\mathbf{M}\mathbf{q}(\dot{\theta} + \dot{\phi})^2 + \mathbf{K}\mathbf{q} + d_4 &= u_4
 \end{aligned} \tag{58.1}$$

Denote $\mathbf{x} = [x_1 \ x_2 \ x_3 \ x_4]^T$, $\mathbf{z} = [x_5 \ x_6 \ x_7 \ x_8]^T$ and $\mathbf{d} = [d_1 \ d_2 \ d_3 \ d_4]^T$ where, $x_1 = R$, $x_2 = \theta$, $x_3 = \theta + \phi$, $x_4 = \mathbf{q}$, $x_5 = \dot{R}$, $x_6 = \dot{\theta}$, $x_7 = \dot{\theta} + \dot{\phi}$, $x_8 = \dot{\mathbf{q}}$, then the dynamic equation can be noted as follows:

$$\begin{cases} \mathbf{z} = \dot{\mathbf{x}} \\ \mathbf{C}(\mathbf{x})\ddot{\mathbf{x}} + \mathbf{f}(\mathbf{x}, \dot{\mathbf{x}}) + \mathbf{d} = \mathbf{u} \end{cases} \tag{58.2}$$

where

$$\mathbf{C}(\mathbf{x}) = \begin{bmatrix} m & & & \\ mx_1^2 & & & \\ & C_0 + \frac{1}{2}\mathbf{x}_4^T\mathbf{M}\mathbf{x}_4 & & \\ & & & \mathbf{M} \end{bmatrix}, \mathbf{f}(\mathbf{x}, \dot{\mathbf{x}}) = \begin{bmatrix} -mx_1\dot{x}_2^2 \\ 2mx_1\dot{x}_1\dot{x}_2 \\ \mathbf{x}_4^T\mathbf{M}\dot{\mathbf{x}}_4\dot{x}_3 \\ \frac{1}{2}\mathbf{M}\mathbf{x}_4\dot{x}_3^2 + \mathbf{K}\mathbf{x}_4 \end{bmatrix}$$

58.3 Controller Design

For the dynamic Eq. (58.2), when the states levels off, there may exist singularity in the state-depend coefficient matrix $C(x)$ due to the small amount of x_1 during the dynamics calculation. Thus, a refined T-S fuzzy dynamic model is introduced to represent the nonlinear characteristics to avoid this phenomenon. $x_1(t)$ is chosen to be the premise variable, then the fuzzy set is defined as $x_1(t) \in \{N_3, N_2, N_1, 0, P_1, P_2, P_3\}$ and the fuzzy membership function is described as Fig. 58.1.

Thus, the i th rule of the T-S fuzzy system can be described as follows [16]:

Plant rule i : if $x_1(t)$ is $N_i(x_1(t))$, then $\chi_i : C_i(x)\ddot{x} + f_i(x, \dot{x}) + d = u$ (Table 58.1).

Based on the T-S fuzzy model, the dynamic equation can be rewritten as follows:

$$\ddot{x} = \sum_{i=1}^j h_i(x_1)C_i^{-1}(x)(u - f(x, \dot{x}) - d), h_i(x_1) = \frac{\mu_i(x_1)}{\sum_{i=1}^p \mu_i(x_1)} \quad (58.3)$$

Lemma 1 [17] It is supposed that there exists a Lyapunov function $V(x, t) \geq 0$ which holds the following inequality.

$$\dot{V}(x, t) \leq -\frac{\pi}{\kappa T_c} \left(V_2^{1-\frac{\kappa}{2}} + V_2^{1+\frac{\kappa}{2}} \right) \quad (58.4)$$

Fig. 58.1 Membership functions of T-S fuzzy sets

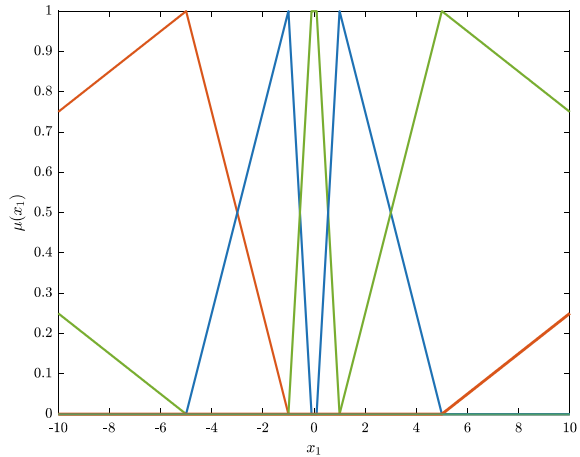


Table 58.1 Fuzzy rules

Rules	R ₁	R ₂	R ₃	R ₄	R ₅	R ₆	R ₇
$x_1(t)$	N_3	N_2	N_1	0	P_1	P_2	P_3

where $0 < \kappa < 1$ is a chosen parameter and T_c is the prescribed control time. Thus, the solution for nonlinear system $\dot{\mathbf{x}} = \boldsymbol{\xi}(\mathbf{x}, t)$ can be stabilized with predefined time T_c .

For dynamic system (58.2), it's defined that $V_1 = \frac{1}{2}\mathbf{x}^T\mathbf{x}$, then the prescribed time sliding mode manifold is designed as Eq. (58.5)

$$\mathbf{s} = \mathbf{z} + \boldsymbol{\tau}, \boldsymbol{\tau} = \frac{1}{\beta_1 T_1} \left(V_1^{-\frac{\beta_1}{2}} + V_1^{\frac{\beta_1}{2}} \right) \mathbf{x} \quad (58.5)$$

When the system states reach the sliding mode manifold, there exists $\mathbf{s} = 0$, thus, according to Lemma 1, the states can be stabilized in prescribed time for $t \rightarrow T_1$.

Proof For $\mathbf{s} = 0$, it can be obtained that $\dot{\mathbf{x}} = \mathbf{z} = -\frac{1}{\beta_1 T_1} \left(V_1^{-\frac{\beta_1}{2}} + V_1^{\frac{\beta_1}{2}} \right) \mathbf{x}$, then the first derivative of V_1 can be denoted as

$$\dot{V}_1 = \frac{1}{2}\mathbf{x}^T\dot{\mathbf{x}} = \frac{1}{2}\mathbf{x}^T \left(-\frac{1}{\beta_1 T_1} \left(V_1^{-\frac{\beta_1}{2}} + V_1^{\frac{\beta_1}{2}} \right) \mathbf{x} \right) = -\frac{1}{\beta_1 T_1} \left(V_1^{1-\frac{\beta_1}{2}} + V_1^{1+\frac{\beta_1}{2}} \right) \quad (58.6)$$

According to Lemma 1, while the states reach the sliding mode manifold, the system states can reach zero with prescribed time.

This completes the proof.

When the states reach the sliding mode manifold, the system can stabilize at T_1 . Nonetheless, it should prove that the states can reach the sliding mode manifold. Thus, it's defined that $V_2 = \frac{1}{2}\mathbf{s}^T\mathbf{s}$, then the prescribed time fuzzy controller can be designed as Eq. (58.7)

$$\begin{aligned} \mathbf{u} = & \mathbf{f}(x, \dot{x}) + \mathbf{d} - \sum_{i=1}^j h_i(x_1) \mathbf{C}_i(\mathbf{x}) \dot{\mathbf{x}} \\ & + \sum_{i=1}^j h_i(x_1) \mathbf{C}_i(\mathbf{x}) \left(-\frac{1}{\beta_1 T_1} \left(V_1^{-\frac{\beta_1}{2}} + V_1^{\frac{\beta_1}{2}} \right) \mathbf{s} \right) - \lambda \mathbf{s} \end{aligned} \quad (58.7)$$

Theorem 1 For given parameters $\beta_1, \beta_2, T_1, T_2, \lambda$, the nonlinear integrated orbit-attitude-vibration system (58.2) can be stabilized in the prescribed time subject to the controller (58.7) with the designed sliding mode manifold (58.5). It's obtained that the convergence time is $T_c = T_1 + T_2$ and the states can converge to zero.

Proof For sliding mode manifold (58.5), the first derivative of \mathbf{s} can be calculated as Eq. (58.8).

$$\dot{\mathbf{s}} = \dot{\mathbf{z}} + \dot{\boldsymbol{\tau}} = \dot{\mathbf{z}} + \sum_{i=1}^j h_i(x_1) \mathbf{C}_i^{-1}(\mathbf{x}) \mathbf{u} - \sum_{i=1}^j h_i(x_1) \mathbf{C}_i^{-1}(\mathbf{x}) (\mathbf{f}(\mathbf{x}, \dot{\mathbf{x}}) + \mathbf{d}) \quad (58.8)$$

Substituting the controller (58.7), the first derivative of V_2 has the following form

$$\begin{aligned}
 \dot{V}_2 &= \frac{1}{2} \dot{s}^T \dot{s} \\
 &= \frac{1}{2} \dot{s}^T \left(\dot{\mathbf{x}} + \sum_{i=1}^j h_i(x_1) \mathbf{C}_i^{-1}(\mathbf{x}) \mathbf{u} - \sum_{i=1}^j h_i(x_1) \mathbf{C}_i^{-1}(\mathbf{x}) (\mathbf{f}(\mathbf{x}, \dot{\mathbf{x}}) + \mathbf{d}) \right) \\
 &= \frac{1}{2} \dot{s}^T \left(\dot{\mathbf{x}} + \sum_{i=1}^j h_i(x_1) \mathbf{C}_i^{-1}(\mathbf{x}) \left(\mathbf{f}(\mathbf{x}, \dot{\mathbf{x}}) + \mathbf{d} - \sum_{i=1}^j h_i(x_1) \mathbf{C}_i(\mathbf{x}) \dot{\mathbf{x}} + \right. \right. \\
 &\quad \left. \left. \sum_{i=1}^j h_i(x_1) \mathbf{C}_i(\mathbf{x}) \left(-\frac{1}{\beta_1 T_1} \left(V_1^{-\frac{\beta_1}{2}} + V_1^{\frac{\beta_1}{2}} \right) \mathbf{s} \right) - \lambda \mathbf{s} \right) \right. \\
 &\quad \left. - \sum_{i=1}^j h_i(x_1) \mathbf{C}_i^{-1}(\mathbf{x}) (\mathbf{f}(\mathbf{x}, \dot{\mathbf{x}}) + \mathbf{d}) \right) \\
 &= -\frac{1}{\beta_2 T_2} \left(V_2^{1-\frac{\beta_2}{2}} + V_2^{1+\frac{\beta_2}{2}} \right) - \lambda \dot{s}^T \mathbf{s} \\
 &\leq -\frac{1}{\beta_2 T_2} \left(V_2^{1-\frac{\beta_2}{2}} + V_2^{1+\frac{\beta_2}{2}} \right) \tag{58.9}
 \end{aligned}$$

Thus, according to Lemma 1, the states can reach the designed sliding mode manifold, i.e. s can converges to zero in the prescribed time T_2 subject to the controller (58.7).

This completes the proof.

Accordingly, it's obtained that the states of system (58.2) can converge to zero in the prescribed time $T_c = T_1 + T_2$.

58.4 Simulation Results

In this section, the effectiveness of the proposed fuzzy prescribed time controller is demonstrated with simulations of closed loop dynamic system. The relevant parameters are chosen as follows

$$\begin{aligned}
 m &= 10000\text{kg}, C_0 = 5000000, M = 1.5, K = 0.001 \\
 T_1 &= 150\text{s}, T_2 = 200\text{s}, \beta_1 = 0.4, \beta_2 = 0.5, \lambda = 50 \\
 \mathbf{d} &= 10^{-3} \times [1 \ 0 \ 0.1 \ 0.01]^T \sin(0.01t) \\
 u_{1 \max} &= 50\text{N}, u_{2 \max} = 50\text{Nm}, u_{3 \max} = 15\text{Nm}, u_{4 \max} = 0.1\text{N}
 \end{aligned}$$

where, m and C_0 is relevant to the quality characteristic of large-scale spacecraft; \mathbf{M} and \mathbf{K} is relevant to the elastic and stiffness properties of the flexible structure (The first-order vibration modal is considered in this paper). Moreover, T_1, T_2 and β_1, β_2 are related to the prescribed stabilization time. Additionally, \mathbf{d} represents the external disturbance and $u_{i \max}$ represents the maximum control force/torque.

Applying the controller (58.7), the simulation results are obtained as Figs. 58.2, 58.3, 58.4, 58.5 and 58.6 where it's obvious that all the states can reach to a small bound at the prescribed 350 s to achieve the control objectives. Time response of radial orbital motion and tangential orbital rotation are shown in Figs 58.2 and 58.3 respectively. At the prescribed 350 s, the radial position and velocity are less than 2×10^{-3} m and 6×10^{-6} m/s respectively, additionally, for the orbital rotation, the tangential rotation and velocity converges to zero. Figure 58.4 depicts the attitude motion of the large-scale spacecraft. When the system states are stable at 350s, the attitude angle is less than 2×10^{-3} rad and the angular velocity is less than 2×10^{-5} rad/s which demonstrates the high precision of control performance. The active vibration response characteristics of the large-scale flexible spacecraft are presented in Fig. 58.5. Based on the active vibration suppression method used in this paper, the modal displacement and modal velocity can converge to zeros rapidly which can reduce the effect of vibration coupling on attitude and orbital motion efficaciously. Finally, Fig. 58.6 shows the variation curve of control force/torque where it's verified that the limited control input can satisfy the actual requirements of control system. Consequently, the simulations results demonstrate that using the proposed fuzzy prescribed time integrated controller, the orbit-attitude-vibration states can be stabilized at the prescribed time in high precision which is significant for the control system design of the large-scale flexible spacecraft.

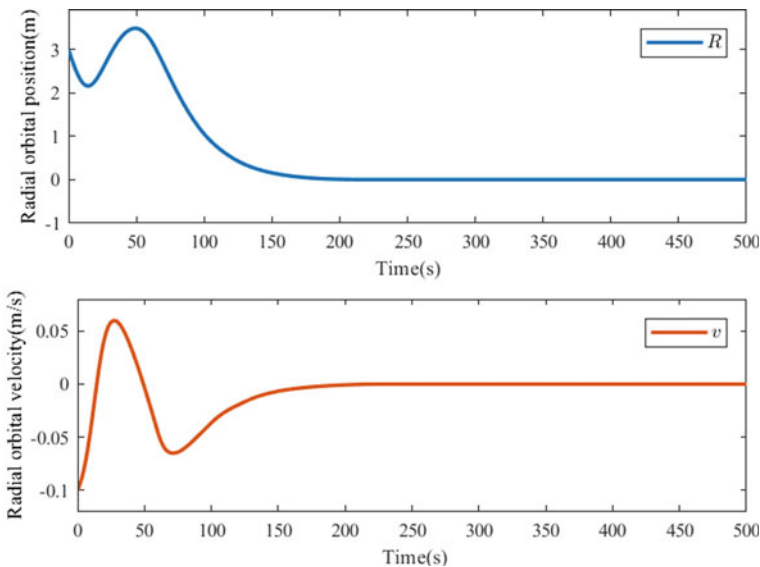


Fig. 58.2 Time response of radial orbital motion

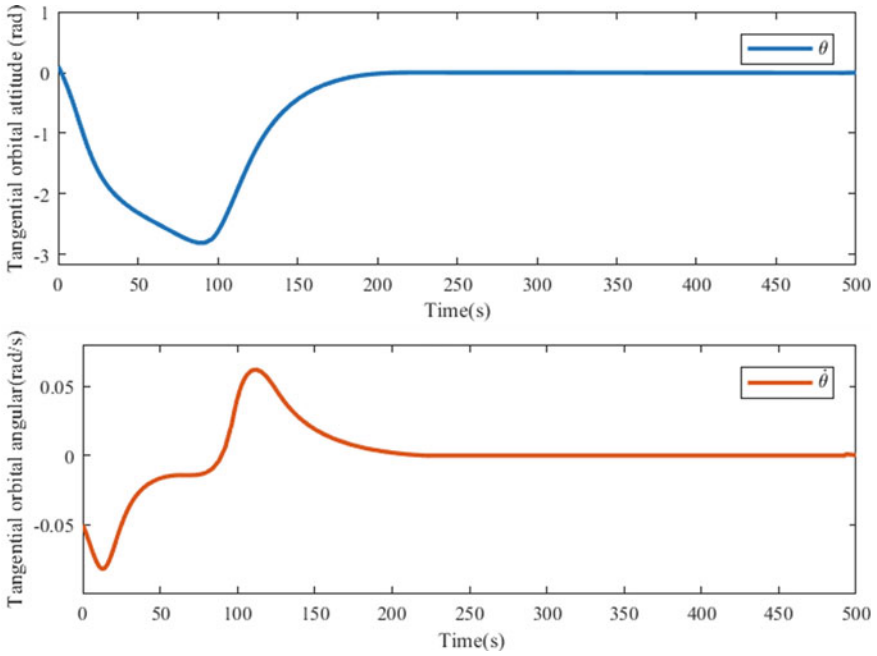


Fig. 58.3 Time response of tangential orbital motion

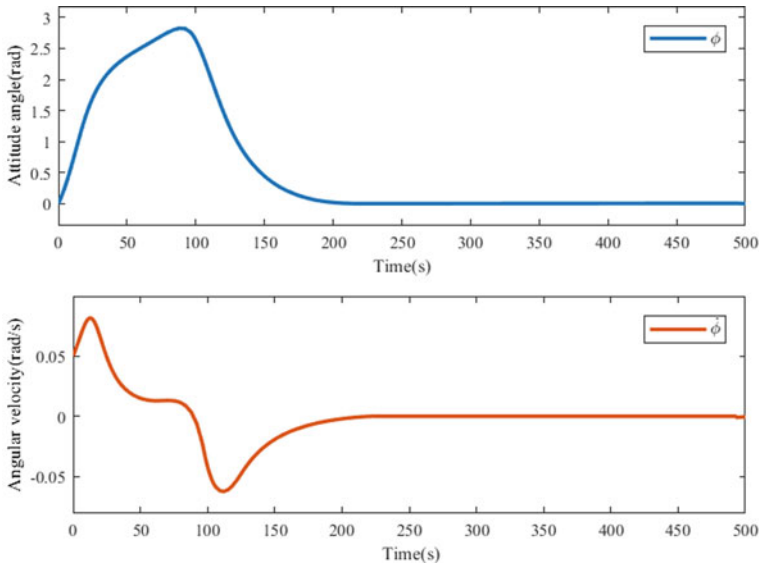


Fig. 58.4 Time response of attitude motion

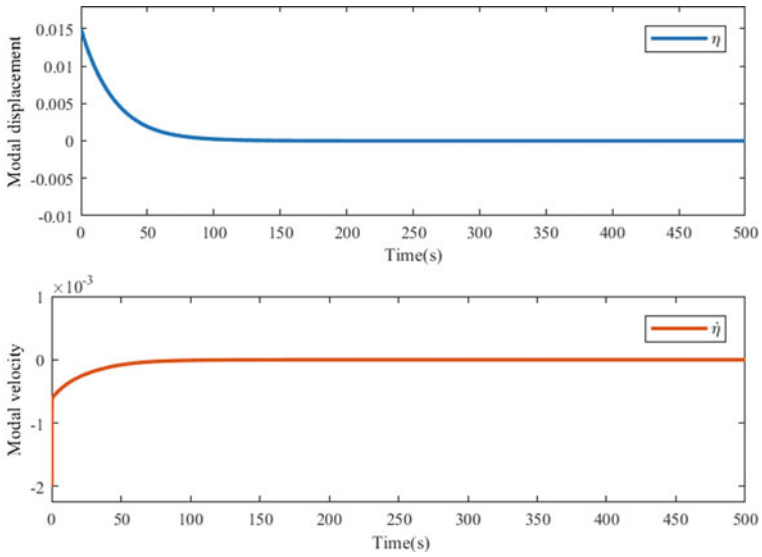


Fig. 58.5 Time response of vibration

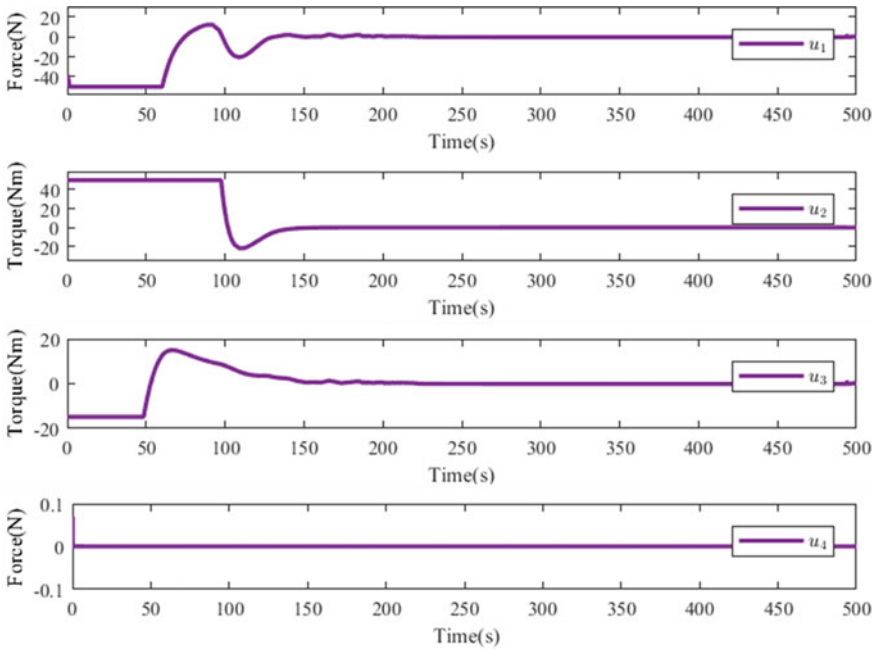


Fig. 58.6 Time response of control force/torque

58.5 Conclusion

This paper investigates the problem of integrated control for large-scale flexible spacecraft. With dynamic analysis, a coupling dynamic model is introduced to depict the motions of orbit, attitude and vibration. Then, a refined T-S fuzzy model is constructed to represent the local nonlinearity and avoid the calculation singularity due to the complex dynamic characteristics. Moreover, a fuzzy prescribed time controller is designed to stabilize the system states in high precision to implement the excellent performance. Finally, simulation results demonstrate the effectiveness of the proposed control strategy. Additionally, the influence of the complex environment will be analyzed specifically for further research, and the system dimensions will be expanded to higher ones to achieve the motion and dynamics modeling completely to accomplish the complex control mission of large-scale flexible spacecraft which is one of the priorities for future work.

Funding Statement This work was supported in part by the National Natural Science Foundation of China under Grants 62103336, 11972026 and U2013206, in part by the Guangdong Basic and Applied Basic Research Foundation under Grants 2021A1515110539 and 2023A1515011666, and in part by Key Research and Development Program of Shaanxi under Grant 2023-YBGY-384.

Conflicts of Interest

The authors declare that they have no conflicts of interest to report regarding the present study.

References

1. Li, Q., Deng, Z.: Coordinated orbit–attitude–vibration control of a sun-facing solar power satellite. *J. Guid. Control. Dyn.* **42**(8), 1863–1869 (2019)
2. Sun, X., Xu, M., Zhong, R.: Dynamic analysis of the tether transportation system using absolute nodal coordinate formulation. *Acta Astronaut.* **139**, 266–277 (2017)
3. Mu, R., Tan, S., Wu, Z., et al.: Coupling dynamics of super large space structures in the presence of environmental disturbances. *Acta Astronaut.* **148**, 385–395 (2018)
4. Ishimura, K., Higuchi, K.: Coupling among pitch motion, axial vibration, and orbital motion of large space structures. *J. Aerosp. Eng.* **21**(2), 61–71 (2008)
5. Wei, Y., Li, Q., Xu, F.: Orbit-attitude-vibration coupled dynamics of tethered solar power satellite. *Adv. Space Res.* **67**(1), 393–400 (2021)
6. Liu, Y., Wu, S., Zhang, K., et al.: Gravitational orbit–attitude coupling dynamics of a large solar power satellite. *Aerosp. Sci. Technol.* **62**, 46–54 (2017)
7. Wang, E., Wu, S., Wu, Z.: Dynamic multi-constrained assembly sequence planning of large space structures considering structural vibration. *Acta Astronaut.* **195**, 27–40 (2022)
8. Zhou, W., Zhang, K., Wu, S., et al.: Distributed cooperative control for vibration suppression of a flexible satellite. *Aerosp. Sci. Technol.* **128**, 107750 (2022)
9. Wang, F., Miao, Y., Li, C., et al.: Attitude control of rigid spacecraft with predefined-time stability. *J. Franklin Inst.* **357**(7), 4212–4221 (2020)
10. Xie, S., Chen, Q., He, X.: Predefined-time approximation-free attitude constraint control of rigid spacecraft. *IEEE Trans. Aerosp. Electron. Syst.* (2022)
11. Xie, S., Chen, Q.: Adaptive nonsingular predefined-time control for attitude stabilization of rigid spacecrafts. *IEEE Trans. Circuits Syst. II Express Briefs* **69**(1), 189–193 (2021)

12. Xu, C., Wu, B., Zhang, Y.: Distributed prescribed-time attitude cooperative control for multiple spacecraft. *Aerosp. Sci. Technol.* **113**, 106699 (2021)
13. Ye, D., Zou, A.M., Sun, Z.: Predefined-time predefined-bounded attitude tracking control for rigid spacecraft. *IEEE Trans. Aerosp. Electron. Syst.* **58**(1), 464–472 (2021)
14. Xiao, B., Wu, X., Cao, L., et al.: Prescribed time attitude tracking control of spacecraft with arbitrary disturbance. *IEEE Trans. Aerosp. Electron. Syst.* (2021)
15. Liu, Y., Wu, S., Zhang, K., et al.: Parametrical excitation model for rigid–flexible coupling system of solar power satellite. *J. Guid. Control. Dyn.* **40**(10), 2674–2681 (2017)
16. Lyu, B., Liu, C., Yue, X.: Hybrid nonfragile intermediate observer-based T-S fuzzy attitude control for flexible spacecraft with input saturation. *Aerosp. Sci. Technol.* **128**, 107753 (2022)
17. Munoz-Vazquez, A.J., Sánchez-Torres, J.D., Jimenez-Rodriguez, E., et al.: Predefined-time robust stabilization of robotic manipulators. *IEEE/ASME Trans. Mechatron.* **24**(3), 1033–1040 (2019)

Chapter 59

Study on the Classification Method of the Usage Severity of Aircraft Structures



Weiye Guo, Yanjun Zhang, Bintuan Wang, and Chengjian Che

Abstract The high overload and high maneuverability in the training course result in the structural damage and the life consumption speed is accelerated, the use of each model is obviously higher than the expected use, which greatly increases the risk of the operation of aircraft. The life design and verification work based on the design load spectrum in the design stage cannot meet the requirements of ensuring the flight safety in the whole life of aircraft. How to ensure the security of active military aircraft under the change of actual use mission has become an urgent problem to be solved. Based on the analysis method of structural fatigue individual aircraft tracking, this paper expounds the design method and task profile of individual aircraft, studies the calculation of equivalent damage of individual aircraft, puts forward three classification methods of usage severity of aircraft, which are mild severity, severity moderate and heavy severity, and carries out the determination of reference equivalent damage for the object aircraft. In addition, the interval classification method is used to classify the usage severity, and the method of the usage severity analysis is provided.

Keywords Individual aircraft tracking · Usage severity · Classification · Structure fatigue

59.1 Preface

The purpose of aircraft structural fatigue individual aircraft tracking (FIAT) analysis is to evaluate the implementation of the training program of aircraft fleet by using monitoring and tracking to evaluate whether or not the conditions (task composition) of the design service life have changed; the second is to analyze and evaluate the life of aircraft fleet according to the previous changes, and to optimize the assignment of training task of aircraft fleet and revise the structural integrity control plan for the service fleet [1]

W. Guo (✉) · Y. Zhang · B. Wang · C. Che
The First Aircraft Design and Research Institute of AVIC, Xi'an 710089, China
e-mail: 954089521@qq.com

Aircraft life determination is generally achieved by life analysis, evaluation and validation under the load spectrum compiled according to the design mission profile [2]. Because the actual load spectrum cannot be obtained in the development stage, there are obvious differences between the design load spectrum and the actual load spectrum. On the other hand, even though the load spectrum of the design stage can reflect the typical use of the aircraft group, but due to the obvious difference between the actual use of the individual aircraft and the expected use conditions, the fixed life conclusion cannot be used directly in the life management, especially at present, the new training program has been widely used in the active military aircraft. The high overload and high maneuverability in the training course result in the structural damage and the life consumption speed is accelerated, the use of each model is obviously higher than the expected use, which greatly increases the risk of the operation of aircraft. The life design and verification work based on the design load spectrum in the design stage cannot meet the requirements of ensuring the flight safety in the whole life of aircraft. How to ensure the security of active military aircraft under the change of actual use mission has become an urgent problem to be solved [3, 4].

The design mission profile of the aircraft gives the expected use of the aircraft, and the load history of each aircraft in the actual use of the aircraft group is obviously different from that of the design mission profile. The actual use of some models has exceeded even the expected use of the design task profiles used at the time of life.

The most commonly used method to evaluate the weight of each flight is to analyze the relative damage relation of each flight according to the equivalent damage theory. This work usually needs to carry out damage calculation based on flight parameters after obtaining a large amount of flight takeoff and landing data. After determining the total damage of each take-off and landing, the damage size of each take-off and landing as the measure of weight evaluation. For fatigue individual aircraft tracking, the evaluation of each flight take-off and landing weight constitutes the most basic data for individual aircraft tracking.

In addition to the above-mentioned quantitative evaluation, a qualitative and semi-quantitative method for evaluating the severity of flight take-off and landing can be developed by using quantitative damage analysis as a benchmark. That is, in the individual aircraft tracking based on the analysis of aircraft use, according to the flight parameters of the classification judgment, the rapid landing caused by the damage is relatively lighter or heavier qualitative classification.

59.2 Aircraft Design Method and Equivalent Damage

The method of aircraft design is usually represented by the aircraft design using the mission profile. The mission profile is a list of mission sequences composed of mission segments and performance parameters that constitute a complete flight. The typical load condition in the static strength design only reflects several limit

conditions on the strength envelope, and the sum of the typical mission profiles of the aircraft reflects all the expected use of the aircraft.

In order to monitor the healthy state of aircraft structure, it is necessary to carry out structural fatigue individual aircraft tracking, and to calculate the equivalent damage under the load spectrum of the actual load history and the design/actual load history as a benchmark for each flight, in order to evaluate the difference of damage accumulation and life consumption caused by the difference in use, Then it analyzes and forecasts the use of the aircraft.

59.2.1 Mission Profile

The type of mission profile is closely related to the type of aircraft. Different types of mission profiles should include: type of mission profiles; percentage of use per mission profile; time of one flight per mission profile; task segments and their sequence; effective load layout of various mission profiles; the number of landings and the form of landings in various mission profiles.

Each task segment of each mission profile shall include: the time spent on each task segment in one flight; each task segment as a percentage of the use of the task; each task segment as a percentage of the total use; and performance parameters within each task segment, such as speed, height, weight, etc.

The mission profile is determined primarily by the use of the aircraft. For a newly designed aircraft, the mission profile of a similar aircraft can be borrowed and then modified appropriately. Active aircraft can be obtained by understanding the aircraft's performance, analyzing flight training programs, flight logs, visiting pilots, and flight measurements [5].

59.2.2 Equivalent Damage Theory

From the point of view of evaluating the use of aircraft, it is necessary to introduce the concept of equivalent damage and establish corresponding methods. The calculation model of equivalent damage includes two aspects: equivalent damage formula and damage index. In the research of structural fatigue individual aircraft tracking, the equivalent damage of reference spectrum (design load spectrum or whole-machine fatigue test load spectrum) should be calculated by different equivalent damage formula, and the final equivalent damage formula and damage index m should be determined [6].

Equivalent damage formula. The current equivalent damage calculation method is generally based on the influence of different average stress (or stress ratio) on the S-N curve, assuming that the stress and overload are linear, each cycle ($\Delta G_i, R_i$) in the load spectrum is converted into a pulsating cycle, and the equivalent damage

calculation formula is established as follows:

$$D = \sum_{i=1}^n (G_{\max,0i})^m \quad (59.1)$$

Among them, $G_{\max,0i}$ is the maximum overload of pulsating cycle, m is the damage index and n is the number of load cycles in the load spectrum.

The method of converting any cycle ($\Delta G_i, R_i$) in the load spectrum into a pulsating cycle is generally based on Odin's formula and the transformation based on equal life curve [6, 7]. The only difference between the two methods is the difference in the equivalent damage reduction formula.

Damage index. The value of damage index will influence the calculation result of equivalent damage. The main metal materials of aircraft body structure are aluminum alloy, high strength steel and titanium alloy. The stress concentration in the key parts is 1.5 ~ 3.0. The load cycle of the main damage in the random spectrum corresponds to the middle life interval. The m value of the pulsation cycle corresponds to the range of 3.5 ~ 5.0. The material, structural form and stress concentration of several key parts of the whole machine will have different m -values. Multiple key parts should be considered in the selection of m -value, so that the equivalent damage energy can represent the structure of the whole machine.

Benchmark Equivalent Damage. The reference load spectrum representing aircraft reference usage is generally composed of some typical mission profiles in a certain proportion. The load spectrum (benchmark spectrum) of aircraft-wide fatigue test is used as the reference for the analysis of flight takeoff and landing damage of individual aircraft, and the equivalent damage is the reference equivalent damage. According to the equivalent damage model determined in the preceding section and the method of determining the damage index, the equivalent damage of the reference spectrum can be determined.

59.3 Classification Method of Aircraft Usage Severity

59.3.1 Classification of Aircraft Usage

According to the actual use of the aircraft, it can be divided into three different levels of severity:

Mild Severity. It indicates that the damage of the body structure caused by the rise and fall is small.

Severity Moderate. It represents that the body structure damage caused by the rise and fall is in the middle.

Heavy Severity. It indicates that the body structure damage caused by the take-off and landing is greater.

In aircraft individual aircraft tracking, the severity of any one take-off and landing can be classified as one of the three different severities.

In order to classify the damage severity of any aircraft in actual use according to three classifications: mild, normal and heavy, it is necessary to find a comparative basis for evaluating the severity of any aircraft in actual use. Generally, the design load spectrum (or measured load spectrum) used for model durability and damage tolerance verification is used as a reference for comparison.

59.3.2 An Interval Method for Classification of Aircraft Severity Usage

Based on the damage calculated in the reference damage, the rise and fall of the benchmark is divided into three types of use (i. e., the division of the damage interval). Considering the neutral position and certain representativeness, one third of the rise and fall represented by the three types of use is preferred.

- (1) Calculating the equivalent damage D of the base landing

$$D = \sum_{k=1}^m \sum_{j=1}^{i_k} D_{k,j} \tag{59.2}$$

Among them, m is the number of mission sections, i_k is the number of k-off and landing of the first section. $D_{k,j}$ is the damage of the first j in the k section, and $D_{k,j}$ is calculated according to the equivalent damage formula.

- (2) The division of the reference damage interval. According to the relationship between the takeoff and landing of a flight of $m * i_k$, the single take-off and landing equivalent damage is divided into a graded interval of severity $[0, D_1]$, $[D_1, D_2]$, $[D_2, D_{max}]$, so that the number of take-off and landing in each interval is n_1, n_2, n_3 and is satisfied:

$$n_1 + n_2 + n_3 = mi_k \tag{59.3}$$

And make n_1, n_2, n_3 approximately equal, i. e. each occupies 1/3 of the total number of ups and downs.

- (3) Choose different classification indexes, such as some function relation (such as maximum, average, median, etc.) $f(x_1, x_2, \dots, x_n)$ between flight parameters, and determine the upper limit of the corresponding interval range B3.

$$B_3 = \max\{[f(x_1, x_2, \dots, x_n)]_i\} \tag{59.4}$$

$$B_3 = \frac{1}{m * i_k} \sum_{i=1}^{m*i_k} [f(x_1, x_2, \dots, x_n)]_i \quad (59.5)$$

$$B_3 = \text{median}\{[f(x_1, x_2, \dots, x_n)]_i\} \quad (59.6)$$

Among them x_1, x_2, \dots, x_n is the parameter obtained by individual aircraft tracking, $f(x_1, x_2, \dots, x_n)$ function can be the expression of multiple linear regression or the load or damage of machine learning. In the example, normal overload maximum, normal overload average, normal overload median can be used.

- (4) Division of intervals. The interval $[0, B_3]$ is divided into three different severity definitions: $[0, B_1]$ represents the rise and fall of mild severity; $[B_1, B_2]$ represents the rise and fall of normal severity; $[B_2, B_3]$ represents the rise and fall of heavier severity. The maximum likelihood estimation of parameters in logarithmic normal density function of reference spectrum adjusts the range of B_1 and B_2 , so that the number of aircraft taking off and landing in $[0, B_1]$, $[B_1, B_2]$, $[B_2, B_3]$ is approximately equal. B_1 and B_2 values were determined according to three different B_3 values.
- (5) Using $[0, B_1]$, $[B_1, B_2]$, $[B_2, B_3]$ as the basis of division, a number of data used in the outfield of aircraft are randomly selected to calculate the consistency with the classification of the above-mentioned usage. It can realize the division of the use of the weight of the fall together. When significant changes occur in aircraft usage, such as changes to the training syllabus, the classification of damage based on baseline usage needs to be reclassified.

59.4 Interval Classification of the Usage Severity of a Certain Type of Aircraft

The reference load spectrum representing aircraft reference usage is generally composed of some typical mission profiles in a certain proportion. The full-scale fatigue test load spectrum of an aircraft (compiled from measured data) consists of eight typical flight mission types, a total of 40 representative flight take-off and landing, and 335 representative take-off and landing (300 flying hours) in a certain proportion, as shown in Table 59.1. Based on 335 random-arranged typical block spectra, the test load spectrum was compiled and the fourfold fatigue test was completed, and the spectrum was used as the reference spectrum.

Figure 59.1 shows the diagram of the flight history curve of the typical take-off and landing center of gravity overload.

According to the statistics of dozens of effective parameters of takeoff and landing, the distribution rules and characteristics of key parameters such as center of gravity overload, bending moment of flat tail root, bending moment of vertical tail root and deflection angle of aileron are determined, and the mean value and standard deviation are calculated. The statistical analysis of typical flight mission profiles is carried out

Table 59.1 Reference spectrum 8 types of typical flight tasks and their proportion

Ordinal number	Typical flight take-off and landing number	Number of occurrences	Ordinal number	Typical flight take-off and landing number	Number of occurrences
1	A-01	1	21	D-08	14
2	A-02	3	22	D-09	8
3	A-03	1	23	D-12	9
4	A-04	1	24	D-13	6
5	A-05	7	25	E-04	29
6	A-06	1	26	E-05	24
7	A-07	2	27	E-06	52
8	A-08	4	28	F-01	25
9	B-01	1	29	F-06	57
10	B-03	1	30	F-09	12
11	B-04	1	31	F-12	11
12	B-05	1	32	G-01	2
13	B-06	2	33	G-02	1
14	B-07	3	34	G-03	1
15	B-08	5	35	G-04	1
16	B-10	1	36	G-05	2
17	C-01	10	37	G-06	3
18	D-01	15	38	H-01	1
19	D-02	8	39	H-04	1
20	D-03	5	40	H-05	3

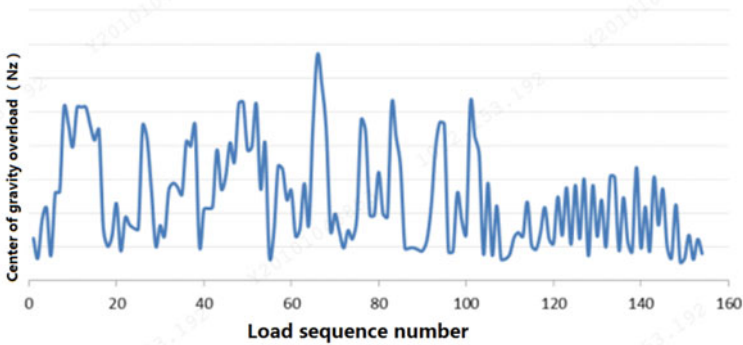


Fig. 59.1 Diagram of the overload process curve of the typical gravity center of take-off and landing

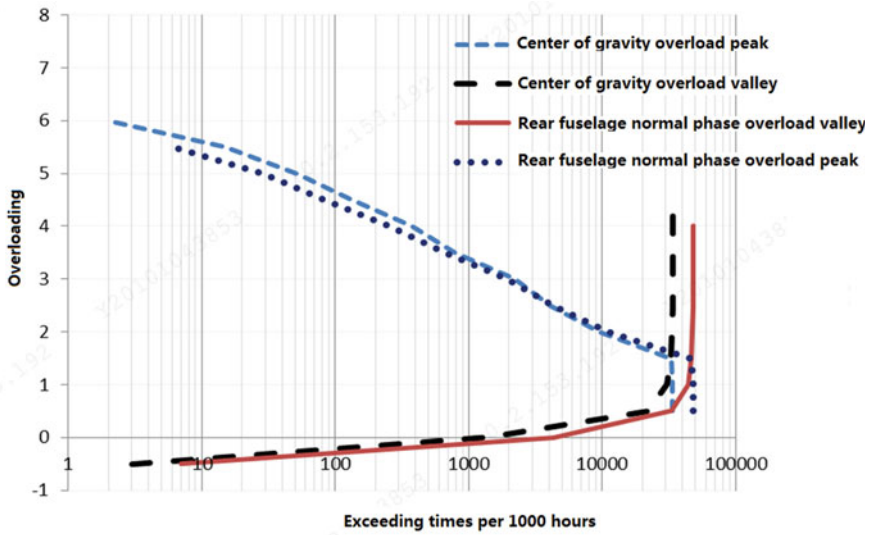


Fig. 59.2 Chart of surpass number curve Per 1000 h

according to the key parameters, which provides the basic data for the merging of mission profiles and the compilation of the measured load spectrum. Figure 59.2 is a schematic diagram of the overtaking times of the center of gravity overload and the rear fuselage normal overload per 1000 flight hours.

By summing up the equivalent damage calculation for each stage of load cycle in the base spectrum, the equivalent damage for each stage of load cycle can be obtained as shown in Table 59.2.

As a result, the total equivalent damage of the single loading block of the reference spectrum is = 144,659, corresponding to 335 takeoff and landing, 400 flying hours. The reference equivalent damage per flight hour (the standard equivalent damage rate) is obtained as follows

$$DR_0 = \frac{D_{jz}}{400} = \frac{144659}{400} = 361.6 \tag{59.7}$$

According to the data processing results of the measured flight parameters of each aircraft in the field, the equivalent damage of the actual flight hours can be obtained by using the equivalent overload of the center of gravity. According to the equivalent damage per flight hour is 361.6, and the equivalent damage per take-off and landing is 323.8.

The relationship between the flight take-off and landing equivalent damage and the maximum overload, the average overload, and the median overload is shown in Fig. 59.3. It can be seen that the relationship between equivalent damage and overload maximum is close.

Table 59.2 Equivalent landing damage of reference spectrum

Ordinal number	Typical flight take-off and landing number	Typical flight take-off and landing damage	Number of occurrences	Ordinal number	Typical flight take-off and landing number	Typical flight take-off and landing damage	Number of occurrences
1	A-01	155.0	1	21	D-08	807.5	14
2	A-02	839.8	3	22	D-09	68.3	8
3	A-03	170.8	1	23	D-12	331.0	9
4	A-04	155.8	1	24	D-13	455.9	6
5	A-05	1808.2	7	25	E-04	25.8	29
6	A-06	371.4	1	26	E-05	177.4	24
7	A-07	568.0	2	27	E-06	355.3	52
8	A-08	1021.4	4	28	F-01	106.4	25
9	B-01	1099.1	1	29	F-06	381.8	57
10	B-03	573.0	1	30	F-09	57.0	12
11	B-04	1069.0	1	31	F-12	27.4	11
12	B-05	681.3	1	32	G-01	988.9	2
13	B-06	1891.5	2	33	G-02	409.1	1
14	B-07	2978.3	3	34	G-03	491.4	1
15	B-08	3849.9	5	35	G-04	668.1	1
16	B-10	582.8	1	36	G-05	752.2	2
17	C-01	53.9	10	37	G-06	1576.4	3
18	D-01	488.0	15	38	H-01	182.7	1
19	D-02	73.8	8	39	H-04	406.1	1
20	D-03	101.9	5	40	H-05	551.7	3

Equivalent damage, $D_{max} = 3850$. The use severity of the three intervals classified according to the size of the take-off and landing injury is (0, 350), (350, 680), (680, 3850). After the interval is divided, the number of take-off and fall of each interval is 14, 13, 13. The classification of the use severity of each landing is shown in Table 59.3.

Selecting the classification index of flying parameter in take-off and landing, the classification index is the maximum value of barycenter normal to overload, the mean value of barycenter normal to overload, and the median value of barycenter overload to determine the upper limit B_3 of the corresponding interval range.

Adjust the range of B_1 and B_2 so that the number of ups and downs in $[0, B_1]$, $[B_1, B_2]$, $[B_2, B_3]$ is approximately equal. B_1 and B_2 values were determined according to three different B_3 values. The maximum N_z interval is (0, 3.15), (3.15, 4.05), (4.05, 5.675); the average N_z interval is (0, 1.3), (1.3, 1.64), (1.64, 2.214); the median N_z interval is (0, 1.26), (1.26, 1.45), (1.45, 2.221).

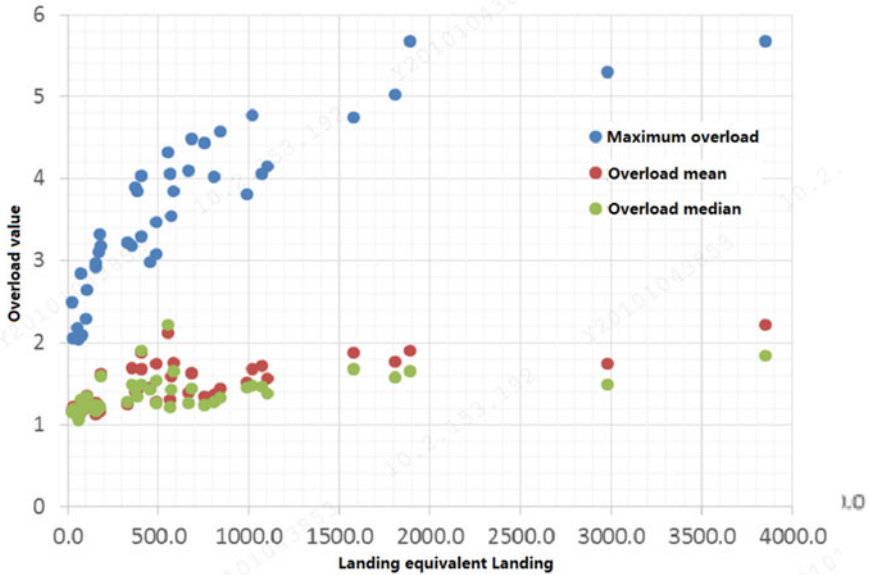


Fig. 59.3 Relationship between overloading and landing damage

Finally, the classification of severity is shown in the table after the damage is divided according to different methods.

According to the classification of severity in Table 59.3, the results of the consistency analysis by interval can be obtained as follows:

- (1) In the case of interval division according to the maximum center of gravity overload, the number of ups and downs in light, medium and heavy use is basically the same, which is 13, 13 and 14. The severity of six ups and downs by maximum center of gravity overload was greater than that by damage, and four of them were smaller than that by damage.
- (2) According to the gravity center normal to the overload mean of the severity of the division, divided into light, medium, heavy three serious use of the same number of ups and downs, 14, 13, 13. The severity of eight ups and downs is larger than that of the damage, and the severity of eight ups and downs is smaller than that of the damage.
- (3) According to the gravity center method, the number of ups and downs under the three serious uses of light, medium and heavy is basically the same, which is 12, 14, 14. The severity of 10 ups and downs by barycenter normal overload median interval is larger than that by damage, and 7 of them are smaller than that by damage.
- (4) The number of ups and downs of the combination of mild and normal use, normal and severe use of the interval is compared with the result of the division of equivalent damage, and the three methods are compared as follows:

Table 59.3 Use severity classification results

Number	Typical flight number	Classification by damage		Classification by maximum Nz		Classification by nz mean		Classification by nz median	
		Damage value	Results	Nz_max	Results	Nz mean	Results	Nz median	Results
1	A-01	155.0	Light	2.923	Light	1.122	Light	1.158	Light
2	A-02	839.8	Heavy	4.573	Heavy	1.443	Middle	1.324	Middle
3	A-03	170.8	Light	3.108	Light	1.228	Light	1.202	Light
4	A-04	155.8	Light	2.971	Light	1.265	Light	1.236	Light
5	A-05	1808.2	Heavy	5.02	Heavy	1.77	Heavy	1.579	Heavy
6	A-06	371.4	Middle	3.898	Middle	1.404	Middle	1.445	Middle
7	A-07	568.0	Middle	4.056	Heavy	1.296	Light	1.212	Light
8	A-08	1021.4	Heavy	4.775	Heavy	1.679	Heavy	1.477	Heavy
9	B-01	1099.1	Heavy	4.146	Heavy	1.569	Middle	1.372	Middle
10	B-03	573.0	Middle	3.542	Middle	1.584	Middle	1.432	Middle
11	B-04	1069.0	Heavy	4.057	Heavy	1.718	Heavy	1.467	Heavy
12	B-05	681.3	Heavy	4.487	Heavy	1.632	Middle	1.435	Middle
13	B-06	1891.5	Heavy	5.671	Heavy	1.898	Heavy	1.654	Heavy
14	B-07	2978.3	Heavy	5.296	Heavy	1.741	Heavy	1.491	Heavy
15	B-08	3849.9	Heavy	5.675	Heavy	2.214	Heavy	1.837	Heavy
16	B-10	582.8	Middle	3.841	Middle	1.749	Heavy	1.65	Heavy
17	C-01	53.9	Light	2.173	Light	1.139	Light	1.152	Light
18	D-01	488.0	Middle	3.08	Light	1.273	Light	1.262	Middle
19	D-02	73.8	Light	2.088	Light	1.158	Light	1.166	Light
20	D-03	101.9	Light	2.29	Light	1.216	Light	1.232	Light
21	D-08	807.5	Heavy	4.015	Middle	1.366	Middle	1.282	Middle
22	D-09	68.3	Light	2.843	Light	1.271	Light	1.307	Middle
23	D-12	331.0	Light	3.214	Middle	1.25	Light	1.276	Middle
24	D-13	455.9	Middle	2.983	Light	1.45	Middle	1.424	Middle
25	E-04	25.8	Light	2.496	Light	1.18	Light	1.15	Light
26	E-05	177.4	Light	3.317	Middle	1.169	Light	1.215	Light
27	E-06	355.3	Middle	3.179	Middle	1.687	Heavy	1.494	Heavy
28	F-01	106.4	Light	2.641	Light	1.351	Middle	1.336	Middle
29	F-06	381.8	Middle	3.845	Middle	1.43	Middle	1.344	Middle
30	F-09	57.0	Light	2.04	Light	1.078	Light	1.048	Light
31	F-12	27.4	Light	2.056	Light	1.214	Light	1.189	Light
32	G-01	988.9	Heavy	3.811	Middle	1.514	Middle	1.45	Middle
33	G-02	409.1	Middle	3.289	Middle	1.884	Heavy	1.902	Heavy
34	G-03	491.4	Middle	3.473	Middle	1.74	Heavy	1.535	Heavy

(continued)

Table 59.3 (continued)

Number	Typical flight number	Classification by damage		Classification by maximum Nz		Classification by nz mean		Classification by nz median	
		Damage value	Results	Nz_max	Results	Nz mean	Results	Nz median	Results
35	G-04	668.1	Middle	4.098	Heavy	1.393	Middle	1.263	Middle
36	G-05	752.2	Heavy	4.433	Heavy	1.338	Middle	1.24	Light
37	G-06	1576.4	Heavy	4.743	Heavy	1.873	Heavy	1.675	Heavy
38	H-01	182.7	Light	3.185	Middle	1.617	Middle	1.586	Heavy
39	H-04	406.1	Middle	4.028	Middle	1.681	Heavy	1.485	Heavy
40	H-05	551.7	Middle	4.322	Heavy	2.115	Heavy	2.221	Heavy

- (5) There are 26 ups and downs of mild and normal use according to the maximum of overload, of which 2 of them are inconsistent with that of damage, and 27 of them by normal and severe use, of which 3 are inconsistent with that of damage. The accuracy of qualitative classification can reach 92.3% (2/26) and 88.9% (3/27) respectively.
- (6) There were 26 ups and downs of mild and normal use according to the mean value of take-off and take-off, 6 of which were inconsistent with that of damage, and 27 of which were normal and severe use, 1 of which was inconsistent. The accuracy of qualitative classification can reach 76.9% (20/26) and 96.3% (26/27) respectively.
- (7) There are 26 ups and downs by the median of overload, of which 5 are different from those by the damage, and 28 by the normal and severe use, of which 4 are different. The accuracy of qualitative classification can reach 80.8% (21/26) and 85.7% (24/28) respectively.

Based on the above results, it is recommended to use the barycenter method to classify the maximum overload type. When the parameters used in the calculation of equivalent damage are different from each other, the recommended parameters for the classification of take-off and landing types may be different.

59.5 Conclusion

In order to ensure the security of active military aircraft under the change of actual use task, based on the individual aircraft monitoring technology of aircraft structure, three classification methods of aircraft use severity are put forward, which are mild, normal and heavy, and the determination of reference equivalent damage is carried out for the object aircraft, and the use severity is classified by interval classification method. This paper provides a method of using weight analysis, and puts forward a feasible theoretical method and a practical case for carrying out individual aircraft tracking and evaluating the use of aircraft.

References

1. Zhi, W., Lei, W.: Overview of the technology of individual aircraft life monitoring and structural health prediction management in foreign countries. In: *Aeronautical Safety and Equipment Maintenance Technology_Proceedings of the Symposium on Aviation Safety and Equipment Maintenance Technology*, pp. 283–291 (2014)
2. Molent, L.: A unified approach to fatigue usage monitoring of fighter aircraft based on F/A-18 experience. *Proc. ICAS*. (1998)
3. Ezhilarasu, C.M.: The application of reasoning to aerospace integrated vehicle health management (IVHM): challenges and opportunities. *Prog. Aerosp. Sci.* **105**, 60–73 (2019)
4. Chiang Kai-shek's motherland: Aircraft Structure load/ Environment Spectrum. Electronic Industry Press (2012)
5. GJB 67.6A-2008.: (2008) Structural strength specification for military aircraft part 6: repeated load, Durability and Damage Tolerance[S].
6. Wenting, L., Zhi, W., Fucheng, S.: *Technical guidelines for individual aircraft life monitoring*. National Defense Industry Press, Beijing (2010)
7. Yanjun, Z., Bintuan, W., Qiang, M. et al.: Study on the equivalent damage calculation model for individual aircraft life monitoring. *Aeronautical Science and Technology*, 30 (09), 101–107 (2019)

Chapter 60

Six Degrees of Freedom Simulation for Skipping Stones Based on Quaternion Method in SPH Framework



Xiang-Shan Guan, Peng-Nan Sun, Yu-Xiang Peng, and Nian-Nian Liu

Abstract Six degrees-of-freedom (6-DOF) motion of structures and fluid–structure interactions (FSI) widely exist in engineering fields. It is significant to study the 6-DOF motion for simulating the motion trajectory and fluid–structure interactions. In this paper, the smoothed particle hydrodynamics (SPH) method combined with improved numerical techniques is used to simulate the fluid–structure interactions, and the 6-DOF equations based on the quaternion method are adopted to simulate the 6-DOF motion of skipping stones in the three-dimensional numerical tank. The accuracy of this method is verified by comparing it with the experimental snapshots, which can prove that the simulation results of skipping stones are in good agreement with the experimental results. As a result, the quaternion method can simulate water entry processes of structures with high-speed spin more accurately and is more suitable for the calculation of 6-DOF motion.

Keywords 6-DOF · Skipping stones · SPH · Quaternion

60.1 Introduction

Fluid–structure interaction phenomena widely exist in nature and engineering, which have been a typical and critical issue in fluid dynamics [1]. One of the most important branches of FSI problems is the water entry problem, which has been investigated for over a hundred years [2].

Von Karmen is a pioneer in the study of the water entry problem [3]. He analyzed the water entry of a wedge and obtained the impact load through a theoretical study.

X.-S. Guan · P.-N. Sun (✉) · Y.-X. Peng · N.-N. Liu
School of Ocean Engineering and Technology, Sun Yat-Sen University and Southern Marine Science and Engineering Guangdong Laboratory (Zhuhai), 519000 Zhuhai, China
e-mail: sunpn@mail.sysu.edu.cn

P.-N. Sun
Key Laboratory of Icing and Anti/De-Icing, China Aerodynamics Research and Development Center, Mianyang 621000, China

In addition to theoretical analysis, an experimental study is also an important tool for studying water entry problems. Due to the development of high-speed cameras and sensors, the dynamic process of the water entry problem can be accurately captured, and the impact load on the structure can also be accurately measured. There are various experimental results for water entry problems, such as skipping stones [4] and water entry of projectiles [5].

The phenomenon of skipping stones is a typical problem of water entry, and it is also a very interesting sport. Many people are obsessed with how many times a stone can bounce on the surface, so the skipping stone game was proposed, which has attracted many enthusiasts. In addition to studying how many times the skipping stone can bounce on the water, researchers are also interested in the mechanism of skipping stones [6]. In recent decades, skipping stones, where the object rebounds from the water surface, have attracted the attention of researchers from all over the world [7]. There are many experimental results about skipping stones. The most famous experiments were carried out by Clanet et al. [6] and Rosellini et al. [4] extended to multiple bounces in the experiment, uncovering four different cavity evolution modes due to different motion responses of the stone. These skipping stone experiments provide sufficient reference and data for researchers to study the details of water entry problems.

In recent years, with the rapid development of computer technology, Computational Fluid Dynamics (CFD) has gradually become an important tool for hydrodynamic research to solve engineering problems [8], which has been widely applied in the simulation of water entry problems. Currently, most of the numerical methods in CFD are based on the Eulerian grid method, which have been widely implemented in commercial software, such as Open Foam and STAR-CCM+.

However, mesh-based methods often need complex algorithms to capture or reconstruct the liquid surface in the simulation of large deformation problems. As a result, mesh-based methods have challenges in the simulation of water entry/exit problems. Compared with the Eulerian grid methods, Lagrangian particle methods are advantageous when simulating the large deformation of fluid interfaces [9]. The Smooth Particle Hydrodynamics (SPH) method is one of the Lagrangian meshless algorithms, which was proposed by Monaghan [10], as well as Lucy [11], and uses a set of Lagrangian particles with physical properties to discretize fluid domains. Thanks to the Lagrangian properties, the SPH method has advantages in capturing the liquid surface and simulating the motion of structures due to the Lagrangian properties, which is beneficial for simulating water entry problems. As a result, more and more researchers have adopted the SPH method to simulate hydrodynamic problems [12–15].

The 6-DOF simulation of three-dimensional structures has always been a challenge in computational mechanics, so it is necessary to improve the calculation accuracy and efficiency. After half a century of development, various numerical improvement techniques and SPH models have been proposed, such as the δ -SPH model [16], Particle Shifting Technique (PST) [17, 18] and Adaptive Particle Refinement (APR) technique [19], which greatly improve the accuracy of the SPH method.

At present, the 6-DOF calculation of SPH rigid particles is mainly based on the Euler angle method. Cheng et al. [20] studied the motion of a ground-effect wing ship in the three-dimensional ditching problems, where the 6-DOF equations of motion based on the Euler angle method are incorporated into the SPH scheme. In their study, the accuracy of the SPH model is validated through the benchmark of three-dimensional stone-skipping. However, the Euler angle method may lead to singularity in special circumstances, such as a skipping stone with high-speed spin. For calculating large body rotations (large pitch/yaw/roll), it is necessary to apply the quaternion-based approach to minimize round-off errors and obtain numerical stability [21, 22].

In this paper, the δ -SPH model combined with improved numerical techniques is used to simulate the water entry process of skipping stones, and the 6-DOF equations based on the quaternion method are adopted to simulate the 6-DOF motion of skipping stones. The single-phase flow model and APR technique are adopted in this paper in order to improve the efficiency of calculations.

The paper is organized as follows: in Sect. 60.2, the SPH model and improved numerical techniques applied in the paper are briefly presented. At the same time, the 6-DOF equations of the quaternion method are introduced. In Sect. 60.3, the numerical model of skipping stones is established. Then the numerical simulation results are obtained and compared with the experimental results, proving the accuracy of quaternion method in 6-DOF motion calculation.

60.2 SPH Model and Quaternion Method

60.2.1 Brief Introduction to SPH Method

Monaghan and Gingold [23] introduced the Equation of State (EOS) in order to solve the pressure based on density, regarding liquids as weakly compressible fluid, and proposed the method known as the Weakly-Compressible SPH (WCSPH). In order to reduce the pressure fluctuations in WCSPH simulations, Antuono et al. [16] proposed the δ -SPH model, which is one of the most successful models.

The governing equations for the δ -SPH model are as follows [16]:

$$\begin{aligned} \frac{D\rho_i}{Dt} &= -\rho_i \sum_j (\mathbf{u}_j - \mathbf{u}_i) \cdot \nabla_i W_{ij} V_j + \delta h c_0 D_i \\ \frac{D\mathbf{u}_i}{Dt} &= -\frac{1}{\rho_i} \sum_j (p_i + p_j) \nabla_i W_{ij} V_j + \mathbf{g} + \alpha h c_0 \frac{\rho_0}{\rho_i} \sum_j \pi_{ij} \nabla_i W_{ij} V_j \\ \frac{D\mathbf{r}_i}{Dt} &= \mathbf{u}_i; \quad p = c_0^2 (\rho - \rho_0) \\ D_i &= 2 \sum_j \psi_{ji} (\mathbf{r}_j - \mathbf{r}_i) \cdot \nabla_i W_{ij} V_j / |\mathbf{r}_j - \mathbf{r}_i|^2 \end{aligned}$$

$$\begin{aligned}\pi_{ij} &= (\mathbf{u}_j - \mathbf{u}_i) \cdot (\mathbf{r}_j - \mathbf{r}_i) / |\mathbf{r}_j - \mathbf{r}_i|^2 \\ \psi_{ij} &= (\rho_j - \rho_i) - 0.5[\langle \nabla \rho \rangle_i^L + \langle \nabla \rho \rangle_j^L] \cdot (\mathbf{r}_j - \mathbf{r}_i)\end{aligned}\quad (60.1)$$

In the above equations, D/Dt represents the material derivative or Lagrangian derivative with respect to time t . ρ , \mathbf{u} , and \mathbf{r} represent the density, velocity vector, and position vector of fluid, respectively. \mathbf{g} is the gravity acceleration. p and V represent the pressure and volume, respectively. The subscripts i and j represent the target particle and the neighboring particle, respectively. W is the kernel function. h and ρ_0 are the smooth length and reference density, respectively.

The last term in the continuity equation is the density dissipation term. The last term in the momentum equation is the artificial viscosity term. c_0 is an artificial sound speed, which is chosen by $c_0 \geq 10 \max(U_{\max}, \sqrt{p_{\max}/\rho_0})$. p_{\max} and U_{\max} are the estimated maximum velocity and pressure of particles. The diffusive coefficients δ and α are constants. δ is generally set as 0.1. α uses a smaller value (0.01–0.02) for low-speed hydrodynamic problems but uses a larger value (about 0.1–0.5) for shock or impact problems.

60.2.2 6-DOF Equations of Quaternion Method

In the present SPH model, the total force and total torque applied on the body can be calculated, which are shown as follows [20]:

$$\begin{aligned}\mathbf{F}_e &= \sum_{i \in \text{fluid}} \sum_{j \in \text{ghost}} V_i V_j (p_i + p_j) \cdot \nabla_i W_{ij} \\ \mathbf{T}_e &= \sum_{i \in \text{fluid}} \sum_{j \in \text{ghost}} V_i V_j \left(\frac{\mathbf{r}_i + \mathbf{r}_j}{2} - \mathbf{d}_o \right) \times [(p_i + p_j) \cdot \nabla_i W_{ij}]\end{aligned}\quad (60.2)$$

Two reference frames $O_e - x_e y_e z_e$ and $O_b - x_b y_b z_b$ are established in order to calculate the 6-DOF motion. The subscripts e and b represent the earth-fixed reference frame and body-fixed reference frame, respectively.

Physical quantities in two reference frames can be converted to each other. The equation is shown as follows:

$$\begin{cases} \mathbf{F}_b = \mathbf{R}^T \mathbf{F}_e \\ \mathbf{T}_b = \mathbf{R}^T \mathbf{T}_e \\ \mathbf{v}_{e,j} = \mathbf{R} \cdot \mathbf{v}_{b,j} \\ \mathbf{a}_{e,j} = \mathbf{R} \cdot \mathbf{a}_{b,j} \end{cases}\quad (60.3)$$

where \mathbf{R} is the transformation matrix, which is defined as [21]:

$$\mathbf{T} = \begin{bmatrix} q_0^2 + q_1^2 - q_2^2 - q_3^2 & 2(q_1q_2 + q_0q_3) & 2(q_1q_3 - q_0q_2) \\ 2(q_1q_2 - q_0q_3) & q_0^2 - q_1^2 + q_2^2 - q_3^2 & 2(q_2q_3 + q_0q_1) \\ 2(q_1q_3 + q_0q_2) & 2(q_2q_3 - q_0q_1) & q_0^2 - q_1^2 - q_2^2 + q_3^2 \end{bmatrix} \quad (60.4)$$

$[q_0, q_1, q_2, q_3]$ are quaternions, which are defined as:

$$\begin{bmatrix} q_0 \\ q_1 \\ q_2 \\ q_3 \end{bmatrix} = \begin{bmatrix} \sin\left(\frac{\alpha}{2}\right) \sin\left(\frac{\beta}{2}\right) \sin\left(\frac{\gamma}{2}\right) + \cos\left(\frac{\alpha}{2}\right) \cos\left(\frac{\beta}{2}\right) \cos\left(\frac{\gamma}{2}\right) \\ -\cos\left(\frac{\alpha}{2}\right) \sin\left(\frac{\beta}{2}\right) \sin\left(\frac{\gamma}{2}\right) + \sin\left(\frac{\alpha}{2}\right) \cos\left(\frac{\beta}{2}\right) \cos\left(\frac{\gamma}{2}\right) \\ \sin\left(\frac{\alpha}{2}\right) \cos\left(\frac{\beta}{2}\right) \sin\left(\frac{\gamma}{2}\right) + \cos\left(\frac{\alpha}{2}\right) \sin\left(\frac{\beta}{2}\right) \cos\left(\frac{\gamma}{2}\right) \\ -\sin\left(\frac{\alpha}{2}\right) \sin\left(\frac{\beta}{2}\right) \cos\left(\frac{\gamma}{2}\right) + \cos\left(\frac{\alpha}{2}\right) \cos\left(\frac{\beta}{2}\right) \sin\left(\frac{\gamma}{2}\right) \end{bmatrix} \quad (60.5)$$

$[\alpha, \beta, \gamma]$ are the Euler angles, which are the transformation angles between two reference frames.

The acceleration and angular acceleration of the rigid body can be determined according to the following formula:

$$\begin{cases} M \frac{d\mathbf{U}_b}{dt} - \boldsymbol{\Omega}_b \times \mathbf{U}_b = \mathbf{F}_b \\ \mathbf{I}_b \frac{d\boldsymbol{\Omega}_b}{dt} + \boldsymbol{\Omega}_b \times \mathbf{I}_b \boldsymbol{\Omega}_b = \mathbf{T}_b \end{cases} \quad (60.6)$$

where \mathbf{U}_b and $\boldsymbol{\Omega}_b$ represent the velocity of rigid centroid and angular velocity of rigid in the body-fixed reference frame. \mathbf{I}_b denotes the moment of inertia with respect to the centroid of the rigid body in the body-fixed reference frame.

The velocity $\mathbf{v}_{b,j}$ and acceleration $\mathbf{a}_{b,j}$ of rigid particles in the body-fixed reference frame can be calculated as follows:

$$\begin{aligned} \mathbf{v}_{b,j} &= \mathbf{U}_o + \boldsymbol{\Omega}_b \times \mathbf{r}_{b,j} \\ \mathbf{a}_{b,j} &= \frac{d\mathbf{U}_o}{dt} + \frac{d\boldsymbol{\Omega}_b}{dt} \times \mathbf{r}_{b,j} + \boldsymbol{\Omega}_b \times (\mathbf{v}_{b,j} - \mathbf{U}_b) \end{aligned} \quad (60.7)$$

The velocity of rigid centroid $\mathbf{U}_e, d\mathbf{q}/dt$ and $\boldsymbol{\Omega}_e$ in the earth-fixed reference frame can be calculated as follows:

$$\begin{cases} \mathbf{U}_e = \mathbf{R}\mathbf{U}_b \\ \frac{d\mathbf{q}}{dt} = \mathbf{Q}_q \boldsymbol{\Omega}_b \\ \boldsymbol{\Omega}_e = \mathbf{Q}_e \boldsymbol{\Omega}_b \end{cases} \quad (60.8)$$

where \mathbf{Q}_q represents the transformation matrix between $\boldsymbol{\Omega}_b$ and $d\mathbf{q}/dt$, which can be shown as follows [22]:

$$\begin{bmatrix} \frac{dq_0}{dt} \\ \frac{dq_1}{dt} \\ \frac{dq_2}{dt} \\ \frac{dq_3}{dt} \end{bmatrix} = \frac{1}{2} \begin{bmatrix} q_0 & -q_1 & -q_2 & -q_3 \\ q_1 & q_0 & -q_3 & q_2 \\ q_2 & q_3 & q_0 & -q_1 \\ q_3 & -q_2 & q_1 & q_0 \end{bmatrix} \begin{bmatrix} 0 \\ \Omega_{bx} \\ \Omega_{by} \\ \Omega_{bz} \end{bmatrix} \tag{60.9}$$

The \mathbf{Q}_e represents the transformation matrix between $\mathbf{\Omega}_b$ and $\mathbf{\Omega}_e$, which can be used in the Euler method and shown as follows [20]:

$$\mathbf{Q}_e = \begin{bmatrix} 1 & \sin \alpha \sin \beta / \cos \beta & \cos \alpha \sin \beta / \cos \beta \\ 0 & \cos \alpha & -\sin \alpha \\ 0 & \sin \alpha / \cos \beta & \cos \alpha / \cos \beta \end{bmatrix} \tag{60.10}$$

According to the above formula, the matrix \mathbf{Q}_e has singular values when the angle reaches 90° , but the singular values do not appear in the transformation matrix \mathbf{Q}_q . Equations 60.3–60.9 are 6-DOF calculation equations based on the quaternion method, which will be embedded in the SPH frame.

60.3 The SPH Simulation of Skipping Stones

The skipping stone is a circular disk with a radius of $R = 25 \text{ mm}$ and a thickness of $h = 2.75 \text{ mm}$. The circular disk obliquely impacts the water surface with different incident angles θ_y , attack angles θ_x , translational velocities v_0 and angular velocities $\mathbf{\Omega}$. The numerical model of a skipping stone is shown in Fig. 60.1.

According to the results of experiments, an initial condition is selected for SPH simulations. The initial condition is the skipping stone with spinning velocity, in which $\theta_x = 20^\circ$, $\theta_y = 18^\circ$, $\Omega_{by} = 10 \text{ rot/s}$ and $v_0 = 3.5 \text{ m/s}$.

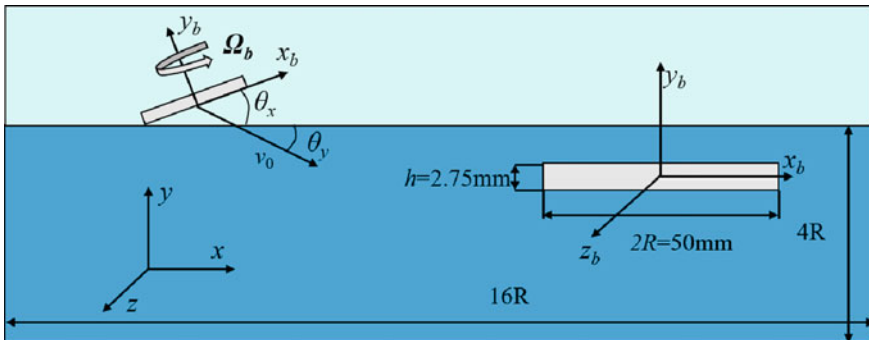


Fig. 60.1 Initial configuration of numerical tank and the geometric parameter of skipping stone

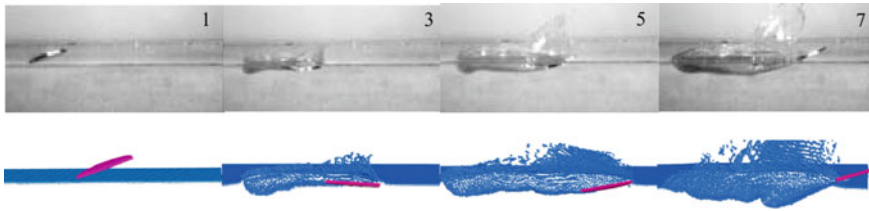


Fig. 60.2 The comparison between simulation results and experimental results [4], in which $\theta_x = 20^\circ$, $\theta_y = 18^\circ$, $\Omega_{by} = 10 \text{ rot/s}$ and $v_0 = 3.5 \text{ m/s}$. The time step between each image is 17.8 ms

The motions of skipping stones under the conditions are simulated, and the simulation results are obtained. The simulation results are in good agreement with the experimental results, which are shown in Fig. 60.2.

The center of the skipping stone is selected as the reference point to describe the trajectory of the stones, then the simulation of STAR-CCM+ is carried out. The comparison of simulation results between the SPH and STAR-CCM+ is shown in Fig. 60.3. The trajectory of the skipping stone simulated by the SPH method is very consistent with the simulation results of STAR-CCM+. The slight difference between the two methods may be due to considering the air effect in STARCCM+.

The center of the skipping stone is selected as the reference point to describe the trajectory of stones, then the simulation of STAR-CCM+ is carried. The comparison of simulation results between the SPH and STAR-CCM+ is shown in Fig. 60.3.

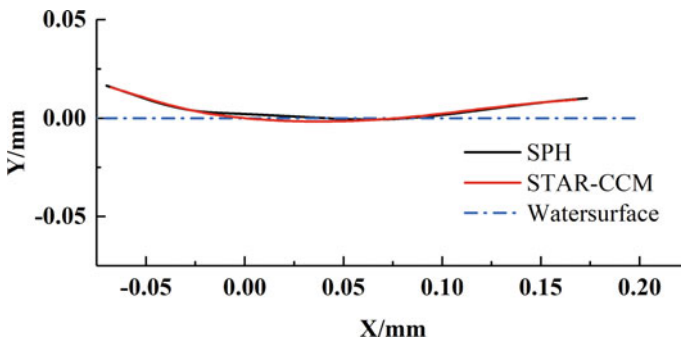


Fig. 60.3 The comparison of centroid between the SPH and STAR-CCM+ during the skipping process, in which $\alpha = 20^\circ$, $\beta = 18^\circ$, $\Omega_{by} = 10 \text{ rot/s}$ and $v_0 = 3.5 \text{ m/s}$

60.4 Conclusions and Prospects

The SPH method based on the quaternion method can simulate the 6-DOF motion of a rigid body with spin, and the simulation results are in good agreement with the experimental results of skipping stones.

The quaternion method solves the singularity problem in the Euler angle method, which can simulate water entry processes of structures with high-speed spin more accurately and is more suitable for the calculation of 6-DOF motion.

In the future, the SPH method based on the quaternion can be applied to the engineering problems, such as the ditching landing of seaplanes. And multiphase flow effect will be considered.

Acknowledgements This research is supported by the Key Laboratory of Icing and Anti/De-icing of CARDC (Grant No. IADL20210301), the National Natural Science Foundation of China (Grant Nos. 52171329 and 12002404), the Natural Science Foundation of Guangdong Province of China (Grant No. 2022A1515012084) and the Innovation Group Project of Southern Marine Science and Engineering Guangdong Laboratory (Zhuhai) (No. SML2022008). The OceanConnect High-Performance Computing Cluster of Sun Yat-sen University that supports the scientific computing in this paper is also acknowledged.

References

1. Lyu, H.G., Deng, R., Sun, P.N., Miao, J.M.: Study on the wedge penetrating fluid interfaces characterized by different density-ratios: numerical investigations with a multi-phase SPH model. *Ocean Eng.* **237**, 109538 (2021)
2. Truscott, T.T., Epps, B.P., Belden, J.: Water entry of projectiles. *Annu. Rev. Fluid Mech.* **46**, 355–378 (2014)
3. Von Karman, T.: The impact on seaplane floats during landing (1929)
4. Rosellini, L., Hersen, F., Clanet, C., Bocquet, L.: Skipping stones. *J. Fluid Mech.* **543**, 137–146 (2005)
5. Weiland, C., Vlachos, P.P.: Time-scale for critical growth of partial and supercavitation development over impulsively translating projectiles. *Int. J. Multiph. Flow* **38**(1), 73–86 (2012)
6. Clanet, C., Hersen, F., Bocquet, L.: Secrets of successful stone-skipping. *Nature* **427**(6969), 29 (2004)
7. Li, C., Wang, C., Wei, Y., Xia, W.: Three-dimensional numerical simulation of cavity dynamics of a stone with different spinning velocities. *Int. J. Multiph. Flow* **129**, 103339 (2020)
8. Zhang, A., Li, S.M., Cui, P., Li, S., Liu, Y.L.: A unified theory for bubble dynamics. *arXiv preprint arXiv:2301.13698* (2023)
9. Luo, M., Khayyer, A., Lin, P.: Particle methods in ocean and coastal engineering. *Appl. Ocean Res.* **114**, 102734 (2021)
10. Gingold, R.A., Monaghan, J.J.: Smoothed particle hydrodynamics: theory and application to non-spherical stars. *Mon. Not. R. Astron. Soc.* **181**(3), 375–389 (1977)
11. Lucy, L.B.: A numerical approach to the testing of the fission hypothesis. *Astron. J.* **82**, 1013–1024 (1977)
12. Liu, M.B., Liu, G.: Smoothed particle hydrodynamics (SPH): an overview and recent developments. *Arch. Comput. Methods Eng.* **17**, 25–76 (2010)

13. Lyu, H.G., Sun, P.N., Huang, X.T., Peng, Y.X., Liu, N.N., Zhang, X., Xu, Y., Zhang, A.M.: SPHydro: promoting smoothed particle hydrodynamics method toward extensive applications in ocean engineering. *Phys. Fluids* **35**(1), 017116 (2023)
14. Lyu, H.G., Sun, P.N., Colagrossi, A., Zhang, A.M.: Towards SPH simulations of cavitating flows with an EoSB cavitation model. *Acta Mech. Sinica* **39**(2), 722158 (2023)
15. Huang, X., Sun, P., Lyu, H., Zhang, A.M.: Water entry problems simulated by an axisymmetric SPH model with vas scheme. *J. Mar. Sci. Appl.* **21**(2), 1–15 (2022)
16. Antuono, M., Colagrossi, A., Marrone, S., Molteni, D.: Free-surface flows solved by means of SPH schemes with numerical diffusive terms. *Comput. Phys. Commun.* **181**(3), 532–549 (2010)
17. Lind, S.J., Xu, R., Stansby, P.K., Rogers, B.D.: Incompressible smoothed particle hydrodynamics for free-surface flows: a generalised diffusion-based algorithm for stability and validations for impulsive flows and propagating waves. *J. Comput. Phys.* **231**(4), 1499–1523 (2012)
18. Sun, P.N., Colagrossi, A., Marrone, S., Zhang, A.M.: The δ plus-SPH model: simple procedures for a further improvement of the SPH scheme. *Comput. Methods Appl. Mech. Eng.* **315**, 25–49 (2017)
19. Barcarolo, D.A., Le Touzé, D., Oger, G., De Vuyst, F.: Adaptive particle refinement and derefinement applied to the smoothed particle hydrodynamics method. *J. Comput. Phys.* **273**, 640–657 (2014)
20. Cheng, H., Ming, F.R., Sun, P.N., Wang, P.P., Zhang, A.M.: Towards the modeling of the ditching of a ground-effect wing ship within the framework of the SPH method. *Appl. Ocean Res.* **82**, 370–384 (2019)
21. Lu, G., Third, J.R., Müller, C.R.: Discrete element models for non-spherical particle systems: from theoretical developments to applications. *Chem. Eng. Sci.* **127**, 425–465 (2015)
22. Yang, Y.: Spacecraft attitude determination and control: quaternion based method. *Annu. Rev. Control.* **36**(2), 198–219 (2012)
23. Monaghan, J.J., Gingold, R.A.: Shock simulation by the particle method SPH. *J. Comput. Phys.* **52**(2), 374–389 (1983)

Chapter 61

Deep Reinforcement Learning-Based Intelligent Decision-Making for Orbital Game of Satellite Swarm



Weizhuo Yu, Xiaokui Yue, Panxing Huang, and Chuang Liu

Abstract Recent years have witnessed the rapid development of aerospace science and technology, and the orbital game technology has shown great potential value in the field of failed satellite maintenance, debris removal, etc. In this case, orbital game is often characterized by nonlinear dynamic model, unknown state information, high randomness, but the existing approaches to deal with game problem are difficult to be applied. The analytical method based on game theory is only applicable to simple scenarios, and it is challenging to find the optimal strategy for such complex scenarios as satellite swarm game. It should be noted that deep reinforcement learning has some research basis in the cooperative decision-making and control of multi-agents. In view of its powerful perception and decision ability, this paper applies deep reinforcement learning to solve the orbital game problem of satellite swarm. Firstly, the game scenario is modeled, where typical constraints, e.g., minimum time, optimal fuel, and collision avoidance, are taken into consideration in the game process, and then the multi-agent reinforcement learning algorithm is developed to solve the optimal maneuver strategy. The algorithm is based on the Actor-Critic architecture and uses a centralized training and decentralized execution approach to solve the optimal joint maneuver strategy. For different task scenarios, the action space, state observation space, and reward space are designed to introduce more rewards that match the specific game tasks to make the algorithm converge quickly, so that the satellite swarm emerges and executes better intelligent strategies to complete the corresponding game task.

Keywords Satellite swarm · Orbital game · Intelligent decision-making · Deep reinforcement learning

W. Yu · X. Yue · C. Liu (✉)

National Key Laboratory of Aerospace Flight Dynamics, School of Astronautics, Northwestern Polytechnical University, Xi'an 710072, China

e-mail: liuchuangforever@msn.com

P. Huang

Science and Technology on Space Intelligent Control Laboratory, Beijing Institute of Control Engineering, Beijing 100094, China

61.1 Introduction

With the advancement of aerospace technology, the degree of spacecraft intelligence is increasing globally. Spacecraft control technology is evolving towards intelligent decision-making and collaborative work, based on traditional orbit control and task allocation technologies [1]. Meanwhile, with the maturity of satellite launching technology, a large number of spacecraft have been launched into space. The increasing complexity of the space environment, as well as the increasing number of defunct satellites and space debris, which will pose a potential threat to orbiting satellites and space stations [2]. Serious collisions may occur if their operating orbits come close to those of normal spacecraft. For the potential threats brought by these non-cooperative targets, traditional orbit control technology can cope with some deterministic scenarios, but it is weak in the game situation of strong uncertainty. Removal of defunct satellites requires safe and precise access to them, which is known as rendezvous and docking technology, before subsequent on-orbit service operations can be carried out [3]. Tasks such as rendezvous, docking and on-orbit control can be abstracted as orbital game problems.

Due to limitations imposed by gravity and fuel, different methods are employed to solve the orbital game problem. To ensure efficient completion of the fuel pursuit task, it is imperative to leverage the dynamic characteristics of the orbit. Scholars worldwide have conducted extensive research on the orbital game problem, resulting in primarily two solutions. The first involves converting the problem into a two-sided optimal control problem and designing an orbital maneuvering strategy based on differential game. By solving these optimal control problems in sequence, the original differential game problem is proved to be equivalent solved [4]. An indirect method called CSCM is proposed in [5], which combines the shooting method and the configuration method, to solve the exact saddle point solution of the three-dimensional orbital pursuit game considering J2 perturbation. A semi-direct method is proposed to solve the three-dimensional orbit pursuit differential game for spacecraft in [6], which has good robustness and convergence. Aiming at the problem of minimum time pursuit differential game with continuous small thrust, the optimal open-loop trajectory is obtained by particle swarm optimization algorithm, and the closed-loop control solution based on the current state is given by Kriging interpolation method in [7]. Aiming at the low efficiency of most calculation-intensive methods for solving differential games, the Sensitivity Method (SM) is applied to the track pursuit game solution in [8]. This method has a high solution efficiency in the area far away from the obstacle surface, but it is more restricted near the obstacle surface. A distributed online mission planning algorithm for multi-spacecraft chase and escape game is proposed in [9]. In addition to the tracker and evader, there are also defenders in the game. The online planning algorithm is based on fuzzy evaluation and Nash equilibrium. Compared with the centralized mission planning algorithm, which has more robustness and faster online solution efficiency.

In recent years, an increasing number of scholars have turned to deep reinforcement learning as a solution for the problem of differential games. This approach

involves placing the game participants in an adversarial simulation environment for training, ultimately resulting in the optimal strategic neural network that attains equilibrium. Despite some challenges that remain to be addressed, this method can effectively handle complex game environments and factor in a range of practical considerations. Furthermore, the intelligent algorithm based on deep reinforcement learning is well-grounded in its ability to address such complex problems. As early as 1995, the reinforcement learning algorithm was applied to solving differential game problems [10]. Through improvement, the algorithm can converge successfully and find the minimax point. Aiming at the problem of dynamic obstacle avoidance, a method combining deep reinforcement learning with prioritized replay patterns is proposed in [11], which can predict the behavior of the current state according to experience, thus reducing the amount of computation and improving the success rate. For the new bionic deformable UAV model designed in [12], the paper adopts the deep deterministic policy gradient (DDPG) algorithm as the control strategy of the bionic deformable UAV, which can make the UAV operate in different tasks and flight rapid autonomous deformation and aerodynamic performance optimization. Based on the Actor-Critic framework in deep learning and combined with a pre-trained network, the pre-trained network is used to complete the task of unmanned aerial vehicles autonomously navigating to their destinations in a discrete three-dimensional environment in [13].

In summary, for the pursuit game problem, the existing methods are mainly based on two ideas. The first is to transform the game problem into a two-point boundary value problem, and then solve it through some other methods, such as power distribution method and particle swarm method. The other is to put both sides of the game into the game environment as an Agent for training, and finally get the optimal strategy under the equilibrium state. This method can be effectively applied to the complex environment, and can take into consideration a variety of practical factors. However, the existing researches mainly focus on the field of robots or unmanned aerial vehicles. For the complex space environment, deep reinforcement learning methods need to be further studied.

To solve the pursuit-evasion problem in a complex satellite environment, an excellent mobility strategy is developed using a complete dynamic model of the relative motion of the satellites. Both satellites are treated as agents for training within a simulation environment. The pursuit and evasion roles and elements are described using game theory, and a cost function is defined as the optimization goal for the learning strategy. A three-dimensional dynamic model is established to describe the state transition in reinforcement learning, and the reinforcement learning algorithm is transformed to solve the orbital game problem. The reward is shaped based on the characteristics of the orbital game and actual factors. Finally, the feasibility of the algorithm is verified in the simulation environment. The remainder of the paper is arranged as follows: Sect. 61.2 presents the problem and provides the dynamics framework. Section 61.3 designs the deep reinforcement learning algorithm. Section 61.4 is simulation and analysis. Section 61.5 is the conclusion.

61.2 Problem Formulation

61.2.1 Orbital Game Model

Based on the mission context of space confrontation and satellite tracking, our satellite swarm has detected a non-cooperative target in proximity. Depending on the prevailing circumstances, our satellites will employ a single or multiple units to pursue the target and achieve capture. This intricate pursuit process constitutes the satellite swarm's chasing game [14].

1. Game Player

The game players are pursuing satellite P (Pursuer) and evading satellite E (Evader).

2. Game State

The game state includes the position and speed of both pursuers' state.

3. Strategy

Strategy can change the state of players. It can be represented by N-dimensional control vectors as $\mathbf{u}_i = [u_1, \dots, u_N]^T$. Generally, strategy is restricted by specific constraints in a bounded set, and all available policy sets are called strategy sets.

4. Equation of Game State

The evolution of game state can be described by a system of differential equations as:

$$\begin{cases} \dot{x}(t) = f(t, x(t), u_1(t), \dots, u_N(t))^T \\ x(0) = x_0 \end{cases} \quad (61.1)$$

5. Cost Function

Each player has his own payment function, and each player wants to minimize that payment function.

$$J_i(u_1, \dots, u_N) = \varphi_i(x(T)) + \int_0^{T_f} g_i(t, x(t), u_1(t), \dots, u_N(t)) dt \quad (61.2)$$

In the pursuit game problem, the pursuer needs to learn the optimal strategy to chase and capture the evader, while the evader also needs to constantly learn the optimal strategy to avoid and stay away from the pursuer. The game between the two sides constitutes a zero-sum differential game problem. However, it is necessary to coordinate and cooperate among the pursuers to complete certain game purposes, and each pursuer is equivalent to a cooperative game problem. Through the modeling of the game model, the mathematical model is used to express the game strategies of both sides. The mathematical model of game strategy of both sides is as follows:

$$\begin{cases} J_{P_i}^* = \min J_{P_i}(\mathbf{r}_E, \mathbf{v}_E, \mathbf{r}_{P_1}, \mathbf{v}_{P_1}, \mathbf{r}_{P_2}, \mathbf{v}_{P_2}, \dots, \mathbf{r}_{P_N}, \mathbf{v}_{P_N}, \mathbf{u}_{P_i}), & (i = 1, 2, \dots, N) \\ J_E^* = \min J_E(\mathbf{r}_E, \mathbf{v}_E, \mathbf{r}_{P_1}, \mathbf{v}_{P_1}, \mathbf{r}_{P_2}, \mathbf{v}_{P_2}, \dots, \mathbf{r}_{P_N}, \mathbf{v}_{P_N}, \mathbf{u}_E) \end{cases} \quad (61.3)$$

where J_{P_i} and J_E are the maneuver strategy cost functions of the pursuer and the evader participating in the game respectively.

The evader and each pursuer in the game optimize their own strategies according to the cost function, aiming to minimize their corresponding cost function. Since the game strategy of each game participant will affect the final game result, both sides of the game must optimize their own strategies to achieve the optimal result during the game process. Therefore, in the game, assuming that both sides are rational, the final strategy will form the Nash equilibrium condition:

$$\begin{cases} J_{P_i}(\mathbf{u}_e^*, \mathbf{u}_{P_i}^*) \leq J(\mathbf{u}_e^*, \mathbf{u}_{P_i}) \\ J_e(\mathbf{u}_{P_i}^*, \mathbf{u}_e^*) \leq J(\mathbf{u}_{P_i}^*, \mathbf{u}_e) \end{cases}, \quad (i = 1, 2, \dots, N) \quad (61.4)$$

When the satellite of one party adopts the action under Nash equilibrium strategy, and the other party adopts the irrational strategy, that is, if the action outside Nash equilibrium strategy is adopted, the objective function of the other party cannot be optimized, then the probability of success of the other party in the game will increase.

Therefore, in the satellite pursuit game model, Nash equilibrium strategy is obtained by solving the above optimization problems, to achieve the optimal maneuver in the pursuit game.

61.2.2 Relative Dynamics Model

In the process of space multi-satellite pursuit game, the perturbation factor is ignored, and the satellite satisfies the basic two-body orbit dynamics. In the orbital coordinate system $Ox_{LVLH}y_{LVLH}z_{LVLH}$, it is assumed that the pursuer orbits around a virtual reference satellite before the game starts [15]. The orbit of the virtual reference satellite is a circular orbit, and the relative distance between the virtual reference satellite and the non-cooperative target is much smaller than the orbit radius of the reference satellite. Because the satellite moves in the relative orbital coordinate system, its dynamics model ignores the high-order small quantities. Then the relative motion of the satellite can be described by C-W equation:

$$\begin{cases} \ddot{x}_i - 2w\dot{y}_i - 3w^2x_i = a_{x_i} \\ \ddot{y}_i + 2w\dot{x}_i = a_{y_i} \\ \ddot{z}_i + w^2z_i = a_{z_i} \end{cases} \quad (61.5)$$

where w is the orbital angular velocity of the reference satellite. x_i, y_i, z_i are the relative position of the i th satellite. $\dot{x}_i, \dot{y}_i, \dot{z}_i$ are the relative speed of the i th satellite. $\ddot{x}_i, \ddot{y}_i, \ddot{z}_i$ are the relative acceleration of the i th satellite. $a_{x_i}, a_{y_i}, a_{z_i}$ are the maneuvering acceleration of the i th satellite, which are also the strategies to be learned.

Next, the thrust acceleration of the satellite is limited:

$$\|a_i\| \leq a_{i_max} \tag{61.6}$$

where a_i is the thrust acceleration of the first satellite. a_{i_max} is the thrust acceleration amplitude of the i th satellite. Based on the actual situation, generally the thrust acceleration amplitude of the pursuer is same. When the number of evaders is less than that of the pursuing satellite, the thrust acceleration amplitude should be bigger than that of the pursuing satellite considering the game balance.

Considering the constraints of collision avoidance and maximum communication range of satellites, it is necessary to limit the maneuvering range of satellites:

$$r_{i_min} \leq r_i \leq r_{i_max} \tag{61.7}$$

Finally, the pursuit success is defined and the position and speed constraints are taken into consideration. Then, the following conditions are available for determining the success of the pursuit:

$$\begin{cases} \min_{i \in [1, N]} \|r_{pi} - r_e\| \leq r_d \\ \|v_{pi} - v_e\|_{\min \|r_{pi} - r\|} \leq v_d \end{cases} \tag{61.8}$$

where r_{pi} represents the position of the i th pursuing satellite. r_e represents the position of the evader. v_{pi} represents the speed of the i th pursuer. v_e represents the speed of the evader. The first part of the judgment condition is that the distance between a satellite in the pursuer and the evader is less than or equal to a certain distance threshold r_d . The second part is that when one of the satellites is closest to the evader, their relative velocity is also less than or equal to a certain velocity threshold v_d . Only when the two parts are satisfied at the same time can the pursuit game behavior be judged to be successful. Otherwise, escape game behavior succeeds.

61.3 Intelligent Decision Modeling

61.3.1 Deep Reinforcement Learning Algorithm

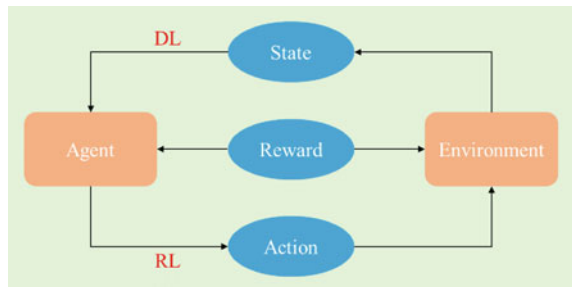
Reinforcement learning focuses on how agents act differently in the environment in order to maximize cumulative rewards. Reinforcement learning is mainly composed of agent, environment, state, action, and reward [16]. The state space is represented by the state set S , and the action space is represented by the action set A , then the interaction process between the agent and the environment is: When a state of a given environment, agent will be based on the current strategy perform an action environmental migration to the new state, at the same time agent from environment are rewarded. According to the reward of environment feedback, the agent updates its own strategy model to learn the optimal decision sequence. Through layer-by-layer combination of neural network, deep learning can finally extract high-dimensional abstract features that can represent the most essential data, with strong representation ability.

Deep reinforcement learning combines the advantages of both deep learning and reinforcement learning while possessing strong feature extraction and excellent autonomous decision-making abilities. This approach enables direct control of an agent’s behavior by processing high-dimensional perception data and achieving end-to-end learning of perception input to control output. The structure of deep reinforcement learning, as shown in Fig. 61.1, comprises two main components: DL, representing the strong feature extraction ability of deep learning, i.e., perception ability, and RL, representing the excellent autonomous decision-making ability of reinforcement learning.

To express cumulative rewards, discount future cumulative rewards are often used instead of:

$$R_t = \sum_{i=t}^T \gamma^i r(s_i, a_i) \tag{61.9}$$

Fig. 61.1 The structure of deep reinforcement learning



where γ is the discount coefficient, r is the reward of each step, s_t is the state of the i th satellite, and a_t is the action of the i th satellite.

When the training reaches a certain step, it is necessary to evaluate the status of the current agent at the time step, which is mainly accomplished by the value function, including the state value function $V^\pi(s)$ and the action-state value function $Q^\pi(s, a)$.

$$V^\pi(s) = E[R_t | s_t = s] \quad (61.10)$$

$$Q^\pi(s, a) = E[R_t | s_t = s, a_t = a] \quad (61.11)$$

Or:

$$\begin{aligned} Q^*(s, a) &= \max_{a \in A} E[R_{t+1} + \gamma Q^*(s_{t+1}, a') | s_t = s, a_t = a] \\ &= \max_{a \in A} \sum_{s', r} p(s', r | s, a) [r + \gamma Q^*(s', a')] \end{aligned} \quad (61.12)$$

where A is the state transition probability.

Generally, deep reinforcement learning algorithms can be divided into three categories, namely, value function method, strategy search method, and hybrid Actor-Critic algorithm type. Typical deep reinforcement learning algorithms include Deep Q-network (DQN), Advantage Actor-Critic (A2C), Deterministic Policy Gradient (DPG), Trust Region Policy Optimization (TRPO), Proximal Policy Optimization (PPO) [17].

DDPG algorithm is a combination of Actor-Critic framework and DQN, which has solved the problem of difficult convergence of DQN [18]. DDPG can be divided into D (Deep) and DPG (Deterministic policy gradient) according to its characteristics. The first D refers to the deeper network structure of DDPG, which inherits the structure of experience pool and double-layer network in DQN, and can improve the learning efficiency of neural network more effectively. The DPG in the second part means that DDPG algorithm adopts deterministic strategy. Actor no longer outputs the probability of each action, but a specific action. Compared with random strategy, DPG greatly reduces the amount of sampled data of the algorithm, improves the efficiency of the algorithm, and is more conducive to network learning in continuous action space.

In terms of network structure, DDPG algorithm applies the framework form of actor-critic, so it has two networks: Actor network and Critic network. At the same time, both Actor and Critic have a dual network structure, with their own Target network and Eval network.

For DDPG algorithm in the case of multiple agents, each agent adopts the DDPG structure, and uses a global Actor-Critic architecture at the same time, making each agent find the optimal joint strategy by using the method of centralized training, decentralized execution. In this way, the strategy of each agent is fully taken into consideration, and it is optimized during the centralized training. During the execution, each agent only uses the observed information to predict, which solves the problem of unstable environment.

The algorithm considers that there are N agents, and each agent should have its own decision network. The output of this decision network is the policy output of the corresponding agent. During the centralized training, each agent uses the observation information to output the corresponding action $a(\pi_i)$ after passing through the decision network [19]. At the same time, each agent uses an evaluation network that can receive global information (including the opponent's action information) to evaluate the output of the agent decision network. The corresponding value function is obtained for each agent output action. The decision network of the agent receives the evaluation signal and adjusts and optimizes its own strategy π_i . In this way, although the Actor network of each agent receives the local observation information output action, under the global evaluation network evaluation correction, the strategy of each agent is the global optimal strategy that takes other agents into consideration. Therefore, when the training is completed and the final execution is completed, the agent can output the strategy action considering the whole world only through local observation information, without the need of other agents' strategies, to achieve the overall optimal effect in the decentralized execution.

61.3.2 Algorithm Design

In the progress of the orbital pursuit game, in order to make the game strategy complete and real, both the pursuer and the evader can be seen as intelligent agents to conduct the pursuit game training together in the environment, and the finally optimized strategy will be able to fully take into consideration the strategy and maneuver output of the other side, to achieve the optimal game purpose. Based on the multi-agent depth deterministic strategy gradient method, this paper uses the decision-evaluation network structure to obtain the optimal cooperative strategy of multiple pursuers. At the same time, the escape satellite is also iterated in the game during the training to achieve the solution of the optimal escape strategy. And each agent will optimize according to the corresponding index to get its optimal strategy, mutual reach Nash Equilibrium [20].

In order to achieve the game purpose, Reward Shaping should be carried out for each agent before training. The degree of conformity between the reward function and the actual task will directly affect the training effect of the agent. Therefore, it is necessary to set different reward functions for each agent according to the actual situation, to introduce the cooperation between its own agent and the confrontation

between its opponent agent. According to the difference of game purpose and method, the reward function of evader game and pursuer game are designed respectively.

Based on the capture conditions defined above, the reward function of the evader is first designed. The purpose of the evader is to avoid being captured by the pursuer to the maximum extent. Therefore, in the environmental interaction training, the reward is divided into the following four parts:

1. Capturing Reward

When an evader is captured by a pursuer, it is punished and the training for this turn is over.

$$R_{e1} = \begin{cases} -1, & i \min_{i=1 \sim N} \|r_{p,i} - r_e\| \leq r_{th} \\ 0, & \text{else} \end{cases} \quad (61.13)$$

2. Leading Reward

Since only the completion of the target reward (R_{e1}) is likely to cause sparse reward which cannot be converged, guiding reward R_{e2} is added. As it approaches the pursuer, greater punishment is given to the evader, to guide the evader to move away from the pursuer:

$$R_{e2} = - \min_{i \in [1, N]} \sqrt{(x_e - x_{p,i})^2 + (y_e - y_{p,i})^2 + (z_e - z_{p,i})^2} \quad (61.14)$$

3. Time Reward

Add time reward R_{e3} , the longer the escape satellite persists without being captured during the game, the greater the reward:

$$R_{e3} = t \quad (61.15)$$

4. Fuel Reward

In the escape process, the evader will consume fuel. In order to guide the evader to learn the game strategy of saving fuel, fuel consumption penalty is introduced:

$$R_{e4} = -\|\Delta v\|_2 \quad (61.16)$$

In summary, the reward design of evader is:

$$Reward_e = \alpha_1 \cdot R_{e1} + \alpha_2 \cdot R_{e2} + \alpha_3 \cdot R_{e3} + \alpha_4 \cdot R_{e4} \quad (61.17)$$

where $\alpha_1, \alpha_2, \alpha_3, \alpha_4$ are the weight coefficients of capture penalty, guide reward, time penalty and fuel consumption penalty respectively, which need to be adjusted according to different task objectives and initial conditions.

In order to make the pursuer capture the evader in the shortest time and with the least energy consumption, while avoiding collisions and getting closer to the destination point, the reward is divided into the following parts [21]:

1. Capturing Reward

When the pursuer successfully captures the evader, a reward is awarded and the training round is over.

$$R_{p1} = \begin{cases} -1, & i \min_{i=1 \sim N} \|\mathbf{r}_{p-i} - \mathbf{r}_e\| \leq r_{th} \\ 0, & else \end{cases} \quad (61.18)$$

2. Leading Reward

Since R_{p1} is prone to sparse rewards that cannot be converged only by completing the target, guiding reward R_{p2} is added. When the distance between the pursuer and the evader decreases at this moment compared with the previous one, the reward will be given, thus guiding the pursuers to approach the evader:

$$R_{p2} = \begin{cases} 1, & (\mathbf{r}_{p-i} - \mathbf{r}_e)_{before} - (\mathbf{r}_{p-i} - \mathbf{r}_e)_{now} < 0 \\ -1, & else \end{cases} \quad (61.19)$$

3. Time Reward

In order to make the pursuer catch up with the evader as soon as possible, time reward is introduced. In the game process, the longer the chasing takes, the greater the penalty is:

$$R_{p3} = -t \quad (61.20)$$

4. Fuel Reward

$$R_{p4} = -\|\Delta v\|_2 \quad (61.21)$$

5. Collision Reward

Considering that satellite swarm needs to meet the collision avoidance constraints in the pursuit process:

$$R_{p5} = \begin{cases} -1, & \min_{i=1 \sim N} \|\mathbf{r}_{pi} - \mathbf{r}_e\| \leq r_{th} \\ 0, & else \end{cases} \quad (61.22)$$

In summary, the rewards for pursuers are:

$$Reward_p = \beta_1 \cdot R_{p1} + \beta_2 \cdot R_{p2} + \beta_3 \cdot R_{p3} + \beta_4 \cdot R_{p4} + \beta_5 \cdot R_{p5} \quad (61.23)$$

where $\beta_1, \beta_2, \beta_3, \beta_4$ are the weight coefficients of capture penalty, guide reward, time penalty and fuel consumption penalty respectively, which need to be adjusted according to different task objectives and initial conditions.

61.4 Simulation and Analysis

61.4.1 Parameter Setting

In this paper, the simulation and verification of the chasing game scenario of swarm satellites in synchronous orbit are carried out. Assume that there is a satellite formation whose virtual primary satellite has an orbital angular velocity of $w = 1.46 \times 10^{-4}$, and one non-cooperative target satellite with similar orbital roots is encountered near the satellite formation. In a relatively close range, the pursuit-evasion game scheme is implemented. When the number of pursuers is dominant, the amplitude of the maneuvering acceleration of the evader is set to be larger than that of the pursuer. The track game simulation of one pursuer, two pursuers and three pursuers chasing one evader was carried out respectively. In scenarios one pursuer-one evader and two pursuers-one evader, the three-dimensional C-W equation is used as the dynamic model. In scenarios three pursuers-one evader, in order to reduce calculation and accelerate training, the z -axis dynamic equation is ignored, and the game double opposers are fixed in the $x - y$ plane. The conditions for successful capture are specified as $r_d = 15$ m and $v_d = 1$ m/s. When this condition is satisfied between any pursuer and evader, the pursuit is successful.

61.4.2 Result Analysis

Through the above experimental parameter setting, after reasonably adjusting the weight value of the reward function and the structure of the neural network, and after training the pursuit game model, the algorithm reaches the convergence, which ensures the success of the pursuer. The dynamic game process effect of the pursuer and the evader is shown in Figs. 61.2, 61.3 and 61.4.

Figure 61.2 shows the game between one pursuer and one evader in three-dimensional space. Figure 61.3 shows the game between two pursuers and one evader in three-dimensional space. Figure 61.4 shows the game between three pursuers and one evader in two-dimensional space. Blue is the track of the pursuers, and red is the track of the evader. The green spheres and circle are the capture areas. During the game, the weight of the time reward item is set relatively small, so the game time is relatively long in the three cases. But from the perspective of the trajectory, in the absence of obstacles, pursuers can move in the direction of capturing the evader. When one pursuer has little difference in maneuvering ability, it can successfully capture the evader through the maneuvering strategy it has learned, to make up for

Fig. 61.2 One pursuer and one evader

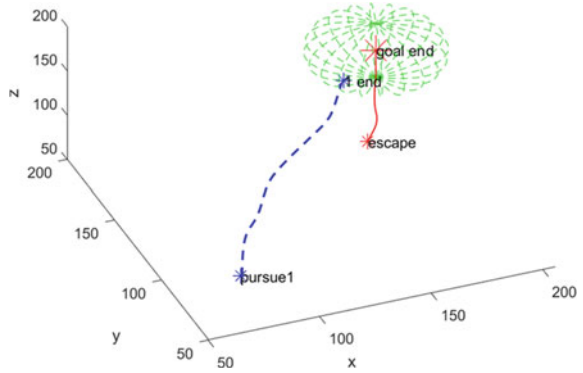


Fig. 61.3 Two pursuers and one evader

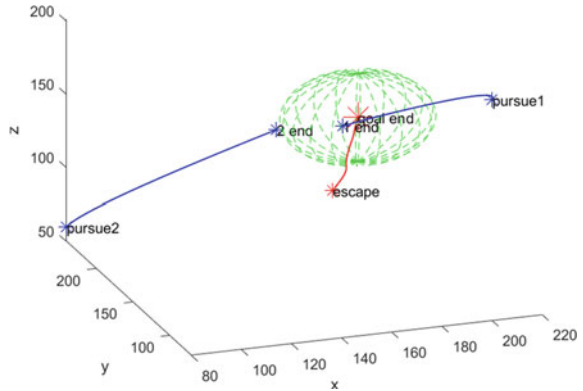
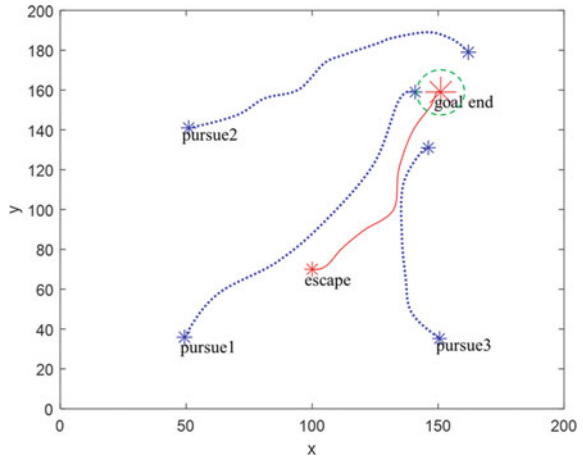


Fig. 61.4 Three pursuers and one evader



the defect of maneuvering ability. Moreover, in the presence of multiple pursuers, the pursuer can also round up the evader if it meets the conditions for successful capture, so that the pursuing satellite swarm can achieve greater advantages in the orbit game.

61.5 Conclusion

In view of the limitations of existing satellite swarm decision-making methods, this paper studies the multi-spacecraft mission decision-making problem based on deep reinforcement learning algorithm, elaborates the principle and characteristics of deep reinforcement learning algorithm, and combines the background of satellite swarm orbit game mission. The model structure of the deep reinforcement learning algorithm is designed from the network structure, state space, action space and reward function respectively. The deep reinforcement learning algorithm is combined with the satellite swarm task decision problem. The experiment proves that the deep reinforcement learning algorithm can solve the intelligent decision problem in the orbital game well.

Acknowledgements This work was supported in part by the National Natural Science Foundation of China under Grants U21B6001, 11972026 and U2013206, in part by Science and Technology on Space Intelligent Control Laboratory under Grant 2021-JCJQ-LB-010-07, and in part by Key Research and Development Program of Shaanxi under Grant 2023-YBGY-384.

References

1. Zhao, L.R., Dang, Z.H., Zhang, Y.L.: Orbital game: concepts, principles and methods. *J. Command Control* **7**(3), 215–224 (2021)
2. Zhou, J.: Manned space rendezvous and docking technology. *Manned Space* **17**(2), 1–8 (2011)
3. Yuan, L.: Spacecraft intelligent autonomous control technology toward uncertain environment. *J. Astronaut.* **42**(7), 839–849 (2021)
4. Sun, S., Zhang, Q., Loxton, R., et al.: Numerical solution of a pursuit-evasion differential game involving two spacecraft in low earth orbit. *J. Ind. Manag. Optim. (JIMO)* **11**(4), 1127–1147 (2015)
5. Li, Z., Zhu, H., Yang, Z., et al.: Saddle point of orbital pursuit-evasion game under J2-perturbed dynamics. *J. Guid. Control Dyn.* **43**(9), 1733–1739 (2020)
6. Pontani, M., Conway, B.A.: Numerical solution of the three-dimensional orbital pursuit-evasion game. *J. Guid. Control Dyn.* **2**(32), 474–487 (2009)
7. Stupik, J., Pontani, M., Conway, B.: Optimal pursuit/evasion spacecraft trajectories in the hill reference frame. In: *AIAA/AAS Astrodynamics Specialist Conference*, p. 4882 (2012)
8. Hafer, W.T., Reed, H.L., Turner, J.D., et al.: Sensitivity methods applied to orbital pursuit evasion. *J. Guid. Control Dyn.* **38**(6), 1118–1126 (2015)
9. Liu, Y., Ye, D., Hao, Y.: Distributed online mission planning for multi-player space pursuit and evasion. *Chin. J. Aeronaut.* **29**(6), 1709–1720 (2016)
10. Harmon, M.E., Baird, L.C., Klopff, A.H.: Reinforcement learning applied to a differential game. *Adapt. Behav.* **4**(1), 3–28 (1995)

11. Liu, B.Y., Ye, X.B., Gao, Y., et al.: Forward-looking imaginative planning framework combined with prioritized replay double DQN. In: International Conference Control, Automation and Robotics, pp. 336–341 (2019)
12. Xu, D., Hui, Z., Liu, Y.Q., et al.: Morphing control of a new bionic morphing UAV with deep reinforcement learning. *Aerosp. Sci. Technol.* **92**, 232–243 (2019)
13. Zhu, Y., Mottaghi, R., Kolve, E., et al.: Target-driven visual navigation in indoor scenes using deep reinforcement learning. In: 2017 IEEE International Conference on Robotics and Automation (ICRA), pp. 3357–3364. IEEE (2017)
14. Liu, B., Ye, X., Gao, Y., et al.: Strategy solution of non-cooperative target pursuit-evasion game based on branching deep reinforcement learning. *Acta Astronaut. Astronaut. Sinica* **41**(10), 348–358 (2020)
15. Wang, C., Ye, D., Sun, Z., et al.: Adaptive game strategy of spacecraft terminal interception. *J. Astronaut.* **41**(3), 309–318 (2020)
16. Lowe, R., Wu, Y., Tamar, A., et al.: Multi-agent actor-critic for mixed cooperative-competitive environments. *Advances in Neural Information Processing Systems*, pp. 6379–6390 (2017)
17. Mnih, V., Kavukcuoglu, K., Silver, D., et al.: Human-level control through deep reinforcement learning. *Nature* **518**(7540), 529–533 (2015)
18. Lillicrap, T., Hunt, J., Pritzel, A., et al.: Continuous control with deep reinforcement learning. *Comput. Sci.* (2015)
19. Zavoli, A., Federici, L.: Reinforcement learning for robust trajectory design of interplanetary missions. *J. Guid. Control Dyn.* **44**(8), 1440–1453 (2021)
20. Hovell, K., Ulrich, S.: Deep reinforcement learning for spacecraft proximity operations guidance. *J. Spacecr. Rocket.* **58**(2), 254–264 (2021)
21. Shirobokov, M., Trofimov, S., Ovchinnikov, M.: Survey of machine learning techniques in spacecraft control design. *Acta Astronaut.* **186**, 87–97 (2021)

Chapter 62

Numerical Studies on the Temperature and Pressure Changes of a Maglev Train Surface Moving Dynamically in a Vacuum Tube



Yunfeng Bi, Haiquan Bi, and Honglin Wang

Abstract The existence of the vacuum tube train can improve the efficiency of transportation. However, the complex aerodynamic phenomena cause drastic environmental fluctuations in the tube, which are concentrated on pressure and temperature. On the background of an under-constructed test platform, using three-dimensional numerical methods, a vacuum tube train model is established to analyze the environmental changes on the surface of the train dynamically during the acceleration process, uniform motion process and deceleration process. The result proposed that the specific aerodynamic phenomena such as shock wave, expansion wave and choked flow, are the main reasons for the changes of pressure and temperature. During the acceleration process, the generation of the shock wave, expansion wave and choked flow causes the drastic changes of the temperature and pressure. During the uniform motion process, a normal shock wave generated in front of the choked flow enhances the increase of temperature and pressure, yielding the maximum values at the end of this process. During the deceleration process, the disappearance of shock wave and the reflection of the expansion waves in the rear cause the sudden changes on the temperature and pressure.

Keywords Vacuum tube · Maglev train · Pressure · Temperature · Numerical study

62.1 Introduction

With the development of the science and technology on the high-speed transportation, vacuum train is studied popularly due to the combinations with the advantages of the magnetic levitation and vacuum technologies [1]. Although this effective transportation has great prospects for development, it also faces several serious problems

Y. Bi · H. Bi (✉) · H. Wang
School of Mechanical Engineering, Southwest Jiaotong University, Chengdu 610031, China
e-mail: bhquan@swjtu.edu.cn

[2]. When the maglev train moves at a high speed in the vacuum tube, complex aerodynamic phenomenon is presented around the train. With the increase of speed, the generation and disappearance of shock waves and choked flow cause drastic environment changes in the vacuum tube and influences the safety of the train in operation [3–5]. The heat generated by the air friction and the aerodynamic effect transfers to the tube wall through the radiation and make the distribution of the temperature uneven [6, 7]. In addition, the drastic change of pressure also influences the structure of the train and the vacuum tube [8].

Numerous researches are studied on the characteristics of the pressure and temperature around the train in a vacuum tube. The relative studies have shown that the aerodynamic thermal effect is quickly strengthened with the blocking ratio [9] and is weakened with the increase of the vacuum degree in the tube [10]. In addition, the generation of shock wave makes the environmental changes more drastic with the acceleration of the train [11]. Zhou et al. [12] proposed that the airflow through the shock wave produces the temperature rise and the temperature on the surfaces of the train has an obvious increase when the shock wave hits the train, yielding a local high-temperature region around the train. Moreover, the wall pressure has a violent fluctuation, which is caused by the generation of the shock wave at the rear end of the train [8]. In addition, the magnitude of the acceleration and deceleration also influences the environment in the tube. Within a certain range, the lower acceleration and deceleration are, the higher maximum and minimum temperature are. However, if the acceleration or deceleration is lower than the certain range, obverse phenomena is presented [13]. what's more, the length of low-pressure and low-temperature region at the rear end of the train is obviously shortened with the increase of the initial ambient temperature [14].

However, the above studies mainly focus on the train under constant speed conditions, not considers the acceleration and deceleration processes. Thus, the pressure and temperature changes during the whole process are not considered. Niu et al. [13] described the variation of aerodynamics during the whole process. But the influence of the tube end is ignored and the operation is simplified. Bi et al. [15] simulated the train moving in a vacuum tube during the whole process, and comprehensively analyzed the aerodynamic characteristics of each motion process.

In summary, based on the under-constructed test platform, this paper analyzed the temperature and pressure changes on the surface of the train during the whole motion process caused by the special aerodynamic phenomena in a vacuum tube using three-dimensional numerical simulation. This study can improve the understanding of temperature and pressure changes on the surface of the train during the whole process and provide suggestions for the establishment of the test platform. The organization of this paper is organized as follows: Sect. 62.2 mainly introduces numerical methods, especially the usage of the isentropic limit and Kantrowitz limit. In Sect. 62.3, computational domain, mesh selection and verification are conducted. And then Sect. 62.4 analyzes the pressure and temperature changes which occurs on the surfaces of the train respectively. Finally, several important conclusions are summarized in Sect. 62.5.

62.2 Methodology

62.2.1 Fundamental Mathematical Model

Continuum theory is commonly considered before numerical calculations in relevant studies of an evacuated tube train. And Knudsen number is as fundamental criteria to estimate the variations of the flow [16]. When the Knudsen number is less than 0.01, the continuum theory is suitable. Thus, the molecular mean free path can be calculated by [17]:

$$\lambda = \frac{k_B T}{\sqrt{2\pi} d_m^2 p} \quad (62.1)$$

where k_B represents the Boltzmann constant, 1.38×10^{-23} , T and p is ambient temperature and pressure respectively, K and Pa. In addition, d_m is the molecular diameter, m. In this paper, 300 K and 506.625 Pa are selected as initial ambient temperature and pressure, the characteristic length is 0.4 m, and the molecular diameter is 3.5×10^{-10} m. Thus, Knudsen number is 7.5×10^{-8} calculated by Eq. 62.1, which is suitable for continuum theory.

In addition, the compressibility of the air should be considered. Therefore, the ideal state equation is adopted in this study. Moreover, the airflow in the vacuum tube belongs to complex three-dimensional transient vicious region. Relevant governing equations are as follow [18]:

$$p = \rho RT \quad (62.2)$$

$$\frac{\partial(\rho\phi)}{\partial t} + \text{div}[\rho(u - u_m)\phi] = \text{div}(\Gamma \text{grad } \phi) + S_i \quad (62.3)$$

where ρ is the air density and R is the specific gas constant, 287.06 J/(kg K). t , u , u_m , ϕ , Γ , S_i are respectively the time, velocity vector of the airflow, migration velocity, flow field flux, diffusion coefficient, and source item.

62.2.2 Isentropic Limit and Kantrowitz Limit

The cross-section area formed by the tube and the train is similar to the Laval nozzle. And with the increase of the airflow, some interesting aerodynamic phenomenon appears during the flow through this structure, such as shock wave and choked flow. Moreover, when the airflow exceeds the supersonic speed, it will be subject to the Kantrowitz limit in addition to the isentropic limit. Without the consideration of shock wave, on the basis of isentropic theory, the isentropic limit can be expressed as [19, 20]:

$$\left(\frac{A_c}{A_t}\right)_{\text{Isentropic}} = M \left(\frac{\gamma + 1}{2}\right)^{\frac{\gamma+1}{2(\gamma-1)}} \left[\left(1 + \frac{\gamma - 1}{2} M^2\right) \right]^{-\frac{\gamma+1}{2(\gamma-1)}} \tag{62.4}$$

where A_c is the cross-sectional area of the gap, A_t is the cross-sectional area of the tube, M is the Mach number, and γ is the specific heat ratio of the gas, 1.4.

After the generation of a shock wave, Kantrowitz limit can be calculated by multiplying the isentropic limit with the total pressure ratio as [21]:

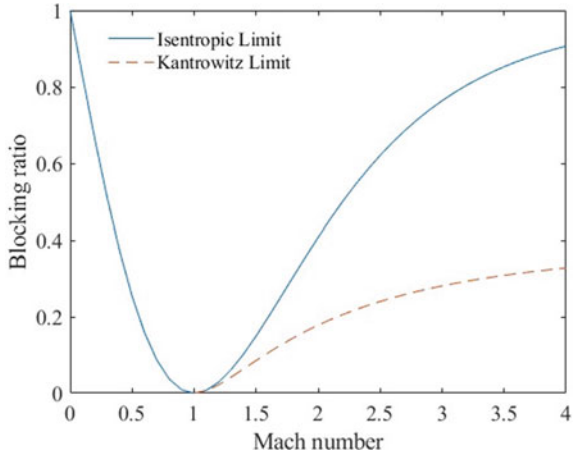
$$\begin{aligned} \left(\frac{A_c}{A_t}\right)_{\text{Kan}} &= M \left(\frac{\gamma + 1}{2}\right)^{\frac{\gamma+1}{2(\gamma-1)}} \left[\left(1 + \frac{\gamma - 1}{2} M^2\right) \right]^{-\frac{\gamma+1}{2(\gamma-1)}} \\ &\times \left[\frac{(\gamma + 1)M^2}{(\gamma - 1)M^2 + 2} \right]^{-\frac{\gamma}{\gamma-1}} \left[\frac{\gamma + 1}{2\gamma M^2 - (\gamma - 1)} \right]^{-\frac{1}{\gamma-1}} \end{aligned} \tag{62.5}$$

What’s more, blocking ratio β is expressed as:

$$\beta = 1 - \frac{A_c}{A_t} \tag{62.6}$$

Combining Eqs. 62.4 and 62.5, the relationship among the blocking ratio, isentropic limit and Kantrowitz limit can be obtained, as shown in Fig. 62.1. Thus, for a certain Mach number of the incoming flow, the generation of choked flow and shock wave depends on the blocking ratio which is greater than the values decided by these two limits.

Fig. 62.1 Isentropic and Kantrowitz limits



62.3 Numerical Model

62.3.1 Computational Model and Boundary Conditions

The total length of this computational domain is 1620 m and the diameter is 3 m, as shown in Fig. 62.2. The length of the train is 6.25 m, and the height is 0.4 m. Thus, the blocking ratio is 0.02958. Moreover, the train is divided into three parts for the sake of analysis.

As for the boundary conditions, the boundaries except for the interior and symmetry faces are stationary walls. The middle domain is considered as moving domain due to the usage of dynamic mesh method. Thus, the middle domain, train surfaces, and interior faces are set as rigid body motion, while the wall of the middle domain is set as faceted deforming motion, as displayed in Fig. 62.3. The movement of motion domain is achieved by the profile, as shown in Fig. 62.4. The train firstly accelerates to 416.67 m/s in 3.7332 s and then moves at this constant speed until 4.2132 s. Finally, it decelerates to static state in 2.8560 s. In addition, the initial ambient temperature is 300 K (26.85 °C) and the initial ambient pressure is 506.625 Pa. A symmetrical model is applied to save computation costs.

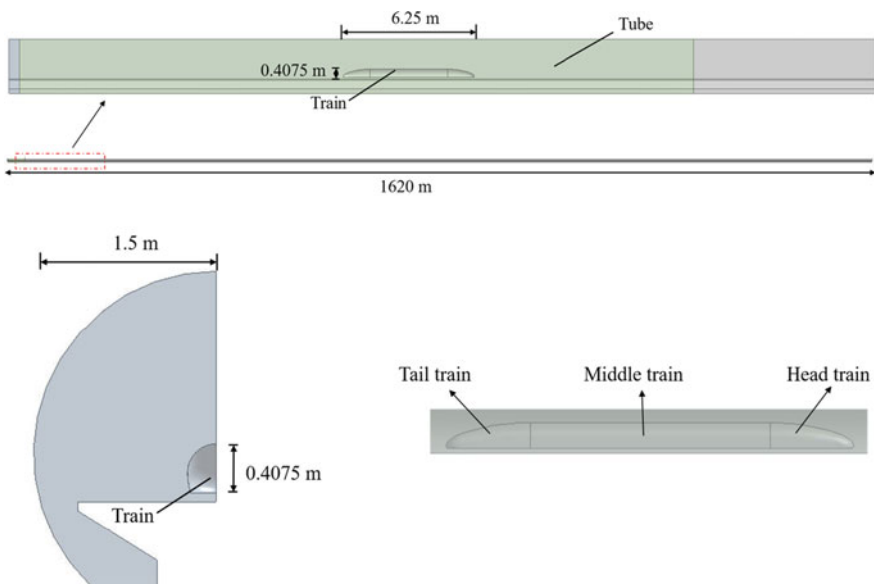


Fig. 62.2 Computational domain

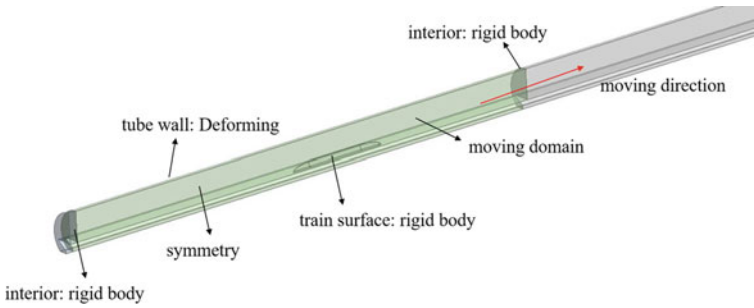
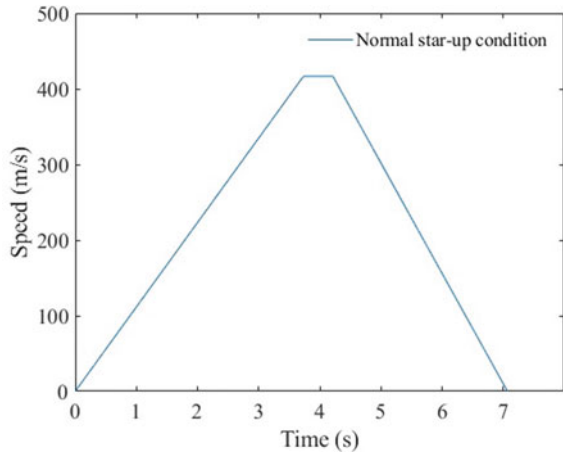


Fig. 62.3 Boundary conditions

Fig. 62.4 Operation conditions



62.3.2 Numerical Mesh

Mesh generation. Based on the requirements of dynamic layering method, a refinement domain should be established to capture the phenomenon around the train, as shown in Fig. 62.5. Moreover, the meshes generated in the front and tail domains are prismatic and tetrahedral meshes are used in the middle domain for adapting complex shapes greatly. Figure 62.6 displays the mesh distribution.

Grid independence. The refinement mesh size is crucial to affect the numerical accuracy due to the surrounding airflow distribution around the train. Thus, three types of meshes are selectively generated. And the total amount of these meshes is respectively 6.74×10^6 , 7.33×10^6 and 12.18×10^6 . Figure 62.7 demonstrates the differences between the results of three meshes for the distribution of temperature and pressure at the nose point of the train, and shows the result of medium mesh is closer to that of fine mesh. Additionally, the results of coarse mesh deviates more from the fine mesh. Consequently, the medium mesh size is suitable for this study.

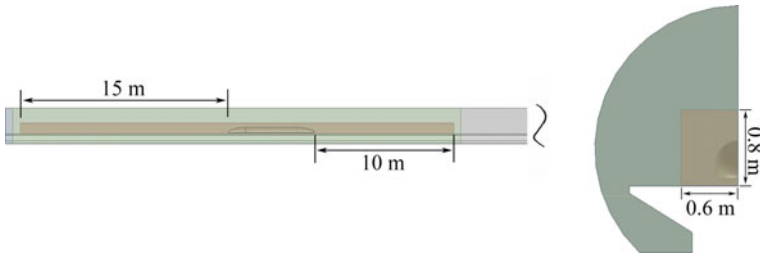


Fig. 62.5 Refinement domain

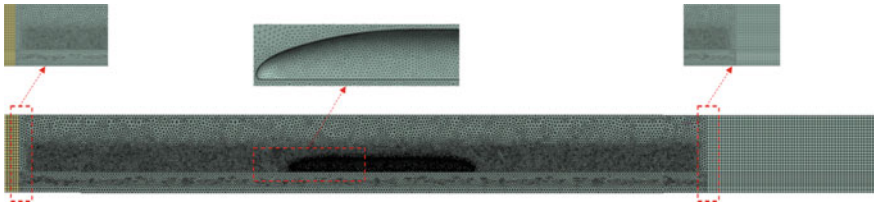


Fig. 62.6 Mesh generation

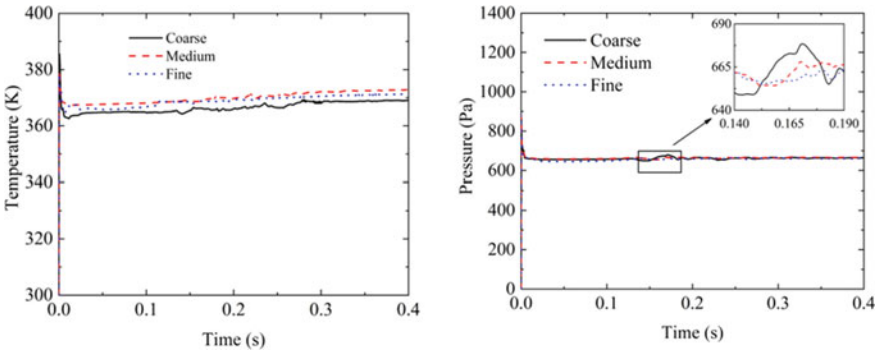


Fig. 62.7 Grid independent analysis of temperature and temperature at the nose point

Verification. In this study, the shear stress transport (SST) $k-\omega$ model is used which combines the advantages of $k-\epsilon$ model and standard $k-\omega$ model and can deal with the turbulence effect, simulating the separation of airflow better [22, 23]. And the RAE 2822 airfoil is commonly used to verify the accuracy of the numerical method [24–26]. This verification of this paper adopts the previous literature [15].

62.4 Result and Discussion

62.4.1 Pressure Distribution on the Surface of the Train

In order to analyze the changes of train surface pressure, monitoring points are set at the nose tip of the head train, the nose tip of the tail train, and the center of the surface of the middle train. The pressure changes of each monitoring point are integrally shown in Fig. 62.8. The pressure at the head train is always higher than other measuring points and reaches the maximum value of 669.86 Pa at the end of the acceleration process.

During the acceleration process, the pressure at the head train continues to rise. As depicted in Fig. 62.9, the pressure at the middle train is less than that at the tail train before t_1 . As the time gradually approaches t_1 , the train speed continues to increase, the airflow velocity in the annular space between the train and the tube increases, and the pressure at the middle train continues to decrease.

Fig. 62.8 The pressure distribution on the surface of the train

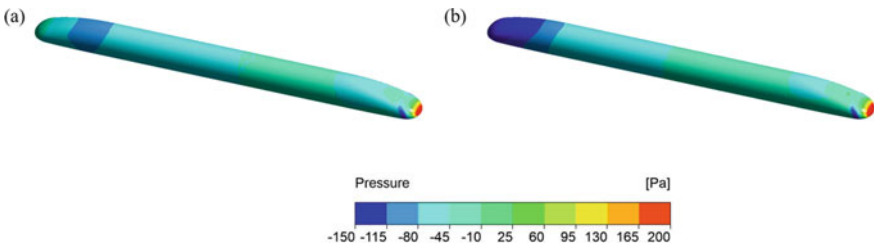
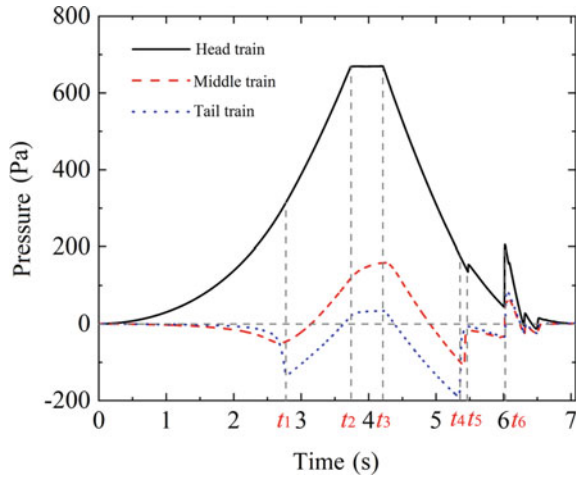


Fig. 62.9 The pressure contours of the train surface **a** $t = 2.6$ s, **b** $t = 2.8$ s

When the airflow velocity reaches the sound velocity at the rear end of the train, expansion wave is generated, making the pressure of the tail train rapidly decrease and lower than that of the middle train. After t_1 , a choked flow is formed in the front of the train, and the positive pressure region gradually diffused to the middle and tail train. Consequently, the pressure at the middle and tail train continues to rise, as shown in Fig. 62.10.

During the uniform motion process, the choked flow continuously strengthens, and the positive pressure region accelerates to the rear end of the train, which makes the pressure of each measuring point at the train surface increase, and the pressure change at the middle train is the greatest. Figure 62.11 describes the pressure distribution of the train surface at the end of uniform motion process.

After t_3 , the train begins to decelerate, the choked flow in the front is relieved rapidly, all the pressure monitoring points decrease rapidly. At t_4 , the pressure at

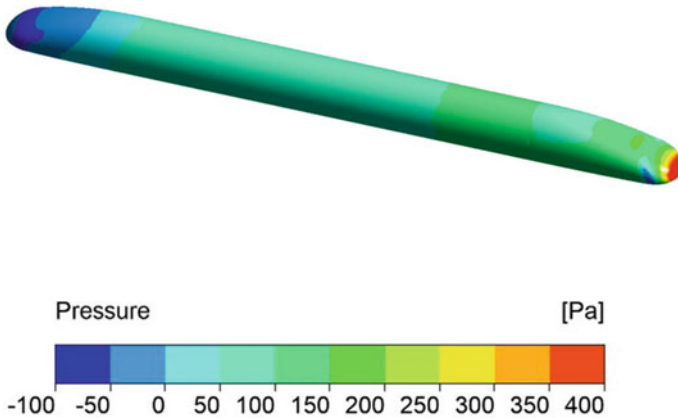


Fig. 62.10 The pressure contour of the train surface at 3.6 s

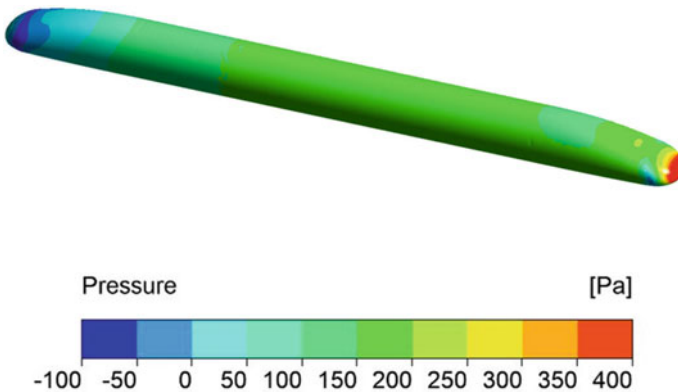


Fig. 62.11 The pressure contour of the train surface at 4.2 s

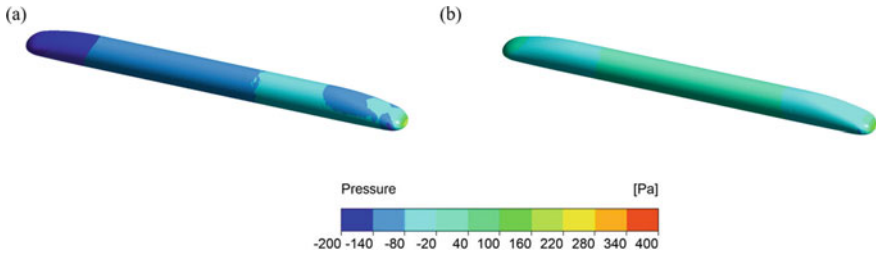


Fig. 62.12 The pressure contours of the train surface **a** $t = 5.3$ s, **b** $t = 5.5$ s

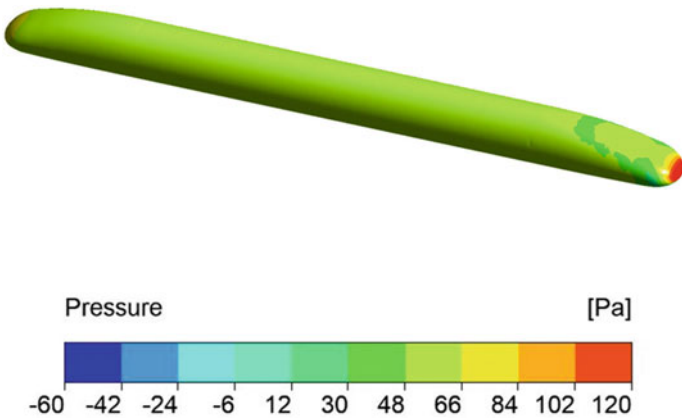


Fig. 62.13 The pressure contour of the train surface at 6.1 s

the tail train reaches the minimum, -191.47 Pa. During the period from t_4 to t_5 as shown in Fig. 62.12, the rapid disappearance of expansion wave and shock wave makes the pressure at the head and tail train increase rapidly, and the pressure at the tail train is higher than that at the middle train again.

Thereafter, at t_6 illustrated in Fig. 62.13, the reflected compression wave hits the train, and the pressure at each measuring point increases rapidly. Finally, the train meets the expansion waves, making the pressure rapid decrease around 6.3 and 6.5 s.

62.4.2 Temperature Distribution on the Surface of the Train

The temperature changes of monitoring points on the surfaces of the train are wholly shown in Fig. 62.14. When the train starts to move, the temperature monitoring point at the middle train is higher due to the higher heat generated by air friction. With the acceleration of the train, the air in front of the train is violently compressed. Therefore, the temperature monitoring point at the head train sharply increases and

is higher than other two monitoring points at the middle and tail train. As the airflow in front of the train accelerates and approaches isentropic limit, the intensity of the vortex at the rear end of the train is sharply strengthened. Thus, the temperature monitoring point at the tail train sharply increases. The generation of the shock wave and the choked flow is at t_1 . Thus, the temperature monitoring point at the tail train quickly decreases, as shown in Fig. 62.15.

With continuous acceleration of the train, the generation of the choked flow strengthens the aerodynamic thermal effect and the high-temperature region develops backwards to the rear end of the train. Consequently, all monitoring points sharply increase in the period of t_1 and t_2 as displayed in Fig. 62.16.

When the train moves at a constant speed, all monitoring points continuously increase caused by the strengthening of the choked flow as shown in Fig. 62.17.

When the train begins to decelerate, the quick affiliation of the choked flow and weakening of the expansion wave make all monitoring points decrease during t_3 and t_4 . Thereafter, in the period of t_4 and t_5 , the choked flow in front of the train is relieved due to the quick disappearance of the shock wave at the rear end of the

Fig. 62.14 The temperature distribution on the surface of the train

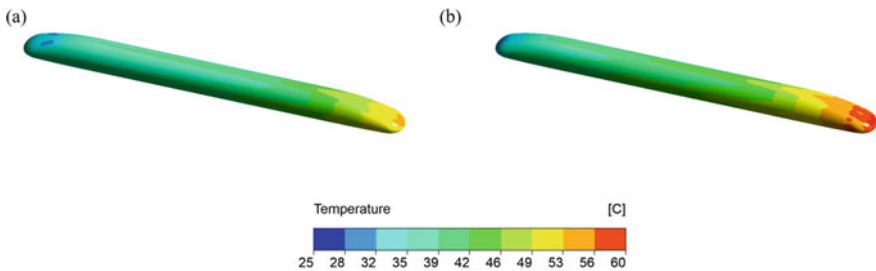
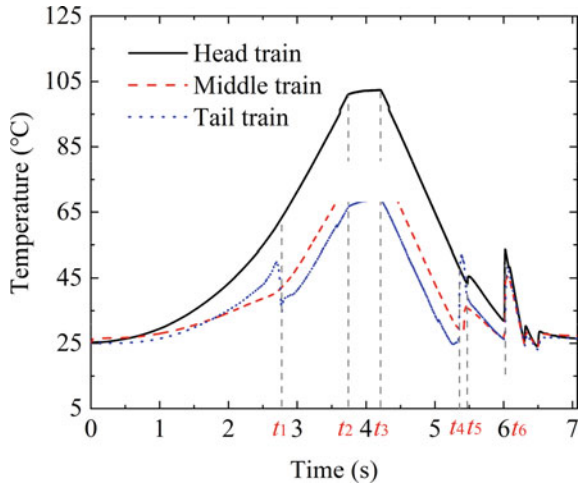


Fig. 62.15 The temperature contours of the train surface **a** $t = 2.6$ s, **b** $t = 2.8$ s

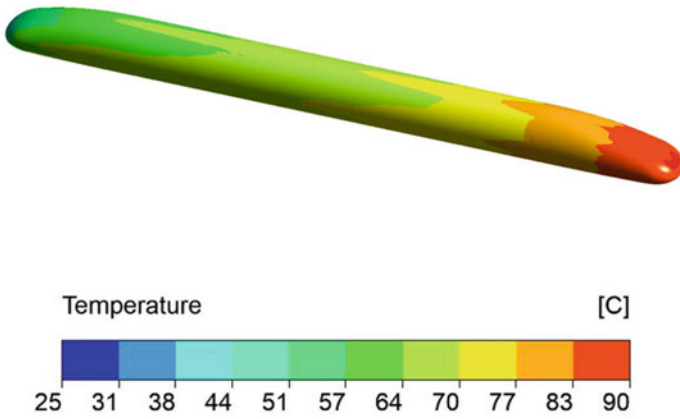


Fig. 62.16 The temperature contour of the train surface at 3.6 s

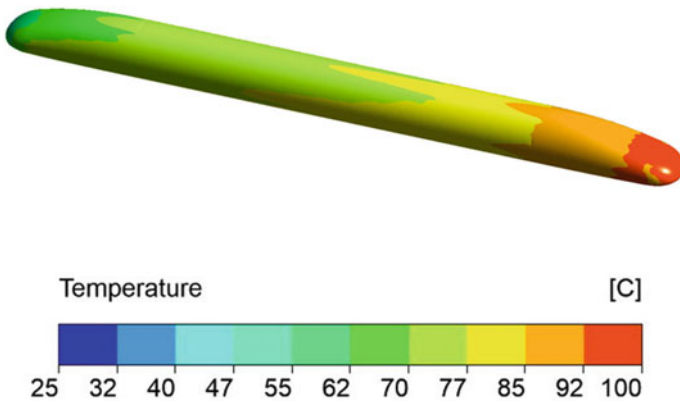


Fig. 62.17 The temperature contour of the train surface at 4.2 s

train. Thus, the temperature monitoring points at the head and middle train sharply decreases. In addition, the disappearance of the expansion wave results in the sharp increase of temperature monitoring point at the tail train. During the t_5 and t_6 as shown in Fig. 62.18, the shock wave and expansion wave at the rear end of the train completely disappear. The temperature at the middle and head train firstly increase and then decreases with the deceleration of the train.

At t_6 , the reflected compression wave with high temperature hits the surface of the train, making all the points sharply increase. Finally, the reflected expansion waves make all the monitoring points decrease, and then increase after t_6 as presented in Fig. 62.19.

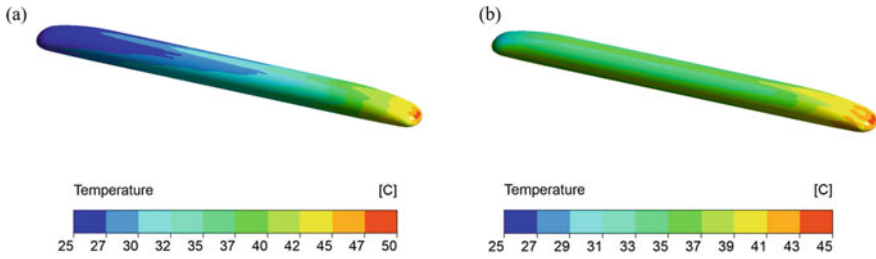


Fig. 62.18 The temperature contours of the train surface **a** $t = 5.3$ s, **b** $t = 5.5$ s

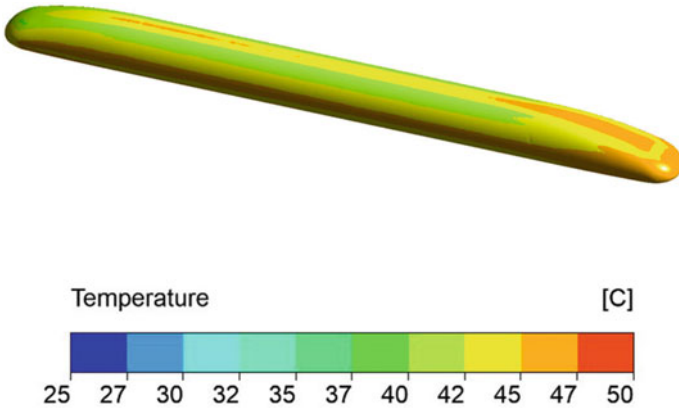


Fig. 62.19 The temperature contour of the train surface at 6.1 s

62.5 Conclusion

In this paper, a three-dimensional model is established to analyze the pressure and temperature changes on the surface of the train caused by the special aerodynamic phenomenon in a vacuum tube. The acceleration and deceleration of the train in operation make serious fluctuations of pressure and temperature, which may influence the safety of the train. Thus, these findings in this study can be served as design suggestions on the establishment of the test platform. The main findings are as follows:

During the acceleration process, expansion waves and shock waves are rapidly generated in the rear end region of the train as the airflow speed in front of the train gradually approaches the isentropic limit. The pressure measuring points at tail and middle train rapidly decreases, and the vortex at the rear end of the train rapidly strengthens, resulting in the vortex influence area with high temperature. In addition, the rhomboid shock wave structure at the rear end of the train makes the pressure and temperature fluctuate rapidly. The phenomenon of choked flow in front of the train

makes the high temperature and high-pressure regions in front of the train develops to the rear end of the train.

During the uniform motion process, the high temperature and high-pressure regions in front of the train continue to develop to the rear end of the train due to the generation of a normal shock wave. As the distance between expansion wave at the rear end and the train increases, the temperature increases caused by the vortex. The maximum pressure at the head measuring point the maximum temperature at the head measuring point both appear at the end of the uniform motion process, which are 669.86 Pa and 101.29 °C, respectively.

During the deceleration process, the influence of the expansion wave at the rear end of the train is strengthened rapidly in the early stage. After the shock wave at the rear end of the train disappears completely, the vortex intensity at the rear end of the train weakens rapidly, which makes the previous vortex break away and generates a local vortex area. Meanwhile, the expansion wave is generated in front of the train and propagates forward relative to the train. When the compression wave hits the tube wall, a local high temperature and high-pressure region is generated, and then the compression wave reflects. When the reflected compression wave hits the train, the vortex intensity at the rear end of the train increases rapidly, and a new vortex region is generated at the rear end of the train. When the expansion waves generated in front of the train and at the rear end of the train hit the tube end, a local low temperature and low-pressure region is generated. Then, when the reflected expansion wave meets the train, the temperature and pressure of the train surface decrease rapidly.

Acknowledgements This work was supported by Sichuan Science and Technology Program (No. 2021YFG0208) and the Fundamental Research Funds for the Central Universities (No. 2682021ZTPY121).

References

1. Shen, Z.: On developing high-speed evacuated tube transportation in China. *Xinan Jiaotong Daxue Xuebao/J. Southwest Jiaotong Univ.* **40**, 133–137 (2005)
2. Zhang, Y., Oster, D., Kumada, M., Yu, J., Li, S.: Key vacuum technology issues to be solved in evacuated tube transportation. *J. Mod. Transp.* **19**, 110–113 (2011)
3. Janzen, R.: TransPod ultra-high-speed tube transportation: dynamics of vehicles and infrastructure. *Procedia Eng.* **199**, 8–17 (2017)
4. Gillani, S.A., Panikulam, V.P., Sadasivan, S., Yaoping, Z.: CFD analysis of aerodynamic drag effects on vacuum tube trains. *J. Appl. Fluid Mech.* **12**, 303–309 (2019)
5. Hou, Z., Zhu, Y., Bo, J., Yang, J.: A quasi-one-dimensional study on global characteristics of tube train flows. *Phys. Fluids* **34**, 026104 (2022)
6. Zhou, Y., Liu, H., Liu, Y., Duan, R., Li, Q.: Simulation of entropy layer in evacuated tube transport at supersonic speed. *Zhenkong Kexue Yu Jishu Xuebao/J. Vac. Sci. Technol.* **34**, 775–780 (2014)
7. Mao, Y., Yang, M., Wang, T., et al.: Influence of vacuum level on heat transfer characteristics of maglev levitation electromagnet module. *Appl. Sci.* **10**(3), 1106 (2020)
8. Kim, T., Kim, K., Kwon, H.: Aerodynamic characteristics of a tube train. *J. Wind Eng. Ind. Aerodyn.* **99**(12), 1187–1196 (2011)

9. Jia, W., Dong, C., Zhou, Y., et al.: Study of thermal-pressure coupling effect in the evacuated tube transportation system on blocking ratio. *J. Eng. Thermophys.* **34**(09), 1745–1748 (2013)
10. Jia, W.: The Characteristic Investigation of Evacuated Tube Transport System on Thermodynamics. Thesis of doctor, Qingdao University of Science & Technology (2013)
11. Niu, J., Sui, Y., Yu, Q., et al.: Numerical study on the impact of Mach number on the coupling effect of aerodynamic heating and aerodynamic pressure caused by a tube train. *J. Wind Eng. Ind. Aerodyn.* **190**, 100–111 (2019)
12. Zhou, P., Zhang, J.: Aerothermal mechanisms induced by the super high-speed evacuated tube maglev train. *Vacuum* **173**, 109142 (2020)
13. Niu, J., Yang, S., Yu, Q., et al.: Effect of acceleration and deceleration of a capsule train running at transonic speed on the flow and heat transfer in the tube. *Aerosp. Sci. Technol.* **105**, 105977 (2020)
14. Bao, S., Hu, X., Wang, J., et al.: Numerical study on the influence of initial ambient temperature on the aerodynamic heating in the tube train system. *Adv. Aerodyn.* **2**(1) (2020)
15. Bi, H., Wang, Z., Wang, H., Zhou, Y.: Aerodynamic phenomena and drag of a maglev train running dynamically in a vacuum tube. *Phys. Fluids* **34**(9), 096111 (2022)
16. Tsien, H.S.: Superaerodynamics, mechanics of rarefied gases. *Collected Works of H. S. Tsien (1938–1956)*, pp. 406–429 (2012)
17. Liu, J., Zhang, J., Zhang, W.: Impacts of pressure, blockage-ratio and speed on aerodynamic drag-force of high-speed trains. *Zhenkong Kexue Yu Jishu Xuebao/J. Vac. Sci. Technol.* **34**, 10–15 (2014)
18. Ebrahimi, E., Amini, Y., Imani, G.: Numerical study of fluid flow and heat transfer characteristics of an oscillating porous circular cylinder in crossflow. *Phys. Fluids* **32**, 023602 (2020)
19. Van Wie, D.M., Kwok, F.T., Walsh, R.F.: Starting characteristics of supersonic inlets. In: 32nd Joint Propulsion Conference and Exhibit (1996)
20. Zhou, P., Zhang, J., Li, T.: Effects of blocking ratio and Mach number on aerodynamic characteristics of the evacuated tube train. *Int. J. Rail Transp.* **8**, 27–44 (2020)
21. Kantrowitz, A., Donaldson, C.: Preliminary investigation of supersonic diffusers. Report No. NACA-WR-L-713, National Advisory Committee for Aeronautics (1945)
22. Li, T., Hemida, H., Zhang, J., Rashidi, M., Flynn, D.: Comparisons of shear stress transport and detached Eddy simulations of the flow around trains. *J. Fluids Eng. Trans. ASME* **140**, 111108 (2018)
23. Menter, F.R.: Two-equation eddy-viscosity turbulence models for engineering applications. *AIAA J.* **32**, 1598–1605 (1994)
24. Cook, P.H., McDonald, M.A., Firmin, M.C.P.: Aerofoil RAE 2822—pressure distributions and boundary layer and wake measurements, experimental data base for computer program assessment. AGARD Report No. AR 138, Advisory Group for Aerospace Research and Development (1979)
25. Garbaruk, A., Shur, M., Strelets, M., Spalart, P.R.: Numerical study of wind-tunnel walls effects on transonic airfoil flow. *AIAA J.* **41**, 1046–1054 (2003)
26. Namgoong, H., Crossley, W.A., Lyrintzis, A.S.: Global optimization issues for transonic airfoil design. In: 9th AIAA/ISSMO Symposium on Multidisciplinary Analysis and Optimization, American Institute of Aeronautics and Astronautics Inc. (2002)

Chapter 63

A Model-Based Pre-feedback Decoupling Control Framework for Ground Flutter Simulation Test



Guiwei Zhang, Weiguang Li, Ximing Zhu, and Zhichun Yang

Abstract Ground flutter simulation test (GFST), which simulates the unsteady aerodynamic force on the structure through the excitation forces generated by shakers, is a semi-physical simulation test method on the ground to verify the aeroelastic stability boundary of the real structure without the wind tunnel. However, when the structure is excited by multiple electrodynamic shakers, the dynamic characteristics of the shakers and the coupling effects between the structure and shakers make the actual exciting forces acting on the structure are usually not equal to the required values that is supposed to be, such as the simulated aerodynamic forces. To deal with this issue, a model-based decoupling control framework for aerodynamic loading system is proposed to trace the simulated aerodynamic force for each shaker, which is divided into the following two parts: (1) the modeling of aerodynamic loading system; (2) the pre-feedback compensation decoupling controller. The state space model of aerodynamic loading system is established with substructure synthesis method, which couples the FEM model of structure to lumped parameters model of shakers. In order to enhance the robustness and control accuracy of the controller, genetic algorithm is used to optimize the model parameters of the aerodynamic loading system model before the decoupling controller is designed. Subsequently, both the excitation force waveform control experiments and the GFSTs are conducted on the GFST system composed of a fin model and four shakers to demonstrate the proposed method. Results show that the aerodynamic loading system can trace the simulated aerodynamics forces accurately within the target frequency range. The model-based pre-feedback compensation decoupling method can effectively eliminate the coupling effects among the shakers, and have the advantage of a simple decoupling network, a wide control frequency range and good robustness. Therefore, using the aerodynamic loading system with the proposed control method can effectively expand the application of ground aeroelastic simulation test.

G. Zhang · W. Li · X. Zhu · Z. Yang (✉)

School of Aeronautics, Northwestern Polytechnical University, Shaanxi 710072, China

e-mail: yangzc@nwpu.edu.cn

G. Zhang

Xi'an Institute of Applied Optics, Shaanxi 710065, China

Keywords Electrodynamic shaker · Multi-exciter · Force control · Pre-feedback compensation · Ground flutter simulation test

63.1 Introduction

The ground flutter simulation test (GFST) models a structural flutter boundary on the ground outside the wind tunnel by using a real structure as the test object and the unsteady aerodynamic force that is distributed on the structure through the excitation force produced by the exciter [1–7]. The ground flutter test system is comprised of a flutter model, a virtual aerodynamic loading control system, and an unsteady aerodynamic real-time reconstruction system, as shown in Fig. 63.1. Among them, the unsteady aerodynamic real-time reconstruction system uses the structural vibration response signal that the sensor has collected as input to calculate the concentrated aerodynamic force of the loading point in real time using the aerodynamic equivalent model and then outputs it to the simulated aerodynamic loading control system. The simulated aerodynamic loading control system then applies the simulated aerodynamic force to the flutter model to excite the flutter model to produce vibration using a limited number of electric exciters. The closed-loop system can ensure that the dynamic response of the flutter model is equivalent to the vibration response of the structure under distributed unsteady aerodynamic excitation in order to predict the aeroelastic stability boundary of the flutter model by adjusting parameters like wind speed and density of the simulated incoming flow.

Electric exciters are frequently used in GFSTs as a common dynamic loading device because of their broad operating frequency range and low waveform distortion. However, due to the dynamic properties of the exciter and the flexibility of the

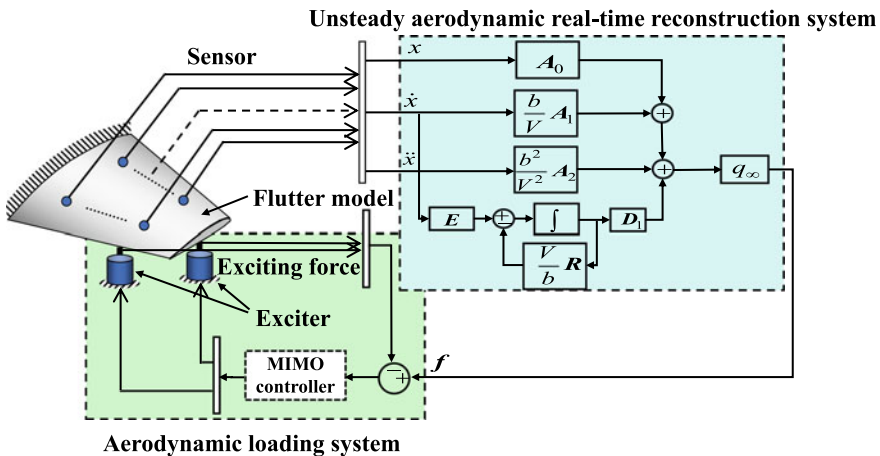


Fig. 63.1 Schematic diagram of ground flutter simulation test

structure, when numerous exciters are used to excite the structure simultaneously, the output force of each exciter is invariably different from the predetermined target excitation force (i.e., simulated unsteady aerodynamic force). Due to this issue, there are two primary categories of common GFST solutions: decoupling control and non-decoupling control. The decoupling control mainly adopts robust control and feedforward decoupling control methods: When designing the feedback controller to achieve the decoupling control of the MIMO (Multiple Input Multiple Output, MIMO) excitation force system, Zeng et al. [1] used the robust H_∞ mixed sensitivity method. The same control method was applied in the literature [2, 8–12]. Wu et al. [13, 14] and Yun et al. [15–17] designed feedforward decoupling controllers based on inverse transfer function (TF). Some publicly available papers [8–21] in Russia demonstrate that for non-decoupling control, they compensate each exciter channel in accordance with the motion data of the excitation point and implement using multiple exciters to simulate aerodynamic force. In order to improve the control effect, Wu et al. [22] used a sliding mode controller.

According to the research [23], the ground flutter simulation test is performed by the decoupling controller when the flexible structure is excited. The majority of the decoupling controllers described in the aforementioned literature rely on the system identification technique to create a mathematical model of the MIMO excitation force system, but the model physical parameters are of little use in practical applications. Additionally, the robust controller based on the state space model will raise the order of the identification model, decrease accuracy [1, 12], and narrow the control bandwidth as the number of excitation points increases, which limits its application space. Furthermore, designing robust controllers is difficult and heavily relies on the designers' prior expertise. The corresponding elements g_{ij} and g_{ji} ($i \neq j$) in the excitation force transfer function matrix do not satisfy reciprocity for the feedforward decoupling control based on the transfer function model because the actual parameters of each exciter and the gain of the power amplifier in the test are not exactly the same [23]. As a result, the decoupling network must identify a sharp increase in the number of transfer functions as the number of excitation sites rises.

This paper develops a pre-feedback decoupling controller based on the coupling system model for the ground flutter simulation test system, which includes four exciters, in order to address the above issues. The output force waveform control test of the exciter and the ground flutter simulation test serve to confirm the viability and accuracy of the controller design method.

63.2 Aerodynamic Loading Control System

63.2.1 Aerodynamic Real-Time Reconstruction System

The aerodynamic equivalent method based on generalized force equivalence in Refs. [10, 24] is used. Specifically, the generalized aerodynamic force in modal coordinates is transformed through coordinate transformation into the dispersed unsteady aerodynamic force on all nodes of the structural finite element model in physical coordinates. To create the frequency domain equivalent model of the unsteady aerodynamic force, the dispersed unsteady aerodynamic force is then equivalently condensed by surface spline interpolation and concentrated to a limited number of loading points. Finally, the frequency domain equivalent aerodynamic model is fitted to the time domain using the minimum state method [25].

A limited number of excitation point/pickup point configurations are typically used to reduce the dimensions of the frequency domain aerodynamic equivalent model and the design challenge of the subsequent aerodynamic loading system controller. The key vibration mode of flutter coupling is chosen as the goal function to optimize the position of the excitation point/vibration pickup point in order to guarantee the accuracy of structural flutter boundary prediction. The equivalent approximation between the equivalent aerodynamic force and the real can be converted into the best approximation between the original mode shape of the aerodynamic mesh nodes and the interpolation mode shape of the aerodynamic grid nodes represented by the excitation point/pick-up point, as stated in Ref. [26]. The modal assurance criterion (MAC) of each order modal shape and the original modal shape expressed by the excitation point/pickup point on the structural grid nodes can be directly established by considering the difference in number and location between the aerodynamic grid nodes and the structural grid nodes as well as the error introduced by the quadratic interpolation. The objective function of the excitation point/pickup point location optimization is defined as Eq. (63.1).

$$\begin{aligned}
 \text{obj} &= \sum_{i=1}^n \eta_i (1 - \text{MAC}_i)^2 \\
 \text{MAC}_i &= \frac{(\boldsymbol{\varphi}_{\text{A},i}^T \boldsymbol{\varphi}_{\text{E},i})^2}{(\boldsymbol{\varphi}_{\text{A},i}^T \boldsymbol{\varphi}_{\text{A},i})(\boldsymbol{\varphi}_{\text{E},i}^T \boldsymbol{\varphi}_{\text{E},i})} \tag{63.1}
 \end{aligned}$$

In the formula, η_i is the contribution of the i -order mode shape to the flutter, MAC_i is the modal confidence criterion value of the i -order mode shape and the original mode shape interpolated by the excitation point/pickup point, $\boldsymbol{\varphi}_{\text{A},i}$ and $\boldsymbol{\varphi}_{\text{E},i}$ are the i -order full-node mode shape calculated by the finite element method and the mode shape interpolated by the excitation point/pickup point, respectively, and n is the modal truncation order.

63.2.2 Aerodynamic Loading System Modeling

The output force of exciters differs from the necessary simulated aerodynamic force because of the coupling between the exciter and the structure [27] and the exciter itself [23]. Therefore, a MIMO excitation force controller needs to be added to the aerodynamic loading control system in addition to exciters and its power amplifiers. The mathematical model of the multi-exciter-structure coupling system must be established prior to developing the MIMO excitation force controller. The two types of prevalent models are theoretical modeling and experimental modeling. One of them, experimental modeling, tests the input and output traits of the coupled system to determine the mathematical model of the system. The theoretical model parameters have a clear physical meaning when compared to the experimental modeling approach, which is useful for analyzing how system parameters affect the exciter excitation force characteristics under multi-point excitation. As a result, the theoretical modeling approach used in this paper establishes a parametric model of the exciter first. The linear model of the electric exciter, which can be divided into circuit part and mechanical part, is shown in Fig. 63.2 when the power amplifier of the exciter uses voltage mode. The circuit part includes power amplifier gain G , moving coil line resistance R , inductance L and back electromotive force E_{back} . I is the current flowing through the moving coil, $E_{\text{back}}(t) = -\kappa_c \dot{z}(t)$, κ_c is the electromechanical coupling constant, and \dot{z} is the moving coil velocity. The mechanical part is an elastically supported moving coil assembly, which can be regarded as a single-degree-of-freedom lumped parameter system with moving coil mass m_s , stiffness k_s and viscous damping c_s , and is driven by electromagnetic force $F_e(t) = \kappa_c I(t)$.

A single exciter can be viewed as an electrical coupling system made up of a single-degree-of-freedom spring mass system and an RL series circuit, according to the operating principle of the exciter. The control equation of the coupling system is [28].

$$\begin{aligned}
 m_s \ddot{z} + c_s \dot{z} + k_s z &= \kappa_c I + F' \\
 L \dot{I} + RI + \kappa_c \dot{z} &= Gu
 \end{aligned}
 \tag{63.2}$$

In the formula, F' is the force of the structure on the exciter. The parameters of the exciter model are determined by experiments. The no-load exciter, which is $F' =$

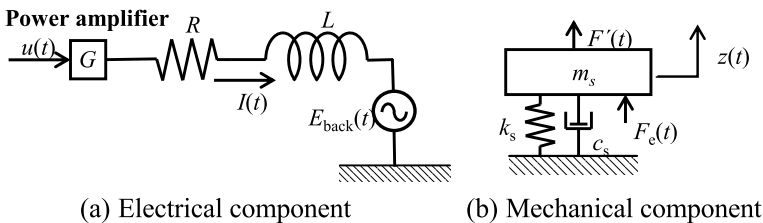


Fig. 63.2 Electrodynamic shaker model

0 N, and the specific identification process reference are used to identify the unknown parameters of the exciter-power amplifier system [23, 27]. When considering the tested structure, the dynamic equation of the tested structure needs to be introduced. The dynamic equation of the structure in modal coordinates is

$$M \ddot{Q} + B \dot{Q} + K Q = 0 \tag{63.3}$$

In the formula, M , B and K are the generalized mass matrix, generalized damping matrix and generalized stiffness matrix of the structure respectively, $Q = [Q_1 \ Q_2 \ \dots \ Q_n]^T$ is the modal coordinate column vector, Φ is the modal shape matrix.

According to the substructure method, considering the double coordination conditions of displacement and force at the connection point between the exciter and the tested structure [29, 30], the dynamic equation of the multi-exciter-structure coupling system can be obtained as follows

$$\begin{aligned} \tilde{M} \ddot{Q} + \tilde{B} \dot{Q} + \tilde{K} Q - \Phi_m^T \kappa_c I &= 0 \\ L \dot{I} + R I + \Phi_m \kappa_c \dot{Q} &= Gu \end{aligned} \tag{63.4}$$

and

$$\begin{cases} \tilde{M} = M + \Phi_m^T m \Phi_m \\ \tilde{B} = B + \Phi_m^T c \Phi_m \\ \tilde{K} = K + \Phi_m^T k \Phi_m \end{cases} \tag{63.5}$$

In the formula, Φ_m is the mode shape matrix corresponding to the degree of freedom of the excitation point, $I = [I_1 \ I_2 \ \dots \ I_q]^T$ is current column vector of exciter, $u = [u_1 \ u_2 \ \dots \ u_q]^T$ is input voltage signal column vector of exciter, where q is the number of exciters. M , c , k , L , R , κ_c , G are diagonal matrices related to exciters, and the diagonal elements are $[m_{s1} \ m_{s2} \ \dots \ m_{sq}]$, $[c_{s1} \ c_{s2} \ \dots \ c_{sq}]$, $[k_{s1} \ k_{s2} \ \dots \ k_{sq}]$, $[L_1 \ L_2 \ \dots \ L_q]$, $[R_1 \ R_2 \ \dots \ R_q]$, $[\kappa_{c1} \ \kappa_{c2} \ \dots \ \kappa_{cq}]$ and $[G_1 \ G_2 \ \dots \ G_q]$.

According to the electromechanical coupling equation of the exciter (63.2), the force of structure at the excitation point i on the exciter is

$$F'_i = m_{si} \Phi_m \ddot{Q} + c_{si} \Phi_m \dot{Q} + k_{si} \Phi_m Q - \kappa_{ci} I_i \tag{63.6}$$

Then the force exerted on the structure by the i th exciter is

$$F_i = \kappa_{ci} I_i - m_{si} \Phi_m \ddot{Q} - c_{si} \Phi_m \dot{Q} - k_{si} \Phi_m Q \tag{63.7}$$

Write the above formula in matrix form

$$F = \kappa_c I - m \Phi_m \ddot{Q} - c \Phi_m \dot{Q} - k \Phi_m Q \tag{63.8}$$

Equations (63.4) and (63.8) can be combined to create the state space equation of the multi-exciter-structure coupling system, from which it is possible to compute the actual excitation force F of the exciter in accordance with the input signal u . In the next part of the model-based pre-feedback compensation decoupling controller design, the transfer function matrix created from the state-space equation can be used.

63.2.3 Model-Based Pre-feedback Compensation Decoupling Control

63.2.3.1 Pre-feedback Compensation Decoupling Principle

Equation (63.6) demonstrates that coupling between loading points due to structural vibration happens for the multi-point excitation vibration system. Since changing the input voltage of an exciter power amplifier typically changes the output force of some or all exciters, the non-diagonal components of the transfer function matrix G_p between the output force of the exciter and the input voltage of the power amplifier are not zero.

The goal of pre-feedback compensation control is to accomplish decoupling by using a dynamic pre-compensation matrix D , where $D \cdot G_p$ is a diagonal matrix or a diagonally dominant matrix.

63.2.3.2 Decoupling Control System Design

The designed decoupling controller structure is shown in Fig. 63.3 using the pre-feedback compensation decoupling control method [31], where f is the target signal vector, F is the exciter output force signal vector, $G_d(s)$ is the feedback channel transfer function matrix, $C(s)$ is the control matrix, and $G_p(s)$ is the transfer function matrix of the exciter output force. $G_p(s)$ is divided into a matrix $G_{p1}(s)$ with only diagonal elements and a matrix $G_{p2}(s)$ without any diagonal elements. The compensation decoupling matrix $D(s)$ is

$$D(s) = [E - D_F(s)]^{-1} \quad (63.9)$$

where E is unit matrix, D_F is the transfer function matrix of the feedback loop in the decoupling controller, and s is the Laplace variable.

In order to realize decoupling of the system shown in Fig. 63.3, the transfer function matrix of the output force of the compensated exciter \tilde{G}_p should be

$$\tilde{G}_p(s) = G_p(s)D(s)$$

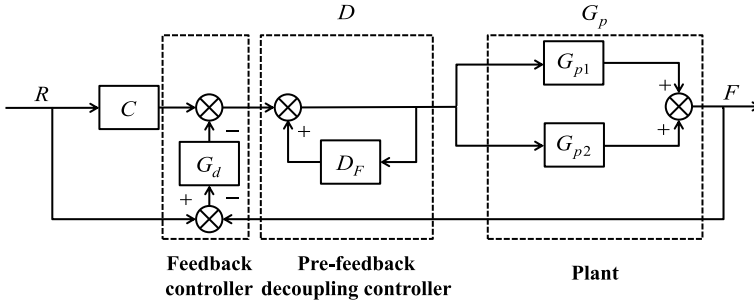


Fig. 63.3 Schematic diagram of pre-feedback compensation decoupling controller

$$= [G_{p1}(s) + G_{p2}(s)][E - D_F(s)]^{-1} \tag{63.10}$$

is a diagonal matrix, let $\tilde{G}_p(s) = G_{p1}(s)$, then

$$[G_{p1}(s) + G_{p2}(s)][E - D_F(s)]^{-1} = G_{p1}(s) \tag{63.11}$$

The elements of $D_F(s)$ are

$$D_{Fij}(s) = \begin{cases} -\frac{g_{ij}(s)}{g_{ii}(s)} & i \neq j \\ 0 & i = j \end{cases} \tag{63.12}$$

It is clear that the elements of $D_F(s)$ are determined by the proportion of off-diagonal to diagonal elements of $G_p(s)$. According to previously published study [23], g_{ij} and g_{ji} only satisfy reciprocity when the parameters of the two exciter models (i, j) are identical. As a result, in order to perform an actual decoupling, it is required to determine the transfer functions G_{p2} of all non-diagonal elements of G_p and the inverse transfer function of the main diagonal G_{p1} .

The decoupling system is equivalent to the unit matrix decoupling method, which not only eliminates the coupling between the original systems but also transforms the forward channel of each channel into a straight link, in order to meet the target requirements of multi-point excitation force control in this paper, let $C(s) = G_{p1}^{-1}(s)$. In general, the tracking error of the MIMO excitation force controller can be decreased when the transfer function matrix of the model is not exactly equal to the actual transfer function matrix by modifying the controller of each channel in the feedback controller $G_d(s)$ to meet the target requirements of multi-point excitation force control.

The denominator order of each transfer function in the inverse transfer function matrix must be greater than or equal to the molecular order in order to execute the inverse transfer function on the semi-physical simulation platform. In order to satisfy this condition, the inverse transfer function is multiplied by the first-order low-pass filter (LPF). Here is the LPF expression:

$$H_{L\text{PF}} = \frac{2\pi f_c}{s + 2\pi f_c} \tag{63.13}$$

where f_c is the cut-off frequency.

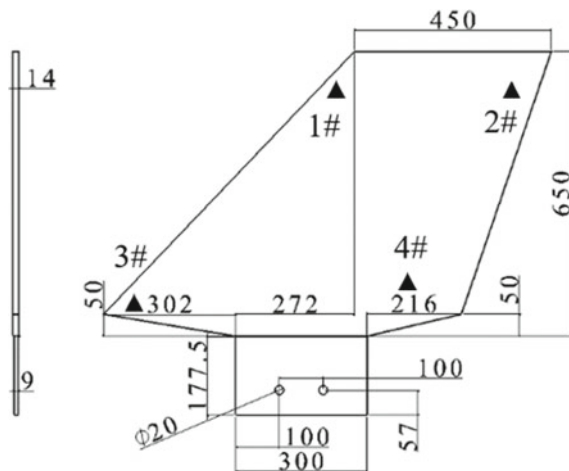
63.3 Experimental Verification

63.3.1 Experimental Arrangement

The output force waveform control test of the exciter and the ground flutter simulation test are conducted, respectively, to confirm the viability of the design method of the simulation aerodynamic loading control system proposed in this paper. A rudder model is used as the test object. The geometric size of rudder structure model is shown in Fig. 63.4. The root fixation restriction is used in the model. By reducing the thickness of the root clamping part, the root stiffness of the actual rudder is simulated. The root thickness is 9 mm, and the rudder surface is a uniform plate with a thickness of 14 mm. The material is aluminum, with $E = 70 \text{ GPa}$, $\nu = 0.3$, $\rho = 2750 \text{ kg/m}^3$. Four pairs of excitation point/pick-up points (alignment) are used in accordance with the unsteady aerodynamic equivalent condensation method described in Sect. 2.1. After refinement, Fig. 63.4 displays the locations of the excitation points. The first two rows of Table 63.2 display the flutter speed and flutter frequency of the rudder structure before and after the aerodynamic equivalent condensation. The outcome demonstrates that the dispersed original aerodynamic characteristics can be accurately described by the aerodynamic equivalent model.

On the semi-physical modeling platform Quarc of the Quanser Company, the aerodynamic real-time reconstruction system and aerodynamic loading control system

Fig. 63.4 Schematic diagram of fin model and locations of shakers



are developed. Four units of the MB Dynamcis Modal 50 exciter and the SL500VCF power amplifier are used in the loading system. To quantify the simulated aerodynamic force output by the exciter, four force sensors (208C02, PCB) are attached to the rudder surface and connected to the exciter through the ejector pin. To gather the vibration response signal of the rudder model, four acceleration sensors (333B30, PCB) and a laser displacement sensor (LK-G150, Keyence) are used.

63.3.2 Model Parameters of Multi-exciter-structure Coupling System

As can be seen from Sect. 2.3.2, the output force transfer function matrix of the exciter must be acquired in order to calculate the controller parameters. First, the finite element model of the rudder structure is created. The finite element model is modified to produce the generalized mass matrix M , the generalized damping matrix B , the generalized stiffness matrix K , and the first four order modal shape matrix Φ based on the findings of the modal tests. The dynamic properties of the system alter when the exciter is coupled to the rudder model. This also demonstrates the coupling impact between the exciter and structure as the first-order frequency changes from 9.669 to 10.117 Hz (a change of 4.63%) and the second-order frequency changes from 33.156 to 32.116 Hz (a change of 3.14%). As described in Sect. 2.2, the parameters of the exciter model are identified by experiments. The results are shown in Table 63.1 [27].

The parameter values in the table are used as the reference values for the respective parameters of each exciter in order to increase the robustness of the controller. To increase the accuracy of the coupling model, genetic algorithm is used to optimize the parameters of the exciter. The transfer function curve calculated by the model

Table 63.1 Parameters of the shaker model

m_s (kg)	c_s (N s/m)	k_s (N/m)	G	L (H)	R (Ω)	κ_c (N/A)
0.1885	1.2202	1.9523×10^3	- 1.6281	4.5252×10^{-4}	2.0598	16.6754

Table 63.2 Comparison of flutter characteristics of the fin model

		Flutter speed (m/s)	Error (%)	Flutter frequency (Hz)	Error (%)
Simulation	Original aerodynamic model	458.5	-	19.2	-
	Aerodynamic equivalent model	454.3	0.91	19.1	0.52
Ground flutter simulation test		464.0	1.20	19.5	1.56

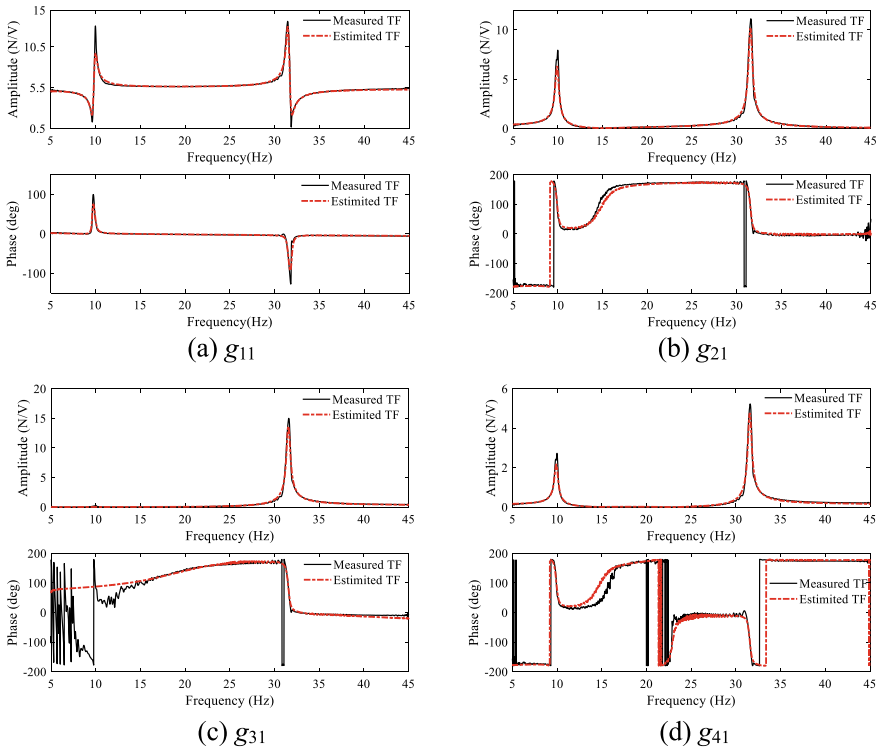


Fig. 63.5 Comparison of the measured TF and the estimated TF, g_{i1} ($i = 1, 2, 3, 4$)

and the transfer function curve measured by the test are shown in Fig. 63.5 in order to confirm the accuracy of the multi-exciter-structure coupling system model. Only the comparison findings of g_{i1} ($i = 1, 2, 3, 4$) are listed in the figure. The established coupling model can accurately reflect the dynamic properties of the multi-exciter-rudder model coupling system, as shown by the diagram, which shows that the calculated transfer function curve is in good agreement with the test transfer function curve in the interest frequency range (5–45 Hz, including the first two resonance frequencies of the system). It is also essential to design a controller to further reduce the coupling effect between the four exciters because of the coupling phenomenon between the structure and the four exciters.

63.3.3 Multi-point Excitation Force Controller Design

The controller block diagram created using the pre-feedback decoupling method mentioned in Sect. 2.3.2 is shown in Fig. 63.3 for the rudder structure vibration system with four exciters. The force sensor collects the exciter output force F and

inputs it into Quarc, which calculates the control output voltage u to operate the exciter and cause the structural vibration. The cutoff frequency f_c of the low-pass filter is chosen as 1000 Hz during the process of finding the inverse transfer function.

63.3.4 Waveform Control Experiment of Output Force of Exciter

When driving four exciters simultaneously, the linear sine sweep signal is used to test the tracking impact of the multi-point excitation force controller on the same frequency reference signal. The linear sweep frequency range is still set to 5–45 Hz, and the sweep duration is 50 s. As shown in Fig. 63.6, the amplitude-frequency and phase-frequency curves between the corresponding input signal f_i and the output force signal F_i of the four exciters after control are contrasted with the curves prior to control. When compared to the unregulated one, the control effect of the output force of exciter is good at resonance frequencies distant from the specimen. The output force gain of the exciter is currently very close to 1, and the phase is very nearly 0° . In particular, the phase tracking error is within $\pm 10^\circ$ and the amplitude tracking error between the output force of exciter and the reference signal is less than 10% in the frequency range of 12–30 Hz. The resilience of the controller is inadequate close to the resonant frequency of the system (10.117 and 32.164 Hz), and the output force of the exciter exhibits a significant tracking error in these frequency ranges. The controller can be used to control the aerodynamic loading system and finish the ground flutter simulation test because the excitation force frequency for the test, or the flutter frequency, is far from the resonance frequency of the system. The following part will include details regarding the results.

63.3.5 Ground Flutter Simulation Test

Whether the ground flutter simulation system of the rudder structure responds with convergent vibration, equal-amplitude vibration, or divergent vibration in reaction to the initial disturbance determines the flutter speed of the system. When the response vibrates with identical amplitude, the flutter speed (the wind speed used in the calculation) is also the frequency of the response. Table 63.2 displays the outcomes of the ground flutter simulation exercise. The initial aerodynamic flutter model characteristics are also provided in the table, and the two are in good agreement. Figure 63.7 compares the simulated force (F_1) produced by the exciter under various experimental wind speeds to the real-time aerodynamic force (f_1) determined by the response at 1# exciter. It is evident that the tracking performance of the MIMO force controller is nearly close to the flutter speed, demonstrating the effectiveness of the

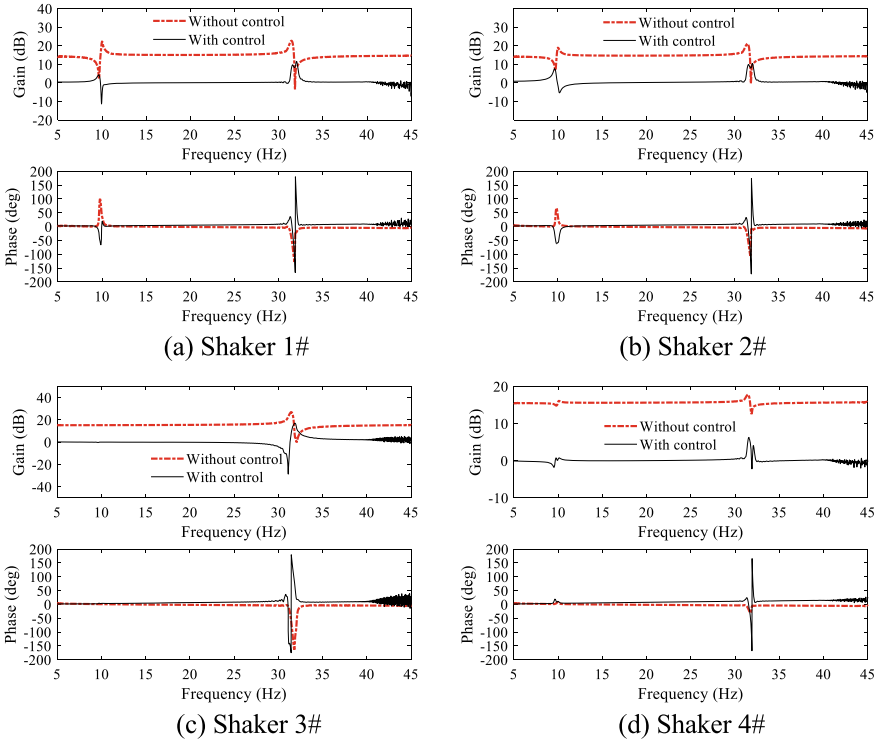
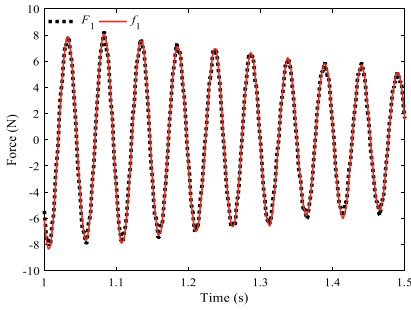
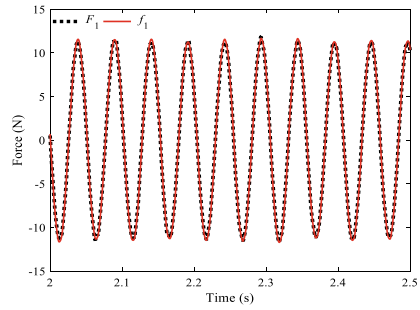


Fig. 63.6 Comparison of the excitation forces of the shakers with control and without control

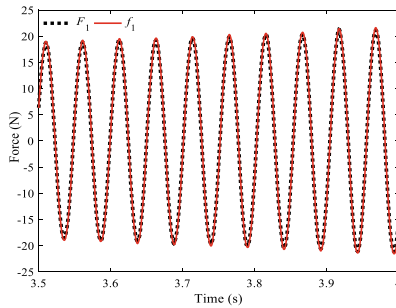
pre-feedback compensation decoupling concept put forth in this paper and the multi-point excitation force controller developed in accordance with it. This controller is suitable for the loading control of the simulated aerodynamic force in the ground flutter simulation test.



(a) $V=463\text{ m/s}$



(b) $V=464\text{ m/s}$



(c) $V=465\text{ m/s}$

Fig. 63.7 Comparisons between the excitation force of Shaker 1 and the reference signal at different experimental simulated wind speeds

63.4 Conclusion

In this paper, a model-based pre-feedback compensation decoupling concept is used to design a multi-point excitation force controller. The output force waveform control test and a ground flutter simulation test of a ground flutter model with four exciters are then performed. The experimental findings demonstrate that the decoupling controller can completely eliminate coupling between the structure and the exciter as well as between numerous exciters. It also has a wide control frequency band. As a result, it can be used in vibration tests that have specific demands on the exciter output force waveform. The following are the major conclusions:

1. Based on model pre-feedback control, a new decoupling control method for simulating unsteady aerodynamic loads is suggested.
2. Compared to the conventional experimental identification model, the physical significance of parameters is obvious, which is useful for analyzing how changing a parameter affects the controller effect and ground flutter test findings.

3. The decoupling controller that was developed has a straightforward structure and a broadly useful frequency range. It can be used for aeroelastic ground simulation tests like wind response ground simulation and flutter ground simulation tests.

References

1. Zeng, J., Kingsbury, D.W., Ritz, E., et al.: GVT-based ground flutter test without wind tunnel. In: Proceeding of 52nd AIAA/ASME/ASCE/AHS/ASC Structures, Structural Dynamics and Materials Conference (2011)
2. Zhang, G., Tan, G., Xu, Q., Gu, Y., Yang, Z.: A study on the impact of dynamic characteristics of a loading system in ground flutter simulation. *J. Vib. Shock* **39**(16), 214–221 (2020). (in Chinese)
3. Deng, Z., Song, H.: Simulation for a bridge section model's wind tunnel test based on feedback control. *J. Vib. Shock* **36**(5), 120–126 (2017). (in Chinese)
4. Liu, C., Liu, Z., Song, H.: The simulation of airfoil flutter characteristic based on active control strategy. *Chin. J. Theor. Appl. Mech.* **51**(2), 333–340 (2019). (in Chinese)
5. Hou, Y., Liu, Z.: Aeroelastic test of large flexible structure based on electromagnetic dry wind tunnel. In: Asia-Pacific International Symposium on Aerospace Technology, pp. 2684–2691 (2019)
6. Hou, Y., Liu, Z.: Quasi modal test of large flexible structure based on electromagnetic dry wind tunnel. *Acta Aerodyn. Sinica* **37**(1), 115–120 (2019). (in Chinese)
7. Hou, Y., Zhu, J., Fu, Z.: Computer aided physical test technology. In: 4th International Conference on Computer Science and Application Engineering, CSAE 2020, October 20, 2020–October 22, 2020. Association for Science and Engineering (ASciE) (2020)
8. Song, Q., Wang, B., Li, X.: Ground flutter simulation test validation based on wing flutter wind tunnel test model. *Eng. Test* **61**(02), 3–7 (2021). (in Chinese)
9. Zhang, Z., Gao, B., Wang, J., et al.: A generalised force equivalence-based modelling method for a dry wind-tunnel flutter test system. *Aeronaut. J.* **125**(1286), 720–741 (2021)
10. Wang, B., Fan, X.: Ground flutter simulation test based on reduced order modeling of aerodynamics by CFD/CSD coupling Method. *Int. J. Appl. Mech.* **11**(01) (2019)
11. Gao, B.: Study on simulation technology of dynamical modeling and controller for the ground flutter test system (Master thesis). China Aerospace Science and Technology Corporation, Beijing (2018). (in Chinese)
12. Song, Q.Z., Yang, Z.C., Wang, W.: Robust control of exciting force for vibration control system with multi-exciters. *Sci. China-Technol. Sci.* **56**(10), 2516–2524 (2013)
13. Ma, C.J., Wu, Z.G., Yang, C.: Determination of the dynamic characteristics of a multi-point excitation system using electrodynamic shakers and control of their exciting force. *J. Vib. Eng. Technol.* **4**(2), 161–173 (2016)
14. Wu, Z.G., Ma, C.J., Yang, C.: New approach to the ground flutter simulation test. *J. Aircr.* **53**(5), 1575–1580 (2016)
15. Yun, J.M., Han, J.H., Lee, Y.K.: MIMO force control of electro-dynamic shaker system using inverse transfer function based controller. *Trans. Korean Soc. Noise Vib. Eng.* **28**(1), 5–13 (2018)
16. Yun, J.M., Han, J.H.: Development of ground vibration test based flutter emulation technique. *Aeronaut. J.* **124**(1279), 1436–1461 (2020)
17. Yun, J.M., Han, J.H.: Application of ground flutter emulation test technique for the passive flutter suppression effect validation. *Int. J. Aeronaut. Space Sci.* (2021)
18. Leonteva, R.V., Smyslov, V.I.: Features of simulating the force actions from a damaged engine at ground vibration tests of an airplane. *TsAGI Sci. J.* **47**(6) (2016)

19. Leonteva, R.V., Pronin, M.A., Smyslov, V.I.: Modeling of Forced Vibrations of the Airplane with the Engine Imbalance at Ground Resonance Tests (2017)
20. Smyslov, V.I.: Tasks of the modal test and reproduction of forces by means of electromechanical simulation. *TsAGI Sci. J.* **48**(8) (2017)
21. Liseykin, G.V., Markin, I.V., Pronin, M.A., et al.: Physical model vibration modeling using artificial flow. *TsAGI Sci. J.* **50**(1) (2019)
22. Wu, Z., Zhang, R., Ma, C., et al.: Aeroelastic semiphysical simulation and wind-tunnel testing validation of a fin-actuator system. *J. Aircr.* **54**(1), 235–245 (2017)
23. Zhang, G., Li, W., Wang, X., et al.: Influence of flexible structure vibration on the excitation forces delivered by multiple electrodynamic shakers. *Mech. Syst. Signal Process.* **169**, 108753 (2022)
24. Zhang, G., Yang, Z., Gu, Y.: New approach to aerodynamic reduction in ground flutter simulation based on generalized aerodynamics. In: *Proceeding of 26th International Congress on Sound and Vibration* (2019)
25. Karpel, M.: Extensions to the minimum-state aeroelastic modeling method. *AIAA J.* **29**(11), 2007–2009 (1991)
26. Xu, Y., Wu, Z., Yang, C.: Simulation of the unsteady aerodynamic forces for ground flutter simulation test. *Acta Aeronaut. Astronaut. Sinica* **33**(11), 1947–1957 (2012). (in Chinese)
27. Zhang, G., Wang, X., Yang, Z.: Study on excitation force characteristics in a coupled shaker-structure system considering structure modes coupling. *Chin. J. Aeronaut.* (2021)
28. Lang, G.F., Snyder, D.: Understanding the physics of electrodynamic shaker performance. *Sound Vib.* **35**(10), 24–33 (2001)
29. Klerk, D.D., Rixen, D., Voormeeren, S.: General framework for dynamic substructuring: history, review and classification of techniques. *AIAA J.* **46**, 1169–1181 (2008)
30. Mayes, R., Ankers, L., Daborn, P., et al.: Optimization of shaker locations for multiple shaker environmental testing. *Exp. Tech.* **44**(3), 283–297 (2020)
31. Hu, H., Han, C., Liu, J., et al.: On multivariable feedback decoupling control systems. *Control Eng. China* **11**(6), 500–502 (2004). (in Chinese)

Chapter 64

Evaluating Contribution of Training Samples for Differentially Private Machine Learning



Yang Lv, Yufu Zou, Simin Wang, Zhe Sun, and Ran Li

Abstract Differential privacy is applied to machine learning for privacy protection because of its formal privacy guarantee. Differentially private algorithm needs to inject enough noise to limit the overall privacy disclosure risk of the training set. In the case of unbalanced data sets, however, this privacy protection intensity is excessive for most datasets, leading to significant loss of utility. In this paper, we adjust the training set by assessing the risk of disclosure of data privacy and its contribution to model accuracy to improve the utility of differentially private ML. Specifically, we quantify the risk of data privacy disclosure through membership inference attacks and evaluate the contribution of data to improving model accuracy through ablation experiments. Our experiments show that when the training set of the model is unbalanced, the model accuracy can be substantially improved by adjusting the training set to our assessment method under the same budget of privacy.

Keywords Differential privacy · Machine learning · Privacy-utility trade off

64.1 Introduction

Machine learning [1, 2] has made great progress, and machine learning models have been deployed in various practical application scenarios, such as face recognition and auxiliary diagnosis [3]. Machine learning models used in practical situations often require a large amount of sensitive data for training, which incorporates the

Y. Lv · Y. Zou · S. Wang · Z. Sun (✉)

Cyberspace Institute of Advanced Technology, Guangzhou University, Guangzhou 510006, China
e-mail: sunzhe@gzhu.edu.cn

R. Li (✉)

College of Artificial Intelligence, Guangdong Mechanical and Electrical Polytechnic, Guangzhou, China
e-mail: liran_503@163.com

Y. Zou

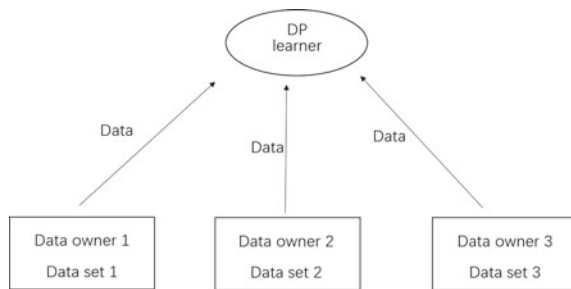
Guangxi Key Laboratory of Cryptography and Information Security, Guilin, China

personal information of data providers [4]. Existing research suggests that machine learning models can capture such sensitive information. This feature of machine learning model can be used by attackers to steal private information in training data. Differential privacy [5] is used in machine learning to prevent the disclosure of training data privacy information. Differential privacy is a standard definition of privacy. It formalizes the effect of privacy protection through strict mathematical proof. The privacy risk is quantified as “privacy loss” [6, 7]. The differential privacy definition was first used for database queries [8], and was later introduced into the machine-learning training algorithm model to protect the privacy of training data and to formally analyze the privacy disclosure risk of training data [9–13].

However, differentially private machine learning will lead to a loss of model utility [14–16]. The machine learning algorithm of differential privacy is to protect the privacy of training data by introducing random noise. The higher the privacy demand means introducing more noise, and the introduction of random noise inevitably leads to a loss of model utility. Particularly in collaborative ML training [17–20] scenarios, as shown in Fig. 64.1, training data comes from different data providers and is passed on to the learner for training. Data privacy risks from different data providers vary, and the degree of improvement in model performance is also different. The way to improve the utility of the model under the premise of ensuring all data privacy is a problem that needs to be solved by the learner.

Some researchers have designed new differential privacy algorithms to improve the usability of machine learning models [15, 21]. A new differentially private machine learning algorithm proposal requires rigorous privacy analysis from a theoretical perspective to prove that it meets the definition of differential privacy. Other researchers, beginning with the definition of differential privacy, have identified a more precise upper bound on privacy disclosure for the existing differential privacy algorithm at the theoretical level [22, 23]. In other words, their work is to show that differential privacy algorithms can theoretically achieve less privacy disclosure under the same noise intensity standard. To avoid designing new theoretical methods for analysing privacy, some models start from a machine learning model architecture and improve the usability of the model under the same privacy protection effect by modifying the activation function of the model without changing the differential privacy algorithm. The current work is based on the data set as a whole, ignoring the differences in privacy disclosure risks caused by the differences in data distribution.

Fig. 64.1 Collaborative ML training



Machine learning algorithms for differential privacy have a strict mathematical definition. To meet the privacy protection requirements of all subsets, it is often necessary to add excessive noise to most subsets at the cost of model utility.

To address the shortcomings of the current work, this paper proposes a system to improve the usability of differentially private machine learning models based on the evaluation of data set contribution. We calculate the contribution of a data set by evaluating the privacy risk of the data set and the improvement of the model performance. Specifically, we use a membership inference attack based evaluation method to evaluate the privacy disclosure risk of data sets. To improve the attack effect of member reasoning attacks on unbalanced data sets, we adopt the shadow training method and set different thresholds according to the data distribution of a subgroup. We measure a subset improvement in model performance through ablation experiments, that is, reducing the effect of the subset on model accuracy by reducing the number of samples in the subset. The change in model accuracy reflects the impact of the existence of the subset on the improvement of model accuracy. We quantify subsets contributions through a quantitative indicator of ‘contribution’, which is a function of the above two analysis results. Based on the contribution of subsets, we adjust the entire training set and remove the low-value subsets from the training set so as to improve the performance of the model on the premise of meeting privacy requirements.

In summary, our contributions are as follows:

- We propose a personalised evaluation scheme in which the system evaluates the value of a subset, i.e. the contribution of a subset to the improvement of the accuracy of the model and the level of privacy protection required by the subset, and then adjusts the dataset according to the evaluation results. Our scheme improves the utility of the model on the premise of meeting the privacy needs of data providers.
- Because of a data set imbalance problem in machine learning, we have improved the membership inference attack method. Experiments show that our method improves the accuracy of attacks.
- We propose ‘contribution’, a quantitative indicator based on the degree of protection imposed by differential privacy and the decline of model accuracy, to quantify the value of subsets. Through ‘contribution’, we can quantify the trade-off of the utility cost and privacy cost of the model. In this way, we can adjust the training set according to our privacy and utility trade-off requirements.
- We experimentally demonstrate the advantage of our method by constructing a training dataset containing multiple unbalanced subsets, and evaluating each subset using the quantitative indicator “contribution. Experimental results suggest that the training set is adjusted in accordance with our evaluation results and that model utility improves while meeting the requirements for privacy protection.

The rest of the paper is organized as follows: In Sect. 64.2, we review the related work. We then briefly introduce the preliminary in Sect. 64.3. In Sect. 64.4, we present the design details of the proposed evaluation scheme. Section 64.5 describes the evaluation and experiments.

64.2 Related Works

Mironov [22] proposed the definition of privacy Rényi Differential Privacy (RDP), which is a natural relaxation of Differential Privacy. RDP analyzes the privacy protection algorithm through Rényi diversity, provides a method to track the accumulated privacy loss, and provides privacy guarantee for the privacy protection algorithm. Triastcyn et al. [23] proposed a differential privacy definition $(\epsilon\mu, \delta\mu)$ -Bayesian differential privacy (BDP), which considers the data distribution of protected data based on the definition of the DP. the difference between BDP and DP is calculation of $\epsilon\mu, \delta\mu$ takes into account the distributions $\mu(x)$ that are more consistent with the machine learning scenario, that is, the training dataset often follows a certain distribution. BDP needs less noise to ensure privacy, and machine learning algorithms that meet the BDP definition are faster and more accurate.

Although these systems improve the usability of the model by designing new differential privacy definitions, implementation of these methods requires that they meet their own specific privacy assumptions.

Zhu et al. [21] proposed a private data publishing system based on the KNN query, called private kNN, to overcome the problem of limited private data for training deep neural networks in visual application. This scheme uses privacy amplification through subsampling and iteratively refining the kNN feature embedding. Compared with the differentially private learning method PATE [24], Private-kNN reduces privacy loss by 90% with the same accuracy. Canonne et al. [15] theoretically analyzed discrete Gaussian noise from three aspects of privacy, utility, and sampling, demonstrated its advantages over continuous Gaussian noise in DP, and derived sampling methods from discrete Gaussian noise; it is also shown that discrete Gaussian noise can achieve the same privacy protection effect as continuous Gaussian noise, and discrete Gaussian noise can overcome the defect that continuous Gaussian noise cannot accurately sample.

These schemes design corresponding differentially private machine learning algorithms according to specific scenarios, so their applications have limitations.

Papernot et al. [16] proposed to use bounded activation functions to prevent activation from exploration during training. By designing a general family of bounded activation functions, the temporary sigmoids, the tradeoffs between privacy and utility are significantly improved. Cheng et al. [25] combine private deep learning with architecture research, this paper designs a new research area and proposes a candidate model training method based on the work of DP. Ye et al. [26]. The privacy protection mechanism of differential privacy is realized by modifying the confidence score vectors. This method can resist membership inference attack and model inversion, and will not cause loss of model classification accuracy.

These schemes improve the utility of machine learning for differential privacy by designing a model architecture suitable for differential privacy, but they are all analyzed from the perspective of the training set as a whole, ignoring the need for differential analysis of the training set in practical applications.

64.3 Preliminary

64.3.1 Differential Privacy in Deep Learning

Differential privacy as a privacy protection definition was proposed by Dwork in 2006 [5], and Dwork has carried out a rigorous mathematical proof of its privacy protection strength.

Definition 1 A randomized mechanism $M: D \rightarrow R$ with domain D and range R satisfies (ϵ, δ) -differential privacy if for any two adjacent inputs $x, x' \in D$ and for any subset of outputs $S \subseteq R$ it holds that

$$Pr[M(x) \in S] \leq \exp(\epsilon)Pr[M(x') \in S] + \delta \quad (64.1)$$

The original definition of ϵ -differential privacy does not include the additive term δ . We use the variant introduced by Dwork et al. [2], which allows for the possibility that plain ϵ -differential privacy is broken with probability δ .

64.3.2 Membership Inference Attack

Membership inference attack [27] is one of the most popular privacy attacks against ML models [28–33]. The goal of membership inference is to determine whether a data sample x is part of the training dataset of a target model. A successful membership inference attack can cause severe privacy risks. For instance, if a model is trained on data samples collected from people with certain sensitive information, then successfully inferring a sample from a person being a member of the model can directly reveal the person’s sensitive information.

We are concerned about the black box membership inference attack [27, 29], that is, the attacker can only judge by the prediction results of the model, and the model architecture and the output of the middle layer are unknown. The architecture of black-box membership inference attack is shown in Fig. 64.2.

64.4 Dataset Evaluation Scheme

Existing work [34–36] takes the training set as a whole as an analytic object, ignoring the differences in the risk of data set privacy disclosure and the degree of improvement in model performance. Our privacy protection scheme includes subsets from different data providers, including quantitative analysis of “privacy needs” and “contribution accuracy. The final evaluation index “contribution” is obtained by comprehensive

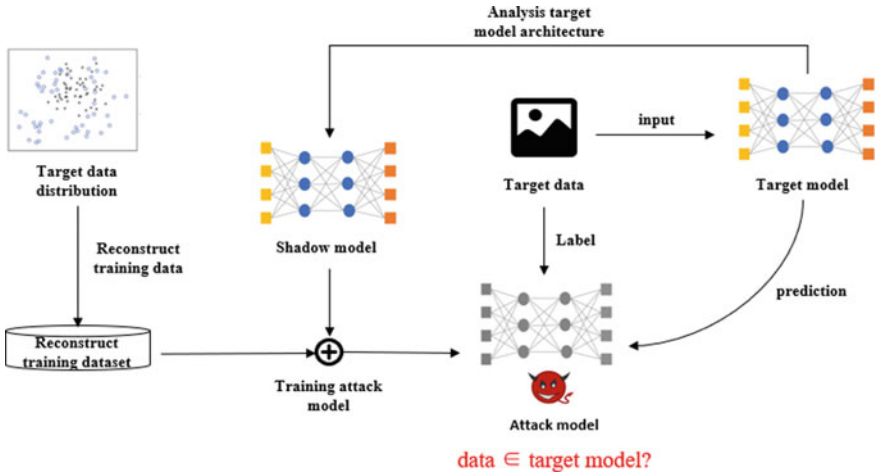


Fig. 64.2 Framework of black-box membership inference attack

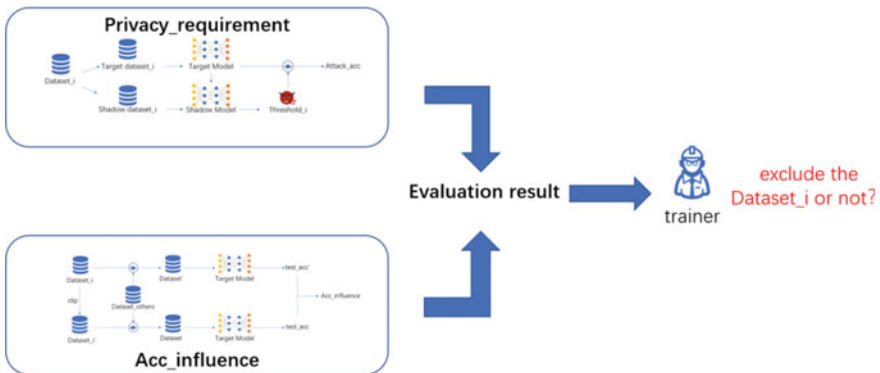


Fig. 64.3 Workflow of the evaluation scheme

analysis of the quantitative results. The size of the index represents the value of the subset to data users. According to the evaluation results, data users make a choice between subsets to improve the usability of the model while meeting the privacy requirements. In this section, we first introduce how to quantify “privacy demand” and “accuracy contribution”, and then propose the definition of “contribution” (Fig. 64.3).

64.4.1 Privacy-Requirement

Prior work pays attention to the privacy protection impact of different privacy algorithms on the whole training set. They define the privacy loss in the differential privacy

definition ϵ as an evaluation indicator of the strength of data set privacy protection. However, the meaning of privacy loss is difficult to understand in practice. Data providers and data users hardly know how much privacy loss value is meaningful for privacy protection for data. Research is to convert the loss of privacy into the success rate of membership inference attacks, and to analyze the training set as a whole to make the degree of privacy disclosure more intuitive. However, different analyses for different data sets are needed in some practical scenarios, such as collaborative machine learning training.

Inspired by [27], we set thresholds for different subgroups by shadow-training. The threshold setting algorithm is as follows:

Algorithm 1 Set the threshold of member inference attack by shadow-training

Data: Loss value of member samples: *member_values*; Loss value of non-member samples: *distribution_values*; threshold of member inference attack: *thre*; Function to sum quantity: *Sum(.)*; Number function: *Num()*

Value_list = *member_values* \cup *distribution_values*

For *value* \in *Value_list*

```

    member_ratio = Sum(member_values > = value) / Num(member_values)
    distribution_ratio = Sum(distribution_values < value) / Num(distribution_
values)
    acc = 0.5*( member_ratio + distribution_ratio)
    If acc > max_acc
        thre, max_acc = value, acc

```

Return *thre*

Compared with the global threshold method in [35, 36], our experiment shows that a subgroup dependent threshold leads to a better performance evaluation when the data set is unbalanced.

It should be emphasized that we use black box membership interference attachments. Attackers can only use the confidence vector of the model, and the model architecture is unknown because such attacks are closer to the real scene.

We interpret the accuracy of the attack as a measure of privacy disclosure risk, *privacy_risk*, and the risk calculation algorithm as follows:

Algorithm 2 Calculate privacy risk

For *num* \in *num_classes*

```

    thre = thre_setting(tr_values[tr_labels == num], te_values[te_labels ==
num])
    tr_mem += Sum(tr_values[tr_labels == num] > = thre)
    te_non_mem += Sum(te_values[te_labels == num] < thre)
return privacy_risk = 0.5*(tr_mem/Num(tr_labels) + te_non_mem/Num(te_labels))

```

The calculation formula of privacy protection degree $Privacy_protect$ is as follows:

$$Privacy_protect(a, b) = privacy_risk(\epsilon_a) - privacy_risk(\epsilon_b) \quad (64.2)$$

$privacy_risk(\epsilon)$ shows when the privacy loss of the privacy protection algorithm is ϵ , privacy loss of dataset. $Privacy_protect(a,b)$ indicates the decrease of privacy loss of dataset i from a to b . We define privacy requirement as $Privacy_requirement$:

$$Privacy_requirement = Privacy_protect(0, \epsilon') \quad (64.3)$$

ϵ' Indicates the privacy loss value when the subset has no privacy risk. Increasing the privacy requirements means more noise needs to be introduced to protect the dataset as a whole.

64.4.2 Acc-Influence

When the impact of the privacy demand on the utility is greater than the impact of the dataset on the accuracy of the model, we think that the dataset has no contribution to the model. We also need to quantify the impact of data sets on model accuracy in order to assess the contribution of data sets to the impact of privacy requirements. We use an ablation study method to assess the effect of the data on model accuracy. We use a model that does not use privacy protection algorithms to evaluate data sets.

The formula for calculating the Acc-influence of the dataset i is as follows:

$$Acc - influence = (acc1 - acc2)/acc1 \quad (64.4)$$

$acc1$ is model precision when using a comprehensive dataset, and $acc2$ is model accuracy when dataset i is absent. It is important to note that each data point is assumed to be independent and identically distributed, meaning that the data scarcity will not affect the overall data distribution.

64.4.3 Sub-contribution

To assess the contribution of the data set, we propose a quantitative indicator of *Sub-con*, defined as the following indicator:

Definition 2 Dataset Di , data distribution D , dataset overall D' , dataset are independent and distributed and belong to distribution D . For a private machine learning model $f(\epsilon)$, the contribution of the data set Di is as follows:

$$Sub-con = (privacy_requirement)/(acc_influence) \quad (64.5)$$

where *privacy_requirement* is the privacy requirement of the D_i data set, and *acc_influence* is the impact of D_i on the improvement of model accuracy. Each of the two privacy and utility parameters is affected by the input of the data, which reflects the effect of the data on the trade-off of a model.

64.5 Empirical Evaluation

We evaluated our proposed method through experiments. First of all, we proved the effectiveness of the proposed membership inference attack. The success rate of the attack reflects the change in privacy loss of differentially private algorithm. Our method intuitively measures the change in privacy risk of each data set before and after the use of the differentially private algorithm. We then estimated the association between *Sub-con* and model utility. Experimental results show that abandoning a data set with low *Sub-con* values can significantly improve the utility of the model while meeting the privacy requirements.

64.5.1 Experimental Setup

Data sets. We use a common benchmark for differentially private ML: CIFAR10. CIFAR10 is dataset consisting of 60,000 $32 \times 32 \times 3$ images of vehicles and animals, split into a train set of 50,000 and a test set of 10,000. We randomly disaggregate the trained sets, then divide the broken data sets into 10 subgroups and count them. We artificially construct unbalanced data sets by dividing the number of samples into subgroups, that is, the samples in the 10 subgroups are independently and identically distributed and have different numbers.

Differentially private ML model. The differentially private algorithm for learning we use is DP-SGD [9]. This algorithm is based on a differentially private version of stochastic gradient descent, we use Opacus to implement DP-SGD, which is a library that enables training PyTorch models with differential privacy.

Attack. We employ the membership inference attack framework proposed in [27]. By training shadow models, we set the corresponding threshold for different subgroups. The attacker determines whether the target sample belongs to the training set according to the threshold. For each subgroup, we divide it into four equal parts, *Dtrain_target*, *Dtest_target*, *Dtrain_shadow*, and *Dtest_shadow*. *Dtrain_shadow* and *Dtest_shadow* are used to train and test shadow models. Based on the test results, shadow models will return a threshold value for each subgroup. *Dtrain_target* and *Dtest_target* are used to evaluate the success rate of the attack target model.

64.5.2 Membership Inference Attack Based on Differentiation Threshold

We evaluated the effectiveness of the proposed attack method against unbalanced data sets. The experimental study was conducted on a model without privacy protections. We compare the effects of two types of threshold-based membership inference attacks, namely our differential threshold method and the global threshold method in the previous scheme; the experimental results are shown in Fig. 64.4. We find that when the data set is unbalanced, our membership inference attack method has a higher success rate.

Membership inference attack is based on the memory of the model to the training data, which is related to the distribution of the data. Previously, the black-box member reasoning attacks were based on a unified threshold [MIA BY FIP], ignoring the impact of different data distributions on model memory. We build shadow models for different data sets and obtain corresponding thresholds to improve the accuracy of the evaluation results.

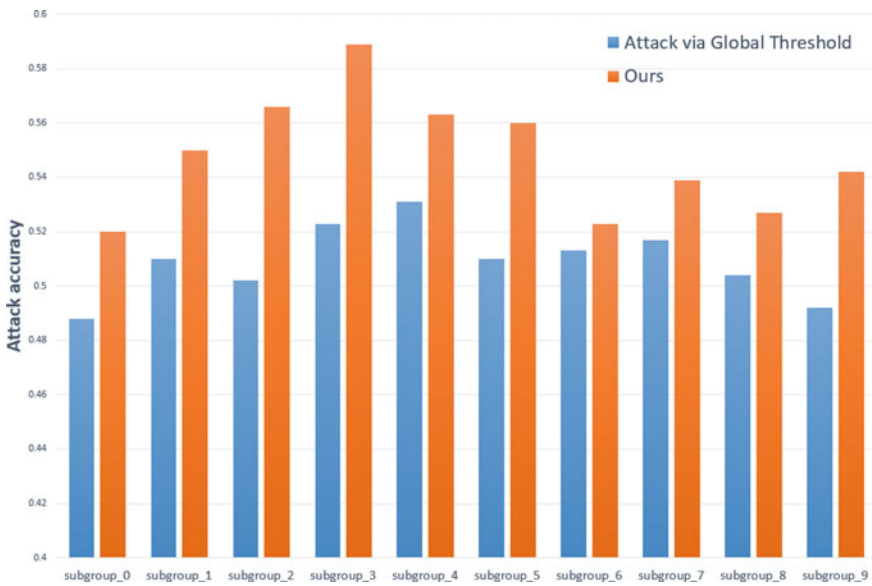


Fig. 64.4 Comparison of membership inference attack results

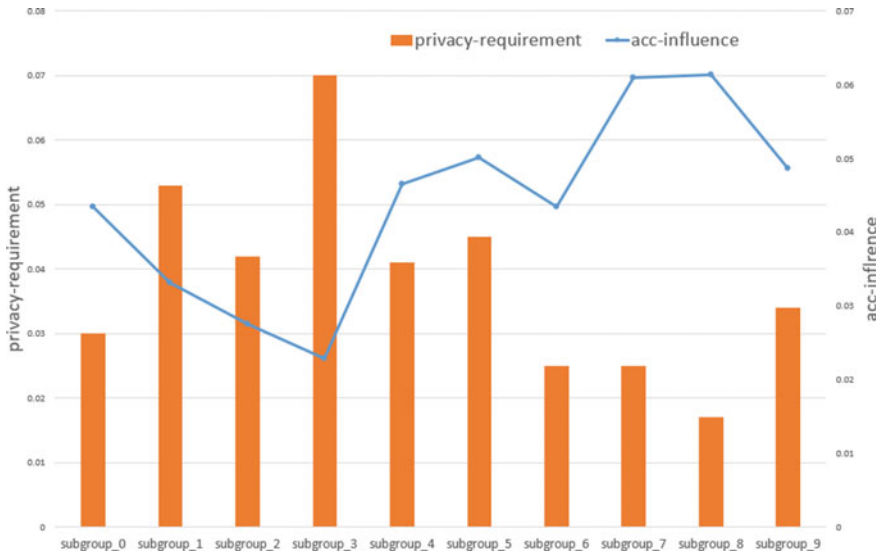


Fig. 64.5 acc_influence and privacy_requirement of each subgroup

64.5.3 Validation of ‘Contribution’

This part of the experiment is to verify our privacy protection methods. We first calculated the “privacy requirements” and “acc. information” of each subgroup, where the experimental results are shown in Fig. 64.5.

According to the results of the experiment, we calculate the *Sub-con* of each subgroup, as shown in Fig. 64.6.

Based on evaluation results, we excluded subgroup_3 from the training dataset and the experimental results are shown in Table 64.1.

It can be seen that our scheme has higher model accuracy under the same level of privacy protection.

While the existence of subgroup_3 helps to improve the generalizability of the model, when considering the privacy protection requirements, the data set causes a decline in the accuracy of the model.

The samples in some data sets are easier to remember by the model, so more noise needs to be added to the privacy protection process to prevent the disclosure of the data. But if that dataset does not improve the performance of the model, mixing that data set into a training set will reduce the model’s accuracy because of the privacy protection effect. Therefore, only when a data set will not seriously reduce the performance of the model due to privacy protection considerations, this data set is worth inclusion in the training.

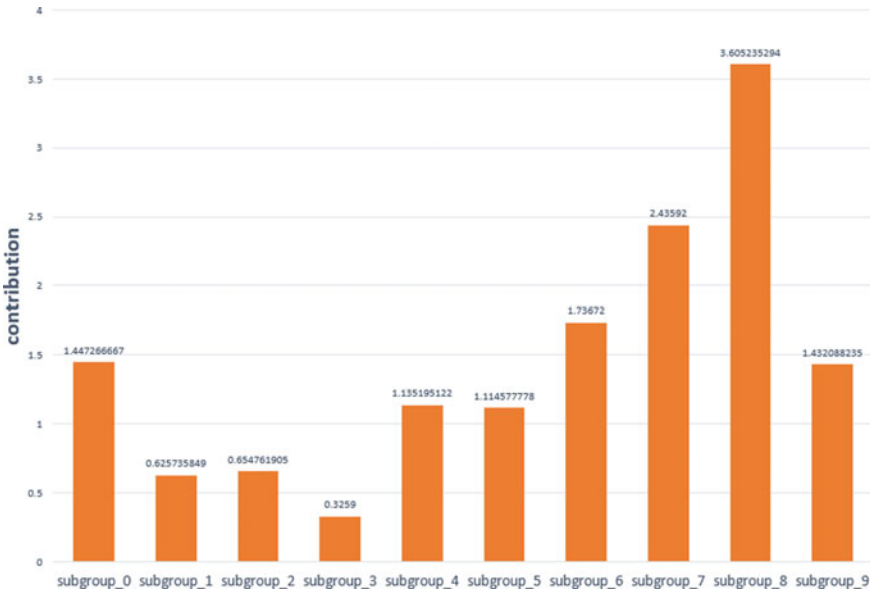


Fig. 64.6 Contribution of different subgroup

Table 64.1 Membership inference attack accuracy and model accuracy

	ϵ	MIA_attack_acc	Model_test_acc
With subgroup_3	85.43	0.512	0.679
Without subgroup_3	85.56	0.510	0.717
Without subgroup_3	88.82	0.509	0.715

64.6 Conclusion

In this work, we modify training data by evaluating the privacy risks of different distributed datasets, and their contribution to model accuracy, to improve the performance of differentially private machine learning models. We use the proposed evaluation method to estimate the contribution of the datasets to the model and make a selection of the datasets according to the evaluation results, so as to improve the performance of the differential privacy machine learning model.

Our experiment found that when certain data sets have little improvement in model accuracy, the model performance will be reduced to ensure the data set privacy requirements. The proposed method can guide model designers to make personalized choices of data sets based on the evaluation results, so as to understand the trade-off between utility and privacy.

Acknowledgements This work was supported in part by the National Natural Science Foundation of China (No. 62002077), in part by Major Research Plan of the National Natural Science

Foundation of China (No. 92167203), in part by Guangdong Basic and Applied Basic Research Foundation (No. 2020A1515110385), in part by Guangzhou Science and Technology Plan Project (No. 2023A03J0119), in part by Guangxi Key Laboratory of Cryptography and Information Security (No. GXIS202119).

References

1. Deng, L., Yu, D.: Deep learning: methods and applications. *Foundations and Trends in Signal Processing*, vol. 7, pp. 197–387 (2014)
2. Nielsen, M.A.: *Neural Networks and Deep Learning*, vol. 25. Determination Press (2015)
3. Carlini, N., Liu, C., Erlingsson, Ú., Kos, J., Song, D.: The secret sharer: evaluating and testing unintended memorization in neural networks. In: 28th USENIX Security Symposium, pp. 267–284 (2019)
4. Cormode, G., Kulkarni, T., Srivastava, D.: Answering range queries under local differential privacy. *Proc. VLDB Endow.* **12**, 1126–1138 (2019)
5. Dwork, C.: Differential privacy. In: *Proceedings of the 33rd International Conference on Automata, Languages and Programming*, vol. 4052 (2006)
6. Kairouz, P., Oh, S., Viswanath, P.: The composition theorem for differential privacy. In: *International Conference on Machine Learning*, pp. 1376–1385 (2015)
7. Dwork, C., Roth, A.: The algorithmic foundations of differential privacy. *Foundations and Trends in Theoretical Computer Science*, vol. 9, pp. 211–407 (2014)
8. Jia, J., Gong, N.Z.: Calibrate: frequency estimation and heavy hitter identification with local differential privacy via incorporating prior knowledge. In: *IEEE Conference on Computer Communications*, pp. 2008–2016 (2019)
9. Abadi, M., Chu, A.: Deep learning with differential privacy. In: *Proceedings of the 2016 ACM SIGSAC Conference on Computer and Communications Security*, pp. 308–318 (2016)
10. Lu, J., Zhang, X.S., Zhao, T., et al.: APRIL: finding the Achilles’ heel on privacy for vision transformers. In: *Proceedings of the IEEE/CVF Conference on Computer Vision and Pattern Recognition*, pp. 10051–10060 (2022)
11. Golatkar, A., Achille, A., Wang, Y.X., et al.: Mixed differential privacy in computer vision. In: *Proceedings of the IEEE/CVF Conference on Computer Vision and Pattern Recognition*, pp. 8376–8386 (2022)
12. Li, Z., Zhang, J., Liu, L., et al.: Auditing privacy defenses in federated learning via generative gradient leakage. In: *Proceedings of the IEEE/CVF Conference on Computer Vision and Pattern Recognition*, pp. 10132–10142 (2022)
13. Tian, Z., Li, M., Qiu, M., Sun, Y., Su, S.: Block-DEF: a secure digital evidence framework using blockchain. *Inf. Sci.* **491**, 151–165 (2019)
14. Mironov, I.: On significance of the least significant bits for differential privacy. In: *Proceedings of the 2012 ACM Conference on Computer and Communications Security*, pp. 650–661 (2012)
15. Canonne, C.L., Kamath, G., Steinke, T.: The discrete Gaussian for differential privacy. *Adv. Neural. Inf. Process. Syst.* **33**, 15676–15688 (2020)
16. Papernot, N., Thakurta, A., Song, S., Chien, S., Erlingsson, Ú.: Tempered sigmoid activations for deep learning with differential privacy. In: *Proceedings of the AAAI Conference on Artificial Intelligence*, vol. 35, No. 10, pp. 9312–9321 (2021)
17. Melis, L., Song, C., Cristofaro, E.D., Shmatikov, V.: Exploiting unintended feature leakage in collaborative learning. In: *IEEE Symposium on Security and Privacy*, pp. 691–706 (2016)
18. Wu, N., Farokhi, F., Smith, D., Kaafar, M.A.: The value of collaboration in convex machine learning with differential privacy. In: *2020 IEEE Symposium on Security and Privacy (SP)*, pp. 304–317. IEEE (2020)

19. Qiu, J., Tian, Z., Du, C., Zuo, Q., Su, S., Fang, B.: A survey on access control in the age of Internet of Things. *IEEE Internet Things J.* **7**(6), 4682–4696 (2020)
20. Tian, Z., Luo, C., Qiu, J., Du, X., Guizani, M.: A distributed deep learning system for web attack detection on edge devices. *IEEE Trans. Ind. Inf.* **16**(3), 1963–1971 (2020)
21. Zhu, Y., Yu, X., Chandraker, M., Wang, Y.X.: Private-knn: practical differential privacy for computer vision. In: *Proceedings of the IEEE/CVF Conference on Computer Vision and Pattern Recognition*, pp. 11854–11862 (2020)
22. Mironov, I.: Rényi differential privacy. In: *2017 IEEE 30th Computer Security Foundations Symposium (CSF)*, pp. 263–275. IEEE (2017)
23. Triastcyn, A., Faltings, B.: Bayesian differential privacy for machine learning. In: *International Conference on Machine Learning*, pp. 9583–9592. PMLR (2020)
24. Jordon, J., Yoon, J., Van Der Schaar, M.: PATE-GAN: generating synthetic data with differential privacy guarantees. In: *International Conference on Learning Representations* (2019)
25. Cheng, A., Wang, J., Zhang, X.S., Chen, Q., Wang, P., Cheng, J.: DPNAS: neural architecture search for deep learning with differential privacy. In: *Proceedings of the AAAI Conference on Artificial Intelligence*, vol. 36, no. 6, pp. 6358–6366 (2022)
26. Ye, D., Shen, S., Zhu, T., Liu, B., Zhou, W.: One parameter defense—defending against data inference attacks via differential privacy. *IEEE Trans. Inf. Forens. Secur.* **17**, 1466–1480 (2022)
27. Shokri, R., Stronati, M., Song, C., Shmatikov, V.: Membership inference attacks against machine learning models. In: *IEEE Symposium on Security and Privacy*, pp. 3–18 (2017)
28. Carlini, N., Chien, S., Nasr, M., et al.: Membership inference attacks from first principles. In: *IEEE Symposium on Security and Privacy (SP)*. IEEE, pp. 1897–1914 (2022)
29. Choquette-Choo, C.A., Tramèr, F., Carlini, N., Papernot, N.: Label-only membership inference attacks. In: *International Conference on Machine Learning*, pp. 1964–1974 (2021)
30. Chen, D., Yu, N., Zhang, Y., Fritz, M.: GAN-Leaks: a taxonomy of membership inference attacks against generative models. In: *ACM SIGSAC Conference on Computer and Communications Security*, pp. 343–362 (2020)
31. Fredrikson, M., Jha, S., Ristenpart, T.: Model inversion attacks that exploit confidence information and basic countermeasures. In: *Proceedings of the 22nd ACM SIGSAC Conference on Computer and Communications Security*, pp. 1322–1333 (2015)
32. Shafiq, M., Tian, Z., Sun, Y., Du, X., Guizani, M.: Selection of effective machine learning algorithm and Bot-IoT attacks traffic identification for internet of things in smart city. *Future Gener. Comput. Syst.* **107**, 433–442 (2020)
33. Shafiq, M., Tian, Z., Bashir, A.K., Du, X., Guizani, M.: CorrAUC: a malicious Bot-IoT traffic detection method in IoT network using machine learning techniques. *IEEE Internet Things J.* **8**(5), 3242–3254 (2021)
34. Jayaraman, B., Evans, D.: Evaluating differentially private machine learning in practice. In: *28th USENIX Security Symposium*, pp. 1895–1912 (2019)
35. Yeom, S., Giacomelli, I., Fredrikson, M., Jha, S.: Privacy risk in machine learning: analyzing the connection to overfitting. In: *IEEE 31st Computer Security Foundations Symposium*, pp. 268–282 (2018)
36. He, X., Zhang, Y.: Quantifying and mitigating privacy risks of contrastive learning. In: *Proceedings of the ACM SIGSAC Conference on Computer and Communications Security*, pp. 845–863 (2021)

Chapter 65

Research on Fire Smoke Control of an Ultra-wide Road Tunnel with Lateral Exhaust



Jing Wang, Haiquan Bi, Bo Lei, Zhicheng Mu, Zhe Liu, and Qingxun Zeng

Abstract The existence of the ultra-wide road tunnels improves the transportation efficiency and promotes economic development. However, fire hazards cannot be ignored. Thus, a single entrance 4-lane road tunnel is selected to explore the fire smoke control effect of an ultra-wide road tunnel with lateral exhaust. First, a scale model experiment is utilized to verify the accuracy of the numerical model and then in the influence of the most unfavorable position of the fire source, the number of open smoke outlets and the amount of smoke exhaust volumes on the smoke control effect of tunnel fire under the lateral exhaust mode is simulated by a three-dimensional model. The results show that the distribution pattern of fire smoke in an ultra-wide road tunnel under the lateral exhaust mode is affected by the lateral position of the fire source. When the fire source is closer to the sidewall of the exhaust duct, the smoke distribution that is inclined to the sidewall of the tunnel is more obvious. Based on the comparison among the time of the smoke spreading to the tunnel entrance, the spreading distance of 60 °C smoke, and the smoke exhaust efficiency under various working conditions, it is concluded that the most unfavorable lateral fire source location is in the middle of the tunnel. What's more, 4 open smoke exhaust ports with 200 m³/s exhaust volume near the fire source can achieve the best smoke control effect.

Keywords Lateral exhaust · Ultra-wide road tunnel · Scale model test · Numerical calculations · Smoke control

J. Wang · H. Bi (✉) · B. Lei · Q. Zeng
School of Mechanical Engineering, Southwest Jiaotong University, Chengdu, China
e-mail: bhquan@swjtu.edu.cn

Z. Mu · Z. Liu
CRRC DALIAN CO., LTD, Dalian, China

65.1 Introduction

Due to the complex and diverse landform, the road tunnel can improve the efficiency of transportation with the advantage of shortening mileage. In recent 10 years, the newly increased mileage of road tunnel in China has exceeded 1100 km every year, and the tunnel has gradually developed from single-tunnel two-lane tunnel to double-tunnel four-lane tunnel, double-tunnel six-lane tunnel, and even double-tunnel eight-lane tunnel [1]. The increase of highway tunnel width can effectively relieve the traffic pressure, but the flattening of tunnel section increases the traffic density and vehicle fire load. Therefore, when the fire occurs in the ultra-wide road tunnel, how to control the smoke of tunnel fire quickly and effectively is crucial to the safety of public transportation.

Most previous studies are based on the smoke exhaust mode at the top of tunnel. Because, the smoke exhaust effect of the smoke exhaust mode at the top of tunnel is better than that of the lateral smoke exhaust mode [2, 3]. However, the application of lateral smoke exhaust mode in the tunnel with limited upper space, two-way lane or two holes and one corridor have significant advantages, which not only saves the tunnel headspace, but also reduces the engineering cost [4, 5]. Therefore, lateral smoke exhaust is widely used in ultra-wide road tunnels.

Compared with traditional tunnels, ultra-wide tunnels have a larger section width-to-height ratio. The increase of tunnel width is conducive to reducing the heat release rate in case of fire [6, 7], delaying the spread of high temperature smoke, accelerating the longitudinal decay rate of smoke temperature along the tunnel. Therefore, the ultra-wide section tunnel has a thinner smoke layer and can hold more smoke gas volume in the case of fire [8, 9].

Several studies declared the feasibility of adopting the top exhaust mode in large-section tunnels [10, 11]. Since the buoyancy effect of smoke is vertical [12], the direction of the top exhaust is consistent with the direction of the smoke buoyancy, so the top exhaust mode is conducive to the smoke exhaust. When the smoke vent is located on the side wall of the tunnel, the suction force generated by the smoke vent is perpendicular to the direction of the smoke buoyancy, and the smoke exhaust effect will be limited.

Therefore, this paper takes single-hole 4-lane road tunnel as the research object to analyze the factors influencing the fire smoke control effect of tunnel under lateral exhaust mode, and the research results can provide reference for the design of lateral exhaust system of ultra-wide road tunnel.

65.2 Numerical Methods

65.2.1 Numerical Model and Boundary Condition

Based on an actual size of a single entrance 4-lane tunnel section, a numerical model is established to analyze the characteristics of lateral smoke exhaust in an ultra-wide road tunnel section, which is 17 m long and 7 m high. In order to capture the whole development of the airflow in the tunnel during numerical simulation, the length of the tunnel model is chosen as 600 m. Moreover, the length and height of the smoke vent is 3 m and 2 m, respectively. The distance between two adjacent smoke vents is 60 m, and the upper edge of the smoke vent is 0.4 m away from the tunnel vault. The illustration of this numerical model is shown in Fig. 65.1.

The tunnel inlet and outlet are set as open boundary, both ends of exhaust passage are considered exhaust boundary. The ambient temperature is 20 °C.

Open boundary shall be adopted at the tunnel inlet and outlet, Exhaust boundary shall be adopted at both ends of exhaust passage, and the ambient temperature shall be set at 20 °C. In order to study the smoke characteristics in the tunnel when the fire develops to the stable stage, the heat release rate of the fire source is assumed as 30 MW during the whole simulation.

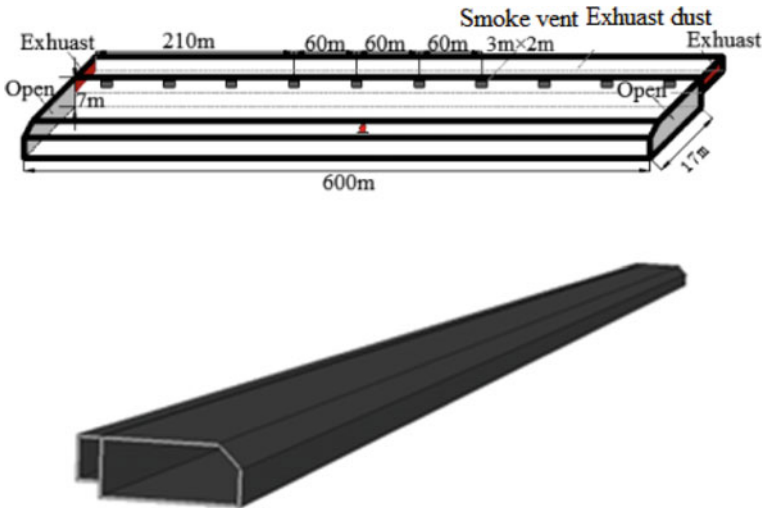


Fig. 65.1 Numerical model of single entrance 4-lane tunnel

65.2.2 Numerical Mesh

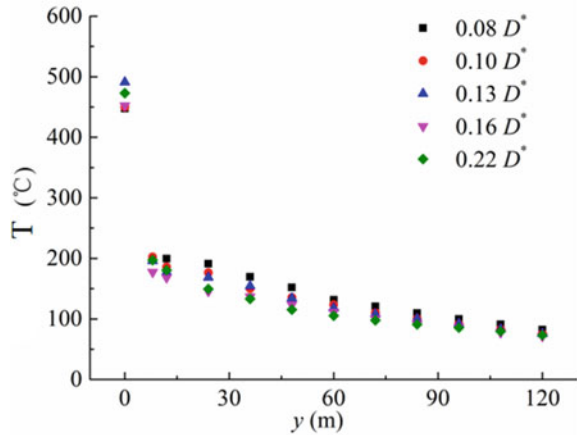
A reasonable mesh size can not only ensure the accuracy of calculation, but also save the computational cost. The selection of the mesh size is based on the characteristic diameter of fire source, which is expressed as:

$$D^* = \left[\frac{Q}{\rho_0 C_p T_0 \sqrt{g}} \right]^{2/5} \tag{65.1}$$

where, D^* is the characteristic diameter of fire source (m), Q is the fire heat release rate (kW), ρ_0 is air density (kg/m^3), C_p is the specific heat capacity ($\text{kJ}/(\text{kg K})$), T_0 is the ambient temperature (K), and g is the acceleration of gravity (m/s^2).

According to Eq. 65.1, the characteristic diameter of fire source is 3.7 m when the heat release rate of fire source is 30 MW. Previous studies have shown that the numerical results are consistent with the experimental results when the mesh size near the fire source is $0.0625\text{--}0.25D^*$ [13]. When the mesh size is $0.1\text{--}0.12D^*$, the average axial velocity and average temperature in the LES (a large-eddy simulation) model have a great deal with the fitting equation obtained through the experiment [14]. Therefore, mesh sizes ranging from $0.08D^*$ to $0.22D^*$ are selected in this paper to conduct independent analysis. By comparing the calculation results of smoke temperature in the tunnel vault under different mesh sizes (as shown in Fig. 65.2), when the mesh size decreases from 0.5 m ($0.13D^*$) to 0.3 m ($0.08D^*$), the flue gas temperature in the tunnel vault is basically unchanged. Therefore, the mesh size is determined to be 0.4 m ($0.1D^*$) and 0.2 m near the fire source in this study.

Fig. 65.2 Vault smoke temperature under different mash sizes



65.2.3 Comparison with Experimental Results

In order to verify the accuracy of the numerical calculation of FDS, a scale ratio experiment was conducted according to the Froude simulation method [15], and an ultra-wide tunnel fire test platform with a 1:20 scale ratio was built. The fire source is placed in the middle of the tunnel, and the heat release rate is 16.8 kW. When the fire occurs, four smoke vents on both sides of the fire source are open, and the exhaust volume of 0.556 m³/s is used for lateral exhaust. Wherein, the size of the smoke vent is 150 mm × 100 mm, and the distance between adjacent exhaust outlets is 3 m. The ambient temperature is set as 29 °C, and the ambient pressure is set as 101 kPa which is consistent with that in the experiment (Fig. 65.3).

The established numerical model based on the tunnel size, test conditions and monitoring equipment settings in the experimental tunnel is shown in Fig. 65.4. The open boundary is adopted at the tunnel opening and Exhaust boundary is adopted at the exhaust flue opening. According to the above analysis of mesh independence of full-size tunnel, the mesh size of the tunnel model is 0.02 m in scale ratio and 0.01 m near the fire source.

The comparison between the experimental results of each lane and the simulated results of FDS is shown in Fig. 65.5. The simulated results of FDS and the experimental results of scale ratio are highly matched, showing the same tendency and regulation on temperature.

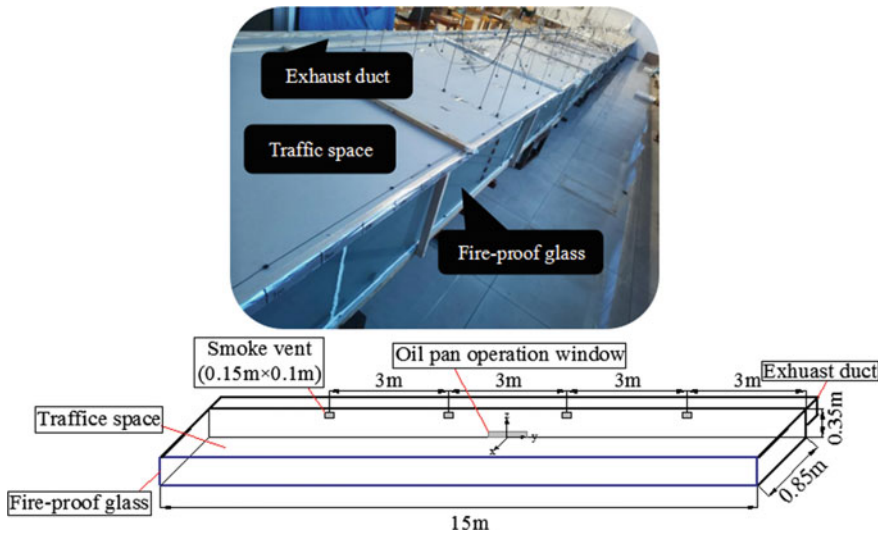


Fig. 65.3 Scale experimental tunnel

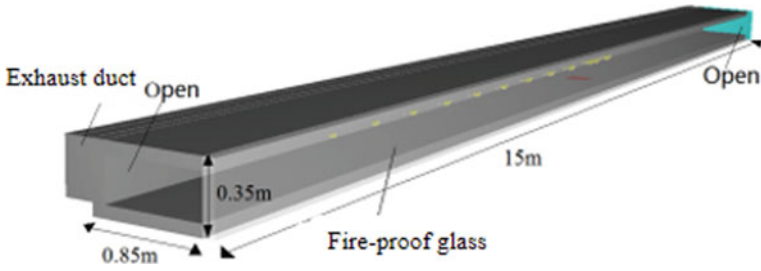


Fig. 65.4 FDS feasibility verification calculation model

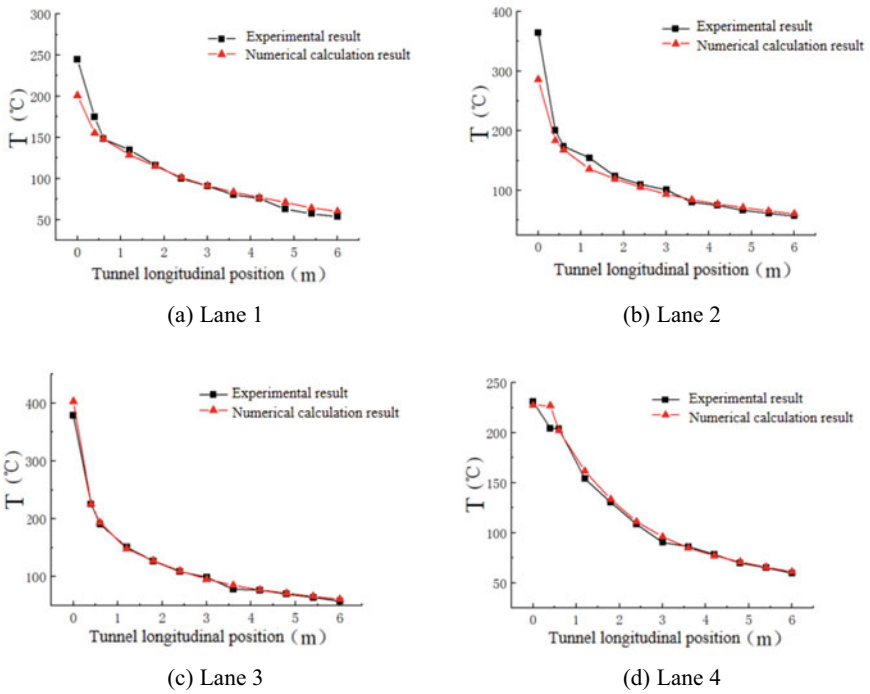


Fig. 65.5 Comparison between test results and FDS calculation results

65.3 Results and Discussion

65.3.1 The Most Unfavorable Fire Source Location of Smoke Control

In order to obtain the transverse fire source position that is most unfavorable to smoke control in the case of fire in the ultra-wide road tunnel, this paper selected three fire source positions for comparative analysis, as depicted in Fig. 65.6. These three positions are close to the side wall of the smoke vent, located in the middle of the tunnel and far away from the side wall of the smoke vent, respectively. In the longitudinal direction, the fire source is placed in the middle of the tunnel.

When smoke exhaust system does not work, there are some different phenomena on the smoke spread between different fire source locations, as illustrated in Fig. 65.7. During the spreading process of smoke that hits the tunnel roof, the smoke flow is limited by the structure of the side wall earlier when the fire source is located near the side wall. And the smoke spread mode above the fire source changes from circular type to semi-circular type. Due to the weaker jet formed at the side wall and less smoke returned to the fire source, more accumulation of the smoke on the opposite side appears. Therefore, the smoke spreads faster on the opposite side of the fire source within a certain longitudinal range.

When the fire source is close to the side wall of the tunnel, more smoke accumulate on the opposite side of the fire source. Besides, the lateral exhaust has a better effect on the smoke spread that is closer to the vent. Therefore, the effect of lateral exhaust mode on smoke spread is different when the fire source is in different transverse

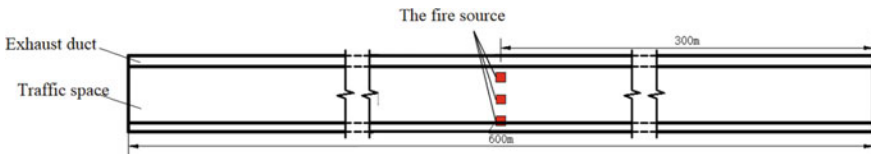
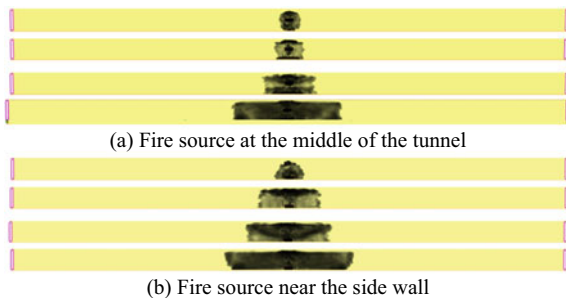


Fig. 65.6 Schematic diagram of the location of the fire source

Fig. 65.7 Comparison of smoke free spreading process of the fire source near the wall and the fire source in the middle of the tunnel



(a) Fire source at the middle of the tunnel

(b) Fire source near the side wall

Table 65.1 Time for the smoke to spread to the tunnel exit

Transverse position of the fire source	No exhaust mode (s)	Lateral exhaust mode (s)
Far away from the side wall of the smoke vent	143	268
In the middle of the tunnel	140	233
Close to the side wall of the smoke vent	142	271

positions. When the fire source is near the side wall of the smoke vent, the oblique propagation of smoke spread is strengthened. On the contrary, the smoke on both sides of the tunnel tends to spread longitude-wise at the same speed earlier.

In addition, the PIARC report [16] states that the centralized exhaust system has the ability to control the smoke spread and minimizes the range of influence caused by high-temperature smoke and toxic gases when a fire occurs in the tunnel. Thus, the time that the smoke spreads to the exit of the tunnel and the distance that 60 °C smoke can spread under the ceiling are considered as criterion to evaluate the smoke control effect [17].

When the fire source is in different transverse positions of the ultra-wide tunnel, the time of the smoke spreading to the tunnel exit is summarized in Table 65.1.

According to the results of fire source at different locations, the time that the smoke spreads to the exit of the tunnel is prolonged 87, 66 and 91% with the comparison of no exhaust mode. In this case, it has a better effect on the smoke control when the fire source is located near the side wall under the lateral exhaust mode.

Figure 65.8 shows the results of 60 °C smoke spread distance under the tunnel ceiling, and the region above the black line represents the smoke range which is higher than 60 °C. The 60 °C smoke is controlled in the tunnel with the usage of lateral exhaust mode. When the fire source is in the middle of the tunnel, the distances of the smoke spread are the farthest whether the exhaust mode is.

In summary, the most unfavorable location of fire source is the middle of an ultra-wide road tunnel.

65.3.2 Number of Smoke Vent Openings

In this section, the influence of the number of open smoke exhausts near the fire source in the tunnel on the smoke control effect under lateral exhaust mode is analyzed through the numerical simulation. The fire source is set as the most unfavorable location in the middle of a single entrance 4-lane road tunnel, and the number of open smoke exhausts is 2, 4, and 6, respectively.

Due to the symmetry of the open smoke vent on both sides of the fire source, the number of open smoke vent has no obvious effect on the smoke spread process. The time that smoke spreads to the tunnel entrance under different numbers of smoke vent is shown in Fig. 65.9. With the increase of the number of smoke vents, the smoke

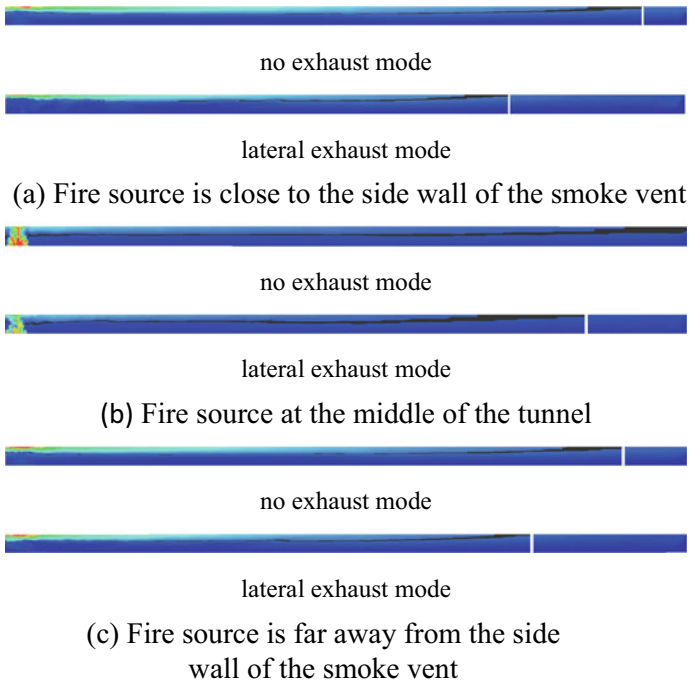
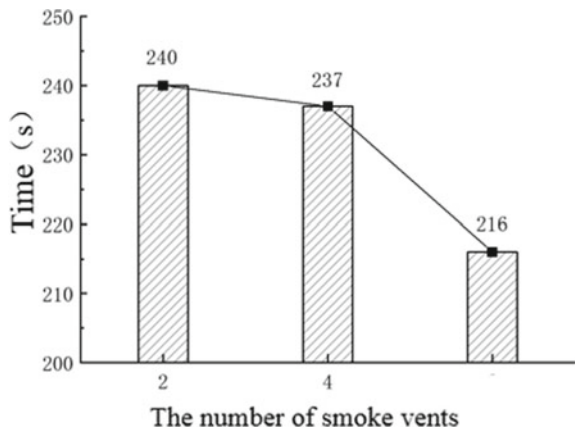


Fig. 65.8 60 °C smoke spread distance

spreads faster to the tunnel entrance. When the number of smoke vents increases from 2 to 4, the spread time is shortened by 1.25%. And when the number of smoke outlets increases from 2 to 6, the spread time is shortened by 10%.

Figure 65.10 shows the spreading distance of 60 °C smoke under the ceiling with different number of open smoke exhausts. When the number of smoke vents

Fig. 65.9 Time for the smoke to spread to the tunnel entrance



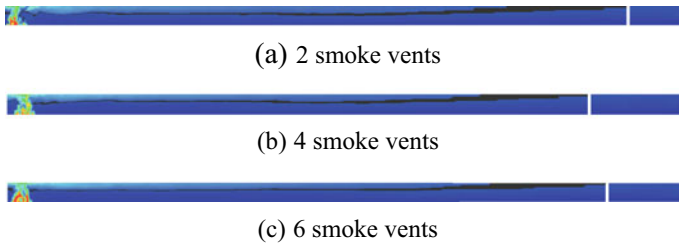


Fig. 65.10 The spread distance of smoke at 60 °C

increases from 2 to 4, the spreading distance of 60 °C smoke is shortened. And when the number of smoke vents is increased to 6, the spreading distance increases.

In order to ensure the most reasonable number of smoke vents that need to be open, it is necessary to analyze the exhaust efficiency under different number of open smoke vents. The exhaust efficiency is deduced based on the amount of CO₂ produced in the event of a fire in the tunnel and the amount of CO₂ emitted from the smoke vents. The expression of exhaust efficiency is as follow:

$$\eta = \frac{m_e}{m_p} \times 100\% \tag{65.2}$$

where η is smoke extraction efficiency, %; m_e is CO₂ emission at smoke outlet, kg/s; m_p is the amount of CO₂ produced by the fire source, kg/s.

Figure 65.11 shows the exhaust efficiency under different number of open smoke vents in lateral exhaust mode. The exhaust efficiency is the highest (73%) when four smoke vents are open. Compared with 2 and 6 open smoke vents, the exhaust efficiency is increased by 5% and 2% respectively. Therefore, the most reasonable number of smoke vents for the lateral exhaust system is 4.

65.3.3 Smoke Exhaust Volumes

As for studying the influence of smoke exhaust volume on the smoke control effect of lateral smoke exhaust system, the fire source is also set in the middle of the tunnel. Four smoke vents near the fire source are open in the lateral exhaust mode. The smoke produced by the heat release rate of 30 MW fire source is 90.82 m³/s, so the minimum smoke exhaust volume in this study is 90 m³/s. The fire scene settings are shown in Table 65.2. The exhaust volume of 0 m³/s represents the operation of no exhaust system.

The time that smoke spreads to the tunnel entrance is extended with the increase of the smoke exhaust volume and increases exponentially (as illustrated in Fig. 65.12). When the exhaust volume is 300 m³/s, the smoke generated by the fire source still overflows the tunnel. But when the exhaust volume increases to 350 m³/s, the smoke

Fig. 65.11 Smoke exhaust efficiency

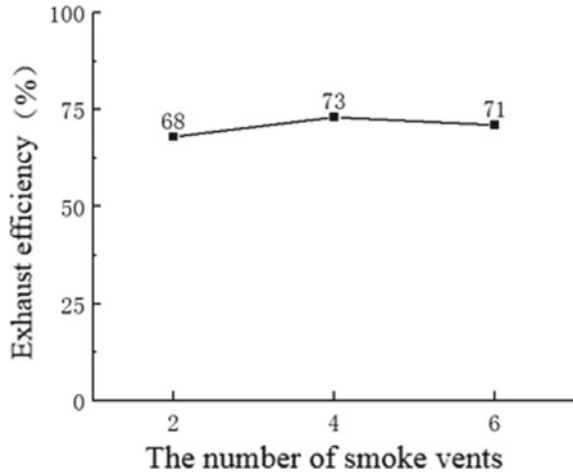


Table 65.2 Fire scene settings

	V (smoke exhaust volumes) (m ³ /s)	Smoke vent opening condition
1	0	No exhaust mode
2	90	Open the four smoke vents near the fire source
3	160	
4	200	
5	260	
6	300	
7	350	
8	400	

is controlled in the tunnel. Thus, higher exhaust volume in lateral exhaust mode can delay the smoke spread, and when the exhaust volume is large enough, the smoke can be controlled inside the ultra-wide tunnel.

Figure 65.13 shows the spread distance of 60 °C smoke under different exhaust volume. When the exhaust volume is 90 m³/s, the 60 °C smoke has been controlled in the tunnel. With the increase of smoke discharge, the spread distance of 60 °C smoke is gradually shortened.

Figure 65.14 shows the exhaust efficiency of different smoke volumes under lateral exhaust mode of an ultra-wide tunnel. With the increase of the exhaust volume, the exhaust efficiency gradually improves. When the exhaust volume is about 250 m³/s, the exhaust efficiency reaches 80%. However, with the further increase of smoke exhaust volume, the growth trend of smoke exhaust efficiency gradually slows down. And when the smoke exhaust volume increases from 90 to 160 m³/s, the smoke exhaust volume increases by 70 m³/s and the smoke exhaust efficiency increases by

Fig. 65.12 The time for the smoke to spread to the tunnel entrance under different smoke exhaust volumes

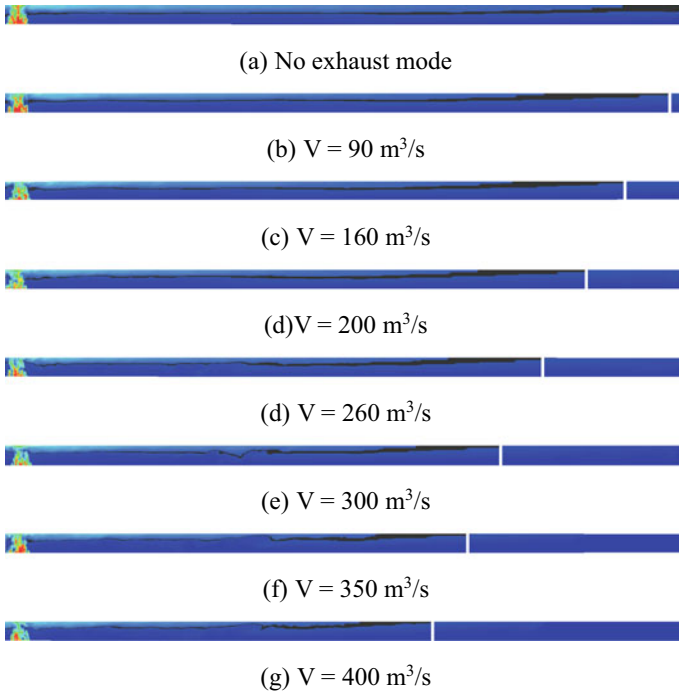
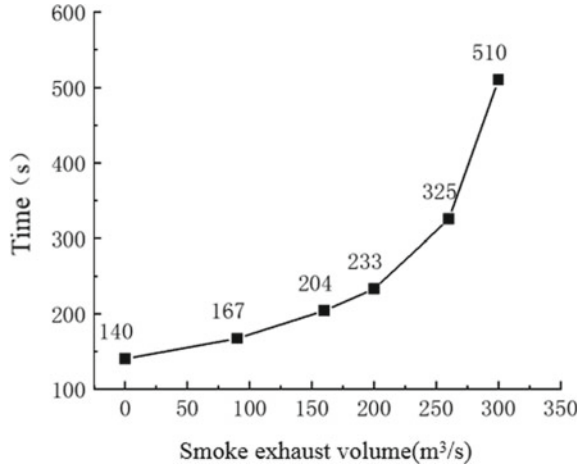
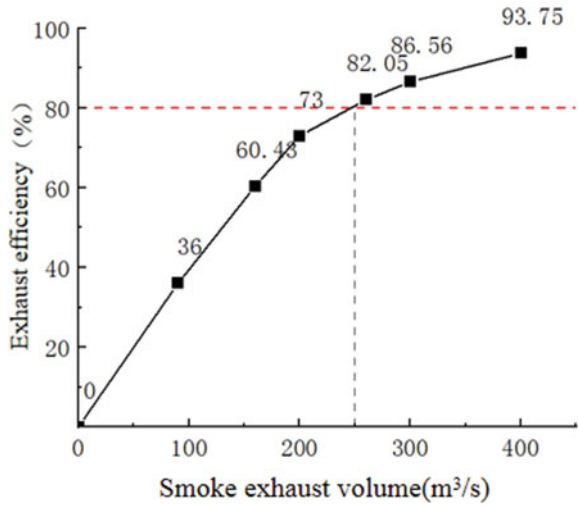


Fig. 65.13 60 °C smoke spread distance under different smoke exhaust volumes

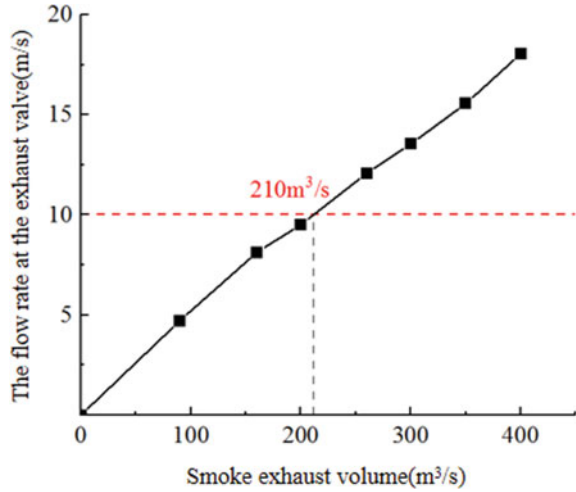
Fig. 65.14 Efficiency of smoke extraction under different smoke extraction volumes



about 24%. When the exhaust volume increases from 300 to 400 m³/s, the exhaust volume increases by 100 m³/s, while the exhaust efficiency only increases by about 7%. Consequently, the increased smoke exhaust volume leads to a decrease in the improvement effect of smoke exhaust efficiency.

Relevant studies require that the flow rate at the exhaust valve should not exceed 10 m/s [18]. Figure 65.15 shows the monitoring results of the flow rate of the smoke exhaust valve under different smoke discharge volumes. When the smoke discharge volume exceeds 200 m³/s, the flow rate of the smoke exhaust valve does not meet the specification requirements. Therefore, in order to ensure the flow rate of the exhaust valve which meets the specification requirements, the maximum exhaust volume should be 200 m³/s when the four smoke vents near the fire source are open.

Fig. 65.15 The flow rate of the exhaust valve under different smoke exhaust volumes



65.4 Conclusion

In this paper, on the basis of an ultra-wide road tunnel with lateral exhaust, a three-dimensional model is established to study the influence of fire source location, the number of opened smoke vent and smoke exhaust volume on the characteristics of smoke spread process. The time that the smoke spreads to the tunnel entrance, the distance of 60 °C smoke spread and the efficiency of the smoke exhaust under different working conditions improve the understanding of the smoke spread. The main conclusions are as follows:

When a fire occurs in an ultra-wide tunnel and the fire source is located near the side wall of the tunnel, if the smoke is in a state of free spread, the spread speed of the smoke near the fire source is less than that away from the fire source. Under the lateral exhaust mode, the flow of smoke is affected by the combined action of buoyancy force and suction force of exhaust port. There are greater differences on the speed of smoke spread between the two sides of the tunnel when the fire source is near the side wall of the smoke vent and the smoke on both sides spreads longitudinally along the tunnel within a certain time when the fire source is far away from the side wall of the smoke vent.

When the smoke spreads freely, the transverse position of the fire source has little effect on the time of the smoke spreading to the tunnel entrance. Under the lateral exhaust mode, by comparing the smoke spread process of the fire source located near the side wall of the smoke vent, the fire source located in the middle of the tunnel, and the fire source located away from the side wall of the smoke vent, it is concluded that the fire source located in the middle of the tunnel is the most unfavorable transverse position of a single entrance 4-lane road tunnel under the lateral exhaust mode.

By comparing the smoke control effect with different amount of lateral smoke vents, the spread distance of smoke is the shortest and the efficiency of smoke exhaust

is the highest with four open lateral smoke vents. Therefore, the most reasonable amount of open smoke vent under lateral exhaust in a single entrance 4-lane road tunnel is four.

With the increase of the smoke exhaust volume within a reasonable range, the smoke exhaust efficiency is improved. In order to meet the requirements of the flow rate of the smoke exhaust valve, the maximum smoke exhaust volume in a single entrance 4-lane road tunnel is 200 m³/s.

References

1. Ciro, C., Paolo, C., Maria, L.D.G., et al.: Numerical simulation of different HGV fire scenarios in curved bi-directional road tunnels and safety evaluation. *Tunnell. Undergr. Space Technol.* **31** (2012)
2. Olivier, V.: Experimental simulations of fire-induced smoke control in tunnels using an “air–helium reduced scale model”: principle, limitations, results and future. *Tunnell. Undergr. Space Technol.* **23**(2), 171–178 (2007)
3. Vauquelin, O., Tello, D.: Definition and experimental evaluation of the smoke “confinement velocity” in tunnel fires. *Fire Saf. J.* **40**(4), 320–330 (2005)
4. Chen, J., Fang, Z., Yuan, J.: Numerical simulation about smoke vent arrangement influence on smoke control in double-decked tunnel. *Procedia Eng.* **52**, 48–55 (2013)
5. Yang, J., Pan, X., Hua, M.: Study on the flow-dynamic characterization of the lateral mechanical extraction system in tunnel fire. *Procedia Eng.* **211**, 888–896 (2018)
6. Xu, Z., Liu, Y., Kang, R., et al.: Study on the reasonable smoke exhaust rate of the crossrange exhaust duct in double-layer shield tunnel. *Procedia Eng.* **84**, 506–513 (2014)
7. Xu, Z., Liu, Q., Lu, H., et al.: Study on the heat exhaust coefficient and smoke flow characteristics under lateral smoke exhaust in tunnel fires. *Fire Mater.* **43**(7), 857–867 (2019)
8. Fan, C., Li, Y., Haukur, I., et al.: Effect of tunnel cross section on gas temperatures and heat fluxes in case of large heat release rate. *Appl. Therm. Eng.* **93**, 405–415 (2016)
9. Ji, J., Bi, Y., Kondapalli, V., et al.: Influence of aspect ratio of tunnel on smoke temperature distribution under ceiling in near field of fire source. *Appl. Therm. Eng.* **106**, 1094–1102 (2016)
10. Zhu, H., Shen, Y., Yan, Z., et al.: A numerical study on the feasibility and efficiency of point smoke extraction strategies in large cross-section shield tunnel fires using CFD modeling. *J. Loss Prev. Process Ind.* **44**, 158–170 (2016)
11. Yan, Z., Zhang, Y., Guo, Q., et al.: Numerical study on the smoke control using point extraction strategy in a large cross-section tunnel in fire. *Tunnell. Undergr. Space Technol.* **82**, 455–467 (2018)
12. Ji, J., Gao, Z.H., Fan, C.G., et al.: Large Eddy Simulation of stack effect on natural smoke exhausting effect in urban road tunnel fires. *Int. J. Heat Mass Transf.* **66**, 531–542 (2013)
13. Zhao, S., Liu, F., Wang, F., et al.: A numerical study on smoke movement in a metro tunnel with a non-axisymmetric cross-section. *Tunnell. Undergr. Space Technol.* **73** (2018)
14. Nele, T., Xavier, D., Bart, M.: CFD study of relation between ventilation velocity and smoke backlayering distance in large closed car parks. *Fire Saf. J.* **48** (2011)
15. Quintiere, J.G.: Scaling applications in fire research. *Fire Saf. J.* **15**(1) (1989)
16. PIARC: Fire and Smoke Control in Road Tunnels. Committee on Road Tunnels. World Road Association (PIARC), Cedex, France (1999)
17. Wang, S.: Study on Characteristics of Smoke Control with One-Side Exhaust Duct in Tunnel Fires and Ventilation Network Calculation. Central South University (2013)
18. Xu, Z., Jiang, X.: Smoke Control Project. China Machine Press, Beijing (2011)

Chapter 66

Deformable Special-Shaped Projectile Impacting Basalt Target: Experiments and Analysis



Guang Ren, Haijun Wu, Heng Dong, Yingqing Lv, and Fenglei Huang

Abstract Using kinetic energy to crush high-strength rocks and then collect particle samples has attracted much attention in the Near-Earth Asteroid (NEA) sampling scheme. In this study, two deformable special-shaped projectiles of tantalum: petal-penetrating type (T1), petal-non-penetrating type (T2), and high-speed (453.0–612.0 m/s) impact experiments, were designed to study the projectile-target interaction and rock fracture mechanisms based on a 14 mm ballistic gun platform. Results shown that deformation of the Special-Shaped Projectile is related to the plasticity of material and projectile configuration; The projectile-target interaction of the T2 is two-phase processes: multi-point simultaneous impact and the Taylor impact, which increase the diameter and depth of the crushing zone and raise the mass of spalled-rock particles about three times than T1. The two-phase processes inspiring to create the projectile's head and cylinder section from different properties of materials respectively. This research inspires the design of the deformable special-shaped projectile and the comprehension of the fracture mechanisms of rocks under high-speed impact.

Keywords Projectile-target interaction · Deformable special-shaped projectile · High-speed impact

66.1 Introduction

In the NEA sampling, the probe shoots a projectile to stimulate regolith particles on the condition of hovering or touching-flying off the asteroid's surface. In 2014, the Japanese Hayabusa2 probe [1] shot an oval tantalum projectile and collected particles of 3.5 g. In 2016, the American OSIRIS-REx probe stimulated regolith by jetting high-pressure gas directly. However, difficulties such as promoting sampling mass

G. Ren · H. Wu · H. Dong (✉) · Y. Lv · F. Huang
State Key Laboratory of Explosion Science and Technology, Beijing Institute of Technology,
South of Zhongguancun, Beijing 100081, China
e-mail: 7520210180@bit.edu.cn

and evaluating the ability of projectiles to spall high-strength rocks under surface regolith are still to be solved.

The assumption of a rigid projectile underlies conventional impact research, simplifying the interaction between the projectile and the target while neglecting the effects of the projectile’s plastic deformation on the diameter, depth, and morphology of the target crushing zone. While the projectile-target interaction of deformable projectiles is quite different from that of rigid projectiles [2, 3], therefore, this study designed petal-penetrating type (T1) and petal-non-penetrating type (T2) deformable projectiles to analyze the influence of deformation on the issues mentioned above. The results are significant in evaluating the ability of spalled rocks and improving the sampling efficiency.

66.2 Experiments

Constrained by the compact design of the probe and the extreme temperature in outer space, tantalum was selected as the projectile material. Tantalum has high density, which can increase the specific kinetic energy; The mechanical characteristics maintain good plasticity and high fracture strain in a wide temperature range (– 100 to 500 °C), and reduce the debris pollution of rock samples caused by projectile impact. The physical properties of tantalum in experiments and the mechanical properties at different temperatures are shown in Table 66.1.

Asteroid rocks have the characteristics of low porosity and high compression strength, so basalt with a quasi-static uniaxial compression strength of 180 MPa was selected as the target material.

T1 (Fig. 66.1a) and T2 (Fig. 66.1b) are the two types of special-shaped projectiles, both with an outer envelope size of $\phi 10.0 * 15.0$ mm. The head of T1 has a petal-shaped structure, and the cylinder section has through preset troughs, with a mass of 10.7 g; The head of T2 is the same as T1, while the cylinder section has no troughs, with a mass of 15.4 g.

Table 66.1 Basic physical and mechanical properties of tantalum (20 °C)

Material	Density (g/cm ³)	Coefficient of thermal expansion (< 100 °C)	Poisson’s ratio	Elastic modulus (GPa)	Yield (– 100 °C) MPa	Yield ^a (500 °C) MPa
Ta	16.6	6.5e–6	0.3	195.0	600.0	360.0

^a The yield strength at 500 °C is calculated based on the modified Johnson–Cook constitutive in paper [4]

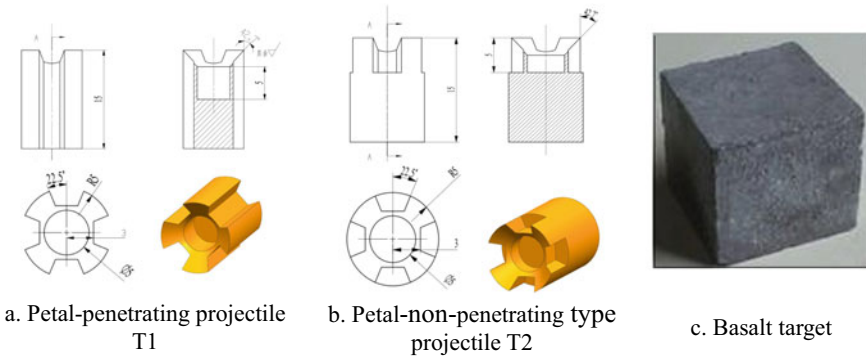


Fig. 66.1 Two types deformable special-shaped projectiles and the target of 200 * 200 * 200 mm

As shown in Fig. 66.2, the experimental platform consists of the ballistic gun, sheller, silver paper, collection box, and high-speed camera system. Set the shutter speed to 1/1500,000 s. Dust and ejected spalled-rock particles make it hard to collect and measure the mass of spalled-rock particles directly. Salt was backfilled into the crushing zone and calculated the rock particles mass by $m_r = (\rho_{\text{rock}}/\rho_{\text{salt}})m_{\text{salt}}$ (Fig. 66.3).

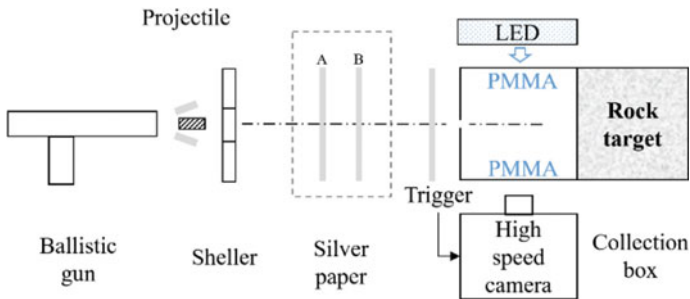
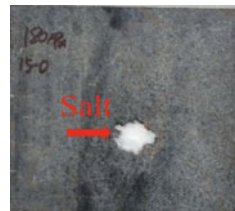


Fig. 66.2 The 14 mm ballistic gun experimental platform

Fig. 66.3 Measurement method of spalled-rock mass



66.3 Experimental Results and Analysis

The experimental data include projectile mass m_p , incidence velocity V_{in} , crushing zone diameter d_c , depth h_c and mass of spalled-rock m_r , as shown in Table 66.2. The typical impact process of T2 at 455.0 m/s is as shown in Fig. 66.4. A is the incident flight attitude, B is the instantaneous state of impact, and it can be seen in (c) that the impact process produces a large number of gravel particles accompanied by bright firelight.

66.3.1 Projectile Deformation Mode and Two-Phase Impact Process

T1 deformation mode at 453.0 m/s is shown in Fig. 66.5a1, a2. The projectile’s petal-shaped head and cylinder section have been torn along the axial trough completely. T2’s deformation mode at 610.0 m/s is shown in Fig. 66.6b1, b2, c1. The petal shaped head was torn (I Type fracture) along the axial, and the cylinder section expanded

Table 66.2 Experimental results with high-speed impact of T1 and T2

Type	m_p (g)	V_{in} (m/s)	d_c (mm)	h_c (mm)	m_r (g)
T1	10.6	453.0	22.0	3.0	0.8
	10.5	458.0	28.0	4.0	2.2
	10.6	599.0	32.0	7.0	2.4
	10.5	600.0	33.0	7.0	2.8
T2	15.7	455.0	38.0	6.0	10.2
	15.7	465.0	40.0	7.0	11.7
	15.6	612.0	57.0	12.0	19.9
	15.7	610.0	55.0	11.0	19.8

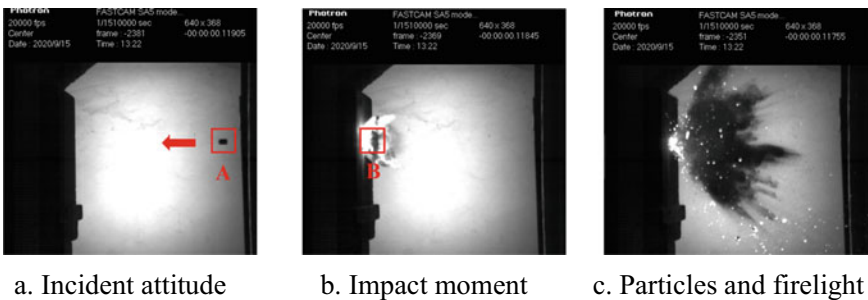


Fig. 66.4 T2 projectile impacts basalt target

radially, forming a bowl-like structure eventually. There was no shear fracture along the cylinder section in axial direction, consistent with the Taylor impact deformation characteristics of plastic materials [5].

T2's deformation mode indicates that the projectile-target interaction can be decoupled into a two-phase impact in time sequence. As shown in Figs. 66.6 and 66.7, the first phase starts from the petal shaped head contacting the rock surface to the end of the head tearing. In the first phase, the simultaneous impact of multiple points formed the initial crack zone and yielded large size rock pieces. The second phase starts from the cylinder section impacting the initial crushing zone, then being compressed until the residual projectile rebounds. In the second phase, the Taylor impact of the cylinder section on the initial crack zone, and the large size pieces yielded in the first impact were crushed into small particles.

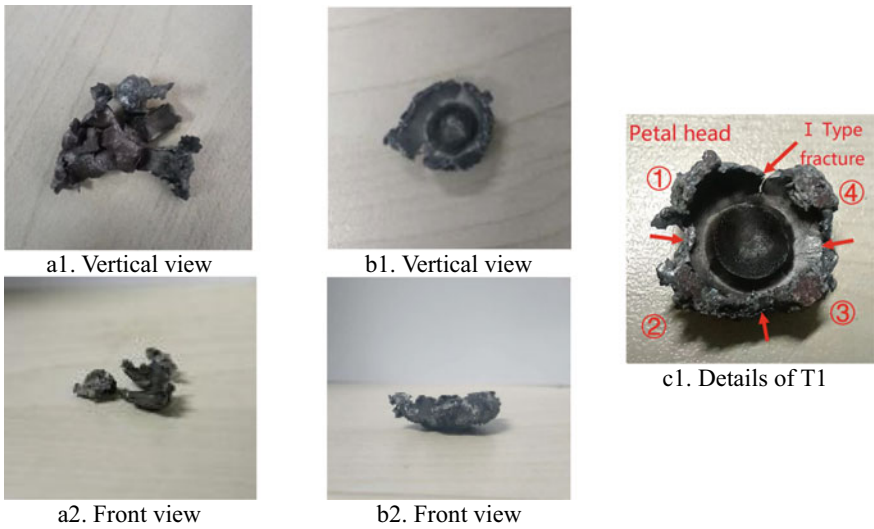


Fig. 66.5 a1, a2 T1's deformation at 453.0 m/s; b1, b2 T2's deformation at 610.0 m/s; c1 deformation mode and fracture characteristics of T1

Fig. 66.6 Multi-point simultaneous impact of petal shaped head



Fig. 66.7 Taylor impact of the cylinder section



66.3.2 Crushing Zone Morphology and Mass of Spalled-Rock

The crushing zone of T1 and T2 at 600.0 and 610.0 m/s is shown in Figs. 66.8 and 66.9. The central area appeared white, covered with powder-like particles, while the edge area was black. It implies that the central area presented compression failure under high hydrostatic pressure, while the edge area was brittle spalling failure dominated by tensile and shear stress [6].

Figure 66.10 shows that the dimensionless depth k ($=h_c/d_p$, the ratio of crush zone depth h_c to projectile diameter d_p) increases linearly with the projectile kinetic energy, and that there was no significant difference in k between T1 and T2. Figure 66.11 shows that the dimensionless diameter d_n ($=d_c/d_p$, the ratio of diameter d_c to projectile diameter d_p) was also linear relationship with the projectile kinetic energy.

In conventional defense studies, researchers tend to focus on single variables such as dimensionless depth k and dimensionless diameter d_n , which are unable to describe the characteristic of crushing zone morphology. In this paper, shape factor

Fig. 66.8 Crushing zone of T1 at 600.0 m/s

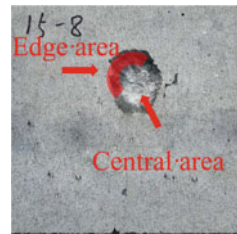


Fig. 66.9 Crushing zone of T2 at 610.0 m/s

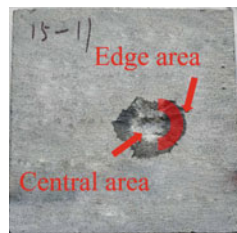


Fig. 66.10 Relationship between dimensionless depth k and projectiles kinetic energy

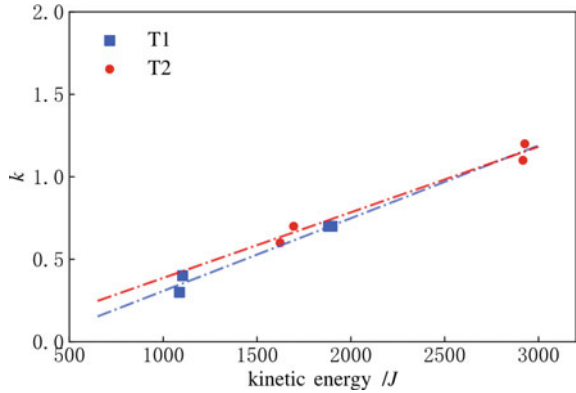
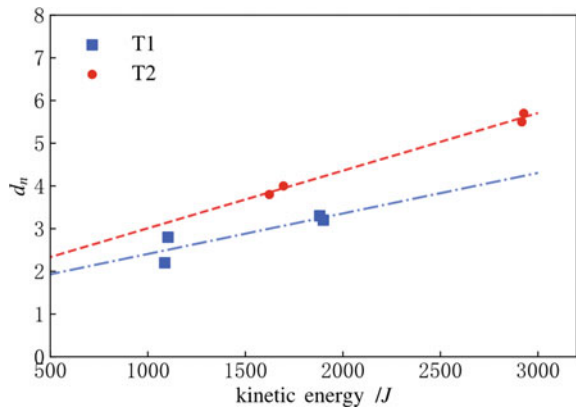


Fig. 66.11 Relationship between dimensionless diameter d_n and kinetic energy



$N (=d_n/k)$ is more preferred. Experimental data of crushing zone formed by an oval copper projectile (deformable body) and an oval steel projectile (rigid body) impact uniaxial compression strength concrete and rocks of 37.9–238.5 MPa at the speed of 400 m/s. is calculated as shown in Fig. 66.12. Compared with the traditional oval rigid projectile, the crushing zone formed by the deformable projectile is flatter [7].

The spalled-rock mass of T2 is 10.2 g at kinetic energy of 1695.0 J, about three times that of T1, 2.8 g, as shown in Fig. 66.13. Obviously, the two-phase impact of T2 formed a more flatter fracture zone morphology, which shows the advantage of increasing the diameter of the crushing zone and the mass of spalled-rock particles.

Fig. 66.12 Shape factor N of crushing zone of targets with different zone strengths

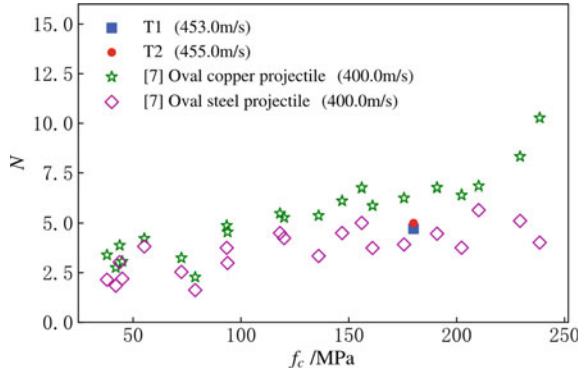
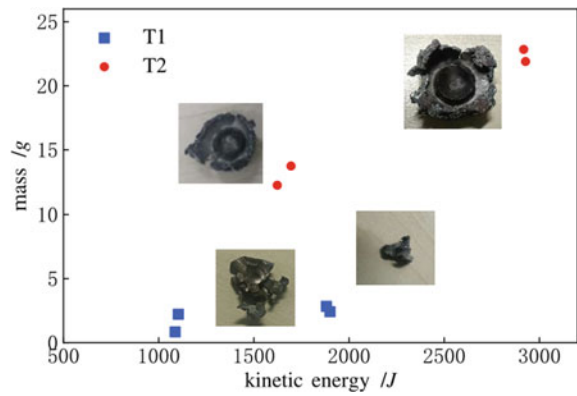


Fig. 66.13 Mass of spalled-rock particles and projectiles kinetic energy



66.4 Conclusion

Based on the background of crushed rock sampling of asteroid detector, two deformable special-shaped projectiles: petal-penetrating type (T1), petal-non-penetrating type (T2), and high-speed (453.0–612.0 m/s) impact experiments were designed to study the projectile-target interaction and rock fracture mechanisms, the conclusions are as follows:

- (1) Deformation of the Special-Shaped Projectile is related to the plasticity of material and projectile configuration. Projectile deformation mode is ‘bowl-like structure’, owing to the torn of projectile head and radial expansion of the projectile cylinder section.
- (2) In high-speed impact, the projectile-target interaction of the petal projectile is a two-phase process. The first phase is a multi-point simultaneous impact, and the second is a Taylor impact, which increases the diameter of the crushing zone and the mass of spalled-rock particles.

- (3) The two-phase impact inspired researchers to create the projectile's head and cylinder section from different properties of materials respectively, which could be the following design and research focus points.

References

1. Sawada, H., Okazaki, R., Tachibana, S., et al.: Hayabusa2 sampler: collection of asteroidal surface material. *Space Sci. Rev.* **208**(1–4), 81–106 (2017)
2. Máca, P., Sovják, R., Konvalinka, P.: Mix design of UHPFRC and its response to projectile impact. *Int. J. Impact Eng.* **63**, 158–163 (2014)
3. Zhang, F., Poh, L.H., Zhang, M.: Resistance of cement-based materials against high-velocity small caliber deformable projectile impact. *Int. J. Impact Eng.* **144**, 103629 (2020)
4. Peng, J.X., et al.: Experiments on dynamic constitutive relations of tantalum. *Explosion and Shock Waves*, pp. 183–187 (2003)
5. Xiao, X., Zhang, W., Wei, G., et al.: Effect of projectile hardness on deformation and fracture behavior in the Taylor impact test. *Mater. Des.* **31**(10), 4913–4920 (2010)
6. Simons, E.C., Weerheijm, J., Toussaint, G., et al.: An experimental and numerical investigation of sphere impact on alumina ceramic. *Int. J. Impact Eng.* **145**, 103670 (2020)
7. Zhang, F., Poh, L.H., Zhang, M.: Resistance of cement-based materials against high-velocity small caliber deformable projectile impact. *Int. J. Impact Eng.* **145**, 103670 (2020)

Chapter 67

Research on the THMC Coupling Model for Enhanced Geothermal Systems Based on the Framework of EDFM



Weitao Zhang, Dongxu Han, Kaituo Jiao, Yujie Chen, Qing Yuan, Liang Gong, and Bo Yu

Abstract The Enhanced Geothermal System (EGS) involves a complex thermo-hydro-mechanical-chemical (THMC) coupling process during long-term heat extraction. However, many models used to solve fractured reservoir problems are computationally time-consuming, especially when dealing with reservoir-scale engineering problems. To address this challenge, this paper proposes a novel THMC coupling model that solves the governing equations using a unified FVM framework based on the embedded discrete fracture model (EDFM). The accuracy of the model is confirmed by comparing the THMC coupling and displacement (M) results with the Fully Resolved Solution Method (FRSM) from MRST software and COMSOL, respectively. Moreover, the model developed is utilized to simulate and analyze the spatiotemporal behavior of pressure, temperature, concentration, and mechanical deformation in EGS. The results suggest that the model is appropriate for effectively assessing the long-term production performance of EGS.

Keywords Enhanced geothermal system · Embedded discrete fracture model · Extended finite volume method · THMC coupling model · Simulation calculation

W. Zhang · L. Gong (✉)

College of New Energy, China University of Petroleum (East China), Qingdao 266580, P.R. China
e-mail: lgong@upc.edu.cn

D. Han (✉) · Y. Chen · B. Yu

Beijing Key Laboratory of Pipeline Critical Technology and Equipment for Deepwater Oil and Gas Development, School of Mechanical Engineering, Beijing Institute of Petrochemical Technology, Beijing 102617, P.R. China
e-mail: handongxubox@bipt.edu.cn

K. Jiao · Q. Yuan

State Key Laboratory of Multiphase Flow in Power Engineering, School of Chemical Engineering and Technology, Xi'an Jiaotong University, Xi'an 710049, P.R. China

67.1 Introduction

Geothermal energy is regarded as a renewable and environmentally friendly energy source that holds enormous potential in meeting worldwide energy requirements while also lowering greenhouse gas emissions [1]. Geothermal energy resources can be categorized into three types based on their applications: shallow geothermal resources, hydrothermal resources, and hot dry rock (HDR) resources [2]. It is estimated that there are over 25×10^{24} J of geothermal reserves in China, and the majority of geothermal resources are found and stored in HDR [3]. However, exploiting HDR resources is challenging because they are primarily located in crystalline basement rocks, which are naturally dry and impermeable at depths of 3–10 km.

The Enhanced Geothermal System (EGS), also known as engineered HDR, has been developed to extract heat from HDR by using hydraulic stimulation to improve formation permeability [4]. Due to the presence of artificial fractures and matrix in EGS, various physical and chemical processes occur in the reservoir during fluid injection and heat extraction [5]. These changes largely depend on the operating conditions and the interaction and coupling of heat transfer (T), fluid flow (H), stress/deformation (M), and geochemical reaction (C) processes in the fractured reservoir. Therefore, a complex THMC coupling process exists for EGS during the long-term heat extraction process. A thorough understanding of these coupled THMC processes is essential for the exploitation of geothermal energy resources.

To date, numerical modeling has become an effective tool for predicting and understanding the THMC coupling process for EGS. Various numerical solvers have been developed to study the multi-physical coupling process for EGS [6]. When dealing with discontinuity problems in fractured reservoirs, many solvers primarily rely on traditional finite element methods that incorporate enriched basis functions, such as the extended finite element method (XFEM), which can be computationally expensive. Deb and Jenny [7] proposed an extended finite volume method (XFVM) for resolving the flow and mechanical failure in fractured reservoirs to address this issue. This method utilizes a discontinuity function for each fracture segment to capture irreversible slip and the stress distribution near the fractures. Li [8] demonstrated that the XFVM is more efficient than the XFEM for deformation simulation in terms of CPU time.

In addition, it is crucial to develop a fast and accurate computational model to characterize fractured reservoirs. Generally, researchers use simplified methods to characterize fractures, including four commonly used fracture models: the equivalent continuous model (ECM), the dual-continuum model (DCM), the discrete fracture model (DFM), and the embedded discrete fracture model (EDFM) [9]. Among these models, EDFM is a better choice for characterizing fractures due to its combination of accuracy and computational efficiency. EDFM uses non-conforming grids to discretize the matrix and fracture system, with the matrix being gridded regardless of the fracture geometry, and fractures being treated as line sources or sink with grids embedded within the matrix grid [10, 11]. This approach is suitable for efficiently evaluating long-term reservoir performance with fracture uncertainties, making it a

highly attractive option [12]. Over the past decade, several numerical methods based on EDFM have been developed to simulate various processes in fractured reservoirs, including fluid migration, heat transfer, solute transport, and rock geomechanics. However, there are limited modeling studies of the THMC coupling process for EGS based on the EDFM and XFVM frameworks.

In this study, we establish and validate a new THMC-coupled model based on the EDFM. This model meshes the rock matrix and fractures separately using two independent structured grids and solves the governing equations within a unified FVM framework, significantly reducing the gridding complexity and greatly improving the computational efficiency. Using this model, we investigate the spatiotemporal evolution of pressure, temperature, concentration, and mechanical deformation in EGS reservoirs. The paper is structured as follows: Sect. 67.2 introduces the mathematical models, followed by the model solution methods in Sect. 67.3. Then, the validation of the model is described in Sect. 67.4, and the application of the model is presented in Sect. 67.5. Lastly, some final remarks are provided in Sect. 67.6.

67.2 Governing Equation

67.2.1 Equations of Fluid Flow

The fluid in the matrix and fractures is assumed to be single-phase and weakly compressible, and its flow is governed by the mass conservation law and Darcy’s law. Based on the EDFM, the mass conservation equation for fluid in the matrix is given [13]

$$\rho_f \phi^m c_t \frac{\partial p^m}{\partial t} - \nabla \cdot \left(\rho_f \frac{\mathbf{k}^m}{\mu_f} \cdot \nabla p^m \right) = \sum_i \rho_f Q^{m-fri} + \rho_f Q_w^m \tag{67.1}$$

and the mass conservation equation for fluid in the *i*th fracture is

$$\rho_f \phi^{fri} c_t \frac{\partial p^{fri}}{\partial t} - \nabla \cdot \left(\rho_f \frac{\mathbf{k}^{fr}}{\mu_f} \cdot \nabla p^{fr} \right) = \rho_f Q^{fri-m} + \sum_j \rho_f Q^{fri-frj} + \rho_f Q_w^{fri} \tag{67.2}$$

where the superscripts *m* and *fr* represent the matrix and fractures, respectively; ρ_f is the fluid density; ϕ is the porosity; c_t is the total compressibility coefficient of rock and fluid; p is the pore fluid pressure; t is time; \mathbf{k} is the permeability tensor; μ_f is the fluid dynamic viscosity; and Q represents the terms indicating the mass flux transfer from fracture to the matrix (superscript *m-fri*), matrix to fracture (superscript *fri-m*), from the *j*th fracture to the *i*th fracture (superscript *fri-frj*), from well to matrix (superscript *m* and subscript *w*), and from well to fracture (superscript *fri* and subscript *w*).

67.2.2 Equations of Heat Transfer

Similarly, two sets of energy equations are established based on the EDFM to describe heat transfer in the matrix and the fractures, respectively. The energy equation for the matrix can be expressed as

$$(\rho c_p)_{eff} \frac{\partial T^m}{\partial t} + \nabla \cdot (\rho_f c_{pf} \mathbf{v}^m T^m) = \nabla \cdot (\lambda_{eff}^m \nabla T^m) + \sum_i E^{m-fri} + E_w^m \quad (67.3)$$

and the energy equation for the *i*th fracture is

$$\begin{aligned} (\rho c_p)_{eff} \frac{\partial T^{fri}}{\partial t} + \nabla \cdot (\rho_f c_{pf} \mathbf{v}^{fri} T^{fri}) &= \nabla \cdot (\lambda_{eff}^{fri} \nabla T^{fri}) + E^{fri-m} \\ &+ \sum_j E^{fri-fri} + E_w^{fri} \end{aligned} \quad (67.4)$$

where *T* is the temperature in the matrix and fracture; $(\rho c_p)_{eff}$ is the effective physical parameter; c_{pf} is the heat capacity of the fluid; \mathbf{v} is the Darcy fluid velocity; λ_{eff} is the effective thermal conductivity; and *E* represents the terms indicating the energy carried by the fluid from the fracture to the matrix (superscript *m-fri*), from the matrix to the fracture (superscript *fri-m*), from one fracture to another fracture (superscript *fri-fri*), from the well to the matrix (superscript *m* and subscript *w*), and from the well to the fracture (superscript *fri* and subscript *w*).

67.2.3 Equations of Solute Transportation

The transportation of solute in the aqueous phase involves reactant diffusion and convection processes. Fick’s law is used to describe solute diffusion and assumes that reactive solutes are in chemical equilibrium with the minerals of the host rock matrix. The solute transport equations for the matrix and the *i*th fracture are given

$$\frac{\partial (\phi^m C^m)}{\partial t} + \nabla \cdot (\mathbf{v}^m C^m) = \nabla \cdot (\phi^m D^m \nabla C^m) + \sum_i \psi^{m-fri} + M_w^m + Q_r^m \quad (67.5)$$

and

$$\begin{aligned} \frac{\partial (\phi^{fri} C^{fri})}{\partial t} + \nabla \cdot (\mathbf{v}^{fri} C^{fri}) &= \nabla \cdot (\phi^{fri} D^{fri} \nabla C^{fri}) + \psi^{fri-m} + \sum_j \psi^{fri-fri} \\ &+ M_w^{fri} + Q_r^{fri} \end{aligned} \quad (67.6)$$

where *C* is the mineral concentration; *D* is the dispersion coefficient; ψ represents the terms indicating the mineral concentration transfer from fracture to the matrix (superscript *m-fri*), from matrix to fracture (superscript *fri-m*), and one fracture to

another fracture (superscript *fri-fri*); *M* represents the terms indicating the mineral concentration transfer from the well to the matrix (superscript *m* and subscript *w*), and from the well to the fracture (superscript *fri* and subscript *w*); *Q_r* is the source term of reaction rate with $Q_r = \phi r_n \rho_s$; *r_n* is the kinetic mineral dissolution/precipitation, as described by the work of Xu [14].

67.2.4 Equations of Mechanical Equilibrium

The fracture network is modeled as a poroelastic medium, which is characterized by a maximum shear strength that the fractures can bear. The linear momentum balance equation in the porous matrix under quasi-static equilibrium is given [15]

$$\nabla \cdot \boldsymbol{\sigma} + \mathbf{f} = 0 \tag{67.7}$$

where $\boldsymbol{\sigma}$ is the total stress tensor, $\boldsymbol{\sigma} = \tilde{\boldsymbol{\sigma}} - a p \tilde{\mathbf{I}} - \beta_T \theta \tilde{\mathbf{I}}$; $\tilde{\boldsymbol{\sigma}}$ is the effective stress tensor; *p* is the local fluid pressure; θ represents temperature change, $\theta = T - T_0$, *T₀* is the reference temperature; *a*, β_T and $\tilde{\mathbf{I}}$ respectively denote the Biot coefficient, thermal expansion factor, and identity tensor; \mathbf{f} is the body force due to gravity. The effective stress $\tilde{\boldsymbol{\sigma}}$ is obtained as

$$\tilde{\boldsymbol{\sigma}} = \lambda (\nabla \cdot \mathbf{u}) \tilde{\mathbf{I}} + G (\nabla \mathbf{u} + \nabla \mathbf{u}^T) \tag{67.8}$$

where λ and *G* are respectively the first lamé constant and the second lamé constant, or shear modulus; \mathbf{u} is the displacement vector, $\mathbf{u} = \{u_x, u_y\}$.

The tensile and shear stress values on the fracture surface are given [7]

$$\boldsymbol{\sigma}_c = -\mathbf{n} \cdot (\tilde{\boldsymbol{\sigma}} \cdot \mathbf{n}) \tag{67.9}$$

and

$$\boldsymbol{\tau} = (\tilde{\mathbf{I}} - \mathbf{nn}) \cdot (\tilde{\boldsymbol{\sigma}} \cdot \mathbf{n}) \tag{67.10}$$

respectively. Here, $\boldsymbol{\sigma}_c$ and $\boldsymbol{\tau}$ are defined concerning the local coordinate axes normal and parallel to the fractures manifold. The unit normal vector to the fracture surface, $\mathbf{n} = \{n_x, n_y\}$.

67.3 Numerical Methods

The coupled computational framework is divided into four parts: hydraulic, thermal, chemical, and mechanical (Fig. 67.1). The coupling between these parts is implemented using a sequential one-way coupled approach. At each time step, the fluid mass conservation equations are first solved to obtain the pressure field of the matrix and fractures. Followed closely after this process is the calculation of the velocity field based on Darcy's law. Then, the temperature field is solved based on the velocity field solution. Next, the reactive solute transport is solved, and the reservoir porosity and permeability, as well as other parameters such as fluid density and viscosity, are updated. This process is repeated iteratively within an inner loop within each time step until the solutions for pressure, temperature, ion concentration, and displacement converged under the given convergence conditions. After that, the mechanical equilibrium equation is solved to obtain the displacement field of the matrix and fractures depending on the variation of pressure and temperature. Finally, when the solution time is reached, data for each variable (\mathbf{p} , T , C , and \mathbf{u}) is output.

The THMC coupling solution process described above is based on the EDFM framework. Equations of fluid flow, heat transfer, and solute transportation are discretized by the classical cell-centered finite volume method (FVM), which can ensure conservation in numerical methods to a large extent. For the mechanical equations, XFVM is employed to discretize the equations. Based on this approach, the displacement solution throughout the solved domain is represented as follows

$$\mathbf{u} \approx \sum_{i=1}^{n_e} \mathbf{u}_i N_i(\mathbf{x}) + \sum_{j=1}^{n_s} (\mathbf{s}_j^n + \mathbf{s}_j^t) N^j(\mathbf{x}) \quad (67.11)$$

where \mathbf{u}_i is the displacement vector at each finite volume node; N_i is the bilinear basis function corresponding to the node; \mathbf{s}^n and \mathbf{s}^t respectively represent the normal and shear displacement vectors on the fracture surface; N^j is the discontinuous basis functions corresponding to each fracture segment; n_e and n_s is the numbers of matrix nodes and fracture segments, respectively. The details of the discretization form for the mechanical equations refer to Deb [16].

67.4 Model Verification

In this section, two cases are presented to verify the proposed model and in-house code. The first case is a THC coupling problem, which is used to demonstrate the efficiency of the THC coupling method within a fractured reservoir based on EDFM. The second case for deformation in the same geometrical is to validate the XFVM code.

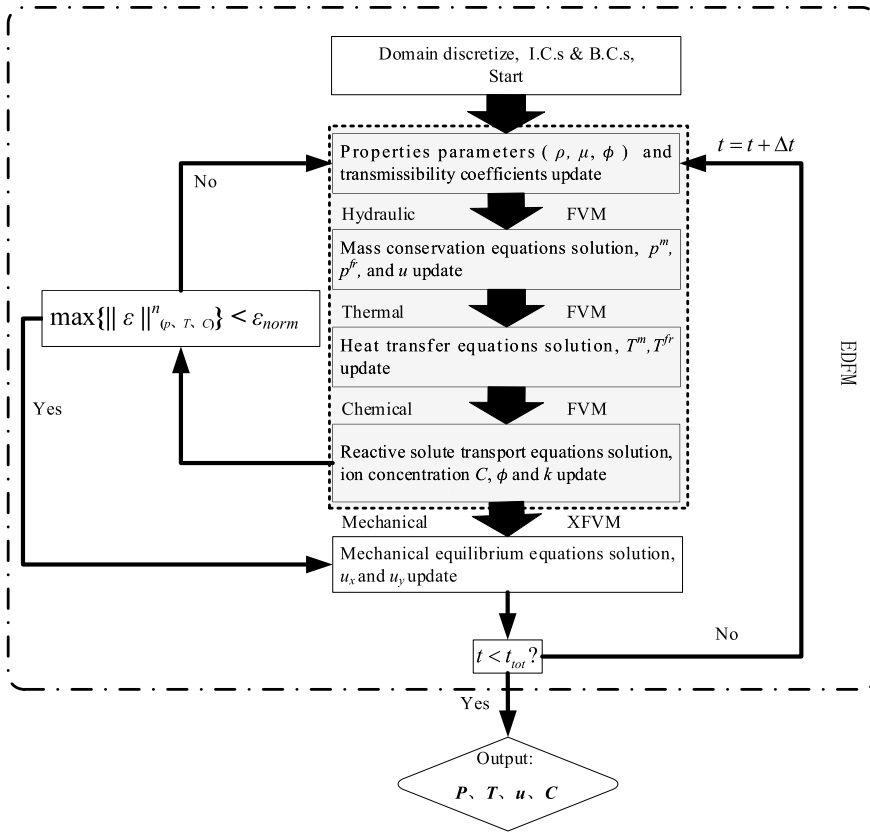


Fig. 67.1 Computational procedure of the proposed THMC coupling model

67.4.1 Verification of THC Coupling Method

The THM coupling model has already been validated in our previous work [9], and will not be repeated here. Solute transportation and kinetic reaction are significantly influenced by variations in fluid seepage velocity and temperature. Therefore, the solutions of pressure, temperature, and concentration field achieved through the THC coupling method are compared to those obtained using the Fully Resolved Solution Method (FRSM) in open-source software MRST, which resolves on a fine-scale grid [17].

Figure 67.2a shows a 2D square domain of a porous medium with a slanted fracture. The results of computational domain meshing based on the EDFM are shown in Fig. 67.2b, with grid numbers of 10,201 and 47 for the matrix and fracture, respectively. The results of the computational domain meshed by the FRSM are shown in Fig. 67.2c, with a total number of grids in the computational of 62,500.

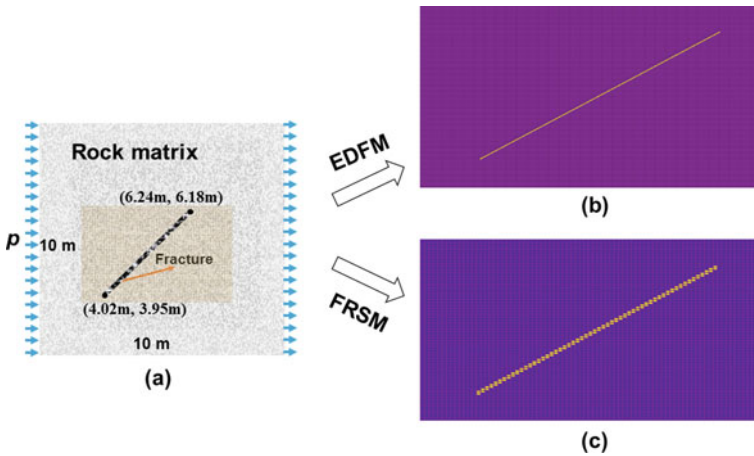


Fig. 67.2 Schematic of the mesh used for the EDFM and FRSM: **a** the computational domain; **b** the meshes of the rock matrix and the fracture generated by EDFM; **c** the meshes of the rock matrix and the fracture generated by FRSM

The initial pressure is 0.1×10^6 Pa, and the pressures at the left and right boundaries are 1.5×10^6 Pa and 0.1×10^6 Pa, respectively. Impermeable boundary conditions are applied at the top and bottom boundaries. The initial temperature is $180 \text{ }^\circ\text{C}$, and the injection temperature at the left boundary is $20 \text{ }^\circ\text{C}$, while the remaining boundaries are adiabatic. The initial concentration is 3.8 mol/m^3 , and the injection concentration at the left boundary is zero, with zero concentration gradient in the remaining boundaries. Other model parameters are given in Table 67.1. The time step is 0.1 day, and the evolutions of the pressure, temperature, and concentration fields over 365 days are shown in Fig. 67.3. The results obtained based on EDFM and FRSM are in good agreement, but the computation time of EDFM (122 s) is much shorter than that of FRSM (721 s), resulting in a computation rate ratio of 1:5.9. This comparison demonstrates the accuracy and efficiency of the proposed model.

67.4.2 Verification of XFVM

To verify the accuracy of XFVM implementation, the numerical results of the displacement field obtained by XFVM are compared with those obtained by XFEM and commercial software (COMSOL), which uses a standard FEM solver. The calculation domain and boundary conditions are shown in Fig. 67.4, with the same geometric dimensions as in Case 1. The top boundary of the domain is subjected to a tensile stress of $\sigma = 1.0 \times 10^6$ Pa, while the bottom side has fixed boundary conditions in the x and y-directions, and the right and left sides have freedom boundary conditions. The mechanical parameters used are as follows: Young’s modulus $E = 5.0 \times 10^{10}$ Pa, and Poisson’s ratio $\nu = 0.3$.

Table 67.1 Parameters of the slanted fractured reservoir

Model parameters	Values	Units
Matrix size	10×10	m
Fracture aperture	0.04	m
Permeability of matrix and fracture	1.0×10^{-16} , 1.0×10^{-11}	m^2
The porosity of the matrix and fracture	0.2, 0.3	–
Fluid viscosity	1.0×10^{-3}	Pa s
The density of rock and fluid	2623, 1000	kg/m^3
Heat conductivity of rock and fluid	2.0, 0.5	W/(m K)
Heat capacity of rock and fluid	1000, 4000	J/(kg K)
Diffusion coefficient	1.0×10^{-9}	m^2/s

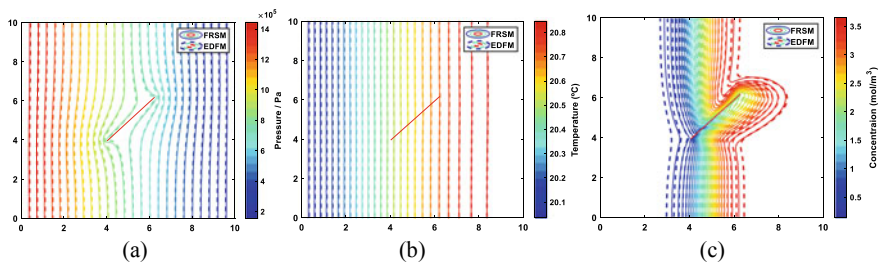


Fig. 67.3 Comparison of the results obtained using EDFM and FRSM: **a** pressure field; **b** temperature field; **c** concentration field

Figure 67.5 shows the displacement fields results in the x and y-directions calculated by XFVM, XFEM, and COMSOL, respectively. The results obtained by XFVM are in good agreement with those obtained by XFEM and COMSOL. To quantify the difference between the methods, we define the Maximum Relative Error (MRE) as $\varepsilon = \max\{|(U_{ref} - U)/U_{ref}|\}$, where U_{ref} represents the displacements determined by XFEM and COMSOL, and U denotes the displacements determined by XFVM. The MRE of the y-direction displacement on line A (Fig. 67.4) between XFVM and XFEM is 5.85%, while the MRE between XFVM and COMSOL is 5.95% (Table 67.2).

67.5 Application and Result

Heat extraction from an EGS is accompanied by a complex THMC coupling process. To fully understand the long-term productivity performance of an EGS reservoir, the proposed model has been applied to simulate and analyze the spatiotemporal behavior under the THMC coupling process during heat extraction.

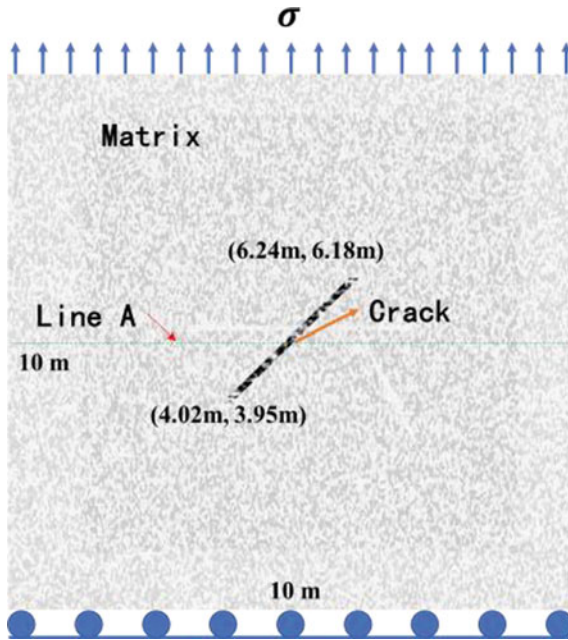


Fig. 67.4 Geometry and boundary conditions of a porous medium containing a slanted fracture

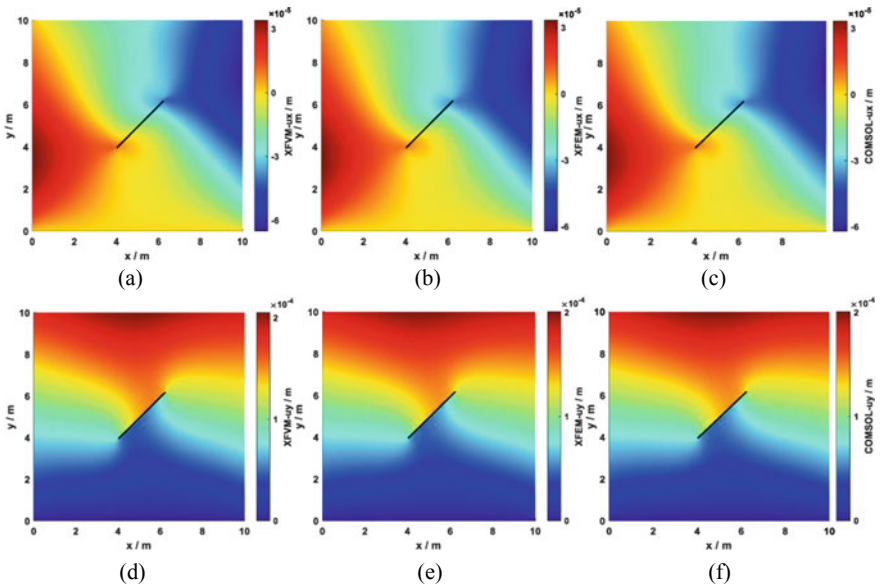


Fig. 67.5 Comparison of displacement fields between XFVM, XFEM, and COMSOL: a–e is the displacement field in the x-direction; d–f is the displacement field in the y-direction

Table 67.2 The MRE for the displacement field in the y-direction on line A

MRE	XFEM	COMSOL
XFVM	5.85%	5.95%

67.5.1 Computational Model

The simulation cases presented in this section aim to demonstrate the feasibility of the proposed model and method. The quartz dissolution/precipitation chemical equivalent formula refers to the work by Tester [18], the rate constant and activity product of quartz are taken from the literature [19]. Figure 67.6a shows a 2D simplified model of an EGS reservoir, which contains 29 fractures embedded in the rock matrix. The injection and production wells are presented by a green and a red point, respectively, with both having a diameter of 0.1 m. Two independent grid systems are used to discretize the matrix and fractures, resulting in a total of 24,731 grids. The matrix is composed of 22,801 structured grids, while the 38 fractures are composed of 1595 grids (Fig. 67.6b).

The initial and boundary conditions are specified as follows. Firstly, the initial values of pressure, temperature, concentration, and displacement are set to 5.0×10^6 Pa, 236 °C, 7.01 mol/m³, and 0 m, respectively. The quartz volume in the reservoir is assumed to account for 66% of the total mineral volume. Secondly, the domain is enclosed by impermeable, adiabatic, and fixed boundary conditions, with zero concentration gradients around the domains. The pressure and temperature of the injection well are set to 15.5×10^6 Pa and 60 °C, respectively, while the pressure of the production well is 4.77×10^6 Pa. The remaining computational parameters for the EGS reservoir are referred to as the Qiabuqia geothermal field [20] and are listed in Table 67.3.

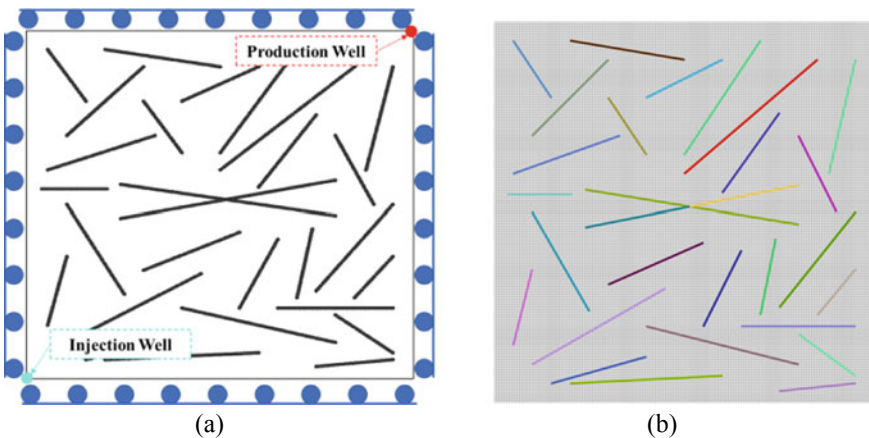


Fig. 67.6 a Schematic of the EGS heat extract model; b the EDFM mesh

Table 67.3 Model parameters for the EGS reservoir

Model parameters	Values	Units
Matrix size	100 × 100	m ²
Fracture aperture	0.001	m
Fracture permeability	1.0 × 10 ⁻¹¹	m ²
Fracture porosity	0.8	–
Fluid viscosity	1.0 × 10 ⁻³	Pa s
The density of rock and fluid	2623, 1000	kg/m ³
Heat conductivity of rock and fluid	3.0, 0.5	W/(m K)
Heat capacity of rock and fluid	980, 4000	J/(kg K)
Poisson's ratio	0.3	–
Young's modulus	5.0 × 10 ¹⁰	Pa
Fluid compressibility	4.4 × 10 ⁻¹⁰	1/Pa
Biot's coefficient	1.0	–
Linear thermal expansion coefficient	5.0 × 10 ⁻⁶	1/K
Diffusion coefficient	1.0 × 10 ⁻⁹	m ² /s

In a fractured reservoir, porosity and permeability are always inhomogeneous. To make the simulation more representative of actual conditions, we employed the Carman-Kozeny empirical formula to generate an inhomogeneous distribution of porosity and permeability [21]. Water density and viscosity variations with temperature and pressure were calculated using the methodology described in Spivey [22].

67.5.2 Computational Model

Figure 67.7 shows the evolution of pressure, temperature, concentration, and displacement in the fractured reservoir over 30 years. It can be observed that the pressure distribution remains inhomogeneous throughout the life of heat production in the EGS (Fig. 67.7a). This is because the fractures are more permeable than the rock matrix, providing the main channel for fluid flow and causing the seepage velocity in fractures to be greater than in the rock matrix, leading to rapid pressure changes. This phenomenon further confirms that fractures are the main fluid pathway in the EGS. In addition, the pressure near the injection well increases distinctly relative to other regions during the first 5 years of heat production. The reason for this is that the low-temperature zone around the injection well is expanding, causing the viscosity of the water to increase and flow impedance to rise.

Heat production in this case can be divided into two stages based on the variation of production temperature: the stable stage during the first 5 years and the declining stage for the following 25 years. Figure 67.7b shows the production temperature

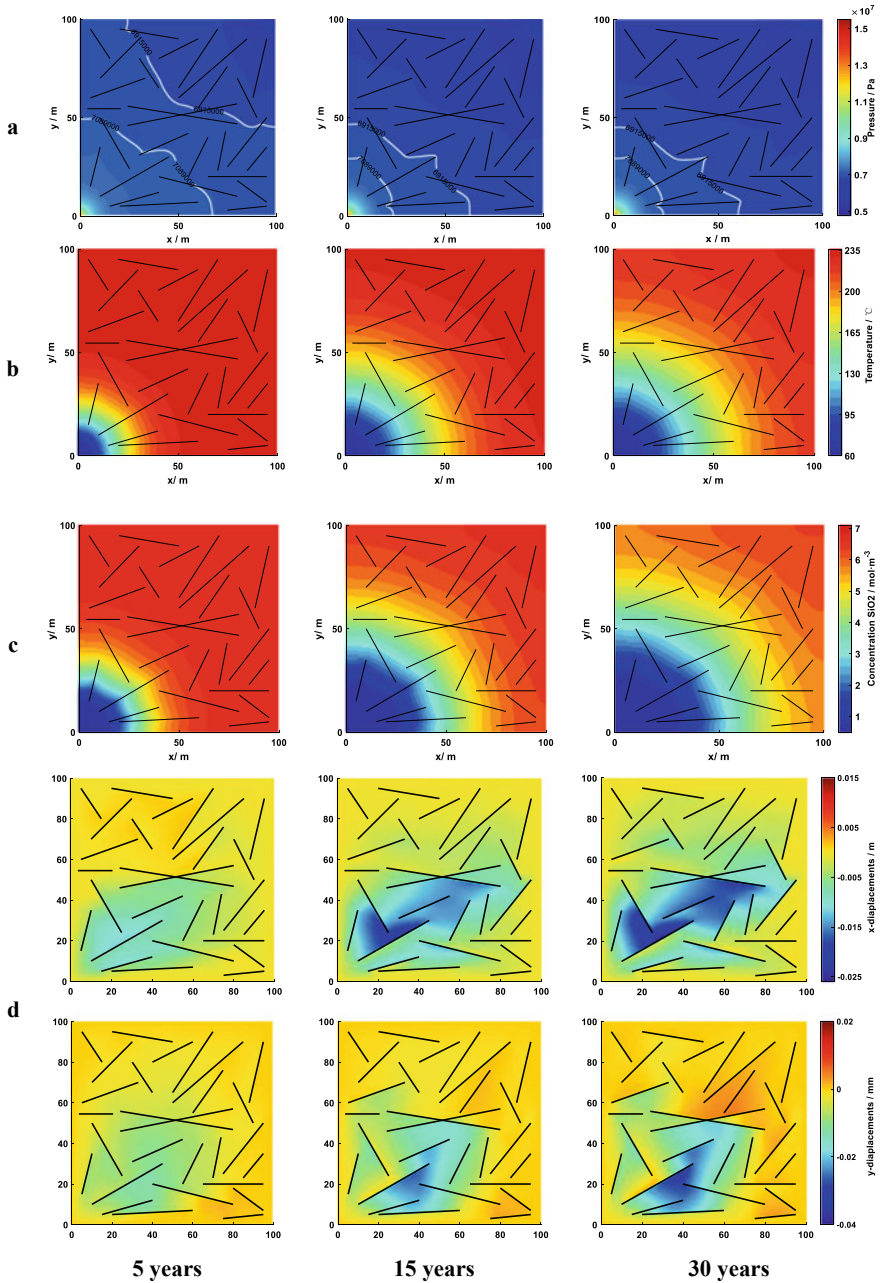


Fig. 67.7 Evolutions of the distribution of **a** pressure, **b** temperature, **c** concentration, and **d** displacement for different years of heat extraction in the EGS reservoir

remains almost constant at 235 °C during the stable stage. This is because the low-temperature zone surrounding the injection wells expands slowly and the temperature drop in most of the rock matrix near the production well is small. During the declining stage, the production temperature starts to significantly decrease when the cooling front expands to the production well. The concentration field evolution shows similar behavior to the temperature field (Fig. 67.7c). However, the concentration changes more noticeably near the fractures. This is because the fractures have higher conductivity than the surrounding rock matrix, and the diffusion coefficient has the same order of magnitude as the fracture permeability.

Figure 67.7d presents the spatial distributions of displacement fields in the x and y directions. The displacement fields in the x- and y-directions mainly occur near the area of fractures. This deformation is mainly caused by changes in fluid pressure, temperature, and chemical dissolution after the long-term cold-water injection. The seepage pressure can decrease the effective stress, leading to changes in the normal tension of the fractures. With the continuous injection of low-temperature water, the rock matrix contracts, and the displacement field redistributes. The thermal stress changes can further open the fracture. During the declining stage, the pressure distribution tends to stabilize, the displacement field is primarily affected by thermal stress. Based on the numerical results, thermal stress from evolving temperatures, particularly around injection wells and fractures, can lead to significant displacement in EGS reservoirs during long-term cold-water injection.

67.6 Conclusion

- (1) A new coupled THMC numerical model is presented based on the EDFM. In this model, the fluid flow, heat transfer, water–rock reaction, and solute transport are solved using the FVM. The XFVM method is employed to characterize the discontinuities of the fractures in the rock matrix and solve the mechanical model. This model is suitable for efficiently evaluating the long-term production performance of EGS within a unified FVM calculation framework.
- (2) The accuracy of the proposed model was verified by comparing the results of THC coupling and displacement (M) with those obtained from FRSM in MRST software and COMSOL, respectively. The results are in good agreement obtained using EDFM and FRSM, but EDFM is more efficient with a computation time ratio of 1:5.9. The displacement solutions obtained using XFVM are almost identical to those provided by XFEM and COMSOL. The MRE of the displacement field in the y-direction between XFVM and XFEM is 5.85%, and between XFVM and COMSOL is 5.95%.
- (3) The proposed model was employed to investigate the THMC evolution of heat production in EGS reservoirs. The results are as follows: (a) as the main channel for fluid flow, fractures make the pressure, temperature, concentration, and deformation variation distinctly near the surrounding areas in the EGS reservoir. (b) While pressure fluctuations in the reservoir have a short-term effect on

displacement changes, the most significant and long-term effect is caused by thermal effects. (c) Regions with high temperature and pressure gradients, such as injection well and fracture surroundings, are more prone to generate large deformation during long-term cold-water injection.

Acknowledgements This work is supported by the National Natural Science Foundation of China (No. 51936001), the Scientific Research Project of Beijing Educational Committee (KZ202110017026), the Beijing Science and Technology Plan (Z221100002722005), and the fund of the Beijing Municipal Education Commission, China (22019821001).

References

1. Vargas, C.A., Caracciolo, L., Ball, P.J.: Geothermal energy as a means to decarbonize the energy mix of megacities. *Commun. Earth Environ.* **3**(1), 66 (2022)
2. Hu, Y., Cheng, H., Tao, S.: Opportunity and challenges in large-scale geothermal energy exploitation in China. *Crit. Rev. Environ. Sci. Technol.* **52**(21), 3813–3834 (2022)
3. Song, G., Song, X., Xu, F., Li, G., Wang, G., Ji, J., Shi, Y.: Numerical parametric investigation of thermal extraction from the enhanced geothermal system based on the thermal-hydraulic-chemical coupling model. *J. Clean. Prod.* **352**, 131609 (2022)
4. McClure, M.W.: Stimulation mechanism and the direction of propagation of microseismicity. In: *Proceedings, Thirty-Ninth Workshop on Geothermal Reservoir Engineering*, Stanford University (2014)
5. Pandey, S.N., Vishal, V., Chaudhuri, A.: Geothermal reservoir modeling in a coupled thermo-hydro-mechanical-chemical approach: a review. *Earth-Sci. Rev.* **185**, 1157–1169 (2018)
6. White, M., Fu, P., McClure, M., Danko, G., Elsworth, D., Sonnenthal, E., Kelkar, S., Podgorney, R.: A suite of benchmark and challenge problems for enhanced geothermal systems. *Geomech. Geophys. Geo-Energy Geo-Resour.* **4**(1), 79–117 (2018)
7. Deb, R., Jenny, P.: Modeling of shear failure in fractured reservoirs with a porous matrix. *Comput. Geosci.* **21**(5), 1119–1134 (2017)
8. Li, T., Han, D., Yang, F., Yu, B., Sun, D., Wei, J.: A comparative study on simulating flow-induced fracture deformation in subsurface media by means of extended FEM and FVM. *Oil Gas Sci. Technol. Revue d'IFP Energies Nouvelles* **75**, 41 (2020)
9. Li, T., Han, D., Yang, F., Li, J., Wang, D., Yu, B., Wei, J.: Modeling study of the thermal-hydraulic-mechanical coupling process for EGS based on the framework of EDFM and XFEM. *Geothermics* **89**, 101953 (2021)
10. Lee, S.H., Lough, M.F., Jensen, C.L.: Hierarchical modeling of flow in naturally fractured formations with multiple length scales. *Water Resour. Res.* **37**(3), 443–455 (2001)
11. Li, L., Lee, S.H.: Efficient field-scale simulation of black oil in a naturally fractured reservoir through discrete fracture networks and homogenized media. *SPE Reserv. Eval. Eng.* **11**(4), 750–758 (2008)
12. Sepehrnoori, K., Xu, Y., Yu, W.: *Embedded Discrete Fracture Modeling and Application in Reservoir Simulation*. Elsevier, Netherlands (2020)
13. Tran, M., Jha, B.: Effect of poroelastic coupling and fracture dynamics on solute transport and geomechanical stability. *Water Resour. Res.* **57**(10), e2021WR029584 (2021)
14. Xu, T., Pruess, K.: *Numerical Simulation of Injectivity Effects of Mineral Scaling and Clay Swelling in a Fractured Geothermal Reservoir* (No. LBNL-55113). Lawrence Berkeley National Lab. (LBNL), Berkeley, CA, US (2004)
15. Aliyu, M.D., Archer, R.A.: Numerical simulation of multifracture HDR geothermal reservoirs. *Renew. Energy* **164**, 541–555 (2021)

16. Deb, R. (2018). Numerical modeling of fluid injection induced shear failure, tensile opening and flow-mechanics coupling. Doctoral dissertation, ETH Zurich.
17. Lie, K.A.: An Introduction to Reservoir Simulation Using MATLAB/GNU Octave: User Guide for the MATLAB Reservoir Simulation Toolbox (MRST). Cambridge University Press, New York, US (2019)
18. Tester, J.W., Worley, W.G., Robinson, B.A., Grigsby, C.O., Feerer, J.L.: Correlating quartz dissolution kinetics in pure water from 25 °C to 625 °C. *Geochim. Cosmochim. Acta* **58**(11), 2407–2420 (1994)
19. Palandri, J.L., Kharaka, Y.K.: A Compilation of Rate Parameters of Water-Mineral Interaction Kinetics for Application to Geochemical Modeling. Geological Survey, Menlo Park, CA, USA (2004)
20. Lei, Z., Zhang, Y., Zhang, S., Fu, L., Hu, Z., Yu, Z., Li, L., Zhou, J.: Electricity generation from a three-horizontal-well enhanced geothermal system in the Qiabuqia geothermal field, China: slickwater fracturing treatments for different reservoir scenarios. *Renew. Energy* **145**, 65–83 (2020)
21. Carman, P.C.: Fluid flow through granular beds. *Chem. Eng. Res. Des.* **15**, 155–166 (1997)
22. Spivey, J.P., McCain, W.D., North, R.: Estimating density, formation volume factor, compressibility, methane solubility, and viscosity for oilfield brines at temperatures from 0 to 275 °C, pressures to 200 MPa, and salinities to 5.7 mole/kg. *J. Can. Petrol. Technol.* **43**(07), 55–60 (2004)

Chapter 68

Synthetic Data: Development Status and Prospects for Military Applications



Jinhui Huang, Junsong Yin, Shuangshuang Wang, and Dezhao Kong

Abstract In the current booming big data boom, many fields still face the problem of data scarcity. Synthetic data, as a new technology in the field of big data, not only tries to retain the main features of the original data for analysis, but also tries to avoid containing information that may cause privacy leakage. Synthetic data provides a new solution for the problems of data security sharing and artificial intelligence training. This paper summarizes the main methods, performance evaluation indexes and application of synthetic data, looks forward to its military application prospect, and puts forward the preliminary idea of military application of synthetic data, which provides reference for the research in related fields.

Keywords Synthetic data · Machine learning · Data insufficiency · Data sharing · Data security · Data privacy preserving

68.1 Introduction

With the innovation breakthrough and integrated application of the new generation of information technologies such as big data, cloud computing, artificial intelligence and the Internet of Things, data is becoming an increasingly prominent strategic resource [1]. The big data industry has ushered in a new period of development opportunities. However, with the booming of big data, many fields are still faced with the problem of data scarcity. On the one hand, the current artificial intelligence is mainly based on

J. Huang (✉) · J. Yin · S. Wang · D. Kong
Academy of Military Science, Beijing 100091, China
e-mail: night098@sina.com

J. Yin
e-mail: yjsnuds@163.com

S. Wang
e-mail: wss2312@163.com

D. Kong
e-mail: kongoptics@126.com

data-driven machine learning, which often requires massive sample data. For areas where the cost of sample data collection and labeling is too high or where there is no sufficient sample data, the existing artificial intelligence methods are faced with great challenges. On the other hand, due to data security, privacy protection and other considerations, some organizations still have concerns about data sharing, which to some extent restricts making the most of existing data resources.

As an effective supplement to real data, synthetic data not only retains the main features of the original data for analysis, but also tries to avoid the information that may cause privacy disclosure, which has attracted more and more attention in recent years [2]. MIT Technology Review selected synthetic data for artificial intelligence as one of the world's top 10 breakthrough technologies in 2022 [3]. Gartner predicts that 60% of the data used for AI training and data analysis will be synthetic by 2024 [4]. Synthetic data provides a possible solution for efficient accumulation of data resources, effective protection of data security, promoting the wide application of big data and development of artificial intelligence.

In a broad sense, data synthesis methods include process-driven method and data-driven method [5]. Among them, the process-driven method builds the corresponding simulation model based on the principle of data generation, and then generates data through simulation operation. Agent-based simulation, discrete event simulation and Monte Carlo simulation all belong to this category. The data-driven method is to build a data generation model based on real data sets, and then generate data based on the model. Considering that there are a lot of special researches on modeling and simulation, and for many fields where data is scarce, it is usually quite difficult to accurately construct the simulation model of data generation process. It is a more feasible method to generate synthetic data based on some existing real data. Therefore, this paper will focus on data-driven synthetic data. Unless otherwise specified, synthetic data in this paper refer to data-driven synthetic data. This paper summarizes the research status of synthetic data from synthesis methods, performance evaluation, application field, and discusses its military application prospects.

68.2 Main Methods of Synthetic Data Generation

The concept of synthetic data was first proposed by Rubin in 1993, and all variables of the original data were interpolated to avoid information leakage [6]. In the same year, Little proposed that only sensitive variables in the original data should be changed to generate part of the synthetic data [7]. In 2003, Reiter further described the problem of data synthesis and proposed an analytical method for partial synthesis data sets. Due to the limitation of the technical conditions at that time, synthetic data was not widely used at the beginning. In recent years, the rapid development of artificial intelligence technology not only puts forward urgent demand for data synthesis, but also provides new methods for data synthesis. Under the traction of data sharing and privacy protection in related fields, a series of data synthesis methods are born. The representative ones are data synthesis methods based on Copula function, data

synthesis methods based on Bayesian network, data synthesis methods based on tree, data synthesis methods based on parameter machine learning, data synthesis methods based on generative adversarial network (GAN).

68.2.1 Data Synthesis Methods Based on Copula Function

The definition of Copula function was given by Nelsen in 1998, which is essentially a multivariate joint distribution function of random variables x_1, x_2, \dots, x_n with edge distributions of $F_{x_1}(x_1), F_{x_2}(x_2), \dots, F_{x_n}(x_n)$ [8]. Because Copula means connection and exchange, Copula function is also called connection function. Copula function can separate the correlation between random variables from the edge distribution of variables, which provides a new idea and method for solving the joint probability distribution of multiple random variables. Synthetic Data Vault (SDV) [9] developed by Patki in 2016 is a typical application of data synthesis method based on Copula function, which is suitable for data modeling and synthesis of relational databases. For each table composed of several rows and columns of data, its generation model consists of distribution (describing the probability distribution of each column of data) and covariance (describing how different columns interact with each other). Among them, for the probability distribution function, Kolmogorov–Smirnov test can be used to determine the distribution function suitable for the current data from a series of alternative functions such as truncated Gaussian distribution, normal distribution and exponential distribution. The covariance can be estimated by Gaussian Copula function. On this basis, a method called Conditional Parameter Aggregation (CPA) is used to analyze the interaction between different tables. For columns with blank values or non-numerical columns, pretreatment is needed first, and then the data generation model is constructed by the above method. Based on the data generation model, data rows can be generated recursively until the data synthesis of the whole database is completed [9]. The data synthesis method based on Copula function has strong interpretability and good applicability to different application scenarios, which is more suitable for the synthesis of tabular data. Toolkits such as SDV [9] and Synthia [10] can be used for data synthesis based on Copula function.

68.2.2 Data Synthesis Methods Based on Bayesian Network

Bayesian network was put forward by Judea Pearl in 1980s. It is a probability graph model which uses Bayesian inference to calculate probability, also called belief network or probabilistic causal network [11, 12]. Bayesian network consists of network structure and conditional probability table. The network structure of Bayesian network is a directed acyclic graph, in which nodes represent random variables and the edges between nodes represent the direct dependence between variables. Each element in the conditional probability table corresponds to a node in

the directed acyclic graph, and the joint conditional probability of this node for all its direct predecessor nodes is stored. Bayesian network combines probability theory, graph theory and decision theory, and can be used as a framework for knowledge representation and probabilistic reasoning. Kaur [13] and Bruera [14] adopt the data synthesis method based on Bayesian network. Firstly, the Bayesian network structure is learned based on existing data, then the relevant parameters of probability distribution function are learned based on existing data and Bayesian network structure, and finally synthetic data is produced based on Bayesian network. Toolkits such as Data synthesizer [15] can be used for data synthesis based on Bayesian networks.

68.2.3 Data Synthesis Methods Based on Tree-Based Machine Learning

Tree-based machine learning algorithm is a common method to solve the problem of supervised learning. When it is used in data synthesis, it can automatically find the characteristics of data and use it for prediction [16]. Classification and regression tree (CART) [17], Bagging [18], random forest [19] and other algorithms can be used for data synthesis. CART algorithm is a widely used decision tree learning method. Based on the training data set, it uses the minimum square error criterion for regression trees and the minimum Gini index criterion for classification trees to select features and recursively construct binary decision trees. Then, branches are continuously subtracted from the bottom of the generated decision tree to the root node to obtain a subtree sequence; Finally, the optimal subtree is selected from multiple subtree sequences by cross-validation method. Bagging algorithm and random forest algorithm both adopt random sampling, that is, after each sample is collected from the training set, the sample is put back so that it may still be collected. Bagging algorithm obtains multiple samples with the same number as the training set samples through multiple rounds of random collection, and constructs decision trees respectively. For classification problems, the category with the most votes in each decision tree is the final category, and for regression problems, the value obtained by arithmetic average of the regression results of each decision tree is the final model output. Random forest algorithm improves the decision tree on the basis of Bagging to further enhance the generalization ability of the model. Toolkits such as Synthpop (SP) [20] and SynGen [21] can be used for tree-based data synthesis.

68.2.4 Data Synthesis Methods Based on Parameter Machine Learning

With sufficient prior knowledge of data, parametric machine learning can be considered to solve the problem of data synthesis. You can assume the specific form of the

objective function or distribution to be learned, and then, through training the data set, based on the learning strategies such as maximum likelihood estimation, maximum posterior probability estimation, empirical risk minimization, structural risk minimization, etc., estimate the relevant parameters, and then generate the synthetic data. Parameter machine learning methods that can be used for data synthesis include linear regression and logical regression [22]. The advantage of data synthesis method based on parametric machine learning is that the speed of learning and training is fast, and less data is needed. However, the way of selecting function form for learning itself also limits the model, and it may be difficult to match the actual objective function in practice. Toolkits such as Synthpop (SP) [20] can be used for data synthesis based on parametric machine learning.

68.2.5 Data Synthesis Methods Based on GAN

GAN was proposed by Ian Goodfellow in 2014, which combines competing generator and discriminator models [23]. By learning the characteristics of the training set data, the generator tries to fit the random noise distribution into similar data with the characteristics of the training set under the guidance of the discriminator. The discriminator is responsible for distinguishing whether the input data is real data or false data generated by the generator and feeding it back to the generator. The two models train alternately in the zero-sum game, and their abilities improve synchronously until they become good enough in their specific tasks [24]. In the limit case, the output of the generator model is indistinguishable from the actual output, and the discriminator model converges to a neutral prediction result of about 0.5. In recent years, a series of data synthesis methods based on GAN, such as SGAN [25], PSGAN [26], TextureGAN [27], MGANs [28], ProGAN [29], BigGANs [30], StyleGAN [31] and ESRGAN+ [32], have been put forward one after another, and have been obtained in the fields of image synthesis. However, data synthesis based on GAN may still encounter a series of problems, such as mode collapse, gradient disappearance, and difficult model convergence, which need further research and solution [33]. ITS-GAN [34] and other toolkits [35] can be used for data synthesis based on GAN.

68.3 Performance Evaluation of Synthetic Data

When generating synthetic data, it is usually necessary to consider both data utility and information leakage risk [36]. The former describes the fidelity of the synthetic data set relative to the original data set, while the latter reflects the risk that the synthetic data will directly or indirectly reveal the original data [5]. The two are contradictory to some extent, and reducing the risk of information leakage often

means the decline of data utility at the same time. When synthesizing data, it is necessary to strike a balance between the two types of targets.

68.3.1 Data Utility

The data utility can be evaluated from the perspectives of general utility, special utility, stability and structural similarity.

General Utility. Universal utility is one of the most commonly used indicators for synthetic data evaluation. ‘Universal’ here means that it is not limited to a specific task, but pays attention to whether the statistical characteristics of the synthetic data set are similar to those of the original data set, which can be further measured from different dimensions such as univariate accuracy, bivariate accuracy and overall distribution accuracy [37]. Univariate accuracy reflects the similarity of statistical characteristics between each variable in the synthetic data set and the corresponding variable in the original data set, which can be measured by indicators such as Hellinger distance [38] and Kullback-Liebler divergence (KL divergence) [5]. Bivariate accuracy reflects the degree of consistency between different variables in the synthetic data set and the original data set, which can be measured by such indicators as pairwise correlation difference (PCD) [5]. The accuracy of overall distribution reflects the similarity between the overall distribution of synthetic data and the original data, which can be measured by such indicators as propensity mean square error (pMSE) [39], log-cluster [40] and support coverage [5].

Special Utility. Special utility is to analyze the original data set and the synthetic data set with the same method and process based on the purpose of the data set and the task requirements, compare the differences of the analysis results, and then evaluate the synthetic data [41]. If the analysis conclusion based on synthetic data is consistent with the analysis conclusion based on original data, it can be considered that synthetic data has high special utility. Sometimes there are public literature based on the original data. At this time, the same analysis can be carried out on the synthetic data, and the analysis results can be compared with the results based on the original data in the literature. It should be noted that in order to ensure the effectiveness of the evaluation, the analysis method must be selected in combination with the actual use of synthetic data [42].

Stability. Because the synthetic data is generated randomly, the synthetic data method can be evaluated by the stability of the generated synthetic data. Firstly, multiple synthetic data sets are generated, and then their general utility is calculated. The fluctuation of general utility can reflect the stability and deviation of synthetic data generation. If there is systematic deviation or significant change, it shows that there is a certain problem in the reliability of the synthetic data generation model [42].

Structural Similarity. From the practical point of view, the structural similarity between synthetic data and original data is sometimes necessary. Structural similarity

means that the synthetic data and the original data have the same variable name, variable type, value range, data structure, table name and file format. This ensures that the code or software used for synthetic data analysis can be directly used for real data analysis without additional development or transformation [42].

68.3.2 Information Leakage Risk

In 2018, Taub proposed to use the Correct Attribution Probability (CAP) to describe the information leakage risk of synthetic data [43]. On this basis, Taub and Elliot put forward the Targeted Correct Attribution Probability (TCAP) in 2019, which has become a commonly used indicator to measure the risk of information disclosure of synthetic data [35, 44].

TCAP method assumes that two data owners each provide a part of the data to construct an original data set. Synthetic data is generated based on this data set. At this time, one of the data owners tries to infer the original data of another data owner by using the synthetic data and some of the original data he has mastered. It can be seen that TCAP method assumes strong conditions, so the evaluation results can reflect the maximum risk of information leakage to some extent [35]. TCAP value is between 0 and 1. If TCAP is close to 0, it means that there is almost no risk of information leakage in the synthetic data; If TCAP is close to 1, it indicates that there is a high risk of information leakage [35].

68.4 Application of Synthetic Data

Synthetic data has been applied in data release, autonomous driving, software testing and other scenarios.

68.4.1 Data Release

Since 2003, the US Bureau of Statistics began to study the validity of synthetic data and the risk of information leakage. Supported by relevant research results, the US Bureau of Statistics, the Internal Revenue Service, the Social Security Bureau and other departments released the information of several sensitive databases such as personal lifetime income data, personal income data, income and project participation data to the public in the form of synthetic data for analysis. Researchers can submit the analysis results based on synthetic data to the US Bureau of Statistics for verification with real data. In this process, we can not only continuously improve the analytical model of researchers, but also continuously improve the data synthesis technology of the US Bureau of Statistics. By providing synthetic data to research groups and

the public, people who have not been exposed to relevant data in the past also have convenient conditions for conducting economic policy research [45]. Encouraged by the relevant research results, the US Bureau of Statistics further increased the release of synthetic data, and many states also provided their own synthetic data [46]. Britain [47], Germany [48, 49] and other countries have also released some sensitive data in the form of synthetic data.

68.4.2 Automatic Driving

Reinforcement learning algorithm is usually used when training unmanned vehicles or unmanned aerial vehicles, and a large number of experiments are needed in the real world to complete the self-learning of agents. The real data collection process is time-consuming and laborious, and the data annotation is also costly. Using synthetic data to construct a virtual three-dimensional experimental environment for artificial intelligence training can greatly save costs [50]. As early as 1989, when researchers at that time tried to solve the problem of autonomous driving by using neural networks, it was found that it was very difficult to train based on images of real road conditions, because it was difficult to traverse various possible scenarios [50]. A series of synthetic data sets for automatic driving training, such as Virtual KITTI [51], VIPER [52], GTAV [53] and SYNTHIA [54], have been put forward successively, covering pictures or video information of various scenes. VIVID has expanded the virtual environment and further increased the interaction with pedestrians [55]. Matterport3D [56], Scannet [57], Gibson env [58], Sun3d [59], etc. constructed indoor scene data sets for home robots or factory robots training. Gazebo [60], AirSim [61], Janus platform [62], FLAME [63] and others provide data generation tools for UAV training.

68.4.3 Software Testing

The quality of test data significantly affects the effect of software testing. In many cases, real data is often difficult to be obtained and used by testers because it is too sensitive, and relying on subjective experience to artificially test data is not only inefficient, but also difficult to ensure coverage. Synthetic data has obvious advantages in the field of software testing because of its high security, strong fidelity, efficient generation and cost saving [64]. A series of test data generation tools based on grammar [65], random walk [66], program execution [67], neural network [68], search [69] and so on have been put forward. Through the optimization and enhancement of synthetic data, the test coverage can be significantly improved.

In addition, in the fields of bioinformatics, natural language processing, Internet of Things, advanced manufacturing, etc., synthetic data has also been concerned and used [50, 64, 70].

68.5 Military Application Prospect of Synthetic Data

In recent years, a series of big data research and development projects have been launched [71–73]. The rapid development of synthetic data technology and its successful application in related fields can bring some enlightenment to the construction of military big data.

68.5.1 Providing a Supplement to Real Data

Synthetic data is a useful supplement to real military data. Military big data not only has the characteristics of large scale, various contents, high processing speed and low value density, but also has the characteristics of high security, strong antagonism and high complexity [74, 75]. Real war sample data are often scarce, and even there is no real sample data for future wars. Synthetic data just provides solutions and methods for the current few-shot/zero-shot learning, and together with the simulation data, it provides a useful supplement for the real data, forming a military data resource system that combines virtual and real data. With the development of military intelligence, the demand for data will be increasing, the importance of synthetic data will continue to increase, and the proportion in data resources will also increase simultaneously.

68.5.2 Promoting Data Sharing

On the one hand, military data highly emphasizes security and puts strong constraints on the open sharing of data, on the other hand, in order to fully tap the value of data, it is necessary to continuously promote the open sharing of data. Synthetic data provides a useful support for the safe sharing of military data. For example, based on the original real data, according to the corresponding requirements, a series of synthetic data sets containing specific contents and meeting the corresponding confidentiality requirements can be generated, which can be opened to specific users according to the authority, so as to facilitate relevant researchers to analyze the data and dig out the potential value of the data without revealing confidential information, as shown in Fig. 68.1.

68.5.3 Accelerate the Development of Military Intelligence

In the future, the intersection and integration of technologies will become more and more obvious. The trend of technology integration determines that synthetic data technology should not develop in isolation. The rapid development of federated

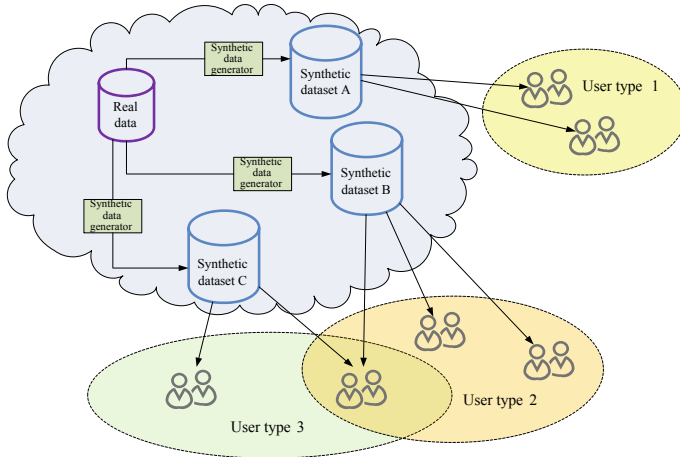


Fig. 68.1 Data sharing on demand based on synthetic data

learning, blockchain, Internet of Things, combat experiments and other technologies provides an opportunity for the integration and development with synthetic data technology. The distributed artificial intelligence training scheme adopted by federal learning, the credible and shared distributed ledger provided by blockchain, the massive data collected by the Internet of Things, and the pre-practice of combat experiments through modeling and simulation all provide opportunities for technological integration and innovation of synthetic data, which is expected to provide strong support for the development of military intelligence.

68.6 Conclusion

Data is being fully integrated into the military field, becoming the driving force of military scientific research, an important basis for scientific decision-making and an important resource for winning the war. As a new technology in the field of big data, synthetic data is expected to play an increasingly important role in data security sharing and military intelligence training. This paper summarizes the main methods, performance evaluation indexes and application of synthetic data, looks forward to its military application prospect, and puts forward the preliminary idea of military application of synthetic data, which provides reference for the research in related fields.

References

1. Jiang, M., Yu, M.-g., Wang, Z.-x.: Thinking on the construction of metadata in the army big data. *J. Command Control* **4**(3), 220–225 (2018). (in Chinese)
2. Kokosi, T., De Stavola, B., Mitra, R., et al.: An overview on synthetic administrative data for research. *Int. J. Popul. Data Sci.* **7**(1) (2022)
3. 2022 10 Breakthrough Technologies. <https://www.technologyreview.com/2022/02/23/1045416/10-breakthrough-technologies-2022/>
4. Noruzman, A.H., Ghani, N.A., Zulkifli, N.S.A.: Gretel.ai: open-source artificial intelligence tool to generate new synthetic data. *Malays. J. Innov. Eng. Appl. Soc. Sci. (MYJIEAS)* **1**(1), 15–22 (2021)
5. Goncalves, A., Ray, P., Soper, B., et al.: Generation and evaluation of synthetic patient data. *BMC Med. Res. Methodol.* **20**(108), 1–40 (2020)
6. Rubin, D.B.: Discussion statistical disclosure limitation. *J. Off. Stat.* **9**, 461–468 (1993)
7. Little, R.: Statistical analysis of masked data. *J. Off. Stat.* **9**(2), 499–522 (1993)
8. Cherubini, U., Luciano, E., Vecchiato, W.: *Copula Method in Finance*. Wiley (2004)
9. Patki, N., Wedge, R., Veeramachaneni, K.: The synthetic data vault. In: *IEEE International Conference on Data Science and Advanced Analytics (DSAA)*, Montreal, QC, Canada, pp. 399–410 (2016)
10. Meyer, D., Nagler, T.: Synthia: multidimensional synthetic data generation in Python. *J. Open Source Softw.* **6**(65), 2863 (2021)
11. Pearl, J.: Bayesian networks: a model of self-activated memory for evidential reasoning. In: *Proceedings of the Cognitive Science Society*, Irvine, pp. 329–334 (1985)
12. Pearl, J.: Markov and Bayesian networks: two graphical representations of probabilistic knowledge. *Probabilistic Reasoning in Intelligent Systems (Revised Second Printing)*, pp. 77–141 (1988)
13. Kaur, D., Sobieski, M., Patil, S., et al.: Application of Bayesian networks to generate synthetic health data. *J. Am. Med. Inform. Assoc.* **28**(4), 801–811 (2021)
14. Bruera, A., Alda, F., Cerbo, F.D.: Generating realistic synthetic curricula vitae for machine learning applications under differential privacy. In: *Proceedings of the Workshop on Ethical and Legal Issues in Human Language Technologies and Multilingual De-identification of Sensitive Data in Language Resources Within the 13th Language Resources and Evaluation Conference*, Marseille, France, pp. 53–63 (2022)
15. Ping, H., Stoyanovich, J., Howe, B.: DataSynthesizer: privacy-preserving synthetic datasets. In: *Proceedings of the 29th International Conference on Scientific and Statistical Database Management*, Chicago, IL, USA, pp. 1–5 (2017)
16. Nowok, B.: Utility of synthetic microdata generated using tree-based methods. *UNECE Statistical Data Confidentiality Work Session*, pp. 1–11 (2015)
17. Breiman, L., Friedman, J.H., Olshen, R.A., et al.: *Classification and Regression Trees (CART)*. CRC Press (1984)
18. Brylla, R., Gutierrez-Osuna, R., Queka, F.: Attribute bagging: improving accuracy of classifier ensembles by using random feature subsets. *Pattern Recogn.* **36**(6), 1291–1302 (2003)
19. Liaw, A., Wiener, M.: Classification and regression by randomForest. *R News* **23**(23) (2002)
20. Nowok, B., Raab, G.M., Dibben, C.: synthpop: bespoke creation of synthetic data in R. *J. Stat. Softw.* **74**(11), 1–16 (2016)
21. Kothare, A., Chaube, S., Moharir, Y., et al.: SynGen: synthetic data generation. In: *2021 International Conference on Computational Intelligence and Computing Applications (ICCICA)*, Nagpur, India, pp. 1–4 (2021)
22. Dankar, F.K., Ibrahim, M.: Fake it till you make it: guidelines for effective synthetic data generation. *Appl. Sci.* **11**, 2158 (2021)
23. Goodfellow, I., Pouget-Abadie, J., Mirza, M., et al.: Generative adversarial nets. In: *Proceedings of the 27th International Conference on Neural Information Processing Systems*, pp. 2672–2680 (2014)

24. Roh, Y., Heo, G., Whang, S.E.: A survey on data collection for machine learning: a big data—AI integration perspective. *IEEE Trans. Knowl. Data Eng.* **33**(4), 1328–1347 (2021)
25. Jetchev, N., Bergmann, U., Vollgraf, R.: Texture synthesis with spatial generative adversarial networks. In: *NIPS 2016*, Barcelona, Spain, pp. 1–11 (2016)
26. Bergmann, U., Jetchev, N., Vollgraf, R.: Learning texture manifolds with the periodic spatial GAN. In: *Proceedings of the 34th International Conference on Machine Learning*, Sydney, Australia (2017)
27. Xian, W., Sangkloy, P., Agrawal, V., et al.: TextureGAN: controlling deep image synthesis with texture patches. In: *2018 IEEE/CVF Conference on Computer Vision and Pattern Recognition*, Salt Lake City, UT, USA, pp. 8456–8465 (2018)
28. Li, C., Wand, M.: Precomputed real-time texture synthesis with Markovian generative adversarial networks. In: Leibe, B., Matas, J., Sebe, N., et al. (eds.) *Computer Vision—ECCV 2016*, vol. 9907, pp. 702–716. Springer, Cham (2016)
29. Karras, T., Aila, T., Laine, S., et al.: (2018) Progressive growing of GANs for improved quality, stability, and variation. In: *The Sixth International Conference on Learning Representations*, Vancouver, BC, Canada, pp. 1–26
30. Brock, A., Donahue, J., Simonyan, K.: Large scale GAN training for high fidelity natural image synthesis. In: *International Conference on Learning Representations (ICLR)*, pp. 1–4 (2019)
31. Karras, T., Laine, S., Aila, T.: A style-based generator architecture for generative adversarial networks. In: *2019 IEEE/CVF Conference on Computer Vision and Pattern Recognition (CVPR)*, pp. 4401–4410 (2019)
32. Rakotonirina, N.C., Rasoanaivo, A.: ESRRGAN+: further improving enhanced super-resolution generative adversarial network. In: *2020 IEEE International Conference on Acoustics, Speech and Signal Processing (ICASSP)*, Barcelona, Spain (2020)
33. Wang, L., Chen, W., Yang, W., et al.: A state-of-the-art review on image synthesis with generative adversarial networks. *IEEE Access* **8**, 63514–63537 (2020)
34. Chen, H., Jajodia, S., Liu, J., et al.: FakeTables: using GANs to generate functional dependency preserving tables with bounded real data. In: *Proceedings of the Twenty-Eighth International Joint Conference on Artificial Intelligence*, Macao, China, pp. 2074–2080 (2019)
35. Little, C., Elliot, M., Allmendinger, R., et al.: Generative Adversarial Networks for Synthetic Data Generation: A Comparative Study. arXiv: <http://arxiv.org/abs/2112.01925> (2021)
36. Little, C., Elliot, M., Allmendinger, R.: Comparing the utility and disclosure risk of synthetic data with samples of microdata. In: *International Conference on Privacy in Statistical Databases*, pp. 234–249 (2022)
37. Dankar, F.K., Ibrahim, M.K., Ismail, L.: A multi-dimensional evaluation of synthetic data generators. *IEEE Access* **10**, 11147–11158 (2022)
38. Cam, L.L., Yang, G.L.: *Asymptotics in Statistic*. World Book Publishing Company (2000)
39. Snoke, J., Raab, G.M., Nowok, B., et al.: General and specific utility measures for synthetic data. *J. R. Stat. Soc. A Stat. Soc.* **181**(3), 663–688 (2018)
40. Woo, M.J., Reiter, J.P., Oganian, A., et al.: Global measures of data utility for microdata masked for disclosure limitation. *J. Privacy Confid.* **1**(1), 111–124 (2009)
41. Hittmeir, M., Ekelhart, A., Mayer, R.: Utility and privacy assessments of synthetic data for regression tasks. In: *2019 IEEE International Conference on Big Data*, Los Angeles, CA, USA, pp. 5763–5772 (2019)
42. El Emam, K.: Seven ways to evaluate the utility of synthetic data. *IEEE Secur. Privacy* **18**(4), 56–59 (2020)
43. Taub, J., Elliot, M., Pampaka, M., et al.: Differential correct attribution probability for synthetic data: an exploration. In: *International Conference on Privacy in Statistical Databases*, vol. 11126, pp. 122–137. Springer (2018)
44. Taub, J., Elliot, M., Raab, G., et al.: Creating the best risk-utility profile: the synthetic data challenge. In: *Joint UNECE/EUROSTAT Work Session on Statistical Data Confidentiality*, Hague, Netherlands, pp. 1–21 (2019)
45. Rankin, D., Black, M., Bond, R., et al.: Reliability of supervised machine learning using synthetic data in health care: model to preserve privacy for data sharing (preprint). *JMIR Med. Inform.* **8**(7), 1–21 (2020)

46. Bonn ery, D., Feng, Y., Henneberger, A.K., et al.: The promise and limitations of synthetic data as a strategy to expand access to state-level multi-agency longitudinal data. *J. Res. Educ. Effect.* **12**(4), 616–647 (2019)
47. Raab, G.M., Nowok, B., Dibben, C.: Guidelines for Producing Useful Synthetic Data. arXiv, <http://arxiv.org/abs/1712.04078> (2017)
48. Drechsler, J.: Synthetic datasets for the German IAB Establishment Panel. In: Joint UNECE/Eurostat Work Session on Statistical Data Confidentiality. Bilbao, Spain (2009)
49. Drechsler, J., Bender, S., R assler, S.: Comparing fully and partially synthetic datasets for statistical disclosure control in the German IAB Establishment Panel. *Trans. Data Privacy* **1**(3), 105–130 (2008)
50. Nikolenko, S.I.: *Synthetic Data for Deep Learning*. Springer, Cham (2021)
51. Gaidon, A., Qiao, W., Cabon, Y., et al.: Virtual worlds as proxy for multi-object tracking analysis. In: 2016 IEEE Conference on Computer Vision and Pattern Recognition (CVPR), Las Vegas, NV, USA, pp. 4340–4349 (2016)
52. Richter, S.R., Hayder, Z., Koltun, V.: Playing for benchmarks. In: 2017 IEEE International Conference on Computer Vision (ICCV), Venice, Italy, pp. 22–29 (2017)
53. Richter, S.R., Vineet, V., Roth, S., et al.: Playing for data: ground truth from computer games. In: Leibe, B., Matas, J., Sebe, N., et al. (eds.) *Computer Vision-ECCV 2016*, pp. 102–118. Springer (2016)
54. Ros, G., Sellart, L., Materzynska, J., et al.: The SYNTHIA dataset: a large collection of synthetic images for semantic segmentation of urban scenes. In: 2016 IEEE Conference on Computer Vision and Pattern Recognition (CVPR), Las Vegas, NV, USA, pp. 3234–3243 (2016)
55. Baker, S., Scharstein, D., Lewis, J.P., et al.: A database and evaluation methodology for optical flow. *Int. J. Comput. Vision* **92**(1), 1–31 (2011)
56. Chang, A., Dai, A., Funkhouser, T., et al.: Matterport3D: learning from RGB-D data in indoor environments. In: 2017 International Conference on 3D Vision, Verona, Italy (2017)
57. Dai, A., Chang, A.X., Savva, M., et al.: ScanNet: richly-annotated 3D reconstructions of indoor scenes. In: *IEEE Conference on Computer Vision and Pattern Recognition (CVPR)*, pp. 2432–2443 (2017)
58. Xia, F., Zamir, A., He, Z.Y., et al.: Gibson Env: real-world perception for embodied agents. In: 2018 IEEE/CVF Conference on Computer Vision and Pattern Recognition, Salt Lake City, UT, USA, pp. 9068–9079 (2018)
59. Xiao, J., Owens, A.H., Torralba, A.: SUN3D: a database of big spaces reconstructed using SfM and object labels. In: 2013 IEEE International Conference on Computer Vision, Sydney, NSW, Australia, pp. 1625–1632 (2013)
60. Koenig, N., Howard, A.: Design and use paradigms for Gazebo, an open-source multi-robot simulator. In: 2004 IEEE/RSJ International Conference on Intelligent Robots and Systems (IROS), Sendai, Japan (2002)
61. Shah, S., Dey, D., Lovett, C., et al.: AirSim: high-fidelity visual and physical simulation for autonomous vehicles. *Field Serv. Robot.* **5**, 621–635 (2018)
62. Gaud, N., Galland, S., Hilaire, V., et al.: An organisational platform for holonic and multiagent systems. In: *Programming Multi-agent Systems*. Springer, Berlin, Heidelberg (2008)
63. Kiran, M., Richmond, P., Holcombe, M., et al.: FLAME: simulating large populations of agents on parallel hardware architectures. In: *Proceedings of the 9th International Conference on Autonomous Agents and Multiagent Systems*, pp. 1633–1636 (2010)
64. Popic, S., Pavkovic, B., Velikic, I., et al.: Data generators: a short survey of techniques and use cases with focus on testing. In: 2019 IEEE 9th International Conference on Consumer Electronics (ICCE-Berlin), Berlin, Germany, pp. 189–194 (2019)
65. Deason, W.H., Brown, D.B., Chang, K.H., et al.: A rule-based software test data generator. *IEEE Trans. Knowl. Data Eng.* **3**(1), 108–117 (1991)
66. Xuan, J., He, J., Ren, Z., et al.: A random walk based algorithm for structural test case generation. In: *Proceedings of 2nd International Conference on Software Engineering and Data Mining (SEDM 2010)*, pp. 583–588 (2010)

67. Jian, Z., Chen, X., Wang, X.: Path-oriented test data generation using symbolic execution and constraint solving techniques. In: Proceedings of the Second International Conference on Software Engineering and Formal Methods, Beijing, China (2004)
68. Hermadi, I., Ahmed, M.A.: Genetic algorithm based test data generator. In: Proceedings of 2003 Congress on Evolutionary Computation, Canberra, ACT, Australia (2003)
69. Malhotra, R., Poornima, Kumar, N.: Automatic test data generator: a tool based on search-based techniques. In: 2016 5th International Conference on Reliability, Infocom Technologies and Optimization (Trends and Future Directions) (ICRITO), Noida, India (2016)
70. Libes, D., Lechevalier, D., Jain, S.: Issues in synthetic data generation for advanced manufacturing. In: 2017 IEEE International Conference on Big Data (Big Data), Boston, MA, pp. 1746–1754 (2017)
71. Zhan, X.-s.: Present situation and prospect of military big data. *Military Abstr.* **5**, 57–61 (2020)
72. Wang, S.-b., Li, X.-m., Pei, Z.-m., et al.: Methodology analysis of cognitive computing system for equipment system of system based on big data. *J. Command Control* **2**(1), 54–59 (2016)
73. Dai, C.-f., Liu, L.-h., Zeng, S.-h., et al.: On military data quality management. *J. Command Control* **2**(4), 322–328 (2016)
74. Zheng, S.-q., Han, L.-b., Wang, J., et al.: The conceptual connotation, development challenges and technical practices of military big data. *J. Command Control* (2022) (Online)
75. Guan, D.-l., Liu, J.-t., Zhou, W.-n.: Thought on key links in the construction and application of military big data. In: Proceedings of the 8th China Command and Control Conference, pp. 142–146 (2020)

Chapter 69

Experimental Study on Aeroacoustic of Counter-Rotating Propeller in Ground Acoustic Environment



Wei Kai, Cao Qi, Yan Qun, Xu Jian, and Xue Dongwen

Abstract According to the performance evaluation and optimization research requirement of counter-rotating propellers aeroacoustics, based on ground acoustic environment, a set of counter-rotating propeller aeroacoustics test platform was built. The aeroacoustic test of counter-rotating propeller was carried out in a semi-anechoic chamber. The aerodynamic performance and far-field noise characteristics of the counter-rotating propeller were obtained, and the distribution of far-field noise were analyzed. The results show that the tension, torque and power increase with the increase of rotating speed. The amplitude distribution of sound pressure level of far-field noise will move with the change of speed. The discrete noise at each passing frequency is also different. The test platform and the test scheme could provide help for the aeroacoustic evaluation and optimization design of counter-rotating propeller under ground takeoff condition.

Keywords Counter-rotating propeller · Aerodynamics · Far-field noise · Test measurement · Directivity

69.1 Introduction

Compared with turbofan engines of the same thrust level, propeller engines have the advantages of high fuel efficiency and good maneuverability. However, there are disadvantages such as large propeller diameter, complicated mechanism design and low flight speed. Counter-rotating propeller, also known as counter-rotating open rotor, has two rows of propellers with opposite rotation. Two rows of propellers increase the number of blades, and the diameter of blades can be appropriately reduced, so as to increase the cruise Mach number and solve some design difficulties of single row propellers. Some data show that the efficiency of contra-rotating

W. Kai (✉) · C. Qi · Y. Qun · X. Jian · X. Dongwen
Aviation Technology Key Laboratory of Aeroacoustics and Vibration, Aircraft Strength Research Institute of China, Aviation Industry Corporation of China Limited, Xi'an, China
e-mail: weikai.258@163.com

propeller can be improved by 6–16% compared with conventional propeller [1]. However, compared with single-row propellers, the interference noise of contra-rotating propellers and the noise of single propellers lead to huge noise. There is no package in the nacelle, and the noise radiates directly into the cabin and surrounding environment. This seriously limits the application and further development of contra-rotating propellers in the civil market [2–4]. With the rise of oil price and stricter restrictions on carbon emissions and noise, it is urgent to solve the noise problem of contra-rotating propellers.

At present, the main methods to study the noise of contra-rotating propeller are numerical simulation and experimental measurement. In terms of numerical simulation, Enviva [5] simulates the unsteady flow field of a contra-rotating rotor by combining computational fluid dynamics (CFD) with computational aeroacoustics (CAA). He used Ffowcs Williams-Hawkings (FW-H) to calculate the far-field noise. The numerical simulation results are in good agreement with the experimental results. The comparison results show that the noise amplitude mainly occurs at the passage frequency and its harmonics of the two rows of blades. GE [4] optimized and designed a low-noise contra-rotating open rotor model based on the blades of GE36 open rotor engine. GE uses the self-developed CFD-CAA software to simulate the aerodynamic and noise performance of the open rotor under cruise conditions, and the results are good. In terms of test measurement, Parrya [7] described the wind tunnel tests of three typical contra-rotating propellers, and analyzed the distribution characteristics of discrete noise and broadband noise in detail. NASA, GE, TsAGI and other laboratories have established the aerodynamic noise test bench of contra-rotating propeller in the wind tunnel. They have successively carried out aerodynamic noise tests in low-speed wind tunnels, high-speed wind tunnels and acoustic wind tunnels, and obtained a large number of test data. These test data guide the subsequent aerodynamic noise optimization design of contra-rotating propeller [8–10].

In the 1980s, GE developed the GE36-UDF open-rotor engine and carried out test flight on the MD-80 aircraft. The test results show that the noise level of this type of engine meets the noise requirements of the third stage of ICAO. Compared with the original engine, the noise and vibration levels are reduced [11–13]. At the same time, Loma designed SR-7 pair of rotor fans and also carried out flight tests [14, 15]. In 2022, the China Aerodynamic Research and Development Center set up an aerodynamic noise test platform for contra-rotating propellers. In the acoustic wind tunnel, the aerodynamic performance and aerodynamic noise tests of contra-rotating propellers were carried out. At the same time, the influence of the rear rotor diameter on the aerodynamic and noise of the contra-rotating propeller is studied by numerical simulation.

The BeiHang University has built a small aerodynamic noise test rig for contra-rotating propellers in the anechoic chamber. The platform uses two motors to drive two rows of propellers, and the flow mechanism between the two rows of propellers is preliminarily studied [16, 17]. Ning and Hu [18] tested the noise of a UAV propeller in the anechoic chamber and evaluated the impact of the blade serrated trailing edge on the noise. Mariono [19] measured the acoustic characteristics of the propeller under different propulsion ratios in the anechoic chamber, and analyzed the noise

characteristics of the propeller under zero propulsion ratio, but the error was large. The aerodynamic noise test in wind tunnel or flight platform is costly and difficult to control the time schedule, which is the obstacle faced by the current research on the aerodynamic noise of contra-rotating propeller. The above aerodynamic noise test scheme in the anechoic chamber can be used for reference, but the test design needs to be improved to reduce the error.

In this paper, a set of aerodynamic noise test platform for contra-rotating propeller is designed. For a set of contra-rotating propellers, the aerodynamic noise test research was carried out at different speed conditions. The aerodynamic performance and far-field noise characteristics of the counter-rotating propeller are evaluated.

69.2 Experimental Principle

The purpose of this test is to evaluate the aerodynamic performance and far-field noise characteristics of counter-rotating propellers. By measuring the pulling force, torque and other parameters of the contra-rotating propeller. The pull coefficient and torque coefficient of the propeller are calculated by formulas (69.1)–(69.4). The aerodynamic performance of counter-rotating propeller can be evaluated according to the above parameters.

$$C_T = \frac{T}{\rho n_s^2 D^4} \quad (69.1)$$

$$C_M = \frac{M}{\rho n_s^2 D^5} \quad (69.2)$$

$$P = 9549 \frac{M}{n} \quad (69.3)$$

$$C_P = \frac{P}{\rho n_s^3 D^5} \quad (69.4)$$

where T is trust, M is torque, C_T is trust coefficient, P is power, and C_P is power coefficient. ρ is the air density, n_s is the propeller rotation speed (r/s), D is the propeller diameter, n is the speed (r/min), and P is the power.

The noise source of contra-rotating propeller is the same as that of single-row propeller, which has obvious directionality. Take the rotation center of the rear row blades of the counter rotating propeller as the origin. The sound intensity of the far-field noise receiving point can be recorded as I , and the average sound intensity of other points at the same distance can be recorded as \bar{I} . Then the directivity factor Q and directivity index DI are defined as:

$$Q = \frac{I}{\bar{I}} \quad (69.5)$$

$$DI = 10 \lg Q = L_{p\theta} - \bar{L}_p \quad (69.6)$$

where $L_{p\theta}$ is the sound pressure level at angle θ on the spherical surface with radius r ; \bar{L}_p is the average sound pressure level measured on the spherical surface with radius r . The directivity index can usually be measured directly. In three-dimensional spherical coordinates, the directivity index $DI(\theta, \varphi)$ in a specific direction has the following relationship with the sound pressure level $L_p(r, \theta, \varphi)$ measured at the distance r .

$$Q(\theta, \varphi) = 10^{-1} \frac{DI(\theta, \varphi)}{10} \quad (69.7)$$

The directivity index of sound source in the ground acoustic environment can be considered as a free field on the reflecting surface, and the directivity index is:

$$DI = L_{pi} - \bar{L}_p + 3 \quad (69.8)$$

where W is the sound pressure level at the distance R from the sound source; E is the average sound pressure level on the test hemisphere. Through formula (69.8), the fluctuation of sound pressure level at each measuring point in the far field relative to the average level is given. In this paper, the noise characteristics of the contra-rotating propeller will be evaluated by the spectrum and directivity of the far-field noise.

69.3 Experimental Device and Scheme

69.3.1 Experimental Platform

With the semi-anechoic chamber as the ground acoustic environment, a set of anti-rotating propeller aerodynamic noise test platform is built, and the schematic diagram is shown in Fig. 69.1. The test platform includes base, slide rail, servo motor, tension sensor, torque sensor, cooling system and control system. The servo motor drives the propeller to rotate through the coupling and gearbox. The tension sensor is installed on the slide rail to measure the tension transmitted by the contra-rotating propeller when it rotates. The torque sensor is connected with the coupling to measure the torque transmitted by the contra-rotating propeller. The base is designed as a streamlined shape, which can reduce the airflow disturbance caused by the test bed. The tester shall measure and control outside the semi-anechoic chamber to ensure safety.

The maximum rotational speed of the contra-rotating propeller test platform is 3500 rpm, the tension measurement range is 0–400 N, and the torque measurement range is 0–400 Nm.

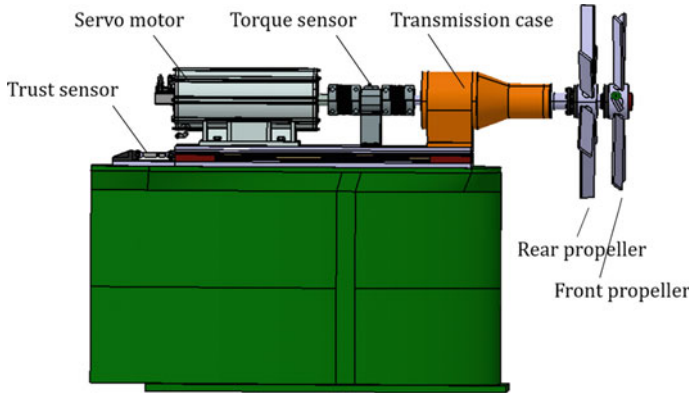


Fig. 69.1 Schematic diagram of test platform

69.3.2 Experimental Conditions

This test was carried out in the semi-anechoic chamber of the China Aircraft Strength Research Institute. The size of the semi-anechoic chamber is $10 * 10 * 8$ m. The test site is shown in Fig. 69.2. The test items include aerodynamic performance test and far-field noise test. The diameter of the contra-rotating propeller is 0.66 m, and there are 6 blades in the front and rear rows. The blades are made of composite materials. NACA0012 airfoil is selected as the blade, and the blade angle at 70% blade height is 20° . Based on the similarity of blade tip Mach number and the ground takeoff condition, the test condition is designed. The rotational speed is set at 1500, 2000, 2500, 2600, 2800 and 3000 rpm, and the relationship between the rotational speed and the aerodynamic performance of the contra-rotating propeller and the far-field noise is studied.

69.3.3 Test Method

The purpose of aerodynamic performance test is to obtain the pull and torque of the contra-rotating propeller. After the test reaches the preset working condition, the tension and torque can be directly read from the control system. A microphone array is arranged in the semi-anechoic chamber to measure the sound pressure at each noise observation point in the far field. The microphone array arrangement is shown in Fig. 69.3.

The microphone array is composed of 12 BK4954 free-field microphones with a distance of 10° . The microphone is uniformly distributed on the circular arc with the rotation center of the rear row propeller as the center and the radius of 3.5 m. The height of the microphone is consistent with the rotation center of the propeller. During the test, the microphone is equipped with a windproof ball in order to reduce the error

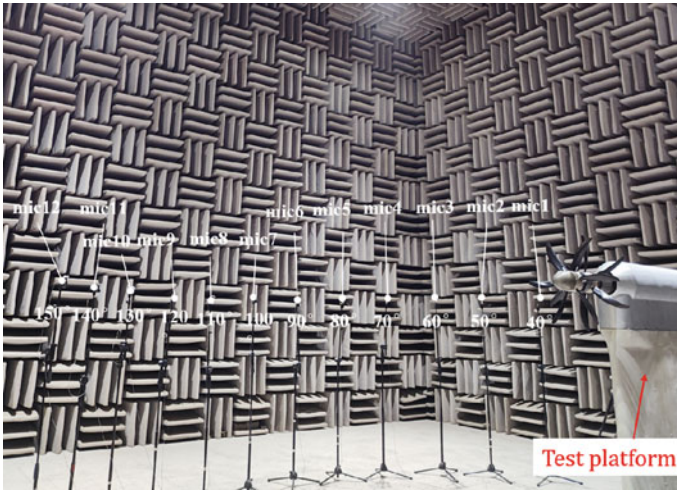


Fig. 69.2 Test site photo

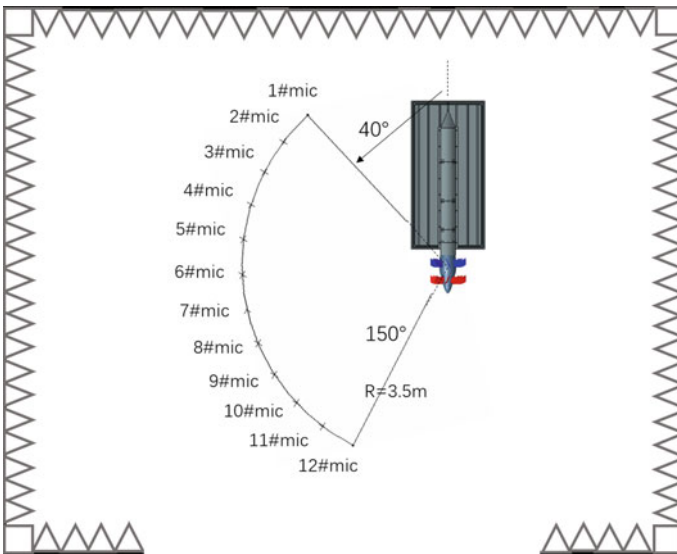


Fig. 69.3 Schematic diagram of microphone array

caused by the rotating turbulence of the propeller. During the test, 12 microphones simultaneously collected 20 s of sound pressure data. The adopted frequency is set at 16384 Hz, and the microphone must be calibrated.

69.4 Experimental Results and Analysis

The test results include aerodynamic performance results and far-field noise results. The aerodynamic performance results are directly measured tension, torque, power and indirectly calculated tension coefficient, torque coefficient and power coefficient. The far field noise is mainly noise frequency spectrum and directivity.

69.4.1 Aerodynamic Results and Analysis

Figure 69.4 shows the test results of the pull force of the counter-rotating propeller at different speeds. It can be seen that the pulling force increases with the increase of rotating speed, and the increase is large. No stall occurs within the measured speed range. Figure 69.5 shows the change of the tension coefficient with the speed. The tension coefficient increases with the increase of the speed, and the increase slows down after 2800 rpm. The tensile force and the coefficient of tensile force increase with the increase of the rotating speed, which indicates that the blade angle and the rotating speed match well in the whole test rotating speed range.

Figure 69.6 shows the torque test results, and Fig. 69.7 shows the torque coefficient results. As can be seen from Fig. 69.6, with the increase of speed, the torque also increases, but the growth rate is small. It can be seen from Fig. 69.7 that the torque coefficient decreases with the increase of speed. From 1500 to 2000 rpm, the torque coefficient decreases greatly; The decrease from 2000 to 3000 rpm slowed down. This shows that in the speed range of 1500–2000 rpm, the matching degree between blade angle and speed is high.

Fig. 69.4 Thrust data of test

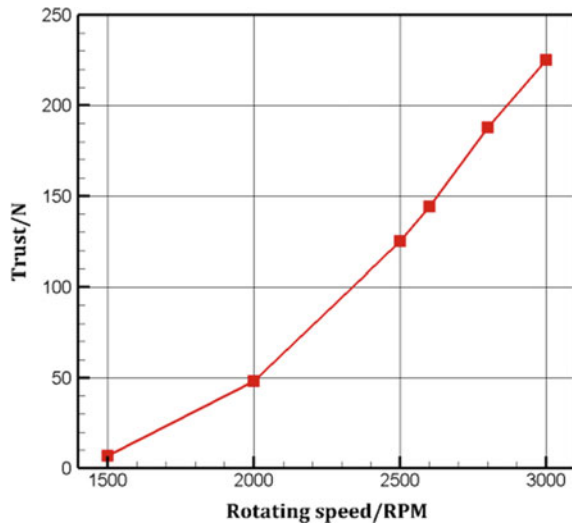


Fig. 69.5 Thrust coefficient data of test

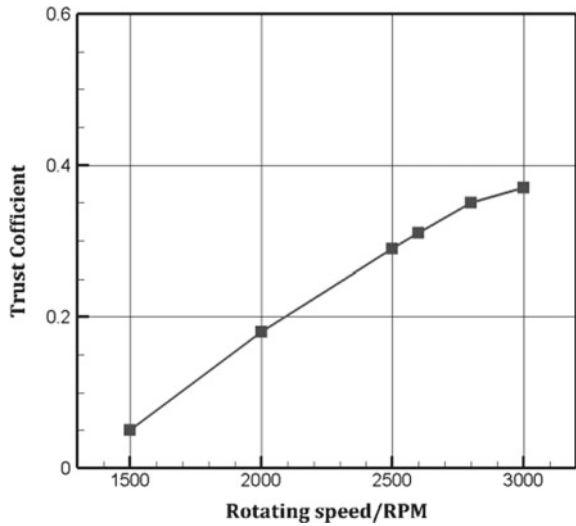
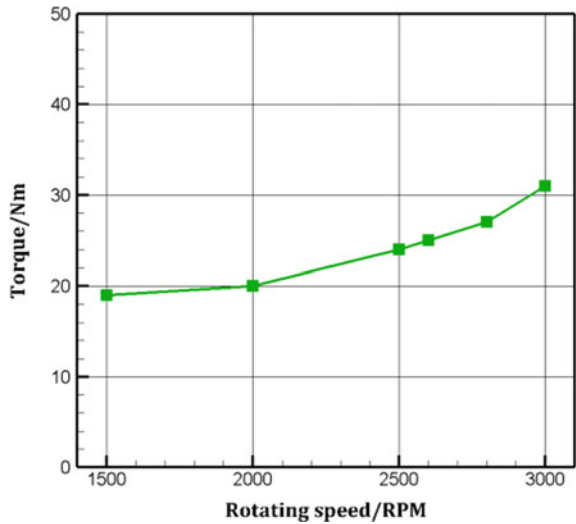


Fig. 69.6 Torque data of test



Figures 69.8 and 69.9 show the relationship between the power, power coefficient and rotational speed of the contra-rotating propeller. It can be seen from Fig. 69.8 that the power increases with the increase of speed, and the increase is obvious. It can be seen from Fig. 69.9 that the power coefficient decreases with the increase of the speed, and the speed of decline is fast in the range of 1500–2000 rpm; In the range of 2000–3000 rpm, the power factor slows down with the speed of speed reduction. These results show that in the speed range of 1500–2000 rpm, the matching degree of blade angle and speed is high, which is consistent with the conclusion in Fig. 69.7.

Fig. 69.7 Torque coefficient data of test

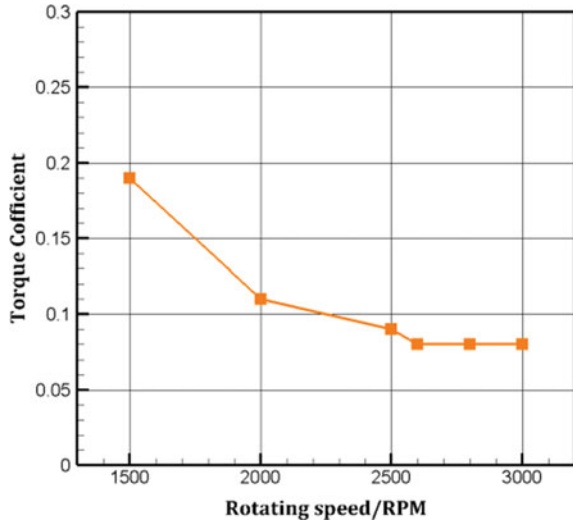
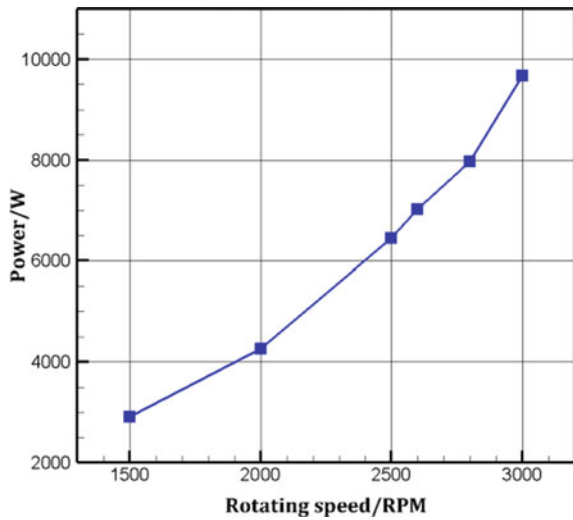
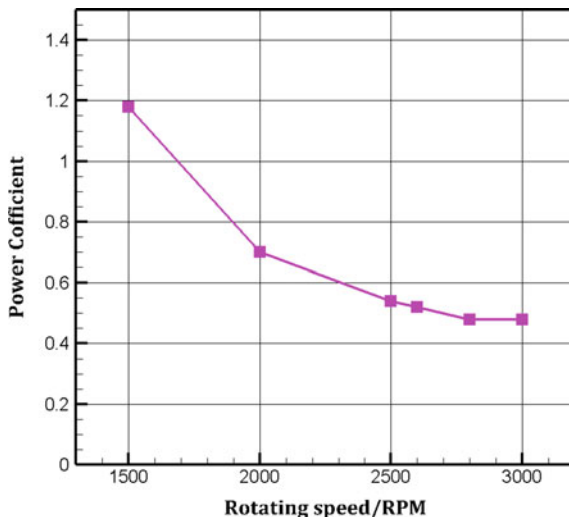


Fig. 69.8 Power data of test



The aerodynamic performance of the contra-rotating propeller is obtained through experiments, which provides a basis for the optimal design of the blade. The aerodynamic noise optimization of contra-rotating propellers is similar to that of single-row propellers. Even when the efficiency of propellers is guaranteed, the noise is minimal. According to the required power and tension requirements, the airfoil of the blade is initially selected and the number of blades is determined.

Fig. 69.9 Power coefficient data of test



69.4.2 Noise Results and Analysis

The far-field noise spectrum of the counter-rotating propeller at 3000 rpm is shown in Fig. 69.10. It can be seen from Fig. 69.10 that the far field noise amplitude of the contra-rotating propeller in this test is within 3000 Hz, and the higher frequency band is mainly broadband noise. The results accord with the general law of aerodynamic noise of contra-rotating propeller.

Fig. 69.10 Spectra of far-field noise of different azimuthal angles at 3000 rpm

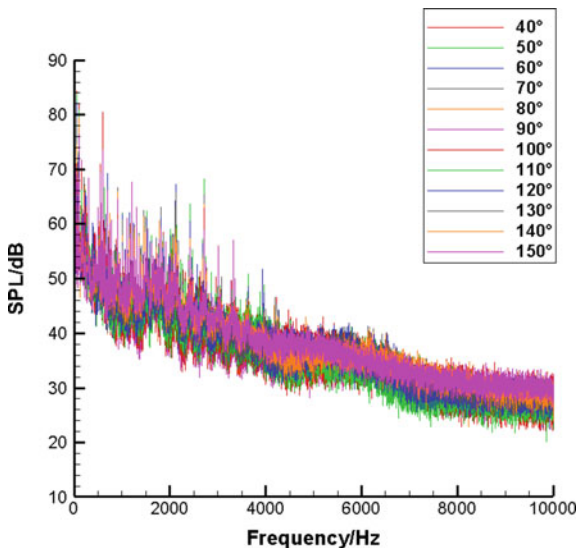


Figure 69.11 shows the noise spectrum of the counter-rotating propeller at the blade passing frequency (BPF). It can be seen that the noise amplitude at the second pass frequency (2BPF) is greater than that at the first pass frequency (1BPF) and the third pass frequency (3BPF). The amplitude of aerodynamic noise of counter rotating propeller mainly appears at 1BPF, 2BPF and 3BPF, indicating that the noise of counter rotating propeller is mainly discrete noise. The discrete noise mainly comes from the load noise of the single row propeller and the interference noise generated by the interaction between the two rows of propeller. The interference noise of counter-rotating propeller is generated at the interference frequency. The interference frequency is the sum of the passing frequencies of the two rows of propellers and their higher-order harmonics. 2BPF is the first order interference frequency, where the noise amplitude is the largest, which conforms to the general law of aerodynamic noise of contra-rotating propeller. The noise amplitude points of the contra-rotating propeller can be obtained, and the noise reduction method can be put forward in combination with the interference noise generation mechanism.

Figure 69.12 shows the far-field noise directivity results of the counter-rotating propeller at 3000 rpm. It can be seen from the figure that compared with 1BPF and 3BPF, the noise sound pressure level at 2BPF is the highest. Compared with other pointing angles, the sound pressure level at 40° is the highest, followed by 90° , which is also the direction with the greatest impact on the environment and cabin. The noise in the range of $110\text{--}150^\circ$ is low. The noise sound pressure level of 1BPF and 2BPF is small, and the direction of the maximum sound pressure level is around 80° , which is slightly forward compared with 3BPF.

From the previous test results, the noise amplitude of the counter-rotating propeller is mainly at 2BPF, which is interference noise. Then, the noise rule at 2BPF can be

Fig. 69.11 Spectrum at blade passing frequency

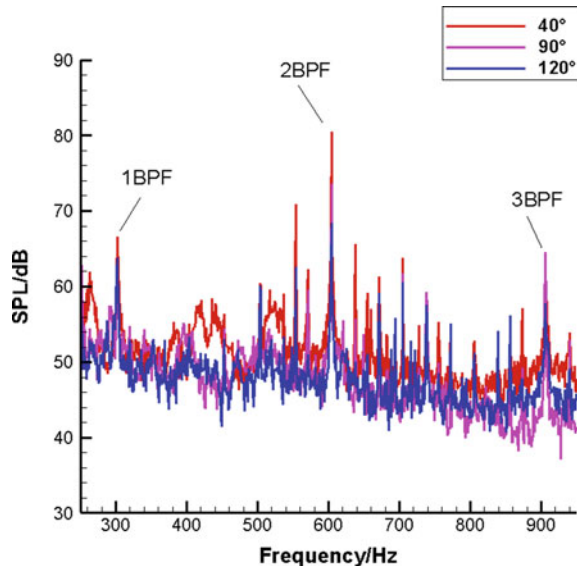
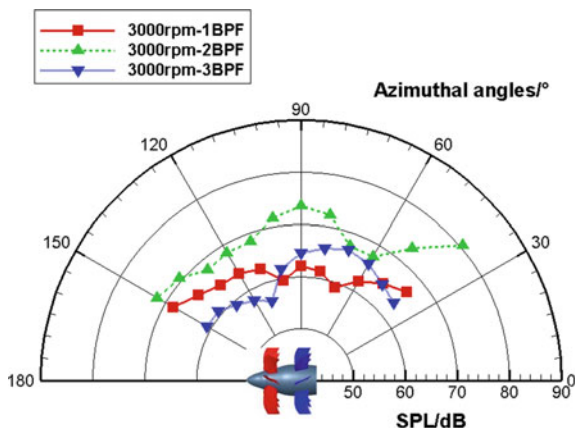


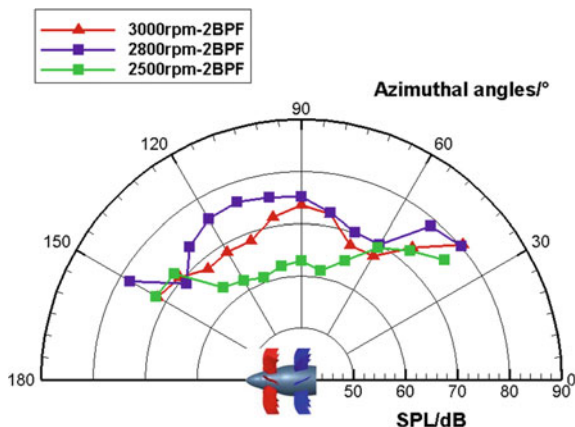
Fig. 69.12 Noise directivity at blade passing frequency—3000 rpm



analyzed through Fig. 69.13. The distribution trend of far-field noise at 2800 and 3000 rpm is similar at each direction, and the amplitude of sound pressure level is the largest at 90° and 40°. The distribution of sound pressure level at 2500 rpm at each direction angle is not consistent with the trend of 2800 and 3000 rpm.

Similar to the generation mechanism of discrete noise of single-row propeller, the discrete noise of counter-rotating propeller is also the result of the propeller periodically cutting the air in the flow field and interacting with it. The noise power is generally the highest in the tip area, so the aerodynamic load can be moved to the inner diameter direction along the peak value of the spanwise distribution to reduce the load noise. The propeller load noise can be reduced by improving the spanwise blade shape or increasing the radial blade width, so as to reduce the discrete noise. On the other hand, the air flow interference between two rows of propellers produces interference noise, which can be reduced in mechanism by adjusting the ratio of the height of two rows of blades or the spacing between two rows of propellers.

Fig. 69.13 Noise directivity at 2BPF at different speeds



69.5 Conclusion

Within the measured speed range, the pull, torque and power of the counter-rotating propeller increase with the increase of the speed. The torque coefficient and power coefficient decrease with the increase of speed, which indicates that there is still room for optimization of the speed design of the contra-rotating propeller. Interference noise is the main noise of contra-rotating propeller. The aerodynamic noise test platform of contra-rotating propeller can be used to evaluate the aerodynamic noise performance of contra-rotating propeller. The load noise can be reduced by improving the spanwise or radial width of the blade. The interference noise is reduced by adjusting the diameter ratio and pitch of the two rows of propellers.

References

1. Hager, R., Vrabel, D.: Advanced turboprop project. NASA SP-495 (1988)
2. Zhou, L., Shi, J., Wang, Z.: Research progress in open-rotor engine. *J. Propuls. Technol.* **40**(7), 1921–1932 (2019). (in Chinese)
3. Kingan, M.J., Parry, A.B.: Acoustic theory of the many bladed contra-rotating propeller: the effects of sweep on noise enhancement and reduction. *J. Sound Vib.* **468**, 89–115 (2020)
4. Parry, A.B., Kingan, M.J.: Acoustic theory of the many bladed contra-rotating propeller: physics of the wake interaction noise critical sources. *J. Fluid Mech.* **880**, 1–12 (2019)
5. Envia, E.: Contra-rotating open rotor tone noise prediction. In: Proceedings of the AIAA/CEAS Aeroacoustics Conference, AIAA, Atlanta, GA, pp. 1027–1042 (2014)
6. Van Zante, D.E., Collier, F., Orton, A.: Progress in open rotor propulsors: The FAA/GE/NASA open rotor test campaign. *Aeronaut. J.* **118**(1208), 1181–1213 (2014)
7. Parry, B. Relative importance of open rotor tone and broadband noise sources //Proceedings of 17th AIAA/CEAS Aeroacoustics Conference. Portland, OR: AIAA, 2011:1075–1087.
8. Hoff, G.E.: Experimental Performance and Acoustic Investigation of Modern, Counterrotating lade Concepts. NASA CR 182158, January 1990
9. Elliott, D.M.: Initial Investigation of the Acoustics of a Counter Rotating Open Rotor Model with Historic Baseline Blades in a Low Speed Wind Tunnel. AIAA-2011-2760 (2011)
10. Dale, E., Van, Z.: The NASA Environmentally Responsible Aviation Project/General Electric Open Rotor Test Campaign. AIAA-2013-0415 (2013)
11. GE36: Design and Systems Engineering. Full scale technology demonstration of a modern counter rotating unducted fan engine concept: design report. NASA CR 180867, January 1987
12. GE36: Design and Systems Engineering. Full scale technology demonstration of a modern counter rotating unducted fan engine concept: component test. NASA CR 180868, January 1987
13. GE36: Design and Systems Engineering. Full scale technology demonstration of a modern counter rotating unducted fan engine concept: engine test. NASA CR 180869, January 1987.
14. Little, B.H., Poland, D.T., Bartel, H.W., et al.: Propfan Test Assessment (PTA): Final Project Report. NASA-CR-185138 (1989)
15. Little, B.H., Bartel, H.W., Reddy, N.N., et al.: Propfan Test Assessment (PTA): Flight Test Report. NASA-CR-182278 (1989)
16. Chen, Z., Jiang, Y., Zhao, Y., et al.: The counter-rotating propellers aerodynamic and aerodynamic noise test technology in wind tunnel. *J. Aerosp. Power.* <https://doi.org/10.13224/j.cnki.jasp.20220476>
17. Cui, P., Tong, F., Feng, H., et al.: Influence of rear rotor diameter on aerodynamic and acoustic characteristics of counter-rotating propeller. *J. Aerosp. Power* **37**(8), 1749–1760 (2022)

18. Ning, Z., Hu, H.: An experimental study on the aerodynamics and aeroacoustic characteristics of small propellers of UAV. In: 54th AIAA Aerospace Sciences Meeting, AIAA 2016-1785, San Diego, USA (2016)
19. Marino, L.: Experimental analysis of UAV propeller noise. In: 16th AIAA/CAES Aeroacoustics Conference, Stockholm, Sweden (2010)

Chapter 70

Enhanced Geothermal System Performance Prediction Based on Deep Learning Neural Networks



Chuan-Yong Zhu, Di Huang, Bo Yu, Liang Gong, and Ming-Hai Xu

Abstract The rapid development of the global economy and the sharp rise in population has increased human demand for energy. Hot dry rock (HDR) geothermal energy has attracted much attention because of its wide distribution, huge reserves, and high stability. Enhanced geothermal systems (EGS) are used for the extraction of HDR, whose recovery performance has a highly non-linear relationship with actual production constraints. Therefore, accurately predicting geothermal productivity is an important task for managing sustainable geothermal systems. In this paper, we use a convolutional neural network (CNN), a long short-term memory network (LSTM), and hybrid models based on a convolutional neural network and a long short-term memory network model (CNN-LSTM) for prediction. The dataset is obtained from numerical simulations on the dynamic economic performance of EGS extraction with different well model parameters and fracture parameters. The performance of different neural networks for geothermal capacity prediction is evaluated comprehensively. The results show that the CNN-LSTM neural network can predict geothermal energy production accurately and stably. Compared with the original LSTM and CNN neural networks, the combined network has the best geothermal capacity prediction accuracy, stability, and generalization ability. This study provides a highly accurate and efficient prediction method for geothermal capacity prediction.

Keywords Geothermal productivity prediction · Deep learning · Long short-term memory · Convolutional neural network

C.-Y. Zhu · D. Huang · L. Gong (✉) · M.-H. Xu
College of New Energy, China University of Petroleum (East China), No. 66, West Changjiang Road, Huangdao District, Qingdao 266580, P. R. China
e-mail: lgong@upc.edu.cn

B. Yu
School of Mechanical Engineering, Beijing Institute of Petrochemical Technology, 19 Qingyuan North Road, Daxing District, Beijing 102617, China

70.1 Introduction

In recent years, due to the extensive use of traditional fossil fuels, problems such as energy shortages and environmental pollution have been caused [1, 2]. Therefore, it is urgent to reduce the use of fossil fuels and find low-carbon renewable energy sources [3]. Hot dry rock (HDR) geothermal resources have the potential to satisfy the world's energy needs in the long term because of their clean and stable nature [4, 5]. However, the most important characteristic of dry heat rock type geothermal resources is that their reservoirs are dense and contain no or little fluid. It is difficult to recover thermal energy by circulating water through the high-temperature reservoir. Therefore, Enhanced Geothermal System (EGS) has been designed to extract thermal energy from dry heat rocks [6]. The EGS process involves complex multi-field coupling processes, and there is a highly nonlinear relationship between its productivity and parameters such as fracture distribution and well network layout. Hence, developing a fast and accurate method for predicting the EGS heat production capacity is crucial to ensure the sustainable utilization of geothermal resources.

Numerical simulation is the most used method for predicting the performance of HDR [7–9]. However, establishing numerical models is a time-consuming and computationally intensive task. Previous studies have proved that deep learning techniques are computationally efficient and cost-effective compared to experimental and numerical methods. As a core technology of artificial intelligence algorithms, deep learning has been widely applied in various scientific and engineering fields in recent years. Researchers have also conducted relevant studies in the geothermal field.

After obtaining EGS extraction data based on numerical simulations, Zhou et al. [10] analyzed the effects of four key factors, i.e., well spacing, injection temperature, injection rate, and fracture permeability, on reservoir performance using an artificial neural network approach. Their results showed that the injection rate had the greatest effect on the total heat extraction rate, followed by the injection temperature and well spacing, while the fracture permeability had the least effect. Gudmundsdottir and Horne [11] compared the predictive power of feedforward and recurrent neural networks based on geothermal data. The results show that simple feedforward neural networks simplify the model structure and reduce the training time. And its prediction performance is better than that of recurrent neural networks. Pandey and Singh [12] used temperature, mass flow rate, pressure, and fracture permeability as input parameters to a neural network for the prediction of recovery temperature. The results showed that the neural network could accurately predict the thermal drawdown of the EGS system. During the extraction process of geothermal energy, reservoir parameters continuously change over time, which is a typical time-series problem. An artificial neural network type called the Long Short Term Memory network (LSTM) has shown great potential for time-series prediction. Shi et al. [13] combined LSTM and Multilayer Perceptron (MLP) neural networks. In this combined model, MLP is used to learn the nonlinear relationship between geothermal energy production and input features, and LSTM is used to memorize the time-series relationships in the data. The results show that the combined neural network has the best geothermal

capacity prediction accuracy, stability, and generalization ability. Gudala and Govindarajan [14] predicted the production temperature by nine influencing parameters. They combined machine learning, response surface modeling, and the Autoregressive Integrated Moving Average model (ARIMA) model. Through training, the accuracy of the integrated ML-RSM-ARIMA model for geothermal production prediction was confirmed. In recent years, researchers have combined LSTM with Convolutional Neural Networks (CNN) to extract both temporal and spatial features, and the CNN-LSTM hybrid model has been applied in different fields. For example, Wang et al. [15] used a region-based CNN-LSTM model with text input for natural language processing; Ullah et al. [16] designed a combined CNN and bidirectional LSTM model to recognize human actions in video sequences; Zhao et al. [17] proposed a CB-LSTM model obtained by combining CNN and LSTM to perform health detection on machines.

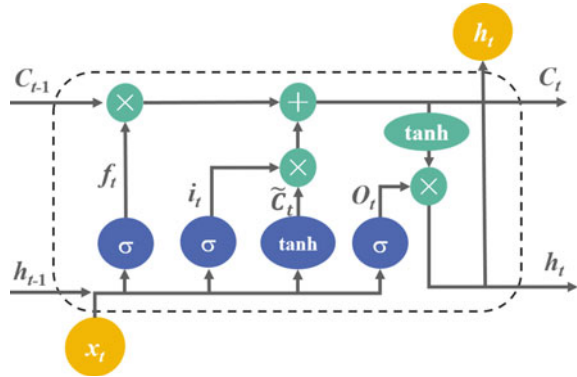
In summary, current research on deep learning-based geothermal prediction still uses simpler artificial neural networks. In addition, most studies use operational parameters such as injection temperature and rate and so on as input features for prediction models. However, in a real geothermal system, the productivity of EGS is directly related to the distribution of reservoir fractures and well location parameters. Therefore, geothermal energy prediction involves multiple input features and dynamic time series. Consequently, it is necessary to build a CNN-LSTM model for geothermal development prediction, where CNN is used to re-eliminate noise and consider correlations among multiple variables, while LSTM is used to handle temporal information. In this paper, we used numerical models to obtain a large amount of production data for EGS under different fracture and injection-production well parameters as the learning dataset. Then a CNN-LSTM combined neural network model was proposed for geothermal energy production prediction and its prediction performance and generalization ability were evaluated. Finally, the prediction performance of the original LSTM, CNN, and LSTM-CNN combination networks were compared.

70.2 Neural Network Description

70.2.1 LSTM Network

Geothermal exploitation is a typical time-series problem with time-varying productivity. Recurrent neural networks have an advantage in dealing with time series problems. Nevertheless, the problem of gradient disappearance may occur if the sequence is too long. To solve this problem, Hochreiter and Schmidhuber [18] proposed a long short-term memory (LSTM) neural network, which improves the basic structure of recurrent neural networks by adding three gating units to each LSTM unit. These units filter out unnecessary information, retain useful information, and transmit it to

Fig. 70.1 Information passing in LSTM cells



the following time point. This allows the LSTM to efficiently process serialized data with long-term dependencies.

As shown in Fig. 70.1, the cell state C_t is the main medium of information transmission in LSTM, flowing throughout the entire information conveyor belt. The cell state at time $t - 1$, C_{t-1} undergoes a process of information filtering and addition through three gate units: the forget gate (Fig. 70.1, f_t), the input gate (Fig. 70.1, i_t), and the output gate (Fig. 70.1, O_t), before being passed on to the cell state at time t , C_t . This vector encompasses a “summary” of all input information processed by the neural network up to time $t + 1$.

The forget gate determines how much of the previous cell state can be retained at the current time step. The input gate determines how much of the new information at this time step will be stored in the cell state. After the calculations of the forgetting gate and input gate are completed, the cell states are updated and passed on. Finally, the output gate is responsible for determining how much information from the cell state should be output to the next layer of the LSTM or as the final output. The expressions are as follows:

$$f_t = \sigma(W_f \cdot [h_{t-1}, x_t] + b_f) \quad (70.1)$$

$$i_t = \sigma(W_i \cdot [h_{t-1}, x_t] + b_i) \quad (70.2)$$

$$\tilde{C}_t = \tanh(W_c \cdot [h_{t-1}, x_t] + b_c) \quad (70.3)$$

$$C_t = f_t * C_{t-1} + i_t * \tilde{C}_t \quad (70.4)$$

$$O_t = \sigma(W_o \cdot [h_{t-1}, x_t] + b_o) \quad (70.5)$$

$$h_t = O_t \cdot \tanh(C_t) \quad (70.6)$$

In Eqs. (70.1)–(70.6), w represents weight. b is bias. σ denotes the sigmoid activation function and \tanh denotes tanh activation function.

70.2.2 CNN Network

CNN is a neural network designed to process images, and its topology is shown in Fig. 70.2. CNN has a deep structure. The weight-sharing structure and translation invariance of CNN enable it to reduce large-scale spatial data to small-scale data without ignoring the local structural information of images. This addresses the issue of slow training performance in conventional neural networks due to a large number of network parameters and the loss of spatial information when images are flattened into vectors.

The basic structure of a CNN consists of an input layer, a convolutional layer, an activation function layer, a pooling layer, a fully connected layer, and an output layer. The input layer mainly operates on the input data. Input data can be in various formats such as 1-D, 2-D, or even n-D. The object of this paper is time series data, so the model uses a 1-D data input format. The essence of the convolution layer is a mutual correlation operation. The detailed steps of the convolution operation are shown in Fig. 70.3. Taking the two-dimensional interrelation operation as an example, the convolution kernel starts from the upper left corner of the input tensor and slides from left to right and from top to bottom. When the convolution window slides to a new position, the part of the tensor contained in the window is multiplied by elements with the convolution kernel tensor. The resulting tensor is then summed to obtain a single scalar value, which yields the output tensor value at this position. The activation function layer aims to enhance the expressiveness of the entire network, and common activation functions include sigmoid, tanh, and RELU. The pooling layer typically comes between consecutive convolution layers, which compresses the amount of data and parameters, thereby reducing overfitting. The pooling layer is used to compress the number of data and parameters thereby reducing overfitting. Pooling methods mainly include average pooling and maximum pooling. Similar to the cross-correlation operator, the pooling window starts from the upper left corner of the input tensor and slides from left to right and top to bottom in the input tensor.

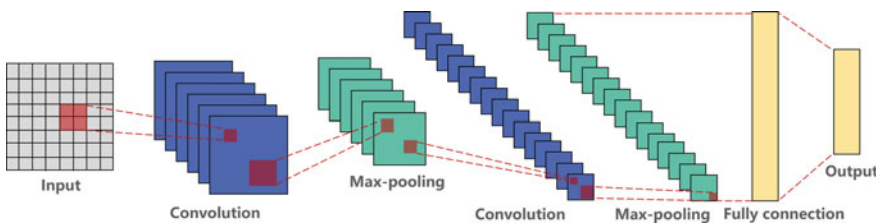


Fig. 70.2 CNN topology

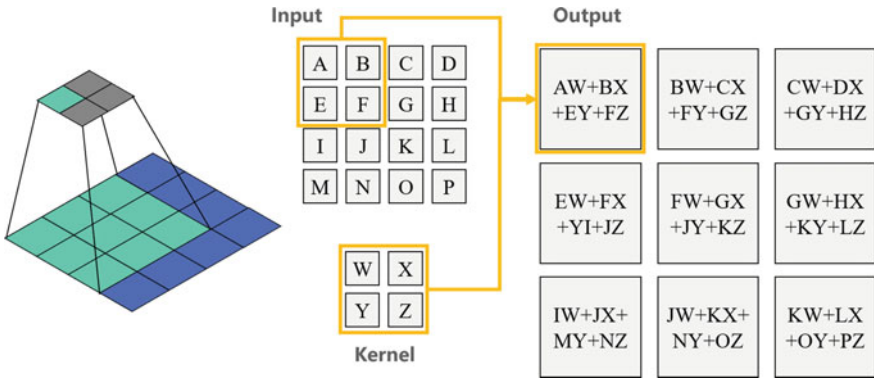
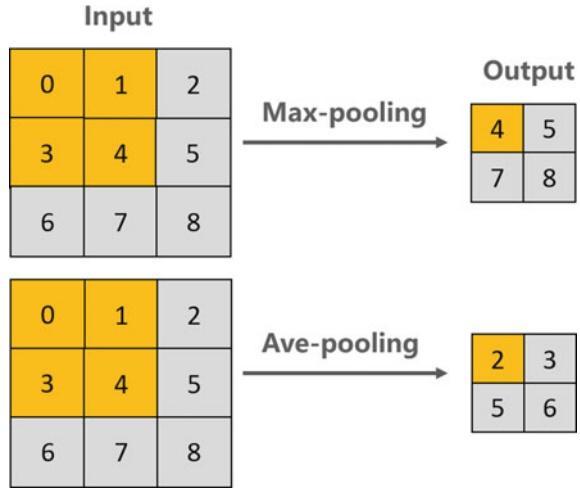


Fig. 70.3 Principles of convolutional layer calculation

Fig. 70.4 Principles of pooling layer calculation



At each position reached by the pooling window, the max-max or average value of the input sub-tensor within the window is calculated, as shown in Fig. 70.4.

70.2.3 LSTM and CNN Combinational Neural Network

The trend of power generation evolution of the EGS system exhibits high dimensionality, nonlinearity, and high time lag. Predicting power generation is a challenging task. CNN can extract features from the input data, and LSTM can learn and remember the historical feature information of nonlinear time series data. If the advantages of these two models were deeply integrated, an accurate model for power

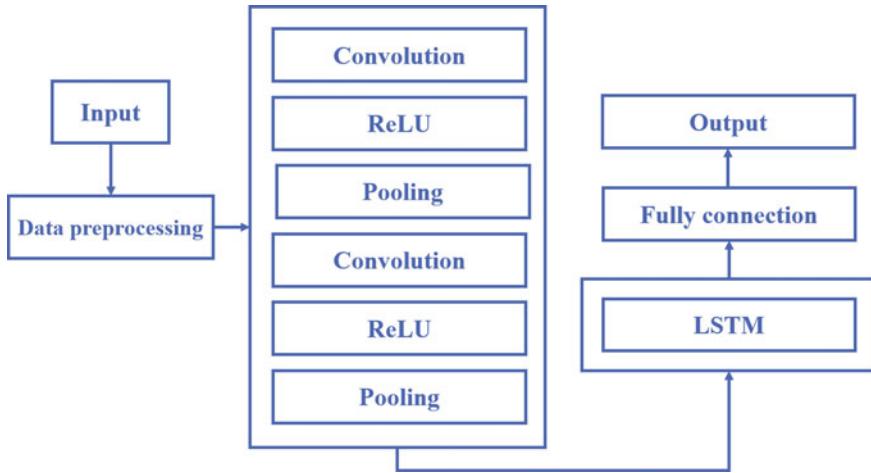


Fig. 70.5 Architecture of proposed CNN-LSTM model

generation prediction can be obtained. Accordingly, this work proposes a generation forecasting model based on a combined CNN-LSTM neural network.

The structure of the CNN-LSTM neural network is shown in Fig. 70.5. After feeding the data into the model, the data preprocessing module is first used to format the original data and divide the data into a training set and a validation set. The preprocessed data are passed into the CNN module, which has two stacked convolutional layers, using ReLU activation functions and pooling layers after each convolutional layer. After utilizing the spatial feature extraction capability of the convolutional layers, we introduce the LSTM part to process the temporal data. In addition, the two neural network submodules in this study are integrated by the tensor processing layer in order to convert the output of the CNN into the input of the LSTM network. Thus, this CNN-LSTM neural network is able to combine the spatial feature extraction of CNN with the ability of LSTM to learn temporal dependencies in time-series data.

70.3 Data Preparation and Preprocessing

70.3.1 Data Preparation

To solve the problem of lack of historical mining data in actual geothermal systems, in this paper, we use TOUGH2-EGS to perform extensive numerical simulations of production data under different well types and fracture distributions. These data constitute the sample database for deep learning. The input features of the neural network prediction model include well length, vertical well spacing, horizontal

Table 70.1 Values of different main controlling factors in big data sample database

Constraints	Values
Well length (m)	100, 150, 200, 250, 300
Vertical well spacing (m)	150, 250, 350, 450, 550
Horizontal well spacing (m)	150, 250, 350, 450, 550
Number of fractures	20, 30, 40, 50, 60
Length of fractures (m)	100, 150, 200, 250, 300
Width of fractures (mm)	1, 3, 5, 7, 9

well spacing, number of fractures, fracture length, and fracture width, as shown in Table 70.1. Five sets of values were assigned to each major control factor, with a total of 15,000 data points. The output parameter is the cumulative power production of the geothermal system.

After building a database for deep learning, the data needs to be pre-processed firstly. Since the data in this paper are derived from numerical simulations, the data set has smooth time intervals and few outliers, which can be normalized. In this study, the raw data were processed using z-score normalization by Eq. (70.7).

$$x' = \frac{x - \mu}{\sigma} \quad (70.7)$$

In the equation, x represents the original feature matrix; x' represents the normalized feature matrix; μ represents the mean value of the original feature matrix; and σ represents the standard deviation of the original feature matrix. Z-score enables the model to read the feature differences in different units by normalizing the raw data of different magnitudes to the range of $[-1, 1]$. Thus, it accelerates the training and convergence of the model.

In deep learning, the sample database is frequently divided into a training set and a validation set. In this study, 80% of the sample data is used to train the model and 20% of the sample data is used to validate the model.

70.3.2 Prediction Accuracy Evaluation

This study uses the root mean square error (RMSE), mean absolute error (MAE), and mean absolute percentage error (MAPE) to evaluate the performance of the neural network model. The expressions are as follows:

$$RMSE = \sqrt{\frac{1}{n} \sum_{i=1}^n (y_i - \hat{y}_i)^2} \quad (70.8)$$

$$MAE = \frac{1}{n} \sum_{i=1}^n |y_i - \hat{y}_i| \quad (70.9)$$

$$MAPE = \frac{1}{n} \sum_{i=1}^n \left[\frac{|y_i - \hat{y}_i|}{\hat{y}_i} \right] \times 100\% \quad (70.10)$$

In the formulas, n represents the number of samples; y_i represents the predicted value; \hat{y}_i represents the actual value.

70.4 Results and Discussions

70.4.1 Effects of Network Structure Parameters

In this section, for the combined CNN-LSTM neural network, we investigate the effects of convolutional kernel size, number of convolutional kernels and pooling method in the CNN module and the effects of the number of hidden layers and the number of hidden layer nodes in the LSTM module on the performance of the neural network. To prevent overfitting, an early stopping mechanism is used in this paper. This means that when the accuracy of the validation set does not improve within a specified number of consecutive training sessions, the model will stop training and output the results.

In CNN, the size of convolutional kernels and the number of convolutional kernels have a direct influence on the performance of the neural network. Figure 70.6 shows the validation set error with different convolutional kernel sizes and the number of convolutional kernels. In CNNs, the size of convolutional kernels is usually odd. In this way, the input and output can be of the same size by padding the same number of rows at the top and bottom and columns of the same size at the left and right sides of the input tensor. Consequently, in this paper, the convolutional kernel sizes are taken as 3, 5, and 7 for comparison. In particular, to ensure that the input and output have the same size, the padding values in this paper are 1, 2, and 3, and the stride is 1 when the size of the convolution kernel is 3, 5, and 7, respectively.

As can be seen from Fig. 70.6a, the error of the CNN-LSTM neural network on the validation set gradually increases as the convolutional kernel size increases. This is because, for the convolutional layers, the stacking of multiple layers of small-sized convolutional kernels can achieve the same perceptual range as a single layer of large-sized convolutional kernels, while having smaller parameters and computational effort. In addition, multiple layers of small-sized convolutional kernels can enhance the depth rather than the width of the neural network, which increases the ability to fit nonlinearities. The RSME, MAPE, and MAE for convolutional kernel size 3 are 0.13, 1.23, and 0.10, respectively, and 0.20, 1.42, and 0.15 for convolutional kernel size 7,

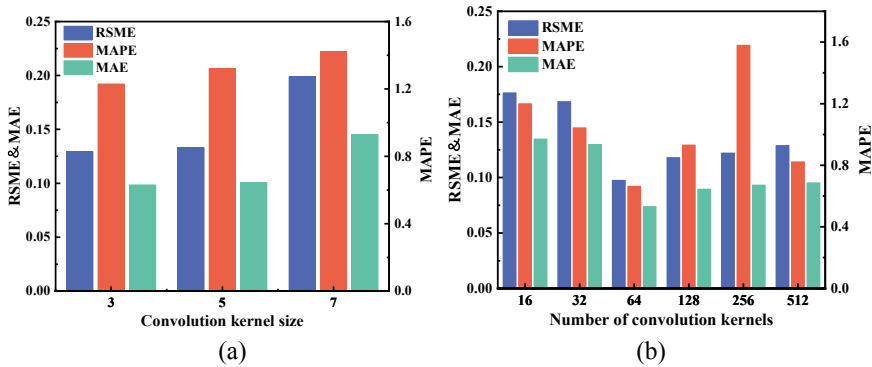


Fig. 70.6 Validation set error under different convolutional kernel sizes (a) and the number of convolutional kernels (b)

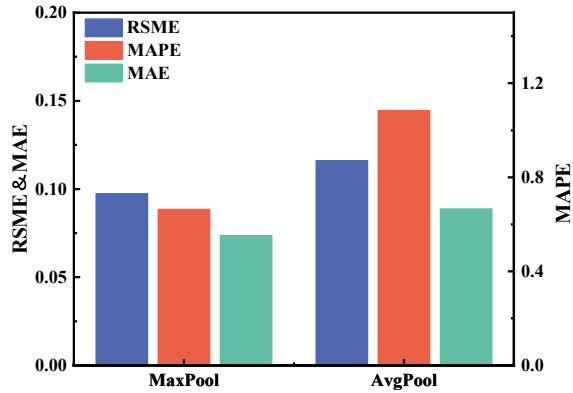
respectively, with an error increase of 54%, 15%, and 50%, respectively. Therefore, in this paper, a convolutional kernel of size 3 is chosen.

The number of convolution kernels means the number of output channels. Each convolution kernel outputs a corresponding result, which is a one-dimensional feature map. Multiple convolution kernels will output a feature map with the corresponding number of channels, which will be stacked together to output a feature map matrix with depth. The number of convolutional kernels is usually chosen as a power of 2. Therefore, in this paper, we study the error on the validation set by taking 16, 32, 64, 128, 256, and 512 convolutional kernels, and the results are shown in Fig. 70.6b. From the figure, it can be observed that when the number of convolutional kernels is too few or too large, it will lead to the increase of the error. Therefore, the final number of convolutional kernels chosen in this paper is 64, which has the smallest error on the validation set.

For the pooling layer, the maximum pooling layer and the average pooling layer are compared in this paper. Figure 70.7 shows the validation set errors under different pooling methods. The results show that the neural network with the maximum pooling layer is better than the average pooling layer. This may be due to the fact that Max-pooling directly selects the most significant features, which can retain more feature texture information. Therefore, the Max pooling method was chosen in this study. In this case, the RMSE is 0.097, MAE is 0.074, and MAPE is 0.664.

The error was investigated for the LSTM module in the CNN-LSTM hybrid neural network under various numbers of hidden layers and hidden nodes. The number of hidden nodes varied from 4 to 512, while the number of hidden layers varied from 1 to 3 in this study. The outcomes are displayed in Fig. 70.8. This image illustrates that when the number of hidden layers increases, it results in an increase in the prediction error. This is due to the possibility of the gradient disappearing when the LSTM layers are too deep, which would increase inaccuracy. Furthermore, as the number of hidden nodes rises, the error steadily reduces, but when the number of hidden nodes reaches 512, the error may increase. To speed up model computation and

Fig. 70.7 Validation set error under different pooling methods



convergence in this study, the number of hidden layers and nodes should be chosen to minimize the model size and structure while ensuring that the total model error is within the acceptable range. As a consequence, 1 hidden layer and 256 nodes were finally chosen. This combination produced the model’s least overall error and best performance, with RMSE, MAPE, and MAE of 0.126, 0.834, and 0.096, respectively.

Another crucial deep learning hyperparameter is the learning rate. The loss function changes more quickly as the learning rate rises, whereas a lower learning rate causes the loss function to change more slowly. However, if the learning rate is too high, the loss function may not approach the local minimum. The convergence complexity of the neural network will dramatically increase and the convergence speed will slow down if the learning rate is too low. Consequently, choosing the right learning rate parameter is crucial for enhancing the effectiveness of deep learning models. In order to balance training duration and model accuracy, this paper employs

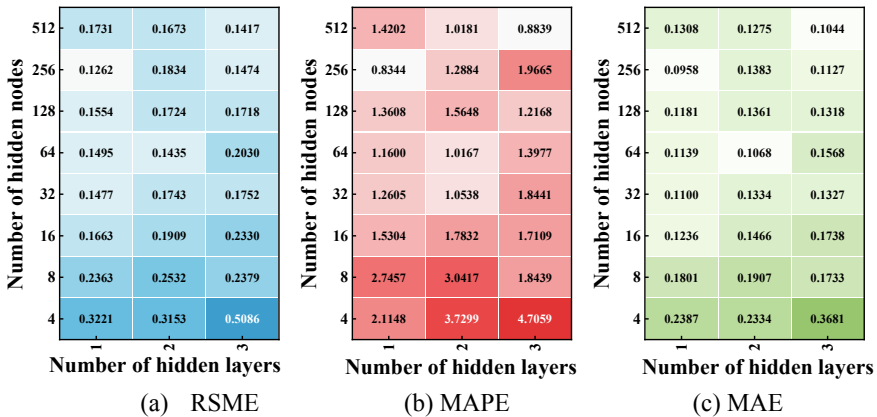


Fig. 70.8 Error comparison of three evaluation indicators with different numbers of hidden layers and nodes in hidden layers

a dynamic learning rate modification technique. The fundamental idea is to choose an initial learning rate and then use an adaptive approach to change it at the conclusion of each training cycle. The learning rate steadily drops as the loss function gets closer to the global optimum, and the model eventually reaches it. This is how it is expressed:

$$LR^* = LR \times \gamma \quad (70.11)$$

In the formula, LR represents the initial learning rate, LR^* represents the dynamically adjusted learning rate, and γ represents the decay rate, which is set to 0.999.

The effect of various initial learning rates on error is depicted in Fig. 70.9. The findings demonstrate that the errors of the three evaluation metrics on the validation set are much bigger when the initial learning rate is set to 0.01 than they are under other learning rates. This is because the gradient cannot converge to a local minimum during the propagation process. The error steadily diminishes as the initial learning rate declines. However, the model might become caught in a local minimum and fail to converge to the global optimum, slowing down convergence dramatically as the learning rate declines. As a result, in this part, the initial learning rate is set to 0.001, at which point all evaluation measures' errors are at their lowest values, and the validation set's RMSE, MAE, and MAPE values are, respectively, 0.094, 0.071, and 1.337.

In conclusion, Table 70.2 displays the key characteristics of the CNN-LSTM neural network. Based on the selection of the aforementioned hyperparameters, an effective neural network model has been created. The validation set's cumulative net power generation's anticipated and actual values are contrasted in Fig. 70.10. The great accuracy of the trained model in prediction is indicated by their good consistency.

Fig. 70.9 Errors on the validation set with different initial learning rates

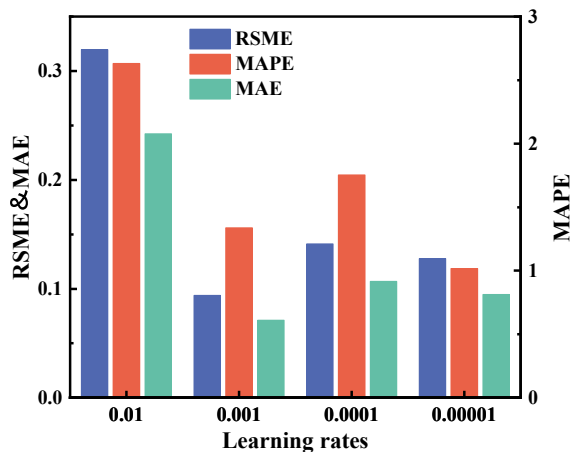
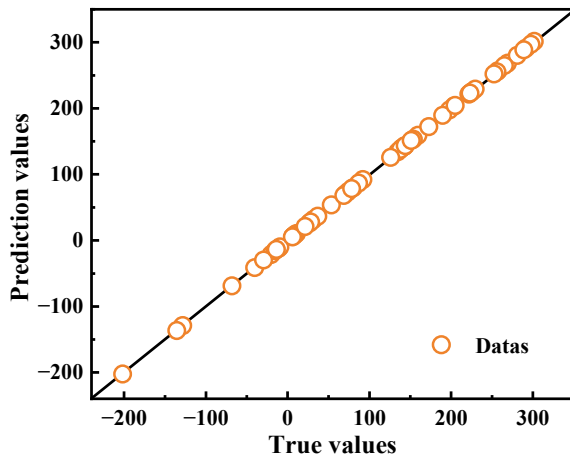


Table 70.2 The main parameters of CNN-LSTM neural network

Main parameters	Values
Kernel size	3
Number of kernels	64
Padding	1
Stride	1
Pooling layer	Max-pooling
Activation layer	ReLU
LSTM hidden nodes	1
LSTM hidden layers	256
Optimizer	Adam

Fig. 70.10 Prediction and true values of the cumulative net generation on the validation set

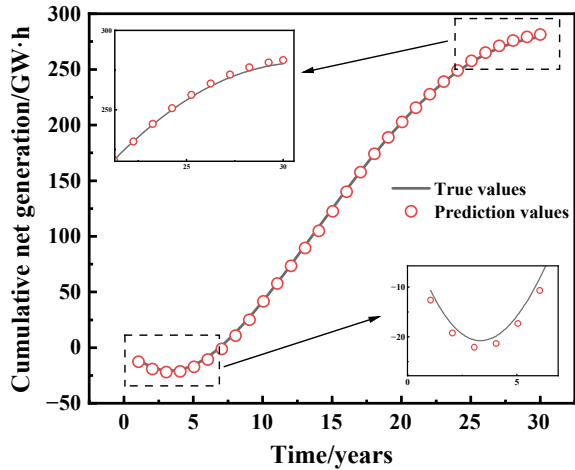


70.4.2 A Case Study of the LSTM-CNN Combinational Network

The CNN-LSTM neural network model performed well at predicting cumulative net power generation in the previous section. Here a new dataset (prediction set) that was not used in the training process is used to assess the generalization ability of this model. In the new dataset, the well length is 120 m, the vertical well spacing is 450 m, the horizontal well spacing is 400 m, the number of fractures is 32, the fracture length is 270 m, and the fracture width is 4 mm. Cumulative net power generation is projected as the output parameter. We will verify the trained model’s accuracy in predicting new geothermal fields using this prediction set.

The prediction results of cumulative net power generation on the prediction set are shown in Fig. 70.11. As can be seen from the figure, the predicted values agree well with the actual values. In the prediction set, the RMSE, MAPE and MAE

Fig. 70.11 The predicted results of the cumulative net generation on the prediction set



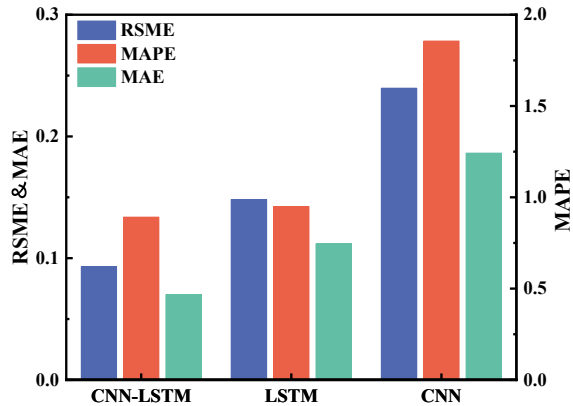
are 0.51, 3.86 and 0.38, respectively. This indicates that the model has excellent prediction accuracy and that the deep learning prediction model of geothermal system performance based on large data has strong universality. It is feasible to correctly and effectively anticipate the cumulative net power generation of a specific production plan when establishing new geothermal fields.

70.4.3 Comparisons of Different Neural Networks

The performance of the original CNN neural network, the LSTM neural network, and the suggested CNN-LSTM neural network in this article were compared in this section. The dataset utilized was the same as previously described. Six parameters were included in the input features: well depth, vertical well spacing, horizontal well spacing, number of fractures, fracture length, and fracture breadth. The output was EGS's cumulative net power production. The dataset was first normalized using the Z-score approach. Next, 80% of the data was utilized for training, while the remaining 20% was used as a validation set. The best prediction models were obtained by optimizing the hyperparameters of each neural network. The performance differences amongst neural networks were investigated by comparing the RSME, MAE, and MAPE of several neural network models.

Figure 70.12 depicts the validation set errors of several neural networks. It can be seen that the prediction results of the combined CNN-LSTM network are lower than the other two neural networks in all three errors. The CNN-LSTM neural network lowered the RSME, MAPE, and MAE by 61.22%, 46.62%, and 62.41%, respectively, when compared to the neural network with the highest error. This is due to the CNN module's data feature extraction capabilities in CNN-LSTM being advantageous for reducing unstable elements and making data features more apparent. It also builds the

Fig. 70.12 Errors of different neural networks on verification sets



groundwork for the LSTM network to extract data temporal properties. Ultimately, the CNN-LSTM network can considerably increase the accuracy and stability of geothermal energy production forecasts by combining the benefits of LSTM and CNN.

70.5 Conclusions

In this study, a CNN-LSTM hybrid neural network is proposed for estimating EGS production capacity. By numerical simulation, a huge data sample library for deep learning was produced, and the input characteristics included six dimensions: well length, vertical well spacing, horizontal well spacing, number of fractures, length of fractures, and width of fractures. The cumulative power generation of EGS was the expected output characteristic. Based on the dataset, a geothermal energy production prediction model for the CNN-LSTM combined network was trained, and the effect of its hyperparameters on prediction performance was investigated. At last, the original LSTM, CNN, and CNN-LSTM combined networks were compared in terms of performance. The main conclusions are as follows: The CNN-LSTM neural network can predict geothermal energy generation with high accuracy. The CNN-LSTM neural network has an RSME prediction error of 0.51 for the prediction set data and suggests high generalization ability. Moreover, comparing the RSME, MAE, and MAPE across different neural network models reveals that the CNN-LSTM combined network may greatly improve geothermal energy production forecast accuracy when compared to the original LSTM and CNN networks.

References

1. Kinney, P.L.: Interactions of climate change, air pollution, and human health. *Curr. Environ. Health Rep.* **5**, 179–186 (2018)
2. Lelieveld, J., Klingmüller, K., Pozzer, A., Burnett, R.T., Haines, A., Ramanathan, V.: Effects of fossil fuel and total anthropogenic emission removal on public health and climate. *Proc. Natl. Acad. Sci. U. S. A.* **116**, 7192–7197 (2019)
3. Danish, Baloch, M.A., Mahmood, N., Zhang, J.W.: Effect of natural resources, renewable energy and economic development on CO₂ emissions in BRICS countries. *Sci. Total Environ.* **678**, 632–638 (2019)
4. Zeng, Y., Tang, L., Wu, N., Cao, Y.: Analysis of influencing factors of production performance of enhanced geothermal system: a case study at Yangbajing geothermal field. *Energy* **127**, 218–235 (2017)
5. Li, K., Bian, H., Liu, C., Zhang, D., Yang, Y.: Comparison of geothermal with solar and wind power generation systems. *Renew. Sustain. Energy Rev.* **42**, 1464–1474 (2015)
6. Kelkar, S., WoldeGabriel, G., Rehfeldt, K.: Lessons learned from the pioneering hot dry rock project at Fenton Hill, USA. *Geothermics* **63**, 5–14 (2016)
7. Wang, S., Zhang, J., Yang, Z., Yin, C., Wang, Y., Zhang, R., et al.: Fully Coupled Thermal-Hydraulic-Mechanical Reservoir Simulation with Non-Isothermal Multiphase Compositional Modeling, Day 3 Wed, 22 Feb 2017, Montgomery, Texas, USA, p. D031S010R002. *SPE* (2017)
8. Chen, P., Sun, J., Lin, C., Zhou, W.: Application of the finite volume method for geomechanics calculation and analysis on temperature dependent poromechanical stress and displacement fields in enhanced geothermal system. *Geothermics* **95**, 102138 (2021)
9. Zheng, J., Fan, T., Dou, B., Cui, G., Tian, H.: A Thermal-hydraulic-mechanical coupling simulation of fluid flow and heat transfer specifically in crossed-rough fractures in a geothermal reservoir. *J. Energy Eng.* **148**, 04022032 (2022)
10. Zhou, L., Zhang, Y., Hu, Z., Yu, Z., Luo, Y., Lei, Y., et al.: Analysis of influencing factors of the production performance of an enhanced geothermal system (EGS) with numerical simulation and artificial neural network (ANN). *Energy Build.* **200**, 31–46 (2019)
11. Gudmundsdottir, H., Horne, R.: Prediction Modeling for Geothermal Reservoirs Using Deep Learning (2020)
12. Pandey, S., Singh, M.: Artificial neural network to predict the thermal drawdown of enhanced geothermal system. *J. Energy Res. Technol.* **143**, 1–19 (2021)
13. Shi, Y., Song, X., Song, G.: Productivity prediction of a multilateral-well geothermal system based on a long short-term memory and multi-layer perceptron combinational neural network. *Appl. Energy* **282**, 116046 (2021)
14. Gudala, M., Govindarajan, S.K.: Numerical investigations on a geothermal reservoir using fully coupled thermo-hydro-geomechanics with integrated RSM-machine learning and ARIMA models. *Geothermics* **96**, 102174 (2021)
15. Wang, J., Yu, L.-C., Lai, K.R., Zhang, X.: Dimensional sentiment analysis using a regional CNN-LSTM model. In: *Proceedings of the 54th Annual Meeting of the Association for Computational Linguistics (Volume 2: Short Papers)*, pp. 225–230. Association for Computational Linguistics, Berlin, Germany (2016)
16. Ullah, A., Ahmad, J., Muhammad, K., Sajjad, M., Baik, S.W.: Action recognition in video sequences using deep bi-directional LSTM with CNN features. *IEEE Access* **6**, 1155–1166 (2018)
17. Zhao, R., Yan, R., Wang, J., Mao, K.: Learning to monitor machine health with convolutional bi-directional LSTM networks. *Sensors* **17**, 273 (2017)
18. Hochreiter, S., Schmidhuber, J.: Long short-term memory. *Neural Comput.* **9**, 1735–1780 (1997)

Chapter 71

The Influence of the Mesh Size on Numerical Simulations of Dynamic Buckling of the Stiffened Cylindrical Shell Subjected to Underwater Explosion Shock Wave



Chen-Xing Qu, Shao-Fei Ren, Peng-Fei Zhao, and Qi Wang

Abstract Dynamic buckling of submerged cylindrical shells subjected to underwater explosion (UNDEX) seriously threatens the safety of structures. Due to fluid–structure interaction, geometric and material nonlinearities, the relevant theoretical, numerical and experimental studies are very limited. Dynamic buckling of a stiffened cylindrical shell subjected to the UNDEX shock wave is numerically studied by the coupled acoustic–structural formulation in ABAQUS/Explicit, and the influence of the mesh size of the cylindrical shell on the buckling behavior is investigated. Both the hydrostatic pressure and the UNDEX shock wave acting on the shell are considered in the finite element model. The mesh size for the static buckling analysis of unstiffened cylindrical shells, $\sqrt{Rt}/2$, is taken as the benchmark of the mesh size of the cylindrical shell, where R is the radius of the cylindrical shell, and t is the thickness of the shell. Then, different smaller mesh sizes of the cylindrical shell and the flow field are adopted. Numerical results show that the mesh size of the cylindrical shell has significant influence on the dynamic buckling of the cylindrical shell subjected to UNDEX shock wave. Furthermore, the suggested mesh size of the cylindrical shell is proposed.

Keywords Cylindrical shell · Underwater explosion · Dynamic buckling · Mesh size

C.-X. Qu · S.-F. Ren (✉) · P.-F. Zhao
College of Shipbuilding Engineering, Harbin Engineering University, Harbin 150001, China
e-mail: renshaofei@hrbeu.edu.cn

Q. Wang
Naval Research Academy, Beijing 100073, China

71.1 Introduction

Stiffened cylindrical shells have been widely used because of their excellent mechanical properties. The buckling failure of such structures under possible loads has attracted much attention, and the static buckling has been extensively studied [1–3]. For dynamic buckling behavior of the shells under dynamic load in the air, there are relatively adequate researches [4, 5]. For submerged cylindrical shells, underwater explosion (UNDEX) can cause serious damage to shells, and previous studies have found that the fluid–structure interaction significantly affects the dynamic responses of submerged cylindrical shells [6], which is quite different from the solid/solid impact problems. UNDEX load consists of shock wave and bubble pulsation. The shock wave has a very high peak pressure and a very short duration, then the shock wave is followed by the bubble pulsation load. The bubble stage is much longer than the shock wave, but its peak pressure is about 20% of that of the shock wave [7]. Geers et al. [8, 9] synthesized the shock wave phase and the bubble pulsation phase, and provided empirical formulas of the UNDEX load. Recent years, there have been quite a number of studies [10–12] on the UNDEX shock wave and the bubble pulsation loads. For example, Zhang et al. [13] established a new theory for the dynamics of oscillating bubbles, which unified different classical bubble dynamics equations, and verified the applicability of the theory by experimental and numerical methods.

However, due to fluid–structure interaction, geometric and material nonlinearities, there are relatively few researches on the dynamic buckling of stiffened cylindrical shells subjected to UNDEX loads. Pedron et al. [14] studied the dynamic buckling of the typical structures subjected to UNDEX. Yuan et al. [15] analyzed the dynamic buckling behavior of stiffened cylindrical shells subjected to shock wave generated by UNDEX, and the Budiansky-Roth (B-R) buckling criterion and the South-well buckling criterion were applied to obtain the critical buckling load of stiffened cylindrical shells. Meanwhile, they also briefly analyzed the influence of the amplitude of the load, mesh size, diameter-thickness ratio, length-diameter ratio and other factors on buckling modes and the critical buckling load. Kwon and Fox [16] experimentally and numerically studied the dynamic buckling of the cylindrical shell subjected to UNDEX, and found that serious dynamic buckling occurred at the ends and the back-side of the cylindrical shell. However, some studies found that under different conditions, the more serious dynamic buckling occurred at the front-side of the cylindrical shell [17, 18]. Nie and Zhang [7] numerically studied the dynamic buckling of the cylindrical shell subjected to UNDEX shock wave by ABAQUS/Explicit, and the hoop and axial buckling modes of the cylindrical shell were analyzed. Ren et al. [19] experimentally investigated the dynamic buckling of a submerged grid-stiffened cylindrical shell subjected to radial intermediate-velocity impact.

Review of the literatures shows that previous works mainly focus on the dynamic buckling of the unstiffened cylindrical shells subjected to UNDEX, and the hydrostatic pressure is neglected due to the small immersion depth of the shell. This work is to numerically study the dynamic buckling of a stiffened cylindrical shell subjected to hydrostatic pressure and UNDEX shock wave by the total wave algorithm of

the coupled acoustic-structural formulation in ABAQUS-Explicit. The influence of the mesh size of the shell on the dynamic buckling are studied. $\sqrt{Rt}/2$ which is used for analyzing the static buckling of unstiffened cylindrical shells is selected as the benchmark of the mesh size of the cylindrical shell [20]. Then, different smaller mesh sizes of the cylindrical shell and the flow filed are adopted, and the suggested mesh size of the cylindrical shells and flow filed is proposed.

71.2 Numerical Method and B-R Dynamic Buckling Criterion

71.2.1 Finite Element Model

Figure 71.1 is the geometric model, which includes a cylindrical shell with a length of 3000 mm and two hemispherical end caps with an inner radius of 750 mm. 16 circumferential T-shaped stiffeners are arranged at equal intervals inside the cylindrical shell. The detailed parameters of the stiffened cylindrical shell are listed in Table 71.1.

The stiffened cylindrical shell is made of HY-80 steel. The Johnson–Cook material model (J–C model) [22] is applied and expressed as follows:

$$\sigma_y = (A + B\varepsilon_p^n)(1 + C \ln \varepsilon_p^*) \tag{71.1}$$

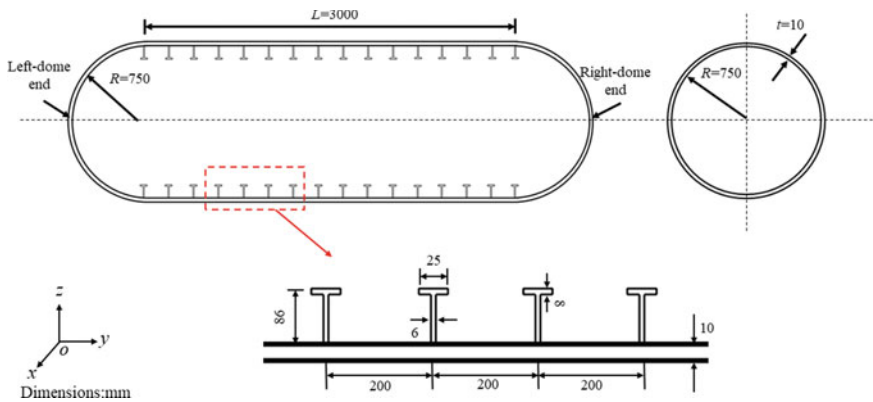


Fig. 71.1 Structural profile of the stiffened cylindrical shell (units of length and thickness: mm)

Table 71.1 Detailed parameters of the stiffened cylindrical shell [21]

Hull thickness	Web height	Web thickness	Flange width	Flange thickness	Frame spacing
10 mm	86 mm	6 mm	25 mm	8 mm	200 mm

where σ_y is the flow stress, ε_p and ε_p^* are the standardized plastic strain, A , B , C , m and n are material parameters.

The mass density ρ , the Young's modulus E , the Poisson's ratio ν , and the constants in J-C model of HY-80 steel are listed in Table 71.2.

The finite element model of the stiffened cylindrical shell and the flow field is established by the ANSYS software. On the premise of ensuring the accuracy and efficiency of the numerical simulations, the radius of the flow field is selected as six times of the radius of the cylindrical shell, and the length of the middle region of the flow field is selected as the same as the length of the shell. The stiffened cylindrical shell is discretized by S4R elements, and the flow field is discretized by AC3D8R elements.

In order to analyze the effect of the mesh size on the dynamic buckling behavior of the stiffened cylindrical shell subjected to UNDEX shock wave, three different mesh sizes are compared in the present work. The buckling of unstiffened shells subjected to static loads has been extensively studied, and the suggested mesh size of the unstiffened cylindrical shell is $\sqrt{Rt}/2$ [20], where R is the radius of the cylindrical shell, and t is the thickness of the shell. Then, $\sqrt{Rt}/2$ is taken as the benchmark of the mesh size of the stiffened cylindrical shell, and two smaller mesh sizes, $\sqrt{Rt}/3$ and $\sqrt{Rt}/4$ of the stiffened shell are considered and compared. The mesh size of the intermediate flow field is the same as the stiffened shell. Then, there are 27,904 shell elements and 1,519,104 solid elements for the mesh size of $\sqrt{Rt}/2$, 41,600 shell elements and 3,744,000 solid elements for the mesh size of $\sqrt{Rt}/3$, and 77,504 shell elements and 5,870,592 solid elements for the mesh size of $\sqrt{Rt}/4$. The finite element model of the stiffened cylindrical shell with the mesh size $\sqrt{Rt}/2$ is shown in Fig. 71.2.

Table 71.2 The material parameters of HY-80 steel [23]

ρ	E	ν	A	B	m	n	C
7746 kg/m ³	211 GPa	0.3	559 MPa	518 MPa	1.14	0.379	0.0268

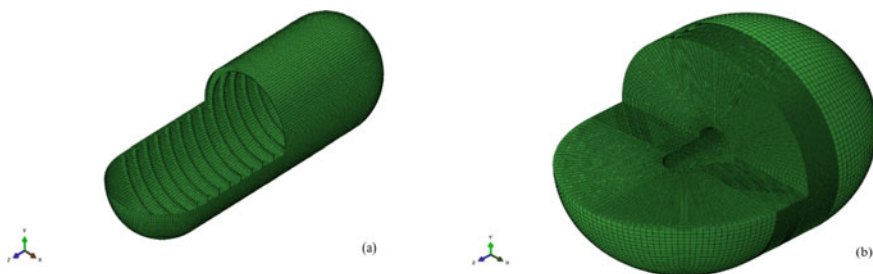


Fig. 71.2 The finite element model of the stiffened cylindrical shell and the flow field with the mesh size of $\sqrt{Rt}/2$

71.2.2 The Coupled Acoustic-Structural Formulation

The coupled acoustic-structural formulation in ABAQUS/Explicit software is applied to calculate the dynamic buckling of the stiffened cylindrical shell subjected to UNDEX shock wave, in which the flow field is treated as an acoustic medium that can transmit the UNDEX load [24]. The density and bulk modulus of the flow field are 1024 kg/m³ and 2.14 GPa, respectively. The total wave algorithm of the coupled acoustic-structural formulation is applied to conduct the numerical simulations, and the semi-empirical formula [25] is used to calculate the UNDEX shock wave load:

$$P(t) = \begin{cases} P_m e^{-\frac{t}{\theta}}, & 0 \leq t < \theta \\ 0.368 P_m \frac{\theta}{t} \left[1 - \left(\frac{t}{t_p} \right)^{1.5} \right], & \theta \leq t \leq t_1 \end{cases} \quad (71.2)$$

$$P_m = \begin{cases} 44.1 \times 10^6 \left(\frac{\sqrt[3]{W}}{d} \right)^{1.5}, & 6 \leq \frac{d}{R_0} < 12 \\ 52.4 \times 10^6 \left(\frac{\sqrt[3]{W}}{d} \right)^{1.13}, & 12 \leq \frac{d}{R_0} < 240 \end{cases} \quad (71.3)$$

$$\theta = \begin{cases} 0.45 R_0 \left(\frac{d}{R_0} \right)^{0.45} \times 10^{-3}, & \frac{d}{R_0} \leq 30 \\ 3.5 \frac{R_0}{c} \sqrt{1g \frac{d}{R_0} - 0.9}, & \frac{d}{R_0} > 30 \end{cases} \quad (71.4)$$

where P_m is the amplitude of the UNDEX shock wave, θ is the decay constant for the spherical shock wave, W is the charge mass, d is the distance from the structure to the explosion center, R_0 is the radius of the spherical charge, c is the speed of sound propagation in water, t_1 is the time when the shock wave pressure drops to the hydrostatic pressure at the corresponding height of the blast core, and t_p is the time from the bubble expansion to the maximum radius to the initiation.

The settings of the total wave algorithm are shown in Fig. 71.3. The source point is at the location of the explosive charge, and the standoff point is the reference point on the outermost surface of the flow field in the total wave algorithm. The outer surface of the flow field is the reference surface. The outer surface of the cylindrical shell and the inner surface of the flow field are tied together to simulate the fluid–structure interaction, and the nonreflecting boundary conditions are set on the outer surface of the flow field.

The mass of TNT is 200 kg, and the distance from the explosive charge to the outer surface of the cylindrical shell is 9.75 m. Because dynamic buckling of stiffened shells subjected to UNDEX has strict conditions, thus, the immersion depth of the stiffened cylindrical shell (H) is changed from 100 m to 475 m to find the buckling condition of the shell, and the case studies are listed in Table 71.3. The pressure–time history curve obtained by the semi-empirical formula with the immersion depth of 475 m is shown in Fig. 71.4.

Some monitoring positions on the stiffened cylindrical shell are selected to determine whether dynamic buckling occurs. The monitoring locations are shown in

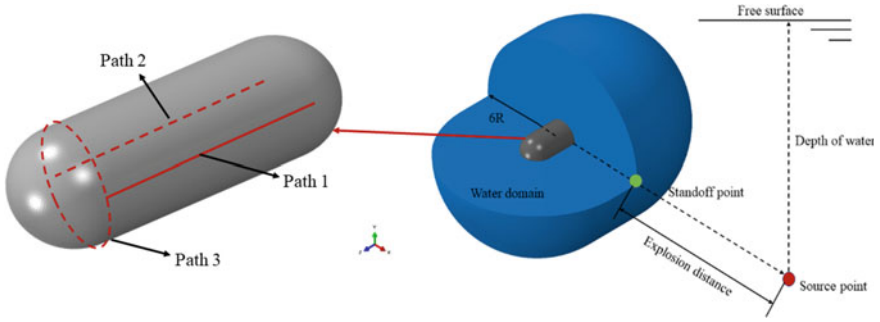


Fig. 71.3 Schematic diagram of the total wave algorithm of the coupled acoustic-structural formulation

Table 71.3 Case studies for different immersion depths of the stiffened cylindrical shell

Case	1	2	3	4	5	6	7
H (m)	100	200	300	400	425	450	475

Fig. 71.4 Pressure–time history curve obtained from the semi-empirical formula

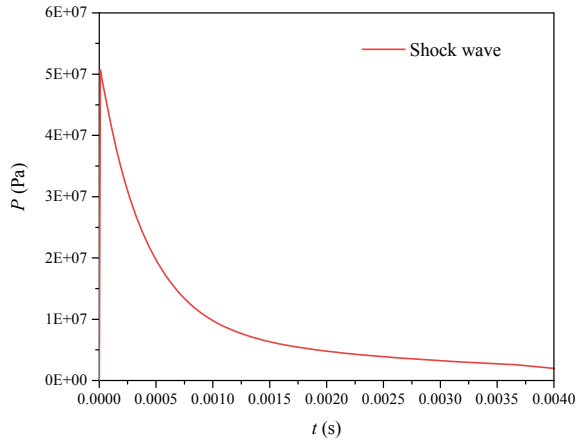


Fig. 71.3, in which Path 1 and Path 2 are along the axial direction of cylindrical shell, while Path 1 is closest to the source point, and Path 2 is farthest from the source point. Path 1 and Path 2 are located on the middle region of the cylindrical shell, and the length of them are 3 m. Path 3 is a circumferential monitoring line in the region near the ends of the shell.

71.2.3 B-R Dynamic Buckling Criterion

Many researchers have proposed a series of dynamic buckling criterion on how to determine the dynamic buckling of structures. The B-R dynamic buckling criterion is selected in the present work. According to this criterion, if the response of the structure changes greatly with a slight increase of the load, then the dynamic buckling occurs, and the corresponding load is the critical dynamic buckling load of the structure. The critical dynamic buckling load determined by the B-R criterion corresponds to the “inflection point” of the load-response curve, which can be found in Fig. 71.6a.

71.3 Results and Discussion

71.3.1 Influence of the Mesh Size on Critical Dynamic Buckling Load

The load-response curve of the stiffened cylindrical shell subjected to UNDEX shock wave were obtained. For the convenience of observation, the hoop plastic strain (ε_c) at the monitoring positions (Path 1, Path 2 and Path 3) of the shell with the mesh size of $\sqrt{Rt}/2$ are shown in Fig. 71.5. In Fig. 71.5c, 0° is the closest position of the stiffened cylindrical shell from the source point, and 180° is the farthest position from the source point.

Due to the symmetry of the numerical model, the Path 1 is divided into regions I and II, the Path 2 is divided into regions III and IV, and the Path 3 is divided into regions V and VI, which is shown in Fig. 71.5. With the increase of the immersion depth, the hoop plastic strain of the shell at regions I and V increases relatively rapidly, while the response in other regions (II, III, IV, VI) does not change significantly. When the immersion depth increases from 400 m to 475 m, the response of the shell in regions I and V increases more rapidly. According to the B-R buckling criterion, it can be concluded that local buckling occurred in regions I and V, which is consistent with the conclusion obtained by Nie and Zhang [7]. However, this phenomenon can not be found in other regions.

The amplitude of the equivalent plastic strain (ε) of the shell in each region was selected as the response parameter, and the immersion depth of the shell was chosen as the load parameter. Then, the load-response curves corresponding to different paths at different regions are shown in Fig. 71.6. For different mesh sizes, there are obvious “inflection points” in load-response curves of the shell in regions I and V, however, there is no obvious “inflection point” in load-response curves of the shell in other regions. It can be concluded that dynamic buckling occurred in regions I and V. According to Fig. 71.6a, it can be concluded that the mesh size has a significant influence on the critical dynamic buckling load of the stiffened cylindrical shell subjected to UNDEX shock wave.

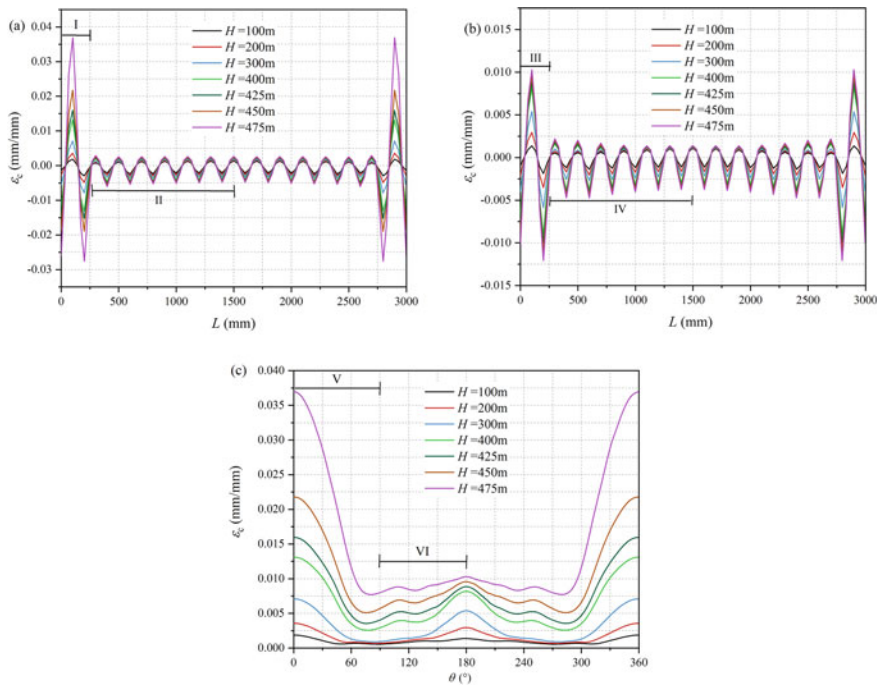


Fig. 7.15 Hoop plastic strain distribution along different paths a Path 1, b Path 2, c Path 3

Figure 7.1.7 shows the equivalent plastic strain nephogram of the stiffened cylindrical shell with the immersion depth of 475 m. It can be found that the smaller mesh size leads to more serious buckling of the shell in local regions. During the calculation, it is found that the critical buckling load of the stiffened cylindrical shell with the mesh size of $\sqrt{Rt}/5$ is basically the same as the critical load of the shell with the mesh size of $\sqrt{Rt}/4$. Then, on the premise of ensuring the calculation efficiency, the mesh size of the stiffened cylindrical shell is selected as $\sqrt{Rt}/4$ when conducting the numerical simulations.

71.3.2 Dynamic Buckling Modes of the Stiffened Cylindrical Shell

According to the above analysis, $\sqrt{Rt}/4$ is selected for the finite element model of the stiffened cylindrical shell and the middle region of the flow field, then the dynamic buckling modes of the stiffened cylindrical shell is analyzed. The axial and hoop plastic strains along Paths 1 and 3 are obtained to monitor buckling modes. For the immersion depth of 475 m, the hoop and axial buckling modes of the shell are shown in Figs. 71.8 and 71.9. Figure 71.8 shows the hoop buckling mode of the

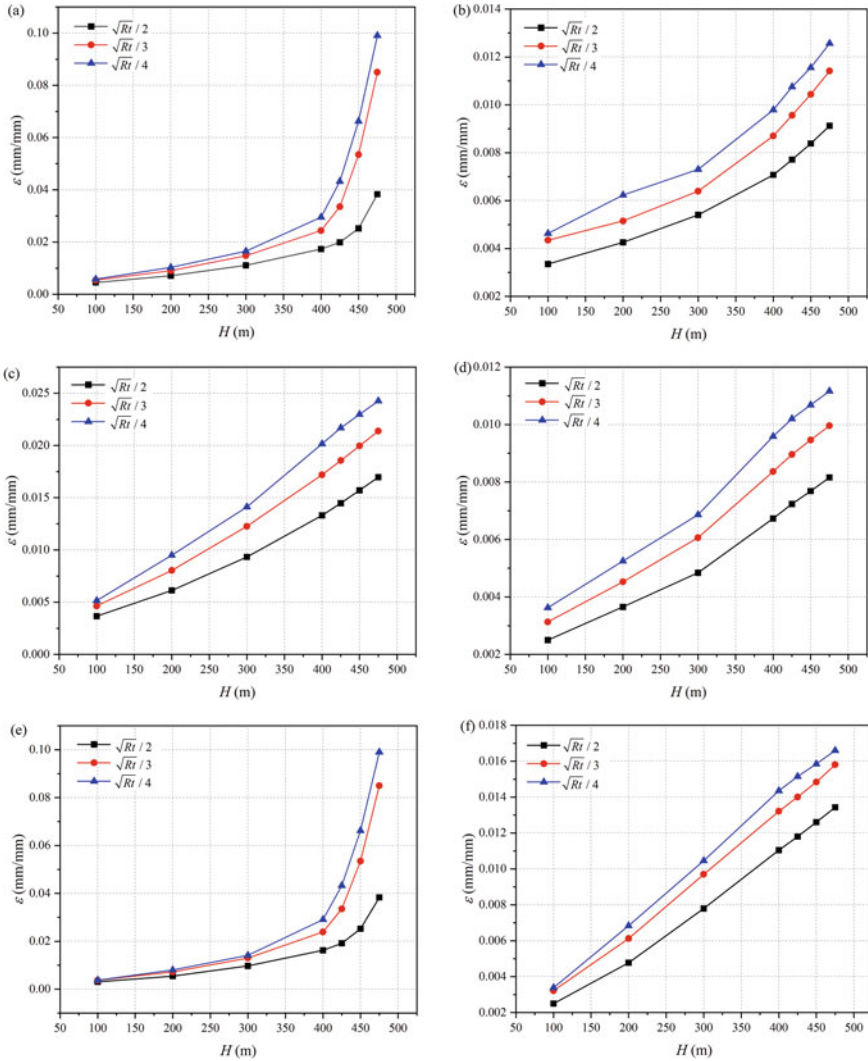


Fig. 71.6 Load-response curves corresponding to different paths at different regions **a** regions I, **b** region II, **c** regions III, **d** region IV, **e** region V, and **f** region VI

stiffened cylindrical shell along Path 3, and Fig. 71.9 shows the axial buckling mode of the shell along Path 1. In these figures, ε_a is the axial plastic strain, ε_e is the plastic strain.

It can be found that the hoop plastic strain is positive and the axial plastic strain is negative along the hoop direction near the end region of the shell. Compared with Figs. 71.5c and 71.8, it is not difficult to find that the range of dynamic buckling failure in the hoop direction near the end region of the shell is about -90° to 90° ,

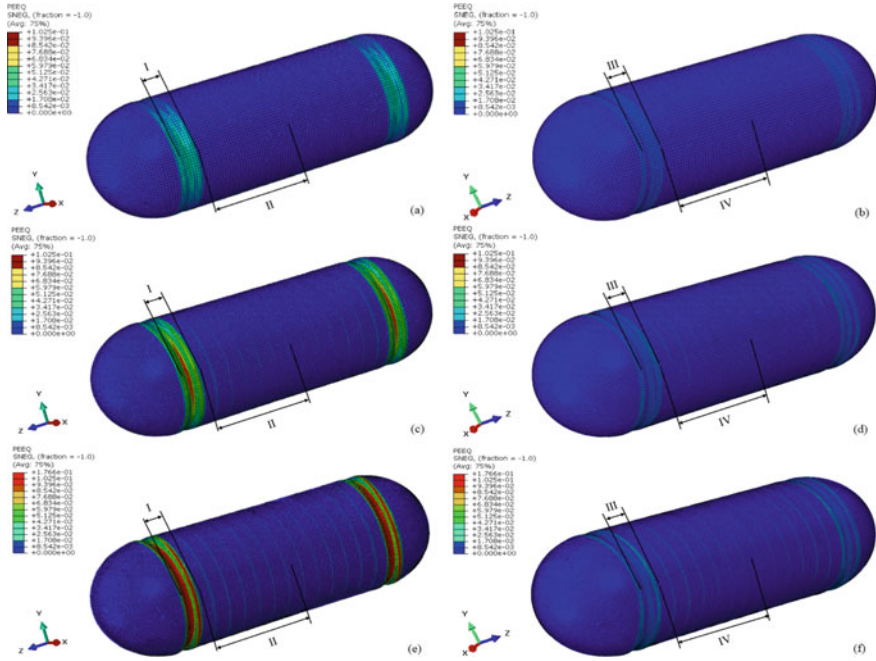
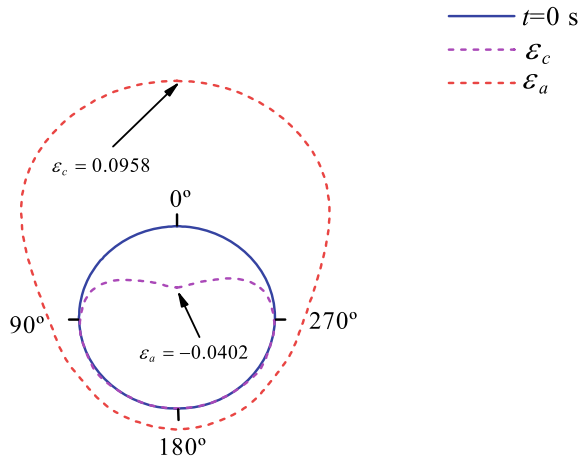


Fig. 71.7 The plastic strain nephogram of the stiffened cylindrical shell with different mesh sizes, **a** and **b** front- and back-sides of the shell with the mesh size of $\sqrt{Rt}/2$, **c** and **d** front- and back-sides of the shell with the mesh size of $\sqrt{Rt}/3$, **e** and **f** front- and back-sides of the shell with the mesh size of $\sqrt{Rt}/4$

Fig. 71.8 Hoop buckling mode of the shell with the mesh size of $\sqrt{Rt}/4$ of Case 7



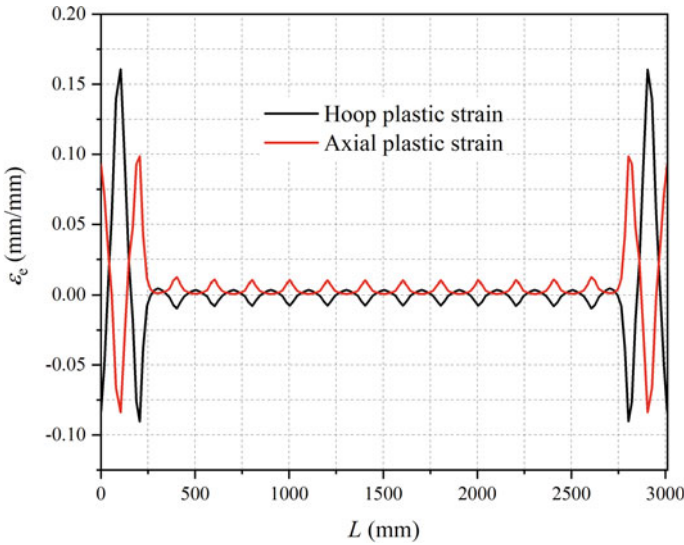


Fig. 71.9 Axial buckling mode of the shell with the mesh size of $\sqrt{Rt}/4$ of Case 7

and in this buckling region, the hoop plastic strain of the shell plays an important role. According to Fig. 71.9, it is found that the hoop and axial plastic strains are alternately arranged along the axis of the buckling region, and when the stiffened cylindrical shell undergoes dynamic buckling subjected to UNDEX shock wave, a relatively obvious buckling half-wave is formed along the axis of the shell in the buckling zone.

71.4 Conclusions

The total wave algorithm in the coupled acoustic-structural formulation of the ABAQUS/Explicit program is used to analyze the influence of the mesh size on the dynamic buckling of the stiffened cylindrical shell subjected to UNDEX shock wave, and the charge mass and the explosion distance are fixed. Then, by comparing numerical results obtained from different immersion depths of the shell, it is found that there are obvious “inflection points” in the load-response curves at typical locations of the stiffened cylindrical shell, which verifies the applicability of the B-R dynamic buckling criterion. By analyzing the numerical results with different mesh sizes, the influence of the mesh size on the dynamic buckling of the stiffened cylindrical shell is investigated. The main conclusions of the present work are as follows:

- (1) Numerical results show that there are obvious “inflection points” in the load-response curves of regions I and V, which indicates that dynamic buckling of the stiffened cylindrical shell occurs near the end caps of the shell, and the B-R dynamic buckling criterion can be used to determine the critical buckling load of the stiffened cylindrical shell subjected to UNDEX shock wave.
- (2) For the dynamic buckling of the stiffened cylindrical shell subjected to UNDEX shock wave, the mesh size of the stiffened cylindrical shell has a significant influence on the critical dynamic buckling load. The widely used mesh size, $\sqrt{Rt}/2$, for static buckling analysis is not suitable for the present problem, and the suggested mesh size of the stiffened cylindrical shell is $\sqrt{Rt}/4$.
- (3) For the stiffened cylindrical shell in the present work, dynamic buckling occurs near the ends of the shell, and the buckling region is distributed from -90° to 90° along the hoop direction.

Acknowledgements This work is supported by the National Natural Science Foundation of China (No. 52171304), and Heilongjiang Provincial Natural Science Foundation of China (No. LH2020E081).

References

1. Zhang, J., Zhang, M., Cui, W.C., Tang, W.X., Wang, F., Pan, B.B.: Elastic-plastic buckling of deep sea spherical pressure hulls. *Mar. Struct.* **57**, 38–51 (2018)
2. Wagner, H.N.R., Hühne, C., Zhang, J., Tang, W., Khakimova, R.: Geometric imperfection and lower-bound analysis of spherical shells under external pressure. *Thin-Walled Struct.* **143**, 106195 (2019)
3. Zingoni, A., Enoma, N.: Strength and stability of spherical-conical shell assemblies under external hydrostatic pressure. *Thin-Walled Struct.* **146**, 106472 (2020)
4. Lindberg, H.E., Florence, A.L.: *Dynamic Pluse Buckling—Theory and Experiment*. Martinus Nijhoff Pub, The Netherlands (1987)
5. Kubiak, T.: *Static and Dynamic Buckling of Thin-Walled Plate Structures*. Springer, Switzerland (2013)
6. Bitter, N.P., Shepherd, J.E.: *Dynamic buckling and fluid-structure interaction of submerged tubular structures. Blast Mitigation—Experimental and Numerical Studies*. Springer, New York (2014)
7. Nie, B.C., Zhang, H.Q.: Hoop and axial plastic buckling modes of submerged cylindrical shells subjected to side-on underwater explosion shock wave. *Mar. Struct.* **84**, 103–200 (2022)
8. Geers, T.L., Hunter, K.S.: An integrated wave-effects model for an underwater explosion bubble. *J. Acoust. Soc. Am.* **111**(4), 1584–1601 (2002)
9. Geers, T.L., Park, C.K.: Optimization of the G&H bubble model. *Shock Vib.* **12**(1), 3–8 (2005)
10. Jin, Z.Y., Yin, C.Y., Chen, Y.: An analytical method for the response of coated plates subjected to one-dimensional underwater weak shock wave. *Shock Vib.* **2014**(pt. 1), 131–136 (2014)
11. Zhang, A.M., Liu, Y.L.: Improved three-dimensional bubble dynamics model based on boundary element method. *J. Comput. Phys.* **294**, 208–223 (2015)
12. Li, T., Zhang, A.M., Wang, S.P.: Bubble interactions and bursting behaviors near a free surface. *Phys. Fluids* **31**(4), 042104 (2019)
13. Zhang, A.M., Li, S.M., Cui, P., Li, S., Liu, Y.L.: A unified theory for bubble dynamics. *Phys. Fluids* **35**, 033323 (2023).

14. Pedron, C.: Dynamic buckling of stiffened cylindrical shells of revolution under a transient lateral pressure shock wave. *Thin-Walled Struct.* **23**(1–4), 85–105 (1995)
15. Yuan, J.H., Zhu, X., Zhang, Z.H.: Dynamic bulking of a ring-stiffened cylindrical shell subjected to underwater explosive loading. *Explos. Shock Wave* **32**(6), 585–591 (2012)
16. Kwon, Y.W., Fox, P.K.: Underwater shock response of a cylinder subjected to a side-on explosion. *Comput. Struct.* **48**(4), 637–646 (1993)
17. Praba, R.P.S., Ramajeyathilagam, K.: Numerical investigations on the large deformation behaviour of ring stiffened cylindrical shell subjected to underwater explosion. *Appl. Ocean Res.* **101**, 102–262 (2020)
18. DeNardo, N., Pinto, M., Shukla, A.: Hydrostatic and shock-initiated instabilities in double-hull composite cylinders. *J. Mech. Phys. Solids* **120**, 96–116 (2017)
19. Ren, S.F., Song, Y., Zhang, A.M., Wang, S.P., Li, P.B.: Experimental study on dynamic buckling of submerged grid-stiffened cylindrical shells under intermediate-velocity impact. *Appl. Ocean Res.* **74**, 237–245 (2018)
20. Wullschleger, L., Meyer-Piening, H.R.: Buckling of geometrically imperfect cylindrical shells—definition of a buckling load. *Int. J. Non-Linear Mech.* **37**, 645–657 (2002)
21. Yin, C., Jin, Z., Chen, Y., et al.: Shock mitigation effects of cellular cladding on submersible hull subjected to deep underwater explosion. *Ocean Eng.* **117**, 221–237 (2016)
22. Johnson, G.R., Cook, W.H.: Fracture characteristics of three metals subjected to various strains, strain rate, temperatures and pressures. *Eng. Fract. Mech.* **12**(1), 31–48 (1985)
23. Bogdan, S., Radosaw, K.: Material properties of HY 80 steel after 55 years of operation for FEM applications. *Materials* **14**(15) (2021)
24. Dassault Systèmes: Abaqus Analysis User’s Manual. Dassault Systemes Simulia Corp., Providence, Rhode Island (2010)
25. Zamyshlyayev, B.V., Yakovlev, Y.S.: Dynamic Loads in Underwater Explosion, AD-757183. Naval Intelligence Support Center, Washington, DC (1973)

Chapter 72

DDoS Detection Based on Sliding Window Entropy and Decision Tree with Programmable Switch



Shurong Zhang, Tianyu Gao, and Junxing Zhang

Abstract Distributed denial-of-service (DDoS) attacks have become a constant threat to modern networks, and how to detect and respond to them is a key challenge for network operators. Data plane programmability is a promising technology that enables fast control loops to detect and mitigate cyberattacks. At the same time, the domain-specific language P4 used by the programmable switch allows users to flexibly customize DDoS detection methods and attack mitigation behaviors, so the programmable switch can bring some new opportunities for DDoS attack detection. This paper proposes an in-network architecture for DDoS attack detection that combines the entropy of statistical measures describing traffic distribution and machine learning models for network devices. The proposed sliding window detection mechanism completes the fine-grained detection of a single packet within the linear time complexity, and the machine learning model can perform secondary detection of the flow of normal packets in the suspected DDoS attack window to improve the accuracy of detection. We evaluated the proposed framework using real publicly available traffic tracing as input to the experiment, the results show that our framework has the advantages of high accuracy, fine-graininess, and coverage of a wide range of attack types compared with state-of-the-art methods, and is completely executed on the data plane.

Keywords In-network computing · P4 · Information entropy · Machine learning · Sliding window

S. Zhang · T. Gao · J. Zhang (✉)

College of Computer Science-College of Software, Inner Mongolia University, 235 Daxue West Road, Saihan District, Hohhot, People's Republic of China

e-mail: junxing@imu.edu.cn

72.1 Introduction

Distributed Denial of Service (DDoS) attacks continue to be a destructive force on today's Internet. According to Kaspersky's Q3 2021 report, there was a significant increase in the number of attacks in the third quarter relative to the previous quarter and last year [1]. At the same time, these attacks are rapidly evolving, with new DDoS attack vectors emerging that pose a serious threat to Internet security.

While meeting the strict requirements for accuracy, latency, throughput, cost and flexibility, how to protect these networks and their clients from DDoS attacks is a major challenge. Traditional solutions tend to use dedicated hardware to distinguish suspicious traffic from legitimate traffic [2–5]. While these hardware can offer the benefits of high accuracy, low latency and high throughput, they are typically expensive and difficult to program and upgrade due to their low flexibility. The recent trend is to use SDN/NFV based systems to detect and respond to DDoS attacks [6–9]. Software-based solutions are more flexible than custom hardware, but analyzing each packet forwarded in software will result in significant overhead in processor time, memory allocation, and network management traffic. Programmable data plane has become a promising alternative to solve the above problems[10]. The advantages of using programmable switches for DDoS attack detection are as follows: (1) High-speed guarantee: Programmable switch-based solutions offer multiple orders of magnitude speed advantages over other DDoS attack solutions. (2) Flexibility: Programmable switches provide the flexibility to support variable attacks. Using a new switch architecture, the defense solution can be flexibly customized to respond to changing attacks.

Previous work can be divided into statistical-based detection schemes and machine-learning-based detection schemes based on the detection method. The scheme to distinguish DDoS attacks by extracting statistical features is fast to detect in a practical environment, but the disadvantage is that it can easily lead to misclassification when the traffic size of normal packets is also large [8, 11]. It has become a trend to use machine learning methods to improve the recognition rate of abnormal network traffic. The method has a high accuracy rate, but requires manual construction of more feature values, parameters, etc., and slow detection speed. Therefore, finding a detection method with high accuracy and high efficiency is a difficult problem for DDoS attacks [12, 13].

Most of the existing solutions for implementing DDoS attacks on programmable switches use IP information entropy-based detection mechanisms. The paper [14] presents the first implementation of information entropy estimation on a programmable switch and implements high accuracy DDoS attack detection based on the entropy value. The paper [15] makes some improvements on previous work by transforming information entropy into normalized network traffic entropy, making it fully applicable to the data plane. But both articles can only detect whether a DDoS attack has occurred within a window, and cannot find DDoS packets. And although the statistical model based on IP information entropy is fast in detection, it has a high false alarm rate and is less scalable when the size of normal traffic packets

is also large. Therefore, we propose a DDoS attack detection mechanism based on programmable switches. Our mechanism combines a statistical model based on IP address information entropy and a machine learning-based model, which achieves high accuracy and fine-grained detection. To the best of our knowledge, we make the following contributions.

With limited programmable switch instructions and limited memory, we design an attack detection mechanism based on a statistical model of IP address information entropy and use sliding windows to accomplish fine-grained detection of individual packets within a linear time complexity.

For the first time, we introduce a machine learning model for DDoS attack detection in a programmable switch, and we introduce a decision tree to re-detect the flow where normal packets are located in the window where a DDoS attack has occurred, improving the accuracy of detection.

We implement the estimation of information entropy in the data plane with low relative error and low memory usage, and incorporate the fluctuating value of the difference in the threshold update model. The results show that our proposed entropy estimation model and threshold update model are fully applicable to data plane DDoS detection.

This paper is organized as follows: In Sect. 72.2, we provide an overview of the architecture used in this paper. In Sect. 72.3, we describe the basis of the detection strategy as well as the specific implementation of the entropy detection mechanism. In Sect. 72.4, we provide the selection of machine learning models and the data plane implementation. In Sect. 72.5, we present our evaluation methodology and the results we obtained. In Sect. 72.6, we conclude the paper with final remarks and perspectives for future work.

72.2 System Overview

The overall architecture is shown in Fig. 72.1. This detection method consists of two sections, which are initial detection based on information entropy and deep detection based on machine learning. Initial detection starts with an initial analysis of the packet, extracts the features used to calculate the entropy value, and then calculates the entropy value within the sliding window and compares it with the traffic characterization module to generate an adaptive threshold to determine whether the current packet is a DDoS packet. The design of sliding windows and observation windows is described in Sect. 72.3. If a DDoS attack is detected in the previous observation window, the flow in which a normal packet is located in the next observation window is marked and sent to the deep detection module for detection of that flow. Initial detection and deep detection are all implemented in the data plane.

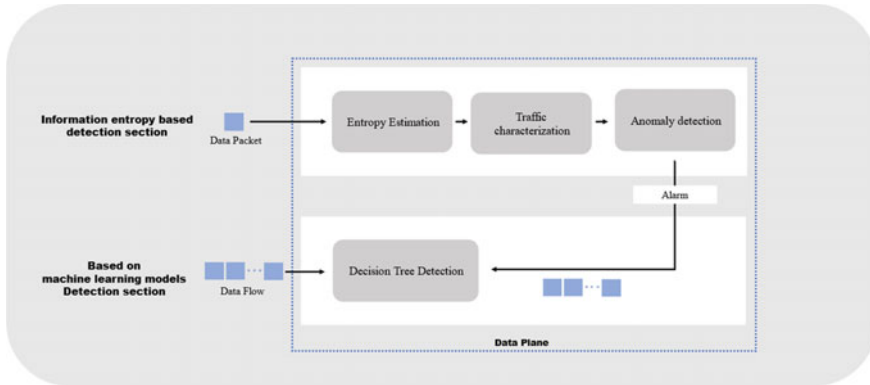


Fig. 72.1 Overall architecture of detection model

72.3 Information Entropy-Based Detection Mechanism

72.3.1 Detection Strategy Foundations

Information entropy is an important concept of information theory that measures the natural amount of uncertainty or randomness of a single random sample of a distribution which has been widely used in the information sciences [16]. Information metrics have shown encouraging results in detecting DDoS attacks. The entropy of random sample x is defined as:

$$H(x) = - \sum_{i=1}^n p(x_i) \log_2(p(x_i))$$

where $X = \{x_1, x_2, x_3, \dots, x_n\}$ and $p(x_i)$ presents the probability of the random event x_i . $p(x_i)$ can be defined as:

$$p(x_i) = \frac{f(x_i)}{m}$$

where $f(x_i)$ represents the number of occurrences of sample x_i and m represents the total number of samples. Thus the entropy value of sample x can be defined as:

$$H(x) = \log_2 m - \frac{1}{m} \sum_{i=1}^n f(x_i) \log_2(f(x_i))$$

The terms other than the constant term in this formula can be expressed as:

$$S = \sum_{i=1}^n f(x_i) \log_2(f(x_i))$$

72.3.2 Model Design

Sliding window design. We timed update the number of packets P_t received by the switch in a fixed time interval and set an observation window of size 2^n , n is the index of the leftmost 1 when P is represented as binary. We estimate the entropy value of the results within the observation window at the end of each observation window and update the threshold value through the traffic characterization module. A fixed size sliding window is set during multiple observation windows, and we set the size of the sliding window to 2^l for computational convenience, and we perform entropy estimation and anomaly detection based on the current sliding window to determine whether the packet is a DDoS packet.

Address frequency estimation. We use the count-min sketch [17] to store packet IP frequency approximations. When updating the frequency, the current IP is calculated by the hash function with d different hash values, and then the corresponding position is added to 1. The approximate value of the frequency is taken as the minimum of all the hash values. Figure 72.2 shows the address frequency estimation when the sketch depth is 1.

Calculation of logarithmic functions. As an important part of implementing information entropy in the data plane, we must implement the logarithm in the data plane.

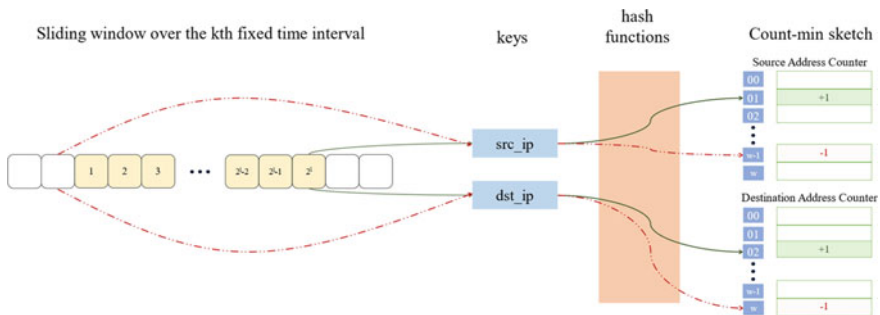


Fig. 72.2 Sliding window sliding and address frequency estimation

The paper [14] proposes the use of efficient TCAM table lookups instead of real-time computationally intensive operations, however, this requires the insertion of a large number of table entries. The paper [18] uses shift operations to estimate the integer and fractional bits of log values but produces a certain relative error. To reduce the occupancy of TCAM and to obtain a small relative error, we present the estimation of log values by storing only the logarithmic values of odd numbers within 2 and half of the observation window size. All log values can be extrapolated or estimated by depositing some of the log values in TCAM and reducing the footprint of TCAM by nearly three quarters.

Entropy estimation. The sliding window size is fixed, so the cumulative entropy parametrization of the first sliding window can be calculated as:

$$S \leftarrow S + f(x_i) \log_2 f(x_i) - (f(x_i) - 1) \log_2(f(x_i) - 1)$$

The entropy value within the sliding window can be expressed as:

$$H(x) = l - S \gg l$$

After each subsequent slide, we update the entropy value by adding the difference between the newly calculated term and its previous value using the interval continuity of the sliding window, and the updated entropy value is calculated as:

$$H(x) \leftarrow H(x) + ((f(x_{out}) - 1) \log_2(f(x_{out}) - 1) - f(x_{out}) \log_2 f(x_{out})) \gg l$$

where $f(x_{out})$ represents the frequency estimate of the outgoing window packets and $f(x_{in})$ represents the frequency estimate of the incoming window packets.

Traffic characterization. The difference between the source IP entropy value and the destination IP entropy value within the k th observation window can be expressed as:

$$D_k = |H_k^{src} - H_k^{dst}|$$

where H_k^{src} represents the source IPs entropy value in the k th observation window and H_k^{dst} represents the destination IPs entropy value in the k th observation window.

Due to the fluctuation of network traffic over time, we set adaptive thresholds and the threshold for the k th observation window is calculated as:

$$M_k = (1 - \alpha)M_{k-1} + \alpha D_k + W_k$$

where W_k is used to characterize the fluctuating value of the normal flow and is calculated as:

$$W_k = (1 - \alpha)W_{k-1} + \alpha|D_k - D_{k-1}|$$

Anomaly detection. We use the difference between the source IP and destination IP entropy values within the sliding window as the basis of detection to compare with the threshold value. The difference between the source IP and destination IP entropy values within the sliding window can be calculated as:

$$D_s = |H(x)_{src} - H(x)_{dst}|$$

where $H(x)_{src}$ represents the source IPs entropy value within the current sliding window and $H(x)_{dst}$ represents the destination IPs entropy value.

72.3.3 Data Implementation

Data plane programming has constraints such as limited instructions, limited memory, and no loop support. To break through these constraints, the observation window and sliding window are updated in the SRAM registers. We implement the sliding window by replacing the IP of the old packet in the register with the IP of the current packet and design the action to classify the IP address by count-min sketch to get the estimated value of the address frequency, and the array corresponding to the hash value is recorded by the SRAM register.

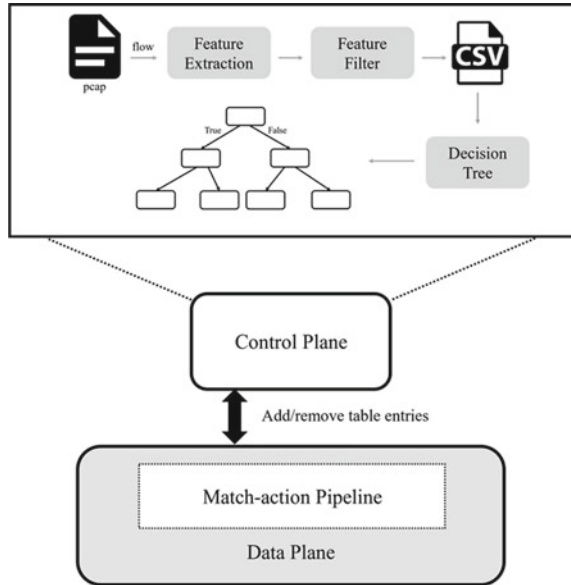
To overcome the challenge that P4, the programming language used in the data plane of this paper, does not support binary logarithmic operations, we use a logarithmic LPM lookup table with a base of two in the entry control block. The binary logarithmic operations are performed by adding static LPM entries to it, and the result is stored in the switch metadata using action. The resulting address frequency estimate is multiplied by the binary logarithm operation value, and then the information entropy estimate of the current sliding window is obtained by each accumulation. We achieve the update of the threshold value by accumulating the difference between the source IPs entropy value and the destination IPs entropy value of the observation window in the SRAM register, and the final judgment of the packet type by the if-else entry.

72.4 Machine Learning Based Detection Mechanisms

72.4.1 Algorithm Design

Figure 72.3 shows the framework of our algorithm, where features can be obtained from external datasets to convert the data into stream-based features. Due to limitations such as P4 not supporting floating-point numbers, it is necessary to filter flow-based features to extract features that can be obtained in programmable switches. After the features are sent into the decision tree for training, the final model is

Fig. 72.3 Machine learning based algorithm flow chart



obtained, and then the model is mapped to the data plane match-action pipeline through translation. The final data plane receives the matching rule set and reacts immediately after receiving the packet.

72.4.2 Algorithm Implementation

A crucial step of machine learning is to accurately identify the research objects and characteristics, that is, to define the features of these objects. The first step of the algorithm is to extract the relevant features of all pcap streams, establish machine learning data sets, and select the wrong features or focus on the classification types of data sets, which may make the model completely invalid [19]. Since P4 does not support floating-point numbers, standard measures such as average calculation and data conversion, and the flow-based features that can be extracted in the data plane are limited, it is necessary to filter the extracted features.

Once the data-centric step is completed, selecting the model type is our next action plan, and we need to make choices that match the expected results. Due to the high complexity of the model, the deep neural network can not be deployed in the data plane. In simple machine learning, the decision tree model is a tree structure, in which each internal node represents a test on an attribute, each branch represents a test output, and each leaf node represents a category. In the data plane, it can be realized through continuous matching of match-action pipelines or if-else judgment conditions. Therefore, the decision tree is selected as the classification model.

The core of the machine learning process is model training. A lot of learning is completed at this stage. Compare the obtained output with the actual output and minimize the difference by trying different weights and deviation values.

After the model classification results are obtained, the tree structure needs to be reproduced in the data plane. Two methods can be used: match-action pipeline and if-else judgment. Here, we use the match-action pipeline to realize continuous matching between different layers and use the table to realize the mapping between layers, Use action to store the classification value in the metadata for the matching of the next table. Finally, use the table defined by us in the entry control block to realize continuous matching.

72.5 Evaluation

72.5.1 Experimental Setup

We implemented the detection mechanism proposed in this paper in bmv2, with the system architecture deployed on a virtual machine running ubuntu 20.04 with four processors and 4 GB RAM, and we also simulated our proposed mechanism using python for evaluation. We use the CAIDA Anonymized Internet Traces 2016 dataset to represent legitimate traffic on the network. To perform the attack, we used the CAIDA DDoS Attack 2007 dataset, which contains anonymized traffic traces from approximately one hour of DDoS attacks.

To evaluate our experiments, We first generate a 60 s traffic trace using the legitimate traffic dataset to set the adaptive threshold correctly, then we generate 60 s DDoS traffic with different attack traffic ratios based on the DDoS attack dataset, and finally, we mix it with legitimate traffic at a fixed interval of 1 s and replay it to evaluate our proposed mechanism.

72.5.2 Evaluation Metrics

Evaluation metrics for entropy estimation. We call \widehat{H}_{src} the estimated traffic entropy of the source IPs in the observation window, and H_{src} its exact value. The relative error is defined as the average of $\frac{|\widehat{H}_{src} - H_{src}|}{H_{src}} \times 100\%$ over 20 consecutive observation windows.

Evaluation metrics for DDoS detection. We considered the true positive rate (TPR), the false positive rate (FPR) and the detection accuracy (Accuracy) as the evaluation metrics. The above metrics are defined as:

$$\begin{aligned} \text{TPR} &= \frac{TP}{TP + FN} \times 100\% \\ \text{FPR} &= \frac{FP}{TN + FP} \times 100\% \\ \text{Accuracy} &= \frac{TP + TN}{TP + TN + FP + FN} \times 100\% \end{aligned}$$

72.5.3 Entropy Estimation Evaluation

We evaluated the effect of the depth and width of the sketch on the relative error of the entropy estimates and compared it with the methods proposed in other papers using count-min sketch for frequency estimation. The scheme DDOSD entropy stored all log values in the LPM lookup table and estimated the entropy values by entropy accumulation. The scheme P4NEntropy proposed by the paper [15] converts the computed information entropy by computing $\log_2 f_i + \frac{1}{\ln 2}$. Figure 72.4 shows the effect of sketch width on the relative error and Fig. 72.5 shows the effect of sketch depth on the relative error. By comparison, we find that the effect of width is more pronounced and our work has a lower occupancy of TCAM than DDOSD [14] entropy and a lower relative error than P4NEntropy [15]. This shows that our proposed mechanism can achieve a trade-off between relative error and a low memory footprint.

Fig. 72.4 Effect of sketch width on entropy estimation relative error

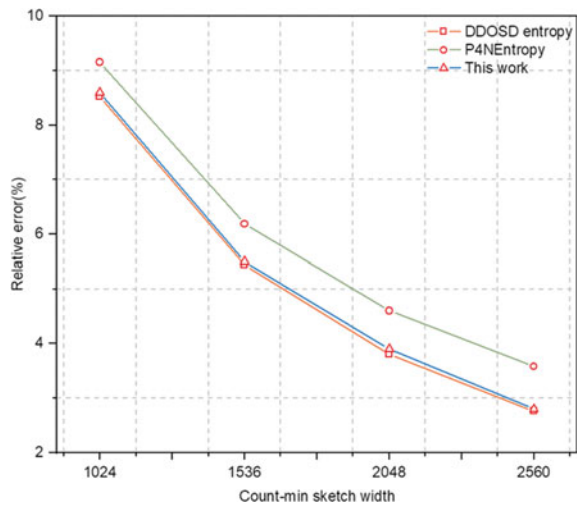
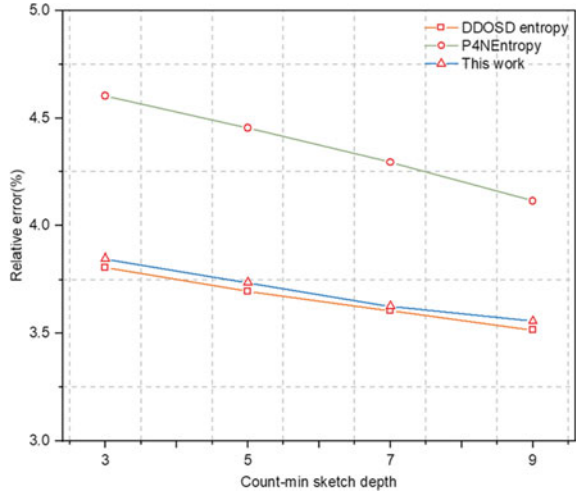


Fig. 72.5 Effect of sketch depth on entropy estimation relative error



72.5.4 Evaluation Based on Packet Detection

Unlike window-based detection, we add a sliding window to estimate the class of the current packet by the entropy value within the sliding window, and we add a decision tree to optimize the packet-based detection mechanism after detecting a DDoS attack in the last observation window.

Figure 72.6 demonstrates the effect of sliding window size on TPR before and after adding the decision tree. Setting the attack ratio to 30%, it can be seen that the true positives for entropy detection are highest at $l = 3$ because the smaller sliding window size better characterizes the class of the last packet within the observation window of the mixed ratio. After adding the decision tree, the true positive rate has improved significantly, and the corrected true positive rate reaches over 99% at $l = 3$.

Fig. 72.6 Sliding window size effect on TPR before and after adding decision tree

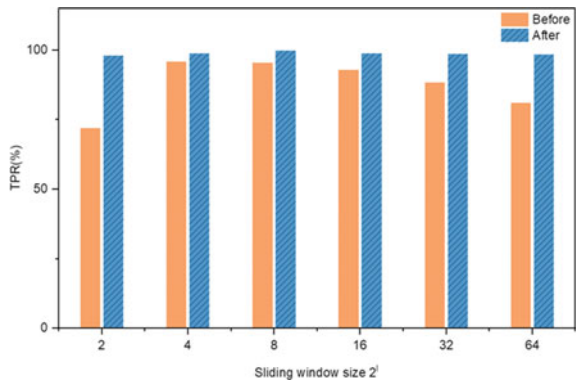
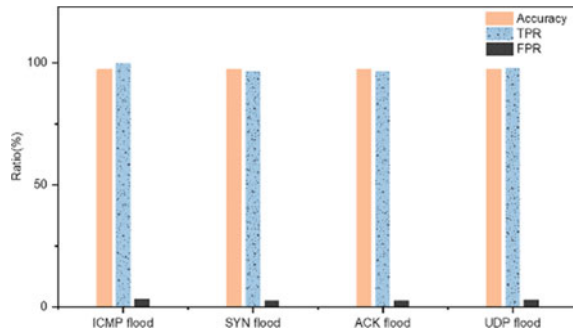


Fig. 72.7 Performance under different types of attacks



We also evaluate the performance of our mechanism on different types of attack traffic, we use a real-world attack traces CAIDA 2007 to simulate a real ICMP flood attack, for the other three attacks, ACK Flood attack, SYN flood attack and UDP attack, we use one of the DDoS attack software hping3 to generate the corresponding attack traffic traces and evaluate them experimentally with a 30% attack traffic ratio.

As shown in Fig. 72.7, our mechanism can complete the detection of a single packet with more than 96% true positives and less than 3% false positives under four different attacks.

72.6 Conclusion and Future Work

DDoS attacks are designed to consume resources and directly affect the availability of servers in the network infrastructure. While significant efforts have been made to detect and mitigate DDoS attacks within a feasible time frame, this type of attack remains one of the major security concerns in the network. In this paper, we propose a framework for detecting DDoS attacks within a network based on the high speed and flexibility of programmable switches, which combines information entropy and machine learning models. We perform tests on our framework using real publicly available traffic traces and show that our framework can perform a fine-grained inspection for a single packet with low memory usage and high accuracy.

For future work, we plan to complete more tests on real devices for performance such as network throughput and explore the performance of the framework for DDoS mitigation, as well as dig into implementing more machine learning-based techniques on programmable switches.

References

1. Kupreev, E.G.A., Badovskaya, O.: Ddos attacks in q3 2021 (2021) [Online]. Available: <https://securelist.com/ddos-attacks-in-q3-2021/104796/>
2. NSFOCUS: Nsfocus anti ddos solution. <https://nsfocusglobal.com/wp-content/uploads/2018/05/Anti-DDoS-Solution.pdf> (2018) [Online]. Accessed 8 July 2019
3. Cisco: Cisco guard xt 5650. <https://www.cisco.com/c/en/us/products/collateral/security/guard-xt-5650a/productdatasheet0900aecd800fa55e.html> (2018) [Online]. Accessed 8 July 2019
4. Arbor Networks APS Series. <https://www.arbornetworks.com/ddos-protection-products/arb-or-aps>. Cisco Guard XT 5650 Series. <https://goo.gl/DoFRBk>
5. Guenane, F., Nogueira, M., Pujolle, G.: Reducing DDoS attacks impact using a hybrid cloud-based firewalling architecture. In: 2014 Global Information Infrastructure and Networking Symposium (GIIS), pp. 1–6. IEEE (2014, Sept)
6. Kokila, R.T., Selvi, S.T., Govindarajan, K.: DDoS detection and analysis in SDN-based environment using support vector machine classifier. In: 2014 Sixth International Conference on Advanced Computing (ICoAC), pp. 205–210. IEEE (2014, Dec)
7. Jero, S., Koch, W., Skowyra, R., Okhravi, H., Nita-Rotaru, C., Bigelow, D.: Identifier binding attacks and defenses in software-defined networks. In: USENIX Security Symposium, pp. 415–432 (2017, Aug)
8. Wang, R., Jia, Z., Ju, L.: An entropy-based distributed DDoS detection mechanism in software-defined networking. In: 2015 IEEE Trustcom/BigDataSE/ISPA, vol. 1, pp. 310–317. IEEE (2015, Aug)
9. Afek, Y., Bremler-Barr, A., Feibish, S.L., Schiff, L.: Detecting heavy flows in the SDN match and action model. *Comput. Netw.* **136**, 1–12 (2018)
10. Sonchack, J., Loehr, D., Rexford, J., Walker, D.: Lucid: a language for control in the data plane. In: Proceedings of the 2021 ACM SIGCOMM 2021 Conference, pp. 731–747 (2021, Aug)
11. Navaz, A.S., Sangeetha, V., Prabhadevi, C.: Entropy based anomaly detection system to prevent DDoS attacks in cloud (2013). arXiv preprint [arXiv:1308.6745](https://arxiv.org/abs/1308.6745)
12. Xavier, B.M., Guimarães, R.S., Comarela, G., Martinello, M.: Programmable switches for in-networking classification. In: IEEE INFOCOM 2021-IEEE Conference on Computer Communications, pp. 1–10. IEEE (2021, May)
13. Musumeci, F., Ionata, V., Paolucci, F., Cugini, F., Tornatore, M.: Machine-learning-assisted DDoS attack detection with P4 language. In: ICC 2020–2020 IEEE International Conference on Communications (ICC), pp. 1–6. IEEE (2020, June)
14. Lapolli, Á.C., Marques, J.A., Gaspary, L.P.: Offloading real-time DDoS attack detection to programmable data planes. In: 2019 IFIP/IEEE Symposium on Integrated Network and Service Management (IM), pp. 19–27. IEEE (2019, Apr)
15. Ding, D., Savi, M., Siracusa, D.: Tracking normalized network traffic entropy to detect DDoS attacks in P4. *IEEE Trans. Dependable Secure Comput.* **19**(6), 4019–4031 (2021)
16. Shannon, C.E.: A mathematical theory of communication. *Bell Syst. Tech. J.* **27**(3), 379–423 (1948)
17. Cormode, G.: Count-Min Sketch (2009)
18. Ding, D., Savi, M., Siracusa, D.: Estimating logarithmic and exponential functions to track network traffic entropy in P4. In: NOMS 2020–2020 IEEE/IFIP Network Operations and Management Symposium, pp. 1–9. IEEE (2020, Apr)
19. Xavier, B.M., Guimarães, R.S., Comarela, G., Martinello, M.: Programmable switches for in-networking classification. In: IEEE INFOCOM 2021-IEEE Conference on Computer Communications, pp. 1–10. IEEE (2021, May)

Chapter 73

Supply Forecast of Shared Parking Spaces in Social Parking Lots Around Primary Schools Based on Shared Parking Spaces



Lu Chu, Jingyuan Wang, and Xiaoyu Ji

Abstract With the increasing proportion of car transportation in the school-wide mode, the traffic jam of different degrees will be formed at the entrance of every primary school in Shenzhen, this phenomenon not only wastes the time of parents and students, affects personal safety, but also causes great pressure to the traffic operation and management around. At present, there is no good solution to this problem, and there is also a lack of in-depth research. As an effective way to ease the parking problem in the city center, “Parking sharing” has attracted the attention of some scholars at home and abroad in recent years. However, most of the existing studies are biased towards the specific parking lot to do a period of time in the future parking supply forecast, and do not take into account the parking demand of primary schools, in the actual operation process, there is a common situation that the prediction precision of shared parking is not enough and can not fully meet the parking demand. Based on the theory of shared parking spaces, this paper transfers the parking demand of primary school to the surrounding social parking lots, which can alleviate the traffic disorder in front of school and ensure the safety, the utility model can also improve the utilization rate of parking spaces in social parking lots. The supply of parking spaces plays an important role in evaluating the social and economic benefits of parking spaces. The supply law of parking spaces is different in different types of allocated parking lots, the trend of free shared berth is different with time. With the aim of improving the clarity and reliability of the information on free parking spaces in car parks, this paper takes three key primary schools in Luohu District as an example, and obtains the time-varying data of historical parking spaces in various types of car parks around primary schools through the parking space sharing platform, the ARIMA and BP neural network models are used to forecast the time span of parking lots in different land use types, and the applicable prediction

L. Chu · J. Wang (✉)

College of Civil and Transportation Engineering, Shenzhen University, Shenzhen 518060, China
e-mail: jiwang@szu.edu.cn

X. Ji

BYD Auto Industry Company Limited, Shenzhen, China

methods of shared parking spaces are found. The results show that the smaller the time span is, the higher the prediction accuracy is. BP neural network model is more suitable for office area and part of commercial area, while ARIMA model is more suitable for residential area. This study has great practical significance for mining the parking supply capacity, reducing the construction of parking facilities and investment, reducing the demand for parking space, optimizing the transportation environment in primary schools, and improving social and public benefits.

Keywords Shared parking · Berth sharing · Pick up and drop off schoolchild · Shared parking forecast

73.1 Introduction

With the acceleration of urbanization, the problem of parking during school hours around primary schools is becoming more and more prominent. How to solve this problem has become the focus of attention of many urban planners and traffic management departments. However, due to the constraints of construction cost, land use and regulations, it is difficult to improve the parking supply in the short term. Meanwhile, according to the 2017 Big Data Report of China Smart Parking Industry, the utilization rate of parking Spaces in more than 90% cities is less than 50% [1]. Therefore, the sharing of parking Spaces between parking lots is considered to be the key approach and effective means to improve the urban parking problem. Among them, real-time and accurate prediction of the free parking space information is an important part of parking sharing.

However, accurate parking berth prediction is not easy. First of all, different types of parking lots have different parking demand and supply levels, which leads to different time variation trends of parking Spaces. Therefore, adopting the same method to forecast may cause large errors [2, 3]. Secondly, there is a time lag between parking demand users submitting reservation applications and arriving at the matching parking lot, and the change of parking lot berth changes dynamically under the influence of many factors. Different forecast time spans will have a great impact on the prediction accuracy [4]. In addition, different parking berth prediction methods have their own advantages and disadvantages and have different adaptability [5, 6].

Aiming at the above problems, this paper adopts the time-varying data of working day berth supply on the platform of shared parking line operated in Luohu District during December 13–24, 2021, and systematically evaluates the commonly used parking lot berth share prediction methods. Firstly, this paper analyzed the time-varying characteristics of parking space occupancy in three types of parking lots: residential area, business area and office area. Then, it used ARIMA model and BP neural network model to predict the parking space occupancy in the future period respectively, and compared and analyzed the prediction accuracy under different prediction time spans such as 5, 10, and 15 min. This paper provides reference for the selection of different parking lot berth prediction methods. This study can

provide some solutions to excavate the supply capacity of existing parking berths, optimize the environment of primary school pickup and drop-off, improve social public benefits and other aspects, and has certain practical significance to promote the sustainable development of berth sharing.

73.2 Literature Review

In recent years, scholars at home and abroad have established a variety of short-term prediction models for berths. Yang et al. [7] proposed a parking berth prediction model based on fuzzy neural network and general BP neural network. However, there was no theoretical basis for the method of training BP neural network with the actual data of the past three moments as input to output the forecast data of the next moment, so the prediction results were not accurate. Based on the data of vehicle arrival time and stay time, Dunning used ARIMA model to predict the availability of parking Spaces in the future period and found that the prediction accuracy decreased with the increase of vehicle arrival rate [8]. Liu et al. proposed a first-order weighted local region method based on chaotic time series to predict berths. Although this method has a good prediction speed, the accuracy of the prediction results needs to be improved [9]. Ji et al. used wavelet neural network and maximum Lyapunov index method respectively to predict the effective berths of parking lots, and the results showed that the former has better prediction accuracy [10]. Based on the parking data of Wujiaochang District in Shanghai, Tang Keshuang et al. selected ARIMA, Kalman filter and BP neural network prediction methods based on model analysis and comparison to forecast the demand of three types of parking lots in business district, office district and sports ground respectively. The results show that the prediction accuracy of Kalman filter is weaker than that of the other two methods. Different prediction methods for different types of parking lots or the same type of parking lots will lead to different prediction accuracy [11]. Ji et al. [12, 13] proposed a parking berth prediction model based on wavelet neural network, wavelet transform and particle swarm wavelet neural network. The latter model is an improvement of the former model, which greatly improves the prediction accuracy compared with the former. But wavelet transform needs a lot of time, so it greatly reduces its training speed. Guo Jiahui and Zhu Jiayou analyzed the main influencing factors of parking in central urban areas with many influencing factors and complex land use, and adopted BP neural network and principal component analysis methods respectively to establish parking demand prediction models to meet people's parking demand [14, 15]. Rajabioun et al. [16] and Klappenecker et al. [17] predicted parking Spaces through mathematical methods. Although this method is easy, but for emergency poor robustness and fault tolerance, the final forecasting result is not ideal.

In summary, ARIMA model and neural network model have strong fault tolerance and robustness, and can identify nonlinear complex systems. It is an effective berth prediction method commonly used at present. However, most of the existing studies are aimed at predicting and verifying the situation of parking supply in a certain

period of time for specific parking lots, and there are few studies on the applicability evaluation of different methods in different types of parking lots. In addition, few existing studies make predictions based on the parking needs in actual scenes, and the prediction of available shared berths for the parking needs of primary school pick-up and drop-off in specific periods is still blank. Therefore, the purpose of this study is to evaluate the applicability of the above two methods for predicting the parking occupancy of different parking lot types and different forecasting time steps around primary school campuses.

73.3 Analysis of Parking Supply Characteristics of Parking Lots Around Primary Schools

According to the conclusion in relevant literature that the appropriate walking distance for berth sharing is 500 m [18], and the proportion of students in key primary schools who go to school by car is far higher than that in ordinary primary schools [19], this paper selects three representative key primary schools in Luohu District, and initially takes 500 m walking distance as the standard to obtain the surrounding parking lots added to the online platform in Luohu District by means of data capture. Moreover, relevant information of parking lot berth is extracted, including land type, available time slot, real-time available number of berths and geographical location. After summary, it is found that the land types of the parking lots around the three primary schools are mainly divided into residential areas, office areas and business areas. Therefore, this section selects typical land parking lots to analyze the general characteristics of the three types. In order to ensure that the analysis results can accurately reflect the rules of berth occupancy of allocated parking lots of different land types, the following criteria are followed in the selection of parking lot samples:

- (1) Building land has single function, relatively independent geographical location, and is not too close to other buildings [20].
- (2) The parking berths are built independently of the parking lot, and there is no combination of berths supply phenomenon.
- (3) The land type of the parking lot has its own typical characteristics.
- (4) It is convenient to obtain the characteristic index of the building.

Moreover, since the parking sharing discussed in this paper is based on the parking demand for primary school pickup and drop-off, only the parking supply data of weekdays from Monday to Friday are selected. Table 73.1 lists the selected objects and data forms.

Table 73.1 Selected objects and data forms of typical parking lot

Type of land use	Survey object	Sample data
Residential area	Maguoling Community	Time-varying data of berth supply on weekdays from December 13, 2021 to December 24, 2021, for a total of 10 days
Business area	Tamai Jewelry Park	
Office area	Shenzhen Antique City	
	Animation Building	
	Luohu Management Office	

73.3.1 Variation Rules of Typical Land-Use Berths

The change of parking Spaces directly affects the external sharing ability of parking lots. According to the dynamic change of parking space occupancy, Wang Bin concluded that parking demand peaks of parking lots with different land types were different, and therefore judged whether each land type was suitable for opening and sharing at a certain time [20]. Therefore, this section also analyzes the supply law of parking berths on weekdays with the representative object of typical land parking lots.

Figure 73.1 shows the time variation rule of average parking supply quantity in 5 different types of parking lots in 10 working days.

As can be seen from Fig. 2.1, the daily variation trend and amplitude of average berths supply in residential areas, office areas and business areas differ greatly, among

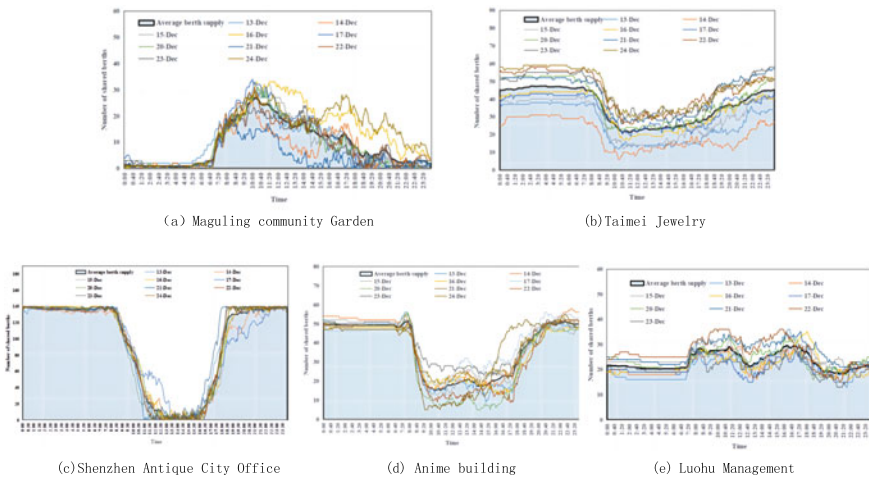


Fig. 73.1 Variation curve of supply quantity of 5 parking lots in 10 working days

which the shared berths in residential areas reflect the characteristics of sufficient berths during the day and shortage of berths at night. The number of shared berths starts to increase at around 7:00, which is consistent with commuting characteristics. Between 10:00 and 12:00, the number of shared berths increases and decreases at other times. The reason is that some residents go home for lunch break, and the number of shared berths declines slowly from afternoon to night. The total number of berths in the business district is large, and the general trend shape of the two representative parking lots is similar. Since morning business hours, the number of shared berths begins to decline. Affected by the parking demand of the land itself, the number of shared berths decreased in different amplitude, but both of them restored the sufficient state of shared berths at around 19:00 in the evening. The office area is divided into local work type and field type, and the change trend of the shared berths of the two parking lots is not the same. The number of shared berths decreases due to the increase in parking demand after 8:00 working hours for work types in this area. During the lunch break, some people went out, and the number of shared berths rebounded, returning to the morning state with the end of the lunch break. The type of field work is the opposite of the type of work in the district.

73.3.2 Overall Variation Characteristics of Berth Share

For the purpose of data forecasting, it is necessary to have an overall grasp of the changing trend of shared berths supply. However, the application of neural network model requires normalization of time series data [21]. Therefore, in order to facilitate the comparison between the two methods, the berths supply rate is used to discuss and analyze the characteristics of shared berths supply, as shown in Table 73.2.

Generally speaking, the variation of the supply rate of shared berths in all types of land parking lots has the following characteristics:

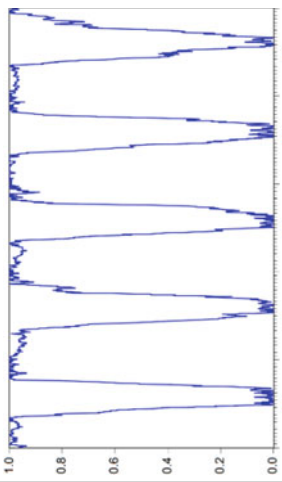
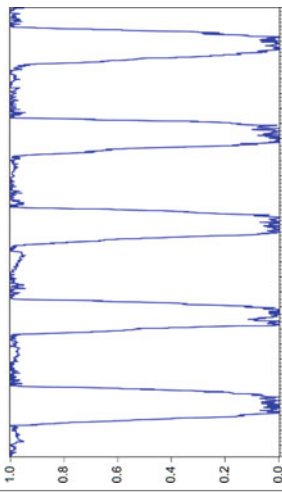
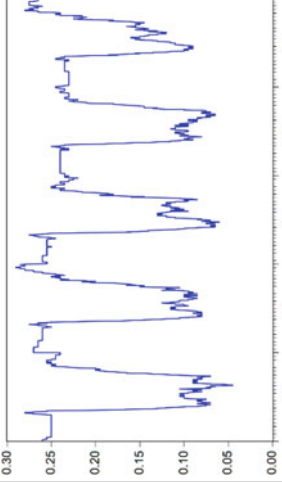
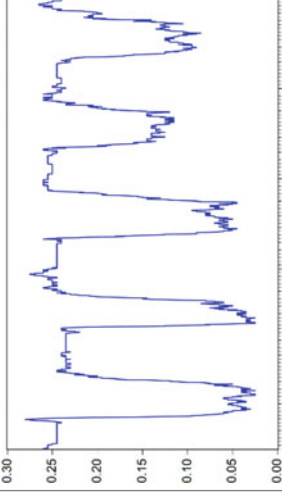
- (1) Time dependence. The berth supply rate of the previous moment has an impact on the berth supply rate of the later moment, because a higher shared berth supply rate will have a selection advantage for parking demand users' decision-making.
- (2) Short-term random volatility. The random fluctuation of the supply rate of shared berths in a single day is relatively obvious in the after-school period, and the variation range of the supply rate of shared berths from day to day is uncertain.
- (3) Long-term periodicity. The supply rate of shared parking Spaces in a single parking lot shows large cyclical fluctuations every one week, which is related to people's travel rules.

Table 73.2 Total variation law of utilization rate of various parking lots

Parking lot	2021/12/13-2021/12/17	2021/12/20-2021/12/24
Residential area		
Business area I		

(continued)

Table 73.2 (continued)

Parking lot	2021/12/13–2021/12/17	2021/12/20–2021/12/24
Business area 2		
Office area 1		

(continued)

Table 73.2 (continued)

Parking lot	2021/12/13–2021/12/17	2021/12/20–2021/12/24
Office area 2		

73.4 Prediction Model

As can be seen from Table 2.2, different types of parking lot share berth supply rates have different periodicity and trend, which belong to the unstable time series data characteristics. ARIMA model and BP neural network model are commonly used to predict unstable time series data, so this paper chooses these two models for comparative analysis. The ARIMA model does not consider the background factors of data generation, and can establish a prediction model only by using the rules among the limited sample time series data. However, the prediction accuracy of the low-order model is low, and the parameter prediction of the high-order model is difficult [22]. BP neural network model has strong self-learning, self-adaptability and fault-tolerance in prediction, especially for time series data with many influencing factors and difficult to fit with mathematical formulas, but it has the disadvantage of falling into local optimization [6].

Based on the above two models, this section conducts comparative analysis on the time series data of shared berths of parking lots of different land types combined with different time spans (5, 10, 15 min), and seeks suitable prediction methods.

73.4.1 ARIMA Model

The prediction expression of ARIMA model is as follows:

$$\begin{cases} \Phi(B)\nabla^d x_t = \Theta(B)\varepsilon_t \\ (E)\varepsilon_t = 0, Var(\varepsilon_t) = \sigma_\varepsilon^2, E(\varepsilon_t \varepsilon_s) = 0, s \neq t \\ E\varepsilon_t x_s = 0, \forall s < t \end{cases} \quad (73.1)$$

Among them: $\nabla^d = (1 - B)^d$, $\Phi(B) = 1 - \varphi_1 B - \dots - \varphi_p B^p$ is the autoregressive coefficient polynomial of the model; $\Theta(B) = 1 - \theta_1 B - \dots - \theta_q B^q$ is the moving smoothness coefficient polynomial of the model; p is the non-seasonal autoregressive order; q is the order of non-seasonal moving average; $\{\varepsilon_t\}$ is a zero-mean white noise sequence. The above model can be denoted as ARIMA (p, d, q).

The steps of using ARIMA model (taking 5 min as an example) to predict the supply rate of shared parking Spaces in each parking lot are as follows:

Step 1. Test the stationarity of the time series of the shared berth supply rate of the parking lot. If it does not meet the requirements of the stationarity sequence, the stationarity is processed by difference operation until the sequence is stationarity.

Step 2. Identify the model according to the autocorrelation coefficient and partial autocorrelation coefficient of the time series of shared berth supply rate, and determine the final p and q values by combining the Bayesian information (BIC) criterion.

$$BIC = k \ln(n) - 2 \ln(L) \quad (73.2)$$

where k is the number of model parameters, n is the number of samples, and L is the maximum likelihood function value of the model.

Step 3. Use the least square method to estimate the model parameters, and judge whether they pass the significance test of the parameters by observing the corresponding P-value of the T statistic of the parameters.

Step 4. Check whether the residual sequence is white noise sequence. If yes, the prediction model is effective in extracting information.

Step 5. Use the calibration model to predict the supply rate of shared berth in real time.

Step 6. Take the predicted value with a time span of 5 min as the historical data for the next prediction, and use the same prediction model as above. Figure 73.2 shows how to construct the model.

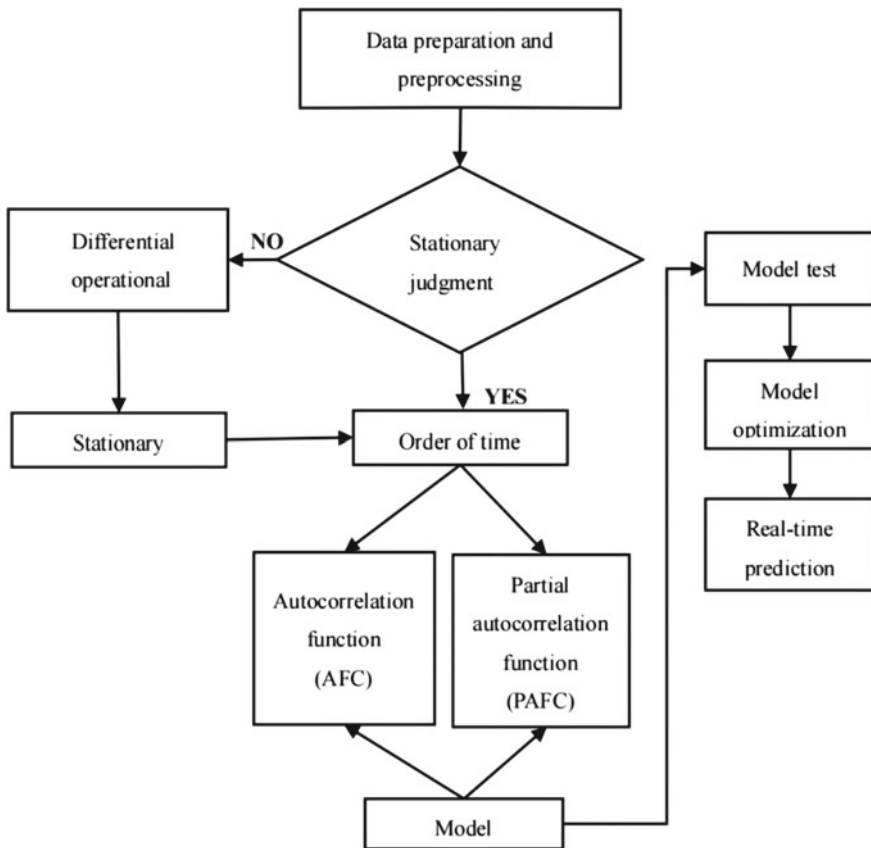


Fig. 73.2 Flowchart of ARIMA model construction (drawn by the author)

73.4.2 BP Neural Network Model

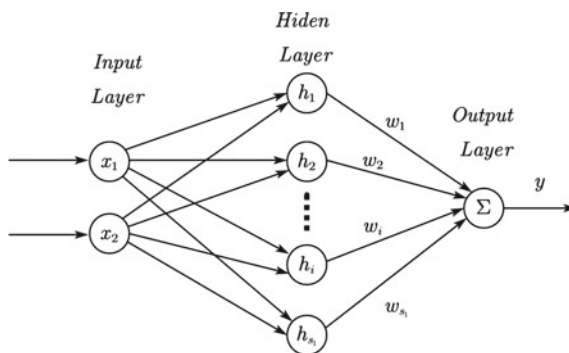
BP neural network is a hierarchical neural network consisting of single input layer, multiple hidden layer and single output layer. Studies have shown that BP neural network can map continuous functions in all closed intervals only by changing the number of neuron nodes in one hidden layer without adding additional hidden layers [23]. Therefore, a three-layer BP neural network model with a single hidden layer is constructed in this section to predict the supply rate of shared parking spaces. The topological structure of the three-layer BP neural network is shown in Fig. 73.3.

The steps to predict the supply rate of shared berth by using BP neural network are as follows:

Step 1. Network training shall be conducted in the way of mentor learning. First, the expected output is given, and then the neural network is trained to perform results infinitely close to the expected output. In order to achieve this goal, BP algorithm (error back propagation) and information forward propagation should be combined. Forward propagation is to calculate the output value according to the input value, while back propagation is used to reverse transfer the error layer by layer to correct the weight and threshold between the layers of the network, and so on until the error between the actual value and the expected value reaches the minimum, and the optimal weight and threshold are obtained;

Step 2. Enter the time series value $(x_1, x_2, x_3, \dots, x_i)$ before a certain time t , predicting the future value after time t $(x_{i+1}, x_{i+2}, \dots, x_{i+k})$, where k is the predicted step size. In the BP neural network, the prediction models with different prediction step sizes are independent of each other. In this paper, the time span of 5 min, 10 min and 15 min is predicted respectively, and the k value is determined respectively according to the selection interval of the original data, and then the prediction is carried out.

Fig. 73.3 Topology structure of three-layer BP neural network



73.5 Determine Model Parameters

In this section, the valid berths of Maguling Community (residential area), Taimei Jewelry (Business area 1), Shenzhen Antique City (Business area 2), Animation Mansion (Office area 1) and Luohu Management Office (Office area 2) during the whole working day from December 13 to 24, 2021 are selected to establish ARIMA and BP neural network models and different model parameters are calibrated according to different time spans (5, 10, 15 min). In the BP neural network method, the three time spans correspond to the prediction step size $k = 1, 2, 3$ respectively. This section takes Office Area 2 as an example to conduct experiments on parameter calibration and prediction process of ARIMA model and BP neural network model respectively.

73.5.1 Parameter Determination of ARIMA Model

(1) Stationarity test

Before the prediction of the ARIMA model, it is necessary to ensure that the time series $\{X_t\}$ of the shared berth input in office area 2 is a stationary series, which is usually tested by ADF. Table 73.3 lists the inspection results.

As shown in the results, for the time series $\{X_t, t \in T\}$, the ADF statistic of $\{X_t\}$ is -6.429 , which is less than the critical value under the significance level of 1, 5 and 10%. Therefore, $\{X_t\}$ is a stationary series.

(2) Model identification and establishment

With 5 min interval, the data changes of parking space supply in different periods within two weeks were counted, and autocorrelation-partial autocorrelation coefficient analysis charts were drawn, as shown in Fig. 73.4.

According to the variation of the autocorrelation coefficient and partial autocorrelation coefficient, the types of censoring and tailing were judged. The model comparison and identification are shown in Table 73.4. The range of parameters p and q is preliminarily determined as follows: $p = 0-5, q = 0-5$. Multiple feasible (p, q) combinations were used for parameter estimation, and the model with smaller BIC was selected as the final model. After calculation, when $p = 2$ and $q = 1$, the BIC value was the minimum, so the final model was determined as ARIMA (2, 0, 1).

Table 73.3 Stability test results

Variable	ADF test values	The ADF cut-off value at the significance level			Prob.
		1%	5%	10%	
X_t	- 6.429	- 3.43	- 2.86	- 2.57	0.000

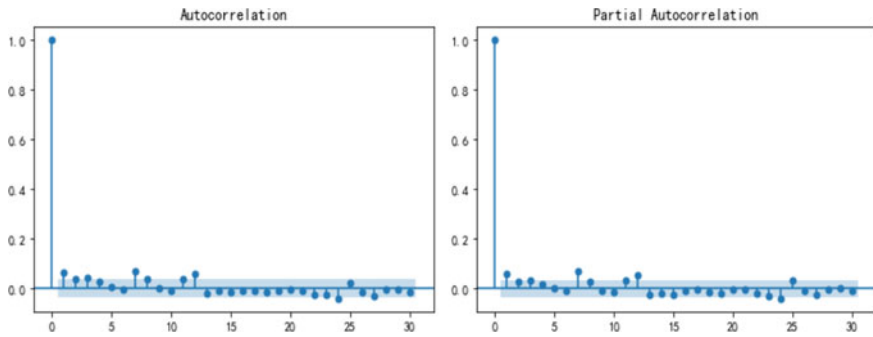


Fig. 73.4 Autocorrelation-partial autocorrelation analysis diagram of shared supply berths of parking lot in office area 2

Table 73.4 Time series model recognition table

Autocorrelation coefficient ρ_t	Partial autocorrelation coefficient φ_{tt}	Selected model
Trailing	P-order truncation	AR (p)
Q-order truncation	Trailing	MA (q)
Trailing	Trailing	ARMA (p, q)

(3) Parameter estimation

Parameter estimation method including the torque estimation, maximum likelihood estimation and least squares method, etc. The maximum likelihood estimation has the highest estimation accuracy when the model probability distribution is known. The least square method is effective to estimate the unknown distribution of the model. Since the probability distribution of time series data of shared supply berths in this paper is unknown, the least square method is used in this section for parameter estimation and calibration of the model. The calibration results of model parameters are shown in Table 73.5.

Observing the regression results of the ARIMA (2, 0, 1) model, the p-values corresponding to the Z-statistics of the parameters are all 0.000, indicating that the

Table 73.5 Regression results of ARIMA (2, 0, 1) model

Variable	Coefficient	Standard error	Z-statistics	P-value
CONST	0.6368	0.019	34.151	0.000
AR (1)	1.9071	0.028	69.201	0.000
AR (2)	- 0.9098	0.027	- 33.653	0.000
MA (1)	- 0.8765	0.034	- 26.045	0.000
R-squared	0.971			

Table 73.6 Stability test results of residual sequence

Variable	ADF test values	The ADF cut-off value at the significance level			P-value
		1%	5%	10%	
Resid	- 14.379	- 3.43	- 2.86	- 2.57	0.000

parameter calibration passes the significance test. R-squared reflects the goodness-of-fit of the model and takes a value between 0 and 1, with closer values to 1 indicating a better model fit. The results show that the value of R-squared is 0.971, so it can be considered that model ARIMA (2, 0, 1) has a good fitting effect.

(4) Model test

In order to test the goodness of model fitting, stationarity and white noise tests should be performed on the residual sequence after parameter estimation. The output results of stationarity test are shown in Table 73.6. It can be seen from the table that the ADF test value is - 14.379, less than the critical value under the significance level of 1, 5 and 10%, which proves that the residual series of this model is a stationary series.

White noise test is a pure random test. If it passes the white noise test, it is a pure random sequence; Conversely, it is proved that the sequence has correlation. Ljung-box was used to extract the residual sequence, and the P value was 0.07605, which was greater than 5% confidence level, so it was considered that the sequence passed the white noise test.

(5) Real-time prediction

The model determined by the above parameters was used to fit and predict the supply of the shared berths in office area 2 on December 24, and the results are shown in Fig. 73.5. It can be seen from the figure that the model is well fitted and can be predicted for shared berths.

(6) Confirm all parameters

According to the above methods and steps, ARIMA model parameter calibration corresponding to each time forecast span of 5 parking lots was completed, and the results were shown in Table 73.7.

It can be seen that the coefficient and residual sequence of the ARIMA prediction model of each parking lot have passed the test and can be predicted.

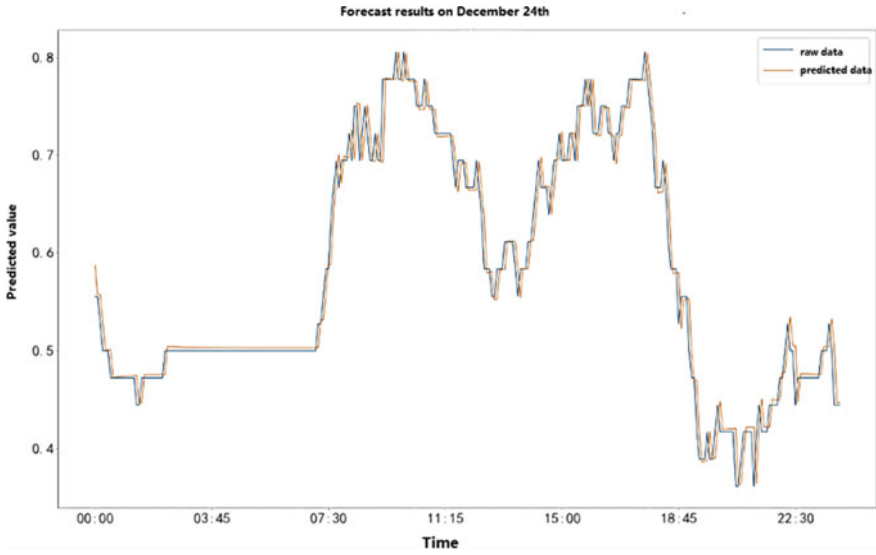


Fig. 73.5 Test results of ARIMA (2, 0, 1) model

Table 73.7 Calibration results of optimal parameters of ARIMA model

Parking lot	Time span	p	d	q	R-squared
Residential area	5 min	2	0	4	0.982
	10 min	5	0	1	0.965
	15 min	2	0	2	0.950
Business area 1	5 min	2	0	2	0.993
	10 min	2	0	1	0.988
	15 min	2	0	1	0.981
Business area 2	5 min	2	0	2	0.997
	10 min	4	0	4	0.991
	15 min	4	0	1	0.990
Office area 1	5 min	2	0	1	0.992
	10 min	2	0	2	0.988
	15 min	5	0	3	0.981
Office area 2	5 min	2	0	1	0.971
	10 min	2	0	1	0.945
	15 min	2	0	1	0.912

73.5.2 Determination of BP Neural Network Model Structure

(1) Structural parameters of neural network

The input layer is the time-varying data $\{X_t\}$ of the shared berths supply rate for 10 working days from December 13, 2021 to December 24, 2021. Taking the whole sequence as a variable to be input, the number of nodes in the input layer is related to the length of defined training data. The number of hidden layers is 1; The output layer is the future time berth supply rate, and the number of neurons is 1. In this paper, the cyclic method is adopted to determine the number of nodes in the hidden layer. In order to avoid sequence underfitting due to too few neurons and sequence overfitting due to too many neurons, the number of nodes in the hidden layer N_h is cyclic values between [6, 12], and the mean square error (MSE) after convergence of each model is obtained. The corresponding value of N_h with the minimum MSE is selected as the optimal structure in this example. Substitute the value of N_h into the network for test and get the results (Table 73.8).

In the table, the number of hidden layer neurons starts to converge when it is 7. Considering the large number of input layer nodes, 12 is selected as the optimal number of hidden layer nodes to ensure the matching degree between the hidden layer and the input layer nodes.

(2) Activation function

At present, the commonly used activation functions include Sigmoid function, tanh function, Purelin function and Relu function. Among them, Sigmoid function and tanh function are nonlinear functions, which have strong network approximation ability, and tanh function is better than Sigmoid function in the zero centered output problem. The forecast object of this paper is the shared berth supply rate of the parking lot in the future continuous periods, which is a regression prediction problem, so the tanh function is adopted in the hidden layer.

(3) Learning rate

The learning rate affects the tuning speed of neural network learning. Research shows that the learning rate generally ranges from 0.01 to 0.8. In order to ensure enough data learning information, 0.01 is adopted in this paper.

(4) Training function

Adam function is an optimization algorithm to search for the global optimum, and introduces quadratic gradient correction, which has certain advantages over trairdx function. Therefore, adam function is selected as the training function.

Table 73.8 Test results of the number of hidden layer neurons

Number of neurons in the hidden layers	6	7	8	9	10	11	12
MSE	0.0114	0.0105	0.0105	0.0106	0.0105	0.0105	0.0105

Table 73.9 BP neural network parameters

Number of the BP neural network layers	Number of neurons			Activation function	Learning rate	Maximum iteration times	Training function
	Input layer	Hidden layer	Output layer				
3	Length of training data	12	1	Tanh	0.01	20	Adam

(5) Maximum number of iterations

The maximum number of iterations is the number of batches in which the entire training data can be reused for model training. The results of a single training model have the condition of underfitting, and it is necessary to extract useful information from the data many times. The maximum number of iterations is related to the convergence of the loss function. When the loss function no longer declines, the number of iterations is considered reasonable. Through relevant data experiments, the maximum number of iterations is selected as 20 in this paper.

After training and learning, mean square error (MSE) is used to determine the optimal weight parameters of BP neural network model. The expression is as follows:

$$MSE = \sum_{t=1}^N \frac{(y(t) - y'(t))^2}{N} \tag{73.3}$$

where $y(t)$ is the actual value of the shared berth supply rate in time period t ; $y'(t)$ is the predicted value of the supply rate of shared berths in time period t ; N is the total number of predicted samples.

In summary, the optimal parameter results of BP neural network are shown in Table 73.9.

73.6 Comparison of Forecast Results

Taking office Area 2 as an example, the prediction results of ARIMA and BP neural network methods are compared, as shown in Fig. 73.6.

In order to more comprehensively evaluate the prediction effect of the two prediction methods and the prediction accuracy under different time spans, it is necessary to make an overall comparison between the predicted data and the actual data to establish the evaluation index of the prediction model, which is embodied in the following two indicators:

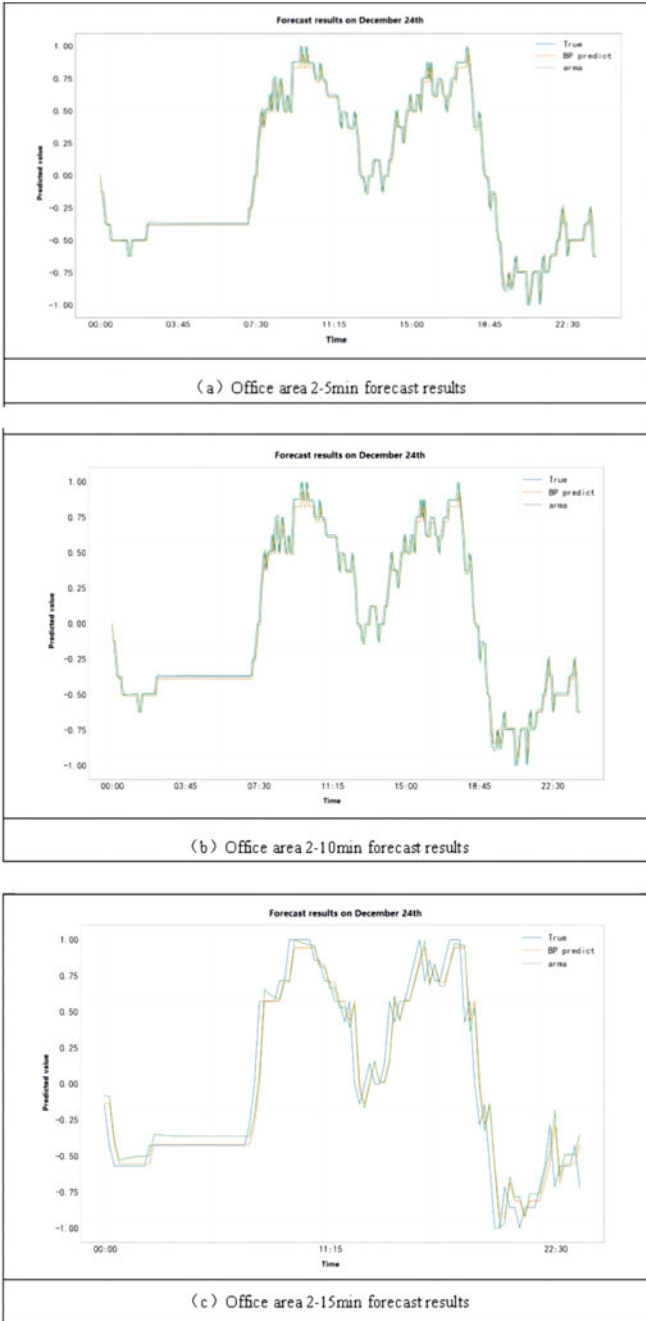


Fig. 73.6 ARIMA/BP neural network prediction results of office area 2

Mean absolute error (E)

$$E = \frac{1}{N} \sum_{t=1}^N |x'_t - x_t| \tag{73.4}$$

Root mean square error (r)

$$r = \sqrt{\sum_{t=1}^N \frac{(x'_t - x_t)^2}{N}} \tag{73.5}$$

where x'_t represents the predicted value of berth at time t ; x_t represents the actual berth value at time t ; N is the total number of predicted samples; The closer E and r are to 0, the higher the prediction accuracy is; otherwise, the greater the prediction error is.

According to the established ARIMA model and BP neural network model, the prediction accuracy of each model is tested by choosing the data of shared berth supply rate of the whole day on December 24, 2021. The results are shown in Table 73.10 (MAE and RMSE represent values of E and r , respectively).

According to the table, it can be seen that:

- (1) When the prediction time span is small, the prediction accuracy of the two methods is good; With the increase of the prediction time span, the two methods have different degrees of reduction in prediction accuracy;

Table 73.10 Comparison of results of prediction methods

Parking lot	Evaluating indicator	ARIMA			BPNN		
		5 min	10 min	15 min	5 min	10 min	15 min
Residential area	MAE	0.0648	0.0936	0.1108	0.0198	0.0198	0.0227
	RMSE	0.0921	0.1362	0.1533	0.0184	0.0184	0.0203
Business area 1	MAE	0.0539	0.0688	0.0817	0.0462	0.0644	0.0791
	RMSE	0.0745	0.0939	0.1186	0.0734	0.0909	0.1151
Business area 2	MAE	0.0319	0.0446	0.0619	0.0476	0.0714	0.1243
	RMSE	0.0475	0.0719	0.0978	0.0557	0.0822	0.1393
Office area 1	MAE	0.0427	0.0583	0.0699	0.0415	0.0614	0.0683
	RMSE	0.0622	0.0910	0.1064	0.0608	0.0907	0.0953
Office area 2	MAE	0.0621	0.0835	0.1837	0.0601	0.0866	0.1340
	RMSE	0.0931	0.1287	0.1228	0.0088	0.0166	0.0346

- (2) When the time span is 5 and 10 min, the overall performance of BP neural network is better than that of ARIMA in residential area and office area 2, but the difference in other areas is not obvious;
- (3) When the time span is 10 and 15 min, the performance of ARIMA for business area 2 is better than BP neural network;
- (4) When the time span is 15 min, the prediction accuracy of BP neural network for office area 2 is significantly higher than that of ARIMA;
- (5) For all time spans, the prediction accuracy of BP neural network for residential areas is better than that of ARIMA, and the change of MAE and RMAE is not obvious with the increase of time span. However, for the prediction of business district 2, ARIMA is generally better than BP neural network.

73.7 Summary

This paper analyzes the variation rules of the shared berths supply rate of three typical parking lots in residential areas, commercial areas and office areas around the three key primary schools in Luohu District. ARIMA model and BP neural network model are used respectively to predict and compare the shared berths supply rate of different parking lots in future periods. The results show that the (1) both of the 2 prediction models have high prediction accuracy for the shared parking supply rate data of the 5 parking lots. (2) With the increase of the prediction time span, the prediction accuracy of the two models will gradually decrease; (3) Different types of land use, applicable forecasting methods are also different. The BP neural network model has the overall prediction advantage for residential area and office area 2, while the ARIMA model has the overall prediction advantage for commercial area 2.

Based on the survey and combined with mathematical modeling analysis, this paper provides a possible solution to solve the problem of pick-up and parking in primary school campuses. However, this study still has some shortcomings: on the one hand, there are only 3 schools in this survey, and all of them are in Luohu District, Shenzhen, which inevitably has some limitations. On the other hand, the selected forecasting method and the extracted data of berth supply rate are limited, and the correlation between parking lots and the randomness caused by weather or other unexpected conditions are not taken into account. In the next step, more data will be used to analyze and compare different forecasting methods. At the same time, integrated models can be considered to make more accurate predictions.

Acknowledgements This paper was supported by the National Natural Science Foundation of China (no. 50908150).

References

1. ETCP Intelligent Parking Industry Research Institute and China Business Data Center. Big Data Report of China Smart Parking Industry (2017)
2. Richter, F., Di Martino, S., Mattfeld, D.C.: Temporal and spatial clustering for a parking prediction service. In: 2014 IEEE 26th International Conference on Tools with Artificial Intelligence, Limassol, Cyprus, pp. 278–282 (2014). <https://doi.org/10.1109/ICTAI.2014.49>
3. Li, Y., Sun, J., Zhang, X.: Fuzzy cluster analysis of urban parking situation. *J. Kunming Univ. Sci. Technol. (Sci. Technol. Ed.)* (02), 62–66 (2008)
4. Liu, S., Guan, H., Yan, H., et al.: Unoccupied parking space prediction of chaotic time series. In: 10th International Conference of Chinese Transportation Professionals, vol 3, pp. 2122–2131. American Society of Civil Engineers (2010)
5. Ji, Y., Tang, D., Guo, W., Blythe, T.P., Wang, W.: Forecasting available parking space with largest Lyapunov exponents method. *J. Central South Univ. English* **21**(4), 1624–1632 (2014)
6. Xiong, Z.B.: Research on GDP time series forecast based on ARIMA and neural network integration. *Math. Stat. Manag.* **30**(02), 306–314 (2011). <https://doi.org/10.13860/j.carolcarrollnkiSLTJ.2011.02.012>
7. Yang, Z., Chen, X.: Intelligent parking guidance system effective parking data prediction technology research. *J. Transp. Syst. Eng. Inf. Technol.* (04), 12–15 (2003). <https://doi.org/10.16097/j.carolcarrollnki.1009-6744.2003.04.003>
8. Dunning, A.E.: Method and system for projecting dynamic parking availability based on an ongoing survey for remote lots with high demand, US (2006)
9. Liu, S., Guan, H., Hai, Y., et al.: Unoccupied parking space prediction of chaotic time series. In: Tenth International Conference of Chinese Transportation Professionals (ICCTP) (2010)
10. Ji, Y., Tang, D., Blythe, P., et al.: Short-term forecasting of available parking space using wavelet neural network model. *Intell. Transp. Syst. IET* **9**(2), 202–209 (2014)
11. Tang, K., Hao, Z., Yixie, B., et al.: Evaluation of parking berth occupancy prediction method. *J. Tongji Univ. Nat. Sci.* (4), 11 (2017)
12. Ji, Y., Tang, D., Blythe, P., Guo, W., Wang, W.: Short-term forecasting of available parking space using wavelet neural network model. *IET Intell. Transp. Syst.* **9**(2) (2015)
13. Ji, Y., Chen, X., Wang, W., Hu, B.: Short-term prediction of effective parking berth based on wavelet transform and particle swarm wavelet neural network model. *J. Jilin Univ. (Eng. Sci.)* **46–48**(02), 399–405 (2016). <https://doi.org/10.13229/j.carolcarrollnkiJdxbgxb201602010>
14. Zhu, J., Bai, H., Wang, Z.: Based on principal component analysis (PCA) of parking demand forecasting research. *J. Intell. City* **2**(5), 43 (2016). <https://doi.org/10.19301/j.carolcarrollnkiZNCS.2016.05.036>
15. Guo, J., Bai, H., Wang, Z.: Research on parking demand prediction based on neural network. *Commun. China* **000**(004), 6–7 (2016). (in Chinese)
16. Rajabioun, T., Foster, B., Ioannou, P.: Intelligent parking assist. In: 21st Mediterranean Conference on Control and Automation, Platania, Greece, pp. 1156–1161 (2013). <https://doi.org/10.1109/MED.2013.6608866>
17. Klappenecker, A., Lee, H., Welch, J.L.: Finding available parking spaces made easy. *Ad Hoc Networks* **12**(Jan), 243–249 (2014)
18. Wu, T.: Research on Parking Resource Matching Based on Berth Sharing Strategy. Chang'an University, Xi'an (2019)
19. He, J., Li, J.: Analysis of transportation characteristics of primary and secondary school students to and from school in Wuhan and suggestions for improvement. *Urban Transp.* (05), 87–91 (2007)
20. Wang, B.: Research on the Matching of Parking Berth Allocation in Urban Central District. Southeast University, Nanjing (2017). (in Chinese)
21. Yong, S., Chunging, L., Yihuai, W., Shukui, Z., Feixiong, L.: A forecasting model for parking guidance system. In: 2009 WRI World Congress on Computer Science and Information Engineering, Los Angeles, CA, USA, pp. 607–611 (2009). <https://doi.org/10.1109/CSIE.2009.1088>

22. Pan, D., Liu, H., Li, Y.: Wind farm wind speed prediction optimization model based on time series analysis and Kalman filter algorithm. *Power Grid Technol.* **32**(7), 5 (2008)
23. FADAREDA: The application of artificial neural networks to mapping of wind speed profile for energy application in Nigeria. *Appl. Energy* **87**(3), 934 (2010)

Chapter 74

Review on the Development of Multi-lateral Well Technology



Qirui Yan, Jianfang Jiang, and Na Zhu

Abstract Multi-lateral well technology is a new drilling technology developed after directional well, lateral drilling and horizontal well technology. As the extension and development of horizontal well technology, multi-lateral well technology has obvious technical and economic advantages in reducing drilling cost and improving recovery efficiency of new and old oil fields. Multi-branch well technology takes drilling and completion technology as the main difficulty to tackle. Multi-branch well technology is a new drilling and completion technology to increase the production of oil and gas well by increasing the drainage area of oil and gas reservoir. It is one of the important technologies in the field of drilling in the twenty-first century. This paper, by investigating the progress of multi-branch well at home and abroad, focuses on the types of multi-branch well and the application of key drilling and completion technologies, as well as the application of multi-branch well technology in the oilfield, and gives an outlook on the current multi-branch well technology.

Keywords Multi-lateral well · Drilling · Completion technique

74.1 Introduction

Multi-lateral well technique refers to drilling two or more lateral holes (secondary holes) into the reservoir in the fundus of the main well of a well, and then drilling a tertiary hole from the secondary hole and connecting it back to a single well hole. Main boreholes can be vertical, directional, or horizontal. Lateral Wells can be directional, horizontal, or wavy lateral Wells.

Multi-lateral well technology is a new drilling technique developed in the mid to late 1990s based on conventional horizontal Wells and lateral Wells, which can obtain

Q. Yan · J. Jiang (✉)
China University of Petroleum, Beijing 102249, China
e-mail: 15103543959@163.com

N. Zhu
SINOPEC Research Institute of Petroleum Engineering Co., Ltd., No. 197 Baisha Road,
Changping District, Beijing 102206, China

maximum total horizontal displacement from a single well hole and drill multiple sets of oil and gas formations at different depths in the same or different directions. In particular, the lateral drilling of old Wells (dead Wells) to dead oil areas can greatly increase the exposed area of oil and gas reservoirs and prolong the life of oil and gas Wells, so as to revive dead Wells, greatly improve the oil reservoir recovery and reduce the comprehensive cost of oil and gas production. With remarkable economic benefits and broad application prospects, it is one of the main process technologies for oil and gas field development in the twenty-first century [1]. Compared with conventional vertical well technology, multi-lateral Wells have the advantages of wide service area, high recovery rate, fast investment recovery and low overall cost.

74.2 Progress of Multi-lateral Well Technology at Home and Abroad

In 1953, the former Soviet Union first drilled the 65/45 lateral horizontal well in the Ishimbai Oil Complex in Kartashev oilfield of Bashkiria Republic. There are three such branch Wells, including one 90° branch horizontal well with 170 m horizontal section. Since then, the technology of branching Wells has spread rapidly.

Horizontal Wells, especially branch horizontal Wells, were popular in the 1950s and 1960s. Lateral horizontal Wells were prized as a way to increase production in many fields in the former Soviet Union, the United States, Canada, Italy and other countries, but the boom did not last long because it was technically uneconomic. In the mid-1970s, with the exception of a few fields in the former Soviet Union and the United States where some lateral horizontal Wells were still being drilled, the rest were stagnant. As oil fields are depleted, oil prices rise and technology improves, lateral-directional Wells and lateral-horizontal Wells are becoming more important again. According to the relevant statistics in 1976, in the former Soviet Union oil producing areas, there are 5–10 branches of 80–300 m long branch highly deviated well and branch horizontal well drilling alone more than 100. Branching well has become one of the important means of increasing oil and gas production and enhancing oil recovery in the former Soviet Union.

In 1979, Richfield Atlantic completed four lateral horizontal Wells in the Emper Abaugh field. The four lateral Wells produced 87,450 m³ of recoverable original reserves, twice as much as the four standard vertical Wells. By 1986, Eastman Christensen had successfully drilled more than 200 lateral short-radius horizontal Wells in more than 60 vertical Wells through various formations using flexible drilling tools, and had successfully sidetracked five lateral Wells in different directions.

Multi-branch Wells have been applied in many domestic oil fields, including Bohai Oil field, Shengli Oil field, Liaohe Oil field, Xinjiang Oil field, Tahe oil field, etc. In September 1998, Nanhai West Company drilled the first multi-bottom well in China with workover rig and sidetracking technology of old well. The combined production of two shafts with electric submersible pump was 3 times of that of a

single inclined well. A double branching well was drilled in Xinjiang Oilfield in 1999. Hai14-20 three-branch well drilled in Liaohe Oilfield in April 2000 is the first self-designed and self-constructed sidetracking three-branch well with independent intellectual property rights. The completion technology level is 4. On the basis of its advanced horizontal well technology, Shengli Oilfield completed the first double-branch horizontal well in September 2000. Since 2000, the application of fishbone branch well in China has increased rapidly. In April 2005, Dagang oilfield was drilled successfully into the first fishbone type horizontal multi-branch well JH2 in onshore oilfield of our country and fills the gap of onshore fishbone type horizontal multi-branch well JH2 in onshore oilfield of our country [2].

74.3 Types and Advantages of Multi-lateral Wells

74.3.1 *Multi-lateral Well Type*

- (1) Superimposed multi-lateral or triple-lateral Wells: Two or three horizontal lateral Wells are drilled laterally in the same direction from one main hole at different intervals.
- (2) Reverse double branching well; Two horizontal holes were drilled laterally from the main hole in different directions.
- (3) Two-dimensional bi-horizontal branching well (Y-type multi-branching well); Two horizontal holes were drilled laterally from one main hole in different directions in the same plane.
- (4) Two-dimensional three horizontal lateral Wells: Three horizontal lateral Wells are drilled laterally from the main hole in the same plane.
- (5) Two-dimensional displacement of four-branch horizontal Wells: one horizontal well is drilled first, and then a new horizontal well is drilled laterally in the same direction with four different positions in the horizontal well.
- (6) Two-dimensional reverse four-horizontal branching well (fishbone type horizontal branching well): one horizontal hole is drilled first, and then multiple horizontal holes in opposite directions are drilled at different positions of the horizontal holes.
- (7) Directional three-lateral horizontal well (U-shaped well): One horizontal or directional well section is drilled first, and then two lateral horizontal Wells are drilled at different positions in the horizontal or directional well section.
- (8) Radial four-lateral horizontal well: Four horizontal or directional sections are drilled laterally from one main hole in different directions and at different intervals.

74.3.2 Multi-lateral Well Advantage

- (1) Different borehole structure, there are multiple branch borehole connections. It can increase the contact area between the well and the reservoir, increase the oil intake area, improve the pumping efficiency, and thus improve the well production and oil and gas recovery.
- (2) It can effectively develop complex oil and gas reservoirs with multiple reservoir intervals, simultaneously develop multiple sets of oil reservoir systems with fewer vertical Wells, and effectively develop heavy oil reservoirs, sagging reservoirs, natural fractures and tight reservoirs to increase the exposed area of the reservoir; It can effectively exploit the complex geological structure of multiple faults and isolated small sections, small oil layer, expand and communicate the regional connectivity between them.
- (3) Improve the dynamic reservoir profile, reduce the coning effect, reduce or delay the potential possibility of sand production, and improve the stress discharge effect.
- (4) Adding lateral holes from the main hole can increase the ratio of effective footage drilled in the reservoir to the total footage drilled, thus reducing the total footage drilled and reducing the drilling cost.
- (5) For the oil fields with near marginal economic benefit, the development cost can be reduced by drilling multiple Wells to make them become economical and effective development oil fields.

74.4 Key Technologies for Multi-lateral Wells

Lateral well drilling and completion technology is an important means to solve the problem of rapid production decline, high production cost and limited notch in old oil fields [3]. Lateral well drilling and completion technology has the following advantages: opening the window in the wellbore to increase the new hole, increase the drainage area, improve the recovery rate and increase the productivity of the old well; It can effectively exploit scattered small fault block and small oil reservoir around the old well to increase the productivity of the old well. Reduce drilling and completion costs and reduce operational time by utilizing the old hole notch.

74.4.1 Lateral Well Drilling Technology

At present, in the world, horizontal Wells, extended reach Wells, branch Wells and other difficult complex Wells are booming, and have been applied on a large scale, traditional drilling technology can not meet the needs of these difficult Wells, must rely on advanced steering technology to ensure the accuracy of the well trajectory.

The highest stage of drilling technology development is automated drilling. The whole process of drilling depends on sensors to measure various parameters, and the use of computer acquisition, comprehensive interpretation and processing, and then issued instructions, and finally by the relevant equipment automatic execution, so that the whole drilling process into an unmanned automatic control process. In the process of drilling automatic control, downhole measurement while drilling and downhole automatic control are the key link and also the key technology. The combination of the two is actually the automatic control technology of well trajectory—steering drilling technology. There are two main guiding modes: geometric guiding and geological guiding. Geometric steering is measured by the downhole MWD tool and transmitted to the control system for timely correction and control of the wellbore trajectory. Geosteering is the ability to control the wellbore trajectory in real time based on geologic parameters (formation lithology, formation layer, reservoir characteristics, etc.) derived from logging while drilling, allowing the bit to drill along the optimal position of the formation. This allows for optimal control without prior knowledge of formation characteristics.

74.4.2 Lateral Well Completion Technology

In recent years, onshore and offshore operators have become increasingly interested in multi-lateral completions for two reasons. First, many late-stage reservoirs now require longer intervals and more complex multi-lateral configurations. Second, multi-lateral well completion technology can better reduce the cost and efficiency of oil and gas development, and effectively solve the industry has been focused on low carbon emission. In a deepwater Stage 5 offshoring project in the Norwegian North Sea, a single well can reduce carbon emissions by 5000–10,000 tonnes.

The multi-lateral well technology is mainly limited by the completion technology, the completion success directly affects the application effect of the multi-lateral well. The difficulty of the bifurcated well completion technology lies in the connection technology between the main hole and the branch hole, which is unique to the branch well technology, and the sealing problem is the most difficult in the branch well completion operation. Therefore, the research on lateral well completion technology mainly focuses on the connection technology of main and branch boreholes in lateral well completion, and its technical level is mainly reflected in three aspects: interface support, interface seal and branch well re-entry.

Interface support means that the completion string of each lateral hole should be connected with the casing of the main hole, and its connection should have mechanical integrity to solve the problems of borehole stability and sand formation. Interface seal means to separate the oil flow of different pressure systems in each branch hole to solve the problem of production separation. Branch well reentry means that each branch well should be connected with the main well hole to realize reentry from the main well hole to any branch hole, so as to meet the requirements of oil production and workover operation [4]. Mechanical integrity must be ensured in order to realize

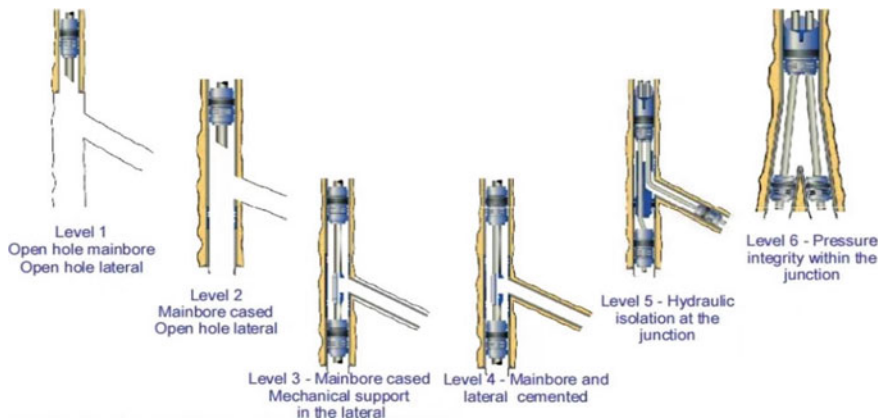


Fig. 74.1 TAML classification

the branch connection between the main hole and the branch, that is, mechanical stability is required at the branch connection. To ensure hydraulic integrity, that is, a certain hydraulic seal is required at branch joints; Ensuring re-entry, i.e., how to achieve selective access to each lateral or primary hole; It is also necessary to ensure that the casing is in place, which requires a more accurate wellbore trajectory.

Multi-lateral completion types. Shell's EricDiggins group held a Technology Advancement forum on multi-laterals in Aberdeen and developed a classification system based on complexity and functionality known as TAML (Technology Advancement Multi Laterals) (Fig. 74.1).

The technology and grading of multi-lateral well completion are evaluated according to three characteristics: connectivity, isolation, and access of linked branching Wells. The grading system of multi-lateral well completion methods is divided into six levels from "easy to difficult".

- (1) Primary completion: Both primary and lateral Wells are open holes. Lateral crossing length and yield control are limited. Completion operations do not separate zones or treat zonal differential pressure.
- (2) Secondary completion: casing and cementing under main well, open hole or just screen without cementing in lateral well. The main-wellbore connection is left open or, where possible, a "breakaway" screen is used in the lateral section, meaning that the screen is placed in the lateral section without mechanical connection to the main casing. It improves the flexibility of the main wellbore and improves the re-entry potential of the lateral interval compared to the primary completion.
- (3) Three-stage completion: casing is used in both the main and lateral Wells, with cement in the main and no cement in the lateral. Three stage completions provide connectivity and accessibility. The lateral-well liners are secured to the main hole through liner hangers, quick-connect systems, or other locking systems,

but are not cemented. There is no hydraulic integrity or pressure seal at the main-branch connection, but there is main-branch accessibility.

- (4) Stage 4 Completion: Both main and lateral Wells are cased and cemented, providing mechanical support connections but no hydraulic integrity. Casing in lateral Wells may also be cemented to the main casing. Both main and lateral Wells can be run in full.
- (5) Stage Five completions: Features three- and four-stage branch connection technology, with the addition of a completion device that provides a pressure seal at the junction of the branch liner and main casing. Hydraulic isolation can be achieved by straddling the lateral and production tubing using auxiliary packers, sleeves, and other completions in the main casing hole. Sidetracking can be done from both main and lateral boreholes.
- (6) Phase 6 completions: Pressure integrity at the connection can be achieved by running casing instead of using downhole completion tools. The six-phase completion system has an integral pressure seal at the junction of the branch and main casing. The connection part of a pressure-proof seal is designed to obtain an integral seal feature or integral formed or formable metal design, which will be valuable in offshore deepwater and subsea installations.

Multi-lateral Well completion requirements

- (1) Oil and gas can re-enter different branches of boreholes through the tripping guide. Maintain optimum connection conditions between the zone and wellbore.
- (2) The oil seepage area between the oil and gas reservoir and the wellbore should be as large as possible.
- (3) Should be able to effectively seal oil, gas and water layer, prevent gas channeling and water channeling, release layer interference.
- (4) Should be able to effectively control the emergence of oil and gas sand, prevent wall collapse, to ensure long-term production of oil Wells.
- (5) Conditions should be available to perform stimulation measures such as zonal water injection, gas injection, fracturing, and acidizing to facilitate artificial lift and downhole operations.

Key technologies of multi-lateral Well completion

- (1) Optimize spatial configuration

In offshore oil fields, the spatial configuration of multi-lateral Wells has a great impact on the success of well completion. Meanwhile, the wellbore stability of lateral Wells is also restricted by the spatial configuration. In deep-sea drilling and completion, well trajectory and geometry must be optimized first. From the point of view of borehole stability, the connection of branch Wells is the most unstable link of borehole wall, and the deviation azimuth of multi-branch Wells should ensure the stability of the connection as much as possible. When the branch is drilled along the direction of maximum horizontal principal stress, the connection is the most stable. When the branch is drilled along the direction of the minimum horizontal principal stress, the horizontal wellbore wall is relatively stable. In order to maximize the productivity of

the branch Wells, the spatial configuration of the branch Wells must be optimized first. On the premise of ensuring the stability of the shaft wall, a reasonable connection relationship between the main and branch Wells can be determined to reduce the interference of each branch section and achieve the best production state.

(2) Ensure the accessibility of multi-lateral Wells

Most of the country's laterals are used in inefficient fields, where production is usually achieved through fracturing. Therefore, each well in a multilateral well must have the ability to re-enter the perforation combination and fracture string. The pre-opened window branch completion device can better solve the problems of re-entry of branch window and long time and high risk of branch casing milling, and realize the re-entry of different branch holes by pulling up the guide. For example, the directional tie-back system of liner hanger developed by the Drilling Technology Research Institute of Shengli Oilfield and the pre-opened window branch completion device can well satisfy the re-drilling capability and ensure the integrity of the branch well [5].

74.5 Multi-lateral Well Application Examples

74.5.1 *Ultra-short Radius Sidetracking Multi-branch Drilling Technology*

“T-drilling technology” through “ultra-short radius sidetracking”, directly complete the window opening, inclining, horizontal drilling and other processes in the reservoir, minimize the ineffective drilling depth, “curve” on the well trajectory; This technology can also realize the drilling and completion of a single well with multiple reservoirs and multiple branches and multiple directions and multiple branches of a single reservoir. By increasing the drainage area, the recovery efficiency can be greatly improved and the cost of oil and gas production can be greatly reduced. Due to loose reservoir cementation and high argillaceous content in well A-1 of C oilfield in the South China Sea, particle migration occurred in the production process of the well, leading to screen plugging and substantial decline in production. The conventional acid plugging removal process measures were ineffective, and T-shaped multi-branch well stimulation technology was successfully adopted [6].

74.5.2 *Application of Multi-branch Wells in Geothermal Resources*

Our Geothermal resources are rich in reserves and have great potential for development and utilization. In order to efficiently develop deep high temperature geothermal resources, Enhanced Geothermal System (EGS) is adopted to provide seepage and

heat transfer channels for heat extraction medium by artificially building reservoir fractures. However, traditional EGS require two Wells to be drilled for injection and production of heat extraction. Due to high hardness and poor drillability of deep rock, the cost of drilling two Wells is high. In order to solve this problem, a new method for exploiting high temperature geothermal resources by multi-branch well EGS is proposed. The multi-branch geothermal system has advantages such as single-well injection-production cycle, large borehole and reservoir contact area, and strong borehole and fracture communication ability. The multi-branch well technology is used to drill two layers of lateral boreholes above the main borehole, in which insulated inner pipe is installed, annulus is sealed by packer, low-temperature fluid is injected into the upper branch borehole, and high-temperature fluid is exploited in the lower branch borehole [7]. Compared with the traditional well matching system, this method can realize the same injection and production well, reduce the number of Wells drilled and reduce the construction cost. In order to realize the economical and efficient development of high temperature geothermal resources, the contact area between borehole and reservoir can be expanded by using branch boreholes, the communication degree between borehole and fracture can be improved, and the injection and production capacity of the system can be improved.

74.5.3 Fishbone SAGD Horizontal Branching Well Drilling Technology

Fishbone type lateral horizontal well refers to drilling 2 or more lateral Wells in the same or different side of horizontal section of horizontal well. According to the horizontal projection diagram, each lateral well is distributed in a pinnate pattern with the main well. From the three-dimensional map, the distribution between each branch hole and the main hole is fishbone. FHW3121SAGD horizontal Wells are a set of fishbone SAGD horizontal Wells deployed by Xinjiang Oilfield Company in the SAGD Development Experimental area of well block No. 45, Fengcheng Oilfield. The Wells drill 4 more branches on both sides of the horizontal section of gas injection well I, with each branch length of 100 m. Conventional SAGD only generates steam cavities in the horizontal section of gas injection Wells, while fishbone SAGD can inject gas to form steam cavities in all four branches except the main borehole, which greatly increases the heating area of heavy oil formations and effectively increases oil drainage [8].

74.5.4 Stage 4 Branching Well Technology

The four level branch well systems with independent intellectual property rights in China are: The branch well system developed by Shengli Drilling Technology

Research Institute, the DF-1 multi-branch well system developed by the Great Wall Drilling Engineering Technology Research Institute, the branch well system developed by Karamay Drilling Technology Research Institute of West Drilling of CPC, and the expansion tube positioning multi-branch well system developed by the Research Institute of Exploration and Development of PetroChina, all of these branch well systems have been applied in the field. It achieved the TAML4 completion level. As of April 2020, the four-stage completion and lateral well technology has been successfully applied to three Wells in Caofeidian 11-1 oilfield, Bohai Sea. Compared with conventional sidetracking methods, the production of three new Wells has been increased while retaining the production of the old Wells. Compared with the newly drilled adjustment Wells, it saves nearly 50% of the construction period and hundreds of millions of yuan of costs. The total recoverable reserves of $9.2 \times 10^4 \text{ m}^3$ of 3 old Wells and $3.8 \times 10^4 \text{ m}^3$ of the remaining recoverable reserves of 3 branch Wells are converted into future production, and the recoverable reserves of the old Wells are increased by 2.5 times. The four-stage drilling and completion technology of main hole/branch hole reentry technology, casing sidetracking window technology, polymer drilling fluid technology, bottom liner cementing technology, and optimized design of supporting sand control string for completion has been successfully applied in three branch Wells of Caofeidian 11-1 oilfield [9].

74.5.5 Stage 5 Lateral Well Technology

The stage 5 lateral well technology is to use the window on the upper part of the existing well to sidetrack, without moving the well location, increase the exposed reservoir area, and greatly improve the oil and gas recovery. Compared with the one to four lateral Wells, the five lateral Wells have three technical advantages: the five lateral well completion technology uses mechanical support to establish a connecting path between the main and lateral Wells; Realize hydraulic seal; For branching holes, subsequent selective re-entry is also available.

Schlumberger's Rapid family of multi-lateral completion systems offers a full range of solutions, ranging from TAML1 to Stage 5, for both new and old well modifications in a variety of environments/well types. The system has the advantages of more flexibility, more reliable connector design and more secure and efficient operation flow. In 2022, the RapidXtreme system successfully completed the first four-stage lateral well with gravel pack sand control in the South China Sea.

74.6 Conclusion and Understanding

- (1) The speed and quality of the development and application of multi-branch well directly affect the survival and development of oil fields. Multi-branch well technology is also one of the most key technologies for oil enterprises to enter the

foreign market. Compared with common directional Wells and horizontal Wells, multi-lateral Wells have the advantages of increasing exposed reservoir area, improving drainage efficiency, improving dynamic profile of oil flow, reducing coning effect, improving gravity drainage effect, adjusting reservoir production vertically, and reducing repeated well intervals and drilling equipment relocation, and reducing platform construction costs.

- (2) Multi-lateral well completion technology is one of the difficulties of multi-lateral well completion technology, mainly the connection technology of main hole and branch hole. Completion technology has many advantages, such as reducing the comprehensive cost of drilling, and can be used as an effective means to develop heavy oil reservoirs, marginal or middle and late oil reservoirs, natural fractures and tight oil reservoirs, and fault block oil reservoirs.
- (3) By analyzing the development of multi-lateral well technology at home and abroad, it can be seen that the drilling and completion technology of foreign branch Wells has been relatively mature, while the application scale and supporting technology of domestic branch Wells have a certain gap compared with the advanced level in the world, and there are few completion systems with independent intellectual property rights. Therefore, it is necessary to devote efforts to technical breakthroughs as soon as possible.

References

1. Zheng, Y., Huang, W.: Fresh security. Review on the development of lateral well technology abroad. *Pet. Drill. Tech.* (04), 54–57 (1997)
2. Yuan, S., Liu, Q., Xiong, J.: Review on development of multi-lateral well technology. *Oilfield Eng. Abroad* **26**(12), 42–44+47 (2010)
3. Fan, B., Hao, Z., Wu, G., Wang, B., Li, Z., Chai, L.: Pipe string structure and pilot test of double-pipe completion in multi-lateral wells. *Oil Field Equipment* **51**(05), 22–27 (2022)
4. Chen, J., Wu, G., Zuo, K., Cao, Y., Yan, W., Chai, L., Zhao, J.: Development trend of five-stage completion technology for lateral wells at home and abroad. *Oil Field Equipment* **48**(04), 80–84 (2019)
5. Yang, L., Liu, X., Liang, L., Tang, Z.: Review on the development of multi-lateral well completion technology. *Inner Mongolia Petrochem. Ind.* **36**(11), 86–88 (2010)
6. Zhang, Y., Yang, J., Lu, Y.: Application of new technology for stimulation technology of T-type multi-branch well in offshore oilfield. *West. Explor. Eng.* **34**(05), 73–75 (2022)
7. Shi, Y., Song, X., Li, G., Xu, F., Cui, Q.: Comparison of heat extraction effects of CO₂ and water in a multi-branch well geothermal system. *Nat. Gas Ind.* **41**(11), 179–190 (2021)
8. Wang, Y., Gao, F., Wang, H., Xu, G., Yang, G., Zhang, J., Zhang, R.: Drilling technology of fishbone SAGD horizontal lateral well. *West. Explor. Eng.* **29**(06), 35–38 (2017)
9. Ma, Y., Wang, K.: Application of four-stage branching drilling and completion technology in Caofeidian 11-1 oilfield. *China Offshore Oil Gas* **32**(03), 124–129 (2020)

Chapter 75

A Robust Nonsingular Double-Boundary CHIEF Method for Full Wave Numbers



Jie Chen, Yu Xiang, and Ziyu Shi

Abstract In this paper, a double-boundary CHIEF method is constructed based on the idea of the combined Helmholtz integral equation formulation (CHIEF) method by adding supplementary equation for overcoming the non-uniqueness of the boundary integral equation at the eigenfrequency. The conventional boundary element method (CBEM) equation is coupled with the virtual indirect boundary element method (VIBEM) equation. Because the CBEM equation and the VIBEM equation are located at different boundaries, their eigenfrequencies are not coincident, which theoretically avoids the failure of the supplementary equation in the traditional CHIEF method. At the same time, according to the equivalence of the coefficient matrix between the CBEM and VIBEM, the singular matrix is obtained indirectly by replacement calculation. Through the analysis and verification of numerical examples, the non-singular dual-boundary CHIEF method proposed in this paper can effectively overcome the non-uniqueness of the conventional boundary element method at the eigenfrequency, and can obtain high-precision and robust results in the full wavenumber domain. The accuracy of the proposed method is much higher than that of CBEM and Burton-Miller method without singular integral processing.

Keywords Boundary element method · Eigenfrequency · Acoustic radiation · Singular integral

J. Chen · Y. Xiang (✉) · Z. Shi
Guangxi Key Laboratory of Automobile Components and Vehicle Technology, Guangxi
University of Science and Technology, Liuzhou 545006, China
e-mail: xiangyu@gxust.edu.cn

J. Chen
College of Mechanical and Automotive Engineering, Guangxi University of Science and
Technology, Liuzhou 545006, China

75.1 Introduction

The conventional boundary element method (CBEM) is the classical method for calculating structural acoustic field problems. This method is not only able to reduce the space dimension of the solved problem, but also its kernel function automatically satisfies the Helmholtz equation and Sommerfeld radiation condition, which is suitable for solving acoustic external problems in infinite and semi-infinite domains [1]. In particular, the coefficient matrix of the method has a dominant main diagonal and small condition number, thus the stability of the numerical solution is excellent. However, CBEM has an inherent defect, i.e., the non-uniqueness of the solution at the eigenfrequency. The combined Helmholtz integral equation formulation (CHIEF) method [2, 3] or Burton-Miller method [5–7] is generally used to solve this problem. However, the supplementary equations of CHIEF method have the potential of failure [3, 4], and Burton Miller method adds the calculation of hypersingular integral [1]. The proposed method takes its roots from the idea of CHIEF method, it associates the combined layer potential virtual indirect boundary element method (VIBEM) equation as a supplementary equation with the CBEM equation, and the singular matrix is indirectly replacement calculated by using the equivalent relationship between the CBEM and VIBEM coefficient matrix. Furthermore, a robust nonsingular double-boundary CHIEF method for full wave numbers is proposed.

75.2 Basic Theories of BEM

75.2.1 CBEM

By configuring field points on the real boundary of the sound source, the conventional boundary integral equation (CBIE) can be discretized into the following matrix equation form:

$$\mathbf{A}_S \mathbf{p} = \mathbf{B}_S \mathbf{q} + \mathbf{p}_{in} \quad (75.1)$$

where \mathbf{p} is the surface sound pressure column vector, \mathbf{q} is the surface sound flux column vector, and \mathbf{p}_{in} is the field point incident sound pressure column vector. Equation (75.1) can be used to calculate the unknown boundary value of radiation and scattering problems very effectively. However, the CBEM cannot give a unique solution to the external acoustic problem at the eigenfrequency of the relevant internal problem. Moreover, because the integral kernel function is a function of the distance between the field point and the source point, there is a problem of singular integration when the field point coincides with the integration source point.

The normal derivative boundary integral equation (NDBIE) can be obtained by taking the derivative of the field points on both sides of the Eq. (75.1), which is written in matrix form:

$$\mathbf{A}_N \mathbf{p} = \mathbf{B}_N \mathbf{q} + \mathbf{q}_{in} \quad (75.2)$$

The commonly used method to overcome non-uniqueness is to obtain Burton-Miller equation through CBIE + α NDBIE linear combination:

$$(\mathbf{A}_S + \alpha \mathbf{A}_N) \mathbf{p} = (\mathbf{B}_S + \alpha \mathbf{B}_N) \mathbf{q} + \mathbf{p}_{in} + \alpha \mathbf{q}_{in} \quad (75.3)$$

where α is the combination coefficient. Because the coefficient matrix of NDBIE is introduced, the calculation accuracy of Eq. (75.3) at the non-eigenfrequency will be lower than that of CBEM, and the problem of hypersingular integration will also be brought, which increases the difficulty of numerical solution.

75.2.2 VIBEM

The virtual indirect boundary method matches the integral relationship between the virtual source strength and the real boundary condition by locating the equivalent source on the virtual boundary of the vibration body, and then obtains the virtual indirect boundary integral equation. For common problems outside the sound field, the virtual indirect boundary element method also has non-uniqueness at the characteristic wave number of the relevant problems corresponding to the virtual boundary. It is easy to overcome the non-uniqueness of the virtual indirect boundary element method by using the method of superposition of monopoles and dipoles, namely the combined layer potential method. The integral equation of VIBEM can be discretized into the following matrix equation form:

$$\mathbf{p} = \mathbf{A}_V \mathbf{w} + \mathbf{p}_{in} \quad (75.4)$$

where \mathbf{w} is the source strength of the equivalent source on the virtual boundary. The derivative of the offsite normal direction of Eq. (75.4) can be obtained:

$$\mathbf{q} = \mathbf{B}_V \mathbf{w} + \mathbf{q}_{in} \quad (75.5)$$

Equations (75.4) and (75.5) are combined to eliminate the source intensity:

$$\mathbf{A}_V^{-1} \mathbf{p} = \mathbf{B}_V^{-1} \mathbf{q} - \mathbf{B}_V^{-1} \mathbf{q}_{in} + \mathbf{A}_V^{-1} \mathbf{p}_{in} \quad (75.6)$$

Although VIBEM calculation is simple and accurate, its generated coefficient matrix \mathbf{A}_V and \mathbf{B}_V is generally ill-conditioned and its numerical solution has poor stability, which is the main reason for limiting its engineering application.

75.3 Double-Boundary CHIEF Method

Based on the idea that the traditional CHIEF method uses the interior point equation as the supplementary equation, we take the VIBEM equation as the supplementary equation, and form the overdetermined equation system by coupling with the CBEM equation:

$$\begin{cases} \text{CBEM} \\ \text{VIBEM} \end{cases} = 0 \quad (75.7)$$

Since the CBEM equation and the VIBEM equation are located at different boundaries and their eigenfrequencies are not coincident, Eq. (75.7) theoretically avoids the problem of the failure of the supplementary equation in the traditional CHIEF method, and can obtain a unique solution at the full wave number. The equation of the double-boundary CHIEF method can be written as follows:

$$\begin{bmatrix} \mathbf{A}_S \\ \mathbf{A}_V^{-1} \end{bmatrix} \mathbf{p} = \begin{bmatrix} \mathbf{B}_S \\ \mathbf{B}_V^{-1} \end{bmatrix} \mathbf{q} - \begin{bmatrix} \mathbf{0} \\ \mathbf{B}_V^{-1} \end{bmatrix} \mathbf{q}_{\text{in}} + \begin{bmatrix} \mathbf{I} \\ \mathbf{A}_V^{-1} \end{bmatrix} \mathbf{p}_{\text{in}} \quad (75.8)$$

The combination scheme can be optimized according to different boundary conditions:

$$\begin{bmatrix} \mathbf{A}_S \\ \mathbf{I} \end{bmatrix} \mathbf{p} = \begin{bmatrix} \mathbf{B}_S \\ \mathbf{A}_V \mathbf{B}_V^{-1} \end{bmatrix} \mathbf{q} - \begin{bmatrix} \mathbf{0} \\ \mathbf{A}_V \mathbf{B}_V^{-1} \end{bmatrix} \mathbf{q}_{\text{in}} + \begin{bmatrix} \mathbf{I} \\ \mathbf{I} \end{bmatrix} \mathbf{p}_{\text{in}} \quad (\text{Neumann}) \quad (75.9)$$

$$\begin{bmatrix} \mathbf{A}_S \\ \mathbf{B}_V \mathbf{A}_V^{-1} \end{bmatrix} \mathbf{p} = \begin{bmatrix} \mathbf{B}_S \\ \mathbf{I} \end{bmatrix} \mathbf{q} - \begin{bmatrix} \mathbf{0} \\ \mathbf{I} \end{bmatrix} \mathbf{q}_{\text{in}} + \begin{bmatrix} \mathbf{I} \\ \mathbf{B}_V \mathbf{A}_V^{-1} \end{bmatrix} \mathbf{p}_{\text{in}} \quad (\text{Dirichlet}) \quad (75.10)$$

75.4 Singular Integral Problem

The accurate calculation of singular integral processing is the key of BEM, and also one of the problems to be considered in the double-boundary CHIEF method proposed in this paper. In the case of boundary element discretization commonly used in two-dimensional or three-dimensional problems, singular integral processing is usually required for \mathbf{B}_S . In this paper, the equivalent relationship between the coefficient matrices of CBEM and VIBEM is used to indirectly replace and calculate singular matrices (Xiang et al. proposed an indirect replacement algorithm for singular matrices in literature [4], and indirectly obtain singular matrices through matrix operations).

$$\mathbf{B}_S = \mathbf{A}_S \mathbf{A}_V \mathbf{B}_V^{-1} \quad (75.11)$$

where \mathbf{B}_S is the singular matrix of CBEM, and \mathbf{A}_S is the nonsingular matrix (for plane element) of CBEM, \mathbf{A}_V and \mathbf{B}_V are coefficient matrices of VIBEM. In this way, the singular matrix \mathbf{B}_S of CBEM can be obtained indirectly through the operation of the other three matrices, thus avoiding the singular integral processing. In addition, the indirect calculation of the matrix not only retains the diagonally dominant characteristic of the CBEM coefficient matrix, but also inherits the high-precision advantage of VIBEM.

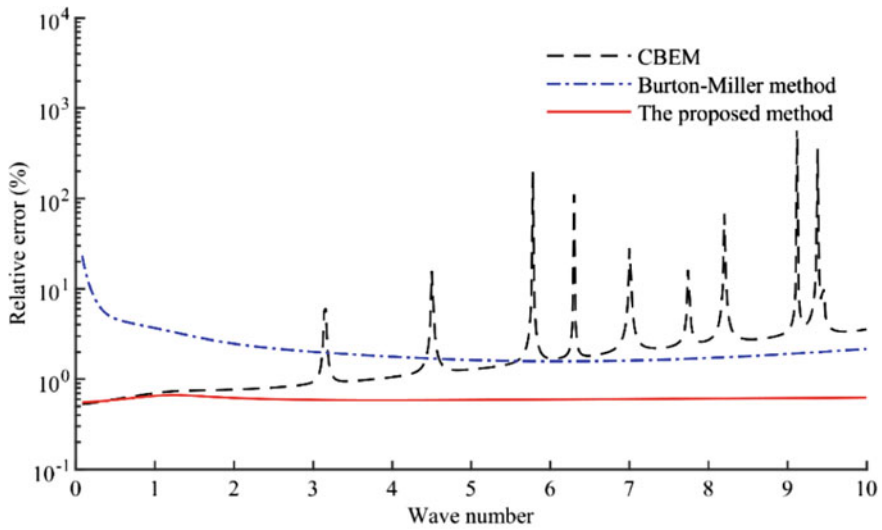
75.5 Numerical Example

The analytical solutions of the radiation problem of the pulsating spherical sound source with the normal vibration velocity of the sound source surface and the scattering problem of sound-soft boundary (Dirichlet boundary) and sound-hard boundary (Neumann boundary) spherical sound source with a unit amplitude of plane incident wave propagating along the z-axis in the forward direction are known, which are used to verify the accuracy and effectiveness of the method in this paper. The triangular plane constant element is used to discretize the spherical boundary, and the number of elements is 246–1534; The element integral is calculated by triangular Gauss–Legendre integral, and the number of integral points is 6.

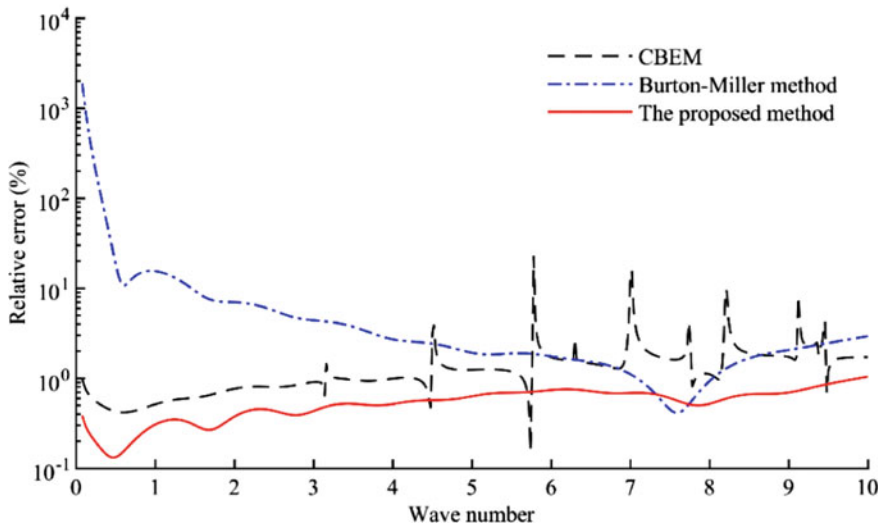
Foremost, the relative error of the surface sound pressure amplitude of the vibrating body is calculated by the method in this paper, and compared with CBEM and Burton-Miller method, the effectiveness of this method to overcome the non-uniqueness problem is judged. Figure 75.1 shows the comparison of the relative error of different models with the change of wave number. The results show that the method in this paper can obtain unique solutions in the whole frequency domain, and has better accuracy than CBEM and Burton-Miller methods.

Secondly, the convergence of this method is analyzed by taking the pulsating sphere as an example. Figure 75.2 shows the relative error comparison between Burton-Miller method and the proposed method when the model is discretized into different elements numbers. The results show that the accuracy of this method is always better than Burton-Miller method under the same number of discrete elements. In addition, it can be seen that the accuracy of the method in this paper in the case of 246 discrete elements is comparable to that of Burton-Miller method in the case of 2808 discrete elements, which fully demonstrates the high accuracy advantage of the method in this paper.

Since the VIBEM coefficient matrix is introduced into this method, and the ill-conditioned problem of the coefficient matrix will greatly affect the stability of the numerical solution, the condition number of the coefficient matrix in this method is also investigated. Figure 75.3 shows the comparison of the condition number of coefficient matrix between CBEM, VIBEM and the proposed method. The results show that the condition number of coefficient matrix of this method is far lower than that of VIBEM.



(a) Sound-soft boundary



(b) Sound-hard boundary

Fig. 75.1 Comparison of relative errors of CBEM, Burton-Miller method and proposed method for calculating surface sound pressure

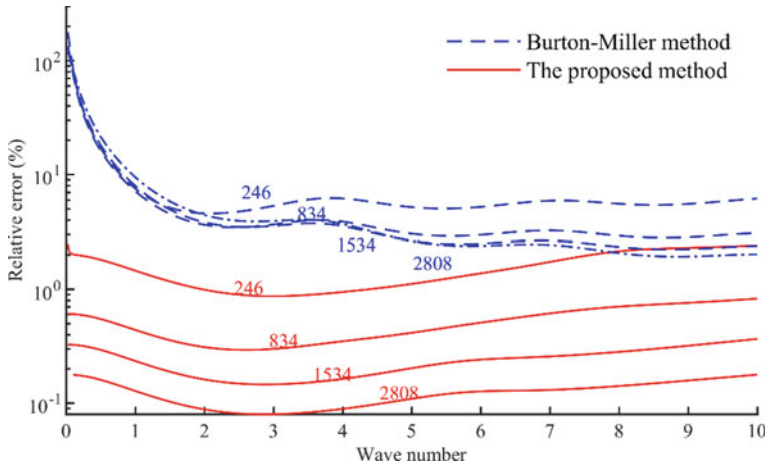
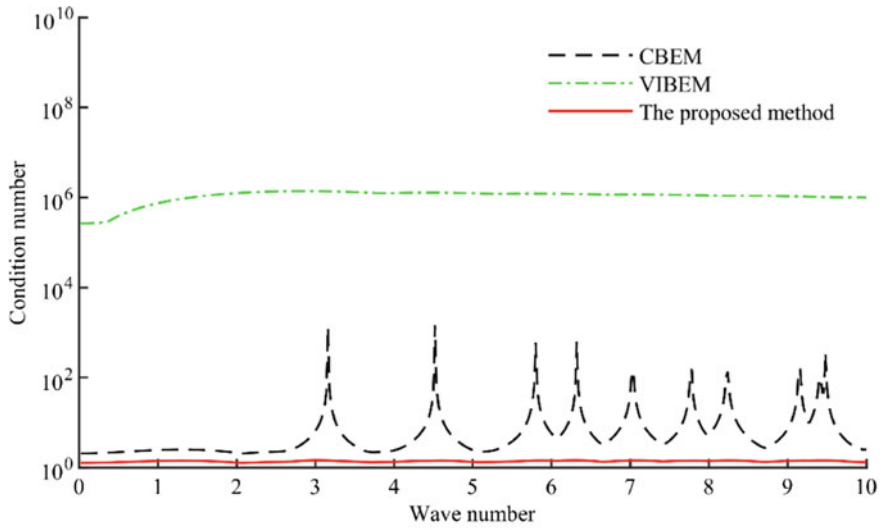


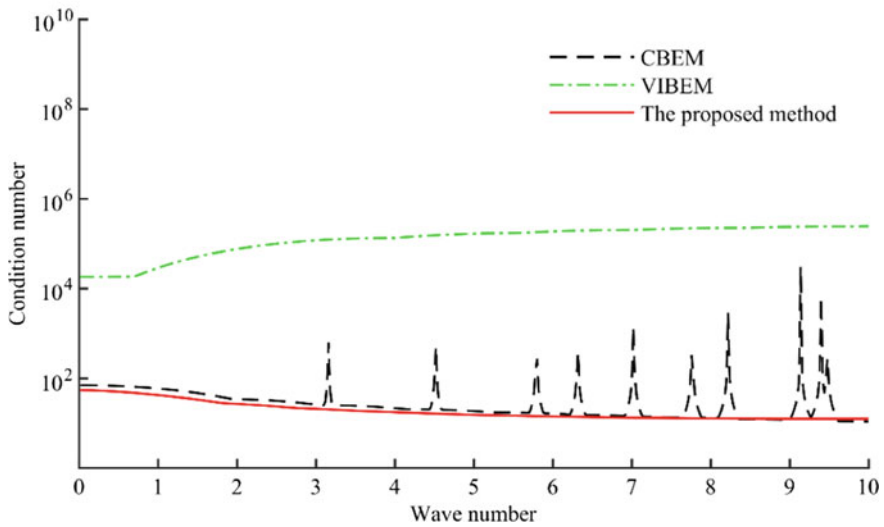
Fig. 75.2 Comparison of relative errors between Burton-Miller method and proposed method when pulsating sphere surface is discretized into different elements

According to the results of numerical examples, the method proposed in this paper can effectively avoid their defects while inheriting the advantages of CBEM and VIBEM. Using this method to calculate radiation and scattering problems can obtain unique solutions in the entire wavenumber domain, and the accuracy of the results is far higher than that of Burton-Miller method without singular integration.

In summary, the non-singular double-boundary CHIEF method proposed in this paper provides an efficient and simple numerical calculation tool for the calculation of medium and large-scale acoustic field analysis problems in the acoustic and related engineering fields. The method proposed in this paper can be combined with the fast multipole method to further improve the computational efficiency of the algorithm, and is expected to efficiently calculate large-scale acoustic problems. At present, research work in this area is ongoing.



(a) Matrix A



(b) Matrix B

Fig. 75.3 Comparison of coefficient matrix condition numbers among CBEM, VIBEM and the proposed method

Acknowledgements This work was supported by the National Natural Science Foundation of China under Grant No. 51775121.

References

1. Liu, Y.J.: On the BEM for acoustic wave problems. *Eng. Anal. Boundary Elem.* **107**, 53–62 (2019)
2. Schenk, H.A.: Improved integral formulation for acoustic radiation problems. *J. Acoust. Soc. Am.* **44**, 41–58 (1968)
3. Chen, I.L., Chen, J.T., Liang, M.T.: Analytical study and numerical experiments for radiation and scattering problems using the CHIEF method. *J. Sound Vib.* **248**, 809–828 (2001)
4. Xiang, Y., Shi, Z.Y.: Full wavenumber high precision combined coupled double boundary element method for solving external acoustic problems. *J. Sound Vib.* **544**, 117392 (2023)
5. Zheng, C.J., Chen, H.B., Gao, H.F., Du, L.: Is the Burton-Miller formulation really free of fictitious eigenfrequencies? *Eng. Anal. Boundary Elem.* **59**, 43–51 (2015)
6. Zheng, C.J., Bi, C.X., Zhang, C.Z., Zhang, Y.B., Chen, H.B.: Fictitious eigenfrequencies in the BEM for interior acoustic problems. *Eng. Anal. Boundary Elem.* **104**, 170–182 (2019)
7. Burton, A.J., Miller, G.F.: The application of integral equation methods to the numerical solution of some exterior boundary-value problems. *Proc. R. Soc. A: Math. Phys. Eng. Sci.* **323**, 201–210 (1971)

Chapter 76

Numerical and Experimental Study on the Construction Process of the Pedestrian Bridge with a Curved Beam and Inclined Arch



Shaocai Zhu , Dan Liu , and Zhiyong Yao 

Abstract This paper investigates the stress and geometry shape of a pedestrian bridge with a curved beam and an inclined arch during the construction process using numerical simulation and field testing. The results reveal that the stress and geometry of the arch ribs and the main beam would vary noticeably as a result of the initial development of the beam-arch combination system after the cable is tensioned, which may result in a significant safety risk. During the whole construction process, the measured stress and geometry of the bridge show a good agreement with the numerical results by means of the finite element (FE) method, and are subjected to the requirements in the design, which indicates that the construction control of the bridge is reasonable. The output of this study can provide important scientific insights as well as practical applications for similar bridges.

Keywords Curved beam and inclined arch pedestrian bridge · Construction process · Numerical simulation · Stress monitoring · Geometry shape

76.1 Introduction

With the rapid development of the economy and the acceleration of urbanization, the pedestrian bridge not only includes the traveling function, but people are also paying increasing attention to the aesthetics of the bridge [1], where the bridge structure with a curved beam and inclined arch has become increasingly popular in urban pedestrian bridges owing to its distinct shape, graceful curve, and sense of science and technology [2–4]. However, the construction process of the pedestrian bridge

S. Zhu

China-Singapore Guangzhou Knowledge City Fiscal Invested Construction Project Management Center, Guangzhou 510700, China

D. Liu · Z. Yao (✉)

School of Civil Engineering, Guangzhou University, Guangzhou 510006, China

e-mail: zhiyongyao@gzhu.edu.cn

with a curved beam and inclined arch usually associates with many structural system transformations as a result of the complex structure [5–8]. Therefore, it is an essential problem that how to ensure that the stress state and geometry shape of the bridge in the construction process are subjected to a safe condition [9, 10].

As an example of the pedestrian bridge with a curved beam and an inclined arch that crosses the main road in Guangzhou city, this paper investigates the variation laws of the stress and geometry of the bridge in the construction process through numerical simulation and field test. The findings of this study can be applied to guide the construction of similar bridges.

76.2 Bridge Overview

The total length of the main bridge is 144.5 m, and the span is arranged as (4 + 26 + 36 + 55 + 22 + 1.5) m. Besides, the three branches with spans of 4.064, 19.0 and 15.128 m are connected to the main bridge as a whole. Figure 76.1 shows the overall layout of the bridge elevation. The main steel beam is a single-cell box with a height of 1.2 m and a width of 4–6 m. The arch rib is a pentagon section, where the arch axis is set as a quadratic parabola, the calculated span is 58 m, the rise is 23.2 m, the rise-span ratio is 1/2.5, and the arch rib is 20° outward. A total of 13 replaceable rib cables with a transverse spacing of 3 m, are arranged symmetrically along both sides of the overall bridge from the center of the main span. The piers, beams, and arch ribs are all prefabricated in the factory and then lifted and welded together on the site to form the final structure.

The construction steps of the bridge are as follows: substructure construction → placing the concrete of the springing stone → installing temporary piers → lifting and welding the beam and arch segments → removing the temporary constraint of the arch rib → tensioning and controlling cable force → removing the temporary pier of the beam → construction of the deck and guardrail.

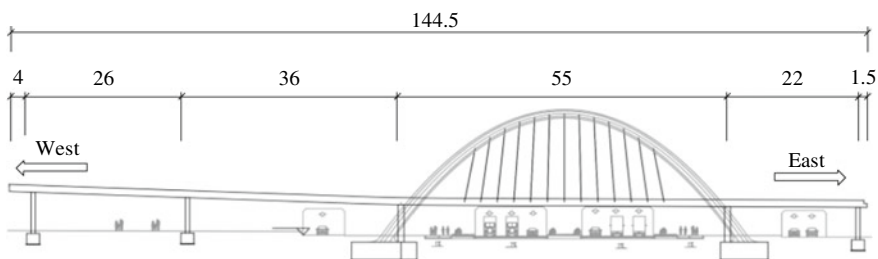


Fig. 76.1 Layout of the bridge elevation (unit: m)

76.3 Construction Monitoring

Monitoring and control are significantly essential to bridge construction, where several important indicators, including the stress state and geometry shape, are measured and compared with the ideal condition to ensure the safety of bridges in the construction process by forecasting, identifying, and analyzing the error.

76.3.1 Monitoring Stages

Lifting and welding the beam and arch segments of the bridge are completed by installing temporary piers, which cannot affect the structure status. However, removing the temporary constraint of the arch rib, tensioning the cable force, and removing the temporary pier of the beam can change the structural system and lead to a complex stress condition. Besides, the construction of the deck and guardrail also will affect the external load that acts on the structure. Thus, there are four significant monitoring stages in the construction process of the bridge, including the removal of temporary constraints of arch ribs, the tension of the cable force, the removal of the temporary pier of the beam, the construction of the deck and guardrail.

76.3.2 Stress Monitoring

Considering the structural characteristics of the bridge and referring to related literatures, Fig. 76.2 shows the stress monitoring layout of the bridge. It can be seen that 5 stress sections are symmetrically arranged in the main span and arch ribs, while only 3 stress sections are arranged in other spans. Finally, there are 16 stress monitoring sections in the whole bridge. For the beam section, four measure points are arranged on the bottom and top surfaces respectively, and two points are monitored on the outer surface of the arch rib, as shown in Fig. 76.3. The surface-type strain gauge is adopted to monitor the stress. In order to easily measure, the handheld acquisition instrument is used to manually collect strain data on the top surface of the beam. However, the data on other points is collected online by installing the wireless transmission module, as shown in Fig. 76.4.

76.3.3 Geometry Monitoring

The geometry shape monitoring of the bridge mainly involves the coordinates of the arch rib and the elevation of the bridge deck. In order to better capture the geometry variation law of the bridge, 9 monitoring sections are arranged symmetrically on

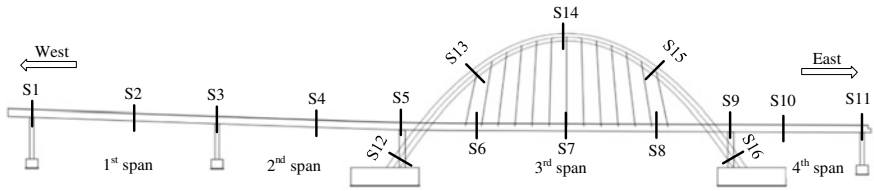


Fig. 76.2 Stress monitoring layout of the bridge

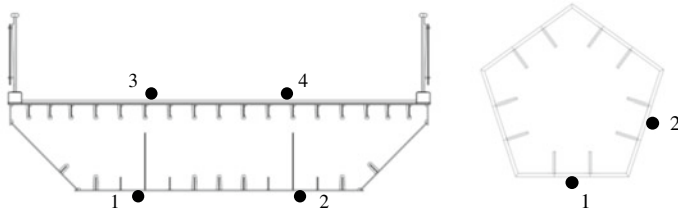
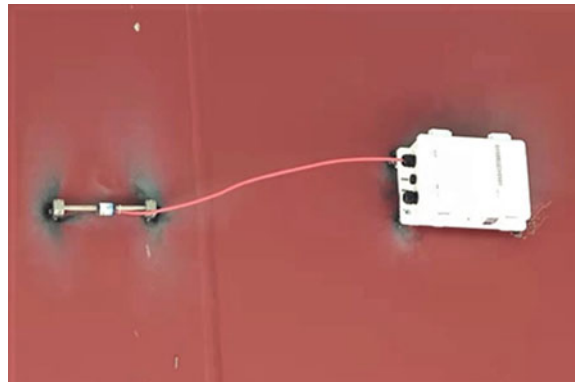


Fig. 76.3 Layout of stress monitoring points of beam and arch sections

Fig. 76.4 Surface-type strain gauge and wireless transmission module



the main span and arch ribs, and 5 monitoring sections are arranged on other spans. Finally, there are 21 geometry shape monitoring points in the whole bridge, as shown in Fig. 76.5. Two elevation observation points of the main beam section are arranged on the outside of the box girder, which can be checked mutually to ensure the accuracy of the results. There are 4 monitoring points on the outside surface of the arch rib for visual observation, as shown in Fig. 76.6. Leica TS60 total station is used in the measurements and the coordinates of the monitoring points can be automatically obtained by a cross reflector that sticks on the surface of the structure as shown in Fig. 76.7.

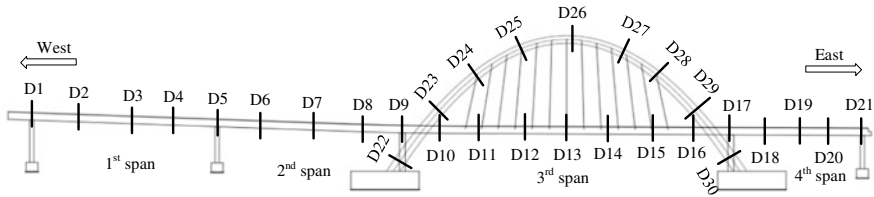


Fig. 76.5 Geometry monitoring layout of the bridge

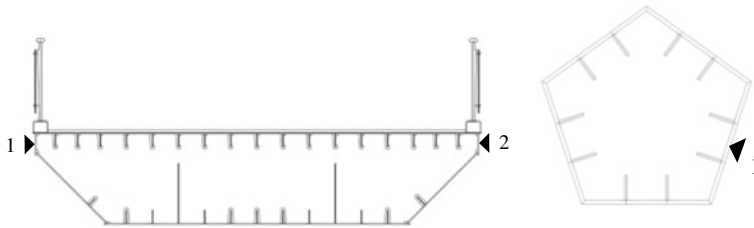


Fig. 76.6 Layout of geometry monitoring points of beam and arch sections



Fig. 76.7 Leica TS60 total station and cross reflector

76.4 Construction Simulation

In order to graphically reproduce the whole construction process of the bridge, a numerical model is established through the FE method, which can predict the state of the bridge at each construction stage in advance. Such work is considerably important to ensure the safety and quality during bridge construction. In this paper, the forward-calculation analysis is applied to obtain the geometry and stress state of the pedestrian bridge with a curved beam and inclined arch in each construction stage, which is also a widely used method in the construction process of a tied arch bridge at present.

The numerical model of the bridge is created using commercial FE software MIDAS/Civil with three-dimensional beam elements modeling the steel box girder, arch, pier, and pile, truss link elements that bear only tension modeling the cable, and

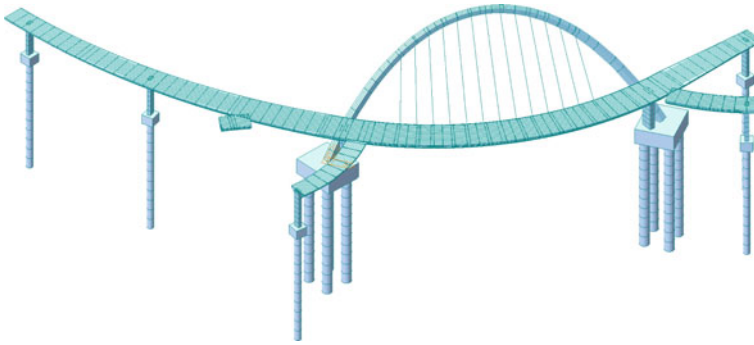


Fig. 76.8 Finite element model of the bridge

spring elements modeling the temporary pier during construction. Finally, a total of 415 nodes, 386 beam elements, 13 truss elements, 20 connecting spring elements, 15 rigid connection elements, and 158 linear spring elements are used in the numerical FE model. Figure 76.8 shows the three-dimensional FE model of the bridge with a curved beam and inclined arch.

The construction process of the bridge is created by activating and deactivating the corresponding elements and boundary conditions in the model, namely activating the components and boundaries involved in this stage, and deactivating those that are not. Thus, it can numerically calculate the geometry and stress results of the bridge through the activation and deactivation procedures in different construction stages.

76.5 Results and Discussions

76.5.1 Stress Results

Figures 76.9 and 76.10 show the calculated and monitored stress of the beam and arch at different construction stages, respectively. It can be seen that when the temporary constraint of the arch is removed, except for the springing stone, the arch rib mainly bears compressive stress under the self-weight of the structure. After the tension of the cable is applied, the arch rib can bear a part of the self-weight of the beam through the cable due to the beam-arch combination system, resulting in a fully compressive stress. It can be observed that the greatest compressive stress is on the springing stone and midpoint of the arch. In the process of removing the temporary piers of the beam and the construction of the deck and guardrail, the stress of the arch remains steady.

After the temporary constraints of the arch are removed, the stress on the beam is small as a result of the support of the temporary pier. However, the tensioned

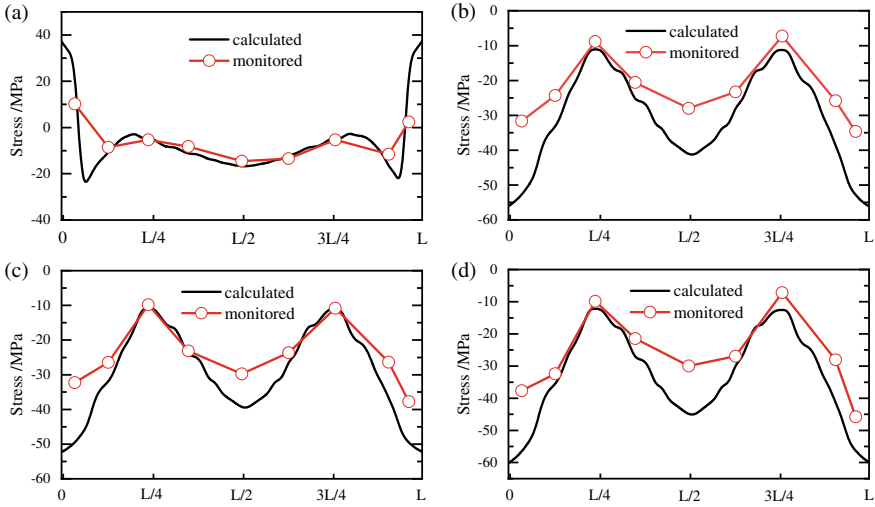


Fig. 76.9 Stress of the arch rib in the construction process of the bridge: **a** removing the temporary constraint of the arch rib; **b** tensioning the cable; **c** removing the temporary pier of the beam; **d** constructing the deck and guardrail

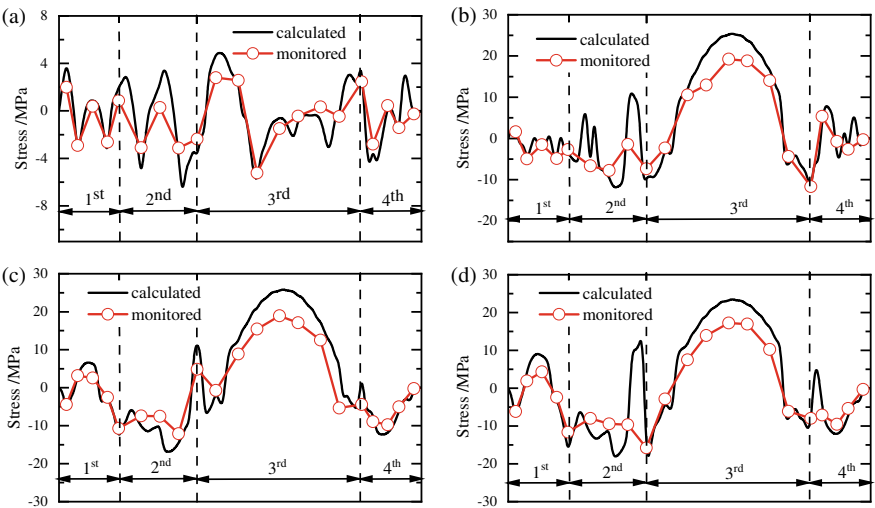


Fig. 76.10 Stress of the beam in the construction process of the bridge: **a** removing the temporary constraint of the arch rib; **b** tensioning the cable; **c** removing the temporary pier of the beam; **d** constructing the deck and guardrail

cable can increase the stress on the middle span of the main beam due to the beam-arch combination system, and the stress on the beam of other spans will also be redistributed. Besides, there is no obvious influence on the stress of the beam in the process of removing the temporary pier of the beam and the construction of the deck and guardrail.

In addition, it can also be found that in the whole construction process, the distribution law of the calculated stress of the arch and main beam is similar to that of the monitored result. However, considering the simplification of the finite element model and some artificial deviations in the construction, the calculated stress will be slightly greater than the monitored result.

76.5.2 Geometry Results

Figure 76.11 shows the calculated and monitored displacement of the arch rib at different construction stages. It can be found that the displacement of the arch rib is symmetrically distributed along the span direction of the bridge in the whole construction process, and there is a greatest displacement in the mid-span of the arch. The tension of the cable also can increase significantly the rib displacement, while there is no obvious influence when the temporary pier of the beam is removed. After the deck and guardrail are installed, the rib displacement will slightly rise to a high level on account of the increase in the self-weight of the structure. In the whole construction process, the monitored displacement of arch ribs is less than that of the calculated result.

The calculated and monitored displacements of the beam in the construction process are shown in Fig. 76.12. It can be seen that there is a small displacement on the beam when the temporary constraint of arch ribs is removed due to the temporary support pier of the beam. The tension of the cable also is essential to the beam displacement, which can give a significant increase at the midspan of the beam. When the temporary pier of the beam is removed, the beam displacement on other spans also increases as a result of the self-weight of the beam. However, the construction of the deck and guardrail leads to a move down on the beam displacement of the main span.

76.6 Conclusions

Through numerical simulation and field measurement for the stress and geometry shape of arch ribs and beams in the construction process of a pedestrian bridge with a curved beam and inclined arch, the main conclusions are as follows:

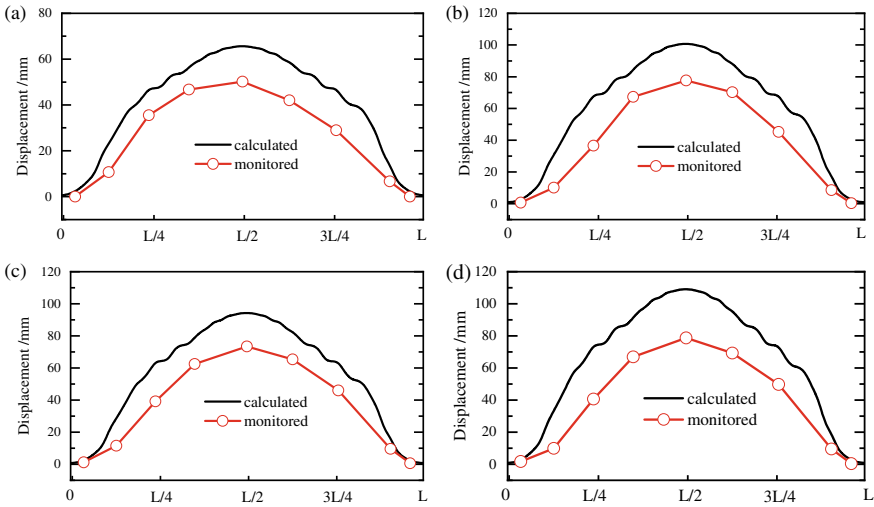


Fig. 76.11 Displacement of the arch rib in the construction process of the bridge: **a** removing the temporary constraint of the arch rib; **b** tensioning the cable; **c** removing the temporary pier of the beam; **d** constructing the deck and guardrail

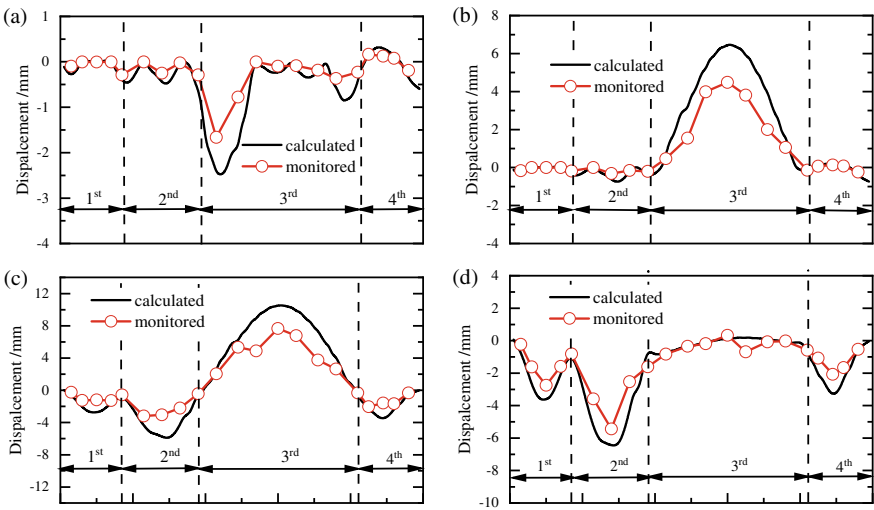


Fig. 76.12 Displacement of the beam in the construction process of the bridge: **a** removing the temporary constraint of the arch rib; **b** tensioning the cable; **c** removing the temporary pier of the beam; **d** constructing the deck and guardrail

- (1) The tension of the cable can result in a significant increase in the stress and displacement on the arch and beam due to the change in the structural system of the bridge, which may pose a great safety risk in the construction process of the bridge with a curved beam and inclined arch. Therefore, more attention and monitoring measures should be taken during the construction stage of the cable tension.
- (2) In the whole construction process, the measured stress and displacement of the arch and beam are in a reasonable range, and give a good agreement in the variation law with the FE simulated result. The results of this study can provide a reference for the construction of similar bridges.

References

1. Tang, M.C.: Forms and aesthetics of bridges. *Engineering* **4**(2), 267–276 (2018). <https://doi.org/10.1016/j.eng.2017.12.013>
2. Zhou, J., Hung, Y., Liu, A.: Walking comfort analysis and vibration control of bridge with curved beam and inclined arch. *Eng. Mech.* **39**(S), 214–220 (2022). <https://doi.org/10.6052/j.issn.1000-4750.2021.05.S043>
3. Huang, H., Liu, B., Zang, Y., Li, F.: Optimum analysis of suspenders tensioning through skewed arch bridge with curved beam. In: *ICCTP 2010: Integrated Transportation Systems: Green, Intelligent, Reliable*, pp. 3366–3372 (2010). [https://doi.org/10.1061/41127\(382\)363](https://doi.org/10.1061/41127(382)363)
4. Lu, P., Zhang, J., Li, D., Zhou, Y., Shi, Q.: Conceptual design and experimental verification study of a special-shaped composite arch bridge. *Structures* **29**, 1380–1389 (2021). <https://doi.org/10.1016/j.istruc.2020.12.018>
5. Sun, J., Li, J., Jiang, Y., Ma, X., Tan, Z., Zhufu, G.: Key construction technology and monitoring of long-span steel box tied arch bridge. *Int. J. Steel Struct.* **23**(1), 191–207 (2023). <https://doi.org/10.1007/s13296-022-00687-y>
6. Ren, W., Wang, X., Tu, P.: Simulation and monitoring of high-speed railway tied-arch bridge construction with arch first and beam late method. *J. Traffic Transp. Eng.* **12**(5), 28–36 (2012). <https://doi.org/10.19818/j.cnki.1671-1637.2012.05.004>
7. Li, Y., Wang, J., Ge, S.: Optimum calculation method for cable force of concrete-filled steel tube arch bridge in inclined cable-stayed construction. *J. Highw. Transp. Res. Dev.* **11**(1), 42–48 (2017). <https://doi.org/10.1061/JHTRCQ.0000549>
8. Wang, Z., Zhang, N., Du, X., Wang, S., Sun, Q.: Multi-objective optimization of cable forces and counterweights for universal cable-stayed Bridges. *J. Adv. Transp.* **2021**, 1–13 (2021). <https://doi.org/10.1155/2021/6615746>
9. Yin, T., Zhang, W., Zhao, Y.B., Sun, X.L.: Construction monitoring technology research on large-span V structure tied arch bridge. *Appl. Mech. Mater.* **351**, 1240–1243 (2013). <https://doi.org/10.4028/www.scientific.net/AMM.351-352.1240>
10. Zhu, L., Chen, T., Chen, L., Han, X., King, W., Wang, L., Zhai, C., Tian, Y.: Temperature effect on cable force of a special-shaped tied-arch bridge. *Heliyon* **8**(11), e11253 (2022). <https://doi.org/10.1016/j.heliyon.2022.e11253>

Chapter 77

Numerical Study on Fracture Formation and Propagation Law in the Perforating Process Based on FEM-SPH Coupling



Xianbo Liu, Jun Li, Wei Lian, Gonghui Liu, Yunfeng Zhao, Shiyuan Xie, Penglin Liu, and Dian Wang

Abstract In the exploration and development of oil and gas wells, perforation completion is the most commonly applied method of well completion. The formation of fracture networks near the wellbore during perforation is directly influenced by fractures near the wellbore, which have direct effects on the flow of hydraulic fracturing fluid. A three-dimensional perforation numerical calculation model is developed using the FEM-SPH coupling method. This is coupled with the theory of impact dynamics. FEM-SPH coupled perforation numerical models have been used to investigate fracture formation and propagation laws during perforation. In the study, it was found that when perforating the rock along the direction of maximum principal stress, a significant number of fractures could be formed. In addition, the length of these fractures was relatively long. Fractures are formed as a result of the radial tensile stress of the rock near the wellbore, and fractures are formed along the radial direction during the perforation process. It is primarily the circumferential tensile stress of the rock that determines the expansion of fractures near the wellbore. Perforation parameters and fracture parameters can be improved by using the research results presented in this paper as a reference.

Keywords FEM-SPH · Perforation process · Crack formation · Crack extension

X. Liu · G. Liu · P. Liu · D. Wang
China University of Petroleum, Beijing 102249, China

J. Li (✉) · W. Lian
China University of Petroleum-Beijing at Karamay, Beijing 834000, China
e-mail: lijun446@vip.163.com

Y. Zhao · S. Xie
Research Institute of Engineering Technology, PetroChina Xinjiang Oilfield Company,
Karamay 834000, China

77.1 Introduction

There are often unconventional oil and gas resources in rocks that have low porosity and low permeability, which limits their efficiency for development. Oil and gas wells have been explored and developed using perforation and hydraulic fracturing in recent years [1, 2]. This has solved the difficult problem of finding and developing reservoirs with low permeability. In order to stimulate unconventional reservoirs through production stimulation, perforation is completed in casing-cement sheath-rock in order to open the oil and gas flow channels, as shown in Fig. 77.1. It has been shown that a significant amount of fractures is generated during the perforation process around the perforation tunnel. This facilitates the formation of complex fracture networks during hydraulic fracturing, resulting in increased oil and gas production.

When the reservoir rock is in its initial state, it maintains a state of stress balance. However, after drilling, the wellbore will redistribute stress across the rock near the wellbore [3, 4]. When the metal jet penetrates the casing and the cement sheath under the action of the detonation pressure, perforation tunnels are formed in the rock. Based on the heterogeneous characteristics of the rock and the high kinetic energy of the jet itself, it is required that fractures develop and expand simultaneously with the formation of perforation channels, as shown in Fig. 77.2. Perforation directions should be arranged in a manner that is conducive to the formation of artificial fractures that are capable of communicating with natural fractures. This will improve hydraulic fracture treatment effects.

Numerical simulations of perforation completion have mostly relied on finite element modeling (FEM), which utilizes the variational principle to discretely solve differential equations. There are several advantages to this method, including its wide

Fig. 77.1 Perforation and completion diagram for an oil and gas well

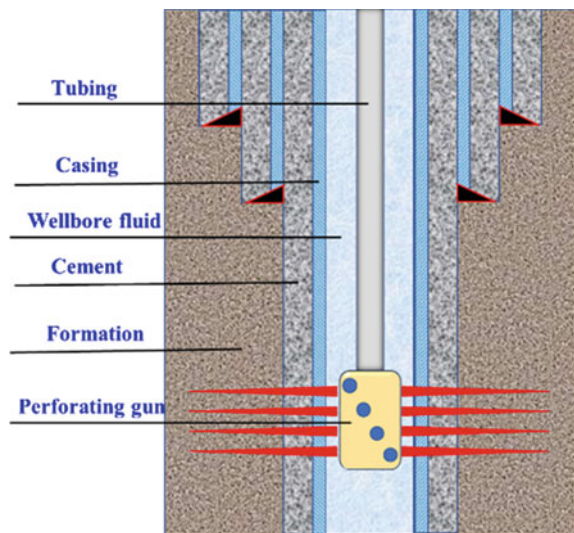
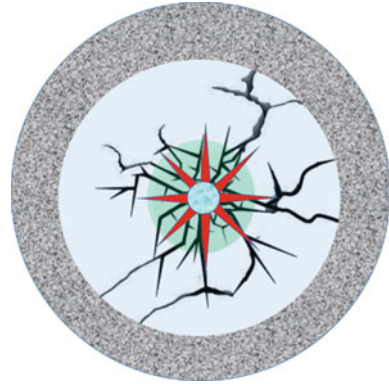


Fig. 77.2 Schematic diagram of fracture propagation near wellbore



application range and high calculation efficiency. It is necessary to note, however, that perforation often results in large deformations and damage to materials. As a result of significant grid distortions, the accuracy of FEM perforation numerical calculations is often reduced, and even the calculation may be interrupted [5–8]. For the purpose of overcoming the limitations of the FEM method, Lucy [9] and Gringold [10] proposed the smoothed particle method (SPH), which is a calculation method that does not provide for grids. It is possible to solve the problem of large deformation of the material during the perforation process by converting all the original FEM elements into particles using the SPH method. Although an adjacent particle search is required as part of SPH calculation, it must be performed at every time step, which results in extremely low SPH calculation efficiency. It is often necessary to use a large number of SPH particles in the study of penetration damage, in order to ensure calculation efficiency and capture damage characteristics.

The coupling algorithm of FEM and SPH is regarded as the most effective method for the solution of the problem of the coexistence of large and small deformation regions in numerical calculations [11, 12]. It is possible to obtain stable calculations using the FEM-SPH coupling algorithm when solving problems concerning large deformation of materials, such as impact explosions, and the calculation results are very accurate [13]. It has been widely used in many industries, but due to the complex perforation completion conditions, it is not widely used for perforation completion.

This paper presents a numerical model of perforation based on the FEM-SPH adaptive coupling method. This model takes into account the perforation completion conditions as well as the rock mechanics parameters downhole. The formation of rock fractures and their propagation during the perforation process were studied using the established numerical model for perforation. Perforation designs of oil and gas wells on site are influenced by this information.

77.2 Theories of FEM-SPH Adaptive Coupling

The SPH method relies on the concept of integral expressions by constructing an integral expression for the field function. To obtain an approximate value of the function, it is necessary to discretize the integral expression of the function through the use of discrete particles [14]:

$$f(x) = \int_{\Omega} f(x') W(x - x', h) dx \quad (77.1)$$

In the formula, Ω is the solution domain, $f(x)$ is an arbitrary function, $W(x - x', h)$ is a smooth function, h is the smooth length, x is the position vector of the approximate value calculation point, x' is the position vector of any point, and dx is the micro-element volume at x' .

The SPH method is to discretize a continuous medium into a particle medium by means of discretization. The discretized solution domain is discretized into a certain number of particle spaces, and each particle has an independent mass and density. The discretized Eq. (77.1) can be expressed as the particle approximation formula:

$$f(x_i) = \sum_{j=1}^N \frac{m_j}{\rho_j} f(x_j) \cdot W(x_i - x_j, h) \quad (77.2)$$

where $f(x_i)$ is the integral approximation of the particle field function at the position x_i , N is the number of particles in the solution domain after discretization, m_j and ρ_j are the mass and density of particle j , respectively. Taking the derivative of Eq. (77.2), the particle approximate expression of the function derivative at any particle can be obtained:

$$\frac{\partial f(x_i)}{\partial x} = \sum_{j=1}^N f(x_j) \frac{m_j}{\rho_j} \frac{\partial W_{ij}}{\partial x} \quad (77.3)$$

where $W_{ij} = (X_i - X_j, h)$, and $\frac{\partial W_{ij}}{\partial x_i} = \frac{x_i - x_j}{d_{ij}} \frac{\partial W_{ij}}{\partial d_{ij}}$ is the distance between particles.

In computational fluid dynamics, the basic governing equations of fluid flow mainly include mass conservation equation and momentum conservation equation.

$$\frac{\partial \rho}{\partial t} + \frac{1}{r} \frac{\partial}{\partial r} (r \rho v_r) + \frac{1}{r} \frac{\partial}{\partial \theta} (\rho v_{\theta}) + \frac{\partial}{\partial z} (\rho v_z) = 0 \quad (77.4)$$

Momentum conservation equation in cylindrical coordinate system:

$$\begin{aligned} \frac{\partial v_r}{\partial t} + v_r \frac{\partial v_r}{\partial r} + \frac{v_\theta}{r} \frac{\partial v_r}{\partial \theta} - \frac{v_\theta^2}{r} + v_z \frac{\partial v_r}{\partial z} &= g_r + \frac{1}{\rho} \left(\frac{1}{r} \frac{\partial}{\partial r} (r \sigma_r) + \frac{1}{r} \frac{\partial \tau_\theta}{\partial \varphi} - \frac{\tau_{\theta\theta}}{r} + \frac{\partial \tau_{zr}}{\partial z} \right) \\ \frac{\partial v_z}{\partial t} + v_r \frac{\partial v_z}{\partial r} + \frac{v_\theta}{r} \frac{\partial v_z}{\partial \theta} + v_z \frac{\partial v_z}{\partial z} &= g_z + \frac{1}{\rho} \left(\frac{1}{r} \frac{\partial (r \tau_{rz})}{\partial r} + \frac{1}{r} \frac{\partial \tau_\theta}{\partial \theta} + \frac{\partial \sigma_z}{\partial z} \right) \end{aligned} \quad (77.5)$$

In the cylindrical coordinate system, Eqs. (77.4) and (77.5) represent radial, circumferential, and axial directions. Xiao et al. used particle approximation expressions to construct the axisymmetric expression of the discrete equations of computational fluid dynamics [7, 8]. The axisymmetric expression of the mass conservation equation after discrete particle expression:

$$\frac{d\rho_i}{dt} = -\frac{\rho_i v_{ri}}{r_i} + \frac{1}{2\pi} \sum_{j=1}^N \frac{m_j}{r_j} \left((v_{ri} - v_{rj}) \frac{\partial W_{ij}}{\partial r_i} + (v_{zi} - v_{zj}) \frac{\partial W_{ij}}{\partial z_i} \right) \quad (77.6)$$

Following the discretization of the particle expression, this is the axisymmetric expression of the momentum conservation equation:

$$\begin{aligned} \frac{dv_{ri}}{dt} &= -\frac{\sigma_{\theta i}}{\rho_i r_i} + 2\pi \sum_{j=1}^N m_j \left(\frac{r_j \sigma_{rj}}{\eta_j^2} + \frac{r_i \sigma_{ri}}{\eta_i^2} \right) \frac{\partial W_{ij}}{\partial r_i} + 2\pi \sum_{j=1}^N m_j \left(\frac{r_j \sigma_{r_{zj}}}{\eta_j^2} + \frac{r_i \sigma_{r_{zi}}}{\eta_i^2} \right) \frac{\partial W_{ij}}{\partial z_i} \\ \frac{dv_{zi}}{dt} &= 2\pi \sum_{j=1}^N m_j \left(\frac{r_j \sigma_{r_{zj}}}{\eta_j^2} + \frac{r_i \sigma_{r_{zi}}}{\eta_i^2} \right) \frac{\partial W_{ij}}{\partial r_i} + 2\pi \sum_{j=1}^N m_j \left(\frac{r_j \sigma_{zj}}{\eta_j^2} + \frac{r_i \sigma_{zi}}{\eta_i^2} \right) \frac{\partial W_{ij}}{\partial z_i} \end{aligned} \quad (77.7)$$

In Eqs. (77.6) and (77.7), r, θ, z respectively represent the radial, circumferential and axial directions in the cylindrical coordinate system, $\eta = 2\pi r \rho$ is the plane density, m is the mass, v is the velocity, and σ is the stress.

77.3 Numerical Model

77.3.1 Geometric Model

Based on this study’s numerical calculations, the overall height of the model is 200 mm, as shown in Fig. 77.3. Both the length and width of the perforation numerical calculation model are 600 mm. According to Saint Venant’s Principle, the perforation channel has a diameter of approximately 10 mm. The height of the perforation model in the perforation numerical simulation is the same as the diameter of the channel. This results in the size effect being ignored in the calculation of perforations. Among the components of the perforating charge are the casing, the perforating charge, and the liner. It is primarily the geometric parameters of the perforating charge that are

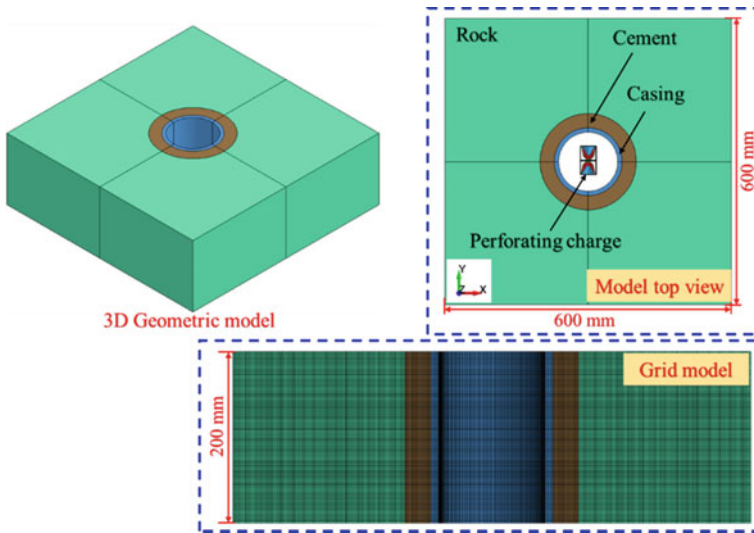


Fig. 77.3 Geometric model of perforation numerical calculation

used in the numerical simulation of perforation. The perforating bullet has a 42 mm charge height in the perforation test. RDX is the type of charge, and the mass of the charge is 28 g. There is a cone angle of 60°, a height of 30 mm, and a thickness of 1.75 mm on the liner. Perforating bullets have a 41 mm caliber in the numerical simulation of perforation.

It is critical to note that the geometric size of the perforating charge and the liner within it are quite different. The grid size of the perforating charge is determined by the liner size of the liner in order to improve perforation accuracy. There are approximately 0.1 mm grid cells in the perforating charge. A regular geometric structure is present on the perforation target. A structured grid has been adopted for the grid units of the perforation target in order to improve calculation efficiency. It is estimated that the grid cell size of the perforation target is 0.12 mm, which can meet the accuracy requirements in the numerical simulation of the perforation process.

77.3.2 Governing Equation

The type of perforating charge used in the perforating numerical calculation model is RDX, and the keyword `*MAT_HIGH_EXPLOSIVE_BURN` is used to describe the perforating charge in ANSYS/LS-DYNA software. And the keyword `*EOS_JWL` is used as the state equation of the explosive, and the JWL (*Jones Wilkins Lee*) mathematical model in the state equation is as follows [15–17]:

$$P = A \left(1 - \frac{\omega}{R_1 v} \right) e^{-R_1 v} + B \left(1 - \frac{\omega}{R_2 v} \right) e^{-R_2 v} + \frac{\omega E}{v} \tag{77.8}$$

where P is the explosive pressure, E is the explosive internal energy per unit mass, A , B , R_1 , R_2 , and ω are material constants. The units of A and B are pressure units, while R_1 , R_2 , and ω are dimensionless constants. v is the specific volume. The values of these parameters are shown in Table 77.1.

Rock’s damage and failure characteristics need to be considered in the numerical calculation of shaped energy perforation. The HJC constitutive model can synthesize the critical characteristics of rock under perforation conditions, such as high deformation, high strain rate, and damage evolution. The HJC model can be used for rock damage description in the numerical calculation of shaped energy perforation [18, 19].

The damage evolution process of the HJC model is mainly characterized by the accumulation of the equivalent plastic strain and plastic volume strain after the material is impacted.

$$D = \sum \frac{\Delta \varepsilon_p + \Delta \mu_p}{\varepsilon_p^f + \mu_p^f} \tag{77.9}$$

$$\varepsilon_p^f + \mu_p^f = D_1 (P^* + T^*)^{D_2} \geq EFMIN \tag{77.10}$$

where $\Delta \varepsilon_p$ and $\Delta \mu_p$ are the equivalent plastic strain and plastic volumetric strain, D_1 , D_2 are material constants, T^* is the normalized maximum tensile hydrostatic pressure, where ε_p^f is equivalent plastic strain, μ_p^f is plastic volume strain, $\varepsilon_p^f + \mu_p^f$ is the total plastic strain under a constant pressure until fracture, $EFMIN$ is amount of plastic strain before fracture [20].

In the HJC model, the state of the material is divided into three stages: the linear elastic stage, the cracking stage, and the compaction stage.

$$P = \begin{cases} K \mu & (0 < P < P_{crush}) \\ P_{crush} + K_{lock}(\mu - \mu_{crush}) & (P_{crush} < P < P_{lock}) \\ K_1 \mu^* + K_2 \mu^{*2} + K_3 \mu^{*3} & (P_{lock} < P) \end{cases} \tag{77.11}$$

$$K_{lock} = \frac{P_{lock} - P_{crush}}{\mu_{lock} - \mu_{crush}} \tag{77.12}$$

$$\mu^* = \frac{\mu - \mu_{lock}}{1 + \mu_{lock}} \tag{77.13}$$

Table 77.1 Material parameters of perforating charges

ρ (g/cm ⁻³)	D (cm/ μ s)	PCJ (GPa)	P (GPa)	A (GPa)	B (GPa)	R_1	R_2	ω
1.63	0.693	27	374	3.2	10	4.15	0.95	0.3

Table 77.2 HJC parameters of cement sheath and rock

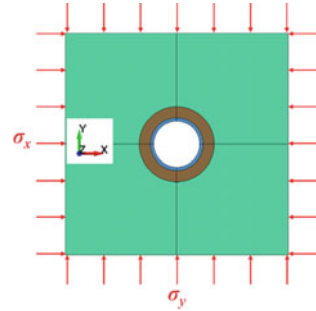
HJC parameter	Value	HJC parameter	Value
Density (g/cm^3)	2.4	Crushing pressure (MPa)	13.2
Shear modulus (GPa)	16.04	Crushing volumetric strain	$6.5\text{e}-4$
Strain rate coefficient	0.007	Damage constant: D_1	0.031
Pressure hardening exponent	0.79	Damage constant: D_2	1
Quasi-static uniaxial compressive strength (MPa)	44.6	Pressure constant: K_1 (GPa)	81
Quasi-static threshold strain rate	$1\text{e}-6$	Pressure constant: K_2 (GPa)	- 91
EFMIN	0.005	Pressure constant: K_3 (GPa)	89

where K is bulk modulus, μ is volumetric strain of the element. P_{crush} is elastic limit pressure, μ_{crush} is the volumetric strain at the elastic limit P_{crush} , P_{lock} is locking pressure, μ_{lock} is locking volumetric strain, K_1 , K_2 , K_3 are material constants. μ^* is corrected volumetric strain. The HJC parameters of rock, in the numerical calculation study of perforation, are mainly determined from references [21, 22], as shown in Table 77.2.

77.3.3 Boundary Conditions

The detonation method of the perforating charge is based on a traditional point detonation method in the numerical simulation of the perforation process. The detonation point of the perforating bullet is located at its head, which is also the source of the numerical model. As a result, the vertical wall stress is applied to the periphery of the perforation target to simulate the stress characteristics of the perforated rock in the downhole, as shown in Fig. 77.4. Perforation numerical simulation is made with non-reflection boundary conditions on the outer wall of the perforation target in order to exclude the influence of the size effect on calculations [23–26]. As long as the boundary is non-reflective, boundary stress wave reflection will not interfere with the calculation results. To establish the numerical model for perforation, the axisymmetric modeling method was used, which greatly improved the calculation efficiency.

Fig. 77.4 Boundary condition setting of perforation numerical calculation model



77.4 The Law of Fracture Propagation and Its Influencing Factors During Perforation

77.4.1 Analyses of Crack Formation and Propagation

The FEM-SPH coupling was used to simulate perforation along the direction of maximum principal stress of rock, as shown in Fig. 77.5. The fractures that occur during the perforation process are distributed on both sides of the perforation tunnel and are relatively short in length. When the fracture propagates along the direction of the minimum principal stress, the perforation process proceeds along the direction corresponding to the maximum principal stress. The maximum principal stress, however, makes it difficult to open the crack, so its length is relatively short. With an increase in the minimum principal stress, fractures formed during perforation gradually increase in length. It is evident that the fracture formed by perforation is far removed from the cement sheath. This is because there is a large difference between the minimum principal stress and the maximum principal stress of the rock. Fractures caused by perforation are concentrated in the rock position near the cement sheath when the minimum principal stress is close to the maximum principal stress. As a result, the number of fractures increases as the minimum principal stress approaches the maximum principal stress. It is not conducive to the formation of fractures when the perforation operation is carried out in the direction of the maximum principal stress of the rock. The length of the fractures is short, which does not allow for the communication of natural fractures during the process.

An analysis of the numerical simulation of perforation along the minimum principal stress direction of rock was carried out using the FEM-SPH coupling, as shown in Fig. 77.6. It is significant to note that a substantial number of artificial fractures are formed as a result of the perforation process. These fractures are usually longer, allowing them to communicate with natural fractures and improve the hydraulic fracturing process. When a fracture propagates along the direction of maximum principal stress, it is accompanied by perforation along the direction of minimum principal stress. It has been noted that when the minimum principal stress in the perforation direction is increased, the number and length of artificial fractures formed during

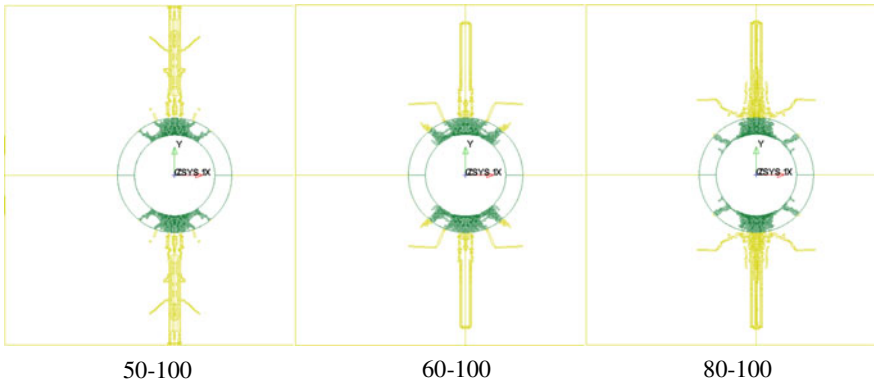


Fig. 77.5 Fracture propagation characteristics during maximum principal stress perforation

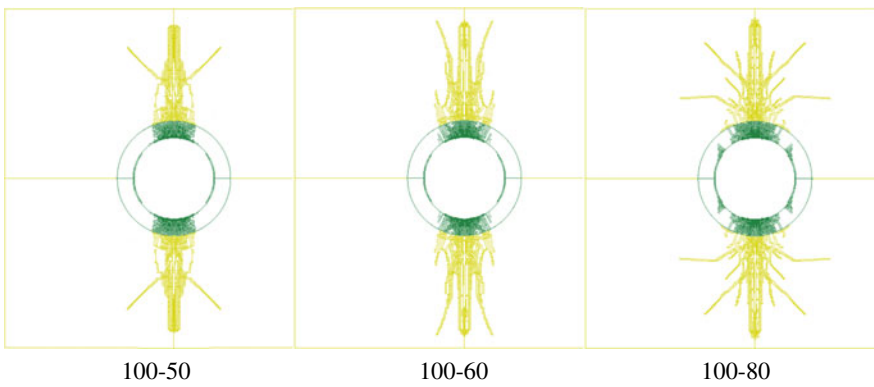


Fig. 77.6 Fracture propagation characteristics when the minimum principal stress is perforated

perforation increase significantly. In cases where the maximum principal stress is close to the minimum principal stress, the crack length has been fully extended.

The most common types of perforation are directional perforations, fixed surface perforations, and spiral perforations. In view of the fact that the first two methods of perforation place higher requirements on reservoirs, axial distribution perforations are the most commonly used perforation design for oil and gas wells. As a method of perforation, axial distributed perforation involves evenly distributing perforating charges around the wellbore in a 360° rotation. In order to minimize the effect of ground stress on fracture formation and expansion during perforation, it is recommended to use spiral perforation methods with non-uniform hole distribution. It is possible to achieve better fracture formation during the hydraulic fracturing process by increasing the number of perforating charges along the direction of the minimum principal stress.

77.4.2 Perforation Fracture Propagation and In-Situ Stress Analysis

The radial stress of the rock near the wellbore is primarily manifested as tensile stress when the perforation direction is in the direction of the maximum principal stress of the reservoir, as shown in Fig. 77.7. In addition to increasing the minimum principal stress, the radial compressive stress at the wellbore also increases gradually, as well as the number and length of fractures. In the crack propagation direction, a zone of compressive stress concentration exists, and the crack cannot propagate further. It has been observed that, in cases where the perforation direction is along the direction of the minimum principal stress of the reservoir, the radial stress of the rock near the wellbore is characterized by tensile stress, which is relatively high, as shown in Fig. 77.8. As soon as cracks in the cement sheath and rock are formed, they expand in the radial direction. This is regardless of whether perforation occurs along the maximum principal stress line or along the minimum principal stress line. Fractures are formed and expanded in direct proportion to the tensile stress during the perforation process.

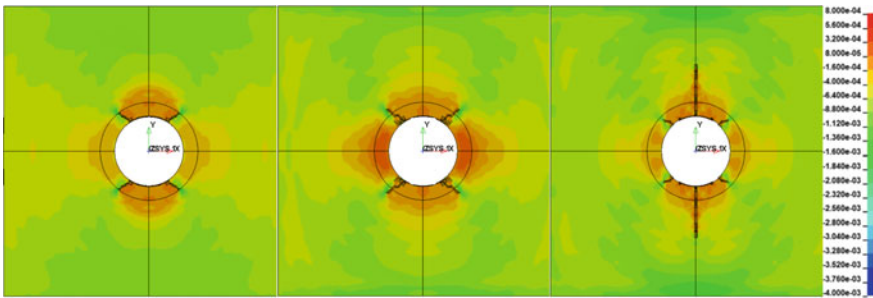


Fig. 77.7 Perforating in the direction of maximum principal stress under different minimum principal stresses

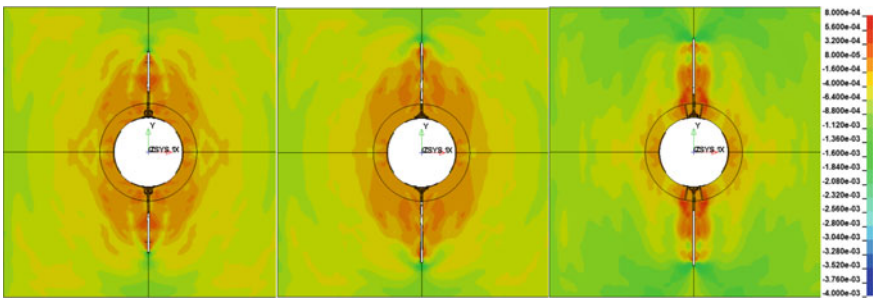


Fig. 77.8 Different maximum principal stress distributions under perforating along the minimum principal stress direction

When there is a compressive stress in the hoop, it will interfere with the development and expansion of cracks, as shown in Fig. 77.9. It is not important whether the perforation occurs along the direction of the maximum principal stress or the minimum principal stress of the rock; however, the hoop stress is compressive stress in the direction perpendicular to the perforation, and cracks are not generated as a result of the perforation process, as shown in Fig. 77.10. Perforation causes a concentration of compressive stress at the tip of the fracture formed in the rock, which causes the fracture to cease propagating. Therefore, during crack propagation, the hoop stress exhibits the characteristics of tensile stress, which is beneficial for further crack propagation.

Fractures typically occur in the direction of the wellbore's radial direction during the perforating process. When perforating, rock tensile stress plays a significant role in the formation and expansion of fractures. It has been noted that the number of fractures is increased when the radial stress around the wellbore is increased. Propagation of fractures is mainly determined by the hoop stress around the wellbore. If the stress characteristic is compressive, regardless of whether it is radial or hoop stress, crack formation and expansion will be hindered.

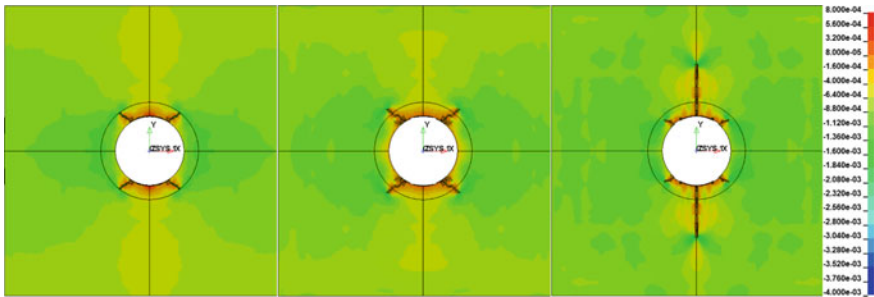


Fig. 77.9 Distribution of hoop stress at different minimum principal stresses when perforating in the maximum principal stress direction

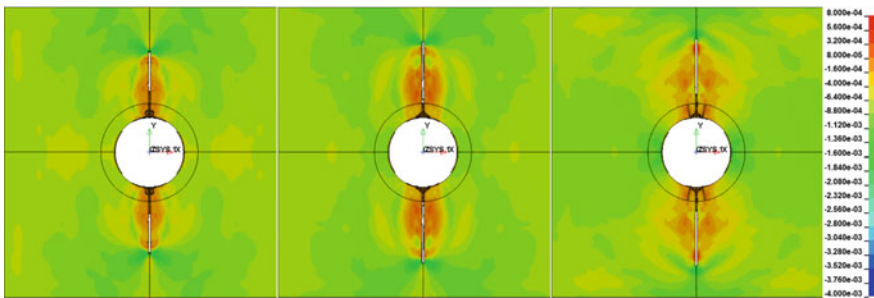


Fig. 77.10 Distribution characteristics of hoop stress at different maximum principal stresses

77.5 Conclusion

An analysis of comparative perforation is presented here along the direction of maximum principal stress and minimum principal stress. A large number of fractures can be formed in a rock after perforation if perforation occurs in the direction of the maximum principal stress. The propagation distance of these fractures is wider when perforation is made along the direction of the maximum principal stress.

It is common for rock fractures to form along the radial direction of the rock when perforating, and fracture expansion is influenced by the hoop stress of the rock. There is a circumferential tensile stress around the circumference of the rock that enables fractures to develop. However, a circumferential compressive stress at the tip of the fracture prevents it from continuing to expand.

When designing spiral perforations, it is suggested that the density of the perforation should be increased in the direction of maximum principal stress. This is an analysis of the law of fracture formation and expansion. Through the use of non-uniform helical perforation technology, fractures in the rock around the wellbore can be created more effectively to facilitate hydraulic fracturing.

Acknowledgements The author thanks China University of Petroleum (Beijing) for its academic and technical support. This paper is supported by Wellbore Integrity Analysis and Optimization System Construction of Shale Oil and Gas Wells During Life Cycle (No. XQZX20220019). This paper is also supported by Study on quantitative calculation model of fault slip induced by multistage fracturing and casing deformation control method in shale gas well (No. 52204018). This paper is also supported by Basic Research on Prevention and Control of Sustained Casing Pressure in Deep and Ultra-Deep Gas Wells in Sichuan Basin (No. U22A20164).

References

1. Wu, K., Olson, J.E.: Mechanisms of simultaneous hydraulic-fracture propagation from multiple perforation clusters in horizontal wells. *SPE J.* **21**(03), 1000–1008 (2016)
2. Lian, W., Li, J., Tao, Q., Du, J., Wang, L., Xi, Y.: Formation mechanism of continuous gas leakage paths in cement sheath during hydraulic fracturing. *Energy Sci. Eng.* **8**(7), 2527–2547 (2020)
3. Gao, Q., Cheng, Y., Han, S., Yan, C., Jiang, L.: Numerical modeling of hydraulic fracture propagation behaviors influenced by pre-existing injection and production wells. *J. Petrol. Sci. Eng.* **172**, 976–987 (2019)
4. Zhang, Z., Guo, J., Liang, H., Liu, Y.: Numerical simulation of skin factors for perforated wells with crushed zone and drilling-fluid damage in tight gas reservoirs. *J. Nat. Gas Sci. Eng.* **90**, 103907 (2021)
5. Elshenawy, T., Li, Q.M.: Influences of target strength and confinement on the penetration depth of an oil well perforator. *Int. J. Impact Eng.* **54**, 130–137 (2013)
6. Elshenawy, T., Elbeih, A., Li, Q.M.: Influence of target strength on the penetration depth of shaped charge jets into RHA targets. *Int. J. Mech. Sci.* **136**, 234–242 (2018)
7. Xiao, Y., Han, X., Hu, D.: A coupling algorithm of finite element method and smoothed particle hydrodynamics for impact computations. *Comput. Mater. Contin.* **23**(1), 9 (2011)

8. Xiao, Y.H., Hu, D.A., Han, X., Yang, G., Long, S.Y.: Simulation of normal perforation of aluminum plates using axisymmetric smoothed particle hydrodynamics with contact algorithm. *Int. J. Comput. Methods* **10**(03), 1350039 (2013)
9. Lucy, L.B.: A numerical approach to the testing of the fission hypothesis. *Astron. J.* **82**, 1013–1024 (1977)
10. Gingold, R.A., Monaghan, J.J.: Smoothed particle hydrodynamics: theory and application to non-spherical stars. *Mon. Not. R. Astron. Soc.* **181**(3), 375–389 (1977)
11. Violeau, D., Rogers, B.D.: Smoothed particle hydrodynamics (SPH) for free-surface flows: past, present and future. *J. Hydraul. Res.* **54**(1), 1–26 (2016)
12. Ye, T., Pan, D., Huang, C., Liu, M.: Smoothed particle hydrodynamics (SPH) for complex fluid flows: recent developments in methodology and applications. *Phys. Fluids* **31**(1), 011301 (2019)
13. Wang, Z., Ma, D., Suo, T., Li, Y., Manes, A.: Investigation into different numerical methods in predicting the response of aluminosilicate glass under quasi-static and impact loading conditions. *Int. J. Mech. Sci.* **196**, 106286 (2021)
14. De'an, H., Chunhan, L., YiHua, X., Xu, H.: Analysis of explosion in concrete by axisymmetric FE-SPH adaptive coupling method. *Eng. Comput.* **31**(4), 758–774 (2014)
15. Burley, M., Campbell, J.E., Dean, J., et al. : Johnson-Cook parameter evaluation from ballistic impact data via iterative FEM modelling. *Int. J. Impact Eng.* **112**, 180–192 (2018). <https://doi.org/10.1016/j.ijimpeng.2017.10.012>
16. Chen, C.Y., Shiuan, J.H., Lan, I.F.: The equation of state of detonation products obtained from cylinder expansion test. *Propell. Explos. Pyrotechn.* **19**(1), 9–14 (1994). <https://doi.org/10.1002/prep.19940190103>
17. LSTC, L.S.D.: Keyword User's Manual, vol. II: Livermore Software Technology Corporation (LSTC) (2007)
18. Ma, G.W., An, X.M.: Numerical simulation of blasting-induced rock fractures. *Int. J. Rock Mech. Min. Sci.* **45**(6), 966–975 (2008). <https://doi.org/10.1016/j.ijrmmms.2007.12.002>
19. Tu, Z., Lu, Y.: Evaluation of typical concrete material models used in hydrocodes for high dynamic response simulations. *Int. J. Impact Eng.* **36**(1): 132–146 (2009). <https://doi.org/10.1016/j.ijimpeng.2007.12.010>
20. Ren, G.M., Wu, H., Fang, Q., Kong, X.Z.: Parameters of Holmquist–Johnson–Cook model for high-strength concrete-like materials under projectile impact. *Int. J. Prot. Struct.* **8**(3), 352–367 (2017).
21. Yan, Y., Guan, Z., Yan, W., et al.: Analysis method of cement sheath damage zone after perforation. In: SPE/IATMI Asia Pacific Oil & Gas Conference and Exhibition. OnePetro (2020).
22. Wang, B., Li, J., Liu, G.H. et al.: Near-wellbore fracture propagation physical simulation based on innovative interlaced fixed perforation [J]. *Petrol. Explor. Dev.* **46**(6), 1187–1196 (2019). [https://doi.org/10.1016/s1876-3804\(19\)60279-x](https://doi.org/10.1016/s1876-3804(19)60279-x)
23. Yan, Y., Guan, Z., Zhang, B., et al.: Numerical investigation of debonding extent development of cementing interfaces during hydraulic fracturing through perforation cluster. *J. Petrol. Sci. Eng.* **197**, 107970 (2021). <https://doi.org/10.1016/j.petrol.2020.107970>
24. Villavicencio, R., Soares, C.G.: Numerical modelling of the boundary conditions on beams struck transversely by a mass. *Int. J. Impact Eng.* **38**(5), 384–396 (2011).
25. Pham, T.M., Hao, H.: Effect of the plastic hinge and boundary conditions on the impact behavior of reinforced concrete beams. *Int. J. Impact Eng.* **102**, 74–85 (2017).
26. Liu, B., Villavicencio, R., Soares, C.G.: Experimental and numerical plastic response and failure of pre-notched transversely impacted beams. *Int. J. Mech. Sci.* **77**, 314–332 (2013).

Chapter 78

Study on Degradation of Prestressed Concrete Beams in Hydrochloric Acid Environment Based on Stochastic Process



Yuwei Wang, Zuanfeng Pan, and Chengye Zhao

Abstract The durability problem of concrete and prestressed concrete structures caused by corrosive effects of various media in the environment has become a hot topic in engineering and academic circles. However, the research results on the deterioration of prestressed concrete performance under various corrosive media in typical industrial environment are still insufficient. Combined with acidic industrial environment of the corrosive medium, the corrosion mechanism of prestressed concrete is clarified, and on this basis, time-varying models of prestressed concrete material with engineering practicability is explored. An original model of concrete strength degradation described with pH is established, and a constitutive model considering the stress corrosion of the prestressed strand is put forward. Based on the stochastic process theory of component resistance and the corrosion degradation model of materials, the time-varying performance analysis of corroded components with bearing capacity is carried out using the statistical theory and the Monte-Carlo event-based simulation. Compared with the existing test results the accuracy of the material deterioration model is verified. At the same time, according to the simulation results, it is concluded that the corrosion of steel bars in the elastic stage has little influence on the mechanical properties, but has great influence on the stiffness and bearing capacity of the beam after cracking.

Keywords Prestressed concrete beam · Hydrochloric · Numerical simulation · Performance degradation

Y. Wang · Z. Pan (✉)

Department of Structural Engineering, Tongji University, Shanghai 200092, China

e-mail: zfpan@tongji.edu.cn

Z. Pan

State Key Lab of Disaster Reduction in Civil Engineering, Tongji University, Shanghai 200092, China

C. Zhao

Powerchina Huadong Engineering Corporation Limited, Hangzhou 311122, China

78.1 Introduction

The performance degradation of prestressed concrete structure is a dynamic process with the development of time. In the environment of corrosive medium, the structural components are eroded by various physical and chemical factors, the material properties are gradually reduced, and the damage is continuously accumulated. Finally, the steel bars corrosion and concrete cracking of the structural components are formed, which leads to a series of safety, applicability and durability problems.

Chloride corrosion is one of the most common concrete structural diseases in engineering. Strong acid is also a typical industrial environment, such as pickling car in metallurgical industry. The combined action of chloride corrosion and strong acid aggravates the performance degradation of prestressed concrete structures [1, 2]. At present, theoretical and experimental research [3–5] for the mechanism of chloride corrosion has been relatively mature, but the deterioration process of prestressed concrete structures in acidic environment is still mainly based on experimental research [6, 7], which is lack of thorough theoretical basis. In general, the alkaline environment plays an important role in maintaining the stability of cement cementitious materials and the passivation of steel bars. However, in the hydrochloric acid corrosion environment, the alkalinity of concrete gradually weakens or even becomes acidic under the penetration of hydrogen ion H^+ and the accompanying chemical reaction, which has a great adverse effect on the concrete strength and passivation film of steel bars [8].

In this study, a material deterioration model is derived from the material corrosion process of concrete and prestressed strands under hydrochloric acid corrosive environment. And on the basis of the material deterioration model, the uncertainty of material and geometric parameters is introduced, the sampling calculation and statistical analysis of the resistance is carried out by Monte-Carlo event-based simulation, the finite element model of four-point bending test of prestressed concrete beams based on the stochastic process is established, the performance degradation process of prestressed concrete beams in hydrochloric acid environment is analyzed, and the accuracy of the material deterioration model is validated by comparing with experimental data.

78.2 Deterioration Model of Materials Under Hydrochloric Acid Corrosion

78.2.1 The Variation of pH Value of Concrete Pore Solution in Acidic Environment

In the acidic environment, referring to the research results of Niu et al. on carbonized concrete [9], the acidification zone of concrete is proposed, and the concept of “acidification depth” is used to characterize the infiltration and corrosion of H⁺. The spatial position of concrete is divided into three parts: unacidified zone, partially acidified zone and completely acidified zone. The distribution of pH is simplified to a three-line model, as shown in Fig. 78.1, which represents the distribution of pH along the height direction of concrete at a given moment. When the time changes, the graph line will move along the x-axis direction at a certain rate, which is determined by the equation of “acidification depth”:

$$X_H = kt^\alpha \tag{78.1}$$

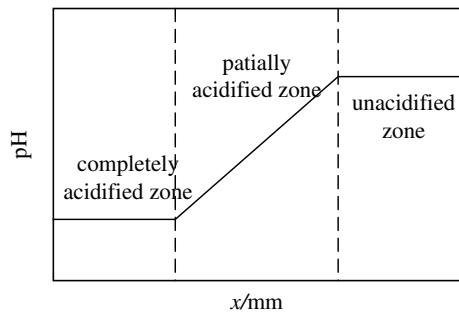
where X_H is acidification depth (mm), k_H is acidification rate coefficient, α is the coefficient related to the corrosion rate.

The undetermined coefficients k_H and α in Eq. (78.1) are obtained by regression analysis of the experimental data of Wang et al. [10], and then the analytical formula of the pH distribution curve is obtained:

$$pH = \begin{cases} 12.5 & \text{(unacidified zone)} \\ 12.5 - \frac{12.5-pH_0}{25} \times (17.6t^{0.7} - x_r) & \text{(partially acidified zone)} \\ pH_0 & \text{(completely acidified zone)} \end{cases} \tag{78.2}$$

where pH_0 is external ambient pH, x_r is depth of measuring point in mm, t is corrosion time (year).

Fig. 78.1 Concrete pore solution pH distribution



78.2.2 Critical Chloride Concentration of Steel Bar Based on pH Value of Pore Solution

Previous studies have shown that the ratio of chloride ions concentration to hydroxide ion concentration $[Cl^-]/[OH^-]$ when the steel bar is depassivated is linearly correlated to the pH value of the concrete pore solution on the surface of the steel bar:

$$\frac{[Cl^-]}{[OH^-]} = k \cdot pH + b \quad (78.3)$$

Since the ionic product of water in solution at a given temperature is constant, the equation for the $[Cl^-]_{cr}$ versus pH can be obtained as:

$$[Cl^-] = (k \cdot pH + b) \times 10^{(pH-14)} \quad (78.4)$$

The chloride ion concentration limit of 0.06% recommended by ACI201.2R [11] and the code GB50164-2011 [12] is used as the critical chloride concentration $[Cl^-]_{cr}$ of prestressed strands in normal alkaline environments, the relationship between the $[Cl^-]_{cr}$ (as a percentage of cement mass) and the pH of the concrete pore solution on the surface of the prestressed strands can be written as:

$$[Cl^-]_{cr} = 9.798 \times (-1.34 \times pH + 18.48) \times 10^{(pH-14)} \times 10^{-3} \times 100\% \quad (78.5)$$

78.2.3 The Strength Degradation Characterized by pH Value

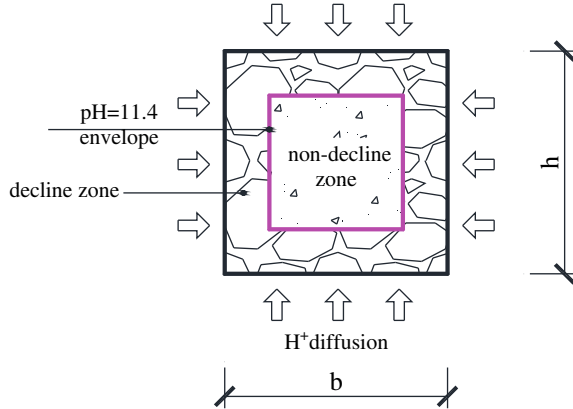
The main hydration products of cement are hydrated calcium silicate (C-S-H), hydrated calcium aluminate (CAH), hydrated calcium aluminate sulfate (AFt/AFm), calcium hydroxide (CH), etc. These products can only exist stably in alkaline environment, and are prone to neutralization or decomposition reaction in acidic environment, resulting in the deterioration of concrete performance. Table 78.1 gives the pH value at which the hydration products in cement can exist stably. The data in the table show that the stability of the main hydration products of cement decreases with the decrease of pH value. When the pH value reaches about 10.4, the stability of all the main hydration products of cement is destroyed, and the normal bonding effect cannot be provided. Therefore, the mechanical indexes such as the strength of concrete also decrease sharply.

Based on the above view, the concrete is divided into two parts: one part is the part with pH less than 11.4, the stability of CAH and CH within this part of concrete has been destroyed, and the strength has been significantly decayed, which is called the decline zone; the second part is the part with pH still greater than 11.4, which is not

Table 78.1 Critical pH values of decomposition of main hydration products

Hydration products	C-S-H	CAH	AFt/AFm	CH
pH values	10.4	11.4	10.7	12.23

Fig. 78.2 Internal partition of concrete in acidic environment



completely eroded, and the cementitious material still has certain bonding strength, so it is called non-decline zone, as shown in Fig. 78.2.

The envelop position of the pH = 11.4 in concrete can be described as:

$$x = 17.6t^{0.7} - \frac{27.5}{12.5 - \text{pH}_0} \text{ (mm)} \tag{78.6}$$

where t is the current time, x_c is defined as the depth (mm) of strength degradation of concrete. Combined with Eq. (78.2), the change process of the area of the non-decline zone and the decline zone with time can be obtained. The ratio of the area of the non-decline zone to the total section is denoted as k_{RS} , which is related to the residual strength of concrete:

$$k_{RS} = \frac{(b - 2x)(h - 2x)}{bh} \tag{78.7}$$

In order to explore the quantitative relationship between the k_{RS} and the residual strength coefficient μ_{RS} , defined as ratio of the strength of acid-eroded concrete to the strength of uneroded concrete, it is considered that μ_{RS} can be expressed as a function of k_{RS} . Through the investigation of the existing acid corrosion concrete strength experimental data [10, 13], the strength loss rate $1 - k_{RS}$ is corrected considering the external environment pH value and the concrete stress state:

$$\mu_{RS} = 1 - k_{pH}k_{\sigma}(1 - k_{RS}) \tag{78.8}$$

where k_{pH} is the correction factor considering the environmental pH, $k_{pH} = 1/pH_0$; k_σ is the correction factor considering the stress level of concrete, $k_\sigma = 1$ in compression and $k_\sigma = 1.1$ in tension.

78.2.4 Equivalent Constitutive Model of Prestressed Strand Considering Stress Corrosion

In addition to the general electrochemical uniform corrosion, the prestressed strand due to its own long-term high tensile stress state, greatly accelerates the corrosion rate under the combined action of external corrosive media, which is called stress corrosion of prestressing strand. The literature [14, 15] gives experimental data of the material properties of prestressed strands in a variety of corrosive environments, and the parameters such as ultimate strength, elastic modulus and strain hardening rate of prestressed strands during corrosion were fitted to obtain the regression equation for prestressed strands under uniform corrosion.

$$f_{pu}(\eta) = f_{pu0} \times (1 - 3.15 \times \eta) \quad (78.9)$$

$$E_p(\eta) = E_{p0} \times (1 - 1.32 \times \eta) \quad (78.10)$$

$$b(\eta) = 1.4\eta + 0.0275 \quad (78.11)$$

where f_{pu0} and E_{p0} are the ultimate strength and elastic modulus of the uncorroded prestressed strand, respectively, and η are the corrosion level of the prestressed strand.

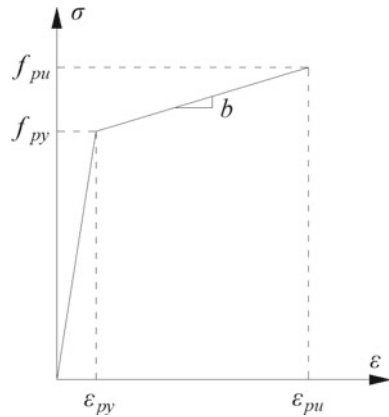
Another important feature of stress corrosion is pitting corrosion. The occurrence of pitting corrosion leads to stress concentration at the location of the corrosion pit. The local stress is much larger than the average tensile stress of the prestressed strand, so that the prestressed strand may suddenly brittle fracture at the corrosion pit. Liu et al. proposed that the maximum stress caused by stress concentration at the corrosion pit has the following relationship with the average tensile stress [16]:

$$\sigma_{\max} = K\sigma_{ave} \quad (78.12)$$

where σ_{\max} is the maximum stress at the corrosion pit, K is the stress concentration amplification factor, and σ_{ave} is the average stress of the prestressed strand.

Equation (78.12) gives the relationship between the average stress of the corroded prestressed strand and the maximum stress at the location of pitting corrosion. The average strain can be derived from the average stress, and the relationship between the maximum stress at the pitting corrosion and the average strain of the prestressed strand can be obtained. It is assumed that the nominal yield stress of prestressed strand is $f_{py} = \sigma_{0.2} = 0.88 f_{pu}$. According to the constitutive relation of prestressed

Fig. 78.3 Constitutive curve of prestressed strand



strand given in Fig. 78.3, the ultimate tensile strain can be obtained as:

$$\epsilon_{pu} = \frac{f_{py}}{E_p} + \frac{f_{pu} - f_{py}}{b \cdot E_p} = \left(0.88 + \frac{0.12}{b}\right) \cdot \frac{f_{py}}{E_p} \tag{78.13}$$

It is assumed that the strand fractures when the maximum local stress reaches the ultimate tensile stress, at which time the average stress of the strand is f_{pu}/K , and the average strain of the strand is:

$$\epsilon = \left(0.88 + \frac{0.12}{b}\right) \cdot \frac{f_{pu}/K}{E_p} \tag{78.14}$$

The strain when the prestressed strand fractures is redefined as the equivalent ultimate tensile strain, and the constitutive relationship of the strand is updated to consider the case of pitting corrosion. At the same time, the value of K varies with the corrosion level η . Substituting Eqs. (78.9)–(78.11) into Eq. (78.14), the equivalent ultimate tensile strain of prestressed strand considering both pitting corrosion and uniform corrosion can be obtained:

$$\epsilon_{pu} = \left(0.88 + \frac{0.12}{b(\eta)}\right) \cdot \frac{f_{pu}(\eta)/K(\eta)}{E_p(\eta)} \tag{78.15}$$

So far, the constitutive relation model of prestressed strand considering both stress corrosion and uniform corrosion is established.

78.3 Numerical Simulation Based on Stochastic Process

78.3.1 Stochastic Process Finite Element Simulation Method

In practical engineering, material properties have uncertainties due to differences in quality, fabrication process, and environmental conditions. In the process of construction, the geometric parameters of components such as section width, height, center of gravity and span are random, and these are the uncertainties of the geometric parameters. The above uncertainties are collected together to reflect the uncertainty of the resistance. Therefore, in numerical simulation, it is necessary to clarify the stochastic distribution model of these parameters to consider the uncertainties of material properties and geometric parameters in components, and to obtain the stochastic distribution function of resistance, which can reflect the performance of components more comprehensively.

Monte-Carlo event-based simulation, also known as statistical simulation method, a computational method based on probability and statistical theory, which can be used to solve the above-mentioned uncertainty problem. Let the function of the structure be $Z = g_X(X)$ and the probability density function of the basic random variable X be $f_X(x)$. Random sampling of X is performed according to $f_X(x)$, and the value of the function Z is calculated with the obtained sample value x . If $Z < 0$, the structure is failure in the simulation. If a total of N simulations are performed, $Z < 0$ occurs N_f times, and when the number of samples N is large enough, it follows from law of large number that the frequency N_f/N of $Z < 0$ converges to the failure probability p_f , namely, the estimated value of p_f is:

$$\hat{p}_f = \frac{N_f}{N} \quad (78.16)$$

Based on the above idea, the time-varying process and probability distribution of key parameters such as materials, geometries and loads in the finite element model are calculated and analyzed through MATLAB, and then input the processed parameters into OpenSEES for finite element model analysis, and finally the data are visualized, the whole numerical simulation process is given in Fig. 78.4.

78.3.2 Introduction of Finite Element Model of Experimental Beam

78.3.2.1 Design Parameters of Prestressed Concrete Beam

To verify the correctness of the material deterioration model, the prestressed concrete beam designed with reference to the literature [17] are simulated and analyzed using OpenSEES and MATLAB. The experimental beam is designed by the pretensioning

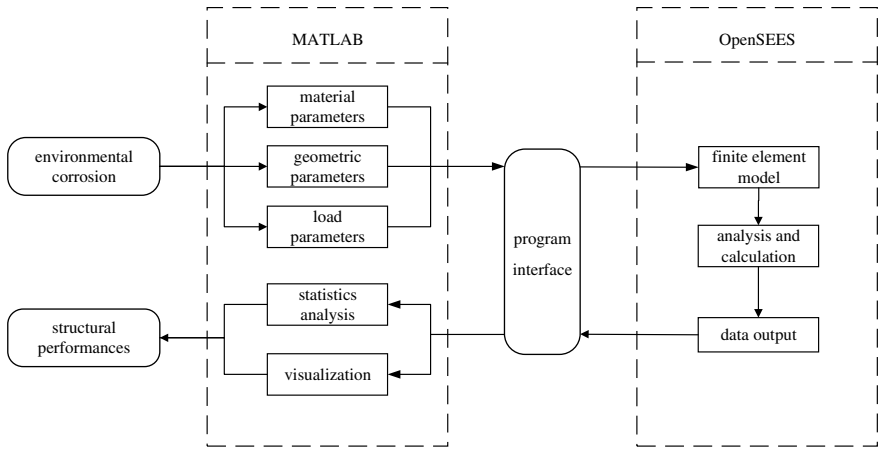


Fig. 78.4 Stochastic finite element simulation analysis process

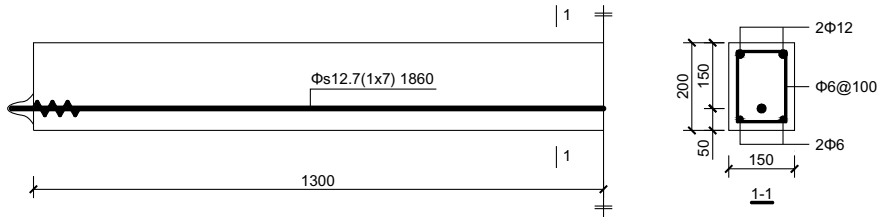


Fig. 78.5 Specimen design

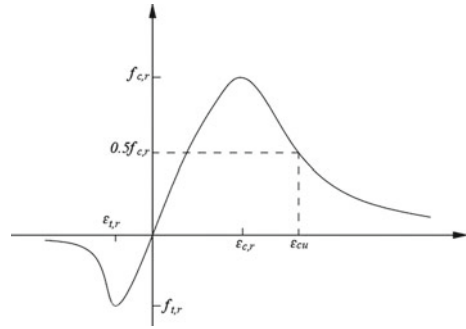
method with the total length of 2600 mm, the calculated span of 2400 mm and beam section size of $b \times h = 150 \text{ mm} \times 200 \text{ mm}$, as shown in Fig. 78.5.

In the numerical simulation, the concrete strength grade is set to C30, the prestressed tendons are $1 \times 7\Phi^s 12.7$ (1860 MPa), and the controlled stretching stress is $\sigma_{con} = 0.75f_{ptk}$. Considering the prestress lose, the effective stress is calculated as $\sigma_{pe} = 1100 \text{ MPa}$. According to the above research conclusions, assuming that the chloride ion content of the specimen is much larger than the critical chloride concentration $[Cl^-]_{cr}$ of the prestressed strand, and it can be considered that the component is corroded at the initial time. The model adopts the three-point loading mode to obtain the vertical deflection of the loading point and the mid-span point.

78.3.2.2 The Material and Geometric Parameters of the Model and Their Probability Statistics

The constitutive model of concrete is described by ConcreteD, which is based on the Code GB50010-2010 [18], as shown in Fig. 78.6. The compressive strength and

Fig. 78.6 Concrete constitutive curve



tensile strength of concrete are calculated by the following formulas:

$$f_{cm} = f_{ck}/(1 - 1.645\delta_c) \tag{78.17}$$

$$f_{tm} = f_{tk}/(1 - 1.645\delta_t) \tag{78.18}$$

where f_{cm} and f_{tm} are the mean values of compressive strength and tensile strength of concrete respectively, f_{ck} and f_{tk} are the standard values of compressive strength and tensile strength of concrete respectively, δ_c and δ_t are the coefficients of variation (COV) of compressive strength and tensile strength respectively, and $\delta_c = \delta_t$ is assumed here.

The parameters $\epsilon_{t,r}$, α_t , $\epsilon_{c,r}$, α_c required in the constitutive model are determined by the Code GB50010-2010 and are given in Table 78.2, which are the initial constitutive parameters of concrete in the uncorroded state, and the parameter changes during corrosion need to be determined in accordance with the material deterioration model.

The constitutive model of ordinary rebar adopts Steel01, the constitutive model of prestressed strand is described by Steel02, which can set the pre-tension stress of strand. Several key constitutive parameters of the prestressed strand are shown in Table 78.3. The values in the table are the initial constitutive parameters of the prestressed strand in the uncorroded state. The change of the constitutive model during the corrosion process is calculated according to the equivalent constitutive model of the prestressed strand.

The uncertainties of material properties and geometric parameters should be considered when establishing the model. Referring to the existing literature and codes, the material and geometric parameters are set as shown in Table 78.4. The table only gives the parameter values of the initial design state, and the specific

Table 78.2 Constitutive parameters of concrete

Parameters	$f_{cm}/(\text{MPa})$	$f_{tm}/(\text{MPa})$	$E_c/(\text{MPa})$	$\epsilon_{c,r}/(10^{-6})$	α_c	$\epsilon_{t,r}/(10^{-6})$	α_t
Mean value	29.2	2.9	30,000	1640	1.36	118	2.81

Table 78.3 Constitutive parameters of prestressed strand

Parameters	$f_{pu}/(\text{MPa})$	$f_{py}/(\text{MPa})$	$\sigma_{pe}/(\text{MPa})$	$E_p/(\text{MPa})$	ε_{pu}
Mean value	1962	1727	1116.2	195,000	0.041

Table 78.4 Statistical parameters for the model

Parameters	Distribution	Mean value	COV
Section dimensions	Normal	150 mm (width) 200 mm (height)	0.02
Concrete covers	Normal	25.5 mm (rebars) 51 mm (strands)	0.30
Sectional area	Normal	Design values	0.08 (rebars) 0.03 (strands)
Concrete strength	Normal	29.2 Mpa (compressive) 2.9 MPa (tension)	0.19
Rebar strength	Normal	300 MPa	0.05
Ultimate tensile strength of strands	Normal	1962 MPa	0.03
Cl-diffusion coeff.	Lognormal	Calculated value	0.035

values in the corrosion process are determined according to the deterioration model mentioned above.

78.4 Results

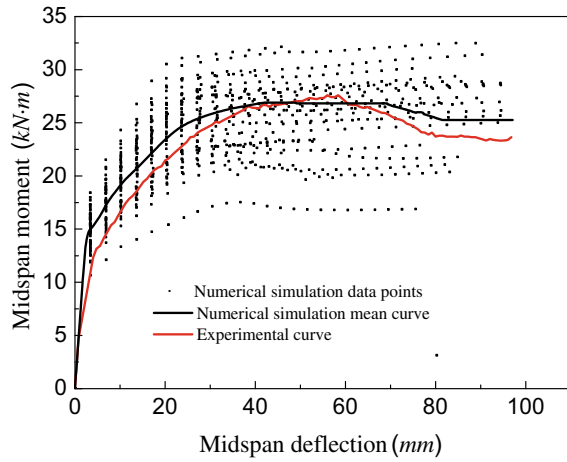
78.4.1 Comparison of Experimental and Simulation Results

Two specimens numbered PRB1 and PRB4 in Reference [17] are selected as simulation objects. The two specimens were placed in indoor environment and outdoor 10% salt solution environment for 13 months of accelerated corrosion test. The actual measured corrosion levels of prestressed strands were 1.73% and 2.87%, respectively.

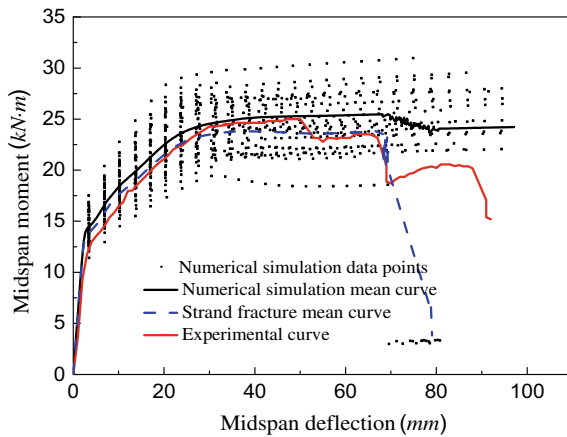
The comparison between the experimental results and the numerical simulation results is given in Fig. 78.7. The experimental curves of PRB1 and PRB4 are mostly located in the relatively dense area of numerical simulation data points, which shows that the selected finite element model can well simulate the mechanical behavior of corroded prestressed beams. In Fig. 78.7b, the experimental curve shows a step-down change, which is due to the excessive corrosion rate of the prestressed strand, and the fracture of prestressing wires occurs during the experiment. Although the bearing capacity in the numerical simulation decreases, it is not as obvious as the experimental curve. The comparative analysis of experimental and simulation results shows that the numerical model can reflect the mechanical behavior of the corroded prestressed

beam well before the bearing capacity of the beam decreases significantly, and it has a good applicability for the analysis of the bearing capacity of the component. However, due to the fracture of prestressing wires, the calculation of finite element software is not convergent and interrupted, which makes the numerical simulation of the failure process of beams is not ideal.

Fig. 78.7 Comparison between experiment and simulation



(a) PRB1



(b) PRB4

78.4.2 Load–Deflection Curves During Corrosion

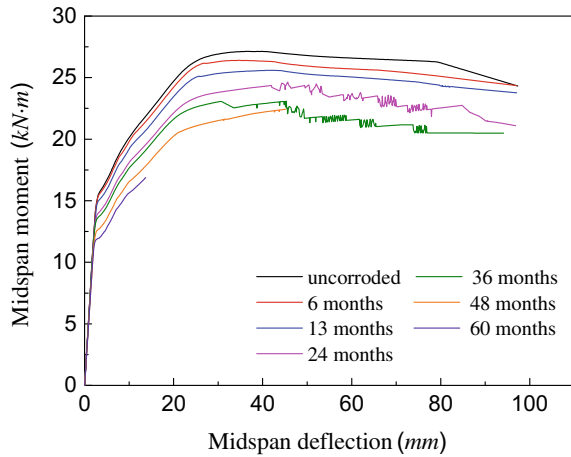
The mean value of the load–deflection curves obtained by the numerical simulation after different service time is shown in Fig. 78.8. It can be seen from curves that the stiffness of the components at different ages is basically the same in the elastic working stage before the beam cracking, indicating that the corrosion of steel bars in the elastic stage has little effect on the mechanical properties of the beam. When the concrete cracks, the stiffness of the beam decreases obviously with the increase of the corrosion degree, which indicates that the corrosion of the prestressed strands has a great influence on the stiffness of the beam after cracking. The longer the corrosion time is, the more obvious the ultimate bearing capacity of the component decreases. The ultimate bearing capacity of the beam corroded for 3 years has been reduced to less than 85% of the uncorroded condition, and the effect of corrosion of prestressed strands is significant. In addition, after the corrosion time of the two components reaches 4 years, the numerical simulation cannot obtain complete mean curves, which is more clearly reflected in Fig. 78.8b. This is because the corrosion level is too large, and the prestressed strand breaks, resulting in the non-convergence of the calculation and interruption, indicating that the prestressed beam has experienced brittle failure.

Table 78.5 gives the bending moment and deflection data of key points such as cracking point, yield point and ultimate point of components at different ages in corresponding corrosion environment. It can be seen from the data in the table that the cracking moment of the two components is reduced by more than 4.5 kN m in the setting age, and the change range is 28.8%. The change of yield point and ultimate point is also obvious. In 4 years, the yield moment of PRB1 decreased by 23%, the yield deflection decreased by 6 mm, the ultimate moment decreased to about 82% of the initial moment, and the corresponding deflection of ultimate load increased by 11%. The yield moment and ultimate moment of PRB4 are reduced by more than 20% in the third year due to the harsher environmental conditions. The comparison of the above characteristic performance points shows that the corrosion of prestressed strands has adverse effects on the crack resistance and bearing capacity of prestressed concrete beams. In the environment of high corrosion medium, the corrosion rate of prestressed strands is accelerated, the performance degradation of beams is also more rapid, and the failure time is greatly advanced.

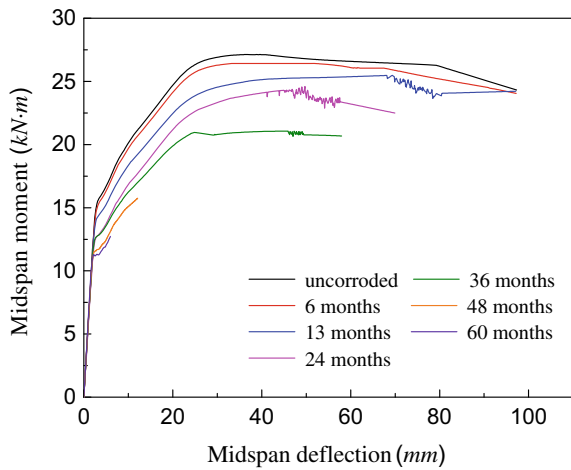
78.4.3 Bearing Capacity of Corroded Prestressed Concrete Beam

The mean-time curve and the COV-time curve of the ultimate moment are shown in Fig. 78.9. Due to the high ambient chloride ion concentration, the corrosion of prestressed strands begins at the initial moment, and the ultimate moment of the beam decreases rapidly with the service age. After reaching the cracking point, the model assumes that the concrete immediately loses the protective effect on the prestressed

Fig. 78.8 Load–deflection curves of model for different service time



(a) PRB1



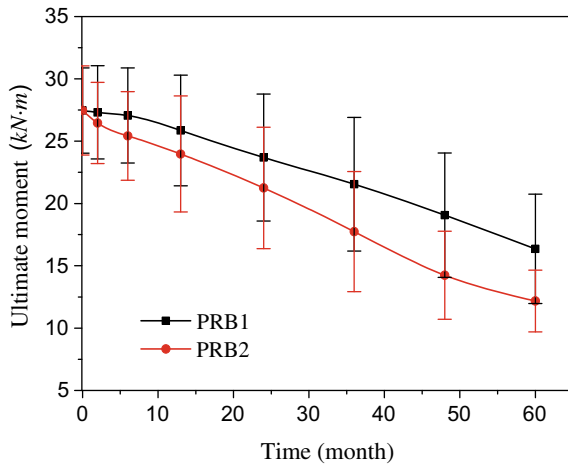
(b) PRB4

strands. The chloride ion concentration on the surface of the prestressed strands reaches the external environment concentration in a very short time, the corrosion rate of the prestressed strands is accelerated, and the curve shows an obvious turning point. Comparing the ultimate moment of PRB1 and PRB4, it can be found that the ultimate moment of PRB4 decreases faster. When the corrosion time is 2.8 years, the ultimate moment of PRB1 decreases to 80% of the initial moment, while the ultimate moment of PRB4 has decreased by about 35%. In general, the simulation results are in good agreement with the theoretical model, reflecting that the proposed model can well simulate the bearing capacity degradation process of corroded prestressed concrete beams.

Table 78.5 Key points data of load–deflection curves in different service periods

Component	Age/ (months)	Cracking moment $M_{cr}/(\text{kN m})$	Yield moment $M_y/(\text{kN m})$	Ultimate moment $M_u/(\text{kN m})$	Yield deflection $f_{dy}/(\text{mm})$	Ultimate deflection $f_{du}/(\text{mm})$
PRB1	0	15.6	26.5	27.1	27.2	40.4
	6	15.4	26.1	26.4	27.0	41.2
	13	14.8	25.2	25.8	26.7	45.7
	24	13.6	23.4	24.5	24.8	45.8
	36	13.2	22.4	23.0	22.5	44.6
	48	12.2	20.5	22.4	21.2	45.0
	60	11.6	–	16.9	–	13.7
PRB4	0	15.6	26.5	27.1	27.2	40.4
	6	14.9	25.8	26.4	25.7	52.2
	13	13.8	23.5	25.4	23.2	65.4
	24	12.2	22.0	24.5	22.3	49.6
	36	12.2	20.9	21.1	24.8	45.8
	48	11.6	–	15.7	–	12.1
	60	11.1	–	12.7	–	5.9

Fig. 78.9 Mean and COV of ultimate moment



It can be seen from the curves that the COV of the bearing capacity of the prestressed beam during the corrosion process generally shows an upward trend. With the deepening of the corrosion degree, the increasing trend of the coefficient of variation is more significant, which is 2 times of the initial time in the third year. The shape of the curve indicates that the greater the concentration of corrosive media in the environment, the greater the corrosion of the prestressed strands and the greater the discrete degree of the bearing capacity of the beam. This phenomenon implies

that the reliability of the beam decreases significantly with corrosion time, when the service life of the beam is much lower than its design life. Therefore, it is clearly inappropriate to use the design moment parameters to assess the durability of prestressed concrete components in corrosive environments, but rather a more reasonable service life assessment needs to be made by considering the real-time corrosiveness.

78.5 Conclusions

The method of quantifying hydrochloric acid corrosion by pH value is proposed to determine the variation of pH of concrete pore solution. The corresponding concrete strength deterioration model is established, which can easily calculate the residual strength of concrete according to environmental conditions.

The concept of equivalent ultimate tensile strain of prestressed strand is proposed, and based on this concept, an equivalent constitutive relationship model considering stress corrosion is established. Compared with the commonly used constitutive model of prestressed strand, the proposed model can well reflect the performance degradation of prestressed strand due to corrosion.

The stochastic process numerical simulation of four-point bending test of prestressed concrete beams is carried out by using OpenSEES and MATLAB, and compared with the experimental data. The numerical simulation results are in good agreement with the experimental results, which shows the accuracy of the proposed deterioration model of materials.

The corrosion of steel bars has little effect on the mechanical properties of the beam in the elastic stage, but has a great influence on the stiffness of the beam after cracking. The greater the concentration of corrosive medium in the environment and the longer the corrosion time, the more obvious the reduction of ultimate bearing capacity and the greater the discrete degree of bearing capacity of the beam, which indicates that the reliability and service life of the beam are also greatly reduced.

Acknowledgements The authors gratefully acknowledge the funding supports of National Key Research and Development Plan, China (2022YFC3801800) and National Natural Science Foundation of China (Grant No. 52038010 and 52078368).

References

1. Zhang, D.W., Zeng, Y., Fang, M.S., et al.: Service life prediction of precast concrete structures exposed to chloride environment. *Adv. Civ. Eng.* **1**, 1–14 (2019)
2. Pепенar, I.: Long-term corrosion behavior of reinforced concrete structures in chloride-based industrial environments: case studies. In: 8th International Structural Engineering and Construction Conference on—Implementing Innovative Ideas in Structural Engineering Project Management, pp. 23–28, Sydney, Australia (2015)

3. Li, Y., Chen, X., Jin, L., Zhang, R.: Experimental and numerical study on chloride transmission in cracked concrete. *Constr. Build. Mater.* **127**, 425–435 (2016)
4. Szweda, Z.: Evaluating the impact of concrete design on the effectiveness of the electrochemical chloride extraction process. *Materials* **16**, 666 (2023)
5. Raczkiwicz, W., Bacharz, M., Bacharz, K., Teodorczyk, M.: Reinforcement corrosion testing in concrete and fiber reinforced concrete specimens exposed to aggressive external factors. *Materials* **16**(3), 1174 (2023)
6. Nnadi, E.O., Lizarazo-Marriaga, J.: Acid corrosion of plain and reinforced concrete sewage systems. *J. Mater. Civ. Eng.* **25**(9), 1353–1356 (2013)
7. Wang, Z.H., Zhu, Z.M., Sun, X., et al.: Deterioration of fracture toughness of concrete under acid rain environment. *Eng. Fail. Anal.* **77**, 76–84 (2017)
8. Vafaei, M., Allahverdi, A., Dong, P., et al.: Durability performance of geopolymer cement based on fly ash and calcium aluminate cement in mild concentration acid solutions. *J. Sustain. Cem. Based Mater.* **8**(5), 290–308 (2019)
9. Niu, D.T.: *Durability and Life Forecast of Reinforced Concrete Structure*. Science Press, Beijing (2003). (in Chinese)
10. Wang, J.B., Niu, D.T.: Nitric acid immersion corrosion of shotcrete lining: diffusion law of hydrogen ions (H^+) and nitrite ions (NO_3^-), and the corrosion mechanism. *Materials Reports* **33**(06), 991–999 (2019). (in Chinese)
11. American Concrete Institute. ACI201.2R-08. Guide to durable concrete (2008)
12. GB 50164-2011. Ministry of Construction of the People's Republic of China. Standard for quality control of concrete. China Architecture & Building Press, Beijing, China (2011). (in Chinese)
13. Yin, Q.X., Hou, M.J., Du, J.M., et al.: Research on the corrosion rate of concrete under different acid solution corrosion. *Concrete* (9), 23–25, 30 (2017)
14. Zeng, Y.H., Gu, X.L., Zhang, W.P., et al.: Study on mechanical properties of corroded prestressed tendons. *J. Build. Mater.* **2**, 169–174 (2010). (in Chinese)
15. Wu, X.F.: Research on mechanical properties and bonding performance of corroded prestressing steel strand. Ph.D. Thesis. Central South University, Changsha, China (2014). (in Chinese)
16. Liu, X., Zhang, W., Gu, X., et al.: Probability distribution model of stress impact factor for corrosion pits of high-strength prestressing wires. *Eng. Struct.* **230**, 111686 (2021)
17. Li, F.M., Yuan, Y.S.: Experimental study on bending property of prestressed concrete beams with corroded steel strands. *J. Build. Struct.* **2**, 78–84 (2010). (in Chinese)
18. GB 50010-2010. Ministry of Construction of the People's Republic of China. Code for design of concrete structures. China Architecture & Building Press, Beijing, China (2010). (in Chinese)

Chapter 79

Prediction Model of Wellbore Temperature Field in Ultra-deep Shale Oil Horizontal Well During Managed Pressure Cementing



Jinlu Liu, Jun Li, Hongwei Yang, Hui Li, and Gonghui Liu

Abstract Horizontal well is the main well type of ultra-deep shale oil exploitation, and the prediction of temperature field in the horizontal well managed pressure cementing (MPC) process is of great significance to the field construction. Based on energy conservation and thermal resistance method, taking conventional three-stage well as an example, the prediction model of wellbore temperature field in ultra-deep horizontal wells of shale oil was established. The effect of well trajectory and fluid performance parameters on temperature field were considered comprehensively to improve the prediction accuracy of the model. A well in China was taken as an example to verify the model, and the model can simulate the changing law of various parameters and has good applicability. The influence factors of temperature field were analyzed. The results show that the temperature of drill pipe and annulus decreases with the increase of cycle time. The formation temperature at wellhead increases with the increase of cycle time, while the formation temperature at bottom hole decreases with the increase of cycle time. The length of horizontal section has little effect on bottom hole temperature. The inlet temperature of cementing fluid has little influence on the long horizontal section. Increasing cementing fluid density, displacement, and time can reduce bottomhole temperature. The research results provide a theoretical basis for the exploration and development of ultra-deep shale oil.

Keywords Ultra-deep shale oil · Horizontal well · Managed pressure cementing · Temperature field

J. Liu · J. Li (✉) · H. Yang · H. Li · G. Liu
China University of Petroleum-Beijing, Changping, Beijing, China
e-mail: lijun446@vip.163.com

79.1 Introduction

The prediction of wellbore temperature field runs through the whole process of drilling and cementing [1], and is also an important basis for other related research. At present, there are three methods to obtain wellbore temperature field during cementing: measurement while cementing, prediction of adjacent well data and prediction of mathematical model [2, 3]. The mathematical model method has become the key research object because of its fast prediction speed and low prediction cost. Its shortcoming is that the prediction accuracy is difficult to guarantee. Therefore, improving the accuracy of temperature field model has become the key of research [4].

Scholars [5–7] have done a lot of research and reached a consensus on the prediction theory of temperature field in vertical Wells. Raymond [8] proposed the first one-dimensional numerical model to predict annulus temperature in vertical Wells under unsteady and quasi-stable conditions. However, the accuracy of calculation results is low because this model neglects the change of thermal and physical parameters of wellbore fluid, well structure and heat source terms. Maubeuge [9] calculated the temperature distribution, believing that in addition to friction resistance, the change of temperature gradient would also lead to heat loss in the heat transfer process. Cheng [10] believed that the traditional dimensionless time calculation formula does not consider the influence of heat capacity. Cheng simplified the dimensionless function to make its accuracy meet the field requirements. The research on horizontal well temperature field model is much less than that of vertical well [11]. Some scholars have proposed a two-dimensional transient heat transfer model to predict formation temperature. The establishment of this temperature field is based on heavy oil formation, but it also has certain reference significance for shale oil.

To sum up, the current research on temperature field mainly focuses on vertical Wells without considering the influence of horizontal well type, which is the main well type of shale oil exploitation. Therefore, it is still of great significance for the further development of temperature field [12, 13].

In this paper, based on energy conservation and thermal resistance method, taking conventional three-stage well as an example, the prediction model of wellbore temperature field in ultra-deep horizontal wells of shale oil was established. The effect of well trajectory and fluid performance parameters on temperature field were considered comprehensively to improve the prediction accuracy of the model. A well in China was taken as an example to verify the model, and the model can simulate the changing law of various parameters and has good applicability. The influence factors of temperature field were analyzed. The research results provide a theoretical basis for the exploration and development of ultra-deep shale oil.

79.2 Horizontal Well Temperature Field Model

79.2.1 Model Assumption

There are many factors affecting the temperature field of the cementing wellbore. In order to facilitate the establishment and subsequent solution of the model, the following assumptions are made: The temperature field of the cementing fluid in the same area only changes in the axial direction; The thermal physical property parameters (density, specific heat and thermal conductivity) of seawater and strata are constant values. Ignoring the influence of casing eccentricity; The displacement process is steady-state displacement; The radial change of seawater temperature around the riser is ignored; In the cement ring area, it is assumed that the heat transfer process from the inner edge of the cement ring to the outer edge of the cement ring is stable, while the heat transfer process from the outer edge of the cement ring to the formation is unsteady.

79.2.2 Physical Model

There are many types of horizontal Wells. The advantages and disadvantages of different well types are introduced in this section, and the physical model of wellbore temperature field is established by taking conventional three-stage type as an example.

Horizontal well pattern. To cope with the complex geological conditions, scholars designed a variety of horizontal well patterns, Include Hook upturned “Spoon type well”, Hook bent down, The hook is bent back “Spoon type well”, Regular double increment, Regular three-stage form. Figure 79.1 shows common horizontal well types. For different well types, the variation law of well trajectory is different, and the temperature field in the MPC process is also different. Among them, the fish-hook well can avoid dead oil area, but its design is complicated and the trajectory control is difficult. In order to reduce the maximum building slope, double increment design is usually used. However, in order to facilitate the reader’s understanding, this paper takes the conventional three-stage formula as an example to establish the corresponding physical model and mathematical model and solve it.

Regular three-stage form. According to the characteristics of conventional three-stage well structure, it is divided into three parts, the first part is vertical section, the second part is inclined section, and the third part is horizontal section. A schematic diagram of heat transfer in the wellbore is given. The heat transfer process is similar regardless of the interval the unit belongs to. The heat transfer process of fluid unit in drill pipe and annulus is analyzed, which is convenient for the establishment of mathematical model (Fig. 79.2).

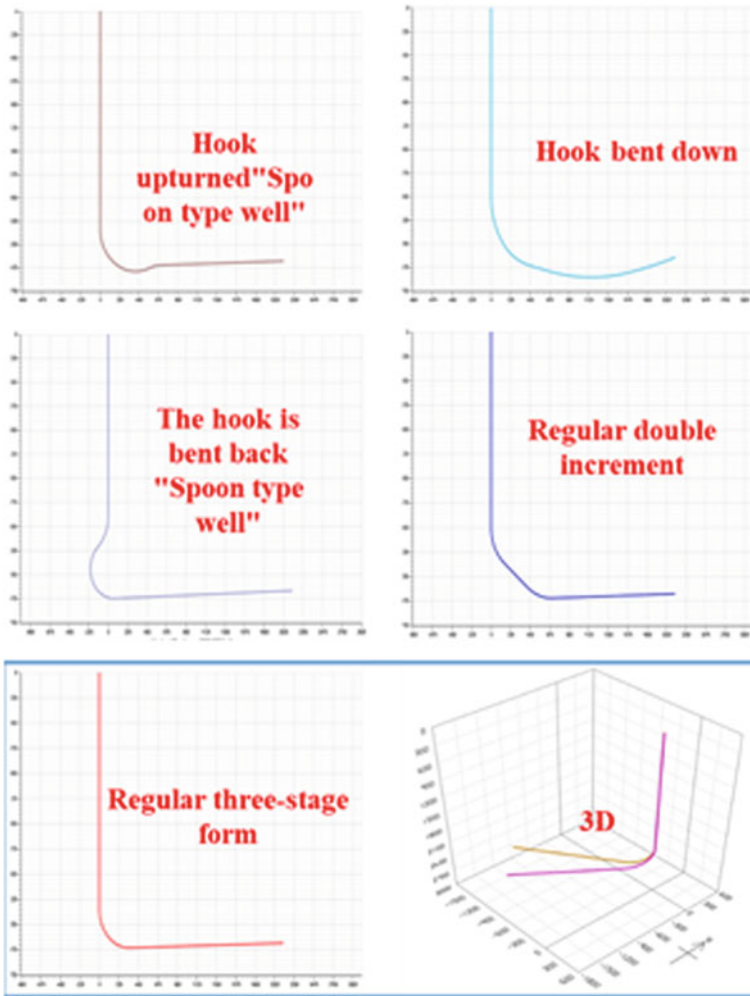


Fig. 79.1 Common horizontal well pattern

79.2.3 Mathematical Model

The corresponding mathematical model is established based on model hypothesis and physical model. As the model of temperature field is relatively mature, this paper focuses on the key equations in the mathematical model and the equations which are different from those in previous studies. The mathematical model is composed of well trajectory description equation, heat conservation equation and auxiliary equation.

Well path description equation. Equations (79.1), (79.2) and (79.3) describe the mathematical relationship between sounding and vertical depth. Equation (79.1) can

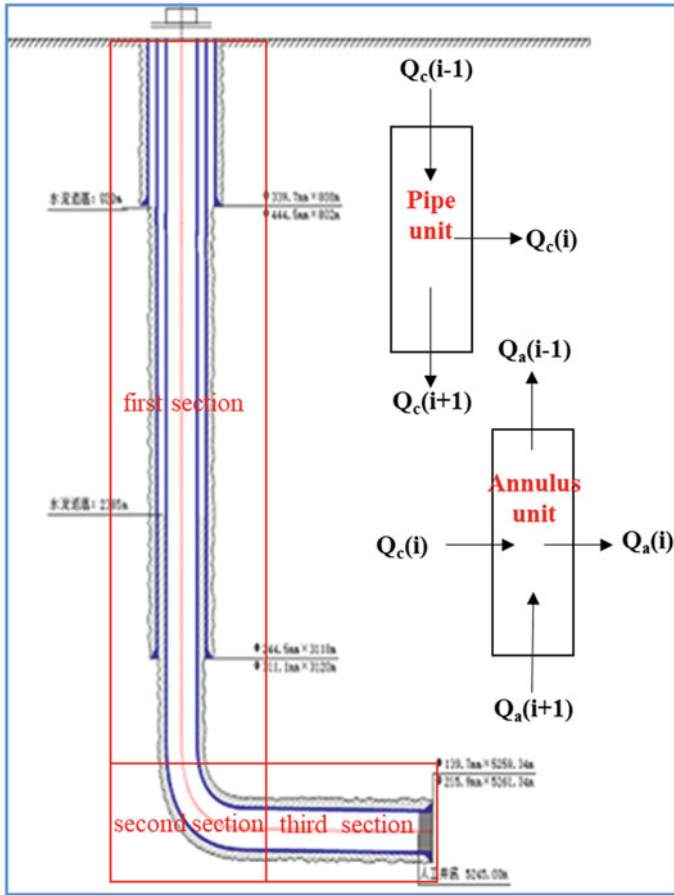


Fig. 79.2 Conventional three-stage depth structure

be used to indicate that vertical well sounding is equal to vertical depth. Equation (79.2) can be used to express the relationship between sounding and vertical depth in the inclined section. For the horizontal segment, vertical depth no longer increases, which can be expressed by Eq. (79.3).

$$VD(i + 1) = VD(i) + dh(i) \tag{79.1}$$

$$VD(i + 1) = VD(i) + dh(i) * \cos \theta \tag{79.2}$$

$$VD(i + 1) = VD(i) \tag{79.3}$$

Energy conservation equation. The energy conservation equation includes Eqs. (79.4), (79.5) and (79.6). These three equations are the core of the horizontal well temperature field calculation. The frictional heat generation is taken as a part of the variation of unit energy in the equation, so it is not shown in the equation.

Equation of fluid energy conservation in drill pipe

$$\Delta Q_c(i) = Q_c(i - 1) - Q_c(i) - Q_c(i + 1) \quad (79.4)$$

Equation of fluid energy conservation in annulus

$$\Delta Q_a(i) = Q_c(i) + Q_a(i + 1) - Q_a(i) - Q_a(i - 1) \quad (79.5)$$

Equation of conservation of formation energy. Only lateral heat transfer is considered for the formation.

$$\Delta Q_f(i) = Q_a(i) - Q_f(i) \quad (79.6)$$

Auxiliary equation. The model considers the effects of temperature and pressure on viscosity and density, and the specific relations are expressed in Eqs. (79.7) and (79.8), respectively.

Effect of temperature and pressure on viscosity

$$\begin{cases} \mu_e = \mu_{e0} \times \exp(\phi) \\ \phi = \xi_p(p - p_0) + \xi_{pp}(p - p_0)^2 + \xi_T(T - T_0) + \xi_{TT}(T - T_0)^2 + \xi_{pT}(p - p_0)(T - T_0) \end{cases} \quad (79.7)$$

Effect of temperature and pressure on density

$$\begin{cases} \rho = \rho_0 \times \exp(\phi) \\ \phi = \xi_p(p - p_0) + \xi_{pp}(p - p_0)^2 + \xi_T(T - T_0) + \xi_{TT}(T - T_0)^2 + \xi_{pT}(p - p_0)(T - T_0) \end{cases} \quad (79.8)$$

Table 79.1 The density and thermodynamic parameters

Parameter	Value	Parameter	Value
Drilling fluid density	1.08	Thermal conductivity of drilling fluid	1.73
Rock density	2.64	Thermal conductivity of rock	2.25
Specific heat of drilling fluid	1674	Thermal conductivity of drill pipe	43.75
Specific heat of drill pipe	400	Specific heat of rock	837

79.3 Model Solution

79.3.1 Initial Conditions and Boundary Conditions

Initial conditions and boundary conditions are the necessary preconditions for solving the equation. Reasonable initial boundary value conditions are beneficial to improve the accuracy and convergence of the model. Equation (79.9) is the initial condition and Eq. (79.10) is the boundary condition.

$$T_c(i)|_{i=0} = T_{in} \quad (79.9)$$

$$T_c(i)|_{i=h} = T_a(i)|_{i=h} \quad (79.10)$$

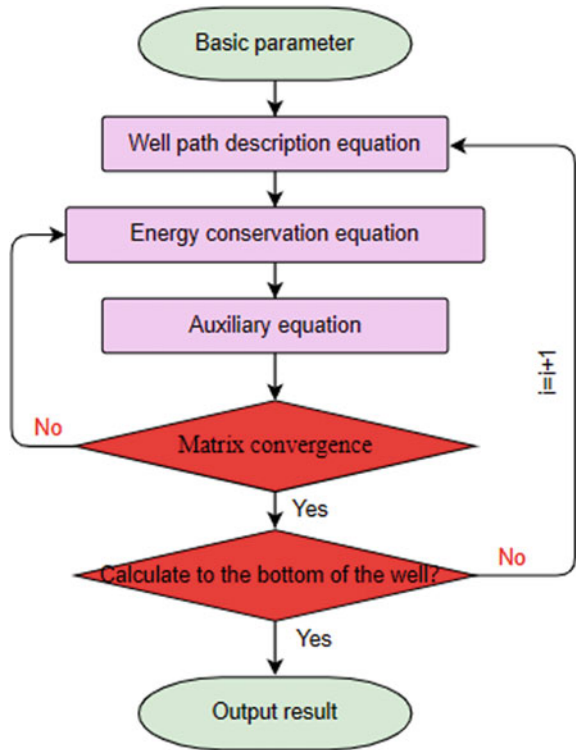
79.3.2 Calculation Parameter

Taking an ultra-deep horizontal well as an example, the model is solved and the calculation results are analyzed. The simulated well depth is 7762.5 m, the length of vertical well is 6000 m, the length of horizontal section is 1200 m, the casing vertical well is 157 mm, the bit diameter is 152.4 mm, the outside diameter of drill pipe is 88.9 mm, the inside diameter of drill pipe is 70.2 mm, the inlet temperature is 40 °C, the surface temperature is 25 °C, and the geothermal gradient is 2.19 °C/100 m. The density and thermodynamic parameters are shown in Table 79.1.

79.3.3 Calculation Process

The mathematical model is discretized, and the initial boundary value conditions and basic parameters are substituted to solve iteratively. Figure 79.3 shows the specific solution process.

Fig. 79.3 Model solving process



79.4 Simulation Result Analysis

79.4.1 Casing Circulating Temperature Field

Figure 79.4 shows the temperature field variation of fluid circulation in the casing over time. As can be seen from the figure, with the increase of well depth, the fluid temperature in the drill string is less than the original temperature except for a distance near the wellhead. At the same time, with the increase of well depth, the temperature increases the fastest in the vertical section, followed by the deviation section, and the slowest in the horizontal section. At the bottom of the hole, there is a significant increase in temperature, which is mainly due to the effect of bit pressure drop. With the increase of cycle time, the fluid temperature in the drill string decreases continuously, with a large amplitude at the bottom hole position.

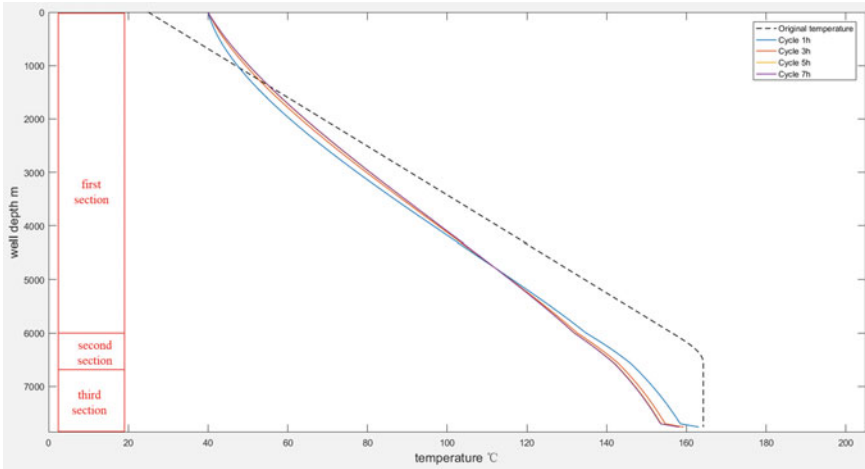


Fig. 79.4 Diagram of temperature field of fluid circulation in casing with time

79.4.2 Annular Circulation Temperature Field

Figure 79.5 shows the variation curve of the temperature field of the fluid circulation in the annulus over time. As can be seen from the figure, with the increase of well depth, the fluid temperature in the annulus is less than the original formation temperature in the well section below the turning point, which is about 4800 m. At the same time, temperature increases fastest in vertical Wells as well as in the drillstring. At the bottom of the hole, there is a significant decrease in temperature, which is mainly due to bit pressure drop, which is contrary to Fig. 79.4. Combined with Fig. 79.4, it can be seen that annular fluid temperature decreases as a whole with the increase of cycle time.

79.4.3 Formation Rock Temperature Field

Figure 79.6a shows the variation of formation radial temperature over time at the wellhead. As can be seen from the figure, with the increase of radial temperature, the formation temperature gradually decreases and approaches the undisturbed formation temperature, which is mainly due to the constant dissipation of heat in the process of transfer. At a certain distance from the wellbore, the formation temperature field will no longer be affected by the circulating wellbore temperature field. With the increase of cycle time, the wellhead formation temperature increases and gradually reaches equilibrium.

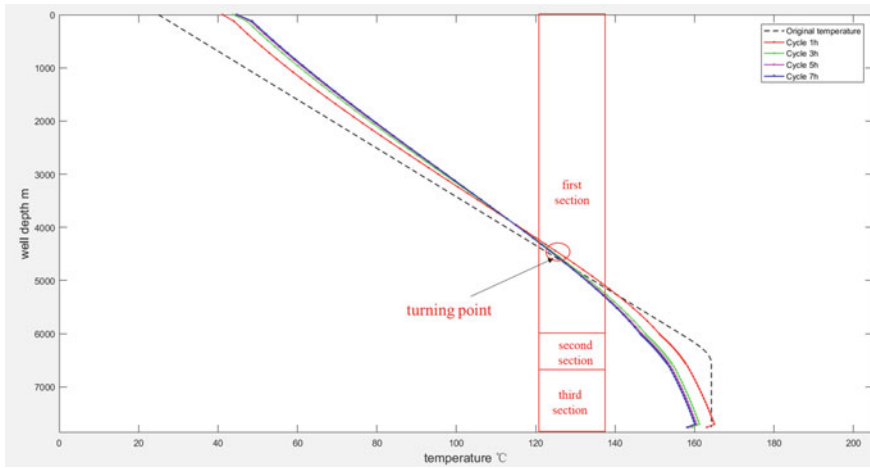


Fig. 79.5 Diagram of temperature field of fluid circulation in annulus with time

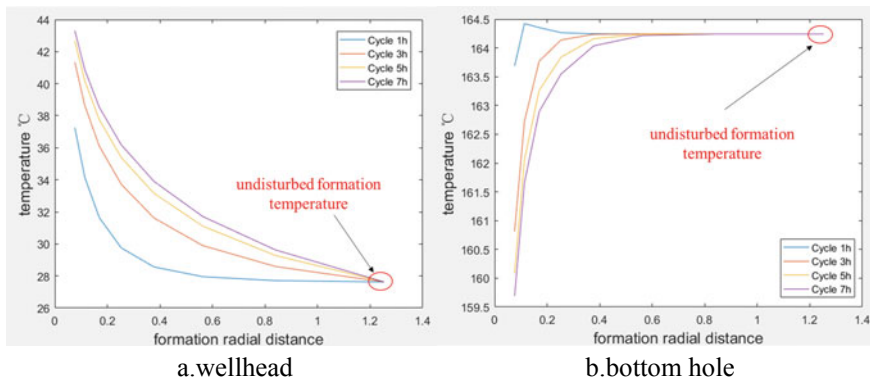


Fig. 79.6 Curve of formation radial temperature with cycle time

Figure 79.6b shows the variation of formation radial temperature at the bottom of the hole over time. As can be seen from the figure, with the increase of radial temperature, the formation temperature gradually increases and approaches the undisturbed formation temperature. This is mainly because the bottom hole temperature is low and the formation continuously transfers heat to the wellbore. Therefore, the farther away from the wellbore, the higher the formation temperature will be. Similarly, at a certain distance from the wellbore, the formation temperature field will not be affected by the circulating temperature field of the wellbore. As the cycle time increases, the bottom hole temperature decreases, which is completely contrary to Fig. 79.6a.

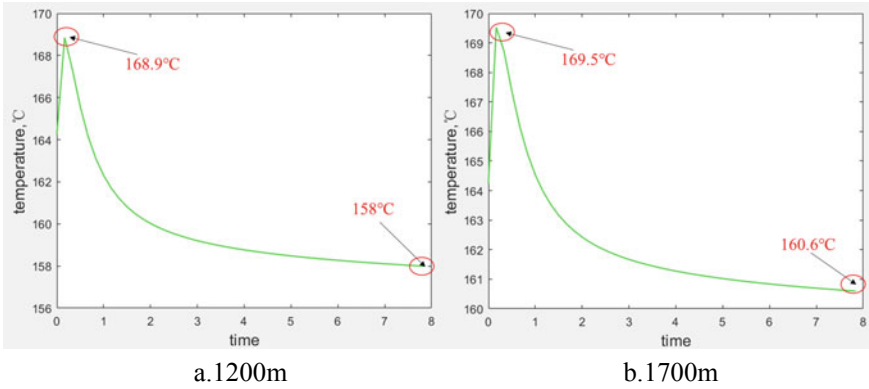


Fig. 79.7 Bottom hole temperature curve with time under different horizontal length

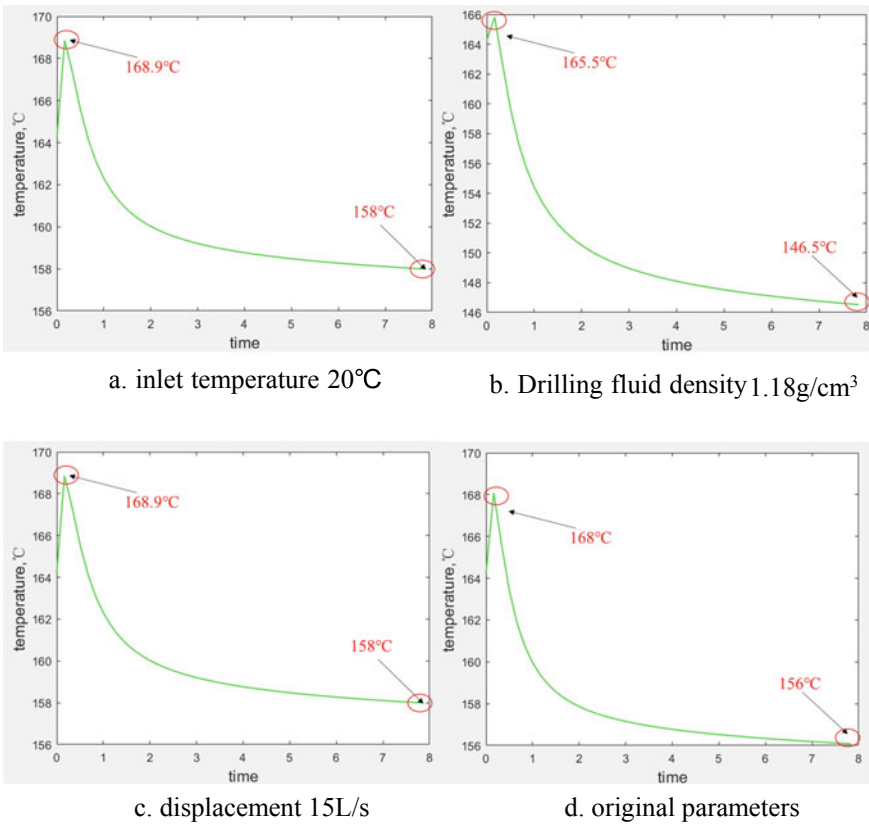


Fig. 79.8 Effect of injection parameters on bottom hole temperature

79.4.4 Effect of Horizontal Section Length on Bottom Hole Temperature

Figure 79.7 shows the variation curve of bottomhole temperature with time under different horizontal length. The length of horizontal segment in Fig. 79.7a is 1200 m, and the length of horizontal segment in Fig. 79.7b is 1700 m. As can be seen from the figure, the length of the horizontal section increases by 500 m, while the maximum temperature increases by only about 0.6 °C, and the temperature increases by about 2.6 °C when it is stable, which is negligible compared with the geothermal gradient. Therefore, it can be concluded that the length of the horizontal section has little influence on the bottom hole temperature, and the wellbore temperature field is relatively stable in the process of MPC the horizontal section.

79.4.5 Effect of Injection Parameter on Bottom Hole Temperature

The influence of injection parameters on bottom hole temperature is analyzed, and the calculation results are shown in Fig. 79.8. Control variable method was adopted to set injection temperature of 20 °C, drilling fluid density of 1.18 g/cm³ and circulation displacement of 15 L/s. Compared with the simulation results of initial parameters (Fig. 79.8d), it can be seen that drilling fluid inlet temperature has little influence on temperature field of long horizontal Wells. Increasing drilling fluid density and circulation rate can reduce bottom hole temperature. It is worth noting that the bottom hole temperature decreases as the cycle time increases. This can be used to adjust the bottom hole temperature in the MPC process to meet the needs of the field construction.

79.5 Conclusion

The prediction model of wellbore temperature field in ultra-deep horizontal wells of shale oil was established. The effect of well trajectory and fluid performance parameters on temperature field were considered comprehensively to improve the prediction accuracy of the model.

The length of horizontal section has little effect on bottom hole temperature. The inlet temperature of drilling fluid has little influence on the long horizontal section. Increasing drilling fluid density, displacement, and time can re-duce bottomhole temperature.

Acknowledgements The authors gratefully acknowledge the Key Program of National Natural Science Foundation of China (Grant No. 51734010), the Study on Casing Deformation Mechanism

and Control Method During Shale Gas Well Fracturing (Grant No. XQZX20220006), the Joint Foundation Program of National Natural Science Foundation of China (Grant No. U22B2072).

References

1. Yang, H., Li, J., Liu, G., Wang, J., Luo, K., Wang, B.: Development of transient heat transfer model for controlled gradient drilling. *Appl. Therm. Eng.* **148**, 331–339 (2018)
2. Arnold, F.C.: Temperature variation in a circulating wellbore fluid. *J. Energy Resour. Technol.* **112**(2), 79–83 (1990)
3. Xiao, D., Hu, Y., Meng, Y.: Research on wellbore temperature control and heat extraction methods while drilling in high-temperature wells. *J. Pet. Sci. Eng.* (2019), 209 (2022)
4. Maud, R.B., Noemie, C., Cyril, C., Myriam, D.: Method for determining at least one parameter that represents a change in a fluid by multi-point near-infrared spectroscopy. EP3881069A1 (2021)
5. Jianhong, F.U., Su, Y., Jiang, W., Zhong, C., Zhengtao, L.I.: Research and application of wellbore transient temperature in deep shale gas horizontal wells (6) (2019)
6. Espinosa-Paredes, G., Espinosa-Martinez, E.G.: A feedback-based inverse heat transfer method to estimate unperturbed temperatures in wellbores. *Energy Convers. Manage.* **50**(1), 140–148 (2009)
7. Garcia-Gutierrez, E.P.: Estimation of static formation temperatures in geothermal wells. *Energy Convers. Manage.* (2003)
8. Raymond, L.R.: Temperature distribution in a circulating drilling fluid. *J. Pet. Technol.* **21**(03), 333–341 (1969)
9. Maubeuge, F., Didek, M.P., Beardsell, M.B., Caltagirone, J.P.: Temperature model for flow in porous media and wellbore. In: *SPWLA Annual Logging Symposium* (1994)
10. Cheng, W.L., Huang, Y.H., Lu, D.T., Yin, H.R.: A novel analytical transient heat-conduction time function for heat transfer in steam injection wells considering the wellbore heat capacity. *Energy* **36**(7), 4080–4088 (2011)
11. Emami-Meybodi, H., Saripalli, H.K., Hassanzadeh, H.: Formation heating by steam circulation in a horizontal wellbore. *Int. J. Heat Mass Transf.* **78**(7), 986–992 (2014)
12. Duong, A.N., Tomberlin, T., Cyrot, M.: A new analytical model for conduction heating during the SAGD circulation phase. In: *International Thermal Operations & Heavy Oil Symposium*
13. Zhang, L.Z.: The flow and heat transfer characteristics of multi-thermal fluid in horizontal wellbore coupled with flow in heavy oil reservoirs. *J. Pet. Sci. Eng.* **122**(Null) (2014)

Chapter 80

A Blockchain Based Documentation Sharing Framework for Copyright Protection



Huanqin Zheng, Yue Xue, Wanjuan Xie, and Zhengzheng Shi

Abstract In the context of the information age, electronic documents have replaced traditional paper documents and become the most commonly used data carrier in work. Compared with traditional paper documents, the cost of electronic documents is lower, and it is convenient for the modification and transmission of information, which brings great convenience to the work of users. However, while electronic documents bring convenience to users, digital copyright infringements are ubiquitous because of their ease of duplication. To protect the user's document security, this paper develops a decentralized electronic document sharing framework based on blockchain non-fungible token (NFT) technology. We have designed an on-chain and off-chain collaborative storage solution for off-chain storage of source files and on-chain storage proofs for file storage. By setting the challenge period and extracting file keyword groups for file duplication detection, the user's copyright is protected. And develop smart contracts based on solidity language, design access control mechanisms, realize copyright deposit certificates, copyright confirmation, copyright infringement detection, and document sharing.

Keywords Documentation sharing · Smart contracts · Decentralized storage · NFT

H. Zheng · Y. Xue
GuangZhou University, No. 230, Waihuan West Road, University City, Panyu District,
Guangzhou 510006, Guangdong, China

W. Xie (✉)
Information Network Engineering and Research Center, South China University of Technology,
Guangzhou 510006, Guangdong, China
e-mail: [wanjuanxie@scut.edu.cn](mailto:wanjianxie@scut.edu.cn)

Z. Shi
National Computer System Engineering Research Institute of China, Beijing, China

80.1 Introduction

With the advent of the information age, the Internet has become the main way for people to work and play, and more and more digital works are disseminated, stored, and used on the Internet. The prosperity of the Internet has also led to ubiquitous digital copyright infringements and frequent online copyright disputes. As the most commonly used data carrier in work, electronic documents have a particularly high probability of being infringed on the Internet.

Traditional document sharing mainly relies on the delivery of centralized systems and the sharing of usage rights, and its essential logic lies in the centralized management, delivery, and marketing of document ownership. Traditional centralized document sharing has the following three disadvantages: (1) In the era of big data, extremely fast transmission speed, easy-to-copy form, and convenient storage make digital publishing works extremely easy to be plagiarized, and users' intellectual property rights cannot be guaranteed. (2) Traditional centralized storage will lead to excessive data centralization, and there are certain security issues. (3) The traditional centralized system lacks an effective incentive mechanism, and users lack the motivation to share resources.

Aiming at the above problems, this paper proposes a document sharing system based on blockchain NFT technology. We store the source file of the document on the off-chain distributed storage system through on-chain and off-chain collaborative storage [1], and store the metadata (encrypted storage address, keyword group, digital signature, creator address, and document content introduction and other information) of the document on the blockchain, casting it into a unique NFT. Utilizing the blockchain's encryption algorithm, non-tamperable, decentralization, time stamp, chain storage and consensus mechanism, and other characteristics can ensure the authenticity and effectiveness of NFT, and confirm and endorse documents. To discuss the sharing, management and business model of electronic documents, and pave the way for promoting the digitization and cross-platform sharing of electronic documents. The research content of this paper is as follows:

(1) Documentation sharing platform framework

Facing the business needs of documentation sharing, clarify the system composition of the document sharing platform, the functions of each component, component interface and data format, and the system business implementation process, and then propose a feasible implementation plan for the document sharing platform.

(2) Technology for verification and confirmation of documentation content

Aiming at the problem that it is difficult to determine the weight of electronic documents, we have designed two document copyright protection technologies in combination with the resource characteristics of documents and existing document protection technologies. The first method is to automatically identify and block duplicate files by extracting keyword phrases of documents for similarity comparison. The second method is to introduce a copyright challenge mechanism, which sets a

week after the document is uploaded as the document's copyright challenge period, allowing all users in the system to challenge the document's copyright during the challenge period.

(3) On-chain and off-chain collaborative storage technology

Aiming at the problem that it is difficult to store large files on the blockchain, the method of generating digital certificates of documentation on the blockchain and the data interaction mode on and off the chain is studied to realize the safe and effective sharing of documentation.

80.2 Research Status

The concept of a blockchain originated from Bitcoin. In 2008, it was proposed by Satoshi Nakamoto in "Bitcoin White Paper: A Peer-to-Peer Electronic Cash System" [2]. It mainly has a decentralized function of digital currency and payment platform, the blockchain at this time is called blockchain 1.0 [3]. After Vitalik Buterin developed Ethereum based on Bitcoin in 2014, he began to enter blockchain 2.0 [4]. The biggest difference between blockchain 2.0 and blockchain 1.0 is that Ethereum provides a Turing-complete programming language solidity, which allows anyone to use solidity to develop and publish new programs on the chain, which run on Ethereum Programs are called smart contracts. Once the smart contract intelligence is released, it cannot be changed and can only be triggered by transactions [5]. The emergence of smart contracts makes it possible to develop complex applications based on blockchain [6].

In recent years, many fields have carried out further research based on smart contracts. Due to their characteristics of decentralization, immutability, and traceability [7], they are widely used to manage and ensure the security of data in various industries. For example, Zhang Guochao published a digital music copyright management system based on blockchain in the field of music copyright protection [7], Zhu Jianming published a blockchain-based dynamic multi-center collaborative authentication model for supply chains [8] in the field of supply chain and Su Liandeng published a blockchain-based decentralized system for archives information in the field of archives management [9].

The research of blockchain in the field of file sharing is still in its infancy, and the research results are few and there are still some deficiencies [10]. At present, only Vimal S in this field has implemented a P2P file-sharing system based on blockchain and IPFS [11] and Guo Qiang published two articles on a teaching resource-sharing system based on blockchain [12]. Both Vimal S and Guo Qiang adopt the storage model of on-chain and off-chain collaborative storage. First, large files are stored on IPFS, and then the storage path of the files is stored on the blockchain. But they also have some deficiencies. The file weight judgment algorithm adopted by Vimal S judges whether the same file exists by judging whether the file hash returned after IPFS stores the file is the same. The disadvantage of this method is that as long as the

content of the file changes a little, the calculated file hash will change accordingly, so the success rate of using this method to judge the weight is poor. Guo Qiang’s article is that the document weight judgment mechanism is single, lacks a certain incentive mechanism, and cannot motivate users to participate in community construction.

After 2021, NFT based on the Ethereum ERC-721 and ERC-1155 standards will become another new field in the financial market. As a token representing digital assets, it is a unique digital item that is scarce, indivisible, and irreplaceable. NFT establishes a new ecosystem of digital asset ownership on the blockchain by storing the actual content as a simple URL string within the metadata. The emergence of NFT also provides a new application practice for the protection of digital copyrights [13].

In general, there are still problems in the document sharing platform based on blockchain that need to be solved. Based on the current research, we combine the latest Ethereum NFT technology to propose further innovations and propose new solutions for documentation sharing.

80.3 Documentation Sharing Platform System Architecture

80.3.1 Architecture Design

As shown in Fig. 80.1, this paper draws on the traditional Web front-end and back-end separation structure and divides the system into a data layer, contract layer, middleware layer, and presentation layer.

- (1) Data layer: Because the cost of storing large files on the blockchain is too high, this system has a total of two storage engines. They are respectively a distributed storage system composed of multiple independent centralized servers and a

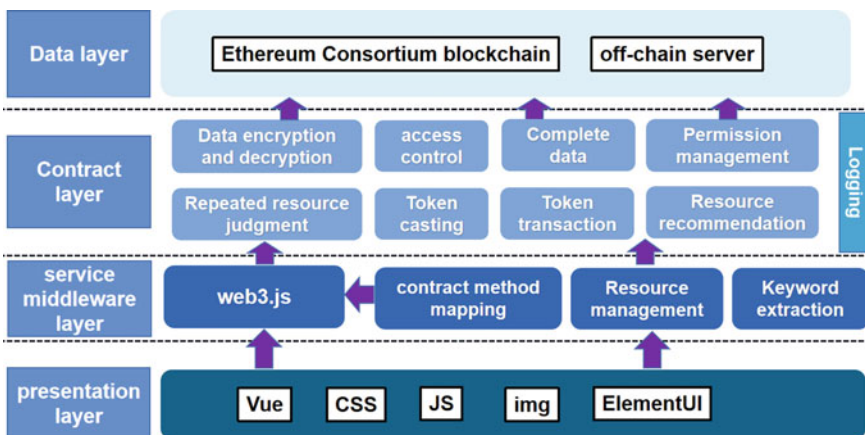


Fig. 80.1 Logical framework of document sharing platform system

private alliance chain based on Ethereum. The alliance chain is used to store structured data such as users' personal information, uploaded documentation metadata, and user operation logs. The off-chain distributed storage system is used to store document source files uploaded by users.

- (2) **Contract layer:** The smart contract in this article is developed using solidity. We have designed multiple business contracts to realize the functional requirements of the system. The functions of the smart contract can be triggered through transactions to realize data reading, writing, and modification.
- (3) **Middleware layer:** As the bridge between the contract layer and the front-end interaction, the middleware layer is mainly composed of two parts. One part is the data interface provided by web3.js, which is used to call the smart contract and realize the transfer of data between the front-end page and the smart contract. The other part is the documentation management module written by python, which realizes the functions of documentation upload, download, keyword extraction, and documentation similarity calculation.
- (4) **Presentation layer:** We use Vue+ElementUI to realize data visualization and display the data obtained from smart contracts to users.

80.3.2 Functional Module Design

80.3.2.1 Technology of Confirming the Rights of Documentation

This paper mainly uses the duplicate checking algorithm and the introduction of the challenge period to review and confirm the rights of documentation during the documentation upload stage, to ensure the originality of documentation.

(1) Similarity comparison of documentation through duplicate checking algorithm

The duplicate checking algorithm used in this paper is to use the Textrank algorithm [14] to extract the keyword groups of documentation for cosine similarity calculation to realize automatic judgment. The TextRank algorithm is improved from Google's PageRank algorithm and is a graph-based sorting algorithm for keyword extraction and document summarization. It uses the co-occurrence information between words in the document to achieve unsupervised keyword extraction. The basic idea of the Textrank algorithm is to use the adjacent relationship between words in the document to build a word network, and then use PageRank to iteratively calculate the rank value of each node. The higher the rank value, the higher the importance. After sorting the rank values, you can get the keyword group for the document.

$$WS(V_i) = (1 - d) + d \sum_{V_j \in \text{In}(V_i)} \left(w_{ji} / \sum_{V_k \in \text{out}(V_j)} w_{jk} \right) WS(V_j) \quad (80.1)$$

Table 80.1 Cosine similarity and document correlation

Cosine similarity	Document correlation
$0 \leq \text{Icos } \theta \leq 0.4$	Irrelevant
$0.4 \leq \text{Icos } \theta \leq 0.8$	Relevant
$0.8 \leq \text{Icos } \theta$	Strong correlation

The algorithm can be expressed as the above formula Eq. (80.1), $S(v_i)$ represents the TextRank value, j and i represent any two words here, W_{ij} represents the weight of the edge. The weight of a word i depends on the composition of each point j in front of i the weight of the (j, i) edge, and the sum of the weights from the point j to other edges.

When users upload documentation, the system will first use the Textrank algorithm to extract the keywords and rank values of the documentation, and then select the top 20 words as the keyword groups of the article after sorting according to the rank values. Then traverse the keyword groups of documentation already stored on the chain, and find the keyword groups that start with the same keyword. The two keyword groups are combined, and the respective rank value vectors of the two keyword groups are generated according to the rank values of the two keyword groups. According to the cosine similarity algorithm, after determining the distance between vectors, the similarity between two documents can be measured by calculating the cosine value between two text vectors. We substitute the two vectors of rank values into the cosine similarity formula: Then the cosine similarity of the two keyword groups can be calculated, and the closer the cosine similarity is to 1, the higher the similarity between the two documents is proved.

Through the results of Experiment 4.2, we have made different definitions according to different thresholds, as shown in Table 80.1 [15].

When the cosine similarity is greater than 0.8, we consider the two documents to be highly similar, directly determine that the same document exists in the system, and reject this upload. When the cosine similarity is between 0.4 and 0.8, we believe that there is a certain correlation between the two teaching documents, but piracy does not necessarily exist. At this time, we will first extract a part of the content of the document for publicity, and send a challenge invitation to the caster who uploaded it first, inviting the caster to challenge the copyright. When the cosine similarity is less than 0.4, we believe that there is no keyword group similar to the uploaded courseware in the system, directly extract a part of the content in the document for publicity, and wait until the end of the challenge period to officially cast the NFT.

(2) Documentation copyright challenge mechanism

Since the keyword group of the document may change after excessive deletion and modification of the document, the weight-judgment algorithm based on keyword similarity cannot be accurately identified. To strengthen the protection of copyright, we introduce the concept of the challenge period.

We require creators to submit 2 FAN coins as a pledge before minting NFTs, and the pledged coins cannot be retrieved during the challenge period. The token FAN

pledged by users is a homogeneous token minted according to ERC-20, which can be obtained through issuing, trading NFT, and participating in copyright challenges.

One week after NFT minting is the NFT copyright challenge period. During this period, the system will extract part of the content of the NFT and publish it in the community, and all users can challenge the copyright of the NFT by providing proof of the existence of piracy in the NFT. Proof materials can be photos and documents, and it is necessary to prove that the NFT has been pirated and that the pirated documents were created before the NFT.

The system sets up 5 notary addresses for review, and the notary checks the evidence submitted by the challenger. If the submitted evidence can effectively prove that there is piracy in the NFT, the NFT will be invalidated, and the challenger will get two FAN coins pledged by the minter. On the contrary, it is considered a failure of the challenge. When the challenge period is over, the tokens pledged by the minter will be returned, and the NFT minting is successful.

Through the above two methods, the system reduces the possibility of repeated uploading of documents and guarantees users' ownership of uploaded resources. In addition, this article also stores all operation logs in the system in the blockchain. When a copyright dispute occurs, the time stamp of the document can be used to assist in judging the ownership of the NFT.

80.3.2.2 Storage Mechanism of Documentation

Due to the limited size of each block of the blockchain, high transaction fees, and the generation of each block requiring a certain amount of consensus time, the current blockchain is more used to process small data such as ledger transactions. When dealing with large-scale data, the blockchain usually adopts the combination of on-chain and off-chain [16], stores the source files of large-scale data under the chain, and then saves the storage address of the documentation to the blockchain.

This article draws on the commonly used solution of combining on-chain and off-chain and adopts the method of storing data source files off-chain and storing digital certificates on-chain. Small data such as users' personal information, operation logs, and metadata of documentation are stored on the chain, and the metadata of documentation is stored off the chain. To ensure data security, the off-chain memory used in this paper is composed of multiple off-chain distributed storage systems built by servers.

When the creator uploads the documentation, the system will first store the documentation on the distributed server under the chain, and then use the asymmetric encryption algorithm to encrypt the storage address of the documentation. The encryption result will be packaged and uploaded together with the keyword group of documentation, resource introduction, creator's digital signature, and other data, and become the metadata of NFT.

When users trade NFT, the system will realize it through two steps. First of all, when the minter sells NFT, he needs to authorize the system first, so that the system has the right to operate NFT. After the system is authorized, it will first use the private

key to decrypt to obtain the storage address of the documentation. According to the storage address of the documentation, the documentation is automatically read, and the keyword groups of the documentation are extracted for similarity calculation. Judge the authenticity of documentation according to the calculation results. When the transaction is concluded, the system will use the buyer's public key to encrypt the storage address of the NFT, and change the owner of the NFT to the buyer's address to complete the transaction.

When a user downloads documentation, the system will first verify the authority to determine whether the user has the authority to download documentation. After the verification is passed, the documentation can be downloaded from the off-chain server. Through the above methods, the privacy and security of documentation can be guaranteed to the greatest extent, and the integrity and authenticity of documentation can also be guaranteed.

80.3.2.3 Documentation Access Control Model Based on Smart Contract

To ensure the confidentiality and integrity of data, this paper proposes the following three access control methods after analyzing the usage scenarios of documentation:

- (1) For different users, we set various roles such as students, teachers, tourists, etc., and give different permissions to different roles, forming a role-based multi-level access control model.
- (2) We set up a dynamic authority control module to support documentation owners to dynamically grant and revoke the authority to visitors [9, 17]. Only users who are authorized by the documentation owner or the owner himself can download the documentation from the off-chain server.
- (3) To stimulate users' enthusiasm for community building, we have also set up an access control method based on the number of uploads. We have set up a variety of hidden functions in the system, and visitors need to reach a certain amount of contribution before they can access it.

To sum up, by setting access control permissions, the system can fully protect the owner's ownership of courseware and stimulate users' enthusiasm for participating in community construction.

80.4 Evaluation

To verify the performance of the system, the test environment used in this paper is Windows 10 operating system configured with CPU Intel Core i5-7300HQ 2.50 GHz and 16 GB memory. The server used is Tencent Cloud Server, equipped with an Ubuntu20.04 system. The alliance chain, front-end, and middleware of the system all run on the server.

After the Ethereum alliance chain is built on the server, the completed smart contract is deployed to the blockchain, and the contract is called through the contract address returned after deployment.

80.4.1 Time Indicator

This paper randomly selects 40 pieces of documentation of different sizes to extract keywords in turn and cast them into NFTs. The total time of each transaction and keyword extraction time is counted to test the time performance of the system.

The keyword extraction experiments of the 40 documentation selected in this test were all successful, and the transactions were completed on the chain. The time of each documentation keyword extraction and the total time of transaction completion is shown in Fig. 80.2.

It can be seen from Fig. 80.2 that the keyword extraction time of documentation is about 2.5 s. The time spent on keyword extraction is mainly affected by the word count of documentation. The time increases with the increase of the word count of documentation, but the increased time can almost be ignored. The total transaction time is about 13 s on average, and the total transaction time includes keyword extraction, document similarity judgment, and transaction consensus. The time taken by the transaction is mainly affected by the speed of the network at the time of upload and the size of the documentation. Through calculation, we can get that the keyword extraction time only accounts for 19.2% of the total transaction time. It is worthwhile to sacrifice a certain amount of time to reduce the risk of the documentation being stolen and uploaded repeatedly.

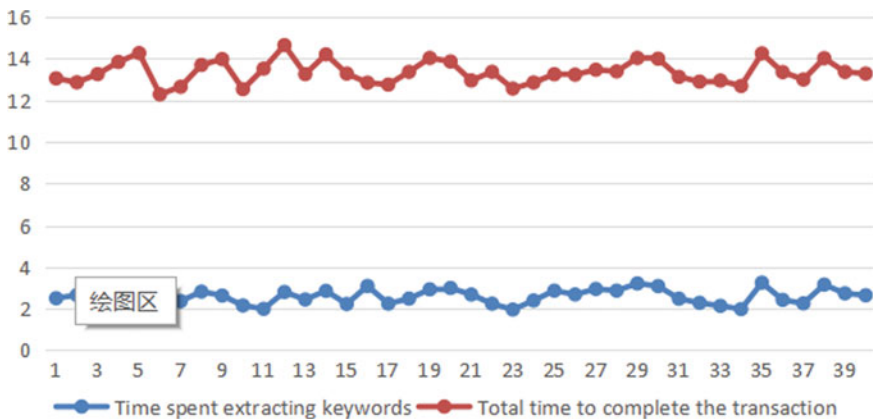


Fig. 80.2 The time of keyword extraction and the total time of transaction completion

80.4.2 Determination of Cosine Similarity Threshold

When judging documentation repeatability, the threshold of cosine similarity is directly related to the scientific nature of the algorithm [18]. To determine the threshold of cosine similarity, this paper randomly extracts 300 different pieces of documentation from the database for similar documentation detection experiments, and randomly selects 100 pieces of documentation as sample documentation for modification. The modified sample documentation and the original 300 documentation are used as a data set to conduct similar documentation detection experiments. We observe the recognition rate of similar documentation by setting different thresholds and selecting the optimal similarity threshold to determine the threshold in this paper.

As can be seen from Fig. 80.3, when the threshold of cosine similarity is set to less than 0.5, we can see that the system has a very high correct rate, and can identify similar documentation 100%, but at the same time, the system also has a high error rate, to easily identify other documentation as similar documentation. When the threshold of cosine similarity is set between 0.5 and 0.8, the system fails to fully identify all similar documentation, but the correct rate of recognition is still above 97%, and the error rate of recognition has also been greatly improved control. When the cosine similarity is set to be greater than 0.8, the accuracy of system recognition is greatly reduced. After analysis, it is concluded that the system failed to correctly identify several groups of similar documentation because the content of the documentation has undergone relatively large changes, resulting in changes in the keyword groups of the documentation, and the system has maintained a high accuracy rate for other documentation.

Finally, for the smart contract-based documentation access control model proposed in this paper, this paper conducts a test experiment of multiple groups

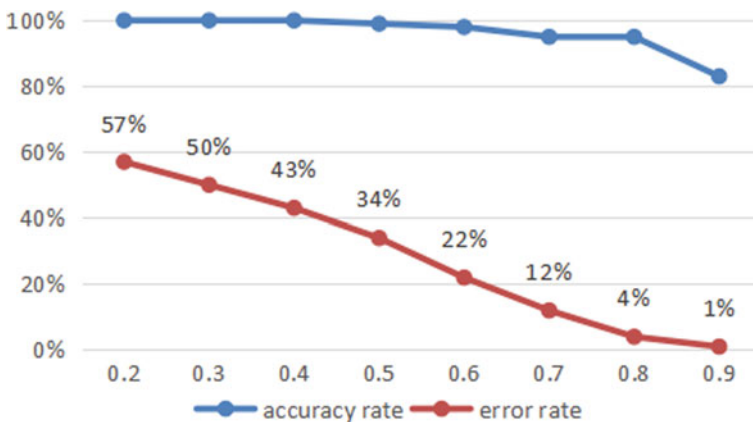


Fig. 80.3 Similar documentation recognition rate

of access documentation. The experimental results prove the feasibility and effectiveness of writing access control logic inside the smart contract, which effectively guarantees the security and privacy of documentation.

80.5 Conclusion

At present, traditional documentation sharing systems are all developed based on centralized servers, relying too much on centralized servers, and there are risks of data loss, resource theft, and information leakage. As a digital proof of digital assets on the chain, NFT has the characteristics of encryption, non-tampering, decentralization, time stamp, and traceability, and has natural technical advantages in the protection of documentation. Based on the existing research, this paper proposes a documentation sharing framework based on blockchain non-fungible token technology and uses the documentation similarity and challenge period mechanism to prevent replay attacks. At the end of the article, we have proved the scientificity and effectiveness of the copyright review mechanism designed in this article through experiments.

Of course, there are still some imperfections in the system. In the future, we will continue to develop new user incentive mechanisms, improve the NFT ecology, and solve the shortage of NFT liquidity, to promote the further integration of NFT and resource sharing.

Funding Statement This work was supported by Guangzhou Higher Education Innovation Group 202032854.

References

1. Tian, Z., Li, M., Qiu, M., Sun, Y., Su, S.: Block-DEF: a secure digital evidence framework using blockchain. *Inf. Sci.* **491**, 151–165 (2019)
2. Nakamoto, S.: Bitcoin: a peer-to-peer electronic cash system. *Decentralized business review* 21260 (2008)
3. Tschorsch, F., Scheuermann, B.: Bitcoin and beyond: a technical survey on decentralized digital currencies. *IEEE Commun. Surv. Tutorials* **18**(3), 2084–2123 (2016)
4. Ding, W.: Block chain based instrument data management system. *China Instrum.* **10**(1), 15–17 (2015)
5. Zhao, H., et al.: Data integrity protection method for microorganism sampling robots based on blockchain technology. *J. Huazhong Univ. Sci. Technol. (Nat. Sci. Ed.)* **43**(s1), 216–219 (2015)
6. Buterin, V.: A next-generation smart contract and decentralized application platform. White paper 3.37, 2-1 (2014)
7. Zhang, G., Tang, H., Chen, J., et al.: Blockchain-based digital music copyright management system. *Comput. Appl.* **41**(4), 945–955 (2021)
8. Zhu, J., Fu, Y.: Blockchain-based supply chain dynamic multi-center collaborative authentication model. *J. Netw. Inf. Secur.* **2**(1), 27–33 (2016)

9. Su, L.: Construction of blockchain support platform for archives information system. University of Chinese Academy of Sciences (Master's thesis of Shenzhen Institutes of Advanced Technology, Chinese Academy of Sciences) (2020)
10. Hu, J., Li, H., Huang, T.: Research on the opening and sharing mechanism of virtual simulation experiment documents in colleges and universities. *Lab. Res. Explor.* **34**(2), 6 (2015)
11. Vimal, S., Srivatsa, S.K.: A new cluster P2P file sharing system based on IPFS and blockchain technology. *J. Ambient Intell. Humanized Comput.* 1–7 (2019)
12. Guo, Q.: Design and implementation of teaching resource sharing system based on block chain. Qufu Normal University (2020)
13. Wei, L., Guo, Y., He, M.: Non-fungible tokens (NFT): logic, application and trend outlook. *Rev. Econ. Res.* (2022)
14. Mihalcea, R., Tarau, P.: TextRank: bringing order into text. In: Proceedings of the 2004 Conference on Empirical Methods in Natural Language Processing (2004)
15. Geng, Z., Hu, H., Han, Y.: Complex network fault detection method and application based on cosine similarity. *J. Beijing Univ. Chem. Technol. (Nat. Sci. Ed.)* **44**(2), 87–94 (2017)
16. Reijers, W., et al.: Now the code runs itself: on-chain and off-chain governance of blockchain technologies. *Topoi* **40**, 821–831 (2021)
17. Qiu, J., Tian, Z., Du, C., Zuo, Q., Su, S., Fang, B.: A survey on access control in the age of internet of things. *IEEE Internet Things J.* **7**(6), 4682–4696 (2020)
18. Song, S., Chen, L., Cheng, H.: Efficient determination of distance thresholds for differential dependencies. *IEEE Trans. Knowl. Data Eng.* **26**(9), 2179–2192 (2013)

Chapter 81

Research on the Design of Blockchain-Based Aviation Physical and Chemical Testing System



Yijian Zhang, Lu Zhang, Jing Xu, Jingyi Du, Zunbo Wei, and Xiaofeng Chen

Abstract As a part of aviation flight guarantee, physical and chemical testing in the aviation industry plays a very important role. The traditional physical and chemical testing industry has problems such as long process waiting time and slow generation of test results and reports. Although laboratory management systems such as the LIMS (Laboratory Information Management System) have improved these problems to a certain extent, the LIMS system has not fundamentally changed the above problems and lead to new problems. Based on the particularity of the aviation physical and chemical testing system, as well as the requirements for high consensus, high synchronization, and high traceability of data, blockchain technology is very suitable as a means of improvement. Based on blockchain technology, this paper designs a new type of the aviation physical and chemical testing system strives to improve the problems existing in the current aviation physical and chemical testing system and improve production efficiency.

Keywords Blockchain · Physical and chemical testing · System architecture · Use case design · Efficiency research

81.1 Introduction

The application of physical and chemical testing and analysis technology is very extensive, and it plays a very important role in scenarios with high system requirements such as aviation and aerospace with high precision, high reliability, and high robustness [1]. In aviation production, manufacturing, maintenance and other units, the main purpose of physical and chemical testing is to check the performance of materials, regularly test the performance and quality of materials, and ensure

Y. Zhang · L. Zhang · J. Xu · J. Du · Z. Wei · X. Chen
Hangzhou Qulian Technology Co., Ltd., Hangzhou, China

X. Chen (✉)
State Key Laboratory of Blockchain and Data Security, Zhejiang University, Hangzhou, China
e-mail: chenxf.alfred@zju.edu.cn

the quality of materials is safe and reliable [2]. Physical and chemical testing is a whole-process technology that runs through from research and development to manufacturing to maintenance.

With the rapid development of the new era, whether it is in the field of military aviation or civil aviation, the research and development and production of spacecraft are developing towards the level of high precision, high integration, and high complexity, and system engineering plays a very important role in it [3], especially in the development of a certain type of aircraft in China, its requirements for metal materials and non-metal materials have reached a new height. With the continuous improvement of material requirements, physical and chemical testing specifications and standardization requirements, inspection and testing data need to be strictly reviewed more than ever, which has become the management focus of compliance laboratories. Optimizing the process and management of physical and chemical testing and the integrated informatization of laboratories are the only way to improve the quality management level of laboratories [4]. The main contributions of this paper are as follows:

- Briefly introduce the physical and chemical testing technology in the aviation field, and analyze the relevant parties and processes of the aviation physical and chemical testing system, list the currently most used LIMS (Laboratory Information Management System), and analyze its disadvantages;
- Based on the current situation of the existing aviation physical and chemical testing system, there are many relevant parties, a large consensus demand, and prolonged message time, etc., the concept of blockchain is introduced for optimization;
- Propose the “blockchain-based aviation physical and chemical testing system”, compare it with the LIMS, design the principles, system architecture, and smart contract functional processes of the blockchain-based aviation physical and chemical testing system, and study the improved system compared with LIMS efficiency improvement;
- Finally, summarize and think about the future of physical and chemical testing system.

81.2 Aeronautical Physical and Chemical Testing Technology Research

81.2.1 Development and Status Quo of Aviation Physical and Chemical Testing Technology

Aeronautical physical and chemical testing technology is produced along with the actual needs of the aviation industry. Physical and chemical testing technology involves various disciplines such as optics, electricity, automation, metrology and testing, material science, and process manufacturing technology [5]. Aeronautical physical and chemical testing objects are divided into two categories: one is metallic

materials, and the other is non-metallic materials. Metal materials are not easy to age and have a long service life, while non-metal materials are easy to age and have many varieties and a wide range of quantities [6]. Therefore, the emphases of physical and chemical testing for the two types of materials are also different.

Physical and chemical testing of metal materials is mainly divided into metallographic structure testing, metal fatigue strength testing, crack growth rate, impact testing, high temperature tensile, high temperature durability and other mechanical performance testing, hydrogen embrittlement testing, salt spray testing, failure analysis, non-destructive testing (Non-destructive testing is often also regarded as an independent department/team, which is distinguished from physical and chemical testing) and so on [7].

Non-metallic materials mainly include: oil, paint, textiles, adhesives, plastics, rubber and other materials. It is characterized by large differences in material properties and a wide variety of tests. Take oil paint as an example: paint film aging test, paint film oil immersion, water immersion test, paint film scratch test, paint film impact resistance test, paint film bending test, oil water content verification, oil particles (large abrasive particles), spectral analysis of oil components, ferrographic analysis and more than ten kinds of tests [8].

For the aviation physical and chemical testing process, it can be mainly divided into three categories.

Incoming factory inspection. The main function is to check the quality of incoming materials;

Periodic verification. During the validity period of the incoming materials, conduct regular tests on the products that have been stored in the warehouse to ensure their usability;

Entrusted testing. That is, the internal department of the unit or the external cooperation unit entrusts the physical and chemical testing laboratory (center) to handle the testing task.

81.2.2 Research on Aeronautical Physical and Chemical Testing Process

Related parties of aviation physical and chemical testing system. In aviation production, manufacturing, use, and maintenance units, there are generally physical and chemical testing laboratories (centers). Unlike general third-party inspection and testing institutions, aviation physical and chemical testing tasks are all internal, that is to say, the sources all come from other departments or cooperative units in the unit, and there is no external inspection, and there is no market behavior [9]. Even so, as an internal system of aviation physical and chemical testing department, its related parties are still complicated, mainly including the following related parties:

- *Test entrusting department.* The test entrusting department is the initiator of a physical and chemical testing process. Its main responsibility is to initiate the

test test entrustment/application form and summarize the test results. The needs of different test entrusting departments are different, and some test entrusting departments have periodicity, will regularly send test commissions and samples; some test commissioning departments depend on production tasks;

- *Test client.* The test client comes from the test commissioning department, who is the sender of the test test order and test samples, and is responsible for receiving the test qualification report/test result notification;
- *Test dispatcher.* The test dispatcher is mainly responsible for receiving the test entrustment/application form, and issuing the test test entrustment form to the corresponding test test personnel. After the test is completed, check the correctness of the test qualification report/test result notice, and write entry account records;
- *Test operator.* The test operator is mainly responsible for filling in the test ledger, recording the test process, cleaning test equipment, conducting test tests, and recording test results;
- *Test report issuer.* In general, the test report issuer and the test operator are not the same person, the most important reason is based on multiple confirmations, and its main responsibility is to issue the test report and stamp the issuer's seal;
- *Test report review personnel.* The test report review personnel are responsible for checking the correctness of the test report and stamping the review personnel seal;
- *Director of the test and testing laboratory (center).* mainly responsible for final confirmation of the correctness of the test pass sheet/test result notification sheet, and stamping the seal of the physical and chemical testing laboratory (center).

As mentioned above, a physical and chemical testing process generally requires the participation of seven relevant parties. There are many participating parties, and the responsibilities of the relevant parties have different focuses and differences [10]. It is necessary to clarify the responsibilities and differences of the relevant parties. Use Case diagram is a method in the Unified Modeling Language (UML) for defining roles and interactions between systems in systems engineering and software engineering. Each use case represents a complete scenario [11]. Physical and chemical testing The use case diagram of the relevant parties of the system is shown in the Fig. 81.1.

Operation process of aviation physical and chemical testing system. The operation of the aviation physical and chemical testing system mainly includes: a single aviation physical and chemical testing entrusted testing process, test data and report output, regular filing and sealing of test data and reports, regular maintenance of test and testing equipment, calibration work, etc. [12]. The relationship between several types of content is shown in the Fig. 81.2.

Based on the rigor of the aviation industry, these four types of processes have an equally important position in actual work. The regular maintenance and calibration of test and testing equipment will directly affect the accuracy of the test results of the test and testing equipment, reducing the range of uncertainty, making it as close as possible to the ground-truth range [13]. However, the aviation industry has a requirement for "data availability" for test data and reports. Although the test data is only responsible for the test sample itself and does not have any long-term validity, its high traceability requirements (it may be archived for five years, ten years or

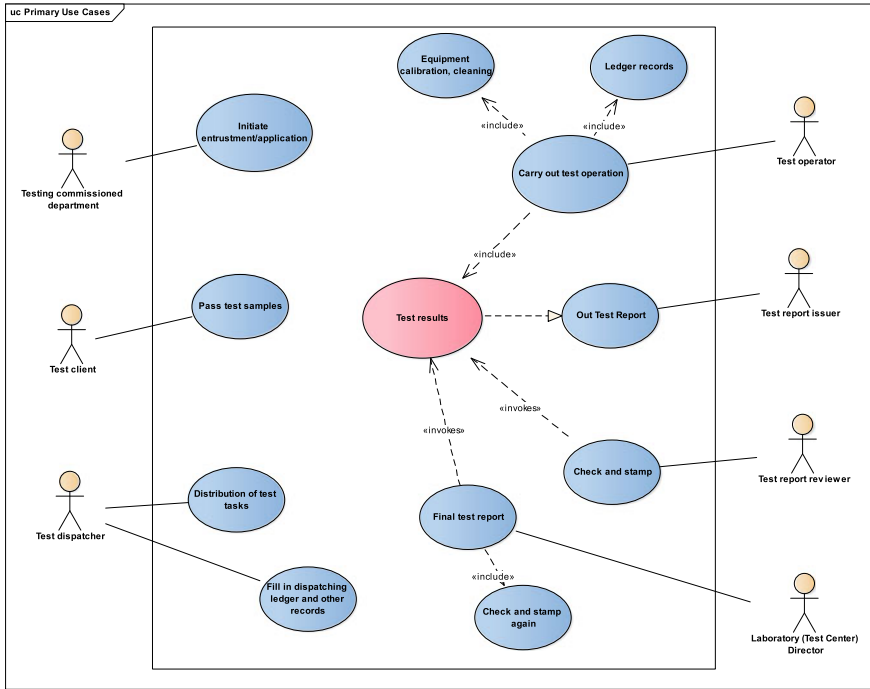


Fig. 81.1 Physical and chemical test process use case diagram

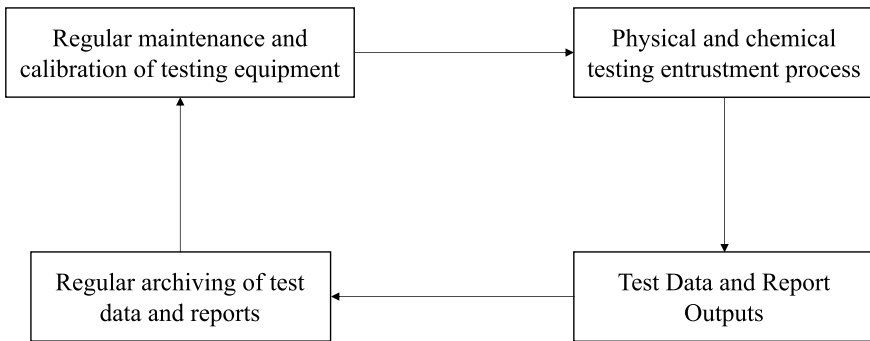


Fig. 81.2 Internal relationship of physical and chemical testing system

more), making the regular archiving and sealing of test data and reports as important as the physical and chemical testing itself.

From the above process, we can see that the entrusted test process of aviation physical and chemical testing involves many related parties, the responsibilities of the related parties are different, and the physical and chemical testing steps are complicated. It is necessary to sort out the context of the process.

81.2.3 Current Situation and Disadvantages of Existing Aeronautical Physical and Chemical Testing System

Based on a certain degree of confidentiality and tradition in the aviation industry and technology, most aviation physical and chemical testing systems adopt the form of paper application form delivery and paper test pass form/test result notice [14]. The form of paper delivery can ensure to a certain extent that the responsibility is assigned to the person, and that problems can be solved through face-to-face communication. However, there are also possible testing data transfer errors and repeated processes (For example, delivery by employees who are not familiar with the process, resulting in the lack of stamping and signature on the paper application form), the need for human delivery, long time flow, etc. [15] problems, the most serious point is that the inspection process is always asynchronous due to paper delivery, the entrusting unit does not know when the sample sent by itself will be tested, what the test result is, whether it needs to re-send the sample, etc. In addition, encountering end-of-month, quarterly, or mass production, equipment overhaul, etc., leads to the accumulation of commissioned test and inspection tasks, and the commissioning unit is always the latest to get the test results [14].

With the in-depth integration of industrialization and industrialization, the laboratory information management system (LIMS) has gradually begun to replace the traditional paper delivery mode. From the beginning of its establishment, LIMS has solved the pain points of the above-mentioned paper delivery mode on the basis of integrating the resources of the laboratory itself and facilitating the unified management of the laboratory [16]. LIMS is based on the local area network, including signal acquisition technology, data transmission, and database management. and other techniques [17]. However, LIMS still has some disadvantages in use.

Use loaded down with trivial details, increase use cost. Under the traditional paper-based delivery mode, roughly 7 types of personnel are required for a physical and chemical inspection entrusted testing process. The LIMS system itself has no intention to reduce the types of personnel involved. This is understandable in itself, because it is based on the rigor of the aviation industry. However, it greatly increases the difficulty of operation for a single category of personnel. Taking physical and chemical testing operators as an example, under the traditional paper delivery mode, he needs to fill in the corresponding test and test ledger, test process records, test and test result records, etc. The LIMS can transfer the writing and viewing of these ledger records to the web, but he may need to click on 3–5 menu bars, and then click on the corresponding second or even third-level menu bars, and need to click on the corresponding confirmation/data send button, missing a single step may lead to out-of-synchronization of data, process freeze, etc., which greatly increases the difficulty of operation for operators and is very cumbersome to use [18]. Taking the testing process as an example, under normal circumstances, the first-level menu of testing in the LIMS system includes three parts: physical and chemical testing application management, physical and chemical testing task management, and physical and chemical testing report management [19].

In the management of physical and chemical testing tasks, there are usually inspection confirmation, unassigned task list, testing task acceptance confirmation, testing task handover, assigned task list, sample list to be inspected, tasks to be reviewed, tasks to be reviewed, reviewed tasks etc. secondary menu of about ten items, corresponding to different parties involved in physical and chemical testing, as shown in the Fig. 81.3, it is a schematic diagram of the secondary menu of physical and chemical testing task management.

The test dispatcher and test operator usually need two to three steps to click on each part of the check-in confirmation, unassigned task list, test task acceptance confirmation, and test task handover menu. In the list of samples to be inspected, in the step of filling in a test result and a test report, it usually takes about 20 clicks, and this does not include the number of clicks to fill in the content of the test report itself. Although there is an operation form for batch filling, this step and the number of clicks are also very cumbersome. As for the subsequent menus such as tasks to be reviewed, tasks to be reviewed, and tasks that have been reviewed, each part also requires three to five steps of clicking operations, regardless of the need to return. In general, even if only the stage of test and testing is considered, a total of about 50 click steps are required, which greatly increases the learning and use costs of relevant parties [20].

There is a lack of consensus on testing data, and testing results are still not timely enough. Although the adoption of LIMS speeds up the entrusting unit’s acquisition of test data and test reports to a certain extent, but LIMS is essentially the same as the paper application mode, and they are all linear, that is to say, the data flows in the form of simplex. Only when the electronic report is finally issued can the entrusting unit know the test results. Therefore, on the one hand, the test data is still unilaterally provided by the physical and chemical testing operators, lacking the participation

Physical and chemical testing task management

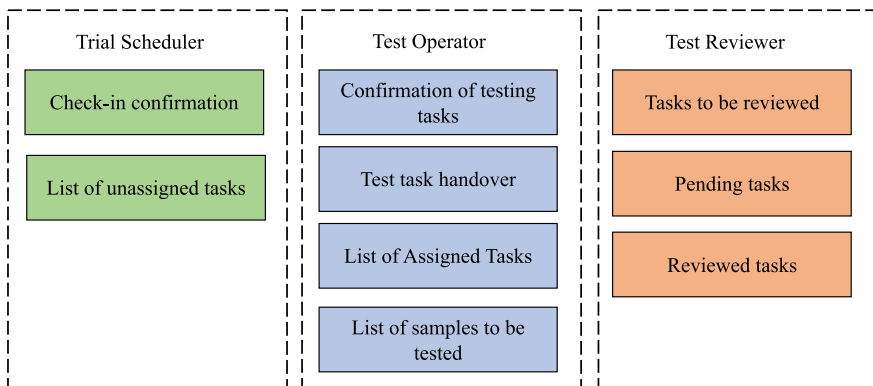


Fig. 81.3 Secondary menu of physical and chemical testing task management

consensus of all parties, especially in the case of large-scale and high-intensity tasks, the transmission delay is particularly obvious [21].

In addition, the LIMS system is still a centralized database software integration system in essence, and there are still risks of data theft and tampering risk issue. Therefore, although the LIMS system has improved some of the pain points of the traditional paper delivery mode, it has increased the use cost and data risks. As a decentralized and distributed technology, blockchain can effectively solve the shortcomings of centralized systems such as LIMS and give full play to its unique advantages. Below we will introduce blockchain technology and try to integrate it with the aviation physical and chemical testing system to provide a new idea for the future development of blockchain and aviation physical and chemical testing systems.

81.3 Blockchain Technology Research

81.3.1 Blockchain Core Technology

Blockchain is a technology that emerged with the virtual currency “Bitcoin”. It first appeared in the article “Bitcoin: A Peer-to-Peer Electronic Cash System” by Satoshi Nakamoto. The essence of blockchain is a decentralized and distributed system [22].

There are three main types of blockchain core technologies: smart contracts, consensus mechanisms, and cryptographic algorithms. The essence of a smart contract is to run an automatically executable program deployed on the blockchain, which provides technical possibilities for the diverse applications of the blockchain [23], through the “oracle machine” technology, the off-chain data required by the smart contract can be transmitted to the chain. The meaning of the consensus mechanism is “multiple node related parties agree on a result”. In the blockchain, it is to ensure the consistency of the distributed system. Imagine that in the blockchain, everyone has an accounting book, and the process of ensuring that the text data on these books is consistent is the consensus mechanism. The algorithm that implements this mechanism is called a consensus algorithm. Cryptographic algorithms can guarantee the immutability of data.

81.3.2 The Advantages and Changes Brought About by Blockchain

The advantages and changes brought about by blockchain:

The data on the chain is consensus and credible. Since the blockchain is distributed, data written to only one database is invalid, that is, “non-consensus”

data. Therefore, writing to the chain means that each user/node has witnessed the generation of the transaction data, so the data is credible and consensus-based. In addition, the data written on the chain is public (in the alliance chain and private chain, it is open to the nodes that join), and each user and node on the chain can synchronize to the data on the chain;

Data on the chain cannot be tampered with. Also based on the distributed nature of the blockchain, it is useless to only change the data of one or a few databases, as long as the data of most nodes (only need to be greater than 51%) is consistent, then the data on the chain cannot be changed, so the data written on the chain is very reliable [24].

Data on the chain can be traced. From the non-tamperable modification mentioned in the previous paragraph, then the traceability of data is meaningful. It is difficult to trace a certain data hard, but in the end it can only be traced back to a string of false data. In addition, the data written on the chain has an unchangeable timestamp, which further guarantees the traceability of the data.

Based on the various disadvantages of the aviation physical and chemical testing system and LIMS system above, the introduction of blockchain technology can better solve these problems [25]:

The test data has reached a consensus, and the entrusting unit can quickly know the test results. In the actual R&D, production, and maintenance tasks of the aviation industry, it will basically not happen that the entrusting unit proceeds to the next step after receiving the “test qualification sheet/test result notification sheet” (although this is contrary to the regulations). But if this rule is followed, then the efficiency will be very low. Therefore, blockchain technology can solve the pain point of data consensus and the urgent need to quickly know the test results. Once the data is uploaded to the chain, all internal users/nodes can be synchronized to this result, changing the traditional simplex linear mode, saving time and effectively promoting the efficiency of production tasks.

The introduction of smart contracts greatly reduces the cost of learning and use. As a code that can run automatically, the smart contract can be designed and executed such as: automatic writing of aviation physical and chemical inspection reports, automatic transmission of aviation physical and chemical inspection reports to internal verification members, etc. it greatly reduces the learning and use costs of operators, and can be designed to write test results and automatically trigger contract execution to quickly form reports.

Based on the immutability and traceability of the data on the chain, it can effectively trace the testing data. Based on the timestamp function, it can effectively eliminate the possibility of forging false testing reports after the event and effectively protect real data. At the same time, it can meet the high traceability requirements of the aviation physical and chemical testing system for reports.

Therefore, based on blockchain technology, designing an aviation physical and chemical testing system has advantages and practical application value. It can effectively solve the disadvantages of the traditional paper delivery mode and LIMS. The following will be related to the design of the blockchain-based aviation physical and chemical testing system.

81.4 Design of the Blockchain-Based Aviation Physical and Chemical Testing System

81.4.1 System Design Principles

Simple process, low learning and operating costs. A major pain point of the LIMS is the complicated process, which increases the learning cost of users. The aviation physical and chemical testing system based on blockchain needs to avoid this problem. The emergence of smart contract technology can convert complex operations on the LIMS system into a piece of automatically executed contract code. On the premise of not reducing the authority and rigor of the test report, the cost of learning and using is greatly reduced.

Fast data synchronization and timely issuance of test reports. Blockchain technology is divided into public chain, alliance chain, private chain and other forms. Based on the confidentiality and access of the aviation industry, the use of alliance chains or private chains can not only effectively protect the privacy and security of testing data, but also speed up the speed of data uploading and synchronization, making this system more practical [26]. In addition, the aviation physical and chemical testing system based on blockchain can use data signal acquisition technology, Internet of Things technology, oracle technology, trusted Unicom on-chain and off-chain data, and through the smart contract technology, it automatically benchmarks and issues test reports, and automatically synchronizes reviewers, reducing the situation of completing a batch of test tasks in the traditional mode and then issuing test reports in batches, speeding up the issuance of test reports and speeding up the efficiency of production tasks.

The data is safe and reliable, meeting the high traceability requirements of the aviation industry. Based on the unchangeable characteristic of “centralization” of the LIMS, the security and reliability of data is actually difficult to guarantee, and risks such as data loss and tampering are prone to occur, and it is difficult to guarantee the traceability of data. Therefore, the aviation physical and chemical testing system based on blockchain should meet the requirements of data security, reliability and high traceability.

Table 81.1 Comparison of LIMS system function menu and the introduction of blockchain technology

A menu	Secondary menu	Changes brought about by blockchain technology*
Physical and chemical testing application management	Application filling, application review, application signature	Data is uploaded to the chain, making it impossible to tamper with
Physical and chemical testing task management	Check-in confirmation, list of unassigned tasks	
	Confirmation of testing tasks, test task handover, list of assigned tasks, list of samples to be tested, writing original test records, equipment ledger records	Write smart contracts and execute them automatically (date on chain, automatic writing, credible circulation automatically, saving operation steps)
	Tasks to be reviewed, pending tasks, reviewed tasks	
Physical and chemical testing report management	Test report writing, report review and signature, report transmission and publication	

*Blockchain technology can ensure that test data written to the chain can be synchronized to all relevant parties after collection

81.4.2 System Design Goals

The original design intention of blockchain-based aviation physical and chemical testing system, is to solve the shortcomings of the traditional paper delivery mode and LIMS system, so it is necessary to compare the improvements and changes that the addition of blockchain technology can bring. As shown in the Table 81.1, it is the functions/menus included in the physical and chemical testing system in the LIMS. As mentioned above, the first-level menu of physical and chemical testing mainly includes Physical and chemical testing application management, Physical and chemical testing task management, physical and chemical testing report management, after the introduction of blockchain technology, the LIMS system is mainly improved and improved in terms of data on-chain, credible and non-tamperable data, credible transfer, smart contracts, and fast synchronization [27].

81.4.3 System Design Goals

Based on the above requirements, the blockchain-based aviation physical and chemical testing system architecture is divided into five layers: infrastructure layer, blockchain platform layer, data transmission layer, core service layer, and application layer. The system architecture design is shown in the Fig. 81.4.

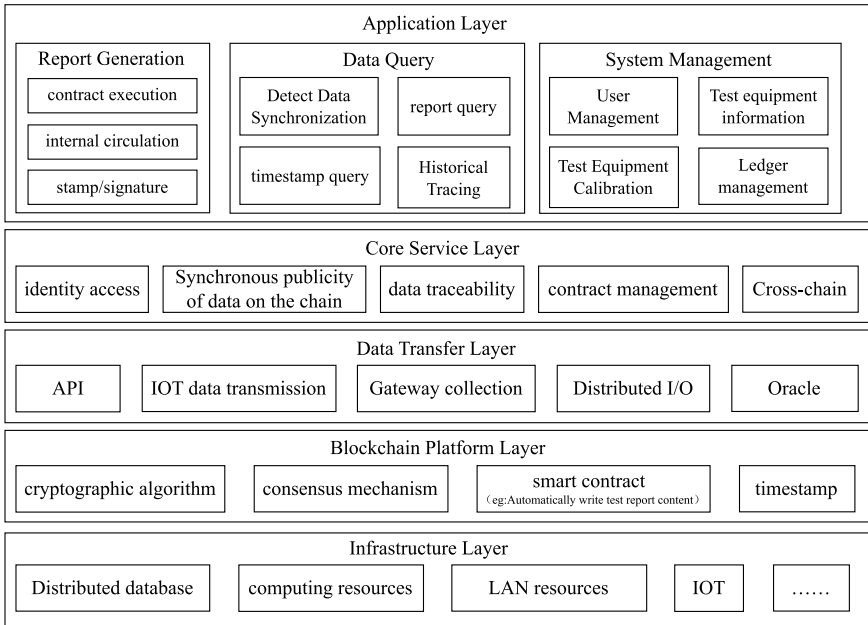


Fig. 81.4 Architecture diagram of blockchain-based aviation physical and chemical testing system

Infrastructure layer. distributed databases, computing resources, local area network resources, Internet of Things technology, etc., which can provide basic facilities for the construction, operation and maintenance of the blockchain-based aviation physical and chemical testing system.

Blockchain platform layer. cryptographic algorithms, consensus mechanisms, smart contracts (such as a program that can automatically write the content of test reports), time stamp functions for on-chain data and test reports, etc. The design of this level not only takes into account the cumbersome forms and operations of the traditional paper delivery mode and the LIMS system, but also uses smart contracts to simplify the steps, and based on cryptographic algorithms, consensus mechanisms and time stamping technology, it ensures data cannot be tampered with, credibility and traceability.

Data transmission layer. Data interface transmission technology (such as API, etc.) that can be connected to the LAN, IOT data transmission technology [28], gateway collection technology, distributed I/O collection and transmission technology [29], the data under the blockchain is credibly transmitted to the “oracle machine” and other content in the chain. This level mainly solves two major problems, one is how to collect the data of test and testing equipment, because not all test and testing equipment has data transmission technology, the solution to this problem can be to replace the supporting equipment, but it is also possible to use gateway collection, IOT data transmission, distributed I/O technology, etc. to transform the equipment so that it can collect and transmit test data; The data

outside the block chain is transmitted to the block chain, which is the “oracle machine” technology [30].

Core service layer. That is, the core function design of the aviation physical and chemical testing system based on blockchain, including: identity access, synchronous disclosure of data on the chain, data traceability, contract management, cross-chain technology (which may be required within the same aviation system), etc. [31].

Application layer. It mainly includes three categories:

- Report generation: contract execution, internal circulation, stamping and signature, etc.;
- Data query: testing data synchronization, report query, timestamp query, historical traceability;
- System management: user management, test equipment information, test equipment verification, ledger management, etc.

The above five levels can address the existing pain points of the aviation physical and chemical testing system at the structural level and effectively change the current status quo. In the application of the blockchain-based aviation physical and chemical testing system, the most important thing is the report generation function based on the smart contract. The following will design this core application function [32].

81.4.4 System Core Function Design

Smart contract functional design for report generation functionality. As mentioned earlier, in the blockchain-based aviation physical and chemical testing system, It is very important to the report generation function, that is, from data generation to collection to the chain, automatic contract execution, preparation of test and test reports, and internal credible circulation, generate the content of the final test qualification report/test result notice. Among them, the most important thing is the design and implementation of the smart contract. The smart contract needs to write the following content, as shown in the Fig. 81.5:

- The test equipment information (to match which standard the test is based on), and the judgment rules in the standard the test is based on, these two are used to make the contract automatically judge whether the test results on the chain are in compliance with the judgment in the standard, that is, whether the test result is qualified;
- External information such as time and weather need to be trusted through the oracle machine to automatically generate test and inspection ledger records. It should be written in the prompts for equipment cleaning before each equipment operation;
- Write the templates of the test ledger, test process record, test pass report/test result notice into the smart contract;

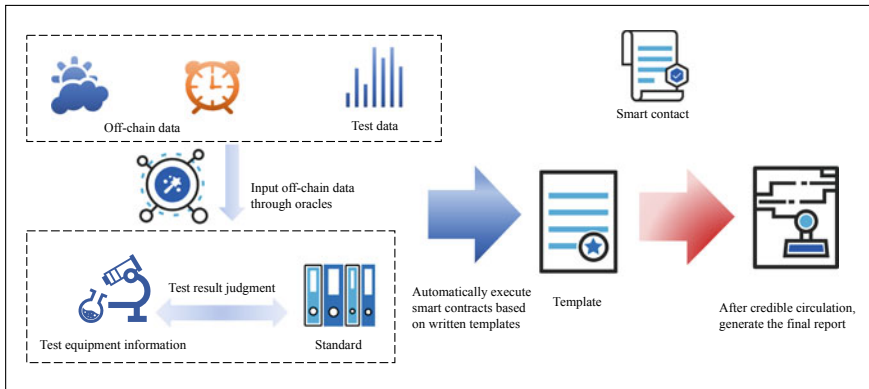


Fig. 81.5 Design diagram of intelligent contract function of the blockchain-based aviation physical and chemical testing system

- After the contract automatically completes the report writing, it needs to transfer the generated content to the designated authorized person for review. During this process, hash algorithm or asymmetric encryption algorithm is used to protect data security [33].

Smart contract process design for report generation functionality. After the smart contract is written, it needs to be deployed on the blockchain for automatic execution. It is necessary to design the state of the smart contract to ensure the consistency of the smart contract design of the system. The state machine diagram is for a certain object in UML, a diagram corresponding to different actions and execution related events in the whole process can scientifically design the change of an object state. The designed blockchain-based aviation physical and chemical testing system smart contract state machine diagram is shown in the Fig. 81.6.

As shown in the figure, after the test operation starts, the external data is uploaded by the oracle machine. After the chain is uploaded, the smart contract starts to be automatically executed, and the test ledger and test process are automatically written to judge the results of the test data.(compared with the corresponding standard), a test pass report will be issued if it is qualified, and a test result notice will be issued if it is unqualified. After generation, the test report will be automatically synchronized to other nodes/users on the chain who need to conduct audit work to generate the final test report, and the smart contract is executed.

81.4.5 System Improvement Efficiency Research

As mentioned above, the blockchain-based aviation physical and chemical testing system can effectively reduce the cost of relevant personnel and improve the synchronization efficiency of testing results. This section will study the specific improvement

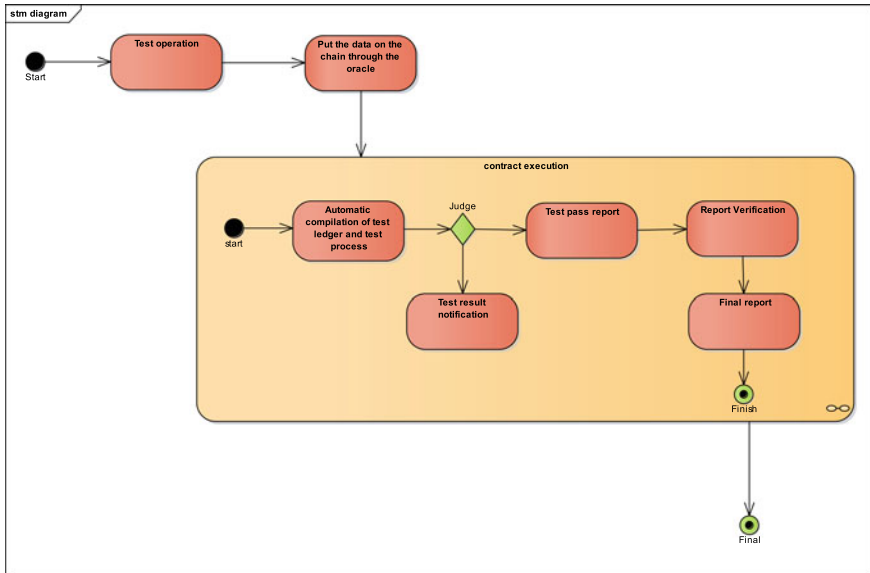


Fig. 81.6 Design diagram of intelligent contract process of the blockchain-based aviation physical and chemical testing system

efficiency. Due to the large number of environmental variables, such as the number of test samples, the number of testing personnel, and the proficiency of system operations, etc., may affect the testing efficiency, this article only uses “system request response time” as the basis for efficiency improvement research. For reference only.

In general, the request response delay of the LIMS system is between 10 and 90 ms. Using python to randomly select random numbers 50 times, the average request response delay is 45.87 ms, as shown in Fig. 81.7 [34].

According to the physical and chemical testing process mentioned above (excluding the early test task application and post-report issuance), it takes about 50 clicks, and the estimated response time of the system request that needs to be spent on the “system click step” is between 512 and 4460 ms, with an average of 2293.59 ms, as shown in Fig. 81.8 [35].

After adopting the blockchain technology, the smart contract can automatically assign the corresponding test tasks to the operator (reduce the operation time of this operation, and the possible situation that the operator does not see the task to be assigned). It can automatically enter the test results and check the standards to automatically judge whether the results are qualified, automatically write the equipment account, the operation of the original test record, and the automatic credible transfer to the auditing parties, etc., but the LIMS system cannot do the above steps. Ultimately, the test operator only needs to check the relevant results. Compared with the LIMS system, the blockchain-based aviation physical and chemical testing system only needs: test result confirmation, equipment ledger confirmation, test original

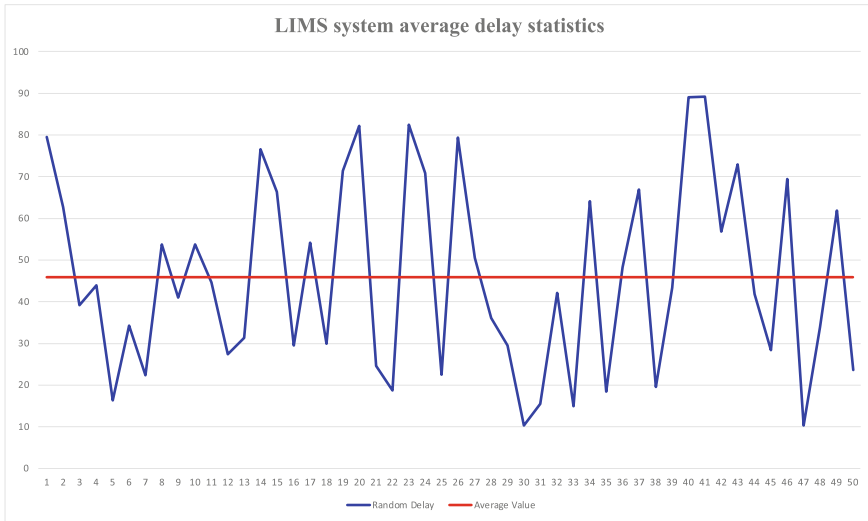


Fig. 81.7 Simulation of LIMS single-click delay using python

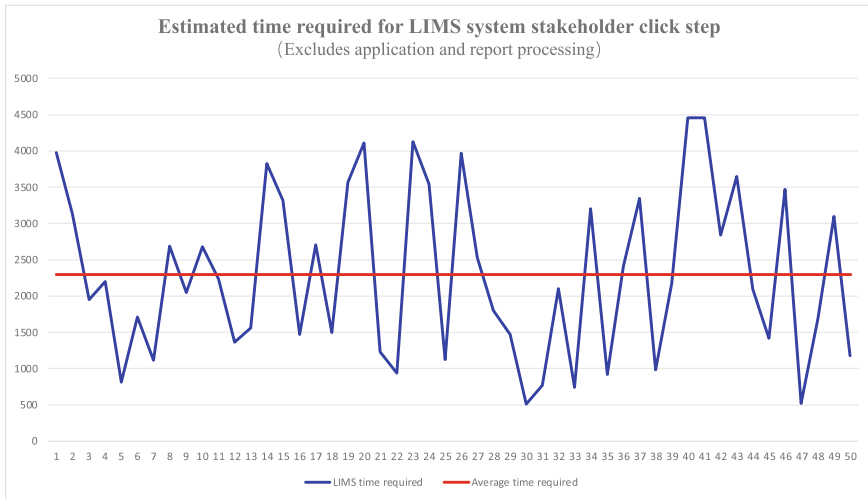


Fig. 81.8 The total delay required for 50 clicks in the LIMS system

record confirmation, test test report confirmation, confirmation of review results and signatures of relevant parties these six steps. The operating click efficiency is 88.00% higher than that of the LIMS, and the click delay (for comparison, the simulated LIMS random delay data is used for calculation), the total request response time range of the blockchain-based aviation physical and chemical testing system is between 61.44

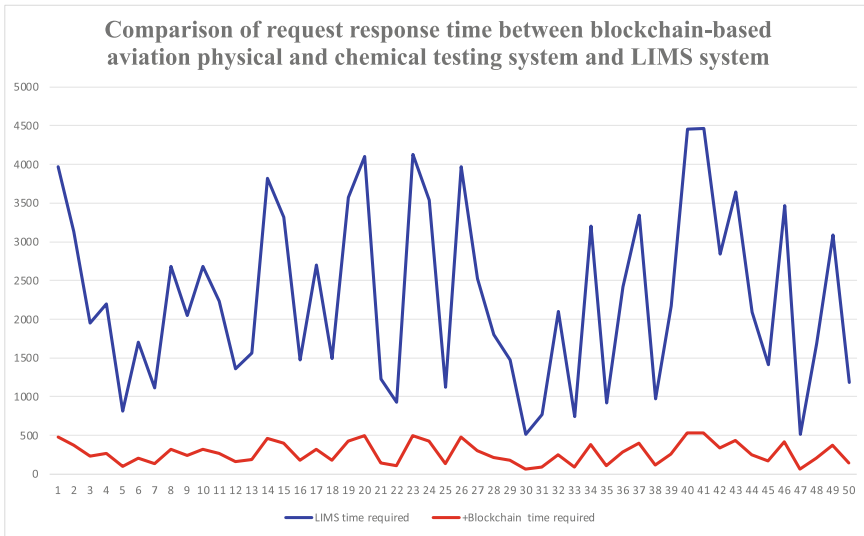


Fig. 81.9 Comparison of the overall required response time between the blockchain-based aviation physical and chemical testing system and the LIMS

and 535.2 ms, the average request response time is 275.23 ms, as shown in Fig. 81.9, and the total request response time is 88.00% higher than that of the LIMS system.

Based on the linear simplex and asynchronous characteristics of the LIMS system, the client of the test test can only know the test results at the end [36]. The physical and chemical test report management stage generally needs four stages: Test report writing, Report Review and Signature, Report transmission and publication, and Final Report Synchronization, even without considering the intermediate waiting and possible return time, only according to the request response delay estimate, the average waiting time is 2476.98 ms, after the improvement of the blockchain technology, the relevant parties can receive the test result data after the test operator confirms the test result. According to the estimated response delay of the request, it is 45.87 ms, and the efficiency is increased by about 98.14%. Of course, the official test report still needs to be reviewed and stamped by various personnel before it can be obtained.

81.5 Summary and Outlook

The disadvantages and defects of the traditional physical and chemical testing system have been around for a long time, and the emergence of the LIMS system has only solved some of the problems, and has not fundamentally solved the problems of the traditional physical and chemical testing system, and has also led to new problems such as high learning costs and complicated steps.

This paper combines blockchain, a data credible, non-tamperable, and highly traceable technology, to effectively solve traditional problems such as slow synchronization of test results, affecting production efficiency, and complicated steps, and can effectively ensure the consensus of testing data, fast synchronization, data traceability and other requirements. This paper clarifies the relevant parties and testing steps through the use case diagram, and clarifies the system architecture of the physical and chemical testing system based on the blockchain through the form of the architecture diagram, and designs the function and process of the key point of the system: the smart contract, ensure that the system meets the requirements of system construction principles such as simple process, low learning and operating costs; fast data synchronization, timely issuance of test reports; safe and reliable data, meeting the requirements of high traceability in the aviation industry, etc., to study the efficiency improvement of the improved system, the successful implementation and promotion of the “block chain + “ type system is inseparable from the advancement of technology on the one hand, and on the other hand, the follow-up of laws and regulations/rules and regulations should also go hand in hand.

Acknowledgements This work was supported by the Key-Area Research and Development Program OF Guangdong Province 2020B0101090003.

References

1. Yi, Y.: Development characteristics and trends of China’s general aviation emerging businesses. *Civ. Aviat. Today* **02**, 48–51 (2021)
2. Zhidong, L.: Periodic verification of reference materials in physical and chemical testing laboratories. *Technol. Mark.* **02**, 197–198 (2020)
3. Staack, I., Amadori, K., Jouannet, C.: A holistic engineering approach to aeronautical product development. *Aeronaut. J.* **123**(1268), 1545–1560 (2019). <https://doi.org/10.1017/aer.2019.51>
4. Zhiming, S., Xiaochen, S., Junzhao, H., Youwen, Z.: Discussion on quality control methods in testing laboratories. *Phys. Chem. Test.-Chem.* **12**, 1466–1469 (2022)
5. Hui, Q.: Analysis of the role of physical and chemical testing in the quality research of metal materials. *China Metal Bull.* **03**, 215–216 (2018)
6. Jun, X., Feng, Z., Yijun, H., Weijie, W., Rongli, M., Xinyun, L.: Aeronautical non-metal physical and chemical testing and laboratory construction. *Aviat. Weapons* **02**, 36–39 (2002). <https://doi.org/10.19297/j.cnki.41-1228/tj.2002.02.013>
7. Peng, L.: The application of physical and chemical testing in the research of metal materials. *China Equip. Eng.* **07**, 149–150 (2021)
8. Jie, Y., Yibo, R., Xing, W., Hui, Z., Yantong, Y.: Characteristics and testing technology analysis of non-metallic materials. *Electron Technol.* **10**, 186–187 (2022)
9. Bolin, Z.: Current status and development trend of non-destructive testing technology for aviation equipment. *China Mil. Civilian* **12**, 54–55 (2022)
10. Jian, M., Li, L., Shuang, W., Wenxiu, Z.: Airport engineering test and laboratory construction. *Lab. Sci.* **04**, 191–193 (2017)
11. Arifin, M.N., Siahaan, D.: Structural and semantic similarity measurement of UML use case diagram. *Lontar Komputer: Jurnal Ilmiah Teknologi Informasi* **11**(2), 88 (2020)

12. Weihua, W.: Construction and Research on Risk Evaluation System of Enterprise Physical and Chemical Testing Laboratory (Master's Thesis, Beijing University of Chemical Technology). <https://kns.cnki.net/KCMS/detail/detail.aspx?dbname=CMFD202101&filename=1020142702.nh> (2020)
13. Chuang, C.: Calculation of product misjudgment rate caused by measurement uncertainty in mechanical inspection. *Ind. Metrol.* **06**, 56–58+64 (2022). <https://doi.org/10.13228/j.boyuan.issn1002-1183.2021.0350>
14. Jianlong, L.: Talking about the necessity of informatization construction of traditional testing and testing laboratories. *Environ. Technol.* **05**, 55–58 (2019)
15. Luping, Z.: Establishment and operation of quality management system in testing laboratories. *Enterp. Reform Manag.* **12**, 35–36 (2015). <https://doi.org/10.13768/j.cnki.cn11-3793/f.2015.2702>
16. Sujuan, S., Chun, X., Rui, W.: Discussion on life cycle laboratory equipment management based on LIMS system. *China Metrol.* **08**, 48–49+61 (2022). <https://doi.org/10.16569/j.cnki.cn11-3720/t.2022.08.044>
17. Dongfang.: Design and implementation of LIMS original record informatization. *Electron. Comp. Inf. Technol.* **04**, 100–103+108 (2022). <https://doi.org/10.19772/j.cnki.2096-4455.2022.4.025>
18. Wenshuang, W., Yajun, Y.: A review of laboratory information management system development. *Electron. Prod. Reliab. Environ. Test.* **S2**, 60–63 (2021)
19. Beibei, X., Jing, D., Tongwen, L., Yankui, L., Bin, Q.: Current status and development of laboratory information management system. *J. Food Saf. Q. Inspection* **11**, 3509–3513 (2014). <https://doi.org/10.19812/j.cnki.jfsq11-5956/ts.2014.11.027>
20. Yueyun, Z.: Construction and management of intelligent laboratory information system. *Inf. Record. Mater.* **11**, 166–168 (2022). <https://doi.org/10.16009/j.cnki.cn13-1295/tq.2022.11.065>
21. Zhuqing, X.: Exploration of effective paths to improve the quality of laboratory construction and management. *Chin. Foreign Enterp. Culture* **07**, 147–148 (2021)
22. Nakamoto, S.: Bitcoin: a peer-to-peer electronic cash system. *Decentralized Bus. Rev.* 21260 (2008)
23. Zou, W., Lo, D., Kochhar, P.S., Le, X.B.D., Xia, X., Feng, Y., Chen, Z., Xu, B.: Smart contract development: challenges and opportunities. *IEEE Trans. Softw. Eng.* **47**(10), 2084–2106 (2019)
24. Alsunaidi, S.J., Alhaidari, F.A.: A survey of consensus algorithms for blockchain technology. In: 2019 International Conference on Computer and Information Sciences (ICIS), pp. 1–6. IEEE (2019)
25. Makridakis, S., Christodoulou, K.: Blockchain: current challenges and future prospects/applications. *Future Internet* **11**(12), 258 (2019)
26. Park, J.S., Kim, J.D.: A study on the development of consortium Blockchain governance framework. *J. Dig. Convergence* **17**(8), 89–94 (2019)
27. Xuedong, S., Ming, L., Xinmin, W.: A review of blockchain development and application. *J. Jilin Univer. (Inf. Sci. Edition)* **05**, 798–804 (2022). <https://doi.org/10.19292/j.cnki.jdxxp.2022.05.016>
28. Shafiq, M., Tian, Z., Bashir, A.K., Du, X., Guizani, M.: CorrAUC: a malicious bot-IoT traffic detection method in IoT network using machine-learning techniques. *IEEE Internet Things J.* **8**(5), 3242–3254 (2020)
29. Xiangtao, Z., Jiebo, H., Zehan, C.: Application of internet of things technology in industrial automation. *Dig. Technol. Appl.* **09**, 120–122 (2022). <https://doi.org/10.19695/j.cnki.cn12-1369.2022.09.38>
30. Qiu, J., Tian, Z., Du, C., Zuo, Q., Su, S., Fang, B.: A survey on access control in the age of internet of things. *IEEE Internet Things J.* **7**(6), 4682–4696 (2020)
31. Yuan, L.: Design and implementation of file management system based on blockchain technology. *Inf. Record. Mater.* **10**, 229–233 (2022). <https://doi.org/10.16009/j.cnki.cn13-1295/tq.2022.10.049>
32. Shafiq, M., Tian, Z., Sun, Y., Du, X., Guizani, M.: Selection of effective machine learning algorithm and Bot-IoT attacks traffic identification for internet of things in smart city. *Futur. Gener. Comput. Syst.* **107**, 433–442 (2020)

33. Yunxia, L., Dasha, H., Yuming, J.: Research on loosely coupling models for on-chain upgrade of smart contracts. *Comput. Appl. Res.* **05**, 1309–1313 (2021). <https://doi.org/10.19734/j.issn.1001-3695.2020.07.0160>
34. Zhang, C.: Research and Implementation of Concurrency Optimization for Internet of Things Systems (Master's Thesis, Beijing University of Posts and Telecommunications). <https://kns.cnki.net/KCMS/detail/detail.aspx?dbname=CMFD202201&filename=1021123493.nh> (2021)
35. Tian, Z., Luo, C., Qiu, J., Du, X., Guizani, M.: A distributed deep learning system for web attack detection on edge devices. *IEEE Trans. Industr. Inf.* **16**(3), 1963–1971 (2019)
36. Tian, Z., Li, M., Qiu, M., Sun, Y., Su, S.: Block-DEF: A secure digital evidence framework using blockchain. *Inf. Sci.* **491**, 151–165 (2019)

Chapter 82

Coupled Axial-Rotational Motion of the Pipe on Cuttings Transport via CFD



Na Zhu, Chenliang Ruan, Heming Zhu, Zhiquan Nie, Wenjun Huang, and Deli Gao

Abstract Inadequate hole cleaning is one of the main reasons for pipe stuck in extended-reach drilling, especially while back reaming. The mechanism of cuttings transport while back reaming is hereby investigated. First, a coupled dynamic layering and sliding method with the Eulerian-Granular approach is established and verified. The sliding mesh method is applied to simulate the pipe rotation, and the layering mesh method is used to simulate the movement in the axial direction. Next, the tripping operation of a connector-furnished pipe is simulated, and the sensitive parameter analysis is conducted. The results demonstrate that cuttings pile up in front of the connector while tripping, which may bring a risk of a stuck pipe. The cuttings pile decreases with the circulation time and rotational speed of the pipe. The tripping velocity has minimal effect on the cuttings distribution after the cuttings pass through the connector. Moreover, the significant flow rate can be more safely employed after the cuttings have passed through the connector furnished with a large diameter, such as the bottom hole assembly. This exploration is an essential guide to predicting and controlling tight spots while tripping.

Keywords Drill cuttings transport · Tripping · Dynamic layering method · Hole cleaning · Connector

N. Zhu · C. Ruan · H. Zhu
SINOPEC Research Institute of Petroleum Engineering Co., Ltd, No. 197 Baisha Road,
Changping District, Beijing 102206, China

Z. Nie (✉)
China National Oil and Gas Exploration and Development Corporation, Building D, State
Investment Building, 6-1 Fuchengmen North Street, Xicheng District, Beijing 100034, China
e-mail: 931819658@qq.com

W. Huang · D. Gao
MOE Key Laboratory of Petroleum Engineering, China University of Petroleum, Beijing 102249,
China

82.1 Introduction

Hole cleaning is regarded as the essential component of any drilling project, fundamentally contributing to the overall efficiency and profitability of any work endeavor [1]. It is largely known that the inadequate execution of hole cleaning may result in a wide array of problems, such as increased equivalent circulating density, formation leakage, low ROP, high drag or torque of the pipe string, or even a stuck pipe accident [2]. Hence, it is essential to recognize that a high proportion (around 54%) of stuck pipe events occur during the execution of tripping or back reaming [3].

Two primary procedures are involved in hole cleaning, namely drilling and washing [4]. However, the importance of cuttings transport under back reaming conditions is similarly important, although current research regarding the effects of this particular aspect is lacking. Current research pertaining to cuttings' transportation is commonly comprised of experimental and theoretical investigations.

The influence of several variables on hole cleaning can be studied experimentally [5–7]. However, the pipe is often assumed to be stationary or merely rotating and does not allow for the dynamic consideration of multiple conditions. Furthermore, specific experiments investigating back reaming, as well as coupling of axial and rotational pipe movement, are complex, more difficult, and scarcely conducted [8].

Layer-modeling and computational fluid dynamics (CFD) are the two primary theoretical approaches used to investigate hole cleaning [9, 10]. However, most layer models are still based exclusively on the two procedures of washing & drilling. Given that the drill pipe rotation mechanism is rather complicated, models of back reaming featuring a coupling of axial and rotational pipe motion have yet to be perfectly simulated.

The CFD method, which aims to determine how cuttings are transported in the annular wellbore, is popular among researchers and readily employed [11, 12]. This method exhibits a select advantage of providing detailed accounts pertaining to the desired properties without needing to limit experimental conditions or layer models [13, 14]. However, even when considering the efficacy and popularity of this approach, no model exists that can accurately forecast cuttings' concentration during back reaming. This lack of investigative methodology is solely attributed to the computational bottleneck created by the immense flow complexity caused by the coupled motion of the pipe [15, 16].

Overall, the back reaming operation is to be simulated via a coupled sliding mesh and layering mesh method. The sliding mesh method is applied to simulate the pipe rotation, and the layering mesh method is used to simulate the movement in the axial direction. A Eulerian-Granular method is to be applied to simulate the two-phase flow to investigate the cuttings transport during back reaming.

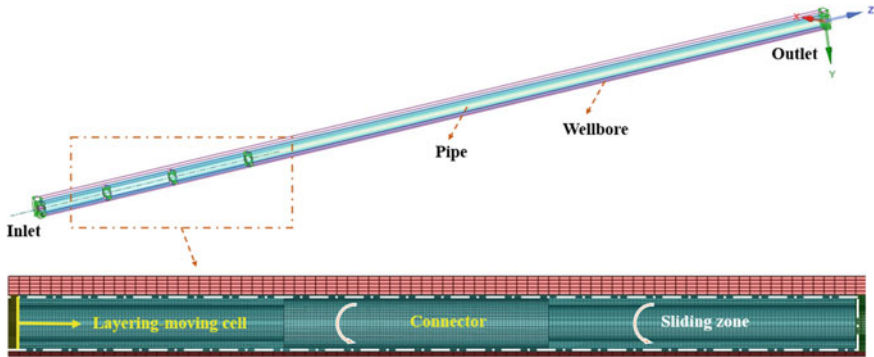


Fig. 82.1 Concept illustration of the back reaming operation with a connector

82.2 Concept of Back Reaming and Methodology

82.2.1 Concept of Back Reaming

Back reaming is a mechanical operation combining pumping, pipe rotating, and extraction from the hole (Fig. 82.1). This method is widely used to avoid tripping out of the hole. However, its use on extended reach wells has garnered a notorious negative connotation for being high risk. Furthermore, the supposed advantages of back reaming for cuttings transport may in fact have an overall negative influence on hole cleaning.

82.2.2 Methodology

A Eulerian-Granular method is applied to simulate the two-phase flow. This method requires less computational resources than the CFD-DEM method and has been extensively used in liquid–solid flows. The detailed equations are presented in Table 82.1.

Besides, to simulate the combined motion of the rotational and axial movement of the pipe during the back reaming operation, the coupled dynamic layering mesh method and sliding mesh method are employed. The dynamic layering mesh method can simulate the axial movement of the pipe, and the sliding mesh method can simulate the pipe rotation.

Thus, a wellbore with a total length of 3 m is simulated, and the length of the connector is 0.25 m. The diameters of the wellbore, pipe and the connector are 0.074, 0.033, and 0.046 m. The fluid is using water, and the solid is the sand particle, with a density of 2500 kg/m^3 , and a diameter of 0.003 m. The eccentricity of the pipe is 0.3. The tripping velocity is 0.1 m/s, and the rotational speed of the pipe is 120 RPM.

Table 82.1 Principal and constitutive equations of the Eulerian-Granular model

Equations	Equation expression	No.
Mass conservation equation	$\frac{\partial}{\partial t}(\alpha_q \rho_q) + \nabla \cdot (\alpha_q \rho_q \vec{v}_q) = \sum_{s=1}^n (\dot{m}_{sq} - \dot{m}_{qs})$	(82.1)
Conservation of momentum	$\begin{aligned} \frac{\partial}{\partial t}(\alpha_q \rho_q \vec{v}_q) + \nabla \cdot (\alpha_q \rho_q \vec{v}_q \vec{v}_q) \\ = -\alpha_q \nabla p + \nabla \cdot \bar{\bar{\tau}}_q + \alpha_q \rho_q \vec{g} \\ + \sum_{s=1}^n (\vec{R}_{sq} + \dot{m}_{sq} \vec{v}_{sq} - \dot{m}_{qs} \vec{v}_{qs}) \\ + (\vec{F}_q + \vec{F}_{lift,q} + \vec{F}_{wl,q} + \vec{F}_{vm,q} + \vec{F}_{td,q}) \end{aligned}$	(82.2)
Granular temperature	$\Theta_s = \frac{1}{3} u_s u_s$	(82.3)
Transport equation	$\begin{aligned} \frac{3}{2} \left[\frac{\partial}{\partial t}(\rho_s \alpha_s \Theta_s) + \nabla \cdot (\rho_s \alpha_s \vec{v}_s \Theta_s) \right] \\ = \left(-p_s \bar{\bar{I}} + \bar{\bar{\tau}}_s \right) : \nabla \cdot \vec{v}_s + \nabla \cdot (k_{\Theta_s} \nabla \Theta_s) - \gamma_{\Theta_s} + \phi_{ls} \end{aligned}$	(82.4)
Solids pressure	$p_s = \alpha_s \rho_s \Theta_s + 2\rho_s(1 + e_{ss})\alpha_s^2 g_{0,ss} \Theta_s$	(82.5)
Solids shear stresses	$\mu_s = \mu_{s,col} + \mu_{s,kin} + \mu_{s,fr}$	(82.6)
Collisional viscosity	$\mu_{s,col} = \frac{4}{5} \alpha_s \rho_s d_s g_{0,ss} + (1 + e_{ss}) \left(\frac{\Theta_s}{\pi} \right)^{1/2}$	(82.7)
Kinetic viscosity	$\mu_{s,kin} = \frac{d_s \rho_s \sqrt{\Theta_s \pi}}{6(3 - e_{ss})} \left[1 + \frac{2}{5} (1 + e_{ss})(3e_{ss} - 1) \alpha_s g_{0,ss} \right]$	(82.8)
Bulk viscosity	$\lambda_s = \frac{4}{3} \alpha_s^2 \rho_s d_s g_{0,ss} (1 + e_{ss}) \left(\frac{\Theta_s}{\pi} \right)^{1/2}$	(82.9)

82.3 Results and Discussion

82.3.1 Impact of the Circulation Time

The simulation of the cuttings bed distribution with the circulation time is investigated. The original dimensionless cuttings bed height is 10% (see Fig. 82.2), and the porosity of the bed layer is 52%. As can be seen, when the time is 0.2 s, part of the cuttings bed has been removed, and there is a cuttings pile in front of the connector (see Fig. 82.3). When the time is 0.6 s, both the cuttings concentration of the cross section and axial section become less. However, the cuttings pile in front of the connector become more obvious. It may be because the cross-sectional area of the connector section is less than that of the pipe body, so the velocity of water is higher than the two ends of the connector. It can also be seen from the streamline of the water in Fig. 82.3 that the velocity in front of the connector is almost zero. Thus, the cuttings become slow and pile up in front of the connector, which brings a stuck pipe risk while tripping out.

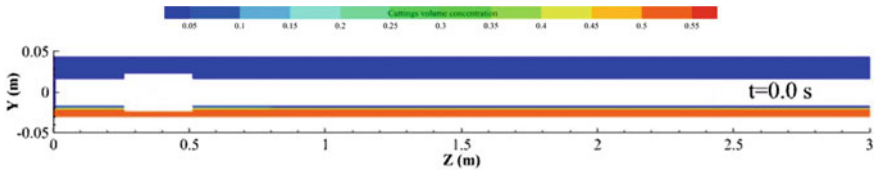


Fig. 82.2 Original cuttings concentration distribution

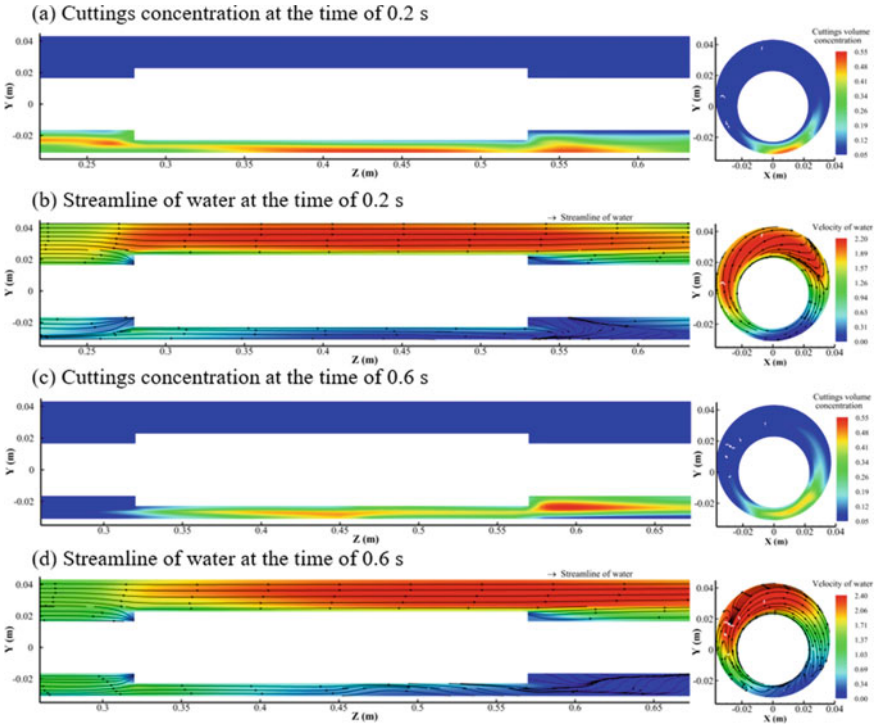


Fig. 82.3 Cuttings concentration and the streamline of water under different circulation time

82.3.2 Impact of the Rotation Speed

The simulation of the cuttings bed distribution with different rotation speeds is depicted in Fig. 82.4. The original dimensionless cuttings bed height is 10%, and the porosity of the bed layer is 52%. The cuttings distributions at a rotation speed of 0 RPM and 60 RPM are depicted in Fig. 82.4, indicating that the higher pipe rotation speed can clean more cuttings and obtain a lower cuttings concentration. The reason is that the pipe rotation can lift the cuttings from the lower side of the pipe to the annulus, so the water flow can bring more cuttings out of the pipe.

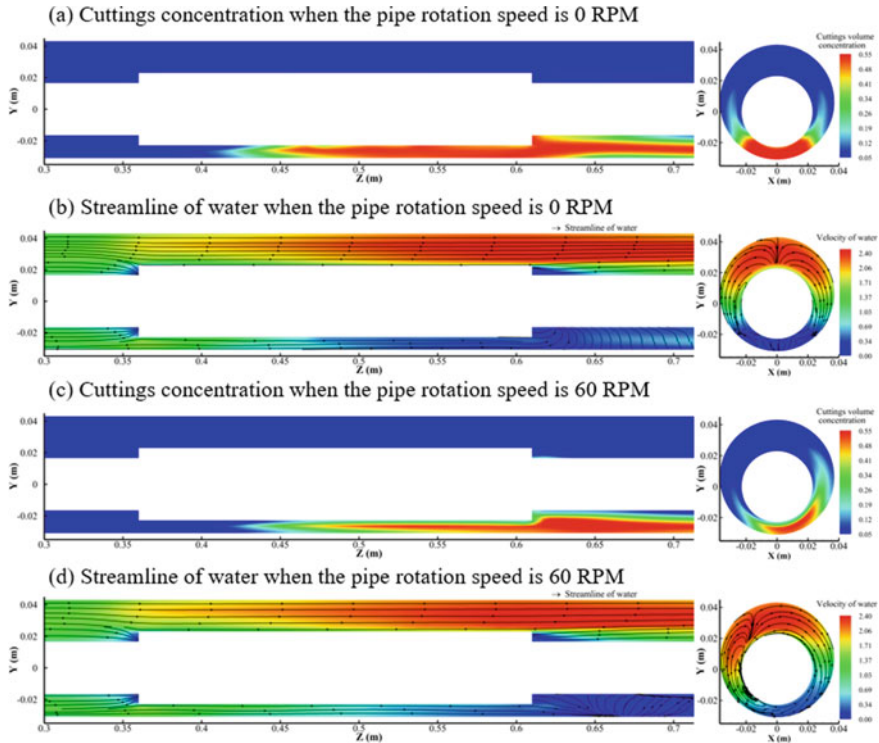


Fig. 82.4 Cuttings concentration and the streamline of water under different pipe rotation speeds

82.3.3 Impact of the Fluid Velocity

The simulation of the cuttings bed distribution with different fluid velocities is depicted in Fig. 82.5. The original dimensionless cuttings bed height is 10%, and the porosity of the bed layer is 52%. The cuttings distributions at a fluid velocity of 0.25 and 0.5 m/s are depicted in Fig. 82.5, indicating that the higher fluid velocity can transport more cuttings and achieve a lower cuttings concentration. The reason is that a higher flow rate can provide a stronger shear force, which can transport the cuttings out of the pipe. However, it also can be seen that, a higher cuttings dune piles up in front of the connector, because when the cuttings have not passed through the connector, a higher flow rate can lead more cuttings to transport to the position of the front of the connector, which has not been transported forward in time. Thus, the higher flow rate should also be applied carefully when the cuttings have not passed through the connector to avoid the pipe getting stuck.

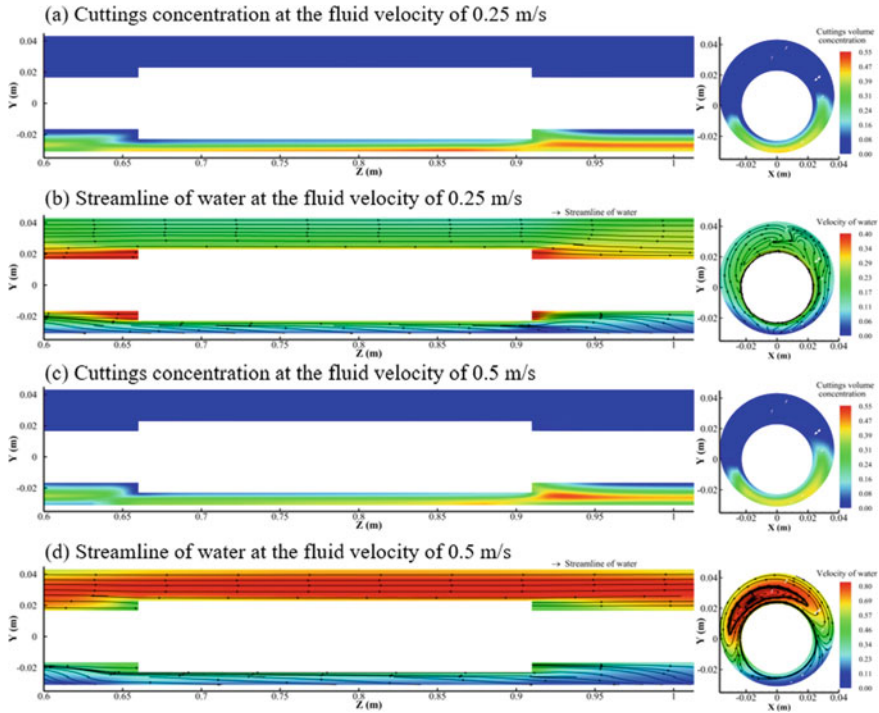


Fig. 82.5 Cuttings concentration and the streamline of water under different fluid velocities

82.3.4 Impact of the Tripping Velocity

The effect of the tripping velocity is investigated in this section. The original dimensionless cuttings bed height is 10%, and the porosity of the bed layer is 52%. The cuttings distributions and the streamline of water at tripping velocities of 0.2, 0.4, and 0.6 m/s are depicted in Figs. 82.6 and 82.7. As shown in Figs. 82.6 and 82.7; the pipe has moved from the position of 0.2–0.6 m at the Z axis, the cuttings concentration at the right end of the connector decreases. The increasing of the tripping velocity does not necessarily lead to a higher cuttings concentration. The reason may be that the connector mainly affects the cuttings around it, such as the pushing function or the differential velocity around the connector. So, when tripping around a connector, it should pay more attention, and after the cuttings pass through the connector, the tripping velocity has very little effect on the cuttings distribution.

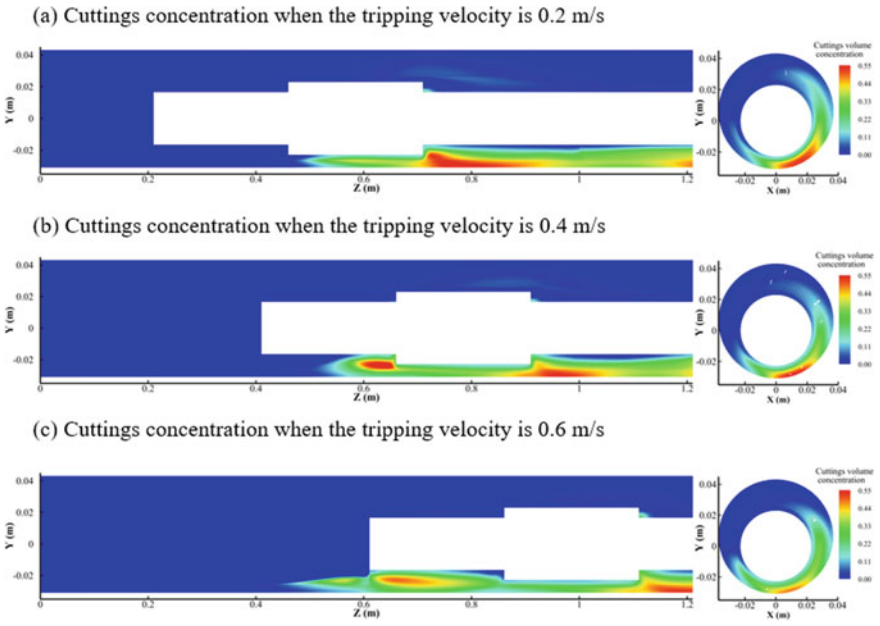


Fig. 82.6 Cuttings concentration of water under different tripping velocities

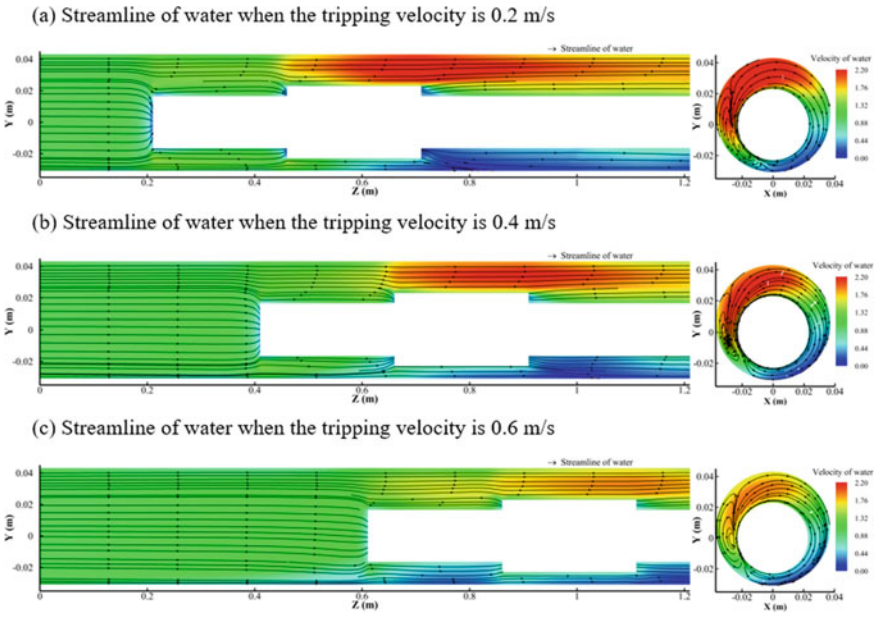


Fig. 82.7 Streamline of water under different tripping velocities

82.4 Results and Discussion

- (1) The back reaming operation is simulated via a coupled sliding mesh and layering mesh method. The sliding mesh method is applied to simulate the pipe rotation, and the layering mesh method is used to simulate the movement in the axial direction.
- (2) During the process of back reaming, there is a cuttings pile in front of the connector, which may bring a risk of stuck pipe. The cuttings pile decreases with the circulation time, the rotational speed of the pipe, and the fluid velocity. The tripping velocity has very little effect on the cuttings distribution after the cuttings pass through the connector.

Acknowledgements The authors gratefully acknowledge the financial support from the Natural Science Foundation of China (Grant Nos. 52222401, 52234002, 51904317 and 52174012), Science Foundation of China University of Petroleum, Beijing (Grant No. ZX20180414), and other projects (ZLZX2020-01-07-01).

References

1. Alshaikh, A.A., Albassam, M.K., Al Gharbi, S.H., Al-Yami, A.S.: Detection of stuck pipe early signs and the way toward automation. In: Abu Dhabi International Petroleum Exhibition and Conference, pp. 12–15. Onepetro, Abu Dhabi, UAE (2018). <https://doi.org/10.2118/192975-MS>
2. Epelle, E.I., Gerogiorgis, D.I.: Drill cuttings transport and deposition in complex annular geometries of deviated oil and gas wells: a multiphase flow analysis of positional variability. *Chem. Eng. Res. Des.* **151**, 214–230 (2019). <https://doi.org/10.1016/j.cherd.2019.09.013>
3. Yarim, G., Uchytel, R.J., May, R.B., Trejo, A.: Stuck pipe prevention—a proactive solution to an old problem, In: SPE Annual Technical Conference and Exhibition, pp. 11–14. Onepetro, California, U.S.A. (2007). <https://doi.org/10.2118/109914-MS>
4. Zhu, N., Huang, W., Gao, D.: Numerical analysis of the stuck pipe mechanism related to the cutting bed under various drilling operations. *J. Pet. Sci. Eng.* **208**, 109783 (2022). <https://doi.org/10.1016/j.petrol.2021.109783>
5. Pandya, S., Ahmed, R., Shah, S.: Effects of particle density on hole cleanout operation in horizontal and inclined wellbores. In: SPE/ICoTA Well Intervention Conference and Exhibition, pp. 26–27. Onepetro, The Woodlands, Texas, USA (2019). <https://doi.org/10.2118/194240-MS>
6. Song, X., Xu, Z., Wang, M., Li, G., Shah, S.N., Pang, Z.: Experimental study on the wellbore-cleaning efficiency of microhole-horizontal-well drilling. *SPE J.* **22**(4), 1189–1200 (2017). <https://doi.org/10.2118/185965-PA>
7. Ozbayoglu, M.E., Saasen, A., Sorgun, M., Svanes, K.: Effect of pipe rotation on hole cleaning for water-based drilling fluids in horizontal and deviated wells. In: IADC/SPE Asia Pacific Drilling Technology Conference and Exhibition, pp. 25–27. Onepetro, Jakarta, Indonesia (2008). <https://doi.org/10.2118/114965-MS>
8. Paranhos Sobrinho, E.S., Escarpini Filho, R.S., Lages, E.N., Anjos, J.L.R., Almeida, L.F.M., Gonçalves, C.: Consideration of backreaming in vertical wells closure modeling in salt rock. *SPE J.* **26**(3), 1092–1109 (2021). <https://doi.org/10.2118/204209-PA>

9. Li, J., Luft, B.: Overview of solids transport studies and applications in oil and gas industry-experimental work. In: SPE Russian Oil and Gas Exploration and Production Technical Conference and Exhibition, pp. 14–16. OnePetro, Moscow, Russia (2014). <https://doi.org/10.2118/171285-MS>
10. Gavignet, A., Sobey, I.: Model aids cuttings transport prediction. *J. Pet. Technol.* **41**(9), 916–921 (1989). <https://doi.org/10.2118/15417-PA>
11. Zhang, F., Wang, Y., Wang, Y., Miska, S., Yu, M.J.S.J.: Modeling of dynamic cuttings transportation during drilling of oil and gas wells by combining 2D CFD and 1D discretization approach. *SPE J.* **25**(3), 1220–1240 (2020). <https://doi.org/10.2118/199902-PA>
12. Heydari, O., Sahraei, E., Skalle, P.: Investigating the impact of drillpipe’s rotation and eccentricity on cuttings transport phenomenon in various horizontal annuluses using computational fluid dynamics (CFD). *J. Pet. Sci. Eng.* **156**, 801–813 (2017). <https://doi.org/10.1016/j.petrol.2017.06.059>
13. Akhshik, S., Behzad, M., Rajabi, M.: CFD-DEM approach to investigate the effect of drill pipe rotation on cuttings transport behavior. *J. Pet. Sci. Eng.* **127**, 229–244 (2015). <https://doi.org/10.1016/j.petrol.2015.01.017>
14. Capecelatro, J., Desjardins, O.: An Euler-Lagrange strategy for simulating particle-laden flows. *J. Comput. Phys.* **238**, 1–13 (2013). <https://doi.org/10.1016/j.jcp.2012.12.015>
15. Basu, D., Das, K., Smart, K., Ofoegbu, G.: Comparison of Eulerian-Granular and discrete element models for simulation of proppant flows in fractured reservoirs. In: ASME International Mechanical Engineering Congress and Exposition, pp. 13–19, American Society of Mechanical Engineers, Houston, Texas (2015). <https://doi.org/10.1115/IMECE2015-50050>
16. Bonamy, D., Chavanis, P.H., Cortet, P.P., Daviaud, F., Dubrulle, B., Renouf, M.: Euler-like modelling of dense granular flows: application to a rotating drum. *Eur. Phys. J. B* **68**, 619–627 (2009). <https://doi.org/10.1140/epjb/e2009-00123-6>

Chapter 83

Design of General SDN Controller System Framework for Multi-domain Heterogeneous Networks



Wenxiao Li, Jianhua Zhao, Huicong Fan, Shijia Zhu, Wandi Liang, Hongguang Yu, and Peng Lin

Abstract The integration of two technologies, Cloud Computing and Software Defined Network (SDN) has placed cooperative orchestration between cloud and network into the focus of attention. However, with the continuous expansion of network scale, the data center would inevitably accommodate multiple SDN network devices which are produced from various manufacturers, and even these devices are associated with different SDN technologies. Therefore, application scenario with multi-domain heterogeneous SDN networks occurs. The interoperability and orchestration of cross-domain services, as well as unified management of devices from multiple domains, have become a challenge. At present, except for OpenFlow, the mainstream technologies for SDN implementation include segment routing technology based on MPLS (SR-MPLS) and that based on IPv6 (SRv6). This paper proposes a general SDN controller system framework. This framework is able to shield the discrepancies, which is caused by different SDN technologies, between northbound interfaces of SDN controllers from multiple manufacturers. Besides, it supports unified management of network resources to solve the difficulties of orchestration of cross-domain service in SDN network. Furthermore, this system framework follows the design principles of high cohesion and low coupling, and regard every adapter that manages one SDN domain with specific technology as one sub-module in the whole adapter module, hence with flexible expansion.

Keywords Software defined network · Segment routing technology · Orchestration of cross-domain service

W. Li · J. Zhao · H. Fan · S. Zhu · W. Liang · H. Yu
Institute of Economy and Technology, State Grid Hebei Electric Power Co, Ltd., Hebei 050023, China

P. Lin (✉)
Beijing VectInfo Technologies Co., Ltd, Beijing 100088, China
e-mail: linpeng@vectinfo.com

83.1 Introduction

In recent years, with the development of cloud computing technology as well as the continuous expansion of scale of networks in cloud data centers, it has become a trend that cloud and network get converged. A few operators and even large enterprises have already possessed their own technologies, which is about the integration of cloud and network, with various degrees of development. This technology is becoming the foundation and key of the novel communication infrastructure [1]. SDN is an innovative network architecture technology, which is emerging in recent years. Due to the flexibility, programmability and scalability of this technology, it is capable to solve the problems faced during cloud computing in large scale networks. The cloud computing network based on SDN will achieve good operation effect in practice and meet demand for the development of cloud computing [2]. However, as the continuous growth of the scope of cloud resource pool and SDN devices deployment, the situation of multi-vendor SDN environment would inevitably emerge, resulting in the demand for intercommunication, unified management and collaborative orchestration in heterogeneous SDN network [3]. In general, the network devices, which are controlled by one controller, from the same SDN domain usually are applied with the same SDN technology, also from the same manufacturer. In the environment of integration between cloud and network, as the scale of cloud computing expands, there may be deployed with multiple multi-vendor SDN products in the cloud resource pool with large scale in one data center [4]. In the scenario of multiple heterogeneous SDN network domains, with regards to devices in different domains, the technologies applied and manufacturers may be not exactly the same. Therefore, it is difficult for the management platform of cloud network in single data center to ensure interoperability and cooperative orchestration of the cross-domain services.

In addition to the current mainstream SDN technologies, OpenFlow and SR-MPLS, which had been applied, a new SDN technology called SRv6 has been realized in some devices. With respect to SRv6, not only the application scenarios and commercial value are now being exploring, but also the industrial standard is still in the draft stage. However, the strengths of SRv6 have been widely recognized by the industry [5]. At present, there have already been a few SDN implementation technologies as shown in Table 83.1. Though during the process of implementation in different SDN technologies different network resources, such as flow tables in OpenFlow and tunnels in SR-MPLS, are required to operate in actual service process, the format or meaning of parameters required by underlying devices are not exactly when orchestrating service. As a consequence, in multi-domain heterogeneous networks, when the service orchestration system in upper layer issues service configuration instructions to underlying devices from top to bottom, it is required to shield discrepancies led by not only different manufacturers but also different SDN techniques.

Table 83.1 The information of current mainstream SDN implementation technology

SDN implementation technology	Application scenario	Scope of service deployment	Main function
OpenFlow	Usually applied in local area network with small scale, not suitable network with large scale	Need to deploy service on all nodes included in service path	Realize division of packets from specific service by flow table, limit service bandwidth through queue
Segment routing based on MPLS(SR-MPLS)	Based on IPv4 applicable to wide area network with large scale	Only need to deploy service on head node and tail node of service path	Realize division of service packets and resource allocation for bandwidth through SR tunnel. Provide function of path centrally calculating
Segment routing based on IPv6(SRv6)	Based on IPv6 applicable to wide area network with large scale	Only need to deploy service on head node and tail node of service path	Define topology and forwarding behavior through segment policies. Provide differentiated forwarding paths and isolate resources for network slices. Provide three-layer programmable space to meet complex requirement of service

83.2 The Challenge of Multi-domain Heterogeneous SDN Network

China Telecom has independently developed the SDN collaborative orchestrator called SDN-O for IDC (Internet Data Center) in scenarios of traffic scheduling intelligently. It interacts with the interface of SDN controllers from multiple vendors to realize cooperative management of the controllers. At present, the SDN-O system has supported the access of SDN controllers from mainstream manufacturers such as Huawei, Cisco, Shanghai Bell, and H3C etc. The interface protocols it supporting include Restful and Netconf etc. China Unicom currently realizes the management of heterogeneous SDN network through self-developed system. Instead of the application, which is developed in upper layer, based on SDN controllers from manufacturers, the system is comparatively independent from the manufacturer's control system through directly connecting with their devices [6]. China Mobile also creatively proposes the concept of POD (Point of Delivery), and apply multi-POD networking structure technology [7]. The comparison of these solutions is shown in Table 83.2.

So far, for the management of SDN devices from different manufacturers, most enterprises have developed service orchestration management systems by themselves to directly manage network devices or SDN controllers. However, some problems still exist.

Table 83.2 Some solutions for management of multi-vendor SDN device from some operators

Operator	Solution
China telecom	Independently develop collaborative orchestrator, which interacts with SDN controllers from multiple vendors, to realize cooperative management of the controllers
China unicom	Independently develop network management system, which directly take charge of devices from vendors by protocols (such as Netconf), to shield interface differences
China mobile	Propose the concept of Point of Delivery (POD), which is centrally managed by a unified cloud management platform. Besides, define and unify the parameters contained in the interface specification to ensure the standardization of northbound interface of SDN controller from multiple manufacturers

- The management protocol of SDN devices produced by some manufacturers may be not available. In orchestration system, it is required to invoke the northbound interface of SDN controllers from these manufacturers to indirectly control network devices, which means that an independent module is needed to develop to interact or manage the SDN controller from one specific manufacturer. It leads to poor scalability in this system.
- The control protocols of network devices from different manufacturers are not exactly the same. when directly managing them, the driver framework provided by manufacturer is required to embed into the module, which is in charge of devices from this manufacturer in the system. As a result, the information exchange between these modules is complex.
- When applying different SDN technologies in service orchestration system, discrepancies between them embody in not only the information models but also the invocation order, entities, and parameters in service process. In upper layer, they are needed to distinguish.

83.3 General SDN Controller System Framework for Multi-domain Heterogeneous Networks

In actual project, from the macroscopic perspective, the layering of management of multi-domain heterogeneous SDN network is shown in Fig. 83.1. And the detail description for each specific layer is as follows:

1. High-Level Application Layer: Other system (such as cloud management platform), which is in the top, interacts with the SDN network management layer below. Through invoking the northbound interface of cross-platform SDN network management platform to proceed instructions issue and service configuration.
2. SDN Network Management Layer: It is mainly composed of a cross-platform SDN network management platform, which is divided into these following functional modules: service orchestration management module, configuration

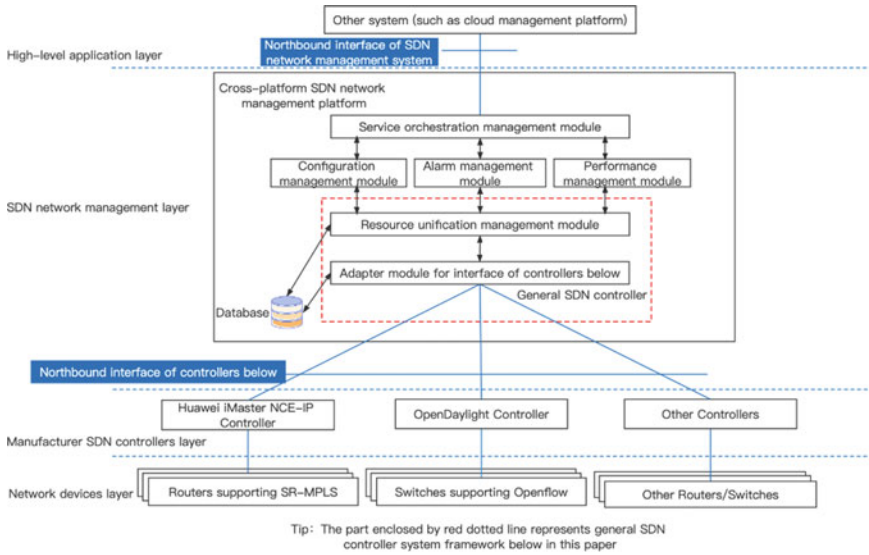


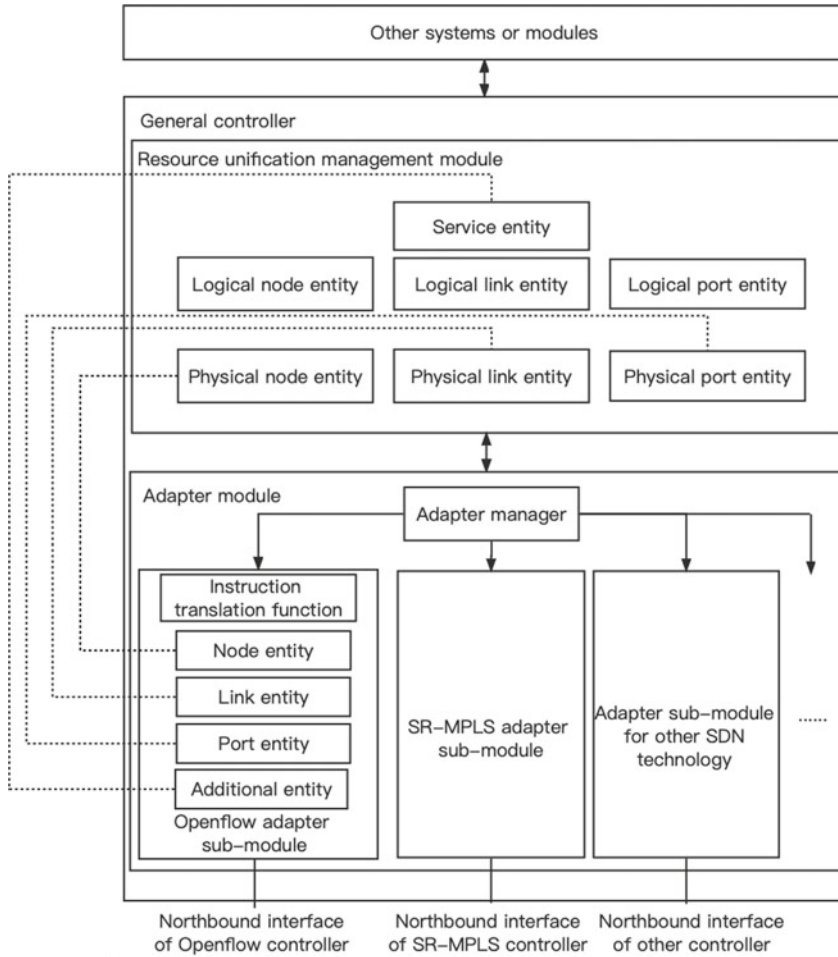
Fig. 83.1. The layering of system in multi-domain heterogeneous SDN network

management module, alarm management module, performance management module, resource unification management module and adapter module for interface of controllers below.

3. **Manufacturer SDN Controllers Layer:** The controller, which is a software with control function, is customized and developed by manufacturers for their respective SDN devices (routers and switches). It is utilized to control the flow table and routing switching strategy in devices as well as monitor device status. Usually, the controller developed by one manufacturer could only manage devices produced by the same manufacturer. Besides, it provides a northbound interface for invocation or secondary development for users. Nevertheless, normally it is not be able to manage devices from other manufacturers. (The controllers deployed in this scenario are Huawei iMaster NCE-IP and OpenDaylight.)
4. **Network devices layer:** Refers to the underlying network devices which are deployed with services. (In this scenario, the router (model Huawei NE8000 M1A) supports SR-MPLS, and SDN switches (model Pica P-5101) supports OpenFlow.)

Among the layers above, the general SDN controller system framework proposed in this paper is made up of the resource unification management module and adapter module in the SDN network management layer. The details inside the system are shown in Fig. 83.2.

The general SDN controller system is composed of two modules which are named resource unification management module and adapter module respectively.



Tip:
 1. Connection of dotted line represents that ID of upper-layer entity is corresponding to ID of lower-layer entity or connected with its other attribute via a foreign key.
 2. Every sub-module in adapter module has the same structure as the one on the far left.

Fig. 83.2 The system frame diagram of general SDN controller

83.3.1 Resource Unification Management Module

The main function of the resource unification management module is to unify the heterogeneous network resources, which locates on different SDN domains in bottom layer, into seven entities for management. So that for modules or systems in upper layer, differences between these domains are eliminated when performing management. This module provides an interface, which is able to be invoked to realize interaction with other systems or modules, such as configuration management module mentioned above.

These seven entities managed by this module can be roughly classified into two categories. Entities, including physical nodes, physical ports and physical links, belongs to one category featuring with objective existence in network. All of them correspond to actual elements can be seen in concrete network. For instance, physical nodes correspond to switches or routers. The rest ones, namely logical nodes, logical ports, logical links and services, belong to the other category. They are abstract and invisible in network. One service consists of three other abstract entities. Therefore, they would change as addition, deletion, or modification of service they belong to.

83.3.2 Adapter Module

The adapter module provides adaptation function for northbound interfaces of different SDN controllers. It maps entities in resource unification management module to those in underlying network to ensure the transmission of correct service instructions to the corresponding SDN controller. This module is composed of an adapter manager and adapter sub-modules that representing different SDN implementation technologies.

The adapter manager, which is considered as the core of the whole adapter module, manages the operations of each sub-module in service process. It receives full command parameters from resource unification management module and decomposes it into the parameters required by each sub-module. Finally, it provides these parameters to each adapter sub-module respectively, as well as inform resource unification module above of the result.

Each adapter sub-module, which stands for a particular SDN implementation technology, possesses with the same partitioning of internal functionality. In each one, the functions are divided into node management, port management, link management, additional entities management and instruction translation.

The node entity in sub-module stores the extended attributes required by a physical device node under this particular SDN technology. It will have one-to-one correlation with a physical node in resource unification management module. So do the port entity and link entity.

Additional entities in sub-module represent the particular entities, which are related to high-level service, are contained in underlying device under this particular SDN technology. For example, in order to meet bandwidth requirement in one service, a queue entity is required to create and utilize in OpenFlow, while bandwidth information will be saved in SR tunnel entity in SR-MPLS. These entities would change as addition, deletion and modification of service, thus attached to service in some extent. Therefore, the foreign key of at least one of their attributes should correspond to ID of one high-level service.

The instruction translation section in sub-module stores the steps of operations performed by sub-module to execute instruction in service process. For example, invoke specific methods in northbound interface of a SDN controller, query required parameters in this sub-module, or create additional entities corresponding to service.

The general controller has advantages with satisfactory scalability from the perspective of design. When there is a requirement to add sub-modules corresponding to other SDN technologies, it only requires to append sub-modules in adapter module according to the same design principle.

83.4 Methodology

83.4.1 Information Model

The UML class diagram of this general controller is shown in Fig. 83.3. In resource unification management module, seven entities mentioned above are not be described here to avoid repetition. Among the newly added entities, IntradomainService represents a sub-service in one SDN domain, and PhysicalNetwork stands for a real physical network containing physical nodes and physical links.

In Fig. 83.3, the sub-modules contained in adapter module are uniformly designed according to the class diagram shown, and dotted line represents that these attributes are connected via a foreign key. In each adapter sub-module, the primary keys, namely ID properties, of nodes, ports and links are respectively to those of physical nodes, physical ports and physical links in resource unification management module through foreign keys, indicating that there always exists a one-to-one mapping of every entity in these types. The additional entities (Entity1...EntityN) in the sub-module all possess a special attribute, which is connected with the primary key of

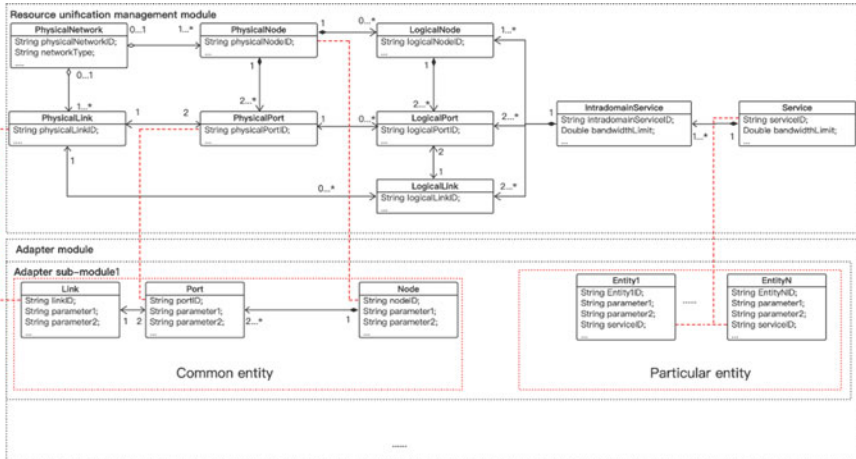


Fig. 83.3 UML class diagram of general controller

a service in the resource unification management module via a foreign key, which indicates their attachments to service.

Among adapter sub-modules, entities of nodes, ports and links belong to common entities of each SDN domain by reason that information of them will be provided however large the internal difference between network devices in different domains. Thus, every sub-module should contain these entities from the perspective of design. These common entities contained in sub-modules possess uncertain extension attributes but with determined relationship of class.

We classify these entities in all SDN domains into common entities and particular entities to summarize the design principle of adapter sub-modules. That is sub-module should include in entities of these four types (links, nodes, ports and additional entities).

83.4.2 Service Implementation Process

Taking creation of a service as an example, the flowchart of implementation is shown in Fig. 83.4. The details and steps are as follows.

1. In order to create a service across multiple domains, other systems or modules require to provide a complete service path and other additional information about this service (such as bandwidth). Through invoking the interface of general controller, service parameters are transmitted into resource unification management module.
2. After receiving request parameters of service, firstly resource unification management module determines whether the syntax and semantic meaning of these parameters are correct. For example, whether service path is correct in current topology or not. After gotten confirmation, parameters including complete service path will be transmitted into adapter manager in adapter module.
3. The adapter manager divides this complete service path into multiple path segments for each SDN domain, and then simultaneously sends parameters containing intra-domain service paths in different SDN domains to all corresponding adapter sub-modules respectively in multi-thread and high-concurrency manner.
4. After one of the adapter sub-modules receives these parameters including intra-domain path in the domain it corresponding to, it will start to performing instruction translation function. By translating, this sub-module will receive invocation sequence of northbound interface of SDN controller in this domain and acquisition procedure of some parameters required when invoking interface. For instance, obtain IDs of head node and tail node in this domain according to the intra-domain service path. And then query their UUIDs for interface invocation by IDs. Besides, it will also receive the process of creating additional entities according to the service information. For example, create a SR tunnel entity

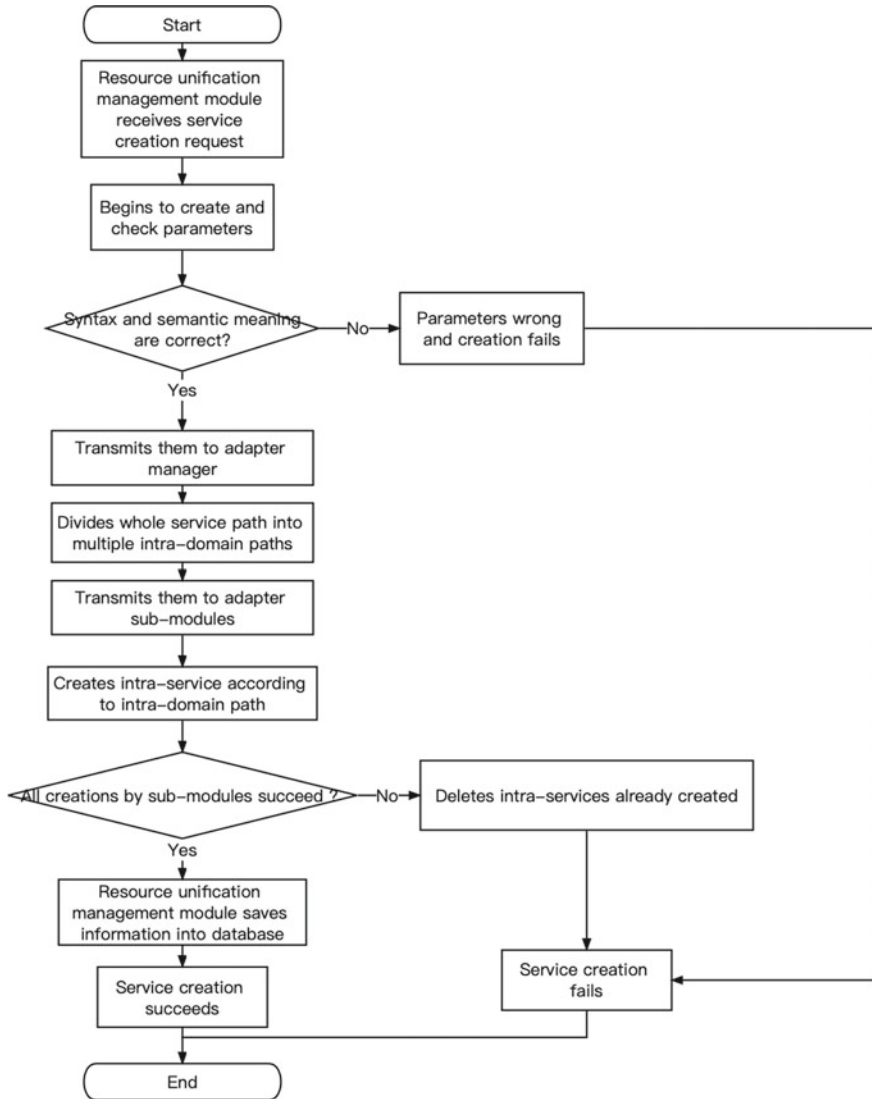


Fig. 83.4 Flowchart of service implementation in general controller

according to loopback IPs and UUIDs of these nodes, service bandwidth and other information.

5. After completing the creation of service process in one domain, adapter sub-module waits for the result from SDN controller below. If result indicates success, it will save additional entities, which is created before, associated with the service to database, and send a successful result back to adapter manager. Otherwise,

additional entities information will not be stored, and a failure result will be returned.

6. The adapter manager collects feedbacks of creation from every adapter sub-module. Only when all of them indicate successful creation, does the manager send successful result to resource unification management module, which will start to create corresponding abstract entities, namely logical nodes, logical ports, logical links, intra-domain services and complete service as well as save them to database. Finally successful message will be sent to upper-layer systems or modules.
7. When any adapter sub-module returns a failure, the adapter manager records other adapter sub-modules that return a successful result. And it sends deletion requests to these sub-modules, which will then execute the deletion process after receiving the request. Through instruction translation, the sub-modules invoke a series of methods in northbound interfaces of SDN controllers below to clear service configuration deployed in underlying device in corresponding domains. At the same time, additional entities related to this failure service will be erased in database.
8. Finally, the adapter manager sends a failure result to resource unification management module, which will next transmit it to upper-layer systems or modules.

83.5 Instance Analysis

The following section will take creation of service as an example to introduce service processes of adapter sub-modules corresponding to two SDN implementation technologies, OpenFlow and SR-MPLS, respectively.

83.5.1 *Design of Service Process of OpenFlow Adapter Sub-module*

Taking creation of a service as an example, the flowchart of service process of OpenFlow adapter sub-module is shown in Fig. 83.5. The details and steps are as follows.

1. After receiving service parameters, the OpenFlow adapter sub-module translates them into a series of instruction sequences via instruction translation function. According to these instructions, firstly this sub-module retrieves information of physical ports, which service path passes through in sequence, as well as physical nodes that they belong to. Then it queries information of parameters required by methods in northbound interface, such as names of bridge in these physical nodes, names of these physical ports in bridge and so on. After that, it activates these

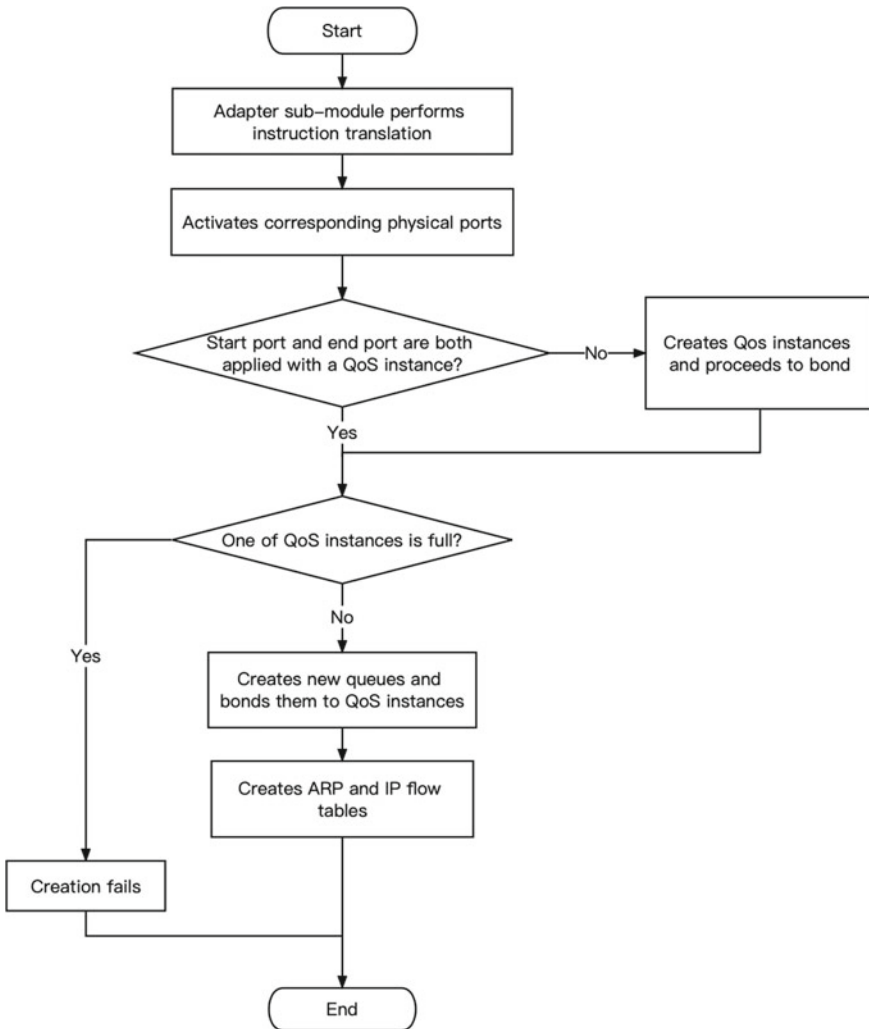


Fig. 83.5 Flowchart of process of service creation in OpenFlow adapter sub-module

ports in turns by invoking methods in northbound interface of OpenDaylight controller. (No invocation if the port is in open state)

2. This sub-module finds the start port and the end port of service path, and judges whether these two ports are applied with a QoS instance respectively. If at least one port not, the same number of QoS instances will be created by controller interface invocation to be bonded to the ports without QoS instance in underlying devices. Besides, QosID distributed by this sub-module and QosUUID generated by OpenDaylight controller will be saved as extensive attributes of the ports into database. (One port can be only applied with one QoS instance at most.)

3. After confirming that both ports are applied with QoS instances, this module continue to determine whether these QoS instances respectively contain 8 rate-limiting queues (One QoS instance can accommodate 8 rate-limiting queues at most). If one of the QoS instances contains 8 queues, which indicates that at least one port has been fully occupied by services, failure result of service creation will be sent back to the adapter manager. Otherwise, creation process will be proceeded by reason that both ports are able to contain more rate-limiting queue.
4. When continuing to perform creation process, this sub-module creates a rate-limiting queue for these two QoS instances respectively by controller interface invocation. The attributes, such as ID, UUID, queue number (range from 0 to 7), service bandwidth, service ID etc., of these two queues that are regarded as additional entities will be saved to database. And then this sub-module appends queues to related QoS instances in underlying devices by invocation of interface of SDN controller.
5. Finally, this sub-module creates ARP and IP flow tables according to information of ports that service path passes by in sequence. (The parameters required by flow tables include datapath ID of bridge in physical node, OpenFlow ID of ports, IP of source and destination terminals, queue number, etc.)
6. This sub-module succeeds in accomplishing creation process of service, after creating flow tables.

83.5.2 Design of Service Process of SR-MPLS Adapter Sub-module

Taking creation of a service as an example, the flowchart of service process of SR-MPLS adapter sub-module is shown in Fig. 83.6. The details and steps are as follows.

1. After receiving service parameters, the SR-MPLS adapter sub-module translates them into a series of instruction sequences via instruction translation function. And then it determines the head node, the tail node and SR labels of links passed by according to service path. It invokes methods in northbound interface of iMaster controller to create two unidirectional SR tunnels at the head node and the tail node respectively according to service bandwidth and information above. Besides, the information of SR tunnels, which are regarded as additional entities by bonded with service ID, will be saved in database.
2. This sub-module invokes controller interface to generate other resources required by service in underlying devices. These are ACL rule, traffic classification and traffic behavior. Besides, the information of these entities, which are regarded as additional entities by bonded with service ID, will be saved into database. And then it continues to invoke methods in northbound interface of controller, so that not only ACL rule, which IPs of source and destination terminals are appended in, is attached to a traffic classification as a matching condition, but also action

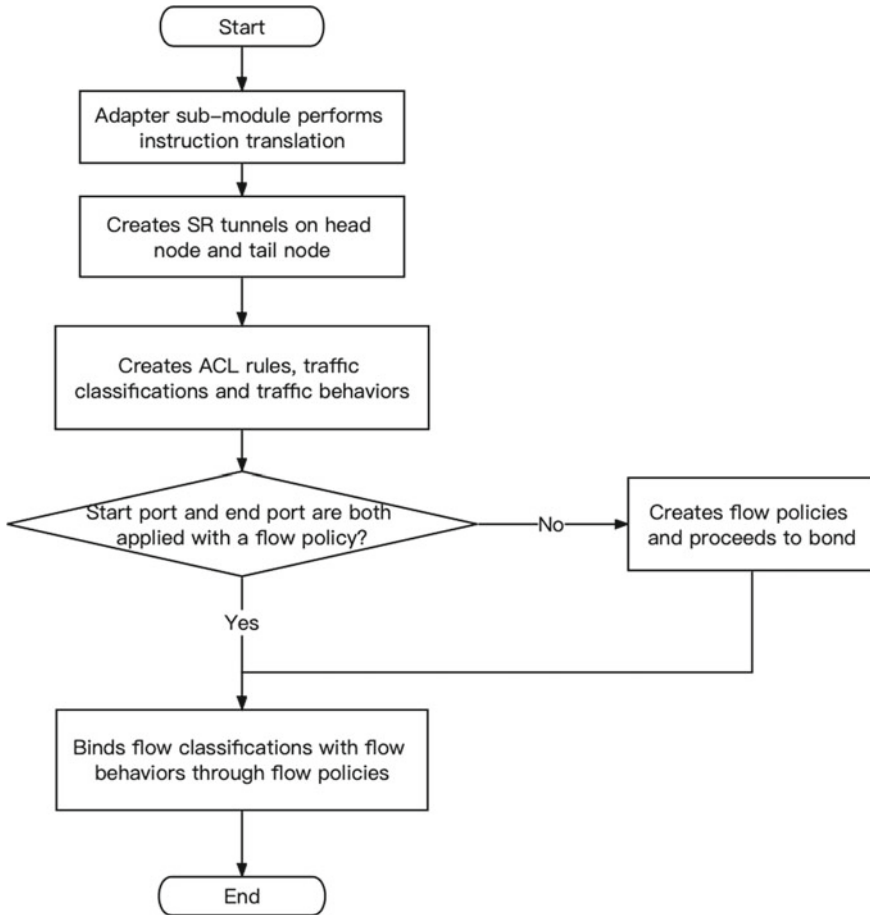


Fig. 83.6 Flowchart of process of service creation in SR-MPLS adapter sub-module

of the flow behavior is set to redirect to a SR tunnel. The process above will be performed twice by reason that there are two SR tunnels.

3. This sub-module finds the start port and the end port of service path, and judges whether these two ports are applied with a flow policy in inbound direction respectively. (One port can be only applied with one flow policy at most). If at least one port not, the same number of flow policies will be created by invocation of controller interface to be bonded to these ports. Besides, flow policy name will be saved as an extensive attribute of the port into database.
4. Finally, this sub-module invokes controller interface, so that flow policies applied on the start node and the end port are used as carriers to bind flow classifications with flow behaviors in underlying devices. After that, when packets of this service enter the start port or the end port, the flow policy bound to this port will come into effect. The packets will be matched by the ACL rule on the flow classification, and

finally be redirected to corresponding SR tunnel. In the end, underlying devices realize communication between terminals of this service.

83.6 Conclusion

Through extracting common traits from different SDN network domains, the general SDN controller system framework proposed in this paper succeeds in unifying and managing network resources to solve the difficulties of orchestration of cross-domain service in multi-domain heterogeneous SDN networks. This system framework divides overall adaptation module into respective sub-modules according to SDN technologies applied in different domains so that discrepancies between technologies only embody in sub-module. Besides, in adapter module, sub-modules provide the same interface to adapter manager, thus with great scalability. When there is a requirement to manage another SDN domain, it only requires to develop a new sub-module in adapter module according to the same interface and design principle.

However, in the scenario that network devices, which applied with the same SDN implementation technology, locate in multiple SDN domains due to being produced by different manufacturers, it is still necessary to develop multiple sub-modules for corresponding domains because of slight differences between northbound interfaces of SDN controllers from different manufacturers. The further optimization object is to ensure that differences between SDN network domains, in which devices are produced from different manufacturers but with the same SDN implementation technologies, should be only embodied in instruction translation function in adapter sub-module. In this scenario, it is still necessary to develop quite different adapter sub-modules to manage devices applied with different SDN implementation technologies.

References

1. Yushen, W., Kai, Y., Wenyun, X.: Research on cloud network integration implementation scheme. *Telecom Power Technol.* **38**(1), 6 (2021)
2. Caiming, L., Rong, W.: network analysis of could computing under SDN context. *China New Telecommun.* **22**(4), 1 (2020)
3. Nan, C., Yongbing, F., Xiaowu, E., et al.: Research on the technology of application—oriented cloud data center network. *Telecommun. Sci.* **30**(9), 6 (2014)
4. Linze, W., Yongbing, F., Zhilan, H., et al.: Design and implementation on orchestrator for heterogeneous SDN data center solutions. *Telecommunications Science* **34**(11), 9 (2018)
5. Hongwei, S., Fengzhi, H.: Research on network slicing technology based on SRv6. *Electric Technol. Softw. Eng.* **16**, 4 (2020)
6. Xiongyan, T., Jichun, M., Chang, C., et al.: Achievements and experiences from SDN transformation of China Unicom 169 network. *Mobile Commun.* **43**(7), 5 (2019)
7. Ruixue, W., Xuetao, X., Sijun, W.: The network architecture and key technologies of China mobile's data center based on SDN. *Mobile Commun.* **43**(7), 6 (2019)

Chapter 84

Systematic Evaluation of the Efficacy and Safety of Rivastigmine in Combination with Memantine for Mild to Moderate Alzheimer's Disease Based on MCMC Algorithm



Hui Yue, Hong-rui Bao, Yan-yin Cui, Wen-xin Hou, and Hong-juan Wen

Abstract *Objective:* To systematically analyze the efficacy and safety of rivastigmine combined with memantine in the treatment of mild to moderate Alzheimer's disease. *Methods:* In this paper we searched the Chinese and English literature from the date of establishment to August 9, 2022, the included studies met the requirements of rivastigmine combined with memantine for the treatment of Alzheimer's disease as the trial group, and rivastigmine or memantine alone for the treatment of Alzheimer's disease was the control group and two researchers performed screening for inclusion, quality evaluation and risk assessment according to the criteria, extracted data and performed statistical analysis of mental status scores and adverse events using generalised linear model Meta-analysis with Markov chain Monte Carlo algorithm. *Results:* The final study included 8 publications containing 382 patients in the trial group and 376 patients in the control group, for a total of 758 patients. 8 studies had a total MMSE assessment score [weighted mean difference (WMD) = 1.52, 95% CI (0.32–2.73), $P = 0.01$] and 5 studies had adverse events [dominance ratio (RR) = 1.09, 95% CI (0.92–1.29), $P = 0.31$], and the results of the reticulated Meta-analysis remained generally consistent with the results of the binary Meta-analysis. *Conclusions:* The MCMC algorithm has a high degree of accuracy, the combination of rivastigmine and memantine has an advantage over single dosing in improving mental status in mild to moderate Alzheimer's disease, MMSE scores are influenced by multiple factors such as age and treatment period, and the combination has a better safety and tolerability profile.

H. Yue · H. Bao · Y. Cui · H. Wen (✉)

School of Health Management, Changchun University of Chinese Medicine, Changchun 130117, China

e-mail: 1007481182@qq.com

W. Hou

University of Melbourne, Melbourne, Australia

Keywords Rivastigmine · Memantine · Alzheimer's disease · MCMC · Systematic evaluation

84.1 Introduction

The pathogenesis of Alzheimer's disease (AD), commonly known as dementia, is not yet clear and there are no specific treatment options [1]. At present, the first-line drugs used for the treatment of AD include cholinesterase inhibitor (rivastigmine) and NMDA receptor antagonists (memantine) [2, 3]. A study has shown that rivastigmine, a cholinesterase inhibitor whose mechanism of action is to inhibit the release of acetylcholine, is used to treat cognitive impairment in early or mid-stage AD, but is less effective in patients with advanced AD. Memantine, on the other hand, is a class of NMDA receptor antagonists that theoretically reduce neuronal damage by inhibiting β -amyloid-induced neuronal hyperexcitability, and is often used in the treatment of mid- to late-stage AD [4]. The two classes of drugs have different mechanisms of action, and theoretically a combination treatment protocol is feasible, but the efficacy of the combination is controversial in different studies [5, 6]. The aim of this study was to use generalized linear model Meta-analysis with Markov chain Monte Carlo algorithm to compare domestic and international clinical studies of rivastigmine combined with memantine with single drug treatment for AD, and to investigate the synergistic effect of the combination of the two drugs, in order to provide an evidence-based basis for clinical treatment protocols for AD.

84.2 Materials and Methods

84.2.1 Search Strategy

The literature search was conducted using subject terms plus free words from the time of database construction to August 9, 2022. Chinese literature was searched in the China Knowledge Network database (CNKI), Wanfang database and Vip database, using "Alzheimer's disease", "Alzheimer's disease", "Alzheimer's disease", "dementia" "Cognitive impairment", "rivastigmine" and "memantine" were used as search terms, and a comprehensive search was conducted to obtain 158 articles on the relevant topics. In English, PubMed, EMBASE and Cochrane Library were searched for the terms, and 324 articles were obtained after a comprehensive search, a total of 482 papers were acquired.

84.2.2 Inclusion and Exclusion Criteria

Inclusion criteria: ① Chinese and English literature; ② clinical controlled studies; ③ clear diagnostic criteria, subjects met the diagnostic criteria for mild to moderate Alzheimer's disease and dementia; ④ combination of rivastigmine and memantine for Alzheimer's disease in the test group and single drug treatment in the control group; ⑤ clear descriptive information and specific interventions for the subjects; ⑥ quantitative statistical indicators, giving means and standard deviations, and complete and error-free data. Exclusion criteria: ① not in line with the content of the study topic; ② incomplete or incorrect information; ③ animal experiments; ④ conference papers, dissertations and journals of the same study, with journals selected for inclusion; ⑤ evaluation indicators not applicable to this study.

84.2.3 Observed Indicators

① The Mental State Simple Evaluation Scale (MMSE), a screening tool for cognitive impairment, has seven main components, with higher scores indicating higher cognitive functioning, has good validity and is widely accepted internationally [7]. ② Adverse drug events (ADES), adverse clinical events that occur during drug therapy and are not related to the purpose of treatment, are important safety monitoring indicators in clinical practice.

84.2.4 Data Extraction and Quality Evaluation

Data extracted for this study included study first author, time of publication, region of publication, diagnostic criteria, mean age, treatment regimen in the trial group, treatment regimen in the control group, evaluation time points, key outcome indicators and quality evaluation scores. The quality of the included literature was evaluated using the modified Jadad evaluation scale and the NOS evaluation scale, which were strictly applied according to the scoring criteria specified in each evaluation scale [8, 9]. The final Jadad score below 4 was classified as low quality literature and above 3 as high quality literature; the NOS score below 3 was classified as low quality literature, 4–6 as moderate quality literature and above 6 as high quality literature.

84.2.5 Methods

Statistical analysis of effect sizes was first performed using binary Meta, with measures expressed as weighted mean differences (WMD) and counts expressed

as dominance ratios (RR). The final validation was done using the Mesh Meta, along with plotting the Network relationship and probability ranking of the various interventions.

The generalised linear model provides a unified modelling framework for Bayesian mesh Meta analysis [10] and consists of a two-part foundation: the likelihood and the connectivity function. Typically the likelihood is defined by some unknown parameters, while the connection function maps these parameters to the whole real number, when the intervention effect can be assumed to be linear, i.e.

$$g(\gamma) = \theta_{ik} = \mu_i + \delta_{ik} \tag{84.1}$$

where g is the linking function, θ is the outcome effect for arm k of study i , and μ is the outcome effect for arm 1 (or the control group) itself. For the random effects model, we assume that the parameter δ is sampled from a random distribution.

$$\delta_{ik} \sim \text{Normal}, (d_{ik}, \sigma^2) \tag{84.2}$$

For fixed effects, the variance is simply set to zero.

When the outcome is a count over a defined period of time, in arm k of study i , r_{ik} is the number of events that occurred during the follow-up period, E_{ik} is the total person-hours, and λ_{ik} is the incidence rate, the likelihood is.

$$r_{ik} \sim \text{Poisson}, (\lambda_{ik}E_{ik}) \tag{84.3}$$

where the parameter to be estimated is λ , the incidence rate. And since the incidence rate can only be taken as a positive number, the connecting function is chosen as a logarithmic function so that the incidence rate can be mapped to the whole real number, i.e.

$$\theta_{ik} = \log(\lambda_{ik}) = \mu_i + \delta_{ik} \tag{84.4}$$

When the ending is continuous data, the central limit theorem guarantees the assumption of a normal distribution (or an approximately normal distribution), so that the likelihood is specified as

$$y_{ik} \sim \text{Normal}, (\theta_{ik}, se_{ik}^2) \tag{84.5}$$

The parameter to be estimated is θ , which is the mean of the k th arm in the i th study. And because of the natural linearity of continuous data, the link function does not need to be transformed in any way, i.e. using its original measure of.

$$\theta_{ik} = \mu_i + \delta_{ik} \tag{84.6}$$

Markov chains [11] in a known random process $\{X(t), t \in T\}$, let n be a positive integer chosen at random arbitrarily, the set of time parameters satisfies $t_1 < t_2, \dots,$

$P(X(t_1) = x_1, \dots, X(t_{n-1}) = x_{n-1}) > 0$, and its conditional distribution satisfies the following relation.

$$\begin{aligned}
 P\{X(t_n) \leq x_n | X(t_{n-1}) = x_{n-1}, \dots, X(t_2) = x_2, X(t_1) = x_1\} \\
 = P\{X(t_n) \leq x_n | X(t_{n-1}) = x_n\}
 \end{aligned}
 \tag{84.7}$$

84.3 Results

84.3.1 Results of the Literature Search

The 482 initially obtained papers were classified and processed, 342 papers were obtained by excluding duplicates, animal experiments and conference reports, and 41 papers were obtained after reading the titles and abstracts and analysing the topics. The literature that met the initial screening criteria was read in full, and eight articles were eventually included in this study [12–19]. The entire screening process was completed by two researchers in strict accordance with the criteria and independently, and any inconsistency in inclusion was resolved by joint consultation between the third researcher. The literature screening process is shown in Fig. 84.1.

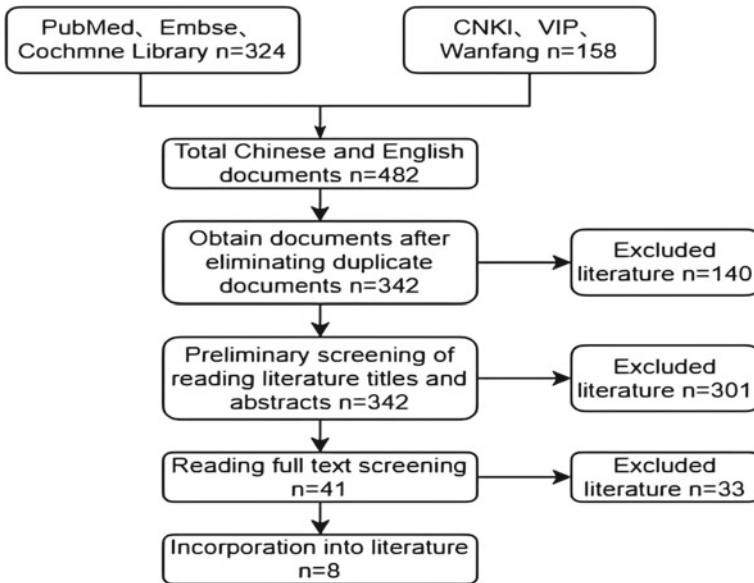


Fig. 84.1 Flow chart of literature screening

84.3.2 Literature Characteristics and Quality Evaluation

The included literature contained one English literature [12] and seven Chinese literature [13–19]. A total of 758 patients were included in the study, comprising 382 cases in the trial group and 376 cases in the control group. Two were of high quality by NOS scale scores and two were of high quality and four were of low quality by Jadad scale scores. Other basic information is shown in Table 84.1.

84.3.3 Meta-analysis Results

MMSE scores. The total MMSE assessment score was included in eight studies, with 381 cases in the test group sample and 376 cases in the control group sample. The heterogeneity of the results was high ($I^2 = 89\%$, $p < 0.00001$), so a random effects model was used. Total MMSE assessment scores were higher in the trial group than in the control group, with a weighted mean difference in MMSE WMD = 1.52, 95% CI (0.32–2.73, $P = 0.01$), as shown in Fig. 84.2. The difference was statistically significant.

Subgroup analysis of MMSE scores. Subgroup analysis was performed according to the difference in the mean age of the subjects and the treatment period, with the maximum mean age ≥ 80 years and treatment period ≥ 24 weeks being the senior long-term treatment group and vice versa for the conventional short-term treatment group, the results of which are shown in Fig. 84.3.

Adverse reactions. In terms of the incidence of adverse events, five clearly stated cases of literature were included for consolidation, with a sample size of 287 cases in the trial group and 280 cases in the control group. The results of the study showed low heterogeneity ($I^2 = 0\%$, $P = 0.66 > 0.1$), whereupon a fixed effects model was used, $RR = 1.09$, 95% CI (0.92–1.29, $P = 0.31$), as shown in Fig. 84.4. The difference was not statistically significant, with no significant difference in adverse events occurring in the combined treatment group compared to the single agent group.

84.3.4 Mesh Meta-analysis

Consistency analysis of outcome indicators MMSE, ADES, PSRF were 1.00, close to 1 indicating good model convergence, so the consistency model was used for the mesh analysis, and the mesh diagrams for the three drug interventions involved in this paper are shown in Fig. 84.5 (A for rivastigmine combined with memantine, B for rivastigmine alone and C for memantine alone).

According to the results of the reticulated meta-analysis, compared with rivastigmine monotherapy, rivastigmine combined with memantine ($MD = 1.28$, 95% CI

Table 84.1 General description of included studies

Author	Area	Diagnostic criteria	Average age (years)	Evaluation indicators	Intervention time	Quality evaluation
Farlow, M.R-2010 [12]	USA	DSM—IV	77.2 ± 8.18 77.3 ± 7.92	ADL\MMSE\ADES	25w	Jadad 3
ZXH-2013 [13]	China	DSM—IV	69.4 ± 12.3 69.4 ± 12.3	ADL\MMSE\ADAS-cog	24w	Jadad 3
XZQ-2015 [14]	China	DSM—IV	73.2 ± 6.9 73.2 ± 6.9	ADL\MMSE	24w	Jadad 3
XJ-2016 [15]	China	DSM—IV	71.9 ± 7.3 69.3 ± 7.8	ADL\MMSE\ADAS-cog	24w	Jadad 4
ZJ-2016 [16]	China	DSM—IV	68.7 ± 4.6 68.7 ± 4.6	ADL\MMSE\ADAS-cog\ADES	25w	NOS 7
HFLY-2019 [17]	China	DSM—IV	73.5 ± 4.8 74.0 ± 5.1	ADL\MMSE\ADES	24w	NOS 7
WYN-2019 [18]	China	DSM—IV	72.2 ± 8.2 74.2 ± 8.5	ADL\MMSE\ADAS-cog\ADES	4w	Jadad 4
FRQ-2021 [19]	China	2018 China Dementia Guidelines	75.3 ± 1.6 75.2 ± 1.7	ADL\MMSE\ADES	6w	Jadad 3

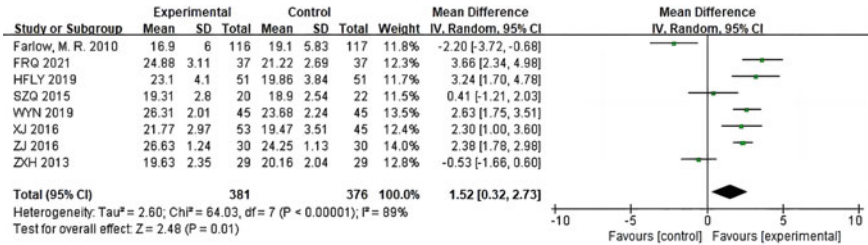


Fig. 84.2 MMSE forest plot after rivastigmine in combination with memantine and monotherapy

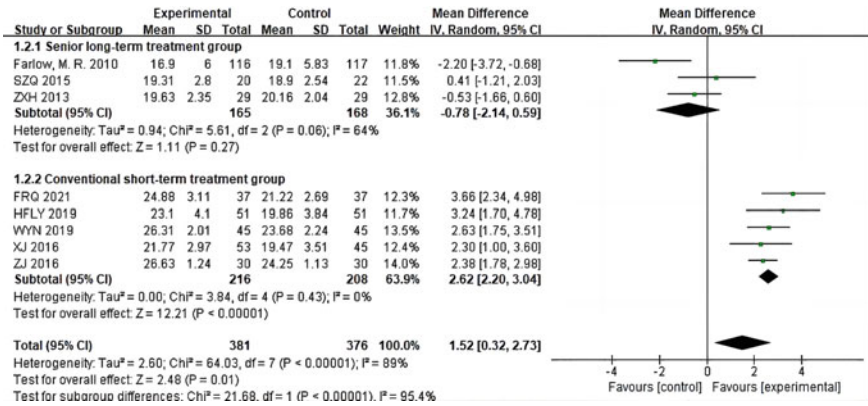


Fig. 84.3 Forest plot of MMSE subgroup analysis after rivastigmine in combination with memantine and monotherapy

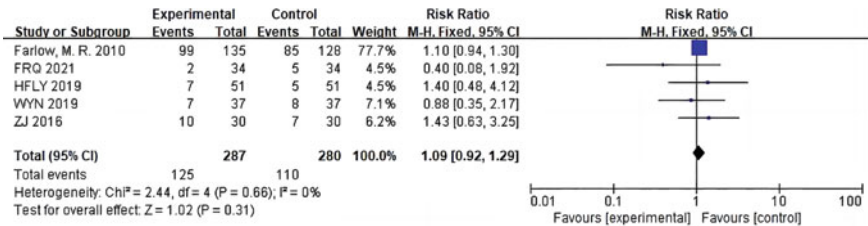


Fig. 84.4 Comparative forest plot analysis of ADEs after rivastigmine in combination with memantine and monotherapy

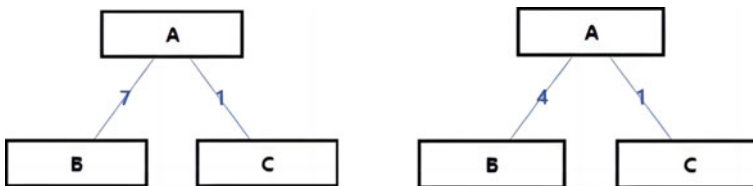


Fig. 84.5 Network diagram of effectiveness and safety of three drug interventions

Table 84.2 Results of mesh meta-analysis of the effectiveness of different drug treatments

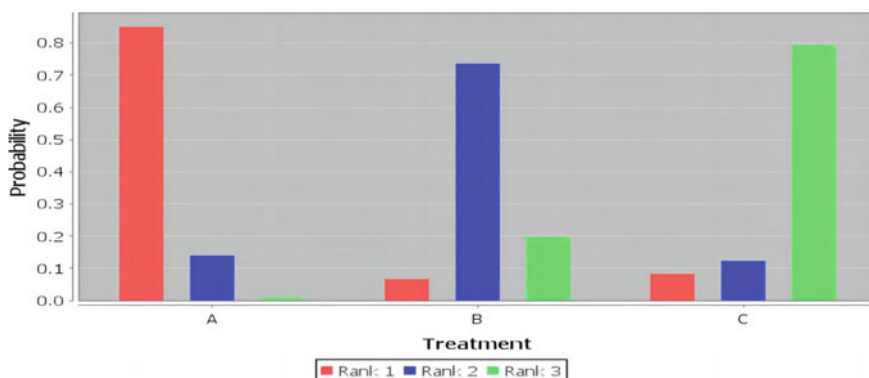
A combination		
1.28 (− 0.61, 3.06)	B rivastigmine	
3.24 (− 1.71, 8.22)	1.94 (− 3.30, 7.22)	C memantine

Table 84.3 Results of mesh meta-analysis on safety of different drug treatments

A combination		
1.13 (0.53, 2.05)	B rivastigmine	
1.53 (0.32, 7.29)	1.36 (0.26, 7.77)	C memantine

(− 0.61 to 3.06, $P < 0.05$); compared with memantine monotherapy, rivastigmine combined with memantine (MD = 3.24, 95% CI (− 1.71 to 8.22, $P < 0.05$); compared with rivastigmine (RR = 1.13, 95% CI (0.53–2.05, $P > 0.05$); safety of rivastigmine combined with memantine compared to monotherapy (RR = 1.53, 95% CI (0.32–7.92), $P > 0.05$); safety of rivastigmine combined with memantine compared to memantine monotherapy (RR = 1.53, 95% CI (0.32–7.92), $P > 0.05$), the results of the reticulated meta-analysis were consistent with the results of the binary meta-analysis remained generally consistent, with significant efficacy and non-significant safety differences for the combination compared to single dosing, as shown in Tables 84.2 and 84.3.

Based on the probability weights, the top three rankings for optimal likelihood of efficiency were: rivastigmine combined with memantine (85%) > rivastigmine alone (74%) > memantine alone (79%). The top three rankings for the optimal likelihood of adverse effects were: memantine alone (61%) > rivastigmine alone (43%) > rivastigmine combined with memantine (44%), as shown in Figs. 84.6 and 84.7 and Table 84.4.

**Fig. 84.6** Probability ranking chart of three drug intervention effects

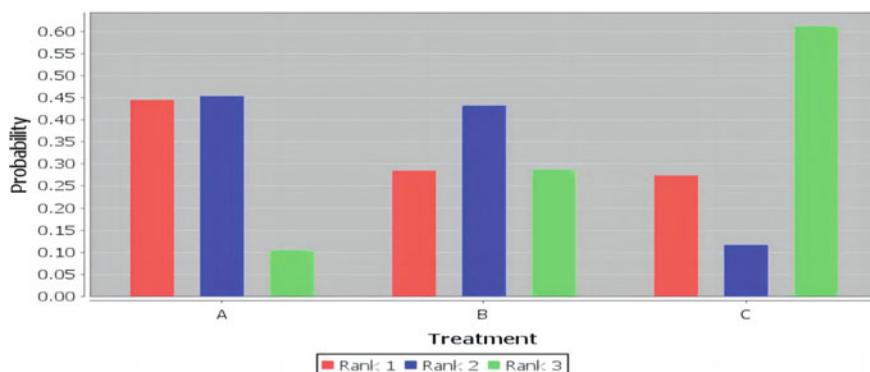


Fig. 84.7 Probability ranking chart of the safety of three drug interventions

Table 84.4 Probability ranking table of efficacy and safety of three drug interventions

Drug	Rank1	Rank2	Rank3	Drug	Rank1	Rank2	Rank3
A	0.85	0.14	0.01	A	0.44	0.45	0.10
B	0.07	0.74	0.20	B	0.28	0.43	0.29
C	0.08	0.12	0.79	C	0.27	0.12	0.61

84.4 Discussion

The study used the Markov chain-Monte Carlo (MCMC) algorithm to synthesize the a priori information about the unknown parameters with the sample information through a Bayesian analysis method, and then based on the posterior information is then inferred from the posterior information to evaluate the outcome variables.

The MCMC algorithm yielded the following results: a combination of efficacy and safety indicators showed that the combination of rivastigmine and memantine was generally effective in improving mental status, and that the combination had some advantages over single-agent treatment, with a relatively stable safety profile. A subgroup analysis showed that the effect of early drug treatment was more pronounced in patients with milder disease at a younger age, while the combination treatment did not show a significant effect compared to monotherapy, but still had a good effect in delaying the course of the disease. The results of the Bayesian mesh meta-analysis were generally consistent with the results of the binary meta-analysis, with the combination being superior to rivastigmine and memantine alone respectively in terms of efficacy, and memantine alone being superior to rivastigmine alone in terms of safety, but the differences were not statistically different.

The MCMC algorithm was simulated using 4 chains based on traditional analyses with an initial value of 2.5, a refinement iteration step size of 10, 20,000 adjusted iterations and 50,000 simulated iterations, and the included data were assessed and processed a priori through a better convergent fit to a consistency model. The posterior

probabilities were used to rank all the interventions analyzed, and the estimates were more accurate and the modelling was more flexible as it overcame the drawbacks of the frequency science method in estimating the maximum likelihood function through constant iterations in parameter estimation, which is prone to instability and biased results. The limitations of this study are that some of the included studies have ambiguous randomization treatments such as randomized grouping and blinding, which have some impact on the quality of the articles, some studies have differences in evaluation time points and diagnostic criteria, and the overall sample size needs to be improved.

References

1. Reitz, C.: Genetic diagnosis and prognosis of Alzheimer's disease: challenges and opportunities. *Expert Rev. Mol. Diagn.* **15**(3), 339–348 (2015)
2. Zhang, L., Fan, Z., Zhang, Z., et al.: Research progress in the pathogenesis of Alzheimer's disease and related therapeutic drugs. *Chin. J. Pharm. Chem.* **31**(06), 438–446+469 (2021)
3. Zhu, J., Zhang, Z., Dong, Y., Chen, N.: Research progress in Alzheimer's disease and its therapeutic drugs. *Chin. Pharmacol. Bull.* **34**(12), 1629–1634 (2018)
4. Zhong, F., Wang, L., Lai, H.: Clinical efficacy of memantine combined with donepezil in the treatment of elderly patients with moderate to severe Alzheimer's disease. *Contemp. Med.* **28**(14), 25–28 (2022)
5. Grossberg, G.T., Manes, F., Allegri, R.F., et al.: The safety, tolerability, and efficacy of once-daily memantine (28 mg): a multinational, randomized, double-blind, placebo-controlled trial in patients with moderate-to-severe Alzheimer's disease taking cholinesterase inhibitors. *CNS Drugs* **27**(6), 469–478 (2013)
6. Choi, S.H., Park, K.W., Na, D.L., et al.: Expect Study Group. Tolerability and efficacy of memantine add-on therapy to rivastigmine transdermal patches in mild to moderate Alzheimer's disease: a multicenter, randomized, open-label, parallel-group study. *Curr. Med. Res. Opin.* **27**(7), 1375–1383 (2011)
7. Zhou, X., Xie, M., Tao, J., et al.: Research and application of the simple mental state examination scale. *Chin. J. Rehabil. Med.* **31**(06), 694–696+706 (2016)
8. Zou, Q.: Adding the modified Jadad method to evaluate the rationality of drug use beyond the instructions: taking naloxone as an example. *Pharm. Clin. Res.* **29**(01), 61–64 (2021)
9. Yuan, M.Z., Li, F., Tian, X., et al.: Risk factors for lung infection in stroke patients: a meta-analysis of observational studies. *Expert Rev. Anti Infect. Ther.* **13**(10), 1289–1298 (2015)
10. Saramago, P., Chuang, L.H., Soares, M.O.: Network meta-analysis of (individual patient) time to event data alongside (aggregate) count data. *BMC Med. Res. Methodol.* **14**, 105 (2014)
11. Fill, J.A.: An interruptible algorithm for perfect sampling via Markov chains. In: Proceedings of the 29th Annual ACM Symposium on Theory of Computing (STOC), pp. 688–695 (1997)
12. Farlow, M.R., Alva, G., Meng, X., Olin, J.T.: A 25-week, open-label trial investigating rivastigmine transdermal patches with concomitant memantine in mild-to-moderate Alzheimer's disease: a post hoc analysis. *Curr. Med. Res. Opin.* **26**(2), 263–269 (2010)
13. Zhang, X.: Clinical efficacy of acetylcholinesterase inhibitors combined with memantine hydrochloride in the treatment of senile dementia. *Chin. J. Gerontol.* **33**(19), 4681–4685 (2013)
14. Shao, Z., Liu, J., Wang, R., et al.: Analysis of the effect of acetylcholinesterase inhibitors combined with memantine hydrochloride in the treatment of Alzheimer's disease. *Chin. J. Clin. Health* **18**(05), 452–456 (2015)
15. Xiao, J., Tan, S., Yun, X., et al.: The effect of combined treatment of memantine hydrochloride and rivastigmine on the ability of daily life of patients with Alzheimer's disease. *Chin. Med. Sci.* **6**(19), 23–27 (2016)

16. Zhang, J., Cao, Y., Li, W.: Analysis of the effect of acetylcholinesterase inhibitors combined with memantine hydrochloride in the treatment of senile dementia. *J. Pract. Clin. Med.* **20**(21), 136–138 (2016)
17. Huang, F., Le, Y.: Clinical efficacy of glutamate receptor antagonist combined with rivastigmine in the treatment of Alzheimer's disease. *J. Pharm. Forum* **40**(12), 95–97 (2019)
18. Wang, Y., Zhang, R., Wang, L., et al.: The effect of memantine combined with rivastigmine on cognitive function and serum homocysteine and uric acid levels in patients with Alzheimer's disease. *China Pharm.* **28**(13), 66–68 (2019)
19. Feng, R., Jin, W., Jia, R.: Analysis of curative effect of memantine combined with rivastigmine tartrate on female patients with Alzheimer's disease. *Contemp. Med.* **19**(17), 116–118 (2021)

Chapter 85

Perlite Pressure Calculation and Finite Element Simulation Study of LNG Storage Tank



Xu Chen, Juan Su, Shuqian Tong, Ye Chen, and Cheng Chen

Abstract Because perlite has good cold insulation effect and is widely used in LNG full capacity tanks, in this paper, the final perlite lateral pressure can be obtained by repeated iterative calculation using Janssen formula, and the perlite lateral pressure is applied to the inner tank of LNG full capacity tanks for statics finite element simulation. The results show that the deformation of the inner tank is within a reasonable range. At the same time, the perlite lateral pressure buckling analysis is carried out for the inner tank of the LNG tank under the empty tank state. The results show that the tank does not buckle under the empty tank state, and the critical buckling pressure of the inner tank is 3.14 times of the applied pressure, which verifies the rationality of the tank design.

Keywords Perlite · Pressure calculation · LNG storage tank inner tank · Buckling analysis · Finite element simulation

85.1 Introduction

As a clean energy, natural gas plays a more important role in modern industry. LNG is easy to store within a relative small volume, so it has obvious advantages in storage and transportation. At present, the full-capacity storage tank has become the mainstream storage tank for liquefied natural gas due to its safety and reliability. Therefore, its importance is self-evident [1–7]. At present, researchers have conducted a lot of research on the structure of the full-capacity storage tank [8, 9]. Large-scale LNG full-capacity storage tanks have high requirements for cold insulation. Perlite is usually used for cold insulation between the inner and outer tanks. Some researchers have conducted related research on the cold insulation performance and pressure calculation of perlite [10–12].

X. Chen (✉) · J. Su · S. Tong · Y. Chen · C. Chen
CNOOC Offshore Oil Engineering Co. Ltd, Tianjin, China
e-mail: Chenxu18@cooec.com.cn

The initial filling of perlite in the full-capacity storage tank has a compressive effect on the elastic felt in the storage tank. This initial pressure can be calculated using the Janssen formula for calculating granular materials [13–15]. The initial pressure causes the elastic felt to shrink, which can be obtained from the compression curve of the elastic felt. The amount of compression causes changes in the thickness of the annular perlite, so the lateral pressure can be recalculated according to the Jensen formula, and this iterative process is repeated until the calculation results converge to obtain the final lateral pressure of the perlite.

85.2 Relevant Dimensions and Material Parameters

Diameter of inner tank in cold state ($-165\text{ }^{\circ}\text{C}$) (Table 85.1):

$$D' = D - D \times \alpha \times \Delta T \quad (85.1)$$

When the inner tank is cold, the radius shrinks:

$$d = (D_i - D')/2 \quad (85.2)$$

According to the Quietflex material data, the temperature change of the inner tank causes the compression of the elastic felt to be 0.235 mm/mm, and the compression of the elastic felt to be df , which can refer to the chart provided by the supplier, as shown in Fig. 85.1.

Table 85.1 Relevant dimensions and material parameters

Inner tank diamete	D_i
Inner diameter of outer tank	D_o
Extreme maximum temperature X7Ni9 steel linear expansion coefficient	$\alpha = 9.2 \times 10^{-6}$
Elastic felt compression caused by temperature changes in the inner tank	0.235 mm/mm
Density of perlite	$\rho = 66\text{ kg/m}^3$
Friction coefficient of perlite	$\mu = 0.70$
Gravitational acceleration	$g = 9.81\text{ m/s}^2$
Shrinkage of elastic felt	df
Elastic felt thickness	tab

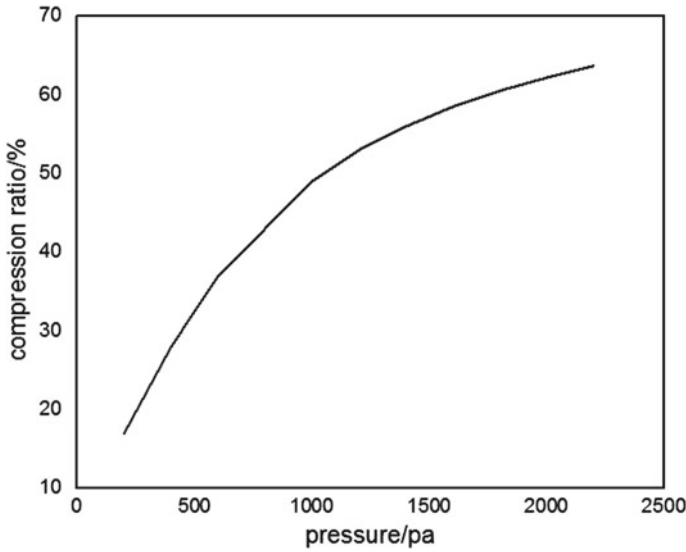


Fig. 85.1 Typical elastic felt curve

85.3 Calculation Method

85.3.1 Calculation Method

The initial pressure is calculated using the Janssen formula for calculating granular materials. The initial pressure causes shrinkage of the elastic felt, which can be obtained from the compression curve of the elastic felt. The amount of compression causes the thickness change of annular perlite, so the lateral pressure can be recalculated according to Janssen formula. Repeat this iterative process until the results converge. The calculation steps are as follows:

- (1) Determine the inner diameter of outer tank (i.e. outer diameter of perlite) and inner tank, as well as the initial thickness of elastic felt, so as to determine the initial inner diameter of perlite (i.e. outer diameter of elastic felt);
- (2) The pressure of perlite is obtained from the outer diameter and inner diameter of perlite according to Janssen formula. This pressure acts on the elastic felt, and the compression rate of elastic felt is obtained from the pressure according to the following figure;
- (3) From the compression rate, we can get the new thickness of elastic felt and the new inner diameter of perlite, calculate the Janssen pressure again, get the new pressure of perlite, and check the compression rate of elastic felt again;
- (4) In this way, until the compression rate of the elastic felt is constant, this compression rate is the final compression rate under the pressure of perlite.

Iterative calculation:

Inner tank radius $R_i = D_i/2$

Outer diameter of perlite $R_o = D_o/2$

Initial value of inner diameter of perlite $R_{pi}(0) = R_i + \text{tab}$.

Janssen formula calculates pressure:

$$p = \frac{(D_o - D_i)\rho g}{4\mu} \left[1 - \exp\left(\frac{-4\mu kh}{D_o - D_i}\right) \right] \quad (85.3)$$

P —pressure of perlite (kPa);

K —lateral pressure coefficient, $k = (1 - \sin \theta)/(1 + \sin \theta)$, θ is the internal friction angle of perlite, generally 30° ;

H —Inner tank height (m).

The Janssen formula is simplified as:

$$P = \rho * g * (R_o - R_{pi})/2\mu \quad (85.4)$$

Iteration formula of original perlite inner diameter:

$$R_{pi(n)=R_{pi}(n-1) - d - \text{tab} * d_f \quad (85.5)$$

When using the original iterative formula for calculation, misunderstandings can easily occur, and it is easy to include d_f as the total compression amount in the calculation, resulting in non convergence of the calculation results.

Improved iteration formula of perlite inner diameter:

$$R_{pi}(n) = R_{pi}(n-1) - d - \text{tab} * df(n=1) \quad (85.6)$$

$$R_{pi}(n) = R_{pi}(n-1) - \text{tab} * \Delta df (n > 1) \quad (85.7)$$

In which, Δdf represents the increase in compression amount.

85.3.2 Trial-Calculation Case

In which, Δdf represents the increase in compression amount.

According to the results of the calculation example, the improved formula is similar to the previous results, and the calculation results converge. Some deviations are due to the former not considering the radius contraction of the inner tank when it is cold.

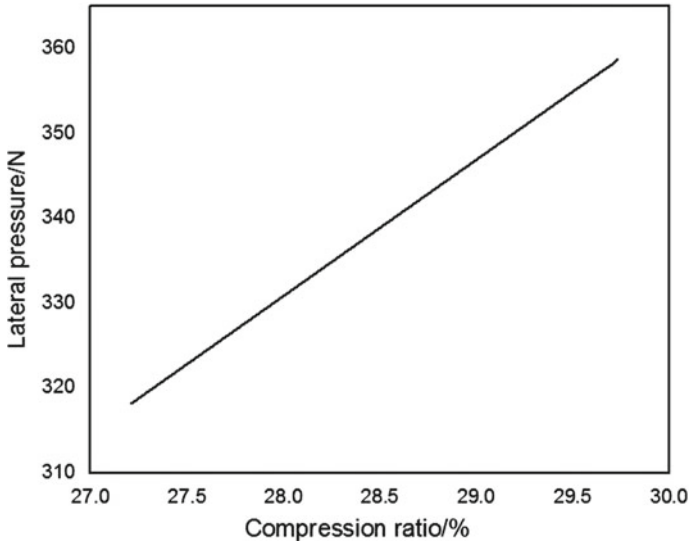


Fig. 85.2 Iterative calculation process of a domestic project

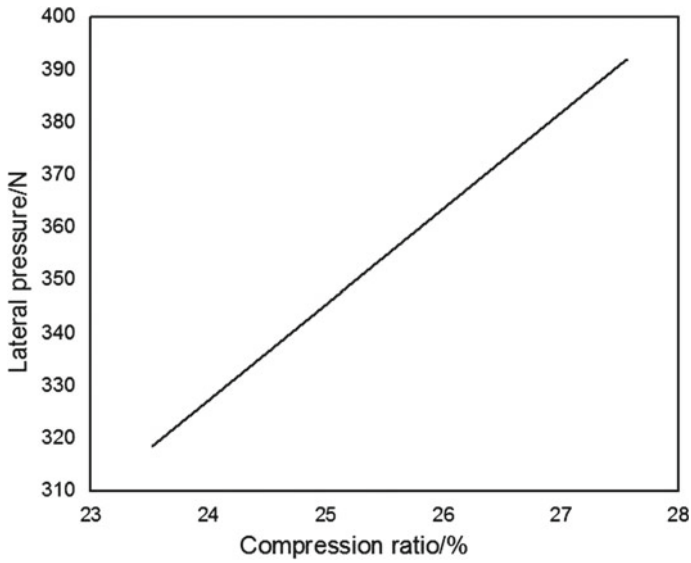


Fig. 85.3 Improved iterative calculation process

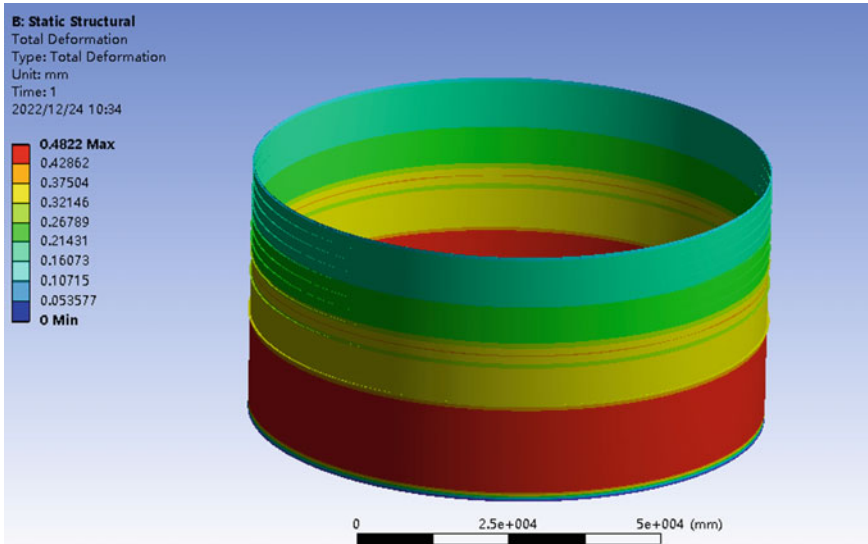


Fig. 85.4 Statics analysis results

85.4 Finite Element Analysis

85.4.1 Statics Analysis

According to the iterative calculation, the final side pressure of perlite is obtained. In order to analyze the deformation of the inner tank of LNG tank under this side pressure, an equal proportion model of the inner tank of LNG tank is established. The deformation of the inner tank under the action of perlite side pressure is shown in Fig. 85.4. According to the deformation results, the deformation of the inner tank under this maximum side pressure is within a reasonable range, so the tank design is reasonable.

85.4.2 Buckling Analysis

Due to the thin-walled cylindrical structure of the inner tank, this type of structure is prone to buckling in engineering. To verify whether the inner tank of LNG storage tanks will buckle, buckling verification analysis should be conducted. The inner tank is only subject to perlite pressure in the empty tank state. During the buckling analysis, perlite pressure is applied to the outside of the tank for buckling analysis. The results are shown in Fig. 85.5. According to the buckling analysis, under this scheme, the critical buckling pressure of the inner tank is 3.14 times of the applied

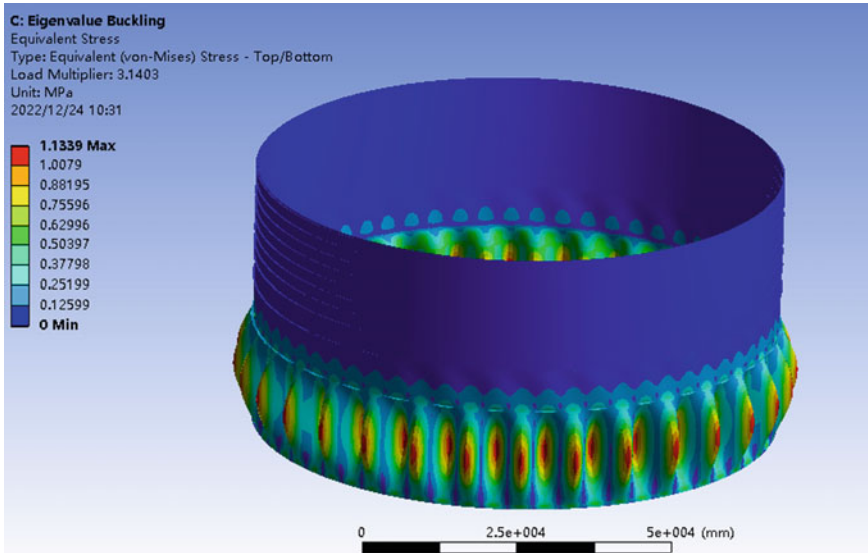


Fig. 85.5 Buckling analysis results of inner tank

pressure, which is greater than the safety factor 3. Therefore, the inner tank will not buckle under this working condition, meeting the design requirements.

85.5 Conclusion

- (1) By using the improved Janssen formula through iterative calculation, convergence and correct results can be obtained;
- (2) Through finite element analysis, it is verified that the deformation of the inner tank under the pressure of perlite is within a reasonable range and will not buckle when the tank is empty.

References

1. Chen, C., Bian, X., Tong, S., Chen, X., Wang, Z., Zhang, J.: Research on the aspect ratio and material consumption of LNG bimetallic full capacity storage tanks. *Petroleum Chem. Equipment* **26**(03), 102–112 (2023)
2. Weng, Z.: Analysis of the structure and performance of full capacity liquefied natural gas (LNG) storage tanks. *Chem. Manage.* (20), 5–6 (2016)
3. Xiang, H., Yang, S.: Exploration of the cold insulation system and its performance for large LNG full capacity storage tanks. In: *The Russian Research Association of Chinese Students*

- and Scholars in Russia. Proceedings of the First Russian Research Symposium of Chinese Students and Scholars in Russia, pp. 119–128 (2016)
4. The construction of China's first independently developed large-scale LNG full capacity storage tank project has started. *Sinopec* (05), 12 (2016)
 5. Zhang, S.: Seismic Response Analysis of 160000 m³ LNG Full Capacity Storage Tank. Harbin Engineering University (2016)
 6. Li, X.: Research on Optimization Design of Large Full Capacity LNG Storage Tank Piles. Tianjin University (2014)
 7. Du, L., Guo, L., Dong, Z., Gao, F., Tang, Y.: Calculation of perlite side pressure in LNG full capacity tank. *Petrochem. Equip.* **42**(06), 47–49 (2013)
 8. Wang, W.: Research on Key Issues in the Design of Large Full Capacity LNG Storage Tanks. Tianjin University (2014)
 9. Liu, S.: Research on the Structure and Performance of Full Capacity Liquefied Natural Gas (LNG) Storage Tanks. South China University of Technology (2009)
 10. Yang, F., Zhang, C., Qu, C., Duan, P.: On site perlite expansion filling technology for large LNG storage tanks. *Gas Heat* **35**(02), 71–76 (2015)
 11. Yang, F., Zhang, C., Huang, H., Zhang, B., Fan, J.: Optimization design of perlite cold insulation for super large LNG storage tanks. *Chem. Equip. Pipeline* **59**(06), 37–46 (2022)
 12. Chen, R., Zhang, G., Xue, F., Zhang, P., Wei, C.: Study on settlement calculation of LNG tank expansion perlite. *Low Temperature Build. Technol.* **43**(09), 149–152 (2021)
 13. Peng, S., Zhou, D., Xie, B.: Analysis of LNG storage tank safety: a comprehensive model approach with ANP and normal cloud. *Appl. Sci.* **12**(23) (2022)
 14. Chung, M., Kim, J., Kim, J.-K.: Feasibility study on the wide and long 9%Ni steel plate for use in the LNG storage inner tank shell. *Steel Compos. Struct.* **32**(5) (2019)
 15. Haddar, M., Hammami, M., Baccar, M.: Numerical parametric study of a cooling system for an LNG storage tank. *Oil Gas Sci. Technol.* **74** (2019)

Chapter 86

Study on the Steel Lazy Wave Riser Configuration via a Simplified Static Model Considering Critical Sensitive Factors



Hui Wang, Ye Chen, Song Liu, Ning He, Zhen Tian, and Jianwen He

Abstract Catenary risers have been broadly adopted for mass transportation between seabed and platform during offshore oil and gas production due to its characteristics such as simple construction and relative low delivery cost. However, because of the dynamic conditions in deep water, a simple steel catenary riser (SCR) is vulnerable to yielding and short fatigue life at the critical sections such as hang-off zone (HOZ) and the touch down zone (TDZ). The conventional SCRs are subjected to even more challenges for ultra-deep field developments. Therefore, many new riser system concepts have been proposed in order to solve the related stress and fatigue challenges, in which steel lazy wave catenary riser (SLWR) is the most popular one in recent years. In this work, a simplified static model and tool based on catenary theory and static equilibrium in mechanics was developed for an initial screening of SLWR configuration in the riser early design phase. According to the analysis, it is implied that each section of the SLWR is conformed to a hyperbolic function numerically. Using the configuration tool developed, a trial calculation case has been carried out assuming a water depth of 1500 m, and the critical sensitive factors including hang-off angle, elevation, and content density have been discussed respectively. The findings can provide certain reference information for the further study and detailed design in the future engineering phases.

Keywords Steel lazy wave riser · Static configuration · Hang-off angle · Vertical elevation · Content density

H. Wang · Y. Chen (✉) · S. Liu · N. He · Z. Tian · J. He
CNOOC Offshore Oil Engineering Co. Ltd, Tianjin, China
e-mail: upcchenye@163.com

86.1 Introduction

The main focusing area for offshore oil and gas field development has been turning from shallow to deep and ultra-deep water depth. Riser systems, which provide flow channels for oil and gas transfer between subsea production systems and floating platforms, play an important role during offshore hydrocarbon production. Up to now, many riser systems including top tension risers, steel catenary risers and hybrid risers have been developed and applied, in conjunction with various floating system concepts. Each of these riser systems, along with hull and mooring systems, has its adaptability and limitations [1].

Steel catenary riser (SCR) is one of the most popular systems adopted in many mid to deep water depth projects, as its construction is relative simple, and cost effectively for installation and delivery. However, because of the severe environmental condition in deepwater and the dynamic response of the platforms, the SCRs are vulnerable to yielding and short fatigue life at the critical sections such as hang-off zone (HOZ) and the touch down zone (TDZ). The conventional SCRs are subjected to even more challenges for ultra-developments, limiting the application of this concept [2]. Consequently, a series of countermeasures need to be adopted to relieve the fatigue, for which steel lazy wave catenary riser (SLWR) is one of the most popular concepts which has been used in several deepwater hydrocarbon production projects in the past ten years [3].

With the assistance of buoyancy modules, the whole steel riser length can be divided into three sections, such as hang-off section, buoyancy section and touch-down section. The buoyancy section could decouple the dynamic motions of the hull platform at the touch down point of the riser. As a result, the riser payloads to the platform can be reduced and the dynamic response of the riser can be controlled reasonably, by which the fatigue and strength performance at each end of the risers can be improved [4, 5].

Generally, the basic configuration of SLWRs is designed and optimized during the preliminary and detailed design, installation phases by certain commercial finite element softwares, like Orcaflex, Flexcom and Abaqus [6]. But the corresponding dynamic analysis based on the complex coupled numerical models always demands a lot of computing power, calculating cycle and post processing [7]. In order to facilitate high-volume screening of SLWR configuration at the beginning of the production projects and improve operation efficiency, a simplified static model based on catenary theory and static equilibrium in mechanics was adopted to evaluate the general impacts of the critical sensitive factors including hang-off angle, turning point elevation and content density etc. The findings can provide certain reference for a qualitative evaluation and an efficient engineering judgement, which are valuable to engineering contractors and operators.

86.2 Numerical Model

A traditional SCR [8], without consideration of potential slight weight variations caused by strakes, marine growth or special shape joints, can be assumed as a cord of uniform density and cross-section subsea pipeline hanging on two ends under gravity and buoyancy, which can be generally expressed by a hyperbolic cosine function in rectangular coordinates according to the classical mathematical theory,

$$y = \alpha \left(\cosh \frac{x}{\alpha} - 1 \right) \tag{86.1}$$

in which the initial catenary curvature radius α can be calculated as,

$$\alpha = \frac{N}{Q} = \frac{\sqrt{1 + \left(\frac{dy}{dx} \right)^2}}{\frac{d^2y}{dx^2}} \tag{86.2}$$

where the Q is the wet weight,

$$Q = (\rho_p - \rho_w) A_p \sqrt{dx^2 + dy^2} \tag{86.3}$$

The relationship between initial catenary curvature k and initial catenary curvature radius α is,

$$k = \frac{1}{\alpha \cosh^2 \frac{x}{\alpha}} = \frac{\alpha}{(\alpha + y)^2} \tag{86.4}$$

The inclination angle β satisfies,

$$\tan \beta = \sinh \frac{x}{\alpha} \tag{86.5}$$

Then the total length of SCR can be obtained by the integral of each point,

$$S = \int \sqrt{\left(\left(\frac{dx}{dx} \right)^2 + \left(\frac{dy}{dx} \right)^2 \right)} dx = \alpha \sinh \frac{x}{\alpha} \tag{86.6}$$

Since SLWR is a special deformation of SCR with a certain segment equipped with external buoyancy modules, whose upward buoyancy per unit length in water is generally designed to be nearly twice the wet weight of the riser pipe self-weight, all the three sections: hang-off section, buoyancy section and touchdown section of the SLWRs should also be governed by hyperbolic cosine functions in static equilibrium, with different characterization coefficients and the same boundary conditions [9–11], as shown in Fig. 86.1.

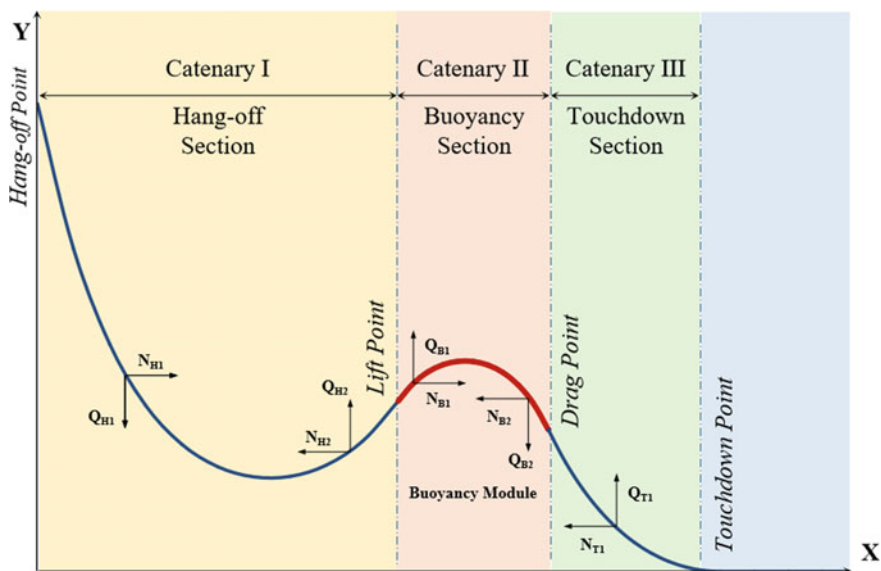


Fig. 86.1 Three catenary sections of SLWR for static analysis

For hang-off section, the Catenary I can be expressed as following,

$$y_H = \alpha_H \left(\cosh \frac{x_H}{\alpha_H} - 1 \right) \tag{86.7}$$

$$\alpha_H = \frac{N_H}{Q_H} = \frac{\sqrt{1 + \left(\frac{dy_H}{dx_H} \right)^2}}{\frac{d^2 y_H}{dx_H^2}} \tag{86.8}$$

$$Q_H = (\rho_p - \rho_w) A_p \sqrt{dx_H^2 + dy_H^2} \tag{86.9}$$

$$k_H = \frac{1}{\alpha_H \cosh^2 \frac{x_H}{\alpha_H}} = \frac{\alpha_H}{(\alpha_H + y_H)^2} \tag{86.10}$$

$$S_H = \int \sqrt{\left(\left(\frac{dx_H}{dx} \right)^2 + \left(\frac{dy_H}{dx} \right)^2 \right)} dx = \alpha_H \sinh \frac{x_H}{\alpha_H} \tag{86.11}$$

For buoyancy section, the Catenary II can be expressed by following equations,

$$y_B = \alpha_B \left(\cosh \frac{x_B}{\alpha_B} - 1 \right) \tag{86.12}$$

$$\alpha_B = \frac{N_B}{Q_B} = \frac{\sqrt{1 + \left(\frac{dy_B}{dx_B}\right)^2}}{\frac{d^2 y_B}{dx_B^2}} \tag{86.13}$$

$$Q_B = (\rho_p - \rho_w)A_p \sqrt{dx_B^2 + dy_B^2} \tag{86.14}$$

$$k_B = \frac{1}{\alpha_B \cosh^2 \frac{x_B}{\alpha_B}} = \frac{\alpha_B}{(\alpha_B + y_B)^2} \tag{86.15}$$

$$S_B = \int \sqrt{\left(\left(\frac{dx_B}{dx}\right)^2 + \left(\frac{dy_B}{dx}\right)^2\right)} dx = \alpha_B \sinh \frac{x_B}{\alpha_B} \tag{86.16}$$

For touchdown section, the Catenary III can be expressed as followings,

$$y_T = \alpha_T \left(\cosh \frac{x_T}{\alpha_T} - 1 \right) \tag{86.17}$$

$$\alpha_T = \frac{N_T}{Q_T} = \frac{\sqrt{1 + \left(\frac{dy_T}{dx_T}\right)^2}}{\frac{d^2 y_T}{dx_T^2}} \tag{86.18}$$

$$Q_T = (\rho_p - \rho_w)A_p \sqrt{dx_T^2 + dy_T^2} \tag{86.19}$$

$$k_T = \frac{1}{\alpha_T \cosh^2 \frac{x_T}{\alpha_T}} = \frac{\alpha_T}{(\alpha_T + y_T)^2} \tag{86.20}$$

$$S_T = \int \sqrt{\left(\left(\frac{dx_T}{dx}\right)^2 + \left(\frac{dy_T}{dx}\right)^2\right)} dx = \alpha_T \sinh \frac{x_T}{\alpha_T} \tag{86.21}$$

Then the total length of the SLWR can be obtained from these three sections,

$$S_{TOTAL} = S_H + S_B + S_T \tag{86.22}$$

As the subsea pipeline and riser can be deemed as a continuum under static equilibrium, the boundary conditions at the lift point between hang-off section and buoyancy section and the drag point between buoyancy section and touchdown section are,

$$N_H = N_B, \quad N_B = N_T \tag{86.23}$$

Table 86.1 Initial screening trial-case basic design data of SLWR static configurations

Terms	Value	Terms	Value
Water depth	1500 m	Buoyancy module density	580 kg/m ³
Sea water density	1025 kg/m ³	Buoyancy per unit	8000 N/m
Outer diameter	12''	Wall thickness	0.027 m
Steel density	7850 kg/m ³	Steel tolerance	10%
Coating density	900 kg/m ³	Coating thickness	0.003 m
Strake weight per unit	30 kg/m	Strake thickness	0.17

86.3 Initial Screening Trial-Case Data of SLWR Configurations

Taking CNOOC Lingshui 17-2 project as a reference and assuming the target water depth as 1500 m, an initial screening trial-case has been carried out for SLWR configuration through the simplified static model, which provides a analysis basis for the subsequent discussion of critical sensitive factors. In order to highlight the variations caused by these sensitive factors, the buoyancy per unit is assumed relatively large here. The design basis data are listed in Table 86.1.

86.4 Impact Discussion of Critical Sensitive Factors

86.4.1 Hang-Off Angle

Hang-off angle, for the scenario when the riser is hung off the platform in nominal without local bending moment at hang-off point, is a critical factor, which not only governs the SLWR configuration design, but also affects the installation difficulty in regard to the top tension. Assuming the hang-off section length as 1600 m and buoyancy section length as 200 m, as listed in Table 86.2, the SLWR static configurations under different hang-off angles are shown in Fig. 86.2.

According to the results, the SLWR static configurations with hang-off angle of 8°, 10° and 12° respectively lead to the turning point of around 388 m, 411 m and

Table 86.2 Control variables for SLWR configuration under different hang-off angles

Control variables	Hang-off section length (m)	Buoyancy section length (m)	Hang-off angle (°)
Group 1	1600	200	8
Group 2	1600	200	10
Group 3	1600	200	12

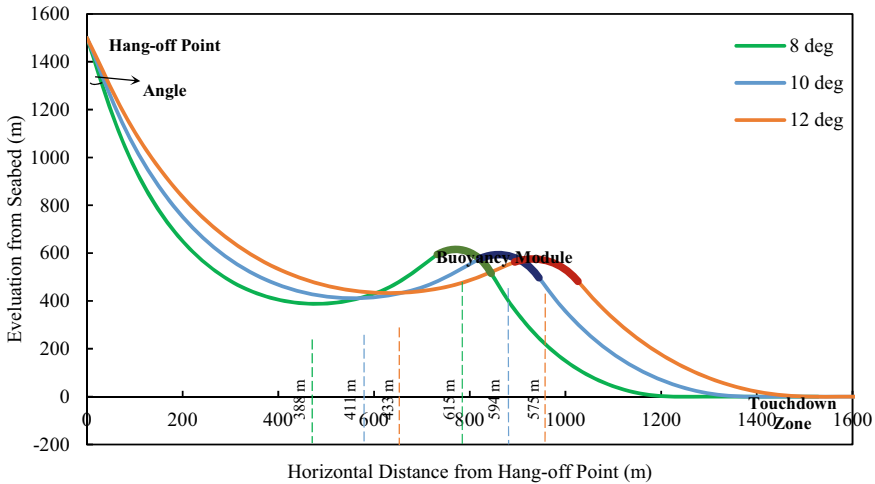


Fig. 86.2 SLWR static configurations of basic design under different hang-off angles

433 m on hang-off section and 615 m, 594 m and 575 m on buoyancy section. The lift point and drag point of the configuration with hang-off angle of 8° is the closest to the hang-off point, resulting a smallest total riser length of nearly 2483 m, followed by that of 10°, and the lift point and drag point of the configuration with hang-off angle of 12° is the furthest to the hang-off point, resulting a largest total riser length of nearly 2524 m. The top tension at hang-off point, horizontal tension and vertical tension of the SLWR static configurations with hang-off angle of 8° are respectively 1820 kN, 253 kN and 1802 kN, lower than those of 10° (1856, 322 and 1827 kN) and 12° (1897, 394 and 1856 kN).

86.4.2 Turning Point Elevation

Vertical elevations of the turning points of both hang-off section and buoyancy section are also critical factors, which should take the seabed topography and steel pipeline fatigue effects into account simultaneously. Given the hang-off angle as 10°, as listed in Table 86.3, the SLWR static configurations under different turning point elevations are shown in Fig. 86.3.

The results indicate that the SLWR static configuration with sagbend turning point elevation of 300 and 600 m on buoyancy section leads to the largest hang-off section length, buoyancy section length, touchdown section length and total riser length, and the corresponding lift point and drag point are furthest to the hang-off point. While the SLWR static configuration with turning point elevation of 550 m on buoyancy section and 400 m on hang-off section leads to the shortest hang-off section length, buoyancy section length, touchdown section length and total riser length, and the

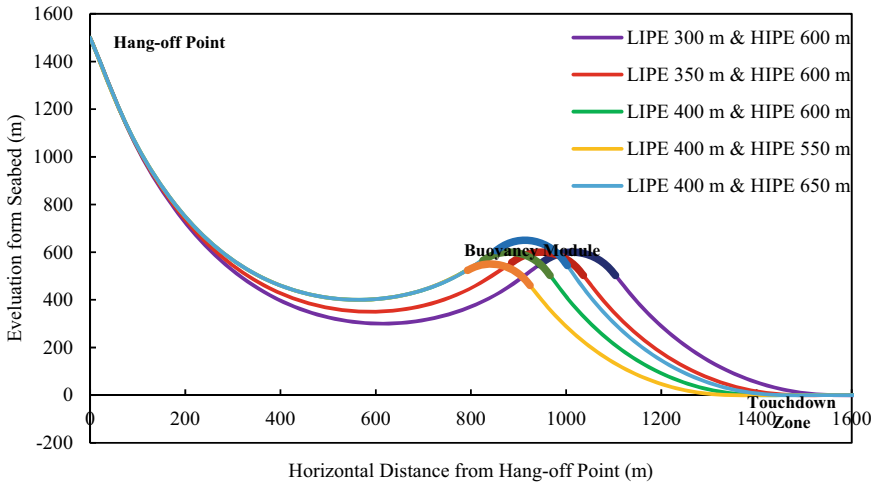


Fig. 86.3 SLWR static configurations of basic design under different vertical elevations

Table 86.3 Control variables for SLWR configuration under different elevations

Control variables	Lowest sagbend point elevation (m)	Highest hogbend point elevation (m)	Hang-off angle (°)
Group 4	300	600	10
Group 5	350	600	10
Group 6	400	600	10
Group 7	400	550	10
Group 8	400	650	10

corresponding lift point and drag point are closest to the hang-off point. It is also implied that the smaller vertical elevation of the sagbend turning point in hang-off section, the larger top tension at hang-off point of SLWR suffers. Under the premise of comprehensive considerations, increasing the vertical elevation of turning point on hang-off section appropriately may be more conducive to alleviating the high stress and fatigue damage of steel pipe.

86.4.3 Content Density

The content density in the pipe may be different at each operation stage, which has impact on the end loads of the whole riser. In this work, three specific conditions, including empty, nominal density (dominated by gas) and flooded, are taken into consideration for discussion, as listed in Table 86.4.

Table 86.4 Control variables for SLWR configuration under different content densities

Control variables	Hang-off section length (m)	Buoyancy section length (m)	Content density (kg/m ³)	Condition
Group 9	1600	200	0	Empty
Group 10	1600	200	165	Nominal operation density
Group 11	1600	200	1025	Flooded

Figure 86.4 shows the SLWR static configurations under different content densities. According to the results, the SLWR static configuration under Empty with the content density of 0 kg/m³ has a hang-off angle of 10.5°, larger than that of 10 degrees under Nominal Density with the content density of 165 kg/m³ and 8° under Flooded with the content density of 1025 kg/m³. The vertical elevations of turning points on hang-off section and buoyancy section under Empty are nearly 418 m and 588 m respectively, higher than those of 387 m and 543 m under Nominal Density, and those of 275 m and 376 m under Flooded. It is indicated that a larger content density always leads to a longer SLWR static configuration (nearly 2252 m under Flooded, 2453 m under Nominal Density and 2509 m under Empty) but a smaller top tension (nearly 2824 kN under Flooded, 2021 kN under Nominal Density and 1868 kN under Empty). Therefore, for safe, reliable and cost-effective production, the different content density under specific conditions should also be considered for the SLWR configuration optimization.

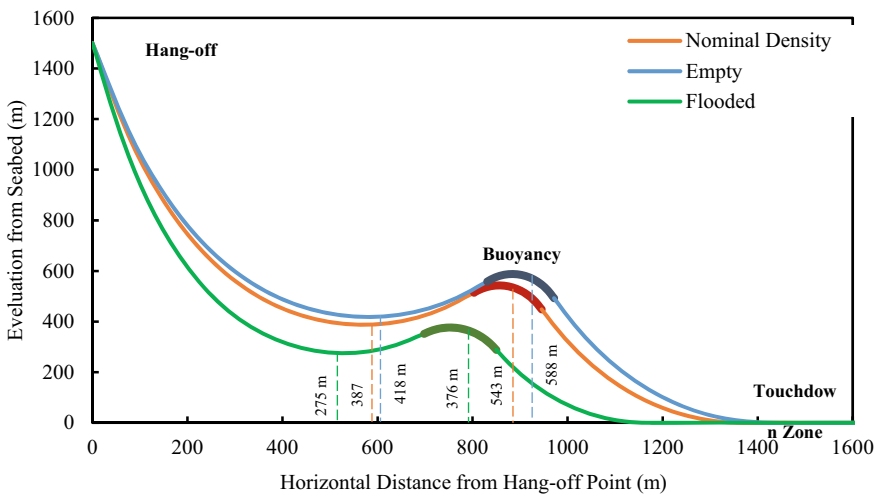


Fig. 86.4 SLWR static configurations of basic design under different content densities

86.5 Conclusion

For a convenient and quick initial screening of SLWR static configuration basic design, this study adopts a simplified static model based on catenary theory and static equilibrium to analyze the impacts of the critical sensitive factors. According to the trial-calculation case study results, the following findings can be concluded.

- (1) A smaller hang-off angle always leads to a lower sagbend turning point of the hang-off section and a higher hogbend turning point of the buoyancy section in the SLWR static configuration, when other conditions are kept the same. Both the corresponding lift point and drag point are closer to the hang-off point, and the total riser length is relative small. All of the top tension, vertical tension and horizontal tension will become larger with a higher hang-off angle, which is unfavorable for riser payload to the platform and the riser could be more favorable to regarding to riser fatigue life.
- (2) A higher vertical elevation of the sagbend turning point of the hang-off section always leads to a smaller length of each section in the SLWR static configuration, if other conditions are assumed to be same. Both the corresponding lift point and drag point are closer to the hang-off point. While a higher vertical elevation of the hogbend turning point of the buoyancy section always leads to a larger length of each section in the SLWR static configuration. Both the corresponding lift point and drag point will be further away from the hang-off point. Under the premise of comprehensive considerations, increasing the vertical elevation of turning point on hang-off section appropriately can reduce the top tension to some extent, which may be helpful to alleviate the high stress and fatigue damage of the steel pipe.
- (3) For a given SLWR configuration, a larger content density in the pipe during operation always leads to a smaller hang-off angle, lower turning points on hang-off section and buoyancy section, a smaller total length of the SLWR suspended section but a larger top tension under the same conditions. Both the corresponding lift point and drag point are further to the hang-off point. During the riser installation and operation, the content density may be variable at different stages, which may have significant impacts on the SLWR static configuration. Therefore, for safe, reliable and cost-effective production, the content density under specific conditions should also be comprehensively considered beforehand.

Appendix

a —initial catenary curvature radius;

k —initial catenary curvature;

N —horizontal force at each point of SCR;

Q —wet weight at each point of SCR;
 S —total SCR length;
 β —inclination angle of catenary;
 a_H , a_B , and a_T —initial catenary curvature radius of SLWR hang-off section, buoyancy section and touchdown section respectively;
 k_H , k_B , and k_T —initial catenary curvature of SLWR hang-off section, buoyancy section and touchdown section respectively;
 N_H , N_B , and N_T —horizontal force at each point of SLWR hang-off section, buoyancy section and touchdown section respectively;
 Q_H , Q_B , and Q_T —wet weight at each point of SLWR hang-off section, buoyancy section and touchdown section respectively;
 S_H , S_B , and S_T —total length of SLWR hang-off section, buoyancy section and touchdown section respectively;
 ρ_p , ρ_{pb} , and ρ_w —density of uniform pipe, pipe with buoyancy module and seawater respectively;
 A_p and A_{pb} —uniform section area of exposed pipe and pipe with buoyancy module respectively.

References

1. Braestrup, M., et al.: Design and Installation of Marine Pipelines. Subsea Pipelines (2005)
2. Bin, Y., Mike, C., David, W., Hugh, T., Kamaldev, R.: Improved SCR design for dynamic vessel applications. In: International Conference on Offshore Mechanics and Arctic Engineering, Shanghai, China, 6–10 June, OMAE2010-20406, pp. 495–504 (2010)
3. Torres, A.L., Gonzalez, E.C., Siqueira, M.Q.D., Dantas, C.M.S., Mourelle, M.M., Silva, R.M.C.D.: Lazy-wave steel rigid risers for turret-moored FPSO. In: International Conference on Offshore Mechanics and Arctic Engineering, Oslo, Norway, 23–28 June, OMAE2002-28124, pp. 203–209 (2002)
4. Wang, J.L., Duan, M.L., Fan, J.K., Liu, Y.J.: Static equilibrium configuration of deepwater steel lazy-wave riser. In: International Offshore and Polar Engineering Conference, Anchorage, Alaska, 30 June, ISOPE-I-13-603 (2013)
5. Ogbeifun, A.M., Oterkus, S., Race, J., Naik, H., Moorthy, D., Bhowmik, S., Ingram, J.: A tabular optimisation technique for steel lazy wave riser. IOP Conf. Ser.: Mater. Sci. Eng. **1052**(1), 012022 (2021)
6. Andrade, E.Q.D., Aguiar, L.L.D., Senra, S.F., Siqueira, E.F.N., Torres, A.L.F.L., Mourelle, M.M.: Optimization procedure of steel lazy wave riser configuration for spread moored FPSOs in deepwater offshore Brazil. In: Offshore Technology Conference, Houston, Texas, USA, 3–6 May, OTC-20777-MS (2010)
7. Li, S.C., Chau, N.: Dynamic Response of Deepwater Lazy-Wave Catenary Riser. Deep Offshore Technology International, Amsterdam, The Netherlands (2010)
8. Lockwood, E.H.: A Book of Curves. Cambridge University Press (1961)
9. Wang, J.L., Duan, M.L., He, T., Cao, J.: Numerical solutions for nonlinear large deformation behaviour of deepwater steel lazy-wave riser. Ships Offshore Struct. **9**(6), 655–668 (2014)

10. Wang, J.L., Duan, M.L.: A nonlinear model for deepwater steel lazy-wave riser configuration with ocean current and internal flow. *Ocean Eng.* **94**, 155–162 (2015)
11. Li, F.H., Guo, H.Y., Gu, H.L., Liu, Z., Li, X.M.: Deformation and stress analysis of the deep-water steel lazy wave riser subjected to internal solitary waves. *J. Ocean Univ. China* **22**(2), 377–392 (2023)

Chapter 87

Numerical Simulation of Breathing Effect Induced by Drilling in Deep-Water Shallow Formations



Honglin Huang, Jun Li, Wentuo Li, Geng Zhang, Hongwei Yang, Jianming Li, Jintao An, Shujie Liu, and Ming Luo

Abstract It is easy to misjudge the breathing effect as kick and take killing measures to cause malignant loss, which will increase the risk and cost of deep-water operation and seriously harm the safety and efficiency of deep-water drilling. In this paper, the mechanism of breathing effect induced by drilling in deep-water shallow formations was studied, and the COMSOL was used to simulate the whole process of breathing effect during drilling in deep-water shallow formations, so as to study the influence of formation characteristics, mud properties and pressure difference on breathing effect. The simulation results show that the breathing effect observed during drilling in deep-water shallow formations belongs to the transient permeability-induced breathing effect. Which is very easy to occur in formations with low elastic modulus, low Poisson's ratio, and high porosity and permeability. However, through using the mud with high viscosity and high yield stress and balanced or near-balanced drilling mode (achieved by reducing displacement and mud density, etc.) is conducive to suppressing the breathing effect. When drilling in formations with low elastic modulus, low Poisson's ratio, high porosity and high permeability, measures should be taken in advance, such as adding filtrate reducer and reducing pump rate, to reduce the impact of breathing effect. The study results can provide some references for the identification, prevention and control the breathing effect during drilling in deep-water shallow formations.

Keywords Deep-water shallow formations · Breathing effect · Formation characteristics · Mud properties · Loss and flowback

H. Huang · W. Li · S. Liu · M. Luo
CNOOC China Limited, Hainan Branch, Haikou 570100, Hainan, China

J. Li (✉) · G. Zhang · H. Yang · J. An
China University of Petroleum-Beijing, Changping, Beijing 102200, China
e-mail: lijun446@vip.163.com

J. Li
China University of Petroleum-Beijing at Karamay, Karamay 834000, Xinjiang, China

J. Li
Hohai University, Nanjing 213022, Jiangsu, China

Nomenclature

R	Penetration radius of drilling fluid (m)
k	Permeability (m^2)
φ	Porosity (Decimal)
ξ	Pore tortuosity (Decimal)
Δp	Pressure difference (MPa)
τ	Yield force (Pa)
q	Volumetric flow rate (m^3/s)
l	Length of the well section (m)
v	Seepage velocity (m/s)
V	Total volume (m^3)
t	Time (s)

87.1 Introduction

Nearly 90% of the global ocean area is the deep water with a depth of more than 1000 m. The oil and gas resources in these areas have become the most important field of global offshore oil and gas exploration and production. According to statistics, about 60% of global marine oil and gas resources are distributed in shallow waters of continental shelf (water depth < 500 m), and the remaining 40% are distributed in deep water (water depth > 500 m) and ultra-deep water (water depth > 1500 m) of continental slope [1]. This confirms the huge exploration potential of oil and gas resources in deep-water areas.

During drilling in deep-water areas, frequent “breathing effect” not only causes mud loss, but also seriously affects kick detection operations. “Breathing effect” refers to the phenomenon that when mud circulates, there will be a small amount, but uninterrupted mud loss in the wellbore, and when mud stops circulating, mud will flow back into the wellbore [2]. When breathing effect is misjudged as kick, excess killing operations can lead to the fractures propagation around the wellbore, which can compromise wellbore stability, cause mud loss, lead to serious drilling accidents, and prolong non-operational time. This undoubtedly increases the risk and cost of offshore deep-water operations and causes serious harm to the safety and efficiency of deepwater drilling [3].

Many researchers have studied the breathing effects occurring in deep formations, but few researchers have conducted detailed studies on the breathing effects observed during drilling in deep-water shallow formations [4–13]. With the characteristics of high cost and high risk of deep-water drilling, we should not ignore any incidents that affect the safety and efficiency of deep-water drilling. In this paper, according to the sedimentary characteristics, lithology and physical properties of deep-water shallow formations, the mechanism of breathing effect observed during drilling in deep-water formations was explored, and a numerical model was established to

simulate the whole process of breathing effect, and the sensitive parameters were discussed. The authors hope that the study results can provide references for the identification, prevention and control breathing effect observed during drilling in deep-water formations.

87.2 Exploration on the Mechanism of Breathing Effect Observed During Drilling in Deep-Water Formations

The first researcher conducting a study on the breathing effects was James A. Gill. But the concept proposed by Gill is “borehole ballooning”. Gill’s description of “ballooning” is vague and does not correspond to most field observations, particularly with respect to the flow back volume of fluid. So in subsequent studies, researchers avoided using the term “ballooning” and gradually replaced it with the term “breathing.”

In the existing researches, the mechanism causing breathing effect is mainly divided into three types [4–13]: (1) Radial elastic expansion of deep well round pipe, such as riser, casing and open hole section; (2) Volume expansion of mud caused by thermal effect in high-temperature and high-pressure wells; (3) Opening and closing of fractures around the wellbore in fractured formation.

A small amount of mud was found to have been lost during drilling in deep-water shallow formations, but it did not affect normal drilling operations. During connecting, the mud pool appears a small increment. This phenomenon is consistent with the breathing effect. However, the conditions in deep-water shallow formations obviously does not match that of the three mechanisms. First, the temperature in deep-water shallow formations is not high (2–4 °C), and the formation pressure is generally hydrostatic pressure. When drilling, seawater or low-density mud is used. The pressure difference between the wellbore and the formation is small. The breathing effect of pipe string or open hole section and fluid expansion does not apply under these conditions. In addition, due to the short deposition time, the formation is characterized by weak cementation, high permeability and strong deformation performance, and there is no micro-fracture system [14]. Mud begin losing before the wellbore pressure reaches the fracture pressure. That is, the breathing effect occurs before the formation fractures occur around the well. Further analysis shows that the breathing effect observed during drilling in deep-water shallow formations were similar to phenomenon observed during fracturing fluid filtration and flowback during fracturing operations, and the mud loss is filtration [15–17]. Therefore, we speculate that the mechanism of breathing effect observed during drilling in deep-water shallow formations belongs to the permeability-induced mechanism.

Figure 87.1 shows the mechanism of permeability-induced breathing effect. Which state can be specifically described as: (1) when the mud is stationary, the wellbore pressure is equal to the hydrostatic pressure or formation pressure, and the wellbore and formation are in a balanced state without fluid exchange; (2) When the mud starts circulating, the wellbore pressure is greater than the formation pressure due

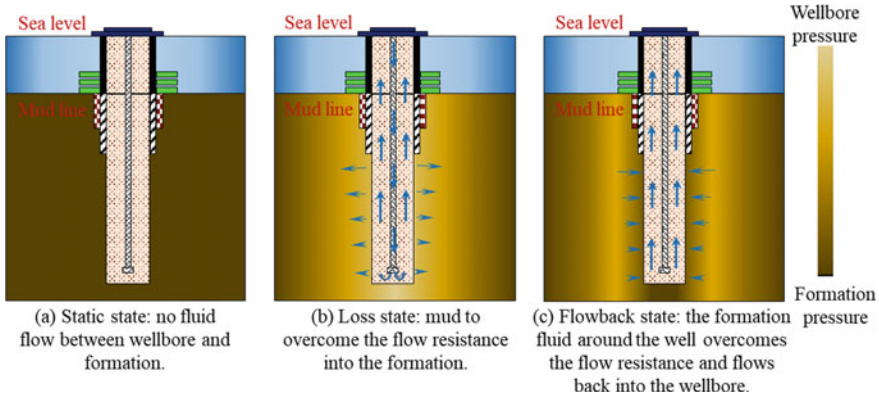


Fig. 87.1 Schematic diagram of permeability-induced breathing effect

to the circulation pressure loss. Under the small pressure difference, the mud penetrates into the formation; (3) When the mud pump is stopped, the circulating pressure loss disappears instantly. At this time, the fluid pressure in the near-wellbore formation is higher than that in the wellbore. Under the instantaneous negative pressure difference, the formation fluid will be discharged back into the wellbore.

87.3 Finite Element Model

87.3.1 Model Establishment

Since light water-based mud or seawater is usually used to drill directly in deep-water shallow formation and rate of penetration is relatively fast, it is assumed that no effective mud cake is formed in the well wall during drilling. COMSOL software was used to build a 3D model of open hole section. Its borehole diameter is ϕ and length is 1 m, and the mud intrusion depth is determined by Eq. (87.1). The outer boundary of the formation is set in a no flow state. The model’s physics field consists of three parts: solid mechanics, Darcy’s law and porous elastic fluid–solid coupling.

$$R = \frac{4\xi \Delta p}{3\tau_0} \sqrt{\frac{2k}{\varphi}} \tag{87.1}$$

The boundary probe is used to monitor the fluid seepage velocity at the well wall, then the fluid flow through the well wall can be expressed as:

$$q = \varphi \pi l v \tag{87.2}$$

Table 87.1 The specific parameters and values

Parameters	Value	Unit	Parameters	Value	Unit
Elastic modulus	3	GPa	Mud viscosity	0.02	Pa s
Poisson's ratio	0.3	Dimensionless	Mud yield stress	3	Pa
Porosity	0.2	Dimensionless	Formation pore pressure	10	MPa
Permeability	1×10^{-12}	m^2	Wellbore pressure	10.3	MPa
Biot coefficient	0.8	Dimensionless	Borehole diameter	0.2159	m

The mud loss volume is obtained by integrating the seepage velocity.

$$V = \int_0^t q \, dt \quad (87.3)$$

87.3.2 Parameter Settings

It is assumed that the formation is linear elastic porous material and the mud is Bingham fluid. The specific parameters and their values are shown in Table 87.1. The formation pore pressure is 10 MPa, and the wellbore pressure is 10.3 MPa when the mud circulates. The mud stops circulating after 1.5 s, the wellbore pressure is equal to the formation pore pressure.

87.3.3 Simulation Results and Verification

Simulation Results. The dynamic changes of formation pressure, mud loss velocity and volume during the process of permeability-induced breathing effect were analyzed. Figure 87.2 shows the change of formation pressure around the wellbore, and Fig. 87.3 shows the situation of mud loss and backflow. According to the settings, the wellbore pressure is 10.3 MPa and the formation pressure is 10 MPa at the initial moment, which is in the condition of the positive pressure difference between the wellbore and the formation. It can be seen from the results that the pressure propagation is very fast and reaches the final invasion in a very short time (< 0.5 s), and the pore pressure around the wellbore is equal to the wellbore pressure within the invasion area. At the moment of time is 1.5 s, the circulating pressure loss disappeared as the mud stopped circulating, and the wellbore pressure instantly dropped to 10 MPa (hydrostatic pressure). At this time, the wellbore and formation are under the negative pressure difference condition, and the formation pressure

around the well propagates into the wellbore and recovers to the wellbore pressure in a very short time. The difference between wellbore pressure and formation pressure is the driving force of fluid flow, and its change time is very short, indicating that permeability-induced breathing effect is instantaneous.

In Fig. 87.3, if the mud loss rate is positive, it means that the wellbore fluid leaks into the formation; if it is negative, it means that the formation fluid flows back into the wellbore. As can be seen from the figure, mud quickly leaked into the formation within a short time after opening the formation, and then reached a stable state soon. At 1.5 s, the formation fluids near the wellbore began to flow back into the wellbore due to the decrease in wellbore pressure, also reaching a stable state in a short time. This is consistent with the dynamic change of formation pressure around the wellbore.

Therefore, the whole process of permeability-induced breathing effect can be divided into three stages:

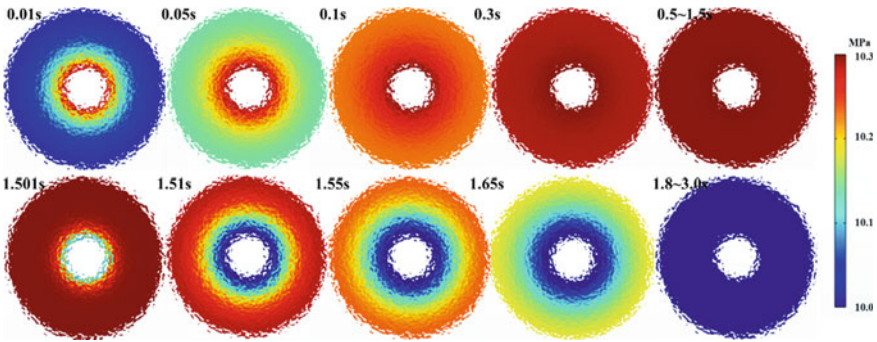


Fig. 87.2 Distribution of pore pressure around wellbore

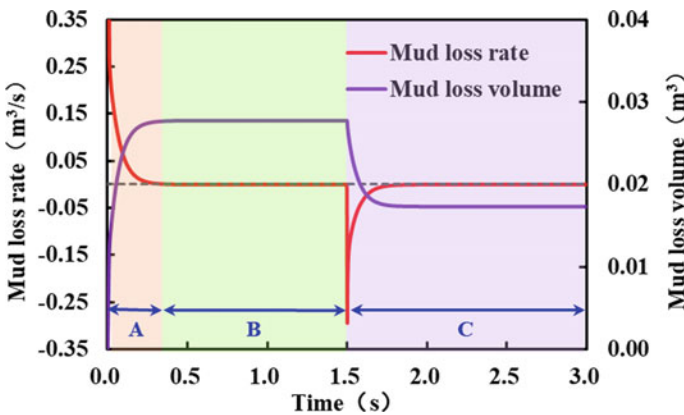


Fig. 87.3 Variation of mud loss velocity and volume at the well wall with time

Stage A: Mud loss stage. At this stage, the mud is pressurized into the formation due to the positive pressure difference. The pressure propagation velocity is very fast, which is related to the formation characteristics of high porosity and permeability. Although the mud continues to leak into the formation at this stage, the flow stops quickly and reaches a relatively stable state due to the pressure spreading quickly to the final penetration depth. This stage is a detailed description of “weak and continuous mud loss” during drilling.

Stage B: Pseudo-steady stage. At this stage, a relatively stable state is achieved between the wellbore and the formation. It can be known that the formation pressure around the wellbore and the mud loss volume remain unchanged. This means that the mud circulates normally through the wellbore and no longer seeps into the formation at this stage. This stage corresponds to the situation where drilling is stopped but the mud in the wellbore is still circulating.

Stage C: Mud flowback stage. At this stage, the mud stops circulating, the wellbore pressure drops, and the negative pressure difference environment appears, deriving the formation fluid to return to the wellbore. It can be known that the formation pressure around the wellbore drops rapidly, and the formation fluid flows back into the wellbore in a very short time. This stage corresponds to the sudden overflow of mud during the pumping stop stage after the normal circulation of drilling operations. As can be seen from Fig. 87.3 that not all of the mud that entered the formation flowed back into the wellbore, but only part of it did. This is due to the need for fluid flow to overcome yield stress.

Model Verification. A breathing effect event observed in a vertical exploration well drilling in deep-water area in South Sea, China was used as a case to verify the accuracy of the model. The water depth is 518 m and the designed well depth is 4300 m. According to the field statistics, the low-temperature resistant water-based mud was used in the 880–980 m well section, and the mud lost slowly during drilling. The total mud loss volume was 3.96 m^3 . The drilling was stopped at 980 m and began to connect. After a period of time, a sudden overflow was observed and the mud in the mud pool increased by 1.35 m^3 . After shut-in, the throttle valve is opened to release the fluid in the wellbore and the gas content is monitored at all times. The results showed that the nozzle flow rate decreases from strong to weak, and gradually returns to zero. At the same time, the wellbore pressure gradually stabilized. The shut-in riser pressure remained roughly the same, indicating that the bottomhole pressure used equalized formation pressure. The shut-in casing pressure was negligible and the returned fluid contained less than 1% hydrocarbons, meaning that no oil or gas entered the wellbore. In other words, this is a breathing effect event, not a kick. Field data were used to simulate the breathing effect event, and specific parameters were shown in Table 87.2.

Table 87.3 shows the comparison of actual mud loss/flowback volume with the simulation results. At the loss stage, the simulation result of mud loss is 3.96 m^3 , with an error of 4.55%. The simulation result of mud flowback volume is 1.21 m^3 , with an error of 10.37%. For the entire breathing effect event, the simulated mud loss volume was 2.57 m^3 , with an error of only 1.53%. It shows that developed model

Table 87.2 Specific simulation parameters

Parameters	Value	Unit	Parameters	Value	Unit
Elastic modulus	3	GPa	Mud viscosity	0.012	Pa s
Poisson's ratio	0.35	Dimensionless	Mud yield stress	3	Pa
Porosity	0.4	Dimensionless	Formation pore pressure	9.89	MPa
Permeability	3.2×10^{-12}	m ²	Wellbore pressure	10.23	MPa
Biot coefficient	0.8	Dimensionless	Borehole diameter	0.66	m

Table 87.3 Simulation results and error analysis

Stage	Mud loss stage	Mud flowback stage	Final moment
Actual situation, m ³	3.96	1.35	2.61
Simulated situation, m ³	3.78	1.21	2.57
Relative error, %	4.55	10.37	1.53

can simulate and explain the breathing effect observed during drilling in deep-water shallow formations.

87.4 Sensitivity Analysis

87.4.1 Influence of Rock Parameters on Permeability-Induced Breathing Effect

Elastic modulus. The elastic modulus is one of the rock mechanical properties. The smaller the elastic modulus is, the easier the rock is to deform. Figure 87.4 shows the variation of mud loss/flowback volume with the formations with different elastic modulus. With the decrease of elastic modulus, both loss and flowback volume increase, that is, the breathing effect is enhanced.

Poisson's ratio. The variation of mud loss/flowback volume with the formations with different Poisson's ratio is showed in Fig. 87.5. With the increase of Poisson's ratio, both mud loss and flowback volume decrease, that is, the breathing effect becomes weaker. However, the change degree of mud loss and flowback volume with Poisson's ratio is lower than that of elastic modulus, indicating that Poisson's ratio has a much weaker influence on breathing effect than the elastic modulus.

Porosity. Porosity directly reflects the formation's ability to store fluid. Figure 87.6 shows the variation of mud loss/flowback volume with the formations with different porosity. With the increase of porosity, both mud loss and flowback volume increase, and the increasing rate also shows a decreasing trend. This indicates that the increase

Fig. 87.4 Variation of mud loss/flowback volume with the formations with different elastic modulus

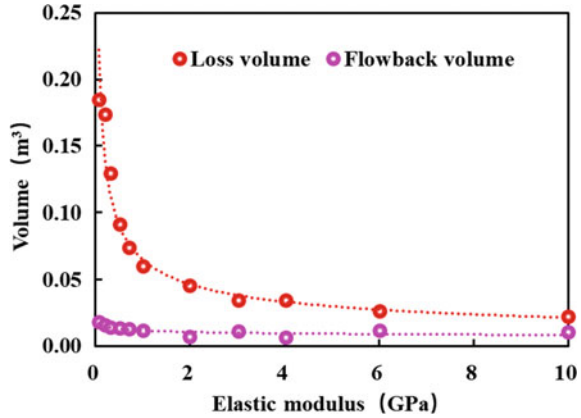
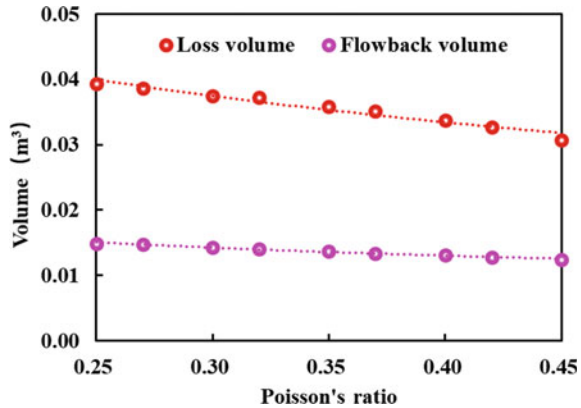


Fig. 87.5 Variation of mud loss/flowback volume with the formations with different Poisson's ratio



of porosity will enhance the breathing effect, but the degree of increase will gradually decrease. Therefore, when drilling into high porosity formation, we should be vigilant and take countermeasures in advance. In the formation with low porosity and undeveloped fractures, permeability-induced breathing effect.

Permeability. Permeability is a direct expression of the ability of fluid to flow in the formation. It can be seen from Eq. (87.1) that in the formation with high permeability, the mud invasion depth will be greater. Figure 87.7 shows the variation of mud loss/flowback volume with the formations with different permeability. With the increase of permeability, the amount of mud loss and flowback volume increased significantly, that is, the degree of respiratory effect was higher. Thus, one of the most important ways to prevent and treat permeability-induced breathing effect is to intervene with formation permeability, which is one of the few formation parameters that can be regulated simply by adding additives such as filtrate reducer to facilitate the development of effective mud cakes. This is important because even small changes can have significant results.

Fig. 87.6 Variation of mud loss/flowback volume with the formations with different porosity

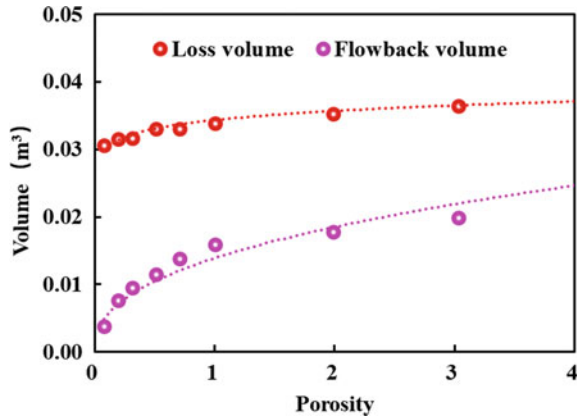
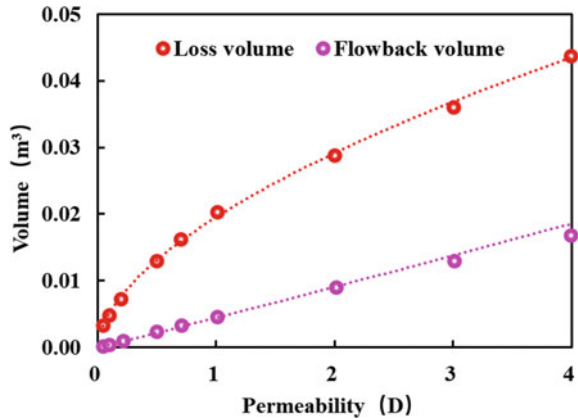


Fig. 87.7 Variation of mud loss/flowback volume with the formations with different permeability



87.4.2 Influence of Mud Properties on Permeability-Induced Breathing Effect

Viscosity. Viscosity is one of the important parameters to reflect the flow resistance of fluid in porous media. The higher the mud viscosity, the higher the flow resistance. Figure 87.8 shows the variation of mud loss/flowback volume with the mud with different viscosity. With the increase of mud viscosity, the mud loss and flowback volume gradually decrease, that is, the more viscous mud is, the lower the degree of permeability-induced breathing effect. Therefore, properly increasing the mud viscosity is helpful to reduce the degree of permeability-induced breathing effect when other conditions remain unchanged. Of course, this also has to do with the fact that the well depth is relatively small. At greater well depth, the increased viscosity is accompanied by an increase in circulating pressure loss and an increase in wellbore pressure, which further increases the degree of breathing effect (as will

Fig. 87.8 Variation of mud loss/flowback volume with the mud with different viscosity

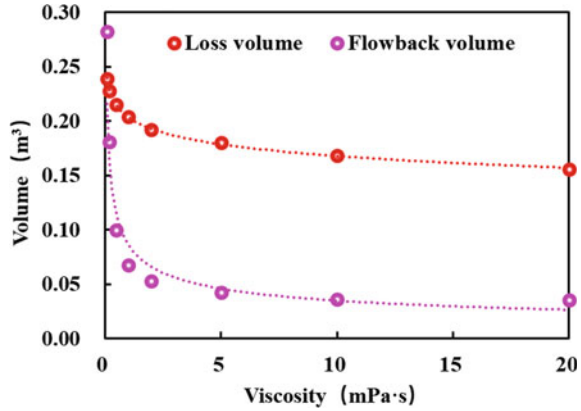
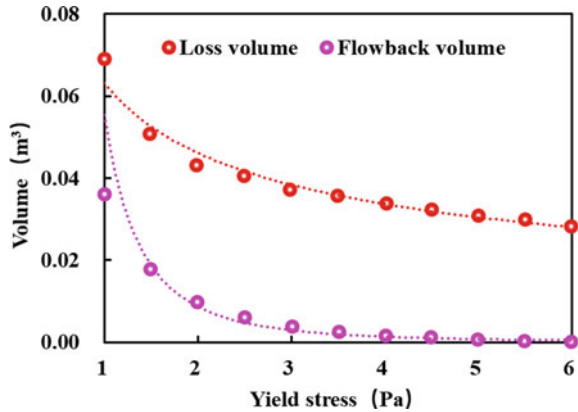


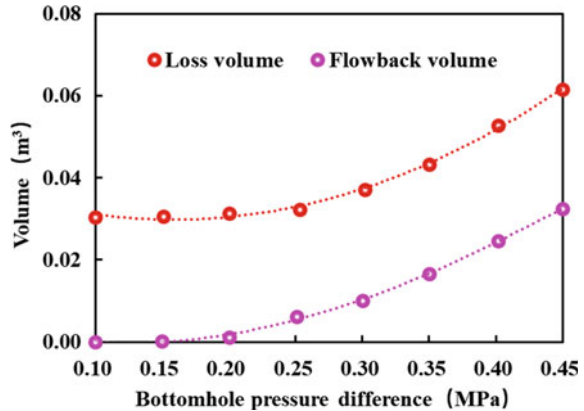
Fig. 87.9 Variation of mud loss/flowback volume with the mud with different yield stress



be demonstrated later). The deeper the well, the greater the effect [18]. Therefore, the mud viscosity design needs to be closely integrated with density, wellbore trajectory, formation characteristics and other parameters.

Yield stress. Yield stress need to be overcome when mud flows. Although the change of yield stress has little effect on the mud flow in the wellbore, the seepage in the porous rock is extremely important. Lietard [19] pointed out that when mud with a positive yield stress invade the formation, the penetration would eventually stop even if no filtrate reducers are used. It can be seen from Eq. (87.1) that the mud invasion depth is negatively correlated with the yield stress. Figure 87.9 shows the variation of mud loss/flowback volume with the mud with different yield stress. The larger the yield stress, the smaller the mud loss and flowback volume. Moreover, with the increase of yield stress, the reduction rate of loss and flowback volume decrease gradually. Therefore, increasing the mud yield stress (by adding inorganic electrolyte, bentonite, etc.) can effectively inhibit the permeability-induced breathing effect.

Fig. 87.10 Variation of mud loss/flowback volume with the different bottomhole pressure difference



87.4.3 Influence of Bottomhole Pressure Difference on Permeability-Induced Breathing Effect

In order to increase the rate of penetration and avoid the formation being contaminated by mud, we generally use balanced or near-balance drilling mode. The pressure difference in wellbore mainly comes from circulating pressure loss and liquid pressure of mud. As can be seen from Fig. 87.10, a small bottomhole pressure difference can effectively weaken the permeability-induced breathing effect. Moreover, with the increase of pressure difference, the increase rate of mud loss and flowback volume also increases. As one of the controllable factors, low pressure difference conditions play a very important role in reducing permeability-induced breathing effect. Reducing mud density and displacement are effective methods.

87.5 Finite Element Model

According to the uniqueness of deep-water shallow formations, a new permeability-induced mechanism is proposed to explain the breathing effect observed during drilling in deep-water shallow formations. A 3D model under fluid–structure coupling condition was established based on COMSOL, and the influences of various factors on permeability-induced breathing effect were analyzed in detail. Here’s what we learned:

1. The permeability-induced mechanism can well explain the phenomenon of breathing effect observed during drilling in deep-water shallow formations, and this breathing effect is completed in a short time.
2. The permeability-induced breathing effect is very easy to occur in formations with low elastic modulus, low Poisson’s ratio and high porosity and permeability. Adding filtrate reducers to reduce the permeability and porosity at the

well wall is helpful to reduce the effect of breathing effect. In addition, the use of high viscosity, high yield stress, low density mud and low displacement drilling method can effectively reduce the degree of permeability-induced breathing effect.

3. It is worth noting that the model is established under hypothetical conditions and has certain limitations, such as idealized formation conditions and poor development of mud cake. The effect of these conditions on permeability-induced breathing effect needs to be further explored.

Acknowledgements The authors acknowledge the support from the National major scientific research instrument research and development project (52227804), the Youth Program of National Natural Science Foundation of China (52104012), the School-Enterprise Cooperation Project (HX20191203), the Key Projects of Scientific Research Plan in Colleges and Universities of Xinjiang Uygur Autonomous Region (XJEDU20211028), the Introduction of Talents Research Launch Project of the China University of Petroleum—Beijing at Karamay “Wellbore Integrity Analysis and Optimization System Construction of Shale Oil and Gas Well Life Cycle”, and the Strategic Cooperation Technology Projects of CNPC and CUPB (ZLZX2020-01-01).

Data Availability Statement

The data that support the findings of this study are available from the corresponding author upon reasonable request.

References

1. Wang, L.X., Pan, J.P., Yang, L.L.: Present conditions and prospect of global deepwater oil and gas exploration and development. *Pet. Sci. Technol. Forum* **39**(2), 31–37 (2020)
2. Huang, H.L., Li, J., Gao, R.Y., Zhang, G., Yang, H.W., Chen, W., Luo, M., Li, W.T.: Investigation of the mechanisms and sensitivity of wellbore breathing effects during drilling in deepwater shallow formations. *Ocean Eng.* **269**, 113405 (2023)
3. Lavrov, A., Tronvoll, J.: Mechanics of borehole ballooning in naturally-fractured formations. In: SPE Middle East Oil and Gas Show and Conference. Society of Petroleum Engineers, OnePetro (2005)
4. Gill, J.A.: How borehole ballooning alters drilling responses. *Oil Gas J.* **87**(11) (1989)
5. Helstrup, O.A., Rahman, M.K., Hossain, M.M., Rahman, S.S.: A practical method for evaluating effects of fracture charging and/or ballooning when drilling high pressure, high temperature (HPHT) wells. In: SPE/IADC Drilling Conference, OnePetro (2001)
6. Atkin, T.: Numerical Modelling to Estimate the Amount of Formation Deformation and its Effect on Cement Integrity. University of Leoben (2019)
7. Elmgerbi, A., Thonhauser, G., Roohi, A., Prohaska, M., Nascimento, A.: General analytical solution for estimating the elastic deformation of an open borehole wall. *Int. J. Sci. Eng. Res.* **7**(1), 1056–1068 (2016)
8. Babu, D.R.: Effect of P- ρ -T behavior of muds on loss/gain during high-temperature deep-well drilling. *J. Petrol. Sci. Eng.* **20**(1–2), 49–62 (1998)
9. Aadnoy, B.S.: *Modern Well Design*. CRC Press (2010)
10. Yuan, Z., Morrell, D., Mayans, A.G., Adariani, Y.H., Bogan, M.: Differentiate drilling fluid thermal expansion, wellbore ballooning and real kick during flow check with an innovative combination of transient simulation and pumps off annular pressure while drilling. In: IADC/SPE Drilling Conference and Exhibition. Society of Petroleum Engineers (2016)

11. Lavrov, A., Tronvoll, J.: Mechanics of borehole ballooning in naturally-fractured formations. In: SPE Middle East Oil and Gas Show and Conference. Society of Petroleum Engineers (2005)
12. Gao, R.Y., Li, J., Liu, G.H., Yang, H.W., Luo, K.D., Zhai, W.B., Zhang, X., Zhang, R.R.: Experimental study on typical characteristics of borehole breathing under different pressure and rock type conditions. *J. Nat. Gas Sci. Eng.* **77**, 103241 (2020)
13. Yang, H.W., Gao, R.Y., Li, J., Lian, W., Guo, B.Y., Wang, W., Huang, H.L.: Dynamic response mechanism of borehole breathing in fractured formations. *Energ. Rep.* **8**, 3360–3374 (2022)
14. Wang, H.H., Yang, J., Liu, Z.L., Xu, J.J., Meng, L.Y., Hong, J.Y., Tian, B., Wang, W.X.: Analysis on the influential factors about the cementing strength of shallow cementing in deep water. *Oil Drilling Prod. Technol.* **41**(3), 277–282 (2019)
15. Zou, D.Y., Zhao, J., Guo, Y.L., Fang, M.Z., Guang, S.: A model for predicting leak-off pressure in permeable-sandstone formations. *Pet. Drilling Tech.* **42**(1), 33–36 (2014)
16. Sun, Y.X., Li, C.L., Bai, X.S., Zhang, L.C., Zhao, J.Y., Guo, C.P.: Study on factors affecting filtration property of drilling fluid with numerical simulation software. *Drilling Fluid Completion Fluid.* **36**(5), 581–586 (2019)
17. Qu, Y.A., Gong, X., Shi, K.L., Liu, Y.F., Ma, G.Q., Wang, X.: Research progress of imbibition and backflow mechanism of fracturing fluids in shale reservoirs. *Contemp. Chem. Ind.* **49**(11), 2532–2535 (2020)
18. An, J.T., Li, J., Huang, H.L., Liu, G.H., Yang, H.W., Zhang, G., Li, W.T.: Mud loss behavior in fractured formation with high temperature and pressure. *Energ. Rep.* **9**, 2638–2652 (2023)
19. Lietard, O.: Permeabilities and skins in naturally fractured reservoirs: an overview and an update for wells at any deviation. In: SPE European Formation Damage Conference. Society of Petroleum Engineers (1999)

Chapter 88

A Review on Vector Form Intrinsic Finite Element Method and Its Application



Y. F. Duan, Y. Fang, S. M. Wang, S. K. Wu, and H. M. Zhang

Abstract The vector form intrinsic finite element (VFIFE) method is a numerical analysis method based on the theory of vector mechanics. With the underlying concepts of point value description, path element and fictitious reverse motion, the numerical model is established for the mechanical behavior of the structure. In comparison with the traditional finite element (FE) methods, there is no assembling for the global stiffness matrices in VFIFE method. VFIFE method can effectively handle the complicated behavior analysis involving large deformation, large displacement, geometric and material non-linearity, contact and collision, fracture and collapse, buckling or wrinkling failure, etc. The differences in basic theory between traditional FE methods and VFIFE method are summarized before demonstrating the recent progress, development and applications in various fields and structures. Existing researches proved the strong capability and high accuracy of VFIFE method. Moreover, the application trends of VFIFE method are discussed, including dynamic behavior of large scale structures, cloud-based high-speed parallel computing, hybrid simulation, and digital twin technology.

Keywords VFIFE · Basic theory · Development · Applications · Trends

88.1 Introduction

Finite element (FE) method, which is based on variational principle and continuum mechanics, is the most commonly used numerical method in solving scientific and engineering problems. However, FE method has inherent difficulties in solving problems involving large deformation, non-linearity or discontinuity [1, 2]. For instance, the problem with large deformation is solved by Lagrangian method in traditional

Y. F. Duan (✉) · Y. Fang · S. K. Wu · H. M. Zhang
College of Civil Engineering and Architecture, Zhejiang University, Hangzhou 310058, China
e-mail: ceyfduan@zju.edu.cn

S. M. Wang
Department of Civil and Environmental Engineering, The Hong Kong Polytechnic University,
Hung Hom, Kowloon, Hong Kong S. A. R., China

© The Author(s), under exclusive license to Springer Nature Switzerland AG 2024
S. Li (ed.), *Computational and Experimental Simulations in Engineering, Mechanisms and Machine Science* 145, https://doi.org/10.1007/978-3-031-42987-3_88

1257

FE method, whereas the FE mesh may be severely deformed under the large deformation, resulting in an ill-conditioned stiffness matrix, which may cause the calculation impossible to continue. The Updated-Lagrangian (UL) or Total-Lagrangian (TL) method [3] are adopted to iteratively solve or modify the stiffness matrices when dealing with geometric nonlinear problems [4], but when it comes to strong geometric non-linearity, the accuracy and efficiency of calculation are difficult to be guaranteed. Traditional FE method uses the continuous displacement approximation function to solving the discontinuity problem, where the high-density mesh is required to ensure the sufficient calculation accuracy, which consequently leads to a large amount of computation.

Currently, many numerical methods, such as the explicit FE method based on co-rotational (CR) coordinate [5, 6], discrete element method (DEM) [7] and extended finite element method (XFEM) [8], have been proposed to make up for the deficiency of traditional FE method in dealing with certain problems. The explicit FE method can deal with the problems of large rotation and small strain of the beam, the plate, the shell and other structures with the CR coordinate theory. However, this method is insufficient in solving the problems with large deformation and large rotation of solid structures since the rigid motion and pure deformation of the solid structures are usually difficult to separate [9]. The DEM can handle the overall motion of discontinuities by separating the discontinuous body into a set of rigid elements. However, the discrete element takes the centroid of the element as the basic node, in which the connection elements between the centroids are established based on the specific problems. When solving a problem by DEM, a large amount of elements are required resulting in the long computation time; moreover, the selection of connection element is difficult for complicated problems [10]. In XFEM, the geometric properties and movement laws of the discontinuity plane are described by additional function (called enrichment function) and level set method, so that the discontinuity problems, such as cracks, voids and inclusion, can be solved. Nonetheless, this method is mainly applied to fracture problem since that the different problems match the different enrichment functions, which are hard to be obtained for complicated problems [11]. The above methods have certain limitations in the behavior analysis of structure, especially in dealing with the complicated behavior of large structure.

In the view of shortcomings of the existing numerical methods in structural behavior analysis, Ting from Purdue University proposed the vector form intrinsic finite element (VFIFE) method based on vector mechanics and numerical calculation [12–13]. Based on physical calculation model of the structure, VFIFE method regards the generalized vector mechanics as the criterion of motion and deformation, and replaces the differential governing equation of the continuous function in traditional behavior analysis with point value [14], which can effectively handle the complicated structural behaviors, including large deformation, large displacement, non-linearity, contact, fracture and multi-body coupling motion and so on. In this paper, the basic theory of VFIFE method is introduced firstly, then the development of element and analysis in VFIFE are illustrated. Meanwhile, the applications in

structural behavior analysis and engineering field are expounded combining with its characteristics and advantages. At the end of the paper, the research trends of VFIFE method in future are given.

88.2 Vector Form Intrinsic Finite Element Theory

Differ from the classical mechanics, VFIFE method adopts a new theory framework with a different set of description concepts and simplified assumptions designed to enable it to be applied to simulate the three-dimensional (3D) structure and to predict the behavior variation of structure motion. There are three underlying concepts in vector form theory: (1) The parameters of the continuous components are described by the point values of a set of spatial points, and the parameters between the space points are calculated by a set of standard interpolation functions. (2) The motion of spatial points is described by the point value of a set of time points, and the processes between the time points are calculated by a set of governing equations, which are regarded as a path element. (3) The motion analysis of the component is described by the particle motion equation and the internal forces between spatial points need to be calculated. Since the internal force is related to pure deformation, the fictitious reverse motion is introduced to calculate the pure deformation. The following is a brief introduction of the three underlying concepts in VFIFE method.

88.2.1 Point Value Description

In classical mechanics, the component is assumed to be composed of an infinite number of points, the spatial location of which is described by a set of differential continuous functions. Differ from that, the assumption in VFIFE method is that a finite number of point location are selected among the infinite points as the independent variables, and the location between points are calculated by a set of standard interpolation functions, which satisfy the condition that the component is a physical continuum.

Figure 88.1 shows a simple example of a straight bar $a-b$, which becomes curved when subjected to external forces. If the straight bar $a-b$ is described by the continuous function (Fig. 88.1a), where the shape function of the bar and the vector function of the force should be given before the analysis. However, the two functions are difficult to be obtained during the numerical analysis. In VFIFE, the shape of the bar is described by a set of points linked by elements, which means the points are time-dependent (Fig. 88.1b). The force can be treated as the concentrated force of each point. These finite points to describe the mechanics behavior are regarded as the motion particles. The motion of each individual particle satisfies Newton's second law. The element is usually used as the smallest entity of the structure in traditional FE method. In contrast, the particle in VFIFE is the carrier of the spatial location,

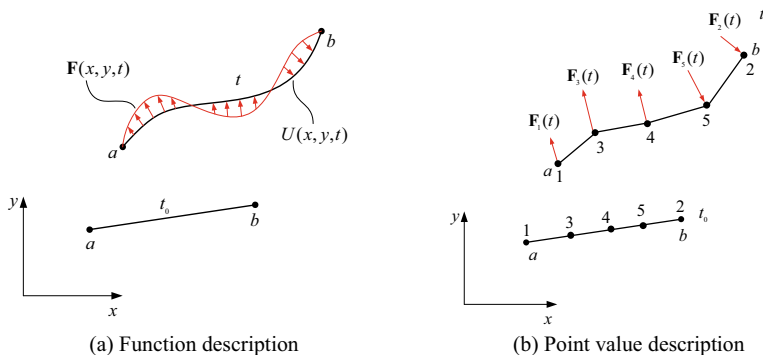


Fig. 88.1 Straight bar $a-b$

mass, force, deformation and boundary condition of the structure, while the element is only used for the relationship between the particles.

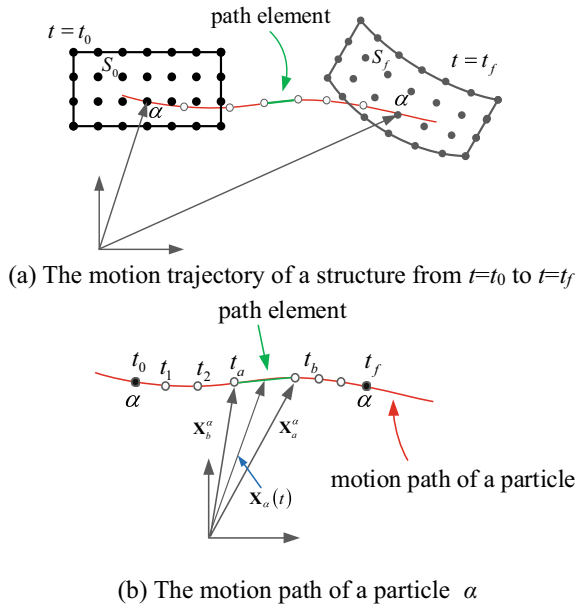
88.2.2 Path Element

In VFIFE, the movement path of each particle on the component is described by a set of time points. Under the action of external force, the location of the particle in a certain time point will move to the location of another time point after a period of time. If the transformation process can be described by a set of standardized governing equations, then this time period is called as a path element (expressed as $t_a \leq t \leq t_b$ in Fig. 88.2). Even if the total deformation is large, it can be assumed that the geometric deformation in any path element is rather small, so that the increment of internal force in a path element can be handled by the theory of large displacement and small deformation. The introduction of path element simplifies the internal force calculation but also deals with the complicated behaviors involving large deformation, large displacement and discontinuity. Figure 88.2 presents a motion trajectory of a particle α .

88.2.3 Fictitious Motion

In VFIFE, each particle follows the Newton's second law and the governing equations are described by motion and displacement formulae of a set of points, where the resultant internal force of the particle is included in motion formula. Since the pure deformation is essentially for calculating the internal force between two particles, fictitious reverse motion is used to obtain the pure deformation. Here is the detail illustration.

Fig. 88.2 A motion trajectory of a particle on a structure



Firstly, it can be assumed that the deformation among the particles within a path element is close to a uniformly deformed state after introducing the point value description and the path element. Secondly, suppose that the element between two particles have the fictitious reverse rigid body motion at the arbitrary time t in a path element, including rigid body translation and rotation and then a fictitious element shape will be obtained (Fig. 88.3). The translation can be defined as the displacement of an arbitrary element node in the time period $t-t_a$, and the rotation can be approximated by the nodal displacement vector. Since the deformation of the element is small within the time period $t-t_a$, the resultant differences between the fictitious shape after the reverse motion and the original shape are the small deformation and small displacement. Therefore, the deformation and internal force of the fictitious shape can be described by the micro-strain and engineering stress. After obtaining the nodal internal force and elemental stress, the bar element is returned to the original spatial position through a positive rigid body motion. In other words, the true internal force and stress can be obtained by converting the force direction of the fictitious shape [14].

88.2.4 Numerical Solution

According to the theory of point value description, the mechanical behavior of the component is described by the position of a finite number of particles. The particle motion can be calculated based on Newton's second law like:

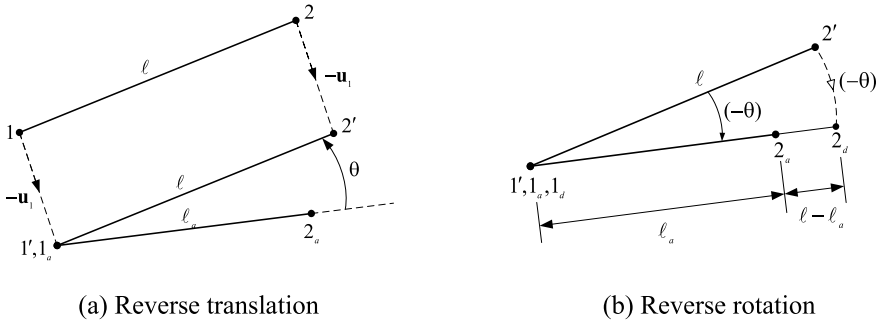


Fig. 88.3 Fictitious reverse motion

$$\mathbf{M}_\alpha \ddot{\mathbf{X}}_\alpha = \mathbf{F}_\alpha^{ext} - \mathbf{F}_\alpha^{int} \tag{88.1}$$

where α is an arbitrary particle of the component, \mathbf{M}_α and $\ddot{\mathbf{X}}_\alpha$ are respectively the mass matrix and acceleration of particle α , \mathbf{F}_α^{ext} and \mathbf{F}_α^{int} are respectively the resultant external force vector and resultant internal force vector of particle α . The calculation of equivalent internal force can be referred to the reference [12].

The explicit central difference method is adopted to solve the equations of motion for particles in VFIFE, avoiding the iterative solution. Each particle is solved independently with the same solution process. Specially, the global stiffness matrix is not assembled during the solving process. Hence, it can handle the complicated 3D problems involving nonlinear or discontinuous issues.

88.3 Development of Vector Form Intrinsic Finite Element Method

In the researches based on vector form intrinsic finite element method, it can be summarized as follows: (1) Developing new element types to adapt to different research objects; (2) Improving the theory or analysis pattern to make VFIFE more stable and extensive; (3) Applications to mechanical behavior analysis and engineering problems. This section contains the first two aspects.

88.3.1 Development of Element Types

Since the planar frame element and solid element based on vector mechanics [15, 17, 13] were firstly proposed, the element types have been continuously developed over the next dozen years. The planar plate and shell element, membrane element, fiber element, fine beam element, 3D element and macroscopic element based on

vector mechanics have been proposed successively, so that the different structural behaviors can be more effectively captured by VFIFE. Meanwhile, the improvement of time integral step, the theory of parallel computing and the proposed deformation coordinate have greatly enhanced the theory of vector mechanics. The development of element types based on VFIFE is briefly described below.

Wu [18] in 2004 developed the tetrahedral solid element in VFIFE and applied it to analyze the motion of 3D solid structure. This study extended the application of VFIFE into 3D entities. In the year of 2006, Wang [19] derived the internal force solution of 3D rigid frame element in VFIFE and carried out a series of dynamic and static force analysis of 3D structures. In 2007, the constant strain triangular membrane element, a new member of the VFIFE family, was proposed by Wu et al. [20] to analyze the spatial motion of the arbitrary 3D membrane structures. The further study of four-node membrane element (as shown in Fig. 88.4) developed by Wu and Ting [21] was finished in 2008, where the spatial quadrilateral was transformed into the plane through the projection relation. The introduction of triangular membrane element and quadrilateral membrane element made the VFIFE more widely used in 3D membrane structures. In 2009, Chang [22] firstly developed two kinds of plate and shell elements in VFIFE, and verified the small displacement problem of plate and shell structures under various boundary conditions, and finally adopted the two proposed elements into the study of harbor engineering issues. Chung [15] combined constant strain triangle (CST) element and discrete Kirchhoff theory (DKT) triangular plate element with the concepts of motion analysis and CR coordinate, and then developed the shell element in VFIFE in 2010, which was focused on analyzing the static small displacement problems and was applied to harbor engineering. Chen [23] further derived the analysis formulae of thin shell element based on VFIFE-DKT (as shown in Fig. 88.5), and discussed the key factors affecting the stability of VFIFE-DKT free motion analysis. Duan et al. [24] firstly combined the traditional fiber element and the VFIFE, developed the vector fiber model (as depicted in Fig. 88.6) and simulated the entire process of earthquake collapse of a mock up long-span cable-stayed bridge. Liu et al. [25] considered the torsion deformation into the fiber beam element and simulated a buried pipeline crossing strike-slip fault. Lin et al. [26] derived the formulae for the fiber beam element simultaneously considering shear and torsion deformation, and simulated the elasto-plastic behavior of structures, which presented higher accuracy than the plastic hinge method. Based on the theory of spatial fine beam model considering the coupling effect of different deformations, Chen et al. [27] proposed the relevant formulae of strain and internal force applied to VFIFE analysis, which demonstrated more efficient and accurate when the beam had a larger depth-span ratio. In 2018, Wang et al. [28] presented the basic formulae of eight-node hexahedral isoparametric solid element, which further expanded the application of VFIFE into the dynamic analysis.

The above microscopic elements can reflect the detailed response of structures, while usually resulting in heavy time consuming. To find a method with the advantages of both microscopic and macroscopic models, a hybrid planar model based on

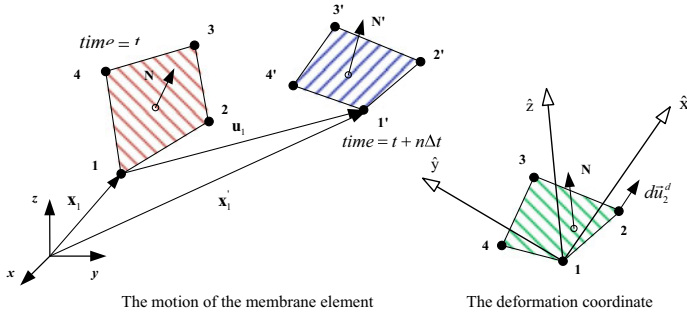


Fig. 88.4 Four-node quadrilateral membrane element (courtesy of [21])

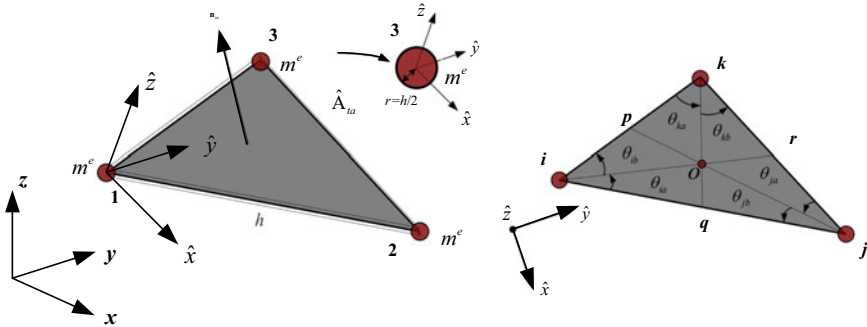


Fig. 88.5 VFIFE-DKT element (courtesy of [23])

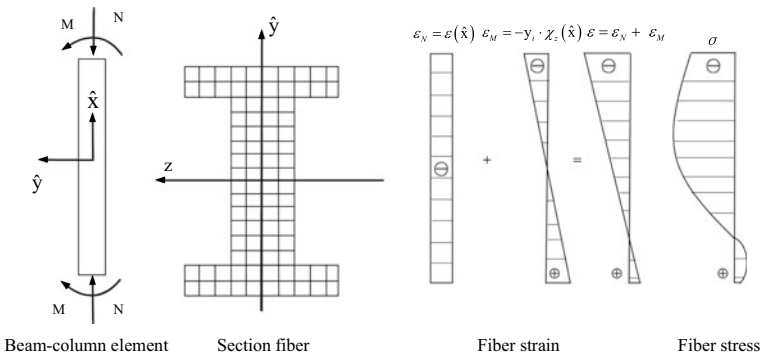


Fig. 88.6 Interaction of axial force and bending moment in a beam-column element (courtesy of [24])

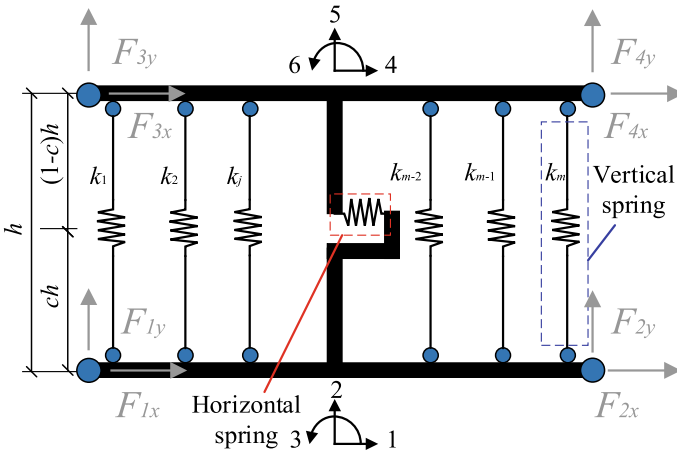


Fig. 88.7 Diagram of V-MVLE model (courtesy of [29])

VFIFE and macroscopic multi-vertical line element (MVLE) is accordingly proposed by Zhang et al. [29], called V-MVLE model (as presented in Fig. 88.7), and compared with the test results of a dozen shear walls to verify the effectiveness and accuracy of the proposed model.

88.3.2 Improvement in Analysis Mode and Theory

Apart from the enrichment of the element types, the development of theory and analysis modes makes the VFIFE method more competent in the behavior analysis of the complicated structures. The time step of central difference method selected in VFIFE is inevitably to be a pretty small value to guarantee the convergence and stability, which may take much long computational time.

The central difference method used in VFIFE is to build a dynamic equilibrium equation, where the external force received by the system usually equilibrates at the discrete time point, while the external force between the two discrete time points cannot be described. In 2008, Li [30] improved the time integration method by introducing the concept of momentum balance into VFIFE analysis. The motion equation was established with the equilibrium of momentum and impulse, whose results showed that based on the momentum balance-based integration method, time step in a wider range can be chose so that huge amount of time can be saved. Since there may be numerical dispersion when solving the Rayleigh damping analysis, Su [31] adopted the implicit time integration method (Newmark- β) in 3D VFIFE analysis. Recently, Wang et al. [32] developed an adaptive explicit algorithm for static simulation and evaluated the system convergence in combination with a dynamic relaxation method (DRM) [33] with kinetic damping and discrete control theory, where the accuracy, stability and efficiency of the method were verified by cases.

Apart from the improvements in integration method, the parallel processing was introduced into speeding computation. Lai [34] introduced a distributed computations technology into the VFIFE analysis in 2006 by personal computer (PC) cluster with message passing interface coding technologies. Since the motion equation for each particle is mutually independent, the particles and elements in the VFIFE can be arranged into different PCs to parallelize the procedures. This method can effectively reduce the computational cost under the great demand of more complex engineering problems. Du proposed the particle distributing mechanism for parallel computation, and verified the low time consuming of the proposed VFIFE parallel computing framework under Spark cluster [35]. Wang et al. [36] recently built a linked-list data structure suitable for parallel processing, and proposed the parallel global and local search algorithms for contact detection, where the numerical cases were compared with those of the ABAQUS/EXPLICIT software and presented much better computational speed.

In the meantime, some scholars made efforts to the detailed improvements of VFIFE, including mass matrix improvement and reverse motion, etc. As mentioned before, the mass of element in VFIFE is replaced by the lumped mass of the particle at both ends of element. However, it is inevitable that there will be a loss of element information and computational accuracy during the establishment process, since the lumped mass matrix cannot truly perform the interaction between particle inertial forces. For this reason, Yuan et al. [37] established the particle motion equation based on the second type of Lagrange equation and derived the consistent mass matrix with the energy principle. The applicability, efficiency and accuracy of the proposed consistent mass matrix were verified, especially in the transient dynamic analysis, the computation of translation and rotation of the rigid body, and the analysis of meshing related structures. For reverse motion modification, Hou et al. [38], Wang et al. [39] and Liu et al. [40] successively simplified the reverse motion of the solid elements (as described in Figs. 88.8, 88.9 and 88.10), showed the good performance in shortening time. Likewise, the side-angle-method by Wang et al. [41] was also provably superior to the traditional centroid-angle-method (as shown in Fig. 88.11) in calculating the rigid body motion, the large deformation and the deformation of complex structure.

Another significant improvement for VFIFE was about the damping form. Typically, a virtual damping was set based on the DRM in conventional VFIFE to accelerate the solution for quasi-static problems. Without the concept of stiffness in VFIFE, the damping cannot be constructed through the structural frequency and structural damping ratio. For this reason, Yu et al. [42] proposed two methods for VFIFE damping form on the basis of the Rayleigh method, the virtual stiffness was established and discussed by simulation and test so that the damping approximation with a higher precision can be verified.

All the above have greatly improved the computational efficiency of the VFIFE method. Compared with the traditional FE method, which requires iterations to solve the huge stiffness matrix, the VFIFE method has more advantages in solving the complex behavior analysis of the structure. By all accounts, the proliferation of this method will continue to grow.

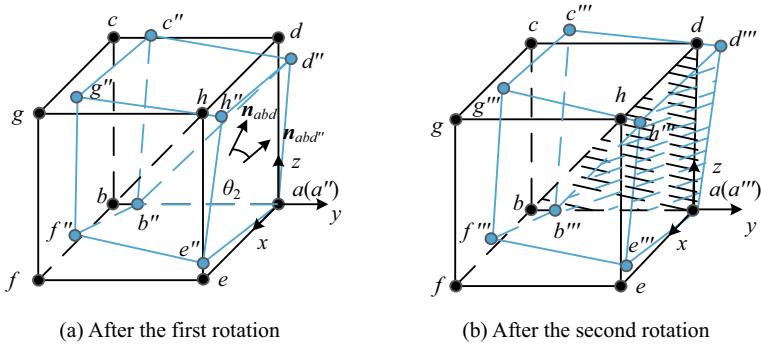


Fig. 88.8 Element position after rigid rotation (courtesy of [38])

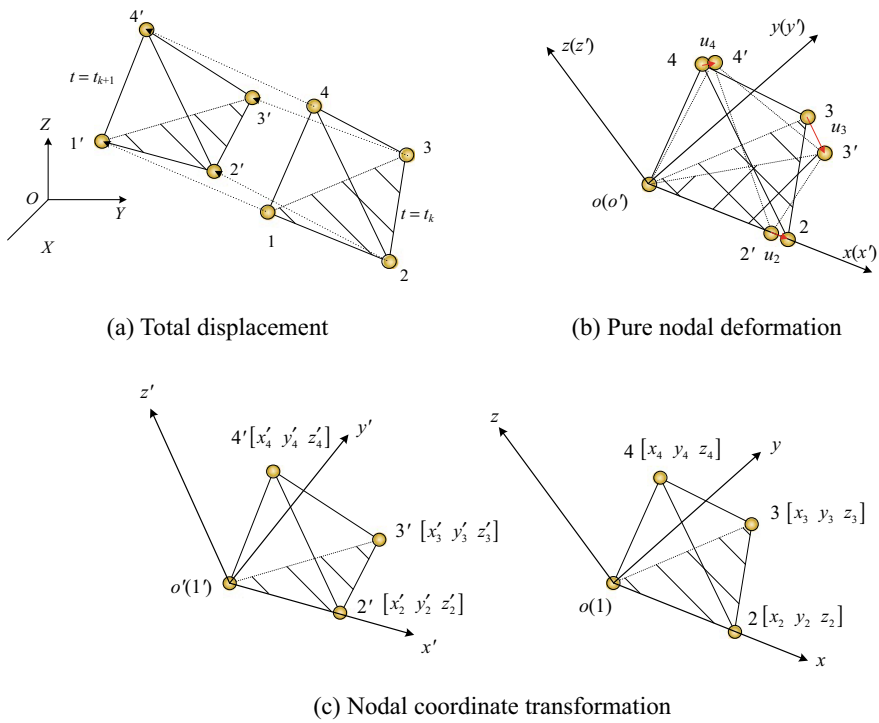
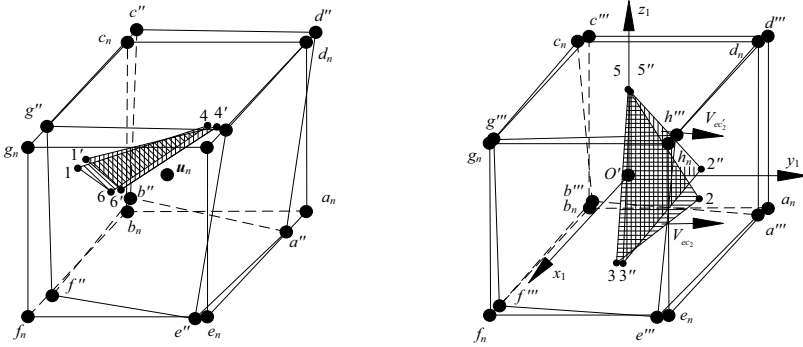
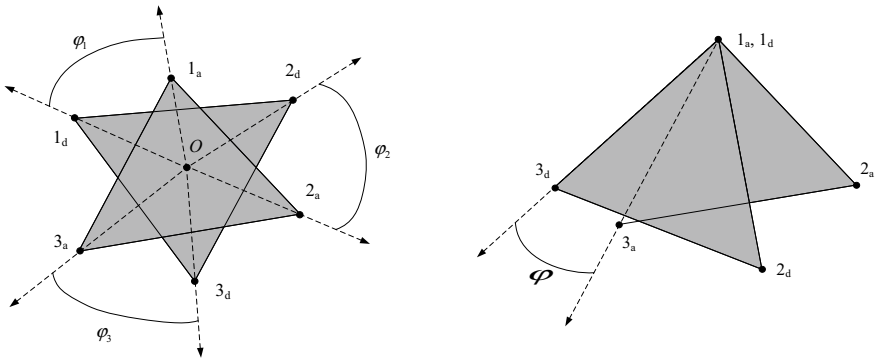


Fig. 88.9 Reverse motion in tetrahedral element (courtesy of [39])



(a) Position after the first reverse rotation (b) Position after the second reverse rotation

Fig. 88.10 Reverse motion in hexahedral element (courtesy of [40])



(a) Centroid-angle-method (b) Side-angle-method

Fig. 88.11 Comparison of two methods for calculating reverse rotation angle in plane (courtesy of [41])

88.4 Application of Vector Form Intrinsic Finite Element Method

From the underlying concepts of vector mechanics, the solution form of VFIFE takes a strong form [17]. In consequence, no solution to matrix equation is required for VFIFE method, and the correlation between particles can be changed at any time. Hence, it can simulate the complex structural behaviors, such as the large deformation, large displacement, geometric non-linearity, material non-linearity, contact non-linearity, fracture and collapse, etc.

88.4.1 Mechanical Behavior Analysis

The mechanical behavior of the structure mainly consist of static behavior, dynamic behavior, mechanism motion, large deformation, large displacement, geometric non-linearity, material non-linearity, contact and collision, buckling and wrinkling, fracture behavior, and the composite behavior composed of the aforementioned behavior, such as dynamic instability and continuous collapse behavior. Since the most of these perform with the non-linearity, it is kind of difficult to solving them using the existed numerical method. Relatively, the proposed VFIFE method has been proven to effectively deal with the sophisticated non-linear behavior.

Static Analysis. The static balance is a common assumption within the traditional structural and strain analysis. In traditional FE method, the static displacement can be obtained by solving matrix equation established based on structural morphology and mechanical behavior. According to the Hooke's law and Newton's law, the structure is definitely deformed under the load action and the change in position is induced by motion. The vibration amplitude of structure will gradually decrease under the energy dissipation mechanism, and eventually the structure converges to an almost static state. On account of this, the VFIFE adds an arbitrary energy dissipation mechanism to the particle motion equation so as to obtain the convergence position of the space particle and the connection particle with respect to time, when calculating the static solution of the structure.

As aforementioned, a dummy damping force \mathbf{F}_α^d can be added into each motion formula, resulting in,

$$\begin{aligned} \mathbf{M}_\alpha \ddot{\mathbf{X}}_\alpha &= \mathbf{F}_\alpha^{ext} - \mathbf{F}_\alpha^{int} - \mathbf{F}_\alpha^d \\ \mathbf{F}_\alpha^d &= \zeta \cdot \mathbf{M}_\alpha \dot{\mathbf{X}}_\alpha \end{aligned} \quad (88.2)$$

where, $\zeta > 0$ is an arbitrary damping factor. It can be an artificially positive value for obtaining the static solution, rather than the physical material damping. Similarly, an extreme slow loading speed can be applied during the numerical calculation.

Xiang [43] conducted a theoretical study on the tensioned cable-membrane structure of the spatial structure and applied it to the analysis of the Shanghai Expo Axis, which showed that the theoretical study of VFIFE for tensioned cable-membrane structure can effectively analyze the mechanical behavior of complex spatial structure systems.

Dynamic Analysis. In traditional FE analysis, different governing equations and solving methods are respectively used in dynamic analysis and static analysis. Moreover, solving dynamic problem is much more complicated than static problem, as well as the computational cost. According to the description of particle motion in Eq. (88.2), apparently, this method is essentially a dynamic solution method, which can tackle the static and dynamic problem with a unified computational flow and solution strategy.

Wang et al. [44] introduced VFIFE to carry out the nonlinear dynamic analysis of reticulated space truss structures with several benchmark problems of features as large rotation and dynamic instability, and demonstrated its accuracy and superior capability. Zhu and Dong et al. conducted the tracking simulation analysis of the whole process of the failure of the oblique cables and the loop cables in the torus-dome tensile structure [45], suspen-dome [46], cable dome [47], and inner-outer combined reticulated shell-string structure [48], and obtained the dynamic response curves of the displacement and internal force of the dome after the cable was broken. For the vehicle induced dynamic simulation, Shih [49] firstly developed the analysis of vehicle-track-bridge interaction behaviors by VFIFE, in which the rail system was simulated by mass spring damping system, and the mechanical models corresponding to six types of vehicle systems were derived. Duan et al. [50] took the influence of rail irregularity and ballast into account, analyzed the train-bridge interaction involving the two-axle and coach models, and further analyzed the train-bridge interaction problem considering the coach-coupler effect [51]. This study demonstrated that the couplers played the significant role in energy-dissipating. Besides, a dual-resonance phenomenon was discovered for the first time (shown in Fig. 88.12). Furthermore, Wang et al. [52] developed a new method which can efficiently model the maglev train-controller-rail-bridge system as well as the dynamic interaction by VFIFE. The above research shows that the VFIFE method can effectively analyze the vehicle-bridge coupling problem.

Geometric Nonlinearity. The geometric non-linearity concludes large geometric deformation, large displacement, large rotation and mechanism motion, etc. It is awfully difficult to solve the differential equations of such non-linear problems by direct analytical method.

As mentioned before, the UL formulation and TL formulation are broadly adopted to solve these problems, while the work induced by unbalanced elemental force cannot come up to zero leading to inaccurate or diverged calculation when the

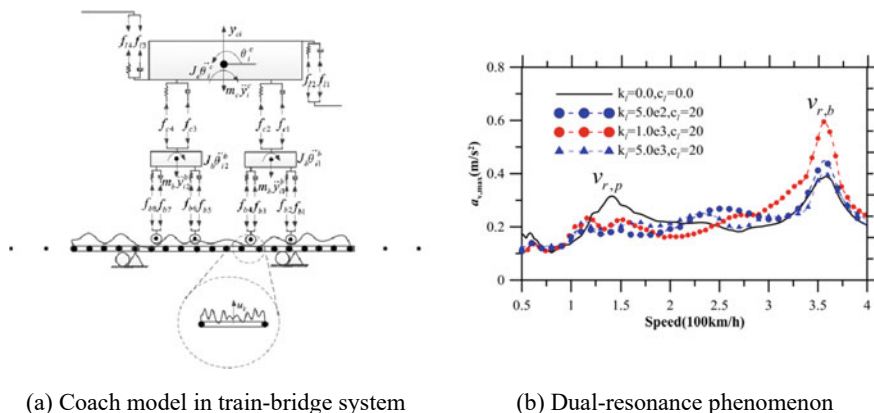


Fig. 88.12 Dual-resonance phenomenon of the train-bridge system (courtesy of [51])

extremely large displacement or rotation occurs. In addition, when the solids undergone a large deformation and was analyzed by CR method, the rigid motion of element was replaced by a convected coordinate system fixed on the particle, resulting in an additional virtual strain and causing the abnormal volume expansion or shrinkage of the element [53], where the special processing method or proper artificial coefficient were required to avoid it [54]. In VFIFE, a convected material frame approach was incorporated, where the updated body geometry at the previous time increment was adopted as the reference frame for kinematic description so that the incremental information such as stresses and strains performed after the time increment can be calculated. Using the fictitious reverse motion in VFIFE enables easy separation of the elemental pure deformation from the rigid-body motion, demonstrating commendable stability in the geometric nonlinear analysis of solid elements.

In 2003, Lai [55] conducted the research on the geometrically nonlinear behavior of planar frame structures, including the analysis of large rigid motion and moderately large geometric deformation, which successfully applied the VFIFE method to nonlinear analysis. Wu et al. [56] firstly applied the VFIFE method into the large deformation of flexible structure, greatly the applicability of VFIFE. The geometric nonlinear analyses of flexible planar frame structures [57], space truss structures [44], three-dimensional membrane structures [20], flexible multi-body systems [9], shell structures [58] and solid structures [59] have been successfully conducted. Besides, Yu, Luo and other scholars applied the VFIFE method into large deformation and large rotation of kinematically indeterminate structures [60] and deployable structures [61].

Material Nonlinearity. Under the load, the structure will undergo large deformation, and may even lead to the material yielding, component fracture and so on. In conventional FE method, it is a quite complicated problem to analyze the dynamic elastic–plastic behavior of structures. The relevant analysis process contains the computational model simplification, the hysteretic model determination, the dynamic load selection, the stiffness matrix modification and the iterative solution of equation, with huge computation resources and long period [62].

In VFIFE method, it can obtain the structural stress and deformation process by the independent particle description. The elastic–plastic behavior is only related to the elemental internal force solution. The elastic-plastics material can directly be introduced as an independent calculation module. Therefore, when analyzing the dynamic elastic–plastic problem by VFIFE, the introduction of complex nonlinear materials will not increase the difficulty of motion analysis.

Chen [63] considered the P- δ effect and utilized plasticity theory to establish the analysis mode of components entering the plastic zone, which could predict the complex behaviors such as the fracture and collapse caused by geometric and material changes. Wang et al. [64] used VFIFE to analyze the nonlinear analysis of the elastic–plastic plane steel frame under dynamic and static loads. The study pointed out that the VFIFE can effectively analyze the structure response of each stage in the dynamic process considering the material non-linearity. To account for

the strain rate effect of material, Wu et al. [57] adopted the Cowper-Symonds viscoplastic constitutive model and bilinear elastic–plastic model with different hardening rules to simulate the motion analysis of frame structures.

Contact and Collision. The contact-collision behavior contains the nonlinearities of material, geometry, and boundary conditions, and the time effect is also required for dynamic behavior analysis.

The commonly FE method to deal with the contact-collision problem is to discretize the area to be solved, simulate the continuum with the finite nodes and constitute the elements by nodes, where the nodes represent the position of the physical quantity to be solved. For contact interface, the distribution and change of the physical quantities between elements are described by Lagrangian multiplier method [65] and penalty function method [66]. However, solving nonlinear problems related to contact and collision behavior becomes more challenging due to geometric discontinuities, which brings difficulties in analysis as the FE method relies on the assumption of an ideal continuum. Another method is to introduce the special elements in the contact region, such as the interface element, gap element, and the spring, to tackle these problems [62, 67, 68], while the solving process is still complicated since the difficulty of FE method in large displacement problem.

VFIFE method is quite different from the traditional FE method in simulating the contact and collision behavior. This complex behavior can be easily simulated by the independent calculation of particles, which is not restricted by the displacement governing equations of contact and collision analysis in the FE method. Furthermore, there are no displacement constraints, and no need to modify the elemental stiffness in the constrained region.

In 2004, Wu [69] analyzed the large deformation and contact behavior of 2D frame structure by VFIFE. Apart from simulating the geometric nonlinear behavior, the contact mechanics was firstly equipped for the frame elements in VFIFE method. On the basis of triangular membrane element of VFIFE theory, Wang [70] proposed the methods of collision detection and response processing for membrane material-to-rigid body, membrane material-to-membrane material. Whereafter, He further studied the complex discontinuous behaviors containing collision-contact, crack-fracture, and penetration for thin-shell structures [71], proved that the VFIFE is greatly advantageous in simulating the complicated strong nonlinear and discontinuous behaviors of thin-shell structures. Apart from the penalty function method, Zhang et al. [72] modified an explicit contact algorithm to avoid the penetration in point-interface contact for thin shell structures. Hou et al. [73] introduced VFIFE with master–slave algorithm and inside-outside algorithm for gear mechanics and contact analysis with complicated interfaces. Liu et al. [74] extended the VFIFE method coupling with smooth particle hydrodynamics into the fluid–solid interaction problems and successfully addressing the nonlinear, fracture and contact problems.

Buckling and Wrinkling Instability. The buckling and wrinkling behavior is a kind of local instability when the structure is subjected to the external forces, with strong nonlinearity, where the FE method and geometrically nonlinear force method are the commonly used for analysis.

For FE method, it usually comes with the problems of singularity of stiffness matrix, or difficulties in convergence of the nonlinear equations. Normally, the arc-length method is adopted for modification so as to overpass the extreme point and track the structural behavior after buckling [75, 16]. However, it is still difficult to analyze the wrinkling behavior of membrane structure. For geometrically nonlinear force method, it separates the geometric topology and constitutive relationship, performs the singular value decomposition of balance matrix, thus replacing the integration of the tangent stiffness matrix, effectively avoiding the singularity of the stiffness matrix. Due to the time-consuming in the singular value decomposition, this method is limited to a certain extent. The VFIFE method describes the structural deformation by the motion of particles with the calculation process of step-by-step, particle-by-particle, it is highly suitable for the analysis of buckling and wrinkling problems.

Yu and Luo [76] simulated the buckling behavior of space structures by bar element, subsequently, Wang realized the buckling simulation of spatial thin-shell structure [77], whose results indicated that the VFIFE method can reach the critical load and track the whole process of large displacement and rotation, structural buckling and post-buckling behavior without any special treatment. Furthermore, without multi-stage loading, the structural loads can be applied to the structure at the initial step of calculation analysis, which is more in line with the engineering practice. In addition, Luo and Zhao conducted additional research on the wrinkling behaviors of thin membrane structures [78, 79], which further proved that the VFIFE method can effectively simulate the wrinkling behavior of the structure with membrane materials.

Yu and Li [80] predicted the buckling loads that initiate local collapse, propagation and crossover, and simulate the dynamic and quasi-static buckling modes for pipelines with practical range of diameter-to-thickness ratios greater than 20 with VFIFE without special processing for the iterative calculation and the stiffness matrix convergence, and achieved the parallel efficiency over 90% for a common computer (12 threads, 4G RAM). Furthermore, they analyzed the buckling failure behavior of subsea buried pipeline crossing seismic faults [81].

Fracture and Collapse. When dealing with discontinuities such as fracture and collapse, the finite element method, discrete element method, mesh-free method or combined method are the traditional analysis tools. For FE method, there are inherent difficulties when it comes to fracture behavior analysis, which need to be combined with other methods to simulate the discontinuous behavior of the structure. Limited by the basic discrete model, the computation cost using discrete element method is greatly increased when establishing the 3D structural model, which is not conducive to the collapse simulation of large structure. For mesh-free method, the approximate functions currently used have no access to the interpolation calculation, so that there are certain difficulties in dealing with boundary conditions and additional approximate methods or numerical methods are combined to meet the boundary conditions. For VFIFE method, on the concept of path element, the fracture occurs at the point of path element and small deformation is regarded within the path element. The fracture only changes the particle force, which means particles can be separated

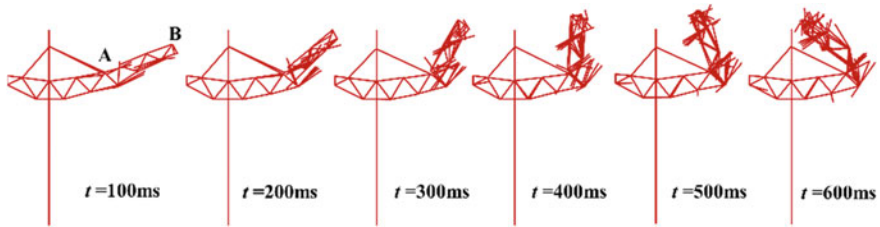


Fig. 88.13 Damage of cantilever roof (courtesy of [84])

from each other without re-updating the grid or particle number. The VFIFE method is therefore a simple and effective method for discontinuous behavior analysis.

Yu et al. [82] evaluated feasibility of the VFIFE method in tracing movement of spatial truss structure after buckling, considering the fracture criteria of truss element and the behavior pattern in post-buckling. In addition, Yu and Luo simulated the whole collapse process of spatial steel structure in multiple dimensions, and studied the failure mechanism during the continuous collapse process [83]. The two classic failure patterns, buckling failure and mechanism failure were further discussed and the effects of different constitutive models and collision algorithms were evaluated [84], in terms of the cantilever roof, truss structure and double-layer reticulated dome (shown in Fig. 88.13). The collapse and fracture analyses of cable-strut tensile structures [45], transmission tower-line system [85], thin-membrane structure [86] have been conducted successively in recent years. Duan et al. [24] simulated the entire-process collapse of earthquake excited cable-stayed bridge with fiber beam-column element model based on VFIFE, in which the eigensystem realization algorithm method was introduced for obtaining the modal parameters. The study provided a foundation for seismic damage prediction and anti-collapse seismic design for cable-stayed bridges.

As for the collapse studies of frame structures, Dalian University of Technology has made significant efforts on it based on VFIFE [80, 81, 88, 89], including the progressive collapse of semi-rigid steel frame structures [90], steel frame with buckling constraint braces [91], steel frame with self-centering energy dissipation support [88] and steel-concrete composite beam frame considering the structural initial deformation [89] (shown in Fig. 88.14).

88.4.2 Engineering Applications

Since the VFIFE method was proposed, it has not only been improved in methods and element types, but also been widely used in engineering fields, such as steel structure, concrete structure, offshore structure, vibration control, and so on. The applications of VFIFE method in each engineering field will be briefly described below.

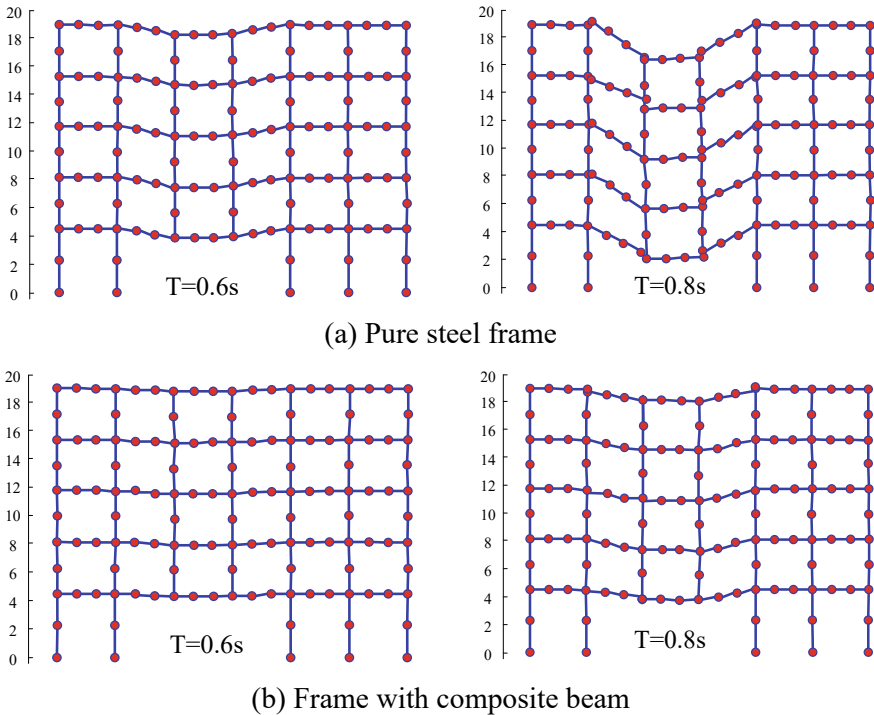


Fig. 88.14 Animation screenshot of collapse simulation (courtesy of [89])

Steel Structure. Due to the high strength, good ductility and plasticity, light weight, easy transportation and installation, excellent seismic and wind resistance, Steel structure is widely employed in building structure.

However, the steel structure is resistant to heat but intolerant to high temperature, with poor fire resistance. The bearing capacity of steel structure decreases rapidly when subjected to high temperature, resulting in the collapse and failure of structure. The traditional fire analysis of steel structure mostly adopts static analysis mode, which is suitable for slow change of temperature and deformation. However, if the temperature changes or the deformation of structure is too fast, especially when predicting the collapse process after structural deformation, it is arduous for the traditional finite element method to deal with such discontinuous deformation because it cannot be in harmony with deformation. Many scholars have applied it to the behavior analysis of steel structure affected by fire.

It was the first time that Chang [92] utilized VFIFE method to analyze beam and column members under different support conditions and different distribution of temperature fields, and on this basis, the mechanical properties of single-span steel frame under ideal temperature field and simulated real fire temperature field were studied and compared. Wei [93] applied VFIFE method to resolve the large deformation problem of the frame structure subjected to fire, and the failure mode

of planar frame after the occurrence of fire can be effectively simulated. Liu [94] conducted in-depth study on the fire simulation of the planar frame and obtained the behavior characteristics of planar frame with temperature effect, considering the material nonlinearity. Lien et al. [95, 96] considered the thermal strain effect and established the analysis model of generalized structural joints that can simultaneously consider the semi-rigid effects of axial force, shear force and bending moment, and simulated the whole process of the multi-layer multi-span steel frame and other structures under fire (shown in Fig. 88.15). The study showed that the fire response of steel structure is significantly affected by the boundary conditions and applied external loads. With regard to semi-rigid joints, Lien et al. [97] further investigated the structural behaviors, involving bifurcation instability, snap-through buckling and the inelastic response with beam element fracture, of steel frame with semi-rigid joints, whose results showed that the semi-rigid joints reduced the structural stiffness so that using simplified rigid joints will overestimate the bearing capacity of structure.

Concrete Structure. Concrete structure, by right of good integrity, easy access to model and great durability, is the most common type of the building structures. However, cracks are prone to occur since the concrete strength is normally low. Since the VFIFE method can simply deal with the geometric and material nonlinearity of the structure, the VFIFE has been applied to the behavior analysis of concrete structures by many scholars.

In 2004, Wang [98] was the first to apply the VFIFE method to nonlinear discontinuous deformation analysis and crack extension of concrete structure. Wu [99] adopted the fiber element to study the behavior of confined concrete structure with carbon fiber reinforced polymer. Zhang [100] utilized the 2D solid element and truss element to respectively model the concrete and steel reinforcement, where the nonlinear elastic model proposed by Darwin and Pecknold was adopted for concrete

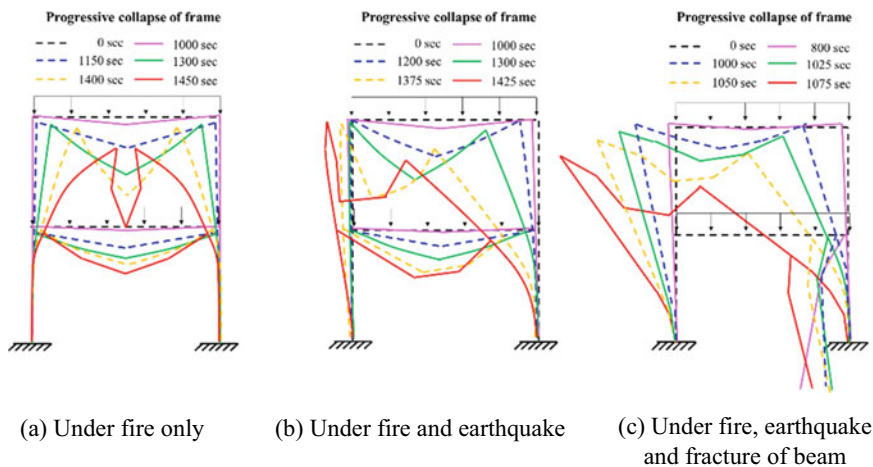


Fig. 88.15 Progressive deformation of the steel frame (courtesy of [96])

and the ideal elastoplastic model was adopted for steel reinforcement, and simulated the nonlinear response of reinforced concrete simply supported beams under the concentrated forces, which was consistent with the test results. Zheng [101] considered the effect of shear force in the fiber section analysis to simulate the behaviors of RC structure under the combined action of axial force, bending moment, and shear force, whose result was consistent with that given by the Response 2000 software of the University of Toronto. Zhang et al. [102, 103] successively proved that the nonlinear behavior of RC shear walls throughout the entire pushover analysis and cyclic loading can be effectively and accurately captured by VFIFE, compared with the test results. The above research shows that the VFIFE method can effectively simulate the sophisticated mechanical behavior of concrete structures.

Offshore Structure. The offshore structures, mostly as multi-degree-of-freedom systems, usually possess the nonlinear large deformation mainly induced from the heavy wave, wind and the marine environment. The other corresponding issues for an offshore structure also draws a lot of attentions, including material fatigue, vibration, and corrosion and so on. The competence of the tradition FE methods is inferior to that of VFIFE for the simulation of nonlinear large deformation behavior and they suffer from their inherent shortcomings.

Tseng [104] applied the VFIFE method to analyze the dynamic responses of rigid-frame offshore structure subjected to the wave force and discussed the behaviors of visco-elastic (VE) dampers applied in the offshore structure, in which the results showed that the lower the natural frequency of the structure is, the better the damping effect is. Chang et al. [105] investigated and discussed the behaviors of several typical offshore template structures of one-bay and two-bay installing the VE dampers and diagonal bracings. The study showed that with the favor of VE dampers, the dynamic responses and resonant responses of the offshore structure can be greatly reduced and the one-bay offshore structure with same span may has better effectiveness for the vibration mitigation. In recent years, Li et al. [106] has embarked on the relevant research in marine risers, verifying the feasibility and good performance of VFIFE-based analysis of marine risers. Besides, Li et al. [107] extended the application of VFIFE to the buoys mooring system, providing a new numerical modeling approach for behavior analysis of buoys mooring system.

Huang [108] investigated the response law of offshore electrical platform under different working conditions, involving the seismic and collision. Yu et al. [109] established a steel catenary riser model integrated with the nonlinear seabed model to develop the trenches by VFIFE. Simulation results prove that the trenches developed only by heave motion or including the low frequency surge motion have a positive effect in reducing the fatigue damage, while the trenches considering static platform offset have little influence. Li et al. [110] proposed a novel VFIFE-based 3D model to study vortex-induced vibration of top-tensioned riser. The comparison with the experiment had proved that the VFIFE method is feasible and effective in predicting the three-dimensional vortex-induced vibration response.

Vibration Control. In addition to the analysis of structural behavior, the VFIFE method can also be used to simulate structural control components and observe the dynamic behaviors of structural control devices.

In 2006, Chen [111] for the first time simulated the passive control devices with VFIFE method, established the reasonable elements that conformed to the dynamic behavior of passive control devices, such as viscous fluid dampers, and discussed the dynamic responses of structure after installing such control devices, which made the application of VFIFE method more engineering-oriented. Chen [44] analyzed the nonlinear dynamic behaviors of the isolated bridges with unseating prevention devices and different nonlinear dampers under large earthquakes, to predict the collapse simulation of bridges. Jui [112] applied the VFIFE method to passive control of 3D frame, establishing the coupling between space frames and rigid bodies, simulating the behaviors of structures with different dampers. Ni et al. [113] established a stay cable, considering the effect of viscous damper, which showed the cable-damper system modeled by VFIFE can accurately simulate the vibration control effect of the damper on the cable. Xu et al. [114, 115] investigated the geometric nonlinearity and axial loading effects of membrane SRA (Synthetic Aperture Radar) antenna structure using VFIFE method, and analyzed the vibration control of SRA antenna structure with piezoelectric sensors and actuators. Zhong [116] and Yin [117] both studied the dynamic behaviors of the frame structures with viscous damper by VFIFE, and proposed the location optimization schemes of dampers with different indices, which provided an effective and reliable method to evaluate the dynamic behavior and failure mode of damping structures.

Construction Simulation. The current research on construction mechanics is mainly based on the time-varying mechanics theory [118], and the construction process is discretized into several construction stages for analysis. Two simulation methods, the element birth and death technology and the step-by-step model technology [119], are often used to discretize and solve the continuous construction process, and both have certain technical drawbacks. Moreover, traditional FE methods often have great difficulties in solving nonlinear problems of such construction processes involving large deformations and large displacements. The whole motion process can be realized in VFIFE analysis of which the realistic continuously changes of exerted forces and operating environment are capable to be simulated. It is easy to add or subtract the model elements or particles in different construction stages during the simulation, directly adding new components to the initial model for analysis. When the boundary conditions change, due to the essentially dynamic solution of VFIFE, there is no need for many changes to the original analysis program.

Liu [120] used VFIFE method for the first time to analyze the simulation of structures in the construction stage, so as to obtain the dynamic responses of structure in each construction stage, where the effects of increasing and decreasing planar frame elements and the changes of boundary conditions were evaluated. Peng et al. [121] carried out the direct analysis and inverse analysis of construction process of cable-strut structures based on VFIFE, verified the proposed method through the analysis of the spoke-type roof structure of Shenzhen Baoan Stadium, simulated

and tracked the whole construction process from the zero state to the final state. Zhu and Guo et al. [122] introduced the tensioning element and realized the whole lifting process simulation of long-span pre-stressed steel structure by controlling the original length of the tensioning element, while the jack element was introduced for the unloading analysis.

Other Fields. Many efforts trying to solve the civil engineering problems have been made and concluded in the above description, meanwhile, the studies on VFIFE in different fields, such as machinery [123, 124], electricity [125–127] and biomedicine [87, 128] are also conducted.

88.5 Future Trends on Vector Form Intrinsic Finite Element Method

With the rapid development for decades, the VFIFE method has been widely used in behavior analysis and failure mode analysis. According to the existed research and analysis, VFIFE method is expected to show a good prospect in the following aspects.

88.5.1 Prediction of Failure Behavior Modes

Accurately predicting and analyzing the behavior modes of structures under extreme conditions, such as earthquakes, typhoons, and explosions, has been a long-standing goal for engineers and researchers. However, due to the influence of many factors, such as the stability and efficiency of the calculation method, the simulation of the behavior or failure mode of the structure group under extreme loads is a complicated yet still not technical problem.

Since the VFIFE method can accurately simulate the true dynamic behavior of a structure without the need to integrate the stiffness matrix, there is no need to solve the large stiffness matrices are also not required to iterate to deal with complex nonlinear behavior. It can be utilized to analyze the structural behavior modes under extreme loads. Since the VFIFE possesses the characteristic of point-value description and independent computation for each particle, which is suitable for analyzing many-body motions and discontinuous behavior, so VFIFE method is promising in analyzing the motion behavior and failure mode of a group of structures in a region under seismic loads to provide an effective computational tool for structural and urban disaster prevention.

88.5.2 Combination of Cloud Computing for High-Speed Parallel Computing

As the preceding description, the VFIFE method adopts an explicit integration procedure without integrated stiffness matrix and the iterative method, where the internal force integration and updating are performed within the element and the displacement is calculated separately for each particle. Therefore, the VFIFE method is capable of being highly parallelizable. It has also been verified by the preceding researches [31, 35].

Cloud computing is an approach that provides universal and convenient on-demand network access to a configurable computing resource sharing pool using network access. The resources contain network, servers, storage, applications, and services, which can be quickly and directly invoked by the users with the low management cost and reduced negotiation with service providers. The hardware infrastructure of cloud computing is typically built on the extensive inexpensive server cluster that offers superior performance and lower costs compared to traditional computing devices. Moreover, the underlying development environment of cloud computing is available to users so that the users can complete the co-development of the underlying structure with their own applications and requirements. The computation is then expanded to the massive server clusters, while using thousands of server nodes to processing and speeding up programs. As a result, the VFIFE computation on a cloud-based platform is expected to enable the parallelization of thousands of servers, which will greatly increase the computation efficiency.

88.5.3 Application on Dynamic Analysis of Large Structure Based on Hybrid Simulation

The hybrid simulation is an increasingly popular testing method to conduct structural analysis by dividing the large civil engineering structures into the numerical substructures that can be accurately simulated by numerical simulation software and the experimental substructures whose performance can only be obtained by experimental means, combining the numerical and experimental methods.

In hybrid simulation, after inputting the environmental excitations, such as seismic waves, to the numerical structure in the personal computer, the relevant response under dynamic loading is resolved by means of numerical integration. The boundary displacement of the numerical substructure is then exerted on the experimental substructure by the actuator, and the experimental reaction force measured by the force sensor is fed back to the numerical model to update the parameters, thus completing the subsequent successive iterations. As for traditional finite element method, the interaction between numerical calculations and experiments in hybrid simulation is inefficient as requiring iterations to solve the kinetic analysis, which is even difficult to achieve real-time hybrid simulation.

Due to the point value description, no iteration is required to solve the dynamic behavior, and the boundary conditions of the element can be simply changed. With the parallel computational characteristics, the computational efficiency by VFIFE can be greatly improved compared to the traditional finite element dynamic analysis. There is a primary trial and verification of VFIFE-based hybrid simulation in the reference [127], accomplished the real time hybrid simulation of a three-story frame structure as the numerical substructure and the attached spring as the experimental substructure, which indicates the feasibility, rationality and efficiency of VFIFE applied in hybrid simulation. The reference only conducted a simple case with linear experimental substructure, many works can be further studied, such as simultaneously considering the complexity of large structure and non-linearity of experimental substructure.

88.5.4 Dynamic Monitoring and Assessment based on Digital Twin Technology

Given the inherent advantages of VFIFE in structural nonlinear simulation, it can be combined with digital twin technology. By continuously collecting and intelligently analyzing the sensor operation data, a real-time updated virtual model based on VFIFE can be established. This enables numerous simulation and validation of the target structure, providing an efficient and novel way for structural health monitoring and assessment.

88.6 Conclusion

The basic concepts and development of VFIFE have been comprehensively reviewed and discussed in this paper. As an innovative method quite differing from traditional FEM, VFIFE method adopts three concepts of point-value description, path element and fictitious inverse motion, to avoid the stiffness matrices integration and iterative analysis existed in traditional FEM. It can effectively simulate the true motion behavior of the structure.

The extensive applications of VFIFE demonstrates the utility and potential of VFIFE as a computational tool to study complex structural behaviors including the non-linearity in material and geometry, collapse, fracture, multi-body motion, etc.

With the advantage of parallel computing, the combination of VFIFE method and cloud-based computing can be considered for large complicated structures, the key problem is how to establish a universal and simple platform while dealing with different problems.

Acknowledgements The research described in this paper was financially supported by the Natural Science Foundation of China (52378318, 52378540), and Zhejiang Provincial Natural Science Foundation of China (LHZ23E080003).

References

1. Lynn, K.M., Isobe, D.: Structural collapse analysis of framed structures under impact loads using ASI-Gauss finite element method. *Int. J. Impact Eng.* **34**(9), 1500–1516 (2007)
2. Zhang, Z.Y., Paulino, G.H.: Extrinsic cohesive modelling of dynamic fracture and micro-branching instability in brittle materials. *Int. J. Numer. Meth. Eng.* **72**(8), 893–923 (2007)
3. Belytschko, T., Liu, W.K., Moran, B.: *Nonlinear Finite Elements for Continua and Structures*, pp. 122–186. Wiley, New York (2000)
4. Oden, J.T.: *Finite Elements of Nonlinear Continua*, pp. 89–115. McGraw-Hill, New York (1972)
5. Wempner, G.: Finite elements, finite rotations and small strains of flexible shells. *Int. J. Solids Struct.* **5**(2), 117–153 (1969)
6. Belytschko, T., Hsieh, B.J.: Nonlinear transient finite element analysis with convected coordinates. *Int. J. Numer. Meth. Eng.* **7**(3), 255–271 (1973)
7. Shi, G., Goodman, R.E.: Discontinuous deformation analysis. In: *Proceedings of the 25th US Symposium on Rock Mechanics*, Evanston, III, p. 1 (1984)
8. Sukumar, N., Moës, N., Moran, B., Belytschko, T.: Extended finite element method for three-dimensional crack modelling. *Int. J. Numer. Meth. Eng.* **48**(11), 1549–1570 (2000)
9. Wu, T.Y., Lee, J.J., Ting, E.C.: Motion analysis of structures (MAS) for flexible multibody systems: planar motion of solids. *Multibody Sys. Dyn.* **20**(3), 197–221 (2008)
10. Liu, K.X., Gao, L.T.: A review on the discrete element method. *Adv. Mech.* **33**(4), 483–490 (2003). (in Chinese)
11. Guo, L.L., Chen, Z.F., Luo, J.R., Chen, G.: A review of the extended finite element method and its applications. *Chin. Q. Mech.* **32**(4), 612–625 (2011). (in Chinese)
12. Ting, E.C., Shih, C.: Fundamentals of a vector form intrinsic finite element: part I. Basic procedure and a plane frame. *J. Mech.* **20**, 113–122 (2004)
13. Ting, E.C., Shih, C.: Fundamentals of a vector form intrinsic finite element: part III. Convected material frame and examples. *J. Mech.* **20**, 133–143 (2004)
14. Ting, E.C., Duan, Y.F., Wu, T.Y.: *Vector Mechanics of Structures*. Science Press (2012)
15. Chung, P.Y.: Development and engineering application of flat shell element by the vector form intrinsic finite element method. Doctor dissertation, National Sun Yat-sen University, Taiwan, China (2010)
16. Crisfield, M.A.: An arc-length method including line searches and accelerations. *Int. J. Numer. Methods Eng.* **19**(2), 1269–1289 (1983)
17. Ting, E.C., Shih, C.: Fundamentals of a vector form intrinsic finite element: part II. Plane solid elements. *J. Mech.* **20**, 123–132 (2004)
18. Wu, C.H.: A study on simulation of motion of 3D solids and establishment of graphical user interface. Master Dissertation, Chung Yuan Christian University, Taiwan, China (2005)
19. Wang, R.C.: Vector-based structural motion analysis. Doctor dissertation, National Central University, Taiwan, China (2006)
20. Wu, T.Y., Wang, C.Y., Chuang, C.C., Ting, E.C.: Motion analysis of 3D membrane structures by a vector form intrinsic finite element. *J. Chin. Inst. Eng.* **30**(6), 961–976 (2007)
21. Wu, T.Y., Ting, E.C.: Large deflection analysis of 3D membrane structures by a 4-node quadrilateral intrinsic element. *Thin-Walled Struct.* **46**(3), 261–275 (2008)
22. Chang, P.Y.: Development and application of plate element by the vector form intrinsic finite element method. Doctor dissertation, National Sun Yat-sen University, Taiwan, China (2009)
23. Chen, S.H.: Development of the vector form DKT thin shell element and motion analyses in shell structures. Doctor dissertation, National Central University, Taiwan, China (2013)
24. Duan, Y.F., He, K., Zhang, H.M., Ting, E.C., Wang, C.Y., Chen, S.K., Wang, R.Z.: Entire-process simulation of earthquake-induced collapse of cable-stayed bridges by vector form intrinsic finite element (VFIFE) method. *Adv. Struct. Eng.* **3**(17), 347–360 (2014)
25. Liu, J., Xu, L., Lin, M.: Simulation of a buried pipeline crossing strike-slip fault based on vector form intrinsic finite element (VFIFE) method with fiber element model. *International Society of Offshore and Polar Engineers*, pp. 977–983 (2016)

26. Lin, X.H., Luo, Y.Z., Tang, J.Z., Wang, W., Zheng, Y.F., Yang, C.: A fiber beam element for the finite particle method considering shear and torsion deformation. *Eng. Mech.* **39**(05), 34–43 (2022). (in Chinese)
27. Yuan, X.F., Chen, C., Duan, Y.F., Qian, R.J.: Elastoplastic analysis with fine beam model of vector form intrinsic finite element. *Adv. Struct. Eng.* **21**(3), 365–379 (2018)
28. Wang, Z., Zhao, Y., Yang, X.L.: Analysis and application of the vector form intrinsic finite element based on the hexahedral grid. *Chin. J. Comput. Mech.* **35**(4), 480–486 (2018). (in Chinese)
29. Zhang, H.M., Fang, Y., Duan, Y.F., Du, G.B.: The V-MVLE model for cyclic failure behavior simulation of planar RC members. *Thin-Walled Struct.* **181**, 110159 (2022)
30. Li, D.C.: A study in time integration method of vector form intrinsic finite element method. Master dissertation, Chung Yuan Christian University, Taiwan, China (2008)
31. Su, C.C.: Numerical simulation on ultimate stage of bridges under earthquakes by 3D vector form intrinsic finite element method. Master dissertation, National Central University, Taiwan, China (2011)
32. Wang, M.L., Chuang, C.C., Lee, J.J.: Development of an adaptive explicit algorithm for static simulation using the vector form intrinsic finite element method. *J. Mech.* **37**, 566–583 (2021)
33. Lewis, W.J.: Dynamic relaxation analysis of the non-linear static response of pretensioned cable roofs. *Comput. Struct.* **18**(6), 989–997 (1984)
34. Lai, J.Y.: Distributed computations of vector form intrinsic finite element method for motion analysis of planar frames. Master dissertation, Chung Yuan Christian University, Taiwan, China (2005)
35. Du, Q.F., Wu, H.: Node distributing technology for parallel computing of spatial truss structure using vector form intrinsic finite element. *J. Tongji Univ. Nat. Sci.* **44**(7), 1121–1129 (2016). (in Chinese)
36. Wang, W., Zheng, Y.F., Tang, J.Z., Yang, C., Luo, Y.Z.: A GPU-based parallel algorithm for 2D large deformation contact problems using the finite particle method. *Comput. Model. Eng. Sci.* **129**(2), 595–626 (2021)
37. Yuan, X.F., Akram, S., Ma, S.: Application of consistent mass matrix to vector form intrinsic finite element. *J. Huazhong Univ. Sci. Technol. Nat. Sci.* **47**(11), 37–42 (2019). (in Chinese)
38. Hou, X.Y., Fang, Z.D.: Solid structure analysis with large deformation of eight-node hexahedral element using vector form intrinsic finite element. *Adv. Struct. Eng.* **21**(6), 852–861 (2018)
39. Wang, R.H., Zhao, Y., Duan, Y.F.: An improved algorithm for reverse motion of solid element in VFIFE. In: *Proceedings of the 17th National Conference on Spatial Structures*, pp. 479–485 (2018)
40. Liu, M.K., Zhang, F.B., Wang, T.Y., Chu, F.L., Cheng, W.D., Liu, Y.M.: Multi-centroid finite point method and its application to the dynamic modeling of industrial robots. *J. Vibr. Shock* **41**(18), 1–8 (2022). (in Chinese)
41. Wang, S.Y., Li, C., Yang, Y.L., Pang, Z.C., Tang, H.Q.: Research on reverse rotation angle calculation method of vector form intrinsic finite element in plane. *J. Central South Univ. Sci. Technol.* **50**(5), 1135–1143 (2019). (in Chinese)
42. Yu, Y., Liu, F.H., Wang, Q.H., Luo, Y.Z., Li, Y.: Study on damping in finite particle method. *Eng. Mech.* **36**(11), 34–40 (2019). (in Chinese)
43. Xiang, X.A.: Theoretical research of cable-membrane structures and application on the expo axis project in Shanghai. Doctor dissertation, Zhejiang University, Hangzhou, China (2010)
44. Wang, C.Y., Wang, R.Z., Chuang, C.C., Wu, T.Y.: Nonlinear dynamic analysis of reticulated space truss structures. *J. Mech.* **22**, 199–212 (2006)
45. Zhu, M.L., Lu, J.Y., Guo, Z.X.: Analysis on progressive collapse resistance of novel torus-dome tensile structure due to cable rupture. *J. Southeast Univ. (Nat. Sci. Ed.)* **46**(5), 1057–1062 (2016). (in Chinese)
46. Zhu, M.L., Dong, S.L.: Failure analysis of suspen-dome by vector form intrinsic finite element method. *J. Zhejiang Univ. (Eng. Sci.)* **46**(09), 1611–1618+1632 (2012). (in Chinese)

47. Zhu, M.L., Dsong, S.H., Yuan, X.F.: Failure analysis of a cable dome due to cable slack or rupture. *Adv. Struct. Eng.* **2**, 259–271 (2013)
48. Liu, H.C., Dong, S.L.: Cable rupture analysis of inner-outer combined reticulated shell-string structure using VFIFE. *Spat. Struct.* **18**(03), 86–96 (2012)
49. Shih, J.Y.: Vehicle-track-bridge interaction analysis by the vector form intrinsic finite element method. Master dissertation, National Central University, Taiwan, China (2010)
50. Duan, Y.F., Wang, S.M., Wang, R.Z., Wang, C.Y., Shih, J.Y., Yun, C.B.: Vector form intrinsic finite-element analysis for train and bridge dynamic interaction. *J. Bridge. Eng.* **23**(1), 04017126 (2018)
51. Duan, Y.F., Wang, S.M., Yau, J.D.: Vector form intrinsic finite element method for analysis of train-bridge interaction problems considering the coach-coupler effect. *Int. J. Struct. Stab. Dyn.* **19**(2), 1950014 (2019)
52. Wang, S.M., Ni, Y.Q., Sun, Y.G., Lu, Y., Duan, Y.F.: Modelling dynamic interaction of maglev train-controller-rail-bridge system by vector mechanics. *J. Sound Vib.* **533**, 117023 (2022)
53. Shabana, A.A.: Flexible multibody dynamics: review of past and recent developments. *Multibody Sys. Dyn.* **1**(2), 189–222 (1997)
54. Jetteur, P., Cescotto, S.: A mixed finite element for the analysis of large inelastic strains. *Int. J. Numer. Meth. Eng.* **31**(2), 229–239 (1991)
55. Lai, C.H.: An Application of vector form intrinsic finite element method on geometrically nonlinear problem for 2D-frames. Master dissertation, Chung Yuan Christian University, Taiwan, China (2003)
56. Wu, T.Y., Wang, R.Z., Wang, C.Y.: Large deflection analysis of flexible planar frames. *J. Chin. Inst. Eng.* **29**, 593–606 (2006)
57. Wu, T.Y., Tsai, W.C., Lee, J.J.: Dynamic elastic-plastic and large deflection analyses of frame structures using motion analysis of structures. *Thin-Walled Struct.* **47**, 1177–1190 (2009)
58. Wu, T.Y.: Dynamic nonlinear analysis of shell structures using a vector form intrinsic finite element. *Eng. Struct.* **56**, 2028–2040 (2013)
59. Wu, T.Y.: Nonlinear analysis of axi-symmetric solid using vector mechanics. *CMES-Comput. Model. Eng. Sci.* **82**(2), 83–112 (2011)
60. Yu, Y., Luo, Y.Z.: Finite particle method for kinematically indeterminate bar assemblies. *J. Zhejiang Univ.-Sci. A* **10**(5), 669–676 (2009)
61. Yu, Y., Luo, Y.Z.: Motion analysis of deployable structures based on the rod hinge element by the finite particle method. *Proc. Inst. Mech. Eng. Part G-J. Aerospace Eng.* **223**(G7), 955–964 (2009)
62. Lynn, K.M., Isobe, D.: Structural collapse analysis of framed structures under impact loads using ASI-Gauss finite element method. *Int. J. Impact Eng.* **34**, 1500–1516 (2007)
63. Chen, C.L.: An application of vector form intrinsic finite element method on elastic-plastic and fragmentary problem for 2D-frames. Master dissertation, Chung Yuan Christian University, Taiwan, China (2005)
64. Wang, R.Z., Tsai, K.C., Lin, B.Z.: Extremely large displacement dynamic analysis of elastic-plastic plane frames. *Earthquake Eng. Struct. Dyn.* **40**, 1515–1533 (2011)
65. Chaudhary, A.B., Bathe, K.J.: A solution method for static and dynamic analysis of three-dimensional contact problems with friction. *Comput. Struct.* **24**(2), 855–873 (1986)
66. Papadopoulos, P., Taylor, R.L.: A mixed formulation for the finite element solution of contact problems. *Comput. Methods Appl. Mech. Eng.* **94**(6), 373–389 (1992)
67. Maison, B.F., Kasai, K.: Dynamics of pounding when two buildings collide. *Struct. Eng. ASCE* **21**, 771–786 (1992)
68. Choi, C.K., Chung, G.T.: A gap element for three-dimensional elasto-plastic contact problems. *Comput. Struct.* **61**(6), 1155–1167 (1996)
69. Wu, S.Y.: Large deformation and contact analysis of 2D frame structure by the vector form intrinsic finite element method. Master dissertation, National Central University (2004)
70. Wang, Z., Zhao, Y.: Vector Form Intrinsic Finite Element method for collision-contact analysis of membrane material. *Chin. J. Comput. Mech.* **31**(3), 378–383 (2014). (in Chinese)

71. Wang, Z., Zhao, Y., Yang, X.L.: Collision-contact, crack-fracture and penetration behavior analysis of thin-shell structures based on vector form intrinsic finite element. *J. Build. Struct.* **37**(6), 53–59 (2016). (in Chinese)
72. Zhang, P.F., Luo, Y.Z., Yang, C.: Buckling analysis of thin shell using the finite particle method. *Eng. Mech.* **34**(2), 12–20 (2017). (in Chinese)
73. Hou, X.Y., Fang, Z.D., Zhang, X.J.: Static contact analysis of spiral bevel gear based on modified VFIFE (vector form intrinsic finite element) method. *Appl. Math. Model.* **60**, 192–207 (2018)
74. Liu, F.H., Yu, Y., Wang, Q.H., Luo, Y.Z.: A coupled smoothed particle hydrodynamic and finite particle method: an efficient approach for fluid-solid interaction problems involving free-surface flow and solid failure. *Eng. Anal. Bound. Elem.* 118 (2020)
75. Riks, E.: An increment approach to the solution of snapping and buckling problems. *Int. J. Solids Struct.* **15**(5), 529–551 (1979)
76. Yu, Y., Luo, Y.Z.: Buckling analysis of structures by the finite particle method. *Eng. Mech.* **26**(10), 23–29 (2009). (in Chinese)
77. Wang, Z., Zhao, Y., Yang, X.L.: Vector form intrinsic finite element method for buckling analysis of thin-shell structures. *J. Central South Univ. Sci. Technol.* **47**(6), 2058–2064 (2016). (in Chinese)
78. Luo, Y.Z., Yang, C.: A vector-form hybrid particle-element method for modeling and nonlinear shell analysis of thin membranes exhibiting wrinkling. *J. Zhejiang Univ.-Sci. A* **15**(5), 331–350 (2014)
79. Wang, Z., Zhao, Y., Yang, X.L.: Analysis of buckling behavior of planar membrane structure. *J. Zhejiang Univ.-Eng. Sci.* **06**, 1116–1122 (2015). (in Chinese)
80. Yu, Y., Li, Z.M., Yu, J.X., Xu, L.G., Zhao, M.R., Cui, Y.P., Wu, H., Duan, Q.H.: Buckling analysis of subsea pipeline with integral buckle arrestor using vector form intrinsic finite thin shell element. *Thin-Walled Struct.* **164**, 107533 (2021)
81. Yu, Y., Li, Z.M., Yu, J.X., Sun, W.Z., Liu, X.W., Ma, J.D., Liu, C.: Buckling failure analysis of subsea buried pipeline crossing strike-slip fault. *Eng. Mech.* **39**(9), 242–256 (2022). (in Chinese)
82. Yu, Y., Zhao, X., Luo, Y.Z.: Multi-snap-through and dynamic fracture based on finite particle method. *J. Constr. Steel Res.* **82**, 142–152 (2013)
83. Yu, Y., Luo, Y.Z.: Structural collapse analysis based on finite particle method I: basic approach. *J. Build. Struct.* **32**(11), 17–26 (2011). (in Chinese)
84. Yu, Y., Paulino, G.H., Luo, Y.Z.: Finite particle method for progressive failure simulation of truss structures. *J. Struct. Eng.-ASCE* **137**(10), 1168–1181 (2011)
85. Wang, W.: Collapse simulation of transmission tower-line system under downburst based on finite particle method. Master dissertation, Huazhong University of Science and Technology, Wuhan, China (2018)
86. Wang, Z., Zhao, Y., Yang, X.L.: Analysis and application of the vector form intrinsic finite element for fracture and penetration of thin-membrane. *Chin. J. Comput. Mech.* **35**(3), 315–320 (2018). (in Chinese)
87. Wang, Y.F.: Research on mechanical properties of cytoskeleton network through three-dimensional form-finding model. Master dissertation, Shanghai Jiao Tong University, Shanghai, China (2017)
88. Lou, Y.M.: Progressive collapse studies of self-centering energy dissipation braces steel frames based on vector form intrinsic finite element method. Master dissertation, Dalian University of Technology, Dalian, China (2020)
89. Wang, J.: Progressive collapse studies of frame with steel-concrete composite beam based on VFIFE method. Master dissertation, Dalian University of Technology, Dalian, China (2020)
90. Qu, J.T., Li, Z.C.: Dynamic analysis of semi-rigid steel frame structures resisting vertical progressive collapse. *J. Dalian Univ. Tech.* **59**(4), 409–416 (2019). (in Chinese)
91. Xue, X.S.: Collapse studies of steel frame with buckling restrained braces on vector form intrinsic finite element method. Master dissertation, Dalian University of Technology, Dalian, China (2020)

92. Chang Ye, J.: Vector form intrinsic finite element analysis of steel structure in fire environment. Master dissertation, National Cheng Kung University, Taiwan, China (2007)
93. Wei, T.L.: Vector form intrinsic finite element method for motion analysis of planar frames with thermal effects. Master dissertation, Chung Yuan Christian University, Taiwan, China (2007)
94. Liu, J.H.: Vector form intrinsic finite element method for planar frames under fire. Master dissertation, Chung Yuan Christian University, Taiwan, China (2008)
95. Lien, K.H.: Vector form intrinsic finite element analysis of steel structures exposed to fire. Master dissertation, National Cheng Kung University, Taiwan, China (2009)
96. Lien, K.H., Chiou, Y.J., Wang, R.Z., Hsiao, P.A.: Vector form intrinsic finite element analysis of nonlinear behavior of steel structures exposed to fire. *Eng. Struct.* **32**, 80–92 (2010)
97. Lien, K.H., Chiou, Y.J., Hsiao, P.A.: Vector form intrinsic finite-element analysis of steel frames with semirigid joints. *Am. Soc. Civil Eng.* **138**, 327–336 (2012)
98. Wang, K.C.: Nonlinear discontinuous deformation analysis of concrete structures. Doctor dissertation, National Central University, Taiwan, China (2004)
99. Wu, J.R.: Numerical simulation analysis for the members with FRP. Master dissertation, Chung Yuan Christian University, Taiwan, China (2008)
100. Zhang, L.W.: Nonlinear analysis of reinforced concrete structures by the VFIFE method. Master dissertation, National Central University, Taiwan, China (2009)
101. Zheng, Z.Y.: A study of the numerical simulation on the flexure-shear behavior of reinforced concrete members. Master dissertation, Chung Yuan Christian University, Taiwan, China (2009)
102. Zhang, H.M., Shan, Y.F., Duan, Y.F., Yun, C.B., Liu, S.: Vector mechanics-based simulation of large deformation behavior in RC shear walls using planar four-node elements. *Struct. Eng. Mech.* **74**(1), 1–18 (2020)
103. Zhang, H.M., Fang, Y., Duan, Y.F.: Seismic and failure behavior simulation for RC shear walls under cyclic loading based on vector form intrinsic finite element. *Structures* **43**, 1834–1853 (2022)
104. Tseng, G.W.: Dynamic analysis of offshore template platform by the vector form intrinsic finite element method. Master dissertation, National Sun Yat-sen University, Taiwan, China (2007)
105. Chang, P.Y., Lee, H.H., Tseng, G.W., Chung, P.Y.: VFIFE method applied for offshore template structures upgraded with damper system. *J. Mar. Sci. Technol.* **18**, 473–483 (2010)
106. Li, X.M., Guo, X.L., Guo, H.Y.: Vector form intrinsic finite element method for nonlinear analysis of three-dimensional marine risers. *Ocean Eng.* **161**, 257–267 (2018)
107. Li, X.M., Zhang, C.X., Liu, Z., Meng, D.: Static configuration and internal forces analysis of buoys mooring system. *Ship Eng.* **42**(1), 128–134 (2020). (in Chinese)
108. Huang, M.Z.: Nonlinear dynamic analysis of offshore electrical platform based on vector form intrinsic finite element. Master dissertation, Tianjin University, Tianjin, China (2019)
109. Yu, Y., Xu, S.B., Yu, J.X., Xu, W.P., Xu, L.X., Xu, L.G.: Influence of seabed trench on the structural behavior of steel catenary riser using the vector form intrinsic finite element method. *Ocean Eng.* **251**, 110963 (2022)
110. Li, X.M., Wei, W.F., Bai, F.T.: A full three-dimensional vortex-induced vibration prediction model for top-tensioned risers based on vector form intrinsic finite element method. *Ocean Eng.* **218**, 108140 (2020)
111. Chen, S.H.: An application of vector form intrinsic finite element method in passive structural control system. Master dissertation, Chung Yuan Christian University, Taiwan, China (2006)
112. Jui, H.C.: Passive control of 3D frame structure using vector form intrinsic finite element method. Master dissertation, Chung Yuan Christian University, Taiwan, China (2008)
113. Ni, Q.B., Duan, Y.F., Gao, B.Q.: Vector form intrinsic finite element (VFIFE) based simulation on vibration control of stay cables. *J. Vibr. Eng.* **27**(02), 238–245 (2014). (in Chinese)
114. Xu, R., Li, D.X., Jiang, J.P., Liu, W.: Nonlinear vibration analysis of membrane SAR antenna structure adopting a vector form intrinsic finite element. *J. Mech.* **31**, 269–277 (2015)

115. Xu, R., Li, D.X., Jiang, J.P., Liu, W.: Adaptive fuzzy vibration control of smart structure with VFIFE modeling. *J. Mech.* **31**, 671–682 (2015)
116. Zhong, J.: Optimum placement of dampers and fracture analysis of frame structures based on vector form intrinsic finite element. Master dissertation, Zhejiang University, Hangzhou, China (2016)
117. Yin, S.Y.: Research on optimization of viscous dampers in concrete frame structures. Master dissertation, Dalian University of Technology, Dalian, China (2019)
118. Wang, G.Y.: On mechanics of time-varying structures. *Chin. Civil Eng. J.* **33**(6), 105–108 (2000). (in Chinese)
119. Liu, X.W., Guo, Y.L.: Construction mechanics analytical procedures for steel structures in view of the geometric nonlinearity. *J. Xi'an Univ. Archit. Technol. (Nat. Sci. Ed.)* **40**(2), 161–169 (2008). (in Chinese)
120. Liu, Y.T.: An application of vector form intrinsic finite element method in construction stage analysis. Master dissertation, Chung Yuan Christian University, Taiwan, China (2007)
121. Peng, T.: Application of vector form intrinsic finite element method in the analysis of cable membrane structures. Master dissertation, Zhejiang University, Hangzhou, China (2012)
122. Zhu, M.L., Chen, X.Q., Guo, Z.X.: Construction analysis on integral lifting of steel structure by the vector form intrinsic finite element. *J. Southeast Univ.* **32**(04), 451–456 (2016)
123. Sun, W.H.: Dynamic analysis of flexible mechanisms using vector form intrinsic finite element method. Master dissertation, Taiwan University, Taiwan, China (2004)
124. Lee, K.H.: Dynamic analysis of flexible mechanisms with clearance using vector form intrinsic finite element method. Master dissertation, Taiwan University, Taiwan, China (2005)
125. Yao, D., Shen, G.H., Pan, F., Xing, Y.L., Guo, Y.: Wind-induced dynamic response of transmission tower using vector-form intrinsic finite element method. *Eng. Mech.* **32**(11), 63–70 (2015)
126. Chen, J.L., Yang, R.C., Ma, R.L.: Integrated simulation of wind turbine based on vector form intrinsic finite element. *J. Hunan Univ. (Nat. Sci.)* **43**(11), 141–148 (2016). (in Chinese)
127. Duan, Y.F., Tao, J.J., Zhang, H.M., Wang, S.M., Yun, C.B.: Real-time hybrid simulation based on vector form intrinsic finite element and field programmable gate array. *Struct. Control. Health Monit.* **26**(1), e2277 (2019)
128. Zhou, P., Huang, S., Chen, Q., He, S.Y., Cai, G.C.: Simulation of skin stretching around the forehead wrinkles in rhytidectomy. *Sens. Imaging* **21**(1), 50 (2020)

Chapter 89

Insight into the Mechanical Behaviour of Cooling Rate-Dependent Blistering Failures in Alumina Films



Ke Wang, Bo Yuan, Xiaofeng Guo, Christopher Harvey, and Simon Wang

Abstract The blistering and spallation failures in alumina films formed on Kanthal substrates have gained significant attention due to the importance of high-temperature materials in various industrial applications. This work aims to investigate the underlying mechanism for the circular interfacial separations that develop spontaneously under the constant compressive residual stresses at room temperature. This study employed analytical mechanical models and finite element simulations that are based on the conventional buckling theories. In detail, the thermal mismatch stress, alumina growth stress and creep of the substrate are included and the linear fracture locus criterion with the fracture toughnesses in mode I and II are used. The finite element model is established and the results reveal the initial separation is essential for blistering triggered by buckling. However, for the originally intact interface, the pockets of energy concentration theories are suggested to use. The present work highlights the difficulties for the blistering and spallation failures in thin films, having significant implications for the design and performance of high-temperature materials.

Keywords Alumina · Cooling rate · Blister · Spallation · Buckling · Pockets of energy concentration

89.1 Introduction

The thermally grown oxide (TGO) layer is of utmost importance to the multi-layer coating system, preventing the oxygen further penetrating into the underneath metallic substrate while bonding the constituent layers, such as the ceramic top coat

K. Wang · B. Yuan · X. Guo (✉)
School of Mechanical Engineering, Inner Mongolia University of Science and Technology,
Baotou 014030, China
e-mail: guoxiaofeng@imust.edu.cn

C. Harvey · S. Wang
Department of Aeronautical and Automotive Engineering, Loughborough University,
Loughborough LE11 3TU, Leicestershire, UK

and the bond coat in the thermal barrier coating system. However, it is frequently seen that the cracking and delamination failure can occur at the interface between the TGO and the metallic substrate, which may be driven by the residual stresses and the interface fracture energy.

Tolpygo and Clarke [1] conducted the pioneering works upon the blistering and spallation failures in the alumina scales formed by oxidation of Fe–Cr–Al Kanthal alloys at high temperatures and cooling in variable rates, as shown in Fig. 89.1. Several valuable phenomena were revealed out of experiments: (a) failures occurred at room temperature under the constant residual stresses rather than during cooling; (b) blisters only appeared at the intermediate cooling rate and nearly no blisters at the very low and very high cooling rate; and (c) the extent of spallation increases with decreasing the alumina thickness. From the conventional mechanical viewpoint, buckling is responsible for this spontaneous failure [2], that is the compressed alumina scale bends away from the substrate when the stress magnitude is sufficiently large or the size of pre-crack at the interface is large. However, it is found that the flaw size at the interface is much smaller than that specified by the buckling theories, and the blisters grew with time at constant stress until abruptly increasing and spalling.

Wang and Harvey [3, 4] proposed a novel mechanical theory to address the problem of spontaneous blistering and spallation failures in alumina scales. They hypothesized that the pockets of energy concentration due to the non-uniform dynamic creep and plastic relaxation at the interface drive the nucleation, growth and spallation. The blister energy, containing the strain energy in the deformed alumina and surface energy while excluding the residual strain energy before interface delamination, is used to describe the growth stages of blisters, based on which theoretical predictions on the blister radius agreed very well with the experimental

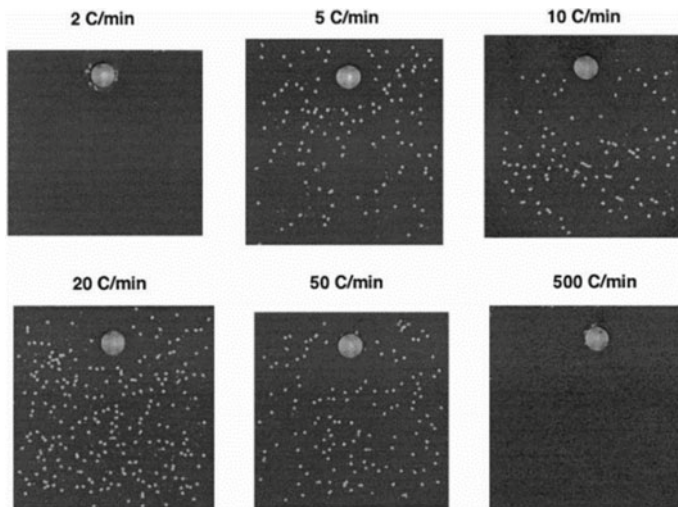


Fig. 89.1 Interface failure at different cooling rates [1]

measurements. However, the mechanical understanding for the pockets of energy concentration has not been fully revealed.

To investigate the blistering and spallation failures, the present work aims to integrate the interface fracture properties with the cooling rate-dependent residual stresses in the alumina scale. It is anticipated to develop a numerical simulation to study the blister growth with the concerns of thermal mismatch stress, alumina growth stress, creep relaxation of the metal substrate, together with the specific interface fracture properties, such as the interface critical separation stresses and fracture toughness. Note that the traditional buckling theories are used in present work for the first attempt to model the failure process. The theories of pockets of energy concentration will be furthermore studied in the future work with the implementation of non-uniform dynamic creep and plastic relaxation at the TGO interface.

89.2 Residual Stresses in Alumina Scales

The pre-cracks at the interface are considered essential for the buckling to occur, and the critical size under the constant stress σ in the alumina scale can be expressed as

$$d = 2.2h\sqrt{E/\sigma}, \quad (89.1)$$

where h represents the scale thickness and E is the Young's modulus of the alumina. After cooling to the room temperature, for a specified constant residual stress σ , the diameter for the circular separation triggered by buckling must be equal or larger than the value given by Eq. (89.1).

During high-temperature oxidation and cooling, the compressive residual stresses are generated in alumina scale, compromising the thermal mismatch stress that is dominant, alumina growth stress due to oxidation under the constraints of geometric boundaries, and stress relaxation resulted by the creep and plastic deformation of the metallic substrate. In detail, the thermal mismatch stress can be evaluated by

$$\sigma_T = \frac{E}{1-\nu} \Delta\alpha \Delta T, \quad (89.2)$$

where ν represents the Poisson's ratio of alumina, $\Delta\alpha$ is the difference of coefficients of thermal expansion between the alumina and the substrate, and ΔT is temperature drop. The details of material properties are presented in Table 89.1. To assess the growth stress, the strains in the lateral and thickness directions, that is, ε_l and ε_t are considered. According to Ref. [5], $\varepsilon_l = 0.001$ and $\varepsilon_t = 0.01$ are taken in present work, which is implemented by using the UEXPAN in-house codes. Furthermore, the creep strain is evaluated by using the conventional Norton's law:

$$\dot{\varepsilon}_{cr} = B\sigma^n, \quad (89.3)$$

Table 89.1 Material properties for the alumina and substrate

Material	Young's modulus (GPa), poisson's ratio	Coefficient of thermal expansion (ppm/°C)
α -Al ₂ O ₃	400, 0.25	8
Kanthal A-1	220, 0.3	15

where $\dot{\epsilon}_{cr}$ is the strain rate, $B = 1.7 \times 10^{-11}$ is the coefficient, σ is the stress, and $n = 5$ is the creep index.

89.3 Interface Fracture Properties

The quadratic nominal stress criterion is used to mode the damage initiation, that is,

$$\left(\frac{t_n}{t_n^0}\right)^2 + \left(\frac{t_s}{t_s^0}\right)^2 = 1, \quad (89.4)$$

where t_n and t_s represent the stresses in the normal and shear directions, respectively; t_n^0 and t_s^0 are critical interface stresses respectively in opening or sliding modes. And $t_n^0 = 140$ MPa and $t_s^0 = 110$ MPa are used in present work.

Furthermore, the cohesive element method is used to describe the crack propagation at the interface between the alumina scale and the substrate. The dependence of the fracture energy on the mode mixity has been defined by the linear failure locus [3, 4]:

$$\frac{G_n}{G_n^e} + \frac{G_s}{G_s^e} = 1, \quad (89.5)$$

where G_n and G_s are the energy release rates respectively for mode I and II fracture; G_n^e and G_s^e are the critical energy release rates respectively. And $G_n^e = 8.6$ N/m and $G_s^e = 43$ N/m are used [3, 4]. When the damage index of cohesive element reaches 1, the element fails.

89.4 Finite Element Simulation and Results

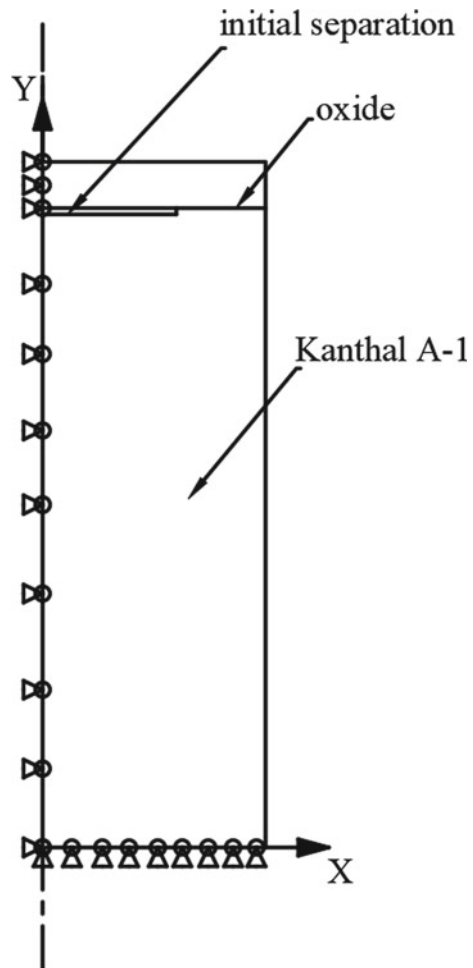
A two-dimensional axisymmetric finite element model is established based on the experiments of Tolygo and Clarke et al. [1, 2]. The model contains two layers, that is, α -Al₂O₃ layer and Kanthal A-1 layer. As shown in Fig. 89.2, the symmetric boundary condition in the x direction is applied to the left of the model, and the periodic boundary condition in the x direction is applied to the right of the model so

that the right boundary has the same displacement in the x direction. In addition, the displacement in the y direction of the bottom is fixed. The thermal loading is divided into two steps: oxidation stage (high temperature, $1200\text{ }^{\circ}\text{C}$) and cooling stage (room temperature, $25\text{ }^{\circ}\text{C}$).

Take one of experiments as an example. The thickness of oxide was $4.9\text{ }\mu\text{m}$, the thickness of metal layer was 5.3 mm , and the cooling rate was $100\text{ }^{\circ}\text{C}/\text{min}$. It was found from the experiment that the diameter of the spallation at the interface was about $150\text{ }\mu\text{m}$ after the cooling stage, and the residual stress away from the oxide spallation was measured about 3.57 GPa . According to Eq. (89.1), the initial buckling diameter in the simulation is set as $98\text{ }\mu\text{m}$.

As shown in Fig. 89.3, the finite element model integrating the residual stresses assessment and interface fracture properties mentioned-above results in the final

Fig. 89.2 Two-dimensional axisymmetric alumina/substrate system model



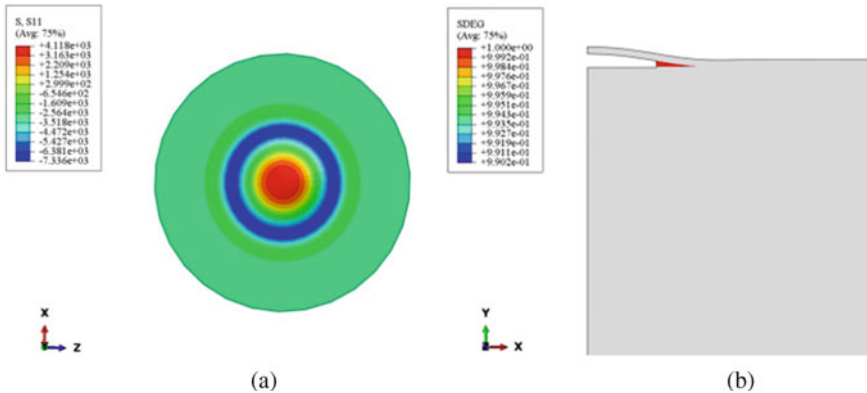


Fig. 89.3 FEM of blistering in alumina. **a** Residual stresses. **b** Interface crack propagation

diameter of blister as $156\ \mu\text{m}$, which is close to the experimental measurement. In the meanwhile, the residual stress remote from the blister is about 3.33 GPa. This indicates that the alumina growth stress, creep and plastic relaxation of the bond coat must be involved. Also, the linear failure locus with the fracture toughness in mode I and II, originally provided by Wang and Harvey [3, 4], are accurate. The mode mixity is of utmost importance for the blister growth. However, it is also noted that the maximum separation stresses and interface stiffness used in the cohesive zone model require further investigation, as these interface properties have not been examined for blistering and spallation in alumina scale within other thickness values. Moreover, it is also found the blisters cannot be generated if the initial interface separation is smaller than the value given by Eq. (89.1), and the experimental observations show no such large pre-cracking at the interface before failure. This directs the next simulation strategy to consider the non-uniform dynamic creep and plastic relaxation at the interface, with smaller interface separation or even without separation, as suggested by Wang and Harvey [3, 4] and experimental observations [1, 2].

89.5 Conclusions

The blistering failure in alumina scales formed on Kanthal alloys is studied in present work. By integrating the thermal mismatch stress, alumina growth stress and creep stress, and the interfacial fracture properties, the circular interfacial separation that develops spontaneously under constant compressive residual stresses is managed to model. It is seen that the pre-crack with critical size must be embedded based on the traditional buckling theories; otherwise, pockets of energy concentration theories are advised for the intact interface. In addition, the linear fracture locus for crack propagation and the mode I and II fracture toughness are applicable for alumina films, which can be further used to investigate the non-uniform dynamic creep and

plastic relaxation of the film/substrate system and to reveal the correlation between the failure and cooling rate and film thickness.

Acknowledgements This work is supported by the National Natural Science Foundation of China (52265021), the central government in guidance of local science and technology development (2022ZY0074), the Natural Science Foundation of Inner Mongolia Autonomous Region (No. 2021MS01011) and Science and Technology Youth Talent Development Program of Inner Mongolia Autonomous Region (No. NJYT22071).

References

1. Tolpygo, V.K., Clarke, D.R.: Spalling failure of α -alumina films grown by oxidation: I. Dependence on cooling rate and metal thickness. *Mater. Sci. Eng. A* **278**, 142–150 (2000)
2. Tolpygo, V.K., Clarke, D.R.: Spalling failure of α -alumina films grown by oxidation. II. Decohesion nucleation and growth. *Mater. Sci. Eng. A*. **278** (2000)
3. Wang, S., Harvey, C.M., Wang, B.: Room temperature spallation of α -alumina films grown by oxidation. *Eng. Fract. Mech.* **178**, 401–415 (2017)
4. Harvey, C.M., Wang, B., Wang, S.: Spallation of thin films driven by pockets of energy concentration. *Theoret. Appl. Fract. Mech.* **92**, 1–12 (2017)
5. He, M.Y., Hutchinson, J.W., Evans, A.G.: Large deformation simulations of cyclic displacement instabilities in thermal barrier systems. *Acta Mater.* **50**(5), 1063–1073 (2002)
6. Zhu, C., Zhao, X., Chen, Y., et al.: Spallation behaviour of alumina scale formed on FeCrAlY alloy after isothermal oxidation. *Oxid. Met.* **85**(3), 391–408 (2016)
7. Zhu, C., Zhao, X., Molchan, I.S., et al.: Effect of cooling rate and substrate thickness on spallation of alumina scale on FeCrAlloy. *Mater. Sci. Eng. A* **528**(29), 8687–8693 (2011)

Chapter 90

Search for Universal Minimum Drag Resistance Underwater Vehicle Hull Using CFD



Harsh Vardhan and Janos Sztipanovits

Abstract In Autonomous Underwater Vehicles (AUVs) design, hull resistance is an important factor in determining the power requirements and range of vehicle and consequently affects battery size, weight, and volume requirement of the design. In this paper, we leverage on AI based optimization algorithm along with Computational Fluid Dynamics (CFD) simulation to study the optimal hull design that minimizes the resistance. By running the CFD based optimization at different operating velocity and turbulence intensity, we want to study/search the possibility of a universal design that will provide least resistance/ near optimal design across all operating condition (operating velocity) and environmental conditions (turbulence intensity). Early result demonstrated that the optimal design found at low velocity and low turbulence condition performs very poor at high velocity and high turbulence conditions. However, design that is optimal at high velocity and high turbulence condition performs near optimal across many considered velocity and turbulence conditions.

Keywords Optimization · Computational fluid dynamics · Bayesian optimization · Reynolds average navier strokes · Underwater vehicle

90.1 Problem Formulation and Approach

AI has proven its potential in system design and operation [1–3]. In this work, we want to leverage AI for finding a universal minimum drag hull shape for AUV. First, we formulate the AUV hull design problem as an optimization problem. Let the hull shape indicated as Λ is defined using a multivariate parameter x , and f is the function that maps a given 3D shape Λ with a drag force (F_d) ($f : \Lambda \rightarrow F_d$). If DS is the design space of search, the optimization problem can be formulated as

$$\Lambda^* = \underset{x \in DS}{\operatorname{argmin}} f(x)$$

H. Vardhan (✉) · J. Sztipanovits

Institute of Software and Integrated Systems, Vanderbilt University, Nashville, TN 37212, USA
e-mail: harsh.vardhan@vanderbilt.edu

The optimization involves running the CFD analysis on chosen hull shape. Since running these CFD simulations are very time-consuming and computationally costly, we chose AI-based Bayesian optimization [4–7] as our optimization algorithm in a loop with CFD analysis to find the optimal design.

Second, we want to study/search for a universal optimal design that is near optimal across all environmental and operating conditions. For creating the different environment and operating conditions for AUV, we consider five different environmental conditions (turbulence intensity of flow {0.1, 2, 5, 10, 20} percent of mean flow velocity) and five different operating conditions (velocity of AUV {1, 2.5, 5, 7.5, 010} in meters/second). The operating velocity and turbulence intensity values are taken from empirical ranges of underwater vehicles' operation. Accordingly, the cartesian product of these two sets creates 25 different scenarios with specific operating velocities and turbulence intensity. By running Bayesian optimization for every 25 scenarios with CFD in the loop, we want to find the optimal hull design in all scenarios.

For running CFD, we chose an open-source simulation tool called openFoam [8] that solves Reynolds-Averaged-Navier Stokes (RANS) [9] with $\kappa - \omega$ Shear Stress Transport ($\kappa - \omega$ SST) [10] as the physical model. The Navies strokes equation is defined below:

$$\rho \frac{d\vec{v}}{dt} = -\nabla p + \mu \nabla^2 v + \rho \vec{g}$$

$$\nabla \cdot \vec{v} = 0$$

For turbulence modeling, we used an improved version of the two-equation turbulence model called $\kappa - \omega$ SST definer by Menter et al. [10] Apart from solving the two equations, the $\kappa - \omega$ SST involves blending functions that ensure gradual changing the $\kappa - \omega$ model of Wilcox to $\kappa - \varepsilon$ model of Jones and Launder from the inner region of a boundary layer to the outer wake region. The two-equation used in $\kappa - \omega$ SST is defined below [11]:

$$\begin{aligned} \frac{\partial(\rho k)}{\partial t} + \frac{\partial(\rho U_i k)}{\partial x_i} &= P_k - \beta^* \rho k \omega + \frac{\partial}{\partial x_i} \left[(\mu + \sigma_k \mu_t) \frac{\partial k}{\partial x_i} \right] \\ \frac{\partial(\rho \omega)}{\partial t} + \frac{\partial(\rho U_i \omega)}{\partial x_i} &= \alpha \rho S^2 - \beta \rho \omega^2 + \frac{\partial}{\partial x_i} \left[(\mu + \sigma_\omega \mu_t) \frac{\partial \omega}{\partial x_i} \right] \\ &+ 2(1 - F_1) \rho \sigma_{\omega 2} \frac{1}{\omega} \frac{\partial k}{\partial x_i} \frac{\partial \omega}{\partial x_i} \end{aligned}$$

The turbulence intensity (I) and mean flow velocity (U) define the initial turbulence energy (k) and its dissipation rate (ω) during the simulation process. These are related by the following equations:

$$k = \frac{3}{2}(UI)^2$$

$$I = \frac{u'}{U}$$

$$u' = \sqrt{\frac{1}{3}(u_x'^2 + u_y'^2 + u_z'^2)}$$

$$U = \sqrt{U_x^2 + U_y^2 + U_z^2}$$

$$\omega = \frac{k^{\frac{1}{2}}}{l * C_{\mu}^{\frac{1}{4}}}$$

Here C_{μ} is the turbulence model constant which usually takes the value 0.09, κ is the turbulent energy, and l is the turbulent length scale. For experimentation, we consider an axisymmetric body of revolution with a fixed hull length (1 m) and fixed fineness ratio (5) that poses a constraint on the hull diameter, which is 0.2 m. The rest of the shape of the hull can be changed by 6 control points across the body by changing its location in space. For each of the 25 experiments, the initial turbulence energy and dissipation rate are provided as initial conditions. The hull has two parts -nose and tail and their lengths can be controlled by the parameter nose_length and the tail_length (tail_length = 1-nose_length (in meters)). By changing the length of the nose, we can move the fineness ratio constraint across the body and provide an optimizer capability to search for a wide variety of shapes. The deep learning-based method has proven potential to capture complex physical phenomenon, but these are very data-hungry models [12, 13]. Accordingly, for the optimization algorithm, we chose Bayesian optimization, since it is a very sample efficient optimization framework involving expensive functions. For modeling our expensive function, we use Gaussian Process non-parametric machine learning architecture to create a probabilistic model of our function (f) and Lower Confidence Bound (LCB) as our acquisition function. The Gaussian process [14] is defined as (Fig. 90.1):

$$p(f) = \mathcal{GP}(f; \mu, K)$$

For any given pair of input points $x, x' \in R^d$, the mean (μ) and covariance (K) are defined as

$$\mu(x) = \mathbb{E}(f(x))$$

$$K = \mathbb{E}[(f(x) - \mu(x))(f(x') - \mu(x')))]$$

We selected Lower Confidence Bound (LCB) as our acquisition function (a) that measures the utility of candidate point in a Bayesian sequential optimization setting

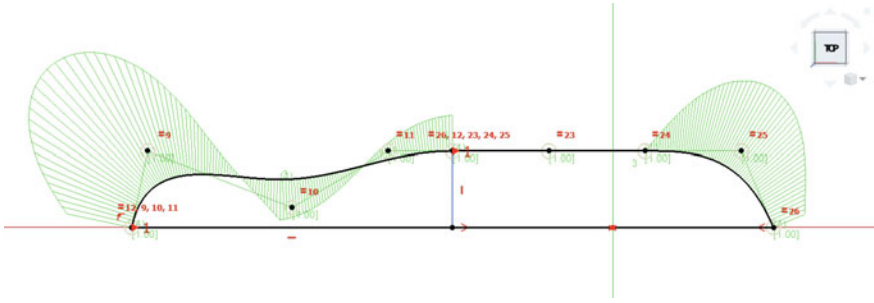


Fig. 90.1 CAD sketch of parametric hull in FreeCAD [15]

since it has good empirical performance and theoretical guarantee to converge to global optimum and is defined below:

$$a_{LCB}(x; \beta) = \mu(x) - \beta\sigma(x); \beta \geq 0(\text{hyper parameter})$$

$$\sigma(x) = \sqrt{K(x, x)}$$

If f' is global optimum and $f(x)$ is the drag of the evaluated sample, a regret function is defined which measure how much have we lost due to selecting a non-optimal sample:

$$r(x) = f' - f(x)$$

$$\min \sum_t^T r(x_t) = \max \sum_t^T f(x_t); T : \text{budget of evaluation}$$

Srinivas et al. [16] proved that with a specific value of β , the regret will go to 0 asymptotically.

$$\beta = \sqrt{(v, \tau_t)}; v = 1 \text{ and } T_t = 2 \log(t^{d/2+2} \pi^2 / 3\delta)$$

$$\lim_{T \rightarrow \infty} R_T / T = 0$$

We used BO-LCB as our optimizer since it is computationally expensive to evaluate each hull using CFD, and BO is a sample efficient sequential design strategy for global optimization [17] and can find the optimal design in a lesser number of evaluations. The design space (DS) of the search is in 7 dimensions (\mathbb{R}^7): six control points with minimum and maximum values in the range are 0 and 0.2 m respectively for every control point. The seventh dimension of design space is the nose_length whose range is between 10–900 cm. The tail_length is a derived parameter and is

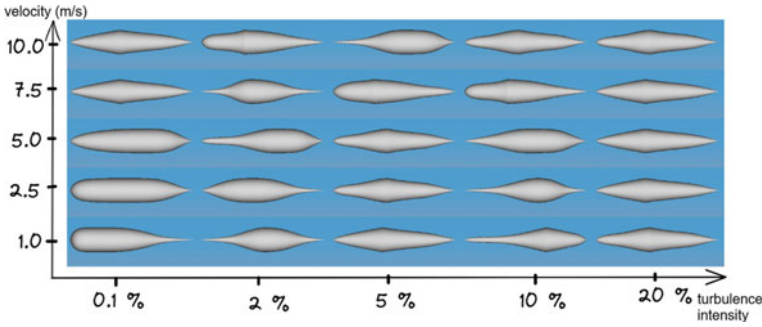


Fig. 90.2 The optimal hull shapes at each scenario after optimization

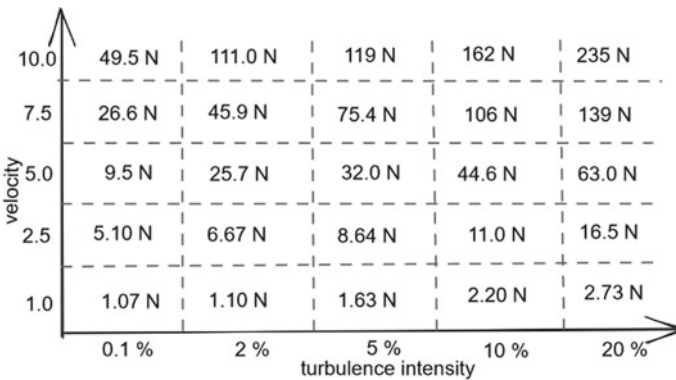


Fig. 90.3 The baseline drag resistances

defined as 1000 cm-nose_length. We ran 100 iterations of sequential BO for each scenario to find the optimal design. The optimal hull shape and their drag resistances are shown in Figs. 90.2 and 90.3 respectively.

90.2 Preliminary Results

At every 25 scenarios, we ran our optimization algorithm until convergence or up to the allocated budget of 100 iterations. At end of the optimization process, the discovered optimal designs are shown in Fig. 90.2 and the related drag force is shown in Fig. 90.3. The preliminary results show that at high turbulence intensity, the optimization converged to a single design (rightmost column of Fig. 90.2). For comparing the performance of optimal designs, in this work, we consider two optimal designs first, the design obtained at lowest turbulence and lowest speed (D1: vel:1 m/s and turbulence 0.1%) and second, the design obtained at highest turbulence and

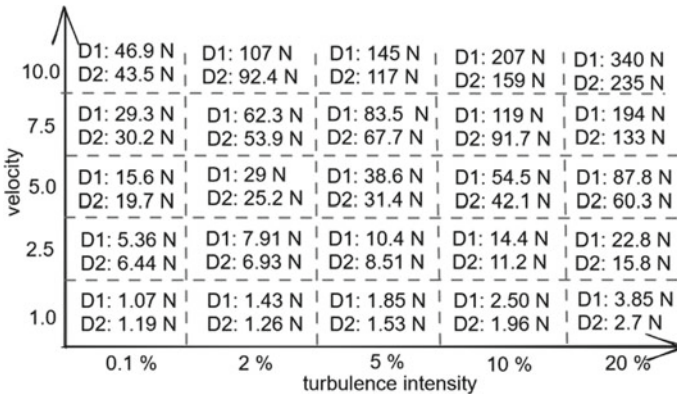
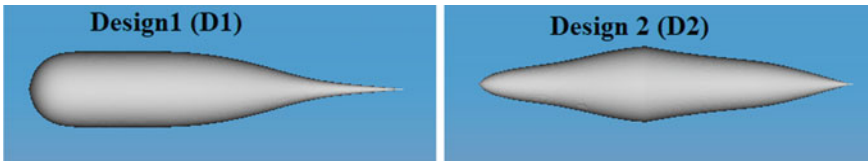


Fig. 90.4 The drag resistances of D1 and D2

highest speed (D2: vel:10 m/s and turbulence 20%)). Once we tested both these designs’ performance in all 25 scenarios, we observed, that design D1 produced more drag in all 24 scenarios while design D2 produced significantly lesser drag resistance in 18 out of 24 scenarios (refer to Fig. 90.4 for drag resistance values).



Also, the drag resistance of design D1 increases significantly at high velocity and high turbulence conditions in comparison to design D2. AI is revolutionizing the engineering design of controllers [18] to classical optimization problems [19–22] by designing a controller just by data or solving complex nonlinear optimization in a sample-efficient manner. In this work, we attempted to find a universal minimum drag hull shape by leveraging computational simulation and AI base optimization methods.

The future direction is to conclude this research by analyzing each 25 optimal design and their performance across all considered environmental and operating conditions.

References

1. Vardhan, H., Volgyesi, P., Sztipanovits, J.: Machine learning assisted propeller design. In: Proceedings of the ACM/IEEE 12th International Conference on Cyber-Physical Systems, pp. 227–228
2. Abbeel, P., Coates, A., Ng, A.Y.: Autonomous helicopter aerobatics through apprenticeship learning. *Int. J. Robot. Res.* **29**(13), 1608–1639 (2010)
3. Vardhan, H., Sztipanovits, J.: Reduced robust random cut forest for out-of-distribution detection in machine learning models. arXiv preprint [arXiv:2206.09247](https://arxiv.org/abs/2206.09247) (2022)
4. Clark, C.E.: The greatest of a finite set of random variables. *Oper. Res.* **9**(2), 145–162 (1961)
5. Moćkus, J.: On bayesian methods for seeking the extremum. In: Optimization Techniques IFIP Technical Conference, pp. 400–404. Springer (1975)
6. Zhilinskias, A.G.: Single-step bayesian search method for an extremum of functions of a single variable. *Cybernetics* **11**(1), 160–166 (1975)
7. Jones, D.R., Schonlau, M., Welch, W.J.: Efficient global optimization of expensive black-box functions. *J. Glob. Optim.* **13**(4), 455–492 (1998)
8. Jasak, H., Jemcov, A., Tukovic, Z., et al.: Openfoam: A c++ library for complex physics simulations. In: International Workshop on Coupled Methods in Numerical Dynamics, vol. 1000, pp. 1–20. IUC Dubrovnik Croatia (2007)
9. Sagaut, P., Terracol, M., Deck, S.: Multiscale and multiresolution approaches in turbulence-LES, DES and Hybrid RANS/LES methods: applications and guidelines. World Sci. (2013)
10. Menter, F.R.: Improved two-equation k-omega turbulence models for aerodynamic flows Tech. Rep. (1992)
11. Vardhan, H., Timalšina, U., Volgyesi, P., Sztipanovits, J.: Data efficient surrogate modeling for engineering design: Ensemble-free batch mode deep active learning for regression. arXiv preprint [arXiv:2211.10360](https://arxiv.org/abs/2211.10360) (2022)
12. Vardhan, H., Sztipanovits, J.: DeepAL for Regression Using ϵ -weighted Hybrid Query Strategy. arXiv preprint [arXiv:2206.13298](https://arxiv.org/abs/2206.13298) (2022)
13. Vardhan, H., Sztipanovits, J.: Deep learning based fea surrogate for subsea pressure vessel. In 2022 6th International Conference on Computer, Software and Modeling (ICCSM), pp. 36–39. IEEE (2022)
14. Rasmussen, C.E.: Gaussian processes in machine learning. In: Summer School on Machine Learning, pp. 63–71. Springer (2003)
15. Riegel, J., Mayer, W., van Havre, Y.: Freecad (2016)
16. Srinivas, N., Krause, A., Kakade, S.M., Seeger, M.W.: Information-theoretic regret bounds for gaussian process optimization in the bandit setting. *IEEE Trans. Inf. Theory* **58**, 3250–3265 (2012)
17. Vardhan, H., Volgyesi, P., Sztipanovits, J.: Constrained Bayesian Optimization for Automatic Underwater Vehicle Hull Design. arXiv preprint [arXiv:2302.14732](https://arxiv.org/abs/2302.14732) (2023)
18. Vardhan, H., Sztipanovits, J.: Rare event failure test case generation in learning-enabled-controllers. In: 2021 6th International Conference on Machine Learning Technologies, pp. 34–40 (2021)
19. Vardhan, H., Sarkar, N.M., Neema, H.: Modeling and optimization of a longitudinally-distributed global solar grid. In: 2019 8th International Conference on Power Systems (ICPS), pp. 1–6. Jaipur, India (2019). <https://doi.org/10.1109/ICPS48983.2019.9067584>
20. Sioshansi R., Conejo, A.J.: Optimization in Engineering, vol. 120. Springer International Publishing, Cham (2017)
21. Hu, X., Eberhart, R.C., Shi, Y.: Engineering optimization with particle swarm. In: Proceedings of the 2003 IEEE Swarm Intelligence Symposium. SIS'03 (Cat. No. 03EX706). IEEE (2003)
22. Vardhan, H., Volgyesi, P., Sztipanovits, J.: Fusion of ML with numerical simulation for optimized propeller design. arXiv preprint [arXiv:2302.14740](https://arxiv.org/abs/2302.14740) (2023)

Chapter 91

Additive Manufacturing Simulation: A Review



Citlaly Castillo, Félix R. Saucedo-Zendejo, and Adrian García

Abstract Additive manufacturing is a printing successive layer process with the capability to manufacture complex geometries. Due to that the process consist on forming layers of material following a previously designed 3D shape, it is useful for many kind of materials as metals, ceramics, polymers, composites and biological systems. For many years, additive manufacturing was only used for prototypes, but now days, by its versatility, it is used in many industries, mainly in automotive and aerospace industry to manufacture components as gearboxes, airboxes, dashboards, motorcycle stands and suspension systems. However, this versatility can be also counterproductive because the measurement and control of the involved variables in this process is complicated, due to the different material's properties. For this reason, a previous simulation results important before to carry out additive manufacturing process. This article is a review of research of additive manufacturing simulations with different materials, as well as their results, focusing on additive manufacturing processes with metals.

Keywords Additive manufacturing · Simulation · Metals

C. Castillo (✉)

Faculty of Chemical Sciences, Autonomous University of Coahuila, 935 Blvd. Venustiano Carranza, República, 25280 Saltillo, Coahuila, Mexico
e-mail: castillo_citlaly@uadec.edu.mx

F. R. Saucedo-Zendejo

Research Center on Applied Mathematics, Autonomous University of Coahuila, Prol. David Berlanga, Colonia 9, Saltillo, Coahuila, Mexico

A. García

Faculty of Metallurgy, Autonomous University of Coahuila, Km 5 Carr. 57, Los Bosques, 25710 Monclova, Coahuila, Mexico

91.1 Introduction

Additive manufacturing (AM) is a revolutionary method that opposes conventional manufacturing processes such as a machining. This process had been used for many years only for the prototype manufacture, although recently, due to its application capacity in different areas, it has managed to revolutionize manufacturing methods. This was a consequence of the first patents for additive manufacturing devices and processes expiring and anyone has access to this type of technology [1].

The automotive and aerospace industries started to use the metal additive manufacturing as an option to manufacture different parts such as gearbox, engine blocks, turbine nozzles, this is because with this method production costs are reduced. However due to metals have different thermal, physical, and chemical properties, it is difficult to measure these variables, which represents a large area of opportunity for mathematical modeling, since carrying out a simulation prior to additive manufacturing is efficient to improve these processes.

This article presents an overview of different additive manufacturing process, as well as a bibliographic review of simulations that have been carried out in metal additive manufacturing processes.

91.2 Additive Manufacturing

91.2.1 Definition and Classification

Additive manufacturing, the technology that was developed in 1986 by the inventor Charles Hull, consists of printing successive layers of materials, its process is known as stereolithography (SLA), followed by developments such as powder fusion, fused deposition modeling (FDM), and contouring.

The complex geometries manufacture is the main advantages that AM presents over traditional manufacturing. Some other benefits of using this manufacturing mechanism are [2]:

- Reduction of manufacturing times
- Less material wastes
- Ability to create lightweight structures
- No molds are needed to manufacture parts.

The American Society for Testing and Materials (ASTM) and International Organization for Standardization (ISO), classify the different additive manufacturing processes, Table 91.1 describes these seven categories [3]:

The two main categories of AM of metals are: Directed Energy Deposition (DED), which includes laser metal deposition (LMD) and powder fusion bed (PFB) including selective laser melting (SLM) [4].

Table 91.1 Additive manufacturing processes classification

Process	Description	Materials
Photopolymerization	A liquid deposit of photopolymeric resin is cured by selective exposure to light (via laser or projector)	UV photocurable resins (various fillers)
Powder bed fusion	A heat source, such as a laser or electron beam is used to selectively melt the powdered materials	Plastics, metals, ceramic powders and sand
Binder jetting	Liquid bonding agents are selectively applied in small layers of powdered material to build parts layer by layer. Binders include organic and inorganic materials	Powdered plastics, metals, ceramic materials, glass and sand
Material jetting	Drops of material are deposited layer by layer to manufacture parts. Common variations include UV curing and photocurable resin blasting	Photopolymers, polymers and waxes
Sheet lamination	The sheet-shaped material is laminate to create an object. This method can be applied in different ways, adhesive or chemical, ultrasonic welding or brazing	Paper, plastics, sheets, metals and ribbons
Material extrusion	Material is extruded through a die to form multi-layered patterns	Thermoplastic Filaments and Pellets (FFF); liquids in siring
Direct energy deposition	Trough laser or electron beam, the powder or wire used are adhered layer by layer until the object is formed	Powder or metal wire and ceramics

LMD plays an important role because this type of process is useful for the manufacture of industrial parts with complex and innovative structures on free-form surfaces, as well as for the reinforcement of light structures, Reconditioning and repair of high-value components and worn dies for metal stamping are just some of its typical applications [5]. It’s an additive manufacturing process that falls within the direct energy deposition classification and is the most widely used in metal additive manufacturing.

In this type of AM, the heat source is a laser beam, is used to melt a material that is supplied in wire or powder form. Once the molten material cools and solidifies the next layer is deposited on top of the solidified layer. Thus a three-dimensional product with designed geometry can be fabricated layer by layer [6]. A wide variety of materials are usually used, the main ones being titanium alloys and stainless steel [7]. Figure 91.1 shows the experimental schematic diagram for an LMD process where the material is used in powder form.

The main advantages that LMD has over other processes are, for example, that its heat source is less intense, therefore the zone affected by the heat is smaller, so the deformation is significantly reduced, in addition the cooling speed is faster, which directs the material to a finer microstructure, this being a positive aspect for it [9].

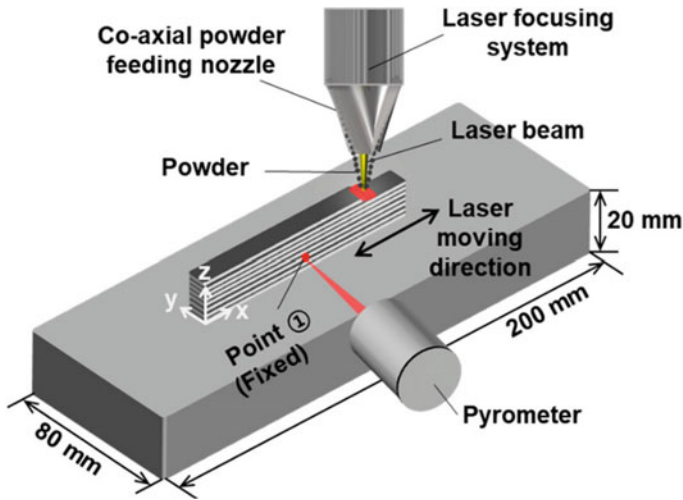


Fig. 91.1 Experimental scheme for the laser metal deposition process [8]

91.2.2 Simulation

The numerical simulation of engineering processes allows to obtain data and predict the behavior of the variables involved before carrying out experimentation, which is useful for every industry to apply it, since it is possible to optimize costs, times and materials, times and materials, as well as explore different alternatives [10].

The measurement of the variables involved in a metal AM process is difficult, due to the small scales that are used. Hence the importance of having preliminary data. Numerical simulations allow the experimental effort to be reduced, since the parameters involved in the AM process can be iterated, according to the type of product and the characteristics with which it is desired to manufacture [11].

In AM processes carried out by LMD the pre-existing material is periodically reheated, creating complex effects such as thermal stresses, local melting, phase transformations and annealing. When building large parts, such as turbine casings or excavator arms, the build is set up experimentally and iterated multiple times for parameter lookup; which implies hours of machine and personal time before achieving the expected results.

Despite the growth in the production of various components using LMD, this process is still not fully efficient and replicable when it comes to aluminum alloys, due to the fact that the temperature distribution is not homogeneous, which is derived from aluminum properties and generates unwanted residual stress, porous microstructures and inconsistent layer geometries.

Due to above Bock [12], used the finite element method to simulate the heat distribution during an LMD process, in which they used an AA5757 aluminum alloy. The results obtained in the simulation were validated experimentally, using the same

alloy as wire and temperature measurements were made with thermocouple and thermography. They observed agreement in both results.

On the other hand, Gu and Li [13], through computational fluid mechanics reported the possible effects of gravity and pressure on DML with wire, for possible space applications. To do this, they used a moving heat source and took into account the various factors involved in the process such as phase change, surface tension, melting, solidification and the properties of the material that depend on temperature.

Dao and Lou [14], performed a mathematical model with smoothed particle hydrodynamics (SPH), a mesh-free Lagrangian method where the coordinates move with the fluid. In that investigation they simulated the heat transfer of dust particles used in an LMD process. Figure 91.2 shows the results obtained from these simulations, which were validated experimentally, demonstrating that the model is stable and efficient to model additive manufacturing processes specifically LMD.

Davyatshin et al. [15], using the smoothed particle hydrodynamics (SPH) simulation method, they modeled the effect of vibration on the hydrodynamic behavior of molten metal droplets in additive manufacturing processes. The numerical tests were carried out with a 12x18H10T steel, which were compared with experimental results using the same steel. This study determined that the value of the coefficient of surface tension depends on the amplitude of the velocity of the vibrations. Figure 91.3 shows the simulation of the behavior of a drop of molten metal when vibration is applied and when vibration is not applied.

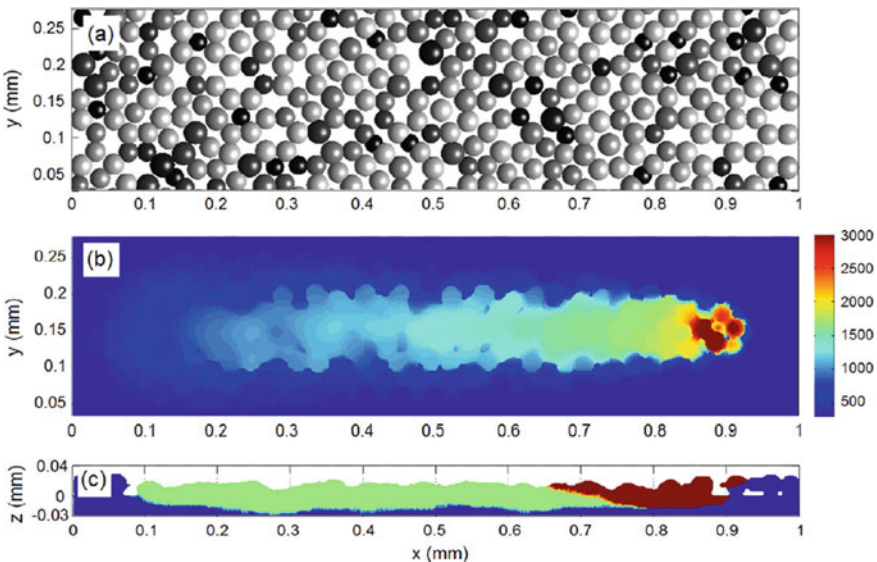


Fig. 91.2 Simulation result of a laser track on a $d_{50} = 27 \mu\text{m}$ powder bed. The laser power is 200 W, $d_{4\sigma}$ is $54 \mu\text{m}$ and scan speed is 2 m/s. **a** Powder distribution; **b** top view of temperature field (K) of the full track with current laser beam at $x = 0.9 \text{ mm}$; **c** side view of the track with material state: blue—original solid (un-melted), green—solidified solid, red—liquid [14]

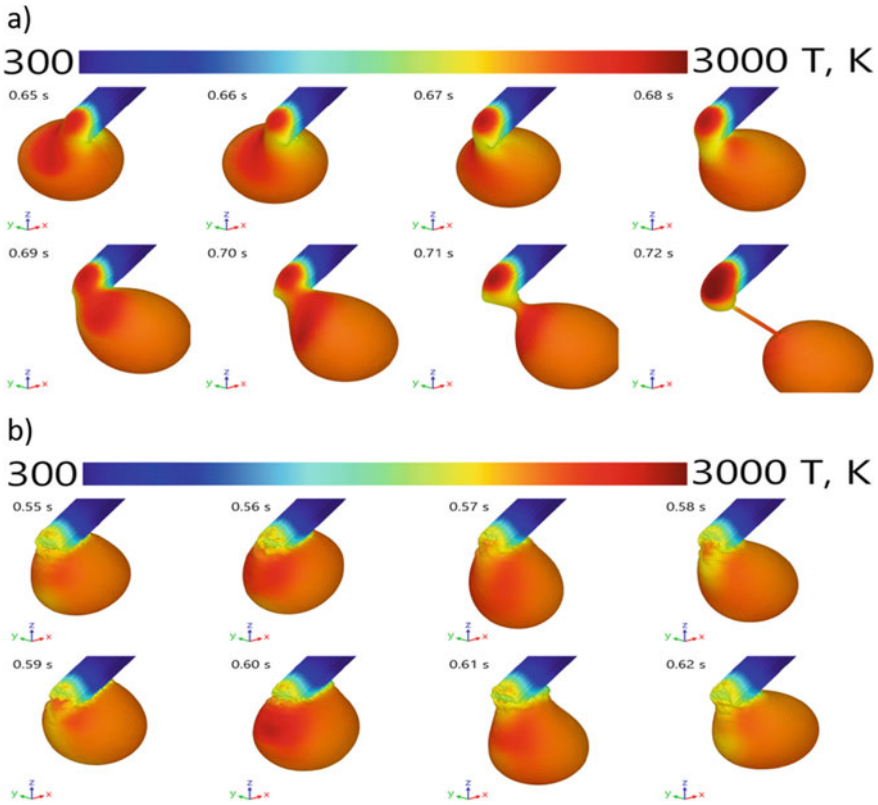


Fig. 91.3 Simulation result. **a** Metal wire melting process without the introduction of vibrating influences; **b** metal wire melting process with the introduction of vibrating influences [15]

In addition, it was concluded that the proposed SPH mathematical model is effective and can be useful to study in greater depth the influence of vibrations in additive manufacturing processes.

Zhu et al. [16] report the first attempt to use artificial intelligence to predict the temperature of the molten pool in additive manufacturing processes, through the physics-informed neural network in which only a small amount of information is used amount of data that is merged with the first physical principles, including the laws of conservation of momentum, mass and energy to carry out the modeling. Figure 91.4 represents a physically informed neural network model applied to a solidification problem.

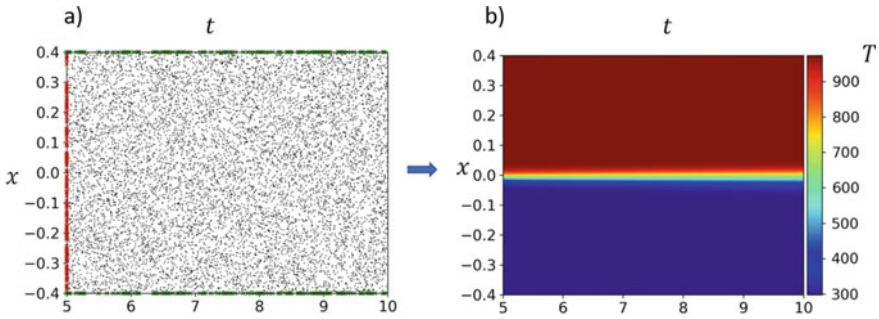


Fig. 91.4 Physics-informed neural network model for solidification problem. **a** Physics-informed neural network setup; **b** temperature prediction [16]

91.3 Conclusions

The positive impact that AM has had recent years in various industries, is mainly because it has been present as an alternative production effective, rapid and lower cost. However, the fact that the different AM methods that currently exist allow the manufacture of pieces or objects from any type of material, regardless of their shape, it is a fundamental part of the growth of this form of manufacturing.

The aerospace and automotive industry have benefited when apply until you want the piece. Thanks to this type of manufacturing, they have significantly reduced the weight of some pieces, which represents a competitive advantage for the aforementioned industries.

According to the researchers who have reported their work, it is concluded that it is possible to carry out the simulation of different phenomena involved in additive manufacturing processes, which, when validated experimentally, have turned out to be efficient.

The numerical modeling is a very useful research tool to study many processes occurring in the weld pool, with a great potential to study the vibration effects on metal flows, and the micro and macro structures formation.

Artificial intelligence is even being used to simulate and predict the behavior of various phenomena involved in additive manufacturing.

References

1. Abdulhameed, O., Al-Ahmari, A., Ameen, W., Mian, S.H.: Additive manufacturing: challenges, trends, and applications. *Adv. Mech. Eng.* **11**(2), 1–27 (2019)
2. Asensio-Lozano, J., Suárez-Peña, B.: Análisis cuantitativo y caracterización morfológica de la aleación 6063. Diferencias microestructurales y mecánicas entre la superficie y el núcleo de barras cilíndricas de colada semicontinua. *Rev. Metal.* **48**(3), 199–212 (2012)

3. Frandsen, C.S., Nielsen, M.M., Chaudhuri, A., Jayaram, J., Govindan, K.: In search for classification and selection of spare parts suitable for additive manufacturing: a literature review. *Int. J. Prod. Res.* **58**(4), 970–996 (2020)
4. Liu, R., Wang, Z., Sparks, T., Liou, F., Newkirk, J.: *Aerospace Applications of Laser Additive Manufacturing*. Elsevier Ltd (2017)
5. Montoya-Zapata, D., et al.: Generation of 2.5D deposition strategies for LMD-based additive manufacturing. *Procedia Comput. Sci.* **180**, 280–289 (2021)
6. Singh, P., Singari, R.M., Mishra, R.S.: A review of study on modeling and simulation of additive manufacturing processes. *Mater. Today Proc.* **56**, 3594–3603 (2022)
7. Biegler, M., Graf, B., Rethmeier, M.: Assessing the predictive capability of numerical additive manufacturing simulations via in-situ distortion measurements on a LMD component during build-up. *Procedia CIRP* **74**, 158–162 (2018)
8. Park, J., Kim, J.Y., Ji, I., Lee, S.H.: Numerical and experimental investigations of laser metal deposition (LMD) using STS 316L. *Appl. Sci.* **10**(14) (2020)
9. Zhong, C., et al.: Laser metal deposition of Ti6Al4V—a brief review. *Appl. Sci.* **10**(3), 1–12 (2020)
10. Carrillo Ledesma, A., González Rosas, K.I., Mendoza Bernal, O.: *Introducción al Método de Diferencias Finitas y su Implementación Computacional*, pp. 37–51 (2021)
11. Stubblefield, G.G., Fraser, K., Phillips, B.J., Jordon, J.B., Allison, P.G.: A meshfree computational framework for the numerical simulation of the solid-state additive manufacturing process, additive friction stir-deposition (AFS-D). *Mater. Des.* **202** (2021)
12. Bock, F.E., Froend, M., Herrnring, J., Enz, J., Kashaev, N., Klusemann, B.: Thermal analysis of laser additive manufacturing of aluminium alloys: experiment and simulation. *AIP Conf. Proc.* **1960** (2018)
13. Gu, H., Li, L.: Computational fluid dynamic simulation of gravity and pressure effects in laser metal deposition for potential additive manufacturing in space. *Int. J. Heat Mass Transf.* **140**, 51–65 (2019)
14. Dao, M.H., Lou, J.: Simulations of laser assisted additive manufacturing by smoothed particle hydrodynamics. *Comput. Methods Appl. Mech. Eng.* **373**, 113491 (2021)
15. Davlyatshin, R.P., Perminov, A.V., Bayandin, Y.V., Castillo-Rodriguez, C., Saucedo-Zendejo, F.R., Trushnikov, D.N.: Numerical modeling of vibration effects on the surface tension of a liquid drop in additive technologies with SPH. *Comput. Part. Mech.* (2022)
16. Zhu, Q., Liu, Z., Yan, J.: Machine learning for metal additive manufacturing: predicting temperature and melt pool fluid dynamics using physics-informed neural networks. *Comput. Mech.* **67**(2), 619–635 (2021)

Chapter 92

A Novel Immersed Framework of Computational Fluid Structure Interaction



Wang Xinyu, Chennakesava Kadapa, and Mei Yue

Abstract The interaction between fluid and immersed solid is a nonlinear multi-physical phenomenon in science and engineering. Due to the challenges of large structural deformation, topological changes in the fluid domain, complexity of the geometry of the structure and computational efficiency and robustness for simulating fluid structure interaction (FSI) problems, developing accurate and efficient finite element numerical methods has always been a research focus in the field of computational fluid dynamics. To overcome these difficulties, we present an efficient stabilised immersed framework involving finite element method called CutFEM and a second-order accurate staggered numerical scheme for fluid–solid coupling. In the following work, we apply this novel framework of computational FSI to several numerical examples to verify the efficiency and robustness of the proposed scheme, and the accuracy is also validated by the results by using the present scheme compared with the reference values.

Keywords Fluid structure interaction · CutFEM · Immersed boundary method · Staggered scheme

92.1 Introduction

Fluid structure interaction is frequently encountered in science and engineering. It specifically refers to the interaction between fluid and immersed solid, which is a nonlinear multi-physical phenomenon. The simulation of FSI is of great significance in science and engineering applications, such as blood flows in arteries and artificial heart valves in biomedicine, various valves, pumps, turbines and vibration of wind

W. Xinyu · M. Yue (✉)

Department of Engineering Mechanics, Dalian University of Technology, Dalian 116024, China
e-mail: meiyue@dlut.edu.cn

C. Kadapa

School of Engineering and the Built Environment, Edinburgh Napier University, Edinburgh EH10 5DT, UK

turbine blades, response of bridges and high-rise buildings to wind and aeroelastic response of aircraft in engineering [1]. Due to the challenges of large structural deformation, topological changes in the fluid domain, complexity of the geometry of the structure and computational efficiency and robustness for simulating fluid structure interaction (FSI) problems, developing efficient and accurate finite element numerical methods has always been a focus and difficulty in the field of engineering. At present, the body-fitted mesh method based on arbitrary Lagrangian-Euler formula (ALE) is the most widely used in commercial software, which requires complex mesh shifting and re-meshing algorithms to capture large deformations of structures. The process of re-meshing includes a data-mapping strategy from old mesh to the new mesh which also introduces error [2]. Hence, low computational efficiency for generating body-fitted meshes and poor convergence for re-meshing algorithms limit the applicability of ALE formulation. To overcome these difficulties, we present an efficient stabilised immersed framework involving finite element method called Cut Finite Element Method (CutFEM) and a second-order accurate staggered numerical scheme for fluid–solid coupling. The key of our immersed framework is to solve the Navier–Stokes equation approximately by using the stabilised finite element method on the fixed background fluid mesh discretised with hierarchical B-splines, which does not need to re-mesh. The weak formulations employ the mixed Galerkin formulation with the streamline-upwind/Petrov Galerkin (SUPG)/pressure-stabilizing/Petrov Galerkin (PSPG) stabilization to obtain the numerical solutions of the incompressible Navier–Stokes equation [3]. At the same time, the weak-coupling staggered scheme is employed to solve the governing equations of fluid and structure in fluid–structure coupling [4]. The application of our computational framework is demonstrated very efficient and robust by simulation [5, 6].

The following work is organized as follows. In Sect. 92.2, we give a brief introduction of our stabilized immersed framework including CutFEM and the staggered scheme. In Sect. 92.3, we demonstrate the efficiency and robustness of the proposed scheme by using some numerical examples.

92.2 Theory

92.2.1 *CutFEM Method*

The fluid is assumed to be viscous, incompressible and laminar in our work. The governing equations of fluid are solved on Cartesian grids discretized by B-spline. The hierarchical B-spline curves can optimize the fluid grids near the immersed solids. Compared with traditional Lagrangian basis functions, B-spline functions have better performance due to their high-order continuity [7].

B-splines are piecewise continuous polynomial functions [8]. Figure 92.1 shows B-spline basis functions for different orders Q_1 , Q_2 and Q_3 , refer to linear, quadratic,

Fig. 92.1 One-dimensional univariate B-spline

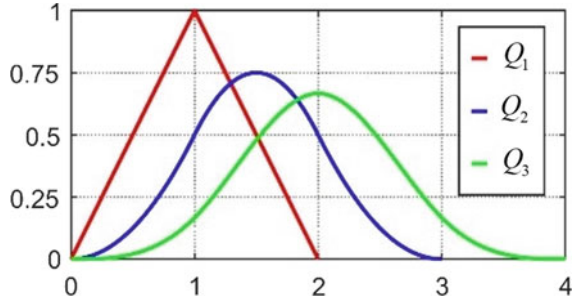
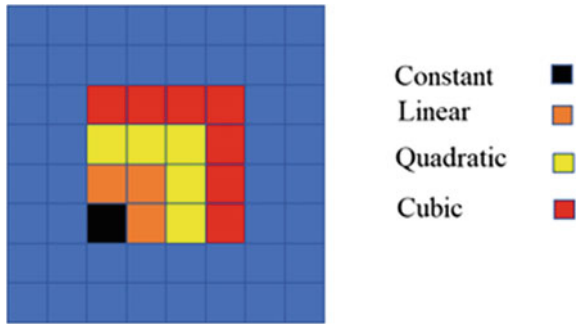


Fig. 92.2 B-Splines in 2D



cubic B-splines, respectively. For spatial discretization of the hierarchical B-spline grid is shown in Fig. 92.2.

For given the knot vector $p = \{\xi_0, \dots, \xi_{n+b+1}\}$, is a non-decreasing set of coordinates, where b is the order of polynomials and n is the number of basis functions used for the construction of B-spline curves, defined in the interval $[\xi_i, \xi_{i+b+1}]$. The B-spline basis functions $N_{i,b}$ are given as [5]

$$N_{i,0}(\xi) = \begin{cases} 1 & \text{if } \xi_i \leq \xi \leq \xi_{i+1} \\ 0 & \text{otherwise} \end{cases} \tag{92.1}$$

$$N_{i,b}(\xi) = \frac{\xi - \xi_i}{\xi_{i+b} - \xi_i} N_{i,b-1}(\xi) + \frac{\xi_{i+b+1} - \xi}{\xi_{i+b+1} - \xi_{i+1}} N_{i+1,b-1}(\xi) \tag{92.2}$$

The current main work presents a new computational framework motivated by the developments in body-unfitted methods proposed by Burman et al. [9]. CutFEM builds on a general finite element formulation for the approximation of PDEs. The basic idea behind CutFEM is to make the discretization as independent as possible of the geometric description and minimize the complexity of mesh generation [9]. Figure 92.3 shows that for a condition consisting of two domains: fluid domain Ω^f

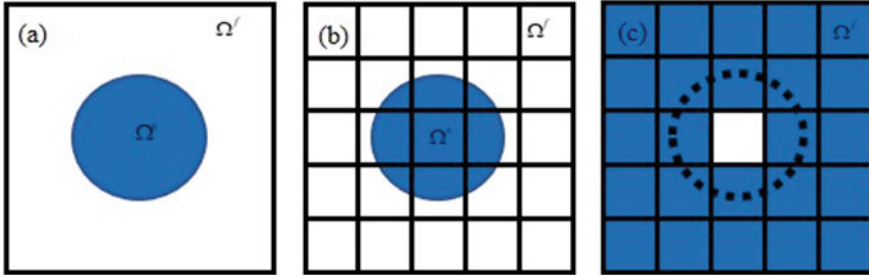


Fig. 92.3 Discretization: **a** geometry consisting of two domains **b** discretization with elements **c** elements belonging to the fluid domain Ω^f

and solid domain Ω^s and some cells of the background grid are cut by the interface between fluid domain and solid domain are cut-cells.

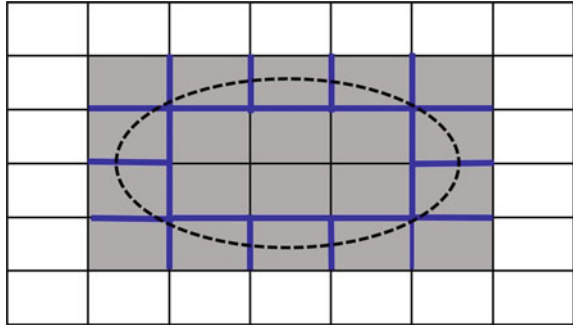
The accurate imposition of interface conditions is the key to the application of CutFEM. Boundary conditions can be imposed on the background grid by using Lagrange multiplier or penalty method [10]. However, the fluid mesh is not aligned with the boundary of the immersed solid, which increases the difficulty of imposing interface conditions. Number of researches have shown in recent studies [3] have proved that Nitsche method is an efficient and accurate strategy for boundary and interface conditions applied to the finite element formulation. Therefore, at the fluid–structure interface, we use Nitsche method to enhance the equilibrium of the fluid–structure interface [11]. Nitsche’s method are applied in combination with the stabilization strategy to avoid the numerical instability associated with very small cutting elements [12]. The terms of Nitsche’s method for enforcing the interface equilibrium conditions are as follows:

$$\begin{aligned}
 B_N^f(\{\mathbf{w}^f, R\}, \{\mathbf{v}^f, p\}) &= \gamma_{N_1} \int_{\Gamma_D} \mathbf{w}^f \cdot (\mathbf{v}^f - \mathbf{v}^s) d\Gamma - \int_{\Gamma_D} \mathbf{w}^f \cdot (\sigma(\{\mathbf{v}^f, p\}) \cdot \mathbf{n}^f) d\Gamma \\
 &\quad - \gamma_{N_2} \int_{\Gamma_D} (\sigma(\{\mathbf{w}^f, R\}) \cdot \mathbf{n}^f) \cdot (\mathbf{v}^f - \mathbf{v}^s) d\Gamma \quad (92.3)
 \end{aligned}$$

where n^f is the unit outward normal on the boundary Γ^f , σ is stress tensor. v^f and v^s is the velocity of the fluid and solid respectively. \mathbf{w}^f and R are weight function of pressure and velocity, respectively. Γ is the boundary of the fluid. γ_{N_1} is a penalty parameter and $\gamma_{N_1} \geq 0$. γ_{N_2} allows to choose between the symmetric $\gamma_{N_2} = 1$ and the unsymmetric $\gamma_{N_2} = -1$ variants of Nitsche’s method [5].

If the intersections of boundary and cut element are very small, the system matrix may be very ill conditioned. The present work follows CutFEM, which uses ghost-penalty terms to alleviate numerical instability and to weakly enforce an appropriate amount of smoothness of the solution across the edges between the cut cells and across the edges between the cut cells and the interior cells (see Fig. 92.4), the ghost

Fig. 92.4 Ghost-penalty operator is applied to the blue boundary



penalty term is defined as

$$B_{GP}^f(\{\mathbf{w}^f, R\}, \{(\mathbf{v}^f, p)\}) = \gamma_{GP}^u \mu \mathcal{G}_1(\mathbf{w}^f, \mathbf{v}^f) + \gamma_{GP}^p \frac{1}{\mu} g_3(R, p) \tag{92.4}$$

where $B_{GP}^f(\{\mathbf{w}^f, R\}, \{(\mathbf{v}^f, p)\})$ is the ghost-penalty term corresponding to the stability of the cut cells. $\mathcal{G}_1(\mathbf{w}^f, \mathbf{v}^f)$ is defined as jump operator as a vector-valued problem. γ_{GP}^u and γ_{GP}^p are the dimensionless ghost penalty parameters for velocity and pressure [5].

92.2.2 Staggered Scheme for Fluid Solid Coupling

The solution approach of fluid–structure coupling has a significant impact on the accuracy and efficiency of FSI numerical method. In FSI problems, the solution strategies are divided into strongly coupled and weakly coupled solution strategies. Based on Dirichlet–Neumann coupling, Dettmer et al. [6] proposed the second order accurate weakly coupled numerical scheme used for our present work.

The steps for the staggered scheme are described as follows. First, update time step $t_{n+1} = t_n + \Delta t$, and then predict force on the solid $F_{n+1}^{s^p}$, solve the solid problem for d_{n+1}^s and v_{n+1}^s using $F_{n+1}^{s^p}$. Then, reposition immersed solid, update cut cell data to get traction force F_{n+1}^f on fluid interface. After that, we introduce the relaxation factor β . The parameter β ($0 < \beta \leq 1$) is defined as the relaxation factor. The value of β influence the stability of the proposed staggered solution strategy. Then use the formula $F_{n+1} = -\beta F_{n+1}^f + (1 - \beta) F_{n+1}^{s^p}$ to correct the traction force on the solid. Finally, proceed to next time step. As demonstrated with the numerical examples [4, 6, 13], the application of this staggered scheme makes the FSI simulation very efficient.

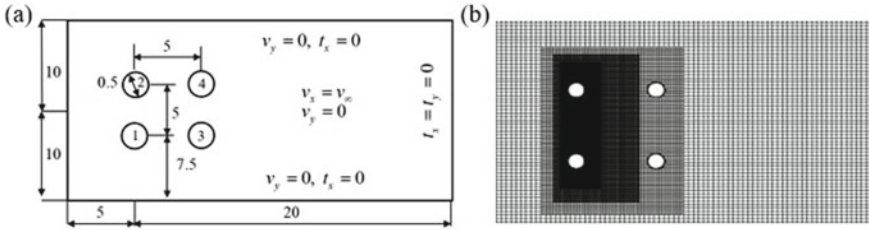


Fig. 92.5 Unsteady flow over cylinder bodies: **a** geometry and boundary condition **b** hierarchical b-spline mesh

92.3 Numerical Examples

92.3.1 Unsteady Flow Over Fixed Circular Bodies for $Re = 100$

The flow over the circular cylinders has always been focus in ocean engineering. The numerical simulations of two-dimensional flow around circular cylinders have been widely used in the field of ocean engineering. Due to the common phenomenon of interference between multiple cylinders, the research on the flow around multiple cylinders is of great significance.

In this numerical example, we employ our stabilized immersed framework to simulate. Figure 92.5 shows the geometry and boundary conditions of the problem and a level-3 hierarchical meshes discretized with B splines for simulations. Properties of the fluid are: density, $\rho^f = 10^3 \text{ kg/m}^3$ and viscosity, $\mu^f = 1 \text{ kg/m s}$. The uniform velocity of $v_\infty = 1.0 \text{ m/s}$ is imposed at the inlet in X-direction so that the Reynolds number is $Re = \rho D v_\infty / \mu = 100$. Figure 92.6 shows flow over multiple fixed circular cylinders for $Re = 100$ of evolution of lift coefficient and drag coefficient, respectively. Due to the interference effect between the two cylinders, the drag coefficients of the upstream and downstream cylinders are different. Figure 92.6a shows the drag coefficients of the upper and lower cylinders with the same vertical y-axis almost overlap. For the upper and lower cylinders located on the same vertical y-axis, the lift curves shown in Fig. 92.6b are symmetric and illustrate that the near wake of two parallel cylinders is symmetrical and opposite. Figures 92.7b and 92.8b depict the symmetrical vortex shedding at the end of cylinders.

92.3.2 Vortex Induced Vibration of a Circular Cylinder

Vortex-induced vibration is one of the main causes of fatigue failure of structures. Therefore, the research on forced vibration and vortex-induced vibration of a cylinder

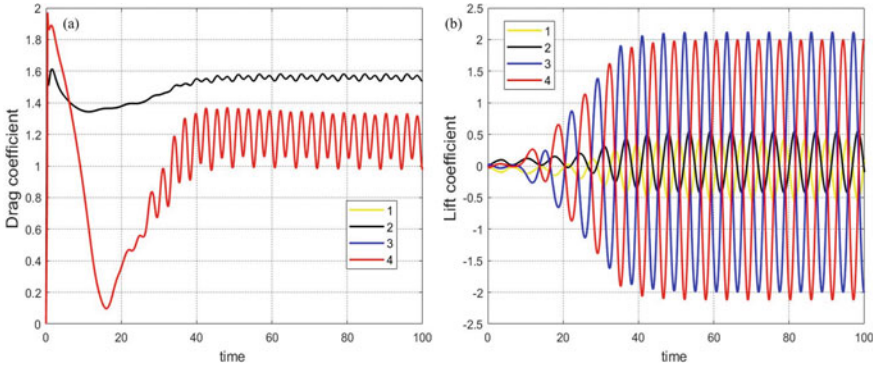


Fig. 92.6 Time history for flow over fixed cylinders of **a** drag coefficient **b** lift coefficient

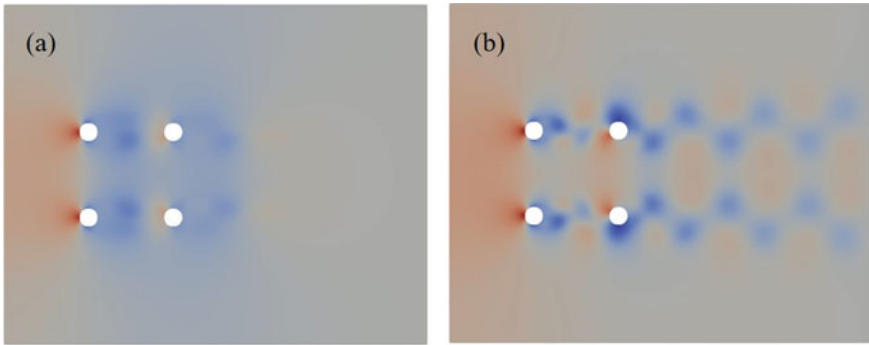


Fig. 92.7 Contours of pressure different time **a** $t = 10$ **b** $t = 100$

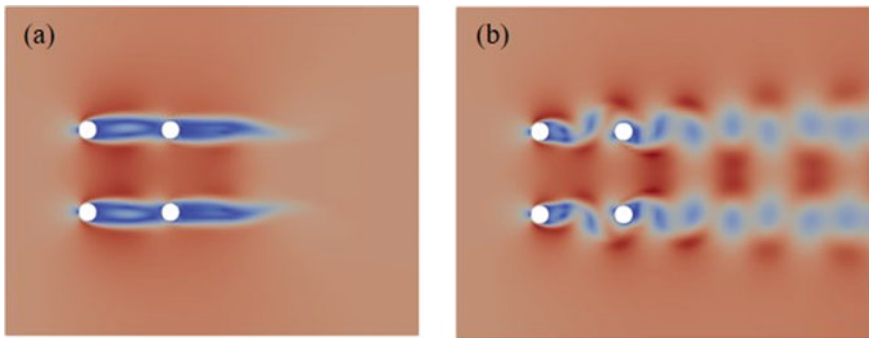


Fig. 92.8 Contours of velocity for different time **a** $t = 10$ **b** $t = 100$

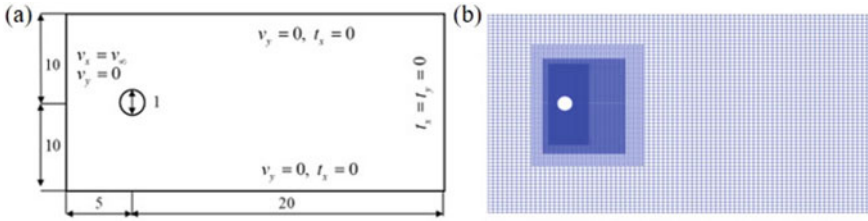


Fig. 92.9 VIV of circular cylinder: **a** geometry and boundary condition **b** hierarchical b-spline mesh

Table 92.1 The vibration response characteristics of cylinder system

Re	Vortex shedding frequency f_s	Normalized displacement
90	0.1440430	0.0012901
100	0.1654053	0.0029205
110	0.1986694	0.3505286
120	0.1989746	0.3394329
130	0.2282715	0.0060493

is of great significance for offshore engineering risers. The numerical example for VIV is concerned with an elastically mounted rigid circular cylinder.

The geometry and boundary conditions of this problem and hierarchical meshes discretized with B splines for simulations are shown as Fig. 92.9. The density of the fluid is $\rho^f = 10^3 \text{ kg/m}^3$ and its viscosity is $\mu^f = 0.1 \text{ kg/m s}$. For this example, we only consider the transverse degree of freedom. The properties of the structure are: mass, $m = 117.10 \text{ g}$, the damping coefficient and stiffness are $c = 0.35317 \text{ g/s}$ and $k = 184.92 \text{ g/s}^2$, respectively. The natural frequency $f_n = 0.2 \text{ Hz}$. We conduct simulations for Re within 90–130. The normalized values of the cylinder’s displacement amplitude and vortex shedding frequency are shown in Table 92.1. It is observed from Fig. 92.10 that there is an interval where the vortex shedding frequency f_s coincides with the natural frequency $f_n = 0.2 \text{ Hz}$. The amplitude performed by the cylinder-spring system has the order of magnitude of the diameter of the cylinder in this Re interval. Figure 92.10 illustrates the amplitude values and the range of Re where the ‘lock-in’ occurs match well with other simulation results from the literature [14–17]. The results above-mentioned illustrate the capability of the immersed FSI framework.

92.3.3 Flexible Beam in Cross Flow

In this numerical example, we focus on the coupling of fluid and a flexible structure. The geometry and boundary conditions of this problem and hierarchical meshes

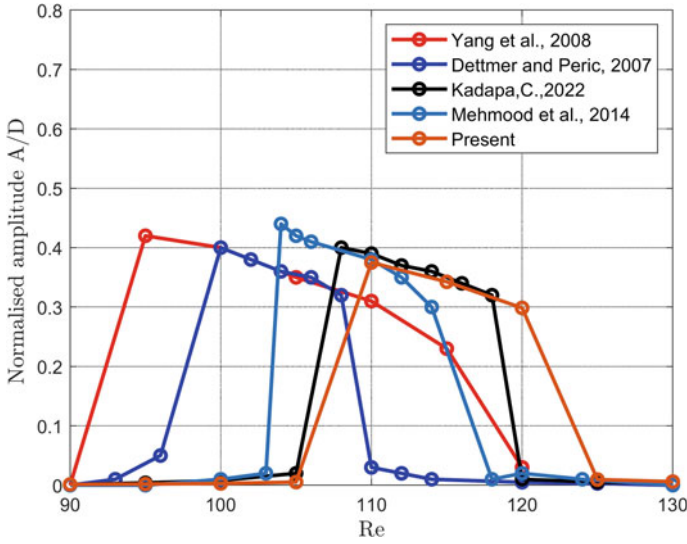


Fig. 92.10 Displacement amplitude of circular cylinder of vortex induced vibration

discretized with B splines for simulations are shown in Fig. 92.11. Properties of fluids: density, $\rho^f = 10^3 \text{ kg/m}^3$, and viscosity, $\mu^f = 0.1 \text{ kg/m s}$. Properties of structure: density, $\rho^s = 10^3 \text{ kg/m}^3$, Young's modulus, $E = 200 \text{ kPa}$ and Poisson's ratio $\nu^s = 0.3$. The inlet velocity is parabolic defined as $v_{in} = 20/6[y(0.6 - y)]$. The time history of lateral displacement of point A and point B is shown in Fig. 92.12. The contour plots of fluid velocity at different times are shown in Fig. 92.13.

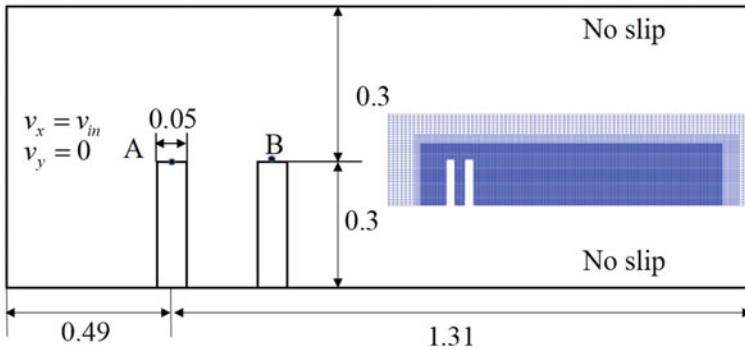


Fig. 92.11 Beam in cross flow: geometry, boundary condition and hierarchical B-spline mesh

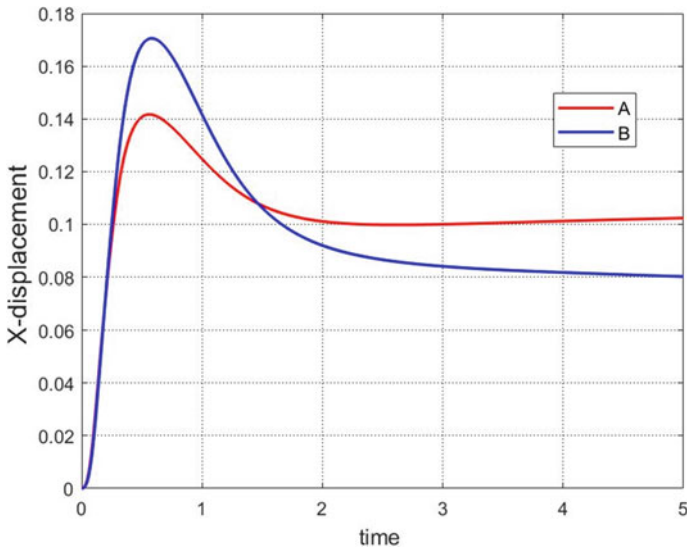


Fig. 92.12 Time history of X-displacement of point A and B

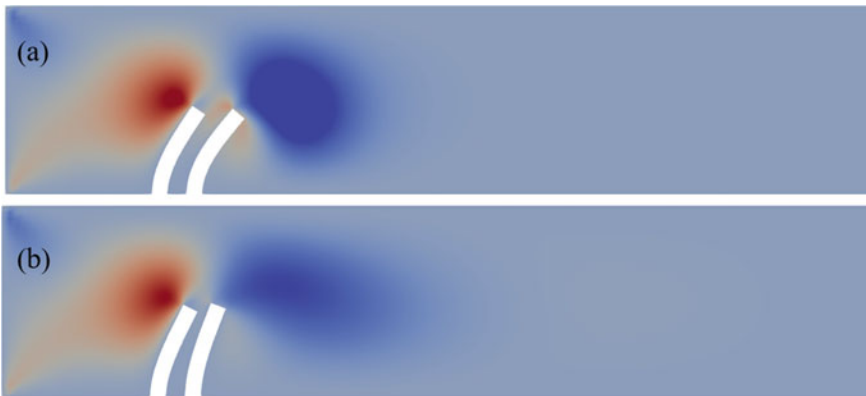


Fig. 92.13 Contour plots of fluid velocity at different times **a** $t = 1$ **b** $t = 5$

92.3.4 Vortex-Induced Vibrations of a Flexible Beam

We take this example as a benchmark example to test the fluid-flexible structure interaction. Figure 92.14 shows hierarchical meshes discretized with B splines and the geometry and boundary conditions of this problem. The density and viscosity of fluid are $\rho^f = 10^3 \text{ kg/m}^3$ and $\mu^f = 1 \text{ kg/m s}$. The properties of this flexible structure are: density is $\rho^s = 10^4 \text{ kg/m}^3$, Young's modulus is $E = 1.4 \times 10^6 \text{ Pa}$ and Poisson's ratio is $\nu^s = 0.4$.

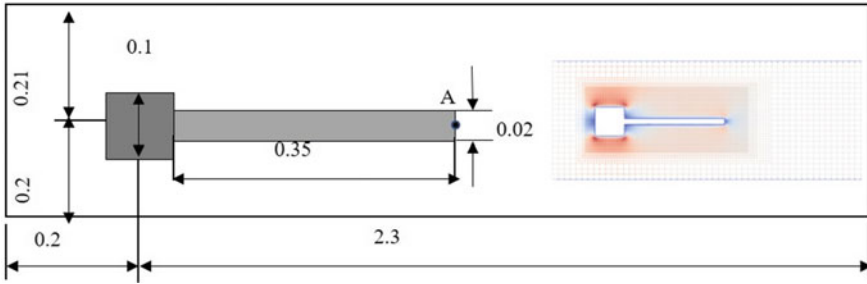


Fig. 92.14 Flexible beam: geometry, boundary condition and hierarchical B-spline mesh

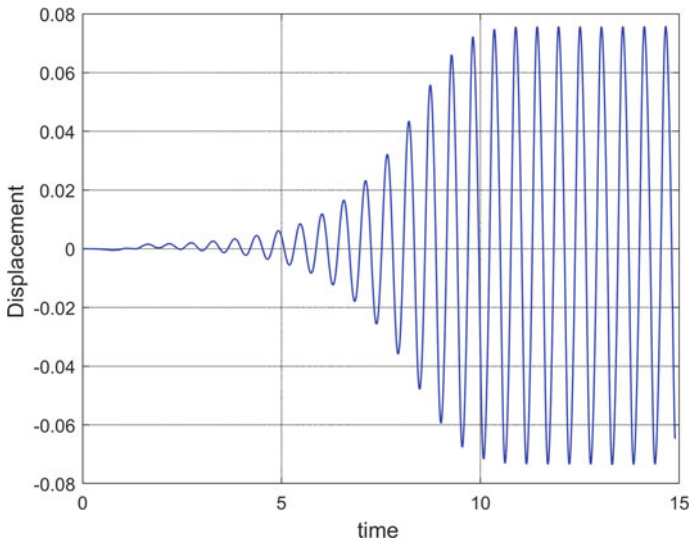


Fig. 92.15 Time history of Y-displacement of point A

The inlet velocity is defined as $v_{in} = 6/0.1681y(0.41 - y)$. The beam attached behind a fixed square body starts to oscillate due to vortices shedding by the corners of the square body.

Evolution of Y-displacement of the beam against time is presented in Fig. 92.15 and it shows the oscillation. Figure 92.16 shows the contour plots of velocity in x direction at two different times for the background meshes discretized with B splines.

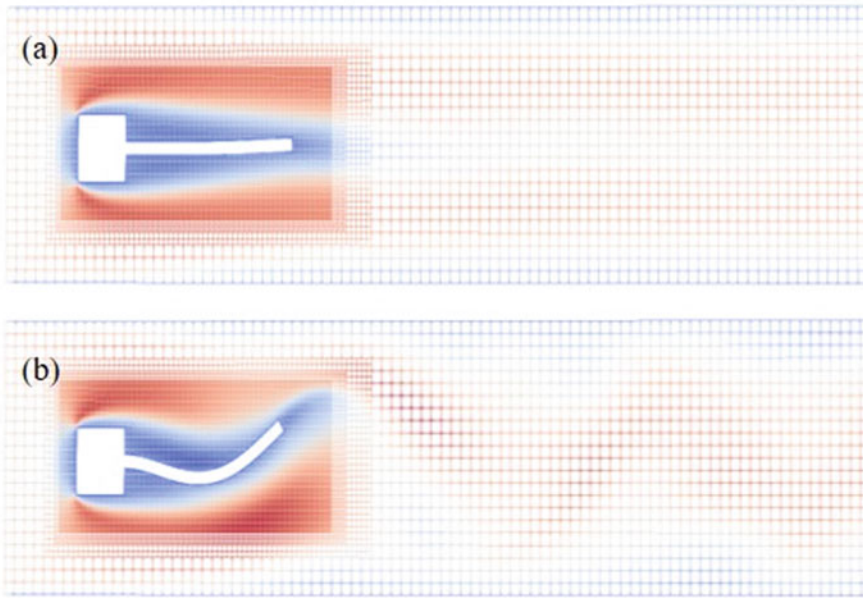


Fig. 92.16 Contour plots of fluid velocity at different times **a** $t = 5$ **b** $t = 12$

92.4 Conclusion

In our paper, we present an immersed stabilised framework for the simulation of fluid–structure interaction problems. We apply this numerical framework to several numerical examples and the robustness of the proposed scheme are demonstrated by the example of vortex induced vibration of flexible beam where the structure undergoes the large deformation, the example of flow over fixed cylinder demonstrated the efficiency of our proposed numerical scheme. As demonstrated with the example of VIV of cylinder, the accuracy is verified by the results obtained with our stabilized scheme are consistent with the reference value. The following research work is expected to employ this proposed framework to high performance computing architecture and large-scale industrial simulation.

References

1. Bazilevs, Y., Takizawa, K., Tezduyar, T.E.: Computational Fluid–Structure Interaction: Methods and Applications. Wiley, United Kingdom (2013)
2. Sahin, M., Mohseni, K.: An arbitrary Lagrangian-Eulerian formulation for the numerical simulation of flow patterns generated by the hydromedusa *Aequorea victoria*. *J. Comput. Phys.* **228**(12), 4588–4605 (2009)

3. Tezduyar, T.E., Mittal, S., Ray, S., et al.: Incompressible flow computations with stabilized bilinear and linear equal-order-interpolation velocity-pressure elements. *Comput. Methods Appl. Mech. Eng.* **95**(2), 221–242 (1992)
4. Kadapa, C., Dettmer, W.G., Perić, D.: Accurate iteration-free mixed-stabilised formulation for laminar incompressible Navier–Stokes: applications to fluid–structure interaction. *J. Fluids Struct.* **97**, 103077 (2020)
5. Kadapa, C., Dettmer, W., Perić, D.: A stabilised immersed framework on hierarchical b-spline grids for fluid-flexible structure interaction with solid–solid contact. *Comput. Methods Appl. Mech. Eng.* **335**, 472–489 (2015)
6. Dettmer, W.G., Lovrić, A., Kadapa, C., et al.: New iterative and staggered solution schemes for incompressible fluid–structure interaction based on Dirichlet–Neumann coupling. *Int. J. Numer. Methods Eng.* **122**(19), 5204–5235 (2021)
7. Schillinger, D., Rank, E.: An unfitted hp-adaptive finite element method based on hierarchical b-splines for interface problems of complex geometry. *Comput. Methods Appl. Mech. Eng.* **200**(47), 3358–3380 (2011)
8. Rübner, T., Cirak, F.: A fixed-grid b-spline finite element technique for fluid–structure interaction. *Int. J. Numer. Methods Fluids* **74**(9), 623–660 (2014)
9. Burman, E., Claus, S., Hansbo, P., et al.: Cutfem: discretizing geometry and partial differential equations. *Int. J. Numer. Methods Eng.* **104**(7), 472–501 (2015)
10. Peskin, C.S.: The immersed boundary method. *Acta Numer.* **11**, 479–517 (2002)
11. Hansbo, P., Hermansson, J., Svedberg, T.: Nitsche’s method combined with space–time finite elements for ale fluid–structure interaction problems. *Comput. Methods Appl. Mech. Eng.* **193**(39–41), 4195–4206 (2004)
12. Dettmer, W., Kadapa, C., Perić, D.: A stabilised immersed boundary method on hierarchical b-spline grids. *Comput. Methods Appl. Mech. Eng.* **311**, 415–437 (2016)
13. Kadapa, C.: A second-order accurate non-intrusive staggered scheme for the interaction of ultra-lightweight rigid bodies with fluid flow. *Ocean Eng.* **217**, 107940 (2020)
14. Yang, J., Preidikman, S., Balaras, E.: A strongly coupled, embedded-boundary method for fluid–structure interactions of elastically mounted rigid bodies. *J. Fluids Struct.* **24**(2), 167–182 (2008)
15. Dettmer, W.G., Perić, D.: A fully implicit computational strategy for strongly coupled fluid–solid interaction. *Arch. Comput. Methods Eng.* **14**(3), 205–247 (2007)
16. Kadapa, C.: A unified simulation framework for fluid–structure–control interaction problems with rigid and flexible structures. *Int. J. Comput. Method* **19**(01), 2150052 (2022)
17. Mehmood, A., Nayfeh, A.H., Hajj, M.R.: Effects of a non-linear energy sink (NES) on vortex-induced vibrations of a circular cylinder. *Nonlinear Dyn.* **77**, 667–680 (2014)

Chapter 93

Mechanical Modeling and Structural Optimization of Spindle System of Static Bias Point the Bit Rotary Steerable System



Tian Chen , Jun Li, and Gonghui Liu

Abstract The fatigue life of the spindle system of the point the bit rotary steerable system largely determines its service life. At present, the mechanical modeling of the spindle system of the point the bit rotary steerable system generally simplifies the force of eccentric rings on the spindle to a known concentrated bias force, and fails to consider the constraint moment of eccentric rings to the spindle, which needs further optimization. Therefore, in this paper, the control and constraint conditions of the tool are considered, and a mechanical model of the biasing spindle with unknown binding force and constrained moment at the eccentric rings is established. On this basis, the geometric and mechanical equations of the spindle system are established, the expressions of deflection and rotation angle at each section of the spindle are derived, and the dimensions of the structure are taken as the known conditions to solve the unknown binding force and the constrained moment. In order to increase the service life of the spindle system, the optimization analysis of the structural dimension parameters involved in the model is carried out to reduce the binding force and constraint moment of the spindle system. According to the analysis results, the optimal value range of the distance ratio from eccentric rings to cantilever bearing and eccentric rings to ball bearing is 2–2.5.

Keywords Point the bit · Rotary steerable system (RSS) · Static bias · Biasing spindle · Mechanical modeling · Structural optimization

T. Chen · J. Li (✉) · G. Liu
College of Petroleum Engineering, China University of Petroleum (Beijing), Beijing, China
e-mail: lijun446@vip.163.com

T. Chen
e-mail: ttc2436@foxmail.com

J. Li
China University of Petroleum (Beijing), Karamay Campus, Xinjiang, China

G. Liu
Beijing University of Technology, Beijing, China

93.1 Introduction

Rotary steerable system (RSS) overcomes the defects of traditional guided drilling, and has the advantages of high drilling efficiency, good hole quality and strong formation adaptability [1]. It has become the new direction of drilling technology development.

RSS can be divided into push the bit and point the bit according to their different guiding modes. According to the different working mode of the bias mechanism, it can be divided into static bias and dynamic bias [2]. At present, international oil technology service companies such as Baker Hughes, Schlumberger and Halliburton have formed a series and commercial rotary steering drilling system. The research and application in China mainly focus on push the bit RSS, the research on directional rotary guide tools is not enough. At present, the mechanical model of offset spindle established by domestic scholars mainly simplifies the force of eccentric rings on the spindle to a certain concentrated bias force [3, 4], but the model does not conform to the control principle, and does not reflect the effect of the eccentric rings on the spindle rotation about the Z-axis. In this paper, the constraint of the spindle under the action of the offset mechanism is reconsidered. Through the mechanical analysis of the spindle of the static bias point the bit RSS, the force condition and its influencing factors of the spindle under the guiding state are studied. The optimization analysis of the size parameter design of the spindle system is carried out, which provides a reference for the design and application of the static bias point the bit RSS.

93.2 Working Principle of Static Bias Point the Bit RSS

The static bias point the bit RSS relies on a set of offset mechanism between the non-rotating outer cylinder and the rotating spindle to offset the spindle, thus generating a deflection angle of a specified size and orientation relative to the original borehole axis. The working principle of the spindle system is shown in Fig. 93.1. The cantilever bearing makes the shell not rotate in the arbitrary axis, and the non-rotating outer cylinder provides a stable working environment for the eccentric ring group and the ball bearing. The eccentric rings exert a displacement deviation of controllable size and direction on the spindle, as shown in Fig. 93.2. It forms a lever with the ball bearing to achieve the purpose of deflecting the bit. The range of the bit deflection angle is determined by the radial dimension of the eccentric ring set, the axial relative position of the ball bearing and eccentric rings.

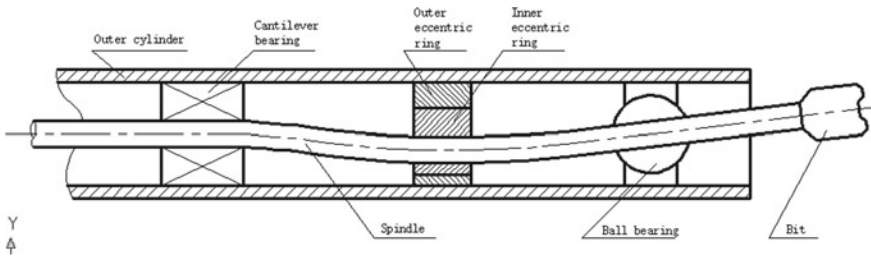


Fig. 93.1 Schematic diagram of spindle system

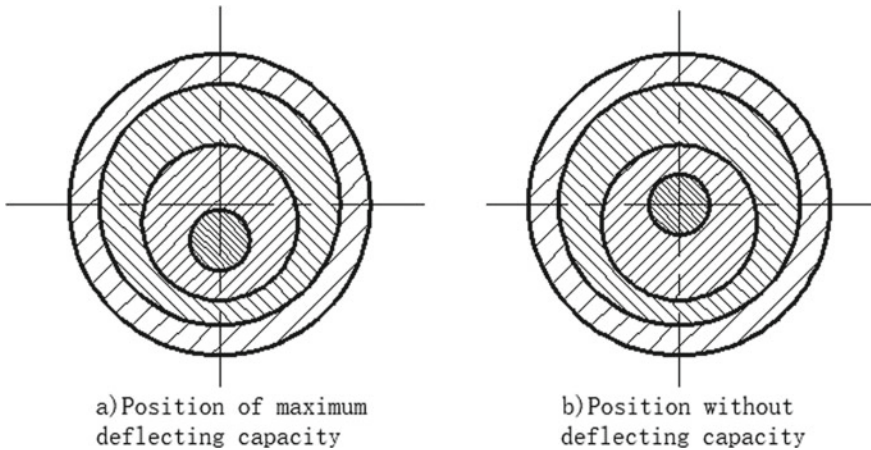


Fig. 93.2 Schematic diagram of eccentric rings

93.3 Mechanical Analysis of Biasing Spindle

93.3.1 Establishment of Mechanical Model of Biasing Spindle

In this paper, the actual constraint condition of the static bias spindle of the point-the-bit RSS is considered. According to the schematic diagram of the static bias point-the-bit RSS, the mechanical model of the displacement working mode of the spindle system is established, as shown in Fig. 93.3.

Hypothesis: The rotational spindle in the bias state is a plane curve. There is no lateral force on the extended ball socket section of the spindle, that is, the counteracting force of the bit on the spindle is along the axis direction. The spindle at the position of maximum deflection capacity is in a small deformation state. The axial friction of the cantilever bearing and eccentric rings on the spindle is ignored.

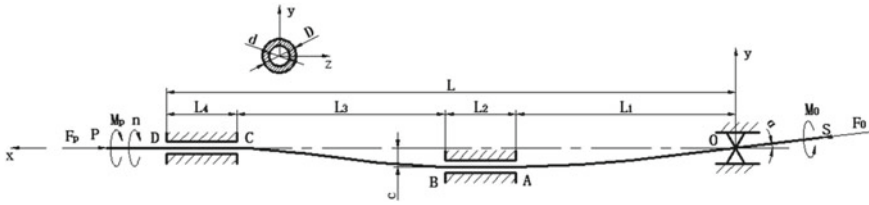


Fig. 93.3 Mechanical model of offset spindle system

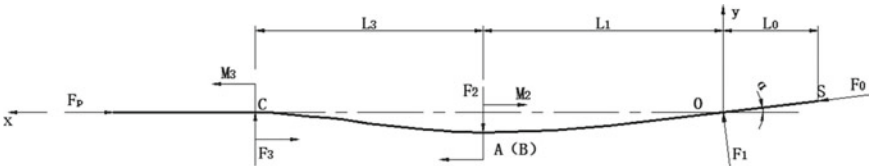


Fig. 93.4 Force analysis diagram of offset spindle

The drilling string is connected at the upper end of the spindle, and the force at point P is simplified as an axial force F_P and a moment M_P . The spindle is connected to the bit, and the force at point S is simplified as an axial force F_0 and a moment M_0 . F_0 and M_0 are known quantities. The eccentric rings make the spindle offset from the original axis by c , the deflection angle of the drill bit is set as α .

The force analysis of the spindle was carried out in the xOy plane. Ignoring the width of the cantilever bearing and the eccentric rings, the action of the cantilever bearing and the eccentric rings on the spindle is simplified as a concentrated force in the y -direction and a plane moment. The force of the ball bearing on the spindle is reduced to a concentrated supporting force perpendicular to the spindle. According to the simplified results, the force on the spindle in the xOy plane is shown in Fig. 93.4. Different from the more common force forking mode [5], in this model, the bias forces and moments of the eccentric ring group against the spindle are taken as unknown quantities, and the bias displacements are taken as known quantities to solve the bias forces and moments.

93.3.2 Establishment and Solution of Mechanical Equations

The spindle of this mechanical model is a statically indeterminate beam, and an in-plane equilibrium equation is established for the spindle as a whole. Equations of mechanical equilibrium are established as shown in Eq. (93.1).

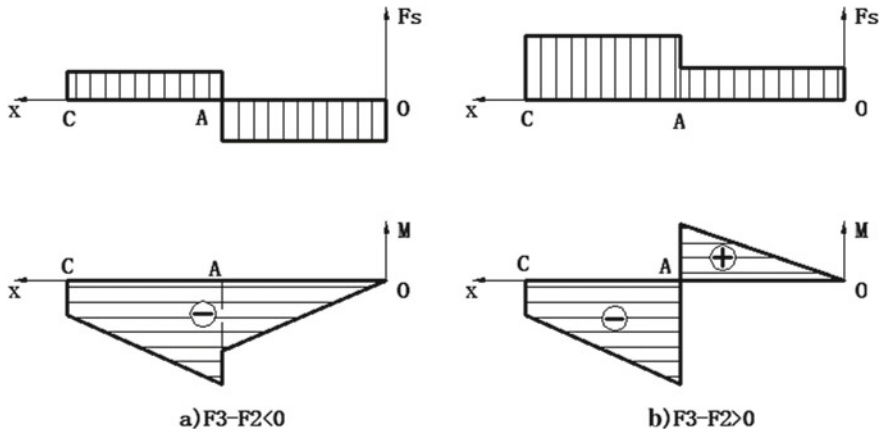


Fig. 93.5 Shear diagram and bending moment diagram of OC section of spindle

$$\begin{cases} \sum F_x = F_0 \cos \alpha + F_1 \sin \alpha - F_p = 0 \\ \sum F_y = F_1 \cos \alpha + F_3 - F_2 - F_0 \sin \alpha = 0 \\ \sum F_z = F_1 \cos \alpha + F_3 - F_2 - F_0 \sin \alpha = 0. \end{cases} \quad (93.1)$$

By analyzing the shear force and bending moment subjected to *OC* section of the spindle, as shown in Eqs. (93.2) and (93.3), the shear bending moment diagram can be obtained, as shown in Fig. 93.5.

$$F_1(x) = \begin{cases} F_3 - F_2, & (0 \leq x \leq L_1) \\ F_3, & (L_1 \leq x \leq L_1 + L_3) \end{cases} \quad (93.2)$$

$$M(x) = \begin{cases} (F_3 - F_2)x, & (0 \leq x \leq L_1) \\ (F_3 - F_2)L_1 - M_2 + F_3(x - L_1), & (L_1 \leq x \leq L_1 + L_3) \end{cases} \quad (93.3)$$

Under the offset position, the approximate differential equation of the torsion crankshaft of the spindle is established by using the deformation coordination condition and the physical relationship between the force and displacement, as shown in in Eq. (93.4), which is used as a supplementary equation to solve the statically indeterminate beam.

$$\frac{d^2\omega}{dx^2} = \frac{M(x)}{EI} \quad (93.4)$$

where, ω is the deflection, $M(x)$ is the bending moment on the cross section at the point, E is elastic modulus of spindle material, and I is the moment of inertia at spindle cross section.

The approximate differential equation of the torsion crankshaft is established for the *OA* section of the spindle, as shown in in Eq. (93.5).

$$\frac{d^2\omega}{dx^2} = \frac{(F_3 - F_2)x}{EI} \tag{93.5}$$

Equation (93.5) is integrated to obtain Eqs. (93.6) and (93.7).

$$\theta(x) = \frac{d\omega}{dx} = \frac{F_3 - F_2}{2EI}x^2 + a_1 \tag{93.6}$$

$$\omega(x) = \frac{F_3 - F_2}{6EI}x^3 + a_1x + b_1 \tag{93.7}$$

where, $\theta(x)$ is the rotation Angle at any section, $\omega(x)$ is the deflection at any section, a_1 and b_1 are the integral constants.

The boundary conditions are shown in Eqs. (93.8) and (93.9).

$$\omega(0) = 0 \tag{93.8}$$

$$\begin{cases} \theta(L_1) = 0 \\ \omega(L_1) = c \end{cases} \tag{93.9}$$

Substitute boundary condition into Eqs. (93.6) and (93.7), and a_1, b_1 can be obtained. Similarly, the expressions of spindle rotation and deflection of AC segment can be obtained, and the expressions of complete spindle rotation and deflection can be obtained as shown in Eqs. (93.10) and (93.11).

$$\theta(x) = \begin{cases} -\frac{3c}{2L_1^3}x^2 + \frac{3c}{2L_1}, & (0 \leq x \leq L_1) \\ \frac{4c\left(2\frac{L_3^2}{L_1^2}-1\right)}{24L_1^3+6L_1^2L_3+3L_3^3}\left[x^2 - 2\left(L_1 + \frac{1}{2}L_3\right)x + L_1^2 + L_1L_3\right], & (L_1 \leq x \leq L_1 + L_3) \end{cases} \tag{93.10}$$

$$\omega(x) = \begin{cases} -\frac{c}{2L_1^3}(x^2 - 3L_1^2x), & (0 \leq x \leq L_1) \\ \left[3x^3 - \left(L_1 + \frac{1}{2}L_3\right)x^2 - \left(L_1^2 + L_1L_3\right)x + 4L_1^3 + \frac{1}{2}L_1^2L_3\right] \\ \times \frac{4c\left(2\frac{L_3^2}{L_1^2}-1\right)}{24L_1^3+6L_1^2L_3+3L_3^3} - 2c, & (L_1 \leq x \leq L_1 + L_3) \end{cases} \tag{93.11}$$

When the tool structure is certain, the parameters $L_1, L_3, c, E,$ and I are known constant values. The expressions of spindle binding force and constraint moment can be obtained by solving the equations as shown in Eqs. (93.12)–(93.17).

$$F_P = \frac{F_0}{\cos \alpha} + \frac{3E I c}{L_1^3} \tan \alpha \tag{93.12}$$

$$F_1 = F_0 \tan \alpha + \frac{3E I c}{L_1^3 \cos \alpha} \tag{93.13}$$

$$F_2 = \frac{8EIc\left(2\frac{L_3^2}{L_1^2} - 1\right)}{24L_1^3 + 6L_1^2L_3 + 3L_3^3} + \frac{3EIc}{L_1^3} \quad (93.14)$$

$$F_3 = \frac{8EIc\left(2\frac{L_3^2}{L_1^2} - 1\right)}{24L_1^3 + 6L_1^2L_3 + 3L_3^3} \quad (93.15)$$

$$M_2 = \frac{8EIc\left(2\frac{L_3^2}{L_1^2} - 1\right)}{24L_1^3 + 6L_1^2L_3 + 3L_3^3} \left(2L_1 + \frac{1}{2}L_3\right) - \frac{3EIc}{L_1^2} \quad (93.16)$$

$$M_3 = \frac{8EIc\left(2\frac{L_3^2}{L_1^2} - 1\right)}{24L_1^3 + 6L_1^2L_3 + 3L_3^3} \left(2L_1 + \frac{3}{2}L_3\right) - \frac{6EIc}{L_1^2} \quad (93.17)$$

where, α is the angle between the bit and the axial direction, and its calculation method is shown in Eq. (93.18).

$$\alpha = \theta(0) = \frac{3c}{2L_1} \quad (93.18)$$

When the structure size is certain, the spindle system at the position of maximum deflection capacity is subjected to stress and deformation as described above. The deviation angle of the bit is determined by the ratio of the maximum eccentricity of the eccentric rings to the distance between the eccentric rings and the ball bearing. Different from the model based on the force working mode, the expression of the deflection angle of the spindle based on the displacement working mode has nothing to do with the material properties of the spindle, and the binding force and moment are related to the material properties of the spindle.

93.4 Structural Optimization Analysis

In order to minimize the binding force on the spindle when the maximum deflection angle of the bit is certain, the structure size is regarded as a variable to optimize the structure size of the spindle system.

According to the derived force expression, F_1 decreases with the increase of L_1 , and the changes of F_2 , F_3 , M_2 and M_3 are affected by multiple size parameters at the same time. Therefore, it is necessary to further analyze the variation of F_2 , F_3 , M_2 and M_3 with the size parameters. The ratio of c to L_1 remains unchanged when the deviation angle of drill bit is constant, and the distance ratio from eccentric rings to cantilever bearing and eccentric rings to ball bearing is defined as n , that is, $L_3/L_1 = n$. When the hole diameter is limited to c , the size of L_1 can be determined according to the required bit deflection angle, while the size of L_3 can be determined by n value. Therefore, in order to study the change of absolute values of F_2 , F_3 , M_2

and M_3 with n value, the influence factors of binding force and moment are y_i (i can be F_2, F_3, M_2 and M_3). When i is different, the meaning and expression of influence factor y_i are different, and the satisfaction relationship is as follows.

$$y_{F2} = \left| \frac{2n^2 - 1}{3n^3 + 6n + 24} + \frac{3}{8} \right| \quad (93.19)$$

$$y_{F3} = \left| \frac{2n^2 - 1}{3n^3 + 6n + 24} \right| \quad (93.20)$$

$$y_{M2} = \left| \frac{8(2n^2 - 1)(2 + \frac{1}{2}n)}{3n^3 + 6n + 24} - 3 \right| \quad (93.21)$$

$$y_{M3} = \left| \frac{8(2n^2 - 1)(2 + \frac{3}{2}n)}{3n^3 + 6n + 24} - 6 \right| \quad (93.22)$$

$$C_1 = \frac{8EIc}{L_1^3} \quad (93.23)$$

$$C_2 = \frac{EIc}{L_1^2} \quad (93.24)$$

$$|F_2| = C_1 y_{F2} \quad (93.25)$$

$$|F_3| = C_1 y_{F3} \quad (93.26)$$

$$|M_2| = C_2 y_{M2} \quad (93.27)$$

$$|M_3| = C_2 y_{M3} \quad (93.28)$$

C_1 and C_2 are constants that can be determined according to tool materials and basic design dimensions.

The optimal range of n value can be obtained by drawing the function curve of the influence factor y_i of constraint force and constraint moment varying with n .

As shown in Fig. 93.6, combined with the calculation results, when n value is about 0.71, $y_{F3}(n)$ value is close to 0. When n value is about 2.99, $y_{F2}(n)$ and $y_{F3}(n)$ values take the maximum value, after that, the coefficient function value gradually decreases, and the values of $y_{F2}(n)$ and $y_{F3}(n)$ are stable in a small range. As shown in Fig. 93.7, when $n < 1$, $y_{M2}(n)$ and $y_{M3}(n)$ are larger, when n is about 2.12, the value of coefficient function $y_{M2}(n)$ is taken as the minimum, when n is about 2.44, the value of $y_{M3}(n)$ reaches the minimum, when n is constant, $|F_2|$, $|F_3|$, $|M_2|$, and $|M_3|$ all decrease with the increase of L_1 .

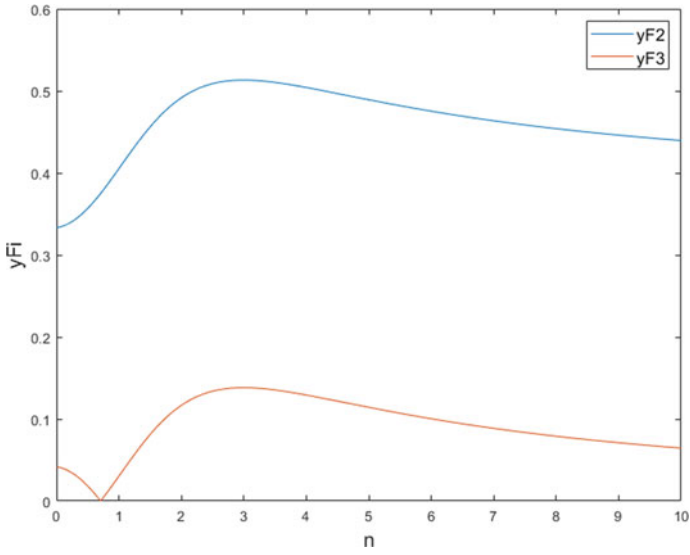


Fig. 93.6 Curve of influence factors y_{F2} and y_{F3} with n value

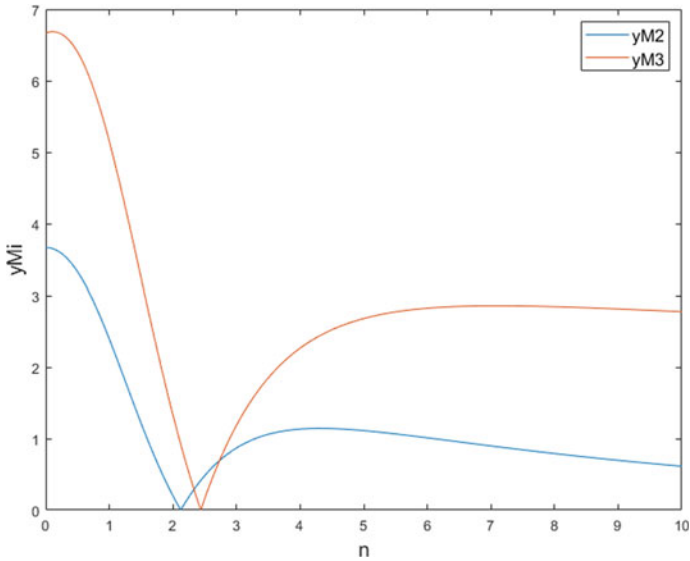


Fig. 93.7 Curve of influence factors y_{M2} and y_{M3} with n value

Combined with numerical calculation and influence factor variation curve, the following suggestions can be put forward for the structural optimization design of spindle system:

- (1) Considering the influence of the value of n on $|F_2|$, $|F_3|$, $|M_2|$, and $|M_3|$, the design value of n is recommended to be 2.12 in order to reduce the binding force and moment and control the length of the structure. Considering the deviation in practical application, the recommended value of n is 2 to 2.5.
- (2) The length ratio n of L_3 to L_1 should be avoided as far as possible, and the value of n should not be less than 1.
- (3) The binding force decreases with the increase of L_1 , but at the same time, the maximum eccentricity (c) of eccentric ring group needs to be increased year on year to ensure that the deflection angle of bit remains unchanged. Considering that the radial size of downhole tools is limited and the length of L_1 should not be too large, the maximum value of L_1 should be taken within the allowable range.

Due to the different simplification of constraints on the eccentric ring set, the optimization conclusions obtained in this paper are different from those obtained by DU's model [3]. The model adopted by Du et al. recommended n value as 2 when $|F_2|$ is the minimum value, which is similar to the recommended n value of 2.12 based on the minimum value of $|M_2|$ in this paper. In this paper, the model satisfies the condition that the spindle angle at the eccentric rings is zero, and the results are more in line with the actual situation, and through the coefficient function curve more directly reflects the variation law of $|F_2|$, $|F_3|$, $|M_2|$, and $|M_3|$ with n values, which is convenient to find the balance point of design under different trends of constraint force and moment.

93.5 Summary

- (1) In this paper, the working principle of static bias point-the-bit rotary steerable system and the constraint of the spindle are considered, and a mechanical model of biasing spindle under displacement working mode which is more in line with the actual working condition of the spindle is established. According to the size of the spindle system, the binding force and moment of the spindle under the maximum offset state, as well as the deflection and rotation angle of each section of the spindle can be calculated.
- (2) According to the established mechanical model, the structure optimization analysis of the spindle system is carried out to reduce the binding force and constraint moment. Under the condition that the maximum deflection angle of the bit is fixed, the relationship between the constraint force, moment, and structure size ratio is studied by numerical calculation and drawing a function curve. The results show that when the maximum deflection angle of the bit and the offset displacement of the spindle are determined, there is an optimal value of the

distance ratio from eccentric rings to cantilever bearing and eccentric rings to ball bearing, which makes the binding force and constraint torque of the spindle smaller.

- (3) The result of optimization analysis is based on the assumption of an ideal model, and the conclusion may have some deviation in engineering application. In this paper, the optimization analysis is carried out to reduce the total force of bearing and eccentric rings on the spindle, and the optimal range of axial dimension proportion of the spindle system is given. If the specific distribution of the binding force on the contact surface is further considered and the optimization analysis is carried out to reduce the stress on the dangerous point of the cross-section, a more detailed structural design optimization scheme can be obtained.

References

1. Wang, W.-P., Yan, W.-H., Peng, Y.: Research on the principle and key structure of rotary steering drilling tools with high build slope. *Mach. Res. Appl.* **29**(05), 127–129 (2016)
2. Wang, K., Li, X.-H., Zhang, G.-W.: Analysis of typical structure and principle of directional rotary steering drilling tools. *Henan Sci. Technol.* **10**, 78–79 (2012)
3. Du, J.-S., Liu, B.-L., Li, Q.-T., Huang, X.-J.: Mechanical model and optimization of offset spindle of directional rotary guidance system. *Petrol. Mach.* (08), 28–31, 35, 103 (2008)
4. Lu, J., Cai, C., Yang, G.-S.: Study on the influence of eccentric ring formation on the performance of directional guidance system. *Miner. Expl. Eng. (Rock Soil Drilling Eng.)* **41**(11), 52–56 (2014)
5. Zhao, J.-Z., Sun, M.-X.: Analysis of working Mode of rotary steering drilling system. *Petrol. Mach.* **06**, 73–75 (2004)

Chapter 94

Calculation Model of Annular Pressure Loss in Slim Hole Considering Drill String Rotation, Eccentricity and Joint



J. T. An, J. Li, G. H. Liu, H. L. Huang, and H. W. Yang

Abstract Slim-hole drilling technology has the advantages of high yield, low environmental protection and low cost, and it has been gradually paid attention to by various oil fields in recent years. However, in hydraulics calculation, especially the calculation of annular pressure loss, the established models by different researchers through laboratory experiments are often not universal and practical. The key point of this problem is that there is a big difference between laboratory experiment parameters and genuine parameters in the field. Therefore, in this study, an annular drilling fluid flow model is established by using numerical simulation technology. Then, a mixed level orthogonal experiment is carried out with four annulus sizes, four groups of drilling fluid rheological parameters, four common annulus flow velocity, four eccentricities and 16 drill pipe rotation speeds, and the experimental results is fitted into an influencing factor of drill string rotation suitable for slim holes. Finally, considering the influence of drill string eccentricity and drill string joint on the annulus pressure loss of slim hole, a model of annulus pressure loss is suitable for slim hole. It can be seen that the calculation results of the model are consistent with the data of laboratory experiments. In addition, to verify the accuracy of the model, the model established in this study was applied to Mahu oilfield, and the average error rate is only 4.6%, which indicates the applicability of this model in the field. Therefore, this model can be applied to design and calculate hydraulic parameters of slim hole and guide engineering practice.

Keywords Slim-hole · Drill pipe rotation speed · Drill pipe eccentricity · Drill string joint · ECD

J. T. An · J. Li (✉) · G. H. Liu · H. L. Huang · H. W. Yang
China University of Petroleum-Beijing, Changping, Beijing 102200, China
e-mail: lijun446@vip.163.com

J. Li
China University of Petroleum-Beijing at Karamay, Karamay 834000, China

H. L. Huang
CNOOC China Limited, Hainan Branch, Haikou 570100, Hainan, China

94.1 Introduction

Slim-hole drilling reduces the amount of work handling drilling fluid and cuttings by 75% compared to conventional drilling, and it relieves environmental pressure and reduces drilling costs. With the improvement of drilling technology, using slim holes has become a trend to exploit oil and gas. However, due to the narrow annulus in the slim hole, the annulus pressure loss is greatly increased, which causes a large error rate with the conventional model applied. The error of predicting ECD may lead to complex accidents such as formation fracture and leakage [1] especially in the formation with a small safe density range.

To establish a more accurate model for the annulus pressure loss in slim holes, a lot of scholars studied the factors sensitivity of the annulus pressure loss by simulations [2, 3] and laboratory experiments [2, 4, 5]. Hansen [2] proposes a model of annular pressure loss in slim holes which can be applied to Newton, Bingham and power law fluids. However, due to the complexity of its solution, it cannot be popularized and applied in the field, and its predictions cannot be verified by the data from the field. Cartalos [6] pointed out that many engineering practices and a large number of experimental observations show that the annulus pressure loss model which only considers drill string rotation cannot produce correct predictions. He proposed a new model for the calculation of annular pressure loss in slim holes, which considers the effects of drill string eccentricity and rotation, as well as the variation of drill string eccentricity along the wellbore. Hacıislamoglu et al. [1] studied the prediction of annulus pressure loss in narrow annulus in the process of slim-hole and coiled tubing drilling. It is noted that the high annulus pressure loss in the small gap leads to ECD close to or even higher than the formation fracture pressure gradient. Therefore, in order to adjust the density and rheology of drilling fluid to ensure the smooth and safe drilling, it is very necessary to accurately predict the annular pressure loss. Compared with the research on the influence of drill string rotation and eccentricity on annulus pressure loss, there are few researches about the influence of drill string joint on annulus pressure loss. Therefore, Enfis [7] from the University of Oklahoma in the United States specifically studies the impact of drill joint on annular pressure loss, and puts forward a model of annular pressure loss in 2011, and points out that the drill joint can increase the annular pressure loss by 30%. Song Xuncheng considers the views proposed by the above scholars, and establishes a model of pressure loss in considering the rotation, eccentricity and joint of drill string. However, the established model of the influence of drill string rotation on annular pressure loss is very poor, and the relationship between rotation and eccentricity is not associated in the research, so the results will have certain errors. Among the previous models, the model about the drill pipe eccentricity and drill pipe joint is pretty complete. But the model of annular pressure loss considering drill string rotation and drill string eccentricity under different drilling fluid rheology needs to be improved. A large number of laboratory experiments using genuine drilling parameters is a feasible way to improve the accuracy of the model, but it is expensive to set up laboratory facilities. Therefore, it is more economical to use the developed CFD numerical simulation technology.

In this study, a numerical simulation model of single-phase annular fluid flow is established by CFD numerical simulation technology, and 32 groups of numerical simulation are designed by using the mixed level orthogonal experimental design method, and the influence factors of drill string rotation are fitted by regression. Then, combined with the drill pipe eccentricity and joint influence factors, a new model of circulating pressure loss in slim holes with higher accuracy is established.

94.2 Basic Calculation Model

94.2.1 Rheological Model of Drilling Fluid

The rheological property of drilling fluid is a basic index to evaluate its performance. Selecting suitable rheological property under different working conditions plays a very important role in improving drilling efficiency (such as efficient cuttings carrying, improving ROP, etc.). The rheological properties of drilling fluid need to be characterized by mathematical equations in the process of calculation of annular hydraulics. Currently, there are three kinds of rheological equations widely used in drilling sites: Bingham plastic equation, power law equation and Herb-Barr equation. The rheological models reflect the physical equation of the relationship between shear stress and shear rate. In the case of one-dimensional shear flow, the above three rheological equations are as follows:

$$\tau = \tau_y + \mu_p \dot{\gamma} \quad (94.1)$$

$$\tau = K \dot{\gamma}^n \quad (94.2)$$

$$\tau = \tau_y + K \dot{\gamma}^n \quad (94.3)$$

where n is liquidity index, dimensionless; μ_p , K are plastic viscosity, consistency coefficient respectively, Pa s ^{n} ; τ_y is yield strength, Pa; $\dot{\gamma}$ is shear stress rate, 1/s; τ is shear stress, Pa.

In order to facilitate the field application, drilling fluid engineers usually choose the Bingham and power law models with two parameters to characterize the performance of drilling fluid. However, laboratory research shows that compared with Bingham and power-law models, the three-parameter H-B model is more consistent with the rheological properties of drilling fluid at low, medium and high shear rates. In order to carry out the hydraulic calculation of slim hole annular flow more accurately, the drilling fluid rheology model is set as the H-B rheology model in this study.

94.2.2 Basic Calculation Model of Annular Pressure Loss in Slim Hole

In the calculation of conventional annulus pressure loss model, the influence of drill pipe eccentricity, rotation, and drill pipe joint is often ignored or weakened. In the process of slim-hole drilling, the cross section between drill string and borehole wall is small. Therefore, the above factors have a prominent influence on annulus pressure loss. If the influence is ignored in calculation, it will cause a large error rate. On the basis of conventional annular pressure loss model, this paper establishes a modified model of single-phase annular pressure loss which is suitable for slim hole considering the correction factors of drill string rotation, eccentricity and drill pipe joint.

$$\Delta P_{sh} = \Delta P \cdot F_E \cdot F_R \cdot F_{con} \quad (94.4)$$

ΔP is the conventional model of annulus pressure loss; F_R is drill string rotation factor, dimensionless; F_E is drill string eccentricity factor, dimensionless; F_{con} is the factor of drill string joint, dimensionless.

In terms of the selection of flow mode of the drilling fluid in slim holes, the flow mode of drilling fluid is basically laminar flow under annular flow velocity in sites due to the small annulus hydraulic diameter. Ahmed confirms this theory by investigating field data, which shows that the Reynolds number of annular drilling fluid flowing in the slime hole is less than 2100 (turbulent critical point). Therefore, in this paper, laminar flow is chosen as the flow mode of conventional model of annulus pressure loss. In the laminar flow case, ΔP of Herschel-Buckley fluid is as follows:

$$\Delta P = \frac{4KL}{D_{hy}} \left(\frac{2n+1}{3n} \frac{12v}{D_{hy}} \right)^n + \left(\frac{2n+1}{n+1} \frac{4L\tau_y}{D_{hy}} \right) \quad (94.5)$$

Reynolds number is a characteristic parameter reflecting liquid flow condition. The generalized Reynolds number under different rheological models can expressed by Eq. (94.6)

$$Re = \frac{12^{1-n} \rho D_{hy}^n v^{2-n}}{K \left(\frac{2n+1}{3n} \right)^n + \left(\frac{2n+1}{n+1} \right) \left(\frac{D_{hy}}{12v} \right)^n \tau_y} \quad (94.6)$$

94.2.3 Calculation Model of Drill String Eccentricity Factor

Calculation method of drill string eccentricity. In the field, the drill string is eccentrically bent in irregular boreholes. Drill pipe eccentricity e can be calculated

as follows:

$$e = 2\delta / (D_h - D_p) \tag{94.7}$$

where, δ is the distance between the center of the drill string and the center of the annulus, m; D_h is the hole diameter, m; D_p is the diameter of drill pipe, m.

In the drilling process of slim-hole horizontal wells, the eccentric state of drill string is relatively complicated. In order to more accurately describe the eccentric state of drill pipe in slim-hole horizontal wells, this paper assumes that the drill string is in sinusoidal eccentric state in vertical and small inclination section (inclination angle $\theta < 60^\circ$). In highly inclined or horizontal sections, the drill string is completely eccentric because of gravity, in which the drill string sinks to the lower side of the annulus (the drill pipe joint is against the wall). The solutions of eccentricity in different well intervals are:

- (1) highly inclined or horizontal sections

$$e = e_{\max} = (D_h - D_{con}) / (D_h - D_p) \tag{94.8}$$

where D_{con} is the diameter of drill pipe joint, m.

- (2) vertical or small inclination section

$$e = e_{\text{avg}} = \sqrt{2(\sqrt{1.5e_{\max} + 1} - 1)} / 3 \tag{94.9}$$

Calculation method of eccentricity factor F_E . When drilling fluid is under laminar flow in the annulus, the drill string eccentricity factor FE can be calculated as follows:

$$F_E = F_{Elam} = 1 - 0.072 \frac{e_{\text{avg}}}{n} \left(\frac{D_p}{D_h}\right)^{0.8454} - 1.5e_{\text{avg}} \sqrt{n} \left(\frac{D_p}{D_h}\right)^{0.1852} + 0.96e_{\text{avg}} \sqrt[3]{n} \left(\frac{D_p}{D_h}\right)^{0.2527} \tag{94.10}$$

where F_{Elam} is the eccentricity factor under laminar flow.

94.2.4 Calculation Method of Influence Factor of Drill String Joint

The joint of drill string is also an important part in the calculation of annular pressure loss in slim hole. In a slim hole annulus, the gap at the drill pipe joint is narrower than at the drill pipe, resulting in faster fluid flow and greater pressure loss. The specific methods for calculating the influence factor Fcon of drill string joint are as follows:

$$F_{\text{con}} = \frac{L_p}{L_p + L_{\text{con}}} + \frac{L_{\text{con}}}{L_p + L_{\text{con}}} \left(\frac{D_p}{D_j} \right)^{4.8} \quad (94.11)$$

where L_{con} is the length of the drill string joint; L_p is the length of drill pipe; D_p is the outside diameter of drill pipe; D_j is the outside diameter of the joint. It is also worth noting that the influence of drill pipe joint is neglected in the conventional calculation model of pressure loss in drill string. In order to obtain a more accurate fluid pressure loss in the drillstring, the effect of the drillstring joint should also be considered in the model of the pressure. The calculation method is to replace the above two diameters with the inner diameter of the drillpipe and the inner diameter of the drillpipe joint.

94.2.5 Calculation Model of Drill String Rotation Factor

The rotation of drill string is often neglected in the conventional well annulus pressure loss model. In fact, not considering string rotation can lead to significant errors (up to 30% or more) when drilling in slim holes. The equation to calculate the drilling string rotation factor F_R involves Taylor number Ta and Reynolds number Re , both of which are related to the annulus flow pattern of drilling fluid. Ta is calculated as follows:

$$Ta = \rho(D_h - D_p)^{n+0.5} D_p^{1.5-n} \omega^{2-n} / 4K \quad (94.12)$$

where ω is the drill pipe rotation angular velocity, rad/s; K is consistency coefficient, n is liquidity index.

Under the conditions of different eccentricity and annular flow velocity, the influence of drill string rotation on annular pressure loss is very different. When the drill string is concentric with the annulus or with low eccentricity, the annulus pressure will decrease as the rotation speed of drill pipe increases due to the shear dilution property of the drilling fluid. When the drill string is in a state of large eccentricity, annulus pressure loss generally increases with the increase of drill pipe rotation speed. The slim-hole model proposed by Song Xuncheng only considers the latter, in which annulus pressure loss increases with the increase of drill pipe rotation speed. Many scholars do not use genuine drilling fluid in laboratory experiments. For an example, Wang Haige chose low viscosity drilling fluid in his experiments, and the universality of relevant models according to his experiments also needs to be further verified.

With the developed CFD numerical simulation technology, the calculation of single-phase flow can reach a higher accuracy. In order to explore the effect of drill pipe rotation on annular pressure loss in the actual drilling site, a CFD numerical simulation model of single-phase annular drilling fluid flow was established in this study. With the method of mixed horizontal orthogonal experiment, four annulus

sizes, four groups of drilling fluid rheological properties (genuine drilling parameters), four annular velocities, four eccentricities and 16 drill pipe speeds are substituted into the CFD numerical model to analyze the influence trend of drill pipe speed on annular pressure loss. Finally, according to the orthogonal experiment results, the regression fitting method is used to establish the calculation model of the influence factors of drill pipe rotation under different annular sizes, drilling fluid properties, annular velocities and eccentricities. The rotation factor FR is expressed as (94.13), whose value expresses the ratio of annular pressure loss with the eccentric and rotating drill string to that with the concentric and not rotating drill string.

$$F_R = \frac{\Delta P_{sh}}{\Delta P_{e=0, \omega=0}} \tag{94.13}$$

94.3 Numerical Simulation of Single Phase Flow of Slim Hole Drilling Fluid

94.3.1 Mixed Horizontal Orthogonal Design of Numerical Simulation Experiment

In order to study the effect of drill string rotation on the annular pressure loss in slim hole, 32 sets of numerical simulation calculations were carried out using the mixed horizontal orthogonal experiment method. The annulus is divided by hexahedron structural grid. The physical model and grid diagram of the annulus are shown in Fig. 94.1, and the specific physical parameters are shown in Table 94.1.

The laminar flow model is selected for research. In order to improve the calculation accuracy, the second-order upwind scheme is selected and the SIMPLE algorithm is applied to accelerate the convergence. The inlet boundary is set as the velocity inlet, the outlet boundary is the pressure outlet, the drill pipe wall and the annulus wall are solid static wall, and there is no slip at the wall; when simulating the rotation of drill string, the corresponding rotation angular velocity is set at the wall of drill pipe.

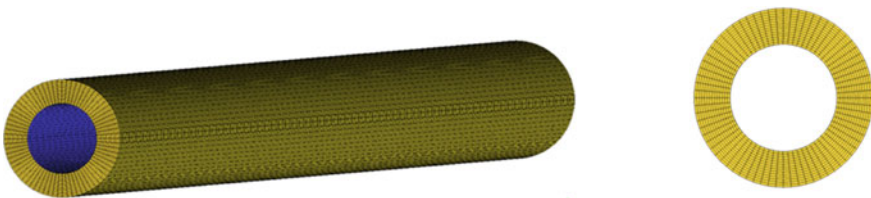


Fig. 94.1 Annulus physical grid diagram

Table 94.1 Physical parameters of numerical simulation

Variables	Values		Unit
Diameter of annulus or drilling pipe	A	Annulus: 150	mm
		Drilling pipe: 90	
	B	Annulus: 150	
		Drilling pipe: 120	
	C	Annulus: 120	
		Drilling pipe: 90	
	D	Annulus: 120	
		Drilling pipe: 72	
Rheological properties	I	Liquidity index n: 0.6841	–
		Consistency coefficient k: 0.6925	Pa s ⁿ
		Yield strength τ_y : 0.016 Pa	Pa
	II	Liquidity index n: 0.799	–
		Consistency coefficient k: 0.4164	Pa s ⁿ
		Yield strength τ_y : 1.042 Pa	Pa
	III	Liquidity index n: 0.8602	–
		Consistency coefficient k: 0.3888	Pa s ⁿ
		Yield strength τ_y : 1.951 Pa	Pa
	IV	Liquidity index n: 0.6599	–
		Consistency coefficient k: 1.453	Pa s ⁿ
		Yield strength τ_y : 2.71 Pa	Pa
Rotation speed of drill pipe	0–150		rpm
Annular flow velocity	0.6–1.2		m/s
Eccentricity	0–0.6		–

The rheological parameters of drilling fluid in the table above are selected from the genuine drilling operations of Mahu oilfield in Xinjiang, so as to ensure that the application range of numerical simulation results is consistent with data from the field. The mixed level orthogonal experiment table is shown in Table 94.2. The experiment has 16 levels of drill pipe rotation which can better reflect the influence of drill pipe rotation on annulus pressure loss.

94.3.2 Regression Fitting Calculation Model of Drill String Rotation Factor

It can be seen from the experimental results that the influence of drill pipe rotation on annular pressure loss is different under different eccentricities. When the drill pipe is concentric or the eccentricity is small, the increase of drill pipe rotation speed

Table 94.2 Mixed horizontal orthogonal test table

Experiment	Rotation speed of drilling pipe (rpm)	Annulus	Drilling fluid	Annular flow rate (m/s)	Eccentricity	Annular pressure loss (Pa)	Annular pressure loss under concentricity (Pa)	F_R
1	0	A	I	0.6	0	1374.75	1374.75	1.0000
2	10	B	II	0.8	0.2	5924	5923	1.0002
3	20	C	III	1	0.4	8370	8360.50	1.0011
4	30	D	IV	1.2	0.6	5091	5032	1.0117
5	40	A	II	0.8	0.4	1804.5	1731.75	1.0420
6	50	B	I	0.6	0.6	3323.5	3373.75	0.9851
7	60	C	IV	1.2	0	13,212.5	13,329.50	0.9912
8	70	D	III	1	0.2	4161	4102.25	1.0143
9	80	B	III	1.2	0	11,275.75	11,387.75	0.9902
10	90	A	IV	1	0.2	3856.25	3816.5	1.0104
11	100	D	I	0.8	0.4	2412.25	2276.25	1.0597
12	110	C	II	0.6	0.6	3806.25	3612.5	1.0536
13	120	B	IV	1	0.4	10,600.25	10,268.25	1.0323
14	130	A	III	1.2	0.6	3344.5	2883.50	1.1599
15	140	D	II	0.6	0	2131.5	2168.5	0.9829
16	150	C	I	0.8	0.2	5230	5315	0.9840
17	0	D	I	1.2	0.2	3279.25	3279.25	1.0000
18	10	C	II	1	0	7356.25	7360.50	0.9994
19	20	B	III	0.8	0.6	6026	6025	1.0002
20	30	A	IV	0.6	0.4	2520.5	2486	1.0139

(continued)

Table 94.2 (continued)

Experiment	Rotation speed of drilling pipe (rpm)	Annulus	Drilling fluid	Annular flow rate (m/s)	Eccentricity	Annular pressure loss (Pa)	Annular pressure loss under concentricity (Pa)	F_R
21	40	D	II	1	0.6	2769.25	2656.25	1.0425
22	50	C	I	1.2	0.4	6547.25	6597.5	0.9924
23	60	B	IV	0.6	0.2	8111.25	8143.25	0.9961
24	70	A	III	0.8	0	2366.25	2380.25	0.9941
25	80	C	III	0.6	0.2	6235	6187	1.0078
26	90	D	IV	0.8	0	4726.25	4783.25	0.9881
27	100	A	I	1	0.6	2026.5	1818	1.1147
28	110	B	II	1.2	0.4	7998.5	7543.25	1.0604
29	120	C	IV	0.8	0.6	7773	7606.50	1.0219
30	130	D	III	0.6	0.4	2661.75	2411.25	1.1039
31	140	A	II	1.2	0.2	2624	2609	1.0057
32	150	B	I	1	0	6113.5	6452	0.9475

will reduce the annulus pressure loss. When the drill pipe is at a high eccentricity, increasing the drill pipe rotation speed leads to an increase in annular pressure loss. This characteristic is the same as the previous experimental results, and it also proves the reliability of the numerical simulation results. In addition, as mentioned above, Taylor number Ta and Reynolds number Re are dimensionless quantities reflecting annular flow state, and it can be seen from the expression that Ta contains annular size and drill pipe diameter, while Re contains rheological parameters of drilling fluid, drilling fluid density and annular velocities. Therefore, in this study, the influence factor of drill string rotation is regressed to be a function of eccentricity e , Teller number Ta and Reynolds number Re according to the results of orthogonal experiment. The specific equation is as (14), and the regression coefficient of this equation is 0.92.

$$\begin{aligned}
 F_R = & 0.985573 - 0.08862e + 0.001892Ta + 0.79744e^2 \\
 & - 1.002e^3 + 0.006966e \cdot Ta - 0.0000167Re + 3.249e \\
 & - 7Re^2 - 5.14e - 10Re^3 + 1.023e - 8Re^2 \cdot Ta - 0.00001142 \cdot Re \cdot Ta \\
 & - 0.0004552e * Re - 0.000002259e^2Re + 8.971e - 7eRe^2 \tag{94.14}
 \end{aligned}$$

Combining the influence factor F_R of drill string rotation with the influence factor F_E of drill string eccentricity and the influence factor F_{con} of drill string joint established above, the calculation model of annular pressure loss is suitable for slim hole in the field.

94.3.3 Model Calculation Results and Law Analysis

Parameters such as annulus size, rheological properties and density of drilling fluid (see Table 94.3 for parameters) is substituted into the model in this paper, and the calculation results are shown in Figs. 94.2, 94.3, 94.4, 94.5 and 94.6.

Table 94.3 Model parameter data

Parameter name	Value	Unit
Annulus inner diameter	154.2	mm
Outside diameter of drill pipe	88.9	mm
Drill pipe speed	0–150	rpm
Annulus return velocity	0.6–1.0	m/s
Eccentricity	0–0.6	–
Drilling fluid rheology	n: 0.42	–
	K: 0.71	Pa s ⁿ
	τ_y : 1.05	Pa
Drilling fluid density	1320	kg/m ³

Fig. 94.2 Eccentricity $e = 0$ pressure loss gradient changes with drill pipe rotation speed

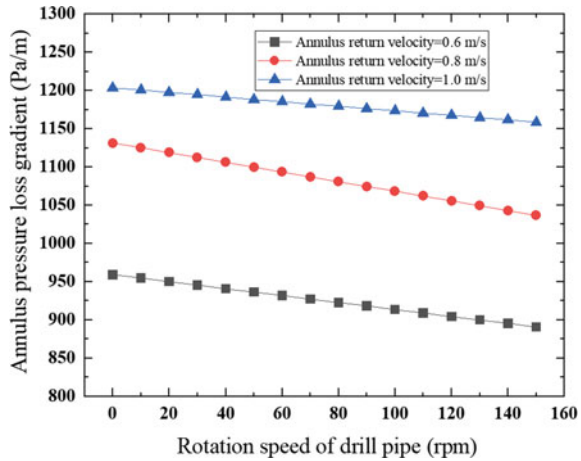
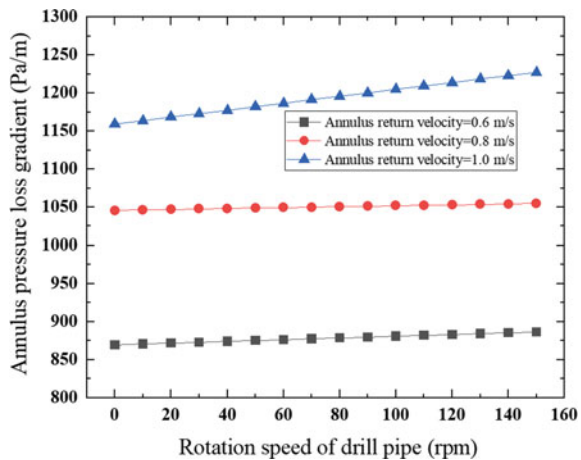


Fig. 94.3 Eccentricity $e = 0.2$ pressure loss gradient changes with drill pipe rotation speed



As can be seen from Figs. 94.2, 94.3, 94.4, 94.5 and 94.6, no matter what eccentricity, annulus pressure loss increases with the increase of drilling fluid flow rate, which conforms to the basic law of hydraulics. When the drill pipe is in a concentric, as shown in Fig. 94.2, the annulus pressure loss decreases with the increase of the drill pipe rotation speed. The results calculated by the regression model are consistent with the experimental results, which also indicates that the Song model is not considered enough in this case. When the drill pipe eccentricity is 0.2 and annular flow velocity is low (0.6 or 0.8 m/s), the effect of drill pipe rotation on annular pressure loss is small. When the annular flow velocity is high (1 m/s), the annular pressure loss also increases with the increase of drill pipe rotation speed. It can be seen that under the condition of the same eccentricity of drill pipe and different annular flow velocity, annulus pressure loss varies with the change law of drill pipe rotation speed. When

Fig. 94.4 Eccentricity $e = 0.4$ pressure loss gradient changes with drill pipe rotation speed

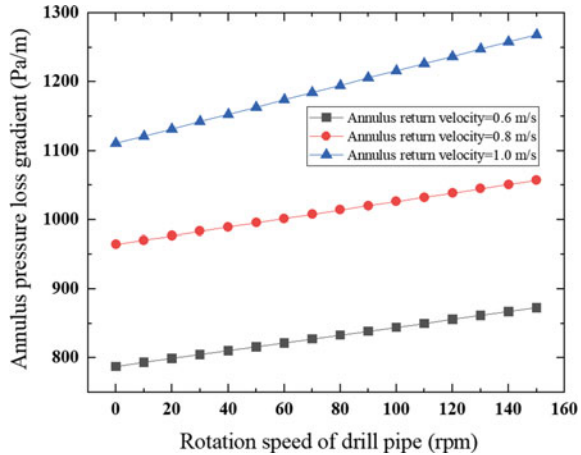
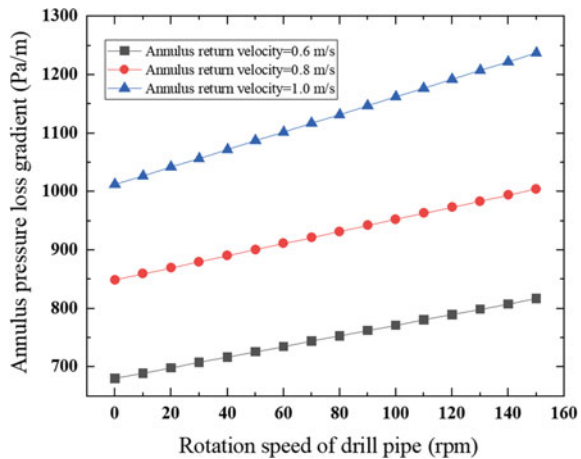


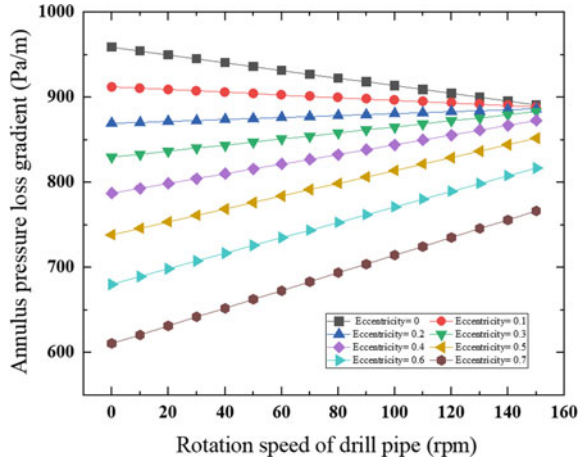
Fig. 94.5 Eccentricity $e = 0.6$ pressure loss gradient changes with drill pipe rotation speed



the drill pipe is at a higher eccentricity, as shown in Figs. 94.4 and 94.5, the drill pipe rotation speed has a greater influence on the annular pressure loss. When the flow rate in the annulus is 1 m/s and the drill pipe rotation speed increases from 0 to 150 rpm, the annulus pressure loss gradient increases from 1012.00 to 1237.23 Pa/m when the eccentricity is 0.6, which is an increase of 22.23%. It can be seen that if the influence of rotation and eccentricity on annulus pressure loss is not considered in the process of slim hole drilling, there is a large error rate.

Comparing Figs. 94.6, 94.7 and 94.8, it can be seen that when drill pipe is not rotating, annular pressure loss decreases with the increase of eccentricity. The influence of eccentricity on annular pressure loss is also different under different annular flow velocity conditions. When the annular flow velocity is 0.6 m/s and the drill pipe rotation speed is 150 rpm, the annular pressure loss gradient reaches its maximum

Fig. 94.6 Annulus return velocity $v = 0.6$ m/s pressure loss gradient versus eccentricity



at the position where the drill pipe is concentric. When the annular flow velocity is 0.8 m/s and the drill pipe rotation speed is greater than 120 rpm, the annular pressure loss gradient under the eccentricity of 0.3 and 0.4 exceeds the annular pressure loss gradient under the concentric condition. When the annular flow velocity is 1 m/s and the drill pipe rotation speed is greater than 60 rpm, the pressure loss gradient under different eccentricities is greater than that under the concentric condition. In conclusion, the influence of drill pipe rotation speed and eccentricity on annular pressure loss is relatively complex and does not show a single response pattern, which also confirms the necessity of established model.

Figures 94.9 and 94.10 reflect the variation curves of annular pressure loss gradient with the diameter reduction rate of borehole under different eccentricity. The drill string sinks at the low side of the annulus and the annulus eccentricity is large in

Fig. 94.7 Annulus return velocity $v = 0.8$ m/s pressure loss gradient versus eccentricity

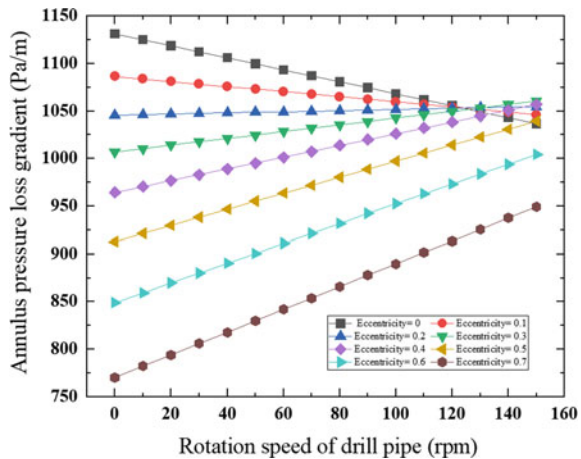
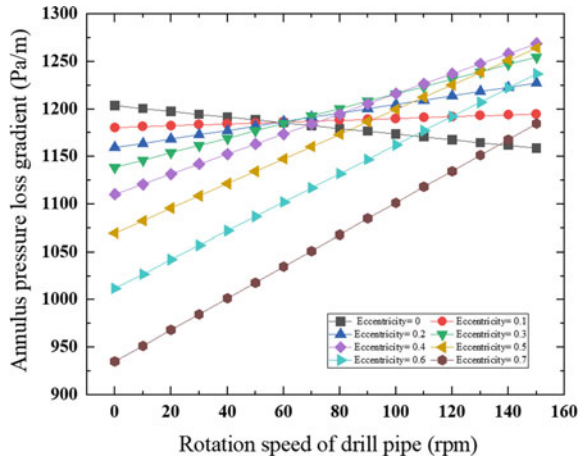


Fig. 94.8 Annulus return velocity $v = 1.0$ m/s pressure loss gradient versus eccentricity



the horizontal section of the slim hole. Figure 94.9 shows the influence of diameter reduction rate of the borehole on annulus pressure loss when the eccentricity is high ($e = 0.7$). When the diameter reduction rate of annulus is 5%, the annulus pressure loss gradient increases by 19.26% compared with that without diameter reduction at different rotation speeds. On the other hand, the average eccentricity of drill pipe is lower in the vertical section of the slim hole due to the buckling of drill pipe. Figure 94.10 reflects the influence of diameter reduction of borehole on annulus pressure loss when the eccentricity is low ($e = 0.3$). When the diameter reduction rate of annulus is 5%, the annular pressure loss gradient increases by 22.99% compared with that when the annular diameter is not reduced at different rotation speeds. In the process of drilling slim hole, especially in the creep prone formation (such as salt rock formation), the influence of diameter reduction should be paid extra attention on to avoid the proliferation of ECD due to diameter reduction, which may lead to more complex downhole accidents such as fracture propagation and leakage.

94.3.4 Field Application of Numerical Mode

The numerical model established in this study is applied to the slim-hole wellbore in Mahu oilfield, Xinjiang, and the model was verified by using the four-way PWD data. Well structure and drilling parameters are shown in Table 94.4.

Figure 94.11 shows the comparison between calculated results and PWD measured data. The mean error rate of ECD in this case is 8.10% with the Song model used, but only 4.6% with our model applied, which indicates the suitability of the model in the field. Therefore, this model can be applied to design and calculate hydraulic parameters of slim hole and guide engineering construction.

Fig. 94.9 Eccentricity $e = 0.7$, annulus return velocity $v = 1$ m/s, pressure loss gradient changes with reducing ratio

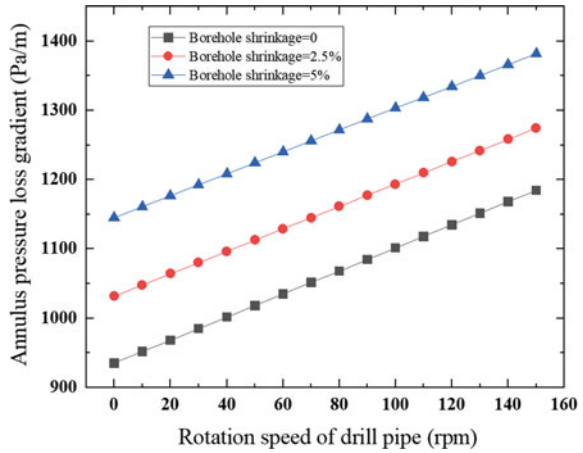


Fig. 94.10 Eccentricity $e = 0.3$, annulus return velocity $v = 1$ m/s, pressure loss gradient changes with reducing ratio

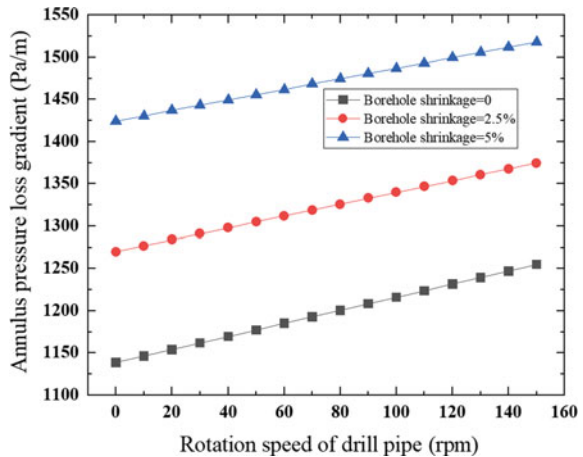
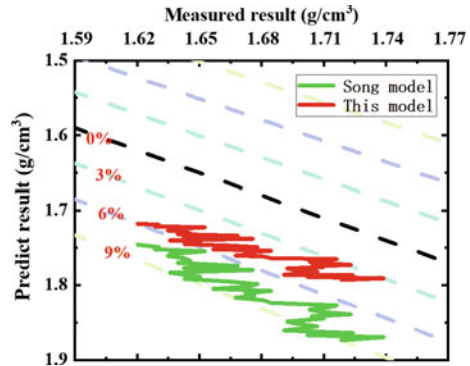


Table 94.4 Well bore structure and drilling parameters of MHHW-X well in Mahu oilfield

Drilling parameters			
Flow rate (L/s)	16	Outer diameter of drill pipe joint (m)	0.124
Vertical depth (m)	3526	Inner diameter of drill pipe joint (m)	0.0635
Measured depth (m)	5719	Inner diameter of heavy drill pipe (m)	0.0635
Outer diameter of drill pipe (m)	0.1651	Outer diameter of heavy drill pipe (m)	0.1016
Inner diameter of drill pipe (m)	0.1016	Joint length (m)	0.51
Inner diameter of casing (m)	0.175	Size of water hole (mm)	11

Fig. 94.11 Relative error between prediction result and measurement result



94.4 Conclusion

Based on the conventional model of annulus pressure loss, a new model is established by adding the influence factors of drill string eccentricity, rotation and joint. To study the influence of rotation on the annulus pressure loss in slim hole, the method of numerical simulation and mixed level orthogonal experimental design is used to substitute the field drilling fluid data to regression fit the drill string rotation factor formula with high accuracy. Conclusions can be drawn from this study as follows:

1. Under the conditions of different eccentricity and annulus flow velocity, the effect of drill pipe rotation speed on annulus pressure loss is different. If a simple single response law model is used, it causes a large error on annulus pressure loss.
2. Hole shrinkage has a great impact on annulus pressure loss no matter in horizontal or vertical sections of horizontal wells. Therefore, in the process of drilling slim hole, especially in the creep prone formation (such as salt rock formation), the influence of hole shrinkage should be paid extra attention to avoid the proliferation of ECD.
3. Compared the predictions of this model with the field measured data of Mahu oilfield in Xinjiang, the average error rate is only 4.6%, which indicates the applicability of this model in the field. Therefore, this model can be well applied to design and calculate hydraulic parameters of slim hole and guide engineering practice.

Acknowledgements The authors acknowledge the support from the National major scientific research instrument research and development project (52227804), the Youth Program of National Natural Science Foundation of China (52104012), the School-Enterprise Cooperation Project (HX20191203), the Key Projects of Scientific Research Plan in Colleges and Universities of Xinjiang Uygur Autonomous Region (XJEDU20211028), the Introduction of Talents Research Launch Project of the China University of Petroleum—Beijing at Karamay “Wellbore Integrity Analysis and Optimization System Construction of Shale Oil and Gas Well Life Cycle”, and the Strategic Cooperation Technology Projects of CNPC and CUPB (ZLZX2020-01-01).

References

1. Hacıislamoglu, M.: Practical pressure loss predictions in realistic annular geometries. In: SPE Annual Technical Conference and Exhibition. OnePetro (1994)
2. Hansen, S.A., Rommetveit, R., Sterri, N., et al.: A new hydraulics model for slim hole drilling applications. In: SPE/IADC Middle East Drilling Technology Conference. OnePetro (1999)
3. Jeng, J., Zhu, K.Q.: Numerical simulation of Taylor Couette flow of Bingham fluids. *J. Nonnewton. Fluid Mech.* **165**(19–20), 1161–1170 (2010)
4. Hansen, S.A., Sterri, N.: Drill pipe rotation effects on frictional pressure losses in slim annuli. In: SPE Annual Technical Conference and Exhibition. OnePetro (1995)
5. Ahmed, R., Miska, S.: Experimental study and modeling of yield power-law fluid flow in annuli with drillpipe rotation. In: IADC/SPE Drilling Conference. OnePetro (2008)
6. Cartalos, U., King, I., Dupuis, D., et al.: Field validated hydraulic model predictions give guidelines for optimal annular flow in slimhole drilling. In: IADC/SPE Drilling Conference. OnePetro (1996)
7. Enfis, M., Ahmed, R., Saasen, A.: The hydraulic effect of tool-joint on annular pressure loss. In: SPE Production and Operations Symposium. OnePetro (2011)
8. Song, X., Wang, G., Guan, Z., et al.: A systematic method for predicting pressure loss in a narrow hole annulus. *Pet. Drilling Tech.* **06**, 11–12 (2004)
9. Tian, Y., Jiang, D., Ma, C., et al.: Numerical simulation of the effects of eccentric rotation of the drill string on annular frictional pressure drop. *Pet. Drilling Tech.* **50**(5), 42–49 (2022)

Chapter 95

A Simulation Model of Resilience Evaluation for Natural Gas Pipeline Network Systems



Zhaoming Yang, Qi Xiang, Qian He, Enrico Zio, Michael Havbro Faber, Huai Su, and Jinjun Zhang

Abstract Resilience is a key component of system safety evaluation and optimization, and research on natural gas pipeline network system (NGPNS) resilience indices and corresponding evaluation is still in early stages. To evaluate the resilience of NGPNS more synthetically and realistically, and to take into account different forms of disruptions, an integrated simulation model combining the topology and operational parameters is provided. The properties of deterministic disruptions, such as earthquakes and equipment breakdowns, are investigated. The maximum flow method and the shortest path method are combined with operational and structural parameters, to assess the amounts and routes of gas supply before and after disturbance; using complex networks theory and graph theory, the traditional view point is changed from the entire system to the affected area. The results can help guide NGPNS topological design and the development of prewarning schemes, including spare gas sources and gas route optimization, as well as pipeline maintenance strategy. They can also aid in the rapid analysis of disturbance consequences and the improvement of NGPNS resilience evaluating accuracy.

Keywords Natural gas pipeline system · Resilience · Maximum flow method · Deterministic disturbance

Z. Yang · Q. Xiang · Q. He · H. Su (✉) · J. Zhang
National Engineering Laboratory for Pipeline Safety/MOE Key Laboratory of Petroleum Engineering/Beijing Key Laboratory of Urban Oil and Gas Distribution Technology, China University of Petroleum-Beijing, Beijing 102249, China
e-mail: suhuai@cup.edu.cn

E. Zio
MINES ParisTech, PSL Research University, CRC, Sophia Antipolis, France

Dipartimento di Energia, Politecnico di Milano, Via La Masa 34, 20156 Milano, Italy

M. H. Faber
Department of the Built Environment, Aalborg University, 9220 Aalborg, Denmark

95.1 Introduction

Resilience is a term with several definitions that refers to a system's or unit's capacity to foresee, resist, absorb, respond to, and recover from a disturbance. Research on NGPNS resilience remains currently in its early stages and is primarily concerned with the reliability and integrity of the system. The present studies mostly concentrate on the approach for resilience evaluation for energy systems in general. In order to assess the resilience of the energy system, Bayesian Networks (BN) and Dynamic Bayesian Networks (DBN) have been widely used [1, 2]. This works well for system with clear topology and process. The in-cascading effects and disturbances for NGPNS are both highly complicated. The network flow system modeling field has used the maximum flow method widely [3]. In complicated networks, it can be utilized for transmission scheduling and route selection. The maximum flow method, specifically for NGPNS, is helpful in simplifying the hydraulic computations. Monte Carlo simulation can be utilized to process the uncertainty [4, 5].

The resilience stages of absorb and adapt, repair, and recovery are discussed. From this point, the assessment for the absorb and adapt stages for an NGPNS in Italy that is resilient to earthquakes has been evaluated using the index technique [6]. The power and heat supply service, and its congestion in both mild and cold winter scenarios, have been the main subjects for the resilience assessment of the NGPNS in Germany [7]. Models and indexes have been examined in order to characterize the resilience of NGPNS in Europe. Although it is unclear how to distinguish between resilience and robustness thoroughly, it has been discovered that NGPNS may be resilient to conflicts, crises, and disruptions [8]. Ecological Network Analysis (ENA) has been applied to study resilience in the instance of the NGPNS in China, with the quantitative index in terms of the traditional ratio of recovery area to loss area [9]. From a different perspective, testing for equipment resilience is also done, such as testing for subsea Christmas tree durability in light of its remaining usable life [2].

The percentage of intermittent solar and wind power generation has steadily increased in recent years due to the reduction of carbon emissions from the world's energy supply. NGPNS has grown in significance for the reliable supply of energy and has been combined with the power grid. The whole system resilience may be increased by increasing system robustness in natural catastrophes [10, 11], as well as taking into account NGPNS within an Integrated Energy System (IES) [11–15].

The following shortages emerge in the current method of analyzing NGPNS resilience.

- (1) there is lack of a framework for evaluating NGPNS supply resilience;
- (2) the quantitative evaluation of NGPNS resilience is not systematic;
- (3) the evaluation frameworks proposed do not capture all network aspects of the practical condition of NGPNS in practice.

95.2 Methodology

In order to transport gas to all nodes after defining the flow direction and volume in the pipelines, the resilience analysis combines operational parameters, such as operating pressure and delivery volume of each pipeline, with structure parameters, such as pipe length, pipe diameter, wall thickness, connection relationships, and node properties. In order to assess the connectedness of the nodes and the occurrence of disturbance events, complex network analysis is used to rank and categorize the pipelines in respect to the degree of each node. The NGPNS is separated into various impacted areas using graph theory, based on community analysis and complicated network analysis. Following that, the supply and topological properties are assessed using evaluation indexes (Fig. 95.1).

In order to analyze the resilience results comprehensively, five indexes are proposed to evaluate the properties of gas supply and topology of the affected areas.

- (1) Gas supply amount ratio:

$$Rat_Q = \frac{\sum Q_i^p}{\sum Q_i^p} \tag{95.1}$$

where Q_i^p is the gas flow in the i th pipe of the affected area after disturbance, and Q_i^p is the gas flow in the i th pipe of the affected area before disturbance.

- (2) Node demand satisfaction:

$$S_i = \frac{Q_i^n}{D_{ei}} \tag{95.2}$$

where Q_i^n is the gas amount which i th node gets in the affected area after disturbance, and D_{ei} is the gas demand amount.

- (3) Pipe number ratio:

$$Rat_n = \frac{n'_p}{n_p} \tag{95.3}$$

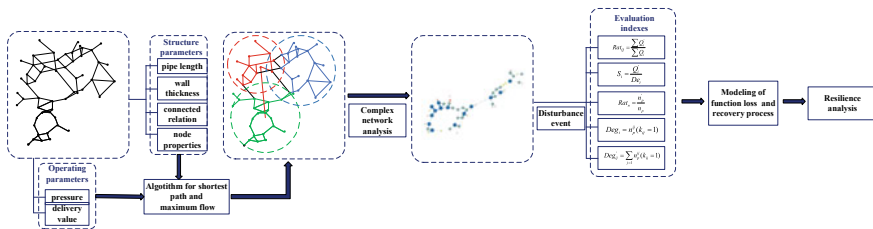


Fig. 95.1 Resilience analysis for deterministic disturbance

where n'_p is the number of pipes which still work in the affected area after disturbance, and n_p is the number of pipes working in the affected area before disturbance.

(4) Direct degrees:

$$Deg_i = n_p^{ij} (k_{ij} = 1) \quad (95.4)$$

where n_p^{ij} is the number of pipes which are connected to the i th node.

(5) Neighbor degrees:

$$Deg'_{ij} = \sum_{j=1} n_p^{ij} (k_{ij} = 1) \quad (95.5)$$

where n_p^{ij} is the number of pipes which are connected to the nodes connected to the i th node. To analyze resilience quantitatively, the following analysis is made.

95.3 Numerical Example

For the purpose of evaluating the supply resilience of NGPNS in respect to deterministic disturbances, the pipeline network system from Europe is used.

95.3.1 NGPNS Sample

The practical system of natural gas pipelines in Europe is used as the calculation's subject [16]. Its structure is displayed in Fig. 95.2, and Table 95.1 displays the pipeline system's specifications. According to Fig. 95.3, network analysis is conducted based on the degrees of each node and community partition. Given the results of this analysis, the following four types of disturbances are considered.

- A. LNG plant No. 11 node failure,
- B. Natural gas storage No. 30 node failure,
- C. Gas transportation station No. 44 node failure,
- D. 19–20 pipe section failure.

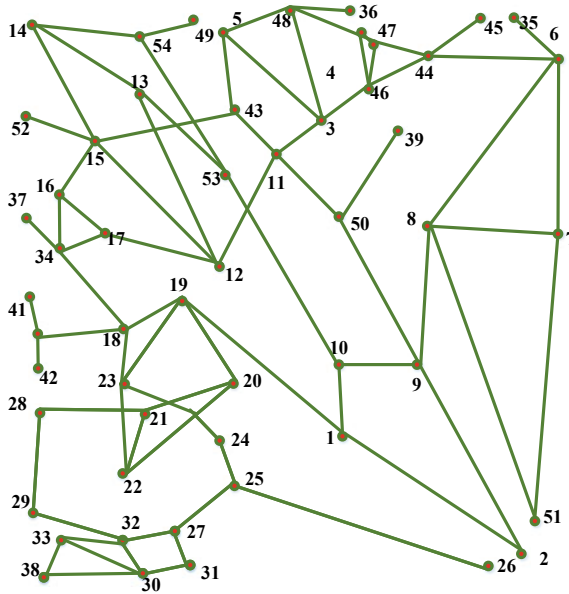


Fig. 95.2 Topology of NGPNS

Table 95.1 Parameters of NGPNS

Node number	Supply source	Demand	Node number	Supply source	Demand	Node number	Supply source	Demand
1	–	–	19	–	–	37	18	1.30
2	–	–	20	19	–	38	30	0.70
3	–	–	21	19	0.54	39	–	1.00
4	3	0.38	22	19	–	40	18	
5	6	3.43	23	19	–	41	18	0.40
6	–	0.57	24	19	–	42	18	0.50
7	6	0.66	25	30	0.60	43	11	1.06
8	6	–	26	30	0.80	44	6	2.82
9	6	–	27	30	3.50	45	6	7.40
10	–	2.02	28	19	6.00	46	3	0.90
11	–	–	29	30	–	47	36	0.68
12	11	0.54	30	–	0.40	48	3	1.17
13	49	1.03	31	30	0.36	49	–	–
14	49	1.30	32	30	–	50	2	–
15	18	0.94	33	30	0.40	51	6	7.00
16	18	0.70	34	18	1.00	52	11	0.98
17	18	0.46	35	6	–	53	49	1.50
18	–	8.40	36	–	1.74	54	49	0.60

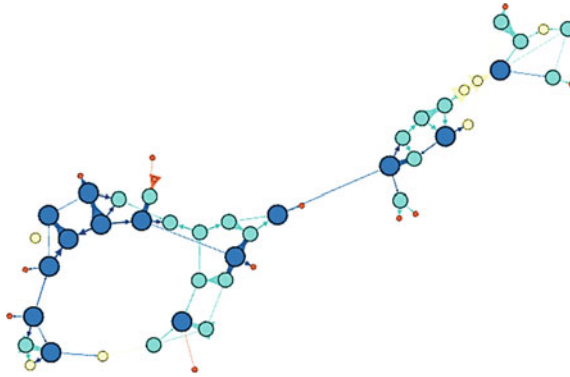


Fig. 95.3 Complex networks analysis of NGPNS based on degrees

95.3.2 Affected Areas Analysis

Figures 95.4, 95.5, 95.6 and 95.7 display the results of applying complex networks analysis and graph theory studies to the NGPNS before and after disruptions of the affected regions. Complex network and graph theory analysis has been used to pinpoint the nodes or pipe sections that might be impacted by the disturbances. Pipe failures are shown in grey, node failures in yellow, and pipes connection changing after disturbances are shown in red. Five indexes are applied to assess the characteristics of the gas supply and the topology of the impacted areas.

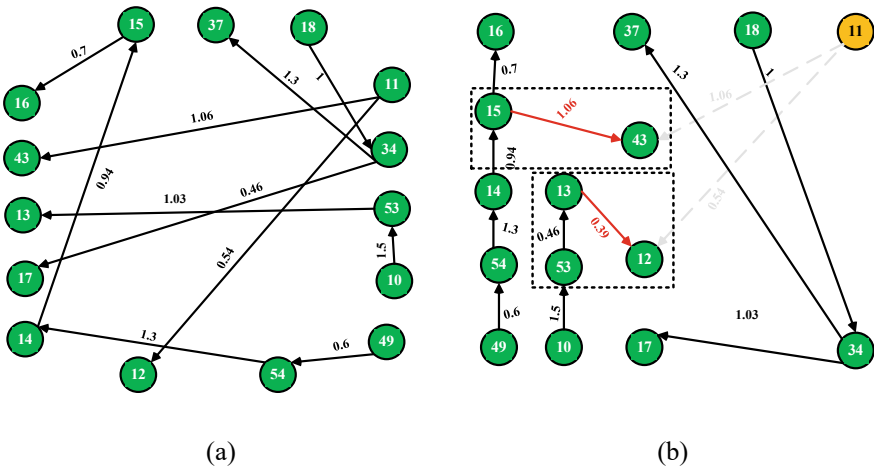


Fig. 95.4 Area of No. 11 node affected by disturbance: **a** before, and **b** after

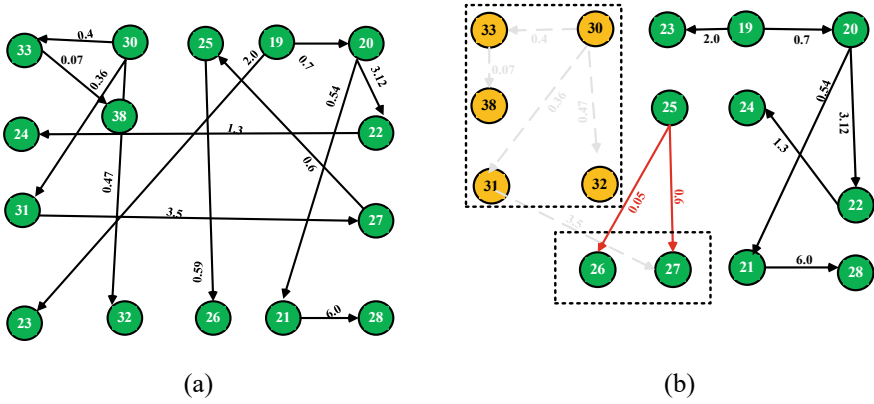


Fig. 95.5 Area of No. 30 node affected by disturbance: **a** before, and **b** after

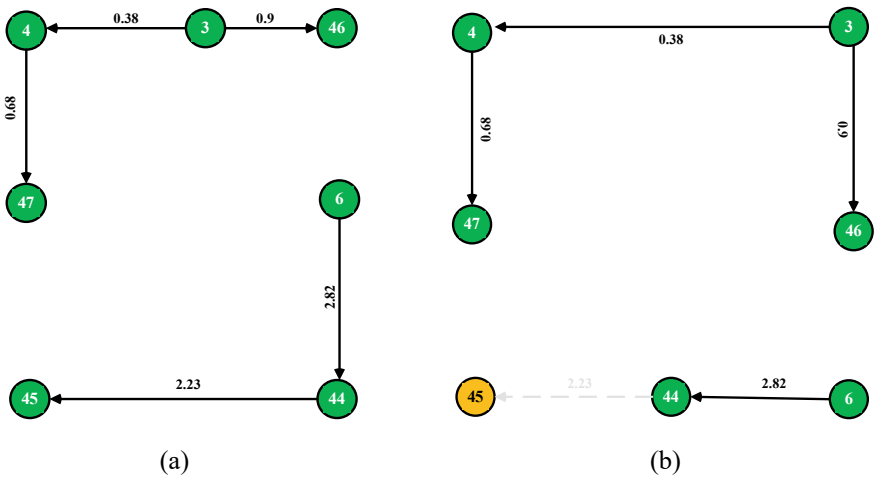


Fig. 95.6 Area of No. 44 node affected by disturbance: **a** before, and **b** after

95.3.3 NGPNS Resilience Analysis

The satisfactions for each node in the impacted areas, following the four disturbances, are displayed in Fig. 95.8, and the formula for the gas supply satisfaction is described in Eq. (95.2). It can be concluded that the gas supply satisfactions depend on (i) the number of pipes connected to a node and the number of pipes connected to neighboring nodes (direct degree and neighbor degree); (ii) the location of the node in the entire system; and (iii) the number of gas sources from which the node is supplied and their gas supply capacities. This is evident when taking into account the indicators of a node's direct degree, neighbor degree, and system degree. In this

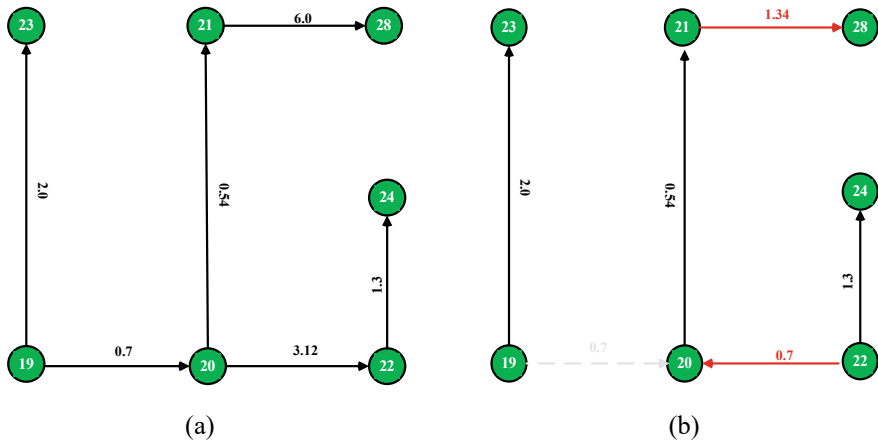


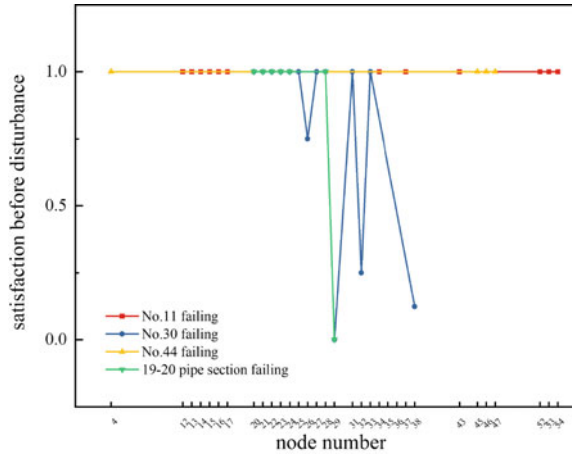
Fig. 95.7 Area of 19–20 section affected by disturbance: **a** before, and **b** after

NGPNS, node No. 32 is directly connected to the disturbance node after by a single pipe disturbance B. The network flow performance analysis shows that the initial gas source before the disturbance is no longer able to supply gas through the alternative route and is unable to do so through other gas sources either. As a result, after node No. 30 failed, the supply of gas to these nodes was not guaranteed. However, other nodes connected to the accident node, such as nodes No. 20 and No. 23, are still able to secure gas supply after the accident (as shown by complex network analysis). There are two reasons for this: firstly, there is an alternative option for supplying gas to the node from the original gas source, and secondly, there is an alternate gas source for the node.

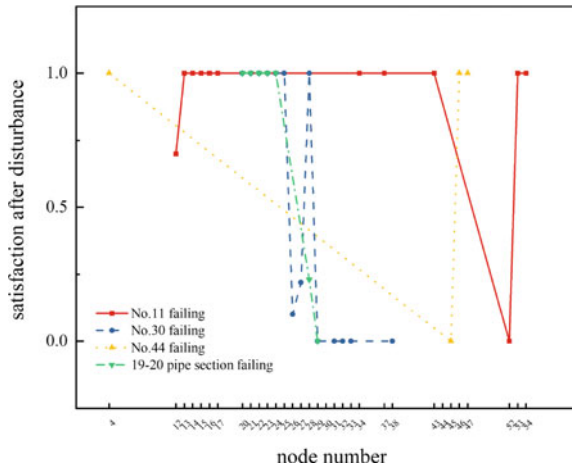
Moreover, Fig. 95.9 demonstrates uniformity in the distribution of the three categories of degrees described in this research. However, in the disturbance of type C, the gas sources 11 and 36 are influencing nodes No. 5 and No. 47, which are connected to node No. 4, which prevents the pipelines connected to these two sources from being categorized under the same affected area, leading to different direct degrees and neighbor degrees values. The discrepancy is due to the fact that there are more gas sources available, making it impossible to split all of the pipes connecting to a node into a single impacted region. In the event that their connected node fails, nodes with uneven system degree and neighbor degree values are assured to get gas from another source, as shown by a comparison of Figs. 95.8 and 95.9.

Under four distinct disturbances, Fig. 95.10 shows the variations in the capacity of the gas transit from the sources to each node. The number of nodes that can still meet the gas supply accounts for 94.33, 98.11, 98.11 and 90.57% of the whole network, respectively, so it can be concluded that the overall gas supply resilience of the NGPNS is good in terms of gas supply capacity of the nodes. As previously said, the reason for that is that there are alternate routes or sources which can supply gas to the affected nodes. For instance, node No. 20 connects directly to node No.

Fig. 95.8 Node satisfaction and supply efficiency



(a) satisfaction before disturbance



(b) satisfaction after disturbance

19 before the failure of the 19–20 pipe section, and the route changes to 19–23–22–20 after the accident. Similarly, when node No. 11 fails, node No. 53, which was previously supplied by No. 11 gas source, is then supplied by No. 10 gas source after the accident.

As can be seen in Fig. 95.1, the combination of the maximum flow method and the shortest path method is efficient at estimating the supply capacity of the NGPNS, assessing the supply resilience, and offering recommendations for rerouting the transmission routes, including switching to alternative sources after disturbance events. It is important to stress that in this case, all nodes are given equal weight in terms of significance and gas supply precedence. Gas should be provided to domestic

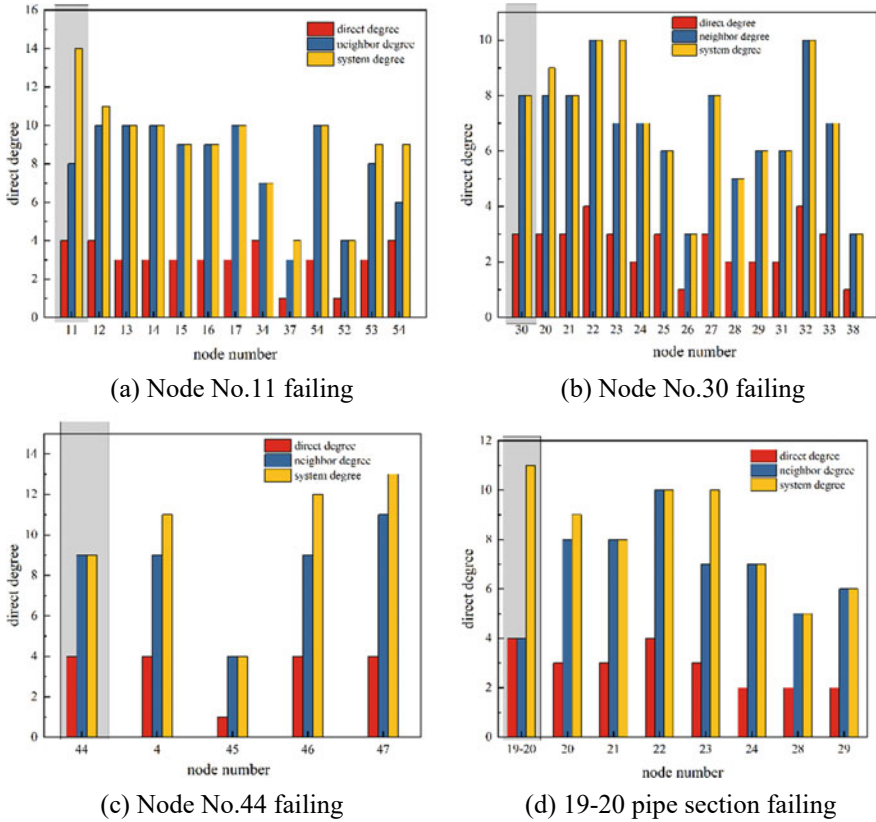


Fig. 95.9 Degrees of each node

consumers firstly after a disruption because, in practice, the supply of gas for residents needs is frequently prioritized over gas for industry. Also, the priority of gas delivery following a disruption varies by city, based on organizational level and population size. For example, Beijing in China has a greater priority than other adjacent cities.

The intricacy of the entire system frequently dilutes the impact of individual nodes on the general resilience of NGPNS. In this research, the affected region is chosen for the study’s focus after being found by complex network analysis, graph theory, and flow performance analysis. Figure 95.11 shows how the gas flows in the impacted regions changed generally before and after the four disturbances. The regions that would not be impacted by the disturbance are removed when the affected areas are divided into communities, which can clarify the effect of the disturbance. Figure 95.11 demonstrates that when pipe section 19–20 fails, 60% of the area’s gas supply is lost, but when nodes 30 and 44 fail, only about 30% of the area’s gas supply is lost. There is only 2% decrease in gas delivery of the Node No. 11 failure, which has the least effect on the related affected region. Figure 95.12 depicts

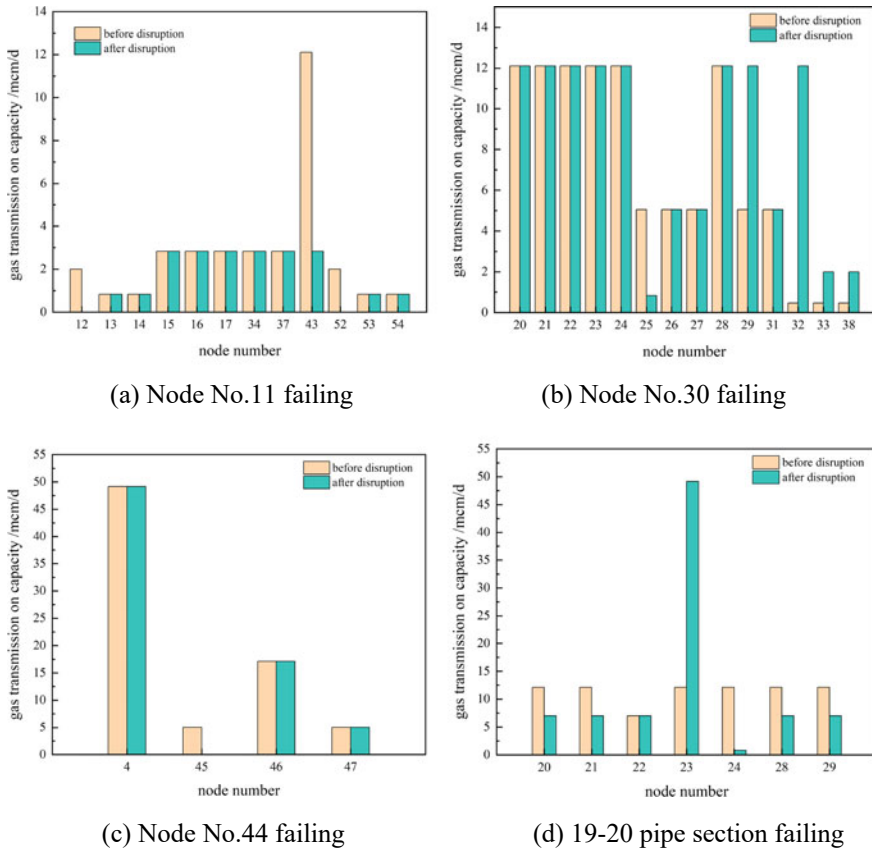


Fig. 95.10 Gas transmission capacity to each node in the case of the four disturbances

the variation in the number of pipelines in operation before and after disturbances, while Fig. 95.13 depicts the variation in the capability of the regional gas transmission system. Combined with Fig. 95.11, it is clear that the failure of nodes or pipe sections results in a reduction in the number of pipes in use. But the extent of the change and the reduction in gas transmission capacity, depend on factors like the location of the failed pipe, and the route that is affected. However, the change in system gas transmission capacity may not be significant. The terms “gas transmission volume” and “gas transmission capacity” should be distinguished. The calculation of gas transmission volume is based on user demand, i.e. the amount of gas provided in the system. The calculation of transmission capacity is determined by the maximum capacity that the system can supply, which is frequently more than the amount of gas supplied. The results also show that the actual gas transmission volume of the NGPNS is more dependent on transmission route than on system capacity.

Fig. 95.11 Comparison of gas supply amount of the system

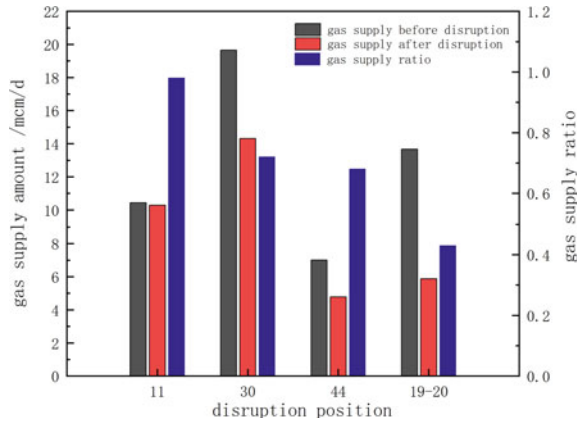


Fig. 95.12 Comparison of effective pipes

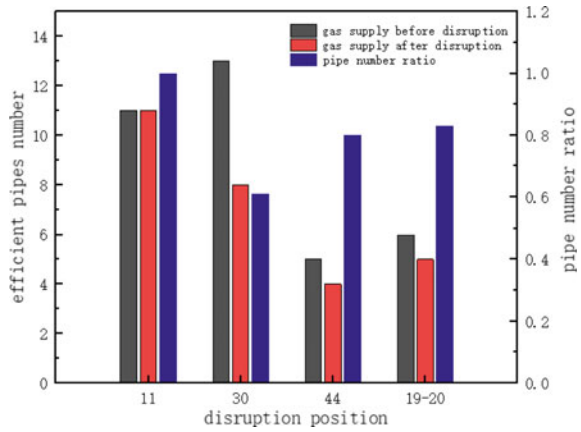
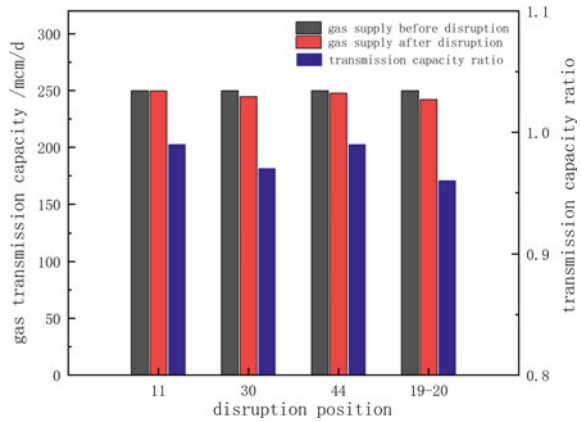


Fig. 95.13 Comparison of transmission capacity



Based on the results, the following actions may be performed to further increase the supply resilience of NGPNS: ① the installation of gas storage, the use of line-pack, and other measures should be taken to extend the effective gas supply duration following the disruption; ② Based on a combination of the prior indexes and network analysis, it is important and necessary that the NGPNS's potential types of disturbances are investigated during the system's design, and alternative gas sources and routes should be established for significant nodes in accordance with the resilience evaluation.

95.4 Conclusions

This study discusses the NGPNS gas supply resilience and defines indicators and assessment models. From deterministic disturbances, the gas supply resilience of NGPNS is evaluated under various types of disturbance occurrences. The research's findings offer recommendations regarding to design and operation of NGPNS.

The complexity network analysis, maximum flow approach, and shortest path method are the key foundations for NGPNS resilience modeling. The maximum flow and shortest path approaches include the structural and operational features of NGPNS, and complex network analysis and graph theory are used to distinguish the impacted areas for a specific failing component of the NGPNS, to evaluate the gas supply resilience.

The analysis of the methods for assessing supply resilience reveals that (i) the combination of the maximum flow method and the shortest path method, which integrate the structural and operational parameters of NGPNS, allows for the capture of the gas supply routing and calculation of the gas supply amount before and after a disturbance occurrence, including the selection of alternate routes and alternate gas sources; (ii) the pipeline system is treated as a network that utilizes the idea of community and the combination of the maximum flow method and shortest path methods, which makes it possible focusing the analysis of the impact of disturbances on the affected areas; (iii) the combination of complex networks and graph theory allows the connection between the geometry of the pipeline network and the gas supply capacity; (iv) the deterministic resilience analysis's findings allow for an explanation of the consequences of adding more gas supply routes and sources.

References

1. Kammouh, O., Gardoni, P., Cimellaro, G.P.: Probabilistic framework to evaluate the resilience of engineering systems using Bayesian and dynamic Bayesian networks. *Reliab. Eng. Syst. Saf.* **198** (2020)
2. Cai, B., Zhang, Y., Wang, H., Liu, Y., Ji, R., Gao, C., et al.: Resilience evaluation methodology of engineering systems with dynamic-Bayesian-network-based degradation and maintenance. *Reliab. Eng. Syst. Saf.* **209**, 107464 (2021)

3. Marino, A., Zio, E.: A framework for the resilience analysis of complex natural gas pipeline networks from a cyber-physical system perspective. *Comput. Ind. Eng.* **162**, 107727 (2021)
4. Rausand, M., Hoyland, A.: *System Reliability Theory: Models, Statistical Methods, and Applications*, vol. 396. John Wiley & Sons (2003)
5. Su, H., Zhang, J., Zio, E., Yang, N., Li, X., Zhang, Z.: An integrated systemic method for supply reliability assessment of natural gas pipeline networks. *Appl. Energy* **209**, 489–501 (2018)
6. Cimellaro, G.P., Villa, O., Bruneau, M.: Resilience-based design of natural gas distribution networks. *J. Infrastruct. Syst.* **21**(1), 1–14 (2015)
7. Hauser, P., Hobbie, H., Mst, D.: Resilience in the German natural gas network: modelling approach for a high-resolution natural gas system. In: *European Energy Market* (2017)
8. Carvalho, R., Buzna, L., Bono, F., Masera, M., Arrowsmith, D.K., Helbing, D.: Resilience of natural gas networks during conflicts, crises and disruptions. *PLoS One* **9**(3) (2014)
9. Xueyi, L., Jinjun, Z., Huai, S., Zio, E.: Resilience assessment of China's natural gas supply system based on ecological network analysis. In: *2019 4th International Conference System Reliability Safety, ICSRS 2019*, pp. 402–406 (2019)
10. He, C., Dai, C., Wu, L., Liu, T.: Robust network hardening strategy for enhancing resilience of integrated electricity and natural gas distribution systems against natural disasters. *IEEE Trans. Power Syst.* **33**(5), 5787–5798 (2018)
11. Di Maio, F., Matteo, F., Guerini, C., Federico, P., Zio, E.: Time-dependent reliability analysis of the reactor building of a nuclear power plant for accounting of its aging and degradation. *Reliab. Eng. Syst. Saf.* **205**, 107173 (2021)
12. Lin, Y., Bie, Z.: Study on the resilience of the integrated energy system. *Energy Procedia* **103**, 171–176 (2016)
13. Li, Y., Li, Z., Wen, F., Shahidehpour, M.: Minimax-regret robust co-optimization for enhancing the resilience of integrated power distribution and natural gas systems. *IEEE Trans. Sustain. Energy* **11**(1), 61–71 (2020)
14. Shao, C., Shahidehpour, M., Wang, X., Wang, X., Wang, B.: Integrated planning of electricity and natural gas transportation systems for enhancing the power grid resilience. *IEEE Trans. Power Syst.* **32**(6), 4418–4429 (2017)
15. Yan, M., He, Y., Shahidehpour, M., Ai, X., Li, Z., Wen, J.: Coordinated regional-district operation of integrated energy systems for resilience enhancement in natural disasters. *IEEE Trans. Smart Grid* **10**(5), 4881–4892 (2018)
16. Praks, P., Kopustinskas, V., Masera, M.: Probabilistic modelling of security of supply in gas networks and evaluation of new infrastructure. *Reliab. Eng. Syst. Saf.* **144**, 254–264 (2015)

Chapter 96

Staged Deployment of LEO Communication Satellite Constellation Based on Real Option Theory



Xuefeng Wang and Shijie Zhang

Abstract In this article, the deployment problem of LEO satellite communication is investigated and analyzed by the financial tool, i.e. real option theory. Traditional methods often neglect the existence of uncertainty and underestimates the value of staged deployment decisions. Real option theory pays more attention to the value of flexibility in large-scale complex engineering system, such as satellite constellation. The objective of this work is to analyze the flexible approach of staged deployment for mega-constellation and deduce the option price equations. Finally, a simple example is given to demonstrate the fact that staged deployment brings the flexibility for the system and real option theory can evaluate this value more exactly.

Keywords Staged deployment · Real option theory · LEO communication satellite constellation

96.1 Introduction

Satellite constellations are groups of satellites with similar function, operating in same or different orbits under shared control [1, 2]. Over the last 15 years a number of communication satellite constellations for personal voice or data communications have been launched and those systems are in low earth orbit, e.g. Iridium and Globalstar. The original target user group of those systems is the global travel businessmen, whose global communication demand cannot be meet by terrestrial cellular networks [3–5]. However, the market prediction for satellite constellation communication services has been proved overly optimistic because of rapid development of terrestrial cellular networks. As a consequence of overestimating the number of users, Iridium had to file for bankruptcy protection in 1999 and Globalstar had to accept the same result in 2002.

X. Wang (✉) · S. Zhang
Harbin Institute of Technology, Harbin 150001, China
e-mail: wangxuefeng@hit.edu.cn

Recently, a number of constellation projects have been proposed and developed to support global communication services with hundreds and even thousands of LEO satellites as the new rapid market demand growth [6, 7]. SpaceX has launched and deployed 1750 satellites to configure the Starlink global broadband communication system and the final constellation consists of 42000 satellites. Amazon has proposed the satellite constellation plan with 3236 satellites named as Kuiper. OneWeb is earliest to apply to Federal Communications Commission (FCC) for frequency licensing for the planned broadband communication services support with 720 satellites, however, what a pity is OneWeb has filed for bankruptcy because of the economic failure caused by COVID-19 pandemic in March 2020.

In the traditional methods, aimed at meeting a predicted users' communication demand, system designers develop and deploy satellite constellations to provide a global coverage [8–11]. However, the market demand or the number of the target users could change drastically during the period of satellite constellation design, research and development. These methods neglect the existence of uncertainty in the process of deployment of project, which could lead to mistakes in decision-making and economic failure. Thus, a flexible method with staged deployment of mega-constellation needs to be studied.

The work is organized as follows. Section 96.2 is the problem statement of staged deployment of the mega constellation. The new method with real option theory is proposed in Sect. 96.3. To illustrate the method highlights, the traditional approach is also analyzed in this section. In Sect. 96.4, some simulation results are given to evaluate the flexibility and then the conclusion could be drawn.

96.2 Problem Statement

Staged deployment is a particular approach which could introduce flexibility in engineering systems. By beginning projects with smaller and cheaper infra-structure, the engineering projects could be deployed progressively with decreasing the risk compared with traditional methods, thereby avoiding the economic failure effectively. When market requirements exceeding the original expectation or there being enough cash flow during development and operation, projects could be upgraded to the next stage with better performance. Differing from methods for a given target, staged deployment method starts with searching an initial architecture which could bring flexibility to decision makers that manage the system to adjust strategies with the change of market conditions. However, there are new problems and challenges to system engineers.

First one is that the possible development and deployment paths need to be determined from the original architecture. A perfect staged deployment is optimization process which satisfies the conditions of Pareto Front, but it is impossible to be realized in the reality. The stages which are already deployed successfully, bring constraints that decrease the level of system freedom with development.

Second problem is that embedding flexibility into engineering system is not costless and the price need to pay is not easy to determine in general. Large scale complex systems always have long deployment period and there is a lot of uncertainty in the process, such as upgrading of technology, changes of policies and component malfunction of system. As a result, it is hard to model systems accurately to predict the outcome that projects could generate in the future.

Compared with traditional methods, real option theory (ROT) could be a better method to deal with complex engineering scenarios that have long development periods with lots of uncertainty. It provides an approach to quantify the value of flexibility for engineering system designers. With this effective mathematic tool, it increases the probability of using opportunities and avoiding risks to bring more profit of projects.

96.3 Staged Development

96.3.1 Traditional Design and Deployment Approach

The fact of previous economic failure for Iridium, Globalstar and OneWeb reveals the intrinsic risk characteristics implied within the traditional deployment approach to build large engineering systems with high-uncertain user demand and high-capital investment. Based on the information from market researches, customers' capacity requirement model could be established via the traditional methods. Assuming that the number of potential customers across global market is subject to uniform distribution over the surface of the earth, the global potential customer provided communication service by constellation system in the first year is

$$PC_0 = k(t_0 + 1) + b \tag{96.1}$$

where t_0 is the initial time point of system deployment, then t_0+1 is the first year under the communication service, k the increment of customers per year, b is the number of customers before deployment of new communication system. In general, system could be recognized as a low-bandwidth system when the data rate is less than 50kps. Otherwise, system is considered as high-bandwidth system. Differing with low- and high-bandwidth, the value selection of k and b is shown as Table 96.1.

Assuming that the increment of customers per year is constant, then the number of potential customers at the end of system deployment is

Table 96.1 Market forecast of communication systems

	k	b
Low-bandwidth system	2.95	49.59
High-bandwidth system	0.51	4.97

$$PC_T = PC_0 + k(T - 1) \quad (96.2)$$

where T is the system lifetime.

According to the Eqs. (96.1) and (96.2), throughout the system lifetime, the total number of potential customers is

$$PC_{tot} = \frac{(PC_0 + PC_T) \cdot T}{2} \quad (96.3)$$

The world land area is 1.489×10^8 km². In developed regions, the terrestrial cellular system is also well deployed to provide communication service for people who are able to afford, whereas in developing regions although there is a large demand of subscribing the service yet fewer people could accept the high price of satellite communication service compared with cellular system. So it is reasonable to assume that the potential customers are evenly distributed over these regions. The number of potential customers per land area is

$$N_{PC} = \frac{PC_{tot}}{A_{land}} \quad (96.4)$$

To meet the communication demand of potential customers, the constellation system should provide enough quantity of channels. Let N_{ch} be the number of channels, it could be computed by

$$N_{ch} = \frac{PC_{tot} \cdot r_{act}}{60 \times 24 \times \frac{365}{12}} \quad (96.5)$$

where r_{act} is the active rate of customers. Let B be the signal channel bandwidth, and K be the frequency re-use factor, then the communication capacity could be calculated by

$$Cap = B \cdot N_{ch} \cdot K \quad (96.6)$$

After the capacity requirement model has been established, the process of satellite constellation design and deployment would be executed by traditional approach with the optimization objective meeting the expected capacity while minimizing cost. Then a trade space for satellite constellation deployment strategies could be architected which is composed by a variety of design options, as shown in Fig. 96.1. Through the exploration in trade space, the optimal design architecture decision could be selected. However, the selected option is designed for the fixed expected customers' capacity requirement. There are lots of source of uncertainty in the economic market and the demand would also vary as the change of external world due to technical, economic, political and other reasons. So it is difficult to reckon the required customers capacity to some extent that it would bring risks into the engineering program. There is sufficient necessity to modify the traditional

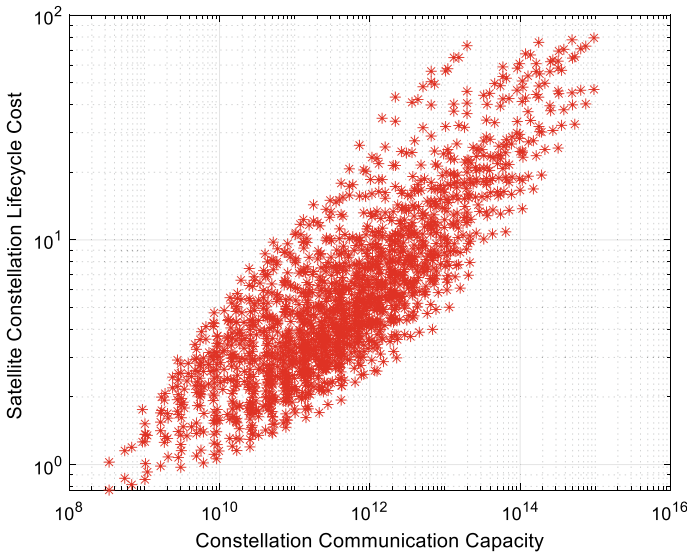


Fig. 96.1 Trade space of constellation architected by traditional approach

approach within the uncertain circumstance condition in order to realizing the flexible engineering deployment strategy.

96.3.2 Flexible Approach: Real Option Analysis

Staged deployment is one approach of introducing flexibility in a system for designing large engineering systems, such as communication satellite constellation, in order to avoid the economic risks as soon as possible. Beginning with an elementary stage, the risk apportionment could be realized through staged deployment of projects. Meanwhile, there is no need to input large amount up-front investment to meet the requirements of majority of customers. When the demand exceeds the current communication capacity and there is good operation circumstance, the satellite constellation system could be deployed into the next stage with better performance. The objective of flexible approach is to determine an initial stage on account of uncertain market economic conditions different from aiming at a fixed expected capacity. Real option theory (ROT) could be an important approach to deal with all of problems above.

A real option could be selected as a technical element introduced into a design architecture, which could bring the right but not the obligation for engineers and skateboarders under the uncertain circumstance [12–22]. The flexibility of staged deployment of the mega-constellation could be provided by real options through changing the system parameters such as orbital inclination and altitude, the number of satellites after initial deployment stage is done. Therefore, there are additional

opportunities to change or modify the configurations of satellite constellations during subsequent stages of development and deployment. The real option theory makes engineers and skateboarders put the emphasis on the value of flexibility rather than technical details. Assuming that there is no challenge to introduce flexibility, the real option theory could be applied to the dynamic uncertain environment compared with the traditional approach [23–28].

Model of Demand Uncertainty. Real option theory is the approach that the option methodology is applied to evaluate the real assets whose value is depended on the relevant financial entity comparing with the financial option approach. To describe the behavior of uncertain economic market, it is assumed that the customer requirement follows a Geometric Brownian Motion (GBM). In the financial fields, this assumption is always used to model the price of a stock X . The model of demand uncertain is given by

$$dX = \alpha X dt + \sigma X dz \quad (96.7)$$

Let X be the current stock price, α is the expected return of this stock, σ is the price volatility, dz is a random variable obeying the standard normal distribution. Figure 96.2 shows the demand variation in 10 years with uncertainty. In option pricing theory, the binomial tree could be a powerful tool to analysis the change of stock price. Considering scenarios with many decision periods, the probable evolution of customer demand could be described by a binomial tree as shown in Fig. 96.3. It is necessary to divide the system lifetime into some intervals when using the binomial tree approach.

Economic Opportunity. Flexibility introduced into systems allows the existence of design and development decision points through program plan periods. At a decision point, the value of parameters that were uncertain are analyzed. Depending on these values, a decision is made to adapt to them in the best possible manner. Since uncertain parameters are observed through time, uncertainty is reduced, thus reducing the risks of the project. Decisions can be of various types, ranging from extending the life of a project to canceling its deployment. This article focuses on the flexibility provided by staged deployment when demand is the uncertain parameter. The decision in this case is about whether or not to move to the next stage in the deployment process. This approach represents an economic opportunity compared to the traditional way of designing systems because it takes current market conditions into account. Two mechanisms explain this advantage. The staged deployment strategy tries to minimize the initial deployment costs by deploying an affordable system but the expenditures associated with transition between two stages can be large [29–32]. However, since those expenditures are pushed towards future times, they are discounted. If r is the discount rate, Q is the cost for deploying a new stage and t is the number of years between the initial deployment of the system and the time the new stage is deployed, the present value of the cost is given by Eq. (96.8)

$$PV(Q) = \frac{Q}{(1+r)^t} \quad (96.8)$$

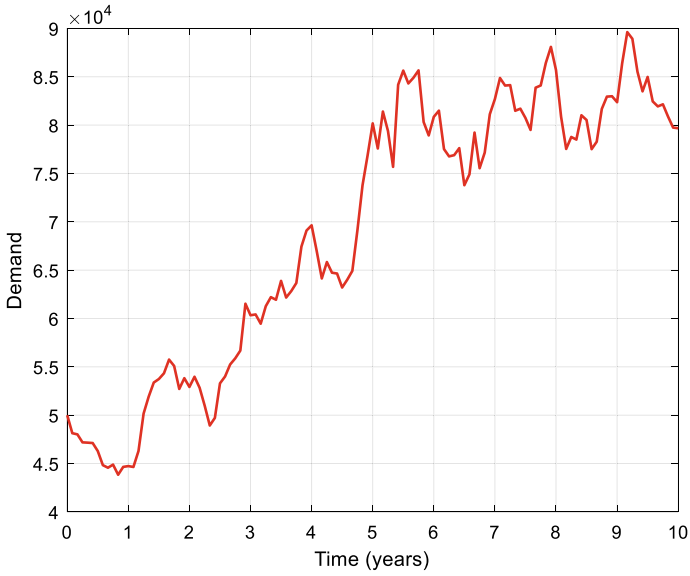


Fig. 96.2 Simulation example of demand model

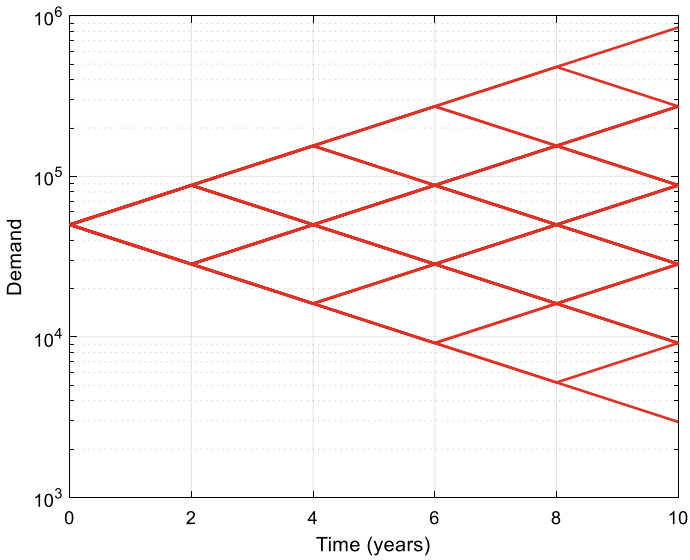


Fig. 96.3 Binomial tree of demand model

The higher t is, the smaller the cost for deploying a new stage is in terms of present value. Consequently, the first economic advantage of staged deployment is that it spreads expenditures in time.

The second mechanism is that the stages are deployed with respect to market conditions. If the market conditions are unfavorable, there is no need to deploy additional capacity. Expenditures are kept low to avoid economic failure [33–35]. On the other hand, if demand is large enough and revenues realized are sufficient, the capacity can be increased [36, 37]. The economic risks are considerably decreased with this approach since stages can be deployed as soon as they can be afforded and when the market conditions are good.

Real Option Model of Staged Deployment. Assumed that X is the revenue cash flow per year which satisfies the Geometric Brownian Motion, $C(t)$ is cost of the t^{th} year, N is the lifetime. The discount value of the revenue cash flow during the lifetime N is given by Eq. (96.9)

$$E\left(\sum_{t=1}^N X e^{-\mu t}\right) = \sum_{t=1}^N E(X) e^{-\mu t} \tag{96.9}$$

According to the characteristic of the GBM

$$\sum_{t=1}^N E(X) e^{-\mu t} = \sum_{t=1}^N X_0 e^{\alpha} e^{-\mu t} = X_0 \sum_{t=1}^N e^{-\delta t} \tag{96.10}$$

Assumed that $V(X)$ is the discount value of net cash flow, we can get the following function.

$$V(X) = X(1 - \tau) \sum_{t=1}^N e^{-\delta t} - (1 - \tau) \sum_{t=1}^N C(t) e^{-\mu t} + \tau \frac{I_1 + I_2}{N} \sum_{t=1}^N e^{-\mu t} \tag{96.11}$$

Let $a = (1 - \tau) \sum_{t=1}^N e^{-\delta t}$, $b = (1 - \tau) \sum_{t=1}^N C(t) e^{-\mu t} - \tau \frac{I_1 + I_2}{N} \sum_{t=1}^N e^{-\mu t}$, the function can be represented as

$$V(X) = aX - b \tag{96.12}$$

Introduce the parameter $A(X)$, let $A(X) = aX$, according to the demonstration above, we can know that $A(X)$ is the discount value of cash flow.

Ito's Lemma: if x is the Ito process and F is the differentiable function, the Ito's differential equation is given by Eq. (96.13)

$$dF = \frac{\partial F}{\partial t} dt + \frac{\partial F}{\partial x} dx + \frac{1}{2} \frac{\partial^2 F}{\partial x^2} (dx)^2 \tag{96.13}$$

Substituting $dx = a(x, t)dt + b(x, t)dz$ into Eq. (96.13), we can get this following form

$$dF = \left[\frac{\partial F}{\partial t} dt + a(x, t) \frac{\partial F}{\partial x} + \frac{1}{2} b^2(x, t) \frac{\partial^2 F}{\partial x^2} \right] dt + b(x, t) \frac{\partial F}{\partial x} dz \tag{96.14}$$

According to Ito's Lemma, $A(X)$ could be represented as

$$dA = \left(\frac{\partial A}{\partial t} dt + \alpha X \frac{\partial A}{\partial X} + \frac{1}{2} \sigma^2 X^2 \frac{\partial^2 A}{\partial X^2} \right) dt + \sigma X \frac{\partial A}{\partial X} dz \tag{96.15}$$

Substituting $\frac{\partial A}{\partial X} = a, \frac{\partial^2 A}{\partial X^2} = 0, \frac{\partial A}{\partial t} = 0$ into Eq. (96.15), we can get the equation

$$dA = \alpha a X dt + \sigma a X dz = \alpha A dt + \sigma A dz \tag{96.16}$$

The Option Value of Second Staged Deployment. Consider the following investment portfolio: $F(A)$ is the value of holding option, the value of the investment portfolio is $\Phi = F(A) - nA$, during the interval dt , the total return of the portfolio is $dF - ndA - n\delta A dt$.

According to the Ito's Lemma, dF satisfies the following form

$$dF = \frac{\partial F}{\partial t} dt + \frac{\partial F}{\partial A} dA + \frac{1}{2} \frac{\partial^2 F}{\partial A^2} (dA)^2 \tag{96.17}$$

Substituting $(dA)^2 = \sigma^2 A^2 dt$ into Eq. (96.17)

$$dF = \frac{\partial F}{\partial t} dt + \frac{\partial F}{\partial A} dA + \frac{1}{2} \sigma^2 A^2 \frac{\partial^2 F}{\partial A^2} dt \tag{96.18}$$

So we can get the form of the portfolio return

$$\frac{\partial F}{\partial t} dt + \frac{\partial F}{\partial A} dA + \frac{1}{2} \sigma^2 A^2 \frac{\partial^2 F}{\partial A^2} dt - ndA - n\delta A dt \tag{96.19}$$

Because the return is risk-neutral

$$r\Phi dt = r[F(A) - nA] = \frac{\partial F}{\partial t} dt + \frac{\partial F}{\partial A} dA + \frac{1}{2}\sigma^2 A^2 \frac{\partial^2 F}{\partial A^2} dt - ndA - n\delta A dt \tag{96.20}$$

Select $n = \frac{\partial F}{\partial A}$, Eq. (96.20) could be represented as

$$\frac{1}{2}\sigma^2 A^2 \frac{\partial^2 F}{\partial A^2} + (r - \delta)A \frac{\partial F}{\partial A} - rF + \frac{\partial F}{\partial t} = 0 \tag{96.21}$$

The boundary conditions need to be satisfied are

$$\begin{aligned} F(A, T_2) &= \max\{A - b - I_2; 0\} \\ F(0, T_2) &= 0 \end{aligned} \tag{96.22}$$

Accordinging the derivation all above, the option value of second staged deployment is

$$\begin{aligned} F(A, t) &= Ae^{-\delta T_2} N(d_1) - (b + I_2)e^{-rT_2} N(d_2) \\ d_1 &= \frac{\ln \frac{A}{b+I_2} + \left(r - \delta + \frac{\sigma^2}{2}\right)T_2}{\sigma \sqrt{T_2}} \\ d_2 &= d_1 - \sigma \sqrt{T_2} \end{aligned} \tag{96.23}$$

$N(X)$ is standard normal distribution function.

The Option Value of First Staged Deployment. Similar to second staged deployment, the option of first staged deployment also satisfies the Eq. (96.21), so we can get the option price equation

$$\begin{aligned} F_{co}(A, 0) &= Ae^{-\delta T_2} M\left(h_1, k_1; \sqrt{\frac{T_1}{T_2}}\right) - (b + I_2)e^{-rT_2} M\left(h_2, k_2; \sqrt{\frac{T_1}{T_2}}\right) \\ &\quad - (b + I_1)e^{-rT_1} N(h_2) \end{aligned} \tag{96.24}$$

With the following parameters

$$\begin{aligned}
 h_1 &= \frac{\ln \frac{A}{A^*} + \left(r - \delta + \frac{\sigma^2}{2}\right)T_1}{\sigma \sqrt{T_1}} \\
 h_2 &= h_1 - \sigma \sqrt{T_1} \\
 k_1 &= \frac{\ln \frac{A}{b+l_2} + \left(r - \delta + \frac{\sigma^2}{2}\right)T_2}{\sigma \sqrt{T_2}} \\
 k_2 &= k_1 - \sigma \sqrt{T_2}
 \end{aligned}
 \tag{96.25}$$

96.4 Scenarios Simulation

Assumed that the lifetime $T = 10$ years, exercise price is 100, after T the expected return is 125, the option value can be plotted as Fig. 96.4.

According to the figure, we could know that when the volatility tends to zero, the uncertainty of the revenue is small, the value of option increases as the volatility.

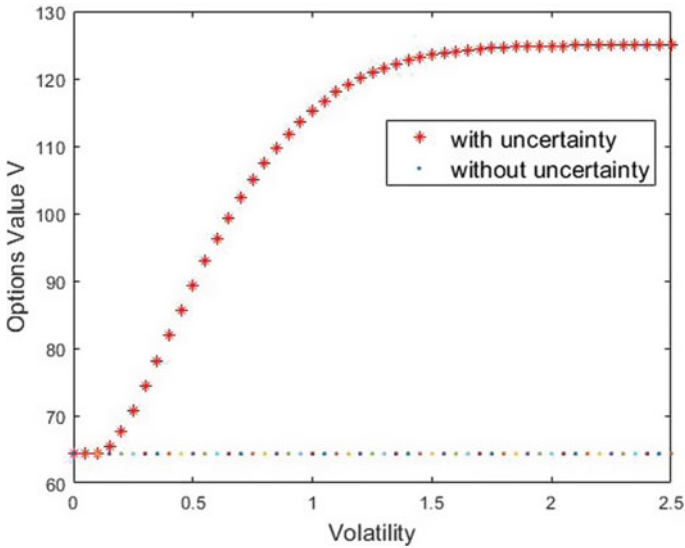


Fig. 96.4 The value of real option

Considering different values of benefit-cost ratio, the changes of option value and flexibility value as volatility change are plotted as Figs. 96.5 and 96.6.

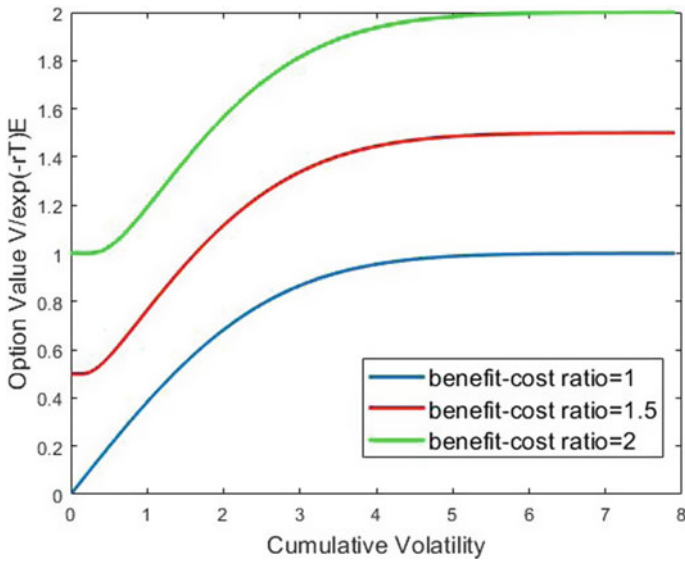


Fig. 96.5 The relationship of volatility and option value

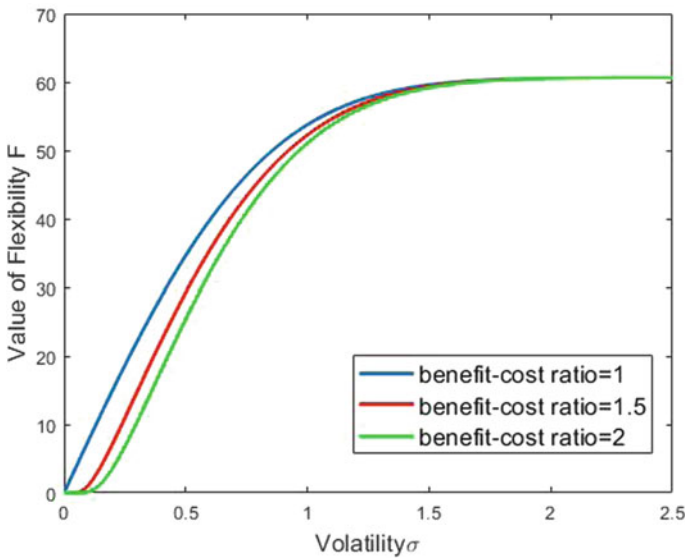


Fig. 96.6 The relationship of volatility and flexibility value

96.5 Conclusion

This paper demonstrates the option value of staged deployment for the communication satellite constellation. Meanwhile, this paper also introduces the option price equation deducing. Through this work, the value of flexibility in the large engineering systems is demonstrated. For the mega-constellations, with the fact of long lifetime and huge development cost, the staged deployment strategy should be adapted in order to avoid the economic failure that Iridium and Globalstar have ever been against. Applying the option pricing equations, the advantages of staged-deployment are analyzed that could bring positive revenues for the systems through the mathematic simulations. In the future work, the more accurate system models will be formed and the value will be estimated more practice significance.

References

1. Khaturia, M., Jha, P., Karandikar, A.: Connecting the unconnected toward frugal 5G network architecture and standardization. *IEEE Commun. Stand. Mag.* **4**(2), 64–71 (2020)
2. Huang, C.: Holographic MIMO surface for 6G wireless networks: opportunities, challenges and trends. *IEEE Wirel. Commun.* **27**(5), 118–125 (2020)
3. Oughton, E., Lehr, E.: Next-G wireless: learning from 5G techno-economics to inform next generation wireless technologies. *Soc. Sci. Res. Netw.* **36**(1), 12–43 (2021)
4. Maral, G., Bousquet, M.: Satellite Communications systems: systems, techniques and technology. *Electron. Radio Eng. J. Inst.* **56**(8), 9–28 (2002)
5. Lorenzo, O., Alessandro, F.: Large constellations assessment and optimization in LEO space debris environment. *Adv. Space Res.* **65**(1), 351–363 (2019)
6. Pauline, J., Koki, H.: Optimal satellite constellation spare strategy using multi-echelon inventory control. *J. Spacecr. Rocket.* **56**(5), 1449–1461 (2019)
7. Ferringer, M.P., Spencer, D.B.: Satellite constellation design tradeoffs using multiple-objective evolutionary computation. *J. Spacecr. Rocket.* **43**(6), 1404–1411 (2012)
8. Weck, O.L.D., Neufville, R.D., Chaize, M.: Staged deployment of communications satellite constellations in low earth orbit. *J. Aerosp. Comput. Inf. Commun.* **5**(1), 119–135 (2004)
9. Sung, W., Sangtae, K., Olivier, D.: Optimization of reconfigurable satellite constellations using simulated annealing and genetic algorithm. *Sensors* **765**(19), 23–52 (2019)
10. Springmann, P.N., De Weck, O.L.: Parametric scaling model for non-geosynchronous communications satellites. *J. Spacecr. Rocket.* **41**(3), 472–477 (2015)
11. Weck, O.D., Zhang, D.D., Jilla, C.: Architecture trade methodology for LEO personal communication systems. *Montreal* **3**(1), 23–56 (2002)
12. Richard, K.: Stochastic inventory control modeling for satellite constellations. *J. Spacecr. Rocket.* **53**(6), 614–620 (2020)
13. Cary, C.G.: Cost per billable minute metric for comparing satellite systems. *J. Spacecr. Rocket.* **34**(6), 837–847 (1997)
14. Chaudhry, A., Yanikomeroğlu, H.: Laser intersatellite links in a starlink constellation: a classification and analysis. *IEEE Veh. Technol. Mag.* **16**(2), 48–56 (2021)
15. Pratt, S.R., Raines, R.A., Fossa, C.E., et al.: An operational and performance overview of the iridium low earth orbit satellite system. *IEEE Commun. Surv. Tutor.* **2**(2), 2–10 (1999)
16. Shaw, G.B., Hastings, D.E.: A generalized analysis methodology for distributed satellite systems. *Mission. Des. Implement. Satell. Constel.* **94**(4), 33–49 (1998)

17. Panggau, Y., Asvial, M.: Analysis of satellite broadband access implementation in Indonesia using costing methodology. In: International Conference on Control, Electronics, Renewable Energy and Communications, pp. 30–35. IEEE, Bandung, Indonesia (2021)
18. Baldesarra, Mark, Miller, David W.: A decision-making framework to determine the value of serviceability in space telescopes. *Proc. Spie.* **35**(2), 6687–6699 (2007)
19. Lamassoure, E.S.: A framework to account for flexibility in modeling the value of on-orbit servicing for space systems. Master's Thesis MIT Dep. Aeronaut. Astronaut. **14**(2), 26–39 (2001)
20. Chaize, M.: Enhancing the economics of communication satellites via orbital reconfigurations and staged deployment. *Mass. Inst. Technol.* **1**(1), 25–52 (2003)
21. Liu, C., Yue, X., Shi, K.: *Spacecraft Attitude Control: A Linear Matrix Inequality Approach*. Elsevier/Science Press, Amsterdam (2022)
22. Markus, G.: Revenue management and resource allocation for communication satellite operators. Massachusetts Institute of Technology (2020)
23. Yoshio, M.: Option pricing in incomplete markets. *Working Papers* **83**(24), 838–840 (2006)
24. Cox, J.C., Ross, S.A., Rubinstein, M.: Option pricing: a simplified approach. *Journal of Financial Economics* **7**(3), 229–263 (1979)
25. Garleanu, N., Pedersen, L.H., Potoshman, A.M.: Demand-based option pricing. Social Science Electronic Publishing (2006)
26. Ron Adner, D.A.L.: What is not a real option: considering boundaries for the application of real options to business strategy. *The Academy of Management Review* (2004)
27. Yeo, K.T., Qiu, F.: The value of management flexibility—a real option approach to investment evaluation. *Int. J. Proj. Manag.* **21**(4), 243–250 (2012)
28. Ding, S., Wang, L., Li, S.: The investment-uncertainty relationship in a real option model. In: International Conference on Business Intelligence and Financial Engineering. IEEE, Beijing **24**(2), 223–240 (2009)
29. Gamba, A., Fusari, N.: Valuing modularity as a real option. *Manag. Sci.* **55**(11), 99–110 (2006)
30. Vonnegut, A.: Real option theories and investment in emerging economies. *Emerg. Mark. Rev.* **1**(1), 82–100 (2000)
31. Ting, S.H.M., Ewald, C.O., Wang, W.K.: On the investment-uncertainty relationship in a real option model with stochastic volatility. *Math. Soc. Sci.* **66**(1), 22–32 (2013)
32. Padhy, R.K., Sahu, S.: A real option based six sigma project evaluation and selection model. *Int. J. Proj. Manag.* **29**(8), 1091–1102 (2011)
33. Cardin, M.A., De Neufville, R., Geltner, D.M.: Design catalogs: a systematic approach to design and value flexibility in engineering systems. *Syst. Eng.* **18**(5), 453–471 (2016)
34. Saleh, J.H., Lamassoure, E., Hastings, D.E.: Space systems flexibility provided by on-orbit servicing. *J. Spacecr. Rocket.* **39**(4), 551–560 (2002)
35. Lafleur, J.M., Saleh, J.H.: Survey of intra- and inter-mission flexibility in space exploration systems. *Acta Astronaut.* **67**(2), 97–107 (2010)
36. Lafleur, J.M.: A Markovian state-space framework for integrating flexibility into space system design decisions. *Dissertations and Theses Gradworks* (2011)
37. Sitterle, V.B., Freeman, D.F., Goerger, S.R., et al.: Systems engineering resiliency: guiding trade-space exploration within an engineered resilient systems context. *Procedia Comput. Sci.* **44**(1), 649–658 (2015)

Chapter 97

Multiphase Flow Model of Gas Hydrate Production Wellbore Based on Double-Layer Continuous Pipe



Geng Zhang, Jun Li, Hongwei Yang, Gonghui Liu, Hui Zhang, Honglin Huang, Jintao An, Wang Chen, and Chao Chen

Abstract In order to research the hydrate decomposition behaviors and multiphase flow characteristics during hydrate mining, a full transient non-isothermal gas-liquid-solid multiphase flow model was established. The model considered the heat and mass transfer due to hydrate phase transition. The calculated results of the model are in good agreement with the measured data of MWD. The model is used to analyze the changes of wellbore temperature and pressure, hydrate decomposition rate, and the volume fraction of each phase over time during the hydrate particles transportation. The numerical simulation results show that: within 2 h before mining, the hydrate decomposition rate is relatively slow, and the volume fraction of each phase in the wellbore changes little; with the increase of time, the volume fraction of each phase in the wellbore varies significantly; it arrives stable state after about 5 h of mining. Meanwhile, the gas volume fraction of the wellhead reaches about 40%. In addition, at the position of the downhole lift pump, the solid-liquid volume fractions both undergo significant mutations. These research results have a particular reference value for the in-depth understanding of the behavior of multiphase flow in hydrate mining.

Keywords Natural gas hydrate · Multiphase flow model · Hydrate decomposition rate · Double-layer continuous pipe · Phase volume fraction

G. Zhang · J. Li (✉) · H. Yang · G. Liu · H. Zhang · J. An · W. Chen · C. Chen
China University of Petroleum-Beijing, Changping, Beijing 102200, China
e-mail: lijun446@vip.163.com

J. Li
China University of Petroleum-Beijing at Karamay, Karamay 834000, China

H. Huang
CNOOC China Limited, Hainan Branch, Haikou 570100, China

97.1 Introduction

Natural gas hydrate (NGH), commonly known as “combustible ice”, is a new type of clean and pollution-free energy. It has the characteristics of wide distribution, high calorific value and high density. At present, hydrate resources found worldwide are mainly stored in polar sandstones and Marine sandstones. This kind of hydrate has good sealing property and can be exploited by conventional mining technology. However, metastable nature gas hydrates stored within a few hundred meters of the seabed have the characteristics of shallow burial depth, no dense cap, loose deposit, low degree of cementation, easy to break and so on. If conventional mining techniques (such as depressurization) are used, it will directly lead to a large amount of decomposition and gasification of hydrates, and then release into the seawater. This will not only cause a waste of resources, but also environmental pollution and damage [1, 2]. Therefore, new mining methods need to be explored.

In response to this challenging problem, Zhou et al. [3–5] proposed a method for mining Marine surface gas hydrate resources through solid fluidization. The basic idea of this method is to crush the deposits containing gas hydrate into small particles, which are treated through the mechanical mining and fluidization process of secondary crushing. And then the hydrate particles are mixed with seawater and piped to an offshore platform for subsequent treatment.

Combined with solid fluidization and the realization of a double gradient through the use of double-walled drill pipe, Wang et al. [6–10] proposed a new method of hydrate mining with double-layer continuous tube. The use of double-layer continuous tube can not only solve the problem of safe drilling in leaky production zone and loose seabed surface, but also broaden the field that conventional drilling technology cannot cover, and ensure the safety of hydrate exploitation. The flow behavior of drilling fluid is used to explain the main flow of the new method (see Fig. 97.1):

- Be pumped into the annulus of double-layer continuous tube by the platform drilling pump through the injection head.
- Passes through a bridge to the inner tube and then drives the turbo motor and downhole lift pump.
- Enters the annulus through the bit water hole to carry cuttings and hydrate slurry through the return hole into the downhole tool annulus.
- Be lifted by downhole pump and returned to the platform processing system after entering the double-layer tube through the bridge channel.

However, in the process of upward transport of hydrate slurry, decomposition will occur, resulting in the wellbore flow pattern from solid-liquid two-phase flow to a complex gas-liquid-solid three-phase flow. At the same time, because the technology is still in the initial stage and the basic theories in all aspects are not mature, there are few studies on the hydrate decomposition law and wellbore multiphase flow law in the process of transportation. Therefore, in this paper, the gas-liquid-solid multiphase transient flow model of wellbore considering hydrate phase transition is established to analyze the hydrate decomposition law and wellbore multiphase

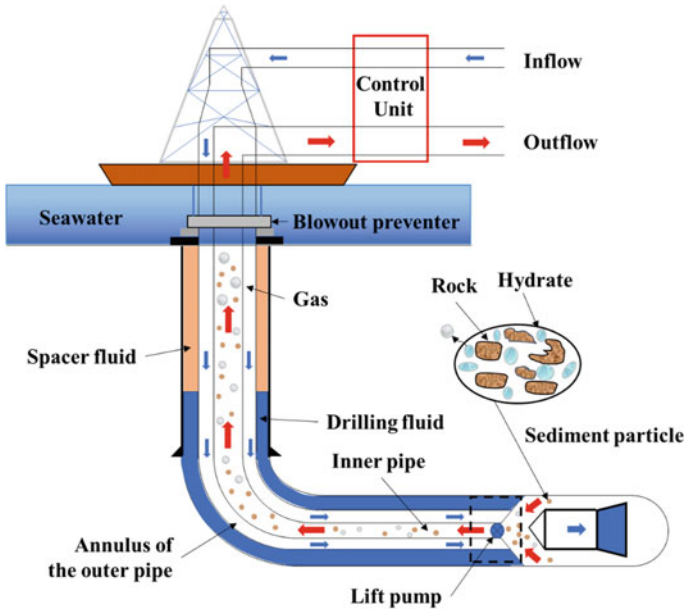


Fig. 97.1 Schematic diagram of hydrate exploitation based on double-layer continuous pipe

flow characteristics during the transportation process. This will provide a theoretical reference for the safe and efficient exploitation of Marine shallow gas hydrate.

97.2 Wellbore Multiphase Flow Model

Scholars have carried out a lot of research on multiphase flow in wellbore. Most of them are based on steady-state flow theory, and have developed three types of multiphase flow models, including homogeneous flow model, split phase flow model and drift flow model, by using laboratory test and field test data and combining with empirical or semi-empirical formulas of multiphase flow characteristic parameters of wellbore under different flow patterns [11–14]. However, researches on wellbore multiphase flow model mainly focus on managed pressure drilling, underbalanced drilling, well control and other fields [15–19], while there are few studies on multiphase flow during hydrate formation drilling [20–22]. Slurry transport is a complex process of multi-phase flow, hydrate phase transition and heat transfer in wellbore. Therefore, a gas-liquid-solid multiphase non-isothermal transient flow model considering hydrate phase transition is established.

97.2.1 Hydrate Decomposition Model

To calculate the hydrate decomposition rate in wellbore, a dynamic hydrate decomposition model under multiphase flow condition was established based on Kim model [23].

$$\dot{m}_h = \left(-\frac{dn_h}{dt} \right)_{T,p} = k_d A_h [f_{eq}(T, p_{eq}) - f(T, p)] \quad (97.1)$$

According to the R-K equation of state, gas fugacity can be calculated by the following equation:

$$\ln(f/p) = Z - 1 - \ln\left(Z - \frac{pb}{RT}\right) - \frac{a}{bRT^{1.5}} \ln\left(1 + \frac{b}{V}\right) \quad (97.2)$$

According to the research of Ryokichi and Ripmeester [24, 25], the decomposition rate constant of hydrate can be expressed as:

$$k_d = \frac{1}{1/k_c^0 e^{(-E_{act}/RT)} + 1/0.347(d_s v_m \rho_m / \mu_m)^{0.62} [\mu_m / (\rho_m D_{AB})]^{1/3} D_{AB} / d_s} \quad (97.3)$$

97.2.2 Hydraulic Model

The gas-liquid-solid three-phase mass conservation equation considering hydrate phase transition can be expressed as:

$$\begin{cases} \frac{\partial(A\rho_g\alpha_g)}{\partial t} + \frac{\partial(A\rho_g\alpha_g v_g)}{\partial z} = A\alpha_s \dot{m}_g \\ \frac{\partial(A\rho_l\alpha_l)}{\partial t} + \frac{\partial(A\rho_l\alpha_l v_l)}{\partial z} = A\alpha_s \dot{m}_l \\ \frac{\partial(A\rho_s\alpha_s)}{\partial t} + \frac{\partial(A\rho_s\alpha_s v_s)}{\partial z} = q_s - A\alpha_s \dot{m}_h \end{cases} \quad (97.4)$$

The gas-liquid-solid three-phase momentum conservation equation considering the pressure drop of downhole lifting pump can be expressed as:

$$\begin{aligned} & \frac{\partial}{\partial t} \sum_{m=g,l,s} (\rho_m \alpha_m v_m A) + \frac{\partial}{\partial z} \sum_{m=g,l,g} (\rho_m \alpha_m v_m^2 A) + \sum_{m=g,l,s} (\rho_m \alpha_m) A g \sin\theta \\ & + \frac{\partial(pA)}{\partial z} + \frac{\partial(p_f A)}{\partial z} + (q_s v_s + q_l v_l) + (\dot{m}_g v_g + \dot{m}_l v_l - \dot{m}_h v_s) = 0 \end{aligned} \tag{97.5}$$

97.2.3 Wellbore Heat Transfer Model

For the upward flow of hydrate slurry in the wellbore, the temperature of the mixed fluid in the wellbore depends on the following processes: (1) heat conduction along the axial direction with fluid movement; (2) Heat exchange between fluid and tube wall; (3) Heat absorption from hydrate decomposition. Therefore, the energy conservation equation of hydrate slurry in wellbore can be expressed as:

$$\begin{aligned} & \frac{\partial}{\partial t} \sum_{m=g,l,s} \left[\rho_m \alpha_m \left(u_m + \frac{1}{2} v_m^2 \right) \right] = \frac{\partial}{\partial z} \sum_{m=g,l,s} \left(\rho_m \alpha_m v_m \left(u_m + \frac{p}{\rho_m} + \frac{1}{2} v_m^2 \right) \right) + \\ & \sum_{m=g,l,s} (\rho_m \alpha_m v_m g \sin\theta) + \frac{Q_{total}}{A} + \sum_{m=g,l,s} \dot{H}_m - \alpha_s \phi \Gamma_h \frac{\rho_h}{M_h} \Delta H_h \end{aligned} \tag{97.6}$$

97.2.4 Auxiliary Equation

Because the heat exchange rate between the mixed fluid and the surrounding environment is dynamic, this point is often ignored in the previous calculation models of non-isothermal multiphase flow. Here, the Nusselt number calculation model established by Gao et al. [26] under bubble flow condition is adopted.

$$Nu = 0.01215 Re^{0.7922} Pr^{0.3} C_T (1 - 0.30577 \alpha_g^{-0.16578}) \tag{97.7}$$

To solve the complex multiphase flow problem, Zuber et al. [27] established a drift flow model considering the phase slip effect. Compared with the homogeneous flow model and the split-phase flow model, the drift flow model is more consistent with the actual flow law and the calculation is simpler. According to the definition of drift flow, the actual velocity of gas phase and solid phase is described as:

$$v_g = c_g v_m + v_{gr} \tag{97.8}$$

$$v_s = c_s v_f - v_{sr} \quad (97.9)$$

The expression of gas distribution coefficient (c_g) is:

$$c_g = \frac{A_e}{1 + (A_e - 1)\gamma^2} \quad (97.10)$$

The expression of gas slip velocity (v_{gr}) is:

$$v_{gr} = \frac{c_g v_c (1 - \alpha_g c_g) K(\alpha_g)}{1 - \alpha_g c_g \left[1 - (\rho_g / \rho_l)^{1/2} \right]} (\cos \theta)^{1/2} (1 + \sin \theta)^2 \quad (97.11)$$

When the distribution coefficient (c_s) of the solid phase is 1, the solid phase sedimentation velocity (v_s) is:

$$v_{sr} = 0.223 \frac{e^{5.03\varphi} \mu_{m'}}{\rho_m' d_s} \sin \theta \left[\sqrt{1 + 0.399g \frac{(\rho_s - \rho_m') \rho_m' d_s^3}{e^{5.03\varphi} \mu_m'^2}} - 1 \right] \quad (97.12)$$

The phase equilibrium temperature in the flow process was calculated by the model established by Dickens and Quinby [28].

$$\frac{1}{T_{eq}} = 3.79 \times 10^{-3} - 2.83 \times 10^{-4} \log p_{eq} \quad (97.13)$$

The downhole lift pump is the key to hydrate exploitation with double-layer continuous tube, and the downhole lift pressure produced by the pump has a crucial effect on the transport efficiency of hydrate slurry. In this paper, the relationship between downhole lifting pressure drop and pump outlet flow rate is obtained by regression of the experimental test data of the downhole lifting pump system.

$$\Delta p = a_0 + a_1 \cos(\omega Q) + b_1 \sin(\omega Q) + a_2 \cos(2\omega Q) + b_2 \sin(2\omega Q) \quad (97.14)$$

When the simulation calculation is carried out, the pump inlet displacement is set to 36 m³/h. The coefficients of the regression model are:

$$\begin{cases} a_0 = 2.09 & a_1 = 1.32 & a_2 = -0.20 \\ b_1 = -0.92 & b_2 = -0.73 & \omega = 0.05 \end{cases} \quad (97.15)$$

97.3 Model Solving and Verification

The governing equation of the model is discretized by a fully implicit difference scheme. Firstly, the governing equations of all the internal nodes in the full computing region are discretized. Then, the discrete equations of the gas-liquid-solid multiphase flow model can be constructed by introducing the boundary conditions. Finally, the equations can be solved by Gauss-Selde iteration method.

Since the hydrate mining technology based on double-layer continuous tube has not been applied in the field, there is a lack of measured data to directly verify the developed model. However, a large number of studies have been carried out on the wellbore heat transfer model, which has been verified by field data. Therefore, conventional drilling temperature measurements can be used to verify the model indirectly, while ignoring the effect of the hydrate phase transition, thus ensuring the accuracy and reliability of the model.

In this paper, the measured temperature data of a high temperature and pressure well drilling in South Sea, China were used to verify the developed model. The well is located at a sea level of 23 m, a water depth of 90 m and a temperature gradient of about 0.045 °C/100m. The detail well structure and drilling hydraulic parameters are shown in Tables 97.1 and 97.2.

Figure 97.2 shows the comparison and error analysis between the measured value of MWD and the calculated value of the developed model. It can be seen from the figure that there is a good consistency between them. The overall error is less

Table 97.1 Structural parameters of wellbore

Structure	Casing outer diameter (in)	Casing inner diameter (in)	Depth (m)	Hole size (in)	Well depth (m)
First layer	30	28	185	36	185
Second layer	20	19	945	26	950
Third layer	13 3/8	12 415	2670	17 1/2	2675
Fourth floor	9 5/8	8.535	3345	12 1/4	3350
Fifth floor	–		–	8 3/8	3711

Table 97.2 Hydraulic parameters of drilling

Well depth (m)	Density of drilling fluid (g/cm ³)	Displacement (L/min)	Bit nozzle area (in ²)
113 ~ 185	1.08	5000	2.70
185 ~ 950	1.08	5000	1.59
950 ~ 2675	1.60	3700	1.78
2675 ~ 3350	1.98	2800	1.34
3350 ~ 3711	2.05	1900	1.25

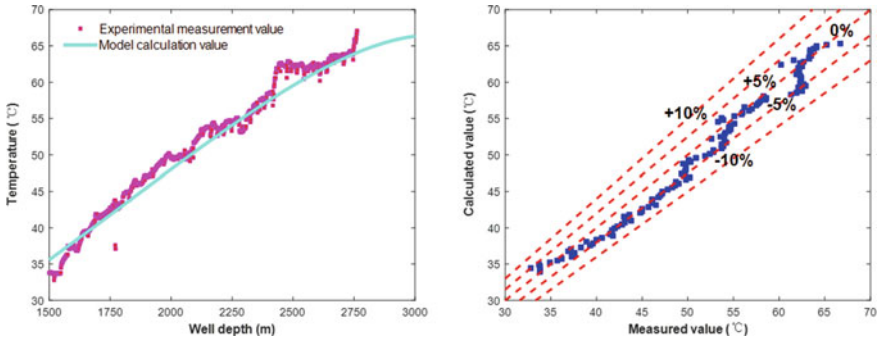


Fig. 97.2 Comparison of calculated values of the model and measured values of MWD

than 10%, and the error is basically controlled within 5%. This indicates that the gas-liquid-solid multiphase non-isothermal transient flow model established in this paper has a certain accuracy.

97.4 Case Analysis

To analyze the multiphase flow law in the process of hydrate exploitation by double-layer continuous tube, a series of numerical simulations were carried out based on the established model to explore the variation law of wellbore temperature pressure, hydrate decomposition rate and volume fraction of each phase with the mining time. Parameters used in numerical simulation are shown in Tables 97.3 and 97.4.

97.4.1 Wellbore Temperature Distribution

Figure 97.3 describes the variation law of wellbore temperature profile and wellhead temperature with the mining time. It can be seen from the figure that, with the increase of production time, the formation heat is continuously carried out by the fluid, and the lower horizontal section and deviated section temperature gradually decreases. However, as the well depth decreases, wellbore temperature changes little in the lower horizontal section and deviated section, and begins to decrease rapidly as it approaches the mud line. At this point, with the decrease of the well depth, the wellbore pressure drops to the critical value of hydrate decomposition, and the hydrate particles in the wellbore begin to decompose.

With the increase of mining time, the wellbore temperature near the wellhead decreases first and then increases. This is mainly due to the increase of heat absorbed by hydrate decomposition along with the time and temperature of exploitation, and

Table 97.3 Basic parameters of simulation

Parameters	Unit	Value	Parameters	Unit	Value
Water depth	m	600	Porosity	dimensionless	0.45
Well depth	m	1500	Hydrate saturation	dimensionless	0.63
Outer double-layer continuous tube outer diameter	m	0.308	Water saturation	dimensionless	0.37
Outer double-layer continuous tube inner diameter	m	0.248	Sea surface temperature	°C	15
Inner double-layer continuous tube outer diameter	m	0.127	Geothermal gradient	°C/m	0.024
Inner double-layer continuous tube inner diameter	m	0.109	Production rate	kg/s	5
Displacement	m ³ /h	36	Cuttings diameter	m	0.003
Injection temperature	°C	20	Wellhead back pressure	MPa	20

Table 97.4 Thermophysical parameters of the medium

Objection	Density	Specific heat capacity	Thermal conductivity
Unit	kg/m ³	J/(kg·°C)	J/(s·m·°C)
Sea water	1025	3890	0.70
Hydrate	900	3100	0.52
Formation	2600	1200	2.10
Pipe string	7800	800	43.00

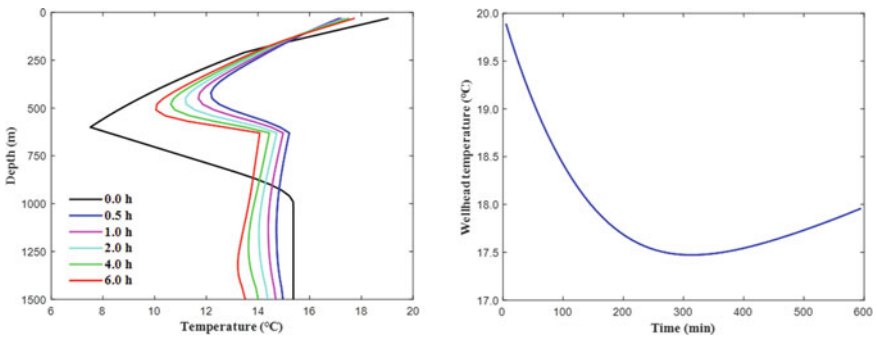


Fig. 97.3 Wellbore temperature varies along well depth or with production time

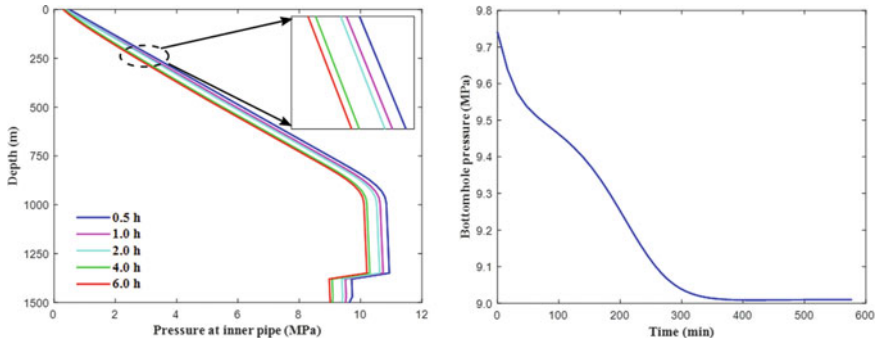


Fig. 97.4 Wellbore pressure varies along well depth or with production time

the gradual decrease of wellbore temperature. However, with the continuous development of production, the volume fraction of gas phase near the wellhead increases, leading to a decrease in the heat conductivity coefficient of the mixed fluid, and then the wellbore temperature rises to a certain extent.

97.4.2 Wellbore Pressure Distribution

Figure 97.4 shows the variation law of pressure in double-layer continuous tube and bottomhole pressure with time during hydrate slurry transportation. As can be seen from the figure, the wellbore pressure gradually decreases with the increase of production time. In addition, it can be found from the change trend of bottomhole pressure that the bottomhole pressure decreases rapidly in the first 5 h of mining, and then gradually begins to stabilize. The main reason for the decrease of pressure in the inner tube is that the density of the mixed fluid decreases due to the gas produced by hydrate decomposition, resulting in the decrease of gravity pressure drop of the mixed fluid. At the same time, as the depth of the well decreases, the inner tube pressure gradually decreases, but the tube pressure in the horizontal section changes little. In addition, after passing through the downhole lift pump, the inner tube pressure increases, which provides some power for the transfer of hydrate slurry.

97.4.3 Hydrate Decomposition Rate

Figure 97.5 describes the variation profile of hydrate decomposition rate along well depth and the variation rule of hydrate decomposition rate at 100 m with time in the process of exploitation. As can be seen from the figure, hydrate particles in the wellbore begin to decompose at about 500 m, and the hydrate decomposition rate increases as the well depth decreases. In addition, the hydrate decomposition rate

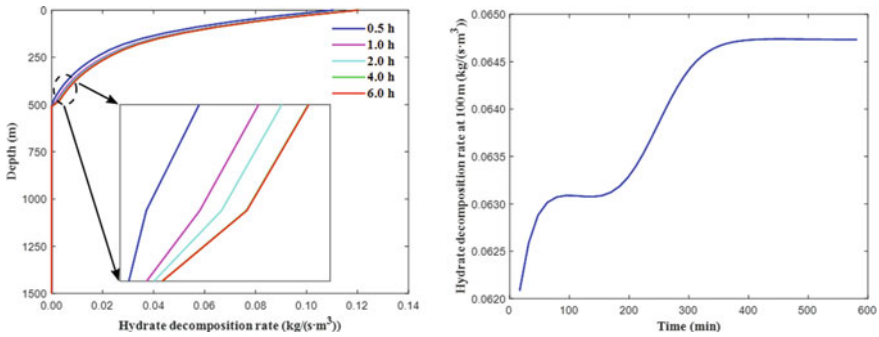


Fig. 97.5 The hydrate decomposition rate varies along well depth or with production time

near the wellhead increases rapidly and then becomes stable with the increase of time. However, there was a short period of slow increase in the initial phase, possibly due to the cooling of the well temperature.

97.4.4 Phase Volume Fraction Distribution

Figure 97.6 describes the variation law of gas phase volume fraction in double-layer continuous tube and gas phase volume fraction at wellhead with time during hydrate exploitation. As can be seen from the figure, with the increase of mining time, the hydrate decomposition amount and rate in the inner tube gradually increase, resulting in the increase of gas phase volume fraction. At the same time, as the depth of the well decreases, the wellbore pressure decreases and the gas expands. In addition, it can be found that the gas phase volume fraction at wellhead changes slowly within first 2 h. With the increase of time, the decomposed gas accumulates to the wellhead continuously, and the gas phase volume fraction at wellhead begins to increase sharply. It reached a stable state about after 5-h production, and the gas phase volume fraction at wellhead reached about 40%.

Figure 97.7 depicts the change of liquid phase volume fraction in the inner tube during hydrate extraction. As can be seen from the figure, the liquid volume fraction in the inner tube increases with increasing well depth. In the lower part of the lift pump, the inner tube is used as the channel for fluid injection, and in the upper part of the lift pump, the inner tube is used as the channel for conveying hydrate slurry. As a result, the liquid fraction of the inner tube at the downhole lift pump mutates. In addition, there is a corresponding abrupt change in the liquid volume fraction of the inner tube at the critical well depth where hydrate begins to decompose. With the increase of mining time, the change of liquid volume fraction in the inner tube is opposite to that of gas volume fraction.

Figure 97.8 describes the variation law of solid phase volume fraction in the inner tube during mining. As can be seen from the figure, the volume fraction of the solid phase in the inner tube increases with increasing well depth. In addition, similar to

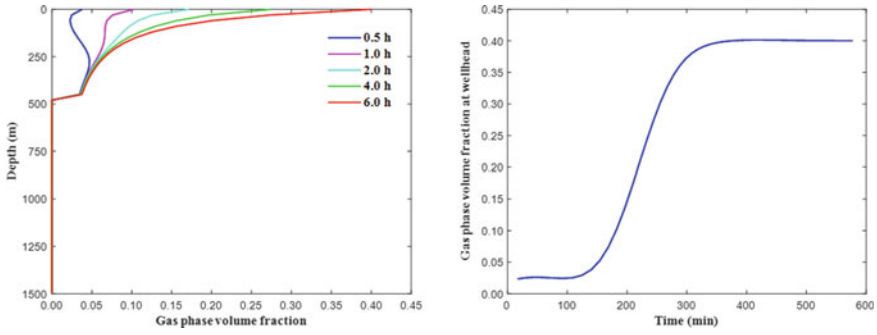


Fig. 97.6 Volume fraction of gas varies along well depth or with production time

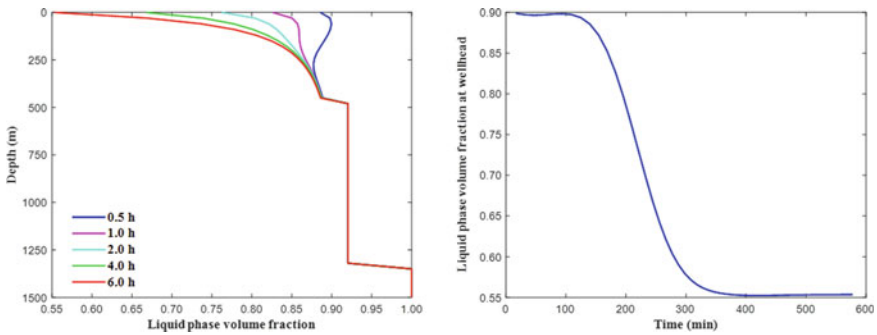


Fig. 97.7 Volume fraction of liquid varies along well depth or with production time

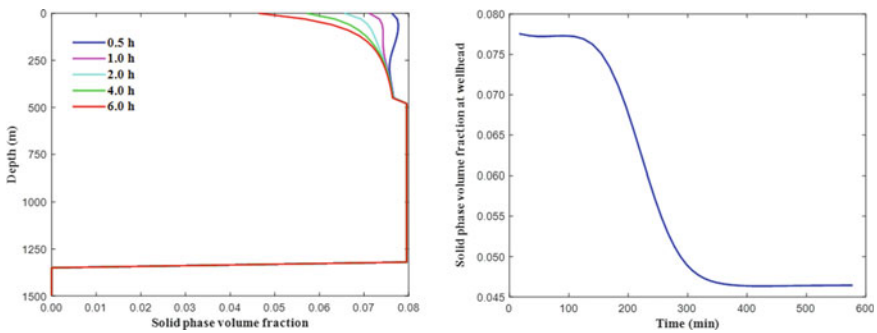


Fig. 97.8 Volume fraction of solid varies along well depth or with production time

the trend of liquid phase volume fraction, solid phase volume fraction at wellhead decreases sharply and then becomes stable with the increase of time. At the same time, the volume fraction of the solid phase in the inner tube changes abruptly due to the change of the flow channel at the location of the downhole lift pump.

97.5 Conclusion

A fully transient non-isothermal gas-liquid-solid multiphase flow model under hydrate phase transition was established, considering the coupling relationship between hydrate phase transition, wellbore multiphase flow and system heat transfer. This model is used to analyze the thermodynamic behavior, hydrate decomposition rate and gas-liquid-solid multiphase flow law in the process of hydrate slurry transportation. The main conclusions are as follows:

- (1) With the increase of mining time, the wellbore temperature in the lower section decreases gradually, while the wellbore temperature in the upper section decreases first and then increases. In the horizontal section and deflection section, the wellbore temperature changes are not significant, and it starts to drop sharply near the mud line and reaches the lowest value.
- (2) When the hydrate slurry is transported upward along the inner tube, the hydrate in the tube reaches the decomposition condition around the mud line. The hydrate decomposition rate and amount increase with the increase of mining time. Correspondingly, the gas phase volume fraction in the wellbore increases, resulting in a gradual decrease in wellbore pressure.
- (3) During the first 2 h of exploitation, the hydrate decomposition rate is relatively slow, and the volume fraction of each phase in the tube changes little. With the increase of time, the volume fraction of each phase in the wellbore changes significantly. It reached a stable state about 5 h after mining. At this time, the volume fraction of well gas phase reaches about 40%.
- (4) In the process of hydrate exploitation, the variation trend of solid and liquid volume fraction are similar. With the increase of well depth, the solid and liquid volume fraction increase gradually. With the increase of time, the solid and liquid integral decrease gradually. In addition, the solid and liquid volume fraction change abruptly at the downhole lift pump location.

Acknowledgements The authors acknowledge the support from the National major scientific research instrument research and development project (52227804), the Youth Program of National Natural Science Foundation of China (52104012), the School-Enterprise Cooperation Project (HX20191203), the Key Projects of Scientific Research Plan in Colleges and Universities of Xinjiang Uygur Autonomous Region (XJEDU20211028), the Introduction of Talents Research Launch Project of the China University of Petroleum-Beijing at Karamay “Wellbore Integrity Analysis and Optimization System Construction of Shale Oil and Gas Well Life Cycle”, and the Strategic Cooperation Technology Projects of CNPC and CUPB (ZLZX2020-01-01).

References

1. Chen, Q., Hu, G.W., Li, Y.L., Wan, Y.Z., Liu, C.L., Wu, N.Y., Liu, Y.: Prospect of new technologies for exploitation of Marine gas hydrate resources. *Mar. Geol. Front.* **454**(09), 46–57 (2020)
2. Sun, Y.B., Cai, F., Li, Q., Yan, G.J., Liang, J., Dong, G., Luo, D., Li, A., Wang, X.X., Zhong, W.J.: Evaluation of natural gas hydrate resources in shallow surface ocean. *Mar. Geol. Front.* **454**(09), 89–95 (2020)
3. Zhao, J.Z., Zhou, S.W., Zhang, L.H., Wu, K.S., Guo, P., Li, Q.P., Fu, Q., Gao, H., Wei, N.: The first global physical simulation experimental systems for the exploitation of marine natural gas hydrates through solid fluidization. *Nat. Gas. Ind.* **37**(9), 15–22 (2017)
4. Zhou, S.W., Zhao, J.Z., Li, Q.P., Chen, W., Zhou, J.L., Wei, N., Guo, P., Sun, W.T.: Optimal design of the engineering parameters for the first global trial production of marine natural gas hydrates through solid fluidization. *Nat. Gas. Ind.* **37**(9), 1–14 (2017)
5. Zhou, S.W., Chen, W., Li, Q.P., Zhou, J.L., Shi, H.S.: Research on the solid fluidization well testing and production for shallow non-diagenetic natural gas hydrate in deep water area. *China Offshore Oil Gas* **29**(4), 1–8 (2017)
6. Wang, G.R., Zhong, L., Liu, Q.Y., Zhou, S.W.: Research on Marine petroleum and hydrate development technology based on dual gradient drilling of double-layer pipe. *Ocean. Eng. Equip. Technol.* **6**(S01), 225–233 (2019)
7. Kang, B., Fan, H.H., Liu, J.G., Wen, Z.X., Deng, S., Wang, S.J., Chen, Y.M., Zhou, Y.J., Feng, G.T., Li, Z.Q. and Yan, X.L.: An efficient gas-lift MPD based on dual-channel drill pipe. In: IADC/SPE Asia Pacific Drilling Technology Conference and Exhibition. OnePetro, 2018
8. Vestavik, O.M., Thorogood, J., Bourdelet, E.: Horizontal drilling with dual channel drill pipe. In: SPE/IADC Drilling Conference and Exhibition, OnePetro, 2017
9. Yang, P., Wang, G.R.: Numerical simulation of transport law of broken particles under solid fluidization jet. *Shipbuild. China* **60**(4), 108–114 (2019)
10. Yang, P., Wang, G.R., Zhou, S.W., Li, Q.P., Zhong, L., Fu, Q., Wang, L.Z., Zhang, C.J.: Development and application of solid fluidization simulation experimental device for non-diagenetic gas hydrate. *Chin. J. Rock Mech. Eng.* **38**(S2), 3512–3519 (2019)
11. Sun, B.J., Wang, Z.Y., Gong, P.B., Song, R.R.: Application of a seven-component multiphase flow model to deepwater well control. *Acta Pet. Sin.* **32**(6), 1042–1049 (2011)
12. Fu, J.H., Su, Y., Jiang, W., Lin, B.: Multiphase flow behavior in deep water drilling: the influence of gas hydrate. *Energy Sci. Eng.* **8**(4), 1386–1403 (2022)
13. Wang, Z., Sun, B.: Annular multiphase flow behavior during deep water drilling and the effect of hydrate phase transition. *Pet. Sci.* **6**(1), 57–63 (2009)
14. Xu, T.T.: Study on gas-liquid-solid three-phase flow mechanism and sand carrying law of water-producing gas Wells. China University of Petroleum (East China) (2018)
15. Wang, Z., Sun, B.: Deepwater gas kick simulation with consideration of the gas hydrate phase transition. *J. Hydrodyn.* **26**(1), 94–103 (2014)
16. Sun, X., Sun, B., Wang, Z.: Wellbore dynamics of kick evolution considering hydrate phase transition on gas bubbles surface during deepwater drilling. In: International Conference on Offshore Mechanics and Arctic Engineering, American Society of Mechanical Engineers, 2017
17. Xu, Y.: Hydrate decomposition mechanism and its influence on drilling safety in deep water drilling. China University of Petroleum (East China) (2017)
18. Zhou, W.J.: Well control technology and parameter calculation of gas hydrate drilling. China University of Petroleum (East China) (2008)
19. Chen, X.: Study on multiphase flow law under the condition of heat and mass transfer between wellbore and formation in underbalanced drilling. Northeast Petroleum University (2015)
20. Fu, W.Q., Wang, Z.Y., Duan, W.G., Zhang, Z.N., Zhang, J.B., Sun, B.J.: Characterizing methane hydrate formation in the non-Newtonian fluid flowing system. *Fuel* **253**, 474–487 (2019)
21. Kvamme, B.: Consistent thermodynamic calculations for hydrate properties and hydrate phase transitions. *J. Chem. Eng. Data* **65**(5), 2872–2893 (2020)

22. Wei, N., Zhao, J.Z., Sun, W.T., Zhou, S.W., Zhang, L.H., Li, Q.P., Fu, Q., Lv, X., Zheng, L.J.: Non-equilibrium multiphase wellbore flow characteristics in solid fluidization exploitation of marine gas hydrate reservoirs. *Nat. Gas Ind. B* **6**(3), 282–292 (2019)
23. Kim, H.C., Bishnoi, P.R., Heidemann, P.A.: Kinetics of methane hydrate decomposition. *Chem. Eng. Sci.* **42**(7), 1645–1653 (1987)
24. Ryokichi, H., Yuki, N., Gen, I., Yosuke, M., Masaki, M.: Gas hydrate decomposition rate in flowing water. *J. Energy Resour. Technol.* **129**(2), 102–106 (2006)
25. Ripmeester, J.A., Alireza, S., Hosseini, B., Alavi, S.: Fundamentals of methane hydrate decomposition. In: *Canadian Unconventional Resources and International Petroleum Conference*, OnePetro, 2010
26. Gao, Y.H., Sun, X.H., Zhao, T.H., Wang, Z.Y., Zhao, X.X., Sun, B.J.: Study on the migration of gas kicks in undulating sections of horizontal wells. *Int. J. Heat Mass Transf.* **127**, 1161–1167 (2018)
27. Zuber, N., Findlay, J.A.: Average volumetric concentration in two phase flow systems. *J. Heat Transfer* **87**(4), 453–468 (1965)
28. Dickens, G.R., Quinby-Hunt, M.S.: Methane hydrate stability in seawater. *Geophys. Res. Lett.* **21**(19), 2115–2118 (1994)

Chapter 98

Multiphase Flow Behaviors and Wellhead Backpressure Responses During Managed Pressure Drilling Well Control Considering Gas Dissolution



Wang Chen, Jun Li, Hongwei Yang, Geng Zhang, and Honglin Huang

Abstract The managed pressure drilling dynamic control (MPDDC) technology of has the advantages of short control time and no need to shut in the well to deal with the gas influx problem. Based on drift flow model and transient solubility calculation model of gas in oil-based drilling fluid, a multi-phase flow model of MPDDC is established. The accuracy and reliability of the model were verified based on the experimental data of gas kick in oil-based drilling fluid. The simulation results show that the change of wellhead back pressure and bottom hole pressure during MPDDC can be divided into three stages with the upward migration of intrusive gas. The multiphase flow behavior and pressure response characteristics of gas dissolution, wellbore heat transfer and kill rate on dynamic well control of managed pressure drilling are discussed and analyzed. Increase drilling fluid displacement (wellhead back pressure, pit gain) during MPDDC. Faster gas kick can be controlled, helping to reduce maximum wellhead back pressure and maximum pit gain. The research results are helpful to improve the calculation accuracy of wellhead back pressure in well control process and provide engineering guidance for MPDDC technology.

Keywords Gas kick · Managed pressure drilling dynamic control · Gas dissolution · Multiphase flow behaviors

W. Chen · H. Yang · G. Zhang
China University of Petroleum-Beijing, 18 Fuxue Road, Changping District, Beijing, China

J. Li (✉)
China University of Petroleum-Beijing at Karamay, 355 Anding Road, Karamay, Xinjiang, China
e-mail: lijun446@vip.163.com

H. Huang
CNOOC China Limited, Hainan Branch, Haikou 570100, Hainan, China

98.1 Introduction

With the continuous increase of wellbore depth in the process of oil and gas development, deep and ultra-deep drilling is faced with many challenges, including narrow safety density window, difficulty in wellbore pressure control, frequent downhole complications such as overflow and leakage [1]. The managed pressure drilling technology has better adaptability to the formation with narrow safety operation window, such as the formation prone to leakage and overflow [2]. However, despite the use of managed pressure drilling technology, gas kick, overflow and other downhole complications also occur from time to time, such as underbalanced gas kick, gravity displacement gas kick, etc. [3]. When gas kick occurs, it is a basic measure to control wellbore pressure discharge and overflow accurately to ensure drilling safety. Traditional wellbore pressure control methods mainly include driller's method, engineer's method and some other special well killing methods, which are mature in theory and field application [4].

With the development of managed pressure drilling technology, managed pressure drilling dynamic control (MPDDC) technology has become an effective means to deal with small or medium scale gas influx and overflow in recent years. The MPDDC is to achieve a new balance in the bottom-formation pressure system by controlling the wellhead throttling manifold system and completely circulating the formation fluid entering the wellbore out of the wellhead when gas influx is detected without shutting in the well. Compared to conventional well control methods, this dynamic well control method greatly improves drilling efficiency and reduces drilling time.

Study on hydrodynamic model in the process of managed pressure drilling. In 2015, He and Udegbunam respectively proposed a transient multiphase fluid dynamic model during gas kick in managed pressure drilling, considering the dissolution of gas in drilling fluid [2, 5]. In 2016, Ma proposed a new multiphase flow model based on coupled conservation equations of mass, momentum, and energy, combined with appropriate auxiliary models, that can be used to simulate transient multiphase flow behavior in the gas and liquid phases of the wellbore [6]. In 2017, Yin proposed a transient multiphase flow model considering the migration of acid gas in vertical and horizontal Wells to solve the problem of acid gas kick [7]. In 2019, Sun proposed a well control method for managed pressure drilling based on wellbore pressure calculation, which adopted a fully coupled multiphase flow model and considered the coupling effect between reservoir and wellbore, gas solubility in drilling fluid and hydrate phase transition [8].

At present, almost all hydrodynamic models of managed pressure drilling are based on empirical solubility model or flash evaporation model [2, 5–8]. They believed that as long as certain conditions of temperature and pressure were satisfied, the gas would immediately dissolve accordingly. Many scholars have studied the mass transfer rate between gas and oil, which shows that the mass transfer rate between gas and crude oil with high Schmidt number is very slow [9]. Therefore, it is necessary to further develop wellbore multiphase flow behavior and pressure response characteristics in the MPDDC process.

In this paper, a MPDDC multiphase flow model is established based on the drift flow model and the transient dissolution rate of gas in oil-based drilling fluid. The characteristics of gas migration and pressure response during well control are studied in detail. The effects of gas dissolution, wellbore heat transfer and kill rate on wellhead back pressure control are discussed. The research results can provide engineering guidance for the MPDDC technology to solve the problem of early gas kick.

98.2 Model Development

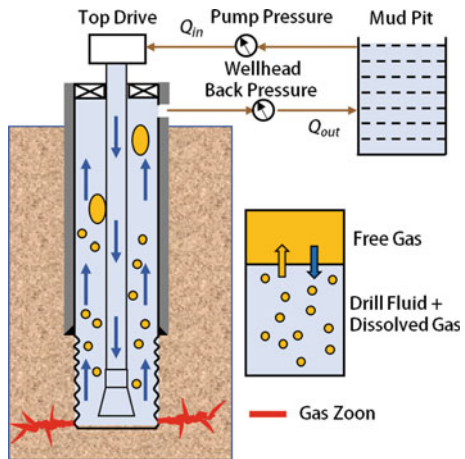
MPDDC has the advantages of simple operation, short control time, and no need to shut in the well to deal with gas influx. The MPDDC process is shown in Fig. 98.1.

When the bit reaches the reservoir, if the wellbore pressure is lower than the formation pore pressure, formation gas will invade the wellbore, resulting in gas kick. With the formation gas invading the wellbore, the mud pool level increases, the outlet velocity increases, and the bottom hole pressure decreases. At some point, surface gas kick detection technology (e.g., incremental mud pool detection or flow difference detection) or real-time bottom-hole pressure monitoring technology (e.g., MWD) or other early gas kick detection technology can identify gas kick and stop it by rapidly increasing wellhead back pressure. After the gas flow stops, the drilling fluid continues to circulate, first moving the gas from the wellbore to the wellhead, and then gradually draining the gas completely out of the wellbore.

In order to establish a multiphase flow model to predict multiphase behavior and pressure response during MPDDC, the main model assumptions are as follows:

- (1) Only one-dimensional flow behavior of fluid in wellbore along the axial direction is considered;

Fig. 98.1 Schematic diagram of MPDDC technology



- (2) In the managed pressure drilling based on oil base drilling fluid, on the one hand, the managed pressure drilling has the ability to identify early gas kick; on the other hand, a large amount of gas is dissolved in the oil base drilling fluid. Therefore, the free gas content in the wellbore is usually not very large, and it is assumed that the gas-liquid two-phase flow in the wellbore is always bubble flow. Flow pattern transition conditions of bubble flow is $\alpha_g < 0.25$ [10];
- (3) Assume that the temperature of the gas is the same as that of the liquid at the same cross section of the wellbore.

98.2.1 Hydrodynamic Model

In the process of gas-liquid two-phase flow in the wellbore, it is assumed that the annulus gas-liquid two-phase flow flows through a static control unit. Considering the phase transformation between free gas and dissolved gas, the mass conservation equation of free gas, drilling fluid and dissolved gas in the control unit is expressed as:

$$\frac{\partial}{\partial t}(A\rho_L\alpha_L) + \frac{\partial}{\partial z}(A\rho_L\alpha_L v_L) = \dot{m}_{g-o} \quad (98.1)$$

$$\frac{\partial}{\partial t}(A\rho_g\alpha_g) + \frac{\partial}{\partial z}(A\rho_g\alpha_g v_g) = \dot{q}_g - \dot{m}_{g-o} \quad (98.2)$$

$$\frac{\partial}{\partial t}(A\rho_L\alpha_L x_{sol}) + \frac{\partial}{\partial z}(A\rho_L\alpha_L x_{sol} v_L) = \dot{m}_{g-o} \quad (98.3)$$

where, ρ is the density, kg/cm^3 ; α is the volume fraction; v is the flow rate, m/s ; \dot{m}_{g-o} is the interphase mass transfer rate, $\text{kg}/(\text{m}\cdot\text{s})$; x_{sol} is the mass fraction of dissolved gas in the drilling fluid; A is the annulus cross-sectional area, m^2 ; t is the time, s ; z is the axial space, m ; the subscripts L , g , o denote the fluid of the drilling mud, the gas, the oil, respectively;

During well control, gas inflow, migration, and expansion will not only affect the rise rate of drilling fluid, resulting in changes in annular friction pressure drop, but also reduce the annulus hydrostatic pressure due to a decrease in the average density of the mixture. To solve the transient multiphase flow model based on the drift flow model, the mixed momentum conservation equation of each component of the multiphase flow is used to solve the model, namely:

$$\begin{aligned} & \frac{\partial}{\partial t} \left(\sum_i A\rho_i\alpha_i v_i \right) + \frac{\partial}{\partial z} \left(\sum_i A\rho_i\alpha_i v_i^2 \right) + \frac{\partial}{\partial z} (AP) \\ & = - \sum_i Af \frac{\rho_i\alpha_i v_i^2}{2d_h} - \sum_i A\rho_i\alpha_i g \sin\theta \quad i = g, L \end{aligned} \quad (98.4)$$

where, P is the wellbore pressure, Pa; f is the friction coefficient; d_h is the equivalent diameter, m; g is the acceleration of gravity, m2/s; θ is the well inclination angle, rad.

98.2.2 Heat Transfer Model

According to the first law of thermodynamics, the two-phase transient heat transfer model of annular air–liquid two-phase flow can be expressed as follows, considering the Joule Thomson effect of gas, heat exchange between fluid in annulus and surrounding environment, and heat convection between formation gas and liquid in intrusive wellbore.

$$\begin{aligned} & \sum_i A\rho_i\alpha_iC_{pi}\left(\frac{\partial T}{\partial t} + v_i\frac{\partial T}{\partial z}\right) - \sum_i A\rho_i\alpha_iC_{pi}C_J\left(\frac{\partial P}{\partial t} + v_i\frac{\partial P}{\partial z}\right) \\ & - \frac{\partial}{\partial t}(AP) + \frac{1}{2}\sum_i\left[\frac{\partial}{\partial t}(A\rho_i\alpha_iv_i^2) + \frac{\partial}{\partial z}(A\rho_i\alpha_iv_i^3)\right] \\ & = Ak_m\left(\frac{\partial^2 T}{\partial r^2} + \frac{1}{r}\frac{\partial T}{\partial r}\right) + \dot{q}_g(\bar{H}_f - H_g) + \sum_i Af\frac{\rho_i\alpha_iv_i^2}{2d_h}v_i - \sum_i A\rho_i\alpha_iv_i g\text{Sin}\theta \end{aligned} \tag{98.5}$$

where, T is the temperature, °C; C_p is the specific heat, J/(kg·°C); C_J is the Joule Thomson effect coefficient; k_m is the thermal conductivity of the mixed fluids, W/(m·K); T_f is the formation temperature, °C; P_f is the formation pressure, Pa; r is the radial space, m.

For a single phase flow area.

$$\begin{aligned} & A\rho_L C_{pL}\left(\frac{\partial T}{\partial t} + v_L\frac{\partial T}{\partial z}\right) - \frac{\partial}{\partial t}(AP) + \frac{1}{2}\left[\frac{\partial}{\partial t}(A\rho_L v_L^2) + \frac{\partial}{\partial z}(A\rho_L v_L^3)\right] \\ & = Ak_L\left(\frac{\partial^2 T}{\partial r^2} + \frac{1}{r}\frac{\partial T}{\partial r}\right) + Af\frac{\rho_L v_L^2}{2d_h}v_L - A\rho_L v_L g\text{Sin}\theta \end{aligned} \tag{98.6}$$

where, k_L is the thermal conductivity of the liquid, W/(m·K).

In addition, the literature is available for transient heat transfer models in stratigraphic regions, thermal and physical parameters of fluids, and convective heat transfer coefficients [11].

98.2.3 Gas Solubility Model

To this end, the interfacial mass transfer theory is adopted here. The upward slip of the gas in the liquid creates a local flow field, as shown in Fig. 98.2.

Diffusions of free gas and dissolved gas on the bubble surface result in dissolution or precipitation of the gas. The direction and rate of gas diffusion are influenced by temperature and pressure, so as the flow regime. Under laminar flow condition, the interaction strength between gas and liquid is weak, and the molecular diffusion mainly occurs at the gas–liquid interface. However, the turbulent flow condition is characterized by intense gas–liquid interaction, and the turbulent diffusion mainly occurs at the gas–liquid interface [12]. Based on the gas diffusion equation on the bubble surface [13], Yang [14] derived the gas diffusion flux at the gas–fluid interface under laminar and turbulent flow, which can well characterize the dynamic gas dissolution process in oil-based drilling fluid. Therefore, Yang’s gas diffusion flux model is employed here to describe the interphase mass transfer rate.

The gas diffusion flux in the laminar flow is:

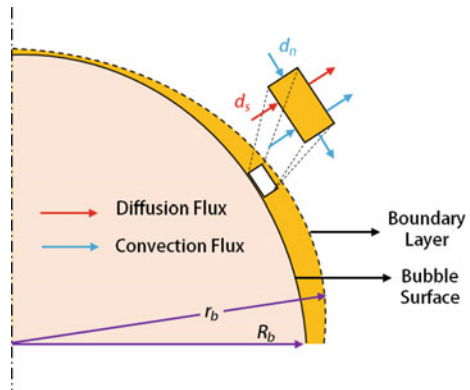
$$J_{g-0}^L = D_{go}^L \left(\frac{\partial C_g}{\partial r_b} \right)_{r_b=R_b} = \frac{4D_{go}(C_{inf} - C_b) \sin \theta_b}{5(\theta_b - \sin \theta_b \cos \theta_b)^{1/3}} \left(\frac{v_\infty}{D_{g0}R_b^2} \right)^{1/3} \quad (98.7)$$

The gas diffusion flux in the turbulent flow is:

$$J_{g-0}^T = D_{go}^T \left(\frac{\partial C_g}{\partial r_b} \right)_{r_b=R_b} = \begin{cases} \sqrt{3/\pi} \beta^{1/2} \varepsilon^{1/6} R_b^{1/6} v_\infty^{1/2} (C_{inf} - C_b) \frac{1 + \cos \theta_b}{\sqrt{2 + \cos \theta_b}} \\ \sqrt{3/\pi} \beta^{1/2} (\varepsilon/\nu_L)^{1/4} R_b^{1/2} v_\infty^{1/2} (C_{inf} - C_b) \frac{1 + \cos \theta_b}{\sqrt{2 + \cos \theta_b}} \end{cases} \quad (98.8)$$

Therefore, the gas–liquid interphase mass transfer rate can be described as:

Fig. 98.2 The local flow field around the upward-sliding bubble



$$\dot{m}_{g-o} = \begin{cases} N_b M_g J_{g-o}^L = \frac{4N_b M_g D_{go} (C_{inf} - C_b) \sin \theta_b}{5(\theta_b - \sin \theta_b \cos \theta_b)^{1/3}} \left(\frac{v_\infty}{D_{go} R_b^2} \right)^{1/3} \\ N_b M_g J_{g-o}^T = \begin{cases} \sqrt{3/\pi} N_b M_g \beta^{1/2} \varepsilon^{1/6} R_b^{1/6} v_\infty^{1/2} \\ (C_{inf} - C_b) \frac{1 + \cos \theta_b}{\sqrt{2 + \cos \theta_b}} \lambda > \lambda_0 \\ \sqrt{3/\pi} N_b M_g \beta^{1/2} (\varepsilon/v_L)^{1/4} R_b^{1/2} v_\infty^{1/2} \\ (C_{inf} - C_b) \frac{1 + \cos \theta_b}{\sqrt{2 + \cos \theta_b}} \lambda < \lambda_0 \end{cases} \end{cases} \quad (98.9)$$

where, J_{g-o}^L is the gas diffusion flux under laminar flow condition, mol/(m²·s); J_{g-o}^T is the gas diffusion flux under turbulent flow condition; mol/(m²·s); M_g is the molar mass, kg/mol; C_g is the gas concentration, mol/m³; C_{inf} is the gas concentration at the gas–liquid interface, mol/m³; C_b is the gas concentration in liquid, mol/m³; θ_b is the angle that deviates from the vertical diameter of the bubble in a clockwise direction, rad; r_b is the radial distance from the bubble center, m; R_b is the radius of the bubble, m; D_{g-o}^L is the molecular gas diffusion coefficient, m²/s; $D_{T go}$ is diffusion coefficient of turbulent flow, m²/s; β is the coefficient; v_L is the kinematic viscosity, m²/s; ζ is the turbulence scale, m; ζ_0 is the Kolmogorov turbulence scale, m; ε is the energy dissipation, J/s; v_∞ is the slip rate, m/s; N_b is the number density of bubbles per volume unit in the wellbore, which can be expressed as:

$$\alpha_g \cdot A \Delta z = N_b \cdot \frac{4}{3} \pi R_b^3 \cdot A \Delta z \quad (98.10)$$

The average radius of bubbles in oil-based drilling fluid can be expressed as [15]:

$$R_b = \frac{\mu_L^{-1/2} v_g^{-10/9} \sigma^{3/5}}{500} \quad (98.11)$$

where, μ_L is the liquid viscosity, Pa s; σ is the gas–liquid surface tension, N/m.

98.2.4 Auxiliary Equation

(1) Interphase slip relation

The drift flow model can well characterize the uneven rate and phase distribution in the multiphase flow. The interphase slip relation can be formulated as:

$$v_g = c_0 v_m + v_\infty \quad (98.13)$$

where, c_0 is the gas distribution coefficient; v_∞ is the gas slip rate, m/s there were many studies on the distribution coefficient and drift flow rate. Shi [16] obtained

continuously varying equations for distribution coefficient c_0 and slip rate v_∞ , which has been widely accepted in multiphase flow calculation. Therefore, Shi's model is used here.

The formula for the gas distribution coefficient c_0 is:

$$c_0 = \frac{A_e}{1 + (A_e - 1)\gamma^2} \tag{98.14}$$

The formula for the gas slip velocity v_∞ is:

$$v_\infty = \frac{c_0 v_c (1 - \alpha_g c_0) K(\alpha_g)}{1 - \alpha_g c_0 \left[1 - \left(\frac{\rho_g}{\rho_L} \right)^{\frac{1}{2}} \right]} (\cos \theta)^{\frac{1}{2}} (1 + \sin \theta)^2 \tag{98.15}$$

where, A_e is the distribution coefficient under the conditions of bubble flow and slug flow; γ is the decreasing term of the profile coefficient; v_c is the characteristic gas velocity, m/s.

(2) Flow friction coefficient

Under the condition of multiphase flow, the circulating pressure loss is closely related to the flow pattern. The cyclic friction under bubble flow condition can be regarded as the cyclic friction of pseudo-steady-state single-phase flow, and the flow friction coefficient is mainly determined by the Reynolds number of miscible fluid [17]:

$$f = \begin{cases} \frac{16}{Re_m} & Re_m \leq 2100 \\ \left[4 \log \left(\frac{\Delta}{3.7065} - \frac{5.0452}{Re_m} \log A \right) \right]^2 & Re_m > 2100 \end{cases} \tag{98.16}$$

Reynolds number in gas-liquid two-phase flow is different from that in single-phase flow. The Reynolds number of a two-phase flow can be expressed as the ratio of the sum of the inertia forces of the phases to the sum of the viscous forces [18]:

$$Re_m = \frac{\rho_g v_g^2 d_h^2 + \rho_L v_L^2 d_h^2}{\mu_g v_g d_h + \mu_L v_L d_h} \tag{98.17}$$

(3) Gas kick rate

When drill bit reaches the reservoir, if the bottom-hole pressure is lower than the formation pressure, the formation gas will enter the wellbore. The gas kick rate of the open hole is [19]:

$$q_g(h_j, t) = \frac{2\pi K_j h_j \left[P_{ej}^2 - P_{bj}^2(t) \right]}{\mu \ln \frac{2.25 K_j t}{r_{wj}^2 \frac{\mu_{gj} c_{tj}}{r_{wj}^2}}} \frac{T_j z_j}{P_{bj} z_{ej} T_{ej}} \rho_{gj} \tag{98.18}$$

where, K is reservoir permeability, D; h is reservoir opening thickness; P_e is reservoir pressure, MPa; P_b is bottom hole pressure, MPa; z is gas compression factor; z_e is gas compression factor under reservoir condition; C_t is the total compressibility, 1/MPa; μ is the viscosity, Pa s; T_e is the reservoir temperature, °C.

(4) Pit gain

During the multiphase flow in oil-based drilling fluid, a portion of the fluid is replaced out of the wellbore by the free gas and the liquid expansion, which results in the variation in the pit gain. The liquid expansion caused by the dissolved gas is usually reflected in the liquid volume coefficient, which can be estimated by the Peng–Robinson gas equation of state. Therefore, the pit gain can be expressed as:

$$V_{pg} = \sum_{j=1}^n V_{pg}(j) = \sum_{j=1}^n [(B_m - B_L)(1 - \alpha_g) + \alpha_g] A_j H_j \tag{98.19}$$

where, V_{pg} is the pit gain, m³; B_{gL} and B_L are the volume coefficient of the mud with and without containing the dissolved gas, respectively; Δz is the length of the opening reservoir, m.

98.2.5 Model Solving

The above transient non-isothermal multiphase flow model is a partial differential form with strong nonlinearity, which is very difficult to solve directly. Therefore, a fully implicit finite difference scheme was adopted to discretize the above governing equation [16]. By solving the discrete model iteratively, the wellbore multiphase flow behavior characteristics under different time and location conditions in the well control process of managed pressure drilling are obtained. The calculation process is shown in Fig. 98.3.

98.3 Model Verification

In this study, the bottom-hole pressure measured by O’ Bryan [20] in the gas kick experiment of oil-based drilling fluid was used to verify the proposed model. O ‘Bryan’s gas kick experiment was conducted in a 1828.8 m offshore test well, which measured and recorded changes in bottom-hole pressure during gas kick. The basic parameters of the experimental well are shown in Table 98.1.

Figure 98.4a shows the bottom-hole pressure measurement results of the experimental well and the bottom-hole pressure change curve calculated by the current model. The experimental process is divided into three stages: (1) cycle gas injection stage; (2) stop the pump stage; (3) cycle exhaust stage. As shown in the figure, the

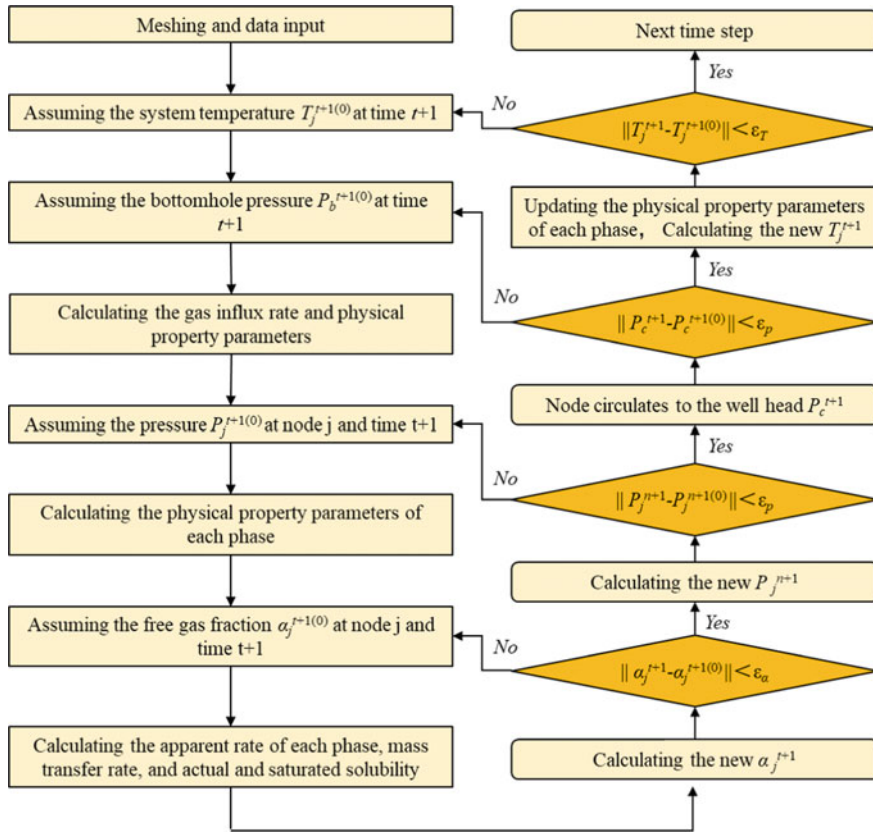


Fig. 98.3 The coupled solution flow of wellbore temperature and pressure under multiphase flow condition

Table 98.1 Basic parameters of experimental well

Parameters	Value	Parameters	Value
Water depth, m	914.4	Well depth, m	1828.8
Drilling fluid density, kg/m ³	982.58	Flow rate, m ³ /s	0.0052
Drilling fluid viscosity, Pa·s	0.022	Outside diameter of pipe, m	0.073
Geothermal gradient, °C	26.7	Borehole diameter, m	0.194
Surface temperature, °C/m	0.0237	Gas injection rate, m ³ /s	0.17

calculation of bottom-hole pressure is in good agreement with the measured data, as heat transfer of wellbore, transient interphase mass transfer and expansion effect of oil-base drilling fluid caused by dissolved gas are considered in the model in this paper. Through the error analysis of the calculation results of the current model and the experimental data (Fig. 98.4b), the error of the calculation results of the model

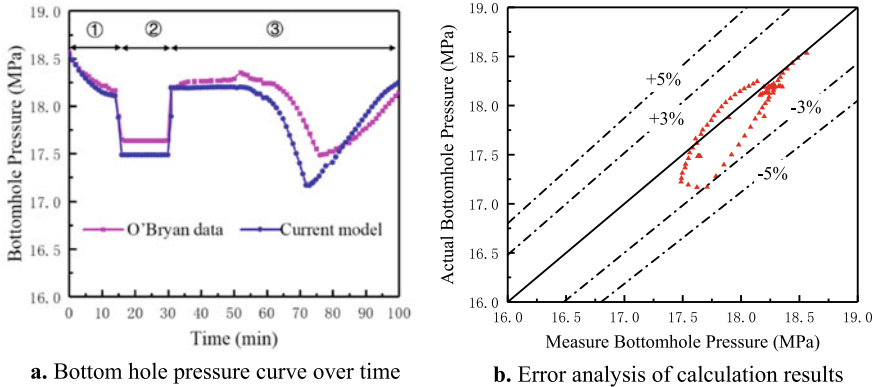


Fig. 98.4 Comparison of experimental results and calculated results

in this paper is less than 5%. Therefore, the accuracy and reliability of the dynamic well control model of managed pressure drilling established in this paper can be guaranteed.

98.4 Results and Discussion

In order to analyze the multiphase flow law and pressure response characteristics in the wellbore during the dynamic well control process of managed pressure drilling, a series of numerical simulations were carried out based on the established model. The effects of gas dissolution, wellbore heat transfer and kill rate on wellbore multiphase behavior during well control are analyzed. The basic parameters used in the simulation are shown in Table 98.2.

Table 98.2 Basic parameters for simulation

Parameters	Value	Parameters	Value
Water depth, m	4500	Drilling fluid thermal conductivity, W/(m·K)	1.02
Drilling fluid density, kg/m ³	1200	Drilling fluid specific heat, J/(kg·°C)	1600
Drilling fluid viscosity, Pa·s	54	Gas thermal conductivity, W/(m·K)	0.03
Flow rate, L/s	30	Gas specific heat, J/(kg·°C)	1012
Inlet temperature, °C	25	Outer diameter of drill string, mm	149.2
Geothermal gradient, °C/100 m	2.4	Inner diameter of casing, mm	244.5
Inner diameter of drill string, mm	127	Drill bit diameter, mm	215.9

98.4.1 Gas Dissolution

(1) Dynamic gas transport

Figure 98.5 shows the distribution of gas volume fraction profiles along the wellbore at different times in the dynamic well control process of managed pressure drilling. After gas kick occurs, due to the density difference between gas and drilling fluid, the gas slippage velocity along the wellbore is higher than the return velocity on drilling fluid, and the gas volume fraction gradually decreases. Because of the high bottom hole pressure, the intrusive gas hardly expands at the bottom hole. When the gas front migrates near the wellhead, the gas expands due to the decrease of wellbore pressure, resulting in the increase of gas volume fraction in the wellbore.

Meanwhile, it can be seen from Fig. 98.5a that gas dissolution has a great impact on gas migration and distribution in the wellbore. The same increment of mud pool is used as the threshold of well gas kick detection. When gas dissolution is not taken into account, the wellhead can detect the overflow 360 s after the occurrence of gas kick at the bottom of the well. At this time, the gas front migrates to 3000 m deep, and the gas content at the bottom of the well is 2%-3%. In the process of controlled pressure circulation exhaust, when the gas migrates to the wellhead, the gas expansion leads to a significant increase in the gas content of the wellbore.

Considering the dissolution of gas in oil-based drilling fluid, gas kick was detected at the wellhead 1438 s after the occurrence of gas kick, as shown in Fig. 98.5b. At this time, the gas front had migrated to the depth of 2340 m. Since most of the gas is dissolved in the drilling fluid, the gas volume fraction in the wellbore is less than 2%, and the gas-liquid two-phase distribution range is about 2100 m. When the gas returns to the wellhead, the decrease of gas solubility and expansion will cause the

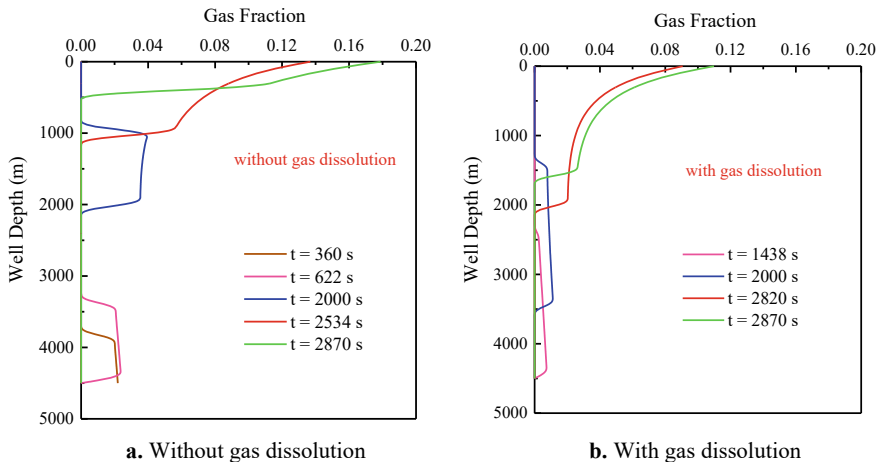


Fig. 98.5 Distribution of gas volume fraction profile along wellbore at different time

gas content of the wellbore to increase dramatically, making the control of wellhead back pressure more difficult.

Therefore, when using oil-based drilling fluid for managed pressure drilling, the occurrence of gas kick is usually hidden and the early kick detection is difficult. When gas kick is detected locally, it is necessary to increase the wellhead back pressure quickly to increase the bottom hole pressure and prevent further gas kick.

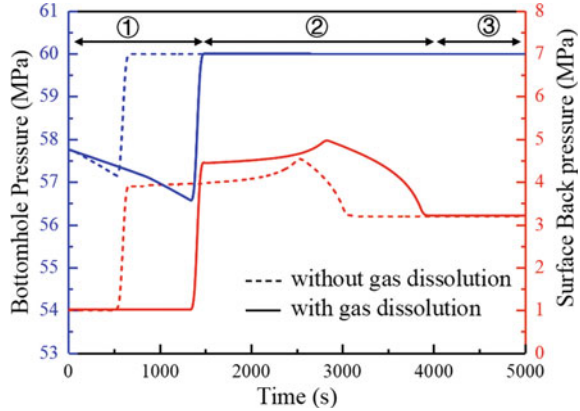
(2) Bottom hole pressure and wellhead back pressure

Figure 98.6 shows the change curves of wellhead back pressure and bottom-hole pressure in the dynamic well control process of managed pressure drilling with or without gas dissolution. In the dynamic well control process of managed pressure drilling, the change of wellbore pressure can be divided into three stages. (1) Bottom gas kick occurs. When the bottom hole pressure is less than the formation pressure, the bottom hole gas keeps invading. With the upward migration and expansion of gas, the hydrostatic column pressure in the wellbore decreases, resulting in a continuous decrease in bottom-hole pressure. (2) controlled pressure circulation exhaust. When the wellhead through pit gain, overflow rate or real-time bottom-hole pressure monitoring to determine the occurrence of gas kick. By quickly adjusting the throttle valve opening, increase the wellhead back pressure, and establish a new pressure balance at the bottom of the well. When gas migrates upward, gas volume fraction in wellbore is affected by interphase mass transfer, gas expansion and other factors, leading to changes in bottom hole pressure. In order to keep the bottom hole pressure constant, it is necessary to dynamically adjust the wellhead back pressure. When the pit gain reaches the maximum, that is, the total gas volume in the wellbore is the maximum, the hydrostatic column pressure is the minimum, and the wellhead back pressure reaches the maximum. As the gas is discharged, the wellhead back pressure gradually drops and then remains stable. (3) Circulating weighted drilling fluid. After the gas is completely discharged from the wellhead, if the wellhead back pressure is high, it is necessary to increase the density of drilling fluid to reduce the wellhead back pressure and prevent gas kick in the next drilling process. If the wellhead back pressure is low, drilling can continue.

According to the analysis of gas migration law, when the dissolution of gas in the oil-based drilling fluid is ignored, the gas kick can be detected at the wellhead about 360 s after the occurrence of the bottom hole, and the well control can be implemented. At this time, as the bottom hole pressure dropped 0.75 MPa, the maximum wellhead back pressure in the process of circulating exhaust was 4.55 MPa. In the actual process of gas kick, because most of the gas will dissolve in the oil-based drilling fluid, taking the same pit gain as the threshold for gas kick discovery will lead to a delay in the time of gas kick discovery at the wellhead, and the wellhead will not detect gas kick until 1438 s after the occurrence of gas kick, so as to start real-time controlled killing and control. At this time, the bottom hole pressure dropped about 1.19 MPa, and the maximum wellhead back pressure required during the circulating exhaust process was 4.98 MPa.

Therefore, in the actual well control process of managed pressure drilling, the actual situation that the gas solubility causes the bottom hole pressure to drop should

Fig. 98.6 Variation curve of bottom hole pressure and inlet back pressure over time



be considered, so as to ensure that the applied wellhead back pressure can balance the bottom hole pressure with the formation pressure.

(3) Outflow response characteristic

Figure 98.7 shows the response characteristics of pit gain and overflow rate in the dynamic well control process of managed pressure drilling. When drilling into an abnormally high pressure formation, the bottom hole pressure falls below the formation pressure and gas begins to invade the wellbore. (1) Gas kick stage. Because of the high bottom hole pressure, there is little expansion of gas. Therefore, the pit gain is approximately linear with the overflow rate increase. (2) Controlled pressure circulation exhaust. When the pit gain reaches the gas penetration detection threshold, the increase in wellhead back pressure causes the pit gain and overflow rate to suddenly drop in a short period of time. As the gas migrates upward and expands, the pit gain and overflow rate increases at an increasing rate until the gas reaches the wellhead and the overflow rate reaches its maximum and begins to decrease. When the overflow rate drops to 0, the pit gain reaches the maximum. And as the gas gradually drains out of the wellhead, the pit gains gradually decrease until all the gas is discharged.

When the dissolution of gas in oil-based drilling fluid is not considered, the pit gain and overflow rate will increase suddenly after gas kick occurs. As the gas migrated upward and expanded, the pit gain and overflow rate increased continuously. When the gas migrated to the wellhead, the maximum pit gain was 2.03m^3 . If the same pit gain is used as the threshold of gas kick detection, the growth rate of pit gain and overflow rate is much lower when considering the dissolution of gas in oil-based drilling fluid. However, due to the longer gas kick time, the actual pit gain (2.26m^3) is significantly increased. Therefore, when using oil-based drilling fluid for managed pressure drilling, the increment threshold of mud pool should be reduced or fine flowmeter should be used as the gas kick detection means to improve the accuracy of early gas kick identification.

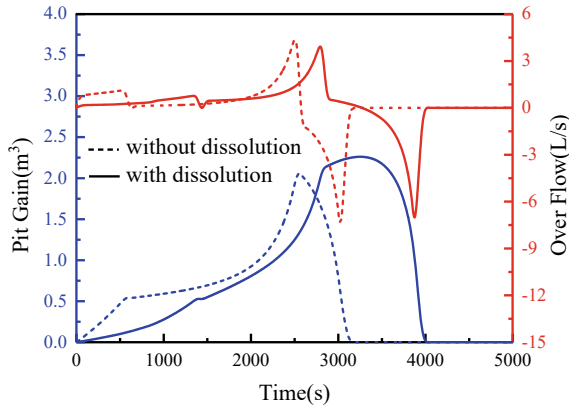


Fig. 98.7 Change curve of pit gain and wellhead overflow rate with time

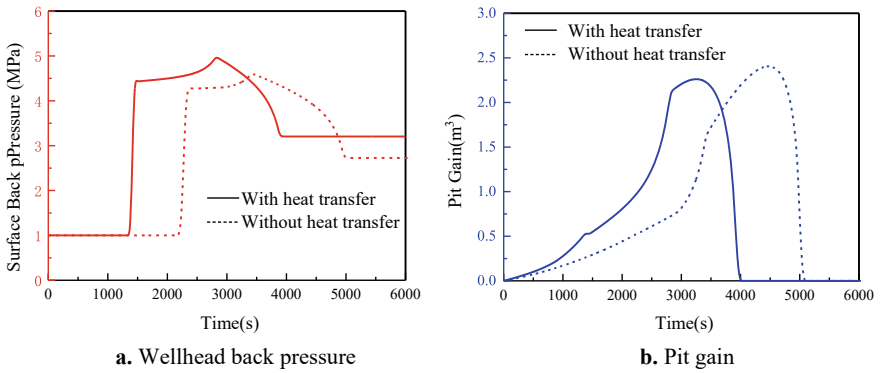


Fig. 98.8 Influence of wellbore heat transfer on dynamic well control in managed pressure drilling

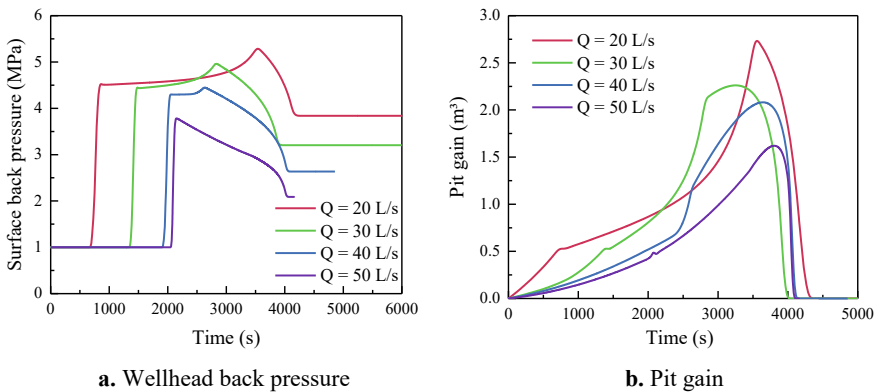


Fig. 98.9 Effect of kill rate on dynamic well control in managed pressure drilling

98.4.2 *Wellbore Heat Transfer*

Figure 98.8a, b show whether the influence of wellbore heat transfer on wellhead back pressure and pit gain in the dynamic well control process of managed pressure drilling is considered

Well heat transfer is not taken into account and the wellbore temperature is always the same as the surface temperature. When wellbore heat transfer is ignored, most of the gas dissolved into the oil-based drilling fluid after gas kick occurs, leading to the time lag of gas kick detected at the wellhead. As gas dissolution will reduce the volume fraction of gas in the wellbore, gas will expand when it migrates to the vicinity of the wellhead. Therefore, low wellhead back pressure is needed to maintain constant bottom-hole pressure in the well control process.

In the dynamic well control process of actual managed pressure drilling, as the formation high temperature gas continuously intrudes into the wellbore, heat transfer occurs between gas and liquid, which makes the wellbore temperature gradually increase. This reduces the solubility of gas under high temperature conditions at the bottom hole, and the high temperature further expands the free gas, resulting in increased gas content in the wellbore. In the early stage of well control, the incremental rise rate of the mud pool is faster and higher wellhead back pressure is required to maintain a constant bottom-hole pressure. Therefore, in the process of dynamic well control parameter design of managed pressure drilling, if the change of wellbore temperature is ignored, the design value of wellhead back pressure may be lower than the actual wellhead back pressure required, resulting in well killing failure.

98.4.3 *Kill Rate*

Figure 98.9a, b respectively show the wellhead back pressure control and pit gain curves in the dynamic well control process of managed pressure drilling under different killing rates. It can be clearly seen from the two figures that the higher the kill rate, the smaller the maximum wellhead back pressure required in the well control process, the smaller the corresponding maximum pit gain, and the lower the requirements for the wellhead back pressure control device.

Taking the rated working pressure of the wellhead equipment as an example, if the kill rate is lower than 30L/s, the maximum wellhead back pressure has exceeded the rated working pressure of the wellhead equipment, and it is difficult to deal with gas influx by using the dynamic wellhead technology of managed pressure drilling.

In this case, the driller or engineer method is used to kill the well to control gas penetration. In the dynamic well control process of managed pressure drilling, the well killing capacity can be increased as much as possible under the condition of ensuring the safety of the wellhead, which can not only reduce the maximum

wellhead back pressure, but also shorten the time of circulating exhaust, which is more conducive to gas influx control.

98.5 Conclusion

In order to study the characteristics of multiphase flow behavior and pressure response in wellbore during the dynamic well control process of managed pressure drilling, a multiphase flow model was established based on the drift flow model and the calculation model of gas instantaneous solubility. The accuracy and reliability of the model were verified based on the experimental data of gas kick in oil-based drilling fluid. The main conclusions of this paper are as follows:

- (1) Gas dissolution in oil-based drilling fluid will lead to a lag in the monitoring time of well gas kick. The increase of bottom gas penetration leads to the increase of bottom hole pressure drop. In the process of killing, it is necessary to ensure a higher wellhead back pressure to balance the bottom hole pressure with the formation pressure. When gas kick is detected at the wellhead, the wellhead back pressure and bottom hole pressure should be increased quickly to prevent further gas kick.
- (2) The change of wellhead back pressure and bottom-hole pressure in the dynamic well control process of managed pressure drilling can be divided into three stages. At the initial stage of gas kick, the pit gain and overflow rate have an approximate linear relationship with the decrease of bottom hole pressure. In the process of recirculating and venting, the pressure and friction resistance of the annulus quiet liquid column change with the gas dissolution and expansion, resulting in a nonlinear relationship between wellhead back pressure and bottom hole pressure.
- (3) When using oil-based drilling fluid for managed pressure drilling, the pit gain threshold should be lowered or fine flowmeter should be used as the gas kick detection means to improve the accuracy of early gas kick identification.
- (4) Due to the increase of wellbore temperature during gas kick, the solubility of gas in drilling fluid decreases. In the initial stage of gas kick, the increment of mud pool is fast. Therefore, higher wellhead back pressure is required to maintain constant bottom-hole pressure when the wellbore temperature is higher.
- (5) In the dynamic well control process of managed pressure drilling, the well killing rate can be increased as much as possible under the condition of ensuring the safety of the wellhead. This can not only reduce the maximum wellhead back pressure, but also reduce the cycle exhaust time, which is more conducive to gas penetration control.

References

1. Nayeem, A.A., Venkatesan, R., Khan, F.: Monitoring of down-hole parameters for early kick detection. *J. Loss Prev. Process Ind.* **40**, 43–54 (2016)
2. He, M., Xu, M., Li, J., et al.: A new two-phase model to simulate sour gas kicks in MPD operations with Water Based Mud. *J. Pet. Sci. Eng.* **159**, 331–343 (2017)
3. Kong, X., Lin, Y., Qiu, Y.: Analysis of gravity displacement and overflow gas kick criteria in managed pressure drilling. *Chinese J. Appl. Mech.* **32**(2), 6 (2015)
4. Hua, J.: Research on safety barrier model based on deepwater well control. China University of Petroleum (East China) (2017)
5. Udegbunam, J.E., Fjelde, K.K., Evje, S., et al.: On the advection-upstream-splitting method hybrid scheme: a simple transient-flow model for managed-pressure-drilling and underbalanced-drilling applications. In: SPE 168960-PA, SPE Drilling & Completion, vol. 30, pp. 98–109 (2) (2015)
6. Ma, Z., Vajargah, A.K., Ambrus, et al.: Multi-phase well control analysis during managed pressure drilling operations. In: SPE 181672-MS, SPE Annual Technical Conference and Exhibition, Dubai, UAE, 26–28 September 2016
7. Yin, B., Liu, G., Li, X.: Multiphase transient flow model in wellbore annuli during gas kick in deepwater drilling based on oil-based mud. *Appl. Math. Model.* **51**, 159–198 (2017)
8. Sun, B., Fu, W., Wang, N., et al.: Multiphase flow modeling of gas kick in oil-based drilling mud. *J. Pet. Sci. Eng.* **174**, 1142–1151 (2019)
9. Nüllig, M., Peters, F.: Experiments on the mass transfer of gas bubbles in mineral oil. *Colloids Surf. A Phys. Eng. Asp.* **540**, 81–89 (2018)
10. Barnea, D.: A unified model for predicting flow-pattern transitions for the whole range of pipe inclinations. *Int. J. Multiph. Flow* **13**(1), 1–12 (1987)
11. Yang, H., et al.: Numerical analysis of transient wellbore thermal behavior in dynamic deepwater multi-gradient drilling. *Energy* **179**, 138–153 (2019)
12. Sun, X., Sun, B., Gao, Y., et al.: A model of multiphase flow dynamics considering the hydrated bubble behaviors and its application to deepwater kick simulation. *J. Energy Resour. Technol.-Trans. Asme.* **140**(8), 082004 (2018)
13. Kelbaliev, G.I.: Mass transfer between a drop or gas bubble and an isotropic turbulent flow. *Theor. Found. Chem. Eng.* **46**(5), 477–485 (2012)
14. Yang, H., et al.: The effect of interfacial mass transfer of slip-rising gas bubbles on two-phase flow in the vertical wellbore/pipeline. *Int. J. Heat Mass Transfer* **150** (2020)
15. Turner, D.J., Miller, K.T., Sloan, E.D.: Direct conversion of water droplets to methane hydrate in crude oil. *Chem. Eng. Sci.* **64**(23), 5066–5072 (2009)
16. Shi, H., Holmes, J.A., Durlifsky, L.J., et al.: Drift-flux modeling of two-phase flow in wellbores. *SPE J.* **10**(1), 24–33 (2005)
17. Chen, N.H.: An explicit equation for friction factor in pipe. *Ind. Eng. Chem. Fundam.* **18**(3), 296–297 (1979)
18. Shannak, B.A.: Frictional pressure drop of gas liquid two-phase flow in pipes. *Nucl. Eng. Des.* **238**(12), 3277–3284 (2008)
19. Sun, B., Sun, X., Wang, Z., et al.: Effects of phase transition on gas kick migration in deepwater horizontal drilling. *J. Nat. Gas Sci. Eng.* **46**, 710–729 (2017)
20. O'bryan, P.L.: Well control problems associated with gas solubility in oil-based drilling fluids (1988)

Chapter 99

Bilinear Auto-Bäcklund Transformation, Shock Waves, Breathers and X-Type Solitons for a (3 + 1)-Dimensional Generalized B-Type Kadomtsev-Petviashvili Equation in a Fluid



Lu Zheng, Bo Tian, Dan-Yu Yang, and Tian-Yu Zhou

Abstract There are abundant nonlinear phenomena in a fluid, such as the nonlinear waves and their interactions. In this paper, a (3+1)-dimensional generalized B-type Kadomtsev-Petviashvili equation in a fluid, which is used to describe the long waves and has the application in water percolation, is investigated. Via the Hirota method, we obtain a bilinear auto-Bäcklund transformation as well as shock-wave, breather and X-type soliton solutions. We graphically show the shock waves and breathers, observe that the amplitudes and shapes of shock waves and breathers keep unchanged during the propagation, and show the X-type soliton on a periodic background. We also analysis the influence of the coefficients in the equation on the above waves.

Keywords Fluid · (3+1)-dimensional generalized B-type Kadomtsev-Petviashvili equation · Bilinear auto-Bäcklund transformation · Shock waves · Breathers · X-type solitons

99.1 Introduction

There are abundant nonlinear phenomena in a fluid, such as the nonlinear waves and their interactions [1–3]. Nonlinear evolution equations (NLEEs) have been involved in nonlinear optics, fluid mechanics, plasma physics and so on [4–11]. Researchers have investigated some NLEEs via several methods including the inverse scattering transformation [12, 13], Hirota method [14–16], Bäcklund transformation (BT) [17, 18], Darboux transformation [19–22] and Lie symmetry analysis [23–25].

Among the NLEEs, Kadomtsev-Petviashvili (KP)-type equations have been studied [26, 27]. A (2+1)-dimensional KP equation has described certain waves on the

L. Zheng · B. Tian (✉) · D.-Y. Yang · T.-Y. Zhou

State Key Laboratory of Information Photonics and Optical Communications, and School of Science, Beijing University of Posts and Telecommunications, 100876 Beijing, China
e-mail: tian_bupt@163.com

© The Author(s), under exclusive license to Springer Nature Switzerland AG 2024

1419

S. Li (ed.), *Computational and Experimental Simulations in Engineering,*

Mechanisms and Machine Science 145,

https://doi.org/10.1007/978-3-031-42987-3_99

surface of a fluid or plasma, as well as internal waves on the interface of two fluids (e.g., two layers of water of different densities) [28]. References [29, 30] have presented a (3+1)-dimensional generalized B-type KP equation in a fluid, i.e.,

$$\alpha u_{xxx} + \beta(u_x u_y)_x + (u_x + u_y + u_z)_t + \gamma u_{xx} + \delta u_{zz} = 0, \tag{99.1}$$

which is used to describe the long waves and has the application in water percolation, where u is a complex differentiable function of the variables x, y, z and t , the subscripts denote the partial derivatives, $\beta \neq 0$, α, γ and δ are the real constants. Bilinear form, bilinear auto-BT, breather, lump, rogue-wave, bright- and dark-soliton solutions for Eq. (99.1) have been constructed [29]. Bilinear auto-BT, Painlevé-type auto-BT, kink soliton, lump and traveling-wave solutions for Eq. (99.1) have been obtained [30].

By virtue of the transformation

$$u = \frac{6\alpha}{\beta} (\ln f)_x, \tag{99.2}$$

Equation (99.1) has been converted into a bilinear form as [29]

$$(\alpha D_x^3 D_y + \gamma D_x^2 + D_t D_x + D_t D_y + D_t D_z + \delta D_z^2) f \cdot f = 0, \tag{99.3}$$

where f is a real differential function of x, y, z and t , while D_x, D_y, D_z and D_t are the bilinear derivative operators defined by [31]

$$\begin{aligned} & D_x^{n_1} D_y^{n_2} D_z^{n_3} D_t^{n_4} M(x, y, z, t) \cdot N(x_1, y_1, z_1, t_1) \\ &= \left(\frac{\partial}{\partial x} - \frac{\partial}{\partial x_1} \right)^{n_1} \left(\frac{\partial}{\partial y} - \frac{\partial}{\partial y_1} \right)^{n_2} \left(\frac{\partial}{\partial z} - \frac{\partial}{\partial z_1} \right)^{n_3} \left(\frac{\partial}{\partial t} - \frac{\partial}{\partial t_1} \right)^{n_4} \\ & M(x, y, z, t) \cdot N(x_1, y_1, z_1, t_1) \Big|_{x_1=x, y_1=y, z_1=z, t_1=t}, \end{aligned} \tag{99.4}$$

with $M(x, y, z, t)$ being a differentiable function with respect to x, y, z and t , $N(x_1, y_1, z_1, t_1)$ being a differentiable function of the independent variables x_1, y_1, z_1 and t_1 , while n_1, n_2, n_3 and n_4 being the non-negative integers.

However, to our knowledge, bilinear-auto BT and breathers which are different from those in Refs. [29, 30] as well as shock-wave and X-type soliton solutions for Eq. (99.1) have not been studied. In Sect. 99.2, we will give a bilinear auto-BT for Eq. (99.1). In Sect. 99.3, we will derive some shock-wave solutions for Eq. (99.1). In Sect. 99.4, we will obtain some breather solutions for Eq. (99.1). In Sect. 99.5, we will derive the X-type soliton solutions for Eq. (99.1). Our conclusions will be given in Sect. 99.6.

99.2 Bilinear Auto-BT for Eq. (99.1)

In this section, we would like to give a bilinear auto-BT for Eq. (99.1). Motivated by Ref. [32], we introduce the following expression of the solutions f and g for Bilinear Form (99.3):

$$\left[(\alpha D_x^3 D_y + \gamma D_x^2 + D_t D_x + D_t D_y + D_t D_z + \delta D_x^2) g \cdot g \right] f^2 - g^2 \left[(\alpha D_x^3 D_y + \gamma D_x^2 + D_t D_x + D_t D_y + D_t D_z + \delta D_x^2) f \cdot f \right] = 0, \quad (99.5)$$

where g is a real differentiable function of x , y , z and t . Via the exchange formulae [31],

$$\begin{aligned} (D_x^2 g \cdot g) f^2 - g^2 (D_x^2 f \cdot f) &= 2D_x(D_x g \cdot f) \cdot (fg), \\ (D_x D_t g \cdot g) f^2 - g^2 (D_x D_t f \cdot f) &= 2D_x(D_t g \cdot f) \cdot (fg), \\ (D_x^3 D_y g \cdot g) f^2 - g^2 (D_x^3 D_y f \cdot f) &= 2D_y(D_x^3 g \cdot f) \cdot (fg) - 6D_x(D_x D_y g \cdot f) \cdot (D_x g \cdot f), \\ D_y(D_x^2 g \cdot f) \cdot (fg) &= D_x(D_x D_y g \cdot f) \cdot (fg) + D_x(D_y g \cdot f) \cdot (D_x g \cdot f), \end{aligned}$$

Eq. (99.5) can be rewritten as

$$\begin{aligned} 0 &= \alpha [(D_x^3 D_y g \cdot g) f^2 - g^2 (D_x^3 D_y f \cdot f)] + \gamma [(D_x^2 g \cdot g) f^2 - g^2 (D_x^2 f \cdot f)] \\ &\quad + [(D_x D_t g \cdot g) f^2 - g^2 (D_x D_t f \cdot f)] + [(D_y D_t g \cdot g) f^2 - g^2 (D_y D_t f \cdot f)] \\ &\quad + [(D_z D_t g \cdot g) f^2 - g^2 (D_z D_t f \cdot f)] + \delta [(D_z^2 g \cdot g) f^2 - g^2 (D_z^2 f \cdot f)] \\ &= 2\alpha D_y(D_x^3 g \cdot f) \cdot (fg) - 6\alpha D_x(D_x D_y g \cdot f) \cdot (D_x g \cdot f) + 2\gamma D_x(D_x g \cdot f) \cdot (fg) \\ &\quad + 2\delta D_z(D_z g \cdot f) \cdot (fg) + 2D_x(D_t g \cdot f) \cdot (fg) \\ &\quad + 2D_y(D_t g \cdot f) \cdot (fg) + 2D_z(D_t g \cdot f) \cdot (fg) \\ &= 2D_y[(\alpha D_x^3 + D_t)g \cdot f] \cdot (fg) \\ &\quad + 2D_x(D_t g \cdot f) \cdot (fg) + 2D_z(D_t g \cdot f) \cdot (fg) \\ &\quad - 6\alpha D_x(D_x D_y g \cdot f) \cdot (D_x g \cdot f) + 6\vartheta D_x(D_z g \cdot f) \cdot (D_x g \cdot f) \\ &\quad + 2\delta D_z(D_z g \cdot f) \cdot (fg) - 6\vartheta D_x(D_z g \cdot f) \cdot (D_x g \cdot f) + 2\gamma D_x(D_x g \cdot f) \cdot (fg) \\ &= 2D_y[(\alpha D_x^3 + D_t)g \cdot f] \cdot (fg) + 2D_x(D_t g \cdot f) \cdot (fg) + 2D_z(D_t g \cdot f) \cdot (fg) \\ &\quad - 6D_x[(\alpha D_x D_y - \vartheta D_z)g \cdot f] \cdot (D_x g \cdot f) + 2\delta D_z(D_z g \cdot f) \cdot (fg) \\ &\quad - 6\vartheta [D_z(D_x^2 g \cdot f) \cdot (fg) - D_x(D_x D_z g \cdot f) \cdot (fg)] + 2\gamma D_x(D_x g \cdot f) \cdot (fg) \\ &= 2D_y[(\alpha D_x^3 + D_t)g \cdot f] \cdot (fg) - 6D_x[(\alpha D_x D_y - \vartheta D_z)g \cdot f] \cdot (D_x g \cdot f) \\ &\quad + 2D_z[(\delta D_z - 3\vartheta D_x^2 + D_t)g \cdot f] \cdot (fg) \\ &\quad + 2D_x[(3\vartheta D_x D_z + \gamma D_x + D_t)g \cdot f] \cdot (fg), \end{aligned}$$

where ϑ is a non-zero constant. Thus, we derive a bilinear auto-BT for Eq. (99.1) as

$$\begin{aligned}
 (\alpha D_x^3 + D_t)g \cdot f &= \lambda_1 fg, \\
 (\alpha D_x D_y - \vartheta D_z)g \cdot f &= \lambda_2 D_x g \cdot f, \\
 (\delta D_z - 3\vartheta D_x^2 + D_t)g \cdot f &= \lambda_3 fg, \\
 (3\vartheta D_x D_z + \gamma D_x + D_t)g \cdot f &= \lambda_4 fg,
 \end{aligned}
 \tag{99.6}$$

with $\lambda_1, \lambda_2, \lambda_3$ and λ_4 as all the constants.

Choosing $f = 1$ as a solution for Bilinear Form (99.3) and substituting it into Bilinear auto-BT (99.6), we obtain that

$$\begin{aligned}
 \alpha g_{xxx} + g_t - \lambda_1 g &= 0, \\
 \alpha g_{xy} - \vartheta g_z - \lambda_2 g_x &= 0, \\
 \delta g_z - 3\vartheta g_{xx} + g_t - \lambda_3 g &= 0, \\
 3\vartheta g_{xz} + \gamma g_x + g_t - \lambda_4 g &= 0.
 \end{aligned}
 \tag{99.7}$$

We take $g = 1 + \varepsilon e^{kx+hy+wz+vt}$ as the exponential-function solutions for Bilinear Form (99.3), where ε, k, h, w and v are the constants. Selecting $\lambda_1 = \lambda_3 = \lambda_4 = 0$ in Expressions (99.7), we get that

$$\begin{aligned}
 h &= \frac{-k^2\alpha + \gamma + 3k\lambda_2}{3k\alpha}, & w &= \frac{k^3\alpha + \sqrt{k^6\alpha^2 + 4k^4\alpha\delta - 4k^2\gamma\delta}}{2\delta}, \\
 v &= -k^3\alpha, & \vartheta &= \frac{-k^3\alpha + \sqrt{k^6\alpha^2 + 4k^4\alpha\delta - 4k^2\gamma\delta}}{6k^2},
 \end{aligned}$$

and derive the exponential-function solutions for Eq. (99.1) as

$$u = \frac{6\alpha\varepsilon k e^{kx+hy+wz+vt}}{\beta(1 + \varepsilon e^{kx+hy+wz+vt})}.$$

99.3 Shock-Wave Solutions for Eq. (99.1)

In this section, to obtain the shock-wave solutions for Eq. (99.1), motivated by Refs. [33, 34], we assume that

$$f = s_1 \tanh^\lambda g_1,
 \tag{99.8}$$

where $g_1 = a_1x + a_2y + a_3z + a_4t$, s_1 is the amplitude of the soliton, and a_i 's ($i = 1, 2, 3, 4$), λ are all the real constants to be determined. Substituting Expression (99.8) into Eq. (99.1), we can derive that

$$\begin{aligned}
 & s_1 \lambda \{ a_1^3 a_2 \alpha (-6 + 11\lambda - 6\lambda^2 + \lambda^3) \tanh^{\lambda-4} g_1 - (\lambda - 1) [-a_4(a_1 + a_2) - a_1^2 \gamma \\
 & - a_3^2 \delta + 4a_1^3 a_2 (2 - 2\lambda + \lambda^2)] \tanh^{\lambda-2} g_1 - 2\lambda [a_4(a_1 + a_2) + a_1^2 \gamma + a_3^2 \delta \\
 & - a_1^3 a_2 \alpha (5 + 3\lambda^2)] \tanh^\lambda g_1 + (1 + \lambda) [a_4(a_1 + a_2) + a_1^2 \gamma + a_3^2 \delta \\
 & - 4a_1^3 a_2 \alpha (2 + 2\lambda + \lambda^2)] \tanh^{\lambda+2} g_1 + a_1^3 a_2 \alpha (6 + 11\lambda + 6\lambda^2 + \lambda^3) \tanh^{\lambda+4} g_1 \\
 & + 2s_1 \lambda a_1^2 a_2 \beta (\lambda - 1) \tanh^{2\lambda-3} g_1 - 2s_1 \lambda a_1^2 a_2 \beta (1 + 3\lambda) \tanh^{2\lambda-1} g_1 \\
 & + 2s_1 \lambda a_1^2 a_2 \beta (1 + 3\lambda) \tanh^{2\lambda+1} g_1 - 2s_1 \lambda a_1^2 a_2 \beta (1 + \lambda) \tanh^{2\lambda+3} g_1 \} = 0.
 \end{aligned} \tag{99.9}$$

From Eq. (99.9), making $\tanh^{\lambda+4} g_1$ and $\tanh^{2\lambda+3} g_1$ equal, we get $\lambda = 1$. Setting the coefficients of $\tanh^{\lambda+4} g_1$, $\tanh^{2\lambda+3} g_1$ and $\tanh^\lambda g_1$ in Eq. (99.9) to zero, we obtain

$$a_1 = \frac{s_1 \beta}{6\alpha}, \quad a_3 = \frac{\sqrt{-108a_4 a_2 \alpha^2 - 18a_4 s_1 \alpha \beta - 2s_1^3 a_2 \beta^3 - 3s_1^2 \beta^2 \gamma}}{6\sqrt{3}\alpha\sqrt{\delta}}, \quad \alpha\sqrt{\delta} \neq 0.$$

Thus, shock-wave solutions for Eq. (99.1) are obtained

$$u = s_1 \tanh \left(a_4 t + a_2 y + \frac{s_1 \beta x}{6\alpha} + \frac{z \sqrt{-108a_4 a_2 \alpha^2 - 18a_4 s_1 \alpha \beta - 2s_1^3 a_2 \beta^3 - 3s_1^2 \beta^2 \gamma}}{6\sqrt{3}\alpha\sqrt{\delta}} \right). \tag{99.10}$$

Figure 99.1 shows the propagation of the shock wave based on Solutions (99.10). We observe that the shock wave propagates stably with the unchanged shape. Furthermore, we investigate the influence of the coefficients in Eq. (99.1) on the amplitude of the shock wave. Comparing Fig. 99.2 with Fig. 99.1(b₂), we find when α , β , γ or δ changes, amplitudes of the shock waves keep unchanged while the values of α , β and δ affect the propagation direction of shock wave.

99.4 Breather Solutions for Eq. (99.1)

In this section, we intend to get the breather solutions for Eq. (99.1) and motivated by Refs. [35–37], we assume that

$$\begin{aligned}
 f &= c_1 \cosh m_1 + c_2 \sin m_2 + c_3, \\
 m_1 &= b_1 x + b_2 y + b_3 z + b_4 t + b_5, \\
 m_2 &= b_6 x + b_7 y + b_8 z + b_9 t + b_{10},
 \end{aligned} \tag{99.11}$$

where c_1, c_2, c_3 and b_j 's ($j = 1, 2, \dots, 10$) are all the real constants to be determined. Substituting Expressions (99.11) into Bilinear Form (99.3), we can derive that

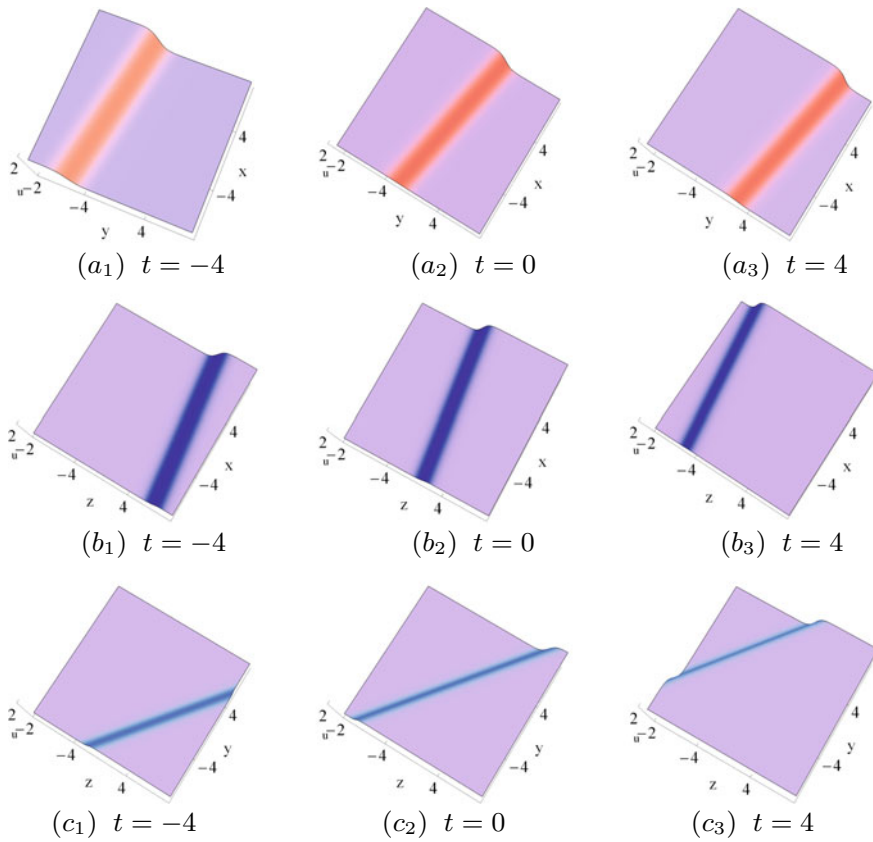


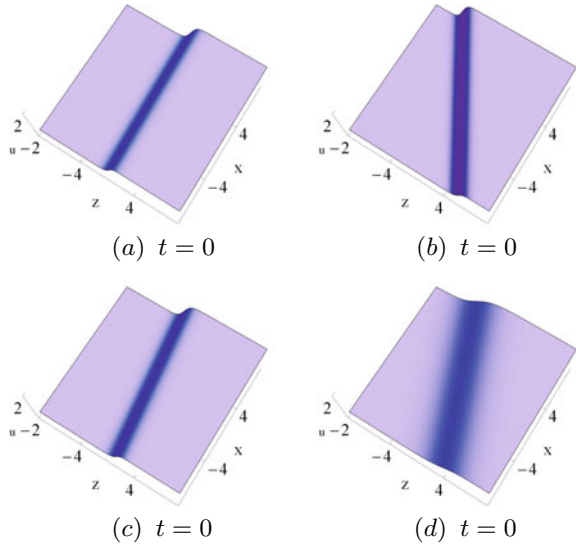
Fig. 99.1 Shock wave via solutions (99.10) with $a_{11} = 2, a_{12} = 1, a_{13} = 1, a_{15} = 1, \alpha = \beta = \gamma = \delta = 1$ and $\mathbf{a} z = 0, \mathbf{b} y = 0,$ and $\mathbf{c} x = 0$

$$\begin{aligned}
 b_1 = 0, \quad b_7 = 0, \quad b_9 &= \frac{-b_6^2\gamma - b_8^2\delta}{b_6 + b_8}, \\
 b_4 &= \frac{b_3 \left[-b_6^3\alpha - 2b_8\delta + b_6\sqrt{b_6^4\alpha^2 - 4(b_6^2\alpha + \gamma)\delta} \right]}{2(b_6 + b_8)}, \\
 b_2 &= \frac{b_3b_6 \left[-b_6^3\alpha - b_6^2b_8\alpha - 2b_6\gamma + 2b_8\delta + (b_6 + b_8)\sqrt{b_6^4\alpha^2 - 4(b_6^2\alpha + \gamma)\delta} \right]}{2(b_6^4\alpha - b_6^3b_8\alpha - b_6^2\gamma + b_8^2\delta)},
 \end{aligned}$$

which need to satisfy the conditions

$$b_6^4\alpha - b_6^3b_8\alpha - b_6^2\gamma + b_8^2\delta \neq 0, \quad b_6 + b_8 \neq 0.$$

Fig. 99.2 The same as Fig. 99.1(b₂) except that: **a** $\alpha = 3$, **b** $\beta = 5$, **c** $\gamma = 7$, and **d** $\delta = 9$



Expressions (99.11) can be rewritten as

$$f = c_1 \cosh m_1 + c_2 \sin m_2 + c_3, \tag{99.12}$$

where

$$m_1 = b_5 + b_3z - \frac{b_3(b_6^3\alpha + 2b_8\delta + b_6\sqrt{b_6^4\alpha^2 - 4(b_6^2\alpha + \gamma)\delta})t}{2(b_6 + b_8)}$$

$$+ \frac{b_3b_6 \left[-b_6^3\alpha - b_6^2b_8\alpha - 2b_6\gamma + 2b_8\delta + (b_8 + b_6)\sqrt{b_6^4\alpha^2 - 4(b_6^2\alpha + \gamma)\delta} \right] y}{2(b_6^4\alpha + b_6^3b_8\alpha + b_6^2\gamma + b_8^2\delta)},$$

$$m_2 = b_{10} + b_6x + b_8z - \frac{(b_6^2\gamma + b_8^2\delta)t}{b_6 + b_8}.$$

Substituting Expression (99.12) into Transformation (99.2), we obtain the breather solutions for Eq. (99.1) as

$$u = \frac{6c_2b_6\alpha \cos\{[b_6(b_{10} + b_8x + b_8z) + b_6^2(x - \gamma t) + b_8(b_{10} + b_8z - b_8\delta t)](b_6 + b_8)^{-1}\}}{\beta (c_3 + c_1 \cosh m_1 + c_2 \sin m_2)}. \tag{99.13}$$

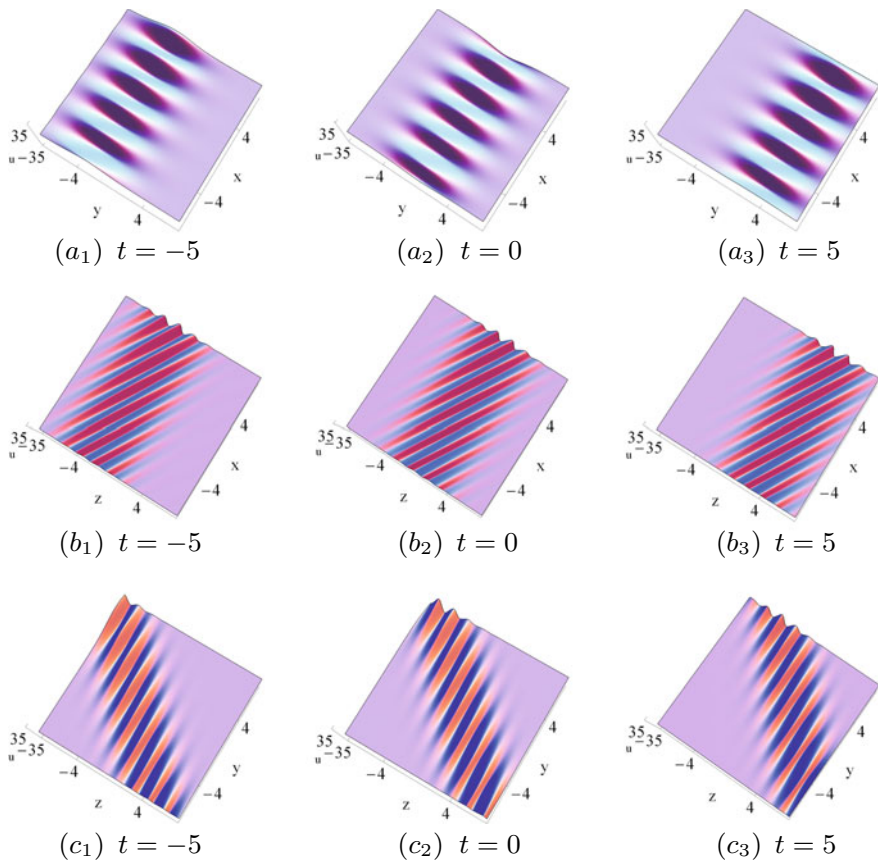
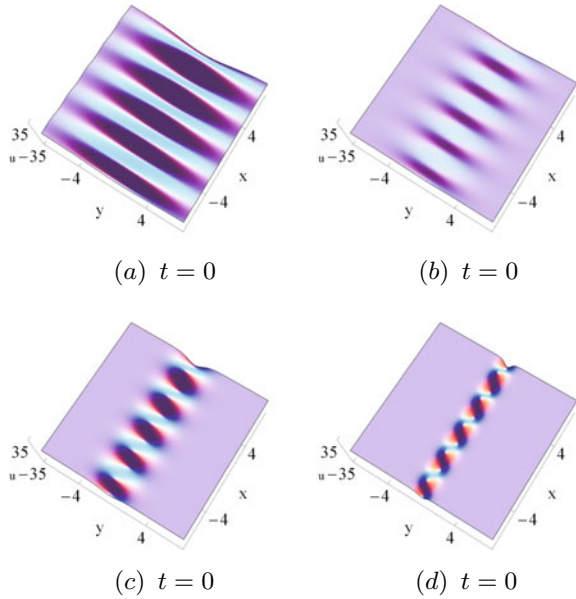


Fig. 99.3 Breather via solutions (99.13) with $c_3 = 3, c_1 = 1, c_2 = 2, b_3 = 1, b_5 = -\frac{1}{2}, b_6 = 2, b_8 = -\frac{7}{2}, b_{10} = \frac{1}{2}, \alpha = 2, \beta = \gamma = \delta = 1$ and $\mathbf{a} z = 0, \mathbf{b} y = 0,$ and $\mathbf{c} x = 0$

Figure 99.3 presents the breather based on Solutions (99.13). We observe that the breather propagates stably with the unchanged shape. Comparing Fig. 99.4a with Fig. 99.3(a₂), we find when α increases, amplitude of the breather increases. Comparing Fig. 99.4(b) with Fig. 99.3(a₂), we observe when β increases, amplitude of the breather decreases. Comparing Fig. 99.4c or d with Fig. 99.3(a₂), we can see when γ or δ increases, amplitude of the breather keeps unchanged while the shape of breather changes.

Fig. 99.4 The same as Fig. 99.3(a₂) except that: **a** $\alpha = \frac{5}{2}$, **b** $\beta = 3$, **c** $\gamma = 6$, and **d** $\delta = \frac{3}{2}$



99.5 X-Type Soliton Solutions for Eq. (99.1)

In this section, to seek the X-type soliton solutions for Eq. (99.1) and motivated by Refs. [38, 39], we assume that

$$\begin{aligned}
 f &= d_1 g_4 + g_5 + d_2 \cos g_6 + d_3 \cosh g_7, \\
 g_4 &= e^{h_1 x + h_2 y + h_3 z + h_4 t + h_5}, \\
 g_5 &= e^{-h_1 x - h_2 y - h_3 z - h_4 t - h_6}, \\
 g_6 &= h_7 x + h_8 y + h_9 z + h_{10} t + h_{11}, \\
 g_7 &= h_{12} x + h_{13} y + h_{14} z + h_{15} t + h_{16},
 \end{aligned}
 \tag{99.14}$$

where d_1, d_2, d_3 and h_q 's ($q = 1, \dots, 16$) are all the constants to be determined. Substituting Expressions (99.14) into Bilinear Form (99.3), we can derive that

$$\begin{aligned}
 h_3 &= \frac{h_2 h_9}{h_8}, \quad h_4 = -\frac{h_2 h_9^2 \delta}{h_8^2 + h_8 h_9}, \quad h_{10} = -\frac{h_9^2 \delta}{h_8 + h_9}, \quad h_1 = h_7 = 0, \\
 h_{13} &= 0, \quad h_{14} = \frac{h_{12}^3 h_8 \alpha + h_{12}^3 h_9 \alpha + 2h_9 h_{12} \delta - h_{12} h_{17} (h_8 + h_9)}{2h_8 \delta}, \\
 h_{15} &= \frac{-h_{12}^3 (2h_8^2 + 2h_8 h_9 + h_9^2) \alpha + h_9 h_{12} [2h_8 h_{17} + h_9 (-2\delta + h_{17})]}{2h_8^2 + 2h_8 h_9}, \\
 h_{17} &= \sqrt{h_{12}^4 \alpha^2 + 4h_{12}^2 \alpha \delta - 4\gamma \delta},
 \end{aligned}$$

which need to satisfy the condition

$$h_8(h_8 + h_9) \neq 0.$$

Expressions (99.14) can be rewritten as

$$f = B_1 + d_2 \cos(h_8y + h_9z - \frac{h_9^2\delta t}{h_8 + h_9} + h_{11}) + d_3 \cosh(h_{12}x + h_{14}z + h_{15}t + h_{16}), \tag{99.15}$$

where

$$B_1 = e^{-h_2y - \frac{h_2h_9z}{h_8} + \frac{h_2h_9^2\delta t}{h_8^2 + h_8h_9} - h_6} + d_1 e^{h_2y + \frac{h_2h_9z}{h_8} - \frac{h_2h_9^2\delta t}{h_8^2 + h_8h_9} + h_5}.$$

Substituting Expression (99.15) into Transformation (99.2), we obtain the X-type soliton solutions for Eq. (99.1) as

$$u = \frac{6d_3h_{12}\alpha \sinh(h_{12}x + h_{14}z + h_{15}t + h_{16})}{\beta \left\{ B_1 + d_2 \cos[h_8y + h_9z - \frac{h_9^2\delta t}{h_8+h_9} + h_{11}] + d_3 \cosh[h_{12}x + h_{14}z + h_{15}t + h_{16}] \right\}}. \tag{99.16}$$

Figure 99.5 shows the X-type soliton on a periodic background based on Solutions (99.16). Comparing Fig. 99.6a with Fig. 99.5(a₂), we find when α increases, amplitudes of the periodic wave and X-type solitons increase and the direction of their propagation alter. Comparing Fig. 99.6b with Fig. 99.5(a₂), we observe when β increases, amplitudes of the periodic wave and X-type solitons decrease. Comparing Fig. 99.6c or d with Fig. 99.5(a₂), we can see when γ or δ increases, amplitudes of the periodic wave and X-type solitons keep unchanged.

99.6 Conclusions

There are abundant nonlinear phenomena in a fluid, such as the nonlinear waves and their interactions. A (3+1)-dimensional generalized B-type KP equation in a fluid, which is used to describe the long waves and has the application in water percolation, i.e., Eq. (99.1), has been investigated in this paper. Based on the Hirota method, we have derived Bilinear Auto-BT (99.6), Shock-Wave Solutions (99.10), Breather Solutions (99.13) and X-type soliton Solutions (99.16). We have observed that the amplitude and shape of the shock wave keep unchanged during the propagation, as shown in Fig. 99.1. Compared with Fig. 99.1(b₂), Fig. 99.2 has displayed the influ-

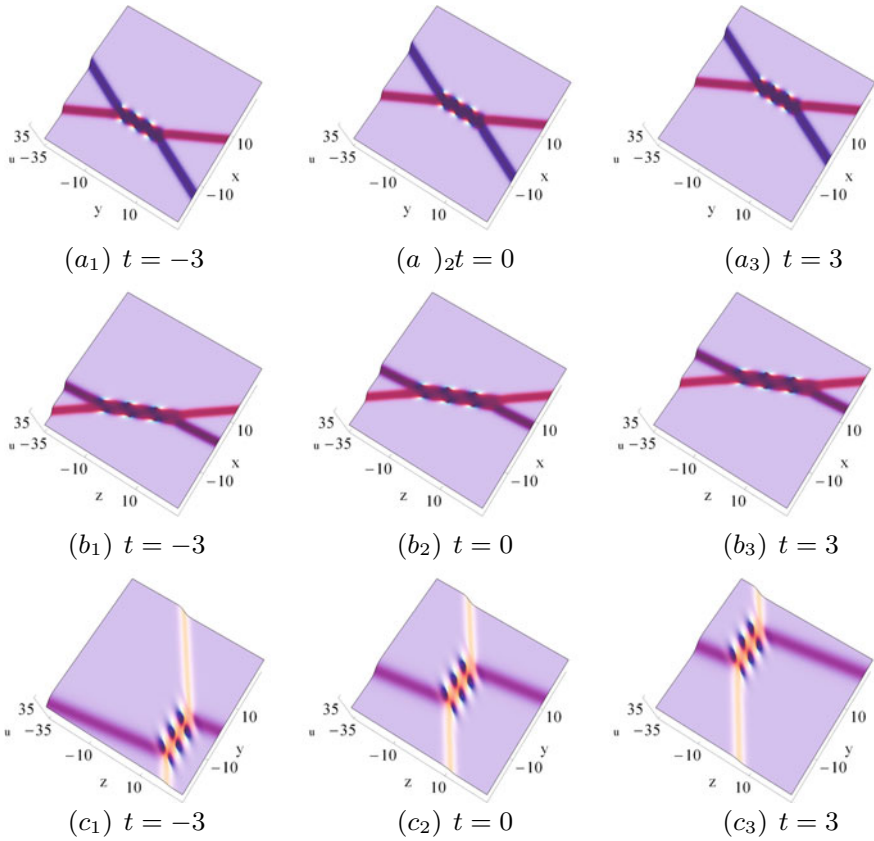
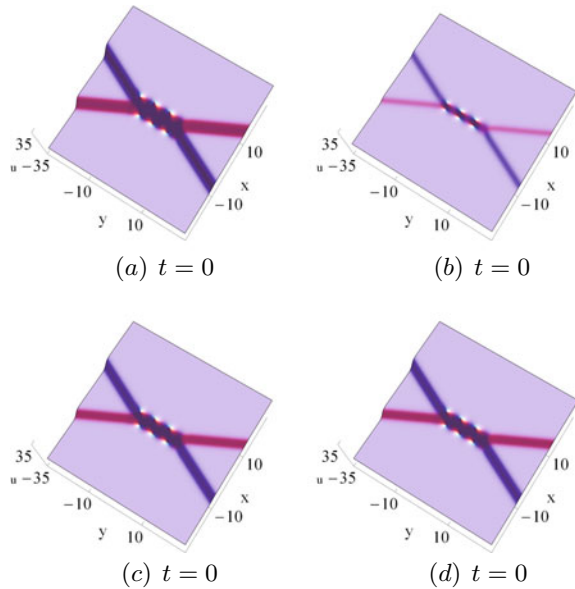


Fig. 99.5 X-type soliton on a periodic background via solutions (99.16) with $d_1 = 3, d_2 = 1, d_3 = \frac{6}{5}, h_2 = 1, h_5 = -8, h_6 = 8, h_8 = \frac{6}{5}, h_9 = \frac{6}{5}, h_{11} = -1, h_{12} = -2, h_{16} = \frac{3}{25}, \alpha = \beta = \gamma = \delta = 1$ and $\mathbf{a} z = 0, \mathbf{b} y = 0,$ and $\mathbf{c} x = 0$

ence of the coefficients α, β, γ and δ in Eq. (99.1) on the shock wave. We have observed the breather which propagates stably along a certain direction and keeps its amplitude unchanged, as shown in Fig. 99.3. Compared with Fig. 99.3(a₂), Fig. 99.4 has displayed the influence of the coefficients α, β, γ and δ in Eq. (99.1) on the breather. We have studied the X-type soliton on a periodic background which keep their amplitudes unchanged, as shown in Fig. 99.5. Compared with Fig. 99.5(a₂), Fig. 99.6 has displayed the influence of the coefficients α, β, γ and δ in Eq. (99.1) on the X-type soliton on a periodic background.

Fig. 99.6 The same as Fig. 99.5(a₂) except that: **a** $\alpha = \frac{3}{2}$, **b** $\beta = 3$, **c** $\gamma = 5$, and **d** $\delta = 7$



Acknowledgements We express our sincere thanks to the Editors and Reviewers for their valuable comments. This work has been supported by the National Natural Science Foundation of China under Grant Nos. 11772017, 11272023 and 11471050, by the Fund of State Key Laboratory of Information Photonics and Optical Communications (Beijing University of Posts and Telecommunications), China (IPOC: 2017ZZ05) and by the Fundamental Research Funds for the Central Universities of China under Grant No. 2011BUPTYB02.

Conflict of Interest Statement

The authors confirm that there are no known conflicts of interest associated with this publication and there has been no significant financial support for this work that could have influenced its outcome.

Data Availability Statement

Some or all data, models, or code generated or used during the study are available from the corresponding author by request.

References

1. Wu, J.W., He, J.T., Lin, J.: Eur. Phys. J. Plus **137**, 814 (2022)
2. Kumar, S., Rani, S., Mann, N.: Eur. Phys. J. Plus **137**, 1226 (2022)
3. Liu, F.Y., Gao, Y.T., Yu, X., Li, L.Q.: Eur. Phys. J. Plus **138**, 6 (2023)
4. Shen, Y., Tian, B., Zhou, T.Y.: Eur. Phys. J. Plus **136**, 572 (2021)
5. Abdelwahed, H.G., El-Shewy, E.K., Alghanim, S., Abdelwahed, M.A.E.: Results Phys. **38**, 105548 (2022)
6. Kumar, S., Mohan, B., Kumar, R.: Nonlinear Dyn. **110**, 693 (2022)
7. Gao, X.Y., Guo, Y.J., Shan, W.R.: Appl. Math. Lett. **132**, 108189 (2022)

8. Shohaib, M., Masood, W., Alyousef, H.A., Siddiq, M., El-Tantawy, S.A.: *Phys. Fluids* **34**, 093107 (2022)
9. Liu, F.Y., Gao, Y.T., Yu, X., Ding, C.C.: *Nonlinear Dyn.* **108**, 1599 (2022)
10. Roshid, M.M., Bairagi, T., Harun-Or-Roshid, Rahman, M.M.: *Partial Differ. Equ. Appl. Math.* **5**, 100354 (2022)
11. Rajan, M.S.M., Veni, S.S.: *Optik* **272**, 173317 (2023)
12. Ablowitz, M.J., Segur, H.: *Solitons and the Inverse Scattering Transform*. SIAM, Philadelphia (1981)
13. Vakhnenko, V.O., Parkes, E.J., Morrison, A.J.: *Chaos Solitons Fract.* **17**, 683 (2003)
14. Shen, Y., Tian, B., Liu, S.H., Yang, D.Y.: *Phys. Scr.* **96**, 075212 (2021)
15. Zhou, T.Y., Tian, B.: *Appl. Math. Lett.* **133**, 108280 (2022)
16. Ahmad, S., Saifullah, S., Khan, A., Inc, M.: *Phys. Lett. A* **450**, 128393 (2022)
17. Butt, A.R., Zil-E-Huma, Raza, N., Inc, M., Alqahtani, R.T.: *Chaos Solitons Fract.* **168**, 113201 (2023)
18. Dong, S., Lan, Z.Z., Gao, B., Shen, Y.J.: *Appl. Math. Lett.* **125**, 107747 (2022)
19. Wang, X., Li, J., Wang, L., Wei, J., Guo, B.W.: *Commun. Theor. Phys.* **72**, 035001 (2020)
20. Wu, X.H., Gao, Y.T., Yu, X., Ding, C.C., Li, L.Q.: *Chaos Solitons Fract.* **162**, 112399 (2022)
21. Wu, X.H., Gao, Y.T., Yu, X., Ding, C.C.: *Chaos Solitons Fract.* **165**, 112786 (2022)
22. Jia, T.T., Gao, Y.T., Yu, X., Li, L.Q.: *Appl. Math. Lett.* **114**, 106702 (2021)
23. Liu, P., Cheng, J., Ren, B., Yang, J.R.: *Chin. Phys. B* **29**, 020201 (2020)
24. Kumar, S., Nisar, K.S., Kumar, A.: *Results Phys.* **28**, 104621 (2021)
25. Liu, F.Y., Gao, Y.T.: *Appl. Math. Lett.* **132**, 108094 (2022)
26. Yuan, Y.Q., Zhao, X.H.: *Phys. Lett. A* **458**, 128592 (2023)
27. Zhao, J., Manafian, J., Zaya, N.E., Mohammed, S.A.: *Math. Method. Appl. Sci.* **44**, 5079 (2021)
28. David, D., Kamran, N., Levi, D., Winternitz, P.: *Phys. Rev. Lett.* **55**, 2111 (1985)
29. Guo, D., Tian, S.F., Wang, X.B., Zhang, T.T.: *E. Asian J. Appl. Math.* **9**, 780 (2019)
30. Ma, Y.X., Tian, B., Qu, Q.X., Wei, C.C., Zhao, X.: *Chin. J. Phys.* **73**, 600 (2021)
31. Hirota, R.: *The Direct Method in Soliton Theory*. Cambridge University Press, New York (2004)
32. Li, L.Q., Gao, Y.T., Yu, X., Jia, T.T., Hu, L., Zhang, C.Y.: *Chin. J. Phys.* **77**, 915 (2022)
33. Biswas, A., Triki, H.: *Appl. Math. Comput.* **217**, 3869 (2018)
34. Triki, H., Jovanoski, Z., Biswas, A.: *Indian J. Phys.* **88**, 71 (2018)
35. Liu, D., Ju, X.D., Ilhan, O.A., Manafian, J., Ismael, H.F.: *Mod. Phys. Lett. B* **20**, 35 (2021)
36. Ilhan, O.A., Manafian, J.: *Mod. Phys. Lett. B* **33**, 1950277 (2019)
37. Zhang, Z., Qi, Z.Q., Li, B.: *Appl. Math. Lett.* **116**, 107004 (2021)
38. Ma, H.C., Wu, H.F., Deng, A.P.: *E. Asian J. Appl. Math.* **11**, 674 (2021)
39. Han, P.F., Bao, T.: *Nonlinear Dyn.* **107**, 1163 (2022)

Chapter 100

Study on Stress Area Law and Detection Range at Key Locations of Natural Gas Station



Gang Liu, Rui Liu, Yang Qin, Fang Yang, and Hang Song

Abstract In recent years, safety accidents have occurred frequently in natural gas pipelines, mostly due to leakage of natural gas pipelines. Most long-distance natural gas pipelines are large-diameter and high pressure pipelines. A large amount of natural gas is stored in the pipeline, which will have serious consequences in case of leakage. The thinning of pipeline wall thickness is an important factor causing the leakage of natural gas pipeline, so it is necessary to monitor the wall thickness of key points of the pipeline. At present, the recognized monitoring points in the industry are elbows and tees of natural gas stations, but no relevant standards have been formulated for the more detailed detection scope of monitoring points. The author uses fluent simulation software to establish the model, and then uses the pressure sensor for on-site detection to modify the model with the detection results. Then, according to the new model, the stress areas of monitoring points (elbows and tees) with different pipe diameter and curve diameter ratio are studied and summarized, and the detection ranges of different monitoring points are determined on this basis. The detection scope provides reference for the daily work of on-site operators, so as to ensure the safe and stable operation of long-distance natural gas pipeline.

Keywords Long distance natural gas pipeline · Stress area · Detection range · Elbow · Tee

In recent years, more and more long-distance natural gas pipelines have been put into operation, and their operation safety has also been widely concerned by the society. Since the lines of long-distance natural gas pipelines are mostly wrapped and buried with anti-corrosion coating, and the corrosion possibility of their steel is also minimized, the corrosion problem of stations is usually considered. During the transportation of natural gas, the gas itself has a certain speed, especially at the elbow and tee, there will be continuous erosion. Because long-term erosion will cause wall thickness thinning, it is necessary to study these locations.

G. Liu (✉) · R. Liu · Y. Qin · F. Yang · H. Song
Sino-Pipeline International Company, Beijing, China
e-mail: fenglangtc@126.com; rui01.liu@cnpc.com.cn

Through literature review, in order to improve the wear resistance of 90° elbow of natural gas transmission pipeline, Huang Kun and others proposed a three-stage bending elbow. Through the three-stage improvement of the bending section of the elbow, the size of secondary flow in the elbow is reduced, the flow field in the elbow is optimized, and the erosion wear condition of the elbow is improved [1]; Song Xiaoqin et al. Studied that the small solid particles entrained in the process of natural gas transmission will produce erosion and wear on the pipeline. The results show that the wear amount increases with the increase of particle diameter, particle density, gas flow rate and bend diameter ratio. The boundary angle is a parameter that can comprehensively evaluate the erosion and wear characteristics of elbow [2]; Huang Yong et al. Studied the wear failure of faucet elbow in reverse circulation drilling. The results show that when gas-solid two-phase flow passes through the elbow, there is a collision concentration area between rock cuttings and wall at 30°, 90° and 150° corners of the elbow, corresponding to the formation of three wall wear areas, of which the wear at 30° corner is the most serious, forming a puncture and leakage point [3]; Liang Guangchuan et al. Established a mathematical model by using finite volume method through FLUENT software, analyzed the changes of flow parameters such as pressure and velocity according to different flow velocities, intuitively and vividly analyzed the impact of flow field on elbow erosion, verified the parts prone to corrosion at the elbow, and provided a basis for studying the impact of hydrodynamic factors on pipeline erosion [4]; Zeng Yongjie and others studied the erosion failure mechanism of natural gas pipeline elbow by using computational fluid dynamics (CFD), analyzed the velocity field and pressure field of elbow, concluded that the large arc surface of elbow is the dangerous surface, and put forward preventive measures to avoid and slow down the erosion failure of elbow [5].

The author uses fluent simulation software to establish the model, and then uses the pressure sensor for on-site detection to modify the model with the detection results. Then, according to the new model, the stress areas of monitoring points (elbows and tees) with different pipe diameter and curve diameter ratio are studied and summarized, and the detection ranges of different monitoring points are determined on this basis. The detection scope provides reference for the daily work of on-site operators, so as to ensure the safe and stable operation of long-distance natural gas pipeline.

100.1 Field Correction Model Data Test and Conclusion

The research project uses vibrating wire surface strain gauge to detect the surface stress of the elbow in gas transmission station, and explores the stress and erosion of the elbow through the change of the elbow surface stress, so as to modify the wall thickness monitoring points and detection range in combination with the simulation calculation of the simulation model.

The working principle of vibrating wire strain gauge is that when the measured object is deformed, it is transmitted to the vibrating wire of the strain gauge through the front and rear seats, so as to change the vibration frequency of the internal vibrating wire, derive the frequency signal through the transmission cable to the reading instrument for reading, and further calculate the stress change of the vibrating wire through the change of vibration frequency, that is, the stress change of the measured object, The stress calculation formula of string vibration strain gauge is:

$$\varepsilon = k\Delta F \quad (100.1)$$

$$\Delta F = F - F_0 \quad (100.2)$$

$$\sigma = \varepsilon E \quad (100.3)$$

where ε is the strain value; σ is the stress value, in MPa; ΔF is the change measured by the strain gauge, in F; K is the measurement sensitivity of the strain gauge, unit: $10^{-6} \varepsilon / F$; F is the vibration frequency modulus measured by the strain gauge, in F; F_0 is the reference value of the strain gauge, in F; E is the elastic modulus, in MPa.

(1) Circumferential test results of bend stress

The vibrating wire strain gauge is installed on the elbow of natural gas station to detect the input of surface stress. During the input detection of 90° compressor outlet elbow, 13 points are set, and one stress detection point is set at an interval of 5° along the axial direction of the outer arch to detect vibration and calculate the stress results; For the 120° manifold inlet elbow, 11 inspection points shall be set at an interval of 5° along the axial direction of the outer arch surface of $20^\circ \sim 70^\circ$; For the 135° air cooler outlet elbow, 13 detection points are set at an interval of 5° along the axial direction of the outer arch surface of $20^\circ \sim 80^\circ$. Each point is detected for 10 min at an interval of 10 s. The average value of the vibration frequency modulus read at each point is shown in Table 100.1, and the calculated results are shown in Fig. 100.1.

From the following results, we can see the distribution law of bend stress in natural gas station at different axial angles. It can be concluded that the surface stress of 90° bend is concentrated at 30° to 60° ; For 120° elbow, the surface stress is concentrated in 40° to 70° ; For 135° elbow, the surface stress changes little, mainly 35° to 65° (subject to the natural gas inlet).

In the Figs. 100.1 and 100.2, a straight line with a circle represents a 90° elbow; The dotted line and triangle represent a 120° elbow; Dashed lines and circles represent 135° elbows;

(2) Axial test results of bending stress

Based on the position of 90° , 120° and 135° elbows with an included angle of 45° with the horizontal direction, the surface stress of the elbow shall be detected along the

Table 100.1 Average value of frequency modulus axial detection point

Elbow angle	Detection point angle	Frequency mode average reading
90	15	3642.6
	30	4646.0
	45	4642.6
	60	4376.1
	70	3732
120	20	3512.9
	30	3778.7
	45	4382.8
	60	4704.0
	70	4322.5
135	20	3638.6
	30	3982.8
	45	4024.0
	60	4002.5
	75	3798.4

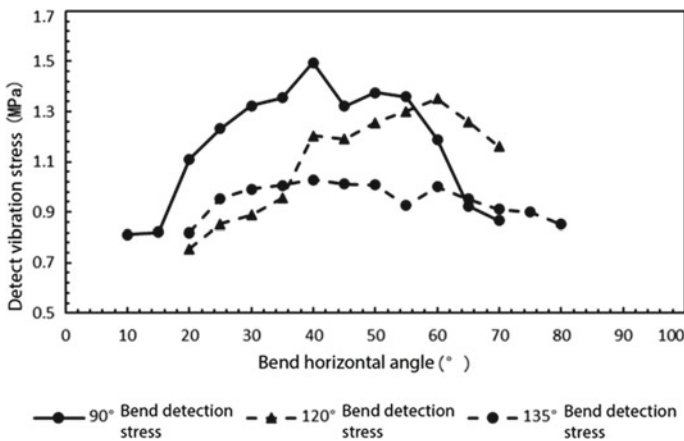


Fig. 100.1 Axial stress test results of elbows at various angles (left), the horizontal axis is the included angle (°), and the vertical axis is the vibration stress (MPa)

pipeline circumferential direction. The vibrating wire strain gauge shall be installed within the distance range of 20 ~ 120 mm from the central axis. The spacing of each detection point is 20 mm. There are 6 points for each elbow. Similarly, each point shall be recorded and tested for 10 min every 10 s, The average value of the obtained vibration frequency modulus is shown in Table 100.2, and the calculated stress value is shown in Fig. 100.2.

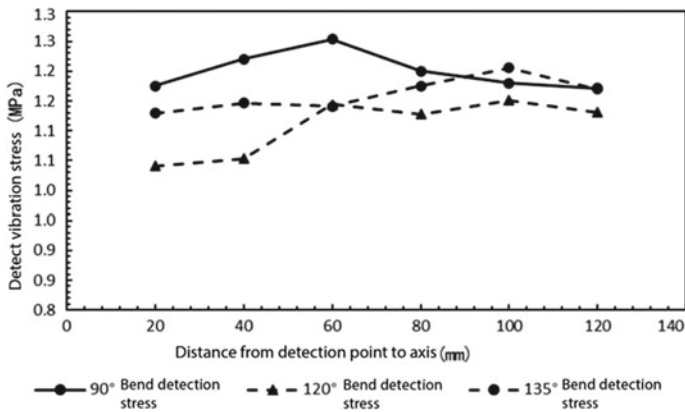


Fig. 100.2 Circumferential stress test results of elbows at various angles (right), the horizontal axis is the distance from the detection point to the axis (mm), and the vertical axis is the vibration stress (MPa)

Table 100.2 Average value of frequency modulus readings at each axial detection point reading of each circumferential detection point

Elbow angle	Distance from inspection point to axis	Detection point angle	Frequency mode average reading
90	40	45	4439.7
	60	45	4507.2
	80	45	4399.7
	100	45	4359.4
120	40	45	4107.2
	60	45	4287.9
	80	45	4255.4
	100	45	4302.9
135	40	45	4293.0
	60	45	4281.3
	80	45	4350.6
	100	45	4410.9

From the above test results, it can be concluded that the surface stress of the bend in natural gas station increases first and then decreases from the central axis to both sides of the pipeline, which has a certain relationship with the impact of fluid and particle erosion. The results are helpful to study the detection scope and monitoring points of the station pipeline in this paper.

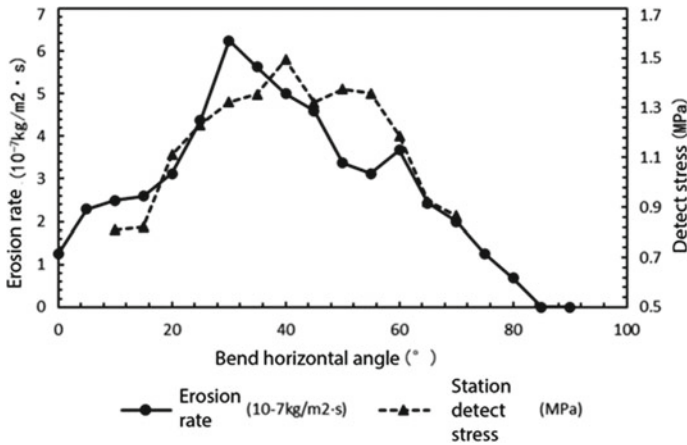


Fig. 100.3 Change curve of erosion rate and detection stress of 90° elbow

(3) Conclusion of comparative analysis

Taking the 90° elbow with 1.5 times the bend diameter ratio at the horizontal inlet and vertical downward outlet as an example, this study compares the stress detection results of gas transmission station with the numerical simulation results of the erosion simulation model, and it can be concluded that the erosion rate or stress varies with the horizontal angle of the elbow α . The curve of angle change is shown in Fig. 100.3.

In Fig. 100.3, a straight line with a circle represents the erosion rate; The dotted line and triangle represent the detection stress; The horizontal axis is the included angle (°); The left vertical axis represents the erosion rate; The vertical axis on the right is the detection stress (MPa).

It can be seen from Fig. 100.3 that the calculation results after numerical simulation of the simulation model increase with the horizontal included angle α . The erosion rate first increases rapidly and then decreases slowly. The area with serious erosion is concentrated in the range of 20° ~ 50° of elbow. However, according to the stress detection results of gas transmission station, the surface stress of the elbow during vibration is mainly concentrated at 30° ~ 60°. Combined with the detection results, we modify the simulation calculation results of the elbow simulation model and analyze the erosion range, as shown in Fig. 100.4.

In the Figs. 100.5 and 100.6, a straight line with a circle represents the erosion rate; The dotted line and triangle represent the detection stress; The horizontal axis is the included angle (°); The left vertical axis represents the erosion rate; The vertical axis on the right is the detection stress (MPa).

Based on the above research, we can conclude that the erosion range of the elbow in the natural gas station is 20° ~ 60°, and the point with the largest erosion rate, that is, the most serious erosion area is concentrated in the 40° ~ 60° (subject to the natural gas inlet), and the wall thickness monitoring of the elbow in the station can be mainly concentrated in this area.

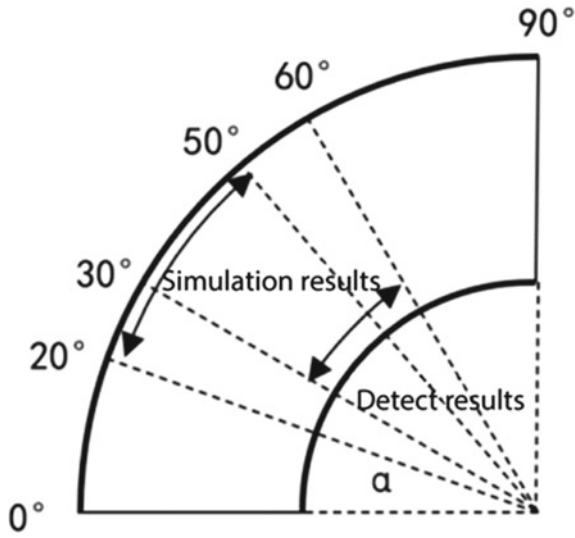


Fig. 100.4 Erosion range correction

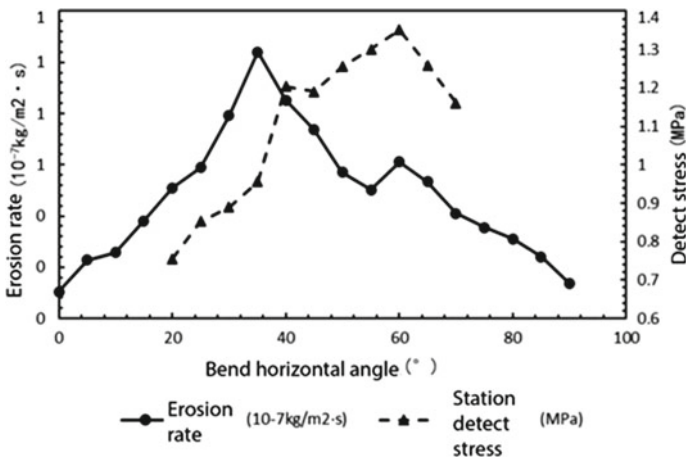


Fig. 100.5 Change curve of erosion rate and detection stress of 120° elbow

For the 120° and 135° natural gas pipeline elbows in the station, combined with the simulation model and the detection results of station, the following elbow angle and erosion rate curves can be obtained, as shown in Fig. 100.5 and Fig. 100.6.

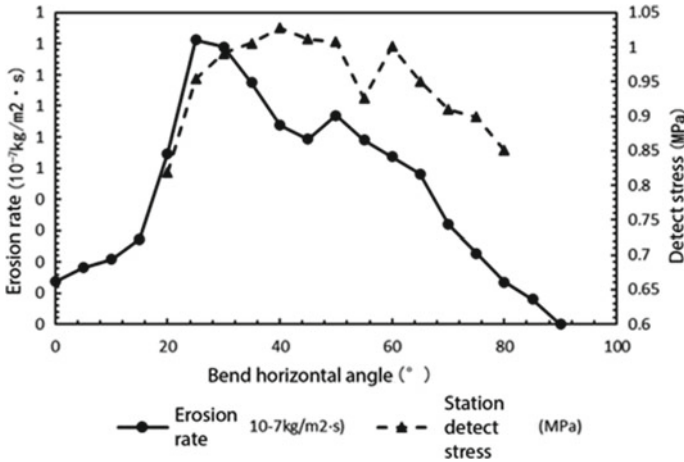


Fig. 100.6 Change curve of erosion rate and detection stress of 135° elbow

It can be seen from Fig. 100.5 that for the erosion of 120° elbow in the station, the wall thickness monitoring range can be concentrated in the range of 30° ~ 65° (subject to the natural gas inlet). It can be seen from Fig. 100.6 that for the erosion of 135° elbow in the station, the wall thickness monitoring range can be concentrated in the range of 25° ~ 70° (subject to the natural gas inlet).

100.2 Suggestions on Detection Range of Key Positions

Based on the above research results, it is suggested that the detection range (location of monitoring points) of the following elbows, tees and reducers:

(1) Suggestions on inspection range of elbow

- (1) For the outer arch surface of the elbow, the axial range is based on the tangent point of the tangent in the incoming direction and the connecting line between the center point (0°). 35° ~ 65° for 90° elbow; 25° ~ 70° for 120° elbow; The angle of 135° elbow is 25° ~ 75°. Take out the arc scribed lines at the above angles, and take 22° scribed lines on the left and right respectively (as shown in Fig. 100.7) based on the center line of the arch surface outside the radial direction. The intersection of the above two scribed lines is the detection range (monitoring point position);

During daily monitoring, if the pipe diameter is greater than 600mm, it is recommended to select four locations in the area for detection (at least two points are on the central axis); If the pipe diameter is less than 300mm, it is recommended to select one position in the area for detection (on the

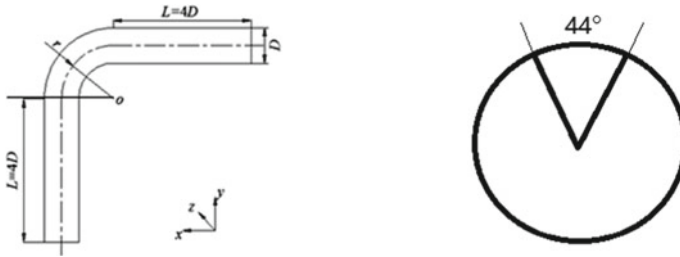


Fig. 100.7 Division of monitoring scope

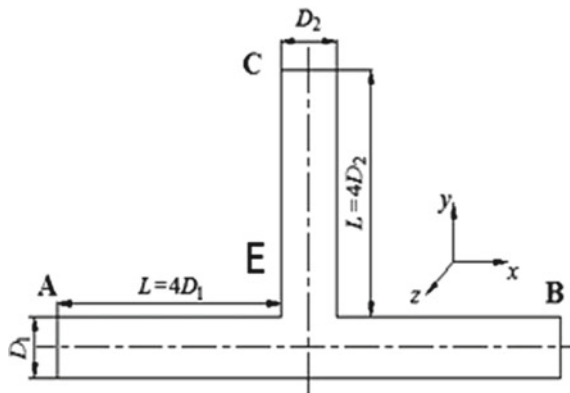
central axis); For the rest, it is recommended to select 2-3 locations in the area for detection (at least one point is on the central axis);

- (2) The negative pressure area is mainly for the 120° and 135° elbows in front of the filter separator. The area is the area where the central axis of the air inlet end is reflected to the ground of the air outlet end through the elbow as the center. Refer to the area taken in (1) (take half of the radial and axial directions respectively), and the detection point is correspondingly reduced by 1.

(2) Suggestions on inspection range of tee

- (1) As shown in Fig. 100.8, if the air flow enters from point B, it is output from point C. It is recommended to select area E as the monitoring point; The selection standard of area E is the area composed of a semi-circular arc with diameter D_2 close to e and a distance d_2 from e to C. Two monitoring points are required in the area;
- (2) As shown in Fig. 100.8, if the air flow enters from point C, it is output from point B. It is recommended to select the ring corresponding to D_2 size for point acquisition monitoring. If point a is closed and the air flows to point

Fig. 100.8 Division of detection range of tee pipe



B, it is recommended to properly translate the D2 ring to point B for point taking monitoring.

- (3) For the reducer with large and small head, if the small head flows to the large head, it is not necessary to detect; If the big end flows to the small end, it is recommended to take points directly below the reducing slightly close to the small diameter.

References

1. Kun, H., Ping, D., Yuepeng, L., et al.: Optimization of erosion resistant structure of 90° elbow in gas-solid two-phase flow. *China Sci. Technol. Work. Saf.* **15**(8), 7
2. Xiaoqin, S., Shiwei, H., Shanshan, Z.: Study on gas-solid two-phase flow wear of 90° elbow. *Drill. Prod. Technol.* **000**(006), 56–59 (2015)
3. Yong, H., Kun, Y., Lihong, Z., et al.: Numerical simulation of faucet elbow wear in reverse circulation drilling. *J. Cent.L South Univ.* **44**(5), 2053–2059 (2013)
4. Guangchuan, L., Chang, N., Qi, L., et al.: Erosion analysis of oil pipeline elbow based on fluent. *Corros. Prot.* **09**, 822–824 (2013)
5. Yongjie, Z.: Study on erosion failure mechanism of natural gas pipeline elbow. *Pet. Chem. Equip.* **14**(002), 44–46 (2011)

Chapter 101

Numerical Simulation of Impact Response of Board-Level Packaging Structure



Xu Long, Yuntao Hu, Tianxiong Su, and Chao Chang

Abstract Board-level drop responses are critical to evaluate the mechanical reliability of solder joints to serve as electrical and mechanical connections in electronic devices to resist failure due to drop impact. In this paper, by applying the elastoplastic constitutive models of solder materials and polymer materials in the BGA packaging structure, drop impact simulations of board-level packaging structure are performed according to the new version of JEDEC revised in 2016, JESD22-B111A for the drop test standard for portable electronic products. Particularly, the Input-G method is adopted, using a semi-sinusoidal acceleration pulse load with a peak of 1500G and a pulse time of 0.5 ms. The overall finite element model establishes a 1/4 model thanks to the symmetry of the board-level packaging structure. According to the simulation results, we explored the failure mode of the solder joint and polymer layer. At the same time, the mechanical reliability of different solder joints in the packaging structure is also discussed according to the production requirements. The results show that the solder joint far away from the center point of the PCB board is subjected to the greatest stress, which is the most vulnerable solder joint. It is found that the stress component in the vertical direction plays a leading role, which can be treated as the peeling stress. Peeling stress is the major reason to cause the crack occurrence and propagation in the solder joint, which is the main failure mode for solder joint. Under the same load, three BGA models with different solder joint distributions are compared.

Keywords Board-level packaging structure · Finite element method · Dynamic response · Drop impact · Input-G method

X. Long (✉)

Research and Development Institute of Northwestern, Polytechnical University,
Shenzhen 518063, China

e-mail: xulong@nwpu.edu.cn

Y. Hu · T. Su

School of Mechanics, Civil Engineering and Architecture, Northwestern Polytechnical University,
Xi'an 710072, People's Republic of China

C. Chang

School of Applied Science, Taiyuan University of Science and Technology, Taiyuan, China

101.1 Introduction

The continuous advancement of science and technology has resulted in the rapid development of portable electronics into the fast lane; consumer demand and use of this has also expanded, raising the reliability requirements of such products, particularly the diversity of uses brought about by drop shock response and device multi-function, miniaturization caused by high power operations and different service environments, and other extreme operating conditions.

Tee et al. [1, 2] proposed the Input-G method in 2004, which applies the reverse acceleration pulse signal obtained after a drop of an electronic component as a boundary condition directly to the location of the four bolt holes of a standard PCB board, except for the PCB board and its fixed package structure, which are negligible according to the experimental principle. Wong et al. [3] investigated the basic dynamics of a PC board under dropped impact loading. Long et al. [4, 5] described the deformation behavior of SAC305 at low to medium strain rates through an improved UCP constitutive model based on unified creep theory, and used the Johnson–cook model to characterize the shock response of the solder at high strain rate at room temperature. Long et al. [6–12] also conducted response studies on constitutive parameters and damage evolution. Mao et al. [13, 14] used machine learning methods to process the results. Xue and Xie et al. [15, 16] studied the stability of solder joints.

101.2 The Board-Level Package Drop Shock Response

101.2.1 Overview of BGA Packages and Related Principles

Surface mount technology is important in ICs because it provides a strong connection between the chip and the carrier. Because of its advantages such as high storage capacity per unit space, low inductance, and a high number of I/Os, the Ball Grid Array (BGA) form is widely used.

The widespread use of BGA package structures in portable electronics makes it difficult to apply in harsh service environments. The mechanical response behavior of interconnect materials under drop shock conditions is investigated in this paper for three different solder joint distributions (14×14) of BGA package structures classified as perimeter type array, full array, and interleaved array, with the specific distribution form shown in Fig. 101.1.

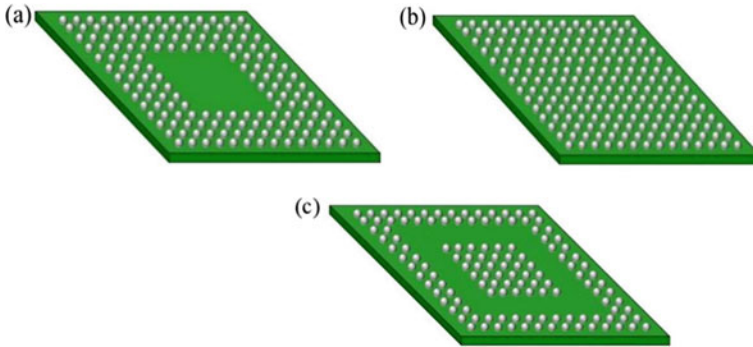


Fig. 101.1 BGA solder joint distribution form

101.2.2 BGA Board-Level Package Drop Reliability Analysis

The U.S. Joint Electron Device Engineering Standards Committee (JEDEC) issued the drop test standard JESD22-B111 for portable electronics in 2003 and revised it in 2016, i.e., standard JESD22-B111A. The standard describes a typical drop impact test experimental setup, mainly consisting of a rail, a drop table, and a rigid base; the test process. The standard PCB board is fixed to the substrate of the drop table by four bolts, as shown in Fig. 101.2a. The impact acceleration pulse application method in the numerical simulation is shown in Fig. 101.2b. The JEDEC standard recommends the use of a Class B peak of 1500 G and a pulse duration of 0.5 ms for the half-sine acceleration pulse load profile, as shown in Fig. 101.2c.

The dynamic impact response obtained from the solder joints under the conditions of a downward facing and horizontal drop of the package structure is larger than the

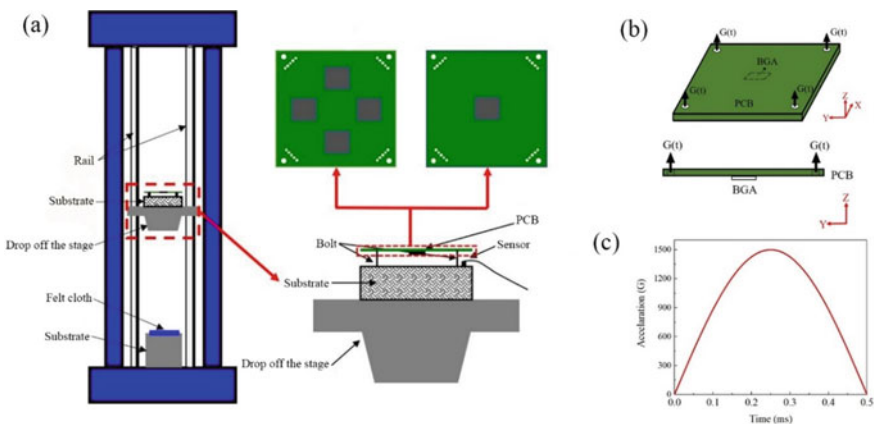


Fig. 101.2 a Sketch of a typical drop impact test setup; b overall model loading method; c half-sine acceleration pulse load curve

response effect obtained from other drop methods and is more prone to failure, so only the simulation content of the horizontal drop of the PCB board was carried out. Also, considering the complexity of the overall model and the computational time, only a board-level model with a BGA package structure affixed to the middle of the PCB is simulated in the numerical simulation process.

101.3 The Board-Level Package Drop Impact Simulation Modeling

101.3.1 Model Building and Material Properties

In the modeling process, the PCB board uses the dimensions specified in the new JEDEC revised standard JESD22-B111A, and according to the standard to establish the four-bolt hole constraint design, according to the actual application in which the load is applied. The global model structure is schematically shown in Fig. 101.3, which is mainly composed of five parts, that is, EMC, Die, Substrate, Solder ball, and PCB. The relevant dimensions of each component are shown in Table 101.1. The relevant dimensions of each component are listed in Table 101.1, where the center spacing between adjacent solder joints is 1 mm.

During the modeling process, multiple components are combined into a new Part by using the Merge technique, while still retaining the sub-interface to ensure the differentiation of the different components and to facilitate the specification of

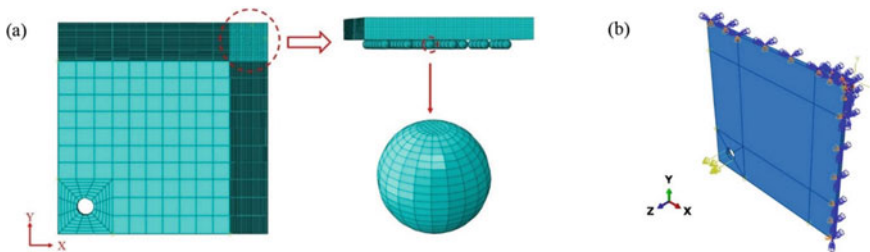


Fig. 101.3 **a** Mesh division; **b** load and boundary conditions

Table 101.1 Dimensions related to each component of the board-level package drop model

Component name	Length (mm)	Width (mm)	Height (mm)
PCB	77	77	1
EMC	15	15	0.61
Die	5	5	0.3
Substrate	15	15	0.36
Solder ball	Φ0.45		0.43

Table 101.2 Material parameters for each component of the board-level package drop model

Component name	Modulus of elasticity (MPa)	Poisson's ratio	Density (kg/m) ³
PCB	22,000	0.28	1800
EMC	15,500	0.3	1180
Die	131,000	0.3	2320
Substrate	18,200	0.25	1200
Solder ball	10,480	0.4	1000

different material properties. The material properties of the solder joints are defined using the Johnson-cook intrinsic model parameters, the material properties of the EMC are defined using the ZWT constitutive model, and the material parameters of the remaining components are shown in Table 101.2.

101.3.2 Mesh Division and Boundary Conditions

According to Table 101.1, the data related to different component sizes can be seen that the solder joint size is much smaller compared to the PCB board size, therefore, in this chapter, different mesh sizes are used for different components in the board-level package structure model during the process, i.e., cutting operations are performed for each component to refine the mesh of solder joints and their contact locations and coarsen the mesh of other parts. In terms of cell type selection, each component in the overall model is chosen to be a hexahedral cell with a 3D solid linear reduction integral of C3D8R, as provided in Fig. 101.3a.

Considering that the whole board-level package structure is centrosymmetric, to reduce the calculation time and improve the calculation efficiency, this section establishes a 1/4 model in the process of carrying out, as shown in Fig. 101.3b. At the same time, symmetry constraints need to be applied on the symmetry surface of the 1/4 model, i.e., translational constraints in the X direction and rotation constraints in the Y and Z directions are applied on the X symmetry surface, and translational constraints in the Y direction and rotation constraints in the X and Z directions are applied on the Y symmetry surface.

For the acceleration load application method of the impact response, the Input-G method is used in the simulation process. By the requirements for the use of this method, the impact load obtained by the PCB board after free fall acts as an acceleration pulse signal at the four bolt holes with the direction vertical up.

101.4 Simulation Results and Analysis

101.4.1 Board-Level Package Drop Shock Response Analysis

According to the drop impact theory, the PCB board with BGA package structure attached to the drop impact response process mainly contains two phases, the first phase is the PCB board subjected to half-sine acceleration pulse load phase, and the second phase is the free vibration phase after the acceleration pulse load disappears. The dynamic impact displacement response cloud of the PCB board in the simulation results is shown in Fig. 101.4a, and the displacement time history curve of its central node is shown in Fig. 101.4b. After the board-level package structure is subjected to a half-sine acceleration pulse impact load, the response at the center of the PCB board is the largest when the analysis step time is 1.3 ms, with an absolute displacement of 2.7 mm and a relative displacement of 1.64 mm.

Figure 101.5a shows the normal stress cloud for the array of solder joints in the package structure. The maximum normal stress for a hazardous solder joint is located at the location where the joint is attached to the PCB and near the edge side of the PCB board, followed by the upper surface where the joint is attached to the substrate and near the center of the substrate. Figure 101.5b shows the stress versus time curve of the solder joint. It can be observed that the value of the positive stress in the perpendicular direction to the PCB (σ_{33}) is much greater than the other component stresses, i.e., the maximum stress is the peel stress, which has a maximum value of 349.69 MPa.

At the maximum moment of the displacement response of the PCB board, the polymer layer is also severely deformed, and at this time the inner and outer stress clouds of the structure are illustrated in Fig. 101.6. It is obvious that the maximum stress of the polymer layer under the drop impact load occurs in its central part and is located on the outer side, while the inner stress value is lower and the interaction with the chip is weaker, which has less effect on the chip.

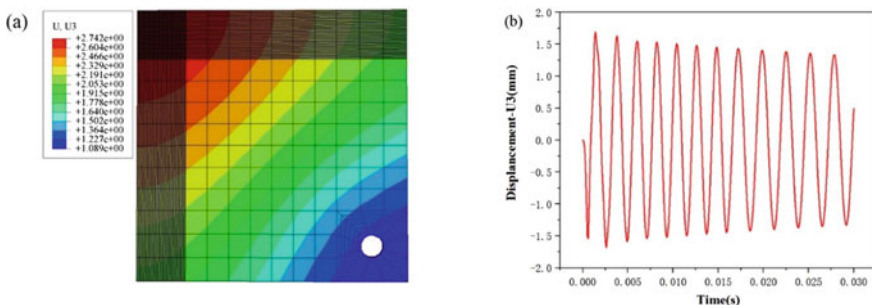


Fig. 101.4 a Displacement response cloud at 1.3 ms; b displacement time course curve of the central node

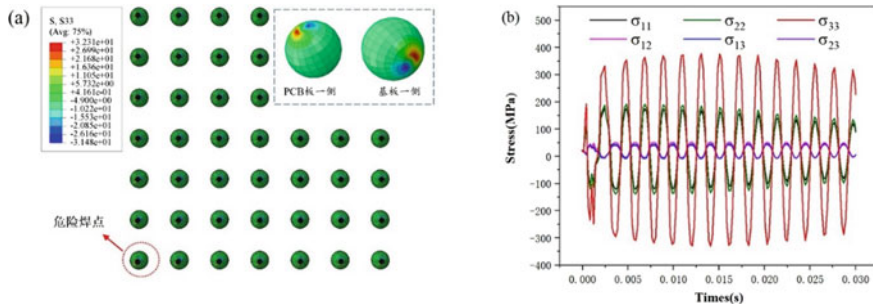


Fig. 101.5 a Normal stress cloud for the weld joint array; b stress versus time curve at the most dangerous weld joint

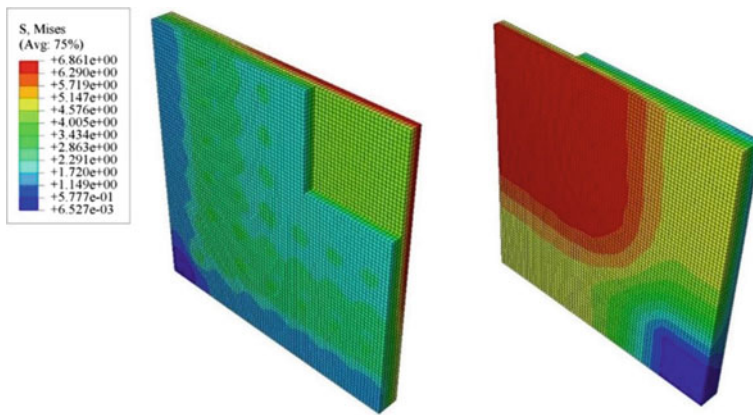


Fig. 101.6 Stress clouds on the inner and outer sides of the polymer layer

101.4.2 Effect of Different Solder Joint Distributions on Drop Impact Response

To study the effect of different solder joint distributions on the drop impact response of the whole board-level package structure in the same package form, three BGA models with different solder joint distributions were selected in the course of this paper. According to the simulation results in Fig. 101.7, there is a good overlap between the three before 8ms, but the displacement peak of solder joint array A is slightly higher than that of solder joint array B and C. This is mainly because solder joint arrays B and C retain the most central solder joint, which plays a restraining role, resulting in a maximum displacement of the A array with the central solder joint removed. This is mainly because solder joint arrays B and C retain the most central solder joint, which acts as a constraint, resulting in a smaller maximum displacement than array A with the central solder joint removed, and a corresponding phase lag.

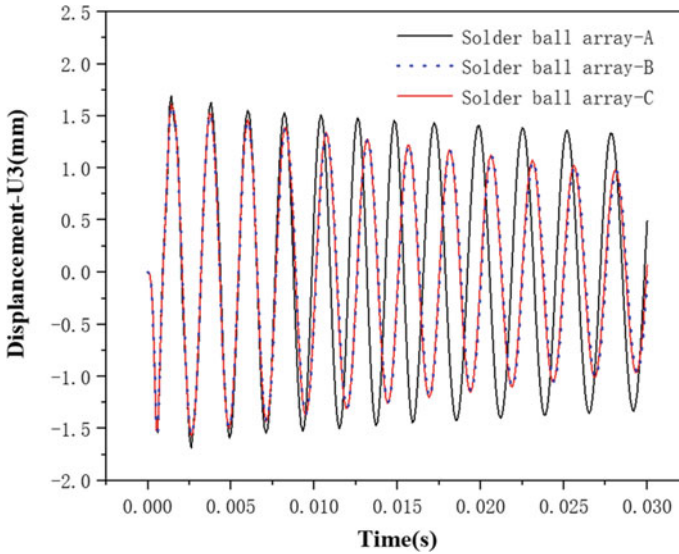


Fig. 101.7 PCB displacement impact response with different solder joint distribution

The displacements of array B and array C tend to be the same, which reflects that the 3 and 4 layers of solder joints have little effect on the displacement.

It is found that peel stress can be considered the main basis for determining the failure of a solder joint. Figure 101.8 shows the peel stress curves of the hazardous joints for three different solder joint distributions. Similar to the displacement impact response of the PCB, there is a significant hysteresis in the peel stress of the hazardous joints of solder joint arrays B and C. The maximum stress is less than the 349.69 MPa of array A. This proves that under the same load, solder joint array A is more likely to be damaged.

The effect of different forms of solder joint distribution on the polymer layer under the same impact load is shown in Fig. 101.9. When the response time reaches 0.6 ms, the Mises stresses in the polymer layer caused by solder joint arrays A, B, and C all reach their maximum values, and after 5 ms, solder joint arrays B and C show a hysteresis phenomenon relative to solder joint array A. At the same time, it makes the Mises stresses in the polymer layer drop faster and their stress values are smaller than those of solder joint array A.

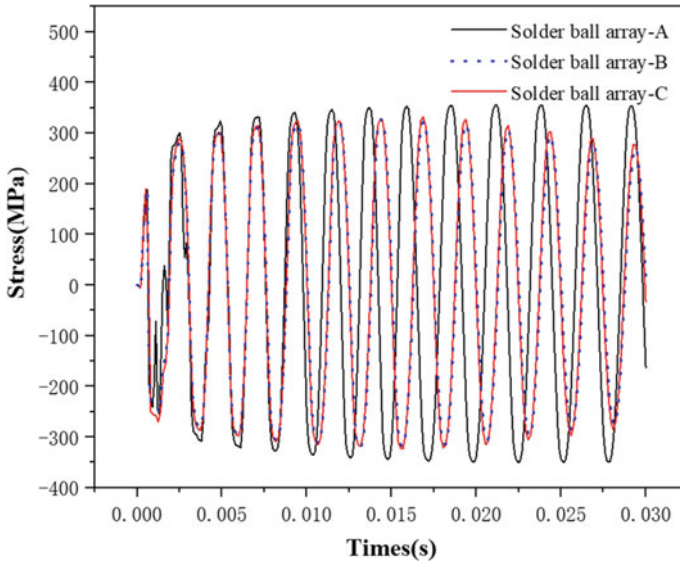


Fig. 101.8 Plots of hazardous solder joint peel stresses for different solder joint distributions

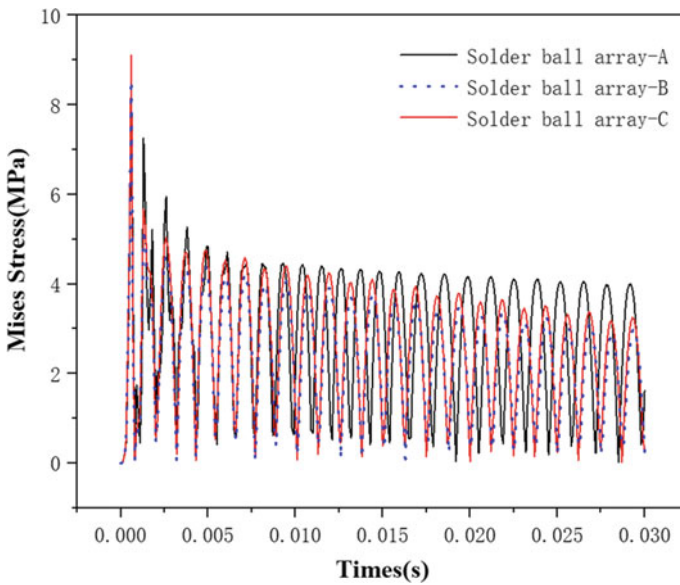


Fig. 101.9 Effect of different solder joint distributions on the polymer layer

101.5 Conclusion

In this paper, by applying the intrinsic structure model of solder joint material and polymer material in BGA package structure, the drop impact simulation of the board-level package is carried out according to the new version of JEDEC drop test standard JESD22-B111A revised in 2016 for portable electronic products, using Input-G method with a peak value of 1500G and a pulse time of 0.5 ms. The overall model is based on the symmetry of the 1/4 model. The results show that the corner solder joints far from the center of the PCB are subjected to the highest stresses and are the most vulnerable hazardous solder joints and that the positive stresses perpendicular to the direction of the PCB are peeling stresses, in addition, the maximum stresses on the polymer layer occur at its outer center. Under the same load, the stress on the solder joint array A is the largest, B, and C array of stress is smaller and very close, indicating that the innermost layer of the solder joint at this time plays a very obvious role in restraint.

Acknowledgements This work was supported by the Guangdong Basic and Applied Basic Research Foundation (No. 2023A1515011170), National Natural Science Foundation of China (No. 52175148), and the Regional Collaboration Project of Shanxi Province (No. 202204041101044).

References

1. Tee, T.Y., Luan, J.E., Pek, E., Lim, C.T., Zhong, Z. (eds.): Novel numerical and experimental analysis of dynamic responses under board level drop test. In: Proceedings of the 5th International Conference on Thermal and Mechanical Simulation and Experiments in Microelectronics and Microsystems, EuroSimE (2004)
2. Tee, T.Y., Luan, J.E., Pek, E., Lim, C.T., Zhong Z. (eds.): Advanced experimental and simulation techniques for analysis of dynamic responses during drop impact. In: Proceedings—Electronic Components and Technology Conference (2004)
3. Wong, E.H., Mai, Y.W., Seah, S.K.W.: Board level drop impact—Fundamental and parametric analysis. *J. Electron. Packag. Trans. ASME*. **127**(4), 496–502 (2005)
4. Long, X., Xu, J., Wang, S., Tang, W., Chang, C.: Understanding the impact response of lead-free solder at high strain rates. *Int. J. Mech. Sci.* **172**, 105416 (2020)
5. Long, X., Su, T., Lu, C., Wang, S., Huang, J., Chang, C.: An insight into dynamic properties of SAC305 lead-free solder under high strain rates and high temperatures. *Int. J. Impact Eng* **175**, 104542 (2023)
6. Long, X., Guo, Y., Su, Y., Siow, K.S., Chen, C.: A new unified creep-plasticity constitutive model coupled with damage for viscoplastic materials subjected to fatigue loading. *Fatigue and Fracture of Engineering Materials and Structures*(2022)
7. Long, X., Guo, Y., Su, Y., Siow, K.S., Chen, C.: Unveiling the damage evolution of SAC305 during fatigue by entropy generation. *Int. J. Mech. Sci.* **244**, 108087 (2023)
8. Long, X., Jia, Q., Shen, Z., Liu, M., Guan, C.: Strain rate shift for constitutive behaviour of sintered silver nanoparticles under nanoindentation. *Mech. Mater.* **158**, 103881 (2021)
9. Long, X., Jia, Q.P., Li, Z., Wen, S.X.: Reverse analysis of constitutive properties of sintered silver particles from nanoindentations. *Int. J. Solids Struct.* **191–192**, 351–362 (2020)

10. Long, X., Mao, M., Lu, C., Li, R., Jia, F.: Modeling of heterogeneous materials at high strain rates with machine learning algorithms trained by finite element simulations. *J. Micromech. Mol. Phys.* **6**(1) (2021)
11. Long, X., Mao, M.-H., Su, T.-X., Su, Y.-T., Tian, M.-K.: Machine learning method to predict dynamic compressive response of concrete-like material at high strain rates. *Defence Technol.* (2022)
12. Long, X., Shen, Z., Jia, Q., Li, J., Dong, R., Su, Y., et al.: Determine the unique constitutive properties of elastoplastic materials from their plastic zone evolution under nanoindentation. *Mech. Mater.* **175**, 104485 (2022)
13. Mao, M., Liu, J., Tian, M., Lin, P., Long, X.: Drop impact analysis of TSV-based 3D packaging structure by PSO-BP and GA-BP neural networks. *China Welding (English Edition)*. **31**(1), 37–46 (2022)
14. Mao, M., Wang, W., Lu, C., Jia, F., Long, X.: Machine learning for board-level drop response of BGA packaging structure. *Microelectron. Reliab.* **134**, 114553 (2022)
15. Xie, D., Gektin, V., Geiger, D. (eds.): Reliability study of high-end Pb-free CBGA solder joint under various thermal cycling test conditions. *Electron. Compon. Technol. Conf.* (2009)
16. Xue, S., Zhang, L., Shenglin, Y.U., Lai, Z., Han, Z., Fangyan, L.U.: Finite element analysis on soldered joint reliability of FCBGA device with different dimensions. *J. Jiangsu Univ. Sci. Technol.* (2007)

Chapter 102

A Graphical Computing-Based Image Registration Method for LED Chips



Pengfei Zheng, Bo Wang, Xiyuan Wan, Jingjing Lou, Jun Lv, Qingdong Luo, and Linsheng Xie

Abstract Image registration is a key problem and a technical difficulty in the field of machine vision and image processing research. For the problems that the detection accuracy of the machine learning method depends on a large number of training samples, and it is difficult to take samples in the LED chip production process, a graphical computing-based LED chip image registration method is proposed. The geometrical representation of the LED chip image features is used to realize the registration of the chip image in the form of geometric calculation. Image morphology processing and Hough transform are used to calculate the registration angle of chip images. With the variational thinking of tessellation grid, a simplified computational model of tessellation grid is proposed to replace the global information with key features of the image for fast registration. The step-by-step generalized image registration algorithm is designed for multiple types of LED chip image characteristics to achieve efficient registration of multiple LED chip images. According to the experimental results of multi-type LED chip image registration, it shows that the proposed graphical computational registration method has a high average registration accuracy and a good registration effect for a variety of LED chip images, which can lay a good foundation for large-scale online detection of LED chip defects.

Keywords LED chip · Image registration · Graphical calculation · Tessellation grid · Defect detection

P. Zheng (✉) · B. Wang · X. Wan · J. Lou · J. Lv · Q. Luo
Yiwu Industrial and Commercial College, Yiwu 322000, China
e-mail: pfzheng@126.com

P. Zheng · L. Xie
East China University of Science and Technology, Shanghai 200237, China

P. Zheng
HC Semitek Corporation, Yiwu 322000, China

102.1 Introduction

Machine vision technology is an interdisciplinary discipline involving artificial intelligence, neurobiology, psychophysics, computer science, image processing, pattern recognition and many other fields. It uses machines instead of human eyes to simulate human visual functions, extracting information from images of objective things, processing and understanding them, and finally using them for practical detection, measurement and control. In recent years, with the booming development of artificial intelligence, machine vision technology has been widely used in many engineering applications. As an important image processing technology, image registration plays an important fundamental role in machine vision applications. Image registration is mainly to solve the problem of geometric correspondence between images obtained under different spatial and temporal conditions and different sensors. Therefore, many scholars have conducted extensive research on the image registration problem. He et al. [1] proposed a novel nonfinite-modality data augmentation for brain image registration. Zhang et al. [2] proposed a mixture model approach based on mesh warping. Lin et al. [3] designed a multi-plane alignment algorithm guided by the disparity map to distinguish one background plane and multiple foreground objects from the image. Chen et al. [4] presented a novel registration method named HMVReg, and implemented the challenging registration task via a three-stage coarse-to-fine alignment. Hernandez-Matas et al. [5] employed a retinal image registration through eye modelling and pose estimation (REMPE) framework, which simultaneously estimated the cameras' relative poses. Gupta et al. [6] discussed on various well known approaches of medical image registration using hardware or software. Teuwen et al. [7] reviewed many applications of automatic image registration in radiation oncology. Song et al. [8] presented a novel cross-modal attention mechanism for correlating features extracted from the multi-modal input images and mapping such correlation to image registration transformation. Sorzano et al. [9] proposed an approach for post-acquisition alignment of tilt series images, which was marker-free, based on patch tracking and integrated in free software. Zheng et al. [10] presented a coarse-to-fine medical image registration method based on progressive images and SURF algorithm (PI-SURF) for higher registration accuracy. Lara-Hernández et al. [11] presented a deformable deep learning-based image registration method for quantitative myocardial perfusion CT examinations, which took into account some unique challenges such as low image quality with less accurate anatomical landmarks, and misalignment caused by cardiac stress, respiration, and patient motion. Gul et al. [12] proposed an accurate method for various high resolution remote sensing image registration. Cocianu et al. [13, 14] presented a new memetic, cluster-based methodology for image registration in case of geometric perturbation model involving translation, rotation and scaling, and a new method to register images in the case of geometric perturbations that included rotations, translations, and non-uniform scaling. Zang et al. [15] proposed a method for registering a patient's chest CT scan to live surgical EBUS views, thereby facilitating accurate image-guided EBUS bronchoscopy. Jiang

et al. [16] proposed a novel image alignment algorithm to cope with the multi-exposed images with saturated regions. Ma et al. [17] proposed an image registration method based on additive edge cosine loss. Marsland et al. [18] discussed how image registration using finite-dimensional planar Lie groups (in contrast to general diffeomorphisms) can be used in this process. Striewski et al. [19] proposed a method to non-rigidly align a three-dimensional (3D) volumetric image with a two-dimensional (2D) planar image representing a projection of the deformed volume. Shao et al. [20] presented an adaptive feature scaling (AFS) mechanism to refine the multi-scale feature maps derived from the HAT module by rescaling channel-wise features in the global receptive field. Mondal et al. [21] proposed a high-speed hardware-based image registration to exploit parallelism and adaptive sampling technique to fulfill the requirement of high-speed portable multimedia devices.

According to different image registration principles, image registration methods can be generally classified into three categories: grayscale based image registration algorithms, feature based image registration algorithms and transform domain based image registration algorithms, all three types of methods have their own advantages and disadvantages and are suitable for different application scenarios. In this paper, we propose an LED image registration method based on geometric dimensionality reduction calculation with LED chip images as the research object.

102.2 Image Pre-processing

102.2.1 Image Denoising and Feature Enhancement

In the sampling process of LED chip images, some random noise will inevitably be generated due to the environment and equipment conditions and other factors. And Gaussian filtering is a weighted average processing of the whole image, whose value is obtained by itself and other pixel values in the neighborhood after weighted average, so Gaussian filtering is a typical linear smooth filtering, which is exactly in line with the characteristics of LED chip image with relatively single object and relatively stable background. Therefore, in this paper, Gaussian filtering is chosen to denoise the chip image, and the two-dimensional Gaussian filtering distribution function as below.

$$G(x, y) = \frac{1}{2\pi\sigma^2} e^{-\frac{x^2+y^2}{2\sigma^2}} \quad (102.1)$$

As shown in Fig. 102.1, Gaussian filtering is used to denoise different types of LED chip images with good results.

In order to retain as many important features as possible in the image and highlight the lithographic circuit graphics in the LED chip image, the image enhancement technique is used to enhance the features of interest (ROI) of the denoised image. The Laplace transform, as a linear transform commonly used in engineering mathematics,

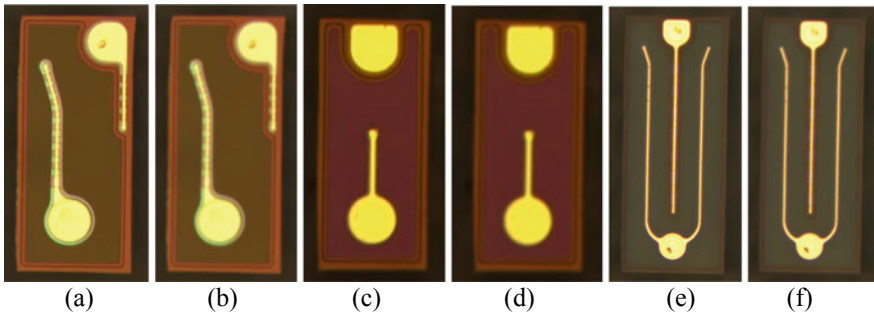


Fig. 102.1 Gaussian filtering effect of different LED chip images

can perform a second-order differentiation operation on the image, which plays the role of highlighting the image edges and increasing the detail features of the image. Therefore, we use the Laplace operator for feature enhancement of chip images, and its enhancement effect is shown in Fig. 102.2. Laplace operator is defined as follows.

$$\nabla^2 f(x, y) = \frac{\partial^2 f}{\partial x^2} + \frac{\partial^2 f}{\partial y^2} \tag{102.2}$$

Its discrete expression is.

$$f(x + 1, y) + f(x - 1, y) + f(x, y + 1) + f(x, y - 1) - 4f(x, y) \tag{102.3}$$

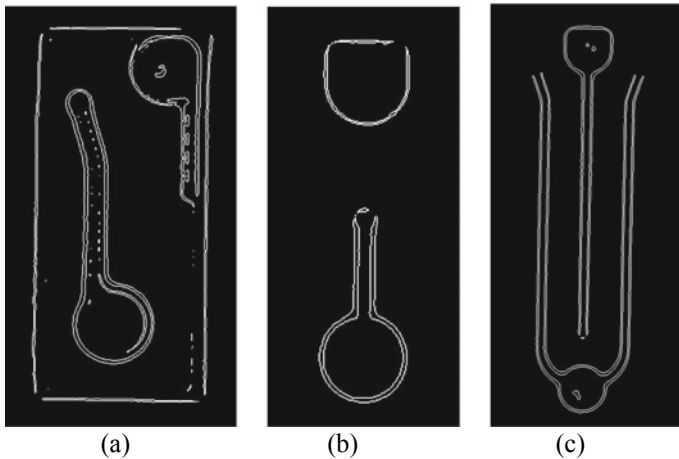


Fig. 102.2 Image enhancement effect

102.2.2 Image Segmentation

In order to better locate important feature regions and reduce the amount of invalid computation, the maximum between-class variance (OTSU) method is used to segment the images and achieve target separation. Maximum interclass variance was proposed by Nobuyuki Otsu, a Japanese scholar, in 1979 as an adaptive threshold determination method. The algorithm assumes that the image can be segmented into two parts, background and target, based on the pixel threshold. Then, this optimal threshold is calculated to distinguish the pixels in these two parts so that the two parts are distinguished with maximum pixel differentiation. Set an image is $I(x, y)$, the total number of pixels is Sum , the segmentation threshold between target and background is T , the number of pixels in the image whose gray value is less than the threshold T is denoted as N_1 , and the number of pixels whose grayness is greater than the threshold T is denoted as N_2 . Then, the background pixel share ω_1 , the target pixel share ω_2 , the average gray value of the background μ_1 , the average gray value of the target μ_2 , the cumulative gray value of the image μ and the inter-class variance g are calculated as follows.

$$\omega_1 = \frac{N_1}{Sum} \quad (102.4)$$

$$\omega_2 = \frac{N_2}{Sum} = 1 - \omega_1 = 1 - \frac{N_1}{Sum} \quad (102.5)$$

$$\mu_1 = \sum_{i=0}^t i * P_r(i|C_0) = \sum_{i=0}^t i * P_i / \sum_{i=0}^t P_i = \frac{\mu_t}{\omega_1} \quad (102.6)$$

$$\mu_2 = \sum_{i=t+1}^{M-1} i * P_r(i|C_1) = \sum_{i=t+1}^{M-1} i * P_i / \sum_{i=t+1}^{M-1} P_i = \frac{\mu - \mu_t}{\omega_2} \quad (102.7)$$

$$\mu = \mu_1 * \omega_1 + \mu_2 * \omega_2 \quad (102.8)$$

$$g = \omega_1 * (\mu - \mu_1)^2 + \omega_2 * (\mu - \mu_2)^2 = \omega_1 * \omega_2 * (\mu_1 - \mu_2)^2 \quad (102.9)$$

As shown in Fig. 102.3, the chip image can be segmented effectively by using the Otsu method, which avoids the interference of invalid background pixels with the uncertainty of subsequent graphical calculations and lays an accurate data base for image registration.

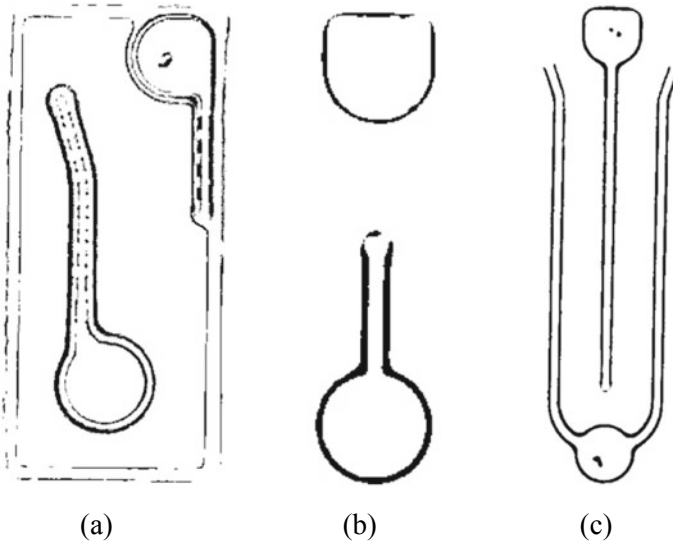


Fig. 102.3 Image segmentation effect

102.3 Image Feature Calculation and Registration

102.3.1 Image Registration Method Design

Based on the above analysis and image pre-processing, we propose a graphical computation-based LED chip image registration method. The method adopts a step-by-step calculation idea, using the tessellation model to reduce the dimensional representation of the image information, and to simplify the calculation and extraction of the image geometric features for the initial positioning of the image to be registered; then, the linear features in the corresponding area between the image to be registered and the image template are identified through the Hough transform, and the corresponding geometric correspondence is obtained by graphical calculation, and the image is fine-tuned again. Finally, according to the established geometric correspondence, feature registration and affine are performed on the image to be registered. The overall flow of the proposed method is shown in Fig. 102.4.

102.3.2 Calculation and Extraction of Image Features

Although the image segmentation algorithm has effectively separated the background from the target, the target features of the LED chip image are all circuits of the PN junction, the graphic structure is slender and occupies a smaller area, compared to

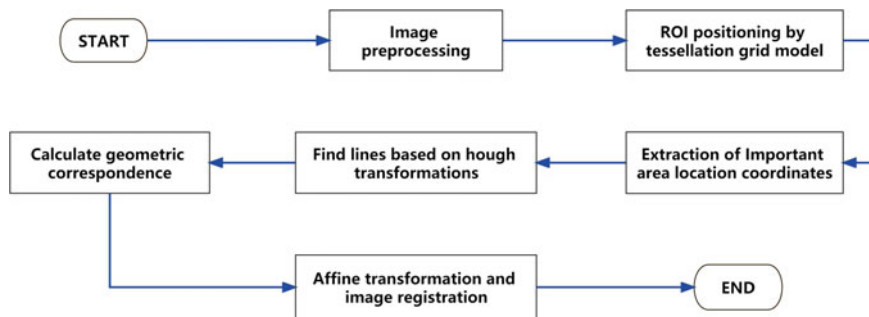


Fig. 102.4 Overall flow chart of the algorithm

the smallest rectangular box of the target features. If the segmented target image is used for direct registration, its computation is still not small. Therefore, in order to reduce the computation of registration to a greater extent, we use the tessellation model to simplify the image and replace the global computation of the target image with several key regions of the target image, which not only can significantly reduce the computation, but also can ensure that the accuracy is not affected. The reason is simple, for two images of the same size (template map and to be registered map), only need to find a number of key points corresponding to one by one, according to which the image registration, other features on the image can naturally correspond. Because the LED chip image does not have spatial distortion or aberration, which is different from the print or textile, if the size of the template image and the image to be registered are not the same, equal scaling can be used to solve.

As shown in Fig. 102.5, we divide the image to be registered into a tessellation grid structure, which can be any size such as 2×2 , 4×4 , 8×8 , etc. This division size depends on the size of the specific chip image. As shown in Fig. 102.6, if A is a chip image template and B is a chip image to be registered. The coordinates of the four corner points (Tp_1, Tp_2, Tp_3, Tp_4) and (Rp_1, Rp_2, Rp_3, Rp_4) of A and B images can be obtained according to the characteristics of the image pixel point coordinates, from which the coordinates of the center point (Tp_0, Rp_0) of the two images can be computed. Based on the value of the coordinates of this center point, the directionality of each image in the plane can be determined, and the azimuth calculation can be obtained by Eq. 102.11. Therefore, we can use the difference between θ_t and θ_r to perform a preliminary rotation correction of the image to be registered. In addition, the registration relationship between the corresponding positions of two images can be initially judged by comparing the number or density of pixel points within the corresponding grid. We use the registration similarity threshold τ to indicate the degree of coincidence of the corresponding grid within the two images, and the smaller the value of τ , the smaller the error and the higher the similarity of the images within the two grids. τ is calculated by Eq. 102.12, where, $\sum_{i,j} \sigma_t(i,j)$ denotes the number of pixel points contained in the tessellation grid in row i and column j of the template image, and $\sum_{i,j} \sigma_r(i,j)$ denotes the number of

pixel points contained in the tessellation grid in row i and column j of the image to be registered. According to the experimental test, the value of τ in this paper is 0.001. When $\tau \leq 0.001$ is satisfied, the correspondence is considered to exist, otherwise, the registration is considered to fail.

$$Tp_0 = (mid(Tp_1, Tp_2, Tp_3, Tp_4), mid(Tp_1, Tp_2, Tp_3, Tp_4))$$

$$Rp_0 = (mid(Rp_1, Rp_2, Rp_3, Rp_4), mid(Rp_1, Rp_2, Rp_3, Rp_4)) \tag{102.10}$$

$$\theta_t = ang(Tp_0 \rightarrow Tp_4), \theta_r = ang(Rp_0 \rightarrow Rp_4) \tag{102.11}$$

$$\tau = \left(\sum_{i,j} \sigma_{t(i,j)} - \sum_{i,j} \sigma_{r(i,j)} \right) / \sum_{i,j} \sigma_{t(i,j)} \tag{102.12}$$

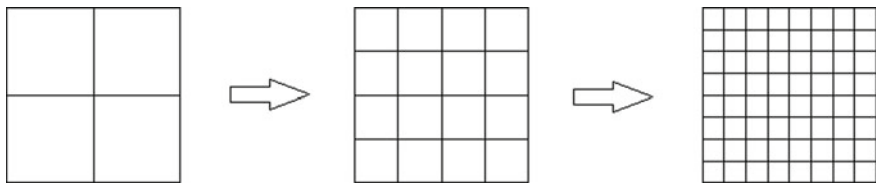


Fig. 102.5 Arbitrary sizes of tessellation grid model

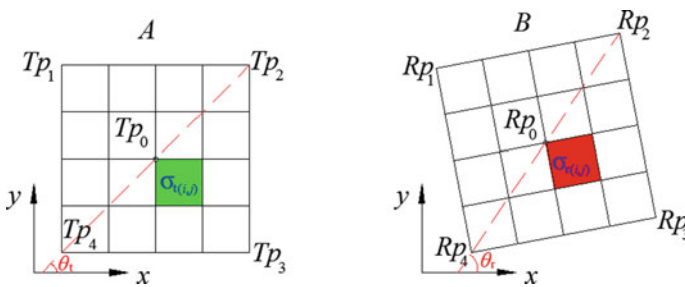


Fig. 102.6 Image feature calculation

102.3.3 Image Registration Based on Graph Computation and Hough Transform

After the initial calibration of the tessellation model, the geometric correspondence between the two registered images can be basically established, but in order to improve the image registration accuracy, we use a combination of graphical computation and Hough transform to align the images again. As shown in Fig. 102.6, the overall determination of the position offset values Δx and Δy between the template image and the image to be registered in x and y directions is performed by calculating the coordinates of the centroids of the grids corresponding to the registration thresholds. The principle of the Hough transform is to transform the points on a particular graph onto a set of parameter spaces and find a solution corresponding to an extreme value based on the cumulative result of the points in the parameter spaces. Since the linear features in the chip image are basically horizontal or vertical lines, we can use the Hough transform to set a specific slope of the line to search for lines in the ROI region. As shown in Fig. 102.7, all the corresponding lines are searched by the Hough transform for direction vector statistics, and the directional relationship between them can be calculated in a simplified way by Eq. 102.14. After the above calculation, we can align the image to be registered with the template image in x and y directions and overall orientation. In order to improve the registration efficiency, the whole process does not need to move the image, but uses data calculation and coordinate mapping for registration display. Finally, the tessellation grids that match the registration relationship are associated, as shown in Fig. 102.8. Obviously, the variation of the tessellation grid size can achieve the purpose of locating the ROI region quickly, while reducing the computation and ensuring the registration accuracy.

$$\begin{aligned}\Delta x &= \sum_{i,j} ((\sigma_{t(i,j)})_{center-x} - (\sigma_{r(i,j)})_{center-x}), \\ \Delta y &= \sum_{i,j} ((\sigma_{t(i,j)})_{center-y} - (\sigma_{r(i,j)})_{center-y}),\end{aligned}\quad (102.13)$$

$$ang_l = \sum_{i=1}^n (ang_{Hough_T_i} - ang_{Hough_L_i}) \quad (102.14)$$

102.4 Experiment and Analysis

In order to verify the effectiveness of the image registration method proposed in this paper, the algorithm is tested on AutoCAD. The experimental environment is Windows 10 operating system with 2.20 GHz main frequency and 8.00 GB of

Fig. 102.7 Search for lines using Hough transform

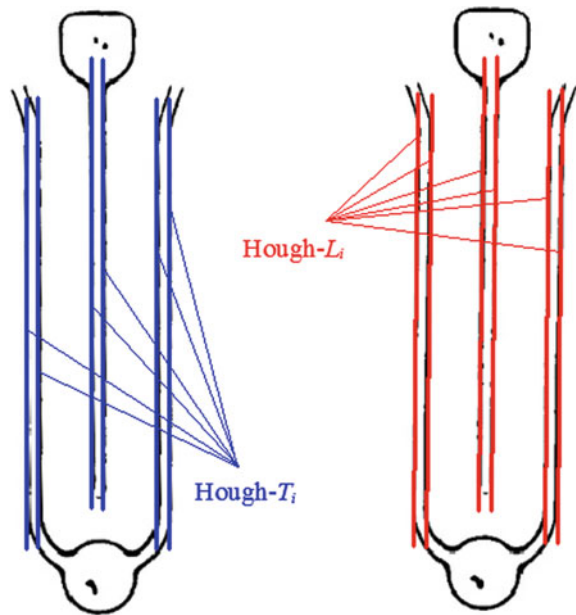
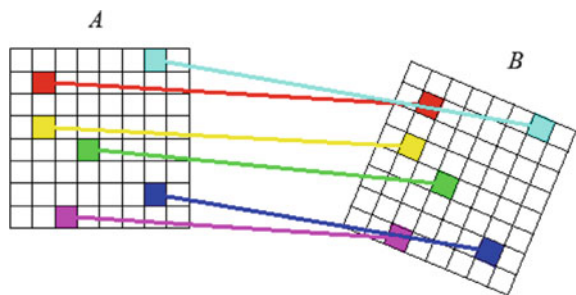


Fig. 102.8 Image alignment model



memory. The experimental images are all from the LED chip images collected on the actual production line of a company, and the registration experiments are conducted by multiple groups of images collected under different equipment and different conditions, and the registration effects are shown in Figs. 102.9 and 102.10.

From the above experiments, it can be seen that: the LED chip image registration method based on graphical computation proposed in this paper is applicable to the registration problem of different types of LED chip images, and the computational efficiency is high and the accuracy can reach the demand of engineering applications. The method uses the partitioning strategy of tessellation grid to reduce the continuous image information into discrete data, which achieves the purpose of dimensionality reduction calculation, has generality, simple operation and good robustness, and is a typical way to solve geometric problems using geometric computation.

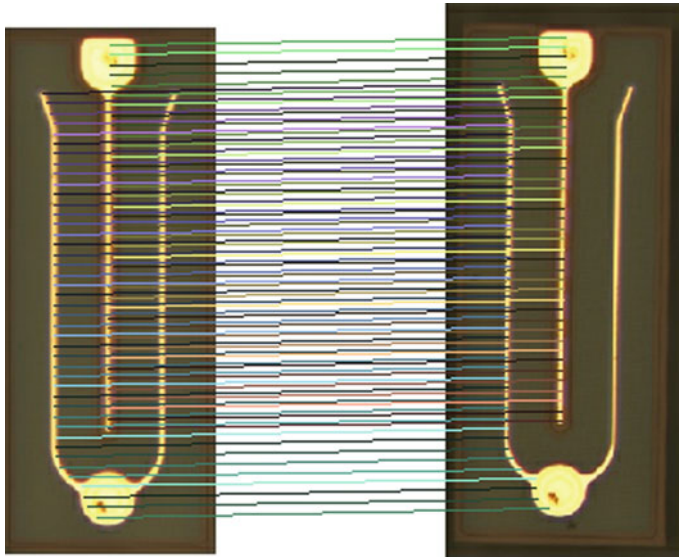


Fig. 102.9 Registration effect of chip 1

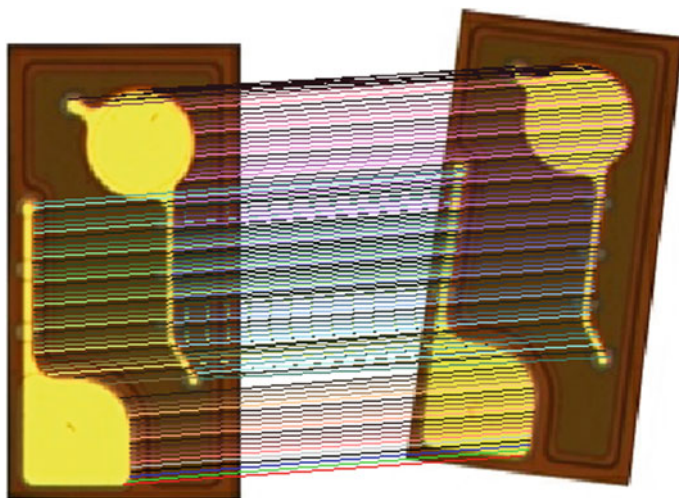


Fig. 102.10 Registration effect of chip 2

102.5 Conclusion

Image registration is a fundamental problem in graphic image processing and pattern recognition. In this paper, we investigate the registration problem of LED chip images and propose a graphical computation-based registration method for LED chip images.

The method uses Gaussian filtering and Laplace transform to denoise and feature enhance the LED chip image in the image pre-processing stage, and the Otsu method is used to segment the image target and background. On this basis, the ROI region in the target object is quickly localized with the help of tessellation grid model, and the pose adjustment and calibration of the image are combined with Hough transform and graphical calculation. Finally, the proposed method is experimented by the LED chip images in actual production, and the experimental results show that the method is more efficient in calculation, has better accuracy, can effectively reduce the calculation volume, meets the practical application requirements of engineering, and has a good development space. The future work will continue to take advantage of the dimensionality reduction of geometric computing, use geometric thinking to solve complex problems of metrics and localization among graphic images, apply it to more engineering fields, and deepen the concept of geometric computing to solve geometric problems.

Funding Statement This study was supported by the Special Project of Scientific Research and Development Center of Higher Education Institutions, Ministry of Education of the People's Republic of China (Grant No. ZJXF2022126), the new product pilot program projects of Zhejiang Province in 2022 (the second batch), China (Grant No. 2022D60SA7020371, 2022D60SA7017931), the public Welfare Science and Technology Research Project of Jinhua, Zhejiang Province, China (Grant No. 2022-4-302, 2022-4-305), and Ywice Special Interest Group on Machine Vision (YSIGMV).

Conflicts of Interest The authors declare that they have no conflicts of interest to report regarding the present study

References

1. He, Y.B., Wang, A.Y., Li, S., et al.: Nonfinite-modality data augmentation for brain image registration. *Comput. Biol. Med.* **147**, 105780 (2022)
2. Zhang, Z.H., Yu, X.H., Yang, X.Q.: Image alignment using mixture models for discontinuous deformations. *Signal Process.* **195**, 108467 (2022)
3. Lin, M.Y., Liu, T.B., Li, Y., et al.: Image stitching by disparity-guided multi-plane alignment. *Sig. Process.* **197**, 108534 (2022)
4. Chen, Z.N., Zhao, S., Hu, K., et al.: A hierarchical and multi-view registration of serial histopathological images. *Process Recogn. Lett.* **152**, 210–217 (2021)
5. Hernandez-Matas, C., Zabulis, X., Argyros, A.A.: Retinal image registration as a tool for supporting clinical applications. *Comput. Methods Programs Biomed.* **199**, 105900 (2021)
6. Gupta, S., Gupta, P., Verma, V.S.: Study on anatomical and functional medical image registration methods. *Neurocomputing* **452**, 534–548 (2021)
7. Teuwen, J., Gouw, Z., Sonke, J.: Artificial intelligence for image registration in radiation oncology. *Semin. Radiat. Oncology* **32**, 330–342 (2022)
8. Song, X.R., Chao, H.Q., Xu, X.: Cross-modal attention for multi-modal image registration. *Med. Image Anal.* **82**, 102612 (2022)
9. Sorzano, C.O., Isidro-Gómez, F., Fernández-Giménez, E., et al.: Improvements on marker-free images alignment for electron tomography. *J. Struct. Biol.* **X 4**, 100037 (2020)
10. Zheng, Q., Wang, Q., Ba, X.J., et al.: A Medical Image Registration Method Based on Progressive Images. *Comput. Math. Methods Med.* **2021**, 4504306 (2021)

11. Lara-Hernández A., Rienmüller T., Juárez I., et al. (2022). Deep learning-based image registration in dynamic myocardial perfusion CT imaging. In: *IEEE transactions on medical imaging*, 3214380 (2022)
12. Gul, S., Memon, S., Naz, B.: Image registration model for remote sensing images. *EAI Endorsed Trans. Internet of Things* **4**(16), 1–6 (2018)
13. Cocianu, C., Uscatu, C.R.: Cluster-based memetic approach of image alignment. *Electronics* **10**, 2606 (2021)
14. Cocianu, C., Uscatu, C.R.: Multi-scale memetic image registration. *Electronics* **11**, 278 (2022)
15. Zang, X.N., Zhao, W.N., Toth, J., et al.: Multimodal registration for image-guided EBUS bronchoscopy. *J. imag* **8**, 189 (2022)
16. Jiang, J., Li, Z.G., Xie, S.L., et al.: Robust alignment of multi-exposed Images with saturated regions. *IEEE Access* **8**, 221689 (2020)
17. Ma, Y.D., Sun, S.Y., Wu, F.J., et al.: Additive margin cosine loss for image registration. *Vis. Comput.* **38**, 1787–1802 (2022)
18. Marsland, S., McLachlan, R., Zarre, R.: Analysing ‘simple’ image registrations. *J. Math. Imag. Vis.* **63**, 528–540 (2021)
19. Striewski, P., Wirth, B.: Elastic 3D–2D image registration. *J. Math Imag. Vis.* **64**, 443–462 (2022)
20. Shao, S.W., Pei, Z.C., Chen, W.H., et al.: A multi-scale unsupervised learning for deformable image registration. *Int. J. Comput. Assist. Radiol. Surg.* **17**, 157–166 (2022)
21. Mondal, P., Banerjee, S.: FPGA-accelerated adaptive projection-based image registration. *J. Real-Time Imag. Proc.* **18**, 113–125 (2021)